Proceedings of the 28th Seismic Research Review: Ground-Based Nuclear Explosion Monitoring Technologies

September 19–21, 2006

Orlando, Florida

Volume I

Seismic Regional Characterization and Wave Propagation
Seismic Event Detection and Location
Seismic Identification and Source Characterization

Approved for Public Release; further dissemination unlimited.

National Nuclear Security Administration

AIR FORCE RESEARCH LABORATORY

LA-UR-06-5471

2006

Proceedings of the 28th Seismic Research Review: Ground-Based Nuclear Explosion Monitoring Technologies

Vol. I

To view these Proceedings online, visit
https://www.nemre.nnsa.doe.gov/review2006

Acknowledgements

The National Nuclear Security Administration (NNSA) and the Air Force Research Laboratory (AFRL) gratefully acknowledge the important contributions of the following people for their work to produce the ***Proceedings of the 28th Seismic Research Review: Ground-Based Nuclear Explosion Monitoring Technologies***.

Authors of papers for excellent research, technical documentation, and cooperation in electronic submission.

Dr. Anton M. Dainty, ***Mr. Robert J. Raistrick***, ***Dr. Frederick R. Schult***, AFRL/VSBYE, and ***Ms. Doris Richards***, ESC/PAM, for review and clearance of abstracts and papers related to AFRL contracts.

Dr. Mark T. Woods and ***Mr. John J. Dwyer***, Air Force Technical Applications Center (AFTAC)/TTR, for review and clearance of abstracts and papers related to AFTAC contracts.

Dr. Stanley D. Ruppert, Lawrence Livermore National Laboratory (LLNL), for assistance in ensuring that the CDs could be read on a variety of platforms and for burning the CDs.

Mr. Marvin A. Wetovsky, Los Alamos National Laboratory (LANL), for overall coordination of the Proceedings development and for technical editing of abstracts and papers. Also, for their contributions to the production of the Proceedings, thanks to ***Ms. Deidré A. Plumlee***, LANL, for composition of the Proceedings covers and format preparation of the electronic submissions; ***Ms. Jody Benson and Ms. Eileen Patterson***, LANL, for supplementary technical editing of papers; ***Ms. AnnMarie Cutler***, LANL, for design and artwork of the CD label; ***Ms. Sandra Valdez***, LANL, for labeling the CDs; ***Mr. Geoff Miller***, ***Ms. Karen LaRue***, ***Ms. Diana Hollis***, ***Mr. Leo Beckstead***, ***Ms. Sandra Bonchin***, and ***Mr. Burton Krohn***, LANL, for classification review of compiled papers; and ***IRM-RMMSO***, LANL, for color printing and binding of the hard copies.

Ms. Leslie A. Casey, NNSA, for review and clearance of abstracts and papers related to NNSA contracts and for NNSA overall support of the Proceedings.

Dr. Leigh S. House, NNSA/LANL; ***Dr. Dave Harris***, LLNL; ***Prof. Ed Garnero***, Arizona State University; ***Dr. Michael Pasyanos***, LLNL; and ***Dr. William Walter,*** LLNL, for their help in creating the guide to seismic phases.

Mr. John K. Yim, Space and Missile Defense Command (SMDC), for review and clearance of abstracts and papers related to SMDC contracts.

Ms. Mary L. Girven, Sandia National Laboratories (SNL), for making everyone's job easier with web-based technology for abstract and paper submission, on-line review and approval tools, and creation of the master files for the hardcopy, CD, and website versions of the Proceedings.

Ms. Guadalupe (Lupe) Massoth, SNL, for providing assistance to Mary Girven on website development.

Dr. David B. Harris, LLNL; ***Mr. Phillip E. Harben***, LLNL; ***Dr. W. Scott Phillips***, LANL; ***Mr. Ward L. Hawkins***, LANL; ***Dr. Dale N. Anderson***, Pacific Northwest National Laboratory (PNNL); ***Dr. Harry S. Miley***, PNNL; ***Dr. Ted W. Bowyer***, PNNL, ***Mr. J. Mark Harris***, SNL; ***Dr. Christopher J. Young***, SNL, and ***Dr. Joseph C. Wehlburg***, NNSA/SNL, for a myriad of internal management and technical reviews of NNSA abstracts and papers.

Table of Contents - Volume I

1. Seismic Regional Characterization and Wave Propagation 1

1-01 **Cong, L. and B. Mitchell**
Continent-Wide Maps of 5-50 S Rayleigh-Wave Attenuation for Eurasia Inferred from Maps of 1-Hz Lg Coda Q and its Frequency Dependence 3

1-02 **Fatehi, A. and K. Koper**
Characterization of P Wave Propagation and Multipathing in the Upper Mantle Beneath South Asia 8

1-03 **Fisk, M. and S. Taylor**
Robust Magnitude and Path Corrections for Regional Seismic Phases in Eurasia by Constrained Inversion and Enhanced Kriging Techniques 15

1-04 **Ford, S., D. Dreger, K. Mayeda, W. Walter, L. Malagnini, and W. Phillips**
Regional Attenuation Method Comparison for Northern California 25

1-05 **Gaherty, J., T. Hong, and L. Zhao**
Regionalization of Crustal and Upper Mantle Q Structure in Eastern Eurasia Using Multiple Regional Waves 33

1-06 **Ghalib, H., G. Aleqabi, B. Ali, B. Saleh, D. Mahmood, I. Gupta, R. Wagner, P. Shore, A. Mahmood, S. Abdullah, O. Shaswar, F. Ibrahim, B. Ali, L. Omar, N. Aziz, N. Ahmed, A. Ali, A. Taqi, and S. Khalaf**
Seismic Characteristics of Northern Iraq and Surrounding Regions 40

1-07 **Helmberger, D., J. Tromp, and A. Rodgers**
Advanced Waveform Simulation for Seismic Monitoring Events 49

1-08 **Herrmann, R., Y. Jeon, H. Yoo, K. Cho, W. Walter, and M. Pasyanos**
Seismic Source and Path Calibration in the Korean Peninsula, Yellow Sea, and Northeast China 60

1-09 **Lay, T., X. Yang, X. Xie, S. Taylor, and M. Arrowsmith**
Development of Regional Phase Tomographic Attenuation Models for Eurasia 71

1-10 **Levshin, A., X. Yang, M. Ritzwoller, M. Barmin, and A. Lowry**
Toward a Rayleigh Wave Attenuation Model for Central Asia 82

1-11 **Mackey, K., H. Hartse, K. Fujita, L. Linkimer, L. Steck, R. Stead, and C. Rowe**
Seismic Characterization of Northeast Asia 93

1-12 **Martin, R., M. Krasovec, S. Romer, M. Toksöz, and L. Gülen**
Extension of the Caucasus Seismic Information Network Study into Central Asia 103

1-13 **Martin, R., M. Krasovec, S. Romer, M. Toksöz, Y. Sun, D. Kalafat, and E. Vergino**
Caucasus Seismic Information Network 114

1-14 **Mooney, W., S. McDonald, and S. Detweiler**
An Updated Eurasian Crustal Model Using Multiple Seismic Methods 120

1-15 **Morozov, I., E. Morozova, C. Zhang, G. Chubak, W. Phillips, and I. Lipovetsky**
Magnitude-Yield and Travel-Time Calibration of Northern Eurasia Using Deep Seismic Sounding Data Sets 130

1-16 **Morozov, I., E. Morozova, S. Smithson, and I. Lipovetsky**
Deep Seismic Sounding Profiles for Seismic Calibration of Northern Eurasia 141

1-17 **Myers, S., J. Wagoner, L. Preston, K. Smith, H. Tkalcic, and S. Larsen**
The Effect of Realistic Geologic Heterogeneity on Local and Regional P/S Amplitude Ratios Based on Numerical Simulations 146

1-18 **Nyblade, A., A. Adams, R. Brazier, Y. Park, and A. Rodgers**
Ground Truth, Magnitude Calibration and Regional Phase Propagation and Detection in the Middle East and Horn of Africa 156

1-19 **Nyblade, A., W. Walter, and R. Gok**
Developing and Exploiting a Unique Seismic Dataset from South African Gold Mines for Source Characterization and Wave Propagation 166

1-20 **Pasyanos, M., W. Walter, M. Flanagan, R. Gok, and G. Franz**
The Use of Geophysical Models for Nuclear Explosion Monitoring 176

1-21 **Pitarka, A., C. Saikia, B. Woods, L. Zhu, and R. Herrmann**
Developing Multiple-Frequency Discriminants for Use with Regional Coda-Amplitude Measurements 186

1-22 **Pulliam, J., M. Sen, and A. Gangopadhyay**
Determination of Crust and Upper Mantle Structure Beneath Africa Using a Global Optimization Based Waveform Modeling Technique 196

1-23 **Reiter, D. and W. Rodi**
Crustal and Upper-Mantle P- and S-Velocity Structure in Central and Southern Asia from Joint Body- and Surface-Wave Inversion 209

1-24 **Reiter, D., A. Ferris, and M. Johnson**
Improved Intermediate-Distance Phase Characterization in Central Asia 219

1-25 **Ritzmann, O., N. Maercklin, J. Faleide, H. Bungum, W. Mooney, and S. Detweiler**
A 3D Geophysical Model of the Crust in the Barents Sea Region: Model Construction and Basement Characterization 229

1-26 **Ritzwoller, M., M. Pasyanos, Y. Yang, A. Levshin, and N. Shapiro**
Progress Toward Broad Band Ambient Noise Tomography in Eurasia 238

1-27 **Romanowicz, B., M. Panning, A. Kim, F. Marone, and D. Dreger**
Calibration of 3D Upper Mantle Structure in Eurasia Using Regional and Teleseismic Full Waveform Seismic Data 249

1-28 **Sandvol, E., E. Zor, B. Xueyang, J. Xie, B. Mitchell, A. Gasanov, and G. Yetirmishli**
Measurements of Regional Phase Q in the Middle East 258

1-29 **Shearer, P. and J. Lawrence**
Transition Zone Wave Propagation: Characterizing Travel-Time and Amplitude Information 267

1-30 **Stevens, J., J. Given, G. Baker, and H. Xu**
Development of Surface Wave Dispersion and Attenuation Maps and Improved Methods for Measuring Surface Waves 273

1-31 **Tibuleac, I., A. Stroujkova, J. Bonner, K. Mayeda, and J. Britton**
Predicting Explosion-Generated Sn and Lg Coda Using Synthetic Seismograms 283

1-32 **Toksöz, M., R. Van der Hilst, Y. Sun, C. Li, and H. Yao**
P and S Wave Velocity Structure of the Crust and Upper Mantle Under China and Surrounding Areas from Body and Surface Wave Tomography 295

1-33 **Xie, X., T. Lay, R. Wu, and Y. He**
Near Source Energy Partitioning for Regional Waves in 2D and 3D Models: Contributions of Free Surface Scattering 304

1-34 **Zhang, H., Y. Liu, C. Thurber, L. Steck, C. Rowe, K. Fujita, and K. Mackey**
Regional-Scale Differential Time Methods: Development and Application to the Siberia Data Set 315

1-35 **Zhang, H., Y. Liu, Z. Xu, X. Song, and C. Thurber**
High-Resolution Seismic Velocity and Attenuation Structure of the Sichuan-Yunnan Region, Southwest China, Using Seismic Catalog and Waveform Data 323

1-36 **Zhang, Z., Y. Shen, L. Zhao, X. Yang, and K. Olsen**
Developing Finite-Frequency Regional Pn Velocity Models 333

1-37 **Zhou, R., B. Stump, R. Herrmann, Y. Chen, and Z. Yang**
Broadband Network Operation and Shear Velocity Structure Beneath the Yanqing-Huailai Basin, NW of Beijing 341

2. Seismic Event Detection and Location 351

2-01 **Anderson, D., W. Walter, D. Carlson, T. Mercier, and S. Taylor**
A Lower Bound on the Standard Error of an Amplitude-Based Regional Discriminant 353

2-02 **Bondár, I., B. Kohl, E. Bergman, K. McLaughlin, H. Israelsson, Y. Kung, J. Given, and E. Engdahl**
Global Ground Truth Data Set with Waveform and Improved Arrival Data 359

2-03 **Bondár, I., K. McLaughlin, and H. Israelsson**
Improved Event Location Uncertainty Estimates 368

2-04 **de la Torre, T., G. Monsalve-Mejia, A. Sheehan, C. Rowe, and M. Begnaud**
Ground Truth Hypocenters and 3D Crustal Velocity Structure in Central Asia from In-Country Networks 377

2-05 **Engdahl, E., E. Bergman, S. Myers, and F. Ryall**
Improved Ground Truth in Southern Asia Using In-Country Data, Analyst Waveform Review, and Advanced Algorithms 387

2-06 **Flanagan, M., E. Matzel, S. van der Lee, H. Bedle, M. Pasyanos, F. Marone, B. Romanowicz, C. Schmid, and A. Rodgers**
Joint Inversion for Three-Dimensional Velocity Structure of the Broader Africa-Eurasia Collision Region 397

2-07 **Flanagan, M., S. Myers, and K. Koper**
Regional Travel-Time Uncertainty and Seismic Location Improvement Using a Three-Dimensional a priori Velocity Model 407

2-08 **Ichinose, G., C. Saikia, D. Helmberger, and M. Simons**
Ground Truth Locations Using Synergy Between Remote Sensing and Seismic Methods: SSSC at IMS Stations for Tibetan Plateau Earthquakes 417

2-09 **Johannesson, G. and J. Sweeney**
Statistical Classification and Prediction of Seismic Event Location Accuracy 427

2-10 **Kerr, J. and D. McClung**
Low-Noise Borehole Triaxial Seismometer -- Phase II 438

2-11 **Ringdal, F., S. Gibbons, and D. Harris**
Adaptive Waveform Correlation Detectors for Arrays: Algorithms for Autonomous Calibration 444

2-12 **Rodgers, A., D. Harris, and M. Pasyanos**
A Model-Based Signal-Processing Approach to Seismic Monitoring 455

2-13 **Rodi, W.**
Error Analysis in the Joint Event Location/Seismic Calibration Inverse Problem 465

2-14 **Rodi, W. and S. Myers**
Modeling Travel-Time Correlations Based on Sensitivity Kernels and Correlated Velocity Anomalies 475

2-15 **Salzberg, D. and M. Marshall**
Seismic Source Locations and Parameters for Sparse Networks by Matching Observed Seismograms to Semi-Empirical Synthetic Seismograms: Improvements to the Phase Spectrum Parameterization 484

2-16 **Schaff, D. and F. Waldhauser**
Improving Magnitude Detection Thresholds Using MultiStation, MultiEvent, and MultiPhase Methods 493

2-17 **Shumway, R.**
Advances in Mixed Signal Processing for Regional and Teleseismic Arrays 503

2-18 **Steck, L., H. Hartse, M. Maceira, J. MacCarthy, C. Rowe, W. Phillips, K. Mackey, K. Fujita, M. Begnaud, and D. Baker**
Pn Tomography, Geophysical Models, Cross-Correlation, and Location in Eurasia 510

2-19 **Stroujkova, A. and D. Reiter**
Regional Depth-Phase Detection and Focal Depth Estimation: Application to Events in Southeast Asia 520

2-20 **Sweeney, J., S. Myers, and J. Wagoner**
Automated Development of 3D Local Travel Time Models 530

2-21 **Yang, T., Y. Shen, and X. Yang**
Finite-Frequency Seismic Tomography for Eastern Eurasia 538

3. Seismic Identification and Source Characterization 547

3-01 **Arrowsmith, S., M. Arrowsmith, M. Hedlin, and B. Stump**
Discrimination of Mining Events Using Regional Seismic and Infrasound Waveforms: Application to the US and Russia 549

3-02 **Bonner, J., M. Pasyanos, H. Hooper, M. Leidig, and D. Harkrider**
A Comparison of Different Surface Wave Magnitude Formulas on a Eurasian Dataset 560

3-03 **Bungum, H., T. Kvaerna, S. Mykkeltveit, N. Maercklin, M. Roth, K. Aastebol, D. Harris, and S. Larsen**
Energy Partitioning for Seismic Events in Fennoscandia and NW Russia 570

3-04 **Fisk, M., T. Lay, and S. Taylor**
Modeling and Empirical Research on Energy Partitioning of Regional Seismic Phases used for Explosion Monitoring 580

3-05 **Ford, S., D. Dreger, and W. Walter**
Identifying Isotropic Events Using an Improved Regional Moment Tensor Inversion Technique 590

3-06 **Gitterman, Y., A. Hofstetter, and V. Pinsky**
Source Features and Scaling of Buried and Surface Experimental Explosions in Israel 597

3-07 **Hong, T., W. Menke, and J. Xie**
Phase Composition of Regional Waves from the Balapan and Degelen Nuclear Explosions and its Implications for Shear-Wave Excitation 607

3-08 **Leidig, M., V. Romanovsky, R. Hansen, R. Martin, R. Grove, J. Bonner, and J. Lewkowicz**
Possible Effects of Frozen Rock on Explosive Coupling 618

3-09 **Mayeda, K., J. Bonner, and H. Hooper**
Regional P-Coda for Stable Estimates of Body Wave Magnitude: Extending the Ms:mb Discriminant to Smaller Events 625

3-10 **Murphy, J., B. Barker, and J. Sultanov**
A Scaling Analysis of Frequency-Dependent Energy Partition for Local and Regional Seismic Phases from Explosions 636

3-11 **Patton, H. and W. Phillips**
Regional Magnitude Research Supporting Broad-Area Monitoring of Small Seismic Events 646

3-12 **Randall, G., X. Yang, H. Hartse, M. Maceira, M. Arrowsmith, and S. Taylor**
Regional Event Identification Research in Asia 654

3-13 **Sammis, C. and R. Biegel**
Preparing for the 2006 Alaska Permafrost Experiment 665

3-14 **Shearer, P. and B. Allmann**
Spectral Studies of Shallow Earthquakes and Explosions in Southern California 674

3-15 **Stevens, J., G. Baker, and H. Xu**
The Physical Basis of the Explosion Source and Generation of Regional Seismic Phases 681

3-16 **Stevens, J., H. Xu, and G. Baker**
Analysis of Shear Wave Generation by Decoupled and Partially Coupled Explosions 693

3-17 **Walter, W., S. Taylor, E. Matzel, R. Gok, S. Heller, and V. Johnson**
Regional Seismic Chemical and Nuclear Explosion Discrimination: Western U.S. Examples 704

Seismic Regional Characterization and Wave Propagation

CONTINENT-WIDE MAPS OF 5-50 S RAYLEIGH-WAVE ATTENUATION FOR EURASIA INFERRED FROM MAPS OF 1-HZ LG CODA Q AND ITS FREQUENCY DEPENDENCE

Lianli Cong[1] and Brian J. Mitchell[2]

Yunnan University[1] and Saint Louis University[2]

Sponsored by Air Force Research Laboratory

Contract No. FA8718-04-C-0021[1,2]

ABSTRACT

The crust of southern Eurasia is characterized by low *Q* values (200-450) for 1-Hz *Lg* coda everywhere from Spain to China. The north-south extent of that low-*Q* zone varies from being relatively narrow in western Europe to being very broad from the Middle East to China. Those variations in both magnitude and width first became apparent with the development of continent-wide tomographic maps of *Lg* coda *Q*. The most recent mappings of *Lg* coda *Q* values at 1 Hz (Q_o), completed over the past year, show that the four regions of lowest Q_o values occur in regions marked by high levels of seismicity. Q_o in stable regions of Eurasia varies between about 450 and 900 with the highest values occurring in the Indian shield, the East European Craton, the Siberian Craton and the Khazakh Platform. The maps reveal relatively, and unexpectedly, low values of Q_o in the Siberian Trap region of Siberia. Variations in the mapped values of the frequency dependence of *Lg* coda *Q* at 1 Hz (η) show no systematic relationships to variations of Q_o in either southern or northern Eurasia.

Plots of point-spreading functions—measures of how well features can be resolved—reveal that features with dimensions as small as 800 to 1000 km can be resolved. The standard error for Q_o throughout a large portion of Eurasia is 50 or smaller and between 50 and 100 in most other regions. An exception to these small errors occurs in a region that extends southwestward from Lake Baykal where they are as large as 200. The Baykal values probably reflect complexities in the deep crust of that region. Standard errors for the frequency dependence of *Q* also show anomalously high values to the southwest of Lake Baykal.

Using values of Q_o and η obtained for *Lg* coda and assuming that η is the same for all frequencies, we have estimated Rayleigh-wave attenuation coefficient (γ_R) values for all of Eurasia at periods of 5, 10, 20 and 50 s. In our studies of Rayleigh-wave attenuation and its regional variation for various periods across Eurasia, we have assumed that the values of Q_o and η obtained from *Lg* coda can be used to infer values of shear-wave *Q* (Q_μ) and its frequency dependence (ζ). In that process we assume Q_o to be equivalent to an average value for shear-wave *Q* in each 3° x 3° cell of Eurasia and that the frequency dependence of shear-wave *Q* can be obtained using an empirically-derived multiplicative factor. We have tested this assumption for several crustal shear-wave *Q* models, one for the Arabian Peninsula, one for the Turkish/Iranian Plateaus and seven for China where both shear-wave *Q* models and *Lg* coda *Q* information are available. We find that the relations $Q_\mu = Q_o^C$ at all depths and $\zeta = 0.8\eta$ for the depth range 0-40 km and $\zeta = 0.5\eta$ for depths greater than 40 km provide realistic estimates for γ_R in the period range 5 – 70 s. We find that 5-s Rayleigh waves vary between 0.5 x 10^{-3} and 5.0 x 10^{-3} km^{-1}, 10-s waves vary between 0.2 and 2.2 x 10^{-3} km^{-1}, 20-s waves vary between 0.1 and 1.1 x 10^{-3} km^{-1} and 50-s waves vary between 0.06 and 0.3 x 10^{-3} km^{-1}. Sediments play a large role in attenuating 5-s and 10-s Rayleigh waves in some regions but have a much smaller effect for 20-s and especially 50-s waves.

OBJECTIVES

Seismic *Q* is an important parameter that affects how rapidly various seismic waves attenuate with distance as they travel through the Earth. Its value can vary both spatially and with frequency. The overall purpose of our research is to better understand details of those variations throughout southern Asia and how they might affect our ability to detect waves generated by small seismic events, to estimate magnitudes and yields of those events, and to determine if they are explosions or earthquakes. To improve understanding in those areas we have focused on two specific objectives. Our first objective has been to expand and improve previously published maps of regional variations of *Lg* coda *Q* across Eurasia with emphasis on regions where path coverage was too sparse to obtain reliable and high-resolution results. Our second objective has been to use those new maps of *Lg* coda *Q* and its frequency dependence at 1 Hz (Q_o and η, respectively) to develop maps of Rayleigh-wave attenuation coefficients for various periods (5–50 s) throughout southern Asia.

RESEARCH ACCOMPLISHED

Lg Coda Q Variation

We presented new maps of Q_o and η, values of *Lg* coda *Q* and its frequency dependence at 1 Hz, for all of Eurasia in our paper for last year's Seismic Research Review meeting (Cong and Mitchell, 2005). Both last year's study and this one use the method developed by Xie and Mitchell (1990) to obtain tomographic maps of Q_o and η. Details about our methodology can be obtained from that paper. In this paper we again present maps of Q_o and η. This repetition of the process will allow comparison of our new maps of Rayleigh-wave attenuation variation for Eurasia with the Q_o. Also, our Q_o and η maps have been slightly revised because of a bug discovered in a new code that we used to determine *Lg* coda *Q* from individual records.

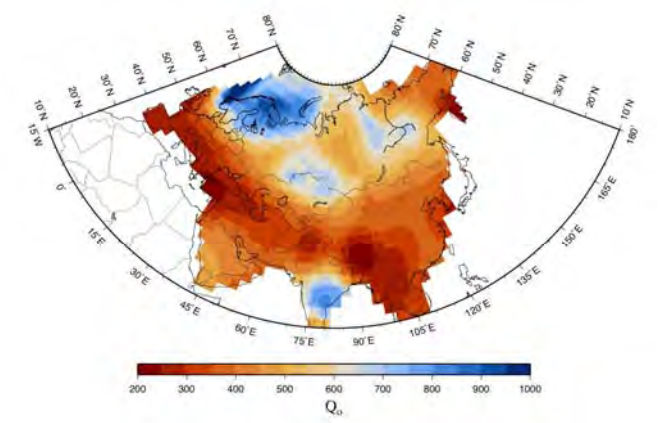


Figure 1. *Lg* coda *Q* at 1 Hz (Q_o) for

Figures 1 and 2 present continent-wide maps of Q_o and η for virtually all of Eurasia. They were constructed using 1383 determinations of those quantities from individual seismic records for paths confined to the Eurasian continent, compared with 440 determinations used by Mitchell et al., 1997 in an earlier study. Data coverage was best in regions where seismicity rates are highest; i.e., in the southern and eastern portions of the continent. The coverage was, however, more than adequate throughout the entire continent.

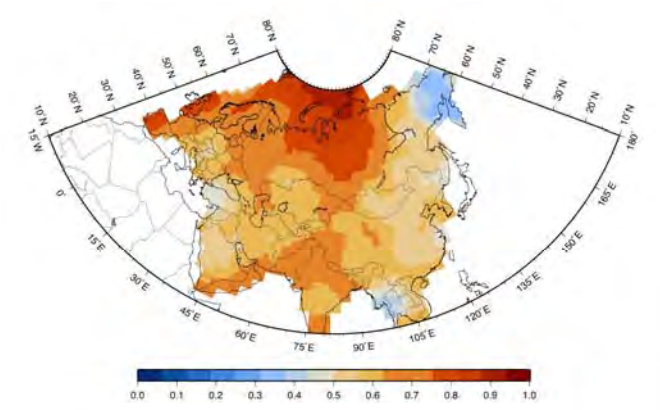


Figure 2. Frequency dependence of *Lg* coda *Q* at 1 Hz (η) for Eurasia.

Figure 1 indicates that, with the exception of the Indian platform, Q_o is generally higher in northern than in southern Eurasia. But even in northern Eurasia unexpectedly low values occur. The most conspicuous of these is in central Siberia where low Q_o values coincide with the most recent mapping of the Siberian Traps (Reichow et al., 2002). The lowest values for Q_o lie in the four regions where seismicity rates are highest. These are the Kamchatka Peninsula in northeastern Asia, the southeastern portion of the Tibetan Plateau, the Hindu Kush region slightly north of India, and western Turkey. The low Q_o in the southeastern Tibetan Plateau extends further to southeast and covers a broad region of enhanced seismicity. The Arabian Peninsula, even though it is a stable

platform over its entire area and contains a shield in the western part of the peninsula, is marked by Q_o values that are lower than most other stable platforms.

The map of η variation in Figure 2 shows no clear relationship to Q_o variation. Low η correlates with low Q_o in Kamchatka in northeastern Siberia, high η correlates with low Q_o in Spain and the variation of the large low-η region in the north-central part of the map appears to be independent of Q_o variation in that region. This differs from some other continents we have studied, such as Africa and South America, where high Q_o values are associated with low η values and low Q_o values with low η values.

Cong and Mitchell (2005) computed point-spreading functions and measures of resolution, at six positions in Eurasia. They showed that our ability to resolve features in the crust was about the same everywhere in the continent and indicated that we could resolve features with dimensions between about 800 km and 1000 km. That paper also showed that the standard error in Q_o determinations was less than 50 in most places and between 50 and 100 in most of the other regions of Eurasia. A region to the southwest of Lake Baikal exhibited a standard error greater than 200. Since data coverage in that region was good, we interpret the high standard error to be due to a severe lateral variation in crustal properties in that region. Those determinations appear in Figure 3. Standard errors for the frequency dependence of *Lg* coda *Q* at 1 Hz (not shown) are less than 0.1 in most places and between 0.1 and 0.2 in most of the rest of Eurasia. Like Q_o, it is higher to the southwest of Lake Baikal.

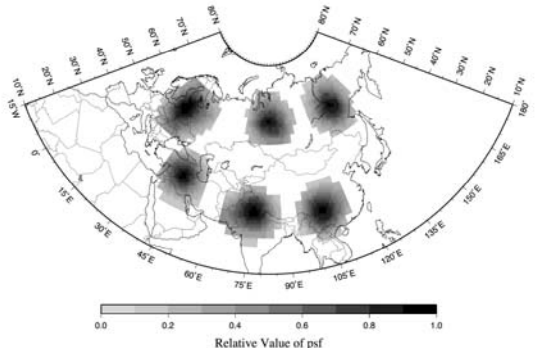


Figure 3. Point spreading function (psf) plots for six selected cells.

Continent-Wide Estimates of Rayleigh-Wave Attenuation Coefficients (γ_R) for Eurasia

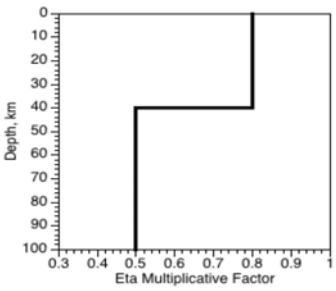


Figure 4. Factor by which Q_o must be multiplied to obtain a good empirical fit

Cong and Mitchell (2005) presented estimates of Rayleigh-wave attenuation coefficients for southern Asia for periods of 10, 20, and 50 s. In this paper we extend those determinations to include all of Eurasia and also add determinations for all of Eurasia at a period of 5 s. In those determinations, we use equations developed by Anderson et al. (1965) to estimate Rayleigh-wave attenuation coefficients from *Lg* coda *Q*. *Lg* coda *Q* can be expressed by the equation

$$Q_{Lg}^{C} = Q_o f^{\eta} \qquad (1)$$

where Q_o is *Lg* coda *Q* at 1 Hz and η is the frequency dependence of *Q* at 1 Hz. At least two studies (Herrmann and Kijko, 1983; Campillo et al., 1985) have found that Q_o in the above equation is a good approximation of the average value of shear-wave *Q* (Q_μ) in the crust. An expression for shear-wave is

$$Q_\mu = Q_o f^{\zeta} \qquad (2)$$

where ζ is the frequency dependence for Q_μ. We take Q_μ in this expression to approximate Q_o. We had initially thought we could let ζ approximate η but found that we could not duplicate measured values of Rayleigh-wave attenuation by doing that. We then, by trial and error, empirically obtained a depth-dependent factor that, when multiplied by η, provided a good fit between γ_R predicted by *Lg* coda *Q* and observed γ_R curves. That factor is 0.8 for the upper 40 km in the Earth and 0.5 at greater depths.

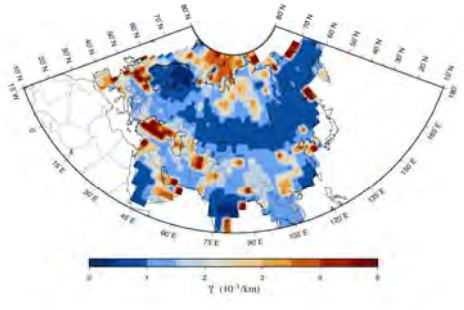


Figure 5. γ_R at a period of 5 s.

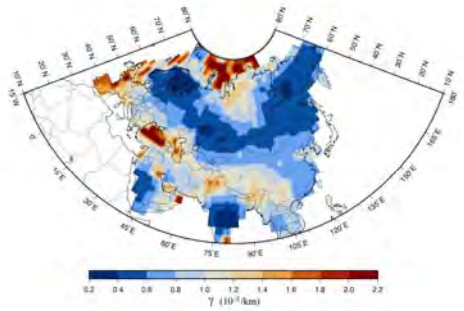


Figure 6. γ_R at a period of 10s.

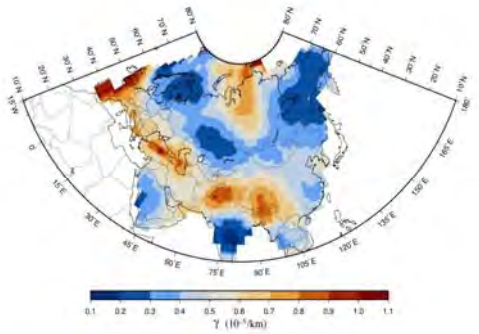


Figure 7. γ_R at a period of 20 s.

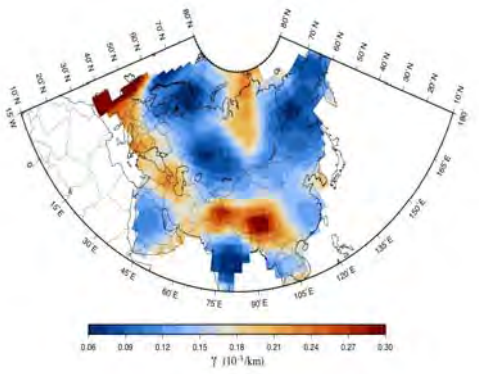


Figure 8. γ_R at a period of 50 s.

Equation 3 shows the equation of Anderson et al. (1965) as modified by Mitchell and Xie (1993) to take into consideration depth-variable frequency dependence of *Q*.

$$\gamma_R = \frac{\pi}{C_R^2 T}\sum_{i=1}^{N}\left[\left(\beta_l \frac{\partial C_R}{\partial \beta_l}\right)_{\omega\rho\alpha} + \frac{1}{2}\left(\alpha_l \frac{\partial C_R}{\partial \alpha_l}\right)_{\omega\rho\beta}\right] Q_{\mu l}^{-1} \qquad (3)$$

In this expression, C_R refers to Rayleigh-wave phase velocity, T to period, β_l to shear-wave velocity in layer l, α_l to compressional-wave velocity in layer l and $Q_{\mu l}$ to shear-wave Q in layer l. The subscripts to the right of the partial derivatives refer to quantities held constant during the differentiation. ρ in those subscripts refers to density. The Rayleigh-wave phase velocities and the partial derivatives in equation 3 were computed for every 3° x 3° cell in our Q_o map using many shear-wave velocity models for Eurasia provided by M. Ritzwoller and A. Levshin.

We have tested the utility of our conversion for several crustal shear-wave *Q* models, one for the Arabian Peninsula, one for the Turkish/Iranian Plateaus, and seven for China where both shear-wave *Q* models and *Lg* coda *Q* information are available. As indicated above we find that the relations $Q_\mu = Q_o^{\,C}$ at all depths and $\zeta = 0.8\eta$ for the depth range 0-40 km and $\zeta = 0.5\eta$ for depths greater than 40 km provide realistic estimates for γ_R in the period range 5–70 s. We find that 5-s Rayleigh waves vary between 1.5 x 10^{-3} and 5.0 x 10^{-3} km^{-1}, 10-s waves vary between 0.2 and 2.2 x 10^{-3} km^{-1}, 20-s waves vary between 0.1 and 1.1 x 10^{-3} km^{-1},and 50-s waves vary between 0.06 and 0.3 x 10^{-3} km^{-1}. Sediments play a large role in attenuating 5-s and 10-s Rayleigh waves but are less important for 20-s and, especially, 50-s waves.

At both 5-and 10-s periods there are several regions where attenuation is quite high. Some of these, such as the Barents north of the continent and the Black Sea region are obviously associated with thick accumulations of sediments. There are also several smaller regions with high attenuation rates. We checked the velocity models for several of these regions and found that all of them were also marked by thick accumulations of low-velocity sediments. As periods increase, the smaller regions with high attenuation disappear and the *Q* variations are broader with fewer small-scale features. This is due to the smaller sensitivity of the longer wavelength waves to detail and to the fact that those waves are less sensitive to near-surface features.

At 50-s periods, the Rayleigh-wave attenuation coefficient map resembles the 1-Hz Lg coda *Q* map. This is probably because the *Lg* coda samples the entire crust and is not, like 5- and 10-s Rayleigh waves, dominated by the upper crust.

Similar to the Q_o map for Lg coda, the 50-s Rayleigh-wave attenuation map shows regions of low-attenuation (or high Q) in the three stable regions of northern Eurasia, as well as the Indian platform. It also shows low attenuation for most of the Arabian Peninsula and southeastern-most Asia in contrast to the relatively high attenuation (or low Q) exhibited by the Q_o map. This occurs because the frequency dependence parameters (η) in Figure 2 are relatively low in both of those regions.

CONCLUSIONS AND RECOMMENDATIONS

New maps of *Lg* coda Q at 1 Hz (Q_o and η) have been used, along with regionalized seismic velocity models, to develop continent-wide maps of Rayleigh-wave attenuation coefficients at periods of 5, 10, 20, and 50 s. The Lg coda Q maps were found to resolve features between about 800 km and 1000 km in dimension and to have relatively low standard deviations everywhere but a region southwest of Lake Baikal. The Rayleigh-wave attenuation coefficient maps were determined, based upon published work, assuming that Q_o in each 3° x 3° cell of Eurasia represents an average value for the shear-wave Q (Q_μ) there and that the frequency dependence of Q_μ can be obtained from an empirically determined depth-dependent multiplicative factor. That factor is 0.8 at depths between 0 and 40 km and 0.5 at greater depths. It was tested for paths in China, the Arabian Peninsula, and the Iran/Turkey Plateaus and was found to be satisfactory in all cases but those where the Q_o or η may not be well determined. We find that 5-s Rayleigh waves vary across Eurasia from 0.5 x 10^{-3} and 5.0 x 10^{-3} km^{-1}, 10-s waves vary from about 0.2 tp 2.2 x 10^{-3} km^{-1}, 20-s waves vary from about 0.1 to 1.1 x 10^{-3} km^{-1},and 50-s waves vary from about 0.06 to 0.3 x 10^{-3} km^{-1}. Sediments play a large role in attenuating 5-s and 10-s Rayleigh waves in some regions but have a much smaller effect for 20-s and especially 50-s waves.

The validity of our empirical relation for obtaining shear-wave Q frequency dependence used in computing Rayleigh-wave attenuation coefficients is, so far, based only upon Rayleigh-wave attenuation information in tectonically active regions. For that reason, we recommend obtaining Rayleigh-wave attenuation measurements for regions in northern Eurasia that are relatively stable. Also, our determinations assume that the ratio of compressional-wave Q to shear-wave Q is equal to 2 in crystalline rock beneath sediments. Recent work suggests that that ratio is closer to 1, at least in tectonically active regions. We recommend conducting combined determinations of compressional-wave Q and shear-wave Q in a variety of tectonic regimes to obtain values for that ratio in the crust.

ACKNOWLEDGMENTS

We thank Jack Xie for making his code for tomographic mapping of Q_o and η available to us. The maps in this paper were prepared using GMT version 3.0 developed by Paul Wessel and H. F. Smith.

REFERENCES

Anderson, D.L., A. Ben-Menahem and C.B. Archambeau (1965). Attenuation of seismic energy in the upper mantle, *J. Geophys. Res.* 70: 1441–1448.

Cong, L., and B.J. Mitchell (2005). Regional variation of Rayleigh-wave attenuation in southern Asia predicted from maps of *Lg* coda *Q* and its frequency dependence at 1 Hz, in *Proceedings of the 27th Seismic Research Review: Ground-Based Nuclear Explosion Monitoring Technologies*, LA-UR-05-6407, Vol. 1, pp. 23.

Mitchell, B.J., Y. Pan, J. Xie and L. Cong (1997). *Lg* coda *Q* variation across Eurasia and its relation to crustal evolution, *J. Geophys. Res.* 102: 22767–22779.

Reichow, M.K., A.D. Saunders, R.V. White, M.S. Pringle, A.I. Al'Mukhamedov, A.I. Medvedev and N.P. Kirda (2002). $^{40}Ar/^{39}Ar$ dates from the West Siberian Basin: Siberian flood basalt province doubled, *Science*, 296: 1846–1849.

Xie, J., and B.J. Mitchell (1990). A back-projection method for imaging large-scale lateral variations of Lg cod Q with application to continental Africa, *Geophys. J. Int*. 100: 161–181.

CHARACTERIZATION OF P WAVE PROPAGATION AND MULTIPATHING IN THE UPPER MANTLE BENEATH SOUTH ASIA

Ali Fatehi and Keith D. Koper

Saint Louis University

Sponsored by Air Force Research Laboratory

Contract No. FA8718-06-C-0003

ABSTRACT

This paper reports on our recent efforts to characterize P wave propagation in the mantle transition zone beneath south Asia, using data from the small aperture seismic array deployed in Chiang Mai, Thailand. This array is located at regional distances from nuclear weapons test sites in China, India, and Pakistan as well as potential test sites in North Korea. We have downloaded and performed quality control on the Chiang Mai Array (CMAR) records of just under 1,700 events (corresponding to about 30,000 traces) that occurred between 1995 and 2005 with primarily continental paths. Each event occurred at distances of 13°–30° from CMAR and had a magnitude of at least 4.0 mb. We have done an initial slowness analysis for a large fraction of these events and obtained the arrival time, ray parameter, and backazimuth for all first arrivals and all dominant later arrivals. For the slowness parameters we have also determined the standard errors that have been generated using a bootstrap-type resampling algorithm.

Our initial results show that observed travel times of later arriving phases obtained from the slant-stack of the data are different from the predictions based on standard earth models such as Preliminary Reference Earth Model (PREM) and IASP91. Ultimately, we will use the slownesses and travel times of these later arriving phases to investigate the properties of the transition zone in our study area, and develop a series of 1D P velocity models for well-sampled geographic corridors.

OBJECTIVES

Detection and location of small magnitude seismic events are two of the current challenges in verification seismology. Local and regional analysis of small magnitude data is of great importance since these events do not produce sufficient teleseismic data. Locally recorded phases such as Pn, Pg, and Lg, show considerable variability in travel time and waveform character from region to region, since they travel in the lithosphere, which is the most heterogeneous layer of the Earth. Regional P waveforms are also complicated since they turn in the mantle transition zone (MTZ). Two global discontinuities at depths of 410 km and 660 km bound the MTZ, and lead to the multipathing of P waves in which several distinct P waves arrive in a short time window. Although the MTZ is less heterogeneous than the lithosphere, it has significant lateral variations as well, which makes the situation even more complicated. Two other seismic discontinuities are also thought to exist, at least in specific regions, at depths near 220 km (Gu et al., 2001) and 520 km (Shearer, 1996; Ryberg et al., 1997).

It is important to understand regional distance P wave propagation in verification studies. Multipathing can reduce the amplitude of the first arriving P wave by partitioning energy into later arriving phases. This defocusing effect should be recognized and accounted for to avoid underestimating the magnitude of the seismic event. Multipathing can also hinder the detection of depth phases. Depth phases from crustal events can arrive in the same time window as later arriving waves from the MTZ. Due to the importance of event depth as a discrimination factor, it is crucial to distinguish between the wave types.

The initial goal of this study is to identify and document P wave multipathing owing to discontinuities and velocity gradients in the upper mantle beneath south Asia. We use data from the CMAR, which is deployed in northern Thailand and consists of 18 short period, vertical component seismometers deployed with an effective aperture of about 10 km. The seismicity covers a wide range of distances and azimuths yielding ray paths that preferentially sample the complicated tectonics of the India-Eurasia collision zone (Figure 1). We use array-processing techniques to determine the subtle differences in arrival time and slowness of multipathed P waves. The travel times and slownesses of the later-arriving P waves will be used to generate 1D velocity models along well-sampled geographic corridors.

RESEARCH ACCOMPLISHED

Development of the CMAR Database

Initially, we compiled a list of 1,706 events that occurred at regional distances (13°–30°) from CMAR, with primarily continental ray paths, between March 1995 and December 2004. Each event had a magnitude of at least 4.0 mb and was reported in the USGS earthquake catalog to have produced a P arrival at CMAR. With help from data technicians at Air Force Technical Applications Center (AFTAC), we were able to download 30-min long segments of CMAR data for 1,697 of the target events. We then used a series of shell scripts to convert the data into individual sac binary files, arrange the files into a coherent directory structure, and fill in relevant header information. Over 60% of the approximately 30,000 traces have been visually inspected, and those with glitches, data gaps, or extraordinary noise levels have been removed from the database.

Array Processing of CMAR Database

Using array-processing techniques has two primary advantages: an increase in signal-to-noise ratio, and the ability to determine the direction (backazimuth and ray parameter) from which seismic energy arrives. Both of these features are important in our analysis of small-amplitude, later-arriving P waves. We used the Generic Array Processing (GAP) software package (Koper, 2005) for the array processing of CMAR data. In GAP, slowness analysis is done in the time domain by repeated beam formation over a grid of potential slowness vectors. A variety of beamforming techniques are available such as simple delay and sum, n^{th} root stacking, and phase-weighted stacking (PSW) (Rost and Thomas, 2002). The non-linear beamforming techniques (i.e., PSW) often lead to a much higher increase in signal-to-noise compared to the $\sqrt{N}$ enhancement expected from linear approaches.

Within GAP Cartesian or polar components of the 2D horizontal slowness vector can be obtained simultaneously. Ray parameter and backazimuth can be inferred while one of them is held constant. There is also the capability of

inferring the relative slowness between two phases or time windows. In all cases uncertainties for slowness parameters are determined with a stochastic bootstrap-type error estimation algorithm (i.e., Tichelaar and Ruff, 1989). For example, when estimating uncertainties associated with the estimate of a horizontal slowness vector, a pseudo-array is generated by randomly resampling the *N* array traces with replacement until *N* traces have been selected. A grid search is then carried out on the pseudo-array to determine the optimal slowness vector. This process is repeated M times to generate a population of optimal slowness vectors. This population is then used to calculate the model covariance matrix, from which a 95% confidence ellipse can be determined. Alternatively, error bounds on either the ray parameter or backazimuth can be estimated from the population of bootstrap solutions.

An example slantstack from GAP is presented in Figure 2. Here the backazimuth was held constant at the expected value (311°) and a series of array beams were calculated for ray parameters varying from 3 s/deg to 15 s/deg in increments of 0.25 s/deg. Each beam was enhanced with phase-stack weighting of order 3, and the amplitude of the beam envelope is plotted. At this distance of 27.7° multipathing can be expected, and indeed the slant-stack shows a few later arrivals from which the first one arrives about 10 s after the primary *P* wave. For this later arriving phase, a grid search could be carried out to obtain the optimal differential ray parameter. The vertical streaking of the energy peaks is caused by the relatively small aperture of CMAR. Figure 3 shows the result of the grid search for the optimal 2D slowness vector for the same event. The grid search is done in a time window bracketing first *P* wave. Beam amplitude is calculated using a 3rd order PSW that significantly amplifies coherent energy while providing less waveform distortion than N-th root stacking (Schimmel and Paulssen, 1997).

We have done the slant-stack and 2D slowness analysis for more than 200 events, which lie within the backazimuth range of 307°–312° (Figure 1). This cluster of events covers the whole distance range of interest (14°–30°) in this study. We compared the results of slant-stacks and 2D slowness analysis with the predictions using reference Earth models. Reference models of the upper mantle are inconsistent with the properties of the later arriving phases. The differential slowness analysis results and travel times from the data often can not be explained by the predicted arrivals of models such as PREM and IASP91. We compared the predictions from IASP91 and PREM to the observed travel times of the first and later arrivals of these set of events, obtained from the slant-stack analysis. We used an automated algorithm to pick the arrival time and ray parameter of all local maxima above a given threshold. The results are shown in Figure 4 for those events with mb $\geq$5.0, with the ray parameters plotted as vectors centered on the corresponding arrival time. The differences in travel time for some of the data are too large to be explained by errors in event locations. The PREM model however, predicts some later arrival phases (the upper branch of the travel time curve), due to a discontinuity at 220 km depth, which correspond to some of the observed data. IASP91 lacks such a discontinuity.

Modeling and Interpretation of CMAR Data

Later arriving phases can be modeled to constrain properties of the transition zone by using ray theory to predict observed differential ray parameters and differential travel times for various hypothetical models. By using differential properties, we can greatly reduce the effects of source mislocation, near source heterogeneities, and array site effects. Differential ray parameters and differential travel times of later arriving phases can be used to develop 1D models of upper mantle for specific, well-sampled geographic corridors to CMAR.

For a given set of observations we will use a niching genetic algorithm (NGA) to determine a suite of acceptable models (Koper et al., 1999). An NGA is a search based method that is more efficient than a simple grid search and appropriate for non-linear problems. For this problem we search for models that explain the differential properties of later arriving phases. Candidate velocity models will be evaluated for geometric arrivals at specific distances using the method of Buland and Chapman (1983).

CONCLUSION AND RECOMMENDATIONS

We have downloaded and performed quality control on the CMAR records of nearly 1,700 seismic events that occurred between 1995 and 2005. We use this data to characterize P wave propagation in the mantle transition zone beneath south Asia. We have done an initial slowness analysis for a cluster of more than 200 events. The backazimuth of these events range form 307° to 312° and their distances from CMAR range from 13°–30°. The results show that for some of the arrivals, there is a big difference between the observed travel times and predicted travel times based on PREM or IASP91 models. The differences in some cases are larger than what that could be explained by mislocation errors. Since we are interested in possible azimuthal dependence in the results, we will

analyze the data, which lie in different backazimuth ranges from CMAR. In the next step we will model the later arriving phases to constrain properties of the transition zone. We will use differential ray parameters and differential travel times of later arriving phases to develop 1D models of upper mantle in our study region.

ACKNOWLEDGEMENTS

We thank Richard "Boomer" Baumstark and Michele Kelly of AFTAC for help in obtaining the CMAR data.

REFERENCES

Buland, R. and C. H. Chapman (1983). The computation of seismic travel times, *Bull. Seism. Soc. Am.* 73: 1,271–1,302.

Gu, Y. J., A. M. Dziewonski, and G. Ekstrom (2001). Preferential detection of the Lehman discontinuity beneath continents, *Geophys. Res. Lett.* 28: 4,655–4,658.

Koper, K. D. (2005). The Generic Array Processing (GAP) software package, Annual SSA Meeting, Lake Tahoe, NV, 2005.

Koper, K. D., M. E. Wysession, and D. A. Wiens (1999). Multimodal function optimization with a niching genetic algorithm: A seismological example, *Bull. Seism. Soc. Am.* 89: 978–988.

Rost, S. and C. Thomas (2002). Array seismology: Methods and applications, *Rev. of Geophys.* 40: 3, 1008, doi:10.1029/2000RG000100.

Ryberg, T., F. Wenzel, A. V. Egorkin, and L. Solodilov (1997). Short-period observation of the 520 km discontinuity in northern Eurasia, *J. Geophys. Res.* 102: 5,413–5,422.

Schimmel, M. and H. Paulssen (1997). Noise reduction and detection of weak, coherent signals through phase weighted stacks, *Geophys. J. Int.* 130: 497–505.

Shearer, P. M. (1996). Transition zone velocity gradients and the 520-km discontinuity, *J. Geophys. Res.* 101: 3053–3066.

Tichelaar, B. W. and L. J. Ruff (1989). How good are our best models? Jacknifing, bootstrapping, and earthquake depth, *Eos Trans. AGU*, 70: 593.

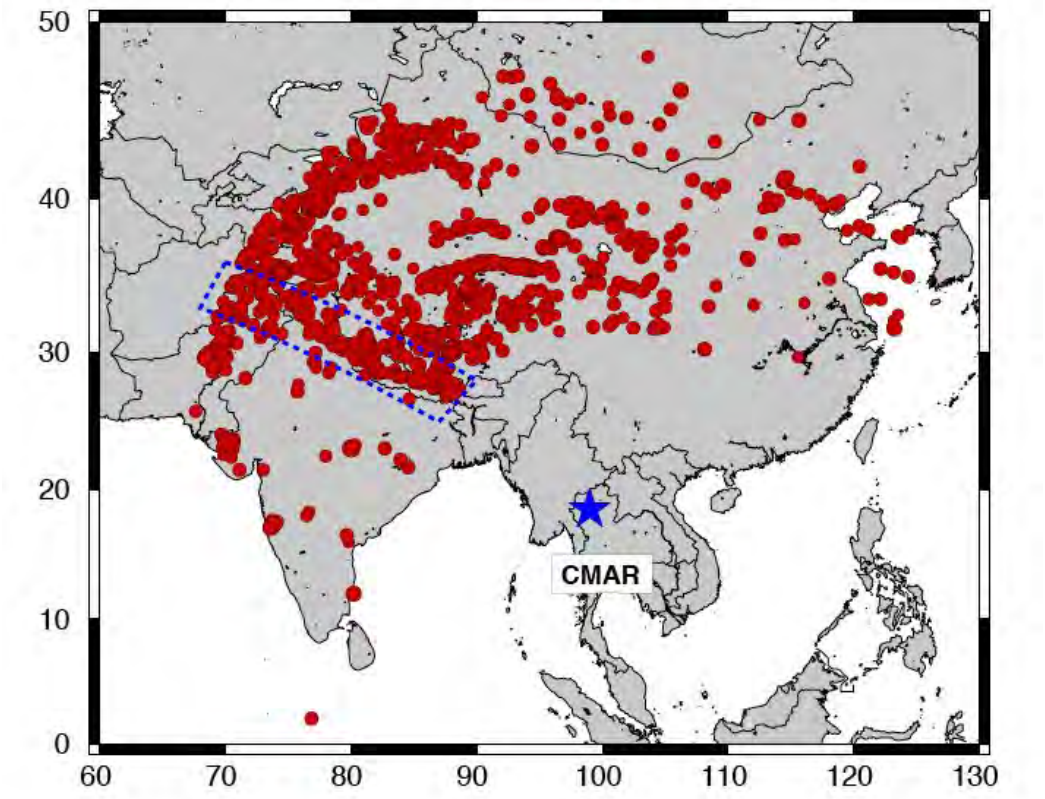


Figure 1. Epicenters for nearly 1,700 seismic events that occurred at distances of 13°–30° from CMAR from Jan. 1995 through Oct. 2005. Only events with primarily continental paths to CMAR were selected. The events inside the dotted blue box have backazimuths from 307° to 312° for which the results of travel time and slowness analysis are presented in this paper.

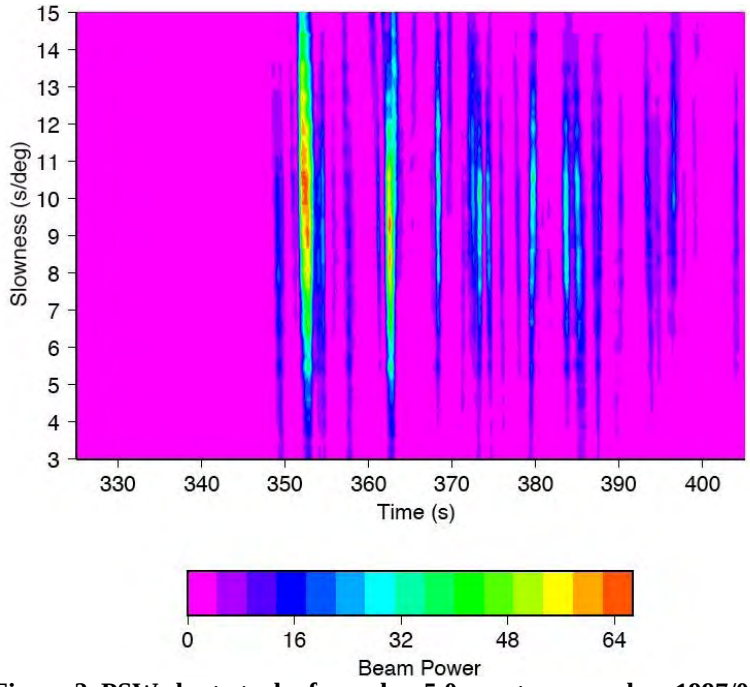


Figure 2. PSW slant-stack of an mb = 5.0 event occurred on 1997/05/31 with a distance of 27.7 from CMAR.

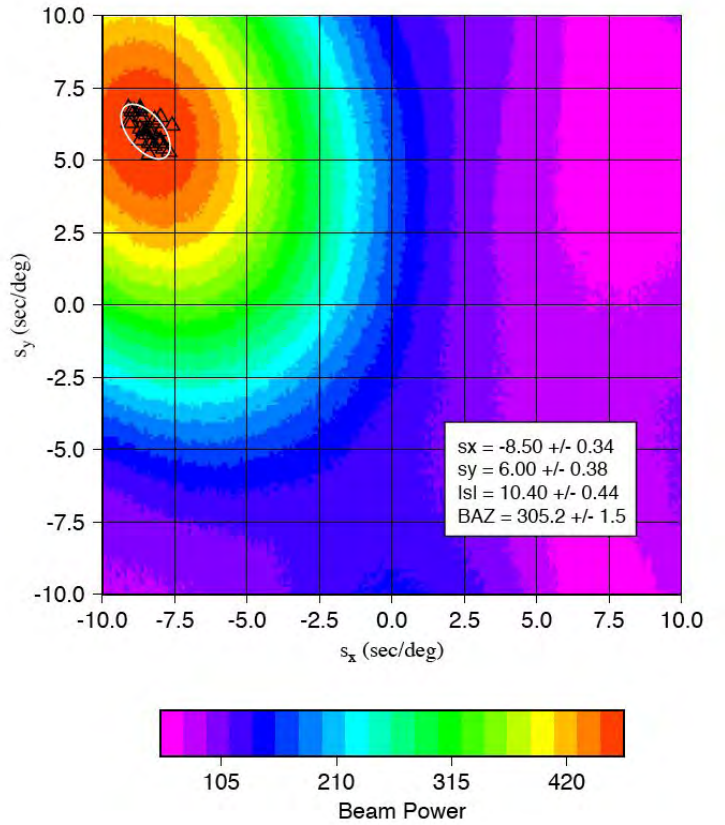


Figure 3. A grid search for the optimal 2D slowness vector in the time window of the first *P* wave for the May 31, 1997, event.

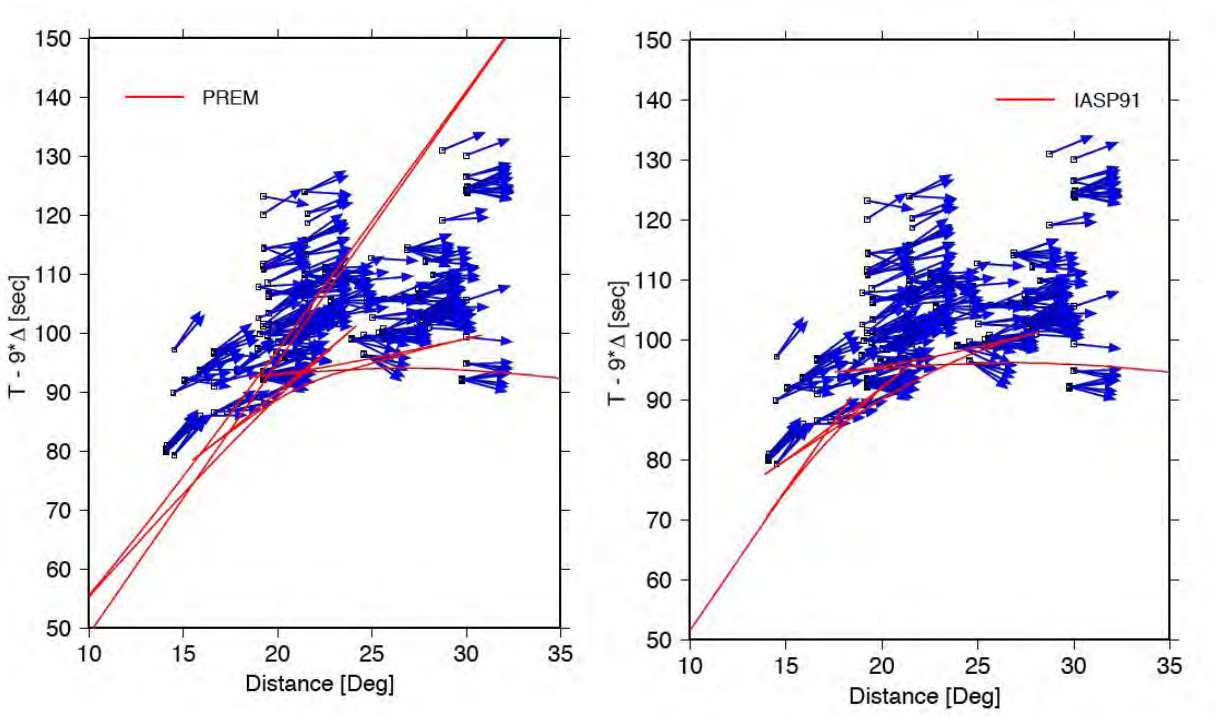


Figure 4. Travel times and slowness vectors (blue arrows) obtained from the slant-stack of the data for events with mb ≥5.0. Red curves are the theoretical travel times for PREM (right) and IASP91 (left) Earth models.

ROBUST MAGNITUDE AND PATH CORRECTIONS FOR REGIONAL SEISMIC PHASES IN EURASIA BY CONSTRAINED INVERSION AND ENHANCED KRIGING TECHNIQUES

Mark D. Fisk[1] and Steven R. Taylor[2]

ATK Mission Research[1] and Rocky Mountain Geophysics, LLC[2]

Sponsored by National Nuclear Security Administration
Office of Nonproliferation Research and Development
Office of Defense Nuclear Nonproliferation

Contract No. DE-AC52-06NA27321[1,2]

ABSTRACT

Many studies have demonstrated the need to apply distance (geometrical spreading and attenuation Q) corrections to regional seismic phases for their reliable use in discrimination procedures. Additional studies have also demonstrated that significant improvements to regional discrimination performance (e.g., using Pn/Sn and Pn/Lg) are obtained by applying station/path-specific (kriged) corrections to regional phase amplitudes or ratios. While substantial advances have been made to develop and apply such capabilities, two key issues have limited their reliability. The first is related to the fact that standard models and procedures used to invert simultaneously for geometrical spreading, frequency-dependent Q, site, and source corner frequency parameters for regional seismic phases include many trade-offs and instabilities over the parameter space. The second is related to concerns that regional phase amplitudes from earthquakes with anomalous mechanisms could significantly bias kriged correction grids and, thereby, bias discrimination results. Both of these issues and their potential impact on discrimination errors are legitimate. Under this new effort, we plan to implement, apply, and evaluate two techniques that will significantly enhance *Q* models and the robustness and reliability of magnitude and path corrections for regional seismic phases. The first is a constrained inversion approach to improve parameter estimates of geometrical spreading and *Q* models for Pn, Pg, Sn and Lg in Eurasia, by eliminating trade-offs with source corner frequencies. This will be accomplished by fitting model source parameters to relative spectra for pairs of nearby earthquakes to constrain the source corner frequencies before estimating *Q* models. The second is to implement, apply, and evaluate an extension to Bayesian kriging, that properly treats localized calibration events which may have anomalous, correlated amplitudes, to provide robust path corrections and appropriate uncertainties for regional phase amplitudes. We will evaluate the corrections and uncertainties using applications to multiple data sets. We plan to deliver these techniques, parametrizations of stress drop, corner frequency scaling, geometrical spreading and *Q* models, and kriged amplitude correction and uncertainty grids for stations in Eurasia, for potential incorporation into the Department of Energy National Nuclear Security Administration (DOE/NNSA) Knowledge Base (KB). We expect that this will significantly enhance nuclear explosion monitoring capabilities in Eurasia.

OBJECTIVES

We are just starting a two-year project to develop and test two methods to improve magnitude and path corrections for regional seismic phase amplitudes. Objectives of the first method, a constrained inversion approach, are to improve estimates of geometrical spreading and *Q* models for Pn, Pg, Sn, Lg in Eurasia, by eliminating trade-offs with source corner frequencies, and to improve source parametrizations in Eurasia, in terms of grids of stress drop and corner frequency scaling. The objective of the second method, an extension to Bayesian kriging, is to provide robust path corrections and uncertainties for regional phase amplitudes, that properly treats localized calibration events that may have anomalous, correlated amplitudes. This project has three main tasks: (Task 1) Assemble multiple data sets of regional seismic recordings of earthquakes throughout broad areas of Eurasia. Apply waveform cross-correlation techniques to determine nearby pairs/clusters of events. Assemble spectral amplitude measurements of Pn, Pg, Sn, Lg for the events. (Task 2) Implement a technique to estimate corner frequencies and scaling parameters for Pn, Pg, Sn, Lg, by fitting relative Brune model spectra to data for pairs of nearby earthquakes of different moments. Compute grids of stress drop and earthquake corner-frequency scaling with moment for Eurasia. Use spectral amplitude data for regional phases and constrained source parametrizations to perform a robust inversion for geometrical spreading and *Q* model parameters. Test and evaluate resulting magnitude and distance corrections on events in Eurasia, using cross-validation methods. (Task 3) Investigate clusters of earthquakes at the Nevada Test Site (NTS) and regions in Eurasia, and assess the potential for events with anomalous, correlated mechanisms to bias kriged amplitude correction grids beyond existing uncertainty estimates. Develop a technique to quantify the correlation of regional phase amplitudes within clusters. Extend a Bayesian kriging method to incorporate these correlation measures in the computation of amplitude correction and uncertainty grids. Test and evaluate the methods on events in Eurasia, using cross-validation techniques. We plan to deliver the techniques, parametrizations of stress drop, corner frequency scaling, geometrical spreading and *Q* models, and kriged amplitude correction and uncertainty grids for stations in Eurasia.

Background and Motivation

Many studies have demonstrated the need to apply distance corrections to regional seismic phases for reliable use in discrimination procedures (e.g., Fisk et al., 1996, 2001; Taylor and Hartse, 1998; Taylor et al., 2002). Additional studies have further demonstrated substantial improvements to regional discrimination performance by applying path-specific corrections to regional phase amplitudes or their ratios (e.g., Pn/Sn and Pn/Lg). While considerable advances have been made to compute and apply such corrections, e.g., MDAC [Magnitude and Distance Amplitude Corrections] (Taylor et al., 2002) and various forms of kriging or Bayesian calibration (e.g., Schultz et al., 1998; Bottone et al., 2002), two key issues have limited their reliability. The first is related to the fact that the models and procedures used to invert simultaneously for geometrical spreading, attenuation Q, site, and source corner-frequency parameters for regional seismic phases include many trade-offs and instabilities over the parameter space (Taylor and Hartse, 1998). The second is related to concerns that regional phase amplitudes from earthquakes with anomalous mechanisms could significantly bias kriged amplitude correction grids and, thereby, bias regional discrimination results. Both of these issues can lead to significant discrimination errors. They also have tractable solutions.

First, it is well known that there are substantial trade-offs between *Q* parameters and source corner frequencies that are very difficult to constrain by standard techniques and available data (e.g., Taylor and Hartse, 1998). Following Taylor et al. (2002), the amplitude spectrum for a given phase and station, for event *i*, may be expressed as

$$A_i(f) = S_i(f, f_c) G(r_i, r_0) \exp\left(-\frac{\pi f}{Q(f) v} r_i\right) P(f), \quad (1)$$

where *f* is the frequency, $S_i(f, f_c)$ is the source spectrum with corner frequency f_c, r_i is the epicentral distance, $Q^{-1}(f)$ is the frequency-dependent attenuation, v is the group velocity, $P(f)$ is a unitless station term, and $G(r, r_0)$ is the frequency-independent geometrical spreading term, assumed to be inversely proportional to distance to a power η, beyond some reference distance r_0. Frequency dependence of *Q* is modeled by a power-law relation of the form

$$Q(f) = Q_0 f^{\gamma}. \quad (2)$$

The logarithm of Equation (1) is used in a grid-search inversion procedure to simultaneously estimate the parameters related to source corner frequency, geometrical spreading, and frequency-dependent Q. Trade-offs between these parameter estimates can have disastrous effects of improperly correcting regional phase amplitudes for distance and magnitude. Figure 1 illustrates the serious nature of this problem for two earthquakes on 27 and 30 January 1999 near the Lop Nor Test Site (LNTS). It shows relative spectra of Pn, Sn, and Lg for the smaller event (Mw 4.38) relative to the larger event (Mw 5.69). The ratios were computed for each phase at 18 stations and then network averaged. Note that both events have similar epicenters and depths of about 20 km, based on well-constrained depth-phase solutions. Thus, path and station effects should cancel out in the relative spectra. Also shown are theoretical predictions, based on a Brune (1970) model for P and S waves, using corner frequency scaling relations for Pn and Lg estimated by Xie and Patton (1999), (XP99, dashed curves) and results by Fisk et al. (2005) by fitting the empirical relative spectra (dotted curves). It is clear that the dashed curves do not match the empirical relative spectra. Also, for a given moment, the XP99 Pn and Lg corner frequencies differ by a factor of about 4.7, quite different than many published results of between 1.73 and 1.0 (e.g., Madariaga, 1976; Choy and Boatwright, 1995; Walter and Taylor, 2002). The disagreement of the XP99 corner frequency relations with many past studies, and the empirical spectral ratios shown here, is presumably due to invalid attenuation corrections for Pn, Lg, or both. Applying these source corrections (dashed curves), based on the XP99 corner frequency relations, would lead to P/S ratios for these earthquakes that are grossly inaccurate, and would likely lead to invalid discrimination results.

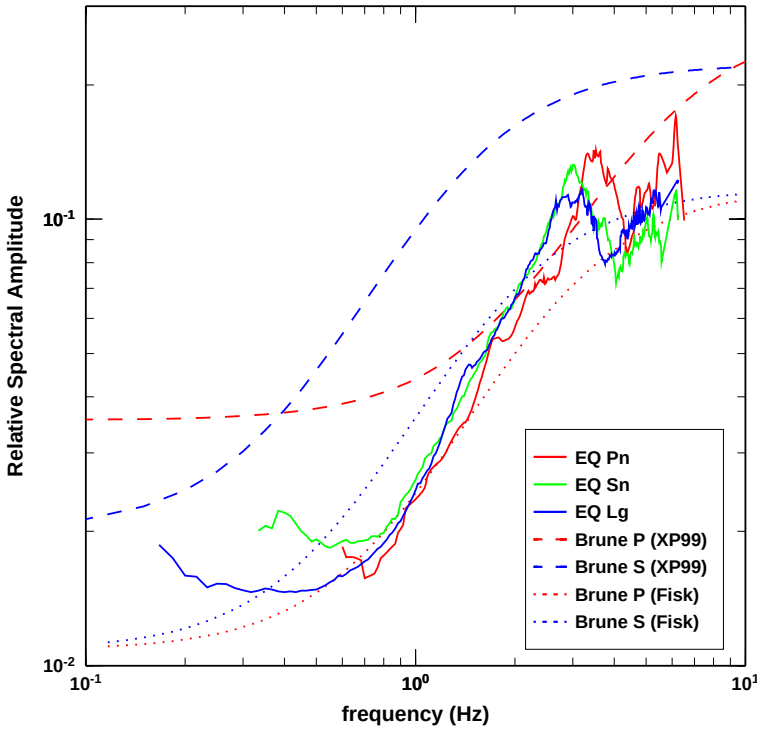


Figure 1. Network-averaged relative spectra of Pn, Sn, and Lg for two earthquakes (Mw 4.38 and 5.69) near LNTS. The empirical ratios were computed by dividing the spectra, for a given phase type, of the smaller event by those of the larger event. Also shown are theoretical predictions for P and S waves, based on a Brune (1970) model, using the corner frequency scaling relations published by XP99 and estimated by Fisk et al. (2005).

In addition, many of the MDAC2 parameters, initially estimated for geometrical spreading and *Q* at stations in Asia, do not seem physically reasonable, based on prior experience in China. They appear to be the result of trade-offs and insufficient constraints in the grid search for these parameter estimates. For example, many of the Pn geometrical spreading coefficients η are estimated to be 2.0 (a restricted upper bound), as compared to more typical estimates of 1.3 for this region of China (e.g., Xie and Patton, 1999; Taylor et al., 2002). Similarly, MDAC2 estimates of Pn Q_0 for regional stations surrounding LNTS are between 560 and 900, in striking contrast to the average Pn Q_0 values of 354

over all paths, estimated by Xie and Patton (1999). At present, it is difficult to assess which, if any, of these *Q* and geometrical spreading parameters are appropriate, but it is clear that there are substantial differences in the reported estimates. To compensate for these problems, MDAC further utilizes a “non-physical” bilinear regression fit to obtain frequency-dependent amplitude corrections as functions of magnitude and distance (Taylor et al., 2002), which seems to provide reasonable corrections, but does not lend much confidence that they are physically appropriate.

While Figure 1 illustrates a serious problem, it also shows a straightforward solution. Since geometrical spreading, *Q*, and site effects are factored out of relative spectra of a given phase for nearby pairs of events with similar mechanisms, the corner frequencies of a Brune model may be fit to the relative spectra, as was done by Fisk et al. (2005) for LNTS earthquakes (cf. Figure 1). Thus, by first eliminating path and station effects, the source parametrization can be constrained reasonably well. Then the inversion for geometrical spreading, Q, and site parameters will be more robust by eliminating the trade-off with corner frequency. The feasibility of this approach depends on sufficient pairs of nearby events to constrain the source parameters over a broad enough spatial extent. Fortunately, Schaff and Richards (2004) showed that about 4200 events in and near China, listed in the Annual Bulletin of Chinese Earthquakes (ABCE) over a 15 year period, have at least one other event with Lg waveform (0.5-5.0 Hz) cross-correlations greater than 0.5. This indicates that there are indeed many pairs of replicated events throughout much of China and surrounding regions that can be exploited for our approach. We expect to find many other such events for other regions throughout Eurasia. Below we describe our plans to collect and process such data and our constrained inversion procedure.

Second, despite compelling demonstrations that kriging of path-specific amplitude corrections can significantly improve regional P/S discrimination performance (e.g., Phillips et al., 1998; Phillips, 1999; Rodgers et al., 1999; Fisk et al., 2001; Bottone et al., 2002; Fan et al., 2002; Taylor et al., 2002), there are concerns regarding the robustness of the amplitude corrections to aberrant calibration data. To first illustrate the substantial benefit obtained by using kriged corrections for Pn/Sn and Pn/Lg, Figure 2 shows the locations of explosions and presumed earthquakes that we used in a global discrimination study, as well as the locations of 52 International Monitoring System (IMS) stations and 4 non-IMS stations with regional recordings of these events. Bottone et al. (2002) and Fisk et al. (2001) described these data sets, the distance corrections for Pn/Sn and Pn/Lg, station-specific kriged correction and uncertainty grids for the amplitude ratios, a discrimination hypothesis test, application of the correction and discrimination techniques to these global data sets, and in-depth analyses of the results for each nuclear test site. They found that an additional 28% of the earthquakes (78% versus 50%) are classified properly by using the Bayesian calibration (kriging) method than just using distance corrections, without misclassifying any of the explosions in either case. However, there are valid concerns that earthquakes with anomalous mechanisms, depths, or paths could significantly bias kriged amplitude correction grids. This is certainly possible, especially for kriging algorithms that fit each data point (e.g., Schultz et al., 1998). The Bayesian kriging method, developed by Bottone et al. (2002), estimates the local mean, weighted by the global average and nearby calibration data relative to the calibration grid point. This approach is far less sensitive to data with anomalously high or low values. Nevertheless, a cluster of events with anomalous amplitudes (such as an aftershock sequence with atypical focal mechanism) could impact the correction surface near those data.

These concerns regarding the correction grids, while justified, must be viewed in the context of the associated uncertainty (variance) grids, which are intended to represent the variability from localized source mechanisms (i.e., residual variance) and from the amount of calibration data in proximity to the correction grid point (i.e., calibration variance). We generally estimate these variances in a conservative manner by using global sets of earthquakes in variogram analysis, which also estimates the correlation length. By properly using conservative estimates of these variances in a discrimination procedure, the overall uncertainty accounts for the fact that earthquakes from a global population can have anomalous amplitudes, that could result in aberrant corrections. This treatment of the uncertainty protects from making erroneous event classifications in poorly calibrated areas (effectively lowering the confidence level due to greater calibration uncertainty). Thus, isolated or limited data points with anomalous amplitudes may impact the correction grid some, but the uncertainties should, and generally do, account for this potential behavior.

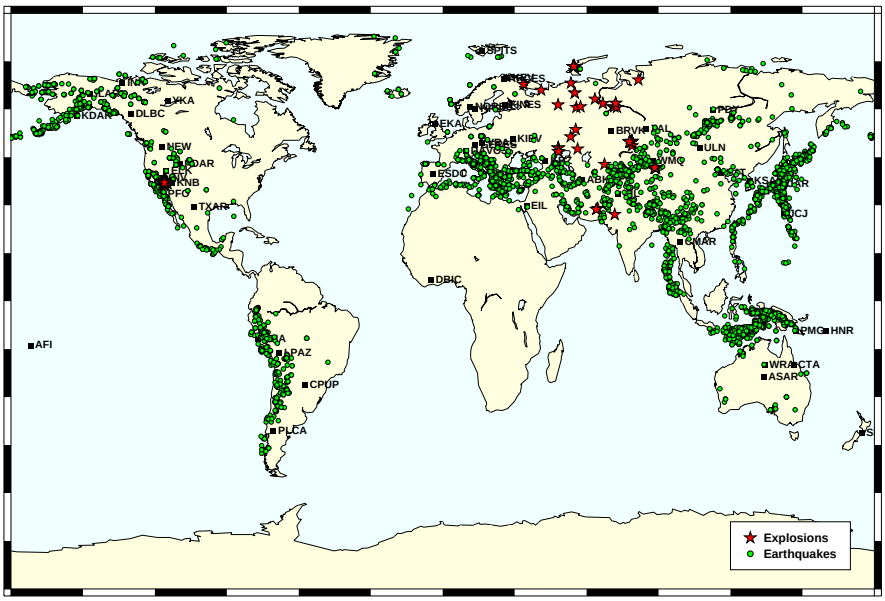


Figure 2. Locations of 161 explosions (stars) and 4173 REB events (circles) above mb 3.5. Locations of 52 IMS and 4 non-IMS stations with regional recordings of these events are also shown.

However, a real problem can arise if there is a localized cluster of many events with atypical amplitudes. In this case, most kriging algorithms reduce the calibration variance without any assessment of how representative or atypical the data might be. Only the correlations, which depend just on relative distances of reference data to the calibration point, are presently used. In such cases, the calibration variance could be reduced to a level where the overall variance does not adequately reflect the potential bias in the correction grid. Indeed, the real problem is that most kriging methods treat clustered calibration data as independent samples, with no assessment of whether they have correlated source mechanisms. If this type of correlation was explicitly treated, then the calibration variance would be reduced more slowly as a function of the number of calibration data. As an extreme case, if all of the waveforms for a cluster of events were perfectly correlated, then the calibration variance should treat this cluster as a single data point, and the uncertainties, based on a global earthquake population, would still conservatively reflect potential anomalies.

As an example of this problem, several aftershock sequences with distinct mechanisms have occurred at the NTS (e.g., Walter et al., 1995). During 1992, about 35 earthquakes in the Little Skull Mountain (LSM) sequence, with depths of 6-12 km, were recorded with good signal-to-noise ratio (SNR) by MNV and KNB. In 1993 and 1994, unusually shallow (1-3 km) earthquakes occurred in Rock Valley (RV), about 10-20 km from the LSM sequence. About 10 of these events have good SNR at MNV and KNB. Walter et al. (1995) showed that Pn/Lg(6-8 Hz) values for the RV events are systematically higher than those for the LSM events (Figure 3), especially at KNB. Figure 4 shows that near NTS the kriged Pn/Lg correction grid for MNV is higher than the global average (green) and the variance grid has its lowest values, where many calibration events are available. Fisk et al. (2001) showed that application of Bayesian kriging (path corrections and uncertainties) to Pn/Lg (6-8 Hz) did not misclassify any NTS explosions and most nearby earthquakes were classified properly, except for the RV earthquakes that were classified as *undetermined*. Thus, although the correction grid for MNV is higher than the global average, the uncertainties are adequate to produce appropriate discrimination results. However, if all of the calibration earthquakes near NTS were like the shallow RV events, the kriged Pn/Lg correction grid would have even much higher values and the calibration variance would still be small. The potential to misclassify explosions with lower Pn/Lg values would be likely, since the RV earthquake mean falls within the explosion population (Figure 3).

This is exactly the type of problem that requires research to know if kriged amplitude correction and uncertainty grids, based on aberrant earthquake clusters, can lead to discrimination errors. It must be resolved before kriged corrections can be applied confidently to broad areas lacking explosion data, where discrimination results cannot be

directly validated. Fortunately, a tractable solution may be implemented by treating correlations of waveforms or amplitude measurements for clusters of events in a manner that properly accounts for the effective independent number of calibration data. In the example above, using only RV earthquakes to calibrate NTS, the effective amount of independent calibration data would be limited by the fact that the mechanisms for these events were similar. Thus, the calibration variance would be relatively large and the discrimination criteria would be aptly conservative.

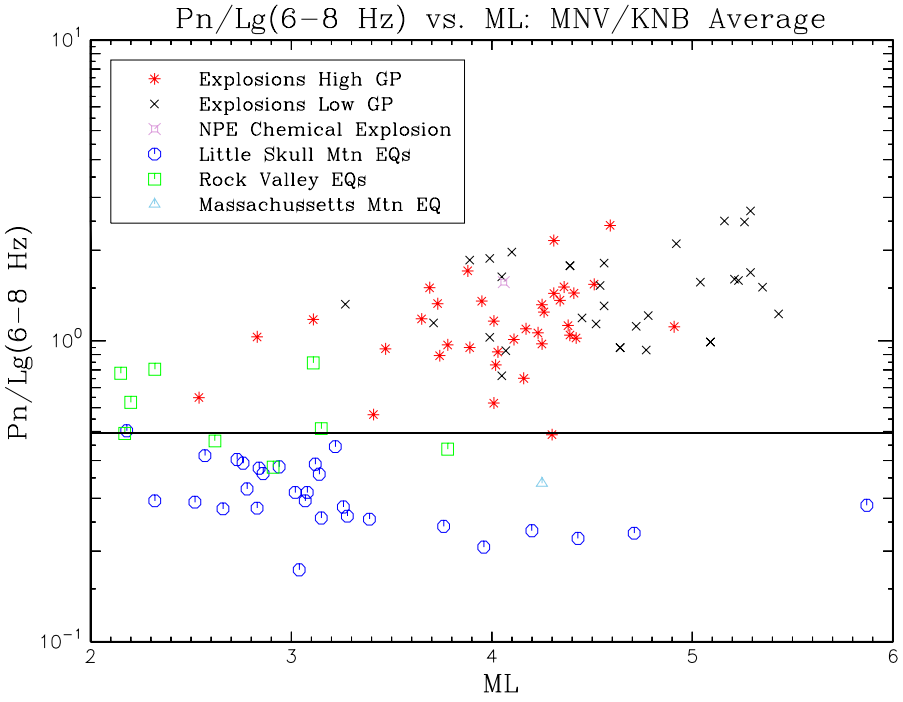


Figure 3. Averaged MNV and KNB Pn/Lg(6-8 Hz) values versus ML for NTS explosions and earthquakes. The line corresponds to the lowest Pn/Lg value for the explosions. Most Rock Valley earthquakes fall above the line.

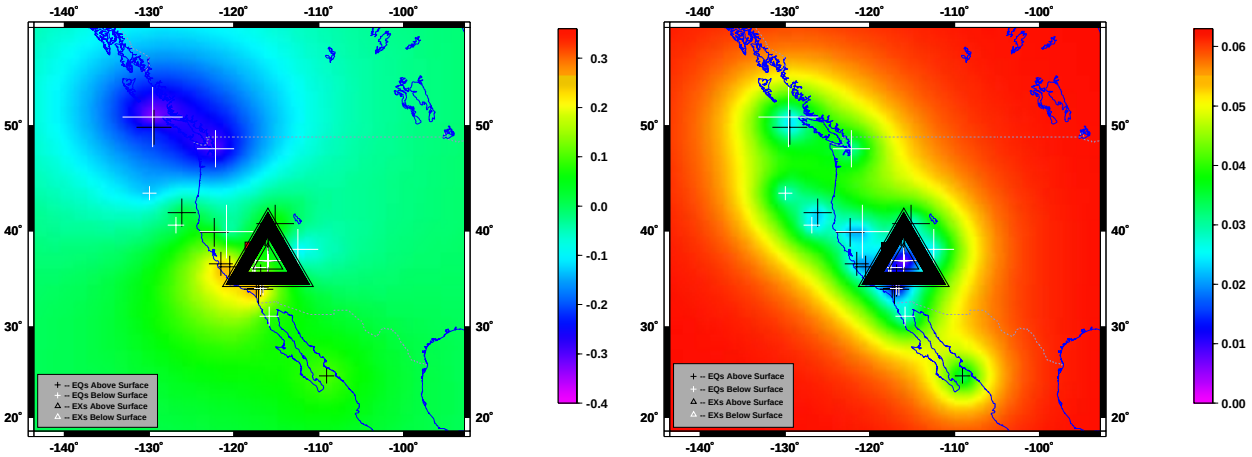


Figure 4. Correction (left) and uncertainty (right) grids for log[Pn/Lg(6–8 Hz)] at MNV. Triangles depict explosions and crosses depict earthquakes. Black (white) markers have values greater (less) than the local value of the correction grid. Marker size is proportional to the absolute difference from the correction surface.

Below we present the data sets, an inversion technique for distance correction parameters that first constrains the source parameters, extension of our Bayesian kriging method, and plans to test and evaluate these techniques.

Data Sets

Several excellent data sets will be considered for this project, to obtain large numbers of pairs or clusters of events in Eurasia. First, we have compiled and processed regional recordings of 4173 presumed earthquakes above mb 3.5 in the Reviewed Event Bulletin (REB) (green circles in Figure 2). We will apply waveform cross-correlation software to various regional phase windows and assess events with significant correlations. Our primary focus will be on Eurasia, but we expect that some interesting event clusters will be found in other regions, that will be useful for investigating effects of anomalous path corrections. Second, regional recordings for several thousand earthquakes in Eurasia exist at LANL (Figure 5). Spectral amplitudes in several frequency bands have already been processed for these events. We plan to assess earthquakes in this large database that have significant waveform cross-correlations for regional phases and utilize these data for our constrained inversion of geometrical spreading and *Q* models for various regional phases, and for our kriging efforts. Third, Schaff and Richards (2004) assembled International Seismological Centre data for over 14,000 events in and near China, listed in the ABCE from 1985 to 2000. They processed Lg waveform cross-correlations to find large subsets of replicating events. We plan to utilize their results to obtain pairs/ clusters of events.

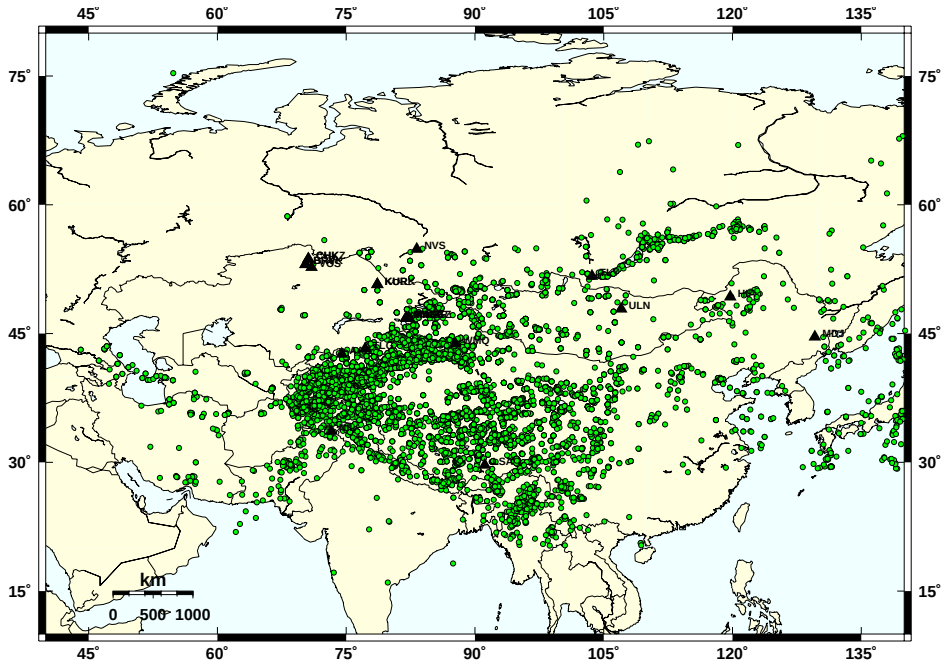


Figure 5. Locations of presumed earthquakes with regional seismic data in the LANL database.

Constrained Inversion Technique

To characterize the source spectral function in Equation (1) for earthquakes, we use a modified Brune (1970) model. For a particular phase type, ξ (P or S), the amplitude spectrum is given by

$$S(f, f_c(\xi)) = \frac{M_0 R_{\theta\phi}(\xi)}{4\pi\sqrt{\rho_s \rho_r v_s(\xi)^5 v_r(\xi)}[1 + (f/f_c(\xi))^2]}, \quad (3)$$

where M_0 is the seismic moment, $R_{\theta\phi}$ is the radiation pattern coefficient for P or S waves, ρ_s and ρ_r are the source and receiver medium densities, v_s and v_r are the source and receiver medium velocities for P or S waves, and f_c is the source corner frequency. For a Brune (1970) dislocation source, the corner frequency is given by

$$f_c(\xi) = c_\xi v_s(\xi)\left(\frac{\sigma_b}{M_0}\right)^{1/3}, \quad (4)$$

where σ_b is the stress drop and c_ξ is a constant that depends on phase type. Cong et al. (1996) and Nuttli (1983) show that corner frequency scaling as $M_0^{-1/4}$ is more appropriate than -1/3 scaling for earthquakes in central Asia. This departure from cube-root scaling can be viewed as a result of non-constant stress drop. Following Walter and Taylor (2002), non-constant stress drop may be treated by defining the apparent stress drop for a given moment, M_0, as

$$\sigma_b = \sigma_b^{(0)}\left(\frac{M_0}{M_0^{(0)}}\right)^{\psi}, \quad (5)$$

where $\sigma_b^{(0)}$ is the stress drop at a reference moment $M_0^{(0)}$. Parameters $\sigma_b^{(0)}$, $M_0^{(0)}$, and ψ may be estimated from data. Instead of doing a grid search for all source and attenuation parameters simultaneously, we will use relative spectra to first estimate and fix the source parameters, and then invert for values of η, Q_0, and γ. That is, for a pair of nearby earthquakes with similar radiation patterns and media, the model relative spectra for a given phase type is given by

$$\frac{A_1(f)}{A_2(f)} = \frac{S_1(f)}{S_2(f)} = \frac{M_0^{(1)}[1 + (f/f_c^{(2)})^2]}{M_0^{(2)}[1 + (f/f_c^{(1)})^2]}. \quad (6)$$

Using pairs of localized earthquakes, we will fit the parameters $\sigma_b^{(0)}$, $M_0^{(0)}$, ψ, and c_P/c_S of this model to empirical relative spectra of regional phases (e.g., as depicted by the dotted curves in Figure 1, above). We will generate grids of stress drop and corner frequency scaling parameters for regional phases in Eurasia. We will the adapt the MDAC algorithm to constrain the source parameters and estimate geometrical spreading, *Q*, and site terms of Equation (1) for stations in Eurasia. We will compare the results among these data sets (and to published results) to assess their robustness. We will then perform a final application using the merged data sets to obtain and evaluate the final results. We will quantify the uncertainties and remaining trade-offs of the estimated source and attenuation parameters in terms of root mean square (RMS) residual misfits and residual sum of squares (RSS) values of the model and empirical relative spectra, and using Principal Components Analysis to assess the eigenvectors that quantify the most relevant contributions to the variance and trade-offs among the parameters, with and without using the source constraints.

Enhanced Bayesian Kriging Methodology

Among other geophysical applications, kriging has been used to calibrate and treat uncertainties of regional phase amplitudes or amplitude ratios (see Bottone et al., 2002; and references therein). Kriging provides optimal prediction at a new location, as a weighted linear combination of reference data, with greater weight given to data that are spatially closer to the prediction location. That is, given *N* reference data values, $x(\mathbf{s}_1), \ldots, x(\mathbf{s}_N)$, at locations $\mathbf{s}_1, \ldots, \mathbf{s}_N$, the optimal predictor for the mean at a location $\mathbf{s}_0$ is given by the weighted linear combination of data:

$$\hat{\mu}(\mathbf{s}_0) = \sum_{i=1}^{N} w_i x(\mathbf{s}_i). \quad (7)$$

In previous applications, $x(\mathbf{s}_i)$ has represented MDAC-corrected amplitudes or distance-corrected amplitude ratios. The set of all predictions, $\hat{\mu}(\mathbf{s}_0)$, over permissible locations $\mathbf{s}_0$, provides a correction grid. The corresponding uncertainty surface, $\sigma^2(\mathbf{s}_0)$, also results from the calculation. This posterior variance and the weights w_i depend on the correlations, ρ_{ij}, between the data means at $\mathbf{s}_i$ and $\mathbf{s}_j$, the calibration variance, σ_c^2, and the residual variance, σ_r^2:

$$w_i = F(\sigma_c^2, \sigma_r^2, \rho_{ij}) \quad (8)$$

$$\sigma^2(s_0) = G(\sigma_c^2, \sigma_r^2, \rho_{ij}). \quad (9)$$

Explicit forms of *F* and *G* depend on the distribution of the $x(\mathbf{s}_i)$, but not on the data themselves. Assuming the $x(\mathbf{s}_i)$ have a normal distribution, the expressions for *F* and *G* have closed forms. The correlations, ρ_{ij}, between the means at $\mathbf{s}_i$ and $\mathbf{s}_j$, are generally assumed to depend only on the distance $\Delta(\mathbf{s}_i,\mathbf{s}_j)$ between $\mathbf{s}_i$ and $\mathbf{s}_j$, and are often taken to be the exponential function $\rho_{ij} = \exp(-\Delta(\mathbf{s}_i, \mathbf{s}_j)/\alpha)$, where α is the correlation length. Input parameters for the kriging

algorithm are σ_c^2, σ_r^2, and α. In practice, they are estimated from data using variogram analysis. Further details regarding this Bayesian kriging approach, variogram analysis, and applications are presented by Bottone et al., 2002.

The issue we plan to redress, that is common to most kriging methods, is that the weights and variances in Equations (8) and (9) treat an effective correlation, based only on the distances of reference data to the calibration point, but do not depend on the intrinsic correlations among clustered events, which could be high if the events have similar mechanisms. In such cases, existing methods compute the weights too high and the variances too low near the cluster, because the data are treated as independent. The first step will be to assess the impact on discrimination performance. Several aftershock sequences are well suited for this analysis. First, we will examine the LSM and RV earthquakes at NTS. We will quantify waveform cross-correlations for events within each cluster and regress these values against the correlation of Pn/Lg values among the events. This information will be used to determine how many independent degrees of freedom actually exist for these data sets and how the weights and variances of the kriging algorithm should be modified to guard against potential discrimination errors. Second, aspects of these analyses will be applied to several known aftershock sequences in Eurasia and other clusters of events found by waveform cross-correlation methods. For example, there are three large earthquake sequences (20-80 events) in India near Bhuj, Chamoli, and Koyna, a sequence of about 70 events near Jiashi in western China, over 30 events near Tabas, Iran, and a large number of aftershocks in Kyrgyzstan during 1998. Third, to examine the effects on discrimination performance we will take one or more earthquakes with the highest P/S ratios near nuclear test sites in China, Pakistan, Kazakhstan, and India and replicate those data, based on the correlations and variances measured for the aftershock sequences elsewhere. We will quantify discrimination performance for these simulated (worst-case) earthquake calibration sets as a function of the number of replicated reference events. We will develop a fundamental improvement to kriging methods by incorporating correlations of waveforms or amplitudes that properly treats the independent degrees of freedom of localized calibration data. We will apply the enhanced kriging algorithm to broad data sets of almost 4200 global REB earthquakes and several thousand earthquakes in Eurasia. We will evaluate the correction and variance grids using cross-validation methods (eliminating entire groups of nearby events) and assess the discrimination performance near known nuclear test sites, based on these final grids.

RESEARCH ACCOMPLISHED

The start date for this contract was too late to obtain results for this paper, but we are working on the first milestone of assembling and processing the data sets.

CONCLUSIONS AND RECOMMENDATIONS

We expect that our innovative inversion technique for constraining source corner frequencies and then estimating attenuation parameters will significantly improve geometrical spreading and *Q* models and the robustness/reliability of magnitude and path corrections for regional seismic phases. Our approach will utilize multiple data sets, assessing and treating trade-offs between *Q* parameters and source corner frequency scaling, and assessing the uncertainties. This effort will also provide improved source characterization for events in Eurasia, in terms of stress drop grids and corner-frequency scaling parameters. We also expect that our research and extension to Bayesian kriging will provide robust path corrections and uncertainties for regional phase amplitudes, generalized to properly treat localized calibration events that may have anomalous, correlated amplitudes. This method will explicitly quantify the resulting variances of regional phase amplitudes in Eurasia. Both of these research areas will be directed at improving regional phase amplitude corrections and the uncertainties throughout major regions of Eurasia. These methods and the resulting amplitude correction and uncertainty terms will be directly applicable for use in existing monitoring systems. The results of this effort will be delivered to LANL for potential incorporation into the DOE/NNSA KB. We expect that this will significantly enhance U.S. nuclear explosion monitoring capabilities in Eurasia.

REFERENCES

Bottone, S., M. D. Fisk, and G. D. McCartor (2002). Regional seismic event characterization using a Bayesian formulation of simple kriging, *Bull. Seism. Soc. Am.* 92: 2277–2296.

Brune, J. N. (1970). Tectonic stress and the spectra of seismic shear waves from earthquakes, *J. Geophys. Res.* 75: 4997–5009.

Choy and Boatwright (1995). Global patterns of radiated seismic energy and apparent stress, *J. Geophys. Res.* 100: 18,205–18,228.

Cong, L., J. Xie and B. J. Mitchell (1996). Excitation and propagation of Lg from earthquakes in central Asia with implications for explosion/earthquake discrimination, *J. Geophys. Res.* 101: 27,779–27,789.

Fan G.-W., T. Lay and S. Bottone (2002). Path corrections for source discriminants: a case study at two international seismic monitoring stations, *Pure and Appl. Geophys., Special Edition on Monitoring the Comprehensive Nuclear-Test-Ban Treaty: Seismic Event Discrimination and Identification*, 159: 651–678.

Fisk, M. D. (2006). Source spectral modeling of regional P/S discriminants at nuclear test sites in China and the Former Soviet Union, in press, *Bull. Seism. Soc. Am.*

Fisk, M. D., S. Bottone, and G. D. McCartor (2001). Regional seismic event characterization using Bayesian calibration, MRC-R-1621, Mission Research Corp., Santa Barbara, CA.

Fisk, M. D., H. L. Gray and G. D. McCartor (1996). Regional discrimination without transporting thresholds, *Bull. Seism. Soc. Am.* 86; 1545–1558.

Fisk, M. D., S. R. Taylor and T. Lay (2005). Modeling and empirical research on energy partitioning of regional seismic phases used for explosion monitoring, in *Proceedings of the 27th Seismic Research Review: Ground-Based Nuclear Explosion Monitoring Technologies*, LA-UR-05-6407, Vol. 1, pp. 539–549.

Madariaga, R. (1976). Dynamics of an expanding circular fault, *Bull. Seism. Soc. Am.* 66: 639–667.

Nuttli, O. W. (1983). Average seismic source-parameter relations for mid-plate earthquakes, *Bull. Seism. Soc. Am.* 73: 519–535.

Phillips, W. S. (1999). Empirical path corrections for regional seismic phases, *Bull. Seism. Soc. Am.* 89: 384–393.

Phillips, W. S., G. E. Randall and S. R. Taylor (1998). Path correction using interpolated amplitude residuals: An example from central China, *Geophys. Res. Lett.* 25: 2729–2732.

Rodgers, A. J., W. R. Walter, C. A. Schultz, S. C. Myers, and T. Lay (1999). A comparison of methodologies for representing path effects on regional P/S discriminants, *Bull. Seism. Soc. Am.* 89: 394–408.

Schaff, D. P. and P. G. Richards (2004). Repeating seismic events in China, *Science* 303: 1176–1178.

Schultz, C. A., S. C. Myers, J. Hipp and C. J. Young (1998). Nonstationary Bayesian Kriging: A predictive technique to generate spatial corrections for seismic detection, location and identification, *Bull. Seism. Soc. Am.* 88: 1275–1288.

Taylor, S. R., and H. E. Hartse (1998). A procedure for estimation of source and propagation amplitude corrections for regional seismic discriminants, *J. Geophys. Res.* 103: 2781-2789.

Taylor, S. R., A. A. Velasco, H. E. Hartse, W. S. Phillips, W. R. Walter, and A. J. Rodgers (2002). Amplitude corrections for regional seismic discriminants, *Pure and Appl. Geophys., Special Edition on Monitoring the Comprehensive Nuclear-Test-Ban Treaty: Seismic Event Discrimination and Identification*, 159: 623–650.

Walter, W. R., K. M. Mayeda, and H. J. Patton (1995). Phase and spectral ratio discrimination between NTS earthquakes and explosions. Part I: Empirical observations, *Bull. Seism. Soc. Am.* 85: 1050–1067.

Walter, W. R. and S. R. Taylor (2002). A Revised Magnitude and Distance Amplitude Correction (MDAC2) Procedure for Regional Seismic Discriminants: Theory and Testing at NTS, *UCRL-ID-146882, LA-UR-02-1008*.

Xie, J. and H. J. Patton (1999). Regional phase excitation and propagation in the Lop Nor region of central Asia and implications for P/Lg discriminants, *J. Geophys. Res.* 104: 941–954.

REGIONAL ATTENUATION METHOD COMPARISON FOR NORTHERN CALIFORNIA

Sean R. Ford[1], Douglas S. Dreger[1], Kevin Mayeda[2], William R. Walter[3], Luca Malagnini[4], and William S. Phillips[5]

University of California, Berkeley[1], Weston Geophysical[2], Lawrence Livermore National Laboratory[3], Istituto Nazionale di Geofisca e Vulcanologia[4], Los Alamos National Laboratory[5]

Sponsored by National Nuclear Security Administration
Office of Nonproliferation Research and Development
Office of Defense Nuclear Nonproliferation

Contract No. DE-FC52-05NA26605[1–5]

ABSTRACT

The measurement of regional attenuation (Q^{-1}) is difficult and can produce method dependent results. The discrepancies among methods are due to differing parameterizations (e.g., geometrical spreading considerations), datasets used (e.g., choice of path lengths and sources), and the methodologies themselves (e.g., measurement in the frequency or time domain). This study aims to quantitatively understand differences in regional attenuation measures by applying multiple techniques to common datasets in a several different regions. Here we show results of applying the methods with controlled parameterization in the well-studied region of northern California with a high-quality dataset from the Berkeley Digital Seismic Network. Specifically, we employ the coda normalization, two-station, reverse two-station, source-pair/receiver-pair, and the new coda-source normalization methods to measure Q of the regional phase, Lg (Q_{Lg}), and its power-law dependence on frequency of the form $Q_0 f^{\alpha}$.

All methods produce similar overall regional patterns in Q_0, with low attenuation in the central Sierra Nevada foothills and high attenuation in the Bay Area and northern Sierras. However, the absolute values of Q_0 can differ by as much as a factor of 1.9 for similar paths and stations. The reverse two-station method produces the smallest variance in Q_0, whereas the source-pair/receiver-pair produces the greatest. Spatial variation in α follows that of Q_0, but has more variability for all methods. This variability may be due to the improper accounting of site effects.

We test the sensitivity of each method to changes in geometrical spreading, Lg frequency bandwidth, the distance range of data, and the Lg window. Change in the geometrical spreading model (r^{γ}) affect all methods and is shown to be an important assumption when extracting Q_{Lg} from path effects. There is a significant change in α when measuring Q at frequencies less than 1 Hz, suggesting the power-law frequency dependence of Q may be different at the lower end of the spectrum. All methods are also affected by the choice of the Lg time window, and careful handpicking of the time window may result in less variance in the measurements. Epicentral distance choice has the most effect on the coda-normalization method, which may be due to the fixed elapsed time that the coda is sampled at for all distances. The reverse two-station method is the most robust technique, which is most probably due to its superior suppression of site effects.

OBJECTIVES

Understanding of regional attenuation can help to correct for the effects of Q and lead to better discrimination of small nuclear tests. Present threshold algorithms rely on Q models that are derived differently, and the models can vary greatly for the same region. For example, recent one-dimensional (1-D) Q studies in South Korea find frequency-dependent Q_{Lg} that at 1 Hz range from 450 to 900 (Chung and Lee, 2003; Chung et al., 2005). It is difficult to learn the cause of such discrepancies because the methods and parameterizations change for each analysis. While individual regional attenuation techniques can determine their own self-consistent Q parameters, it then becomes a challenge to reconcile new results with other parameterizations in the literature, or to use them in algorithms that may employ different assumptions. These inconsistencies limit the ability to extend prior studies to understand new regions. In order to better understand the effects of different methods and parameterizations on Q models, we implement four popular methods and one new method to measure Q_{Lg} with a high-quality dataset from the Berkeley Digital Seismic Network (BDSN). This analysis allows for an "apples-to-apples" comparison of different attenuation methods and their assumptions. With this knowledge, future attenuation studies can more knowledgeably interpret Q models.

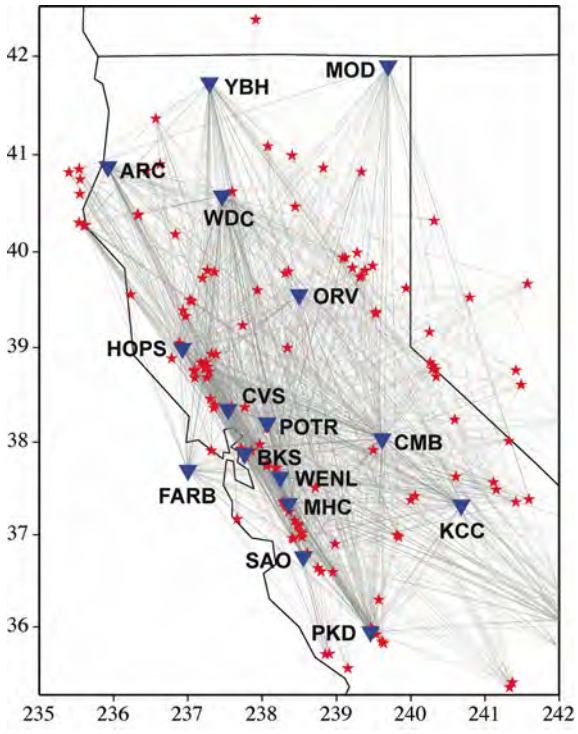


Figure 1. Map of events (red stars), stations (blue inverted triangles), and path coverage (grey lines) employed in this study.

RESEARCH ACCOMPLISHED

The dataset consists of 158 earthquakes recorded at 16 broadband (20 sps) three-component stations of the BDSN between 1992 and 2004 (Figure 1). Records were inspected for a high signal-to-noise ratio and chosen to have a good spatial distribution. Magnitude (mb) ranges from 2.2 to 6.5 (San Simeon event). Distance ranges from 3 to 800 km. Interstation distance ranges from 30 to 670 km. This wide distribution of data parameters allows for sensitivity testing to a given dataset. With this dataset we calculate Q_{Lg} by fitting the power-law model, $Q_0 f^{\alpha}$, in Northern California using five different methods. The first two methods use the seismic coda to correct for the source effect. These methods can produce best-fit power-law parameters for specific stations. The last three methods use the spectral ratio technique to correct for source, and possibly site effects. These methods produce best-fit power-law parameters for specific interstation paths. The two types of methods are briefly introduced and the results compared using the parameterization given in Table 1.

Coda Normalization Method (CNM)

CNM uses the coda as a proxy for the source and removes it from the Lg spectrum (Aki, 1980; Yoshimoto et al., 1993). The amplitude is then least-squares fit as a function of distance in small frequency bands for each station, where the slope is related to path attenuation, Q^{-1}. Q^{-1} at the center frequency of each band then reveals a power-law Q model for each station. Results from this method are given in Figure 2a.

Table 1. Method parameterization

Parameter	Value
Lg velocity (km/s)	3.5
Spreading exponent	0.5
Lg velocity window (km/s)	2.5 - 3.5
Component	N-S
Epicentral distance (km)	100 - 400
Measurement bandwidth (Hz)	0.2 - 8
SNR	> 2
Interstation distance (km)	50 - 500
Azimuthal window (°)	15

Coda-source normalization method (CSM)

CSM uses the 1-D coda-source spectra previously calculated in the study by Mayeda et al. (2005) and

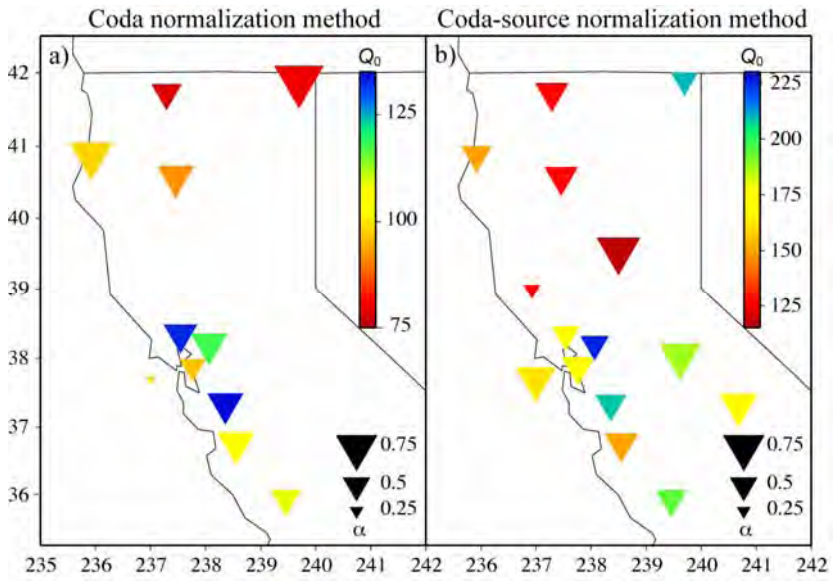


Figure 2. Spatial variability in the power-law fit parameters ($Q_0 f^{\alpha}$) for the coda normalization method (left) and coda-source normalization method (right). Note the similar scales for the parameter α and different scales for Q_0.

removes it from the Lg spectrum in small frequency bands (Walter et al., 2006). Q^{-1} is calculated for each of these bands for each event-station path. In this application of CSM all paths to a common station are fit to find a power-law Q model for each station. Results from this method are given in Figure 2b.

Comparison of CSM and CNM

Since both CNM and CSM give a result for each station, we compare these results by finding the percent deviation

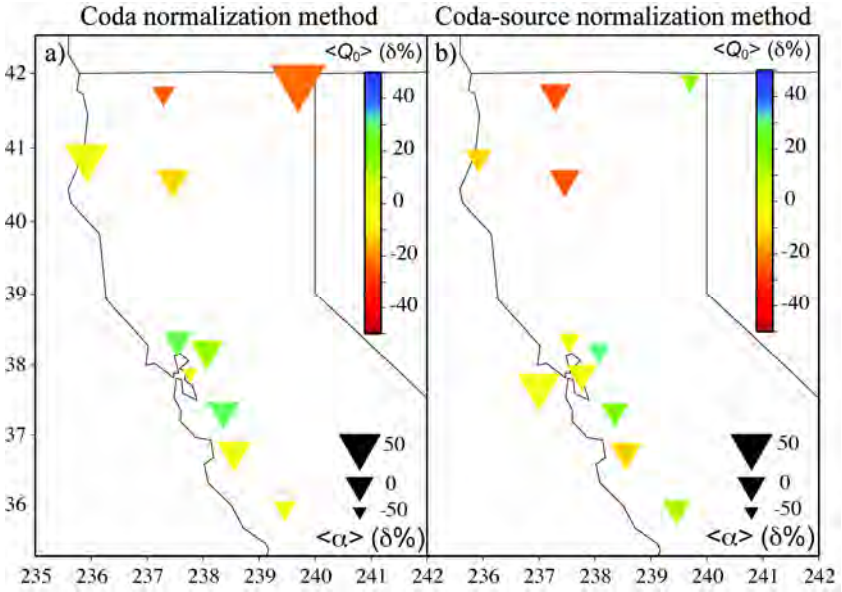


Figure 3. Spatial variability in the percent deviation from the method average power-law fit parameters ($Q_0 f^{\alpha}$) for the coda normalization method (left) and coda-source normalization method (right). The average model ($Q_{Lg} = \langle Q_0 \rangle f^{\langle \alpha \rangle}$) given by CNM is $104 f^{0.61}$ and from CSM is $172 f^{0.57}$.

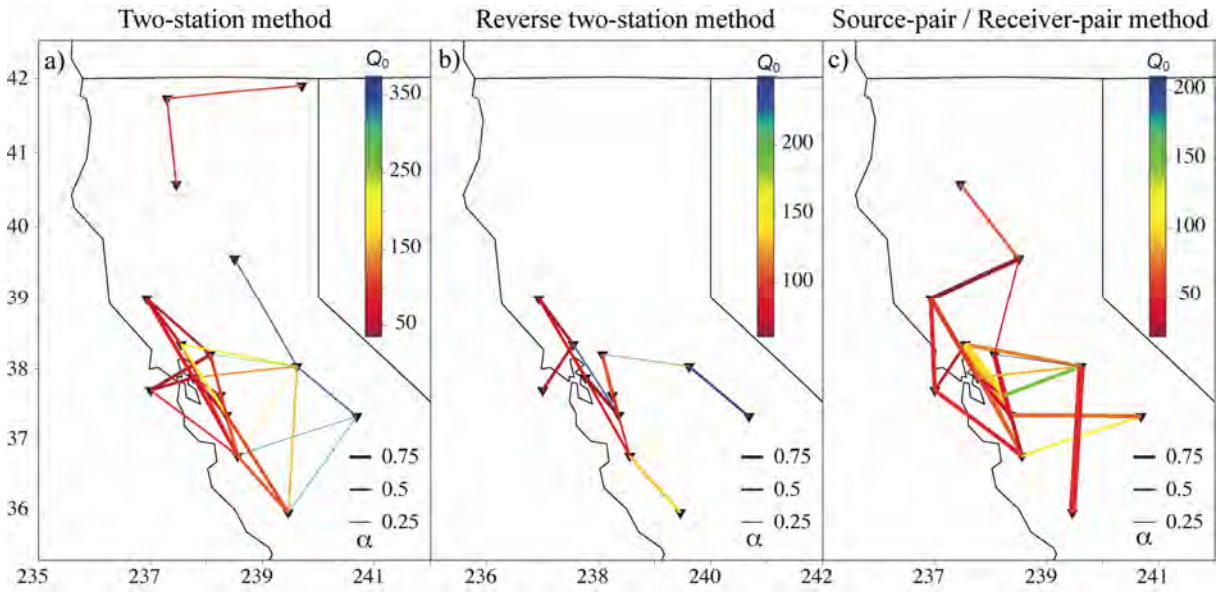


Figure 4. Spatial variability in the power-law fit parameters ($Q_0 f^{\alpha}$) for the three spectral ratio methods. Note the similar scales for the parameter α and different scales for Q_0.

of each station from the average $Q_0 f^{\alpha}$ produced for each method . Comparisons are mapped in Figure 3a-b for robust solutions. The average Q_{Lg} model given by the CNM is $104 f^{0.61}$, while the CSM produces an average of $172 f^{0.57}$. The absolute difference in Q_{Lg} models may be due to the absence of a site correction in the CSM. There is overall relative agreement in the two methods, with low Q in the northern part of the study region and variable Q in the Bay Area. This Bay Area variance may be due to paths crossing different tectonic regimes to reach these stations and forming an average fit. Stations MOD, FARB, and POTR appear to have a strong difference in measured $Q_0 f^{\alpha}$. However, the fit to a power-law model is poor at frequencies > 2 Hz, and the comparison for a power-law model may be flawed for these stations. Stations BKS and MHC are consistently lesser or greater, respectively, than the average for each method, but there is a large percent deviation for the two stations. A possible reason for this deviation may be that the effective SNR is different for the two methods. The signal in the SNR calculation for the CSM is the Lg energy, while the signal for the CNM is the coda. Therefore, it is possible that noisier data is used in the CSM, though this effect would most probably be seen across all stations and not just these two.

Two-Station Method (TSM)

TSM takes the spectral ratio of Lg recorded at two different stations along the same narrow path from an event (Xie, 2002; Xie and Mitchell, 1990). We restricted the path to fall in an azimuthal window of 15°. The ratio removes the common source term and the amplitude is fit in the log domain so that the slope is α and the intercept is Q. Results from this method are given in Figure 4a.

Reverse Two-Station Method (RTSM)

RTSM uses two TSM setups where an event is on either side of the station pair in a narrow azimuthal window (Chun et al., 1987; Fan and Lay, 2003). The two ratios are combined to remove the common source and site terms and the amplitude is fit in the log domain so that the slope is α and the intercept is Q. Results from this method are given in Figure 4b.

Source-Pair / Receiver-Pair Method (SPRPM)

SPRPM is basically the RTSM with a relaxation on the narrow azimuthal window requirement (Shih et al., 1994). Results from this method are given in Figure 4c.

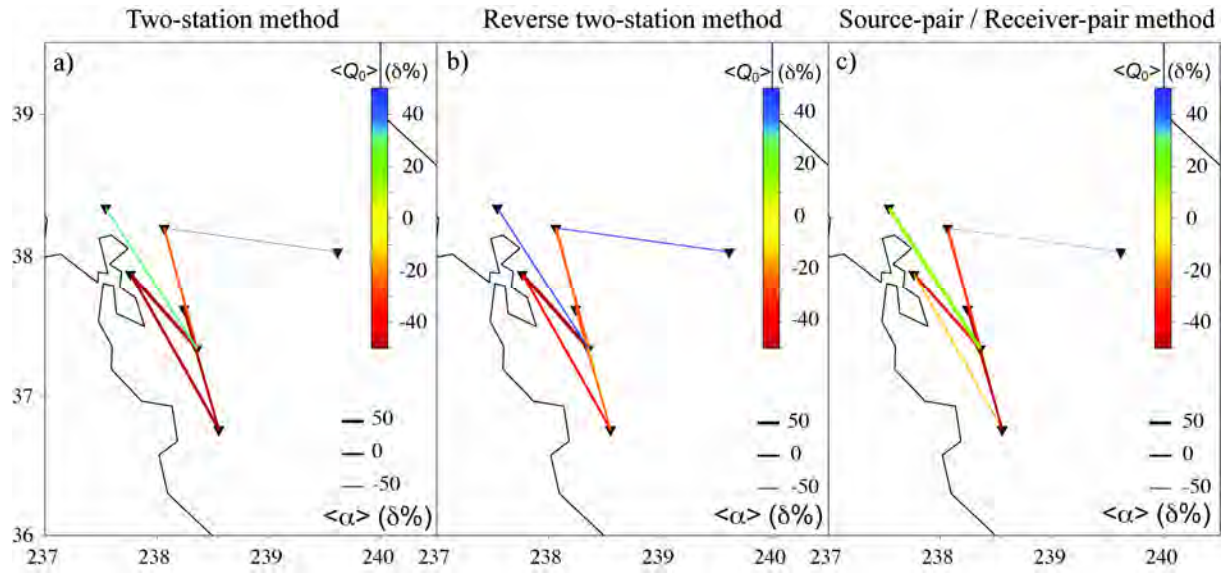


Figure 5. Spatial variability in the percent deviation from the method average power-law fit parameters ($Q_0 f^{\alpha}$) for the three spectral ratio methods. The average model ($Q_{Lg} = \langle Q_0 \rangle f^{\langle \alpha \rangle}$) given by TSM is $132 f^{0.53}$, by RTSM is $121 f^{0.52}$, and by SPRP is $76 f^{0.76}$.

Comparison of TSM, RTSM, and SPRPM

Since TSM, RTSM, and SPRPM give a result for interstation paths, we compare these results by finding the percent deviation of each interstation path from the average $Q_0 f^{\alpha}$ produced for each method. Comparisons are mapped in Figure 4a-c when a solution was calculated for all methods.

The average Q_{Lg} model given by the TSM is $132 f^{0.53}$, by RTSM is $121 f^{0.52}$, and by SPRP is $76 f^{0.76}$. Values of Q_0 are fairly uniform with greater than average and lesser than average consistent across each method. A notable exception is the path from MHC to SAO, where the TSM calculates a greater than average Q_0 and the other methods find a less than average Q_0. There is also a large deviation from mean values for the path from CMB to POTR. The mean value of Q_0 and α for SPRPM are very low for the region. The power-law exponent, α, varies widely among all methods. This may be due to the variance in the spectral amplitudes. More robust methods of spectrum estimation may reduce the variance.

Sensitivity Tests

We investigated how the choice of parameterization affects the results. In each test only one parameter was varied and $Q_0 f^{\alpha}$ was calculated with each of the methods. The varied parameters were geometrical spreading dependence (r^{γ}), measurement bandwidth, epicentral distance of the data, and the Lg window (Table 2). This range of parameterization was

Table 2. Sensitivity test parameterization (varied values in red).

Parameter	Test 1	Test 2	Test 3	Test 4
Lg velocity (km/s)	3.5	3.5	3.5	3.5
Spreading exponent (r^{γ})	0.83	0.5	0.5	0.5
Lg velocity window (km/s)	2.6 - 3.5	2.6 - 3.5	2.6 - 3.5	3.0 - 3.6
Component	Vertical	Vertical	Vertical	Vertical
Epicentral distance (km)	100 - 400	100 - 400	100 - 700	100 - 400
Interstation distance (km)	50 - 500	50 - 500	50 - 500	50 - 500
Measurement bandwidth (Hz)	0.5 - 8	0.25 - 4	0.5 - 8	0.5 - 8
SNR	> 2	> 2	> 2	> 2
Coda critical time (s)	150	150	150	150
Azimuthal window (deg)	15	15	15	15

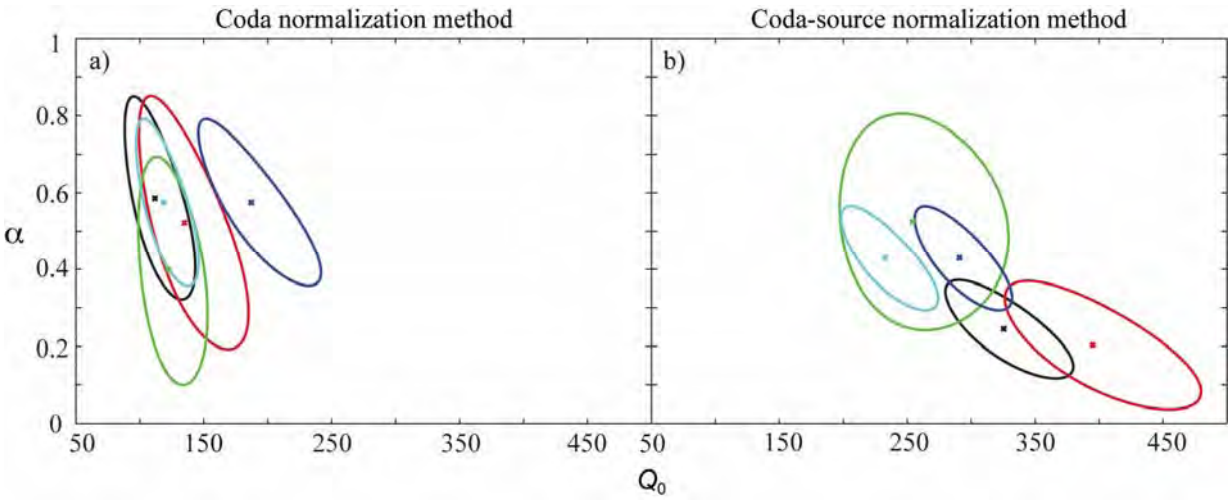


Figure 6. 95% confidence ellipses for the power-law model parameters for station PKD calculated by the coda normalization (left) and coda-source normalization (right) methods obtained by the original parameterization (black), and by varying the spreading exponent (red), bandwidth (green), distance (dark blue), and time window (light blue). The small cross is the best-fitting parameter estimate.

chosen based on the values used in previous studies.

All methods were affected by a change in spreading exponent, where there is a systematic increase in both Q_0 and α as the spreading exponent increases. Also, when more of the spectrum below 1 Hz is sampled, α can change significantly. The methods that use a maximum Lg amplitude in the time domain to measure Q_{Lg}, CNM and SPRP, are less sensitive to Lg window choice than the other methods. However, CNM is affected by epicentral distance, which may be due to the fixed time that the coda is sampled for all distances. The RTSM is the most robust and resistant to changes in parameterization.

In order to better visualize the sensitivity of the methods to varied parameterization, we produce 1-D power-law *Q* models for a common station, PKD, for the coda-based methods (Figure 6), and a common path, MHC to POTR, for the spectral ratio based methods (Figure 7). Error in these 1-D fits is calculated and we produce 95% confidence ellipses for each of the power-law model parameters (Aster et al., 2005). Figures 6 and 7 allow for an analysis of both the epistemic (model-based) uncertainty due to the relative location of the ellipse and aleatoric (random, data-based) uncertainty due to the size of the ellipse.

Estimates of the power-law parameters, Q_0 and α, have a complex relationship with parameterization choice. The most variance in Q_0 is given by the CSM (~200 - 500), while there is a large variance in α calculated with the SPRPM (~0.6 - 1.8). However, for all methods (with the possible exception of the RTSM) the 95% confidence region is large and the range of the parameter estimates is greater than is given by previous 1-D Q_{Lg} studies, which often only present one choice of parameterization.

CONCLUSIONS AND RECOMMENDATIONS

There is lateral variability in Q_{Lg} at 1 Hz and the power-law dependence on frequency in Northern California. The spatial variability is similar to that found by Mayeda et al. (2005), where there is high attenuation in the northern region of the study area and variable attenuation in the Bay Area. Trends in calculated power-law parameters are similar among the methods investigated in this study, though there is large variability in the absolute values for $Q_{Lg}f^{\alpha}$. The coda-based methods can produce a power-law *Q* model for each raypath, and though in this study we report station averages, these methods lend themselves more naturally *Q* tomography. The two station methods are more restrictive in data selection and *Q* tomography may be difficult in regions without dense station coverage and high seismicity.

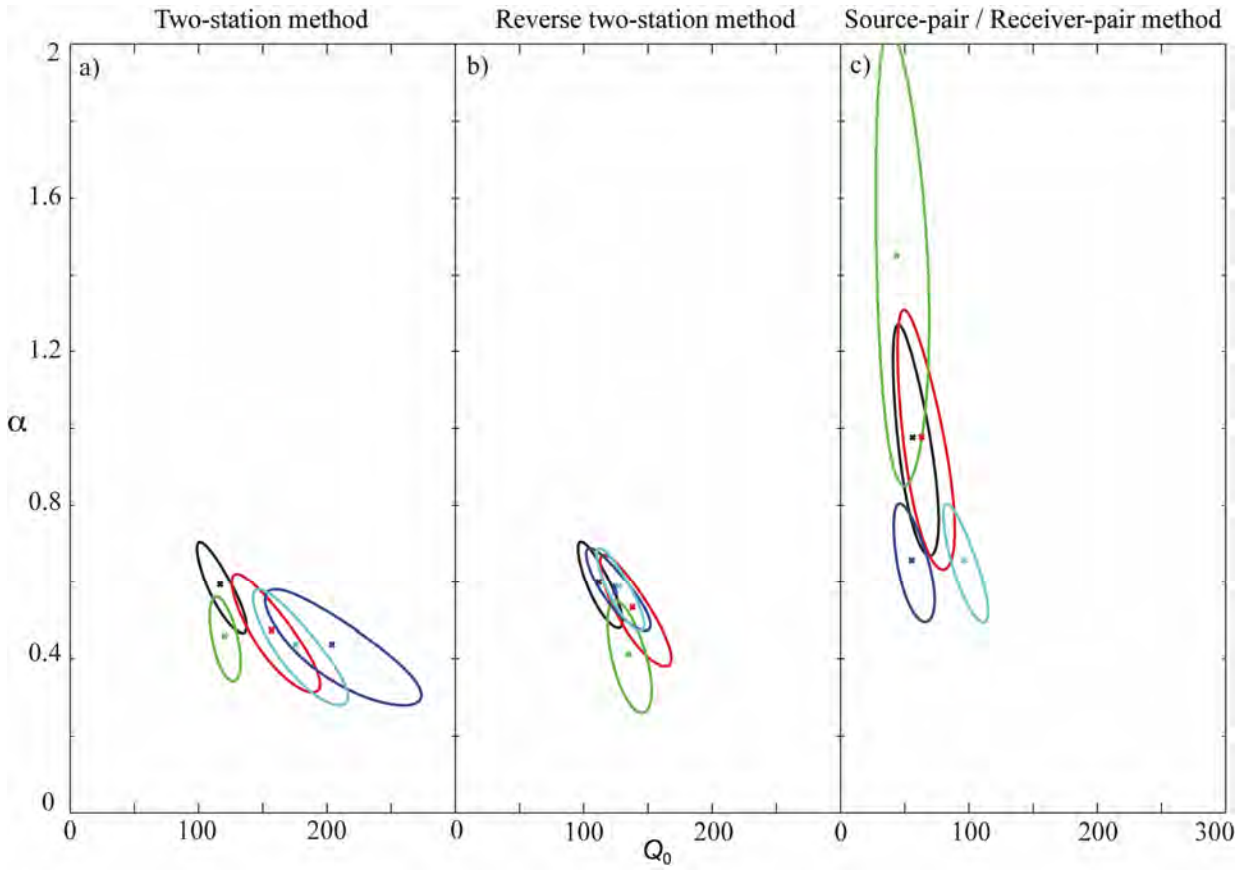


Figure 7. 95% confidence ellipses for the power-law model parameters for the path MHC to POTR calculated by (a) the TSM (b) the RTSM, and (c) the SPRPM obtained by the original parameterization (black), and by varying the spreading exponent (red), bandwidth (green), distance (dark blue), and time window (light blue). The small cross is the best-fitting parameter estimate.

The choice of spreading exponent, distance, and measurement window has a large influence on the best-fit power-law parameter estimates. Unless the parameterization choice can be constrained from a priori information, regional attenuation studies should search the entire solution space in order to report useful power-law *Q* models.

REFERENCES

Aki, K. (1980). Attenuation Of Shear-Waves In The Lithosphere For Frequencies From 0.05 To 25 Hz, *Phys. Earth Planet. Inter.*, 21: 50–60.

Aster, R. C., and B. Borchers, and C. H. Thurber (2005). *Parameter Estimation and Inverse Problems*. San Diego: Elsevier Academic Press.

Chun, K. Y., G. F. West, R. J. Kokoski, and C. Samson (1987). A Novel Technique For Measuring Lg Attenuation - Results From Eastern Canada Between 1-Hz To 10-Hz, *Bull Seism Soc.* 77: 398–419.

Chung, T. W., and K. W. Lee (2003). A study of high-frequency Q(Lg)(-1) in the crust of South Korea, *Bull Seism Soc.* 93: 1401–1406.

Chung, T. W., Y. K. Park, I. B. Kang, and K. Lee (2005). Crustal Q(Lg)(-1) in South Korea using the source pair/receiver pair method, *Bull Seism Soc.* 95: 512–520.

Fan, G. W., and T. Lay (2003). Strong Lg wave attenuation in the Northern and Eastern Tibetan Plateau measured by a two-station/two-event stacking method, *Geophys. Res. Lett.* 30.

Mayeda, K., L. Malagnini, W. S. Phillips, W. R. Walter, and D. Dreger (2005). 2-D or not 2-D, that is the question: A northern California test, *Geophys. Res. Lett.* 32.

Shih, X. R., K. Y. Chun, and T. Zhu (1994). Attenuation Of 1-6-S-L(G) Waves In Eurasia, *J. Geophys. Res.* 99: 23859–23873.

Walter, W. R., K. Mayeda, L. Malagnini, L. Scognamiglio (2006). Regional body-wave attenuation using a coda source normalization method: application to MEDNET records of earthquake in central Italy, *Seism. Res. Lett.* 77: 260.

Xie, J. K. (2002). Lg Q in the eastern Tibetan Plateau, *Bull Seism Soc.*, 92: 871–876.

Xie, J., and B. J. Mitchell (1990). Attenuation Of Multiphase Surface-Waves In The Basin And Range Province.1. Lg And Lg Coda, *Geophys. J. Int.* 102: 121–137.

Yoshimoto, K., H. Sato, and M. Ohtake (1993). Frequency-Dependent Attenuation Of P-Wave And S-Wave In The Kanto Area, Japan, Based On The Coda-Normalization Method, *Geophys. J. Int.* 114: 165–174.

REGIONALIZATION OF CRUSTAL AND UPPER MANTLE Q STRUCTURE IN EASTERN EURASIA USING MULTIPLE REGIONAL WAVES

James B. Gaherty[1], Tae-Kyung Hong[1], and Li Zhao[2]

Lamont Doherty Earth Observatory, Columbia University[1] and Institute of Earth Sciences of Academia [2]

Sponsored by Air Force Research Laboratory

Contract No. F19628-03-C-0122[1,2]

ABSTRACT

We map lateral variations of upper-mantle Q in eastern Eurasia using a new inversion procedure based on three-dimensional partial-derivative (Fréchet) kernels. In our initial analysis, we utilize Rayleigh waves with periods longer than ~15 s, derived from regional and near-teleseismic earthquakes. We have collected and begun analysis on over 11000 vertical-component seismograms, derived from over 150 events with Mw > 6 that occurred within the eastern Eurasia region (10˚-60˚N, 70˚-140˚E) between 2000-2006. The data were recorded on 71 broadband seismic stations within eastern Eurasia (10˚-60˚N, 80˚-140˚E). The data are evaluated for signal-to-noise within the band of interest by comparing the records to complete normal-mode synthetic seismograms for radially symmetric and transversely anisotropic reference models. We then make mutually consistent measurements of frequency-dependent traveltime and amplitude anomalies for surface waves by cross-correlation between records and synthetics. We use coupled normal-mode summation to compute the three-dimensional Fréchet kernels of these traveltime and amplitude anomalies to both the elastic wave speeds and Q values. The initial model for Q is extracted from a recent global model of upper-mantle attenuation. The frequency-dependent traveltime and amplitude anomalies will be jointly inverted for three-dimensional models of both elastic (v_s) and anelastic structures. This coupled inversion will allow us to account for the effects on amplitudes from elastic heterogeneities such as scattering, focusing and defocusing, as well as the effects of anelastic dispersion on the traveltimes. The regional models will provide lateral resolution of upper-mantle Q that will be as high as the data permit. The models will be compared to other models of upper-mantle Q derived from higher-frequency Pn and Sn observations, as well as crustal Q models of Pg and Lg, providing a means to assess the process controlling seismic attenuation at different frequencies.

OBJECTIVES

Accurate event detection, identification, and characterization are critical components of the US nuclear monitoring program. A necessity for improving these estimates is the more accurate estimation of seismic attenuation rate (or its inverse, Q), which controls the amplitudes of seismic phases upon which the assessments are based. Q is known to vary widely in continental regions, making reliable estimates of it critically important, but also quite difficult. Q is also frequency dependent, which makes it difficult to determine whether Q estimates derived from different phases with different frequency characteristics are a result of intrinsic frequency dependence, or differences in structural sampling. Finally, Q estimates are derived from seismic amplitudes, which are also strongly dependent on elastic effects such as wavefield focusing and scattering. As a result, robust tomographic (3D) quantification of Q on regional scales remains in its infancy.

We address this problem by applying a comprehensive waveform analysis and inversion scheme to simultaneously estimate 3D variations in shear velocity (v_s) and shear attenuation (Q_μ) from Rayleigh waves recorded in eastern Eurasia. The analysis technique characterizes phase and amplitude residuals between recorded and synthetic Rayleigh waves, and inverts them using new three-dimensional sensitivity (Fréchet) kernels for structural perturbations. The analysis will span a frequency band from 0.01-0.08 Hz, with the low frequency estimates providing a stable long-wavelength framework from which we bootstrap to higher frequency. We focus on Rayleigh waves because they provide spatial and depth constraints on Q_μ in the upper mantle and crust across a broad frequency band. In Eurasia, Rayleigh waves from regional and near-teleseismic events give good spatial coverage, and can quantify large-scale regional trends and the effects of long-wavelength scattering. The resulting model spans all of China, the Korean peninsula, and much of Southeast Asia, and can be used to place localized high-frequency observations (e.g. Lg, Pg, Sn, Pn) into a larger regional context.

RESEARCH ACCOMPLISHED

Data Collection

Our data set consists of broadband Rayleigh waves that traverse Eastern Eurasia. The seismic records were recorded on instruments from the IRIS GSN, cooperating networks such as the CDSN, and several IRIS PASSCAL experiments from Asia. All data were collected from IRIS DMC. The stations used are distributed in the region from 10˚N - 60˚N and 80˚E - 140˚E. We used stations recording either an LHZ or BHZ components, with a total of 71 stations. Events occurred in the region between 10˚N - 60˚N and 70˚E - 140˚E in the time period between 2000 and 2006. The magnitudes are greater than Mw 6. The total number of events collected was 151. The initial dataset was cleaned to remove data with a signal-to-noise level of less than approximately 2 in the central portion of the frequency band (0.02-0.1 Hz), as well as data clearly contaminated by glitches or other problems. The final number of records used is 3135 from 146 events. The final event and station distribution is shown in Figure 1a, while Figure 1b depicts the spatial path coverage associated with this data.

Cross-Correlation Analysis

We analyze these data using a cross-correlation analysis, where the phase-delay times and differential amplitudes of observed Rayleigh waves are measured relative to complete normal-mode synthetic seismograms as a function of frequency across the 0.01-0.08 Hz band (Gee and Jordan, 1992; Gaherty et al., 1996). As described more fully in the following paragraphs, this methodology utilizes synthetic seismograms of a target wavegroup (in this case the fundamental-mode Rayleigh waves) to estimate phase delays and relative amplitudes of the observed arrival relative to the synthetic as a function of frequency. The synthetic wavegroup, called an “isolation filter”, is cross-correlated with both the data and a complete synthetic seismogram. The resulting cross-correlagrams are windowed and narrow-band (Gaussian) filtered at discrete frequency intervals between 0.01 and 0.08 Hz, and the peak phase and amplitude of each correlagram is estimated at each frequency. Referencing the observations to a synthetic/isolation-filter cross-correlation in this fashion allows us to account for interference from unmodeled wavegroups and minimizes bias associated with windowing and filtering. The synthetics are complete from 0-80 mHz (all periods longer than 12.5 s), and are calculated for a reference models constructed from a composite of iasp91 for mantle shear and compressional velocities; Crust 2.0 for local crustal velocity perturbations (Laske et al., 2001); a mantle Q_μ profile for the China region extracted from a recent global model (Dalton and Ekström, 2006); and a crustal Q_μ profile derived from analysis of regional phases (Jemberie and Mitchell, 2004).

These observations characterize the observed wavefield characteristics in a manner similar to traditional estimates of phase velocity and spectral amplitudes. They differ from the traditional estimates in that they are relative to a reference model (similar to travel-time residuals), and thus can be directly inverted for improved velocity and Q structure using a linearized Gaussian-Bayesian approach (e.g. Gaherty et al., 1996; Chen et al., 2006). In particular, the travel-time (phase) and relative amplitude observations quantify discrepancies δd between the recorded and synthetic seismograms. Every anomaly δd observed on a record from a specific source-receiver pair can be related to the perturbation of a model parameter δc through a linear integral over the volume of the earth model:

$$\delta d(\mathbf{r}_R;\mathbf{r}_S) = \int_{\oplus} K_c^d(\mathbf{r}_R;\mathbf{r};\mathbf{r}_S)[\delta c(\mathbf{r})/c^0(\mathbf{r})]d^3\mathbf{r}\,, \qquad (1)$$

where $\mathbf{r}$ is a position in space and the subscripts S and R indicate the source and receiver, respectively. The quantity $K_c^d(\mathbf{r}_R;\mathbf{r};\mathbf{r}_S)$, referred to as the Fréchet kernel, represents the degree to which the observed anomaly δd is dependent on the local model perturbation $\delta c(\mathbf{r})$ relative to its unperturbed value $c^0(\mathbf{r})$, where a superscript 0 indicates a quantity in the reference model. Thus $K_c^d(\mathbf{r}_R;\mathbf{r};\mathbf{r}_S)$ is also often called the sensitivity kernel. In our case, we calculate three such kernels for each observable; the sensitivity of the phase-delay with respect to shear-velocity perturbations in the crust and mantle; the sensitivity of relative amplitude with respect to these shear-velocity perturbations (due to focusing and other wavefield effects); and the sensitivity of relative amplitude with respect to shear attenuation.

We quantify the difference between the seismic record of a given component $u(\mathbf{r}_R;\mathbf{r}_S)$ and the corresponding synthetic $u^0(\mathbf{r}_R;\mathbf{r}_S)$ through their cross-correlation

$$C(t) = u^0(\mathbf{r}_R,t;\mathbf{r}_S) \otimes u(\mathbf{r}_R,t;\mathbf{r}_S) = \int_{-\infty}^{\infty} u^0(\mathbf{r}_R,\tau;\mathbf{r}_S)u(\mathbf{r}_R,t+\tau;\mathbf{r}_S)d\tau. \qquad (2)$$

Defining the traveltime anomaly δT as the lag time at which the cross-correlagram reaches its maximum, we can obtain the expression (Dahlen et al. 2000; Zhao et al. 2000):

$$\delta T = -\int_{-\infty}^{\infty} \dot{u}^0(\mathbf{r}_R,t;\mathbf{r}_S)\delta u(\mathbf{r}_R,t;\mathbf{r}_S)dt \Big/ \int_{-\infty}^{\infty}[\dot{u}^0(\mathbf{r}_R,t;\mathbf{r}_S)]^2 dt\,, \qquad (3)$$

where $\dot{u}^0$ is the time derivatives of u^0, and $\delta u = u - u^0$ is the waveform perturbation. The traveltime anomaly δT is defined such that a positive value indicates a delay of the recorded waveform relative to the synthetic. Upon applying the representation theorem (e.g. Aki & Richards 2000) and the Born approximation, the waveform perturbation can be expressed as (e.g. Zhao et al. 2005)

$$\delta\mathbf{u}(\mathbf{r}_R,t;\mathbf{r}_S) = \int_{\oplus}\int_0^t [\nabla\mathbf{G}^0(\mathbf{r}_R,t-\tau;\mathbf{r})]^{213} : [\delta\rho(\mathbf{r})\mathbf{I}\partial_{\tau\tau} - \delta\mathbf{C}(\mathbf{r})] : [\nabla\mathbf{u}^0(\mathbf{r},\tau;\mathbf{r}_S)]d\tau\, d^3\mathbf{r}, \quad (4)$$

where $\delta\rho(\mathbf{r})$ and $\delta\mathbf{C}(\mathbf{r})$ are the model perturbations in density and the fourth-order elasticity tensor, respectively, $\mathbf{I}$ is the fourth-order identity tensor, and the symbol $[\cdot]^{213}$ indicates the transposition of a third-order tensor between its first and second indices (Ben-Menahem & Singh 1981), i.e., $[\cdot]^{213}_{ijk} = [\cdot]_{jik}$. For the perturbation of any specific structural parameter such as the *S*-wave speed v_s, the expression for its delay-time Fréchet kernel can be derived by selecting the elements of $\delta\mathbf{C}(\mathbf{r})$ in eq. (4) corresponding to vs, substituting the resulting equation for $\delta\mathbf{u}(\mathbf{r}_R;\mathbf{r}_S)$ into eq. (3) and identifying the kernel for the spatial integral. Figure 2 provides an example of the travel-time kernel with respect to v_s for a representative Rayleigh wave observation. In practice, the cross-correlagram in (2) is narrow-band filtered around a series of discrete frequencies to obtain a set of frequency-dependent delay-time measurements $\delta T(\omega_i)$. The frequency-dependent delay times $\delta T(\omega_i)$ can still be expressed as in eq.(3) except that $\dot{u}^0$ is also narrow-band filtered.

As described in Zhao (2006), we define the amplitude anomaly in terms of the maximum amplitude $C_M = C(\delta T)$ of the cross-correlogram

$$\delta A = \frac{C_M - \tilde{C}_M}{\tilde{C}_M}, \tag{5}$$

where $\tilde{C}_M$ is the maximum amplitude of the auto-correlagram of the synthetic u^0:

$$\tilde{C}(t) = u^0(\mathbf{r}_R, t; \mathbf{r}_S) \otimes u^0(\mathbf{r}_R, t; \mathbf{r}_S) = \int_{-\infty}^{\infty} u^0(\mathbf{r}_R, \tau; \mathbf{r}_S) u^0(\mathbf{r}_R, t+\tau; \mathbf{r}_S) d\tau. \tag{6}$$

Upon using the delay time in (3), we can derive the expression for the amplitude anomaly

$$\delta A = \int_{-\infty}^{\infty} u^0(\mathbf{r}_R, t; \mathbf{r}_S) \delta u(\mathbf{r}_R, t; \mathbf{r}_S) dt \Big/ \int_{-\infty}^{\infty} [u^0(\mathbf{r}_R, t; \mathbf{r}_S)]^2 dt. \tag{7}$$

If the waveform perturbation $\delta\mathbf{u}(\mathbf{r}_R; \mathbf{r}_S)$ represents wavefield effects such as focusing or defocusing, the amplitude anomaly can be expressed in terms of perturbations in elastic structure (e.g. Zhao et al., 2005). Figure 3 provides an example of the travel-time kernel with respect to v_s for the representative Rayleigh wave observation. When intrinsic attenuation is taken into account, the (real) elasticity tensor in eq.(4) is replaced by a complex tensor:

$$\begin{aligned} C_{jklm} = &\left\{ \kappa(\omega)[1 + iQ_\kappa^{-1}(\omega)] - \frac{2}{3}\mu(\omega)[1 + iQ_\mu^{-1}(\omega)] \right\} \delta_{jk}\delta_{lm} \\ &+ \mu(\omega)[1 + iQ_\mu^{-1}(\omega)](\delta_{jl}\delta_{km} + \delta_{jm}\delta_{kl}) + \gamma_{jklm}, \end{aligned} \tag{8}$$

where Q_κ and Q_μ are the quality factors for the incompressibility κ and the shear modulus μ, respectively. In (8), the elasticity tensor has been decomposed into a purely isotropic part expressed in terms of κ and μ and a purely anisotropic part γ_{jklm}, and the intrinsic attenuation of only the purely isotropic part is considered (Dahlen & Tromp 1998). Substituting the complex elasticity tensor in eq. (8) into (4), we can obtain a linear relation between the waveform perturbation $\delta\mathbf{u}(\mathbf{r}_R; \mathbf{r}_S)$ and the perturbations δQ_κ and δQ_μ. From this linear relation and eq. (7) we can derive the expressions for the Fréchet kernels of the amplitude anomaly for δQ_κ and δQ_μ. Like the delay times, the amplitude anomaly can also be measured from barrow-band filtered cross-correlagrams to obtain a set of frequency-dependent amplitude anomalies. In practice, fundamental-mode surfaces waves in the 0.01-0.1 band have little sensitivity to Q_κ, and our modeling incorporates only variations in Q_μ. Figure 4 provides an example of a sensitivity kernel for the amplitude anomaly with respect to shear attenuation for the representative Rayleigh wave.

We utilize this procedure to measure, and calculate 3D sensitivity kernels for, frequency-dependent relative travel-time and amplitude observations for the 3100+ Rayleigh waves depicted in Figure 1b. These observations will be inverted for spatial variations in shear velocity and shear attenuation. Our joint velocity/Q inversion will allow us to explicitly incorporate focusing/defocusing effects in the analysis, providing for more robust estimates of Q_μ.

CONCLUSIONS AND RECOMMENDATIONS

Rayleigh waves traversing the eastern Eurasia region provide self-consistent constraints on mantle and crustal attenuation across a broad frequency band. The available data provide good spatial coverage across China, the Korean peninsula, and much of Southeast Asia. Using a cross-correlation analysis, relative phase and amplitude behavior of these waveforms can be quantified, and realistic 3D sensitivity kernels can be formulated for these observations with respect to both elastic and anelastic structure. These data and associated kernels will provide the basis for a tomographic inversion for v_s and Q_μ in the crust and upper mantle throughout the region.

ACKNOWLEDGEMENTS

Colleen Dalton provided the 1D model for Q in the mantle used as our reference model. Jack Xie provided helpful advice in the direction of this research following his transfer to AFRL.

REFERENCES

Aki, K. & Richards, P. G. (2002). *Quantitative Seismology*, second edition, University Science Books, Sausalito, CA.

Ben-Menahem, A. and Singh, S. J. (1981). *Seismic Waves and Sources*, Springer-Verlag, New York, NY.

Chen, P., L. Zhao, and T.H. Jordan (2006). Generalized seismological data functional for broadband seismic waveform inversion, *Geophys. J. Int.* in preparation.

Dahlen, F. A. and Baig, A. M. (2002). Fréchet kernels for body-wave amplitudes, *Geophys. J. Int*. 150: 440–466.

Dahlen, F. A., Hung, S.-H. and Nolet, G. (2000). Fréchet kernels for finite-frequency traveltimes: I. Theory, *Geophys. J. Int*. 141: 157–174.

Dalton, C.A. and G. Ekstrom (2006). Global models of surface wave attenuation, *J. Geophys. Res.* 111: B05317, doi:10029/2005JB003997.

Dziewonski, A. M. & Anderson, D. L. (1981). Preliminary Reference Earth Model (PREM), *Phys. Earth Planet. Inter*. 25: 297–356.

Gaherty, J.B., T.H. Jordan, and L.S. Gee (1996). Seismic structure of the upper mantle in a central Pacific corridor, *J. Geophys. Res.* 101: 22,291–22,309.

Gee, L. S., and T. H. Jordan (1992). Generalized seismological data functionals, *Geophys. J. Int. 111*, 363–390.

Laske, G., G. Masters, and C. Reif (2001). CRUST 2.0, A New Global Crustal Model at 2x2 Degrees, http://mahi.ucsd.edu/Gabi/rem.html.

Jemborie, A.L. and B.J. Mitchell, (2004). Shear wave *Q* structure and its lateral variation in the crust of China and surrounding regions, *Geophys. J. Int.* 157: 363–380.

Zhao, L. (2006). Full-wave Fréchet kernels for Q tomography, *in preparation*.

Zhao, L., Jordan, T. H. & Chapman, C. H. (2000). Three-dimensional Fréchet differential kernels for seismic delay times, *Geophys. J. Int*. 141: 558–576.

Zhao, L., Jordan, T. H., Olsen, K. B. & Chen, P. (2005). Fréchet kernels for imaging regional Earth structure based on three-dimensional reference models, *Bull. Seismol. Soc. Am*. 95: 2066–2080.

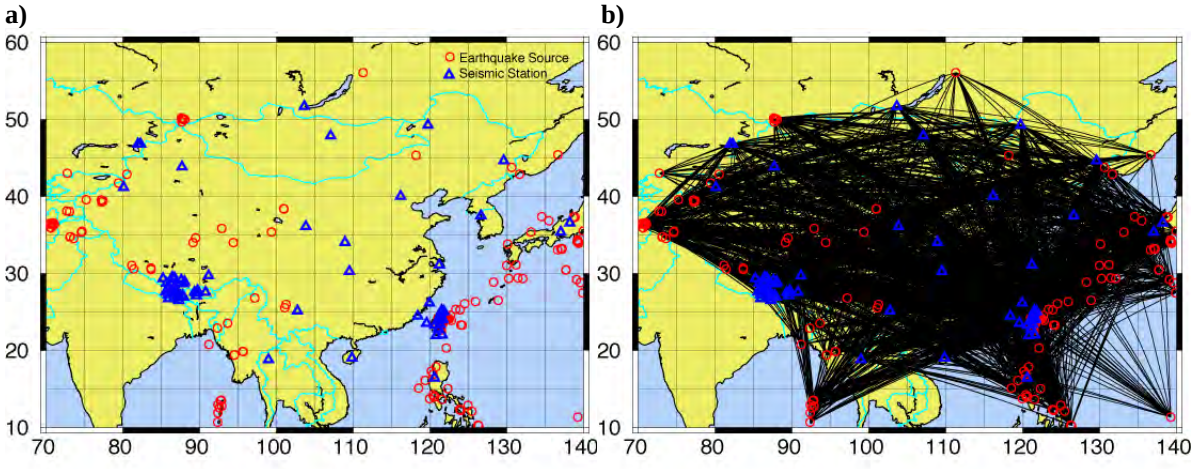


Figure 1. Sources and receivers and associated path coverage of Rayleigh waves selected for cross-correlation analysis. (a) Source (circles) and receiver (triangles) distribution. Total number of sources is 146, and total number of receivers is 71. (b) Total path coverage (3135 paths) provided by final clean dataset.

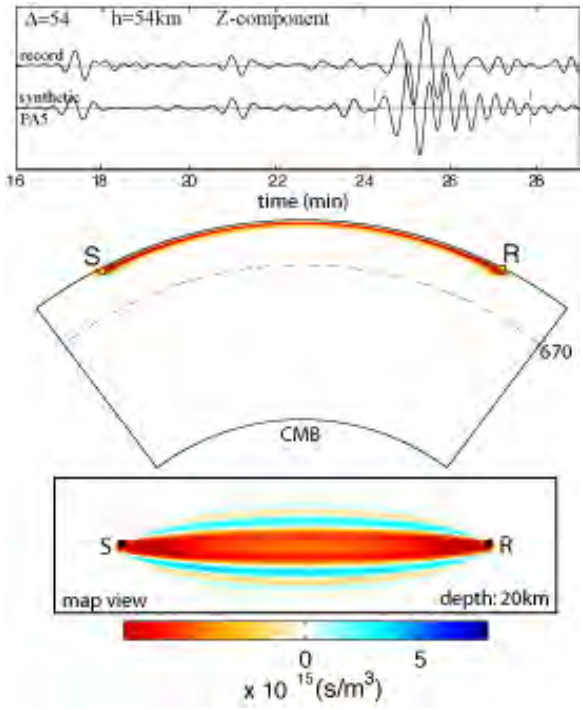


Figure 2. Partial derivative kernels for phase-delay with respect to shear velocity, for a typical Rayleigh wave observation. (top panel) Broadband (5-60 mHz) Rayleigh waveform selected for analysis (dashed lines represent window). (middle panel) Cross-section of kernel within the vertical source-receiver plane. (bottom panel) Plan view of kernel at depth 20 km.

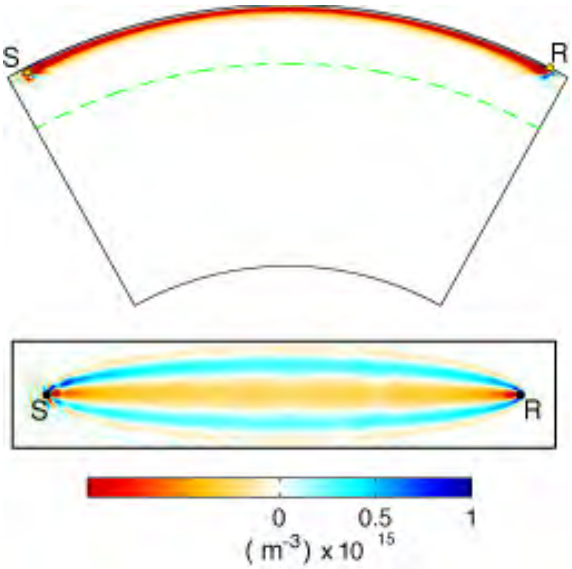


Figure 3. Partial derivative kernels for relative amplitude with respect to shear velocity, for the example Rayleigh-wave observation in Figure 1. (top panel) Cross-section of kernels within the vertical source-receiver plane. (bottom panel) Plan view of kernel at depth 20 km.

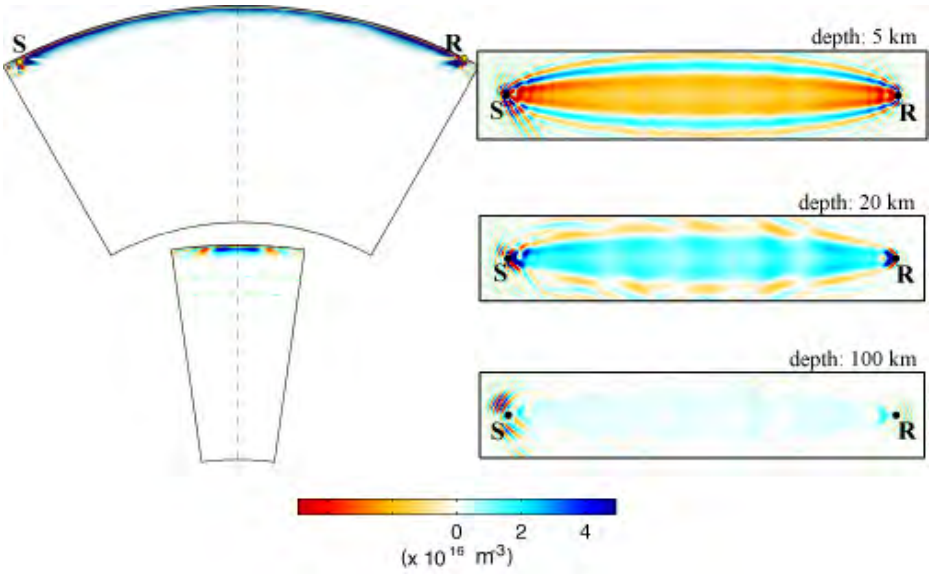


Figure 4. Partial derivative kernels for relative amplitude with respect to Q_μ, for the same Rayleigh wave example from Figure 2. (left) Cross-sections of kernels within the vertical source-receiver plane, as well as perpendicular to the path, midway between source and receiver. (right) Plan view of kernels at depths of 5, 20, and 100 km. In all kernels, color scale is such that blue indicates regions where an increase in Q_μ will produce an increase in predicted Rayleigh-wave amplitude.

SEISMIC CHARACTERISTICS OF NORTHERN IRAQ AND SURROUNDING REGIONS

Hafidh A. A. Ghalib[1], Ghassan I. Aleqabi[2], Bakir S. Ali[3], Borhan I. Saleh[3], Dawood S. Mahmood[4, 5], Indra N. Gupta[1], Robert A. Wagner[1], Patrick J. Shore[2], Aras Mahmood[3], Shaho Abdullah[3], Omar K. Shaswar[7, 8], Fadhil Ibrahim[6], Basoz Ali[3], Layla Omar[3], Nokhsha I. Aziz[3], Nian H. Ahmed[3], Ali A. Ali[5], Abdul-Karem A. Taqi[5], and Samira R. Khalaf[5]

Multimax, Inc.[1], Washington University in Saint Louis[2], Sulaimaniyah Seismological Observatory[3], Iraq Meteorological Organization[4], Baghdad Seismological Observatory[5], Erbil Seismological Observatory[6], Sulaimaniyah University[7], and University of Baghdad[8]

Sponsored by Air Force Research Laboratory

Contract No. FA8718-04-C-0016

ABSTRACT

This is a preliminary report on a field experiment to collect seismological data from the Middle East. Starting in November 2005, a network of 10 broadband seismic stations was deployed in stages over a period of 9 months throughout northern, northeastern, and central Iraq. The spatial distribution covers a large portion of the folded and foothill zones west of the Zagros continental collision boundary of the Arabian plate. These three-component digital stations have since been recording continuously at a rate of 100 Hz, yielding a rapidly growing database of numerous high quality local, regional, and teleseismic events that are characteristic of this relatively young and exceedingly active seismotectonic setting. Initial review of collected data and published bulletins confirms that a large number of small events (magnitude < 4) are either not being recorded or not being detected by distant stations, and/or they are not being reported by the scarce number of neighboring seismic stations in Turkey and Iran. Premature loss of Iraq Seismological Network (ISN) assets and contributions over the past two decades has further exacerbated this problem. Initial review of recorded seismograms, including high frequency phases, shows lateral variations, indicating signal blockage and attenuation that will require thorough mapping for the characteristics of wave propagation in the region to be understood. In addition, location of small events and relocation of internationally reported ones seem to identify source regions and trends that will be investigated in more detail when better velocity models are developed. Seismograms of events associated with these sources show remarkable similarity. Plans and preparations to utilize receiver functions and dispersion of surface waves are underway.

OBJECTIVE

Interaction between the Arabian, Eurasian, African, and Indian plates is the primary force defining the present-day seismotectonic framework of the Middle East. Figure 1 shows that interplate seismicity is significantly more important than intraplate activity. The plate margin seismicity is associated with a variety of boundaries that include spreading zones in the Gulf of Aden and the Red Sea, the transform fault along the Dead Sea rift and East Anatolia, the Bitlis suture in eastern Turkey, the northwest-southeast trending Zagros thrust zone, the Makran east-west trending continental margin and subduction zone, and the Owen fracture zone in the Arabian Sea. The apparently aseismic Arabian plate interior features an exposed young shield, a deformed platform and a foredeep that consists of extraordinarily thick layers of sediments and evaporites. Structural faults and folds cross these major tectonic regions.

Several investigators attributed the observed low intraplate seismicity to the lack of regional and local seismic stations, and to the scarce reporting of events by existing networks in and around the Arabian plate (Adams and Barazangi, 1984; Ghalib et al., 1985). Another feature of the interplate seismicity is its non-uniform distribution along the plate boundaries (e.g., the Zagros thrust zone), which seems to correlate with the presence of local seismic networks or individual stations (e.g., stations TAB and SHI and, more recently, the local Iranian networks along the central Zagros region).

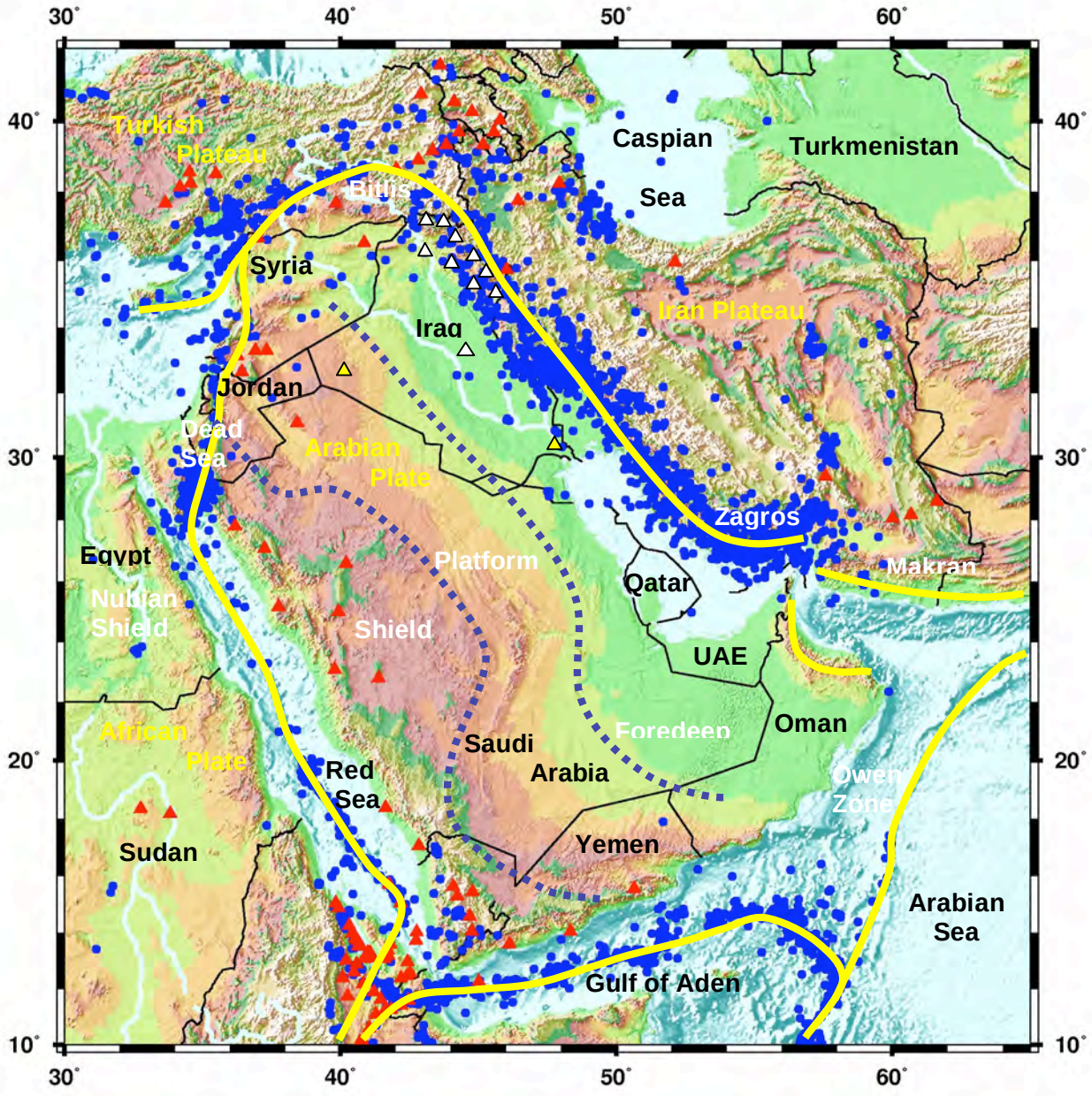


Figure 1. Map of the Arabian Peninsula and surrounding regions. The major geographic, tectonic, and geologic features are labeled. The plate boundaries are marked with yellow lines. Earthquakes and volcanoes are shown as blue circles and red triangles, respectively. White triangles represent the 10 stations that compose the North Iraq Seismological Network (NISN). The yellow triangles reflect the location of some Iraq Seismological Network (ISN) stations, currently not operational.

To study the seismicity and seismotectonic setting of the Arabian plate, its seismotectonic boundaries, and the surrounding regions, this effort commenced with the deployment of a network of broadband seismic stations in north and northeast Iraq to the south of the Bitlis suture zone and to the east and southeast of the Zagros thrust zone, an area that was partially monitored by the severely damaged five ISN stations. This ISN network was composed of stations BHD, SLY, MSL, RTB, and BSR outside the cities of Baghdad, Sulaimaniyah, Mosul, Al Rutba, and Basra, respectively. The instrumentation at these five stations included short-, intermediate-, and long-period analog as well as some digital systems procured from various vendors and manufacturers.

The primary objectives of this deployment effort are as follows:

1. Collect and analyze high-quality ground-truth seismic data from this area of Iraq and the surrounding region.
2. Precisely locate the events and characterize the signal and propagation of high-frequency waves in the region.
3. Estimate the seismic velocity and attenuation structures of the study area using the dispersion and receiver functions of observed surface and body waves, respectively.

RESEARCH ACCOMPLISHED

This is the first technical report on an effort in progress that entails the deployment and operation of a broadband seismological network of 10 stations to record local and regional seismic activity in north Iraq and the surrounding countries of Iran and Turkey, where the Zagros and Taurus (Bitlis) tectonic zones meet. Figure 2 shows the location and spatial distribution of these stations throughout Kurdistan province. In August 2005, the first two stations, KSLY and ERBL, were deployed temporarily at Sulaimaniyah and Erbil seismological observatories until the desired remote sites were surveyed and prepared for long-term deployment. These stations were later shut down and the instrumentation relocated to more remote and significantly quieter sites to complement the planned distribution and coverage of the NISN (see Figure 2).

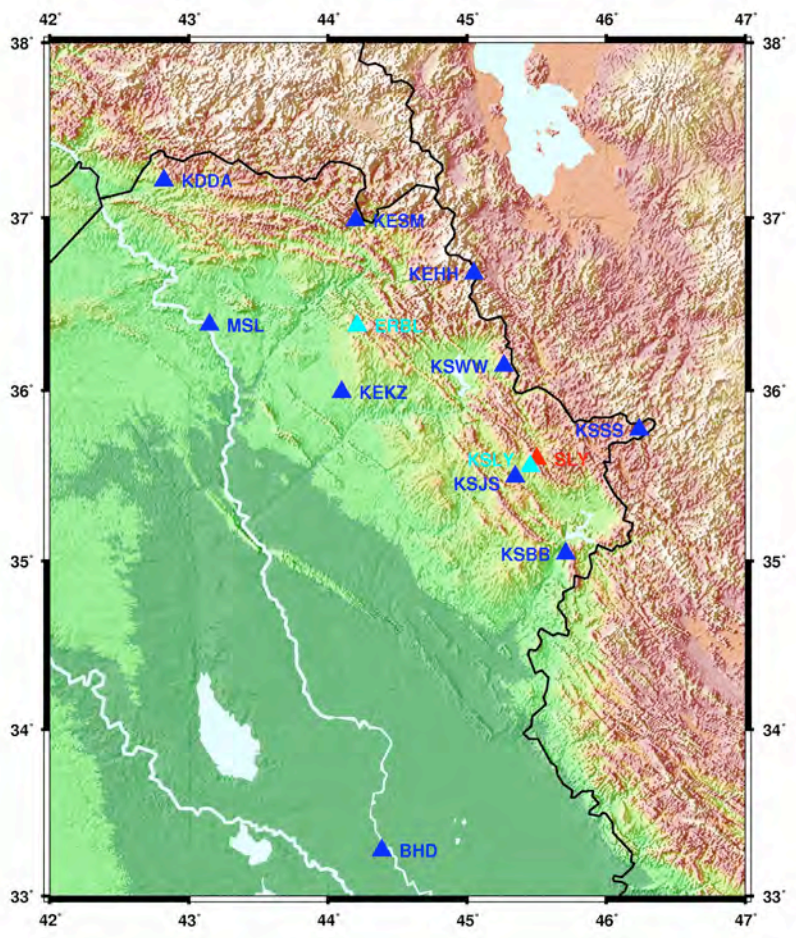


Figure 2. A map showing the distribution of NISN stations. The station locations are marked with blue triangles. Stations ERBL and KSLY (aqua triangles) are the temporary sites of these two stations. Station SLY (red triangle) belongs to the ISN. Stations BHD, MSL, and SLY are also part of the original ISN.

Figure 3 shows photographs of three of the stations in the foothills and along the NW-SE trending axis of the Zagros tectonic boundary. The photographs are of stations (a) KSSS, (b) KSWW, and (c) KEMS. The instrumentation for these 10 stations is provided by the Incorporated Research Institutions for Seismological Research (IRIS), PASSCAL Instruments Center. They have been continuously recording and storing on-site three-component data at 100 Hz. The data have been retrieved manually once every three months during maintenance visits to the sites.

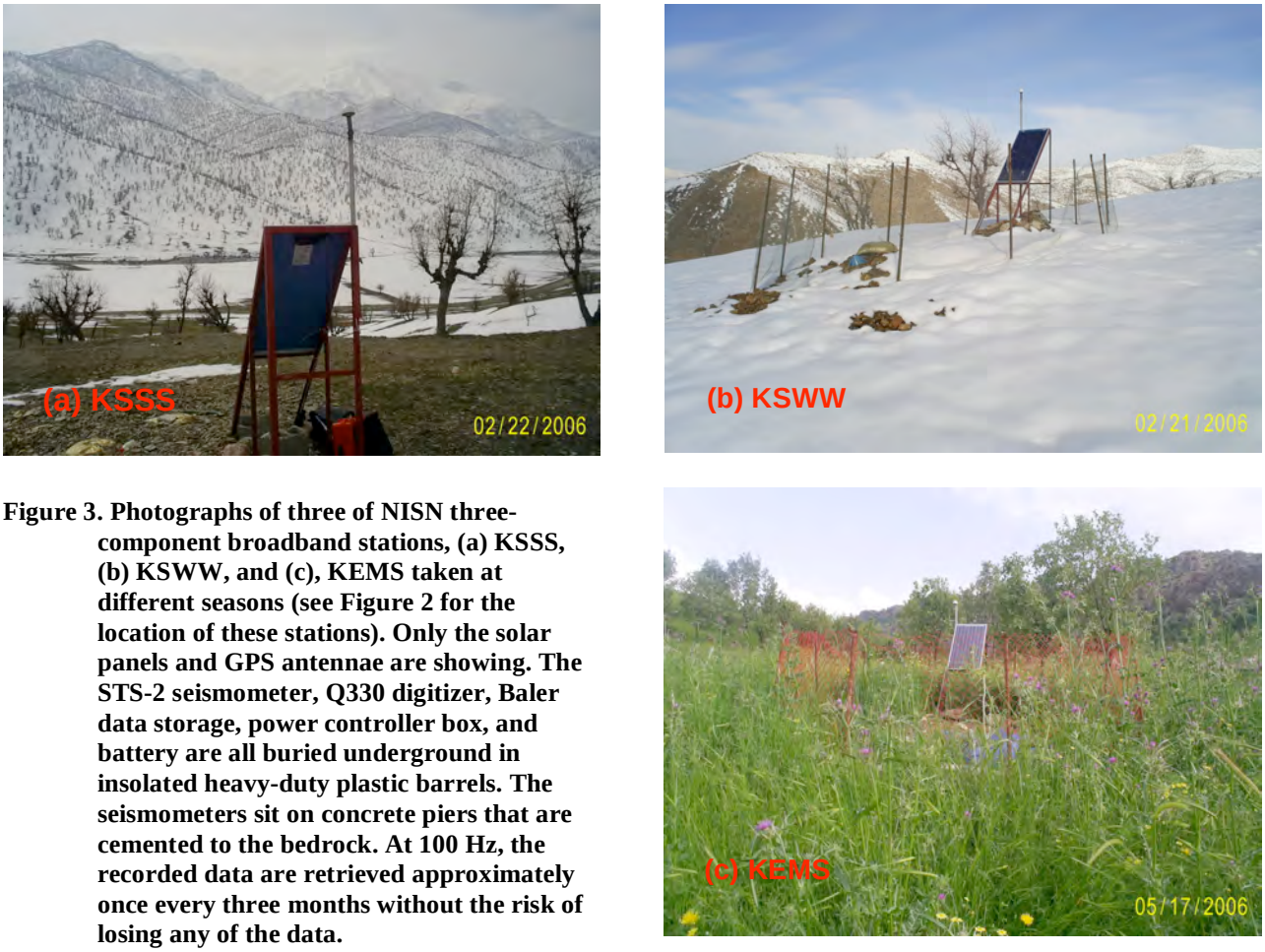


Figure 3. Photographs of three of NISN three-component broadband stations, (a) KSSS, (b) KSWW, and (c), KEMS taken at different seasons (see Figure 2 for the location of these stations). Only the solar panels and GPS antennae are showing. The STS-2 seismometer, Q330 digitizer, Baler data storage, power controller box, and battery are all buried underground in insolated heavy-duty plastic barrels. The seismometers sit on concrete piers that are cemented to the bedrock. At 100 Hz, the recorded data are retrieved approximately once every three months without the risk of losing any of the data.

Deployment of NISN stations took place in stages and over a 6-month period. The majority of the stations (8 out of 10) were deployed during November 2005. The installations of instruments at station BHD in Baghdad and at station MSL in Mosul were delayed until April 2006 due to the unrest in both cities. The parameters for all stations are given in Table 1.

Table 1. Parameters of the North Iraq Seismological Network (NISN)

North Iraq Seismological Network (NISN)						
No.	**Station Name**	**Latitude (degrees)**	**Longitude (degrees)**	**Elevation (meters)**	**Installation Date**	**Removal Date**
1	KSBB	35.0415	45.7092	550	11/25/2005	
2	KSSS	35.7696	46.2362	1515	11/26/2005	
3	KSWW	36.1493	45.2624	1310	11/28/2005	
4	KSJS	35.4965	45.3452	825	11/27/2005	
5	KEHH	36.6764	45.0470	1725	11/30/2005	
6	KESM	36.9846	44.1981	1000	12/01/2005	
7	KDDA	37.2125	42.8207	750	12/02/2005	
8	KEKZ	35.9893	44.0970	450	12/03/2005	
9	MSL	36.3817	43.1483	242	04/06/2006	
10	BHD	33.2744	44.3858	32	04/11/2006	
11	KSLY	35.5559	45.4534	912	08/23/2005	04/04/2006
12	ERBL	36.3772	44.2086		08/21/2005	11/29/2005

The Zagros is a relatively young orogenic belt known for its high level of seismicity. To date, eight NISN stations (excluding BHD and MSL) have provided approximately 40 gigabytes of high-quality local, regional, and teleseismic data. More data, including stations BHD and MSL, will become available shortly. Figure 4 shows a map of 190 events (red solid circles) recorded by NISN from November 30, 2005, to January 8, 2006, located using a generalized velocity model for the Zagros fold and thrust zones (Pasyanos et al., 2004). In an attempt to understand the capability and performance of the NISN, the events reported by the U.S. Geological Survey (USGS, blue crosses) and the International Seismological Center (ISC, green crosses) are also included.

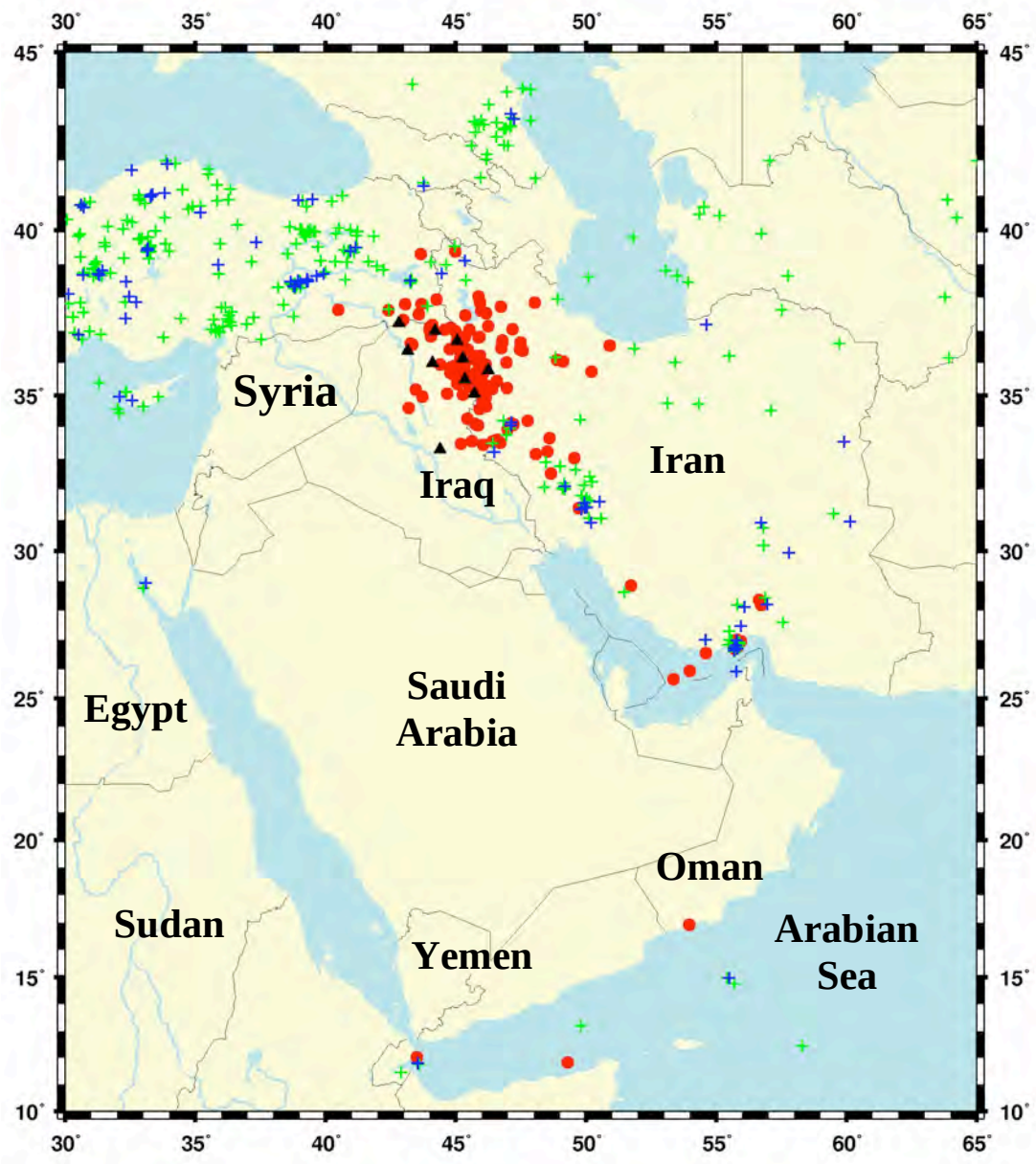


Figure 4. A map showing the location of 190 events recorded by NISN (red solid circles) for the period November 30, 2005, to January 8, 2006, ISC (green crosses), and the USGS (blue crosses) for the same period.

Although it is too early to draw affirmative conclusions, it is evident that most of the events recorded by NISN are found in neither the ISC nor USGS bulletins. The histogram in Figure 5 shows that during the period November 30, 2005, to January 8, 2006, NISN has recorded over five and eight times the number of events reported by the ISC and USGS, respectively. One obvious explanation is that many of the unreported events are small and may not have been detectable by regional stations in Turkey and Iran. Second, the degradation of ISN capability has significantly impacted monitor events in this region. Also noteworthy is that many of the events reported by the USGS and ISC seem to cluster around the local stations in Iran and Turkey that reported their parameters, leaving a major section of the Zagros and its foothills and folded belt to be covered by NISN in an effective and comprehensive manner.

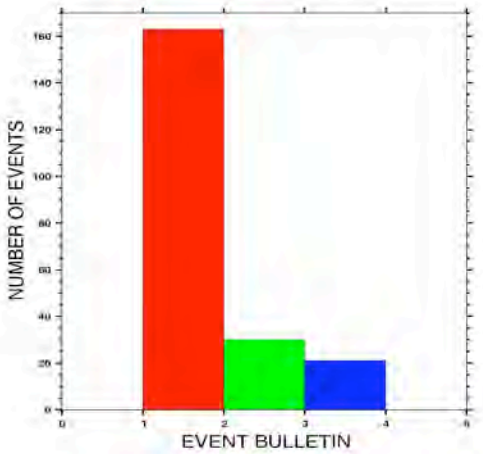


Figure 5. A histogram showing the number of events reported by NISN (red bar), ISC (green bar), and USGS (blue bar) for the same time period.

Figure 6 presents sample waveforms recorded by NISN stations. Example A shows waveforms from an event recorded at eight NISN stations in which the primary regional phases Pn, Pg, Sn, and Lg are clearly identified on most traces. According to the USGS, this event occurred on December 26, 2005, at 23:15:53.4, 49.1713°N, 49.2201°E, 32 km, m_b = 5.1. The epicentral distances and azimuths range from about 130–140 km and 2°–5°, respectively. Example B shows the waveforms of a regional event near Bandar Abbas in Iran, recorded at station KSSS. According to the USGS, this event occurred on November 30, 2005, at 15:19:54, 26.76°N, 55.82°E, m_b = 6.0, and it was felt throughout several of the Arabian Gulf countries, including the United Arab Emirates. In this case, the Pn, Sn, and LR phases are pronounced due to their propagation paths, which coincide with the axis of the thick sedimentary column of the Arabian foredeep.

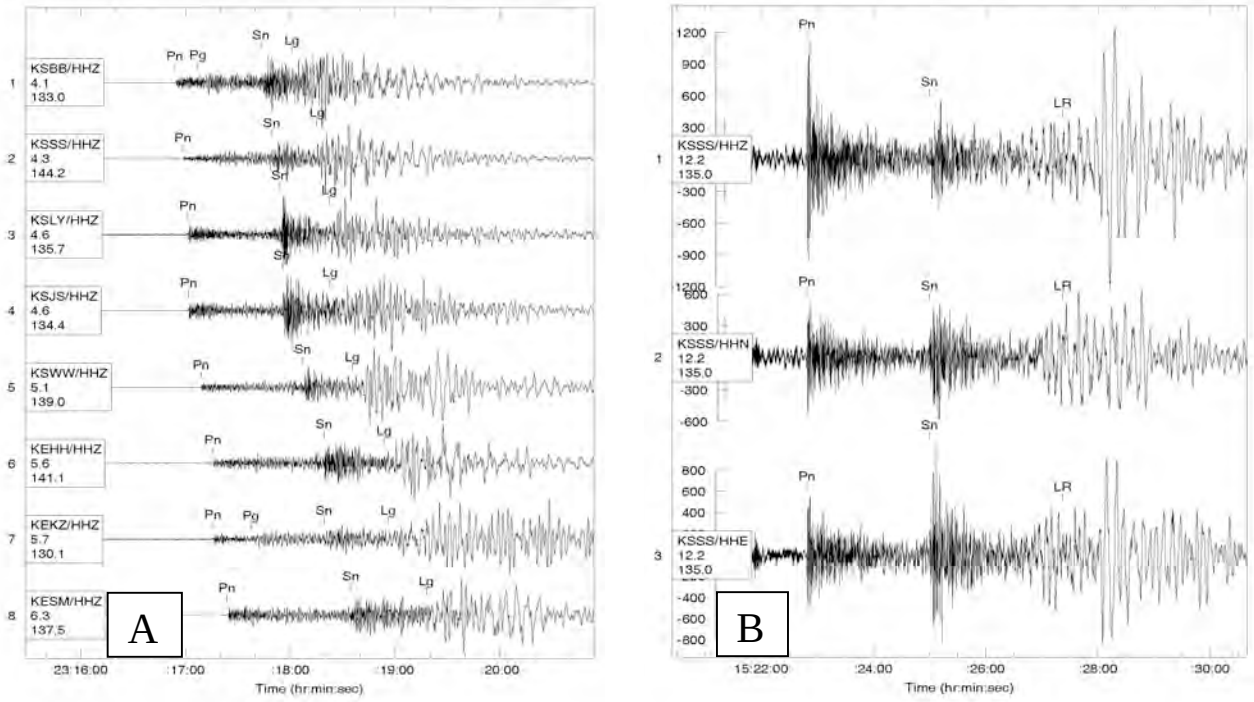


Figure 6. Sample waveforms recorded at eight NISN stations showing the quality of recorded data and pronounced arrival of Pn, Pg, Sn, Lg, and LR phases.

At this stage of the effort, data from all 10 NISN stations (including BHD and MSL) are being analyzed to satisfy the first and subsequent objectives of this project, as stated earlier. The analyses include reformatting the data in

accordance with CSS 3.0 and SAC, identifying observed phases, evaluating the path effects on propagating waves from different azimuths, and locating the events using published models for the region.

In the next example (Figure 7), the vertical component waveforms from three events recorded at station KSWW are presented to illustrate the influence of the Zagros tectonic structure on wave propagation. Studies have shown that some of the regional phases (e.g., Sn and Lg) can be attenuated or blocked from propagating across or along the major structural features. In Figure 7, the top waveform, whose backazimuth is about 29^{o}, reveals clear Pn, Pg, and Lg but no clear Sn crossing the Zagros-Bitlis zone, whereas, the second waveform reveals Pn and Sn but no Pg or Lg traveling along the Zagros axis. In contrast, events with a propagation path from west or south (bottom waveform) exhibit unobstructed propagation of Pn, Pg, Sn, and Lg phases.

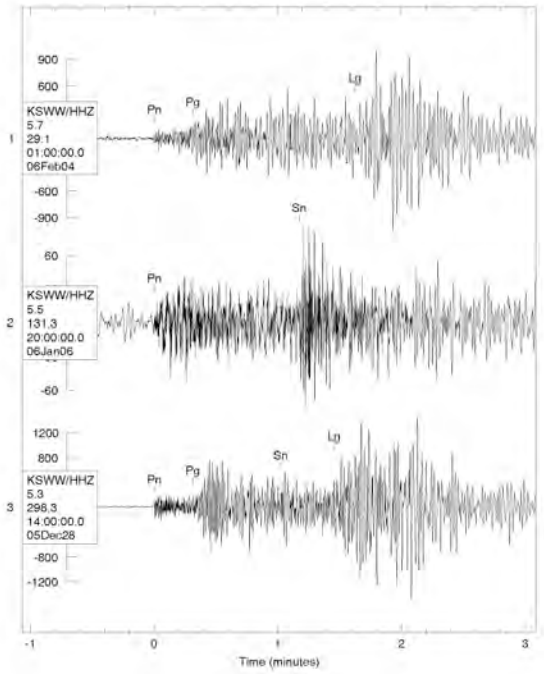


Figure 7. An example showing the impact of tectonic structures (in the form of attenuation or signal blockage) on wave propagation of various azimuths on regional phases Pn, Pg, Sn, and Lg.

Finally, to satisfy the second and third objectives of this effort, preparation to estimate the velocity models along different paths and beneath the 10 NISN station is also underway. Figure 8 shows example of a shear velocity model derived from the inversion of a Rayleigh wave propagating along a path that traverses the region from Bandar Abbas in Iran to station ERBL. Data from many more events along this path will be combined at a later date to provide better estimates and constraints of the dispersion curves and estimated models. Furthermore, joint inversions using the dispersion and receiver functions of observed surface and body waves, respectively, will be attempted to provide more detailed and precise representation of the variation of the velocity model throughout the study area.

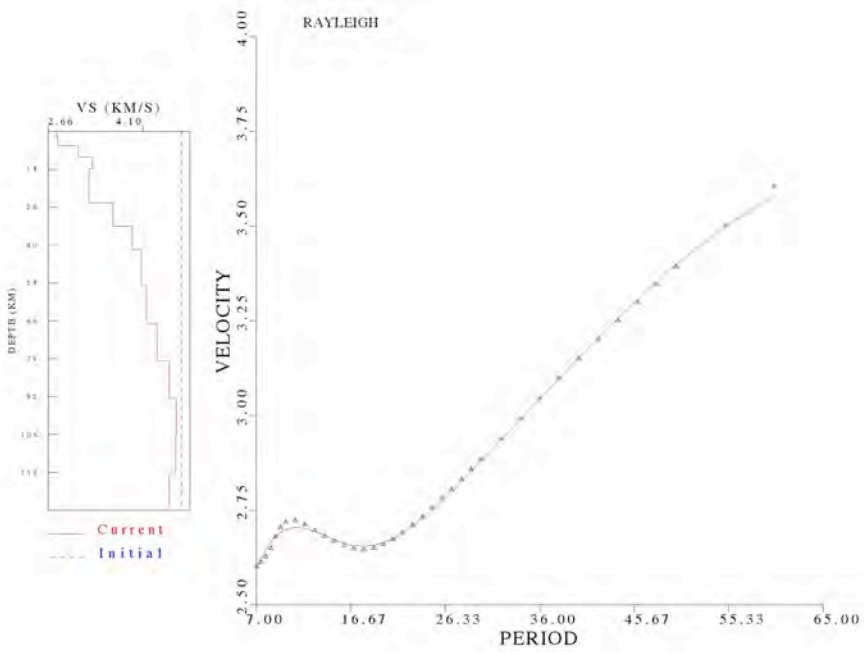


Figure 8. An example of a shear velocity model calculated from the inversion of a Rayleigh wave recorded at station ERBL, whose propagation path traversed the NW-SE trend of the thick sediments of the Arabian plate foredeep.

CONCLUSIONS AND RECOMMENDATIONS

This research effort is in its early stage of accomplishment. To date, the network of 10 NISN stations have been installed and are collecting three-component seismic data. Analyzed waveforms show remarkable quality and a wealth of information about the signal propagation at various azimuths and across major tectonic provinces. Preparations to further exploit these data to estimate the velocity and attenuation models of the study area are underway.

Preliminary evaluation of the data collected to date leads one to recommend expanding the NISN array to cover a larger area of the Zagros and its foothills. This will not only help to draw better three-dimensional models of the physical parameters and properties of the region but will also map the geological and tectonic features for better monitoring of earthquakes throughout the Middle East. Furthermore, it is invaluable to not only continue but also to expand our collaboration with the Iraqi institutions.

ACKNOWLEDGEMENTS

All maps were generated using the Generic Mapping Tools (GMT) by Wessel and Smith (1998). Thanks to Jonathan Creasy for locating the events and to Roland Gritto for reviewing the manuscript.

REFERENCES

Adams, R. D. and M. Barazangi (1984). Seismotectonic and seismology in the Arab region: A brief summary and future plans, *Bull. Seism. Soc. Am.* 74: 1011–1030.

Ghalib, H. A. A., D. R. Russell, and A. Kijiko (1985). Optimal design of a seismological network for the Arabian countries, *Pure Appl. Geophys*. 122: 694–712.

Pasyanos, M. E., W. R. Walter, M. Flanagan, P. Goldstein, and J. Bhattacharyya (2004). Building and testing *a priori* geophysical models for western Eurasia and North Africa, *Pure Appl. Geophys.* 166: 47.

Wessel, P. and W. H. F. Smith (1998). New, improved version of Generic Mapping Tools released, *EOS, Trans. Amer. Geophys. U.* 79: 579.

ADVANCED WAVEFORM SIMULATION FOR SEISMIC MONITORING EVENTS

Donald V. Helmberger[1], Jeroen Tromp[1], and Arthur J. Rodgers[2]

California Institute of Technology[1] and Lawrence Livermore National Laboratory[2]

Sponsored by National Nuclear Security Administration
Office of Nonproliferation Research and Engineering
Office of Defense Nuclear Nonproliferation

Contract No. DE-FC52-06NA27319[1,2]

ABSTRACT

To lower monitoring thresholds to detect and locate small seismic events and identify nuclear explosions from natural seismicity maximum information must be extracted from limited available data. For small events (M<4.0) only a few stations may observe the event above background noise at regional or far-regional distances. Additional information on the location, depth and source is embedded in the waveforms, but isolating their contributions proves difficult. Three-component recording at two stations coupled with a few P-wave picks is sufficient to refine locations, depth, and source parameters. Several methodologies have been attempted to address these seismograms mainly associated with either calibration or wave equation analysis. While satisfying the wave equation has intellectual merit, the great complexity of the earth continues to limit its usefulness, especially at higher frequency. In contrast, calibration methods seem to be the most practical in solving the problems involving the location and identification of small events. Note that some of the best small event discriminants involve the excitation of energy in the 5 to 10 Hz range where waveform modeling is in its infancy. Moreover, if some calibration events are available, the coda magnitude methodology developed by Mayeda and his colleagues proves very useful. To extend this calibration method to moment-rate estimates requires additional information about source time histories of the calibration events, where a cluster of different size events (main plus aftershocks) becomes particularly useful.

Our main objective is to join these two approaches by using waveform modeling at the longer periods, station-path timing corrections, and frequency-dependent amplitude corrections at frequencies above .5 Hz. In particular, we have made some progress by using 3 to 15s periods to develop 2D phase delay corrections (Maps) for Airy Phase Rayleigh and Love Waves for Southern California. Three component recordings at two stations coupled with a few P-wave picks proves very effective to refine locations, depths, and source parameters when compared against results for 150 stations. For still smaller events, we developed a method to work in the .5 to .2 Hz band (essentially the short-period band), and invert P-waveforms for source parameters down to $M_w = 2$ using station calibration. These events can be used to calibrate P-waves for still smaller events working in the 8 to 2 Hz range. This allows the modeling of short-period array P-wave data where numerous events can be examined in terms of source excitation, mining blasts, small explosions, major accidents, etc. Accurate estimates of m_b (P-wave energy) can be used in combination with SP/LP ratio, Woods and Helmberger (1997) to produce an effective discriminant for small magnitudes.

OBJECTIVE

Our main objective is to develop methods for locating and identifying seismic events, focusing primarily on earthquakes but including mining blasts and explosions. To advance methodologies, we want to use our computational resources to address both deterministic approaches as well as developing a better physical understanding of scattering where frequency-dependent coda magnitudes prove so effective. While the latter is apparently source-radiation pattern free (above some cut-off frequency), the direct phases are not and thus the combination should be even more effective in discrimination. In this report, we concentrate on the direct phases and produce a very well recorded set of events ($2<M<5$) which can be used for calibration and scattering models.

RESEARCH ACCOMPLISHED

We begin with a brief review of modeling and how we intend to use the larger events ($M>3.5$) as "Master events" to select simple paths and develop frequency-dependent station corrections. These refinements can then be used to address directivity effects for the larger events ($M>3.5$).

Our basic idea is to explore the large number of seismic stations in Southern California (SC) to develop useful techniques. Since earthquake occurrence in Southern California has been one of the highest in the world, we have a natural laboratory to observe seismic wave complexity generated by different types of earthquakes in a variety of tectonic settings. The number of events recorded is huge but the earthquake catalog Southern California Seismic Network (SCSN) is still dominated by information generated by the short-period array, namely, location and focal-mechanism plots based on travel time and first motion polarity picks. The relative locations has greatly increased in resolution with the cross-correlation methodology, where the first few seconds of P-waves are used in establishing onset timing differentials, Waldhauser and Ellsworth (2000) and Shearer et al. (2005). More recently, the latter researchers have used this same window to estimate Brune-type source parameters with considerable success.

The change over from short-period vertical-type seismology to broadband waveform modeling is facing considerable challenges caused by propagational complexity. At long-periods, LP>6s, these features are less severe and have been modeled remarkably well even for regions along the extended Los Angeles basin, Liu et al. (2004) and Tromp et al. (2005). However, automated methods still use longer period surface-waves and apply a CMT-type solution. These solutions for larger events agree well with the Harvard Centroid Moment Tensors but apparently agree less well with the depth estimates given in the SCSN files. The sensitivity of long-period surface-wave to depth is relatively low. A more accurate determination is possible with the use of depth phases, Helmberger and Wood (1996). Thus including bodywaves into source inversions proves quite useful in constraining possible solutions and are combined in a hybrid method developed by Zhao and Helmberger (1994). This approach called the "cut and paste" (CAP) method breaks the seismograms into segments, upper panel of Fig. 1, and fits the waveforms independently. Synthetics for a model, 1D in this exercise, are stored as a function of distance and depth for the fundamental fault systems, strike-slip, dip-slip, and 45° dip-slip. Combinations of these three synthetics based on weighting determined by possible strike (θ), slip (λ), and dip (δ) are used to obtain the best solution, Zhao and Helmberger (1994), Zhu and Helmberger (1996), and Tan and Helmberger (2006). The source mechanism is obtained by applying a direct grid search through all possible combinations to find the global minimum of misfit between the data and synthetics. In this search, a range of time shifts are allowed between portions of the seismograms when correlating with synthetics to account for crustal variation not included in the model. For example, the observed Pnl waves (extended P-waves) are too early by .7s at PAS and by .36s at GSC, see Fig. 2 for a phase delay map used to predict these delays for surface waves. The cross-correlation values are given in the second row of numbers. The best depth is obtained by fitting a curve through the best fitting grid solutions, and estimating the minimum.

The bottom of Fig. 1 displays how two stations can be used to determine location, depth, origin time, and mechanism simultaneously. The white lines show possible locations based on the P-wave travel time picks for these two stations. If station delays are small, the preferred location would fall along the slice (±.05). If there are delays at any one station, the location will be shifted as displayed. If we knew the surface waves travel time delays, we could also search for the best combination of unknowns by allowing the source to be

situated at every node in a cube and searching for the best mechanism for that position, *Tan et al.* (2006). Adding P-waves with calibrated paths greatly strengthens this approach by fixing the location and nodes. The surface waves then help to fix the depth and moment. We think such a methodology can be used to study events with the sparse datasets, especially when combined with coda-magnitudes.

The rapid expansion of TriNet array has allowed applications of the earlier developed techniques to a much larger data set, Tan and Helmberger (2006), where we have retrieved the source parameters of 250 earthquakes that occurred between 1998-2005 with the so-called "cut and paste" source estimation technique. The two-station methodology was used at the two stations, PAS and GSC (Fig. 1) and tested against the results of the full array. Nearly 80% of the events can be located by these two stations to within 5 km with accurate depth and mechanism estimates, using the phase-delay maps for Love and Rayleigh waves as in Fig. 2. This particular map was generated directly from modeling local events but given the similarity of Fig. 2 with tomographic imaging, Figure 1 of Ritzwoller et al. (2005), it appears they can be generated by synthetic means which will be discussed in the poster. Moreover, high resolution models are presently being developed for particular regions, Rodgers et al. (1999). Although retrieving source mechanisms of magnitude ~3.5 or above events has become a routine process with redundant waveform data from the dense TriNet array, smaller events can hardly be addressed by such long-period (>5 sec) inversions due to the poor signal to noise ratio. Moreover, the second order source characteristics of the magnitude 4 events, such as finite fault and rupture directivity, remain unresolved in the long-period frequency band.

An effective way to address these problems is to model waveform data at shorter periods. However, the unmodeled structural effect often becomes overwhelming, where one has to face the inherent trade-offs between source complexity and structural heterogeneity. Under such circumstances, analyzing clustered events of different sizes provides a practical way to "separate" the source from the structural effect. Figure 3 displays a typical comparison between the records at the same station GSC from three clustered events near Big Bear. While the smaller events are depleted in long-period (5-20 sec) energy, all the three events display very similar signals in the higher frequency bands. This implies propagational stability along the path. Although what has caused the complexity is unclear, the most important information conveyed in Fig. 3 is the possibility of a "two-way" calibration process. First, we can use the magnitude 4 event with the known source mechanism to calibrate the path effect on short-period records, so that smaller events can be studied. Secondly, the smaller events can provide empirical Green's functions at high frequency for studying the detailed rupture process of the big event. Although we only address events with magnitude down to two here, the same methodology has a potential for even smaller events working in the 2 to 8 Hz window.

a) Determining mall earthquake focal mechanisms using high frequency P-waves

In this section, we will demonstrate the two major steps in terms of using high frequency P-waves, namely, path calibration, and short period P-wave inversion. We concentrate on the first P arrival (mainly P_g and P_n phases), since they are the most easily isolated and understood in terms of crustal complexity. The frequency band of 0.5-2Hz is selected, where small events with M_L down to ~2.0 have good signal to noise ratio, while detailed rupture processes of bigger events are mostly filtered out.

The 2003 Big Bear sequence started with a magnitude 5 mainshock and produced about 100 aftershocks with magnitudes down to 2 in the following couple of months. Among them, six events have adequate signal to noise ratio for the LP inversion. The discrepancies between the observed P-waves and the synthetics in the SP-band are mainly manifested as amplitude differences. For quantification purposes, we define the function of "Amplitude Amplification Factor" (AAF) as

$$AAF = \sqrt{\frac{\int u^2(t)\,dt}{\int s^2(t)\,dt}}, \qquad (1)$$

where u(t) and s(t) are the data and synthetics, respectively. The integration is over a 2 sec window centered on the onset of P wave. It appears that the most anomalous AAFs occur for the stations in the basins. In particular, these stations are consistently characterized by large AAFS (>1) on the vertical component, but small AAFs (<1) on the radial component. This discrepancy between the vertical and radial components has been noted by many previous investigators (e.g., Savage and Helmberger, 2004). By comparing the AAFs derived from all the calibration events, particularly, the thrust and the strike-slip events, we found a large number (~70) of stations display stable, and mechanism-independent AAFs, which suggest the amplitude discrepancy of the synthetic P-waves could be corrected to model the observations, hence determine the earthquake focal mechanism.

We invert the short-period P waves with a similar grid-search approach as in the long-period inversion, where we minimize the L2 norm of the misfit between the data and synthetics:

$$e = \left\| u(t) - AAF \,.\, s\,(t) \right\|. \tag{2}$$

The AAFs in equation (1) are taken as the averages of the AAFs derived from the calibration events. The validation test with respect to the calibration events shows remarkable agreement between the results from short-period P-wave inversions and their known LP solutions (Tan and Helmberger, 2006a). Moreover, the advantage of adding the AAF corrections is clearly displayed in Fig. 4 where the results with and without the AAF corrections for the calibration event 13936432 are compared. Note that this works for events independent of mechanism indicating that the correction is primarily caused at the station. We also conducted statistic tests on the calibration events using subsets of the recording stations to mimic the poor coverage smaller events will face, in an attempt to quantify how many stations are needed for a reliable solution. We have demonstrated that one would need 15 stations, or 10 stations with the largest azimuthal gap less than 90° to obtain accurate results, (Tan and Helmberger, 2006). Although we have used only regional data, any distance can be included to enhance coverage, including far-regional and teleseismic, if calibrated in the SP-band.

With reasonably accurate mechanisms of small events, we can greatly increase the population and generate record sections of events at a single station, (see Figure 5). These events ranges in magnitude from 2.1 (13936196) to 5.1 (13935988). The top two-thirds are mostly small strike-slip events with similar seismograms. The lower portion of the section contains some larger events with some thrust events (bottommost trace), with changes in polarities in secondary arrivals.

b) Rupture Directivity

A direct consequence of rupture propagation on a fault plane is the azimuthal dependence of the observed source time function (STF). In brief, if a seismic station is located along the rupture propagation direction, the STF is narrower and has higher amplitude. For a station located such that the rupture is propagating away from it, the STF will be spread out and have a smaller amplitude. Instead of using inaccurate Green's functions, Hartzell (1978) demonstrated the feasibility of modeling the strong ground motion of a large earthquake using records from its own aftershocks as Green's functions. This empirical Green's function (EGF) approach assumes the large event and the EGF events occur at a similar location and have a similar focal mechanism, so that they share nearly the same propagational effect, and a linear scaling between their source terms exists at the same stations. Since we can rotate an aftershock to be the same mechanism as the target event, the method becomes particularly useful. We estimate the relative source time function, RSTF (t), specified by the convolution of two triangles, rise time and rupture time. We force the rise time to be independent of azimuth and solve by grid search. We illustrate the process in Fig. 6 for event 13937492, third trace from the bottom of Fig. 5, for a sample of azimuths. Preliminary results from Tan and Helmberger (2006b) indicate that most events larger than 3.5 have recognizable patterns but events in clusters show a great deal of variability in rise time (stress-drop). Because those frequencies are in the bandpass used in discriminants, they become a crucial issue for explaining anomalous data points in both energy ratio discriminants, i.e., Woods and Helmberger (1997), and P-S high frequency ratios, Walter et al. (2002).

CONCLUSIONS AND RECOMMENDATIONS

In summary, we demonstrate that regional seismograms from as few as two stations suffice to determine both the source location and mechanism provided that we have path calibration. For the 200 events tested here, the two station solutions agree well with those from the entire TriNet array except for a few cases. We also demonstrated that the magnitude 4 events with known source mechanisms can be used to calibrate the path effects on the short-period (0.5-2 sec) P waves, so that the corrected P waves can be modeled for determining focal mechanisms of the smaller events within clusters. The correction is formulated in terms of a station-specific "Amplitude Amplification Factor" (AAF), whose origin is mainly due to the site effect. Second, we show that the smaller events with radiation pattern corrections provide excellent empirical Green's functions (EGFs) for investigating the detailed rupture processes of the magnitude 4 events.

Future plans include (1) the extension of SP calibration to S-waves to constrain radiation pattern, (2) defining the portion of the recordings that are radiation pattern free (coda), (3) developing a better understanding of scattering in terms of surface structure, (4) using these measures to study mining blasts and local explosions, and (5) include the above information into a new SP/LP discriminate, Woods and Helmberger (1997) and testing at various test sites.

REFERENCES

Hartzell, S. H. (1978). Earthquake aftershocks as Green's functions, *Geophys. Res. Lett.* 5: 1–4.

Helmberger, D. V. and B. Woods (1996). Regional Source Parameters, Seismic Energy, and Discrimination, *Monitoring a Comprehensive Test Ban Treaty, E. S. Husebye and A. M. Dainty (eds.)*, Kluwer Academic Publishers: 365–383.

Helmberger, D. V., X. J. Song, and L. Zhu (2001). Crustal complexity from regional waveform tomography: Aftershocks of the 1992 Landers earthquake, California, *J. Geophys. Res.* 106: (B1): 609–620.

Helmberger, Don V. and S. Ni (2005). Approximate 3D Body-Wave Synthetics for Tomographic Models, *Bull. Seismol. Soc. Am.* 95: (1): 212–224.

Liu, Q., J. Polet, D. Komatitsch, and J. Tromp (2004). Spectral-element moment tensor inversions for earthquakes in Southern California, *Bull. Seismol. Soc. Am.* 94: 1748–1761.

Ritzwoller, Michael, N. Shapiro, M. Pasyanos, G. Bensen, and Y. Yang (2005). Short Period Surface Wave Dispersion Measurements from Ambient Seismic Noise in North Africa, the Middle East, and Central Asia, in *27th Seismic Research Review: Ground-based Nuclear Explosion Monitoring Technologies*, LA-UR-05-6407, Vol. 1, 161–170.

Rodgers, A., W. Walter, R. Mellors, A. M. S. Al-Amri, and Y.-S. Zhang (1999). Lithospheric structure of the Arabian Shield and Platform from complete regional waveform modeling and surface wave group velocities, *Geophys. J. Int.* 138: 871–878.

Savage, B. and D. V. Helmberger (2004). Site response from incident *Pnl* waves, *Bull. Seismol. Soc. Am.*, 94 (1): 357–362.

Shearer, Peter, E. Hauksson, and G. Lin (2005). Southern California hypocenter relocation with waveform cross-correlation, Part 2: Results using source-specific station terms and cluster analysis, *Bull. Seismol. Soc. Am*. 95 (3): 904–915.

Tan, Ying, L. Zhu, D. V. Helmberger, and C. Saikia (2006). Locating and Modeling Regional Earthquakes with Two Stations, *J. Geophys. Res*. 111(B1): 306–320.

Tan, Ying and D. V. Helmberger (2006a). A new method for determining small earthquake focal mechanisms using short-period P waves, submitted to *Bull. Seismol. Soc. Am.*

Tan, Ying and D. V. Helmberger (2006b). Rupture Directivity of the 2003 Big Bear aftershocks, submitted to *Bull. Seismol. Soc. Am.*

Tromp, Jeroen, Carl Tape, and Qinya Liu (2005). Seismic tomography, adjoint methods, time reversal, and banana-donut kernels, Geophys. J. Int. 160: 195–216.

Waldhauser, F. and W. Ellsworth (2000). A Double-Difference Earthquake Location Algorithm: Method and Application to the Northern Hayward Fault, California, *Bull. Seismol. Soc. Am*., 90 (6): 1353–1368.

Walter, W. R., A. J. Rodgers, M. E. Pasyanos, K. M. Mayeda, and A. Sicherman (2002). Identification in western Eurasian: Regional Body-Wave Corrections and Surface-Wave Tomography Models to improve discrimination, in *Proceedings of the 24th Seismic Research Review – Nuclear Explosion Monitoring: Innovation and Integration*, LA-UR-02-5048, Vol. 1, pp. 592–600.

Woods, B. B. and D. V. Helmberger (1997). Regional Seismic Discriminants using Wavetrain Energy Ratios, *BSSA* 87 (3): 589-605.

Zhao, L. S. and D. V. Helmberger (1993). Source retrieval from broadband regional seismograms: Hindu Kush region, *Phys. Earth Planet. Inter*. 78: 69-95.

Zhao, L.-S. and D. V. Helmberger (1994). Source Estimation from Broadband Regional Seismograms, *Bull. Seismol. Soc. Am*. 84: 91-104.

Zhu, Lupei and D. V. Helmberger (1996). Advancement in Source Estimation Techniques Using Broadband Regional Seismograms, *Bull. Seismol. Soc. Am.* 86 (5): 1634–1641.

Zhu, Lupei, D. V. Helmberger, C. K. Saikia, and B. B. Woods (1997). Regional waveform calibration in the Pamir-Hindu Kush region, *J. Geophys. Res.* 102 (B10): 22,799–22,813.

Zhu, L., Y. Tan, D. V. Helmberger, and C. Saikia (2005). Locating and Modeling Regional Earthquakes, Part I: Calibration of the Tibetan Plateau, *Pure Applied Geophys.*, in press.

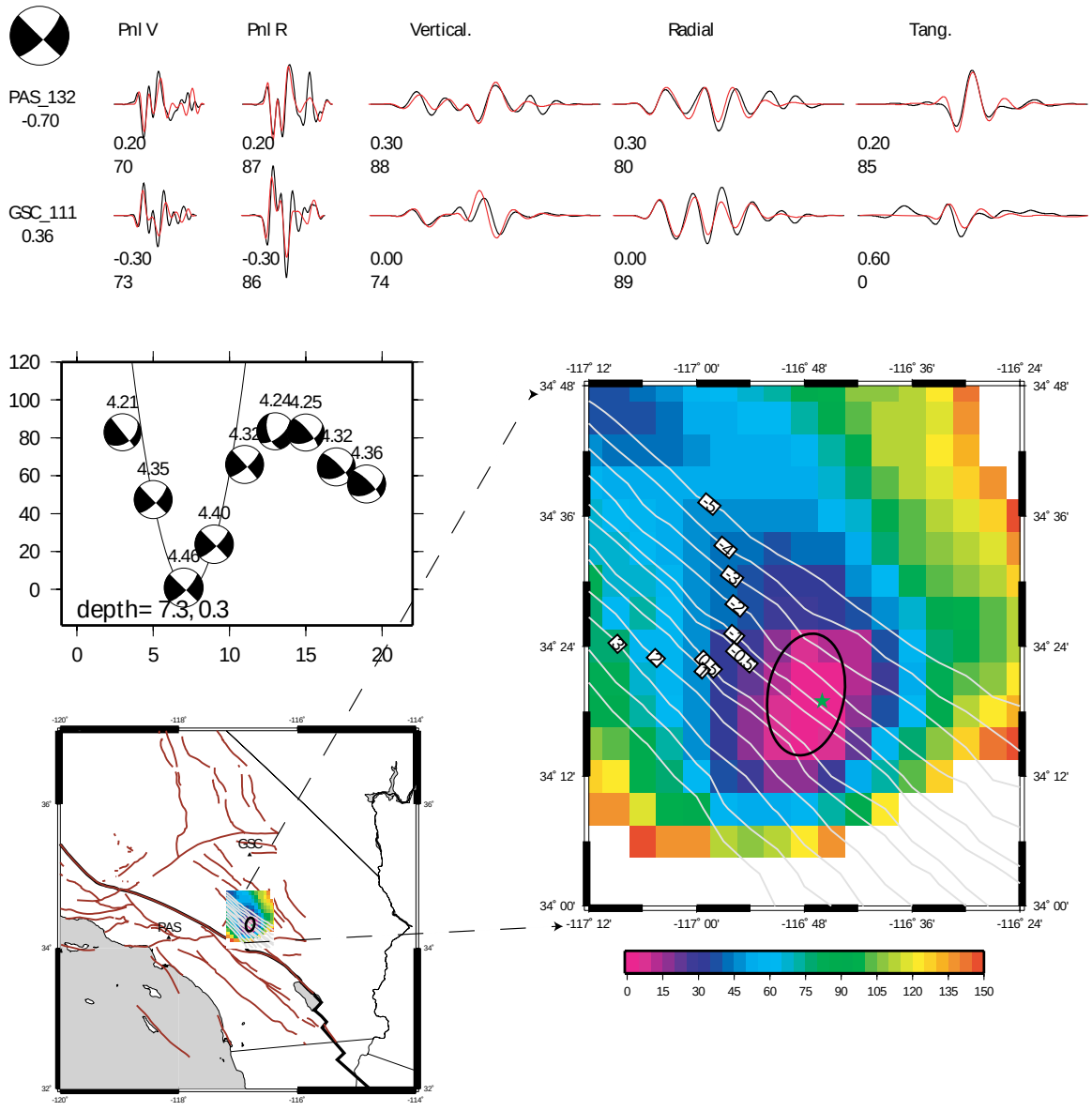


Figure 1. Demonstration of how to determine the location and mechanism simultaneously by searching various positions in a cube. The resolution based on misfit error for a 2D section at the preferred depth (7.3 km) is displayed. The various trade-offs can be seen in a 3D image. Note that if these two P-wave paths have zero corrections, we could fix the location to within a few km.

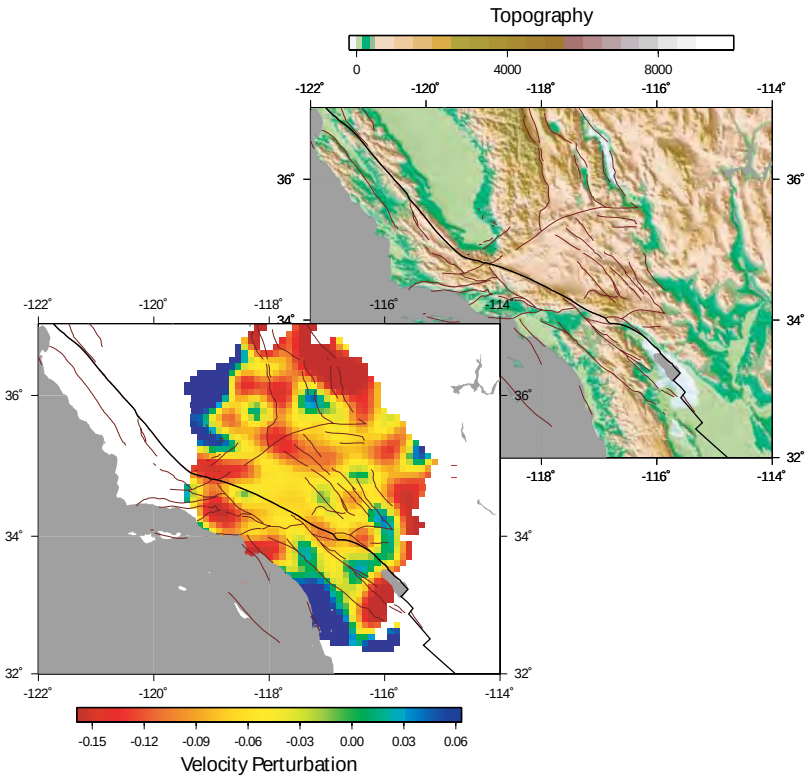


Figure 2. Comparison of the Rayleigh delay map against the topography.

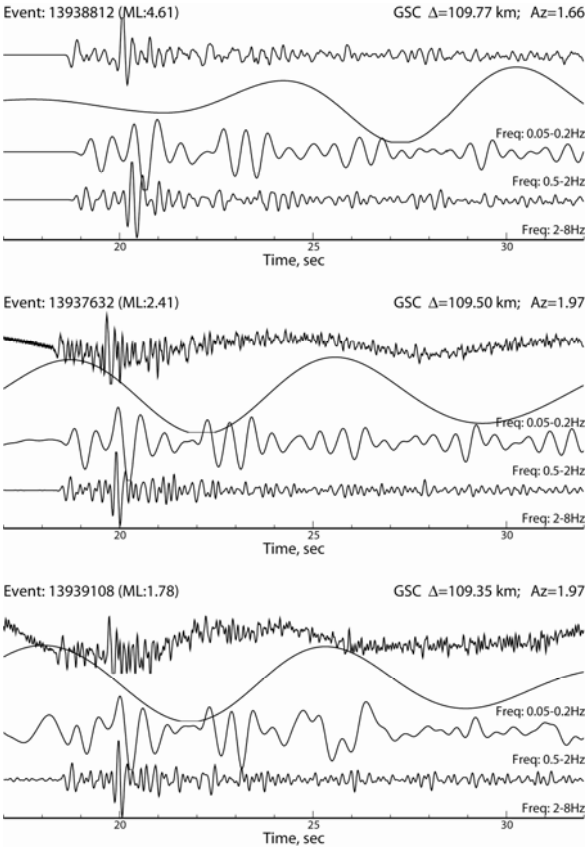


Figure 3. This figure displays the comparisons among the records from clustered, but different-sized events, M_L = 4.6, 2.4 and 1.8. For each event, the four traces from the top to bottom are the original vertical component broadband record, and the filtered records featuring different frequency bands.

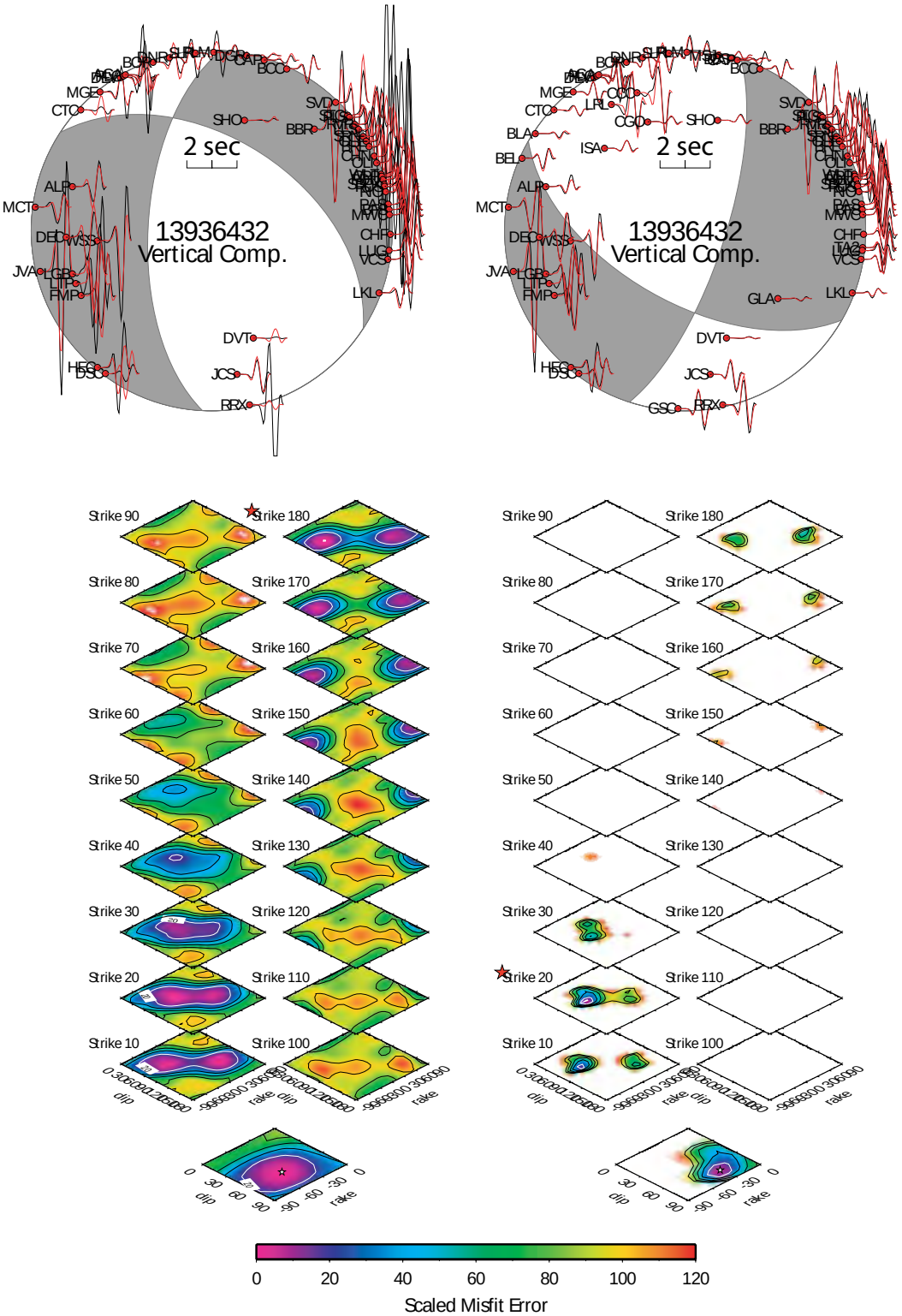


Figure 4. (Top) The resulted P-wave waveform fits on the vertical component from the short-period inversions without (left) and with AAF corrections (right) for the event 13936432 (bottom). The resolution of the solutions from short-period inversions for the event 13936432 without (left) and with AAF corrections (right) is displayed as the scaled waveform misfit errors. A red star indicates where the best solution resides with the blow up of the slice at the bottom. The white contours of 20% variance increase are displayed as the uncertainty estimates.

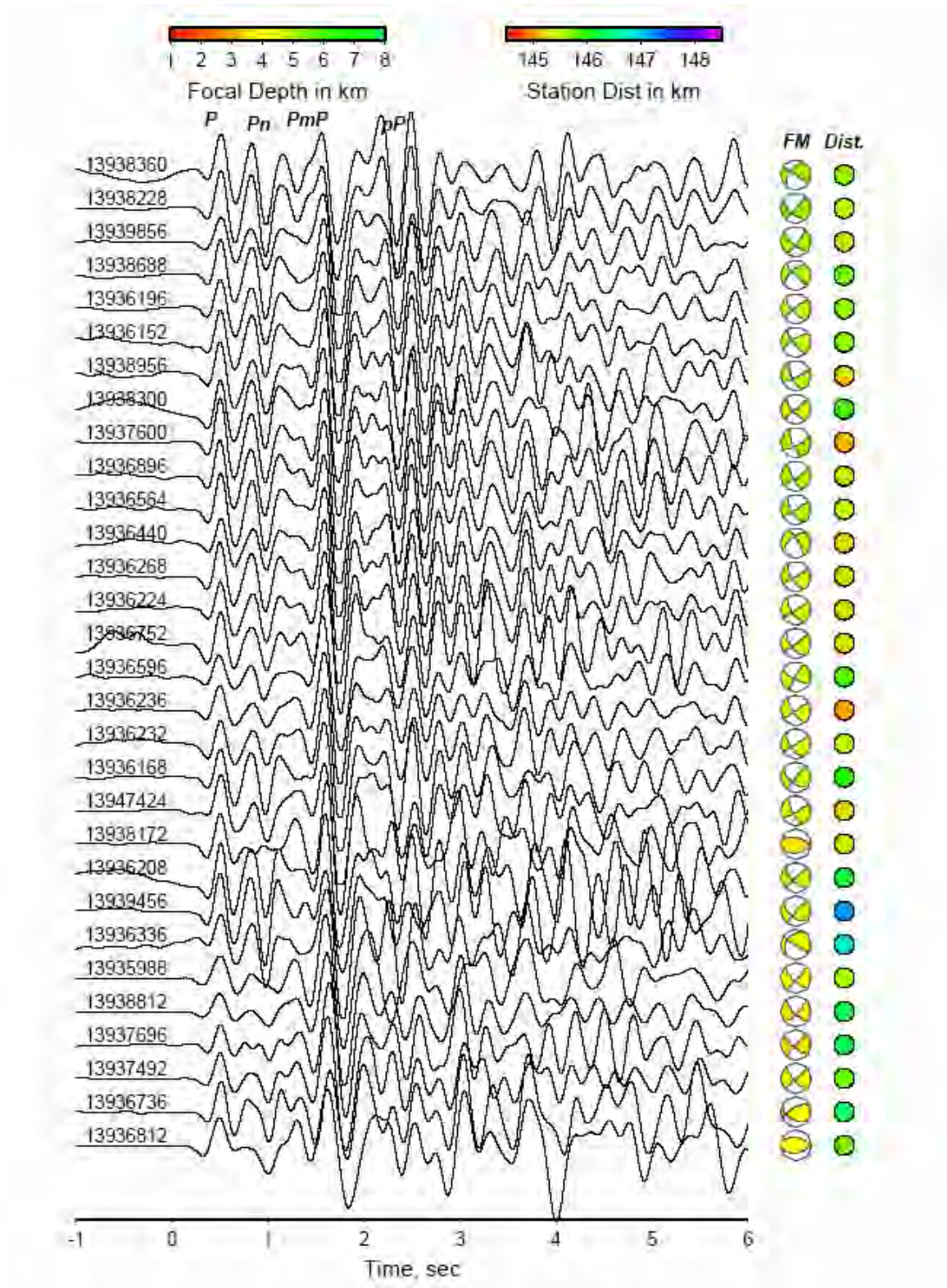


Figure 5. The vertical component records at station DPP from the clustered events of the 2003 Big Bear sequence. The traces are ordered with the separations between P and PmP increasing from the top to the bottom. Note the Pn phase changes sign for the thrust events due to the radiation pattern (bottom trace).

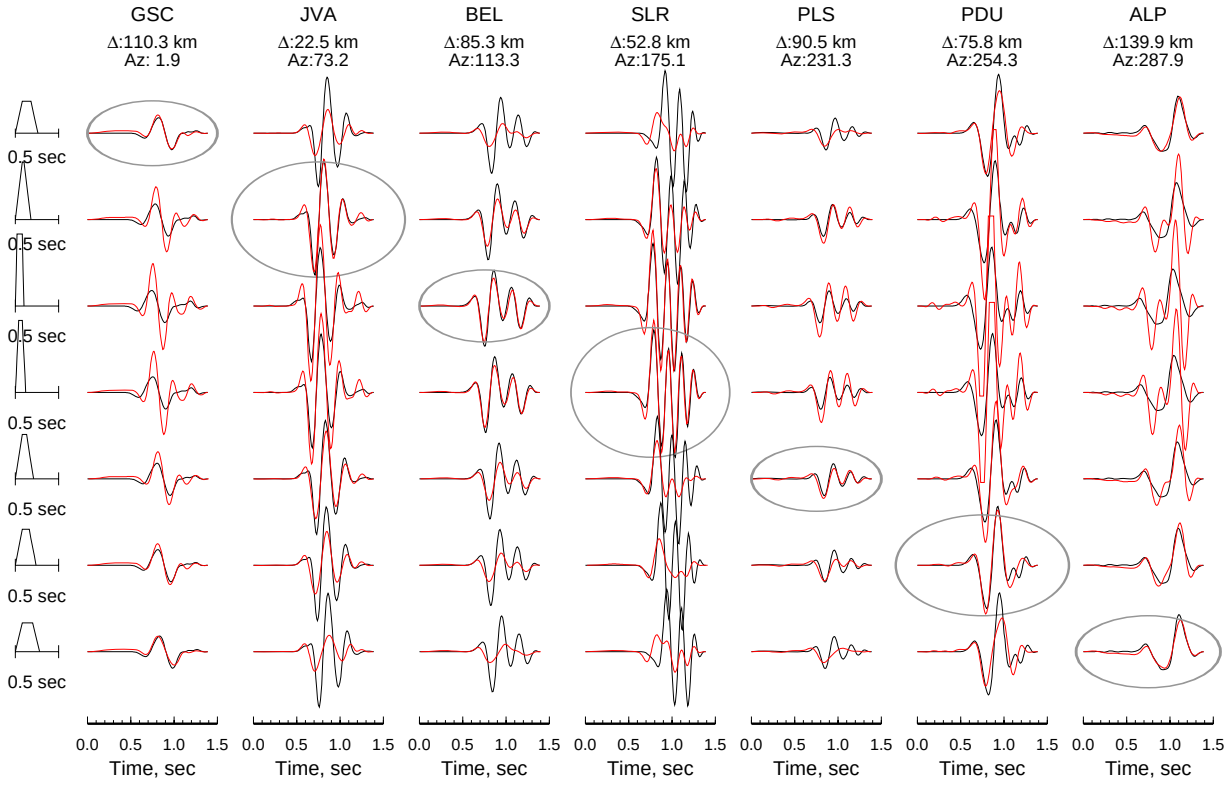


Figure 6. The selected waveform fits (Vertical P-waves) between the records from event 13937492 (black) and the "synthetics" (red) using the records from event 13937632 as EGFs. The relative source time functions (RSTFs) are given to the left. Plotted are the absolute amplitudes, except that a scaling factor of ¼, ½, and 2 has been applied to the stations JVA, PDU, and PLS respectively for the display purpose. The obtained best RSTFs for the stations are circled. Note the apparent azimuthal pattern of the RSTFs.

SEISMIC SOURCE AND PATH CALIBRATION IN THE KOREAN PENINSULA, YELLOW SEA, AND NORTHEAST CHINA

R. B. Herrmann[1], Y. S. Jeon[1], H.J. Yoo[2], K. H. Cho[2], W. R. Walter[3], and M. Pasyanos[3]

Saint Louis University[1], Seoul National University[2], and Lawrence Livermore National Laboratory[3]

Sponsored by National Nuclear Security Administration
Office of Nonproliferation Research and Development
Office of Defense Nuclear Nonproliferation

Contract Nos. DE-FC52-04NA25539[1,2] and W-7405-ENG-48[3]

ABSTRACT

The technique joint inversion of surface-wave dispersion and teleseismic P-wave receiver functions is used as a tool to derive a three-dimensional image of crustal velocities in the southern part of the Korean Peninsula. The station-specific surface-wave dispersion consists of two components—a long-period (10–150 s) Rayleigh-wave phase velocity dispersion for the peninsula and short period (0.5–20 s) tomographic Rayleigh- and Love-wave group velocity dispersion based on an analysis of >2100 empirical Green's functions derived from the cross-correlation of ground noise. When combined with teleseismic P-wave receiver functions from broadband, short-period, and acceleration sensors at 58 sites, a three-dimensional picture of the south Korean crust results. Spatial variations are seen in the depth to the Moho (28–32 km) and the degree of an upper crustal shear-wave velocity gradient from 3.0 to 3.5 km/s. Shear-wave velocities in the upper kilometer are typically greater than 3.0 km/s except in the southeast in the volcanoclastic Gyeongsang basin where the velocities are 5%–10% lower. An average velocity structure is used for moment tensor inversion.

OBJECTIVES

The primary focus is the determination of moment magnitudes for earthquakes in the Korean Peninsula, Yellow Sea and Northeast China region for use in calibration of coda based seismic moment determination. The source parameters are to be determined from the inversion of broadband waveforms of earthquakes in the region. To address the lack of large earthquakes, inversion of small earthquakes requires calibration of the shear-wave velocities in the upper crust in order to use the predominant signal in the higher frequency band of 0.05–0.2 Hz.

RESEARCH ACCOMPLISHED

Significant progress has been made in the characterization of the three-dimensional velocity structure of the southern half of the Korean Peninsula. Cho et al. (2006) mapped the variation of 1–20 s surface-wave group velocities in the study area. Yoo et al., (2006) used these and other surface-wave dispersion results together with teleseismic P-wave receiver functions at 80 sites to image the depth to the Moho and three-dimensional shear-wave velocity structure.

Study Area

The Korean Peninsula, Figure 1, situated at the eastern margin of the Eurasian continent, is a tectonic assemblage of two Phanerozoic mobile belts; the Imjingang belt and the Ogcheon fold belt, three Precambrian basement terrains; Nangrim, Gyeonggi, and Yeongnam Massifs from north to south, and one volcanoclastic basin, i.e., Gyeongsang basin (Chough et al., 2000). The Nangrim and the Gyeonggi massifs are separated by the Imjingang belt, which is a narrow suture zone recording high grade metamorphic events during the Late Permian to Early Triassic periods. The Gyeonggi and Yeongnam massifs are separated by the north-east trending Ogcheon belt, which is a fold and thrust belt involving Precambrian to Jurassic rocks. The Ogcheon belt and the Yeongnam massif contact at the Honam shear zone, north-east trending dextral strike-slip shear zone (ca. 400 km long and 80 km wide and both are overlain unconformably by Cretaceous sedimentary rocks). The volcanoclastic Gyeongsang basin covers the southeastern part of the Yeongnam massif. The tectonic affinity of the Korean Peninsula has been an enigma for a long time. The entire peninsula was traditionally regarded as an extension of the North China Block (also called the Sino-Korea Craton/Block). However, recent geological and petrophysical studies revealed that the Imjingang Belt and the Okchon Fold Belt (and Honam Shear Zone) could be the collision zone between the North China Block (Sino-Korea Craton) and the South China Block (Yangze Craton).

Digital Seismic Data

Digital seismology in Korea began with the installation of the Incorporated Research Institutions for Seismology (IRIS) station that is now at Inchon. Subsequently the Korean Institute of Geoscience and Mineral Resources (KIGAM) installed some broadband stations. In 2000, the Korean Meteorological Administration (KMA) digital seismic network became operational. The KMA network has a backbone of broadband stations, some additional short-period stations, and a dense network of accelerometers transmitting continuous data to the analysis center in Seoul. In addition, additional broadband sensors and accelerometers are operated by the Korean Electric Power Research Institute (KEPRI). For the surface-wave studies we used data from the broadband stations of KMA and KIGAM, approximately 15 at the time, for phase velocity determination, and waveforms from KMA broadband and acceleration channels for the group velocity analysis (Cho. et al., 2006). Receiver functions were determined from the KMA, KIGAM and KEPRI broadband channels and selected KMA short-period and acceleration channels. Figure 2 presents the location of the sites providing the group velocities and the receiver functions that we used in the study. The dense distribution of the stations permits us to examine the 3-D crustal structure in detail.

Surface-Wave Dispersion

The surface-wave data consists of two components. A peninsula average Rayleigh-wave phase velocity in the 10–50 s range, and tomographic estimates of the Rayleigh and Love wave group velocities in the 0.5–20 s period range determined using a 12.5 x 12.5 km grid for the southern part of the peninsula.

To obtain the phase velocities at longer periods, we applied the p-omega technique of McMechan and Yedlin (1981) to teleseismic Rayleigh waves observed on the Peninsula. The fundamental mode surface-wave was extracted using a combination of multiple filter analysis and phase matched filtering, a great circle path was assumed to project the

station observations onto a pseudo-linear array for analysis, and the phase velocities were determined. The Korean average Rayleigh wave phase velocity dispersion was determined in the 10–150 period range from about ten distant earthquakes. In spite of scatter, at the longer periods, the dispersion agreed with the Harvard tomography.

Cho K. H. et al. (2006) derived tomographic maps of Rayleigh- and Love-wave group velocity dispersion from inter-station empirical Green's functions obtained from the cross-correlation of ground noise (Shapiro et al., 2005). Group velocities were obtained from the empirical Green's functions for over 2100 inter-station paths in the 0.5–20 s period band. Because of the path density, they used a 12.5 x 12.5 km grid to create a tomographic dispersion image for each measured period. Figure 3 shows the Rayleigh-wave tomography results for selected periods. For our application, we associate the dispersion at a station with the nearest tomographic grid value. This is justified by the wavelengths considered and the smoothing used for the tomography. Figure 4 shows the dispersion data used at one KMA station, CHJ, for example.

Receiver Functions

Receiver functions are filters which predict a filtered version of a horizontal component from the vertical component trace (Ammon, 1997). This study uses P-wave radial receiver functions. To obtain these, teleseismic waveforms with a good P-wave signal are selected. The receiver function is estimated using the iterative time-domain deconvolution technique of Ligorria and Ammon (1999), which is an implementation of the Kikuchi and Kanamori (1982) technique. The time-domain Gaussian pulses used correspond to low-pass filters with frequencies of 0.3 and 1.0 Hz. Because of high-frequency noise, we did not attempt to use Gaussian filters with higher corner frequencies. In addition we did not try to use longer time-domain pulses, e.g., lower frequency data, because of long-period noise and because of the limited resolution of such data. In the terminology of Ligorria and Ammon (1999), we used the filter parameters alpha = 1.0 and 2.5.

A multi-step process was used to determine if a given receiver function should be used in the inversion for structure. The first criterion required that the derived receiver function predict 80% of the filtered radial signal power. This criterion is a quality check on the deconvolution stage. Given the large data sets and our unwillingness to subjectively exclude data, unrealistic receiver functions with the first pulse negative, passed this criterion since the deconvolution is a purely mathematical procedure that knows nothing of elastic wave propagation.

The second criterion involved using all acceptable receiver functions for the joint inversion of surface-wave dispersion and receiver functions at a station. The reduction of variance between each observed and predicted receiver function is obtained from this process. Predictions are made for the final crustal model and are thus constrained by elastic wave propagation theory. Of the receiver functions used, we used only those that fit 80% of the observed signal power. This stage rejected many signals for the final inversion. Of the 95 stations initially considered, only 80 stations had 2 or more good receiver functions. The locations of these stations are shown in Figure. 2a. Table 1 gives the station names, coordinates, and the final number of receiver functions used for the site.

We were able to have so many stations available for analysis because we obtained receiver functions from broadband (STS-2), short-period (SS-1) and acceleration (Episensor) channels of the 20 Hz archived data stream. Since STS-2 and SS-1 sites also had Episensor channels, we were able to verify that the acceleration channels could give good receiver functions. The possibility of using the acceleration channels was suggested by the success in obtaining empirical inter-station Green's functions from them, which is because these channels in Korea are more sensitive than is typical. The use of these data is made easier since there seems to be little azimuthal dependence on the receiver function and since the P-wave transverse receiver function is usually small.

Joint Inversion Structure

Joint inversion of receiver functions and surface-wave dispersion was first proposed by Özalaybey et al. (1997). It has been used by Juliá et al. (2000), Herrmann et al., (2001), Chang et al., (2004), and Chang and Baag (2005). The iterative least-squares joint inversion used here is described by Herrmann and Ammon (2002). Surface-wave dispersion partial derivatives are computed analytically while receiver function partial derivatives are computed numerically. The inversion fixes the Vp/Vs ratio in each layer and recomputes layer density from the P-wave velocity after each iteration. A differential smoothing constraint is applied with the objective of finding the simplest model that fits the data set. The smoothing constraint is implemented by solving for the change in the velocity

contrast at layer boundaries rather than solving for the changes in the individual layer velocities. The starting model used at all sites consists of 85 layers to a depth of 580 km. From a depth of 50 km to the bottom, the model is AK135-F Continental Model (http://wwwrses.anu.edu.au/seismology/ak135/ak135f.html). The upper 50 km of the model consists of layers (four 1 km and twenty-three 2 km) having the same velocities as AK135-F at 50 km. The velocity jumps at the layers boundaries are not permitted to change from 380 km to the bottom of the model. They are permitted to change slightly from 80–380 km, and they are permitted to change in the upper 80 km. The high initial velocities of the crust provide a uniform unbiased starting model for the inversion. No a priori assumptions about the location of the Moho are made. In addition no persistent artifacts of crustal layer boundaries appear in the solution. Starting with a continental upper mantle, and permitting a significant departure from the starting model only in the upper 80 km, ensure that the lower part of the model does not depart from the global seismology experience. The choice of crustal layer thicknesses of 2.0 km is appropriate because of the lack of resolution with fundamental mode surface-wave dispersion, and the receiver function resolution for the filters used.

As mentioned above, we performed the joint inversion twice, first with all receiver functions associated with a successful deconvolution, and second with just those for which the model provided at least an 80% variance reduction in fit. Since it is the receiver functions, which provide the constraints on velocity model discontinuities, we will focus only on those 80 sites which had 2 or more receiver functions. At common stations, we have compared our inverted models with those from the recent work of Chang et al. (2004) and Chang and Baag (2005). The models are similar.

Rather than presenting all 80 crustal models, and to test the usefulness of our approach to image the three-dimensional crust, we present the results as a contour map of Moho depth and vertical sections. Presenting the Moho depth estimates as a contoured surface is a compromise because the Moho probably does not change in depth as a smoothly varying surface everywhere, but it presents the most effective means to view the data. To make the Moho contour map, we assign the Moho where the shear wave velocity increases to or is >4.2 km/s in each model and then applied “minimum curvature technique” (Smith and Wessel, 1990) for interpolation. The Moho depth varies from about 26 km to 38 km and 32.7 km in average (Figure 5). It is deeper in the southern and central parts of the peninsula. It is to be noted that the variation of Moho topography of the east coast differs from that of the west and south coasts. Figure 6 shows representative two-dimensional crustal shear-wave velocity slices along diagonal paths across the study area.

MOMENT TENSOR INVERSIONS

Using the moment tensor inversion techniques and velocity model developed for SRR 2005, we have continued to use regional broadband waveforms for the determination of earthquake source parameters for earthquakes in the study region. Our tabulation now consists of solutions for 27 earthquakes and is available at the web page

http://www.eas.slu.edu/Earthquake_Center/MECH.KR/

As additional earthquakes occur, we will include them in this tabulation.

CONCLUSION(S) AND RECOMMENDATIONS

The striking difference between the Moho depth in the southern and eastern parts of the peninsula reflect the tectonic origins the crust. A working hypothesis is that the velocity models derived in the northwestern part of South Korea may be applicable to the entire northern part of the peninsula. The previously reported model for waveform inversion for source properties still applies.

ACKNOWLEDGEMENTS

Maps were created using Generic Mapping Tools, or GMT (Wessel and Smith, 1995).

REFERENCES

Ammon (1997). An overview of receiver-function analysis, http://eqseis.geosc.psu.edu/~cammon/HTML/RftnDocs/rftn01.html.

Ammon, C. J., G. E. Randall, and G. Zandt (1990). On the nonuniqueness of receiver function analysis, *J. Geophys. Res.* 95: 15,303–15,318.

Chang, S. and C. Baag (2005). Crustal Structure in southern Korea from joint analysis of teleseismic receiver functions and surface-wave dispersion, *Bull. Seism. Soc. Am.* 95: 1,516–1534.

Chang, S., C. Baag, and C. A. Langston (2004). Joint analysis of teleseismic receiver functions and surface wave dispersion using the genetic algorithm, *Bull. Seism. Soc. Am.* 94: 691–704.

Cho, H.-M., C.-E. Baag, J. M. Lee, W. M. Moon, H. Jung, K. Y. Kim, and I. Asudeh (2006). Crustal velocity structure across the southern Korean Peninsula from seismic refraction survey, *GRL* 33: L06307, doi:10.1029/2005/GL025145.

Cho, K. H., R. B. Herrmann, C. J. Ammon, and K. Lee (2006). Imaging the upper crust of the Korean Peninsula by surface-wave tomography, *Bull. Seism. Soc. Am.* (in review).

Chough, S. K., S.-T. Kwon, J.-H. Ree, and D. K. Choi (2000). Tectonic and sedimentary evolution of the Korean peninsula: a review and new view, *Earth-Sci. Rev.* 52: 175–235.

Herrmann, R. B., C. J. Ammon, and J. Juliá (2001). Application of joint receiver-function surface-wave dispersion for local structure in Eurasia, in *Proceedings of the 23rd Seismic Research Review: Worldwide Monitoring of Nuclear Explosions*, LA-UR-01-4454, Vol. 1, pp. 46–54.

Kikuchi, M. and H. Kanamori (1982). Inversion of complex body waves, *Bull. Seism. Soc. Am.* 72: 491–506.

Juliá, J., C. J. Ammon, R. B. Herrmann, and A. M. Correig (2000). Joint inversion of receiver function and surface wave dispersion observations, *Geophys. J. Int.* 143: 99–112.

Ligorria, J. P. and C. J. Ammon (1999). Iterative deconvolution of teleseismic seismograms and receiver function estimation, *Bull. Seism. Soc. Am.* 89: 1,395–1,400.

McMechan, G. A. and M. J. Yedlin (1981). Analysis of dispersive waves by wave field transformation, *Geophys.* 46: 869–874.

Min, K. and M. Cho (1998). Metamorphic evolution of the northwestern Ogcheon metamorphic belt, South Korea, *Lithos* 43: 31–51.

Özalaybey, S., M. K. Savage, A. F. Sheehan, J. N. Louie, and J. N. Brune (1997). Shear-wave velocity structure in the northern Basin and Range province from the combined analysis of receiver functions and surface waves, *Bull. Seism. Soc. Am.* 87: 183–199.

Shapiro, N. M. M. Campillo, L. Stehly, and M. H. Ritzwoller (2005). High resolution surface wave tomography from ambient seismic noise, *Science* 307: 1,615–1,618.

Smith, W. H. F. and P. Wessel (1990). Gridding with continuous curvature splines in tension, *Geophys.* 55: |293–305.

Wessel, P. and Smith, W. (1995). New version of the generic mapping tools released. *EOS Trans. AGU* 76: 329.

Yoo, H. J., R. B. Herrmann, K. H. Cho, and K. Lee (2006). Imaging the three-dimensional crust of the Korean Peninsula by joint inversion of surface-wave dispersion and teleseismic receiver functions, *Bull. Seism. Soc. Am.* (in review).

Table 1. Station locations and number of receiver functions used

Sta	Lat	Lon	N	Sta	Lat	Lon	N	Sta	Lat	Lon	N
KWJ	35.16	126.99	156	HDB	35.73	129.40	21	IMS	35.61	127.29	7
HUK	34.68	125.45	139	GKP1	35.89	128.61	21	HAC	35.56	128.17	7
DGY	37.69	128.67	136	SWO	37.27	126.97	15	DDC	37.89	127.06	7
AND	36.57	128.71	128	BRD	37.97	124.63	15	MAS	35.17	128.57	6
CHC	37.78	127.81	113	SKC	38.29	128.52	14	HOC	37.68	127.88	6
CHO	35.82	127.15	107	BUS	35.25	129.11	13	BUY	36.27	126.92	5
DAG	35.77	128.90	104	INJ	38.05	128.17	11	CWO	38.08	127.52	5
YGN	35.40	126.42	83	YOW	37.17	128.46	10	MOP	34.81	126.38	5
CHI	35.20	128.12	75	ULC	36.99	129.41	10	TOH	37.50	129.12	5
UCN	37.08	129.38	70	SOS	36.78	126.49	10	YAP	37.48	127.49	5
PUS	35.10	129.03	63	CPN	36.22	127.99	10	CHY	36.94	128.92	4
SES	36.79	126.45	60	CEA	36.82	127.26	10	KOH	34.61	127.27	4
SEO	37.49	126.92	56	WON	37.33	127.94	9	KUJ	34.88	128.60	4
ULJ	36.70	129.41	47	HAN	34.57	126.57	9	KUM	36.12	128.32	4
TJN	36.38	127.36	42	EUS	36.35	128.69	9	MIY	35.49	128.74	4
CHU	37.89	127.73	40	YJD	37.47	126.43	8	NAW	35.40	127.33	4
WSN	35.72	129.47	36	YOS	34.74	127.74	8	SUC	35.07	127.24	4
KAN	37.74	128.89	36	YOD	36.53	129.41	8	YOC	35.97	128.95	4
TEJ	36.37	127.37	35	POR	36.32	126.56	8	CEJ	36.64	127.44	3
SNU	37.45	126.96	34	JEC	37.15	128.19	8	PHA	36.19	129.37	3
KRN	35.33	129.30	33	CHA	36.77	127.12	8	BGD	34.16	126.56	2
TAG	35.88	128.62	32	WAN	34.39	126.70	7	BOE	36.49	127.74	2
KUC	35.67	127.91	32	ULS	35.55	129.32	7	KMS	36.10	127.48	2
KUS	36.02	126.83	30	NAH	34.82	127.93	7	PUA	35.72	126.72	2
CHJ	36.87	127.98	25	MUS	37.89	126.76	7	SAC	35.41	127.88	2
JEU	35.49	126.93	23	MUG	36.62	128.15	7	TOY	34.85	128.44	2
ICN	37.29	127.42	23	JAH	34.69	126.92	7				

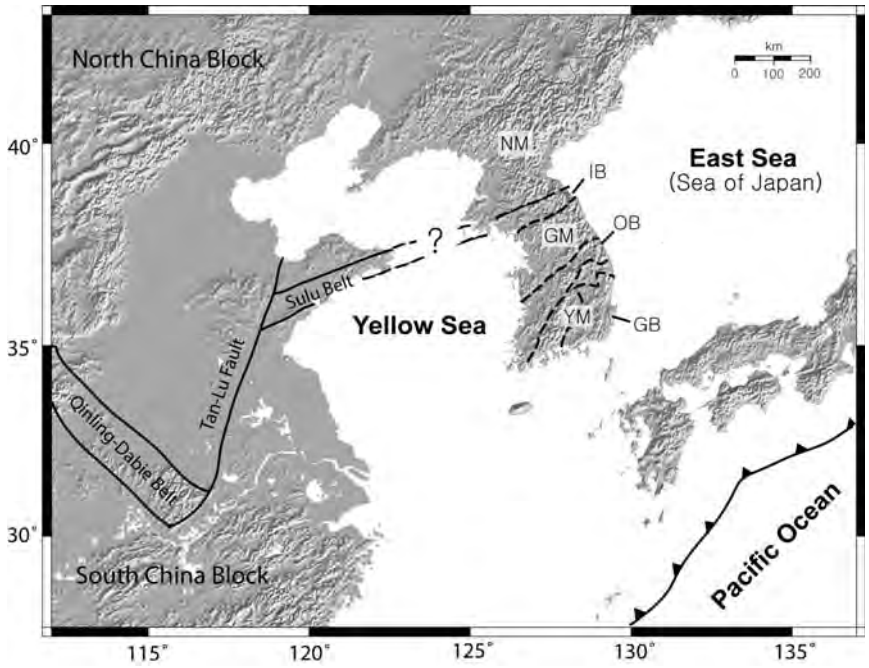


Figure 1. Tectonic map of the Korean Peninsula and adjacent area (modified from Min and Cho, 1998; Chough et al., 2000). Major tectonic provinces are separated by dashed lines. NM, Nangrim massif; GM, Gyeonggi massif; YM, Yeongnam massif; IB, Imjingang belt; OB, Ogcheon fold belt; GB Gyeongsang basin. The topography is from ETOPO02.

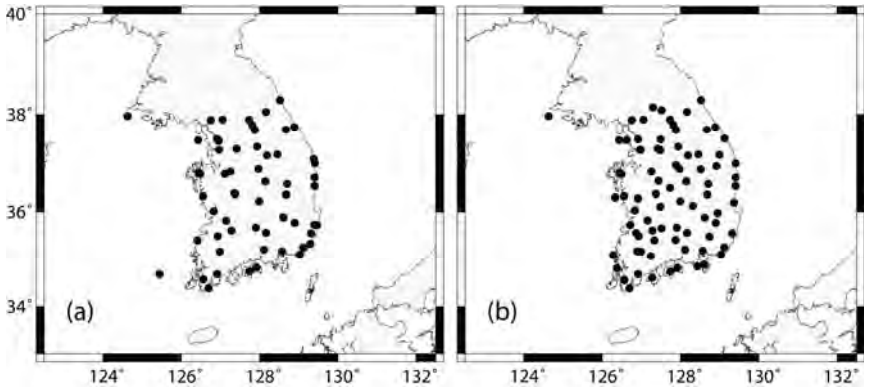


Figure 2. Location of stations used in this study. (a) Stations used for receiver function determination. (b) Stations used for group velocity determination from inter-station Green's functions from the cross-correlation of seismic noise.

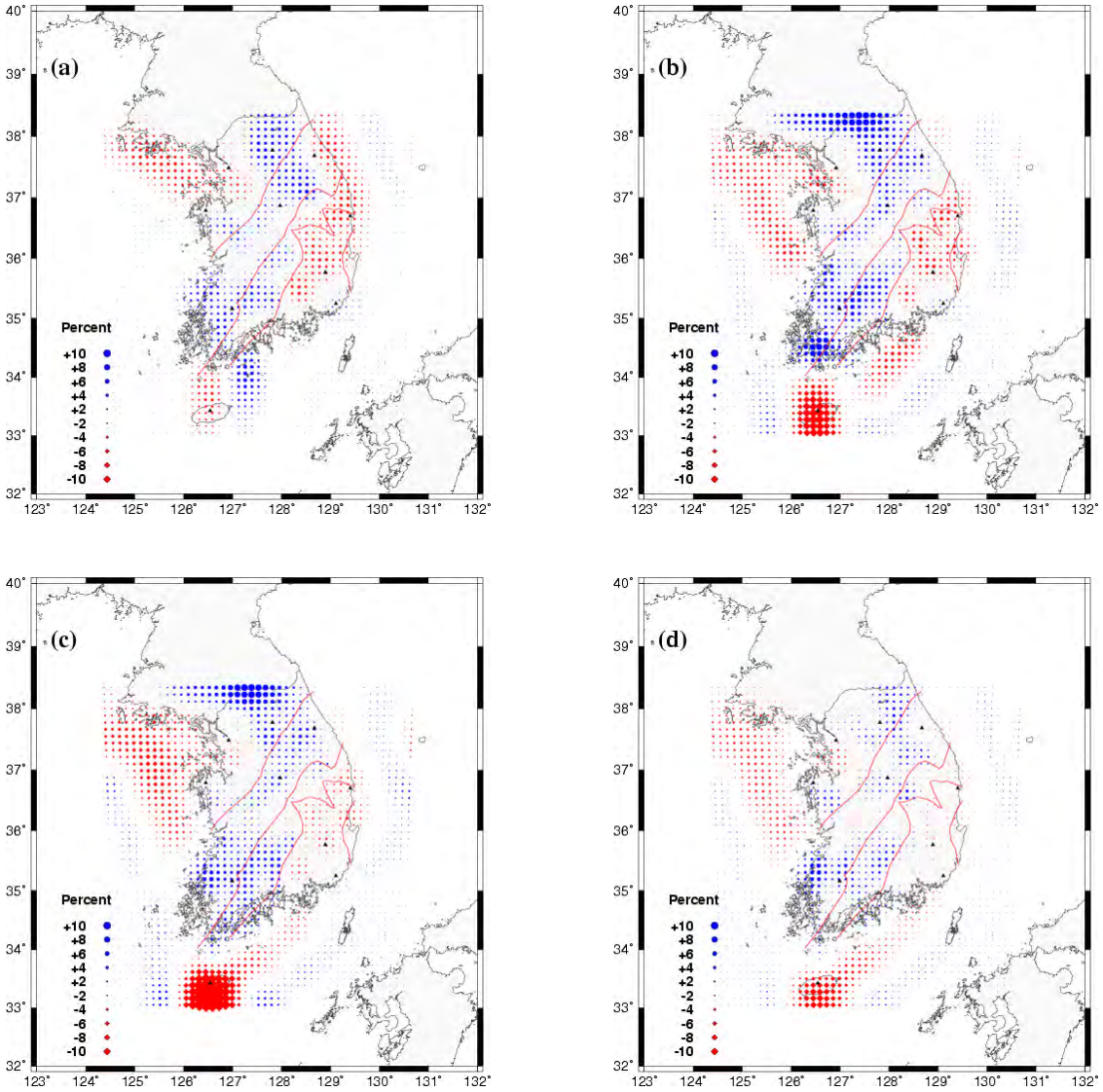


Figure 3. Rayleigh-wave group velocity tomography results for periods of 1.0 (a), 2.0 (b), 3.0 (c) and 6.0 (d) seconds. The boundary lines on the Peninsula separate the major tectonic units Gyeonggi massif, Okcheon fold belt, Yeongnam massif and Gyeongsang basin (Chough et al, 2000; Cho, H.M. et al., 2006).

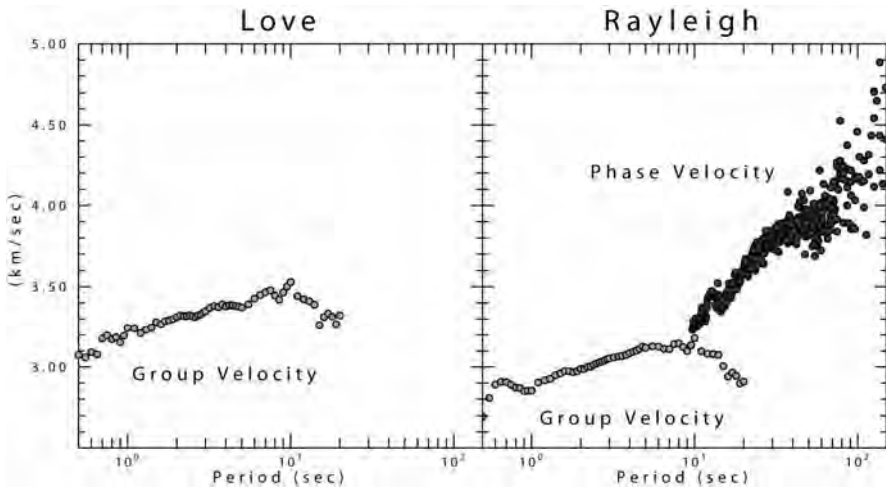


Figure. 4. Dispersion data used for the station CHJ (36.87N, 127.97E). The group velocities are indicated by the lighter shade of gray, and the phase velocities by the darker.

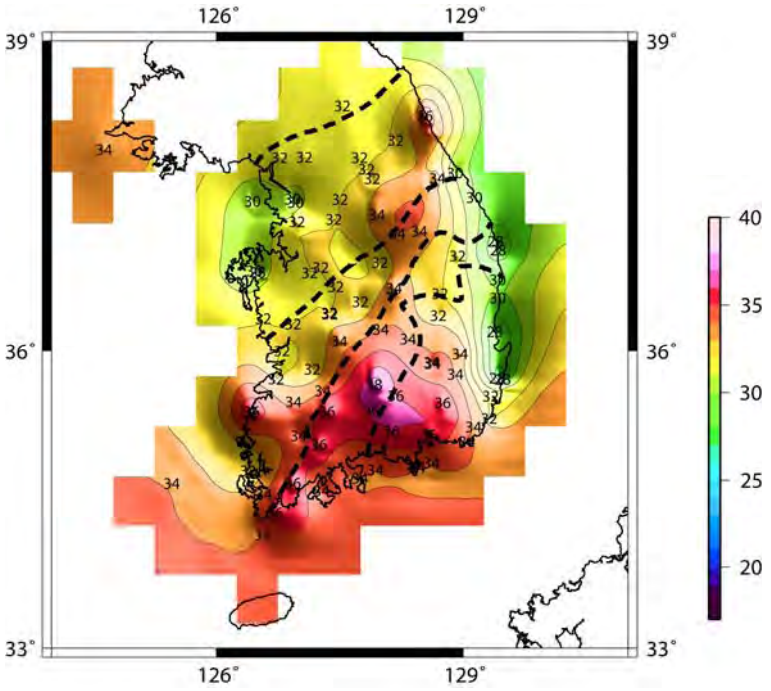


Figure 5. Distribution of the Moho depths in southern Korean Peninsula. Interplolation is performed using "minimum curvature technique" (Smith and Wessel, 1990). Locations and Moho depths used in the interpolation are shown in the map. Major tectonic boundaries are shown as dashed lines.

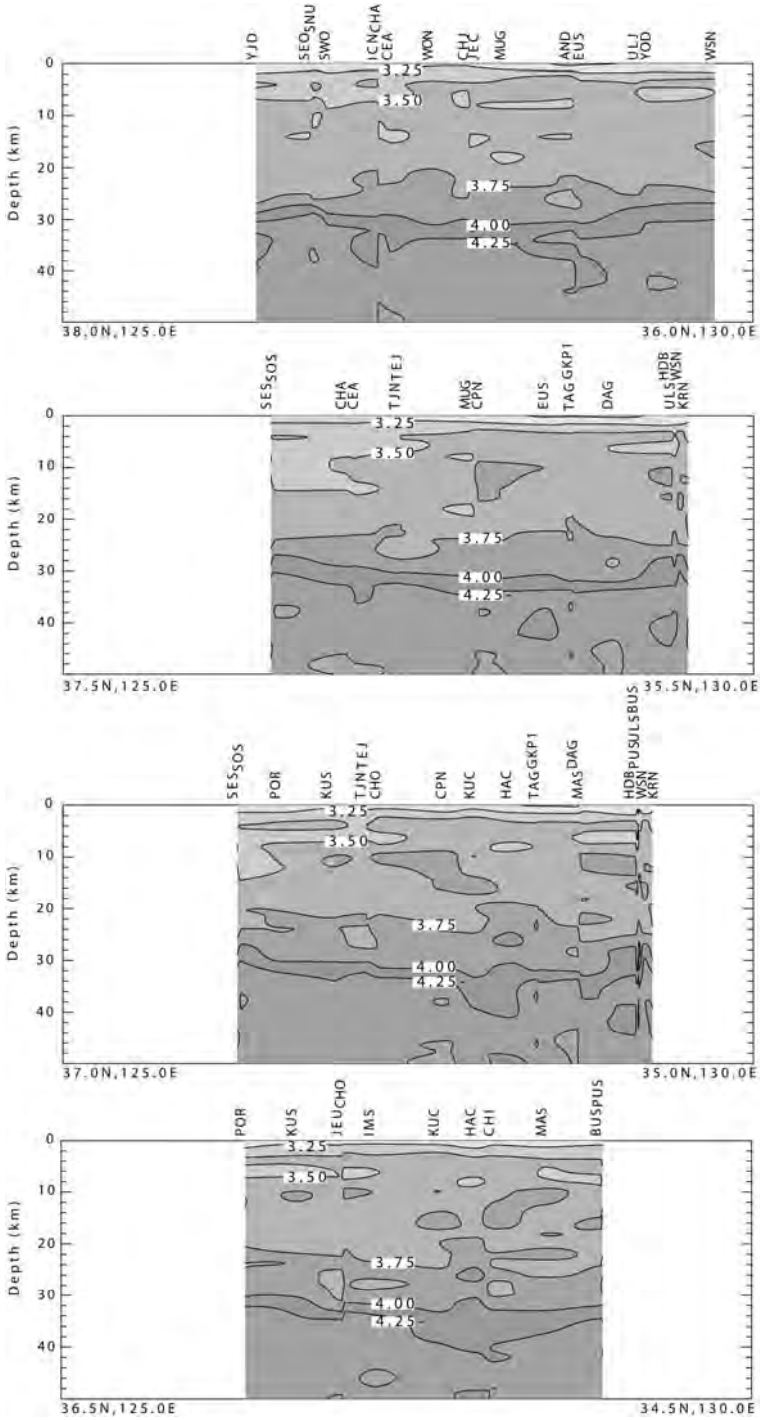


Figure 6. Northwest-southeast diagonal shear-wave velocity profiles across the study area arranged from north to south. The coordinates of the profile are given at the bottom of each plot. Contours are given at every 0.25 km/s and the 3.00 to 4.25 km/s contours are indicated.

DEVELOPMENT OF REGIONAL PHASE TOMOGRAPHIC ATTENUATION MODELS FOR EURASIA

Thorne Lay[1], Xiaoning (David) Yang[2], Xiao-Bi Xie[1], Steven R. Taylor[3], and Marie D. Arrowsmith[2]

University of California, Santa Cruz[1], Los Alamos National Laboratory[2], and Rocky Mountain Geophysics, LLC[3]

Sponsored by National Nuclear Security Administration
Office of Nonproliferation Research and Development
Office of Defense Nuclear Nonproliferation

Contract Nos. DE-FC52-05NA26606[1] and W-7405-ENG-36[2,3]

ABSTRACT

We are developing regional-phase (*Pn, Pg, Sn, Lg*) tomographic attenuation models for Eurasia. The models will be integrated into the National Nuclear Security Administration (NNSA) Knowledge Base and used in the Magnitude and Distance Amplitude Correction (MDAC) station calibration for the development of regional seismic discriminants. Our current focus is on *Pn*, an important phase in seismic event identification. Accurately accounting for regional-phase geometric spreading is critical for the development of useful attenuation models. This is particularly true for *Pn* phases because the propagation nature of these waves renders them acutely sensitive to upper mantle velocity gradients and complexity and effects of sphericity. Even for very simple velocity models, *Pn* geometric spreading can vary with frequency and range, trading off with any attenuation parameterization.

We have been conducting one-dimensional numerical modeling of *Pn* propagation in seismic velocity models representative of different regions of eastern Asia. Velocity models commonly specify constant velocities in the mantle lid (the depth range from the Moho down to any low velocity zone), although there is almost never any direct empirical constraint on the actual lid velocity gradient, which could be negative, zero, or positive, and is likely embedded within complex laterally varying fine-scale structure. If the mantle lid *P*-velocity decreases with depth in proportion to the expected gradient for Earth flattening, approximating a constant velocity half-space, true head-wave spreading is expected, with frequency-independent geometric spreading proportional to Δ^{-2} at large range. A stronger overall negative gradient in lid velocity will give scattering heterogeneity control of the effective *Pn* spreading, and the behavior will depend on the heterogeneity spectrum. If the lid velocity is constant, or has positive gradient, the Earth's sphericity has a dominant role in shaping the *Pn* amplitude decay, as a result of evolution from headwave-like behavior at close ranges to diving ray behavior at larger ranges. To represent the general behavior of *Pn* amplitude decay in a spherical Earth with constant or smoothly increasing lid velocity, we provide a new *Pn* geometric-spreading model in the form of a polynomial. This model has significant differences from standard power law decay models. Exploration of long-range propagation of *Pn* in two-dimensional (2D) models is being initiated to assess the robustness of any geometric spreading corrections based on one-dimensional (1D) models, drawing upon laterally varying regional velocity structures. Given that the geometric spreading relations are nonlinearly dependent on a very poorly resolved Earth parameter (velocity gradient in the mantle lid), we are assessing the relative merits of various reference geometric spreading terms and resulting trade-offs with attenuation models.

To prepare for the attenuation tomographic inversion, we have been collecting and measuring regional-phase amplitude data from the Incorporated Research Institutions for Seismology (IRIS) Data Management Center (DMC) and from the Los Alamos National Laboratory (LANL) Ground-Based Nuclear Explosion Monitoring Research and Engineering (GNEMRE) program database. Initial amplitude measurements exhibit similar decay behavior for *Pn* to what we find in synthetic data. To improve our data coverage, we are conducting further data collection, phase picking, and amplitude measurement. Assessment of the transition from mantle lid refractions to transition zone diving arrivals is underway. Since our region of interest encompasses most of Eurasia from the equator to the North Pole, simple regular gridding methods such as dividing the region with latitude and longitude lines would result in cells with drastically different cell sizes for the tomographic inversion. To avoid this problem and to optimize the resolution of the tomographic model based on data distribution, we have implemented several gridding schemes. They include equal-area-cell gridding and variable-area-cell gridding based on criteria such as the number of path hits. These gridding schemes will be tested in future tomographic inversions to find an optimum gridding method.

OBJECTIVE

The objective of this project is to develop 1-Hz, 2D, regional-phase (*Pn, Pg, Sn* and *Lg*) tomographic attenuation models for Eurasia. The models will be used in MDAC for improved event identification.

RESEARCH ACCOMPLISHED

Pn Geometric Spreading

Accurately accounting for geometric spreading is critical for the development of meaningful regional-phase attenuation models. This is particularly true for *Pn* and *Sn* waves because the nature of their wave propagation renders them acutely sensitive to upper mantle velocity structure and the Earth's sphericity. Even simple 1D velocity models can produce geometric spreading of *Pn* and *Sn* that is strongly dependent on frequency and range (e.g., Sereno and Given, 1990). If frequency dependence of the geometric spreading actually occurs and is neglected, the attenuation model will acquire incorrect frequency dependence. Similar arrival times of *Pg* and *Pn* phases and *Pn* and *P* phases at their respective crossover distances result in rapidly changing *P*-wave amplitudes, difficulty in phase isolation and identification, and uncertainty in appropriate specification of the propagation path and geometric spreading at these distances. Lateral variation of Moho topography and upper-mantle lid velocity and fine scale heterogeneity of the lower crust and/or mantle lid further introduce 2D and three-dimensional (3D) complexities into *Pn* and *Sn* spreading (e.g., Ryberg et al., 2000; Nielsen and Thybo, 2003; Nielsen et al., 2003).

We have been conducting 1D numerical modeling of *Pn* propagation in velocity models representative of different regions of eastern Asia. The reflectivity method (Kennett, 1983; Randall, 1994), which generates complete seismograms for 1D velocity models, is used for the modeling. The velocity models considered are those used by Yang (2002), a 1D model for the Tien Shan region (Roecker et al., 1993), and a one-layer-crust model used by Sereno and Given (1990). These models are plotted in Figure 1. Commonly, such regional velocity models are obtained for flat-layered structures with sphericity being ignored, and the mantle velocities involve simple constant velocity half space assumptions. In such cases, mapping the structures into radially symmetric spherical models would imply a mild negative gradient throughout the structure (the inverse of an Earth flattening approximation). Alternatively, these 1D models may directly represent spherical model velocity profiles, in which case an Earth flattening approximation is needed before application of the reflectivity method. This issue seems trivial and is of minor importance for most regional phases, but for *Pn* and *Sn* waves traveling in the mantle lid below the Moho, the velocity gradient in the lid is of great importance for geometric spreading of the phase. Unfortunately, the reality is that the velocity gradient is almost never well constrained, and there is likely to be small-scale velocity heterogeneity that is only grossly approximated by any simple mantle velocity model.

If we assume that the models in Figure 1 are flat-Earth models with constant velocity half-spaces, we expect that true head waves will result. Figure 2 shows the computed 1-Hz *Pn* amplitude decay for an impulse isotropic source of 10^{15} Nm in strength at 15-km depth in these models. We calculated the synthetics for source-receiver distances between 200 km and 1500 km, with the frequency band extending to 10 Hz. The amplitudes were measured on vertical components. We approximated the elastic propagation using a very high Q of 100,000 for both *P* and *S* waves. Asymptotic analysis (Yang, 2002) confirmed that the results are similar to those for an elastic medium. The decay of the *Pn* amplitudes follows the theoretical prediction for head-wave geometric spreading (Aki and Richards, 2002), with amplitudes at large distances falling off proportional to Δ^{-2}. No frequency dependence of the amplitude decay is observed, which is again consistent with theory for a pure head wave. By plotting the amplitudes as functions of angular distance, we are effectively assuming that in the corresponding spherical models, the velocity gradients are slightly negative. The small differences in the decay rate between these models at short source-receiver distances (< 5°) are caused by the differences in crustal thickness. The absolute *Pn* amplitudes differ by a factor of two at most at longer source-receiver distances. This is due to the wave excitation effects of different source-region medium properties (*P*-wave velocity and density, in this case) and surface receiver function properties (*P*- and *S*-wave velocities and density).

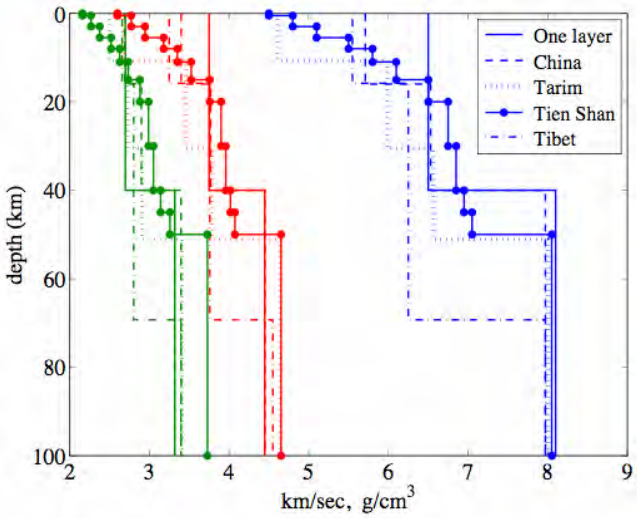


Figure 1. Crustal models used in the *Pn* modeling. Blue lines are P-wave velocities. Red lines are S-wave velocities. Green lines are densities.

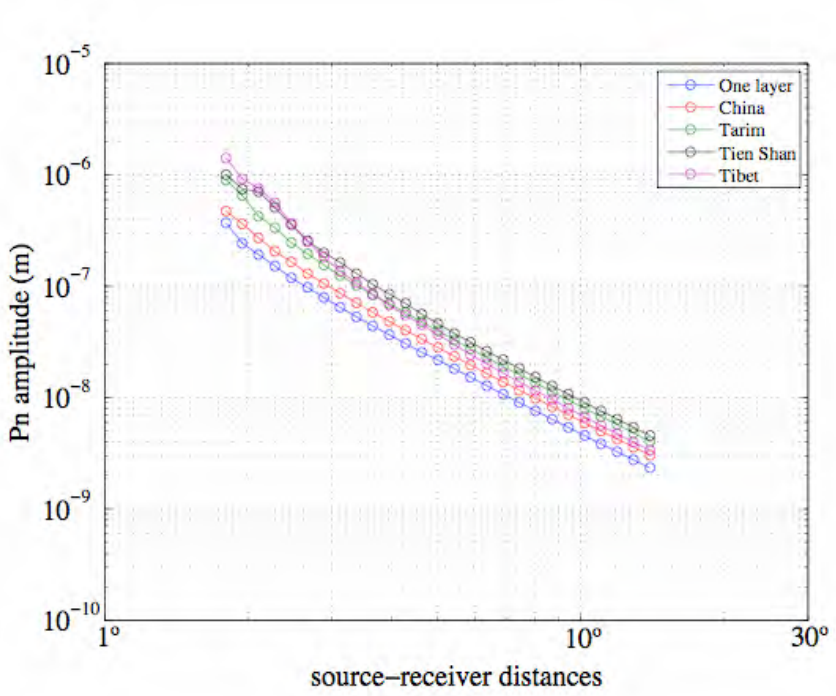


Figure 2. 1-Hz *Pn* amplitude decay in elastic crustal models from Figure 1 where the models are assumed to be for flat-layered structures and hence have constant velocity half-spaces below the Moho. The amplitudes are plotted as a function of angular epicentral distance to provide a mapping to spherical geometry. The corresponding spherical velocity models would have a slight negative gradient in each constant velocity layer in Figure 1. The decay rate beyond 3° is proportional to Δ^{-2}, as expected for head waves. No frequency dependence is observed for the corresponding synthetics.

If we now assume that the structures in Figure 1 are actually for spherical Earth models, we need to map them to flat structures. We use a standard Earth-Flattening Transformation (EFT) (Müller, 1985) and then approximate the inhomogeneous, slightly positive mantle velocity gradient that results by a stack of homogeneous layers for the reflectivity modeling. Impulse responses were again computed with frequencies out to 10 Hz. Figure 3 plots the

1-Hz *Pn* amplitude decay for the various models after the EFT. The decay rates change dramatically beyond about 3°–4° from those in Figure 2 due to the acute sensitivity to velocity gradient in the lid. This nonlinear sensitivity to the sub-Moho velocity gradient has long been known (e.g., Hill, 1973), but is seldom explicitly accounted for in decisions about geometric spreading corrections for *Pn* phases.

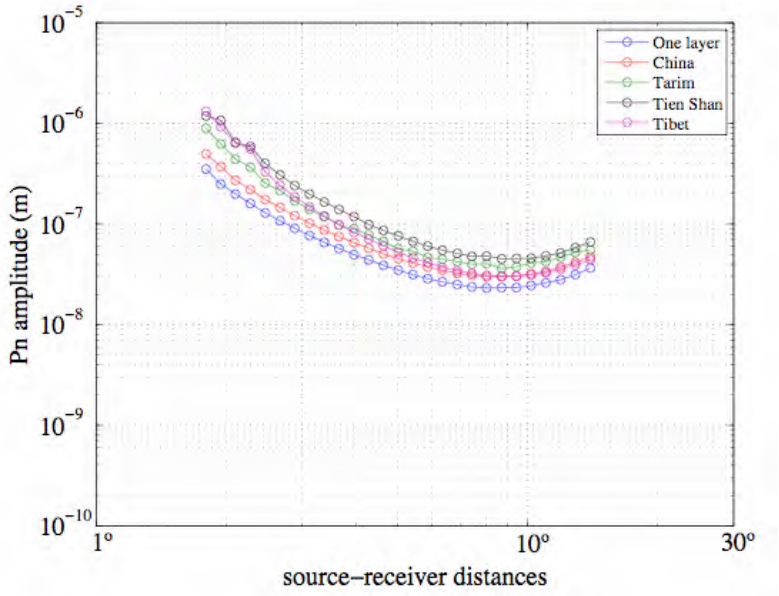


Figure 3. 1-Hz Pn amplitude decay for the elastic crustal models in Figure 1, when those models are assumed to be appropriate for spherical geometry and an EFT is applied prior to modeling. Strong frequency dependence is observed (not shown), with higher frequencies having similarly shaped curves with lower rates of decay and amplitude minima at closer distances.

Comparison of Figure 2 and Figure 3 indicates that *Pn* geometric spreading in a spherical Earth with a constant velocity mantle lid cannot be represented by the geometric-spreading of a head wave or a simple power-law model. This behavior is the same as demonstrated by Sereno and Given (1990), with the curvature of the amplitude decay representing a transition from quasi-head-wave-type decay with strong distance dependence to diving ray behavior with a spherical wave expansion type spreading. Frequency dependence results from the lateral sensitivity along the wavefront to this transition in behavior. The bottoming depths of the turning rays are all within the upper 100 km of the mantle. Increasing the velocity gradients in the mantle lid to positive gradients rather than constant velocities will reduce the turning depths and decrease the amplitude decay further, but the magnitude of this effect has not yet been quantified.

In order to accurately model *Pn* geometric spreading in spherical models with constant mantle lid velocities, we propose a polynomial parameterization based on the numerical modeling results shown in Figure 3. The logarithmic amplitude decay curves in Figure 3 can be well fit by a geometric spreading representation of the form:

$$A(\log_{10}\Delta)^2+B(\log_{10}\Delta) \quad (1)$$

In Eq. (1) Δ is source-receiver distance in angular degrees, and A and B are constants. One of the reasons for choosing a polynomial of degree two for the new model is to keep it as simple as possible while achieving a reasonable fit to the data. Table 1 lists the polynomial coefficients obtained by fitting this model to different curves in Figure 3.

Table 1. Coefficients of the polynomial (1) from fitting the curves in Figure 3.

Velocity Model	A	B
One layer	2.50	–4.66
China	2.62	–4.86
Tarim	2.89	–5.39
Tien Shan	2.93	–5.62
Tibet	3.40	–6.43
mean and std.	**2.87±0.35**	**–5.39±0.70**

To illustrate how the geometric-spreading model we propose fits the synthetics, we compare the model with the synthetic amplitudes and two power-law models in Figure 4. Synthetic data for the one crustal layer velocity model are used for this comparison. The polynomial model was calculated using the mean values of coefficients A and B.

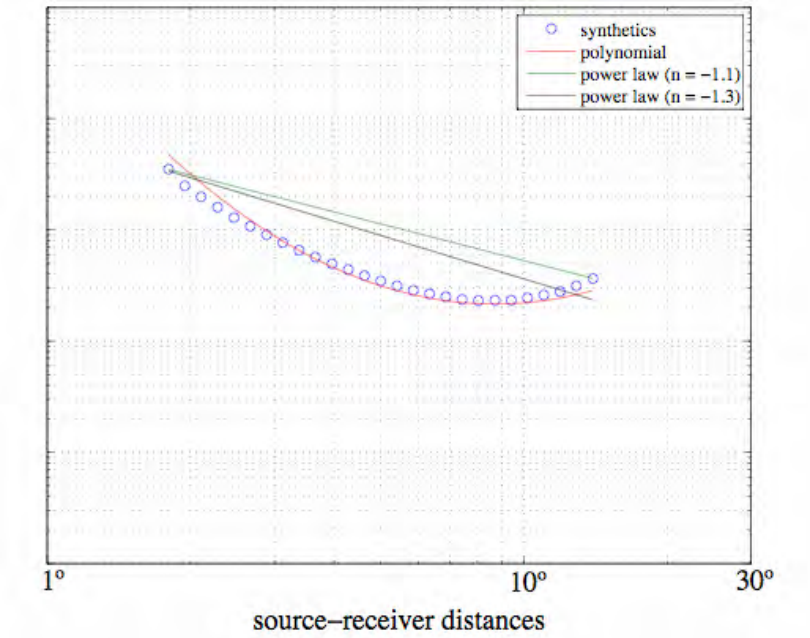


Figure 4. Comparison between the computed *Pn* amplitude decay for the one crustal layer velocity model, the proposed polynomial geometric-spreading model, and two power-law spreading models (Δ^n).

The exponents –1.1 and –1.3 used for the power-law models represent the range of values generally used or estimated by researchers (e.g., Sereno, et al., 1988; Zhu, et al., 1991; Taylor, et al., 2002). These empirical values are clearly much higher than the -2 exponent for purely head-wave spreading. Although not perfect, the averaged polynomial model fits the synthetics reasonably well, whereas the power-law models only approximate the data overall and match the distance trend closely only within a limited distance range, e.g., between 4° and 7° for a model with n = –1.3. In addition to accounting for the effects of the Earth's sphericity (the transition from head wave to diving wave behavior) at longer source-receiver distances, the polynomial model also fits the data better at short distances (<3°) where the effect of the difference between the source-receiver distance and the length of the path segment that *Pn* travels in the mantle is apparent. This effect is manifested in the theoretical prediction of head-wave geometric spreading $\Delta^{-1/2}L^{-3/2}$, where L is the length of the path segment that the head wave travels in the mantle (Aki and Richards, 2002). If the reference Earth model for geometric spreading calculation is taken as a simple model with constant velocity in the mantle lid, the polynomial form of geometric spreading correction is an appropriate choice. But, it should be recognized that this means that a complex frequency dependence is predicted, and different polynomial coefficients are needed for each frequency. Given the absence of direct constraint on a reasonable lid velocity gradient, this is a situation where the default assumption of constant velocity (as the simplest choice of reference model) leads to a specific, but complex geometric spreading representation. With further

modeling of stronger positive gradients and laterally heterogeneous models we will assess whether the specific functional form of the spreading and its frequency dependence are robust enough to serve as a reference model or not.

In the context of nuclear-explosion monitoring, the most important distance range for current MDAC applications is from about 2°–3° to 14° (~1550 km) where *Pn* is the first arrival. Beyond this range, diving waves from the mantle transition zone become the first arrival, and upper-mantle triplications occur between 15° and 22° (Stein and Wysession, 2003). These triplications cause the initial *P*-wave amplitudes to change rapidly, which in turn would seriously degrade the performance of MDAC. Consideration of full mantle models extending below the lid structure is important for assessing the behavior at larger distances.

The existence of a positive upper mantle lid velocity gradient zone in parts of Eurasia has been reported in the literature (e.g., Zhao and Xie, 1993; Morozova, et al., 1999; Nielsen et al., 2003). This would enhance the effects we see in Figure 3, but modeling is needed to assess the relationship between lid gradient and perturbation of the spreading corrections. The lid gradient zone is likely to be variable in thickness (e.g., on the order of a hundred kilometers), depending on whether a low velocity zone is present. It is also clear that there are large variations in crustal thickness in Eurasia, as well as strong lateral variations in lid velocities. These are aspects of the velocity structure that are better characterized than the lid velocity gradients, and an assessment is needed of how much realistic lateral variations modify the results from 1D situations. It is likely that the effects will be pronounced for the frequency dependence of the *Pn* spreading, as it appears to be closely linked to the degree to which finite frequency waves sample the head wave phenomenon versus diving ray phenomena. Finite difference calculations are being pursued to shed light on this issue. The goal will be to determine a relatively robust reference spreading behavior for *Pn* that can be justified lacking precise constraint on the velocity gradient in the lid to which there is such strong nonlinear sensitivity.

Data Collection and Amplitude Measurement

We have finished a first round of data collection and amplitude measurement. We have made about 4000 1-Hz *P* amplitude measurements from over 3000 events and 84 stations in Eurasia (Figure 5). We used a semiautomatic amplitude-measurement procedure based on analyst picks and nominal *Pn* travel times to measure *Pn* amplitudes from the dataset that we assembled through requests from the IRIS DMC. Figure 6 shows the measured 1-Hz *Pn* to *P* amplitudes that have signal-to-noise ratio of 2 or larger. The amplitudes have been corrected for source size. Superimposed on the plot are the averaged polynomial *Pn* geometric-spreading model that we proposed and synthesized *Pn* to *P* geometric spreading for model AK135 (Kennett et al., 1995). The onset of triplication effects is apparent both in the measured data and in the AK135 synthetics at around 16°.

Figure 7 shows the path coverage of the measured amplitudes that have source-receiver distances equal to or shorter than 1500 km. Based on this information, we are currently conducting the second round of data collection, phase picking, and amplitude measurement using data from the LANL GNEMRE database to improve the path coverage in certain areas.

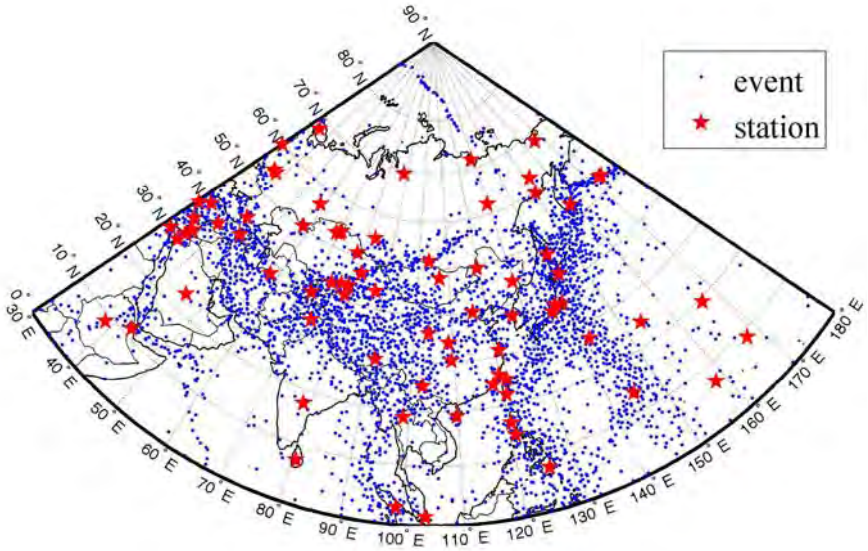


Figure 5. Event and station distribution for the first round of data collection and amplitude measurement.

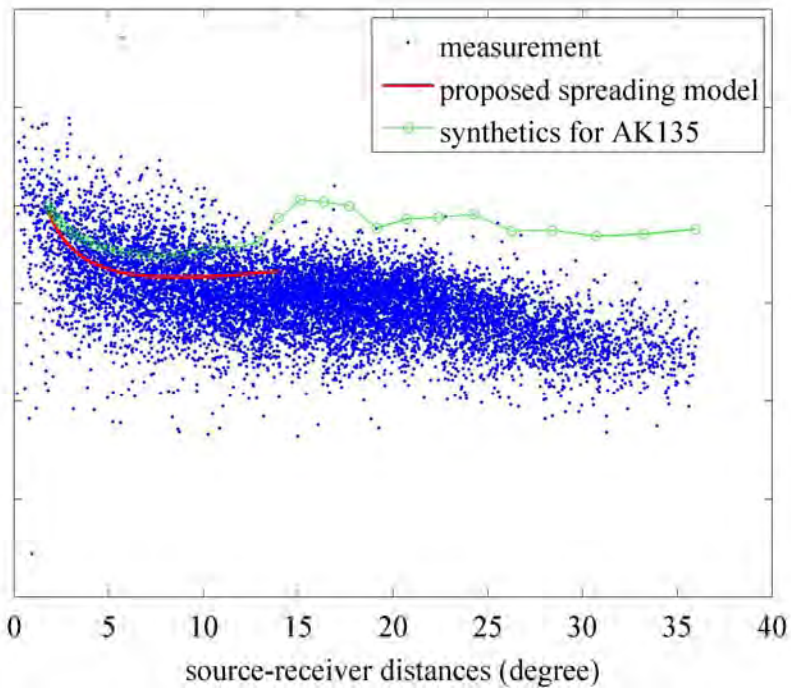


Figure 6. Measured 1-Hz *Pn* to *P* wave amplitudes along with the proposed *Pn* geometric-spreading model and synthetic *Pn* to *P* first-arrival amplitude decay in the AK135 model. Triplication effects can be seen both in the measurements and in the synthesized data. Some observations at closer ranges are likely to be contaminated by *Pg* arrivals.

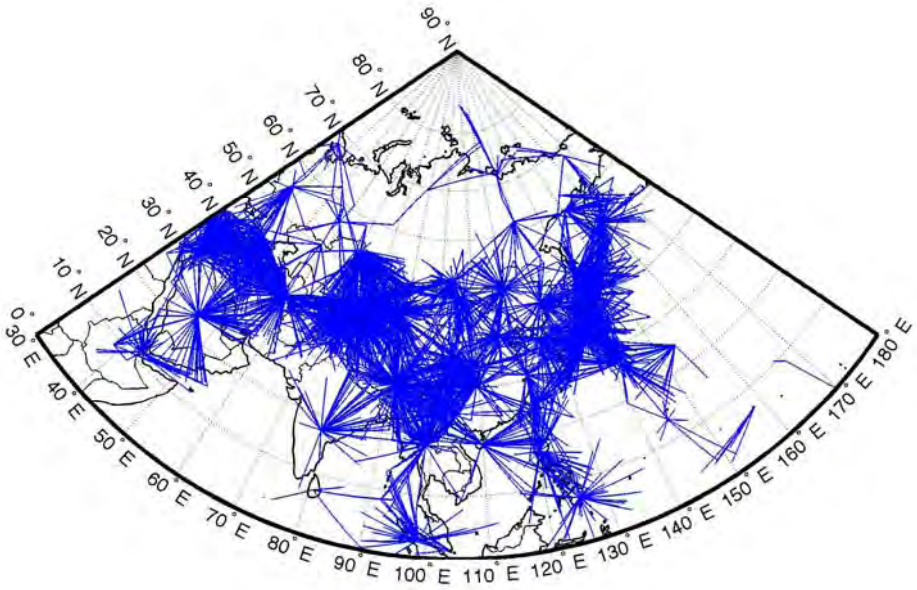


Figure 7. Path coverage of measured *Pn* amplitudes within 1500 km from the corresponding sources.

Inversion Gridding Schemes

Because the region for which we plan to develop regional-phase tomographic attenuation models (e.g., Figure 5) encompasses a large area including the North Pole, simple gridding methods such as dividing the region with longitude and latitude lines are not suitable. To address this issue, we implemented several alternative gridding schemes based on the method developed by Spakman and Bijwaard (2001). In order to impose similar spatial resolutions for regions with different latitudes, we implemented an equal-area-cell gridding scheme. An example is given in Figure 8. To further adjust the resolution according to the data-sampling rate, we also implemented a variable-area-cell gridding scheme based on the number of path hits in a cell. The variable-area cells can be constructed using regular cells as building blocks. Figure 9 shows one of the variable-area-cell griddings that was built upon a grid of regular cells of 0.5°. The sizes of the cells in the figure are based on the sampling of the data shown in Figure 7. In addition to using regular cells as building blocks, we can also use equal-area cells (Figure 8) as building blocks in the construction of variable-area cells. Figure 10 shows such an example. These different gridding schemes will be tested in future inversions of regional-phase attenuation models.

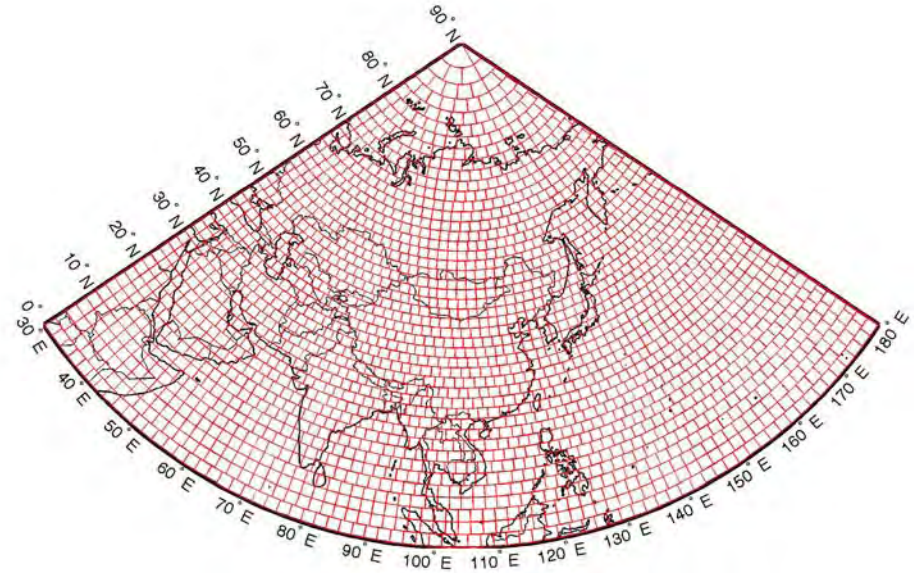


Figure 8. An equal-area-cell gridding of Eurasia with a cell size of 2°×2° at the equator.

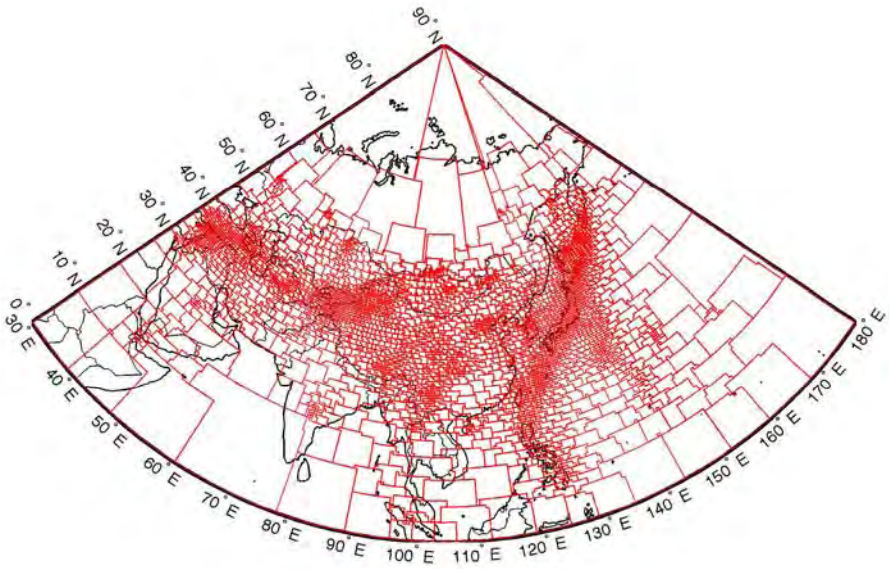


Figure 9. A variable-area-cell gridding of Eurasia based on the number of path hits. Regular cells of 0.5° in size were used as building blocks.

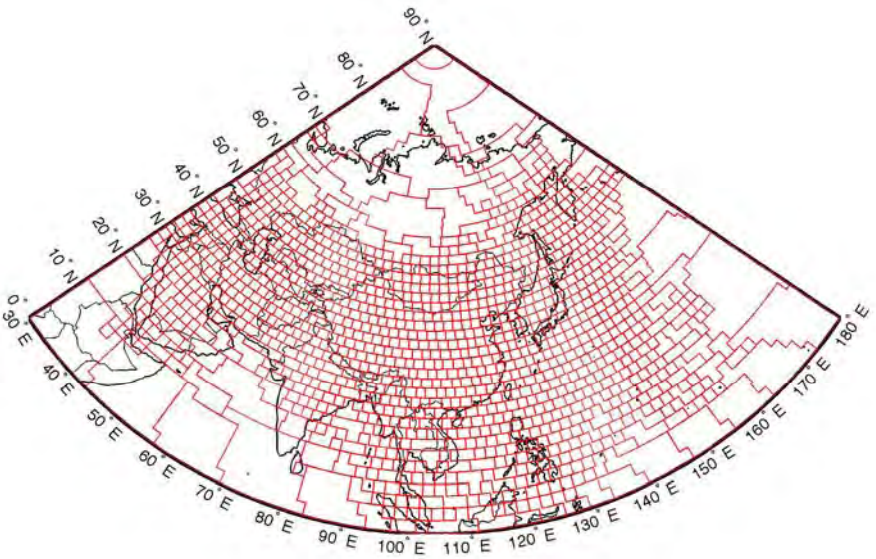


Figure 10. A variable-area-cell gridding of Eurasia based on the number of path hits. Equal-area cells (Figure 8) were used as building blocks.

CONCLUSIONS AND RECOMMENDATIONS

We are developing 2D, 1-Hz regional-phase attenuation models for Eurasia to be used in MDAC event identification. Our focus here has been on investigating *Pn* geometric spreading and attenuation. *Pn* geometric spreading is a surprisingly complex issue, with strong (nonlinear) dependence on poorly constrained velocity gradients in the mantle lid. A 1D modeling method for structures with constant lid velocities demonstrates that *Pn* geometric spreading is more complex than that of a conical head wave and cannot be modeled adequately by a power-law spreading model. For such models, we propose a new *Pn* geometric-spreading model in the form of a polynomial of degree 2 as a function of the logarithm of source-receiver distance. This model fits the synthesized 1-Hz *Pn* amplitude decay well within 15° from the source. Such models predict strong frequency dependence, and

different polynomials are needed for each frequency. Evaluation of the effects of positive lid gradients and cross-over with transition zone triplications is being pursued. We are also conducting modeling of *Pn* geometric spreading in a laterally heterogeneous medium, using profiles from regional 3D velocity models. The intent is to evaluate what reference structure and associated geometric spreading representation make sense to use for attenuation analysis, given the fact that precise information on lid velocity gradients is almost always lacking.

We are continuing our data collection and amplitude measurement effort. We have made about 4,000 reliable 1-Hz *Pn* to *P* amplitude measurements that provide adequate coverage for certain regions of Eurasia. We are making more measurements to improve the coverage for other regions. To optimize the cell parameterization of future tomographic inversions, we implemented several gridding schemes to address the issue of varying model spatial resolution.

ACKNOWLEDGEMENTS

We are grateful to George Randall of LANL for his reflectivity code and his insight on the problem of wave propagation in layered medium that helped understand the synthetic seismograms. Many helpful discussions with Scott Phillips of LANL improved the quality of this research. Diane Baker, Hans Hartse, Michael Begnaud, and Richard Stead of LANL were involved in the data collection, amplitude measurement, and quality control. Our data were obtained from IRIS DMC.

REFERENCES

Aki, K. and P. G. Richards (2002). *Quantitative Seismology*. Sausalito, California: University Science Books.

Hill, D. (1973). Critically refracted waves in a spherically symmetric radially heterogeneous earth model, *Geophy. J. R. Astr. Soc*. 34: 149–177.

Kennett, B. L. N. (1983). *Seismic Wave Propagation in Stratified Media*. London: Cambridge University Press.

Kennett, B. L. N., E. R. Engdahl, and R. Buland (1995). Constraints on seismic velocities in the Earth from travel times, *Geophys. J. Int.* 122: 108–124.

Morozova, E. A., I. B. Morozov, S. B. Smithson, and S. L. Solodilov (1999). Heterogeneity of the uppermost mantle beneath Russian Eurasia from the ultra-long-range profile QUARTZ, *J. Geophys. Res*., 104: 20,329–20,348.

Müller, G (1985). The reflectivity method: A tutorial, *J. Geophys.* 58: 153–174.

Nielsen, L., and T. Thybo (2003). The origin of teleseismic *Pn* waves: Multiple crustal scattering of upper mantle whispering gallery phases, *J. Geophys. Res.* 108: No. B10, 2460, doi:10.1029/2003JB002487.

Nielsen, L., H. Thybo, I. B. Morozov, S. B. Smithson, and L. Solodilov (2003). Teleseismic *Pn* arrivals: Influence of mantle velocity gradient and crustal scattering, *Geophys. J. Int.* 152: F1–F7.

Randall, G. E. (1994). Efficient calculation of complete differential seismograms for laterally homogeneous earth models, *Geophys. J. Int*. 118: 245–254.

Roecker, S. W., T. M. Sabitova, L. P. Vinnik, Y. A. Burmakov, M. I. Golyanov, R. Mamatkanova, and L. Munirova (1993). Three-dimensional elastic wave structure of the western and central Tien Shan, *J. Geophys. Res.* 98: 15,779–15,795.

Ryberg, T., M. Tittgemeyer, and F. Wenzel (2000). Finite difference modeling of P-wave scattering in the upper mantle, *Geophys. J. Int.*, 141: 787–800.

Sereno, T. J., S. R. Bratt, and T. C. Bache (1988). Simultaneous inversion of regional wave spectra for attenuation and seismic moment in Scandinavia, *J. Geophys. Res.* 93: 2,019–2,035.

Sereno, T. J. and J. W. Given (1990). Pn attenuation for a spherically symmetric earth model, *Geophys. Res. Lett.* 17: pp. 1,141–1,144.

Spakman, W. and H. Bijwaard (2001). Optimization of cell parameterizations for tomographic inverse problems, *Pure Appl. Geophys.* 158: pp. 1,401–1,423.

Stein, S. and M. Wysession (2003). *An Introduction to Seismology, Earthquakes, and Earth Structure*. Blackwell Publishing, Malden, USA.

Taylor, S. R., A. A. Velasco, H. E. Hartse, W. S. Phillips, W. R. Walter, and A. J. Rodgers (2002). Amplitude corrections for regional seismic discriminants, *Pure Appl. Geophys.* 159: pp. 623–650.

Yang, X. (2002). A numerical investigation of Lg geometrical spreading, *Bull. Seismo. Soc. Am.* 92: pp. 3,067–3,079.

Zhao, L. S. and J. Xie (1993). Lateral variations in compressional velocities beneath the Tibetan Plateau from Pn traveltime tomography, *Geophys. J. Int.* 115: pp. 1,070–1,084.

Zhu, T., K. Y. Chun, and G. F. West (1991). Geometrical spreading and Q of Pn waves: an investigative study in eastern Canada, *Bull. Seism. Soc. Am.* 81: pp. 882–896.

TOWARD A RAYLEIGH WAVE ATTENUATION MODEL FOR CENTRAL ASIA

Anatoli L. Levshin[1], Xiaoning (David) Yang[2], Michael H. Ritzwoller[1], Mikhail P. Barmin[1], and Anthony R. Lowry[1]

University of Colorado at Boulder[1] and Los Alamos National Laboratory[2]

Sponsored by National Nuclear Security Administration
Office of Nonproliferation Research and Development
Office of Defense Nuclear Nonproliferation

Contracts Nos. DE-FC52-05NA26608[1] and W-7405-ENG-36[2]

ABSTRACT

We report on progress toward an attenuation model for short-period (10-25 s) Rayleigh waves in Central Asia. This model will be defined by maps of attenuation across the region of study in the specified period band. The model is designed to calibrate the regional surface wave magnitude scale and to extend the teleseismic M_S-m_b event discriminant to regional distances. In order to apply the M_S-m_b discriminant to regional-distance monitoring, a modified M_S formula using shorter-period (< 20) surface wave amplitudes is required (e.g., Marshall and Basham, 1972; Bonner et al., 2006; Russell, 2006). Work is progressing in three stages: (1) data accumulation and amplitude measurement, (2) estimation of attenuation coefficients, and (3) tomography. To date, efforts have been devoted primarily to the first stage.

The first stage in the model construction is the measurement of Rayleigh-wave spectral amplitudes. Inherent difficulties result from multipathing and scattering of short-period surface waves crossing strong lateral inhomogeneities in the crust. To overcome these difficulties, we apply the Surface Wave Amplitude Measurement Tool (SWAMTOOL) designed at Los Alamos National Laboratory (LANL), which incorporates dispersion analysis, phase-matched filtering, and additional means to estimate the quality and reliability of the measurements. We have enhanced SWAMTOOL by providing improved options for phase-matched filtering of the surface wave signals. The similarity of the results now obtained with SWAMTOOL and the Frequency-Time Analysis (FTAN) algorithm designed at CU-Boulder, as well as numerous repeatability tests, confirm the validity of the measurements. We currently are collecting and processing both two-station and single-station waveform data. The existing broadband station distribution and the pattern of seismicity provide a sufficient number of spectral amplitude measurements between 12 and 20 s for the construction of the 2-D tomographic maps of attenuation coefficients. Measurements at periods below about 12 s are too scarce for tomographic inversion.

In the second stage of the work, spectral attenuation coefficients are estimated using both interstation amplitude measurements and single-station measurements, corrected for the source and receiver terms. Current work focuses on simulated data, which demonstrate the existence of a strong dependence of Rayleigh-wave amplitude spectra on source parameters, particularly the source depth, and the structure of the crust near the source and receiver regions that grows as periods decrease. It is, therefore, necessary to include additional variables related to the source into the inversion of the observed data and also to apply an existing 3-D model of the Eurasian crust in the data inversion. Work is now beginning to transition to this next stage, the estimation of attenuation coefficients from the observations. Particular emphasis is now being placed on accounting for uncertainties in source parameters and variations in the 3-D structure of the Central Asian crust.

OBJECTIVES

The objectives of the study are (1) to develop short-period (10–18 s), two-dimensional (2-D) Rayleigh-wave attenuation models for Central Asia, along with associated uncertainty statistics, through a tomographic approach, and (2) to calibrate Russell's (2006) M_S formula with these models for the same region.

RESEARCH ACCOMPLISHED

Introduction

Knowledge of the losses of seismic energy during the propagation of the wave from the source to receivers is essential for the estimation of the surface wave magnitude M_S and the seismic moment of the source. This is especially important for monitoring underground nuclear explosions, in which the estimation of M_S is used as a part of the most robust seismic discriminant, the M_S-m_b discriminant. In order to apply this discriminant to regional-distance monitoring, a modified M_S formula using shorter-period (< 20) surface wave amplitudes is required (e.g., Marshall and Basham, 1972; Bonner et al., 2006; Russell, 2006). The purpose of this work is to construct short-period (10–18 s) 2-D Rayleigh-wave attenuation models for Central Asia and to use them to calibrate M_S formula of Russell (2006).

We are currently in this study's first stage, in which we have collected and processed broadband records following seismic events within and around Central Asia. To determine the amplitude spectra of the surface waves, we apply the SWAMTOOL (Yang at al., 2004, 2005). Early applications indicated the need to enhance SWAMTOOL by improving the phase-matched filtering of the surface waves. This paper summarizes the resulting improvements, the comparisons of SWAMTOOL measurements with those from FTAN (Levshin et al., 1989; Ritzwoller and Levshin, 1998) and characterizes the observed data set of spectral amplitude measurements.

The next phase of this study will be the estimation of attenuation coefficients from the observed spectral amplitudes using both single-station and interstation measurements. Measurements of the first type must be corrected for the source and receiver terms and the latter for the receiver terms. At this stage of work, we will focus on simulating these effects and evaluating their influence on the observed attenuation coefficients.

Elements of Theory

We assume that surface waves propagate in a laterally and radially inhomogeneous medium, in which elastic and anelastic parameters change smoothly along the Earth's surface. The term "smoothly" means that the changes of these parameters (wave speeds, densities, thicknesses of layers, Q_s along the distance of a wavelength) are small (e.g., Woodhouse, 1974; Levshin et al., 1989). Surface waves are generated by a point source with a moment tensor **M**. The tensor and coordinates of the source, including depth *h*, are presumed to be known. Then the amplitude spectrum $U(\omega)$ of the surface wave mode recorded by a receiver situated on the Earth's surface at the epicentral distance Δ and in azimuthal direction φ from the epicenter can be presented approximately as

$$U(\omega) = S(\omega, h, \varphi, \mathbf{M}(\omega)) \times P(\Delta, \omega) \times R(\omega) \quad .$$

Here, ω is a frequency in rad/s. The source term *S* depends also on the Earth's structure near the source. The propagation term *P* is defined by the elastic and anelastic structure between the source and receiver. Assuming that the wave propagates along the great circle between source and receiver, we have

$$P = \frac{\exp(-\omega \int_L \frac{dl}{2u(\omega,l)Q_s(\omega,l)})}{\sqrt{k(\omega) r_o \sin\Delta}} = \frac{\exp(-\int_L \alpha_s(\omega,l)dl}{\sqrt{k(\omega) r_o \sin\Delta}} \quad ,$$

where r_0 is the Earth's radius, u is group velocity, k is wavenumber, Q_s is the surface wave Q-factor, and α_s is the surface wave attenuation coefficient. The integral $I = \int_L \alpha_s(\omega, l)dl$ is taken along the great circle through the source and receiver. The receiver term R depends on the structure near the receiver and the frequency response of the instrument. In the case when we have two stations at approximately the same azimuth φ from the source, it is possible to use the ratio of two observed spectra $U_1(\omega)$ and $U_2(\omega)$ to find the integral I_{12}

$$I_{12} = \int_{L_{12}} \alpha_s(\omega, l)dl = \ln\left[\frac{U_1 R_2 \sqrt{\sin \Delta_1}}{U_2 R_1 \sqrt{\sin \Delta_2}}\right],$$

where L_{12} is the path between stations and $\Delta_2 > \Delta_1$. Our goal is to find the values of integrals $I(\omega_i)$ and $I_{12}(\omega_i)$ for all appropriate combinations of receivers and stations or pairs of stations for a set of values of frequencies ω_i in the frequency band of study.

Data Collection

We are currently collecting and processing surface wave waveform data. In the first stage of data collection, we processed around 100 events that occurred in and around Eurasia in 2003–2005. Several global and regional broadband networks have existed in Eurasia during the considered time interval. These include Global Seismographic Network (GSN), International Monitoring System (IMS), GEOSCOPE, GEOFON, Mediterranean Seismic Network (MEDNET), China Seismological Digital Network (CDSN), Kyrgyz Seismic Network (KNET), Kazakhstan Seismic Network (KAZNET), and others available through the IRIS Data Management Center (IRIS DMC). More than 10,000 broadband records of about 100 stations were selected for processing. The map with the event and station distribution used at this stage of work is shown in Figure 1. Records were converted from the Standard for the Exchange of Earthquake Data (SEED) into the Seismic Analysis Code (SAC) format and transformed into ground displacement.

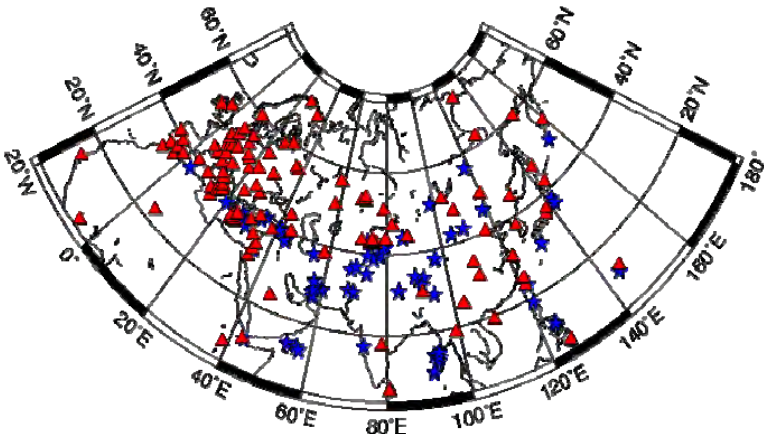


Figure 1. Distribution of epicenters (stars) and stations (triangles) selected for spectral amplitude measurements.

Measurements

The accuracy of surface wave attenuation measurements is affected by uncertainties in source-parameter estimates and site responses and by medium elastic effects, with medium elastic effects such as multipathing, focusing, defocusing, and off-great-circle propagation being among the principal sources of error (Mitchell, 1995; Selby and Woodhouse, 2000). As part of a previous 20 s surface wave attenuation study, LANL researchers designed a SWAMTOOL to address some of these uncertainties (Yang et al., 2004).

We developed several SWAMTOOL improvements, which provide more opportunities for efficient phase-matched filtering of the signal (e.g., Herrin and Goforth, 1977; Russell et al., 1988). A snapshot of SWAMTOOL data processing for an event in Tibet on 04/10/2004 with Ms = 5.1, recorded by the station KMI, is shown in Figure 2. The first step in the analysis of a selected signal (upper right window) is transforming it into the frequency-time domain (upper left window) and tracing the maximum amplitude as a function of frequency ("raw" group velocity curve). Depending on the pattern on the diagram, an analyst makes a decision about the presence and frequency range of the desired signal, i.e., the fundamental mode of the Rayleigh wave. The analyst may either (1) reject the record, (2) construct a phase-matched filter based on prediction from a recently developed surface-wave group velocity model (e.g., Ritzwoller and Levshin, 1998; Levshin and Ritzwoller, 2003; Stevens et al., 2001; Levshin et al., 2003), (3) construct a phase-matched filter using the raw group velocity curve in a chosen frequency range, or (4) construct a phase-matched filter using the curve he/she draws across the diagram.

The filtered signal is then windowed in the time domain to suppress noise and is used for measuring the amplitude spectrum (lower left window). This filtering process and other aspects of the measurement tool (lower right window), such as the analysis of the theoretical source spectrum and radiation pattern and the comparison of observed and geometrical back-azimuths, are designed to reduce the bias caused by multipathing and focusing/defocusing.

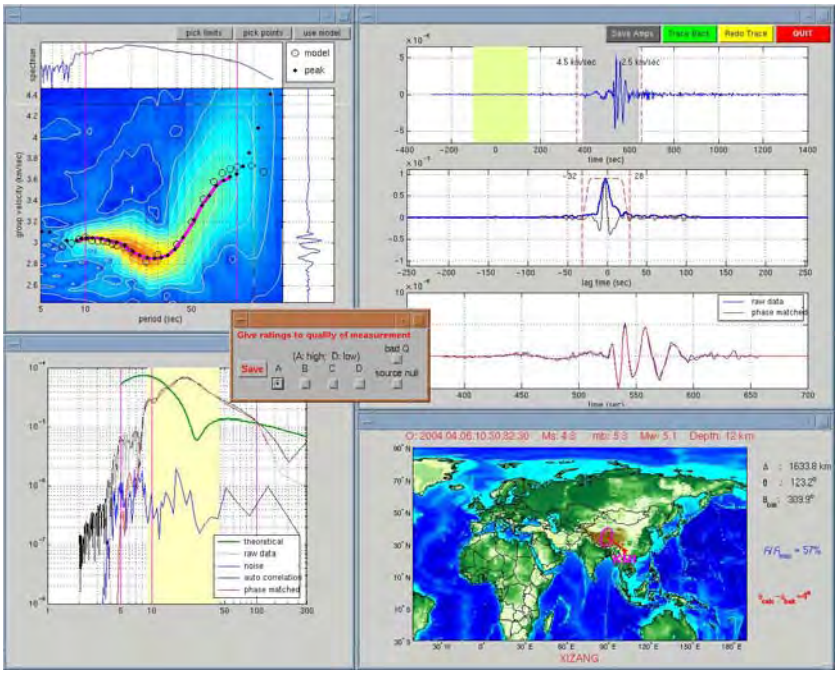


Figure 2. Snapshot of SWAMTOOL for an event in Tibet recorded by station KMI.

The similarity of the results now obtained with SWAMTOOL and the FTAN algorithm designed at CU-Boulder, as well as numerous repeatability tests, confirm the validity of the measurements (Figure 3).

Characterization of the Spectral Amplitude Data

More than 6,000 spectral amplitude measurements were obtained using SWAMTOOL interactively. The amount of measurements significantly varies with period. The paths corresponding to the measurements at different periods are shown in Figure 4. Figure 5 shows the number of measured spectral amplitudes as a function of period. The existing broadband station distribution and the pattern of seismicity provide a sufficient number of source/station spectral amplitude measurements in a 12 to 20 s period for the construction of the 2-D tomographic maps of attenuation

coefficients. Measurements at periods below about 12 s are too scarce. Figure 6 characterizes aspects of the observed data set. The M_b magnitudes of the selected events vary from 4 to 7, with dominant magnitudes near 5. The M_s magnitudes are mostly in the 5 to 6 range. Epicentral distances widely vary from 500 to 8000 km with most path lengths between 2000 and 6000 km. Source depths (according to the Preliminary Determination of Epicenters [PDE] catalog) are between 5 and 40 km. Note the significant difference between source depths provided by the Harvard-Centroid-Moment Tensor (CMT) and PDE catalogs (Figure 6d). The peak of the distribution in Figure 6d is caused by different default values in the PDE and CMT catalog when event depth is ill-constrained (10 km for PDE, 15 km for CMT). This indeterminacy of event depths applied a significant side-constraint on the use of amplitude spectra data, as discussed further in this report.

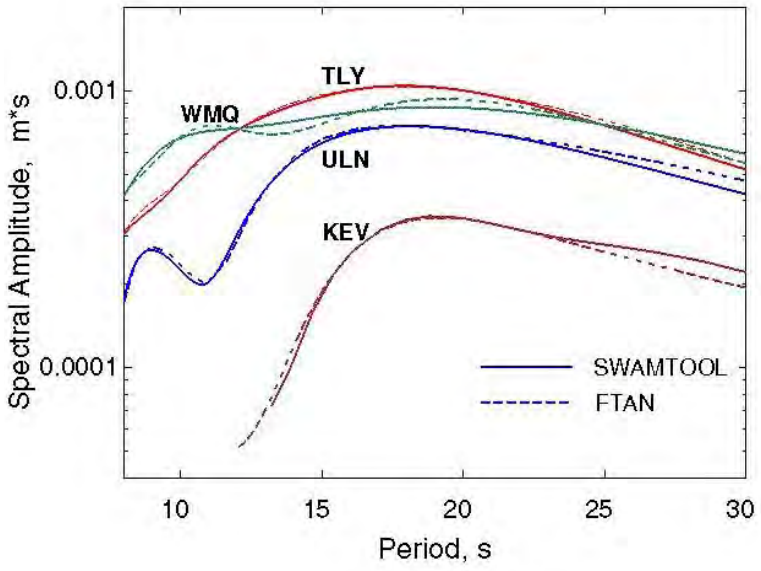


Figure 3. Comparison of the spectral amplitude measurements made with SWAMTOOL and FTAN from an earthquake on 06/01/2005 near the India-China border region (Ms = 5.7).

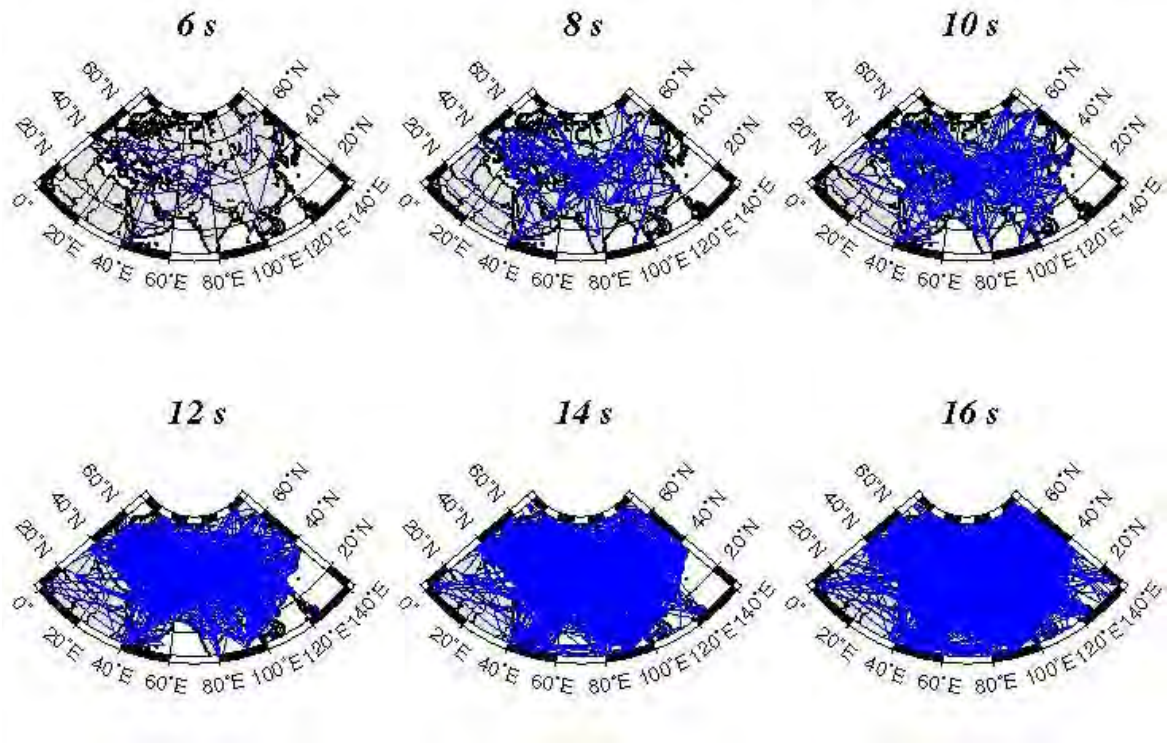


Figure 4. Paths for which the spectral amplitudes were measured at indicated periods.

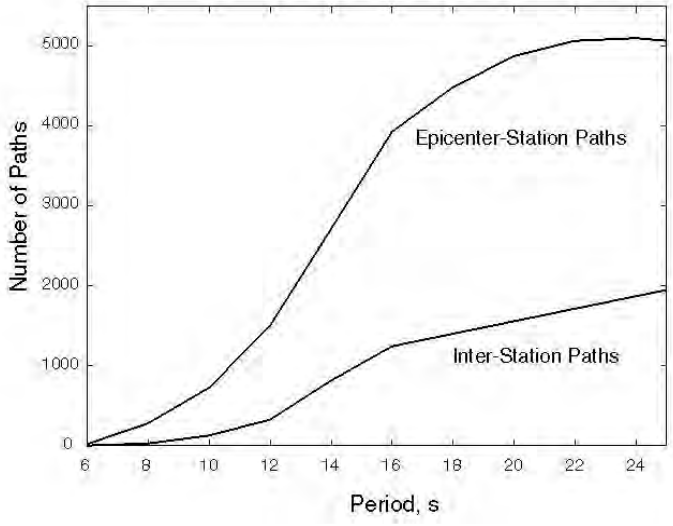


Figure 5. Numbers of selected epicenter/station paths and interstation paths as functions of periods.

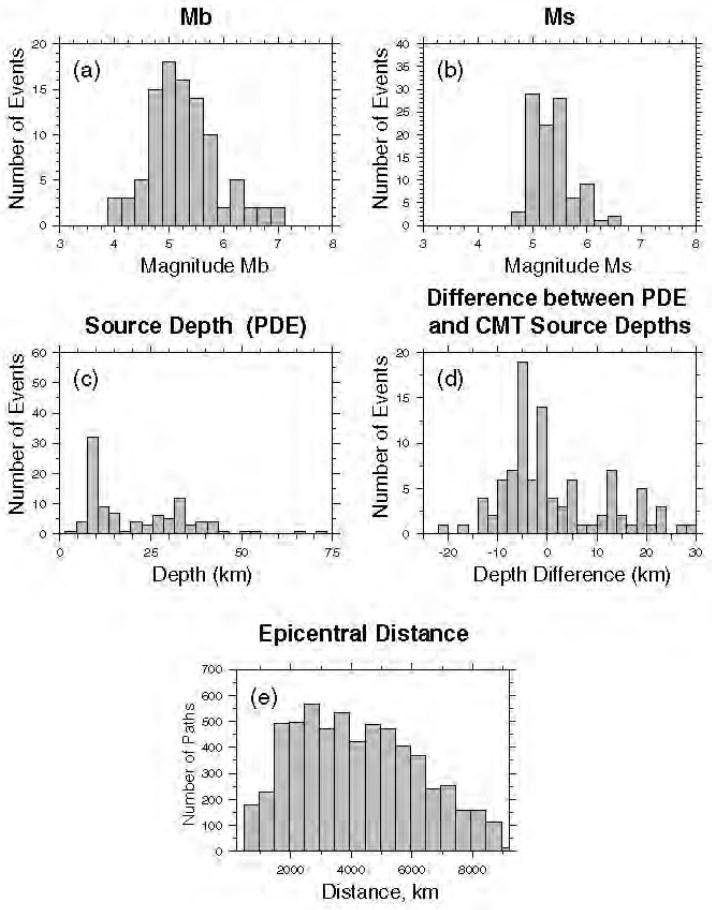


Figure 6. Histograms characterizing the events and paths in the data set.

Figure 7 demonstrates the repeatability of measurements for the set of closely spaced events (doublets) in Turkey. The almost-identical events should generate quite similar amplitude spectra. However, an ~10% difference in amplitudes is observed at short periods, even after the normalization by the slightly different seismic moments, Mo. This may be caused by slight differences in source depths not reflected in the PDE catalog.

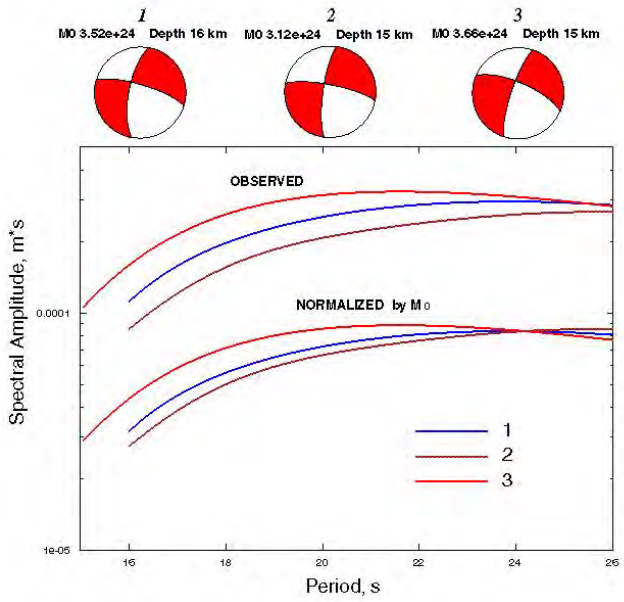


Figure 7. Similarity of amplitude spectra for three close local events in Turkey.

The effect of uncertainties in source parameters may be mitigated by using the interstation measurements. We select for such measurements the stations that are at nearly the same azimuth from the epicenter (with a difference of less than 1 degree). The number of such measurements as a function of period is presented in Figure 5. Figure 8 shows two examples of interstation combinations. In the left panel, spectra observed from three stations in the KNET network are compared with the spectrum observed at station ARU, about ~2000 km from KNET. The close similarity of spectra observed at different KNET stations and their compatibility with the spectrum observed at ARU are evident. In the right panel of Figure 8, the compatibility of spectra obtained by station USP (KNET) and KURK (KAZNET) is similarly demonstrated.

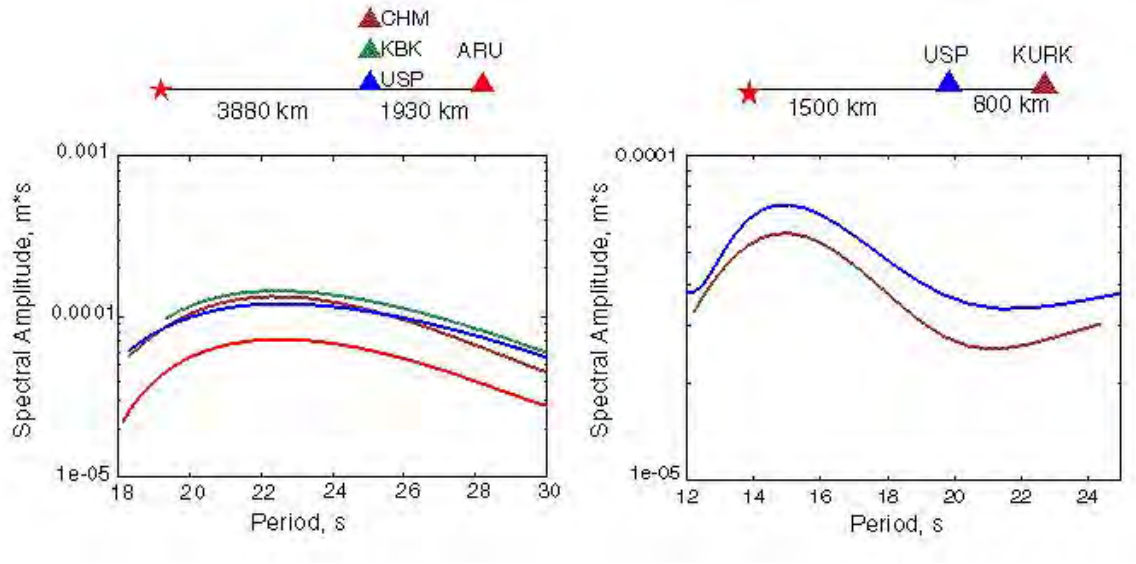


Figure 8. Examples of interstation measurements by stations of KAZNET and KNET networks: event near Andaman Islands (left); event in Pakistan (right).

Interpreting Amplitude Spectra Measurements

The transition from amplitude spectra to attenuation coefficients for the source to receiver paths is based on information about the source mechanism and depth, which is usually taken from the Harvard-CMT catalog. Uncertainties in CMT solutions for the best double couple orientation and source depth have a strong influence on the attenuation coefficients. We illustrate this by simulating the effects of uncertainties in source mechanism, when strike, dip, and slip determining the best couple are varied by ±5 degrees (Figure 9, left). The simulation is performed for a realistic crustal model and source parameters. Variations in the amplitude spectrum are on the order of 10%. More dramatic effects are produced by the uncertainty in the source depth (Figure 9, right). The maximum uncertainty in the spectrum occurs where the source excitation function experiences a minimum near the source depth. Although the details will depend on source mechanism and local structure, this simulation shows that a 5 km error in source depth (see Figure 5d, comparing depth estimates from different catalogs) may produce up to a 50% error in the spectral measurements at periods between 10 s and 20 s. If the event depth is known to lie between 15 and 25 km, the amplitude spectra are expected to be similar between 10 and 20 s. Spectra in this period range are very sensitive to the depth of shallower events. Interstation measurements are significantly less sensitive to these factors, but the number of these measurements is much lower than for source/receiver measurements (Figure 5).

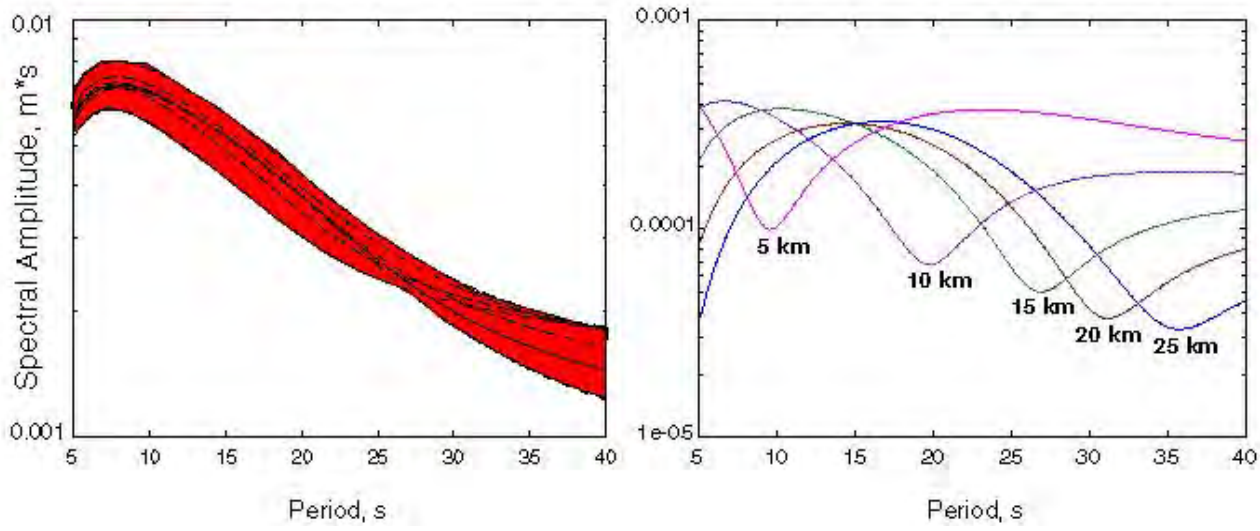


Figure 9. Effects of uncertainties in source parameters. The red stripe (left) corresponds to the possible range of spectral amplitudes when strike, dip, and slip, determining the best couple, vary by±5%. The source depth (right) varies from 5 to 30 km.

Effects of Lateral Inhomogeneities

Uncertainties in the 3-D structure of the crust may also distort the estimated attenuation coefficients. This may happen because of significant differences in the crustal structure near the source and receiver locations (single-station case) or near the location of the receivers (interstation case).

Shown in Figure 10 is a simulated example is shown in Figure 10 for dramatically different crustal structures at source and receiver. This effect is not as severe as the effect of uncertainty in source depth. In addition, its effect can be ameliorated in the transition from amplitude spectra to attenuation coefficients by using an existing 3-D model of the Eurasian crust (e.g., Shapiro and Ritzwoller, 2002).

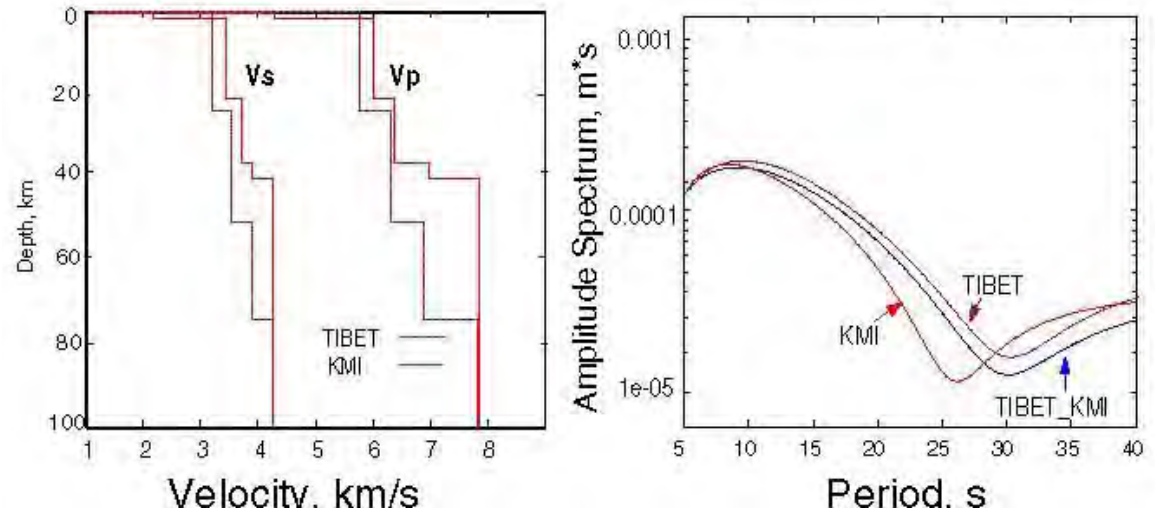


Figure 10. The differences in synthetic amplitude spectra for the path from Tibet to station KMI and a realistic source mechanism. Crustal models under the source (TIBET) and receiver (KMI) are shown on the left. Synthetic amplitude spectra for three different simulations appear on the right. The TIBET curve is for the TIBET model at both event and station locations; the KMI curve is for the KMI model at both location. The TIBET-KMI curve is for the TIBET model near the source and KMI model under the station.

CONCLUSIONS AND RECOMMENDATIONS

We described here the first stage of the study dedicated to the construction of the attenuation model for short-period waves across Central Asia. Only three years (2003-2005) of data have been used up to now.

The modified SWAMTOOL technique permits reliable measurement of surface-wave amplitude spectra and evaluation of the quality of measurements. We found that the existing networks and the pattern of seismicity will provide a significant amount of data on spectral amplitudes for periods in the range 12-20 s, appropriate for 2-D tomographic inversion for attenuation coefficients. Data for shorter periods are too scarce for tomographic inversion.

The synthetic examples demonstrate the strong dependence of the Rayleigh-wave amplitude spectra on source parameters, particularly the source depth and the structure of the crust at source and receiver regions. This implies the necessity to include some additional unknowns related to the source into the inversion of observed data and to use an existing 3-D model of the Eurasian crust in the data-inversion process. Inclusion of additional unknowns such as a source depth, seismic moment, and angles determining source geometry will address some of the uncertainties discussed in this report.

We plan to continue data acquisition and processing as well as developing the robust algorithm for data inversion, taking into account uncertainties in source parameters and the 3-D structure of the Eurasian crust.

ACKNOWLEDGEMENTS

The authors highly appreciate the opportunity to receive digital records from IRIS DMC, GEOSCOPE, and GEOFON.

REFERENCES

Bonner, J. L., D. R. Russel, D. G. Harkrider, D. T. Reiter, and R. B. Herrmann (2006). Development of a time-domain, variable-period surface wave magnitude measurement procedure for application at regional and teleseismic distances, *Bull. Seism. Soc. Am*. 96: 678-696.

Herrin, E. E. and T. T. Goforth (1977). Phase-matched filters: Application to the study of Rayleigh waves, *Bull. Seism. Soc. Am*. 67: 1259-1275.

Levshin, A. L., T. B. Yanovskaya, A. V. Lander, B. G. Bukchin, M. P. Barmin, L. I. Ratnikova, and E. N Its (1989). *Seismic Surface Waves in Laterally Inhomogeneous Earth*. (Ed. V.I. Keilis-Borok), Kluwer Publ. House.

Levshin, A. L. and M. H. Ritzwoller (2003). Discrimination, Detection, Depth, Location, and Wave Propagation Studies Using Intermediate Period Surface Waves in the Middle East, Central Asia, and the Far East, Technical Report DTRA-TR-01-28, Defense Threat Reduction Agency, 120 pp.

Levshin, A. L., J. L. Stevens, M. H. Ritzwoller, D. A. Adams, and G. E. Baker (2003). Improvement of Detection and Discrimination Using Short Period (7s-15s) Surface Waves in W. China, N. India, Pakistan and Environs, Final Report, submitted to Defense Threat Reduction Agency, 49 pp.

Marshall, P. D. and P. W. Basham (1972). Discrimination between earthquakes and underground explosions employing an improved Ms scale, *Geophys. J. R. Astr. Soc*. 28: 431-458.

Mitchell, B. J. (1995). Anelastic structure and evolution of the continental crust and upper mantle from seismic surface wave attenuation, *Rev. Geophys*. 33: 441-462.

Ritzwoller, M. H. and A. L. Levshin (1998). Eurasian surface wave tomography: Group velocities, *J. Geophys. Res.* 103: 4839-4878.

Russell, D. R., R. B. Herrman, and H. Hwang (1988). Application of frequency-variable filters to surface wave amplitude analysis, *Bull. Seism. Soc. Am*. 78: 339-354.

Russell, D. R. (2006). Development of a time-domain, variable-period surface wave magnitude measurement procedure for application at regional and teleseismic distances, Part I: Theory, *Bull. Seism. Soc. Am*. 96: 665-677.

Selby, N. D. and J. H. Woodhouse (2000). Controls on Rayleigh wave amplitudes: Attenuation and focusing, *Geophys. J. Int.* 142: 933-940.

Shapiro, N. M. and M. H. Ritzwoller (2002). Monte-Carlo inversion for a global shear-velocity m\model of the crust and upper mantle, *Geophys. J. Int*. 151: 88-105.

Stevens, J. L., D. A. Adams, and G. E. Baker (2001). Improved surface wave detection and measurement using phase-matched filtering with a global one-degree dispersion model, in *Proceedings of the 23rd Seismic Research Review: Worldwide Monitoring of Nuclear Explosions*, LA-UR-01-4454, Vol. 1, 420-430.

Woodhouse, J. H. (1974). Surface waves in a laterally varying layered structure, *Geophys. J. Roy. Astr. Soc*. 37: 461-490.

Yang, X., S. R. Taylor, and H. J. Patton (2004). The 20-s Rayleigh wave attenuation tomography for central and southeastern Asia, *J. Geophys. Res.* 108, B12304, doi:10.1029/2004JB003193.

Yang, X, A. R. Lowry, A. L. Levshin, and M. H. Ritzwoller (2005). Toward a Rayleigh wave attenuation model for Eurasia and calibrating a new M_S formula, in *Proceedings of the 27th Seismic Research Review, Ground-Based Nuclear Explosion Monitoring Technologies*, LA-UR-05-6407, 259-265.

SEISMIC CHARACTERIZATION OF NORTHEAST ASIA

Kevin G. Mackey[1], Hans E. Hartse[2], Kazuya Fujita[1], Lepolt Linkimer[1], Lee K. Steck[2], Richard J. Stead[2], and Charlotte A. Rowe[2]

Michigan State University[1] and Los Alamos National Laboratory[2]

Sponsored by National Nuclear Security Administration
Office of Nonproliferation Research and Development
Office of Defense Nuclear Nonproliferation

Contract Nos. DE-FC52-2004NA25540[1] and W-7405-ENG-36[2]

ABSTRACT

Our project of seismic characterization of northeast Asia continues on a multi-faceted approach concentrating on eastern Russia. The field work aspects of the project are addressing additional seismic station installations and calibration of existing digital stations. Seismic station deployments include permanent and temporary stations deployed in Chukotka, temporary stations deployed in the vicinity of Yakutsk, one aftershock study station for the April 19 2006, M_w 7.6 Koryak Highlands earthquake, and a planned 5 station temporary deployment in the Stanovoi Range in southern Yakutia. We also are planning permanent station deployments in the Amur region. As the existing digital stations include a diverse set of instruments and recorders, many with poorly defined characteristics and no established calibration procedure, we are obtaining empirical calibrations for remote unknown stations. The empirical calibrations are obtained by co-locating a calibrated reference station at each remote station and conducting a comparative analysis of both stations' recordings.

Our Siberia database enhancements for this past year include: (1) addition of about 8000 new events primarily from the Yakutsk and Magadan networks and mostly from between the years 1995 and 2005, (2) addition of about 11,000 mining explosions from between the years 1979 and 1997, (3) reconciliation of seismic instrument names noted within the database, and (4) general quality control efforts primarily targeting unmerged, multi-author origins and resolution of duplicated arrival information.

Using our arrival time data set we have been exploring the viability of differential Pn travel-time tomography across eastern Siberia. To date, we have observed the expected results of higher velocities under the Siberian platform, with generally lower velocities under the tectonically active regions in the central and eastern portions of our study area.

We have also continued our studies of the Russian K-class (Energy) system and the relationship between K-class and magnitude scales. Because K-class and magnitude are determined independently, we have calculated region specific orthogonal regressions between K-class and m_b and M_S. The relationships vary somewhat from network to network but major differences are noted for the Sakhalin, Kamchatka, and Kuril networks where local computational methodologies were used to account for perceived differences in attenuation.

In order to discriminate industrial explosions from earthquakes that were recorded during the latter portion of the analog period (1985-2000), we have examined amplitude ratios calculated from data reported in regional seismic bulletins. The best results are obtained using an average of ratios from several stations with correct event discrimination as high as 90 %.

OBJECTIVES

The main objective of our current research is to improve the overall seismic characterization of northeastern Asia. To accomplish this we seek to develop a complete seismicity database and use this database to discriminate industrial explosions, develop velocity models, and understand the relationship between the sizes and locations of events.

RESEARCH ACCOMPLISHED

The Russian K-class System and its Relation to Magnitudes

The size of local and regional earthquakes in the former Soviet Union (FSU) has been given by the energy class (K-class) system since the late 1950s. The nature, origin, and methodology of this system is poorly known to western seismologists studying Soviet and Russian seismological data, and yet of great interest to those conducting detailed research on the seismicity of the FSU. As the primary means of quantifying the size of small events in the FSU, understanding the K-class system is critical in the analysis of FSU seismological data. K-class data are also often used as the basis for magnitude values given in international catalogs. When the annual *Zemletrayseniya v SSSR* ("Earthquakes in the USSR") began to be compiled in 1962, almost all of the regional networks estimated K for their part of the catalog using the method of Rautian (1958); now, energy class is calculated for almost all of the regional earthquakes in the Former Soviet Union (Figure 1). The relationship between K-class and magnitude has also been a great interest of seismologists working with data from the FSU. To examine the empirical relationship between magnitude and K-class, we tabulated M_b and M_S magnitudes as reported by the International Seismological Centre (ISC), and K-class values reported in *Zemletryaseniya v SSSR* and its successor publication, *Zemletryaseniya Severnoi Evrazii* for each of the seismic regions for 1970-1997. Because K-class and magnitude are both independent variables with their own uncertainties, one can not simply calculate a regression holding one as the dependent variable. We thus calculated an orthogonal regression (see Figure 2 for an example) which minimizes the sum of the squares of the distance to the regression line. It should be noted that K-class is calculated, and calibrated, for events generally smaller than K = 10 – 11 (m_b ~ 4), while teleseismic magnitudes are calculated for larger events. For smaller events of m_b (or M_S) around 4, magnitude is often calculated with very few stations, or using stations with potentially weak arrivals, thus increasing the uncertainty and scatter.

All regressions were standardized to the form

$$\text{Magnitude} = c + s\,(K - 14)$$

This formulation eliminates having sign variations on c and makes comparisons clearer in the range for which K-class and magnitude are both calculated ($9 \le K \le 14$).

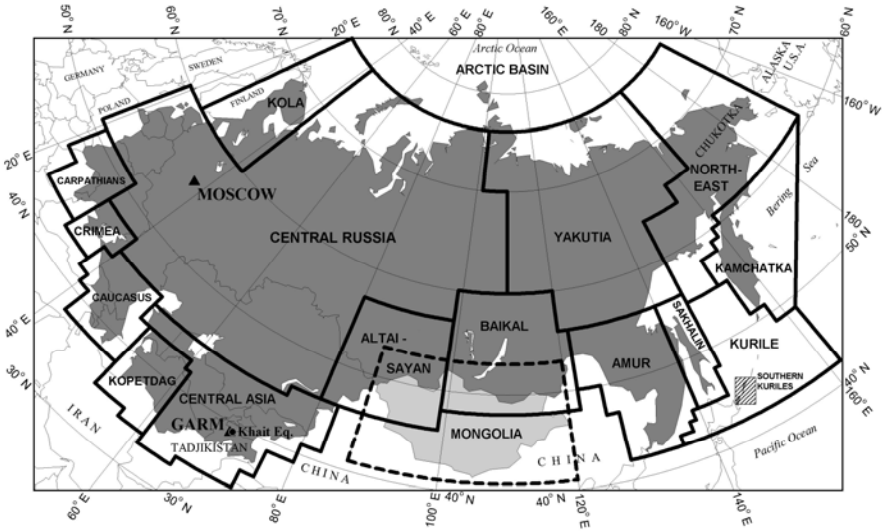


Figure 1. Index map showing boundaries between regional networks in the Former Soviet Union. Individual regressions between K-class and magnitude were calculated for each region.

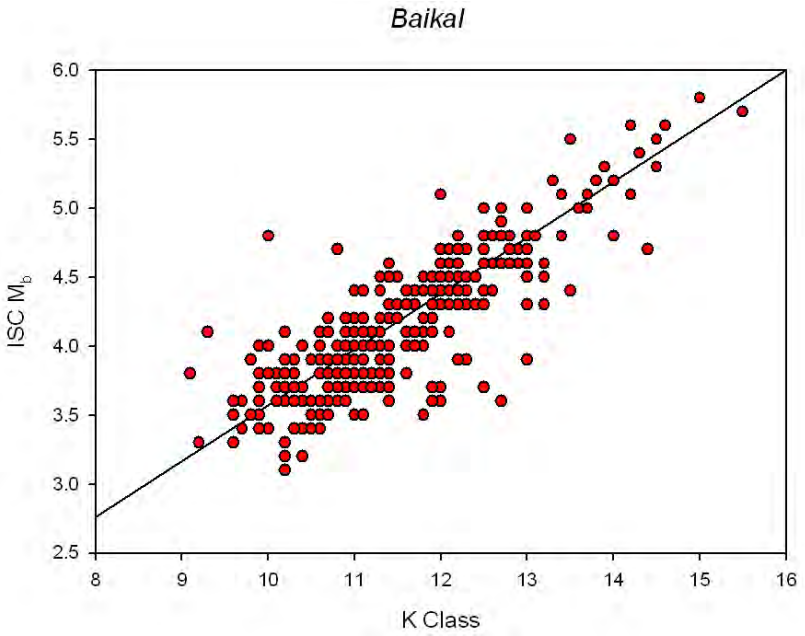


Figure 2. Sample orthogonal regression between K-class and ISC magnitude (m_b).

The m_b regressions (Table I) are generally similar, close to 5.41 + 0.43 (K – 14), in the K-class range of interest ($9 \leq K \leq 14$) except for Crimea, Sakhalin, Kuril, and Kamchatka (Figure 3). Crimea, Sakhalin, and Kamchatka have higher c and s values than the other regions, while Kuril has a similar slope, but higher c. As noted above, the three Far Eastern regions use a different formulation for K, and are therefore expected to be different from the rest of the FSU; the difference for the Crimea may reflect a smaller number of data points. It is interesting that the Kuril regression differs from both Sakhalin (which administers the Kuril network) and Kamchatka (which is tectonically similar).

The intercepts (c) for the Sakhalin m_b relationship and Central Asia regressions are close to those calculated by Solov'ev and Solov'eva (1967; 6.59 + 0.55 (K_S – 14)), and Bune et al. (1960; 5.48 + 0.55 (K – 14)), respectively; however, the slopes differ by more than 0.1 in both cases.

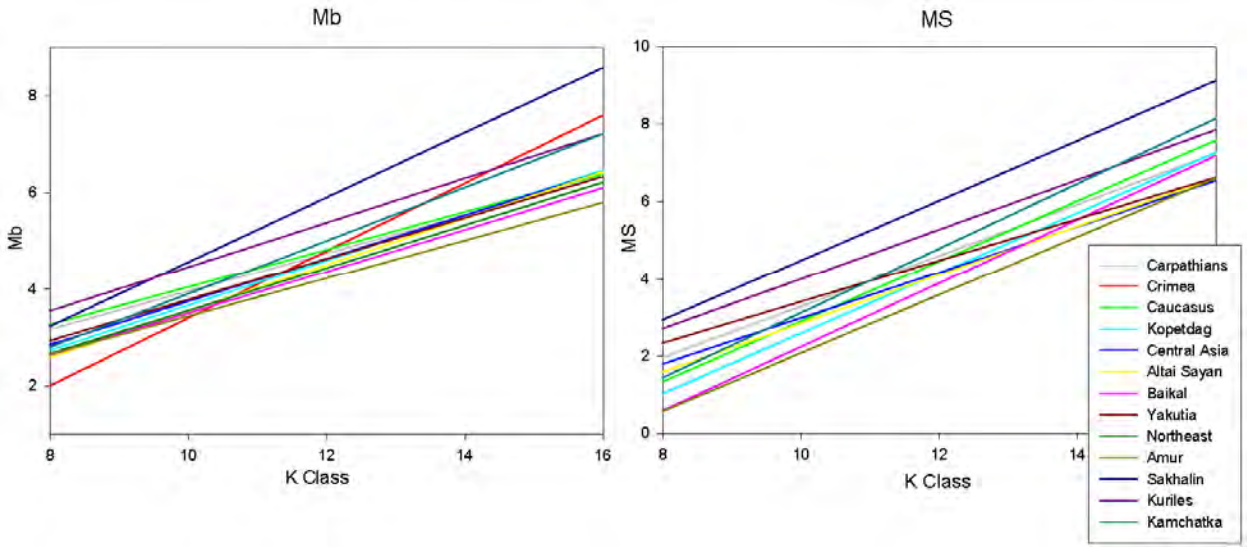


Figure 3. Comparisons of orthogonal regressions between K-class and a) m_b and b) M_S for various regions of the FSU.

The M_S regressions are more variable (Table 1; Figure 3), reflecting the fact that the methodology and frequencies used for calculating m_b and K are more similar than those for determining M_S. Slopes for the M_S values fall into three general groups; those near 0.8 (Caucasus, Turkmenistan, Baikal, Amur, Sakhalin, and Kamchatka), those near 0.6 (Carpathians, Central Asia, Altai-Sayan, Kuril), and those near 0.5 (Yakutia). The Carpathians are based on very limited data. The c values are generally near 5.5 except for the three Far Eastern regions ($c > 6.4$), and the Caucasus and the Crimea ($c \sim 6.0$). In general, however, most of the curves are fairly close to each other in the $10 \leq K \leq 14$ range. Sakhalin has an abnormally high intercept (as it did for m_b).

We present here our preferred results, but note, however, that both c and s can vary considerably depending on different regression methodology and algorithms, data sets used, cut-off magnitudes and K-classes, and to what degree the data are cleaned. Variations in c of 0.5 and in s of 0.1 are easy to obtain.

K-class is calculated from, and calibrated to, short-period instruments. Therefore like m_b, K-class saturates; because of the similarity in the frequency response of FSU and western short- period seismometers, this probably occurs at about the same level ($K \approx 16$-17).

Because of the standard of using magnitude in the west, many regional events in western catalogs are reported with magnitude calculated from K-class using a locally derived regression. Examples include the data for the Crimea and Chukotka (although the Chukotka relationship is particularly abnormal) in the *New Catalog of Strong Earthquakes in the USSR* (Kondorskaya and Shebalin, 1977), the digital SSR catalog distributed by the US Geological Survey, and the Kamchatka data in the International Seismological Centre catalog. However, this is not always explicitly stated, causing confusion as to what the primary measurement was and how it was derived.

Table 1. Regressions between K Class and ISC Magnitude

Region	m_b	M_S
Carpathians	5.5382 + 0.3966 (K-14)	5.9198 + 0.6613 (K-14)
Crimea	6.2001 + 0.6992 (K-14)	Insufficient Data
Caucasus	5.6014 + 0.3910 (K-14)	6.0221 + 0.7818 (K-14)
Kopetdag	5.5332 + 0.4673 (K-14)	5.7114 + 0.7811 (K-14)
Central Asia	5.5332 + 0.4490 (K-14)	5.3636 + 0.5943 (K-14)
Altai - Sayan	5.4650 + 0.4823 (K-14)	5.3686 + 0.6327 (K-14)
Baikal	5.2298 + 0.4337 (K-14)	5.5397 + 0.8276 (K-14)
Yakutia	5.4871 + 0.4270 (K-14)	5.5524 + 0.5387 (K-14)
Northeast	5.3288 + 0.4452 (K-14)	Insufficient Data
Amur	5.0080 + 0.3943 (K-14)	5.1003 + 0.7547 (K-14)
Sakhalin	7.2456 + 0.6688 (K_S-14)	7.5682 + 0.7727 (K_S-14)
Kuril*	6.2958 + 0.4602 (K_S-14)	6.5628 + 0.6422 (K_S-14)
Kamchatka	6.1060 + 0.5518 (K_F-14)	6.4744 + 0.8380 (K_F-14)

* see text for calculation methodology

Explosion Discrimination

Contamination of the seismicity catalog from mining and industrial explosions continues to be a problem for both historic seismicity as well as current events. Using historic analog data we have completed the first amplitude based study to address discrimination of individual events. We extracted 484 events from the seismicity database of which 237 are local nighttime occurring earthquakes and 247 are known daytime explosions. Events were extracted in two regions, Magadan – Northern Yakutia, and Southern Yakutia (Figure 4). For each event, all available Pg and Sg amplitudes were added to the database to construct ratios. For approximately 100 events, additional amplitudes were read directly from the original seismograms in the archives of the Yakutsk and Magadan seismic networks. All earthquake and explosion data utilized here were recorded on photo paper and using only short period instruments. Although we were unable to conduct any frequency analysis due to the analog nature of the records and the lack of such information in the bulletins, the response of the seismometers restricts recorded signals to higher frequencies (1-5 Hz), which other studies indicate are generally better for explosion discrimination. Events extracted cover the

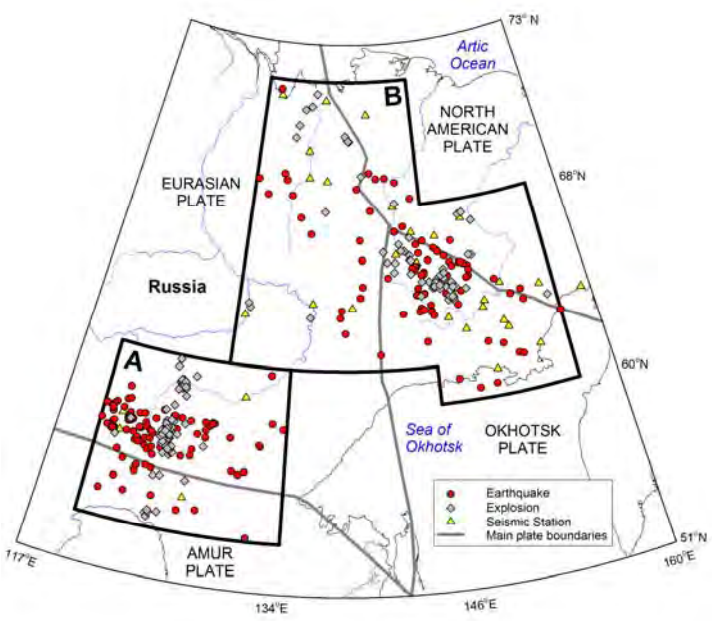


Figure 4. Study regions where Pg/Sg explosion discrimination studies were undertaken showing earthquakes, explosions, and seismic stations used. A. Southern Yakutia region. B. Magadan – Northern Yakutia region.

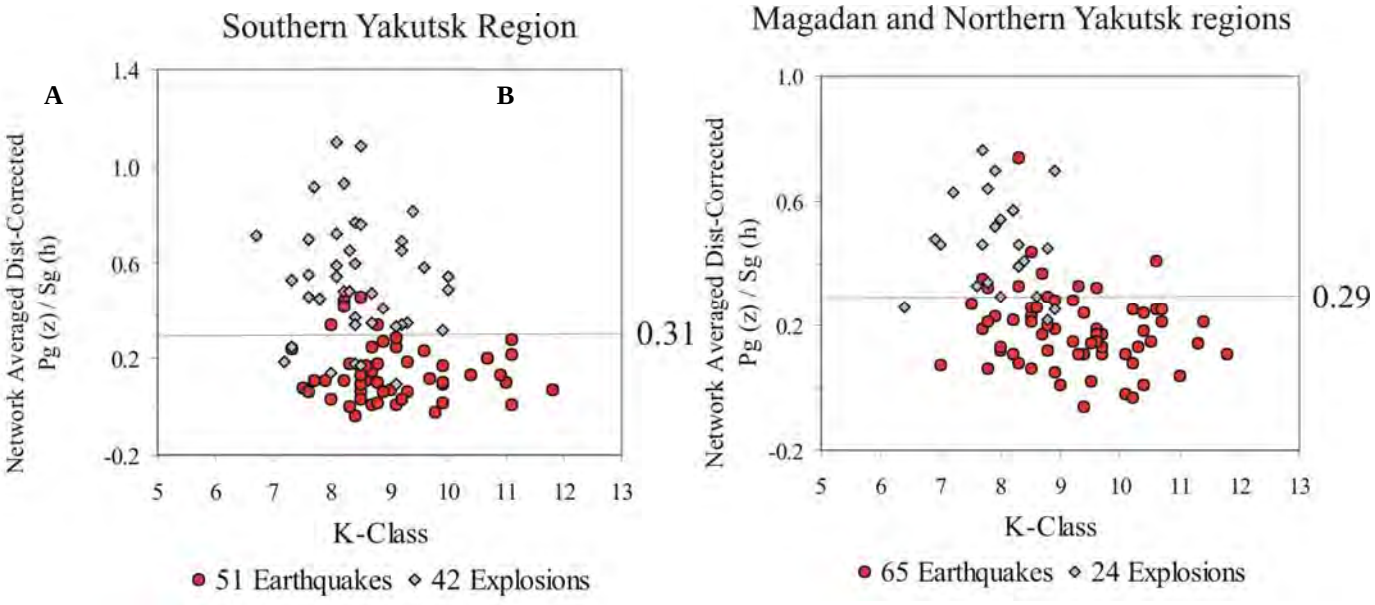


Figure 5. Network averaged-distance corrected Pg_z/Sg_h ratio discrimination plots for the Southern Yakutia (A) and Magadan – Northern Yakutia (B) regions. With this discrimination plot, critical values of 0.31 and 0.29 respectively correctly separate 87% of the events.

time interval 1985-2000, with a magnitude range of 1.5 to 4.9 for earthquakes and 1.4 to 3.9 for explosions. For each region we calculated 5 different Pg/Sg ratios,varying by components (Pg_z/Sg_z, Pg_h/Sg_h, Pg_h/Sg_z, Pg_z/Sg_h, and full vector Pg/Sg), and evaluated the discrimination effectiveness of these ratios against event size, event distance, with and without distance corrections applied, and ratios averaged over the network for individual events. Only events where a minimum of three stations had ratios were used to calculate network averages. Figure 5 (A and B) illustrate

the discrimination plot using the Pg_z/Sg_h ratio with distance correction applied and network averages for the Southern Yakutia and Northern Yakutia - Magadan regions, respectively. For each discrimination plot constructed, the best value that distinguishes earthquakes from explosions (critical value) was calculated. The relative number of earthquakes and explosions was normalized in this calculation. For the Pg_z/Sg_h ratio, 86 to 87% of the events are correctly classified using the best critical values for both study regions using the network averaged ratios (Figure 6, A and B). Although some other ratios perform slightly better, the Pg_z/Sg_h ratio is the most practical to use in evaluation of existing data sets as it is these amplitudes most often recorded in the historic event bulletins.

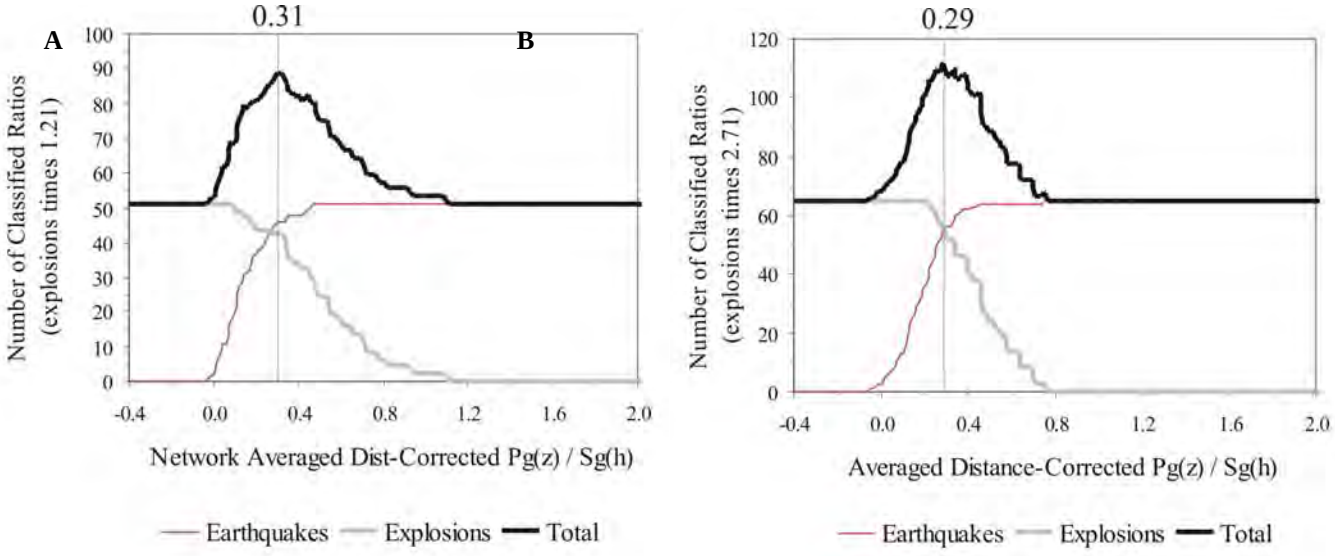


Figure 6. Network averaged-distance corrected Pg_z/Sg_h ratio critical value determination for the Southern Yakutia (A) and Magadan – Northern Yakutia (B) regions (see Figure 5).

Overall, the network average Pg_h/Sg_h, Pg_z/Sg_h, and full vector Pg/Sg ratio appear to discriminate earthquakes best, with successful discrimination ranging from 86.4 to 91.7%, while the Pg_z/Sg_z and Pg_h/Sg_z, ratios are poorer with successful discrimination ranging from 78.5 to 81.3% (Table 2). The network averaged ratios always discriminate better than individual ratios. Surprisingly, we found that the inclusion of a distance correction had little effect on the ability of a ratio to discriminate, though this may be a result of small events at only local and near regional distances.

Table 2. Summary of successful discrimination percentages using different amplitude ratios and methods.

Discrimant	Raw Phase Ratio		Distance Corrected Ratio		Network Averaged Ratio		Net. Avg.-Dist. Corr. Ratio	
	S. Yak.	Mag.	S. Yak.	Mag.	S. Yak.	Mag.	S. Yak.	Mag.
Pg(h)/Sg(h)	71.3%	70.7%	71.0%	70.0%	89.1%	91.0%	89.1%	91.7%
Pg(z)/Sg(z)	65.4%	63.8%	66.6%	63.8%	78.5%	78.1%	80.1%	79.1%
Pg(h)/Sg(z)	69.4%	62.8%	69.4%	63.3%	81.3%	80.2%	80.6%	80.2%
Pg(z)/Sg(h)	68.0%	67.0%	68.6%	66.0%	86.8%	86.4%	86.8%	86.1%
Full Vector	71.2%	70.9%	71.6%	70.8%	87.9%	91.7%	89.1%	91.7%

Database Improvements

Over the past year we have been working quality-control issues and adding additional information to the MSU Siberia database. Most quality-control issues have involved combing origin information from (typically) two or three separate origins into single events. These situations occurred because network operators have sometimes reported the same event more than once, but from separate bulletins. A few hundred of these cases were resolved (from over 245,000 total events). We added approximately 8000 new events, including location, arrival time, and amplitude information, to the database. Most events were from the Magadan and Yakutsk networks covering the years 1995 to 2005.

We also added around 11,000 mining explosions to the database. Most of these explosion records were derived from individual station operator's notes. In the Russian Far East station operators often note approximate times (to within the nearest minute) when waves from an explosion at a known mine arrive at their station. Sometimes station operators call mining companies to confirm explosion times and locations. Hence, even though many of these mining events were never formally located, records of time and approximate source location were often available. These mining explosions are from the Magadan and Yakutsk networks. The MSU Siberia database now holds origin information for over 11,700 mining explosions.

Station Calibrations

One of the long term problems with the established digital stations in eastern Russia deals with station calibrations. The majority of digital stations operating in our field area combine various short period Russian sensors with either Russian or U.S. digitization systems. Accurate calibrations of the merged systems has been difficult due to this diverse set of seismometers and recorders, many with poorly defined characteristics and no established calibration procedure. We have therefore established an empirical calibration procedure for the remote, unknown stations. The empirical calibrations are obtained by co-locating a calibrated reference station (a Geotech Instruments KS-2000 broadband seismometer recorded on a Geotech Instruments Smart24 recorder) at each remote station over a sufficient time interval to record multiple local, regional, and teleseismic events (see Figure 7).

To begin this calibration process, we first located the Geotech system at station MA2 adjacent to the GSN STS1 seismometer, which has operated for over a decade. Using STS1 response information provided by the IRIS Data Management Center and response information from Geotech, we confirmed that we could successfully correct the KS-2000 raw records (ground velocity in digital counts) into displacement (in meters) and obtain a close match to the corrected STS-1 records. Figure 8 compares the corrected KS-2000 and STS1 records from a deep, eastern Afghanistan event (December 12, 2005, mb near 5.7, depth near 220 km). Both the broadband and short-period records match well. Thus we have now obtained a calibrated pole-zero file for the KS-2000 system.

With the transportable KS-2000 system calibrated, we have been moving the system to other Magadan network sites throughout winter, spring, and summer of 2006. We now have joint records at stations OCHR and SUUS (Russian SM3 seismometers). During instrument co-locations, OCHR recorded the large Koryak earthquake of April 20, 2006, (Mw 7.6, see Figure 7). Based on reported SM3 free period and damping constant values (Mackey et al., 2005) we designed a pole-zero file for the SM3, and then instrument-corrected the SM3 and KS-2000 event records into displacement (in meters). Figure 9 shows the quite close match between displacement records from a local earthquake (top) and from the Koryak earthquake (bottom). We applied a high pass filter to these records because the SM3 is a short-period sensor. We plan to refine our SM3 calibration at OCHR, and then continue efforts to include SUUS and other Magadan network stations where Russian recording systems are deployed.

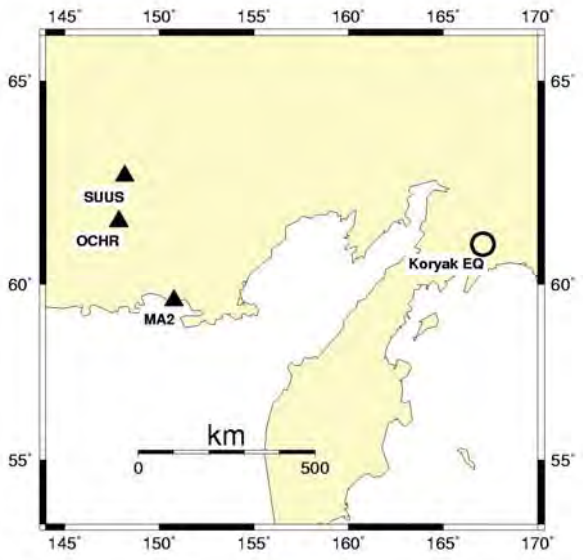


Figure 7. Locations of Magadan network stations discussed in text and location of April 20, 2006, Koryak earthquake (see text).

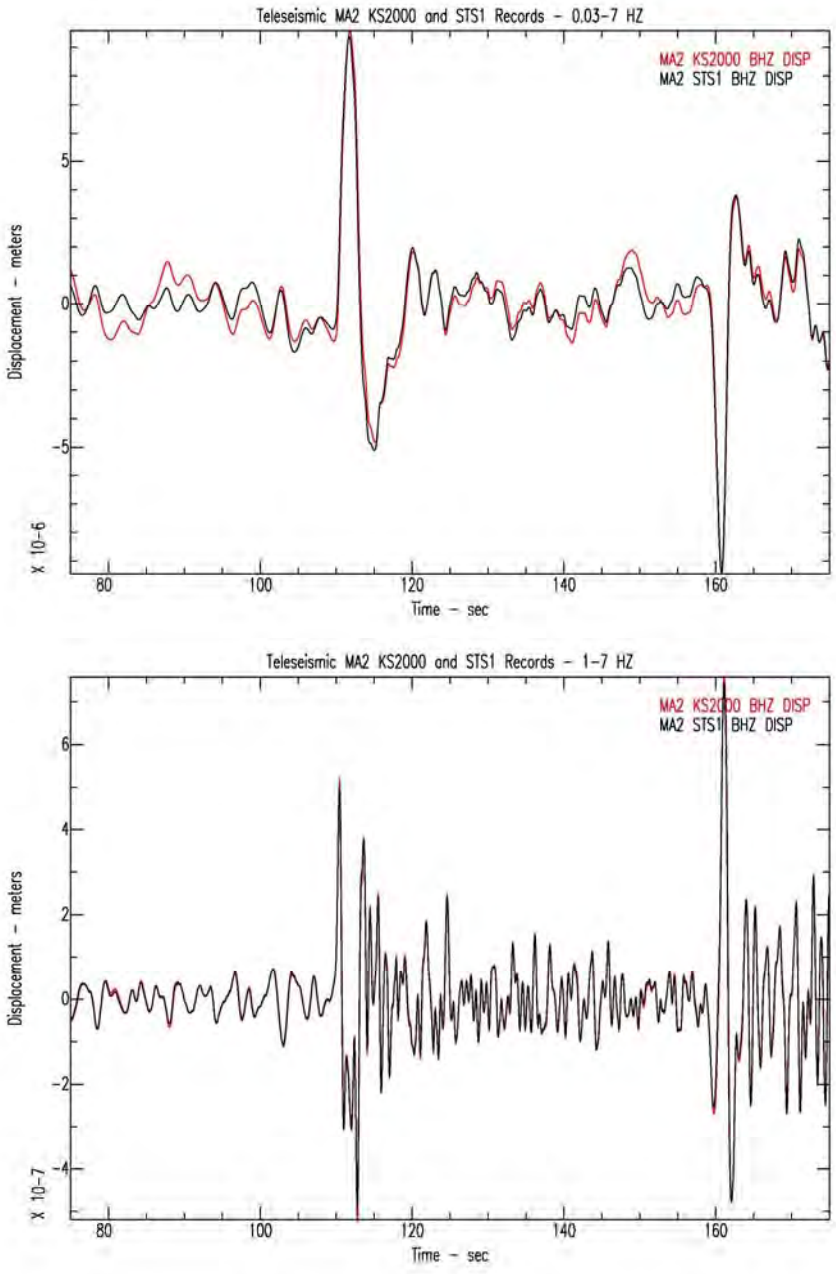


Figure 8. Station MA2 STS1 (black) and KS2000 (red) records corrected to displacement in meters. Top shows broadband records of a deep teleseism from eastern Afghanistan. Bottom shows a filtered short-period comparison.

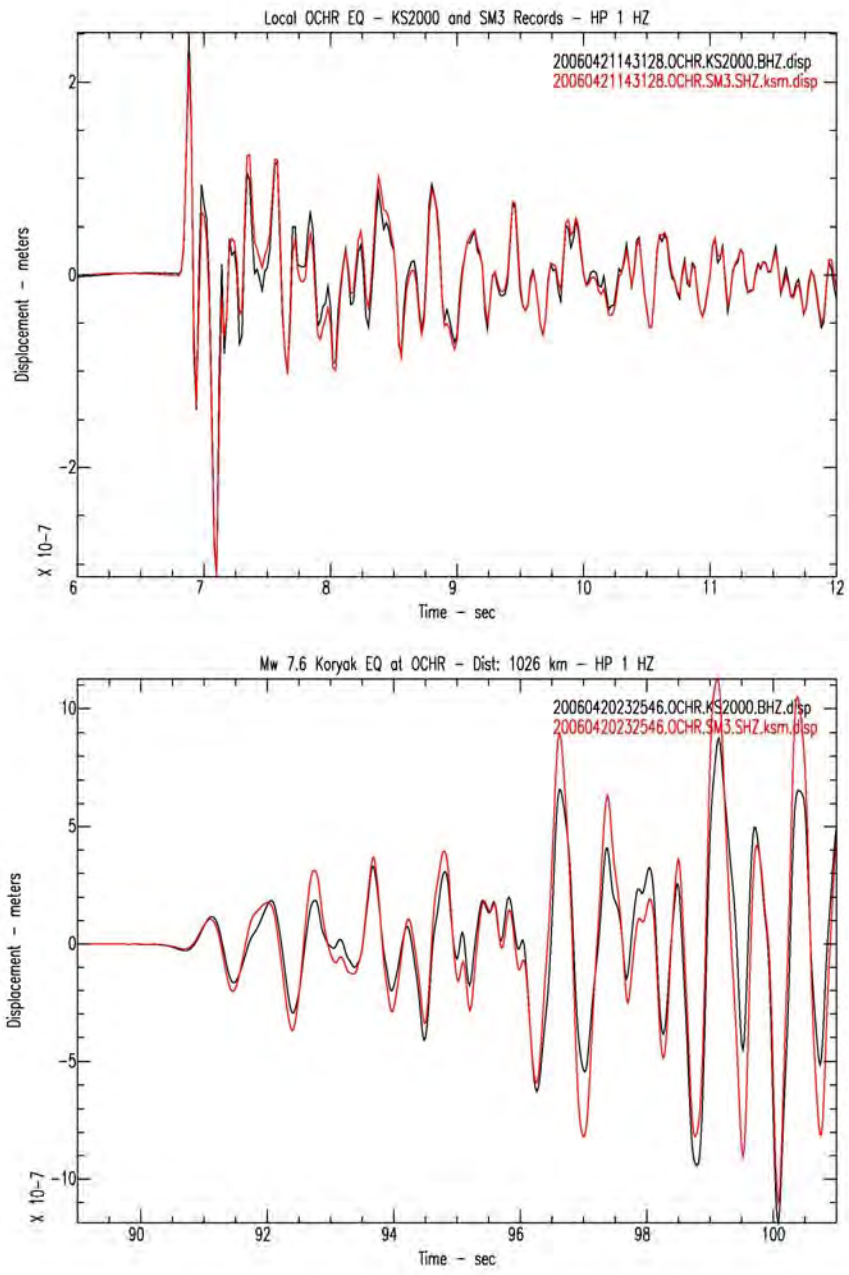


Figure 9. Instrument-corrected displacement records from OCHR. Top compares SM3 SHZ record (in red) to KS2000 BHZ record for a local earthquake. Bottom compares records from the large Koryak earthquake of April 20, 2006 (Mw 7.6). Records are high-pass filtered at 1 Hz.

Pn Tomography

Preliminary results of the use of differential Pn tomography (e.g., Phillips et al., 2005) as applied to the relocated eastern Russian catalog, a part of this study, are discussed in this volume in the paper by Steck et al. (2006, these Proceedings).

CONCLUSION(S) AND RECOMMENDATIONS

We continue to improve our seismicity characterization of northeast Russia with improvements in the seismicity database, discrimination of industrial explosions, station calibrations, and ongoing fieldwork.

ACKNOWLEDGEMENTS

We would like to thank T. Rautian, V. Khalturin, A. Kendall, and M. Nichols for discussions and assistance on K-class and its relation to magnitude. We also thank George Randall for valuable assistance regarding our instrument calibration efforts.

REFERENCES

Bune, V. I., M. V. Gzovsky, K. K. Zapol'sky, V. I. Keilis-Borok, V. N. Krestnikov, L. I. Malinovskaya, I. L. Nersesov, G. I. Pavlova, T. G. Rautian, G. I. Reisner, Y. V. Riznichenko, V. I. and Khalturin (Y. V. Riznichenko, editor) (1960). *Methods for the Detailed Study of Seismicity*, Moscow: Izdatel'stvo Akademii Nauk SSSR, 327 pp. (in Russian).

Mackey, K., K. Fujita, L. V. Gunbina, B. Koz'min, and S. Shibaev (2005). Final Report: Regional-scale ground-truth studies of northeast Russia, Part 9: Seismic stations of northeast Russia: Magadan and Yakutsk networks, LA-UR-06-0697, 424 pp.

Phillips, W.S., C.A. Rowe and L.K. Steck, 2005. The use of interstation seismic phase arrival differences to account for regional path variability, *Geophys. Res. Lett.* 32: L11301, doi:10.1029/2005GL022558 .

Rautian, T. G. (1958). Attenuation of seismic waves and the energy of earthquakes, I, *Trudy Institut Seismostoikogo Stroitel'stva i Seismologii Akademiya Nauk Tadjikskoi SSR* **7**: 41–85 (in Russian).

Kondorskaya, N. V., and N. A. Shebalin (editors) (1977). *New Catalog of Strong Earthquakes in the Territory of the USSR from Ancient Times to 1975*, Moscow: Nauka, 534 pp. (in Russian).

Solov'ev, S. L., and O. N. Solov'eva (1967). The relationship between the energy class and magnitude of Kuril earthquakes, *Izvestiya, Academy of Sciences of the USSR, Earth Physics Series* 3; 79–84.

EXTENSION OF THE CAUCASUS SEISMIC INFORMATION NETWORK STUDY INTO CENTRAL ASIA

Randolph Martin[1], Mary L. Krasovec[1], Spring Romer[1], M. Nafi Toksöz[2], and Levent Gülen[2]

New England Research[1] and Massachusetts Institute of Technology[2]

Sponsored by National Nuclear Security Administration
Office of Nonproliferation Research and Development
Office of Defense Nuclear Nonproliferation

Contract Nos. DE-AC-52-04NA25612[1] and NNSA-4-45[2]

ABSTRACT

The Central Asian Seismic Research Initiative (CASRI) is an extension of the Caucasus Seismic Information Network (CauSIN). Both projects seek to build knowledge bases of geological, geophysical, and seismic information in their respective regions and to use crustal modeling techniques to create a combined model of the regions to aid in seismic monitoring.

Tectonically, the most complex region in central Asia is the Tien Shan region. It is an intracontinental convergence region consisting of igneous and metamorphic ranges and major basins. The east-west trending morphology is the result of reactivation of the old structures in the late Cenozoic. Folding, thrusting and high-angle reverse faults are the most dominant forms of deformation.

The crust upper mantle structure of the region, primarily based on global tomography and receiver function analysis, is highly variable. New seismic data from local and regional stations are becoming available. We will use the travel-time data to generate a 3-D Moho map and the associated P_n velocity model for the region.

OBJECTIVES

The primary goal of this project is to develop a database of geology, tectonics, and seismicity for central Asia which covers Kazakhstan, Uzbekistan, Kyrgyzstan, and Tajikistan, basically extending and complimenting the work that we have accomplished for the CauSIN project countries (Georgia, Armenia, Azerbaijan, and northeastern Turkey) in the west (Figure 1).

We will be able to improve the event locations with this new data base which will include data from denser seismic networks that have improved and upgraded instrumentation with broadband seismometers, calibration events (mining and quarry blasts), improved models, and better location algorithms (e.g., double difference, multiple-event grid search etc).

We will obtain 3-D crust/upper mantle structure in the Central Asia using data from local seismic stations as well as other stations operated as part of the national networks. Extensive geological and geophysical data (e.g., surface seismic reflection profiles, gravity maps) as well as seismic data will be utilized in the construction of the lithospheric models.

RESEARCH ACCOMPLISHED

One of the deliverables of the CauSIN and CASRI projects is a geological map compilation covering the Caucasus and the central Asia region. Such a geological map was prepared in Arc geographical information system (GIS) digital format (Figure 2). The geological map of Asia and Europe (1:5,000,000 scale) that was originally compiled by Tingdong et al. (1997) was used, different sheets were merged seamlessly, and the map projection was converted into the Lambert equal-area projection.

Since most of the seismic activity that occurs in the CASRI countries is associated with the Tien Shan, an extensive literature survey was carried out, and this paper summarizes the detailed technical report that was prepared on the active tectonics of the Tien Shan, Central Asia (Gülen and Toksöz, 2006).

Geology and Tectonics of the Tien Shan

The active tectonics of central Asia is a consequence of the continental collision and the continuing continental convergence between the Indian and the Eurasian plates. This continental collision is considered to be the most important geological event of the Cenozoic era because it has created a 2500 km long mountain chain, the Himalayas, that contains the highest elevations on earth, and an immense plateau, Tibet, that has an average elevation of more than 5,000 m and an areal extent of 700,000 km^2. It also tectonically reactivated and uplifted the 2,500-km-long Tien Shan ranges 1,500 km to the north.

The Tien Shan is a prominent mountain belt of central Asia that rises north of the Pamir and the Tarim Basin and extends for 2,500 km from the Kizil Kum in the west to the Gobi Desert in the east (Figure 3). It is bounded by the Kazakh Platform and the Junggar (Dzungarian) Basin in the north. The Tien Shan is composed of E-W trending mountain ranges of mainly Paleozoic rocks that are separated by intermountain basins filled with Mesozoic and Cenozoic sediments, and its width increases towards the west, reaching 400 km at 76°E (Burtman, 1975; Tapponnier and Molnar, 1979; Avouac et al., 1993). A major NW–SE trending, right-lateral strike-slip fault, the Talas-Fergana Fault forms a major discontinuity between the western Tien Shan (Chatkal Ranges) and the central Tien Shan.

The structure of the greater part of the Tien Shan was formed in the Late Paleozoic and it was an active tectonic era of crustal deformation evidenced by widespread folding, trust and strike-slip faulting (Burtman, 1975; Tapponnier and Molnar, 1979; Burtman, 1980). Metamorphosed Carboniferous ophiolites mark the suture of the northward subducting Turkestan Paleozoic ocean along the long axis of the Tien Shan in the north. (Lee et al., 1982; Khain, 1985; Watson et al., 1987; Dewey et al., 1988; Burtman et al., 1996). The Tien Shan basement was fully amalgamated to Eurasia along the Tien Shan Suture Zone by the end of the Paleozoic (Burtman, 1975, Tapponnier and Molnar, 1979; Avouac et al., 1993).

Active Crustal Deformation and Shortening in the Tien Shan

The present E–W trending morphology, high elevation, and structure of the Tien Shan, which contains a number of mountain ranges and intermountain basins squeezed between them, is formed mainly as a result of late Cenozoic tectonics. In general, folding, thrusting, and high angle reverse faulting are by far the most dominant form of deformation in the Tien Shan. The E-W trending, active thrust systems form the northern and southern boundaries of the Tien Shan mountain range (Molnar and Tapponnier, 1975; Tapponnier and Molnar, 1979; Yin et al., 1998). Mostly, the marginal fold and thrust belts of the Tien Shan Ranges have a structural vergence that is toward the flanking basins, such as the Junggar and Tarim basins to the north and south, respectively, but there are well-developed exceptional structures that have an opposite vergence as well (Burchfiel et al., 1999). In fact, thrust faulting extensively defines the boundaries of almost all the mountain ranges and basins within the Tien Shan and along its boundaries (Cobbold et al., 1996; Burbank et al., 1999; Abdrakhmatov et al., 2002; Thompson et al., 2002).

For example Issyk Kul, Suusamyr, Kochkor, Naryn, At-Bashi, and Aksay are such intermontaine basins that are bounded by E–W trending thrust faults at the basin boundaries (Figure 3).

Recent GPS measurements carried out by numerous campaigns through multilateral collaborations provide important data on the rates of crustal shortening in the Tien Shan (Abdrakhmatov et al., 1996; Wang et al., 2001; Reigber et al., 2001) and the rest of Asia. These measurements confirm active shortening rates of about 20 mm yr^{-1} for the Tien Shan. Wang et al. (2001) also measured the India-Eurasia convergence rate by GPS and they obtained 38 mm yr^{-1}, which suggests that the crustal shortening in the central Tien Shan takes up about half of the total convergence between India and Eurasia.

Talas-Fergana Strike-Slip Fault

The Talas-Fergana Fault is a major right-lateral strike slip fault that runs from the northwestern corner of the Tarim Basin, traverses the Tien Shan Ranges for about 500 km in the northwest direction, and extends well into the Kazakh Platform with a total length of over 1500 km (Figure 3; Burtman, 1975; Tapponnier and Molnar, 1979; Burtman, 1980; Burtman et al., 1996). This fault separates the Chatkal Ranges (the NW corner of the Tien Shan), the Fergana Basin, and the Alay Ranges (Tien Shan Range north of the Pamir) from the central Tien Shan and it consists of two major segments. The Talas-Fergana Fault, after crossing the Tien Shan Ranges, makes a right step-over in the north and continues in the Kazakh Platform. This northwestern segment is also referred to as the Karatau Fault (Burtman et al., 1996). On satellite images and high resolution shuttle radar topographic mission (SRTM) images it can be seen clearly that numerous thrust faults of the Tien Shan Ranges, on both sides of the Talas-Fergana strike-slip fault, abruptly terminate along the fault trace indicating that the Talas-Fergana Fault forms a major crustal discontinuity.

The Talas-Fergana Fault originated during the intense tectonic activity occurred in this region in the late Paleozoic time (Burtman, 1975; 1980). The Paleozoic igneous intrusions and tectonic structures have been displaced right-laterally ~ 180 km along the Talas-Fergana Fault and the amount of right-lateral displacement is estimated to be 60 ± 10 km since the early Cretaceous time (Burtman et al., 1996). The lack of seismic activity along this fault during the entire instrumental period is rather interesting and may suggest that The Talas-Fergana fault is presently locked and the present-day activity appears to stem from the active shortening on both sides of the fault (Ghose et al., 1998a,b).

Seismicity of the Tien Shan

The Tien Shan is seismically very active (Figure 4) and this is not surprising, because the entire region is characterized by roughly E-W trending active thrust faults, both along its outer margins, as well as along the numerous intermontane basin margins with the bounding mountain ranges.

One of the important characteristics of the Tien Shan seismicity is its shallow crustal nature. Although, excluding the Pamir region, a few events appear to be deeper than 50 km, there is no clear evidence of earthquakes occurring in the continental mantle lithosphere of the Tien Shan (north of 40°N), and the seismic activity is confined to the continental crust (Chen and Molnar, 1983; Maggi et al., 2000). As

pointed out by Maggi et al. (2000), among the events that have well determined centroid depths constrained by teleseismic and regional P and SH body wave modeling, only 10 events occurred at the depth range of 20–44 km, and the majority of them have depths less than 20 km.

The focal mechanism solutions for the earthquakes in the Tien Shan region indicate predominantly thrust events, with roughly E-W trending fault planes, that provide evidence for the overall N-S active crustal shortening of the Tien Shan (Ni, 1978; Tapponnier and Molnar, 1979; Nelson et al., 1987; Ghose et al.,1998a,b).

Another important feature of the Tien Shan seismicity is a general relationship between the geological structure and the earthquake magnitude. For example, in the Gissar-Kokshal area, north of the Tadjik Basin, the low angle frontal thrusts that move over sedimentary rocks are associated with small magnitude earthquakes, while moderate size ($M < 5.5$) earthquakes occur on crustal thrust ramps that have higher dips, and major strain releases ($5.5 > M > 8.1$) occur along the basement thrusts that form the Tien Shan margin (Leith and Simpson, 1986). This general relationship appears to be valid for the Tien Shan and probably for most of the active fold and thrust belts of the world.

During the last 120 years 12 large earthquakes ($M \geq 7$) occurred along the northern and southern margins of the Tien Shan (Chen and Molnar, 1977; Tapponnier and Molnar, 1979; Molnar and Ghose, 2000; Abdrakhmatov et al., 2002). Among these Verny (the old name for Almaty, 1887, M = 7.3), Chilik (1889, M = 8.3), Manas (1906, M = 8.3), Kemin (1911, M = 8.2), Chatkal (1946, M = 7.5), and Suusamyr (1992, M = 7.3) earthquakes occurred along the northern margin. The large earthquakes that occurred along the southern margin are: Kashgar (1902, M = 7.8), Karatagh (1907, double shock with M = 7.3 and 7.4), Khait (1949, M = 7.4), and Wuqia (1985, M = 7.6).

The Lithospheric Structure of the Tien Shan

The lithospheric structure of the Tien Shan is extremely variable and therefore complex starting from the surface, through the crust, to all the way down to the mantle (Figure 5). Since the nineties many studies have been carried out to reveal the lithospheric structure of the Tien Shan (Kosarev et al., 1993; Roecker et al., 1993; Cotton and Avouac, 1994; Ghose et al., 1998a,b; Bump and Sheehan, 1998; Oreshin et al., 2002; Vinnik et al., 2002a,b; Poupinet et al., 2002; Vinnik et al., 2004; Kumar et al., 2005).

The first P receiver function application in the Tien Shan indicated significant crustal velocity differences on both sides of the Talas-Fergana Fault (Koserev et al., 1993). The crustal velocities are 10% higher on the west side of the Talas-Fergana Fault at the 10–35 km depth range and the areas east of the fault are associated with lower mantle velocities, low Q, and shorth-wavelength variations in anisotrophy. These differences were interpreted as due to mantle upwelling, which may have contributed to the vertical uplift of the Tien Shan ranges on the west side of the Talas-Fergana Fault.

P and S wave tomographic study of Roecker et al. (1993) determined that the Chu and Fergana Basins have 7 km and 10 km thick sediments, respectively. The differences on both sides of the Fergana Fault were confirmed (Roecker et al., 1993; Ghose et al., 1998a,b) and they suggested that the 10% lower mantle velocities on the west side of the Talas-Fergana Fault, beneath the central Tien Shan exceed 150 km depth, but no deeper than 300 km.

Surface wave-dispersion, P and S tomography and receiver function studies have produced Moho depth values in the range of 45 to 70 km in the Tien Shan (Roecker et al., 1993; Cotton and Avouac, 1994; Mahdi and Pavlis, 1998; Bump and Sheehan, 1998; Oreshin et al., 2002; Vinnik et al., 2002 & 2004; Kumar et al, 2005). This reported range in Moho depth is real and demonstrates the extremely variable nature of the lithospheric structure in the Tien Shan.

Using simulated annealing technique, Vinnik et al. (2004) inverted P and S receiver functions together for 40 broad-band stations to obtain receiver function tomographic images of the Tien Shan lithosphere. The P and S receiver function tomography indicates that the Moho depth varies between 45 km to about 70 km beneath the Tien Shan. The Kazakh Platform, the Tarim Basin have thinner crust (~45 km), whereas within

the Tien Shan Ranges, west of the Lake Issyk-Kul the crustal thickness reaches up to 70 km. The crust is thin (~45 km) beneath the Naryn Basin and the immediate west of the Talas-Fergana Fault. Interestingly, the elevated crustal thickness correlates with a thickened "basaltic" layer (Vs ~ 4.0 km s^{-1}) in the lower crust and the presence of low-velocity zones in the uppermost mantle, suggesting that recent magmatic underplating is also responsible for crustal thickening in addition to the crustal shortening (Vinnik et al., 2004).

The lithosphere and asthenospere boundary (LAB) in the Tien Shan and surrounding regions vary significantly based on another S receiver function study by Kumar et al. (2005). They found that, along a N-S profile at 75°E, the LAB is 130 km deep beneath the Kazakh Platform and 90 km deep beneath the Tien Shan (40°–41°N) confirming the results obtained by Oreshin et al. (2001) and Vinnik et al. (2004). The lithospheric thickness is 180 km in the Tarim Basin and the LAB starts dipping toward south reaching a depth of 270 km beneath Pamir, where it correlates with the intermediate-depth seismicity, which is interpreted as an evidence for the continental subduction of the Asian lithosphere (Kumar et al., 2005). This geometry of the LAB correlates well and forms the upper boundary of a low-velocity anomaly dipping toward south from a depth of 90 km beneath the Tien Shan to 300 km beneath the Karakoram imaged by surface wave tomography (Freiderich, 2003).

Similarly, southward subduction of the Tarim plate with ~ 45° angle, down to ~300 km depth beneath northwestern Tibet has been suggested based on the results obtained from receiver function and P-wave tomography (Wittlinger et al., 2004).

On the other hand, teleseismic receiver function analysis (Poupinet et al., 2002) and seismic refraction/wide-angle-reflection studies (Zhao et al., 2003; 2006) along a northeast trending profile from the Tarim Basin to the Junggar Basin suggest that the Moho at the northern margin of the Tarim basin dips north beneath the Tien Shan. Also the Moho at the southern margin of the Junggar Basin dips south beneath the Tien Shan. The results obtained from a larger scale P-wave tomographic study of the southeast Asia (Li et al., 2006) appear to confirm only the southward subduction of the Junggar lithosphere. However, this does not necessarily rule out the northward subduction of the Tarim lithosphere, because as reported by Li et al. (2006) the resolution of their P-wave tomographic model beneath the Tarim Basin is rather poor. Furthermore, they state that no prominent high velocity is detected beneath the Tarim Basin, which is contradicted by the results obtained from surface wave velocity inversion, receiver function tomography, and P-wave tomography (Villaseñor et al., 2001; Vinnik et al., 2004; Sun and Toksöz, 2006).

CONCLUSIONS AND RECOMMENDATIONS

The current structure of the Tien Shan is formed by the reactivation of Paleozoic structures in the Late Cenozoic due to the India-Asia plate collision. Roughly east-west trending folding, thrusting and high-angle reverse faulting is the dominant form of crustal deformation. The Tien Shan region has high seismic activity, and many large earthquakes that have predominantly thrust faulting mechanisms occurred in the region. Based on the GPS measurements the active crustal shortening rate is 20 mm yr^{-1} in the Tien Shan. This rate corresponds to the half of the total plate convergence between the Indian and Eurasian plates. The lithospheric structure of the Tien Shan is extremely complex, and the Moho depth varies between 45–70 km. The thicker crust correlates with a thickened basaltic layer in the lower crust and the presence of low-velocity zones in the upper-mantle. Seismic tomographic and S-receiver function studies indicate a southward dipping LAB that suggests the southward subduction of the continental lithosphere in the western Tien Shan. The lithospheric mantle beneath the Junggar Basin appears to subduct southward beneath the Tien Shan. Our recommendation for the next step in this research is to integrate tectonic models with the crustal structure which will be determined from new data from local networks in the participating countries.

REFERENCES

Abdrakhmatov, K. Y. et al. (1996). Relatively recent construction of the Tien Shan inferred from GPS measurements of present day crustal deformation rates, *Nature*, 384: 450–453.

Abdrakhmatov, K. Y., K. D. Djanuzakov, and D. Delvaux (2002). Active tectonics and seismic hazards of the Issyk-Kul Basin in the Kyrgyz Tian Shan, in *Lake Issyk-Kul: Its Natural Environment*, J. Klerkx and B. Imanackunov (Eds.).Norwell, Massachusetts: Kluwer Academic Publishers, pp. 147–160.

Avouac, J. P., P. Tapponnier, M. Bai, H. You, and G. Wang (1993). Active thrusting and folding along the northern Tien Shan and Late Cenozoic rotation of the Tarim relative to Dzungaria and Kazakhstan, *J. Geophys. Res*. 98: 6,755–6,804.

Bump, H. A. and A. F. Sheehan (1998) Crustal thickness variations across the northern Tien Shan from teleseismic receiver functions, *Geophys. Res. Lett.* 25: 1,055–1,058.

Burbank D. W., J. K. McLean, M. Bullen, K. Y. Abdrakhmatov, and M. M. Miller (1999). Partitioning of intermontane basins by thrust-related folding, Tien Shan, Kyrgyzistan, *Basin Res.* 11: 75–92.

Burchfiel, B. C., E. T. Brown, Q. Deng, X. Feng, J. Li, P. Molnar, J. Shi, Z. Wu, H. You (1999). Crustal shortening on the margins of the Tien Shan, Xinjiang, China, *Int. Geol. Rev*. 41: 665–700.

Burtman, V. S. (1975). Structural geology of the Variscan Tien Shan, USSR, *Am. J. Sci*. 272-A: 157–186.

Burtman, V. S. (1980). Faults in middle Asia, *Am. J. Sci*. 280: 725–744.

Burtman, V. S., S. F. Skobelev, and P. Molnar (1996). Late Cenozoic slip on the Talas-Ferghana fault, the Tien Shan, central Asia, *Geol. Soc. Am. Bull*. 108: 1,004–1,021.

Chen, W. P. and P. Molnar (1983). Focal depths of intracontinental and intraplate earthquakes and their implications for the thermal and mechanical properties of the lithosphere, *J. Geophys. Res*. 88: 4,183–4,214.

Cobbold, P. R., E. Sadybakasov, and J. C. Thomas (1996). Cenozoic transpression and basin development, Kyrgyz Tien Shan, central Asia, in *Geodynamic Evolution of Sedimentary Basins*, F. Roure, N. Ellouz, V. S. Shein, and I. Skvortsov (Eds.). Paris: Technip, 181–202.

Cotton, F. and J. P. Avouac (1994). Crustal and upper-mantle structure under the Tien Shan from surface-wave dispersion, *Phys. Earth Planet Int*. 84: 95–109.

Dewey, J. F., R. M. Shackleton, C. Chang, and Y. Sun (1988). The tectonic evolution of the Tibetan Plateau, in The Geological Evolution of Tibet C. Chang, R. M. Shackleton, J. F. Dewey, and J. Yin (Eds.). Royal Society of London Philosophical Transactions, pp. 379–413.

Friederich, W. (2003). The S-velocity structure of the east Asian mantle from inversion of shear and surface waveforms, *Geophys. J. Int*. 153: 88–102.

Ghose, S., M. W. Hamburger, and C. J. Ammon (1998a). Source parameters of moderate-sized earthquakes in the Tien Shan, central Asia from regional moment tensor inversion, *Geophys. Res. Lett*. 25: 3,181–3,184.

Ghose, S., M. W. Hamburger, and J. Virieux (1998b). Three-dimensional velocity structure and earthquake locations beneath the northern Tien Shan of Kyrgyzstan, central Asia, *J. Geophys. Res.* 103: 2,725–2,748.

Gülen, L. and M. N. Toksöz (2006). Active Tectonics of the Tien Shan, central Asia, Earth Resources Laboratory, Massachusetts Institute of Technology report, 88 pp.

Khain, V. E. (1985). *Geology of the USSR, First Part: Old Cratons and Paleozoic Fold Belts*. Berlin: Gebrüder Borntraeger, 264 pp.

Kosarev, G. L., N. V. Petersen, and L. P. Vinnik (1993). Receiver functions for the Tien Shan analog broadband network: Contrasts in the evolution of structures across the Talasso-Fergana Fault, *J. Geophys. Res*. 98: 4,437–4,448.

Kumar, P., X. Yuan, R. Kind, and G. L. Kosarev (2005). The lithosphere-asthenosphere boundary in the Tien Shan-Karakoram region from S receiver functions: Evidence for continental subduction, *Geophys. Res. Lett.* 32: L07305, doi: 10.1029/2004GL022291.

Lee, C. Y., Q. Wang, X. Liu, and Y. Tang (1982). Explanatory notes to the tectonic map of Asia, Beijing: Institute of Geology and Geophysics, Chinese Academy of Sciences, 49 pp.

Leith, W. and D. W. Simpson (1986). Seismic domains within the Gissar-Kokshal seismic zone, Soviet central Asia, *J. Geophys. Res*. 91: 689–699.

Li, C., R. D. van der Hilst, and M. N. Toksöz (2006). Constraining P-wave velocity variations in the upper mantle beneath Southeast Asia, *Phys. Earth Planet. Int.* 154: 180–195.

Maggi, A., J. A. Jackson, K. Priestley, and C. Baker (2000). A re-assessment of focal depth distributions in southern Iran, the Tien Shan and northern India: Do earthquakes really occur in the continental mantle? *Geophys. J. Int*. 143: 629–661.

Mahdi, H. and G. L. Pavlis (1998). Velocity variations in the crust and upper mantle beneath the Tien Shan inferred from Rayleigh wave dispersion: Implications for tectonic and dynamic processes, *J. Geophys. Res.* 103: 2,693–2,703.

Molnar, P. and P. Tapponnier (1975). Cenozoic tectonics of Asia, *Science* 189: 419–426.

Molnar, P. and S. Ghose (2000). Seismic moments of major earthquakes and the rate of shortening across the Tien Shan, *Geophys. Res. Lett*. 27: 2,377–2,380.

Nelson, M. R., R. McCaffrey, and P. Molnar (1987). Source parameters for 11 earthquakes in the Tien Shan, central Asia, determined by P and SH waveform inversion, *J. Geophys. Res*. 92: 12,629–12,648.

Ni, J. (1978). Contemporary tectonics in the Tien Shan region, *Earth Planet Sci. Lett*. 41: 347–354.

Oreshin, S., L. P. Vinnik, D. Peregoudov (2002). Lithosphere and asthenosphere of the Tien Shan imaged by S receiver functions, *Geophys. Res. Lett.* 29: 1191, 10.1029/2001GL014441.

Poupinet, G., J. P. Avouac, M. Jiang, S. Wei, E. Kissling, G. Herquel, J. Guilbert, A. Paul, G. Wittlinger, H. Su, and J. C. Thomas (2002). Intracontinental subduction and Paleozoic inheritance of the lithosphere suggested by a teleseismic experiment across the Chinese Tien Shan, *Terra Nova*, 14: 18–24.

Reigber, C., G. W. Michel, R. Galas, D. Angerman, J. Klotz, J. Y. Chen, A. Papschev, R. Arslanov, V. E. Tzurkov, and M. C. Ishanov (2001). New space geodetic constraints on the distribution of deformation in Central Asia, *Earth Planet. Sci. Lett*. 191: 157–165.

Roecker, S. W., T. M. Sabitova, L. P. Vinnik, Y. A. Burmakov, M. I. Golvanov, R. Mamatkanova, and L. Munirova (1993). Three-dimensional elastic wave velocity structure of the western and central Tien Shan, *J. Geophys. Res*. 98: 15,779–15,795.

Sun, Y. and M. N. Toksöz (2006). Crustal structure of China and surrounding regions from P wave traveltime tomography, *J. Geophys. Res*. 111: B03310 doi:10.1029/2005JB003962.

Tapponnier, P. and P. Molnar (1979). Active faulting and Cenozoic tectonics of the Tien Shan, Mongolia, and Baykal regions, *J. Geophys. Res*. 84: 3425–3459.

Thompson, S. C., R. J. Weldon, C. M. Rubin, K. Abrakhmatov, P. Molnar, and G. W. Berger (2002). Late Quaternary slip rates across the central Tien Shan, Kyrgyzstan, central Asia, *J. Geophys. Res*. 107(B9): 2203, doi:10.1029/2001JB000596.

Tingdong, L., et al. (1997). *Geological Map of Asia and Europe* (Scale: 1:5,000,000). Beijing: Geological Publishing Housea.

Villaseñor, A., M. H. Ritzwoller, A. L. Levshin, M. P. Barmin, E. R. Engdahl, W. Spakman, and J. Trampert (2001). Shear velocity structure of central Eurasia from inversion of surface wave velocities, *Phys. Earth Planet. Int.* 123: 169–184.

Vinnik, L. P., S. W. Roecker, G. L. Kosarev, S. I. Oreshin, and I. Y. Koulakov (2002a). Crustal structure and dynamics of the Tien Shan, *Geophys. Res. Lett*. 29: 2047, doi: 10.1029/2002GL015531.

Vinnik, L. P., D. Peregoudov, L. Makeyeva, and S. Oreshin (2002b,).Towards 3-D fabric in the continental lithosphere and astenosphere: The Tien Shan, *Geophys. Res. Lett.* 29: 1795, 10.1029/2001GL014588.

Vinnik, L. P., C. Reigber, I. M. Aleshin, G. L. Koserev, M. K. Kaban, S. I. Oreshin, and S. W. Roecker (2004). Receiver function tomography of the central Tien Shan, *Earth Planet. Sci. Lett*. 225: 131–146.

Wang, Q., et al. (2001). Present-day crustal deformation in China constrained by global positioning system measurements, *Science* 294: 574–577.

Watson, M. P., A. B. Hayward, D. N. Parkinson, and Z. Zhang (1987). Plate tectonic history, basic development and petroleum source rock deposition of onshore China, *J. Mar. Petr. Geol*. 4: 205–225.

Wittlinger, G., J. Vergne, P. Tapponnier, V. Farra, G. Poupinet, M. Jiang, H. Su, G. Herquel, A. Paul (2004). Teleseismic imaging of the subducting lithosphere and Moho offsets beneath western Tibet, *Earth Planet. Sci. Lett*. 221: 117–130.

Yin, A., S. Nie, P. Craig, M. T. Harrison, F. J. Ryerson, Q. Xianglin, and Y. Geng (1998). Late Cenozoic tectonic evolution of the southern Chinese Tien Shan, *Tectonics* 17: 1–27.

Zhao, J., G. Liu, Z. Lu, X. Zhang, and G. Zhao (2003). Lithosperic structure and dynamic processes of the Tian Shan orogenic belt and the Junggar basin, *Tectonophys.* 376: 199–239.

Zhao, J., H, Liu, S. Pei, S. Jia, B. Liu, J. Zhang, and J. Fan (2006). A geophysical transect of the lithosphere across the eastern Tienshan orojen, (submitted).

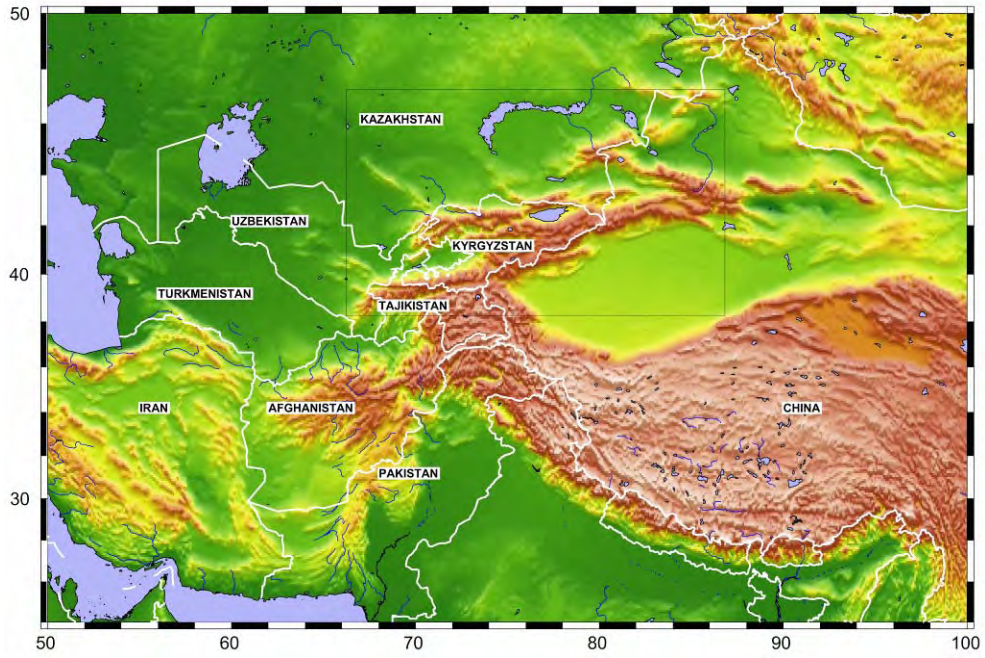


Figure 1. CASRI project area political boundaries and topography.

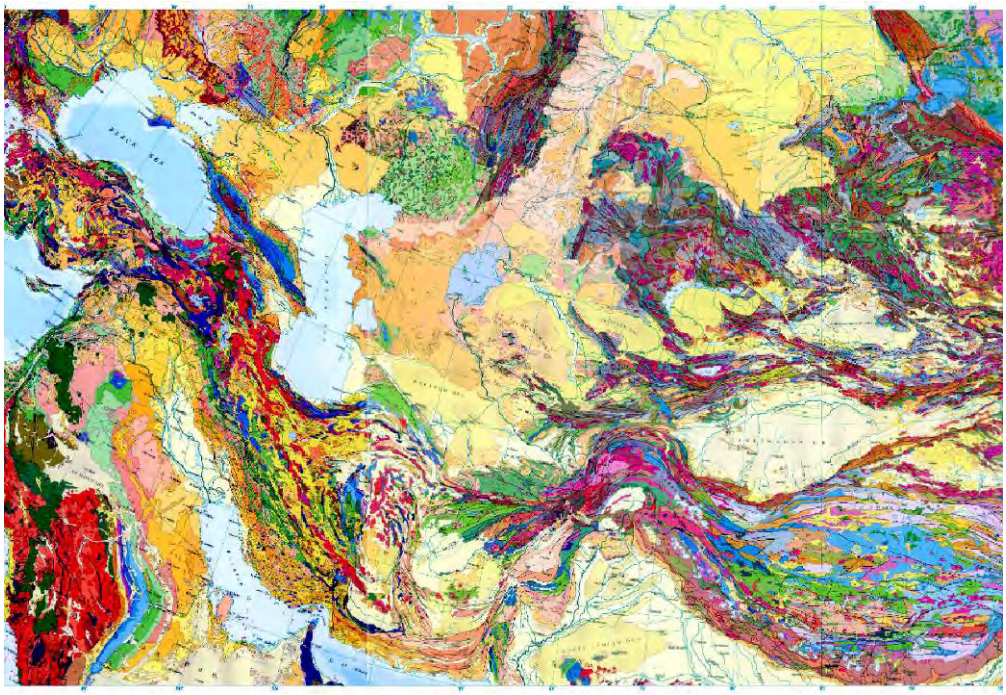


Figure 2. Geological map compilation of the CauSIN and CASRI regions.

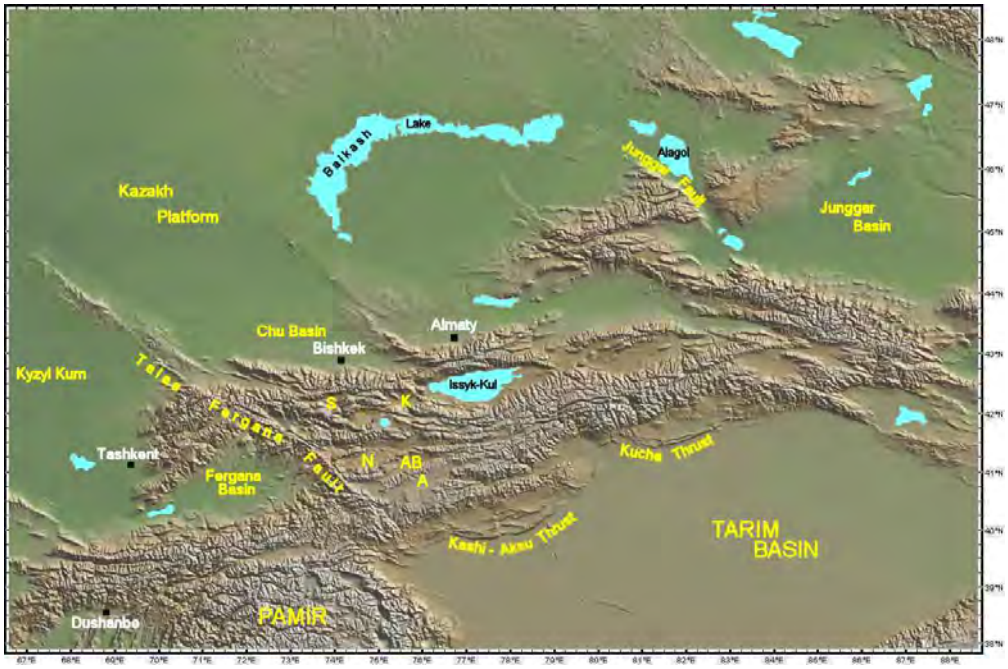


Figure 3. Shuttle Radar Topographic Mission (SRTM) image showing tectonics and topography of the Tien Shan and surrounding regions. The east-west trending lineaments are the active thrust faults in the Tien Shan. Basins are S, Suusamyr; K, Kochkor; N, Naryn; AB, At-Bashi; and A, Aksay.

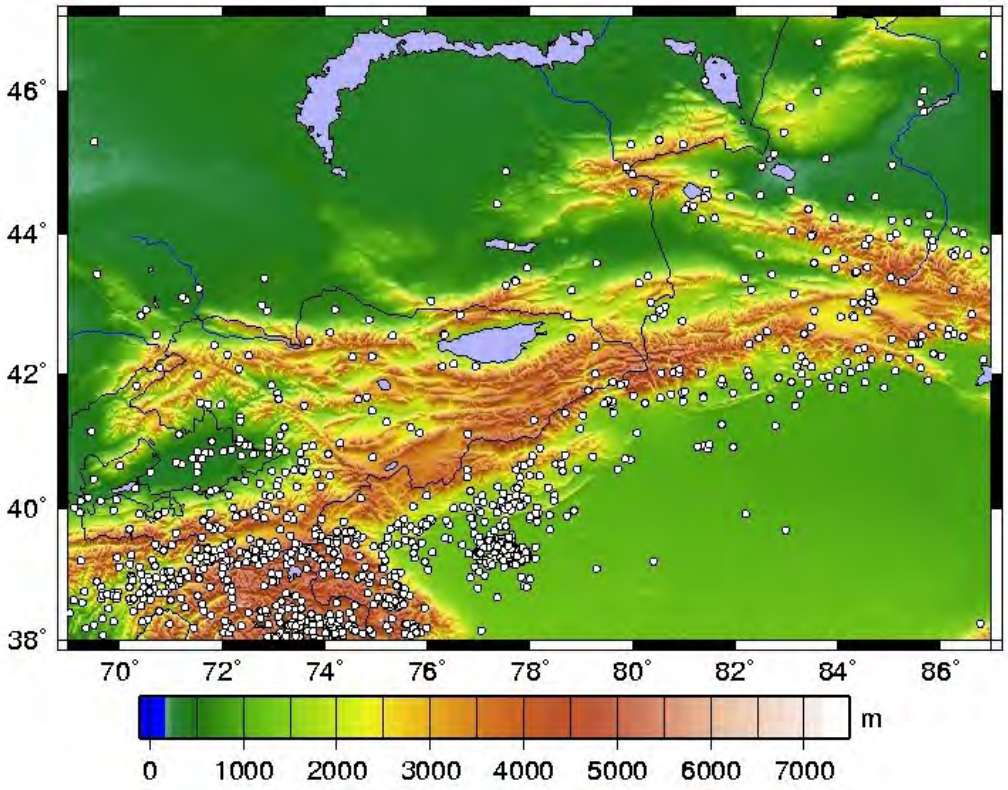


Figure 4. Seismicity map of the Tien Shan and surrounding regions. The seismicity data cover the events with M>4 for the period 2000-2004 from the ISC Comprehensive database.

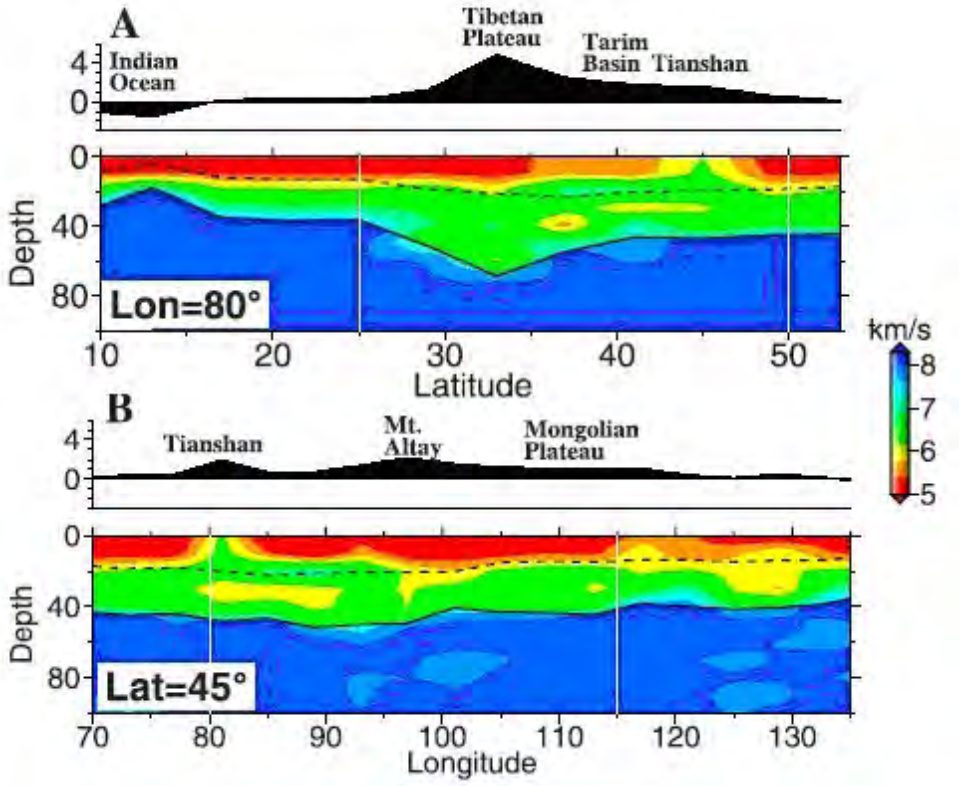


Figure 5. Cross sections showing P-wave velocity variations along N-S (A) and E–W (B) directions beneath central Asia (Sun and Toksöz, 2006). The dashed lines indicate the Conrad discontinuity.

CAUCASUS SEISMIC INFORMATION NETWORK

Randolph Martin[1], Mary L. Krasovec[1], Spring Romer[1], M. Nafi Toksöz[2], Youshun Sun[2], Dogan Kalafat[2], and Eileen S. Vergino[3]

New England Research[1], Massachusetts Institute of Technology[2], and Lawrence Livermore National Laboratory[3]

Sponsored by National Nuclear Security Administration
Office of Nonproliferation Research and Development
Office of Defense Nuclear Nonproliferation

Contract Nos. DE-AC52-03NA99600[1], NNSA-03-2S[2], and W-7405-ENG-48[3]

ABSTRACT

The Caucasus Seismic Information Network (CauSIN) seeks to build a knowledge base of geological, geophysical, and seismic information in the Caucasus and to use crustal modeling techniques to create a model of the region to aid in seismic monitoring.

Over the past year, we have expanded our knowledge base in the CauSIN region. The Republic of Georgia has expanded its digital network, and we are receiving new data from them as events occur. Azerbaijan has a 13-station kinemetric array. No data had been received from this array until the beginning of 2006, but we are currently working with local scientists on extracting the data and developing catalogs that will be made available to all participants in the program.

A joint effort with our colleagues at the Massachusetts Institute of Technology has led to 3D modeling results. The method follows Hearn's (1996) approach and computation method, inverting Pn travel-time residuals for the lateral velocity variation and anisotropy within the mantle lid. Initial results show relatively low Pn velocities under the Lesser Caucasus, eastern Turkey, and northern Iran. Relatively higher Pn velocities occur under the eastern portion of the Black Sea and the southern Caspian Sea, and also extend into the eastern edge of Azerbaijan.

OBJECTIVE

The primary goal of this project is to develop a database of geology and active tectonics in the Caucasus and Central Asian regions. Data will include localized shallow crustal structure obtained from geophysical surveys for oil exploration.

With this new database, we will be able to improve earthquake location and identify potential "ground truth" (GT) events. The dense network, calibration events (mining and quarry blasts), improved models, and better location algorithms (including multiple-event grid search, and double difference) will improve the event locations. Scientists at collaborating countries are very eager to assist with this task, since improved locations will aid in the identification of active faults.

With the ground truth events to serve as validation, we will obtain a detailed crust/upper mantle structure in the Caucasus, eastern Turkey, and northwestern Iran, using data from newly installed seismic stations as well other stations operated as part of the national networks. The model will incorporate the extensive geological and geophysical data (e.g., surface seismic reflection profiles, gravity maps) as well as the seismic data.

RESEARCH ACCOMPLISHED

Crustal Modeling: Methodology

Following Hearn's (1996) approach and computation method, P_n travel-time residuals are inverted for the lateral velocity variation and anisotropy within the mantle lid. Within the epicentral distances considered in this study, the P_n ray paths can be modeled as refracted rays traveling along the Moho discontinuity. The variation of seismic velocity within the uppermost mantle is parameterized by subdividing the surface of the uppermost mantle in a 2D grid of square cells with dimensions of 30 km by 30 km. The P_n travel-time residuals are described as the sum of three time terms:

$$t_{ij} = a_i + b_j + \sum d_{ijk}(s_k + A_k \cos 2\varphi + B_k \sin 2\varphi)$$

where t_{ij} is the travel time residual for the ray from event j to station i; a_i is the static delay for station i, depending on the crust thickness and velocity beneath the station; b_j is the static delay for event j, not only depending on the crust thickness and velocity beneath the event, but also on the event focal depth; d_{ijk} is the distance traveled by ray ij in mantle cell k; s_k is the slowness perturbation for cell k; A_k and B_k are the anisotropic coefficients for cell k; and φ is the back azimuth angle. The unknown quantities in the equation are a_i, b_j, s_k, A_k and B_k. As a first approximation, seismic anisotropy in the mantle is assumed to be described by a 2φ azimuthal variation. The magnitude of anisotropy for cell k is given by $(A_k^2 + B_k^2)^{1/2}$ and the azimuthal angle θ of the fast direction of P_n propagation is given by $1/2\arctan(B_k/A_k)$. The sum is calculated over all cells through which the ray travels in the uppermost mantle. Further details of the tomography technique used here can be found in Hearn (1996). A set of Laplacian damping equations regularizes the solution, and two damping constants are separately applied to the unknown slowness and anisotropic coefficients. A proper pair of damping constants is chosen to balance the error size and the resolution width. In this approach the trade-off between velocity and anisotropy variations is a crucial issue, which has been examined by using different combinations of damping parameters for both velocity and anisotropy. In this study the main features of the velocity and anisotropy fields are observed to be significantly stable, even though the extent of the velocity anomalies and the amount of anisotropy vary slightly for different combinations of the damping constants.

Crustal Modeling: Results

Figures 1 through 5 show preliminary results of applying this tomography method to the CauSIN time picks database, which has been recently extended to include data from local Turkish networks.

Figure 1 shows the ray paths used in the tomography; there are 41,682 Pn rays from 5,465 events to 245 stations. Figure 2 shows preliminary results of 3D tomography for lateral variations in P_n velocity. Areas of thicker continental crust throughout the central Caucasus show lower velocities, while the oceanic crust under the Black and Caspian seas show higher velocities. The region of higher velocity under the eastern portion of Azerbaijan is most likely due to high velocities in the oceanic crust under the south Caspian Sea. Poor coverage of ray paths in this part of the study area has resulted in smearing the feature toward the west. Similarly, the high velocity in the northern part of the image is most likely from a basin structure north of the Greater Caucasus.

Figure 3 shows station delays for P_n travel-times, while Figure 4 shows event delays for Pn travel-times. Finally, Figure 5 shows travel-time residuals before and after inversion. The standard deviation of travel-time residuals is reduced from 1.28 sec to 0.92 sec.

This tomography result will improve the coverage once data are received from our colleagues in Azerbaijan. We will also extend the study region past the Caspian Sea into central Asia when this dataset is joined with data being collected for the Central Asian Seismic Research Initiative (CASRI) project in central Asia.

CONCLUSIONS AND RECOMMENDATIONS

The P_n velocities shown in Figure 2 have similar features to those obtained by Al-Lazki et al. (2004). High P_n velocities are dominant under eastern Azerbaijan/ southern Caspian and under eastern Black Sea. The extent of the anomalies require further confirmation. Because of the distribution of earthquake epicenters and stations, rays traversing the area are mostly NW-SE. It is important to ensure that there is no "smearing" along the dominant ray direction.

We are in the process of extending our data coverage to the south and east, which should improve the image of the high velocity zone under the south Caspian Sea. It will be more difficult to improve data coverage in the north, as there is very little seismicity north of the greater Caucasus and very few stations. We hope that combining this data with data from networks in the Central Asian countries (as part of the CASRI project) will be beneficial to the image quality in the northern and eastern region of the CauSIN study area.

REFERENCES

Al-Lazki, A. I., E. Sandvol, D. Seber, M. Barazangi, N. Turkelli, and R. Mohamad (2004). Pn tomography imaging of mantle lid velocity and anisotrophy at the junction of the Arabian, Eurasian and African plates, *Geophys. J. Int.* 158: 1,024–1,040.

Hearn, T. M. (1996). Anisotropic Pn tomography in the western United States, *J. Geophys. Res.* 101: 8,403–8,414.

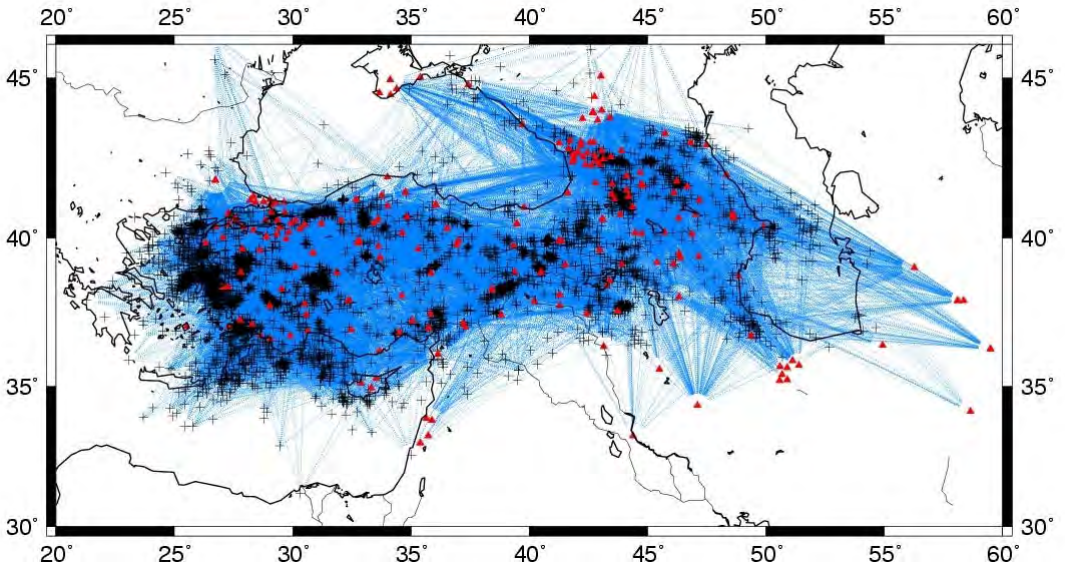


Figure 1. Ray paths for Pn travel times. As shown here, 41682 Pn rays were obtained from 5465 events (black crosses) recorded by 245 stations (red triangles).

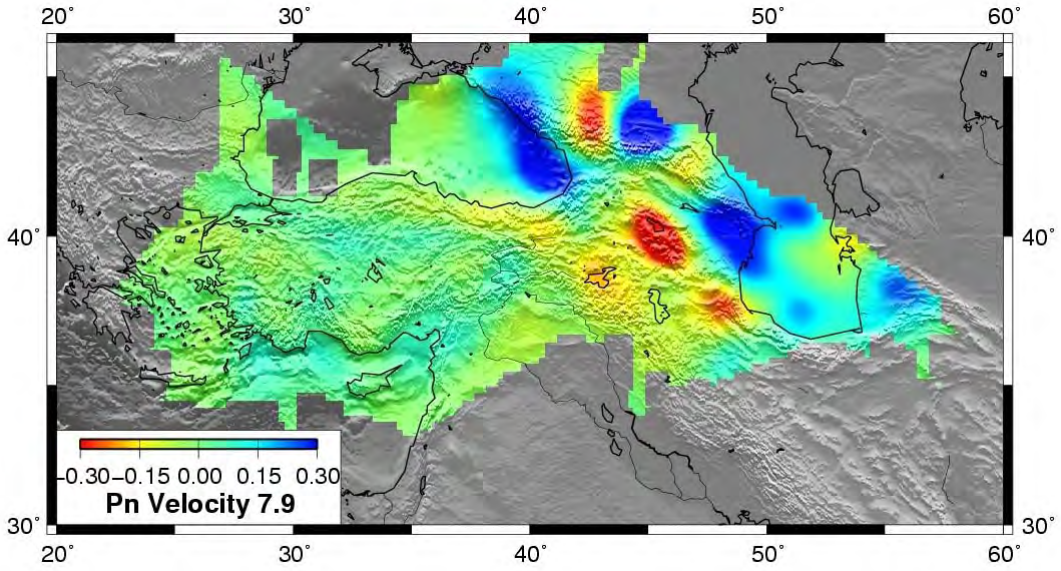


Figure 2. Imaged Pn velocity lateral variations. Average Pn velocity is 7.9km/s, and variation corresponds with color, red representing lower velocity than the average and blue denoting higher velocity.

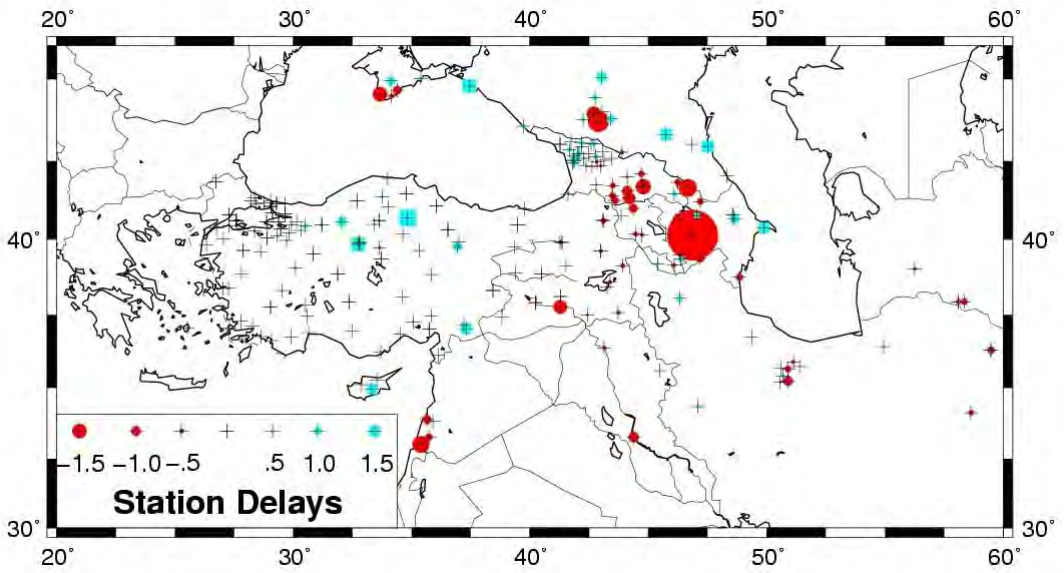


Figure 3. Station delays for Pn travel times. Crosses represent stations. Circles indicate early arrival times and squares indicate late arrival times, with their size proportional to delay amount.

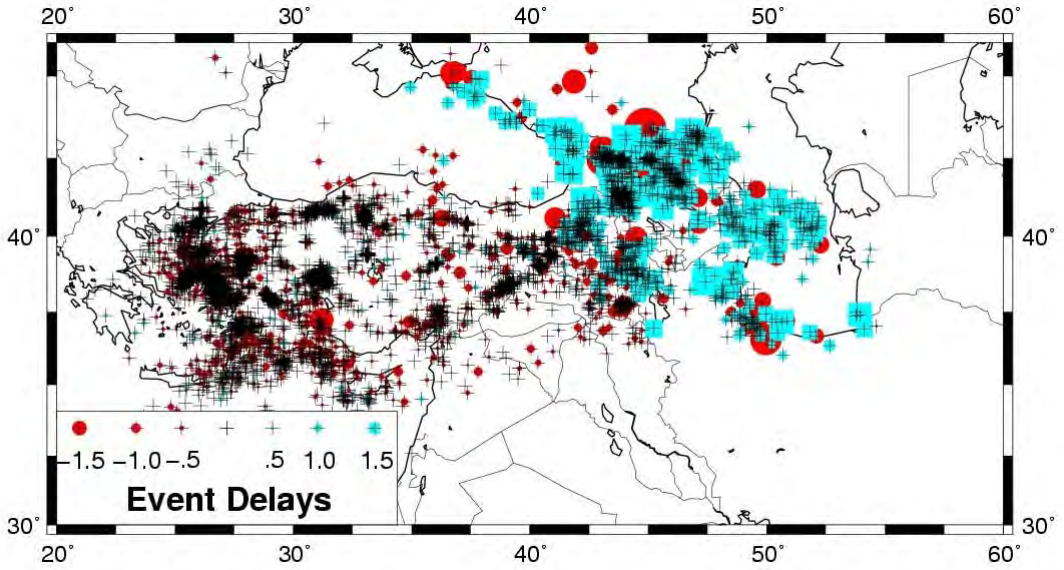


Figure 4. Event delays for Pn travel times. Crosses represent events. Circles indicate early arrival times and squares indicate late arrival times, with their size proportional to delay amount.

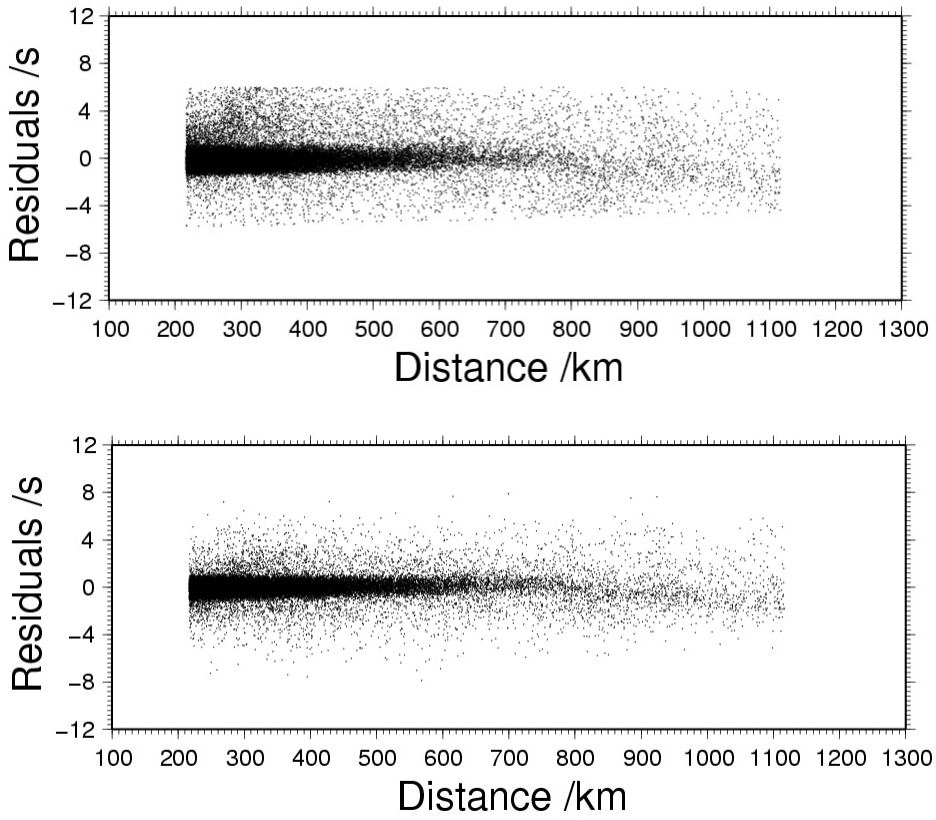


Figure 5. Travel time residuals before inversion (top panel) and after inversion (bottom panel). The standard deviation of travel time residuals decreased to 0.92 s from 1.28 s.

AN UPDATED EURASIAN CRUSTAL MODEL USING MULTIPLE SEISMIC METHODS

Walter D. Mooney, Susan McDonald, and Shane Detweiler

U.S. Geological Survey

Sponsored by National Nuclear Security Administration
Office of Nonproliferation Research and Development
Office of Defense Nuclear Nonproliferation

Contract No. DE-AI04-2000AL66517

ABSTRACT

An updated $2^o \times 2^o$ crustal model for greater Eurasia is being completed from (1) synthesizing existing models, such as WENA 1.0, the new Barents Sea model, and P-wave velocity model for India and Pakistan (WINPAK); (2) regional seismic compressional phase/regional seismic shear phase (Pn/Sn) tomography data; (3) our ongoing compilation of published seismic models for the crust, based on active- and passive-source seismology; and (4) observed and calculated seismic surface wave group and phase velocity maps. In particular, three controlled source studies from China and India completed by the U.S. Geological Survey and colleagues in the past year are contributing to this updated Eurasian crustal model. These include: (1) three short (20–35 km) seismic reflection profiles from the immediate region of the 2001 Mw 7.7 Bhuj (western India) earthquake that yielded a crustal thickening from 35 to 45 km over a distance of about 50 km from the northern margin of the Gulf of Kutch to the epicentral zone of the earthquake; (2) a compilation of over 90 seismic refraction/wide-angle reflection profiles, with a cumulative length of more than sixty thousand kilometers, across mainland China that have shown a mid-crustal low-velocity layer in unstable regions; and (3) a 1000-km-long geophysical profile from Darlag-Lanzhou-Jingbian extending from the Songpan-Ganzi terrane to the Ordos basin in the NE margin of the Tibetan plateau that yielded a 2-D seismic velocity profile from which crustal composition and continental dynamics of the Tibetan plateau are inferred. New crustal depth and velocity maps for greater Eurasia have been compiled, which incorporate the results from the above three studies and other relevant controlled source experiments. This updated compilation of Eurasian Pn and Sn data in CRUST 2.2 will yield more detailed models of the Earth's structure and subsequently more accurate seismic monitoring. Well-resolved crustal models are critical for determining event locations and size estimations.

OBJECTIVE

Our primary objective is to produce an updated 2º × 2º Eurasian Crustal and Pn/Sn model that can be applied to the problem of improving seismic event location accuracy. The compilation of additional data from previously unavailable regions will add to the understanding of lithospheric structure, and will allow us to develop new and more accurate models for the region. These models will in turn, give better resolution and detection capabilities for individuals wishing to: (1) locate and constrain seismic events, (2) determine regional magnitude equivalents, (3) calculate attenuation coefficients, and (4) describe amplitude variations.

RESEARCH ACCOMPLISHED

In order to meet the above objective, we have completed several investigations of crustal structure in Asia that improve the resolution of the 2º × 2º model. These investigations include seismic reflection profiles in the Kutch (Bhuj) epicentral region of western India and the northeastern Tibetan Plateau, as well as a refined determination of Pn velocity structure throughout mainland China. Data from these studies and those of other researchers are being compiled into an updated CRUST 2.2 Eurasian Model.

Data quality is mainly dependent on the general amount and distribution of appropriate first-order data such as deep seismic wide-angle experiments covering the entire crustal column down to the Moho-discontinuity. On the basis of regional geological and tectonic history, nearby and statistical data, second-order parameters (e.g., thermodynamic) and other model compilations, a model may be "derived." During later steps these models are tested and validated against independent geophysical data. Therefore, acquiring new and accurate wide-angle seismic data, especially in complex boundary regimes such as the contact between the Indian and Eurasian plates, is critical to the improvement of a 2º × 2º Eurasian Crustal model by significantly reducing the effect of interpolating a priori estimations of crustal velocity. This paper presents the results of three reflection, refraction, or deep seismic sounding surveys in the complex boundary regime between the Indian and Eurasian plates.

In India, research was done to determine the seismic structure and thickness of the crust at and adjacent to the epicenter of the 2001 Mw 7.7 Bhuj earthquake, fortuitously near the Indian nuclear test site. Seismic refraction data was taken from a 1997 survey with three seismic lines that were 20–35-km-long (Figure 1). Data from these seismic profiles were used to determine crustal reflectivity patterns and to bring out the lateral variations in the crustal configuration, which may significantly increase our understanding of the seismicity in the region. Each seismic reflection profile imaged a highly reflective 35–45-km-thick crust.

Seismic refraction data were collected using two 60-channel DFS-V recording systems (NGRI, 2000). The receiver spacing was 100 m, while the shot interval was 7–8 km. Holes drilled up to 20–30 m were utilized to detonate explosives varying between 50–500 kg, depending upon the shot-receiver distances. The data were reprocessed into three common-depth point (CDP) reflection profiles. The seismic survey delineated the basement configuration and the sediments that are sometimes "hidden" under higher velocity Deccan volcanics. The refraction data, however, indicated some basement faults, either directly observable in the form of fault-plane-reflections or in terms of a sudden change in the basement depth, suggesting that a re-analysis of the data sets is likely to bring out seismotectonically important information for the upper and lower crust.

The single-fold 'refraction' data were next subjected to Kirchhoff pre-stack depth migration along each of the three line segments A, B and C, with 4, 3 and 4 shots, respectively (Figure 1). Pre-stack depth migration has become an important tool for obtaining quality images from seismic data acquired in geologically complex regions (Yilmaz, 1987; Audebert et al., 1997). The depth migration consists of an estimation of a velocity-depth model and the calculation of an appropriate Green's function. The migration places structures in their true spatial locations by applying the Green's function to each reflecting location using a travel-time map that relates time and amplitude from each surface location to a region of subsurface points.

The results indicated that away from the epicentral region of the 2001 Bhuj earthquake (lines A and B), the crust is generally highly reflective, while the crust beneath line C is less reflective. Prominent sub-basement

near horizontal reflection horizons evident at depths of 18–20 km and 30 km beneath lines B and C correspond to the upper and lower crust, respectively. The thickness of the crust increases from 35 km near the coast to nearly 45 km in the region near the Bhuj earthquake. In addition, an upper mantle reflective horizon was imaged ~10–15 km below the Moho, which suggests an earlier period of extension. Figure 2 is a 3-D model of all reflective surfaces discovered through this re-analysis of the 1997 survey data. Overall, the Kutch tectonic setting was revealed to be a complex system rather than a simple rift model of extended and thinned crust. The region may be undergoing compressive deformation under the stress regime of the India-Eurasia collision, resulting in a thickened, highly reflective crust.

Similar work was done in mainland China, with the goal of producing new, updated contour maps of crustal thickness (Figure 3) and Pn velocity (Figure 4) for inclusion in our Eurasian model. The results of more than 90 seismic refraction / wide-angle surveys were used for our new crustal model, compared to 41 profiles used in previous studies.

One such useful Chinese profile was 1,000-km-long and ran from Darlag-Lanzhou-Jingbian extending from the Songpan-Ganzi terrane to the Ordos basin in the NE margin of the Tibetan plateau (Figure 5). This profile examined the interaction between the Tibetan plateau and the Sino-Korean platform, and also imaged the deep driving mechanisms of tectonic deformation. A 2-D velocity structure was constructed from P- and S-waves, from which we inferred the composition of the crust using Poisson's ratio, and evaluated the continental dynamics in the NE margin of the Tibetan plateau based on the seismic refraction data (Figure 6; Li et al., 2002; Liu et al., 2003).

Along the Darlag-Lanzhou-Jingbian seismic profile, twelve charges were fired at nine shot points numbered SP1 to SP9 (Figure 5). All charges were fired in boreholes except for the water shot at SP1. Each charge size was about 2 tons. The seismic energy was recorded by 200 portable digital seismographs, DAS-1, developed by the Geophysical Exploration Center of the China Earthquake Administration (CEA). Three-component geophones were used for the whole profile and the receiver spacing was 1.5–2 km. High-quality P- and S-wave data were acquired. The vertical-component and the horizontal-component parallel with the profile were used to identify P- and S-waves, respectively. Record sections were plotted with reduction velocities of 6.00 km/s and 3.46 km/s for P- and S-waves, respectively. In order to match the P-wave arrival times, the timescale used for S-waves was compressed by a factor of 0.58 on the S-wave record section. To improve the signal-to-noise ratio, the data were filtered with band passes of 0–10 Hz and 0–6 Hz, respectively, for P- and S-waves. A 3-D velocity structure was derived from Vp-σ values, which indicated that the crust had a more felsic composition in the upper layers that changed into a more intermediate composition at the base (Figure 7).

From the calculated P- and S-wave velocity structure and Poisson's ratio, it was also discovered that the crust could be divided into two layers and its thickness increased from northeast to southwest (Figure 7). While the thickness of the lower crust increased from 22 km to 38 km, the total crustal thickness increased from 42 km beneath the Ordos basin to 63 km in the Songpan-Ganzi terrane south of the Kunlun fault. Low-velocity zones, possibly indicative of partial melting, were also discovered in the West-Oinling Shan and in the Haiyuan arcuate tectonic region, in addition to other anomalous structures that resulted from tectonic activity between the Tibetan Plateau and the Sino-Korean and Gobi Ala Shan platforms. The tectonic setting throughout China ranges from the Archean core of the Sino-Korean Platform to the active continent-continent collision in the Tibetan Plateau, and a well-defined knowledge of crustal structure in these diverse geologic settings can be extrapolated throughout other regions in our Eurasian crustal model.

As mentioned previously, increased data coverage with improvements in data quality has led to a significantly more accurate crustal contour map (Figure 3). This highly detailed map revealed a north-south-trending belt at 103°–105° E with a strong lateral gradient in crustal thickness, and an apparent relationship between crustal thickness and tectonic setting. The crust appears thinner near depressions and basins, including the Tarim basin, the Junggar basin, the Qaidam basin, the Sichuan basin, and the Jiang-Han basin. However, in tectonically uplifted areas such as the Tibetan plateau, the Thailhanf and Daxingan Ling mountains, and the Tianshan mountains, the crust is thicker than in its surroundings.

The Chinese DSS profiles were compared to tomographic studies, revealing that the earthquake tomography techniques tended to yield more reliable Pn velocities. We reasoned that the DSS profiles had a higher density of shot points and recording stations, and were therefore more useful for determining the Moho depth. Earthquake tomography however, with a larger number of travel-time paths, could be averaged to yield more accurate estimates of actual Pn velocities. Crustal thicknesses derived from these two techniques generally were within ± 3–5 km of each other. These observations regarding the usefulness of various seismic techniques to determine particular crustal parameters can be applied to our updated Eurasian crustal model.

One of the first steps in compiling a new Eurasian crustal model is comparing previously existing regional models (e.g., Nataf and Ricard, 1996; Mooney et al., 1998; Pasyanos et al., 2004), and evaluating them based on their technique and data quality. We constructed separate databases for each technique, e.g., (1) active source models, (2) surface wave models, (3) seismic tomography models, and (4) receiver function models. Integration of such varied models required some discrimination of data and model quality, and we expect that a suite of models will emerge from which we will develop a "best fit" composite model. Discrepancies between input models are resolved based on the best available data, sometimes on a subjective basis.

Following past practice, we are creating our $2^o \times 2^o$ Eurasian model in terms of eight layers: (1) ice, (2) water, (3) soft sediments, (4) hard sediments, (5) crystalline upper, (6) middle, (7) lower crust, and (8) uppermost mantle (Pn and Sn). The first seven layers are required so that we can accurately model the thickness of the crust, and therefore, obtain accurate Pn/Sn results. Both P- and S-wave velocities are specified in each layer. Only with this information will we be better able to resolve and compensate for transition zone structures and the mantle gradient effect, thus improving accuracy in our location/discrimination efforts. At present, the USGS database includes more than 9,000 data points (more than seven times the number available for CRUST 2.0). A preliminary Eurasian depth to Moho map (Figure 8) at $2^o \times 2^o$ resolution has already been developed, though this will improve dramatically once the CRUST 2.2 database is complete.

CONCLUSIONS & RECOMMENDATIONS

The accumulated efforts that have gone into developing these numerous regional seismic models, such as this one, are well-justified by several factors. First, new seismic constraints accumulate rapidly each year, and a focused regional approach permits the careful consideration and inclusion of all new measurements. Second, whereas previous models were mainly based on active-source seismic profiles, the new regional models make use of many more data types, such as receiver functions, short-period surface wave inversions, travel-time tomography, and gravity data. The result is that regional models often provide better locations than global models when tested with GT05 and GT10 ground truth events.

CRUST 2.2 incorporates the most recent crustal velocity measurements throughout Eurasia. Relationships between phase and group velocities and three-dimensional isotropic Earth structure form the basis of forward and inverse modeling procedures that are routinely implemented (e.g., Trampert and Woodhouse, 1995; Ekström et al., 1997; Pollitz, 1999; Hazler et al., 2001). Once the model is complete, we shall test both the consistency of group velocity measurements with existing Earth models and invert available measurements for three-dimensional crust and upper mantle structure in Eurasia. The additional resolution provided by these data is expected to fill in numerous gaps in crust and upper mantle structure provided by other means (primarily seismic refraction). It is our recommendation that this improved crustal model be expanded to incorporate the entire globe.

REFERENCES

Audebert, F., D. Nichols, T. Rekdal, B. Biondi, D. Lumley, and H. Urdaneta (1997). Imaging complex geologic structure with single-arrival Kirchhoff Prestack depth migration, *Geophys.* 62: 1,533–1,543.

Bassin, C., G. Laske and G. Masters (2000). The current limits of resolution for surface wave tomography in *North America, EOS Trans. AGU* 81: F897.

Christensen, N. I. and W. D. Mooney (1995). Seismic velocity structure and composition of the continental crust: A global view. *J. Geophys. Res*. 101: 9,761–9,788.

Ekström, G., J. Tromp, and E. F. W. Larson (1997). Measurement and global models of surface wave propagation. *J. Geophys. Res*. 102: 8,137–8,157.

Hazler, S. E., A. F. Sheehan, D. E. McNamara, and W. R. Walter (2001). One-dimensional shear velocity structure of northern Africa from Rayleigh wave group velocity dispersion, *Pure Appl. Geophys*. 158: 1,475–1,493.

Li, S. L., X. K. Zhang, C. K. Zhang, J. R. Zhao, and S. X. Cheng (2002). A preliminary study on the crustal velocity structure of Maqin-Lanzhou-Jingbian by means of deep seismic sounding profile. *Chinese J. Geophys*. 45: 210–217 (in Chinese, with English abstract).

Li, S. L., W. D. Mooney, and J. Fan (2006). Crustal structure of China from deep seismic sounding data. *Tectonophys.* 420: 239–252.

Liu, B. F., S. L. Li, X. K. Zhang, C. K. Zhang, Q. F. Ren, and Y. Hai (2003). Study of crustal structure with S-wave data from Maqin-Jingbian profile, *Acta Seismol. Sin.* 16: 92–98.

Malik, J. N., P. S. Sohoni, S. S. Merh, and R. V. Karanth (2000). Palaeoseismology and neotectonism of Kachchh, western India, in *Active Fault Research for the New Millennium, Proceedings of the Hokudan International Symposium and School on Active Faulting*, K. Okumura, H. Goto, and K. Takada (Eds.).

Mooney, W. D., G. Laske, and T. G. Masters (1998). CRUST 5.1: A global crustal model at 5º × 5º. *J. Geophys. Res.* 103: 727–747.

Nataf, H. C. and Y. Ricard (1996). 3SMAC: An a priori tomographic model of the upper mantle based on geophysical modeling, *Phys. Earth Planet. Int.* 95: 101–122.

NGRI (2000). Integrated geophysical studies for hydrocarbon exploration, Kutch, India, technical report NGRI-2000-EXP-296.

Pasyanos, M. E., W. R. Walter, M. P. Flanagan, P. Goldstein, and J. Bhattacharyya (2004). Building and testing an a priori geophysical model for western Eurasia and North Africa, *Pure Appl. Geophys*. 161: 235–281.

Pollitz, F. F. (1999). Regional velocity structure in northern California from inversion of scattered seismic surface waves, *J. Geophys. Res.* 104: 15,043–15,072.

Trampert J. and J. H. Woodhouse (1995). Global phase velocity maps of Love and Rayleigh waves between 40 and 150 seconds, *Geophys. J. Int*. 122: 675–690.

Yilmaz, D. (1987). *Seismic Data Processing*. Tulsa, Oklahoma: SEG Publishing.

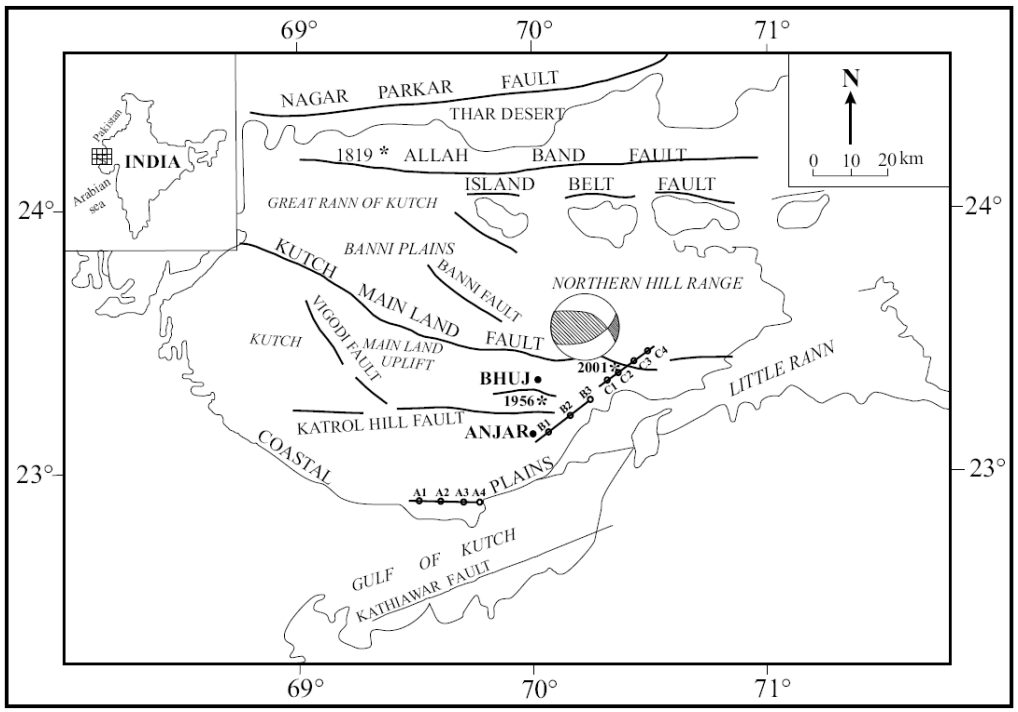


Figure 1. Tectonic map of Kutch showing major fault systems (adapted from Malik et al., 2000). The epicenters of the 2001 Bhuj earthquake (23, 36N, 70.34E) as well as two earlier events of 1819 and 1956 are indicated by asterisks. The focal mechanism of the 2001 earthquake is also shown. The three seismic lines (A, B, C) that were studied are shown by thick solid lines with corresponding shot points (open circles). Solid circles indicate towns.

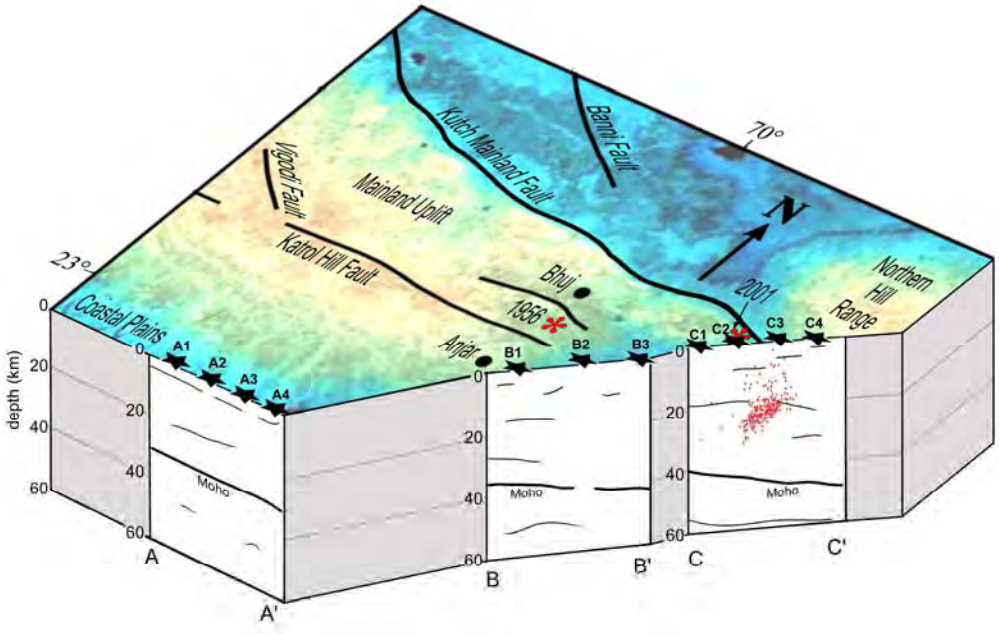


Figure 2. This is a 3-D representation of reflective surfaces within the crust and the location of 2001 seismic activity in the Bhuj region (red dots). Shot points are indicated by black stars, the epicenters of historical earthquakes are marked by red stars. Surface faults are also labeled.

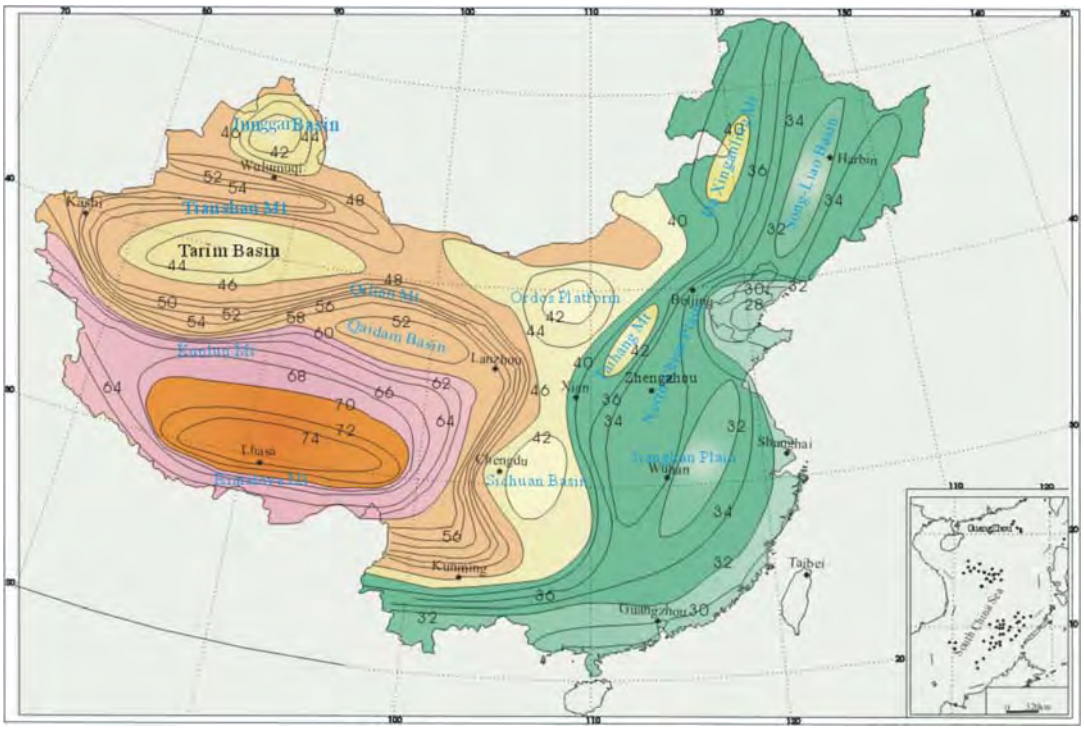


Figure 3. Contour map of crustal thickness obtained from DSS data. Contour internal is 2 km. Crustal thickness ranges from 28–46 km in eastern China, and from 42–74 km in western China. The margins of the Tibetan Plateau are marked by a steep gradient in crustal thickness (from Li et al., 2006).

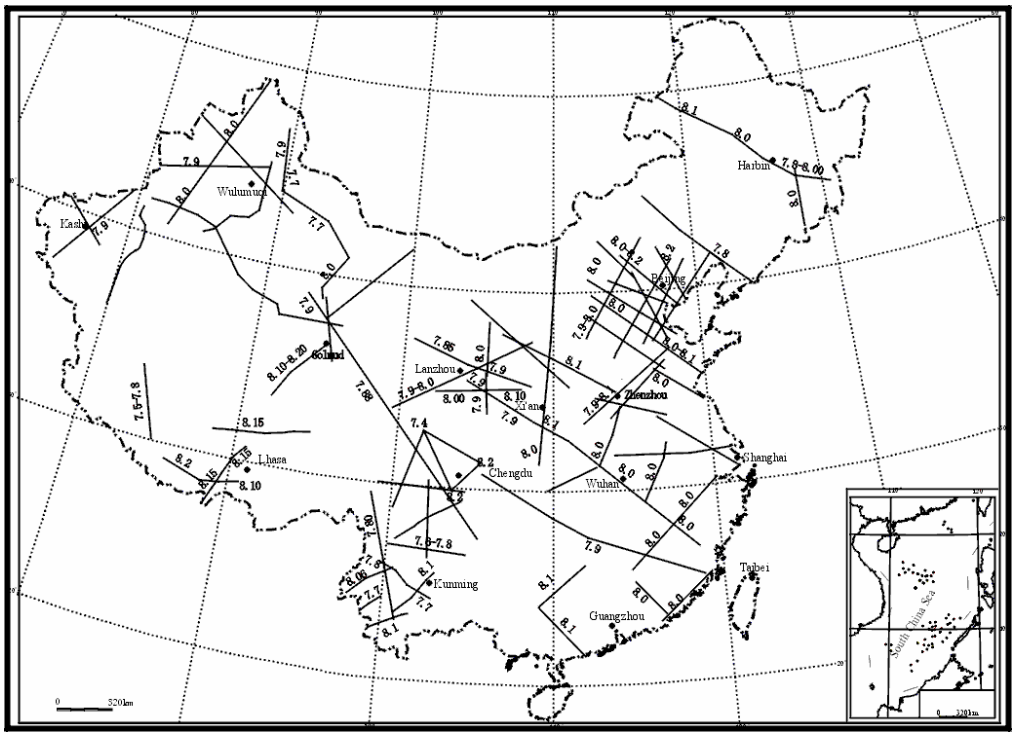


Figure 4. Seismic velocities of the uppermost mantle from Pn waves. Pn velocities are generally lower in eastern China as compared with those of the Tibetan Plateau (from Li et al., 2006).

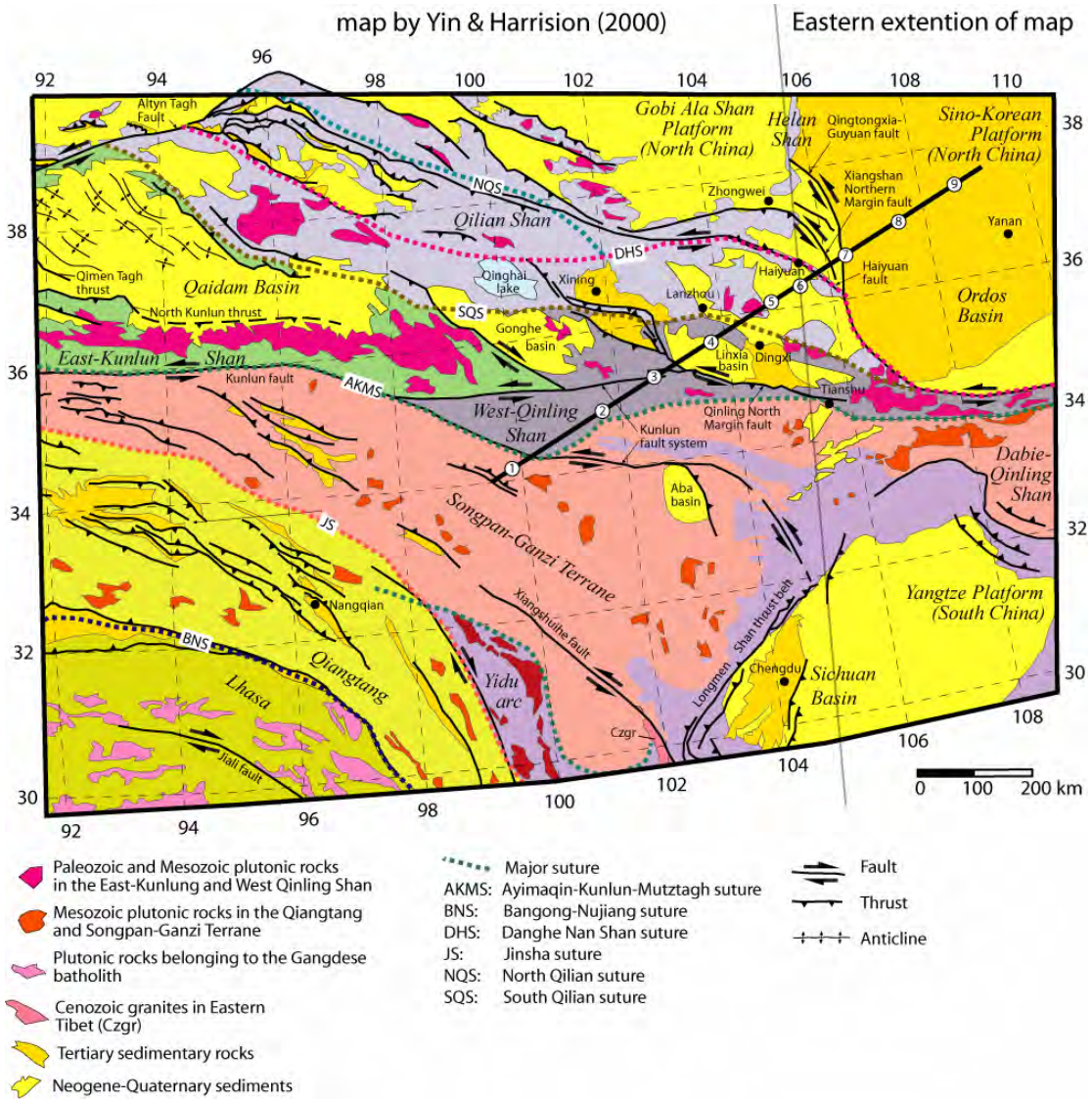


Figure 5. Tectonic map of the NE Tibetan plateau. The seismic profile is indicated by a solid black line with circled numbers 1 through 9, which indicate shot point locations. The southernmost shot point (SP1) is located in the Songpan-Ganzi terrane near Darlag. The northernmost shot point (SP9) is located in the Ordos basin near Jingbian. The seismic profile crosses, in addition, the Qinling-Qilian fold system (SP2 to SP6) and the Haiyuan arcuate tectonic belt (SP7).

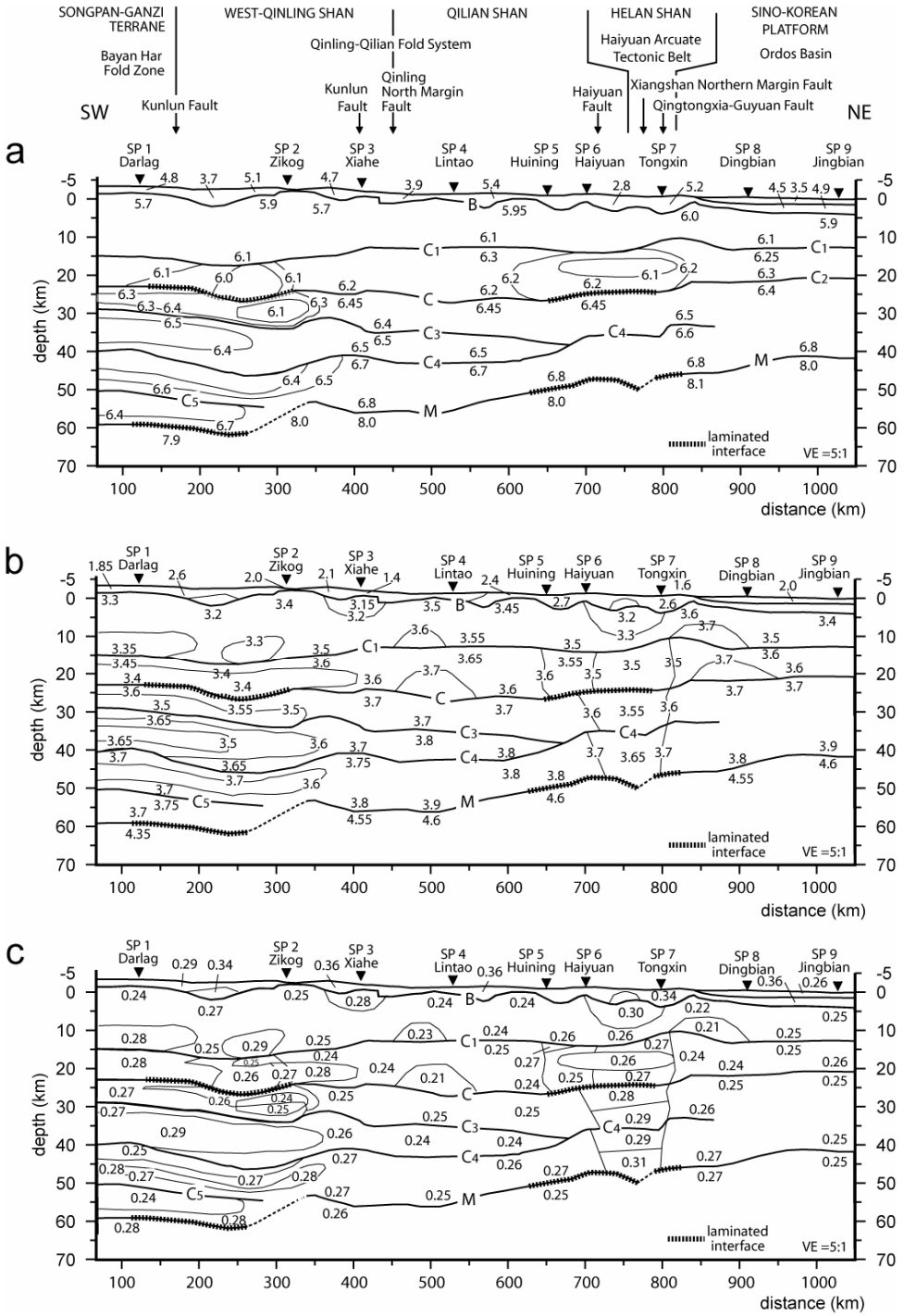


Figure 6. Two-dimensional crustal velocity structure along the Darlag-Lanzhou-Jingbian profile reaching from the Songpan-Ganzi terrane in the southwest to Ordos basin in the northeast. The top panel shows the tectonic units, faults, and thrust which are crossed by the profile. (a) Crustal P-wave velocity model (V_p), (b) the crustal S-wave velocity model (V_s), and (c) Poisson's ratio σ (equivalently, V_p/V_s ratio). The top of the crystalline basement is indicated by B, the Conrad discontinuity by a C and the crust-mantle boundary by M. The upper crust lies between B and the C, and the lower crust between C and M. C1 and C3 to C5 indicate further interfaces in the upper and lower crust, respectively. The cross-sections are shown with a vertical exaggeration of 1:5.

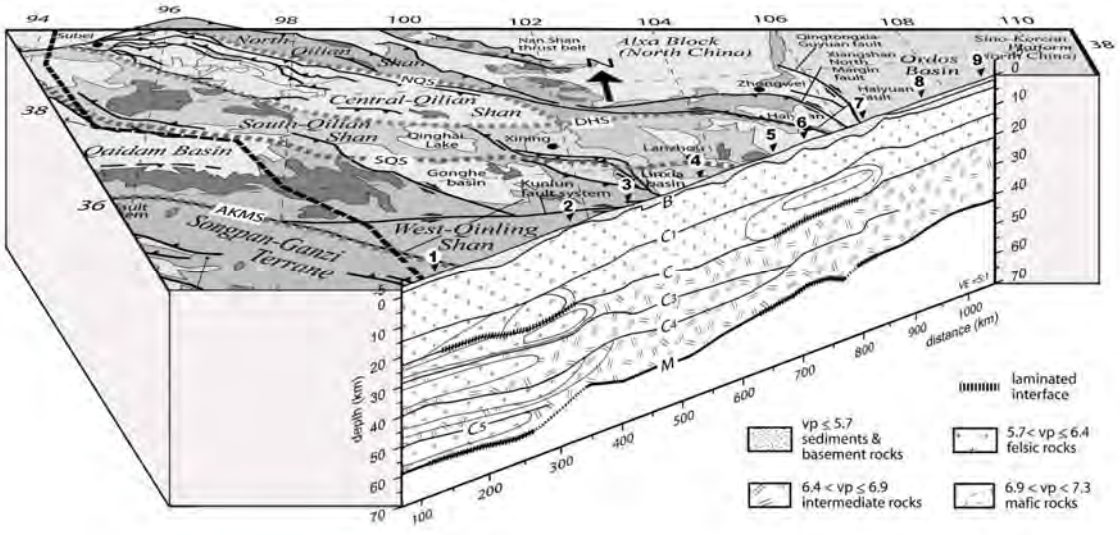


Figure 7. Three-dimensional perspective view of the compositional structure of the crust along the Darlag-Lanzhou-Jingbian profile. The composition is derived from the P-wave velocity structure whereby felsic, intermediate and mafic material is identified through velocity intervals according to Christensen and Mooney (1995).

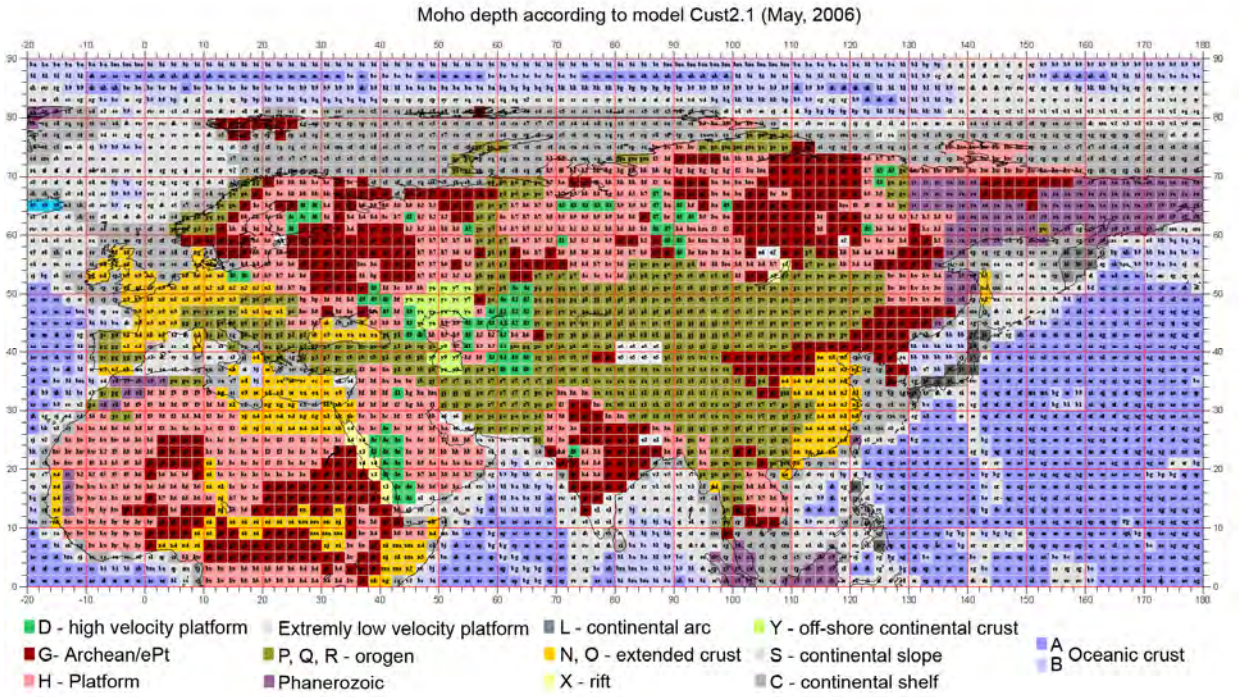


Figure 8. The USGS CRUST 2.1 model covering Eurasia, the Middle East and Northern Africa. This map is depth to Moho, with crustal types shown. This map was compiled using six times the number of active and passive source seismic data points than were used to construct the earlier CRUST 2.0 model (Bassin, et al., 2000).

MAGNITUDE-YIELD AND TRAVEL-TIME CALIBRATION OF NORTHERN EURASIA USING DEEP SEISMIC SOUNDING DATA SETS

Igor B. Morozov[1], Elena A. Morozova[2], Chaoying Zhang[1], Glenn Chubak[1], W. Scott Phillips[3], and Igor A. Lipovetsky[4]

University of Saskatchewan[1], University of Wyoming[2], Los Alamos National Laboratory[3], and Center GEON/Vniigeophysika[4]

Sponsored by Air Force Research Laboratory

and

National Nuclear Security Administration
Office of Nonproliferation Research and Development
Office of Defense Nuclear Nonproliferation

Contract Nos. DE-FC52-05NA26609[1,2], DTRA01-01-C-0057[1,4], and W-7405-ENG-36[3]

ABSTRACT

Travel-time and magnitude-yield calibration of Northern Eurasia, which is largely aseismic, can be improved by using the large chemical and peaceful nuclear explosion (PNEs) seismic data sets that resulted from the Soviet Deep Seismic Sounding (DSS) program. Eleven major data sets of this program have recently been digitized and become available to nuclear test monitoring research. In this study, we extend this database by including the source ground truth parameters (charge types, sizes, and other relevant information where available) of the chemical explosions and digitizing several earthquake data sets acquired along the DSS profiles. For seamless data exchange with the test monitoring community, we incorporate the waveforms and ancillary data into the National Nuclear Security Agency (NNSA) database schema.

To date, we have assembled a database of frequency-dependent coda parameters from the PNEs and performed their preliminary interpretation. By utilizing a newly developed, parallelized version of the one-dimensional (1D) *reflectivity* program, we also extended synthetic modeling to the full DSS frequency band (0.5-20 Hz) in velocity models of realistic crustal complexity. This modeling suggests that compared to the mantle, the crust plays the most significant role in relating the observed coda decay parameter (Q) to the intrinsic (elastic and inelastic) dependence, and also that leaking of the seismic energy into the mantle could account for the strong frequency dependence of the observed coda Q. Based on the resulting empirical relationships, we improve our previous measurements of the bulk crustal $Q(f)$ along profile QUARTZ.

In the ongoing work, we will further utilize the DSS data sets for 1) coda magnitude analysis for chemical and nuclear explosions; 2) derivation of empirical magnitude (apparent coda source spectra) yield relationships for small explosion events; and 3) examination of the variability of the derived coda calibration parameters (particularly crustal attenuation), along and across the profiles, correlating this variability with geology and tectonics of the area. Additionally, the goals of this project include derivation of a P-wave travel-time calibration model for Northern Eurasia with an unusually well-constrained and detailed crustal and uppermost mantle structure based on the chemical explosion data. These efforts should ultimately lead to a unified three-dimensional/two-dimensional (3D/2D) calibration model of Northern Eurasia including travel times, stable coda magnitudes, and magnitude-yield relations. This model will bridge the gap between Europe, central Asia, the European Arctic, and eastern Siberia and provide additional calibration information for further work in these areas.

OBJECTIVES

The general objective of this study is to derive stable and transportable regional magnitudes of smaller events and other seismic calibration information by using nuclear and chemical-explosion data sets acquired by the Russian Deep Seismic Sounding (DSS) program (Figure 1). By contrast to the paucity of natural seismicity in Northern Eurasia, DSS data sets provide unusually dense and uniform coverage of this vast area with hundreds of chemical explosions and dozens of Peaceful Nuclear Explosions (PNEs). In this report, we focus on development of approaches for coda magnitude calibration, which have been shown to yield stable magnitude/yield relationships. The specific objectives of this study are the following:

- To extend the database of DSS recordings by including the source ground truth parameters and adding several earthquake data sets acquired along the DSS profiles.
- To develop improved tools for DSS data exchange between the participants of this project and also with other users of DSS data sets.
- To develop an improved $Q(f)$ parameterization suitable for coda magnitude calibration using numerical modeling, demonstrate its physically attractive properties, and substantiate it by numerical modeling and observations.

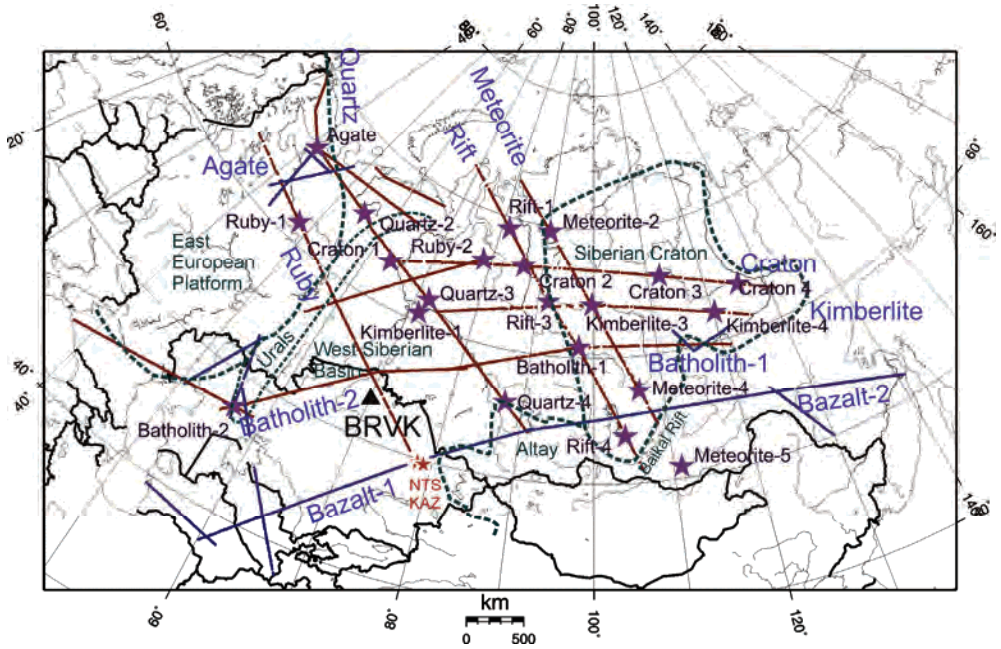


Figure 1. Location map of DSS PNE projects of this project. Projects are labeled in blue, and labeled purple stars show the PNEs. The data set also includes two Semipalatinsk nuclear test site explosions (red). Parameters of the PNEs were reported by Sultanov et al (1999). Major tectonic units are indicated in green. Small brown circles (appearing as lines at station spacing of 10-15 km) are PNE recording stations, and blue circles are chemical-explosion recording stations. Each profile also contains from 30 to 150 chemical explosions. Borovoye IMS station is also indicated (BRVK).

RESEARCH ACCOMPLISHED

Data

Because DSS data sets bridge the gap between controlled-source and earthquake seismology, data formats accepted in these areas are only marginally suitable for maintaining DSS data. The data format that we used for exporting DSS PNE over the years (an extension of PASSCAL SEGY) has caused occasional difficulties in data transfer and in a few cases required custom reformatting. The volumes of chemical-shot data sets could present significantly greater challenge in such reformatting (30-150 shots per profile as opposed to 2-4 PNEs). For seamless data exchange between the participants of this project (University of Saskatchewan and Los Alamos National Laboratory) with the test monitoring community, we incorporated the waveforms and ancillary data into the NNSA database schema. The procedure is currently undergoing extensive testing using the chemical-explosion data sets.

Center GEON (Moscow, Russia) has started digitalization of earthquake records from profiles AGATE-1 (465 seismograms), BATHOLITH-2 (135 seismograms), BAZALT-2 (680 seismograms), and QUARTZ (710 seismograms) (Figure 1). This work is currently in progress.

Coda Analysis and Modeling

To date, we have assembled a database of frequency-dependent coda parameters from the PNEs and performed their preliminary interpretation. By utilizing a newly developed, parallelized version of the 1D *reflectivity* program, we also extended synthetic modeling to the full DSS frequency band (0.5-20 Hz) and in velocity models of realistic crustal complexity.

In most cases, the *Lg* coda *Q* observed from earthquake and PNE records shows significant frequency dependence. This dependence could complicate coda magnitude calibration, and understanding of the processes contributing to frequency-dependent coda attenuation is critical for the development of a correct and robust calibration model. In practical terms, it is essential to develop a parameterization of the coda $Q(f)$ dependence that would reflect the fundamental physical processes and crustal properties involved. With such parameterization, the resulting calibration model would stand a better chance for being portable, and its parameters could potentially be stable across broader areas and geological environments.

The attenuation of seismic waves is usually described by the "quality" parameter *Q* (e.g., Knopoff, 1964). However, depending on the type of observations (e.g., body-wave, *Lg*, or coda *Q*) and the method used to measure *Q*, different energy loss mechanisms may be important, leading to different $Q(f)$ functional forms. Customarily, the frequency-dependent quality factor, $Q(f)$, is described by a two-parameter power law:

$$Q(f) = Q_0 \left(f \Big/ f_0 \right)^{\eta} , \qquad (1)$$

where f_0 is some reference frequency often taken to be 1 Hz. Both Q_0 and exponent η are considered constant (typically, η>0) within the frequency band of interest. The power-law dependence appears to be generally dictated by convenience and represents a suitable parameterization in most cases. From several *Lg Q* and *Lg* coda *Q* studies, the frequency-dependence parameter η typically ranges from ~0.1 to near 1.0 (e.g., Nuttli, 1973; Mitchell, 1975; Frankel, 1991; Benz et al., 1997; Mitchell et al., 1997, 1998; McNamara, 2001; Erickson et al., 2004). Visco-elastic rheological models were also proposed to explain observations of frequency-dependent *Q* in Earth materials (Liu et al., 1976). Correlation to tectonics appears to suggest that active tectonic regions are generally characterized by low Q_0 and high η, while stable cratons – by higher Q_0 and lower η (Erickson et al., 2004).

However, note that frequency-dependent *Q* is typically measured from the amplitude decay rates in the time domain. This method relies on the ability to accurately compensate the geometrical spreading effects, and errors in the geometrical spreading would manifest themselves as a frequency-dependent *Q*. Dainty (1981) suggested that for *S*-waves at 1-30 Hz, the observed frequency dependence could be best described using the following expression (Warren, 1972):

$$\frac{1}{Q(f)} = \frac{1}{Q} + \frac{g_0 v}{2\pi f} , \qquad (2)$$

where Q is the quality factor for intrinsic (anelastic) attenuation, v is the S-wave velocity, and g_0 is the turbidity describing the elastic attenuation. If larger scatterers dominate the scattering, g_0 could be considered constant (Dainty, 1981), leading to an alternative form (2) for $Q(f)$. The second term in this expression is essentially an additional geometrical spreading (geometrical scattering) effect, which may dominate the observations (Dainty, 1981),

Although both two-parameter forms (1) and (2) can be used for describing experimental data (owing to significant uncertainties in the latter), their implications for development of suitable calibration models could be significant. In the following, we present some observations from Soviet PNEs and coda modeling results. Both of these results favor the $Q(f)$ model (2).

Observations of frequency-dependent coda Q

The initial interpretation of the frequency-dependent coda in PNE QUARTZ-4 (Morozov and Smithson, 2000) used form (1) for $Q(f)$. The measurements of *Lg* coda Q were performed for a location near the Mezenskaya Depression (near the position of PNE QUARTZ-2 in Figure 1), and resulted in Q_0=350 (at f_0=1 Hz) and η=0.13 in relation (1). (Figure 2; Morozov and Smithson, 2000). The somewhat low Q_0 value was explained as caused by thick sediments within the depression, and low η appeared in agreement with the stable East European Platform.

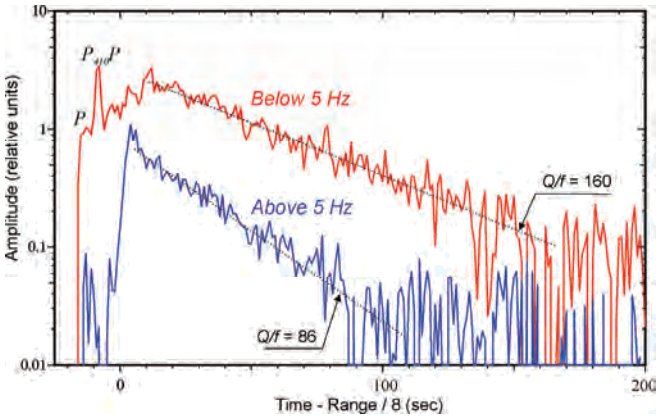


Figure 2. Amplitude-time decay for *Lg* coda from PNE QUARTZ-4, measured near the position of PNE QUARTZ-2 (Figure 1Error! Reference source not found.**). Note the increasing amplitude decay rate with frequency; this increase is indicative of seismic attenuation. *Q*/*f* values measured from the slopes are given in the labels.**

Similar measurements using the records from profiles KIMBERLITE and METEORITE in Siberia lead to strikingly different results. The logarithms of *Lg* coda amplitudes measured from PNE Kimberlite-3 at a station within the Siberian craton show approximately frequency-independent decays with time (Figure 3). To account for such frequency-independent decay rate in relation (1), Q should be proportional to the frequency ($\eta \approx 1$). From eq. (1) Q_0 was estimated as ~200 for *Lg* coda and 400 for the *S*-wave coda, with both values appearing surprisingly low for this cratonic area and also in disagreement with observations of *Pg* propagating to ~1700 km in this area (Morozov et al., 2005).

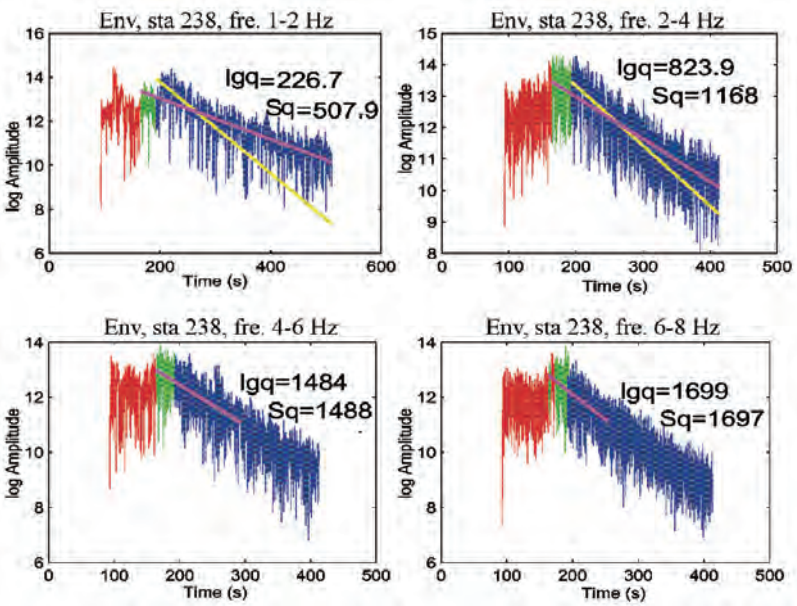


Figure 3. Amplitude envelope of vertical-component record from station 238 from PNE Kimberlie-3 filtered within 1-2, 2-4, 4-6, and 6-8 Hz frequency bands (labeled). Estimated coda *Q* for the *S*-wave and *Lg* coda windows are indicated. Note that these *Q* values quickly increase with frequency. Also note that at the same time, temporal slopes of log(amplitudes) appear to be independent on the frequency bands.

High $\eta \approx 1$ values in relation (1) would imply that attenuation is quickly reduced with frequency. As we argued previously (Morozov et al., 2005), for coda waves, attenuation decreasing with frequency would mean that the total volume of scatterers drops nearly linearly at smaller scale lengths. Although this could be possible, it still appears unlikely, as scaling laws suggest increasing abundance of heterogeneities (e.g., faults and topographic features) at smaller scales. In addition the $\eta \approx 1$ value itself appears suspicious, as it represents rather extreme case of frequency-dependent $Q(f)$ that in fact corresponds to frequency-independent amplitude decay, which could be also attributed to geometrical spreading.

To account for these observations, Morozov et al. (2005) argued that instead of the commonly used coda attenuation relation:

$$\frac{d\log A}{dt} \approx -\frac{\pi f}{Q(f)}, \qquad (3)$$

a simple linear relation could be more appropriate, at least for describing the amplitude decay of PNE arrival coda:

$$\frac{d\log A}{dt} \approx -\gamma - \frac{\pi f}{Q_{coda}}. \qquad (4)$$

Here, γ is the uncompensated geometrical spreading, and Q_{coda} is the attenuation parameter. Because only two parameters describing the $d\log A(f)/dt$ dependence are retained (as it is only practical in the actual measurements), the attenuation is frequency-independent. Note that the empirical expression (4) is equivalent to (2), with $\gamma = g_0 v/2\pi$ in the case of scattering described by Dainty (1981).

Notably, application of the dependence (4) instead of (1) to QUARTZ-4 (Figure 2) and KIMBERLITE-3 (Figure 3) observations showed that for both data sets, geometrical factors were similar, $\gamma \approx 0.003$ s^{-1}, with crustal attenuation (which should predominantly be related to Q_S) $Q_{coda} \approx 470$ for QUARTZ and $Q_{coda} = \infty$ for KIMBERLITE (Morozov et al., 2005). In agreement with the observations of an unusually efficiently propagating *Pg* within the Siberian Craton, its crust should indeed possess a very low attenuation. Close geometrical factors both east and west of the Uralian belt (Figure 1) could also be expected, as crustal thickness is similar in both of these areas. If γ is confirmed

to be stable or correlated with known crustal properties, it could become a useful and transportable calibration parameter. Robust regional values of geometrical spreading could be utilized to correct the observed coda *Q* values (Morozov et al., 2005).

Numerical Model of Coda Q

Useful insights into the nature of a frequency-dependent coda *Q* can be gleaned from numerical modeling. Using synthetic modeling, one could try a range of (frequency-independent) crustal *Q* values, simulate the coda wavefields, measure the resulting coda amplitude decays within different frequency bands, measure the resulting coda log-amplitude slopes (4), from which the effective coda $Q_{coda}(f)$ (eq. (1)) can be estimated. Note that even for a frequency-independent crustal *Q*, the resulting Q_{coda} is likely to depend on the frequency - and this is confirmed by our numerical experiment below.

We re-implemented our earlier modeling attempt (Morozov et al., 2002), with modifications including an improved (parallelized) version of the one-dimensional (1D) reflectivity program (Fuchs and Muller, 1971) and utilizing a Beowulf cluster computer. These modifications allowed us to increase the frequency band to 20 Hz, offset ranges to 3000 km, and improve the sampling in Monte-Carlo computations (Morozov et al., 2002). In addition, fidelity of the synthetics (signal/numerical noise ratio) was improved by using longer modeling times and unaliased phase velocity spectra in *reflectivity* computations (Fuchs and Muller, 1971), also facilitated by code parallelization.

The modeling proceeded as follows. First, several 1D crustal and upper mantle velocity models were created. The models contained crustal layering and complex mantle structures leading to synthetic wavefields with strong and complex *P*, *S*, *Pg*, and *Lg* wavetrains. For each of these models, a range of crustal *Q* was tested while keeping the distribution of mantle *Q* as determined by Morozov et al. (1998). For each value of crustal *Q*, synthetic wavefields were precomputed and used as the source field *u* and Green's function *G* in the following single-scattering integral:

$$\tilde{u}_{coda}(r,t) = R\int ds dt' A(s) u(s,t') * G(s,t' \mid r,t), \qquad (4)$$

where *s* is the surface integration point, *A* is the scattering potential, *R* is the receiver site factor, and '*' denotes time convolution (Figure 4). For simplicity (and also recognizing that the strongest heterogeneity is located in the near-surface), scattering points were placed close to the surface, and therefore the integration was carried out over the 2-D surface of the model (Figure 4). In this simulation, the scattering potential was assumed uniform, $A(s)=1$, and only one receiver position at 2900 km from the source was considered. Integration (4) was performed using the Monte-Carlo method, by random sampling of the 2500-km square in 30 parallel runs of the code with 2000 scattering points in each of run (Figure 4).

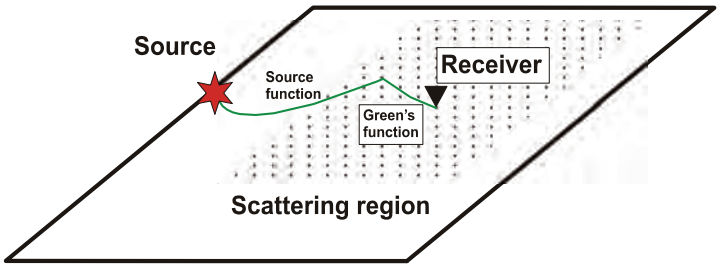


Figure 4. Surface scattering model. Seismic energy originates at the source, scatters from uniformly distributed Monte-Carlo-sampled surface points, and is detected at receiver. Source and Green's functions are precomputed using the 1-D reflectivity approach (Fuchs and Muller, 1971).

Because of the wavefield complexity, the scattered field is also very complex and consists of an interplay of various scattering modes ($P \rightarrow P$, $P \rightarrow Pg$, $S \rightarrow P$, etc. (Figure 4). However, fortunately for our analysis, different source phases are incoherent between each other, and consequently the power (intensity) of the scattered wavefield (4) is the sum of the intensities of the field caused by the different source phases. Therefore, the different primary arrivals can be considered independently, in a way similar to the coda decomposition model by Morozov and Smithson (2000). Below, we only consider the coda of the source *P*-wave, which was obtained by muting the source $u(s,t)$ in

expression (4) leaving only the time window corresponding to the primary body *P*-wave arrival. The results should thus represent the dependence of the *P*-wave coda *Q* on crustal *Q* and frequency, even though the *P*-wave coda is usually overprinted with secondary events and is difficult to measure from PNE data (Morozov and Smithson, 2000).

Below, we present numerical tests using two crustal/mantle models: "Quartz-4," based on the structure derived from 2D inversion of PNE profile QUARTZ (Morozova et al., 1999) and the same model with crustal complexity (layering) increased by introduction of a lower-velocity sedimentary layer and increased intracrustal contrasts and gradient in the uppermost mantle (Figure 5). In this model, a greater portion of the energy should return to the surface earlier. Examples of the Green's function sections for the "complex crust" model within two frequency bands are shown in Figure 6. Note the dependence of the Green's functions on the frequency.

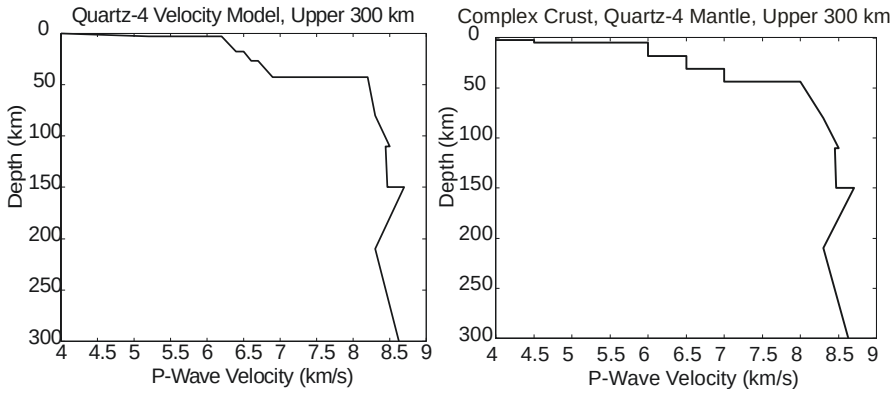


Figure 5. Upper 300 km of 1D velocity models discussed in this report. *Left*: PNE Quartz-4 model by Morozova et. al. (1999). *Right*: "complex crust" model, with modified 5-layer crust and Quartz-4 mantle with somewhat increased gradient in the uppermost mantle gradient.

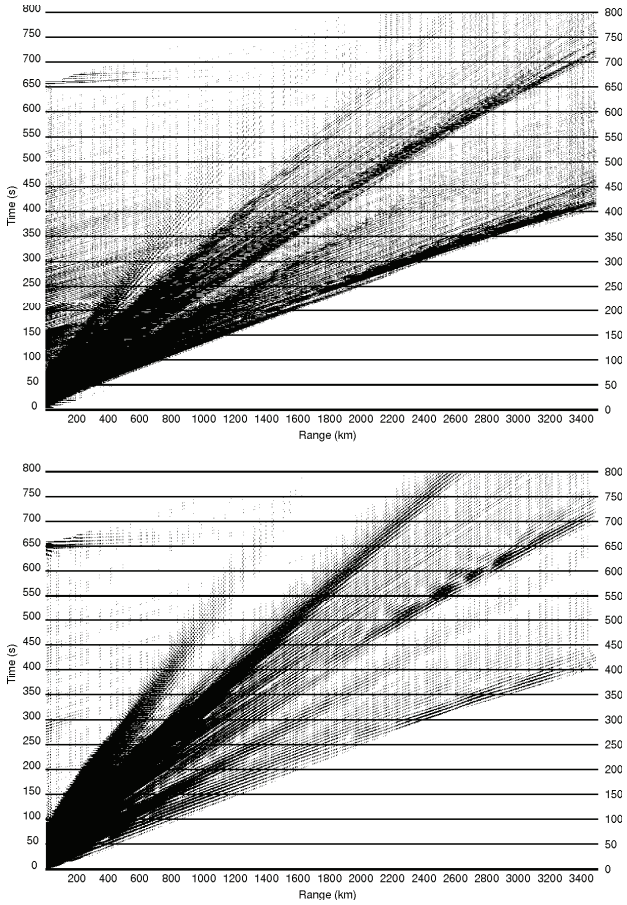


Figure 6. Synthetic Green's function computed using the "complex crust" model (Figure 4). *Top*: unfiltered vertical-component records; *Bottom*: the same record filtered within 0.1-0.2 Hz frequency band.

The dependence of the logarithms of the resulting coda amplitudes at the receiver (Figure 4) on recording time for crustal Q=550 in the "complex crust" is shown in Figure 7. This plot was obtained by computing logarithms of instantaneous amplitudes (envelopes) of the records obtained from each of the ~30 statistical simulations, followed by stacking the resulting logarithms. The resulting records show very good continuity and linearity, and the slopes can be measured with ~1% accuracy using the standard linear regression (Figure 7). We found that this approach serves as a good proxy for robust regression.

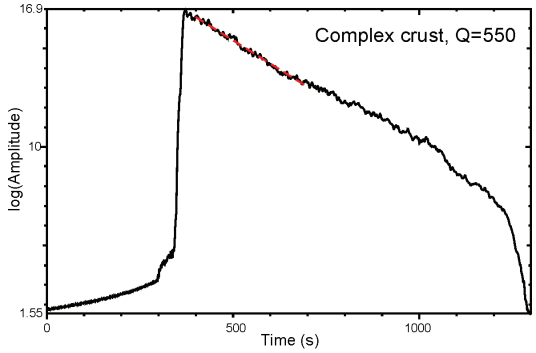


Figure 7. Modelled *P*-wave coda in the "complex crust" model. Note the linear slope allowing accurate log(*A*)/*dt* measurements (dashed red line).

By filtering the resulting coda synthetics (prior to stacking described above) within narrow pass-bands, frequency-dependent coda slopes similar to the one shown in Figure 7 were produced. By using relation (3), these slopes were transformed into coda Q values shown in Figure 8. In all cases we have studied so far, and similarly to PNE observations above, the resulting Q_{coda} values are nearly proportional to the frequency (Figure 8).

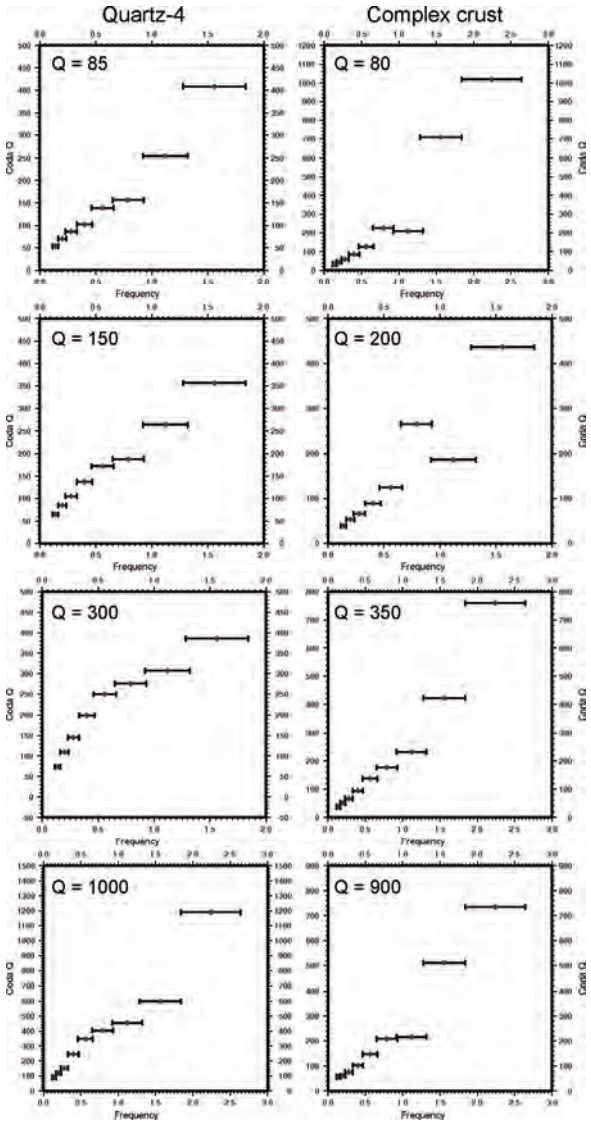


Figure 8. Coda Q as functions of frequency, inverted from the synthetic coda log-amplitude slopes using relation (3). Note the near-linear frequency dependence of $Q_{coda}(f)$. Error bars represent bandwidths of the filters applied to the synthetics.

Interpretation

Because our rheological models contain no relaxation mechanisms, attenuation in all parts of the models should be frequency-independent. The strong positive frequency dependence observed in the models (Figure 8) suggests that the high-frequency energy propagates to farther distances more efficiently than by traveling through the attenuating crust. This means that the coda amplitude decay (Figure 7) is controlled more by geometrical factors (refraction into the mantle, scattering on crustal discontinuities) than by anelastic attenuation. Consequently, although taken as empirical descriptions of the coda variation with frequency, $Q_{coda}(f)$ dependencies (Figure 8) provide a description of the observations, and Q_{coda} values themselves could still be difficult to relate to any meaningful crustal rheology.

Therefore, their value for seismic calibration and regionalization could also be difficult to ascertain without a detailed knowledge of the crustal structure and extensive modeling.

By contrast, direct comparison of the original coda log-amplitude slope measurements (Figure 7) shows that the synthetics are consistent with equations (2) and (4) (Figure 9). For Quartz-4 model, the time-frequency behavior of coda amplitudes can be explained by the geometrical spreading (elastic attenuation, cf. Dainty 1981) factor $\gamma \approx 0.55$ and $Q_{coda} \approx 2.5\ Q$ [eq. (4)]). Note that as expected, the coda Q is higher than the crustal S-wave and P-wave Q's used to parameterize the model, apparently because part of the energy propagates through the mantle, which has lower attenuation. Factor 2.5 relating the crustal Q to Q_{coda} should apparently depend on the structure; detailed analysis of this dependence will be addressed in further research.

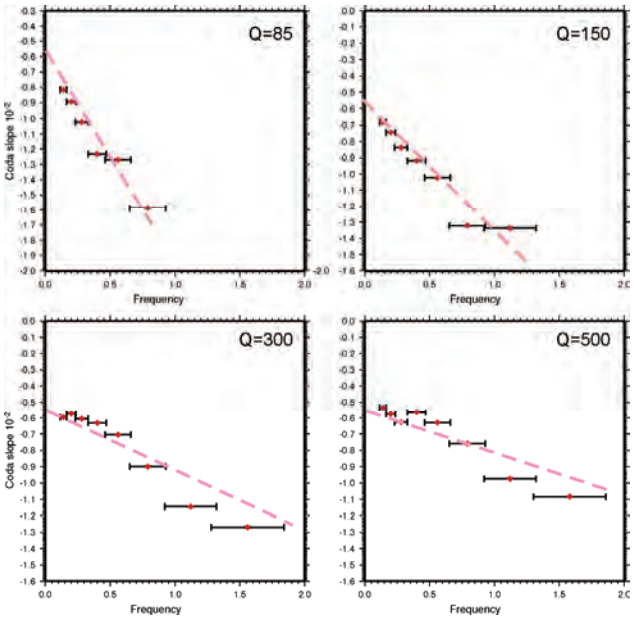


Figure 9. Logarithmic coda amplitude slopes as functions of frequency in Quartz-4 model. Dashed pink lines correspond to dependence (4) with $\gamma = 0.55$ and $Q_{coda} = 2.5\ Q$.

CONCLUSIONS AND RECOMMENDATIONS

Analysis of the frequency-dependent *Lg* coda Q from DSS PNE profiles indicates significant differences in attenuation properties between the East European Platform and West Siberian Basin and Siberian Craton. To explain these variations, we propose to abandon the customary $Q(f)=Q_0 f^{\eta}$ model for frequency-dependent coda attenuation and use geometrical spreading and frequency-independent attenuation. In this model, the geometrical spreading is consistent between the two studied areas, and the attenuation appears to be very low within the Siberian Craton, in agreement with other observations.

The proposed coda model was tested by numerical modeling of P-wave coda in PNE wavefields. Coda synthetics computed using a velocity, attenuation, and density structure close to that of the East European Platform and SW part of the West Siberian Basin show good correspondence with the model. Modeling results show that the geometric spreading factor for this area equals approximately 0.55, and the effective coda Q is approximately 2.5 times the crustal S-wave Q. These results suggest that 1) geometrical spreading (elastic attenuation) dominates PNE coda amplitudes decays, 2) the observed coda Q_{coda} derived by using the modified model could be useful to constrain the intrinsic crustal Q, and 3) modeling should be used to calibrate the $Q_{coda}(Q)$ dependence that should be also related to the crustal structure.

REFERENCES

Benz, H., A. Frankel, and D. Boore (1997). Regional Lg attenuation in the continental United States, *Bull. Seis. Soc. Am*. 87: 600–619.

Erickson, D., D. E. McNamara, and H. Benz (2005). Frequency-dependent Lg Q within the continental United States, *Bull. Seism. Soc. Am*. 94: 1630–1643.

Frankel, A. (1991). Mechanism of seismic attenuation in the crust: scattering and inelasticity in New York state, South Africa, and southern California, *J. Geophys. Res.*, 96, 17441-17457.

Fuchs, K., and G. Müller, (1971). Computation of synthetic seismograms with the reflectivity method and comparison with observations, *J. R. Astronom. Soc., 23*, 417–433

Knopoff, L. (1964). *Rev. Geophys*. 2: 625-660.

Liu, H. P., Anderson, D. L., Kanamori, H. (1976). Velocity dispersion due to anelasticity: implications for seismology and mantle composition, *Geophysical Journal of the Royal Astronomical Society* 47: 41–58.

McNamara, D. E. (2000). Frequency-dependent *Lg* attenuation in south-central Alaska, *Geophys. Res. Lett*. 27: 3949–3952.

Mitchell, B. (1975). Regional Rayleigh wave attenuation in North America, *J. Geophys. Res*., 80: 4904–4916.

Mitchell, B. J., Cong, L. (1998). *Lg* coda Q and its relation to the structure and evolution of continents: a global Perspective, *Pure Appl. Geophys*. 153: 655–663.

Mitchell, B. J., Pan, Y., Xie, J., Cong, L. (1997). *Lg* coda Q variation across Eurasia and its relation to crustal evolution, *J. Geophys. Res*. 102: 22767–22779.

Morozov, I. B., and S. B. Smithson (2000). Coda of long-range arrivals from nuclear explosions, *Bull. Seism. Soc. Am.* 90: 929–939.

Morozov, I. B., E. A. Morozova, S. B. Smithson, and L. N. Solodilov, (1998). 2-D image of seismic attenuation beneath the Deep Seismic Sounding profile “Quartz”, Russia, *Pure and Applied Geoph*. 153: 311–348.

Morozov, I. B., Smithson, S. B., Li, H., and Duenow, J. N. (2002). Amplitude analysis and modeling of peaceful nuclear explosion recordings, in *Proceedings of 24th Seismic Research Review—Nuclear Explosion Monitoring: Innovation and Integration*, LA-UR-02-5048, Vol. 1, pp. 117–124.

Morozov, I., Li, H., Zheng, H., and Smithson, S. B. (2005). Observations and modeling of frequency-dependent lg coda from Peaceful Nuclear Explosions, in *Proceedings of 27th Seismic Research Review: Ground-Based Nuclear Explosion Monitoring Technologies*, LA-UR-05-6407, Vol. 1, 104–112.

Morozova, E. A., I. B. Morozov, S. B. Smithson, and L. N Solodilov (1999). Heterogeneity of the uppermost mantle beneath the ultra-long range profile “Quartz,” Russian Eurasia, *J. Geophys. Res.* 104: (B9), 20: 329–20, 348.

Nuttli, O. (1973). Seismic wave attenuation and magnitude relations for eastern North America, *J. Geophys. Res*., 78: 876–885.

Schueller, W., I. B. Morozov, and S. B. Smithson (1997). Crustal and uppermost mantle velocity structure of northern Eurasia along the profile Quartz, *Bull. Seism. Soc. Am.* 87: 414–426.

Sultanov, D. D., J. R. Murphy, and Kh. D. Rubinstein (1999). A seismic source summary for Soviet Peaceful Nuclear Explosions, *Bull. Seism. Soc. Am*. 89: 640–647.

Warren, N. (1972). Q and structure, *Earth, Moon, and Planets*, 4: (3-4), 430–441, Springer Netherlands.

DEEP SEISMIC SOUNDING PROFILES FOR SEISMIC CALIBRATION OF NORTHERN EURASIA

Igor B. Morozov,[1,2] Elena A. Morozova,[1,2] Scott B. Smithson,[2] and Igor A. Lipovetsky[3]

University of Saskatchewan[1], University of Wyoming[2], and Center GEON/Vniigeophysika [3]

Sponsored by Air Force Research Laboratory

Contract No. DTRA01-01-C-0081[1,2,3]

ABSTRACT

For nearly twelve years, the Center for Geophysical and Geoecological Studies (GEON, now a part of Vniigeophysika, Moscow, Russia) has been cooperating with the University of Wyoming, and now also with the University of Saskatchewan, in digitization and preservation of digital records from the unique ultra-long range Deep Seismic Sounding (DSS) profiles using Peaceful Nuclear Explosions (PNEs). These efforts have resulted in 22 PNEs and several hundred chemical explosion datasets that are now distributed through the Incorporated Research Institutions for Seismology (IRIS) and broadly available for seismological and nuclear test monitoring research. To date, complete sets of records from projects AGATE, BAZALT, BATHOLITH, CRATON, KIMBERLITE, RIFT, RUBY, and QUARTZ were delivered to IRIS and AFRL. Due to poor recording conditions, only three PNEs could be digitized from project METEORITE. However, chemical-explosion records from project SPAT have became available and should be delivered in the near future.

DSS PNE profiles were recorded by GEON (the Special Geophysical Expedition at the time) from the early 1970's through late 1980's using 200-400 three-component analog instruments deployed in a grid of lines traversing much of the territory of the Former USSR. Each profile recorded one to four PNEs and several dozen of chemical explosions at the same receiver locations. Long listening times (up to ~600 sec after the first arrivals) allowed recording of the secondary phases (*S*, *Lg*, *Pg*, *Rg*) critical for nuclear test monitoring. The energies of the PNEs ($m_b \approx 5$) were sufficient for reliable recordings beyond 3000 km, which included consistent reflections from the mantle transition zone and several reflections from the core-mantle boundary. Chemical explosions of 5-12 tons yielded clear reflections from ~100-km depths and were recorded to 300-600-km distance.

In the context of nuclear test monitoring, the DSS datasets provide nearly the only dense three-component recordings of regional phases in the aseismic regions of Northern Eurasia. PNE data sets cover the intermediate distance ranges (~0-3200 km) and bridge the gap between controlled-source and earthquake seismology. The records allow detailed measurements of phase amplitude ratios and coda attenuation in different directions from most PNEs. Dense, linear, and reversed systems of DSS observations lead to unusually detailed models of the crust and uppermost mantle over 4000-km long geotraverses. These models can be combined to form a well-constrained 3D structural model, which can also be integrated with empirical phase calibration information, leading to a unified calibration model of Northern Eurasia.

OBJECTIVES

This report gives an update of our four-year project aimed at digitization, verification, and editing the key part of the unique collection of Soviet DSS datasets using PNEs. The PNE datasets were the only ones in the history of seismology where nuclear-explosion sources were specially designed for seismic exploration and detonated into densely recorded, reversed linear profiles of three-component seismographs. The final objective of the project is to make the data broadly available to the seismic monitoring and research communities.

The PNE profiles originally targeted the deep crustal and mantel structures. However, fortunately for seismic nuclear test monitoring (emerging at about the time the DSS PNE program ended), these profiles provided long (200-600 s) records and contain large numbers of recordings of the key regional phases (*P*, *S*, *Lg*, and *Pg*). The profiles also covered much of the aseismic parts of Northern Eurasia that would be difficult to calibrate by other means. These historic data thus provide unique opportunities to develop and test seismic nuclear discrimination techniques and study regional wave propagation through complex lithospheric structures.

Below, we provide updates to our previous reports on data deliveries at the 24th through 27th Seismic Research Reviews.

RESEARCH ACCOMPLISHED

The data are being digitized at Center GEON, Moscow, processed and edited at the University of Wyoming, and recently also at the University of Saskatchewan (Canada). The data delivered and archived at IRIS currently include 18 PNEs and 522 chemical-explosions recorded in eleven major DSS PNE projects (Figure 1). The project is near completion, with all data except those from profile METEORITE delivered.

The updated project schedule is shown in the table below. To date, we have delivered the data from all planned projects to IRIS and AFRL, with the exception of METEORITE. The analysis of the status of the field datasets by GEON has shown that the chemical-shot records from this project conducted in 1977 are practically unrecoverable. In replacement to these datasets, it was determined that the data from project SPAT can be digitized and included in data deliveries. We are currently pursuing this option, and GEON (which is now a part of Vniigeophysika) is carrying out digitization of this profile. Note that SPAT represents a NW-SW direction of profiling that was under-represented in the database so far.

DSS PNE data have been widely recognized as an unparalleled source of seismic information about the detailed structure of the upper mantle down to 400- to 800-km depths (e.g., Kozlovsky, 1990; Morozova et al., 1999). PNE yields of ~7 – 23 kton provided reliable seismic recording throughout the full recording. Several PNE record sections (BATHOLITH, CRATON-1, and QUARTZ-4) show reflections from the Earth's core. On a typical PNE profile, 3 – 4 nuclear explosions were recorded at up to 400 of three-component seismograph stations with nominal spacing of 10 to 15 km. About 50 – 80 chemical explosions (typically, each 3000 – 5000 kg, with some shots up to 15000 kg) per profile were also recorded to enable interpretation of crustal and uppermost mantle structures. The locations, depths, yields, and times of the PNEs, and descriptions of the source media were given by Sultanov et al. (1999).

PNE data sets of the DSS program cover an intermediate distance range between 0 – 3200 km bridging the gap between the conventional controlled source, earthquake, and nuclear–explosion-monitoring seismology. Dense, linear systems of PNE- and chemical-explosion profiles cross a variety of contrasting tectonic structures in Northern Eurasia and result in unusually detailed models of the crust and uppermost mantle over 4000-km long geotraverses (Yegorkin, 1992; Pavlenkova, 1996). Some of the recent interpretations were performed by Egorkin and Mikhaltsev (1990), Mechie et al. (1993, 1997), Cipar et al. (1993), Priestley et al., (1994), Ryberg et. al. (1995, 1996), Schueller et al., (1997), Lorenz et al. (1997), Morozov et al. (1998a), and Morozova et al. (1999). These datasets also provide virtually the only dense three-component recordings of regional phases in aseismic regions of Northern Eurasia. Some of our recent results related to nuclear test monitoring were presented in Morozov (1998b), Morozov and Smithson (2000, 2002), and Morozov et al. (2005).

Table 1. Updated planned and actual data delivery schedule as of September, 2006.

#	Data set	Raw data delivery from GEON to UWyo (months)		Edited and reduced data delivered to IRIS DMS (months)	
		planned	*Actual*	*planned*	*actual*
1	QUARTZ	-	-	12/2001	12/2002
2	CRATON	02/2002	10/2002	08/2002	11/2002
3	KIMBERLITE	05/2002	11/2002	11/2002	11/2002,10/2003(chemical)
4	RIFT	08/2002	11/2002	05/2003	10/2003
5	RUBY	02/2003	02/2003	10/2003	02/2004
6	AGATE (5 profiles)	08/2003	07/2003	05/2004	06/2004
7	BATHOLITH-1 (3 profiles)	10/2003	12/2003	11/2004	12/2004
8	BATHOLITH-2** (4 profiles)	03/2004	12/2003	11/2004	12/2004
9	BAZALT-1** (3 profiles)	06/2004	01/2004	06/2005	07/2005
10	BAZALT-2 **(2 profiles)	10/2004	09/2004	06/2005	07/2005
11	METEORITE***	03/2005*		11/2005	

*Only chemical explosion data sets need to be delivered to UWYO. Delivery delayed.
**Only chemical explosions used in these projects.
***Due to loss of the original field material, chemical-shot data from project METEORITE are now deemed unrecoverable. Data from project SPAT are currently being digitized in replacement of this project.

CONCLUSIONS AND RECOMMENDATIONS

As a result of this effort, the broad seismological and seismic monitoring communities are obtaining a set of digital recordings of a large number of nuclear explosions recorded across a variety of propagation paths to the distances of ~3000 km. The available PNE and chemical-explosion datasets from eleven major Russian seismic projects should make important contributions into the studies research of regional seismic phases, into seismic calibration of the region and into help develop transportable seismic discriminants in Northern Asia. Availability of the unique PNE recordings would foster research in nuclear test monitoring. In addition, from a broader scientific perspective, the digitized DSS recordings and models of the upper mantle could also provide ideal reference and calibration data sets for the detailed structure of the upper mantle targeted by the US Array.

REFERENCES

Cipar, J., K. F. Priestley, A. V. Egorkin, and N. I. Pavlenkova (1993). The Yamal Peninsula-Lake Baikal deep seismic sounding profile, *Geophys. Res. Lett.* 20: (15), 1631–1634.

Egorkin, A. V. and A. V. Mikhaltsev (1990). The Results of Seismic Investigations along Geotraverses, in Super-Deep Continental Drilling and Deep Geophysical Sounding, K. Fuchs, Y. A. Kozlovsky, A. I. Krivtsov and M. D. Zoback (Editors), Super-Deep Continental Drilling and Deep Geophysical Sounding, Springer, Berlin, 111–119.

Kozlovsky, Y. A. (1990). The USSR Integrated Program of Continental Crust Investigations and Studies of the Earth's Deep Structure under the Globus Project, in Super-Deep Continental Drilling and Deep Geophysical Sounding, Fuchs K., Kozlovsky Y. A., Krivtsov A. I. and Zoback M. D. (Editors), Springer, Berlin, 90–103.

Lorenz, F., F. Wenzel, and J. Mechie (1997). Lateral heterogeneity implications from 2-D nuclear-seismic travel-time inversion, in: Fuchs, K. (Ed.) Upper mantle heterogeneities from active and passive seismology, pp. 237–248, Kluwer Academic Publ., Dordrecht.

Mechie, J., A. V. Egorkin, K. Fuchs, T. Ryberg, L. Solodilov, and F. Wenzel (1993). P-wave velocity structure beneath northern Eurasia from long-range recordings along the profile Quartz, Phys. *Earth Planet Inter*., 79, 269–286.

Mechie, J., A. V. Egorkin, L. Solodilov, K. Fuchs, F. Lorenz, and F. Wenzel (1997). Major features of the mantle velocity structure beneath northern Eurasia from long-range seismic recordings of peaceful nuclear

explosions, in: Fuchs, K. (Ed.) Upper mantle heterogeneities from active and passive seismology, pp. 33-50, Kluwer Academic Publ., Dordrecht.

Morozov, I. B., E. A. Morozova, S. B. Smithson, P. G. Richards, V. I. Khalturin, and L. N. Solodilov (2005). 3-D first-arrival regional calibration model of northern Eurasia, *Bull. Seismol. Soc. Am* 95: (3), 951–964, doi:10.1785/0120030173.

Morozov, I. B., and Smithson, S. B. (2002). Imaging crustal structure along refraction profiles using multicomponent recordings of first-arrival coda, *Bull. Seismol. Soc. Am.* 98: (8), 3080–3086.

Morozov, I. B. (2001). Comment on "High-frequency wave propagation in the uppermost mantle" by T. Ryberg and F. Wenzel, *J. Geophys. Res*., 106, 30,715–30,718.

Morozov, I. B., and S. B. Smithson (2000). Coda of long-range arrivals from nuclear explosions, *Bull. Seism. Soc. Am.* 90: 929–939.

Morozov, I. B., E. A. Morozova, and S. B. Smithson, (1998a). On the nature of the teleseismic Pn phase observed in the recordings from the ultra-long range profile "Quartz", Russia, *Bull. Seismol. Soc. Am*. 88: (1), 62–73.

Morozov, I. B., E. A. Morozova, S. B. Smithson, and L. N. Solodilov. (1998b). 2-D image of seismic attenuation beneath the Deep Seismic Sounding profile "Quartz", Russia, *Pure and Applied Geoph*. 153: 311–348.

Morozova, E. A., I. B. Morozov, S. B. Smithson, and L. N Solodilov (1999). Heterogeneity of the uppermost mantle beneath the ultra-long range profile "Quartz," Russian Eurasia, *J. Geophys. Res.* 104: (B9), 20: 329–20,348.

Pavlenkova, N. I., (1996). General features of the uppermost mantle stratification from long-range seismic profiles, *Tectonophysics* 264: 261–278.

Priestley, K. F., J. Cipar, A. Egorkin, and N. I. Pavlenkova (1994). Upper-mantle velocity structure beneath the Siberian Platform, *Geophysical Journal International* 118: (2), 369–378.

Ryberg, T., F. Wenzel, J. Mechie, A. Egorkin, K. Fuchs, and L. Solodilov (1996). Two-dimensional velocity structure beneath Northern Eurasia derived from the super long-range seismic profile Quartz, *Bull. Seismol. Soc. Am*. 86: 857–867.

Ryberg, T., K. Fuchs, A. V. Egorkin, and L. Solodilov (1995). Observations of high-frequency teleseismic *Pn* on the long-range Quartz profile across northern Eurasia, *J. Geophys. Res.* 100: 18151–18163.

Schueller, W., I. B. Morozov, and S. B. Smithson (1997). Crustal and uppermost mantle velocity structure of northern Eurasia along the profile Quartz, *Bull. Seismol. Soc. Am.* 87: 414–426.

Yegorkin, A. V. (1992). Crustal structure along seismic geotraverses, *International Geology Review*, 34: (4), 345–362.

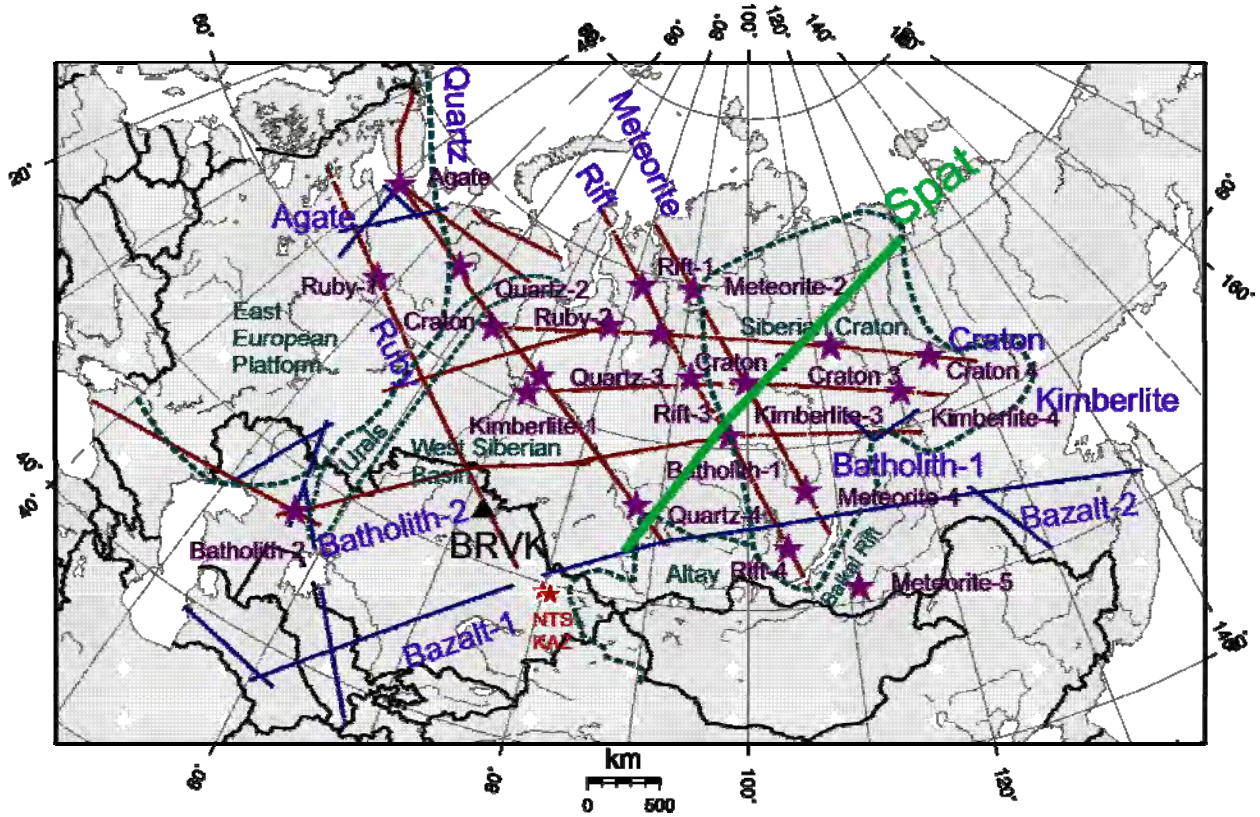


Figure 1 Eleven DSS PNE projects of this study (blue labels). With the exception for project METEORITE, all data were already delivered to IRIS and AFRL. Profile SPAT proposed as a replacement to METEORITE is shown schematically in green. Coordinates and other parameters of the PNEs used in these profiles were reported by Sultanov et al. (1999). Major tectonic units are indicated in dark green. Note the extent of systematic, continuous profiling, with PNEs (labeled stars) detonated at the nodes of a 2-D recording grid. Small brown circles are PNE recording stations, and blue circles are chemical-explosion recording stations. Project RUBY also recorded two Semipalatinsk nuclear test site explosions (red).

THE EFFECT OF REALISTIC GEOLOGIC HETEROGENEITY ON LOCAL AND REGIONAL P/S AMPLITUDE RATIOS BASED ON NUMERICAL SIMULATIONS

Stephen C. Myers[1], Jeffery Wagoner[1], Leiph Preston[2], Ken Smith[2], Hrvoje Tkalcic[1], and Shawn Larsen[1]

Lawrence Livermore National Laboratory[1] and University of Nevada, Reno[2]

Sponsored by National Nuclear Security Administration
Office of Nonproliferation Research and Development
Office of Defense Nuclear Nonproliferation

Contract Nos. W-7405-ENG-48[1] and DE-FC03-02SF22656[2]

ABSTRACT

Generation of S-waves from explosion sources continues to be an intriguing area of seismological research. Empirical studies document a general decrease in regional S-phase amplitudes (compared to P phases) for explosions sources. Although the decrease in S-phase amplitude for explosive (compressional) sources is intuitive, a physical understanding of the dominant mechanism(s) that contribute to S-phase excitation does not currently exist. Despite the success of regional discriminant and magnitude methods that rely on decreased S-phase amplitude for explosion sources, instances remain – primarily in the ~1Hz band – where explosions produce anomalously large S-phase amplitudes that confound regional methods. In this study, we investigate the effect of realistic earth structure on the local and regional wavefield for explosive sources. We develop a detailed model of the Nevada Test Site (NTS) and southern Basin and Range, and simulate seismic propagation through the model using a full-elastic, finite-difference method. Our simulations are based on the Nonproliferation Experiment (NPE) explosion at the NTS, which was well recorded at permanent and temporary stations.

Much of our effort is devoted to construction of the earth model, translating the geologic model to seismic velocity, and validating seismic simulations. To construct the model we make use of the extensive geologic database covering the NTS as well as numerous published and unpublished geological and geophysical studies. The topographic representation for the NTS is based on a digital elevation model (DEM) with 10-meter resolution, and the southern Basin and Range DEM is 100-meter resolution. The geologic detail and accurate topography at the NTS provides a realistic rendition of the geologic structure near the NPE shot. We estimate seismic velocity in the upper crust by translating geologic units into either a constant velocity or – for units that span a significant depth range – a velocity/depth profile. Velocity structure of the lower crust and upper mantle, as well as crustal thickness, is adapted from published profiles in the southern Basin and Range. Validation of the velocity structure is accomplished by simulating both phase and amplitude characteristics of local and regional recordings of the NPE. Simulations and observed travel times are in excellent agreement for both P and S phases at local and regional distances. Local-distance simulations and observed seismograms, which tend to be less than one wavelength in distance from the source, are also in excellent agreement when an isotropic source is used and the model includes a topographic free surface. A Compensated Linear Vector Dipole (CLVD) source was also tested with poor results. At regional distance the first few swings of the simulated and observed Pn phase are in good agreement, but later swings do not necessarily agree in phase (dominant frequency ~1 Hz). However, the average amplitude of simulated and observed phases is in good agreement. Using this validated model we have conducted two tests to date: 1) regional simulations with a flat free surface and 2) simulations with an explosion event at mid crustal depth. Both simulations suggest that the topographic free surface has a strong effect on the production of regional S phases. With a flat free surface, the generation of regional S waves is significantly reduced; most of the converted energy is propagated into the mantle. For an explosion source at mid-crustal depth, appreciable S waves are not generated until the wavefield interacts with shallow structure and the free surface. The diminished amplitude of the P waves by the time they reach the free surface, and the reduced curvature of the wavefront, results in a significant reduction in the amplitude of converted S waves. While not conclusive our simulations to date suggest that near source complexity is a major contributor to the generation of S waves from explosions. In the case of the NPE, topography is the dominant scatterer.

OBJECTIVE

Regional monitoring relies heavily on comparisons of P- and S-phase amplitudes (Pomeroy et al., 1982; Walter et al., 1995). Further, widely used methods of determining magnitude make use of Lg and Lg coda amplitudes (e.g., Nuttli, 1986; Mayeda and Walter, 1996; Patton, 2001), and regional S-phases often add important arrival-time observations to limited, small-magnitude datasets used for location (Mayeda and Walter, 1996, Myers et al., 1999).

Most investigators agree that appreciable energy from the explosions is converted to S waves near the source, but the dominant P-to-S transfer mechanism is not agreed upon. Several physically reasonable transfer mechanisms are proposed, including P-to-S conversion at the free surface, spall, scattering of short-period surface waves, tectonic release, and rock-damage (e.g., Vogfjord, 1997; Day and Mclaughlin, 1991; Gupta et al., 1992; Wallace et al., 1985; Johnson and Sammis, 2001). Each mechanism fits a subset of observations, and each mechanism, with the exception of surface-wave scattering, is understood from first principles. Currently, the Rg-to-S mechanism is represented by an empirical transfer function (e.g. Gupta et al., 1992; Patton, 2001).

This project aims to study the physical process of near-source scattering to establish a fundamental understanding of this phenomenon. Our recent progress is in the areas of model construction, and pursuant numerical experiments on the effect of near-source topography, and event depth are presented below.

RESEARCH ACCOMPLISHED

In previous years of this project, we developed a detailed upper-crustal model centered on the 1993 NPE shot (Figure 1). The local model is 20 km on a side (including depth), and construction of the model leverages the extensive LLNL database of geological and geophysical information that includes mapping, bore-hole logs, seismic surveys, and gravity surveys (e.g. Healey et al. 1963). While much of LLNL geological database is unpublished, it constitutes a wealth of knowledge that was accumulated over decades of study at the NTS.

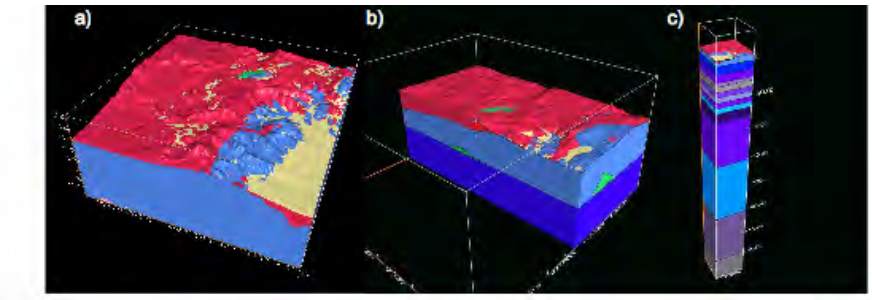


Figure 1. Local model around NPE shot determined from detailed geologic and geophysical studies. a) The entire local model. b) Cross section through the NPE shot. c) Local model merged into a lithospheric velocity stack.

The local model is imbedded in a regional model that extends to ~400 km from the NPE source (Figure 2). The default velocity structure is a one-dimensional model based on work of Patton and Taylor (1984). Deviation from the default model is based on published studies in the region. The current version of the model includes variations in upper-crustal structure based on regional geologic maps of Nevada, Utah, California, and Arizona. We assume that crystalline rocks are continuous into the lower crust, and that basin depths are proportional to the magnitude of local gravity anomalies (e.g., Blakely et al., 1997). The lower crustal velocities and Moho depth are modified based on the work of Zandt et al. (1995) and Mooney et al. (1998). Minor modifications to mantle velocities are based on refraction profiles summarized in Mooney et al. (1998). In specific areas we have incorporated tomographic studies, such as Biasi (2005) and Preston et al. (2005).

Considerable effort has been put into translating EarthVision models – as seen in Figures 1 and 2 – into seismic models. We have developed a suite of codes that translate geologic units into either a constant P wave, S wave, and density, or into a geologic unit may be translated into a specified portion of a velocity/depth profile. Generally, the upper crust is modeled as constant velocity units, such as sedimentary units and granite bodies. The lower crust and

upper mantle are modeled as smooth velocity vs. depth profiles, which are allowed to change laterally. Modeling the lower crust and upper mantle with smooth velocity profiles, as opposed to discrete layers, eliminates nuisance reflections and conversions from P to S energy.

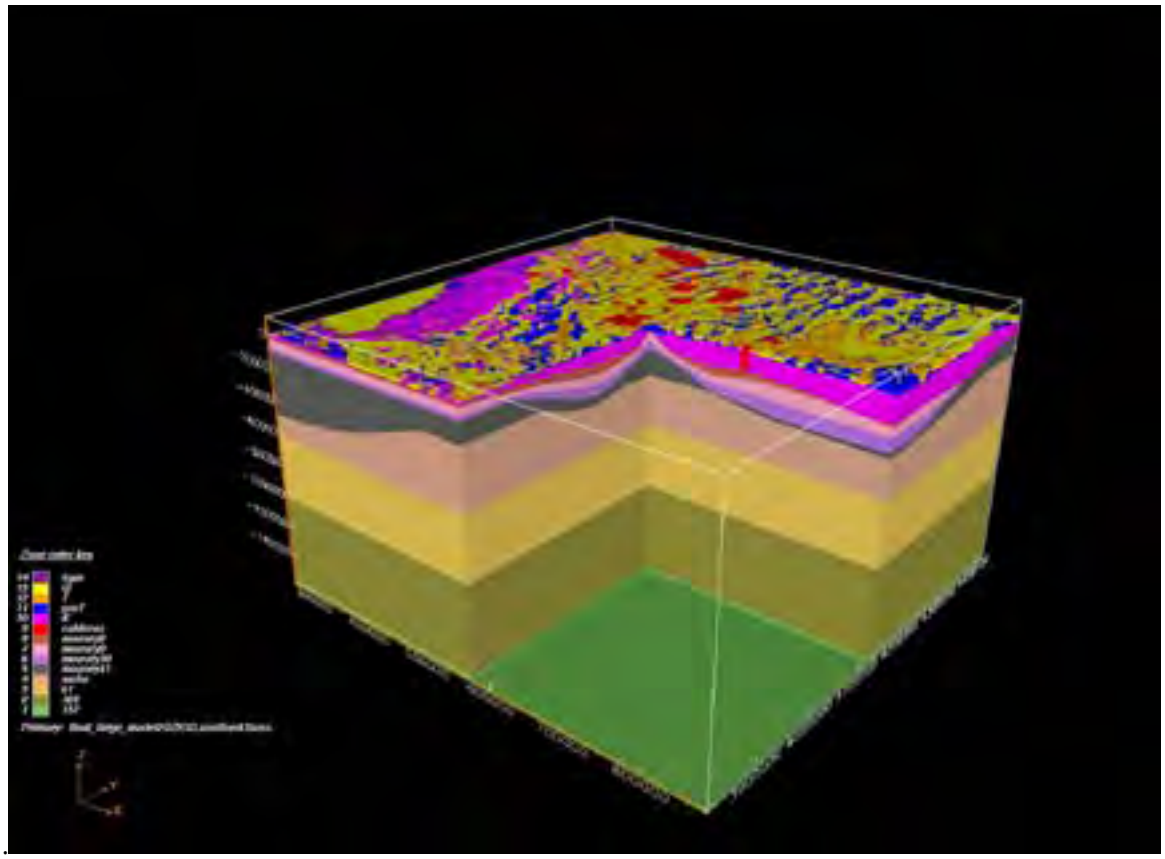


Figure 2. Regional geologic model centered on the Nevada Test Site. The model extends into California (to the left), Utah and Arizona (to the right). The model is a compilation of: geologic mapping; seismic profiles, receiver functions, and tomography; gravity modeling for basin structure.

Model Validation using NPE Observations

We use the E3D code of Larsen and Grieger (1998) for seismic simulations. E3D is a full elastic code that allows the input of a general geologic structure, including the free surfaces. All of our simulations use a grid spacing of 60 m, which enables interpretation to 3 or 4 Hz.

Our numerical simulations are based on the 1993 NPE. The NPE was a 1-kiloton chemical explosion at the NTS. NPE details and research reports can be found in Denny and Stull (1994). Figure 3 shows the extensive network of stations that recorded the NPE. We have compiled all these recordings to validate our model. We begin with the local recordings, which we used both to validate the near-source model and to estimate the NPE moment tensor.

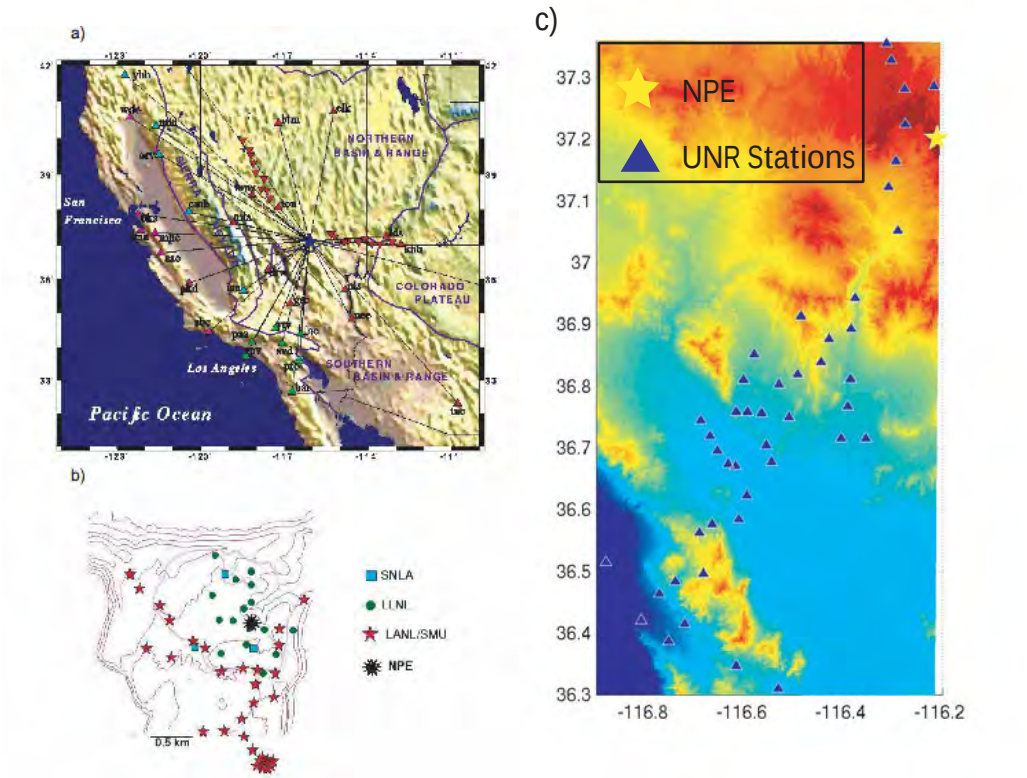


Figure 3. Stations with recordings of the NPE shot. We have compiled waveforms from all of these stations.

Figure 4 shows an example waveform (black) from a station that is approximately 2 km from the NPE. Simulations (red) with combinations of isotropic (Figure 4 a,b) and CLVD (Figure 4 c,d) moment tensors and topographic free surface (Figure 4 a,c) and flat free surface (Figure 4 b,d) are compared with the data. It is clear that the isotropic source in a model that includes the topographic free surface is the best fit to the data. Comparisons with other local data (not shown) are similar, and we conclude that the NPE is best modeled as an isotropic source.

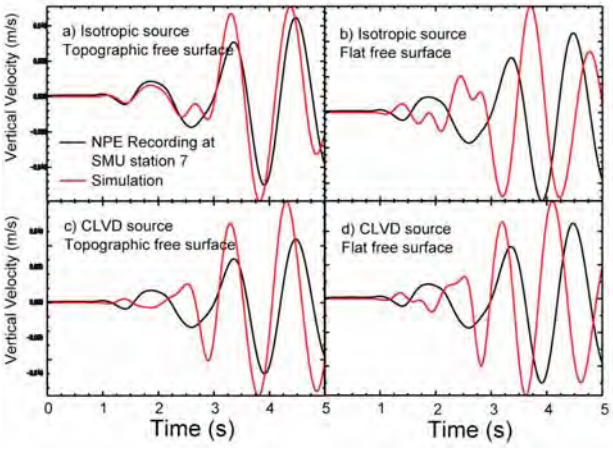


Figure 4. Recorded (black) and simulated (red) displacement seismograms for the NPE shot. These 3-dimensional simulations make use of the local NPE model (see above). Event-station distance is approximately 2 km. a) Simulation with isotropic moment tensor and free surface based on DEM. b) Simulation with isotropic source and flat free surface. c) Simulation with CLVD moment tensor with DEM free surface. d) Simulation with CLVD moment tensor and flat free surface. The NPE is best modeled as an isotropic source. Simulation with a realistic free surface is essential to match the data.

Figure 5 is an example of our regional validation effort. In this example we use the temporary, broadband (STS-2 sensor) deployment fielded by the University of Arizona. The cross section is color coded to P-wave velocity, which was taken from our regional 3-dimensional model. The upper crust is characterized by Paleozoic sedimentary rocks, which are interrupted by low-velocity basins. Velocity in the mid- and lower crust primarily increases with depth, but we include minor lateral variation in velocity as well as changes in Moho depth based on the work of Zandt et al. (1995). The interface between light and dark red in the lower quarter of the cross section is the Moho. We have superimposed a snap shot of the seismic wavefield on the cross section to demonstrate the complexity that results from this relatively simple model.

The traces shown in Figure 5 compare recorded (black) and synthetic (red) velocity seismograms. Both velocity and synthetic records are band passed between 0.7 Hz and 3 Hz. Amplitudes are normalized because geometric spreading in the 2-dimensional synthetics is incorrect. In general, the comparison of observed and synthetic data is favorable. The degree of waveform complexity is nearly identical, and it would be difficult to tell which trace is real based on simple inspection. The relative amplitudes of the real and synthetic waveforms are also in good agreement (with the notable exception of station 8, where synthetic amplitudes after the first arrival are too large). Although the phase is matched in many instances (particularly the first arrival), we cannot claim to have simulated phase reliably. Nonetheless, the overall agreement between observed and synthetic data is very good, especially considering that the model was not directly derived from the data. Figure 5b shows cumulative energy for the 6 recordings and synthetics. In most cases, the cumulative energy curves of data and synthetics are in good agreement. We also note that synthetic estimates are high in some case and low in others, i.e., there is not a consistent bias across all stations. We find that the overall model performance is good and that variability can be attributed to station site effects.

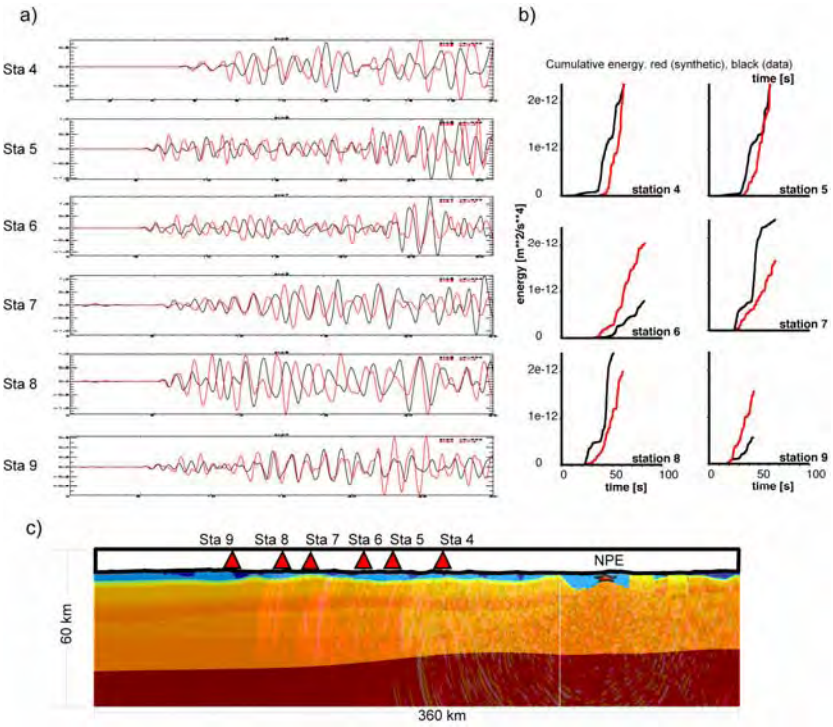


Figure 5. Model validation with regional seismic simulations of the U. Arizona broadband deployment (line extending east from NPE in Figure 2). a) Vertical velocity recordings of the NPE between 0.7 Hz and 3 Hz (black) with synthetics (red) for comparison. Amplitudes are normalized. A separate 2-dimensional simulation was made for each of the stations to account for slight azimuth variations in structure. The general character of the observed seismograms is matched by the synthetics, suggesting that the regional model is a good representation of true structure. b) Cumulative energy for observed and synthetic waveforms in a). c) Cross-section shows a snap shot of the seismic wavefield overlain on a P-wave velocity for the station 9 simulation; west is to the right. The transition from red to near black in the lower quarter of the cross section is the Moho.

Observed and synthetic P/S ratios are in good (but not perfect) agreement (Figure 6). In a band pass of 0.5 Hz to 1.0 Hz the data are biased towards higher P/S ratios. We are currently working to understand the bias, but we note that the bias is only a couple tenths, which is well within the spread of most empirical P/S plots. In the 1.0 Hz to 3.0 Hz band, P/S ratios for both data and synthetics increase, suggesting that our model is characterizing the wavefield at these frequencies.

Table 1: P/S ratio for data and synthetics

	0.5 to 1.0 Hz		1.0 to 3.0 Hz	
	data	synth	data	synth
sta4	0.504	0.143	1.568	0.374
sta5	0.592	0.200	0.551	0.601
sta6	0.153	0.230	0.336	0.424
sta7	0.724	0.518	0.860	1.290
sta8	1.032	0.406	1.665	0.469
sta9	0.741	0.480	0.934	0.802

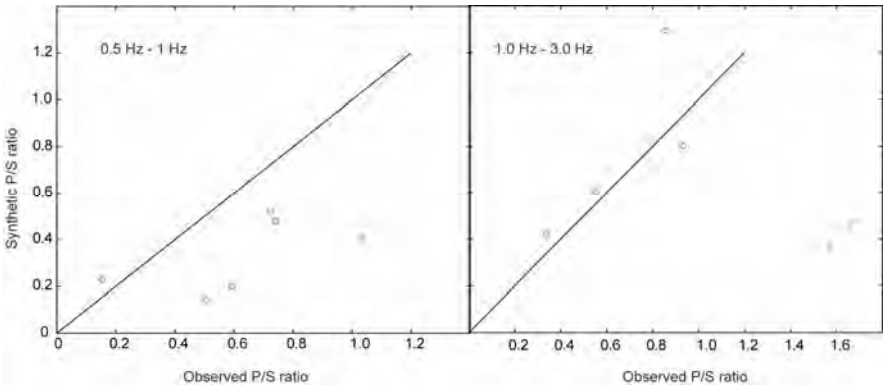


Figure 6: Comparison of observed and synthetic P/S ratios.

The Effect of Topography on P/S Ratios

Figure 7 is a map-view snap shot of a local simulation with and without topography (note that these are the same simulations that produced the synthetic seismograms in Figure 4 a,b). The topographic level at the NPE epicenter is applied uniformly in the flat free surface simulation with surface velocities filled to the flat free surface or with truncation of the structure (depending on whether the elevation is lower or higher than at the NPE). Figure 7 shows that local topography immediately imparts disorder (scattering) into the wavefield.

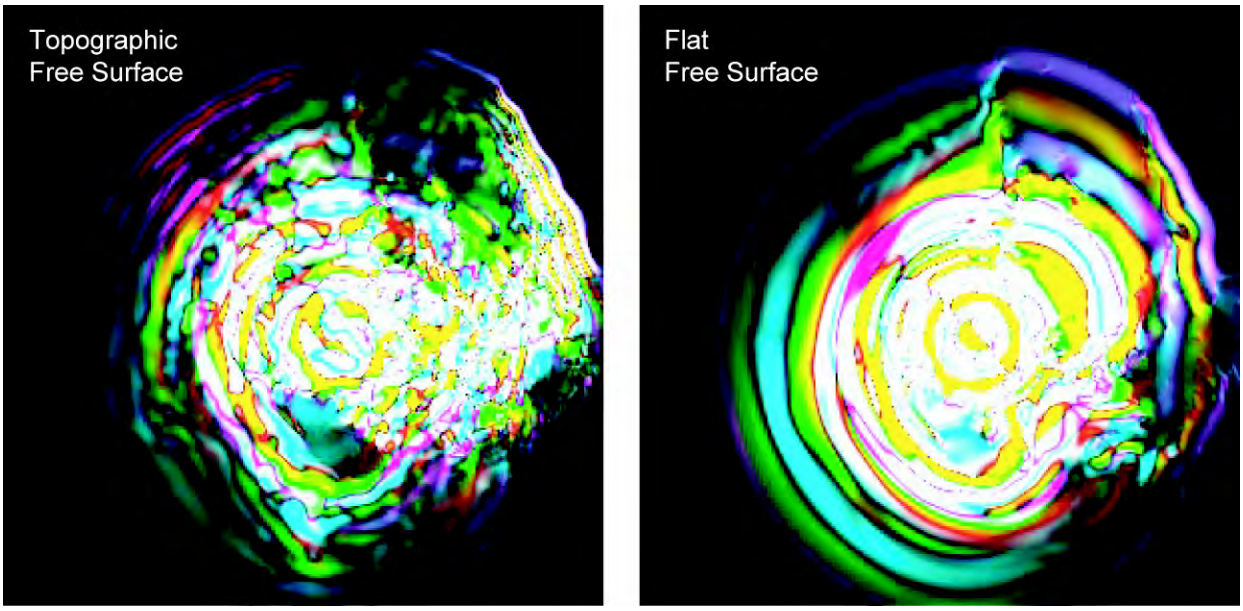


Figure 7. Map view of simulations with topographic free surface based on a digital elevation model (left) and flat free surface (right). Red, magenta and blue colors are P-waves. Green and yellow colors are S-waves. The map views shown above are 20 km on a side. Images are snap shots at approximately 5.5 seconds after event origin time and are at the lowest topographic elevation in the model. Detailed geologic structure from local mapping and geophysical studies is included in both simulations. Inclusion of realistic topography complicates the wave field considerably with appreciably more scattering.

Figure 8 shows synthetic spectra and seismograms of P-potential and S-potential at approximately 5 km from the source (taken from the simulations shown in Figure 7). In all cases, the S-potential exceeds the P-potential, which is presumably the result of free surface effects. However, the real topographic free surface results in a frequency-dependent P/S ratio. In fact, the P/S ratio is significantly decreased at frequencies close to 1 Hz. Although these results are preliminary, the qualitative similarities in the frequency dependence of observed P/S ratios (mentioned in the Objectives section) and the synthetic P/S ratios for simulations that include real topography is suggestive. Further testing and rigor will determine whether topographic scattering is the primary mechanism for S waves in the 1 Hz band.

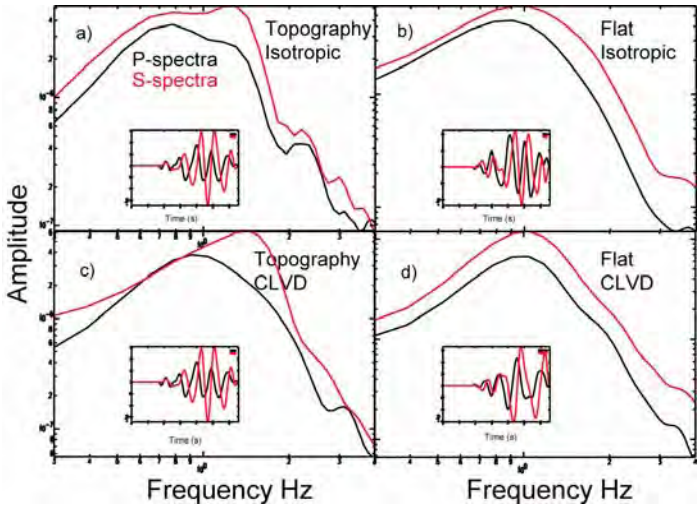


Figure 8. P (black) and S (red) displacement spectra and seismograms for simulations of the NPE shot (Simulations shown in Figure 7). These 3-dimensional simulations make use of the local NPE model (see above). The inset seismograms are P-potential (black) and S-potential (red) for a location approximately 5 km from the source. The spectra are derived from P and S potential seismograms. a) Simulation with isotropic moment tensor and free surface based on digital elevation model (DEM). b) Simulation with isotropic source and flat free surface. c) Simulation with compensated linear vector dipole (CLVD) moment tensor with DEM free surface. d) Simulation with CLVD moment tensor and flat free surface. Both isotropic and CLVD moment tensors produce a distinctly frequency-dependent P/S ratio.

The Effect of Source Depth on P/S Ratios

Results presented above suggest that near-source scattering, particularly scattering off of the free surface, boosts the amplitude of radiated S waves at the expense of P-wave amplitudes. We test this hypothesis by comparing the simulation of a shallow source with a simulation of a deep (mid crustal) source (Figure 9). Near-source heterogeneity for the shallow source (upper-crustal structure and topography) is considerable. Near-source heterogeneity for the deep source, where velocity is changing smoothly with depth, is minor. In both instances the source is isotropic (explosion) with the same moment. The model is approximately 300 km wide and 150 km deep. Some artifacts from reflections off of the side of the model are evident, but these artifacts do not muddle the overall picture.

The difference between the shallow- and deep-source simulations is striking. For the shallow source, S waves grow to large amplitudes within seconds. The large S waves radiate from the source in all directions. Therefore, S-waves are observed to propagate at steep angles into the mantle (and could propagate to teleseismic distances), as well as at shallow angles into the crustal waveguide to regional distances. For the deep source, S waves are all but absent until the P-wave enters the upper crust. Notable conversion to S-waves does occur, but the S-wave amplitudes are significantly smaller than they are for the shallow source. Much of the S-wave energy is trapped in the upper crust, forming a P-coda. S energy that escapes local, upper-crustal structures (e.g., basins) is reflected downward at steep angles. Therefore, the majority of the S energy that escapes the upper crust is transmitted into the mantle, and little energy is trapped in the crustal waveguide.

CONCLUSIONS AND RECOMMENDATIONS

We have constructed a regional model centered on the NTS based on published and unpublished studies. The starting point of the regional model is a 1-dimensional model that is based on surface-wave studies. We include significant 3-dimensional modifications to the 1-dimensional model based on receiver function, refraction, reflection, and gravity studies. The regional model includes a detailed upper crustal model centered on the NPE explosion. This local model is constrained by geologic maps, borehole data, and geophysical studies at the NTS. The local model is seamlessly imbedded into a regional model to enable realistic simulations of NTS sources to regional distance.

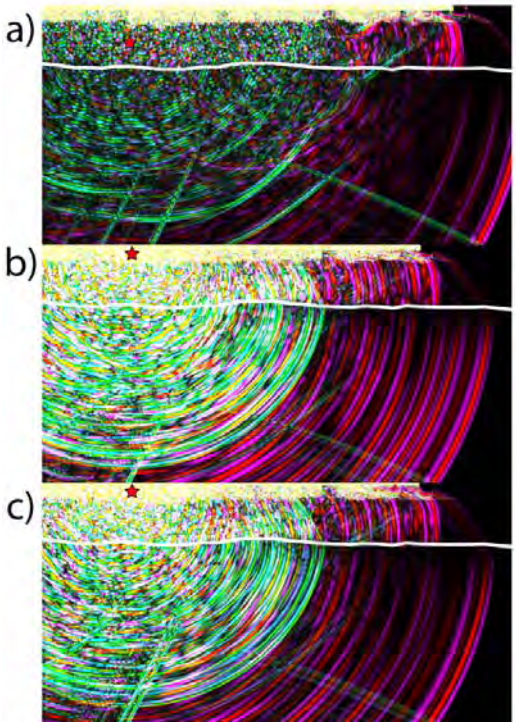


Figure 9. Regional, 2-dimensional simulation showing the difference between a) mid-crustal source, b) shallow source with complex geology and flat topography, and c) shallow source with complex geology and topographic free surface. In each case the source is isotropic. The model is approximately 300 km wide and 150 km deep. Snap shots are at approximately 75 seconds after the source origin time. P waves are red, and S waves are green and yellow. The shallow sources generate vastly more S waves (green and yellow) than the deeper source. The intensity of Pg (red and blue crustal phase on the right side of each panel) is greater for the deeper source.

Validation of the model is based on recordings and simulations of the NPE shot, as well as phase travel-times from NTS explosions. Validation of the local model is complete and the model reliably predicts local NPE waveforms. Validation of the regional model is on-going. Although we do not predict regional waveforms above ~1Hz, arrival times and relative amplitudes of regional phases are reliably predicted.

Local 3-dimensional simulations demonstrate that topographic scattering is an important source of S-wave generation for the NPE. We find that topographic scattering peaks S-wave amplitudes at approximately 1 Hz, which is in agreement with observations in many instances (at NTS and other locales). Topographic scattering produces a disordered wavefield and scatters energy in all directions. Simulations with a flat free surface produce S waves, but little frequency dependence is observed.

Regional simulations demonstrate that a shallow NPE source produces appreciable S waves that radiate at a large range of ray parameters. For shallow sources, S waves generated through structural and topographic scattering propagate in all directions. This means that the S waves propagate at steep angles into the mantle (and would presumably continue to teleseismic distance) as well as into the regional waveguide to form Sn and/or Lg. Our results are consistent with those of similar numerical studies (e.g., Xie et al., 2005). When the equivalent NPE source is placed in the mid crust, S-wave generation is significantly diminished. S waves are generated as the P wave traverses the upper crust and reflects off of the topographic free surface, but S waves that escape the upper crust travel at steep angles and are largely transmitted into the mantle.

ACKNOWLEDGEMENTS

We acknowledge the LLNL containment program for generous access to their extensive database of geologic and geophysical studies at the NTS. We also would like to than Glenn Biasi and Walter Mooney for providing regional geophysical information.

REFERENCES

Blakely, R. J., R. C. Jachens, J. P. Calzia, and V. E. Langenheim (1997). Cenozoic basins of the Death Valley extended terrane as reflected in regional-scale gravity anomalies, L.A. Wright and B.W. Troxel, eds., Cenozoic Basins of the Death Valley Region: Boulder, CO, *Geol. Soc. Am. Special Paper 333*.

Biasi, G. (2005). Mantle lithospheric clues to Walker Lane evolution, presented at the 2005 SSA meeting, Incline, NV.

Day, S., and K. Mclaughlin (1991). Seismic source representations for spall, *Bull. Seismol. Soc. Am*. 81: 191–201.

Denny, M. D., S. P. Stull (1994). Proceedings of the Symposium on the Non-Proliferation Experiment (NPE): Results and Implications for Test Ban Treaties, Rockville Maryland; Lawrence Livermore National Laboratory.

Gupta, I. N., W. W. Chan, and R. A. Wagner (1992). A comparison of regional phases from underground nuclear explosions at East Kazakh and Nevada Test Sites, *Bull. Seismol. Soc. Am*. 82: 352–382.

Healey, D. L. and Miller, C. H. (1963). Gravity survey of the Gold Meadows Stock, Nevada Test Site, Nye County, Nevada. *USGS Technical Letter NTS-40*.

Johnson, L.R., and C.G. Sammis (2001). Effects of rock damage on seismic waves generated by explosions, *Pageoph*, 158, 1869–1908.

Larsen, S., and J. Grieger (1998). Elastic modeling initiative, Part III: 3-D computational modeling, in *Soc. Expl. Geophys. Conference Proceedings*, 6: 1803–1806.

Mayeda, K., and W. Walter (1996). Moment, energy, stress drop, and source spectra of western United States earthquakes from regional coda envelopes, *Jour. Geophys. Res*. 101: 11,195–11,208.

Myers, S.C., W.R. Walter, K. Mayeda, L. Glenn (1999). Observations in support of Rg scattering as a source for explosion S waves: regional and local recordings of the 1997 Kazakhstan depth of burial experiment, *Bull. Seismol. Soc. Am*. 89: 544–549.

Mooney, W., G. Laske, G. Masters (1998). Crust 5.1: a global crustal model at 5x5 degrees, *Jour. Geophys. Res*. 103: 727–747.

Nuttli, O. W. (1986). Yield estimates of Nevada Test Site explosions obtained from seismic Lg waves, *J. Geophys. Res*. 91: 2137–2151.

Patton, H. J. and S. R. Taylor (1984). Q-structure of the basin and range from surface waves, *Jour. Geophys. Res*. 89: (NB8) 6929–6940.

Patton, H. J. (2001). Regional magnitude scaling, tranportability, and Ms:mb discrimination at small magnitudes, *Pageoph* 158: 1951–2015.

Pomeroy, P., W. Best, and T. McEvilly (1982). Test ban treaty verification with regional data - a review, *Bull. Seismol. Soc. Am*. 72: S89-S129.

Preston, L., K. Smith, and D. vonSeggern (2005). 3D velocity structure of the Yucca Mountain, *Seismo. Soc. Am. Spring meeting*, presented at the 2005 SSA meeting, Incline, NV .

Vogfjord, K. (1997). Effect of explosion depth and earth structure on the excitation of Lg waves: S* revisited, *Bull. Seismol. Soc. Am*. 87: 1100–1114.

Wallace, T., D. Helmberger, and G. Engen (1985). Evidence for tectonic release from underground nuclear explosions in long period S waves, *Bull. Seismol. Soc. Am*. 75: 157–174.

Walter, W., K, Mayeda, and H. Patton (1995). Phase and spectral ratio discrimination between NTS earthquakes and explosions: Part I: empirical observations, *Bull. Seismol. Soc. Am*. 85: 1050–1067.

Xie, X. B., Z. Ge, T. Lay, Investigating Explosion source energy partitioning and Lg-wave excitation using a finite-difference plus slowness analysis method, Bull. Seism. Soc. Am., 95, 2412-2427, 2005.

Zandt, G. SC Myers, TC Wallace (1995). Curst and mantle structure across the Basin and Range – Colorado plateau at 37° north latitude and implications for Cenozoic extension mechanism, *Jour. Geophys. Res*. 100: 10,592–10,548.

GROUND TRUTH, MAGNITUDE CALIBRATION AND REGIONAL PHASE PROPAGATION AND DETECTION IN THE MIDDLE EAST AND HORN OF AFRICA

Andrew A. Nyblade[1], Aubreya Adams[1], Richard A. Brazier[1], Yongcheol Park[1], and Arthur Rodgers[2]

Penn State University[1] and Lawrence Livermore National Laboratory[2]

Sponsored by National Nuclear Security Administration
Office of Nonproliferation Research and Development
Office of Defense Nuclear Nonproliferation

Contract Nos. DE-FC52-05NA26602[1] and W-7405-ENG-48[2]

ABSTRACT

In this project, we are exploiting unique and open source seismic data sets to improve seismic monitoring across the Middle East (including the Iranian Plateau, Zagros Mountains, Arabian Peninsula, Turkish Plateau, Gulf of Aqaba, Dead Sea Rift) and the Horn of Africa (including the northern part of the East African Rift, Afar Depression, southern Red Sea and Gulf of Aden). The data sets are being used to perform three related tasks. 1) We are determining moment tensors, moment magnitudes and source depths for regional events in the magnitude 3.0 to 6.0 range. 2) These events are being used to characterize high-frequency (0.5-16 Hz) regional phase attenuation and detection thresholds, especially from events in Iran recorded at stations across the Arabian Peninsula. 3) We are collecting location ground truth at GT5 (local) and GT20 (regional) levels for seismic events with M > 2.5, including source geometry information and source depths.

In the first phase of this project, seismograms from earthquakes in the Zagros Mountains recorded at regional distances have been inverted for moment tensors, and source depths for the earthquakes have been determined via waveform matching. Early studies of the distribution of seismicity in the Zagros region found evidence for earthquakes in the upper mantle. But subsequent relocations of teleseismic earthquakes suggest that source depths are generally much shallower, lying mainly within the upper crust. Nine events with magnitudes between 5 and 6 have been studied so far. Source depths for six of the events are within the upper crust, and three are located within the lower crust. The uncertainty in the source depths of the lower crustal events allows for the possibility that some of them may have even nucleated within the upper mantle. Eight events have thrust mechanisms and one has a strike-slip mechanism.

We also report estimates of three-dimensional P- and S-wave velocity structure of the upper mantle beneath the Arabian Peninsula obtained from travel time tomography. Travel time measurements were obtained using a data set provided by King Abdulaziz City for Science and Technology (KACST) for the Saudi Arabia National Digital Seismic Network. The network consists of 38 stations (27 broadband and 11 short period). We augmented the KACST data with delay times measured from permanent stations in the region and the 1995-7 Saudi Arabian PASSCAL Experiment. Tomographic images reveal a low velocity feature in the upper mantle stretching north-south beneath the central portion of the Arabian Shield.

OBJECTIVES

The objective of this effort is to determine ground truth source parameters (depth, moment, focal mechanism) for earthquakes in the Middle East. For this reporting period we focused on events in the Zagros Mountains of Iran using unique broadband waveforms from regional stations. Source moments will be used to calibrate coda wave moment magnitudes (Mayeda et al., 2003) and to model high-frequency regional body-wave amplitude spectra with the Magnitude-Distance Amplitude Correction (MDAC) methodology (Walter and Taylor, 2002). In subsequent periods, we will determine models of the propagation characteristics, including attenuation, of high-frequency regional phases. These models will then be used to estimate detection thresholds by comparing model-based predictions of signal amplitudes to background noise levels.

RESEARCH ACCOMPLISHED

Introduction

In this project, we are exploiting unique and open source seismic data sets to improve seismic monitoring for the Middle East (including the Iranian Plateau, Zagros Mountains, Arabian Peninsula, Turkish Plateau, Gulf of Aqaba, and Dead Sea Rift) and the Horn of Africa (including the northern part of the East African Rift, Afar Depression, southern Red Sea, and Gulf of Aden). Broadband waveform data sets are being used to perform three related tasks. 1) We are determining moment tensors, moment magnitudes and source depths for regional events in the magnitude 3.0 to 5.0 range. 2) These events are being used to characterize high-frequency (0.5-16 Hz) regional phase attenuation and detection thresholds, especially from events in Iran recorded at stations across the Arabian Peninsula. 3) We are collecting location ground truth at GT5 (local) and GT20 (regional) levels for seismic events with M > 2.5, including source geometry information and source depths.

The results of this research will enhance monitoring capabilities within the study region by improving our understanding of high frequency regional phase attenuation and how this attenuation affects detection thresholds. Accurate hypocentral locations of M>2.5 seismic events are needed to construct travel time correction surfaces, which are of fundamental importance to ground-based nuclear explosion monitoring.

The work completed so far in this project has focused on obtaining well constrained source parameters for magnitude 5.0 and greater events in the Zagros Mountains of Iran that have been well recorded at regional distances. Focal mechanisms have been obtained through standard moment tensor inversion of regional waveforms, and a grid search procedure has been applied to find the source depth that produces the best fit to the regional waveforms. As part of this project, we have also imaged three-dimensional P- and S-wave velocity structure of the upper mantle beneath the Arabian Peninsula using teleseismic travel time tomography. We have completed travel time measurements and inversion for a data set provided by KACST for the Saudi Arabia National Digital Seismic Network. The network consists of 38 stations (27 broadband and 11 short period). We augmented the KACST data with delay times measured from permanent (GNS/IMS) stations in the region (RAYN, EIL and MRNI) and the 1995-7 Saudi Arabian PASSCAL Experiment (Vernon and Berger, 1998).

Background

The Arabian Shield consists of late Proterozoic crystalline basement overlain by Tertiary and Quaternary volcanic rocks in some places. The break-up of the Arabian Plate from Africa initiated at about 30-35 million years ago (Ma), with the formation of the Red Sea-Gulf of Aden rift system (Coleman and McGuire, 1988). Volcanism was widespread between 30 and 12 Ma, and uplift of the Arabian Shield occurred at about 13 Ma (Coleman and McGuire, 1988). The volcanism and uplift are thought to be related to the presence of hot upper mantle (Camp and Roobol, 1992). The uplifted Arabian Shield contains two major features: one is the
Makkah-Madinah-Nafud (MMN) volcanic line in the south and the other is the Ha'il-Rutbah Arch in the north (Figure 1). The MMN volcanic line, extending north-south, has been the major site of volcanism in Saudi Arabia over the past 10 Ma and the Ha'il-Rutbah Arch has been the site of several periods of uplift (Camp and Roobol, 1992).

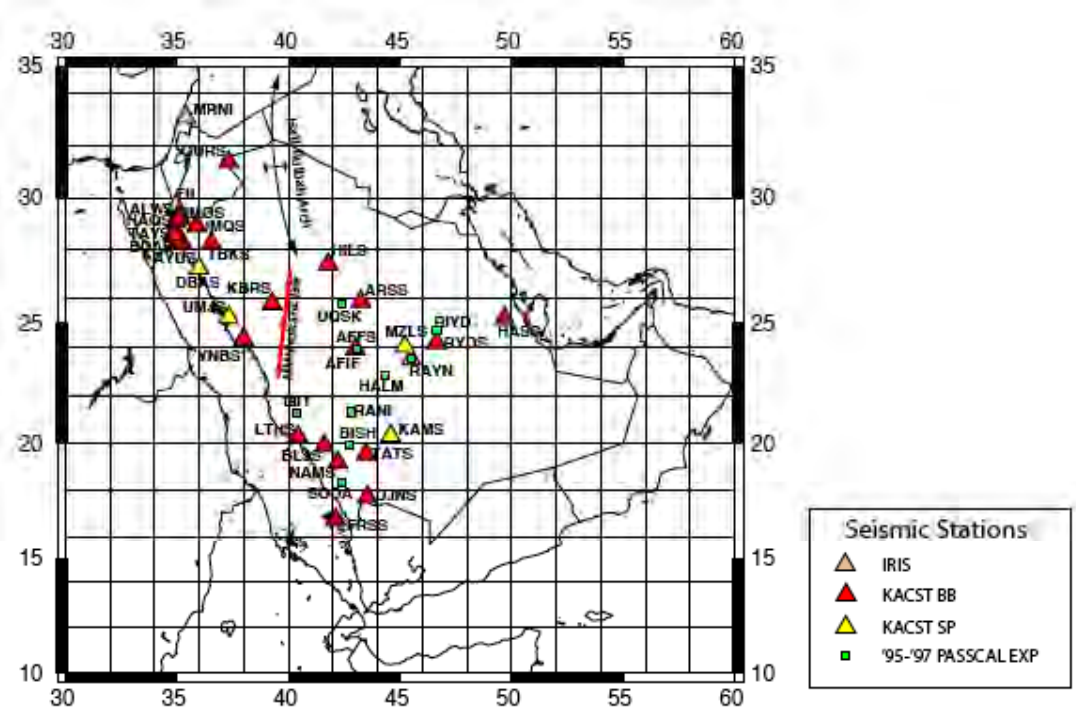


Figure 1. Map showing seismic stations in the Arabian Peninsula used in this study. KACST stations belong to the Saudi Arabia Digital National Seismic network.

The Zagros Mountain Belt, one of the world's most seismically active mountain ranges, marks the convergent boundary between the Arabian and Eurasian plates in southwestern Iran (Figure 2). The upper 11 km of the crust consists of folded sedimentary layers, while the lower 36 km of the crust are composed of faulted crystalline basement rock. The most prominent fault exposed at the surface is the Zagros Main Thrust, which marks the northern extent of seismicity associated with the Zagros Mountains and separates the Zagros Mountains from the Central Iranian Plateau. The Moho dips to the northeast from a depth of 40 km beneath the Persian Gulf to a maximum depth of approximately 65-70 km beneath the Zagros Main Thrust (Paul et al., 2006). Early studies of the distribution of seismicity in the Zagros region found evidence for earthquakes in the upper mantle (Nowroozi, 1971; Bird et al., 1975). Subsequent recalculations of teleseismic earthquakes indicated that source depths were much shallower, lying within the upper crust (Maggi et al., 2000, 2002).



Figure 2. Colored topography map of the Middle East showing the location of the main plates and the Zagros Mountains.

Zagros Earthquakes

Source depths and focal mechanisms for nine new events have been obtained (Table 1). A grid search method was used to determine the source parameters of each event. First, regional waveforms for each event were inverted for a moment tensor over a range of potential source depths. Synthetic seismograms were then computed using a reflectivity code for each source mechanism and compared to observed waveforms. In addition to the KACST and PASSCAL stations, data recorded at regional distances on open stations to the north and east were used, providing fairly good azimuth ray coverage for each event. The quality of the visual fit between the synthetic and observed waveforms, along with the root mean square error, were used to determine the best-fitting focal mechanism and associated source depth.

The locations of the events are shown in Figure 3. Most of the events studied occurred within the central portion of the Zagros Mountains where there are the best constraints on crustal structure provided by receiver function and gravity studies. Figure 4 summarizes graphically the results for the nine events, and shows a selection of the waveform fits for each event. Eight events have thrust mechanisms and one has a strike-slip mechanism. Source depths for six of the events are within the upper crust, and three are located within the lower crust. The uncertainty in the source depths of the lower crustal events allows for the possibility that some of them may have even nucleated within the upper mantle. The depth distribution of the events with uncertainties is shown in Figure 5.

Table 1a. Source parameters for events in the Zagros Mountains. Event letters are the same as in Figure 3.

Event Letter	Event ID Number	Date MM/DD/YYYY	Time	M0	Mw	Mw CMT	Strike/Dip/Rake (Plane 1)	Strike/Dip/Rake (plane 2)
A	9962	11/13/1998	13:01:10	1.35E+24	5.4	5.4	144.21/65.33/120.95	269.05/38.80/41.76
B	1320614	10/31/1999	15:09:40	7.13E+23	5.2	5.2	158.09/69.17/102.39	306.38/24.10/60.58
C	776913	05/06/1999	23:00:53	5.44E+26	7.1	6.2	19.15/10.66/-6.79	115.83/88.75/259.41
D	9816	10/05/1998	02:20:36	1.26E+24	5.4	5.4	40.91/85.77/206.56	308.80/63.51/-4.73
E	4070289	03/01/2000	20:06:29	1.93E+23	4.8	5.0	298.57/49.98/134.73	61.56/57.04/50.03
F	1326382	03/01/2000	20:06:28	1.78E+23	4.8	5.1	112.26/33.89/122.73	254.50/62.03/70.04
G	1582024	02/17/2002	13:03:53	1.01E+24	5.3	5.5	109.24/10.24/76.99	302.46/80.03/92.33
H	4357281	07/10/2003	17:40:16	4.64E+24	5.7	5.6	343.19/6.42/35.13	218.22/86.31/95.26
I	1559906	04/13/2001	01:04:27	3.93E+23	5	5.1	96.81/14.85/134.62	231.21/79.49/79.45

Table 1b. Moment tensors and source depth for events in the Zagros Mountains. Event letters are the same as in Figure 3.

Event Letter	Mxx	Mxy	Mxz	Myy	Myz	Mzz	Depth
A	8.67E+10	3.73E+10	-4.49E+09	5.16E+09	-9.42E+10	-9.19E+10	12 (+-2)
B	2.35E+10	1.97E+10	-1.13E+10	2.72E+10	-5.13E+10	-5.08E+10	12 (+-2)
C	9.18E+12	1.99E+12	4.85E+13	-1.84E+13	1.86E+13	9.25E+12	54 (+15/-8)
D	-1.18E+11	2.13E+10	3.33E+10	1.04E+11	-4.42E+10	1.35E+10	35 (+15/-5)
E	1.79E+10	2.01E+08	-1.97E+09	-4.28E+09	1.04E+10	-1.36E+10	9 (+-3)
F	1.66E+10	7.22E+08	8.33E+09	-3.64E+09	-4.28E+09	-1.30E+10	9 (+-3)
G	2.85E+10	1.84E+10	7.94E+10	2.29E+09	5.09E+10	-3.08E+10	4 (+-2)
H	4.01E+08	1.31E+10	2.90E+11	8.04E+10	-3.54E+11	-8.08E+10	39 (+10/- 15)
I	1.52E+10	5.69E+08	2.55E+10	2.08E+09	-2.50E+10	-1.73E+10	8 (+-3)

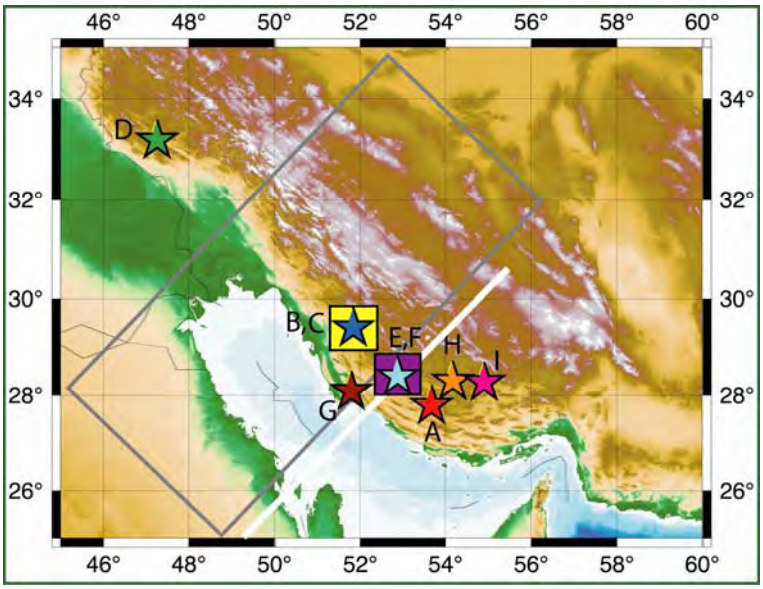


Figure 3. Map of Zagros Mountains and Persian Gulf showing the locations of earthquakes studied. Letters correspond to the events in Table 1. The grey box shows the area where crustal thickness has been constrained using gravity data and the white line shows where crustal thickness has been imaged using receiver functions.

The focal depth of earthquakes can affect the excitation of regional phases, particularly the guided Lg phase, which is composed of higher mode surfaces waves whose amplitudes are strongly depth dependent. The source parameters determined above can be used to infer how focal mechanism and depth might impact regional phase S-wave generation and how this might in turn impact P/S discriminants. Two nearby events (A & H) were recorded at station HILS on the northern Arabian Shield. These events had similar magnitudes (5.4 versus 5.7) and although both are thrust mechanisms their strikes are slightly different. These events have significantly different depths with event A in the upper crust and event H in the lower crust (or upper mantle, but less likely). The high-frequency (0.5-5 Hz) responses of these events are shown in Figure 6. Note that Lg is weaker with respect to the Pn for the deeper event (H), making the Pn/Lg ratio discriminant more explosion-like for this event. This suggests a possible depth-dependence of the Lg amplitude (and Pn/Lg ratio discriminant). Alternatively, the further event (H) may be located in a region of thicker crust, which leads to disruption of the crustal waveguide along the path to HILS. Both explanations would cause additional scatter in body-wave discriminants, compounding discrimination strategies. These observations will be explored in further work on this project.

Body Wave Tomography

Upper mantle structure strongly impacts the propagation of regional Pn and Sn phases. We report velocity structure of the upper mantle reported from teleseismic P- and S-body waves. While this study elucidates deep upper mantle structure, there are likely relationships with structure directly below the crust. To investigate upper mantle structure under the Arabian Shield, we measured and inverted relative travel times from stations across the Arabian Peninsula. We augmented the KACST data with delay times measured from permanent stations in the region (RAYN, EIL and MRNI) and the 1995-7 Saudi Arabian PASSCAL Experiment data set. Figure 1 shows the locations of seismic stations used in this study. We computed travel time differences for two nearly co-located stations (AFFS and AFIF in Figure 1) between KACST and the PASSCAL networks in order to investigate possible biases between these data sets before combining all delay times from different seismic networks. We sorted events recorded on the common stations by back azimuth and distance and measured P-wave travel time residuals from arrival times subtracted from a theoretical travel time. The trends of the residuals with back-azimuth and distance are very similar and indicate no bias between the travel time residuals for the common stations.

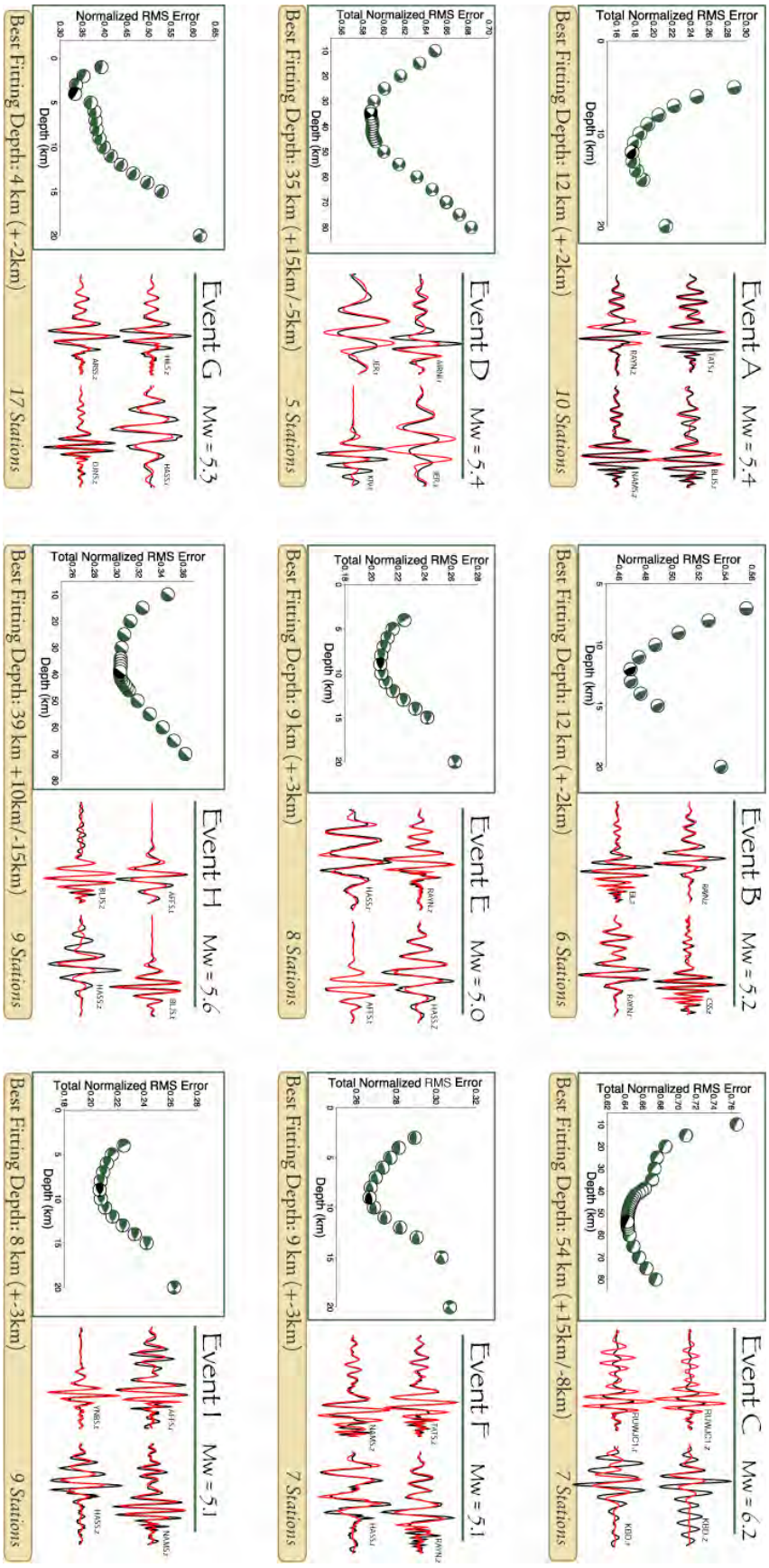


Figure 4. Results from moment tensor inversion and grid search of source depth for nine events studied in the Zagros Mountains. For each event, the graph to the left shows focal mechanism as a function of source depth plotted against RMS error. The focal mechanism and source depth that yields the best fitting synthetics to the data is noted with the black beach ball. Selected waveforms are shown on the right side of each panel. Observed waveforms are in black and synthetics are in red. Event letters are the same as in Table 1 and Figure 3.

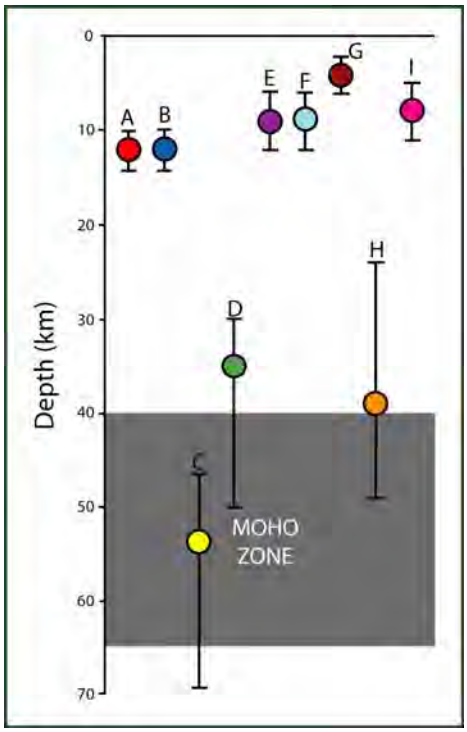


Figure 5. Plot showing source depths for the nine events studied from the Zagros Mountains. Error bars correspond to the uncertainties given in Figure 4. The "Moho Zone" represents the range of Moho depths across the Zagros Mountains within proximity of the earthquakes, as reported from gravity and receiver function studies. Event letters are the same as in Table 1 and Figures 3 and 4.

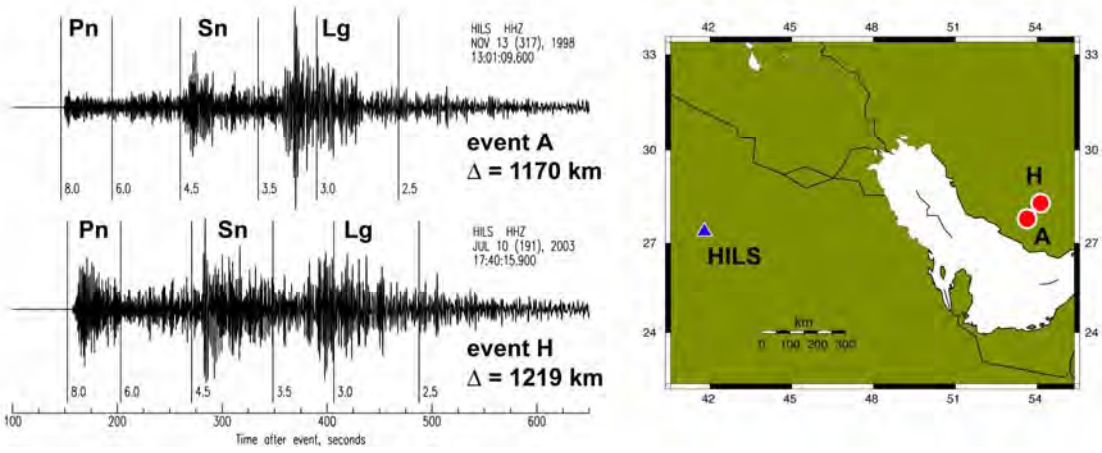


Figure 6. (left) Vertical component waveforms (filtered 0.5-5 Hz) for events A (top) and H (bottom) at station HILS (Al Hail, Saudi Arabia). (right) These events are closely located with event H slightly further away.

For the data sets, we computed relative arrival time residuals using a multi-channel cross-correlation (MCCC) method and inverted for a three dimensional velocity model using the method of VanDecar (1991). For the inversion, we parameterized travel time slowness using a grid of knots comprised of 34 knots in depth, 56 knots latitude between 12.0° N and 37.0° N and 56 knots in longitude between 29.5° E and 55.0° E. The horizontal knot spacing is one third of a degree, and the vertical knot spacing is 25 km in

the inner region of seismic array (17.4° N-30.7° N, 35.5° E-48.5° E, and 0-200 km depth). We used the IASPEI91 model (Kennett and Engdahl, 1991) as the initial model for the inversion.

Results for the P-wave Tomography

We used 401 earthquakes resulting in 3,416 ray paths with P- and PKP-wave arrivals. The majority of the events are located in the western Pacific Rim between back azimuths of 15 and 150 degrees, but the events are distributed over a wide range of back azimuths. The waveforms were filtered with a zero-phase two-pole Butterworth filter between 0.5 to 2 Hz before the relative travel-time residuals were computed. The MCCC procedure was performed over a three-second window on the filtered data. A final model was selected by investigating the way in which changes in regularization levels (flattening and smoothing values) affect the reduction in travel time residuals. To determine a preferred model, 2,000 iterations of the conjugate gradient procedure are performed with several different pairs of flattening and smoothing values. For our preferred model, we have chosen a model with the values of 1,600 for flattening and 3,200 for smoothing.

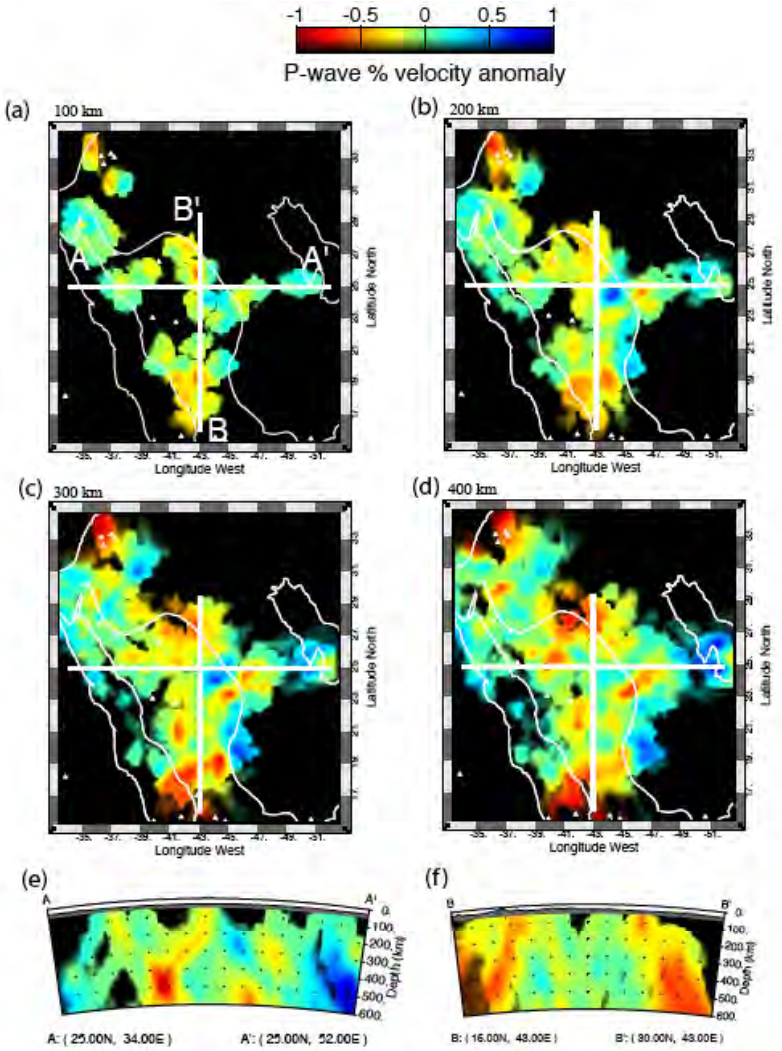


Figure 7. Results of P wave tomography. (a–d) Depth slices through the model at depths of 100, 200, 300 and 400 km. (e-f) vertical slices through the model along E-W (e) and N-S (f) profiles denoted with white lines in a–d.

Figure 7 shows depth slices (a-d) and vertical cross-sections (e and f) through the model. A preliminary interpretation of these features would suggest that low velocities beneath the Gulf of Aqaba and southern

Arabian Shield and Red Sea are related to mantle upwelling and seafloor spreading. Low velocities beneath the northern Arabian Shield may be related to volcanic centers. The origins of the low velocity features near the eastern edge of the Arabian Shield and western edge of the Arabian Platform are unknown.

Results from the S-wave Tomography

For the S-wave model, we used 201 earthquakes resulting in 1,602 ray paths with S- and SKS-wave arrivals. Although the total number of rays for the S-wave model is half of the rays for the P-wave model, the event distribution shows better coverage of back azimuth. The signal processing procedures for the S-wave data are exactly the same as for the P-wave data, but traces were filtered over a lower frequency band (0.04 to 0.1 Hz), and relative arrival time residuals were computed by the MCCC method using a fifteen-second window. As a result we could use the short-period stations for the P-wave analysis, but were limited to data from the broadband stations for the S wave model. The first order velocity variations seen in the S model are similar to the P model, and therefore we do not show the S wave model here.

CONCLUSION(S) AND RECOMMENDATIONS

We reported progress on the determination of ground truth source parameters (focal depths and mechanisms, seismic moments) for earthquakes in the Zagros Mountains. These moments can be used to calibrate coda wave magnitudes and to model high frequency regional phase amplitude spectra with the MDAC methodology. We will explore the effect of location and focal depth on regional phase amplitudes and discriminants and estimate propagation properties (including attenuation, quality factors). Regional phase propagation models (derived from the MDAC methodology) will be developed to improve understanding of high frequency body-wave discriminants and amplitude detection thresholds in the Middle East.

ACKNOWLEDGEMENTS

The facilities of the IRIS Data Management System, and specifically the Incorporated Research Institutions for Seismology (IRIS) Data Management Center (DMS), were used for access to waveform and metadata required in this study. The IRIS DMS is funded through the National Science Foundation and specifically the GEO Directorate through the Instrumentation and Facilities Program of the National Science Foundation under Cooperative Agreement EAR-0004370.

REFERENCES

Bird, P., M. N. Toksoz, and N. H. Sleep (1975). Thermal and mechanical models of continent-continentconvergence zones, *J. Geophys. Res*. 80: 4405–4416.

Camp, V. E., and M. J. Roobol (1992). Upwelling asthenosphere beneath western Arabia and its regional implications, *J. Geophys. Res.* 97: 15255–15271.

Coleman, R. G., and A. V. McGuire (1988). Magma Systems Related To The Red-Sea Opening, *Tectonophysics*, 150: 77–100.

Crosson, R. S. (1990). Determination of teleseismic relative phase arrival times using multi-channel cross correlation and least-squares, *Bull. Seism. Soc. Am.* 80: 150–169.

Kennett, B. and E. R. Engdahl (1991). Travel times for global earthquake location and phase identification, *Geophys. J. Int.* 105: 429–465.

Maggi, A., J. Jackson, K. Priestley and C. Baker (2000). A re-assessment of focal depth distributions insouthern Iran, the Tien Sha and northern India: do earthquakes really occur in the continentalmantle?, *Geophys. J. Int.* 143: 629–661.

Maggi, A., K. Priestley and J. Jackson (2002). Focal depths of moderate to large earthquakes in Iran. *Journal of Seismology and Earthquake Engineering* 4: 1–10.

Mayeda, K., A. Hofstetter, J. O'Boyle and W. Walter (2003). Stable and transportable regional magnitudes based on coda-derived moment-rate spectra, *Bull. Seism. Soc. Am.*, 93, 224–239.

Nowroozi, A. A. (1971). Seismotectonics of the Persian Plateau Eastern Turkey, Caucasus, and Hindu-Kush Regions, *Bull. Seism. Soc. Am*. 61: 317–342.

Paul, A., A. Kaviani, D. Hatzfeld, J. Vergne and Mohammad Moktari (2006). Seismological evidence forcrustal scale thrusting in the Zagros mountain belt, submitted to *Geophys. J. Int.*

VanDecar, J. C. (1991). Upper mantle structure of the Cascadia subduction zone from non-linear teleseismic travel time inversion, Ph. D. Thesis, Univ. of Washington, Seattle, WA.

Vernon, F., and J. Berger (1998). Broadband seismic characterization of the Arabian Shield, Final Scientific Technical Report, Department of Energy Contract No. F 19628-95-K-0015, 36 pp.

Walter, W. and S. Taylor (2002). A revised magnitude and distance amplitude correction (MDAC2)procedure for regional seismic discriminants, Lawrence Livermore National Laboratory technicalreport UCRL-ID-146882.

DEVELOPING AND EXPLOITING A UNIQUE SEISMIC DATASET FROM SOUTH AFRICAN GOLD MINES FOR SOURCE CHARACTERIZATION AND WAVE PROPAGATION

Andrew A. Nyblade[1], William Walter[2], and Rengin Gok[2]

Penn State University[1] and Lawrence Livermore National Laboratory[2]

Sponsored by National Nuclear Security Administration
Office of Nonproliferation Research and Development
Office of Defense Nuclear Nonproliferation

Contract No. DE-FC52-06NA27320[1,2]

ABSTRACT

In this project, we are developing and exploiting a unique seismic dataset to address the characteristics of small seismic events and the associated seismic signals observed at local (< 200 km) and regional (< 2000 km) distances. The dataset is being developed using mining-induced events from three deep gold mines in South Africa recorded on in-mine networks (< 1 km) comprised of hundreds of high-frequency sensors, a network of five broadband seismic stations installed as part of this project at the surface around the mines (1–50 km), and a network of 16 existing broadband seismic stations at local/regional distances (50–1000 km) from the mines. The final dataset will contain: (1) events spanning 5 orders of magnitude (M from ~-1 to 3) well recorded at a wide range of local and regional distances, (2) events from a range of source depths (0–4 km), and (3) events from a variety of source types correlated with in-mine information, such as pillar collapse and shear failure.

We are exploiting the dataset to improve U.S. operational capabilities to monitor for low-yield nuclear tests by analyzing the mining-induced events in 10 areas of interest. We are gathering and analyzing hundreds of events with M>2.5 and many more selected smaller events, including point explosions (mine blasts), mine-related stress release, mining activities, and shallow earthquakes. We are creating cataloged information on origin times and locations (GT 0), source parameters, focal mechanisms, coda-derived source spectra, coda magnitudes, local-to-regional phase propagation characteristics, relative P and S excitation, source apparent stress variation, and local-to-regional body-wave amplitude ratios that can discriminate between the different source categories. We are systematically analyzing the direct body-wave and coda wave properties of these events in terms of variability with source type, depth, magnitude, distance and other characterization factors. These direct and coda wave amplitudes are of fundamental importance to yield estimation and source type discrimination.

INTRODUCTION

In this project we are developing and exploiting a unique seismic dataset for addressing the characteristics of small seismic events and the associated seismic signals observed at local (< 200 km) and regional (< 2000 km) distances. The dataset is being developed using mining-induced events from three deep gold mines in South Africa recorded on in-mine networks comprised of hundreds of high-frequency sensors, a network of five broadband seismic stations installed at the surface around the mines, and a network of 16 broadband seismic stations at local/regional distances from the mines (Figure 1). The in-mine data are providing high-fidelity recordings of the seismic wave field at distances of a few meters to a few kilometers from the source. The surface mine network is providing broadband recordings of the wave field at distances of 1–2 km from the source out to distances of about 50 km, and the local/regional stations are providing broadband recordings from about 50 km out to distances of ~1000 km.

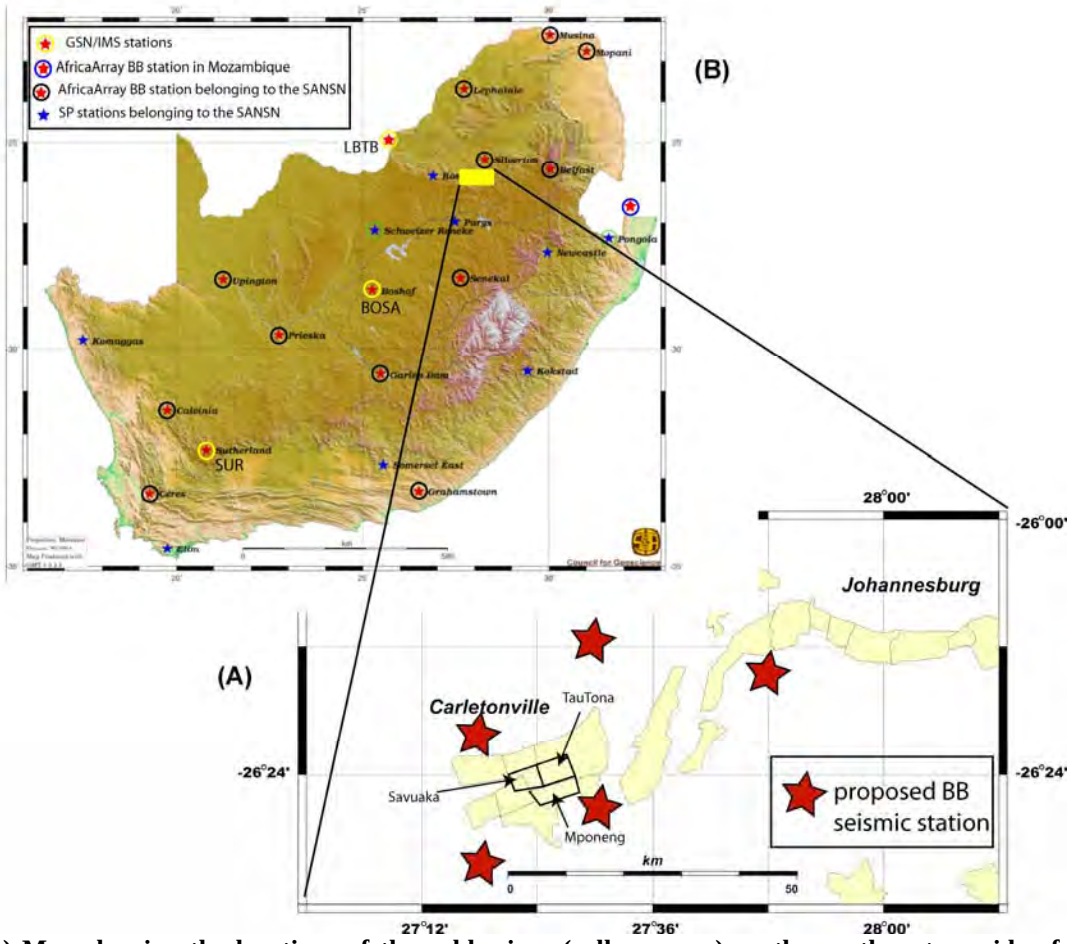


Figure 1. (A) Map showing the locations of the gold mines (yellow areas) on the northwestern side of the Witwatersrand basin (Far West Rand region). Data for this project come from the three mines labeled. The red stars show preliminary station locations of the surface mine network that is being constructed. (B) Map showing location of broadband (BB) stations at local and regional distances.

This dataset will be unique in that it will contain (1) events spanning 5 orders of magnitude (M from ~-1 to 3) well recorded at a wide range of local and regional distances, (2) events from a range of source depths (0-4 km), and (3) events from a variety of source types (e.g., normal faulting, strike-slip faulting, mine blasts, pure double-couple events, isotropic events). In addition, the dataset will include details of mine plans that will enable us to correlate certain mining events with mining activities, such as blasting and pillar collapse, and investigate the influence of mine cavities and lithology on wave propagation. We plan to exploit the dataset by using the mining events in 10 related areas of research aimed at improving U.S. operational capabilities to monitor for low-yield nuclear tests: (1) create an event catalog with accurate origin times and locations; (2) determine seismic moment, radiated energy,

corner frequency, and stress drop; (3) obtain focal mechanisms from moment tensor inversion; (4) define several categories of event types (shear slip, tensile failure with volumetric component, explosions) using focal mechanisms and in-mine observations (e.g., pillar collapse); (5) define and calibrate a coda Mw scale for southern Africa; (6) determine Mw for all cataloged events using calibrated coda techniques; (7) investigate the effects of depth and source mechanism on the coda-derived source spectra and evaluate the potential of using coda spectral peaking as a depth discriminant; (8) define and calibrate local-to-regional phase (direct P and S, Pn, Pg, Sn, and Lg) propagation characteristics, including the use of the magnitude and distance amplitude corrections (MDAC) technique to determine appropriate geometrical spreading and frequency dependent Q values for the region; (9) characterize relative P and S excitation and source apparent stress resulting from variations in source parameters, including magnitude, mechanism, depth, rock characteristics and source type; (10) define regional phase ratios that can discriminate between the different source categories, and compare these discriminants and their performance with ongoing work done for other types of mining events, such as in Scandinavia and the western U.S.

Data

As mentioned above, three complimentary datasets are being assembled in this project: (1) High-frequency in-mine seismic data from three mines along the northwestern edge of the Witwatersrand basin; (2) Seismograms from mine events recorded at distances of 1 to 50 km will be provided by five new broadband stations installed and operated by the Council for Geoscience; and (3) Broadband recordings of the mine events at local and regional distances will be provided by twelve *AfricaArray* stations in South Africa that are part of the South African National Seismic Network (SANSN), International Monitoring System (IMS) stations BOSA (South Africa) and LBTB (Botswana), a ground station network (GSN) station (SUR, South Africa), and an *AfricaArray* station in southern Mozambique.

Gold Mines and Mining Seismicity. The Witwatersrand basin is part of a granite-greenstone complex constituting the basement of the Kaapvaal craton. The basement evolved between 3.8 and 2.8 billion years ago and has remained relatively stable except for the development of stratified basins. Subsidence of the Witwatersrand basin probably began before basement evolution was complete and resulted in the deposition of three major stratigraphic units: the Dominion Group, the Witwatersrand Supergroup, and the Ventersdorp Supergroup. Most of the gold is mined from the quartzites (commonly referred to as reefs) within the Witwatersrand Supergoup.

The mining activities of the Witwatersrand basin induce thousands of seismic events per day, many of which are larger than M=2. The data are recorded at depth (1–5 km) by arrays of three-component geophones operated by AngloGold Ashanti, Ltd. and Integrated Seismic Systems International (ISSI). We will obtain from three mines (Mponeng, Savuka, and TauTona) in the Far West Rand region (80 km southwest of Johannesburg; Figure 1a), waveforms from over 500,000 mining-induced events recorded on hundreds of high-frequency geophones within the mines. Based on seismicity rates in these mines, the dataset will contain between 20 to 35 M>3 events per year, about 200 events per year between magnitude 2 and 3, and hundreds of mining blasts (mostly M<0).

These mines are some of the deepest in the world and extract ore from two gold-bearing quartzites, the Ventersdorp Contact Reef and the Carbon Leader Reef (Figure 2). These two units are separated by 900 m vertically, extend 2–4 km below the surface, and dip to the south at 21 degrees (Figure 2). The mines contain faults and dykes with two major trends: N 5^{o} E and N 96^{0} E. Some of the faults have been reactivated by the mining, providing sources for many of the larger events.

Details of the geology within the mines have been determined by underground mapping, surface surveys, and well logs from deep boreholes. Densities of major lithologies present in the mines have been measured from rock samples, and the shear and bulk modulus of the lithologies have been determined using Vs and Vp measurements from test-blasting.

The geophones sample at frequencies of 400–10,000 Hz and are located at depth on the quartzite reefs. The station spacing underground is on the order of 100 m in the active mining zones. Because there are two horizons being mined simultaneously, event depth is well-constrained by the geophones at different depths, especially compared to other mining-induced datasets in which the seismometers are usually situated on a single plane.

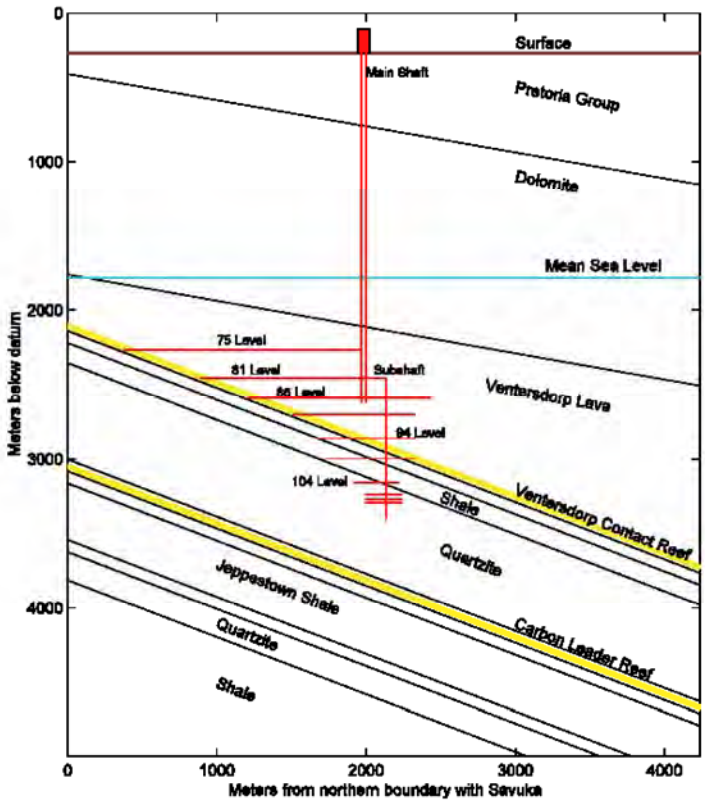


Figure 2. Cross-section through main shaft of the Mponeng mine looking east. The two gold-bearing horizons are marked in yellow. The datum is measured from an elevation in Johannesburg, so it is above the ground surface.

In order to determine the locations of the mine events, ISSI technicians routinely pick P-wave and S-wave arrival times and run a ray-tracing algorithm. This method of locating events is successful (uncertainties are on the order of 10–20 m) because the geologic setting of the Far West Rand consists of layers without appreciable lateral heterogeneities. The layered velocity model used is based on geologic units that have been determined by underground surveying and mapping as well as surface-based refraction profiles and borehole data. The accuracy of the velocity model has been verified by test blasting used to determine wavespeeds through various strata.

The ray-tracing algorithm is outlined in Mendecki (1993, 1997). In general, a system of equations consisting of arrival time and azimuth information is constructed, and the minimum of the residuals of these measurements is found with respect to the system's L1 norm. Using the L1 norm prevents large outliers from having too great an effect on the results (Prugger and Gendzwill, 1988; Jeffreys, 1932). In order to improve locations of events of special interest, the "arrival time difference" method or "master event" method is used to refine the location determined by ray-tracing (Spence, 1980). In this case, the master event will be a test blast whose precise location is well known, and other events in a nearby cluster are relocated relative to the master event based on arrival time differences. To relocate events, they must be close enough to the master event so that the seismic waves travel through the same geologic structures. This ensures that only location differences contribute to arrival-time differences among the events in a cluster.

Surface Mine Network. Mining-induced events from the three mines described above will be recorded at distances of 1 to 50 km using a new permanent, surface mine network comprised of broadband seismic stations. The surface mine network will also provide data from many thousands of other events that occur in other deep mines around the Witwatersrand basin for which we will not obtain in-mine data, including many hundreds of events with M>2.5. The location of the proposed stations with respect to the three mines is shown in Figure 1A.

Local/Regional Broadband Seismic Network. Sixteen permanent broadband seismic stations across southern Africa will provide high-quality seismograms of the mining-induced events, data that will compliment the data from

the in-mine and mine surface networks. The locations of the local/regional stations are shown in Figure 1B. Twelve of the stations are part of the SANSN, and data from these stations are being archived as *AfricaArray* data at the IRIS data management center. These stations are equipped with a 24 bit data loggers and broadband sensors (STS-2, Guralp 40T, KS 2000). Two of the sixteen stations are IMS stations (BOSA in South Africa and LBTB in Botswana) and one is an IRIS GSN station (SUR in South Africa). The final station is a new *AfricaArray* station in southern Mozambique at Changalane and equipped with a 24-bit digitizer and a Guralp CMG-3T sensor.

OBJECTIVES

In this section we provide details of how the seismic data will be modeled and analyzed to meet the research objectives for each of the research areas identified in the Introduction.

Create an Event Catalogue with Accurate Times and Locations. The in-mine network operators routinely locate and catalog events, and we will obtain these catalogs and use them as a starting point to create an event catalog with accurate origin times and locations in universal coordinates. Each mine network is operated independently using a local coordinate system and a different timing system. We will transform station and events locations into a universal coordinate system and use the 5-station surface mine network to calibrate the timing of each in-mine network by using larger, well-recorded events. An ML magnitude will also be included in the catalog based on the ML scale used routinely by the Council for Geoscience in their event bulletins. As the mining-induced event locations are typically constrained to within 10 to 20 meters by the mine network operators, we will not need to relocate any of the events.

Determine Source Parameters. In work recently completed (Richardson et al., 2004, 2005), we have determined for 27 M>2.5 mine events in the Far West gold fields recorded between 1998 and 1999 seismic moment, radiated energy, corner frequency, and stress drop using the method of Richardson and Jordan (2002), which was adapted from the spectral method first developed by Andrews (1986). In order to determine source parameters, we median-stacked each event's spectra and integrated the results up to the Nyquist frequency to determine the integral of the displacement power spectra, the integral of the velocity power spectra, and the acceleration power spectral level. These parameters were then used to determine the source parameters radiated energy, seismic moment, and static stress drop using the equations provided in Richardson et al. (2004, 2005). During the three year duration of this project we anticipate recording over 100 M>2.5 events from the three mines described above, and we will use the in-mine data to determine seismic moment, radiated energy, corner frequency and stress drop using the same method.

Obtain Focal Mechanisms from Moment Tensor Inversion. We will determine focal mechanisms for events with M>2.5 and a select number of smaller events using moment tensor inversion of the in-mine data. One important difference between mine tremors and natural earthquakes is the effect of mining voids on the recorded waveforms. The voids can influence the frequency content of the seismograms, cause focusing and defocusing of the wave field, as well as cause unexpected amplifications. In addition, the moment tensor calculated for an event near the free surface of a stope, for example, can have a significant isotropic component related to the closure or convergence of the excavation. The mining geometry also can influence source parameters calculated for an event. For example, the seismic moment calculated for a crushed pillar would have contributions from the failure of the pillar as well as from the convergence of the surrounding stope. (Gay et al., 1995, McGarr, 1992; Milev et al., 2005; Napier et al., 2005).

Many of the past open studies of small (M<5) event mechanisms in the mining environment have been limited by the quality of the available seismic data, and therefore a number of inconsistent interpretations have been published. Studies that analyzed P- and S-wave first motions interpreted fractures around stope faces as having isotropic components consistent with implosional mechanisms. These fractures have been assumed to be related to closure of excavations and crushing of rock ahead of the stope face (Joughin, 1966; Joughin and Jager, 1983; McGarr, 1992). First-motion studies have also concluded that explosional isotropic events occur occasionally.

However, all of these results have been debated because the coverage of the focal sphere often proved inadequate to reject a pure double-couple solution (Wong and McGarr, 1990). In addition, other first-motion studies and waveform analyses found predominantly double-couple sources (McGarr, 1971; Spottiswoode and McGarr, 1975). Recent developments using moment-tensor inversions corroborate evidence that both pure double-couple and mechanisms with significant isotropic explosional components exist in mine settings (Sellers et al., 2003; Wright et al., 2003; Talebi and Young, 1990; Feignier and Young, 1992; McGarr, 1992; Baker and Young, 1997; Gibowicz, 1997).

We will invert the in-mine data to determine moment tensor solutions for all events with M>2.5, and a select number of smaller events. We anticipate that a number of the events will have non-double couple mechanisms, based on previous results from other researchers. To help characterize the non-double couple mechanisms, these mechanisms will be examined further using regional full waveform modeling following an approach that was developed for modeling other non-double couple sources, such as large mine collapses in Wyoming (Pechmann et al., 1995) and Germany (Bowers and Walter, 2002).

Define Several Categories of Event Types. Using the focal mechanisms and in-mine observations, we will define several categories of event types, such as shear slip, tensile failure with volumetric component, and explosions. The mine plans will be very important for correlating with focal mechanisms to categorize event types, as will the records of blasting in the mines.

Defining and Calibrating a Coda Mw Scale for Southern Africa. Determining meaningful and accurate measures of the size of seismic events is a critical part of characterizing and cataloging the seismicity in a region. For the southern Africa region, we want to define a useful scale that can cover the expected range of mining induced and natural events from about magnitude -1 to 4. Teleseismic magnitudes such as mb and Ms are limited mainly to events greater than magnitude 4. Local magnitudes scales such as ML are valid for comparing relative sizes of events within the region but make it difficult to compare events across regions such as with other parts of the world. Local magnitude scales are also difficult to relate to fundamental physical properties of the source. For these reasons seismic moment magnitude has become the measure of choice for modern digital networks (e.g., Pasyanos et al., 1996; Kubo et al. 2002). However, if waveform modeling were required to determine the moments, it would be difficult to systematically determine moments for events less than about 3.0. Techniques based on regional coda envelopes (Mayeda and Walter, 1996; Mayeda et al., 2003) offer the potential to determine seismic moments for events over the entire range of interest down to magnitude -1 with local and in-mine data.

The scattered seismic energy following the direct phase arrivals (e.g., Lg or Sn) is called the seismic coda. Techniques measuring the amplitude of seismic coda on local and regional envelopes have provided some of the most stable measures of source spectra available (e.g., Mayeda and Walter, 1996; Mayeda et al. 2003). Comparisons with amplitudes from the direct phases have shown that coda-based amplitude measures have 3–5 times smaller standard deviations when the amplitudes determined at two stations are compared. This means that a single station can provide as accurate a measure of source amplitude as a 9-to-25 station averaged measure of a direct arrival. Thus coda-based measures are ideal for smaller events and sparse station networks.

To determine coda based source spectra and moments we will first calibrate for path and site effects in each narrow frequency band using a set of well-recorded events distributed in distance. Then we will tie the lower frequencies to moments determined from waveform modeled events in the region. For southern Africa there are a few larger events that have previously been modeled (e.g., Bowers, 1997) as well as some of the smaller mine events (Richardson et al., 2004, 2005). As part of this project we will perform additional moment tensor inversions of mining events as well as a few of the largest events using regional waveform modeling techniques to improve our calibrations. Finally a number of very small events will be used as empirical Green functions to determine the high-frequency corrections. These events are chosen such that their corner frequencies are higher than the calibration frequencies, and we can assume their spectra is flat.

Determining Coda Source Spectra and Mw for Selected Catalogued Events. Once the regional stations are calibrated, we will use existing LLNL scripts to calculate coda derived source spectra and Mw. Processing will be done for the subset of cataloged events selected for detailed analysis as part of this project.

Analyzing Depth Effects on Coda-Derived Source Spectra. The displacement source spectra of normal tectonic depth earthquakes (e.g., 5–20 km) determined from local and regional coda envelopes have typical Brune (1970) style shapes: flat at long periods and then falling off at frequencies above a corner frequency. In contrast very shallow events (<1 km) produce unusual “peaked” source spectra when the coda method is calibrated using normal depth earthquakes (e.g., Mayeda and Walter, 1996; Myers et al., 1999).

The coda derived source spectral shape differences appear to depend on the differences in the excitation of coda as a function of depth. It has been hypothesized that this peaking is related to the stronger excitation with shallower depth of the fundamental Rayleigh wave Rg that is then scattered into the coda (e.g. Myers et al., 1999). If quantified these shape differences could be exploited to flag very shallow events for nuclear monitoring purposes. The mine-induced seismicity completely covers the depth range of interest of 0 to 4 km depth. The in-mine network will provide very good control on the source depth so this effect can be investigated. In addition we will use the

moment tensor results to explore the effect of focal mechanism on the coda spectra as well. In particular we want to see if the coda spectral shapes differ for events with isotropic components when compared with double-couple events.

Local-to-Regional Phase Propagation Characteristics. In southern Africa, the local P and S phases as well as all four major regional phases Pn, Pg, Sn, and Lg propagate and can be identified in seismograms. In order to be able to compare events of different distances or sizes with each other, we need to be able to correct for source and path effects. Walter and Taylor (2002) developed a procedure to do this called Magnitude Distance Amplitude Correction (MDAC). The MDAC method includes path corrections due to geometrical spreading, frequency dependent attenuation, and site effects. The MDAC process also simultaneously corrects for source effects by removing a generalized Brune (1970) style spectra. It corrects both local P and S phases as well as the four regional phases in all frequencies allowing the researcher the freedom to explore any possible ratio of body-wave amplitudes. In this project we will use a much larger dataset to determine optimal MDAC parameters for the broadband stations in the region. We will explore the variability of the body wave amplitudes as a function of local to regional distance. These MDAC corrections will allow us to investigate both source parameter and discriminant behavior for the southern Africa events.

Source Parameters and Scaling. The regional amplitudes and their ratios show very large variation in southern Africa. We want to try and understand this scatter in terms of variations in source parameters such as relative P and S excitation and apparent stress with mechanism, depth, rock type and other source region properties. We will take advantage of the in-mine data to look for correlations of seismic properties observed regionally with what is known to have happened near the source.

Regional Phase Amplitude Ratio Discriminants. It is well established that amplitude ratios of regional body-wave phases at frequencies of 1 Hz and higher can discriminate explosions from earthquakes (e.g. Bennett and Murphy, 1986; Taylor et al., 1988; Baumgardt and Young, 1990; Dysart and Pulli, 1990; Kim et al., 1993; Walter et al., 1995; Taylor, 1996; Fisk et al., 1996; Hartse et al., 1997; Rodgers and Walter, 2002, and Taylor et al., 2002). Such ratios include ratios of P phases to S phases (phase ratios), low frequencies to high frequencies within a phase (spectral ratios) and ratios of high frequency in one phase to low frequencies in another (cross-spectral ratios). We will explore how well some of these ratios can discriminate between the different source categories of mine region events. These may include shear slip, tensile failure with volumetric component, and explosions. We will compare these discriminants and their performance with ongoing work done for other types of mining events and other major mining regions, such as in Scandinavia (e.g. Bungum et al., 2004) and the western U.S. (e.g. Leidig et al. 2004).

ACKNOWLEDGEMENTS

This project is being conducted by a team of researchers at Penn State, LLNL, and in South Africa at the Council for Geoscience, the Council for Scientific and Industrial Research, and the University of the Witwatersrand.

REFERENCES

Andrews, D. J. (1986). Objective determination of source parameters and similarity of earthquakes of different size, in *Earthquake Source Mechanics*, S. Das, J. Boatwright, C. H. Scholz, eds, vol. 6 of Geophysical Monograph 37: pp. 259–267, Am. Geophys. Union.

Baker, C., R. P. Young (1997). Evidence for extensile crack initiation in point source time-dependent moment tensor solutions, *Bull. Seism. Soc. Am.* 87: 1442–1453.

Baumgardt, D. R. and G. B. Young (1990). Regional seimsic waveform discriminants and case-based event identification using regional arrays, *Bull. Seism. Soc. Am.* 80: 1874–1892.

Bennett, T. J. and J. R. Murphy (1986). Analysis of seismic discrimination capabilities using regional data from western United States events, *Bull. Seism. Soc. Am.* 76: 1069–1086.

Bowers, D. (1997). The October 30, 1994 seismic disturbance in South Africa: Earthquake or large rockburst? *J. Geophys. Res.* 102: 9843–9857.

Bowers. D., and W. Walter (2002). Discriminating between large mine collpases and explosions using teleseismic P waves, *PAGEOPH, 159,* 803-830.

Bungum H., T. Kverna, S. Mykkeltveit, M. Roth, V. Oye, K. Aastebol, D. B. Harris, and S. C. Larsen (2004). Energy portioning for seismic events in Fennoscandia and NW Russia, in *Proceedings of the 26th Seismic Research Review: Trends in Nuclear Explosion Monitoring*, LA-UR-04-5801, Vol. 1, pp. 387–396.

Brune, J. (1970). Tectonic stress and the spectra from seismic shear waves earthquakes, *J. Geophys. Res.* 75: 4997–5009.

Dysart, P. S. and J. J. Pulli (1990). Regional seismic event classification at the NORESS array: seismological measurements and the use of trained neural networks, *Bull. Seism. Soc. Am.* 80: 1910–1933.

Feignier, B., R. P. Young(1992). Moment tensor inversion of induced microseismic events: Evidence of non-shear failures in the -4 < m < -2 moment magnitude range, *Geophys. Res. Lett.* 19: 1503–1506.

Fisk, M. D., H. L. Gray, and G. D. McCartor (1996). Regional event discrimination without transporting thresholds, *Bull. Seism. Soc. Am.* 86: 1545–1558.

Gay, N.C., Durrheim, R.J., Spottiswoode, S.M. & van der Merwe, A.J. (1995). Effect of Geology, in-situ stress, and mining methods on seismicity in Southern African gold and platinum Mines, 8th Intl. Congress on Rock Mechanics, Tokyo, Japan, Balkema, pp. 1321–1325.

Gibowicz, S. J. (1997). An anatomy of a seismic sequence in a deep gold mine, *Pure Appl. Geophys.* 150: 393–414.

Gupta, I. N., W. W. Chan, and R. A. Wagner (1992). A comparison of regional phases from underground nuclear explosions at East Kazakh and Nevada Test Sites, *Bull Seism. Soc. Am.* 82: 352–382.

Hartse, H., S. R. Taylor, W. S. Phillips, and G. E. Randall (1997). A preliminary study of regional seismic discrimination in Central Asia with an emphasis on Western China, *Bull. Seism. Soc. Am.* 87: 551–568.

James, D. E., M. J. Fouch, J. C. VanDecar, S. van der Lee and Kaapvaal Seismic Group (2001). Tectospheric structure beneath southern Africa, *Geophys. Res. Lett.*, 28: 2485–2488.

Jeffreys, H. (1932). An alternative to the rejection of observations, *Proc. R. Soc. Lond. Ser A,* 137: 78–87.

Joughin, N. C. (1966). The measurement and analysis of earth motion resulting from underground rock failure, Ph.D. thesis, University of the Witwatersrand.

Joughin, N. C., A. J. Jager (1983). Fracture of rock at stope faces in South African gold mines, in *Rockbursts: Prediction and control*, L. Richards, ed, pp. 53–66, Inst. Min. and Metall., London.

Kim, W.-Y., D. W. Simpson, and P. G. Richards (1993). Discrimination of earthquakes and explosions in eastern United States using regional high-frequency data, *Geophys. Res. Lett.* 20 : 1507–1510.

Kubo, A., E. Fukuyama, H. Kawai, K. Nonomura (2002). NIED seismic moment tensor catalogue for regional earthquakes around Japan: quality test and application, *Tectonophysics* 356: 23–48.

Leidig, M. R., B. W. Stump, J. L. Bonner, C. T. Hayward, A. A. Velasco, Diane F. Baker, H. Hooper, W. R. Walter, X. Yang, R. Zhou, C. L. Edwards, M. D. Renwald, and J. F. Lewkowicz (2004). Source phenomenology experiments in Arizona in *Proceedings of the 26th Seismic Research Review: Trends in Nuclear Explosion Monitoring*, LA-UR-04-5801, Vol. 1, pp. 427–438.

Mayeda, K. and W. R. Walter, Moment (1996). energy, stress drop and source spectra of western United States earthquakes from regional coda envelopes, *J. Geophys. Res.* 101: 11,195–11,208, 1996.

Mayeda, K., A. Hofstetter, J. L. O'Boyle and W. R. Walter (2003). Stable and transportable regional coda magnitudes based on coda-derived moment rate spectra, *Bull. Seism. Soc. Am.* 93: 224–239.

McGarr, A. (1971). Violent deformation of rock near deep-level tabular excavations seismic events, *Bull. Seism. Soc. Am.*, 61: 1453–1466.

McGarr, A. (1992). Moment tensors of ten Witwatersrand mine tremors, *Pure Appl. Geophys.* 139: 781–800.

Mendecki, A. J., ed. (1997). *Seismic Monitoring in Mines*, Chapman and Hall.

Mendecki, A. J. (1993). Real time quantitative seismology in mines, Keynote lecture in *Proc. 3rd Intl. Symp. on Rockbursts and Seismicity in Mines*, edited by R. P. Young, Balkema, Rotterdam, 1141–1144.

Milev, A. M., Hildyard, M. W., Linzer, L. M., and Spottiswoode, S.M. (2005). Underground Micro-seismic Monitoring of Pillar Systems to Evaluate Mechanism of Failure, 6th Intl Symposium on Rockbursts and Seismicity in mines, Perth, Australia, pp 239–246.

Myers, S. C., W. R. Walter, K. Mayeda and L. Glenn (1999). Observations in support of Rg scattering as a source for explosion S waves: regional and local recordings of the Kazakhstan depth of burial experiment, *Bull. Seism. Soc. Am.* 89: 544–549.

Napier J. A. L., Spottiswoode S. M., Sellers, E., Hildyard, M.W., Linzer, L. M., & Kataka, M.O. (2005). New criteria for rockmass stability and control using integration of seismicity and numerical modeling. SIM 02 03 01. Final SIMRAC Project Report. 141p.

Pasyanos, M.E., D.S. Dreger, and B. Romanowicz (1996). Toward Real-Time Estimation of Regional Moment Tensors, *Bull. Seism. Soc. Amer.*, 86: 1255–1269.

Pechmann, J. C., W. R. Walter, S. J. Nava, and W. J. Arabasz (1995). The February 3, 1995, M_L 5.1 seismic event in the trona mining district of southwestern Wyoming, *Seism. Res. Lett.* 66: 25–34.

Prugger, A. F. and D. J. Gendzwill (1988). Microearthquake location: A non-linear approach that makes use of a simplex stepping procedure, *Bull. Seism. Soc. Am.* 78; 799–815.

Richardson, E., T. H. Jordan (2002). Seismicity in deep gold mines of South Africa: Implications for tectonic earthquakes, *Bull. Seism. Soc. Am.*

Richardson, E., A. A. Nyblade, W. R. Walter, and A. J. Rodgers (2004). Seismic source characterization and energy partitioning from in-mine and regional broadband data in South Africa, in *Proceedings of the 26th Seismic Research Review: Trends in Nuclear Explosion Monitoring*, LA-UR-04-5801, Vol. 1, pp. 467–474.

Richardson, E., A.A. Nyblade, W. R. Walter, and A.J. Rodgers (2005). Seismic source characterization and energy partitioning from in-mine and regional broadband data in South Africa, in *Proceedings of the 27th Seismic Research Review: Ground-Based Nuclear Explosion Monitoring Technologies*, LA-UR-05-6407, Vol. 2, pp. 622–631.

Rodgers, A. J. and W. R. Walter (2002). Seismic Discrimination of the May 11, 1998, Indian Nuclear Test with Short-Period Regional Data From Station NIL (Nilore, Pakistan), *Pure Appl. Geophys.* 159: 679–700.

Sellers, E.J., Kataka, M.O. & Linzer, L.M. (2003). Source parameters of acoustic emission eventsand scaling with mining-induced seismicity, *Journal of Geophysical Research*, 108: No. B9, 2418–2430.

Spence, W. (1980). Relative epicenter determination using P-wave arrival-time differences, *Bull. Seism. Soc. Am.* 70: 171–183.

Spottiswoode, S. M. and A. McGarr (1975). Source parameters of tremors in a deep-level gold mine, *Bull. Seism. Soc. Am.* 65: 93–112.

Talebi, S., R. P. Young (1990). Characterizing microseismicity associated with stope development, in *Rockbursts and Seismicity in Mines*, C. Fairhurst, ed, pp. 189–194, Balkema, Rotterdam.

Taylor, S. R., N. W. Sherman and M. D. Denny (1988). Spectral discrimination between NTS explosions and western United States earthquakes at regional distances, *Bull. Seism. Soc. Am.* 78; 1563–1579.

Taylor, S. (1996). Analysis of high-frequency Pg/Lg ratios from NTS explosions and Western U.S. earthquakes, *Bull. Seism. Soc. Am.* 86: 1042–1053.

Taylor, S., A. Velasco, H. Hartse, W. S. Philips, W. R. Walter, and A. Rodgers (2002). Amplitude corrections for regional discrimination, *Pure. App. Geophys*. 159: 623–650.

Walter, W. R., K. Mayeda, and H. J. Patton (1995). Phase and spectral ratio discrimination between NTS earthquakes and explosions Part 1: Empirical observations, *Bull. Seism. Soc. Am.* 85: 1050–1067.

Walter, W. R. and S. R. Taylor (2002). A revised magnitude and distance amplitude correction (MDAC2) procedure for regional seismic discriminants: theory and testing at NTS, Lawrence Livermore National Laboratory Report, UCRL-ID-146882.

Wong, I. G., A. McGarr (1990). Implosional failure in mining-induced seismicity: A critical review, in *Rockbursts and Seismicity in Mines*, C. Fairhurst, ed, pp. 45-51, Balkema, Rotterdam.

Wright, C., Kijko, A.J., Linzer, L.M. & Smith, M., Recent research in earth structure, earthquake and mine seismology, and seismic hazard evaluation in South Africa. South African Journal of Science, Vol 99, July/August, 389 – 394, 2003.

THE USE OF GEOPHYSICAL MODELS FOR NUCLEAR EXPLOSION MONITORING

Michael E. Pasyanos, William R. Walter, Megan Flanagan, Rengin Gok, and Gregory A. Franz

Lawrence Livermore National Laboratory

Sponsored by National Nuclear Security Administration
Office of Nonproliferation Research and Development
Office of Defense Nuclear Nonproliferation

Contract No. W-7405-ENG-48

ABSTRACT

Geophysical models constitute an important component of calibration for nuclear explosion monitoring. Models take a wide variety of forms and scales and are used in a number of ways. We will focus on several of them here. The first that we discuss are regional tomography models. They can be constructed as 2-D, 2 1/2 D, or 3-D, depending on how the crust and upper mantle are parameterized, each having certain advantages (speed, accuracy, etc.). In any form, these are used to predict regional travel times such as Pn and Sn. The times derived by the models can be used as corrections to our arrival times, or simply as a background model for empirical measurements. We are also developing a number of fully 3-D models, including a priori geophysical models and stochastic models. The a priori WENA (Western Eurasia North Africa) model is a large-scale model that has been shown to compare favorably against a number of data sets and has been recently demonstrated to improve both travel-time and location estimates. We have also been using the Markov Chain Monte Carlo (MCMC) technique to produce stochastic models in the Yellow Sea–Korean Peninsula (YSKP) region. We are continuing to make improvements to this model by going to higher resolution and by incorporating more data sets to further narrow the range of acceptable models.

We maintain our efforts to develop models of surface wave dispersion and attenuation, and apply the results. Ambient noise tomography is being employed to further improve the resolution of the group velocities in certain regions as presented by Ritzwoller et al. (2006, these Proceedings). The maps are being used to isolate the fundamental mode surface wave and ensure that the signal passes dispersion and backazimuth tests when making Ms measurements, as presented by Bonner et al. (2006, these Proceedings). Attenuation models can be used to make corrections to surface wave amplitudes to account for regional amplitude variations that are important at shorter periods. We have been testing model-based attenuation models, as well as investigating the correlations between dispersion and attenuation. Surface wave group velocities can be inverted either alone, or in conjunction with other data, to derive models of the crust and upper mantle structure. We are using receiver functions, in joint inversions with the surface waves, to produce profiles directly under seismic stations throughout the region. By assembling the results from many stations, we can see how regional seismic phases are affected by complicated upper mantle structure, including lithospheric thickness and anisotropy. We will be showing the latest results from a study using data from the Eastern Turkey Seismic Experiment (ETSE) deployment. The joint inversion is used to map the boundary of the lithospheric hole in eastern Turkey where the phase Sn is blocked.

OBJECTIVE

Geophysical models constitute an important component of calibration for nuclear explosion monitoring. Models take a wide variety of forms and scales and are used in a number of ways. We will focus on several of them that have been developed at Lawrence Livermore National Laboratory (LLNL). Regional tomography models, such as those for upper mantle head-waves Pn and Sn, can be used to predict regional travel times. We are also developing a number of fully 3-D models, including a priori geophysical models and stochastic models. Stochastic models are data-driven models generated using an MCMC technique. This method combines a priori information with geophysical data from multiple sources (and varying sensitivities) to produce models that are most consistent with the constraints. We next consider surface wave models of velocity and attenuation. The dispersion models can be used to construct phase-matched filters, which can improve weak surface wave signal and calculate regionally determined M_S. Attenuation models can be used to further correct the surface wave amplitudes. Dispersion models can be used either alone or in conjunction with other data, such as receiver functions, to construct 3-D velocity models of the lithosphere. This method is a reliable way of obtaining the local velocity structure near a station from teleseismic events.

RESEARCH ACCOMPLISHED

Regional Tomography Models

Regional tomography models can be used to predict the travel times of regional phases such as Pn and Sn. While details of the various methodologies vary, they all generally tomographically distribute the slowness along the upper mantle leg of the path, while either inverting or making some sort of correction for the crustal legs. The advantages of such a method is that the tomography can be used to help estimate travel times of these regional phases, even when no direct measurements have been made at a particular station. Due to the propagation path of these phases, however, the spatial coverage is generally limited to a relatively narrow swath around seismic areas within about 1500 km from events, making it of limited use in aseismic regions. Another potential problem is that normalization in the tomography can dampen the full amplitude of the velocity anomalies.

Still, the utility of tomography is evident. Figure 1 shows P-wave velocities in the upper mantle determined from tomographic inversion. Paths were limited to ground truth (GT) events (Bondar et al., 2004), but still resulted in about 90,000 observations. The path map shows excellent coverage of western and central Europe, the Middle East, central Asia and south Asia. Coverage is poor in the ocean, North Africa, and Russia. The model shows fast velocities beneath oceans and old crust (India, the Russian Platform) and slow velocities beneath Red Sea, East African Rift, and the Tethys Belt. These models can be used to predict the travel time of these regional phases.

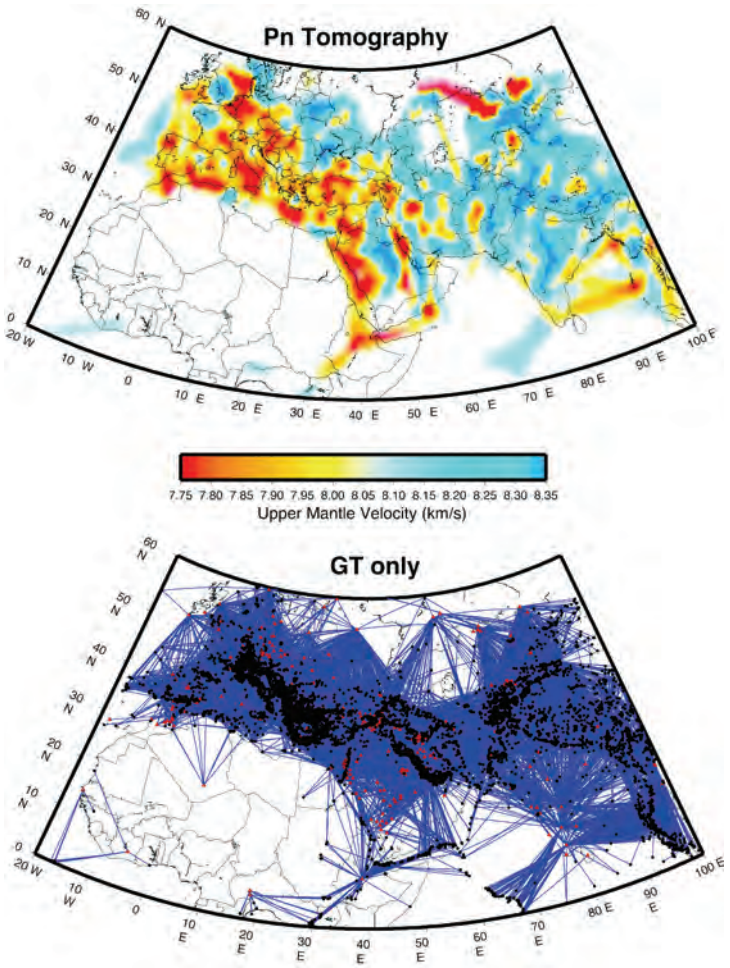


Figure 1. Uppermost mantle P-wave velocities derived from tomographic inversion (a) upper mantle velocities at 1º resolution and (b) the corresponding path map (Pasyanos et al., 2004).

A Priori Models

The WENA model is an a priori 3-D model for western Eurasia and North Africa (Pasyanos et al., 2004). Models like WENA can serve as background values for travel time correction surfaces and other derived parameters. We have demonstrated our ability to improve regional travel-time prediction and seismic event location accuracy using this model (Flanagan et al., 2006). Travel-time residuals are assessed relative to the IASPEI91 model (Kennett et al., 1995) for approximately 6,000 Pg, Pn, and P arrivals, from seismic events having 2σ epicenter accuracy between 1 km and 25 km (GT1 and GT25, respectively), recorded at 39 stations throughout the model region. Ray paths range in length between 0° and 40° (local, regional, and near teleseismic) providing depth sounding that spans the crust and upper mantle. The dataset also provides representative geographic sampling across Eurasia and North Africa including aseismic areas.

The WENA1.0 model markedly improves travel-time predictions for most stations with an average variance reduction of 29% for all ray paths from the GT25 events; when we consider GT5 and better events alone the variance reduction is 49%. For location tests we use 196 geographically distributed GT5 and better events. In 134 cases (68% of the events), locations are improved, and average mislocation is reduced from 24.9 km to 17.7 km. We develop a travel time uncertainty model (Figure 2) that is used to calculate location coverage ellipses. The coverage ellipses for WENA1.0 are validated to be representative of epicenter error and are smaller than those for IASPEI91 by 37%.

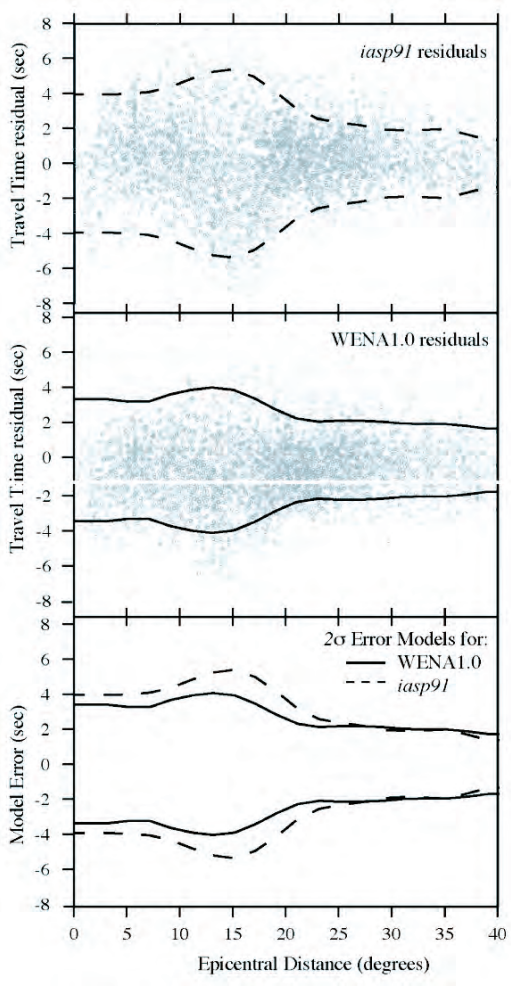


Figure 2. Distance-dependent uncertainty models for the IASPEI91 (top) and WENA1.0 (middle) velocity models. Note the nonstationarity and correlation in the travel-time uncertainty between 10° and 23° epicentral distance; uncertainty increases and errors are correlated (Flanagan et al., 2006).

In Figure 3, we find that the IASPEI91 variogram is non-stationary (levels off at the sill then increases again). The non stationarity is caused by long-period features in the travel time residual structure. WENA1.0 improves prediction of long-period residual features, and the variogram is relatively flat after the sill is reached. In some cases the sill value in the WENA1.0 variogram is reduced overall relative to the IASPEI91 variogram (e.g., station NUR), indicating that the 3-D model reduces the background variance. We conclude that a priori models are directly applicable where data coverage limits tomographic and empirical approaches, and the development of the uncertainty model enables merging of a priori and data-driven approaches using Bayesian techniques.

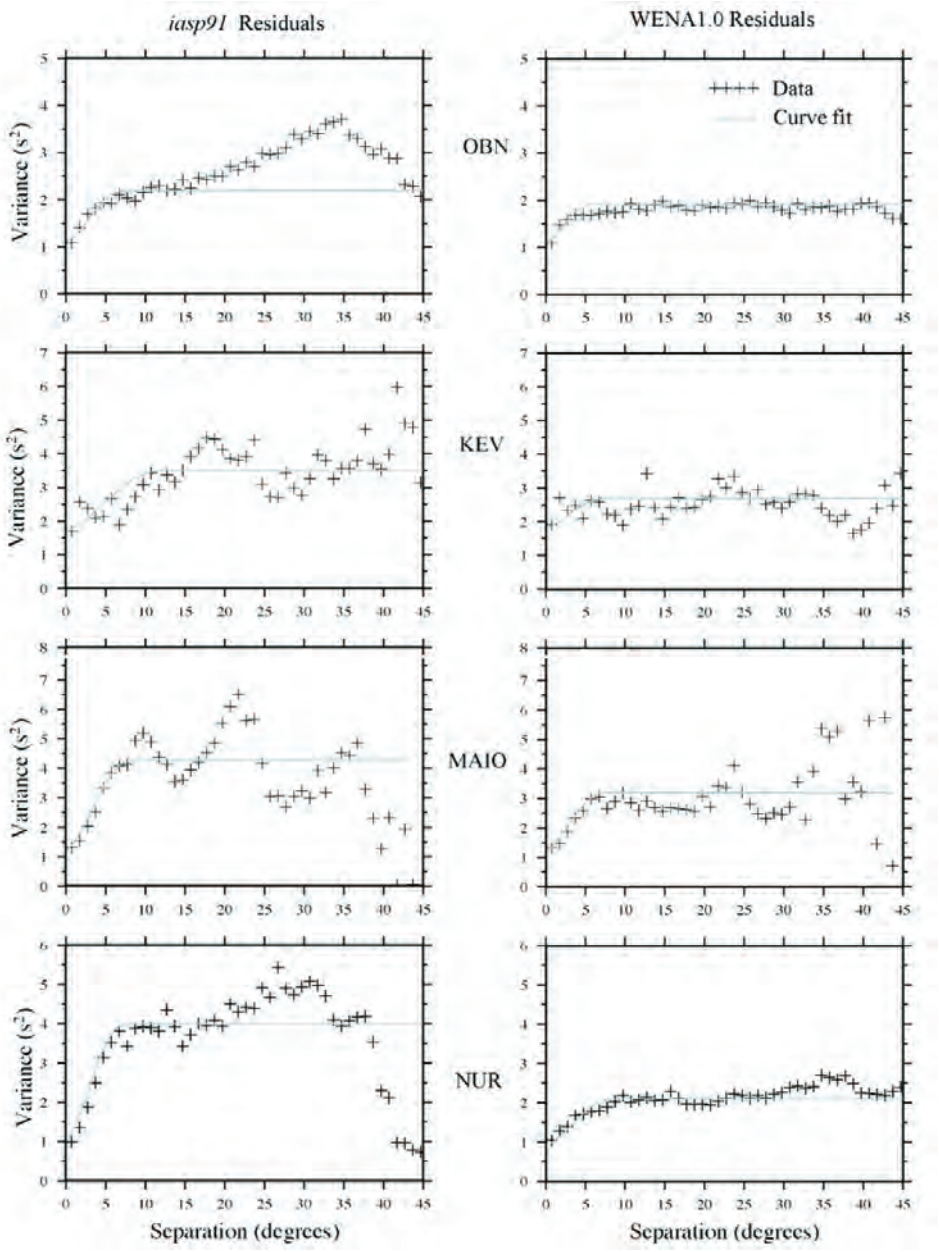


Figure 3. Variograms of travel time residuals at stations OBN, KEV, MAIO, and NUR for both the WENA1.0 and IASPEI91 velocity models. Crosses are the data variogram values in 1.0 degree bins; solid lines are the model variograms determined by curve fitting (Flanagan et al., 2006).

Stochastic Geophysical Models

We have been using the MCMC method to generate 3-D, data-driven stochastic models. We use MCMC to sample models from a prior distribution, test them against multiple data types in a staged approach, and develop a posterior distribution of seismic models that are most consistent with multiple seismic data sets (Pasyanos et al., 2006). This approach has several advantages over a single deterministic model. First, we are able to easily incorporate prior information on the model, such as the a priori geophysical models that were discussed earlier. Secondly, with this technique, we are able to reconcile different data types that can be used to constrain the model. We can also estimate the uncertainties of model parameters, properly migrating data uncertainties into model uncertainties. The method

does not constrain models to be normally distributed, but instead allows non-Gaussian or multi-modal distributions. Finally, we can estimate uncertainties on predicted observable signals, such as would be required to apply this model as a correction surface.

We use this method to determine the crust and upper mantle structure of the YSKP region using surface wave dispersion data, body wave travel time data, gravity, and receiver functions (Pasyanos et al., 2006). Figure 4 shows a crustal thickness map and corresponding uncertainties, taken by calculating the mean and standard deviation of the posterior distribution. One can see the thinning associated with the oceanic crust of the Pacific Ocean and Sea of Japan. We also use this model to predict waveforms using a spectral element model (Komatitsch et al., 2002; Rodgers et al., 2006, these Proceedings).

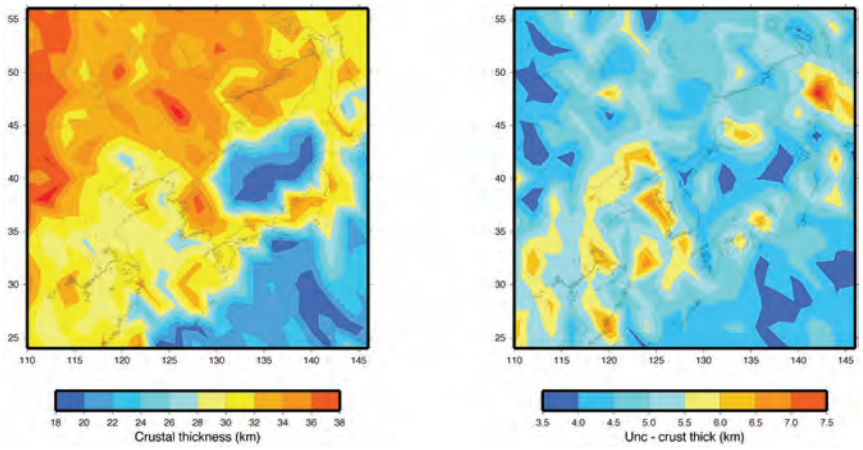


Figure 4. A crustal thickness map of the YSKP region determined using stochastic inversion methods, along with its associated uncertainties (Pasyanos et al., 2006).

Surface Wave Models

Over the past several years, LLNL has been developing surface wave models in Eurasia for nuclear explosion monitoring (Pasyanos et al., 2001; Pasyanos, 2005). Dispersion measurements are made using multiple narrow-band filters on deconvolved displacement data from the LLNL Seismic Research Knowledge Base (SRKB). We continue to improve upon our surface wave model by adding more paths, generally by taking advantage of new datasets, but also by revisiting stations with more recent events. Most recently, we have added measurements from stations in the Mediterranean (e.g., MIDSEA, Libya), India as presented by Bonner et al. (2006, these Proceedings), southern and central Africa, Alaska, and Siberia, including several PASSCAL deployments. To date, over 100,000 seismograms have been analyzed to determine the individual group velocities of 7–150 s Rayleigh and Love waves. Overall, we have made good quality dispersion measurements for 30,000 Rayleigh and 20,000 Love wave paths. Using a conjugate gradient method, we then tomographically invert these measurements to produce group velocity maps for Love and Rayleigh waves.

The group velocity models continue to improve in several ways. First, with more measurements, we have been able to expand the region of coverage to all of Eurasia and into Africa. By increasing the density of coverage in existing regions, we have increased the resolution of our model. Finally, we have been able to provide more reliable maps at short periods, expanding the frequency coverage down to 7 s period. We are able to resolve structural features associated with the tectonics of the region (Pasyanos, 2005). Path coverage will be further improved in the future by the use of cross-correlation of ambient seismic noise to derive the Green function between two stations, and from which the dispersion characteristics can be derived, as presented by Ritzwoller et al. (2006, these Proceedings). The benefits of this method in seismology have been dramatically demonstrated for southern California in Shapiro et al. (2005).

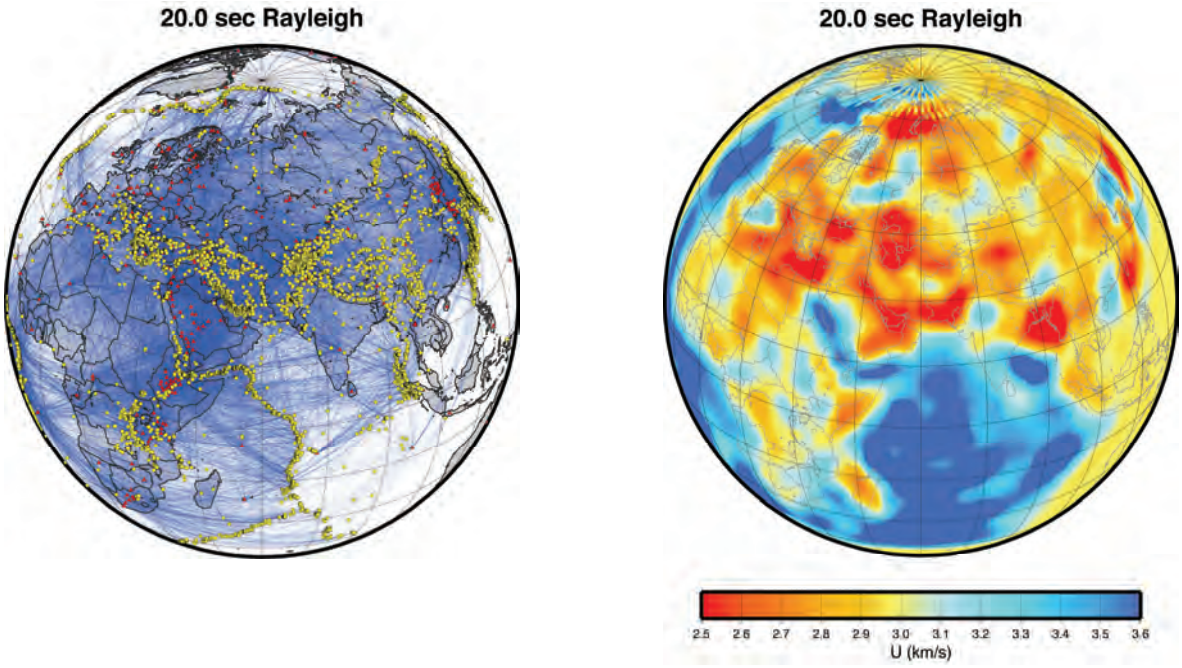


Figure 5. Surface wave dispersion maps for 20 s Rayleigh waves. (a) Path map showing coverage of the Eurasian and African continents. (b) Group velocity map of the same region (Pasyanos, 2005).

One application of surface wave models is to invert the results to derive models of the crust and upper mantle structure. This is particularly useful in aseismic regions that are poorly sampled by other datasets. By combining the surface wave data with other data, we can reduce the non-uniqueness inherent in the profile inversions performed using only surface wave data. In the next section, for example, we will be using the surface wave data in combination with teleseismic receiver functions.

Another application of the group velocities is to construct phase-matched filters in combination with regional surface-wave magnitude formulas to improve the mb:Ms discriminant and extend it to smaller magnitude events. Phase matched filtering has been shown to effectively winnow out any unwanted signals from the surface wave signal. Regional surface wave magnitudes calculated using narrow-band filters (Russell, 2006) from the cleaned signal show a more consistent magnitude value between periods, as presented by Bonner et al. (2006, these Proceedings).

Ms magnitudes can be further improved by making corrections based on surface wave attenuation maps.
One approach is to calculate model-based attenuation values from geophysical models, such as the WENA model (Pasyanos et al., 2004). An example of such a map is shown in Figure 6 for 15 s Rayleigh waves. Attenuation is high (Q is low) where we find large sedimentary basins, either oceanic or continental. Low Q is found in regions with fast, competent upper crust and is particularly low in abyssal oceanic crust. These model-based maps could be tested and validated by comparing model-based predictions to empirical maps in regions where these have been developed.

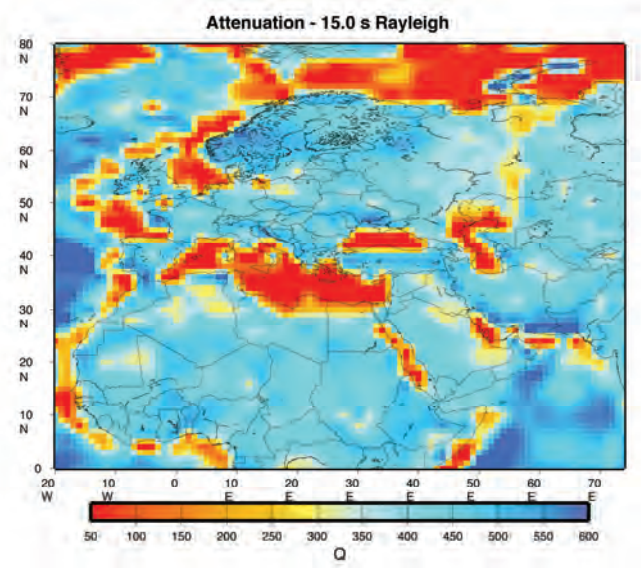


Figure 6. Map of the model-based surface wave attenuation parameter Q for 15 s Rayleigh waves.

Another approach would be to take both the attenuation and dispersion measurements and derive a relationship between the two. For example, we have correlated the group velocity tomography models to the surface wave attenuation model of Selby et al. (2001) to see if there are correlations between the two. Similar correlations could be made with other global models of surface wave attenuation (e.g. Dalton and Ekström, 2006) but currently only for long periods. We have also correlated the velocity model to the model-based attenuation maps. Figure 7 shows the correlation for 20 s where, although there is a lot of scatter, we can clearly see the trend between the two parameters (solid line). Here, we find that in regions with thick sediments that have both slow velocities and high attenuation, the group velocities are slow and the attenuation parameter $\gamma = \frac{\pi}{UQT}$ is high. In contrast, on the other end of the plot in oceanic crust, the velocities are high while the attenuation is low. Once such relationships have been established, then attenuation models can be easily constructed. One of the advantages of this technique is that the resolution would far-exceed the resolution available performing an attenuation tomography.

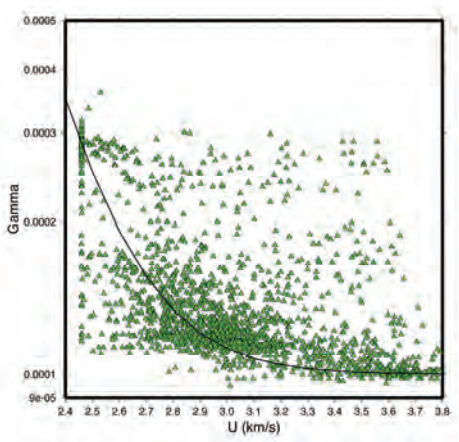


Figure 7. A comparison of tomographically-based group velocities and model-based attenuation parameters.

Receiver Function Profiles

We are also using receiver functions, in joint inversions with the surface waves, to produce profiles directly under seismic stations throughout the region. These two data types are complementary since receiver functions are sensitive to velocity contrasts, and surface waves are sensitive to depth-averaged velocity.

Here, we have applied this methodology to stations from the ETSE IRIS program that manages seismic equipment (PASSCAL) deployment (Gok et al., 2006). We jointly invert for the S-wave velocity structure, Moho depth and mantle-lid (lithospheric mantle) thickness. We also estimated the transverse anisotropy due to Love and Rayleigh wave propagation discrepancies.

We found anomalously low shear wave velocities underneath the Anatolian Plateau. Average crustal thickness is 36 km in the Arabian Plate, 44 km in Anatolian Block and 48 km in the Anatolian Plateau (Figure 8). We observe very low shear wave velocities at the crustal portion (30–38 km) of the northeastern part of the Anatolian Plateau. The lithospheric mantle thickness is either not thick enough to resolve it or it is completely removed underneath the Anatolian Plateau. The shear velocities and anisotropy down to 100 km depth suggest that the average lithosphere-asthenosphere boundary in the Arabian Plate is about 90 km and 70 km in Anatolian block. The study reveals three different lithospheric structures in eastern Turkey: Anatolian plateau (east of Karliova junction), Anatolian block and the northernmost portion of the Arabian plate. The boundaries of differences in lithospheric structure coincide with the major tectonic boundaries.

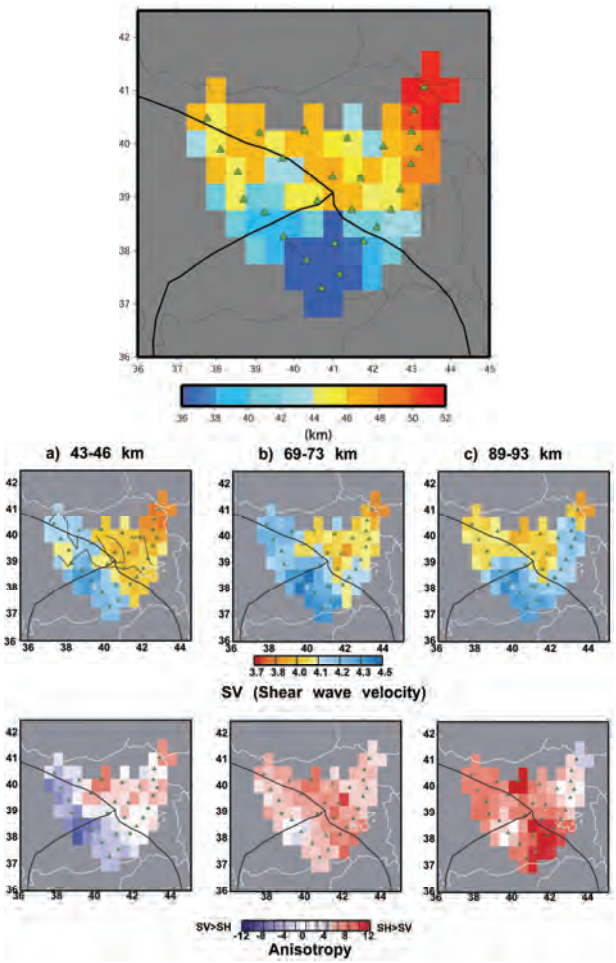


Figure 8. Results from the joint inversion of receiver functions and surface waves from ETSE stations in eastern Turkey. Upper figure: crustal thickness map. Lower figure: shear wave velocity and anisotropy for several mantle depth slices (Gok et al., 2006).

CONCLUSIONS AND RECOMMENDATIONS

Geophysical models are used in a variety of ways for nuclear explosion monitoring. We have presented a variety of models being developed at LLNL, often in coordination with other institutions, including regional tomography models, a priori models, stochastic models, surface wave models, and receiver function models. They can be used to calibrate and represent the calibration of structure under stations, predict travel times, assess phase behavior, and improve discrimination.

REFERENCES

Bondar, I., S. C. Myers, E. R. Engdahl, and E. A. Bergman (2004). Epicentre accuracy based on seismic network criteria, *Geophys. J. Int.* 156: 483–496.

Dalton, C. A. and G. Ekström (2006). Global models of surface wave attenuation, *J. Geophys. Res.* 111: B05317, doi:10.1029/2005JB003997.

Flanagan, M. P., S. C. Myers, and K. D. Koper (2006). Regional travel-time uncertainty and seismic location improvement using a 3-dimensional a priori velocity model, *Bull. Seism. Soc. Amer*. (submitted).

Gok, R., M. E. Pasyanos, and E. Zor (2006). Lithospheric structure of the continent-continent collision zone: Eastern Turkey, *J. Geophys. Res.* (submitted).

Kennett, B. L. N., E. R. Engdahl, and R. Buland (1995). Travel times for global earthquake location and phase association, *Geophys. J. Int.* 122: 108–124.

Komatitsch, D., J. Ritsema, J. Tromp (2002). The spectral-element method, Beowulf computing, and global seismology, *Science*, 298: 1,737–1,742.

Pasyanos, M. E., W. R. Walter, and S. E. Hazler (2001). A surface wave dispersion study of the Middle East and North Africa for monitoring the comprehensive nuclear-test-ban treaty, *Pure Appl. Geophys.* 158: 1,445–1,474.

Pasyanos, M. E., W. R. Walter, M. P. Flanagan, P. Goldstein, and J. Bhattacharyya (2004). Building and testing an a priori geophysical model for western Eurasia and North Africa, *Pure Appl. Geophys.* 161: 235–281.

Pasyanos, M. E. (2005). A variable-resolution surface wave dispersion study of Eurasia, North Africa, and surrounding regions, *J. Geophys. Res*. 110: B12301, doi:10.1029/2005JB003749.

Pasyanos, M. E., G. A. Franz, and A. L. Ramirez (2006). Reconciling data using Markov Chain Monte Carlo: An application to the Yellow Sea–Korean Peninsula region, *J. Geophys. Res*. 111: B03313, doi:10.1029/2005JB003851.

Russell, D. R. (2006). Development of a time-domain, variable-period surface wave magnitude measurement procedure for application at regional and teleseismic distances. Part I: Theory, *Bull. Seism. Soc. Amer.* 96: 665–677.

Selby, N. (2001). Association of Rayleigh waves using back azimuth measurements: Application to test ban verification, *Bull. Seism. Soc. Am.* 91: 580–593.

Shapiro, N. M., M. Campillo, L. Stehly, and M. H. Ritzwoller (2005). High resolution surface wave tomography from ambient seismic noise, *Science*, 307: 1,615–1,618.

DEVELOPING MULTIPLE-FREQUENCY DISCRIMINANTS FOR USE WITH REGIONAL CODA-AMPLITUDE MEASUREMENTS

Arben Pitarka[1], Chandan Saikia[1a], Bradley Woods[1], Lupei Zhu[2], and Robert Herrmann[2]

URS Group Inc.[1] and Saint Louis University[2]

Sponsored by National Nuclear Security Administration
Office of Nonproliferation Research and Development
Office of Defense Nuclear Nonproliferation

Contract Nos. DE-AC52-04NA225545[1] and DE-FC52-04NA25546[2]

ABSTRACT

We are performing analyses of coda waves for a large number of seismic events recorded in southwest China, the Korean Peninsula and Nepal with the objective of developing multiple-frequency discriminants for small events. Our analyses of recorded and simulated Lg coda waves indicate a regional dependency of wave scattering effect on coda waves. Besides magnitude estimates for small seismic events and Q analyses, we are examining several possible sources of wave propagation scattering and their frequency-dependent effects on the amplitude of coda waves. Initial analyses of three-dimensional finite-difference simulation results suggest distinguished scattering effects as a function of the location and size of the scattering bodies.

[a] Chandan Saikia has moved on to AFTAC.

OBJECTIVES

We are investigating the possibility of using regional coda wave characteristics, such as multiple narrow band spectral amplitudes, for discriminating small seismic events. Broad-band waveform observations made in regions with various tectonic regimes show clear differences of coda source spectra characteristics between normal depth earthquakes (h> 5 km) and shallow events, and explosions in particular. Based on data analyses and 3D simulation of scattering effects on coda waves, using velocity models with small-scale random heterogeneities, we are investigating the amplitude and frequency content of coda waves and their sensitivity to structural heterogeneities in the crust. Our study is focused on regions where good quality data are available, including the Korean Peninsula, southwestern China, and Nepal.

RESEARCH ACCOMPLISHED

At present, we have completed the first task of our investigation, which involved broad-band waveform data gathering, and estimates of the focal mechanism and seismic moment of selected earthquakes. We have collected and modeled regional seismograms for 54 seismic events that occurred in China and were recorded by stations of the local Chinese network (Zhu et al., 2005). Their moment magnitude M_w ranges from 4.3 to 5.5. In addition we collected available waveforms of regional events recorded at stations LSA, HIA, LZH, WMQ, and other stations in China that lie within 30^o of the events. Our database also includes regional waveforms recorded by the temporary HIMNT seismic network stations operating in Nepal from selected events located in Nepal. Among them, 20 were selected for estimating the seismic moment, depth, and M_w for amplitude scaling and calibration of the M_w vs. coda magnitude relation. We also estimated focal mechanism, depth, and seismic moments for recent earthquakes that occurred in the Korean Peninsula.

The Chinese data are being processed in analyses of Q, and calibration of M_w vs. coda magnitude in multiple frequency bands (Mayeda et al., 2003). The procedure for estimating source spectrum and path Q using Lg and coda waves is based on well established techniques (Herrmann 1980). Figure 1 shows the locations of the InDepth3 array stations and the 1999/03/13 Mw4.5 earthquake that we have analyzed. Multiple frequency window spectral amplitudes of this event indicate wave scattering which is significant at some stations depending on the stations location. The origin of the high-frequency scattering affecting mainly the Lg coda waves (above 1Hz) could be due either to deep or shallow crustal structure complexities along the wave path or in the source region (e.g., Dainty 1996; Wu et al.,2000). Lg wave shows evidence of scattering from small-scale structures. Other causes of scattering could also be large-scale structural complexities such as crustal thinning or multipatthing (e.g., Ni and Barazangi, 1983; Phillips et al., 2000).

To examine potential sources of wave propagation scattering we have calculated synthetic seismograms for point sources buried at different shallow depths using a parallelised 3D finite-difference code (Pitarka, 1999). Our finite difference code solves the stress-velocity wave equations in a heterogeneous medium using staggered grids. The technique for generating the 3D velocity model on a regular grid with variable spacing allows for inclusion of small-scale complexities and surface topography as well. The technique we use to model free surface topography is an extension of the formalism that we have applied to modeling wave propagation in media with curved free surface (Pitarka and Irikura, 1996). The performance of our free-surface boundary condition technique at handling Lg coda waves for flat free surface and very long distances was compared with that of the FK method of Saikia (1994) for a shallow source. Also the technique has been validated against other standard and accurate techniques for modeling surface topography such as 2D-Boundary Element Method (BEM) and the 2D-Discrete Wavenumber-Boundary Integral Equation method of Takenaka et al. (1996).

An essential feature of the regional models used in the analyses is the location of the structures causing the scattering. In our models such structural bodies are located immediately below the array, around the source or along the wave path. We looked at the relative contribution of wave-field scattering on different frequency bands of Lg and coda waves due to localized and highly heterogeneous small scale bodies embedded in a planar layered velocity model. They are randomly distributed near the source, along the top 5km of the crust, or along the Moho boundary. The spatial fluctuations of the correlation function of the medium's random velocity is modeled by the Von Karman function. The Fourier transform of the correlation function represents the power spectrum density. The von Karman correlation function in 3D is given by Goff and Jordan (1988):

$$C(\vec{r}) = \frac{4\pi\nu H^2 r^{\nu} K_{\nu}(\vec{r})}{K_{\nu}(0)} \quad \text{(Equation 1)}$$

where r is the lag vector, H^2 is the variance, ν is the Hurst number ($0 < \nu < 1$), and K_ν is the modified Bessel function of order ν. The Fourier transform of the von Karman correlation function is,

$$P(\vec{k}) = \frac{4\pi\nu H^2}{K_{\nu}(0)} \frac{a_x^2 + a_y^2 + a_z^2}{(1+k^2)^{\nu+3/2}} \quad \text{(Equation 2)}$$

where the lag vector r, and wave-number vector k is,

$$\vec{r} = \sqrt{\frac{x^2}{a_x^2} + \frac{y^2}{a_y^2} + \frac{z^2}{a_z^2}}, \; \vec{k} = \sqrt{k_x^2 a_x^2 + k_y^2 a_y^2 + k_z^2 a_z^2} \quad \text{(Equation 3 and 4)}$$

and a_x, a_y, and a_z are characteristic scales of the medium along the 3 dimensions and k_x, k_y, and k_z are the wave-number components. The velocity within the scattering body varies from 2–6%. In our simulations we used variable correlation lengths, which depend on the size of the scattering body.

Figure 2 shows cross sections of several 3D velocity models used in our simulations of scattering effects. They are named Model1, Model2, Model3, Model4, and Model5, respectively. Model1 is a reference crustal model with multiple planar layers. In Model2, the top 6 km of the crust is made randomly heterogeneous. In Model3, the source is surrounded by a scattering body with a large volume of 40 x 30 x 6 km. In Model4, the scattering body is located in the receivers range 250–300 km in the top 6 km of the crust. Model5 includes a 5-km thick scattering region located along the Moho boundary. In our simulations, we used grids with variable spacing that enable calculations that are accurate up to 1.3 Hz. In order to separate scattering effects due to structural complexities from those caused by the intrinsic attenuation we used relatively high Q values. The effect of Q in the considered frequency ranges certainly merits attention, but this is the scope of the next phase in our study.

Results of selected simulations are shown in Figures 3, 4, and 5. In these figures, we show seismograms of the vertical component of ground motion velocity. The synthetic motion is calculated at 15 receivers that are regularly spaced between 180 km and 320 km epicentral distances. The four sets of seismograms correspond to the four crustal models described above. The seismograms are band-pass filtered in the frequency ranges of 0–1.3 Hz, 0.5–1.3 Hz, and 1.0–1.3 Hz. As expected, Model1 (Figure 3a, left panel) produces seismograms with clear high frequency Sn and Sg phases and well developed Lg waves. This is partly due to the laterally homogeneous layers and the shallow depth of the seismic source. They facilitate trapping of the waves within the shallow layers. Because of their lower frequency content the Lg coda waves are completely absent in the frequency range 1.0–1.3 Hz for this model (Figure 3c, left panel). A much different frequency content and amplitude of such dominating phases is obtained with Model2 and Model3 which differ from each other only by the spatial extent of the scattering area. The synthetic waveforms in both cases (Figures 3, and 4, right panels) show relatively broad-band scattering effects.

The shallow crustal scattering in Model2 reduces the amplitude of the Sg waves by at least a factor of two in the frequency range 0.5–1.3 Hz (Figure 3b, right panel). It does not affect the Sn wave significantly, since this wave travels less across the scattering region. The effect of scattering is clear in the frequency range 1.0–1.3Hz where the scattered coda waves with high-frequency content dominate the waveforms (Figure 3c, right panel). Such waves are completely absent in Model1.

Model3 demonstrates that scattering due to large-scale heterogeneities around the source has important implications in the amplitude of coda waves (Figure 4, right panel). While responsible for generating high-frequency coda waves the near-source scattering decreases the amplitude of other phases discussed here by a factor of two. Compared with Model2, the coda waves in this case seem to be less energetic at high frequencies (>1.0 Hz), but not at intermediate frequencies (0.5–1Hz). This finding suggests that, although very local, crustal heterogeneities around the source can have significant effects on coda waves and other important phases that are used in discriminating small seismic

events (Xie et.al., 2005). Local scattering in the receivers' range of 250–300 km calculated with Model4 has small effects only at receivers beyond this range in the forward direction (Figure5). This model does not produce significant back scattering effects in the considered frequency range. Model5 was used to investigate the effect of a weaker Moho boundary contrast caused by random heterogeneities along the boundary. This model produced very negligible effects on coda waves. Surprisingly, the effect on amplitude of Sn wave is also very small. We plan to further investigate the effect of the Moho boundary on different types of waves in relation with correlation lengths and maximum velocity fluctuations used in modeling the medium's random velocity.

CONCLUSIONS AND RECOMMENDATIONS

Data analyses and simulations indicate that the amplitude of Sn, Sg, and Lg coda waves are significantly affected by scattering in the crust. Multiple frequency-band analyses of simulated waves indicate that wave scattering affects the amplitude of coda waves even at intermediate frequencies (0.5–1Hz). We have found the following:

1. The amplitude and duration of Lg coda waves, which is controlled by wave scattering, depend on the location and size of the scattering body. Coda waves are more energetic in the presence of scattering bodies around the source, or in the shallow part of the crust. They are much less energetic when the scattering body is beneath the recording station.

2. While very efficient at increasing the amplitude of coda waves, scattering due to random structural heterogeneities in the source region decreases the amplitude of both Sg and Sn phases significantly.

3. In contrast, scattering due to random heterogeneities in the shallow part of the crust affects Sg phase but not Sn phase. If robust, these features could help identifying the location of bodies with strong scattering in the crust.

REFERENCES

Dainty, A. (1996). The influence of seismic scattering on monitoring, in *Monitoring a Comprehensive Test Ban Treaty, E.S. Husebye and A.M. Dainty*, 663–688.

Goff, J. A. and T. H. Jordan (1988). Stochastic modeling of seafloor morphology: Inversion of sea beam data for second-order statistics, *J. Geophys. Res*. 93: 13589–13608.

Herrrmann, R. B. (1980). Q estimates using the coda of local earthquakes. *Bull. Seis. Soc. Am*, 389–399.

Mayeda K. M., A. Hofstetter, J. L.O'Boyle, and W. R. Walter (2003). Stable and transportable regional magnitudes based on coda-derived moment rate spectra, *Bull. Seis. Soc. Am*. 93: 224–239.

Ni, J. and M. Barazangi (1983). High frequency seismic wave propagation beneath the Indian shield, Himalayan Arc, Tibetian Plateau, and surrounding regions: high uppermost mantle velocities and efficient Sn propagation beneath Tibet, *Geophys.Jour. Roy. Astron. Soc*. 72: 655–689.

Phillips, W. S. and K. Aki (1986). Site amplification of coda waves from local earthquakes in central California, *Bull. Seism. Soc. Am*. 76: 627–648.

Phillips, W. S., H. E. Hartse, S. R. Taylor, and G. E. Randall (2000). 1 Hz Lg Q tomography in central Asia, *Geophys. Res. Lett*. 27: 3425–3428.

Pitarka, A. (1999). 3D elastic finite-difference modeling of seismic motion using staggered grid with nonuniform spacing, *Bull. Seis. Soc. Am.* 89: 54–68.

Pitarka, A. and K. Irikura (1996). Modeling 3D surface topography by finite-difference method: Kobe-JMA station site, Japan case study. *GRL*, 20: 2729–2732.

Saikia, C. K. (1994). Modified frequency-wave-number algorithm for regional seismograms using Filon's quadrature-modeling of L(g) waves in eastern North America, *Geophys. J. Int.* 118*:* 142–158.

Takenaka, H. B., L.Kennett, and H. Fujiwara (1996). Effect of 2-D topography and 3-D seismic wave field using a 2.5-D discrete wavenuber-boundary integral equation method, *Geophys. J.Int.* 124:741–755.

Wu, Ru-Shan, S. Jin, and Xiao-Bi Xie (2000). Seismic wave propagation and scattering in heterogeneous crustal waveguides using screen propagators: I SH-waves, *Bull. Seismol. Soc. Am.* 90: 401–413.

Xie, X., T. Lay, and R. Wu (2005). Near-source energy partitioning for regional waves in 2D and 3D models, contributions of S^{*}-to-Lg and P-to-Lg scattering. in *Proceedings of the 27th Seismic Research Review:Ground-based Nuclear Explosion Monitoring Technologies*, LA-UR-05-6407, Vol 1, pp. 249–258.

Zhu, L., Y. Tan, D. V. Hemberger, and C. K. Saikia (2005). Locating and modeling regional seismograms, Part I: Calibration of Tibetan Plateau, *J. Geophy. Res*.

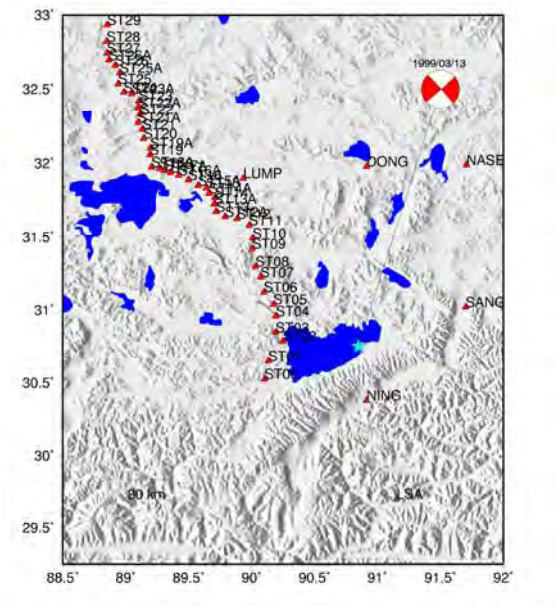


Figure 1. **Location map of the InDepth3 stations and the 1999/03/13 06:03:57utc earthquake.**

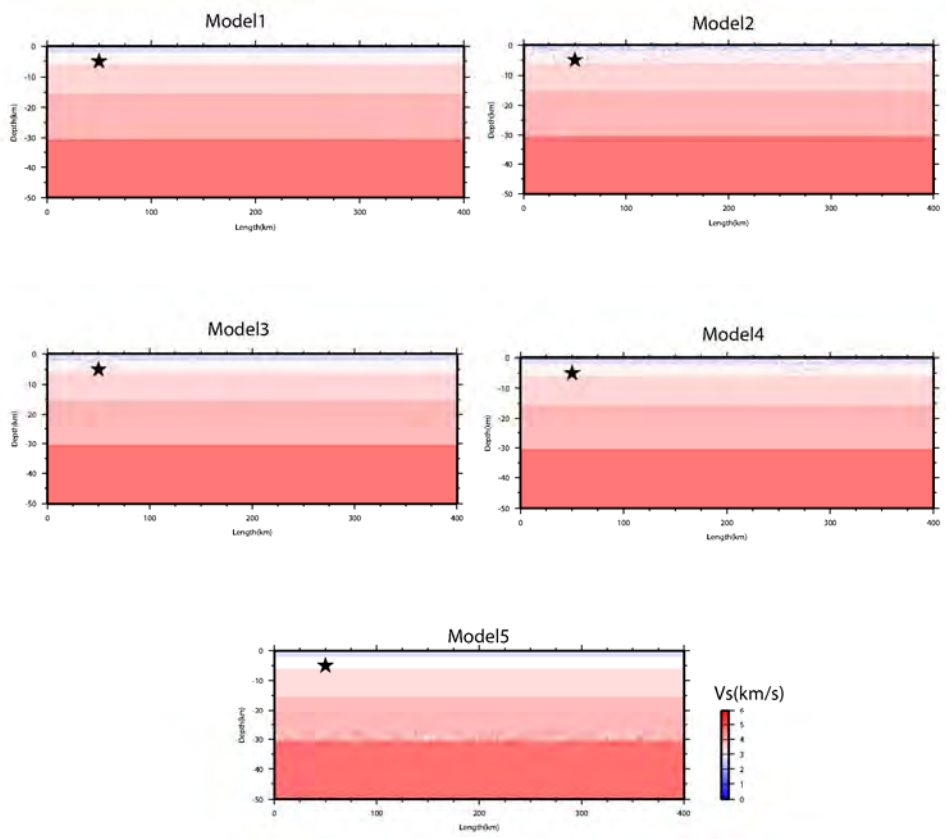


Figure 2. Cross sections of 3D models used in simulations of wave scattering effects.

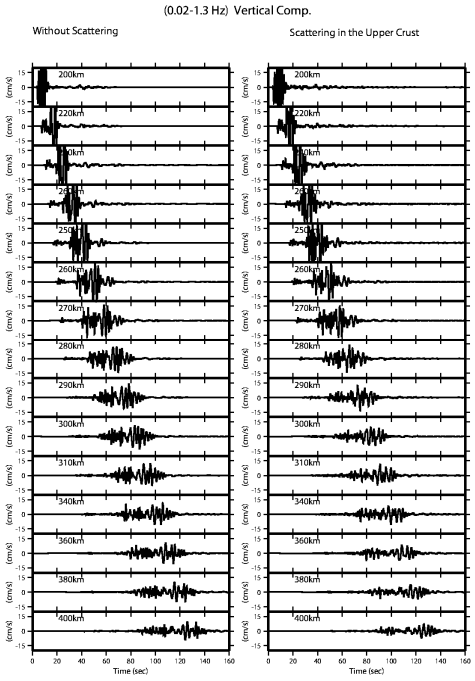


Figure3a. Comparison of velocity seismograms calculated with a 3D crustal velocity model without scattering (left panel) and with scattering in the top layers (right panel), band-pass filtered at 0.-1.3 Hz.

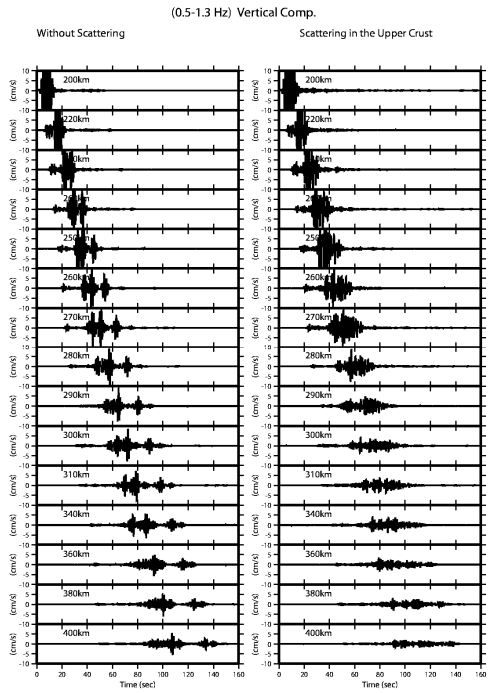


Figure3b. Same as Figure 3a, but band-pass filtered at 0.5-1.3 Hz.

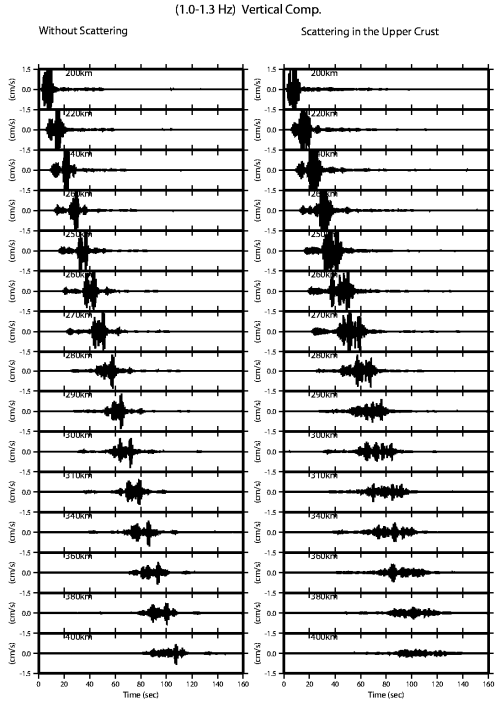


Figure3c. Same as Figure 3a, but band-pass filtered at 1.0-1.3 Hz.

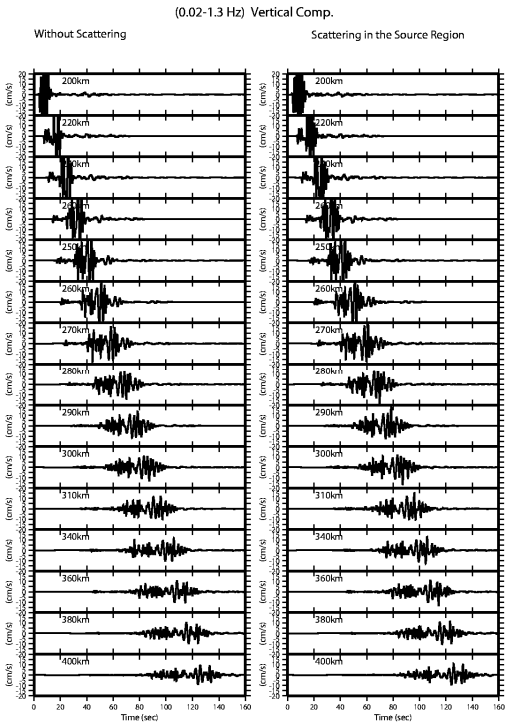


Figure4a. Comparison of velocity seismograms calculated with a 3D crustal velocity model without scattering (left panel) and with scattering in the source region (right panel), band-pass filtered at 0.-1.3 Hz.

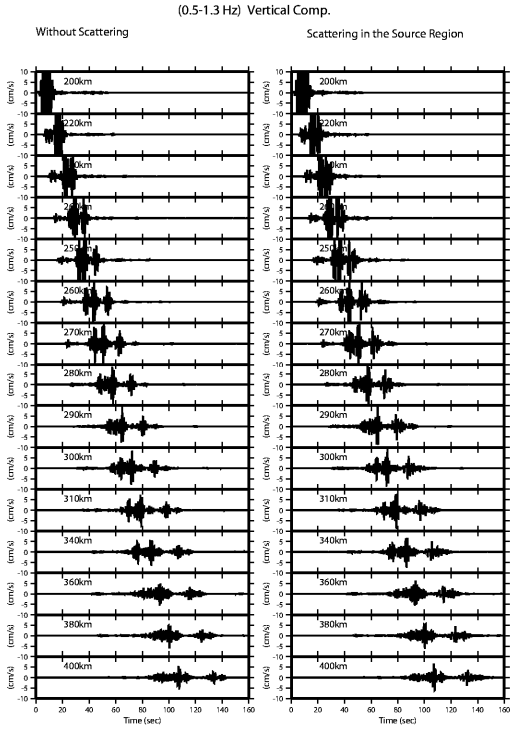


Figure4b. Same as Figure 4a, but band-pass filtered at 0.5-1.3 Hz.

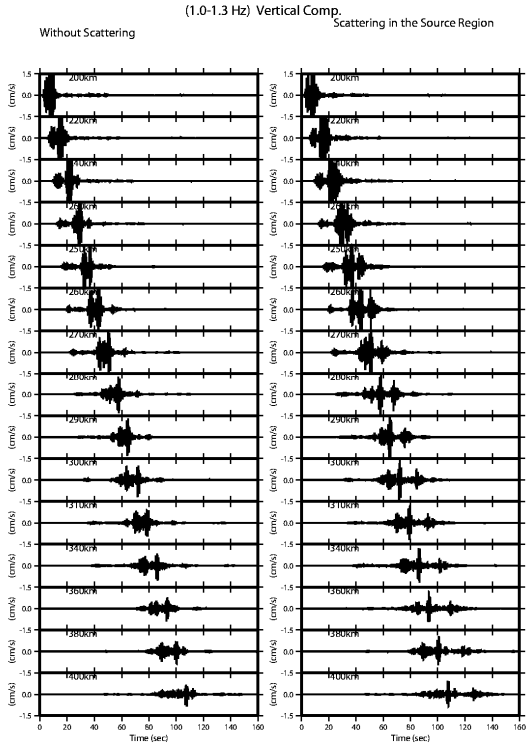


Figure4c. Same as Figure 4a, but band-pass filtered at 1.0-1.3 Hz.

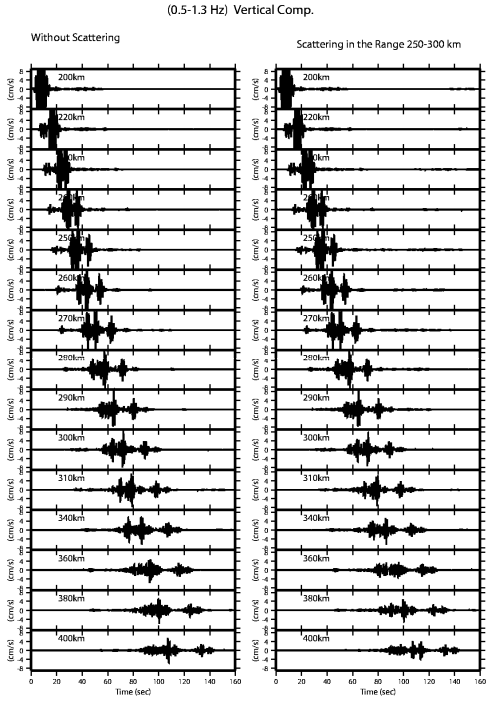


Figure5a. Comparison of velocity seismograms calculated with a 3D crustal velocity model without scattering (left panel) and with scattering in the receivers region in the 250-300km range (right panel), band-pass filtered at 0.5-1.3 Hz.

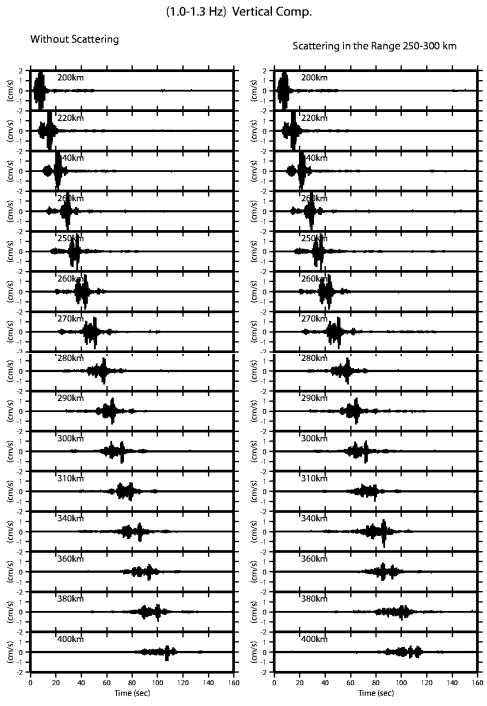


Figure5b. **Same as Figure 5a, but band-pass filtered at 1.0-1.3 Hz.**

DETERMINATION OF CRUST AND UPPER MANTLE STRUCTURE BENEATH AFRICA USING A GLOBAL OPTIMIZATION BASED WAVEFORM MODELING TECHNIQUE

Jay Pulliam, Mrinal K. Sen, and Abhijit Gangopadhyay

University of Texas at Austin

Sponsored by Air Force Research Laboratory

Contract No. FA8718-04-C-0014

ABSTRACT

During the initial years of the project, a waveform modeling program based on the reflectivity method and incorporating a global optimization algorithm, was developed. Assuming a one-dimensional, isotropic, layered Earth, the method computes synthetic seismograms by distributing independent computations for different ray parameters across multiple processors, providing nearly a linear decrease in computation time with the number of processors. During the inversion process, the method implements a global optimization algorithm using very fast simulated annealing (VFSA). Global optimization allows for searching within a broad spectrum of models in order to find the global minimum, and eliminates dependency on the starting model. In particular, VFSA is advantageous because it allows for larger sampling of the model space during the early stages of the inversion process, and much narrower sampling in the model space as the inversion converges and the temperature decreases, while still allowing the search to escape local minima. Additionally, the ability of VFSA to perform different perturbations for different model parameters allows for individual control of each parameter and the incorporation of *a priori* information. The method also uses statistical tools such as computation of the posterior probability density (PPD) function and the parameter correlation matrix, so as to evaluate the uniqueness of a particular model obtained by searching the model space, and the trade-offs between individual model parameters therein.

The waveform modeling approach has now been applied to ground truth data recorded in twelve permanent broadband seismographic stations spanning the African continent. The waveforms modeled included S, Sp, SsPmP, and shear-coupled PL (SPL) phases from deep (200–800 km) earthquakes of magnitude 5.5 to 7.0 located at distances of 30 to 80 degrees. Earthquake data that satisfy the search criteria described above are sparse, however. Seventeen events meeting the above criteria were available for analysis. Forward computation of the synthetic seismograms was performed using models from independent receiver function studies (wherever available) as an initial velocity model for the crust. Preliminary reference earth model (PREM) was used for mantle velocities below the receiver function models. The global optimization algorithm with several hundreds of iterations was then implemented. This algorithm perturbs the crust and upper mantle velocity structure (up to ~100 km depth) within user-specified bounds to generate synthetic seismograms that best fit the data. The results show that the final velocity models obtained from the application of this method for various stations in the African continent correlate well with those obtained from receiver function techniques. In particular, more detailed crust and upper mantle structure was obtained for seismographic stations located in north and west Africa, where prior studies are sparse. Broad tectonic observations were supported by the models generated using this method; specific refinements of the models for some stations are underway.

Overall, the method is successful in determining the crust and upper mantle structure of the African continent. Notable advantages of this method include ability to simultaneously model all the waveforms, assess uncertainties in model parameters, finding a range of acceptable models that explain the data, and avoiding a dependence of the final model on the starting model. Furthermore, it differs from other commonly used methods in the fact that it provides a direct measurement of P and S wave velocities simultaneously. Also, the use of the SPL phase wherever available improves constraints on the models of the lower crust and upper mantle.

OBJECTIVES

We describe a technique based on waveform fitting by synthetic seismograms, and demonstrate its application to determine the crust and upper mantle structure beneath the continent of Africa. Our technique utilizes the reflectivity method (Kennett, 1983) to compute the synthetic seismograms for an earthquake recorded at a particular seismic station and implements a global optimization algorithm using VFSA (Ingber, 1989; Sen and Stoffa, 1995) to invert for the crust and upper mantle structure beneath the station. Our technique is complimentary to the existing receiver function analysis method (e.g., Owens et al., 1987; Ammon, 1991) and retains its advantages, yet minimizes its potential limitations when the derived structural models are used to locate and determine the focal depths of small, regional events.

RESEARCH ACCOMPLISHED

Modeling Method

Following the development of the forward problem described in Pulliam and Sen (2005), we perform an optimization procedure to determine the best model for a given source-receiver pair. In this analysis we employ a "global optimization algorithm" which is only weakly dependent on the choice of the initial model. In particular, we use a method called VFSA, which is a variant of simulated annealing (SA) aimed at making the computations more efficient (Ingber, 1989; Sen and Stoffa, 1995). To further illustrate the VFSA technique, a simplified flow-chart is shown in Figure 1. The method starts with an initial model (m^0) with an associated error or energy, $E(m^0)$. It then draws a new model, m^{new}, among a distribution of models from a temperature (T) dependent Cauchy-like distribution, r(T), centered on the current model (Figure 1). The associated error or energy, $E(m^{new})$, is then computed and compared with $E(m^0)$ (Figure 1). If the change in energy (δE) is less than or equal to zero, the new model is accepted and replaces the initial model. However, if the above condition is not satisfied, m^{new} is accepted with a probability of $[e^{\delta E/T}]$ (Figure 1). This rule of probabilistic acceptance in SA allows it to escape a local minimum. The processes of model generation and acceptance are repeated a large number of times with the annealing temperature gradually decreasing according to a predefined cooling schedule (Figure 1). VFSA is more efficient than the traditional SA because it allows for larger sampling of the model space during the early stages of the waveform fitting, and much narrower sampling in the model space as the procedure converges and the temperature decreases, while still allowing the search to escape from the local minima. Additionally, the ability to perform different perturbations for different model parameters allows for individual control of each parameter and the incorporation of *a priori* information (Sen and Stoffa, 1995).

Solutions to geophysical inverse problems are often nonunique. It is therefore necessary to explore the model space and thus identify the range of models that fit the data, and perhaps to identify characteristics of the models that are required by the data, rather than which simply are allowed by the data. VFSA conducts such a search efficiently, and the products of multiple such searches enable us to evaluate the uncertainty in a single, best-fitting solution. This evaluation is particularly necessary in seismic waveform modeling because more than one model can often explain the observed data equally well, and trade-offs between different model parameters are common (Pulliam and Sen, 2005). The waveform inversion method we use in this study incorporates important statistical tools that allow the user to evaluate the uniqueness, and physical feasibility of the resulting model. The most useful of these tools in evaluating the results' reliability are the posterior probability density (PPD) function, and the parameter correlation matrix. To estimate these statistical parameters we cast the inverse problem in a Bayesian framework (e.g., Sen and Stoffa, 1995), and employ "importance sampling" based on a Gibbs' sampler (GS) (Sen and Stoffa, 1995; Pulliam and Sen, 2005). The goal of "importance sampling" is to concentrate sample points in the regions that are the most "significant," in some sense (perhaps, for example, where the error function is rapidly varying, or many acceptable solutions lie). Because this concentration is achieved using a Gibbs' probability distribution, it has been named the "Gibbs' sampler" (Sen and Stoffa, 1995). The PPD function $[\sigma(\mathbf{m}|\mathbf{d}_{obs})]$ is defined as a product of a likelihood function $[e^{-E(\mathbf{m})}]$, and prior probability density function, $p(\mathbf{m})$. The prior probability density function $p(\mathbf{m})$, describes the available information on the model without the knowledge of the data and defines the probability of the model $\mathbf{m}$ independent of the data. The likelihood function defines the data misfit and its choice depends on the distribution of error in the data (Sen and Stoffa, 1995). Sen and Stoffa (1996) examined several different approaches to sampling models from the PPD and concluded that a multiple-VFSA based approach, though theoretically approximate, is the most efficient. Here, we have employed the fast multiple-VFSA algorithm to estimate uncertainties. We compute approximate marginal PPD and posterior correlation matrices to characterize uncertainties in the derived results. The

posterior correlation matrix measures the relative trade-off between individual model parameters and is computed by normalizing the covariance between two model parameters (Sen and Stoffa, 1996).

Application

We apply the modeling method outlined above to data from large-magnitude, deep-focus earthquakes recorded teleseismically at twelve permanent broadband seismic stations spanning the continent of Africa (Figure 2). A total of seventeen earthquakes are used in this study selected from the global catalog of Harvard Centroid Moment Tensors (CMT) (1976–2004) (Table 1). Seven of these are located in the Hindu Kush, three in southern Bolivia, two each in Argentina, and the Java Sea, and one each in Afghanistan, South Sandwich Islands, and southern Sumatra. The focal depths of these earthquakes range between 200 km–600 km, and their magnitudes lie between 5.5–7.0. Since the goal of this study is to also model the SPL phase that is generated close to the seismic station, we choose such a focal depth range to eliminate the (SPL) phase generated at the earthquake source. Epicentral distances from the seismic stations of the selected earthquakes are between 30° and 80° so as to avoid possible incorporation of phases that interacted with the earth's core. Based on our selection criteria, earthquake data available from the seismic stations in Africa are sparse. Hence, the numbers of earthquakes recorded by each station range from 1 to 9 and azimuthal coverage is poor. In spite of the sparse set of source-receiver pairs available for modeling, we are able to obtain reliable azimuthally dependent models in some cases.

Table 1. List of earthquakes used in this study

Event Number	Date (yyyy/mm/dd)	Time (hr:min:sec)	Latitude	Longitude	Focal Depth (km)	Magnitude	Region
1	1990/07/13	14:27:24.8	36.46 N	70.80 E	218	5.6	Hindu Kush
2	1991/06/23	21:31:58.33	26.82 S	63.40 W	581	6.4	Santiago del Estero, Argentina
3	1993/08/09	11:44:08.306	36.42 N	70.72 E	210	5.8	Hindu Kush
4	1993/08/09	12:48:29.404	36.36 N	70.85 E	230	6.3	Hindu Kush
5	1994/06/30	09:31:04.212	36.25 N	71.08 E	233	6.1	Afghanistan
6	1994/10/25	00:58:47.987	36.30 N	70.91 E	244	5.9	Hindu Kush
7	1994/11/15	20:27:46.338	5.61 S	110.2 E	559	6.2	Java Sea
8	1994/12/07	03:47:10.307	23.46 S	66.74 W	243	5.6	Jujuy Province, Argentina
9	1995/05/13	21:07:41.552	5.22 S	108.92 E	554	5.7	Java Sea
10	1997/01/23	02:24:53.890	22 S	65.72 W	276	6.4	Southern Bolivia
11	1997/10/05	18:14:56.228	59.74 S	29.20 W	273.9	6.0	South Sandwich Islands
12	1997/12/17	05:55:49.933	36.39 N	70.77 E	207	5.5	Hindu Kush
13	1998/03/21	18:26:09.8	36.43 N	70.13 E	227.8	5.8	Hindu Kush
14	1999/09/15	03:11:17.074	20.93 S	67.28 W	218	6.0	Southern Bolivia
15	2002/03/03	12:12:00.183	36.43 N	70.44 E	209	6.3	Hindu Kush
16	2003/07/27	11:49:52.347	20.13 S	65.18 W	345.3	5.9	Southern Bolivia
17	2004/07/25	14:44:40.148	2.43 S	103.98 E	582.1	6.8	Southern Sumatra, Indonesia

Results of this Application

Below, we report results of waveform fitting for selected teleseismic earthquakes recorded in Africa. A comment on amplitude matches: The most successful match between synthetics and data would be one in which the synthetic waveform matched the data exactly—wiggle for wiggle. This is unrealistic for several reasons, including the fact that models used to compute synthetics are layered, isotropic, limited to ten to sixteen layers, and have fixed attenuation (Q) values. Further, the source time function is assumed to be Gaussian and its focal mechanism is assumed to be correctly represented by Harvard's CMT solution. To minimize complexities in the source time function we avoid very large earthquakes. Given the uncertainties in model Q and focal mechanisms, which will largely control relative amplitudes of various phases, we focus our fitting criteria on matching each phase's arrival time, polarity, and pulse character. Fitting the amplitude of each phase, while desirable, is deemed to be of lesser importance.

West Africa

The region encompassing north and west Africa includes the seismic stations of TAM, DBIC, MBO, and MDT (Figure 2). Among these stations, TAM recorded data of better quality; examples of the waveform fits for events 1, 3, and 6 (Table 1) recorded at TAM are shown in Figure 3a. We observe S, SP, and SsPmP phases consistently on all these event seismograms, and they correlate well with the synthetics generated by the optimization technique (Figure 3a). On event 3, we also observe a prominent SPL phase and the synthetics match it well (Figure 3a). Particle motion diagrams for the corresponding time window on both data and synthetics confirm this observation (Figure 3b). We observe prograde elliptical particle motion, which is diagnostic of the SPL phase, on both diagrams (Figure 3b). Except for event 3, none of the others have any signature of the SPL phase, as confirmed by particle motion diagrams for corresponding time windows. This observation—that one source-receiver pair would show SPL while other, similar paths would not—is unexpected and we cannot explain it.

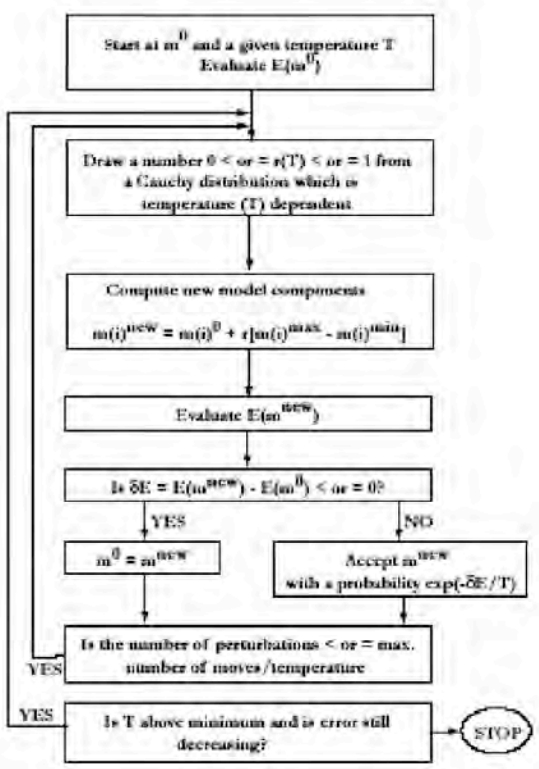


Figure 1. Flow-chart elaborating the very fast simulated annealing (VFSA) algorithm used in this study for the waveform inversion by global optimization (Modified from Sen and Stoffa, 1995). $E(m^0)$-error function for the initial model m^0, $E(m^{new})$-error function for the new model m^{new}, T-temperature, r(T)-temperature dependent Cauchy-like distribution.

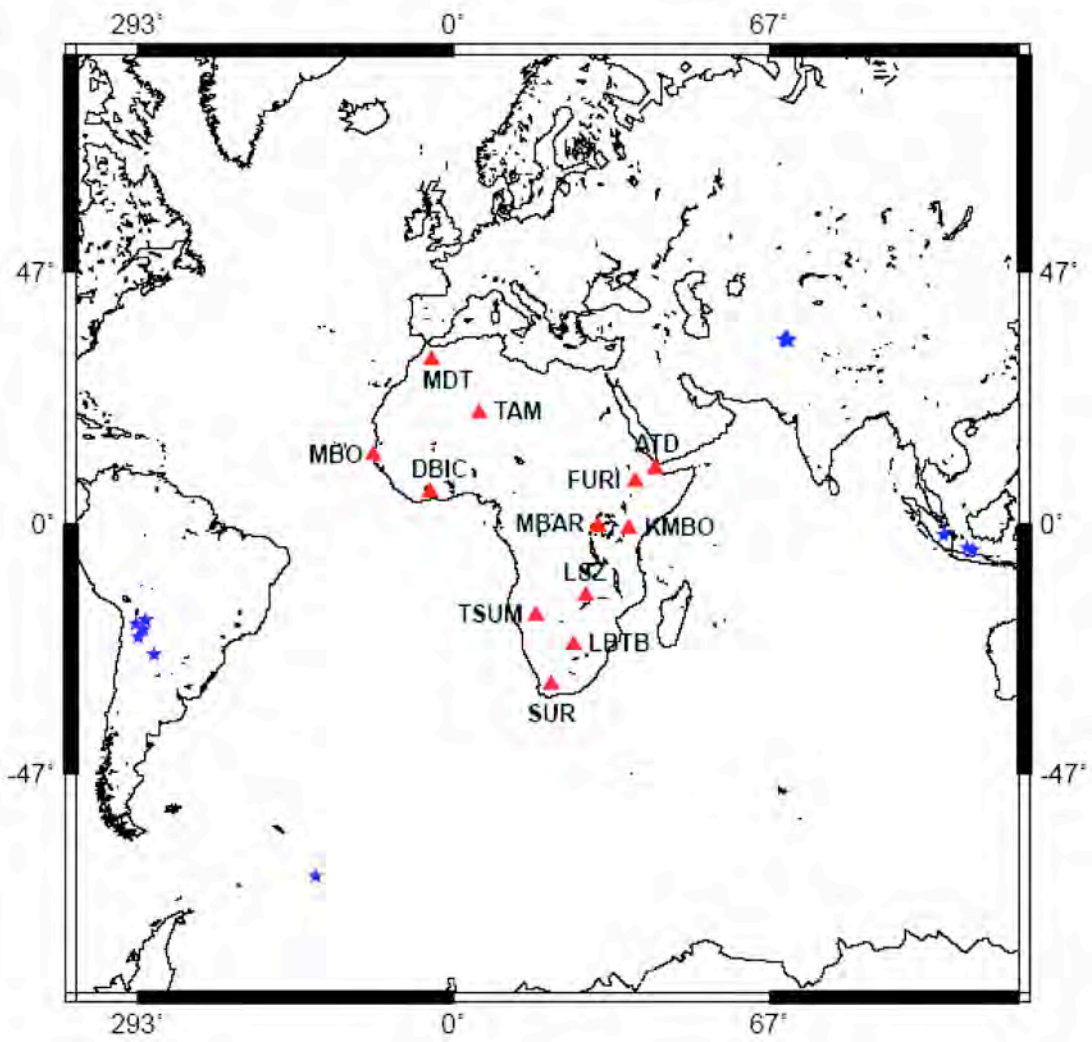


Figure 2. Map showing locations of the earthquakes used in this study (blue stars) and the permanent broadband seismic stations in the African continent (red triangles) that have recorded these earthquakes. The respective station codes are shown adjacent to each seismic station.

Based on the waveform-fitting results for all six events recorded at TAM, we generate P- and S-wave velocity models up to a depth of 100 km (Figure 3c). We observe some variability in the models (Figure 3c), and hence compute the uncertainties for each model using the statistical tools described earlier to choose the "best" model. In Figure 3d, we show examples of parameter correlation matrices computed from the modeling results of events 1 and 3 (Table 1). Each small square along an axis of the parameter correlation matrix, either horizontally or vertically, represents a model parameter (Figure 3d). Since every model layer consists of four independent model parameters (V_p, V_s, thickness, and density), four small squares combined together represent a model layer on both axes (Figure 3d). Correlation values range between –1 and 1 and are symmetric about the diagonal of the matrix, hence, for clarity, we show only values below the diagonal (Figure 3d). Values along the diagonal are ones, simply indicating that each parameter is perfectly correlated with itself. Off-diagonal colored squares indicate significant cross-correlation (trade-offs) between corresponding model parameters. In the parameter correlation matrices for both events (Figure 3d), layers comprising the upper crust have greater independence, as indicated by the sparse distribution of off-diagonal cross-correlations whose absolute values are greater than ±0.5 (colored squares). Also, for both events, the level of tradeoffs among model parameters in these shallow layers is similar (Figure 3d). For event 1, however, the layers comprising the lower crust and upper mantle have larger off-diagonal cross-correlations, indicating significant tradeoffs (Figure 3d). On the contrary, for event 3, even the lower crustal and upper mantle layers appear better constrained (Figure 3d). Intriguingly, the SPL phase is also observed in the

seismogram of event 3 but not in that of event 1 (Figure 3a). This observation attests to the fact that, if SPL is present in the seismogram and is well modeled, we are able to better constrain the structure of the lower crust and upper mantle. This result, which is expected, due to the sensitivity of SPL to those parts of the model (Figure 1b), drives our decision to generate velocity models down to the Moho for seismic stations at which SPL is not observed.

We observe and successfully fit S and SP phases in seismograms recorded at DBIC and at MBO. The SsPmP phase appears on the vertical-component seismograms of events 13 at DBIC and event 16 at MBO but is absent on their radial-component seismograms. We do not observe the SPL phase in seismograms recorded at DBIC but do so at MBO in the seismograms of event 16. The SPL phase is prominent on both vertical and radial component seismograms of event 16 recorded at MBO, which we confirm with particle motion diagrams that show prograde elliptical motion for the corresponding time window. At MDT, within the time-window expected to contain the phases analyzed in this study, we are unable to clearly identify them and they appear to be contaminated by interfering arrivals, and hence are also not well-correlated with the synthetics generated by the waveform inversion process. Station MDT is located near the Atlas Mountains in Morocco, and so may be underlain by complicated three-dimensional structure, which the waveform modeling program used in this study is unable to model accurately. The lack of correlation between synthetic seismograms and data at MDT is likely a consequence of this limitation.

East Africa

Stations ATD, FURI, KMBO, and MBAR are situated within and on the flanks of the active East African rift system and waves recorded at these stations sample the complicated three-dimensional, anisotropic structure beneath the rift (Ayele et al., 2004; Dugda and Nyblade, 2006). Three-dimensional structure is manifested in the seismograms as numerous, possibly scattered, refracted, or split, phase arrivals with strong interference amongst themselves. Anisotropy inferred from shear-wave splitting studies has also been reported for stations ATD, FURI, and KMBO by Ayele et al. (2004). The waveform inversion method we use in this study is capable of estimating only one-dimensional (although azimuthally dependent) structure only, hence waveforms for events recorded at these stations are not precisely correlated in some cases. On both the vertical and radial component seismograms of most events at ATD, FURI, KMBO, and MBAR, we observe S and SsPmP phases. On the other hand, except at MBAR, we observe the SP phase only on the vertical component for these events. Only at FURI, for event 12 (Table 1), and MBAR, for event 15 (Table 1), do we see SPL phases in the seismograms.

Southern Africa

Seismic stations TSUM, LSZ, LBTB, and SUR are located in southern Africa (Figure 2). However, for the lone event recorded at SUR, we are able to identify only the direct S phase, and thus we do not attempt to generate P- and S-wave velocity models for SUR. We observe and successfully fit S, SP, and SsPmP phases on events 13 and 14 (Table 1) recorded at TSUM, event 9 (Table 1) recorded at LSZ, and event 11 (Table 1) at LBTB. But, except for event 13 at TSUM, we are able to identify the SP phase on both the vertical and radial component seismograms at TSUM, LSZ, and LBTB. Similarly, the SsPmP phase is only identifable on the vertical component seismogram for events 14 and 9 recorded at TSUM and LSZ respectively. It is, however, absent on the seismograms for event 13 at TSUM. We do not observe the SPL phase in the seismograms of any event recorded at these stations.

Summary of Models

Figures 4a–d show P- and S-wave velocity models for the north and west African stations of TAM, DBIC, MBO, and MDT. Estimates of crustal thickness beneath these stations range between 36 km and 42 km (Figures 4a–d), comparable to regional estimates of 34 km to 40 km by Pasyanos et al. (2004). We also note that the crust is slightly thicker in west Africa, e.g. beneath stations DBIC and MBO (~41–42 km) (Figures 4b and 4c), compared to the seismic stations TAM and MDT in north Africa (~36 km–38 km) (Figures 4a and 4d). A similar observation was also made earlier by Pasyanos and Walter (2002) using surface wave dispersion tomography, and by Marone et al. (2003) using joint inversion of local, regional, and teleseismic data. Except for TAM, the crust below all the stations appears to be fairly simple in structure (Figures 4a–d) (Sandvol et al., 1998), suggesting that it is minimally affected by large-scale tectonic processes. However, a middle to lower crustal low-velocity zone obtained beneath all the seismic stations in the region (Figures 4a–d), indicate possible local tectonic influences. Our estimate of crustal thickness beneath TAM (~36 km) is similar to that obtained from receiver function studies by Sandvol et al. (1998) (38 ± 2 km) (Figure 4a), from Rayleigh wave group velocity dispersion studies by Hazler et al. (2001) (43 ± 5 km), and from surface-wave dispersion tomography by Pasyanos and Walter (2002) (~40 km). TAM is close to the location of the Hoggar hot spot but, as noted by Sandvol et al. (1998), the crustal thickness indicates that a mantle plume has not significantly altered the crust here. However, in contrast to the model of Sandvol et al. (1998), the

crustal P- and S-wave velocities we obtain in this study at TAM are both slightly lower (Figure 4a). These velocities at TAM range between 6.25 km/s–6.8 km/s, and 3.1 km/s–3.9 km/s, respectively (Figure 4a). Upper mantle P-wave velocities exhibit a gradational increase with depth below the Moho, whereas the S-wave velocities are nearly constant (4 km/s–4.2 km/s) within that range of depths (Figure 4a). Furthermore, we also obtain an anomalous low-velocity zone of ~5 km thickness at the base of the upper crust (Figure 4a) that appears to be well constrained based on the uncertainty estimates described earlier (Figure 3d). However, we are unable to confirm the existence of this layer from any other independent studies.

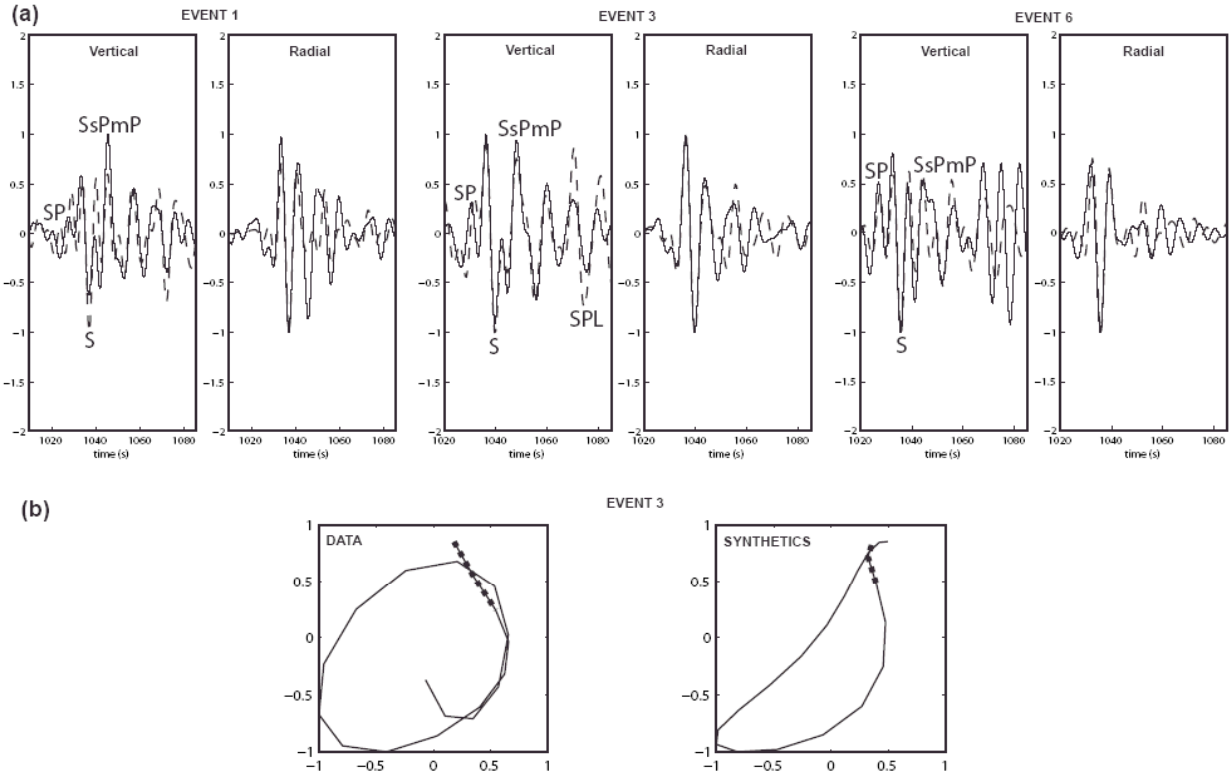


Figure 3. (a) Vertical and radial component seismograms for events 1, 3, and 6 (Table 1) recorded at TAM showing the observed (solid line) and synthetic (dashed line) waveforms. The correlated waveforms are indicated on the panels. (b) Particle motion diagrams for the portion of the waveforms in the time window (1077–1085 s) on the data and synthetics for event 3 showing prograde ellipitical motion diagnostic of the SPL phase. The dotted portions of the diagrams indicate beginning of the motion. Figure 3 is continued on next page.

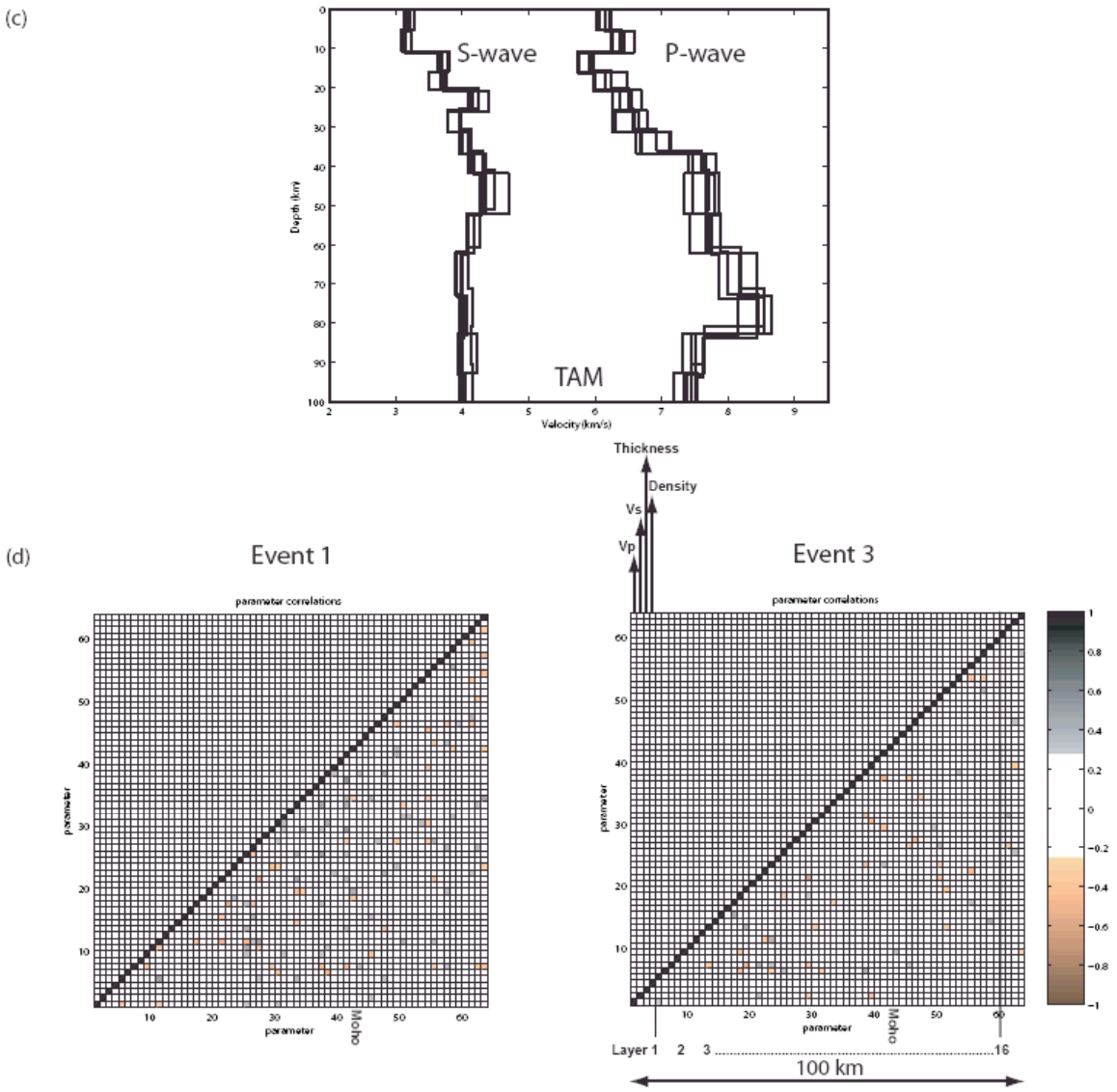


Figure 3 continued. (c) P- and S-wave velocity models up to 100 km for station TAM from the inversion results for individual events recorded at TAM. (d) Model parameter correlation matrices for events 1 (left panel) and 3 (right panel). Each small square represents a model parameter (Vp, Vs, thickness of layer, and density) on both the axes. The correlations range between –1 and 1. Sparse off-diagonal colored squares in the lower crust-upper mantle in event 3 (right panel) compared to that in event 1 (left panel) indicate better resolution and confidence (less tradeoff) in this region.

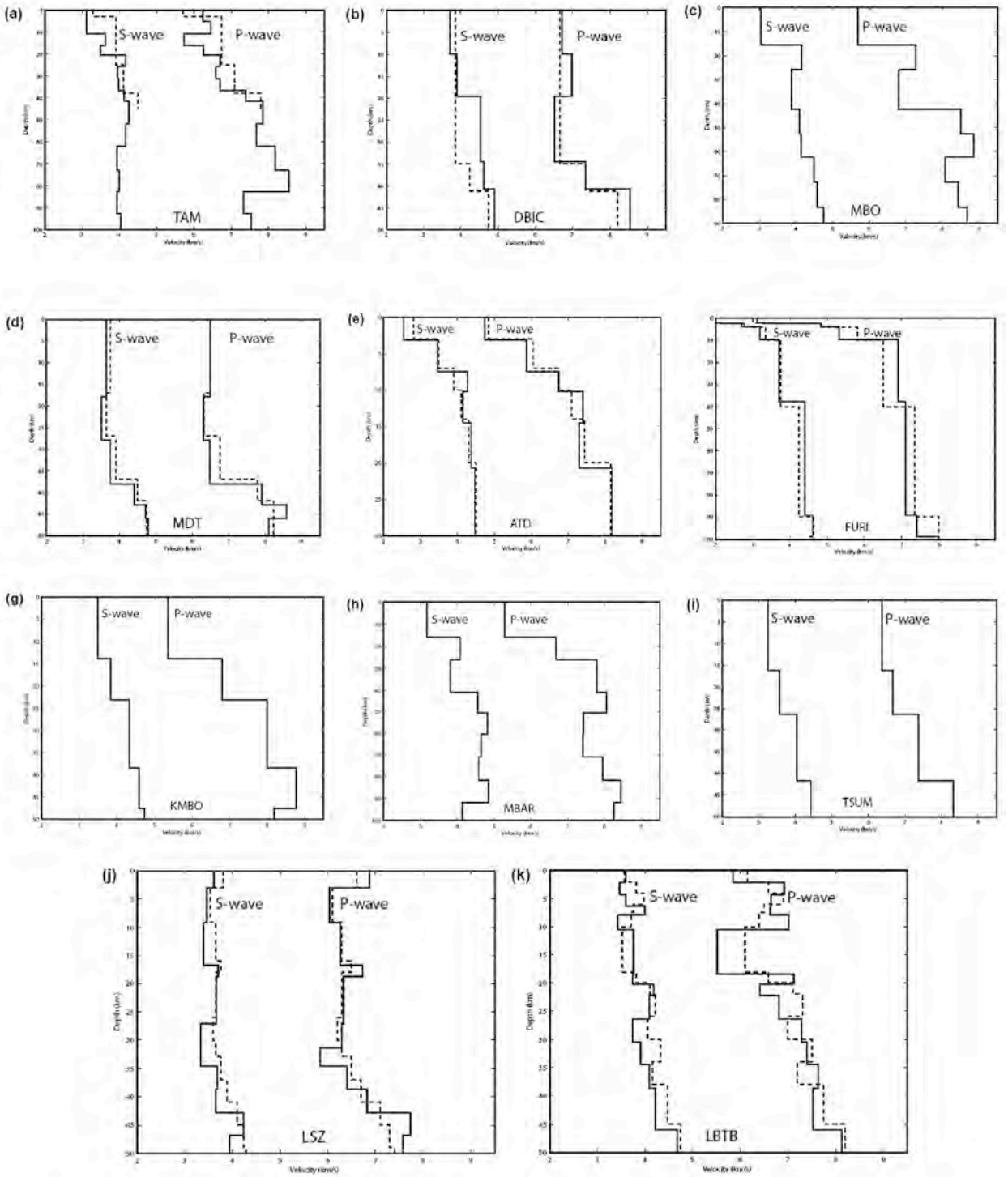


Figure 4. P- and S-wave velocity models (solid lines) obtained for (a) TAM (b) DBIC (c) MBO (d) MDT (e) ATD (f) FURI (g) KMBO (h) MBAR (i) TSUM (j) LSZ (k) LBTB. The P- and S-wave velocity models (broken lines) in (a), (b), (d), and (e) are from receiver function studies by Sandvol et al. (1998), in (f) are from receiver function studies by Ayele et al. (2004), and in (j) and (k) are from receiver function studies by Midzi and Ottemoller (2001).

At the west African coastal station DBIC, we obtain a Moho depth of ~41 km which is similar to that obtained by Sandvol et al. (1998) (~40 ± 2.3 km) (Figure 4b). P-wave velocities range between 6.7 km/s–7 km/s in the upper crust, and 6.5 km/s–7.3 km/s in the lower crust (Figure 4b). On the contrary, S-wave velocities show a gradational increase in the crust with depth from 3.7 km/s–4.7 km/s (Figure 4b). Anomalous V_p/V_s ratios are thus caused by a low P-wave velocity zone of ~15 km thickness in the lower crust. However, due to the trade-offs between the model parameters in this depth range, we conclude that this anomaly is not well-constrained. Beneath MBO, any prior P- and/or S-wave velocity models are absent. Sandvol et al. (1998) had analyzed seismic data recorded at MBO but the anomalous data did not allow them to estimate a velocity model. We obtain a crustal thickness of ~42 km (Figure 4c), which is similar to that found underneath other stations in the region. A regional crustal thickness of 43 ± 5 km obtained from Rayleigh wave group velocity dispersion studies (Hazler et al., 2001) correlates well with the results of this study at MBO. The P- and S-wave velocities at MBO in the crust range between 5.6 km/s–7.2 km/s, and 3.1 km/s–4.1 km/s, respectively (Figure 4c). We also observe an anomalous lower crustal, approximately 15 km-thick zone of relatively low P- and S-wave velocities (6.8 km/s and 3.8 km/s) beneath MBO (Figure 4c). Our P- and S-wave velocity models beneath MDT predict a Moho depth of ~38 km (Figure 4d). Surprisingly, even with the poor waveform fit by synthetics to the event recorded at MDT, this result is consistent with the estimates obtained by Sandvol et al. (1998) (36 ± 1.3 km). As also noted by Sandvol et al. (1998) and Pasyanos and Walter (2002), the slightly shallower Moho at MDT, compared to that at DBIC and MBO, indicates that in spite of its proximity to the Atlas Mountains, there is no crustal thickening associated with them, and a significant root is absent beneath the mountains. Sandvol et al. (1998) concluded that this may be a possible outcome of the fact that there existed a failed rift earlier which was subsequently inverted. In this study, beneath MDT, we obtain average P- and S-wave velocities in the crust of ~6.4 km/s and 3.7 km/s, respectively, except in a low-velocity zone of ~10 km thickness in the lower crust where these are 6.2 km/s and 3.4 km/s, respectively (Figure 4d). A similar zone has also been postulated by the earlier velocity model obtained from receiver function studies (Sandvol et al., 1998). However, because of poor waveform fits at MDT in this study, we are unable to postulate the existence of this zone.

For East Africa, we generate P- and S-wave velocity models beneath seismic stations ATD, FURI, KMBO, and MBAR, which are shown in Figures 4e–h. Located within and on the flanks of the East African Rift System, which is relatively well studied, these stations are situated in active tectonic domains. Except beneath ATD (Figure 4e), where the crust is significantly thin compared to the other stations in the region (Figures 4f–h), the Moho is generally between ~38 km–41 km deep. The estimate of crustal thickness beneath ATD, however, is the subject of an active debate. Using a grid search method to model receiver functions for eleven earthquakes recorded at ATD, Sandvol et al. (1998) obtained a crustal thickness of ~10 km (Figure 4e). But, Dugda and Nyblade (2006) used H-κ analysis of receiver functions and predicted a crustal thickness of ~23 ± 1.5 km beneath ATD, consistent with earlier results from inversion of gravity data for the general area by Tiberi et al. (2005). In this study, our velocity model beneath ATD shows comparable velocity discontinuities at ~10 km and ~21 km depths (Figure 4e), suggesting that either of these depths could be interpreted as the Moho. However, the layer at 10 km depth appears to be poorly constrained compared to the layer at ~21 km depth, as evidenced from the PPD and the parameter correlation matrix computations. Therefore, we prefer a crustal thickness of ~21 km. Irrespective of the debate on the crustal thickness at ATD, the crust beneath it is significantly thinner than the crust beneath other seismic stations in east Africa (Figures 4f–h). Located within the Afar depression, close to the coast of the Red Sea on the eastern edge of the African continent, such a thin crust is expected at ATD because of highly stretched continental crust (Sandvol et al., 1998). The P- and S-wave velocities in the crust at ATD range between 4.7 km/s–7.2 km/s, and 2.5 km/s–4.3 km/s, respectively (Figure 4e). Crustal P-wave velocities below about 5 km depth are relatively high and, as noted by Dugda and Nyblade (2006), could indicate a highly mafic composition caused by igneous rock emplacement during the syn-rift stage. Figure 4f shows the preferred P- and S-wave velocity models beneath FURI which is situated in the northern part of the western Ethiopian plateau. We obtain an estimate of crustal thickness beneath FURI of ~39 km, which is similar to that obtained using receiver function analyses by Ayele et al. (2004) (~40 km), and Dugda et al. (2005) (~44 km). The ~40 km thick crust beneath FURI, which is located close to the border of the western Ethiopian plateau and the Afar depression, is also consistent with previous refraction studies of Berckhemer et al. (1975) as reported by Ayele et al. (2004). Crustal P- and S-wave velocities below ~5 km depth at FURI range between 5.3 km/s–6.8 km/s, and 3.2 km/s–3.6 km/s, respectively (Figure 4f). In addition, beneath FURI, our results also predict an ~50 km thick layer immediately below the Moho in the upper mantle that has P- and S-wave velocities of ~7.1 km/s and ~4.3 km/s, respectively, which are anomalously slow (Figure 4f). A similar layer with P- and S-wave velocities of ~7.4 km/s and ~4.2 km/s, respectively, was also obtained by Ayele et al. (2004) (Figure 4f). As noted by Ayele et al. (2004), this anomalously slow layer possibly indicates altered lithospheric material, and supports the result from Rayleigh wave dispersion by Knox et al. (1999), of an approximately 100 km thick

lithosphere beneath FURI. Station KMBO is located in Kenya, close to the southern end of the eastern branch of the East African Rift System, but outside its edge. Beneath KMBO our estimate of the crustal thickness is ~38 km (Figure 4g). This estimate is similar to that obtained using receiver function analysis by Dugda et al. (2005) (~41 km). Crustal P- and S-wave velocities show a gradational increase with depth and range between 5.4 km/s–8 km/s, and 3.5 km/s–4.5 km/s, respectively (Figure 4g). The velocity structure beneath KMBO appears to be fairly simple. Although it has relatively high P-wave velocities in the lower crust (Figure 4g), it is otherwise typical of cratonic regions. Seismic station MBAR is located between the western boundary of the Tanzania craton and the western branch of the East African Rift System. Due to poor correlation of some of the observed phases with synthetics, and the availability of only one event, the velocity model beneath MBAR is poorly constrained. Nevertheless, our estimate of crustal thickness beneath MBAR, to our knowledge the first of its kind, is ~41 km (Figure 4h), and is consistent with that obtained from other stations in the region. Crustal P- and S-wave velocities at MBAR range between 5.3 km/s–7.7 km/s, and 3.2 km/s–3.8 km/s, respectively (Figure 4h). Our model also predicts a low P-wave velocity (~7.2 km/s) layer beneath the crust (Figure 4h). Such a layer promotes the generation of the SPL phase near the station, which we observe in both data and synthetics for the event recorded at MBAR. Therefore, in spite of the poorly constrained model obtained in this study, we cannot rule out the possibility of its existence.

In southern Africa we generated P- and S-wave velocity models beneath the seismic stations TSUM, LSZ, and LBTB (Figures 4i–k). Although we analyzed seismic data recorded at SUR, due to the lack of identifiable phases, we do not generate P- and S-wave velocity models for the station. Similar to most of the results in north and west Africa, our results for southern Africa are representative of stable shield regions. However, in general, we obtain slightly higher crustal thicknesses ranging between ~42 km and 46 km (Figures 4i–k). We also predict crustal low velocity zones as discussed later in our models beneath two of the three stations in southern Africa. Beneath TSUM, to our knowledge, no prior velocity model exists. Thus, the velocity model obtained from our study at TSUM is the first of its kind. We obtained a crustal thickness beneath TSUM of ~42 km (Figure 4i). The velocities of P- and S-waves in the crust range between 6.3 km/s–7.3 km/s, and 3.2 km/s–4 km/s, respectively (Figure 4i). These results are similar to those obtained for the seismic stations in north and west Africa and are therefore representative of stable shield regions. We do not obtain any anomalous P- and S-wave velocity zones beneath TSUM (Figure 4i). At LSZ, our study indicates that the Moho is located at a depth of ~43 km (Figure 4j), which is consistent with that obtained by Midzi and Ottemöller (2001) (~40–43 km). The crustal P-wave velocity is nearly constant (~6.2 km/s) between ~8 km to 32 km depth (Figure 4j). Below ~32 km depth, P-wave velocities increase rather sharply from ~6.2 km/s to 7.8 km/s at the Moho (Figure 4j). The crustal S-wave velocities range between ~3.6 km/s and 3.8 km/s (Figure 4j). We also obtain a lower crustal low-velocity zone of ~5–8 km thickness in our velocity model for LSZ (Figure 4j), consistent with models for seismic stations elsewhere in Africa in the cratonic regions. Such a phenomenon was also noted by Midzi and Ottemöller (2001). Figure 4k shows the P- and S-wave velocity models beneath LBTB obtained in our study. There appears to be a broad crust–mantle transition zone beneath LBTB and the upper bound of the estimate of crustal thickness beneath LBTB is ~46 km (Figure 4k). Midzi and Ottemöller (2001) also noted the same and predicted a crust-mantle transition zone between 37-45 km. The crustal P- and S-wave velocities beneath LBTB range between 5.8 km/s–7.5 km/s, and 3.5 km/s–4.2 km/s, respectively, except for a distinct low P-velocity (5.4 km/s) zone of ~8 km thickness in the upper crust between 10 km–20 km depth (Figure 4k). Such a low-velocity zone was also obtained by Midzi and Ottemöller (2001) at similar depths, however, the P-wave velocities predicted from our study for this zone are significantly lower than those predicted by Midzi and Ottemöller (2001). Given its appearance beneath other cratonic seismic stations in Africa, the crustal low-velocity zone appears to be a general characteristic of the region.

CONCLUSIONS AND RECOMMENDATIONS

In this paper, we discuss a waveform fitting technique that relies on a parallelized reflectivity method to compute synthetic seismograms and implements a global optimization algorithm using VFSA. We also demonstrate the application of the method to determine one-dimensional, azimuthally dependent, crust and upper mantle P- and S-wave velocity structure beneath broadband seismic stations across the continent of Africa. Our technique avoids dependence of the final results on the initial model, and we are able to compute synthetic seismograms that contain all the possible phases for a prescribed source–receiver path, and obtain direct estimates of the P- and S-wave velocities beneath seismic stations. Statistical tools incorporated in the technique allow us to assess uncertainties associated with our models and estimate tradeoffs between model parameters in different layers. The use of the SPL phase as shown in the study, enhances our constraints for lower crust and upper mantle structure beneath the seismic stations.

Applied to large-magnitude, deep-focus earthquakes recorded teleseismically in Africa, our method successfully produced crust and upper mantle (wherever SPL was observed) P- and S-wave velocity models, that are consistent with earlier models, in the sense that they fall within the associated uncertainties we found with the products of multiple VFSA runs. For some seismic stations, our study provided such velocity models that are the first of their kind. Our models were also consistent with the regional tectonics of Africa. While the technique described here provided layered, one-dimensional models, a dataset that includes a broader azimuthal distribution of earthquakes for each station would allow this source-receiver-based technique to produce better azimuthally-dependent models, and thus a more detailed view of the earth's structure. We plan to apply this method to determine the crust and upper mantle structure beneath China and the Middle East.

ACKNOWLEDGEMENTS

Data were obtained from the Incorporated Research Institutions for Seismology (IRIS).

REFERENCES

Ammon, C. J. (1991). The isolation of receiver effects from teleseismic P wave fronts, *Bull. Seis. Soc. Am.* 81: 2,504–2,510.

Ayele, A., G. Stuart, and J. M. Kendall (2004). Insights into rifting from shear wave splitting and receiver functions: An example from Ethiopia, *Geophys. J. Int.* 157: 354–362.

Berckhemer, H. et al. (1975). *Afar Depression of Ethiopia, in Schweizerbart*, Vol. 1, A. Pilger and A. E. Rosler (Eds.). Stuttgart: Schweizerbart'sche Verlagsbuchhandlung, Science Publishers, 89–107.

Dugda, M. T. and A. A. Nyblade (2006). New constraints on crustal structure in eastern Afar from the analysis of receiver functions and surface wave dispersion in Djibouti, in *The Structure and Evolution of the East African Rift System in the Afar Volcanic Province*, Yirgu, G., C. J. Ebinger, and P. K. H. Maguire (Eds.). London: Geological Society of London, Special Publications, Vol. 259, pp. 241–253.

Dugda, M. T., A. A. Nyblade, J. Julià, C. A. Langston, C. J. Ammon, and S. Simiyu (2005). Crustal structure in Ethiopia and Kenya from receiver function analysis: Implications for rift development in eastern Africa, *J. Geophys. Res.* 110: B01303, doi:10.1029/2004JB003065.

Hazler, S. E., A. F. Sheehan, D. E. McNamara, and W. R. Walter (2001). One-dimensional shear velocity structure of northern Africa from Rayleigh wave group velocity dispersion, *Pure Appl. Geophys.* 158: 1,475–1,493.

Ingber, L. (1989). Very fast simulated reannealing, *Math. Comput. Modeling*, 12: 967–993.

Kennett, B. L. N. (1983). *Seismic Wave Propagation in Stratified Media*. Cambridge: Cambridge University Press.

Knox, R., A. Nyblade, and C. Langston (1999). Upper mantle S velocities beneath Afar and western Saudi Arabia from Rayleigh wave dispersion, *Geophys. Res. Lett.* 25: 4,233–4,236.

Marone, F., M. van der Meijde, S. van der Lee, and D. Giardini (2003). Joint inversion of local, regional and teleseismic data for crustal thickness in the Eurasia-Africa plate boundary region, *Geophys. J. Int.* 154: 499–514.

Midzi, V. and L. Ottemöller (2001). Receiver function structure beneath three southern Africa seismic broadband stations, *Tectonophysics* 339: 443–454.

Owens, T. J., S. R. Taylor, and G. Zandt (1987). Crustal structure at regional seismic test network stations determined from inversion of broadband teleseismic P waveforms, *Bull. Seismol. Soc. Am.* 77: 631–662.

Pasyanos, M. E. and W. R. Walter (2002). Crust and upper-mantle structure of North Africa, Europe and the Middle East from inversion of surface waves, *Geophys. J. Int.*, 149: 463–481.

Pasyanos, M. E., W. R. Walter, M. P. Flanagan, P. Goldstein, and J. Bhattacharyya (2004). Building and testing an *a priori* geophysical model for western Eurasia and North Africa, *Pageoph.* 161: 235–281.

Pulliam, J. and M. K. Sen (2005). Assessing uncertainties in waveform modeling of the crust and upper mantle, in *Proceedings of the 27th Seismic Research Review: Ground-Based Nuclear Explosion Monitoring Technologies*, LA-UR-o5-6407, Vol. 1, pp. 152–160.

Sandvol, E., D. Seber, A. Calvert, and M. Barazangi (1998). Grid search modeling of receiver functions: Implications for crustal structure in the Middle East and North Africa, *J. Geophys. Res.* 103: 26,899–26,917.

Sen, M. K. and P. L. Stoffa (1995). *Global Optimization Methods in Geophysical Inversion*, Netherlands: Elsevier Science Publishing Company.

Sen, M. K. and P. L. Stoffa (1996). Bayesian inference, Gibbs' sampler and uncertainty estimation in geophysical inversion, *Geophys. Prospecting* 44: 313–350.

Tiberi, C., C. Ebinger, V. Ballu, G. Stuart, and B. Oluma (2005). Inverse models of gravity data from the Red Sea–Aden–East African rifts triple junction zone, *Geophys. J. Int.* 163: 775–787.

CRUSTAL AND UPPER-MANTLE *P*- AND *S*-VELOCITY STRUCTURE IN CENTRAL AND SOUTHERN ASIA FROM JOINT BODY- AND SURFACE-WAVE INVERSION

Delaine Reiter[1] and William Rodi[2]

Weston Geophysical Corporation[1] and Earth Resources Laboratory, Massachusetts Institute of Technology[2]

Sponsored by Air Force Research Laboratory

Contract No. FA8718-04-C-0027

ABSTRACT

Accurate travel-time predictions for regional seismic phases are essential for locating small seismic events with the accuracy needed for nuclear monitoring decisions. Travel times calculated through 3D Earth models have the best chance of achieving acceptable prediction errors, if the models are constrained by sufficient data. With this motivation, we have developed a joint body-wave/surface-wave inversion method to derive self-consistent 3D *P* and *S* velocity models for the crust and upper mantle. For body waves, our approach employs 3D finite-difference ray tracing to calculate first-arrival travel times through a 3D velocity model. Modeling of surface-wave dispersion is done using a two-step procedure. In the first step we apply 1D dispersion modeling to the velocity-depth profile at each point of a latitude/longitude grid to calculate phase- and group-velocity dispersion curves. The second step employs 2D finite-difference ray tracing to the resulting phase-velocity maps, period by period, and then integrates the group-velocity maps along the derived ray paths to obtain group delays. The use of 2D ray tracing accounts approximately for the non-great-circle propagation of surface waves in 3D Earth structures.

Our inversion approach follows these procedures in reverse. For surface waves, 2D tomography is applied to fit group-velocity maps to observed group delays along particular source-receiver paths, and then a 1D inversion technique is applied to the resulting group-velocity dispersion curve for each geographic grid point to determine an updated *S*-wave velocity-depth profile for the point. For body waves, 3D tomography is applied directly to the first-arrival travel-time residuals for observed source-receiver pairs to update the *P*-wave velocity model. An important element of our inversion approach, which serves to couple the body-wave and surface-wave problems more tightly and accommodate their differing spatial sensitivities to Earth structure, is the use of prior velocity constraints in each inversion step, determined from bounds on Poisson's ratio and the velocities themselves as a function of depth and tectonic regime.

To date, we have developed a basic version of our modeling and inversion procedures and have begun to apply them to a large region covering southern and central Asia, with the goal of determining crustal and upper-mantle structure to a depth of approximately 400 km. The surface-wave dispersion database includes group-velocity measurements provided by groups at the University of Colorado and Lawrence Livermore National Laboratory. Body-wave travel times are collected from the Engdahl, van der Hilst and Buland, EHB (1998) bulletin, screened to include first-arrival times for regional source-receiver distances and shallow event depths. Our initial model for the region is a hybrid of the CRUST2.0 3D model of crust and lid velocities (Bassin et al., 2000) and the global 1D AK135 model. In this paper we show results from the first exercise of our approach, in which we derive *P* and *S* velocity models independently from body and surface waves, respectively. This exercise allows us to determine whether the data sets and our assumed velocity and Poison's ratio constraints are all mutually consistent.

OBJECTIVES

The development and validation of accurate 3D velocity models of the crust and upper mantle for regions of nuclear monitoring interest remains a important goal for the Air Force Technical Applications Center (AFTAC). Systematic biases caused by inadequately modeled Earth structures cause errors in the estimation of geophysical parameters such as the travel times and amplitudes of regional seismic phases. More accurate and reliable estimates of these quantities (especially in aseismic regions) will improve nuclear monitoring efforts to detect, locate and discriminate regional events. Therefore, we have developed a joint 3D inversion technique that incorporates both compressional-wave travel times and Rayleigh-wave group velocity measurements to determine the full *P* and *S* velocity structure of the crust and upper mantle.

In this paper we report on the application of the first iteration of our inversion technique to data from the broad region shown in Figure 1. This region, extending from 10-50°N and 40-110°E, covers some of the most tectonically complex areas on Earth.

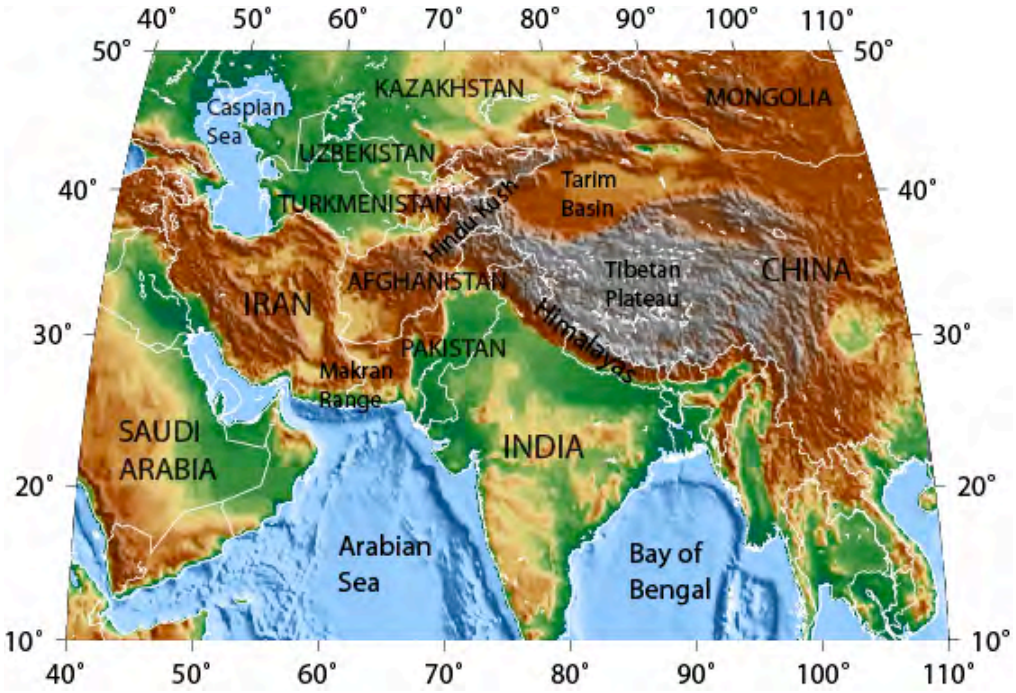


Figure 1. Topographic map of study region, which encompasses most of central and southern Asia, as well as portions of the Middle East.

RESEARCH ACCOMPLISHED

Joint Inversion Approach

The algorithms we are developing perform a joint, nonlinear inversion of body-wave travel times and surface-wave group delays to obtain fully 3D regional models of the crust and upper mantle. Problem nonlinearity is handled by iterating over linearized inversion steps, with the aid of finite-difference ray tracing techniques to perform the necessary forward modeling in the updated Earth model at each iteration step.

At each step of the iteration, we perform linearized body-wave and surface-wave inversion as separate procedures. The body-wave data, comprising only first-arrival *P*-wave times, are used to update the P velocity model (*Vp*). The surface-wave dispersion data are used to update the *S*-wave model (*Vs*), ignoring the small dependence of Rayleigh wave dispersion on P velocity. This sequential approach allows us to avoid some of the pitfalls associated with large simultaneous inverse problems. The separate inversions are coupled, however, through the prior information applied to the velocity functions.

The prior information used in each linearized inversion is of two types. First, we apply constraints on the size and spatial smoothness of velocity perturbations using a standard Tikhonov regularization approach (Tikhonov and Arsenin, 1977). The Tikhonov stabilizing functional in our case is based on a geo-statistical formulation whereby a prior variance and horizontal and vertical correlation distances are used in lieu of a simple regularization parameter (Rodi et al., 2005). The second form of prior information consists of upper and lower bounds on the *P* and *S* velocities, which are allowed to vary with depth and tectonic regime. The velocity bounds are determined in part from bounds on Poisson's ratio. Figure 2 illustrates this concept. The green six-sided admissible region in *Vp*-*Vs* space follows from constraints that might be appropriate for a point in the upper mantle: 7.7 <= *Vp* <= 8.4 km/s, 4.2 <= *Vs* <= 4.7 km/s, and Poisson's ratio (σ) between 0.25 and 0.30. If the current model velocities are 8.20 and 4.55 (black circle), the body-wave inversion would use the *Vp* bounds indicated by the horizontal line, while the surface-wave inversion would use the *Vs* bounds indicated by the vertical line. The Poisson's ratio constraints, in particular, couple the body-wave and surface-wave inversions in a way that ensures consistency between the *P* and *S* velocity models.

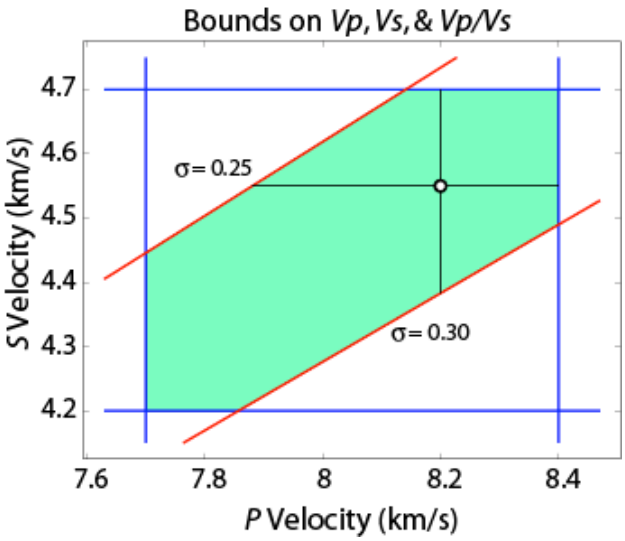


Figure 2. Illustration of the inversion bounds strategy for *Vp* and *Vs* for a sample point in the upper mantle. The upper and lower bounds on *Vp*, *Vs* and Poisson's ratio are allowed to vary with depth and tectonic regime.

To date, we have performed only the first step of the nonlinear iteration, using a 3D Earth model for the initial (reference) model. This paper presents the results of this first step and a preliminary analysis of the consistency between the body-wave and surface-wave data sets. This is an essential step toward the difficult goal of reconciling these disparate data sets, which constrain different aspects of the Earth's seismic structure.

In the next sections we present details on the travel-time and group-velocity dispersion data sets used in our inversion, followed by details and results of the inversion procedure.

Body-wave (Travel-Time) and Surface-Wave (Rayleigh Dispersion) Data Sets

Compressional-wave Travel-Time Database: The travel times we use in the *P*-wave tomography are taken from the EHB bulletin (Engdahl et al., 1998). We extracted arrivals from 1988-2004 having event and station locations within

0-60°N, 30-120°N and event depths between 0-200 km, including only first-arriving phases denoted *Pg*, *Pb* or *Pn* and which were defining phases for the EHB locations. To ensure small epicentral mislocations in the events, we required the secondary azimuth gap for a given event to be less than or equal to 130º (Bondár, Meyers, et al., 2004) and the number of teleseismic arrivals to be at least 15. The data set satisfying these criteria comprised 124,080 arrivals from 6,079 events and 735 stations.

We compressed this data set by forming summary events on a regular grid having 0.5-degree spacing in latitude and longitude and containing 13 nodes in depth between 0 and 200 km, with the depth spacing per node increasing from 5 to 20 km. For each summary-event node and each station/phase type, a summary travel-time residual (relative to the AK135 Earth model) was formed by averaging the individual residuals for the events near that node. Following this compression, stations containing fewer than 25 arrivals were dropped from the data set. The use of summary events acknowledges the redundant sensitivity of individual data to the Earth model (which is on a 1-degree grid) and, combined with the station-dropping rule, reduces the ray-tracing requirements for the inversion substantially.

The final database used in the body-wave tomography contained 76,355 arrivals for 2,998 summary events and 438 stations. The data spanned epicentral distances to 18.7 degrees, and the travel-time residuals (relative to AK135) ranged from -8.0 to 8.8 s with a root-mean-square (RMS) error of 2.5 s. The path coverage for the travel-time database is shown in Figure 2; it demonstrates that we have excellent coverage for nearly our entire study region, with the exception of the eastern tip of Saudi Arabia, where there is low seismicity and a paucity of station coverage.

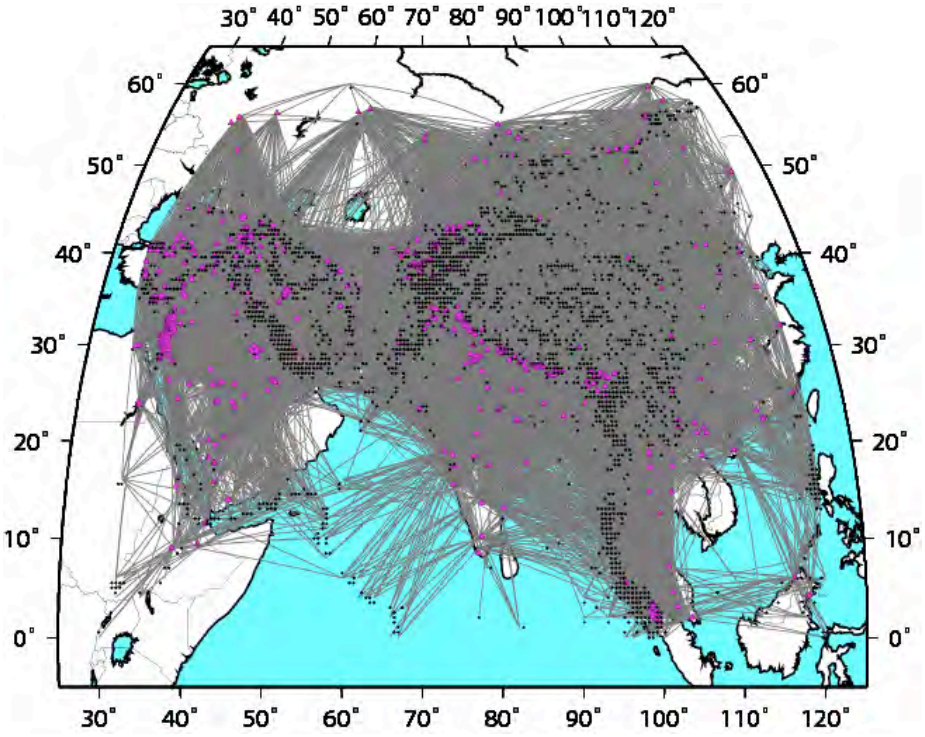


Figure 3. Path coverage for the summary-event *P*-wave travel-time data set, displayed with great-circle rays between event and station location. Purple triangles represent stations, and black dots are the summary-event locations.

Surface-wave Dispersion Database: The surface-wave dispersion database was collected from several sources, but primarily consists of measurements made by the University of Colorado at Boulder (CUB) group (Ritzwoller and Levshin, 1998) and the Lawrence Livermore National Laboratory (Pasyanos, pers. comm.). Some measurements in the region were also made by the Weston Geophysical internal group. To eliminate potential outliers in the data set, we performed a period-by-period grooming of the data, in which we retained a group velocity measurement if it was within two standard deviations of the mean group velocity for that period. This exercise resulted in a database of

61,200 fundamental-mode Rayleigh group velocity picks, for periods of T = 10-16, 18, 20, 25, 30, 35, 40, 50, 60, 70, 80, 90, 100, 120, 125 and 150 seconds. A depiction of the great-circle path coverage over our study region is shown in Figure 4. The 'footprint' or overall coverage of this data set is slightly smaller in geographical extent than that of the body-wave travel-time data set, which will become more apparent in the final inversion results. We plan to increase our group velocity data coverage to match that of the travel-time database for our final inversion runs.

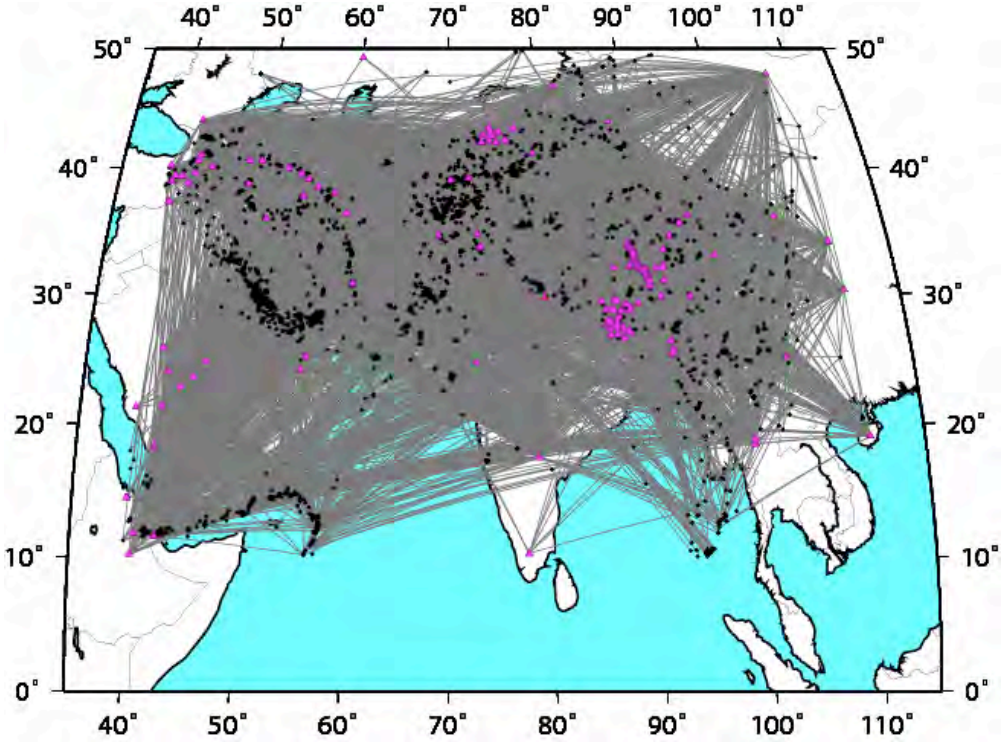


Figure 4. Path coverage for the surface-wave dispersion data set, depicted with great-circle rays between event and station locations. Purple triangles represent stations, and black dots are the event locations.

Initial Model

The initial Earth model we used for both the body-wave and surface-wave tomographies is a composite 3D model consisting of the CRUST2.0 model (Bassin et al., 2000) for the crust and the 1D AK1355 reference model (Kennett et al., 1995) for the mantle. The CRUST2.0 *Pn* velocities were ignored in favor of the AK135 velocities (*Vp* = 8.04 km/s, *Vs* = 4.48 km/s at the top of the mantle). However, the CRUST2.0 variable Moho depth was retained and accommodated by vertical compression or extension of the AK135 mantle thickness to a depth of 210 km.

A first attempt at deriving realistic velocity bounds was done as follows. First, we assigned nominal bounds for each layer of the crust based on the velocity values occurring in CRUST2.0, but not attempting to cover the entire variation in CRUST2.0 velocities. We set nominal bounds for depth-dependent mantle velocities to be the AK135 values plus or minus a fixed amount (±0.2, for *P* velocity, and ±0.1 for *S* velocity). Table 1 shows these nominal bounds, including ones chosen for specific Poisson's ratio. Second, we modified the nominal bounds on velocity to vary with the tectonic regimes assigned in CRUST2.0. Namely, the admissible range of velocities for a given regime was expanded to include (with an additional buffer) the highest and lowest values that occur (worldwide) in that regime. This exercise recognized only the major regimes identified in CRUST2.0 with leading letters A-Z (e.g., "Platform," "Archean," "Proterozoic," "extended crust"). The resulting bounds on velocity thus varied both geographically and with depth.

Table 1. Nominal bounds on velocities and Poisson's ratio (σ) for the inversion as a function of model unit.

Model Unit	*Vp* (km/s)	*Vs* (km/s)	Poisson's ratio (σ)
Upper Crust	5.8 – 6.2	3.2 – 3.5	0.23 – 0.34
Middle Crust	6.1 – 6.8	3.4 – 3.8	0.24 – 0.33
Lower Crust	6.7 – 7.2	3.7 – 4.1	0.25 – 0.32
Mantle (relative to AK135)	± 0.2	± 0.1	± 0.26 – 0.31

Travel-Time Tomography for the Compressional Velocity Model

The 3D tomography method developed for this project is an extension of the method developed by Reiter et al. (2005). Forward modeling of travel times in a 3D velocity model is done with the finite-difference method of Podvin and Lecomte (1991) as implemented by Lomax et al. (2001). We extended this software with algorithms for mapping Earth models in spherical coordinates to flat-Earth, Cartesian models, as needed by the P-L algorithm, and for generating the partial derivatives (sensitivities) of the calculated travel-times with respect to the velocity model parameters.

As noted above, each iteration of our joint inversion method performs linearized tomography, (i.e. with the travel-time sensitivities held fixed). The linearized problem is solved as a regularized least-squares problem, with the regularization functional serving to constrain the size and spatial smoothness of velocity perturbations in a geostatistical sense (see above). We invoke velocity bounds with the use of a parameter mapping technique; we solve directly for an unconstrained variable that is mapped onto a finite range of velocity values. This mapping technique changes the least-squares problem from a linear to a nonlinear one, even though the forward problem is linearized. We use a *nonlinear* conjugate gradients technique to obtain the solution.

The body-wave tomography results shown at the end of the paper were obtained with the following choices for smoothing parameters. The prior standard deviation of *Vp* was set to 2% of the reference model velocity. The correlation distances were 500 km and 100 km in the horizontal and vertical directions, respectively. The velocity was allowed to vary in the crust below the sediment layers of the CRUST2.0 model and to a depth of 410 km in the mantle. No smoothing was applied across the crustal interfaces (separating upper, middle and lower crust) or across the Moho discontinuity.

Surface-Wave Inversion for the Shear Velocity Model

Forward modeling and inversion of surface-wave dispersion are each performed as two-step procedures. The following sections describe each step of these procedures.

Forward Modeling of Group Delays. Our approach for modeling surface wave dispersion in a 3D Earth employs the same approximation used by Stevens and Adams (1999), Ritzwoller and Levshin (1998) and others, which states that the phase delay, or phase travel time, between an event and a station is obtained as an integral of the local phase velocity along a travel path. Our procedure, however, uses a minimum-time path through the phase-velocity structure instead of a great-circle path, as we now describe.

We calculate phase delays in a two-step process. The first step is to compute the dispersion response for each geographic grid point of the 3D Earth model, as determined by the 1D velocity/density profile defined for each point. We perform these dispersion calculations using software adapted from a set of modal summation codes (Herrmann, 2002). Implicit in the use of these codes is an "Earth-flattening" transformation that corrects for the Earth's sphericity.

Once we have completed the dispersion calculations over the geographic grid, we collate the output from these calculations at the frequencies of interest to produce a set of phase- and group-velocity maps. The next step in the dispersion forward-modeling process is the calculation of phase-delay (or "phase-time") maps from the phase-velocity maps, using the P-L ray tracer. Surface-wave path delays are typically found by integrating along the great circle connecting the source and receiver points (Woodhouse and Dziewonski, 1984), which is correct for a 1D

Earth model in which the local dispersion is the same at each latitude and longitude. However, lateral heterogeneities in the crust and upper mantle can cause both Rayleigh and Love waves to deviate laterally relative to the great-circle path. A better approximation to phase and group travel times is found by integrating the phase and group slownesses along the minimum-time path through the frequency-specific, 2D phase velocity map. We have adapted the P-L ray-tracing technique we use in body-wave modeling to additionally obtain phase and group delays for the source-receiver paths in our group-velocity database.

For the group delay, we integrate the group velocities along the minimum phase-time ray path. In the P-L method, a ray path is represented by the sensitivities of the phase travel time to the phase velocities of cells. We compute the cell sensitivities using the same algorithm that calculates sensitivities for body-wave travel times. The sensitivities of travel times to cell slownesses are computed using recursive back-propagation of node-to-node and node-to-cell dependencies from any given receiver point (event position) toward the source (station position). Consistent with the underlying ray theory, the resulting sensitivities are concentrated along a trajectory of cells connecting the source and receiver points, and this trajectory defines the P-L version of a ray path. For example, Figure 5 displays three examples of the ray-path sensitivities (out of more than 61,000 paths) found using our forward-modeling approach. In each subplot we show both the 2D sensitivities and the great-circle path between station and event at a particular period. The results demonstrate the significant off-path deviations that can occur, even at mid-range periods.

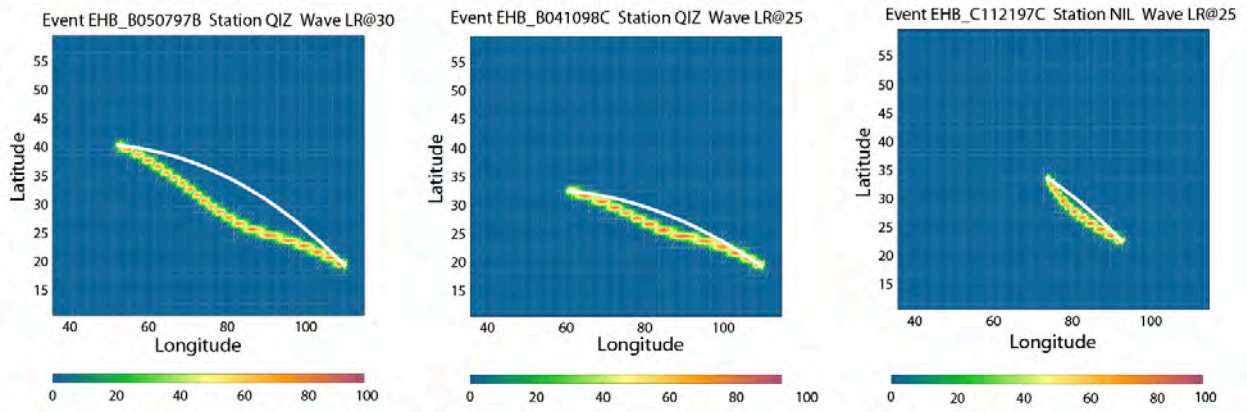


Figure 5. Examples of surface-wave ray-path sensitivities. White lines represent the great-circle path between the source and receiver for a particular period. Colored pixels show the sensitivities (or ray paths) derived by ray-tracing through a 2D phase-velocity map. Significant departures from great-circle-path travel can be seen, even for fairly short paths (right-hand subplot).

Group Velocity Tomography. To produce an updated set of group velocity maps that become the input to the 1D dispersion profile inversion, we employ the same tomography technique that is used to invert the body-wave travel times. The data are now observed group delays along particular source-receiver paths, for a set of frequencies, and the 3D model parameter is now group velocity as a function of latitude, longitude and period. The depth coordinate used in the body-wave tomography is replaced with logarithmic period, with an appropriate correlation "distance" assigned to accomplish some degree of smoothing over period (20% of the period in the results presented here). A departure from the body-wave tomography technique is that group velocity bounds were set to be two prior standard deviations from the reference model values. In other words, we did not derive the group-velocity bounds that are implied by the shear-velocity bounds for the Earth. In the results presented here, the prior standard deviation of group velocity was set to 3% of the initial model values, implying that the velocity bounds were 6% from the reference values.

A subset of the resulting group velocity maps is shown in Figure 6, for periods of 15, 25, 35, 40, 60 and 80 seconds. Comparison of our group velocity maps with those of other authors indicates good agreement on most long-wavelength features, with differences restricted to smaller-scale features and specific velocity variations.

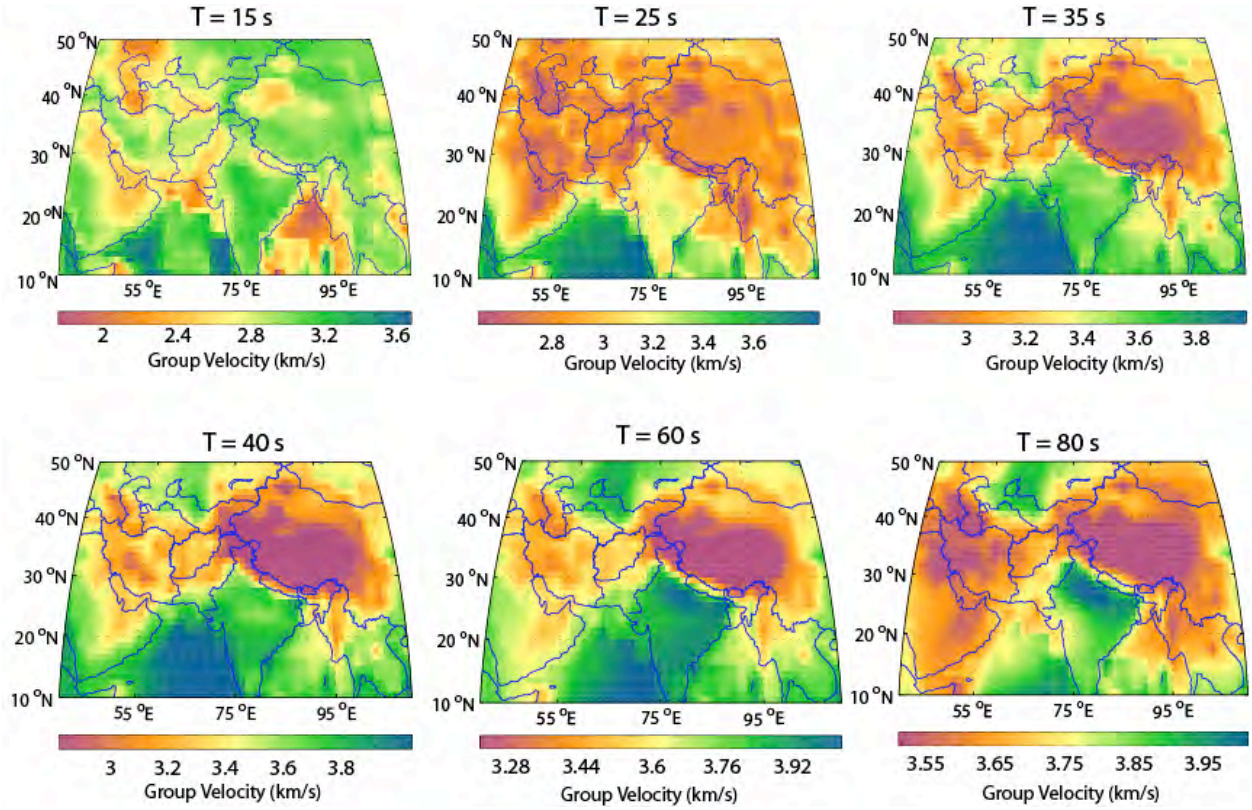


Figure 6. Results from the group velocity tomography at various periods. The results indicate strong correlation with tectonic features such as the Tibetan Plateau, Tarim Basin, continental India and the Arabian Peninsula. Note that the color maps are *not* normalized across all periods.

Dispersion Profile Inversion: Following the tomographic inversion of the group delays to retrieve a set of group velocity maps at a set of twenty-three discrete frequencies, we invert individual dispersion curves as a function of period collected from the set of group velocity maps. The result is an *S*-velocity profile as a function of depth at a single latitude and longitude point. We solve this inversion problem by minimizing a Tikhonov-regularized objective function with a bounded-value least-squares (BVLS) code (Stark and Parker, 1995). We impose upper and lower velocity bounds on the inversion, using the values described previously. We can also restrict the model to allow changes in certain 'depth zones', depending on the confidence we have in the resolving power of our data. As in the body-wave tomography, we allowed changes to the velocity model for layers in the upper, middle and lower crust, and in the upper mantle to a depth of 410 km.

Joint Inversion Results: Iteration 1

In Figure 7 we show our *Vp* and *Vs* model after completing one iteration of our joint inversion technique. Each row in the figure displays a single layer or depth horizon from the geographic model over the study region. In the top row we show the *Vp*, *Vs* and depth of the model at the top of the lower crust unit. The depth at the top of this unit varies from 8 – 40 km depth. The middle row shows the inversion results from the uppermost mantle node, corresponding to what many researchers denote the 'lid' velocity. In the bottom row of the plot, we show the velocities from a level in the model that varies from 150-174 km depth. It is interesting to note both the correlated and anti-correlated features of this model, some of which are seemingly counter-intuitive. However, without mapping the inverted *Vs* model to a prior model for the *Vp* tomography, perhaps by using a Poisson's ratio half-way between the bounds, it is difficult to determine if the models are self-consistent. These post-inversion analyses are some of the next steps to be performed before we begin to iterate the inversion.

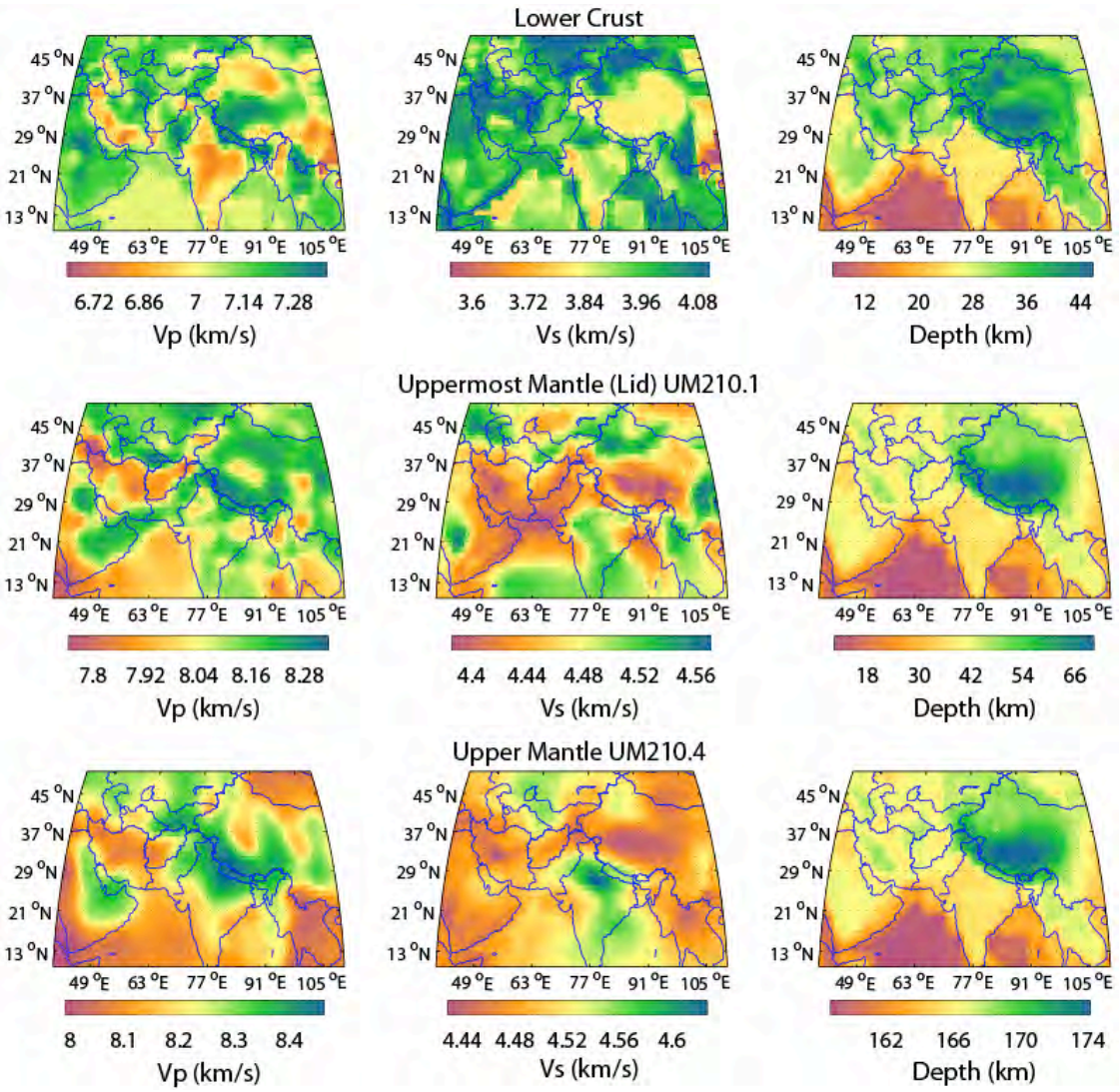


Figure 7. Compressional and shear-velocity results from the first iteration of the joint inversion method. Each row displays a nodal map of *Vp, Vs* and depth from the inversion model. The top row displays the result from the lower crust; middle row shows the map from the uppermost-mantle (i.e. the lid velocity); and the bottom row shows upper-mantle velocities at 150-174 km depth.

CONCLUSIONS AND RECOMMENDATIONS

In this paper we presented the basic components of our nonlinear 3D inversion algorithm, which have applied in a first-iteration step. The results appear reasonable in relation to other available models (for example, the CUB model of Ritzwoller et al. [2002]) and the known tectonics of the region. While our *Vp* and *Vs* models show some similarity, we must still evaluate the consistency of our data sets and prior velocity constraints, since we did attempt to correlate the *Vp* and *Vs* models. As we proceed to further inversion iterations, we will address these and other questions. For example, we do not know the effects of nonlinearity; that is, how strongly the ray paths will change after re-tracing them in the new model. Another factor in the nonlinearity is the potential need to relocate the earthquakes in the travel-time tomography. These issues, among others, will be addressed prior to completion of the inversion model.

Once we have developed a final model, we will validate it by relocating a ground-truth (GT) database of explosions and shallow earthquakes in the region (Bondár, Engdahl, et al., 2004) and comparing the travel-time predictions for the arrivals in the database. In addition, we will perform full-waveform modeling for paths of interest in the region to determine the goodness-of-fit for both the body and surface waves to our new joint compressional and shear-wave velocity model.

ACKNOWLEDGEMENTS

We gratefully acknowledge the contribution of the surface-wave dispersion data sets provided by the CUB and LLNL groups. Some of the figures in the paper were created using the Generic Mapping Tools (Wessel and Smith, 1991; 1995).

REFERENCES

Bassin, C., G. Laske and G. Masters (2000). The Current Limits of Resolution for Surface Wave Tomography in North America, *EOS Trans AGU*, 81, F897.

Bondár, I., E. R. Engdahl, X. Yang, H. A. A. Ghalib, A. Hofstetter, V. Kirichenko, R. Wagner, I. Gupta, G. Ekström, E. Bergman, H. Israelsson and K. McLaughlin (2004). Collection of a reference event set for regional and teleseismic location calibration, *Bull. Seism. Soc. Amer.*, 94, 1528-1545.

Bondár, I., S. C. Myers, E. R. Engdahl, and E. A. Bergman (2004). Epicentre accuracy based on seismic network criteria, *Geophys. J. Int'l*., 156, 483-496.

Engdahl E. R., R. van der Hilst, and R. Buland (1998). Global teleseismic earthquake relocation with improved travel times and procedures for depth determination, *Bull. Seism. Soc. Amer.*, 88, 722-743.

Herrmann, R. B. (2002), *Computer Programs in Seismology*, Version 3.20, St. Louis University.

Kennett, B. L. N., and E. R. Engdahl (1991). Travel times for global earthquake location and phase identification, *Geophys. J. Int*., 105, 429-465.

Kennett, B. L .N. Engdahl, E. R., and Buland R. (1995). Constraints on seismic velocities in the Earth from travel times, *Geophys. J. Int'l.*, 122, 108-124.

Lomax, A., A. Zollo, P. Capuano, and J. Virieux (2001). Precise, absoute earthquake location under Somma-Vesuvius volcano using a new 3D velocity model, *Geophys. J. Int'l.*, 146**,** 313-331.

Podvin, P., and I. Lecomte (1991). Finite difference computation of travel times in very contrasted velocity models: a massively parallel approach and its associated tools, *Geophys. J. Int.*, 105, 271-284.

Reiter, D., W. Rodi, and M. Johnson (2005). Development of a tomographic upper-mantle velocity model beneath Pakistan and northern India for improved regional seismic event location, *Bull. Seis. Soc. Amer*., 95, 926-940.

Ritzwoller, M. H., and A. L. Levshin (1998). Eurasian surface wave tomography: Group velocities, *J. Geophys. Res*., 103, B3, 4839-4878.

Ritzwoller, M. H., N. M. Shapiro, M. P. Barmin and A. L. Levshin (2002). Global surface wave diffraction tomography, *J. Geophys. Res*., 107**,** doi: 10.1029/2002JB001777.

Rodi, W., C. A. Schultz, G. Johannessen, and S. C. Myers (2005). Grid-search location methods for ground-truth collection from local and regional seismic networks, *Final Technical Report* to National Nuclear Security Administration, Dept. of Energy, Contract Nos. DE-FC03-01SF22397 and W-7405-ENG-48.

Stark, P. B. and R. L. Parker (1995). Bounded-variable least-squares: an algorithm and applications, *Comput. Stat.*, 10, 129-141.

Stevens, J. L., and D. A. Adams (1999). Improved surface wave detection and measurement using phase-matched filtering and improved regionalized models, in the *Proceedings of the 21st Annual Seismic Research Symposium*, Las Vegas, NV, 274-282.

Tikhonov, A. N., and V. Y. Arsenin (1977). *Solutions of Ill-Posed Problems*, Winston & Sons, Washington, DC.

Wessel, P., and W. H. F. Smith (1991). Free software helps map and display data, *Eos Trans. AGU*, 72, 441, 445-446.

Wessel, P., and W. H. F. Smith (1995). New version of the Generic Mapping Tools released, *Eos Trans. AGU*, 76, 329.

Woodhouse, J. H., and A. M. Dziewonski (1984). Mapping the upper mantle: three-dimensional modeling of Earth structure by inversion of seismic waveforms, *J. Geophys. Res*., 89, 5953-5986.

IMPROVED INTERMEDIATE-DISTANCE PHASE CHARACTERIZATION IN CENTRAL ASIA

Delaine Reiter, Aaron Ferris, and Michelle Johnson

Weston Geophysical Corporation

Sponsored by Air Force Research Laboratory

Contract No. FA8718-06-C-0002

ABSTRACT

Accurate knowledge of waveform characteristics observed at far-regional and near-teleseismic distances is critically important for regions in which arrays are sparsely located. Significant body-wave phase complexities that are observed at distances between 13-30°. These complexities produce uncertainties in phase identification and errors in phase arrival-time estimation. Our research project focuses on two principal tasks designed to improve the identification and characterization of body-wave phases observed at intermediate distances in Central Asia.

In the first task we are investigating array-processing techniques to improve estimates of phase arrival times, amplitudes, slownesses and back azimuths from events at intermediate distances. At epicentral distances of 13-30° seismic waves interact with upper mantle discontinuities, and multiple body-wave arrivals often occur over 4-20 second time windows on the seismogram. To enhance and distinguish between these multiple arrivals of similar frequency content, we are investigating the capabilities of vespagram, semblance-stacking, MUltiple Signal Classification (MUSIC) and cross-correlation techniques. We are extensively testing and validating these algorithms to determine the optimum detection and identification procedures to use on observed data. Our primary data sources are the Kazakhstan regional arrays in Makanchi (MKAR) and Karatau (KKAR).

In our second task we have begun a study of the seismic velocity and discontinuity structure beneath Central Asia. Accounting for known seismic heterogeneity will allow us to more accurately predict the travel-time characteristics of intermediate-distance body-wave phases, which in turn will help us to distinguish between poor phase identification and path-related behavior at these distances. We are collecting and reconciling previously published receiver-function models for stations in our study area. We plan to append several of the available global upper-mantle models to the base of these receiver functions and use the resulting 1-D velocity models in full-waveform synthetic studies.

OBJECTIVES

This project is focused on improving body-wave seismic phase characterization at far-regional and near-teleseismic distances. At distances of approximately 1500-2800 km from a seismic event, propagation complexities arise that cause significant difficulties in the interpretation of seismograms. At these distances seismic waves sample upper-mantle low-velocity zones (LVZ) and discontinuities at approximately 410 and 660 km depth. This interaction results in triplications and interference phenomena in wave propagation, which consequently produce uncertainties and errors in bulletin phase picks. We demonstrate this phenomenon in Figure 1a, in which we plotted *Pn/P* travel-time residuals as a function of epicentral distance. To generate this figure, we retrieved the International Seismological Centre (ISC) bulletins for the years 1999-2001 from the Flinn-Engdahl Seismic Regions 26-30, 47 and 48 (see http://neic.usgs.gov/neis/epic/fer.html), which include most of Asia and areas of the Middle East. We filtered this data set to include all events with ISC depths less than 40 km that were located by more than 25 stations. In Figure 1a, we plotted the residuals (gray dots) with respect to the IASPEI91 global 1D model (Kennett and Engdahl, 1991) for associated, first-arriving *P*-wave picks between 10-30°. Then we calculated the density (number) of residual picks in boxes of 0.5° by 0.5 seconds and superposed a smoothed version of the resulting image over the individual picks. The two dashed black lines show the travel-time differences between branches *C'B'- A'B'* and *CB - AB* in Figure 1b, which depicts the *iasp91* travel-time curves for upper-mantle arrivals.

Figure 1a clearly shows a high-density region of travel-time residuals that are associated with the 410-km phase triplication (occurring at 14-18° epicentral distance). There is also considerable structure to the residuals in the regional to far-regional range, revealed by the negative bias of residuals at distances between 10-17°. While this particular data set does not reveal an increase in phase residuals associated with the 660-km discontinuity (i.e., the *CB* travel-time branch), we have observed such an effect for other time ranges and in other bulletins (e.g., the National Earthquake Information Center [NEIC]). This type of residual behavior as a function of epicentral distance is also present in the phase picks used to locate events at the ISC (i.e., the time-defining phases), but other agencies restrict their location travel-time picks more aggressively, making the phenomenon shown in Figure 1a less apparent.

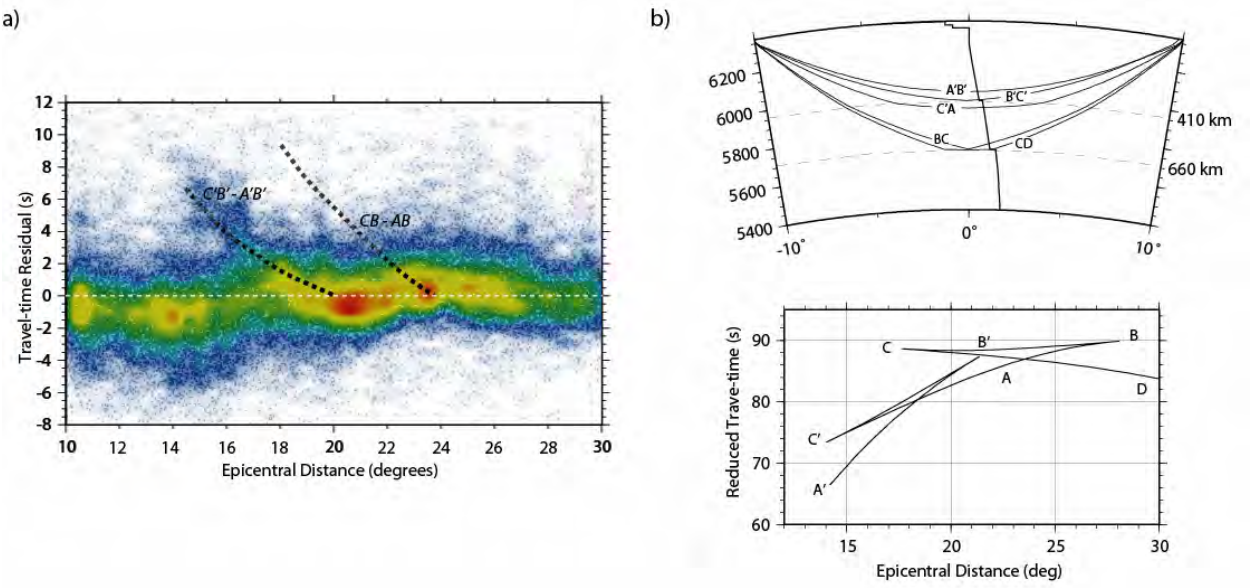


Figure 1: a) Associated *P/Pn* phase residuals (with respect to the global 1D *iasp91* model) from ISC bulletins in Asia (1999-2001) as a function of epicentral distance. Heavy black dashed lines show the travel-time difference between secondary and primary upper-mantle phase branches of the *iasp91* travel-time curves. b) Ray-path illustrations (top) and reduced travel times (bottom) for phases that sample upper-mantle discontinuities at 410 and 660 km depths. The two predominant triplication effects from this set of arrivals occur at distances between approximately 14-18° and 20-24°.

The variation of the residuals shown in Figure 1 illustrates the fundamental question we wish to address in our research project: What are the causes of heterogeneous behavior in travel-time residuals at the distance range between 13-30°? There are likely to be two primary causes for the residuals shown in Figure 1: 1) phase misidentification and 2) unaccounted-for crustal and upper-mantle heterogeneity. In our study, we are quantitatively examining the causes of phase residuals and uncertainties at these distances, trying to determine whether they might be due either to poor phase identification or upper-mantle heterogeneity (or both). Our goal is to ensure that the techniques and results developed will be directly applicable to the regional monitoring problem.

Thus, our research objectives focus on 1) array-processing techniques capable of distinguishing between closely-spaced arrivals; and 2) studies of upper-mantle heterogeneity between 150-700 km depths at intermediate distances from arrays and stations in Central Asia. The results of these studies will produce a methodology to characterize body-wave phases in Central Asia observed at intermediate distances using small-aperture arrays. Our deliverables will also include 'templates' of typical events and associated phase behavior, supported by accurate velocity models, in specific regions such as Iran, Turkmenistan, Pakistan, northern India, and western China.

RESEARCH ACCOMPLISHED

The objective of our research project is a better understanding of the behavior of primary and secondary body-wave arrivals at distances between 13-30°, which will lead to more accurate location and discrimination efforts, particularly for small events. Therefore, we are studying ways to improve the identification and characterization of phases at intermediate distances observed in Central Asia. We believe that a study of this type will help to reduce the uncertainties currently associated with phases observed at these distances.

To address the phase misidentification problem, we are developing array-based methods that can differentiate between closely-spaced arrivals in the seismogram. The use of arrays has the potential to reduce phase misidentification, primarily because of the greater confidence in the phase analysis that multiple recordings of a very similar wavefield provide. Array methods allow seismologists to resolve subsurface features at a finer scale and examine waveform features in great detail with more confidence. However, there is a significant complication with array observations at intermediate distances, in that the small aperture of current regional arrays is poorly designed to resolve small slowness variations in the early *P*-wave coda. Our research will address this complication through the development and adaptation of array methods to our specific problem.

To address the problem of seismic velocity heterogeneities as they pertain to understanding phase arrivals at intermediate epicentral distances, we have begun a study of the crust and upper-mantle velocity (and discontinuity) structure in the regions surrounding the MKAR and KKAR regional arrays in Kazakhstan. There is an extensive body of previous research on tectonic and seismic structure in the broad region surrounding Kazakhstan that we can draw upon, but we will augment the previous research by closely examining the velocity structure in the mantle from ~400-700 km depths and the seismic phases that sample that structure.

We are applying the array techniques we develop to data from Central Asia. For the current project, we will concentrate on the available data from the small-aperture arrays in MKAR and KKAR, which have been reporting since 2002 and early 2003 for MKAR and KKAR, respectively. Figure 2 shows the location of the MKAR and KKAR arrays as well as the abundant seismicity (from the 1973-2004 NEIC bulletins) at distances between 13-30° from each array. The pink and blue annular regions surrounding each array are simple cartoons of the surface region where intermediate-distance phases bottom before arriving at MKAR or KKAR.

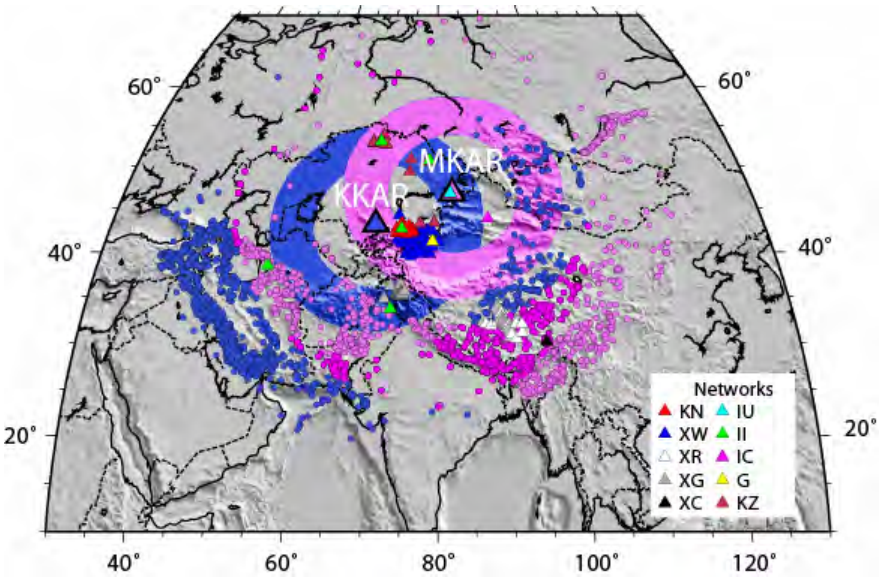


Figure 2. Map of the study region and US AEDS arrays (MKAR and KKAR) in Central Asia. Earthquakes at intermediate distances from the arrays (from the 1973-2004 NEIC bulletins) are plotted, with annular regions showing the surface expressions of upper-mantle transition zones sampled by the earthquakes. Also plotted are the open networks and stations in the region (available from the Incorporated Research Institutions for Seismology [IRIS]).

MKAR/KKAR Earthquake Database

To provide a test bed for our analysis techniques, we are collecting data from moderate-sized events observed at the MKAR and KKAR arrays. We populate the database with events that are well located teleseismically and have Harvard Centroid Moment Tensor (CMT) solutions (Dziewonski et al., 1981) associated with them. To date we have collected waveforms for 198 earthquakes appearing in the EHB (Engdahl et al., 1998) bulletin, comprised of 83 KKAR and 115 MKAR recordings. Figure 3 shows the event locations of our current earthquake database. We note that all of the events currently in the data set were observed at distances between 14-18° from at least one of the arrays, since we intend to focus our initial studies on the 410-km mantle discontinuity.

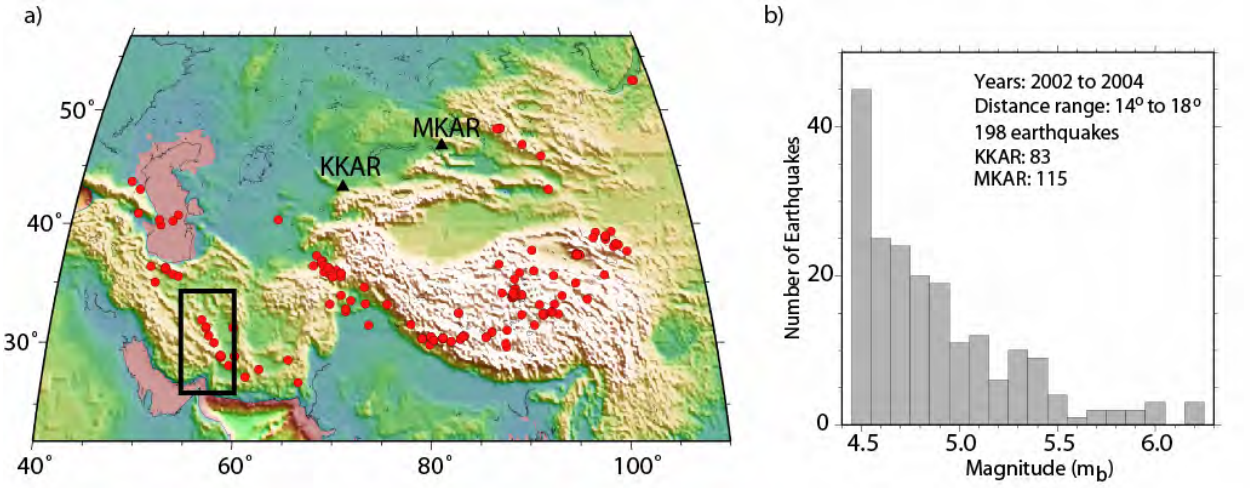


Figure 3. a) Distribution of our current test-bed database of earthquakes at intermediate distances from MKAR and/or KKAR. b) Histogram showing the magnitude distribution of the database (all events have Harvard CMTs associated with them).

To illustrate the waveform variability we see in our data set, Figure 4 displays a record section from several southern Iran earthquakes (m_b ~ 4.5-6.0) recorded at the KKAR array. The black box in Figure 3 outlines the location of the events shown in Figure 4. Each vertical-component waveform in Figure 4 is aligned on the analyst-picked *P* arrival and filtered between 0.1 – 1.75 Hz. We note that most of the *P* arrivals are emergent, and while there are indications of similarities in the secondary arrivals, the waveforms do not reveal any strong overlapping characteristics. Since these events are observed at KKAR inside a small epicentral and azimuthal range, it will be necessary to extract considerable information about the sources, path structure, and event locations in order to make some conclusions about the body-wave phases seen at the arrays and nearby broadband stations.

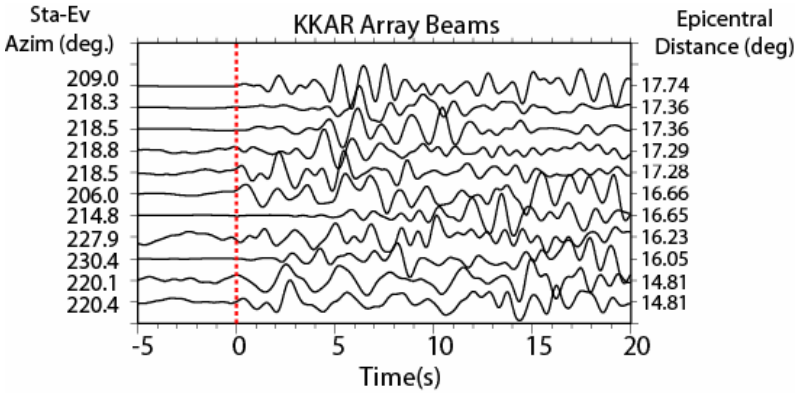


Figure 4. Waveform section showing the KKAR array beams from earthquakes inside the orange box in Figure 3a. All waveforms have been aligned on their direct *P*-wave arrival time from the EHB bulletin. Note that even though the events are arriving from a tight back azimuth and epicentral distance range at KKAR, they exhibit significant variation in their initial arrivals.

Array-Processing Techniques for Improved Intermediate-Distance Phase Characterization

To improve phase characterization at far-regional and near-teleseismic distances, we will need analysis techniques that can separate closely-spaced arrivals related to transition-zone discontinuities. We are examining the capabilities of array-based techniques such as vespagram, improved frequency-wavenumber (*f-k*), and cross-correlation, all of which can produce accurate estimates of phase travel times, azimuths, and slownesses.

For example, there are many classical and recently improved *f-k* techniques available from the technical literature. We are developing a version of the MUSIC estimator (Schisselé et al., 2004), which utilizes a continuous wavelet transform (CWT) to help identify the time windows in which coherent phases exist. Once the user has defined this window, the MUSIC estimate returns estimates of the propagation characteristics of the analyzed phase.

Another analysis technique that may hold promise for triplicated phase arrivals is a modification of a traditional vespagram (the velocity spectral method, also known as the 'slant-stack' method). Vespagrams display seismic signals recorded at an array in terms of the energy content of the incoming signal as a function of the slowness (Davies *et al.*, 1971). Vespagram analysis is used in diverse applications, including mapping transition-zone discontinuities in the Pacific using precursors to *PP* (Rost and Weber, 2002) and processing small events from mines in northwestern Russia (Gibbons and Kvaerna, 2002). In traditional vespagram analysis, the energy in the array data is displayed as a function of horizontal slownesses and back azimuth. However, the linear vespagram cannot always resolve arrivals that have very similar slownesses. To address this, the n^{th} -root vespagram (Muirhead and Datt, 1976) takes the n^{th}-root (n=2,3,4,…) of the amplitudes of all array traces prior to performing the slant-stack or vespagram calculation.

To illustrate the methods described above, we analyzed an event in Tibet that was observed at the MKAR and KKAR arrays. Figure 5a shows the location of the Kazakhstan arrays, as well as the Harvard CMT solution for the event, which occurred at the edge of the Tibetan Plateau (Qinghai, China). In Figure 5b we display the 1D *P* and *S* velocity model we used to predict P-wave travel times using the Tau-P Toolkit (Crotwell et al., 1999). This velocity model is a composite profile derived from the CRUST2.0 model (Bassin et al., 2000) and the IASPEI91 1D

reference model (Kennett and Engdahl, 1991) mid-way between the arrays and the event. Figure 5c shows the first 20-40 seconds of unfiltered short-period data from the nine-element MKAR and KKAR arrays, which observed the event at distances of 14.11° and 20.54°, respectively. Table 1 provides event location and magnitude information extracted from several seismic bulletins.

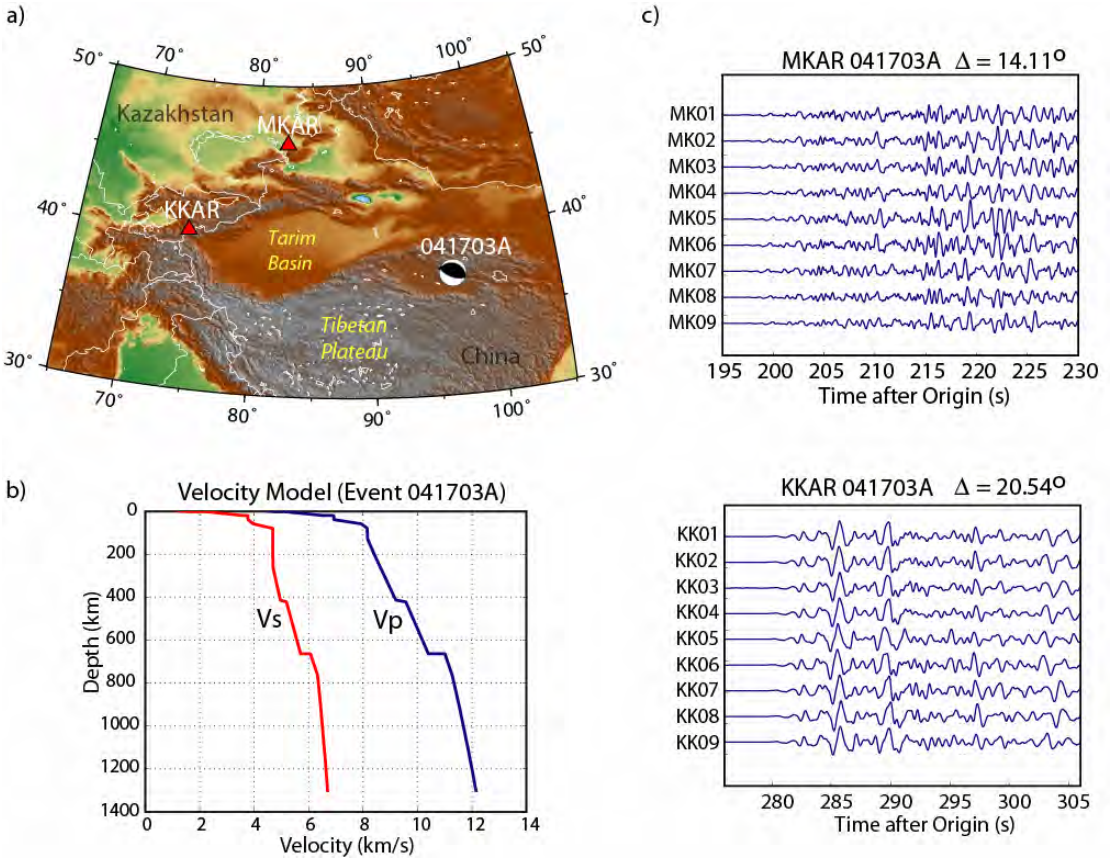


Figure 4. Event in Tibet (EVID 041703) used to illustrate analysis techniques. a) Regional map including event and array locations and the published Harvard CMT solution; b) 1D velocity model used to predict the travel times of triplicated *P* phases; and c) MKAR and KKAR array gathers recorded for the event.

Table 1. Location and magnitude information from several agencies for the Tibetan event shown in Figure 5.

Event 041703 Origin Parameters					
Agency	**Origin Time**	**Latitude**	**Longitude**	**Depth (km)**	**Magnitude**
IDC	00:48:38.09	37.52	96.67	0.0f	5.7 (mb)
NEIC	00:48:38.58	37.53	96.48	14.0f	6.4 (MW)
HRVD	00:48:46.30	37.53	96.45	16.0	6.2 (mb)
ISC	00:48:38.63	37.52	96.51	15.0f	6.2 (mb)

Figure 6 shows results from applying both MUSIC and vespagram analysis to the KKAR recordings of Event 041703. In Figure 6a, we show the 1st-root (i.e., classic slant-stack) vespagram of the unfiltered array data beneath the KKAR array beam. In both figures, the array beam was calculated using the predicted *P*-slowness from the IASPEI9*1* model (Kennett and Engdahl, 1991) and the back azimuth from the ISC event location. The results clearly illustrate the difficulties in resolving the phase arrival velocity at small-aperture arrays with the classic vespagram

method. To confidently identify the different triplicated *P* arrivals from the upper mantle, we need phase velocity resolution on the order of ~0.5 km/s.

In Figure 6b, we show the results from applying the MUSIC estimator to arrival P2 shown in the top subplot of the array beam. The results indicate that the MUSIC technique estimates a well-constrained phase velocity that corresponds to the *P660* arrival time predicted by the IASPEI91 model. From these initial results, we can see that the MUSIC estimator shows promise; however, the classic vespagram method requires further enhancement.

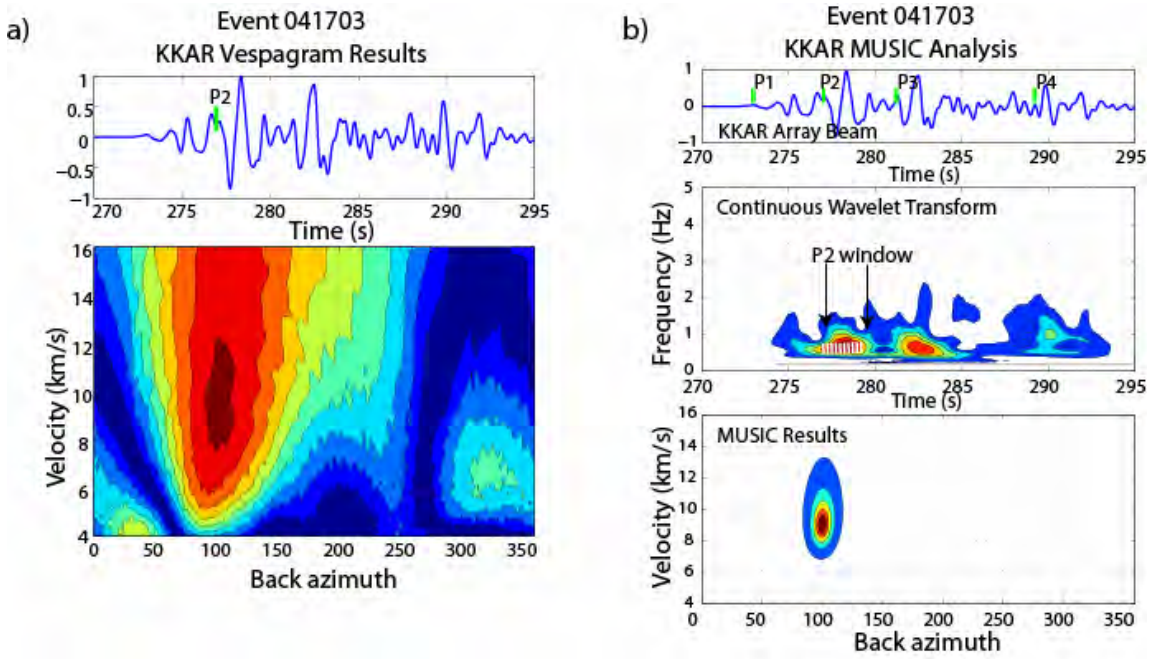


Figure 5. a) KKAR array beam for Event 041703 (top) and single-root (or classical slant-stack) vespagram analysis (bottom) applied to large-amplitude arrival P2; b) KKAR array beam (top), continuous wavelet transform (middle) and MUSIC estimator (bottom) applied to the P2 window outlined in white in the wavelet transform subplot. The results show that the classical vespagram technique does not have the slowness resolving power of the MUSIC estimation technique.

To address the deficiency in the classical vespagram analysis, we are developing modifications that can be used to better quantify the wave propagation characteristics. For example, Figure 7 shows the 4th-root vespagram analysis for a 4-second window that includes 2 seconds of the initial *P* phase at the KKAR array (Figure 7a). Even though we applied the 4th-root vespa process, the phase-velocity is still not well-resolved. In this case, the vespa process incorrectly estimates a phase velocity of 32.5 km/s for this arrival (shown as the orange dot in Figure 7b), whereas the theoretical phase velocity is 10.2 km/s. This lack of slowness resolution is an inherent obstacle in analyzing events at intermediate distances using small-aperture arrays and classical methods. However, an examination of the gradient of the vespa amplitude versus phase velocity shows a maximum gradient change at 9.7 km/s. This is remarkably near the theoretical phase velocity of 10.2 km/s (Figure 6c). This preliminary observation suggests that an enhanced vespagram method, which takes into account the gradient of the vespa amplitude, might be able to increase the slowness resolution of arrivals from intermediate-distance events.

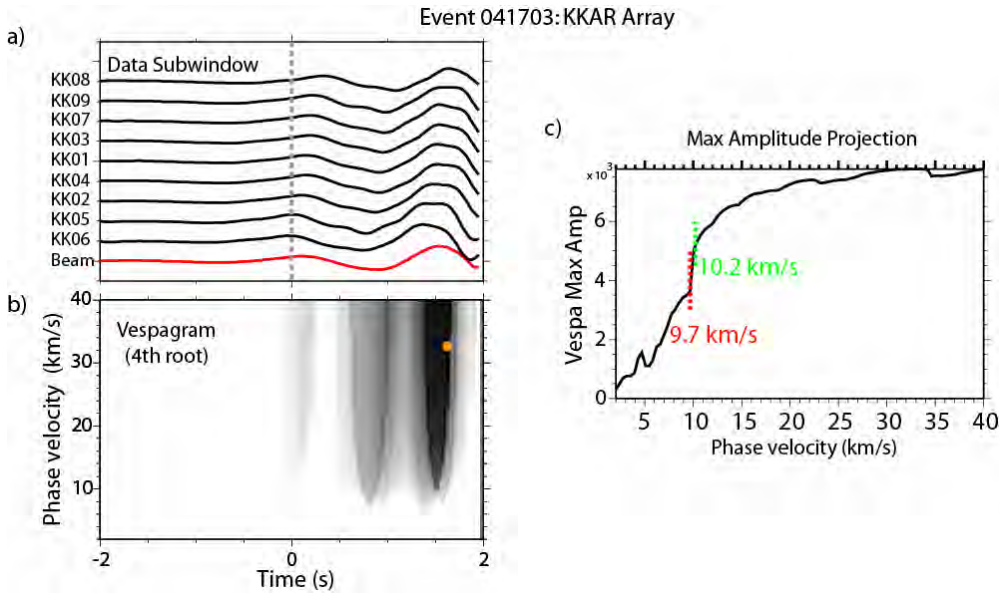


Figure 6. a) Sub-windowed KKAR data from the initial *P*-wave phases. The *P* arrival at the closest station is aligned to zero-offset (dashed line), and the best beam resulting from the vespa analysis is shown in red. b) Vespagram (4th-root) of the signals shown in (a). Gray scale represents the beam power for different stacking velocities. The orange dot marks the phase velocity that produces the best beam (red waveform in a). c) A projection of the vespa image along ~1.6 sec showing the variation of vespa amplitude to phase velocity. The green dashed line marks the theoretical *P*-wave phase velocity, and red dashed line marks the maximum gradient in slope along the projection.

Upper-Mantle Structure Studies Using Full-Waveform Modeling

There are abundant sources of data in central Asia for the study of phase characterization through waveform modeling. In China and northern India, there have been many experiments and resulting studies of the tectonics and seismic velocity structure. A few of the relevant experiments include the INDEPTH experiment (International Deep Profiling of Tibet and Himalaya; 52 seismographs deployed across central Tibet; Zhao et al., 1993), and experiments in Nepal/Tibet (Schulte-Pelkum et al., 2005) and Pakistan (Meltzer et al., 1996).

In countries of the Former Soviet Union, temporary experiments around the Caspian Sea and permanent regional networks such as KNET in the Tien Shan of Kyrgystan have produced data and regional velocity models to describe wave propagation (e.g., Ghose et al., 1998; Martynov et al., 2004). There are also several in-country networks (for example, in Turkmenistan and Uzbekistan) that provide their data to IRIS; the data from these networks could be used to provide important constraints on the seismic velocity structure in the surrounding regions.

We are compiling pre-existing information on the lithospheric and upper-mantle structure in our study region that has a direct bearing on the phase characterization from events at intermediate epicentral distances. This includes information regarding crust and upper-mantle velocity structure, such as the sub-vertical velocity high below Tibet that may document the down-welling of the Indian mantle lithosphere beneath Tibet (Tilmann et al., 2003), as well as the 20-km topographic change in the 410-km discontinuity across the Kazakh shield and the Tien Shan. Incorporating information such as in these two examples will be crucial in understanding the effects of mantle heterogeneity on phase arrivals from intermediate-distance events.

Many receiver function (RF) studies have been performed in our region, for stations in Iran (Hatzfeld et al., 2003), northeastern India and Tibet (Mitra et al., 2005), and the Tien Shan in Kyrghystan (Bump and Sheehan, 1998; Oreshin et al., 2002), among many others. RF analysis is used to determine the crust and upper mantle structure immediately beneath three-component broadband stations. The resulting velocity structure is based on modeling the amplitudes of *P* to *S* conversions and their reverberations in teleseismic *P*-wave coda, following deconvolution of the vertical component from the radial and transverse components of broadband data. We are concentrating on RF

models, because information about the discontinuity structure provided by these models may prove to be more useful in phase characterization than models from tomographic studies. We have gathered the available literature detailing RF-based models from previous studies. Figure 7 shows the RF station coverage we have discovered to date in the literature; we have started to compile these models and compare them to the other regional velocity models that are available for the crust and upper mantle. Following this exercise we will supplement our collection of RF models wherever we have gaps in our coverage, using available data from stations within the circular regions shown in Figure 2.

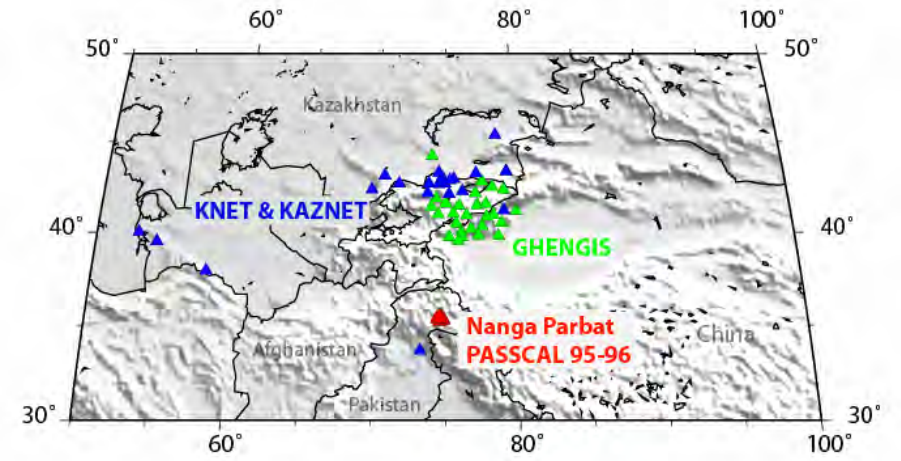


Figure 7. The stations (triangles) indicate locations where a receiver-function model in our study region has been published in the seismological literature. We are collecting the models for the purpose of full-waveform modeling to improve phase characterization of the early portion of the *P* waveform at intermediate distances.

As have other researchers (Rodgers and Schwartz, 1998; Leborgne et al., 1999), we will initially focus on developing representative 1D models for paths of interests. We will not create new models of the transition-zone structure, since other researchers have published in-depth studies of the mantle transition zones in our region. We will instead derive models of the transition zone from published 1D and 3D mantle models. These mantle models will be appended to the high-resolution crust and uppermost mantle RF models to create path-appropriate composite 1D models, and the results used for synthetic waveform generation.

We will generate waveform synthetics using the 1D reflectivity (Kennett, 1988) method. Our primary goal will be to explain the phase travel-time behavior observed at the MKAR and KKAR arrays. It is likely that, rather than modeling random events, we will collect and identify 'templates' of typical events and associated phase behavior, supported by accurate velocity models, in specific regions such as southern Iran, Turkmenistan, Pakistan, northern India, and western China.

CONCLUSIONS AND RECOMMENDATIONS

Our study of intermediate-distance phase characterization will accomplish two important nuclear monitoring objectives. First, we are developing and testing array-based techniques that will improve the identification of closely-spaced phases observed at intermediate epicentral distances. So far, no comprehensive array-based approach has been attempted (by either the national laboratories or the external research community) to resolve the difficult problem of identifying seismic phases in this important distance range. These techniques will be a strong contribution from the project that could be applied to other array data and monitoring applications.

We are also developing information and associated results on transition-zone velocity and discontinuity structure in Central Asia. This information will distill and augment the results from previous and ongoing tectonic studies of the region. While many studies have focused on crust and mantle structure for the upper 200 km in central Asia, we will perform full-waveform modeling using composite models that include additional transition-zone structure at depths between 400-700 km. It is this deeper structure (in conjunction with accurate models between the surface and ~250

km) that has the strongest effect on the succession of phases observed at distances of 13-30°. In summary, our efforts to combine array-based signal processing and waveform modeling to better understand complex phase behavior should in turn lead to better event location and discrimination capabilities at lower magnitudes.

REFERENCES

Bassin, C., G. Laske and G. Masters (2000). The Current Limits of Resolution for Surface Wave Tomography in North America, *EOS Trans AGU*, 81, F897.

Bump, H. A., and A. F. Sheehan (1998). Crustal thickness variations across the northern Tien Shan from teleseismic receiver functions, G*eophys. Res. Ltrs.* 25: 1055–1058.

Crotwell, H.P., T.J. Owens, and J. Ritsema (1999). The TauP Toolkit: Flexible seismic travel-time and raypath utilities, *Seis. Res. Ltrs.* 70: 15–170.

Davies, D., E. J. Kelly, and J. R. Filson (1971). Vespa process for analysis of seismic signals, *Nature Phys. Sci*. 232: 8–13.

Dziewonski, A.M., T.-A. Chou and J.H. Woodhouse (1981). Determination of earthquake source parameters from waveform data for studies of global and regional seismicity, *J. Geophys. Res*. 86: 2825–2852.

Engdahl E. R., R. van der Hilst, and R. Buland (1998). Global teleseismic earthquake relocation with improved travel times and procedures for depth determination, *Bull. Seism. Soc. Amer*. 88: 722–743.

Ghose, S., M. W. Hamburger, and J. Virieux (1998). Three-dimensional velocity structure and earthquake locations beneath the northern Tien Shan of Kyrgyzstan, central Asia, *J. Geophys. Res.*: 103: 2,725–2,748.

Gibbons, S., and T. Kvaerna (2002). Analysis and processing of events from the Kovdor Mine, Kola, NW Russia, *NORSAR Contribution 793*, http://www.norsar.no/seismology/research/kovdor/kolareport.pdf.

Hatzfeld, D., M. Tatar, K. Priestley, and M. Ghafory-Ashtiany (2003). Seismological constraints on the crustal structure beneath the Zagros Mountain belt (Iran), *Geophys. J. Int.* 155: 403–410.

Kennett, B. L. N., and E. R. Engdahl (1991). Travel times for global earthquake location and phase identification, *Geophys. J. Int*. 105: 429–465.

Kennett, B.L.N. (1988). *Systematic Approximations to the Seismic Wave Field*, Chapter III.1 in Seismological Algorithms**,** ed. D.J. Doornbos, Academic Press.

Leborgne, S., and R. Madariaga (1999). Body waveform modeling of east Mediterranean earthquakes at intermediate distances (17-30) with a Gaussian beam summation method, *J. Geophys. Res*. 104: 28,813–28,828.

Martynov, V. G., F. L. Vernon, D. L. Kilb, and S. W. Roecker (2004). Directional variations in travel-time residuals of teleseismic *P* waves in the crust and mantle beneath Northern Tien Shan, *Bull. Seis. Soc. Amer* 94: 650–664.

Meltzer, A. S., P. K. Zeitler, M. L. Schoemann, B. C. Beaudoin, L. Seeber, and J. G. Armbruster (1996). The Nanga Parbat Seismic Experiment, *Eos Trans. AGU (Supplement)* **77**: 688.

Mitra, S., K. Priestley, A. K. Bhattacharyya, and V. K. Gaur (2005). Crustal structure and earthquake focal depths beneath northeastern India and southern Tibet, *Geophys. J. Int.* 160: 227–248.

Muirhead, K. J., and R. Datt (1976). The N-th root process applied to seismic array data, *Geophys. J. R. Astron. Soc*. 47: 197–210.

Oreshin, S., L. Vinnik, and D. Peregoudov (2002). Lithosphere and asthenosphere of the Tien Shan imaged by *S* receiver functions, *Geophys. Res. Ltrs.* 29: doi:10.1029/2001GL014441.

Rodgers, A. J., and S. Y. Schwartz (1998). Lithospheric structure of the Qiangtang Terrane, northern Tibetan Plateau, from complete regional waveform modeling: Evidence for partial melt, *J. Geophys. Res*. 103: 7,137–7,152.

Rost, S., and M. Weber (2002). The upper mantle transition zone discontinuities in the Pacific as determined by short-period array data, *Earth Planet Sci. Ltrs.* 204: 347–361.

Schisselé, E., J. Guilbert, S. Gaffet, and Y. Cansi (2004). Accurate time–frequency–wavenumber analysis to study coda waves, *Geophys. J. Intl*. 158: (2), 577–591.

Schulte-Pelkum, V., G. Monsalve, A. Sheehan, M. R. Pandey, S. Sapkota, R. Bilham, and F. Wu (2005). Imaging the Indian subcontinent beneath the Himalaya, Nature, 435, 1,222–1,226.

Tilmann, F., J. Ni and the INDEPTH II Team (2003). Seismic Imaging of the Downwelling Indian Lithosphere Beneath Central Tibet, *Science*, 300: (5624), 1424–1427, DOI: 10.1126/science.1082777 .

Zhao, W., K. D. Nelson, and the Project INDEPTH Team (1993). Deep seismic reflection evidence for continental underthrusting beneath southern Tibet, *Nature* 366: 557–559.

A 3D GEOPHYSICAL MODEL OF THE CRUST IN THE BARENTS SEA REGION: MODEL CONSTRUCTION AND BASEMENT CHARACTERIZATION

Oliver Ritzmann[1], Nils Maercklin[2], Jan Inge Faleide[1,2],
Hilmar Bungum[1,2], Walter D. Mooney[3], and Shane T. Detweiler[3]

University of Oslo[1], NORSAR[2], and U.S. Geological Survey[3]

Sponsored by National Nuclear Security Administration
Office of Nonproliferation Research and Development
Office of Defense Nuclear Nonproliferation

Contract No. DE-A104-2000AL66517[1,2,3]

ABSTRACT

We here present BARENTS50, a new 3D geophysical model of the crust in the Barents Sea region. The target region of interest comprises northern Norway and Finland, parts of the Kola Peninsula and the East European lowlands. Novaya Zemlya, the Kara Sea and Franz-Josef Land terminate the region to the east, while the Norwegian-Greenland Sea marks the western boundary. In total, 680 one-dimensional seismic velocity profiles were compiled, mostly by sampling 2D seismic velocity transects, from seismic refraction profiles, every 25 km. Seismic reflection data in the western Barents Sea were further used for density modeling and subsequent density-to-velocity conversion. Velocities from these profiles were binned into two sedimentary and three crystalline crustal layers. The first step of the compilation comprised the layer-wise interpolation of the velocities and thicknesses. Within the different geological provinces of the study region, linear relationships between the thickness of the sedimentary rocks and the thickness of the remaining crystalline crust are observed. We therefore used the separately compiled (area-wide) sediment thickness data to adjust the crystalline crustal thickness according to the sedimentary thickness where no constraints from 1D velocity profiles existed. The BARENTS50 model is based on an equidistant hexagonal grid with a node spacing of 50 km. The P-wave velocity model was used for gravity modeling in order to obtain 3D density structure in the study region. A better fit to the observed gravity was achieved using a grid search algorithm which focused on the density contrast of the sediment-basement interface. The high resolution of 50 km is an improvement compared to older geophysical models. The BARENTS50 model is available at http://www.norsar.no/barents3d.

OBJECTIVES

We provide a new, high-resolution 3D geophysical model of the Barents Sea region, including Novaya Zemlya, using an updated data compilation. Our model aims to be precise enough both for further basic geological research and for the detection, location and characterization of small events in the greater Barents Sea region.

RESEARCH ACCOMPLISHED

Three-dimensional seismic models of the Earth's crust and mantle play important roles in the detection and classification of seismic events. Seismic waves which cross the Moho discontinuity experience traveltime delays, since the crust has relatively low seismic velocities compared to the upper mantle. The crustal structure often contains inhomogeneities such as sedimentary basins with very low seismic velocities. Accurate velocity models of the crust and upper mantle are therefore required tools for seismic event detection, location, discrimination, source inversion and for subsequent traveltime modeling. Once a 3D model is extended by the addition of other physical rock properties, such as the S-wave velocity, the density structure or the Q-structure, it will also provide general capabilities for lithological and geological interpretations.

Previously, velocity models were developed at a variety of scales, such as local, regional, plate, or global scales. They were based on numerous methods of study, such as body and surface-wave tomography, receiver function analysis, thermodynamic modeling or, as carried out here, by compiling first-order velocity data from active seismic refraction experiments. The data coverage eventually limits the model quality, and crustal seismic experiments are mostly distributed unevenly. The velocity compilation for the Barents Sea region, as documented in this paper, is based on a large amount of first-order data (Figure 1).

Global-scale seismic models reveal resolutions of 0.5º to 5º constructed along the Earth’s longitude-latitude geographical grid. This configuration is particularly problematic at high latitudes since poor data coverage contrasts with the large number of grid nodes. We therefore chose to use an equidistant grid with a node spacing of 50 km to exploit the input data properly.

The compilation strategy for the BARENTS50 model has been as follows: We collected all available velocity data based on seismic refraction experiments in the target region. A number of profiles were obtained during this study from density modeling along deep seismic reflection profiles and subsequent density-to-velocity conversion. Subsequently, the seismic velocities and layer thicknesses were interpolated layer-by-layer. We observed different linear relationships between the sediment thickness and the thickness of the crystalline crust in the different provinces of our target region. A compiled sediment thickness map was used to adjust the crystalline crustal thicknesses where no database constraints were given. The 3D velocity structure was then converted into density and used for gravity modeling, in order to obtain the 3D density structure. A programmed grid search algorithm helped to obtain a better fit to the observed gravity field. The 3D model of Levshin et al. (2005) was used to extend our model into the upper mantle. The S-wave structure for the crustal section was estimated using crustal P/S-wave ratios from same model.

In order to demonstrate the improvements of the newly developed BARENTS50 model we have compared it to commonly applied 3D models. To this end, Figure 2 shows the (one-way) traveltimes of seismic P-waves from sea level down to the Moho discontinuity in comparison to 3SMAC (Nataf & Ricard, 1996), CRUST2.0 (Bassin et al., 2000) and WENA1.0 (Pasyanos et al., 2004). These illustrations represent roughly the expected traveltime delay for incoming seismic waves, caused by the relatively low seismic velocities of the crust compared to the mantle. The most significant improvement is the increased resolution of 50 km (Fig. 2a) compared to the very smooth fields derived from other models. Generally, the defined geological provinces have a strong effect on the traveltime distribution. Strong gradients in the traveltime are achieved if neighboring provinces are very different in the calculated regression (Fig. 3). The large traveltime obtained at 73°N/40°E is located at a prominent change of the heading along the profile AR-1 by Sakoulina et al. (2003). This is the only location where the traveltime map (Fig. 2a) reflects the input data distribution (Fig. 1). Here, we did not adjust the crystalline crustal thicknesses, since nearby data constraints were given.

The western continent-ocean transition (COT) is clearly visible in the BARENTS50 model; here the traveltimes drop from ca. 5 to 4 s towards the west. The WENA1.0 (Fig. 2b) model shows the COT similar to our model,

although the Moho is about 1.0 s deeper. Local positive undulations in the traveltimes along the COT in the CRUST2.0 (Fig. 2c) model are most likely due to local deposition centers and high accumulation of glacial sediments, with no traveltime effect in the BARENTS50 model. The average traveltime in the western Barents Sea is about 5.0 s and slightly higher in the east (ca. 6.0-6.5 s; Fig. 2a). This trend is approximately matched by the CRUST2.0 model. The 3SMAC model is notable here, since a strong positive traveltime anomaly is located centrally on the Barents shelf (Fig. 2d). The Barents Sea is represented by a 1D structure in the WENA1.0 model so that local anomalies are absent. Onshore Fennoscandia, 3SMAC and CRUST2.0 match well the trend of lower traveltimes in the Caledonian Orogen and towards the Kola Peninsula; again, WENA1.0 incorporates an average model that does not account for regional features of 200-400 km width. Prominent differences between all models occur as well in the region of the Novaya Zemlya Fold Belt and the Kara Sea. While 3SMAC shows no N-S striking anomalies along Novaya Zemlya, the remaining models obviously account for the structure of the foldbelt. WENA1.0 shows a remarkably mismatch with a traveltime of more than 8 s due to a regional crust thickness of 47 km. Here, the differences are locally to more than 3.0 s.

Transects through the 3D velocity model reveal for the first time simplified geological sections through the European Arctic from the Norwegian-Greenland Sea, across the continental margin, to the Barents Sea, the Novaya Zemlya Foldbelt and into the Kara Sea region. The 3D construction of the sedimentary basins can be interpreted with the crystalline crustal units and Moho topography below. Depth to Moho is shown in Figure 4. With respect to the chosen approach of regionalization, most of the geological provinces reveal a homogenous crustal structure. Naturally, the denser the data coverage the more complex is the local structure of the model. The crustal construction is more differentiated and the Moho topography more pronounced in the west, where the majority of data constraints are provided. Here, the Paleozoic and Mesozoic rifting history in the western Barents Sea resulted in a complex array of basins and basement highs which supposedly are inherited from the Caledonian consolidation phase (Gudlaugsson et al., 1998).

A fundamental step during the velocity model compilation was the adjustment of the crustal thickness according to the linear and province-related relationships between the sediment thickness and the thickness of the remaining crust (Fig. 3). The fundamental consideration behind this approach is that subsidence and the development of sediment basins is coeval with the flexure and/or thinning of the underlain crust. Regional conditions, such as density of the crust and mantle, the strain and stress rates, the viscosity and strength of the crust and, obviously, the sediment supply result therefore in a specific (local) thickness relation between the sedimentary cover and the remaining crust. Simple models of crustal extension (e.g., McKenzie, 1978) show that after the cooling of the stretched lithosphere (>120 Ma) the relation between basin depth and crystalline crust follows a straight line similar to an Airy-type isostatic compensation model (e.g., Watts, 2001). Prior to the state of thermal equilibrium the ratio between basin depth (sediment thickness) and thinned crystalline crust is slightly curvilinear. If, for example, the density of the crust is increased, the straight lines get steeper slopes; similarly, we expect other regional parameters to contribute to the final trend of the relationship. The earliest rift period in the Barents and Kara Seas is supposed in late Cambrian times (510 Ma; O'Leary et al., 2004), while the latest phase of rift-related subsidence and deposition was in the Early Cretaceous (100 Ma; Faleide et al., 1993). Additional extension has also been suggested in Late Cretaceous-Early Cenozoic times, following the break-up along the western Barents Sea margin; nevertheless a straight or slightly curvilinear relationship can be expected.

Figure 3 shows, despite the scatter, that most distribution patterns reveal linear trends which can satisfactorily be expressed through linear regressions. The standard deviations for the sediment (x-axis) and crystalline crustal thicknesses (y-axis) do not exceed 20% of the observed thicknesses and are often considerably lower. The scatter is highest in the case of the thinned continental crust in the western Barents Sea (Fig. 3; prov. 24) where the standard deviation is 4.2 at sediment thicknesses between 0 and 15 km. Fitting the data by linear regression in this province is problematic since rifting and break-up occurred in Late Cretaceous and Eocene times and the thermal subsidence is probably not completed. Other provinces show very low scatter such as the Nordkapp Basin (prov. 10) or the basement highs off NW Novaya Zemlya (prov. 16).

The different y-axis intercepts and slopes in the different provinces (Fig. 3) provide estimates for the zero-sediment thickness and resistance to crustal thinning, respectively. Zero-sediment thicknesses range between 30 km in some provinces (e.g., prov. 17, Nordkapp Basin) to more than 45 km (e.g., prov. 14, Gardabanken High). A low slope indicates a mantle updoming below sedimentary basins (e.g., prov. 12, South Kara Basin; slope -2.0), while in

provinces with a higher slope (e.g., prov. 23, Cretaceous Volcanic Province; slope -0.7) the crust-mantle boundary is flat-lying or slightly down-warped below the sedimentary basin.

The basaltic layers of the oceanic crust in the Norwegian-Greenland Sea thin rapidly with increasing latitude while the sediment thickness decreases. Our developed model preserves very well the results of the crustal studies of Breivik et al., (2003) and Ritzmann et al. (2004) at the latitudes of Bjørnøya and northern Svalbard, respectively. The basaltic lower crustal layer 3 thins towards the north, while the upper layer 2 remains approximately constant in thickness. This suggests that magmatic activity at the oceanic spreading center is decreased with decreasing spreading rates in the narrow corridor between Eurasia and Greenland. Therefore, the traveltime through the crust and water column is about 1 sec higher in the south off the western Barents Sea (Fig. 2a).

The Barents Sea is surrounded by thick crustal complexes to the south while the crust of the Novaya Zemlya Microplate thins rapidly towards the east, indicating a transition to the Kara Sea province in the east (prov. 12), where the Moho topography is very rough and characterized by local domes (Fig. 4). These strong lateral thickness variations are well-constrained by the seismic velocity models compiled during this study (Fig. 1) and documented by the low slope in the thickness relationship of the Kara Sea province (Fig. 3).

The continental crust of northern Norway and the Kola Peninsula shows similar large thicknesses. In Fennoscandia the maximum Moho depth of 52.4 km is observed. The crustal thicknesses are also in agreement with results from unpublished receiver function analyses of the MASI99 experiment in northern Norway (Hoehne, 2001). The majority of the stations derived similar thicknesses, within a range of 1 to 3 km, to our model. Larger deviations are given in the northern coastal areas where receiver function analyses indicate shallower depth of about 40 km, where our model is founded on the FENNOLORA-experiment by Guggisberg et al. (1991) and the work of Helminsen (2002).

CONCLUSIONS AND RECOMMENDATIONS

The present study provides a new and detailed crustal velocity model, BARENTS50, for the Barents Sea region with a resolution of 50 km, and with a new compilation strategy based on geological provinces (or regionalization). Other approaches for model compilations using velocity function from seismic refraction experiments are purely based on mathematical solutions such as continuous curvature gridding or kriging methods. Other 3D models evolved from gravity modeling based on isostatic and flexural principles (e.g., Kimbell et al. 2004) or from the inversion of surface-wave dispersion data (e.g., Shapiro & Ritzwoller, 2002). The fundamental problem of all approaches, including the present one, is the non-uniqueness or ambiguity of the resulting models, which is most striking when using gravity modeling (size and shape of the anomalous body versus its density contrast). In our case, the chosen input are mostly ray tracing based models which are also ambiguous, since traveltime, layer thickness and seismic velocities are convertible parameters. Any geophysical feature of the finally constructed model (such as traveltime delays) or geological interpretation (such as the shape and extent of a lower crustal body) are naturally uncertain and, if not treated with care, can lead to false interpretations. However, the principle of layer thickness adjustments based on thickness relationships originated from the detailed analysis of the very simple but consistent dataset. The new method for adjusting the crustal thickness was particularly applicable in the Barents Sea region which is largely covered by riftogenic sedimentary basins. At this stage, it remains unclear, however, to what extent this technique is applicable to other regions worldwide. Further study is required.

Our model was already used as primary input for a new surface-wave inversion and improved, along with an extended set of recordings (Levshin et al., 2005) the mantle model comprehensively. In addition, the model provides assistance for studies of various geodynamic problems concerning the plate tectonic setting of the Barents Sea region, basin formation processes or the distribution of magmatism. Studies of the regional isostatic and thermal states and local gravity and basin modellings are backed up thanks to the availability of a complete lithosphere model.

In conclusion, the combination of a consistent seismic database and a reliable methodology to use secondary geological constraints (depth-to-basement data and thickness relations) helped significantly to establish a new higher-resolution geophysical model of the greater Barents Sea region.

REFERENCES

Bassin, C., G. Laske, and G. Masters (2000). The current limits of resolution for surface wave tomography in North America, EOS Trans. *AGU* 81: F879.

Breivik, A.J., R. Mjelde, P. Grogan, H. Shimamura, Y. Murai, and Y. Nishimura (2003). Crustal structure and transform margin development south of Svalbard on ocean bottom seismometer data, *Tectonophysics* 369: 37–70.

Faleide, J.I., E. Vagnes, and S.T. Gudlaugsson (1993). Late Mesozoic-Cenozoic evolution of the south-western Barents Sea in a regional rift-shear tectonic setting, *Mar. Petr. Geol*. 10: 186–214.

Gudlaugsson, S.T., J.I. Faleide, S.E. Johansen, and A.J. Breivik (1998). Late paleozoic structural development of the South-western Barents Sea, *Mar. Petr. Geol*. 15: 73–102.

Guggisberg, B., W. Kaminski, and C. Prodehl (1991). Crustal structure of the Fennoscandian Shield; a traveltime interpretation of the long-range FENNOLORA seismic refraction profile, *Tectonophysics* 195: 105–137.

Helminsen, L. (2002). Skorpestuktur i Finnmark og det sydvestlige Barentshav. Unpublished Master Thesis, Geological Department, University of Oslo, Oslo.

Hoehne, J. (2001). Untersuchungen der Geschwindigkeitsstruktur der Kruste und des oberen Mantels der Finnmark aus den Daten des MASI 99 Projektes. Unpublished diploma thesis, Institut für Geowissenschaften, Fachbereich Geophysik, Universitaet Potsdam, Potsdam.

Kimbell, G.F., R.W. Gadliff, J.D. Ritchie, A.S.D. Walker, and J.P. Williamson (2004). Regional three-dimensional gravity modelling of the NA Atlantic margin, *Basin Research* 16: 259–278.

Levshin, A., J. Schweitzer, C. Weidle, N. Maercklin, N. Shapiro, and M. Ritzwoller (2005). Surface wave tomography of the European Arctic, *EOS Trans. AGU* 86: (52), Fall Meet. Suppl., Abstract S51E-1053.

McKenzie, D. (1978). Some remarks on the development of sedimentary basins, *E. Planet. Sci. Let*. 40: 25–32.

Nataf, H.-C. and Y. Ricard (1996). 3SMAC: An a priori tomographic model of the upper mantle based on geophysical modeling, *Phys. Earth Planet. Inter*. 95: 101–122.

O'Leary, N., N. White, S. Tull, V. Bashiov, V. Kuprin, L. Natapov, and D. Macdonald (2004). Evolution of the Timan-Pechora and South Barents Sea basins. *Geol. Mag*. 141: (2), 141–160.

Pasyanos, M.E., W.R. Walter, M.P. Flanagan, P. Goldstein, and J. Bhattacharyya (2004). Building and testing an a priori Geophysical Model for western Eurasia and North Africa, *Pure appl. geophys.* 161: 235–281.

Ritzmann, O., W. Jokat, W. Czuba, A. Guterch, R. Mjelde, R. and Y. Nishimura (2004). A deep seismic transect in northwestern Svalbard at Kongsfjorden (Ny Ålesund) and the implications for Cenozoic break-up from Greenland: A sheared margin study. *Geophys. J. Int*. 157, 683–702.

Sakoulina, T.S., Yu. V. Roslov, and N.M. Ivanova (2003). Deep seismic investigations in the Barents and Kara seas. Rus. Acad. Sci. Physics of the Solid Earth 39: (6), 438–452.

Shapiro, N. M. and M.H. Ritzwoller (2002). Monte-Carlo inversion for a global shear velocity model of the crust and upper mantle, *Geophys. J. Int*. 151: 88–105.

Watts, A.B. (2001). Isostasy and Flexure of the lithosphere, Cambridge University Press, Cambridge, 458 pp.

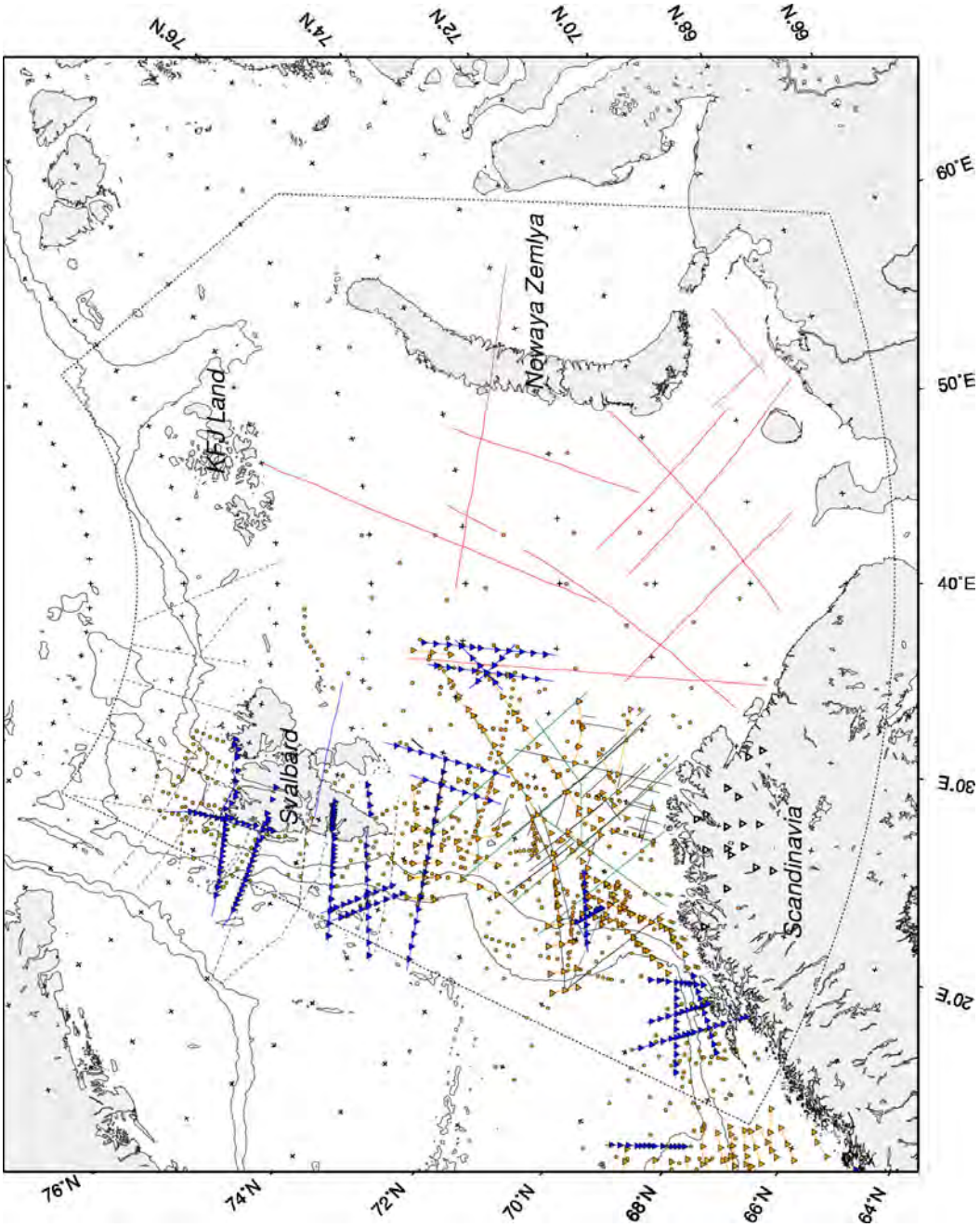


Figure 1. Location map showing principal (seismic) data coverage of the target region between Northern Scandinavia, Svalbard, Kaiser-Franz-Josef Land and Novaya Zemlya. Blue lines and blue triangles indicate deep seismic wide-angle profiles, yellow lines and yellow triangles indicate ESP profiles taken from velocity database at UiO, yellow dots indicate minor 1D-velocity profiles taken from velocity database at UiO (partly unreversed, sonarbuoys, etc.), green lines indicate IKU deep seismic MCS data that can be linked to ESP-profiles, black lines (western Barents Sea) indicate additional published MSC data, dashed lines (north and west of the Svalbard Archipelago) indicate compiled seismic transects, dotted red lines indicate MCS and wide-angle seismic lines acquired by Russian institutions and provided by MAGE (Marine Arctic Geological Expedition, Murmansk) and SMNG (Sevmorneftegeofizika: Offshore Oil and Gas Exploration, Murmansk). The bathymetry is shown with 4000, 2000 and 500 m isocontours.

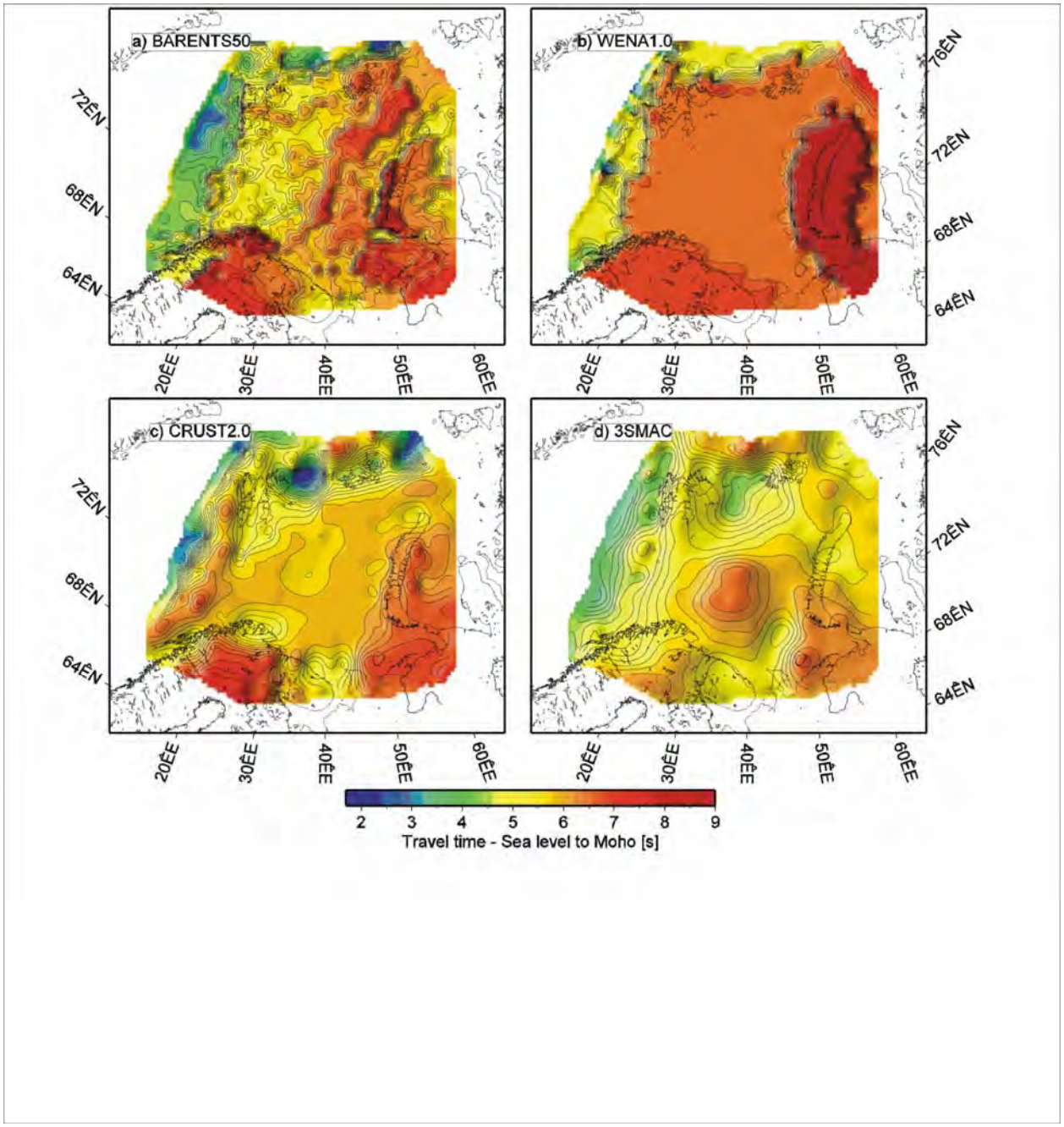


Figure 2. Traveltimes down to the Moho discontinuity. a). BARENTS50, this study. b). WENA1.0 (Pasyanos et al., 2004). c). CRUST2.0 (Bassin et al. 2000). d). 3SMAC (Nataf & Ricard 1996).

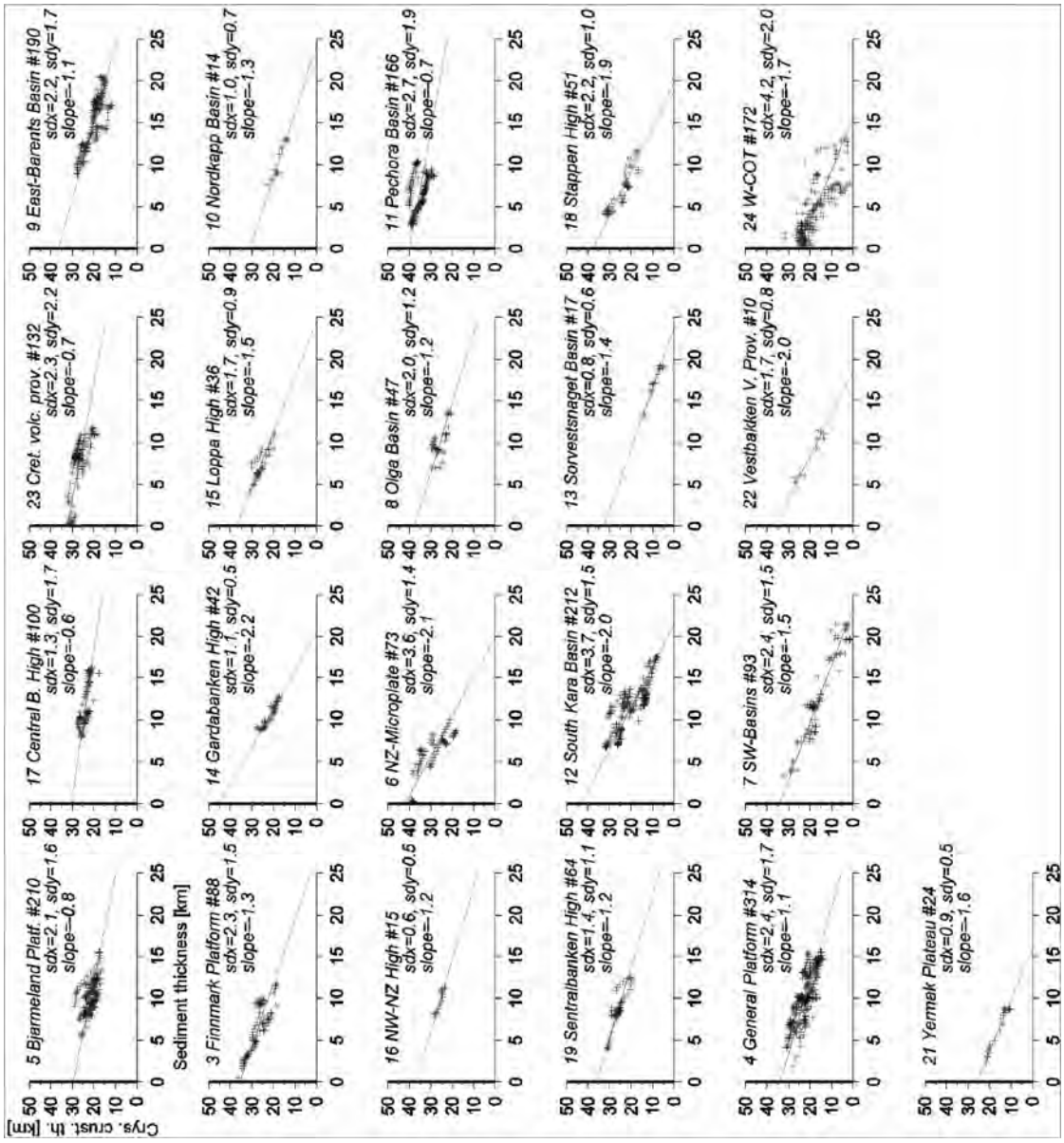


Figure 3. Sediment thickness plotted against crystalline crustal thickness for all provinces (excluding sediment-free cratons, oceanic crustal domains and regions overprinted by convergent tectonics). Black crosses are datapoints extracted from the profile database. The solid lines show the calculated linear regressions. The total number of observations is given after the #-sign. The sdx and sdy values give the standard deviations of the sediment thickness and crystalline crustal thickness, respectively.

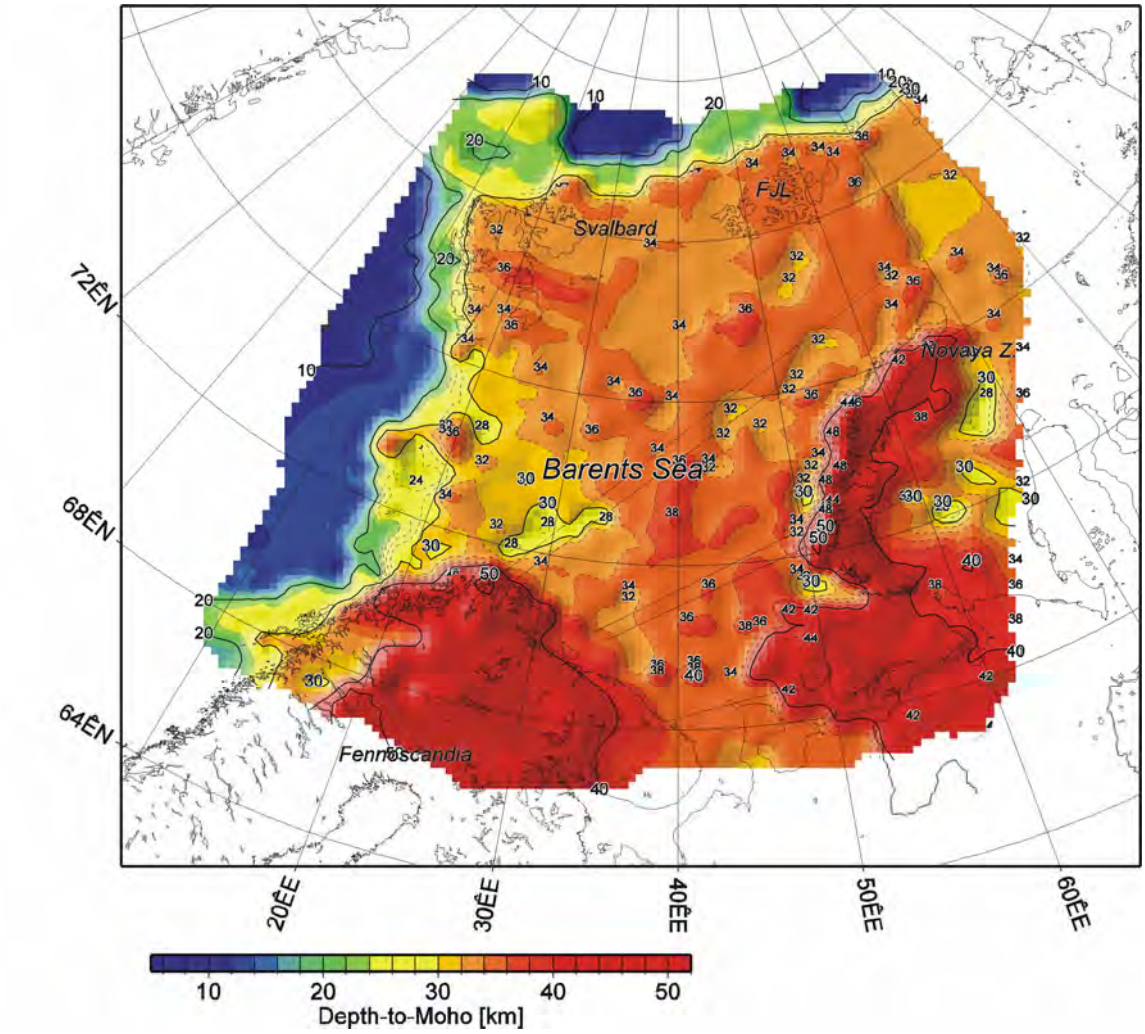


Figure 4. Depth-to-Moho from the BARENTS50 model. Provinces in the central Barents Sea, Novaya Zemlya and Kara Sea show detailed contouring (every 2 km, dashed; other contours: 10 km, solid).

PROGRESS TOWARD BROAD BAND AMBIENT NOISE TOMOGRAPHY IN EURASIA

Michael H. Ritzwoller[1], Michael Pasyanos[2], Yingjie Yang[1], Anatoli L. Levshin[1], and Nikolai M. Shapiro[1]

University of Colorado at Boulder[1] and Lawrence Livermore National Laboratory[2]

Sponsored by National Nuclear Security Administration
Office of Nonproliferation Research and Development
Office of Defense Nuclear Nonproliferation

Contract Nos. DE-FC52-20-05NA26607[1] and W-7406-ENG-48[2]

ABSTRACT

We extend ambient noise surface wave tomography both in band width (6–50 s period) and geographical extent (across much of Europe) compared with previous applications. The data are taken from about 125 broad band seismic stations from the Global Seismographic Network (GSN) and the Observatories and Research for European Seismology (Orfeus) Virtual European Broadband Seismic Network (VEBSN). Cross-correlations are computed in daily segments, stacked over one-year (2004), and Rayleigh wave group disperson curves from 6–50 s periods are measured using a phase-matched filter, frequency-time analysis technique. We estimate measurement uncertainties using the seasonal variation of the dispersion curves revealed in three-month time series. On average, uncertainties in group delays increase with periods from ~3 to ~7 s from periods of 10–50 s, respectively. Group speed maps at periods from 8–40 s are estimated, and the resulting path coverage is denser and displays a more uniform azimuthal distribution than from earthquake-emitted surface waves. The fit of the group speed maps to the ambient noise data is significantly improved below 30 s compared with the fit achieved with earthquake data. Average resolution is estimated to be about 100 km at 10 s periods, but degrades with increasing periods and toward the periphery of the study region. The resulting ambient noise group speed maps demonstrate significant agreement with known geologic and tectonic features. In particular, the signatures of sedimentary basins and crustal thickness are revealed clearly in the maps. These results are evidence that surface wave tomography based on cross-correlations of long time-series of ambient noise data can be achieved over a broad period band on nearly a continental scale and yield higher resolution and more reliable group speed maps than based on traditional earthquake-based measurements. Final application of the method in Europe would benefit from processing a second year of data in order to increase the signal-to-noise level, improve the uncertainty estimates, and increase the size of the dataset. Application of ambient noise tomography to other areas with dense station coverage in Eurasia is a natural extension of this work.

OBJECTIVE

The goal of this research is to develop a new method to obtain surface wave dispersion measurements based on ambient seismic noise and to produce a new dataset of interstation group velocity measurements. These new data are used to produce improved group velocity tomographic maps, particularly at short periods (< 20 s).

RESEARCH ACCOMPLISHED

Introduction

Traditional inference of seismic wave speeds in Earth's interior is based on observations of waves emitted by earthquakes or human-made explosions. Surface wave tomography has proven particularly useful in imaging Earth's crust and uppermost mantle on both regional and global scales. Because they propagate in a region directly beneath Earth's surface, surface waves typically generate better path coverage of the upper regions of Earth than body waves with the same distribution of seismic stations. There are, however, basic limitations to earthquake-based surface wave tomography independent of the number of broadband stations available. First, due to the uneven distribution of earthquakes around the world, seismic surface waves only sample certain preferential azimuths. In addition, in aseismic regions surface wave dispersion can be measured only from distant earthquakes. Second, it is difficult to obtain high-quality short-period (<20 s) dispersion measurements from teleseismic events due to intrinsic attenuation and scattering along ray paths. It is, however, the short-period waves that are most useful to constrain the structure of the crust and uppermost mantle. Third, inversions of seismic surface waves require some information about sources, such as earthquake hypocentral locations and moment tensors in some cases, which have a substantial intrinsic inaccuracy, particularly for small events. Some of the problems that beset traditional earthquake surface wave tomography can be alleviated by observations made on diffuse wavefields (e.g., ambient noise, scattered coda waves). Theoretical research has shown that, under the right circumstances, the time-derivative of the cross-correlation of records of ambient noise from two seismic stations provides an estimate of the Green function between the stations, modulated by the spectrum of the noise source (Weaver and Lobkis, 2001, 2004; Derode et al., 2003; Snieder, 2004;). Ambient noise tomography has been applied successfully at very short periods over small regions (e.g., in S. California, Shapiro et al., 2005 and Sabra et al., 2005; in S. Korea, Cho et al., 2006). The purpose of this research is to determine whether ambient noise Rayleigh wave tomography can be applied reliably on a nearly continental scale and extended from short (~6 s) to intermediate periods (~50 s). More details about this method are given by Yang et al. (2006). Final application of the method in Eurasia would benefit from adding a second year of data in order to improve the signal level, dispersion measurements, and uncertainty estimates.

Data Processing and Group Velocity Measurements

Europe is an excellent region to test ambient noise surface wave tomography. Broad band seismic station coverage is dense across much of the continent and the substantial a priori knowledge of geological structures allows us to evaluate the reliability of the resulting group velocity maps. We have collected continuous vertical-component seismic data from 125 stations including data from the GSN and the VEBSN (Figure 1) over the 12 months of 2004. About 110 of these stations returned useful data.

The data processing procedure that is applied here is very similar to that discussed at greater length in the paper by Bensen et al. (2006). The data processing method was evolved significantly since the first work by Shapiro et al. (2005). Using vertical-component seismic data implies that the resulting cross-correlations contain only Rayleigh wave signals. Data are processed one day at a time for each station after being decimated to 1 sample per second and are band-pass filtered in the period band from 5–150 s after the daily trend, the mean and the instrument response are removed. Data are then normalized in time and whitened over the frequency-band of interest prior to cross-correlation.

After the time-series has been processed for each day, we then compute daily cross-correlations in the period band from 5–150 s and then stack the results into a set of three-month and one-year time series. The three-month stacks are used to investigate the seasonal variability of the measurements, which is the basis for the error analysis and is part of the data selection procedure discussed further below. An example of a broad band (5–50 s) symmetric-component cross-correlation for the station pair Ibbenbueren, Germany (IBBN) and Hungary (TIRR) is shown in Figure 2 together with the cross-correlation filtered into five frequency sub-bands. Rayleigh waves emerge clearly in each frequency band with the longer period waves arriving earlier.

To begin to evaluate the quality of the cross-correlations quantitatively, we calculate the signal-to-noise ratio (SNR)

for each cross-correlation. SNR is defined as the ratio of the peak amplitude within a time window containing the signals to the root-mean-square of noise trailing the signal arrival window. Because the SNR can vary strongly with frequency, we filter the broad band cross-correlations into three narrower pass-bands at 8–25 s, 20–50 s and 33–70 s and compute the SNR in each band. We reject cross-correlations with SNR less than 7 in each band. Group velocity curves are measured on the estimated Green functions that emerge from both the three-month and one-year stacks in each of the three period bands using automatic Frequency Time Analysis (FTAN) as described by Bensen et al. (2006) in detail.

Data Selection and Uncertainty Estimation

The automated measurement procedure must be followed by the application of criteria to select the data. We apply three general types of criteria: (1) SNR, (2) repeatability of the measurements (particularly seasonal variability), and (3) coherence across the set of measurements. The formal uncertainty analysis is based on seasonal variability.

First, we reject a cross-correlation if its SNR < 7. Figure 3a shows an example histogram of the distribution of SNR for signals band-pass filtered between 20 and 50 s. Distributions are similar in the other two pass-bands, between 8 and 25 s and between 33 and 70 s.

Second, for a measurement to be accepted, it needs to be repeatable in the sense that measurements obtained at different times should be similar. The repeatability criterion is based on quantifying seasonal variability. To do so, we select 12 over lapping three-month time-series for each station pair. Figure 4 shows an example of the seasonal variability in the observed dispersion curves. The dispersion curves that are used for tomography here are taken from the 12-month stacks. The standard deviation is computed for a station-pair if more than 4 three-month stacks have a SNR > 7. The measurement is retained if the standard deviation is less than 100 m/sec. It is rejected if the standard deviation either cannot be computed due to the fact that too few measurements can be obtained on the 3-month stacks or if the standard deviation is too large. The effect of this step in eliminating measurements is shown in Figure 3b. Figures 3d and 3e show the average measurement uncertainties taken over the entire European data set. Average uncertainties of group velocities and group arrival times increase with periods from ~0.02 km/s or ~3 s at 10 s periods to 0.09 km/s or 7.5 s at 50 s period.

Third, we require that the measurements cohere with one another across the data set. Incoherent measurements that disagree with other measurements in the data set are identified during tomography.

Finally, we find that to obtain a reliable measurement, the stations must be separated by at least three wavelengths.

The number of measurements that remain after all criteria have been applied is shown in Figure 3b. Less than a third of the original measurements are retained for tomography. The least satisfying part of the procedure is eliminating what appears to be a good measurement on the 12-month stack because the uncertainty estimate could not be determined, usually because of an insufficient number of high SNR 3-month stacks. To retain a higher percentage of measurements, it will be necessary to process two or more years of data. This would increase the SNRs of the seasonal stacks and be preferable over a single year of data. Bensen et al. (2006) discusses this further.

Surface Wave Tomography

The dispersion measurements of Rayleigh waves from one-year cross-correlations are used to invert for group velocity maps on a $1^{o} \times 1^{o}$ grid across Europe using the tomographic method of Barmin et al. (2001). Uncertainty estimates exist for every measurement, and have been used as weights in the inversion. Resolution is estimated using the method described by Barmin et al. (2001) with modifications presented by Levshin et al. (2005).

Group speed tomography is performed in two steps. The first step generates overly smoothed maps at each period in order to identify and reject any remaining bad measurements. The over-smoothed model is able to fit most data fairly well. We discard group velocity measurements with travel time residuals larger than 15 s, which is about the root mean square (RMS) value of the travel time residuals at most periods. The number of paths remaining after this step of data reduction is shown in Figure 3b.

The second step of tomography is the construction of the final maps. Maps are defined relative to the reference maps computed from the 3-D model of Shapiro and Ritzwoller (2002). In an important sense, the reference maps already have a priori information imposed on crustal structure. The 3-D model itself was constructed as a perturbation to a

starting model that included information about sediments and crustal thicknesses. For this reason, we choose to seek only smooth perturbations to the reference maps.

Examples of path density and resolution are shown in Figure 5 for the 16 s measurements. Results are similar from 10–50 s periods. Path density is highest in the center of Europe and gradually degrades toward the edge of the study region. Average resolution is estimated to be about 100 km in the center of the study region in Europe, and like path density degrades toward the periphery of the map where station coverage is minimal.

The results of group velocity tomography at 10, 16, 20, 30, and 40 s periods are shown in Figures 6 and 7a. Figure 7b illustrates that the perturbations to the reference model introduced during tomography are smooth and occur only in regions where path coverage is high, predominantly in the center of the region of study. In most of the Mediterranean Sea, the Atlantic Ocean, North Africa, the Iberian Peninsula, and far eastern Europe, the perturbations are small and the estimated maps are very similar to the reference maps. Many of the observed anomalies are correlated with known geological units, which is discussed further in the following paragraphs.

At the short-period end of this study (8–20 s), group velocities are dominantly sensitive to shear velocities in the upper crust. Because the seismic velocities of sediments are very low, short-period low velocity anomalies are a good indicator of sedimentary basins. At the intermediate periods of this study (25–40 s), Rayleigh waves are primarily sensitive to crustal thickness and the shear velocities in the lower crust and uppermost mantle. To aid assessment, Figure 6e and 6f presents a map of sediment thickness from CRUST1.0, which Laske and Masters digitized across most of Europe from the EXXON Tectonic Map of the World (Laske and Masters, 1997), and a map of crustal thickness taken from CRUST2.0 (Bassin, et al., 2000). We identify the names of several geological units on these maps, mainly sedimentary basins and mountain ranges.

The 10 s and 16 s group speed maps in Figures 6 and 7 exhibit low velocity anomalies associated with most of the known sedimentary basins across Europe. In regions of high data coverage, low-velocity anomalies are observed in the North Sea Basin, the Silesian Basin (North Germany, Poland), the Pannonian Basin (Hungary, Slovakia), the Po Basin (North Italy), the Rhone Basin (Southern France), and the Adriatic Sea. At intermediate periods (25–40 s), the estimated maps exhibit low-velocity anomalies associated with the Alps, the Carpathians and the mountains in the Balkan region. The low velocity anomalies are probably caused by deeper crustal roots beneath mountain regions that occur due to isostatic compensation. The general reduction in Rayleigh wave velocity in the eastern part of the 30–40 s maps in Figure 6 is probably related to the general thickening of the crust toward the east European craton.

Figure 8a shows the improvement in fit to the measured dispersion curves achieved by the resulting group velocity maps, expressed as the variance reduction relative to the predicted group velocity maps. In addition, variance reduction relative to the average across each map is shown. Variance reductions relative to predicted group velocity (solid line) are larger at short periods (< 25 s) and smaller at long periods (>35 s) than relative to the average (dashed line). Variance reductions are highest at short periods and gradually decrease with periods. The observed trend of variance reductions is caused by group speed anomalies being largest at short periods and also because the 3-D model is more reliable for the longer periods. The RMS group velocity and travel time misfits after tomography are also shown in Figures 8b and 8c. Travel time misfit of the final data set is~5–6 s and is nearly independent of periods.

CONCLUSIONS

In this study, we use ambient noise data recorded at 125 broad band seismic stations available from the GSN, Orfeus, and VEBSN. All dispersion measurements have uncertainty estimates that derive from observations of seasonal variability. The data set would benefit from time-series of 2 or more years, which would allow more uncertainties to be measured and, therefore, more measurements will pass the selection criterion.

Group velocity maps at periods from 8 to 50 s are obtained using ambient noise tomography. These maps provide a significant improvement in the understanding of surface wave dispersion in Europe, particularly at periods below about 20 s. This study has denser and more uniform data coverage and demonstrates higher resolution than pervious studies, which have relied on traditional earthquake-based surface wave tomography. The group velocity maps agree well with known geologic features, such as sedimentary basins and the lateral variation of crustal thickness. Observations at short periods (8–20 s) provide entirely new constraints on sediment thickness, crustal thickness, and the shear velocity structure of crust.

In summary, this study demonstrates that surface wave tomography based on cross-correlations of long time-series of ambient noise data can be achieved over a broad period band on a nearly continental scale and yield higher resolution and more reliable group velocity maps than based on traditional earthquake-based measurements.

ACKNOWLEDGEMENTS

All of the data used in this research were downloaded from the continuous ftp database of the Orfeus Data Center and from the IRIS Data Management Center. In particular, the authors are deeply grateful to the data contributors to the VEBSN, a partnership of more than 30 local, regional and global arrays and network. The list of contributors is located at

http://www.orfeus-eu.org/meredian/vebsn-contributors.htm.

REFERENCES

Barmin, M. P., M. H. Ritzwoller, and A. L. Levshin (2001). A fast and reliable method for surface wave tomography, *Pure Appl. Geophys.* 158: 1,351–1,375.

Bassin, C., G. Laske, and G. Masters (2000). The current limits of resolution for surface wave tomography in North America, *EOS Trans AGU* 81: F897.

Bensen, G. D., M. P. Barmin, F.-C. Lin, M. P. Moschetti, Y. Yang, A. L. Levshin, N. M.Shapiro, and M. H. Ritzwoller (2006). Obtaining robust group and phase speed curves for ambient noise tomography (in preparation).

Cho, K. H., R. B. Hermann, C. J. Ammon, and K. Lee (2006). Imaging the upper crust of the Korean Peninsula by surface-wave tomography, *Bull. Seism. Soc, Amer.* (submitted).

Derode, A., E. Larose, M. Tanter, J. de Rosny, A. Tourim, M. Campillo, and M. Fink (2003). Recovering the Green's function from filed-field correlations in an open scattering medium (L), *J. Acoust. Soc. Am.* 113: 2973–2976.

Laske, G. and G. Masters (1997). A global digital map of sediment thickness, *EOS Trans. AGU* 78: F483.

Levshin, A. L., M. P. Barmin, M. H. Ritzwoller, and J. Trampert (2005). Minor-arc and major-arc global surface wave diffraction tomography, *Phys. Earth Planet. Ints.* 149: 205–223.

Sabra, K. G., P. Gerstoft, P. Roux, W. A. Kuperman, and M. C. Fehler (2005). Surface wave tomography from microseism in southern California, *Geophys. Res. Lett.* 32: L14311, doi:10.1029/2005GL023155.

Shapiro, N. M. and M. H. Ritzwoller (2002). Monte-Carlo inversion for a global shear velocity model of the crust and upper mantle, *Geophys. J. Int.* 151: 88–105.

Shapiro, N. M., M. Campillo, L. Stehly, and M. H. Ritzwoller (2005). High resolution surface wave tomography from ambient seismic noise, *Science* 307: 1,615–1,618.

Snieder, R. (2004). Extracting the Green's function from the correlation of coda waves: A derivation based on stationary phase, *Phys.Rev. E*. 69: 046610.

Weaver, R. L. and O. I. Lobkis, (2001). On the emergence of the Green's function in the correlations of a diffuse field, *J. Acoust. Soc. Am.* 110: 3,011–3,017.

Weaver, R.L. and O.I. Lobkis (2004). Diffuse fields in open systems and the emergence of the Green's function, *J. Acoust. Soc. Am.* 116: 2,731-2,734.

Yang, Y., M.H. Ritzwoller, A. L. Levshin, and N. M. Shapiro (2006). Ambient noise Rayleigh wave tomography across Europe, *Geophys. J. Int.* (submitted).

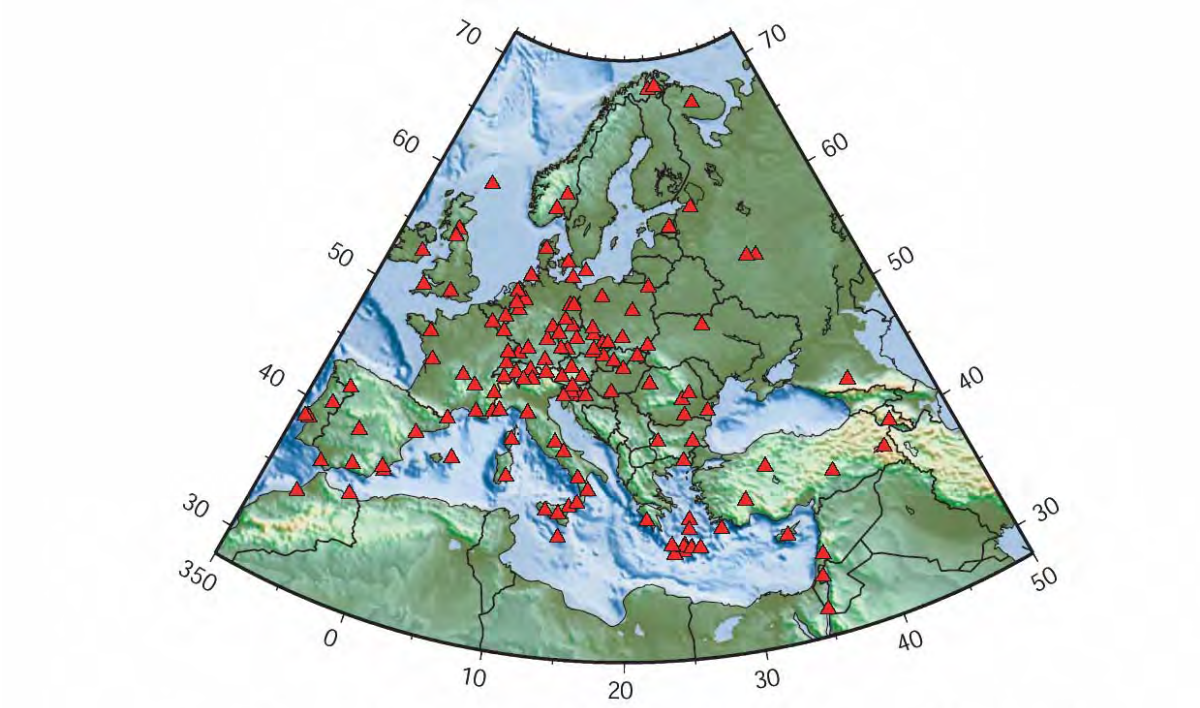


Figure 1. Broad band seismic stations in Europe used in this study, marked by red triangles.

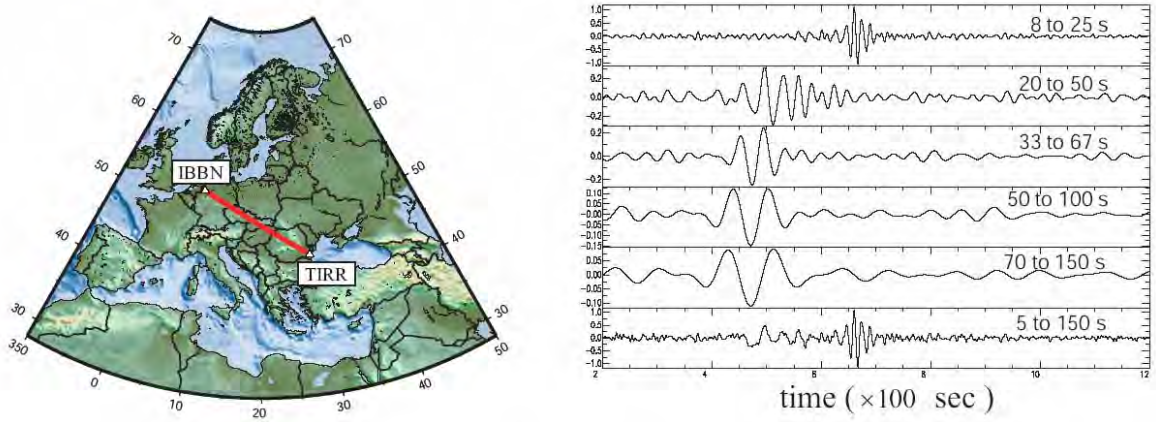


Figure 2. Example of a 12-month broad band symmetric-component cross-correlation between the station pair IBBN and TIRR. The red line shows the great-circle linking the two stations. The broad band cross-correlation is filtered into five sub-bands. Note the clear normal dispersion of the Rayleigh waves, with the longer periods arriving earlier.

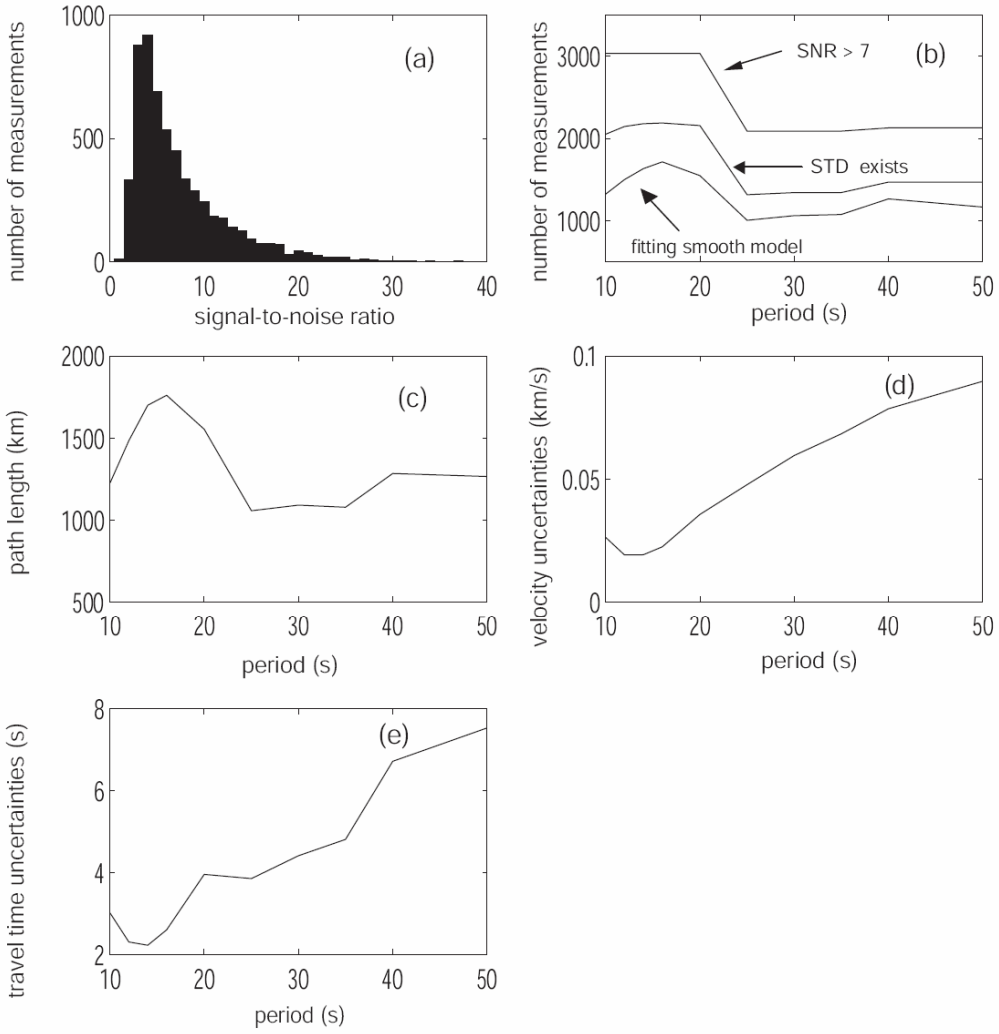


Figure 3. (a) Number of measurements versus signal-to-noise ration from the 12-month stacked cross-correlations between 20 and 50 s periods. (b) Number of measurements remaining after several steps in data reduction. (c) Average path length of the accepted dispersion measurements. (d) Average group speed uncertainties versus periods. (e) Average travel time uncertainties versus periods.

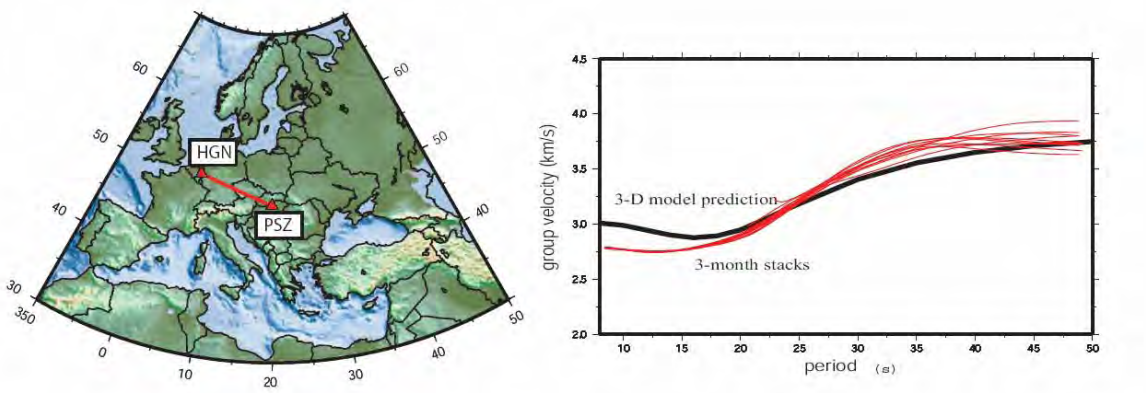


Figure 4. An example of seasonal variability of the dispersion measurements. (left) The path considered is between stations HGN (Heijmans Groeve, Netherlands) and PSZ (Piszkes-teto, Hungary). (right) The red curves are group velocity measurements obtained on twelve 3-month cross-correlations band-pass filtered from 8 to 50 s periods. The black line is the prediction from the global 3-D model (Shapiro and Ritzwoller 2002).

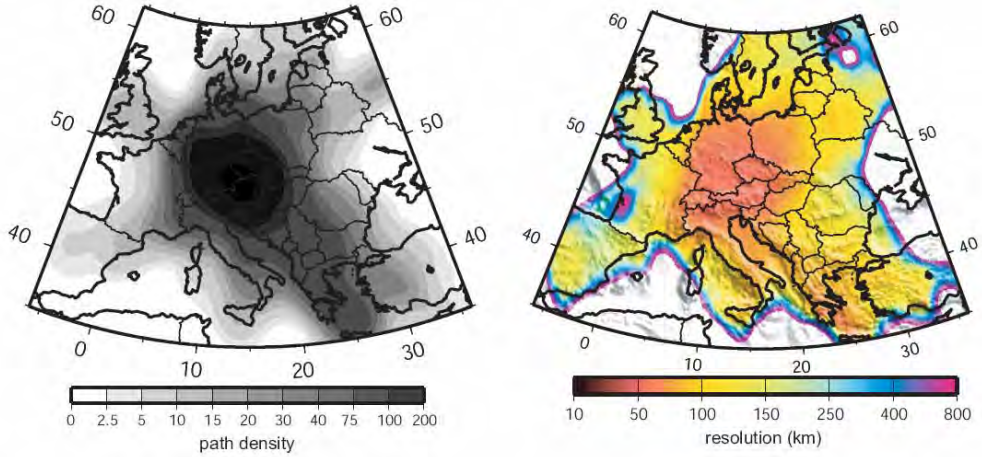


Figure 5. Path density (left) and resolution estimates (right) at 16 s periods. Path density is defined as the number of rays intersecting a 111 km x 111 km square cell. Resolution is presented in units of km, and is defined as the standard deviation of a 2-D Gaussian fit to the resolution surface at each model node.

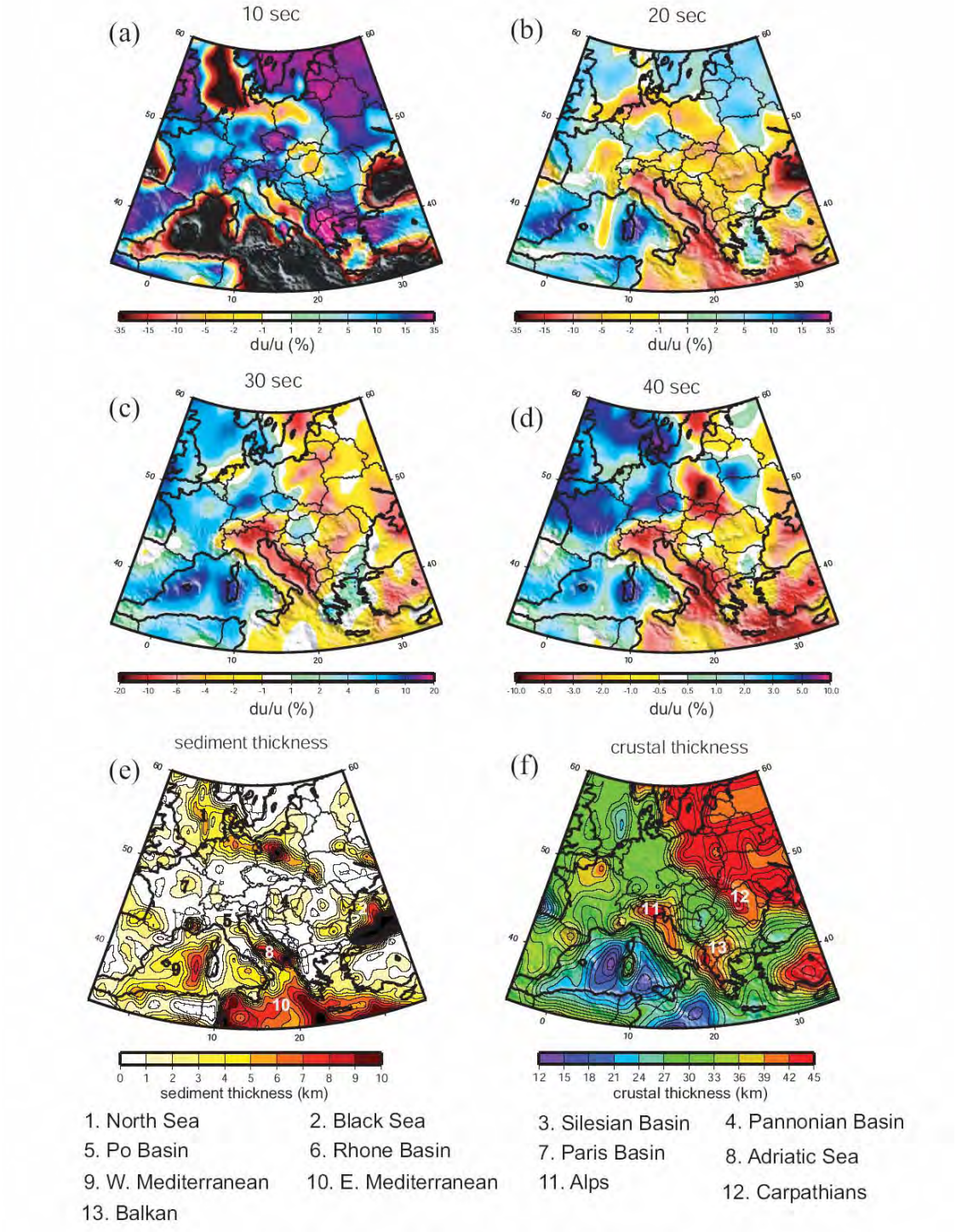


Figure 6. (a–d) Estimated group speed maps at 10, 20, 30, and 40 s periods. Maps are presented as a perturbation from the average across the map in percent. (c) and (f) Maps of sediment thickness and crustal thickness (Bassin et al., 2000; Laske and Masters, 1997). The locations of geological units discussed in the text are marked approximately.

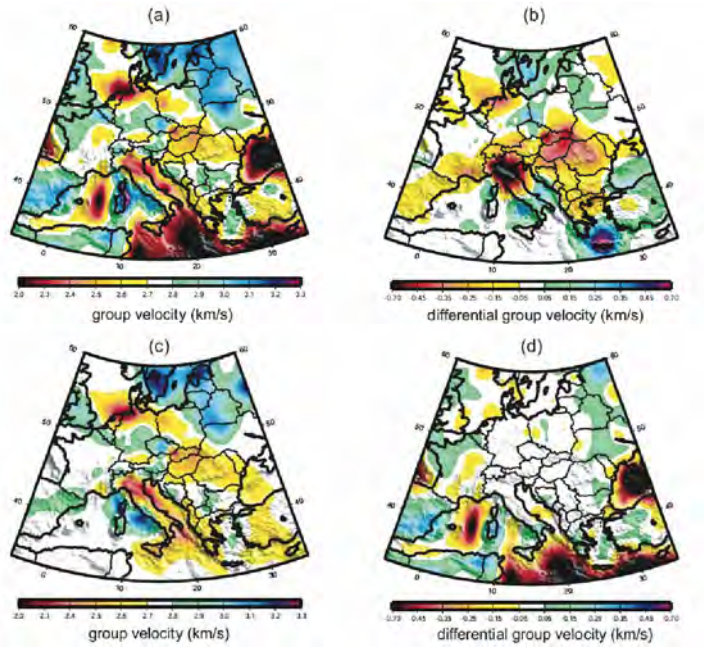


Figure 7. Group speed maps at 16 s periods. (a) Estimated group speed map. A reference map has been used as a starting model in the inversion. (b) Difference between the estimated map in (a) and the reference map. (c) Estimated group speed map determined without a reference map. Comparison should be made with (a). (d) Difference between the two estimated maps in (a) and (c).

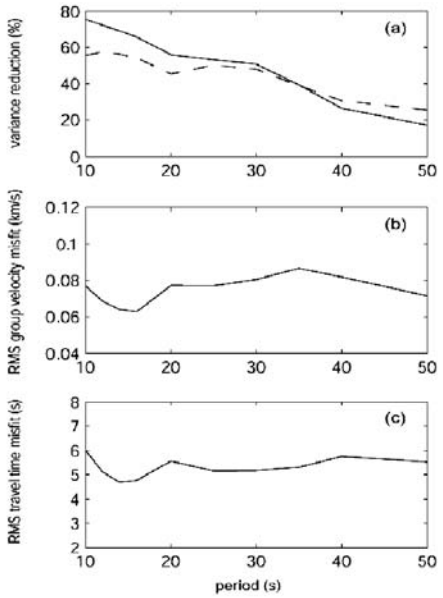


Figure 8. Various misfit statistics for the estimated group speed maps to the observations taken after all stages of data rejection are complete. (Top) Misfit is represented as reduction of variance delivered by (solid line) the estimated maps relative to the predicted group velocity maps from the global 3-D model (Shapiro and Ritzwoller, 2002) and (dashed line) the average velocity across each map. (Middle) RMS group velocity misfit presented versus period. (Bottom) RMS travel time misfit presented versus period.

CALIBRATION OF 3D UPPER MANTLE STRUCTURE IN EURASIA USING REGIONAL AND TELESEISMIC FULL WAVEFORM SEISMIC DATA

Barbara Romanowicz, Mark Panning, Ahyi Kim, Federica Marone, and Douglas S. Dreger

University of California, Berkeley

Sponsored by National Nuclear Security Administration
Office of Nonproliferation Research and Development
Office of Defense Nuclear Nonproliferation

Contract No. DE-FC52-04NA25543

ABSTRACT

We present progress in the development of a new approach to develop and evaluate earth models at the regional scale that utilizes full waveform seismograms.

Adequate path calibrations are crucial for improving the accuracy of seismic event location and origin time, size, and mechanism, as required for Comprehensive Nuclear-Test-Ban Treaty (CTBT) monitoring. There is considerable information on structure in broadband seismograms that is currently not fully utilized. The limitations have been largely theoretical. The development and application to solid earth problems of powerful numerical techniques, such as the Spectral Element Method (SEM), has opened a new era, and theoretically, it should be possible to compute the complete predicted wavefield accurately without any restrictions on the strength or spatial extent of heterogeneity. This approach requires considerable computational power, which is currently not fully reachable in practice.

We have implemented an approach which relies on a cascade of increasingly accurate theoretical approximations for the computation of the seismic wavefield to develop a model of regional structure for the area of Eurasia located between longitudes of 30 and 150 degrees E, and latitudes of -10 to 60 degrees North. The selected area is highly heterogeneous, presenting a challenge for calibration purposes, but it is well surrounded by earthquake sources and a significant number of high quality broadband digital stations exist, for which data are readily accessible through Incorporated Research Institutions for Seismology (IRIS) and the Federation of Digital Seismic Networks (FDSN).

The initial model is derived from a large database of teleseismic surface waveforms using well-developed theoretical approximations, the Path Average Approximation (PAVA) and Nonlinear Asymptotic Coupling Theory (NACT). Both approaches assume waveforms are only sensitive to structure along the great circle path between source and receiver, which is adequate for the development of a smooth velocity model. This model is already parameterized and developed at relatively short wavelengths on the order of 200 km in the best-sampled regions and 400 km elsewhere.

We are refining this velocity model in a smaller subregion using a more accurate theoretical approach. We utilize an implementation of a 3D Born approximation, which takes into account the contribution to the waveform from single scattering throughout the model, including points off of the great circle path, which has been shown to accurately represent the wavefield in several situations where approximations such as PAVA and NACT are problematic.

The Born approximation has already been used to perform a preliminary inversion of regional waveforms for a smaller subregion between longitudes 90 and 145 degrees E, and latitudes 15 and 40 degrees N with a subset of the original dataset consisting of the source-receiver pairs contained within the region. However, to improve resolution, we are implementing an inversion scheme where PAVA and NACT are used to compute sensitivity outside the region and the Born approach inside the region. This inversion is being complemented by forward modeling of regional broadband waveforms using 2D and 3D finite element codes. This allows us to better constrain shorter wavelength and crustal structure.

There is also now a regional implementation of the SEM code available, and work is underway to refine the model further using a novel inverse approach where the synthetic seismograms in the inversion are calculated with SEM using a stacked-source approach.

OBJECTIVES

The primary objective of this research is to develop and apply an approach to utilize increasingly advanced theoretical frameworks and numerical methods in order to obtain improved regional seismic structure calibration. Specifically, a large-scale regional Eurasian model has been developed from a large dataset of seismic waveforms using the PAVA and NACT (Li and Romanowicz, 1995), which are well-developed normal-mode based approaches which consider 1D and 2D waveform sensitivity respectively along the great-circle path between source and receiver. We are now refining this model in a smaller region using a linear implementation of Born single-scattering theory (Capdeville, 2005), which more accurately represents the 3D sensitivity of the seismic wavefield, as well as comparing using a non-linear modified implementation of the Born kernels. Finally, we will utilize the SEM, a numerical approach that accurately models both 3D and non-linear effects (e.g., Faccioli et al., 1996; Komatitsch and Vilotte, 1998; Komatitsch and Tromp, 1999), which is now being adapted to the regional case. To conserve computational resources for this step we will restrict the use of spectral elements to the upper mantle by coupling to a normal mode solution (Capdeville et al., 2002) and applying Perfectly Matched Layer (PML) boundary conditions. Additionally we plan to utilize a novel approach with stacked sources (Capdeville et al., 2003) to further speed computation.

A further objective of this research is to perform validation and improved calibration of the model described above using a variety of approaches and datasets, including ground truth datasets from the Knowledge Base. Specifically, we plan to apply teleseismic receiver function modeling, regional broadband data forward modeling, and surface wave group velocity measurements to test and improve the model using data not included in the original inversion. While these additional datasets can help improve all aspects of the model, we anticipate the greatest improvement in the shallow structure, particularly the crust, which is not as well constrained by the longer-period data used in the initial model development.

This research can then serve as a proof of concept for applying a similar approach to the calibration of seismic structure in other regions of the Earth.

RESEARCH ACCOMPLISHED

A global dataset of surface wave waveforms crossing the region of interest was collected. We started from the existing waveform database that was collected at Berkeley over the last 10 years for the construction of global mantle tomographic models (Li and Romanowicz, 1996; Megnin and Romanowicz, 2000; Gung et al., 2003; Panning and Romanowicz, 2004). The goal was to complement this global database in the region of interest. After choosing data from 20 new events, and adding in the data from the existing dataset, we now have 38,826 3-component waveforms from 393 events recorded at 169 stations. The data has been processed using an automated algorithm, which removes glitches, and checks for many common problems related to timing, poor instrument response, and excessively noisy windows. A weighting scheme has been applied to insure even distribution of data across the region.

We have developed a starting radially anisotropic model using NACT (Li and Romanowicz, 1995) which covers the large Eurasian region (Figures 1 and 2). This model is parameterized laterally in spherical splines. The isotropic velocity (Figure 1) is parameterized in level 6 splines, which correspond to lateral resolution of ~200 km, while the radial anisotropic parameter ξ (V_{SH}^2/V_{SV}^2) (Figure 2), which is less well-constrained, is parameterized in level 5 splines, which have resolution of ~400 km.

We have nearly completed the technical work on developing the theoretical and numerical approaches which consider 3D waveform sensitivity. A regional version of the SEM code is in final debugging in collaboration with researchers at Institut de Physique du Globe de Paris (IPGP). This code takes the well-developed global SEM code, and modifies it to limit the lateral and radial extent of the volume by implementing PML boundary conditions on all sides except the free surface, which effectively eliminate spurious reflections from the lateral boundaries of the region. The final technical work on this code is some debugging on the implementation of attenuation and interpolation of the 3D velocity model. However, while preparation of that code continues, we have proceeded to develop a complementary 3D inversion approach, which incorporates many of the advantages of the coupled spectral element method (CSEM) inversion approach discussed in the proposal. As shown in previous reports for this project, very similar accuracy in defining the partial derivatives with respect to model parameters can be obtained using a 3D implementation of the Born (single scattering) approximation. For this reason, we intend to use

this approach for definition of the partial derivatives with respect to model parameters for the development of the final model using SEM for the forward calculations, as using the numerical approach for partial derivatives becomes prohibitively expensive for models with large number of model parameters. We have also adapted this approach to directly invert our surface wave dataset until the availability of the SEM code. Because the Born approach is somewhat less numerically intensive than the CSEM-based inversion, an added benefit is that stacking of sources is no longer required, and therefore the waveforms can be divided into packets. Using packets is advantageous as it allows us to only use the highest quality data from the waveform dataset, while removing noisy portions of the seismograms.

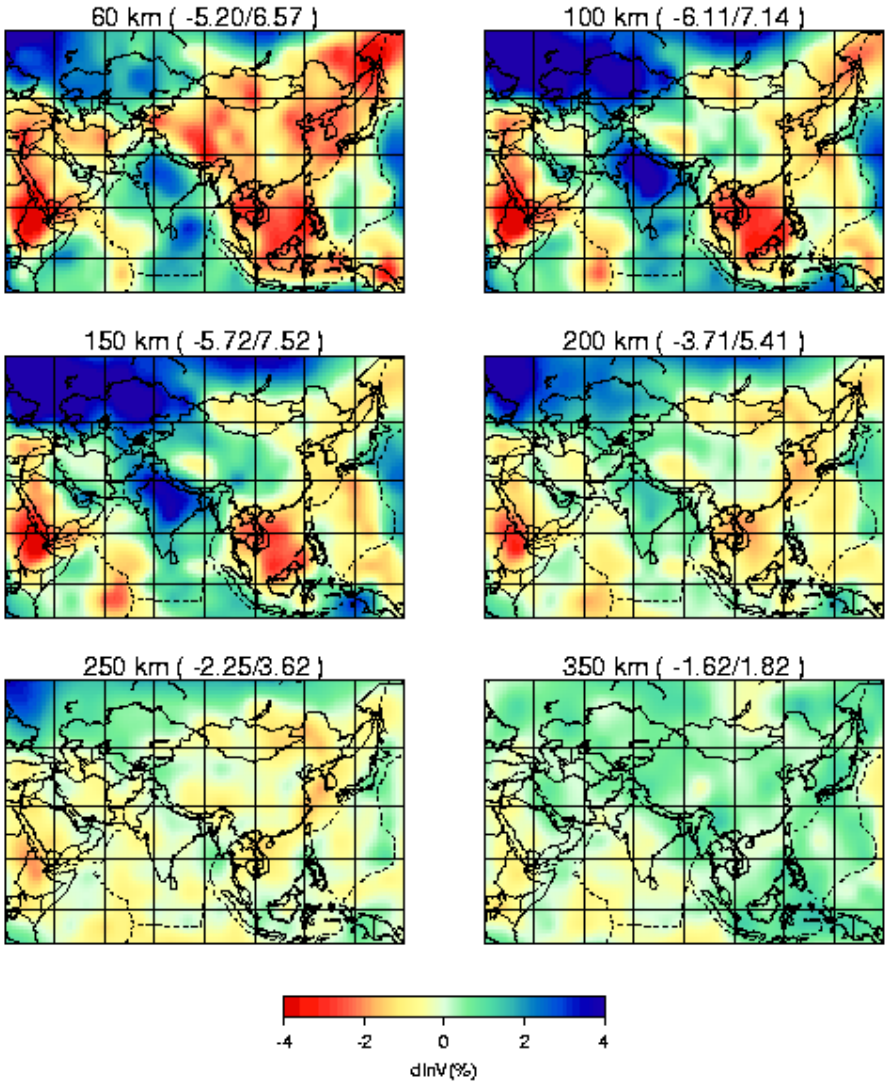


Figure 1. Starting isotropic shear velocity model derived using NACT. The lateral parameterization in terms of level-6 spherical splines, gives a resolution of ~200 km. Values are shown as percent perturbations to the isotropic velocity of the reference model, PREM.

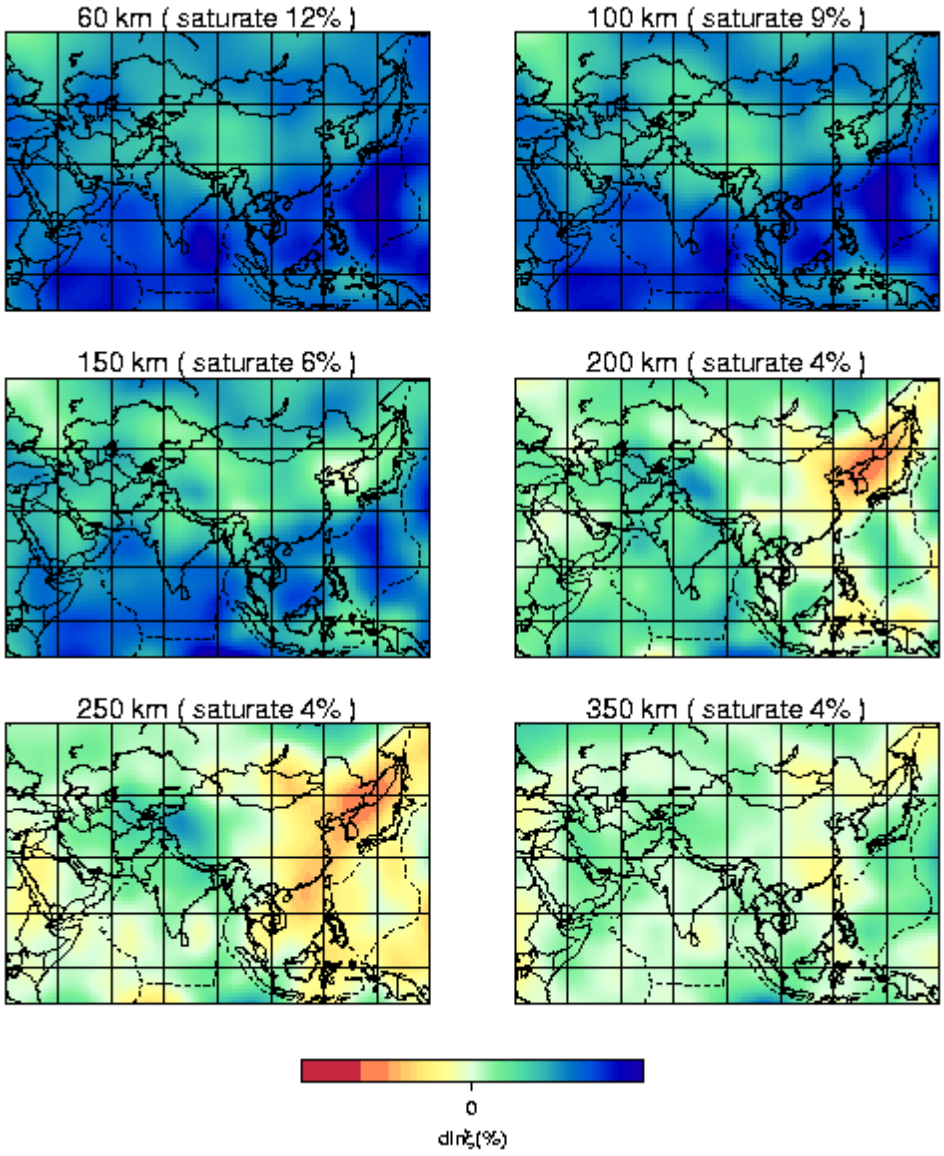


Figure 2. Maps of ξ (V_{SH}^2/V_{SV}^2) for the starting model. Values are shown relative to an isotropic model (ξ=1.0), including the anisotropy of the starting model above 220 km. Blue regions represent regions where $V_{SH}>V_{SV}$ and red regions where $V_{SV}>V_{SH}$.

While awaiting the SEM inversion, we have been exploring preliminary refinements of the model using 3D sensitivity in the subregion using vertical component records from 180 events where the source-receiver paths are contained within the larger region. For this preliminary work, we are focusing on isotropic velocity expanded in level 5 splines in order to determine what partial derivative approach will give the best results when used in conjunction with the regional SEM code. We explore two different implementations of 3D Born single-scattering theory. The first approach maps the effect of structure into linear perturbations to the amplitude of the reference seismogram (Capdeville, 2005). The 3D sensitivity of this approach provides a great improvement over previous approaches which neglect off-path sensitivity for some complex paths (Figure 3). For some relatively simple paths through strong anomalies, however, a linear amplitude perturbation approach can be outperformed by an approach that instead perturbs the phase of the reference seismogram such as the PAVA (Woodhouse and Dziewonski, 1984) (Figure 4), which is non-linear in amplitude. For this reason we choose to also explore an implementation where the effect of the average structure along the great-circle path is treated as a perturbation to the phase of the seismogram

as in PAVA, while the effects of 3D sensitivity including off-path sensitivity are included as a linear amplitude perturbation. This can be easily accomplished because we can show that the linearized version of PAVA is already included due to coupling between modes of different frequencies along a given dispersion branch (Romanowicz, 1987), and we can subtract this contribution from our linear Born kernels, and replace it with the non-linear contribution from PAVA.

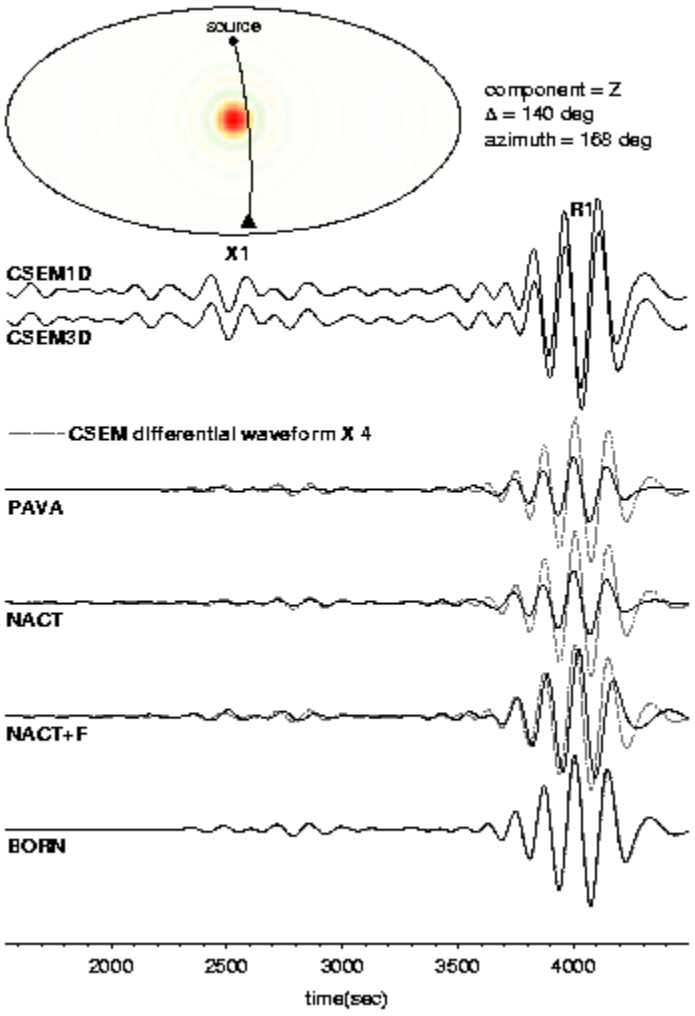


Figure 3. Synthetic test of various theoretical approaches for a path grazing the edge of 5% slow anomaly. The top two traces are synthetics calculated in SEM for the 1D reference model and the 3D perturbation shown at top. The bottom four traces are differential seismograms (3D synthetic minus reference trace) calculated for 4 different theoretical approaches (solid) plotted over the SEM differential seismograms (dotted). PAVA and NACT are asymptotic approaches with 1D and 2D sensitivity respectively constrained to the great-circle path, while NACT+F uses derivatives of structure across the path to approximate the effects of focusing. Born is the 3D implementation of single-scattering discussed in the text.

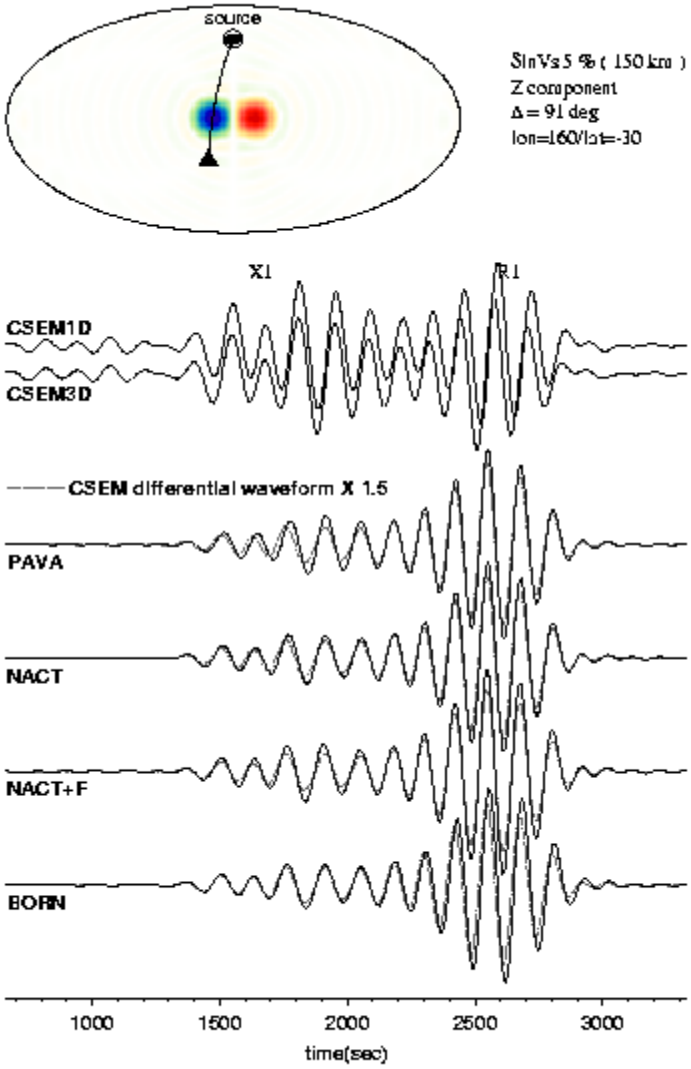


Figure 4. Same as Figure 3 for a different velocity model and a path through the center of a 5% fast anomaly. While all approximations have similar performance, note that the first 3 approaches, which perturb the phase of the seismogram perform slightly better, particularly for the fundamental mode R1.

We develop two models of the subregion using these two Born implementations. Structure outside the subregion is modeled using NACT in both cases. Because the preliminary models are developed with only vertical component data, anisotropy is constrained to be equal to the reference model within the region. From depths of 100 km to 250 km, the two models (Figures 5 and 6) are in good agreement. At a depth of 60 km, the results are more unstable, with relatively large differences between models developed with linear Born (Figure 5), modified non-linear Born (Figure 6), and one developed with NACT using the same dataset and the same relatively low level of resolution (not shown). Work is ongoing to determine the origin of this instability. However, the stable structure at depth in agreement with other models of the region shows that the partial derivatives calculated in this manner should be useful when developing the final model using SEM. Further work is needed to determine whether there is an advantage to be gained by using the modified non-linear Born kernels rather than the linear partials in the final inversion.

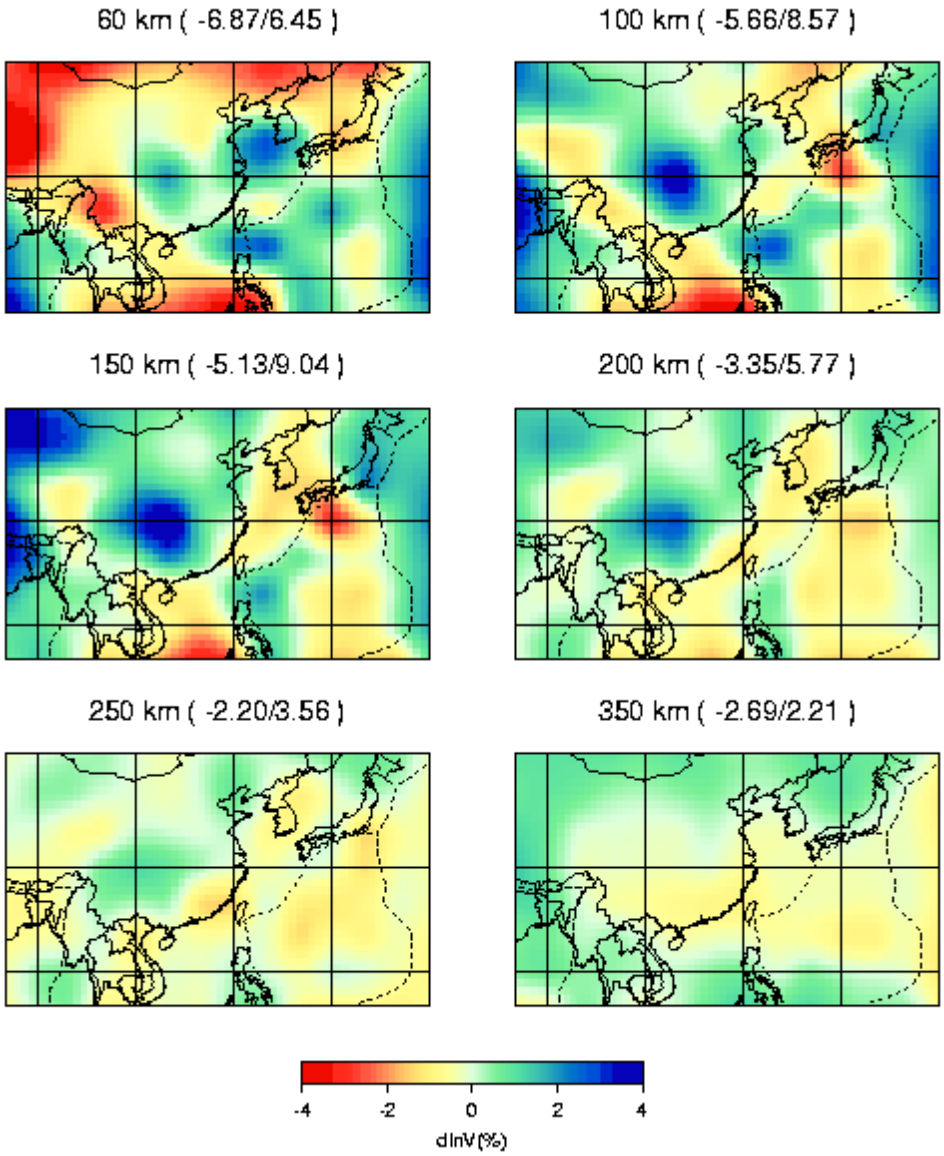


Figure 5. Shear velocity model developed using linear Born kernels for 180 events recorded on the vertical component. Values shown are perturbations relative to the isotropic average of the reference model.

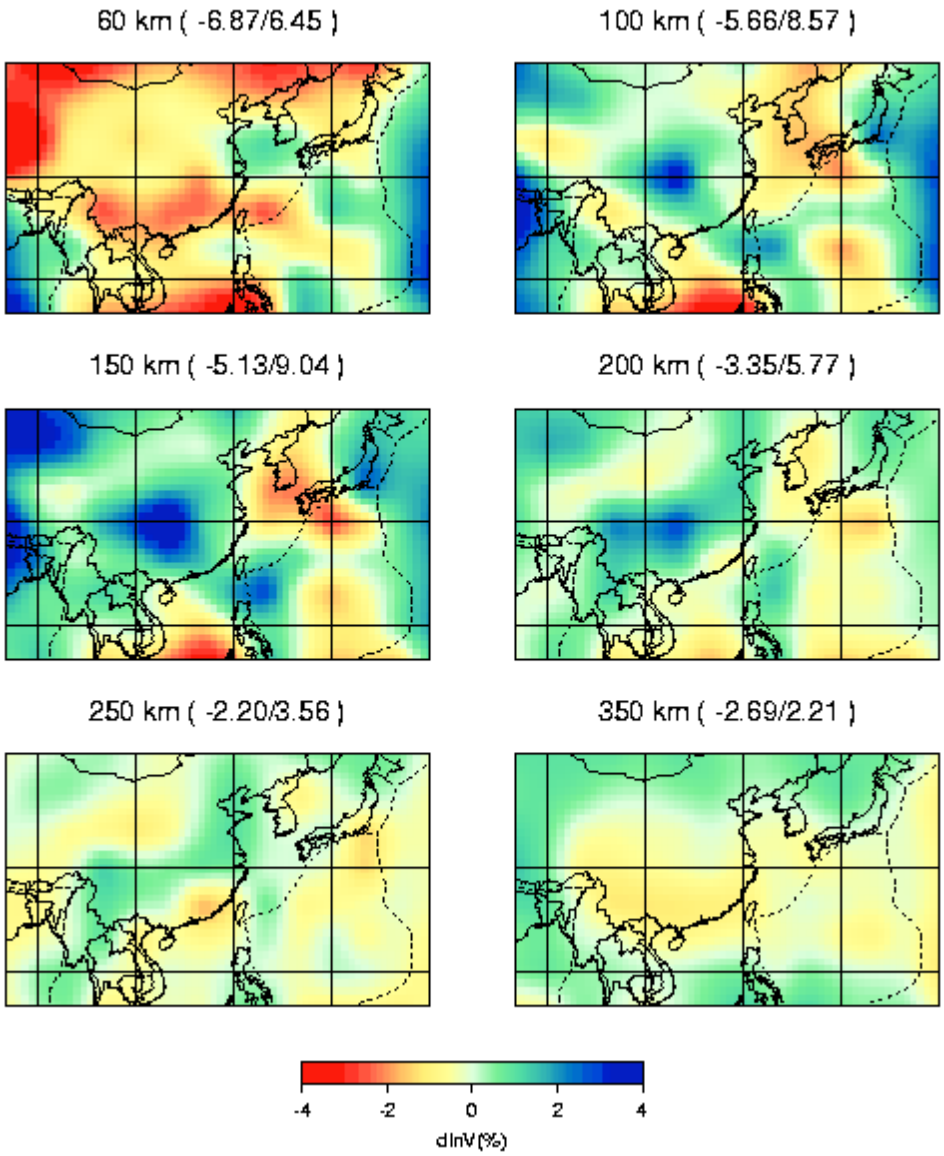


Figure 6. Same as Figure 5 for the model developed using the modified non-linear Born partial derivatives.

CONCLUSIONS AND RECOMMENDATIONS

Using better theoretical and numerical approaches in regional tomographic modeling is very important for adequate seismic path calibration. Here a 3D implementation of Born scattering theory is shown to accurately model 3D effects for a few particular structures, while potential improvements to the method are also explored. This approach should allow for relatively rapid calculation of partial derivatives for use in an inversion based on the regional implementation of SEM.

Further work on using SEM, a numerical approach which takes into account 3D and nonlinear effects, in an inversion should offer continued improvement of the model. Additionally, other approaches and datasets, including ground truth datasets from the Knowledge Base, teleseismic receiver functions, broadband waveform forward modeling, and surface wave group velocities allow for validation and improvement of the model.

ACKNOWLEDGEMENTS

We would like to acknowledge Yann Capdeville and Paul Cupillard at IPGP for extensive work on both the Born and SEM codes. Many computations were performed using computing resources obtained through a startup allocation at the National Energy Research Scientific Computing Center from the DOE Office of Science Geosciences division.

REFERENCES

Capdeville, Y., E. Chaljub, J. P. Vilotte, and J. P. Montagner (2002). Coupling the spectral element method with a modal solution for elastic wave propagation in global earth models, *Geophys. J. Int.* 152: 34–66.

Capdeville, Y., B. Romanowicz, and Y. Gung (2003). Global seismic waveform tomography based on the spectral element method, abstract, joint AGU/EGS/EUG Meeting, Nice, April 2003.

Capdeville, Y. (2005). An efficient Born normal mode method to compute sensitivity kernels and synthetic seismograms in the Earth, *Geophys. J. Int.* 163: 639–646.

Faccioli, E., F. Maggio, A. Quarteroni, and A. Tagliani (1996). Spectral-domain decomposition methods for the solution of acoustic and elastic wave equations, *Geophysics* 61: 1160–1174.

Gung, Y., M. Panning, and B. Romanowicz (2003). Global anisotropy and the thickness of continents, *Nature* 422: 707–711

Komatitsch, D. and J. P. Vilotte (1998). The spectral element method: an effective tool to simulate the seismic response of 2D and 3D geological structures, *Bull. Seism. Soc. Am.* 88: 368–392.

Komatitsch, D. and J. Tromp (1999). Introduction to the spectral-element method for 3-D seismic wave propagation, *Geophys. J. Int.* 139: 806–822.

Li, X. D. and B. Romanowicz (1995). Comparison of global waveform inversions with and without considering cross branch coupling, *Geophys. J. Int.* 121: 695–709.

Li, X. D. and B. Romanowicz (1996). Global mantle shear velocity model developed using nonlinear asymptotic coupling theory, *J. Geophys. Res.* 101: 22,245–22,273.

Megnin, C. and B. Romanowicz (2000). The 3D shear velocity structure of the mantle from the inversion of body, surface and higher mode waveforms, *Geophys. J. Int.* 143: 709–728.

Panning, M. and B. Romanowicz (2004). Inferences on flow at the base of Earth's mantle based on seismic anisotropy, *Science* 303: 351–353

Romanowicz, B. (1987). Multiplet-multiplet coupling due to lateral heterogeneity: asymptotic effects on the amplitude and frequency of Earth's normal modes, *Geophys. J. R. Astr. Soc.* 90: 75–100.

Woodhouse, J.H. and A.M. Dziewonski (1984). Mapping the upper mantle: Three dimensional modeling of Earth's structure by inversion of seismic waveforms, *J. Geophys. Res.* 89: 5953–5986.

Measurements of Regional Phase Q in the Middle East

Eric Sandvol[1], Ekrem Zor[2], Bao Xueyang[1], Jiakang Xie[3], Brian Mitchell[4], Arif H. Gasanov[5], and Gurban Yetirmishli[5]

University of Missouri[1], TUBITAK Marmara Research Center[2],
Air Force Research Laboratory[3], St. Louis University [4], and Azerbeycan National Academy of Science [5]

Sponsored by National Nuclear Security Administration
Office of Nonproliferation Research and Development
Office of Defense Nuclear Nonproliferation

Contract Nos. DE-FC52-03NA99518[1], DE-FC52-03NA99519[3], and DE-FC52-03NA99520[4]

ABSTRACT

In order to construct reliable frequency-dependent Q models for both Lg and Pg, we have used approximately 5,000 waveforms from approximately 200 events recorded by 10 permanent and temporary networks throughout the Middle East. Waveforms with unstable values that had higher standards were separated from the final data file used in our model. Using these waveforms, we have developed a tomographic model with frequency-dependent Q using direct Lg waves in this region. Our tomographic model of Lg Q_o is consistent with previous, more-qualitative Lg attenuation models that showed inefficient or blocked Lg across the Eurasian-Arabian plate boundary. We have also found, similar to the previous models, efficient Lg propagation throughout much of the Arabian Plate. The lowest Q_o values found were located in the East Anatolian Plateau (~70 to 100) and East Anatolian Fault Zone (~80 to 120). The systematic variations appear to correlate with regions where there is evidence of Sn-to-Lg converted energy leaking into the Lg group velocity window.

We have also measured Pg across the Middle East, including the Arabian Platform and the Arabian Shield. We have manually picked the Pg group velocity window for the seismograms used in the Q-calculations. We also used this process to identify the seismic waveforms where there was a clear Pg phase. In general, we found lower Pg-Q within the Arabian Platform and less Pg attenuation for much of the Arabian Shield. Not surprisingly, we found that the Pg-Q does not vary as much as Lg Q; however, the general trend is the same: low Q within the plateau and high Q within the stable Arabian Plate. The frequency dependence, however, is different than what we have found for Lg. We have found a higher eta (η~0.4) for Pg as compared with Lg. Resolution tests of 2 x 2 cell size for our Pg-Q tomography indicate that we have very good resolution throughout much of the Anatolian plateau. Currently, we cannot resolve details within much of the northern Arabian Plate or the Dead Sea Fault System (DSFS). We still expect to improve on our existing coverage by including waveform data from the Syrian National Seismic Network (SNSN). The SNSN is currently installing several broadband seismometers that will be very important because they are located along key regions of the northern DSFS, and they have reliable instrument response information.

OBJECTIVES

The objective of this study is to obtain laterally varying Q models for multiple regional waves, including Lg, Pg, and Pn, for the Middle East. We are developing Q models that have the highest possible lateral resolution. For some waves such as Lg and Pg, the resulting Q model will be in the form of a tomographic Q map; for other waves such as Sn, the resulting Q models may be region specific. We will divide the Middle East into several sub-regions of constant Q. Blockage effects will be represented by low effective Q values in the models.

Challenges Associated with Regional Phase Q Measurements

It is well known that the attenuation rate of regional waves, including the high-frequency Lg, Pg, Sn, and Pn waves and the lower-frequency surface waves, is highly variable over major continents. Reliable knowledge of the lateral variation in regional wave attenuation rate, or its inverse, Q, is extremely important for event detection and identification in the nuclear monitoring program. The preferred way to acquire this knowledge is to conduct tomographic mapping of regional wave Q. However, in contrast to the wide success in seismic velocity tomography since the 1970s, there has been relatively little progress in Q tomography. The main obstacle is the difficulty in obtaining reliable measurements of Q. The observed amplitude of high-frequency waveforms is affected by a number of factors, including (1) possible non-isotropic source radiation patterns; (2) source spectra that may be only grossly described by a seismic moment and a corner frequency; (3) geometrical spreading terms caused by the wave front expansion which, in complex 3D Earth structures, may cause focusing and defocusing; and (4) potential site responses caused by local structural complications under the seismic stations. Effects of these factors are difficult to correct, causing biases in Q measurement. We have assembled a unique waveform database with reliable instrument response information for both the short period and broadband stations (Figure 1).

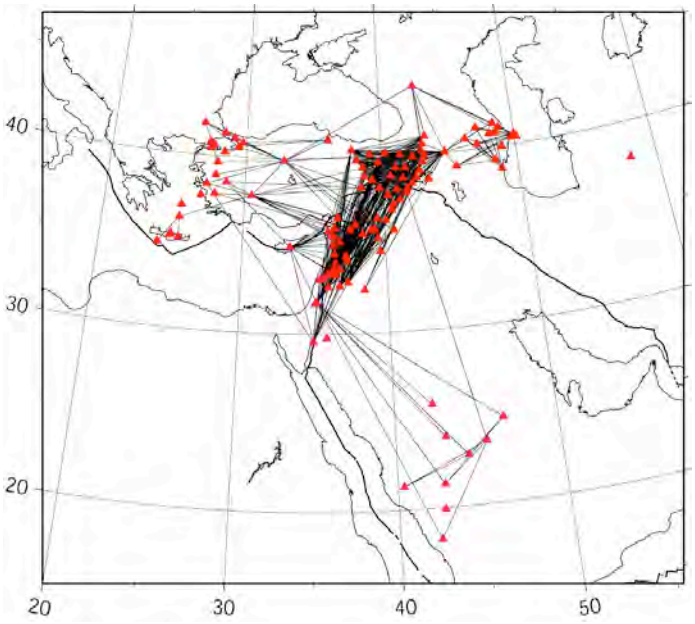


Figure 1. The current two station paths for Turkey and surrounding regions that we have used for both Pg and Lg. We have determined reliable Q measurements for all existing paths.

RESEARCH ACCOMPLISHED

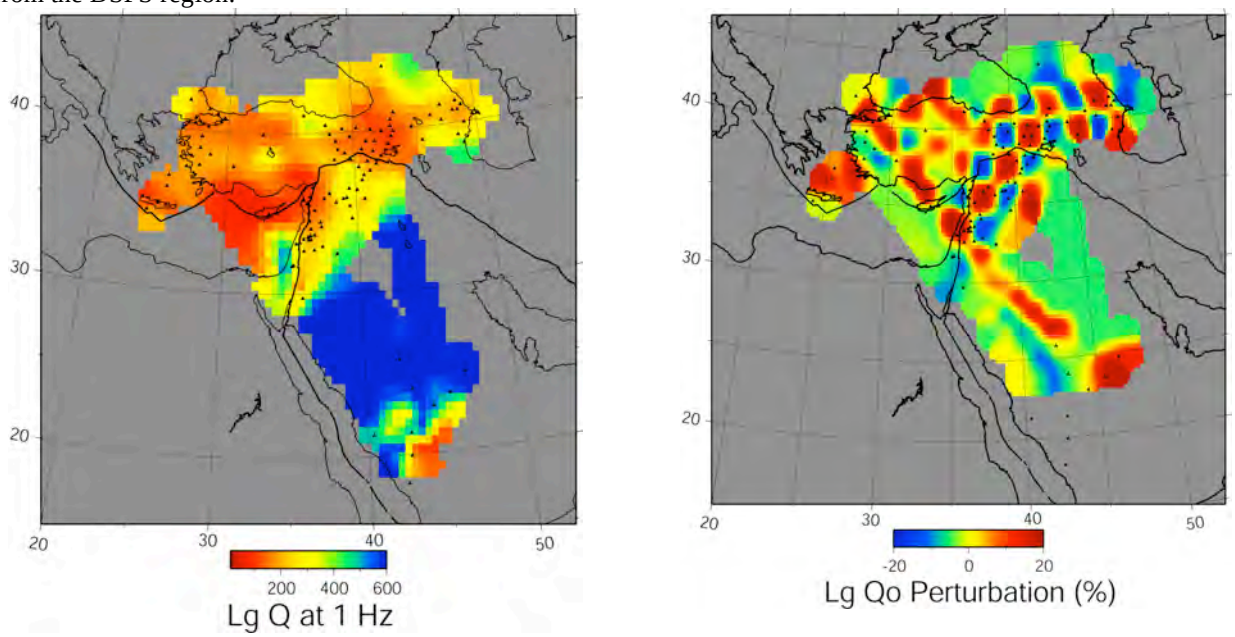
We determined the possible two-station paths aligned with every source. To define the alignment we use an angle $\delta\theta$, which is the difference between the azimuths from the source and the two stations. The choice of $\delta\theta_{max}$ is less restrictive for Lg than for many other phases. The Q_o and η values may contain errors because of the effects of *Lg* attenuation outside the path and a non-isotropic source radiation pattern using non-zero $\delta\theta$. In order to minimize this error, we chose to set $\delta\theta_{max}$ to 15°, as explained by Xie et al. (2004), based on results of Der et al. (1984). The second important parameter in this method is the inter-station distance (Δ_{ij}). The potential error caused by Δ_{ij} is strongly related to the estimated Q_o value for the corresponding path and can be estimated by using the equation given by Xie et al. (2004):

$$\frac{\delta Q_0}{Q_0} \approx 1.1\left(\frac{Q_0}{\Delta_{ij}}\right) \qquad (1)$$

In order to keep this error lower than 35% with a given modeling error value (δx) as 0.2, the inter-station ratio between Q_o and Δ_{ij} should not be greater than 1.6. By applying the criterion of $\delta\theta_{max}$ = ±15° and the inter-station ratio = 1.6 to the ~2300 Lg spectra, we have found 1,383 two-station paths from approximately 140 regional events (Figure 1). When calculating Lg Q_o and η, we did not fix the Lg window on the waveform because Lg velocity typically varies by 20% from one region to another, as emphasized by Nuttli (1973). We define our frequency dependent Q model using Q_o and η using the following relation:

$$Q(f) = f^{\eta-1} Q_0 \qquad (2)$$

We also show two interesting inter-station paths crossing the western Taurus Mountains in southern Anatolia and the eastern Mediterranean. Exceptionally low to normal Lg Q_o valus have also been found for stations ISP-MALT (~150-315) and CSS-EIL (~300). The relatively higher values beneath the western Taurus Mountains may be related to the root of the mountain. In the eastern Mediterranean, we observe what appears to be a relatively fast (3.9 km/s group velocity) phase for the inter-station path between Israel and Cyprus (Figure 1). It is not classified as Sn because it arrives much later than a typical Sn. The usual Sn window is plotted in the figure using the upper mantle velocity between 4.5 and 4.7 km/s. With its relatively fast group velocity and its path through oceanic crust, this is probably energy converted from Sn to Lg. The conversion is probably occurring along the northern coast of the Sinai, west of the southern DSFS. This conversion will bias our Q measurements upward along the eastern Mediterranean. It is interesting to note, however, that the Lg Q values are consistent with the number we obtained from the DSFS region.



(a) **(b)**

Figure 2. (a) Our current Lg Q tomography for the Middle East and surrounding regions. (b) Resolution checkerboard test using the two-station paths shown in Figure 1.

Mapping Variations in Lg Q_o and η

Of the 1,383 two-station pairs, those paths with standard deviations greater than 50% from the linear regression were excluded from the tomography. This model is a significant improvement for the Dead Sea Fault region, where we have added approximately 600 new two-station paths using data from the SNSN. Even though this is primarily a short period network, we were able to verify that we have accurate instrument response data for all 26 short period stations in the SNSN using reverse two-station paths.

We have defined a two-station blocked Lg path as a two-station pair, where Lg is observed at the closest station and then not observed at the more-distant station. Hence, we know that the Lg blockage is occurring between the two

stations. After averaging repeated observations from 296 unblocked two-station paths, the resulting Lg Q_o values were used to obtain a laterally varying Q_o model, as shown in Figure 2a, using a 1º x 1º cell size. We used the average Lg Q_o of 148 for the initial constant Q_o model for the study area. From the total of 720 cells, 198 were sampled and used. The variance reduction is 43% over an initial constant Q model, corresponding to 70% variance reduction in predicted amplitudes. Although stable measurements of inter-station η values are much more difficult to obtain than those of Q_o values, as stated by Xie et al. (2004), an attempt has been made to invert for laterally varying η values and their deviation from the linear regression.

In order to increase path coverage and resolution, we supplemented the 296 unblocked paths with 154 blocked paths in our tomographic model. In order to estimate the Q values for these blocked paths, we used the equation below:

$$\frac{V_{Lg}}{\pi \Delta_{ij}} ln\left(\left(\sqrt{\frac{\Delta_i}{\Delta_j}}\right) A_{loss}\right) = f^{1-\eta} Q_0^{-1} \qquad (3)$$

We have assumed a $V_{Lg} = 3.5$ *km/s* and $A_{loss} = 99.0$. This represents a 99% amplitude loss from the first (i^{th}) station to the second (j^{th}) for $f = 1$ *Hz*. We term this value the maximum allowable Lg Q_o. Of course the actual Q_o value is probably less than this value. Attenuation perturbations of ±20% were used to calculate a synthetic data set. By using a series of checkerboards with different cell sizes, we estimated that the smallest easily distinguished cell size is 2º x 2º. The checkerboard test for the tomographic inversion is shown in Figure 2b. As can be seen from this figure, we have excellent resolution for the areas where we have good coverage in terms of crossing rays. In the areas where we do not have enough crossing rays, such as in the Arabian Plate, smearing reduces the resolution.

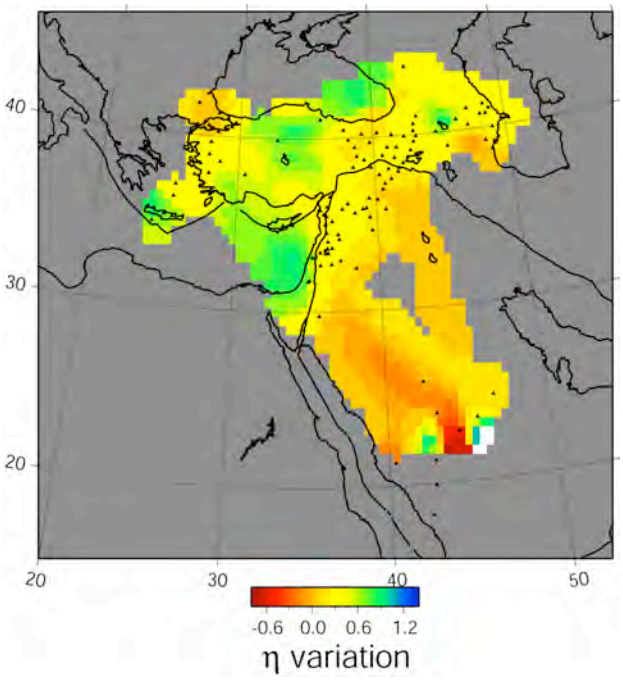
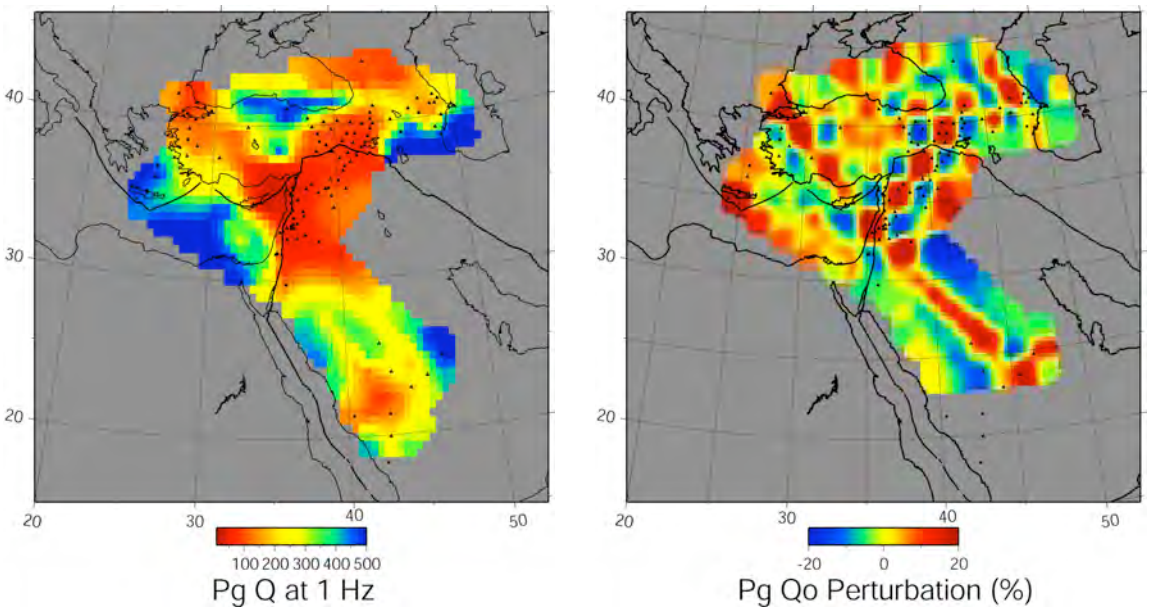


Figure 3. Frequency dependence for Lg attenuation in the Middle East. In general, we observe lower η values where we have higher Q values.

We also finalized our model for the frequency dependence of Lg Q. Figure 3 shows our map of η for the northern Middle East. We found an anomalously low average η for the Middle East (0.22). We also found large regions of negative η. We found a correlation between large Q values and small η values that is consistent with frequency-dependent coda-Q measurements. The spatial variation in η also suggests that these anomalously low Q measurements might be, to some extent, a function of Sn-to-Lg converted energy.

Comparison with Coda Measurements (e.g., Cong and Mitchell, 1998)
Given the larger number of available coda-Q measurements, it is important to compare frequency dependent Q models for the Middle East. The most comprehensive Lg coda-Q model for the Middle East is Cong and Mitchell (1998). The comparison of the two Lg Q models reveals a number of important consistencies and some interesting differences. Overall, the direct phase and coda measurements demonstrate a strong and relatively rapid increase in attenuation across the Arabian-Eurasian plate boundary and relatively small attenuation across the Arabian Shield. The direct phase methods have some further complexity that must be verified but suggest that much of the Lg attenuation in the Middle East is concentrated within the fault zones.

In terms of the frequency dependence of the coda and direct Lg Q measurements, the coda measurements of η are consistently larger. This has been true not just for the Middle East but also for measurements throughout Eurasia. However, we do observe consistent spatial variations of η. This includes the finding of smaller values for the Arabian Shield (–0.1 for the direct phase and 0.4 for coda) and larger values for the Anatolian plateau (0.5 for direct phase and 1.0 for the coda measurements).



(a) **(b)**

Figure 4. (a) Our current Pg Q tomography for the Middle East and surrounding regions. (b) Resolution checkerboard test using Pg two-station paths. This model suggests that we have good resolution for most of the northern Arabian-African-Eurasian plate boundaries but are still lacking data resolution within much of the Arabian plate.

Mapping Variations in Pg Q_o and η
We have also created a Pg-Q model for the Middle East. We measured Pg across the Arabian platform and the Arabian shield. We manually picked the Pg group velocity window for the seismograms used in the Q calculations. We also used this process to identify the seismic waveforms where there was a clear Pg phase. In general, we found Pg-Q values between 100-200 for northern Arabian Plate and Anatolian Plateau and between 200 and 300 for the Arabian Shield (Figure 4). Similar to our Lg Q model, this model has very good resolution for most of the northern Middle East, including the DSFS, Anatolian Plateau, and Lesser Caucasus. It is important to note that we have assumed an "Lg-like" geometrical spreading function for Pg; however, this assumed function should not greatly affect relative variations in Pg attenuation. We have begun work on estimating the Pg geometrical spreading term and have preliminary results suggesting that it does not vary a great deal across the Middle East.

The Lg and Pg Q models are fairly consistent with regional variations in amplitude ratios for the region. The low Pg Q along the Dead Sea Fault helps to explain the relatively large Lg/Pg amplitude ratios that we have observed there (Sandvol et al., 2001).

Not surprisingly, we found that the Pg-Q does not vary quite as much as Lg Q; however, the general trend is the same: low Q within the plateau and high Q within the stable Arabian Plate. Our estimated η value, however, is higher (~0.4) for Pg than for Lg (Figure 5). This observation is consistent with the idea that some of the anomalously low frequency dependence for Lg is caused by high frequency energy leaking into the crust because this effect might be different for Pn-to-Pg converted energy.

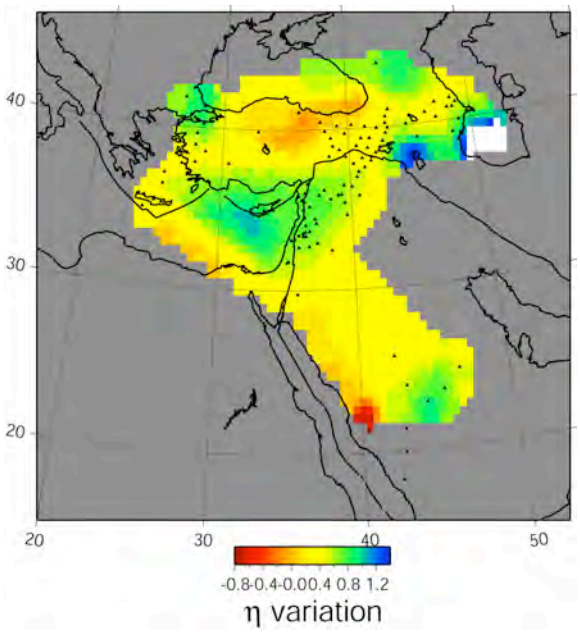


Figure 5 Frequency dependence for Pg. The average η value for the Middle East is 0.25. We have found relatively constant frequency dependence. The only significant variation occurs in regions where we have relatively low resolution (see Figure 4b.).

CONCLUSION(S) AND RECOMMENDATIONS

In this study, we processed a large set of new broadband waveform data to obtain an Lg Q model for much of the Middle East. The resulting tomographic model in Figure 2a clearly shows the variation in Lg Q across the boundary between the Arabian Plate and the Turkish Plateau portion of the Eurasian Plate. The Lg Q_o values are generally higher within the Arabian Plate than beneath the Turkish Plateau. Other studies have similarly concluded that Lg propagation in the Turkish-Iranian Plateau is usually blocked or highly attenuated (Sandvol et al., 2001; Al-Damegh et al., 2004). We also observe substantial variation in Lg Q_o values within the Arabian Plate itself; we observe higher values beneath the Arabian Shield than beneath the Arabian and northern Arabian Platforms. These higher values could be due, in part, to systematic errors, given the lack of crossing paths in this portion of our model. Similarly, the Turkish Plateau also shows some significant variation in crustal attenuation, with normal Lg Q_o values observed beneath the central Taurus Mountains and very low Lg Q_o values beneath the eastern Anatolian Plateau and western Turkey around the Menderes Massif. Of course some sub-regions are not sampled by the two-station paths because of the lack of stations in central Anatolia from south to north.

High Pg and Lg attenuation values within the Anatolian Plateau (Q_o ~100 to 200) may be caused by a combination of scattering and intrinsic attenuation. Scattering attenuation is due to the tectonic complexity, and the intrinsic attenuation could be due to the wide spread crustal melting. However, the low Q_o values in the eastern Anatolian Plateau (~70 to 100) and portions of western Turkey (~60 to 150) are probably due to the widespread Quaternary volcanism. In western Turkey, there is a correlation with the location of the young volcanism, and the geothermal activity (İlkışık, 1995; Göktürkler et al., 2003). Zhu et al. (2006) have shown that the crustal thickness of western Turkey probably does not change rapidly enough to reduce or block the Lg phases and heavily attenuate Pg. Similarly, the receiver function waveform inversion in eastern Turkey has suggested that there is no rapid change in the crustal thickness across the Bitlis Suture and East Anatolian Fault Zone. They also observed localized mid-

crustal seismic low-velocity zones scattered throughout the eastern Anatolian Plateau. These low-velocity zones might be an indication of partial melt within the eastern Turkey crust (Zor et al., 2003). This inference is also supported by the widespread young (less than 6 Ma) volcanism in the region (e.g., Keskin, 2003) and low Pn velocities (Hearn and Ni, 1994; Al-Lazki et al., 2004) coupled with high Sn attenuation (Gok et al., 2003; Al-Damegh et al., 2004) as an indication of anomalously hot lithosphere.

Beneath the western Taurus Mountains in southern Anatolia, relatively normal Pg and Lg Q_o values (~200-300) have been found. These relatively higher values may be related to the root of the mountain that would comprise a stable continental crustal waveguide like that in southernmost Tibet in the general region of the high Himalayas (>300) (Xie et al., 2004). Furthermore, the sedimentary cover is limited in this region, which might also improve the efficiency of Lg propagation in this region. It is important to note that our paths are all parallel to the strike of the mountain front. Gok (2000) suggests that paths that are perpendicular to the Taurides tend to be inefficient or blocked. We were unable to test this because of the lack of perpendicular two-station paths in this region. For northeastern Turkey, the Caucasus, and Azerbaijan, we also found some low-to-normal Lg Q_o values (~170-180), as well as some blocked two-station paths.

We found large variations in Pg and Lg Q_o for paths crossing the Arabian Peninsula (~300-800). Our Lg Q_o values are roughly consistent with the observations from Lg coda-Q (350-500) by Mitchell et al. (1997) and Cong and Mitchell (1998). However, they did not observe Lg Q_o values as high as ours (~800) in the Arabian Plate. This slight inconsistency may be caused by the difference in sampling area between direct Lg and Lg coda. However, it is important to note that we still have relatively few paths crossing the Arabian Shield; therefore, systematic errors caused by the effect of lateral changes in the crustal structure may have a large effect on our measurements. The northern Arabian Platform crust has low-to-normal Lg Q_o values (~300-350). In addition, we observe high Q_o values (~670-800) for the southern Arabian Plate, where previous Lg/Pg studies show little attenuation. This is probably due to the lack of any substantial sedimentary cover in the Arabian Shield. We also observe lower Q values (~550) for paths crossing the northern and southern Arabian Platform, where the sedimentary layer is thicker than for the western Arabian Plate. Additionally, we have found a dramatic decrease in Lg Q_o across the Arabian-Eurasian plate boundary. This is due to a fundamental difference in the rheology of the Anatolian crust compared with the Arabian crust. Paths to the south of the Bitlis Suture have Lg Q_o values of ~350-550, but the paths crossing the Bitlis Suture have an Lg Q_o of ~200. This decrease may be related to the higher intrinsic attenuation from partial melt in the eastern Anatolian Plateau. In contrast, the Pg Q values are uniformly low throughout the northernmost Arabian Plate and into the Anatolian Plateau.

We have found that in order to achieve sufficiently dense two-station paths to cover the Middle East, it is necessary to integrate data from a variety of temporary and permanent, short-period and broadband seismic stations. Using these large data sets, it is possible to construct a reliable model for Lg Q throughout the northern portions of the Middle East and DSFS. We are currently in the process of calculating Q models for Pn, Pg, and Lg.

Clearly, one of the most challenging aspects of calculating Lg in the Middle East is the large number of blocked paths. Therefore, it is critical to accumulate a large number of waveforms at local and near-regional distances in order to better constrain the Q in the very high attenuation zones such as the eastern Anatolian Plateau. Prior work has established the blockage zones, and these blocked paths will also be used to help create a robust attenuation model for the majority of the Middle East. It is therefore essential that more data be collected for these regions of exceptionally low Lg Q, such as the lesser and possibly greater Caucasus and western Turkey.

After we finalize our Lg Q model, we expect to include more than 1,400 two-station paths using Newton-like nonlinear method for inversion with multiple colocated events. Pg and Lg Q_o and η values measured using these methods are of very high quality because they are not subject to the trade-off between source and path parameters. Therefore in the tomographic inversion of laterally varying Q_o and η values, the input Q_o and η values along approximately 900 paths will be used to derive a more long-wavelength Q map for those regions of the Middle East with good two-station path coverage.

It is also important that the two-station Q measurements and coda-based methods are reconciled, especially the systematic variations in the frequency dependence of coda-Q and the direct-phase Q. We plan to apply available methods for Lg Q determination in order to better quantify the potential differences in the techniques. This should help build a more-robust model for high-frequency wave attenuation in the Middle East. Furthermore, our model

needs to be further validated using calibration events with well-known source spectra.

ACKNOWLEDGEMENTS

We would like to thank Randa Mohamad and Dr. Niyazi Turkelli for providing data from the SNSN and the KOERI network, respectively, and for assisting in the analysis of portions of the data. We would also like to thank Dr. Rob Mellors for providing data from the Azerbaijan Seismic Network and Dr. Arthur Rodgers for providing data from two Lawrence Livermore National Laboratory broadband stations in Jordan.

REFERENCES

Al-Damegh, K., E. Sandvol, A. Al-Lazki, and M. Barazangi (2004). Regional seismic wave propagation (Lg and Sn) and Pn attenuation in the Arabian Plate and surrounding regions, *Geophys. J. Int.* 157: 775-795.

Al-Lazki, A., E. Sandvol, D. Seber, M. Barazangi, N. Turkelli, and R. Mohamad (2004). Pn tomographic imaging of mantle lid velocity and anisotrophy at the junction of the Arabian, Eurasian and African Plates, *Geophys. J. Int.* 158: 1024-1040.

Cong, L. and B. Mitchell (1998). Lg coda Q and its relation to the geology and tectonics of the Middle East, *Pure appl. geophys*. 153: 563-585.

Der, Z., M. E. Marshal, A. O'Donnell, and T. W. McElfresh (1984). Spatial coherence structure attenuation the Lg phase, site effects, and interpretation of the Lg coda, *Bull. Seismol. Soc. Am.* 74: 1125-1148.

Gok, R. (2000). Regional wave propagation in Turkey and surrounding regions, *Geophys. Res. Lett.* 27: 429-432.

Gok, R., E. Sandvol, N. Turkelli, D. Seber, and M. Barazangi (2003). Sn attenuation in the Anatolian and Iranian Plateaus and surrounding regions, *Geophys. Res. Lett.* 30: 8042, doi:10.1029/2003GL018020.

Göktürkler, G., Salk, M., and Sari, C. (2003). The numerical modelling of the conductive heat flow in western Anatolia, *The Journal of the Balkan Geophysical Society* 6: 1-15.

Hearn, T., and J. Ni (1994). Pn velocities beneath continental collision zones: the Turkish-Iranian Plateau, *Geophys. J. Int.* 117: 273-283.

İlkişik, O.M., (1995). Regional heat flow in western Anatolia using silica temperature estimates from thermal springs, *Tectonophy.* 244: 1-3, 175-184.

Keskin, M. (2003). Magma generation by slab steepening and breakoff beneath a subduction-accretion complex: An alternative model for collision-related volcanism in Eastern Anatolia, Turkey, *Geophys. Res. Lett.* 30: 8046, doi: 10.1029/2003GL018019.

Mitchell, B. J., Y. Pan, J. Xie, and L. Cong (1997). Lg coda Q variation across Eurasia and its relation to crustal evolution, *J. Geophys. Res*. 102: 22767-22779.

Nuttli, O.W. (1973). Seismic wave attenuation and magnitude relations for eastern North America, *J. Geophys. Res.* 78: 5212-5218.

Sandvol, E., K. Al-Damegh, A. Calvert, D. Seber, M. Barazangi, R. Mohamad, R. Gok, N. Turkelli, and C. Gurbuz (2001). Tomographic imaging of observed regional wave propagation in the Middle East, *Pure Appl. Geophys.* 158: 1121-1163.

Xie, J., R. Gok, J. Ni, and Y. Aoki (2004). Lateral variations of crustal seismic attenuation along the INDEPTH profiles in Tibet from Lg Q inversion, *J. Geophys. Res*. 109: B10308, doi:10.1029/2004JB002988.

Zhu, L., B. Mitchell, N. Akyol, I. Çemen, and K. Kekovalı (2006). Crustal thickness variation in the Aegean region and its implications for the extension of continental crust, *J. Geophys. Res.* 111: doi:10.1029/2005JB003770.

Zor, E., E. Sandvol, C. Gurbuz, N. Turkelli, D. Seber, and M. Barazangi (2003). The crustal structure of the east Anatolian Plateau from receiver functions, *Geophys. Res. Lett.* 30: 8044, doi:10.1029/2003GL018192.

TRANSITION ZONE WAVE PROPAGATION: CHARACTERIZING TRAVEL-TIME AND AMPLITUDE INFORMATION

Peter M. Shearer and Jesse F. Lawrence

University of California San Diego

Sponsored by Air Force Research Laboratory

Contract No. FA8718-06-C-0005

ABSTRACT

We characterize transition-zone seismic wave propagation by mapping and calibrating the travel-time and amplitude behavior of P waves traveling through the transition zone at epicentral distances from 13 to 30 degrees and modeling the triplications resulting from the 410- and 660-km discontinuities. We have built an online database of waveforms from the IRIS FARM archive, which consists of broadband data from the global seismic networks as well as portable seismic arrays deployed in PASSCAL experiments. We process the data to compute source and station amplitude terms to correct for different magnitude sources and near-receiver site effects as well as errors in the instrument response functions. We then compute both global and regional stacks to obtain the average time and amplitude of the wavefield within the 13- to 30-degree distance interval. Because the timing of the secondary branches is variable, we implement an envelope-function stacking method to obtain robust results. We model our data stacks using WKBJ synthetic seismograms and a niching genetic algorithm to explore the model space of different transition-zone velocity structures. We compare these results with long-wavelength models of 410- and 660-km discontinuity topography obtained from SS precursors and more detailed images beneath individual seismic stations derived from receiver functions. Our goal is to produce integrated transition-zone models of seismic velocity and discontinuity topography that will improve our ability to locate and estimate magnitudes of events recorded at regional distances.

OBJECTIVES

This project studies the effects of heterogeneous transition zone structure on seismic travel times and amplitudes. Accurate predictions of P- and S-wave travel times and amplitudes at distances between 13 and 30 degrees are hindered by the sensitivity of the multiple travel-time branches at these distances to variable structure in the mantle transition zone. Both discontinuity topography and bulk seismic velocity anomalies perturb seismic ray paths, which cause focusing and defocusing effects on wave amplitudes as well as travel-time anomalies. However, travel time and amplitude information is critical for locating and estimating magnitudes of target events. By comparing regional variations of triplication amplitudes and travel times with predictions of 3D seismic velocity models, we will obtain improvements in mantle transition zone models, as well as in the estimated locations and magnitudes of recorded events.

The effect of the mantle discontinuities at 410- and 660-km depth is shown in Figure 1, which depicts a series of P-wave ray paths between 13 and 35 degrees. Retrograde branches result from the velocity jump at each of the discontinuities, causing the familiar double triplication centered at about 20 degrees. However, the positions of these branches are sensitive to the discontinuity depths, which typically vary by 30 km or more (e.g., Shearer, 1990, 1991, 1993; Shearer and Masters, 1992; Flanagan and Shearer, 1998a,b; Gu et al., 1998), and to the size of the velocity jumps at the discontinuities, which also exhibit considerable variation (e.g., Melbourne and Helmberger, 1998; Shearer and Flanagan, 1999; Chambers et al., 2005). In addition, there is some sensitivity to 3D velocity variations in the transition zone.

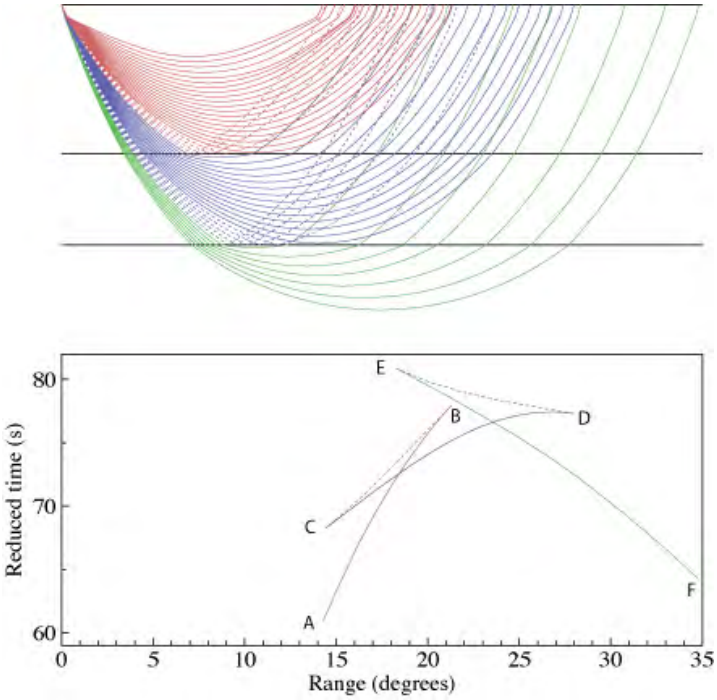


Figure 1. Discontinuities in the mantle transition zone at 410- and 660-km depths cause a pair of triplications in P- and S-wave arrivals between ~15 and 30 degrees. The ray paths (top) are color-coded and correspond to the different branches in the travel-time curve plotted below (reduced at 10 s/degree). The AB branch consists of direct waves that bottom above the 410-km discontinuity (red solid). The BC branch reflects at 410 km (red dashed). The CD and DE branches bottom above and reflect off the 660-km discontinuity (blue solid and dashed). The EF branch bottoms in the lower mantle. This figure is adopted from Shearer (2000).

We plan a series of tests to compare observed P- and S-wave travel times and amplitudes with predictions based on the best current models. These tests will illuminate the strengths and weaknesses of these models and determine if the models are sufficient to explain anomalous travel times and amplitudes at these distances (and consequently

check the robustness of our current event locations and amplitude predictions). This project also will compare global and regional travel-time data sets with thousands of new measurements of travel times and amplitudes recorded at both temporary and permanent seismic stations. These new measurements will focus on obtaining times and amplitudes for all triplication phases, not just the first arrivals. Where data coverage is sufficient, we intend to improve portions of our current models by integrating these new measurements into hybrid models. This will yield more accurate earthquake locations and magnitude estimates for these regions. It may also be possible to interpolate these models to some extent to improve our transition zone models for low data coverage regions.

The triplications cause difficulties for traditional methods of source location, magnitude estimation, and inversions for 3D velocity structure. Therefore, triplication data are typically avoided for seismic tomography and source location. However, details of the triplications can be useful for characterizing heterogeneity and calculating better source locations. With sufficient data, the secondary branches can be used to model variations in discontinuity topography and seismic velocity. Once the structural properties are determined, the high sensitivity of triplication travel-time and amplitude fluctuations to source location and magnitude make triplications ideal for determining source characteristics. However, without an appropriate transition zone model, these times cannot yield accurate times or amplitudes.

The relevance of our results for nuclear test monitoring is that better structural models of transition zone structure will reduce source location and magnitude uncertainties. The anomalous arrival times and amplitudes between 13 and 30 degrees currently limit the usefulness of regional phase data in calculating accurate source locations and event magnitudes. However, records from closer distances are not likely to be available in many parts of the world and small magnitude events are often not well recorded at longer distances because of the sharp drop in P and S amplitudes that occurs just beyond 30 degrees. Thus, unraveling the complexities of the travel-time triplications and improving our models of the transition zone are likely to be critical for accurate monitoring of a significant number of target events.

RESEARCH ACCOMPLISHED

Our initial efforts have concentrated on assembling a database of waveforms from the IRIS FARM archive, which consists of broadband data from the global seismic networks as well as portable seismic arrays deployed in PASSCAL experiments. This involves transferring the data from the IRIS DMC, running the READSEED program to convert them from the SEED format to SAC, and then running a program to convert them to the GFS format that we use for subsequent processing. The GFS files are currently being stored on a RAID system, with both mirroring and tape backup for redundancy in the event of hardware failures. Configuring the RAID system took considerable time, as well as sorting out some of the timing difficulties associated with multiple time windows in the FARM archive, but now we have transferred almost all of the data to our RAID system.

We have also completed computing index files and signal-to-noise estimates for the P and S arrivals, which facilitates later processing and provides a check on the timing integrity of the GFS waveforms. Our basic approach is to measure the signal-to-noise as the ratio between the maximum amplitude (peak to trough) in a time window that contains the phase of interest and a pre-event noise window of equal length. Because the raw data are broadband, we perform this operation separately for different frequency bands.

Finally, we have begun preliminary time and amplitude stacks for the transition zone wavefield and are writing software to isolate station and event correction terms. We also are adapting a WKBJ synthetic seismogram code to generate suites of model predictions for comparison to the data. Our analyses so far have concentrated on characterizing the globally averaged wavefield as a starting reference point for studies of regional variations. Because the position of the triplicated phases is highly variable, we have adopted an envelope-stacking approach that is robust with respect to travel time variations. A simple measure of amplitude versus distance for shallow events (<30 km depth) is provided by the maximum amplitude within a given frequency band. To obtain meaningful results, however, first it is necessary to apply empirical corrections for source size and station gain (or local site effects). We compute these terms iteratively using a robust least-squares method that automatically downweights data outliers.

Results of this analysis for P-waves from earthquakes between 1981 and 2004 are shown in Figure 2, compared to synthetic seismogram predictions for three different models of upper mantle discontinuity depths. Notice that the

amplitude peaks between 15 and 25 degrees as a result of the focusing of energy from the steep velocity gradients through the transition zone. The overall amplitude versus distance behavior is similar to that obtained by Veith and Clawson (1972) for magnitude calibration. Our synthetic seismograms are computed using a WKBJ method, which provides comparable results to reflectivity synthetics at much less computational cost. The advantage of WKBJ is that it will enable us to explore the data fits provided by testing thousands of different models.

The fit between data and synthetics is not perfect and we plan to test whether this reflects limited sampling of model space or a more fundamental problem. In addition to the velocity and Q structure through the transition zone, there are questions regarding exactly how to best filter the data and how to simulate the averaging process (which combines data from many different source-receiver paths and transition zone structures). Our ultimate goal is to perform this modeling separately among different regions.

Some idea of the coverage of the transition zone that we are likely to achieve is shown in Figure 3, which is based on stations and sources contained in the FARM database between 1981 and 2001. The best coverage is in the Middle East and southeastern Asia where it should be possible to completely resolve the mantle triplications.

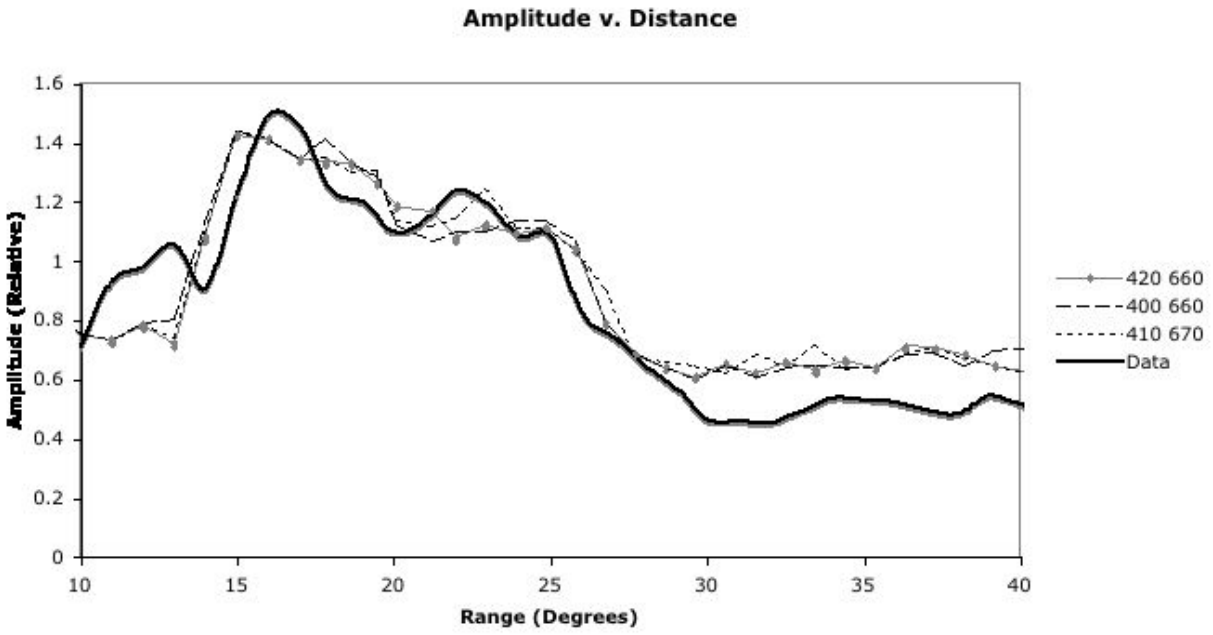


Figure 2. Observed average amplitude versus epicentral distance for shallow earthquakes in the IRIS FARM database. Empirical corrections have been applied for source and station differences. The largest amplitudes occur near 17 degrees and amplitudes are nearly constant beyond 30 degrees.

CONCLUSIONS AND RECOMMENDATIONS

This IRIS FARM database provides a large resource for probing transition zone structure and for characterizing seismic wave propagation through this region at epicentral distances from 13 to 30 degrees. Travel-time and amplitude anomalies reflect large regional differences in upper-mantle discontinuity topography, which can be mapped using synthetic seismograms and compared to long-wavelength models of seismic velocity and discontinuity topography. We anticipate rapid progress on this project now that most of the preliminary data processing and archiving is complete.

ACKNOWLEDGEMENTS

We thank Kris Walker for his work in assembling the FARM database.

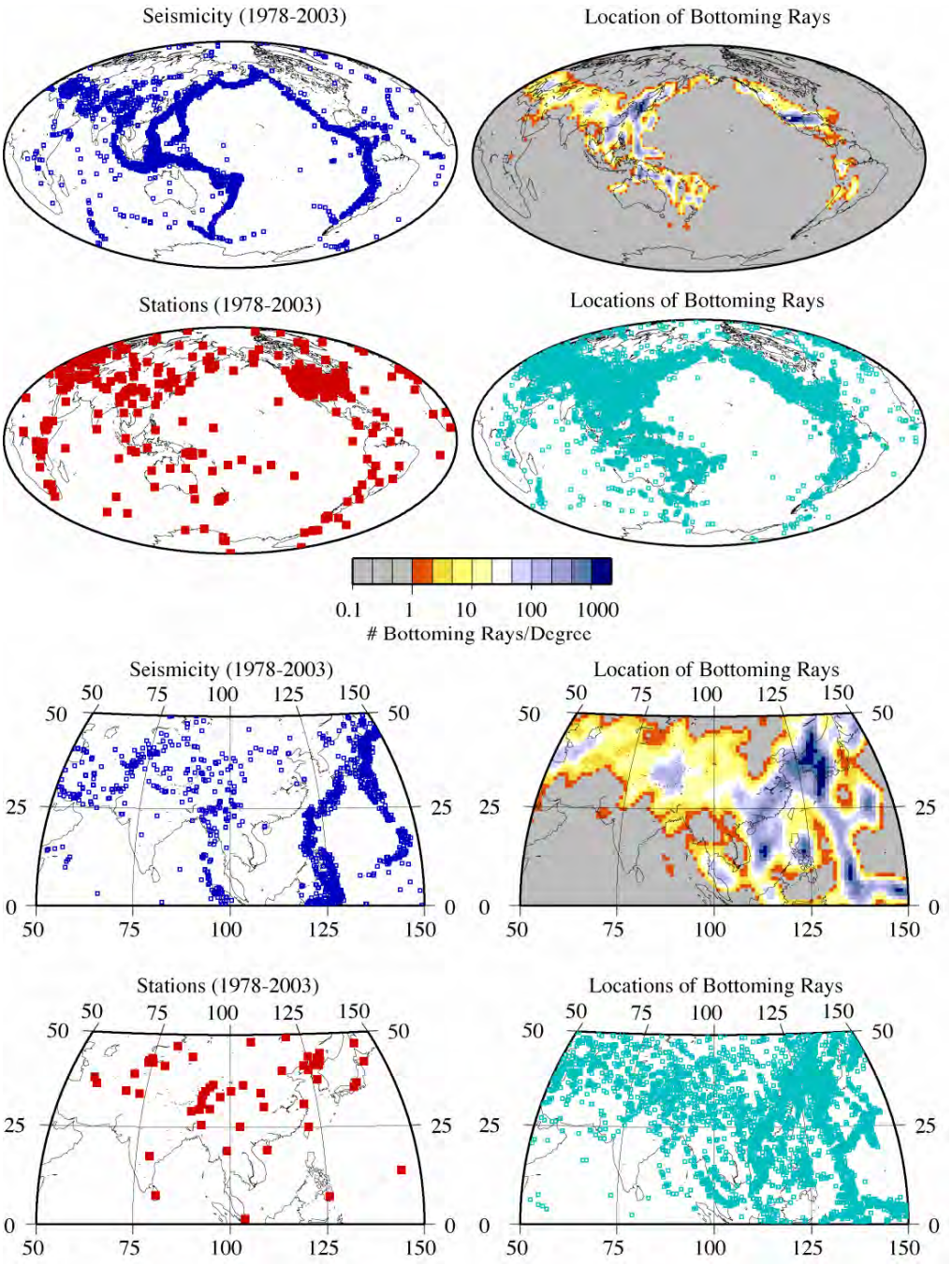


Figure 3. Seismicity and station locations for the IRIS FARM data (left panels) and midpoints of rays for source-receiver distances between 13 and 33 degrees (right panels). Global results are shown in the top four panels; regional results for Asia are shown in the bottom four panels.

REFERENCES

Chambers, K., A. Deuss, and J. H. Woodhouse (2005). Reflectivity of the 410-km discontinuity from PP and SS precursors, *J. Geophys. Res*. 110: B02301, doi:10.1029/2004JB003345.

Flanagan, M. P. and P. M. Shearer (1998a). Global mapping of topography on transition zone velocity discontinuities by stacking SS precursors, *J. Geophys Res.* 102: pp. 2,673–2,692.

Flanagan, M. P. and P. M. Shearer (1998b). Topography on the 410-km seismic velocity discontinuity near subduction zones from stacking of sS, sP, and pP precursors, *J. Geophys. Res.*:103: 21, pp. 165-21, 182.

Gu, Y., A. M. Dziewonski, and C. B. Agee (1998). Global decorrelation of the topography of transition zone discontinuities, *Earth Planet. Sci. Lett*., Vol. 157, pp. 57–76.

Melbourne, T. and D. Helmberger (1998). Fine structure of the 410-km discontinuity, *J. Geophys. Res*. 103: pp. 10,091–10,102.

Shearer, P. M. (1990). Seismic imaging of upper-mantle structure with new evidence for a 520-km discontinuity, *Nature* 344**:** pp. 121–126.

Shearer, P. M. (1991). Constraints on upper-mantle discontinuities from observations of long-period reflected and converted phases, *J. Geophys. Res*. 96: pp. 18,147–18,182.

Shearer, P. M. (1993). Global mapping of upper mantle reflectors from long-period SS precursors, *Geophys. J. Int.* 115**:** pp. 878–904.

Shearer, P. M. (2000). Upper mantle seismic discontinuities, *in Earth's Deep Interior: Mineral Physics and Tomography from the Atomic to the Global Scale, AGU Geophysical Monograph 117*, pp. 115–131.

Shearer, P. M. and M. P. Flanagan (1999). Seismic velocity and density jumps across the 410- and 660-kilometer discontinuities, *Science* 285: pp. 1,545–1,548.

Shearer, P. M. and T. G. Masters (1992). Global mapping of topography on the 660 km discontinuity, *Nature* 355**:** pp. 791–796.

Veith, K. F. and G. E. Clawson (1972). Magnitude from short-period P-wave data, *Bull. Seismol. Soc. Am.* 62: pp. 435–452.

DEVELOPMENT OF SURFACE WAVE DISPERSION AND ATTENUATION MAPS AND IMPROVED METHODS FOR MEASURING SURFACE WAVES

Jeffry L. Stevens, Jeffrey W. Given, G. Eli Baker and Heming Xu

Science Applications International Corporation

Sponsored by Air Force Research Laboratory

Contract No. FA8718-05-C-0023

ABSTRACT

The objective of this project is to optimize measurement of surface waves, particularly at regional and local distances and at periods of 8–15 s. An important part of the project is the development of global regionalized dispersion and attenuation maps, with a particular focus on determining attenuation maps for Eurasia in the 8–15 s period band. Both the dispersion and attenuation maps are corrected for scattering and diffraction from heterogeneous earth structure, and amplitude correction "maps" are also being developed.

Surface wave propagation in the frequency band of interest is strongly affected by heterogeneous earth structure as well as attenuation, particularly along paths crossing deep sedimentary basins. Two such basins of interest in Eurasia are the Tarim Basin in Western China, and the West Siberian Basin. Explosions within these basins generate unusually high amplitude and persistent high frequency fundamental mode surface waves. The Quartz3 and Kimberlite peaceful nuclear explosions (PNEs) were conducted in the West Siberian Basin, and their data give a particularly good sampling of the surface wave propagation across the basin, so we are analyzing these events in detail.

We implemented the algorithm of Zhou et al. (2004) for calculating finite frequency sensitivity kernels for dispersion and amplitude variations, and have been testing the algorithms using the one-degree dispersion maps of Stevens et al. (2005). We performed a large test inversion similar to our earlier great circle path inversions, but using the finite frequency sensitivity kernels. While the inversion looks reasonable, it is not yet clear whether the results fit the data significantly better than the simpler great-circle representation. Amplitude corrections predicted by the Born approximation for the one degree model seem unreasonably large on long paths. This likely reflects the limit of the approximation when large velocity contrasts are encountered.

In order to validate and improve the results, we test whether the Born approximation is giving correct results for structural variations of the magnitude present in the Stevens et al. (2005) models at the frequencies of interest. We compare theoretical Rayleigh wave spectra derived using the Born approximation with those calculated by a 3D finite difference method. The test model was the Tarim Basin structure embedded in a uniform structure typical of the Eurasian shield regions. The source was located immediately east of the basin and the predicted wavefields were compared out to several hundred km west of the basin. The Born approximation is generally consistent with the finite-difference results, but there are localized, strong interference effects in the finite-difference results not apparent in the Born calculation. As expected, the approximation is less accurate at 10 s periods than at 20 s because of the larger phase velocity variation at shorter periods.

We define a path corrected time domain magnitude, which combines the time domain narrow-band surface wave magnitude procedure of Russell (2006) with the path corrected spectral magnitude of Stevens and McLaughlin (2001). The dispersion and attenuation corrections being developed in this project will be used to define regionalized correction factors for this magnitude.

OBJECTIVES

The objective of this project is to optimize measurement of surface waves, particularly at regional and local distances and at periods of 8–15 s. An important part of the project is the development of global regionalized dispersion and attenuation maps, with a particular focus on determining attenuation maps for Eurasia in the 8–15 s period band. Both the dispersion and attenuation maps are being corrected for scattering and diffraction from heterogeneous earth structure.

RESEARCH ACCOMPLISHED

Overview

Surface wave amplitudes are affected by both attenuation and earth structure. The effect on surface wave amplitudes of propagation normal to variations in earth structure is predicted fairly well by energy conservation. Propagation along paths at grazing incidence to large structure variations, however, are much more difficult to predict. Our main interest in this project is on understanding amplitude variations in 8–15 s surface waves. In this frequency band, surface waves may be affected as strongly or more strongly by earth structure than by intrinsic attenuation, particularly along shorter paths. Our goal is therefore to be able to model and correct for both of these effects. Our plan for doing so is illustrated in Figure 1.

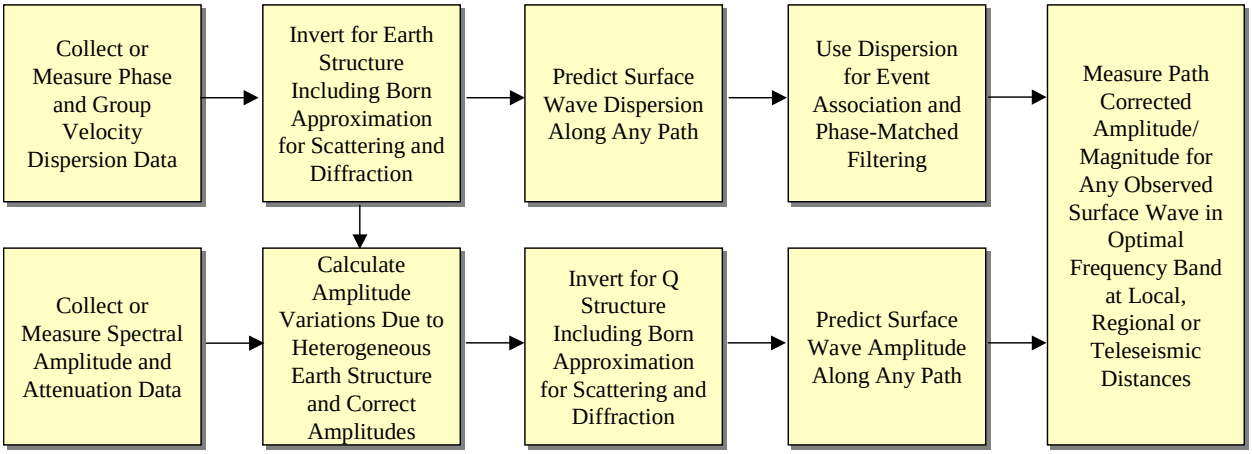


Figure 1. Overview of the surface wave dispersion and attenuation project.

In an earlier project (Stevens et al., 2005) we developed global, regionalized dispersion models that allow the phase and group velocity to be calculated between any two points on the earth. We did this by accumulating a large data set consisting of more than one million dispersion measurements derived by a number of researchers, and then inverting this data set to determine earth structure, which in turn was used to generate dispersion maps at all frequencies. In that project, we modeled surface waves in a heterogeneous earth using the following approximations: (1) surface waves propagate along great circle paths, (2) surface wave phase and group velocities and anelastic attenuation can be modeled using a path integral between source and receiver, and (3) energy is conserved with no mode conversion across material boundaries. This approximation is quite good for large parts of the world, particularly at lower frequencies, but the unmodeled variations become important in regions of structural complexity.

In the first year of this project, we have focused on understanding the variations in surface wave dispersion and amplitude caused by heterogeneous earth structure. We have recalculated our tomographic inversions using finite frequency Born sensitivity kernels in place of the great circle path integrals. We have calculated amplitude variations along Eurasian paths using the resulting earth models, again using the Born approximation to calculate amplitude variations. We are looking in detail at surface waves propagating in highly heterogeneous regions, and trying to understand and model their behavior. Two particularly heterogeneous areas in Eurasia are the Siberian Basin and the Tarim Basin, and so we have been analyzing surface waves in these areas in detail. Our plan is to

develop Born amplitude corrections first, to assess their performance by comparison with data, and then to incorporate the amplitude corrections into inversions for surface wave attenuation. The combination of the attenuation correction and amplitude corrections is necessary to allow accurate prediction of surface wave amplitudes.

Surface Wave Amplitude Predictability

An important goal of this project is to be able to predict surface wave amplitudes in both simple and complex structures, to determine under what conditions the more complicated calculations for laterally heterogeneous structure are required, and under what conditions the approximations generally used for calculating surface waves in complex structures become inadequate. In the following, we discuss calculations of surface waves in simple and complex structures.

Surface Wave Propagation in Simple Structures

We define "simple structures" to mean those structures in which the surface wave propagation is normal to all changes in structure, and lateral changes in structure are negligible. In that case we can predict surface wave amplitude and phase using an approximation originally due to McGarr (1969) that uses propagation of surface waves along great circle paths with conservation of energy across material interfaces and no mode conversion. With these approximations, surface wave propagation in a heterogeneous, anelastic structure takes the following form, separating source, path and receiver (notation follows Harkrider et al, 1994):

$$u_z(\omega,r,\varphi) = \frac{1}{\sqrt{a_e \sin\left(r/a_e\right)}} \sqrt{\frac{2A_{R_1}}{\pi\omega c_1^{\,2}}} \sqrt{c_2 A_{R_2}} \exp\left[i\left(\pi/4 - \omega r / c_p - \gamma_p r\right)\right] F_s(\omega,\varphi,h) \ , \qquad \textbf{(1)}$$

where ω is angular frequency, r is source to receiver distance, h is source depth, a_e is the radius of the earth, φ is azimuth, A_R is the Rayleigh wave amplitude function, c is phase velocity, γ is the attenuation coefficient, and the subscripts *1*, *2*, and *p* refer to parameters derived from the source region structure, parameters derived from the receiver region structure, and parameters which are defined by path averages, respectively. All source properties are contained in the function F_s. For an isotropic explosion source, the Rayleigh wave spectrum can be written:

$$u_z(\omega,r) = M_0^{'} \frac{S_1^x(\omega,h_x) S_2(\omega) \exp[-\gamma_p(\omega) r + i(\varphi_0 - \omega r / c_p(\omega))]}{\sqrt{a_e \sin(r/a_e)}} \ , \qquad (2)$$

where φ_0 is the initial phase equal to -3π/4, S_1^x depends on the source region elastic structure and the explosion source depth, and S_2 depends on the receiver region elastic structure. $M_0^{'} = \frac{3\beta^2}{\alpha^2} M_0$ where M_0 is the explosion isotropic moment. $M_0^{'}$ is defined this way so that the function S_1^x does not depend explicitly on the material properties at the source depth. More details are given in Stevens and McLaughlin (2001) and Stevens and Murphy (2001).

Surface Wave Propagation in Complex Structures

In more complex structures, Equations (1) and (2) may be inadequate to describe surface waves. Consequently, we have been testing algorithms that may be more appropriate for these structures. We implemented the algorithms of Zhou et al. (2004) for calculating finite frequency sensitivity kernels for dispersion and amplitude variations. Using the forward scattering, forward propagating approximation, the phase and amplitude corrections are:

$$\delta\phi = \iint K_\phi^c \left(\delta c/c\right) d\Omega \ , \text{ where } \ K_\phi^c = -\frac{2k^{3/2} \sin\left[k\left(\Delta' + \Delta'' - \Delta\right) + \pi/4\right]}{\sqrt{8\pi \sin\Delta' \sin\Delta''/\sin\Delta}} \ \text{ and} \qquad (3)$$

$$\delta \ln A = \iint K_A^c \left(\delta c/c\right) d\Omega \ , \text{ where } K_A^c = -\frac{2k^{3/2} \cos\left[k\left(\Delta' + \Delta'' - \Delta\right) + \pi/4\right]}{\sqrt{8\pi \sin\Delta' \sin\Delta''/\sin\Delta}} \ , \qquad (4)$$

where distance is in radians, k is wavenumber, and Δ', Δ" and Δ refer to the source to scatterer, scatterer to receiver, and source to receiver distances, respectively. The integrals run over the entire earth's surface, although in practice

(and in this paper) are limited to the first Fresnel zone, which is defined by $k(\Delta' + \Delta'' - \Delta) < 3\pi/4$. Dahlen and Zhou (2006) extend these equations to derive group delay and intrinsic attenuation kernels.

Application of Corrections to Surface Wave Amplitudes

We have been testing the algorithms described above using the 1 degree dispersion maps of Stevens et al. (2005). While the results are reasonable for prediction of dispersion variations, the predicted amplitude corrections seem unreasonably large, particularly on long paths. Consequently, we have been investigating how model roughness affects amplitudes. Figure 2 shows the 10 s phase velocity model for Eurasia; Figure 3 shows the predicted amplitude variation for paths through this region from the Lop Nor test site using the model shown in Figure 2 directly, and using a "smoothed" version of the amplitude variation in which the phase slowness was modeled with a bilinear function instead of discrete blocks. For both of the amplitude figures, the anomalies have been truncated where they exceed $\log_{10}$(amplitude) = 0.6. The amplitude variations become quite large on longer paths, and it is not clear whether the Born approximation is giving reasonable answers on these paths.

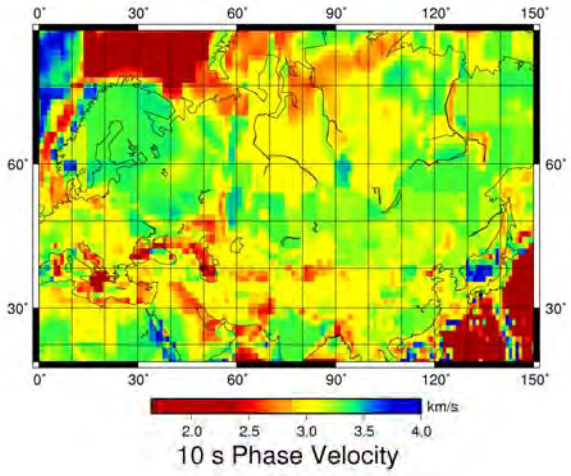


Figure 2. Eurasian phase velocity model at 10 s from Stevens et al. (2005).

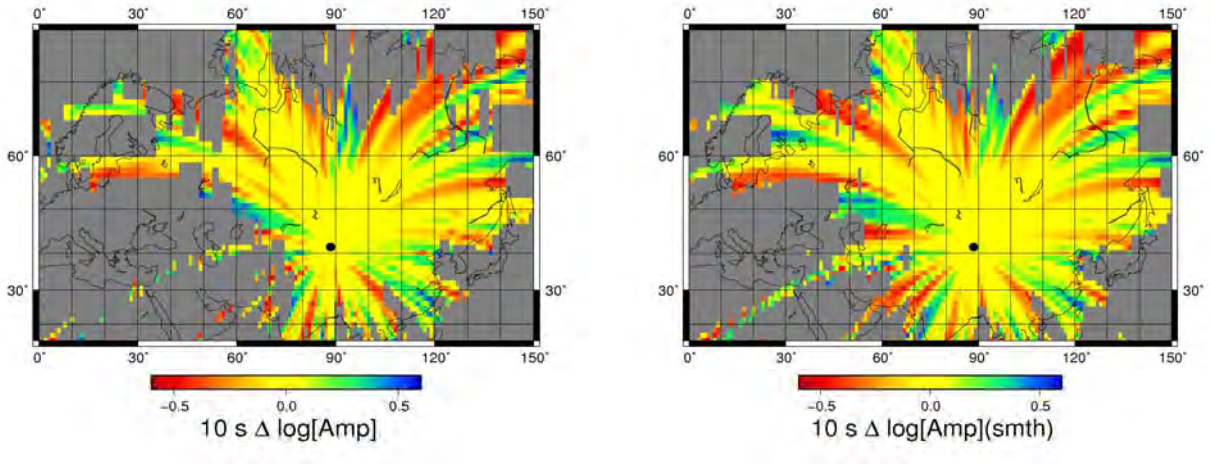


Figure 3. Left—predicted amplitude variations at 10 s through the phase velocity model of Figure 2 on paths out of Lop Nor. Right—same, but the velocity model has been smoothed by modeling it as a bilinear rather than piecewise discontinuous function.

In order to validate/correct the results, we need to determine whether the Born approximation is giving correct results for structural variations of the magnitude present in the Stevens et al. (2005) models, and at the frequencies of interest. To do this, we performed a test case of a structure for the Tarim Basin embedded in a uniform structure typical of shield regions of Eurasia, such as those that surround the Tarim Basin (Figure 4). We then performed a Born approximation calculation and a 3D finite difference calculation for a source located just east of the Tarim Basin and examined the wavefield for several hundred km west of the Tarim Basin. The results showed that although the Born approximation is generally consistent with the finite difference results, there are noticeable interference effects leading to high and low amplitudes in the finite difference calculation that are not present in the Born approximation. The differences are significantly larger at 10 s than at 20 s.

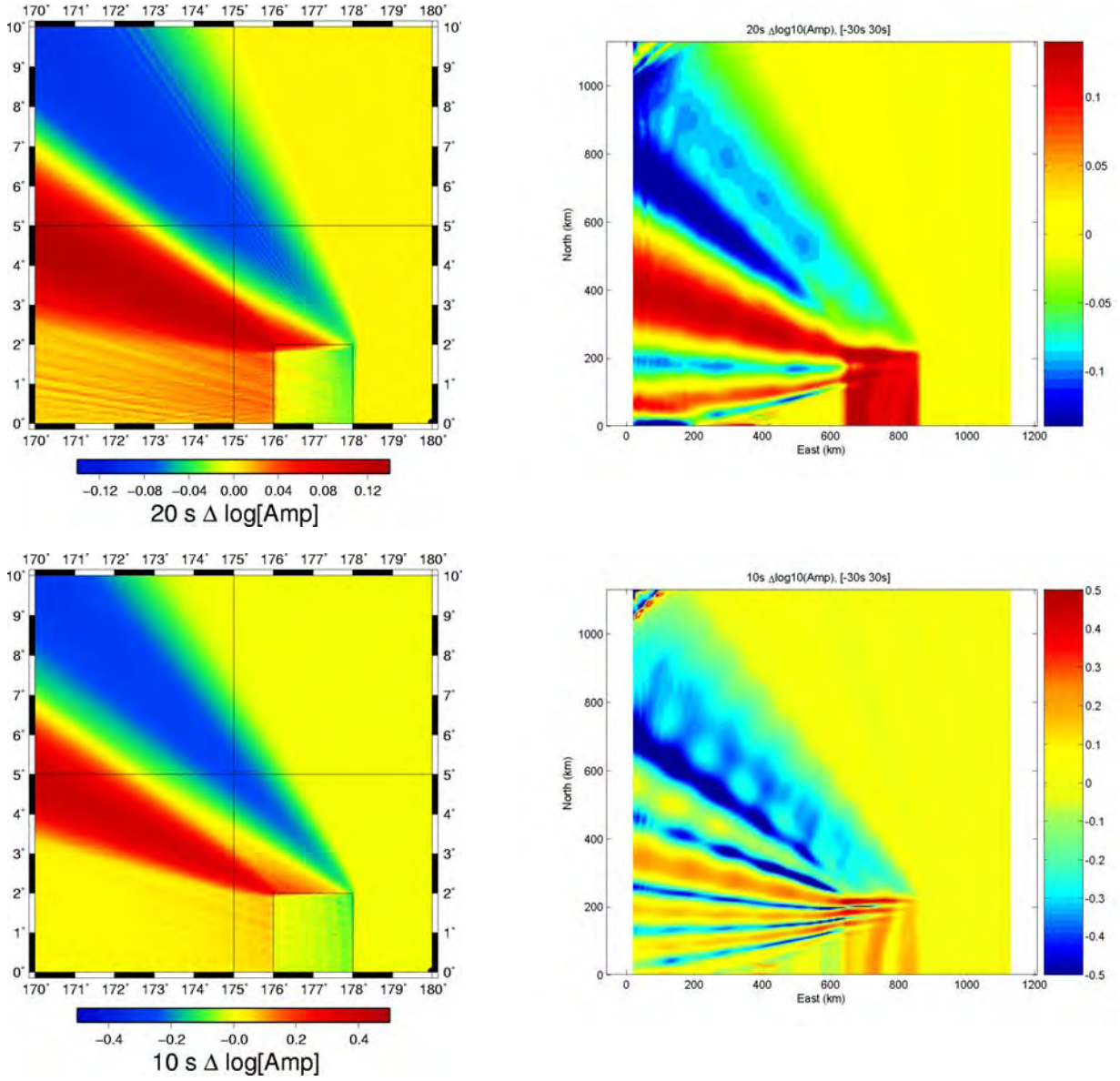


Figure 4. Comparison of Born approximation (left) with finite difference calculation (right) of amplitude perturbations at 20 s (top) and 10 s (bottom). The rectangular inclusion is modeled after the Tarim Basin structure, and the external structure after a Eurasian shield earth structure. The source is on the horizontal axis at the right edge of the plot. There is general agreement in the features of the two calculations. The amplitude is increased in a band above and to the left of the inclusion in both cases, and decreased above that. However, there are some interference effects in the finite difference calculation that are not reproduced in the Born calculation.

One reason for this increase in complexity is illustrated in Figure 5. Propagation of the cylindrical wave leaving the source through the Tarim Basin model leads to a strong diffracted wave generated by the wavefront passing along the top of the basin. This secondary wave interferes with the direct wave and complicates analysis, particularly in the interpretation of spectra. Since the first order Born approximation only models the direct wave, it cannot reproduce this strongly diffracted secondary wave, although it may do an adequate job of predicting the primary arrival. Also shown in Figure 5 are two observed waveforms that traveled through the Tarim Basin. There are two distinct surface wave arrivals similar to the figure on the left. Although we have not done sufficient analysis to say that the split in these seismograms was due to the effect illustrated in the left figure, it does suggest that strong diffraction may be responsible.

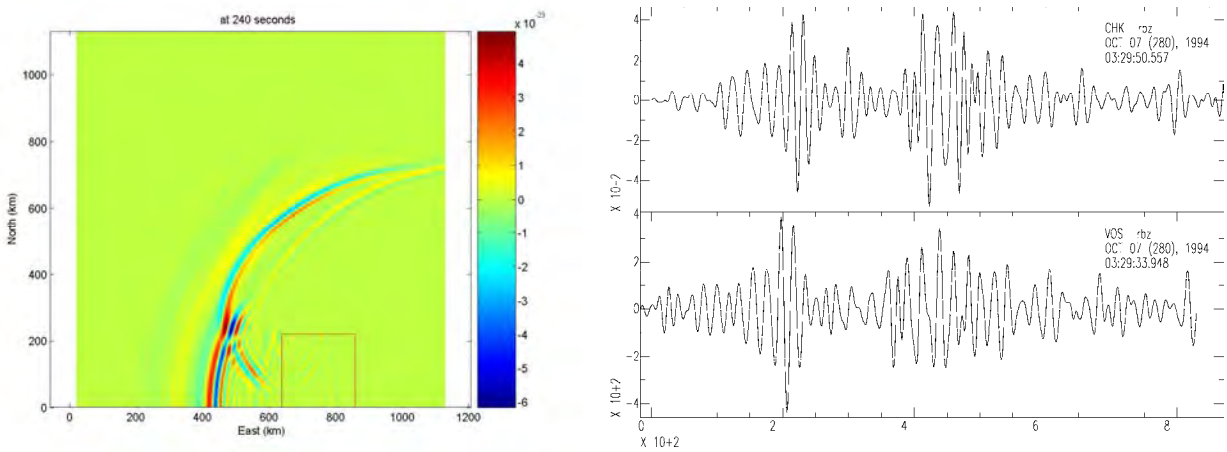


Figure 5. Vertical component velocity after propagation across the low velocity basin (left). There is a strong diffracted wave that interferes with the direct wave. The right figure shows two observed waveforms that passed through the Tarim Basin and have two distinct surface wave arrivals.

Application of Corrections to Inversion for Earth Structure

As discussed earlier, our plan is to incorporate Born corrections for scattering and diffraction into our tomographic inversion scheme. Although we are primarily interested in amplitude estimates, it is necessary to first recalculate the dispersion inversions for earth structure in order to account correctly for the structural effects on amplitude. We have incorporated the finite frequency sensitivity kernels (Equation 3) into our inversion code, and rerun the global tomographic inversions (Stevens et al., 2005) with these corrections. As of this writing, we are still evaluating the results. The changes from the previous inversion are modest in most areas, so more analysis is needed to determine whether results represent an improvement over the inversion using great circle paths. We anticipate that the inversions will give more realistic earth structure with slightly improved data fits in areas of strong lateral heterogeneity.

Data Analysis

We have been identifying data sets in Eurasia that can be used to determine attenuation, as well as dispersion, from 5 to 20 s surface waves. These data sets include nuclear test data, PNEs of the former Soviet Union, moderate size earthquakes recorded at the International Monitoring System (IMS) stations with Harvard Centroid Movement Tensor (CMT) solutions, and deep seismic sounding (DSS) data. The DSS data are potentially very interesting, even though the instrument response of the short period geophones used in those studies is not optimal for longer period (~10–20 s) surface waves. Two of the DSS explosions, Kimberlite 1 (8.5 kt) and Quartz 3 (22 kt), were detonated within the Siberian Basin, and showed very strong surface waves along the entire seismic line, even at long periods. Recordings of both events outside of the basin at 3,300 km, at the very quiet IRIS/GSN station KONO, have surface waves of the amplitude expected from 8.5 and 22 Kt explosions at that distance. This suggests that long period site amplifications may be especially high within the basin. Figure 6 shows data from Kimberlite 1 recorded at 349 km, in 5 passbands (left) and synthetics for a basin structure (right). An interesting characteristic of the data that can be

seen in this figure is that while the synthetic seismogram exhibits smoothly increasing dispersion between low and high frequencies, the data show more of a discontinuous jump. That is, the Rg data near 1 Hz is consistent with the synthetic, and the main arrival of the long period surface wave at the lowest frequencies is also consistent with the synthetic, however there is not a smooth transition between them. Instead, the Rg and long period surface waves or appears almost as two distinct phases, with the long period part of the data growing with decreasing frequency and the Rg decreasing with decreasing frequency.

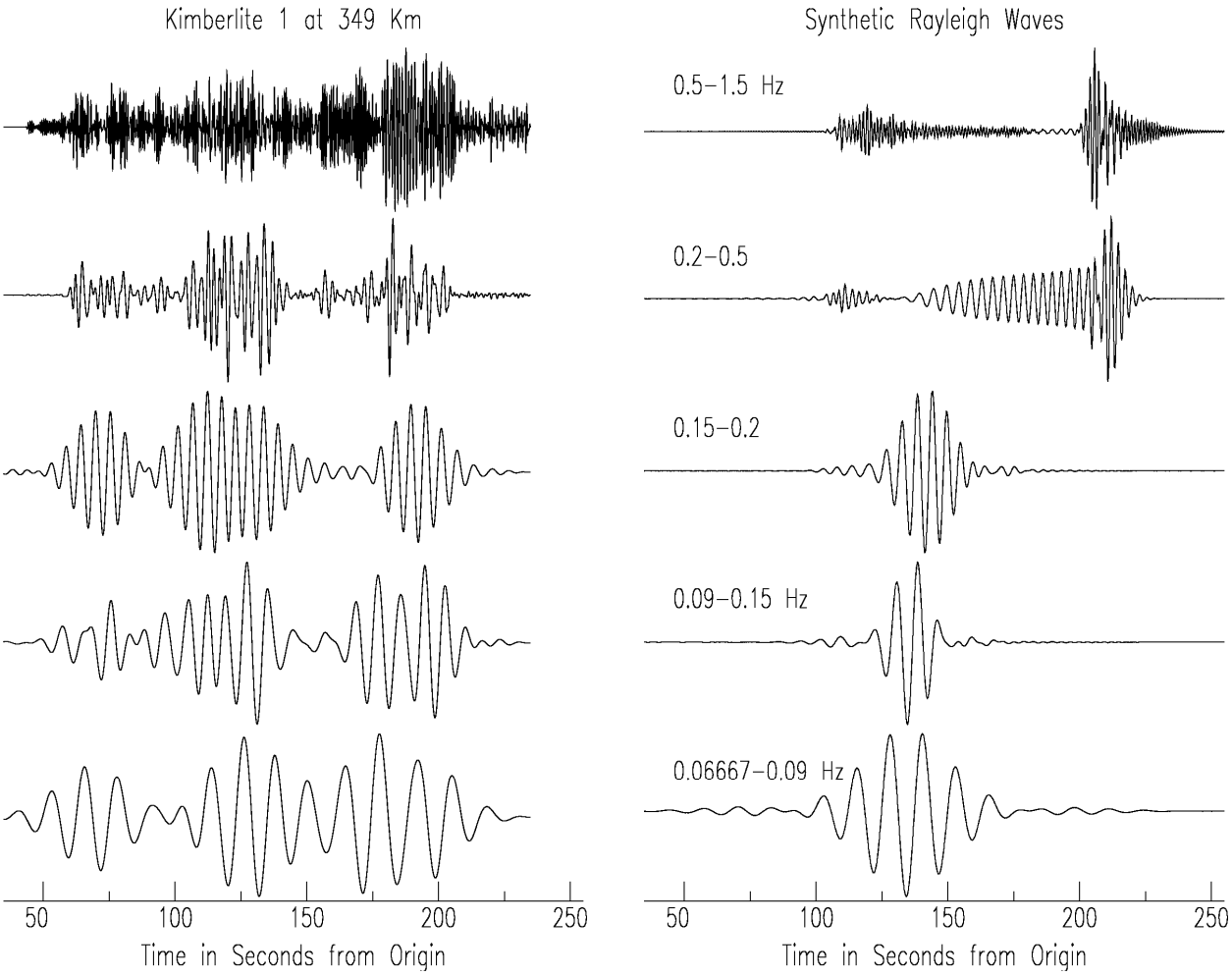


Figure 6. Vertical component Kimberlite-1 record at 349 km (left) in 5 passbands (centered approximately on 1, 3.5, 6, 9, and 13 s from top down), and corresponding synthetics for the first five modes for a Siberian Basin structure.

Regionalization and Improvement of Surface Wave Magnitudes

Regionalization of earth structure, dispersion, and attenuation allows surface wave magnitude estimates to be made more consistent by taking into account regional differences. In addition, consistent surface wave measurement at short distances requires a different procedure than has traditionally been used. Surface wave measurements have typically been made by measuring a time domain amplitude at a period near 20 s and then calculating a surface wave magnitude M_s. This procedure is problematic at regional distances because the surface wave is not well dispersed and a distinct 20 s arrival may not be present. It is possible to measure time domain amplitudes at higher frequencies with corrections (e.g. Marshall and Basham, 1972), however measurements may be inaccurate due to differences in dispersion caused by differences in earth structure. Stevens and McLaughlin (2001) suggested as an alternative replacing time domain measurements with a path corrected spectral magnitude. Russell (2006) proposed a time domain magnitude based on a Butterworth filtered signal, which similarly removes many of the problems associated with time domain magnitudes at close distances. In the following, we suggest a regionalized version of the Russell magnitude which then corresponds to a path corrected time domain magnitude.

Path Corrected Spectral Magnitudes

The path corrected spectral magnitude, $\log M_0$, is calculated by dividing the observed surface wave spectrum by the Green's function for an explosion of unit moment and taking the logarithm of this ratio, averaged over any desired frequency band. The path corrected spectral magnitude is defined as the logarithm of:

$$M_0^{'} = \left| U(\omega, r, \theta) \Big/ \left(\frac{S_1^x(\omega, h_x) S_2(\omega) \exp[-\gamma_p(\omega) r]}{\sqrt{a_e \sin(r / a_e)}} \right) \right|, \tag{5}$$

where U is the observed surface wave spectrum, and as above S_1^x depends on the source region elastic structure and the explosion source depth, S_2 depends on the receiver region elastic structure, and γ_p is the attenuation coefficient that depends on the attenuation integrated over the path between the source and receiver. All of the functions in equation 5 are easily derived from plane-layered earth models (Stevens and McLaughlin, 2001) and allow the measurement to be regionalized to account for differences in earth structure at the source and receiver and due to attenuation along the path. Regionalized path corrected spectral magnitudes incorporate geographic variations in source excitation and attenuation. It can be measured over different frequency bands to optimize the signal-to-noise ratio. M_s and $\log M_0$ share some limitations: spectra from earthquakes vary due to source mechanism and depth, and errors can occur if the measurement is made in a spectral dip or at high frequencies for a deep event. Azimuthal variations in amplitude caused by focal mechanism also affect the amplitudes of both $\log M_0$ and M_s. $\log M_0$ can also be corrected for structural heterogeneity using the amplitude corrections described earlier.

Path Corrected Time Domain Magnitudes

Russell (2006) proposed a new type of surface wave magnitude $M_{s(b)}$ which differs from a traditional 20 s magnitude in that it uses a Butterworth filter to measure a time domain amplitude in a narrow band around any desired frequency, and then applies a correction for the source function similar to the explosion source function used in the path corrected spectral magnitude described above. The main purpose of $M_{s(b)}$ is to allow surface waves to be measured at regional distances at higher frequencies. Bonner et al. (2006) showed that it gave consistent results in a test study. The magnitude is defined by

$$M_{s(b)} = \log(A_b) + \frac{1}{2}\log(\sin\Delta) + 0.0031\left(\frac{20}{T}\right)^{1.8}\Delta - 0.66\log\left(\frac{20}{T}\right) - \log(f_c) - 0.43, \tag{6}$$

where A_b is the filtered amplitude, T is the measured period, and f_c is the Butterworth filter width. It is instructive to compare the terms in the Russell magnitude with the Rezapour and Pearce (1998) M_s and the path corrected spectral magnitude $\log M_0$ described above. This is shown in Table 1.

Table 1. Comparison of time domain and spectral magnitude measurement and correction terms

Magnitude Type	Amplitude Measure	Source	Receiver	Geometric Spreading	Attenuation	Dispersion	Filter	Norm
M_s	log(A/T)			$\frac{1}{2}\log(\sin\Delta)$	0.0046Δ	$\frac{1}{3}\log\Delta$		2.37
$M_{s(b)}$	$\log(A_b)$	$-0.66\log\left(\frac{20}{T}\right)$		$\frac{1}{2}\log(\sin\Delta)$	$.0031\left(\frac{20}{T}\right)^{1.8}\Delta$		$-\log(f_c)$	-0.43
$\log M_0$	$\log(U_z)$	$-\log(S_1)$	$-\log(S_2)$	$\frac{1}{2}\log(\sin\Delta)$	$\gamma_p\Delta\log e$			$\frac{1}{2}\log a_e$

Note that each magnitude makes a slightly different set of corrections. $\log M_0$ corrects for both source and receiver structure based on earth models at those locations and an explosion Green's function at the source. Similarly, $M_{s(b)}$ applies a source correction based on typical explosion source excitation. The Airy phase dispersion correction accounts for superposition of waves with similar group velocities, and is needed only in the time domain. $M_{s(b)}$ uses a Butterworth filter that is sufficiently narrow to avoid this problem. The filter correction corrects for the width of the Butterworth filter. The normalization for the two M_s measurements is chosen to make it consistent with historical M_s magnitudes at a chosen distance range. $\log M_0$ has natural units of log moment and is not otherwise normalized; however, Stevens and McLaughlin (2001) showed that subtracting 11.75 makes $\log M_0$ consistent with the Rezapour and Pearce M_s. Attenuation for M_s is an empirical correction based on a very large number of 20 s measurements. $M_{s(b)}$ similarly uses an empirical attenuation correction, but also includes an empirical correction for the change in attenuation with frequency; $\log M_0$ uses attenuation calculated from earth (velocity, density, and Q) models along a source to receiver path.

A path corrected time domain magnitude can be derived by combining the path corrected spectral magnitude with $M_{s(b)}$, using the source and path corrections from earth models to replace the empirical average corrections. We define the path corrected time domain magnitude $M_{s(bp)}$ as

$$M_{s(bp)} = \log(A_b) + \frac{1}{2}\log(\sin\Delta) + \gamma_p\Delta\log e - \log(S_1) - \log(S_2) - \log(f_c) + C_{bp}, \quad (7)$$

where C_{bp} is a constant chosen to make $M_{s(bp)}$ consistent with historical magnitudes. Although equation 7 may appear more complicated than equation 6, the functions S_1, S_2, and γ_p are easily tabulated and stored in files, and a computer can quickly calculate them for any path based on a simple lookup table. There is substantial regional variation in these quantities that should be removed to ensure consistent measurements (examples of S_1, S_2, and γ for continental and oceanic structures are shown in Stevens and McLaughlin, 1996). Another advantage of this approach is that it can ensure that f_c, which must be less than a minimum value calculated from the group velocity ($f_c < 0.6/\left(T\sqrt{\Delta}\right)$, delta in degrees) is always set appropriately.

None of the magnitude measurements described above include correction for amplitude variations caused by laterally heterogeneous earth structure. To do so requires an additional term that depends on the earth structure in the Fresnel zone surrounding the source to receiver path. The extra term can in principle be calculated using Equation 4, although as discussed previously, the accuracy of this correction particularly for long paths and complex structures requires further investigation.

CONCLUSIONS AND RECOMMENDATIONS

We have incorporated corrections for scattering and diffraction based on the Born approximation into modeling of surface wave amplitude and phase in complex structures, and into inversion of dispersion for earth structure. We have performed a large finite difference calculation for comparison with the Born approximation results to assess its accuracy and range of applicability. We have performed a preliminary global tomographic inversion including the Born corrections. We are continuing to investigate the effect of complex structure on surface waves. This is particularly important for our goal of understanding and predicting surface waves in Eurasia in the 8–15 s period band, as these are strongly affected by earth structure in cases of strong heterogeneity such as occurs in the Tarim Basin and Siberian Basin. We are continuing to investigate the most appropriate amplitude corrections to incorporate into path corrected time domain surface wave magnitudes.

REFERENCES

Bonner, J. L., D. R. Russell, D. G. Harkrider, D. T. Reiter, and R. B. Herrmann (2006). Development of a time-domain, variable period surface-wave magnitude measurement procedure for application at regional and teleseismic distances—Part II: Application and M_s-m_b performance, *Bull. Seism. Soc. Am.*, 96: 678–696, doi: 10.1785/0120050056.

Dahlen, F. A. and Y. Zhou (2006). Surface-wave group-delay and attenuation kernels, *Geophys. J. Int.* 165: 545–554, doi: 10.1111/j.1365-246X.2006.02913.x.

Harkrider, D. G., J. L. Stevens, and C. B. Archambeau (1994). Theoretical Rayleigh and Love waves from an explosion in prestressed source regions, *Bull. Seism. Soc. Am.* 84: 1,410–1,442.

Marshall, P. D. and P. W. Basham (1972). Discrimination between earthquakes and underground nuclear explosions employing an improved M_s scale, *Geophys. J. R. Astr. Soc*. 28: 431–458.

McGarr, A. (1969). Amplitude variations of Rayleigh waves—Propagation across a continental margin, *Bull. Seism. Soc. Am.* 59: 1,281–1,305.

Rezapour, M. and R. G. Pearce (1998). Bias in surface-wave magnitude Ms due to inadequate distance corrections," *Bull. Seism. Soc. Am*. 88: 43–61.

Russell, D. R. (2006). Development of a time-domain, variable period surface-wave magnitude measurement procedure for application at regional and teleseismic distances—Part I: Theory, *Bull. Seism. Soc. Am.*, 96: 665–677, doi: 10.1785/0120050055.

Stevens, J. L. and K. L. McLaughlin (1996). Regionalized maximum likelihood surface wave analysis, Maxwell Technologies technical report submitted to Phillips Laboratory, PL-TR-96-2273, SSS-DTR-96-15562, September.

Stevens, J. L. and K. L. McLaughlin (2001). Optimization of surface wave identification and measurement, *Pure Appl. Geophys.* 158: 1,547–1,582.

Stevens, J. L. and J. R. Murphy (2001). Yield estimation from surface wave amplitudes, *Pure Appl. Geophys.* 158: 2,227–2,251.

Stevens, J. L., D. A. Adams, G. E. Baker, M. G. Eneva, and H. Xu (2005). Improved surface wave dispersion models, amplitude measurements and azimuth estimates, SAIC final report submitted to AFRL under contract DTRA01-01-C-0082, March.

Zhou, Y., F. A. Dahlen, and G. Nolet (2004). Three-dimensional sensitivity kernels for surface wave observables, *Geophys. J. Int*. 158: 142–168.

PREDICTING EXPLOSION-GENERATED *Sn* AND *Lg* CODA USING SYNTHETIC SEISMOGRAMS

Ileana M. Tibuleac[1], Anastasia Stroujkova[2], Jessie L. Bonner[2], Kevin Mayeda[2], and James Britton[2]

University of Nevada at Reno[1] and Weston Geophysical Corporation[2]

Sponsored by National Nuclear Security Administration
Office of Nonproliferation Research and Development
Office of Defense Nuclear Nonproliferation

Contract No. DE-AC52-05NA26610[1,2]

ABSTRACT

Recent examinations of the characteristics of coda-derived *Sn* and *Lg* spectra for yield estimation have shown that the spectral peak of Nevada Test Site (NTS) explosion spectra is depth-of-burial dependent, and that this peak is shifted to higher frequencies for Lop Nor explosions at the same depths. To confidently use coda-based yield formulas, we need to understand and predict coda spectral shape variations with depth, source media, velocity structure, topography, and geological heterogeneity. Thus, we have undertaken a coda modeling study to predict *Sn* and *Lg* coda.

During the initial stages of this research, we have acquired and parameterized deterministic 6º x 6º velocity and attenuation models for the Nevada, Shagan, Degelen, Novaya Zemlya, and Lop Nor Test Sites. Near-source data are used to constrain density and attenuation profiles for the upper five km at several test sites. The upper crust velocity profiles are quilted into a background velocity profile at depths greater than five km. Topography from digital elevation models will eventually be incorporated into the model development. The models are parameterized for use in a modified version of the Generalized Fourier Method in two and three dimensions (GFM2D/3D). The new GFM algorithm will soon include a coordinate transform that allows for variable gridding in the upper few kilometers of the model and simulation of the topography at finer scales. The smaller grid size in the upper crust allows for an increase in the accuracy of the *Sn* and *Lg* synthetics.

We modify these models to include stochastic heterogeneities of varying correlation lengths within the crust. Three parameters—correlation length, Hurst number, and fractional velocity perturbation of the heterogeneities—are used to construct different realizations of random media. Building the stochastic model is not trivial, since a large number of medium and source-specific parameters affect the results. We discuss possibilities for heterogeneity parameter estimation using available seismic and geological data. Lateral correlation and coherence measures between seismic traces are estimated from clusters of nuclear explosions and well-log data. This, and information from elevation and geological maps, as well as satellite imagery, are used to generate synthetic waveforms we compare to the observed data. We assess the relative importance of variables such as heterogeneity location, model grid size, stochastic model parameters, and source type and depth in shaping the *Lg* coda.

Multiple runs with different realizations of stochastic velocity are needed to calculate average amplitude envelopes of the seismic traces for every set of the stochastic parameters. We calibrate these parameters by matching synthetic earthquake *Sn* and *Lg* coda envelopes to local earthquakes with well-defined moments and mechanisms. Once the deterministic and stochastic models have been generated, we will use GFM2D/3D to generate regional-distance synthetics for monopole explosions at depths ranging from 0.25 km to 1 km for all test-site models. We will then superpose secondary source effects, such as spall and compensated linear-vector dipole (CLVD) sources, on the monopole synthetics. Finally, we will derive *Sn* and *Lg* coda spectra from the synthetics, estimate moments, and yields from these spectra, and compare to observed data from each test site. If successful, this method may be used to estimate the *Sn* and *Lg* coda properties for yield estimation of explosions at historical test sites or for broad, uncalibrated regions where we will likely have little information on velocity structure.

OBJECTIVE

Our objective is to determine why the current mechanisms for *Sn* and *Lg* generation from explosions often produce stable coda magnitudes that are transportable between test sites. We aim is to understand and predict *Lg* and *Sn* coda spectral shapes with variations in source depth, material properties, velocity structure, topography, and geological heterogeneity. We will use 2D/3D modeling techniques to estimate synthetic explosion coda for five nuclear test sites as well as for regions without nuclear testing history.

RESEARCH ACCOMPLISHED

For sparse local and regional seismic networks and small events (< ~1 kt), one of the most stable and unbiased methods for yield and magnitude estimation is based on *Sn* and *Lg* coda envelopes (Mayeda, 1993). Coda-derived spectra have characteristics that require in-depth investigation, so that any possible bias can be accounted for when lower bounds on yields are reported. For example, the peaks of coda-derived Nevada Test Site (NTS) and Lop Nor explosion spectra are depth-of-burial dependent, however, the peaks are shifted to higher frequencies at Lop Nor.

We plan to compare observed local and regional *Sn* and *Lg* coda spectra to coda-derived source spectra for simulated explosions at the Nevada (NTS), Shagan (STS), Degelen (DTS), Novaya Zemlya (NZ) and Lop Nor (LN) Test Sites. Our coda investigation methodology consists of: 1) Compilation and parameterization of seismic velocity models consisting of deterministic material models with stochastic perturbations. Estimation of the effect of deterministic and stochastic model parameters on *Lg* propagation and structure; 2) Calibration of stochastic variations at the each test site using nearby earthquake data. Synthetic waveforms are created using a Generalized Fourier Method (GFM; Orrey et al., 2002) and 3) Calculation of 2D/3D synthetics for composite source models of varying depths and moments for each test site. An illustration of our progress in developing this methodology is presented below with results for earthquakes that occurred at the Nevada Test Site.

Methodology for Nevada Test Site Earthquakes and Explosions

Data. *Lg* coda from an earthquake recorded at MNV that occurred on June 29, 1992, 10:31:02.4 is modeled using combined deterministic and stochastic velocity models for the NTS-MNV (Mina, Nevada) path. This m_b 4.3 magnitude earthquake was a 5 km deep aftershock of the M_L 5.6 – 5.8 Little Skull Mountain, Nevada, June 29,1992, earthquake, which occurred in the SW portion of NTS, 20 km from Yucca Mountain. The aftershock was located 256.8 km from MNV, at a back azimuth of 138.2 deg. We assume that the aftershock and the main event located near Little Skull Mountain have the same mechanism, which was listed in the Harvard Centroid Moment Tensor (CMT) catalog. We used these CMT parameters to generate synthetic seismograms for the aftershock. A second earthquake occurred on June 14, 2002, 12:40:44 and recorded at NV11 (a station of the Mina, Nevada seismic array NVAR located less than 100 m from MNV), is used for comparison of the *Lg* coda.

To evaluate stochastic model parameter estimation using correlation of well-located event sequences, we use a dataset provided by Lawrence Livermore National Laboratory (LLNL), (Springer et al., 2002) of 247 NTS nuclear explosions ranging from 200-1500 m depth, recorded at MNV. Seismic velocities derived from geophone logs in boreholes 0.8 km deep at Pahute Mesa are also used to estimate shallow stochastic parameters. This database (Fergusson et al., 1994) was provided by Los Alamos National Laboratory.

Models. *Lg* coda for the events near Little Skull Mountain is modeled using deterministic and combined deterministic and stochastic velocity models for the path between NTS and MNV.

Deterministic Model Generation. The background velocity structure for NTS (see Figure 1; Tibuleac et al., 2005) is based on a regional model for the Basin and Range similar to the model developed by Benz et al. (1991). The velocities in the upper crust are based on borehole data, geologic and gravity data, refraction studies and seismic experiments (McLaughlin et al. 1983; Stump and Johnson, 1984; Ferguson et al., 1994; Stevens et al., 1991). The model is parameterized for use in *GFM 2D*, with grid spacing of either 0.25 km or 0.125 km. The 0.250 km grid has 1183 nodes in the X direction (~298 km) and 385 nodes (~96 km) in the Z direction, for a total of 0.45 million nodes. For this grid spacing, we are able to accurately model *Lg* up to 1.6 Hz. The 0.125 km grid has a total of 1.5 million nodes and can accurately model *Lg* up to 3.2 Hz. The edges of the grid have absorbing boundary conditions

to suppress artificial reflections. To avoid edge effects, the actual side boundaries of the grid are located 40 grid points (for 0.250 km grid spacing) and 70 grid points (for 0.125 km grid spacing) from either end of the model.

Stochastic Model Generation. Generating stochastic models (Tibuleac et al., 2005) is not trivial, considering the number of variables involved. Given the time required to run a model (4 hrs. for 0.250 km grid, 36 hrs for 0.125 km grid, 2D) we simultaneously investigate a) using seismic information in the region, to constrain the stochastic model parameters; and b) efficiently modifying the model for a best fit of the observed envelopes. We will combine the results of these calculations to build the final stochastic model.

Using Existing Seismic Information in the Region to Constrain Stochastic Model Parameters. To address the non-uniqueness inherent in our method, stochastic parameters at each test site are restricted within the bounds of the results from literature searches and satellite imagery correlation-length analyses. Since this information is not always available, it is important to evaluate alternative methods for stochastic parameter development such as correlation and coherence studies and well-log data.

Crosscorrelation Studies. We have estimated model stochastic parameters by correlating well-located nuclear explosions on NTS. This technique will be further applied, with appropriate modifications, to earthquakes in regions with no history of nuclear testing. We use seismograms from three clusters of NTS nuclear explosions as a virtual seismic array that records seismograms from a single source located at the real seismic receiver (the seismic station MNV). Source and receiver positions are virtually interchangeable because of the reciprocity of the Green's function of elastodynamics. We assume differences in phase characteristics (such as *Pn, Pg* and *Lg*) to reflect scattering from stochastic heterogeneity beneath the 'virtual array'.

We assume that the phase crosscorrelation maxima variation as a function of inter-event distance reflects a von Karman (Pullammanapalil, 1997) distribution of seismic velocity heterogeneity in the media. The maximum value of the absolute crosscorrelation of normalized and filtered (0.6 – 1.5 Hz and 0.6 – 4 Hz) waveforms in equal length *Pn, Pg* and *Lg* windows of each two events is averaged as a function of event separation (offset). The crosscorrelation maxim for the normalized entire event waveforms is also calculated. We use explosions within the same depth range (0.1 – 0.2 km; 0.2 – 0.4 km; 0.4 – 0.6 km; 0.6 – 0.8 km and 0.8 – 1.5 km) to estimate horizontal correlation.

Maxim crosscorrelation variation averaged to yield a single value at each spatial lag as a function of horizontal inter-event distance is shown in Figure 2. Since we are interested in the mean properties of the region, the figure is a summary of the results for all three clusters and all depth intervals. The von Karman correlation length for *Lg* phases is between 0.4 -1.1 km, with Hurst numbers (Pullammanapalil, 1997) between 0.3 and 0.7 for waveforms in two frequency intervals. We obtain inconsistent *Pn* results, possibly because the maxim crosscorrelation value for the *Pn* arrivals is the maxim value of the source function crosscorrelation (see explanation below) and does not vary with distance. At 256 km from NTS, *Pn* is a very weak and short phase, which might affect the results. Also, the real medium could have more than one fractal dimension as well as more than one correlation length or could be described by a distribution that is not von Karman The *Pg* correlation function variation is not a good approximation of a von Karman variation. Our experiments with waveforms generated by convolving random Green's functions with a random source function show that saturation of the crosscorrelation maxim values in Figure 1 is partly due to source similarity.

Coherence Studies. For NTS nuclear explosions we also measure seismic phase coherence (*Pg, Lg direct, Lg coda*) in different frequency ranges and estimated dominant heterogeneity dimensions. Direct wave scattering on heterogeneity inside the Earth produces coda (Nishizawa et al., 1997) and the energy transfer is controlled by the scattering characteristics of the media. Coda is the most coherent for most efficient scattering, when the wavelength λ is proportional to the size of heterogeneity *d* (Yomogida et al., 1998), that is, for

$$\frac{\lambda}{\pi} < d < \frac{3\lambda}{2\pi}$$

Therefore, dominant heterogeneity scale can be determined from the coherence maxima. The exact relationship between dominant heterogeneity dimension and von Karman correlation length is still to be established; however,

some authors consider the dominant heterogeneity dimension as the correlation length. Maxim coherence frequency is estimated in two cases: 1) horizontal coherence.for nuclear explosions at the same depth in each region and 2) vertical coherence, for nuclear explosions with $m_b < 5$ at different depth in 2 km^2 regions on the surface. Heterogeneity dimension is estimated to be between 0.7 and 1.9 km for raw *Pg* and between 0.2 and 1.8 km for *Lg* arrivals on the horizontal and vertical direction for the same set of 247 nuclear explosions. Waveform coherence function in the same region varies for each phase. A consistent feature is the *Lg* coda coherence, which is best between 1 and 4 Hz.

Auxillary Data Studies: Borehole Velocity Analysis. We use seismic velocity derived from geophone logs in boreholes at Pahute Mesa to estimate vertical stochastic media parameters at NTS (see Fergusson et al., 1994 for the borehole location).Whether to remove the general trend in the borehole data is not generally agreed upon (Dollan et al., 1998). We have performed our calculations with and without the general velocity trend removed. We assume the horizontal velocity variations are small and randomly distributed with depth within the 15 km length borehole region. The mean of autocorrelation borehole velocity functions is shown in Figure 2 (blue line). Von Karman correlation functions with parameters shown in Table 1 are the best L1 fit (measurement of fit of model to data) to the observed data and are represented with red lines in both plots. The Hurst number is very similar in both cases, however, the correlation length is twice as large for the case when the general trend is not removed. Our results from well log data are consistent with strong shallow heterogeneity with short wavelengths and are well modeled by a von Karman distribution.

Table 1. Von Karman distribution parameters from L1 interpolation of the mean autocorrelation curves in Figure 1. The vertical correlation is a_z (km) and the Hurst number is H. These values are valid down to 800 m depth.

General trend removed		**General trend not removed, each mean removed instead**	
a_z(km)	**H**	**a_z (km)**	**H**
0.04	0.6	0.08	0.5

Efficiently Modifying the Model for a Best Fit of the Observed Envelopes. It is important to model the entire *Lg* phase for best fit of the synthetic and observed waveforms. Mayeda and Walter, (1996) use the *Lg* envelope starting with the *direct Lg* maxim amplitude up to tens to several hundreds of seconds into the coda for coda magnitude estimation. Also, results from numerous studies (Rautian and Khalturin, 1978; Sherbaum et al., 1991; Spudick and Botswick, 1987; Der et al., 1984; Dainty and Tocksoz, 1990; Xie, 1996 and Shapiro et al., 2002) suggest that the *Lg* phase is composed of the least of two regimes. The earliest part of the *Lg*, the *direct Lg*, is spatially more coherent and composed of forward scattered waves with the same direction as the *S* waves and coda, arriving from a variety of directions.The early portion of coda is different from station to station; however, the coda of band-pass filtered seismograms have a common shape at all stations after about two times and always after three times the S-wave travel time from the source to the receiver. The later part of the coda tends to be comprised of multiple scattered waves and is described as a diffusion regime.

Out of a large number of possibilities, we identify the deterministic and stochastic parameters most likely to shape *Lg* and *Lg* coda. We design experiments to evaluate the effect of heterogeneity distribution in the crust on the *Lg* envelope. Effects of source mechanism and depth on coda are further quantified. While our focus remains *Lg* coda modeling, when choosing the best heterogeneity distribution and parameters we aim for the synthetic waveforms to also fit the first arrivals and their coda.

The Effect of Heterogeneity Location on Lg coda. To determine the location of the stochastic perturbations which most influence *Lg* coda, we construct models with different perturbation location within the crust (Table 2). The first model, SD1 has perturbations located at the Conrad discontinuity (from 15 km to 21 km deep). SD2 contains perturbations on top of the Moho, between 29.8 km and 32 km depth. We use a correlation length of 0.8 km with 10% velocity variation for the SD2 model. SD3 has stochastic perturbations distributed throughout the entire crust. Receivers are 0.5 km deep for model SD4 laying on the top of 1-km thick stochastic perturbations. Before the variable grid is implemented into GFM, using model SD4 was the closest to simulate topography effects. Model SD5 has perturbations confined to the upper 6 km of the crust. All the models, except for SD4, have receivers at the surface. We choose fractional perturbation of 10% for both velocity and density. Intrinsic attenuation was not added to these models. Our parameter choice is in accord with the stochastic parameters derived for the observed data.

Table 2. Stochastic parameters for the models used for synthetic waveform generation. We choose the notation SD to represent a stochastic model superposed on the deterministic model described by Tibuleac et al. (2005). D is depth (km), a_x is horizontal correlation length, a_z is vertical correlation length, % represents the fractional velocity and density perturbation in each model and H is the Hurst number. The stochastic layers in the models are represented by "x."

Depth km	Parameters				Models				
	$a_{x\ (km)}$	$a_{z\ (km)}$	H	%	SD1	SD2	SD3	SD4	SD5
0-0.5	0.5	0.25	0.5	10	-	-	x	-	x
0.5-1.5	0.5	0.25	0.5	10	-	-	x	x	x
0-1.5 - 3	0.5	0.25	0.5	10	-	-	x	-	x
3-4	0.6	0.3	0.5	10	-	-	x	-	x
4-5.5	0.6	0.3	0.5	10	-	-	x	-	x
5.5-6	0.8	0.3	0.5	10	-	-	x	-	x
6-15	0.8	0.3	0.5	10	-	-	x	-	-
15-21	1	0.3	0.5	10	x	-	x	-	-
6-24.4	1	0.3	0.5	10	-	-	x	-	-
24.4-27.8	0.8	0.8	0.5	10	-	-	x	-	-
27.8-29.8	0.8	0.8	0.5	10	-	-	x	-	-
29.8-32	1	0.3	0.5	10	-	x	-	-	-
32+	-	-	-	-	-	-	-	-	-

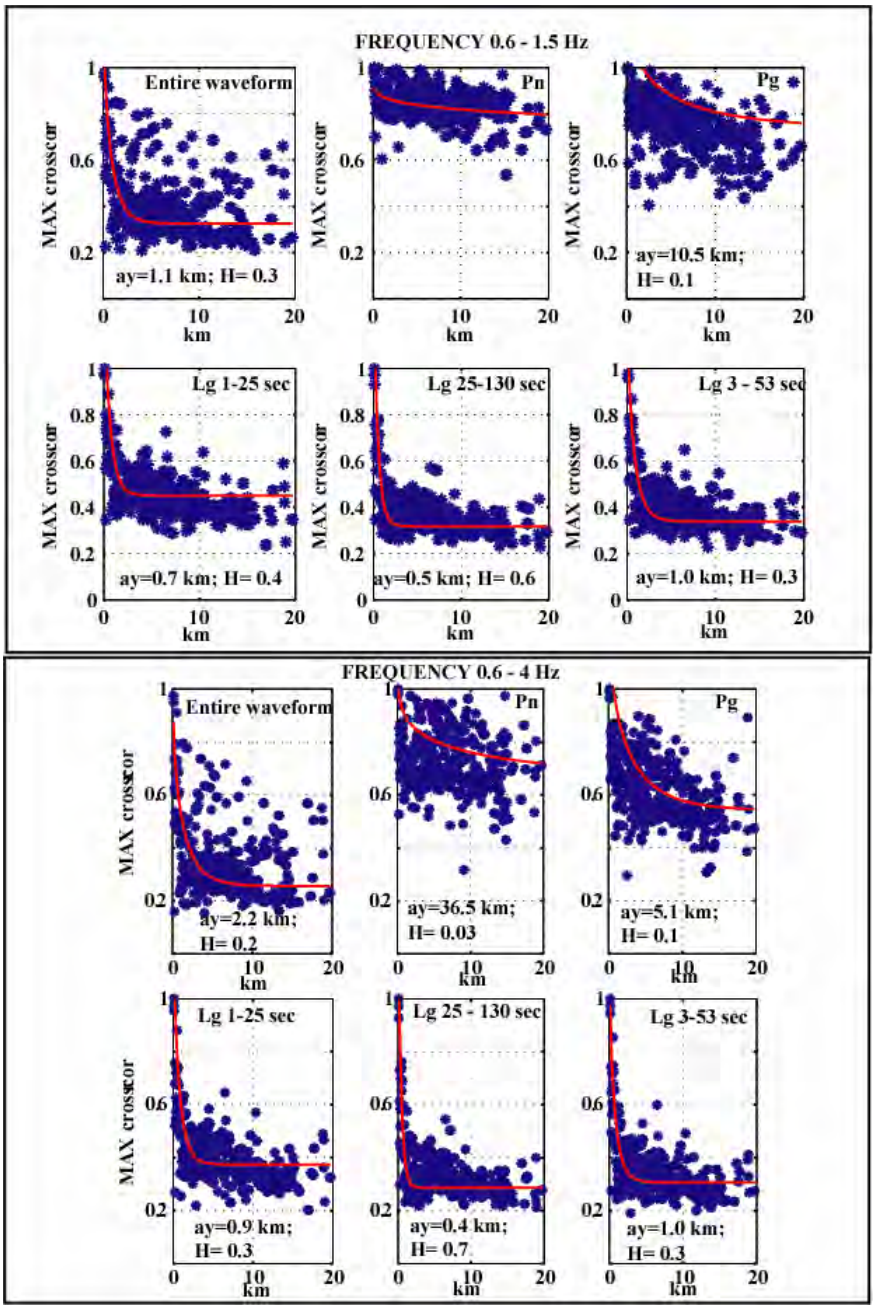


Figure 1. Variation of the crosscorrelation maxima with inter-event distance in a frequency range of 0.6 – 1.5 Hz (upper plots) and 0.6 – 4 Hz (lower plots) for the whole waveform (upper left plot), *Pn* window (upper middle plot), *Pg* window (upper right plot), direct *Lg* window (lower left plot), *Lg* coda window (middle plot) and the transitional *Lg* arrival (right plot). The crosscorrelation maxima as a function of inter-event distance are calculated for each of the depth intervals and the results are shown here for all depths and all clusters. The continuous line represents the L1 interpolated von Karman model correlation variation with the saturation value added. The estimated horizontal correlation value (a_y) and the Hurst number (H) are represented in each plot. The unrealistic values estimated for the *Pn* are omitted. Note the offsets are much larger than the characteristic length, therefore we have a robust measure of the correlation function.

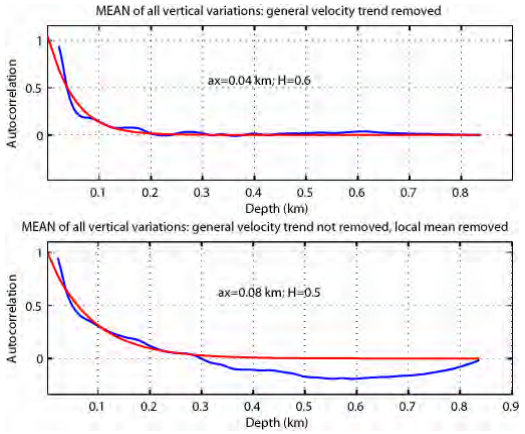


Figure 2. Upper plot: Autocorrelation mean for all wells (blue) and the L1 norm fit (red) of a von Karman autocorrelation function. The general velocity trend was removed at each well. Lower plot: Autocorrelation mean for all wells (blue) and the L1 norm fit (red) of a von Karman autocorrelation function when the general trend was not removed. The von Karman parameters of the best fit are shown in each plot.

Figure 3 shows a comparison of the observed waveforms (g and h) and the synthetic waveforms without (a) and with (b-f) random velocity variations in the model for 0.250 km grid. In the three upper plots, we observe large 1-Hz surface waves that are typically not observed in regional data near NTS. Adding crustal heterogeneity (d-f) forward- and back scatters more energy into the *Lg* coda. The best correspondence of synthetic and observed *Lg* coda is obtained for a model with stochastic heterogeneity only in the upper 6 km of the crust (f). Adding heterogeneity into the whole crust (d) produces more scattering than in the recorded waveform, mostly for first arrivals. Variable heterogeneity in a 1 km thick layer on top of the crust affects more the later part of *Lg* coda (however, the resulting coda amplitude is ten times less than the SD5 coda amplitude) and affects less the direct *Lg*.

Significant amplitude noise is observed before the event for models SD3 and SD5. The inaccuracy of the GFM method at high frequencies produces frequency-dependent errors in phase and group velocity, i.e. 'grid dispersion' (Frankel and Clayton, 1986). The errors are a function of the wavelength to grid spacing ratio and can produce effects in the synthetic seismograms similar to those of attenuation. We observe that a smaller grid size model reduces the amplitude of numerical noise. However, a comparison of waveforms propagated through the SD5 model with 0.25 km and 0.125 km grid spacing shows that the finer grid produces a lower amplitude event signal as well as slightly more coda. One possible reason is that the variance in a medium with a finer grid depends on the Nyquist wavenumber $k_{Nyq} = \pi / h$, where h is the grid spacing (Frankel and Clayton, 1986, eq. B2). The variance of a finer sampled medium is larger. In the spatial domain it is equivalent to truncating the correlation function at zero offset. Therefore, future investigations will address normalization of the discrete random media to correspond to a continuous media with a given variance.

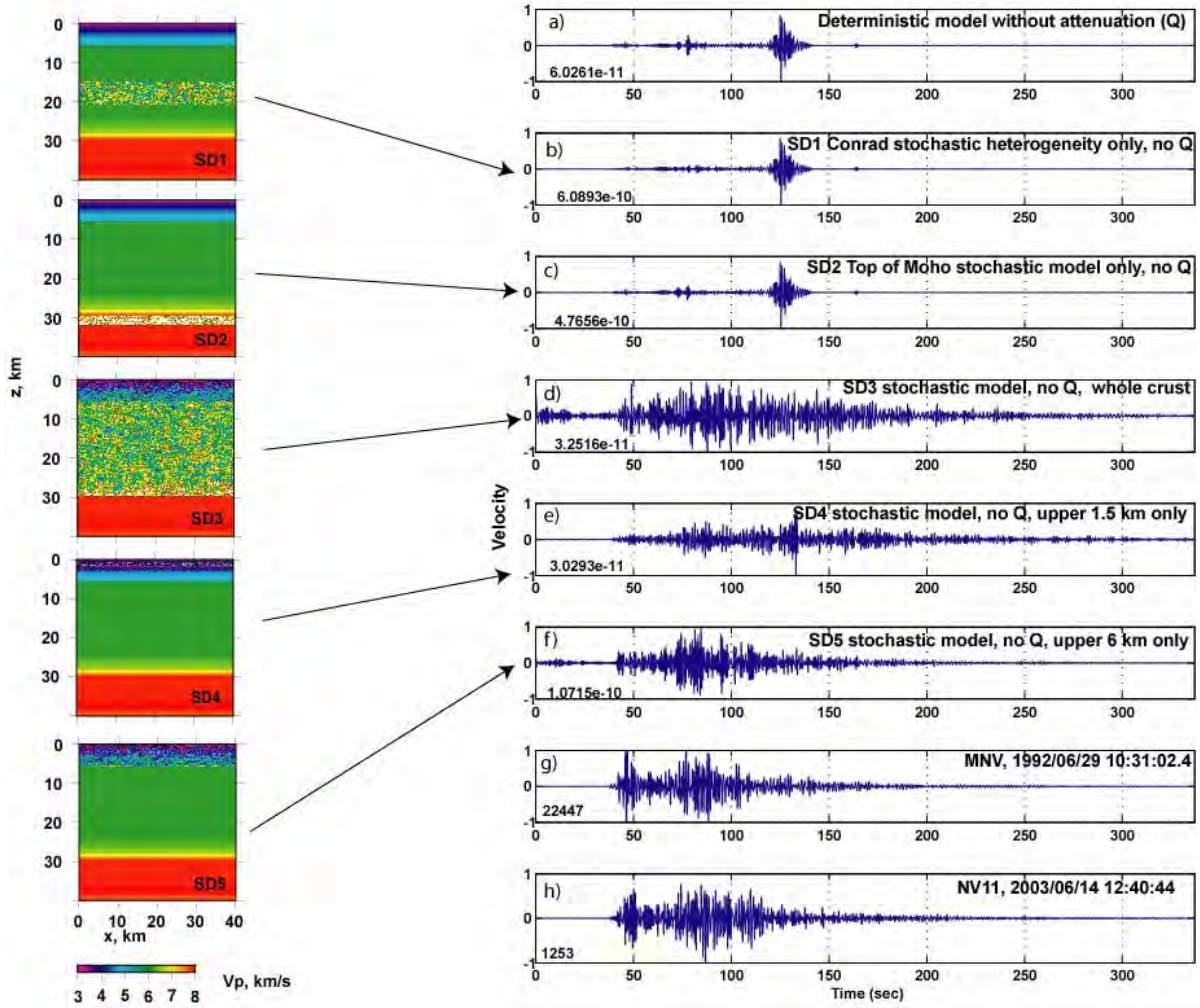


Figure 3. (Left) Stochastic models superposed on the deterministic model used for *Lg* coda simulations. (Right) A comparison of observed waveforms (g,h) and synthetics propagating in the 2D NTS-MNV velocity model without (a) and with (b-f) stochastic variations. The *Lg* phase arrives at a time lag of 73 sec. Waveforms represent velocity in nm/s filtered from 0.5 to 1.6 Hz with a zero-phase, 4 pole Butterworth forward and reverse filter. The waveforms are normalized to the largest *Lg* amplitude value (shown in the lower left corner) between 0.5 and 1.6 Hz. Large 1 Hz surface wave arrivals at 140 seconds lag (upper three plots) are removed by introducing stochastic perturbations in the deterministic model. In plots (d-f) more energy is scattered in the *Lg* coda. Note low-amplitude direct-wave *Lg* arrivals when the stochastic heterogeneity is located at the Conrad depth.

The Effect on Direct Lg of Moho Depth and Seismic Velocity Value at the Surface. If the direct *Lg* and coda waveforms propagate through the same parts of the crust, an SD5 model with 65 km deep crust will affect direct *Lg* as well as its coda. On the contrary, if coda is formed mostly at the surface, where 3 km/s velocities dominate, then a higher velocity (6 km/s) in the upper 6 km of model SD5 will mostly affect coda. Our simulations show that a high-velocity upper layer with stochastic composition (same parameters as for SD5, with 6 km/s in the upper layer instead of 3 km/s) significantly diminishes both *Pg* and *Lg* coda while a 65-km deep Moho does not significantly affect the *Lg* coda. Also, reverberations from Moho are present following direct *Lg*, however Moho depth is a less important factor in the coda envelope shape than the upper layer seismic velocity.

The Effect of Source Mechanism on Lg Coda. An explosion source mechanism is also used in model SD5 and the results are compared to the two recorded events at MNV and NV11 described in Figure 4. We observe that source mechanism has a slight effect on *Lg* coda envelope shape for double-couple and explosion-type sources at the same depth (Figure 4, first and sixth plots in upper inset). Source mechanism is important for event amplitude and the shape and amplitude of the first arrivals. Further investigations are necessary to quantify these effects.

The Effect of Source Depth on Coda. Earthquake and explosion sources were placed at different depths in the SD5 model, with 0.250 km and 0.125 km grid spacing. A decrease in coda high-frequency content with depth is observed for different explosions in the NTS velocity model. Figure 4 shows explosions at different depths in the SD5 model. Depth effects are better modeled using a finer grid (Figure 4, second inset, grid size 0.125 km).

Effects of Variable Correlation Lengths on Direct Lg and Lg Coda. Synthetic waveforms from models with correlation lengths two, four, and eight times larger than in the SD5 model with 0.250 km grid spacing (with the same aspect ration on vertical and horizontal) show that the longer the correlation length, the higher the relative energy in longer wavelengths and the longer the coda duration.

Effects of Variable Hurst Numbers on the Envelope and Frequency of Direct Lg and Lg Coda. Synthetic waveforms from models with characteristic Hurst numberS 0.3 and 0.8 are compared to waveforms from model SD5. The Hurst number is important for amplitude as well as for the shape of the coda. The more rugged the medium (lower H) the more high-frequency coda is observed**.**

Effects of Seismic Velocity Perturbations on Coda Frequency and Amplitude. We observe important effects of heterogeneity dimension on the coda. We observe lower amplitude, longer coda when the 10% velocity perturbation in model SD5 is replaced with 5% velocity perturbation.

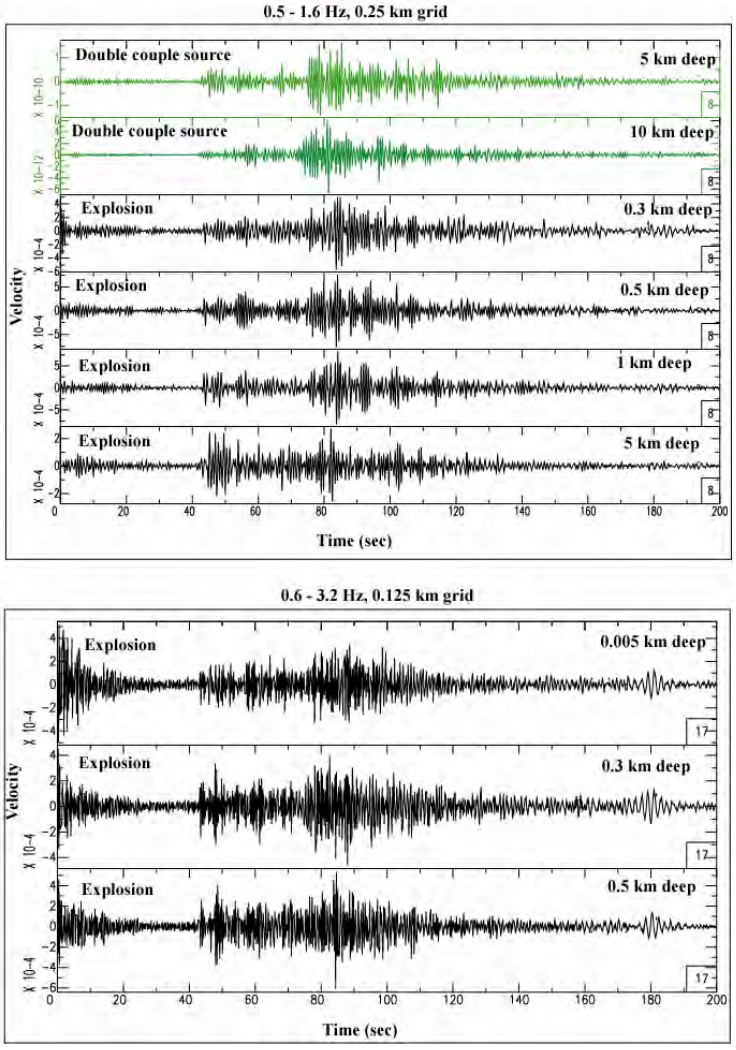


Figure 4. Synthetic seismograms for earthquakes and explosions at different depths for 0.25 km grid size (upper plots) and 0.125 km grid size (lower plots) in model SD5. The frequency range, mechanism, and depth are shown for each plot. Note less high-frequency energy with increasing depth. Also note a model artifact (due to the sharp variation in heterogeneity at 6 km depth) at time lag 180 sec.

CONCLUSIONS

Studies of seismic and borehole data at NTS have the potential to provide constraints for the stochastic model parameters. Reliable coda modeling is only possible when considering the entire waveform. While the effect of Moho depth and the source mechanism is important for direct *P* and Lg, their effect is less important for the *Lg* coda than the effect of the heterogeneity location relative to the model surface. Seismic velocity perturbations and correlation length are important for *Lg* coda shape, and their values can be constrained by fitting the first arrivals as well. So far, we have considered a simple 2D deterministic model for the path between the NTS and MNV. A 3D model consisting of laterally inhomogeneous structures will affect the coda energy partitioning. In a future model, the heterogeneity edge will need to be smoothed.

The next stage of modeling development will be the addition of attenuation and topography. We will use digital elevation models for NTS in order to simulate *Rg* scattering from topography, which has been shown to be a primary constituent of explosion-generated shear waves. This scattering will contribute to the coda signatures for our synthetics. We will then systematically modify the random velocity heterogeneities to improve the match between the observed and synthetic data. Three dimensional strip models will also be developed to examine the scattering

efficiency of 2D media in comparison to 3D simulations. Multiple runs with different realizations of stochastic velocity will be needed to find average amplitude envelopes of the seismic traces for every set of the stochastic parameters. These parameters will then be calibrated by matching synthetic earthquake *Sn* and *Lg* coda envelopes to local earthquakes with well-defined moments and mechanisms. We will quantify possible biases in the yields between test sites and relate them to the choice of, or combination of, *Sn* and *Lg* mechanisms. Finally, we will use our techniques to estimate the *Sn* and *Lg* coda spectra for explosions in uncalibrated regions.

ACKNOWLEDGEMENTS

We thank Mr. Allen Cogbill for providing velocity data at Pahute Mesa and professor John Fergusson for help with the Pahute Mesa well log data. We wish to thank Dr. Jeffrey Orrey for his continued support on the GFM2D/3D code.

REFERENCES

Benz, H. M., Unger, J. D., Leith, W. and V. Ryaboy (1991). The Norilsk DSS Profile in Northern Siberia: interpretation of the velocity structure and comparison with basin and range and New England profiling results, in *Abstracts of the 13th Annual PL/DARPA Seismic Research Symposium*, 85–100.

Dainty, A. M. and M.N. Toksoz (1990). Array analysis of seismic scattering, *Bull. Seism. Soc. Am.*, 80: (6), 2242–2260.

Der, Z., M. E. Marshall, A. O'Donnell, and T. W. McElfresh (1984). Spatial coherence structure and attenuation the *Lg* phase, site effects, and interpretation of the *Lg* coda, *Bull. Seism. Soc. Am.* 74: 1125–1148.

Ferguson, J.F., Cogbill, A.H., and Warren, R.G. (1994). A geophysical-geological transect of the Silent Canyon caldera complex, Pahute Mesa, Nevada, *J. Geophys. Res.* 99: 4323–4339.

Frankel, A. and R.W. Clayton (1986). Finite difference simulations of seismic scattering: implications for the propagation of short-period seismic waves in the crust and models of crustal heterogeneity. *J. Geophys. Res.* 91: No. B6: 6465:6489.

Mayeda, K. M. (1993). mb(*Lg*Coda): a stable single station estimator of magnitude, *BSSA*, 83: 851–861.

Mayeda K. and W. Walter (1996). Moment, energy, stress drop, and source spectra of western U.S. earthquakes. *J. Geophys. Res.* 101**:** 11195–11208.

McLaughlin, KL, L. R. Johnson, LR and T.V. McEvilly (1983). Two-dimensional array measurements of near-source ground accelerations, *Bull. Seis. Soc. Am.* 73:349–375.

Nishizawa, O., T. Satoh, X. Lei, and Y. Kuwahara (1997). Laboratory studies of seismic wave propagation in inhomogeneous media using a laser Doppler vibrometer, *Bull. Seism. Soc. Am.* 87**:** 809 –823.

Orrey, J. L., C. B. Archambeau and G. A. Frazier (2002). Complete seismic wavefield synthesis with a pseudospectral method: The Generalized Fourier Method, revised manuscript to be submitted to *Geophys. J. Int.*

Pullammanapalil, S., A. Levander, S. Larkin (1997). Estimation of crustal stochastic parameters from seismic exploration data, *J. Geophys. Res*. 102: 15269–15286.

Rautian, T. G. and V. I. Khalturin (1978). The use of the coda for determination of the earthquake source spectrum, *Bull. Seism. Soc. Am.* 68: 923–948.

Scherbaum F., D. Gillard and N. Deichmann (1991). Slowness power spectrum analysis of the coda composition of two microearthquake clusters in northern Switzerland, *Phys. Earth. Planet. Inter*. 67: 137–161.

Shapiro, N. M., M. Campillo, L. Margerin, S. K. Singh, V. Kostoglodov, and J. Pacheco (2000). The Energy Partitioning and the Diffusive Character of the Seismic Coda, *Bull. Seis. Soc. Am.* 90: (3), 655–665.

Springer, D. L., G. A. Pawloski, J. L. Ricca, R. F. Rohrer and D. K. Smith (2002). Seismic source summary for all U. S. below surface nuclear explosions, *Bull. Seism. Soc. Am.* 92: 1806–1846.

Spudich, P., and Bostwick, T. (1987). Studies of the seismic coda using an earthquake cluster as a buried seismograph array, *J. Geophys. Res.* 92: 10526–10546.

Stevens, J. L., T. G. Berker, S. M. Day, K. L. McLaughlin, N. Rimer and B. Shkoller (1991). Simulation of teleseismic body waves, regional seismograms, and Rayleigh wave phase shifts using two-dimensional, nonlinear models of explosion sources, *Explosion Source Phenomenology, Geophysical Monograph 65*, Copyright 1991, American Geophysical Union: 239–252.

Stump, B. W. and L. R. Johnson (1984). Near-field source characterization of contained nuclear explosions in tuff, *Bull. Seism. Soc. Am.* 74: 1–26.

Tibuleac, I. M., A. Stroujkova, J. L. Bonner and K. Mayeda (2005). Predicting explosion generated Lg and Sn using synthetic seismograms, in *27th Seismic Research Review: Ground-Based Nuclear Explosion Monitoring Technologies*, Vol. 1, pp. 214–221.

Xie, J., L. Cong, B.J. Mitchell, and J.-M. Chiu (1996). Complexities in high-frequency seismic waveforms due to three-dimensional structure in the New Madrid Seismic Zone, *J. Geophys. Res.* 101: (B3): 5751–5778.

P AND S WAVE VELOCITY STRUCTURE OF THE CRUST AND UPPER MANTLE UNDER CHINA AND SURROUNDING AREAS FROM BODY AND SURFACE WAVE TOMOGRAPHY

M. Nafi Toksöz, Robert D. Van der Hilst, Youshun Sun, Chang Li, and Huajian Yao

Massachusetts Institute of Technology

Sponsored by Air Force Research Laboratory

Contract No. FA8718-04-C-0018

ABSTRACT

The objective of this project is to use a combination of travel-time and surface wave tomography to obtain compressional and shear wave velocity distributions in the crust and upper mantle under China and surrounding areas.

Three-dimensional (3-D) P and S wave velocity structures, based on travel-time tomography, are developed for the crust and the upper mantle transition zone for China and surrounding areas. P and S wave arrival time data from the Annual Bulletin of Chinese Earthquakes (ABCE) are used for the regional travel-time tomography of the crust and uppermost mantle. The International Seismology Centre (ISC/EHB) travel times are used with the crustal structure to extend the velocity models into the mantle. The shallow velocity models correlate well with the major geologic features, such as the Tibet Plateau and the basins. P and S wave velocity structures in general are well-correlated. Lateral variations of shear velocities, which exceed 6% at some places, are larger than P velocity variations.

The current effort is directed to two areas: (1) obtaining a regional crust/uppermost mantle 3-D shear wave velocity model from the travel times and (2) obtaining high-resolution, regional velocity models where additional data from local networks make it feasible to undertake the tomographic inversions. Tibet and southwestern regions are the primary regions in these studies.

OBJECTIVES

The primary goal of this project is to obtain compressional and shear wave velocity distributions in the crust and upper mantle under China and surrounding areas using a combination of travel-time and surface wave tomography. The first phase of the study is directed at producing a P wave velocity model based on travel-time tomography.

RESEARCH ACCOMPLISHED

Introduction

In this paper we present a 3-D shear wave velocity structure for the crust and upper mantle under China and surrounding regions obtained using local and regional travel-times and surface waves.

The available S wave velocity models of the crust and upper mantle in China and the surrounding area have been obtained using different approaches. Global models such as CUB 1.0 (Shapiro and Ritzwoller, 2002) and the SAIC 1° x 1° model (Stevens et al., 2001) were constructed from group and phase velocity dispersion measurements of surface waves. The global model CRUST 2.0 (Laske et al., 2001) was constructed from seismic refraction data and developed from the CRUST 5.1 model (Mooney, 1998) and a 1° x 1° sediment map (Laske and Masters, 1997). Only P wave velocities are inverted by travel-time tomography. The S wave velocities in the model are obtained by empirical Vp/Vs ratios or compiled from other sources. For East Asia, mantle S velocity models were obtained from shear and surface waveforms (Friederich, 2003). Lateral spatial resolution of the models is larger than 200 km.

Regional models were constructed by Sn and/or Pn tomography (Ritzwoller et al., 2002; Hearn and Ni, 2001; Pei et al., 2004) and from surface waves (Wu et al., 1997, Lebedev and Nolet, 2003; Huang et al., 2002; Song et al. 1991; Zhu et al., 2002). P and S wave tomography have been performed in several local regions in China (Xu et al., 2002; Huang et al., 2002; Yu et al., 2003; Huang and Zhao, 2004;). Xu et al. (2002) used P and S wave arrival times of local, regional and teleseismic events recorded by Chinese and Kyrgyzstan seismic networks to derive crust and upper mantle velocity structures beneath western China. The grid spacing is 1.5° x 1.5° in the horizontal direction and about 10 km (in the crust) and 50 km (in uppermost mantle) in the vertical direction. Crustal structure models beneath north and east China, including Beijing and surrounding regions, were obtained by Zhu et al. (1990), Yu et al. (2003) and Huang and Zhao (2004) with a P and S wave tomography. Huang et al. (2002) inverted the lithospheric structure in southwest China from local/regional travel-time data. A number of studies carried out in the Tien Shan (Roecker et al., 1993; Poupinet et al., 2002; Vinnik et al., 2002, 2004) and Hindukush (Koulakov and Sobolev, 2006) regions, that include parts of western China, show heterogeneous crust/upper mantle structures with crustal thickness varying between 40 and 70 km. All these models provide detailed crustal structures in specific regions. A detailed map for the whole China area remains to be developed.

During the last two decades, many digital seismic stations were installed in China. The large database of high-quality recorded arrival times provides an unprecedented opportunity to determine a detailed 3-D crustal structure under the region. Using these data, Sun and Toksöz (2006) derived a 3-D P wave velocity structure for the crust and uppermost mantle. In the present work, we use the tomographic constraint from the P wave study along with the S wave travel times to determine a 3-D shear wave velocity structure of the crust and upper mantle under this region.

Data and Method

For this work, we selected shear wave arrival time data from the Annual Bulletin of Chinese Earthquakes (ABCE) (IG-CSB, 1990–2002). In this database there are 25,000 earthquakes, 220 stations, and 450,000 S wave ray paths in China and the surrounding areas in the January 1990 to December 2002 time period. Figure 1 shows earthquake epicenters and stations in China. The selection of earthquakes is based on the following criteria: (1) events that occurred in the study area with magnitudes greater than M 3.0 (except for the northwest area with less seismicity, where we included earthquakes with M 2.5–3.0); (2) all selected events were recorded by at least 15 stations; and (3) earthquakes were selected to provide a uniform distribution of hypocenters in the study area. With these criteria, 262,000 S wave arrival times from 12,215 earthquakes were selected to determine the S wave velocity structure. The reading accuracy of S wave arrival times is, in general, 0.1–0.4 s. Figure 1 shows the epicentral distribution of the 12,215 selected earthquakes.

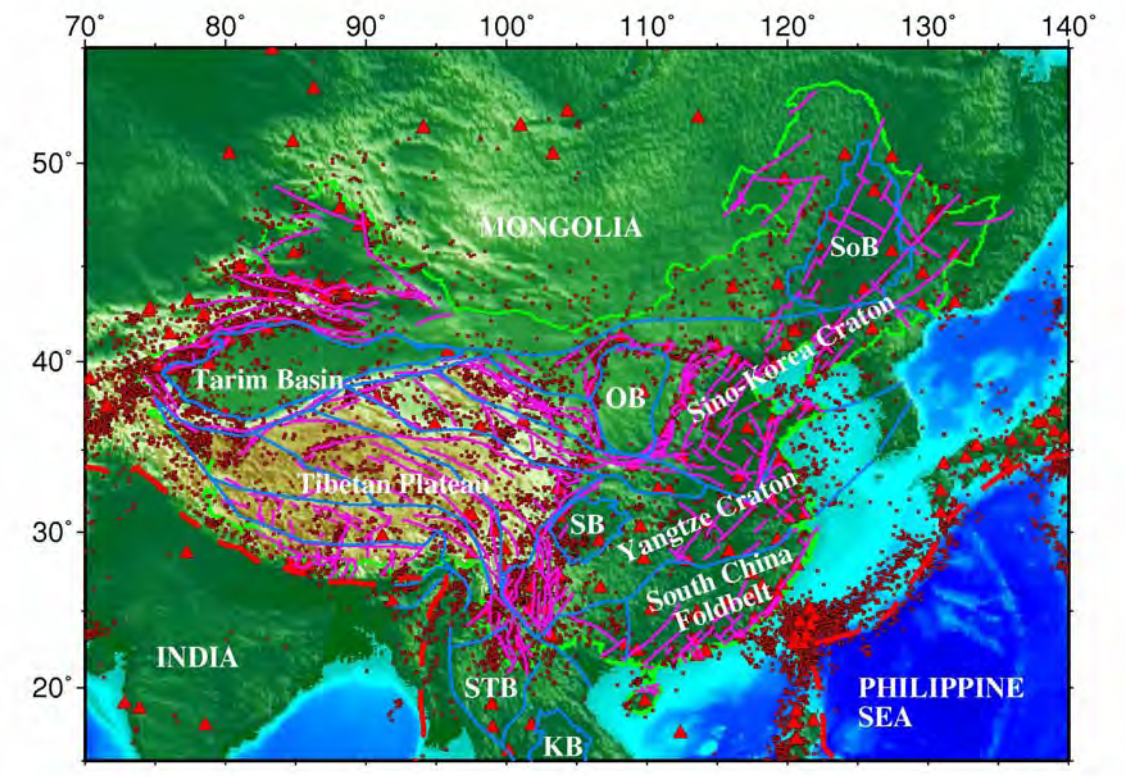


Figure 1. Shown are 512 earthquakes (M > 6.0 from January 1978 to May 2004), 220 stations, active faults, and major tectonic boundaries in China and the surrounding area. Earthquake epicenters are shown in red dots and stations are shown in red triangles. The yellow line shows the boundary of China. Active faults in the China area are shown in purple lines and tectonic sutures are shown in blue lines, where SoB: Songliao Basin; OB: Ordos Basin; SB: Sichuan Basin; KB: Khorat Basin; STB: Shan Thai Block; IB: Indochina Block.

To determine the shear velocity structure from arrival time data, we used the tomographic method of Zhao et al. (1992). This method has the following features: (1) It accommodates discontinuities such as the Moho. A 3-D grid is set up in the model to express the 3-D structure. Velocity perturbations at the grid nodes are the unknown parameters. The velocity perturbation at any point in the model is calculated by linearly interpolating the velocity perturbation at the eight grid nodes surrounding that point. (2) It calculates travel times and ray paths using an efficient 3-D ray-tracing technique (Zhao et al., 1992). It uses iteratively the pseudobending technique of Um and Thurber (1987). Station elevations are taken into account in the ray tracing. (3) It uses a LSQR algorithm (Paige and Saunders, 1982) with a damping regularization to solve the large and sparse system of equations, inherent in the tomographic problem. The LSQR algorithm has been used by a number of researchers (Nolet, 1985; Spakman and Nolet, 1988; Papazachos and Nolet, 1997), and is an efficient algorithm to solve problems with large sparse systems. (4) The nonlinear tomographic problem is solved by conducting linear inversions iteratively.

For the shear wave tomography we follow a procedure very similar to the one used for the P wave tomography (Sun and Toksöz, 2006). We adopt a grid spacing of 1° × 1° in the horizontal direction, and 10 km in depth. We also set grids at the depths of 1 km, 2 km, 5 km and 7 km to sample the sediment layer. We use a starting 1-D model (Figure 2) based on the average 1-D P wave model. We put into the starting model the Moho depth obtained from the P wave tomography, which is consistent between the Moho depths in this region by different researchers (Mooney, 1998; Hearn et al., 2004; Sun at el, 2004; Sun and Toksöz, 2006). In the study area, the Moho depth ranges from 30 km in the east to 78 km. During the tomographic inversion, the Moho geometry is fixed and only the velocities at grid nodes are determined.

The earthquake hypocentral parameters are those determined by P wave tomography. They are kept constant during S wave inversion. We chose the value of 25.0 for the damping parameters to balance between the reduction of

travel-time residuals and the smoothness of the 3-D velocity model obtained. The root mean square (RMS) travel-time residual decreased by 35% from 0.98 s to 0.72 s by the inversion. Spatial resolution was evaluated using a checkerboard test (Spakman and Nolet, 1988; Zhao et al., 1992).

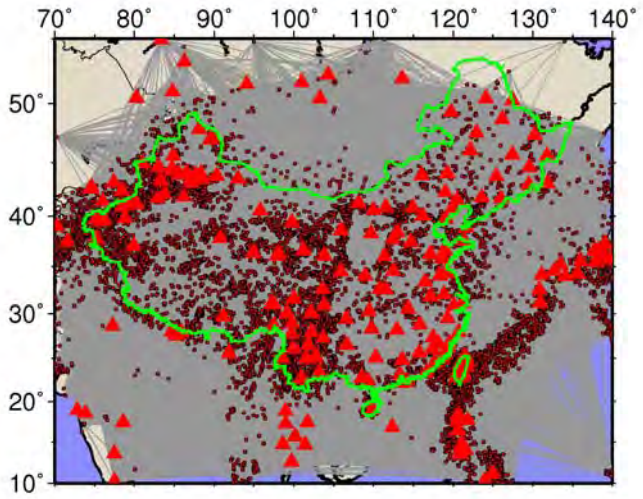


Figure 2. Shown are 25,000 earthquakes, 220 stations, and 450,000 ray paths in China and the surrounding area. Earthquake epicenters are shown in black circles and stations are shown in red triangles. The green line shows the boundary of China.

Results

The 3-D shear wave velocity models are shown in Figures 3–5. Figure 3 shows the Moho depth map taken from P tomography and used as an input to S wave tomography. On the right are the Sn velocities. Depth slices of shear velocities are shown in Figure 4. North-south and east-west cross sections of shear velocities are shown in Figure 5. The lateral variation of S wave velocities exceeds 6% in the study area, indicating the heterogeneities in the crust and upper mantle in this region. Prominent features in the figures are the thick crust under Tibet with low velocity, low Sn velocities in NE China (rift zone) and high Sn velocities under Tibet at 80 km depth.

In the cross sections (Figure 5), there is a prominent low velocity zone in the mid-crust at a depth around 40 km under Tibet. This feature is consistent with other observations of similar velocity decrease and shear wave attenuation increase in the mid- to lower-crust under Tibet. Higher velocities under the Sichuan Basin and under Mount Altay extend into the mantle, as do the lower velocities under the rift system south of the Bohai Bay.

In an earlier study (Sun and Toksöz, 2006), 3-D P wave velocity models were obtained through a tomographic inversion similar to those used in this study for S waves. It would be informative to compare the results. Figure 5 shows N-S cross sections of P and S wave velocities. There is good correlation between the P and S velocities under Tibet. Lower velocities in the mid-crust appear both in the P and S tomograms. The low velocity zone is more prominent in the S velocities.

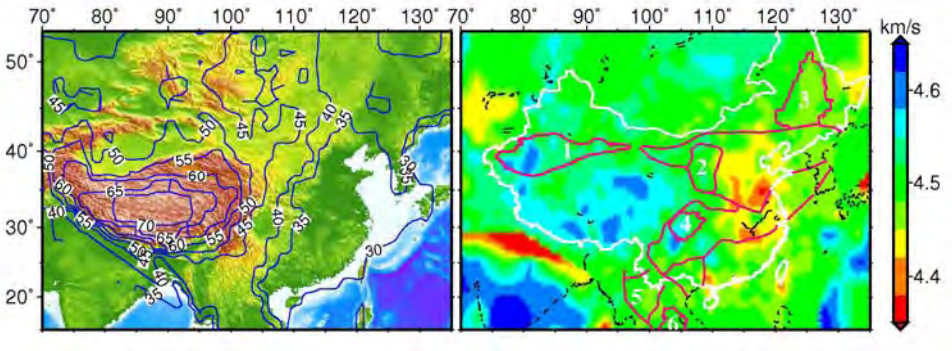


Figure 3. Depth of the Moho discontinuity (left) and Sn velocity distribution obtained (right) in the present study area. The Moho depths are shown in contours. 1: Tarim Basin; 2: Ordos Basin; 3: Songliao Basin; 4: Sichuan Basin; 5: Shan Thai Block; 6: Khorat Basin.

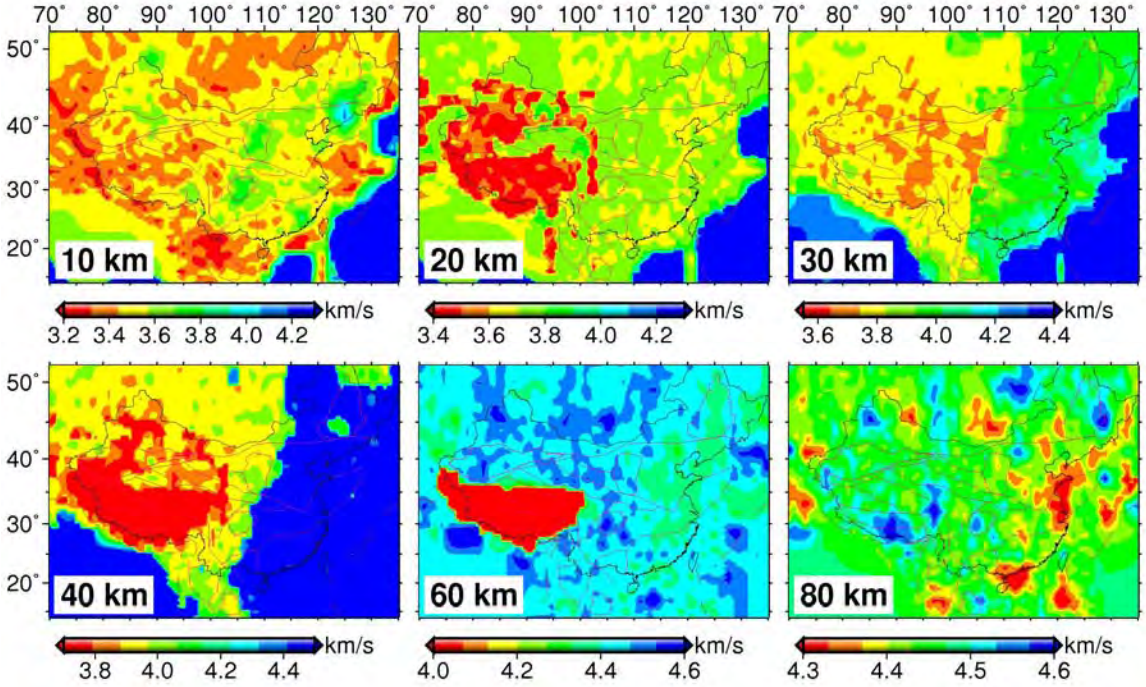


Figure 4. S wave velocity image at each depth slice. The depth of each layer is shown at the lower left corner of each map.

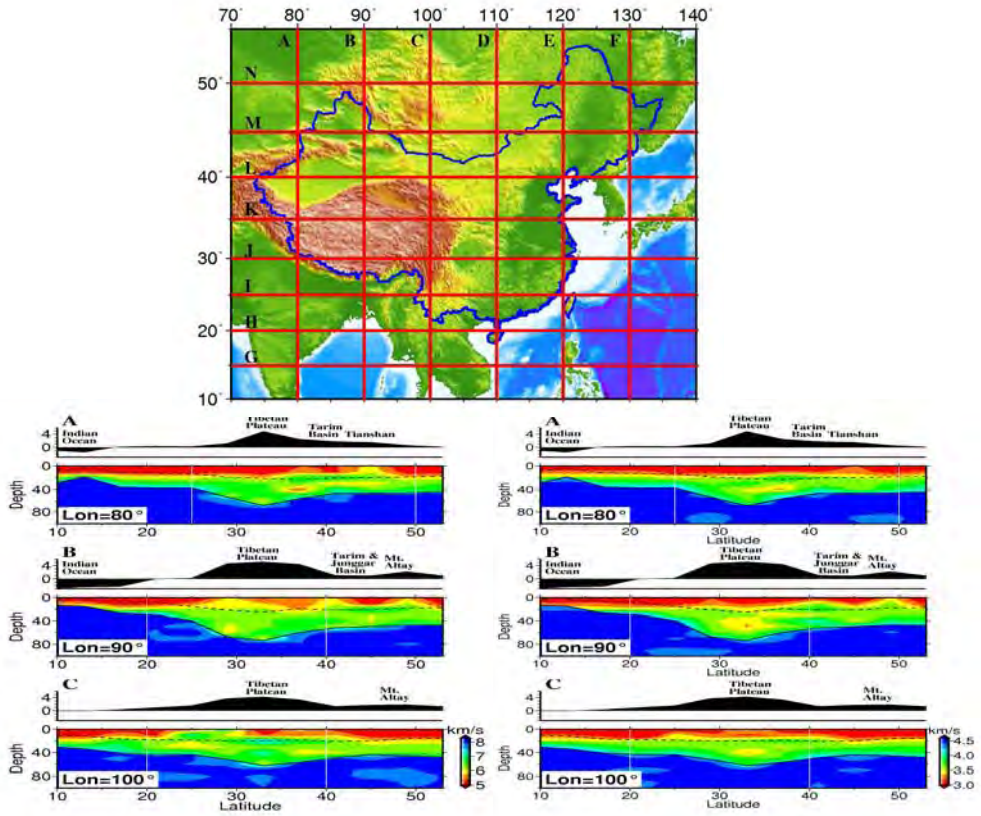


Figure 5. P (left) and S (right) vertical velocity profiles of the crust and uppermost mantle at 80°, 90°, and 100° E longitudes. The profile locations are shown in the upper figure

To extend the velocities into the upper mantle, we use teleseismic travel-time data for P waves and multi-mode surface waves for the shear waves. To minimize the "smearing effect" of crustal structures into the upper mantle, the upper 80 km of the model velocity is constrained by the regional tomography. The regional and teleseismic data from the ISC/EHB database are used for the mantle tomography. The data and tomographic inversion are described by Li et al. (2006). The S wave velocities are obtained by surface wave tomography (Lebedev et al., 2005).

Figure 6 shows the preliminary results for upper mantle P and S wave velocity variations in southern and western China at a depth of 250 km. The color bars and spatial resolutions are different for P and S velocity variations. Note the extension of high velocities under the Sichuan and Ordos basins to 250 km. The relative variations in S wave velocities are greater than those of the P waves.

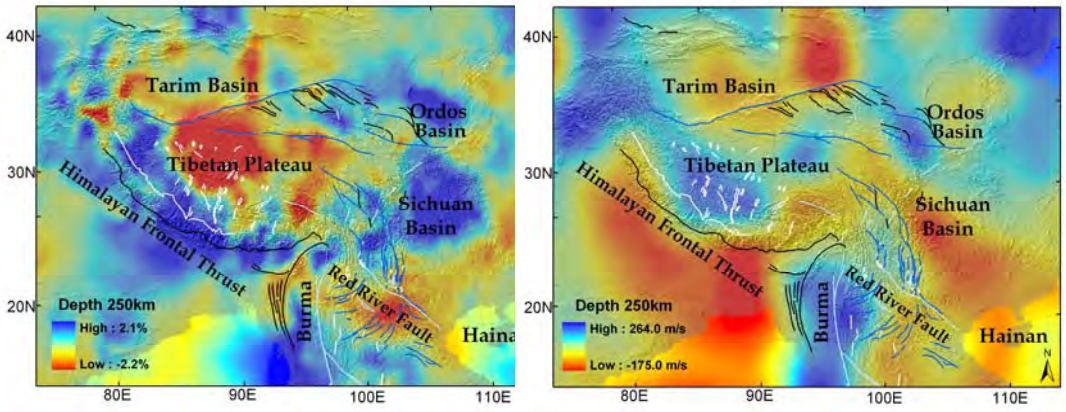


Figure 6. P wave velocity (left) and S wave velocity (right) at the depth of 250 km.

CONCLUSIONS

The 3-D shear-wave velocity models of the crust and upper mantle, obtained by S wave travel-time tomography, reveals pronounced lateral heterogeneities under China and surrounding regions. The velocity models exhibit the following features.

.

1. At the upper crust, down to 20 km depth, velocity variations strongly correlate with the major geological features.

2. There is a strong contrast between the regions to the east of 110°E longitude and the west. In eastern China, where crustal thickness is about 35 km or less, velocity variations are relatively small. Lower velocities delineate the rift structure of NE China. In the region to the west of 110°E longitude the crustal velocities are much more variable. Crustal thickness varies between 35 km and 78 km. The roots of prominent features such as the Tibet, Tarim, Sichuan and Ordos basins, dominate the subsurface velocity structures.

3. There is a prominent low velocity zone in the middle crust (around 40 km depth) under central Tibet. Shear velocity decreases by as much as 6% relative to the values north of Tibet and Tarim basin.

4. In general, there is good correlation between the P wave and S wave velocity variations. However, relative magnitudes of the variations (i.e. percentage velocity changes) are different in different regions. For example, the shear velocity decrease in the mid-crust under Tibet is twice as large as that of P velocity, percentage wise.

5. In the upper mantle, the percentage variation of shear velocities is greater than those of P velocities.

REFERENCES

Friederich, W. (2003). The S velocity structure of the East Asian mantle from inversion of shear and surface waveforms, *Geophys. J. Int.* 153: 88–102.

Hearn, T. M. and J. F. Ni (2001). Tomography and location problems in China using regional travel-time data, in *Proceedings of the 23rd Seismic Research Review: Worldwide Monitoring of Nuclear Explosions*, LA-UR-01-4454, Vol. 1, pp. 27–45.

Hearn, T. M., S. Wang, J. F. Ni, Z. Xu, Y. Yu, and X. Zhang (2004). Uppermost mantle velocities beneath China and surrounding regions, *J. Geophys. Res.* 109: doi:10.1029/2003JB002874.

Huang, J. and D. Zhao (2004). Crustal heterogeneity and seismotectonics of the Chinese capital region. *Tectonophysics* 385: 159–180.

Huang, J., D. Zhao, and S. Zheng (2002). Lithospheric structure and its relationship to seismic and volcanic activity in southwest China. *J. Geophys. Res.* 107: doi:10.1029/2000JB000137.

Institute of Geophysics, China Seismological Bureau (IG-CSB), 1990–2003. *Annual Bulletin of Chinese Earthquakes (ABCE).* Beijing: Seismological Publishing House.

Koulakov, I. and S. V. Sobolev (2006). A tomographic image of Indian lithosphere break-off beneath the Pamir-Hinkukush region, *Geophys. J. Int.* 164: 425–440.

Laske, G. and G. Masters (1997). A global digital map of sediments thickness, *EOS* 78: F483 (abstract).

Laske, G., G. Masters, and C. Reif (2001). CRUST 2.0: A new global crustal model at 2x2 degrees, http://mahi.ucsd.edu/Gabi/rem.dir/crust/crust2.html (last accessed July 2005).

Lebedev, S. and G. Nolet (2003). Upper mantle beneath southeast Asia from S velocity tomography. *J. Geophys. Res.* 108: doi 10.1029/2000JB000073.

Lebedev, S., G. Nolet, T. Meier, and R. D. van der Hilst (2005). Automated multimode inversion of surface and S waveforms, *Geophys. J. Int*. 162: 951–964.

Li, C., R. D. van der Hilst, and M. N. Toksöz (2006). Constraining P wave velocity variations in the upper mantle beneath Southeast Asia, *Phys. Earth Planet. Inter.* 154: 180¨C 195.

Mooney, W. D. (1998). CRUST 5.1: A global crustal model at 5° x 5°. *J. Geophys. Res.* 103: 727–747.

Nolet, G. (1985). Solving and resolving inadequate and noisy tomographic systems, *J. Comput. Phys.* 61: 463–482.

Paige, C. and M. Saunders (1982). LSQR: An algorithm for sparse linear equations and sparse least squares. *ACM Trans. Math. Software* 8: 471.

Papazachos, C. B. and G. Nolet (1997). P and S deep velocity structure of the Hellenic area obtained by robust nonlinear inversion of travel-times, *J. Geophys. Res.* 102: 8,349–8,367.

Pei, S., Z. Xu, and S. Wang (2004). Discussion on origin of Pn velocity variation in China and adjacent region. *Acta Seismol. Sin.* 26: 1–10 (in Chinese).

Poupinet, G., J. P. Avouac, M. Jiang, S. Wei., E. Kissling, G. Herquel, J. Guilbert, A. Paul, G. Wittlinger, H. Su, and J. C. Thomas (2002). Intracontinental subduction and Paleozoic inheritance of the lithosphere suggested by a teleseismic experiment across the Chinese Tien Shan, *Terra Nova* 14: 18–24.

Ritzwoller, M. H., M. P. Barmin, A. Villasenor, A. L. Levshin, and E. R. Engdahl (2002). Pn and Sn tomography across Eurasia to improve regional seismic event locations. *Tectonophys.* 358: 39–55.

Roecker, S. W., T. M. Sabitova, L. P. Vinnik, Y. A. Burmakov, M. I. Golvanov, R. Mamtkanova, and L. Munirova (1993). Three-dimensional elastic wave velocity structure of the western and central Tien Shan, *J. Geophys. Res.* 98: 15,779–15,795.

Shapiro, N. M. and M. H. Ritzwoller (2002). Monte Carlo inversion for a global shear velocity model of the crust and upper mantle. *Geophys. J. Int.* 151: 88–105.

Song, Z. H., C. Q. An, G. Y. Chen, L. H. Chen, Z. Zhuang, Z. W. Fu, and J. F. Hu (1991). Study on 3-D velocity structure and anisotropy beneath west China from the Love wave dispersion. *Acta Geophys. Sin.* 34: 694–707 (in Chinese).

Spakman, W. and G. Nolet (1988). Imaging algorithms, accuracy and resolution in delay time tomography, in *Mathematical Geophysics*, N. Vlar et al. (Eds.). Norwell, Massachusetts: D. Reidel, pp. 155–187

Stevens, J. L., D. A. Adams, and G. E. Baker (2001). Improved surface wave detection and measurement using phase-matched filtering with a global one-degree dispersion model, in *Proceedings of the 23rd Seismic Research Review: Worldwide Monitoring of Nuclear Explosions*, LA-UR-01-4454, Vol. 1, pp 420–430.

Sun, Y. and M.N. Toksöz (2006). Crustal structure of China and surrounding regions from P wave traveltime tomography, *J. Geophys Res.* 111: B03310, doi:10.1029/2005JB003962.

Sun, Y., X. Li, S. Kuleli, F. D. Morgan, and M. N. Toksöz (2004). Adaptive moving window method for 3-D P velocity tomography and its application in China. *Bull. Seism. Soc. Am.* 94: 740–746.

Um, J. and C. Thurber (1987). A fast algorithm for two-point seismic ray tracing. *Bull. Seism. Soc. Am.* 77: 972–986.

Vinnik, L. P., S. W. Roecker, G. L. Kosarev, S. I. Oreshin, and I. Y. Koulakov (2002). Crustal structure and dynamics of the Tien Shan, *Geophys. Res. Lett.* 29: 2047, doi 10.1029/2002GL015531.

Vinnik, L. P. C. Reigber, I. M. Aleshin, G. L. Koserev, M. K. Kaban, S. I. Oreshin, and S. W. Roecker (2004). Receiver function tomography of the central Tien Shan, *Earth Planet. Sci. Lett.* 225: 131–146.

Wu, F. T., A. L. Levshin, and V. M. Kozhevnikov (1997). Rayleigh wave group velocity tomography of Siberia, China, and vicinity. *Pure Appl. Geophys.* 149*:* 447–473.

Xu, Y., F. Liu, J. Liu, and H. Chen (2002). Crust and upper mantle structure beneath western China from P wave travel-time tomography. *J. Geophys. Res*. 107: doi 10.1029/2001JB000402.

Yu, X., Y. Chen, and P. Wang (2003). Three-dimensional P wave velocity structure in Beijing-Tianjin-Tangshan area. *Acta Seismol. Sin.* 25: 1–14.

Zhao, D., A. Hasegawa, and S. Horiuchi (1992). Tomographic imaging of P and S wave velocity structure beneath northeastern Japan. *J. Geophys. Res*. 97: 19,909–19,928.

Zhu, J., J. Cao, X. Cai, Z. Yan, and X. Cao (2002). High resolution surface wave tomography in east Asia and west pacific marginal sea. *Chinese J. Geophys*. 45: 679–698.

Zhu, L., R. Zeng, and F. Liu (1990). 3-D P wave velocity structure under the Beijing network area. *Acta Geophys. Sin*. 33: 267–277 (in Chinese).

NEAR SOURCE ENERGY PARTITIONING FOR REGIONAL WAVES IN 2D AND 3D MODELS: CONTRIBUTIONS OF FREE SURFACE SCATTERING

Xiao-Bi Xie, Thorne Lay, Ru-Shan Wu, and Yaofeng He

University of California, Santa Cruz

Sponsored by Air Force Research Laboratory

Contract No. FA8718-05-C-0021

ABSTRACT

Regional seismic phases have become of central importance for low-yield nuclear event size estimation and discrimination. However, the lack of fundamental understanding of the physics controlling regional wave energy partitioning remains a major concern for high-confidence applications of regional phases in nuclear monitoring. Due to the complex excitation and energy partitioning processes involved in regional phase formation, it is difficult to separate the contributions of different excitation mechanisms in the observed data. Given this situation, numerical simulations can play an important role for understanding the excitation of regional phases.

We have developed a regional seismic wave numerical modeling method to investigate energy partitioning for explosion-generated signals. Our approach is to separate the problem into consideration of near-source energy partitioning effects apart from long-range propagation effects. This is achieved by combining the near source simulation, e.g., finite-difference modeling or boundary-element modeling, with a slowness analysis method. This method allows very fine near source models to be used to investigate the near-source energy partitioning process explicitly. A localized slowness analysis tracks the energy partitioning instead of a time consuming mode formation by long distance propagator. Recent empirical demonstrations that explosion generated shear waves have a corner frequency that scales approximately as $V_s(S)/R_e$ (Fisk, 2006), where R_e is the elastic radius and $V_s(S)$ is the source shear velocity, indicate the importance of very near-source processes for the energy partitioning. Our initial work has involved *P*-to-*S* energy conversion by near-source scattering, which intrinsically scales the *S* energy generation relative to the *P*-waves without systematically shifting the corner frequency of the explosion *S*-waves. We are now exploring mechanisms that may account for the corner frequency shift between *P* and *S* signals for explosions that preserve the yield scaling behavior. Scattering of *Rg*-to-*S* is one such mechanism, as *Rg* forms with a lower frequency content than *P*. The most effective mechanism for scattering of *Rg* is rough surface topography, although shallow crustal heterogeneity can be important too.

In this report, we apply a combined boundary element simulation and slowness analysis method to investigate the effect of near-source topographic scattering on the explosion source energy partitioning. Random free surface models with exponential power spectrum, variable rms fluctuations and correlation lengths are used in the calculation. In addition, we test the effects of intrinsic attenuation and source depth on the scattering process. The frequency dependence on different parameters is investigated. The results show that couplings caused by surface scattering do occur between the body and surface waves, and these processes influence the overall partitioning of the explosion energy. Additional trapped waveguide energy can be generated by the interaction between an explosion source and near-source topographic fluctuations. The source depth, rms value, correlation length and attenuation all affect this process.

OBJECTIVE

With the current emphasis on global monitoring for low-yield nuclear tests, regional seismic phases such as *Lg* have become very important for magnitude and yield estimation of underground nuclear tests (e.g. Nuttli, 1986; Patton, 2001). In addition, various *P*/*S*-type amplitude ratios for high frequency regional phases (e.g. *Pn*/*Sn*, *Pn*/*Lg*, *Pg*/*Lg*, *Pg*/*Sn*) have become important for event discrimination (e.g., Taylor et al., 1989; Kim et al., 1993, 1997; Walter et al., 1995; Fisk et al., 1996; Taylor, 1996; Taylor and Hartse, 1997; Hartse et al., 1997; Fan and Lay, 1998a–c; Xie, 2002; Bottone et al., 2002). The applications of regional phases for yield estimation and event discrimination are largely based on empirical approaches, and while very promising in many cases, there are major questions about the nature of excitation of *S*-wave dominated phases such as *Lg*. Numerous excitation processes have been proposed. The complex excitation and energy partitioning processes associated with regional phases make it difficult to empirically separate the contribution of individual energy partitioning mechanisms by data analysis. Numerical modeling approaches are thus of great importance for investigating the excitation and propagation of regional phases (e.g., Xie and Lay, 1994; Wu, et al., 2000a, b; Bonner et al., 2003; Stevens et al., 2003; Myers et al., 2003, 2005; Xie, et al., 2005a, b).

Although there are continuing controversies about the dominant *P*-to-*S* transfer mechanisms affecting regional phases, most investigators agree that appreciable energy from explosion sources is converted to *S*-waves in the near-source region. Fisk (2006) demonstrates that the *S*-wave excitation for explosions scales with explosion yield and has a corner frequency shift relative to *P* energy proportional to the source region velocity ratio *Vs(S)/Vp(S)*. Several possible near-source energy excitation mechanisms have been proposed to explain the generation of regional *Lg*-wave. Among these models, the near source coupling between *P*-, *S*- and the *Rg*-waves due to the scattering on a rugged free surface may play an important role for *Lg*-wave excitation. This has been investigated by different authors from both observational and theoretical perspectives. From data analysis, Gupta et al. (1992, 2005) suggested that near-source scattering of explosion-generated *Rg* into *S* makes a significant contribution to the low-frequency *Lg*. Patton and Taylor (1995) analyzed the *Lg* spectral ratios from Nevada Test Site (NTS) explosions and suggested that the *Lg*–wave is generated by near-source scattering of *Rg*-waves into body waves, which become trapped in the crust. Patton and Taylor (1995) and Gupta et al. (1997) introduced the theoretical model of spall source to explain the observed similarity between the *Rg* and *Lg* spectrum. McLaughlin and Jih (1988) used finite-difference simulation to investigate topography influences on teleseismic *P*-waveforms, and indicated possible *Rg*-to-*P* scattering due to the near source topography. Several more recent studies, e.g., Bonner et al. (2003), Myers et al. (2003), and Wu et al. (2003), also provided strong evidence in favor of the *Rg*-to-*S* scattering mechanism for the generation of the low frequency *S* and *Lg* for explosions. Myers et al. (2005), using numerical simulation, investigated the effect of topography on the *P*-to-*S* conversion. They concluded that near-source topography and geologic complexity in the upper crust strongly contribute to the generation of S-waves. Xie et al. (2005a, b) investigated the contribution of shallow scattering on the explosive source energy partitioning and calculated the frequency dependent *Lg* excitation functions. They found that the high-frequency *Lg* energy is from *P*-*pS*-to-*Lg* and *P*-to-*Lg* scattering, and the low-frequency energy comes from *Rg*-to-*Lg* scattering.

With the existence of a rugged free surface, the actual coupling between waves in the near source region is expected to be rather complex affecting the very formation of *Rg*, so it important to study this phenomenon with the source excitation in the model, not simply as a propagation effect. The scattering at the free surface can change the propagation direction of *pP*- and *pS*-waves causing some of their energy to become trapped in the crustal waveguide to contribute to the *Lg*-wave. A rugged free surface or shallow heterogeneity also provides coupling between the surface wave and body waves. Both body-wave to surface-wave and surface-wave to body-wave scattering could occur. Multiple scattering, source depth and attenuation in the shallow layers are all factors that may affect the result and should be considered in the investigation. Source depth, attenuation and statistical features of the surface fluctuation may add frequency dependency to the energy partitioning process. In this report, we use the 2D *P-SV* boundary-element simulation (Ge et al., 2005) and slowness analysis method (Xie et al., 2005a) to investigate the effect of topographic scattering on the explosion source energy partitioning. Topographic models with different rms fluctuations and correlation lengths are used in the numerical simulations, and their effects are examined.

RESEARCH ACCOMPLISHED

The Boundary Element Simulation

The boundary element method is formulated in terms of integrals along boundaries so that the traction-free condition on the free surface can be naturally treated. The method provides a geometrically accurate description of irregular boundaries. Among different numerical simulation methods such as the finite-difference method, the boundary integral method is more suitable for modeling complex reflections from the rugged topography. We use the 2D elastic boundary element method developed in the previous stage of this project (Ge et al., 2005) to simulate the effect of free surface scattering on the explosion source energy partitioning. The following is a brief description of the boundary element method.

Consider the layered crustal model shown in Figure 1. Each layer Ω has constant velocities and density but the free surface and the interfaces can be irregular. Γ_1 and Γ_2 are the free surface and the interface. Γ_∞ is the radiation boundary marked with dash lines. Based on the representation theorem (e.g., Aki and Richards, 1980), the wavefield within each layer can be expressed using the integral along its boundary (Ge et al., 2005)

$$\mathbf{C}(\mathbf{r})\mathbf{u}(\mathbf{r})+\int_\Gamma\left[\mathbf{u}(\mathbf{r}')\Sigma(\mathbf{r},\mathbf{r}')-\mathbf{t}(\mathbf{r}')\mathbf{G}(\mathbf{r},\mathbf{r}')\right]d\Gamma(\mathbf{r}')=\int_\Omega\mathbf{f}(\mathbf{r}',\omega)\mathbf{G}(\mathbf{r},\mathbf{r}')d\Omega(\mathbf{r}'), \tag{1}$$

where $\mathbf{u}(\mathbf{r})$ is the displacement, $\mathbf{r}$ is the position of observation point and $\mathbf{r}'$ is the scattering point, $\mathbf{t}(\mathbf{r}')$ is the traction vector on the boundary, the coefficient $\mathbf{C}(\mathbf{r})$ generally depends on the local geometry at $\mathbf{r}$, and $\mathbf{G}(\mathbf{r},\mathbf{r}')$ and $\mathbf{\Sigma}(\mathbf{r},\mathbf{r}')$ are the Green's functions for displacements and traction, respectively. $\mathbf{C}(\mathbf{r})$, $\mathbf{\Sigma}(\mathbf{r},\mathbf{r}')$ and $\mathbf{G}(\mathbf{r},\mathbf{r}')$ are all 2×2 matrices for a 2 D *P-SV* problems. $\mathbf{f}(\mathbf{r},\omega)$ is the body force distribution in the model. The green's functions $\mathbf{G}(\mathbf{r},\mathbf{r}')$ and $\mathbf{\Sigma}(\mathbf{r},\mathbf{r}')$ can be calculated using the elastic wave equation in unbounded homogeneous medium.

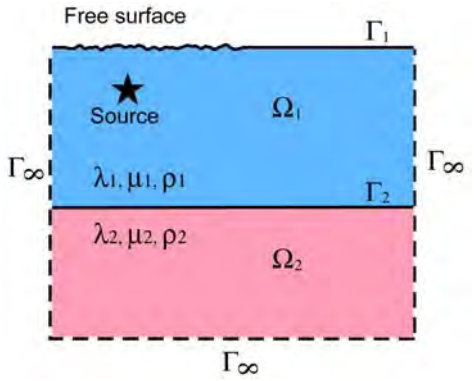


Figure 1. Geometry of a layered crustal model.

Taking the two-layer model as an example, using a delta distributed source $\mathbf{f}(\mathbf{r},\omega)=\mathbf{f}(\omega)\delta(\mathbf{r}_0)$, and considering the traction free boundary condition on the free surface and radiation boundary condition for Γ_∞, the equations for the first and second layers can be modified as (Ge et al., 2005)

$$\mathbf{C}(\mathbf{r})\mathbf{u}(\mathbf{r})+\int_{\Gamma_1}\Sigma(\mathbf{r},\mathbf{r}')\mathbf{u}(\mathbf{r}')d\mathbf{r}'+\int_{\Gamma_2}[\Sigma(\mathbf{r},\mathbf{r}')\mathbf{u}(\mathbf{r}')-\mathbf{G}(\mathbf{r},\mathbf{r}')\mathbf{t}(\mathbf{r}')]d\mathbf{r}'=\mathbf{G}(\mathbf{r},\mathbf{r}_0)\mathbf{f}(\omega) \tag{2}$$

and

$$\mathbf{C}(\mathbf{r})\mathbf{u}(\mathbf{r})+\int_{\Gamma_2}[\Sigma(\mathbf{r},\mathbf{r}')\mathbf{u}(\mathbf{r}')-\mathbf{G}(\mathbf{r},\mathbf{r}')\mathbf{t}(\mathbf{r}')]d\mathbf{r}'=0 \tag{3}$$

Equations (2) and (3) simultaneously provide the basis for calculating the wave propagation in a model with rugged free surface. The displacement $\mathbf{u}(\mathbf{r})$ on both Γ_1 and Γ_2 can be discretized and solved from these equations. Finally, the internal displacement field can be calculated from their boundary values using Equation (1).

Investigating the Boundary Scattering Using the Slowness Analysis Method

We use the slowness analysis method (Xie et al., 2005a) developed in this project to analyze the wavefield generated from the boundary element calculation and investigate the near source energy partitioning with the presence of free surface fluctuations. Figure 2 shows the configurations of calculations. In this simple example, we use two-layer models with different free surface parameters and source depths for boundary element calculations. The velocities and densities are listed in Table 1. The topographic fluctuation has an exponential power spectrum and a correlation length of 0.5 km. The fluctuations are located above the source and extend in both directions for 20 km. Illustrated in Figure 2(a) is the model with 150 m rms fluctuation (maximum peak to trough is 625 m), and in Figure 2(b) is the model with 300 m rms fluctuation (maximum peak to trough is 1,281 m). The source depths used in these calculations are 500 m and 3,000 m, respectively. The synthetic seismograms are generated in a vertical array of 41×60 receivers located between epicentral distances 30 and 50 km and depths 0 and 30 km. Figure 3 shows the snap shots of wavefield in the vertical array.

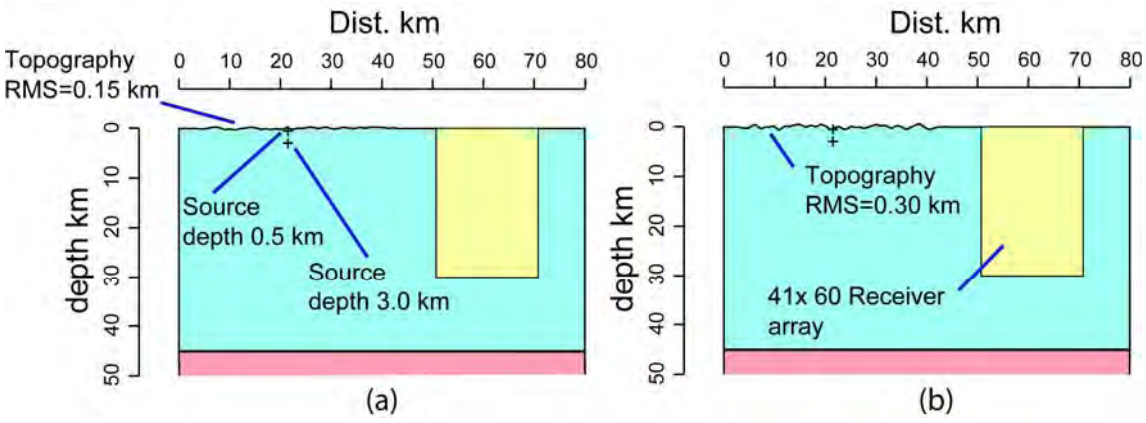


Figure 2. Cartoon showing the boundary element calculations and slowness analysis. Details given in the text.

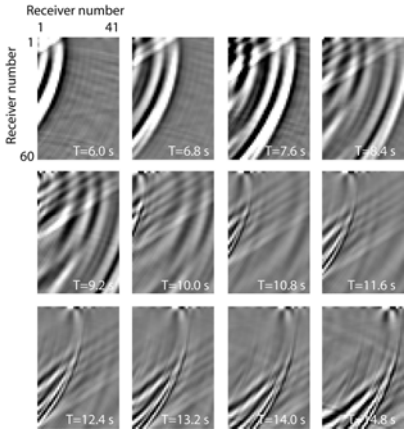


Figure 3. Wavefield snapshots from the vertical receiver array. Each time frame is independently normalized.

The synthetic seismograms are analyzed using the slowness analysis method (Xie et al. 2005a) to demonstrate how the energy partitioning is affected by the free surface fluctuations and the source depths. Illustrated in Figure 4 is the energy distribution in the horizontal-slowness and depth domain for different free surfaces and source depths. The red vertical lines indicate the upper mantle *S*-wave slowness. To the left of these lines, the waves have incidence angles steeper than the critical angle on the Moho and the energy will leak to the upper mantle through multiple reflections. To the right of these lines, total reflection will keep the energy in the crustal wave guide to contribute to the *Lg*-wave. In Figure 4, row (a) is for a flat free surface and a deeper explosion source. As expected, this configuration generates neither noticeable trapped energy nor clear *Rg*-wave. Row (b) is for a flat free surface and a shallow explosion source. The trapped energy is from *S**-wave. *Rg*-energy can be seen at very shallow depth for the shallow source. Row (c) is for a deeper explosion source and a free surface with 150 m rms fluctuation. Comparing with row (a), the existence of surface fluctuation generates considerable trapped energy from free surface scattering. Although the source is located at a depth of 3.0 km, the *Rg* energy can now be seen at shallow depth. This enhanced *Rg*-wave comes from the free surface scattering, which can be treated as shallow secondary sources. In rows (d) to (f), with shallower source or larger rms free surface fluctuations, a lot of trapped energy can be generated from the interaction between an explosion source and topographic fluctuations.

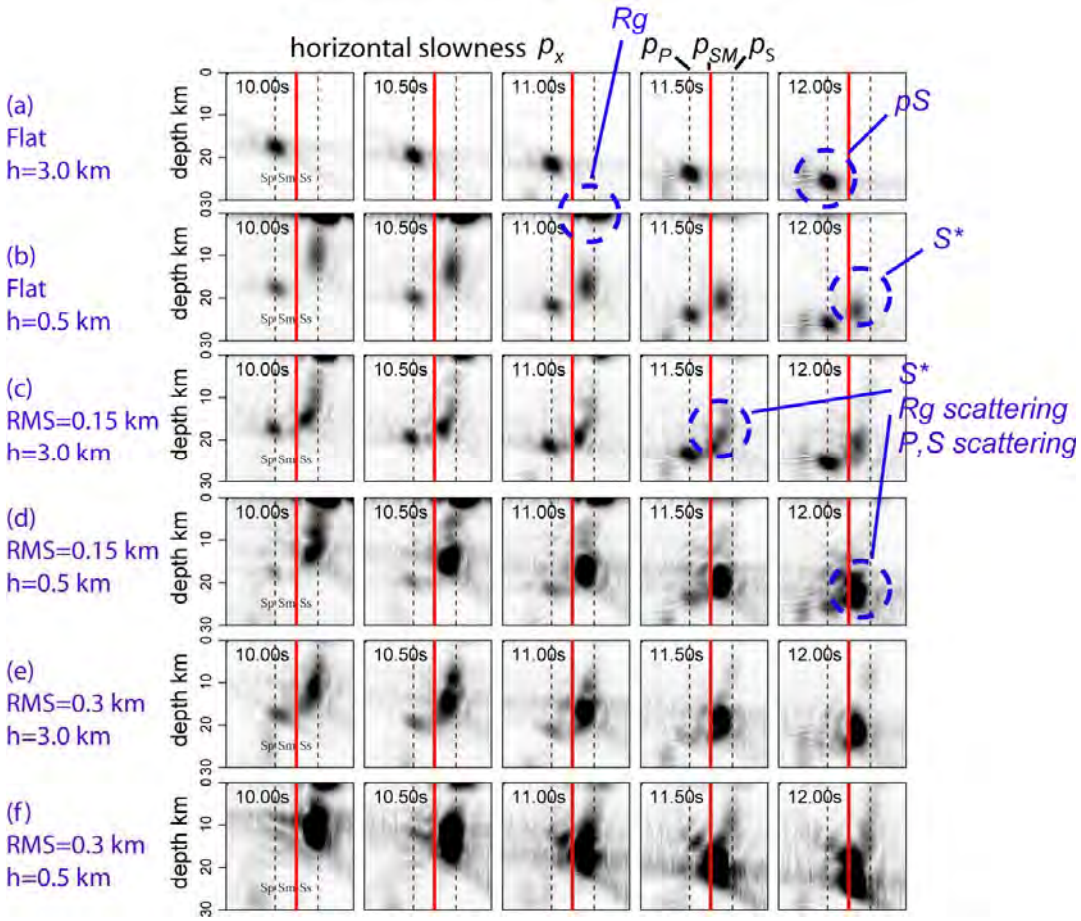


Figure 4. Slowness analysis for models with different source depths and free surface parameters. In each small panel, the horizontal coordinate is horizontal slowness and the vertical coordinate is depth. The red vertical lines indicate the upper mantle *S*-wave slowness which separates energy that leaks out of the waveguide (to the left) from energy trapped in the wave guide (to the right) that forms *Lg*.

The Effect of Surface Scattering on Energy Partitioning

We can symbolically write the near-source energy partitioning process for an explosion source as

$$E^K(p,f) = S(f)R^K(p,f), \tag{4}$$

where $E^K(p,f)$ is the near-source energy partitioned to the type *K* wave (*K* can be *P*, *S*, *Lg* , *Rg* or other wave types), p is the slowness, f is the frequency, and $S(f)$ is the spectrum of an isotropic explosion source. The $R^K(p,f)$ is the response of the near source structure to excite type *K* wave and can be expressed as

$$R^K(p,f) = R_F^K(p,f) + \sum_J R_F^J(p,f)T^{J\to K}(p,f), \tag{5}$$

where $R_F^K(p,f)$ is the response of a flat layered earth model and $T^{J\to K}(p,f)$ is the energy transfer function due to secondary effects such as near-source scattering or spall. In this study, we focus on the contribution from the surface scattering. The response function R_F^K partitions the source energy into different phases. The transfer function $T^{J\to K}$ provides the *J*-to-*K* coupling, which further modifies the partitioning by moving energy from one phase to another. The combined effect of R_F^K and $T^{J\to K}$ forms R^K, which partitions the energy radiated from an isotropic source into the *K*-wave energy distributed in slowness and frequency domains and this energy will later develop into different regional phases at remote distances. We allow $T^{J\to K}$ to take either positive or negative values. For example, if *J* type wave loses energy due to scattering, then $T^{J\to J}$ could be negative. Investigating these response and transfer functions provides a way to estimate the underlying process of energy partitioning. Due to the complex mechanisms involved, the actual near-source energy partitioning can be highly complex. Factors such as the source depth, local layered structure, attenuation, random velocity perturbations and free surface fluctuations all affect the partitioning. These effects often apply to the partitioning in a coupled way and the entire process may not necessarily be linear or simply separated. We will use numerical modeling to simulate the complex partitioning process and use slowness analysis to calculate these response functions. The above symbolic equations can provide us with a basic relationship to understand this process. The partitioning process relates to the space and time variables as well (Xie et al., 2005). We apply proper space and time windows to separate different phases for analysis. For simplicity, we omit the discussions on these variables.

Rg-to-*Lg* Coupling Due to Scattering from a Rugged Free Surface

To demonstrate the *Rg*-wave scattering on a rugged free surface, we calculate synthetic seismograms for the two-layer velocity model listed in Table 1. The source depth is 0.5 km. The random surface fluctuation is located between epicentral distances 5 and 25 km. It has a correlation length of 0.5 km and rms values vary between 0.0 and 0.4 km. The results of slowness analysis are shown in Figure 5 with different rows for models with different rms fluctuations. The *Rg* energy is located at depths less than 3 km and with a slowness similar to the *S*-wave. In row (a) with rms = 0, the *Rg*-wave is generated by the explosion source and a flat earth model. It arrives at the receiver array between 12 and 15 s and is labeled as “direct *Rg*-wave.” The existence of rough free surface can cause scattering of different waves and redistribute their energy. As shallow secondary sources, these scattering interactions generate *Rg*-waves. In rows (b) to (d), there are early scattered *Rg*-waves between 10 and 12 s. They arrive earlier than the direct *Rg* because part of their wave path travels with faster body wave speed. We label this as “scattered *Rg*-wave.” The amplitudes of *Rg*-waves depend on the same rms fluctuations that excite the scattered *Rg* but the roughness attenuates both direct and scattered *Rg*. The scattered energy may go to body waves as well. In row (e), due to strong scattering from a very rugged free surface, both direct and scattered *Rg*-waves are very weak.

Table 1. Two-layer velocity model

Bottom of layer (km)	V_P (km/s)	V_S (km/s)	ρ (g/cm^3)
45	6.5	3.6	2.9
infinity	8.0	4.5	3.3

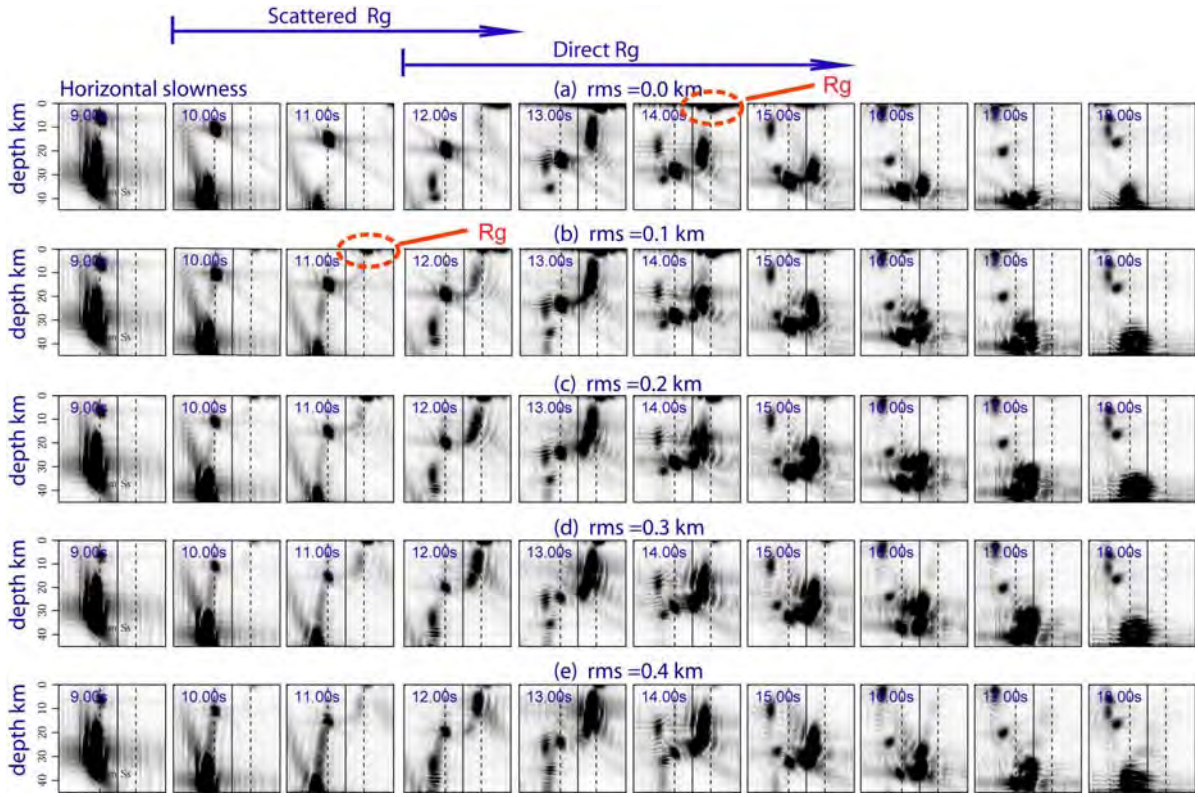


Figure 5. The slowness analysis for models with different rms topographic fluctuations. In each time frame the horizontal coordinate is the horizontal slowness and vertical coordinate is the depth. The *Rg* energy is located near the surface, with a slowness similar to the S-wave. Source depth is 0.5 km.

Applying proper frequency, slowness, time, and space windows to the slowness analysis result shown in Figure 5, we can separate the energy and estimate the excitation of different phases (Xie et al., 2005). For this purpose, we first calculate synthetic seismograms for a three-layer velocity model listed in Table 2. We use a source depth of 0.5 km. The random surface fluctuation is located above the source and extended in both directions for 20 km. The correlation length is 0.5 km and rms values vary between 0.0 and 0.4 km. A series of band pass filters are used to obtain responses between 0.75 and 4.0 Hz. In Figure 6, the top row illustrates the near-source responses of (a) direct *Rg*, (b) scattered *Rg* and (c) *Lg* as functions of frequency and rms surface fluctuations. For response function R^{Rg_direct}, the energy is mainly located at low frequencies and decreases with the increasing rms values. Note that the histograms labeled with rms = 0 indicate the response of a flat earth model.

Table 2. Three-layer velocity model

Bottom of layer (km)	V_P (km/s)	V_S (km/s)	ρ (g/cm^3)
10	5.6	3.2	2.7
45	6.5	3.8	2.9
Infinity	8.0	4.5	3.3

The contribution of the surface scattering can be calculated by subtracting the flat earth response from the total response (see Equation (5). The negative values of the differences shown in Figure 6 (d) indicate the energy loss of direct *Rg* due to the scattering attenuation, which is strong for larger rms values. The response of scattering *Rg* in Figure 6 (b) increases with increasing rms up to a moderate rms value, then decreases with further increasing rms. This suggests that small to moderate topographic fluctuation can excite secondary *Rg*-wave, but a very bumpy free surface will prevent the formation and propagation of *Rg*-waves. Because the time window of the direct *Rg* has some overlap with the scattered *Rg*, there is some energy in the scattered *Rg* window even for a flat earth model.

By subtracting this energy, we can obtain the pure scattering contribution, which is shown in Figure 6 (e). We see that this response is comprised of both low and high frequency contributions. It is possible that the former mainly comes from the *Rg*-to-*Rg* scattering and the later comes from body wave to surface wave scattering.

Shown in Figures 6 (c) and (f) are *Lg*-wave response R^{Lg} and separated scattering contribution $R^{Lg} - R_F^{Lg}$. The contribution of scattering to the *Lg*-wave is proportional to the rms values. Again, the contribution includes high frequency content which likely comes from the scattering of body waves to *Lg*, and low frequency content which mainly comes from *Rg*-to-*Lg* scattering. However, the low frequency content cannot be fully explained with the *Rg* energy loss. Although the low frequency spectrum of $R^{Lg} - R_F^{Lg}$ almost mirrors the shape of the $R^{Rg_direct} - R_F^{Rg_direct}$ spectrum, *Rg*-to-*Lg* coupling does not provide quite enough energy to *Lg*—this can be recognized by comparing the scales of (d) and (f). A possible explanation is that the additional low frequency *Lg* energy is provided by the body waves as well. A broadband body wave may excite low frequency S-waves if the surface scattering serves as shallow secondary sources. For example, a mechanism similar to the generation of *S** can provide a frequency dependent transfer function $T^{body \to Lg}$ in Equation (5). To verify this, additional study is required.

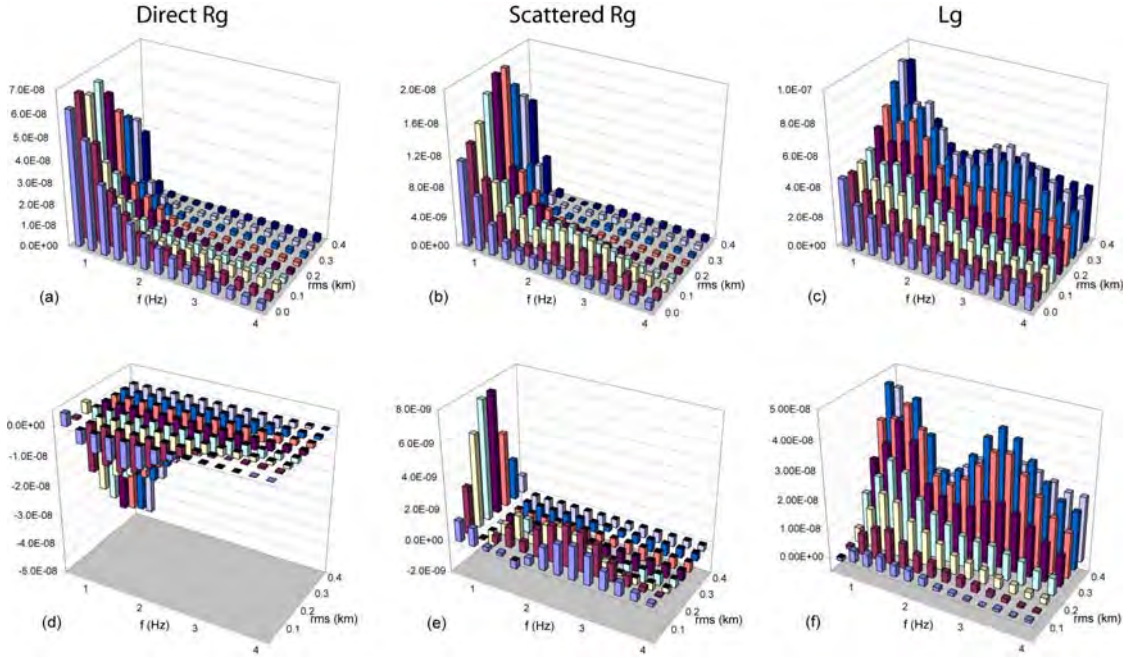


Figure 6. Top row: the near source responses of direct *Rg*, scattered *Rg* and the *Lg*-waves as functions of frequency and rms fluctuations, with (a) R^{Rg_direct}, (b) R^{Rg_scatt} and (c) R^{Lg}. Bottom row: the contributions of surface scattering to these responses, with (d) $R^{Rg_direct} - R_F^{Rg_direct}$, (e) $R^{Rg_scatt} - R_F^{Rg_scatt}$ and (f) $R^{Lg} - R_F^{Lg}$.

The Effect of Attenuation on the Energy Partitioning

Scattering from topographic fluctuations occurs within the topmost crust, which is usually a low *Q* layer. This attenuation will strongly affect the scattering and energy partitioning of an explosion source. To test the effect of attenuation, we introduce intrinsic attenuation in the boundary element calculation. We use the same source parameters, free surface parameters, and velocity model as used in Figure 6 except replacing the infinite *Q* in the top 10 km with $Q_P = 100$ and $Q_S = 50$. The results are shown in Figure 7. Comparing Figure 7 with Figure 6, two prominent features can be identified. First, compared to the purely elastic case, there is considerable energy loss in the model with intrinsic attenuation. For example, the maximum energy level drops 40% for direct *Rg*-wave, 70% for scattered *Rg*-wave, and 40% for *Lg*-wave. Second, the short period waves undergo more attenuation than long period waves. This is especially true for the scattered *Rg*-wave and the *Lg*-wave. By using rather low *Q* values in this calculation, this should give a maximum effect of the attenuation.

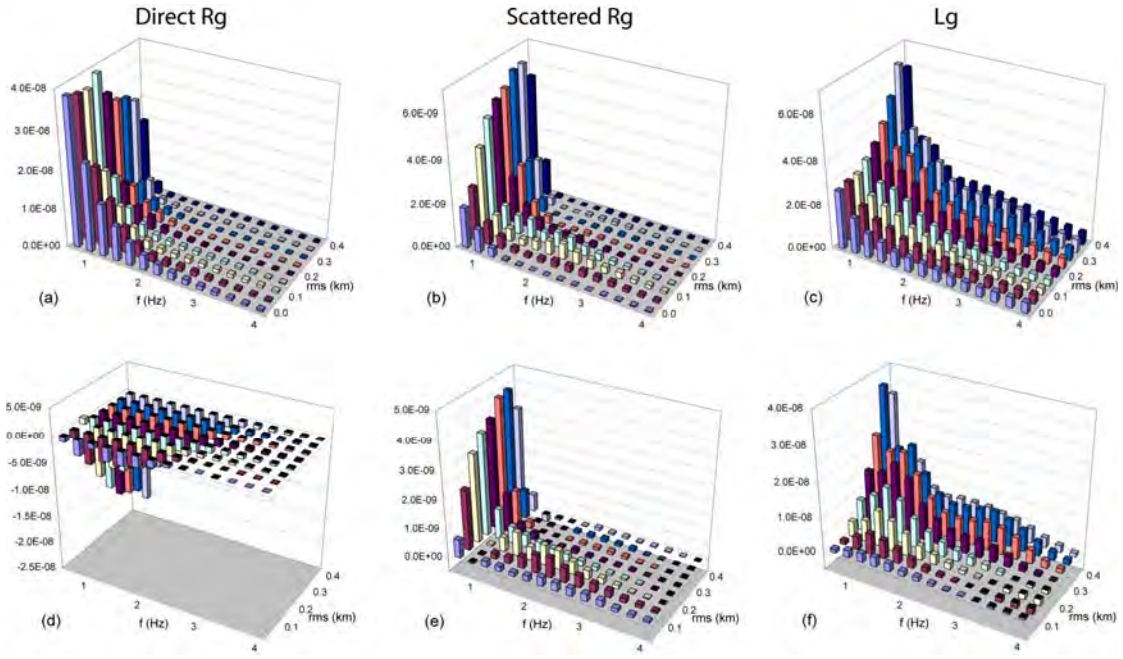


Figure 7. Similar to that shown in Figure 6, except low *Q* values are used in the top layer.

CONCLUSIONS AND RECOMMENDATIONS

We used the 2D *P-SV* boundary-element simulation and slowness analysis method to investigate the effect of topographic scattering on the near-source energy partitioning. Topographic models with different rms fluctuations and correlation lengths and different source depths and attenuation were investigated using numerical simulations. The result revealed that the surface scattering has strong effect on *Rg*-waves. The scattering process can excite the *Rg*-wave for a moderately rugged topography but prevent the formation of *Rg*-wave if the surface is becoming too rugged. The free surface scattering can increase the *Lg*-wave energy. It is possible that both *Rg* and body waves contribute to the *Lg*-wave through surface scattering. The effect of intrinsic attenuation on the energy partitioning was also studied.

The numerical simulation and slowness analysis accomplished in this report are 2D. We did not consider the energy partitioned to the *SH* component. In addition, in many cases, the effect of the 2D scattering may not be exactly the same as the 3D scattering. Expansion of the analysis to full 3D models should be pursued. Consideration of the P/S spectral behavior is also planned for future analysis.

ACKNOWLEDGEMENT

The authors wish to thank Dr. Zengxi Ge for many discussions and kindly providing the boundary element code.

REFERENCES

Aki, K. and Richards, P. G. (1980). *Quantitative Seismology. Theory and Methods.* San Francisco: W.H. Freeman.

Bonner, J. B., H. J. Patton, A. C. Rosca, H. Hooper, J. Orrey, M. Leidig, and I. Gupta (2003). Aspects of Rg and Lg generation from the Shagan depth of burial explosions, in *Proceedings of the 25th Seismic Research Review—Nuclear Explosion Monitoring: Building the Knowledge Base*, LA-UR-03-6029, Vol. 2, pp. 384–394.

Bottone, S., M. D. Fisk, and G. D. McCartor (2002). Regional seismic event characterization using a Bayesian formulation of simple kriging, *Bull. Seism. Soc. Am*. 92: 2,277–2,296.

Fan, G. W. and T. Lay (1998a). Statistical analysis of irregular waveguide influences on regional seismic discriminants in China, *Bull. Seism. Soc. Am*. 88: 74–88.

Fan, G. W. and T. Lay (1998b). Regionalized versus single-station wave-guide effects on seismic discriminants in western China, *Bull. Seism. Soc. Am*. 88: 1,260–1,274.

Fan, G. W. and T. Lay (1998c). Statistical analysis of irregular waveguide influences on regional seismic discriminants in China: Additional results for Pn/Sn, Pn/Lg and Pg/Sn, *Bull. Seism. Soc. Am*. 88: 1,504–1,510.

Fisk, M. D., H. L. Gray, and G. D. McCartor (1996). Regional discrimination without transporting thresholds, *Bull. Seism. Soc. Am*. 86: 1,545–1,558.

Fisk, M. D. (2006). Source spectral modeling of regional *P*/*S* discriminants at nuclear test sites in China and the former Soviet Union, *Bull. Seism. Soc. Am*. (in press).

Ge, Z., L. Y. Fu, and R. S. Wu (2005). P-SV Wavefield connection technique for regional wave propagation simulation, *Bull. Seism. Soc. Am.* 95: 1,375–1,386.

Gupta, I. N., W. Chan, and R. Wagner (1992). A comparison of regional phases from underground nuclear explosions at East Kazakh and Nevada test sites, *Bull. Seism. Soc, Am*. 82: 352–382.

Gupta, I. N., T. Zhang, and R. A. Wagner (1997). Low-frequency Lg from NTS and Kazakh nuclear explosions: Observations and interpretations, *Bull. Seism. Soc. Am*. 87: 1,115–1,125.

Gupta, I. N., W. W. Chan, and R. A. Wagner (2005). Regional source discrimination of small events based on the use of Lg wavetrain, *Bull. Seism. Soc. Am*. 95: 341–346.

Hartse, H. E., S. R. Taylor, W. S. Phillips, and G. E., Randall (1997). A preliminary study of regional seismic discrimination in central Asia with emphasis on western China, *Bull. Seism. Soc. Am*. 87: 551–568.

Kim, W. Y., V. Aharonian, A. L. Lerner-Lam, and P. G. Richards (1997). Discrimination of earthquakes and explosions in southern Russia using regional high-frequency three-component data from IRIS/JSP Caucasus Network, *Bull. Seism. Soc. Am*. 87: 569–588.

Kim, W. Y., D. W. Simpson, and P. G. Richards (1993). Discrimination of earthquakes and explosions in the eastern United States using regional high-frequency data, *Geophys. Res. Lett.* 20: 1,507–1,510.

McLaughlin, K. L. and R. S. Jih (1988). Scattering from near-source topography: Teleseismic observations and numerical simulations, *Bull. Seism. Soc. Am.* 78: 1,399–1,414.

Myers, S. C., J. L. Wagoner, S. C. Larsen, A. Rodgers, K. Mayeda, K. D. Smith, and W. R. Walter (2003). Simulation of regional explosion S-phases (SIRES) project, in *Proceedings of the 25th Seismic Research Review—Nuclear Explosion Monitoring: Building the Knowledge Base*, LA-UR-03-6029, Vol. 1, pp. 117–124.

Myers, S. C., J. Wagoner, L. Preston, K. Smith, and S. Larsen (2005). The effect of realistic geologic heterogeneity on local and regional P/S amplitude ratios based on numerical simulations, in *Proceedings of the 27th Seismic Research Review: Ground-Based Nuclear Explosion Monitoring Technologies*, LA-UR-05-6407, Vol. 1, pp. 123–132.

Nuttli, O. W. (1986). Yield estimates of Nevada Test Site explosions obtained from Lg waves, *J. Geophys. Res*. 91: 2,137–2,151.

Patton, H. J. (2001). Regional magnitude scaling, transportability, and Ms:mb discrimination at small magnitudes, *Pageoph*, 158: 1,951–2,015.

Patton, H. J. and S. R. Taylor (1995). Analysis of Lg spectral ratios from NTS explosions: Implications for the source mechanisms of spall and the generation of Lg waves, *Bull. Seism. Soc. Am*. 85: 220–236.

Stevens, J. L., G. E. Baker, H. Xu, T. J. Bennett, N. Rimer, and S. M. Day (2003). The physical basis of Lg generation by explosion sources, in *Proceedings of the 25th Seismic Research Review—Nuclear Explosion Monitoring: Building the Knowledge Base*, LA-UR-03-6029, Vol. 2, pp. 456–465.

Taylor, S. R. (1996). Analysis of high frequency Pn/Lg ratios from NTS explosions and western U.S. earthquakes, *Bull. Seism. Soc. Am*. 86: 1,042–1,053.

Taylor, S. R., M. D. Denny, E. S. Vergino, and R. E. Glaser (1989). Regional discrimination between NTS explosions and western U.S. earthquakes, *Bull. Seism. Soc. Am*. 79: 1,142–1,176.

Taylor, S. R. and H. E. Hartse (1997). An evaluation of generalized likelihood ratio outlier detection to identification of seismic events in Western China, *Bull. Seism. Soc. Am*. 87: 824–831.

Walter, W. R., K. M. Mayeda, and H. Patton (1995). Phase and spectral ratio discrimination between NTS earthquakes and explosions—Part I: Empirical observations, *Bull. Seism. Soc. Am.* 85: 1,050–1,067.

Wu, R. S., S. Jin, and X. B. Xie (2000a). Seismic wave propagation and scattering in heterogeneous crustal waveguides using screen propagators: I SH waves, *Bull. Seism. Soc. Am*. 90: 401–413.

Wu, R. S., S. Jin, and X. B. Xie (2000b). Energy partition and attenuation of Lg waves by numerical simulations using screen propagators, *Phys. Earth and Planet. Inter*. 120: 227–243.

Wu, R. S., X. B. Xie, Z. Ge, X. Wu, and T. Lay (2003). Quantifying source excitation and path effects for high-frequency regional waves, in *Proceedings of the 25th Seismic Research Review—Nuclear Explosion Monitoring: Building the Knowledge Base*, LA-UR-03-6029, Vol. 1, pp. 172–181.

Xie, J. (2002). Source scaling of Pn and Lg spectra and their ratios from explosions in central Asia: Implications for the identification of small seismic events at regional distances, *J. Geophys. Res.* 107: B7, 10.1029/2001JB000509.

Xie, X. B. and T. Lay (1994). The excitation of Lg waves by explosions: A finite-difference investigation, *Bull. Seism. Soc. Am.* 84: 324–342.

Xie, X. B., Z. Ge, and T. Lay (2005a). Investigating explosion source energy partitioning and Lg-wave excitation using a finite-Difference plus slowness analysis method, *Bull. Seism. Soc. Am*. 95: 2,412–2,427.

Xie, X. B., T. Lay, and R. S. Wu (2005b). Near source energy partitioning for regional waves in 2d and 3d models, contributions of S*-to-Lg and P-to-Lg scattering, in *Proceedings of the 27th Seismic Research Review: Ground-Based Nuclear Explosion Monitoring Technologies*, LA-UR-05-6407, Vol. 1, pp. 249–258.

REGIONAL-SCALE DIFFERENTIAL TIME METHODS: DEVELOPMENT AND APPLICATION TO THE SIBERIA DATA SET

H. Zhang[1], Y. Liu[1], C. Thurber[1], L. Steck[2], and C. Rowe[2], K. Fujita[3], and K. Mackey[3]

University of Wisconsin-Madison[1], Los Alamos National Laboratory[2], Michigan State University[3]

Sponsored by National Nuclear Security Administration
Office of Nonproliferation Research and Development
Office of Defense Nuclear Nonproliferation

Contract No. DE-FC52-06NA27325[1,2,3]

ABSTRACT

The University of Wisconsin-Madison (UW-Madison) group is developing improved methodologies for regional-scale three-dimensional (3D) seismic tomography, and is working collaboratively with Los Alamos National Laboratory (LANL) and Michigan State University (MSU) on applications of these methods to the Siberia data set assembled by MSU. The tomographic study proposed here will emphasize the accretionary regions to the south and east of the Siberian craton, providing the first detailed 3D look at the seismic structure of continental eastern Russia.

There are four main tasks in this project: (1) an extension of our development of double-difference (DD) seismic tomography to the use of station-pair residual differences, including incorporation of a new method for resolution matrix calculation; (2) testing, refinement, and adaptation of a method for spherical-earth finite-difference (SEFD) travel time calculations for use in DD tomography; (3) an extension of our Cartesian adaptive-grid DD tomography algorithm to spherical coordinates; and (4) collaborative work among the UW-Madison, LANL, and MSU groups to apply these analysis tools to the Siberia data set.

Our work under Task 1 has so far focused on the incorporation and testing of the new resolution matrix calculation method in an existing DD tomography code. The PROPACK package developed by Larsen (1998) is able to efficiently and accurately estimate singular values and vectors for large matrices based on the Lanczos bidiagonalization with partial reorthogonalization (BPRO). We have made substantial progress towards incorporating the PROPACK package into the double-difference seismic tomography code tomoDD, allowing its use to estimate the model resolution matrix for large seismic tomography problems. Compared to previous LSQR-based methods for estimating the model resolution matrix, the PROPACK-based method accurately calculates the full resolution matrix and thus gives a complete description of how well the model is resolved.

Task 2 involves the testing, refinement, and adaptation of a new method for SEFD travel time calculations developed by S. Roecker. The basic concept is the extension of a standard Cartesian FD travel time algorithm to the spherical case by (1) developing a mesh in radius, co-latitude, and longitude; (2) expression of the FD derivatives in a form appropriate to the spherical mesh; and (3) the construction of "stencils" to calculate extrapolated travel times. S. Roecker has developed this code, and we have begun to test it against another existing SEFD code (Flanagan et al., 2000, 2006). We will then integrate it into our DD tomography algorithms.

Our other work planned for Year 1 includes: acquire and enter additional seismic phase data from eastern Siberia into the MSU Siberia data base (MSU); parse newly acquired datasets into NNSA Schema tables (LANL); load and integrate new data from LANL and MSU into the LANL research knowledge base (LANL); advance and apply interstation travel-time distance inversion method for catalog pick quality control to Siberia data set (LANL); develop P and S datasets from LANL research knowledge base for use in DD tomography and participate in the application of DD tomography (LANL); apply new DD tomography algorithms to the Siberia data delivered by MSU and LANL (3 subregions) (UW-Madison).

OBJECTIVES

The UW-Madison is investigating and developing new and improved methodologies for regional-scale three-dimensional (3D) seismic tomography using a combination of event- and station-pair arrival time differences, and is working collaboratively with LANL and MSU on applications to their Siberia data set. The tomographic work proposed here will provide a more reliable velocity model for both the crust and upper mantle of the accretionary regions to the south and east of the Siberian craton. The resulting model will be compared against previous Russian work and interpreted in the context of regional geology. In addition to the high-velocity cratons and low-velocity rift regions, we hope to identify velocity variations associated with the various types of terranes in the Russian northeast and the Mongol-Okhotsk suture zone.

The components of our proposed work are (1) algorithm development and resolution and uncertainty analysis of event-pair and station-pair residual difference inversion techniques, (2) true spherical-earth (SE) finite-difference (FD) travel time calculations adapted for tomographic inversion algorithms, (3) SE adaptive grid seismic tomography, and (4) application of these methods to the MSU and LANL Siberia data set.

Task 1 is an extension of our recent development of double-difference (DD) seismic tomography using event-pair residual differences (Zhang and Thurber, 2003) to the use of station-pair residual differences (Steck et al., 2004; Phillips et al., 2005). The latter is somewhat akin to teleseismic tomography but with the sources contained within the model region. Event-pair 3D and station-pair two-dimensional (2D) inversion algorithms currently exist. By 2D, we mean a 2D “map” of variable Pn velocity, similar to the method of Hearn (1996). We will extend the station-pair inversion to model 3D structure, and we will develop inversion algorithms that include both event-pair and station-pair residual differences, as well as absolute data. We will also carry out a resolution and uncertainty analysis for these algorithms on synthetic datasets, similar to that of Wolfe (2002). We further propose to incorporate an approximate SVD algorithm into the DD tomography code to compute approximate resolution and/or covariance matrices, based on the Lanczos BPRO.

Task 2 involves the testing, refinement, and adaptation of a new method for SEFD travel time calculations. The basic concept is the extension of a standard Cartesian FD travel time algorithm (Vidale, 1990) to the spherical case by developing a mesh in radius, co-latitude, and longitude, expression of the FD derivatives in a form appropriate to the spherical mesh, and the construction of “stencils" to calculate extrapolated travel times. Roecker has developed this code, and we propose to first test it against another existing SEFD code (Flanagan et al., 2000, 2006) and then integrate it into our DD tomography algorithms.

Task 3 is an extension of our recent development of a Cartesian adaptive-grid DD seismic tomography algorithm (Zhang and Thurber, 2005) to spherical coordinates. The technique utilizes extremely flexible tetrahedral model volumes (allowing virtually unconstrained node geometries), sophisticated 3D interpolation methods, and a system for adding or removing nodes based on the density of ray path sampling. The aim is to stabilize the inversion and at the same time maximize the spatial resolution of the inversion. The goal of this task is to adapt the Cartesian algorithm to spherical coordinates by integrating a SEFD travel time algorithm. While this appears to be straightforward in concept, in practice it will be a difficult challenge. We will also develop a new way of adding or removing nodes based on the approximate resolution estimated from the BPRO algorithm in addition to ray sampling density.

Finally, for Task 4, the UW-Madison, MSU, and LANL groups will work collaboratively to apply these analysis tools to the Siberia data set. The applications will be done in different stages, starting with smaller-scale subregions and progressing to the entire region. This effort will provide the first detailed 3D velocity model of continental eastern Russia. We will also generate travel time correction surfaces based on the obtained 3D models that can be used to improve seismic event locations in this region. Finally we will interpret velocity variations in terms of geology and tectonics and attempt a structural regionalization of the study area. Our efforts in Year 1 are concentrated in Tasks 1 and 2.

RESEARCH ACCOMPLISHED

Resolution Matrix Calculation

The primary goal of geophysical inverse problems is to estimate the unknown model parameters from a set of observations. In addition, it is also important to characterize how reliable the resulting model parameters are through a resolution analysis. For smaller problems, the model resolution can be evaluated using a model resolution matrix estimated using the singular value decomposition (SVD) of the sensitivity matrix. For some tomography problems, however, there may be hundreds of thousands to millions of observations and tens to hundreds of thousands of model parameters (Vasco et al., 2003). The SVD algorithm is not practical for such large problems because it requires large CPU memory space and is very time-consuming (Dongarra et al., 1978).

In practice, synthetic tests are generally used to estimate the model resolution and uncertainty by applying the same inversion algorithm to a synthetic data set having the same data distribution as the real data. These synthetic tests include checkerboard test (Humphreys and Clayton, 1988), restoration test (Zhao et al., 1992) and statistical analysis methods such as "jackknifing" and "bootstrapping" (Tichelaar and Ruff, 1989). However, these tests suffer the shortcomings of measuring the sensitivity only with respect to fixed cell or grid patterns (Leveque et al., 1993; Nolet et al., 1999). Soldati and Boschi (2005) contend that the checkerboard test does not provide more valuable information than a simple plot of data coverage. The "jackknifing" and "bootstrapping" methods are computationally very expensive and of questionable use for large tomographic systems (Nolet et al., 1999).

Several researchers have suggested using an LSQR-based method to estimate the model resolution and covariance matrices for large seismic tomography problems (Berryman, 1994a, b; Zhang and McMechan, 1995; Minkoff, 1996; Vasco et al., 1999; Yao et al., 1999; Vasco et al., 2003). LSQR is now a standard algorithm for solving large inverse problems and its core is based on the Lanczos bidiagonalization process (Paige and Saunders, 1982). The central concept of this method is to use Ritz values and vectors resulting from the Lanczos bidiagonalization process to approximate singular values and vectors and then to estimate model resolution and covariance matrices (e.g. Zhang and McMechan, 1995; Vasco et al., 1999). The major argument against using this method is that the Ritz vectors resulting from a limited number of Lanczos bidiagonalization iterations only span a portion of the model space and thus could not provide adequate estimates of model resolution and covariance matrices (Deal and Nolet, 1996; Nolet et al., 1999). However, Yao et al. (1999) contended that although the resolution matrix estimated in this way may not be a good approximation to the full resolution matrix, it is a "full and adequate description" of the properties of the subspace model that the data can actually solve.

Because of the controversies over the validity of the LSQR-based method, the checkerboard resolution test is still the "standard" method to check the reliability of model parameters for seismic tomography applications (Tryggvason et al., 2002), with the exception of a very few studies (e.g. Vasco et al., 1999, 2003; Van Avendonk et al., 2004). The LSQR-based model resolution and covariance matrices estimation is seldom applied in the practical large-scale geophysical inverse problems. Instead, Nolet et al. (1999) proposed an explicit expression for the approximate inverse matrix using a one-step projection method. Although this one-step projection method may give a reasonable estimation of the resolution matrix under some circumstances, i.e. when $\mathbf{AA}^T$ is diagonally dominant (Nolet et al., 1999, 2001), it may fail to approximate the full resolution matrix because it ignores the iterations required to converge in the conjugate gradient method when solving the Penrose condition $\mathbf{AA}^{-1} = \mathbf{I}$ (Yao et al., 2001). One approach to estimate the full resolution matrix is to apply parallel Cholesky factorization to the matrix $\mathbf{A}^T\mathbf{A}$, an approach that is feasible and efficient on shared-memory multiprocessor servers (Boschi, 2003; Soldati and Boschi, 2005). This approach may potentially lose its accuracy since the matrix $\mathbf{A}^T\mathbf{A}$ is more ill-conditioned than the matrix $\mathbf{A}$ and it cannot calculate singular values and vectors that are important to assess the stability of the system.

Recently, a package called PROPACK that can accurately estimate the singular values and vectors for sparse matrices was developed by Larsen (1998). The PROPACK package is still based on the Lanczos bidiagonalization process but it is able to estimate the larger singular values and vectors more accurately. This method is shown to be very efficient for estimating the full model resolution matrix for inverse problems having hundreds of thousands of observations and tens of thousands of model parameters. Using this method, estimating the full model resolution matrix is no longer a significant challenge for large inverse problems.

With the ability of using the PROPACK package to accurately and efficiently estimate the singular values and vectors for a large sensitivity matrix, it is then straightforward to construct the covariance matrix in a similar way to that for estimating the resolution matrix (Aster et al., 2005). Therefore, a strict uncertainty analysis for large geophysical inverse problems is possible, although we note that the solution from the regularized system is biased by the applied regularization methods (Aster et al., 2005).

Preliminary results from applying this approach to a test dataset from Mt. Etna, Italy, have proven successful and provide a number of additional findings. It is generally reasonable to use ray sampling density to describe model resolution in a qualitative manner. Furthermore, the model resolution estimated for just velocity inversion always overestimates that for the true simultaneous inversion, but in a relatively predictable manner. Our results also confirm that the DD seismic tomography method is better able to characterize the source region structure with substantially higher resolution than is obtained via conventional tomography. With availability of the PROPACK package for efficiently estimating the singular values for large sensitivity matrices, we can also easily estimate optimal smoothing parameters for seismic tomography problems.

Spherical-Grid Finite-Difference Travel Time Calculation

The eikonal equation in spherical coordinates is:

$$(dt/dr)^2 + (1/r\ dt/d\theta)^2 + (1/(r \sin\theta)\ dt/d\phi)^2 = s^2 \tag{1}$$

where r is the radius from center of earth, dr is positive away from the center, $|dr| = h$, θ is the co-latitude (0° at North Pole, 90° at the equator), $d\theta$ is positive to the south, $|d\theta| = \Theta$, ϕ is longitude, $d\phi$ is positive to the south, $|d\phi| = \Phi$, and s is slowness.
To solve this system, we must account for the differences in r, θ, and ϕ for each node in the mesh. Thus, for each node i we assign r_i, θ_i, ϕ_i, and also signs for directional purposes. It is then necessary to derive expressions for each of the "stencils" used in the algorithm. For example, for Scheme A of Vidale (1990), the algorithm computes the time at one point given the times at 7 adjacent points (thus 7 of the eight points of a cell are known).

Referring to Figure 1 and Table 1, the FD derivatives are:

$$\begin{aligned} dt/dr &= [(t_4 - t_0) + (t_5 - t_1) + (t_6 - t_2) + (t_7 - t_3)]\ /4 \\ 1/r\ dt/d\theta &= [(t_0 - t_3)/r_1 + (t_1 - t_2)/r_1 + (t_4 - t_7)\ /r_2 + (t_5 - t_6)\ /r_2]\ /4\Theta \\ 1/(r \sin\theta)\ dt/d\phi &= [(t_0 - t_1)/(r_1 \sin\theta_2) + (t_3 - t_2)/(r_1 \sin\theta_1) + (t_4 - t_5)/(r_2 \sin\theta_2) + (t_5 - t_6)/(r_2 \sin\theta_1)]/4\Theta \end{aligned} \tag{2}$$

From these equations, it can be shown that the eikonal equation for this stencil is

$$\begin{aligned} s^2 = &\left[\sum_{i=0}^{7} t_i^2 + 2\sum_{i=0}^{6} t_i g_i \sum_{j=i+1}^{7} t_j g_j\right] \Big/ 16h^2 + \left[\sum_{i=0}^{7} (t_i/r_i)^2 + 2\sum_{i=0}^{6} t_i n_i/r_i \sum_{j=i+1}^{7} t_j n_j/r_j\right] \Big/ 16\Theta^2 \\ &+ \left[\sum_{i=0}^{7} (t_i/(r_i \sin\theta_i))^2 + 2\sum_{i=0}^{6} t_i m_i/(r_i \sin\theta_i) \sum_{j=i+1}^{7} t_j m_j/(r_j \sin\theta_j)\right] \Big/ 16\Phi^2 \end{aligned} \tag{3}$$

This expression can be rewritten in the form $at_7^2 + bt_7 + c = 0$, which is then solved for t_7, given the values for t_0 through t_6. Comparable equations can be derived for the "edge" and "face" stencils of Vidale (1990).

The first step is to validate the algorithm. This will be done by comparing calculated travel times against analytic solutions for simple earth models and against calculated travel times from the sphere-in-a-box code (Flanagan et al., 2000, 2006). In fact, this will provide a valuable validation of the latter code in the process. If we find discrepancies, then we will need to expand the evaluation to include another spherical-earth code, most likely an existing shooting method. Preliminary work indicates that the Roecker algorithm is quite accurate, and is less sensitive to accuracy issues related to grid spacing than the "sphere-in-a-box" algorithm due to the former method's intrinsic spherical geometry.

The second step will be to integrate the SEFD code into the regional-scale DD tomography code (tomoFDD; Zhang et al., 2004). This will require significant coding changes, as the tomoFDD code has an underlying Cartesian system. This step will be time-consuming, but in the end will provide a tremendously valuable tool for regional and even global seismic tomography. The same code can also be used for single- or multiple-event location.

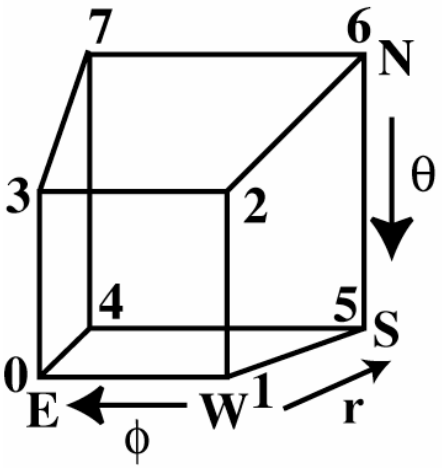


Figure 1. Geometry of a basic cell for the spherical-earth FD calculation of travel times.

Table 1. Convention on point numbering; the signs are the coefficients for the derivatives dt/dr, dt/dθ, and dt/dϕ as shown below.

Point	Position	r	θ	ϕ	r Sign (g)	θ Sign (n)	ϕ Sign (m)
0	Deep SE	r_1	θ_2	ϕ_2	-1	1	1
1	Deep SW	r_1	θ_2	ϕ_1	-1	1	-1
2	Deep NW	r_1	θ_1	ϕ_1	-1	-1	-1
3	Deep NE	r_1	θ_1	ϕ_2	-1	-1	1
4	Shallow SE	r_2	θ_2	ϕ_2	1	1	1
5	Shallow SW	r_2	θ_2	ϕ_1	1	1	-1
6	Shallow NW	r_2	θ_1	ϕ_1	1	-1	-1
7	Shallow NE	r_2	θ_1	ϕ_2	1	-1	1

Other Year-1 work

In addition to the work mentioned above, in Year 1 MSU will acquire and enter additional seismic phase data from eastern Siberia into the MSU Siberia data base. LANL will parse newly acquired datasets into NNSA Schema tables, load and integrate new data from LANL and MSU into the LANL research knowledge base, and advance and apply interstation travel-time distance inversion method for catalog pick quality control to Siberia data set. UW-Madison will apply new DD tomography algorithms to the Siberia data delivered by MSU and LANL. LANL will participate in the application of DD tomography.

CONCLUSIONS AND RECOMMENDATIONS

Although our 3-year project has just begun, we already have some conclusions and recommendations. Our preliminary tests make it clear that the computation of the resolution matrix (and potentially the covariance matrix as well) with PROPACK will be quite accurate, thus providing a practical means for obtaining this fundamental information for large inverse problems. Similarly, the true SEFD algorithm devised by Roecker apparently can achieve excellent accuracy, and likely can do so over a range of scales of spherical models, from regional to whole-Earth. If further testing confirms these preliminary findings, then we would recommend broad adoption of these approaches for resolution and travel time calculations for large-scale problems.

ACKNOWLEDGEMENTS

We thank Steve Roecker and Megan Flanagan for sharing their SEFD travel time calculation codes.

REFERENCES

Aster, R. C., B. Borchers, and C. H. Thurber (2005). Parameter estimation and inverse problems, Elsevier Academic Press, Burlington, MA, 301 pp.

Berryman, J. G. (2000a). Analysis of approximate inverses in tomography I. Resolution analysis of common inverse, *Optimization and Engineering* 1: 87–115.

Berryman, J.G. (2000b). Analysis of approximate inverses in tomography II. Iterative Inverses, *Optimization and Engineering* 1: 437–473.

Boschi, L. (2003). Measures of resolution in global body wave tomography, *Geophys. Res. Lett*. 30: doi:10.1029/2003GL018222.

Deal, M. M., and G. Nolet (1996). Comment on 'Estimation of resolution and covariance for large matrix inversions' by J. Zhang and G.A. McMechan, *Geophys. J. Int.* 127: 245–250.

Dongarra, J., J. R Bunch, C. F. Moler, and G. W. Stewart (1978). LINPACK Users Guide, SIAM Publications, Philadelphia.

Flanagan, M. P., S. C. Myers, C. A. Schultz, M. E. Pasyanos, and J.Bhattacharyya (2000). Three-dimensional a priori model constraints and uncertainties for improving seismic location, in *Proceedings of the 22nd Seismic Research Symposium: Technologies for Monitoring the CTBT,* Vol. 2, pp. 129–136.

Flanagan, M. P., S. C. Myers, and K. D. Koper (2006). Regional travel-time uncertainty and seismic location improvement using a 3 dimensional a priori velocity model, *Bull. Seism. Soc. Am*., submitted.

Hearn, T.M. (1996), Anisotropic Pn tomography in the western United States, *J. Geophys. Res*. 101: 8403–8414.

Humphreys, E. and R. W Clayton (1988). Adaptation of back projection tomography to seismic travel time problems, *J. Geophys. Res.*, 93: 1073–1085.

Larsen, R. M. (1998). Lanczos bidiagonalization with partial reorthogonalization, Department of Computer Science, Aarhus University, Technical Report, DAIMI PB-357.

Leveque, J. J., L. Rivera, and G. Wittlinger (1993). On the use of the checkerboard test to assess the resolution of tomographic inversions, *Geophys. J. Int*. 115: 313–318.

Minkoff, S. E. (1996). A computationally feasible approximation resolution matrix for seismic inverse problems, *Geophys. J. Int*. 126: 345–359.

Nolet, G., R. Montelli, and J. Virieux (1999). Explicit, approximate expressions for the resolution and a posteriori covariance of massive tomographic systems, *Geophys. J. Int*. 138: 36–44.

Nolet, G., R. Montelli, and J. Virieux (2001). Reply to comment by Z. S. Yao, R. G. Roberts, and A. Tryggvason on 'Explicit, approximate expressions for the resolution and a posteriori covariance of massive tomographic systems,' *Geophys. J. Int*. 145: 315.

Paige, C. C. and M. A. Saunders (1982). LSQR: an algorithm for sparse linear equations and sparse least squares, ACM Trans. *Mathematical Software* 8: 43–71.

Phillips, W.S., C.A. Rowe, and L.K. Steck (2005). The use of interstation P wave arrival time differences to account for regional path variability, *Geophys. Res. Lett.* 32: L11301, doi:10.1029/2005GL022558.

Soldati, G., and, L. Boschi (2005). The resolution of whole Earth seismic tomographic models, *Geophys. J. Int*. 161: 143–153.

Steck, L., C. Rowe, M. Begnaud, W. Phillips, V. Gee, and A. Velasco (2004). Advancing seismic event location through difference constraints and three- dimensional models, in *Proceedings of the 26th Seismic Research Review: Trends in Nuclear Explosion Monitoring*, LA-UR-04-5801, Vol. 1, pp. 346–355.

Tichelaar, B. W., and L.R. Ruff (1989). How good are our best models?, EOS, *Trans. Am. Geophys. Un*., 70: 593–606.

Tryggvason, A., S. T. Rognvaldsson, and O. G. Flovenz (2002). Three-dimensional imaging of the P- and S-wave velocity structure and earthquake locations beneath Southwest Iceland, *Geophys. J. Int.* 151: 848–866.

Van Avendonk, H. J. A., D. J. Shillington, W. S. Holbrook, and M. J. Hornbach (2004). Inferring crustal structure in the Aleutian island arc from a sparse wide-angle seismic data set, Geochemistry, *Geophysics, Geosystems*, 5, Q08008, doi:10.1029/2003GC000664.

Vasco, D. W., L. R. Johnson, and O. Marques (1999). Global Earth structure: inference and assessment, *Geophys. J. Int.*, 137: 381–407.

Vasco, D. W., L. R. Johnson, and O. Marques (2003). Resolution, uncertainty, and whole Earth tomography, *J. Geophys. Res.* 108: 2022.

Vidale, J. E. (1990). Finite-difference calculation of traveltimes in three dimensions, *Geophysics* 55: 521-526.

Wolfe, C. J. (2002). On the mathematics of using difference operators to relocate earthquakes, *Bull. Seism. Soc. Am.* 92: 2879–2892.

Yao, Z. S., R. G. Roberts, and A. Tryggvason (1999). Calculating resolution and covariance matrices for seismic tomography with the LSQR method, *Geophys. J. Int.* 138: 886–894.

Zhang, H., and C. Thurber (2005). Adaptive-mesh seismic tomography based on tetrahedral and Voronoi diagrams: application to the SAFOD site, Parkfield, CA, *J. Geophys. Res.* 110: B04303, doi 10.1029/2004JB003186.

Zhang, H., and C. H. Thurber (2003). Double-difference tomography: The method and its application to the Hayward fault, California, *Bull. Seismol. Soc. Am.* 93: 1875–1889.

Zhang, H., C. Thurber, D. Shelly, S. Ide, G. Beroza, and A. Hasegawa (2004). High-resolution subducting slab structure beneath Northern Honshu, Japan, revealed by double-difference tomography, *Geology* 32: 361–364.

Zhang, J., and G. A. McMechan (1995). Estimation of resolution and covariance for large matrix inversions, *Geophys. J. Int.* 121: 409–426.

Zhao, D., A. Hasegawa, and H. Kanamori (1992). Tomographic imaging of P and S wave velocity structure beneath northeastern Japan, *J. Geophys. Res.* 97: 19,909–19,928.

HIGH-RESOLUTION SEISMIC VELOCITY AND ATTENUATION STRUCTURE OF THE SICHUAN-YUNNAN REGION, SOUTHWEST CHINA, USING SEISMIC CATALOG AND WAVEFORM DATA

Haijiang Zhang[1], Yunfeng Liu[1], Zhen Xu[2], Xiaodong Song[2], and Clifford H. Thurber[1]

[1]University of Wisconsin-Madison, [2]University of Illinois at Urbana-Champaign

Sponsored by Air Force Research Laboratory

Contract No. FA8718-05-C-0016

ABSTRACT

The Sichuan-Yunnan region in southwestern China lies in the transition zone between the uplifted Tibetan plateau to the west and the Yangtze continental platform to the east. This region has a very complicated geological structure and is one of the most active areas of continental earthquakes in the world. This two-year project is to develop high-resolution models of the velocity and attenuation structure of the Sichuan-Yunnan region (latitudes ~97–108^{o}E and longitudes ~21–35^{o}N) using seismic catalog and waveform data.

There are four main components in this project: (1) using waveform alignment methods (waveform cross-correlation and bispectrum analysis) to obtain more accurate differential arrival times, (2) using regional scale adaptive-grid double-difference tomography to obtain detailed P- and S-wave velocity models of the Sichuan-Yunnan region, (3) using the adaptive-grid "triple-difference" seismic attenuation method to determine the detailed attenuation structure for both Qp and Qs for this region, and (4) assembling a ground truth database.

Our current effort is to determine a high-resolution velocity model and a preliminary attenuation model for the Yunnan region using seismic catalog and waveform data. We collected catalog and waveform data from the China Seismological Bureau (newly named China Earthquake Administration), Sichuan, and Yunnan provincial bureaus, and the Incorporated Research Institute for Seismology (IRIS) data management center. We measured more accurate differential times using a waveform alignment algorithm BCSEIS. We developed regional scale adaptive-grid double-difference tomography based on tetrahedral diagrams that deals properly with the curvature of the Earth and has the ability to automatically adapt the inversion grid according to the data distribution. We also modified the code to include the function to invert the Q model using absolute and differential t* values. The absolute t* values are calculated from the amplitude spectrum based on an Ω-square source model with a single corner frequency. The differential t* values are calculated from spectral ratios for two event and station pairs in order to cancel source and site effects. Our next effort is to measure differential times and absolute and differential t* values for the Sichuan region and obtain detailed velocity and attenuation models. Finally we will assemble a ground truth database for the region of size approximately 1300 km × 1000 km.

OBJECTIVES

The routine practice of locating seismic events based on a one-dimensional velocity model inevitably introduces bias into locations. Using a high-resolution three-dimensional seismic velocity model significantly improves seismic event location accuracy and thus helps satisfy the goal of nuclear explosion monitoring. In addition to seismic event locations, seismic wave amplitudes are also important in discriminating between earthquakes and explosions. As seismic waves travel through an anelastic and heterogeneous medium, their amplitudes will be attenuated, and knowledge of the attenuation structure is vital to correct the distortion. Our research program aims to develop high-resolution models of the velocity and attenuation structure of the Sichuan-Yunnan region (latitudes ~97–108^{o}E and longitudes ~21–35^{o}N) that is located in southwest China using seismic catalog and waveform data. This research project falls in topic 2 (Seismic Calibration and Ground Truth Collection) in an effort to "develop models that calibrate earth velocity and attenuation structure." The Sichuan-Yunnan region lies in the transition zone between the uplifted Tibetan plateau to the west and the Yangtze continental platform to the east. This region has a very complicated geological structure and is one of the most active areas of continental earthquakes in the world.

Our research program consists of four components: (1) using waveform alignment methods (waveform cross-correlation and bispectrum analysis) to obtain more accurate differential arrival times, (2) using regional scale adaptive-grid double-difference tomography to obtain detailed P- and S-wave velocity models of the Sichuan-Yunnan region, (3) using the adaptive-grid "triple-difference" seismic attenuation method to determine the detailed attenuation structure for both Qp and Qs for this region, and (4) assembling a ground truth database. In this paper, we will focus on our accomplishments on the velocity and attenuation models for the Yunnan region.

RESEARCH ACCOMPLISHED

Background

The Sichuan-Yunnan region lies in an active transition zone between the Yangtze platform to the east and the Tibetan plateau to the west and is generally believed to have had its origin in the collision between the Indian plate and the Eurasian plate about 45 Ma ago. This continental collision led to active tectonic deformation on a larger scale and created a high level of seismicity. There are seven major active seismic zones (belts) in this region including Longmen Shan, Xianshuihe, Anninghe, Xiaojiang, Red River, Lancang-Gengma, and Tengchong-Longling (Chan et al., 2001). Most, but not all, of the earthquakes in these belts are associated with fault zones that are identified at the surface. Obtaining a high-resolution seismic velocity model for this region and precise earthquake locations will help delineate fault zones at depth more clearly and facilitate their association with surface fault traces. Several magnitude 7 earthquakes occurred in this region in the last twenty years. Recent examples are the 1995 Menglian earthquake (M=7.3) and the 1996 Lijiang earthquake (M=7.0).

There have been some local to regional seismic tomography studies in this region. Chan et al., (2001) and Wang et al., (2003) used both P and S arrival data from 4,625 local and regional earthquakes recorded at 174 stations to determine a three-dimensional (3D) model of the crust and upper mantle. The horizontal grid spacing was 0.5 degrees between latitudes 25–34^{o}N and longitudes 97–105^{o}E. Their findings showed that southwestern China is characterized by low average velocity in the crust and upper mantle, large crustal thickness variations, the existence of a high-conductivity layer in the crust and/or upper mantle, and a high heat flow value (Wang et al., 2003). Yang et al., (2004) conducted a simultaneous inversion to determine the velocity structure and event locations using Pg and Sg picks on 193 stations from 9,988 earthquakes during the period of 1992 to 1999. Their P-wave velocity model, with a horizontal grid spacing of 1°, shows strong heterogeneity (velocity contrast) across the faults. Liu et al. (2005) used a combination of 602 local and regional earthquakes and 102 teleseismic events to determine a 3D P-wave velocity model with a horizontal grid spacing of 0.5° for this region. They imaged a relatively low-velocity anomaly over a large region at depths of 20 to 50 km that may indicate a mechanically weak north-south tectonic belt between Tibet and Eastern China.

Waveform Cross-Correlation Using the Bispectrum (BS) Method, BCSEIS

Researchers using cross-correlation (CC) to align waveforms often choose those time delay estimates with CC coefficients above a specified threshold. For example, Schaff et al., (2002) only select those time delays with CC values larger than 0.70 and mean coherences above 0.70. The selection of an optimum threshold value for waveform cross-correlation is important but difficult. If it is set too high, then only a limited number of very accurate

differential time data are available for further analysis. If the threshold value is set too low, then many unreliable differential time estimates are used which will negatively affect the relocation and tomography results.

The BCSEIS algorithm that we adopted for measuring waveform CC times works in the third-order spectral domain and can suppress correlated Gaussian or low-skewness noise sources (Nikias and Raghuveer, 1987; Nikias and Pan, 1988). BCSEIS employs a third-order spectral method to calculate two additional time delay estimates with both the raw (unfiltered) and band-pass filtered waveforms, and uses them to verify (select or reject) the one computed with the CC technique using the filtered waveforms (Du et al., 2004a). Thus this BS verification process can reject unreliable CC time delay estimates and also can accept additional CC time delays even if their associated CC coefficients are smaller than a nominal threshold value if they pass the BS verification procedure (Du et al., 2004).

We have calculated differential times for 618 events recorded by 27 stations in Yunnan Province using BCSEIS (Figure 1). We found that the calculated differential times with different filtering are slightly different for some waveform pairs. To assure that the results are not affected by filtering, we tested several different filters. We found that the default Butterworth filter with 3 poles and 2 passes in BCSEIS changes the waveform shape around the first arrivals significantly. After testing different filtering, we decided to choose a Butterworth filter with 2 poles and 1 pass in our correlation computation. We also tested different window sizes to find a suitable one for our analysis. In total, at this point we have calculated 8,717 waveform delay times using the BCSEIS algorithm.

Figure 2 shows several examples of highly similar waveforms for pairs of events recorded at the station YS08 (the CC value is labeled at the bottom of the trace). Note that the manual picks align relatively well after the waveforms are aligned using measured relative times, verifying the quality of the hand picked absolute times. The time window we chose here is 30 samples before and 97 samples after the preliminary P arrival pick.

Double-Difference Tomography

The double-difference (DD) seismic tomography method makes use of both absolute and more accurate relative arrival times (Zhang and Thurber, 2003). DD tomography is a generalization of DD location (Waldhauser and Ellsworth, 2000); it simultaneously solves for the 3D velocity structure and seismic event locations. DD tomography uses an evolving weighting scheme for the absolute and differential arrival times in order to determine the velocity structure from larger scale to smaller scale. This method yields more accurate event locations and velocity structure near the source region than standard tomography, which uses only absolute arrival times. It has the unique ability to sharpen the velocity image near the source region because of the combination of the higher accuracy of the differential time data and the concentration of the corresponding model derivatives in the source region. The latter results from the cancellation of model derivative terms where the ray paths overlap away from the source region.

In the “sphere-in-a-box” version of DD tomography, the curvature of the Earth is explicitly taken into account. Following Flanagan et al., (2000), we solve this problem by parameterizing a spherical surface inside a Cartesian volume of grid nodes. Finite-difference ray tracing algorithms (Podvin and Lecomte, 1991) are used for calculating travel times and ray paths. We have successfully finished developing the adaptive-mesh “sphere-in-a-box” version of the DD tomography code. Previously the code had difficulty saving ray path information to adapt the inversion mesh due to the limitation of memory space (Zhang and Thurber, 2005). We overcame this challenge by modifying the code to save ray density information on an intermediate grid and then project it back to the adaptive inversion mesh.

We also modified the code by finding a way to apply the smoothing constraint to the inversion mesh. Previously, we set up an intermediate regular grid and then projected the smoothing weights on it to the inversion mesh (Zhang and Thurber, 2005). This could deteriorate the advantage of using an adaptive mesh to resolve the fine scale structure because the spatial scale of the structure is limited by the size of the intermediate grid. We now have found a way to efficiently search the natural neighbors for each inversion mesh node and are able to directly apply the first-order smoothing constraint.

The adaptive-mesh DD tomography code is further modified by also adding new nodes at the midpoints of tetrahedral edges when a tetrahedron is sampled by many rays, as determined by a threshold level. The previous strategy was to only add new nodes to the center of one tetrahedron. The new strategy will be helpful for more uniformly distributing the inversion mesh nodes.

Measurement of the Absolute t* Values

Under the assumption of an Ω-square source model, the amplitude spectrum for a given event at the observing station j can be related to the attenuation and source parameters as follows:

$$\ln(A_j(f)) = \ln(\Omega_{0j}) - \ln(1 + (f/f_c)^2) - \pi f t_j^*, \quad (1)$$

where A_j is spectral amplitude at frequency f for the event observed at station j, Ω_{0j} is the amplitude asymptote at zero frequency, f_c is corner frequency for the event, and t_j^* is the attenuation parameter defined as

$$t_j^* = \int_{raypath} \frac{dr}{V_j(r)Q_j(r)}. \quad (2)$$

We fit spectral amplitude data to equation (1) within the range of frequencies with adequate signal-to-noise ratio to calculate t* values. We use the multitaper method of spectral analysis (Park et al., 1987) to calculate amplitude spectra from the windowed vertical waveforms around the P arrivals. We also estimate the noise spectra from the seismograms in a window right before the signal window.

In the traditional signal-taper analysis, portions of the waveforms of interest are excluded from analysis as a trade-off for reducing the spectral leakage. In the multitaper approach, a family of statistically independent spectral estimates is computed from a signal using a set of orthogonal tapers that are referred to as discrete prolate spheriodal sequences (DPSS). Averaging over this ensemble of spectra yields an estimate with much lower variance than that from single-taper methods. Stable spectral estimation is of importance for a robust measurement of t* values.

Figure 3 shows samples of seismograms recorded at two stations HQ11 and EY24 for two events with magnitude 3.3 and 4.0, respectively. The signal windows used for amplitude spectrum calculations are indicated by vertical lines in the figure. The corresponding multitaper spectra estimated from these seismograms are shown in Figure 4. In each panel of the figure, the calculated amplitude spectra are shown as solid lines, while the noise spectra are represented by dotted lines. The fits of spectral amplitude data to equation (1) are demonstrated with dashed lines. We obtain a set of Ω, f_c and t* values from the fits as shown in each panel of the figure (Figure 4).

Measurement of Differential t* Values Using Two Events and Two Stations

The above approach for measuring absolute t* values may potentially suffer limitations when there is significant site response at some stations. We have proposed to use two events and two stations to remove source signature and site response from the spectral amplitude. For a pair of nearby events i and j observed at a pair of nearby stations l and m, we form the ratio of ratios

$$\frac{A_{il}(f)/A_{im}(f)}{A_{jl}(f)/A_{jm}(f)} = C(r)\,\frac{\exp(-\pi f(t_{il}^* + t_{jm}^*))}{\exp(-\pi f(t_{im}^* + t_{jl}^*))}, \quad (3)$$

where C(r) is a ratio of ratios of the geometrical spreading terms (assumed to be independent of frequency), with the instrument responses and source spectral amplitudes canceling out (assuming that the radiated source spectra from a given event at two nearby stations are approximately equal). Taking the natural log, we arrive at

$$\ln\left(\frac{A_{il}(f)/A_{im}(f)}{A_{jl}(f)/A_{jm}(f)}\right) = \ln C(r) + f\pi\left((t_{jl}^* - t_{il}^*) - (t_{jm}^* - t_{im}^*)\right), \quad (4)$$

which is a linear function of frequency and can be fit to determine the observed t* difference term.

Figure 5 shows the calculated spectral ratios from the above two stations and two events. We fit spectral ratios to the linear equation (4) and get the differential t* value defined in the equation (4) as 0.0066. The differential t* value calculated directly from the measured absolute t* values is 0.0070. These two values are close; however, the measured differential t* values from spectral ratios are free from station effects and are not affected by the source

model assumption. These differential t* values can be used to solve for the Q model in a way similar to DD tomography. We note that the multitaper method also improves the robustness of spectral ratios significantly.

Velocity and Attenuation Tomographic Results

At present, we collected and analyzed more catalog data for ~3,800 events and 26 stations in the Yunnan region (Figure 1). Each selected event has at least 8 observations. There are 42,500 P and S times (50% each). We applied the regular-grid DD tomography code (0.5^o grid spacing in latitude and longitude and 5 km in depth) to this data set and the new velocity model (Figure 6a) shows different features due to better ray coverage and data quality from previous results that we reported in last year's proceedings paper. For example, the low-velocity anomaly around longitude 100^o from depths of 20 km to 50 km disappears in the new model. The arrival time residuals decrease from ~964 ms for the previous data set to ~357 ms for the new data set. We also included 8,717 P-wave waveform-derived CC times from 618 events and 26 stations in the inversion. Even with this limited number of CC times, the results are very promising (Figure 6b). In comparison, the resulting event locations show more linear features and the velocity model shows sharper velocity boundaries near faults (Figure 6b). We expect to improve the event locations and velocity model once we have more waveform CC measurements. We then applied the adaptive-mesh DD tomography code to the same data set. The new strategy of adding new nodes at the middle points of tetrahedral lines when a tetrahedron is sampled by many rays is helpful for more uniformly distributing the inversion mesh nodes. Compared to the model from the regional-grid inversion shown in Figure 6a, the new model (Figure 6c) shows more fine features due to fine inversion mesh nodes in places where there are more rays.

Figures 7a and b show horizontal slices of the P- and S-wave velocity models at depths of 15 and 35 km, respectively. Both horizontal slices and cross sections show strong lateral velocity heterogeneities, consistent with the nature of active fault zones in this region. Strong velocity contrasts are evident across major faults, such as the Xiaojiang Fault and Red River Fault (Figures 6 and 7). The relocated earthquakes show relatively well-defined vertical linear features, corresponding to major faults at the surface (Figure 7). There is a low-velocity zone between the Nujiang fault and Red River fault, corresponding to the Sanjiang Fold System. Figure 7c shows horizontal slices of the Qp model at a depth of 15 and 25 km, derived from 3873 absolute P-wave t* values for 425 events and 26 stations. This preliminary attenuation model also shows low Qp values corresponding to the low velocity anomaly between the Xiaojiang Fault and Red River Fault, consistent with thick sedimentary layers in the region. We are confident that with more t* measurements from local and regional earthquakes, we will be able to characterize the attenuation structure at much higher resolution.

CONCLUSIONS AND RECOMMENDATIONS

We have applied the adaptive-mesh "sphere-in-a-box" version of DD tomography code to the Yunnan region using catalog P and S picks and waveform CC times. Both P- and S-wave velocity models show strong velocity heterogeneities, consistent with the nature of active transition zone between the Yangtze platform to the east and the Tibetan plateau to the west. Strong velocity contrasts are evident across some major fault zones and the relocated earthquakes show relatively well-defined vertical linear features. The code is also modified to include absolute and differential t* values to determine the attenuation model.

We are in the process of measuring more waveform CC times and absolute and differential t* values for the Yunnan region. A better velocity model and a more complete attenuation model will be reported in the Seismic Research Review meeting in September. After the meeting, our focus will shift to the Sichuan region. Both velocity and attenuation models will be calculated for the Yunnan-Sichuan region.

ACKNOWLEDGEMENTS

We are grateful to Megan Flanagan for allowing us to use the FD code in our "sphere-in-a-box" version of the DD tomography code. We thank Youshun Sun for providing us his compiled picks for the Sichuan-Yunnan region.

REFERENCES

Chan, W. W., C. Y. Wang, and W. D. Mooney (2001). 3-D crustal structure in southwestern China, in *Proceedings of the 23rd Seismic Research Review: Worldwide Monitoring of Nuclear Explosions*, LA-UR-01-4454, Vol. 1: pp. 12–20.

Du, W. X., C. H. Thurber, and D. Eberhart-Phillips (2004). Earthquake relocation using cross-correlation time delay estimates verified with the bispectrum method, *Bull. Seismol. Soc. Am.* 94: 856–866.

Flanagan, M. P., S. C. Myers, C. A. Schultz, M. E. Pasyanos, and J. Bhattacharyya (2000). Three-dimensional a priori model constraints and uncertainties for improving seismic location, in *Proceedings of the 22nd Annual DoD/DOE Seismic Research Symposium: Planning for Verification of and Compliance with the Comprehensive Nuclear-Test-Ban Treaty (CTBT)*, Vol. 2, pp, 129–136.

Liu, Y., X. Xhang, J. He, F. Liu, and H. Sun (2005). Three-dimensional velocity images of the crust and upper mantle beneath the north-south zone in China, *Bull. Seismol. Soc. Am.* 95: 916–925.

Nikias, C. L. and R. Pan (1988). Time delay estimation in unknown Gaussian spatially correlated noise, *IEEE Trans. Acoust. Speech Signal Process* 36: 1,706–1,714.

Nikias, C. L. and M. R. Raghuveer (1987). Bispectrum estimation: A digital signal processing framework, in *Proc. IEEE*, Vol. 75, pp. 869–891.

Park, J., C. R. Lindberg, and F. L. Vernon III (1987). Multitaper spectral analysis of high-frequency seismograms, *J. Geophys. Res.* 92: 12,675–12,684.

Podvin, P. and I. Lecomte (1991). Finite difference computation of travel times in very contrasted velocity models: a massively parallel approach and its associated tools, *Geophys. J. Int.* 105: 271–284.

Schaff, D. P., G. H. R. Bokelmann, G. C. Beroza, F. Waldhauser, and W. L. Ellsworth (2002). High-resolution image of Calaveras Fault seismicity, *J. Geophys. Res.* 107: 2186, doi:10.1029/2001JB000633.

Waldhauser, F. and W. L. Ellsworth (2000). A double-difference earthquake location algorithm: Method and application to the northern Hayward fault, CA, *Bull. Seismol. Soc. Am.* 90: 1,353–1,368.

Wang, C.-Y., W. W. Chan, and W. D. Mooney (2003). Three-dimensional velocity structure of crust and upper mantle in southwestern China and its tectonic implications, *J. Geophys. Res.* 108: 2442, doi:10.1029/2002JB001973.

Yang, Z.-X., X.-W. Yu, Y.-J. Zheng, Y.-T. Chen, X.-X. Ni, and W. Chan (2004). Earthquake relocation and 3-dimensional crustal structure of P-wave velocity in central-western China, *Acta Seismologica Sinica* 17: 20–30.

Zhang, H. and C. H. Thurber (2003). Double-difference tomography: The method and its application to the Hayward fault, California, *Bull. Seismol. Soc. Am.* 93: 1,875–1,889.

Zhang, H. and C. H. Thurber (2005). Adaptive mesh seismic tomography based on tetrahedral and Voronoi diagrams: Application to Parkfield, California, *J. Geophys. Res.* 110, B04303, doi:10.1029/2004JB003186.

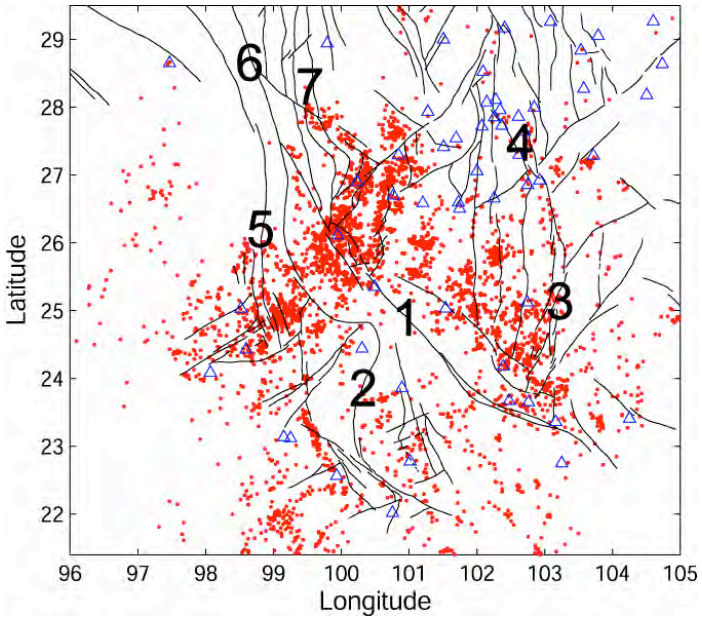


Figure 1. Location of mapped faults (black lines) in the Yunnan region. Earthquakes (red dots) are relocated using the double-difference tomography method with waveform cross-correlation differential times. Triangles indicate the local network stations.

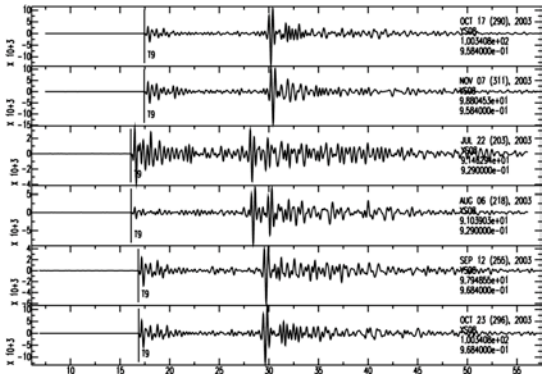


Figure 2. Similar waveforms observed on station YS08 aligned by CC times.

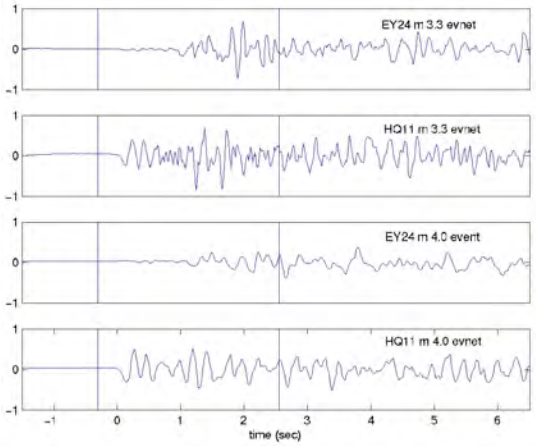


Figure 3. Waveforms at two nearby stations EY24 and HQ11 from two nearby events.

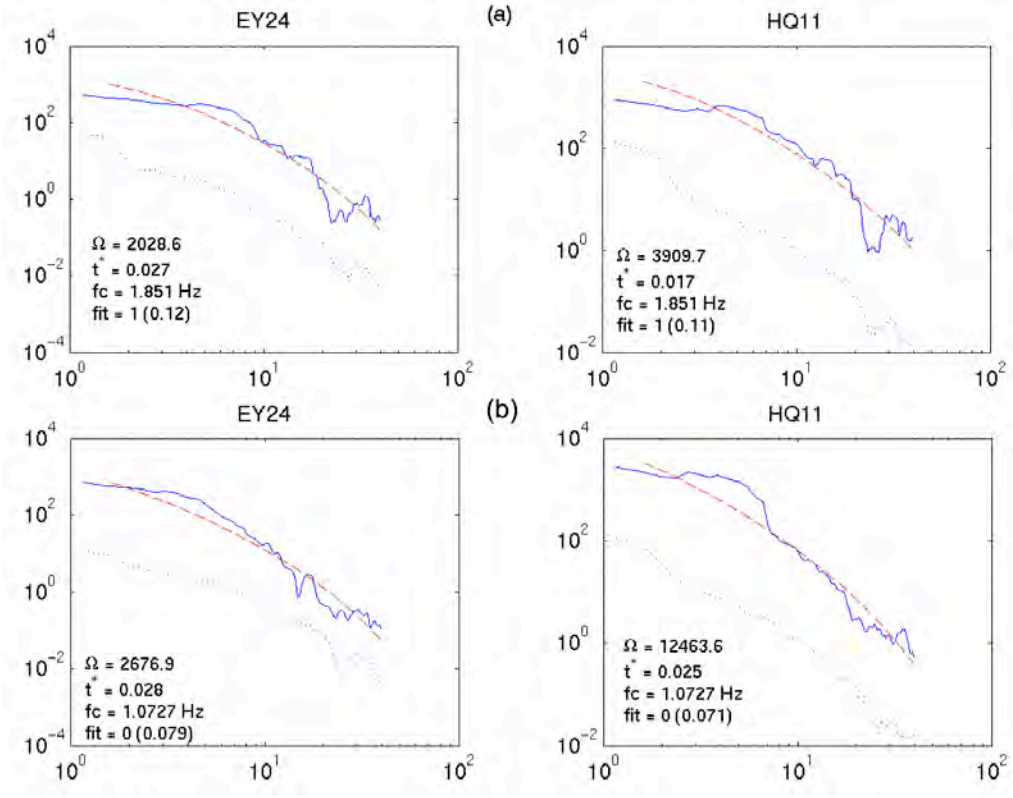


Figure 4. Spectral fitting based on Equation 1 to estimate t* values. Blue solid line: original spectra. Red dashed line: fitting spectra. Blue dots: noise spectra.

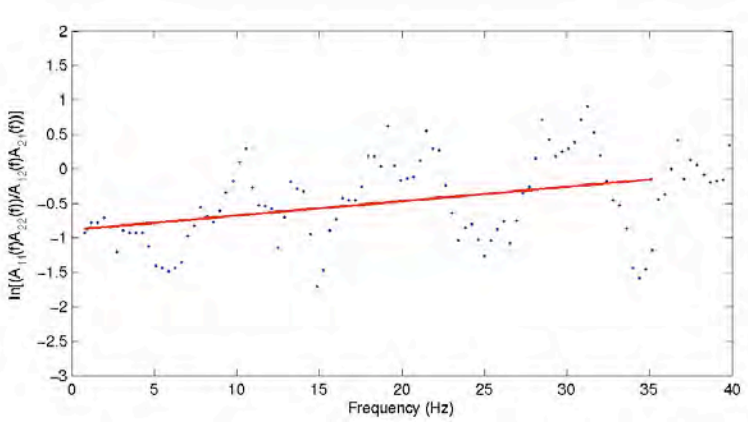


Figure 5. Differential t* measurements using spectral ratios for two events and two stations shown in Figure 4.

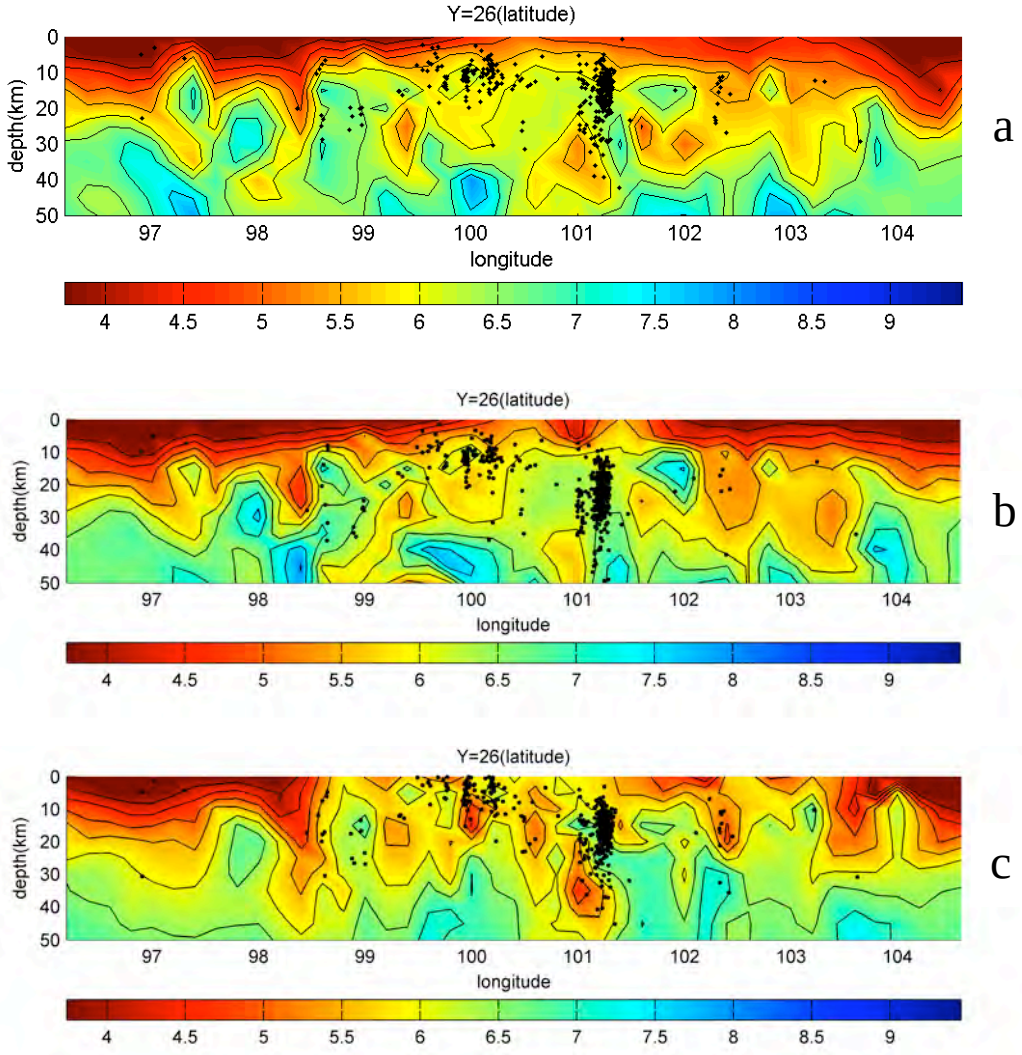


Figure 6. Cross-sections of P-wave velocity model at latitude of 26° from applying the regular-grid DD tomography code to the (a) new catalog data set and (b) new catalog data set plus cross-correlation times and (c) from applying the adaptive-mesh DD tomography code to the new catalog data.

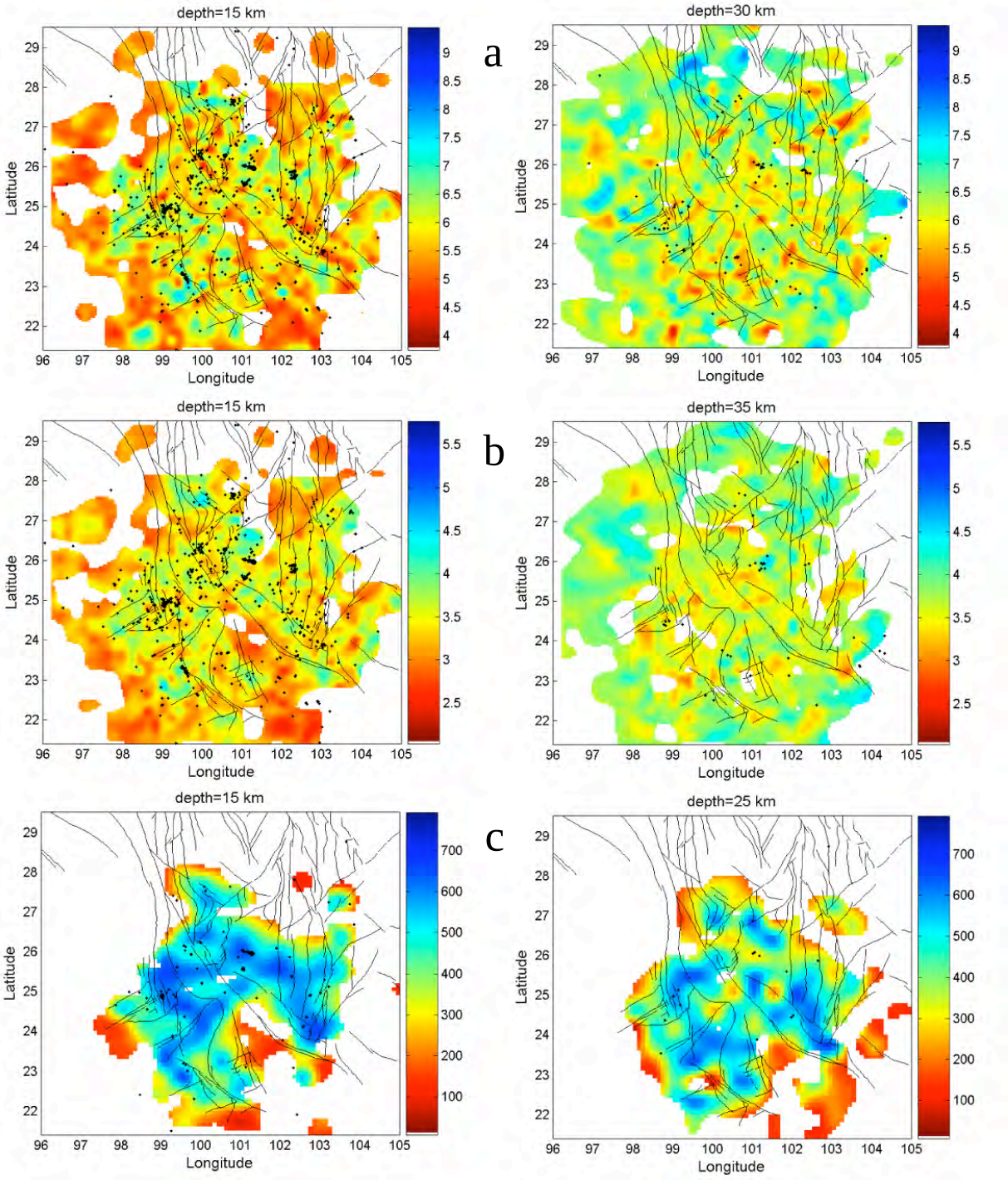


Figure 7. Map view of (a) P-wave velocity model, (b) S-wave velocity model, and (c) Q model from applying the adaptive-mesh DD tomography code to the new catalog data, at the depths indicated.

DEVELOPING FINITE-FREQUENCY REGIONAL PN VELOCITY MODELS

Zhigang Zhang[2], Yang Shen[2], Li Zhao[3], Xiaoping Yang[1], and Kim Olsen[4]

Science Applications International Corporation[1], University of Rhode Island[2], University of Southern California[3], and San Diego State University[4]

Sponsored by Air Force Research Laboratory

Contract No. FA8718-06-C-0014[1–4]

ABSTRACT

Head waves and Pn waves in particular are important in studying the predominantly layered velocity structure of the Earth and discriminating the seismic sources. Conventional studies of head waves have used high-frequency (ray) approximation in wave propagation. While recent studies have shown the diffractive nature and the three-dimensional (3-D) sensitivities of finite-frequency turning waves, analogs of head waves in a continuous velocity structure, the finite-frequency effects and sensitivity kernels of head waves are yet to be carefully examined. We present the results of a numerical study on the finite-frequency behavior of head waves. A reference model with a low-velocity layer over a high-velocity half-space is used. Velocity anomalies of various sizes are placed on either side of the interface at different locations. A 3-D fourth-order staggered-grid finite-difference method is used to calculate synthetic waveforms, and travel time anomalies are measured by cross-correlations of seismograms for models with and without velocity anomalies. The results show that finite-frequency head waves are sensitive to the 3-D velocity perturbation in a more complex way than predicted by ray theory. The peak travel time sensitivity is located near the two piercing points at which the head wave reaches and leaves the interface. The sensitivity is much smaller elsewhere on the ray path. Fresnel zones can be observed from the pattern of positive and negative sensitivities, with the strongest negative sensitivity in the first Fresnel zone. Unlike turning waves, the head wave has a nonzero sensitivity right beneath the interface along the source-receiver path. But at some distance below the interface, the sensitivity has a local minimum. We are in the process of constructing 3-D full-wave sensitivity kernels from 3-D reference velocity models and compare the measured travel time anomalies with the predictions from the 3-D sensitivity kernels.

This is the beginning of a three-year effort to develop accurate, seamless velocity models in Eurasia at local, regional, and teleseismic scales under a self-consistent theory for finite-frequency seismic waves. We will construct the 3-D Finite-Frequency Seismic Tomography (FFST) velocity model for Eurasia and refine it for selected areas of interest (AOIs) and develop finite-frequency attenuation models for the AOIs. Broadband waveforms and ground truth (GT) data will be collected, and frequency-dependent travel times and amplitude measurements will be obtained from waveform cross-correlation.

OBJECTIVES

Our main objectives are to establish a process for developing refined local velocity models and attenuation structure using a newly developed, fully 3-D, finite-frequency waveform-based approach (Zhao et al., 2005). We will obtain FFST velocity models for Eurasia and refine crustal and shallow upper mantle velocity models for selected AOIs. Combining these two levels of velocity models under the unified finite-frequency theory, we will obtain integrated, seamless, finite-frequency kernel-based velocity models at local, regional, and teleseismic scales. A critical component of this project is to understand the finite frequency behavior of head waves, in particular Pn waves, which provides important information about the velocity structure around the crust-mantle boundary. Tomographic models based on the finite frequency effects of head waves (Pn) will likely provide a new and more accurate 3-D view of the boundaries of the Earth's interior, important constraints not only on the location and discrimination of the seismic sources, but also on the geological processes of the Earth.

RESEARCH ACCOMPLISHED

Previous Studies

Usually as the first arrival at regional distances, Pn waves are of prime importance in determining accurate locations of seismic events, source mechanisms, as well as the physical and chemical states of the uppermost mantle. There have been numerous tomographic studies of Pn velocity structure at various scales and localities (e.g., Hearn et al., 1991; Hearn, 1996; Ritzwoller et al., 2002; Liang et al., 2004). In previous Pn tomographic studies, the sensitivity of Pn waves to the velocity structure beneath the Moho is collapsed vertically and horizontally to a ray path right beneath the Moho under high-frequency (ray) approximation. Although many researchers recognize that the real Pn wave usually dips deeper into the mantle as epicentral distances increase and correct for the propagation distances empirically (e.g., Ritzwoller et al., 2002), the inversion is usually parameterized as a 2-D problem in latitude and longitude variations. Yet as all observed seismic waves, the Pn wave has a finite frequency range and may be sensitive to the 3-D structure surrounding the geometric ray path. Understanding the finite-frequency sensitivity of Pn waves is important for improving Pn tomography and related source location and discrimination. While recent studies have shown the diffractive nature and the 3-D sensitivities of finite-frequency turning waves (Dahlen et al., 2000; Hung et al., 2000; Zhao et al., 2000; Zhao et al., 2005; Tromp et al., 2005), analogs of head waves in a continuous velocity structure, the finite-frequency effects and sensitivity kernels of head waves are yet to be carefully examined.

At the regional and global (mantle) scales, the 3-D "banana-doughnut" travel-time sensitivity kernels (Dahlen et al., 2000; Hung et al., 2000; Zhao et al., 2000) represent a major advance from the conventional ray theory as the finite-frequency kernels account for wavefront healing and other diffractional effects. The "banana-doughnut" kernels have been used in global (Montelli et al., 2004) and regional (Hung et al., 2004; Shen and Hung, 2004; Yang et al., 2006) tomographic studies. The use of fully broadband seismic records has shown a significant improvement in the resolution of the velocity structure compared to ray-based models (Hung et al., 2004). We note that the kernels used in these studies are constructed using a 1-D reference Earth model due to computational constraints with respect to the scales of the studies. These tomographic inversions are performed under the assumption that the velocity perturbations are relatively small. This assumption is reasonable at regional and global (mantle) scales as demonstrated by the results of the initial finite-frequency tomographic studies.

At local (crustal) scales, large and sharp velocity variations are common and the 1D reference approach becomes inadequate. It is thus necessary to use a 3-D velocity model as the reference to calculate the sensitivity kernels for further improvement of the velocity model. Constructing 3-D sensitivity kernels from 3-D reference velocity models (hereinafter, fully 3-D kernels) is made possible by the ever-increasing power of computation and recent advances in seismic algorithms (Tromp et al., 2005; Zhao et al., 2005). This new approach eliminates both the high-frequency (ray) and structural averaging approximations and provides a powerful tool to further refine 3-D velocity structure. Furthermore, the new approach provides a straightforward way to utilize any segment of the waveform, and thus the rich information in the broadband waveforms. This is particularly important for small events, which are often recorded by only a few stations. In contrast, the traditional approach for tomography model and source studies depends heavily on the first arrivals due to the difficulties in unambiguously identifying later phases.

We report the initial results of a numerical study of the finite-frequency behavior of head waves. A 3-D finite difference code (Olsen, 1994) is used to simulate wave propagation. Traveltime anomalies are measured by cross-correlations of seismograms for models with and without velocity anomalies. The results indicate that finite-frequency head waves are sensitive to the 3-D velocity perturbation in a more complex way than predicted by ray theory. We are also calculating 3-D full-wave sensitivity kernels from 3-D reference models using the method of Zhao et al. (2005). The measured travel time anomalies will be compared with the values predicted by the 3-D sensitivity kernels.

Preliminary Results

In this initial waveform simulation study, we use a simple reference model with a low-velocity layer overlying a high-velocity half space (Figure 1). The same approach can be applied to 3-D reference models. We use an explosive source, a Gaussian derivative function with a dominant period of 1.2 seconds, in the simulations. A cylindrical velocity anomaly with a radius of 3.2 km and height of 1.6 km is placed in various locations within the high velocity layer. Table 1 shows the velocity parameters of the two layers and the anomaly. The grid spacing is 400 m, and the time length is 20 s with time interval of 0.02 s. Pn travel time delays are measures by cross-correlating Pn waveforms for models with and without the velocity perturbation (Figure 2).

Figure 3a shows the Pn travel time anomalies determined from waveform cross-correlation for models with a low-velocity anomaly right beneath the interface. Positive values indicate travel time delays. The two horizontal axes are the horizontal coordinates of the model. Because of the symmetry about the source-receiver path, calculations are carried out for only half of the model. The travel time delays (sensitivities) have two local maxima near the points where the theoretical ray of the head wave enters and leaves the interface. The asymmetry between the source and receiver sides is attributed to the fact that the source is closer to the interface than the receiver. Unlike turning waves, the travel time anomaly is nonzero along the ray path beneath the interface. Interestingly, there is a local minimum near the piecing point at the receiver side. Such a feature is not observed at the source side because the source is closer to the interface than the receiver and the near-field effects at the source dominate. Figure 3b shows the results for the perturbations with the upper surface of the input anomaly 1.6 km below the interface. The most notable difference is that there is now a local minimum near the center of the source-receiver path, which is analogous to the “doughnut” hole in the sensitivity kernel of the turning wave.

The pattern of positive (delay) and negative (early arrival) travel times and the amplitude variations are consistent with the calculated Fresnel zones (Figure 4). Within the first Fresnel zone, velocity perturbations contribute significantly to the travel time delays as measured by cross-correlation.

Table 1. Reference velocity model and input anomaly

	Vp (m/s)	Vs (m/s)	Attenuation
Upper layer	5207	3189	no
Lower layer	9058	5307	no
Anomaly	8500	5100	no

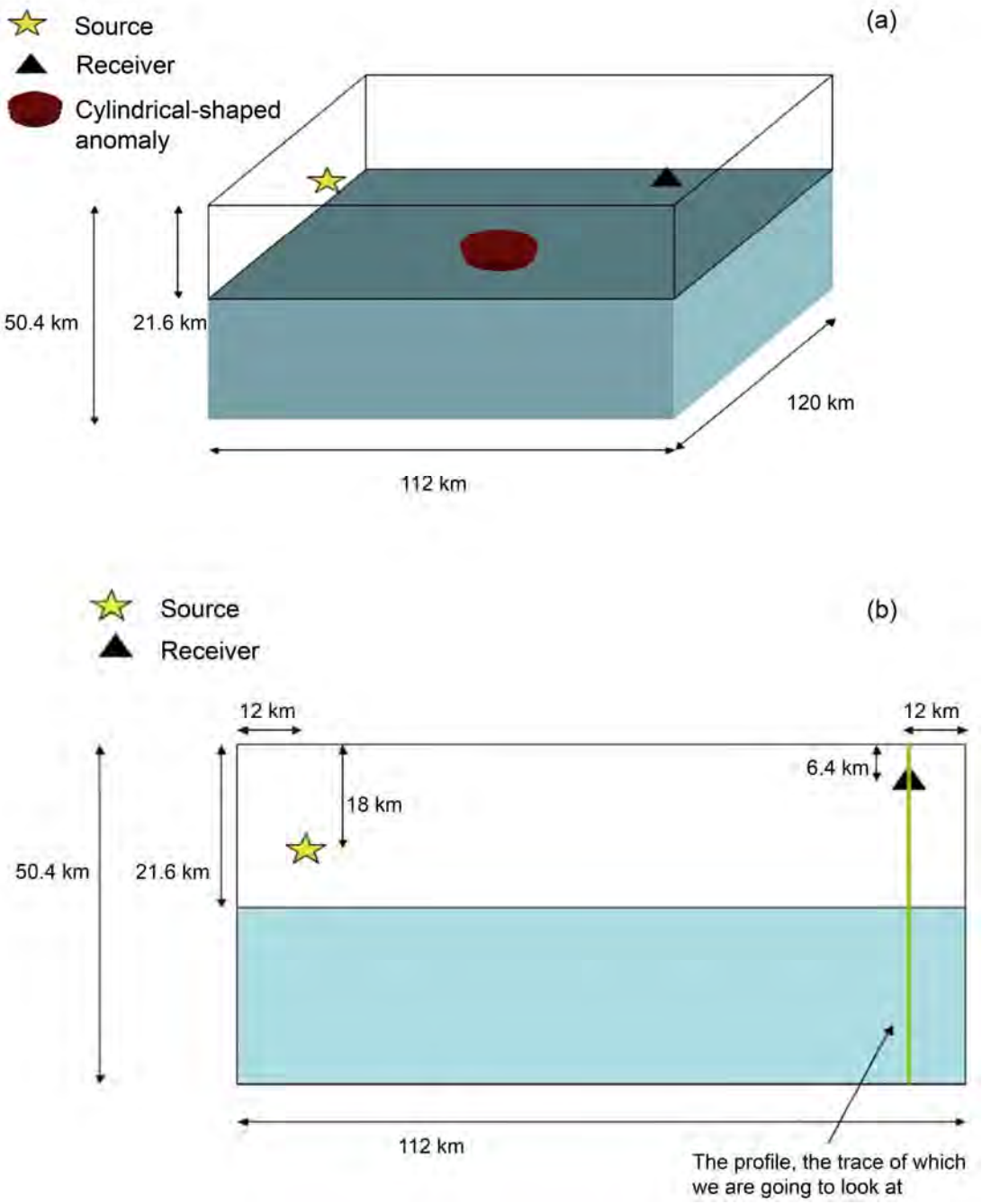


Figure 1. Schematic figure showing the geometry of the 3-D two-layered model. (a) Star represents the explosive source used in wave simulations. Triangle marks the receiver. The red cylindical represents a velocity perturbation beneath the interface. The velocities of the layers can be found in Table 1. (b) The vertical profile containing the source and the receiver. The star presents the location of the source. The black triangle is the location of the receiver. The model and the source-receiver geometry are designed so that the head wave is separated clearly from other phases, including waves reflected from the side and bottom boundaries due to imperfect absorption of seismic energy at the boundaries.

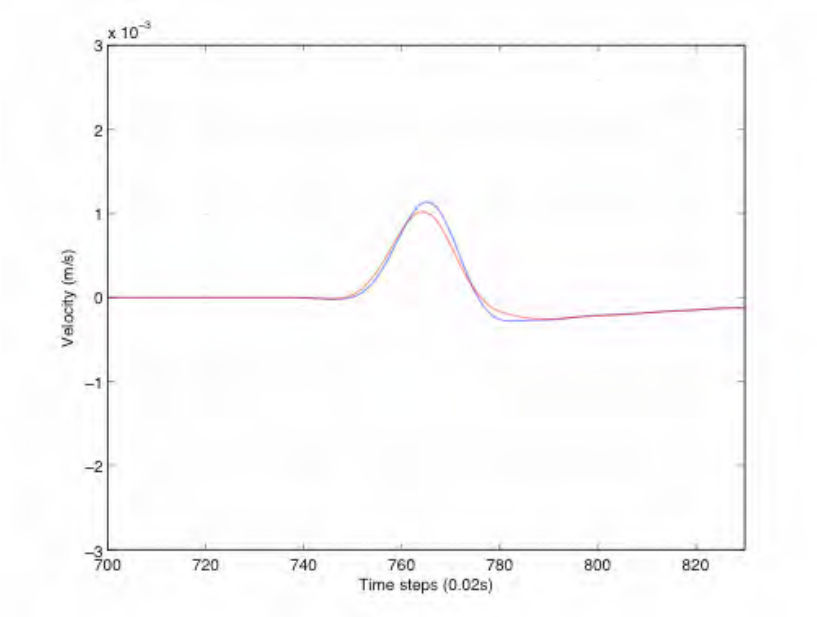
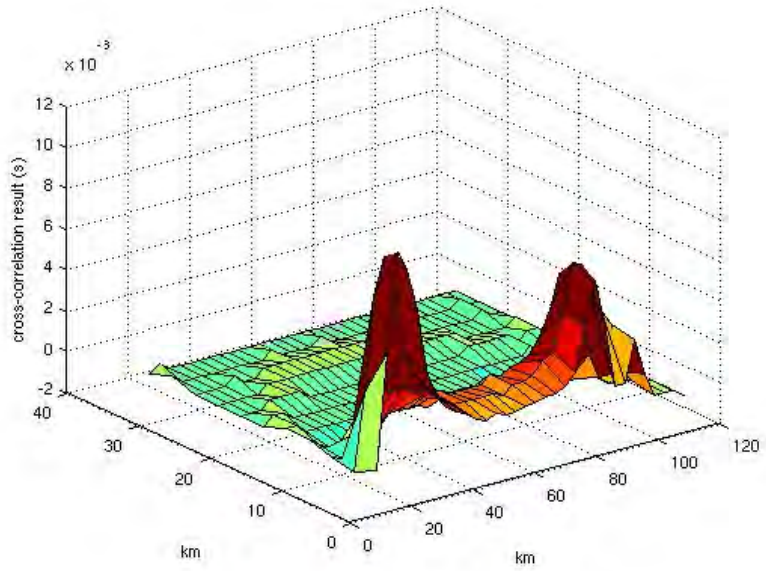
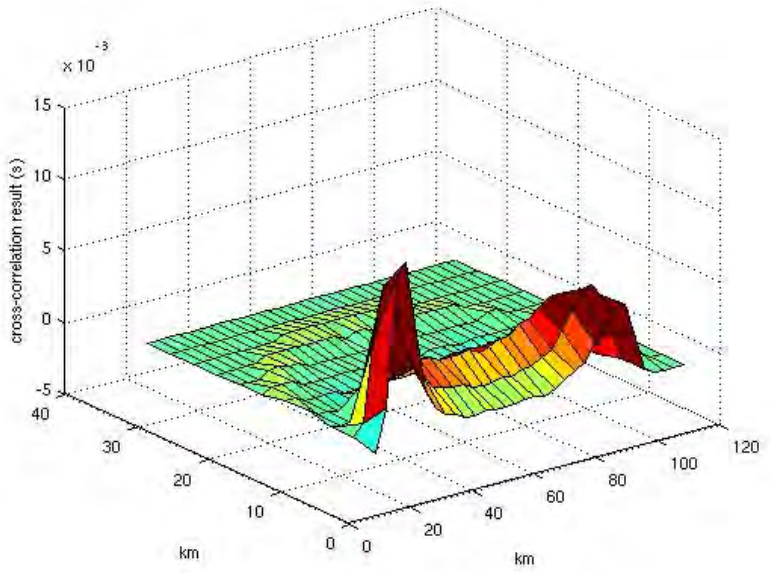


Figure 2. Comparison of the head wave calculated from reference model (red line) and that calculated from a model with a velocity perturbation below the interface in Figure 1 (blue line). The horizontal axis unit is time step with a time interval of 0.02 s. The vertical axis is the velocity.



(a)



(b)

Figure 3. (a) The travel time delays measured by cross-correlation for a moving velocity perturbation right beneath the layer interface with a 5% velocity reduction in a cylinder with a radius of 3.2 km and a height of 4 km. (b) The travel time delay measurements for the same sized velocity anomaly 1.6 km below the layer interface. The x-axis is the distance in the direction of the source and receiver path measured from the side of the model; the y-axis is the distance to the source-receiver plane. The two peaks of the travel time sensitivity are located near the two piecing points of the head wave ray path entering and leaving the bottom layer. Within the first Fresnel zone, velocity perturbations contribute significantly to the travel time delays as measured by cross-correlation. Notice the negative values in the second Fresnel zone and positive values in the third Fresnel zone.

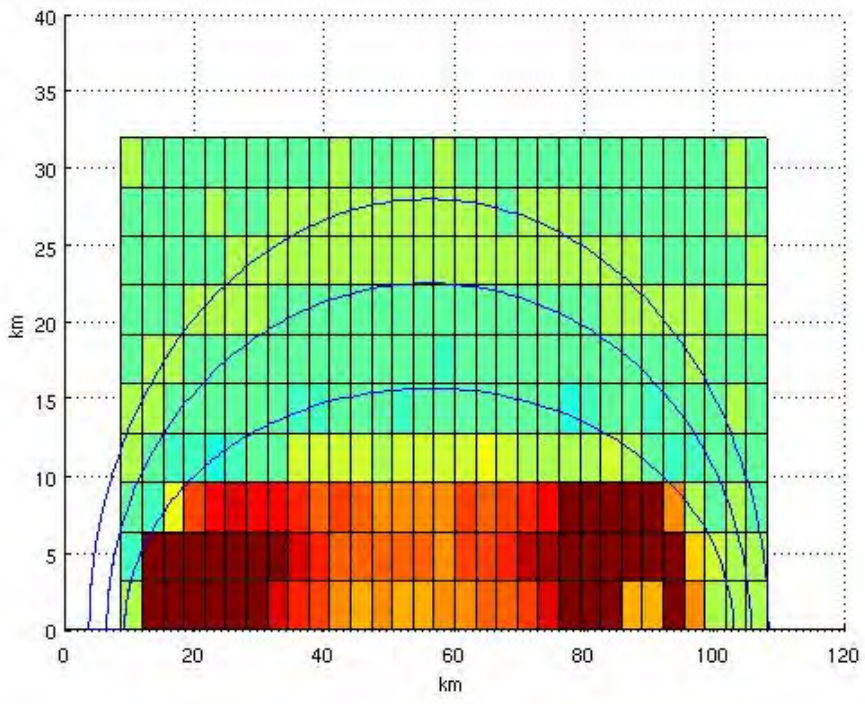


Figure 4. A comparison of the calculated Fresnel zones (blue lines) and the measured travel time delays. The blue lines mark the boundary of the first (innermost), second and third Fresnel zone. The pattern of the travel time sensitivity can be explained by the Fresnel zones.

CONCLUSION(S) AND RECOMMENDATIONS

The travel time anomaly of the finite-frequency head waves measured by waveform cross-correlation is very different from that predicted by the ray theory. While in the ray theory the travel time anomaly is sensitive only to velocity perturbation along the geometric ray path and the sensitivity is the same along the ray path, our results show that realistic head waves with finite frequencies are sensitive to the 3-D structure in a more complex way. The peak travel time sensitivity is located near the two piecing points of the geometric ray of the head wave entering and leaving the interface. The sensitivity is much smaller at other points on the ray path. The pattern of positive and negative sensitivities is consistent with the Fresnel zones, with the travel time anomaly most sensitive to velocity perturbations in the first Fresnel zone. Unlike the turning waves, the sensitivity right beneath the interface is nonzero along the source-receiver path. A few kilometers below the interface, there is a local minimum near the center of the source-receiver path, analogous to the “doughnut” hole in the sensitivity kernels of turning waves.

We are in the processes of constructing 3-D sensitivity kernels for head waves using the method of Zhao et al. (2005) and are exploring how 3-D velocity variations affect the finite-frequency behavior of head waves (Pn waves). The simulations not only help us gain a physical understanding of the finite-frequency behavior of head waves, but also provide us a means to compare the travel time delays measured by waveform cross-correlations and calculations from the sensitivity kernels. We will apply the 3-D Pn sensitivity kernels to image the velocity structure at the selected areas of interest.

REFERENCES

Dalen, F., S. Hung, and G. Nolet (2000). Frechet kernels for finite-frequency travel times—I. Theory, *Geophys. J. Int*. 141: 157–174.

Hearn, T. M. (1996). Anisotropy Pn tomography in the west United States, *J. Geophys. Res.* 101: 8,403– 8,414.

Hearn, T., Beghoul, N., Barazangi, M. (1991). Tomography of the Western United States from regional arrival times, *J. Geophys. Res.* 96: 16,369–16,381.

Hung, S., F. Dalen, and G. Nolet (2000). Frechet kernels of finite-frequency travel times—II. Examples, *Geophys. J. Int.* 141: 175–203.

Hung, S.-H., Y. Shen, and L.-Y. Chiao (2004). Imaging seismic velocity structure beneath the Iceland hotspot: A finite-frequency approach, *J. Geophys. Res.* 109: B08305, doi:10.1029/2003JB002889.

Liang, C., X. Song, and J. Huang (2004). Tomographic inversion of Pn travel times in China, *J. Geophys. Res.* 109: B11304, doi:10.1029/2003JB002789.

Montelli, R., G. Nolet, F. Dalen, G. Masters, E. R. Engdahl, and S. Hung (2004). Finite-frequency tomography reveals a variety of plumes in the mantle, *Science* 303: 339–343.

Olsen, K. B. (1994). Simulation of three-dimensional wave propagation in the Salt Lake Basin, Ph.D. Thesis, University of Utah, Salt Lake City, Utah.

Ritzwoller, M. H., M. P. Barmin, A. Willasenor, A. L. Levshin, and E. R. Engdahl (2002), Pn and Sn tomography across Eurasia to improve regional seismic event locations, *Tectonophysics*, 358: 39–55.

Shen, Y. and S.-H. Hung (2004). Ridge-like upwelling in the uppermost lower mantle beneath eastern Africa from finite-freuqency seismic tomography, *Eos Trans. AGU* 85, Fall Meet. Suppl., Abs. U41A-0720.

Tromp, J., C. Tape, and Q. Liu (2005). Seismic tomography, adjoint methods, time reversal and banana doughnut kernels, *Geophys. J. Int.* 160: 195–216.

Yang, T., Y. Shen, S.-H. Hung, S. van der Lee, and S. C. Solomon (2006). Upper mantle structure beneath the Azores hotspot from finite frequency seismic tomography, *Earth Planet. Sci. Lett.* (in revision).

Zhao, L., T. H. Jordan, and C. H. Chapman (2000), Three-dimensional Fréchet differential kernels for seismic delay times, *Geophys. J. Int*. 141: 558–576.

Zhao, L., T. Jordan, K. Olsen, and P. Chen (2005). Frechet kernels for imaging regional Earth structure based on three-dimensional reference models, *Bull. Seismo. Soc. Am*. 95: 2,066–2,080.

BROADBAND NETWORK OPERATION AND SHEAR VELOCITY STRUCTURE BENEATH THE YANQING-HUAILAI BASIN, NW OF BEIJING

Rong-Mao Zhou[1], Brian W. Stump[1], Robert B. Herrmann[2],
Yun-Tai Chen[3], and Zhi-Xian Yang[3]

Southern Methodist University[1], Saint Louis University[2],
and Institute of Geophysics, China Earthquake Administration[3]

Sponsored by Air Force Technical Application Center

Contract No. FA8718-05-C-0020

ABSTRACT

We continue the operation of the Southern Methodist University-Institute of Geophysics, China Earthquake Administration (IGPCEA) broadband seismic network. The current operating network includes 3 stations NW of Beijing and 10 stations in Haicheng, NE China.

We conducted joint inversion of teleseismic received functions and surface wave phase velocities for crustal shear velocity structure. The focus area of the joint inversion is the Yanqing-Huailai Basin, 120 km northwest of Beijing. The data set is from a broadband seismic network that is part of a PASSCAL deployment in the basin and includes 34 teleseismic events from 2003 to 2005.

Within the Yanqing-Huailai Basin, earthquake risk and propagation path assessment are important because of the basin's historical seismicity and proximity to Beijing's large population. This setting motivated the deployment of portable broadband instruments consisting of STS-2 seismometers deployed in hard rock vaults and recorded on Quanterra Q-330 digitizer and Baler. The high-quality data set recorded by 7 stations around the basin provides us the opportunity to study the detailed velocity structure beneath this region using both teleseismic and regional signals.

The receiver functions from the teleseismic events are simple and similar around the Yanqing-Huailai Basin. They exhibit little variation with azimuth. The inverted velocity models reflect small path differences and are consistent with the shallow local geology. The resulting velocity models all produce a positive gradient from surface to approximately 5 km with shear wave velocity increasing from 2.4-2.7 km/sec to 3.4 km/sec. A low velocity layer was found to start between 5 and 10 km with shear velocity dropping to 3.1 km/sec and extending to about 13 km.

Long period surface wave observations (20-100 sec) are used to further constrain the crust and upper mantle. The crustal components of these models are developed and compared to shallow crustal structures determined from the analysis of intermediate period (2-15 sec) surface waves generated by moderate size regional events and recorded at the same stations. The regional analysis produces shear wave models for the top 15 km of the crust that are consistent with the models constrained by teleseismic data.

OBJECTIVES

The goals of the collaborative study between the SMU and the IGPCEA (formerly IGCSB) are to develop a database of earthquakes and human-induced events; to refine event locations in Yanqing-Huailai Basin and Haicheng area; to understand source characterization of natural and human-induced events; and to separate source and propagation path effects at regional distance.

The deployment of the broadband seismic network operated by SMU and IGPCEA has been completed. The current operating network includes 3 stations around the Yanqing-Huailai Basin, NW of Beijing and 10 stations in the Haicheng, NE China (Figure 1). The seismic data have been archived into the Incorporated Research Institutions for Seismology (IRIS) Data Management System Portable Data Collection Center (DMC) database.

Beijing and Haicheng are two regions of historical natural and human-induced seismicity as well as a seismic hazard. The region includes the site of the first successful earthquake prediction in 1975 near Haicheng and the great Tangshan earthquake in 1976. The broadband seismic network provides near-source and regional coverage for the study area. Data from this network have been used to constrain the preliminary velocity structure around Beijing (Zhou, 2004) from surface wave study and investigate event discrimination for mining explosions (Zhou et al., 2006).

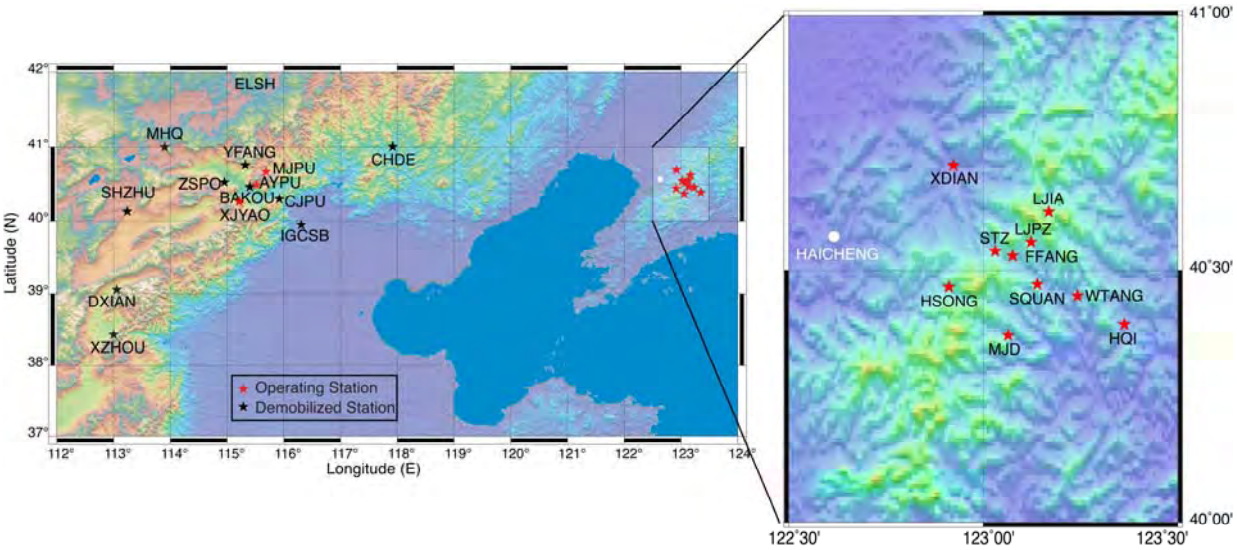


Figure 1. Map of the SMU-IGPCEA Broadband Seismic Network (Operating stations: red stars; Demobilized stations: black stars)

RESEARCH ACCOMPLISHED

Operation of the Broadband SMU-IGPCEA Network

The deployment of the broadband SMU-IGPCEA network was completed and is summarized in Figure 1. To date, 13 broadband seismic stations are operating, including 3 stations (AYPU, MJPU and XJYAO) around the Yanqing-Huailai Basin and 10 stations in Haicheng, Liaoning Province. Data through December 2005 have been converted to SEED format and archived at IRIS DMC.

Shear Structure Beneath the Yanqing-Huailai Basin

Regional Setting and Seismicity

The Yanqing-Huailai Basin is located in the area of 40°00′N – 40°38′N and 115°04′E – 116°14′E, about 90 to 140 km northwest of Beijing, China (Figure 2). The Yanqing-Huailai basin is a collection of four intermountain basins:

Yanqing, Huailai, Zhuolu and Fanshan basin (Zhang et al., 1996), in which the Yanqing and Huailai basins are two sub parallel elongated half-graben basins bounded to their NNW by normal faults (Pavlides et al., 1999). Historically, two large earthquakes occurred in Yanqing-Huailai Basin. One was the Huailai earthquake with magnitude 6.5 on September 8, 1337; the other one was the Shacheng earthquake with magnitude 6.75, near Shacheng on July 12, 1720 (Fig. 2). Recently, the seismicity is increasing in this area. Based on signals recorded by the Beijing Telemetered Seismograph Network, China Seismological Bureau, there are 15 to 20 earthquakes with magnitude equal or greater than 2.0 every year in the Yanqing-Huailai basin and its adjoining area (Chen et al., 1998). On July 20, 1995, a M_L 4.1 earthquake occurred in the Yanqing-Huailai Basin followed by approximately 450 aftershocks (Chen et al., 1998).

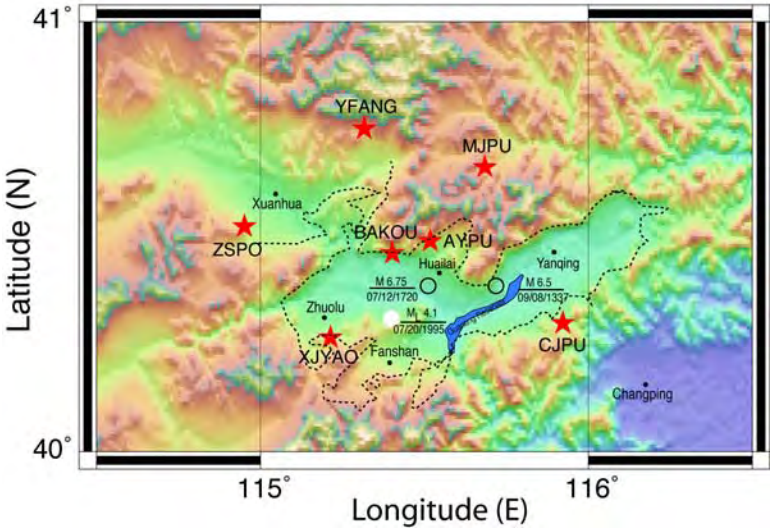


Figure 2. Topographic map of Yanqing-Huailai Basin (dotted line) and adjacent area. Broadband seismic stations of the SMU-IGPCEA Huailai Seismic Network are designated as stars. Open circles are locations of two historical earthquakes in 1337 and 1720. The white dot is the epicenter of a M_L 4.1 earthquake on July 20, 1995. Solid dots are towns in the area.

Receiver Functions

Thirty-four, high signal-to-noise ratio, teleseismic events with great circle epicentral distances in the range of 30-80 degrees from 2003 to 2005 have been chosen for the receiver function and surface wave joint inversion. Source parameters of these events were obtained from the Preliminary Determination of Epicenters (PDE) bulletins provided by the United States Geology Survey (USGS) National Earthquake Information Center (NEIC) and are listed in Table 1. Figure 3 is the map of these 34 teleseismic events with azimuthal equidistant projection centered at AYPU. The distribution of teleseismic sources illustrated the coverage in which the local earth structure is well sampled by the events from the three azimuths to the northeast, southeast and southwest. The three-component seismograms of a magnitude 6.2 event (2003089, which occurred at -3.17°N and 127.54°E on March 30, 2003) are presented in Figure 4 as a typical example of data recorded by the SMU-IGPCEA broadband seismic network.

Receiver functions are extracted from the three-component broadband recordings of teleseismic *P* waves at distances ranging from 30° to 80° (Figure 3). The extraction procedure is described by Langston (1979) and consists of a deconvolution of vertical component seismograms from the radial and transverse components. The deconvolution is performed in the frequency domain using a Gaussian filter and spectral trough filler. It is important to recognize that these receiver functions, although developed from *P* waveforms, are most sensitive to the shear velocity structure beneath the station, since *P* to *S* conversions dominate the horizontal components after source effects are eliminated (Owens et al., 1984). Ammon et al. (1991) suggest that the absolute amplitude of a receiver function supplies an additional constraint on the near-surface shear wave velocity, which also helps avoid inaccuracies due to the presence of dipping layers (Cassidy, 1992).

Table 1. Event Parameters

Even Code	Date (Y-M-D)	Time (hhmmss.mm)	Latitude (°N)	Longitude (°E)	Magnitude	Depth (km)	Distance to AYPU (degree)	AYPU Back-Azimuth (degree)
2003076	2003-03-17	163617.31	51.27	177.98	7.1	33	43.4030	53.841
2003089	2003-03-30	181334.09	-3.17	127.54	6.2	33	45.0290	162.9029
2003141	2003-05-21	184420.10	36.96	3.63	6.9	12	80.5659	311.2685
2003166	2003-06-15	192433.15	51.55	176.92	6.5	20	42.7017	53.6157
2003174	2003-06-23	121234.47	51.44	176.78	7.0	20	42.6352	53.798
2003339	2003-12-05	212609.48	55.54	165.78	6.7	10	35.8562	47.9734
2003360	2003-12-26	015652.44	29.00	58.31	6.8	10	47.5414	274.7492
2004039	2004-02-08	085851.80	-3.66	135.34	6.9	25	47.7394	152.7885
2004107	2004-04-16	215705.41	-5.21	102.72	6.0	44	47.1908	197.498
2004114	2004-04-23	015030.22	-9.36	122.84	6.7	65	50.3108	170.5935
2004162	2004-06-10	151957.75	55.68	160.00	6.9	188	32.6250	47.1192
2004180	2004-06-28	094947.00	54.80	-134.25	6.8	20	67.7271	35.7656
2004316	2004-11-11	212641.15	-8.15	124.87	7.5	10	49.4031	167.7677
2004353	2004-12-18	064619.87	48.84	156.31	6.2	11	29.7939	59.9279
2005022	2005-01-22	203017.35	-7.73	159.48	6.5	29	62.9309	129.4202
2005023	2005-01-23	201012.15	-1.20	119.93	6.3	11	41.8874	173.3834
2005036	2005-02-05	033425.73	16.01	145.87	6.6	142	35.9156	124.1009
2005036-2	2005-02-05	122318.94	5.29	123.34	7.1	525	35.8981	166.6349
2005046	2005-02-15	144225.85	4.76	126.42	6.6	39	37.0547	161.7708
2005050	2005-02-19	000443.59	-5.56	122.13	6.5	10	46.4530	170.9008
2005061	2005-03-02	104212.23	-6.53	129.93	7.1	201	48.8588	160.8297
2005089	2005-03-30	161941.10	2.99	95.41	6.4	22	41.6663	211.0916
2005093	2005-04-03	005921.42	0.37	98.32	6.0	30	43.0583	205.6601
2005093-2	2005-04-03	031056.47	2.02	97.94	6.3	36	41.6333	207.0177
2005099	2005-04-09	151627.89	56.17	-154.52	6.0	14	57.3372	41.3998
2005100	2005-04-10	102911.28	-1.64	99.61	6.7	19	44.5634	202.981
2005100-2	2005-04-10	172439.40	-1.59	99.72	6.4	30	44.4830	202.8524
2005106	2005-04-16	163803.90	1.81	97.66	6.4	31	41.9274	207.3021
2005118	2005-04-28	140733.70	2.13	96.80	6.3	22	41.9354	208.6745
2005130	2005-05-10	010905.10	-6.23	103.14	6.4	17	48.0911	196.6372
2005134	2005-05-14	050518.48	0.59	98.46	6.8	34	42.8045	205.5722
2005139	2005-05-19	015452.85	1.99	97.04	6.9	30	41.9789	208.2643
2005165	2005-06-14	171016.64	51.23	179.41	6.8	51	44.2879	53.6387
2005186	2005-07-05	015202.95	1.82	97.08	6.8	21	42.1231	208.1173

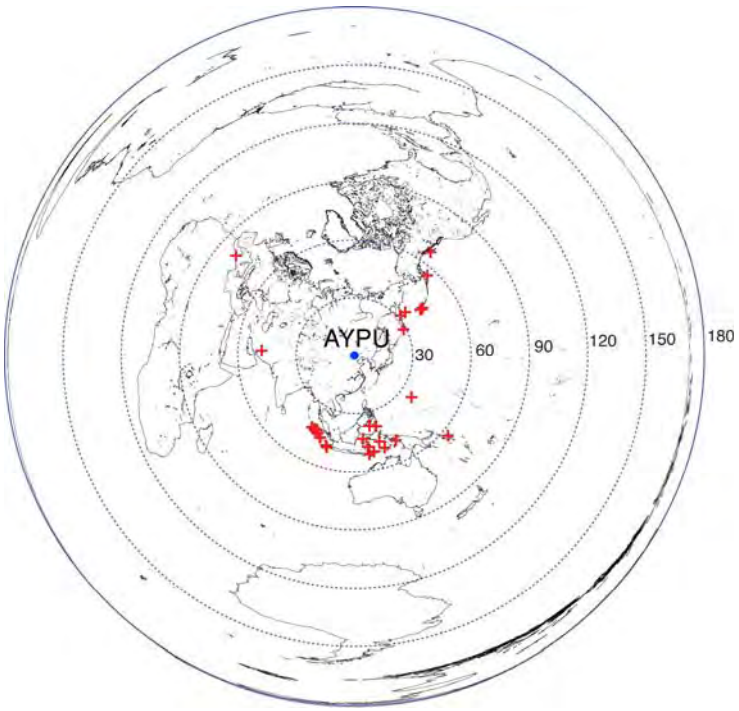


Figure 3. Map (azimuth equidistant projection centered at AYPU) of events (plus) used in the receiver function study. Dotted lines are great circle distance ranges in degrees from AYPU (dot).

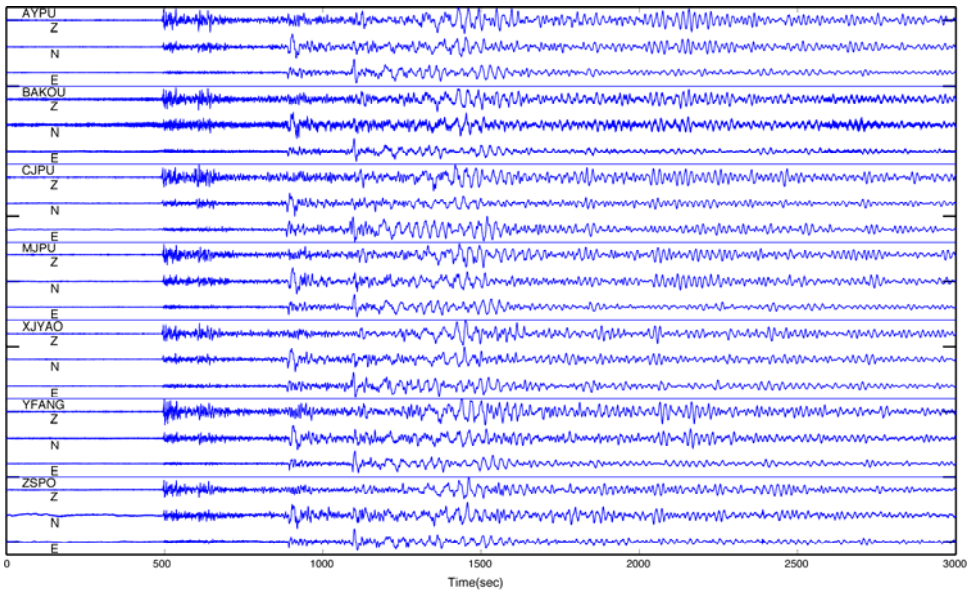


Figure 4. Three components seismograms from Event 2003089 recorded by the network.

Typical radial component receiver functions from Event 2003089 with different Gaussian filter parameters at 6 stations of the SMU-IGPCEA broadband seismic network are reproduced in Figure 5. The signal to noise ratio at BAKOU was low on the north and east component for this event and so data from this station for this event are not included in the subsequent analysis.

The receiver functions were extracted from all 34 events in Table 1 and Figure 3. The radial component receiver functions at stations AYPU and XJYAO are plotted as a function of azimuth in Figure 6. The radial component receiver functions are simple, have little azimuthal variation and are similar around the Yanqing-Huailai Basin. This similarity led us to a simple one dimensional receiver function analysis.

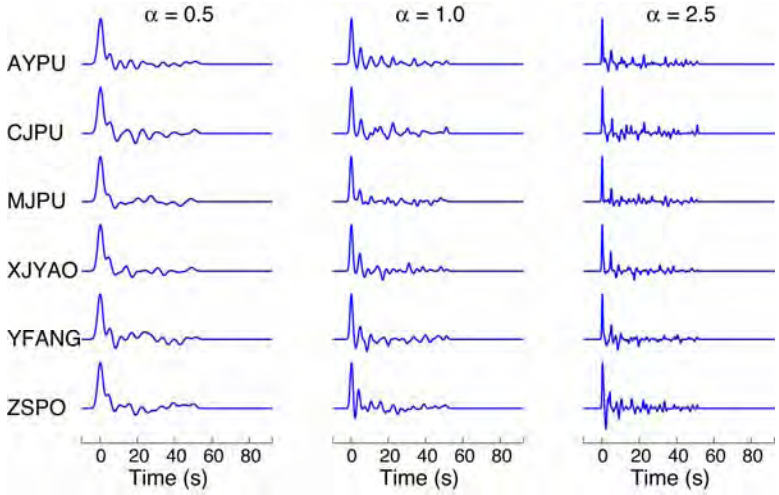


Figure 5. Receiver functions from Event 2003089 on March 30, 2003 with Gaussian window parameters α of 0.5 (left), 1.0 (mid) and 2.5 (right).

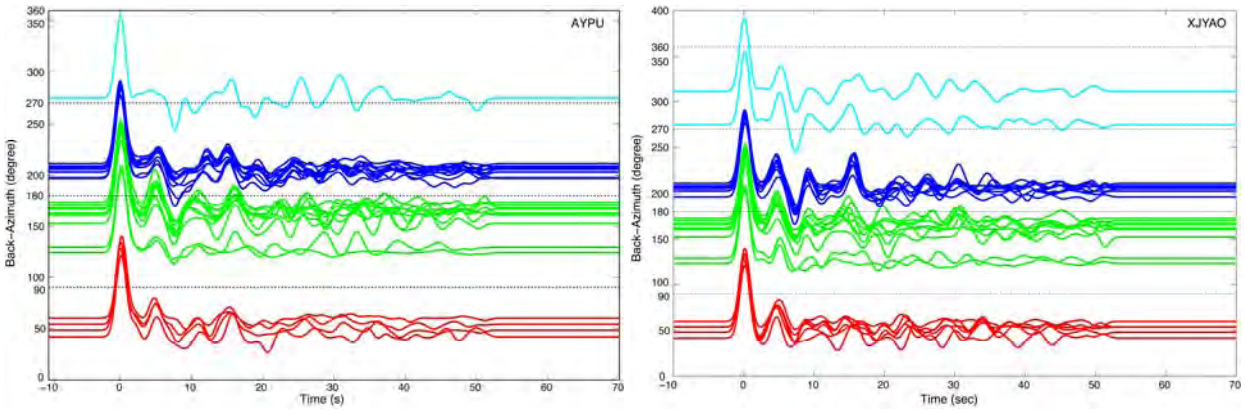


Figure 6. Receiver functions versus back-azimuth for all events recorded at stations AYPU (27 events) and XJYAO (27 events).

Surface Wave

McMechan and Yedlin (1981) described a technique to obtain phase velocity dispersion from an array of seismic traces. This technique relies on a p-τ stack followed by transformation into the p-ω domain (Mokhtar et al., 1988) and is applied to our data set. For each teleseismic event in our data set, the long period surface waves were extracted by using the Multiple Filter Analysis (Dziewonski et al., 1969) and Phase Matched Filtering (Herrin and Goforth, 1977). The fundamental mode Rayleigh waves extracted from Event 2003089 in the period range of 20 to 100 seconds are reproduced in Figure 7. Group velocity dispersion curves from 20 to 100 sec in period were recovered and phase velocity stacks from 3.45 to 4.20 km/sec are also included in Figure 7.

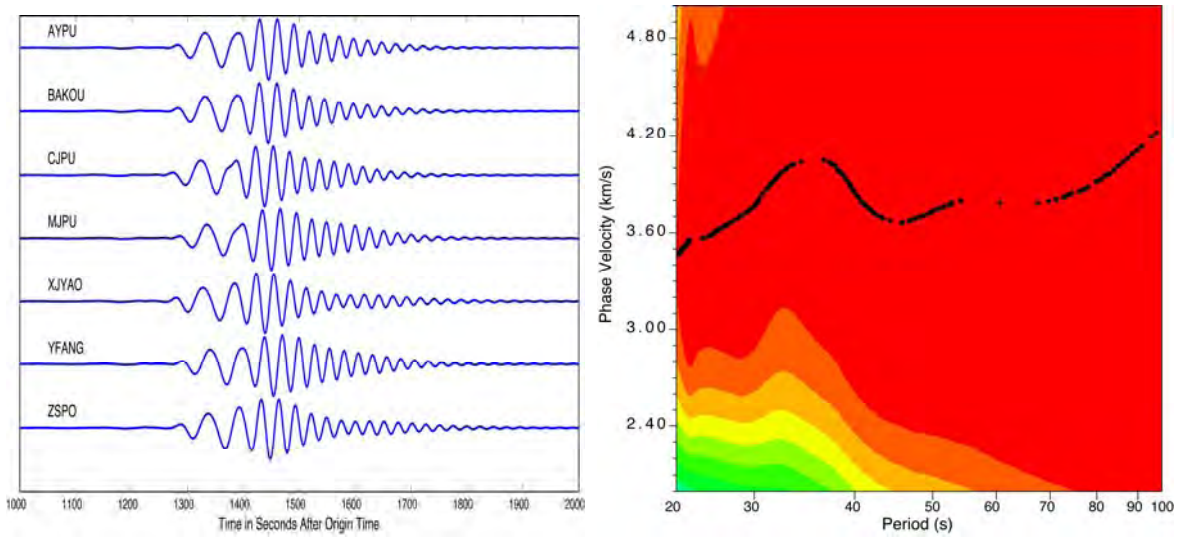


Figure 7. Left: Fundamental Rayleigh waves extracted from Event 2003089 and Right: Phase velocity stacks of the Rayleigh waves for Event 2003089.

Joint Inversion

A joint inversion of the receiver functions and phase velocities across the Yanqing-Huailai Basin has been conducted. The starting model is given in Figure 8 in black with the velocity model resulting from the joint inversion in green. Observed (blue) and predicted (red) receiver functions at station AYPU are also plotted. The predicted receiver functions fit the observed well for the events at all azimuths and distance ranges. The resulting velocity models at each station are summarized in Figure 9. All stations give consistent velocity models except CJPU and ZSPO, which only recorded useful data for 8 and 10 events, respectively. There are differences in the very shallow portions of the models as illustrated by top 2 km for stations in the Yanqing-Huailai Basin which have

a slower shear velocity of about 2.4 km/sec compared to stations outside the basin. All velocity models have a positive velocity gradient from surface to approximately 5 km with shear wave velocity increasing from 2.35/2.8 km/sec to 3.4 km/sec. All models have a low velocity zone in the upper crust starting between 5 and 10 km with a shear velocity oft 3.2 km/sec. A slight negative gradient in velocity starts at about 15 km resulting in an extended constant velocity layer to approximately 25 km. The crustal thickness in this region is between 35 and 42 km from studies of wide-angle reflection and refraction surveys (Zhang et al., 1996; and Zhao et al., 2005) that is consistent with our models.

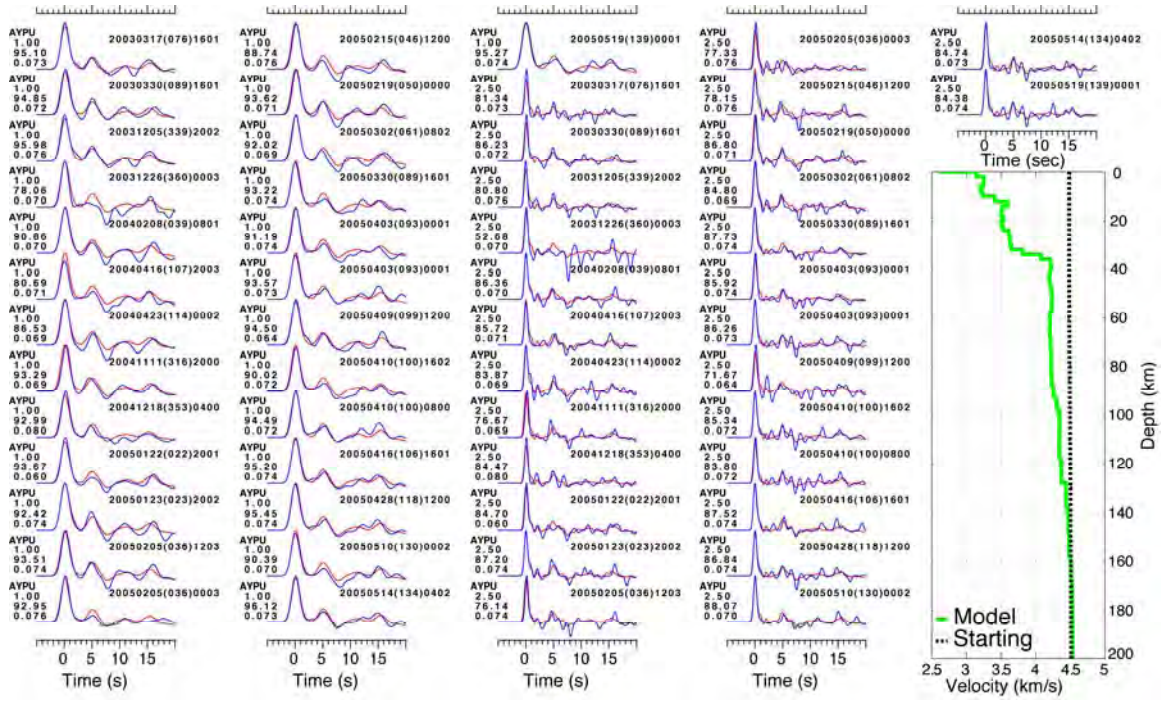


Figure 8. Comparison between observed (blue) and predicted receiver functions (red) at AYPU. The starting shear wave velocity model is the dashed black line and the velocity model from the joint inversion at AYPU is given in green.

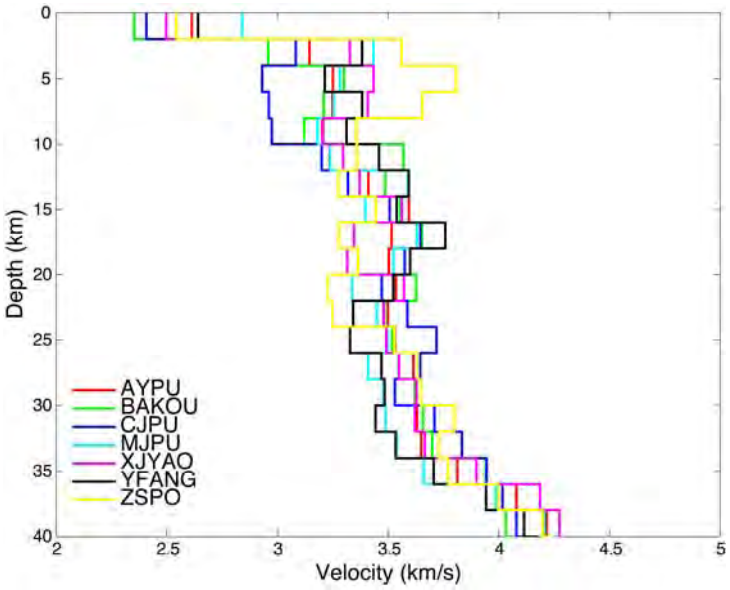


Figure 9. Velocity models resulting from joint inversion at all 7 stations in and around the Yanqing-Huailai Basin.

Model Comparison

An average shear velocity model was estimated by inverting all the receiver functions from the 7 network stations. This average velocity model is compared to the published velocity model based on the wide-angle reflection and refraction profile along the Fengzhen-Huailai-Shunyi (Zhang et al., 1996; and Zhao et al., 2005) in Figure 10. The predicted first arrival times of P and S wave from the two models are also compared in the figure. The *P* wave arrival times for the two models agree to 300 km. The *S* wave arrival times agree to about 170 km with our model predicting later arrival times for *S* waves at the larger ranges.

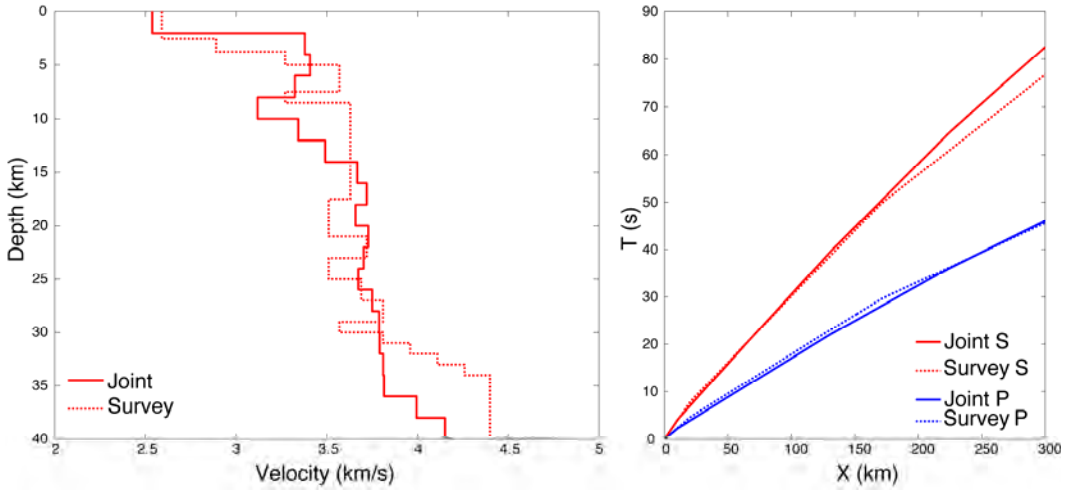


Figure 10. Left: Comparison between the joint inversion model (solid red) and the model from a wide-angle reflection and refraction survey (dotted red). Right: Predicted first arrival times of P (blue) and S wave (red) for jointed inversion model (solid) and the model from a wide-angle reflection and refraction survey (dotted).

CONCLUSIONS AND RECOMMENDATIONS

The operation of the SMU-IGPCEA broadband seismic network is continuing. The data through December 2005 has been archived at the IRIS DMC.

A joint inversion of teleseismic receiver functions and surface wave phase velocities for crustal shear velocity structure beneath the Yanqing-Huailai Basin has been completed. The inversion results indicate that the top 2 km beneath the Yanqing-Huailai Basin has a slower shear velocity of about 2.4 km/sec compared to stations outside the basin. A positive velocity gradient exists at all stations to a depth of 5 km with S wave velocity increasing to 3.4 km/sec. A low velocity layer was found to start between 5 and 10 km with shear velocity dropping to 3.1 km/sec and extending to about 13 km. Crustal thickness around Yanqing-Huailai basin is about 40 km consistent with the wide-angle reflection and refraction survey results.

Predicted first arrival times of *P* waves from the joint inversion model fit well with the wide-angle reflection and refraction results to distances of 300 km. The new shear wave model predicts S arrivals that are late relative to previous model beyond 170 km.

The velocity models from inversion at stations CJPU and ZSPO are different from the others because of the smaller number of the events recorded. This difference suggests that more events should be added to the inversion procedure in the future.

ACKNOWLEDGEMENTS

The authors would like to thank Chris Hayward, Mary Templeton, Eliana Arias, Xiang-Wei Yu, Xiang-Tong Xu and Shi-Yu Bai for their help with network installation, data collection and archive. A large portion of the success of this experiment is due to the outstanding help and support of the seismological bureaus and seismic station operators in these regions. IRIS PASSCAL Instrument Center provided the STS-2 seismometers, Quanterra Q-330 and Baler systems.

REFERENCES

Ammon, C. J. (1991). The isolation of receiver effects from teleseismic P waveforms, *Bull. Seism. Soc. Am.* 81**:** 2504–2510.

Cassidy, J. F. (1992). Numerical experiments in broadband receiver function analysis, *Bull. Seism. Soc. Am.* 82**:** 1453–1474.

Chen, Y.-T., X.-T. Xu, X.-W. Yu, and P.-D. Wang (1998). Observations and interpretation of seismic ground motion and earthquake hazard mitigation in the Beijing area, *South China Journal of Seismology* 18**:** 2–8 (in Chinese with English abstract).

Dziewonski, A., S. Bloch, and M. Landisman (1969). A technique for the analysis of transient seismic signals, *Bull. Seism. Soc. Am.* 59**:** 427–444.

Herrin, E. and T. Goforth (1977). Phase-matched filters: application to the study of Rayleigh waves, *Bull. Seism. Soc. Am.* 67**:** 1259–1275.

Langston, A. C. (1979). Structure under Mount Rainier, Washington, inferred from teleseismic body waves, *J. Geophys. Res.* 84**:** 4749–4762.

McMechan, G. A. and M. J. Yedlin (1981). Analysis of dispersive waves by wave field transformation, *Geophysics* 46**:** 869–874.

Mokhtar, T. A., R. B. Herrmann, and D. R. Russell (1988). Seismic velocity and Q model for the shallow structure of the Arabian shield from short period Rayleigh waves, *Geophysics* 53: 1379–1387.

Owens, J. T., G. Zandt and S. R. Taylor (1984). Seismic evidence for an ancient rift beneath the Cumberland Plateau, Tennessee: A detailed analysis of broadband teleseismic P waveforms, *J. Geophys. Res.* 89**:** 7783–7795.

Pavlides, B. S., N. C. Zouros, Z.-J. Fang, S.-P. Cheng, M. D. Tranos, and A. A. Chatzipetros (1999). Geometry, kinematics and morphotectonics of the Yanqing-Huailai active faults (northern China), *Tectonophysics* 308**:** 99–118.

Zhao, J.-R., X.-K. Zhang, C.-K. Zhang, J.-S. Zhang, B.-F. Liu, Q.-F. Ren, S.-Z. Pan, and Y. Hai (2005). The heterogeneous characteristics of crust-mantle structures and the seismic activities in the northwest Beijing region, *ACTA Seismologica Sinica* 18**:** 125–134.

Zhang, X.-K., C.-Y. Wang, G.-D. Liu, J.-L. Song, L.-L. Luo, T. Wu, and J.-C. Wu (1996). Fine crustal structure in Yanqing-Huailai region by deep seismic reflection profiling, *Chinese J Geophys* 39**:** 356~364 (in Chinese with English abstract).

Zhou, R.-M. (2004). Intermediate period surface waves from mining explosions for crustal structure and source studies: application in the Western USA and Northeast China. *Ph. D. Dissertation*, Southern Methodist University, pp 240.

Zhou, R.-M., B. W. Stump, and C. T. Hayward (2006). M_s:m_b discrimination study of mining explosions in Wyoming, USA and Qianan, China. *Bull. Seismo. Soc. Am.* ***96,*** No.5, in press.

Seismic Event Detection and Location

A LOWER BOUND ON THE STANDARD ERROR OF AN AMPLITUDE-BASED REGIONAL DISCRIMINANT

D. N. Anderson[1], W. R. Walter[2], D. K. Carlson[1], T. M. Mercier[1], S. R. Taylor[3]

Pacific Northwest National Laboratory[1], Lawrence Livermore National Laboratory[2], and
Rocky Mountain Geophysics, LLC[3]

Sponsored by National Nuclear Security Administration
Office of Nonproliferation Research and Development
Office of Defense Nuclear Nonproliferation

Contract Nos. DE-AC06-76RLO 1830[1,3] and W-7405-ENG-48[2]

ABSTRACT

Wave path, magnitude, and signal processing corrections made to observed regional amplitudes fundamentally contain information regarding only the seismic source. These corrected amplitudes can then be used in ratios to discriminate between earthquakes and explosions. Source effects that are due to depth, focal mechanism, local material property and apparent stress variability that cannot easily be determined still remain in the signal. These effects establish a lower bound on the amplitude variability for new events, even after path and magnitude corrections are applied. We develop a general strategy to account for amplitude correction inadequacy by appropriately partitioning error. The proposed mathematics are built from random effects analysis of variance (ANOVA) and have application potential to a variety of amplitude correction theories, for example, see Taylor and Hartse (1998), Taylor et al. (2002), and Walter and Taylor (2002). The error components from random-effects ANOVA are the basis for a general station-averaged regional discriminant formulation. The standard error of the discriminant has a lower bound of amplitude correction error. The developed methods are demonstrated for a suite of Nevada Test Site (NTS) events observed at regional stations.

OBJECTIVES

In Taylor and Hartse (1998), Taylor et al. (2002), and Walter and Taylor (2002), the magnitude and distance amplitude correction (MDAC) technique corrects regional phase amplitudes independent of distance and magnitude. MDAC is a simple, physically based model that accounts for propagation effects, such as geometrical spreading and *Q*, and corrects amplitudes, assuming an earthquake model. MDAC P and S phase amplitude ratios can then be used to discriminate between earthquakes and explosions. Because of complex explosion source phenomenology, it is not obvious which discriminants or combination of discriminants will best separate earthquake and explosion populations. The MDAC technique provides the latitude to form a diversity of discriminants by mixing phases and signal-processing frequencies. Until now, no attempt has been made to obtain a realistic estimate of the error budget associated with MDAC amplitudes used to construct seismic discriminants.

The approach presented in this paper develops the mathematics to form a station-averaged discriminant, with the proper standard error, from multiple stations. Through MDAC we correct amplitudes and adopt the position that any remaining physical structure, not indicative of source, is a random model inadequacy effect. MDAC can be augmented with additional corrections and the basic multi-station model holds. This approach to discriminant formulation properly forms the variance of the discriminant with two components. Station noise is reduced through station averaging, and the model inadequacy variance component only decreases with improvements in physical path correction theory.

RESEARCH ACCOMPLISHED

Established signal-processing research treats amplitudes as lognormally distributed random variables; therefore, in log space, properly formed differences between amplitudes are Gaussian-based discriminants. The conceptual representation of the proposed model is

$$\log(Amplitude) = \eta(Source, Path) + Bias + EventEffect + Noise, \quad (1)$$

where $\eta(Source, Path)$ is MDAC; *Bias* is a constant effect that is due to source only; *EventEffect* is a random effect that varies from event to event and represents model inadequacy from effects such as depth, focal mechanism, local material properties, and apparent stress variability; and *Noise* represents measurement and ambient noise, also a random variable.

The mathematical statistics formulation of Equation (1) is

$$Y_{ijk} = \eta_{ijk} + \mu_i + E_j + \varepsilon_{ijk}, \quad (2)$$

where Y_{ijk} is the log amplitude for source $i = \{0,1\}$, event $j = \{1, 2, \ldots, m_i\}$, and station $k = \{1, 2, \ldots, n_{ij}\}$. In other words, the source *i* event *j* amplitude observed by station *k* equals the sum of a known source/path effect (MDAC), a constant bias effect, a random event adjustment, and a noise effect particular to the source and event. Equation (2) is a *mixed effect* linear mode—see Searle (1971) for details.

The E_j are modeled as independent Gaussian random variables with mean zero and variance τ^2, whereas the $\varepsilon_{(ij)k}$ are modeled as independent Gaussian random variables with mean zero and variance σ^2. Furthermore, E_j and $\varepsilon_{(ij)k}$ are independent across all subscripts.

Statistical Properties of a Station-Averaged Amplitude

The statistical properties of the Y_{ijk} in Equation (2) are written as $\mathbf{Y} = \boldsymbol{\theta} + \boldsymbol{\Omega}$, where $\mathbf{Y} \sim MVN(\boldsymbol{\theta}, \boldsymbol{\Omega})$, where

$$\boldsymbol{\theta} = \begin{bmatrix} \mu_i + \eta_{j1} \\ \mu_i + \eta_{j2} \\ \vdots \\ \mu_i + \eta_{jn_{ij}} \end{bmatrix} \text{ and } \boldsymbol{\Omega} = \begin{bmatrix} \tau^2 + \sigma^2 & \tau^2 & \tau^2 & \cdots & \tau^2 \\ \tau^2 & \tau^2 + \sigma^2 & \tau^2 & \cdots & \tau^2 \\ \tau^2 & \tau^2 & \tau^2 + \sigma^2 & & \vdots \\ \vdots & & & \tau^2 + \sigma^2 & \tau^2 \\ \tau^2 & \cdots & \tau^2 & \tau^2 & \tau^2 + \sigma^2 \end{bmatrix}.$$

MDAC corrections applied to $\mathbf{Y}$ give $\mathbf{X} = \begin{bmatrix} Y_{ij1} - \eta_{j1} & Y_{ij2} - \eta_{j2} & \cdots & Y_{ijn_{ij}} - \eta_{jn_{ij}} \end{bmatrix}^T$, which is multivariate Gaussian with mean vector $\mathbf{1}\mu_i$ and covariance matrix $\boldsymbol{\Omega}$. The station-averaged amplitude, $\overline{\mathbf{X}}_{ij} = \mathbf{1}^T \mathbf{X}_{ij} / n_{ij}$, is Gaussian with mean μ_i and variance $\tau^2 + \sigma^2 / n_{ij}$.

Excluding the E_j term in the model in Equation (2) implies that η is unbiased and that the variance of $\overline{X}_{ij}$ is σ^2 / n_{ij} —the variance of $\overline{X}_{ij}$ becomes small as n_{ij} increases. Omitting E_j results in a model that is fundamentally inconsistent with physical basis because station averaging will not eliminate all noise corrupting a seismic source signal.

Model Properties

The expected value of the MDAC corrected amplitudes is $\mathrm{E}[X_{0jk}] = \mu_0$ for earthquakes and $\mathrm{E}[X_{1jk}] = \mu_1$ for explosions. The covariance matrix intuitively says that the variance of an amplitude is composed of model inadequacy and station noise. The correlation $\left(\tau^2 / \left(\tau^2 + \sigma^2\right)\right)$ between amplitudes implies that increased adjustment to η to fit data increases dependency between stations observing an event. Minimal adjustment to η is conceptually equivalent to the stations being incoherent, which in turn minimizes the variance of an amplitude through station averaging.

Discriminant Formulation

For this development, a discriminant is constructed from two different amplitudes (with different functions η and parameter values μ_i) that are statistically independent (uncorrelated). For specific regional phases, the discriminant equation can be represented with meaningful subscripts. For example, for a given event and source, the station average $\overline{P}_g$ is Gaussian with mean μ_{Pg} and variance ${\tau_{Pg}}^2 + {\sigma_{Pg}}^2 / n_{Pg}$, and the station average $\overline{L}_g$ is Gaussian with mean μ_{Lg} and variance ${\tau_{Lg}}^2 + {\sigma_{Lg}}^2 / n_{Lg}$. Note that if only stations observing a discriminant are used, then $n_{Pg} = n_{Lg}$; however, this constraint on discriminant construction is not necessary—using all available station amplitudes to construct a discriminant is theoretically sound if the MDAC correction is of good quality. The standard error of the P_g versus L_g discriminant is

$$SE_{\overline{P}g - \overline{L}g} = \sqrt{\tau_{Pg}^2 + \frac{\sigma_{Pg}^2}{n_{Pg}} + \tau_{Lg}^2 + \frac{\sigma_{Lg}^2}{n_{Lg}}}. \quad (3)$$

Standardizing observed discriminants relative to the explosion population mean ($\mu_{Pg} - \mu_{Lg}$) and adjusting for uncertainty gives

$$Z_{\overline{P}g - \overline{L}g} = \frac{\left(\overline{P}g - \overline{L}g\right) - \left(\mu_{\overline{P}g} - \mu_{\overline{L}g}\right)}{SE_{\overline{P}g - \overline{L}g}}. \quad (4)$$

The model in Equation (4) implies that $Z_{\overline{Pg}-\overline{Lg}}$ has different means for the explosion and earthquake populations and the same variance for both populations. Values of $Z_{\overline{Pg}-\overline{Lg}}$ below a decision threshold predict an earthquake as the source identification, otherwise an explosion is predicted.

CONCLUSIONS AND RECOMMENDATIONS

Analysis Example

The data used to illustrate the discriminant shown in Equation (4) are events at the NTS. Events were observed with combinations of four seismic stations: Kanab, Utah (KNB); Elko, Nevada (ELK); Landers, California (LAC); and Berkeley, California (CMB). MDAC amplitudes between 6 and 8 Hertz from these stations were averaged in the calculation of $Z_{\overline{Pg}-\overline{Lg}}$. The dataset consists of 56 earthquakes (EQ) and 159 explosions (EX), for a total of 215 events. Event magnitudes (Mw) ran between 2.6 and 7.1. The spatial distribution of events is given in Figures 1 and 2. Model performance is summarized in Table 1.

Table 1. Performance of the MDAC ratios for NTS events. Columns represent predictions by the discrimination method; rows are the true classifications.

	Predicted EX	Predicted EQ
EX	144	15
EQ	2	54

CONCLUSIONS AND RECOMMENDATIONS

The analysis demonstrates the performance of an MDAC regional discriminant derived from the model in Equation (2). The analysis also illustrates the sharp difference that is possible between model-based and empirical-based decision thresholds. An obvious but important observation is that the empirical-based threshold fits the tail of the observed data and is therefore strongly influenced by outlying calibration data. The model-based threshold uses the calibration data to fit model parameters that are more robust to calibration data. If solid theory is in place to support a model—e.g., Equation (2)—then a model-based decision threshold should prove to be more accurate in future event identification.

Regional amplitudes of varying or constant frequencies should be incorporated into statistically based discrimination frameworks if their underlying mathematical and probabilistic structure can be understood. The appropriate standard error to use for the regional MDAC amplitude ratios is one that incorporates both model inadequacy and ambient station noise. The random effects model presented above correctly leads to a standard error for station averaging with a lower bound that conforms to physical basis. The model also properly represents the correlation of station observed amplitudes when the theoretical amplitude correction is poor.

ACKNOWLEDGEMENTS

Rick Schult of the Air Force Research Laboratory has continually provided expertise, insight, and constructive comments regarding the development of discriminants. The authors also acknowledge Gordon Kraft of Quantum Technology Services, Inc., for his input toward discriminant formulation.

REFERENCES

Searle, S. (1971). *Linear Models.* New York: John Wiley & Sons, Inc.

Taylor, S. and H. Hartse (1998). A procedure for estimation of source and propagation amplitude corrections for regional seismic discriminants, *J. Geophy. Res.* 103: 2781–2789.

Taylor, S., A. Velasco, H. Hartse, W. Phillips, W. Walter, and A. Rodgers (2002). Amplitude corrections for regional seismic discriminants, *Pure App. Geophys.* 159: 623–650.

Walter, W. and S. Taylor (2002). A revised magnitude and distance amplitude correction (MDAC2) procedure for regional seismic discriminants: Theory and testing at NTS, Los Alamos National Laboratory report LA-UR-02-1008.

FIGURES

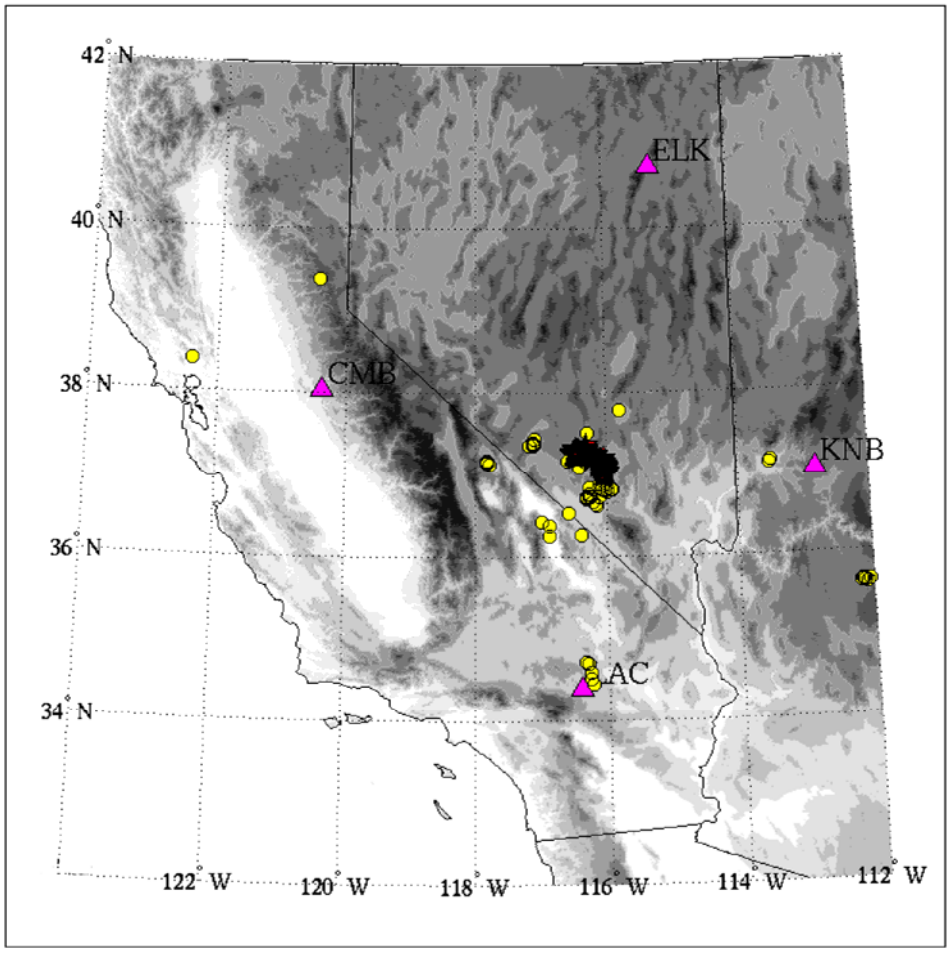


Figure 1. NTS events and stations used in the analysis example. Explosions are red stars, earthquakes are yellow circles, and stations are pink triangles.

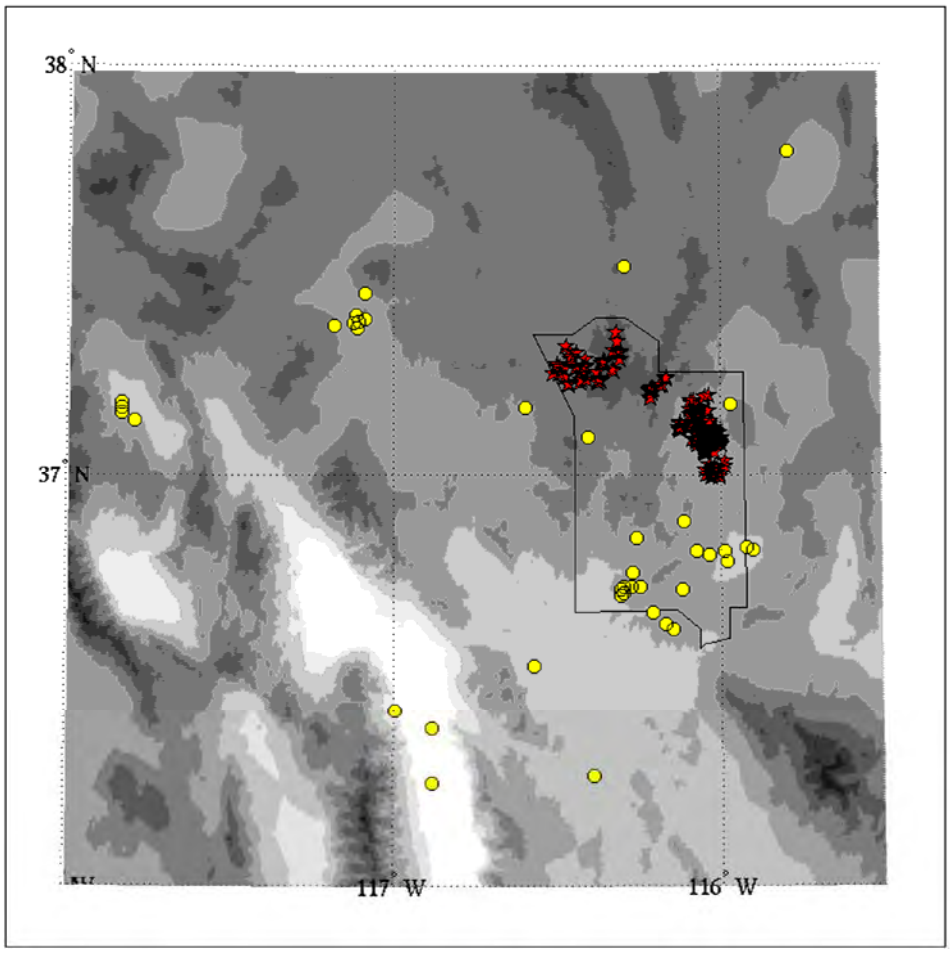


Figure 2. A closer view of NTS events used in the analysis example. Explosions are red stars and earthquakes are yellow circles.

GLOBAL GROUND TRUTH DATA SET WITH WAVEFORM AND IMPROVED ARRIVAL DATA

István Bondár[1], Ben Kohl[1], Eric Bergman[2], Keith McLaughlin[1], Hans Israelsson[1], Yu-Long Kung[1], Jeff Given[1], and Eric R. Engdahl[3]

Science Applications International Corporation[1], Global Seismological Services[2], and University of Colorado at Boulder[3]

Sponsored by Air Force Research Laboratory

Contract No. FA8718-04-C-0020

ABSTRACT

The main objective of this three-year research project is to produce a quality-controlled global GT0-5 event set, accompanied with waveform and groomed arrival time data sets. Our efforts are directed toward developing and refining methodologies for generating new ground-truth (GT) events through multiple-event location analysis.

To accomplish this goal, we have developed the hybrid HDC-RCA (hypocentroidal decomposition and reciprocal cluster analysis) methodology. The HDC analysis determines accurate event location patterns relative to a provisional cluster centroid using regional and teleseismic phases. The RCA analysis then determines the accurate location of the cluster centroid using local phases only. RCA accomplishes this by keeping the event and station patterns fixed and relocates the station centroid using the events as fictitious stations. Because both relative station and relative event patterns are fixed and multiple events are typically recorded at each station, solving for the cluster hypocentroid represents an overdetermined inversion problem that is robust with respect to strong local seismic-velocity biases.

We have extended our multiple-event location technique, RCA, to obtain unconstrained depth estimates for the hypocentroid of the event cluster. We have validated the methodology using synthetic and real event clusters. We performed a large-scale Monte Carlo experiment on a synthetic event cluster to develop applicability criteria for the HDC-RCA methodology. We sought local network geometries under which RCA produces GT5 events at a high confidence level. We found that if the combined secondary azimuthal gap (taking into account all event-station pairs entering the RCA inversion) is less than 180°, RCA recovers the true event centroid within 5 km at the 90% confidence level. Furthermore, if there are one or more stations within 30 km of the true cluster centroid, the hypocentroid (epicenter and depth of the cluster centroid) are both recovered within 5 km at the 95% confidence level. The hybrid HDC-RCA method may produce GT5 (epicenter and depth) event locations that are not produced by local or teleseismic network location methods alone.

We report new GT5 event locations (90% and 95% confidence) produced by the HDC-RCA methodology for event clusters from Romania, Honshu, South Africa, Hawaii, Mona Passage, Ethiopia, Southern Italy, Nepal, and Honduras.

OBJECTIVE

The objective of the research project is to produce new high-confidence GT events of GT5 from an updated EHB (Engdahl et al., 1998) bulletin on a global scale. In order to achieve this goal we have developed a novel hybrid method, the HDC-RCA analysis, which allows us to identify new GT events without the reliance on dense local networks or prior GT information.

RESEARCH ACCOMPLISHED

To generate new GT5 events we have developed the two-tier HDCA-RCA methodology. HDC (Jordan and Sverdrup, 1981; Engdahl et al., 2004) determines accurate event location patterns relative to a provisional hypocentroid using regional and teleseismic phases. RCA analysis (Bondár et al., 2005), using local phases only, determines the accurate location of the cluster centroid by keeping the event and station patterns fixed. Since regional and teleseismic data usually lack the resolution to resolve the full depth pattern in a cluster, event depths are typically fixed in the HDC analysis to a best educated guess, based on analysis of individual events with depth phases, waveform analyses, or prior local data. Fixing event depths to nominal values projects the depth errors into the origin times. We have extended the RCA algorithm so that it solves for the cluster hypocentroid (epicenter, depth, and origin time shift). We have also enabled RCA to use secondary phases (Sg, Sb) in the inversion process.

Multiple-event location techniques implicitly rely on the assumption that the events in a cluster and the stations used in the inversion are well-connected. To ensure strong cluster connectivity, we employ a graph theory approach. An event cluster can be viewed as an undirected graph, where the vertices are the events and stations, and the edges are the ray paths. An undirected graph is biconnected if at least two different paths exist between any two vertices (Orwant et al., 1999). Biconnectivity ensures that there are neither isolated vertices in the graph nor bridges whose removal would cause the graph to fall into disconnected pieces. Graph density, the ratio between the actual number of edges in the graph and the number of edges in the fully connected graph, offers a metric to characterize the cluster connectivity. To build a cluster for HDC analysis, we extract the largest biconnected graph from the initial EHB cluster for stations in the 3°–90° epicentral distance range. Similarly, for the RCA cluster we extract the largest biconnected graph from the HDC output for stations in the 0°–1.5° distance range.

Preliminary RCA Applicability Criteria

In order to develop applicability criteria for the RCA similar to those of Bondár et al (2004), which would indicate whether the combined HDC-RCA analysis will reliably produce GT5 events from a cluster, we have performed a Monte Carlo experiment on a synthetic cluster. To generate the synthetic cluster, we distributed Yucca Flat GT0 nuclear explosions along a provisional fault plane (Figure 1a), hence creating a synthetic cluster of events of GT0 accuracy in both location and depth, with hypocentroid depth of 15.4 km. The arrival times are generated as iasp91 (Kennett and Engdahl, 1991) predictions at local (Pg), regional (Pn), and teleseismic (P) stations. We added distance and azimuth dependent delays (Figure 1b) to the arrival times to imitate separate local, regional, and teleseismic biases. We then relocated the events with EvLoc, using Pn and P phases in the 3°–90° distance range and keeping the depth fixed, introducing a 12 km location bias. This constitutes the input synthetic bulletin for the RCA Monte Carlo experiment. Figure 1c shows the RCA station network. Note that Pg arrival times are generated for every event at every station, thus producing a fully connected RCA cluster. Furthermore, the Pg arrival time bias is roughly equivalent to ±5% velocity perturbation with respect to iasp91, stations being increasingly slow to the SW and increasingly fast to the NE.

In the course of the Monte Carlo experiment, we model the HDC depth estimation procedures by fixing the entire cluster to a provisional depth of 5, 10, 15, 20, or 25 km. Since this introduces a depth error, we adjust the origin times in order to project the depth differences between the assumed and true depths into origin time errors. We randomly select stations (5, 6, 7, 8) and events (10, 12, 14, 16) and perturb the biased Pg arrival times with random Gaussian noise, assuming 0.5 s standard deviation normal picking errors. We generate 500 realizations for each combination for a total of 40,000 realizations. For each realization, we perform an RCA analysis and generate various metrics to measure the quality of the results.

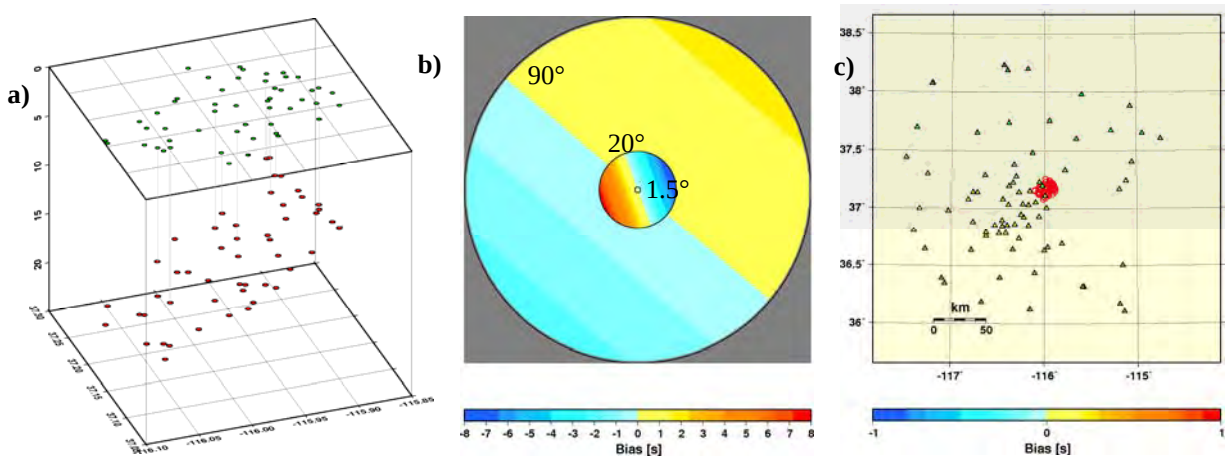


Figure 1. (a) Synthetic event cluster to validate RCA depth inversion applicability criteria. (b) Arrival time delays (biases) applied to Pg, Pn, and P iasp91 predictions. (c) RCA local network geometry. The biased Pg arrival times represent ±5% crustal velocity perturbations in a worst case scenario.

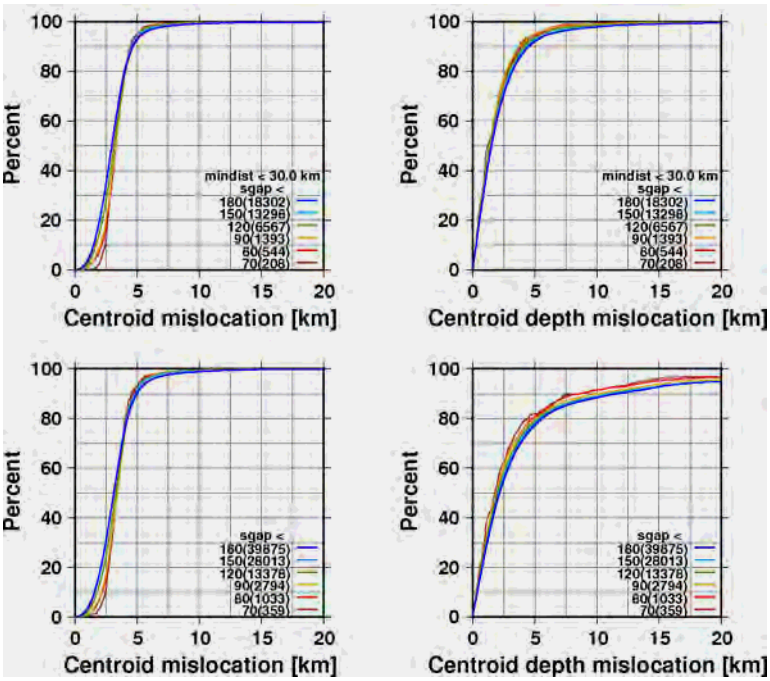


Figure 2. Cumulative distributions of centroid mislocation and centroid depth mislocation for combined secondary gaps less than a specific threshold (bottom) and with station(s) within 30 km from the cluster centroid (top). When there is a nearby station, both the epicenter and the depth of the cluster centroid are recovered with high accuracy.

We found that the combined secondary azimuthal gap, defined as the largest secondary azimuthal gap when considering the azimuths of all ray paths, provides a robust metric that predicts the quality of the RCA results. The lower panels in Figure 2 show the cumulative distributions of the centroid horizontal and depth mislocation for combined secondary gaps less than a specific threshold. The numbers in parentheses next to the combined secondary azimuthal gap threshold in the legend denote the corresponding number of realizations. The figure shows that we recover the true cluster centroid location within 5 km at the 90% confidence level when the combined secondary gap is less than 180°. However, this alone does not guarantee that the centroid depth is recovered with high accuracy and reliability. Not surprisingly, we need at least one station in the close vicinity of the cluster centroid to provide a constraint on the hypocentroid depth. This is illustrated in the upper panel of Figure 2. When there is at least one station within 30 km of the cluster centroid and the combined secondary gap is less than 180°, the epicenter of the cluster centroid is recovered within 5 km at the 95% confidence level, and the centroid depth is recovered within 5 km at the 90% confidence level. Hence, for a fully connected cluster, the above conditions provide GT5 applicability criteria for the cluster centroid, analogous to the GT5 criteria of Bondár et al. (2004) for single-event locations. The GT5 cluster centroid criteria are necessary (but not sufficient) conditions to generate GT5 events. Once the absolute location of the cluster centroid is pinned down with high accuracy, we promote events to the GT5 category if the semi-major axis of their combined absolute error ellipses (HDC+RCA), scaled to the 95% confidence level, is less than 5 km.

HDC-RCA Clusters

When we extract an event cluster from the EHB bulletin, we typically select a core set of clustered events that were recorded by both local (RCA) and regional/teleseismic (HDC) stations. We add regional/teleseismic-only events to the cluster to improve HDC performance. From this initial cluster we select a strongly connected graph of events and regional/teleseismic stations to facilitate robust HDC analysis. We then test for the RCA applicability criteria; if there is little hope of locating the cluster centroid with GT5 accuracy, we may skip the entire cluster and move on to the next cluster. Prior to HDC analysis, we establish the best depth estimates by waveform analysis or the analysis of individual events with depth phases and fix the event depths to the best depth estimates. The HDC analysis produces accurate relative locations and updates the phase identifications so that they are consistent with the fixed depth and ak135 (Kennett et al., 1995) predictions. HDC analysis may also remove observations (eventually entire events or stations) as outliers. From the HDC output cluster, we select a strongly connected graph of events and local stations for the RCA analysis and test again for the applicability criteria. If there are no stations within 30 km from the cluster centroid, we solve only for the horizontal shift of the cluster centroid by keeping the depths and origin times fixed to the HDC depth; otherwise, we solve for all model parameters (horizontal, vertical, and origin time shifts). We prefer to use local velocity models, especially for the depth inversion. We then shift the entire cluster to eliminate the HDC cluster centroid mislocation and identify GT5 events based on their combined absolute error ellipses (HDC+RCA), scaled to the 95% confidence level. Below we present some examples of HDC-RCA clusters.

Our first example is from the Welkom gold mines, South Africa. Figure 3a shows the RCA network geometry of 92 events and 8 stations. This is a very well connected cluster with a graph density of 0.53 and a combined secondary azimuthal gap of 66°. There are also two stations within 30 km of the cluster centroid. By using 553 Pb, Pn, Sb, and Sn phases, RCA shifted the HDC cluster west by 4.5 km (Figure 3b) and increased the hypocentroid depth from 7.5 km to 7.8 km. We promoted 84 events to GT5 level. In this cluster there are 3 EHB events that satisfy the Bondár et al. (2004) GT5 selection criteria for single-event locations, and their locations are consistent with the RCA results (Figure 3c). However, one might think that the 7.8 km hypocentroid depth is too deep for rockbursts. Hartnady (1990) and Richardson et al. (2005) note that natural seismicity does exist in the Kaapvaal craton, unrelated to mining activities. One of the events (1994/10/30, mb=5.7) in this cluster was studied in detail by Fan and Wallace (1995). Based on waveform inversion they concluded that the event was an earthquake with a source depth between 9 and 12 km. On the other hand, Bennett et al. (1996) identified this event as a rockburst, and Bowers (1997) reached the same conclusion, based also on waveform inversion, and put the event at 2.5 km depth. Given that the cluster most likely contains both earthquakes and rockbursts, the HDC-RCA cluster centroid depth is probably an acceptable compromise between the rockburst and earthquake populations. All of these published depth solutions fall within 5 km of the 7.8 km RCA hypocentroid depth.

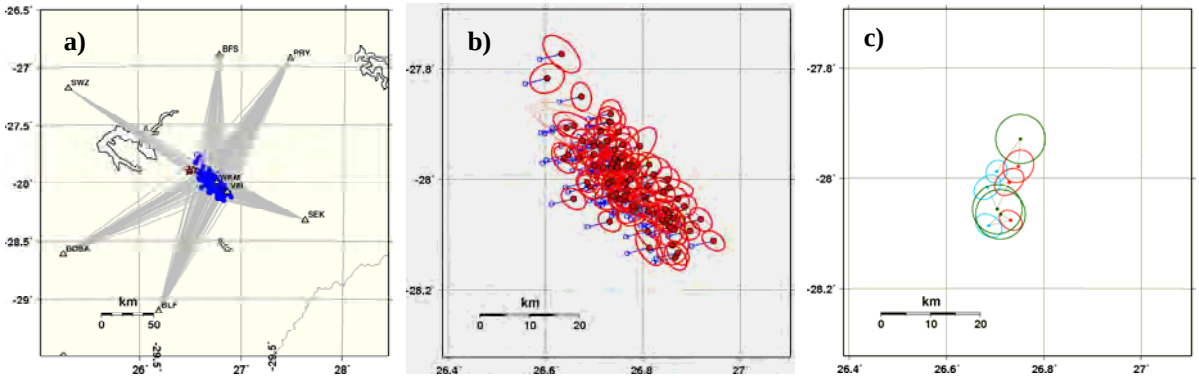


Figure 3. (a) RCA geometry for the Welkom, South Africa, cluster. Triangles denote stations; blue circles represent HDC solutions. (b) RCA shifts the HDC (blue) locations to RCA (red) locations. Eighty-four RCA absolute error ellipses plotted with thick red were promoted to GT5 level. (c) HDC (blue) and RCA (red) locations are consistent with three existing GT5 events (green).

Our next example (Figure 4) is from the south flank of Kilauea Volcano, Hawaii. The RCA cluster consists of 58 stations and 56 events, with a combined secondary gap of 12° and with 27 stations within 30 km of the cluster centroid. We used a local velocity model (Klein, 1981) for Pg and Sg travel times. In the HDC analysis, the event depths were fixed to prior local network solutions. Despite the very dense local network, only 22 events satisfy the original Bondár et al. (2004) criteria. RCA, however, promoted to GT5 status all 56 events, including the two offshore events near the underwater volcano, Loihi, off the coast of Hawaii and more than 20 km outside the local network.

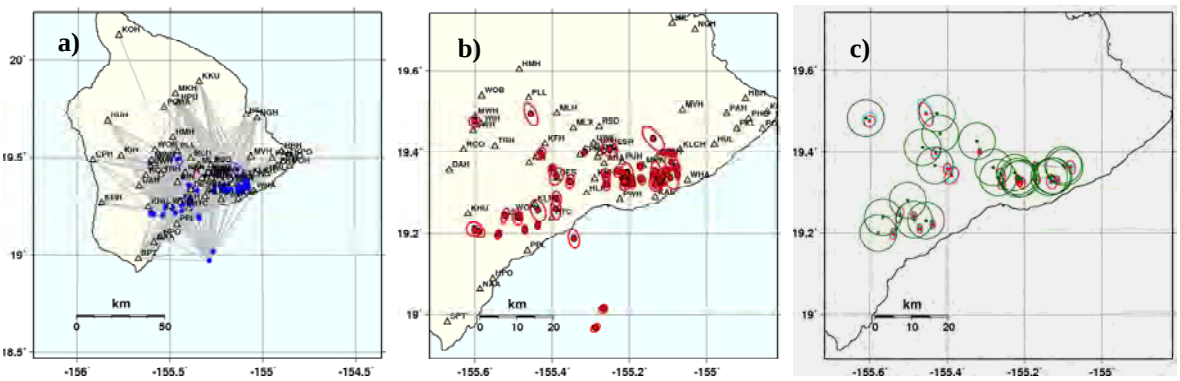


Figure 4. (a) RCA geometry for the Kilauea Volcano south flank, Hawaii cluster. Triangles denote stations; blue circles represent the HDC solutions. (b) RCA promoted all 56 events to GT5 category. (c) HDC (blue) and RCA (red) locations are consistent with 22 existing GT5 events (green).

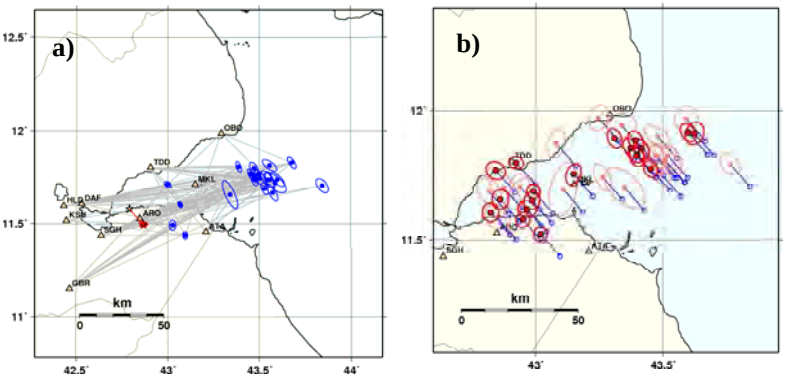


Figure 5. (a) RCA geometry for the Gulf of Tadjoura, Djibouti cluster. Triangles denote stations; blue circles represent the HDC solutions. (b) RCA shift between the HDC (blue) and RCA (red) locations. RCA absolute error ellipses plotted with thick red represent 19 events promoted to GT5 level.

Figure 5 shows an event cluster in the Gulf of Tadjoura, Djibouti. The cluster is located at the triple junction of the Gulf of Aden ridge and the Red Sea and East African rifts. Of the 40 HDC events, 21 events and 10 local stations were used to perform an RCA analysis. The combined secondary azimuthal gap is 126°, and there are two stations within 30 km of the cluster centroid. Again, we used local velocity model (Dugda and Nyblade, 2006) predictions for 115 Pg and Sg phases. RCA shifted the cluster 12.5 km NW and increased the cluster centroid depth from the HDC best estimate 10 km to 12.6 km. We promoted 19 events to the GT5 category.

As we already noted, we can resolve the hypocentroid depth with high confidence only if there are stations in the close vicinity of the cluster centroid. The choice of the local velocity model used in the inversion also plays some role. Figure 6 compares the local velocity models for several clusters to the iasp91 global 1D velocity model. For the clusters in Vrancea, Romania, and Taiwan, the iasp91 depth solutions were in quite good agreement with those obtained from local velocity models (Ma et al., 2001) for Taiwan and a 1D velocity model derived from the 3D tomographic model (Landes et al., 2004) by M. Popa. On the other hand, iasp91 produced non-sensical depth for the Gulf of Tadjoura cluster. Figure 6 indicates that the local velocity model derived from receiver function analysis for the Gulf of Tadjoura (Dugda and Nyblade, 2006) deviates the most from iasp91. Hence, depth is only as good as the local velocity model, and the proper choice of local velocity models is important for reliable depth determination.

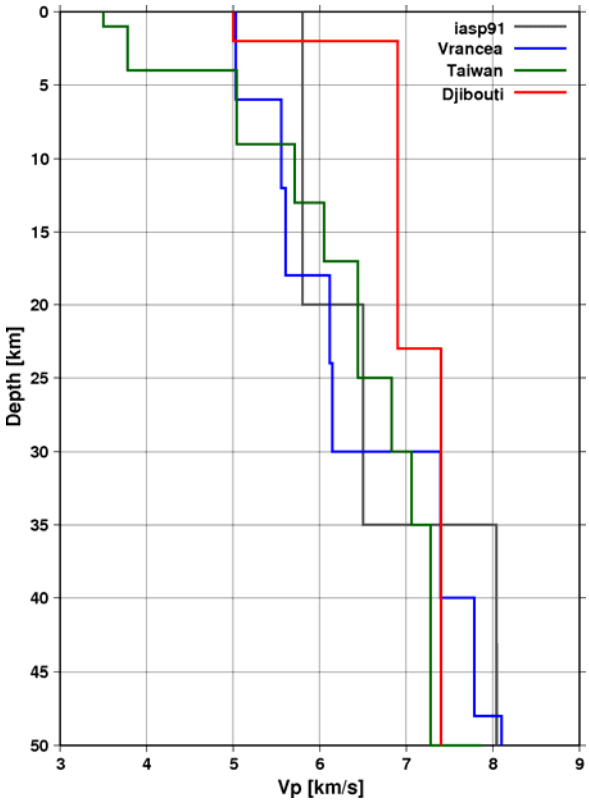


Figure 6. Local velocity models compared to iasp91.

It should be noted that failing the RCA applicability criteria does not mean that the locations are wrong; it only means that the cluster centroid cannot be recovered with GT5 accuracy at a high confidence level. This is illustrated in Figure 7. Figure 7 (a-b) shows the RCA geometry for an event cluster in the Mona Passage. All stations are located on Puerto Rico, and all the events occurred offshore, representing a combined secondary azimuthal gap of 275°. Therefore, even though some of the absolute error ellipses are small, we cannot promote any events to the GT5 category because we cannot determine the cluster centroid location as GT5 with high confidence. Figure 7 (c-d) shows another example, this one for an event cluster in the West Azores. The stations are located on São Miguel Island, and all events are offshore. The combined secondary azimuthal gap in this case is 355°, representing the worst geometry we have encountered so far. Nevertheless, the locations are not inconsistent with the tectonic settings, indicated by the bathymetry and the plate boundaries.

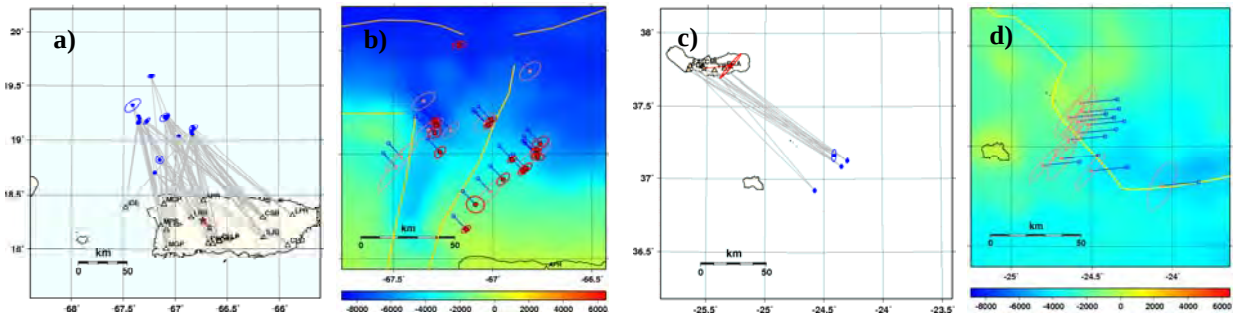


Figure 7. (a) RCA geometry for the Mona Passage cluster (Puerto Rico). (b) HDC (blue) and RCA (red) locations plotted over the bathymetry map. Yellow lines show the Mona Passage transform faults and the Puerto Rico trough. (c) RCA network geometry for the West Azores cluster. (d) HDC (blue) and RCA (red) locations plotted over the bathymetry map. The yellow line shows the plate boundary between Europe and Africa. The HDC-RCA locations, while of unknown confidence, are consistent with the tectonic settings.

The table below summarizes the clusters we have processed so far, ordered by their combined secondary azimuthal gaps. For those clusters that passed the RCA applicability criteria, we identify a significant number of GT5 events at a 90% or 95% confidence level.

Cluster	Sgap	Centroid confidence	GT5
Kileaua, Hawaii	12	95%, with depth constraint	56
Picerno, S. Italy	20	95%, with depth constraint	58
Vrancea, Romania	29	95%, with depth constraint	23
Chi-Chi, Taiwan	46	95%, with depth constraint	25
Welkom, S. Africa	66	95%, with depth constraint	84
Owase, W. Honshu	74	95%, with depth constraint	14
Gulf of Tadjoura, Djibouti	126	95%, with depth constraint	19
Gulf of Fonseca, Honduras	132	90%, no depth constraint	9
Galwa, W. Nepal	203	Stable solution, unknown confidence	None
Mona Passage, Puerto Rico	275	Stable solution, unknown confidence	None
São Miguel, Azores	355	Stable solution, unknown confidence	None

CONCLUSIONS AND RECOMMENDATIONS

We have extended the RCA algorithm to solve for all model parameters of the cluster hypocentroid (horizontal, vertical, and origin time shifts). Secondary phases (Sg, Sb) are also included in the RCA inversion. We use graph theory methods to ensure strong connectivity between stations and events in a cluster.

We have developed preliminary RCA applicability criteria for a fully connected cluster. The criteria are analogous to the single-event location GT5 selection criteria of Bondár et al (2004), but in this case they refer to the cluster centroid. According to the criteria,

- the cluster centroid epicenter is $GT5_{90\%}$ if the combined secondary azimuthal gap is less than 180°;
- the cluster centroid epicenter is $GT5_{95\%}$ and the centroid depth $GT5_{90\%}$ if the combined secondary azimuthal gap is less than 180° and there are stations within 30 km of the cluster centroid epicenter.

We have pointed out the importance of local velocity models to obtain reliable depth estimates. We will further refine the above applicability criteria for more realistic, partially connected clusters (i.e., when each station records only a subset of events).

We have begun the systematic processing of HDC-RCA clusters extracted from an updated EHB (Engdahl et al., 1998) bulletin and demonstrated that once the RCA applicability criteria are met, we are able to produce larger numbers of high-confidence GT5 events that would not result from any previous analysis.

ACKNOWLEDGEMENT

We thank Michaela Popa (National Institute for Earth Physics, Bucharest, Romania) for providing us with a 1D velocity model for the Vrancea region.

REFERENCES

Bennett, T. J., M. E. Marshall, B. W. Barker, and J. R. Murphy (1996). Use of seismic signal characteristics to identify several recent rockbursts, *Seism. Res. Let.* 67: 32.

Bondár, I., S. C. Myers, E. R. Engdahl, and E. A. Bergman (2004). Epicentre accuracy based on seismic network criteria, *Geophys. J. Int.* 156: 1–14, doi: 10.1046/j.1365-246X.2004.02070.x.

Bondár, I., B. Kohl, E. Bergman, K. McLaughlin, H. Israelsson, Y-L. Kung, P. Piraino, and E. R. Engdahl (2005). Global ground truth data set with waveform and improved arrival data, in *Proceedings of the 27th Seismic Research Review: Trends in Nuclear Explosion Monitoring*, LA-UR-05-6407, Vol. 1, pp. 289–298.

Bowers, D. (1997). The October 30, 1994, seismic disturbance in South Africa: Earthquake or large rockburst?, *J. Geophys. Res*. 102: 9843–9857.

Dugda, M. T. and A. A. Nyblade (2006). New constraints on crustal structure in eastern Afar from the analysis of receiver functions and surface dispersion in Djibouti, in *The Afar Volcanic Province within the East African Rift System*, Yirgu, G., C. J. Ebinger and P. K. H. Maguire (Eds.), London: Geological Society, Special Publications, Vol. 259, pp. 239–251.

Engdahl, E. R., E. A. Bergman, S. C. Myers, and F. Ryall (2004). Improved ground truth in Southern Asia using in-country data, analyst waveform review and advanced algorithms, in *Proceedings of the 26th Seismic Research Review: Trends in Nuclear Explosion Monitoring*, LA-UR-04-5801, Vol. 1, pp. 257–266.

Engdahl, E. R., R. D. van der Hilst, and R. P. Buland (1998). Global teleseismic earthquake relocation with improved travel times and procedures for depth determination, *Bull. Seism. Soc. Am.* 88: 722–743.

Fan, G. and T. Wallace (1995). Focal mechanism of a recent event in South Africa: A study using a sparse very broadband network, *Seism. Res. Let.* 66: 5, 13–18.

Hartnady, C. J. H. (1990). Seismicity and plate boundary evolution in southeastern Africa, *S. Afr. J. Geol*. 93: 473–484.

Jordan, T. H. and K. A. Sverdrup (1981). Teleseismic location techniques and their application to earthquake clusters in the south-central Pacific, *Bull. Seism. Soc. Am.* 71: 1105–1130.

Kennett, B. L. N. and E. R. Engdahl (1991). Travel times for global earthquake location and phase identification, *Geophys. J. Int*. 105: 429–465.

Kennett, B. L. N., E. R. Engdahl, and R. P. Buland (1995). Constraints on seismic velocities in the Earth from travel times, *Geophys. J. Int*. 122: 108–124.

Klein, F. W. (1981). A linear gradient crustal model for south Hawaii, *Bull. Seism. Soc. Am.* 71: 1503–1510.

Landes, M., W. Fielitz, F. Hauser, M. Popa, and CALIXTO Group (2004). 3-D upper crustal tomographic structure across the Vrancea seismic zone, Romania, *Tectonophysics*, 382: 85–102.

Ma, K-F., J. Mori, S-J. Lee, and S. B. Yu (2001). Spatial and temporal distribution of slip for the 1999 Chi-Chi, Taiwan, earthquake, *Bull. Seism. Soc. Am.* 91: 1069–1087.

Orwant, J., J. Hietaniemi, and J. Macdonald (1999). *Mastering Algorithms with Perl*. Sebastopol: O'Reilly & Associates, Inc.

Richardson, E. B. A. A. Nyblade, W. R. Walter, K. Mayeda, and L. Lowe (2005). Seismic source characterization and energy partitioning from in-mine and regional broadband data in South Africa, in *Proceedings of the 27th Seismic Research Review: Trends in Nuclear Explosion Monitoring*, LA-UR-05-6407, Vol. 1, pp. 622–631.

IMPROVED EVENT LOCATION UNCERTAINTY ESTIMATES

István Bondár[1], Keith McLaughlin[1], and Hans Israelsson[1]

[1]Science Applications International Corporation

Sponsored by Air Force Research Laboratory

Contract No. FA8718-05-C-0018

ABSTRACT

While many recent studies aimed to reduce location bias by introducing improved travel-time corrections, less effort was devoted to the complete estimation of location uncertainty, despite the fact that formal error ellipses are often overly optimistic. Since most location algorithms assume that the observations are independent, correlated systematic errors that are due to similar ray paths inevitably result in underestimated location uncertainties. Furthermore, the tails of real seismic data distributions are heavier than Gaussian. The main objectives of this project are to develop, test, and validate methodologies to estimate location uncertainties in the presence of correlated, systematic, and non-Gaussian errors. Particular attention is paid to robust and transportable models for a travel-time covariance matrix.

To address correlated errors, we estimate the spatial correlation structure in arrival-time data using variogram models. We developed a methodology based on copula theory to derive robust, data-driven variogram models. For validation purposes, we use GT0-2 event clusters. These include the Nevada, Lop Nor, Semipalatinsk, and Novaya Zemlya test sites, as well as the Azgir Peaceful Nuclear Explosions and the Lubin, Poland, mine-related events. Using ground-truth (GT) clusters allows us to calculate “ground truth” residuals with respect to the GT locations for a specific velocity model. We show the improvements in variogram estimates when using global 3D models instead of the iasp91 model. The proper choice of the underlying velocity model is especially important for regional phases.

To address issues embodied by real data distributions, we performed fully controlled experiments using known high signal-to-noise ratio (SNR) waveforms, scaled down to several magnitude levels and embedded in clean noise to derive models of measurement errors. We model these measurement errors as a series of generalized extreme value distributions whose parameters (location, scale, and shape) depend on the measured SNR. This allows us to model the increasing picking error bias and the increasingly heavier tails of the residual distributions with decreasing SNR.

We have incorporated the full covariance matrix estimate in a linearized location algorithm. We show that by taking into account the correlated error structure with a robust transportable station-station correlation model, we achieve 90% coverage (i.e., the 90% error ellipse covers the true location 90% of the time), for sparse, unbalanced networks. Furthermore, the coverage statistics do not deteriorate with an increasing number of stations. Future work will incorporate SNR-dependent, non-Gaussian arrival-time measurement errors.

OBJECTIVES

The objectives of this project are to develop methodologies to estimate location uncertainties in the presence of correlated, systematic model errors and to characterize measurement errors as a function of signal parameters such as phase and SNR. The improved understanding of the complete error budget described by the full covariance matrix is incorporated into a linearized location algorithm, leading to more robust estimates of location uncertainty. The ultimate goal of this project is to develop transportable error models that will provide reliable location uncertainty estimates for small events recorded only by a few stations.

RESEARCH ACCOMPLISHED

The motivation for this project is the observation that location uncertainty estimates are often underestimated, that is, the error ellipses scaled to the 90% confidence level do not contain 90% of the true locations. While most recent location calibration studies focused on producing improved travel-time predictions to reduce location bias, less effort was devoted to obtaining reliable formal error ellipses. Linearized location algorithms typically rely on the assumption that the observations are independent and the residuals are Gaussian distributed. Unfortunately, these two assumptions are almost always violated. Many researchers have pointed out (e.g., Buland, 1986; Anderson, 1982) that the distribution of measurement errors is non-Gaussian and better described by non-zero mean, skewed, heavy-tailed distributions. Furthermore, station distributions are far from uniform, and observations are not independent. Closely spaced stations sample similar ray paths and thus introduce correlated systematic errors. This redundancy in the observations reduces the effective number of degrees of freedom, thus ignoring the correlated structure inevitably results in underestimated location uncertainty estimates.

In this project we focus on the treatment of correlated errors combined with non-Gaussian, non-zero-mean, heavy-tailed, skewed distributions of reading errors. Figure 1 illustrates our research strategy. Both the measurement and model errors are described by their covariance matrices, where the full data covariance matrix (C_D) is represented by the sum of the reading error (C_R) and network (C_N) covariance matrices. The network covariance matrix describes the correlated error structure and is estimated by variogram analyses. The reading errors are modeled by a general extreme value distribution, with parameters slowly increasing with decreasing SNR. The full data covariance matrix is incorporated in a linearized inversion scheme. Because of the non-Gaussian error distributions, the linearized inversion provides only an approximation of the solution; we will develop a hypothesis test to justify the validity of the "linearized" estimates.

<table>
<tr><td>Measurement error</td><td>Model error</td><td>Measurement error</td><td>Model error</td><td>Measurement error</td><td>Model error</td><td></td></tr>
<tr><td>Gaussian

IID observations</td><td>Uncorrelated

IID observations</td><td>Gaussian

IID observations</td><td>Correlated

Station-station variogram models</td><td>Non-Gaussian

SNR-dependent bias and variance</td><td>Correlated

Station-station variogram models</td><td></td></tr>
<tr><td colspan="2">Linearized inversion (diagonal covariance matrix)
BASELINE</td><td colspan="2">Linearized inversion with correlated errors
(full covariance matrix)</td><td colspan="2">Approximated by linearized inversion with correlated errors
(full covariance matrix)</td><td>Copula-based hypothesis test for the validity of linear approach</td></tr>
</table>

Figure 1. Progress and strategy of research. Gray indicates the current state of the art linearized location algorithm. Validation test results are presented in this paper for the green stage (recent progress); yellow and orange represent planned future development.

All the methodologies developed in the course of this project are tested and validated using GT event clusters, including GT0-2 underground nuclear explosions from Yucca Flat and Pahute Mesa, Balapan and Degelen mountains, Novaya Zemlya, Azgir, and Lop Nor, as well as mining explosions from the Lubin mines.

Network Covariance Matrix

The network covariance matrix accounts for the spatially correlated travel-time structure that is due to similar ray paths. We use variogram analysis to estimate the correlation structure in the data. In order to obtain robust variogram estimates, we use an entire GT event cluster. The variogram in geostatistical analysis is defined by the equation

$$\gamma(\mathrm{h}) = \left\langle \left(\delta\mathrm{t}(\Delta) - \delta\mathrm{t}(\Delta+\mathrm{h})\right)^2 \right\rangle = \sigma^2_{\mathrm{sill}} - \mathrm{Corr}(\mathrm{h})\sigma^2_{\mathrm{sill}} = \sigma^2_{\mathrm{sill}} - \mathrm{Cov}(\mathrm{h}), \quad (1)$$

where σ^2_{sill} denotes the background variance, $\delta t(\Delta)$ and $\delta t(\Delta + h)$ are the GT residuals (residuals with respect to the GT location, using a specific Earth model) at station pairs of common events, and h is the station separation. We employ copula formalism (Nelsen, 1999; Frees and Valdez, 1998; Genest and Rivest, 1993) to determine robust variogram models. A copula couples marginal distributions to form the joint probability distribution: $H(x,y) = C(F(x), G(y))$. In other words, the copula describes the joint distribution of the order statistics $u = F(h)$ and $\mathrm{v} = \mathrm{G}\left(\left(\delta\mathrm{t}(\Delta) - \delta\mathrm{t}(\Delta+\mathrm{h})\right)^2\right)$. We have evaluated a number of copulas and found that the Clayton copula, defined as $\mathrm{C}(\mathrm{u},\mathrm{v}) = \left(\mathrm{u}^{-\alpha} + \mathrm{v}^{-\alpha} - 1\right)^{-1/\alpha}$, $\alpha \in (0,\infty)$, provides the best fit to the data (Bondár et al, 2005). We define the robust variogram model as the median regression curve of the residual difference squares for station pairs of common events with respect to station separation. Using the copula formalism, the median regression curve simply becomes the solution of the equation

$$\mathrm{C}(\mathrm{v}\,|\,\mathrm{u}) = \frac{\partial \mathrm{C}(\mathrm{u},\mathrm{v})}{\partial \mathrm{u}} = 0.5, \text{ which yields } \gamma(\mathrm{h}) = \mathrm{G}^{-1}\left(\left[1 + \mathrm{u}^{-\alpha}\left(0.5^{-\alpha/(\alpha+1)} - 1\right)\right]^{-1/\alpha}\right), \mathrm{u} \in [0,1]. \quad (2)$$

Thus, the copula formalism offers a fully data-driven approach to derive robust, monotonically increasing variogram models that are free from Gaussian assumptions and provide analytic expressions parameterized by the order statistics. Having derived a variogram model, the estimates for the elements of the network covariance matrix are

$$\mathrm{C_N}(\mathrm{i},\mathrm{j}) = \sigma^2_{\mathrm{sill}} - \gamma\left(\Delta(\mathrm{sta_i},\mathrm{sta_j})\right). \quad (3)$$

Note that the isotropic variogram model defined by Eq. (1) does not account for azimuthal variations in the correlation structure. Hence, the proper choice of the underlying velocity model to calculate residuals becomes important, especially for regional phases. Figure 2 shows the Pn variograms obtained for Yucca Flat, Azgir, and Lop Nor GT event clusters when using iasp91 (Kennett and Engdahl, 1991) predictions to calculate GT residuals. The variance of the residuals, indicated by the binned median (blue line), increases significantly at far regional distances, where stations from different tectonic provinces are mixed together. This is poorly modeled by the isotropic variogram model, shown by the red line.

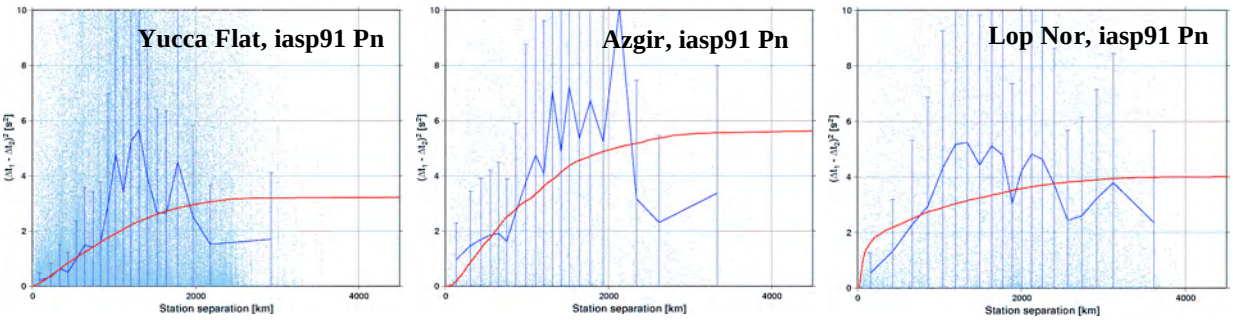


Figure 2. Pn variograms for three GT event clusters using iasp91 predictions. The blue lines represent the median of every 5 percentiles; the red lines indicate the copula variogram models. Because of the unmodeled velocity structure by the iasp91 model, the isotropic variogram model provides a poor approximation of the correlation structure.

To remedy these shortcomings, we recalculate the GT residuals using the global upper-mantle CUB2 model (Shapiro and Ritzwoller, 2004). The CUB2 model was extensively validated in Eurasia (Ritzwoller et al., 2003; Yang et al., 2004), but here we show an example for Pn observations from Yucca Flat events. Figure 3 shows the Pn travel-time correction surface relative to iasp91 predictions and the comparison of the iasp91 and CUB2 GT residuals as a function of epicentral distance. The CUB2 residuals are closer to zero mean than the iasp91 ones, indicating that the CUB2 significantly reduces the path effects that were left unmodeled by iasp91.

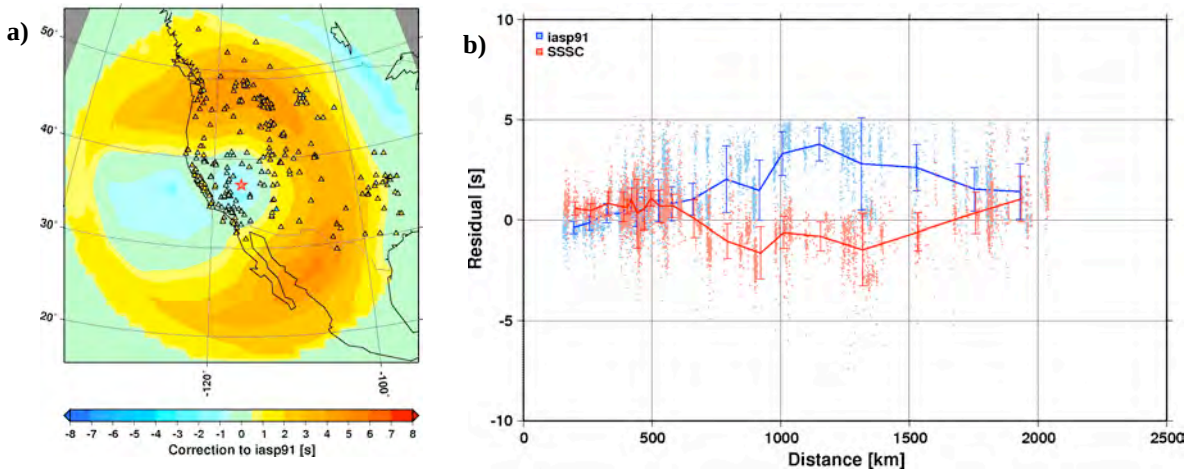


Figure 3. (a) CUB2 Pn travel-time correction surface to iasp91 centered on Yucca Flat (star). The 289 stations with Pn readings are shown as triangles. (b) GT residuals using iasp91 (blue) and CUB2 (red) as a function of epicentral distance.

Figure 4 shows the Pn variograms for the same event clusters as above, but now using the CUB2 predictions. The isotropic variogram models not only fit the observations better but also reflect a 50%–60% variance reduction typically achieved by the CUB2 model over iasp91.

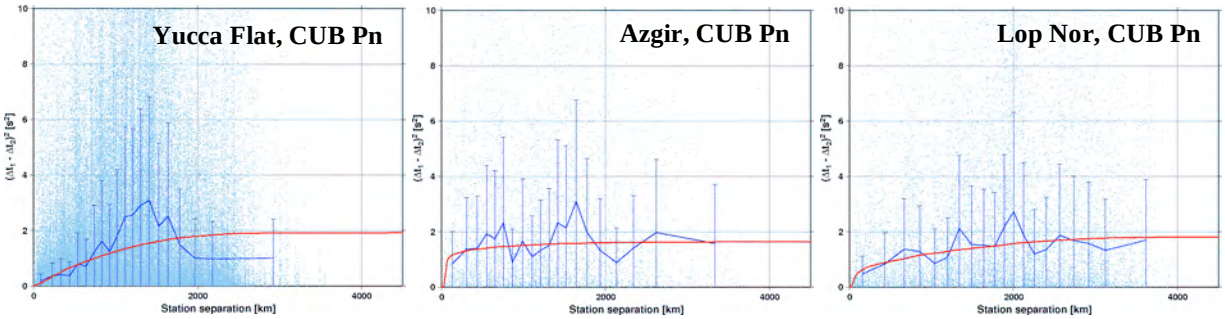


Figure 4. Pn variograms for three GT event clusters using CUB2. The blue lines represent the median of every 5 percentiles, the red lines indicate the copula variogram models. Using a calibrated Earth model, the isotropic variogram models provide acceptable descriptions of the correlation structures.

Figure 5 shows the comparison of the Pn variogram models derived for the various GT event clusters when using iasp91 or CUB2 travel-time predictions. The variance reduction provided by the calibrated CUB2 predictions is reflected in the reduced and remarkably consistent background variance (sill).

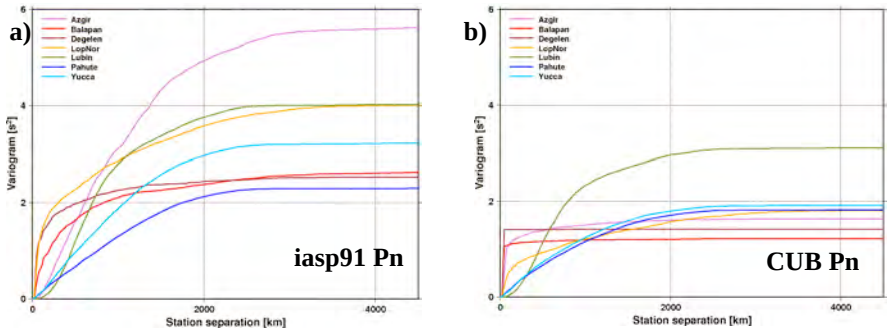


Figure 5. Pn variogram models for GT event clusters using (a) iasp91 and (b) CUB2 predictions. The CUB2 model produces much more consistent variograms, with reduced background variance (sill).

Modified Location Algorithm

Standard linearized location algorithms assume independent Gaussian errors and solve the inversion problem by an iterative, weighted least-squares algorithm by minimizing the expression $(d - Gm)^T C_R^{-1} (d - Gm)$, which is equivalent to solving the equation $WGm = Wd$, where G is the (NxM) design matrix containing the travel time derivatives for an event-station path, m is the ($Mx1$) model adjustment vector $[\Delta T, \Delta x, \Delta y, \Delta z]^T$, d is the ($Nx1$) vector of time residuals, and $W = C_R^{-1/2}$ is the diagonal (NxN) weight matrix. The $G_W m = d_W$ equation is often solved by singular value decomposition, which yields $G_W^{-1} = V_W \Lambda_W^{-1} U_W^T$ and thus the model adjustment of $m_{est} = G_W^{-1} d_W$. At each iteration the model vector is adjusted such that $m_{j+1} = m_j + m_{est}$. Once a convergent solution is obtained, the location uncertainty is defined by the *a posteriori* model covariance matrix, $C_M = G^{-1} C_R G^{-1^T} = V_W \Lambda_W^{-2} V_W^T$, which is typically scaled to the 90% confidence level. This linearized location algorithm constitutes our baseline, against which we measure improvements in location uncertainty estimates.

In the presence of correlated systematic errors, the data covariance matrix is no longer diagonal. Our modified linearized location algorithm seeks a transformed set of equations $WGm = Wd$, in which the data covariance matrix is diagonal. To ensure this, we solve the inversion problem in the eigen coordinate system in which the transformed observations are independent. The singular value decomposition of the full data covariance matrix is written as $C_D = U_D \Lambda_D V_D^T$, where Λ_D is the diagonal matrix of eigenvalues and the columns of U_D contain the eigenvectors of C_D. We keep the first p largest eigenvalues from the cumulative eigenvalue spectrum such that 95% of the total variance is explained: $\sum_j^p \lambda_j \Big/ \sum_i^N \lambda_i \geq 0.95$. We then define p as the effective number of degrees of freedom of the data, with an N-p dimension null space. Note that the 95% total variance level is somewhat arbitrary but a conservative and workable choice. Let $C_D = BB^T$, with $B = U_p \Lambda_p^{1/2}$, then the projection matrix $W = B^{-1} = \Lambda_p^{-1/2} U_p^T$ orthogonalizes the data set and projects redundant observations into the null space. After applying the projections $G_W = \Lambda_p^{-1/2} U_p^T G$ and $d_W = \Lambda_p^{-1/2} U_p^T d$, the formalism remains the same as in the baseline algorithm, but now d_W represents linear combinations of the observed residuals, the "eigen residuals."

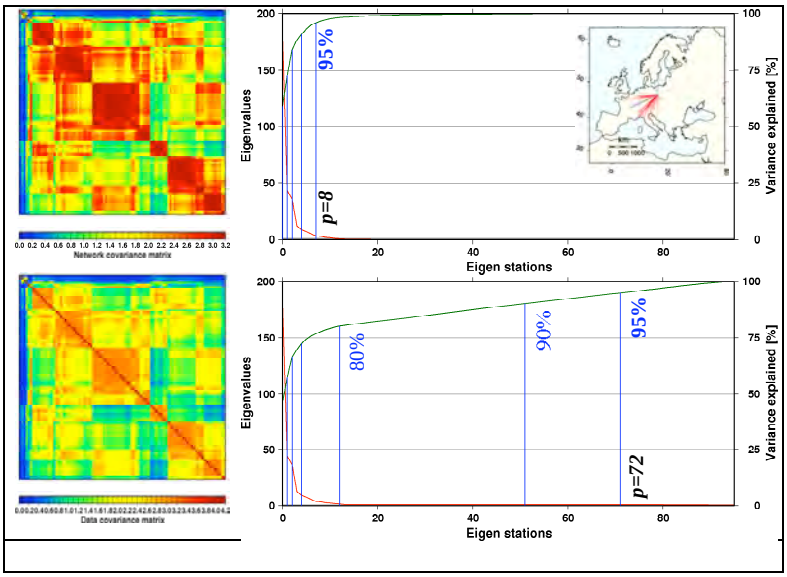


Figure 6. Upper panel: Network covariance matrix for a Lubin rockburst and its corresponding eigenvalue spectrum (red line). The green line shows the cumulative sum of eigenvalues as a percentage of the total sum. Only 8 eigenvalues are needed to explain 95% of the total variance. Bottom panel: Full data covariance matrix and its eigenvalue spectrum. Random picking errors blur the correlation structure and reduce the data redundancy.

The process is illustrated for a Lubin, Poland, event that occurred on May 26, 1995. Pn was reported at 96 stations, representing a dense but rather unbalanced network, as shown in the Figure 6 inset. The upper panel of Figure 6 shows the network covariance matrix and its corresponding cumulative eigenvalue spectrum. The network covariance matrix has been arranged by its nearest-neighbor ordering of stations, and it exhibits a quasi–block-diagonal structure. Because many observations are strongly correlated, the first 8 largest eigenvalues explain 95% of the total covariance. In other words, 92% of the data carry redundant information. When the measurement (picking) error covariance matrix (assuming uniform, 0.5 s reading errors) is added to the network covariance matrix (lower panel), the reading errors weaken the correlation strength but leave the correlation pattern unchanged. Because of this "blurred" correlation structure, more eigenvalues are needed to explain 95% of the cumulative variance.

In general, when the picks suffer from large measurement errors, the correlation structure is blurred by the random noise of picking errors. However, when the onsets are picked very accurately, the correlation structure becomes very important for obtaining reliable location uncertainty estimates. Figure 7 shows location results with the assumption of independent observations compared with those accounting for correlated errors. When the correlation structure is accounted for, not only does the error ellipse cover the GT location but the mislocation is also reduced from 15.6 km to 5.5 km.

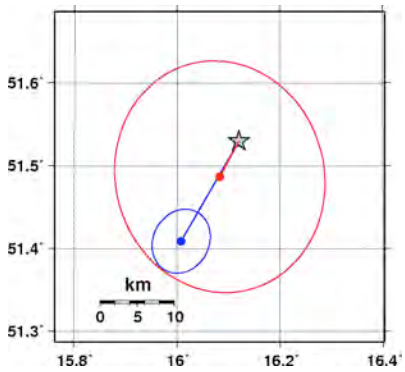


Figure 7. Relocation and 90% uncertainties of a Lubin GT1 event (star) using independence assumption (blue) and accounting for correlated errors (red).

Validation Tests

To validate the improved location uncertainty estimates that are due to the full data covariance matrix, we carried out two experiments using a set of events from each GT event cluster. In each experiment we located the events by both the baseline (independent error assumption) and the modified (correlated errors) location algorithms. We assume uniform, 0.5 s standard deviation measurement errors. For Pn we use the CUB2 travel-time model and construct the network covariance matrices from the variogram models obtained with CUB2 predictions. For teleseismic P we use iasp91 travel-time predictions.

The first experiment is designed to measure the robustness of the location uncertainty estimates against increasing levels of data redundancy. We locate events with an increasing number of stations of optimal azimuthal coverage and measure the mislocation, the area of the 90% error ellipse, and the GT coverage (whether the error ellipse contains the GT location). Figure 8 summarizes these results. When the correlated errors are accounted for, the improved relative weighting scheme reduces location errors. Since the inversion is performed in the eigensystem, redundant data are projected out and can no longer conspire to increase mislocation. The remaining mislocation represents the bias introduced by imperfect travel-time predictions. Furthermore, as the information content carried by the network is exhausted, the size of the 90% error ellipse stabilizes, while maintaining GT coverage. Thus, incorporating the correlated data structure in the location algorithm provides robust location uncertainty estimates unaffected by an increasing degree of redundant information.

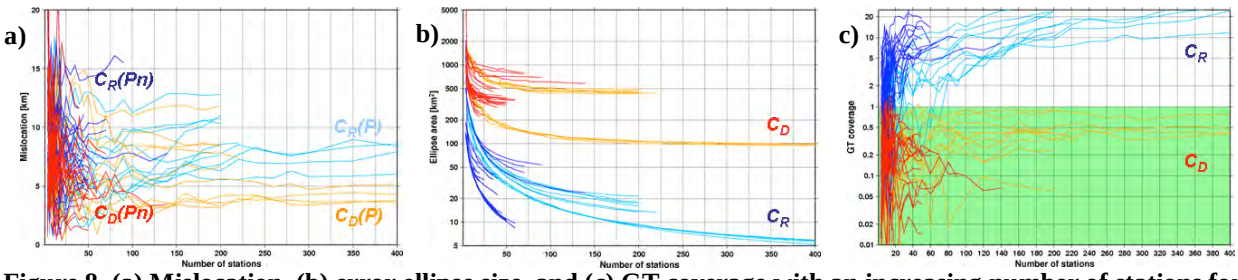


Figure 8. (a) Mislocation, (b) error ellipse size, and (c) GT coverage with an increasing number of stations for an optimal network. Baseline location algorithm (independent error assumption) results are shown in blue; modified location algorithm (correlated errors) results are shown in red.

The second experiment is designed to measure the trustworthiness of the location uncertainty estimates for suboptimal networks. We locate events with randomly selected networks of 5, 8, 10, 20, and 50 stations (1000 realizations each) and measure the distribution of the coverage parameter (normalized distance inside vs outside the 90% ellipse). Note that under Gaussian assumptions, the coverage parameter follows a χ^2 distribution with 2 degrees of freedom. The actual GT coverage is the percentile value, where the coverage parameter equals to one. For honest 90% confidence error ellipses, this should obviously occur at the 90th percentile. Figure 9 shows the results for sparse and dense networks. While the assumption of independent observations produces abysmal coverage, taking into account the correlated error structure maintains 90% coverage for sparse, unbalanced networks. For dense networks, the coverage falls somewhat below 90%, and the deviation from the theoretical χ^2 distribution may indicate residual unmodeled nonlinear dependence structures or non-Gaussian effects.

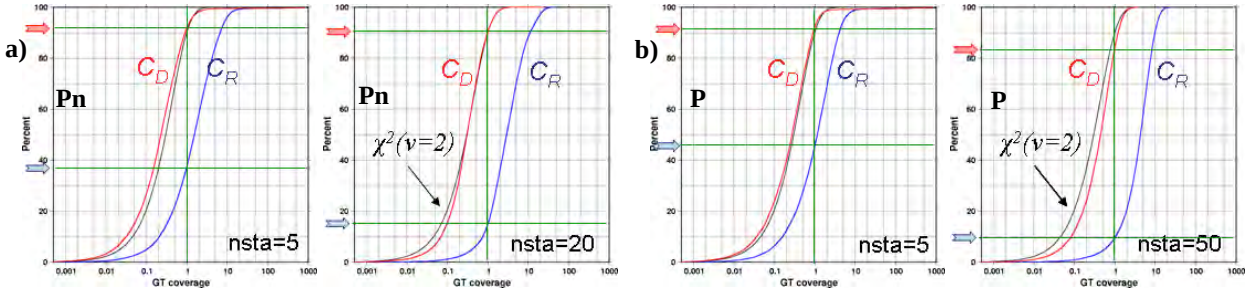


Figure 9. (a) Pn and (b) P coverage statistics for suboptimal sparse and dense networks. The cumulative distribution of coverage parameters is shown in blue when events are located assuming independent errors and in red when using the full data covariance matrix. The theoretical distribution is drawn in black. When correlated errors are accounted for (red), the 90% confidence ellipse covers the true location for 90% of the realizations.

Preliminary Model of Measurement Errors

Measurement errors are typically modeled as Gaussian, zero-mean processes. However, picking errors of onset times suffer from heavy tails (Buland, 1986) and are skewed, as weak emergent arrivals are typically picked too late (Anderson, 1982). Measurement errors also suffer from systematic errors, as onset times along the same ray paths are systematically picked late with decreasing event size, or more precisely, with decreasing SNR (e.g., Douglas et al., 1997, 2005). Douglas et al. (2005) point out that automatic detections are more likely affected by the systematic errors than are manual picks made by experienced analysts. Systematic reading errors introduce location bias, especially for small events recorded by sparse, unbalanced regional networks.

To develop models of measurement error bias and variance, we follow the methodology developed by Kohl et al (2004, 2005). The methodology scales known, high-SNR signals (explosions and/or earthquakes) down to various magnitude levels and embeds them in clean background noise, thus enabling large-scale controlled experiments. We generated some 22,000 realizations of earthquake waveforms from the Lop Nor region scaled to the range of mb 2.5–6.0, as well as some 9,000 realizations of Lop Nor explosion waveforms (mb 2.5–5.7), each embedded in different realizations of clean noise. Since the onset time and the SNR of the embedded signals are exactly known, running a signal detector allows us to derive improved measurement error models conditional on SNR. Figure 10 shows the delays of the automatic picks with respect to the true onset times for first arriving phases with SNRs larger than 3.5. It is apparent that the onsets are picked increasingly late, with decreasing SNR. Furthermore, the bias and the scatter around the bias are much smaller for the more-impulsive explosion signals, and picking errors on the earthquake signals exhibit heavier tails.

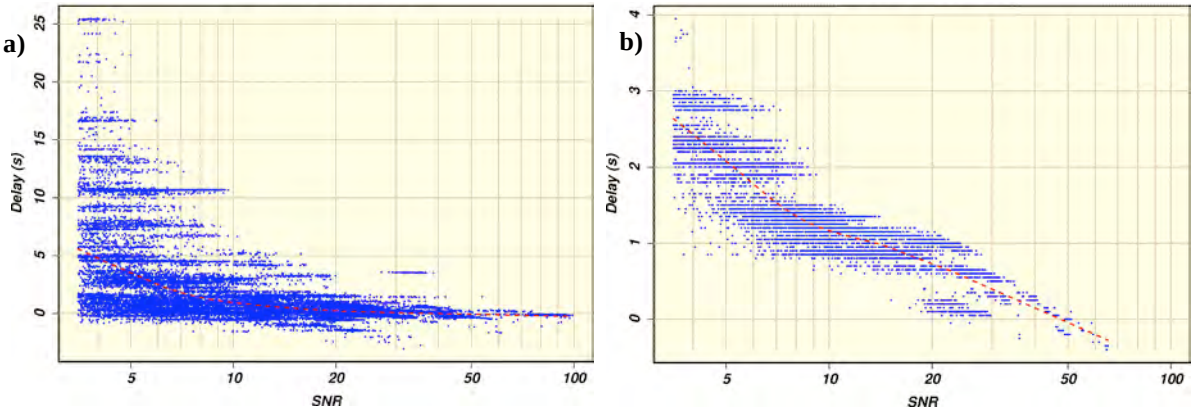


Figure 10. Delay of automatic first-arriving P picks relative to true onset times for (a) earthquake and (b) explosion waveforms. Picking errors of earthquake seismograms exhibit larger bias and scatter and suffer from heavier tails than those from explosions.

To model this increasing bias, scatter and skewness with decreasing SNR, we fit a series of general extreme value (GEV) distributions to the residual distribution as a function of SNR. Figure 11 illustrates the preliminary, SNR-dependent measurement error models for the earthquake and explosion picks. The location, scale, and shape parameters of the GEV distributions vary slowly with SNR, allowing for continuous change in reading errors. The increasing reading error bias with decreasing SNR (dashed lines in Figure 11) introduces systematic, correlated picking errors for a fixed event. However, once the bias is corrected for, the reading errors become nearly independent; thus, the reading error covariance matrix may still be approximated by a diagonal matrix.

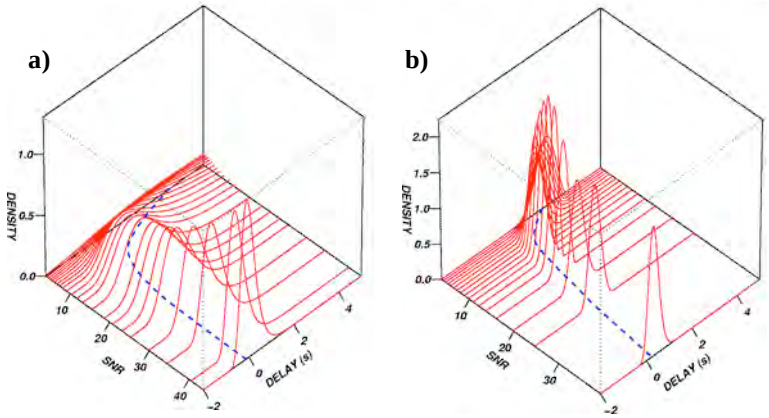


Figure 11. Measurement error models for (a) earthquake and (b) explosion signals for first-arriving P presented as a series of GEV distributions, with parameters slowly changing with SNR.

CONCLUSIONS AND RECOMMENDATIONS

We have developed methodologies to obtain robust estimates of network covariance matrices through copula-based variogram models. We have shown that the CUB2 global upper-mantle model provides significant variance reduction over the iasp91 model for regional Pn and thus produces reliable isotropic variogram models. We have developed a modified linearized location algorithm to incorporate the full, non-diagonal data covariance matrix in the inversion problem. Validation tests demonstrated that when the correlated data structure is taken into account, we

- obtain robust location uncertainty estimates, unaffected by the amount of redundant information,
- reduce mislocation that is due to conspiring errors, and
- achieve 90% coverage 90% of the time for both sparse and dense unbalanced networks.

While the variogram models for the various GT event clusters produce slightly different covariance matrices, the overall correlation structures are similar as the correlation varies the most at relatively small station separations (up to a few hundred kilometers). Preliminary tests indicate that it is possible to develop generic transportable variogram models for both Pn and P that will err on the conservative side and may work well anywhere on the globe.

We have developed preliminary measurement error models for first-arriving phases. We model the bias and scatter of picking errors by a series of GEV distributions whose parameters change slowly with decreasing SNR. In the next stage of this project, we will incorporate these non-Gaussian picking error models into our modified linearized location algorithm, hence utilizing a complete covariance matrix based on spatially correlated and SNR dependent errors. A hypothesis test will then be developed to verify when the linearized approach is valid.

REFERENCES

Anderson, K. R. (1982). Robust earthquake location using M estimates, *Phys. Earth Planet. Int*. 30: 119–130.

Bondár, I., K. McLaughlin, and H. Israelsson (2005). Improved event location uncertainty estimates, in *Proceedings of the 27th Seismic Research Review: Trends in Nuclear Explosion Monitoring*, LA-UR-05-6407, Vol 1, pp. 299–307.

Buland, R. (1986). Uniform reduction error analysis, *Bull. Seism. Soc. Am*. 76: 217–230.

Douglas, A., D. Bowers, and J.B. Young (1997). On the onset of P seismograms, *Geophys. J. Int.* 129: 681–690.

Douglas, A., J. B. Young, D. Bowers, and M. Lewis (2005). Variation in reading error in P times for explosions with body-wave magnitude, *Phys. Earth Planet. Int*. 152: 1–6.

Frees, E. W. and E. A. Valdez (1998). Understanding relationships using copulas, *North Am. Actuarial J*. 2: 1–25.

Genest, C. and L-P. Rivest (1993). Statistical inference procedures for bivariate Archimedean copulas, *J. Am. Stat. Assoc*. 88: 1034–1043.

Kennett, B. L. N. and E. R. Engdahl (1991). Travel times for global earthquake location and phase identification, *Geophys. J. Int*. 105: 429–465.

Kohl, B., T. J. Bennett, I. Bondár, B. Barker, W. Nagy, C. Reasoner, and J. Hanson (2004). Development of a network data set for evaluating detection and network processing performance, in *Proceedings of the 26th Seismic Research Review: Trends in Nuclear Explosion Monitoring*, LA-UR-04-5801, Vol. 2, pp. 725–734.

Kohl, B., T. J. Bennett, I. Bondár, B. Barker, W. Nagy, C. Reasoner, H. Israelsson, and P. Piraino (2005). Development of a network data set for evaluating detection and network processing performance, in *Proceedings of the 27th Seismic Research Review: Trends in Nuclear Explosion Monitoring*, LA-UR-05-6407, Vol. 2, pp. 917–926.

Nelsen, R. B. (1999). *An Introduction to Copulas*. Lecture Notes in Statistics 139, New York: Springer Verla.

Ritzwoller, M. H., N. M. Shapiro, E. A. Levshin, E. A. Bergman, and E. R. Engdahl (2003). Ability of a global three-dimensional model to locate regional events, *J. Geophys. Res*. 108(B7): 2353, 10.1029/2002JB002167.

Shapiro, N. M. and M. H. Ritzwoller (2004). Thermodynamic constraints on seismic inversions, *Geophys. J. Int.* 157: 1175–1188, doi:10.1111/j.1365-246X.2004.02254.x.

Yang, X., I. Bondár, J. Bhattacharyya, M. Ritzwoller, N. Shapiro, M. Antolik, G. Ekström, H. Israelsson, and K. McLaughlin (2004). Validation of regional and teleseismic travel-time models by relocating GT events, *Bull. Seism. Soc. Am.* 94: 897–919.

GROUND TRUTH HYPOCENTERS AND 3D CRUSTAL VELOCITY STRUCTURE IN CENTRAL ASIA FROM IN-COUNTRY NETWORKS

Thomas de la Torre[1], Gaspar Monsalve-Mejia[1], Anne F. Sheehan[1], Charlotte Rowe[2], and Michael Begnaud[2]

University of Colorado at Boulder[1] and Los Alamos National Laboratory[2]

Sponsored by National Nuclear Security Administration
Office of Nonproliferation Research and Development
Office of Defense Nuclear Nonproliferation

Contract Nos. DE-FC52-04NA25544[1] and W-7405-ENG-36[2]

ABSTRACT

The Himalayan Nepal Tibet Seismic Experiment (HIMNT) consisted of 28 broadband STS2 seismometers deployed throughout eastern Nepal and the southern Tibetan Plateau during 2001–2003. The data set is unique, with many stations in remote and difficult to access locations. Ground truth coverage in this portion of Asia is sparse and no permanent stations exist in most of the area covered by the HIMNT network. Thus this unique data set is able to provide reference events where none previously existed. With the ray coverage afforded us by the HIMNT and other regional stations and local network data, we are able to improve the regional and local velocity model as well, through 3D tomographic inversion.

We have examined the entire continuous HIMNT seismic data set and have picked and located over 1600 regional and local events, ranging in magnitude from 1 to 5.5. Initial hypocenters are determined using a priori 1D velocity models and a weighted least squares location algorithm. Relocations using the 1D velocity models result in 33 events that pass the ground truth (GT) criteria of Bondar et al. (2004) for GT5. We further refine the earthquake hypocenters by inverting for 2D and 3D velocity structure with earthquake relocation using the code SIMUL2000. These 2D and 3D locations should increase the number of ground truth events available. Teleseismic receiver function analysis is used to further constrain the crustal thickness variations and the geometry of the major interfaces. The Vp/Vs structure obtained from local earthquake tomography shows a noticeable contrast between the Indian Plate and the overlying thrust sheet, at the bottom of which we find a region of high S-wave speed. Upper mantle P-wave speeds in the study are unusually high, but do not appear to be related to anisotropy. Earthquake hypocenters delineate several distinct groupings that correlate with tectonics of the collision zone. Crustal earthquakes show alignments with depths less than 25 km along the region of highest relief of the Himalayan Front. Clusters of upper mantle earthquakes are found beneath the High Himalaya, in the southern Tibetan Plateau, and beneath southern Nepal. We observe earthquake hypocenters over a large range of depths, beneath Nepal from near-surface to 65 km depth, and beneath the Tibetan Plateau from near-surface to 90 km depth. Earthquakes show a bimodal distribution with depth, with the greatest concentration of seismic events in the upper crust and around Moho depth.

Development of our GT catalog includes moment tensor analysis and waveform modeling of GT events with particular attention to depth control. We have determined focal mechanisms from moment tensor inversion and first motion polarities for twelve of the largest and best recorded local earthquakes recorded during the HIMNT experiment and one ground truth event. We performed a grid search over source depth and different velocity model to examine the sensitivity of the fault plane solution and focal depth to crustal thickness and speed variations. The mostly strike-slip focal mechanisms at sub-Moho depths indicate a right lateral shear zone in the upper mantle beneath the Himalayas and the southern Tibetan Plateau. The new ground truth events can be used to calibrate station-centric correction surfaces and increase the ability to accurately locate and identify seismic events in these regions.

OBJECTIVES

The goal of this project is to contribute to the database of ground truth seismic events in central Asia using data from the Himalayan Nepal Tibet Seismic Experiment (HIMNT) network and other regional seismic data.

RESEARCH ACCOMPLISHED

HIMNT Deployment

The Himalayan Nepal Tibet Seismic Experiment (HIMNT) was a National Science Foundation (Program for Array Studies of the Continental Lithosphere PASSCAL) deployment in Nepal and Tibet in 2001–2003 (Figure 1). HIMNT was the first broadband seismic experiment to simultaneously cover the plains of southern Nepal, the Lesser and Greater Himalaya, and the Southern Tibetan Plateau. The HIMNT experiment included the deployment of twenty-eight three-component broadband seismic stations, which recorded continuously at a sample rate of 40–50 sps. Although the project has primarily tectonic objectives, the high-quality data collected are ideal for ground truth data for monitoring purposes. HIMNT stations were installed with approximately 40–50 km station spacing, covering a 2D area approximately 300 km wide east-west by 300 km north-south.

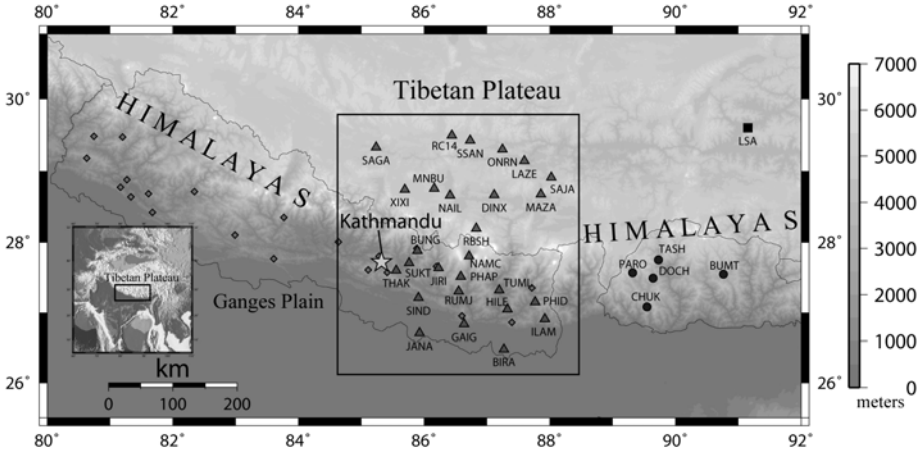


Figure 1. Topography of the study area and HIMNT broadband seismic 2001–2003 station network, triangles inside the rectangle. The moment tensor study was supplemented with data from the 2002 Bhutan broadband experiment (circles), the permanent Global Seismic Network station LSA (square), and the permanent National Seismological Network of Nepal (diamonds). A four letter code for each broadband station is shown.

Three-Dimensional Seismic Velocity Structure

We used P and S arrival time data from 542 earthquakes recorded by the network in order to simultaneously invert for earthquake location, and P-wave speed (Vp) and P- to S-wave speed ratio (Vp/Vs) for a 3D grid of nodes. A total of 5767 P-wave arrivals and 4801 S-wave arrivals were inverted using a method developed by Thurber (1983, 1993) and Eberhart-Phillips (1986), with the program SIMUL2000. The idea was to find the model that minimized the arrival time residuals at the stations. The technique consisted of an iterative damped least squares minimization algorithm. The travel times of the waves between source and receiver were determined by an approximate ray-tracing method (Thurber, 1983).

Several model parameterizations were tested, using an approach similar to that described by Husen et al. (2000), Eberhart-Phillips (1990), and Eberhart-Phillips and Michael (1998) in which we started solving for velocity structure at coarse grids of nodes, and progressively went to finer ones. The best model

parameterization was chosen based on arrival time misfit and the spread function of the resolution matrix. This function measured how similar the model resolution matrix is to the identity matrix (Menke, 1989; Toomey and Foulger, 1989; Michelini and McEvilly, 1991). The chosen model has a 50 km node spacing in the north-south and east-west directions and a vertical node separation of around 15 km. Depths went from surface to 70 km below sea level. After inversion, the obtained RMS arrival time residual was 0.31 s.

Figure 2 illustrates the values of P-wave speed at six different depths beneath the area of the network. Only areas with an associated diagonal resolution greater than 0.2 are shown. Similarly, Figure 3 shows Vp:Vs ratios for the same depths. This 3D velocity structure is then used in order to locate earthquakes in the study area, as discussed in the next section.

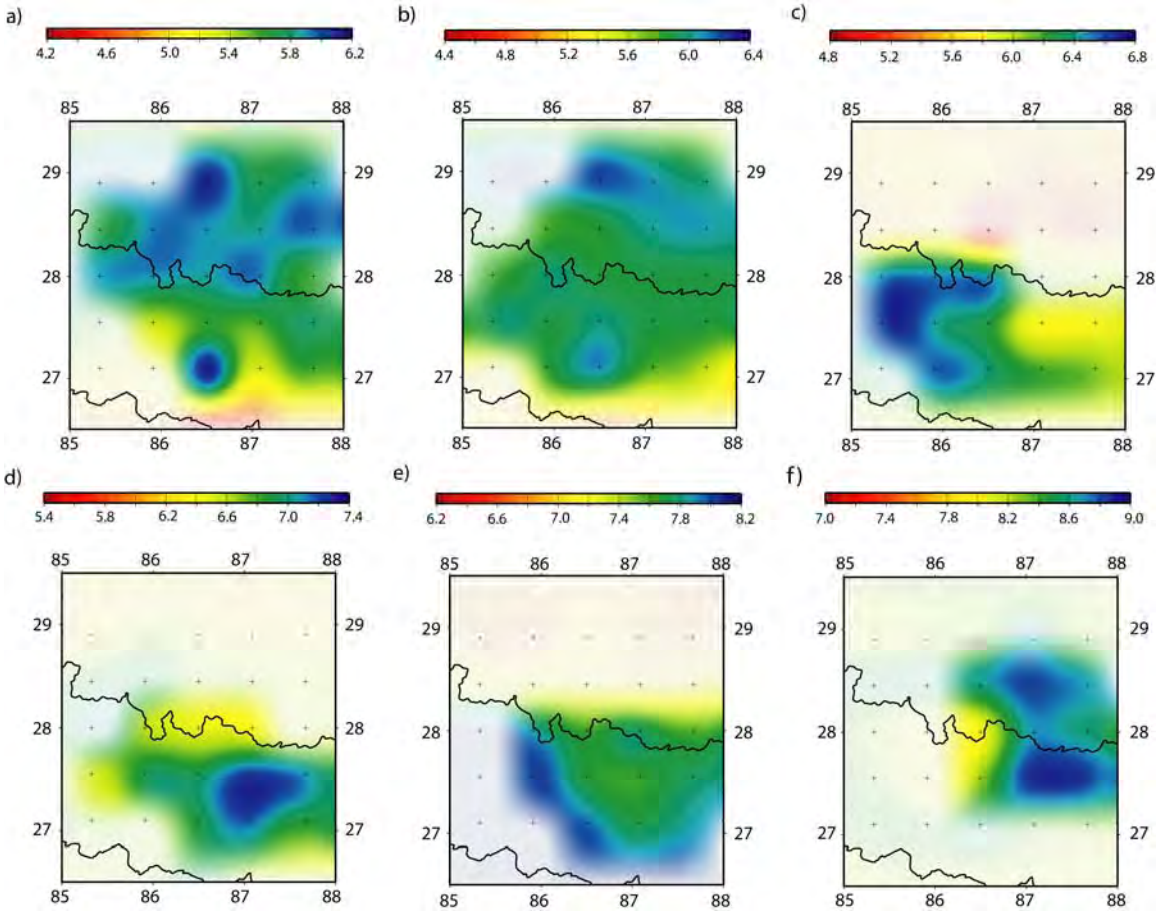


Figure 2. Three-dimensional velocity model used for earthquake locations. Horizontal sections of P-wave speed in km/s at different depths are shown. Only areas with an associated diagonal resolution greater than 0.2 are shown. Areas with smaller resolution are faded out. Vp is mapped at six depths below sea level *z* : a) z = 3 km, b) z = 15 km, c) z = 25 km, d) z = 40 km, e) z = 55 km, and f) z = 70 km.

Earthquake Locations with a 3D Velocity Model

We identified 1649 earthquakes between October 2001 and March 2003 by picking P and S arrival times. All these earthquakes were relocated using 3D velocity models (Figures 2 and 3) and the local magnitude was determined using the routine *dbml* from the BRTT Antelope Package. Earthquake local magnitudes range from 1 to 5.5.

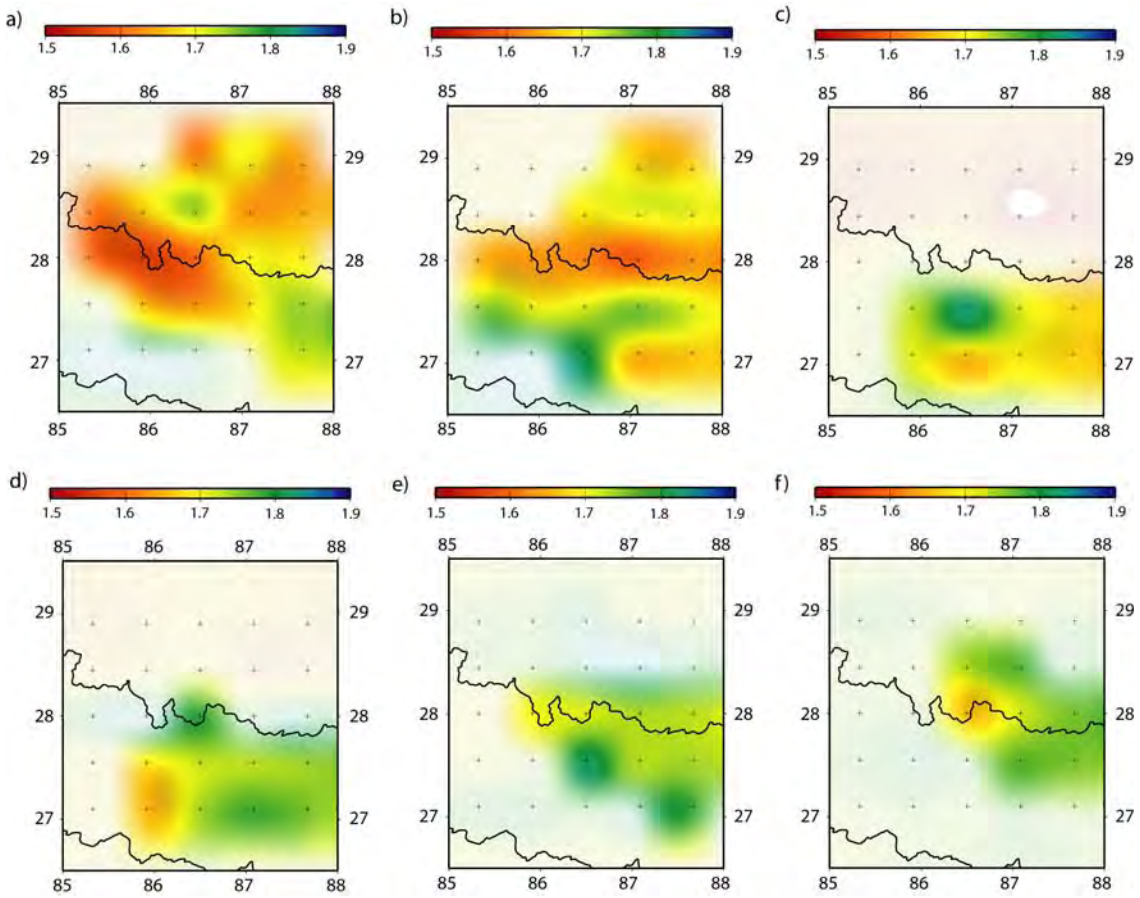


Figure 3. Horizontal sections of P to S-wave speed ratios (Vp/Vs) at different depths are shown. Only areas with an associated diagonal resolution greater than 0.2 are shown. Areas with smaller resolution are faded out. Vp/Vs is mapped at six depths below sea level *z* : a) z = 3 km, b) z = 15 km, c) z = 25 km, d) z = 40 km, e) z = 55 km, and f) z = 70 km.

Earthquake locations were encountered using the NonLinLoc software (Lomax, 2004), which determines probabilistic, non-linear earthquake locations in 3D structures. We use the model illustrated in Figures 2 and 3 in order to locate the set of 1649 earthquakes. NonLinLoc uses a global optimization method where for each set of arrival times corresponding to one earthquake, the whole model space is searched, preventing convergence towards local minima. This method gives better solutions than earthquake location algorithms used previously, which consisted of local optimization methods. We used a nested grid-search algorithm in order to find the location with the highest probability density function. The model was extended in all directions so that events out of the resolved portion of the velocity model could be located. Figure 4 shows a map view of the earthquake locations in the study area, with colors denoting hypocenter depth and sizes indicating earthquake local magnitude. Earthquake depths go from surface to approximately 90 km below sea level.

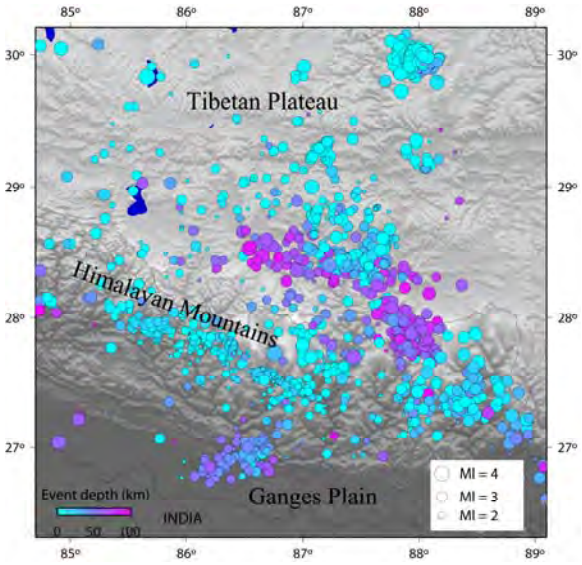


Figure 4. **Map view of the whole set of earthquake locations using the NonLinLoc software. Events are size-scaled by magnitude and color-scaled by depth.**

Moment Tensor and Source Parameter Analysis

We calculated moment tensor inversions for thirteen earthquakes using the moment tensor method of Ammon and Randall (1994) with data collected from the HIMNT experiment, the Bhutan PASSCAL network, and the Global Seismic Network (GSN, station LSA). We created Green's functions for the radial, transverse, and vertical components from 1D velocity models using the reflectivity method of Randall (1994). Since crustal thickness and topography vary dramatically across the study region, we used velocity models with variable speeds and Moho depths to obtain an average fault plane solution and focal depth. We modeled the whole waveform for each component of each station between 5–100 s. Figure 5 illustrates the lower hemisphere projections of the thirteen events at their epicenter locations. Focal mechanisms were verified with take-off angle and first motion polarities from the broadband data and with seismograms collected from the permanent short period vertical component network of the National Seismic Center of the Department of Mines and Geology of Nepal. Figure 6 illustrates the seismicity and focal mechanisms for earthquakes at focal depth range 60–100 km from the HIMNT experiment and four focal mechanism solutions from past studies. This cluster of earthquakes trending NW-SE and the mostly strike slip focal mechanisms suggest a possible shear zone under the Himalayas and the southern Tibetan Plateau.

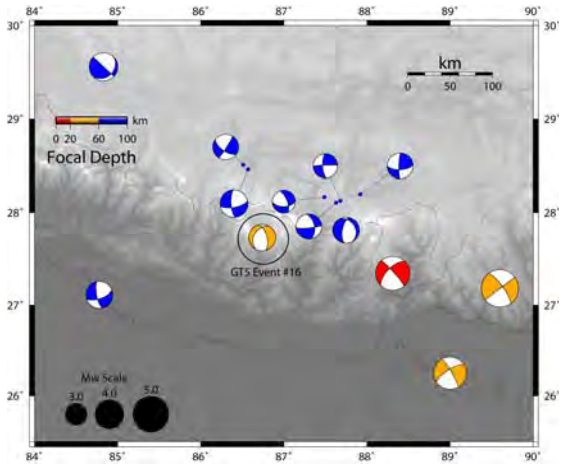


Figure 5. Focal mechanisms for thirteen events located in Figure 4. One earthquake (circled) was determined to be also a GT5 event.

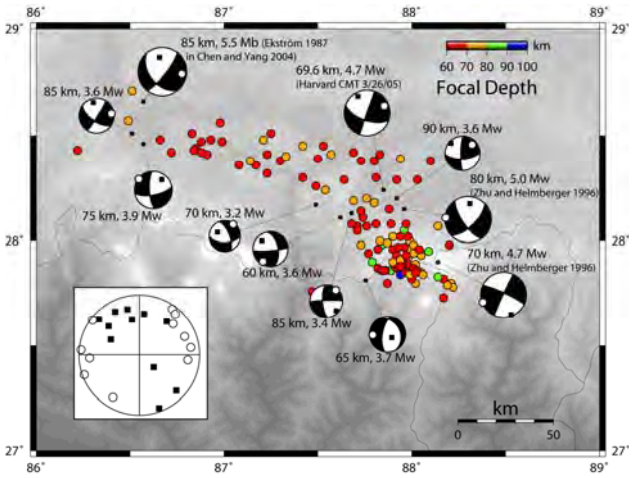


Figure 6. Fault plane solutions from this experiment coupled with solutions from other studies show predominant strike-slip faulting and possibly one normal faulting event 60–100 km under the Himalayas and the southern Tibetan Plateau. Insert illustrates lower hemisphere projections of P-axis orientations (closed squares) and T-axis orientations (open circles).

Ground Truth Events

After the use of advanced earthquake location algorithms we found hypocenters for hundreds of events detected as part of the HIMNT experiment. A subset of these events can be used to improve the database of seismic event ground thruth (GT) information for central and south Asia. According to Bondar et al. (2003), candidate events at the GT5 confidence level must be recorded at 10 or more stations within 250 km, the azimuthal gap should be less than 110°, the secondary azimuthal gap has to be less than 160°, and at least one of the stations should locate within 30 km from the epicenter. A total of 33 of the earthquake events recorded by the HIMNT network meet the Bondar et al. (2003) criteria (Table 1, Figure 7). Their local magnitudes range from 1.61 to 3.79. Figure 7a illustrates the 95% confidence level ellipses for these events in map view. The hypocenter projections onto a north-south vertical plane with the 95% confidence level vertical error bars are shown in Figure 7b.

We determined the source parameters by moment tensor inversion for one GT5 event (#16 in Table 1, Figure 8). The other events were not analyzed for source parameters since their signal-to-noise ratios were not large enough for the moment tensor inversion method we used. A 1D velocity model was extracted from 3D tomographic velocity model for input into the moment tensor inversion. The hypocenter using the NonLinLoc software was at a depth of 26.25 ± 1.3 km while the minimum moment tensor depth was at 32 km. We did not correct for station elevations (2.2 km above sea level on average for this event) for the moment tensor inversion, so the focal depth should be corrected to at least ~ 29.8 km.

Table 1. Candidate events at the GT5 confidence level

	ºN	ºE	Depth (km)	Date	Time (UTC)	M_L
1	27.5579	86.7601	14.75	10/27/2001	16:48:49	2.46
2	26.9256	86.5315	42.00	12/20/2001	7:36:34	2.41
3	27.0336	86.6301	32.00	1/7/2002	18:05:26	2.03
4	28.3926	86.7775	67.75	1/13/2002	14:32:09	2.88
5	27.3554	86.747	2.25	1/21/2002	3:47:20	2.41
6	27.5669	86.6307	13.00	1/25/2002	20:32:55	1.9
7	27.5646	86.6282	11.00	1/25/2002	21:48:21	2.5
8	27.7851	86.3894	25.50	2/3/2002	7:41:58	3.79
9	27.7986	86.3817	9.00	2/3/2002	10:04:12	2.32
10	26.7569	86.3803	54.25	3/1/2002	23:21:06	2.53
11	27.5196	86.8894	17.00	3/17/2002	22:05:11	2.6
12	27.5916	86.6333	14.50	3/26/2002	18:48:48	2.27
13	27.5174	86.1233	15.25	4/9/2002	7:23:23	2.98
14	27.8009	86.191	6.00	4/25/2002	6:22:01	2.14
15	26.7681	86.2518	48.50	4/30/2002	18:33:02	2.47
16	27.7289	86.7555	26.25	5/2/2002	17:35:30	4.2
17	27.8526	86.2799	18.00	6/22/2002	22:25:13	2.7
18	27.1754	86.8022	43.25	7/2/2002	20:28:52	2.27
19	27.2834	87.1848	< 1	7/12/2002	17:25:03	1.61
20	27.0741	85.771	5.25	7/23/2002	23:16:47	2.96
21	28.7459	87.3071	6.00	7/24/2002	8:33:20	2.45
22	28.6829	87.7452	5.00	8/1/2002	20:29:30	3.33
23	28.6671	86.5064	77.25	8/7/2002	17:29:40	2.62
24	27.6456	86.4759	7.25	8/16/2002	6:23:47	2.97
25	28.5546	87.7232	12.25	9/2/2002	12:02:52	2.53
26	27.3644	87.3627	24.00	9/3/2002	8:46:39	2.08
27	27.7199	85.9218	< 1	9/6/2002	14:46:04	1.93
28	28.5794	86.86	64.25	9/22/2002	9:34:59	2.33
29	27.5804	86.6104	19.25	10/2/2002	21:35:14	2.81
30	28.9259	86.3188	< 1	10/16/2002	21:05:35	2.58
31	28.9146	86.3034	< 1	10/16/2002	21:08:09	2.39
32	27.0561	87.4512	16.00	10/25/2002	14:58:27	2.62
33	28.5546	86.9982	59.50	8/26/2002	2:31:53	2.6

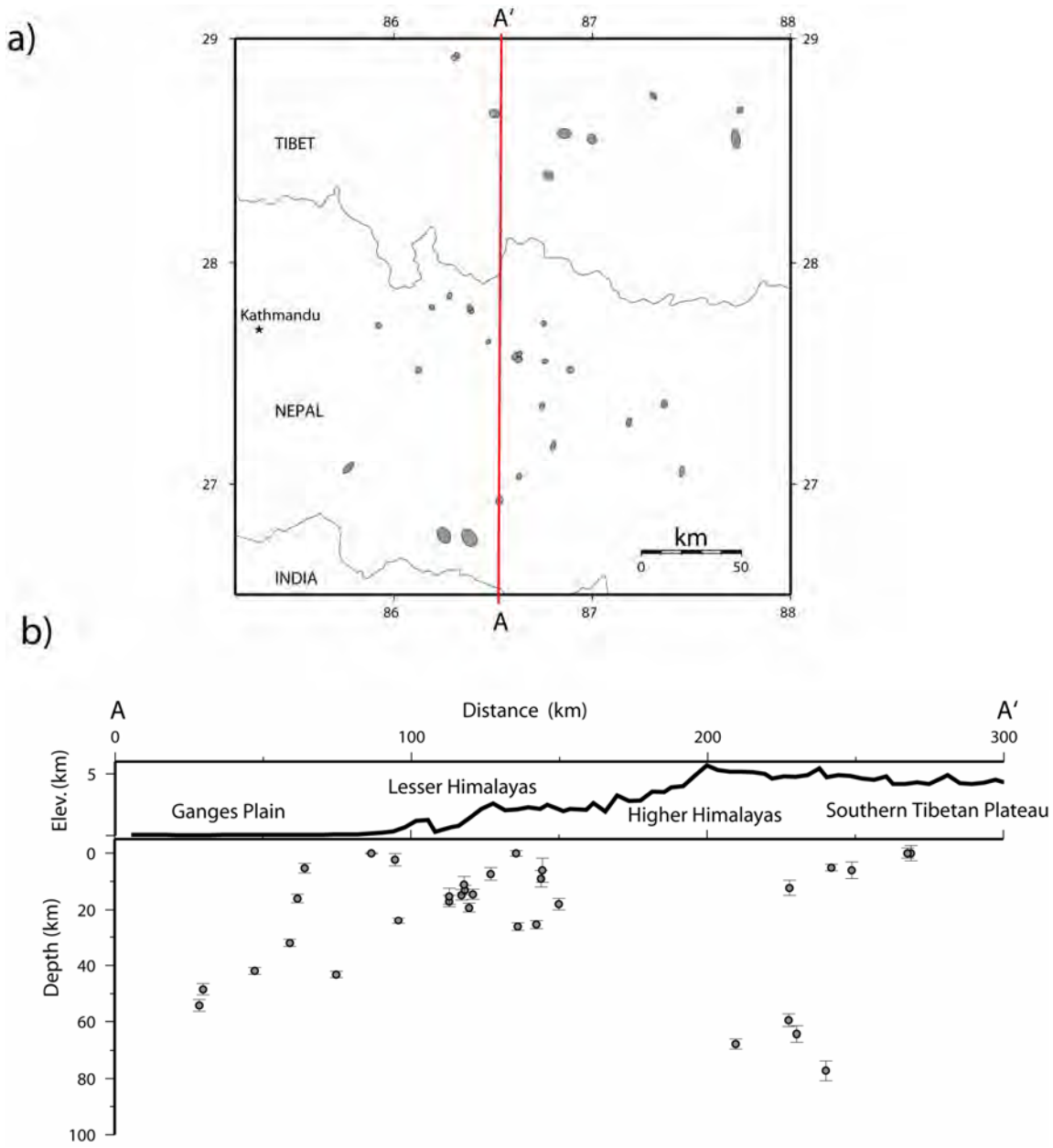


Figure 7. Location of the candidates for GT5 events (Bondar et al., 2003). a) Map view of the candidate event locations with their associated 95% confidence level ellipses. Red line marks the location of cross-section in part (b). b) North-south cross-section of the study area with the event projections and their associated 95% confidence level vertical uncertainties.

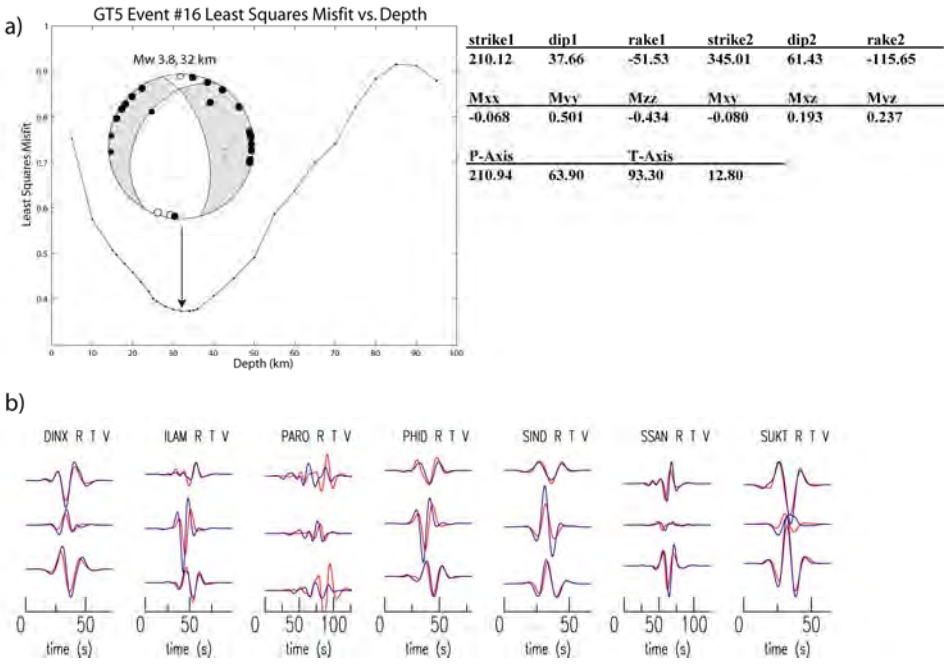


Figure 8. Moment tensor solution for GT event #16 (Table 1) using the 1D velocity extracted from the 3D tomographic velocity model in this analysis. a) A minimum misfit normal faulting solution occurs at a focal depth of 32 km or 29.8 km relative to sea level. Compressive first motion (closed circles), dilational first motion (open circles). b) Data (blue) plotted versus synthetic (red) seismograms at the 32 km focal depth solution.

CONCLUSIONS AND RECOMMENDATIONS

Use of in-country networks contributes to ground truth location determination in central Asia, important for validation of regional velocity models and correction surfaces. Through travel time and moment tensor inversions, we have obtained a regional 3D velocity model profile and source parameters for thirteen events. Examination of the 1649 earthquakes detected by the HIMNT network indicated 33 high-quality ground truth events not included in global catalogs. These ground truth events will contribute to the National Nuclear Security Administration (NNSA) Knowledge Base, which will be used to calibrate station-centric correction surfaces and increase the ability to accurately locate and identify seismic events in these regions.

REFERENCES

Ammon, C. J., G. E. Randall (1994). Deviatoric moment tensor inversion, http//:eqseis.geosc.psu.edu/~cammon/HTML/MTinvDocs/mtinv01.html, 2005.

Bondar, I., S. C. Myers, E.R. Engdahl, and E.A. Bergman (2004). Epicentre accuracy based on seismic network criteria, *Geophys. J. Int.* 156: 483–496.

Chen, W. P. and Z. H. Yang (2004). Earthquakes beneath the Himalayas and Tibet: Evidence for strong lithospheric mantle, *Science* 304: 1949–1952.

Eberhart-Phillips, D. (1986). Three-dimensional velocity structure in the northern California coast ranges from inversion of local earthquake arrival times, *Bull. Seismol. Soc. Am.* 76: 1025–1052.

Eberhart-Phillips, D. (1990. Three-dimensional P and S velocity structure in the Coalinga region, California, *J. Geophys. Res.* 95: 15343–15363.

Eberhart-Phillips, D. and A. J. Michael (1998). Seismotectonics of the Loma Prieta, California, region determined from three-dimensional Vp, Vp/Vs and seismicity, *J. Geophys. Res.* 103: 21099–21120.

Harvard University Department of Geological Sciences (2005), *Centroid Moment Tensor Catalog*, www.seismology.harvard.edu/CMTsearch.html

Husen, S., E. Kissling, and E. Flueh (2000). Local earthquake tomography of shallow subduction in north Chile: A combined on-shore and off-shore study, *J. Geophys. Res.* 105: 28183–28198.

Lomax, A. (2004). Probabilistic, non-linear, global-search earthquake location in 3D media, NonLinLoc Version 3.03, Anthony Lomax Scientific Software, Mouans-Sartoux, France.

Menke, W. (1989). *Geophysical Data \Analysis: Discrete Inverse Theory*. Academic Press.

Michelini, A. and T. V. McEvilly (1991). Seismological studies at Parkfield.—I. Simultaneous inversion for velocity structure and hypocenters using cubic B-splines parameterization, *Bull. Seismol. Soc. Am.* 81: 524–552.

Randall, G. E. (1994). Efficient calculation of complete differential seismograms for laterally homogenous earth models, *Geophys. J. Int.* 118: 245–254.

Thurber, C. (1983). Earthquake locations and three-dimensional crustal structure in the Coyote Lake area, central California, *J. Geophys. Res.* 88: 8226–8236.

Thurber, C. (1993). Local earthquake tomography: Velocities and Vp/Vs—Theory, in *Seismic Tomography: Theory and Practice*, H. M. Iyer and K. Hirahara (Eds.). New York: Chapman and Hall, pp. 563–583.

Toomey, D. R., and G. R. Foulger (1989). Tomographic inversion of local earthquake data from the Hengill-Grensdalur central volcano complex, Iceland, *J. Geophys. Res.* 94: 17497–17510.

Zhu, L. P. and D. V. Helmberger (1996). Intermediate depth earthquakes beneath the India-Tibet collision zone, *Geophys. Res. Lett.* 23: 435–438.

IMPROVED GROUND TRUTH IN SOUTHERN ASIA USING IN-COUNTRY DATA, ANALYST WAVEFORM REVIEW, AND ADVANCED ALGORITHMS

Eric R. Engdahl[1], Eric A. Bergman[1], Stephen C. Myers[2], and Floriana Ryall[2]

University of Colorado[1] and Lawrence Livermore National Laboratory[2]

Sponsored by National Nuclear Security Administration
Office of Nonproliferation Research and Development
Office of Defense Nuclear Nonproliferation

Contract Nos. DE-FC52-03NA99516[1] and W-7405-ENG-482[2]

ABSTRACT

This research has the goal of developing in-country data sets that can be used to improve ground-based monitoring capabilities in Southeast Asia, by providing information needed to develop and test more accurate travel time models for seismic phases that propagate in the crust and upper mantle. These in-country arrival times have been associated with the arrival times of known earthquakes reported by international agencies, and relocated. This has resulted in a highly reviewed catalog of earthquakes in the Iran region for the period 1918-2005 for events larger than about magnitude 4.0. In collaboration with Cambridge colleagues, the new catalog has been used to assess focal depth distributions throughout Iran. A principal result of this study is that the geographic pattern of depth distributions revealed by the relatively small number of earthquakes (~167) with depths constrained by waveform modeling (+/- 4 km) are now in agreement with the much larger number of depths (~1229) determined using reanalysis of ISC arrival-times (+/-10 km), within their respective errors. This is a significant advance, as outliers and future events with apparently anomalous depths can be readily identified and, if necessary, further investigated.

The patterns of reliable focal depth distributions have been interpreted in the context of Middle Eastern active tectonics. Most earthquakes in the Iranian continental lithosphere occur in the upper crust, with the crustal shortening produced by continental collision apparently accommodated entirely by thickening and distributed deformation, rather than by subduction of crust into the mantle. In the Zagros Mountains nearly all earthquakes are confined to the upper crust (depths < 20 km), and there is no evidence for a seismically active subducted slab dipping northeast beneath central Iran. By contrast, in southeastern Iran, where the Arabian sea floor is being subducted beneath the Makran coast, low-level earthquake activity occurs in the upper crust as well as to depths of at least 150 km within a northward-dipping subducting slab. Near the Oman Line, a transitional region between inter-continent collision in the Zagros and oceanic subduction in the Makran, seismicity extends to depths up to 30-45 km in the crust, consistent with low-angle thrusting of Arabian basement beneath central Iran in this region. In north-central Iran, along the Alborz mountain belt, seismic activity occurs primarily in the upper crust but with some infrequent events in the lower crust, particularly in the western part of the belt (the Talesh), where the south Caspian basin underthrusts NorthWestern Iran. Earthquakes that occur in a band across the central Caspian, following the Apsheron sill between Azerbaijan and Turkmenistan, have depths in the range of 30–100 km, increasing northwards. These are thought to be connected with either incipient or remnant northeast subduction of the south Caspian Basin basement beneath the east-west trending Apsheron-Balkhan sill. Curiously, in this region of genuine mantle seismicity, there is no evidence for earthquakes shallower than 30 km.

In addition to uniform analysis of regional seismicity, we continue to conduct detailed analysis of historic and newly occurring event clusters (generally aftershock sequences) using multiple-event techniques and local data sets. These studies have produced numerous events with epicenter accuracy of 5 km and better (GT5). Absolute locations of such clusters are constrained using reference event information for one or more of the cluster events provided by local networks, aftershock deployments, or from non-seismic (e.g., InSAR or geological mapping) information. When both location and origin time can be calibrated for a cluster through use of reference event information, we are able to estimate the true travel times to all reporting stations. These estimates are the basis for improved models of the crust and upper mantle, which in the future will permit far more accurate routine earthquake locations using regional seismic data.

OBJECTIVES

This research seeks to improve the database of ground truth information and velocity models useful for calibration in southern Asia with the following objectives: (1) Aggressive pursuit of in-country data acquisition, especially the collection of ground truth at GT5 level or better for events of magnitude 2.5 and larger recorded by dense local networks, including associated velocity models; (2) Expanded analyst review of relevant regional waveforms for ground truth events by the comprehensive re-picking of phase arrival times from all available waveforms, with special attention to the regional phases Pg, P*, Pn, Sg, S* and Sn; and (3) Application of advanced algorithms, such as those used for multiple event relocation, to refine and validate all available ground truth data, to achieve the optimal selection of data for analysis, to better understand the uncertainties of the results, and to handle the error budget as realistically as possible.

RESEARCH ACCOMPLISHED

Relocation and Assessment of Seismicity in the Iran Region

The aim of a recently published study (Engdahl et al., 2006) is to produce a comprehensive catalog of all instrumentally recorded events for the Iran region and to summarize the patterns seen in this relocated seismicity, in particular the patterns of reliable focal depth distributions, within their active tectonic context.

Engdahl et al. (1998) have shown that hypocenter determination can be significantly improved by using, in addition to direct P and S phases, the arrival times of core phases PKiKP (reflected off the inner core) and PKPdf (transmitted through the inner core), and the teleseismic depth phases (pP, pwP and sP) in the relocation procedure. Epicenter constraints are improved by the inclusion of S-wave and P-core phases because their travel-time derivatives differ significantly in magnitude from direct P, while depth-origin time trade-off is ameliorated by the inclusion of depth phases (pP, pwP, sP) because their travel time derivatives are opposite in sign to those of direct P. The Engdahl et al. (1998) methodology (hereafter referred to as EHB) is applied, with special attention to focal depth, to more than 2000 instrumentally recorded earthquakes occurring in the study region during the period 1918-2004 that are well-constrained by teleseismic arrival times reported to the International Seismological Summary (ISS), the International Seismological Centre (ISC) and the U.S Geological Survey's National Earthquake Information Center (NEIC).

EHB Epicenter and Depth Estimates

Engdahl and Bergman (2001) determined highly accurate relative locations for a number of teleseismically well-recorded earthquake clusters in Iran using a multiple event location method. When well-determined local-network (calibration) locations for a subset of events in the clusters are reconciled with the corresponding teleseismic relative locations, the absolute epicenter accuracy for many events in the clusters can be determined to 5 km or better. EHB epicenters for 80 earthquakes were compared to a set of these highly accurate absolute epicenters. The average and median mislocation errors were 9.2 +/- 5.2 km and 8.9 +/-4.9 km, respectively. The direction of EHB mislocation, though consistent for events in individual clusters, was variable across Iran. This can be accounted for by lateral variations in Earth structure and station coverage between individual clusters. We conclude that the EHB teleseismic epicenter bias for earthquakes in this region is ~10 km.

The EHB procedure was used to determine unconstrained depth solutions of 151 events that were also modeled using long-period P and SH waveforms for the time period post-1962. Each event had more than five reported short-period arrivals that could be identified as pP or sP depth phases. Starting depths were set at the waveform depths, which have an estimated accuracy of ~4 km in the Iran region, to avoid secondary minima in the depth determination. Differences between the waveform and EHB depths for most events were within 10 km of the corresponding waveform depths, with a maximum difference no larger than 15 km. To process the entire database, we relied on a careful review of the EHB starting depths, the EHB assignment of teleseismic depth phases, and the effects of reading errors on these phases. The reviewed EHB depth estimates were sufficiently accurate to resolve robust differences in focal depth distribution within the crust and upper mantle throughout the study region, and showed patterns in agreement with the more accurate, though numerically far fewer, long-period body-wave inversion depths. One principal result of this study is that the patterns of depth distributions revealed by the relatively small number of earthquakes (~167), whose depths (+/- 4 km) are confirmed by waveform modeling, are now in agreement with the much larger number (~1,229) whose EHB depths (+/-10 km) have been reassessed, within their respective errors.

Regional Distribution of Seismicity

There are 2,227 earthquakes that occurred in the Iran region that have well-constrained (secondary teleseismic azimuth gap < 180 degrees) epicenters for the period 1918-2004 based on phase arrival times reported to the ISS, ISC, and USGS/NEIC. Of these events, 1,226 have depths estimated from EHB-associated depth phases or from waveforms (primarily during the post-1964 period). EHB events with unconstrained depths based on first arriving P arrival times alone are usually poorly determined and have been set to default depths based on the regional medians of nearby better determined depth estimates. This ensures that, when other depth constraints for an event are not available, the use of an inappropriate depth does not unduly bias the relocated epicenter. The new locations for all events (color coded by depth) are plotted in Figure 1a, along with known major faults. Figure 1b is similar except only events having depths determined by P and SH body wave modeling are shown. The comparison is important because it shows the geographical coverage, and also reveals places where EHB depths do not have direct waveform confirmation and hence are particularly interesting for future earthquakes.

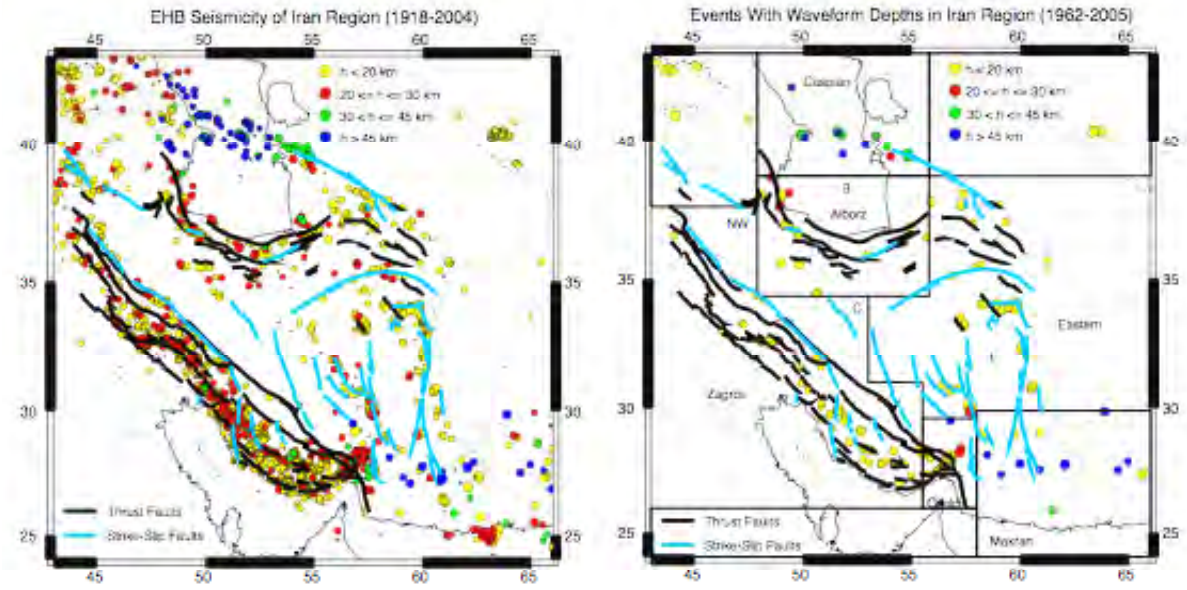


Figure 1. (a) EHB regionalized seismicity in the Iran region (1918-2004). (b) Regionalized seismicity in the Iran region for events with depths determined by P and SH body-wave modeling (1962-2004). The boxes outline the six regions (Caspian, Alborz, Zagros, Oman Line, Makran and Eastern) in which the patterns of seismicity and depth distribution will be discussed Also shown in both figures are thrust (black) and strike-slip (blue) faults.

Central Caspian Region – Offshore Deep and Onshore Shallower Seismicity

Earthquakes in this region occur over a wide range of depths (Figure 2a) with a median depth of 40 +/-15 km, but this generalization hides a clear geographical pattern to the distribution of focal depths. A band of earthquakes crossing the central Caspian beneath the Apscheron-Balkhan sill and continuing onshore in the east includes many earthquakes in the mantle, some as deep as 80 km but none shallower than 30 km. The deepest earthquakes are on the northern side of this zone, but there are an insufficient number of them to define a dipping mantle slab (Jackson et al., 2002). South of this trans-Caspian band, the South Caspian basin itself is apparently aseismic. Crustal thickness varies across the region. Given the uncertainty about the nature of the high-velocity basement beneath the thick sediments of the South Caspian basin, the events at depths between 30 and 50 km beneath the Apscheron-Balkhan sill, whose focal mechanisms show predominantly normal faulting with an ESE strike (Jackson et al., 2002), are difficult to interpret. Several events that lie on the north side of the sill between 70 and 80 km depth are clearly in the mantle, and are thought to represent either the last oceanic remnant of subduction of a now-closed ocean basin or the incipient northeast subduction of the South Caspian basin basement beneath the sill (Jackson et al., 2002). This subduction is a process that appears to occur aseismically at shallow depths, with the lack of earthquakes in the basin indicating that it behaves as a roughly 300 x 300 km^2 relatively rigid block within the

Eurasia-Iran-Arabia collision zone. There is no evidence for seismicity deeper than 100 km, suggesting that the subduction is either slow or young (Jackson et al., 2002).

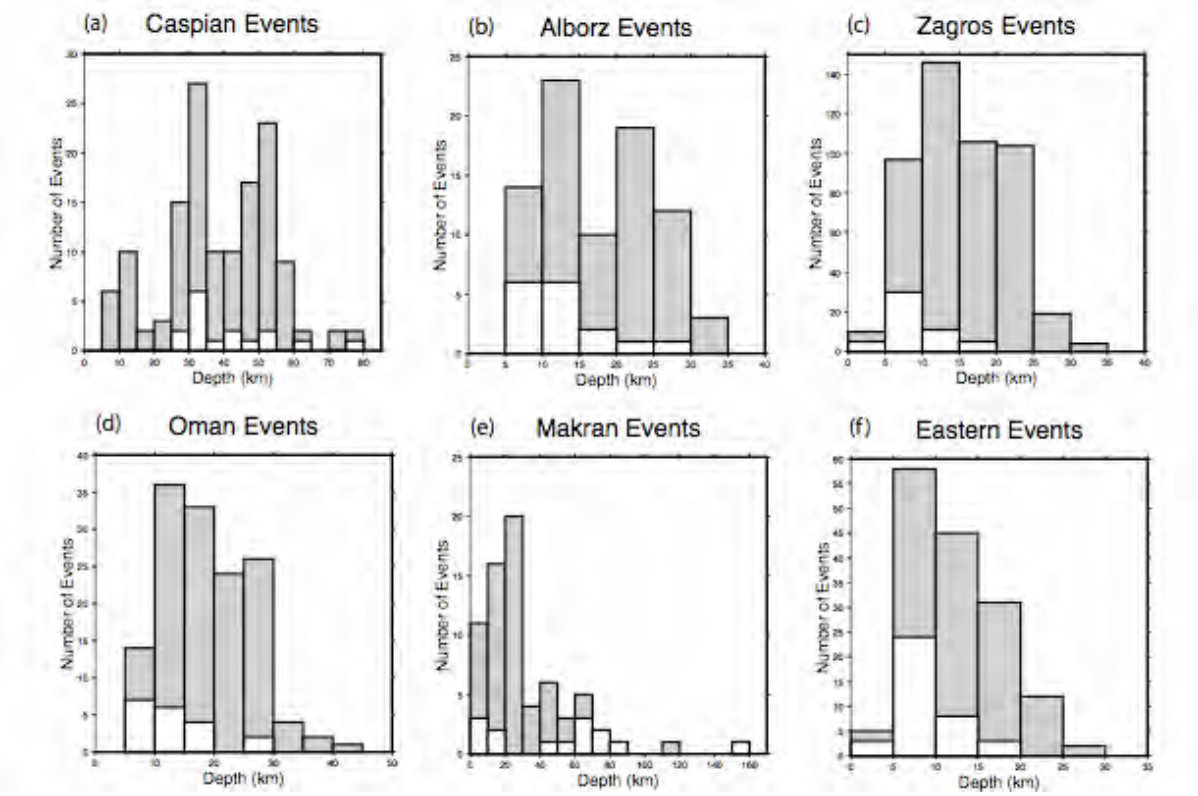


Figure 2. Earthquake depth distribution by region (depths determined by waveform modeling are not shaded): (a) Caspian, (b) Alborz, (c) Zagros, (d) Oman Line, (e) Makran, (f) Eastern.

Alborz Region - Seismicity Throughout the Crust

Roughly 50% of the ~20 mm/yr north-to-south convergence between Arabia and Iran is accommodated in the Alborz region, between the southern Caspian and central Iran. Earthquakes in this region along the Alborz Mountains and other southern Caspian basin active border regions to the southwest and east occur at all depths in the crust (Figure 2b) with a median depth of 20 +/-8 km. However, this generalization hides a clear geographical variation in the known depths. Along the western side of the South Caspian basin, beneath the western Alborz, earthquakes occur to depths of ~30 km, generally on low-angle thrusts, indicating underthrusting of the Caspian sea floor beneath the coast (Jackson et al., 2002). East of 50^{o}E all waveform-modeled depths are shallower than 15 km, but there are a few EHB depths of up to 35 km (Figure 1a). A receiver function result in the central Alborz Mountains shows that the crust is ~35 km thick, with a structure typical of continents. The western Alborz, with its low-angle underthrusting, is tectonically distinct from the central and eastern Alborz, which is dominated by strike-slip and high-angle reverse faulting at shallower depths.

Zagros Region - Seismicity Mostly in the Upper Crust

The Zagros Mountains of SW Iran form a linear intracontinental fold-and-thrust belt about 1,200 km long, trending northwest-southeast between the Arabian shield and central Iran, with a width varying between 200 and 300 km. Roughly 50% of the convergence rate between the Arabia Plate and the continental crust of central Iran is accommodated in the Zagros by north-south crustal shortening oblique to the strike of the belt over much of its length. Of particular interest is whether or not the earthquake depths in this region show any evidence for intracontinental subduction. In their review of waveform-modeled depths in the Zagros, Talebian and Jackson (2004) found no earthquakes deeper than 20 km anywhere except near the Oman Line in the extreme SE Zagros. In the revised EHB database presented here, nearly all earthquakes in the Zagros are less than 30 km in depth (Figure 2c), a result consistent, given the expected uncertainty of 10 km, with the waveform-modeled data. The median

depth in Figure 2c is 15 +/-7 km. However, EHB depths may be slightly overestimated in this region because of slower velocities at depth-phase bounce points in comparison with the faster crustal velocities of the ak 135 model. Moreover, with a 10 km uncertainty in EHB depth estimates, most of these events probably occur within the upper crystalline crust but beneath the sedimentary layer. Hence, beneath the Zagros there is no evidence in the form of mantle earthquakes or structure for present-day active subduction of continental crust, with shortening apparently accommodated entirely by crustal thickening and distributed deformation (Talebian and Jackson, 2004).

Oman Line Region - Transition from Shallow Zagros to Subcrustal Makran Seismicity

The Oman Line is a geological syntaxis, where the faults and folds of the Zagros bend dramatically to connect with those of the Makran. The region is a transition from the continent-continent collision of the Zagros to the subduction of the Arabian plate beneath the Makran coast, and is geologically complex. Global Positioning System (GPS) measurements indicate north-to-south convergence between Oman and central Iran of about 11 mm/yr, expressed as a mixture of shortening and north-to-south right-lateral strike-slip on the eastern side of the syntaxis. In the west and central part of the syntaxis, waveform modeling shows earthquakes increasing in depth northwards, from typically 8-12 km near the coast to as much as 28 km at a location 50 km north of the geological suture (the Main Zagros Thrust) that represents the join between Arabian and Iranian rocks (Talebian and Jackson 2002). The deepest earthquakes are all low-angle thrusts, dipping gently northwards, and represent one of the few places where a case can be made for underthrusting of the Arabian basement beneath central Iran; but only by a distance of 50 km to a depth of ~30 km. The eastern limit of the Oman Line region in Figure 1b is drawn so as to exclude most of the Makran subduction zone, but one earthquake at 100 km is included in its northern part. EHB seismicity within the box extends to depths of about 40 km (Figure 2d), consistent with the waveform data summarized above, with a median depth of 20 +/-8 km. The EHB dataset contains earthquakes on the eastern side of the syntaxis at 30–40 km (Figure 1a), but these have not been confirmed by waveform modeling.

Makran Region - Low-Level, Upper-Crustal, and Subduction-Celated Cantle Seismicity

East of 57.3°E, most of the ~30 mm/yr shortening produced by Arabia-Eurasia convergence is accommodated by the Makran subduction zone. The Makran region has earthquakes both at upper crustal depths and at depths well in excess of 40 km (Figure 2e) with a median depth of 25 +/-19 km. The deeper events apparently occur within a shallow (~26°) northward dipping slab. These mantle-depth events in the Makran result from subduction of the Indian ocean beneath the relatively stable Lut and Afghan continental blocks. The Afghan block east of 60°E is now effectively part of undeforming Eurasia, separated from the Lut by the north-to-south right-lateral Sistan shear zone. An along-strike plot of seismicity (Figure 3) shows how earthquakes in the Oman Line zone merge at ~57.3°E into lower-level seismicity beneath the Makran coastal ranges.

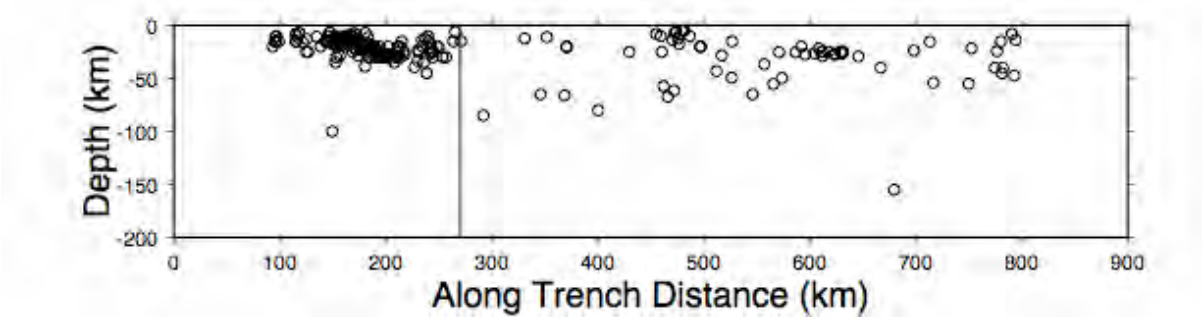


Figure 3. Earthquakes in the Oman Line and Makran regions of Figure 1 plotted along trench strike.

Eastern Iran - Upper Crustal Seismicity Surrounding the Aseismic Lut and Central Iran Blocks

Seismicity in eastern Iran mostly surrounds the stable aseismic blocks of central Iran (Figure 1a). North-south right-lateral shear between central Iran and Afghanistan is about 10-12 mm/yr, mostly accommodated by north-to-south strike-slip faults on the east and west sides of the Lut block. It is probable that most of this shear occurs on the eastern side, whereas north of the Lut the shear is taken up by east-west left-lateral faults that rotate clockwise (Walker and Jackson, 2004). This whole region has been the source of many large earthquakes, many producing surface rupture, in both modern and historic times (Walker and Jackson, 2004). Earthquakes with waveform-modeled depths are all shallower than ~20 km in this region, a pattern seen also in the larger EHB database (Figures 1 and 2f), which has a median depth of 12 +/-5 km.

Iran Ground Truth Data

Critical to our ground truth data discovery and acquisition process are collaborative arrangements that have been made with key organizations in southern Asia. These arrangements are built on exchanges that are mutually beneficial to the parties involved, usually based on our applying advanced techniques to refine locations of the host country's natural seismicity in return for access to in-country ground truth information. In Iran, informal arrangements have been established with the International Institute of Earthquake Engineering and Seismology (IIEES) and the University of Tehran, Institute of Geophysics, during several visits. These arrangements provide a forum for gathering and assessing potential ground truth data, and collecting waveform and phase reading data for events of interest from local and regional stations in Iran. We are also in contact with several groups developing ground truth locations from InSAR-detected ground displacement and other satellite-based location methods that provide important constraints independent of seismic observations. Much new ground truth information in Iran is now being obtained from these sources as an ongoing activity.

Validation through critical examination of the data and procedures that were used in the local network or InSAR location of a proposed ground truth event is an internal process. Therefore, an external validation process, one that utilizes other information as a crosscheck on the reported or derived (using HYPOSAT) local network location, is highly desirable. We use Hypocentroidal Decomposition (HDC), a powerful algorithm for multiple event relocation, as a tool for discovery and validation of ground truth data. HDC is applicable in situations in which several candidate ground truth events and/or InSAR signals are located in a limited region, and in cases where other seismic activity in the area can be localized to known faults and other geologic features. The essence of the validation process is to compare the relative locations in space and time of events based on their ground truth locations, and the relative locations revealed by HDC. An added bonus of the validation process is the generation of additional ground truth events that are of GT5 quality.

Validation of Iran Ground Truth Data

The HDC method for validation yields improved accuracy for both the relative and absolute locations of clustered earthquakes. The gist of the method is to use a multiple event relocation method with regional and teleseismic phase arrival times to constrain relative locations of clustered earthquakes and then to calibrate the absolute location of the cluster by obtaining independent information on the absolute location of one or more members of the cluster. For each cluster there is independent information on location that helps to calibrate the absolute locations. The HDC analysis includes further refinement of the data set by making empirical estimates of readings errors and using these estimates to help identify outliers. These steps yield significant improvements in accuracy and resolution for the relocations. Of course, the main benefit of HDC analysis is to largely remove the biasing effects (path anomalies) of lateral heterogeneity in the Earth, which permits much better resolution of the relative locations of cluster earthquakes.

We have recently extended the calibration process to take into account the uncertainties in calibration data in estimating an optimal calibration shift for the cluster. We also estimate a term to account for the inconsistency between multiple calibration events. Our final estimate of local accuracy for events in calibrated clusters includes all these sources of uncertainty, as well as the uncertainty in relative locations derived from the HDC analysis.

We report here on ground truth studies of four clusters in Iran that are based on recent large earthquakes: Bam (December 2003), Baladeh (May 2004), Zarand (March 2005), and Qeshm (November 2005). In comparison with our previous HDC studies in this region, the data sets of arrival times for these clusters have many more readings from Iranian seismograph stations at near and regional distances. We have obtained these readings through our enhanced collaborative relationship with colleagues at several institutions. The in-country readings have three main advantages:

- They provide critical azimuthal coverage for some events that greatly improves the resolution of relative locations.
- They make it possible to include additional events in the clusters, to improve the statistical power of the HDC analysis and derived parameters, such as empirical path anomalies.
- They provide new paths for which empirical travel times can be estimated, paths that are especially useful for studies of crustal and upper-mantle velocity heterogeneity in the study region.

The four clusters that have been calibrated are shown in Figure 4:

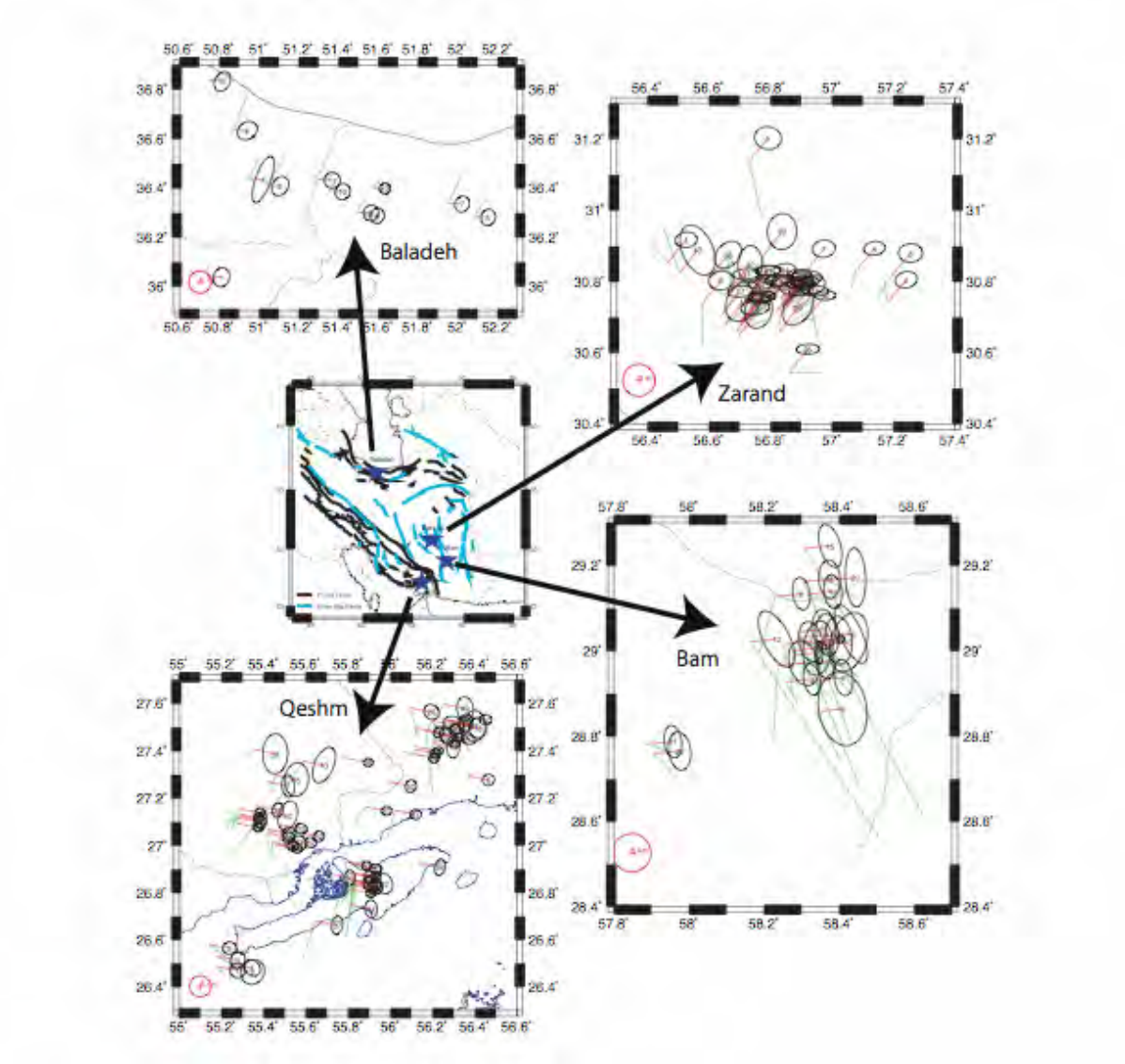


Figure 4. Location map of four earthquake clusters in the Iran region that have been calibrated, and detail maps of the HDC analysis for each cluster. Each figure contains a red circle with 5 km radius in the lower left corner for scale. Green lines show the change in location through the HDC analysis. Red lines show the shift applied to the hypocentroid (thus, the same for each event) to best match the calibration data. Confidence ellipses are at 90% confidence level and include the contribution of uncertainty in relative location from HDC analysis, the calculated uncertainty of the calibration shift, and a component that accounts for discrepancy between multiple calibration data.

Bam Cluster

The Bam cluster begins with the December 26, 2003 mainshock (Mw 6.6) that heavily damaged the city of Bam, and includes 21 subsequent earthquakes through October 7, 2004. Most of the subsequent events can be considered aftershocks, but the last two events in the cluster, on October 6 and 7, 2004 (#21 and 22 in the corresponding panel of Figure 4) are located about 40 km southeast of the seismicity directly associated with the 2003 mainshock.

Calibration of this cluster is based on locating the December 26, 2003 mainshock on the fault revealed by analysis of InSAR data (Talebian et al., 2004; Jackson et al., 2006) and the aftershock survey (M. Tatar, personal comm.). The position along the fault (near the southern end) is constrained by the S-P time of a strong motion instrument in the city of Bam, at the north end of the fault (Bouchon et al., 2006). The depth is well-constrained by waveform modeling at 6 km, but we have no constraint on origin time for this event (the strong motion instrument clock is not calibrated). Fortunately, the aftershock survey provided a reliable location and origin time for an aftershock on January 11, 2004 that is also included in the cluster, and this provides the calibration for origin time. Calibration of the Bam cluster required a shift of 6.9 km at an azimuth of 84° and a shift of -0.24 s in origin time. Ten of the events in the cluster have calibrated locations at GT5 accuracy or better.

Baladeh Cluster

The Baladeh cluster is a small cluster based on the destructive earthquake of May 28, 2004 (Mw 6.3), in the Alborz Mountains north of Tehran (#7 in the corresponding panel of Figure 4). The cluster includes 5 aftershocks, two of which were well-located by a temporary deployment of seismographs (M. Tatar, personal comm.). To increase the resolution of the HDC analysis, we expanded the size of the cluster to include some earlier earthquakes within about 50 km of the May 2004 sequence. The shifts required to satisfy the two calibration events were rather consistent; the weighted average shift that was used to calibrate the cluster is 6.1 km at an azimuth of 93°, and +0.92 s in origin time. Eleven of the events in the cluster have calibrated locations at GT5 accuracy or better.

Zarand Cluster

The Zarand cluster is based on the destructive earthquake of February 22, 2005 (Mw 6.4) and its aftershocks (#8-42 in the corresponding panel of Figure 4). Events 1-7 are earlier events in the area, some of which were also large and damaging.

Calibration of the Zarand cluster is based on the analysis of InSAR, geological, and seismological data by Talebian et al., 2006. This provides a strong constraint on the location and depth of the mainshock hypocenter, but unfortunately does not constrain origin time. There was a temporary deployment to record aftershocks of this earthquake and we are presently waiting for this data to be made available. We are optimistic that the temporary deployment captured one or more of the lengthy and energetic aftershock sequences of this event, allowing improved calibration of the cluster's location, and also providing calibration for origin time. A shift of 9.3 km at an azimuth of 39° is needed to bring the cluster into agreement with the calibration location. Thirty-six of the events in the cluster have calibrated locations at GT5 accuracy or better.

Qeshm Cluster

The Qeshm cluster is based on the Mw 6.0 earthquake of November 27, 2005, and aftershocks that have continued until very recently (#52-62 in the corresponding panel of Figure 4). To gain statistical power for the HDC analysis and gain a better perspective on the seismicity patterns in this region, we enlarged the cluster to include earlier events within about 70 km (Figure 4).

Calibration of the Qeshm cluster is based on a preliminary analysis of InSAR data (J. Jackson, personal comm.) that provides constraint on the location and focal depth of the November 27, 2005 mainshock. There was a very successful aftershock deployment to which we will have access, but analysis of the data has not yet been completed. We are optimistic that these data will provide additional constraint on location calibration, and also provide calibration data for origin time. A shift of 10.1 km at an azimuth of 101° is needed to bring the cluster into agreement with the calibration location. Fifty-two of the events in the cluster have calibrated locations at GT5 accuracy or better.

Regional Path Anomalies

We use the calibrated cluster arrival time data to infer empirical path anomalies (relative to the global model ak135) from each cluster source region to surrounding seismic stations. Figure 5 shows the results for Pg, Pn, and P phases at regional stations for the four clusters in Figure 4. There is broad consistency of path anomalies at most azimuths,

including those observed at stations in Iran. The early arrivals at stations in Saudi Arabia reflect propagation across the Arabian shield. The path anomalies can be the result both of variations in bulk velocity and differences in ray path geometry caused by lateral heterogeneity.

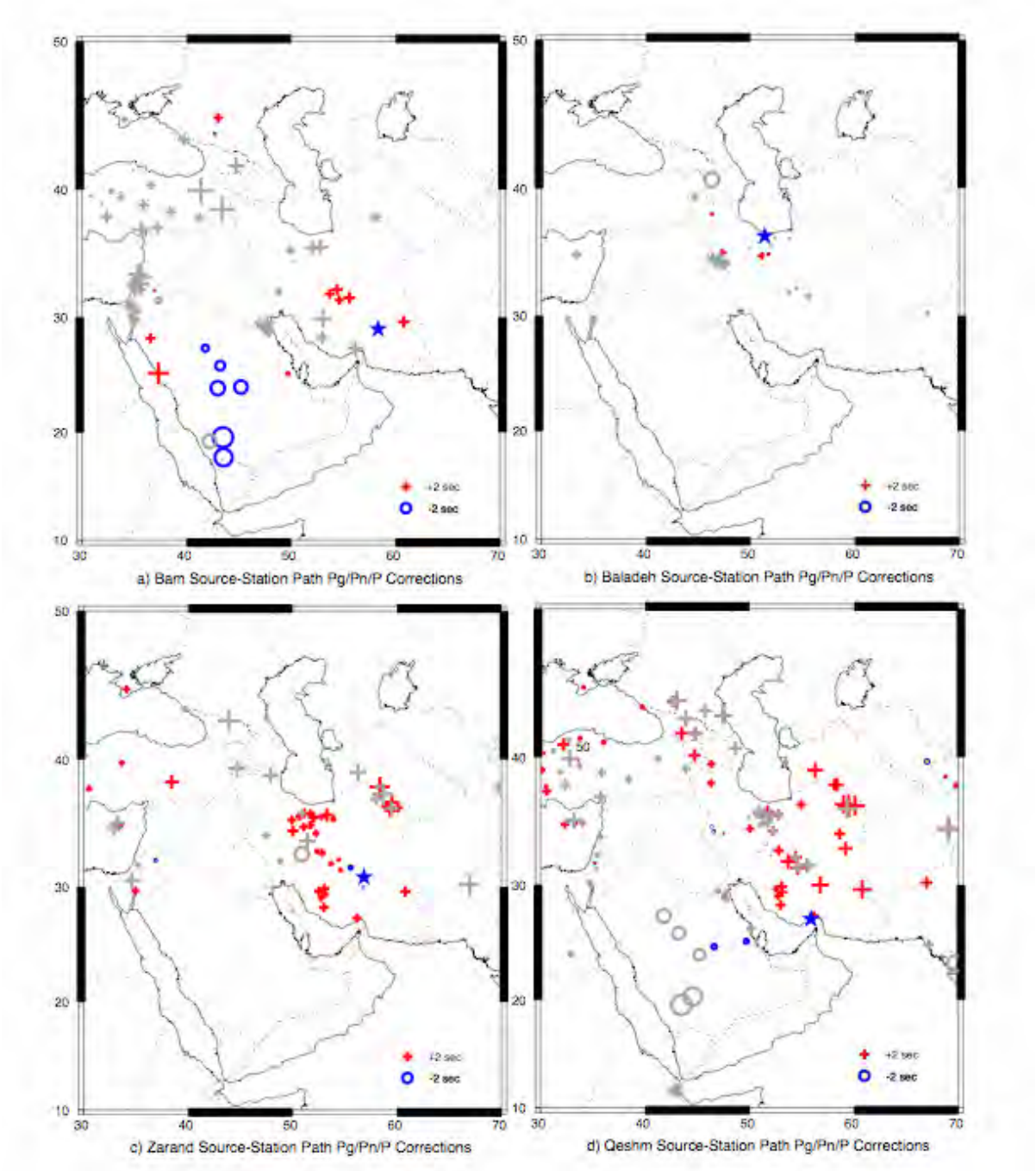


Figure 5. Empirical path anomalies (relative to ak135) for Pn and P phases from (a) Bam, (b) Baladeh, (c) Zarand, and (d) Qeshm clusters. Blue stars show cluster centroids. See Figure 4 for details of clusters. Crosses are late arrivals; circles are early arrivals. Symbol size scales with anomaly. Symbols in color are median anomalies based on 5 or more readings. Grey symbols are based on 2-4 readings.

CONCLUSIONS AND RECOMMENDATIONS

We have relocated Iranian earthquakes occurring between 1918 and 2004. The image of seismic activity occurring at the boundaries between distinct tectonic blocks is sharpened, and event depths are refined. This is a significant advance, as outliers and future events with apparently anomalous depths can be readily identified and, if necessary, further investigated. Our results suggest that the vast majority of Iranian events occur in the upper crust. Lower crustal locations are confirmed in the Oman Line and Alborz regions. Mantle events are associated with the Makran subduction zone and in remnant subduction north of the southern Caspian Sea. Iranian seismicity is the result of the early stages of continent/continent collision between the Arabian Peninsula and Eurasia. Distinct tectonic blocks are responding to the nascent collision through relative motion, resulting in seismicity at the boundaries. Areas of heightened strain (collision with the Oman Peninsula and drastic variations in crustal structure around the southern Caspian) result in lower crustal seismicity.

We have developed new ground truth events and calibrated earthquake locations in Iran, based on detailed multiple event relocation and use of calibration data, both from local seismic network data and from InSAR data. We have been able to include substantial numbers of phase readings at in-country seismograph stations that have improved the quality and quantity of calibrated earthquake locations in this region. We are continuing to develop resources for local network data inside Iran and expect these efforts to lead to new ground truth events and resulting data on empirical path anomalies that will substantially improve location capabilities in this region.

ACKNOWLEDGEMENTS

We are grateful to James Jackson and Keith Priestley at Bullard Laboratories, Cambridge University, and the scientific staff at the International Institute of Earthquake Engineering and Seismology, and at the University of Tehran, Institute of Geophysics, for providing the data used in this study and helping in its interpretation.

REFERENCES

Bouchon, M., D. Hatzfeld, J. A. Jackson, and E. Haghshenas (2006). Some insight on why Bam (Iran) was destroyed by an earthquake of relatively moderate size, *Geophys. Res. Lett*. Vol. 33, L09309, doi:10.1029/2006GL025906

Engdahl, E. R., R.D. Van der Hilst and R. P. Buland (1998). Global teleseismic earthquake relocation with improved travel times and procedures for depth determination, *Bull. Seism. Soc. Amer*., Vol. 88, pp. 722–743.

Engdahl, E. R. and E.A. Bergman (2001). Validation and generation of reference by cluster analysis, location workshop, oral presentation, and poster presentation, in *Proceedings of the 23rd Seismic Research Review: Worldwide Monitoring of Nuclear Explosions*, LA-UR-01-4454, Vol. 1, pp. 205–214.

Engdahl, E. R., J. A. Jackson, S. C. Myers, E. A. Bergman and K. Priestley (2006). Relocation and assessment of seismicity in the Iran region, *Geophys. J. Int*., in press.

Jackson, J., K. Priestley, M. Allen and M. Berberian (2002). Active tectonics of the South Caspian basin, *Geophys. J. Int*. 148: pp. 214–245.

Jackson J., M. Bouchon, E. Fielding, G. Funning, M. Ghorashi, D. Hatzfeld, H. Nazari, B. Parsons, K. Priestley, M. Talebian, M. Tatar, R. Walker and T. Wright (2006). Seismotectonic aspects of the 26 December 2003 Bam, Iran, earthquake, *Geophys. J. Int.*, in press.

Talebian, M., E. J. Fielding, G. J. Funning, M. Ghorashi, J. Jackson, H. Nazari, B. Parsons, K. Priestley, P. A. Rosen, R. Walker, and T. J. Wright (2004). The 2003 Bam (Iran) earthquake: Rupture of a blind strike-slip fault, *Geophys. Res. Lett* 31: L11611, doi:10.1029/2004GL020058.

Talebian, M., and J. Jackson (2002). A reappraisal of earthquake focal mechanisms and active shortening in the Zagros mountains of Iran, *Geophys. J. Int*. 156: pp. 1–21.

Talebian, M., J. Biggs, M. Bolourchi, A. Copley, A. Ghassemi, M. Gorashi. J. Hollingsworth, J. Jackson, E. Nissen, B. Oveisi, B. Parsons and K. Priestley (2006). The Dahuiyeh (Zarand) earthquake of 2005 February 22 in central Iran: reactivation of an intramountain reverse fault. *J. Int*. 164: pp. 137–148.

Walker and Jackson (2004). Active tectonics and late Cenozoic strain distribution in central and eastern Iran, *Tectonics*, 23: doi:10.1029/2003TC001529.

JOINT INVERSION FOR THREE-DIMENSIONAL VELOCITY STRUCTURE OF THE BROADER AFRICA-EURASIA COLLISION REGION

Megan P. Flanagan[2], Eric M. Matzel[2], Suzan van der Lee[1], Heather Bedle[1], Michael E. Pasyanos[2], Federica Marone[3], Barbara Romanowicz[3], Christian Schmid[4], and Arthur J. Rodgers[2]

Northwestern University[1], Lawrence Livermore National Laboratory[2], UC Berkeley[3], ETH Zurich[4]

Sponsored by National Nuclear Security Administration
Office of Nonproliferation Research and Development
Office of Defense Nuclear Nonproliferation

Contract No. DE-FC52-04NA25541[1], W-7405-ENG-48[2], and DE-FC52-04NA25542[3]

ABSTRACT

We report on progress towards a new, comprehensive three-dimensional model of shear velocity in a broad region extending from the western Mediterranean Sea to the Hindu Kush and encompassing northeastern Africa, the Arabian Peninsula, and the Middle East. Our model will be an integration of regional waveform constraints, surface wave group velocity measurements, teleseismic *P* and *S* arrival times, and crustal thickness estimates. These measurements are made from a combination of MIDSEA, PASSCAL, GeoScope, Geofon, GSN, IDA, MedNet, and local deployments throughout the region. The data offer complementary sensitivity to crust and mantle structures and are jointly inverted to image the complexity of this tectonically diverse area.

We are in the process of assembling each of these data sets and testing the joint inversion for subsets of the data. In this phase of the project we focus on compiling crustal thickness constraints from literature, computing group velocity dispersion measurements, and fitting regional fundamental and higher mode Rayleigh waveforms using the partitioned waveform inversion (PWI) technique. To date we have accumulated over 300 crustal thicknesses from receiver functions, reflection/refraction profiles, and gravity surveys. We have measured Love and Rayleigh wave group velocities for hundreds of new paths recorded at the MIDSEA stations and combined them with thousands of existing paths transecting the region. These new paths have better defined the distribution of anomalies particularly with respect to the boundaries of sedimentary basins at short periods. In addition we have inverted over 3,800 waveforms traversing the Arabian Peninsula, Iran, Afghanistan, the Nubian shield, east African rift zone, and the Russian Platform which extends our original coverage significantly to the east and north.

We also demonstrate the proposed new data-inversion methodology and discuss results from combining these new measurements in a preliminary joint inversion for shear velocity structure. The combined data coverage will ensure that our three-dimensional model comprises the crust, upper mantle, and transition zone with spatially varying, but useful resolution that will allow better calibration of both travel times and waveforms for monitoring throughout the Middle East and North Africa.

OBJECTIVES

Our primary objective is developing a new 3-D S-velocity model for the Middle East and Mediterranean region, including North Africa, southern Europe, and Arabia that

1) is resolved in aseismic regions,
2) is resolved throughout the upper mantle (to 660 km),
3) resolves laterally varying crustal thickness,
4) contains laterally varying vertical velocity gradients,
5) is simultaneously compatible with multiple data sets,
6) utilizes several recent, unique waveform data sets, and
7) includes uncertainties of the model parameters.

These features would increase the model's ability to predict and calibrate regional travel times and waveforms, thereby providing improved event locations, focal mechanisms, and other event discriminants.

Secondly, we aim to convert the 3-D *S*-velocity model to a 3-D *P*-velocity model, using both literature on elastic properties (and their partial derivatives with temperature and pressure) of mantle rocks and empirical information provided by measured arrival times of teleseismic *P* and *P*ms waves.

Our third objective is to test both the *S*-and *P*-wave models' ability to predict regional *P* and *S* travel times, deflect wave paths and deform waveforms, and assess their effects first on the studied seismograms (travel times and amplitudes) and subsequently on the 3-D models derived from these data.

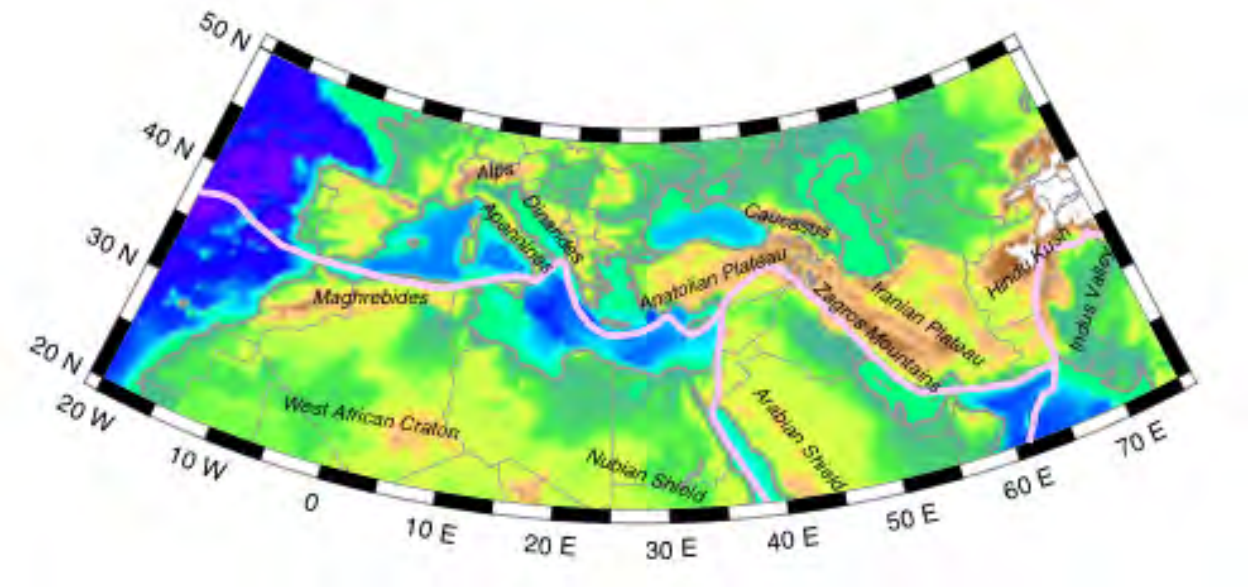


Figure 1. Topographic map of the study region. The pink line is the NUVEL1-A (DeMets et al., 1990) representation of the Eurasia-Africa-Arabia plate boundary.

The study region is centered around the Africa-Arabia-Eurasia triple junction (Figure 1), and extends west to the Africa-Eurasia-North America junction at the Azores, just off the map, and east to the Arabia-Eurasia-Indian Plate junction. The NUVEL1-A (DeMets et al., 1990) representation of these plate boundaries is shown by the pink line in Figure 1. The interaction of these six major tectonic plates with each other and with several microplates within an area ofone quarter of the Earth's circumference yields this region rich with tectonic complexity. The three-dimensional structure of the upper mantle and crust are correspondingly complex. We plan to capture various renditions of this structurally complicated part of the world in one *S*-velocity model through the joint inversion of several different types of seismic data simultaneously; the new model will refine our understanding of the structure and tectonics in this region of the Earth.

RESEARCH ACCOMPLISHED

We have examined over 13,000 available waveforms from the Lawrence Livermore National Laboratory (LLNL) database which sample North Africa and the Middle East and successfully fit about 3800 of them using the non-linear inversion procedure employed by previous partitioned waveform inversion studies (van der Lee and Nolet, 1997: Marone et al. 2004). Six event-station paths for which we have estimated path-average structure are shown in Figure 2 . Earthquakes are indicated by their Harvard Centroid Moment Tensor (CMT) solutions. These six paths sample some of the diversity of geologic/tectonic environments in our study region (Figure 1). The velocity structures were estimated using the average continental model MC35 as a starting model (Van der Lee and Nolet, 1997), however we chose an appropriate crustal thickness for each path (in 5 km increments) based on *a priori* reported estimates. The inversion procedure estimates the perturbations to the starting model by non-linear optimization (Nolet, 1990; van der Lee and Nolet, 1997).

Example Waveform Fits

The waveform fits and resulting shear-velocity profiles for these paths are shown in Figure 3. These models show: 1) faster crustal velocities and slightly faster mantle velocities for the Nubian shield (evid 4074 to AMBATZ); 2) lower velocities in the crust and upper mantle for path crossing the East African Rift (evid 4163 to BGCA); 3) faster crustal and low sub-Moho velocities path from the Gulf of Aden across the Arabian Shield (evid 1325416 to KTLNET); and 4) faster velocities for paths traversing the Russian Platform to the north (evid 6732 to KEV and evid 1323044 to BYKNET).

We attempt to fit both the fundamental and higher mode *S*-waveforms on all three vertical, radial, and transverse components if possible. The following panels show the data (black) and synthetic seismograms for the final model (red). The frequency content of the data and synthetic is different for each fit and generally covers the band 0.006 to 0.1 Hz. The starting model often predicts significant phase differences relative to the data for both the S- and Rayleigh waves. The path across the Nubian Shield (4074-AMBATZ) is faster than the MC35 starting model, and the crustal velocities along this path are quite high. This is consistent with fast crustal velocities in the Arabian Shield (1325416-KTLNET) (e.g., Mokhtar and Al-Saeed, 1994; Sandvol et al., 1998; Rodgers et al., 1999; Julia et al., 2003). It is worth noting that the Red Sea broke up the Nubian-Arabian Shield and these provinces could have similar crustal petrology. Both provinces have volcanics and it has been speculated that mafic intrusion may explain the higher crustal velocities.

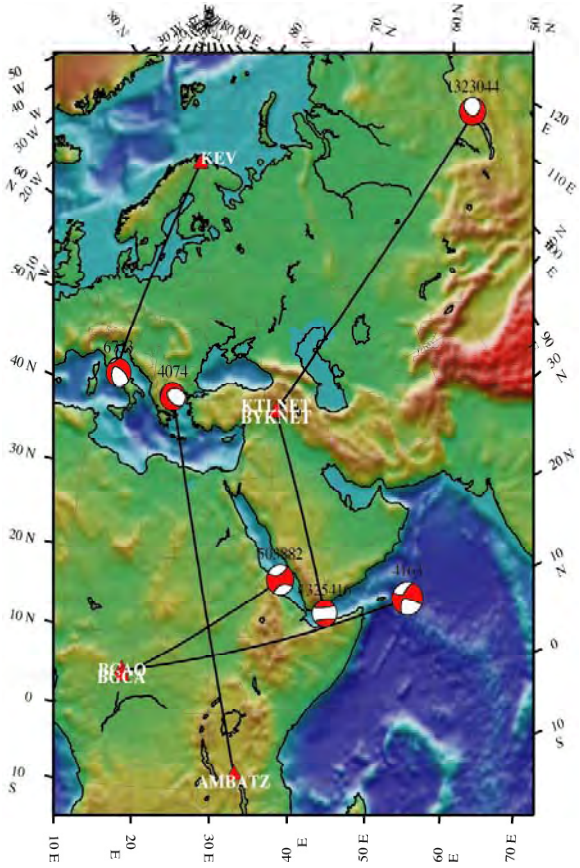
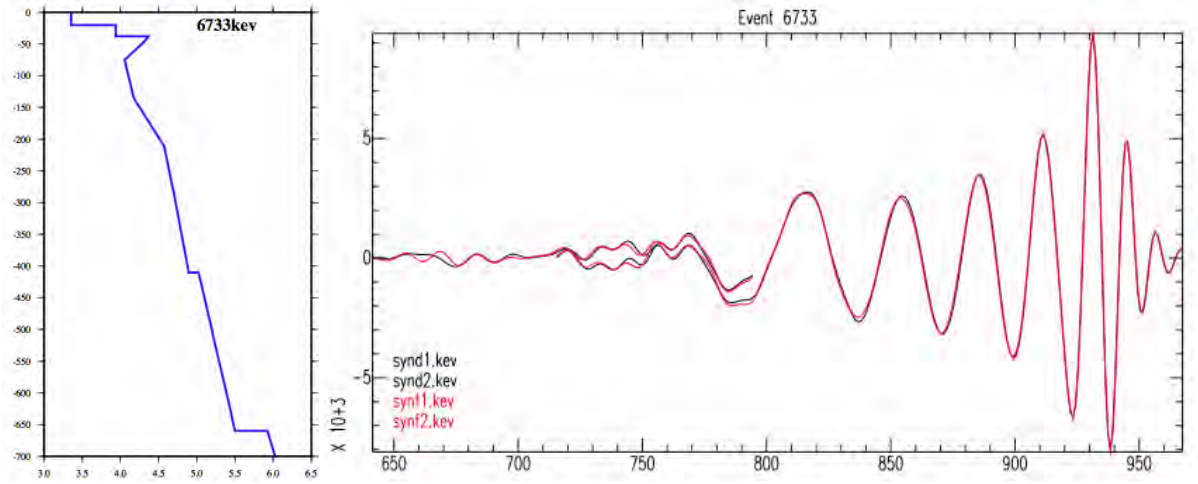
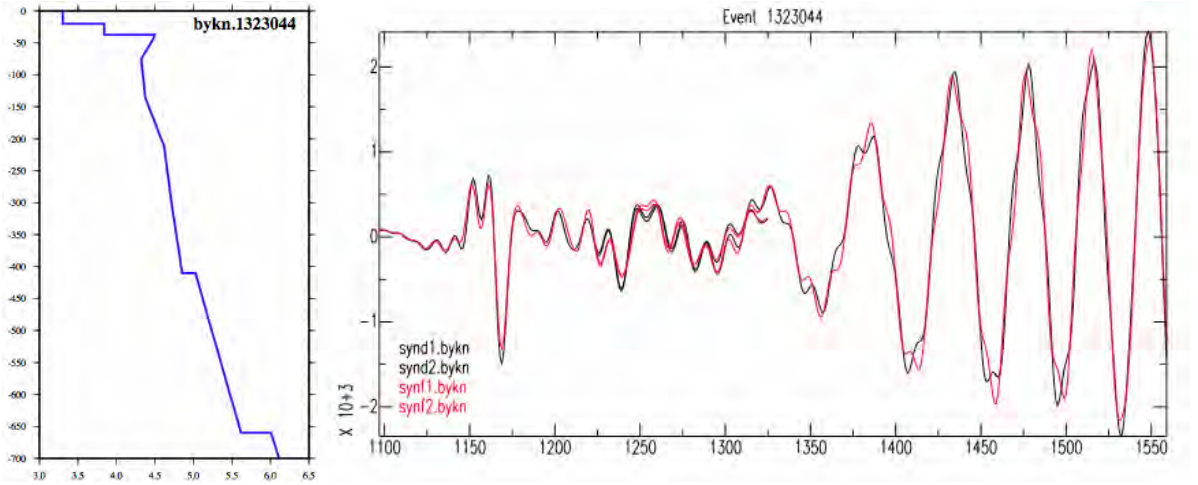


Figure 2. Map of the Western Eurasia and Africa showing six earthquakes and paths for which we fit waveforms. The events are indicated by their moment tensor and identified by their eventid (evid) number. Stations are shown as red triangles.

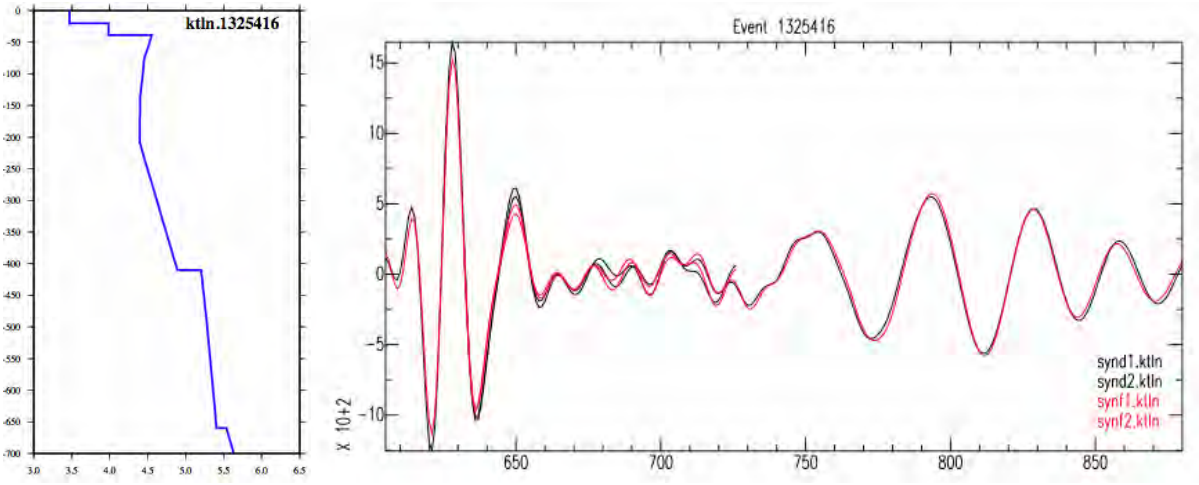
The inferred mantle velocities beneath the Nubian Shield are slightly faster than the starting model. However, reported mantle velocities beneath the Arabian Shield are lower than average (e.g., Mokhtar and Al-Saeed, 1994; Rodgers et al., 1999, Maggi and Priestley, 2005).



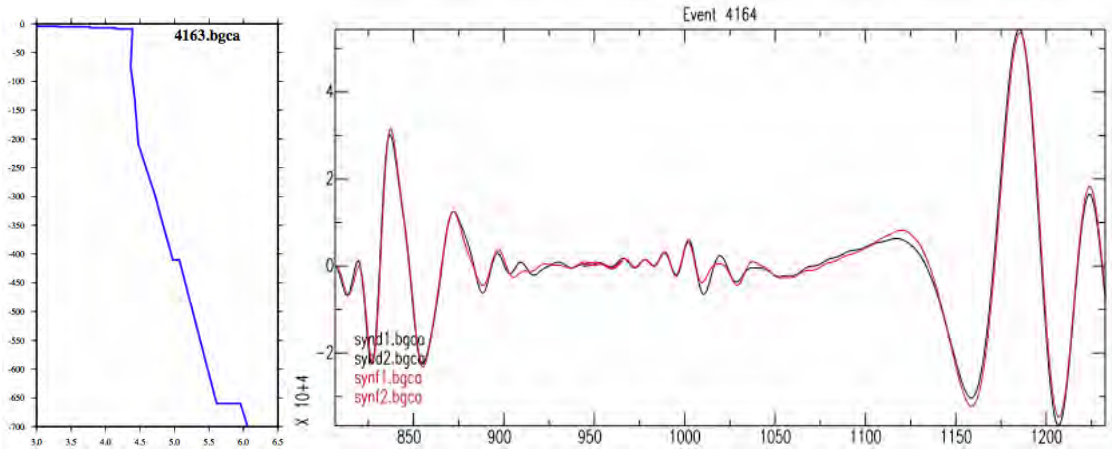
Event 6733 / Station KEV / Transverse component



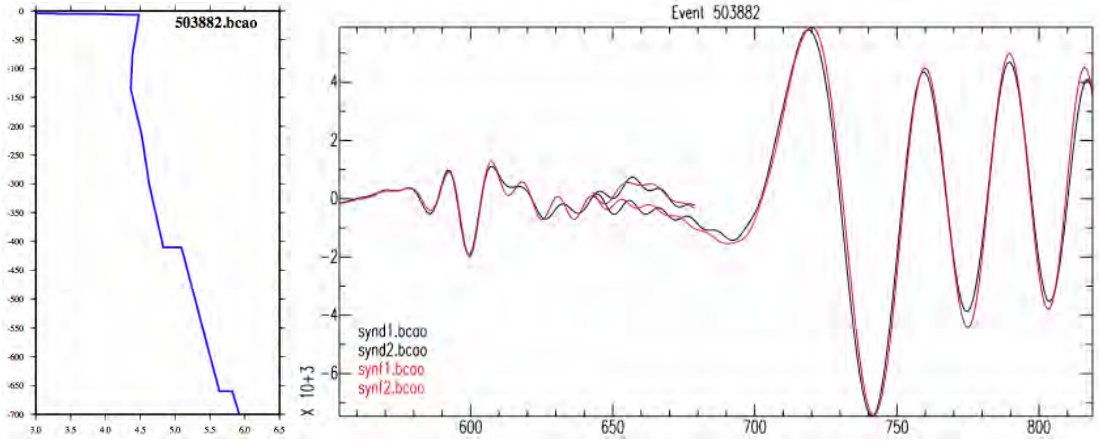
Event 1323044 / Station BYKNET /Transverse component



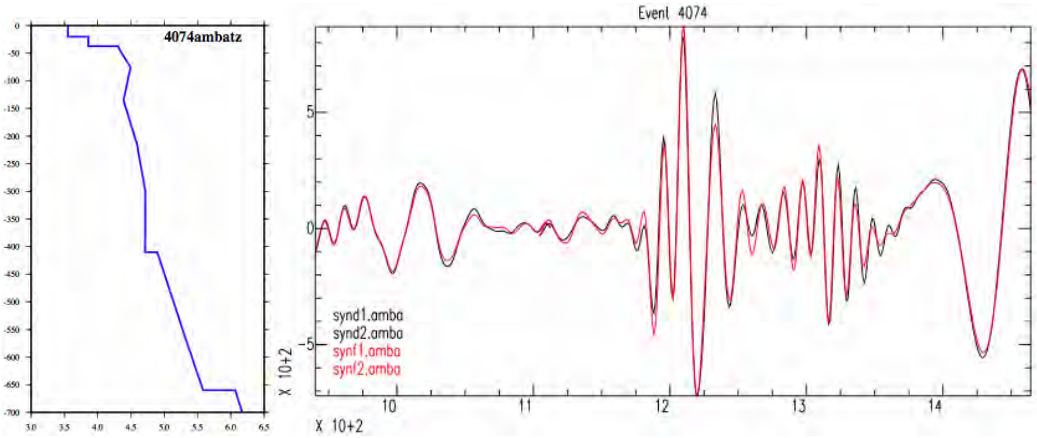
Event 1325416 / Station KTLNET / Radial component



Event 4163 / Station BGCA / Radial component



Event 503882 / Station BCAO / Vertical component



Event 4074 / Station AMBATZ / Vertical component

Figure 3. Example waveform fits (right) and resulting shear velocity profiles (left) for the six paths shown in Figure 2. Data (filtered) is shown in black and the fits in red for three tangential, radial, and vertical components. Note, in some cases the entire wave train is fit (evids 4163 and 4074), and sometimes the body and surface waves are cut and fit separately (evids 6733, 1323044, 1325416, and 503882).

The total ray path coverage is extensive from both the original MIDSEA dataset (Marone et al., 2004) and from data in the LLNL database (shown in Figure 4). We are able to extend the model area significantly to the east and achieve dense sampling of the Arabian Shield, Iran, Afghanistan, and Pakistan. We also have good coverage of northeast Africa, the Red Sea, and parts of the Russian Platform. The 1-D constraints obtained from these ~3,800 waveform fits will be combined with other data sets in the joint inversion for shear velocity structure.

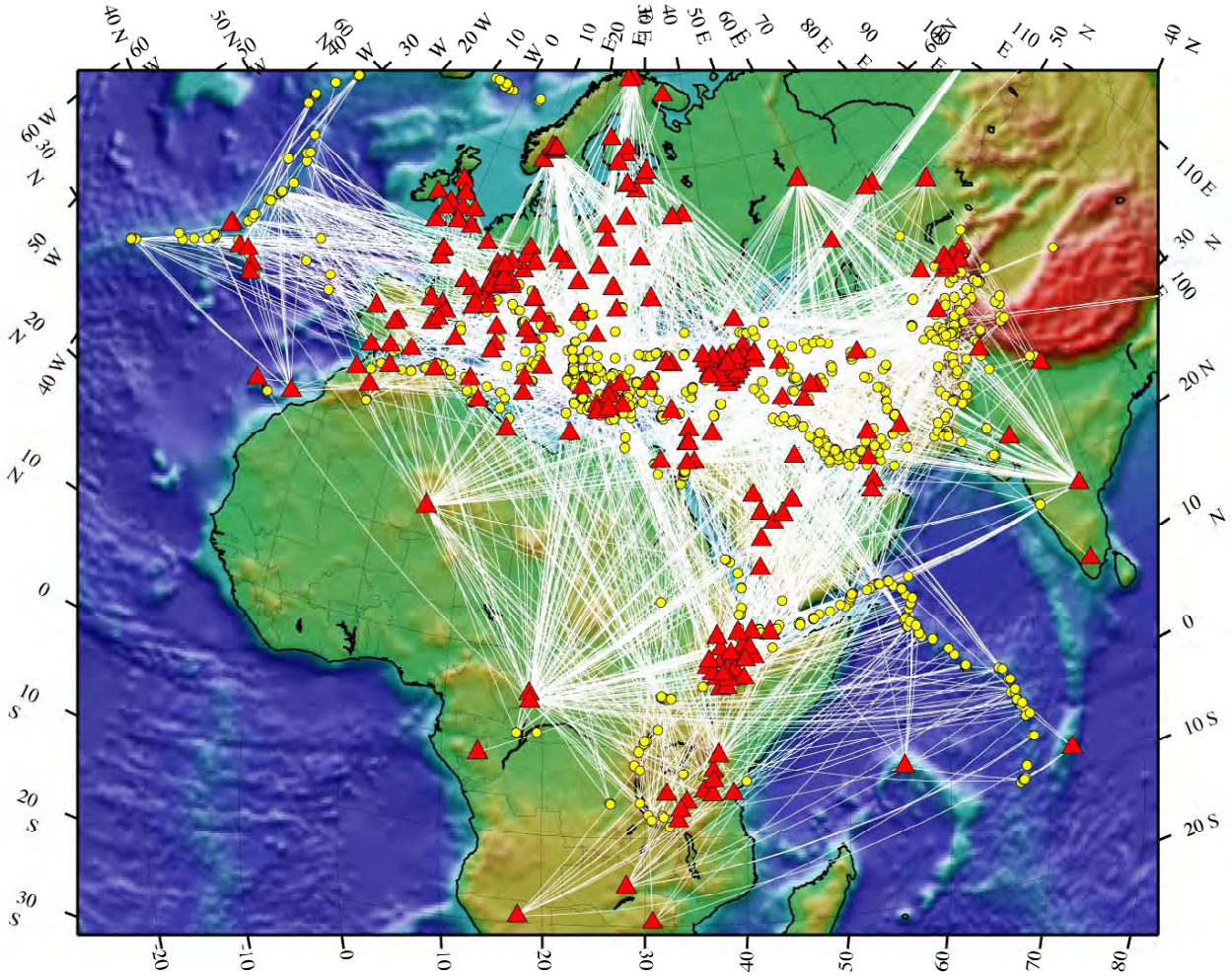


Figure 4. Map of raypath coverage showing all source-receiver paths for the region combining events (yellow circles) with Mb > 5.0 to all recording broadband stations (red triangles) at offsets between 5 and 50 degrees. This represents approximately 3,800 paths from both MIDSEA and LLNL databases.

Surface Wave Group Velocities

We have continued to measure group velocities of Rayleigh waves and use them to update previous group velocity maps (Figure 5). Twenty second Rayleigh waves are very sensitive to crustal structure, which is reflected in the stark group velocity contrast seen in Figure 5 between the oceanic (and Red Sea) regions and the slower continental regions, with thicker crust. Pinpointing the cause of the group velocity differences within continental regions awaits

the analysis of the depth distribution of the *S*-velocity anomalies that give rise to the anomalous group velocities. The contrast between the Nubian Shield and Arabian peninsula is, however, qualitatively consistent with the waveform fits and their constraints on upper mantle structure, which show relatively high velocity in the uppermost mantle beneath northeast Africa. This consistency supports the anticipated benefits of a joint inversion as we plan to incorporate the individual group velocity measurements for each path in the joint inversion.

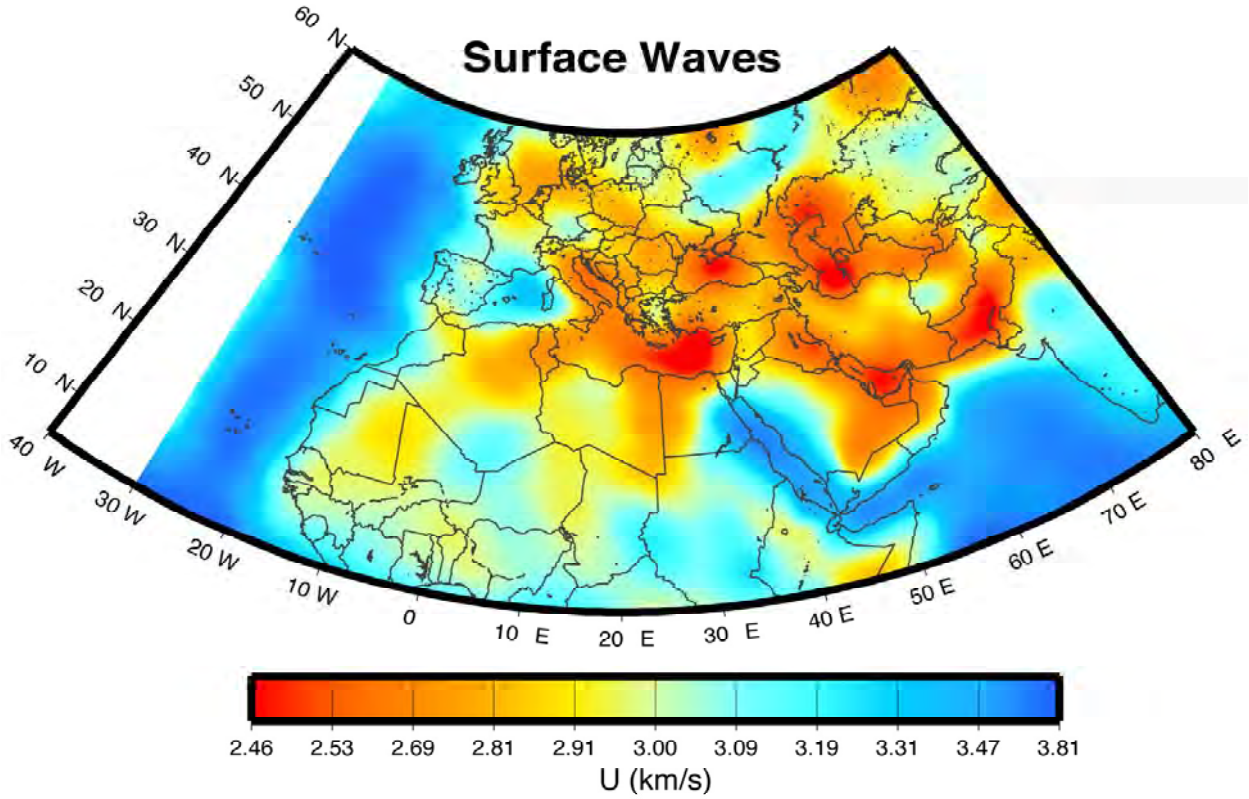


Figure 5. Inferred spatial variation in group velocity (U) for 20 second Rayleigh waves (Pasyanos, 2005).

Crustal Thickness Constraints

We include estimates of crustal thickness as point constraints in the joint inversion and thus compile such measurements from several published studies as shown in Figure 6. We plan to investigate the spatial statistics of these crustal thickness estimates including outlier removal and declustering if necessary before we include them in the joint inversion.

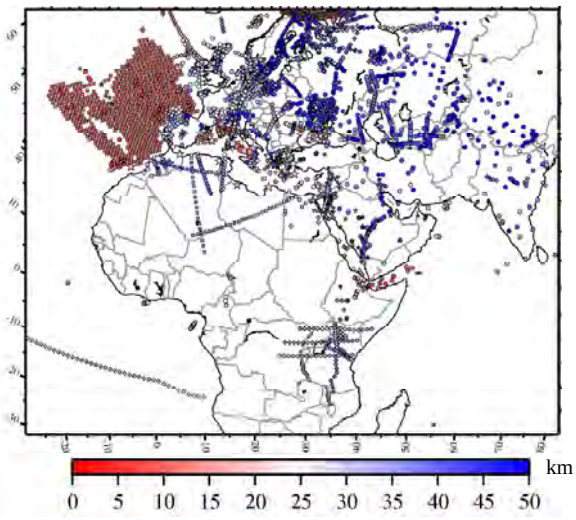


Figure 6. Estimates of crustal thickness including the Mooney et al. (1998) database (circles), receiver function studies (stars), refraction and reflection profiles (squares), and gravity surveys (triangles). The dense points in the Atlantic Ocean are artificially imposed constraints from the MIDSEA study (Marone et al., 2004) due to sparse path coverage from waveform fits.

Teleseismic *S*- and *P*-wave Arrival Times

We plan to include teleseismic *S*- and *P*-wave arrival times and we have collected these data from two different sources thus far (Figure 7).

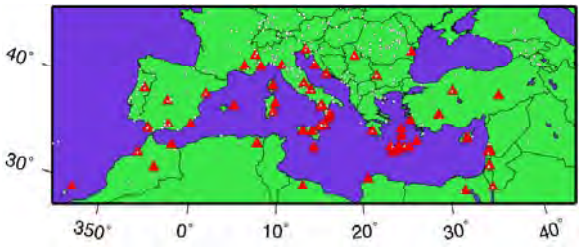


Figure 7. Map of stations used with arrival time data. White circles represent stations for which we extracted absolute delay times from the Engdahl et al. (1998) reprocessed ISC, while red triangles are stations with high-quality relative S-wave delays (between 30 and 90°) obtained using using cross-correlation (Schmid et al., 2006).

Preliminary Inversion Results

To achieve our primary objectives we are developing software that handles the joint inversion of constraints from regional waveform fits, crustal estimates, group velocities, and teleseismic arrival times. We have completed the software for jointly inverting regional waveforms, crustal estimates, and teleseismic arrival times. The joint inversion code has been tested on the teleseismic *S* arrival time data set of Schmid et al. (2006) and the data derived from regional waveform fitting from Marone et al. (2004). The results are encouraging, showing only a percent or two increase in the variance reduction obtained in the linear inversion of both data sets compared to their individual inversions (Schmid et al., 2006). The resolving power of the joint data sets, however, has increased dramatically: the teleseismic data add more lateral resolution to the regional waveform data, while the regional waveform data add more depth resolution to the teleseismic data. The resolved depth range of the combined data sets has doubled with respect to their individual depth ranges. The regional waveform data resolve the upper mantle more strongly while the teleseismic arrival times resolve the lower mantle more strongly. Where the two data sets overlap in spatial sensitivity, (e.g., in the transition zone), the resolving power of the combined data is superior to that of each of the data sets alone.

Upper mantle shear velocity anomalies based on a current inversion of radial and vertical component waveform fits with the crustal constraints is shown in Figure 8. Red regions indicate slower velocities and blue indicate fast. Note the low velocity anomaly beneath the Atlantic Ridge, East Africa Rift, and western Saudi Arabia while fast velocities are seen to the north. These preliminary results are broadly consistent with results from the literature and we do not interpret them further at this point as they are an intermediate step in the whole joint inversion process.

The strength of a joint inversion of different types of seismic data lies in the various data sets being both redundant and complementary. The redundancy is needed to increase accuracy and to ensure that all data sets measure the same structural phenomena. The data sets need to be complementary to increase resolving power over a larger volume of mantle and crust and thereby reduce trade-offs, e.g., between crustal thickness and uppermost mantle velocity, inherent in each type of seismic data set.

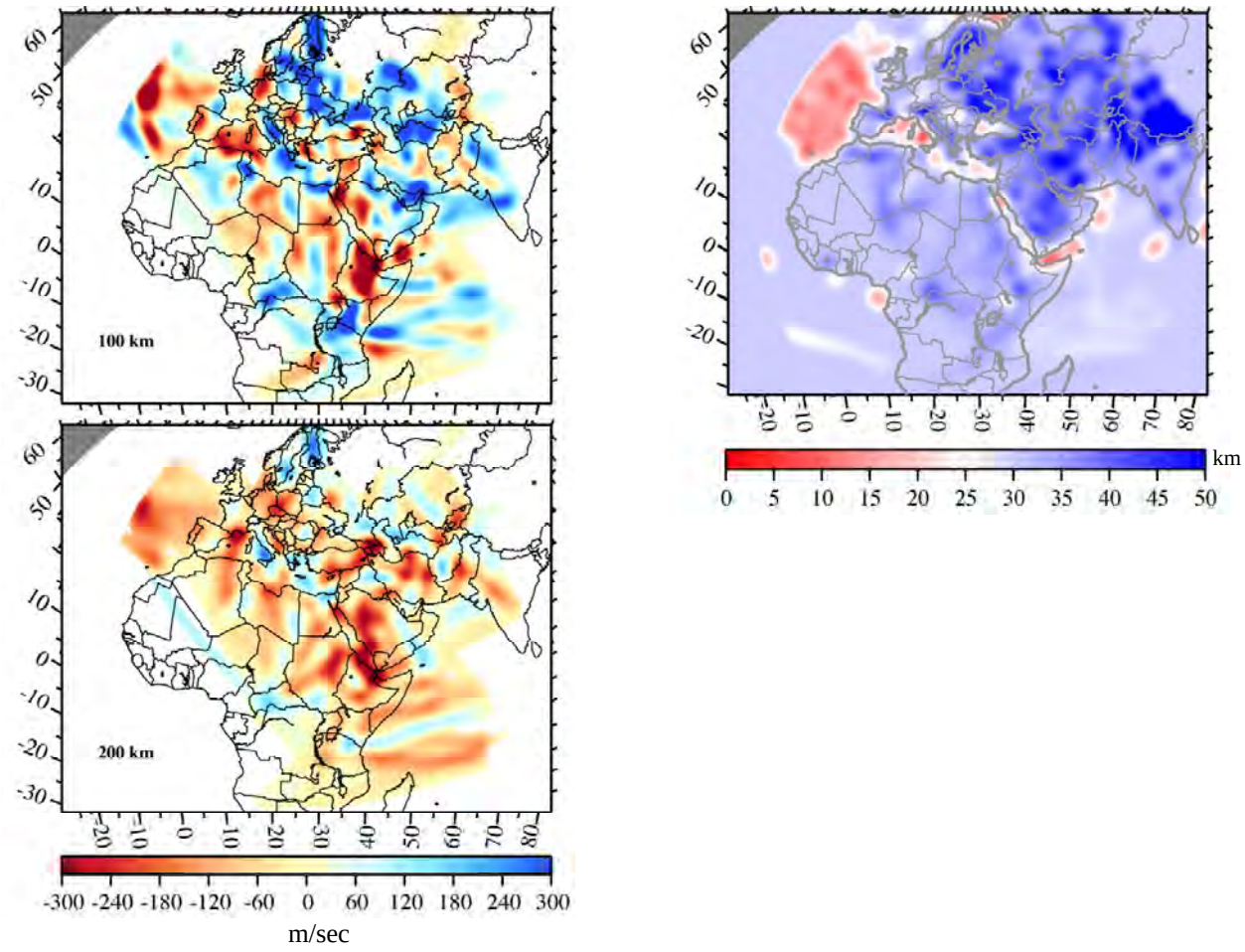


Figure 8. Results from inversion of the regional waveform constraints and crustal thickness estimates. Shear wave velocities at depths of 100 and 200 km are shown to the left where fast (blue) and slow (red) deviations from the starting model are seen. To the right is the resulting map of Moho depth that in some places is driven by the input Moho constraints (from Figure 6). The waveform constraints have been used to interpolate between existing point estimates of crustal thickness in the inversion process to produce this smooth representation.

CONCLUSIONS AND RECOMMENDATIONS

The broad consistency between seismic velocity anomalies inferred from teleseismic arrival times, Rayleigh wave group velocities, and regional waveforms shown here implies that these different types of data sets are at least in part redundant. The consistency further shows that the data sets record the same structural phenomena, despite differences in size and character between typical sensitivity kernels for each data set. This conclusion is further supported by an analysis of how teleseismic delay times depend on frequency (Schmid et al., 2006) and that the teleseismic arrival times and the regional waveforms are highly complementary. The shared sensitivity, though different in character, of receiver functions and Rayleigh wave group velocities to crustal structure is anticipated to separate crustal effects on the observed data from mantle causes when included in the joint inversion.

Preliminary results from data analysis for the Middle East show that this part of the study region is slower on average than typical one-dimensional global velocity models. Marone et al. (2004) and Maggi and Priestley (2005) show that the same is true for the parts of the study region to the west and east, respectively. This allows for a fairly

simple set of one-dimensional starting models, yielding a more uniform treatment of data recorded throughout the region.

ACKNOWLEDGEMENTS

Rick Benson of IRIS guided the conversion of the MIDSEA data to SEED format, and Terri Hauk loaded it into the LLNL database.

REFERENCES

DeMets, C. R.G. Gordon, D.F. Argus, and S. Stein (1990), Current plate motions, *Geophys. J. Int*. 101: 425–478.

Engdahl, E.R., van der Hilst, R. and Buland, R. (1998). Global teleseismic earthquake relocation with improved travel times and procedures for depth determination, *Bull. Seis. Soc. Am*. 88: 722–743.

Hatzfeld, D., M. Tartar, K. Priestley and M. Ghafory-Astiany (2003). Seismological constraints on the crustal structure beneath the Zagros Mountain belt (Iran), *Geophys. J. Int.* 155: 403–410.

Julia, J., C. Ammon and R. Herrmann (2003). Lithospheric structure of the Arabian Shield from the joint inversion of receiver functions and surface wave group velocities, *Tectonophysics* 371: 1–21.

Maggi, A. and K. Priestley (2005). Surface waveform tomography of the Turkish-Iranian Plateau, *Geophys. J. Int*. 160: 1068–1080.

Marone, F., S. Van der Lee, and D. Giardini (2004). 3-D upper mantle *S*-velocity model for the Eurasia-Africa plate boundary region, *Geophys. J. Int*. 158: 109–130.

Mokhtar, T. and M. Al-Saeed (1994). Shear wave velocity structures of the Arabian Peninsula, *Tectonophysics* 230: 105–125.

Mooney, W.D., G. Laske, and T.G. Masters (1998). CRUST 5.1: A global crustal model at 5° x 5°, *J. Geophys. Res*. 103: 727–747.

Nolet, G. (1990). Partitioned waveform inversion and 2-dimensional structure under the network of autonomously recording seismographs, *J. Geophys. Res*. 95: 8499–8512.

Pasyanos, M. E. (2005). A varible-resolution surface wave dispersion study of Eurasia, North Africa, and surrounding regions, *J. Geophys. Res*. 110: B12301, doi:10.1029/2005JB003749.

Rodgers, A., W. Walter, R. Mellors, A. M. S. Al-Amri and Y. S. Zhang (1999). Lithospheric structure of the Arabian Shield and Platform from complete regional waveform modeling and surface wave group velocities, *Geophys. J. Int.* 138: 871–878.

Schmid, C., S. van der Lee, J. C. Vandecar, E. R. Engdahl, and D. Giardini (2006). 3-dimensional S-velocity of the mantle in the African-Eurasia plate boundary region from phase arrival times and regional waveforms, *J. Geophys. Res*., in review

Sandvol, E., D. Seber, M. Barazangi, F. Vernon, R. Mellors, and A. Al-Amri (1998). Lithospheric seismic velocity discontinuities beneath the Arabian Shield, *Geophys. Res. Lett*. 25: 2873–2876.

Van der Lee, S., and G. Nolet (1997). Upper-mantle S-velocity structure of North America, J. Geophys. Res., 102:22,815–22,838.

Van der Lee, S., F. Marone, M. van der Meijde, D. Giardini, A. Deschamps, L. Margheriti, P. Burkett, S. C. Soloman, P. M. Alves, M. Chouliaras, A. Eshwehdi, A. Suleiman, H. Gashut, M. Herak, R. Oritz, J. M. Davila, A. Ugalde, J. Vila, and K. Yelles (2001), Eurasia-Africa plate boundary region yields new seismographic data, Eos Trans. AGU, 82: (51), 637–646.

REGIONAL TRAVEL-TIME UNCERTAINTY AND SEISMIC LOCATION IMPROVEMENT USING A THREE-DIMENSIONAL *A PRIORI* VELOCITY MODEL

Megan P. Flanagan[1], Stephen C. Myers[1], and Keith D. Koper[2]

Lawrence Livermore National Laboratory[1] and Saint Louis University[2]

Sponsored by National Nuclear Security Administration
Office of Nonproliferation Research and Development
Office of Defense Nuclear Nonproliferation

Contract No. W-7405-ENG-48[1,2]

ABSTRACT

We demonstrate our ability to improve regional travel-time prediction and seismic event location accuracy using an *a priori* 3-D velocity model of Western Eurasia and North Africa (WENA1.0). Travel-time residuals are assessed relative to the IASPEI91 model for approximately 6,000 *Pg*, *Pn*, and *P* arrivals, from seismic events having *2s* epicenter accuracy between 1 km and 25 km (GT1 and GT25, respectively), recorded at 39 stations throughout the model region. Ray paths range in length between 0° and 40° (local, regional, and near teleseismic) providing depth sounding that spans the crust and upper mantle. The dataset also provides representative geographic sampling across Eurasia and North Africa including aseismic areas. The WENA1.0 model markedly improves travel-time predictions for most stations with an average variance reduction of 29% for all ray paths from the GT25 events; when we consider GT5 and better events alone the variance reduction is 49%. For location tests we use 196 geographically distributed GT5 and better events. In 134 cases (68% of the events), locations are improved, and average mislocation is reduced from 24.9 km to 17.7 km. We develop a travel time uncertainty model that is used to calculate location coverage ellipses. The coverage ellipses for WENA1.0 are validated to be representative of epicenter error and are smaller than those for IASPEI91 by 37%. We conclude that *a priori* models are directly applicable where data coverage limits tomographic and empirical approaches, and the development of the uncertainty model enables merging of *a priori* and data-driven approaches using Bayesian techniques.

OBJECTIVES

Our objective is to improve regional travel time prediction, improve the accuracy of seismic location estimates, and reduce the uncertainty of the estimated locations. As we focus on the geographic region of Western Eurasia, the Middle East, and North Africa, we develop, test, and validate 3-D model-based travel-time prediction models for 39 stations in the study region. Improvement in travel-time prediction is quantified, and final calibrations are tested in an end-to-end relocation of 196 events with know location accuracy between 1 km and 5 km (GT5). Improvement in both location and uncertainty estimates are assessed.

RESEARCH ACCOMPLISHED

Validation Data Sets

We validate improvement in travel-time prediction using well-recorded events with accurate locations. Each validation event meets either the network-coverage accuracy criteria of Bondár et al. (2004) or the location accuracy is constrained by non-seismic means (e.g., explosions with known sources). Epicenter accuracy ranges from perfect (known locations) to 25 km for events constrained with a teleseismic network. A procedure similar to the leave-one-out validation described in (Myers and Schulz, 2000) is used to check the consistency of each arrival-time observation. This procedure is a considerable improvement over outlier removal based on statistics of the whole population, because local trends and biases are taken into consideration. Culling based on location accuracy and arrival-time consistency produces a self-consistent data set of accurate travel-time measurements. Ray paths for the validation data set are shown in Figure 1. Ray path coverage is excellent over much of the region, and our new data set provides considerable improvement in ray coverage for aseismic regions, such as North Africa.

Our ultimate goal is to improve regional-network location accuracy. We test location performance by relocating 196 events with an epicenter accuracy of 5 km or better (Figure 1): GT1(10), GT3(2), and GT5(184). The GT1 events are peaceful nuclear explosions (PNE) taken from the catalog of explosions scattered across the former Soviet Union and reported to have an accuracy of 1 km (Sultanov et al., 1999). The GT3 events are explosions at the Novaya Zemlya test site as sometimes these locations are known very well from non-seismic analysis such as satellite imagery. Several of the GT5 events are generated from the cluster analyses of researchers Engdahl and Bergman (2001).

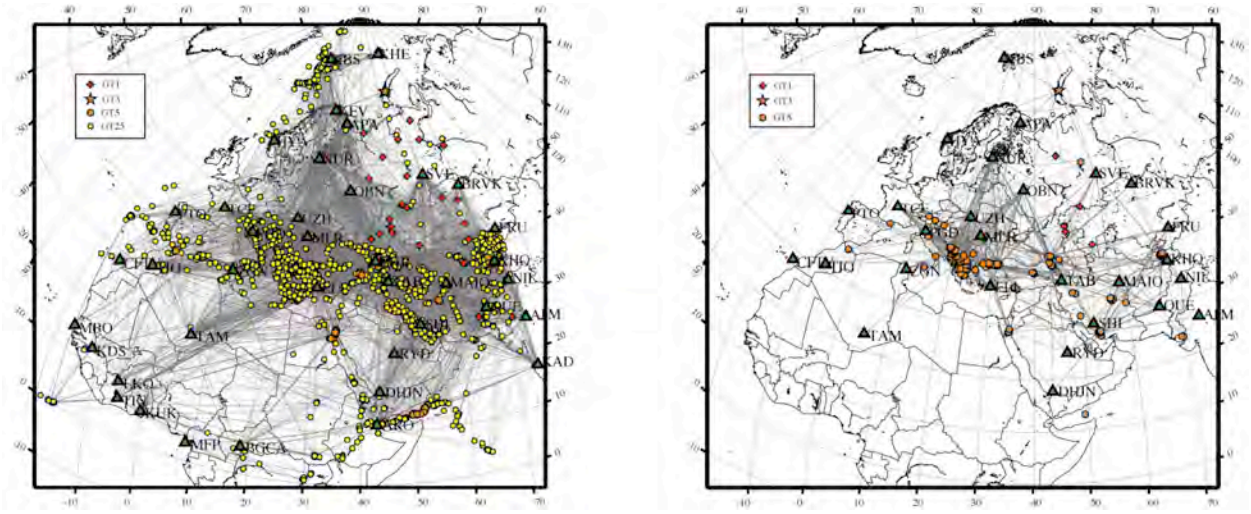


Figure 1. (Left) Map of raypaths from the GT25 and better events to 39 stations (green triangles) showing good coverage of the entire model region. A total 2,367 events (GT1:45, GT3;6, GT5:63, and GT25: 2260 generate 5,767 arrivals to stations ranging from 0° to 50° epicentral distance. (Right) The 195 GT5 reference events used to test location accuracy and the 27 station networks used for relocation.

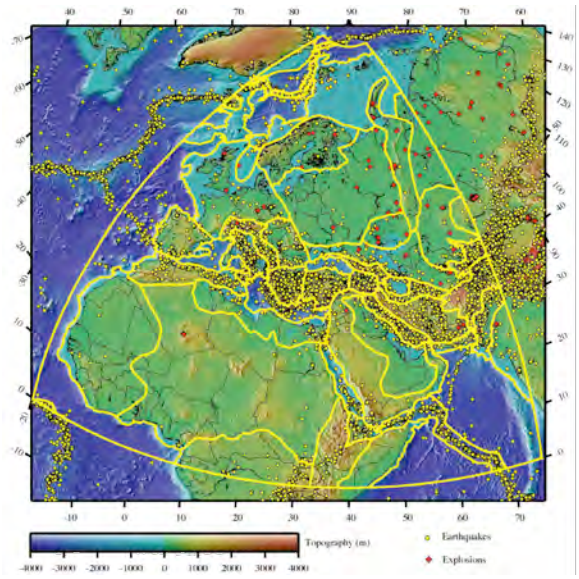


Figure 2. Crustal regionalization used in the WENA1.0 geophysical model. There are 45 base models, outlined in yellow, which describe *P*- and *S*-wave velocities, density, and *Q* (Pasyanos et al., 2004).

WENA1.0 Geophysical Model

We demonstrate improvement in travel-time prediction of *P*-waves and regional location performance using the *a priori* WENA1.0 model of Pasyanos, et al. (2004) (Figures 2 and 3). WENA1.0 is a 3-D Earth model of the crust and upper mantle that is made up of geophysically distinct regions. Each regional velocity model is determined using prior geophysical studies and analogy with similar geologic provinces. Because the regional models are developed independently, the WENA1.0 is an *a priori* model that is not based on any one data set. Because the model is developed using geophysical analogy, it is particularly applicable to aseismic regions where calibration data are sparse. Model resolution is 1° by 1°, and the data are primarily compiled from: Exxon Map, Crust 5.1, topography, seismicity, phase blockages, *Pn* tomography, surface-waves, receiver functions, sediment map of researchers Laske and Masters (1997), crustal regionalizations by Bhattacharyya et al. (2000) and Walter et al. (2000), and mantle model 3SAC by Nataf and Ricard (1996). The WENA1.0 model has been extensively evaluated using a number of data sets, including surface wave dispersion measurements, teleseismic receiver functions, gravity, and waveform fits (Pasyanos et al., 2004).

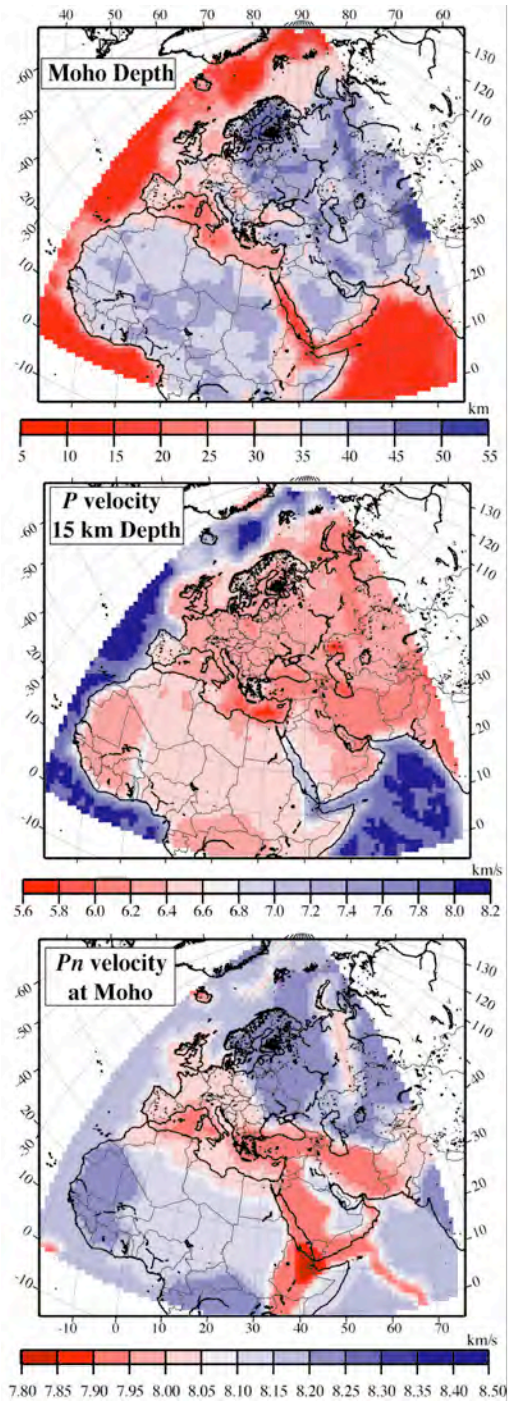


Figure 3. Example of geophysical features of the WENA1.0 model: depth to Moho (Top), *P*-wave velocity at 15 km depth (Center), and *Pn* velocity directly beneath the Moho (Bottom).

3-D Finite Difference Travel-Time Calculations

We use the finite-difference method of Vidale (1988) with modifications by Hole and Zelt (1995) to compute travel times through the WENA1.0 velocity model. This technique propagates wave fronts radially outward from a point source using each grid (or time) point as a secondary source for each successive grid point. This procedure is more efficient and accurate than ray tracing as it is able to treat sharp velocity gradients which produce refracted, diffracted, or head waves in addition to direct phases. Furthermore, by taking advantage of travel-time reciprocity, we place the ray-tracing source at the station locations and calculate travel-times to a 3-D grid of points in the earth. Using this approach, the ray tracer is run once for each station, and travel-time predictions are estimated through interpolate of the travel-time prediction grid.

The finite difference code is modified to allows us to compute travel times out to regional and near-teleseismic distances (~13° to 30°). We apply a Cartesian to spherical coordinate transformation to the source and receiver locations that are input to the code (Flanagan et al., 2006). Therefore, instead of using an earth flattening approach (which may not be applicable to 3-D models), we literally create a spherical grid of points. The code is run in a volume of dimensions of roughly 35° by 50° laterally and 1,500 to 2,200 km deep with a grid spacing of 5 km. The grid spacing is determined empirically as a trade-off between the accuracy of the travel-time prediction and computer memory limitations, and we find that a grid spacing of 5 km provides a reasonable accuracy (i.e., timing errors of approximately 0.25 s, Figure 4).

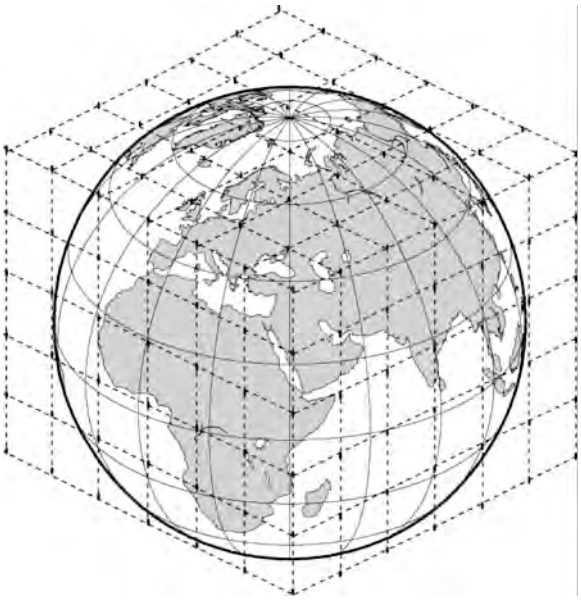


Figure 4. The "sphere in a box" parameterization for the finite difference (FD) code. The source, station, and velocity models are known in spherical coordinates while the FD code operates on a Cartesian grid. We apply a spherical to Cartesian coordinate transform to the input and output of the code to ensure accurate travel time calculations for a spherical earth.

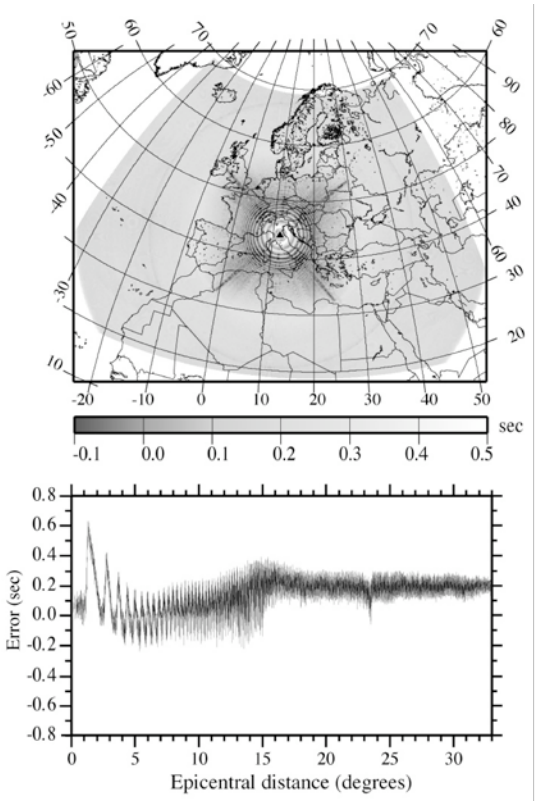


Figure 5. Estimates of computational error in the travel times predicted using the 3-D finite difference code relative to theoretical arrival times computed using a 1-D ray-tracer with the IASPEI91 model. (Top) Map view of errors at 10 km depth; note the errors vary with both distance and azimuth. (Bottom) Plot of errors as a function of distance from the source.

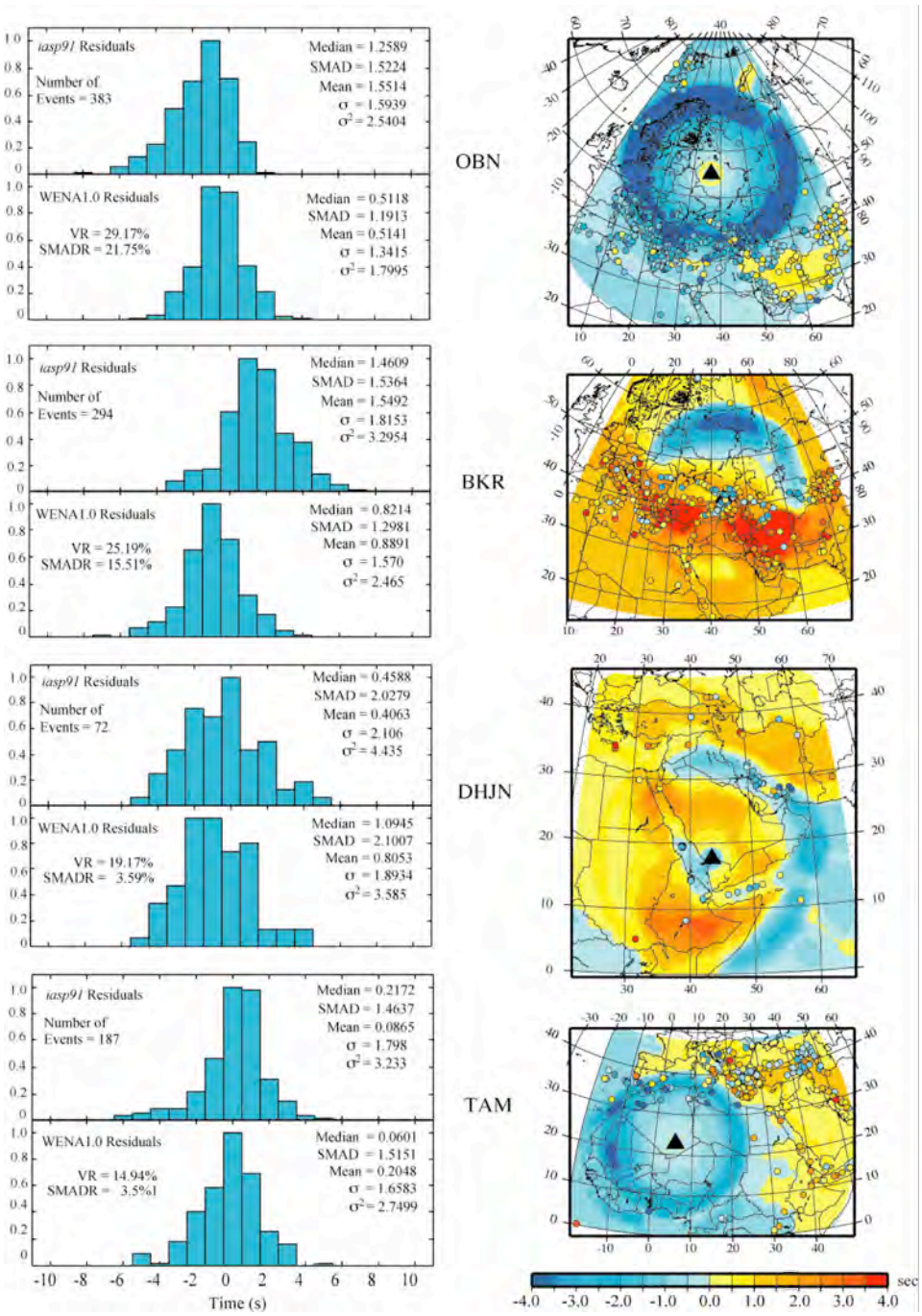


Figure 6. (Left) Histograms of GT25-IASPEI91 and GT25-WENA1.0 residuals showing the variance reduction (VR) for observed times at different stations. While WENA1.0 does not improve travel-time prediction in all cases, we find that prediction is improved by 29% for the whole GT25 data set. (Right) Travel-time residual surfaces at 10 km depth; these model-based correction surfaces are computed by subtracting the IASPEI91 predicted time from the WENA1.0 predicted time. The (GT25-IASPEI91) residuals are plotted on top of the correction surfaces for direct comparison. Note that although these surfaces were derived without any of these data, they reflect the trends in many places, and the remaining misfit should be due to either structure not captured in the model or conflicting picking errors.

Result 1: Improvement in Travel-Time Prediction

We compute 3-D travel-time prediction models for first arriving *P*-wave travel times predicted by the FD algorithm. The total predicted arrival time is computed along a regular latitude and longitude grid with 25 km sampling. Depth is regularly sampled at intervals of 10 km down to 50 km. Each prediction provides station-specific travel times for regional to near-teleseismic distances, which can be used to locate regional-distance events. The difference between WENA1.0 and IASPEI91 travel-time predictions at 4 stations is shown in Figure 6. This example is for a source depth of 10 km. We find travel time differences of up to 6 sec relative to IASPEI91. Extreme differences in travel-time prediction are generally caused by anomalous upper-mantle velocity, thick crust, and/or thick sediments. Note the patterns in these correction surfaces correlate with the structural features in the WENA1.0 model; fast predictions are seen to the north (e.g., Russian platform) while slow anomalies are seen in the south (e.g., Turkey, Mediterranean, Iran). Variation in residual variance is generally on the order of 20% to 30% for the 39 stations we tested, but performance at any given station is quite variable with improvement ranging from 50% (e.g., KDS, APA) to negligible (PGD, RYD).

Result 2: Uncertainty Model for WENA1.0

Travel-time prediction uncertainty is commonly distance dependent. Distance dependent uncertainty results from velocity-model errors that cause cumulatively more bias in travel-time prediction with distance. In this study we fit a distance dependent uncertainty model using our validation data set. The simple fitting procedure entails calculating the mean and spread of the residual distribution in distance bins. Statistics of each bin are then used to determine the uncertainty at a given confidence in each distance bin. The distance-dependent uncertainty for WENA1.0 and IASPEI91 is shown in Figure 7. Because the uncertainty model is based on a data set that covers nearly all of WENA, it is applicable over the whole model.

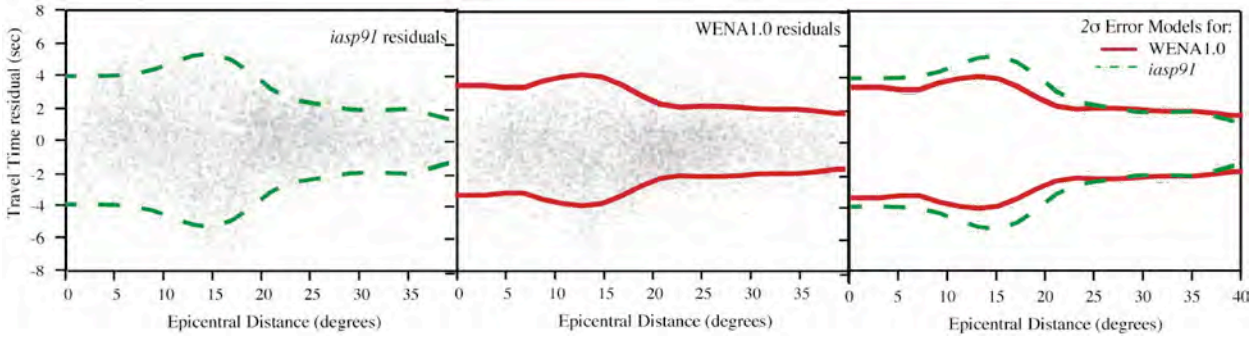


Figure 7. Distance-dependent uncertainty for IASPEI91 and WENA1.0. Note the non-stationarity and correlation in travel time uncertainty between 1,000 and 2,800 km; uncertainty increases and errors are correlated (negative bias).

We use variogram modeling to assess the spatial statistics of the travel-time residuals. This approach examines the difference between residuals as a function of inter-event distance. Example variogram analysis is shown in Figure 8; note that the variograms do not approach zero for points that are nearly co-located (i.e., data are not perfectly correlated) due to errors associated with determining travel-time residuals. However, it is apparent that the variograms reach minima (correlation is maximum) for points close together, and the variograms increase (correlation decreases) as points become separated by greater distance. Overall the IASPEI91 variograms are azimuthally non-stationary beyond 6° to 7° and have higher covariance as compared with the WENA1.0 variograms at the same distance. The WENA1.0 variograms appear more stationary after 6° to 7° and have smaller sill values (lower overall variance). Variogram analysis shows that the 3-D WENA1.0 model accomplishes two goals: improving the travel time prediction by reducing the overall variance of residuals, and reducing the non-stationarity of the uncertainties. The 3-D model removes the long-period structure in residuals, as ideally we want to account for all correlated structure and just be left with random error (Flanagan et al., 2006). Ultimately we want an azimuthally invariant uncertainty model because a simpler uncertainty model means that the 3-D velocity model is predicting the 3-D structure, so errors are more consistent and error ellipses are truly representative of location accuracy.

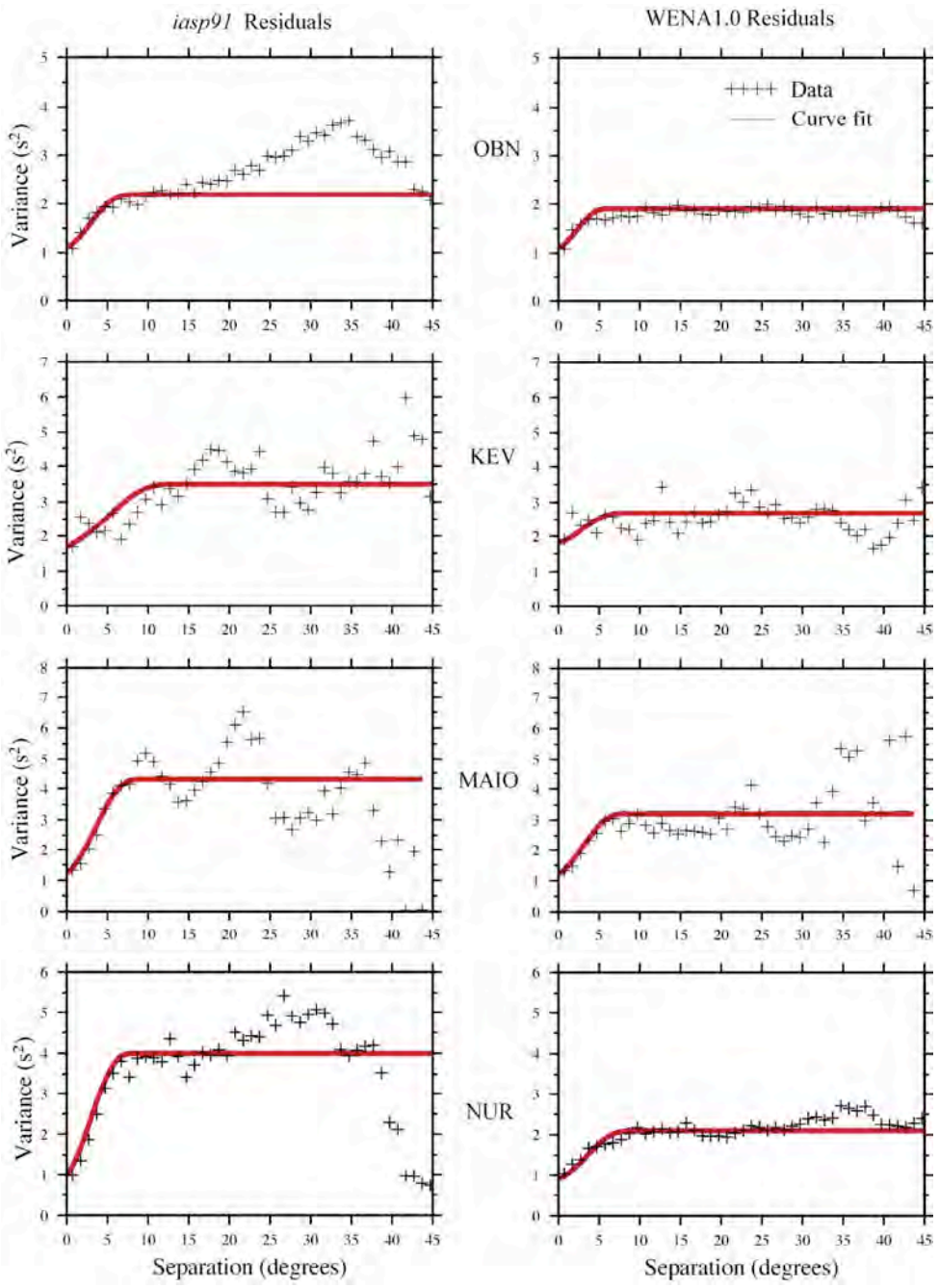


Figure 8. Variograms of travel time residuals at stations OBN, KEV, MAIO, and NUR for both the WENA1.0 and IASPEI91 velocity models. Crosses are the data variogram values in 1.0° bins; solid lines are the model variograms determined by curve fitting. The sill is the background variance of the data, the range is the distance at which correlation between points is zero, and the nugget is the covariance of co-located points. The IASPEI91 variogram is non-stationary (levels off at the sill then increases again). The non-stationarity is caused by long-period features in the residual structure. WENA1.0 improves prediction of long-period residual features, and the variogram is relatively flat after the sill is reached.

Result 3: Improvement in Location Using WENA1.0

Our derived distance-dependent error model is now combined with our model-based correction surfaces to essentially provide a set of station-based 3-D travel-time tables with errors that can be used for computing seismic event locations. We compare event relocations with and without the travel-time corrections and use the statistics of mislocation, error ellipse area, 95% coverage, and location misfit vectors to evaluate location improvement. The geographic distribution of the relocated GT5 events and associated raypaths are seen in Figure 9 for events that moved more than 5 km (the GT level) and had a secondary azimuthal gap of less than 270°. Examining the individual raypaths along which travel time (and thus the location) is improved (red) or degraded (blue) by WENA1.0 allows us to qualitatively assess where the model is performing best. WENA1.0 shows improved location calibration on the Russian Platform, European Arctic, Middle East, South Asia, East African Rift, Anatolian Plateau, and parts of the Mediterranean, however, there are many individual paths (Figure 9, left) that show conflicting results. Most of the improvements occur in the northern and eastern parts on the model, while the most equivocal results are in the Hellenic Arc in the Mediterranean. Because the amount of location improvement scales with the size of the symbols, the greatest improvement can be seen by the larger red triangles, regardless of secondary azimuthal gap criteria, indicating that WENA1.0 improves location accuracy in more instances and to a greater extent.

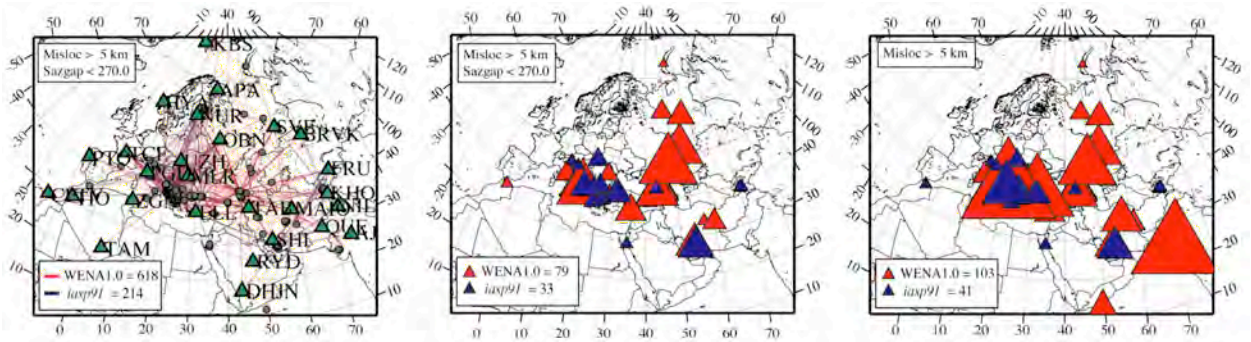


Figure 9. (left) Individual raypaths from GT5 events (gray circles) and stations (green triangles) used in relocation tests that depict specific paths along which the travel time prediction and thus the locations are improved (red lines) or degraded (blue lines). We plot only those events that moved more than 5 km (the GT level) and had a secondary azimuthal gap of less than 270° which resulted in 618 paths being better predicted while 214 paths were degraded. (center) Geographic distribution of the 79 GT5 events which where better located by WENA1.0 (red triangles) and the 33 events which were degraded (blue triangles) again for relocation greater than 5 km and secondary azimuthal gap of less than 270°. The amount of location improvement scales with size of the symbols. (right) Same as center plot for relocation greater than 5 km and no secondary azimuthal gap restriction.

While the average IASPEI91 mislocation is 24.9 km, it is 17.7 km for WENA1.0. Figure 10 illustrates distributions of relative difference in epicenter mislocation for the GT5 validation dataset using both velocity and uncertainty models. Symbols above the diagonal line are improvements using WENA1.0 while below the line are degradations. Difference in epicenter mislocation is also shown in histogram form in Figure 10 where negative values indicate improvement with WENA1.0. This represents an improvement in location of 7.1 km and agrees with other calibration efforts that use 3-D velocity models and GT10 or better reference events (e.g., Ritzwoller et al., 2003; Yang et al., 2004; Murphy et al., 2005).

We next consider the quality of the network geometry on our relocations, as it is a large factor in the resulting accuracy (Bondár et al., 2004). We examine mislocation as a function of primary and secondary azimuthal gap, and number of stations having a defining pick. When the total number of stations used to locate is small (less than five) the location is not well constrained by either velocity model. The average location error grows as the number of stations decreases, with degradation increasing rapidly at about 10 to 11 stations. Note that for any number of stations WENA1.0 almost always performs better than IASPEI91 even when more than 10 stations are used. When the primary azgap is greater than 180° and or the secondary azgap is greater than 270° the station geometry is poor and both models do a poor job of predicting an accurate location, as even small model and pick errors are magnified into large location errors. However, the mean and standard deviation of the distributions are smaller for the 3-D

WENA1.0 model than for the 1D IASPEI91 model. The secondary azgap in particular proved to be an important indicator of the robustness of the final locations, thus we chose a cutoff at 270° for the remaining analysis.

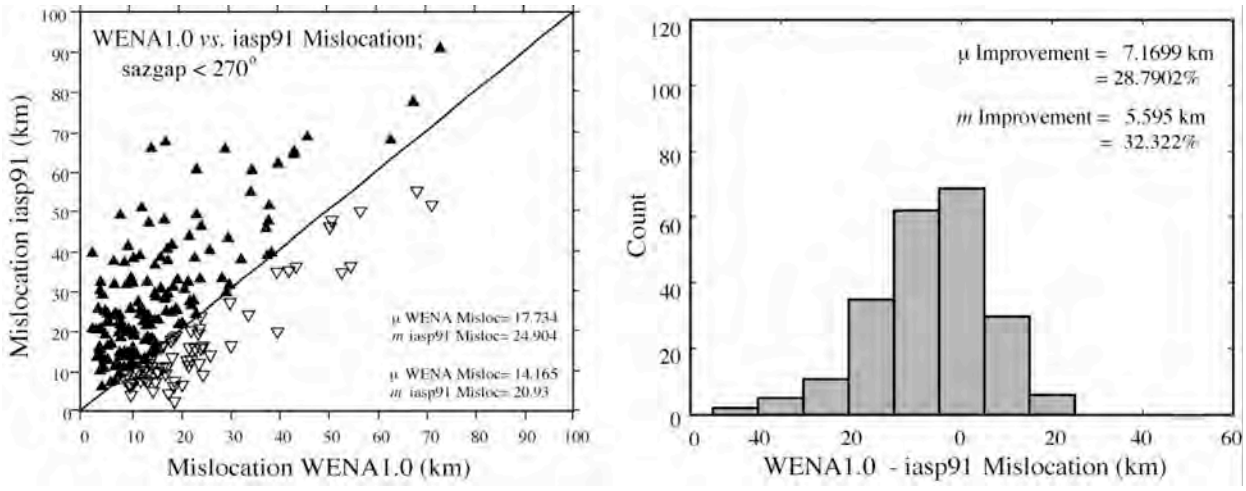


Figure 10. (Left) Scatter plot of WENA1.0 and IASPEI91 epicenter mislocations (in km) for the GT5 validation dataset using relocated events with secondary azimuthal gaps of less than 270°. Symbols above the diagonal line indicate improvements in location using WENA1.0 (filled triangles) while symbols below the line indicate degradations (open triangles). (Right) Histogram of the difference in epicenter mislocation (WENA1.0-IASPEI91) using the GT5 validation dataset. Note the mean (*m*) and median (*m*) improvement in location provided by WENA1.0 is 7.1699 km and 5.595 km, respectively.

Finally we evaluate the coverage ellipses for the GT5 relocations. Determining representative error ellipses is a critical component of location accuracy, as they must adequately describe the random chance that the true location is within the bounds of the ellipse (Myers and Schultz, 2000). Error ellipse coverage is defined as the percentage of GT locations that fall within the corresponding 95% confidence ellipse. As shown in Figure 11 the median area or error ellipse was reduced by 37% while the conservative modeling errors assured 94% coverage for WENA1.0. The reduction of both mean (2,391 km^2) and median (2,009 km^2) error ellipse area is substantial at 37% and is a direct consequence of the WENA1.0 uncertainty model variances used to compute the error ellipse. This is consistent with our finding that WENA1.0 both improves location accuracy and uncertainty. For WENA1.0 the known location lies within the 95% confidence ellipse 94% of the time and for IASPEI91 it is only 90% of the time. This suggests that the WENA1.0 95% confidence ellipses are actually meaningful and that our derived error model is representative of true location accuracy. The observation that the IASPEI91 relocation is only inside the 95% ellipse 90% of the time is noteworthy and is likely the result of correlated error that is not accounted for in propagation of errors.

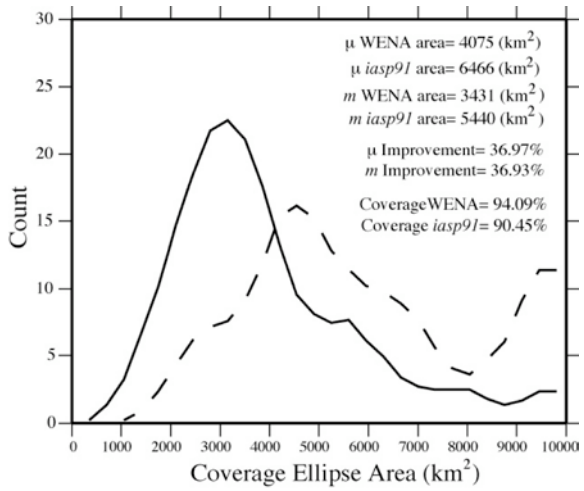


Figure 11. Distribution of WENA1.0 (solid line) and IASPEI91 (dashed line) coverage ellipse areas for GT5 events having secondary azimuthal gaps greater than 270°. For WENA1.0 the known location lies within the 95% confidence ellipse 94% of the time and for IASPEI91 it is 90% of the time. Both the mean and median area of the coverage ellipse for WENA1.0 relocations are smaller than for IASPEI91 by 37% indicating how WENA1.0 reduces the size of the coverage ellipse and yields a more accurate location.

Studies aimed at evaluating the location capabilities of certain models or location techniques commonly concentrate exclusively on the accuracy of the locations relative to some benchmark. Although this is an important component of the present study, we conclude that the ability to model regional travel time data is an equally good measure by which to assess the quality of 3-D models. This is because evaluations based on mislocation alone may not account for the variations in network geometry from one region to another (or from event to event temporally), different mixes of (defining) regional phases, and uneven quality of reported travel times.

CONCLUSIONS AND RECOMMENDATIONS

We tested the applicability of the WENA1.0 model for regional seismic location. Tests include travel-time prediction performance for a large GT25 validation data set, and improvements in location accuracy for a limited, geographically distributed set of GT5 validation events. Our main findings are as follows. First, the 3-D finite difference approach used here, with the Cartesian to spherical coordinate transformation, is a significant advance for travel time prediction at regional to teleseismic distances. Second, a carefully validated set of reference events with good geographical coverage is essential for model-based location calibration. Third, WENA1.0 achieves a statistically significant improvement in travel time prediction over IASPEI91 with a variance reduction of 29% for all GT25 events and 49% for GT5. Fourth, a distance dependent, travel time uncertainty model is developed for WENA1.0 and IASPEI91, and WENA1.0 travel time uncertainties are noticeably smaller than IASPEI91 in particular in the critical range of 0° to 25°. These representative uncertainties are key to our ability to compute realistic coverage ellipses for the relocated GT5 events. Finally, tests of location improvement suggest that WENA1.0 improves epicenter accuracy by about 30% (~7 km) over IASPEI91, and it improves more events than it degrades. Uncertainty estimates are representative of observed mislocation with a mean decrease in ellipse area of 37%, and resulting coverage ellipses are representative of true location error for WENA1.0.

REFERENCES

Bondár, I., S. C. Myers, E. R. Engdahl, and E. A. Bergman (2004). Epicenter accuracy based on seismic network criteria, *Geophys. J. Int*, 156: 483–496.

Flanagan, M. P., C. Myers, and K. D. Koper (2006). Regional travel-time uncertainty and seismic location improvement using a 3-dimensional *a priori* velocity model, *Bull. Seism. Soc. Amer*. (in review).

Hole, J. A. and B. C. Zelt (1995). 3-D finite difference reflection travel times, *Geophys. J. Int.* 121: 427–434.

Murphy, J. R., W. Rodi, M. Johnson, D. D. Sultanov, T. J. Bennett, M. N. Toksoz, V. Ovtchinnikov, B. W. Barker, D. T. Reiter, A. C. Rosca, and Y. Shchukin (2005). Calibration of International Monitoring System (IMS) stations in central and eastern Asia for improved seismic event location, *Bull. Seism. Soc. Amer*. 95: 951–964, doi: 10.1785/0120030173.

Myers, S. C. and C. A. Schultz (2000). Improving sparse network seismic location with Bayesian kriging and teleseismically constrained calibration events, *Bull. Seism. Soc. Am.* 90: 199–211.

Pasyanos, M. E., W. R. Walter, M. P. Flanagan, P. Goldstein, and J. Bhattacharyya (2004). Building and testing an *a priori* geophysical model for western Eurasia and North Africa, *Pure Appl. Geophys*. 161: 235–281.

Ritzwoller, M. H., N. M. Shapiro, A. Levshin, E. A. Bergman, and E. R. Engdahl (2003). The ability of a global 3D model to locate regional events, *J. Geophys. Res.* 108: 2353, doi 10.1029/2002JB002167.

Sultanov, D.D., J. R. Murphy, and Kh. D. Rubinstein (1999). A seismic source summary for Soviet peaceful nuclear explosions, *Bull. Seism. Soc. Am.* 89: 640–647.

Yang, X., I. Bondár, J. Bhattacharyya, M. Ritzwoller, N. Shapiro, M. Antolik, G. Ekström, H. Israelsson, and K. McLaughlin (2004). Validation of regional and teleseismic travel-time models by relocating ground-truth events, *Bull. Seism. Soc. Amer*. 94: 897–919.

GROUND TRUTH LOCATIONS USING SYNERGY BETWEEN REMOTE SENSING AND SEISMIC METHODS: SSSC AT IMS STATIONS FOR TIBETAN PLATEAU EARTHQUAKES

Gene A. Ichinose[1], Chandan K. Saikia[2*], Donald V. Helmberger[3], and Mark Simons[3]

URS Group, Inc.[1,2] and California Institute of Technology[3]

Sponsored by National Nuclear Security Administration
Office of Nonproliferation Research and Development
Office of Defense Nuclear Nonproliferation

Contract No. DE-AC52-03NA99505[1,2,3]

ABSTRACT

The objective of this project is to collect and create earthquake ground truth (GT) locations for calibration of methods and data, which locate, identify, and discriminate explosions and earthquakes. The method involves identifying seismic events which are candidates for Synthetic Aperture Radar Interferometry (InSAR) analysis and then combine and invert the seismic and geodetic data to create high quality source parameters and GT locations for small to moderate sized and shallow earthquakes in North Africa, Middle East, and Asia. In addition, we provide P-wave travel time corrections known as Source Specific Station Corrections (SSSCs) for the International Monitoring System (IMS) based on these GT locations.

We selected ten of the largest earthquakes (M > 4) recorded by the Sino-US Program for Array Seismic Studies of the Continental Lithosphere array between 1991 and 1992 previously analyzed by Zhu et al. (2006) using calibration and CAP methodologies. We first estimated the locations and depths using the regional centroid moment tensor (RCMT) inversion method by inverting the long period filtered complete three component displacement records. The moment tensors are very similar to the CAP regional fault parameters (RFPs) including mechanism, depth and scalar moment. There are some slight differences in location for events with the largest azimuthal gap resulting in poor centriod location resolution. We used the CAP and RCMT solutions to generate SSSCs. We recalculated the earthquake origin times and travel-time residuals relative to the global IASPEI91 layered Earth velocity model based on the fixed location and depth. We then estimated the SSSCs at all stations reporting P-wave arrival times and gridded them using two techniques for developing a global correction surface. We used the continuous curvature spline (CCS) and the nearest neighbor gridding algorithms. The nearest neighbor scheme assumes that the correction is zero outside of a distance search radius while the CCS generates a smoothly varying surface.

We relocated earthquakes listed in the International Seismological Centre (ISC) catalog from 1980 to 2004 using these SSSCs. In one example, we relocated 130 earthquakes using the direct grid search locator method for the Qaidam Basin and Qilan Shan region of the Qinghai Province. These earthquakes appear to be mislocated to the southwest by an average of 40 km relative to ISC locations. As many others have previously indicated, the ISC catalog depths are also over estimated and most earthquakes in this region are less then 10 km in depth. These preliminary results assume that the calibration earthquakes have high quality GT locations. Since the CAP and RCMT methods still assume velocity models and the station distributions are not optimal, then there may be some bias but including geodetic data from remote sensing data from InSAR analysis should provide independent constraints. The earthquake grid search locator indicates that the depth is poorly resolved for many of the earthquakes even with the SSSCs, therefore high-quality broadband waveform data will continue to be important for identifying shallow regional earthquakes ideal for InSAR analysis.

*Chandan K. Saikia has moved on to AFTAC.

OBJECTIVES

The objective of this project is to collect and create earthquake GT locations for calibration of methods and data, which locate, identify, and discriminate explosions and earthquakes. Large calibration explosions provide the best GT locations but are rare and limited in geographical distribution. Earthquakes are much more abundant but usually poorly located in space and time because of the sparse spatial distribution in high quality seismic instruments and complex Earth structure. The best approach is to combine the traditional seismic data with the line of sight ground displacements caused by explosions and earthquakes recorded by orbiting satellites based on the Synthetic Aperture Radar Interferometry (InSAR) technique (e.g., Rosen et al., 2000). The overall goal of this ongoing study is to identify seismic events which are candidates for this InSAR analysis and then combine and invert the seismic and geodetic data to create high quality locations and source parameters (e.g., Lohman et al., 2002) for small to moderate sized (4.5 < Magnitude < 6.5) and shallow (< 10 km) earthquakes in North Africa, Middle East, and Asia. In addition, we will provide P-wave travel time corrections in the form of SSSCs for the International Monitoring System (IMS) based on these new GT locations.

RESEARCH ACCOMPLISHED

In previous proceedings, Saikia et al. (2002, 2003, 2004, 2005) have analyzed and reported the results for the following earthquakes using seismic waveform and geodetic data:

1. 1999/04/30 (Mw 4.9) Southern Iran earthquake
2. 1997/05/05 Southern Iran earthquake
3. 1997/09/18 Southern Iran earthquake
4. 1997/11/08 (Mw 7.6) Manyi, Tibet earthquake
5. 2001/03/05 (Mw 5.7) Tibet earthquake (Manyi aftershock)
6. 1998/01/10 (Mw 5.7) Northeast China earthquake
7. 1999/12/12 Algerian earthquake
8. 1997/03/20 Tunisian earthquake
9. 1998/08/27 (Mw 6.4) Southern Xinjian Province, China earthquake

Although the early success of this methodology proved promising, we have later found some difficulty in identifying shallow and small earthquakes for InSAR analysis. Ordering and processing the InSAR data is costly and time consuming and some analyzed earthquakes have not provided usable results primarily due to poor magnitude and depth selection. InSAR data quality including atmospheric noise and topographical uncertainty also limits the data availability to some extent. Success has been made with larger earthquakes but their usefulness for GT is limited due to the uncertainty in hypocenter and origin time relative to centroid solution defined from InSAR. In summary we have concluded that (1) InSAR and seismic data produce similar earthquake source parameters and both are often needed to better constrain a unique GT location, depth, and mechanism, (2) ISC global earthquake locations are often over estimated in depth, (3) the use of SSSC constrained by InSAR defined GT locations improve the locations of smaller localized seismic events including GT events which were left out as validation examples.

In this report we continue to explore earthquakes for which we can derive GT locations within the Tibetan Plateau by first examining ISC phase data and high quality PASSCAL and IRIS seismic waveform data. We continue to focus on this region because of the availability of travel time data from local network earthquake catalogs but work will also continue in other regions of Asia including the Korean Peninsula, Northern Africa and the Middle East (including Arabian Peninsula and Caspian Sea regions).

Regional Centriod Moment Tensor Inversion

We performed a regional centriod moment tensor (RCMT) inversion on regional waveforms recoded by the Sino-US PASSCAL seismic experiment on the Tibetan Plateau (Owens et al., 1993). We selected ten of the largest earthquakes (M > 4) recorded by the array from 1991 to 1992 (Table 1, Figure 1) previously analyzed by Zhu et al. (2006) and Tan et al (2006) using calibration and CAP methodologies (Zhu and Helmberger, 1996b). We inverted the three component long period filtered (100–10 s) displacements (Figure 2) and performed a grid search for the best fitting centriod longitude, latitude, depth, and origin time (e.g., Ritsema and Lay, 1995) while maximizing the variance reduction and percent double couple component (Table 2). We assume a 1D Tibet velocity model (e.g., Zhu

et al. 2006) that works well in generating realistic f-κ synthetic seismograms (e.g., Zhu et al., 1996a; Rodgers and Schwartz, 1998; Saikia et al. 2002) for this region. The model has a 61 km thick crust with a P-wave velocity of 6.2 km/s and a 4 km thick shallow low velocity layer of 4.7 km/s. The upper mantle is 8.2 km/s.

The RCMT results are shown in Figure 1, indicating that the moment tensors are very similar to the CAP regional fault parameters (RFP) compared with Zhu et al. (2006), including mechanism, depth, and moment. There are some slight differences in location, primarily for earthquakes located outside of the array with the largest azimuthal gap in station coverage. A centriod solution is necessary because some of the CAP locations were inadequate and led to some RCMT with artificially high Compensated Linear Vector Dipole (CLVD) components. In some cases we included seismic waveform data recorded by the China Digital Seismic Network (CDSN) and IRIS stations that improve the azimuthal coverage and the moment tensors but may introduce artifacts and biases in the centriod location due to the velocity model complexity outside of the plateau. Because of this complexity, we instead used the CAP solutions to generate SSSCs. The RCMT centroid locations led to very different and complex SSSCs relative to the much smoother ones based on the CAP RFPs.

Source-Specific Station Corrections at IMS Seismic Stations

We recalculated the earthquake origin times and travel-time residuals relative to the global IASPEI91 layered Earth velocity model based on the fixed location and depth estimated from the CAP methodology (Zhu et al., 2006). We will order and analyze InSAR data for these events in the future. We estimated the SSSCs at seismic stations reporting P-wave arrival times and gridded them using two techniques for developing a global correction surface for this region. We used was the continuous curvature spline (CCS) gridding algorithm (Smith and Wessel, 1990) shown in Figure 3 and the nearest neighbor gridding algorithm (e.g., Wessel and Smith, 1998) shown in Figure 4. The Nearest Neighbor scheme assumes that the correction is zero where no data is present (outside of a 15° distance search radius) while the CCS generates a much smoother interpolated surface.

Northern Tibet Earthquake Relocations Using SSSCs

We selected ISC catalog earthquakes between 1980 and 2004 within 200 km radius of each of the calibration events for relocations with the SSSCs. We use a direct grid search scheme to relocate the earthquakes and select the locations with the lowest root-mean-square (RMS) error. The relocations are fast because of the use of pre-computed lookup tables in LOCSAT format using the TauP program (Crotwell et al., 1999). The tables are read in and interpolated using a cubic spline interpolation method. We also iterate over hypocenter depths for the precomputed travel times in the tables. Origin times are updated for each grid point to minimize any biases in the average residual before the RMS error calculation. Figure 5 shows examples of the relocations. The RMS error for the optimal depth and origin time is plotted for one of the calibration earthquakes and then used to relocate other nearby earthquakes. As a validation, the calibration earthquake shown in Figure 5 is relocated to within 5.7 km of the CAP solution using the SSSCs but is mislocated by 48.7 km to the southwest near the ISC location. These accuracy estimates are consistent with cluster analysis (Engdahl and Bergman, 2001) and we expect the relocated earthquakes to be promoted to at least GT5 or GT10 status. Figure 5 also shows that the minimum RMS error do not vary significantly (<10%) over a radius of < 5 to 10 km around the best solution (Figure 6) so the data can only resolve the location to within 5 to 10 km particularly when teleseismic phase data are included in the relocation. The addition of local phase arrival times greatly improves the resolution.

Figure 7 shows the locations for 130 ISC catalog earthquakes in the Qaidam Basin and Qilan Shan region of the Qinghai Province between 1980 and 2004 within a 200 km radius of the 1991/09/02 (Julian Day 245) earthquake shown in Figure 5. The ISC locations are shown relative to the grid search relocations using the SSSC that is estimated by using the continuous spline interpolation gridding scheme (Figure 3). Figure 8 is similar to Figure 7 but the SSSC is estimated using the nearest-neighbor gridding scheme (Figure 4). The results are very similar because the phase arrival times are recorded from the same global regions of at least the past 24 years; therefore, it is not significant to have travel time information from all regions for constructing SSSC surfaces.

CONCLUSIONS AND RECOMMENDATIONS

Earthquakes in the ISC catalog appear to be mislocated to the southwest by an average of 40 km in the Qaidam Basin and Qilan Shan region of the Qinghai Province. As many others have indicated, the ISC catalog depths are often over estimated and most earthquakes in this region are less then 10 km in depth. These preliminary results

assume that the calibration earthquakes have high quality GT locations. Since the CAP and RCMT methods still assume velocity models, there may be some inherent bias in the GT locations and SSSCs. InSAR should provide independent constraints for GT and can be combined with this seismic analysis. We confirm that all ten of the calibration earthquakes we examined in Table 1 are shallow and the ones with Mw > 4.8 should provide good InSAR results. We also have additional local network phase arrival data from Chinese earthquake catalogs for 1996 to 2000 that can be used to better validate the relocations, improve the SSSCs, or constrain GT locations. We can also provide SSSCs relative to other global 1D velocity models, regionalized models including Regionalized Upper-Mantle models and also with 3D crustal and upper-mantle CUB shear wave velocity model (e.g., Shapiro and Ritzwoller, 2002).

REFERENCES

Crotwell, P. H., T. J. Owens, and J. Ritsema (1999). The TauP Toolkit: Flexible seismic travel-time and ray-path utilities, *Seismol. Res. Lett*. 70: 154–160.

Engdahl, E. R. and E. A. Bergman (2001). Validation and generation of reference events by cluster analysis, in *Proceedings of the 23rd Seismic Research Review: Worldwide Monitoring of Nuclear Explosions*, LA-UR-01-4454, Vol. 1, pp. 205–214.

Lohman, R., M. Simons, and B. Savage (2002). Location and mechanism of the Little Skull Mountain earthquake as constrained by satellite radar interferometry and seismic waveform modeling, *J. Geophys. Res*. 107 (B6): 10.1029/2001JB000627.

Owens, T. J., G. E. Randall, F. T. Wu, and R. S. Zeng(1993). PASSCAL instrument performance during the Tibetan Plateau passive seismic experiment, *BSSA* 83: 1957–1970.

Rodgers, A. J. and S. Y. Schwartz (1998). Lithospheric structure of the Qiangtang Terrane, northern Tibetan Plateau, from complete regional waveform modeling: Evidence for partial melt, *J. Geophys. Res*. 103 (B4): 7137–7152.

Ritsema, J. and T. Lay (1995). Long period regional wave moment tensor inversion for earthquakes in the western United States, *J. Geophys. Res*. 100: 9853–9864.

Rosen, P. A., S. Hensley, I. Joughin, F. K. Li, S. N. Madsen, E. Rodriguez, and R. M. Goldstein (2000). Synthetic aperture radar Interferometry, in *Proceedings of the IEEE*, Vol. 88, pp. 333–382.

Saikia, C. K., H. K. Thio, D. V. Helmberger, G. Ichinose, and C. Ji (2005). Ground truth locations using synergy between remote sensing and seismic methods—Application to Chinese and North African earthquakes, in *Proceedings of the 27th Seismic Research Review: Ground-Based Nuclear Explosion Monitoring Technologies*, LA-UR-05-6407, Vol. 1, pp. 443–453.

Saikia, C. K., J. Chen, G. Ichinose, D. V. Helmberger, A. O. Konca, and M. Simons (2004). Ground truth locations using synergy between remote sensing and seismic methods—Application to Chinese earthquakes, in *Proceedings of the 26th Seismic Research Review: Trends in Nuclear Explosion Monitoring*, LA-UR-04-5801, Vol. 1, pp. 328–337.

Saikia, C. K., R. Lohman, G. Ichinose, and M. Simons (2003). Ground truth locations using a synergy between INSAR and seismic methods, in *Proceedings of the 25th Seismic Research Review—Nuclear Explosion Monitoring: Building the Knowledge Base*, LA-UR-03-6029, Vol. 1, pp. 324–333.

Saikia, C. K., R. Lohman, G. Ichinose, D. V. Helmberger, M. Simons, and P. Rosen (2002). Ground truth locations—A synergy of seismic and synthetic aperture radar interferometric methods, in *Proceedings of the 24th Seismic Research Review—Nuclear Explosion Monitoring: Innovation and Integration*, LA-UR-02-5048, Vol. 1, pp. 420–429.

Shapiro, N. M. and M. H. Ritzwoller (2002). Monte-Carlo inversion for a global shear-velocity model of the crust and upper-mantle, *Geophys. J. Int*. 151: 88–105.

Smith, W. H. F. and P. Wessel (1990). Gridding with continuous curvature splines in tension, *Geophysics,* 55: 293–305.

Wessel, P. and W. H. F. Smith (1998). New, improved version of Generic Mapping Tools released, *EOS Trans. AGU* 79: 579.

Zhu, L. and D. V. Helmberger (1996a). Intermediate depth earthquakes beneath the India-Tibet collision zone, *Geophys. Res. Lett.* 23: 435–438.

Zhu, L. and D. V. Helmberger (1996b). Advancement in source estimation techniques using broadband regional seismograms, *Bull. Seismol. Soc. Am.* 86: 1634–1641.

Zhu, L., Y. Tan, D. V. Helmberger, and C. K. Saikia (2006). Calibration of the Tibetan Plateau using regional seismic waveforms, *Pure Appl. Geophys*. (submitted).

Table 1. Tibet Plateau calibration earthquakes

Julian Day	Date (y/m/d)	Origin Time	sec	Latitude (°N)	Longitude (°E)	Z (km)	M1	Type 1	M2	Type 2	Agency	Regional Location
222	1991/08/10	20:21	52.7	33.874	92.191	15	4.5	mb	4.8	Ms	ISC	Qinghai Province
			52.5	33.970	92.180	10	4.7	Mw	-	-	CAP	
			54.0	33.900	92.200	8	4.8	Mw	-	-	RMTI	
245	1991/09/02	11:05	50.5	37.408	95.384	10	5.3	mb	4.8	Ms	ISC	Qinghai Province
			47.0	37.770	95.570	12	4.7	Mw	-	-	CAP	
			52.0	37.440	95.540	14	4.9	Mw	-	-	RMTI	
263	1991/09/20	11:16	11.7	36.177	100.058	13	5.4	mb	5.1	Ms	ISC	Qinghai Province
			10.8	36.240	100.160	12	4.9	Mw	-	-	CAP	
			10.0	36.300	100.100	13	5.0	Mw	-	-	RMTI	
325	1991/11/21	13:37	43.8	33.736	90.237	49	4.0	mb	-	Ms	ISC	Qinghai Province
			38.6	34.020	90.140	5	4.5	Mw	-	-	CAP	
			38.0	33.950	90.100	5	4.6	Mw	-	-	RMTI	
348	1991/12/14	08:20	23.7	33.925	88.842	31	5.1	mb	4.6	Ms	ISC	Xizang
			19.0	34.040	88.830	5	4.8	Mw	-	-	CAP	
			22.0	33.900	88.950	4	4.9	Mw	-	-	RMTI	
357a	1991/12/23	01:58	25.0	33.898	88.887	32	5.2	mb	4.6	Ms	ISC	Xizang
			20.5	34.050	88.840	5	4.8	Mw	-	-	CAP	
			28.0	33.800	89.100	4	4.9	Mw	-	-	RMTI	
357b	1991/12/23	02:14	56.0	33.897	88.965	48	4.8	mb	-	Ms	ISC	Xizang
			50.7	34.010	88.860	5	4.5	Mw	-	-	CAP	
			52.0	33.800	88.900	4	4.6	Mw	-	-	RMTI	
34	1992/02/03	15:44	22.6	34.452	93.260	10	4.9	mb	4.5	Ms	ISC	Qinghai Province
			22.7	34.600	93.230	5	4.5	Mw	-	-	CAP	
			24.0	34.500	93.300	4	4.5	Mw	-	-	RMTI	
37	1992/02/06	03:35	15.0	29.608	95.639	15	5.5	mb	4.9	Ms	ISC	India-China
			15.0	29.710	95.660	5	5.0	Mw	-	-	CAP	Border Region
			15.0	29.700	95.900	4	5.0	Mw	-	-	RMTI	
104	1992/04/13	03:47	50.7	31.948	88.306	35	4.4	mb	4.4	Ms	ISC	Xizang
			45.3	31.750	88.220	5	4.5	Mw	-	-	CAP	
			48.0	31.700	88.400	4	4.6	Mw	-	-	RMTI	

Table 2. Tibetan Plateau moment tensors and focal mechanisms

Julian Day	TYPE	Nodal Plane 1 (Strike°/Dip°/Rake°)	Nodal Plane 2 (Strike°/Dip°/Rake°)	Mo (dyne*cm)	Mw	OT (sec)	Z (km)	DC (%)	VRED (%)
222	RMTI	249/70/4	158/86/160	2.03×10^{23}	4.8	54	8	97	91.6
	CAP	252/83/2		1.40×10^{23}	4.7	53	10		
245	RMTI	103/50/70	313/44/112	2.68×10^{23}	4.9	52	14	93	62.5
	CAP	102/61/79		1.40×10^{23}	4.7	47	12		
263	RMTI	109/59/62	334/41/127	3.64×10^{23}	5	10	13	96	90.2
	CAP	99/76/60		2.79×10^{23}	4.9	11	12		
325	RMTI	71/81/-11	162/80/-170	1.08×10^{23}	4.6	38	5	100	88.2
	CAP	251/60/-16		7.00×10^{23}	4.5	39	5		
348	RMTI	216/45/-66	4/50/-112	2.51×10^{23}	4.9	22	4	93	86.5
	CAP	212/30/-72		1.97×10^{23}	4.8	19	5		
357a	RMTI	196/40/-90	16/50/-90	2.50×10^{23}	4.9	28	4	97	86.5
	CAP	210/31/-70		1.97×10^{23}	4.8	20	5		
357b	RMTI	168/43/-95	356/47/-85	8.77×10^{23}	4.6	52	4	94	87.4
	CAP	358/60/-87		7.00×10^{22}	4.5	51	5		
34	RMTI	293/35/66	141/58/106	6.17×10^{22}	4.5	24	4	88	80
	CAP	107/19/53		7.00×10^{22}	4.5	23	5		
37	RMTI	3/56/64	224/42/123	4.32×10^{23}	5	15	4	87	81.5
	CAP	0/61/60		3.94×10^{23}	5	15	5		
104	RMTI	147/56/-173	53/84/-35	9.42×10^{22}	4.6	48	4	100	78.5
	CAP	227/49/-23		7.00×10^{22}	4.5	45	5		

Table 3. SSSC at IMS stations (N—nearest neighbor algorithm/S—continuous spline interpolation)

Station	Longitude	Latitude	SSSC(N)	SSSC(S)		Station	Longitude	Latitude	SSSC(N)	SSSC(S)
PS01	-70.6	-40.7	0	-4.7		PS27	10.8	60.8	0.23	0.67
PS02	134.3	-19.9	-5.41	-5.49		PS28	25.5	69.5	1.5	1.59
PS03	133.9	-23.7	-4.62	-4.66		PS29	73.3	33.7	-3.03	-3.16
PS04	141.6	-31.9	-4.9	-4.83		PS30	-57.3	-26.3	0	-3.81
PS05	62.9	-67.6	0	-7.44		PS31	127.9	37.5	0.74	0.12
PS06	-68.1	-16.3	0	-3.06		PS32	42.9	43.7	-0.24	-0.13
PS07	-48	-15.6	0	-3.15		PS33	84.8	53.9	0.63	0.44
PS08	-95.9	50.2	0.68	1.21		PS34	88	69	0.91	1.08
PS09	-114.6	62.5	1.24	1.37		PS35	112.6	59.6	1.72	2.05
PS10	-66.8	54.8	0.89	0.89		PS36	157.8	53.1	1.46	1.03
PS11	18.4	5.2	0	-2.03		PS37	132	44.2	1.14	0.85
PS12	119.7	49.3	0.63	1.72		PS39	25.6	-28.6	-3.41	-4.34
PS13	103.8	36.1	0.25	0.3		PS40	-4	39.7	1.31	1.3
PS14	-74.3	4.9	0	-1.6		PS41	99	18.8	-4.75	-4.59
PS15	-4.9	6.7	-1.53	-1.59		PS42	8.7	35.6	1.07	0.38
PS16	33	26	0.49	-0.51		PS43	32.8	39.9	-0.52	0
PS17	28.1	61.4	0.89	1.23		PS44	58.1	37.9	-1.18	-1.04
PS18	-149.6	-17.6	0	-2.48		PS45	29.1	50.4	0.27	0.53
PS19	13.7	48.9	1.19	1.19		PS46	-103.7	29.3	0.65	0.59
PS21	51.4	35.8	1.08	-0.29		PS47	-118.2	38.4	2.6	1.74
PS22	138.2	36.5	-1.88	-1.59		PS48	-109.6	42.8	1.69	1.79
PS23	82	46.8	-1.53	-0.89		PS49	-146.9	64.8	2.67	2.82
PS24	37.2	-1.1	0	-2.9		PS50	161.9	-77.5	0	-7.4
PS25	106.8	48	6.28	3.75						

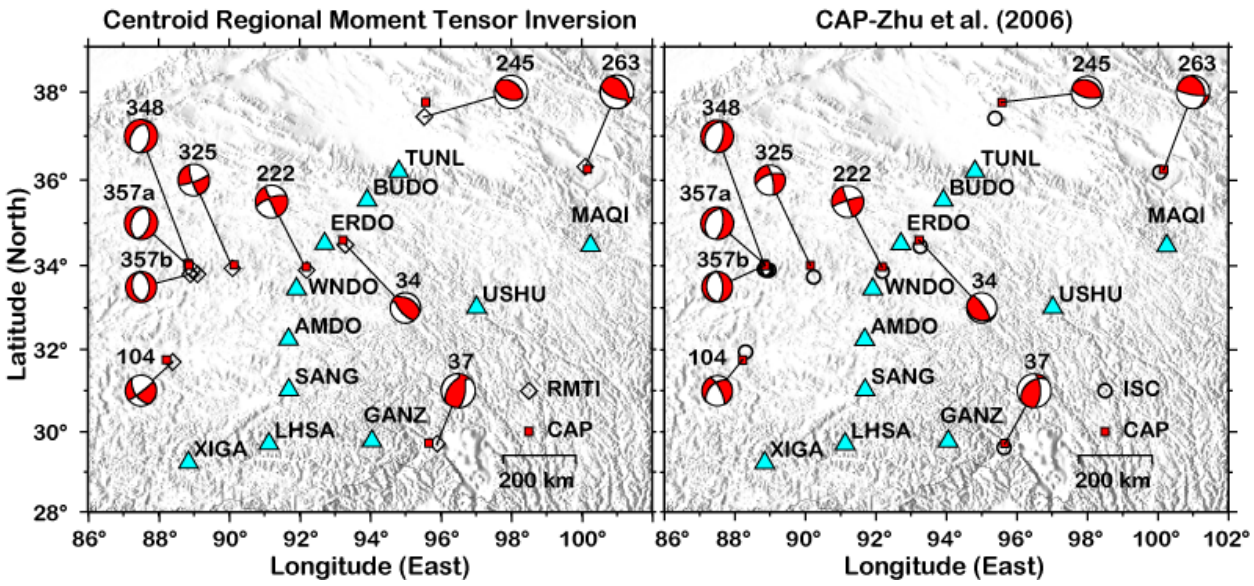


Figure 1. Regional centriod moment tensor solutions (left side) and CAP (right side) and calibration results (Zhu et al., 2006) estimated using broadband regional waveform data from PASSCAL deployment of seismic stations.

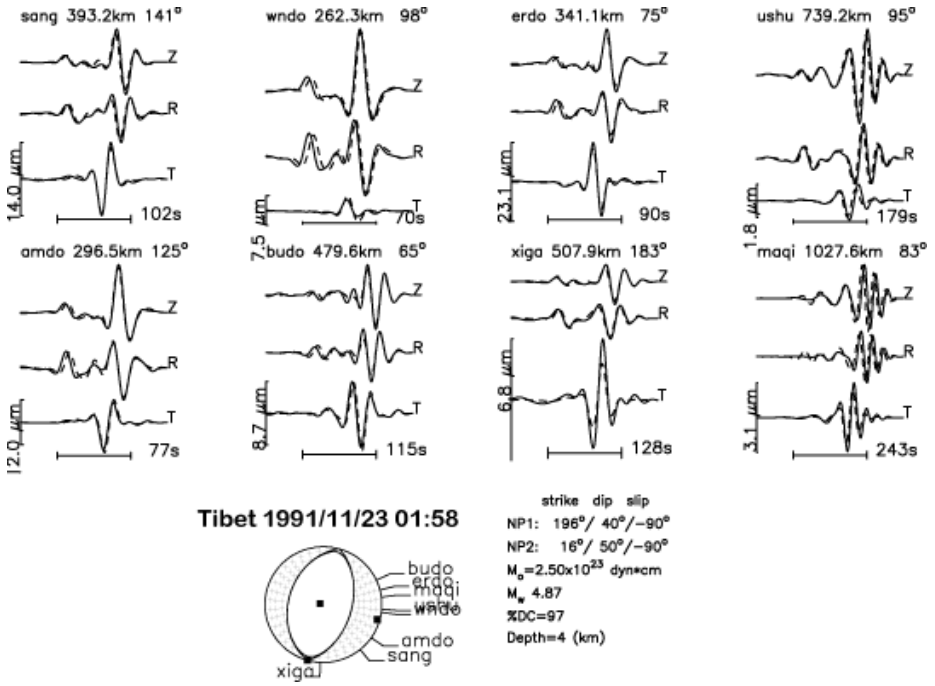


Figure 2. Regional centriod moment tensor solutions of event 357a (Figure 1, Tables 1 and 2) estimated using broadband regional waveform data from PASSCAL deployment of high quality seismic array. The centriod (location, depth, and origin time) was also estimated using direct grid search scheme. We used the 1D Tibet model layered Earth model for calculating the f-k Green's functions (e.g., Zhu et al., 2006).

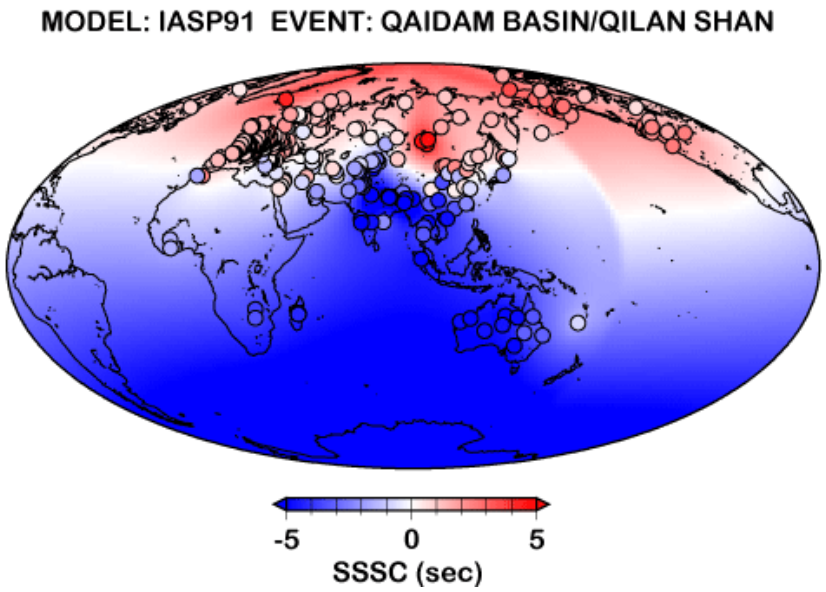


Figure 3. SSSC surface relative to IASPEI91 layered Earth model. We used a continuous curvature spline gridding algorithm to construct a global correction surface. The dots shown are a group of average station residuals from earthquakes in northern Tibet, Qaidam basin and Qilan Shan region.

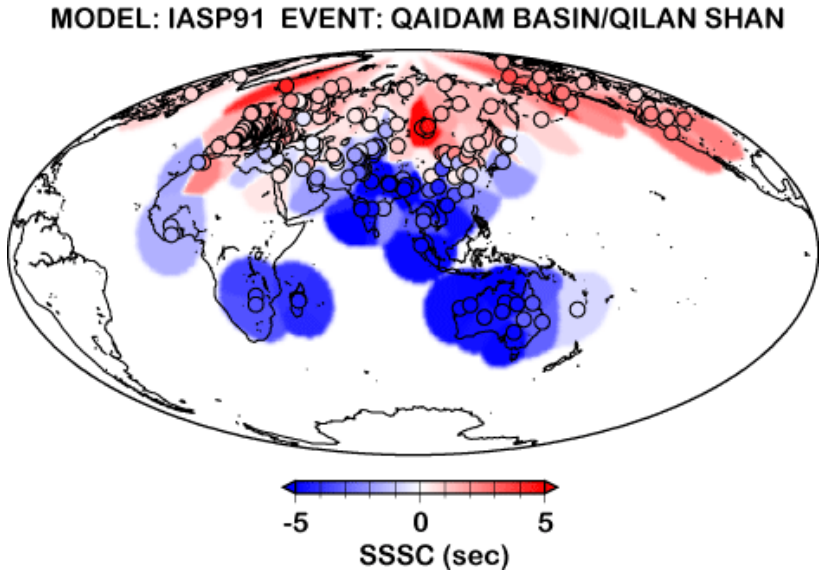


Figure 4. SSSC surface relative to IASPEI91 layered Earth model. We used a nearest neighbor gridding algorithm to construct a global surface. The dots shown are a group of average station residuals from earthquakes in northern Tibet, the Qaidam basin and the Qilan Shan region. The major difference for this gridding scheme, compared with the nearest neighbor method in Figure 3, is that the correction is not constrained to zero in areas without data and the curvature spline method generates a smoother correction surface.

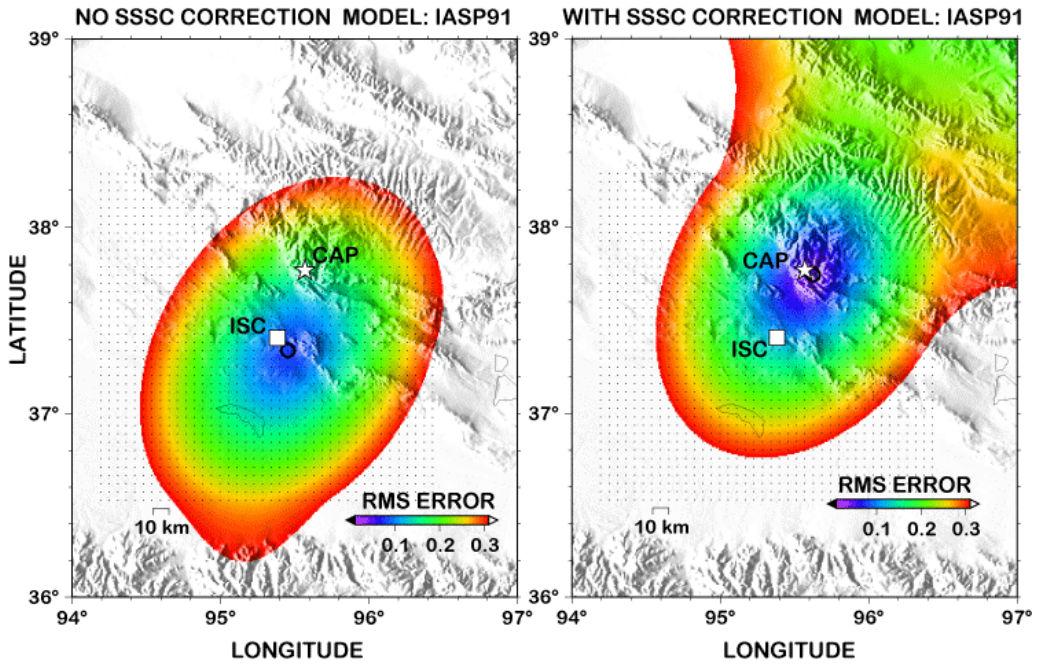


Figure 5. Direct grid search relocations of the 1991/09/02 (Julian Day 245 in Table 1; Figure 1) GT calibration earthquakes with and without SSSC. The root-mean-square (RMS) residuals are contoured at different depths based on the IASPEI91 layered Earth velocity model. The individual grid points (1600) are also shown to indicate where the RMS residual surface is constrained. The best fit location shown as the circle is less than 5 km from the CAP solution with the SSSC but mislocated by 40 km to the southwest without the SSSC.

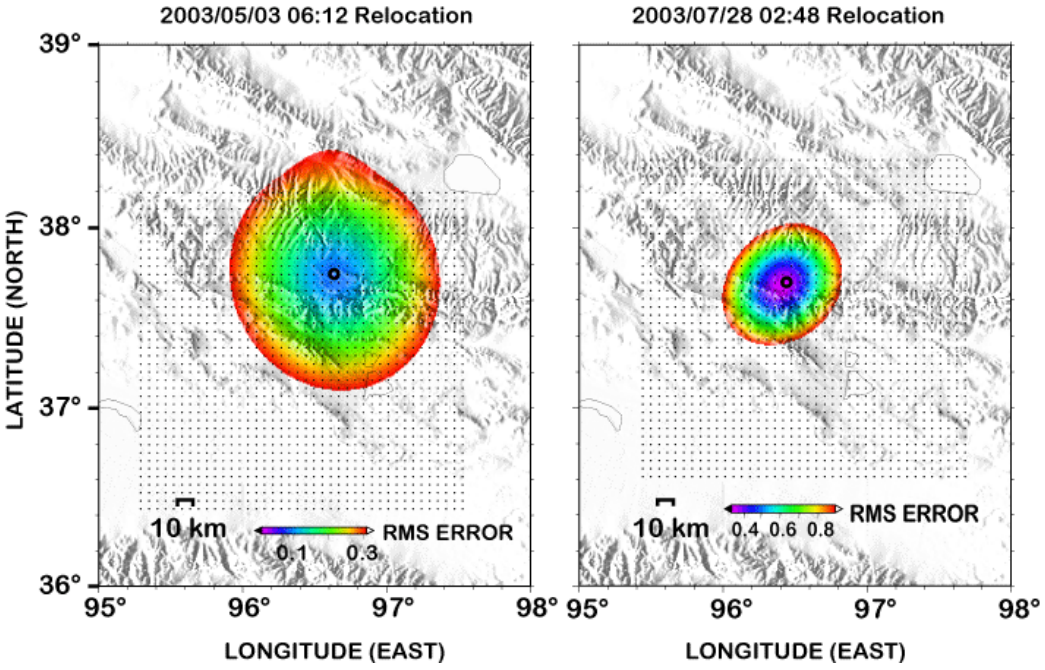


Figure 6. Direct grid search relocation results for two selected individual earthquakes with SSSC not from the GT calibration subset. The RMS residuals for the events are contoured at different depths based on the IASPEI91 layered Earth velocity model. The individual grid points (1600) are also shown to indicate where the RMS residual surface is constrained. The RMS error scale is different in the right panel.

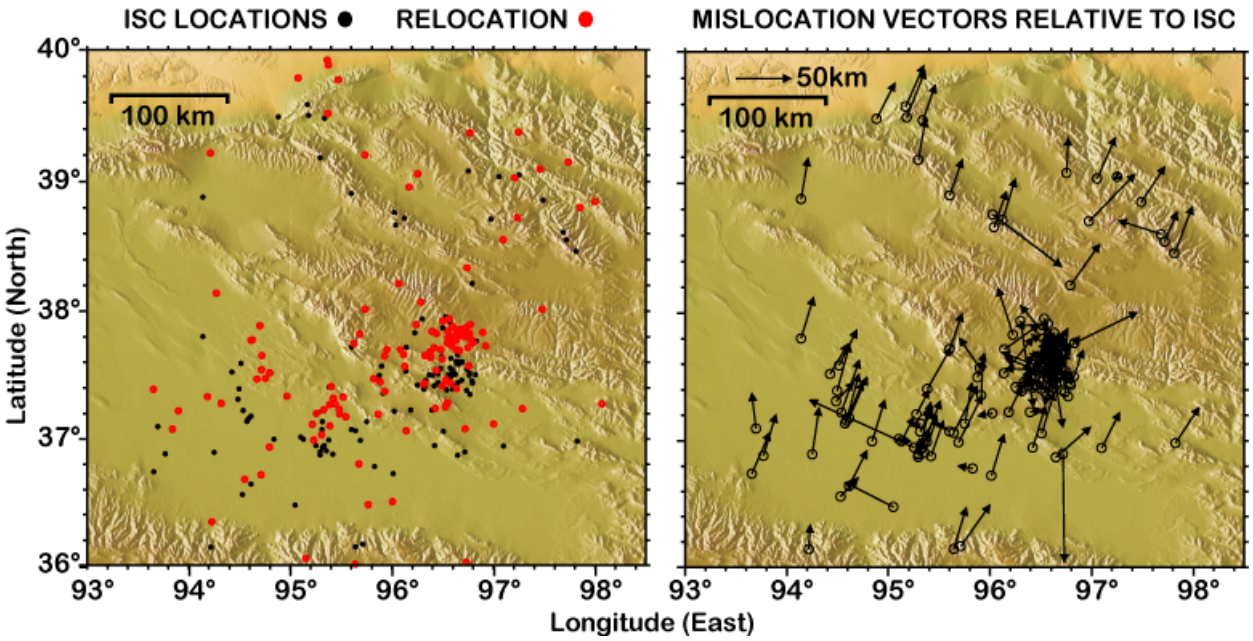


Figure 7. Direct grid search earthquake relocations for ISC catalog events between 1980 and 2004 using IASPEI91 layered Earth model and SSSC derived by the curvature spline fitting method shown in Figure 3b.

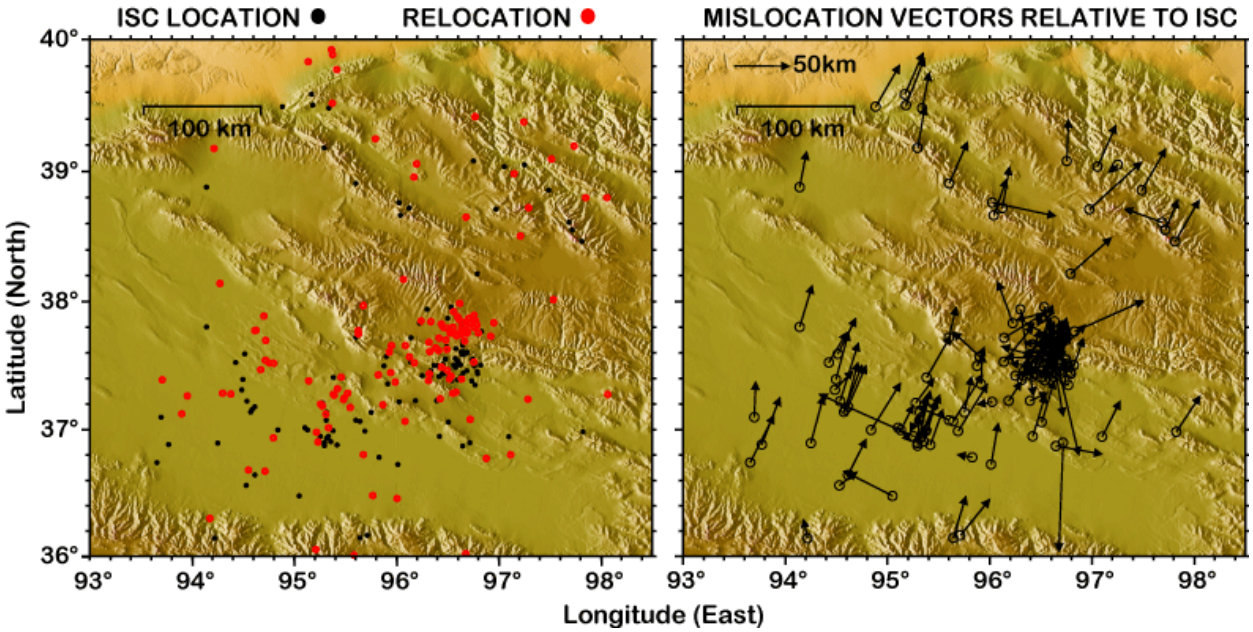


Figure 8. Direct grid search earthquake relocations for ISC catalog events between 1980 and 2004 using IASPEI91 layered Earth model and SSSC derived by the nearest neighbor fitting method shown in Figure 3a.

STATISTICAL CLASSIFICATION AND PREDICTION OF SEISMIC EVENT LOCATION ACCURACY

Gardar Johannesson and Jerry J. Sweeney

Lawrence Livermore National Laboratory

Sponsored by National Nuclear Security Administration
Office of Nonproliferation Research and Development
Office of Defense Nuclear Nonproliferation

Contract No. W-7405-ENG-48

ABSTRACT

In this paper we address the question of how to assign a statistically meaningful error estimate to the location accuracy of an individual seismic event contained in an international seismic bulletin—in this case the U.S. Geological Survey National Earthquake Information Center Reviewed Event Bulletin (NEIC REB). Our approach is to use a training dataset of ground-truth events, for this study obtained from the Middle East-North Africa region, and apply a wide variety of statistical methods. Using the distance between the catalog location and the ground-truth (GT) location of an event as the dependent variable, we examine the influence of the available catalog variables: distance to nearest station, number of detecting phases, primary azimuthal gap, secondary azimuthal gap, and magnitude. We examine several different regression and classification methods and look at their success rate and efficiency as location classifiers for GT5 to GT25. As expected, the classification error rate is inversely related to GT level; but we found it varied only slightly between the different methods. The analysis reveals that representative GT levels that can be obtained from the catalog for one type of regression model are $GT25_{95}$, $GT20_{90}$, $GT15_{80}$, $GT10_{70}$, and $GT5_{50}$ (using the nomenclature of Bondar et al., 2004). We also present an approach for using the statistical model to determine the probability that a given event is at a given level of ground truth, i.e., determine P for GTn_P where n is the level of ground truth. Advantages of regression methods over classification methods are that they make better use of the information in the data and they allow one to construct a classifier based simply on the predicted accuracy of the location, which can then be weighted. We hope that this study will inspire further investigation of the use of formal statistical regression and classification methods to quantify the accuracy of reported seismic locations in bulletins.

OBJECTIVES

Use of GT seismic events to calibrate seismic travel times has become an important way of calibrating seismic stations and regions for improved location accuracy. Statistical methods, such as those introduced by Myers and Schultz (2000), produce spatial travel time corrections based on calibration to ground truth data which itself can have different degrees of uncertainty. Obviously, earthquake and explosion sources will be of variable quality due to different uncertainties in origin time and hypocenter; but as long as the statistical uncertainty in the location of a source event is known or can be estimated, this possible variance can be incorporated in the analysis. In order to calibrate stations over wide areas of the globe, evenly spaced distributions of large numbers of ground truth events are desired. One means of acquiring a large number of ground truth events is to extract them from published catalogs of events, such as the International Seismological Centre (ISC) and the U. S. National Earthquake Information Center (NEIC). The key to being able to use these sources of ground truth is knowing what criteria to use for selection and how to estimate the uncertainty in the accuracy of the ground truth; i.e., what is the level of ground truth (5, 10, 15, 20 km error, etc.) and level of certainty about that level (95%, 90%, 67%, 50% confidence, etc.). Other considerations also come into play, such as how efficient is the selection process.

The objective of this study is to provide a careful statistical assessment of the whole range of parameters available from a published catalog (the NEIC reviewed event bulletin—REB), examine the relative merits of individual or combinations of parameters, examine different types of statistical classification schemes, and assess the ability of these schemes to successfully classify ground-truth events in an international bulletin.

RESEARCH ACCOMPLISHED

Data Used in the Study

Ground-truth events used in this study are those used in an initial study by Sweeney (1998), with five additional event collections added. The seismic reference events are from earthquakes and aftershocks that have been accurately located with temporary arrays of instruments in a local network or with a relatively dense regional array with an accuracy of at least 5 km and selected explosions. While the number of reference events used in this study is statistically significant, it is not as large as that used in other studies, such as Bondar et al. (2004). However, the purpose of this study is not to come up with a definitive answer to the question of event selection, but rather to illustrate a rigorous statistical approach that can be used with any reference data.

For the study we focus on six parameters available from published bulletins. The dependent variable (the variable of interest) is the distance between the catalog location and the ground truth location (which we denote by "**dist**"). The independent (explanatory) variables we consider are the number of defining phases ("**N**"), the largest azimuthal gap between stations recording the event ("**gap**"), the largest azimuthal gap filled by a single station (Bondar et al., 2004—"**gap2**"), the smallest distance between the event location and a recording station ("**sta**"), and the magnitude (typically m_b) of the event ("**mag**"). We use the open-source statistical computing language R (R Development Core Team, 2004) for our analysis. The R environment has emerged as the tool of choice in the statistical community for developing and testing new statistical procedures.

For the data set of 69 records, 48 events (69.6%) have **dist** less than 15km, 54 events (78.3%) have **dist** less than 20 km, and 56 events (81.2%) have **dist** less than 25km. Histograms of the variables (Figure 1) generally show a left tail tendency, in particular for **dist**, **N**, and **sta**. To reduce the impact of extreme values (e.g., large values) in our analysis, the **dist**, **N**, and **sta (in degrees)** variables were logarithmic (base-10) transformed. Scatter plots of log(**dist**) versus the explanatory variables are shown in Figure 2. We observe (1) an expected positive relationship between log(**dist**) and **gap**, **gap2**, and log(**sta**), (2) an expected negative relationship between log(**dist**) and log(**N**), and (3) a somewhat surprising positive-then-negative relationship between log(**dist**) and **mag**. Finally, Figure 3 shows a scatter plot matrix of the explanatory variables. We observe a strong correlation between log(**N**), **gap**, **gap2**, and **mag**, as might be expected since a large magnitude (**mag**) event is typically observed at many stations (**N**) yielding a small azimuthal gap (**gap** and **gap2**). However, the distance to the closest station (**sta**) is observed to have little correlation to the remaining four explanatory variables.

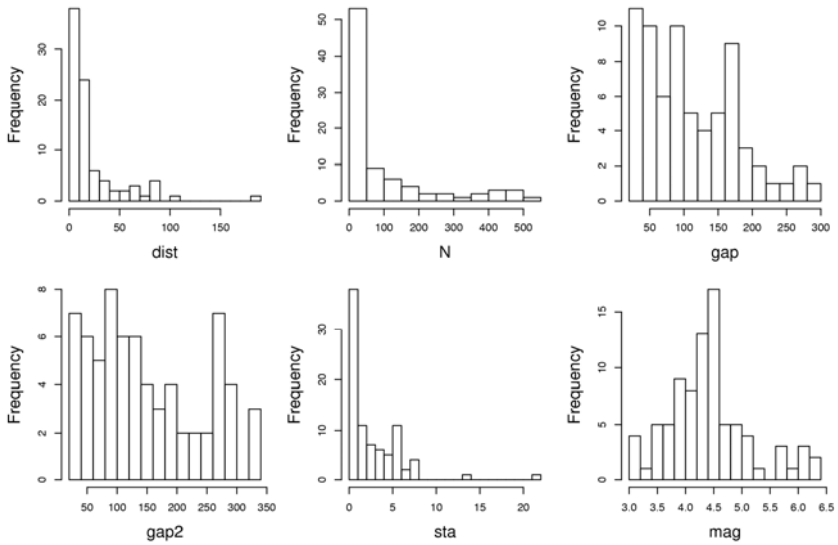


Figure 1. Histograms of the six variables of interest in the NEIC dataset.

The result of using the GT20 and GT25 classification criteria given by Bonder et al. (2004) to the 69 events in the full data sets is given in Table 1. The Bonder et al. classification rule has a very low error rate for the events that are predicted to be GT20 or GT25 events, 3.2% for GT20 events, and 0.0% for GT25 events. We refer to this error rate as type-I error rate; that is an event is classified as a GT event, but it is not a GT event. However, the Bonder et al. classification rule has a very high, what we refer to as type-II, error rate: an event is classified as not being a GT event, but it is a GT event. As a result, the total classification error rate is high (36.2% for both GT20 and GT25 events). This makes the classification rule very inefficient at classifying GT events. For example, of the 54 GT20 events in our set of data, 30 are classified as GT20 events, while 24 are not; we also note that the type-I error for the Bondar et al. GT5 criteria is 50% (2 events misclassified out of 4 predicted) for our GT reference set.

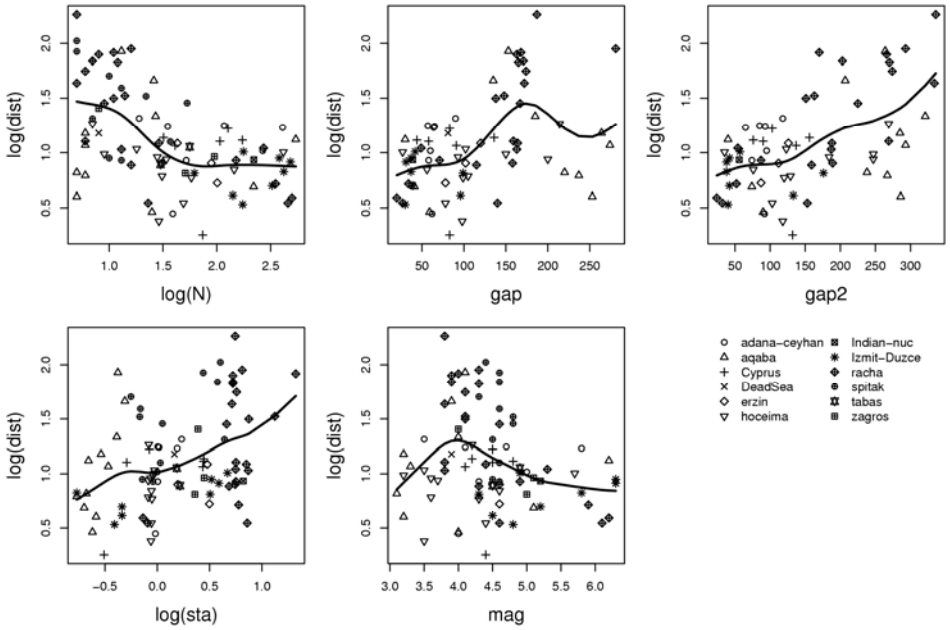


Figure 2. Scatter plot of log(dist) versus the five potential explanatory variables (with N and sta log10 transformed). A superimposed smoothing-spline trend line is also shown on each panel.

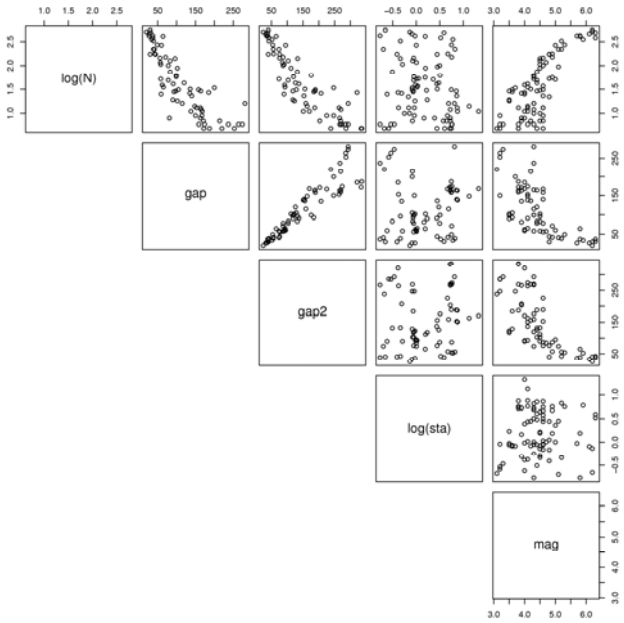


Figure 3. A scatter plot matrix of the potential explanatory variables.

Table 1. Classification results of GT20 and GT25 events using the classification rules of Bondar et al. (2004). The column headings "P>20" and "P<20" denote events predicted (classified) to be non-GT20 and GT20, respectively, and the row headings "O>20" and "O<20" denote events observed to be non-GT20 and GT20 events, respectively. The entry 30 in the left table shows the number of events that are both observed and predicted to be GT20 events, and the number 31 shows the total (Tot) number of predicted GT20 events. The entry "P<20 Err" gives the classification error in predicting GT20 event (given by 1/31), and the entry "Tot Err" gives the total classification error [given by (1+24)/69].

GT20	GT25
P>20 P<20 Tot **O>20** 14 1 15 **O<20** 24 30 54 **Tot** 38 31 69 **P<20 Err** = 3.2% **Tot Err** = 36.2%	**P>25 P<25 Tot** **O>25** 13 0 13 **O<25** 25 31 56 **Tot** 38 31 69 **P<25 Err** = 0.0% **Tot Err** = 36.2%

Analysis: Regression Methods

In our analysis, we considered two groups of statistics-based classification schemes: those based on regression techniques and those based on classification techniques. We first discuss the regression methods.

Following a standard regression notation (see, e.g., Hastie et al., 2001, Chapter 3), let Y = the output/response variable, which is equal to log(**dist**) in our case, and let

$$X = (X_1, ..., X_p) \qquad (1)$$

be a vector of *p* input variables. The set of input variables does not only include the available explanatory variables, but can also include transformations of those and in general any known function of the available explanatory variables.

For example,

$$X_1 = \log(\mathbf{N}),\ X_2 = \log(\mathbf{sta}),\ X_3 = \log(\mathbf{N}) \times \log(\mathbf{sta}) \quad (2)$$

is a set of $p = 3$ input variables. Using the input variables, let

$$f(X) = \text{a given model (function) for predicting } Y \text{ given the input } X, \quad (3)$$

and note that $f(X)$ typically depends on some unknown parameters that need to be specified. The unknown parameters are estimated from observed data that consists of responses, $y_1, \ldots, y_N$,with associated inputs, $x_1, \ldots, x_N$, where $x_i = (x_{i1}, \ldots, x_{ip})$. We denote by

$$\hat{f}(X) = \text{ the model prediction } f(X) \text{ with parameters obtained from the data.} \quad (4)$$

That is, an estimate of the unknown parameters is obtained from the data and simply "plugged" into the model $f(X)$.

The predictor $f(X)$ can be used to create a simple threshold classifier of "is $Y < y$?" versus "is $Y \geq y$?," where y is a given threshold number. Such classifiers can be written as

$$G(X) = \begin{cases} 1 & \text{if } f(X) < y, \\ 0 & \text{otherwise.} \end{cases} \quad (5)$$

Given the estimated predictor $\hat{f}(X)$, one can derive the classifier $\hat{G}(X)$ by simply "plugging in" $\hat{f}(X)$ instead of $f(X)$ in the expression for $G(X)$ above.

In accessing the accuracy of the classifier $\hat{G}(X)$ one can apply it to the data used to estimate the unknown parameters associated with $f(X)$. However, that is in general not considered a good practice as the same data set is used to both estimate (train) the classifier and validate it. An alternative and widely used approach is cross validation (see, e.g., Hastie et al., 2001, Chapter 7.10). An *M*-fold cross validation splits the available data into *M* parts of roughly equal size and for each part uses the remaining *M-1* parts to re-estimate $f(X)$ which is then used to predict the data part left out; this requires *M* re-estimations of the model. If each data part consists of a single observation (i.e., *M* is equal to the number of observations in the data set), then it is often referred to as leave-one-out cross-validation. We applied two regression methods to the NEIC data set: first a classical linear regression and a more adaptive and flexible regression approach.

In linear regression we seek a predictor of *Y* of the linear form,

$$f(X) = \beta_0 + \sum_{j=1}^{p} X_j \beta_j, \quad (6)$$

where the β_j's are unknown parameters to be estimated from the data. Here we shall consider least squares regression where an estimate of $\beta = (\beta_0, \beta_1, \ldots, \beta_p)$ is obtained by minimizing the residual sum of squares,

$$RSS(\beta) = \sum_{i=1}^{N} (y_i - f(x_i))^2 = \sum_{i=1}^{N} \left(y_i - \beta_0 - \sum_{j=1}^{p} \beta_j x_{ij} \right)^2. \quad (7)$$

For details, see, e.g., Hastie et al. (2001).

Of the five explanatory variables we have available, we have the option of including them as main-effects (e.g., $X_j = \log(\mathbf{N})$), as 2-way interactions (e.g., $X_j = \log(\mathbf{N}) \times \log(\mathbf{sta})$), as 3-way interactions (e.g., $X_j = \log(\mathbf{N}) \times \log(\mathbf{sta}) \times \mathbf{mag}$), all the way up to a 5-way interaction. We used an automatic stepwise selection using the Akaike information criterion (AIC) via the stepAIC function available in the MASS package of R; see Venables and Ripley (2002, page 172) and Hastie et al. (2001, Chapter 7).

The model with the lowest AIC statistics selected by stepAIC from the multiple starting models has four input variables and is given by

$$\hat{f}(X) = 0.0121 + 0.00314 \times \mathbf{gap2} + 1.35 \times \log(\mathbf{sta}) + 0.120 \times \mathbf{mag} - 0.240 \times \log(\mathbf{sta}) \times \mathbf{mag}. \quad (8)$$

A scatter plot of the observed **dist** versus the predicted **dist** from the above model has an $R^2 = 0.53$. The term **gap2** has an expected positive contribution to the predictor, while the joint contribution of log(**sta**) and **mag** is harder to judge. A classification of GT15, GT20, and GT25 events was carried out using the threshold classifier described above and a leave-one-out cross-validation; results are given in Table 2.

Table 2. Cross-validation classification results for the linear regression model in classifying GT15, GT20, and GT25 events.

GT15	GT20	GT25
P>15 P<15 Tot	**P>20 P<20 Tot**	**P>25 P<25 Tot**
O>15 13 8 21	**O>20** 11 4 15	**O>25** 10 3 13
O<15 8 40 48	**O<20** 5 49 54	**O<25** 2 54 56
Tot 21 48 69	**Tot** 16 53 69	**Tot** 12 57 69
P<15 Err = 16.7%	**P<20 Err** = 7.5%	**P<25 Err** = 5.3%
Tot Err = 23.2%	**Tot Err** = 13.0%	**Tot Err** = 7.2%

As an alternative to the above, multiple adaptive regression splines (MARS) expresses the impact of each explanatory variable via a combination of piecewise linear terms; see Friedman (1991) for details and Hastie et al. (2001), Chapter 9.4, for a short overview. We let $X_1, X_2, \ldots, X_p$ be our set of explanatory variables. MARS performs a linear regression with input variables selected from the set

$$\{ (X_j - k)_+, (k - X_j)_+ \} \text{ for } j = 1, \ldots, p \text{ and } k \in \{x_{1j}, x_{2j}, \ldots, x_{Nj}\}, \quad (9)$$

where the piecewise linear terms $(X_j - k)_+$ and $(k - X_j)_+$ are given by

$$(X_j - k)_+ = \begin{cases} X_j - k & \text{if } x > k, \\ 0 & \text{otherwise,} \end{cases} \quad \text{and} \quad (k - X_j)_+ = \begin{cases} k - X_j & \text{if k} < x, \\ 0 & \text{otherwise.} \end{cases} \quad (10)$$

Figure 4 shows the two piecewise linear functions above in the case when X_j = **gap2** and k = 150. If all the observed values of the explanatory variables (i.e., the x_{ij}'s for each j) are different, this results in a set of $2Np$ possible input variables; that is 690 input variables when p = 5 and N = 69 as in our case. To select among these input variables and all possible interactions, MARS uses a forward stepwise selection of variables (i.e., starting with an empty set of variables and then adding variables in a stepwise fashion), which is then followed by a backward elimination of variables. The final model is of the former,

$$f(X) = \beta_0 + \sum_{m=1}^{M} \beta_m h_m(X), \quad (11)$$

in the case when M input terms are selected, where each $h_m(X)$ is one of the input variables or a product of two or more input variables. The parameters $b_0, b_1, \ldots, b_M$ are estimated by minimizing the residual sum of squares, as in the previous case of linear regression. The size (M) of the final model selected is automatically decided on using the generalized cross-validation (GCV) criterion (e.g., Hastie et al., 2001, Chapter 9.4).

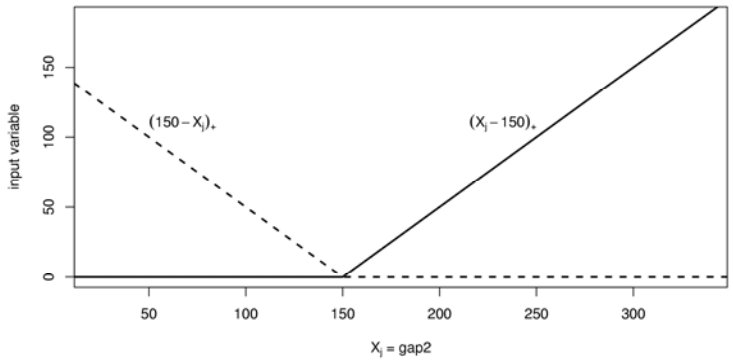


Figure 4. A pair of piecewise linear terms with a knot at 150 used by MARS for the explanatory variable gap2.

The final model selected when we applied MARS to our data with a main-effects-only restriction had only two input variables, and is given by

$$\hat{f}(X) = 1.10 + 0.00361 \times (\mathbf{gap2} - 132)_+ - 0.347 \times (0.723 - \log(\mathbf{sta}))_+ . \qquad (12)$$

The two input variables reflect the marginal relationship seen in Figure 2. The selected MARS model with main-effects and two-way interactions ended up incorporating six input variables and is given by,

$$\begin{aligned} \hat{f}(X) = {} & 0.843 + 0.00894 \times (\mathbf{gap2} - 132)_+ \times (0.723 - \log(\mathbf{sta}))_+ \\ & - 0.00985 \times (\log(\mathbf{N}) - 1.11)_+ \times (\mathbf{gap2} - 132)_+ \\ & - 0.0239 \times (\mathbf{gap} - 135)_+ \times (0.723 - \log(\mathbf{sta}))_+ \\ & + 0.0202 \times (\mathbf{gap} - 153)_+ - 0.169 \times (\mathbf{gap} - 167)_+ \times (\log(\mathbf{sta}) - 0.723)_+ \\ & + 0.510 \times (2.07 - \log(\mathbf{N}))_+ \times (\log(\mathbf{sta}) + 0.0655)_+ . \end{aligned} \qquad (13)$$

Note that of the six input variables there is only one main-effect.

The MARS model with six input variables is seen to perform better in classifying GT15 and GT20 events then the linear regression model presented in Table 2, but is slightly worse at classifying GT25 events. Even with just two input variables (i.e., the simpler MARS model), one is able to extract a considerable amount of information about the GT accuracy of the events.

Alternative Classification Rules

In addition to the classification methods above, we want take into account the uncertainty associated with the accuracy of the predictor $\hat{f}(X)$ (i.e., a predictor of log(**dist)** in our case). In addition, we might want to "penalize" differently for misclassifying a non-GT event as a GT event (i.e., a type I error) versus misclassifying a GT event as non-GT event (i.e., a type II error). Regression models produce a single best prediction and also yield a probability distribution for the predictor. This in turn allows for the computation of

$$\Pr(\hat{f}(X) < d) \text{ = the probability that } \hat{f}(X) < d \text{ for a given threshold value } d. \qquad (14)$$

The analysis revealed that, of the 69 events, 54 (78%) have established distance below the 75% threshold, 61 (88%) below the 90% threshold, and all 69 events are below the 95% threshold. Hence, the confidence intervals are in reasonable agreement with the empirical results given the size of the data set (however, given a sufficiently large data set, one might prefer to use the empirically derived confidence probabilities rather than the theoretical ones if there is a large discrepancy between the two).

Confidence levels may seem to be picked arbitrarily, but there is a connection between the confidence level and the cost associated with misclassification that might help in selecting an appropriate confidence level for classification.

Let

c_I = the cost of misclassifying a non-GT event as a GT event (type I error). (15)

and

c_{II} = the cost of misclassifying a GT event as a non-GT event (type II error). (16)

A classification rule can then be based on minimizing the expected loss of the action taken. The resulting classifier can be shown to be (see e.g., Hastie et al., 2001, Chapter 2.4)

$$G(X) = \begin{cases} 1 & \text{if } \Pr(\hat{f}(X) < d) > c_I / (c_I + c_{II}), \\ 0 & \text{otherwise.} \end{cases} \quad (17)$$

Hence, a classifier that classifies an event as a GT15 event with 90% confidence can be seen as a classifier where c_I is assumed to be nine times higher than c_{II}.

Table 3 shows the number of events classified as GT5, 10, 15, 20, and 25 events at various confidence level using the MARS 2 model. The top section of Table 4 shows the classification results when using the MARS 2 model to classify GT15 events at three different confidence levels (i.e., with three different misclassification cost assumptions). As expected, the (empirical) accuracy of the classifier increases with increasing confidence, but its efficiency (in number of events labeled as GT15) decreases. The table also shows that, using this model, it is not possible to obtain better than $GT5_{50}$, $GT10_{70}$, $GT15_{80}$ events from the NEIC REB.

Table 3. Number of events (out of 69) classified as GT5, 10, 15, 20, and 25 events at five different confidence levels using the MARS 2 model and the classifier in (2). The bottom row shows the actual (established) number of events at each GT level.

	GT5	GT10	GT15	GT20	GT25
50%	3	45	51	52	54
60%	0	39	48	51	53
70%	0	35	44	48	51
80%	0	2	40	45	46
90%	0	0	2	39	44
Est.	12	33	48	54	56

Table 4. Cross-validation classification results for classifying GT15, 20, and 25 events using different methods.

Method	GT15 at 50%	GT15 at 80%	GT15 at 90%
MARS 2	**P>15 P<15 Tot** **O>15** 15 6 21 **O<15** 3 45 48 **Tot** 18 51 69 **P<15 Err** = 11.8% **Tot Err** = 13.0%	**P>15 P<15 Tot** **O>15** 17 4 21 **O<15** 12 36 48 **Tot** 29 40 69 **P<15 Err** = 10.0% Tot Err **= 23.2%**	**P>15 P<15 Tot** **O>15** 21 0 21 **O<15** 46 2 48 **Tot** 67 2 69 **P<15 Err** = 0.0% **Tot Err** = 66.7%
	GT15	**GT20**	**GT25**
LDA	**P>15 P<15 Tot** **O>15** 13 8 21 **O<15** 5 43 48 **Tot** 18 51 69 **P<15 Err** = 15.7% **Tot Err** = 18.8%	**P>20 P<20 Tot** **O>20** 11 4 15 **O<20** 3 51 54 **Tot** 14 55 69 **P<20 Err** = 7.3% **Tot Err** = 10.1%	**P>25 P<25 Tot** **O>25** 11 2 13 **O<25** 2 54 56 **Tot** 13 56 69 **P<25 Err** = 3.6% **Tot Err** = 5.8%
Classification Tree	**P>15 P<15 Tot** **O>15** 14 7 21 **O<15** 7 41 48 **Tot** 21 48 69 **P<15 Err** = 14.6% **Tot Err** = 20.3%	**P>20 P<20 Tot** **O>20** 11 4 15 **O<20** 7 47 54 **Tot** 18 51 69 **P<20 Err** = 7.8% **Tot Err** = 15.9%	**P>25 P<25 Tot** **O>25** 9 4 13 **O<25** 6 50 56 **Tot** 15 54 69 **P<25 Err** = 7.4% **Tot Err** = 14.5%

Classification Methods

An alternative to the regression approach is to perform a direct classification of a derived group variable. In this case the response variable is not the recorded log(**dist**) variable, as in case of regression, but simply an indicator variable, indicating if an observed event is, for example, a GT15 event or not. In a more general notation, denote by

$$G = \text{a reponse group variable (indicator)} \tag{18}$$

that is either equal to 0 or 1, corresponding to two possible outcomes or groups (this can be easily extended to more than two groups). As in regression, associated with G is a vector of input variables $X = (X_1, \ldots, X_p)$. Our goal is then to derive a model for

$$\Pr(G = 1 \mid X = x) = \text{the probabilit y that } G = 1, \text{ given that } X = x, \tag{19}$$

and then classify the (unknown) event associated with the input x to group 1 ($G = 1$) if $\Pr(G = 1 \mid X = x) > 0.5$, otherwise classify to group 0 ($G = 0$); see, for example Hastie et al. (2001, chapter 2.4). This classification rule assumes an equal loss in misclassifying a group 1 event as a group 0 event and a group 0 event as a group 1 event. An unequal loss results in a threshold value for $\Pr(G = 1 \mid X = x)$ that is different from 0.5 (one that is identical to the threshold value for the regression-derived classifier in above).

In deriving the probability model $\Pr(G = 1 \mid X = x)$ we have available a *training* data set that consists of the 69 records in the NEIC data set, where the group variable is, for example, in the case of GT15 events, given by

$$g_i = 1 \text{ if } \mathbf{dist}_i < 15\text{km}, \; g_i = 0 \text{ otherwise} \tag{20}$$

for the $i = 1, \ldots, 69$ observations in the data set. Note that a separate classifier is needed to classify GT20 and GT25 events. We applied two classification procedures to the NEIC data, a linear discrimination analysis (LDA) and a binary classification tree.

LDA (see, e.g., Hastie et al., 2001, Chapter 4.3) models the conditional probability of $G = 1$, given $X = x$, as

$$\Pr(G = 1 \mid X = x) = \frac{\pi_1 \varphi(x; \mu_1, \Sigma)}{\pi_0 \varphi(x; \mu_0, \Sigma) + \pi_1 \varphi(x; \mu_1, \Sigma)} \tag{21}$$

where $\varphi(x; \mu, \Sigma)$ denotes the probability density of a multivariate normal distribution evaluated at x with mean vector μ and variance-covariance matrix Σ and $\pi_0 + \pi_1 = 1$ ($0 \le \pi_g \le 1$, $g = 1,2$). The π_0 and π_1 are the *prior* probabilities that $G = 1$ or $G = 0$, respectively (i.e., our prior believes that the event to be classified belongs to group 1 or 0 typically based on the frequency of the two groups in the available data). The two multivariate normal distributions specify the distribution of the input variable X conditional on knowing the group it is associated with. Note, we assume that the two groups have different mean vectors (μ_0 and μ_1) but have the same variance-covariance matrix Σ. Quadratic discrimination analysis (QDA) is an extension of LDA where the two groups are allowed to have different variance-covariance matrices.

We conducted (three) LDA of the NEIC data set to classify GT15, GT20, and GT25 events using the 1DA function in the MASS package of R (Venables and Ripley, 2002, Chapter 12). After exploring a number of models using the leave-one-out cross-validation process, we selected the following set of input variables:

For GT15: log(**N**), **mag**, log(**N**)×**mag**
For GT20 and GT25: log(**N**), **gap2**, log(**sta**), log(**N**)×log(**sta**)

A number of other models come close to the above selected models, so these are not unique. The cross-validation results for these three classifiers are shown in the middle of Table 4. The LDA does well when compared to the classifier derived from the linear regression model, but is slightly worse than the MARS-derived classifier for GT15 and GT25 events.

In its most common form, a tree-based classification (see, e.g., Hastie et al., 2001, Chapter 9.2) consists of a sequence of binary decision rules (binary splits), where each decision rule is based on a feedback from a single input variable. For a continuous input variable X, a binary split takes (loosely) the form "if $X < a$, do this …, else, do that …". One can visualize this sequence of binary splits as a tree, where the decision process starts at the root-node of the tree. The first split creates two branches off the root-node connecting to two children nodes, which again have their own branches connecting them to their own children nodes, etc. At the terminal nodes of the tree (at the leaves), a classification decision is made as to if $G = 1$ or $G = 0$ based on the proportion of group 1 versus group 0 training data assigned to each terminal node. Using the training data set, the tree is grown in a sequential fashion, starting at the root-node. At each node, an "impurity measure" is computed to judge among the many splits possible (i.e., which input variable to use and where to threshold); see Hastie et al. (2001), Chapter 9.2. The tree is grown this way to a large size, typically until there are only very few training observations left in each terminal node. This large tree is then "pruned" using a "cost-complexity" measure

$$R_\alpha = R + \alpha \times (\text{tree size}), \tag{22}$$

where R is a measure on the fidelity to the data (e.g., classification error rate), the tree size is given by the number of splits, and $a > 0$ is a control parameter. The pruning process consists of joining nonterminal nodes together in an optimal way, as guided by the cost-complexity function. Depending on how severely the cost-complexity function penalizes for the tree size (i.e., the value of a), the pruning process yields a subset of trees, each one optimal for a given range of a. The final three selected among those are then carried out via cross-validation; see Hastie et al. (2001), Chapter 9.2, for further details.

We conducted tree-based classification using the rpart function in the rpart package of R; see Therneau and Atkinsson (1997) and Venables and Ripley (2002), Chapter 9. In our application we followed closely the approach outlined in Venables and Ripley (2002, pages 261–266), which uses cross-validation for model selection. The final (pruned) classification tree for GT15 events is very simple, with two splits; the first one on "**N < 27.5**," and if that is true, a second split is carried out using "**sta ≥ 0.275**." The final classification tree for GT20 events (not shown) was identical to the final GT15 classification tree, except the second split was on "**sta ≥ 0.375**." For GT25 events, the first split was on "**N < 17**," and the second split on "**sta ≥ 0.275**." The leave-one-out cross-validation classification results for the three trees are given in bottom of Table 4. These simple classification trees are seen to perform worse than LDA, particularly for GT20 and GT25 events.

CONCLUSIONS AND RECOMMENDATIONS

The detailed application of the four classification methods presented in this study yielded cross-validated total classification error-rates ranging from 13.0%–27.5% for GT15 events, 8.7%–15.9% for GT20 events, and 5.8%–14.5% for GT25 events (see Tables 1–4). The total classification error-rate accounts both for misclassifying non-GT event as GT event and for misclassifying a GT event as non-GT event. However, we are more concerned with misclassifying a non-GT event as GT, since the selected GT events might be used to calibrate event location procedures. It is thus more appropriate to use a classifier that penalizes more for misclassifying non-GT events as GT events, such as the regression-based classifier. Such a classifier would yield a higher total classification error-rate, but a smaller GT classification error-rate and fewer events classified as GT events. The balance between GT classification accuracy and efficiency (i.e., number of GT events classified) has to be decided by the user with the usage of the resulting classified GT events in mind.

In addition to the four classification methods discussed here, we also tested other methods including support vector machine, nearest neighbor, and neural network classifiers (see, e.g., Hastie et al., 2001). These methods yielded classification error-rates in the range reported above for the classifiers presented in this study. The four methods presented here were selected as representatives for their class of techniques (broadly described as "linear" and "non-linear" regression and classification). One advantage of carrying out regression is that a single model is estimated and used to predict the location accuracy (expected distance from true location) of various events. In addition, the regression approach takes better advantage of the information in the data as it models directly the distance between the established true location of the event and the predicted one versus simply carrying out classification on a binary GT variable derived by thresholding the established distance. An alternative is to simply report the predicted accuracy (**dist**) of each event. When those events are used, for example, to calibrate a seismic event location procedure, the predicted accuracy of the events can be used to construct weights that reflect their accuracy (e.g., one over **dist** squared).

It is the authors' hope that this study will inspire further investigation of the use of formal statistical regression and classification methods to quantify the accuracy of reported seismic location in international bulletins and the real benefits and performance of such methods.

REFERENCES

Bondar, I., S. C. Myers, E. R. Engdahl, and E. A. Bergman (2004). Epicentre accuracy based on seismic network criteria, *Geophys. J. Int.* 156: 483–496.

Friedmann, J. (1991). Multivariate adaptive regression splines (with discussion). *Annals of Statistics* 19: 1–141.

Hastie T., R. Tibshirani, and J. Friedman (2001). *The Elements of Statistical Learning*. New York: Springer.

Myers, S. C. and C. A. Schultz (2000). Improving sparse network seismic location with Bayesian kriging and teleseismically constrained calibration events, *Bull. Seism. Soc. Am.* 90: 199–211.

R Development Core Team (2004). *R: A Language and Environment for Statistical Computing*. Vienna, Austria: R Foundation for Statistical Computing (http://www.R-project.org).

Sweeney, J. J. (1998). Criteria for selecting accurate event locations from the NEIC and ISC Bulletins, Lawrence Livermore National Laboratory report UCRL-JC-130655.

Therneau, T. M. and E. J. Atkinson (1997). An introduction to recursive partitioning using RPART routines, Mayo Foundation technical report.

Venables, W. N. and R. D. Ripley (2002). *Modern Applied Statistics with S*, Fourth Ed. New York: Springer.

LOW-NOISE BOREHOLE TRIAXIAL SEISMOMETER—PHASE II

James D. Kerr and David W. McClung

Geotech Instruments, LLC

Contract No: DE-FG02-03ER83667

Sponsored by National Nuclear Security Administration
Office of Nonproliferation Research and Development
Office of Defense Nuclear Nonproliferation

ABSTRACT

This paper describes the preliminary design of a low-noise borehole triaxial seismometer for use in networks of seismic stations for monitoring underground nuclear explosions. The design assumes the use of the latest technology of broadband seismic instrumentation. Each parameter of the seismometer is defined in terms of the known physical limits of the parameter. These limits are defined by the commercially available components and the physical size constraints. A prototype has been built along with accessory equipment and successfully installed in a borehole. Noise testing is to be completed by the end of 2006.

OBJECTIVES

The goal of this Small Business Innovative Research (SBIR) Phase II contract is to design a low-noise borehole triaxial seismometer for use in networks of seismic stations for monitoring underground nuclear explosions. The design assumes the use of the latest technology of broadband seismic instrumentation. Each parameter of the seismometer is defined in terms of the known physical limits of the parameter. These limits are defined by the commercially available components and the physical size constraints. A prototype design has been built that meets the size requirements.

The design goals set out for the SBIR are for a triaxial seismometer that can be deployed in 7-in. boreholes at a depth of 100 m. The instrument must operate over a bandwidth of 0.2 to 16 Hz, with a response flat to velocity or acceleration. Two instruments may be used to meet the requirements. The self-noise of the instrument(s) must be 6 dB below the U.S. Geological Survey (USGS) low-noise model over the full bandwidth and have a dynamic range of 120 dB. Self-calibration within 5% of amplitude and within 5º for phase over the bandwidth is a requirement. The instrument must have low power requirements and a high reliability when operated unattended in harsh environments.

RESEARCH ACCOMPLISHED

For Phase II, a prototype seismometer has been built, including all accessory equipment required for installation in a borehole. The seismometer uses the modules similar to the KS2000 surface modules with redesigned electronics.

Hole locks strain relief and stabilizers have also been designed and built along with the hole lock installation tool. These tools have been used to successfully install the seismometer in a borehole.

Figure 1 shows the seismometer and accessories ready for lowering into a borehole.



Figure 1. Prototype seismometer and accessories.

The seismometer is 3.5 in. in diameter and approximately 96 in. in length. It can fit into a 4.15 in. minimum diameter casing.

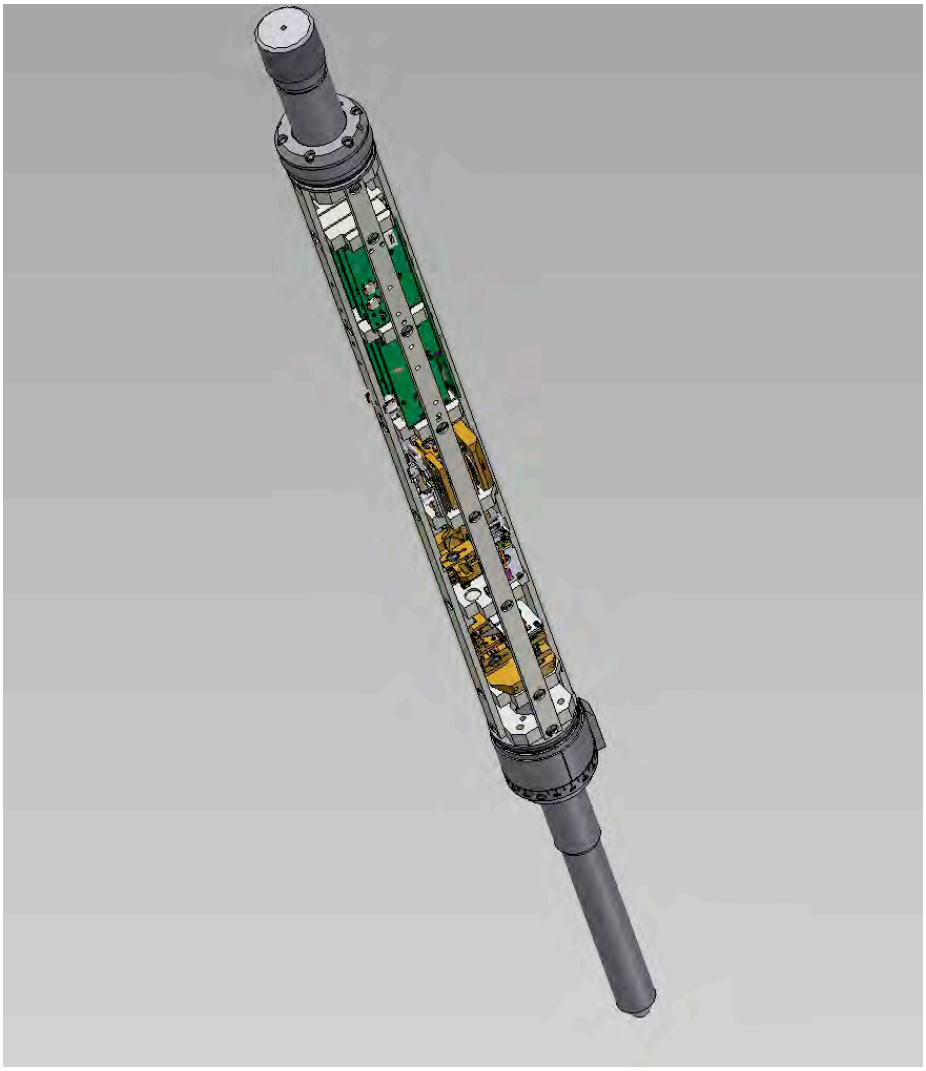


Figure 2. Internal seismometer.

Figure 2 is a CAD drawing of the internal seismometer.

Figure 3 shows the hole lock installation tool, and Figure 4 shows the hole lock.



Figure 3. Hole lock installation tool.



Figure 4. Hole lock.

The next step in this development is to install two or more verticals in the package and install the seismometer in a quiet site to verify the noise characteristics of the seismometer. This testing is scheduled for the latter part of 2006.

CONCLUSIONS AND RECOMMENDATIONS

One of the questions to be considered in this preliminary study was to determine if it was feasible to achieve a seismometer self-noise level at least 6 dB below the USGS low-noise model over the frequency range of 0.2 to 16 Hz. A second question was, could it be done with one instrument, or would two instruments be required. Based on the preliminary theoretical study of Phase I, only one instrument will be required. The requirements for the electronics, suspension, and basic sensors can be achieved with current technology based on the experience with and the history of the KS36000, KS54000 and similar designs.

It is recommended that Phase II continue with the development and testing of prototypes.

ADAPTIVE WAVEFORM CORRELATION DETECTORS FOR ARRAYS: ALGORITHMS FOR AUTONOMOUS CALIBRATION

Frode Ringdal[1], Steven J. Gibbons[1], and David B. Harris[2]

NORSAR[1] and Lawrence Livermore National Laboratory[2]

Sponsored by National Nuclear Security Administration
Office of Nonproliferation Research and Development
Office of Defense Nuclear Nonproliferation

Contract Nos. DE-FC52-05NA26604[1] and W-7405-ENG-48[2]

ABSTRACT

It can be demonstrated that waveform correlation detectors can detect seismic events up to an order of magnitude smaller than traditional energy detectors. Such detectors work by measuring the degree of similarity between the incoming data stream and a template of representative waveforms from an event at a site of interest. Whereas STA/LTA detectors require a significant arrival of energy over a relatively short time interval, correlation detectors utilize the full available waveform and can exploit the characteristic coda which is typically unique to a given source region and often contains the largest amplitudes in the wavetrain. Correlation detectors over arrays are particularly effective since correlation coefficient traces are coherent over arrays or networks of arbitrary dimensions, even when the waveforms at the different sites are incoherent. The greatest disadvantage of such detectors is the requirement of a template waveform. There are many unresolved issues regarding the use of such detectors in operational seismic monitoring. For instance, for a given master event, how far away can a subsequent seismic event be, and how different can the source mechanism and magnitude be, such that it is still detected by the same waveform template.

We have examined an interesting sequence of earthquakes in the north of Norway which has allowed many of these issues to be addressed simultaneously. The events are approximately 600 km from the (large-aperture) NORSAR and (small-aperture) ARCES array stations. Local stations within 20 km of the epicenters have provided confirmation and stable magnitude estimates for all events. Using a waveform template extracted from an m_b=3.5 event, the NORSAR and ARCES arrays were both able to detect events down to m_b=0.5, including many aftershocks concealed within the coda of larger events. This is a clear order of magnitude detection threshold improvement for ARCES and an even greater effective improvement for the NORSAR array over which these high frequency regional signals are incoherent. The false alarm rate at the small-aperture arrays is far higher than for the NORSAR array since the high similarity of the waveforms across small arrays, necessary for traditional array processing, appears to degrade the performance of the array-based correlation detectors. False alarms are usually identified by measuring misalignment of the correlation coefficient traces, although this becomes more challenging for weaker events. We present an example whereby the alignment of correlation maxima allows us to detect and measure a case of erroneous instrumental timing.

Subspace detectors generalize the matched filter concept to detect signals from a particular source that exhibit significant variation, expressed as a signal subspace of dimension greater than one. We have developed interactive software that assists the development of subspace detectors from a collection of master events in the source region of interest by allowing the user to select the dimension of the detector to maximize the probability of detection at a fixed false alarm rate. This new software has been tested on especially well-constrained event clusters in eastern California observed by the NVAR array. Double-difference locations from the Hauksson SCSN catalog provide ground truth with a number of stations in close proximity to the sequences of interest. The results from this study are mixed. Signals from one sequence, near the Long Valley Caldera, are well-characterized by a subspace of dimension one; an array correlation detector performs well in this case, as in the northern Norway example. Two other sequences show large signal diversity for events within fairly compact source regions (<~3-4 km). In these cases subspace detectors perform better than correlation detectors, but still do not capture the majority of events. The issue appears to be smaller events with source mechanisms substantially different from those of larger master events. We are developing a number of strategies for dealing with this problem, including an iterative approach for expanding the subspace as event magnitude decreases.

OBJECTIVE

The overall objective of this three-year study is to develop and test a new advanced, automatic approach to seismic detection using waveform correlation, with special application to seismic arrays. The principal goal is to develop an adaptive processing algorithm. By this we mean that the detector is initiated using a basic set of reference ("master") events to be used in the correlation process, and then an automatic algorithm is applied successively to provide improved performance by extending the set of master events selectively and strategically. These additional master events are generated by an independent, conventional detection system. A periodic analyst review will then be applied to verify the performance and, if necessary, adjust and consolidate the master event set.

RESEARCH ACCOMPLISHED

In the first year of this project, we have focused on three different aspects of waveform correlation detectors. Firstly, we have addressed how great an improvement in the detection threshold for low-magnitude events is possible under various scenarios for repeating events in a small geographical region. Secondly, we have examined how the use of correlation detectors over arrays and networks can be exploited to expose and measure problems with instrumental timing. Thirdly, we have investigated how the use of higher dimension subspace detectors allows an improvement in event detectability even when significant waveform variation is observed between different events from a highly confined region. These issues are discussed in the following sections.

The Detection of Low-Magnitude Seismic Events Using Array-Based Waveform Correlation: A Case Study in Northern Norway

The Rana region of Norway is the site of constant intraplate seismicity (Hicks et al. 2000) and, on June 24 2005, was the site of an m_b = 3.5 event which was well recorded at all the Fennoscandian International Monitoring System (IMS) array stations in addition to the National Seismic Networks of Norway and Finland (Figure 1). An m_b = 2.4 event on April 28, 2005, had been located to almost the same location and subsequent analysis of the waveforms recorded at regional distances indicated very high correlation coefficients between the two events at frequencies up to 10 Hz. The high waveform similarity indicates that the spatial separation between the events is very small (see Geller and Mueller, 1980) and waveform templates were extracted from the June 24 event to attempt to detect occurrences of smaller events from this location which were not detected using traditional array processing. We focused upon the NORSAR array at a distance of approximately 600 km from the earthquake epicenters. The large inter-site distances on this teleseismic array preclude the effective processing of high-frequency regional phases using traditional array methods for small-aperture arrays due to the lack of waveform similarity between sites. However, as was demonstrated by Gibbons and Ringdal (2006), the correlation coefficient channels are coherent over arbitrarily spaced networks and arrays even when the waveforms are not (the condition of waveform similarity between sites is replaced by a condition of waveform similarity between events). The waveform templates for the initial investigation were bandpass filtered between 2.0 and 8.0 Hz, and a 120.0 second long segment was cut for each of the 42 short-period vertical channels. The array correlation beam rarely exceeded a value of 0.005, and a detection threshold of 0.03 was exceeded a total number of 32 times throughout the calender year 2005. On only three occasions did these detections correspond to events from the Rana region which were detected by the IMS arrays: the April 28 event, the June 24 event (a trivial self-correlation detection), and a third event on December 15 with an estimated magnitude 3.0.

Due to the high seismicity in this region, several 3-component stations of the Norwegian National Seismic Network (NNSN) are placed close to the site of the Rana earthquakes (Figure 1); the permanent stations at Stokkvågen (STOK), Meløy (MELS) and Mo i Rana (MOR8) were augmented in the summer of 2005 with temporary stations STOK1 and STOK2, both within 15 km of the assumed epicenter. These stations have provided us with the necessary confirmation of the occurrence of events in this region corresponding to 31 of the 32 correlation detections on the NORSAR array (the remaining marginal detection appears to be a false alarm). Several of the NORSAR detections occurred with a short time separation and one such sequence of detections (on April 28) is displayed in Figure 1. The first and largest correlation peak corresponds to the m_b=2.4 event which was detected at regional distances. The second peak occurs approximately 90 seconds later, during the coda of the main event. Even without the observations at local distances, the evidence that this correlation peak corresponds to a true aftershock is quite strong in that similar correlation detections are observed at essentially the same time at all the Fennoscandian IMS arrays.

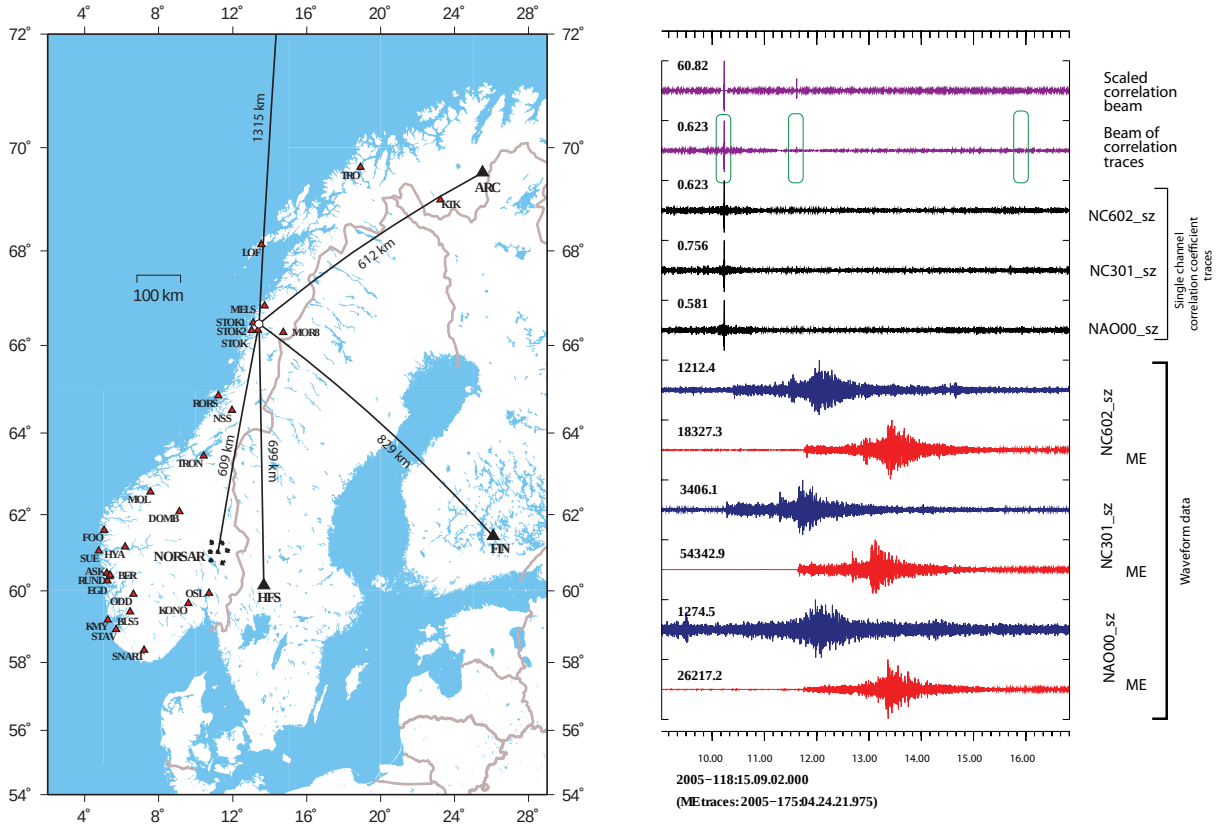


Figure 1. (left) Approximate location of the Rana earthquake sequence relative to the four Fennoscandian IMS array stations (black triangles) and the seismic stations of the Norwegian National Seismic Network (NNSN: red triangles). The line leading Northwards leads towards the SPITS IMS seismic array on the island of Spitsbergen. (right) Detection of an m_b=1.4 aftershock to an m_b=2.4 earthquake on April 28, 2005, in the Rana region of Northern Norway using multichannel waveform correlation on the large aperture NORSAR array at a distance of over 600 km. The master event signals (red traces) result from a magnitude 3.5 earthquake on June 24, 2005, in the same region, and are aligned with the April 28 data (blue traces) according to the first aftershock detection. Only the main shock can be detected on the single channel correlation coefficient trace; the numerous aftershocks are only detected using array processing of the correlation coefficient channels. The green rings mark detections on the array correlation beam. The third detection comprises two distinct correlation maxima, both close to the detection threshold.

Due to the short epicentral distances, the NNSN recordings give the clearest picture of this sequence and the STOK recording is shown for all 3 components in Figure 2. Unlike on the regional distance seismograms, the aftershock signals are observed clearly over the rapidly diminishing coda. The third and most marginal detection is seen to correspond to two distinct events with very similar waveforms separated by no more than 2 seconds. The radiation pattern from these earthquakes is such that the STOK station observes very little P-energy (always over an order of magnitude smaller than S) and, even at the short distances involved, the P-arrivals from these small events are not observed above the noise. Careful inspection of the correlation beam on the NORSAR array reveals two peaks resolved with the correct inter-event spacing. The aftershocks were not detected when templates of only 60 seconds of the P-coda were used; detections were however made when 60 second long templates of the Lg phase and coda were used.

The similarity of the STOK waveforms from event to event, together with the excellent signal-to-noise ratio (SNR) for the S-phases, provides excellent control of the event magnitudes. Applying a logarithmic scaling argument to the

STOK waveforms indicates that the smallest of the detected events were approximately m_b=0.5. This is at least an order of magnitude detectability improvement for the ARCES array and an even greater effective improvement for NORSAR given the lack of array gain for high frequency signals. All events detected by the 42 element NORSAR array could also be detected by the 25 element ARCES array. However, with the threshold set to detect the smallest of these events, the ARCES array generated many more false alarms. The tendency of small-aperture arrays to produce spurious correlation detections was documented by Gibbons and Ringdal (2006), who found that the vast majority of such false alarms could be screened out automatically by measuring the alignment of the correlation coefficient traces. This method is less effective for marginal detections when far longer waveform templates are used, and it remains one of the greatest challenges for the remainder of this project to find robust methods of maintaining high sensitivity together with a low false alarm rate for small-aperture regional arrays. The northern Norway study is described in detail in Gibbons et al. (2006).

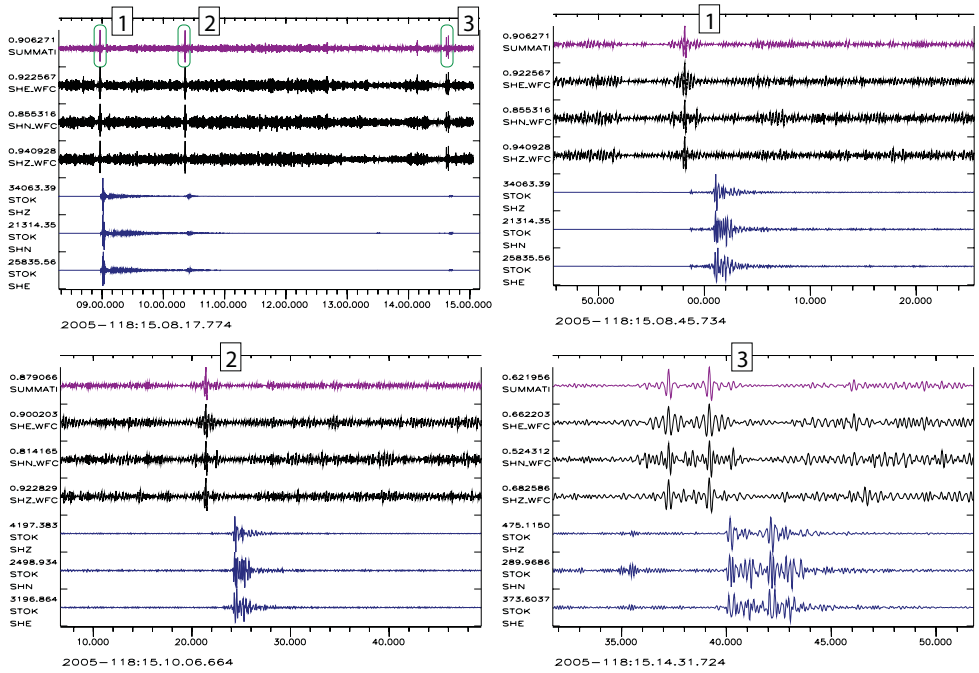


Figure 2. Part of the April 28, 2005, Rana earthquake sequence as recorded by the Stokkvågen 3-component station of the NNSN at a distance of approximately 15 km from the earthquake epicenter. The top left panel shows a seven minute long time window which (correcting for the difference in traveltimes) corresponds to the interval shown in Figure 1 for the NORSAR array. The remaining panels provide a close-up view at the times indicated. In each panel, the blue traces are STOK data from April 28, bandpass filtered between 2.5 and 8.0 Hz, the black traces show the componentwise correlation coefficients with filtered STOK data from the June 24, 2005, event (waveforms not shown), and the magenta trace indicates the mean of the 3 single com-ponent correlation traces.

The Use of Repeating Seismic Events to Control and Measure Erroneous Instrumental Timing

Gibbons and Ringdal (2006) pointed out that if two seismic events are co-located, since the travel time to a given station is identical for both events, the time separating the start of the waveform template for the first event and the maximum of the correlation coefficient channel (whereby the second event is detected) should be identical for all stations. This is the basis by which we can perform coherent beamforming of correlation coefficient traces over sparse networks even when the actual waveforms show no similarity whatsoever. If this is not the case (and the difference cannot be ascribed to waveform dissimilarity - whether due to differences in the seismic sources or to a low SNR) then we have to conclude that there is an inconsistency in instrumental timing at one (or both) of the stations at the time of one (or both) of the events. An event in the vicinity of Novaya Zemlya on March 5, 2006, was

well-recorded by the SPITS and ARCES arrays and also by the broadband station KBS on Spitsbergen (Figure 3). The arrival times for the Pn and Sn phases for the KBS station could not be reconciled with those at the array stations and the residuals obtained by various attempts to locate the event indicated that a consistent offset in the timing at KBS was to blame.

The operators of the station confirmed that a technical fault had occurred with the station on February 17, 2006, which was repaired on March 22, 2006. Continuous real-time correlation detectors have been run on SPITS data at NORSAR for some time to detect microseismic activity at the Barentsburg coal mine, the source of many almost-repeating seismic signals. Many of the Barentsburg events were recorded by both the SPITS array and the KBS station. Measurements of correlation maxima at both stations for many events before, during, and following the period effected by the technical fault allowed us to measure that at the time of the Novaya Zemlya event, the time stamp at the KBS station was approximately 8.07 seconds earlier than the actual UTC time (Figure 4). With the corresponding correction applied to the arrival time estimates, a well-constrained location is obtained for the Novaya Zemlya event including the KBS phase determinations. This study is described in full in Gibbons (2006).

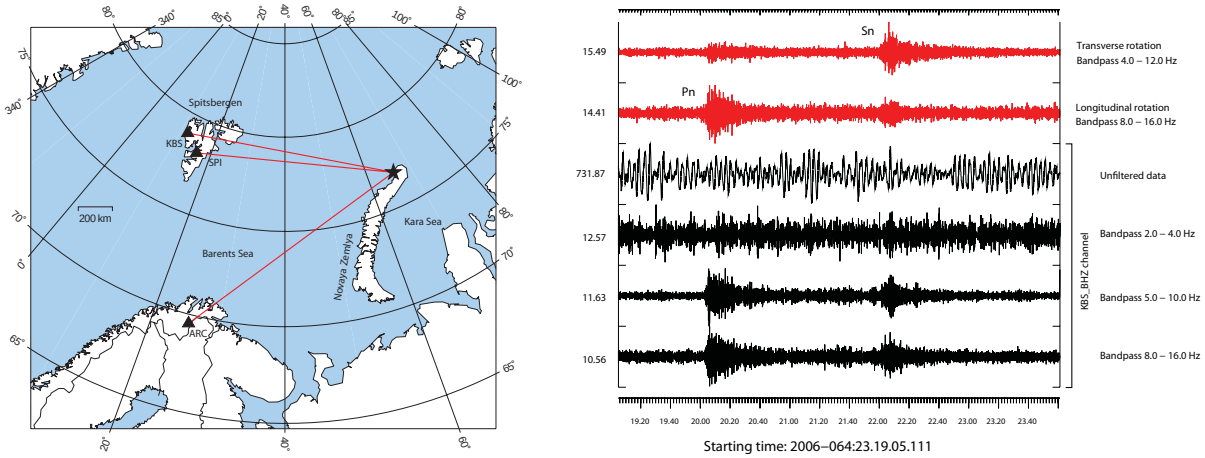


Figure 3. Left panel: location of the IMS arrays ARCES and SPITS and the IRIS/GEOFON/AWI 3-component station KBS at Ny Ålesund, Kings Bay, on Spitsbergen together with the fully automatic GBF location estimate for the March 5, 2006, event on or close to Novaya Zemlya. Right panel: waveforms from the Novaya Zemlya event recorded at the KBS station. Due to an instrumental technical fault, the time-stamp for the KBS station could not be relied upon and attempts to locate the Novaya Zemlya event using phase determinations from ARCES, SPITS, and KBS demonstrate that the time-stamp at KBS must be too early by several seconds.

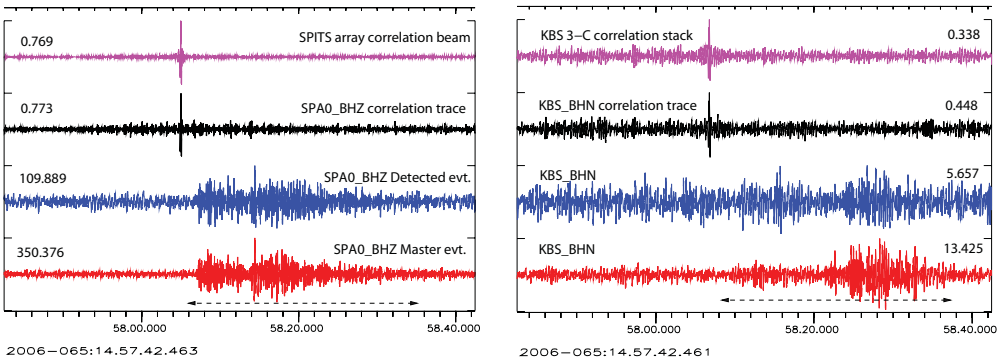


Figure 4. Detection by waveform correlation of the first identified rockburst at the Barentsburg coal mine, Spitsbergen, following the March 5, 2006, Novaya Zemlya event using the SPITS array (distance 50 km) and the KBS 3-component station (distance 120 km). The master event used is the first identified Barentsburg event following the repair of the KBS station on March 22, 2006. All data are bandpass filtered between 3.0 and 6.0 Hz and a 30.0 second waveform template is extracted for all available channels at both stations beginning at the estimated onset time of the first P-arrival. The SPITS waveform template begins at a time 2006-081:23.25.07.15000 and the interpolated correlation coefficient maximum at SPITS occurs at a time 2006-065:14.58.05.00229. The KBS waveform template begins at a time 2006-081:23.25.17.00760 and the interpolated correlation coefficient maximum at KBS occurs at a time 2006-065:14.58.06.78268.

Detection Studies in the Western US

To gain experience with correlation detector performance in a quite different tectonic setting, we are testing and applying correlation and subspace detectors to event clusters in eastern California using the NVAR array. The general setting and array geometry are shown in Figure 5. Studies in this region benefit from the double-difference catalogue produced by Hauksson et al. (2003), which provides good relative event locations importan to understanding how event waveform correlations are influenced by waveform proximity.

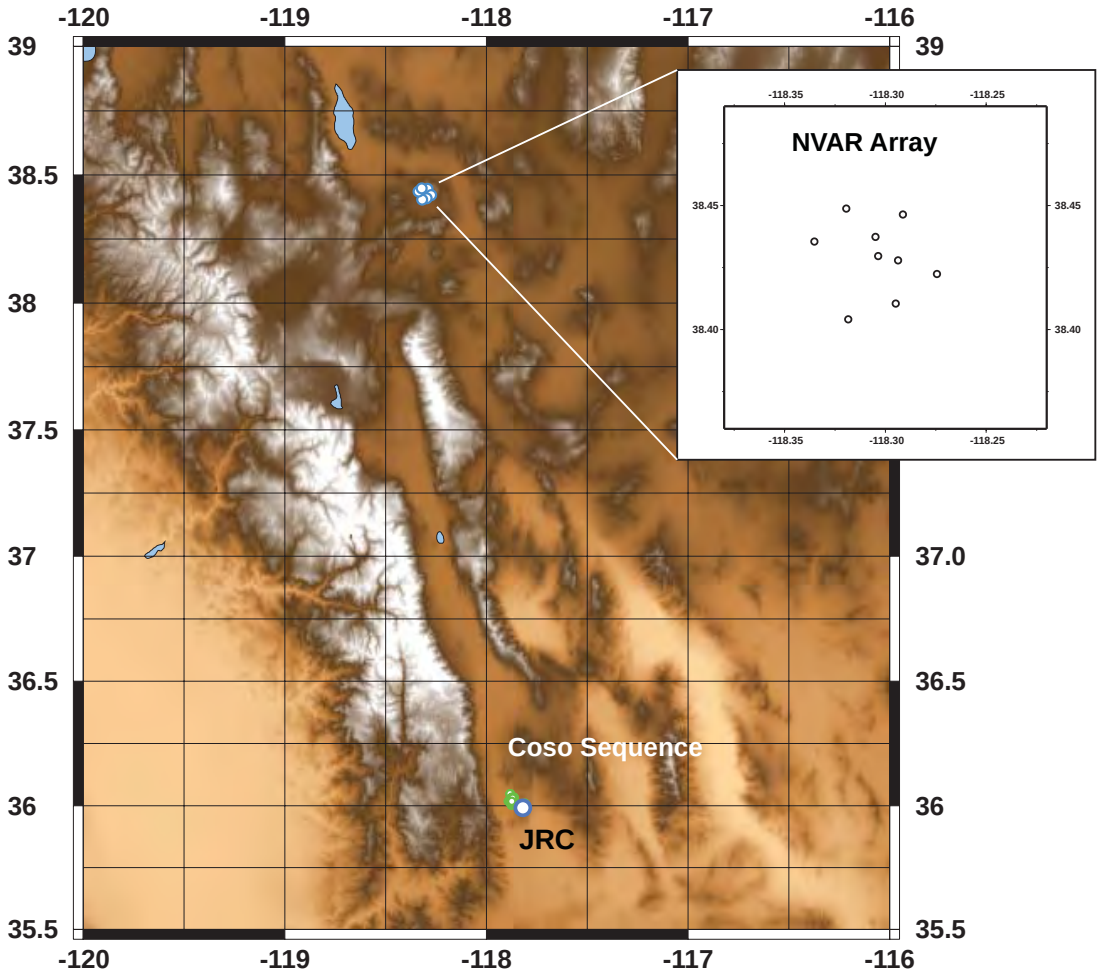


Figure 5. Location of the NVAR array (blue and white symbols) in western Nevada and the 2001 Coso sequence (green and white symbols) in southeastern California. Nine elements of the array were used to construct and apply detectors. The other elements of the array had significant data gaps or poor signal to noise ratio. The Coso sequence and two others in eastern California were chosen for study because of the availability of double-difference locations (Hauksson et al., 2003). While the overall sequence consisted of more the 3500 events (as reported in the catalog), 406 occurring in a 3-day period and in a fairly compact region were selected for study. Reported catalog magnitudes ranged from 0.4 to 3.9 for these events.

We describe one particular cluster here approximately 270 kilometers south of the NVAR array. This cluster of 406 events is part of a larger sequence just north of the geothermal region in Coso, southeastern California (Figure 5). The smaller cluster occurred in 2001 (Julian days 195-197) and had reported magnitudes ranging from 0.4 to 3.9. A local broadband station, JRC, within 5 kilometers of the cluster provides further ground truth information on the sequence.

A set of 29 events with magnitudes above 2.8 were used to characterize the events in the cluster - these are shown in Figure as green crosses. They were drawn from a longer time interval (195-211), but included many of the larger events in the detection interval. Waveforms from the 29 events were extracted from the NVAR data stream; a sample of these recorded at station NV01 are displayed in Figure 6. The figure shows screenshots from a new tool written to select and align waveform data, and compute subspace representations with user-selected parameters (filter band,

representation dimension, etc.). Besides a waveform display, used to screen bad events and channels, the tool has a correlator that aligns the waveforms, and a dendrogram display allowing the user to set clustering thresholds and select clusters. It also has a series of subspace panels that display the fidelity of representation (energy capture, shown in the figure) of waveforms and the probability of detection (at a fixed, selectable false alarm probability) both as a function of the subspace dimension. These analytical tools allow the user to select a subspace (correlator operator) dimension. The tool finally allows the user to write a detector definition file which can be used by a separate code to run the detector against a continuous (multichannel) data stream. In this instance, an 8-dimension detector was constructed and applied against the 9 channels of continuous NVAR data for the 3-day interval 2001:195-197.

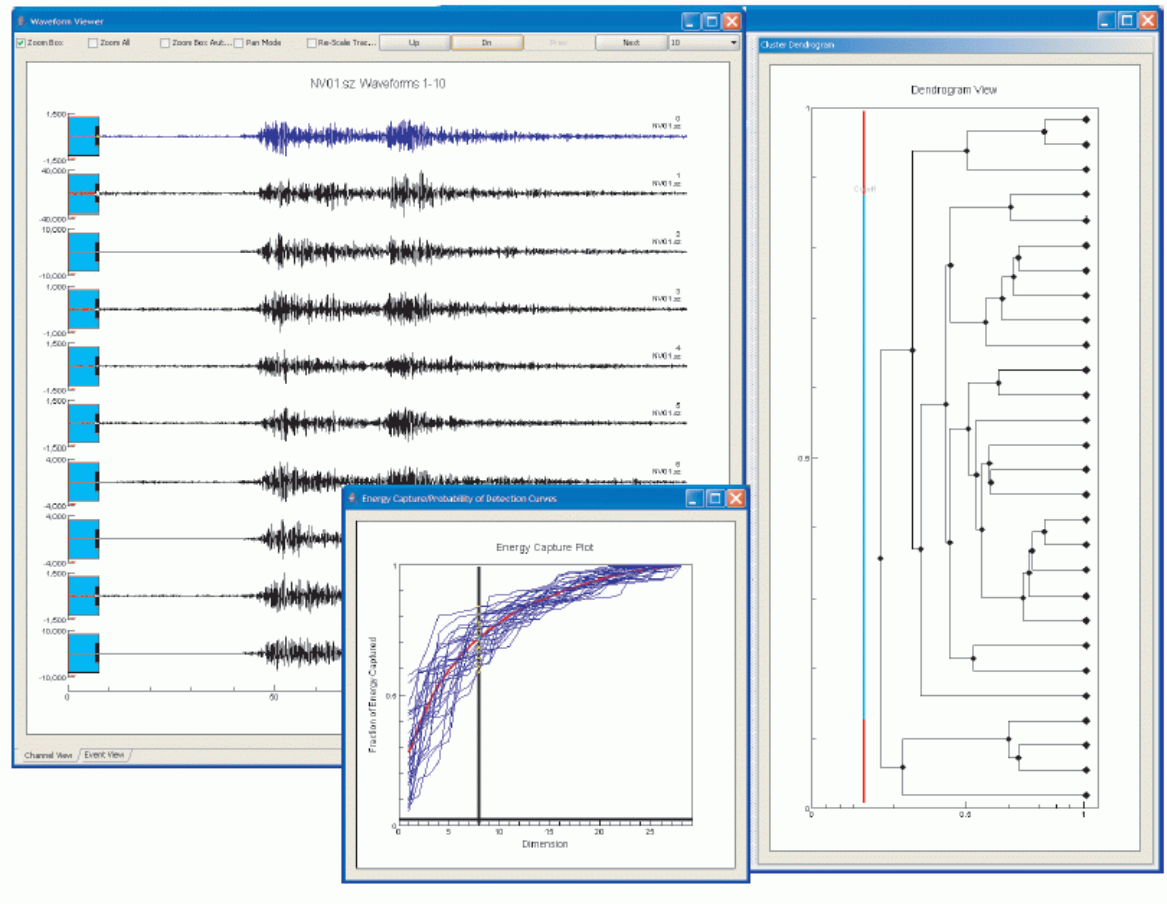


Figure 6. Screen shots from a new tool showing several of the steps in constructing a subspace detector for the Coso sequence with data from the NVAR array. A waveform display tool (at left) allows the user to screen bad events and bad channels. A correlator aligns the waveforms and provides measurements for building a dendrogram display (at right). The dendrogram allows the user to define and select event clusters. A series of subspace panels (one shown at center: energy capture as a function of subspace dimension) allow the user to select a window on the aligned waveforms and choose a subspace dimension.

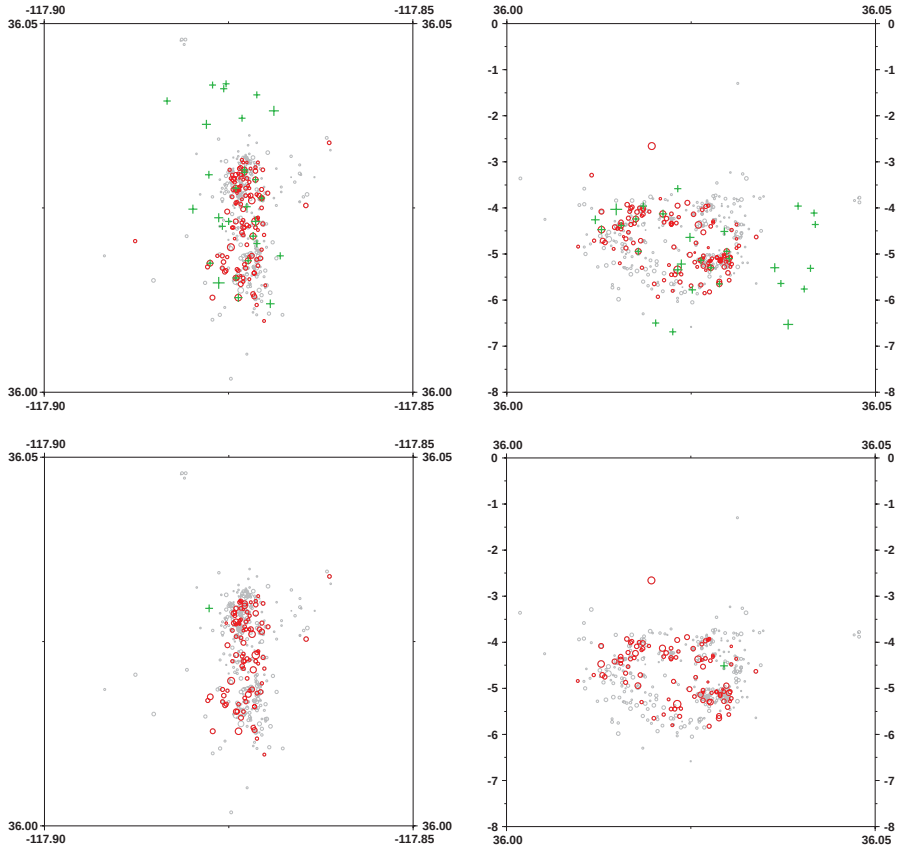


Figure 7. Detail maps showing the spatial distribution of training events (green), detected events (red) and undetected events (grey). Results for the 8-dimension subspace detector are on top and for a correlation detector are on the bottom. The maps show the distribution of events in latitude and longitude (left) and latitude and depth (right). Symbol size is scaled to event magnitude.

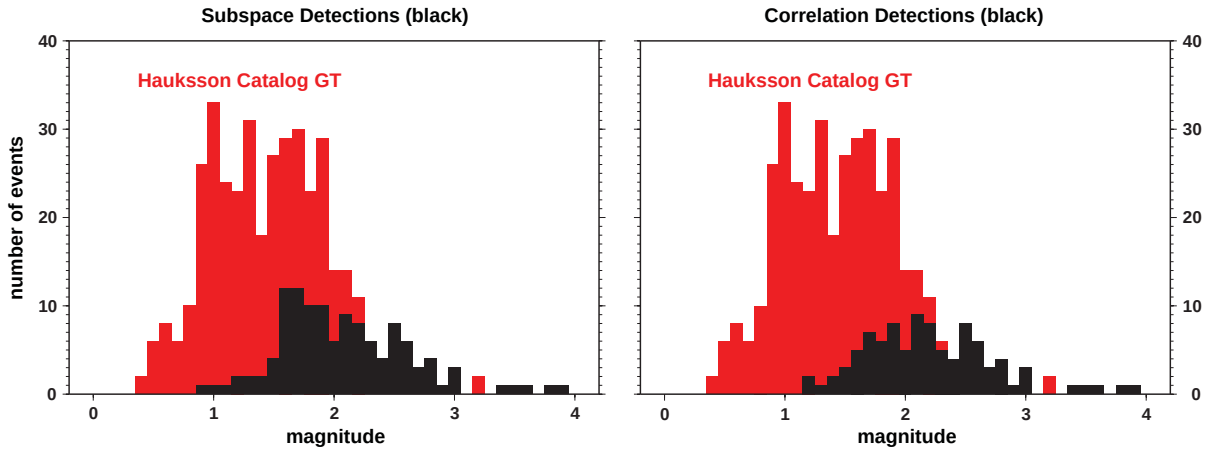


Figure 8. Histograms of detected events in this sequence in black for the subspace detector (left) and the correlator (right). The histogram for the Hauksson catalog is shown in red behind the detector histograms. Waveform representation is a significant challenge for this sequence.

The results of the detection operation are shown in Figures 7 and 8. Figure 7 contains maps of the 406 events comprising the cluster in question. The green crosses indicate the reference events, the red circles indicate detected events and the grey circles indicate undetected events. Results for the 8-dimension multichannel subspace detector are shown at the top: 120 events were detected after adjusting the detection threshold (to 0.03) to allow only 2 presumed false alarms (defined as events not reconcilable against the Hauksson catalog). At left in Figure 8 is a histogram (in black) of the 120 detections reconciled against the catalog as a function of catalog magnitude. Behind the histogram of detections is another histogram (in red) of all the catalog events. Comparison of the two histograms makes it clear that the subspace detector missed at least half the events between magnitudes 1.5 and 2.2, and two magnitude 3.2 events (these were in coda of still larger events).

For comparison, a multichannel correlation detector was developed using one event (shown as the green cross in the bottom of Figure 7) and a similar detection operation was performed. Adjusting the detection threshold (to 0.0125) to allow the same number (2) of unreconciled triggers as in the subspace detector case, this detector found 95 events distributed about as widely as for the subspace detector. The correlation detector threshold was substantially lower than the subspace detector because of the fact that the 8 basis functions of the subspace detector significantly raise the noise floor of the detection statistic (while simultaneously raising the values of the statistic for actual events).

We can only speculate about the reasons for the relatively poor performance of both detector types in this case (compared to almost complete detections in other instances). From cursory examinations of the three-component signals observed at the local station JRC, it does appear that the mechanisms of the events not detected are significantly different from the larger events used for design. One hypothesis consistent with the observations is that the larger events have principal axis orientations aligned with the dominant stress field in the region, and thus have relatively uniform mechanisms. This hypothesis would explain neatly why the correlation detector performed nearly as well as the subspace detector designed from 29 events: the additional 28 events would add relatively little information to the representation relevant to the smaller events. In this view, the smaller events might have relatively random orientations.

CONCLUSIONS AND RECOMMENDATIONS

In the first year of this project, we have demonstrated a significant lowering of the detection threshold using the multichannel waveform correlation method in a number of different scenarios; continuous real-time online correlation detectors have been implemented for an increasing number of test cases on all of the arrays operated by NORSAR. In the example presented here, the signal from an m_b=3.5 event in northern Norway was successfully used as a template to detect events in the immediate vicinity down to m_b=0.5 at distances of over 600 km. The improvement in detection capability appears to be greater for large aperture seismic arrays. False alarms (i.e. spurious correlations) are generally identified by measuring the alignment of peaks in the correlation coefficient traces at different sites in the array. This becomes a greater challenge for very weak signals on small-aperture arrays and will be a main focus of future work. The alignment of correlation peaks has also proved very useful in the identification, measurement, and correction of erroneous timing at seismic stations. This property alone should motivate a large scale initiative to identify sources of repeating seismic events.

The greatest drawback of matched filter detectors is the requirement that we have a representative waveform to use as a detection template. Whilst we are encountering surprisingly many situations in which correlation detectors are highly effective, we have also identified a number of situations where very closely spaced events display a very high degree of waveform dissimilarity and where correlation detectors subsequently miss a large number of events. In a case study in the western United States, using NVAR array data from the Coso earthquake sequence from 2001 (at a distance of 270 km), multidimensional subspace detectors were found to perform only modestly better than a correlation detector. Large numbers of events went undetected by either correlation or subspace detectors, suggesting that the smaller magnitude events in this sequence may display greater diversity in mechanism than the larger events used to design the detection templates.

ACKNOWLEDGEMENTS

We are grateful to Mathilde Bøttger Sørensen and Jens Havskov from the Department of Earth Sciences at the University of Bergen (UiB), Norway for providing data from the STOK station. The Norwegian National Seismic Network is operated by the UiB and supported by Oljeindustriens Lands Forening (OLF) and the Faculty of Mathematics and Natural Sciences, UiB.

REFERENCES

Geller, R. J. and Mueller, C. S. (1980). Four similar earthquakes in Central California, in *Geophys. Res. Lett*., 7: 821-824.

Gibbons, S. J. (2006). On the identification and documentation of timing errors: an example at the KBS station, Spitsbergen, *Seism. Res. Lett*., in press.

Gibbons, S. J., Bøttger Sørensen, M., Harris, D. B. and Ringdal, F. (2006),.The detection and location of low magnitude earthquakes in northern Norway using multichannel waveform correlation at regional distances, manuscript submitted to *Phys. Earth Planet. Int.*, under review.

Gibbons, S. J. and Ringdal, F. (2006). The detection of low magnitude seismic events using array-based waveform correlation, in *Geophys. J. Int*., 165: 149-166.

Hauksson, E., W-C. Chi, P. Shearer, and A. Michael (2003). Comprehensive waveform cross-correlation of southern California seismograms: Part 1. Refined hypocenters obtained using the double-difference method and tectonic implications (abstract), Fall Ann. Meeting, American Geophys. Union. Dec. 8-12, San Francisco, CA.

Hicks, E. C., Bungum, H. and Lindholm, C. D. (2000). Seismic activity, inferred crustal stresses and seismotectonics in the Rana region, Northern Norway, *Quaternary Science Reviews*, 19: 1423-1436.

A MODEL-BASED SIGNAL-PROCESSING APPROACH TO SEISMIC MONITORING

Arthur J. Rodgers, David B. Harris, and Michael E. Pasyanos

Lawrence Livermore National Laboratory

Sponsored by Lawrence Livermore National Laboratory

Contract No. LDRD-05-ERD-019

ABSTRACT

Recent applications of correlation methods to seismological problems illustrate the power of coherent signal processing applied to seismic waveforms. Examples of these applications include detection of low amplitude signals buried in ambient noise and cross-correlation of sets of waveforms to form event clusters and accurately measure delay times for event relocation and/or earth structure. These methods rely on the exploitation of the similarity of individual waveforms and have been successfully applied to large sets of empirical observations. However, in cases with little or no empirical event data, such as aseismic regions or exotic event types, correlation methods will likely fail due to the lack of previously observed similar waveforms.

This study seeks to use a suite of model-based signals computed for three-dimensional Earth models to form the basis for correlation detection using the subspace method. To demonstrate the method we modeled broadband regional seismograms for a moderate (M~5) earthquake near the China-North Korea border. Synthetic seismograms are computed with the Spectral Element Method for a suite of long-wavelength (2 degree) seismic velocity models inferred with the Markov Chain Monte-Carlo (MCMC) method. MCMC uses stochastic sampling to fit multiple data sets but unlike conventional inversions that estimate a single “optimal” model, MCMC results in a suite of models that sample the model space and incorporate uncertainty through variability of the models. The variability reflects our ignorance of Earth structure, due to limited resolution, data and model errors. The variability in 3D earth models produces variability in the seismic waveform response for the paths of interest. Model-based signals are combined using the subspace method where the set of synthetic signals are decomposed into an orthogonal basis by singular-value decomposition (SVD). The observed waveforms are represented with a linear combination of eigenvectors (signals) associated with the most significant eigenvalues of the SVD. We demonstrate the ability of model-based signals to represent intermediate period (down to 10 s) seismograms. Further work will require higher frequency synthetic seismograms and the inclusion of shorter wavelength velocity structure, whether inferred from various seismic data sets or generated by forward calculations through realizations of a stochastic model.

OBJECTIVES

Current methods for seismic monitoring of underground nuclear explosions are heavily dependent on the use of measured quantities from seismograms and deterministic models of Earth structure. For example, seismic events are typically located by minimizing the difference between the observed and predicted arrival times of major P- and S-wave phases from one-dimensional Earth models and source-specific station corrections. This procedure works well when the event is large enough to be observed at a number of stations with high signal-to-noise ratio and the travel time predictions are accurate. However, detection of signals above ambient noise can be difficult for small magnitude events, even at regional distance where there may be at most a few stations recording the event with adequate signal-to-noise (SNR) ratios. Furthermore, if the regional structure is poorly known, as frequently occurs, large bias may result in the location from errors in the travel time predictions. This study attempts to advance the basic methodology of seismic monitoring by using a suite of model-based signals and coherent signal-processing to detect signals in noisy data.

In the past large (> 10 kT) underground nuclear tests at known test sites were detected, located and identified using observations at teleseismic distances (> 2500 km) and the wealth of knowledge gained from previous tests, often from nearly the same location. As new nuclear states emerge it has become increasingly important to monitor broad regions without previous explosion observations. For aseismic regions, monitoring is challenged by the lack of empirical (earthquake- and/or explosion-derived) constraints on travel times, surface wave dispersion and amplitudes for traditional location and identification processing. Significant progress has been made in the development of earth models to predict seismic observables, such as travel times, surface wave dispersion and full waveforms. Recent studies have demonstrated the efficacy of three-dimensional earth models to improve event location using travel times (e.g. Johnson and Vincent, 2002; Ritzwoller et al., 2003; Murphy et al., 2005; Morozov et al., 2005; Li et al., 2006; Flanagan et al., 2006). Similarly, tomographic models of surface group velocity dispersion improve surface wave magnitude estimates through the application of phased-matched filtering (Pasyanos et al., 1999; Stevens and Adams, 2000).

Another challenge impeding the lowering of detection thresholds to monitor small explosions is the difficulty detecting signals with low SNR. Conventional short-term/long-term average (STA/LTA) detectors require elevated signal power in a particular frequency band relative to the preceding noise and are inherently limited when signal power approaches the ambient background noise level. However, waveform correlation methods make use of more information, namely the repeated temporal structure of the waveform. The similarity is measured by the correlation function between a template waveform and a continuous data stream and a high value is obtained when the streaming waveform is the similar to the template (van Trees, 1968). This process, also called a matched filter, is an optimal detector in the presence of white Gaussian background noise and offers great sensitivity. However, it requires perfect knowledge of the signal. Formal statistical analysis provides a rigorous quantification of the probability of detection versus false alarm (i.e. the receiver-operator curve) for a given correlation value.

The application of matched filter detectors to seismology is challenged by the complexity introduced by the source (e.g., focal mechanism, depth, magnitude) and path effects on the resulting waveform(s). Geller and Mueller (1980) concluded that waveforms for adjacent events can be highly correlated when filtered in a sufficiently low-frequency band and the events have similar source parameters and are separated by no more than a quarter of the dominant wavelength. Others (Harris, 1991) argue that waveform correlation is significant out to event separations of one to two wavelengths, which is consistent with correlation lengths observed in the reciprocal problem of waveform coherence for a single event across an array aperture (Mykkeltveit et al., 1984). This phenomenon has been exploited to identify nearby mining explosions (e.g., Israelsson, 1990; Harris, 1991) and measure precise relative arrival times of adjacent nuclear explosions (e.g., Thurber et al., 2001; Waldhauser et al., 2004). Recently, correlation methods have been applied to large earthquake data sets covering active faults with dense local network data (Waldhauser and Ellsworth, 2000; Schaff et al., 2004) or the entire Chinese territory with regional network data (Schaff and Richards, 2004). Gibbons and Ringdal (2006) reported reduction in the detection thresholds for events in the European Arctic using single-channel and array-based matched filters and showed how array frequency-wavenumber analysis provides additional screening power.

Matched filters work well to detect repeating events that produce identical signals. However, seismic sources often generate related events with variations in source mechanism, time history and location that produce similar, but not identical waveforms. As a consequence, there is some uncertainty about the signals to be detected. If a collection of

template waveforms can be assembled that spans the range of signals likely to be produced by a particular source, a subspace detector (Harris, 1989, 1997; Harris et al., 2006) can be developed to detect signals from that source. Subspace detectors operate by correlating a linear combination of a set of orthonormal basis waveforms against an incoming data stream to detect signals that lie in the subspace spanned by the basis (hence the name "subspace detector"). The linear combination is chosen to maximize the correlation at each time step. The basis is developed from the singular value decomposition of a matrix constructed from the representative template waveforms. The basis consists of the left singular vectors corresponding to the most significant singular values in the decomposition.

The objective of this study is to test a new method to monitor events in aseismic regions with detectors employing model-based subspaces rather than empirical subspaces. Our goal is to detect events at regional distances at lower thresholds. Subspace detectors with empirically-derived basis functions have successfully detected clusters of mining explosions and small earthquakes from swarms (Harris et al., 2006) at lower monitoring thresholds than can be obtained with conventional power (STA/LTA) detectors. In such applications, path effects are calibrated with previously-observed waveforms and signals uncertainty is due principally to source effects, such as emplacement or near-source material properties, source-time function and/or focal mechanism. The present application focuses on uncertainty introduced by path effects, in situations where no previously-observed event waveforms are available. In this application, a basis is generated from a collection of representative template signals computed from a suite of fully three-dimensional (3D) earth models with the source parameters kept fixed. While model-based signals for 3D earth models are presently expensive to calculate even for intermediate frequency ranges, this project represents an attempt to advance monitoring science through the use of model-based signals for waveform matching. We expect the present study could be extended in the future to include higher-frequency synthetics and higher resolution earth models. Future efforts may also attempt to include source variability as well.

RESEARCH ACCOMPLISHED

The purpose of this project is to explore the feasibility of applying the subspace detection algorithm to model-based signals. The investigation focuses on regional seismograms from an earthquake in eastern Asia. Models are derived from the Markov chain Monte Carlo algorithm (Pasyanos et al., 2006). Signals are computed for 3D models using the spectral element method (Komatitsch and Vilotte, 1998; Komatitsch and Tromp, 1999). This effort was started in October 2004 as a Laboratory Directed Research and Development (LDRD) Project. The LDRD Program at LLNL supports internally competed projects for the development of new capabilities.

Study Area

For this proof of concept study we considered a moderate sized earthquake occurring near the China-North Korea border. The event occurred on January 11, 2002 and had a moment magnitude (M_W) of 4.89. Figure 1 (left) shows the study area, the event and station locations.

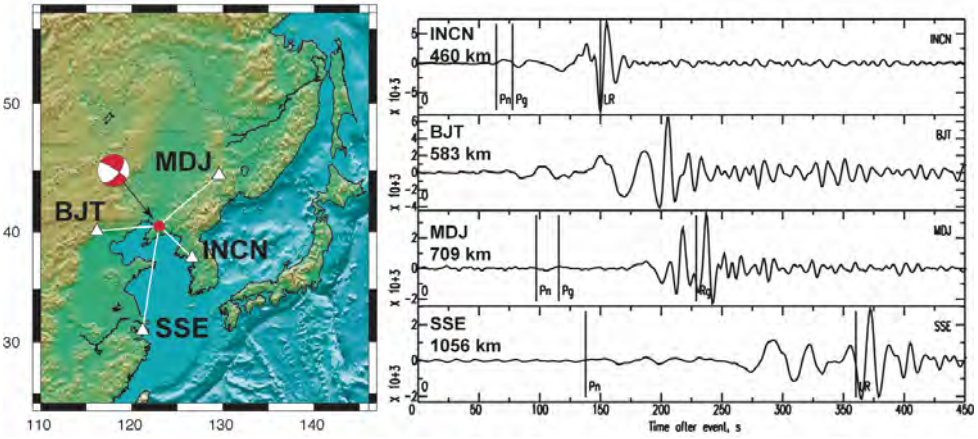


Figure 1. (left) Map of eastern Asia showing the earthquake (red circle, focal mechanism) we studied and regional distance stations (white triangles) that recorded the event. (right) Vertical component waveforms (filtered 0.0125-0.1 Hz) from the event at the four regional stations. The station names and epicentral distances are indicated next to each waveform.

Focal parameters were determined by William Walter (see Acknowledgements). Also shown in Figure 1 are the vertical component waveforms. Broadband waveforms were obtained from four regional stations operated by the Chinese Digital Seismic Network (CDSN, stations BJT, MDJ, SSE) and the Global Seismic Network (GSN, station INCN). These have good SNR for the surface waves at the frequencies of interest for this study. The instrument response was removed, the waveforms were integrated to displacement and the horizontal components were rotated to radial and transverse components.

Stochastic Earth Models

Models of the study region were derived from the Markov Chain Monte Carlo (MCMC) algorithm using surface wave group velocity dispersion, body-wave travel times, receiver functions and gravity (Pasyanos et al., 2006). The MCMC approach is probabilistic in nature, relying on a prior distribution of all model parameters. It computes the difference between all observations and model predictions and then accepts or rejects a model based on a likelihood measure. Codes to implement the MCMC algorithm were developed at LLNL. The approach is computationally intensive and the calculations were performed on the MCR cluster operated by Livermore Computing. The MCMC algorithm results in a set of posterior models that map the solution space. The approach has several advantages over conventional deterministic inversions: it allows for multiple data sets, it maps data and model uncertainties through the process and does not rely on normal statistics.

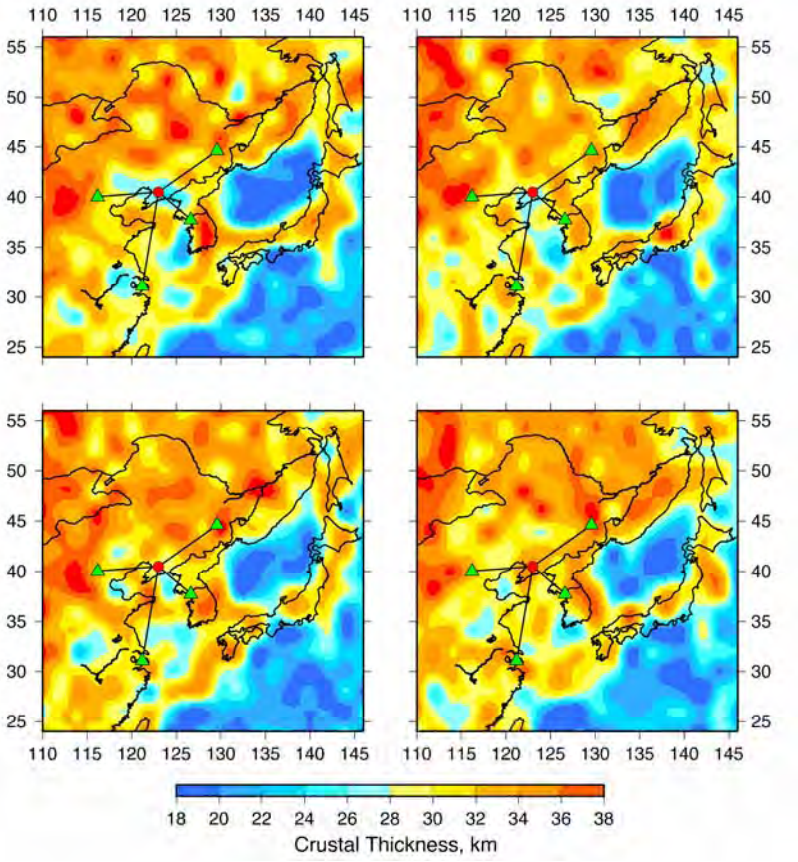


Figure 2. Crustal thickness for four MCMC models of the Yellow Sea-Korean Peninsula region. The event (red circle), stations (green triangles) and paths (black lines) of our data set are also shown.

We used a suite of MCMC models for the study region to compute the response of the event at the four regional stations (Figure 1). Models specify the seismic compressional and shear velocities (v_P and v_S, respectively) and density (ρ) on a regular 2º by 2º grid in longitude and latitude. The models represent five crustal layers of variable thickness spanning the surface of the solid earth to the Moho and are underlain by a mantle half-space. We smoothed the models and embedded them in the CUB2.0 model (Shapiro and Ritzwoller, 2002) which is registered

on the same grid. Figure 2 shows the crustal thickness estimates of four models. Note that the large-scale features of these models are similar, such as the ocean-continent differences. However, details of the model at any specific point or along any path reflect uncertainty in our estimates of the true structure. These 3D model differences will result in different template waveforms when the complete response is computed.

Synthetic Seismograms

We computed synthetic seismograms for this study using the spectral element method (SEM) code SPECFEM3D developed by Komatitsch and Tromp (1999) and Komatitsch et al. (2002). SPECFEM3D is a parallel code for computing the response of a fully 3D earth model to moment tensor loading. It is based on a finite element (FE) mesh of the spherical earth and uses high order polynomials along the edges of the elements sampled at unevenly spaced points. The points are chosen judiciously so that orthogonality relations result in simple and exact expressions for the motions at each time step, avoiding the inversion of large a linear system common to FE algorithms.

We modified the SPECFEM3D code to use the MCMC models embedded in the CUB2.0 model. Calculations were performed to compute the response at the four regional stations keeping the source parameters fixed. Each run was made on 144 CPU's of the MCR cluster and ran for approximately nine hours to compute the response from 0-0.2 Hz. We have since made improvements to allow for higher frequency calculations with the same resources. Figure 3 shows the resulting model-based waveform templates compared to the observed data. Generally the model-based signals show very consistent body-waves, with only slight variations in the timing of arrivals. However, the surface waves, especially the later arriving short-period energy, displays differences likely related to dispersion and scattering. Note especially the data and synthetics for station BJT. This path crosses the sedimentary structure of the Bohai Basin and the data reveal a complex response.

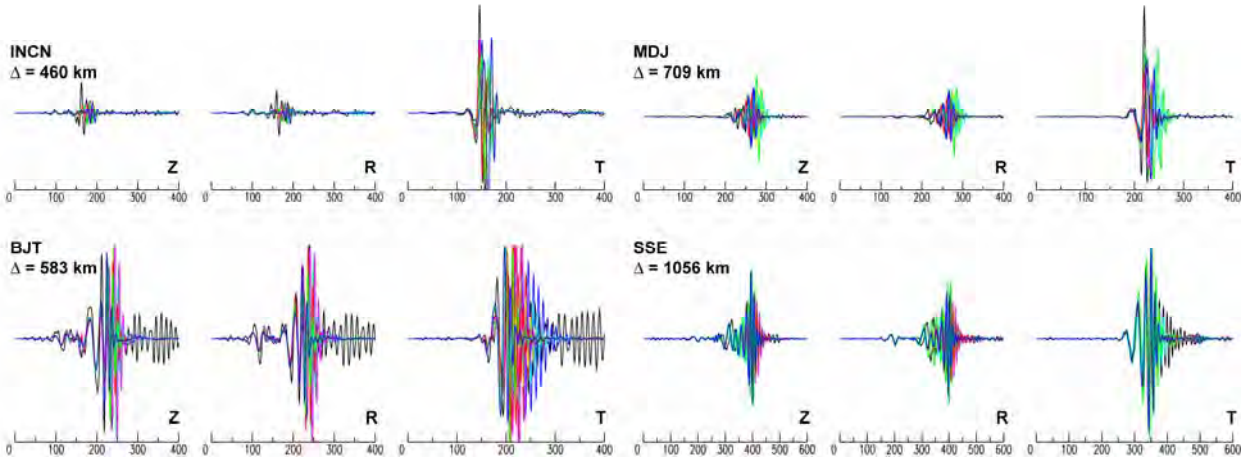


Figure 3. Three-component observed (black) and synthetic (colored) waveforms for the four regional stations. There are synthetic signals for nine different models. Z, R, T corresponds to vertical, radial and transverse components, respectively. Data and synthetics are filtered 0.01-0.1 Hz. Note that the time scale is different for station SSE.

Subspace Analysis

The subspace analysis was performed for each station separately. Each three-component waveform (observed and synthetic) was multiplexed in channel sequential order, with *M* total points. The *N* model-based templates were treated as vectors and formed a matrix of length *M* and width *N*. Following the subspace methodology the matrix of template waveforms was decomposed into its singular vectors and sorted by most-significant singular value. For this study we computed model-based signals for nine models (*N*=9). The length of signal time windows for each station varied such that the entire surface wave and coda were captured (400-600 s, similar to Figure 3).

The dimension of the subspace is a significant design parameter subject to a tradeoff between the probability of detection and the probability of false alarm. The larger the number of significant singular vectors used to represent the observed waveform the better will be the fit to potential signals and the higher the probability of detection. However, using a larger subspace introduces a possibility for a misleading high noise correlations and consequent false alarms. Determination of the subspace dimension is made, in part, by considering the "energy capture". This is the fractional energy of each template waveform represented by the singular vector basis of dimension *1* to *N*. When all singular vectors are used, each of the N design templates will be perfectly represented. The energy capture is computed for each of the *N* original template waveforms and plotted as a function of the subspace dimension. Figure 4 shows the energy capture for the waveform templates computed for station BJT and using three different frequency bands.

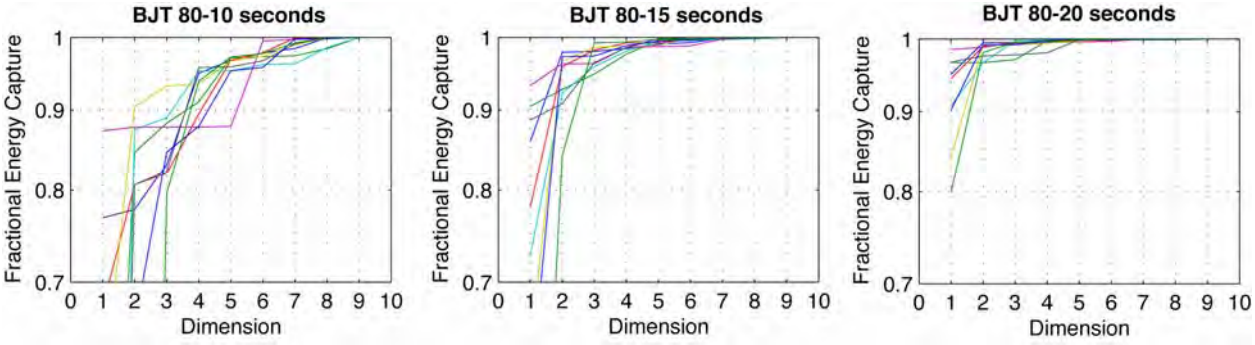


Figure 4. The energy capture for templates computed for station BJT in three different frequency bands 0.0125-0.1 Hz (left), 0.0125-0.067 Hz (center) and 0.0125-0.05 Hz (right).

The energy capture shown in Figure 4 indicates that for the low frequency case a subspace dimension of only one or two is needed to represent 95% of the power in each original template waveform. However, the subspace dimension needed to represent the basis signals increases as the bandwidth increases. For the bands 0.0125-0.067 Hz and 0.0125-0.1 Hz we use subspace dimensions of 3 and 5, respectively. The subspace dimension must increase as additional complexity is added in the broader bandwidth waveforms. The key for the subspace methodology to work effectively is for the subspace dimension to increase slowly as the bandwidth increases.

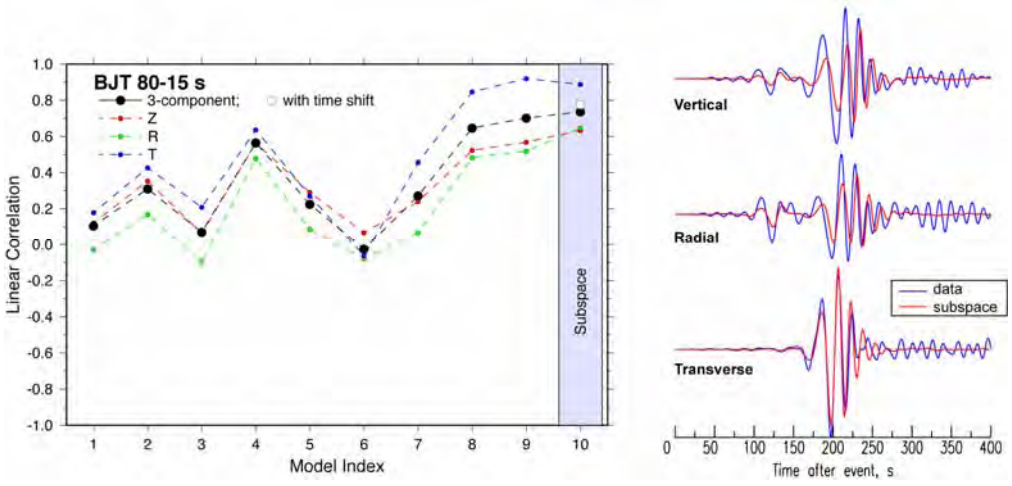


Figure 5. (left) Linear correlation between the observed waveforms and the nine individual MCMC model-based signals, the tenth model is the subspace result, using a subspace dimension of three. The linear correlation is plotted for the three-component (black circles) and individual components (colored circles). (right) The resulting fit between the observed (blue) and subspace detector (red) waveforms.

The subspace representation is then applied to the observed waveforms. To evaluate the performance of the subspace detector we compute the linear correlation between the three-component synthetics for the nine individual MCMC models and for the subspace. Figure 5 shows the linear correlations for the waveforms observed at BJT using the frequency band 0.0125-0.067 Hz and a subspace dimension of 3.

The linear correlations between the observed and individual model-based signals (model indices 1-9) vary between about 0.0 and 0.7. The subspace results in an improved waveform fit over any individual model. While values greater than about 0.5 indicate fairly good waveform similarity the subspace result (about 0.7) should be compared with the average correlation for the individual models (about 0.4) because there is no reason to choose any single model from the MCMC model set. Notice that the resulting waveform for the subspace has the proper surface wave dispersion. For these frequencies the individual model-based signals do not reproduce the late-arriving scattered surface wave energy that was not present in the basis waveforms (Figure 3).

The performance of the subspace representation, as measured by the increase in the linear correlation between the observed and the individual model-based and subspace signals, improves as the bandwidth is increased. Figure 6 shows the three-component linear correlations between the model-based and observed signals for three frequency bands. Increasing the bandwidth introduces additional complexity in the observed and model-based signals and the improvement in linear correlation for the subspace is most dramatic for the broadest band comparisons (80-10 seconds).

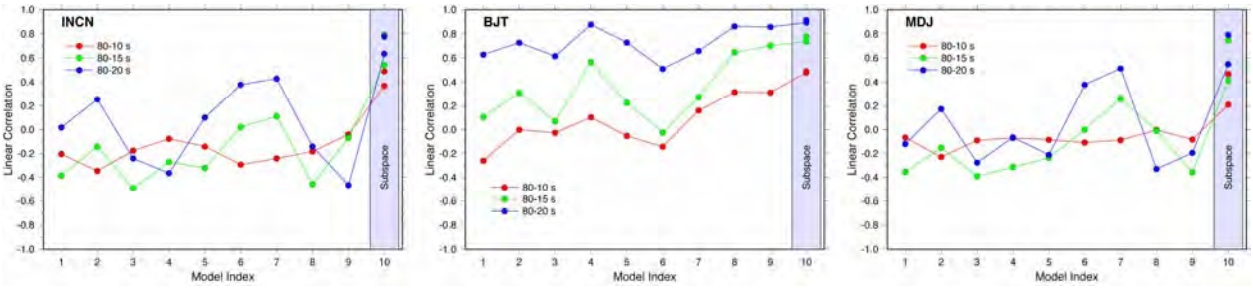


Figure 6. Linear correlations between model-based signals (individual, 1-9, and subspace) and the observed three-component waveforms at three stations INCN (left), BJT (center) and MDJ (right). For each station the analysis was performed in three different frequency bands, indicated by the different colors: 0.0125-0.1, 0.0125-0.067 and 0.0125-0.05 Hz corresponding to period bands 80-10 (red), 80-15 (green) and 80-20 (blue) s.

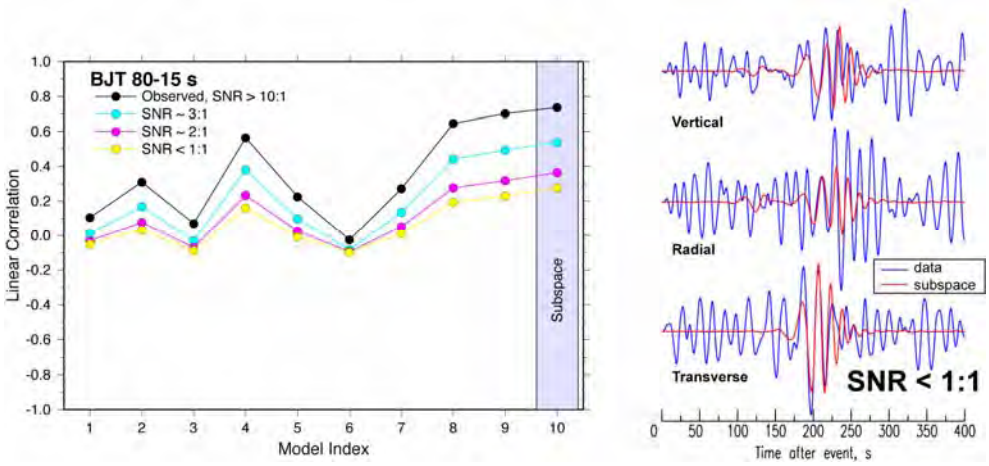


Figure 7. (left) Linear correlation between the observed and individual model-based and subspace signals for station BJT (80-15 s) with the addition of noise. The observed waveform has a SNR to greater than 10:1. The addition of noise degrades the correlations, however, the subspace still improves the representation of the observed signal over the individual model-base signals. (right) The observed (blue) waveforms with noise added to overwhelm the signal and the subspace signal (red) show that the correlation is still possible.

The most dramatic increases in linear correlation between the observed and model-based signals is seen for stations INCN and MDJ. The broadband (80-10 s) comparisons are quite poor for the individual model-based signals, but these all increase dramatically when combined with the subspace methodology.

Finally, we tested the effect of adding noise to the observed signals in order to lower the SNR and found that we can still obtain improvements in the linear correlation with the subspace representation over the individual model-based signals (Figure 7).

CONCLUSIONS AND RECOMMENDATIONS

While limited in scope, this study demonstrates the feasibility of using model-based signals and the subspace representation of signals to improve monitoring of aseismic regions and lower detection thresholds. Correlation methods promise to lower detection thresholds below the 2:1 SNR limitation of conventional STA/LTA methods. The subspace method combines model-based signals to reproduce the temporal structure of observed waveforms as is required for coherent processing of incoming data streams. Although we have not yet tested this strategy on a continuous data stream we intend to use codes developed for empirical template waveforms to test signal detection capabilities (e.g. Harris et al., 2006).

The synthetic seismograms used in this study incorporated fully three-dimensional variability of earth structure, however the long-wavelength representations can be improved to be more realistic. We are currently completing a suite of higher resolution MCMC models of the Yellow Sea-Korean Peninsula region. These will be 1º by 1º rather than the 2º by 2º models we used above. The finer structure will result in more complex synthetic seismograms. Geophysical models will improve in their resolution and accuracy as more data become available and inference methods evolve. The MCMC algorithm is ideal for improving knowledge of earth structure because it can incorporate different data types and map uncertainties through to predictions of observables, such as complete waveforms. When resolution of earth structure is limited to a certain scale, stochastic (random) heterogeneity could be added to 3D earth models to mimic the effects of complex unresolved small-scale structure.

We are also attempting to increase the frequency content of the model-based signals. A new elastic finite difference code is being developed at LLNL (Nilsson et al., 2006) and we are working to use this code for future synthetic seismogram calculations. The code runs in parallel and scales effectively from 1 to 1024 CPU's. While the computation of synthetics seismograms used in this study is expensive, we envision that these calculations will become more accessible in the future.

ACKNOWLEDGEMENTS

We are grateful Sean Ford and Tim Paik who developed some of the software used in this study. Jeroen Tromp and Dimitri Komatitsch developed the SPECFEM3D code and we are grateful to them for making it openly available. JoAnne Levatin assisted with the SPECFEM3D calculations and model manipulations. Al Franz ran the MCMC models. MCMC models and synthetic seismograms were computed on the MCR LINUX cluster operated by Livermore Computing. We thank Bill Walter for providing the source parameters for the January 11, 2000 earthquake we studied. Waveform and parameter data were read from the LLNL Seismic Research Database operated by Stan Ruppert, Doug Dodge and Terri Hauk.

The facilities of the IRIS Data Management System, and specifically the IRIS Data Management Center, were used for access to waveform and metadata required in this study. The IRIS DMS is funded through the National Science Foundation and specifically the GEO Directorate through the Instrumentation and Facilities Program of the National Science Foundation under Cooperative Agreement EAR-0004370.

REFERENCES

Flanagan, M. P., S. C. Myers, and K. D. Koper (2006). Regional travel-time uncertainty and seismic location improvement use a 3-dimensional *a priori* velocity model, *Bull. Seism. Soc. Am.*, submitted.

Geller and Mueller (2006). Four similar earthquakes in central California, *Geophys. Res. Lett.* 7: 821–824.

Gibbons, S. and F. Ringdal (2006). The detection of low magnitude seismic events using array-based waveform correlation, *Geophys. J. Int.* 165:149–166.

Harris, D. (1989). Characterizing source regions with signal subspace methods: theory and computational methods, Lawrence Livermore National Laboratory, Internal Document UCID-02148, Livermore, CA, 41 pp.

Harris, D. (1991). A waveform correlation method for identifying quarry explosions, *Bull. Seism. Soc. Am*. 81: 2395–24187.

Harris, D. (1997). Waveform correlation methods for identifying populations of calibration events, in *Proceedings of the 19th Annual Seismic Research Symposium on Monitoring a Comprehensive TestBan Treaty*, September 23–25, 1997, pp. 604–614.

Harris, D., A. Rodgers, M. Pasyanos, S. Myers, J. Levatin, A. Franz and J. Tromp (2006). Trends in detection in earthquake seismology, presentation at the 151st Meeting of the Acoustic Society of America, June 6, 2006, UCRL-PRES-222128.

Israelsson, H. (1990). Correlation of waveforms from closely spaced regional events, *Bull. Seism. Soc. Am*. 80: 2177–2193.

Johnson, M., and C. Vincent (2002). Development and testing of a 3-D velocity model for improved event location: A case study for the India-Pakistan region, *Bull. Seism. Soc. Amer*. 92: 2893–2910.

Komatitsch, D. and J.-P. Vilotte (1998). The spectral element method: an efficient tool to simulate the seismic response of 2D and 3D geologic structures, *Bull. Seism Soc. Am*. 88: 368–392.

Komatitsch, D. and J. Tromp (1999). Introduction to the spectral element method for three-dimensional seismic wave propagation, *Geophys. J. Int.* 139: 806–822.

Komatitsch, D., J. Ritsema and J. Tromp (2002). The Spectral-Element Method, Beowolf computing and global seismology, *Science* 298: 1737–1742.

Morozov, I. B., E. A. Morozova, S. B. Smithson, P. G. Richards, V. I. Khalturin, and L. N. Solodilov (2005). 3D First-Arrival Regional Calibration Model of Northern Eurasia *Bull. Seism. Soc. Amer*. 95: 951–964.

Murphy, J., Rodi W, Johnson M, Sultanov DD, Bennett TJ, Toksoz MN, Ovtchinnikov V, Barker BW, Reiter DT, Rosca AC, Shchukin Y (2005). Calibration of international monitoring system (IMS) stations in central and eastern Asia for improved seismic event location, *Bull. Seismo. Soc. Am.* 95: (4), 1535–1560.

Mykkeltveit, S. and H. Bungum (1984). Processing of regional seismic events using data from small-aperture arrays *Bull. Seismo. Soc. Am* 74: 2313–2333.

Pasyanos, M. , W. Walter, S. Ford and S. Hazler (1999). Improved Ms:mb discrimination using phase matched filters derived from regional surface wave tomography, in *Proceedings of the 21st Annual Seismic Research Symposium*: *Technologies for Monitoring the Comprehensive Nuclear-Test-Ban Treaty,* Vol. 1, pp. 565–571.

Pasyanos, M, A. Franz and A. Ramirez (2006). Reconciling a geophysical models to data using a Markov chain Monte Carlo algorithm: An application to the Yellow Sea-Korean Peninsula region, *J. Geophys.. Res*. 111: B03313.

Nilsson, S., N.A. Petersson, B. Sjogreen, H.-O. Kreiss (2006). Stable difference approximations for the second order elastic wave equation in second order formulation, Submitted to SIAM Journal on Numerical Analysis, UCRL-JRNL-222276.

Ritzwoller, M. H., N. M. Shapiro, A. Levshin, E. A. Bergman, and E. R. Engdahl (2003). The ability of a global 3-D model to locate regional events, *J. Geophys. Res.* 108**:** 2353, doi 10.1029/2002JB002167.

Schaff, D., G. Bokelmann, W. Ellsworth, E. Zanzerkia, F. Waldhauser and G. Beroza (2004). OptimizingCorrelation Techniques for Improved Earthquake Location, *Bull. Seism. Soc. Am*. 94: 705–721.

Schaff, D. and P. Richards (2004). Repeating seismic events in China, *Science* 303: 1176–1178.

Shapiro, N.M. and M.H. Ritzwoller, (2002). Monte-Carlo inversion for a global shear velocity model of the crust and upper mantle, *Geophys. J. Int.* 151: 88–105.

Stevens, J. and D. Adams (2000). Improved surface wave detection and measurement using phase-matched filteringand improved regional models, in *Proceedings of the 22nd Annual Seismic Research Symposium*: *Planning for Verification of and Compliance with the Comprehensive Nuclear-Test-Ban Treaty (CTBT)*, Vol. 1, pp. 145–154.

Thurber, C., C. Trabant, F. Haslinger and R. Hartog (2001). Nuclear explosion locations at the Balapan, Kazakhstannuclear test site: the effects of high-precision arrival times and three-dimensional structure, *Phys. Earthplanet. Inter*. 123: 283–301.

van Trees, H. (1968). *Detection, Estimation and Modulation Theory*, John Wiley and Sons, Inc., New York.

Waldhauser, F. and W. Ellsworth (2000). A double-difference earthquake location algorithm: method and application to the Northern Hayward Fault, *Bull. Seism. Soc. Am*. 90: 1353–1368.

Waldhauser, F., D. Schaff, P. Richards and W.-Y. Kim (2004). Lop nor revisted: underground explosion locations1976-1996 from double difference analysis of regional and teleseismic data, *Bull. Seism. Soc. Am*. 94: 1879–1889.

ERROR ANALYSIS IN THE JOINT EVENT LOCATION/SEISMIC CALIBRATION INVERSE PROBLEM

William Rodi

Massachusetts Institute of Technology

Sponsored by Air Force Research Laboratory

Contract No. F19628-03-C-0109

ABSTRACT

This project is developing new mathematical and computational techniques for analyzing the uncertainty in seismic event locations, as induced by observational errors and errors in travel-time models. The analysis is being done in the context of the multiple-event inverse problem, in which the locations of multiple events are inferred jointly with travel-time corrections for the event-station paths. The premise is that one of the events is the target of the uncertainty analysis while the others are calibration events that serve to constrain the path corrections within some level of error. An uncertainty analysis on the coupled location/calibration inverse problem leads to the notion of a "multiple-event" confidence region on the target event location, which accounts implicitly for errors in the inferred path corrections, including the effects of uncertainty in the calibration event locations. The approach we have developed considers the nonlinearity of the forward problem and allows the use of non-Gaussian models for data errors and soft or hard constraints on the problem parameters.

The project has addressed mainly the basic multiple-event location problem, wherein travel-time corrections comprise a simple time term for each station/phase combination in the data set. We have developed a numerical scheme for computing multiple-event confidence regions for this problem, based on grid search and Monte Carlo sampling techniques. Given the computationally intensive nature of the approach, some approximations were developed to reduce the computational effort. Experiments with data from the Nevada Test Site validated the approach and demonstrated the adequacy of the approximations when the location uncertainty is not too large. A modification of the approach we are investigating, which offers the possibility of additional efficiency, is the computation of multiple-event confidence regions defined in a Bayesian sense. Moreover, we are investigating an extension of our multiple-event location algorithm to the case where travel-time corrections are parametrized as a function of the event location.

OBJECTIVE

This project is developing new mathematical and computational techniques for quantifying the errors in seismic event locations, including the effects of observational errors and errors in the travel-time forward model. Our approach associates the latter, or *model errors*, with the uncertainty in path travel-time corrections that have been inferred from calibration data. We thus analyze event location uncertainty in the context of the joint location/calibration inverse problem: using arrival time data from multiple events and stations to simultaneously locate the events and estimate calibration parameters that determine the travel-time corrections. Calibration parameters can be as simple as time terms at stations or as complex as a 3D velocity model. Our approach treats one of the multiple events as a new event under investigation and the remaining events as calibration events. Performing uncertainty analysis on the joint location/calibration problem accounts for the key sources of error in the new event location, including picking errors in the arrival times for the new *and* calibration events and errors in the calibration event locations. We are addressing this joint inverse problem with numerical techniques, like grid search and Monte-Carlo simulation, that avoid the limitations of analytic approaches to uncertainty analysis in large inverse problems. These limitations include the restriction to Gaussian data errors, the necessity of using a linear approximation to the travel-time forward model, and restricted mechanisms for incorporating *a priori* constraints on the unknowns.

In previous years' efforts, we implemented and tested this approach to event location uncertainty for a relatively simple, but widely used, parameterization for travel-time corrections (time terms). These efforts demonstrated the conceptual validity of the approach, which could be validated quantitatively in simple situations but which revealed the practical difficulties associated with its computational intensity. Here we report on some incremental improvements to the uncertainty algorithm we have developed.

RESEARCH ACCOMPLISHED

Summary of Approach

Rodi (2004, 2005) presented the mathematical formulation of the joint location/calibration inverse problem and maximum-likelihood uncertainty approach that are the basis for this project. To summarize, we write the joint inverse problem as

$$d_{ij} = T_j(\mathbf{x}_i) + t_i + c_{ij} + e_{ij}\,, \tag{1}$$

where i indexes each of m seismic events and j indexes each of n station/phase combinations that have been observed from one or more of the events. Then, d_{ij} denotes the arrival-time observation for the ith event and jth station/phase ((i,j)th path), $\mathbf{x}_i$ and t_i are the origin parameters (hypocenter and time, respectively) of the ith event, T_j is a model-based travel-time function for the jth station/phase, c_{ij} is a correction to this function for path (i,j), and e_{ij} is an observational error. This equation holds only for the paths (i,j) for which data have been observed. The joint location/calibration problem is often referred to as the *multiple-event location* problem. The project has focused on the "basic" multiple-event location problem whereby the path corrections are assumed to be event-independent (see Jordan and Sverdrup, 1981, and Pavlis and Booker, 1983):

$$c_{ij} = a_j\,. \tag{2}$$

The unknown parameters of the inverse problem are then the event hypocenters and origin times, $\mathbf{x}_i$, t_i, $i = 1,\ldots,m$, and the time terms for the station/phase combinations: a_j, $j = 1,\ldots, n$.

The premise of our approach is that one of the events (e.g., $i = 1$) is the target of the location uncertainty analysis, while the remaining events ($i = 2,\ldots,m$) are calibration events, whose data provide information about the a_j. Generally, prior information is available to constrain the location of one or more of the calibration events.

The likelihood function for the multiple-event location problem is determined, in part, by the assumed probability distribution of the observational errors in the data, e_{ij}. We take this to be a *generalized Gaussian* distribution of order p (Billings et al, 1994). Additionally, the likelihood function depends on the prior information available for the calibration event locations. Rodi (2005) discusses the use of hard and soft prior constraints on an event location.

The latter, which we consider in this paper, take the form of a prior probability distribution on the event hypocenter. As with the data errors, we allow this distribution to be of the generalized Gaussian type.

Given these assumptions, the likelihood function for the basic multiple-event location problem is given by

$$-\log L = \text{const} + \frac{1}{p}\sum_{ij}\frac{1}{\left(\sigma_{ij}\right)^{p}}\left|d_{ij} - T_j\left(\mathbf{x}_i\right) - t_i - a_j\right|^{p} + \sum_{i}\frac{1}{p_{0i}\left(\sigma_{ij}\right)^{p_{0i}}}\left\|\mathbf{x}_i - \mathbf{x}_{0i}\right\|^{p_{0i}} , \tag{3}$$

where || || denotes the Euclidean distance in space. The prior information on the *i*th event location is specified by a prior location estimate, $\mathbf{x}_{0i}$; a standard error, σ_{0i}; and a generalized Gaussian order, p_{0i}, where we generally assume $p_{0j} \geq 2$. The generalized Gaussian order for the data errors is p ($1 \leq p \leq 2$), and the data standard errors are σ_{0i}. For the purpose of exposition, we assume the data standard errors are known.

Location Confidence Regions

Our approach to uncertainty analysis in the joint location/calibration inverse problem separates the unknown parameters into two vectors: **p**, containing the subset of "target" parameters on which a confidence region is desired—and **q**, containing the remaining "nuisance" parameters. For example, if $\mathbf{p} = \mathbf{x}_1$ (the hypocenter of the target event) then

$$\mathbf{q} = (t_1, \mathbf{x}_2, t_2, \ldots, \mathbf{x}_m, t_m, a_1, a_2, \ldots, a_n) . \tag{4}$$

To consider a confidence region on the *epicenter* of the target event, we would move its depth parameter, z_1, from **p** to **q**. Given this separation of parameters, we will show the likelihood function as $L(\mathbf{p},\mathbf{q};\mathbf{d})$, where **d** denotes the vector of arrival-time observations, d_{ij}.

A confidence region on **p** is determined by the behavior of the likelihood function L as a function of **p**, encompassing the points that yield the largest values of L. Throughout this project, we have defined such regions using the approach of Neyman-Pearson (N-P) hypothesis testing. We take as a test statistic, $\tau(\mathbf{p},\mathbf{d})$, the log likelihood ratio given by

$$\begin{aligned}\tau(\mathbf{p},\mathbf{d}) &= \log\max_{\mathbf{p},\mathbf{q}} L(\mathbf{p},\mathbf{q};\mathbf{d}) - \log\max_{\mathbf{q}} L(\mathbf{p},\mathbf{q};\mathbf{d}) \\ &\equiv \log L(\mathbf{p}^*,\mathbf{q}^*;\mathbf{d}) - \log\max_{\mathbf{q}} L(\mathbf{p},\mathbf{q};\mathbf{d}).\end{aligned} , \tag{5}$$

where $(\mathbf{p}^*,\mathbf{q}^*)$ denotes the maximum-likelihood solution for the parameters. We see that τ compares the likelihoods that are achieved with **p** fixed to a particular value (second term of τ) and with **p** free to vary (first term). In each case **q** is free. A N-P confidence region on **p** at confidence level β (e.g. $\beta = 95\%$) is the locus of points satisfying

$$\tau(\mathbf{p}, \mathbf{d}) \leq \tau_\beta(\mathbf{p}) , \tag{6}$$

where $\tau_\beta(\mathbf{p})$ is a critical value of the probability distribution of τ, as induced by the distribution of the data errors:

$$\text{Prob}\left\{\tau(\mathbf{p}, \mathbf{d}) \leq \tau_\beta(\mathbf{p}) \mid \mathbf{p}\right\} = \beta. \tag{7}$$

In writing this and Equation (6), we have allowed for the possibility that the distribution of τ may depend on **p**, but we have tacitly assumed that is does not depend on the nuisance parameters.

We have developed a two-step numerical algorithm to implement the N-P approach to confidence regions. The first step maps the test-statistic, $\tau(\mathbf{p}, \mathbf{d})$, on a grid in **p**-space. This entails minimizing the likelihood function with respect to **q** with **p** fixed in turn to each point on the grid. The second step performs Monte Carlo simulation to infer the critical values $\tau_\beta(\mathbf{p})$. This entails maximizing L with respect to **q**, with **p** fixed and free, for each of many realizations of synthetic data. Both steps of this algorithm are computationally intensive because they involve repeated

maximization of L, i.e., repeated solution of a multiple-event location problem involving many location and calibration parameters.

Needless to say, this formulation applies to the single-event location problem and "single-event confidence regions" by removing the travel-time corrections, a_j, and the calibration events and their data from the problem (i.e., $a_j = 0$, $m = 1$).

Monte Carlo Short Cuts

When data and prior errors are Gaussian ($p = p_{0i} = 2$) and when the model-based travel-time functions can be approximated as linear, τ_β does not depend on **p**. In general, however, τ_β might depend on **p,** indicating the need to perform a separate Monte Carlo simulation with each value of **p** on the sampling grid used for the "true" parameters in calculating synthetic data realizations. This is not practical for realistic problems, and our algorithm performs Monte Carlo simulation only with **p** set to its maximum-likelihood estimate, **p***. That is, Equation (6) is replaced with

$$\tau(\mathbf{p}, \mathbf{d}) \le \tau_\beta(\mathbf{p}^*). \tag{8}$$

This approximation has been assumed by others who have computed numerical confidence regions on seismic event locations (e.g., Wilcock and Toomey, 1991). However, to the extent that the dependence on **p** exists, the confidence regions based on Equation (8) lose the "confidence property," i.e., the region includes the true parameter vector with probability β, regardless of what the true parameter vector is.

A second significant short cut we have implemented pertains to the nuisance parameters. In the Gaussian/linear case, the probability distribution of τ (which is chi-squared) depends only on the dimensionality of **p**, regardless of what, if any, nuisance parameters there are. As a result, **q** can be ignored for the purpose of determining τ_β. In a Monte Carlo simulation of τ_β, this implies that the likelihood maximization with synthetic data realizations can treat **q** as fixed. In the location/calibration problem, most of the computational benefit of doing this is achieved by fixing the calibration event locations so that each likelihood maximization involves the work of single-event, rather than multiple-event, location.

Quasi-Bayesian Confidence Regions

In Bayesian inference, the likelihood function we defined in Equation (3), including the factor for prior information on the parameters, is treated as an unnormalized *posterior* probability density function on the parameters. A Bayesian confidence region on **p** at confidence level β is a region in **p**-space, P_β, which includes a proportion β of the posterior probability density:

$$\int_{P_\beta} d\mathbf{p} \int_{Q_1} d\mathbf{q} L(\mathbf{p}, \mathbf{q}; \mathbf{d}) = \beta \int_{P_1} d\mathbf{p} \int_{Q_1} d\mathbf{q} L(\mathbf{p}, \mathbf{q}; \mathbf{d}), \tag{9}$$

where P_1 and Q_1 denote the entire **p**-space and **q**-space, respectively. In a Gaussian/linear problem, Bayesian confidence regions coincide with N-P regions and thus posses the confidence property. In general, however, the two types of regions differ, and Bayesian ones do not necessarily have the confidence property.

The difference between N-P and Bayesian confidence regions in the presence of nonlinearity is illustrated in Figure 1. This is a "toy" problem involving one unknown parameter—event depth—and a single datum that is taken to be a direct estimate of the depth. We introduce nonlinearity into the problem in the form of the hard constraint that the true event depth (horizontal axis) cannot be negative, even though the depth estimate (vertical axis) might be, such as when arrival times yield an "airquake" as the best-fitting solution for an event location. Intuitively, the positivity constraint on depth should affect a confidence region on depth when the depth estimate is near $z = 0$, and we can see from the figure that it does. The case in the left panel assumes that the depth estimate has a Gaussian distribution ($p = 2$) while the case on the right assumes a Laplace distribution ($p = 1$). The green lines in each plot trace the confidence limits for a N-P confidence intervals, which possess the confidence property. The red dots are

the approximate N-P confidence intervals that result when the critical value τ_β is considered only for the estimated (maximum-likelihood) value of depth, as per Equation (8), and the blue dots mark the Bayesian confidence limits. Generally, the approximate N-P intervals are smaller than the Bayesian intervals for shallow depth estimates, showing they are more influenced by the positivity constraint. Which one better represents the exact N-P intervals depends on the type of data distribution used.

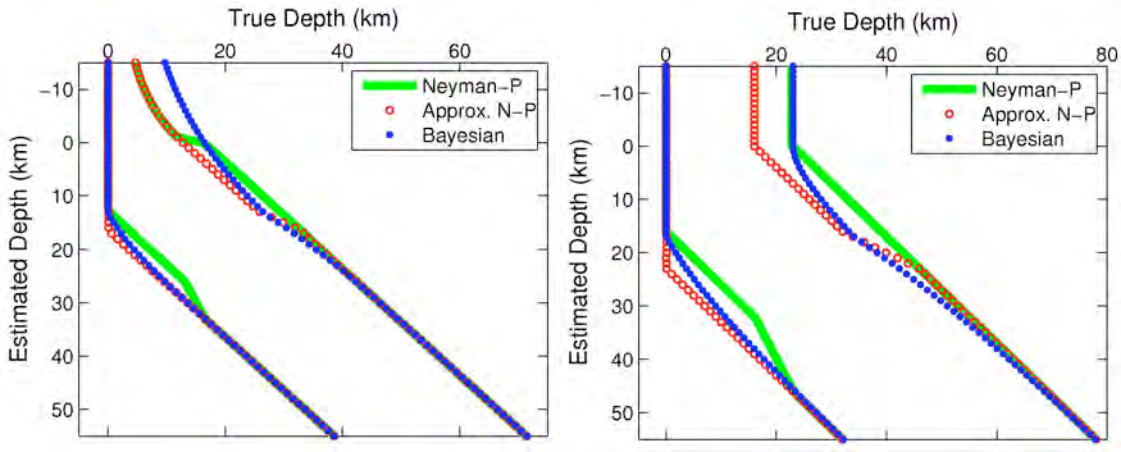


Figure 1. Confidence intervals on event depth in a fictitious problem involving a direct estimate of depth, which is either Gaussian (left panel) or Laplace (right) distributed, with a standard error of 10 km in each case. Three types of confidence limits (at β = 90%) are shown, each as a function of the depth estimate itself (vertical axis): exact N-P (green line), approximate N-P (red dots), and Bayesian (blue dots). The corresponding confidence interval is the range of true depth between these limits.

It is straightforward to modify our numerical algorithm to compute Bayesian confidence regions if we make an additional approximation, namely, replacing the integration over the nuisance parameters **q** in Equation (9) with maximization. (Acknowledging this approximation, we will call the resulting confidence regions "quasi-Bayesian.") Considering the definition of τ in Equation (5), Equation (9) becomes equivalent to Equation (6), with a single τ_β computed as the solution of

$$\int_{\tau(\mathbf{p},\mathbf{d})\le\tau_\beta} d\mathbf{p}\, e^{-\tau(\mathbf{p},\mathbf{d})} = \beta \int_{\tau(\mathbf{p},\mathbf{d})<\infty} d\mathbf{p}\, e^{-\tau(\mathbf{p},\mathbf{d})}. \qquad (10)$$

Application to NTS Data

We are testing our new uncertainty analysis techniques on regional seismic arrival times from NTS explosions, for which precise locations and origin times are known (Walter et al., 2003). The results shown here are based on a subset of the available data set, comprising 262 Pn arrivals from 33 explosions at Pahute Mesa and Rainier Mesa. This subset included arrivals from the 27 stations that spanned the epicentral distance range 1,5°–9° and had Pn arrivals for at least 2 of the 33 events.

When computing a confidence region on the location of one of the events (the "target" event), the remaining 32 events were treated as calibration events. Only one calibration event was assigned a finite ground truth (GT) level; a relatively well-recorded Rainier Mesa explosion (16 Pn arrivals). Its assigned GT accuracy was varied between 0 and 5 km. The depths of all events were fixed to their true values in these tests. The origin times of all events, including the GT calibration event, were unconstrained. The IASP91 travel-time tables were used for the forward model.

Figure 2 compares the epicenter solutions obtained with single-event location (zero travel-time corrections) with multiple-event solutions obtained with varying GT levels for the GT-calibration event. We see that the multiple-event solutions achieve greater accuracy in the *relative* locations between events, but the absolute event mislocations become larger as the location constraint on the GT-calibration event is relaxed.

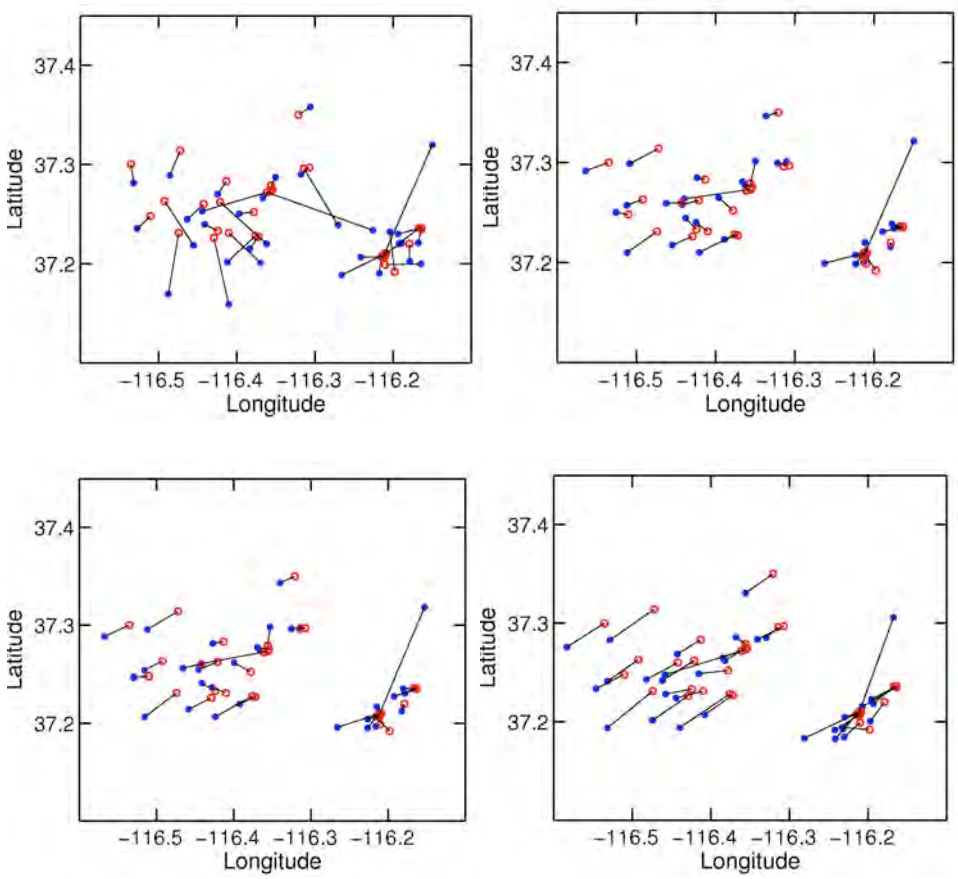


Figure 2. Four epicenter solutions for 33 NTS explosions in the Pahute Mesa and Rainier Mesa testing areas. Each solution location (blue dot) is connected by a line to the corresponding true (GT0) epicenter of the event (red circle). Top left: Solution obtained with single-event location (travel-time corrections set to zero). Top right: Solution obtained with multiple-event location with the location of one well-recorded Rainier Mesa event (37.21°N, 116.21°W) held fixed (GT0 constraint). Bottom: Multiple-event location solutions with the same Rainier Mesa event treated as GT2 (bottom left) and GT5 (bottom right).

Single-Event and Multiple-Event Confidence Regions

Figure 3 compares single-event and multiple-event confidence regions for a Pahute Mesa event with relatively few arrivals (6 Pn arrivals). The regions were calculated using a Gaussian distribution for observational errors (p = 2). The colored areas are the confidence regions, for different confidence levels, computed with our two-step (approximate N-P) numerical algorithm. The single-event regions (left) do not include the effect of errors in travel-time corrections (model errors) and agree almost exactly with analytically derived confidence ellipses based on only the picking error variance (shown for β = 95%).

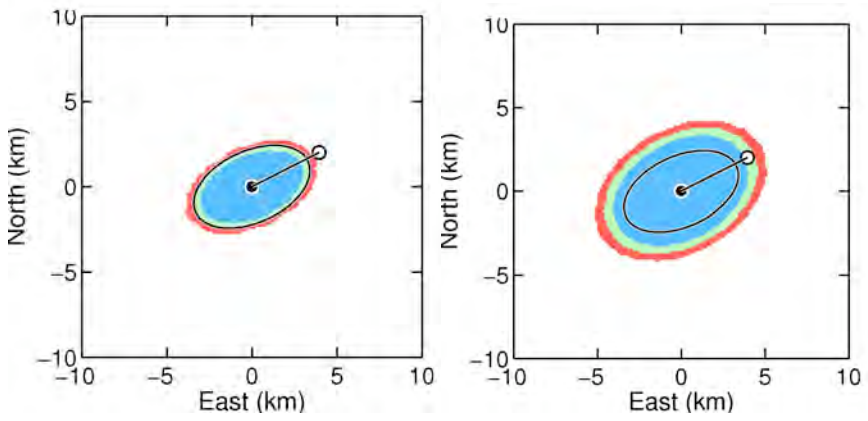


Figure 3. Epicenter confidence regions for a Pahute Mesa explosion with 6 Pn arrivals, computed with our two-step numerical algorithm. Left: Single-event confidence regions (path travel-time corrections assumed known). Right: Multiple-event confidence regions, treating a well-recorded Rainier Mesa event as a GT0 calibration event. Confidence regions are shown for 90%, 95%, and 98% confidence (blue, green, and red, respectively). In each frame the black circle marks the maximum-likelihood solution for the event location, and the white circle is its GT0 location (from Walter et al., 2003). The error distribution for picking errors was assumed to be Gaussian (p = 2). The ellipse in each frame is the conventional 95% *single-event* confidence ellipse, computed analytically under the Gaussian/linear assumption.

The multiple-event confidence regions (right panel) are larger because they account for the additional location uncertainty induced by uncertainty in the estimated travel-time corrections. The multiple-event confidence regions in this case assumed that the GT event at Rainier Mesa was GT0. Therefore, the confidence regions do not account for any location uncertainty in this calibration event.

Monte Carlo Simulation vs. Likelihood Integration

Figure 4 shows multiple-event confidence regions for the same Pahute Mesa target event just considered, computed two different ways. The results in the top row used the same two-step procedure used for Figure 3 (approximate N-P confidence regions). The results in the bottom row are quasi-Bayesian (q-B) confidence regions. The two types of confidence regions are generated from the same numerical mapping of the test statistic (τ) as a function of epicenter, but they use different critical values of the test statistic (τ_β) to determine which contour of τ corresponds to each confidence level. The N-P regions determine τ_β with Monte Carlo simulation (doing 500 realizations), while the q-B regions use likelihood integration, as discussed earlier.

The left panels of Figure 4 assume a GT0 calibration event (the top left panel repeats the right panel of Figure 3.) The center and right panels, respectively, assume the GT-calibration event is GT2 and GT5. We see that the confidence regions grow as the GT level is increased (see Rodi (2005) for additional examples). Comparing the two methods (top vs. bottom panels), we see that the quasi-Bayesian confidence regions are smaller. This owes to the fact that likelihood integration yielded smaller values of τ_β than did Monte Carlo simulation.

Table 1 compares the critical statistics determined by the two methods with the value predicted by the Gaussian/linear theory. The critical values from likelihood integration and the linear/Gaussian theory agree in both the single-event and multiple-event cases, but the Monte Carlo values are larger than either in the multiple-event cases. A discrepancy from the Gaussian/linear values can only be due to nonlinearity (since Gaussian data and prior errors were assumed). However, we would expect the effect of nonlinearity to increase as the GT level of the GT-calibration event increases, but the Monte-Carlo values do not increase. Based on this comparison, we tentatively prefer the likelihood-integration method for determining τ_β. The remaining examples of this paper show quasi-Bayesian confidence regions.

Table 1. Comparison of critical τ values from Monte Carlo simulation (M.C.), likelihood integration (L.I.) and Gaussian/linear theory $\left(\frac{1}{2}\chi_2^2\right)$

	β = 90%			β = 95%		
Case	M.C.	L.I.	$\frac{1}{2}\chi_2^2$	M.C.	L.I.	$\frac{1}{2}\chi_2^2$
S-E	2.34	2.27	2.30	2.89	2.94	3.00
M-E (GT0)	2.86	2.31	2.30	3.66	2.98	3.00
M-E (GT2)	2.87	2.37	2.30	3.66	3.09	3.00
M-E (GT5)	2.87	2.29	2.30	3.65	3.01	3.00

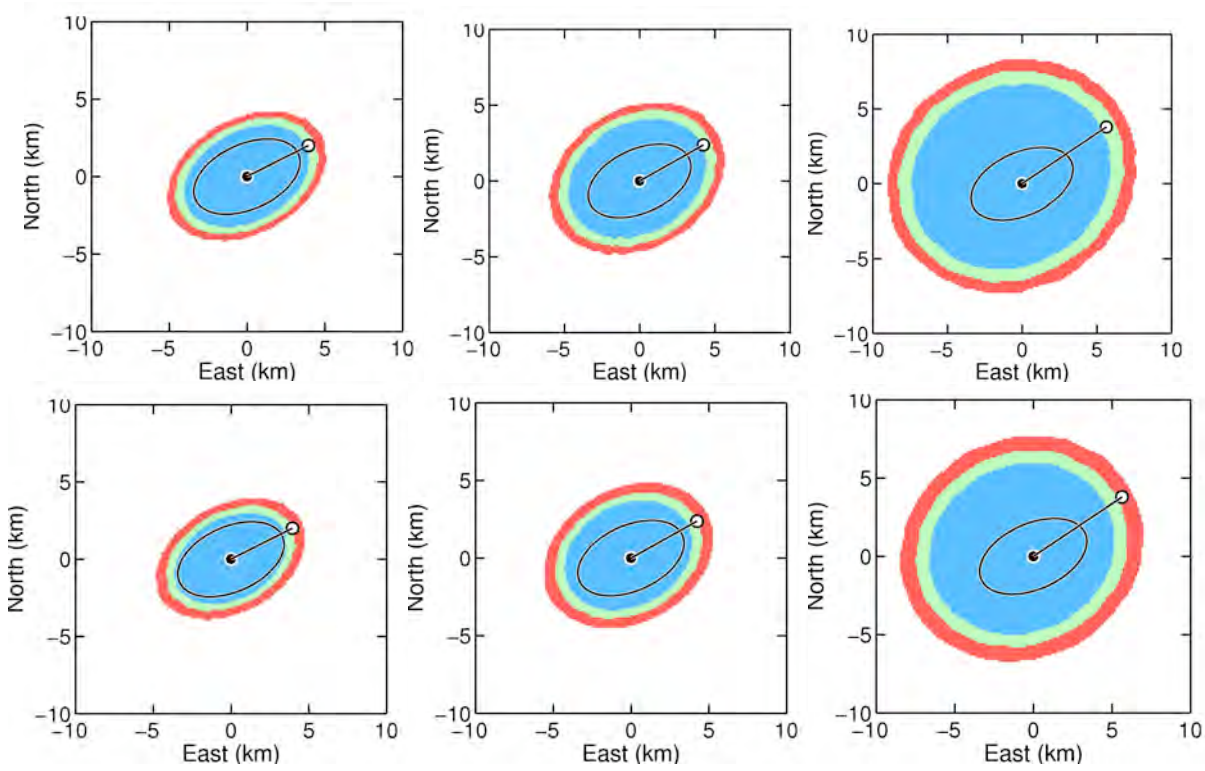


Figure 4. Approximate N-P (top) and quasi-Bayesian (bottom) multiple-event confidence regions for the same Pahute Mesa explosion considered in Figure 3. The Rainier Mesa GT-calibration event is assumed to be GT0 (left), GT2 (center), or GT5 (right). A Gaussian error model is used for both the picking errors and the prior location error ($p = p_0 = 2$). Plotting conventions are the same as Figure 3.

Non-Gaussian Error Models

The examples shown above assumed Gaussian data errors (p = 2) and a Gaussian prior error on the GT-calibration event at Rainier Mesa (p_0 = 2). Using other tests with NTS data, Rodi (2005) showed that increasing p_0 ("hardening" the GT constraint) caused confidence regions to become non-elliptical, especially in the GT5 case. Figure 5 illustrates this for the target event we have been considering.

Our final test shows the effect of using a non-Gaussian probability distribution for the observational errors. Figure 6 shows single-event and multiple-event confidence regions (same target event) for two values of the generalized Gaussian distribution: p = 1.5 (top) and 1.25 (bottom). The confidence regions depart from an elliptical shape more

for p = 1.25 (bottom panels) than for p = 1.5, as expected. The non-ellipticity is most noticeable in the single-event regions, which are most strongly influenced by the picking error distribution.

These results also show the numerical challenge of automatically, but efficiently, gridding the test statistic when its behavior departs significantly from a quadratic function (see lower panels). Our current scheme designs a mapping grid in advance (guided by the conventional error ellipse parameters), but these tests indicate the need for an adaptive gridding scheme.

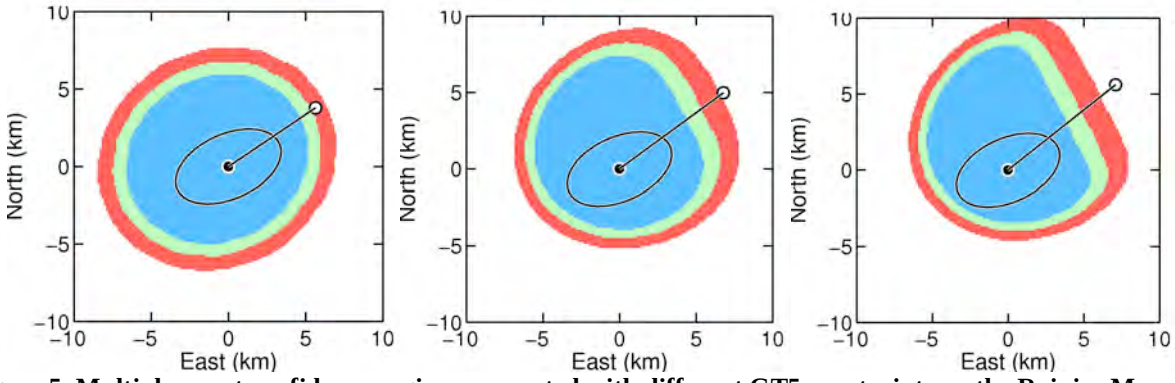


Figure 5. Multiple-event confidence regions computed with different GT5 constraints on the Rainier Mesa calibration event: generalized Gaussian orders p_0 = 2, 5, and 20 (left, center, and right, respectively). The GT5 constraint is at 90% confidence in each case. The data errors are assumed to be Gaussian. The target event is the same as in previous figures.

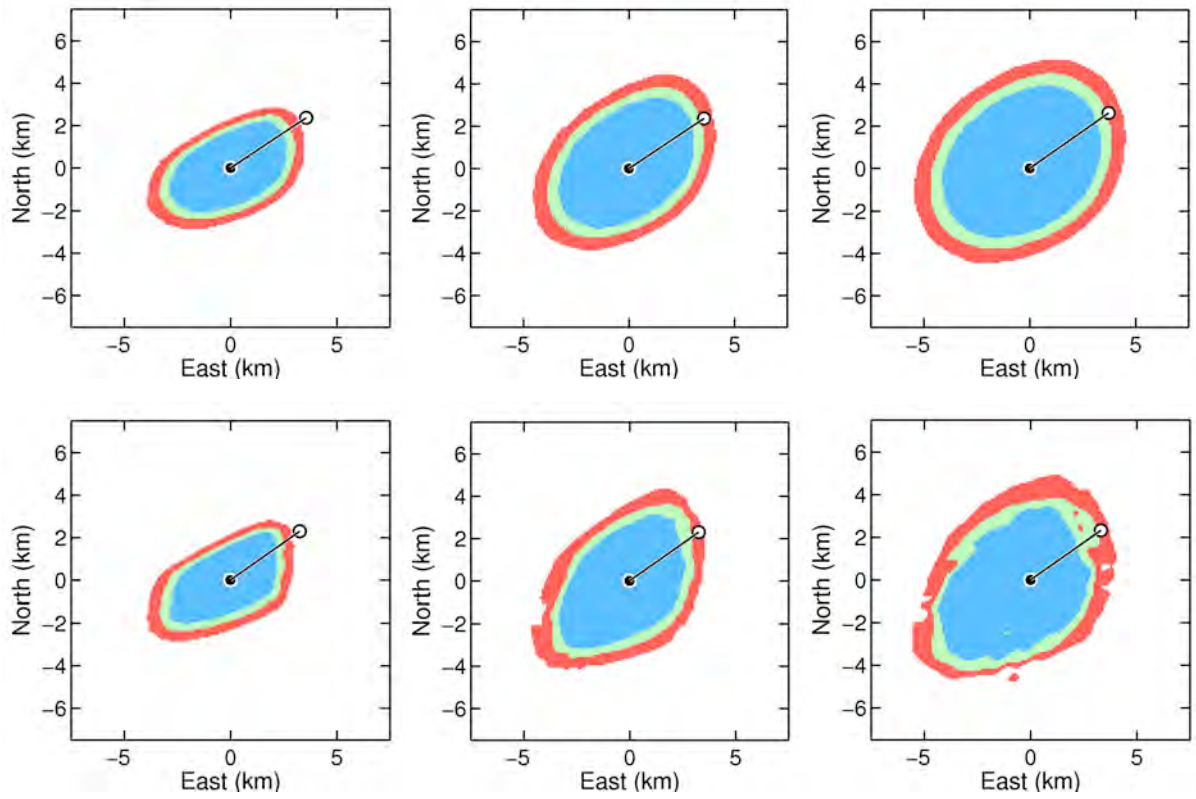


Figure 6: Single-event (left) and multiple-event confidence regions computed using two non-Gaussian probability distributions for picking errors: generalized Gaussian orders p =1.5 (top) and 1.25 (bottom). The prior error on the GT-calibration event for the multiple-event regions is either GT0 (center panels) or GT2 (right), with a Gaussian prior error assumed for the latter.

CONCLUSIONS AND RECOMMENDATIONS

The project has made significant progress in the development of a new approach to event location uncertainty analysis. The approach is based on the framework of the joint location/calibration inverse problem, which considers the effects of both picking and model errors on event location errors. We have implemented numerical techniques for computing "multiple-event" confidence regions without need of the conventional assumptions of Gaussian errors and linearity of the forward problem. Our recent work has focused on additional enhancements to the computational efficiency of the approach, which have led to the alternative of using likelihood integration to replace the Monte Carlo simulation step of our original algorithm. This alternative is tantamount to a Bayesian approach to uncertainty but can also be viewed as just a different computational short cut for approximating the exact confidence regions defined by N-P hypothesis testing. Our results to date suggest that this new approximation may in fact be more accurate. It is apparent, however, that further work is needed to produce reliable calculations when error distributions depart significantly from Gaussian and confidence regions from ellipses.

The practicality of our approach for more complex parameterizations of travel-time corrections, such as velocity models, is in question at this point. However, our future plans include pursuing a more-efficient scheme for generating likelihood functions on a grid (e.g., using linearization with respect to "nuisance" parameters), and this may alter the outlook. In any event, extending our approach to more-complex parameterizations remains a feasible task for research that we intend to pursue during the final year of the project.

REFERENCES

Billings, S. D., M. S. Sambridge, and B. L. N. Kennett (1994). Errors in hypocenter location: Picking, model and magnitude dependence, *Bull. Seism. Soc. Am.* 84: pp. 1,978–1,990.

Jordan, T. H. and K. A. Sverdrup (1981). Teleseismic location techniques and their application to earthquake clusters in the south-central Pacific, *Bull. Seism. Soc. Am.* 71: pp. 1,105–1,130.

Pavlis, G. L. and J. R. Booker (1983). Progressive multiple event location (PMEL), *Bull. Seism. Soc. Am.* 73: pp. 1753–1777.

Rodi, W. (2004). Error analysis in the joint event location/seismic calibration inverse problem, in *Proceedings of the 26th Seismic Research Review: Trends in Nuclear Explosion Monitoring*, LA-UR-04-5801, Vol. 1, pp. 307–316.

Rodi, W. (2005). Error analysis in the joint event location/seismic calibration inverse problem, in *Proceedings of the 27th Seismic Research Review: Ground-Based Nuclear Explosion Monitoring Technologies*, LA-UR-05-6407, Vol. 1, pp. 433–442.

Walter, W. R., K. D. Smith, J. L. O'Boyle, T. F. Hauk, F. Ryall, S. D. Ruppert, S. C. Myers, M. Anderson, and D. A. Dodge (2003). Improving the fundamental understanding of regional seismic signal processing with a unique western United States dataset, in *Proceedings of the 25th Seismic Reearch Review—Nuclear Explosion Monitoring: Building the Knowledge Base*, Vol.2 , pp. 486–484.

Wilcock, W. S. D. and D. R. Toomey (1991). Estimating hypocentral uncertainties for marine microearthquake surveys: A comparison of the generalized inverse and grid search methods, *Mar. Geophys. Res.* 13: pp. 161–171.

MODELING TRAVEL-TIME CORRELATIONS BASED ON SENSITIVITY KERNELS AND CORRELATED VELOCITY ANOMALIES

William Rodi[1] and Stephen S. Myers[2]

Massachusetts Institute of Technology[1] and Lawrence Livermore National Laboratory[2]

Sponsored by National Nuclear Security Administration
Office of Nonproliferation Research and Development
Office of Defense Nuclear Nonproliferation

Contract No. DE-FC52-05NA26603[1] and W-7405-ENG-48[2]

ABSTRACT

The errors in the travel times predicted by a reference Earth model are correlated between different event-station paths when the paths are sufficiently close to one another, reflecting the fact that the velocity anomalies not represented in the reference model are correlated over a finite spatial extent. Previous studies have shown that ignoring these error correlations can induce large biases in seismic event locations when the observing network of stations is far from uniform. Event location algorithms have begun recently to account for travel-time correlations with the use of non-diagonal covariance matrices in the optimality criteria they employ, but the covariance values used have been either empirical or calculated from simple geometrical considerations. The goal of this project is to develop an approach to modeling travel-time correlations based on the physics of seismic travel times and geostatistical descriptions of the Earth's velocity heterogeneity. Our approach involves a two-step process: calculating travel-time sensitivity kernels for various event-station paths, and integrating the kernels, pairwise, with a specified correlation function for velocity anomalies. These steps yield the covariance matrix for the travel-time predictions among the given paths. This paper describes and illustrates the numerical techniques we are developing to perform the required calculations. Our initial focus has been on infinite-frequency travel times, but our approach will also address finite-frequency travel times to determine how the finite width of sensitivity kernels affects travel-time correlations.

OBJECTIVE

Seismic event location algorithms typically assume that errors in the seismic arrival-time data are statistically independent, or uncorrelated. In the case of regional and teleseismic arrivals, however, a significant component of the data errors are prediction errors in the model-based travel times used by the location algorithm—or "model errors"—rather than the "pick errors" committed in the measurement process. Model errors are attributable to velocity anomalies in the Earth that are not rendered in the velocity model used for travel-time prediction. When the observing stations are sufficiently close to one another, their model errors will be correlated. While it is now standard practice in nuclear monitoring applications for event location algorithms to assign error *variances* that include the contribution from model prediction errors, the algorithms generally set the error *covariances* to zero; correlations are ignored. Doing so can seriously degrade location accuracy when the distribution of seismic stations is far from uniform, as was shown, for example, by Chang et al. (1983) and Yang et al. (2004).

This project is using a model-based approach to investigate correlations between the travel-time prediction errors that are induced by velocity heterogeneities in the Earth. We are developing techniques to calculate covariance matrices of travel-time model errors by integrating travel-time sensitivity kernels with plausible correlation functions describing the velocity heterogeneity of the crust and upper mantle. Our initial focus is on first Pn arrivals (epicentral distances between about 2° and 20°) and infinite-frequency travel times, whose sensitivities are concentrated along geometrical rays. Later, the project will address direct teleseismic arrivals (to about 90°) and finite-frequency travel times, whose sensitivities are given by spatially distributed banana-doughnut kernels (e.g., Zhao et al., 1999; Dahlen et al., 2000; Hung et al., 2000). An important issue we will consider is whether the spatial extent of banana-doughnut kernels causes a significant increase in model-error correlations.

This paper formulates our approach to modeling travel-time correlations and describes some of the numerical techniques we have developed thus far, illustrated with an example involving Pn correlations between stations in Asia.

RESEARCH ACCOMPLISHED

Formulation of Approach

Given a set of n arrival time data from an event, one can decompose the data errors as (for $i = 1,\ldots,n$)

$$e_i = e_{\mathrm{p},i} + e_{\mathrm{m},i} \tag{1}$$

where the first term is the *pick*, or measurement, error and the second term is the *model* error, or error in the model-based travel-time prediction. Location algorithms such as EvLoc assume the above decomposition and set the data variances accordingly as

$$\sigma_i^2 = \sigma_{\mathrm{p},i}^2 + \sigma_{\mathrm{m},i}^2. \tag{2}$$

However, the errors for different i are assumed uncorrelated. The problem we are addressing is the calculation of a full covariance matrix for model errors, having components $\sigma_{\mathrm{m},ij}$ defined by

$$\sigma_{\mathrm{m},ij} = \mathrm{E}[e_{\mathrm{m},i}\, e_{\mathrm{m},j}]. \tag{3}$$

E[] denotes the expectation operator.

To calculate the model error covariance matrix, we are making two simplifying assumptions: (1) that the travel-time dependence on velocity is well-approximated as a linear departure from the reference Earth model used for travel-time prediction, and (2) that 3D velocity heterogeneity can be described by a Gaussian random field. Considering only P-wave arrivals, let $v_0(\mathbf{x})$ denote the P velocity function for the reference model, and let $v_E(\mathbf{x})$ denote the Earth's true (and unknown) velocity function. Then, model errors can be linked to the slowness difference, which we denote $m(\mathbf{x})$:

$$m(\mathbf{x}) = v_E^{-1}(\mathbf{x}) - v_0^{-1}(\mathbf{x}). \tag{4}$$

Linearization of the travel-time dependence on slowness implies that the model error in the *i*th datum is given by

$$e_{\mathrm{m},i} = \int a_i(\mathbf{x})\, m(\mathbf{x})\, d\mathbf{x} \tag{5}$$

where $a_i(\mathbf{x})$ is the first-order sensitivity kernel of the ith travel-time functional, as evaluated at v_0. In the high-frequency limit, this kernel is concentrated along the geometrical ray connecting the event and station locations. For finite frequency, it is spatially distributed around this ray. In either case, we point out that the model error is a function of the event *and* station locations.

Now consider a geostatistical description of $m(\mathbf{x})$, assuming it to be a Gaussian random field with zero mean at all points and having a specified covariance between any two points, as described by a covariance function $C(\mathbf{x},\mathbf{x}')$:

$$\mathrm{E}\left[m(\mathbf{x})\right] = 0 \tag{6}$$

$$E\left[m(\mathbf{x})m(\mathbf{x}')\right] = C(\mathbf{x},\mathbf{x}'). \tag{7}$$

The covariance between two model errors is then given by

$$\sigma_{\mathrm{m},ij} = \int d\mathbf{x}\, a_i(\mathbf{x}) \int d\mathbf{x}'\, C(\mathbf{x},\mathbf{x}')\, a_j(\mathbf{x}'). \tag{8}$$

The core task of this project is the evaluation of the double volume integral in this equation.

Equation (8) implies that the extent to which model errors are correlated depends on how strongly correlated the velocity field is *and* on how spatially distributed the sensitivity kernels are. Our project is considering both effects.

Velocity Model Covariance Functions

Geostatistical methods for data interpolation (kriging, e.g. Deutsch and Journel, 1998; Schultz et al., 1998) typically specify the covariance function, $C(\mathbf{x},\mathbf{x}')$, directly and, assuming stationarity, allow it to be a function only of the separation between the points $\mathbf{x}$ and $\mathbf{x}'$:

$$C(\mathbf{x},\mathbf{x}') = \rho(\mathbf{x}-\mathbf{x}'), \tag{9}$$

where ρ is called the *correlation* function. Simple examples of correlation functions are ones of the *Gaussian* type,

$$\rho(\mathbf{x}-\mathbf{x}') = \sigma_0^2 \exp\left[-\frac{|\mathbf{x}-\mathbf{x}'|^2}{2\lambda^2}\right], \tag{10}$$

which characterize smoothly varying velocity fluctuations, and ones of the *exponential* type,

$$\rho(\mathbf{x}-\mathbf{x}') = \sigma_0^2 \exp\left[-\frac{|\mathbf{x}-\mathbf{x}'|}{\lambda}\right], \tag{11}$$

for rougher fluctuations. (Note: the random field described by a correlation function has a Gaussian probability distribution—i.e., is a *Gaussian* random field—regardless of the type of correlation function.) In these expressions, σ_0^2 is the variance of the slowness field and λ is a correlation length. These examples define *isotropic* fields, having the same spatial statistics in all directions.

An indirect way to specify a model covariance function is through the operator inverse of $C(\mathbf{x},\mathbf{x}')$, which we denote *D*, such that

$$DC(\mathbf{x},\mathbf{x}') = \delta(\mathbf{x}-\mathbf{x}'). \tag{12}$$

If we take *D* to be a differential operator, then $C(\mathbf{x},\mathbf{x}')$ is its Green's function. Rodi et al. (2003) implemented this approach with *D* as

$$D = \frac{\text{const}}{\lambda_1^2\lambda_2\sigma_0^2}\left[\delta(\mathbf{x}) - \frac{1}{(2l-3)}\left(\frac{\lambda_1^2}{r^2}\nabla_1^2 + \lambda_2^2\frac{\partial^2}{\partial z^2}\right)\right]^l, \quad l \geq 2. \tag{13}$$

Here, l is an integer specifying the order of the operator; ∇_1^2 is the horizontal Laplacian operator; λ_1 and λ_2 are horizontal and vertical correlation lengths, respectively; and σ_0^2 is a prior variance. The Gaussian and exponential type correlation functions correspond to $l = \infty$ and l = 2, respectively. An advantage of this approach is that one can introduce non-stationarity by allowing (smooth) spatial variations in σ_0 and $\lambda_{1,2}$, while preserving the essential properties of $C(\mathbf{x},\mathbf{x}')$ as a proper covariance function (e.g., positive-definiteness).

The indirect method of specifying the covariance operator is the basis of numerical techniques we have developed thus far for computing model-error covariance matrices.

Numerical Techniques

The numerical techniques we have developed apply to a discrete model parameterization. We thus replace the model function $m(\mathbf{x})$ with a *k*-dimensional vector **m**; the sensitivity kernels $a_i(\mathbf{x})$ with sensitivity vectors $\mathbf{a}_i$; and the operators *C* and *D* with matrices **C** and **D**. We require that

$$\mathbf{DC} = \mathbf{I}, \tag{14}$$

where **I** is the $k \times k$ identity matrix. This requirement implies that **C** and **D** cannot be independently generated as discrete approximations to *C* and *D*.

In the discrete formulation, the double integral of equation (8) becomes the quadratic matrix expression

$$\sigma_{\mathrm{m},ij} = \mathbf{a}_i^T\mathbf{C}\mathbf{a}_j. \tag{15}$$

Let us also define the $n \times k$ sensitivity matrix having the $\mathbf{a}_i$ as its rows:

$$\mathbf{A} = \left(\mathbf{a}_1 \;\; \mathbf{a}_2 \;\; \cdot \;\; \mathbf{a}_n\right)^T. \tag{16}$$

If we let the $\sigma_{\mathrm{m},ij}$ be the components of an $n \times n$ matrix $\mathbf{\Sigma}_\mathrm{m}$, we can rewrite equation (15) as

$$\Sigma_\mathrm{m} = \mathbf{ACA}^T. \tag{17}$$

$\mathbf{\Sigma}_\mathrm{m}$ is the covariance matrix of the *n* model errors. We can now say that the core task of this project is the evaluation of the matrix product in equation (17).

We have formulated a numerical method for computing $\mathbf{\Sigma}_\mathrm{m}$ given **D** and **A** as input. It applies to the situation where the matrix **D** is given explicitly as a finite-difference approximation to the differential operator *D*, with **C** being defined implicitly as the inverse of **D** as per equation (14). However, our technique avoids the step of generating **C** from **D** with matrix inversion.

Instead, our approach solves a minimization problem for each datum, *i* = 1, 2, *n*, stated as

$$\left(\mathbf{n}_i - \mathbf{A}\mathbf{m}_i\right)^T \Sigma_\mathrm{p}^{-1}\left(\mathbf{n}_i - \mathbf{A}\mathbf{m}_i\right) + \mathbf{m}_i D\mathbf{m}_i = \text{minimum} \tag{18}$$

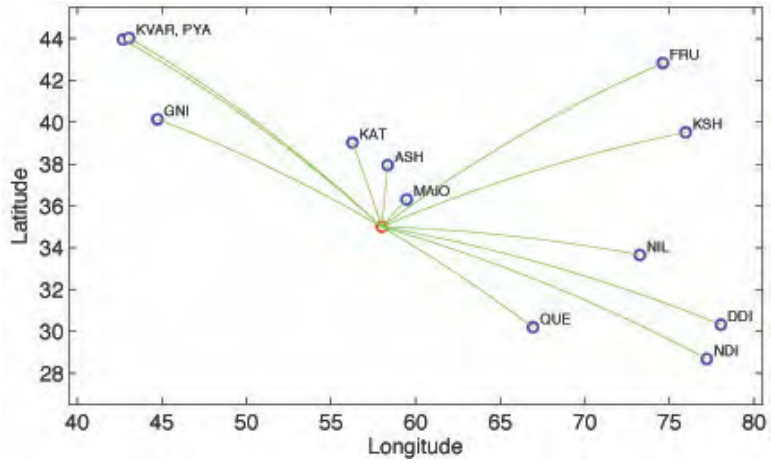


Figure 1. Event/station geometry used for testing our travel-time covariance modeling algorithm. The event location (red circle) is for one of the summary events formed by Reiter and Rodi (2006, these Proceedings) for their body-wave tomography application in south/central Asia. The summary event had Pn arrivals for 12 stations (blue circles).

where $\mathbf{\Sigma}_\mathrm{p}$ is the diagonal covariance matrix for pick errors, and $\mathbf{n}_i$ is the ith column of the $n \times n$ identity matrix. We compute the solution, $\mathbf{m}_i$, of each minimization problem iteratively using the conjugate gradients method, since $\mathbf{D}$ and $\mathbf{A}$ are sparse matrices. To see how $\mathbf{\Sigma}_\mathrm{m}$ can be generated from the resulting solutions, let us consider analytical expressions for the solutions, given by

$$\mathbf{m}_i = \mathbf{C}\mathbf{A}^T \left(\mathbf{A}\mathbf{C}\mathbf{A}^T + \Sigma_\mathrm{p}\right)^{-1} \mathbf{n}_i. \tag{19}$$

The residual vectors can then be written:

$$\mathbf{r}_i \equiv \mathbf{n}_i - \mathbf{A}\mathbf{m}_i = \Sigma_\mathrm{p}\left(\mathbf{A}\mathbf{C}\mathbf{A}^T + \Sigma_\mathrm{p}\right)^{-1} \mathbf{n}_i. \tag{20}$$

Arranging all n residual vectors into a matrix **R,**

$$\mathbf{R} = \begin{pmatrix} \mathbf{r}_1 & \mathbf{r}_2 & \cdots & \mathbf{r}_n \end{pmatrix}, \tag{21}$$

we find

$$\mathbf{R} = \Sigma_\mathrm{p}\left(\mathbf{A}\mathbf{C}\mathbf{A}^T + \Sigma_\mathrm{p}\right)^{-1}. \tag{22}$$

A location algorithm uses the inverse of the covariance matrix for the total errors (pick plus model). This is given as

$$\left(\Sigma_\mathrm{p} + \Sigma_\mathrm{m}\right)^{-1} \equiv \left(\Sigma_\mathrm{p} + \mathbf{A}\mathbf{C}\mathbf{A}^T\right)^{-1} = \Sigma_\mathrm{p}^{-1}\mathbf{R}. \tag{23}$$

The model-error covariance matrix, which is not needed explicitly for location but is the object of our study, is obtained with the additional calculation:

$$\Sigma_\mathrm{m} \equiv \mathbf{A}\mathbf{C}\mathbf{A}^T = \left(\Sigma_\mathrm{p}^{-1}\mathbf{R}\right)^{-1} - \Sigma_\mathrm{p}. \tag{24}$$

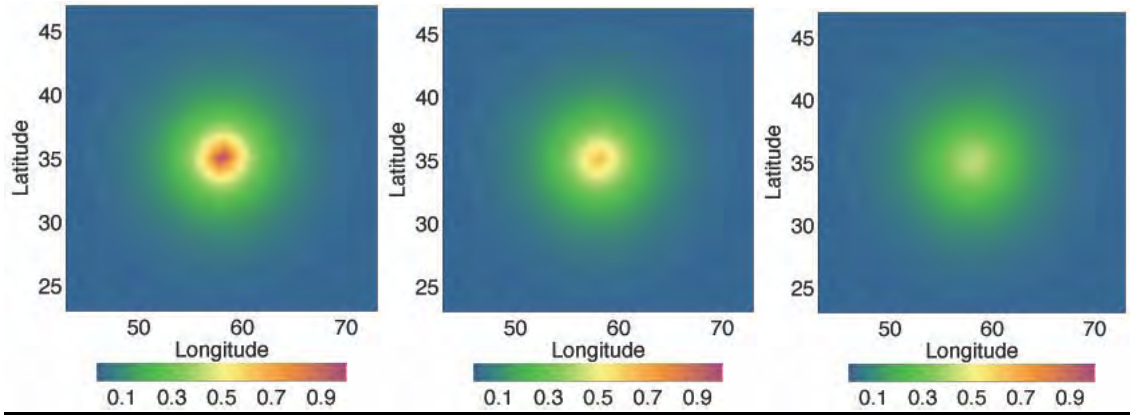


Figure 2. Horizontal slices of a 3D correlation function at depths of approximately 40 km (left panel), 80 km (center) and 120 km (right). The value at each point is the correlation coefficient between the slowness at that point and the slowness at the fixed point: 35°N, 58°E, z = 40 km. The correlation function was computed numerically by solving a differential equation using the differential operator of equation (13). The operator was assigned order l = 2, horizontal correlation length λ_1 = 300 km, and vertical correlation length λ_2 = 100 km.

It is informative to recognize that each minimization problem solved with this method, equation (18), is essentially *single-event* tomography, i.e. velocity tomography using data from only one event.

Numerical Results

We have tested our numerical approach on the event/station geometry shown in Figure 1. The example is extracted from the body-wave tomography data set developed by Reiter and Rodi (2006). The event is one of the summary events they generated from the EHB (Engdahl et al., 1998) data base for the years 1988–2004. The summary event—located at 35°N, 58°E (northeastern Iran) with a depth of 15 km—is associated with Pn arrivals from 12 stations, ranging from 1.8° to 17.5° in epicentral distance and spanning 180° in azimuth. We performed our calculations using the sensitivity vectors (discretized kernels) generated by Reiter and Rodi (2006, these Proceedings), which they computed using finite difference raytracing in a 3D reference Earth model.

We defined the velocity model covariance function indirectly with the differential operator D of equation (13), represented as a differencing matrix (**D**) in spherical coordinates. The order of the differential operator (l) was set to 2, implying a correlation function of the exponential type. The horizontal and vertical correlation lengths (λ_1 and λ_2) were set to 300 km and 100 km, respectively. The slowness standard deviation (σ_0) was set to 2% of the slowness itself at each point of the reference model. We constructed the differential operator to omit vertical derivatives across the Moho discontinuity, implying that velocity anomalies in the crust and mantle are uncorrelated. This crust/mantle decoupling, and the variation of σ_0 with position, are two mechanisms for non-stationarity that are easily accomplished with the differential operator approach.

To demonstrate the equivalence of specifying the model covariance function directly and indirectly, we computed $C(\mathbf{x},\mathbf{x}_0)$ for a fixed point $\mathbf{x}_0$. We chose this point as 35°N, 58°E (the summary event epicenter) with a depth at the top of the mantle. The computation entailed solving the linear system

$$\mathbf{D}\mathbf{c}_0 = \mathbf{n}_0 \tag{25}$$

with the vector $\mathbf{n}_0$ being an appropriate column of the identity matrix and the solution vector $\mathbf{c}_0$ being a discrete approximation to the desired covariance function. The solution function is zero in the crust (because of the crust/mantle decoupling). Figure 2 shows horizontal slices of the function for three depths in the mantle. The function has been scaled by the inverse variance so that it becomes a correlation function, with a peak value of one

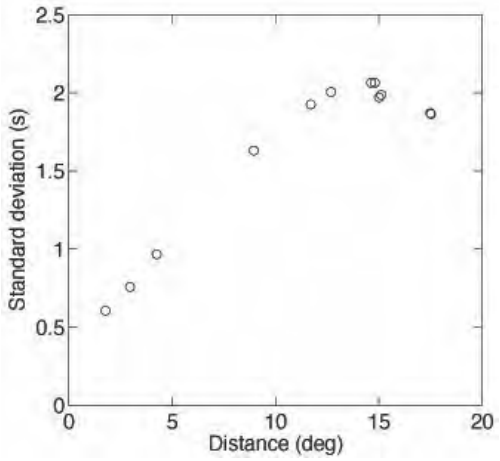


Figure 3. Standard deviation of model error as a function of epicentral distance.

at $\mathbf{x} = \mathbf{x}_0$. We see that the numerically computed correlation function displays spatial behavior consistent with the input parameters, including both its lateral decay from the peak point and its decay with depth.

Our main test was to calculate the 12×12 covariance matrix, $\mathbf{\Sigma}_m$, for the model errors at the 12 stations. This involved solving the single-event tomography problems of equation (18) and then evaluating equation (24) with the resulting matrix of data residuals.

We show the results in two parts. The standard deviations of the model errors, obtained as the square root of the diagonal elements of the covariance matrix, are listed in Table 1 and plotted as a function of epicentral distance in Figure 3. The plot displays the expected increase with epicentral distance, but leveling off beyond about 12°. The model-error standard deviation at the two farthest stations (17.5°) is slightly less than some closer stations, which may reflect the deeper sampling of Pn rays at far regional distances or, possibly, azimuthal variation due to the use of a 3D reference model. We point out that Pn model-error standard deviations of 2 s and less, as these are, are not very large; this reflects our use of 2% for the Earth velocity standard deviation, which underestimates at least the crustal component of the heterogeneity.

The second part of the model-error covariance results consists of the correlation coefficients between model errors at different stations. Table 2 lists the full 12×12 correlation matrix, obtained by dividing each row and column of the covariance matrix ($\mathbf{\Sigma}_m$) by the appropriate standard deviation. The correlation matrix is symmetric and has unit diagonal, so there are 66 independent coefficients in the table, corresponding to the number of possible station pairs. The 66 values are plotted in Figure 4 as a function of the azimuth difference between the two stations in a pair. Looking at Table 2, we see that the highest correlations are between stations at similar locations, e.g. 0.99 for KVAR/PYA and 0.91 for DDI/NDI. The three closest stations (ASH, KAT, MAIO) also have highly correlated errors. From Figure 4 we see that the correlation coefficient generally decreases with the azimuth difference between stations. One would expect a monotonic decrease if the stations were equidistant from the event and the reference model were 1D, neither of which is the case. Stations MAIO and FRU, for example, are at similar azimuths but at very different distances and have a correlation of only 0.24. We also note that the correlation coefficient between any two stations is never below 0.1, which must be due to the fact that all the raypaths sense the structure within one correlation length of the event hypocenter.

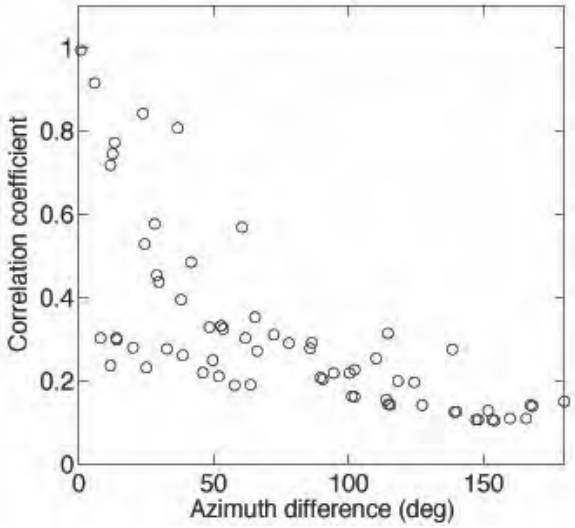


Figure 4: Correlation coefficient between model-error pairs as a function of azimuth difference.

CONCLUSIONS AND RECOMMENDATIONS

Our initial efforts in this project confirm the feasibility of using a model-based approach to investigate the correlation structure of travel-time model errors, as a function of event location and seismic network geometry. The need to account for error correlations in seismic event location algorithms has been demonstrated in several previous studies (e.g. Yang et al., 2004) but the estimation of correlations has been restricted primarily to empirical studies in data rich areas (e.g., Myers and Schultz, 2000). We expect the approach we are developing to provide a useful tool for extrapolating such studies to data poor (aseismic) areas, taking the principles of seismic wave propagation and our knowledge of Earth structure heterogeneity into account.

Table 1. Standard deviation of model errors

Station	*Dist. (deg)*	*Az. (deg)*	*Std. dev. (s)*
ASH	2.96	5.4	0.76
DDI	17.51	99.8	1.86
FRU	15.10	53.9	1.99
GNI	11.70	299.9	1.93
KAT	4.25	341.5	0.97
KSH	15.00	67.2	1.97
KVAR	14.80	311.7	2.07
MAIO	1.77	42.1	0.61
NDI	17.49	105.8	1.87
NIL	12.68	91.8	2.00
PYA	14.62	312.6	2.07
QUE	8.94	112.0	1.63

Table 2. Correlation coefficient between model errors

	ASH	DDI	FRU	GNI	KAT	KSH	KVAR	MAIO	NDI	NIL	PYA	QUE
ASH	1.00	.22	.33	.35	.84	.30	.32	.81	.22	.29	.33	.31
DDI	.22	1.00	.22	.11	.20	.28	.11	.19	.91	.30	.11	.28
FRU	.33	.22	1.00	.16	.31	.77	.16	.24	.21	.40	.16	.27
GNI	.35	.11	.16	1.00	.48	.14	.72	.23	.11	.13	.74	.15
KAT	.84	.20	.31	.48	1.00	.28	.44	.57	.20	.25	.45	.27
KSH	.30	.28	.77	.14	.28	1.00	.14	.23	.26	.53	.14	.33
KVAR	.32	.11	.16	.72	.44	.14	1.00	.20	.11	.12	.99	.14
MAIO	.81	.19	.24	.23	.57	.23	.20	1.00	.19	.25	.21	.29
NDI	.22	.91	.21	.11	.20	.26	.11	.19	1.00	.30	.11	.30
NIL	.29	.30	.40	.13	.25	.53	.12	.25	.30	1.00	.13	.58
PYA	.33	.11	.16	.74	.45	.14	.99	.21	.11	.13	1.00	.14
QUE	.31	.28	.27	.15	.27	.33	.14	.29	.30	.58	.14	1.00

ACKNOWLEDGMENTS

We are very grateful to Prof. Vernon Cormier of the University of Connecticut for collaborating with us on seismic-wave propagation theory and the future extension of our approach to finite-frequency travel times.

REFERENCES

Chang, A. C., R.H. Shumway, R. R. Blandford and B. W. Barker (1983). Two methods to improve location estimates—preliminary results, *Bull. Seism. Soc. Am.* 73: 281–295.

Dahlen, F.A., S.-H. Hung and G. Nolet (2000). Fréchet kernels for finite-frequency traveltimes I. Theory, *Geophys. J. Int.* 141: 157–174.

Deutsch, C. V. and A. G. Journel (1998). *GSLIB: Geostatistical Software Library and User's Guide*, 2nd ed., Oxford University Press, Inc., New York, 369 pp.

Engdahl E. R., R. van der Hilst and R. Buland (1998). Global teleseismic earthquake relocation with improved travel times and procedures for depth determination, *Bull. Seism. Soc. Am.* 88: 722–743.

Hung, S.-H., F. A. Dahlen and G. Nolet (2000). Fréchet kernels for finite-frequency traveltimes II. Examples, *Geophys. J. Int.* 141: 175–203.

Myers, S. C., and C. A. Schultz (2000). Improving sparse network seismic locations with Bayesian kriging and teleseismically constrained calibration events, *Bull. Seism. Soc. Am.* 90: 199–211.

Reiter, D. and W. Rodi (2006). Crustal and upper-mantle P- and S-velocity structure in central and southern Asia from joint body- and surface-wave inversion, in current Proceedings.

Rodi, W., S. C. Myers and C. A. Schultz (2003). Grid-search location methods for ground-truth collection from local and regional seismic networks, in *Proceedings of 25th Seismic Research Review—Nuclear Explosion Monitoring: Building the Knowledge Base*, LA-UR-03-6029, Vol. 1, pp. 311–319.

Schultz, C.A., S.C. Myers, J. Hipp and C.J. Young (1998). Nonstationary Bayesian kriging: a predictive technique to generate spatial corrections for seismic detection, location, and identification, *Bull. Seism. Soc. Am.* 88: 1275–1288.

Yang, X., I. Bondár, J. Bhattacharyya, M. Ritzwoller, N. Shapiro, M. Antolik, G. Ekström, H. Israelsson and K. McLaughlin (2004). Validation of regional and teleseismic travel-time models by relocating ground-truth events, *Bull. Seism. Soc. Am. 94:* 897–919.

Zhao, L., T.H. Jordan and C.H. Chapman (2000). Three-dimensional Fréchet differential kernels for seismic delay times, *Geophys. J. Int., 141*, 558–576.

SEISMIC SOURCE LOCATIONS AND PARAMETERS FOR SPARSE NETWORKS BY MATCHING OBSERVED SEISMOGRAMS TO SEMI-EMPIRICAL SYNTHETIC SEISMOGRAMS: IMPROVEMENTS TO THE PHASE SPECTRUM PARAMETERIZATION

David. Salzberg and Margaret Marshall

Science Applications International Corporation

Sponsored by Air Force Research Laboratory

Contract No. FA8718-05-C-0019

ABSTRACT

The purpose of this study is to demonstrate the feasibility of full-waveform earthquake location using semi-empirical synthetic waveforms and received data from as few as two regional stations. We previously used a parameterization of the semi-empirical correction (or filter) that assumed range invariant phase spectrum of the correction term. That approach works very well if the two events are close (<10 km). However, with greater event separation, the empirical filter is unable to correct the synthetic to match the data, particularly at higher frequencies (Salzberg et al., 2005).

By modifying the parameterization of the semi-empirical correction to allow for a range dependent phase spectrum, the empirical filter is able to correct the synthetic to match the data even when the event separation is large (> 50 km), and in particular, in cases where the range invariant phase correction fails. The improved parameterization characterizes the spectrum in terms of wave number and range. This approach requires us to isolate individual propagating modes as such. Currently, only the fundamental Rayleigh wave is used. In this method, the ray-theory P-wave arrival time is used for time reference; the synthetic is lagged by the predicted arrival time, and the data uses the measured arrival time. With this technique, we are able to obtain GT5 or better locations using the long-period (>30 second) Rayleigh waves. Also, we are able to simulate the waveforms from a nuclear explosion (JUNCTION) using the Little Skull Mountain Earthquake.

We will present comparisons of the results using both the new approach and the old approach by utilizing ground truth (GT) for a data set of events in California. In particular, we will determine the range at which the accuracy of the new approach (using the long period surface waves) exceeds the old approach (using broadband signals). In addition, we will determine the separation at which the new phase parameterization is no longer able to simulate the observations.

OBJECTIVE(S)

The objective of the research is to provide a method that gives accurate locations (GT5) and source mechanisms using a sparse regional network when two or more seismic stations record the event. Tests using synthetic waveforms indicate that location accuracy on the order of 300–500 km^2 and depth uncertainty of less than 5 km can be obtained with recordings from only two stations low pass-filtered at 0.5 Hz using hold waveforms, or .1 Hz when using just the Rayleigh waves. The objective if this paper is to present the semi-empirical (or empirically filtered) method using a range-dependent empirical filter, and to evaluate the results with the new parameterization when compared to the old parameterization.

RESEARCH ACCOMPLISHED

- Measured the Group Velocity Curves of all reviewed waveforms
- Identified two workable clusters
- Determined the 1-D path specific velocity models
- Processed events to determine frequency dependence of the method
- Identified and corrected problems with the original methodology
- Demonstrated the ability to locate earthquakes and explosions to better than GT5
- Demonstrated the ability to locate small events (M = 4.1)
- Demonstrated the ability to transform waveforms with different mechanisms

Approach

In this section we present our technique for empirical filtering. First, an overview of our approach is presented, followed by a derivation of the approach. The overall goal of our approach is to find a filter that transforms synthetic seismograms into the observed data. When comparing the synthetic waveform with real data, a match is not possible unless the velocity model is well defined. Furthermore, errors in the synthetic waveforms translate into errors in the resolved location and source parameters. Consequently, the primary limitation in matched waveform processing is the ability to produce high-fidelity simulations based on an imperfect environmental model.

One approach that can be used to improve the quality of the synthetic waveforms is to empirically determine a filter that characterizes the propagation portion of the synthetic waveform, yet still use the theoretical excitation (Salzberg, 1996; Velasco et al., 1994). These empirically filtered Green's Functions can then be employed to characterize the seismic wavefield recorded at a seismic station or array using sources from a reasonably homogeneous source region.

In our ongoing project, we defined the filter as a static function of frequency. This approach works well if the two events are co-located. However, any significant separation in range yields a poor empirical filter. This is caused by a phase shift from the difference in propagation distances. To compensate for this, we propose to represent the phase of the empirical filter in wave number space. With this approach, the empirically filtered synthetic seismogram, u_e is

$$u_e(\omega, r) = \frac{s(\omega)}{u(\omega, r_o)} \cdot e^{i\Delta k(r - r_o)} \cdot u(\omega, r), \tag{1}$$

where, u is the synthetic seismogram, s is the observed seismogram, r_o is the range to the reference event, r is the range to the new event, and Δk is the wave number corresponding to the phase mismatch reference data and synthetic.

This change significantly improves our ability to match the data to the empirically filtered synthetic seismogram, when there is a substantial distance between the new event and the reference event; or, when r-r_o is large (50 km or more) compared to the static phase approach. The approach will, of course, also work at shorter ranges. However, when the events are close, r-r_o approaches 0, and the formulation reverts to

$$u_e\left(\omega,r\right)=\frac{s\left(\omega\right)}{u\left(\omega,r_o\right)}\cdot u\left(\omega,r\right), \tag{2}$$

or

$$u_e\left(\omega,r\right)=\Delta u\left(\omega,r_o\right)\cdot u\left(\omega,r\right), \tag{3}$$

where

$$\Delta u\left(\omega,r_o\right)=\frac{s\left(\omega\right)}{u\left(\omega,r_o\right)}, \tag{4}$$

which is the approach used in our current Air Force Research Laboratory (AFRL) project.

Proposed Wave Number (K-Space Parameterization)

In this section, the *k-space* parameterization will be described. At the end of the derivation, the resulting formulation is Equation (2).

Parameterizing our classic formulation, shown in Equation (4) in terms of amplitude and phase yields:

$$\Delta u(\omega,r_o)=\left|\frac{s\left(\omega\right)}{u\left(\omega,r_o\right)}\right|\cdot e^{i\left(\phi_s-\phi_{u_o}\right)}=\Delta A\left(\omega\right)\cdot e^{i\Delta\phi}. \tag{5}$$

This approach works well if the events are close together, or if there is a dominant phase in the data (e.g., Rayleigh). In the case where the spatial separation of the events approaches or is greater than the wavelength of the highest frequency energy used, the increasing time separation of the body waves and phase mismatch of the surface waves result in increased misfit, as increases occur in the separation of the reference and the second event.

An alternative, range dependent phase parameterization will provide better agreement of the waveforms in these cases. Treating the waveform as a sum of propagating modes, the modes can be represented as a range dependent amplitude and range dependent phase, or

$$u\left(\omega,t,k,r\right)=\sum_n A_n\left(\omega,r\right)\cdot e^{i\left(k_n r-\omega t\right)}, \tag{6}$$

where u is the displacement, A is the amplitude, k is the wavenumber, and n is the mode.

Using this formulation for both the data and the synthetic waveform (and assuming that the modes of the data can be separated), Equations (5) and (6) can be combined to parameterize the phase misfit to terms of the wave number and distance, or

$$\Delta\phi=\Delta\phi_{reference}-\Delta\phi_{synthetic}=\left(k_{reference}\cdot r_{reference}-\omega\cdot t_{reference}\right)-\left(k_{synthetic}\cdot r_{synthetic}-\omega\cdot t_{synthetic}\right). \tag{7}$$

Assuming the reference time for the data and the synthetic is the same, and the synthetic was computed for the observed distance, then

$$\Delta\phi=\left(k_{reference}\cdot r-\omega\cdot t\right)-\left(k_{synethic}\cdot r-\omega\cdot t\right)=\left(k_{reference}-k_{synethic}\right)\cdot r=\Delta k\cdot r\ . \tag{8}$$

For each propagating mode, assigning the reference event range to be r_o, allows the empirically filtered waveform for the specific propagating mode at range r to be expressed as

$$u_e(\omega, r) = \frac{s(\omega)}{u(\omega, r_o)} \cdot e^{i\Delta k(r - r_o)} \cdot u(\omega, r), \tag{9}$$

which is Equation (1).

With real data, it is not feasible to separate each propagating mode exactly. However, it is possible to apply time-frequency windowing functions to isolate the body waves from the surface waves.

Examples of the Approach

Two Components of NVAR

This process is demonstrated using two broadband components of the NVAR recording a Parkfield, CA, aftershock, as shown in Figure 1. This test is desirable because, with multiple components recording the same wavefield, source uncertainty is eliminated. Computing synthetic waveforms at both distances, and using the observed Rayleigh wave from NV32 (range = 328km) to determine the filter to transform the 344 km synthetic (which is the distance to NV33), it is possible to accurately simulate the waveform. Comparing the synthetic using the range dependent phase correction to the existing constant phase technique shows that the new approach does a better job simulating the Rayleigh wave than using the existing constant phase method, as shown in Figure 2.

Furthermore, the correct distance separation between the stations can be determined by matching the Rayleigh waveforms (with time relative to the P arrival time), as shown in Figure 3.

San Simeon Event Using Parkfield as a Reference Event

In our presentation at the 2005 SRR (Salzberg et al., 2005), we presented an example where the semi-empirical synthetic seismogram location approach was unable to resolve the event location; those results are shown in Figure 4. With the range-dependent formulation, we are able to correctly resolve the event location, as shown in Figure 5, even though the San Simeon Event was small (M_w=4.1), relatively far from the reference event (60 km), and a difference mechanism (Reverse vs. Strike Slip).

Sensitivity Analysis of GT Events (NTS Nuclear Explosions)

In order to evaluate the solution quality of the approach, we have applied it to Nevada Test Site (NTS) nuclear explosions recorded at PAS and Albuquerque (ANMO). Our primary concern is the sensitivity using different frequency bands. As such, the data were processed using surface waves over a variety of frequency bands. We found that we were able to locate the event HOYA using JUNCTION as a reference event in range and depth to within one grid spacing of GT, as shown in Figure 6. The uncertainty in our estimates, though, were on the order of 2–4 km, with the area of ambiguity being about 5 km^2 (2 σ) or 20 km^2 (3 σ), in when looking at broadband surface waves (filtered to periods between 100 and 7 seconds) as shown in Figure 7.

Locating Little Skull Mountain Earthquake Using NTS Explosions as Reference Events

As a final example, the NTS explosion JUNCTION is used as a reference event for locating the Little Skull Mountain (LSM) earthquake. The geographic context of the events and the station is shown in Figure 8. Our two-dimension (range and depth) examples show that we were able to approximately locate the LSM earthquake, as shown in Figure 9. The absence of GT renders it impossible to assess the accuracy of the results.

CONCLUSIONS AND RECOMMENDATIONS

The range-dependent (wave number based) parameterization of the semi-empirical synthetic approach allows for the waveform-matched location to within a few kilometers using P-wave arrival times for reference and the Rayleigh waveform, though the quality of the depth resolution is uncertain. With this, earthquakes and explosions can be relocated using GT events (either earthquakes or explosions) as reference events. In order to improve the technique to provide for better depth estimates, the P-wave and S-wave arrivals (and depth phases) should be included in the processing.

ACKNOWLEDGEMENTS

All waveform data was obtained from the Incorporated Research Institutions for Seismology (IRIS) Data Management Center. The International Data Center (IDC) event locations were from the SMDC Monitoring Research Web Page.

REFERENCES

Salzberg, D. H. (1996). Simultaneous inversion of moderate earthquakes using body and surface waves: Methodology and applications to the study of the tectonics of Taiwan, Ph.D. thesis, State University of New York, Binghamton, NY.

Salzberg, D. H., K. E. Votaw, and M. E. Marshall (2005). Seismic source locations and parameters for sparse networks by matching observed seismograms to semi-empirical synthetic seismograms, in *Proceedings of the 27th Seismic Research Review: Ground-Based Nuclear Explosion Monitoring Technologies*, LA-UR-05-6407, Vol. 1, 454–462

Velasco, A. A., C. J. Ammon, and T. Lay (1994). Recent large earthquakes near Cape Mendocino and in the Gorda Plate: Broadband source time functions, fault orientations and rupture complexities, *J. Geophys. Res.* 99: 711–728.

FIGURES

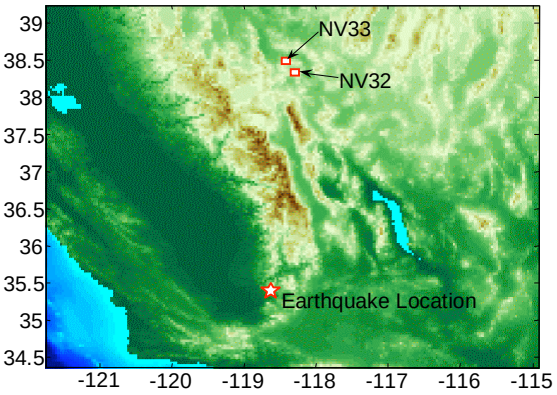


Figure 1. The geographic context of the two NVAR components to the earthquake.

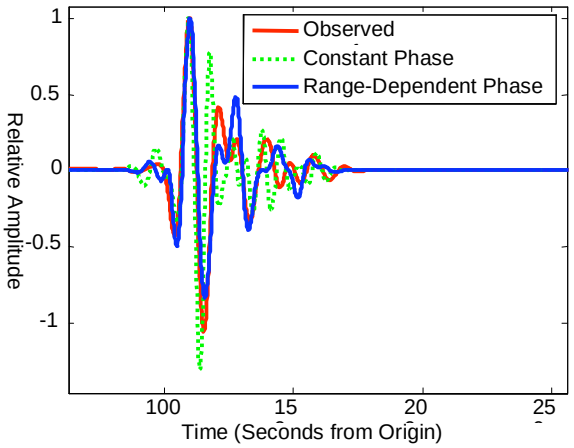


Figure 2. The observed Rayleigh wave recorded at NV33 compared with semi-empirical synthetic based on the constant-phase approach and the range-dependent approach. Note the range-dependent phase (based on wave number) filter does a much better job of fitting the observed data than does the synthetic waveform.

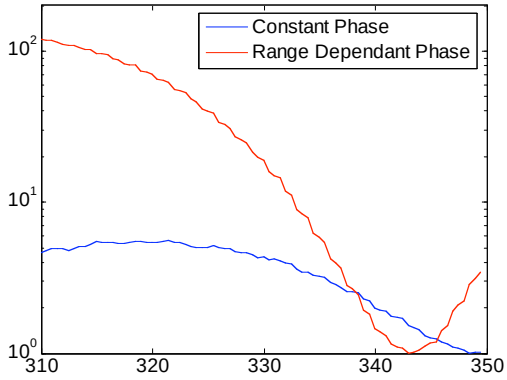


Figure 3. The optimal range determined using the constant phase approach and the range-dependent phase approach. The range-dependent phase is able to resolve the location of NV33 accurately, as the GT range is 344 km.

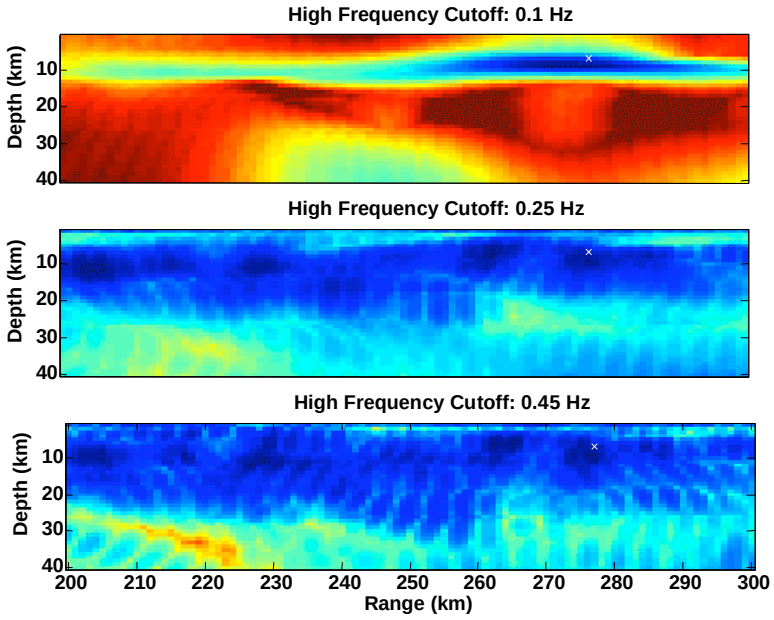


Figure 4. The range-invariant empirical filter only poorly resolves the event location when the new event and reference event are more than a few kilometers. At high frequencies, a minimum was not obtained. At low frequencies (below 0.1 Hz), a broad minimum was obtained. However, the uncertainty is approximately 30 km.

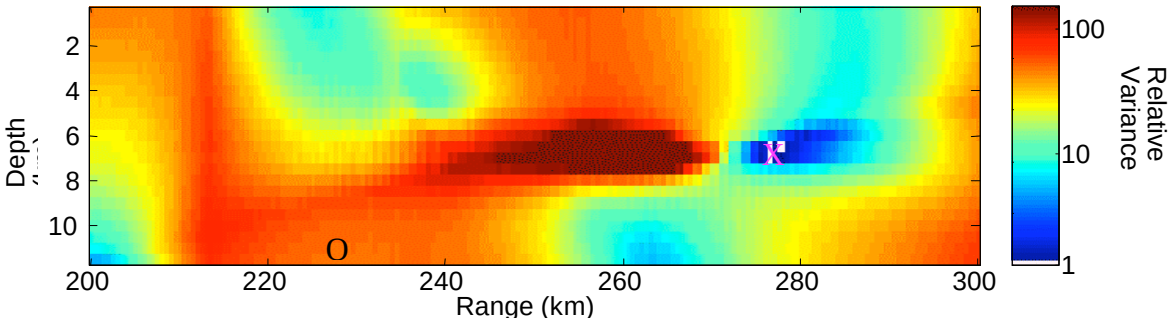


Figure 5. Relocating the same event discussed in Figure 4, but using the range-dependent (wave number based) approach. X marks the GT location, which coincides with the minimum in variance. The reference event, shown by the black O is approximately 50 km. Given the sharpness of the minima, it is clear that the range-dependent approach did obtain a good solution for the event.

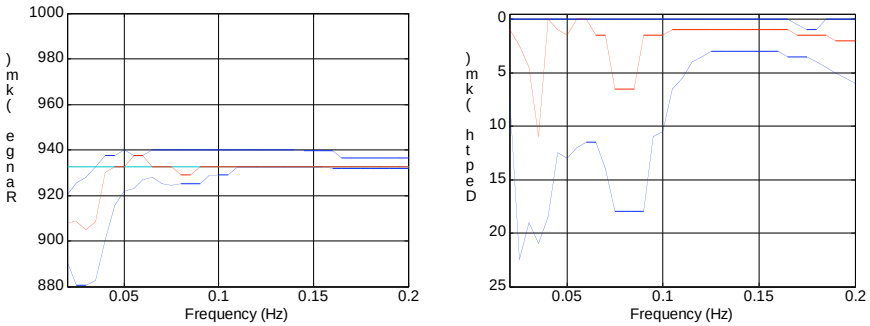


Figure 6. The location sensitivity vs. processing frequency of the HOYA NTS nuclear explosion, using the JUNCTION explosion as a reference event. The blue lines represent the 2 σ errors, based on variance, and the red line is the location of the minimum variance. GT is shown by the cyan line on the range plot and is approximately 300 m on the depth plot. From this, it is clear that the most accurate and precise event locations occur when higher-frequency data are used.

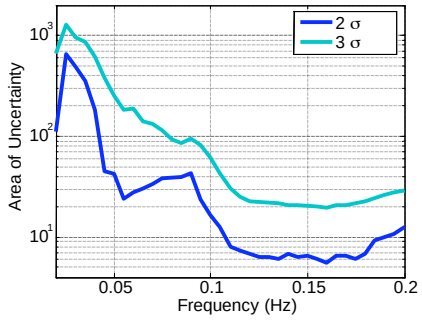


Figure 7. The 2-D area of uncertainty of the HOYA NTS nuclear explosion, using the JUNCTION explosion as a reference event. Note that the minimum uncertainty, which is about 5 km^2, occurs when using data with a low-pass filter of around 7 s (0.15 Hz).

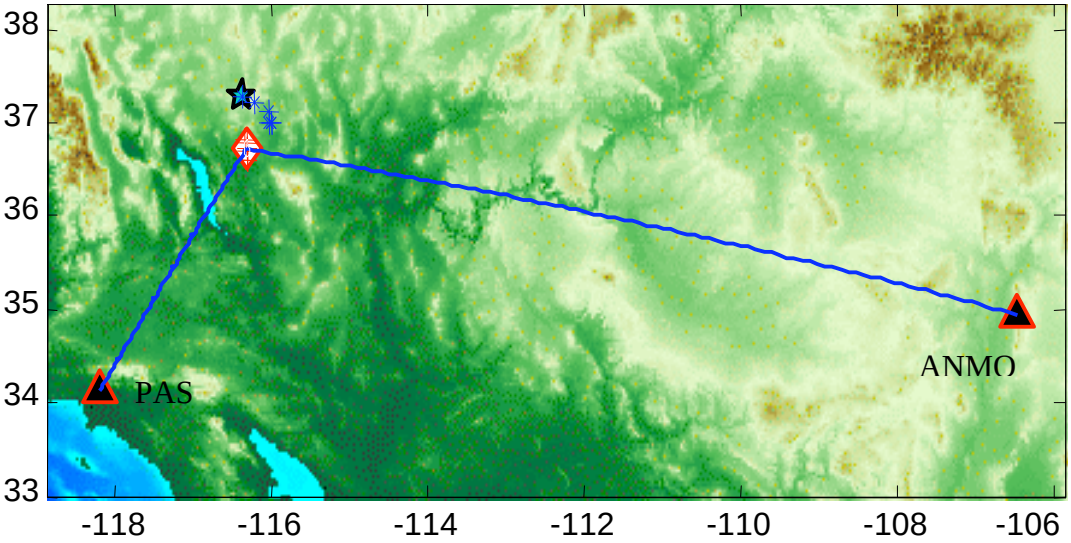


Figure 8. The geographic context of the NTS explosions (blue) and the LSM earthquake (red diamond).

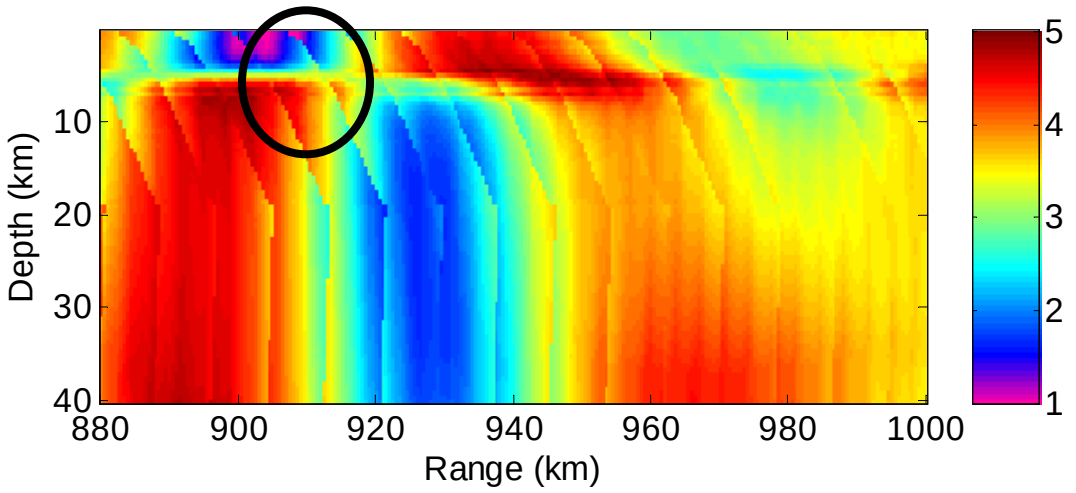


Figure 9. Locating the LSM earthquake using the JUNCTION explosion as a reference event. The GT location is shown by the black ellipse centered near 910 km in range. Note that the location uncertainty overlaps with minimum in residual (magenta region).

IMPROVING MAGNITUDE DETECTION THRESHOLDS USING MULTISTATION, MULTIEVENT, AND MULTIPHASE METHODS

David P. Schaff and Felix Waldhauser

Lamont-Doherty Earth Observatory, Columbia University

Sponsored by Air Force Research Laboratory

Contract No. FA8718-05-C-0022

ABSTRACT

Research was conducted on a correlation detector (multievent and multiphase) for semiempirical synthetic tests and a regional case study in Xiuyan, China. The semiempirical runs took a 50 s window on an Lg-wave recorded at 750 km distance filtered from 1 to 3 Hz and embedded it 300,000 times in real, continuous, background seismic noise. The noise was selected for 36 days spread throughout the year to capture diurnal and seasonal variations. No screening for random, unknown signals in the noise was performed. A correlation detector has a 50% probability of detection with 1.5 false alarms per day for a signal-to-noise ratio (SNR) of 0.32, which corresponds to a full magnitude unit reduction in detection threshold over a standard STA/LTA technique. A scaled cross correlation coefficient performs slightly better with 1 false alarm per day and has fewer false triggers on unknown, random signals. Summing the cross correlation traces together for all three components enhances the detection signal similar to beamforming. A correlation detector summing the three components together has a 96% probability of detection with zero false alarms in 36 days for a SNR of 0.32. The case study looked at 90 events in Xiuyan, China, recorded at stations 500 to 1500 km away. Clear detection spikes are observed on all three components agreeing to the nearest sample allowing for constructive interference on the summation of the correlation traces. In contrast, detection maximums for unknown, random signals do not align to the nearest sample on the three components and destructively interfere with the summation. This is probably the single best indication of a true detection, the fact that three independent components all show clear spikes to the nearest sample. It is also observed that semisimilar events can provide useful detections (events that are not exactly co-located or don't have identical mechanisms). Two examples of an aftershock buried in the coda of a larger event demonstrate new detections that were not previously reported in the available catalogs. A scaled cross correlation detector is able to detect 90 out of 90 or 100% of the events in the catalog using Pg, Pn, and Lg phases, whereas a standard STA/LTA detector like that employed by the Prototype International Data Center (pIDC) finds 10 out of 90 or 11%. Comparison with a known local/regional catalog shows this represents a 1.3 unit reduction in magnitude threshold.

OBJECTIVES

Research will be conducted on techniques for generating a multiphase detection bulletin derived by two means: station array processing (multistation) and source array processing (multievent). Comparison and quantification of improvement over standard P-wave, single-event, single-station procession will be evaluated.

RESEARCH ACCOMPLISHED

Introduction

The first year of this project has focused on a correlation detector or multievent technique. Waveform cross correlation has a long history of improving locations and identifying events (e.g., Poupinet et al., 1984; Harris, 1991). Recently it appears that large percentages of events may be similar enough to enable correlation detectors to be applied on a broad scale (Schaff and Richards, 2004; Schaff and Waldhauser, 2005). Figure 1 shows an Lg-wave recorded 750 km away embedded in various levels of real background seismic noise. The waveforms are filtered from 1 to 3 Hz. Signal-to-noise ratio (SNR) values are shown to the left and are computed as a mean absolute value like an STA/LTA filter uses. A standard trigger used by the pIDC of 3.2 shows a corresponding signal that an energy detector (STA/LTA) would find in this case corresponding to a magnitude 3.5. The relationship between SNR and magnitude is

$$\mathrm{Mag} = \log(\mathrm{SNR}) + 4.3 - \log(\mathrm{SNR}_{\mathrm{Mag}=4.3}) \; .$$

Reducing the detection threshold by 0.5 magnitude units it can be seen that the SNR drops to one. It is impossible for an STA/LTA filter to detect a signal at the noise level. To reduce the detection threshold by a full magnitude unit to 2.5 corresponds to an SNR of 0.32 or where the signal is one-third of the noise level. Figure 2 displays the cross correlation traces for each of these signals correlated with the master template. Clear detection spikes can be seen all the way down to magnitude 2.5 giving us the first indication that a correlation detector can reduce the detection threshold by a full magnitude unit. In the next section we will explore if such detections occur with acceptably low false alarm rates.

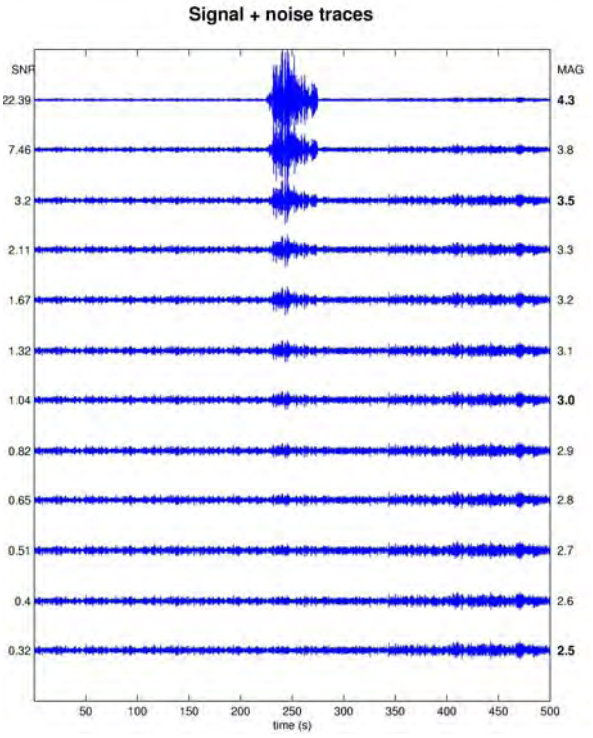


Figure 1. Lg-wave signals embedded in increasing noise.

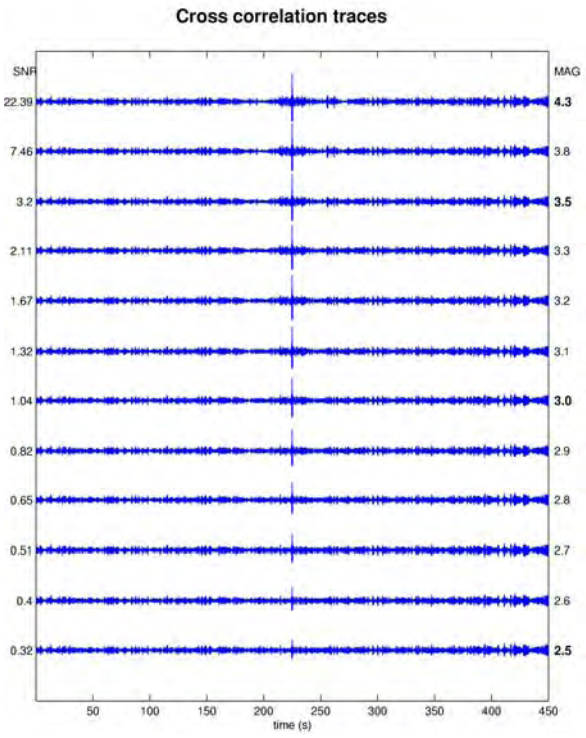


Figure 2. Cross correlation traces corresponding to Figure 1.

Figure 3 shows the maximum cross correlation coefficient (CC) as a function of SNR highlighting the three magnitudes of interest. It can be seen that detecting half a magnitude unit lower at 3.0 would easily be picked up with a cross correlation coefficient above 0.8. Remember that this corresponds to a signal right at the noise level. To detect a full magnitude unit lower, however, at 2.5 has a low CC of 0.367. Normally this type of measurement would be discarded for location purposes even though there was a clear detection spike relative to background levels. The reason can be seen in Figure 4 where you have two dissimilar traces in the top panel. The cross correlation function of these two waveforms corresponds to the first trace in the middle panel with a coefficient of 0.364. Therefore, even though these two waveforms are unrelated they have a similar coefficient to the case of an identical signal buried in noise (0.367). The second trace in the middle panel is the last correlation trace from Figure 2 corresponding to a SNR of 0.32. A detection threshold of 0.35 would trigger on both of these examples. The first case would be a false alarm, whereas only the second is the true detection that we want to capture. One solution to this problem is to note that in the second case the maximum is high relative to background values. We can apply an STA/LTA filter to the cross correlation traces, which is shown in the bottom panel. We choose for the window length of the STA one sample and the window of the LTA 20 s. Here the maximums differ by a substantial amount (5.8 for the dissimilar case and 8.3 for the identical signal buried in noise). Gibbons and Ringdal (2006) employ a similar procedure that they call a "scaled CC," where they scale the CC by the root mean square (RMS) within some window of the background levels. Because our STA/LTA filter uses mean absolute value we divide by that instead of RMS but the effect is basically the same. It can readily be seen that a scaled CC threshold of 6 would weed out the dissimilar case and would leave us with the true detection. We will use this value later as our threshold in our case study in Xiuyan, China.

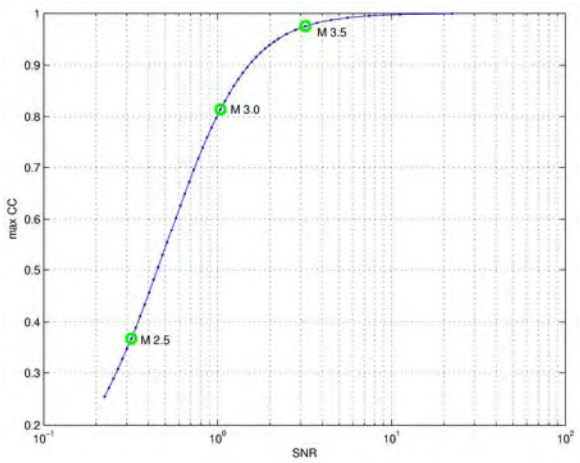


Figure 3. Maximum CC as a function of SNR from Figure 2.

Next we examine how the correlations perform for all three components. In Figure 5 we cross correlate signals for the BHN, BHE, and BHZ components in the top panel with the same signals plus noise in the second panel (SNR = 0.32) to obtain the cross correlation traces in the third panel with CCs around 0.3 as before and clear detection spikes at 225 s. If we stack the cross correlation traces we see that the spikes constructively interfere and give a new maximum of 0.97. There is an overall enhancement in the spike because the background levels deconstructively interfere. We can estimate the level of this enhancement. Define $R = \frac{\max cc}{\sigma}$. Assume σ^2 is the variance for all three components. For the stack the variances add, $\sigma^2_{stack} = 3\sigma^2$. Then $R_{stack} = \frac{3\max cc}{\sqrt{3\sigma^2}} = \sqrt{3}R = 1.732R$. We see that the variances of the three components do add to 0.0137, which is close to 0.0139 of the stack, indicating that they are approximately normally distributed. Also R_{stack} is enhanced by 1.7 times the average R as expected. This is the same improvement in signal enhancement that is achieved by beam forming.

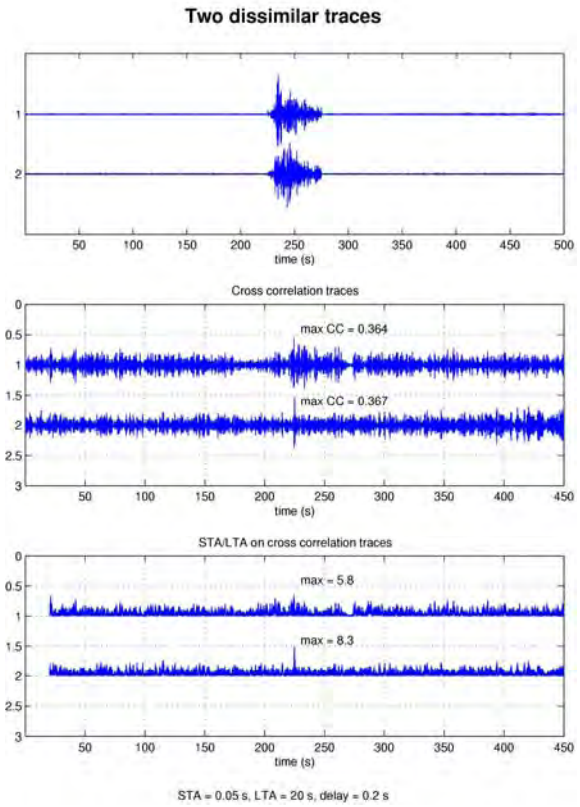


Figure 4. Two dissimilar traces would produce a false alarm with CC but not with a scaled CC.

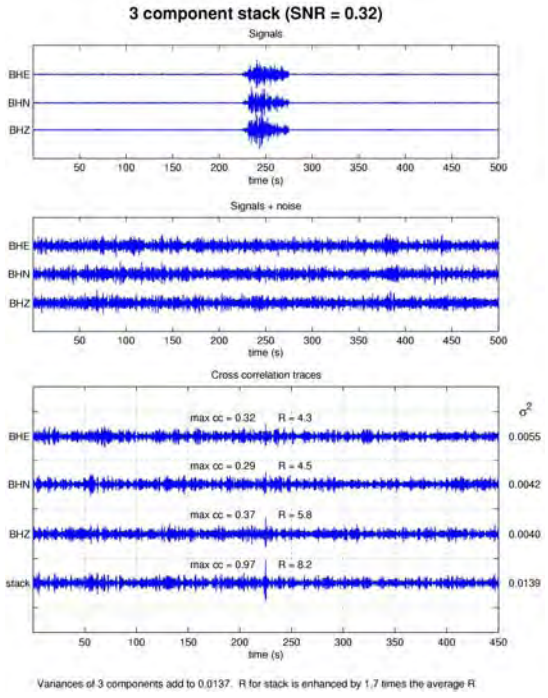


Figure 5. Three components enhance the detection spike.

Semiempirical Synthetic Runs

Now we look more in detail at statistics of detection and false alarm rates. We take 36 days of real seismic noise spread throughout the year to capture diurnal and seasonal variations. The noise also contains random seismic signals of unknown origin that have not been removed. For the master signal we choose a 50 s window on the Lg-wave of Figure 1 recorded at 750 km distance. The waveforms are all filtered from 1 to 3 Hz. The sample rate is 20 Hz. We embed the signal in the noise ~300,000 times. The noise comprises 62 million samples. Figure 6 shows the histograms for the signal and noise distributions for CC for a SNR of 0.32. There is a clear separation between the two allowing for detections to be made with a certain threshold. The mean CC is about 0.35 for the signal buried in noise as before. A Receiver Operating Characteristic plot in the lower panel shows probability of detection as a function of probability of false alarm, which can be computed from the top panel. For a probability of detection of 0.5, there is less than one in a million chance of a false alarm. Given the number of samples per day at 20 Hz this corresponds to 1.5 false alarms per day. This is a reasonable false alarm rate, and so we therefore conclude that a correlation detector is able to detect a signal buried in the noise one full magnitude unit lower than a standard energy detector. Figure 7 shows the same signal and noise distributions for a SNR of 0.32 but this time for the scaled CC or signed STA/LTA on the CC trace. Again a clear separation of the distributions is obvious. The mean of the signal buried in noise is around 6. This time, however, the probability of detection at 0.5 corresponds to a slightly lower false alarm rate of one per day.

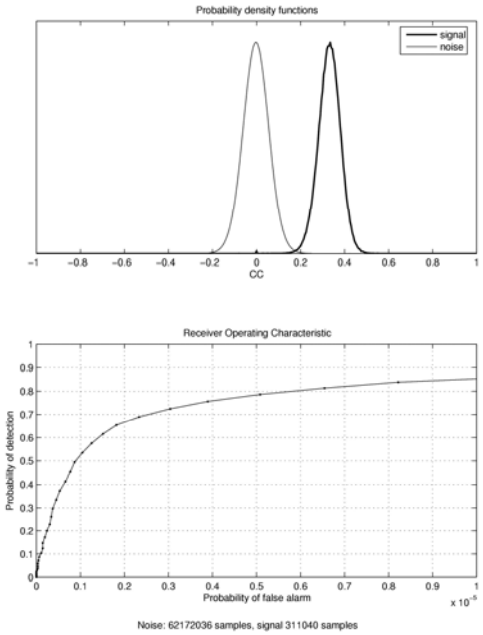


Figure 6. Statistics for a signal buried in noise (SNR = 0.32) for CC.

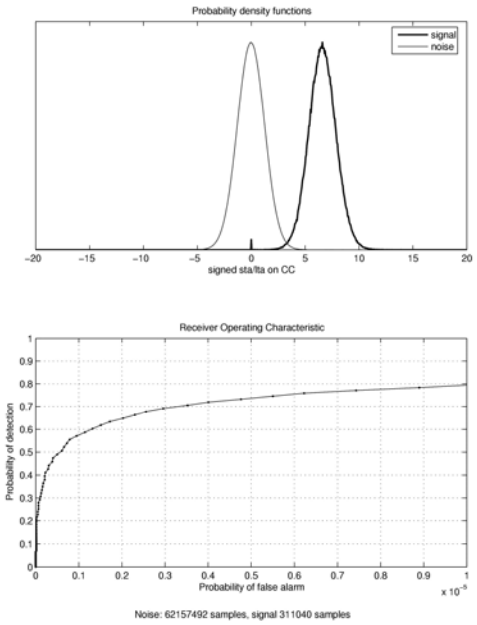


Figure 7. Statistics for a signal buried in noise (SNR = 0.32) for scaled CC.

If we increase the SNR to 1.012, corresponding to half a magnitude unit reduction in detection threshold over an STA/LTA filter then we see in Figure 8 that the signal and noise distributions are extremely well separated. The mean CC for the signal is above 0.7 indicating a high degree of similarity. In this case there are zero false alarms for the entire 36 days considered at a probability of detection of 99.996%. This is rather remarkable that even though the signal is at the noise level there is nearly a 100% probability of detection with a zero false alarm rate. Figure 9 is the same as Figure 6 for a signal buried in noise at the SNR = 0.32 level except all three components are used to enhance the detection as seen in Figure 5. Note that the mean CC is about the same but that the width of both the signal and noise distributions has been reduced by summing the variances. The narrower distributions cause less overlap of the probability density functions and produce a better Receiver Operating Characteristic curve. This time there are zero false alarms in 36 days with a probability of detection of 96.5% compared to the one false alarm per day rate at the 50% level before.

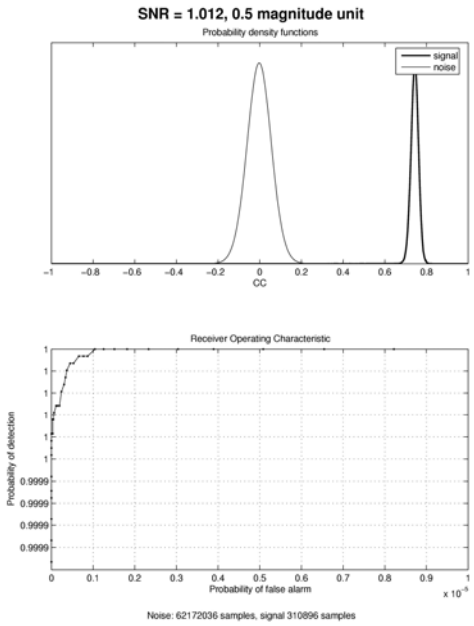


Figure 8. Statistics for a signal buried in noise (SNR = 1.012) for CC.

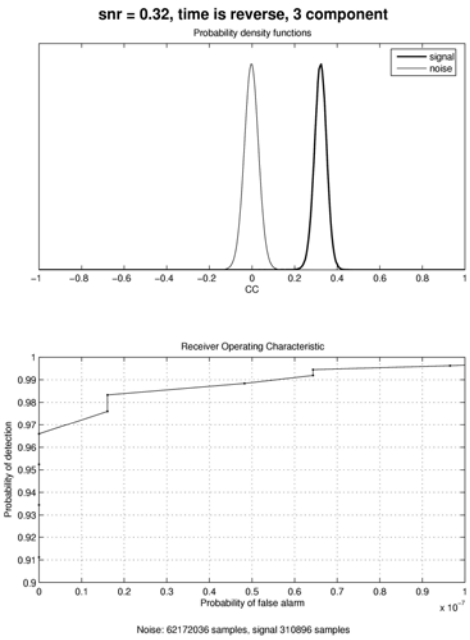


Figure 9. Statistics for a signal buried in noise (SNR = 0.32) for CC with three component enhancement.

1999 Xiuyan, China, Case Study

Ninety events are examined in the 1999 Xiuyan, China, earthquake sequence recorded at stations 500 to 1,500 km away. The cross correlation matrix for station IC.BJT is shown in Figure 10. The windows chosen are centered on the Lg-waves filtered from 0.5 to 5 Hz. Clusters of similar events appear with warm colors as blocks on the diagonal. Several values of the CC are quite high above 0.8. Other colors in cyan are at the 0.35 range that we were looking at before for the detection of a small signal buried in noise. The question is whether these values provide reliable detections. Figure 11 shows the cross correlation traces for the events in the cluster from indices 56 to 79. It is seen that there are clear detection spikes on the vertical, north, and east components. In addition, it can be seen that the spikes constructively interfere and are enhanced on the average of the three components compared to the background levels. This is the clearest indication that we have a true detection for these events—the fact that the spikes all align to the nearest sample for basically three independent tests. Visual inspection of the cross correlation traces for the other clusters in Figure 10 shows similar behavior.

If the waveforms do not correspond to a similar event this phenomenon is not observed on the three components. Figure 12 shows the case where correlations are made with an unknown dissimilar signal. The bottom panel shows the cross correlation traces in different colors for the waveforms on the three components of the top panel. The annotated text occurs where the cross correlation is a maximum for each component (CC). Although the values are in a similar range to the case of a buried signal in noise (0.27, 0.34, 0.23) it is seen that they occur over 100 s apart from each other. The average does not constructively interfere but is much less at 0.16 and is 17 s away from the nearest peak on any component. This is strikingly different than the correlation spikes that align to the nearest sample for the case in Figure 11.

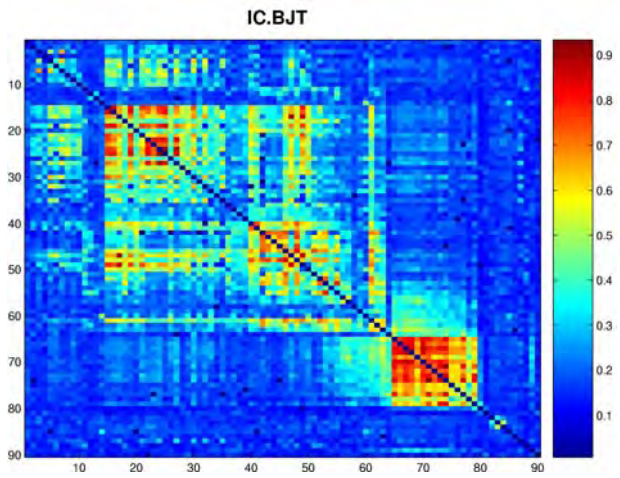


Figure 10. Cross correlation matrix for 90 events in Xiuyan, China.

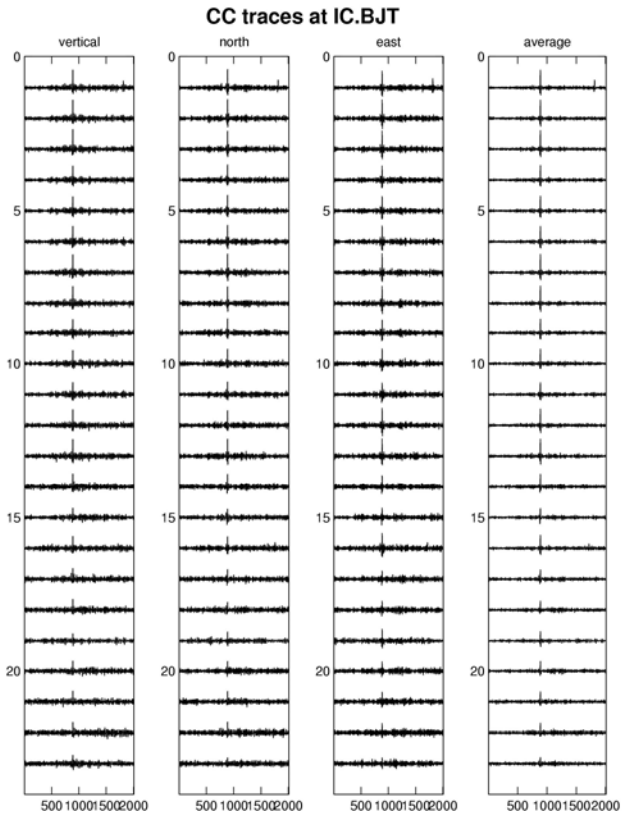


Figure 11. Cross correlation traces for 24 events.

To automatically detect the spikes above the background levels, we use a scaled CC, using a threshold of 6. Running this for all five regional stations and the phase Pg, Pn, and Lg gives the results shown in Figure 13. A blue dot means that event pair in the matrix satisfied the detection threshold of 6. Again similar events are arranged to be blocks on the diagonal. The number beside each phase is the number of events at that station matching the criterion out of 90. The largest amplitude Lg-wave that also has the longest duration of energy in the window produces the best detections and at station MDJ detects 90 out of 90, or 100% of the events. Stations BJT and HIA also have a high number of detected events for Lg. Pg is the next most detected phase and then Pn. Multiphase detections and detections at multiple stations further ensure that these are true detections.

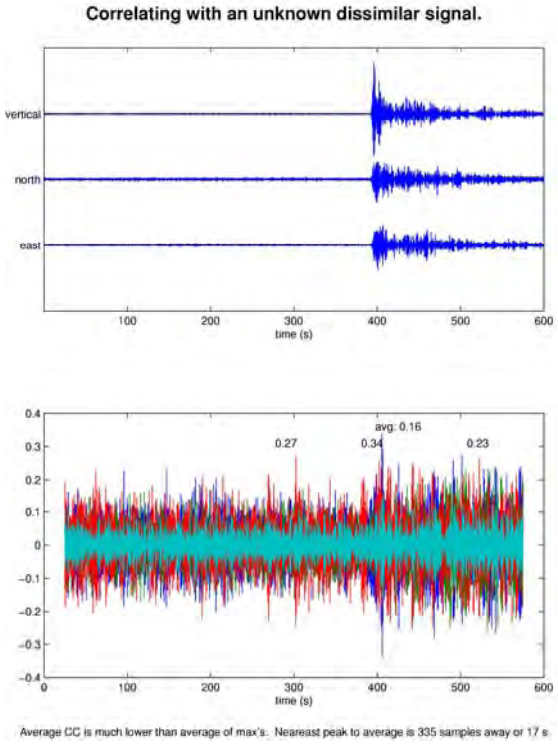


Figure 12. Cross correlation traces for three components of a dissimilar event.

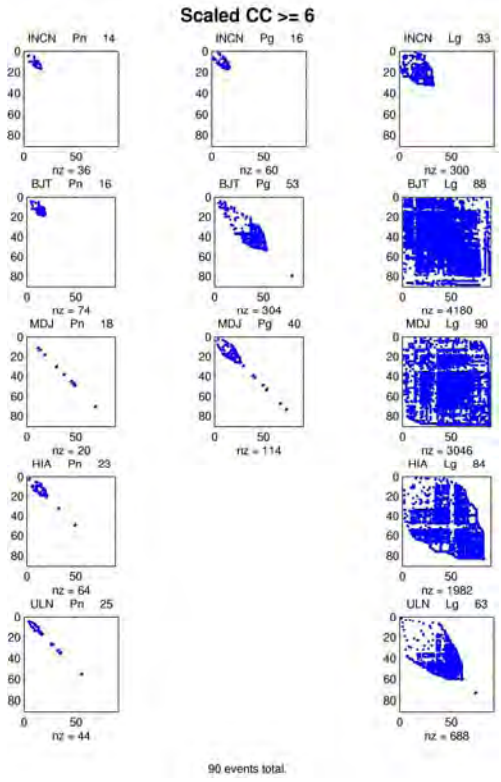


Figure 13. Detection matrices based on scaled CC for 90 events.

CONCLUSIONS AND RECOMMENDATIONS

- CC can detect one magnitude unit lower than STA/LTA.
- Three component averaging enhances the same as beam forming.
- CC has 50% probability of detection at 1.5 false alarm/day for SNR 0.32.
- Scaled CC has 50% probability of detection at 1 false alarm/day for SNR 0.32 because it has fewer triggers on unknown random signals.
- CC on 3 comp. has 96% probability of detection with zero false alarms in 36 days for SNR 0.32.
- 1999 Xiuyan, China, case study shows a CC detector finds 90 out of 90, or 100% of the events, whereas a STA/LTA detector like the pIDC finds 10 out 90, or 11%.
- Comparison with a known local/regional catalog shows this represents a 1.3 unit reduction in magnitude threshold.

ACKNOWLEDGEMENTS

We are grateful to the operators of the Chinese Digital Seismic Network (CDSN) and to the IRIS data management center for archiving the waveforms used in this project.

REFERENCES

Gibbons, S. J. and F. Ringdal (2006). The detection of low magnitude seismic events using array-based waveform correlation, *Geophys. J. Int.* 165: 149–166.

Harris, D. B. (1991). A waveform correlation method for identifying quarry explosions, *Bull. Seism. Soc. Am.* 81: 2395–2418.

Poupinet, G., W. L. Ellsworth, and J. Frechet (1984). Monitoring velocity variations in the crust using earthquake doublets: An application to the Calaveras Fault, California, *J. Geophys. Res.* 89: 5719–5731.

Schaff, D. P. and P. G. Richards (2004). Repeating seismic events in China, *Science* 303: 1176–1178.

Schaff, D. P. and F. Waldhauser (2005). Waveform cross-correlation-based differential travel-time measurements at the Northern California Seismic Network, *Bull. Seism. Soc. Am.* 95: 2446–2461.

ADVANCES IN MIXED SIGNAL PROCESSING FOR REGIONAL AND TELESEISMIC ARRAYS

Robert H. Shumway

University of California, Davis

Sponsored by Air Force Research Laboratory

Contract No. FA8718-04-C-0013

ABSTRACT

In this project, we have considered a number of possible approaches to resolving mixtures of propagating signals and noises over seismic arrays. The problem is important because there will often be interfering noise sources, extraneous signals, or mixtures of phases that will be organized as plane waves. Analyzing such mixtures using conventional beam-forming and other methods will produce distorted velocities and azimuths and may even give incorrect magnitudes. One interesting result of this study is that beam-forming, single-signal F-Statistics as well as typical high resolution multiple-signal estimators from engineering literature, such as the Multiple Signal Characteristic (MUSIC) algorithm all suffer from the above problems for some very common situations involving regional and teleseismic data.

We have approached the problem by showing that the multiple-signal plane-wave model is essentially in the form of a nonlinear regression in the frequency domain so that a sequential approach to isolating component signals analogous to stepwise linear regression can be applied. This approach provides a sequence of tests showing the power contribution of each component of a mixture and yields estimators for velocities and azimuths and their uncertainties. In the first year, we used this regression model, coupled with a corrected form of Akaike's Information Criterion (AICC) to settle on a final mixture. Applying the AICC as a model selection criterion yielded three signals known to have occurred on this long-period mixture and a decomposition of a regional earthquake into a known signal and a propagating noise.

In the second year of the contract, we have concentrated on deconvolving the mixtures obtained using the inverse Fourier components of the signals isolated in the above nonlinear regression model. Applying the approach to the long period mixture previously analyzed produces estimated waveforms for the two known simultaneously occurring earthquakes and for a noise component originating from South Pacific storms. We also show an analysis of a regional event from China that contains a signal and a strong propagating noise component. Deconvolving the mixture produces a waveform for the signal that shows a potential depth phase that cannot be seen in the original waveforms.

OBJECTIVES

This project is aimed at applying recently modified array signal processing techniques to problems involving single and multiple signals observed on teleseismic and regional arrays. We are focused on Topic 3 (Seismic Detection, Location and Discrimination) with particular emphasis on proposing "new techniques to enhance signal detection and parameter estimation (e.g., azimuth, phase velocity) in strongly heterogeneous media."

Specifically, we have developed the sequential F-statistic and model selection criterion AICC as off-line techniques for determining the number of signals in a possible mixture of propagating signals and noises. This includes specifying estimators for velocities and azimuths of the components along with their estimated uncertainties. Finally, the estimated velocities and azimuths enable deconvolutions producing separate estimators for each of the component waveforms. A set of MATLAB subroutines has been developed that can be merged into off-line software for investigative research purposes.

RESEARCH ACCOMPLISHED

Several algorithms, such as the sequential F-detector considered here and the MUSIC algorithm, are available that offer promise for handling array data with low signal-to-nose ratios and contamination from interfering signals. In this project, we have first investigated the performance of currently available algorithms on teleseismic and regional data containing mixed signals in order to demonstrate the superior performance of the sequential F-statistic. A sequential analysis of power using the F-statistic is employed that estimates the correct number of signals and their velocities and azimuths. This is contrasted with results using conventional F-K estimators that do not handle the mixed signal case.

Approaches to detecting signals on arrays all focus on the basic model that expresses the observed channel as sums of delayed signals and a unique noise process. The delays are functionally dependent on velocity and azimuth if the signals are propagating plane waves (this is the assumption that is usually made). Methods that are commonly in use for analyzing such data when a single signal is assumed to be present can be roughly categorized as (1) beam-forming and plotting the power as a function of slowness, which can be converted to estimators of velocity and azimuth, (2) beam-forming converted to an F-statistic by dividing by an estimator of the noise power (see Shumway, 1983; Shumway et al., 1999; Blandford, 2002, a, b) (3) Capon's estimator (see Capon, 1969), (4) MUSIC (Schmidt, 1979; Stoica and Nehorai, 1989) and (5) cross correlation (Tribuleac and Herrin, 1997). Only the MUSIC estimator listed above seems to be at all appropriate for analyzing the mixed signal case. The first four of the above estimators are available as the MATLAB subroutine *beam_sl.m*.

In the first year of this contract, we have concentrated on developing the multiple signal F-detector as an improvement over conventional detectors, such as those given above or the currently favored ratio of short term to long term mean squares (STA/LTA). The multiple signal F-detector fits successively higher order nonlinear regression models as the potential number of propagating signals or noises are increased. The number of propagating signals present is selected using the corrected information theoretic criterion of Hurvich and Tsai (1989). The software is available as the MATLAB subroutine *mul_sig_sl.m*. Technical difficulties in applying the Cramer lower bound approach to getting the variances has necessitated the use of the frequency domain bootstrap (Paparoditis and Politis, 1999) as an alternative. Software in the form of the MATLAB subroutine *mul_boot_sl.m* now computes the detection results along with standard deviations and confidence intervals for velocity and azimuth from the bootstrap distribution for data containing an arbitrary number of signals. Empirical results indicate that the distribution is approximately normal but this is not necessary for the validity of the bootstrap confidence intervals.

Analysis with Conventional Detectors

Conventional methods, such as 1–5 above, have met with varying degrees of success when they have been applied in practice in cases where there are known to be interfering signals. We can illustrate some of the pitfalls by considering the two events shown in Figures 1 and 2. Both events in this section were analyzed using the MATLAB software *beam_sl.*

Figure 1 shows one channel from the seven channels containing a mixture of two simultaneously occurring earthquakes, one from South Africa and the other from the Philippines, observed at the USAEDS long-period seismic array in Korea. The correct back-azimuths for these events are 226 degrees and 198 degrees. Yet simple

time delay estimation for this event gives a back-azimuth of 203 degrees, which is closer to the second of the above two signals but still off by 5 degrees. Beam forming or the F-statistic (equivalent to semblance) also produces an estimated azimuth of 203 degrees with a 95% confidence interval (200, 206), not including either of the known signals. The Capon and MUSIC estimators gave 207 and 212 degrees respectively, still between the two correct azimuths. However the analysis using AICC and the sequential F-detector in the next section shows that there are actually three signals (see Tables 1 and 2) in this mixture at 223 (South Africa) degrees, 200 (Philippines) degrees and 130 degrees (South Pacific storm).

Figure 2 shows a noisy event from China, namely the well-located event 1991101_1325, used by Stroujkova and Reiter (2006, these Proceedings). In this case, estimated azimuths were 284, 283, and 288 degrees respectively with velocities 8.1, 10.8 and 10.5 km/s, respectively. All detectors indicating a single signal used the full 50 s of data to retain sufficient degrees of freedom over the relatively narrow bandwidths for the signal (2Hz). The Capon and MUSIC estimators indicated second signals at 291 and 286 degrees with lower velocities (6.2, 6.6 km/s), probably corresponding to a later phase. An analysis of the noise preceding the signal over a lower frequency range indicated two noises, one at about 130 degrees and one at about 236 degrees using all methods. We will find in the next section that the signal band includes two signals (see Tables 3 and 4), one at 286 degrees and one at 148 degrees with relatively high confidence.

Analysis with the Multiple Signal F-Detector

The analysis of multiple signals involves considering a succession of nonlinear regression models written in the frequency domain with parameters expressed in terms of slowness. Beginning with the single-signal model with an estimated set of slowness coordinates, we consider an alternative model with two signals. The likelihood ratio test for a two-signal model against a single-signal model yields a monotone function of an F-statistic. The numerator is the difference between the error power under the two-signal model and the error power under the single-signal model and represents the reduction in power possible from the added signal. This reduction is scaled by the noise power under the full model and a function of the number of parameters and the error degrees of freedom. The sequential fitting of more signals continues one at a time until no more added signals are statistically significant. The final estimated velocities and azimuths are those obtained under the best model. Because the F-statistic at each stage involves the nonlinear parameter slowness, we use the corrected AIC, say AICC of Hurvich and Tsai (1989). The computations in this section were done using the MATLAB subroutine *mul_sig_sl.m*.

Standard errors and confidence intervals for velocities and azimuths are computed using the frequency domain bootstrap of Paparoditis and Politis (1999) adapted to the nonlinear regression case under the multiple-signal model. This involves reconstructing the frequency domain observations from the regression model evaluated at the maximum likelihood estimators for slowness. The residuals from this model will be roughly independent and constitute the basic resampling population. To reconstruct a bootstrap sample of the data, draw a sample of these residuals with replacement and use the nonlinear regression model to reconstitute a pseudo-sample of the observed data. The estimated velocity and azimuth computed from this pseudo-sample constitute the first pair of estimated parameters. Repeat the above procedure a large number of times (500) and retain the estimators. The sampling distribution of these estimators yields the standard deviations and the 95% confidence intervals shown in Tables 1–4 below. The bootstrap software can be accessed through the subroutine *mul_boot.m*.

Tables 1 and 2 show the results of the sequential F-tests applied to the long period event and give the confidence intervals resulting from the best model. Note that the first signal identified at azimuth 203 degrees accounts for 85% of the total power and still gives an estimated azimuth midway between the two known azimuths of the mixture. The F-detector is highly significant. Adding a second signal to the model substantially increases the percentage of power accounted for and still yields a highly significant F. Testing for the third signal again produces a highly significant F-statistic and increases the power accounted for to 98%. The fourth potential signal adds a negligible amount to the power accounted for and shows a fairly small F value which is still significant. However, because it only accounts for 1% additional power and the AICC values are minimized for the three-signal model, we take that model as our final configuration.

Table 1. Analysis of power for long period mixture. Sequential F-tests and AICC model selection.

Source	Added Power	F-Statistic	AICC	% Power
First Signal	396	36.3	-1.23	86
Second Signal	43	9.9	-1.86	95
Third Signal	14	7.9	-2.23	98
Fourth Signal	3	2.2	-1.59	99

Table 2 shows the estimated azimuths for the three component signals as 200, 223, and 130 degrees. The first two match up well with the known values but the third has not been identified from alternate records as a real seismic signal. Possibly this third signal is a coherent noise source; there was a known storm in the South Pacific at this time which corresponds to the third azimuth. Confidence intervals include the true azimuths for the two known earthquakes.

Table 2. Estimated velocities and azimuths for single-signal and best model for long period mixture. True azimuths are 226 and 198 degrees respectively. Confidence intervals are from the bootstrap distribution.

Model	Azimuth(Velocity)	95% Azimuth	95% Velocity
Single-Signal	203(3.85)	(200, 206)	(3.8, 3.9)
Three-Signal	200(3.5)	(196, 203)	(3.4, 3.6)
	223(3.9)	(218, 228)	(3.8, 4.0)
	130(4.0)	(125, 133)	(3.8, 4.1)

Tables 3 and 4 repeat the analysis on the regional earthquake from China recorded at the Korean Seismic Array (KSAR) analyzed by Stroujkova and Reiter (2006, these Proceedings) who noted the substantial noise present in the P and pP windows at approximately 150 degrees. The first channel for the China event, shown in Figure 2, exhibits the typical nature of regional recordings characterized by high noise levels and multiple arrivals. In this case, substantially less power is accounted for by the signal components than in the teleseismic case. The F-statistic and AICC settle on the two-signal model with the F-statistic marginally significant for the third signal. The third signal adds little power (4%) to the power accounted for and there is a clear minimum in the model selection criterion AICC at the two-signal model. The total power accounted for by the signal and noise only amounts to 54%.

Table 4 gives the estimated azimuths and velocities for the China event, and we note agreement between the single-signal and two-signal models. Note the smaller velocity for the noise component, namely in the neighborhood of 3 km/s. This is less than half that of the primary signal and may indicate that the noise is propagating more slowly than the primary signal. Note that this result agrees with the noise analysis preceding the signal that indicated estimated velocities in the 3–5 km/s range.

Table 3. Analysis of power for regional mixture. Sequential F-Tests and AICC model selection.

Source	Added Power	F-Statistic	AICC	% Power
First Signal	251	7.5	-.0485	32
Second Signal	138	5.2	-.2067	50
Third Signal	.30	1.2	-.1223	54

Table 4. Estimated velocities and azimuths with 95% confidence intervals for China event.

Model	Azimuth(Velocity)	95% Azimuth	95% Velocity
Single-Signal	286.1(8.1)	(284.9, 287.9)	(8.0, 8.3)
Two-Signal	286.4(8.1)	(285.2, 287.9)	(7.9, 8.2)
	148.1(3.0)	(145.9, 149.7)	(2.9, 3.2)

Deconvolution of Component Signals and Noises

Figures 1 and 2 give the estimated signals that follow from the velocities and azimuths implied by Figures 1–4. The deconvolutions are done using the MATLAB subroutine *mul_decon.m*.

The most prominent signal is from South Africa (228 degrees) and clearly shows in the region between 800 and 11,400 points (30 s). The smaller signal from the Philippines (196 degrees) is less prominent and appears to model parts not accounted for by the first signal. The noise component fills in the region before the first signal and accounts for the burst at the end of the data.

The second deconvolution corresponding to the two components noted in the previous section gives the estimated signal and noise components in the regional data. The estimated noise component from 148 degrees shows the character of the low frequency noise before the signal enters. The estimated signal from 286 degrees shows the depth phase pP much more clearly than does the single channel mixture. In this case, one obtains from the plot a delay of about 4.6 s, which is comparable to that obtained by Stroujkova and Reiter (2006). We also note the noise reduction capabilities of the two-signal beam.

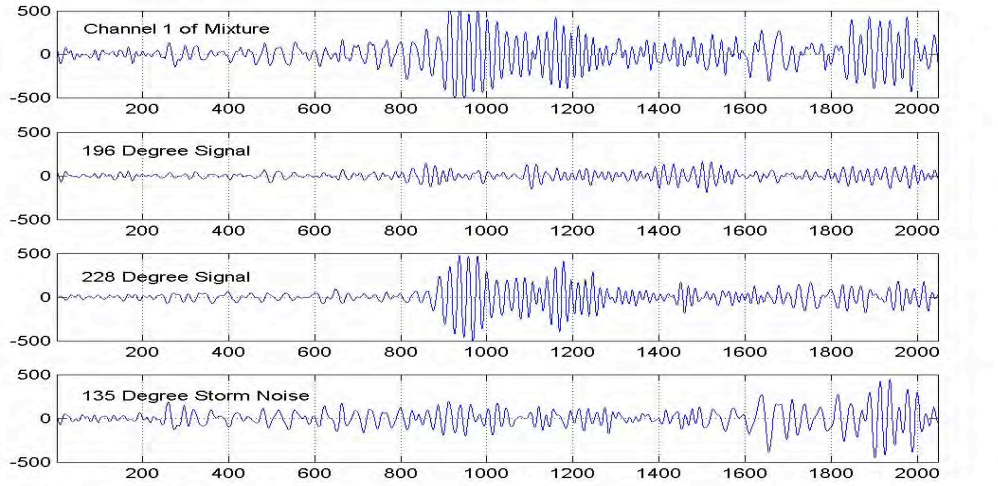


Figure 1. Deconvolution for long-period mixture of two signals and a noise source.

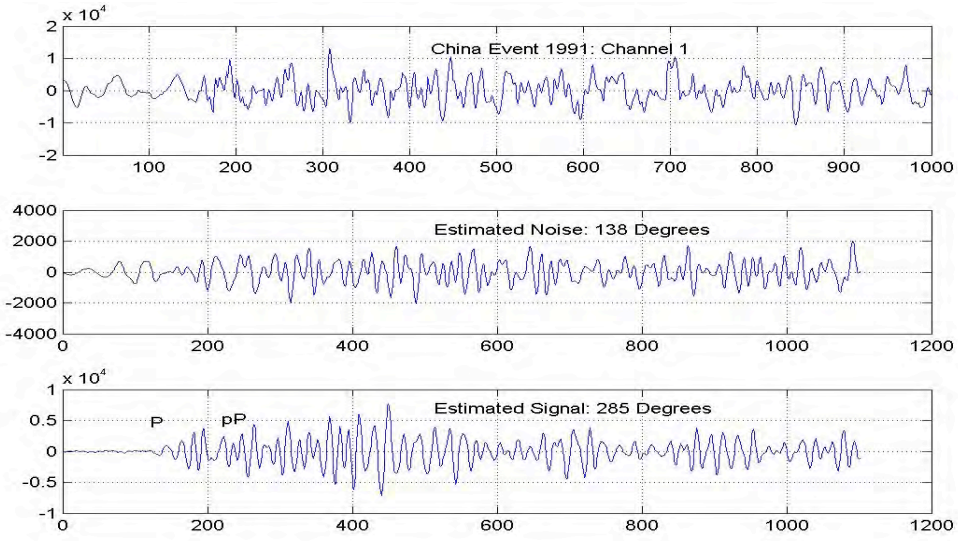


Figure 2. Deconvolution of 1991 China event containing a signal from 285 degrees and an apparent noise source.

CONCLUSIONS AND RECOMMENDATIONS

This work was primarily motivated by the problem of detecting mixtures of signals on teleseismic and regional arrays. Such undetected mixtures are shown to give incorrect velocities and azimuths when treated by traditional single-signal detection methods based on cross-correlation or frequency wave-number methods. Furthermore, the separation of interfering phases and coherent noise sources should improve detection statistics and lead to improvements in location and magnitude estimates.

Using current improved computing platforms, such as MATLAB, makes the nonlinear estimation problems implicit in multiple-signal modeling tractable and easy to implement. Using early work involving multiple-signal estimation (Shumway, 1970) and its extensions to wave-number methods (Smart, 1972, 1976), we are able to formulate the problem in a regression framework that leads to a sequential detection approach for reliably determining the number of signals and coherent noises present along with their estimated velocities and azimuths. We have provided methods for comparing detection performance using the F-statistic, the AICC model selection statistic, and confidence intervals for the velocities and azimuths using the bootstrap. Finally, we have show that the regression model provides a method for deconvolving the component signals and have shown results for both long and short period seismic data.

ACKNOWLEDGEMENTS

Gene Smart and Dean Clauter of the Air Force Technical Applications Center (AFTAC) have graciously provided the data used in this analysis as well as valuable insights into potential methods of analysis. In particular, the previous seminal work of Smart (1972, 1976) is gratefully acknowledged. I am grateful to Anastasia Stroujkova and Delaine Reiter of Weston for providing the data from the regional Chinese event and making available their preprint.

REFERENCES

Blandford, R. R. (2002a). Detection and azimuth estimation by infrasonic arrays as a function of array aperture and signal coherence, Air Force Technical Applications Center AFTAC-TR-02-007.

Blandford, R. R. (2002b). A plan of development for detection systems for seismic and infrasound arrays. Air Force Technical Applications Center AFTAC-TR-02-005.

Capon, J. (1969). High-resolution frequency-wavenumber spectrum analysis. *Proc. IEEE*, 57: 1.408–1.418.

Hurvich, C. M. and C.-L. Tsai (1989). Regression and time series model selection in small samples. *Biometrika* 76: 297–307.

Paparoditis, E. and D. N. Politis (1999). The local bootstrap for periodogram statistics. *J. Time Series Anal.* 20: 193–222.

Schmidt, R. O (1979). Multiple emitter location and signal parameter estimation, in *Proceedings of the RADC Spectral Estimation Workshop*, pp. 243–258.

Shumway, R. H. (1970). Applied regression and analysis of variance for stationary time series. *J. Amer. Statist. Assoc*. 65: 1,527–1,546

Shumway, R. H. (1983). Replicated time series regression: An approach to signal estimation and detection. *Handbook of Statistics 3*: *Time Series in the Frequency Domain*, D. R. Brillinger and P. R. Krishnaiah (Eds.). Ch. 18, pp. 383–408.

Shumway, R. H., S. E. Kim and R. R. Blandford (1999). Nonlinear estimation for time series observed on arrays. Ch. 7 in *Asymptotics, Nonparametrics and Time Series*, S. Ghosh (Ed.). New York: Marcel Dekker, pp. 227–258.

Smart E. (1972). FKCOMB, A Fast General-Purpose Array Processor, *Seismic Array Analysis Center*, Teledyne Geotech, 20 December 1972.

Smart, E. (1976). Linear high-resolution frequency-wavenumber analysis, Ph,D. dissertation, Southern Methodist University.

Stoica, P. and A. Nehorai (1989). Music, maximum likelihood, and Cramer-Rao lower Bound, *IEEE Trans. Acoustics, Speech and Signal Processing* 37: 720–741.

Stroujkova, A. and D. Reiter (2006). Improving focal depth estimates: Studies of depth-phase detection at regional distances, in current Proceedings.

Tribuleac, I. M. and E. T. Herrin (1997). Calibration studies at TXAR, *Seis. Res. Lett.* 68: 353–365.

Pn TOMOGRAPHY, GEOPHYSICAL MODELS, CROSS CORRELATION, AND LOCATION IN EURASIA

Lee K. Steck[1], Hans E. Hartse[1], Monica Maceira[1], Jonathan K. MacCarthy[1], Charlotte A. Rowe[1], W. Scott Phillips[1], Kevin G. Mackey[2], Kazuya Fujita[2], Michael L. Begnaud[1], and Diane F. Baker[1]

Los Alamos National Laboratory[1] and Michigan State University[2]

Sponsored by National Nuclear Security Administration
Office of Nonproliferation Research and Development
Office of Defense Nuclear Nonproliferation

Contract Nos. W-7405-ENG-36[1] and DE-FC52-2004NA25540[2]

ABSTRACT

This paper covers several facets of the location and geophysical modeling efforts at Los Alamos National Laboratory (LANL). In location we continue to develop kriged correction surfaces for Eurasian stations and show results from relocations of GT25 or better events using small (3 to 10 station) regional networks in Asia. With empirical corrections, locations for 70% of tested events were improved using first P only, while 82% improved using first P and first S arrivals. We are exploring model-based corrections using velocity models derived from Pn tomography of China and Siberia. Relocations in Asia using travel times calculated from Pn velocity perturbations show a 10-30% improvement over IASPEI91 travel times alone; similar tests will be performed in northeastern Asia. Pn tomography in northeastern Asia indicates higher velocities under the Siberian platform, with generally lower velocities under regions of more active tectonics. In Central Asia, we are using correlation repicking, satellite imagery and pattern recognition software to identify potential mines and tie correlated seismic events to mining locations. The pattern recognition software has identified several mining locations that we are linking to clusters of correlated seismic events, which are identified from the Kazakh National Data Center (KNDC) bulletins. For geophysical models, we have recently developed a new joint inversion method using gravity and surface wave group velocity data. This method has been applied to the Tarim and Junggar basins and shows high upper mantle velocities beneath the Tarim, with differences in lower-crust and upper-mantle shear velocities between the eastern and western Tarim.

OBJECTIVES

The objective of these studies is to improve our ability to locate and discriminate seismic events in Asia. Our approach relies on the acquisition of ground truth (GT) for empirical corrections and the development of regional velocity models upon which travel time, azimuth, and slowness correction surfaces can be built. In this paper we present results from model development in Siberia and the Tarim Basin, identification of mining explosions in central Asia, and regional station calibration in Asia.

RESEARCH ACCOMPLISHED

Regional Station Calibration in Asia

We are exploring the location performance of small, poorly configured regional seismic networks in Asia. Our stations have been calibrated using GT ranging from 1 km to 25 km, and typical relocations involved from 3 to 12 stations using both primary and secondary phases. Stations and events used in the tests are shown in Figure 1. Network performance is shown in Figures 2 and 3.

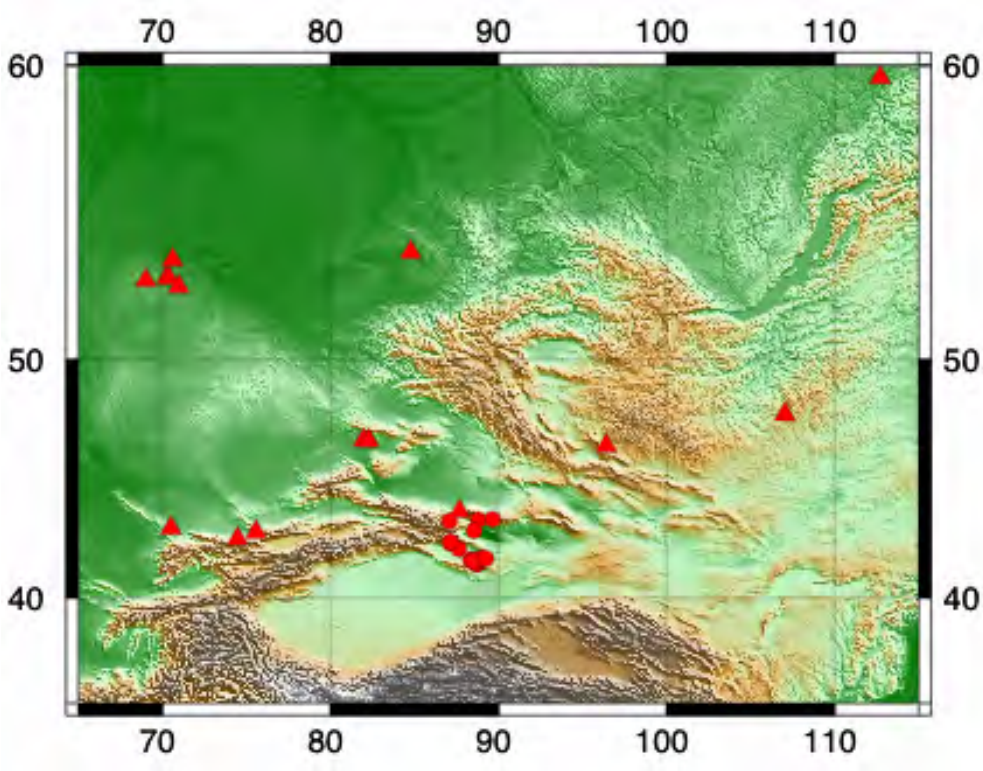


Figure 1. Stations (triangles) and events (circles) used in our tests.

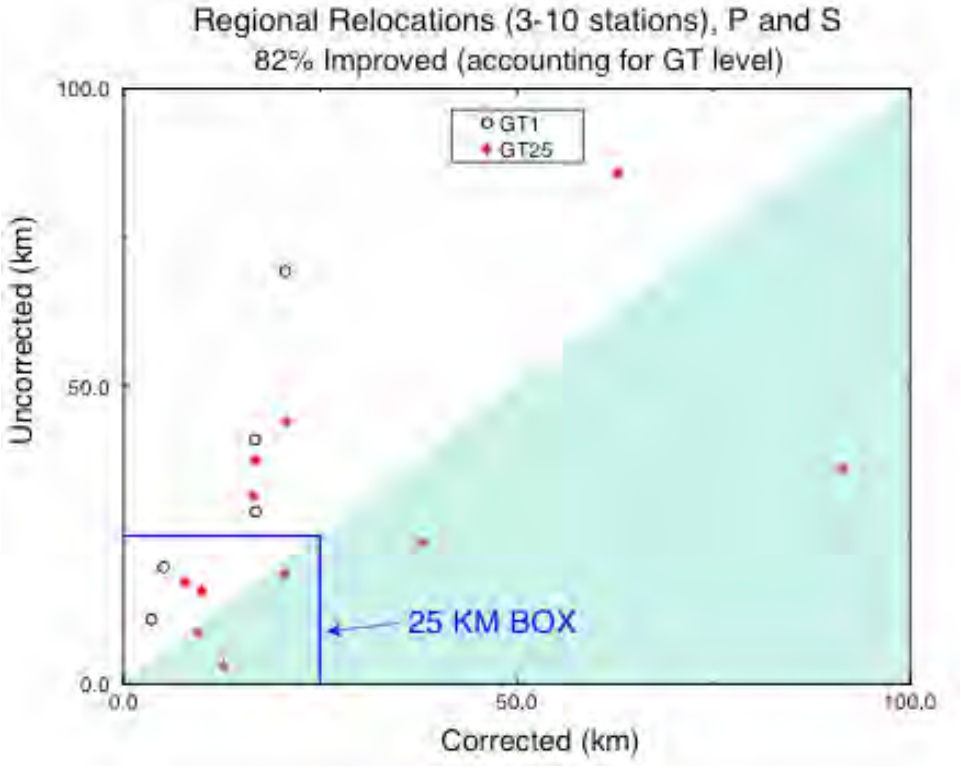


Figure 2. Network performance comparing mislocations using kriged travel time correction surfaces to mislocations with no corrections.

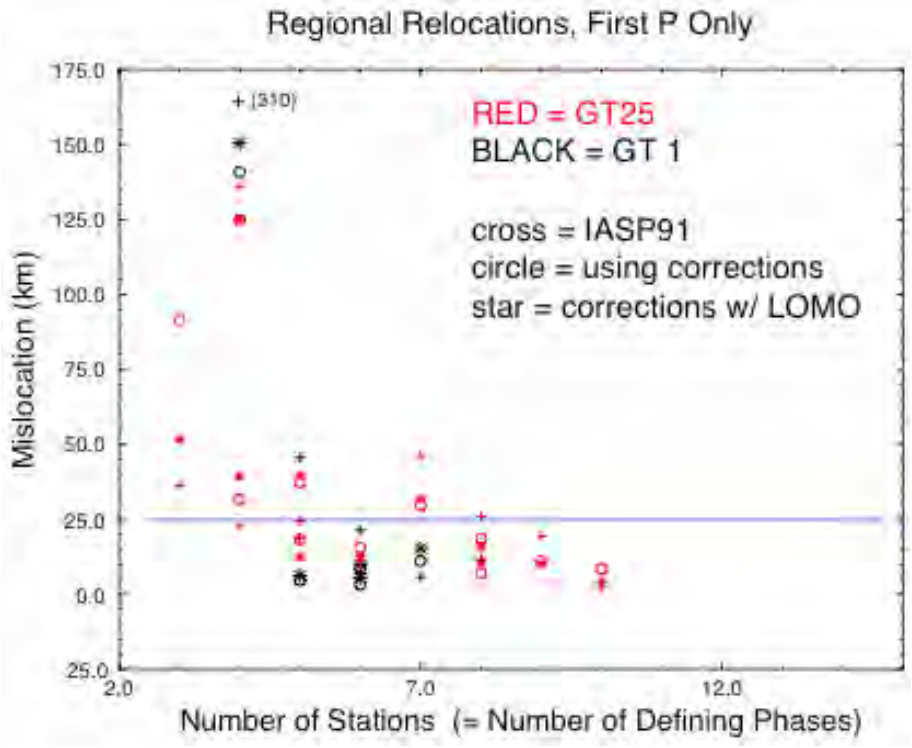


Figure 3. Mislocations with IASPEI91 only (crosses), kriged correction surfaces (circles), and leave-one-out relocations with correction surfaces (stars). In these tests, only first P was used. The blue line indicates a mislocation of 25 km.

Pn Tomography of Siberia

We have applied the method of Phillips et al. (2005) to invert for Pn velocities in Siberia (Steck et al., 2005). We apply the technique to events from the Michigan State University eastern Russia seismic database, following a relocation of the full catalog within a consistent base model (IASPEI91) and incorporation and association of phase arrivals from other sources where applicable. For this study we restrict our test to source-receiver distance of 2 – 20 degrees. The eastern Russia database provides us with differential raypaths for 459 stations, yielding 27,291 station pair combinations with a catalog of 65,489 earthquakes between 45^{o} and 80^{o} N, 100^{o} to 175^{o} E. This resulted in 666,387 differential paths from which to invert for the Pn slowness perturbations and station corrections. Pn tomography in northeastern Russia indicates higher velocities under the Siberian platform, with generally lower velocities under regions of more active tectonics (Figure 4).

Joint Inversion of Surface Wave and Gravity Data in the Tarim Basin

We implement and apply a method to jointly invert surface-wave group velocities and free-air gravity observations. Surface-wave dispersion measurements are sensitive to seismic shear-wave velocities, and the gravity measurements supply constraints on rock density variations. Our goal is to obtain a self-consistent three-dimensional shear-velocity-density model with increased resolution of shallow geologic structures. To obtain the 3-D shear-wave velocity model we parameterize it in terms of one-dimensional (1-D), depth-dependent velocity profiles determined at the center of each cell in a grid of 1° by 1°. In each cell we consider two sets of data points: fundamental-mode group velocities and free-air gravity anomalies. Our approach to joint inversion is very similar and basically follows the scheme described by Julià et al. (2000), except for the implementation of gravity anomaly contributions.

We apply the method to investigate the structure of the crust and upper mantle beneath two large central Asia sedimentary basins: the Tarim and Junggar. The basins have thick sediment sections that produce substantial

regional gravity variations (up to several hundred mGal). We used gravity observations extracted from the global gravity model derived from the Gravity Recovery and Climate Experiment (GRACE) satellite mission (Tapley et al., 2005). We combine the gravity anomalies with high-resolution surface-wave slowness tomographic maps that provide group velocity dispersion values in the period range between 8 and 100 s for a grid of locations across central Asia. To integrate these data, we use a relationship between seismic velocity and density constructed through the combination of two empirical relations: one determined by Nafe and Drake (1963), most appropriate for sedimentary rocks, and a linear Birch's Law (Birch, 1961) more applicable to denser rocks (the basement) (Figure 4). An iterative, damped least squares inversion including smoothing is used to jointly model both data sets, using shear-velocity variations as the primary model parameters.

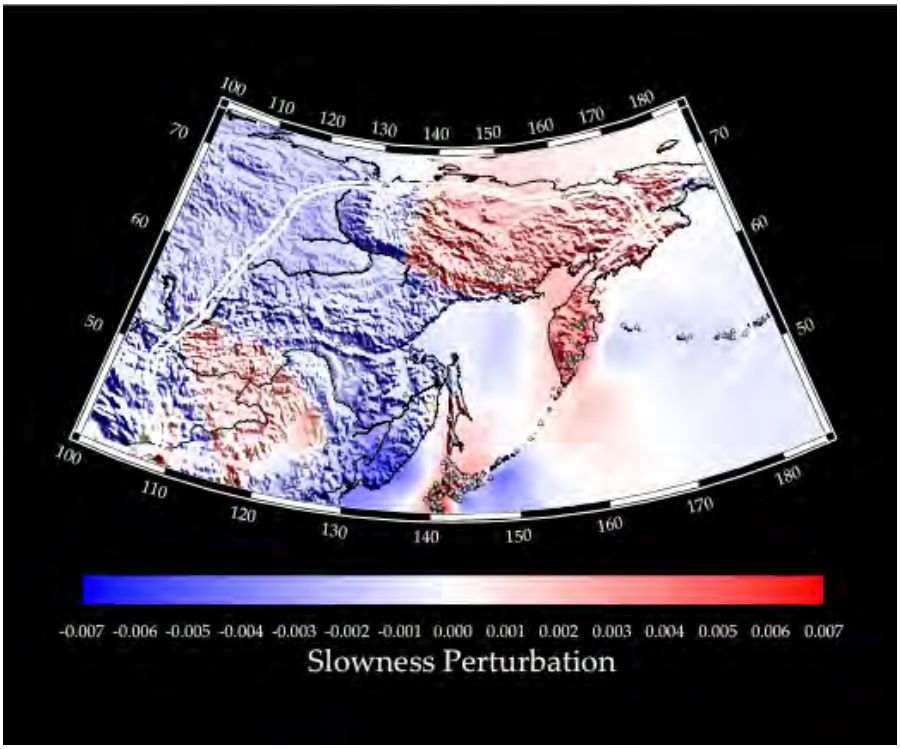


Figure 4. Pn tomography results for northeastern Russia from Rowe et al., 2006.

Results show high upper-mantle shear velocities beneath the Tarim basin and suggest differences in lower-crust and upper-mantle shear velocities between the eastern and western Tarim (Figure 5). At shallow depths, the images are dominated by slow velocities in the Tarim and Junggar basins. This is a predictable result because of the clear presence of low velocities associated with the known major sedimentary basins in the tomographic images at short periods (Maceira et al., 2005). However, the seismic structure in these basins shows slower velocities than without including the gravity in the inversion process. We think that this is an improvement of our 3-D model since seismic discrimination has proven the need for slower velocities at shorter periods (i.e., shallower layers) in those sedimentary basins (see Acknowledgements). Velocity images at mid-crustal depths show differences between eastern and western Tarim. Deeper in the crust and upper mantle, fast velocity regions are found beneath the basins. This is usually interpreted as an indication of old, cold, thick lithospheric blocks that have not been greatly deformed or modified by tectonic activity since their emplacement. The upper mantle velocity slice at 55-km depth shows once more differences between the east and west part of the Tarim basin. In this case, western Tarim displays faster velocities than the eastern side, in good agreement with previous observations (Liang and Song, 2004; Sun and Toksöz, 2006). Depth slices at deeper depths are somewhat puzzling. It could be that the near-surface model cannot explain the higher wavenumber data in the GRACE observations and these then get mapped to greater depths where constraints are weaker. Future work will seek even better models. This could be accomplished by reducing the grid sampling and using many more cells or with additional lateral smoothing with depth (based on the wavelengths that sample those depths). The value of jointly inverting surface wave and gravity data is clear (Figure 6). It is well known that traditional inversion techniques of surface wave dispersion data for seismic structure suffer from poor

resolution and non-uniqueness, especially when a single surface wave mode is used. Joint inversion approaches can help alleviate the problem (Figure 7).

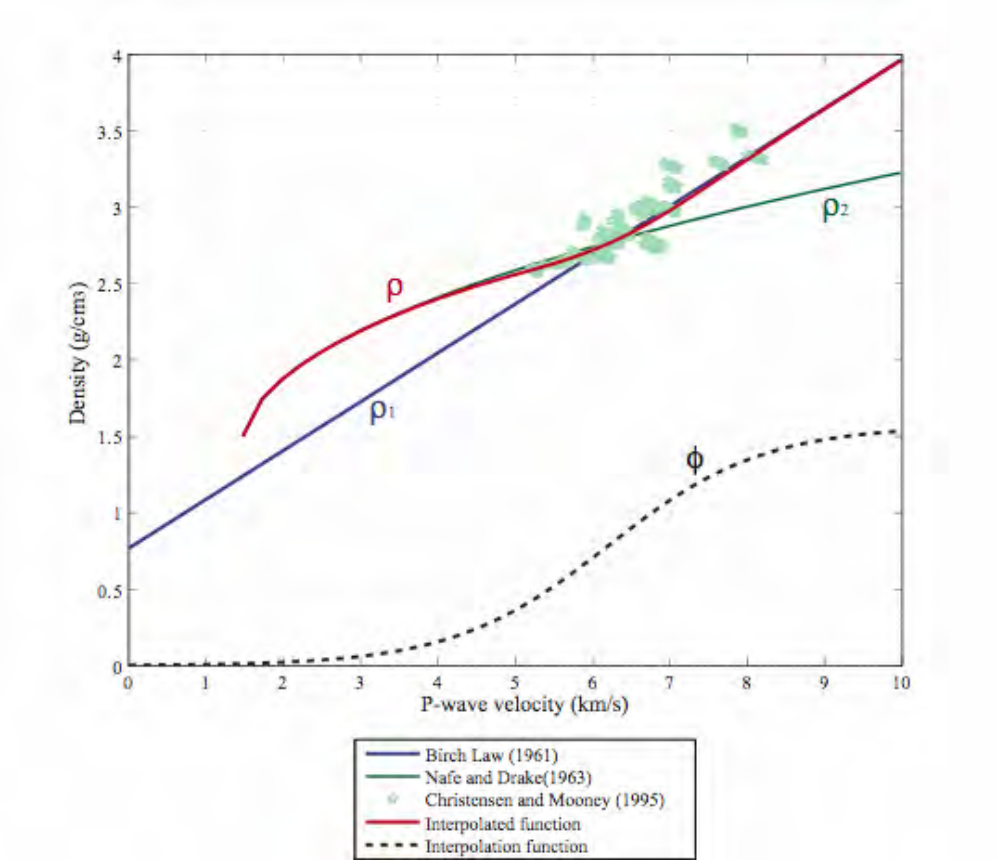


Figure 5. Relationships between P-wave velocity and density used in this study. The solid green line is Onizawa et al. (2002) polynomial fit to laboratory measurements on sediments and sedimentary rocks summarized by Nafe and Drake (1963). The solid blue line is the empirical linear relationship known as Birch's law (1961). Using the interpolation function represented by the dashed black line, we constructed our own relationship by combination of the two empirical ones. The interpolated function is represented by the solid red line. Light green stars are rock measurements performed by Christensen and Mooney (1995) at different depths and temperatures.

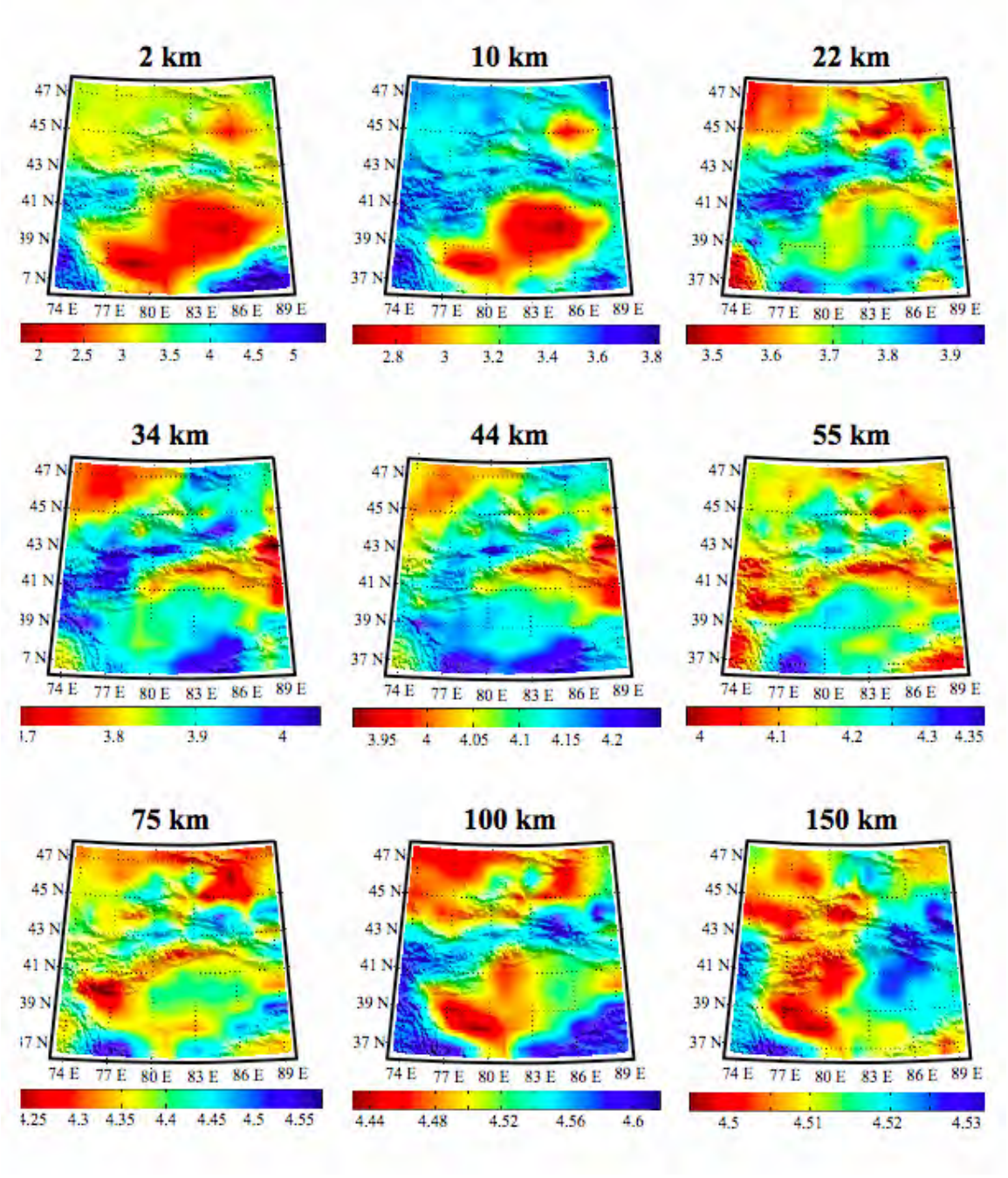


Figure 6. S-wave velocity model at constant depth slices. The depth of each image is shown at the top of each map. Velocity values are expressed in km/s. Note the color scheme is different for each image.

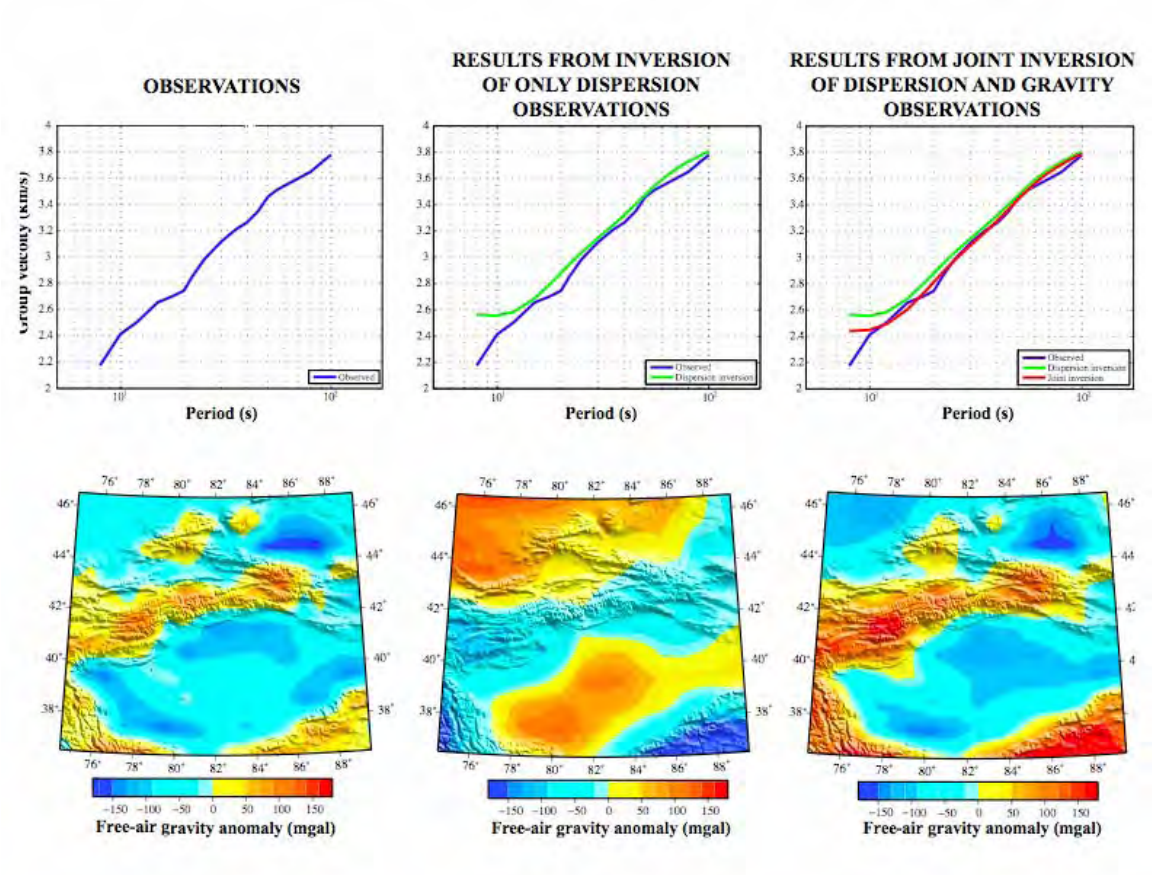


Figure 7. Comparison of data fits from the inversion of only surface wave dispersion observations and from the joint inversion of dispersion and gravity observations. Top panels from left to right: surface wave dispersion data for a typical cell (blue line); fit to the dispersion data from inverting only dispersion data (green line); fit to the dispersion data from the joint inversion (red line). Bottom panels from left to right: GRACE data for the region under study; predicted free-air gravity anomalies from the model resulting from inverting only dispersion observations; predicted free-air gravity anomalies from the model resulting from the joint inversion.

Mining Explosions in Central Asia

In this effort we are exploring the combined use of correlation arrival time picking using the cross-coherency-correlation method of Rowe et al. (2002) and the clustering/stacking approach of Rowe et al. (2004), in combination with satellite imagery to identify mining locations and repeating events in central Asia. The goals of this effort are: (1) build seismicity catalogs of GT mining explosions, (2) create libraries of mine images, (3) create libraries of reference waveforms to accommodate the catalogs and images. Figure 8 shows bins of event origin time-of-day reported in Kazakh National Data Center bulletins and reveals areas where presumed man-made sources dominate the seismicity (gold and yellow bins). By identifying highly correlated waveforms at both array MKAR and station KURK we have identified events whose origins must be similarly located (Figure 9). Relocations of the events using the cross correlation re-picks identifies tight clusters that can be tied to mine locations (Figure 10). We are using a pattern recognition algorithm, GENIEPro, trained on known mining sites (Figure 11), to identify new mine locations in satellite imagery based on association of identified spatial patterns and features common to both known mine sites and new areas of interest. We plan to tie the re-picked and re-located seismicity to these mine locations. Future work where we will use our assembled GT information includes mining explosion discrimination studies, traveltime correction surface refinement, and azimuth correction surface estimation.

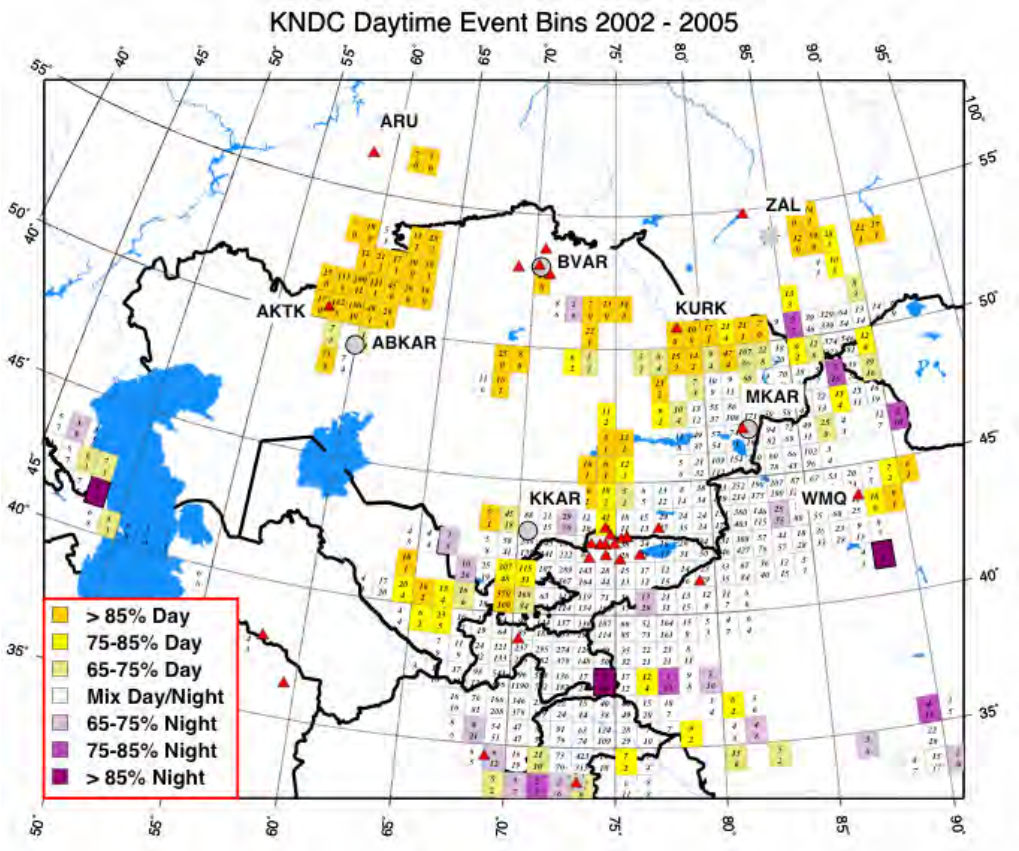


Figure 8. Time-of-day bins for KNDC seismicity.

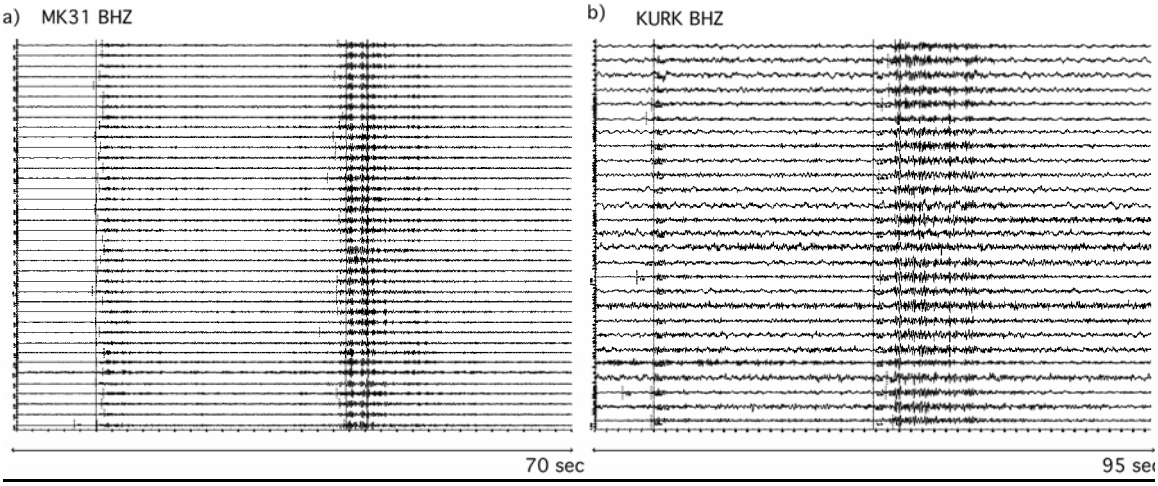


Figure 9. Correlated seismic events in Central Asia, presumed to originate at a mine. Aligned waveforms from stations MK31 (a) and KURK (b) are shown.

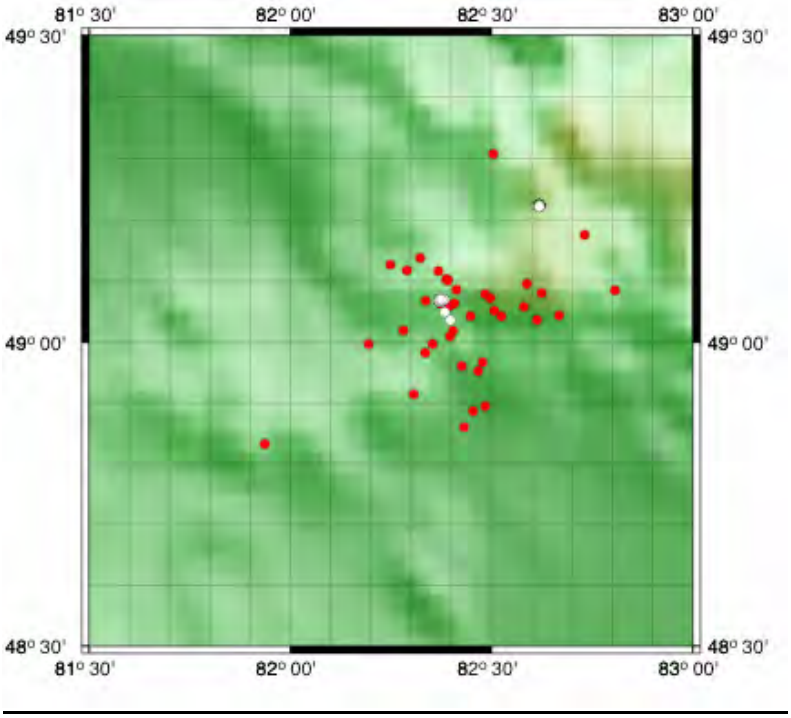


Figure 10. Catalog locations (red circles) and our relocations using correlation picks (white circles).

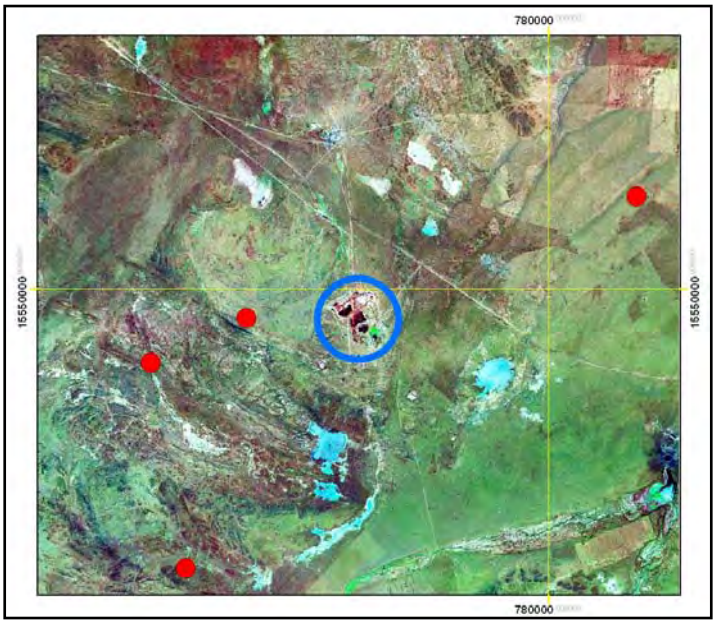


Figure 11. Satellite image showing a mine location in Central Asia. Red circles are catalog seismic locations.

CONCLUSIONS AND RECOMMENDATIONS

We continue to expand our research efforts to improve discrimination and location in Asia. We present new methods of model development that improve location ability in Asia. In addition, synergistic efforts combining seismics, satellite imagery and pattern recognition software show great promise. We recommend these efforts be continued and expanded.

ACKNOWLEDGEMENTS

We gratefully acknowledge valuable discussions with Howard H. Patton.

REFERENCES

Birch, F. (1961). The velocity of compressional waves in rocks to 10 kilobars, Part 2, *J. Geophys. Res.* 66: 2199–2224.

Christensen, N. I. and W. D. Mooney (1995). Seismic velocity structure and composition of the continental crust: A global view, *J. Geophys. Res.* 100: 9761–9788.

Julià J., C. J. Ammon, R. B. Herrmann, and A. M. Correig (2000). Joint inversion of receiver function and surface wave dispersion observations, *Geophys. J. Int.* 143: 99–112.

Liang, C., X. Song, and J. Huang (2004). Tomographic inversion of Pn travel times in China, *J. Geophys. Res.* 109: B11304, doi:10.1029/2003JB002789.

Maceira, M., S. R. Taylor, C. J. Ammon, X. Yang, and A. A. Velasco (2005). High-resolution Rayleigh wave slowness tomography of central Asia, *J. Geophys. Res.* 110: B06304, doi:10.1029/2004JB003429.

Nafe, J. E., and C. L. Drake (1963). Physical properties of marine sediments, in *The Sea*, Vol. 3, edited by M. N. Hill, pp. 794–815: Interscience, New York.

Onizawa, S., H. Mikada, H. Watanabe, and S. Sakashita (2002). A method for simultaneous velocity and density inversion and its application to exploration of subsurface structure beneath Izu-Oshima volcano, Japan, *Earth Planets Space*, 54: 803–817.

Phillips, W. S., C. A. Rowe, and L. K. Steck (2005), The use of interstation P wave arrival time differences to account for regional path variability, *Geophys. Res. Lett.* 32: L11301, doi:10.1029/2005GL022558.

Rowe, C.A., R. C. Aster, B. Borchers, and C. J. Young (2002), An automatic, adaptive algorithm for refining phase picks in large seismic data sets, *Bull. Seismol. Soc. Amer.* 92: 1660–1674.

Rowe C., H. Thurber, and R. A. White (2004). Dome growth behavior at Soufriere Hills Volcano, Montserrat, revealed by relocation of volcanic event swarms, 1995-1996, *Jour. Volc. Geotherm. Res.* 134: 199–221.

Rowe, C., L. Steck, W. Phillips, M. Begnaud, R. Stead, H. Hartse, K. Mackey, and K. Fujita (2006). Pn tomography and location in Eurasia, Proceedings, 24th General Assembly of the International Association of Seismology and Physics of the Earth's Interior, October, 2005, Santiago, Chile.

Steck, L.K., Rowe, C.A., W.S. Phillips, H. Hartse, K. Mackey, and K. Fujita (2005). Differential travel-time Pn tomography in northeast Asia, *EOS*, Transactions, AGU. 86: (52), Fall. Meet. Suppl., Abstract T54A-02.

Sun, Y. and M. N. Toksöz (2006). Crustal structure of China and surrounding regions from P wave traveltime tomography, *J. Geophys. Res*. 111: doi:10.1029/2005JB003962.

Tapley, B., J. Ries, S. Bettadpur, D. Chambers, M. Cheng, F. Condi, B. Gunter, Z. Kang, P. Nagel, R. Pastor, T. Pekker, S. Poole, and F. Wang (2005). GGM02 - An improved Earth gravity field model from GRACE, *J. Geodesy*, DOI 10.1007/s00190-005-0480-z.

REGIONAL DEPTH-PHASE DETECTION AND FOCAL DEPTH ESTIMATION: APPLICATION TO EVENTS IN SOUTHEAST ASIA

Anastasia Stroujkova and Delaine Reiter

Weston Geophysical Corporation

Sponsored by National Nuclear Security Administration
Office of Nonproliferation Research and Development
Office of Defense Nuclear Nonproliferation

Contract No. DE-FG02-03ER83820

ABSTRACT

The accurate estimation of the depth of small, regionally recorded events continues to be an important and difficult monitoring research problem. Our previous studies on detecting regional-distance depth phases using cepstral techniques have yielded only a moderate level of success. Therefore, we are investigating other waveform characteristics and detection techniques that can enhance the accuracy of regional focal depth estimation. In particular, we are combining enhanced signal processing in the complex *Pn* coda of regional seismograms, sparse-network hypocenter locations, and surface-wave inversions for depth and focal mechanism to determine an event's focal depth.

Our work during the preceding year was two-fold. First, we continued research into developing improved array-processing techniques for regional depth-phase detection. The cepstral F-statistic method that we have employed in the past (Bonner et al., 2002) cannot be used to reliably identify depth phases on its own. Other evidence must be used to help determine whether the phase in question is truly a depth phase. For example, apparent velocities, amplitudes and the frequency content of both the direct arrival and suspected surface reflections should be taken into consideration. We used a variety of array methods to estimate apparent phase velocities, including beam-forming, semblance analysis, MUltiple SIgnal Classification (MUSIC) (e.g., Capon, 1969; Schissele et al., 2004), and cross-correlation (e.g., Cansi, 1995; Tibuleac and Herrin, 1997). To facilitate the processing and comparison of results, we developed a MATLAB-based processing tool, which allows application of the various techniques in a single environment.

The second part of our research effort involved the comparison of different depth estimates obtained by both body- and surface-wave techniques. For example, we used a grid-search, multiple-event location method (Rodi, 2005) to estimate hypocenters from body-wave arrivals observed on sparse networks of regional stations. We studied the influence of different factors on the resulting focal depth estimate, such as the velocity model and network geometry. In addition, we applied surface-wave analysis, which can also be used to determine event focal mechanism (Herrmann, 2002), to our regional network data. The surface-wave analyses in turn can provide useful information on the relative amplitudes of the direct and surface reflected arrivals.

To validate our approach and provide quality control for our solutions, we applied the techniques to moderated-sized events (m_b ~ 4.5-6.0) with independently determined focal mechanisms. In this paper we illustrate the techniques using regional events observed at the KSAR (Wonju, South Korea) teleseismic array and other nearby broadband three-component stations. Our results indicate that the techniques can produce excellent agreement between the various depth estimates. However, in some cases there remains great variability between different depth estimates. This variability (as expected) is strongly related to validity of the velocity model employed, and to a lesser extent the recording station coverage.

OBJECTIVES

The accurate identification of regional seismic depth phases such as *pPn* and *sPn* is a formidable task. Depth phases are the primary tool that seismologists use to constrain the depth of a seismic event. When depth phases from an event are detected, an accurate source depth is easily found by using the delay times of the depth phases relative to the *P* wave and a velocity profile near the source. Some of the available techniques to determine source depth from depth-phase data include body-wave modeling (Saikia and Helmberger, 1997; Goldstein and Dodge, 1998), beam forming (Murphy et al., 1999; Woodgold, 1999), and relative-amplitude techniques (Pearce, 1977). In our previous studies, we have utilized the seismic cepstrum, which is defined as the Fourier transform of the log of the spectrum of a time domain signal (Bogert et al., 1963; Oppenheim and Schafer, 1975). The cepstrum is designed to detect the periodicity that occurs in the power spectrum when echoes are present in the original signal due to the interference of the direct (*P*) and depth (*pP* and/or *sP*) phases.

Reiter and Shumway (1999) formulated a cepstral F statistic for depth estimation problems using a classical approach to detecting a signal in a number of stationarily-correlated time series. The method attaches a statistical significance level to peaks in the beamed cepstra of seismic data caused by echoes in the signal. The results provided in Bonner et al. (2002) suggest that the cepstral F-statistic method (CFSM) is best applied at epicentral distances greater than 15°, where teleseismic *pP* and *sP* are the most commonly observed depth phases. However, the determination of depth at regional distances for small-to-intermediate sized crustal depth events remains an important, difficult and unsolved seismological problem.

To address this deficiency in regional depth estimation, we have developed three techniques to obtain regional focal depth estimates. These techniques include ‘assisted’ cepstral processing, sparse-network travel-time locations and surface-wave dispersion inversion. To demonstrate our techniques, we have applied them to moderate-sized events located within regional distances of the KSAR seismic array in South Korea. Only regional stations were used in the processing in order to mimic small events recorded by a limited number of regional stations.

RESEARCH ACCOMPLISHED

Enhanced Cepstral Processing: Application to KSAR Data

As we noted in the previous section, the CFSM (Bonner et al., 2002) cannot be used to reliably identify regional depth phases on its own. While pre-processing techniques such as wavelet denoising have shown some promise in improving cepstral estimates, additional evidence must be used to confirm whether a phase detected by the CFSM is truly a depth phase. For example, apparent velocities, amplitudes and the frequency content of both the direct arrival and suspected surface reflections should be taken into consideration. Therefore, to estimate apparent phase velocities and back azimuths of *Pn* coda arrivals we have tested a variety of array methods, including beam-forming, semblance analysis, MUltiple SIgnal Classification (MUSIC) (Capon, 1969; Schisselé et al., 2004), and cross-correlation (Cansi, 1995; Tibuleac and Herrin, 1997). To facilitate the array processing and comparison of results, we developed a MATLAB-based processing tool, which allows application of all of these techniques in a single environment. Optional pre-processing tools in our MATLAB Graphical User Interface (GUI) include glitch removal, Fourier filtering, and wavelet denoising. This useful new tool is proving to be very adaptable; for example, we are also using it to identify upper-mantle triplicated *P*-wave phases observed at far-regional distances.

To illustrate our depth phase identification techniques at regional distances, we applied them to well-located events observed at regional distances from the KSAR (Wonju, South Korea) teleseismic array and other nearby broadband three-component stations. Five of the events have known focal mechanisms from the Harvard Centroid Moment Tensor (CMT) catalog (Figure 1). Table 1 provides the parameters of the events used in this study, including the depth estimates from the International Seismic Centre (ISC), the Experimental International Data Center (EIDC), and Harvard catalogs.

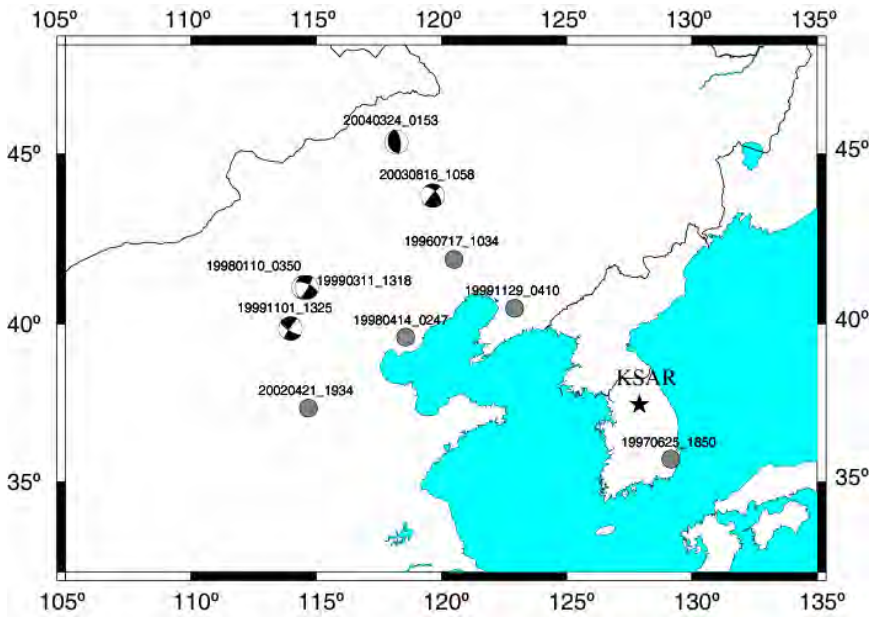


Figure 1. Map showing the locations of study events. Focal mechanisms are shown for the events with available Harvard CMT solutions

Table 1. List of study events recorded at KSAR, with the ISC epicenter and the depths published by the ISC, EIDC and Harvard catalogs. Epicenter locations and magnitudes are given by ISC, with the exception of the event 20040324_0153 (EIDC).

Event Origin (ymmdd_hhmm)	Lat, ºN	Lon, ºE	Depth			m_b
			ISC	EIDC	Harvard	
Events with Harvard CMT						
19980110_0350	41.14	114.52	16.7	4.8	15	5.3
19990311_1318	41.16	114.69	27	17	33	4.5
19991101_1325	39.91	114.05	0.0	10	15	4.7
20030816_1058	43.81	119.74	23.2	8.8	30	4.7
20040324_0153	45.38	118.15	…	18	13	5.4
Other events						
19960717_1034	42.00	120.48	0.0	15.7	…	4.4
19970625_1850	35.75	129.17	13.5	13.5	…	4.2
19980414_0247	39.73	118.74	0.0	23.0	…	4.2
19991129_0410	40.39	122.95	38.6	10.0	…	4.5
20020421_1934	37.43	114.77	23.9	24.0	…	4.3

In previous work, Reiter et al. (2004) demonstrated the benefits of using wavelet denoising before applying the CFSM. Figure 2 shows the results from applying the CFSM with and without wavelet denoising to two of the events in Table 1. Both event records exhibit typical regional Pn with long codas and no clear depth phase candidate. Event 19991101_1325, shown in Figure 2a, has significant pre-event noise. After applying wavelet denoising in the 6th-level decomposition, the pre-event noise is removed; however, the coda behavior doesn't change significantly (Figure 2b). The cepstral F-statistic of the wavelet-denoised

trace is almost identical to the one performed on the raw data; i.e., both results retain several false cepstral peaks.

Figures 2c and 2d show the results for Event 20020421_1934. For this example, the wavelet denoising at the 5th decomposition level removes a significant amount of *Pn* coda energy. The cepstral F-statistic also shows fewer false hits for the denoised data. The correct *pPn* arrival is one of the cepstral peaks, and it can be clearly identified on the seismic trace because of its similarity to the direct arrival. Note that both events appear to have complex source-time functions with more than one peak. In both cases the CFSM detected on the second peaks of the source-time functions, because they produce echoes similar to surface reflections.

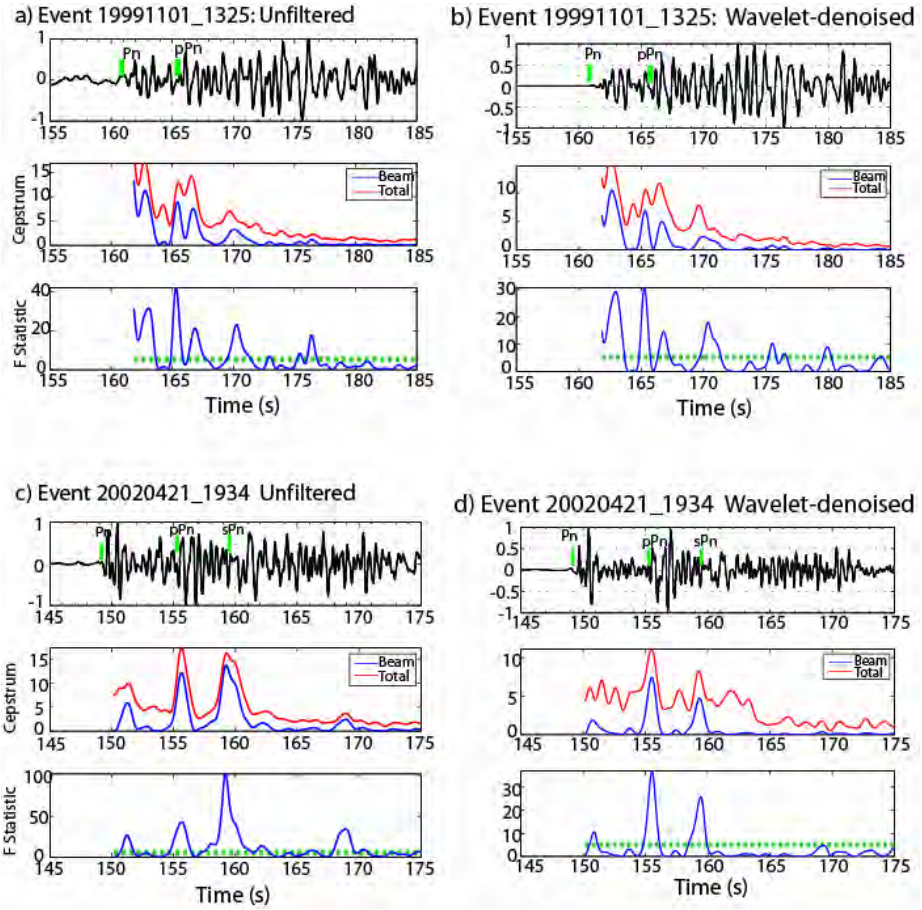


Figure 2. Application of the CFSM to KSAR events before and after wavelet denoising. Each subpanel shows the array beam (top), the beam and total cepstra (middle plot), and the cepstral F-statistic with a green dashed 99% significance level (bottom). a) Event 19991101_1325 using unfiltered data; b) Event 19991101_1325 with wavelet denoising applied at decomposition level 6; c) Event 20020421_1934 using unfiltered data; d) Event 20020421_1934 with wavelet denoising at decomposition level 5.

To help confirm cepstral detections of regional depth-phase arrivals, we apply a version of the MUSIC estimator (Schisselé et al., 2004), which utilizes a continuous wavelet transform (CWT) to help identify the time windows in which coherent phases exist. Once the user has defined a processing window, the MUSIC estimator calculates the propagation characteristics of the analyzed phase. In Figure 3 we show the results of applying the MUSIC estimator algorithm to the KSAR data for the two events analyzed in Figure 2. Figure 3a shows the estimator applied to both the *Pn* arrival (the time-frequency window is denoted by a horizontal white line in the CWT subplot) and to our candidate *pPn* arrival.

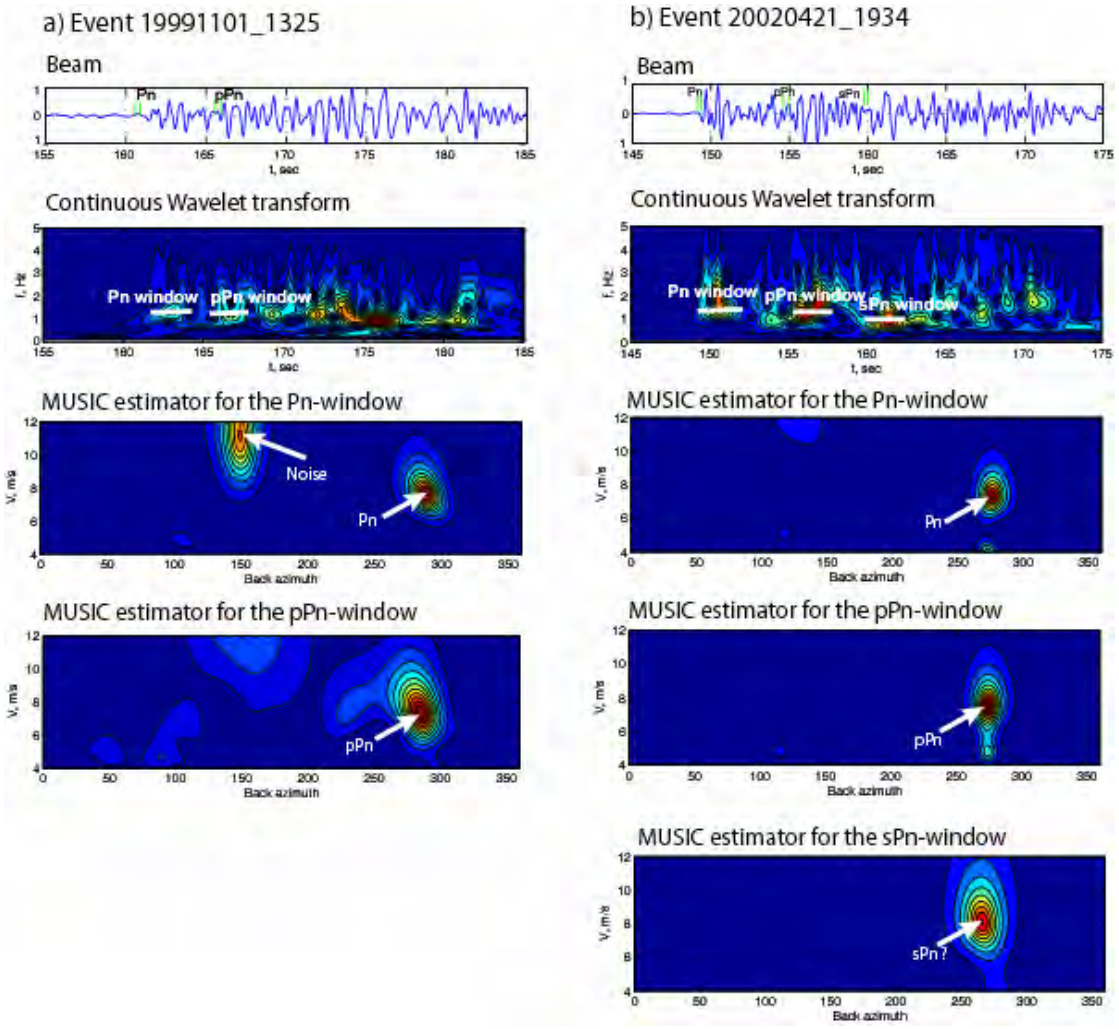


Figure 3. MUSIC estimator analysis of the direct *Pn* and candidate depth phases for a) Event 19991101_1325 and b) Event 20020421_1934.

As Figure 2 demonstrates, in most cases the CFSM produces more than one significant peak corresponding to suspected depth phases. To select the best depth phase candidates, we compute propagation parameters for the first arrival and for all other arrivals with a peak in the F-statistics, as shown in Figure 3. The secondary arrivals with the highest degree of similarity are selected as the best depth-phase candidates. Using this approach we estimated cepstra for the ten events in Table 1, and then found event depths by matching (*pPn-Pn*) travel time differences computed with the one-dimensional (1-D) *IASPEI91* reference model (Kennett and Engdahl, 1991). Table 2 shows the results of this analysis and compares the depth estimates derived from primary phases only to those that include the depth-phase arrival picks.

Sparse-Network Regional Location and Focal Depth Estimates Using a Grid-Search Algorithm

For the second depth estimation technique, we computed event hypocenters from a sparse network of regional observations using a Grid-search Multiple-Event Location algorithm (GMEL), which was initially developed at the Massachusetts Institute of Technology (Rodi and Toksöz, 2000; 2001). The algorithm employs a recursive grid-search technique to find the best-fitting location parameters (origin time and hypocenter) of an event, and a Monte Carlo method to determine confidence regions on the location parameters.

Routine network location procedures do not include regional depth-phase arrivals, which can lead to large uncertainties on the depths of small events observed only at regional distances. Reiter et al. (2002) demonstrated that the addition of regional depth-phase arrivals to the primary *Pn* arrivals in a sparse-network location procedure results in significantly better confidence on the depth estimate. Thus, we examined the effect of including CFSM-estimated *pPn* and *sPn* arrival times at KSAR in the GMEL relocation exercise. To supplement these travel-time picks, we included MUSIC-derived depth-phase candidate arrivals at some of the other regional three-component broadband stations. We also used available catalog *Pn* and *Sn* arrival picks for the regional stations located within 12º from each event. Figure 4 shows a comparison between confidence regions obtained with and without regional depth-phase travel times (Figures 4a and 4b, respectively). Adding correctly identified regional depth-phase picks to the location procedure significantly constrains the depth in the confidence regions.

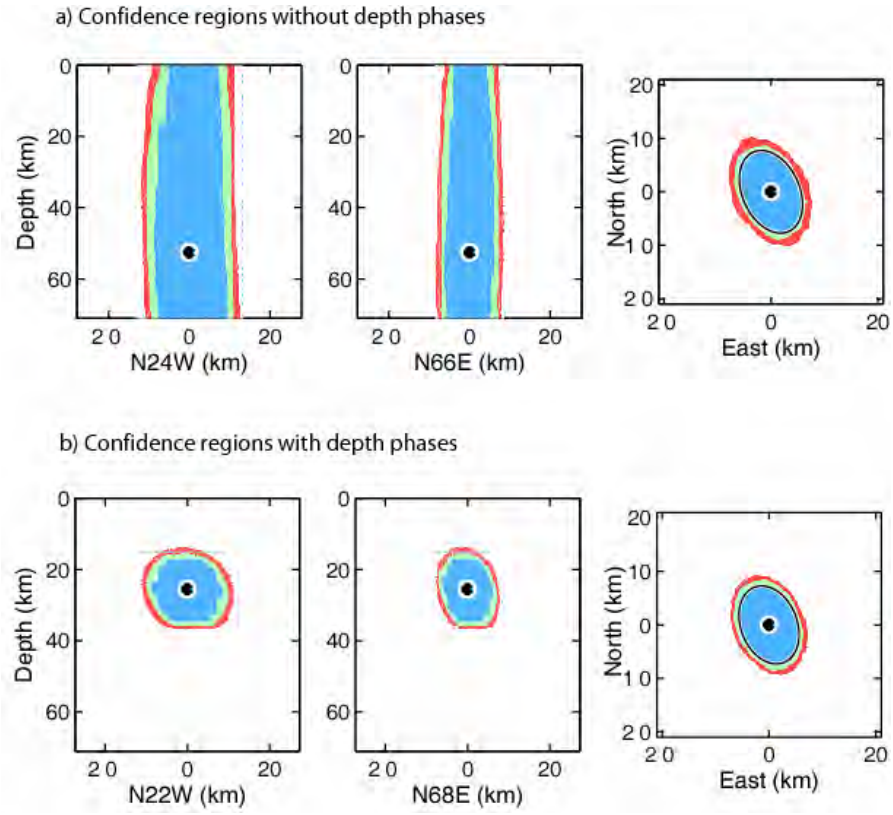


Figure 4. GMEL location confidence intervals for Event 20020421_1934. Each panel shows the depth confidence regions (above 95%) in the left and middle subplots and the epicentral confidence region in the right subplot. The black dot shows the best-fitting hypocenter. a) sparse-network location performed without additional regional depth-phase picks; b) sparse-network location performed with regional depth-phase picks. The results in b) demonstrate improved depth constraints.

Table 2 summarizes the results of depth estimates for the 10 events shown in Table 1. The results indicate that there is a reasonably good agreement between the inversion results and the depths estimated directly from cepstra.

Depth Estimates and Focal Mechanisms from Surface-Wave Inversions

Regional surface-wave observations present another source of data that we can use to estimate both event depth and focal mechanism. Tsai and Aki (1970) and Douglas et al. (1971) demonstrated that Rayleigh

waves can produce notches in the amplitude spectrum. The frequency at which these notches occur is dependent on both the hypocenter depth and the observed azimuth from the event epicenter to the station. This approach has been used successfully by other researchers such as Nguyen and Herrmann (1992) and Patton (1998).

In this study we used the source inversion codes written by Dr. Robert Herrmann of St. Louis University. He has developed and published programs to invert the spectral amplitudes of Rayleigh and Love waves in his Computer Programs in Seismology software package (Herrmann and Ammon, 2002). We used Herrmann's program *srfgrd96* (aka *surf96*), which is a grid-search inversion technique that determines the combination of moment, depth and focal mechanism that minimizes the misfit between observed and predicted surface-wave amplitude spectra. The input required for the inversion consists of the amplitudes of the fundamental Rayleigh and Love waves and a 1-D regional Earth model. The program searches over a model space of moment M_0, depth h, strike ϕ, dip δ, and rake λ to find best-fitting solutions based on the observed amplitude spectra.

We applied *srfgrd96* to the 10 events listed in Table 1. To pick surface wave dispersion curves we used 3-component broadband data from stations located at regional distances from the events. As before, we performed the inversion using the *IASPEI91* reference model; Table 2 includes these results in the column marked '*surf96'*. In general the agreement between the depth estimates contained in the three right-hand columns is quite good.

Table 2. Depth estimates for the events in Table 1 using the three techniques discussed in the paper. Numbers in brackets show numbers of data points used for the event location (number of phase travel times for GMEL and number of stations for which dispersion curves were measured).

Event	Depth (EIDC bulletin)	Depth (km) estimated with *IASPEI91*			
		GMEL: no pPn (# of phases)	GMEL: with pPn (# of phases)	*surf96* (# of stations)	Cepstrum
Events with Harvard CMT					
19980110_0350	4.8	35.0 (16)	12.0 (19)	14 (4)	14.2
19990311_1318	17	0.0 (24)	10.9 (28)	9 (7)	9.7
19991101_1325	10	18.2 (16)	17.9 (20)	17 (6)	19.2
20030816_1058	8.8	35.0 (22)	19.1 (24)	13 (5)	16
20040324_0153	18	0.0 (14)	15.0 (17)	9 (5)	19
Other events					
19960717_1034	15.7	0.0 (8)	16.3 (10)	5 (3)	8.9
19970625_1850	13.5	2.8 (29)	11.6 (32)	13 (5)	11.4
19980414_0247	23.0	35.0 (13)	3.7 (16)	8 (7)	9.7
19991129_0410	10.0	0.01 (15)	9.7 (18)	11 (3)	13.8
20020421_1934	24.0	52.6 (20)	26.4 (24)	21 (3)	27.3

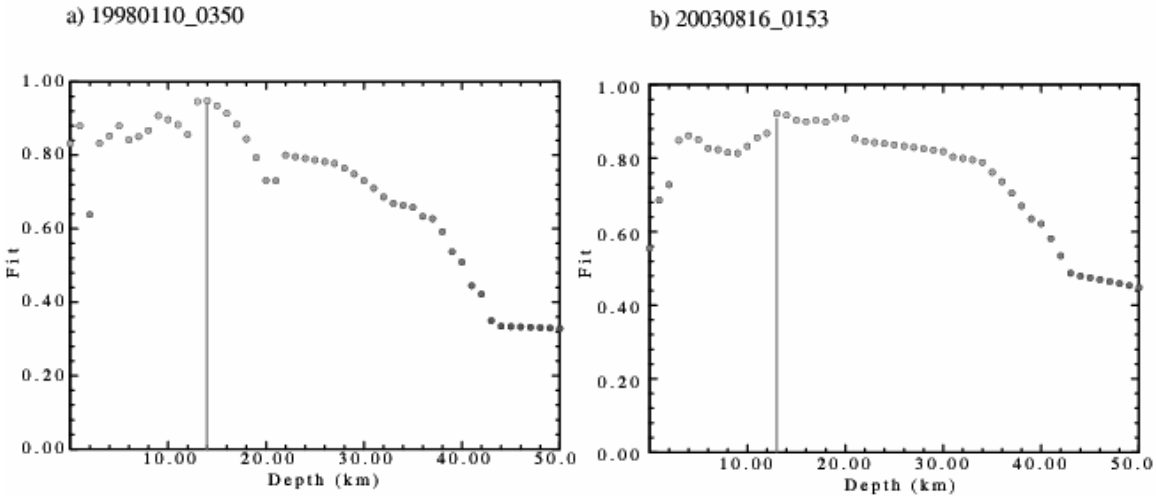


Figure 5. Confidence levels calculated by the surface-wave amplitude inversion routine *srfgrd96* for a) Event 19980110_0350 and b) Event 20030816_1058. Vertical lines show the estimated depth of the event.

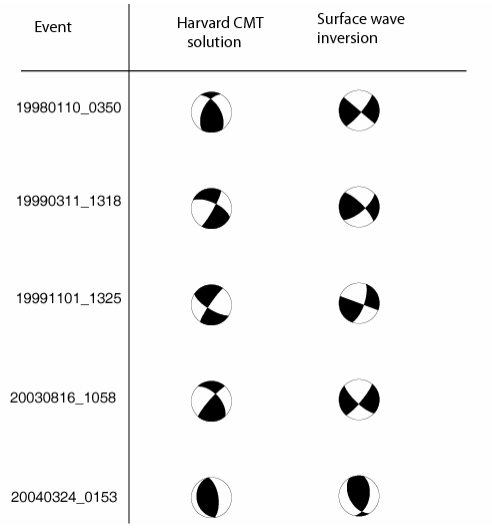


Figure 6. Comparison of the Harvard CMT catalog solutions for events in Table 1 with the ones determined by surface-wave inversion of the regional data.

In Figure 5 we show two examples of the fit in depth estimated by the surface-wave amplitude inversion routine. Figure 6 shows the focal plane solutions computed from the regional station data compared to the Harvard CMT solutions for the relevant events in Table 1. Four out of five focal-plane solutions are in good agreement with the Harvard catalog. Only one event (19980110_0350) resulted in a poor match, even though the surface-wave depth estimate is in good agreement with the cepstral and network location depth estimates. This mismatch in focal solution is likely caused by the small number of stations used in the inversion procedure (4, as indicated in Table 2).

CONCLUSIONS AND RECOMMENDATIONS

We continue to study the problem of determining accurate focal depths for regionally-recorded (small) events. In this paper we combined and compared three different techniques to obtain estimates of focal depths for earthquakes. These techniques included enhanced cepstral processing, in which we supplement cepstral detections of regional phases with additional information such as the phase velocities and back azimuths of candidate phases. This additional information aids in the accurate identification of a depth-phase arrival, which can then be directly inverted for depth or used as a constraint in our second depth-estimation technique: regional network travel-time locations. The third method we have tested is the inversion of surface-wave amplitudes for focal depths and mechanisms using regional station data. While this method shows some promise, it is hampered by its sensitivity to the velocity model used and the requirement for many stations to provide solution stability. However, we may be able to use the surface-wave inversions to confirm or eliminate depths calculated by enhanced cepstral processing and network travel-time locations

We have applied our techniques to data from several seismic arrays in Asia and reported in this paper on results from the KSAR array in South Korea. With this array event depths estimated using depth-phase information show better consistency and lower sensitivity to the velocity model, but this is not always the case.

Our future focus will be to statistically combine the estimates from the different techniques to provide quantitative confidence levels on regional focal depths derived using multiple methods. In addition, we will continue to develop and test additional methodologies to improve the accurate detection of regional depth phases and estimates of event focal depth.

REFERENCES

Bogert, B. P., M. J. R. Healy and J. W. Tukey (1963). The quefrency analysis of time series for echoes: cepstrum, pseudo-autocovariance, cross-cepstrum and saphe cracking, in *Proceedings of a Symposium on Time Series Analysis*, ed. M. Rosenblatt, John Wiley and Sons, Inc., New York.

Bonner, J. L, D. T. Reiter, and R. H. Shumway (2002). Application of a cepstral F statistic for improved depth estimation, *Bull. Seism. Soc. Am* 92: 1675–1693.

Cansi, Y. (1995). Earthquake location applied to a mini-array: K-spectrum versus correlation method, *Geophys. Res. Lett.* 20: (17), 1819–1822.

Capon, J. (1969). High-resolution frequency-wavenumber spectrum analysis, *Proc. of the IEEE*, 57: p. 1408–1418.

Douglas, A., J. A. Hudson and V. K. Kembhavi (1971). The relative excitation of seismic surface and body waves by point sources, *Geophys. J. R. Astr. Soc*. 23: 451–460.

Goldstein, P., and D. Dodge (1998). Depth and mechanism estimation using waveform modeling, in *Proceedings of the 20th Annual Seismic Research Symposium on Monitoring a Comprehensive Test Ban Treaty (CTBT)*, pp. 238–247.

Herrmann, R., and C. Ammon (2002). Surface waves, receiver functions and crustal structure, in *Computer programs in seismolo*gy.

Herrmann, R., Y.-S. Jeon, W. Walter, and M. Pasyanos (2005). Seismic source and path calibration in the Korean Peninsula, Yellow Sea and Northeast China, in *Proceedings of the 27th Seismic Research Review: Ground-Based Nuclear Explosion Monitoring Technologies*, LA-UR-05-6407, Vol. 1, pp. 42–51.

Kennett B. L. N., and E. R. Engdahl (1991). Travel times for global earthquake location and phase identification, *Geophys. J. Int.* 105: 429–465.

Melton, R. S., and L. F. Bailey (1957). Multiple signal correlators, *Geophys.* 22: 565–588.

Murphy, J. R., R. W. Cook, and W. L. Rodi (1999). Improved focal depth determination for use in CTBT monitoring, in *Proceedings of the 21st Seismic Research Symposium: Technologies for Monitoring the Comprehensive Nuclear-Test Ban Treaty*, LA-UR-99-4700, Vol. 1, 50–55.

Nguyen, B. V., and R. B. Herrmann (1992). Determination of source parameters for central and eastern North American earthquakes (1982-1986), *Seism. Res. Lett.* 63**:** 567–586.

Oppenheim, A. V., and R. W. Schafer (1975). *Digital Signal Processing*, Prentice Hall, New York.

Patton, H. J. (1998). Bias in the centroid moment tensor for central Asian earthquakes: evidence from regional surface wave data, *J. Geophys. Res*. 103: 26963–26974.

Pearce, R. G. (1977). Fault plane solutions using relative amplitudes of *P* and *pP*, *Geophys. J. R. Astr. Soc*. 50: 381–394.

Reiter, D. T., and R. H. Shumway (1999). Improved seismic event depth estimate using cepstral analysis, in *Proceedings of the 21st Seismic Research Symposium: Technologies for Monitoring the Comprehensive Nuclear-Test Ban Treaty*, LA-UR-99-4700, Vol. 1, pp. 599–606.

Reiter, D. T., J. L. Bonner, C. E. Vincent and J. Britton (2002). Incorporating secondary phases in 3-D regional seismic event location: application to the sparse network problem, in *Proceedings of the 24th Seismic Research Review—Nuclear Explosion Monitoring: Innovation and Integration,* LA-UR-02-5048, Vol. 1, pp. 375–384.

Reiter, D., A. Rosca, H. Hooper, J. Bonner, C. Vincent and W. Rodi (2003). Improved regional seismic event location using 3-D velocity models, Final Report, Contract DTRA01-00-C-0098.

Reiter, D. T., J. L. Bonner, and R. Shumway (2004). Development of innovative filtering techniques for improved depth phase detection at regional distances, in *Proceedings of the 26th Seismic Research Review: Trends in Nuclear Explosion Monitoring,* LA-UR-04-5801, Vol. 1, pp. 287–296.

Rodi, W. (2005). The grid-search multiple event location (GMEL) algorithm reference manual (rodi@erl.mit.edu), Massachusetts Institute of Technology.

Rodi, W. and M. N. Toksöz (2000), Grid-search techniques for seismic event location, in *Proceedings of the 22nd Annual DoD/DOE Seismic Research Symposium*: *Planning for Verification of and Compliance with the Comprehensive Nuclear-Test-Ban Treaty (CTBT)*, Vol. 2, pp. 339–348.

Rodi, W., and M. N. Toksöz (2001). Uncertainty analysis in seismic event location, in *Proceedings of the 23rd Seismic Research Review: Worldwide Monitoring of Nuclear Explosions,* LA-UR-01-4454, Vol. 1, pp. 324–332.

Saikia, C. K. and D. V. Helmberger (1997). Approximation of rupture directivity in regional phases using upgoing and downgoing wave fields, *Bull. Seism. Soc. Am.* 87: 987–998.

Schisselé, E., J. Guilbert, S. Gaffet, and Y. Cansi (2004). Accurate time–frequency–wavenumber analysis to study coda waves, *Geophys. J. Intl.* 158: (2), 577–591.

Shumway, R. H., S. E. Kim, and R. R. Blandford (1999). Nonlinear estimation for time series observed on arrays, Chapter 7, S. Ghosh ed., *Asymptotics, Nonparameterics and Time Series*, New York: Marcel Dekker.

Tibuleac, I. M. and Herrin, E, (1997), Calibration Studies at TXAR, *Seismological Res. Lett.* 68: 353–365.

Tsai, Y. B., and K. Aki (1970), Precise focal depth determination from amplitude spectra of surface waves, *J. Geophys. Res*. 75: 5729–5743.

Woodgold, C. R. D. (1999), Wide-aperture beamforming of depth phases by timescale contraction, *Bull. Seis. Soc. Am*. 89: 165–177.

AUTOMATED DEVELOPMENT OF 3D LOCAL TRAVEL TIME MODELS

Jerry J. Sweeney, Stephen C. Myers, and Jeffrey L. Wagoner

Lawrence Livermore National Laboratory

Sponsored by National Nuclear Security Administration
Office of Nonproliferation Research and Development
Office of Defense Nuclear Nonproliferation

Contract No. W-7405-ENG-48

ABSTRACT

Intuition suggests that use of three-dimensional (3D) seismic travel time models will lead to improvements in event location by minimizing travel time residuals and local bias. Testing this intuition has been difficult in the past because of a lack of 3D modeling and location codes and the effort involved with generating 3D models. Software now available allows us to easily generate 3D velocity models, calculate travel times over a grid, and compute event locations with the grid search method. This paper describes how we have developed and are evaluating a local (100 km x 100 km x 40 km, 1 km grid spacing) velocity model grid for the Nevada Test Site (NTS). A 3D geological model of NTS has been developed from this highly characterized area's voluminous available data: well logs; core and chip samples; gravity, magnetic, and seismic refraction surveys; and surface geology. This 3D geology has been digitized using EarthVision software (widely used in the oil industry). From the digitized geology, we have created a 3D grid file containing simplified geologic units: alluvium, tuff, Paleozoic bedrock, middle crust, and mantle (top of unit defined by the Moho). We then use a script to assign a velocity to each geologic unit in the grid file, with a velocity gradient for the middle crust unit, and generate a 3D grid file of slowness. This slowness file (for P or S phases) can then be used directly by the open-source code NLLoc (Lomax and Virieux, 2000) to generate separate travel time files for each station in the area to each grid point—NLLoc uses the Podvin and Lecompte (1991) finite difference algorithm. Once the set of travel time files is created for each station of the grid, NLLoc is then used to locate events via a grid search algorithm, compute synthetic travel times for an event, and compute location statistics. We are using travel time data (precisely known origin time and location) from the WATUSI surface chemical explosion at the Big Explosion Experimental Facility (BEEF) as ground truth and stations of the University of Nevada, Reno, local network to calibrate the velocities used in the model. Because the calibration is based on a surface event, travel times are particularly sensitive to shallow crustal velocities. The end result (after iteratively adjusting velocities used for the shallow geologic units) is a velocity model with a mean of the travel time residuals very close to zero. The model results in a location error for WATUSI of less than 1 km. The real advantage of the 3D model is demonstrated by the fact that the location determines a shallow depth for the event, a result not obtainable with a simple one-dimensional (1D) layered velocity model.

OBJECTIVES

The seismic velocity structure of the Earth is known to be relatively homogeneous at the teleseismic scale compared to the regional scale (Ritzwoller, et al., 2003). At the regional scale, tectonic style (fold belts, rift structure, sedimentary basins, etc.) plays an increasingly important role because the seismic ray paths are confined to the crust and upper mantle. At the scale of local seismic networks (200 km or less), ray paths are confined mainly to the upper crust, and local geologic heterogeneity becomes even more important for locating events, especially in the case of sparse networks or networks with poor azimuthal coverage. Thus, one objective for improving seismic event locations at the local scale is to develop a 3D velocity model. The objectives of this study are to develop an automated method of producing a 3D velocity model, apply the method to produce a 3D velocity model of NTS, and test and validate this model using local ground truth events.

Development of local three-dimensional seismic velocity models has several objectives:

- The computer code used to locate events needs to be able to accommodate 3D models. For reasons of computational efficiency, most existing location codes (with the exception of special research codes used in particular areas, such as volcanic studies areas) in the past have used 1D (flat layer) velocity models. Recently, however, grid search location codes have become available that accommodate 3D velocity models.

- A 3D velocity grid needs a grid spacing at least on the order of the seismic wavelength, which can be on the order of 1–2 km for shallow sedimentary deposits with low seismic velocities. These relatively small grid spacings may necessitate large grid files, which are challenging but not prohibitive in a computational sense, but can be prohibitive in the sense of actually putting the 3D grid model together. Clearly, is it not practical to assemble a gridded velocity model on the order of 400,000 elements (100 km by 100 km by 40 km) or larger without automated methods. Thus we need to develop an automated method to produce such grid files.

- Grid spacings of 1–2 km may seem to be quite fine in terms of the area covered by a local seismic network, but compared to the level of detail of geologic mapping or characterization at the local level, this scale is very coarse (it is rare for an individual geologic formation to be as thick as 1 km or more). An important question is how to “down sample” (or, using phraseology familiar to signal processing, “decimate”) geologic information into what is important for the velocity model.

- Once a representative grid with geologic elements has been defined, the next objective is to assign seismic velocities to separate units.

- The final objective is to test and validate the model.

RESEARCH ACCOMPLISHED

Development of the Geology Grid Model

To develop and test our approach for automated generation of a local 3D velocity model, we chose the NTS and surrounding region for several reasons:

- Prior to 1992, extensive efforts were put forth to map and characterize the geology of NTS for the underground nuclear testing program. The hundreds of boreholes drilled and logged and extensive mapping and geophysical surveys carried out have resulted in NTS being an extremely well-characterized region.

- Over the past several years much of the geological and geophysical data from NTS has been digitally compiled into a 3D geologic model that includes detailed local topography. This model is digitally archived in a geographical information system (GIS) format compatible with many different GIS software applications. This digital archive and the software application allow us to easily generate grid files of geology from different areas covered by the model.

- The University of Nevada, Reno (UNR), operates a local seismic network within NTS funded by the Department of Energy (DOE) Yucca Mountain Repository program. UNR also operates additional seismic stations in south-central Nevada as part of their Southern Great Basin Seismic Network (SGBSN—refer to http://www.seismo.unr.edu/). Lawrence Livermore National Laboratory (LLNL) has access to both catalog and waveform data from these stations.

- Because of ongoing chemical explosives and ordinance testing at NTS, several large known explosion sources are available as ground truth events that can be used to test and verify the velocity modeling approach.

EarthVision (Dynamic Graphics, Inc.) is a 3D modeling code used extensively at LLNL to build and visualize 3D geologic models (Figure 1). The goal of these models is to characterize and better understand the subsurface geology. You can rotate, slice, peel, and clone 3D structural and property models for effective evaluation and verification. Also built within the framework are 3D property models of the 3D geologic model that are used to evaluate and visualize the spatial distribution of physical properties. Contour maps, isochore maps, and cross sections derived from 3D models provide easily understood representations of faults and stratigraphy. You can seamlessly integrate seismic interpretation in time with your depth model. These precise 3D models are easily updated with new data. We integrate all geophysical and geological data into one database. These models provide the ability to calculate volumes of individual layers or reservoirs.

The 3D geologic model of NTS was constructed using EarthVision software from a much larger model of the southern Great Basin that was generated for an investigation of the 1993 nonproliferation experiment (NPE) explosion. This regional model includes detailed constraints at the Nevada Test Site based on the extensive geologic and geophysical studies. Gross structure of the crust and upper mantle is taken from regional surface-wave studies. Variations in crustal thickness are based on receiver function analysis and a compilation of reflection/refraction studies. Upper-crustal constraints are derived from geologic maps and detailed studies of sedimentary basin geometry throughout the study area. The free surface is based on 10 m resolution elevation data at the NTS and a 90 m digital elevation model (DEM) elsewhere. The Great Basin model extends to a depth of 150 km, and the NTS model goes to a depth of 38.8 km.

The NTS model incorporates much of the detailed geologic data that was collected for the underground nuclear test program. Literally hundreds of boreholes provide subsurface stratigraphic data that is used to constrain the stratigraphic units. Numerous geophysical surveys are also available to aid the definition of the basins. Faults are not included in this model.

In order to make the initial study model computationally tractable, we limited the size aerially to 100 km by 100 km, with depth to 40 km. For a 1 km grid spacing, this results in 400,000 grid elements. The geographical coordinates of the geographically aligned grid are defined by the southwest corner of the upper surface of the grid at latitude 36.753 longitude -116.775. The grid search location code that we chose to use for this study (see below) uses a flat earth geometry, but station corrections can be included to account for topography differences. Because all of the ground truth events that we have are explosions occurring at the ground surface in Yucca Flat, we chose to use the elevation of Yucca Flat, 1200 m, as the surface datum for the velocity model.

The next decision to make concerning the geology model was which units to include, e.g., the number of different geologic units to be used in the model. We made this choice mainly based on what would be a relatively simple starting point and what made sense with respect to what we thought would have the most impact on the seismic velocity structure. The geologic units were divided into the following from upper to lower: alluvium, volcanic tuff, undivided Paleozoic units, lower crust, upper mantle. The EarthVision code was then used to define and extract these units and assemble them into a 3D binary grid file. Each element in the grid was assigned a code for the geology type. Using a scripting code, the binary elements of the grid file were converted into a binary file of seismic slowness (travel time per unit length, or inverse velocity in km/s for a 1 km grid). This slowness file could then be used to compute travel times in the location code, as described below. A representation of the slowness model is shown in Figure 2 with N-S and E-W cross sections going through the center of the model. Representative velocities used in the figure are alluvium 2.0 km/s, tuff 2.5 km/s, Paleozoic 5.0 km/s, lower crust 6.0–6.5 km/s (as a gradient), and upper mantle 7.8 km/s. Values for these velocities were initially chosen based on known studies for relatively shallow depths (McKague 1980; Howard, 1985) and regional seismic studies (Hoffman and Mooney, 1984; Patton

and Taylor, 1984). Adjustments to the initial velocities used were made iteratively in the testing and validation process, as described below.

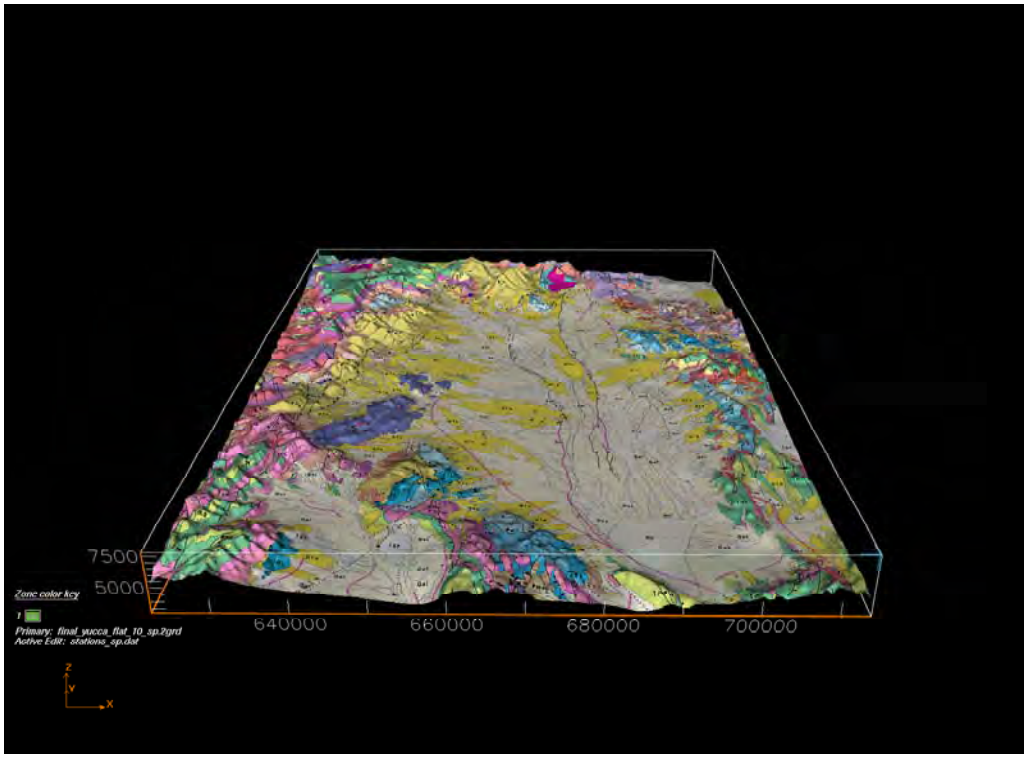


Figure 1. Surface representation of a portion of the NTS geologic model. The elevation is in feet; the horizontal scale is in Nevada coordinates. Surface geology has been draped over the topography.

Incorporation of the Geology Model into the Location Code

The general purpose, probabilistic nonlinear grid search location code NLLoc, developed by Anthony Lomax (Lomax and Virieux, 2000) is ideal for our objectives. The open-source code (refer to http://alomax.free.fr/nlloc/index.html) has the capability to generate 3D travel times from a 3D velocity model via the finite difference algorithm developed by Podvin and Lecompte (1991). Using the input slowness (velocity) model described above, travel times are computed from each station location to every cell in the grid and stored in travel time files. These travel times are then used, via an oct-tree sampling method, to compute the location of seismic events over the grid. A Metropolis-Gibbs sampling method is used to develop probability density functions so that nonlinear effects on the location uncertainty can be examined. The code does not incorporate elevation differences into the travel time model, but station corrections can be included to make a rough approximation to elevation differences affecting travel times.

An additional advantage of the NLLoc software is that it includes a module, called Grid2GMT, which generates scripts for creating maps via the Generic Mapping Tools (GMT) open-source software (Wessel and Smith, 1991). The module makes it particularly easy to generate horizontal and vertical sections (Figures 2 and 3) through the velocity model grid as well as produce similar sections of contoured travel time in addition to the usual maps of station locations and event locations. The capability is particularly important in checking for model artifacts and inconsistencies in large grid files.

Testing, Modifying, and Validating the Model

As can be seen in Figure 2, the distribution of seismic stations is concentrated near the southwest boundary of NTS in the vicinity of the Yucca Mountain nuclear repository with a few additional stations surrounding Yucca Flats (the large yellow area with the word "WATUSI" in it). WATUSI was an 18,000 lb surface explosion detonated at the surface in September 2002. The exact location and origin time of this event are known, it was well recorded on all of the stations, and it is centrally located in the network, thus this explosion provides an excellent ground truth event for testing the 3D velocity model.

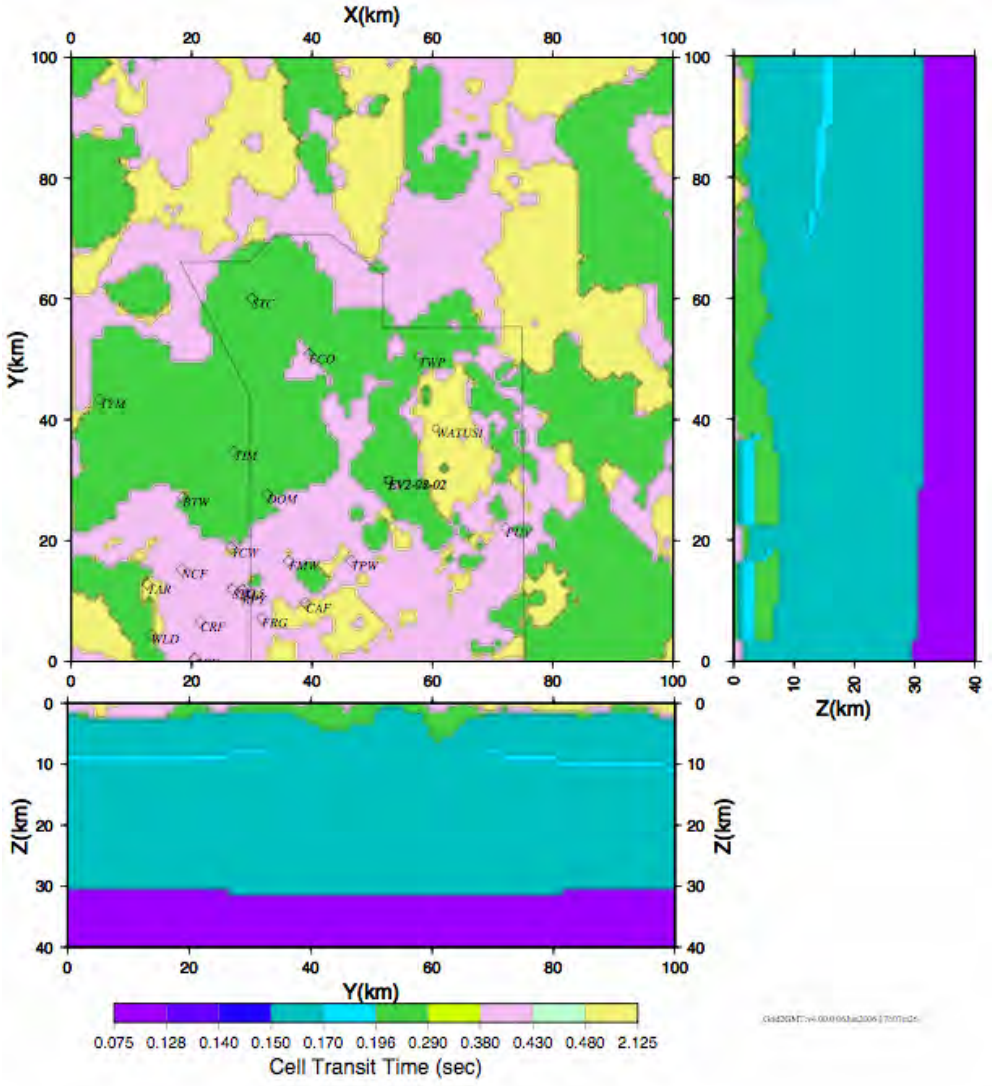


Figure 2. Map view and cross sections (through the middle of the map) of the geologic map grid used in this study. The NTS boundary is shown by straight lines. Diamond symbols are locations of seismic stations', circles are locations of explosion events used for ground truth. Color contours refer to cell transit time (slowness) assigned to individual geologic units as discussed in the text. The color scheme refers to geology units as follows: alluvium—yellow, tuff—pink, Paleozoic—green, lower crust—blue, upper mantle—purple.

The procedure we used was as follows: the initial velocity model, developed as described above, was used to develop files of travel time from each station to every grid point using the Grid2Time module of NLLoc. These travel time files were then used to compute the travel time from each station to the known location of the WATUSI event. These travel times were then compared with the observed travel times for WATUSI. By comparing travel

time differences for different stations with the velocity model along the path between WATUSI and the station (e.g., Figure 3), we can make some guesses about how to adjust the velocity for certain geologic units. We then adjusted the velocities for specific units in the model and repeated the process. If we assume that the picking errors are less than 0.1 s, then our goal in adjusting the velocity model should be to get the mean difference between the observed and predicted travel times to be less than 0.1 s.

In the process of these iterations of the velocity model, we discovered that, because the velocity model has a flat surface with the datum of 1200 m, some of the area (northwest corner of NTS) has a surface above the datum and some (southeast corner) has a surface below the datum. In gridding the velocity model, geology above the datum is missing, and geology below the datum was generated as a different unit with very low velocity (air). This only became obvious after we carefully examined the first run of the model. We corrected this effect by modeling the area below the datum as an upward continuation of the surface geology until the surface datum was reached. In this area (below the datum), stations will need a negative time correction (advance) to account for the elevation difference; in areas above the datum a positive time correction (delay) is needed to account for the additional travel time through the higher topography. Initially, we make these elevation station corrections at a specific station by simply dividing the difference of station elevation from the datum (1200 m) by the velocity of the geologic unit at the surface in the particular area.

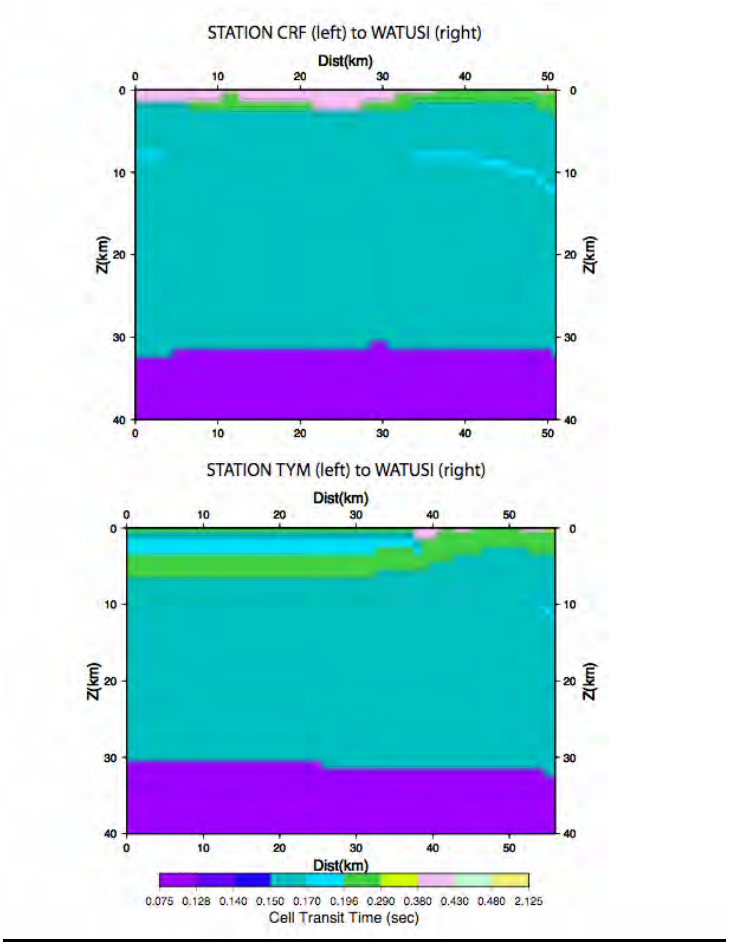


Figure 3. Cross sections through the velocity model (cell transit time is seconds is shown) for paths between the WATUSI explosion (upper right corner) and the station indicated (upper left corner). Color scale and geologic units are the same as for Figure 2.

By plotting the observed and computed travel time with distance, we can compare the differences for each station. By making plots like Figure 3, we can try to determine which part of the model is affecting the travel time and adjust the velocities of geologic units accordingly. Note that we do not change any of the spatial relationships of the model; we only change the velocity assigned to a particular geologic unit. Figure 4 (which is normalized to a velocity of 6.0 km/s) shows considerable variations in travel time (0.6–1.3 s) that are undoubtedly related to velocity heterogeneity. For the model comparison shown in Figure 4, stations DOM, SCF, and TYM have significantly fast arrivals, while stations TWP, PUV, TPW, ECO, and FRG have significantly slow arrivals. Velocity of the alluvial layer under Yucca Flats, where the source WATUSI event is located, generally affects all of the stations equally, while delays or advances at individual stations depend mainly on the geology beneath the station, but also somewhat on particulars of the overall path. The current model (results shown in Figure 4) has a mean travel time residual with respect to the observed travel times of about 0.15 s. When we use this model to locate the WATUSI event using the grid search code NLLoc, the location error of the hypocenter is less than 1 km (the size of a grid element). The nonlinearity of the location solution, however, is notable by the sensitivity of the depth determination to the value of the P/S velocity ratio. (For the current model, we do not use separate P and S velocity models, although the NLLoc code supports this option.) In varying the P/S velocity ratio from 1.80 to 1.95, we found that shallow depths were obtained in the location for values between 1.85 and 1.90, but the depth jumps to 10 km or more for values outside this range.

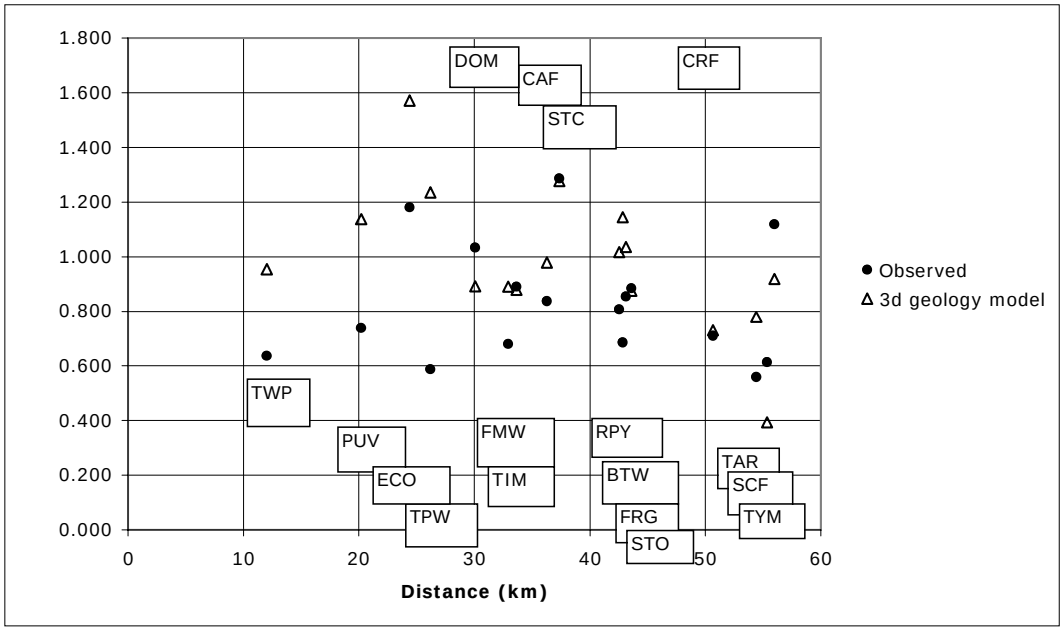


Figure 4. Plot of observed (dots) and calculated (triangles) travel times from the WATUSI explosion to the seismic stations. Calculated travel times are based on the geology-based travel time model. Refer to Figure 2 for station locations. Travel times are normalized to a P wave velocity of 6.0 km/s.

CONCLUSION(S) AND RECOMMENDATIONS

We have demonstrated that local 3D velocity models can be easily generated automatically using commercially available geological modeling GIS software. We can then compute travel times over a 3D grid using the open source software NLLoc. We have begun to assess the value of this modeling approach for improving local seismic event locations in relatively small (100 km x 100 km) areas using NTS as a test case. Visual tools available with NLLoc help us to analyze how seismic velocity in individual geologic units can affect station travel times due to lateral and vertical geologic heterogeneity. Once we have optimized the 3D geologic model (at least for the case of ground truth data we have available), we will be able to study the effects of the network configuration on location results and ultimately assess the value of 3D models over simpler models for location of seismic events at the 40–100 km distance scale with sparse networks.

REFERENCES

Hoffman, L. R. and W. D. Mooney (1984). A seismic study of Yucca Mountain and vicinity, southern Nevada: Data report and preliminary results, U. S. Geological Survey Open-File report, 83–588.

Howard, N. W. (1985). Variation in properties of nuclear test areas and media at the Nevada Test Site, Lawrence Livermore National Laboratory report UCRL-53721.

Lomax, A. and J. Virieux (2000), Probabalistic earthquake location in 3D and layered models, in *Advances in Seismic Event Location*, C. H. Thurber and N. Rabinowitz (Eds.). Netherlands: Kluwer Academic Publishers, pp. 101–134.

McKague, H. L. (1980). Summary of measured medium properties of Paleozoic rocks at the Nevada Test Site, Lawrence Livermore National Laboratory report UCRL-52884.

Patton, H. J. and S. R. Taylor (1984). Q structure of the basin and range from surface waves, *J. Geophys. Res.* 89: B8, 6,929–6,940.

Podvin, P. and I. Lecompte (1991). Finite difference computations of travel times in very contrasted velocity models: A massively parallel approach and its associated tools, *Geophys. J. Int.* 105: 271–284.

Ritzwoller, M. H., N. M. Shapiro, A. L. Levshin, E. A. Bergman, and E. R. Engdahl (2003). Ability of a global three-dimensional model to locate regional events, *J. Geophys. Res.* 108: B7, 2353, doi:10.1029/2002JB002167.

Wessel, P. and W. H. F. Smith (1991). Free software helps map and display data, *EOS Trans. Am. Geophys. Union*, 72: 441.

FINITE-FREQUENCY SEISMIC TOMOGRAPHY FOR EASTERN EURASIA

Ting Yang[2], Yang Shen[2], and Xiaoping Yang[1]

Science Applications International Corporation[1] and University of Rhode Island[2]

Sponsored by Air Force Research Laboratory

Contract No. FA8718-05-C-0017[1,2]

ABSTRACT

Seismic calibration for nuclear explosion monitoring requires accurate, high-resolution 3-D velocity models. Although seismic event locations have been improved recently using more accurate travel times measured by waveform cross-correlation, ray-based models and predictions are not strictly self-consistent with travel times measured by waveform cross-correlation, which are sensitive to 3-D velocity perturbations around the geometric ray paths. Finite-frequency seismic tomography (FFST), which utilizes the 3-D sensitivity kernels to determine the structure that best fits the observations from waveform cross-correlation, provides a self-consistent approach in model development and event location.

We apply the FFST method to determine the crustal and mantle velocity structure beneath eastern Eurasia. Taking advantage of the broadband feature of seismic records, we measure P-wave (primary wave) relative delay times by waveform cross-correlation in three frequency bands (0.03–0.1 Hz, 0.1–0.5 Hz, and 0.5–2.0 Hz). The measurements are inverted jointly to constrain velocity heterogeneities with different distances from the central geometric rays. The effect of strong variations in crustal structure beneath this region on travel time data is removed by conducting a frequency-dependent crustal correction. A comprehensive data set, including waveforms from the publicly accessible sources and other seismic networks in the region, has been collected for this study. Our preliminary model has similar patterns of high- and low- velocity but higher magnitude anomalies than ray-based tomographic models. The resolution checkerboard tests suggest that the resolution is better beneath eastern China, reflecting the better sampling in that part of the model in the current data set. The procedures for computing frequency-dependent travel time corrections from the finite-frequency model have been developed and tested in relocating ground truth (GT) events.

This is the second year of a three-year effort to improve seismic calibration in eastern Eurasia. We will continue processing data to improve the 3-D FFST velocity model and construct an S-velocity model. The final model will be developed using joint body and surface waves, and wave propagation in the transition zone will be simulated. We will continue collecting waveforms and ground-truth (GT) data for model construction and validation.

OBJECTIVES

Our main objectives are (1) to develop P and S velocity models beneath eastern Eurasia by conducting a joint body- and surface-wave tomography based on finite-frequency seismic waves, and (2) to carry out seismic calibration and validate the model and location improvement using GT data. Three-dimensional full waveform simulations will also be conducted to model wave propagation through the transition zone and seismic anisotropy.

RESEARCH ACCOMPLISHED

Data Processing

We collect and utilize a comprehensive data set to construct the new earth model beneath eastern Eurasia. Figure 1 shows the stations in the study region with broadband data. So far we have collected data from the Incorporated Research Institutions for Seismology (IRIS), Global Seismographic Network (GSN), Japanese F-net and JISNET, and Taiwan Broadband Seismic Network, as well as unique sources including permanent and portable seismic stations throughout the study area (e.g., part of the Chinese Digital Seismic Network). Other networks, including the International Monitoring System (IMS) and most of the Program for the Array Seismic Studies of the Continental Lithosphere (PASSCAL) are being extracted and processed.

We process P-waves from global earthquakes in the updated Engdahl-van der Hilst-Buland (EHB) bulletins from 2001 to 2004 and the National Earthquake Information Center (NEIC) bulletins for more recent events with magnitude greater than 5.5 recorded by the seismic stations in eastern Eurasia. The broadband waveforms of the P-waves are filtered in high, intermediate, and low-frequency bands (0.5–2.0, 0.1–0.5, and 0.03–0.1 Hz, respectively) to help isolate the microseism and utilize the broad frequency range of the seismic records. We use an automated waveform cross-correction (VanDecar and Crosson, 1990) routine to measure the relative travel time delays of the arrivals in each frequency band for each event. The signal-to-noise ratio threshold is set to 20 for automated data selection in each frequency band, and each selected record is also examined manually for consistency. The signal-to-noise ratio is defined as the ratio of the peak-to-peak amplitude of the main arrival to the standard deviation of the time series in an 80-s window before the main arrival. Figure 2 shows the distribution of the events and phases in our data set.

The study region spans 20°S to 60°N and 60°E to 160°E. The tomographic model extends to 2500 km deep and is parameterized by a 128 × 128 × 64 grid with spacing of 0.625°, 0.806°, and 39 km in latitude, longitude, and depth, respectively. Details of the FFST methodology used in this work are given in Hung et al. (2004) and Yang et al., (2005). The inversion of the massive matrix is approximated by the iterative solution of the LSQR algorithm (Paige et al., 1982). The norm damping factor of the inversion is determined by the trade-off analysis of model roughness versus variance reduction (Menke, 1989).

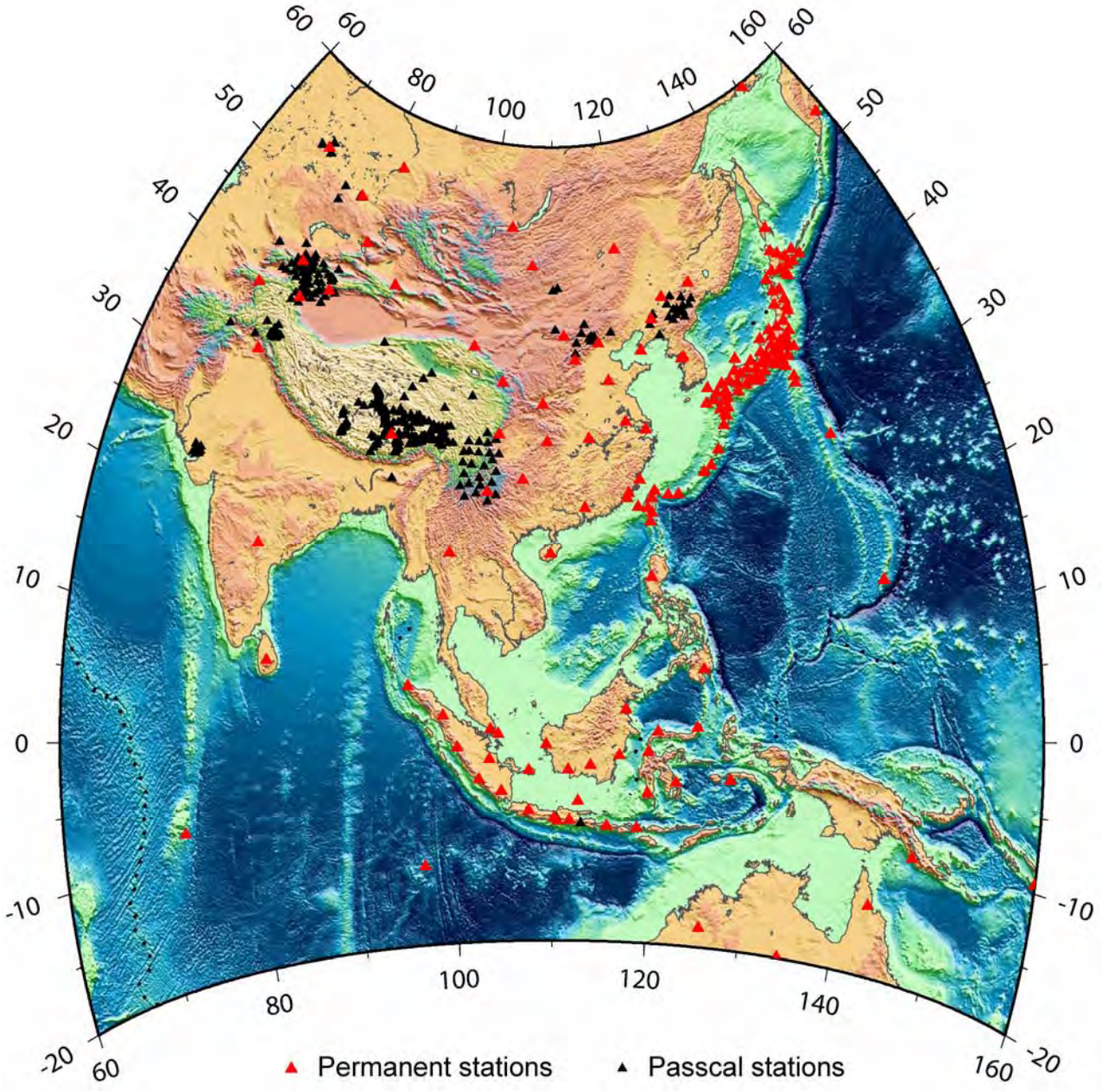


Figure 1. Triangles mark the locations of broadband seismic stations in Eastern Eurasia (red: Permanent stations; black: PASSCAL stations). Data from the PASSCAL stations will be included in our final model.

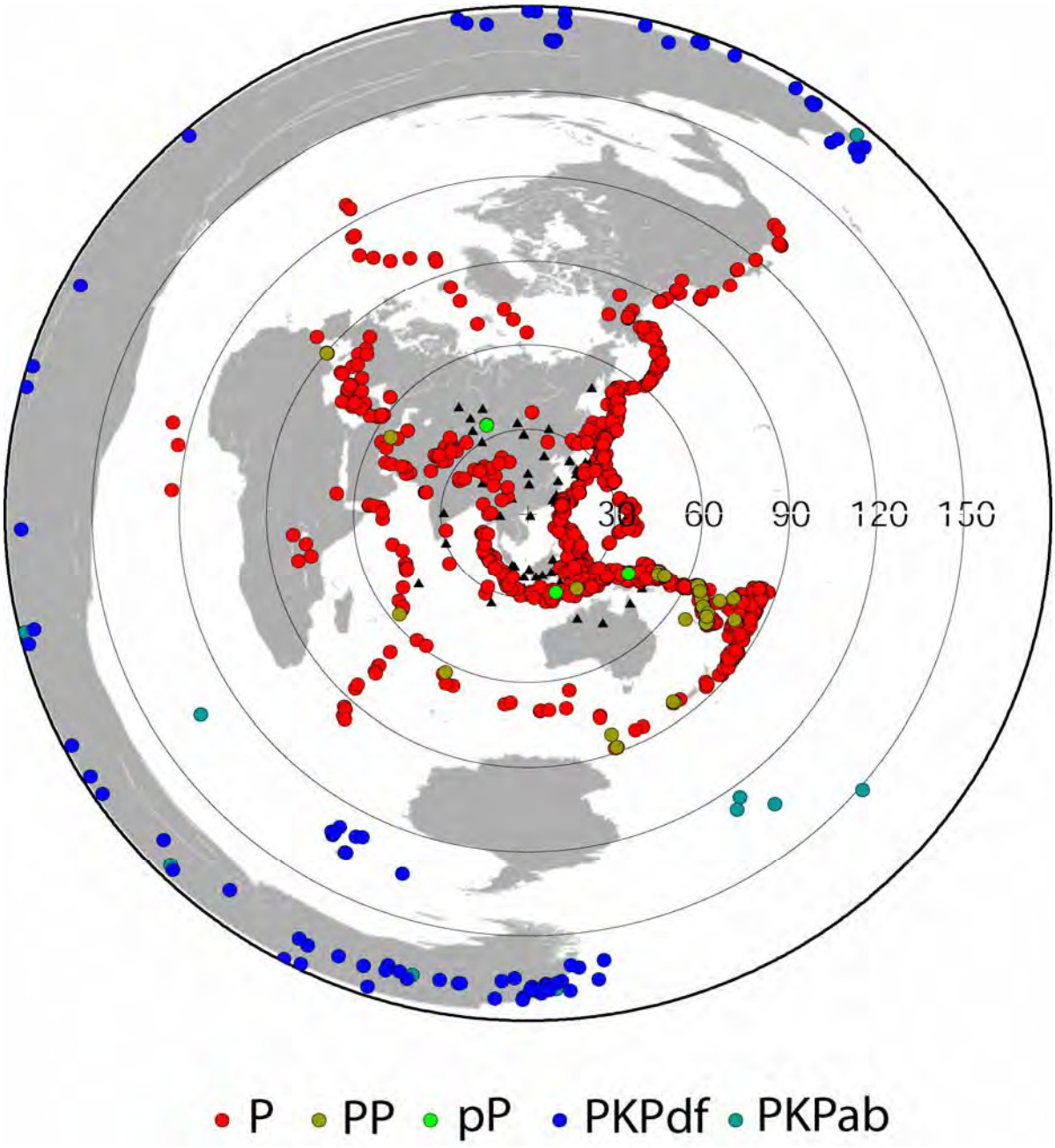


Figure 2. Locations of the earthquakes with useful phases (color circles) and stations (triangles) in the study region. The projection is centered at Hainan, China. Numbers mark the distance in degrees from the center of map projection.

Crustal Correction

Removing the crustal signature from teleseismic travel times is an important procedure to reduce the tradeoff between crustal and mantle velocity heterogeneities in seismic tomography. In regions having large variations like Eastern Eurasia, this is particularly important. Because reverberations of long- and short-period body wave arrivals in the crust affect the waveforms of the direct arrivals differently, the crustal effects on travel times measured by waveform cross-correlation are frequency dependent. With synthetic responses of selected crustal models we have shown (Figure 3) the importance of frequency-dependent crustal corrections to finite-frequency body-wave travel time tomography. The differences in crustal correction between long- and short-period body waves at the same station can be as large as 0.6 s, depending on the crustal thickness, velocity contrast at the Moho, and layering within the crust.

The frequency-dependent crustal correction can be approximated, to the first order, by cross-correlating the impulse responses of a crust model filtered in a narrow frequency band (Yang and Shen, 2006). We use a crustal model from Sun et al. (2005) for stations in China, and CRUST2.0 (crustal model) (Bassin et al., 2000) for stations elsewhere to calculate the travel time difference with respect to IASP91 for the three frequency bands, and apply those frequency dependent adjustments to teleseismic travel times.

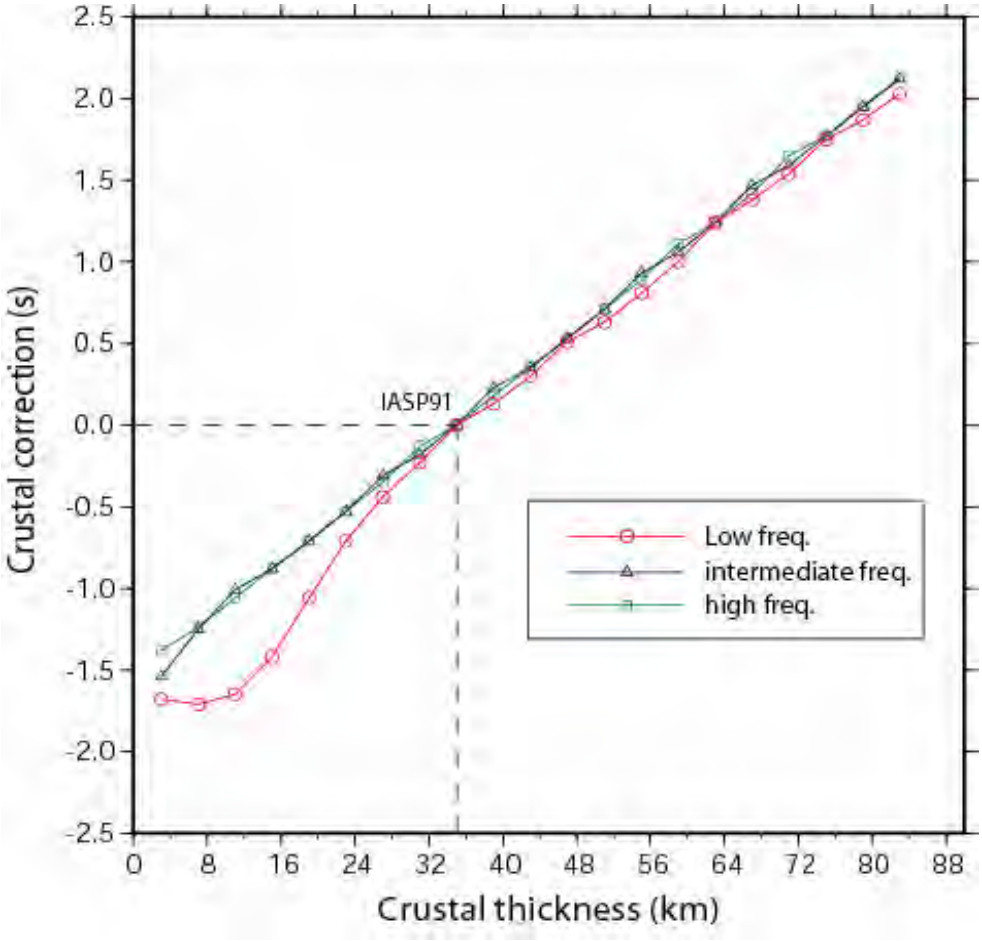


Figure 3. Effect of the crustal thickness on crustal corrections for the high- (0.5–2.0 Hz), intermediate- (0.1–0.5 Hz) and low- (0.03–0.1 Hz) frequency signals from a synthetic experiment. The crust is a two-layer model with the same Vp, Vs and density as those of IASP91. The thicknesses of the upper and lower crust are increased or decreased by the same amount in each calculation.

Preliminary Results

Figure 4 shows the sampling density from high, intermediate, and low frequency P-waves from teleseismic earthquakes in our data set. Because of the relatively narrow "banana-doughnut" sensitivity kernels of high-frequency P-waves, the sampling of high-frequency P-waves (Figure 4a) resembles that in ray theory. At intermediate and low frequencies, the broad sensitivity kernels provide a more smooth coverage of the structure. FFST combines the sensitivity kernels in all frequency bands in the inversion. There is a good data coverage in the depth range of 400–1500 km, but large gaps exist in the shallow upper mantle and crust due to the sparse station distribution. Other datasets (e.g., PASSCAL and IMS) and surface bouncing phases (pP, PP) will reduce the gaps.

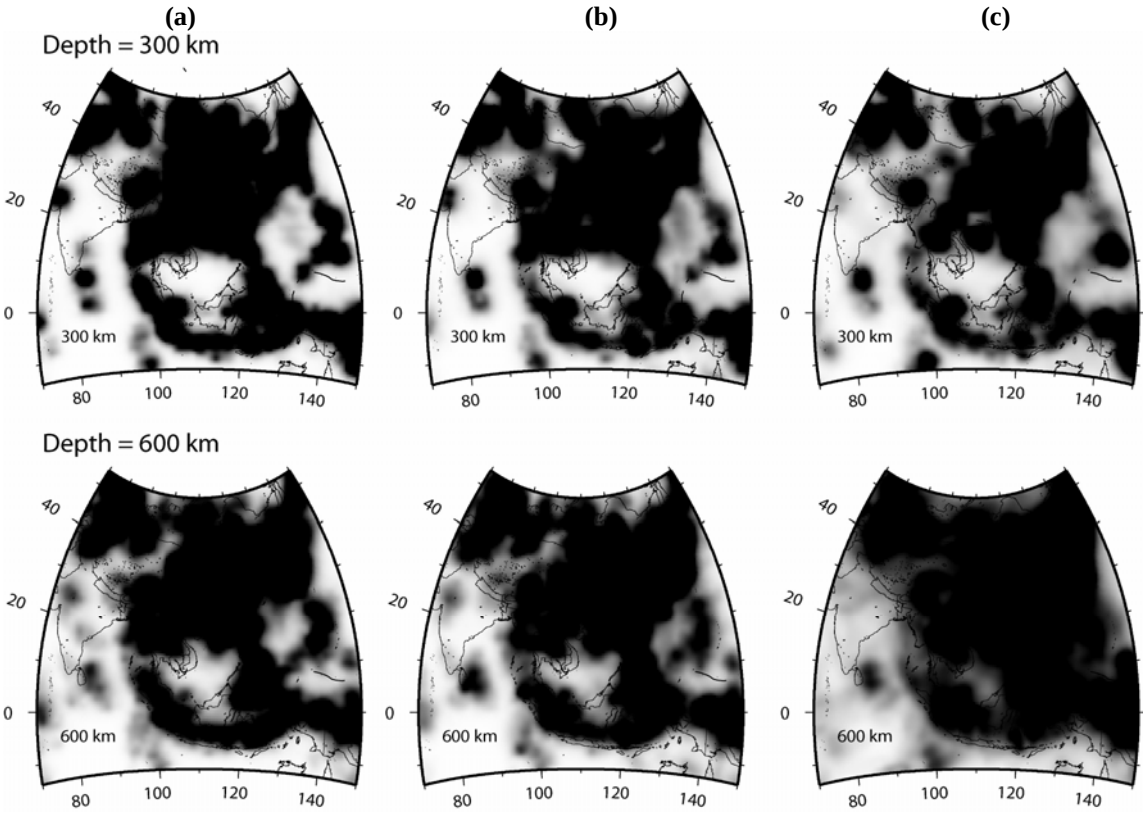


Figure 4. Sampling of the model space by 3-D sensitivity kernels of P-waves at (a) high (left column), (b) intermediate (middle column) and (c) low (right column) frequencies at 300 km (top row) and 600 km (bottom row) depth. Because of the broad sensitivity kernels, low-frequency arrivals reduce the gaps in the sampling of the higher frequency data.

Figure 5 shows the velocity anomalies at 225 and 525 km depth in our preliminary model. A comparison with the previous studies (e.g., Li et al., 2006) shows that our model has similar patterns of high and low velocity anomaly distribution but a higher magnitude than those ray-based tomographic models, indicating the 3-D sensitivity kernels are able to account for the wavefront healing effect of realistic seismic wave propagations. The resolution checkerboard tests suggest that the resolution is good beneath eastern China and along the Japanese island, reflecting the better data coverage and sampling in those regions. We will carry out the finite frequency surface wave tomography to provide higher resolution in the shallow structure and complement the body wave model.

So far we have established the process for model validation using GT event relocation. We developed the code for calculating relative travel time corrections from the kernels using the preliminary P-model. Travel time corrections were computed for IMS stations in Eurasia and applied to sample GT events for testing. We continue collecting GT data and will conduct event relocation to assess our new version of the 3-D velocity model.

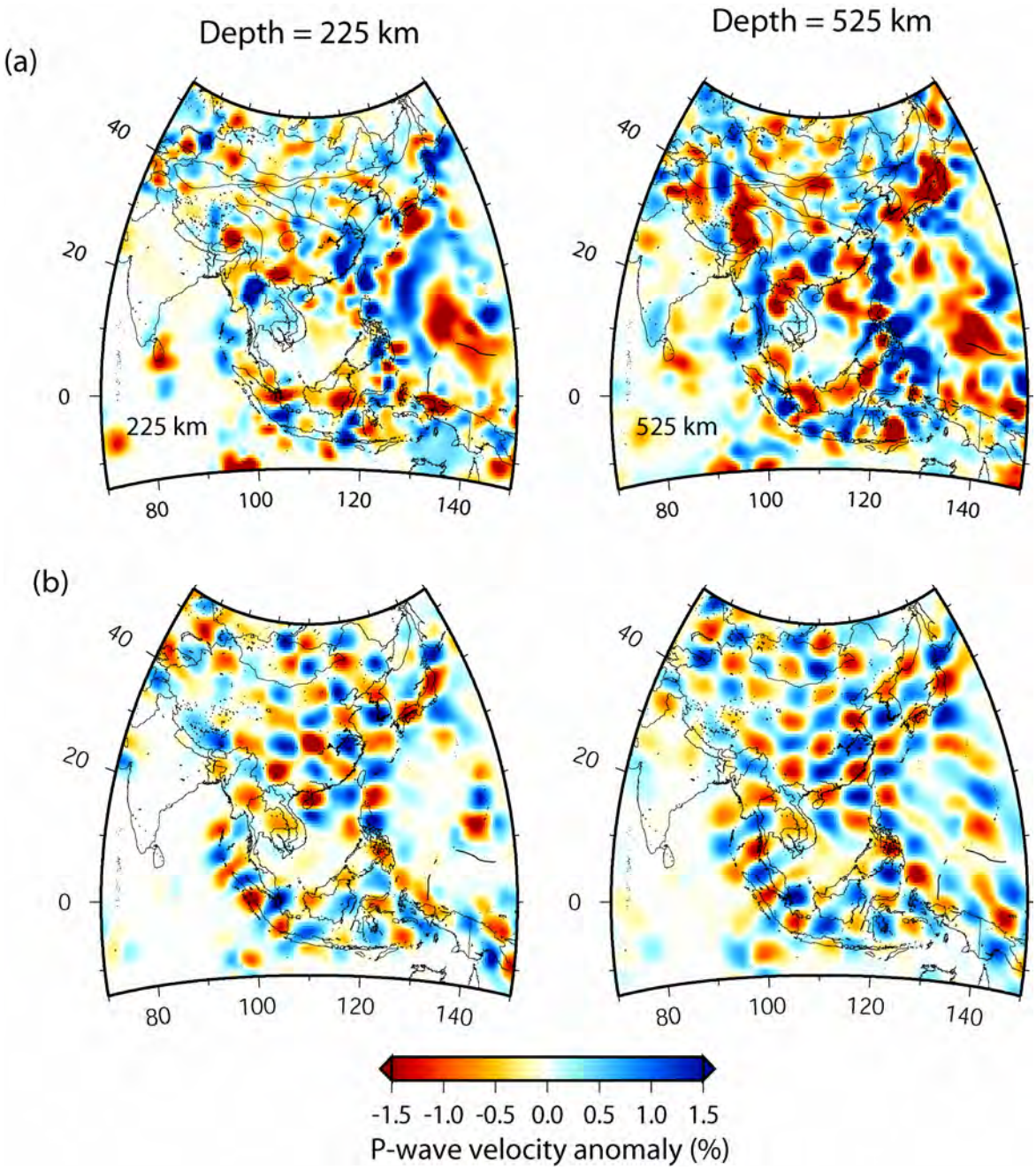


Figure 5. (a) Two horizontal slices of the tomographic model at 225 km and 525 km depth showing the velocity perturbation distribution in the mantle beneath Eastern Eurasia. (b) The checkerboard resolution tests. The structure beneath eastern China is better resolved due to a better sampling in the current dataset.

CONCLUSIONS AND RECOMENDATIONS

In this work we use a 3-D finite-frequency kernel-based approach to improve seismic calibration for nuclear explosion monitoring in eastern Eurasia. We collect and process a comprehensive data set using waveform cross-correlation to construct the FFST models. Preliminary tomographic inversions using finite-frequency kernels have demonstrated improvement in resolution compared to those based on ray theory. The initial model shows similar patterns compared to the previous studies using the ray-based approach but has higher magnitude anomalies. We will continue to process the remaining available earthquake waveforms and carry out the joint body and surface wave finite frequency tomography. The 3-D velocity models will be used in improving seismic calibration in Eurasia. The procedures for computing frequency-dependent travel time corrections from the finite-frequency model have been developed and tested in relocating GT events.

ACKNOWLEDGEMENTS

We thank Bob Engdahl, Bill Rodi, Delaine Reiter, Richard Stead, Chinese collaborators, and the IRIS Data Management Center (DMC) for providing valuable information and help. The figures are made using GMT (Wessel and Smith, Free Software helps map and display date, EOS, 441–445, 1991).

REFERENCES

Bassin, C., G. Laske, and G. Masters (2000). The current limits of resolution for surface wave tomography in North America, *EOS, Trans. Am. Geophys. Un.* 81: F897.

Hung, S.-H., Y. Shen, and L.-Y. Chiao (2004). Imaging seismic velocity structure beneath the Iceland hot spot: A finite frequency approach, *J. Geophy. Res.* 109: doi: 10.1029/2003JB002889.

Li, C., R. D. ver der Hilst, and M. N. Toksoz (2006). Constraining P-wave velocity variations in the upper mantle beneath Southeast Asia, *Phys. Earth Planet. Interiors* 154: 180–195.

Menke, W. (1989). *Geophysical Data Analysis: Discrete Inverse Theory*. Academic, San Diego: Academic.

Paige, C. C. and M. A. Saunders (1982). LSQR: An algorithm for sparse linear-equations and sparse least-squares, *Trans. Math. Software* 8: 3–71.

Sun, Y., L. Xu, S. Kuleli, F. D. Morgan, and M. N. Toksoz (2004). Adaptive moving window method for 3-D P-velocity tomography and its application in China. *Bull. Seism. Soc. Am.* 94: 740–746.

VanDecar, J. C. and R. S. Crosson (1990). Determination of teleseismic relative phase arrival times using multi-channel cross-correlation and least squares, *Bull. Seismol. Soc. Am*. 80: 150–169.

Yang, T. and Y. Shen (2006). Frequency dependent crustal correction for finite frequency seismic tomography, *Bull. Seism. Soc. Am.* (in press).

Yang, T., Y. Shen, and X. Yang (2005). Crustal and mantle structure beneath Eastern Eurasia from finite frequency seismic tomography (FFST), in Proceedings of the 27th Seismic Research Review: Ground-based Nuclear Explosion Monitoring Technologies, LA-UR-05-6407, Vol. 1, pp. 479–488.

Seismic Identification and Source Characterization

DISCRIMINATION OF MINING EVENTS USING REGIONAL SEISMIC AND INFRASOUND WAVEFORMS: APPLICATION TO THE US AND RUSSIA

Stephen J. Arrowsmith[1], Marie D. Arrowsmith[2], Michael A.H. Hedlin[1] and Brian W. Stump[2]

University of California, San Diego[1] and Southern Methodist University[2]

Sponsored by National Nuclear Security Administration
Office of Nonproliferation Research and Development
Office of Defense Nuclear Nonproliferation

Contract Nos. DE-FC52-03NA99511[1] and DE-FC52-03NA99510[2]

ABSTRACT

Historically, event characterization has focused on the task of separating earthquakes and explosions. However, with the increasing availability of high-quality regional seismic data, including seismic array data, there is a need to characterize smaller events (mb 3.5 and below). The present challenge of seismic event identification therefore includes the task of identifying mining explosions, which fall within this lower range of magnitudes. The increasing availability of infrasound data, and in particular the advent of the International Monitoring System (IMS) infrasound array, affords new opportunities in the combined use of seismic and acoustic data for the discrimination of mining explosions. As detailed in last year's report, we have assembled a comprehensive database of earthquakes and mining explosions in three mining regions in the US and in the Altai-Sayan mining region in Russia. By establishing a good working relationship with a large mine operator in Wyoming, we have obtained a detailed ground-truth dataset of explosions in the Powder River basin. By focusing on this region initially, we have developed and tested three types of discrimination algorithms based on high-frequency phase amplitude measurements, spectral content and infrasound.

An algorithm for identifying delay-fired mining explosions by exploiting the time-independent spectral modulations produced by such explosions has been developed. This algorithm has been enhanced to make it applicable to seismic arrays. By applying the algorithm to the dataset of earthquakes and explosions at the Pinedale seismic array (PDAR) in Wyoming, it is shown that the use of array data significantly improves the discriminant. In a blind test, the method successfully identifies 97% of the events out of a group of 76 earthquakes and large delay-fired mining explosions (cast blasts).

The potential of infrasound for contributing to the event identification scheme is assessed using data from the PDIAR infrasound array in Wyoming, which is co-located with the PDAR array. Acoustic detections at the PDIAR array, generated using an array-based signal detection algorithm, are compared with predicted arrival times of cast blast acoustic signals. Predicted arrival times are based on ground-truth information from the mine, which have been adjusted by seismic observations. For one year of data, over fifty percent of cast blasts are associated with detections during July and August, with significantly fewer detections at other times of year. This result suggests that the use of infrasound has good potential for contributing to our identification scheme, although the potential is possibly seasonally dependent.

Amplitude ratios at PDAR have been considered for separating delay-fired mining blasts from nearby earthquakes (within 1,000 km of the Wyoming coal mine). Historically, in other regions, high-frequency P/S ratios have been successful at discriminating these types of events; however, in this region that discriminant fails. We believe this is due to a combination of both path effects (as described in Goforth and Zhou, 2006; Zhou and Stump, 2004) and variability in the source. In order to discover more about the role of source variability in successfully discriminating mining events, current work is designed to minimize the role of path effects by developing regional phase attenuation tomography models of the western US.

In order to assess the portability of the various discriminants tested in Wyoming to different regions, the above techniques are being applied to the dataset acquired for the Altai-Sayan region in Russia. Initial results on this effort are presented.

OBJECTIVES

Enhancements of Comprehensive Ground Truth Database

In order to relate discriminant performance to physical source processes, we have obtained more detailed ground truth information on a number of shots recorded at the PDAR. We have also obtained ground truth information on additional shots for testing the use of infrasound as a potential discriminant.

Further Development of Discriminants and Application to the Subset of Data

We have continued the development of the three discriminants discussed in Arrowsmith et al. (2005): time-varying spectral estimation, infrasound and amplitude ratios. A time-varying spectral estimation method is developed for application to single-component or three-component seismographs, and for either single stations or arrays. We have begun the development of an infrasound discriminant by evaluating the probability of observing infrasound signals from ground truth mining explosions, and how this varies with time-of-year. We also give progress on the amplitude ratio discriminant, in which we are working to refine the path corrections applied to the amplitude measurements via developing regional phase attenuation models of the western US. As outlined in Arrowsmith et al. (2005), we have developed a high-quality training dataset for application and testing of discriminants. We present the results of applying each of the three discriminants to the training dataset.

RESEARCH ACCOMPLISHED

Enhancements of Comprehensive Ground Truth Database

Arrowsmith et al. (2005) outline the development of a comprehensive ground truth database using earthquakes and mining events in three mining regions of the US (the Powder River Basin, southeast Arizona and northwestern Minnesota) and in the Altai-Sayan region in Russia. Due to the high-quality ground truth and close ties with local mining operators, the Powder River Basin has been chosen as a training dataset for the application and testing of regional discriminants. We have improved the training dataset outlined in Arrowsmith et al. (2005) by obtaining more detailed information on select mining explosions and by obtaining ground truth on additional mine shots.

The new ground truth information includes detailed shot-time information for a number of select cast blasts (i.e., number of shots in blast sequence, inter-shot delay times, inter-row delay times and depths of charges). This new information allows us to model regional waveforms from these complicated blast sequences and will be useful in further improving and testing the regional discriminants. The detailed ground truth information should allow us to relate discriminant performance to the source physics.

The development and testing of a regional discriminant based on infrasound data requires a ground truth dataset of mining explosions and earthquakes that covers every season, in order to properly assess the effect of seasonal changes of the atmosphere. The training dataset described in Arrowsmith et al. (2005) has been extended to include additional mining explosions and earthquakes in order to ensure that each season is adequately sampled.

Further Development of Discriminants and Application to the Subset of Data

Time-Varying Spectral Estimation Discriminant

We have developed a methodology for identifying delay-fired mining explosions that utilizes time-independent spectral modulations. The methodology is described in detail in Arrowsmith et al. (2006a) and the extension of the methodology for seismic arrays is described in Arrowsmith et al. (2006b). The methodology is applied to the training dataset described above (which consists of 98 mining explosions and 43 earthquakes), and shown in Figure 1. Briefly, rather than discriminating between two or more possible event classes, the technique can identify simply whether or not an event is a delay-fired mining explosion. The technique can provide seven separate discriminants based on the binary spectrograms of seismic events recorded at a three-component seismograph. Examples of binary spectrograms for a typical earthquake and cast blast in the training dataset are shown in Figure 2.

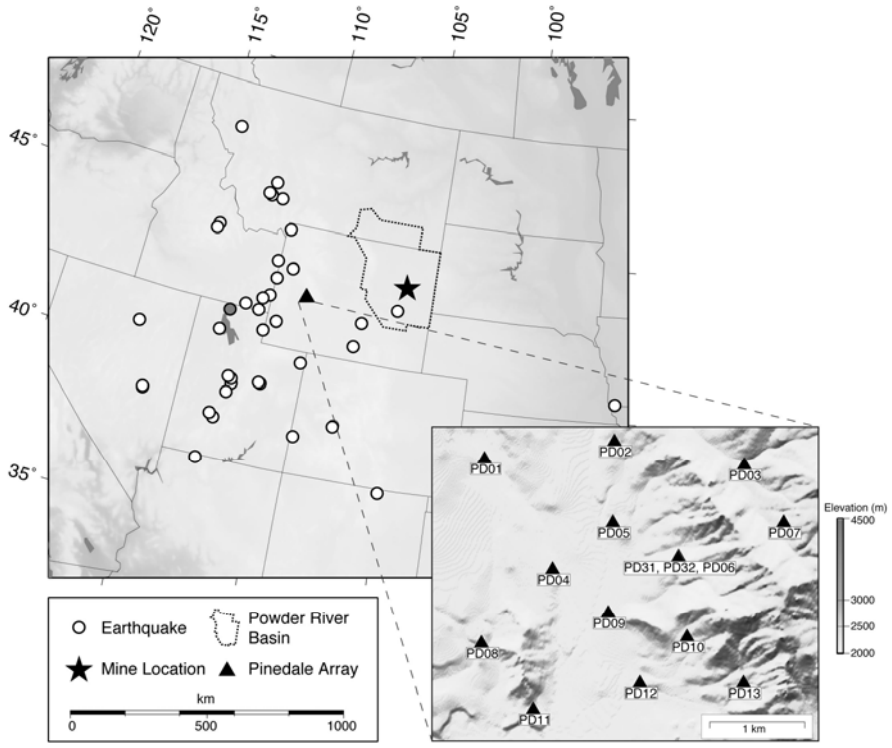


Figure 1. Location map of the study area showing the location of the PDAR seismic array (black triangle), the mine location (black star) and the locations of earthquakes in the dataset (circles). The location of the one misclassified earthquake is shown by the shaded circle, white circles represent the remaining earthquakes. Inset: Detailed map of the PDAR seismic array showing the locations of the 15 separate sensors.

The seven discriminants include the cepstral mean, the three values of cross-correlation of the binary spectrograms (evaluated on all three components) and the three values of autocorrelation of the binary spectrograms (on each component separately). To calculate the cepstral mean we first compute the two-dimensional Fourier transform of the binary spectrogram matrices, providing a 2D cepstral matrix. It is then straightforward to isolate energy periodic in frequency and independent of time, yielding 1D cepstra. The separate 1D cepstra from each of the individual components are then stacked and averaged over the first few cepstral coefficients. We have found the cepstral mean to be a more effective discriminant than simply taking the value of the maximum cepstral peak.

The seven discriminants exploit similar properties of the binary spectrograms: the regular pattern of spectral scalloping, its time independence and the correlation on all three components. Therefore, the discriminants are not completely independent of each other, providing some redundant information about the nature of the source. We perform a simple feature selection procedure in order to ensure that the addition of each discriminant is significant, and therefore that each discriminant contributes to the overall separation between delay-fired mining explosions and the remaining event population. The feature selection procedure also identifies the best combinations of d discriminants to use (where $1 \le d \le 7$). We start by identifying the best single discriminant (using the Mahalanobis distance as a measure of discriminant quality). Next, we identify the best combination of d discriminants, where d = 2,3…,7. At each step, we calculate an F statistic as a guide to determine whether the addition of the new discriminant is significant. The F-statistic (Hand, 1981; Taylor and Hartse, 1997) is given by the following:

$$F \sim \frac{(n-d-1)n_1 n_2 (D_d^2 - D_{d'}^2)}{(d-d')[n(n-2) + n_1 n_2 D_{d'}^2]}, \quad (1)$$

where n is the total number of events, n_1 is the number of earthquakes, n_2 is the number of delay-fired mine blasts, d is the total number of discriminants and d' is the number of discriminants for a particular iteration. $D_d^2 - D_{d'}^2$ is the difference in the Mahalanobis distance on the subset of d and d' discriminants. F is then compared with the tabulated F distribution for (d-d') and (n-d-1) degrees of freedom to examine whether the addition of the new discriminant is significant. The top panel in Figure 3 indicates which discriminant or discriminants are selected after each step in which a new discriminant is added. In the discussion that follows, and in Figure 3, we use Z, N and E to refer to the vertical, north and east component recordings respectively. In the figure, "auto" denotes the autocorrelation of a binary spectrogram on an individual component, "cc" denotes the cross-correlation between binary spectrograms recorded on two components, and "Mean cep" denotes the mean cepstrum. The corresponding Mahalanobis distance and F-statistic are also shown for each step in order to illustrate whether the addition of a new discriminant is significant. The overall Mahalanobis distance between the earthquakes and cast blasts increases as each new discriminant is added, however the final two discriminants [cc(Z&N) and cc(Z&E)] do not result in a significant increase in the Mahalanobis distance. This observation fits with the F-statistics that show that five of the seven discriminants improve the discrimination significantly but that the poorest two discriminants do not. Therefore, cc(Z&N) and cc(Z&E) could have been removed from the discrimination procedure without degrading the overall performance. However, the inclusion of the two discriminants does not degrade the Mahalanobis distance between the two groups and we have included them in our results.

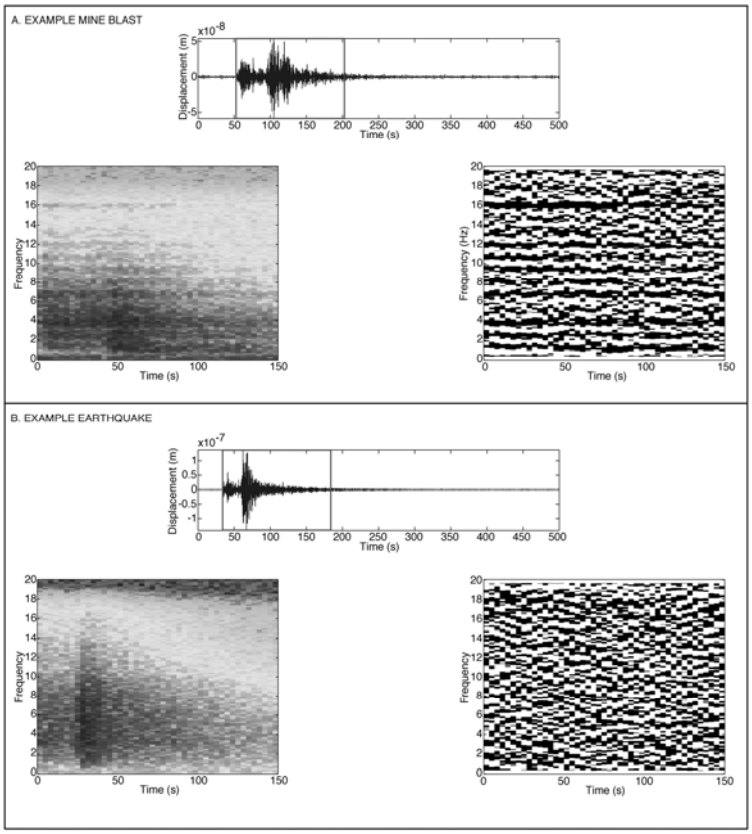


Figure 2. Input seismic waveforms with corresponding spectrograms and binary spectrograms for two example events. For each event, the portion of the waveform used in the computation of the spectrograms is shown. The first event, an example mine blast, exhibits clear spectral modulations that are time independent. The second event, which is a typical earthquake, shows no evidence of spectral modulations.

For a single-component seismogram, only two separate discriminants are computed (cepstral mean and autocorrelation on the vertical component). For any given station, the algorithm can effectively be tuned with a

reference set of events, in order to maximize the success rate in identifying delay-fired and non-delay-fired events. This is accomplished by searching for the optimum values of the free parameters that maximize the separation between the two classes of reference events using the mean Mahalanobis distance. The free parameters in the methodology are the spectrogram duration (*w*), the averaging windows used in converting the spectrograms into binary form (*sp1* and *sp2*), and the window over which the mean cepstral value is evaluated (*cep*). The results of the optimization procedure applied to the training dataset show that the performance of this technique is highly dependent on the values of the input parameters (Figure 4). An inherent assumption in this approach is that the nature of delay-fired blasting in a particular area does not vary significantly, and that delay times between individual shots and rows in blasting arrays are similar. Otherwise it could be possible that a single optimum set of input parameters would not exist, as the optimum parameters would be different for each source.

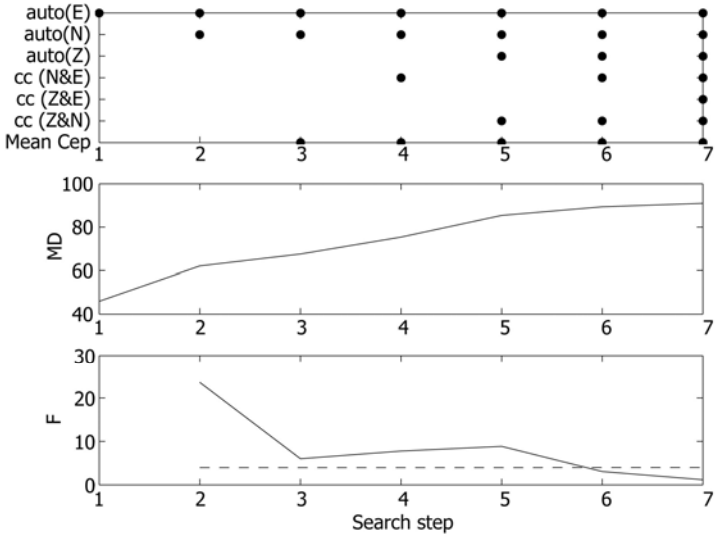


Figure 3. Results of the seven-step feature selection procedure. Each step represents the optimum combination of d discriminants (1≤d≤7). Top panel: Dots indicate the optimum combination of discriminants for each search step. Middle panel: Mahalanobis distance between the earthquake and cast blast groups calculated for each search step (using the appropriate number of discriminants). Bottom panel: Calculated F-statistic from Equation 4 (solid line) and corresponding tabulated value of the F distribution for (d-d') and (n-d-1) degrees of freedom (dashed line).

We have developed a procedure to correct for the effect of pre-event noise, which can exhibit low amplitude spectral modulations. First, we compute a spectrogram of the pre-event noise and evaluate the mean scaled logarithm of the pre-event spectrogram in each frequency band ($\overline{x}_{f(pre)}$). Next, we compute the following parameter for each pixel in the spectrogram of the signal:

$$\alpha = \left| x_{tf} - \overline{x}_{f(pre)} \right|, \tag{2}$$

where x_{tf} is the scaled logarithm of the signal spectrogram at time *t* and frequency *f*. We then randomize the pixels in the binary spectrogram where $\propto$ is less than a threshold value.

For array data, we evaluate a spectrogram for each element of the array separately, and stack the spectrograms from all the array elements. Since each spectrogram is computed for a time window that begins at the picked first arrival at each array element (with duration *w* set as a free parameter), they can be stacked without the need for aligning based on the speed and direction of the incoming wavefront. The results of applying the methodology to 43 earthquakes and 98 delay-fired mining explosions (Figure 1) are shown in Figure 5. The cast overburden shots separate well from the earthquakes, although the smaller shot types do not (for description of shot types see Table 1). The separation improves if (1) the full PDAR array is used (rather than an individual instrument) and (2) the noise correction is applied to remove pre-event noise. In a drop-one event test, this method can identify 97.4% of the earthquakes and cast blasts (i.e., 74 out of the 76 events are identified correctly). The two events that are classified incorrectly (Figure 1) appear to be failures of this methodology. We hope that by combining this discrimination procedure with the other regional discriminants that these misidentified events would be successfully identified.

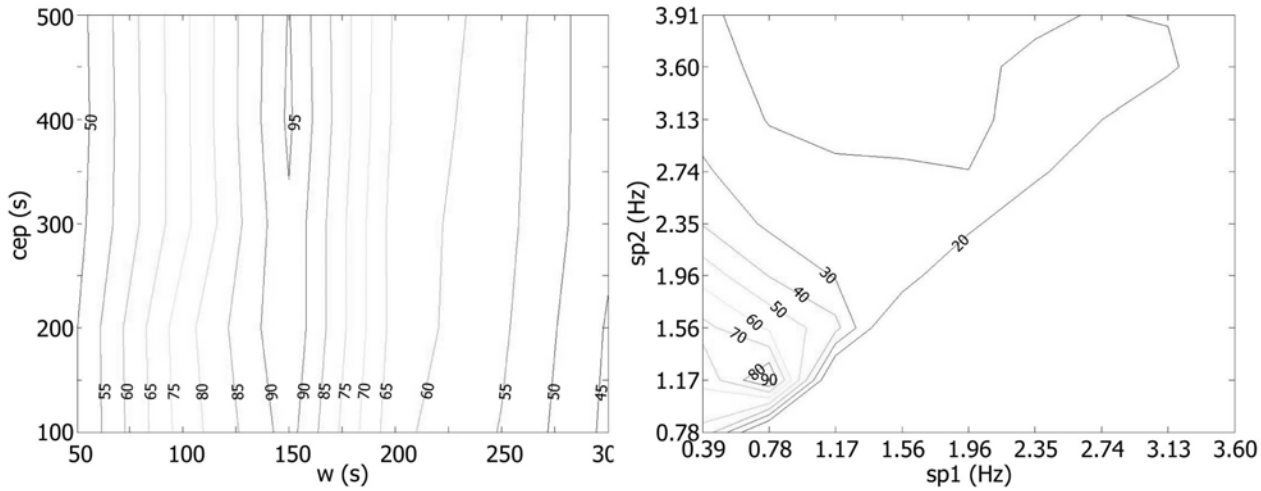


Figure 4. Cross-sections of the objective function (Mahalanobis distance) that show the optimal input parameters. Left panel: Mahalanobis distance as a function of *cep* and *w* with *sp1* and *sp2* held at their optimal values. Right panel: Mahalanobis distance as a function of *sp1* and *sp2* with *cep* and *w* held at their optimal values. Note the requirement that *sp2*>*sp1*.

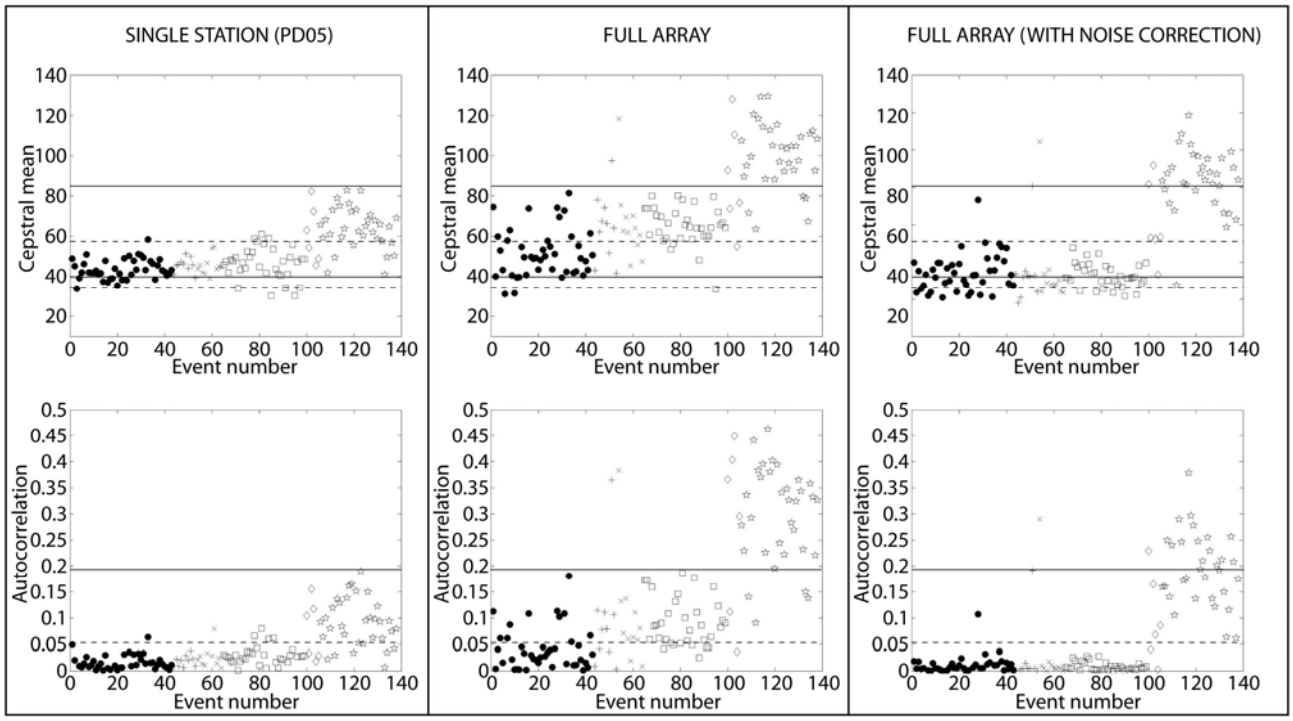


Figure 5. Values of the two discriminants (cepstral mean—top , autocorrelation—bottom) obtained for each event using a single station only (left), the full array stack (middle) and the full array stack with the noise correction applied (right). Black circles represent earthquakes, plus signs represent parting shots, crosses represent coal extraction shots in the upper coal seam, open squares represent coal extraction shots in the main coal seam, open diamonds represent TS overburden blasts and open stars represent cast overburden shots (refer to Table 1 for more information on shot types). The solid lines show the extreme upper and lower bounds of discriminants evaluated from 50 samples of stacked pre-event noise spectrograms (using all 15 array elements). The dashed lines show the equivalent upper and lower bounds for a single array element (i.e., without stacking).

Table 1. Blast types for a large coal mine in the Powder River Basin, Wyoming

Blast Type	Description	Min Yield (lb)	Max Yield (lb)
Cast Overburden	Overburden is cast and removed into adjacent empty pit	300,000	2,500,000
TS Overburden	Blasts in overburden material to be excavated by shovels loading into trucks	100,000	600,000
Coal - Main	Blasts in the main coal seam, which is 60–70 ft in thickness	20,000	200,000
Coal - Upper	Blasts in the upper coal seam, which is 10 ft in thickness	2,000	10,000
Parting	Blasts of waste material layer between the upper and lower coal seam, ranging from 0 to 40 ft in thickness	200	500

Infrasound Discriminant

We are currently developing a discriminant based on the presence (or absence) of a regional infrasound signal. The premise of the discriminant is surface sources generate more infrasound than equivalent sources located at depth. Therefore, infrasound has the potential to be used as an effective depth-discriminant, and the presence of an infrasound signal associated with an event would support the hypothesis that the event was a mining explosion rather than an earthquake. The first step in developing this discriminant is to assess the relative probabilities that ground-truth mining explosions or earthquakes are associated with infrasound signals. Since atmospheric temperatures and winds (which vary seasonally) affect infrasound propagation, it is important that these relative probabilities are assessed as a function of time of year. To this end, we have assembled a dataset of ground truth mining explosions that cover every month of the year.

We have developed a simple automatic procedure to search for an associated infrasound signal from each mining explosion based on signal arrival time and back azimuth. We have obtained waveform data from the PDIAR infrasound array in Wyoming (Figure 1). Signal detections are obtained using the Progressive Multichannel Cross-Correlation procedure (PMCC) (Cansi, 1995), which is an array-based algorithm that uses cross-correlation of the waveforms from the separate array elements to determine signal detections (with associated back azimuths, speeds, etc.). For each ground-truth mining explosion, the predicted arrival time (using a celerity of 300 m/s) and true great-circle back azimuth are calculated. We then search for detections from the PMCC algorithm with an arrival time and back azimuth that match the predictions (within an appropriate time-window and back azimuth range that reflect deviations from the assumed celerity of 300 m/s and true back azimuth). Figure 6 shows the relationship between the actual numbers of cast blasts (for which we have been able to obtain waveform data at PDIAR) and the corresponding number of associated detections (using an allowed time-offset of +10 minutes and azimuth-offset of –5 degrees). In July and August, greater than 50% of explosions are associated with detections, whereas during other months there are no detections (except November, when there are unusually many ground truth explosions). This fits with our knowledge of stratospheric wind directions, which assist stratospheric returns from east to west during the summer, but inhibit returns during winter months. This indicates that the use of infrasound as a discriminant will likely be seasonally dependent.

The next steps in the development of this discriminant will be (1) to further study detections that are associated with mining explosions in order to improve confidence in the tie-in and (2) to repeat this analysis for the earthquakes in the training dataset. If the results obtained indicate that there is potential for infrasound as a discriminant, we will work on developing an automatic infrasound discriminant and evaluating procedures for integrating the discriminant with the results from other regional discriminants.

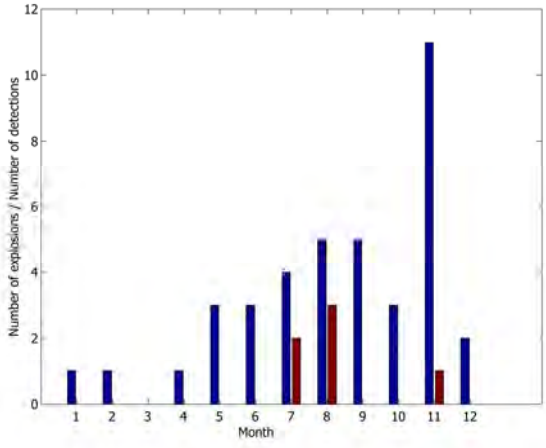


Figure 6. Number of explosions with corresponding waveform data (blue bars) and number of associated detections with ground truth mining explosions (red bars) as a function of month of the year.

Amplitude Ratio Discriminant

Previously, we tested traditionally well-performing discriminants, such as high-frequency P_g/L_g, on regional phase amplitudes from the events shown in Figure 1 recorded at the PDAR. The phase amplitudes were corrected for path and source effects using the MDAC methodology (Walter and Taylor, 2002). We chose a simple 1D path correction based on an average Q model along the path between the mine and the Pinedale array. The results (Figure 7) indicate that this is a poorly performing discriminant, evidenced by variability in P_g and L_g amplitudes for similar event types at high frequencies.

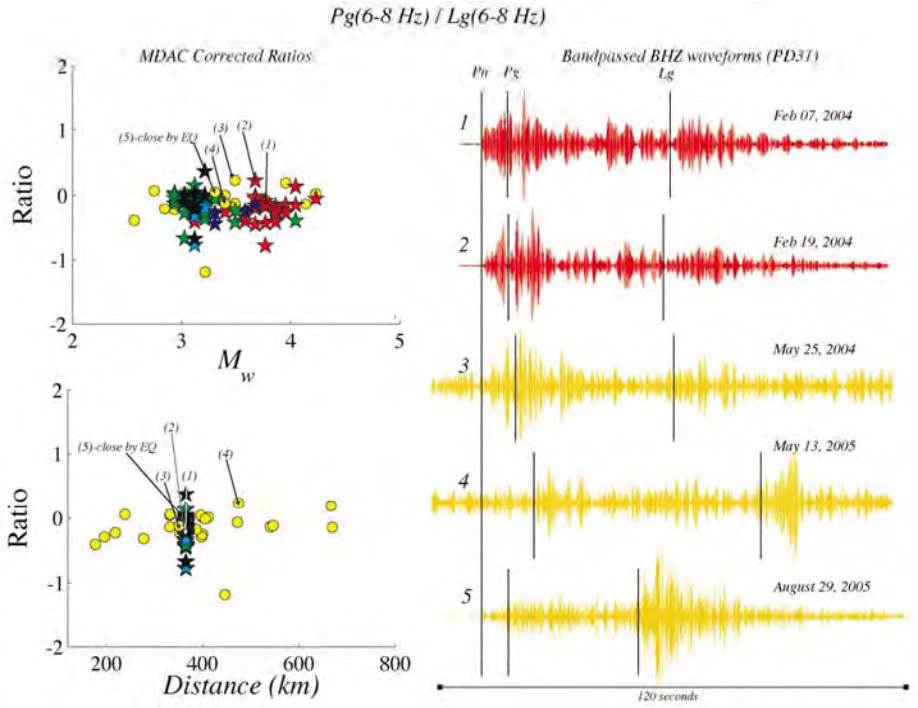


Figure 7. (Left) MDAC corrected P_g/L_g (6-8 Hz) amplitude ratio for mining events (colored stars) and earthquakes (yellow circles) as a function of M_w and distance. (Right) Selected waveforms for two cast blasts (red) and three earthquakes (yellow) with regional phase window onset times marked.

In order to investigate why the discriminant performs as it does, we need to first determine if the 1D path correction is adequate for this region so that we can rule out underlying path effects as the cause for the poor discriminant performance. Previous studies in this geographic region have shown that path effects greatly influence regional waveforms (Zhou and Stump, 2004; Goforth and Zhou, 2006), indicating that simple 1D path corrections may in fact be inadequate. Therefore, we are developing 2D path corrections via construction of attenuation tomography maps of the western United States for the regional phases. Such maps can be imported into the MDAC processing scheme and allow for path corrections based on variable Q along a given path.

We are in the process of our first round of data collection, which includes gathering earthquake information for earthquakes with magnitudes > 4.0 in the region [120 W 104W 30N 50N] recorded at broadband stations in the same region. This effort has amounted in 488 earthquakes recorded about 35 stations. We have also incorporated earthquake data from the western US database developed by Walter et al. (2003). Figure 8 summarizes the data we have collected thus far. As our data coverage is limited in the Intermountain and Great Plains regions, our next round of data collection efforts will focus on smaller magnitude events recorded at stations in the northern and middle Rocky Mountains and Great Plains. The processing scheme on this data includes making regional phase picks and amplitude measurements, using coda magnitude methodology to obtain reliable moments, and finally, to apply inversion techniques similar to those utilized by Lay et al. (2006).

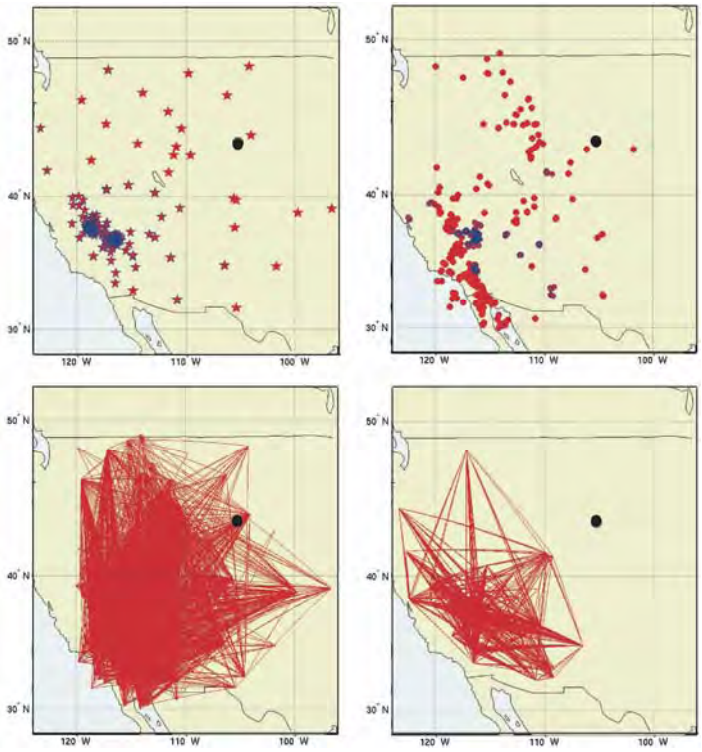


Figure 8. Summary of data gathered in the first round of collection efforts for the attenuation tomography study of the western US. The top left figure shows stations, where red stars represent new stations utilized and blue stars represent those incorporated from the Walter et al. (2003) dataset. Red stars outlined in blue are overlapping stations. The top right figure shows events used, with the same color scheme as the stations plot. The bottom left figure illustrates path coverage for the new data added for this study. The bottom right figure shows path coverage for the Walter et al. (2003) dataset. In all figures, the black circle indicates the location of the Wyoming coal mine referred to in this paper.

CONCLUSIONS AND RECOMMENDATIONS

This report builds on the work discussed in Arrowsmith et al. (2005) in two primary ways: (1) enhancement of ground truth testing dataset and (2) development of discriminants and application to testing dataset. Under the first point we have obtained the following: (a) improved ground truth on select cast blasts for the purpose of relating discriminant performance to source physics, and (b) ground truth on additional shots for testing the infrasound discriminant. Under the second point, we have outlined significant progress in developing three regional discriminants: time-varying spectral estimation, infrasound and amplitude ratios. A new time-varying spectral estimation is discussed, which is applicable to seismic arrays and successfully identifies 97.4% of events from a testing dataset of 43 earthquakes and 33 cast blasts. We outline the initial work on developing an infrasound discriminant, whereby we have begun evaluating the probability of detecting infrasound signals from cast blasts and found a strong seasonal dependence, with over 50% of events being associated with detections in July and August. We also give progress on the amplitude ratio discriminant; because significant variability was seen in regional waveforms, we are working to refine the path corrections applied to the amplitude measurements via developing regional phase attenuation models of the western US. Future work will focus on three main issues: (1) continued development of the three discriminants outlined in this report, (2) development of additional discriminants (e.g., correlation, mb/Ms), and (3) development of a scheme for integrating all the regional discriminants into a comprehensive discrimination package.

ACKNOWLEDGEMENTS

We thank Steve Taylor of Rocky Mountain Geophysics for his help with the feature selection procedure; Steve Beil of ArchCoal for providing ground truth shot time data; and Michele Kelley at AFTAC for her help in providing us with PDIAR data.

REFERENCES

Arrowsmith, M. D., S. J. Arrowsmith, B. Stump, and M. Hedlin (2005). Discrimination of small events using regional waveforms: Application to seismic events in the US and Russia, in *Proceedings of the 27th Seismic Research Review: Ground Based Nuclear Explosion Monitoring Technologies*, LA-UR-05-6407, Vol. 1, 498–508.

Arrowsmith, S. J., M. D. Arrowsmith, M. A. H. Hedlin, and B. Stump (2006a). Discrimination of delay-fired mining events in Wyoming using an automatic time-frequency discriminant, *BSSA* (revised and submitted).

Arrowsmith, S. J., M. A. H. Hedlin, M. D. Arrowsmith, and B. Stump (2006b). Identification of delay-fired mining explosions using seismic arrays: Application to the PDAR array in Wyoming, USA, *BSSA* (submitted).

Cansi, Y. (1995). An automated seismic event processing for detection and location: The P.M.C.C. method, *Geophys. Res. Lett.* 22: 1,021–1,024.

Goforth, T. T. and R. Zhou (2006). Characteristics of seismic waves produced by surface mining operations, 32nd Annual Conference of the International Society of Explosives Engineers, International Society of Explosives Engineers, January 29–February 1, 2006, Dallas, TX.

Hand, D. J. (1981). *Discrimination and Classification*. New York: Wiley.

Lay, T., X. Xie, X. Yang, and M. Arrowsmith (2006). Development of regional phase tomographic attenuation models for Eurasia, in current Proceedings.

Taylor, S. R. and H. E. Hartse (1997). An evaluation of generalized likelihood ratio outlier detection to identification of seismic events in Western China, *Bull. Seism. Soc. Am.* 87: 413–421.

Walter, W., K. Smith, J. O'Boyle, T. Hauk, F. Ryall, S. Ruppert, S. Myers, M. Anderson, and D. Dodge (2003). Improving the fundamental understanding of regional seismic signal processing with a unique Western United States dataset, in *Proceedings of the 25th Seismic Research Review—Nuclear Explosion Monitoring: Building the Knowledge Base*, LAUR-03-6029, Vol. 2, 486–494.

Walter, W. R. and S. R. Taylor (2002). A revised magnitude and distance amplitude correction (MDAC2) procedure for regional seismic discriminants: Theory and testing at NTS, Lawrence Livermore National Laboratory report UCRL-ID-146882, pp. 1–13.

Zhou, R.-M. and B. W. Stump (2004). Rayleigh waves generated by mining explosions and upper crustal structure around the Powder River basin, Wyoming, *Bull. Seism. Soc. Am.* 94, 1,410–1,429.

A COMPARISON OF DIFFERENT SURFACE WAVE MAGNITUDE FORMULAS ON A EURASIAN DATASET

Jessie Bonner[1], Michael Pasyanos[2], Heather Hooper[1], Mark Leidig[1], and David Harkrider[1]

Weston Geophysical Corporation[1] and Lawrence Livermore National Laboratory[2]

Sponsored by National Nuclear Security Administration
Office of Nonproliferation Research and Development
Office of Defense Nuclear Nonproliferation

Contract Nos. DE-AC52-04NA25547[1] and W-7405-ENG-48[2]

ABSTRACT

One of the most robust methods for discriminating between explosions and earthquakes is the relative difference between the body wave (m_b) and surface wave (M_s) magnitudes for a seismic event. Most M_s formulas have been developed for teleseismic distances and for Rayleigh waves in the period range of 17–23 s. For earthquakes of small-to-intermediate magnitude and explosions recorded at regional distances, the amplitudes of Rayleigh waves in this period range may be below background noise levels; however, shorter period surface waves (< 15 s) may still be extracted and processed using phase-match filtering. Thus, calibrated and transportable formulas, which allow for estimation of M_s at regional distances at the period of maximum amplitude (between 5 and 25 s), can be used to lower the M_s thresholds for small earthquakes and explosions in Europe and Asia. Additionally, these calibrated formulas may be able to significantly reduce the variance in M_s estimates for larger events in the region.

During the past year, we have continued our research into improving M_s measurements. We have developed *evalsurf*, a Matlab program that estimates variable-period magnitudes using the Russell (2006) and M_s Variable-Period, Maximum Magnitude Estimation (VMAX) measurement technique (Bonner et al. 2006) and compares these magnitudes to the popular formulas of Marshall and Basham (1972) and Rezapour and Pearce (1998*). Evalsurf* uses the updated Lawrence Livermore National Laboratory (LLNL) group velocity models (Pasyanos, 2005) to phase-match filter the fundamental mode Rayleigh waves. The models are also used to ensure that the signal passes a dispersion test prior to processing the event for a magnitude. A backazimuth test must also be passed before estimating the M_s (VMAX), Marshall and Basham (1972), and Rezapour and Pearce (1998) magnitudes.

We have applied the program to 240 Eurasian earthquakes recorded on 1 to 21 stations at distances of up to 7,000 km. The M_s(VMAX) and Marshall and Basham surface wave magnitudes were measured at periods between 8 and 25 s and 10 and 40 s, respectively. The Rezapour and Pearce magnitudes were estimated at periods between 18 and 22 s in order to closely mimic processing routines at the International Data Center. We used the Murphy et al. (1997) screening criterion for M_s—m_b to determine the percentage of single-station estimates that screened as earthquakes by each technique. Out of 2,484 station-source pairs, we screened 95.7%, 93.8%, and 89.3% using M_s(VMAX), Marshall and Basham, and Rezapour and Pearce, respectively. We note that for our smaller explosion population (102 estimates), each technique had the same number of single-station estimates that screened as earthquakes: three. For network-averaged magnitudes, there were no misclassified nuclear explosions for any of the three techniques. The M_s(VMAX) technique showed the smallest average interstation standard deviation (0.22 m.u.) followed by the Marshall and Basham (0.26 m.u.) and Rezapour and Pearce (0.27 m.u.) methods.

These results suggest that the M_s(VMAX) technique provides optimal earthquake screening in our Eurasian study region. During the final year of this project, we will develop M_s threshold maps for regions of monitoring concern using the variable-period M_s(VMAX) formula and improved signal processing techniques.

OBJECTIVES

Developing a methodology for calculating surface wave magnitudes that is valid at both regional and teleseismic distances, applicable to events of variable sizes and signal-to-noise ratios, calibrated for variable structure and propagation, and easy to automate in an operational setting, is an important monitoring goal. Our objectives are to create such a methodology, and to use it to lower M_s estimation and detection thresholds. We hope that the method will provide a seamless tie between M_s estimation at regional and teleseismic distances.

Our methodology includes the following:

1. Extending the geographic coverage of existing group velocity tomography maps to our entire study area, as well as extending the maps to periods of 10 s or less,
2. Using a semi-automated Rayleigh wave detector to verify that the waveforms contain fundamental-mode Rayleigh waves,
3. Using the updated group velocity maps and automated phase-match filtering to extract the surface waves from the waveforms,
4. Using a variable-period maximum amplitude M_s formula based on Russell (2006) to calculate M_s,
5. Comparing the broadband formula and others for regional distance applications at a number of stations in the study area, and
6. Developing empirical and theoretical M_s threshold maps of the study area.

We have made progress in all aspects of our research with the exception of the final task (Task 6), and the results are included in the following sections of this review paper. During the final year of the research project, we will develop empirical and theoretical threshold maps based on our current research findings.

RESEARCH ACCOMPLISHED

Updates to Group Velocity Models

We have updated the LLNL group velocity models in southern Asia (Figure 1). The results highlight the Indian shield region as relatively fast compared with the slower regions associated with the Himalayas and Bay of Bengal. We continue to update the group velocity models for southern Asia at periods greater than 10 s as data become available.

Processing Improvements

We provide an example of our processing using the program *evalsurf*. The data are examined to ensure that they pass dispersion and backazimuth tests before being narrow-band filtered. Then the amplitude is recorded and the magnitude is calculated. Figure 2 shows an example of waveform data for an event in Iran recorded at station AAK at a distance of 2,010 km. The rotated traces in Figure 2 show the Love wave coming in at approximately 570 s on the transverse component and the Rayleigh wave coming in at about 650 s on the radial and vertical components. The red line on the vertical trace shows the phase-match filtered trace, which looks very similar to the original trace, since this event had a good signal-to-noise-ratio. The great circle path for the event is shown in Figure 3, superposed on the LLNL group velocity maps for the region.

Figure 4 shows the dispersion test, in which the dispersion of the trace (illustrated by the colored contours) is compared to that predicted from the surface wave model (white squares with uncertainty bars connected by the dashed white line). For this event the comparison is favorable, indicating that the energy from the event is coming in at the expected arrival time for most periods. Figure 5 shows the backazimuth test. The horizontal traces are rotated to maximize the cross-correlation of the Hilbert-transformed vertical component and the radial component for a number of backazimuths (Chael, 1997; Selby, 2001). In this example, the estimated backazimuth is 246°, while the true backazimuth is 240°, indicating that the event is arriving from the expected direction

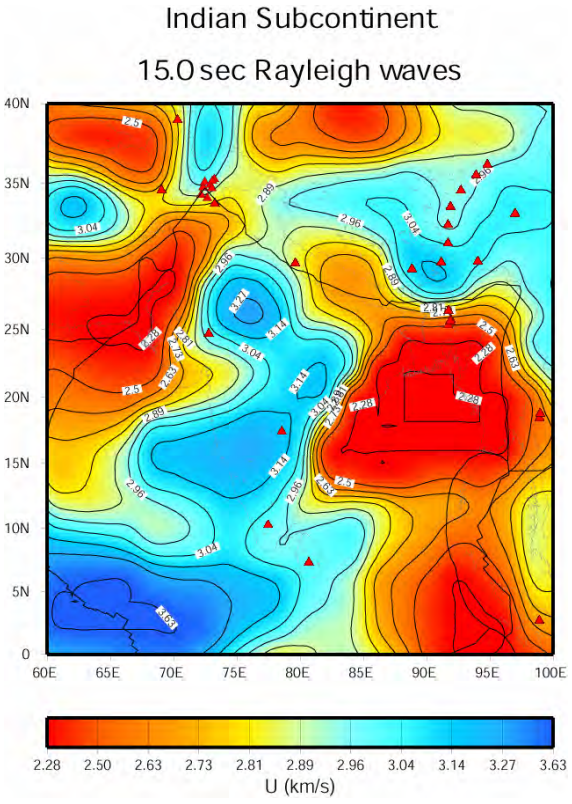


Figure 1. Tomographic inversion of Rayleigh wave dispersion curves at 15-s period for southern Asia.

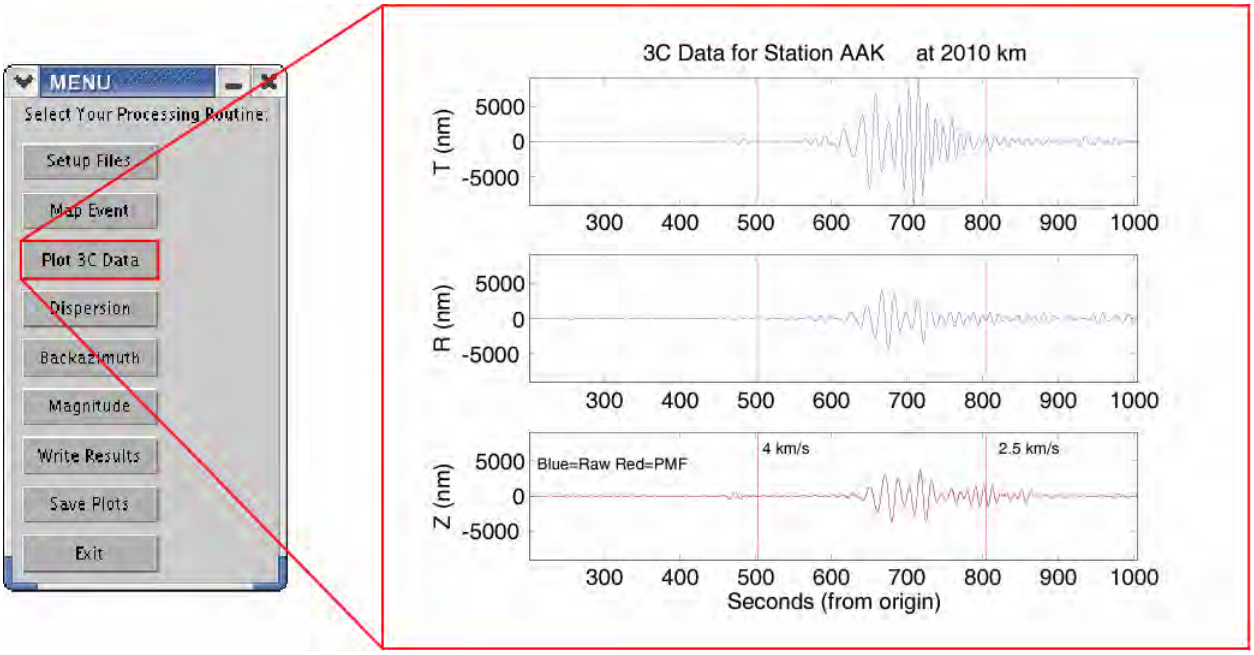


Figure 2. Waveform data and phase-match filtering for an event in Iran recorded at station AAK.

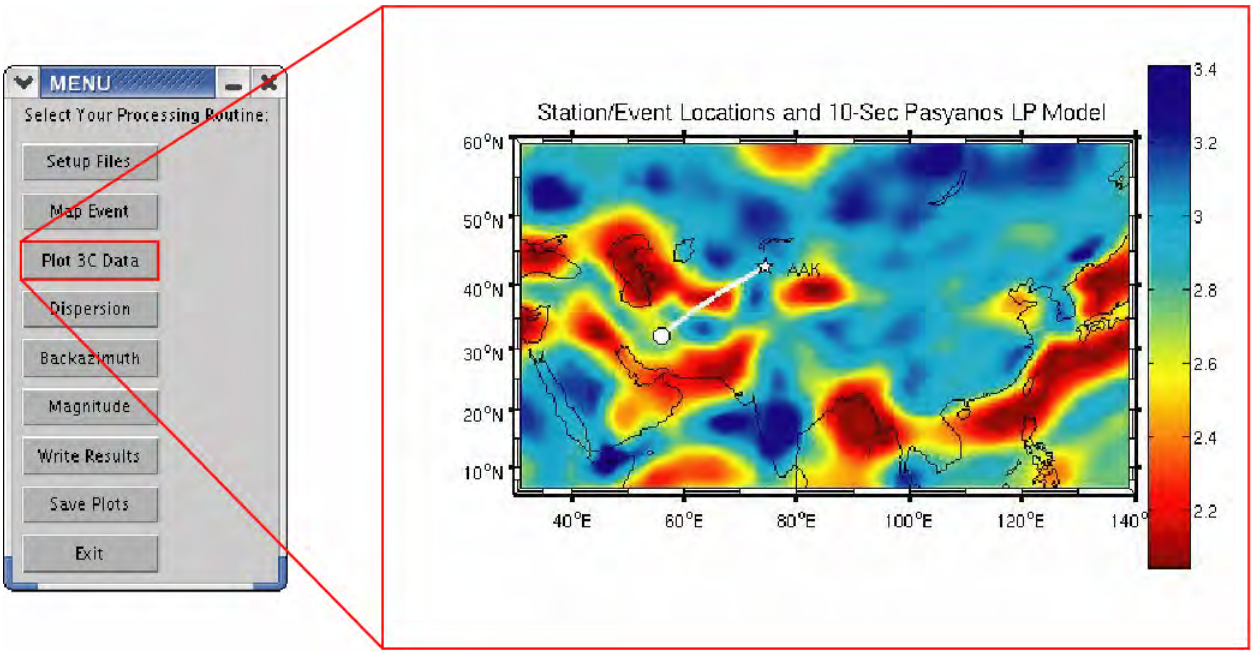


Figure 3. LLNL 10-s group velocity map, event and station locations, and great circle path for the data shown in Figure 2.

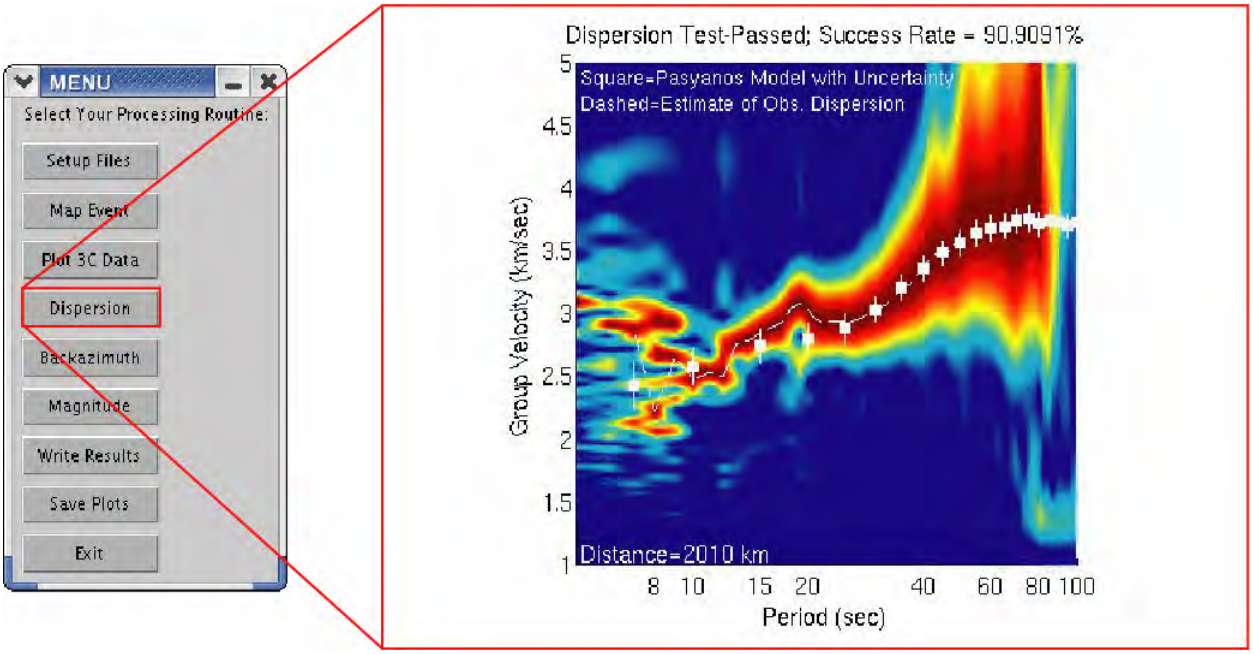


Figure 4. Dispersion test for the data shown in Figure 2.

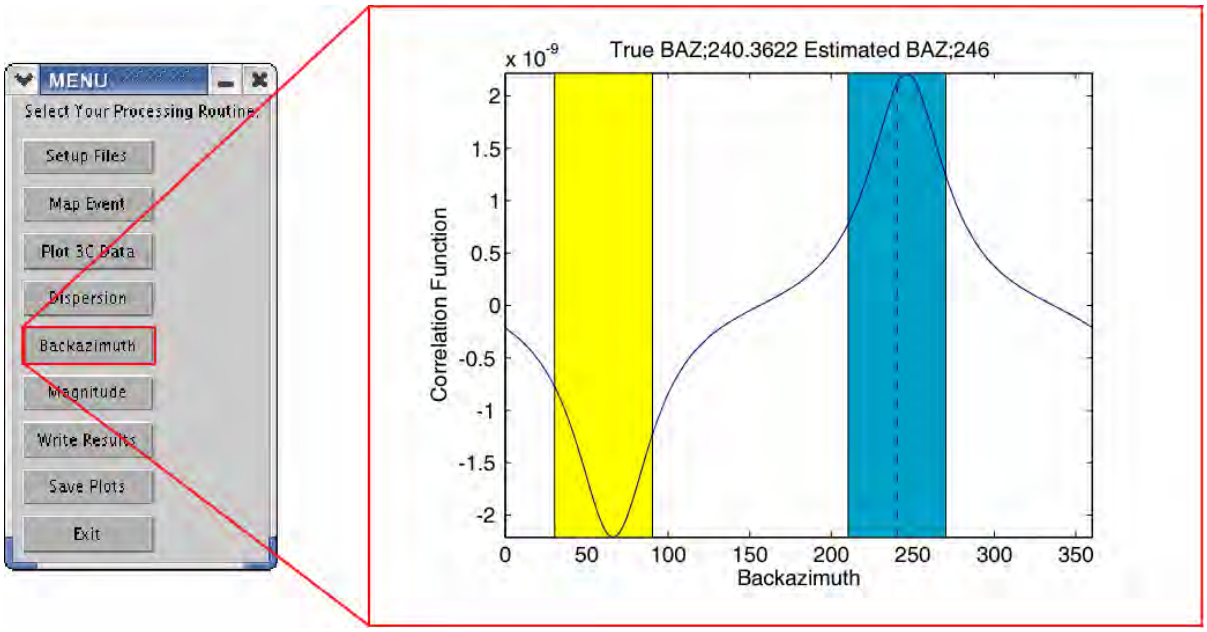


Figure 5. Backazimuth test for the data shown in Figure 2.

Once we are satisfied that we have identified Rayleigh waves with the correct velocity and backazimuth for the event of interest, we calculate surface wave magnitudes using the Rezapour and Pearce (1998), Marshall and Basham (1971), and VMAX (Russell, 2006; Bonner et al. 2006) methods. For this analysis, Rezapour and Pearce (1998) magnitudes are only calculated at periods between 18 and 22 s in order to closely mimic processing routines at the International Data Center. We consider surface waves with periods between 8 and 25 s for the VMAX magnitudes, and surface waves with periods between 10 and 40 s for the Marshall and Basham (1971) magnitudes. The results for this event (Figure 6) and most events analyzed in this study show that the magnitudes from all 3 techniques are within 0.2 m.u. of each other.

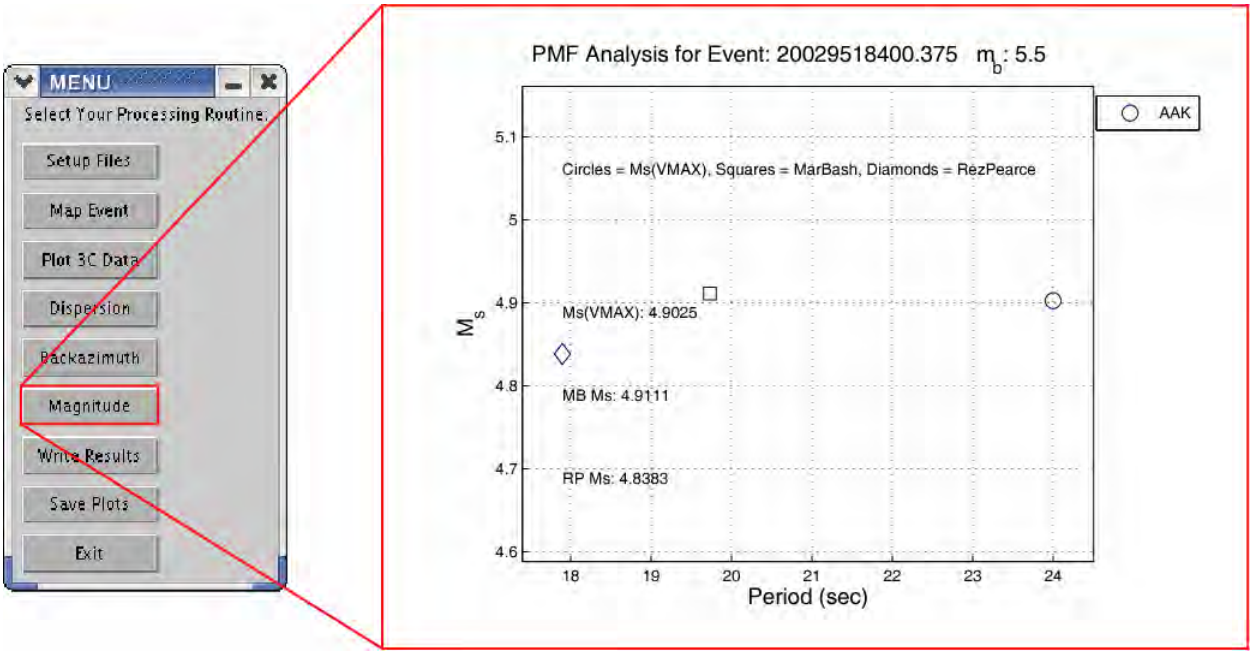


Figure 6. Surface-wave magnitudes for the data shown in Figure 2.

Why Variable Periods?

In Figure 7, we demonstrate one of the reasons why we use variable-period surface waves**.** We have plotted M_s vs. backazimuth for a different earthquake in Iran using the VMAX technique (top panel), Marshall and Basham's variable-period formula (middle panel), and Rezapour and Pearce's formula (which is for periods of 18–22 s only) (lower panel). For this particular event, the slightly sinusoidal nature of the M_s measurements for the Rezapour and Pearce formula (lower panel) demonstrates the effects of a spectral hole at approximately 20 s at some backazimuths, which is a result of the earthquake focal mechanism. Note that the VMAX and Marshall and Basham techniques do not show this pattern, since these techniques ignore the hole. This results in lowered network variance (the variance of M_s calculated using VMAX is usually lower than Marshall and Basham as shown here, even though both are variable period) and a larger M_s estimate. Lowered network variance and larger M_s estimates both improve discrimination.

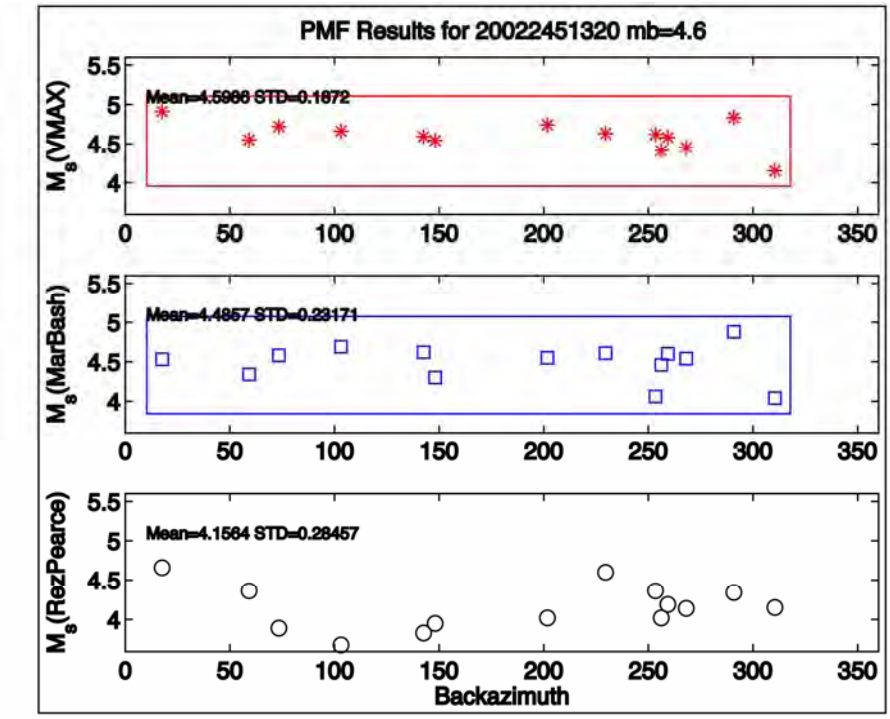


Figure 7. M_s as a function of backazimuth for the three M_s formulas.

Application in Central Asia

We have applied a number of surface wave magnitude formulas to events in Central Asia (Figure 8) at regional distances. We have made M_s estimates for 261 events (240 earthquakes, 3 mine events, and 18 nuclear explosions). Results are shown in Figure 9. The top panels show m_b: M_s, where the surface wave magnitude has been calculated using the Rezapour and Pearce (1998) formula. In the middle panels, we use the formula of Marshall and Basham (1972). We have used the path correction P(T) for continental Eurasia. The bottom panels show M_s calculated using the VMAX formula. For each set, the figure to the right uses the same formula on waveforms that have been phase-match filtered. In each figure, earthquakes are shown as green circles, chemical explosions as yellow diamonds, and nuclear explosions as red triangles. While m_b: M_s easily discriminates the nuclear explosions, the chemical shots generally fall along the earthquake trend. The average interstation deviations of the magnitudes (without phase-match filtering) are 0.24, 0.24, and 0.21 m.u. for each of the formulas, respectively. In this dataset, using phase-match filtering reduces the magnitude variance slightly for earthquakes, but much more significantly for explosions.

We have also examined these techniques for single-station magnitude estimation. We used the Murphy et al. (1997) screening criterion for M_s—m_b to determine the percentage of single-station estimates that screened as earthquakes using each technique. Out of 2,484 station-source pairs, we screened 95.7%, 93.8%, and 89.3% using VMAX, Marshall and Basham, and Rezapour and Pearce, respectively (Figure 10). We note that for our smaller explosion population (102 single-station estimates), each technique had the same number of single-station estimates that screened as earthquakes: three. For network-averaged magnitudes, there were no misclassified nuclear explosions for any of the three techniques.

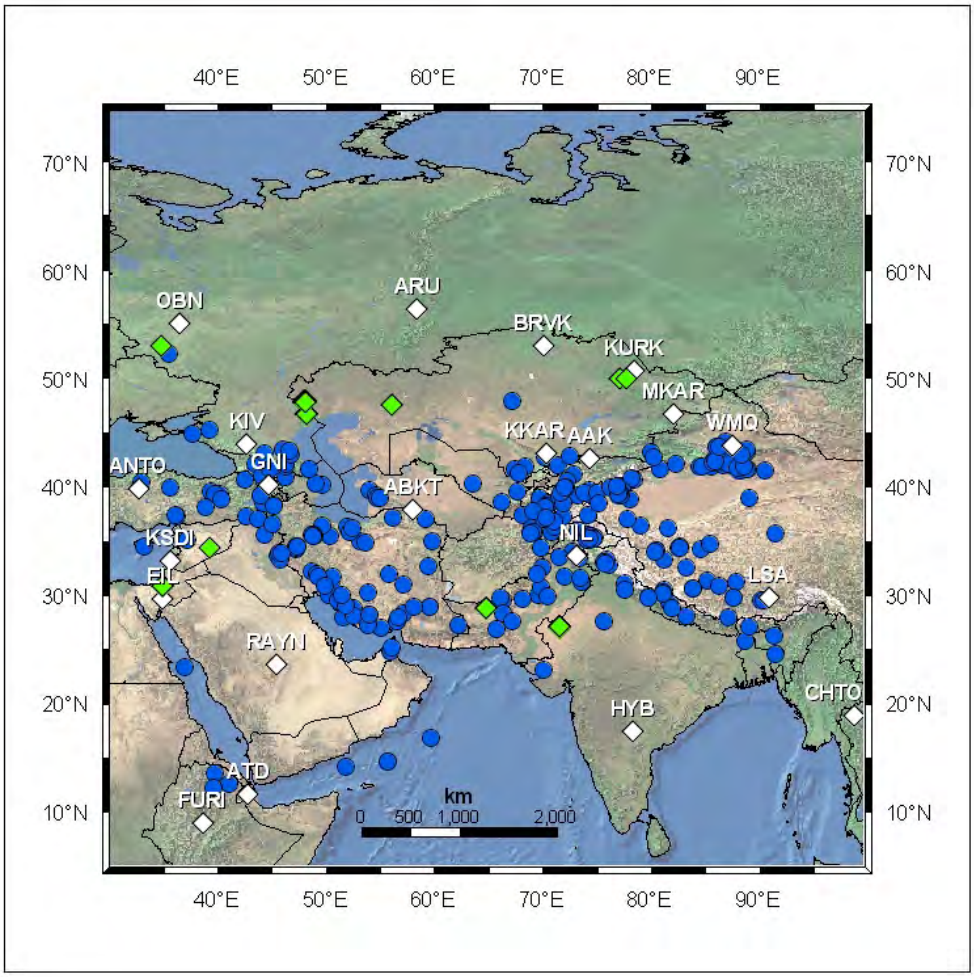


Figure 8. Locations of events and stations in Central Asia used for our study.

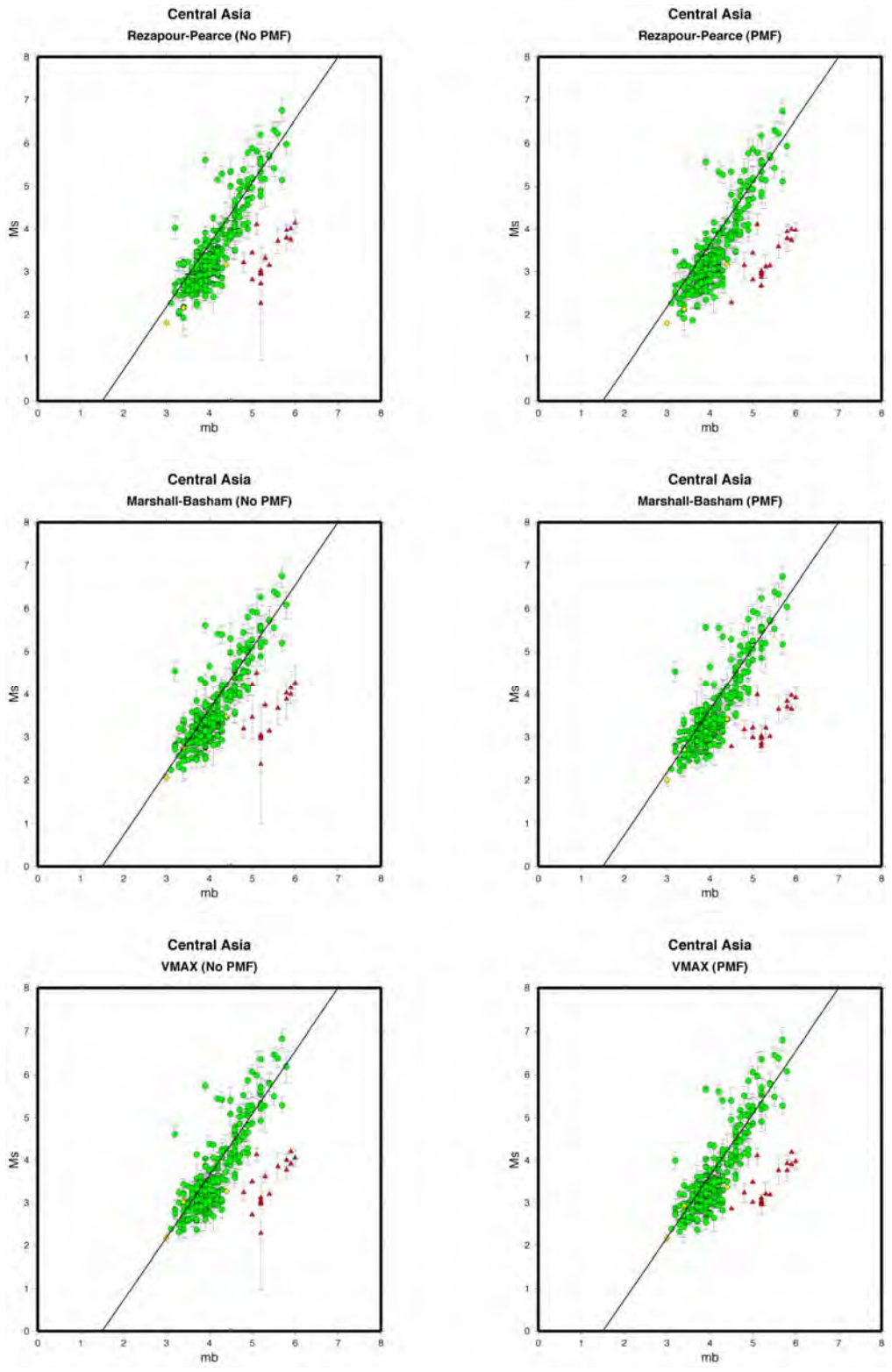


Figure 9. m_b: M_s for Central Asia using the Rezapour and Pearce (top), Marshall and Basham (middle), and VMAX (bottom) formulas without (left) and with (right) phase-match filtering. Red triangles represent nuclear explosions, green circles are earthquakes, and yellow circles are mining explosions.

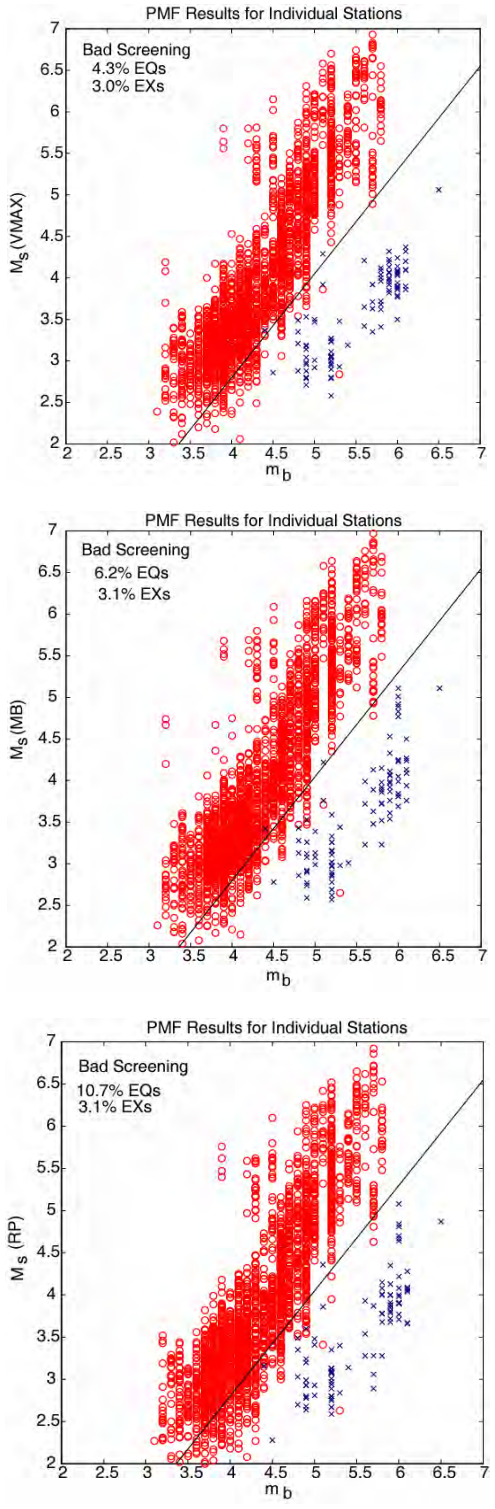


Figure 10. Single-station surface wave magnitude estimates for earthquakes (circles) and explosions (x) in Central Asia. The line is the event screening criterion from Murphy et al. (1997). VMAX (top), Marshall and Basham (middle), and Rezapour and Pearce (bottom).

CONCLUSIONS AND RECOMMENDATIONS

The VMAX appears to provide a better and more consistent estimate of source size, particularly for smaller events and at shorter distances, and especially when combined with phase-match filtering. This combination of methods not only results in the most robust M_s estimate, but also produces the best m_b:M_s discriminant.

REFERENCES

Bonner, J. L., D. Russell, D. Harkrider, D. Reiter, and R. Herrmann (2006). Development of a time-domain, variable-period surface wave magnitude measurement procedure for application at regional and teleseismic distances—Part II: Application and Ms-mb performance, *Bull. Seism. Soc. Amer.* 96: 678–696.

Chael, E. P. (1997). An automated Rayleigh-wave detection algorithm, *Bull. Seism. Soc. Am.* 87: 157–163.

Marshall, P. D. and P. W. Basham (1972). Discrimination between earthquakes and underground explosions employing an improved Ms scale, *Geophys. J. R. Astr. Soc.* 29: 431–458.

Murphy, J. R., B. W. Barker, and M. E. Marshall (1997). Event screening at the IDC using the Ms/mb discriminant. Maxwell Technologies final report, 23 pp.

Pasyanos, M. E. (2005). A variable-resolution surface wave dispersion study of Eurasia, North Africa, and surrounding regions, *J. Geophys. Res.* 110: B12301.

Rezapour, M. and R. G. Pearce (1998). Bias in surface-wave magnitude Ms due to inadequate distance correction, *Bull. Seism. Soc. Am.* 88: 43–61.

Russell, D. R. (2006). Development of a time-domain, variable-period surface wave magnitude measurement procedure for application at regional and teleseismic distances—Part I: Theory, *Bull. Seism. Soc. Amer.* 96: 665–677.

Selby, N. (2001). Association of Rayleigh waves using backazimuth measurements: Application to test ban verification, *Bull. Seism. Soc. Am.* 91: 580–593.

ENERGY PARTITIONING FOR SEISMIC EVENTS IN FENNOSCANDIA AND NW RUSSIA

Hilmar Bungum[1], Tormod Kvaerna[1], Svein Mykkeltveit[1], Nils Maercklin[1], Michael Roth[1], Ketil Aastebol[1], David B. Harris[2], and Shawn Larsen[2]

NORSAR[1] and Lawrence Livermore National Laboratory[2]

Sponsored by National Nuclear Security Administration
Office of Nonproliferation Research and Development
Office of Defense Nuclear Nonproliferation

Contract Nos. DE-FC03-02SF22636[1] and W-7405-ENG-48[2]

ABSTRACT

In this three-year project we have been addressing the problem of energy partitioning at distances ranging from very local to regional for various kinds of seismic sources. On the local and regional scale (20-220 km) we have targeted events from the region offshore of Western Norway, where we have both natural earthquake activity and frequent underwater explosions carried out by the Norwegian Navy. On the small scale we have focused on analysis of observations from an in-mine network of 16-18 sensors in the Pyhäsalmi mine in central Finland. This analysis has been supplemented with 3-D finite difference wave propagation simulations in a realistic mine model to investigate the physical mechanisms that partition seismic energy in the near source region in and around the underground mine.

The results from modeling and analysis of local and regional data show that mean S/P amplitude ratios for explosions and natural events differ at individual stations and are in general higher for natural events and frequency bands above 3 Hz. However, the distributions of S/P ratios for explosions and natural events overlap in all analyzed frequency bands. Thus, for individual events in our study area, S/P amplitude ratios can only assist the discrimination between an explosion and a natural event. This observation is supported by synthetic seismograms calculated for simple 1-D models, which demonstrate that explosions generate shear-wave energy if they are fired close to an interface with a strong material contrast (as is the case for most explosions), e.g., free surface or the ocean bottom. The larger difference in S/P ratios between earthquakes and explosions for higher frequencies can be explained by the fact that at low frequencies (larger wavelengths), discontinuities and structural heterogeneities in the explosion source region are stronger generators of converted S energy. The S* phase, for example, is most efficiently generated whenever an explosion source is located close to (within one wavelength) a strong discontinuity.

High-frequency (50-400 Hz) S/P ratios for mine blasts (explosions) and rockbursts recorded at the Pyhäsalmi in-mine network do not show any significant dependency on the distance to the events, which ranges between 40 and 400 m. The Pyhäsalmi explosions have generally lower S/P ratios than the rockbursts for all frequencies, but the difference is far too small to be significant for classification purposes. S/P ratios for explosions and rockbursts located in the same small area of the mine show results very similar to those for the full data set. This indicates that the observed differences in S/P ratios between explosions and rockbursts are due to differences in the source characteristics, and not to propagation effects along paths in the mine.

Three-dimensional finite-difference simulations were used to model seismic events within the Pyhäsalmi mine. In particular, a January 26, 2003, rockburst was modeled at frequencies of 50 Hz (4 m grid) and 100 Hz (2 m grid). We were able to match the characteristics of the observed data at 50 Hz particularly well, and the characteristics of the 100 Hz data reasonably well. The simulations showed that significant shear-energy can be produced due to the geologic and structural heterogeneities within the mine. In fact, mode-converted shear-energy generated from mine heterogeneity can dominate the compressional energy from an explosive source. A strong correlation is observed between the distance of a source from a mine heterogeneity and the magnitude of generated shear-energy. The ratio of shear to compressional energy is about a factor of two larger when the source is located within one wavelength from a mine heterogeneity. The simulations also suggest that excavated mine volumes are significantly stronger contributors to shear-energy generation than are geologic heterogeneities.

OBJECTIVE

The main objective of this project has been to increase the (nuclear) explosion monitoring effectiveness through improved understanding of basic earthquake and explosion phenomenology. What this entails is detailed characterization and understanding of how the seismic energy is generated from these phenomena (including simple and complex explosions; rockbursts, i.e., stress release in mines; and ordinary tectonic earthquakes, all at different depths and in different geological environments) and how this energy is partitioned between P and S waves. Specific questions are as follows:

- How is the generation and partitioning of seismic energy affected by properties of the source region medium and overburden, the local structure, and the surrounding tectonic structure?
- What are the significant measurable effects of the partitioning of the seismic energy into various regional P and S phases, especially at higher frequencies?
- What is the physical basis for a measurable property, such as magnitude, that can be directly related to the yield of a fully coupled explosion, and how can emplacement conditions affect the observations?

RESEARCH ACCOMPLISHED

This three-year project started on September 30, 2002 and was a collaboration between the Norwegian Seismic Array (NORSAR)—as the lead organization—and Lawrence Livermore National Laboratory (LLNL). The closing date for the award was September 30, 2005, and the results from the project have been reported at previous Seismic Research Reviews (Bungum et al., 2003, 2004, 2005). The project results were summarized in the "Final Technical Report" of January 31, 2006, and included a new section on modeling of shear-waves from explosions in water. This section is included in this paper, together with a summary of the results previously presented in SRR papers and the "Final Technical Report".

Recent Studies on Energy Partitioning

Generally, explosions occur very close to the Earth's surface, which is characterized by sharp discontinuities (free surface, groundwater table, transition between unconsolidated sediments to solid rock, etc.). The interaction of a seismic source with such discontinuities can generate unexpected source radiation patterns and partitioning between P- and S-wave energy. Even in the simplest case of a homogeneous medium bounded by a free surface, an explosive source can generate different types of shear-wave energy, if it is close (within one wavelength) to an interface with a strong impedance contrast, like the free surface or the ocean bottom (e.g., Roth and Holliger, 2000).

There is an ongoing discussion about the dominant P-to-S transfer mechanism. It is generally agreed that significant S-wave energy from explosions is generated in the near-source region; several such near-source energy excitation mechanisms have been investigated, including P-to-Lg scattering, pS-to-Lg conversion at the free surface, Rg-to-Lg coupling, S*-to-Lg conversion, spall excitation of S, tectonic release, and rock damage. S* is a non-geometric wave generated by P-to-S conversion whenever an explosion source is located close (within one wavelength) to the free surface (Fertig, 1984).

Recently, Myers at al. (2005) analyzed recordings from the 1993 non-proliferation experiment (NPE) at the Nevada Test Site (NTS), accompanied with wavefield simulation in a detailed geological model of the area. They found that near-source topography and geological complexity in the upper crust strongly contributed to the S waves from the NPE shot.

Xie et al. (2005) conducted numerical wavefield simulations for shallow explosions in media with 3%-7% random velocity fluctuations. Their results show that S*-Lg scattering is stronger for low frequencies and shallow depths, whereas P-Lg scattering is stronger for high frequencies. Three dimensional simulations showed considerable P-pS-SH or SV-SH generation with a 7% velocity and density perturbations. Tangential Lg energies from explosions are often observed as large as those on the vertical components (Stevens et al., 2003).

The so-called Arizona source phenomenology experiment (Bonner et al., 2005) showed that the designed test shots and mining explosions are good surrogates for nuclear explosions because the magnitude- and distance-corrected Pg/Lg amplitude ratios fall in the range of those for nuclear explosions at NTS. Differences in depth of burial and single versus multiple shots have only a small effect on the amplitude ratios.

Analysis of Semipalatinsk underground nuclear explosions (UNEs) recorded at the Borovoye station at a distance of 680 km show that Rg-to-S scattering does not appear to be a dominant mechanism for the Lg excitation from Semipalatinsk UNEs (Hong and Xie, 2005). The geology of the source region appears to influence the strength of mantle shear-waves in the expected Sn window, where slower near-surface velocities in the source region seem to enhance shear-waves. Less dependency on source region geology is found for the Lg waves, which also have lower frequencies than Sn. The results from this study imply that the source region geology tends to make strong influence on the strength of higher-frequency shear-waves.

Scaling analysis of Sn/Pn and Lg/Pn spectral ratios at Borovoye for Semipalatinsk explosions (Murphy et al., 2005) indicate an Sn/Lg source generation mechanism compatible with a linear frequency-independent conversion of direct P-wave energy from the explosions.

In order to estimate the effect of strong scatterers in the near-source region, Toksöz et al. (2005) conducted 3-D wavefield modeling in media with well-defined tunnels, chambers, shafts, or surface topography. Their simulations show that a tunnel near an explosion acts as a very strong scatterer. P-to-S scattering is much stronger than P-to-P, and some energy is scattered into SH. A hill or a mesa above the explosion source causes strong scattering of the surface waves.

In this project we have further addressed the problem of energy partitioning at distances ranging from very local to regional for various kinds of seismic sources. On the local and regional scale (20-220 km), we have targeted events from the region offshore of Western Norway, where we have both natural earthquake activity as well as frequent underwater explosions carried out by the Norwegian Navy.

On the small scale we have focused on analysis of observations from an in-mine network of 16-18 sensors in the Pyhäsalmi mine in central Finland. This analysis has been supplemented with 3-D finite-difference wave propagation simulations in a realistic mine model to investigate the physical mechanisms that partition seismic energy in the near-source region in and around the underground mine.

Modeling of Shear-Waves from Explosions in Water

In order to investigate S waves generated from explosions in water, we have conducted additional calculations using a frequency-wave number code (Wang, 1999), allowing both the source and the receivers to be located at depth. We have replaced the uppermost 200 m of the Fennoscandian crustal model with water, shown in Figure 1, and put the sensors at a depth of 210 m, i.e. 10 m below the sea bottom. Figure 2 shows the vertical-component synthetic seismograms for an explosion source in water at a depth of 10 m. The dominant frequency of the signal pulse is about 2 Hz.

The large Rg phase and the resonance effect of the water layer on Rg is not very interesting in our context, as the continuous water waveguide carrying the Rg phase is generally absent for the propagation paths addressed in this study; i.e., events located offshore Western Norway recorded at land stations of the National Norwegian Seismic Network (NNSN). However, the modeled amplitudes of the P and S body wave phases provide useful insight into the degree of S-wave energy generated

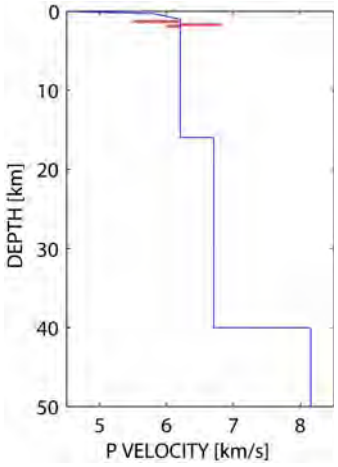


Figure 1. Average crustal P-velocity model for Fennoscandia (blue). A perturbation for the upper crust is shown in red.

from explosion sources, and show that similar mechanisms also are in effect for more realistic complex media. It can be seen from Figure 2 that the first-arriving S phase has a comparable amplitude to the P phase, at least for distances greater than 100 km. The effect of reverberations in the water layer is seen as coda energy related to the different arrivals.

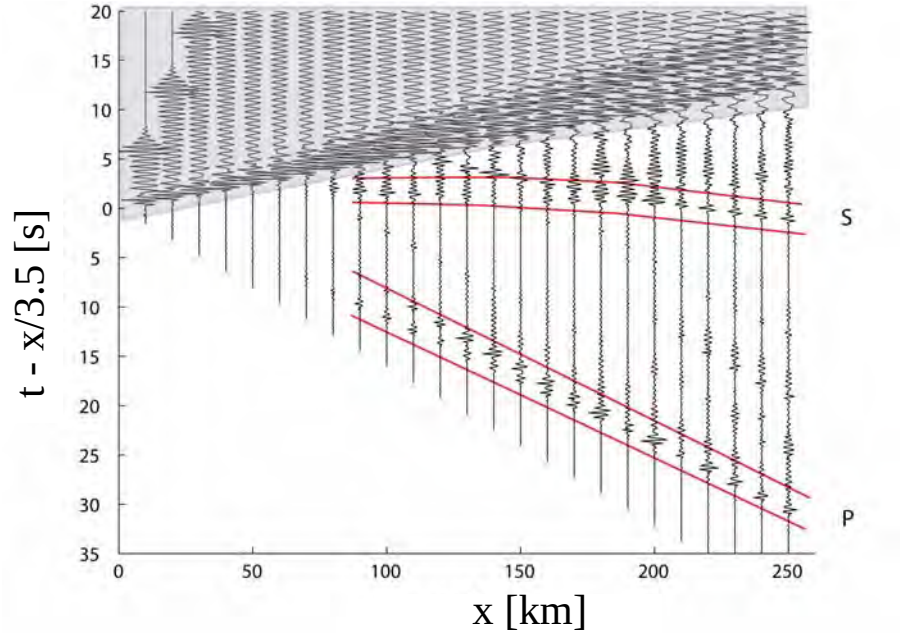


Figure 2.

Trace-normalized vertical component seismogram section for an explosion in water at a depth of 10 m, as described in the text. Rg is the dominant phase (shaded area), but is not important in this discussion of shear-waves. Significant energy travels with S-wave velocities, generated by interaction between the source and the sea bottom. The S-wave amplitudes are comparable to those of the P phase.

For comparison, we show in Figure 3 a similar wavefield simulation, but now without the 200 m water layer. Rg still has the largest amplitudes, now propagating with higher velocity than in the case shown in Figure 3. Also in this case, some shear-energy can be observed, but with an amplitude 2-3 times smaller than P.

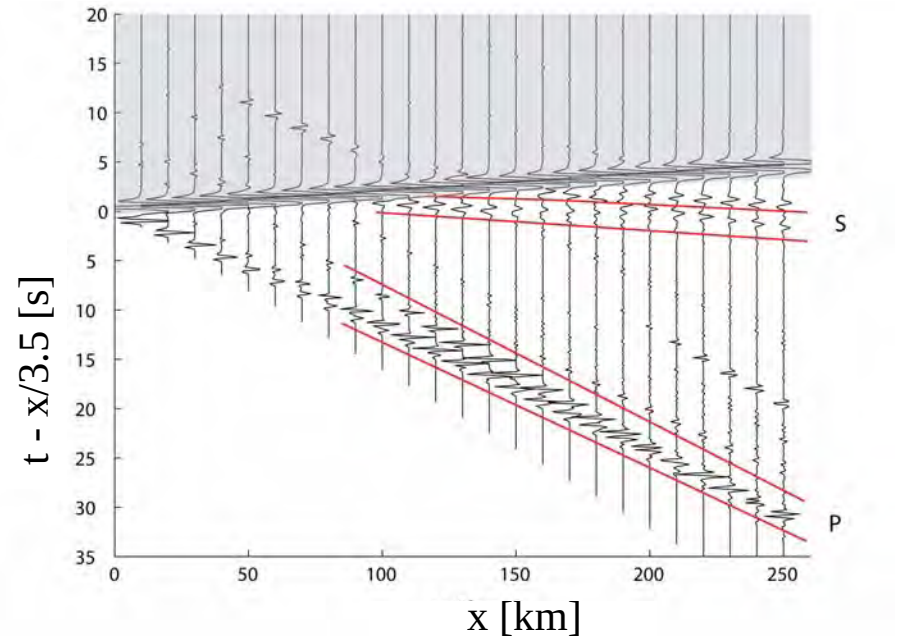


Figure 3.

Trace-normalized vertical component seismogram section for an explosion at a depth of 10 m into the crust, as described in the text. Rg is the dominant phase (shaded area) but is not important in this discussion of shear-waves. Some energy travels with S-wave velocities, generated by interaction between the source and the free surface. The S-wave amplitudes are 2-3 times smaller than those of the P phase.

Energy Partitioning for Seismic Events near the Coast of Western Norway; Summary of Analysis and Modeling Results

The database used in this study has been seismic phase arrival times, source locations, and waveform data of natural events and underwater explosions recorded at seven selected three-component stations in Western Norway between 1997 and 2004 (Figure 4). The seismic stations are part of the permanent NNSN, and the data were provided by the University of Bergen (UiB). The selected source region is located around 60N, 5E, where both event types, earthquakes and explosions, occur.

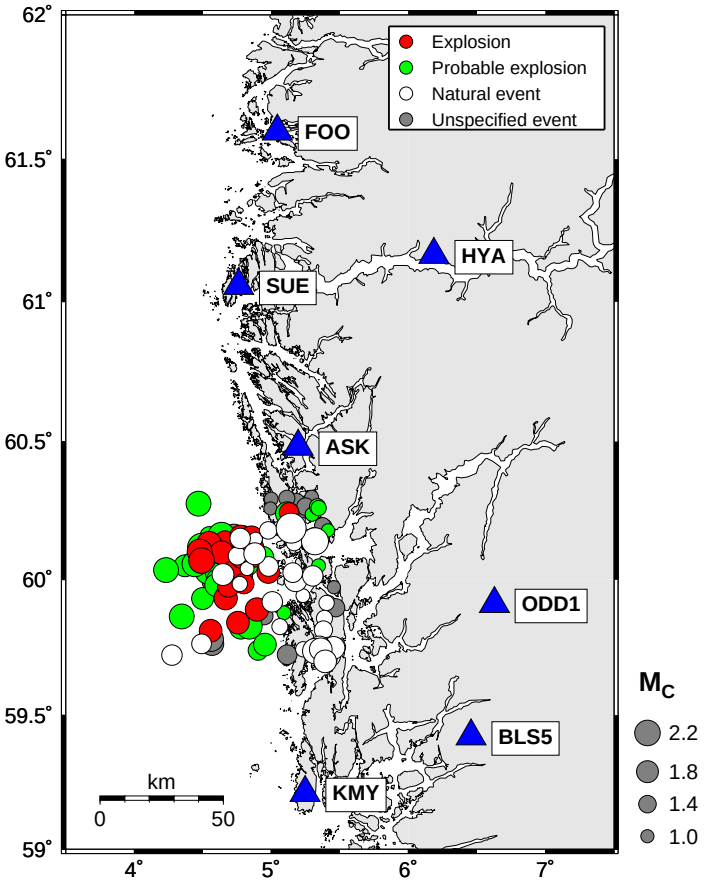


Figure 4. Seismic three-component short-period stations (triangles) and events used for this study: ASK = Askøy, BLS5 = Blåsjø, FOO = Florø, HYA = Høyanger, KMY = Karmøy, ODD1 = Odda, and SUE = Sulen.

The results obtained during the analysis of this data set and the associated modeling efforts can be summarized as follows:

- The S/P ratios of the analyzed data sets give only an indication of the source type. Variation of layer topography and 3-D heterogeneities can focus and defocus P- as well as S-wave amplitudes in different ways. This variation in S/P ratio is one reason for the width of the observed distributions and the overlap between the data sets.
- For the analyzed data set, there is a larger difference in S/P ratios between earthquakes and explosions for higher frequencies. This can be explained by the fact that, at low frequencies (larger wavelengths), discontinuities and structural heterogeneities in the explosion source region are stronger generators of converted S energy. The S* phase, for example, is most efficiently generated whenever an explosion source is located close to (within one wavelength) a strong discontinuity.
- The path dependence of the observed S/P amplitude ratios may also get a significant contribution from lateral heterogeneities in the source region, producing variable levels of P-to-S conversion in different directions from the source.
- Mean S/P amplitude ratios for explosions and natural events differ at individual stations and are in general higher for natural events and frequency bands above 3 Hz. However, the distributions of S/P ratios for explosions and natural events overlap in all analyzed frequency bands. Thus, for individual events in our study area, S/P amplitude ratios can only assist the discrimination between an explosion or a natural event.
- Synthetic seismograms calculated for simple 1-D models demonstrate that explosions also generate shear-wave energy if they are fired close to an interface with a strong material contrast (as is the case for most explosions), such as the free surface or the ocean bottom.
- A single force source generates much stronger S waves than an explosion. The same is assumed to hold for double-couple sources averaged over the radiation pattern.
- Synthetic seismogram calculations confirm that the generation of S-type energy at impedance contrasts later along the ray paths contribute essentially only to the seismic coda of the direct P and S arrivals. This coda energy does

not dominate the amplitude behavior of the seismograms. Therefore, in simple 1-D models, S/P-ratios can be used as a discrimination criterion.

Analysis of In-Mine Data from the Pyhäsalmi Ore Mine, Central Finland

The Pyhäsalmi mine in central Finland has been a key element in our research, and we have been provided with all data from the in-mine seismic monitoring system that became operational in January 2003. This data set consisted by the end of 2005 of more than 30,000 seismic events, including the mine blasts (explosions). An interesting observation from the mine blast is the occurrence of shear-wave energy at the in-mine seismic stations (see Figure 5). The results from analysis of mine blasts and natural events (rockbursts) are summarized below:

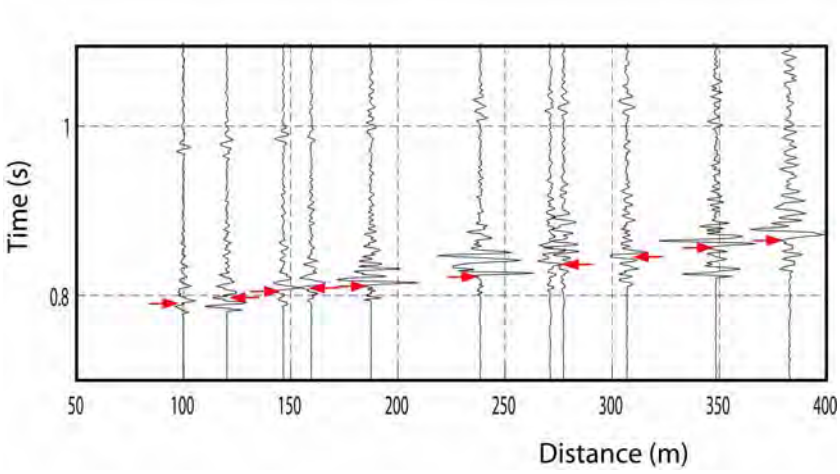


Figure 5.

Record section in the Pyhäsalmi in-mine network for a single detonation of a ripple-fired production shot. For each of the three-component sensors, we have chosen the component having the largest S phase. We have not included vertical-component observations where the rays approach the sensors at steep angles, as the S-arrivals on these sensors have very small amplitudes. The S arrivals are indicated with arrows.

- There is significant generation of S waves from production explosions in the Pyhäsalmi mine. Strong S-wave generation from explosions is observed at all distances and all frequencies considered in this study.
- The S/P ratios of explosions are, on the average, only marginally smaller than the S/P ratios of rockbursts. The overlap of the two populations is so large that the S/P ratio does not appear to be a useful discriminant for this data set.
- The observed S/P ratios do not show any significant dependency on the distance to the source, either for explosions or rockbursts.
- The observed S/P ratios also do not show any clear dependency on frequency bands among the frequencies considered in this study.
- Our results confirm that the major part of the S-wave energy for the explosions is generated in the near-source region.

Modeling of In-Mine Data

There is a lower limit to the distances at which we can practically observe signals at the Pyhäsalmi in-mine network, e.g., it would not be possible to carry out a mine blast in the immediate vicinity of a seismic sensor without risking damage to the hardware. The analysis of S/P ratios showed that there is a lower distance limit at which we can separate P and S energy for the frequencies of interest, and we have consequently no information on the S/P ratios for the first tens of meters from the source. To further investigate the physical mechanisms that partition seismic energy in the near-source region, we have conducted wavefield modeling studies of the Pyhäsalmi mine. Our efforts centered around three primary activities:

- Validation of our seismic modeling techniques in the presence of underground voids.
- Comparison of observed data from seismic events at the Pyhäsalmi mine with synthetic data generated using a 3-D finite-difference wave-propagation code and a 3-D geologic model of the mine.
- Synthetic sensitivity tests to determine the cause and characteristics of shear-energy generation in the near-source region.

The first two activities served to demonstrate our ability to model seismic wave propagation in a mine environment. The third activity was directed at the generation mechanisms for mode-converted shear-energy.

The E3D finite-difference code was used for many of the seismic simulations performed during this study (Larsen and Schultz, 1995; Larsen and Grieger, 1998). For this project, the E3D code utilized a 3-D geologic model of the Pyhäsalmi mine (see Figure 6). The model parameterized the different geologic and structural components of the mine on a regular grid. The geologic components included the background rock and ore bodies. The structural components included excavated regions such as tunnels, voids, and backfilled material produced by mine activity. The 3-D model was 500 m in all three dimensions. The material P-wave and S-wave velocities and the material densities have been discretized onto uniformly spaced grids of 2- and 4-m spacing. The E3D code utilized these discretized grids.

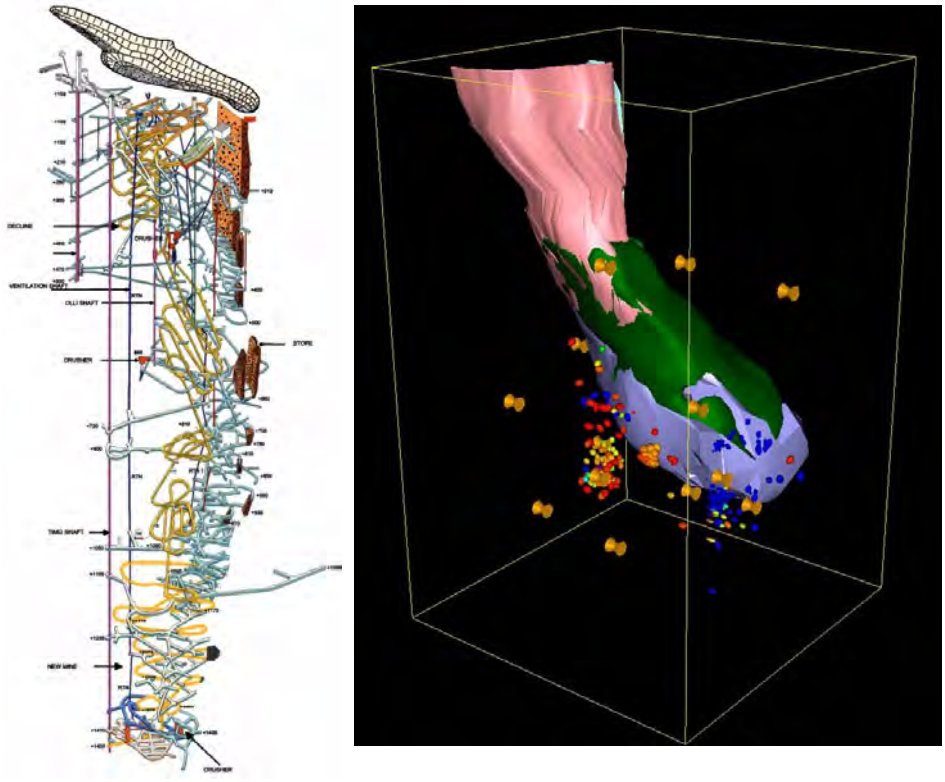


Figure 6.

The left-hand part of the figure shows the shafts and access tunnels of the Pyhäsalmi mine from the surface down to a depth of 1500 m. The right-hand part of the figure shows a 3-D model of the mine, for the depth range 800 - 1500 m. Green represents copper ore, blue represents zinc ore, and pink represent backfilled material. The locations of the initial 16 in-mine monitoring stations are indicated by yellow symbols. Events comprise mine blasts and microearthquakes during September 2003.

Below is a brief summary of our finite-difference modeling efforts. It includes the modeling of observed data from real seismic events within the Pyhäsalmi mine, as well as sensitivity studies.

- **Finite-Difference Modeling of Observed Data**
  Three-dimensional finite-difference simulations were used to model seismic events within the Pyhäsalmi mine. In particular, a January 26, 2003, rockburst was modeled at frequencies of 50 Hz (4 m grid) and 100 Hz (2 grid). We were able to match the characteristics of the observed data at 50 Hz particularly well and the characteristics of the 100 Hz data reasonably well. These results validate the reliability of our simulations.

- **Heterogeneity-Induced Shear-Energy Generation**
  Two Dimensional and 3-D finite-difference simulations were performed to investigate shear-energy generation within the Pyhäsalmi mine. We found that significant shear-energy can be produced due to the geologic and structural heterogeneities within the mine. In fact, mode-converted shear-energy generated from mine heterogeneity can dominate the compressional energy from an explosive source.
- **Correlation between Source Location and Shear-Energy Generation**
  Multiple suites of over 15,000 2-D finite-difference simulations were performed to quantify and investigate the correlation between source location and the magnitude of shear-energy generated within the Pyhäsalmi mine. A strong correlation is observed between the distance of a source from a mine heterogeneity and the magnitude of generated shear-energy. The ratio of shear to compressional energy is about a factor of two larger when the source is located within one wavelength from a mine heterogeneity.
- **Mine Excavation vs Geologic Heterogeneity**
  Finite-difference simulations at 50 Hz suggest that mine excavation is a significantly stronger contributor to shear-energy generation than is geologic heterogeneity.
- **Shear-Energy Generation from Non-Explosive Sources**
  Finite-difference simulations reveal that the magnitude of shear-energy generated as part of a shear-producing source mechanism (e.g., rockburst, mine collapse) can be as large or larger than that caused by an explosion close to a heterogeneity within the mine.
- **Finite-Difference Modeling of Voids**
  Similar synthetic waveforms are produced when the excavated regions within the Pyhäsalmi mine model are filled with air or water.

CONCLUSIONS AND RECOMMENDATIONS

In this project we have addressed the problem of energy partitioning at distances ranging from very local to regional for various kinds of seismic sources. On the local and regional scale (20-220 km), we have targeted events from offshore Western Norway, where we have both natural earthquake activity and frequent underwater explosions.

On the small scale we have focused on analysis of observations from an in-mine network of 16-18 sensors in the Pyhäsalmi mine in central Finland. This analysis has been supplemented with 3-D finite-difference wave propagation simulations in a realistic mine model to investigate the physical mechanisms that partition seismic energy in the near source region in and around the underground mine.

The results from modeling and analysis of local and regional data show that mean S/P amplitude ratios for explosions and natural events differ at individual stations and are in general higher for natural events and frequency bands above 3 Hz. However, the distributions of S/P ratios for explosions and natural events overlap in all analyzed frequency bands. Thus, for individual events in our study area, S/P amplitude ratios can only assist the discrimination between an explosion and a natural event.

This observation is supported by synthetic seismograms calculated for simple 1-D models, which demonstrate that explosions also generate shear-wave energy if they are fired close to an interface with a strong material contrast (as is the case for most explosions), e.g., free surface, the ocean bottom. The larger difference in S/P ratios between earthquakes and explosions for higher frequencies can be explained by the fact that at low frequencies (larger wavelengths), discontinuities and structural heterogeneities in the explosion source region are stronger generators of converted S energy. The S* phase, for example, is most efficiently generated whenever an explosion source is located close to (within one wavelength) a strong discontinuity.

The Pyhäsalmi explosions have generally lower S/P ratios than the rockbursts for all frequencies, but the difference is far too small to be significant for classification purposes. The maxima for the explosion distributions are all below 2, whereas they are all above 2 for the rockbursts. The rockbursts also have a wider distribution of S/P ratios, which can be explained by the variability of the radiation patterns from the rockburst sources. S/P ratios for explosions and rockbursts located in the same small area of the mine show results very similar to those for the full data set. This indicates that the observed differences in S/P ratios between explosions and rockbursts are due to differences in the source characteristics and not to propagation effects along paths in the mine.

Three-dimensional finite-difference simulations were used to model seismic events within the Pyhäsalmi mine. In particular, a January 26, 2003 rockburst was modeled at frequencies of 50 Hz (4 meter grid) and 100 Hz (2 meter grid). We were able to match the characteristics of the observed data at 50 Hz particularly well, and the characteristics of the 100 Hz data reasonably well. These results help validate the reliability of our simulations.

The simulations showed that significant shear-energy can be produced due to the geologic and structural heterogeneities within the mine. In fact, mode-converted shear-energy generated from mine heterogeneity can dominate the compressional energy from an explosive source. A strong correlation is observed between the distance of a source from a mine heterogeneity and the magnitude of generated shear-energy. The ratio of shear-energy to compressional-energy is about a factor of two larger when the source is located within one wavelength from a mine heterogeneity. The simulations also suggest that mine excavation is a significantly stronger contributor to shear-energy generation than geologic heterogeneity. However, the simulations reveal that the magnitude of shear-energy generated as part of a shear-producing source mechanism (e.g., rockburst, mine collapse) can be as large or larger than that caused by heterogeneity within the mine.

It is also interesting to note that analysis and modeling at the local/regional scale provide results that are in accordance with the results obtained from analysis and modeling of in-mine data. Both studies show that strong discontinuities in the source region are efficient generators of P-to-S converted energy, although at very different frequencies for the different scales investigated. The large overlap in the populations of S/P ratios for explosions and natural seismic events at both scales supports this interpretation.

In order to get further insight into the problem of energy partitioning between P- and S-waves from different types of seismic sources, we recommend further studies that include controlled explosion field experiments with near-source recording. Specifically, fully-coupled, contained explosions could be conducted in proximity to production-style shots, such as in the Pyhäsalmi mine. In this way the physical processes comprising small-scale explosions could be separated in order to enable prediction of the observables from larger and more complex explosions. Such observations should be supplemented with numerical simulations of shear-wave energy generated directly by nonlinear source effects, as well as by linear propagation effects such as scattering from the free interfaces of the mine.

The populations of S/P ratios for explosions and natural seismic events of the data sets analyzed in this study show a large overlap and therefore cannot be used as a unique discriminant. The possibility of integrating S/P ratios with existing or new measurements should therefore be investigated further, aimed at improving the discrimination potential.

REFERENCES

Bungum, H., T. Kvaerna, S. Mykkeltveit, M. Roth, K. Astebol, D. B. Harris, and S. Larsen (2003). Energy partitioning for seismic events in Fennoscandia and NW Russia," in *Proceedings of the 25th Seismic Research Review - Nuclear Explosion Monitoring: Building the Knowledge Base,* LA-UR-03-6029, Vol.2, pp. 394–404.

Bungum, H., T. Kvaerna, S. Mykkeltveit, M. Roth, V. Oye, K. Astebol, D. B. Harris and S. Larsen (2004). Energy partitioning for seismic events in Fennoscandia and NW Russia." in *Proceedings of the 26th Seismic Research Review - Nuclear Explosion Monitoring: Trends in Nuclear Explosion Monitoring,* LA-UR-04-5801, Vol. 2, pp. 387–396.

Bungum, H., T. Kvaerna, S. Mykkeltveit, N. Maercklin, M. Roth, V. Oye, K. Astebol, D. B. Harris and S. Larsen (2005). Energy partitioning for seismic events in Fennoscandia and NW Russia." in *Proceedings of the 27th*

Seismic Research Review - Ground-based Nuclear Explosion Monitoring Technologies, LA-UR-05-6407, Vol. 1, pp. 529–538.

Bonner, J. L, B. Stump, M. Leidig, X. Yang, R. Zhou, T. S. Kim, W. R. Walter, A. Velasco, C. Hayward, D. Baker, C. L. Edwards, S. Harder, H. Hooper, T. Glenn, C. Zeiler, R. Gok, J. Britton, and J.F. Lewkowicz (2005). Source phenomenology experiments in Arizona, in *Proceedings of the 27th Seismic Research Review, Ground-based Nuclear Explosion Monitoring Technologies*, LA-UR-05-6407, Vol. 1, pp. 519–528.

Fertig, J. (1984). Shear waves by an explosive point-source: The Earth surface as a generator of converted P-S waves, *Geophysical Prospecting*, 32, 1–17.

Hong, T.-K. and J. Xie (2005). Source array analysis on the composition of regional waves from Balapan explosions in the near-source region, in *Proceedings of the 27th Seismic Research Review, Ground-based Nuclear Explosion Monitoring Technologies*, LA-UR-05-6407, Vol. 1, pp. 561–569.

Larsen, S. C., and C. A. Schultz (1995). ELAS3D: 2D/3D elastic finite-difference wave propagation code, UCRL-MA-121792, 18 pp.

Larsen, S. and J. Grieger (1998). Elastic modeling initiative, Part III: 3-D computational modeling, in *Soc. Expl. Geophys.* Confer. Proceed., 68 ;1803–1806, and Lawrence Livermore National Laboratory Technical Report UCRL-JC-130224.

Larsen, S., T. Kvaerna, M. Roth, K. Aastebol, and D. Harris (2005). Simulations of energy partitioning from seismic events in underground mines, in SSA spring meeting and Lawrence Livermore National Laboratory Technical Report UCRL-ABS-209001.

Murphy, J. R., B. W. Barker and J. Sultanov (2005). A scaling analysis of frequency dependent energy partitioning for local and regional seismic phases from explosions, in *Proceedings of the 27th Seismic Research Review, Ground-based Nuclear Explosion Monitoring Technologies*, LA-UR-05-6407, Vol. 1, pp. 597–605.

Myers, S. C, J. Wagoner, L. Preston, K. Smith, and S. Larsen (2005). The effect of realistic geologic heterogeneity on local and regional P/S amplitude ratios based on numerical simulations, in *Proceedings of the 27th Seismic Research Review, Ground-based Nuclear Explosion Monitoring Technologies*, LA-UR-05-6407, Vol. 1, pp. 123–132.

Roth, M. and K. Holliger (2000): The non-geometric wave in high-resolution seismic data: Observations and modelling. *Geophys. J. Int.*, 140, F5–F11.

Stevens, J. L., G. E. Barker, H. Xu, T. J. Bennett, N. Rimer, and S. M. Day (2003). The physical basis of Lg generation by explosion sources, in *Proceedings of the 25th Seismic Research Review, Nuclear Explosion Monitoring: Building the Knowledge Base*, LA-UR-03-6029, Vol. 2, pp. 456–465.

Toksöz, M. N., S. Chi, Y. Zhang, E. Sze, and R. Lu (2005). Characterization of an explosion source in a complex medium by modeling and wavelet domain inversion, in *Proceedings of the 27th Seismic Research Review, Ground-based Nuclear Explosion Monitoring Technologies*, LA-UR-05-6407, Vol. 1, pp. 683–692.

Wang, R. (1999). A simple orthonormalization method for stable and efficient computation of Green's functions. *Bull. Seism. Soc. Am.*, 89: 733–741.

Xie, X-B, T. Lay, and R-S Wu (2005). Near-source energy partitioning for regional waves in 2D and 3D models, contributions of S*-to-Lg and P-to-Lg scattering, in *Proceedings of the 27th Seismic Research Review, Ground-based Nuclear Explosion Monitoring Technologies*, LA-UR-05-6407, Vol. 1, pp. 249–258.

MODELING AND EMPIRICAL RESEARCH ON ENERGY PARTITIONING OF REGIONAL SEISMIC PHASES USED FOR EXPLOSION MONITORING

Mark D. Fisk[1], Thorne Lay[2], and Steven R. Taylor[3]

ATK Mission Research[1], University of California, Santa Cruz[2], and Rocky Mountain Geophysics, LLC[3]

Sponsored by National Nuclear Security Administration
Office of Nonproliferation Research and Development
Office of Defense Nuclear Nonproliferation

Contract Nos. DE-AC52-04NA25536[1], DE-FC52-04NA25537[2], and W-7405-ENG-36[3]

ABSTRACT

To gain theoretical insight into regional P/S discriminants and their frequency-dependent performance, source and attenuation models are used to predict spectra of regional seismic phases (Pn, Sn, and Lg) for nuclear explosions and selected earthquakes near the Lop Nor, Semipalatinsk (Balapan and Degelen Mountain), and Novaya Zemlya test sites in China and the former Soviet Union. A modified Brune (1970) model is used to predict P- and S-source terms for earthquakes. A Mueller/Murphy (1971) model is used for explosions, including a new conjecture that the S waves may be modeled by the same functional form as for P waves, but with corner frequency reduced by the ratio of near-source shear and compressional velocities. Results indicate that the frequency dependence of Pn/Sn and Pn/Lg discrimination performance at all of these hard-rock test sites is primarily due to differences in the corner frequencies of P and S waves for explosions, qualitatively consistent with observations by Xie and Patton (1999) for Pn/Lg at Lop Nor. P/S discrimination emerges at the explosion S-wave corner frequency and saturates at the P-wave corner frequency. In addition to explaining why P/S discriminants perform better at higher frequencies, these results suggest that their application should be restricted by a magnitude threshold and/or to frequencies near or above the explosion Pn corner frequency for a given source size, which can lead to practical monitoring limitations. Approximate scaling of the explosion S-wave corner frequency with elastic radius as $v_s(S)/R_e$ at all of these test sites suggests that major contributions to the phenomenon of S-wave generation from explosions may have a similar length scale as for P waves from explosions. The explicit physical mechanism of this near-source S generation is still being investigated.

Similar analyses are applied to nuclear explosions at the Nevada test site (NTS) and nearby earthquakes. Explicit information regarding geophysical working-point properties, depth of burial, and some announced yields for NTS explosions (Springer et al., 2002) is utilized for the modeling efforts. Geophysical effects on regional phases are examined for Yucca Flat, Pahute Mesa, and Rainier Mesa, as functions of media properties (type, density, velocities, gas porosity), source yield and depth, and for explosions above or below the water table.

Numerical simulation efforts are being initiated by UCSC to examine the partitioning and variability of regional seismic phases for various path and station effects, using the information (source models, etc.) obtained thus far by ATK/Mission Research. Using suites of explosion signals from each test site recorded at sets of stations, an attempt is made to isolate the near-source and near-receiver contributions to the variability of Pn arrivals. The basic strategy involves constraining the overall path effect by using closely spaced events recorded at a given station or closely spaced stations for a given source. Spectral and time domain measurements, corrected for event-averaged properties from multiple stations, are used to quantify the site or source region contributions. These measures will guide synthetic modeling with variable crustal properties beneath arrays of stations or arrays of sources.

OBJECTIVES

This is a three-year project to investigate energy partitioning of local and regional seismic phases to better understand mechanisms of P/S discriminants. We are analyzing Pn, Pg, Sn, and Lg spectra for underground nuclear explosions (UNEs) and earthquakes, and correcting for distance and source size, so that the variability of each type of phase may be assessed. We are comparing the corrected spectra to source models to explain the dependence of P/S discriminants on frequency, source size, and geophysical properties. Objectives are to quantify these aspects for explosions and earthquakes near the Lop Nor, Semipalatinsk, Novaya Zemlya, and Nevada test sites (LNTS, STS, NZTS, and NTS, respectively). We plan to interpret the variability of observations in terms of geophysical mechanisms by using complex elastic-screen simulations spanning relevant spectral content (0.1 to 10 Hz) for distances of at least 0 to 600 km and considering realistic models with multi-scale heterogeneity, rough Moho, topography, and other boundaries.

RESEARCH ACCOMPLISHED

The results of two studies are summarized below. The first focuses on spectral modeling of regional phases and P/S discriminants at the LNTS, STS, and NZTS in China and the former Soviet Union. Results for these hard-rock test sites were published by Fisk (2006). The second focuses on spectral analyses for explosions in tuff, rhyolite, and alluvium at NTS and for nearby earthquakes. In both studies, extended Mueller/Murphy (1971) (MM71) and Brune (1970) models are used to predict source terms of P and S waves for UNEs and earthquakes, respectively.

Spectral Modeling of Regional P/S Discriminants at Nuclear Test Sites in China and the Former Soviet Union

Fisk (2006) compared model and empirical spectra of Pn, Sn, and Lg for UNEs and earthquakes at LNTS in China, STS in Kazakhstan, and NZTS in the Arctic region of northern Russia. Distinctive aspects of this study are that (1) explicit models of P- and S-wave corner frequencies are provided in terms of near-source P and S velocities, and either stress drop and moment for earthquakes or elastic radius (which depends on yield and depth of burial) for explosions; and (2) the behavior of Pn/Sn and Pn/Lg is investigated at all of these test sites. Specifically new to this study, the explosion S waves are modeled using the same MM71 function as for P waves (as by Xie and Patton, 1999), but with Sn and Lg corner frequency reduced by the ratio of near-source S and P velocities: $v_s(S)/v_s(P)$. This is analogous to the extension of the Brune model for earthquake P and S waves, with the corner frequencies depending on the P and S velocities (as by Taylor et al., 2002). The same MM71 and Brune models are used at all hard-rock test sites.

Figure 1 shows locations of explosions, earthquakes, and digital seismic stations within 2000 km of LNTS and STS (except for TLY and ULN). Many STS UNEs up to 1989 were recorded digitally by BRV (Borovoye, Kazakhstan) and WMQ (Urumqi, China). More recent events, including LNTS UNEs since mid 1994, were recorded digitally by up to 19 regional stations in Kazakhstan, Kyrgyzstan, Pakistan, Russia, Mongolia, and China. Instrument-corrected spectra of Pn, Pg, Sn, and/or Lg were processed for 9 UNEs since 1992 at LNTS and 156 nearby earthquakes. To model the UNEs, yields (W) were estimated using mb = 0.75 log W + 4.4, and scaled depth of burial was assumed. Earthquakes on 1999/01/27 (mb 3.95) and 1999/01/30 (mb 5.40) are particularly useful because they were at LNTS. Spectra were also processed for 51 UNEs (47 by BRV and 28 by WMQ) at STS between 1983 and 1989, and 87 earthquakes (mb 3.2 to 5.5) in the Reviewed Event Bulletin (REB) from 1995 to 2002. An mb 3.8 earthquake (labeled by *jdate* 1996086 in Figure 1) was closest to STS and was recorded by 17 regional stations, including BRVK and WMQ. A yield of 115 kt and depth of 600 m (Sykes and Ekström, 1989; Murphy and Barker, 2001) were used to compute model results for the Soviet JVE on 1988/09/14. For all other Balapan explosions, yields were estimated using mb = 0.75 log W + 4.45 (Murphy and Barker, 2001), and assuming scaled depth of $h = 122\ W^{1/3}$. Murphy (pers. comm., 2005) provided yields and depths from the Institute for the Dynamics of the Geospheres (IDG) in Moscow, Russia for 23 Degelen UNEs between 1964 and 1989, although it is not clear how the IDG determined the values or what the uncertainties are.

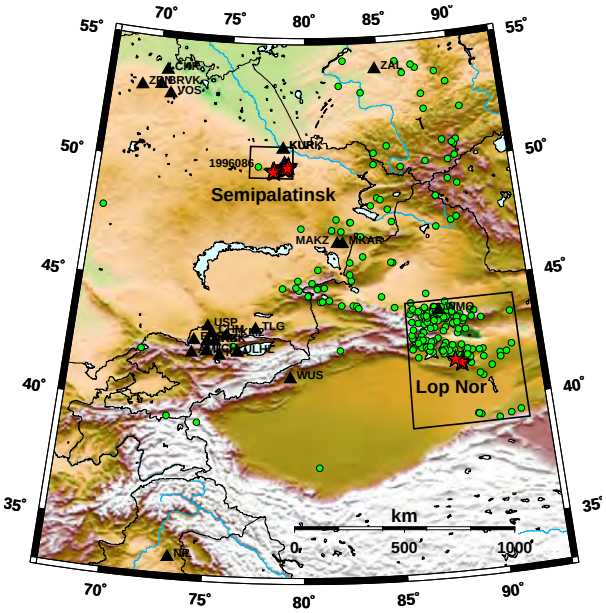


Figure 1. Locations of nuclear explosions (stars), earthquakes (circles), and seismic stations (triangles) within regional distances of LNTS and STS.

Figure 2 shows events at or near NZTS, recorded by NORSAR, NORES, ARCES, and/or KEV. Locations and magnitudes were compiled from Ringdal (1997), NORSAR (1999), and the ISC. ARCES, NORES, and KEV recorded only 3 to 6 NZTS UNEs from 1982 to 1990, with a limited mb range of 5.5 to 5.8, which do not allow study of source scaling effects. From 1976 to 1990 NORSAR recorded 17 UNEs (mb 3.8 to 6.0) at the test site near Matochkin Shar. Most NORSAR elements were clipped for most of these UNEs. The NAO01 element includes some short-period recordings at high gain (sz), and many at low gain (slz; gain reduced by 30 dB), that were not clipped. Thus, NAO01 data are the most useful for this P/S study at NZTS. Since NORSAR is over 20 degrees away, adequate S-wave signal-to-noise ratio (SNR) for these events is limited to below about 3 to 4 Hz. Based on analysis by Murphy and Barker (2001), the same mb:yield relation is used for NZTS and STS. It is also interesting to consider aftershocks – perhaps the only ground-truth earthquakes in the vicinity – that were triggered by megaton UNEs in 1973 and 1974 (e.g., Israelsson et al., 1974), including the largest UNE (3.5 mt) at the southern (Krasino) area on 1973/10/27. Three of the larger aftershocks (mb 4.5–4.6) and the 1986/08/01 Kara Sea event, identified as an earthquake by Marshall et al. (1989), are considered.

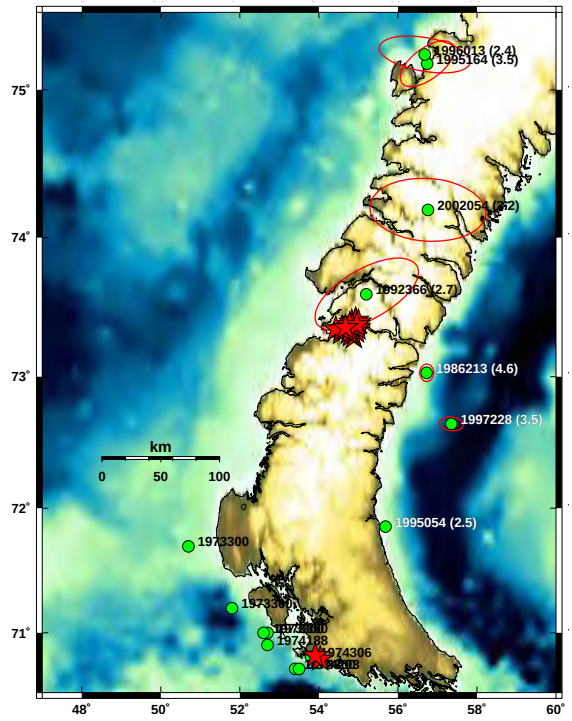


Figure 2. Locations of UNEs (stars) and other events (circles) recorded by KEV, ARCES, NORES, and/or NORSAR. Circles at the southern end of NZ represent aftershocks, induced by megaton-range UNEs. Julian dates, mb values (in parentheses), and location error ellipses are shown for selected events.

Spectra of regional seismic phases were modeled for the Lop Nor, Degelen, Balapan, and Novaya Zemlya test sites, using extended Brune and MM71 source models, and attenuation and station corrections that were estimated for the various paths and stations. (See Fisk, 2006, for details.) Figure 3, for example, compares instrument-corrected Pn, Sn, and Lg spectra to model predictions at MAK (top) for the 1999/01/30 earthquake (left) and the 1996/06/08 UNE at LNTS (right) and at WMQ (bottom) for the 1996/03/26 earthquake (left) and the 1988/09/14 JVE at STS (right). The gray curves in each plot show the model predictions. Since the station terms were computed using the nearby earthquake data, the model comparisons to the earthquake spectra are expected to agree quite well, at least over the frequency range for which the spectra have adequate SNR. The model and empirical spectra for the explosions also compare quite well and provide independent indication that the attenuation and station corrections are reasonable.

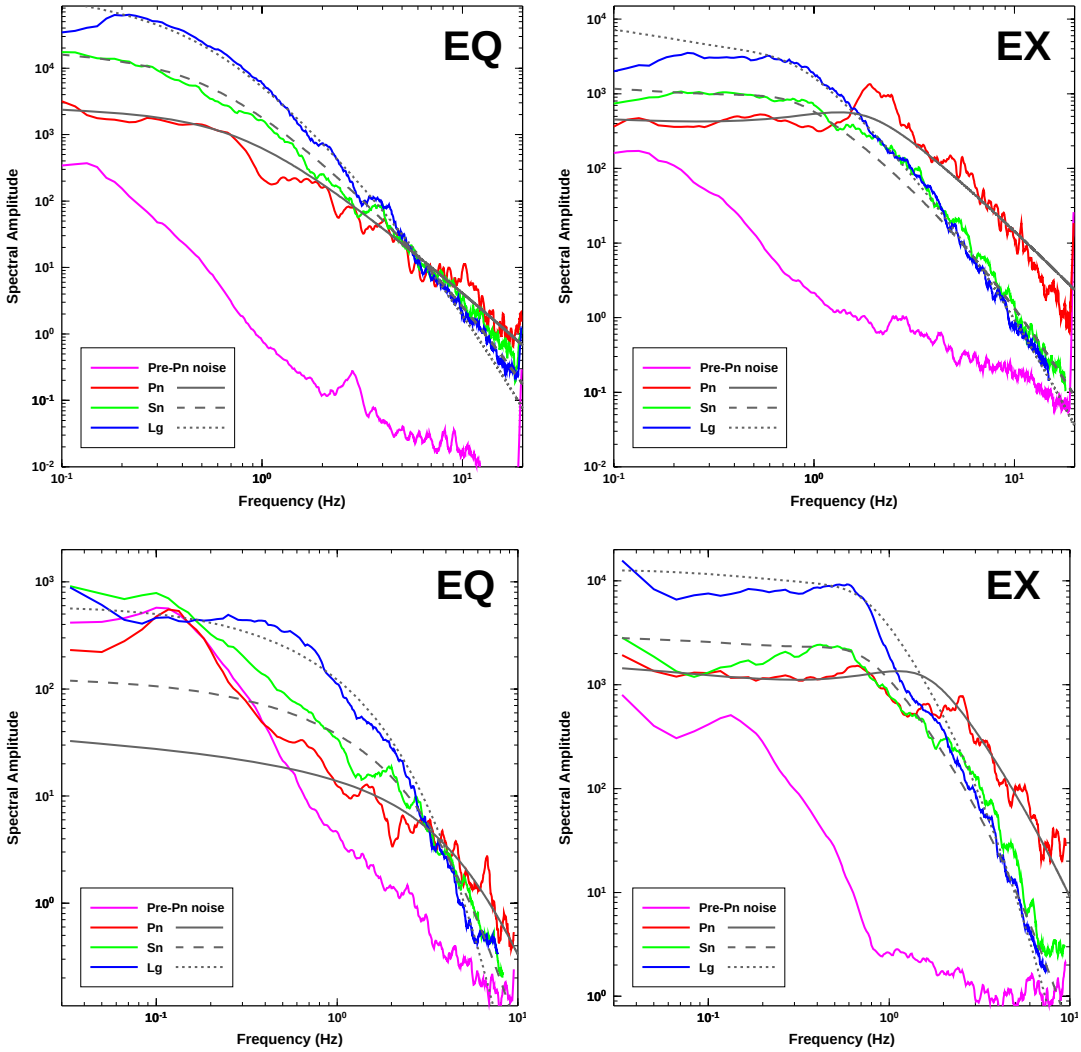


Figure 3. Instrument-corrected Pn, Sn, and Lg spectra at MAK (top) for the 1999/01/30 earthquake (left) and 1996/06/08 UNE (right) and at WMQ (bottom) for a 1996/03/26 earthquake (left) and 1988/09/14 JVE (right). Corresponding model predictions, including attenuation and station terms, are also shown (gray curves).

Figure 4 shows Pn/Sn spectral ratios for 9 LNTS UNEs (magenta curves), the two 1996 UNEs (red curves), and two 1999 earthquakes (green curves), using preliminary distance and station corrections, and then network averaging. (A plot of the Pn/Lg spectral ratios is very similar.) Model results are shown for the 1996 UNEs and 1999 earthquakes (black and gray curves, respectively). They seem to adequately fit the data and indicate that the frequency dependence of P/S discrimination performance is mainly due to different corner frequencies of P and S waves for explosions. Note that, using either the modified Brune or MM71 models, the ratio of high-frequency to low-frequency asymptotic limits of P/S spectral ratios for earthquakes and explosions is given by the ratio of P to S corner frequencies squared. Thus, frequency-dependent discrimination performance is governed by the ratio of the corner frequencies squared and dominated by the event type for which the P and S corner frequencies differ the most. The separation of P/S ratios for earthquakes and explosions is mainly due to the ratio of S and P velocities in the extended Brune model, and a constant k of explosion S-wave coupling (introduced by Fisk, 2006), that was empirically fit for each test site.

Figure 5 shows Pn/Lg spectral ratios at WMQ for 18 UNEs at Balapan, averaged in three mb bins (13 at mb 5.9-6.2, 3 at mb 5.4-5.8, and 2 at mb 4.9-5.1), and for the 1996/03/26 earthquake using WMQ data only (cyan) and averaging over 17 stations (green). Corresponding model results are depicted by the black and gray curves. Figure 6 shows Pn/

Lg spectral ratios at WMQ, corrected for attenuation and site terms, for 6 Degelen UNEs (red curves). The gray curve in each plot is the Brune model result for the earthquake. The solid black curves are the MM71 results for each UNE, using the yields and depths provided by the IDG. The dashed curves are model results using the yields provided and scaled depth of burial. Above about 0.3 Hz, the model results in Figures 5 and 6 seem to suitably predict the empirical Pn/Lg spectral ratios, considering that only one station is used. They do not compare as well below about 0.3 Hz because the Pn attenuation and station corrections are poorly constrained at lower frequencies (cf. bottom left plot of Figure 3) and Pn signals are biased higher by noise. The extended MM71 model, with different corner frequencies for P and S waves, seems to adequately predict Pn/Lg discrimination at STS, as at LNTS.

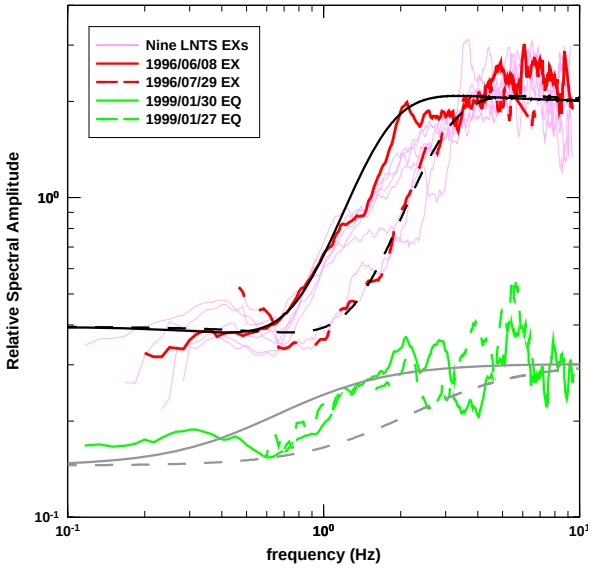


Figure 4. Network-averaged Pn/Sn spectral ratios, corrected for attenuation and station effects, for nine LNTS explosions and two January 1999 earthquakes. Model predictions are shown for the 1996 explosions and the 1999 earthquakes (black and gray curves).

Last, P/S spectral ratios were examined for events at NZTS. Ringdal et al. (1998) noted that P/S ratios in the 1–3 Hz band appear to depend on magnitude for these UNEs, with the smaller ones having lower P/S ratios. Figure 7 shows P/S spectral ratios (for 17 NZTS UNEs), corrected for attenuation and site effects, and averaged in two mb bins (red curves), and for the earthquakes (green and cyan curves). Model predictions are shown for the UNEs (black curves) and an mb 4.6 earthquake (gray curve). The explosion P and S corner frequencies were both increased by 20%, for shale/sandstone at NZTS (Khalturin et al., 2005), compared to granite at LNTS and STS. However, the P and S corner frequencies for NZTS UNEs were still scaled as the ratio of the P and S velocities. Hence, these model results indicate the same explanation of frequency-dependent P/S discrimination performance and dependence on source size, in terms of the relative explosion P and S corner frequencies.

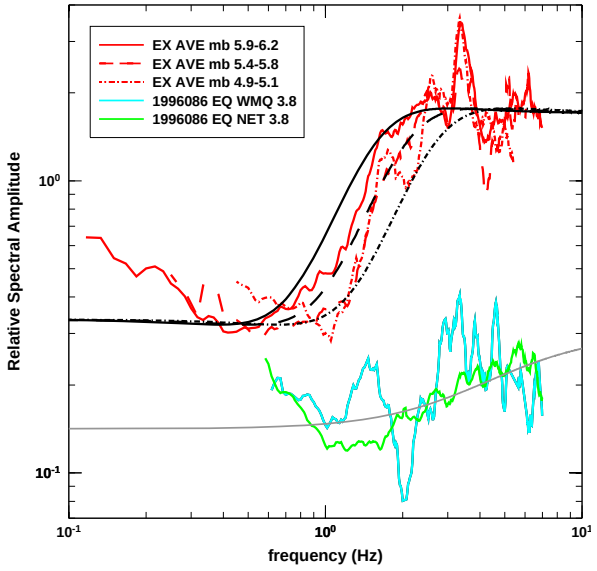


Figure 5. Model and empirical Pn/Lg spectral ratios at WMQ for 18 Balapan UNEs, averaged in three mb bins, and the 1996/03/26 earthquake.

Analysis of Regional P/Lg Discriminants at NTS

We processed Pn, Pg, and Lg spectra for 69 explosions and 38 earthquakes at or near NTS, that were provided by Dr. Walter of LLNL. Figure 8 shows locations of the events. We corrected the spectra for distance and station effects, based on parameters from Walter and Taylor (2002). We have been comparing spectral scaling for various phases and spectral ratios (Pg/Lg and Pn/Lg) to model calculations, using extended Brune and MM71 models for P and S phases, with appropriate geophysical parameters for NTS. For this modeling work, we have utilized explicit information regarding working-point (WP) material properties, depths, and some announced yields for NTS UNEs (Springer et al., 2002).

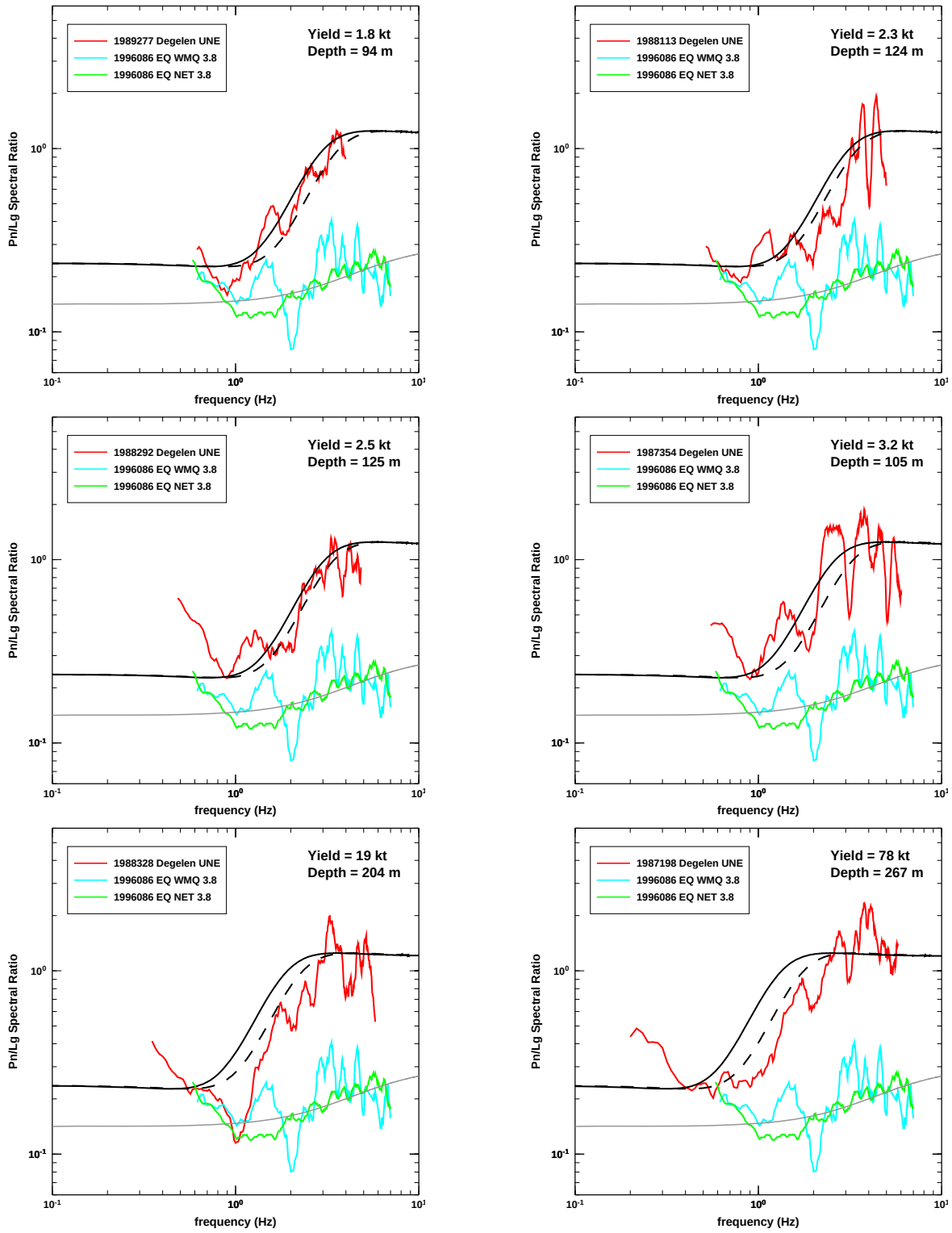


Figure 6. Comparison of empirical and model Pn/Lg spectral ratios at WMQ for 6 Degelen explosions and the 1996/03/26 earthquake. The model results were computed using the yields reported by the IDG and either the depths reported (solid black) or scaled depths (dashed black).

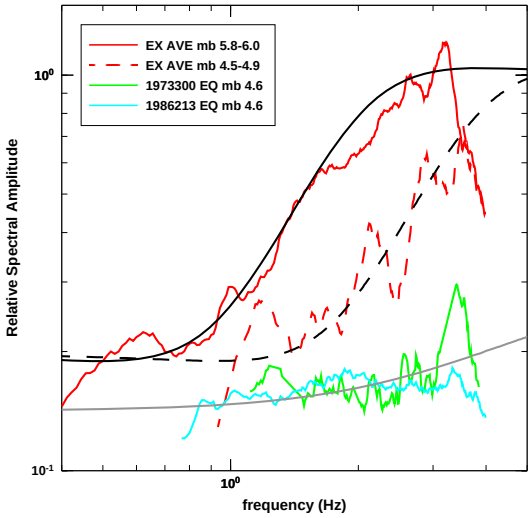


Figure 7. Corrected P/S spectral ratios at NAO01 for 17 NZTS UNEs, averaged in two mb bins, the 1986 Kara Sea event, and an aftershock in 1973. The black and gray curves depict corresponding model results.

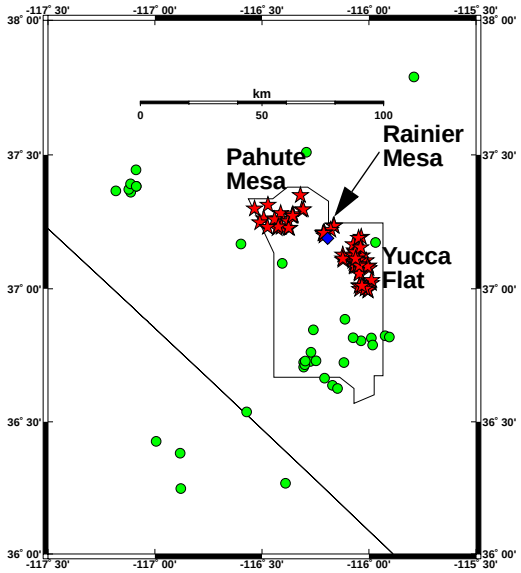


Figure 8. Locations of earthquakes (circles), UNEs (stars), and the NPE (diamond) at NTS.

Among other investigations, we examined whether NTS UNEs exhibit similar relative scaling of P and S corner frequencies as UNEs at the other (hard rock) test sites. To do this, we fit the corner frequencies of a generic MM71 model to the corrected Pn, Pg, and Lg spectra that minimizes the RMS residuals. Figure 9 shows examples of Pn, Pg, and Lg spectra, corrected for instrument response, distance, and site effects, and averaged over ELK, KNB, LAC, and MNV, for two explosions, one at Rainier Mesa (RM) and one at Yucca Flat (YF). Also shown are the fits of MM71 to these corrected spectra.

Figure 10 shows the estimated Pn, Pg, and Lg corner frequencies versus yield for UNEs at RM (top) and at YF (bottom) with gas porosities less than 10%. Also shown are theoretical (MM71) P-wave corner frequencies (gray circles), using the depth and WP material properties for each UNE from Springer et al. (2002). Since each set of these shots were in media with similar properties (e.g., densities of 1.88 to 1.97 g/cm^3 for RM) and at fairly similar depths, the mean properties and depths for each set were used to compute the gray lines, which scale as $W^{-1/3}$. The dashed gray lines are simply shifted lower. The Pn, Pg, and Lg corner frequencies appear to all have similar trends with yield, and fairly consistent with the theoretical predictions. Pg shows the most deviation from the theoretical. Lg shows the best agreement with the theoretical MM71 corner frequency scaling.

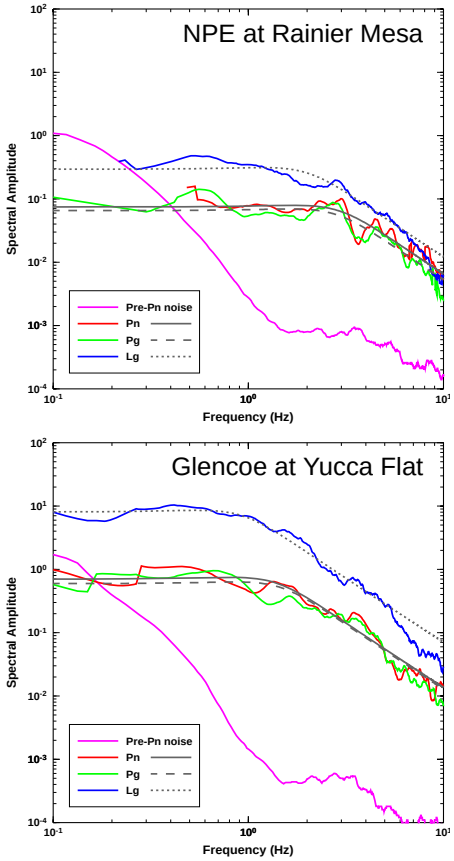


Figure 9. Comparison of model fits to corrected and network-averaged Pn, Pg, and Lg spectra for the Non-Proliferation Experiment (NPE) and Glencoe.

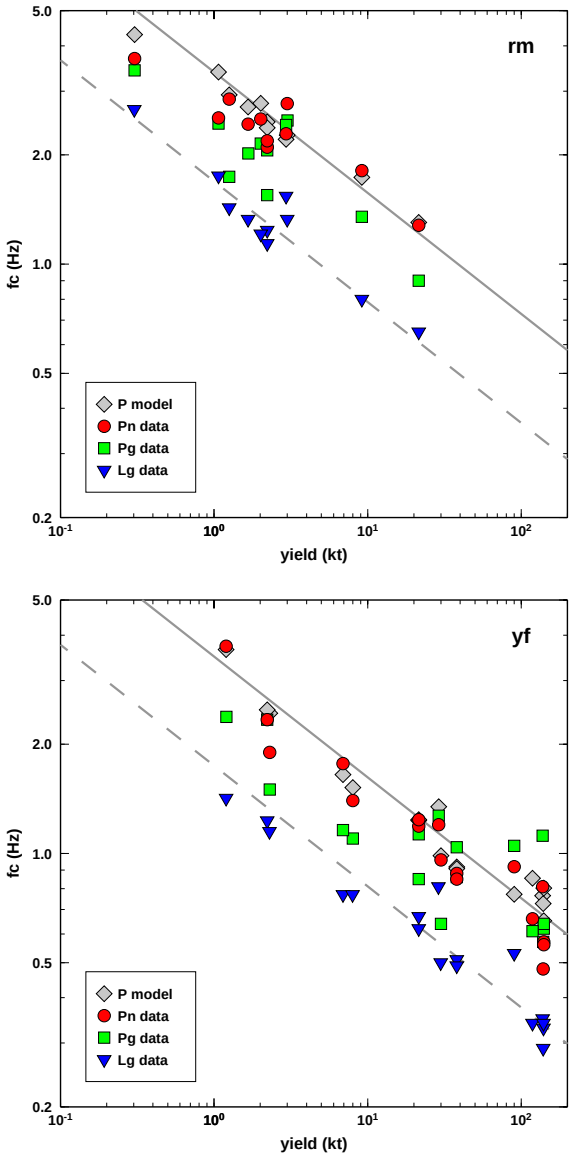


Figure 10. Estimated corner frequencies of Pn, Pg, and Lg versus yield for UNEs at RM (top) and below the water table at YF (bottom). Gray lines are model predictions using the mean material properties and depths for each respective set. Gray dots are MM71 P-wave corner frequencies using the explicit material properties and depths for each explosion.

Since material properties and depths for UNEs at Pahute Mesa have greater variations, we plot the log difference of empirical corner frequencies, relative to MM71 model results for P waves, versus yield (Figure 11). The lack of trends in the residuals suggests good agreement between the empirical and MM71 corner frequencies, as well as similar corner frequency scaling for Pg and Lg. We also examined UNEs above the water table at YF. These data exhibit similar behavior, although there is much more scatter, presumably due to greater variations in the material type (tuff and alluvium) and gas porosity. Despite greater scatter in the data at NTS than at hard-rock test sites, it appears that explosion Lg corner frequencies exhibit similar scaling as P waves, as was observed at LNTS, STS, and NZTS.

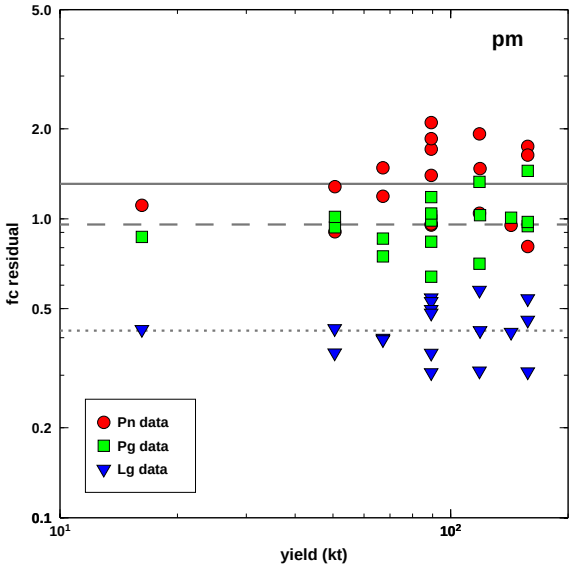


Figure 11. Residuals of model and empirical Pn, Pg, and Lg log corner frequencies versus yield for UNEs at Pahute Mesa. Model results were computed using MM71 for P waves and the depths and WP material properties for each UNE from Springer et al. (2002).

CONCLUSIONS AND RECOMMENDATIONS

Extended MM71 and Brune models were first used to predict source spectra of P and S waves for UNEs and earthquakes near LNTS, STS (Balapan and Degelen), and NZTS. Key results from this study (Fisk, 2006) are as follows. First, frequency dependence of regional P/S discriminants appears to be mainly due to differences in P and S corner frequencies for explosions. The modified Brune and MM71 models used here both predict that the ratio of high-frequency to low-frequency asymptotes of P/S spectral ratios equals the ratio of the P to S corner frequencies squared. Using geophysical parameters from Taylor et al. (2002) and Stevens and Day (1985), model predictions of this ratio are about 2 for the earthquakes and about 5 for explosions. Note that the same relative corner frequency scaling was used for explosion P and S waves throughout this study. Thus, the model provides the same interpretation of frequency-dependent Pn/Sn

and Pn/Lg discrimination at all of the hard-rock test sites examined here. Namely, P/S discrimination begins to emerge predominantly at the explosion S-wave corner frequency and saturates at the explosion P-wave corner frequency. This theoretical result is in agreement with empirical experience obtained over several decades. Also, the dependence of P/S spectral ratios on explosion size at all of these test sites (i.e., lower P/S ratios for smaller explosions at frequencies between the P and S corner frequencies) is qualitatively consistent with observations by Xie and Patton (1999) for LNTS and Ringdal et al. (1998) for NZTS, now with a consistent model-based explanation. An important caveat regarding these results is that limited GT information is available on explosive yield, depth of burial, and other emplacement conditions. Some details of the quantitative results may change if more accurate or explicit information becomes available. However, the conjecture of the relative explosion P and S corner frequencies, which seems to explain the main frequency dependence of P/S discrimination, does not depend on the explicit parameters (i.e., the ratio was the same for all explosions at the hard-rock test sites).

Second, in addition to explaining why P/S discriminants typically perform better at higher frequencies, these results suggest that their application should be restricted by a magnitude threshold and/or to frequencies near or above the explosion Pn corner frequency for a given source size. This can lead to practical monitoring limitations, depending on the size of the explosion, the proximity of regional stations, and SNR, which must be evaluated on a case-specific basis. For example, Figure 6 illustrates that useful discrimination is achieved for explosions down to ~1 kt or perhaps lower at STS, using WMQ recordings at distances of about 1000 km. The performance will degrade for smaller explosions or ones recorded by farther or noisier stations, as SNR degrades near or above the Pn corner frequency. However, a compensating factor is that smaller explosions have more relative high-frequency content in their seismic signals, so (as Figure 6 also indicates) the performance does not degrade as rapidly with yield as might be expected.

Third, the apparent scaling of the explosion S-wave corner frequency with the elastic radius as $\omega_0(S) = v_s(S)/R_e$ at all of the Lop Nor, Degelen, Balapan, and Novaya Zemlya test sites is either an inexplicable coincidence or it suggests that explosion S waves are generated predominantly at a similar length scale as explosion P waves. One would expect that explosion P and S waves would have the same corner frequencies if the S waves are from linear P-to-S conversion, such as at the free surface near the source or by heterogeneities along the path. Alternatively, one would not expect to find any consistent relationship between explosion P and S corner frequencies if the S waves are generated by nonlinear spall effects that can vary greatly with emplacement conditions (e.g., overburden and vertical borehole versus tunnel). While the explicit physical mechanism for near-source S-wave generation is not yet understood, the implications are important regarding where and perhaps how S waves are generated by explosions.

Preliminary results for NTS require further review, but seem to indicate that Lg corner frequencies scale approximately as a constant factor of P corner frequency scaling, as at other nuclear test sites on hard rock. If these results are correct, then they corroborate a very important effect, i.e., that explosion S waves are being generated predominantly near the source. We have also been investigating variations in overall coupling strength of various seismic phases, which appear to be greater than at hard-rock test sites, and effects of spectral modulations on P/Lg discriminants at NTS. Numerical simulations are planned to investigate various near-source and scattering effects that might explain these variations.

We plan to continue our modeling and analysis efforts for NTS, including examination of geophysical effects for Yucca Flat, Pahute Mesa, and Rainier Mesa, based on the type of media, density, velocities, gas porosity, yield, depth of burial, and for UNEs above or below the water table. More work is needed to examine the behavior of P/S discriminants for other geological region types and many more events, but a consistent model-based understanding of P/S discrimination seems to be emerging. Such understanding could potentially be used to predict discrimination performance, on average, for regions with sufficient information. Considerably more work is required to understand regional phase variability due to a multitude of path (scattering) and station effects. More theoretical and numerical-simulation work is also needed to understand the explicit physical mechanism of near-source S generation.

ACKNOWLEDGMENTS

We are grateful to Gary McCartor, Howard Patton, and Jiakang Xie for many useful discussions, and to Scott Phillips, George Randall, and Bill Walter for providing seismic data, moments, stress drop values, and attenuation parameters.

REFERENCES

Brune, J. N. (1970). Tectonic stress and the spectra of seismic shear waves from earthquakes, *J. Geophys. Res.*, 75: 4997–5009.

Fisk, M. D. (2006). Source spectral modeling of regional P/S discriminants at nuclear test sites in China and the former Soviet Union, in press, *Bull. Seism. Soc. Am.*

Israelsson, H., R. Shunga, O. Dahlman (1974). Aftershocks caused by the Novaya Zemlya explosion on October 27, 1973, *Nature*, 247: 450–452.

Khalturin, V. I., T. G. Rautian, P. G. Richards, and W. S. Leith (2005). A review of nuclear testing by the Soviet Union at Novaya Zemlya, 1955-1990, *Science and Global Security*, 13, 1–42.

Marshall, P. D., R. C. Stewart, and R. C. Lilwall (1989). The seismic disturbance on 1986 August 1 near Novaya Zemlya: a source of concern?, *Geophysical Journal* 98: 565–573.

Mueller, C. S. and J. R. Murphy (1971). Seismic characteristics of underground nuclear detonations Part I: seismic spectrum scaling, *Bull. Seism. Soc. Am.* 61: 1675–1692.

Murphy, J. R. and B. W. Barker (2001). Application of network-averaged teleseismic P-wave spectra to seismic yield estimation of underground nuclear explosions, *Pure and Appl. Geophys., Special Edition on Monitoring the Comprehensive Nuclear-Test-Ban Treaty: Source Processes and Explosion Yield Estimation*, 158: 2123–2171.

NORSAR (1999). Novaya Zemlya Explosions 1971–1990 Research and Development Database, Seismic records from the large aperture NORSAR array in CSS3.0 format, June, 1999.

Ringdal, F. (1997). Study of low-magnitude seismic events near the Novaya Zemlya nuclear test site, *Bull. Seism. Soc. Am.*, 87: 1563–1575.

Ringdal, F., E. Kremenetskaya, V. Asming, T. Kvaerna, J. Fyen, and J. Schweitzer (1998). Seismic Monitoring of the Barents/Kara Sea Region, in *Proceedings of the 20th Annual Seismic Research Symposium on Monitoring a Comprehensive Test Ban Treaty*, pp. 21–23.

Springer, D. L., G. A. Pawloski, J. L. Ricca, R. F. Rohrer, and D. K. Smith (2002). Seismic source summary for all U.S. below-surface nuclear explosions, *Bull. Seism. Soc. Am.* 92: 1806–1840.

Stevens, J. L. and S. M. Day (1985). The physical basis of the mb:Ms and variable frequency magnitude methods for earthquake/explosion discrimination, *J. Geophys. Res.* 90: 3009–3020.

Sykes, L. R. and G. Ekström (1989). Comparison of seismic and hydrodynamic yield determinations for the Soviet joint verification experiment of 1988, *Proc. Natl. Acad. Sci.* 86: 3456–3460.

Taylor, S. R., A. A. Velasco, H. E. Hartse, W. S. Phillips, W. R. Walter, and A. J. Rodgers (2002). Amplitude corrections for regional seismic discriminants, *Pure and Appl. Geophys., Special Edition on Monitoring the Comprehensive Nuclear-Test-Ban Treaty: Seismic Event Discrimination and Identification*, 159: 623-650.

Walter, W. R. and S. R. Taylor (2002). A Revised Magnitude and Distance Amplitude Correction (MDAC2) Procedure for Regional Seismic Discriminants: Theory and Testing at NTS, *UCRL-ID-146882, LA-UR-02-1008*.

Xie, J. and H. J. Patton (1999). Regional phase excitation and propagation in the Lop Nor region of central Asia and implications for P/Lg discriminants, *J. Geophys. Res.* 104: 941–954.

IDENTIFYING ISOTROPIC EVENTS USING AN IMPROVED REGIONAL MOMENT TENSOR INVERSION TECHNIQUE

Sean R. Ford[1], Douglas S. Dreger[1], and William R. Walter[2]

University of California, Berkeley[1] and Lawrence Livermore National Laboratory[2]

Sponsored by National Nuclear Security Administration
Office of Nonproliferation Research and Development
Office of Defense Nuclear Nonproliferation

Contract No. DE-SC52-05NA26703[1,2]

ABSTRACT

Seismic moment tensor analysis at local, regional and teleseismic distances has become routine practice. Commonly it involves solving for the deviatoric moment tensor, which is suitable for tectonic earthquakes, and characterizing complexity that might be present due to complex fault geometry or fluid processes in volcanic environments. The general seismic moment tensor also allows for recovery of an isotropic component, which is important in nuclear explosion sources, but which has also been shown to be difficult to resolve.

We have recently corrected a regional distance full moment tensor inversion scheme that greatly increases the stability of moment tensor inversions, and has allowed recovery of isotropic components in volcanic events and nuclear explosions that can be shown to be statistically significant with a high level of confidence. These results suggest that the regional distance moment tensor approach may possibly be used for the discrimination of nuclear explosions from earthquakes. Volcanic events and other seismic sources such as mine collapses also produce anomalous radiation patterns and introduce complexity in distinguishing nuclear explosions from such events. Nevertheless, a complete seismic moment tensor method will provide the capability of distinguishing events based on deviation from the expected double-couple for earthquakes and can identify anomalous events for further scrutiny.

We will investigate performance of the improved moment tensor analysis in the presence of noise and using imperfect velocity structure and Green's functions using both synthetic (controlled experiment) and real data for tectonic and volcanic earthquakes, mine collapses, and nuclear explosions. For nuclear explosions we will test the method for a range of tectonic release strengths, from small up to well known cases where tectonic release seems to dominate and the Rayleigh waves have reversed polarity. We seek to understand the performance of the method under a range of recording conditions from excellent azimuthal coverage to cases of very sparse coverage of one to two stations as might be expected for smaller events of interest. This analysis will be used to determine the magnitude range where reasonably well-constrained solutions can be obtained.

OBJECTIVES

This research seeks to apply a regional distance complete moment tensor approach to tectonic, volcanic and man-made seismic events in order to document performance in the ability to identify and characterize anomalous (non-double-couple) seismic radiation. Identification of events with demonstrably significant non-double-couple components can aid in nuclear event screening and possibly discrimination. The ability of the methodology to characterize the relative amounts of deviatoric and isotropic source components, the similarity of those components with prior events in the source region, and the ability to constrain the source depth all provide utility in investigating events that may appear anomalous using more traditional discrimination techniques.

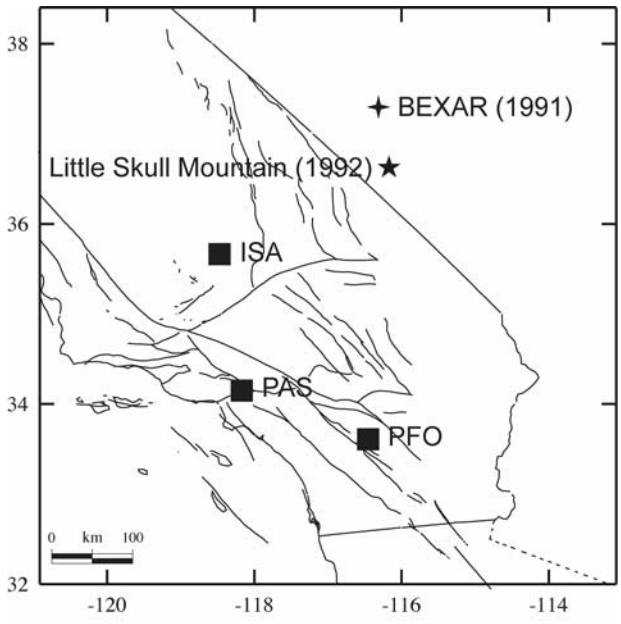


Figure1. Map of stations (squares), earthquakes (star), and explosions (four-pointed star) used in the study.

Large mining collapses, explosions, and volcanic events produce unusual radiation characteristics and seismic moment tensor solutions (see review by Julian et al., 1998). We will apply the regional moment tensor method to a wide range of events in order to characterize the range of moment tensor solutions for different event type and environment. The event populations to be studied include underground nuclear tests, mine collapses, and earthquakes in both the western United States (Walter et al., 2003), and Eurasia, including the 1998 Indian nuclear tests. We will learn what can and cannot be resolved by moment tensor analysis, and what can be found that could help distinguish such mining and natural events from nuclear tests.

Though the full time-domain waveform inversion for the complete moment tensor is a linear operation, there are several choices of parameterization with a nonlinear effect on the solution. For example, the velocity model employed to construct the Green's function is a large source of solution variability and a several models may produce a well-fit solution (Sileny et al., 1992). Our research will emphasize solution significance, resolution, and error analysis through a series of synthetic and observed sensitivity tests. We will probe the solution space and document the point at which it is no longer possible to recover reliable information.

RESEARCH ACCOMPLISHED

We have implemented the time-domain full regional waveform inversion for the complete moment tensor devised by Minson and Dreger (2006) after Herrman and Hutchensen (1993) based on the work of Langston (1981). In general, synthetic seismograms are represented as the linear combination of fundamental Green's functions where the weights on these Green's functions are the individual moment tensor elements. Synthetic displacement seismograms are calculated with a frequency-wavenumber integration method (Saikia, 1994) for a one-dimensional (1-D) velocity model (Table 1) of eastern California and western Nevada (Song et al., 1996). The synthetic data is filtered with a 4-pole acausal Butterworth filter between 0.02 and 0.05 Hz. At these frequencies, where the dominant wavelengths are approximately 100 km, we assume a point source for the low-magnitude ($M_W \leq 5.6$) regional events investigated in this study. Data are collected from the TERRAscope network stations, ISA, PAS, and PFO (Figure 1). We remove the instrument response, rotate to the great-circle frame, integrate to obtain displacement, and filter similarly to the synthetic seismograms.

Table 1. 1-D velocity model (Song et al., 1996)

Thick (km)	V_α (km/s)	V_β (km/s)	ρ (g/cc)	Q_α	Q_β
2.5	3.6	2.05	2.2	100.0	40.0
32.5	6.1	3.57	2.8	286.0	172.0
∞	7.85	4.53	3.3	600.0	300.0

We calibrate the algorithm by calculating the full and deviatoric moment tensor for the 1992 Little Skull Mountain event (Figure 1). The deviatoric solution is

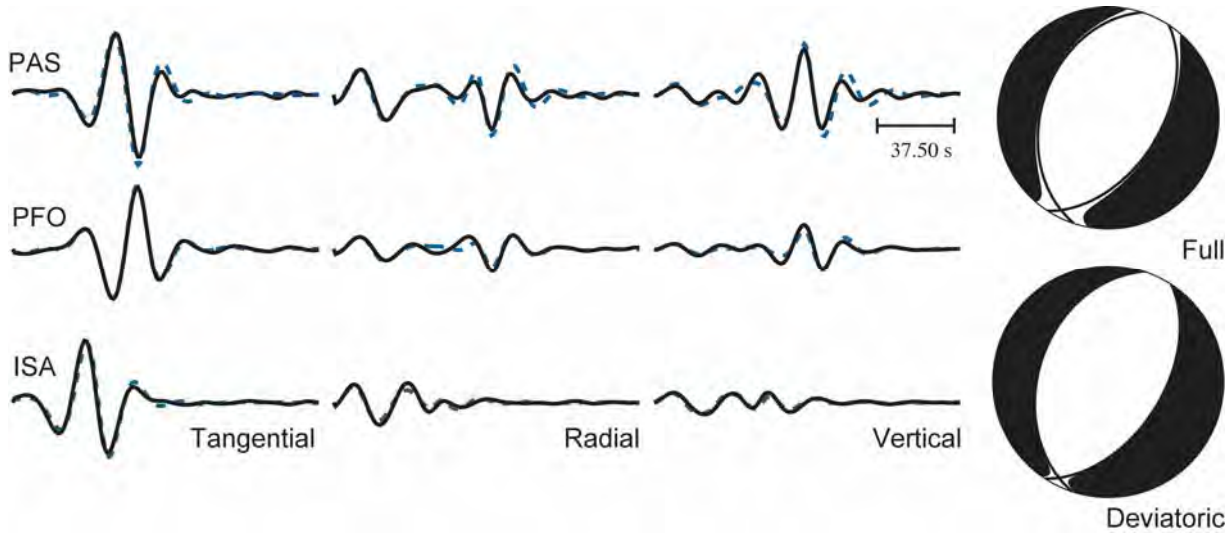


Figure 2. Moment tensor analysis of 1992 Little Skull Mountain earthquake. Data (solid line) and synthetics (dashed blue line) produced by inversion in the 20-50 s passband and resulting full and deviatoric (zero trace) focal spheres with best-fit double-couple planes (black lines), where the size of the deviatoric sphere is relative to the total scalar moment contribution.

obtained by constraining the trace of the moment tensor to be zero. Our result fits the data very well where goodness of fit is measured with percent variance reduction

$$VR = \left(1 - \frac{(d-s)^2}{d^2}\right) \times 100, \qquad (1)$$

where d is the data and s is the synthetic sample, and the solution is summed over all samples for each station and component. The solution has a VR of 92.5% and is highly similar to the double-couple solution of Walter (1993), the deviatoric solution of Ichinose et al. (2003), and the full solution of Dreger and Woods (2002), where we assume a source depth of 9 km. The deviatoric component of the full moment tensor is decomposed to a double-couple and compensated linear vector dipole (CLVD) that share the orientation of the major axis. The 1992 Little Skull Mountain event is almost purely double-couple and there is little change between the full and deviatoric solutions (Figure 2). The best-fit double-couple mechanism produces source parameters of strike 35° and 196°, rake -78° and

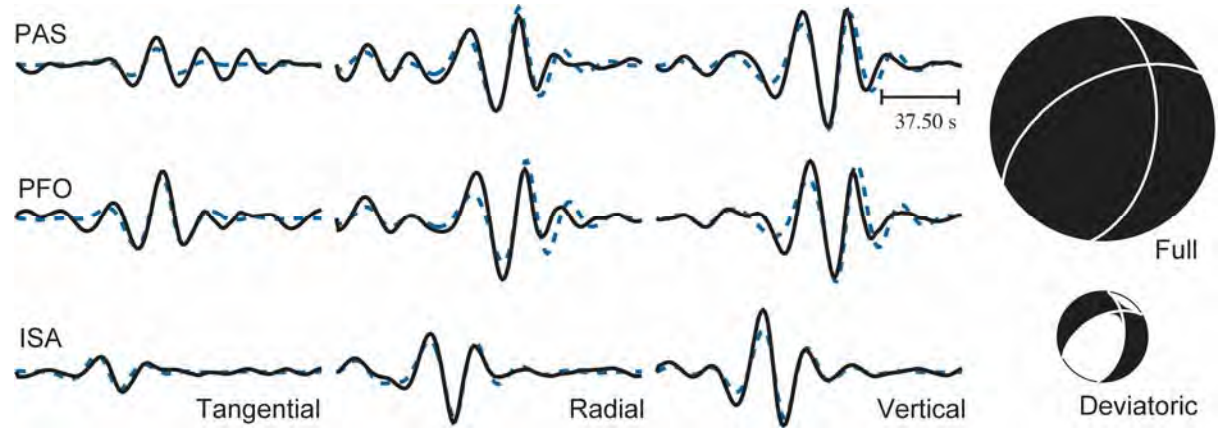


Figure 3. Moment tensor analysis of 1991 NTS test, BEXAR. See Figure 2 caption for figure details.

-104°, and dip 50° and 42°, for the two focal planes, respectively. The total scalar moment (M_0) is 2.92×10^{24} dyne-cm, which results in an M_W of 5.58.

With the same algorithm we calculate the full moment tensor for the 1991 Nevada nuclear test site explosion, BEXAR (m_b=5.6 and M_S=4.2, NEIC; Figure 1). The solution has a *VR* of 80.5% and is similar to the full solution of Minson and Dreger (2006), where we assume a source depth of 1 km. The moment tensor has a large isotropic component, and the ratio of deviatoric moment (M_{DEV}) to isotropic moment (M_{ISO}) is 0.65 (Figure 3), where the M_0 is 4.79×10^{22} dyne-cm (M_W of 4.39). M_{ISO} and M_{DEV} are defined according to Bowers and Hudson (1999) and $M_0 = M_{ISO} + M_{DEV}$.

It is difficult to grasp the source-type from the standard focal mechanism plot. Following the source-type analysis described in Hudson et al. (1989) we calculate 2ε and k, which are given by

$$\varepsilon = \frac{-m_1}{|m_3|} \tag{2}$$

and

$$k = \frac{M_{ISO}}{|M_{ISO}| + |m_3|}, \tag{3}$$

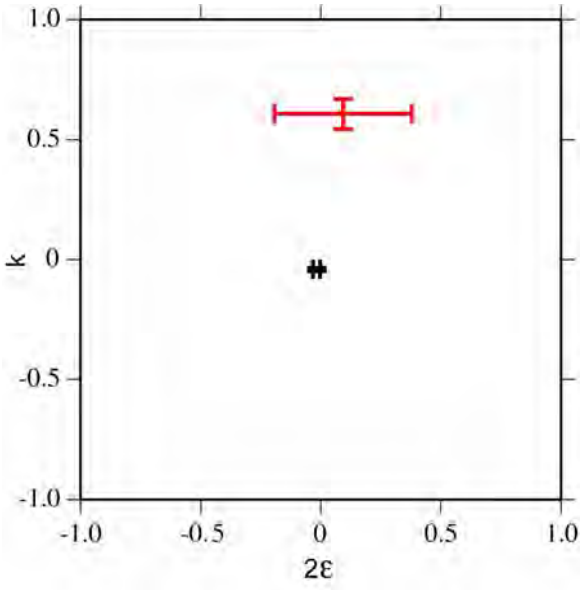


Figure 4. Source type plot for Little Skull Mountain (black) and BEXAR (red), with standard error (bars).

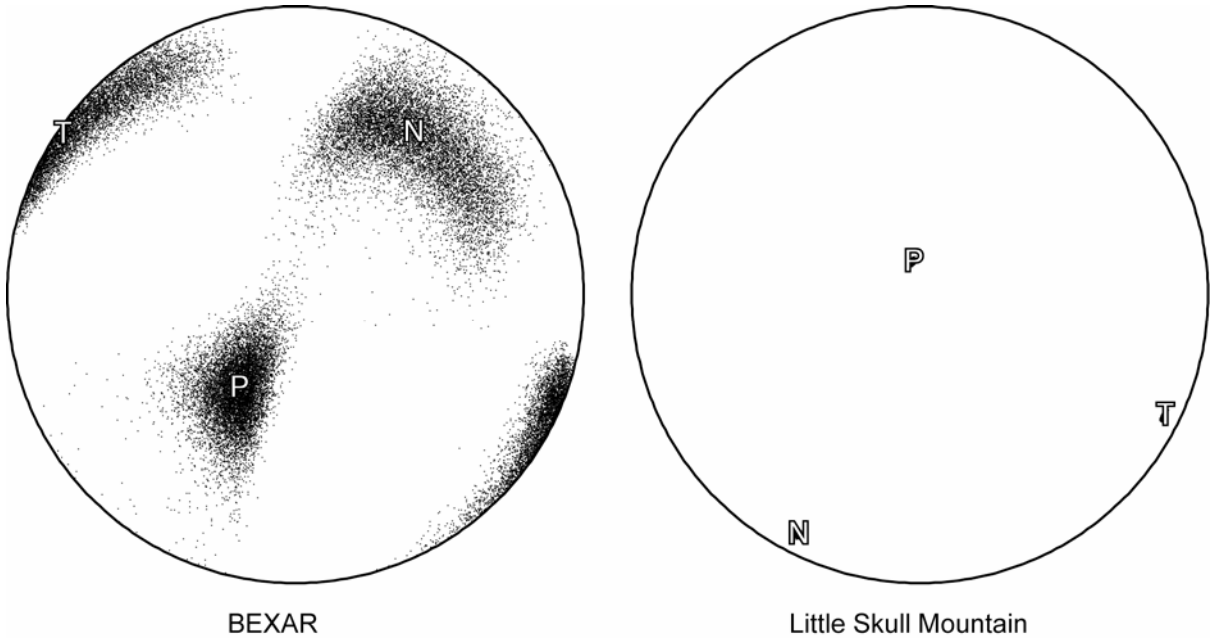


Figure 5. Scatter density of principal axes with best fit axes marked by the T, P, and N for the BEXAR test (left) and Little Skull Mountain earthquake (right).

where m_1 and m_3 are the deviatoric principal moments which are ordered $|m_1| \leq |m_2| \leq |m_3|$. ε is a measurement of the departure of the deviatoric component from a pure double-couple mechanism, and is 0 for a pure double-couple and ±0.5 for a pure CLVD. k is a measure of the volume change, where +1 would be a full explosion and -1 a full implosion. ε and k for the Little Skull Mountain earthquake and NTS explosion, BEXAR are given in Figure 4. Error in the values is derived from the standard error in the moment tensor elements given by the estimated covariance matrix obtained in the weighted least-squares inversion. Figure 4 shows that the Little Skull Mountain earthquake is within the error of being a perfect double-couple event ($2\varepsilon = 0$) with no volume change ($k = 0$). The BEXAR test, on the other hand, has a large volume increase with a large variance in the deviatoric source.

Error in the principal axes is analyzed by plotting the best-fit and scatter density of the axes of minimum compression (T), maximum compression (P) and null (N). The scatter density plot is obtained by randomly selecting moment tensor elements assuming a normal distribution for each element described by the standard error (given by the estimated covariance matrix), and diagonalizing the resulting moment tensor to obtain the principal axes. Principal axes plots for the Little Skull Mountain earthquake and NTS explosion, BEXAR are given in Figure 5. The axes for the Little Skull Mountain event are well constrained, while those for the BEXAR test are more variable. However, the BEXAR test axes do not deviate greatly from the axes of for the Little Skull Mountain event, and could both be the result of a similar tectonic stresses.

In an effort to better characterize the source significance we adopt the source convention described in Riedesel and Jordan (1989). Vectors are defined describing the general,

$$\mathrm{MT} = \sum_{i=1}^{3} M_i \mathbf{M}_i \qquad (4)$$

double-couple,

$$\mathrm{DC} = \mathbf{M_1} - \mathbf{M_3} \qquad (5)$$

isotropic,

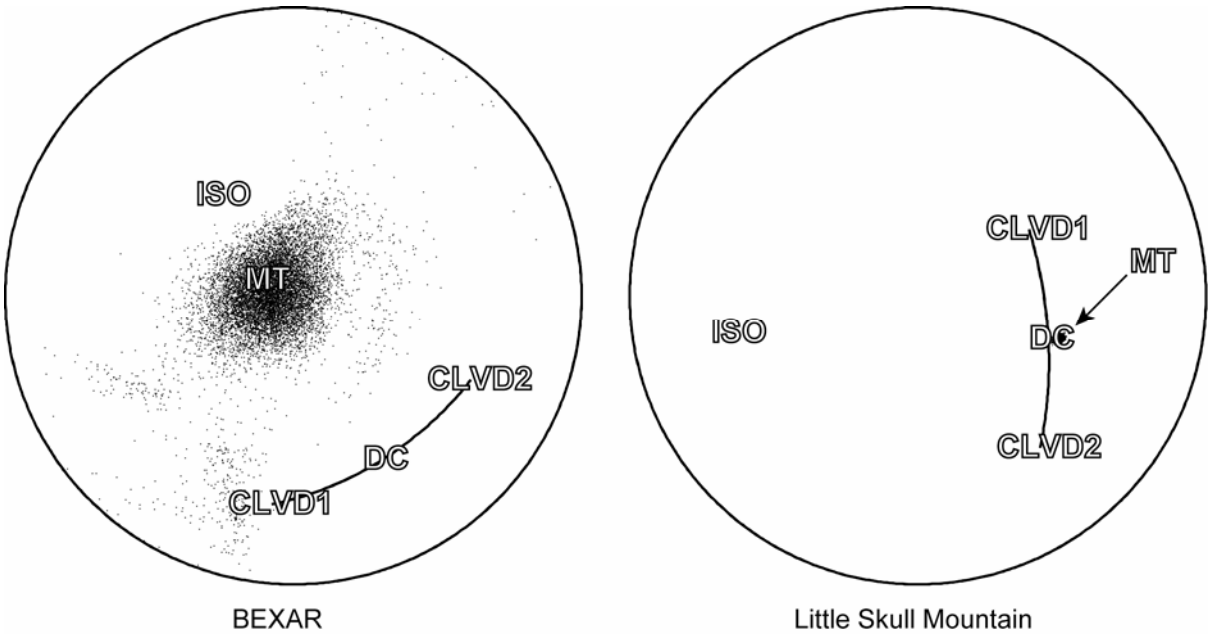


Figure 6. Source vector plot with density plot of general source vector, MT, for the BEXAR test (left) and Little Skull Mountain earthquake (right). See text for definition of vectors. The great-circle line connecting the CLVD1, DC, and CLVD2 vectors defines the purely deviatoric solution space.

$$\mathrm{ISO} = \sum_{i=1}^{3} \mathbf{M}_i \qquad (6)$$

and CLVD sources,

$$\mathrm{CLVD1} = \mathbf{M}_1 - \frac{\mathbf{M}_2}{2} - \frac{\mathbf{M_3}}{2}; \;\; \mathrm{CLVD2} = \frac{\mathbf{M_1}}{2} + \frac{\mathbf{M}_2}{2} - \mathbf{M_3} \qquad (7)$$

where $\mathbf{M_1}$, $\mathbf{M_2}$, and $\mathbf{M_3}$ are the T, N, and P axes, respectively, and M_1, M_2, and M_3 are the principal moments. The source vectors are subspaces of the space defined by the principle axes of the moment tensor. The vectors are plotted on the focal sphere (similar to the T, N, and P axes) for the Little Skull Mountain earthquake and NTS explosion, BEXAR in Figure 6. The general source vector, MT, for the Little Skull Mountain event lies on the great-circle connecting the double-couple and CLVD sources. This great-circle defines the subspace on which MT must lie if the source is purely deviatoric. The MT vector is also collinear with the DC vector, which is to say that the source is almost purely double-couple. The MT vector for the BEXAR test lies well off the line defining the deviatoric solution space. The scatter density of possible MT vectors is also plotted and none of them intersect the deviatoric solution space, which is to say that the solution has a significant isotropic component. Density contours of the distribution will allow for percent confidence statements.

CONCLUSIONS AND RECOMMENDATIONS

The 1992 Little Skull Mountain event is a well-constrained, highly double-couple earthquake with an M_W of 5.6. The 1991 NTS nuclear test, BEXAR (m_b=5.6 and M_S=4.2, NEIC), has a significant positive isotropic component with an M_W of 4.4. The deviatoric components of both events may be responding to the same general Basin and Range stress field of NW-SE extension. Analysis of ε versus k and the source vectors described above allows for an interpretation of the source with error. There are several sources of error in the moment tensor inversion, and the probabilistic method used in this study has the ability to incorporate those sources and produce empirical probability densities of the analyzed parameters (i.e., ε, k, and the source vectors). For example, several velocity models could be used to create the Green's functions for the linear inversion. Each of the moment tensor solutions and their associated scatter density could then be plotted as in Figures 4-6. These types of plots would aid in the understanding of how parameterization choice nonlinearly affects the moment tensor solutions, and help map the solution space of 'best-fit' moment tensors.

The analysis presented here shows that high quality solutions can be obtained for sparsely-recorded events at regional distances, and that these solutions have the potential to discriminate between volume changing (explosions) and double-couple (earthquakes) sources. In the future, we will test the sensitivity of the inversion to noise and non-ideal station spacing. We will also increase the population of moment tensors for man-made and natural events that deviate from the well recorded, large magnitude, small tectonic release cases presented here. Only an analysis of a wide range of events in different environments will allow for a true comparison of explosion and earthquake moment tensor populations.

ACKNOWLEDGEMENTS

Figures were made with Generic Mapping Tools (Wessell and Smith, 1998).

REFERENCES

Bowers, D. and J. A. Hudson (1999). Defining the scalar moment of a seismic source with a general moment tensor, *Bull. Seism. Soc.* 89: (5): 1390-1394.

Dreger, D., and B. Woods (2002). Regional distance seismic moment tensors of nuclear explosions, *Tectonophysics*, 356(1-3): 139–94156.

Herrmann, R. B., and K. Hutchensen (1993). Quantification of m_{Lg} for small explosion, Phillips Laboratory Report PL-TR-93-2070.

Hudson, J. A., R. G. Pearce, and R. M. Rogers (1989). Source type plot for the inversion of the moment tensor, *J. Geophys. Res.* 94(B1): 765–774.

Ichinose, G. A., J. G. Anderson, K. D. Smith, and Y. Zeng (2003). Source parameters of Eastern California and Western Nevada earthquakes from regional moment tensor inversion.

Julian, B.R., A. D. Miller, and G. R. Foulger (1998). Non-double-couple earthquakes 1: Theory, *Rev. Geophys.* 36: 525–549.

Langston, C. A. (1981). Source inversion of seismic waveforms: The Koyna, India, earthquakes of 13 September 1967, *Bull. Seism. Soc. Am.* 71: (1): 1–24.

Minson, S. and D. Dreger (2006). Improved seismic moment tensor inversion, to be submitted to *Geophys. J. Int.*

Riedesel, M. A., and T. H. Jordan (1989). Display and assessment of seismic moment tensors, *Bull. Seism. Soc.* 79(1): 85–100.

Saikia, C. K. (1994). Modified frequency-wavenumber algorithm for regional seismograms using Filon's quadrature: modelling Lg waves in eastern North America, *Geophys. J. Int.* 118: 142–158.

Sileny, J., G. F. Panza, and P. Campus (1992). Waveform inversion for point source moment tensor retrieval with variable hypocentral depth and structural model, *Geophys. J. Int.* 109: 259–74.

Song, X. J., D. V. Helmberger, and L Zhao (1996). Broad-band modelling of regional seismograms: The basin and range crustal structure, *Geophys. J. Int.* 125: (1): 15–29.

Walter, W. R. (1993). Source parameters of the June 29, 1992, Little Skull Mountain earthquake from complete regional wave-forms at a single station, *Geophys. Res. Lett.*, 20: (5): 403–406.

Walter, W. R., K. D. Smith, J. L. O'Boyle, T. F. Hauk, F. Ryall, S. D. Ruppert, S. C. Myers, R. Abbot, and D. A. Dodge (2003). An assembled western United Stares dataset for regional seismic analysis, Lawrence Livermore National Laboratory Report, UCRL-TR-206630.

Wessel, P. and W. H. F. Smith (1998). New, improved version of generic mapping tools released, *Eos Trans. AGU*, 79: 579–579.

SOURCE FEATURES AND SCALING OF BURIED AND SURFACE EXPERIMENTAL EXPLOSIONS IN ISRAEL

Yefim Gitterman, Abraham Hofstetter, and Vladimir Pinsky

Geophysical Institute of Israel

Sponsored by Air Force Research Laboratory

Contract F19628-03-C-0124

ABSTRACT

During the second year of the project additional observations were collected to study empirical features of seismic energy generation for different explosion seismic sources, and how this energy is partitioned between P, S, and surface waves, in specific geological conditions and tectonic settings of the Middle East. The observations concern buried experimental explosions and surface military detonations, for which Ground Truth information (GT0) and blast design parameters were collected.

We analyzed source features and scaling for single-fired, surface explosions at Sayarim military range near Eilat, observed at near-source 3C portable short period (SP) seismometers and regional International Monitoring System (IMS) broadband (BB) stations. A dataset of combined observations of seismic and infrasound waves at collocated sensors was also collected, with S-wave manifestation at distances of up to 150 km. Ground-truth data for 19 explosions in a broad charge weight range (100-8500 kg), recorded at numerous portable and permanent SP and BB stations, facilitated the analysis of energetic characteristics of seismic signals depending on the yield. Source scaling parameters were determined for regional phases observed at BB station EIL (33-38 km). Obtained estimations and waveform features for the surface seismic sources were compared to nearby Sayarim buried (borehole) experimental explosions conducted by the Geophysical Institute of Israel (GII) in 2004, recorded also at EIL. After correction the data for the distance and type of explosives, the scaling power law parameter for P-waves (0.91) with maximal amplitudes was found similar to that for the buried explosions (0.93). The new jSTAR software developed at GII was applied to collected seismograms for the energy generation analysis.

Analysis of Bet-Alpha buried explosions, conducted by GII in 2005 at a basalt quarry and recorded at BB MMLI station, confirmed that amplitudes of regional phases and local magnitudes are well correlated with the scaled depth. Coda-derived moment-rate spectra techniques were applied to BB records for determination of stable regional magnitude for some large-scale calibration explosions conducted by GII: A series of three depth of burial (DOB) experimental explosions of near-spherical charges (five tons of Ammonium Nitrate Fuel Oil [ANFO]) at different depths (22, 43, and 63 m) at Rotem phosphate quarry is scheduled for July 2006. During preparations of the experiment, a number of test shots were conducted in marl rocks to elaborate optimal blast design parameters. Large cavities (up to 3 m) were created at significant depths (up to 63 m) using a special technique, and a number of fully coupled and partially decoupled test explosions were conducted and recorded by numerous portable seismic sensors and permanent stations.

OBJECTIVES

The main objectives of the project are 1) conduction of experimental single-fired explosions of special design; 2) elaboration and verification of empirical source scaling relationships, estimating dependence of seismic wave parameters on different source features; and 3) quantifying the coupling and specific seismic source features, including energy generation analysis and partitioning into various regional phases.

RESEARCH ACCOMPLISHED

During the second year we collected an extensive Ground Truth dataset of surface explosion seismic sources. The collected data were used for 1) analysis of energetic characteristics of seismic signals depending on the yield and estimation of source scaling parameters for regional phases; and 2) comparison of the scaling parameters, waveforms and spectral features to nearby buried explosions observed at the same BB station.

Data of Bet-Alpha explosion series (2005) were used to analyze peak amplitudes and local magnitudes versus charge weight, scaled depth and explosives type. Coda-derived moment-rate spectra technique was applied to BB records for determination of stable regional magnitude for some large-scale calibration explosions conducted by GII.

During preparations of experimental explosions of near-spherical charges at different depths (planned for July 2006), several small test shots were conducted to elaborate optimal blast design parameters and to create large size cavities. The test shots were recorded by portable near-source sensors and used for the energy generation analysis.

In the waveform analysis we used new jSTAR software developed at GII that provides joint processing of different data formats for SP and BB stations (Polozov and Pinsky, 2005).

Collection of Data and Ground-Truth Information for Sayarim Surface Military Detonations.

GT0 data and records for 13 explosions were collected in May-June 1998 during a joint experiment of Israel Defense Forces (IDF) and the US Army Corps of Engineers at the Sayarim military range (Gitterman et al., 2001). The point-like single charges in the range 215-2200 kg of different configurations and explosive composition (TNT, ANFO and Khanit) were detonated on the ground surface (Lat 29.9378ºN, Lon. 34.8185ºE). A similar explosion series of half-spherical charges at about the same site (Lat. 29.95429ºN, Lon. 34.82911ºE) was conducted in October 2003. We collected data for three shots (Figure 1, Table 1). A significant feature of all the shots was that the charges consisted of pure explosives of exactly known weight.

To extend the observation distance range for surface seismic sources, we used data of nearby large explosions (4.5-8.5 tons) intended to destroy outdated ammunition. We visited the explosion site (Lat. 29.99140ºN, Lon. 34.80469ºE) on December 6 and 7, 2005, observed and collected GT0 for three shots, which we placed on the land surface and exposed to the air (Figure 2). Equivalent TNT charge weight was estimated considering shell casing and different explosive types (Table 1).

We measured detonation time and recorded seismic and acoustic waves by near-source portable seismic stations. (A low-frequency infrasound sensor Chaparral 2 was installed in 2005 at the village of Zofar at 73 km; high-quality signals were observed that will be used in a future research).

All selected explosions were well recorded by IMS BB station EIL; some shots were observed also at SP ISN stations (up to 150 km), and close BB stations HRFI, KZIT (in 2003, 2005).

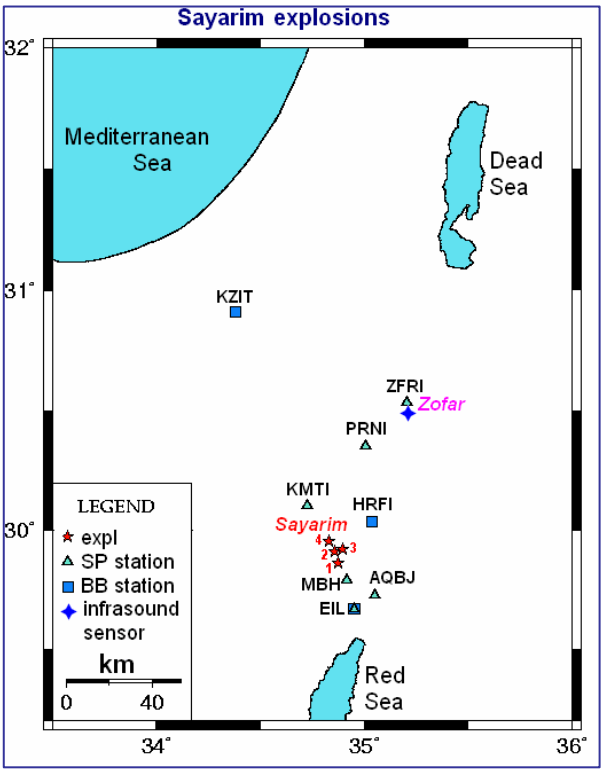


Figure 1. Controlled Sayarim explosions and recording stations: 1 - buried charge-weight series in 2004; 2 & 3 – surface experimental series in 1998 & 2003; 4 –detonations of old ammunition in 2005.

Table 1. Collected Ground Truth parameters (GT0) of surface experimental shots and detonations of old ammunition at Sayarim military range.

Ex. No	Date	O.T.	Charge W, kg	Design	TNT equiv.§	Distance to EIL, km
1	20.05.98	11:37:47.5*	830	TNT cylinder, d~1m, h~1.5m, detonation down	830	32.2
2	24.05.98	14:37:13.70	830	TNT half-spherical, detonation up	830	
3	26.05.98	14:44:02:69	1000	ANFO, detonation down	800	
4	28.05.98	12:25:29*	1000	ANFO	800	
5	02.06.98	09:18:46.67	480	TNT half-spherical, detonation up	480	
6	02.06.98	16:30:18*				
7	03.06.98	09:08:57*				
8	03.06.98	15:50:35.68				
9	03.06.98	16:31:06.16				
10	04.06.98	16:43:58.90	1000	ANFO	800	
11	07.06.98	15:16:56.8*	202	H6, warhead MK83	215	
12	08.06.98	09:49:07.9*	1025	830 TNT (cubic), 195 ANFO	986	
13	08.06.98	16:15:58.0*	2200	TNT+hanit	2200	
14	27.10.03	11:30:44.75	830	TNT half-spherical	830	33.5
15	30.10.03	10:59:29.60	830	TNT half-spherical	830	
16	06.11.03	09:00:31.00	100	TNT cylinder	100	
17	06.12.05	14:18:47.5*	8500	7.5 ton henamit (emulsion) 1 ton TNT (ammunition shells)	7375	38.3
18	07.12.05	13:24:38.6*	4680	4.23 ton henamit (emulsion) 0.45 ton compositeB (ammun. mines)	4086	38.6
19	07.12.05	13:30:15.8*	8570	7.57 ton henamit (emulsion) 1 ton TNT (ammunition shells)	7434	38.3

* O.T. is estimated from records of close SP and BB stations;
§ Explosive TNT equivalent: ANFO – 80%, henamit – 85%, compositeB – 109%.



Figure 2. Sayarim ammunition explosion on Dec. 6, 2005 (Ex.17). Industrial explosive (ANFO-like emulsion Henamit) was added to provide full demolition of the shells (left). The right photo is made from a distance ~3 km, with a large zoom (courtesy of Y. Hamashdyan of IDF).

The three explosions in 2003 were also recorded by portable stations of a special design. The acoustic sensors (low-frequency electret condenser microphone put in a resonance box) were grouped in triangles, each side 100 m long, forming a tripartite array (Figure 3). Each array included a vertical SP seismometer (L4C) collocated with one of the microphones. Acoustic sensors geometry is configured to provide better estimation of source location, which was a major goal of the observations (Pinsky et al., 2005).

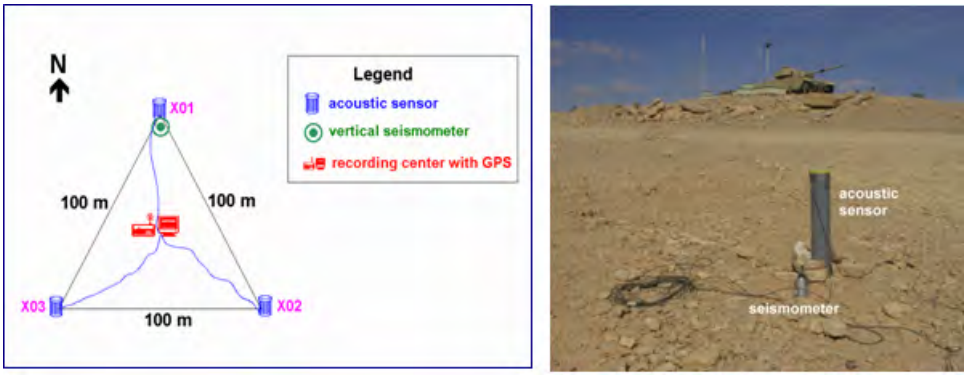


Figure 3. Observations in 1998: (a) Configuration of a hybrid seismic/acoustic portable tripartite array; (b) installed sensors in the Northern apex of the station triangle during one of the shots.

Energy Generation and Source Yield Scaling for Sayarim Surface Explosions.

Strong infrasound phases were observed at seismic channels of local SP and BB stations, which in some cases show much higher amplitudes than seismic waves (Figure 4). Figure 4 also demonstrates a striking example of antipodal manifestation of acoustic phases of the same explosion at two SP stations situated at the same epicentral distance but in opposite directions (Ex.14, Oct. 27, 2003), and the ratio was changed to the opposite on another day (Ex.16, Nov. 6, 2003). These observations correspond to the well known fact that acoustic amplitudes and phase propagation time depend strongly on atmospheric conditions along the infrasound propagation path, especially the altitude distribution of wind direction and velocity (Stump et al., 2002).

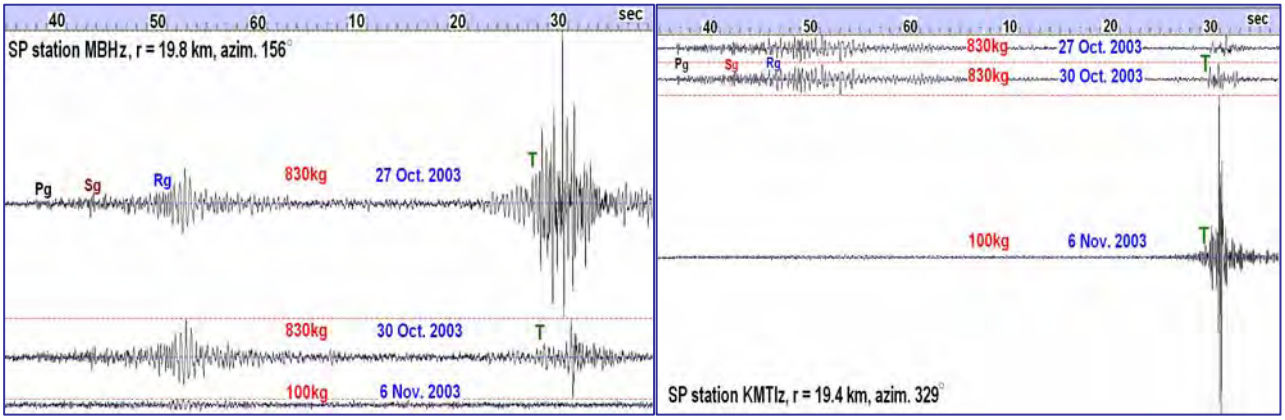


Figure 4. Observations of diverse acoustic phases (T) from surface shots in 2003 at two ISN seismic stations (plotted in absolute scale, filter 1-15 Hz is applied).

The extensive GT0 dataset of about 20 closely-spaced explosions in the broad range of charges 100-8500 kg, recorded at numerous SP and BB stations, facilitate the analysis of seismic energy generation depending on the yield. For a preliminary analysis of energetic characteristics we selected observations at IMS BB station EIL, located at 32-38 km from the explosions (Table 1). Spectra of pre-signal noise showed energy maximum at ~0.2-0.3 Hz, mostly up to ~1 Hz, then seismograms were filtered in the frequency band of 1-20 Hz for 80-Hz data and 1-10 Hz for 20-Hz data (Figure 5). Initially we measured maximal signal amplitudes which are closely correlated with the energy of

radiated seismic waves. For Sayarim shots, observed at the EIL station, maximal amplitudes are presented in first arrivals of P phase (Pg), while S waves are not manifested clearly (Figure 5a). Amplitude spectral shapes of seismic phases are found coherent in general for the five times charge increase (Figure 6). For surface (Rg) waves the dominant frequency and simple spectral shape are about the same for the four shots, only the maximal spectral amplitude is raised ~4 times, whereas spectra of P (Pg) phase are more complicated and the dominant frequency is varied from 2.8 Hz for the largest explosion to 5-6 Hz for smaller shots.

a **b**

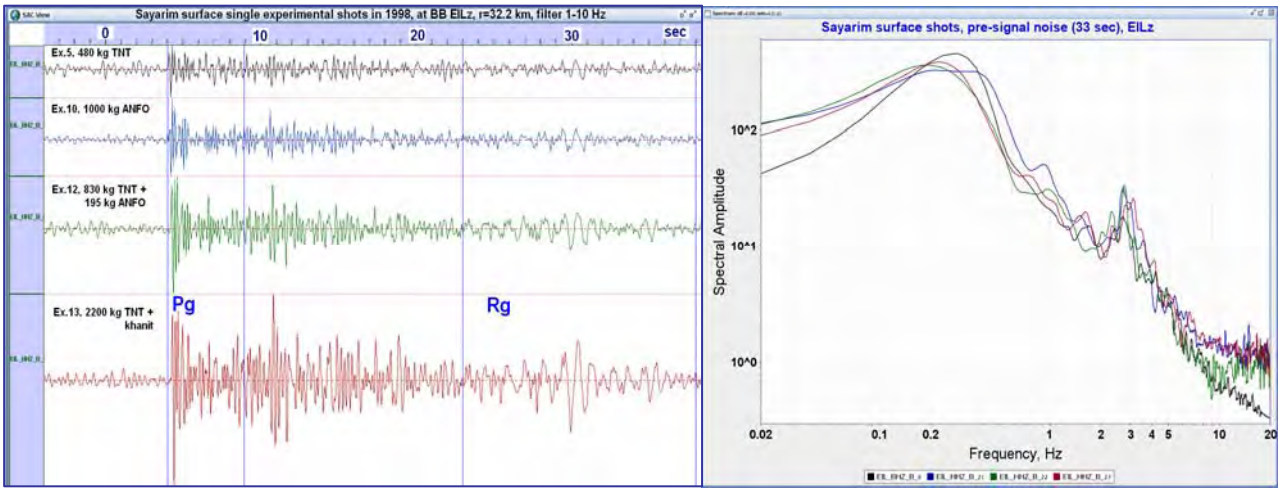


Figure 5. (a) Seismograms (in absolute scale) of 4 selected Sayarim surface explosions at BB station EIL (vertical), low-frequency noise (f<1 Hz) is filtered, vertical lines show windows for spectral analysis; (b) spectra of pre-signal noise (curve colors fit the appropriate seismograms).

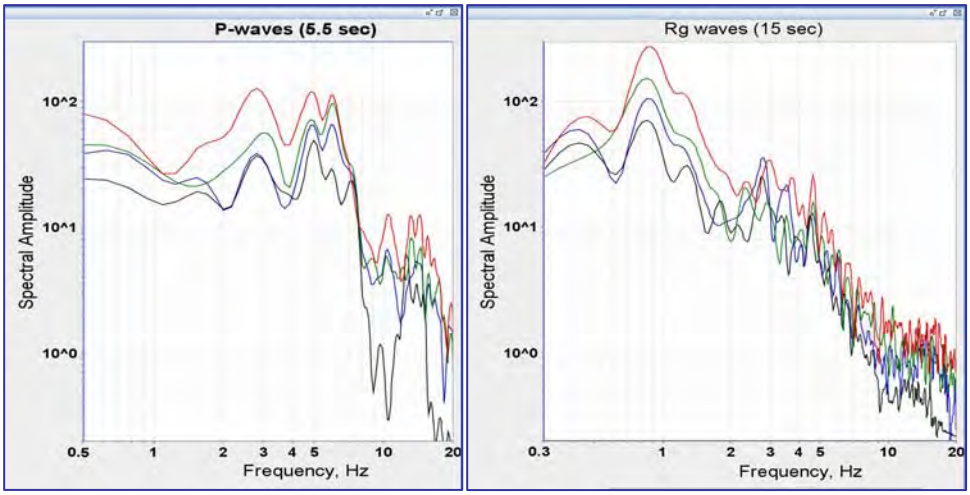


Figure 6. Spectra of P waves and surface waves (Rg) at EIL (vertical) for 4 explosions (the data were pre-filtered in the 0.5-20 Hz band). Curve colors fit the seismograms on Figure 5.

We evaluated a source scaling relationship of surface shots constrained by records at BB station EIL. Measured peak amplitudes (Pg phase) were corrected (Table 1) for distance r (VPA~ $r^{-1.7}$, r_0=35 km) and for various explosives (ANFO energy - ~80% of TNT) (Gitterman et al., 2001). The corrected Vertical Peak Amplitudes (VPA, micron/sec) are plotted against charge weight W (kg) for 19 shots (Figure 7). The data were fitted with the power law equation:

$$VPA_{(mic/sec)} = a*W_{(kg)}^{b} \quad (1)$$

The r.m.s. procedure produced estimates of a = 0.0002258 and b = 0.918 for Pg phase at EIL.

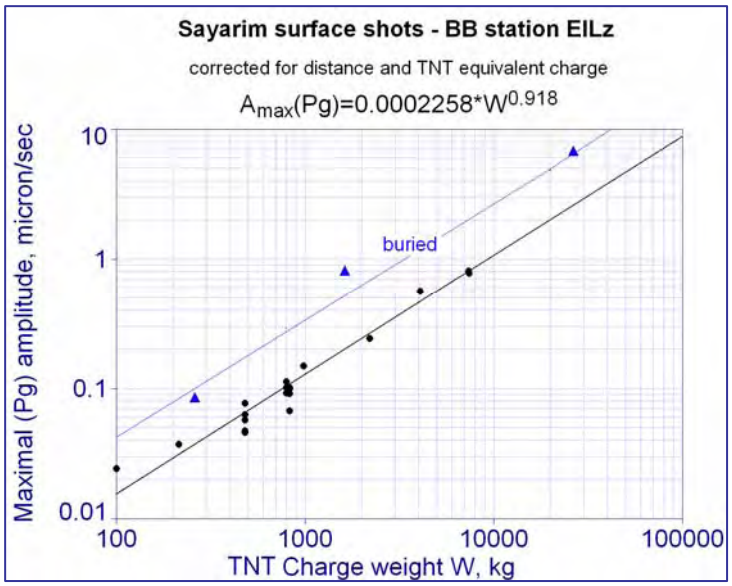


Figure 7. Yield scaling of surface seismic sources at BB station EIL. Data of 3 buried (borehole) Sayarim experimental explosions (2004) at EIL are also shown for comparison (▲).

Comparison of Surface and Buried Seismic Sources.

The very high scaling power law parameter for P-waves b=0.918 is similar to b=0.93 for the nearby buried explosions (in boreholes of large diameter ~0.6-0.7 m, depth 20 m) conducted by GII in 2004, observed at the same BB station EIL (Gitterman et al., 2005) (Figure 7). A lower *b*-value could be expected due to a small charge-rock contact surface for single surface charges resulting in a decrease of explosive energy share transferred to the ground for larger shots. Supposedly the 3 ammunition detonations with the largest multiple charges, placed on a large enough area ~25 m^2 (see Figure 2) (compared to a small area 1-3 m^2 for other single experimental shots in the dataset), produced enhanced Pg-amplitudes, resulting in the high *b*-value.

We compared waveforms and spectra for Sayarim surface and buried (2004) explosions. A comparison sample is presented on Figure 8 for a pair of sources with similar charge weight ~2 tons, observed at BB station EIL, with the same propagation path (North-South). (The buried explosion was in a single borehole, partially contained, with the scaled depth h=1.4 $m/kg^{1/3}$). Both explosions produce maximal amplitudes in P waves on vertical component and clear Rg wave at vertical and about-radial (NS) components, but S-wave manifestation is different: evident Sg arrival at about-transversal (EW) component is found for the buried shot, whereas it is not visible on the surface shot record.

a **b** **c**

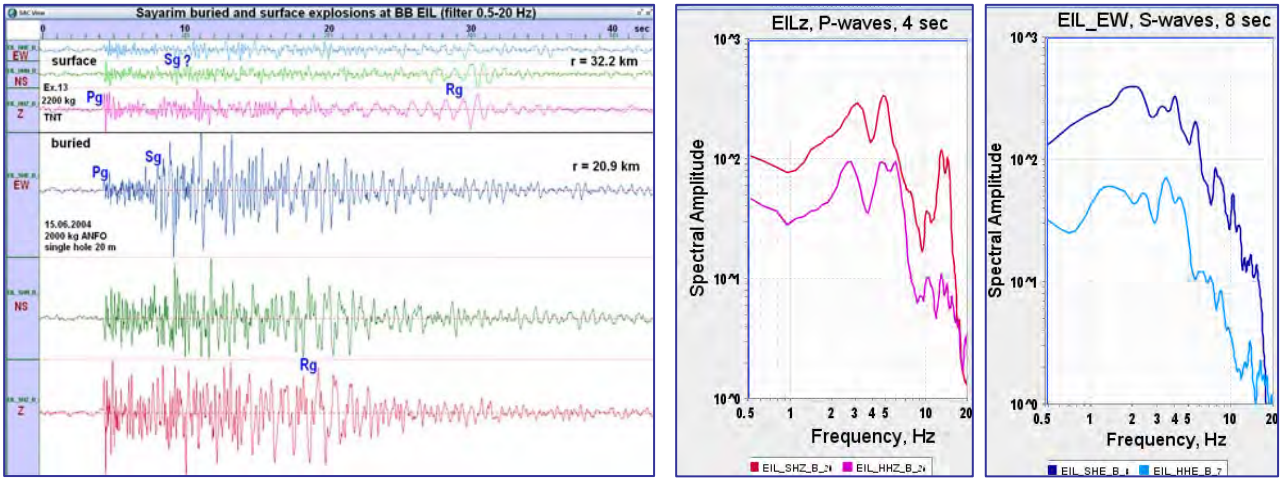


Figure 8. Seismograms in absolute scale (a) and spectra of Pg (b) and Sg (c) for surface and buried shots at EIL. Spectra colors fit appropriate seismograms.

Arrival of Rg, carrying most of the signal energy, cannot be found due to a small distance range, and the Rg group velocity is rather low: 1.0-1.3 km/sec (for close distances 21-32 km). No significant difference or shift to low frequency is found in spectral shapes of Pg and Sg waves for the surface shot comparing to the buried one (Figure 8,b,c) (see Stevens et al., 2003).

Energy Estimations for Bet-Alpha Explosion Series.

We estimated relative seismic energy generated by 4 Bet-Alpha explosions conducted by GII on a basalt quarry (Gitterman et al., 2005). All the shots were well recorded at CNF BB station MMLI located at r=13 km (Figure 9). Maximal vector amplitude and seismic energy for the whole signal (in time window 20 sec) were calculated from measured peak amplitudes for 3 components. Energy values (ratio) relative to the first explosion of 0.5-ton ANFO (Table 2, Figure 10a) were also estimated.

Table 2. Maximal amplitudes, local magnitudes, and energy from Bet-Alpha explosions at BB station MMLI.

Charge, ton	Mag. M_L	Peak Vector, counts	Amplit. Ratio	Energy, counts	Energy Ratio
0.5 (ANFO) single hole	1.5	4147	1	654947	1
0.5 (TNT) single hole	1.5	4330	1.04	689228	1.05
2 (ANFO) two holes	1.4	3277	0.79	429110	0.66
20 (ANFO) 20 holes	2.6	25248	6.1	19822576	30.3

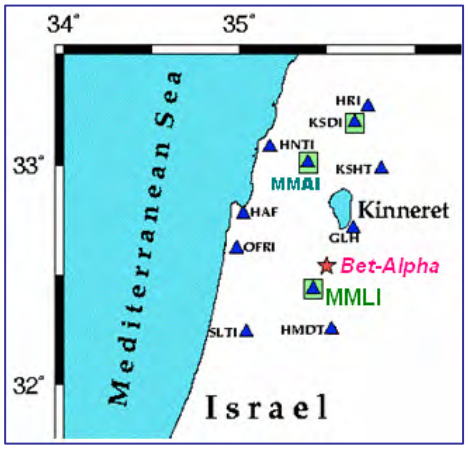


Figure 9. Bet-Alpha explosions and recording stations (symbols are the same as on Figure 1).

a **b**

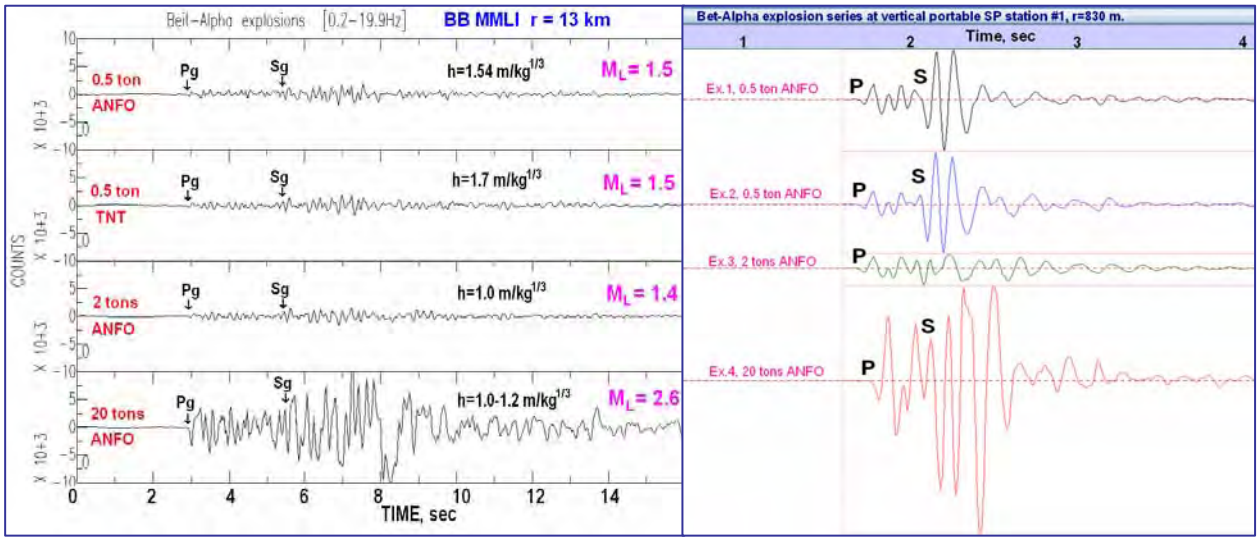


Figure 10. Seismograms (in absolute scale) of Bet-Alpha shots show reduced amplitudes and magnitudes under insufficient scaled charge depth *h* at close BB (a) and portable SP station at ~1 km (b).

For this local seismic observation, a relatively small increase 4-5% in amplitude/energy values is found for a 0.5-ton TNT shot compared with a 0.5-ton ANFO shot. Reduced amplitudes and an energy drop are found for the larger poorly-contained 2-ton shot (in two boreholes), resulting in a low local magnitude of M_L=1.4 compared with a fully-contained 0.5 ton shot with M_L=1.5 (Figure 10a). More significant energy decrease is observed at a near-source portable SP station (Figure 10b). For the largest calibration, a 20-ton shot with the estimated magnitude of M_L=2.6 is also relatively small according to empirical relationship for simultaneous blasts in boreholes (Gitterman, 1998); seismic energy is increased more than 30 times, relative to 0.5-ton shots, that is conformed to about one unit magnitude (M_L) raise.

Analysis of seismic source features and blast design parameters for Bet-Alpha experiment shows that the main reason of reduced seismic strength is smaller, insufficient scaled charge depth $h=H/W^{1/3}$, where H is depth from the surface to the charge center, m, and W is charge weight, kg. The scaled depth for the 0.5 ton shot h=1.54 m/kg$^{1/3}$ is found large enough to provide full containment of the explosion, whereas two larger shots of 2 tons (h=1.0 m/kg$^{1/3}$) and 20 tons (h=1.0-1.2 m/kg$^{1/3}$) produced rock outbreaks and energy losses into the air. These effects, clearly seen on explosion photos and video-records, provide an explanation of reduced magnitudes for the two explosions. The obtained data show the importance of scaled DOB charges as a crucial factor of seismic coupling.

Coda-Derived Moment-Rate Magnitude.

Coda-derived moment-rate spectra technique (Mayeda et al., 2003) was applied to BB records for determination of stable regional magnitude for some large-scale calibration explosions conducted by GII: Dead Sea underwater explosions 2-tons and 5-tons in November 1999 (Gitterman and Shapira, 2001) and Sayarim valley explosion 32.5 tons in June 2004 (Gitterman et al., 2004). For Dead Sea explosions we used recordings of BB IMS stations MRNI (at distance 164 km) and EIL (212 km), for the Sayarim explosion we used data of CNF BB station HRFI (27 km).

Obtained moment-magnitude values fit well to local (duration) magnitudes estimated from Israel network SP stations (Figure 11).

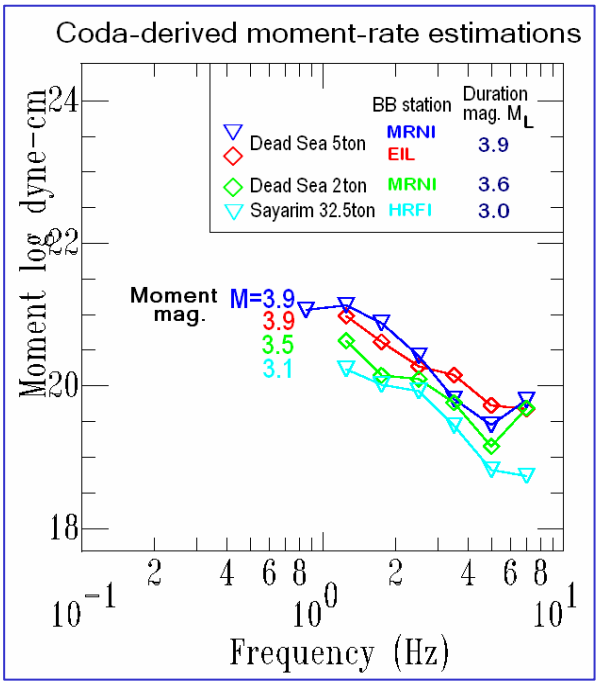


Figure 11. Coda-magnitude estimations for large-scale calibration explosions conducted by GII.

Preparation of a DOB Explosion Series.

During a long time we have been conducting direct preparations of the DOB experiment, that includes three explosions of the same charge at different depths: 22 m, 43 m, and 63 m. One of the main goals of the experiment is to observe regional phases at remote stations, especially at the IMS array AS49 (MMAI) at Mt. Meron, located at ~200 km from a planned explosion site. According to the recent revised magnitude-charge relationship (Gitterman at al., 2005) the charge ~5 tons should be used to provide explosion magnitudes M_L~2.4-2.5 necessary for such observation.

A special complicated design and technology are utilized, developed by Tamar Advanced Quarrying Ltd. (B. Hayoun) and Rotem Amfert Negev Ltd. (U. Yasur, Y. Levi): deployment of explosives in a cavity, created beforehand by a small charge, thus forming near-spherical sources (Figure 12). For the planned ANFO explosives (density ~0.8 gr/cm^3) the diameter of a cavity capable to accommodate this charge is ~2.3-2.5 m. The most important conditions for such an experiment are homogeneity of rock media for all the sources (i.e., for depths 15-65 m), and plasticity of the rocks allowing creation of large cavities (suitable for consolidated sediments of medium strength).



Figure 12. Snapshots of the GeoVISION borehole camera video-records show a borehole inner view before (left) and after (right) a small preparatory explosion. The measuring strip (~80 cm length) attached to the camera is exposed as almost straightened over the created cavity bottom.

Geophysical surveys (seismic refraction and reflection profiles, and microgravity) are also planned at the experiment site by the GII team, in order to estimate the homogeneity of the upper layer and obtain the sub-surface velocity model in the near-source zone. Another important goal will be the evaluation of radius and volume of non-linear source zones created after the explosions, which supposedly should have different size (Figure 13), for characterization of the signal strength and corner frequency and correlation with observed local magnitude and features of regional phases.

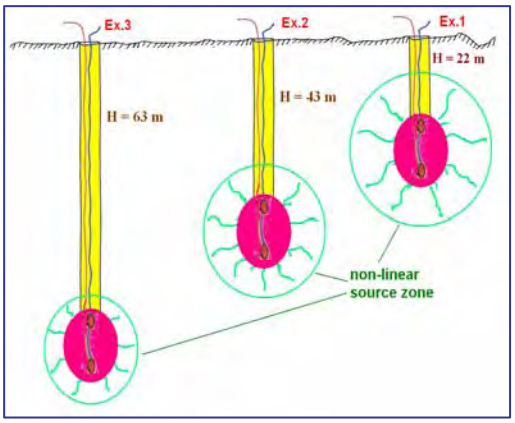


Figure 13. Schematic view of supposed diverse non-linear zones for explosions at different depths.

There is no known and ready technique to create the large size cavity (~2.5 m) at depths more than 60 m in soft consolidated sediments using a vertical borehole with the diameter 6.5", and prevent possible rock-falls in the cavity or borehole blockage. Therefore, a special trial explosion series was conducted (in marl rocks, on Rotem phosphate quarry area) in April-June 2006, before the main DOB experiment. The main goal of the trial series was to test an existing technique (that was used before to produce much smaller cavities) and estimate the optimal small charge or series of charges for creation of appropriate cavities (Figure 14). A number of cavities were created at depths 25-63 m, with maximal size up to 3 m. A part of the trial shots were recorded by several portable seismic instruments (SP 3C stations, accelerometers and engineer sensors) at distances 0.2-5 km, the data are being analyzed, and the results will be used for tuning the observation system during the DOB experiment.



It was revealed that these trial cavities cannot be used for the DOB experiment (with charges of 5 tons), due to a ground shaking hazard for a nearby (~500 m) quarry laboratory building. Nevertheless, we found that they present a good chance for conducting of a decoupling experiment (with smaller charges and decreased seismic strength, permitted for this site).

Due to the very complicated technical realization of the experiment, the preparation activities took several months, more time than planned. The experiment is scheduled for July 2006.

Figure 14. A trial shot (~300 kg ANFO) in a hole with depth 63 m. Ejection of gases and dust lasted ~30 sec, a cavity of ~3m size was created.

CONCLUSIONS AND RECOMMENDATIONS

1) The project event database was extended to study empirical features of seismic energy generation for different wave phases from GT0 surface military explosions in broad range of charge weight and design features.

2) These specific surface sources are different from buried (borehole) sources in generation of seismic energy and waveforms, especially due to radiation of strong acoustic waves, taking most of explosion energy and propagating in atmosphere to large distances. In some cases (depending on atmosphere conditions), strong acoustic phases are found at remote seismic SP and BB IMS stations. Combined interpretation of obtained seismic and infrasound signals may contribute to the analysis of energy generation, source characterization, and related identification task.

3) The extensive GT0 dataset of closely-spaced surface explosions in a broad range of charges, recorded at IMS BB station EIL, facilitated the analysis of seismic energy generation depending on the yield. The scaling power law parameter for P-waves (0.91) with maximal amplitudes was found similar to that for the buried explosions (0.93). Comparison with nearby Sayarim borehole experiment recorded also at EIL demonstrated similar spectral shapes and regional waveforms, except of Sg phase at the transversal component. In the following research this analysis should be conducted for other energetic parameters, in different frequency bands, and for other phases (Sg, Rg) observed at records of EIL and other SP and BB stations from surface and buried shots.

4) The results obtained for Bet-Alpha borehole experiment confirm the importance of scaled depth of buried charges as a crucial factor in seismic coupling well correlated with amplitudes of regional phases and local magnitudes. The experiment contributed to the study of explosion source features in specific geological settings (basalt quarry).

5) A specific blasting technique was used for creation of large (up to 3 m size) and deep (up to 63 m) near-spherical cavities in soft sediments, during preparation of a DOB experiment scheduled for July 2006. Preliminary analysis of obtained results shows that such cavities could be used for a cheap decoupling experiment.

ACKNOWLEDGEMENTS

We thank the IDF personnel for the help in collecting GT0 data for Sayarim military detonations. We appreciate the great efforts of engineers and workers of Tamar Advanced Quarrying Ltd and Rotem Amfert Negev Ltd. involved in preparation of the planned complicated DOB experiment. We also wish to thank Mr. A. Polozov for his permanent support in data processing and analysis by his new software, jSTAR.

REFERENCES

Gitterman, Y. 1998. Magnitude yield correlation and amplitude attenuation of chemical explosions in the Middle East, in *Proceedings of the 20th Annual Seismic Research Symposium on Monitoring a CTBT*, pp. 302–311.

Gitterman, Y. and A. Shapira (2001). Dead Sea Seismic Calibration Experiment contributes to CTBT Monitoring, *Seism. Res. Lett.* 72: (2), March/April 2001, pp. 159–170.

Gitterman, Y., V. Pinsky, and A. Shapira (2001). Improvements in Monitoring the CTBT in the Middle East by the Israel Seismic Network, Contract DSWA01-97-C-0151, Final Report DTRA–TR-01-35, 196 pp.

Gitterman, Y., V. Pinsky, K. Solomi, R. Hofstetter, C. Gurbuz, and M. Ergin (2004). Using ground truth events for travel time calibration and studying seismic energy generation and partitioning into various regional phases, in *Proceedings of the 26th Seismic Research Review: Trends in Nuclear Explosion Monitoring*, LA-UR-04-5801, Vol. 1, pp. 61–72.

Gitterman, Y., V. Pinsky, A. Hofstetter (2005). Using ground truth explosions for studying seismic energy generation and partitioning into various regional phases, in *Proceedings of 27th Seismic Research Review Ground-Based Nuclear Explosion Monitoring Technologies*, LA-UR-05-6407, Vol. 1, pp. 550–560.

Mayeda, K., Hofstetter, A., O'Boyle, J. and Walter, W. (2003). Stable and transportable regional magnitudes based on coda-derived moment-rate spectra, *BSSA* 93: 224–239.

Pinsky, V., Y. Gitterman, A. Hofstetter, A. Shapira (2005). Robust location of surface explosions by a network of acoustic arrays, *Geophys. Res. Lett.* 33: L02317, doi:10.1029/2005GL024304.

Polozov, A., Pinsky V. (2005). New software jSTAR for seismic network and array data processing and joint seismological database. GII Rep. 546/185/05, 27 pp.

Stevens, J. L., Rimer, N., Xu, H., Baker, G. E., Murphy, J. R., Barker, B.W., Lindholm, C., Ringdal, F., Gibbons, S., Kværna, T., and Kitov, I. (2003). Analysis and simulation of cavity-decoupled chemical explosions, in *Proceedings of the 25th Seismic Research Review- Nuclear Explosion Monitoring: Building the Knowledge Base*, LA-UR-03-6029, Vol. 1, pp. 466–475.

Stump, B. W., S. M. McKenna, C. Hayward, and T.-S. Kim (2002). Seismic and infrasound data and models at near-regional distances, in *Proceedings of the 24 th Seismic Research Review-Nuclear Explosion Monitoring: Innovation and Integration*, LA-UR-02-5048, Vol. 2, pp. 572–581.

PHASE COMPOSITION OF REGIONAL WAVES FROM THE BALAPAN AND DEGELEN NUCLEAR EXPLOSIONS AND ITS IMPLICATIONS FOR SHEAR-WAVE EXCITATION

Tae-Kyung Hong[1], William Menke[1], and Jiakang Xie[1,2]

Lamont-Doherty Earth Observatory of Columbia University[1] and AFRL/VSBYE[2]

Sponsored by National Nuclear Security Administration
Office of Nonproliferation Research and Development
Office of Defense Nuclear Nonproliferation

Contract No. DE-FC52-03NA99514[1,2]

ABSTRACT

We analyze historic Balapan and Degelen underground nuclear explosion (UNE) seismograms that were recorded at the Borovoye seismic station in Kazakhstan. We examine the phase composition of waves as they leave the source region using a frequency-slowness source-array analysis. The Degelen UNEs are located ~50 km SW of the Balapan UNEs. We measure the phase velocities of various regional phases (Pn, Pg, Sn, Lg, Rg). We compare the phase composition between the Balapan and Degelen data. We find that the phase compositions of waves from both test sites are similar. From the analysis, we observe that the phase velocities of Lg and Rg are distinctively different. This difference indicates that the dominant waves composing Lg and Rg are originated separately in the source region, which does not support the proposed Rg-to-S scattering mechanism for the explanation of regional shear-wave excitation. To confirm this inference, we expand the study for examination of phase composition of regional coda for the Balapan UNEs. We examine whether the source-array analysis can resolve Rg scattered waves. Strong Rg scattered waves are observed in the coda in the frequency range of 0.2-0.8 Hz. We map the origins of scattered waves, and find that the scattered energy is excited from lateral heterogeneities in the crust. From the overall observations, we infer that the Rg scattering is clearly present, but does not appear to be a dominant mechanism for excitation of regional shear waves from the Balapan and Degelen UNEs.

OBJECTIVES

The objective of this research project is to examine the properties of regional phases (*Pn*, *Pg*, *Sn*, *Lg*, *Rg*) from UNEs and to understand the shear-wave excitation mechanism. Hundreds of clustered UNEs in central Asia and Nevada between the 1970s and 1990s were recorded at common regional stations. The common-station records for clustered UNEs can be treated as array records under the reciprocity theorem. Analyses of source-array records allow us to investigate the properties of wavefields in the near source region. We analyze regional waveform data of the Balapan and Degelen UNEs that were recorded at the Borovoye seismic station.

A frequency-wavenumber (F-K) method is applied to the source-array records to explore the phase composition of regional waves from UNEs as they leave the source. In each frequency band we estimate the powers of various phases, including direct body and surface waves and scattered/multipathed waves. We examine whether previously proposed mechanisms for regional shear-wave excitation are compatible to observed phase composition.

RESEARCH ACCOMPLISHED

Under the reciprocity theorem, velocity seismograms from clustered explosion sources can be regarded as seismograms at an array of fictitious strain meters buried at the source locations, recording a single force acting at the station location (Spudich and Bostwick, 1987; Xie et al., 1996). We apply an F-K method to the source-array seismograms, and investigate the phase composition of regional waves as they leave the source region. We analyze seismic waveform data for the Balapan and Degelen UNEs, recoded at the Borovoye seismic station (BRV), Kazakhstan. We examine the phase composition of the coda, and compare it with the properties of main phases. We infer the shear-wave excitation mechanism along with the properties of main phases.

Data and local geology

We analyze vertical short-period seismic records at BRV for UNEs at the Balapan and Degelen nuclear test site during 1968-1989 (Fig. 1). The recording system of BRV is composed of a set of vertical short-period seismometers (Kim et al., 2001; Hong and Xie, 2005). We analyze seismograms recorded at SKM-3 seismometers with a natural period of 2.0 s and sampling rates of 0.032 and 0.096 s. The records display high signal-to-noise ratios (SNR>50 dB). Both low- and high-gain seismograms are available. The epicentral distances vary between 680 and 697 km. The event magnitudes (m_b) are between 4.8 and 6.2, with 58 out of the total 67 events having magnitudes larger than 5.5 (Marshall et al., 1985; Kim et al., 2001). High-precision hypocentral locations of the UNEs are measured geodetically (NNCRK, 1999; Thurber et al., 2001).

High-accuracy or ground truth information is available for 10 UNEs between 1985 and 1989 (Adushkin et al., 1997). For all UNEs, teleseismically determined origin times are also available from multiple sources, such as the International Seismological Centre (ISC) and Thurber et al. (2001). The azimuths for the great-circle directions between the UNEs and BRV are 302º-304º.

The upper crust of the northeastern subregion of the Balapan test site has lower shear velocities by ~0.4 km/s relative to the southwestern subregion due to difference in surface geology [Ringdal et al., 1992; Bonner et al., 2001]. The seismic velocities gradually increase with depth and reach 8.0 km/s for *P* and 4.7 km/s for *S* in the mantle lid (Quin and Thurber, 1992). The crustal basement along the great-circle path between the Balapan test site and the Borovoye observatory are composed of precambrian and early palaeozoic hard rocks (Levashova et al., 2003), which enables to collect unique waveform data set with high signal-to-noise ratio.

In the analysis of seismic coda, we use low-gain records for early coda and high-gain records for late coda (lapse time > 400 s) to avoid the digital round-off error. We check every record section, and confirm no apparent contamination in the coda by any earthquakes.

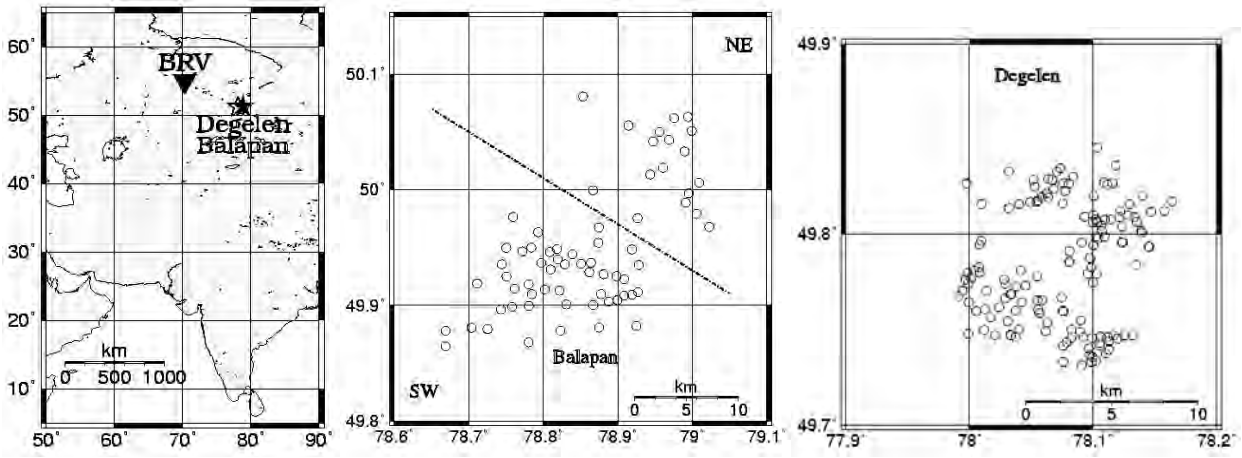


Figure 1. A map showing locations of the Borovoye seismic station (BRV) and the Balapan and Degelen nuclear test sites (left), and locations of nuclear explosions in the Balapan (middle) and Degelen (right) test sites. The explosion sources in the Balapan test site can be grouped into NE and SW subregions according to the velocity and geological structure.

Frequency-wavenumber (F-K) analysis

We analyze frequency-slowness power spectra of source-array records using a conventional F-K technique to study the phase velocities of the waves in source region. In the original geometry, the analysis yields the phase composition of the wavelets leaving the explosion sources. The slowness power spectrum (P_c) at angular frequency ω and wavenumber **k** (=ω**s**, where **s** is the slowness vector) is determined by

$$P_c(\omega\mathbf{s},\omega) = \left|U(\omega\mathbf{s},\omega)\right|^2, \qquad (1)$$

where U is the double-Fourier transform of the waveforms $u(\mathbf{r},t)$ recorded at location **r** in the reciprocal geometry. When a seismic wave is approximately nondispersive in a finite frequency range, coherent power spectral features can be enhanced by stacking the $P_c(\omega\mathbf{s}, \omega)$ over frequencies (ω) (Spudich and Bostwick, 1987):

$$P_w(\mathbf{s}) = \frac{1}{N}\sum_{j=1}^{N} P_c(\omega_j\mathbf{s},\omega_j)\cdot\frac{1}{m_j}, \qquad (2)$$

where N is the number of discrete frequencies, ω_j is the jth angular frequency, P_W is the stacked slowness power spectrum, and m_j is a normalization (whitening) factor. P_W indicates the relative strength of a plane wave leaving the source region in a finite frequency range. The pre-whitening normalization corrects for instrument response and seismic attenuation (Spudich and Bostwick, 1987).

Regional phases from the Balapan and Degelen UNEs

We apply the F-K analysis to the Balapan and Delegen source-array data, and compare the properties of regional phases between the test sites. In Figure 3, the slowness power spectrum of *Pn* waves has a maximum value at horizontal slowness (s_h) of 0.125 s/km, which corresponds to *P* waves travelling in the uppermost mantle with a phase velocity (v_h) of 8.0 km/s (Quin and Thurber, 1992). The azimuths of the maximum power are 302°-304° that agree with the great-circle azimuths of events.

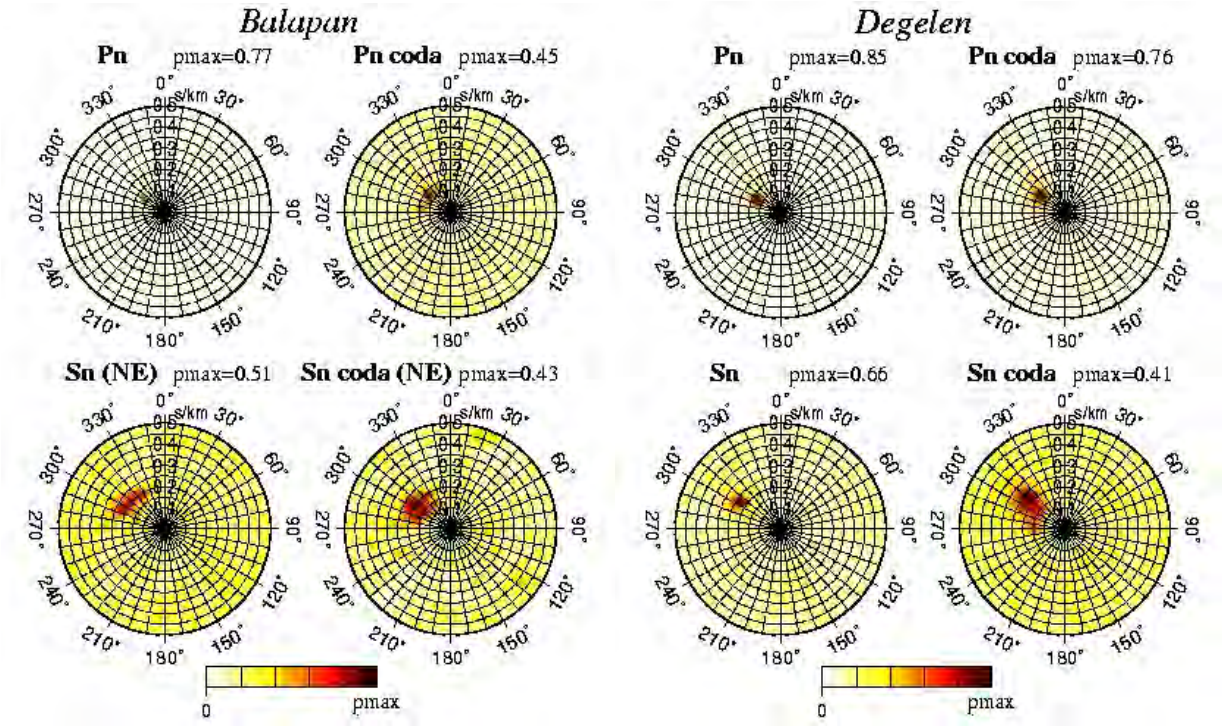


Figure 2. Slowness power spectra of the Balapan (left) and Degelen (right) UNE records for *Pn*, *Pn* coda, *Sn*, and *Sn* coda. Parameter pmax indicates the maximum normalized power ($0 \leq pmax \leq 1$). The event lapse-time windows for *Pn*, *Pn* coda, *Sn*, and *Sn* coda are 92-96 s, 125-130 s, 162-170 s, and 174-182 s, respectively. The frequency band used is 0.5-3.0 Hz.

The slowness power spectrum of the expected *Sn* window, which is observed in a group velocity window of 4.0-4.3 km/s, exhibits a dominant horizontal slowness of 0.205 s/km (Figure 2). Some energy with s_h of 0.14 s/km (v_h=7.1 km/s) is mixed in the *Sn* and *Sn* coda and spreads into multiple azimuths. This observation implies that *Sn* and *Sn* coda are composed of multiple forward scattered lower crustal (*Pg*) waves. The phase with s_h of 0.205 s/km (v_h=4.8 km/s) is the shear wave propagating in the uppermost mantle. The phase velocities of *Pn* and *Sn* coda are similar to those of *Pn* and *Sn* (Figure 3). But, the azimuthal distributions of the maximum slowness power spectra of the coda are wider than those of the *Pn* and *Sn* . This difference indicates that the waves constituting the coda tend to undergo forward scattering in the near source region. The azimuthal span of slowness power spectra of coda increases with time, indicating that the scattered rays tend to increasingly deviate from the great-circle azimuth toward later coda.

The *Lg* waves are composed of crust-guided shear waves, with group velocity of 3.0 to 3.6 km/s (e.g., Kennett, 2002). The dominant phase in the expected *Lg* window has a v_h of 4.2 km/s at frequencies up to 2.0 Hz, and coherency of the phase in the *Lg* window degrades at frequencies above 1.5 Hz (Figure 5). This phase velocity is typical of *Lg* observed in conventional receiver array analysis (e.g., Der et al., 1984).

Rg wave is dominant in a frequency range around 0.2-0.8 Hz. The dominant phase velocity in that window is 3.0 km/s at frequencies between 0.5 and 0.8 Hz, and appears to increase gradually with frequency up to 1.5 Hz (Figure 6). At the higher frequencies (>1.5 Hz), the coherency in the slowness power spectra decrease drastically owing to a lack of coherent high-frequency energy. The observed high phase velocities (~4.0 km/s) in frequency range 0.8-1.5 are high for the typical *Rg* phase velocity. These high phase velocities suggest that high-frequency energy is originated from forward-scattered higher mode or *Lg* waves.

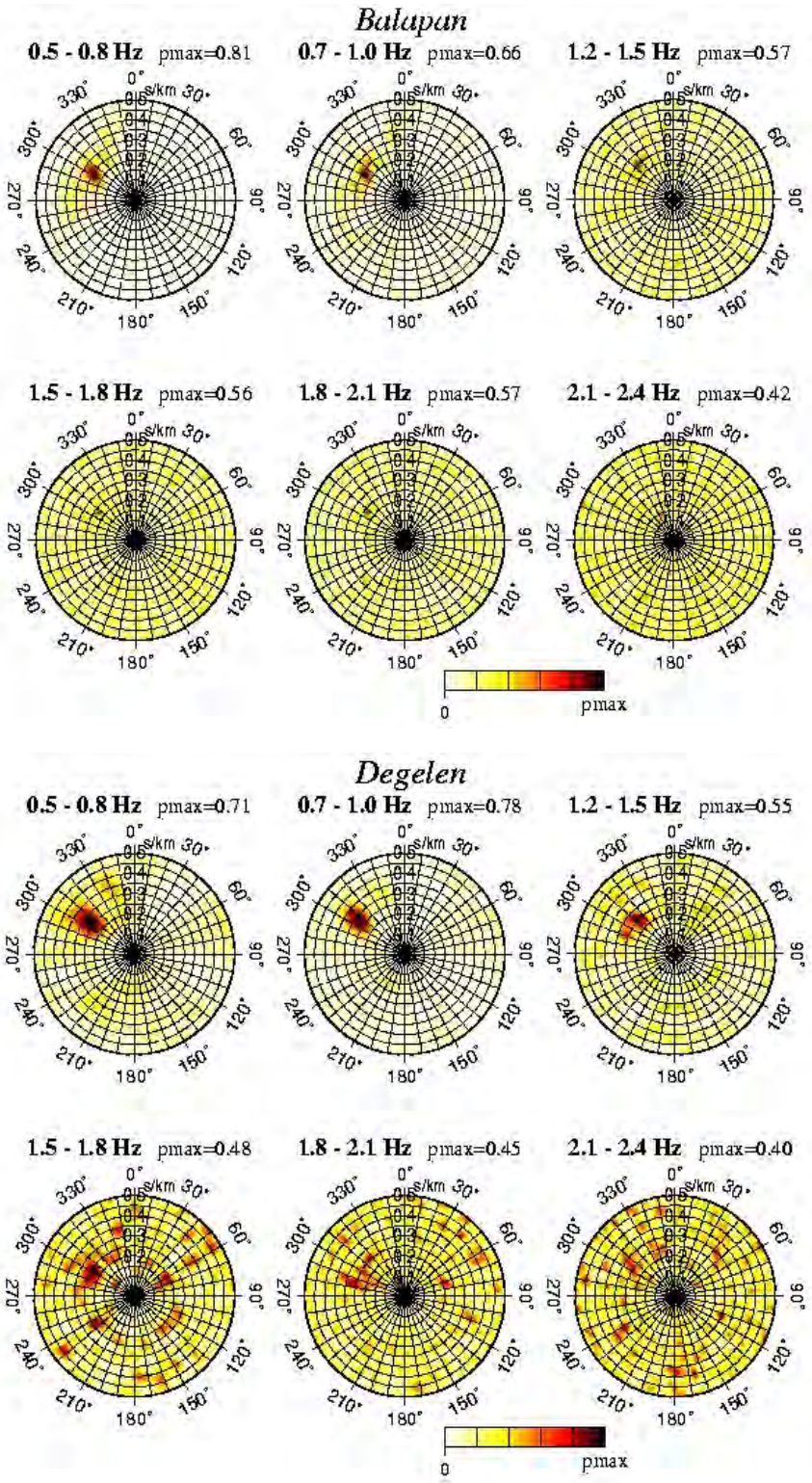


Figure 3. Slowness power spectra of the *Lg* window for various frequency bands. The dominant phase with phase velocity of 4.2 km/s is observed in frequency range between 0.5 and 2.0 Hz, above which the coherency in slowness power spectra degrades.

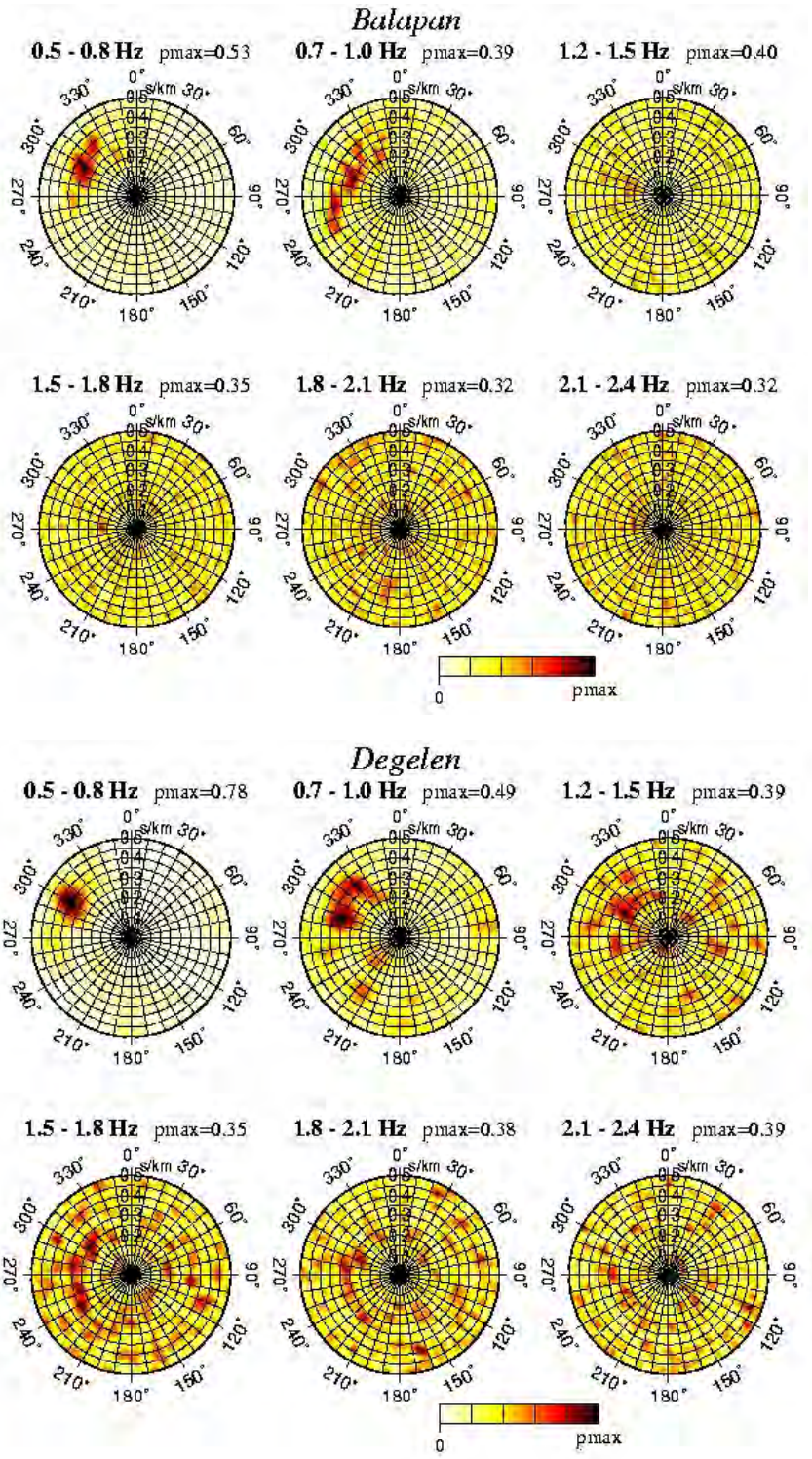


Figure 4. Slowness power spectra of the expected *Rg* window for various frequencies. The phase velocity of *Rg* is 3.0 km/s at frequencies between 0.5 and 0.8 Hz, which is the dominant frequency range of coherent *Rg* signal. Phases at higher frequencies appear to be scattered *Lg* and body waves with higher phase velocities. Note the coherency generally degrades with frequency.

Phase Composition of Regional Coda

We examine the phase composition of the coda from the Balapan UNEs in frequency ranges: 0.2-0.4 Hz, 0.4-0.8 Hz, 0.8-1.6 Hz, and 1.6-3.2 Hz. We observe strong and coherent scattered energy with a phase velocity of 3.0 km/s in the slowness power spectra at frequency bands of 0.2-0.4 Hz and 0.4-0.8 Hz (Fig. 5). This phase velocity corresponds to the typical *Rg* phase velocity observed in this region (Hong and Xie, 2005). Also, the dominant frequency range, 0.2-0.8 Hz, is consistent with the observed *Rg* frequency content of Hong and Xie (2005). This phase, but with variational azimuths, is consistently observed over the entire coda section of array records with a time length of 900 s, about 4 times the *Rg* traveltime. The azimuths of the maximum lowness power spectra of 0.2-0.4 Hz and 0.4-0.8 Hz are different from that for the great-circle direction (~303.9 ^{o}), and change with time. On the other hand, the phase composition of high-frequency coda (0.8-1.6 Hz, 1.6-3.2 Hz), appear to be diffusive.

This coherent *Rg*-origin energy in low-frequency coda can be extracted using a beamforming technique based on slant-stacking (Kanasewich, 1981). A beamforming of the source-array records collects unimodal wavelets leaving the source in a narrow azimuth range. This analysis allows us to quantify the energy of specific phase as function of initial radiation direction. The temporal variation of azimuths in Figure 6 indicates that the *Rg* waves with various initial radiation directions join in the coda. Such *Rg* waves require a change (or, multiple changes) of propagation direction to be recorded at a station located away from the initial radiation direction. We observe the coherent *Rg* phase up to at least 900 s of lapse time, which corresponds to a propagation distance of at least 2,700 km. However, we observe no apparent *Rg* arrivals in the coda section and exponentially decreasing coda amplitude with time. These observations suggest that the coherent energy is generated from scattering on crustal heterogeneities.

In Figure 7, we present the phase composition of coda in terms of regional phases radiated from the source. We quantify the constituent energy of coda by assessing the slowness power spectra. Three sets of regional phases (*P, S, Rg*) are considered. The *P* phase includes *Pn* and *Pg*, and the *S* phase includes *Sn* and *Lg*. We set the slowness ranges by 0.12-0.17 s/km for *P* and 0.20-0.25 s/km for *S* and 0.29-0.42 s/km for the *Rg* phase (Hong and Xie, 2005). We correct for the background diffuse energy so that we estimate only the actual composition of identifiable energy.

Rg constitutes 10-18 % (~14 % on average) of coda energy in frequencies 0.2-0.4 Hz. *P*- and *S*-origin energy constitutes 0-2 % (~1 % on average) and 2-5 % (~3 % on average), respectively. Energy from unidentifiable sources constitutes ~80 %. The influence of major phases is weakened with frequency. The *Rg* phase constitutes 6-11 % (~8 % on average) of coda energy in frequency range 0.4-0.8 Hz. The energy of the other phases constitutes 0-4 % in this frequency range. In higher frequencies 0.8-1.6 Hz and 1.6-3.2 Hz, energy from identifiable phases is rarely observed. This phase composition indicates that no apparent energy from regional phases is observed and these high-frequency wavefields are diffused.

The magnitude of scattering is strong when the wavelength is comparable to the size of the heterogeneities (Hong, 2004). Thus, high-frequency waves interact strongly with small-scale heterogeneities that are distributed rather uniformly in the crust and the mantle lid. On the other hand, the observation of coherent *Rg* scattered energy suggests that the lateral heterogeneities responsible for the *Rg* scattering are spatially localized. In addition, the magnitude of *Rg* scattering appears to be discriminatively stronger than those from other phases.

Implication for Shear-Wave Excitation Mechanism

From the F-K source-array analysis, we observe scattered waves originated from *Rg* phase. The observation of *Rg*-origin scattered waves supports the idea that *Rg* wave can be a source for significant shear waves (e.g., Gupta et al., 1992). However, such strong *Rg*-origin waves are observed only after the main *Rg* phase. In a recent study with the same data set, Hong and Xie (2005) have shown that major regional shear-wave phases, *Sn* and *Lg*, have their unique phase velocities. The unique phase velocities of regional shear waves that are different from the *Rg* phase velocity imply that the regional shear waves were not originated from *Rg* waves (Hong and Xie, 2005). However, we observe strong *Rg*-origin energy in the coda. These observations indicate that *Rg* scattering is certainly active in regional propagation, but is not a major source responsible for the excitation of regional shear waves from UNEs, although it can still contribute as a minor source.

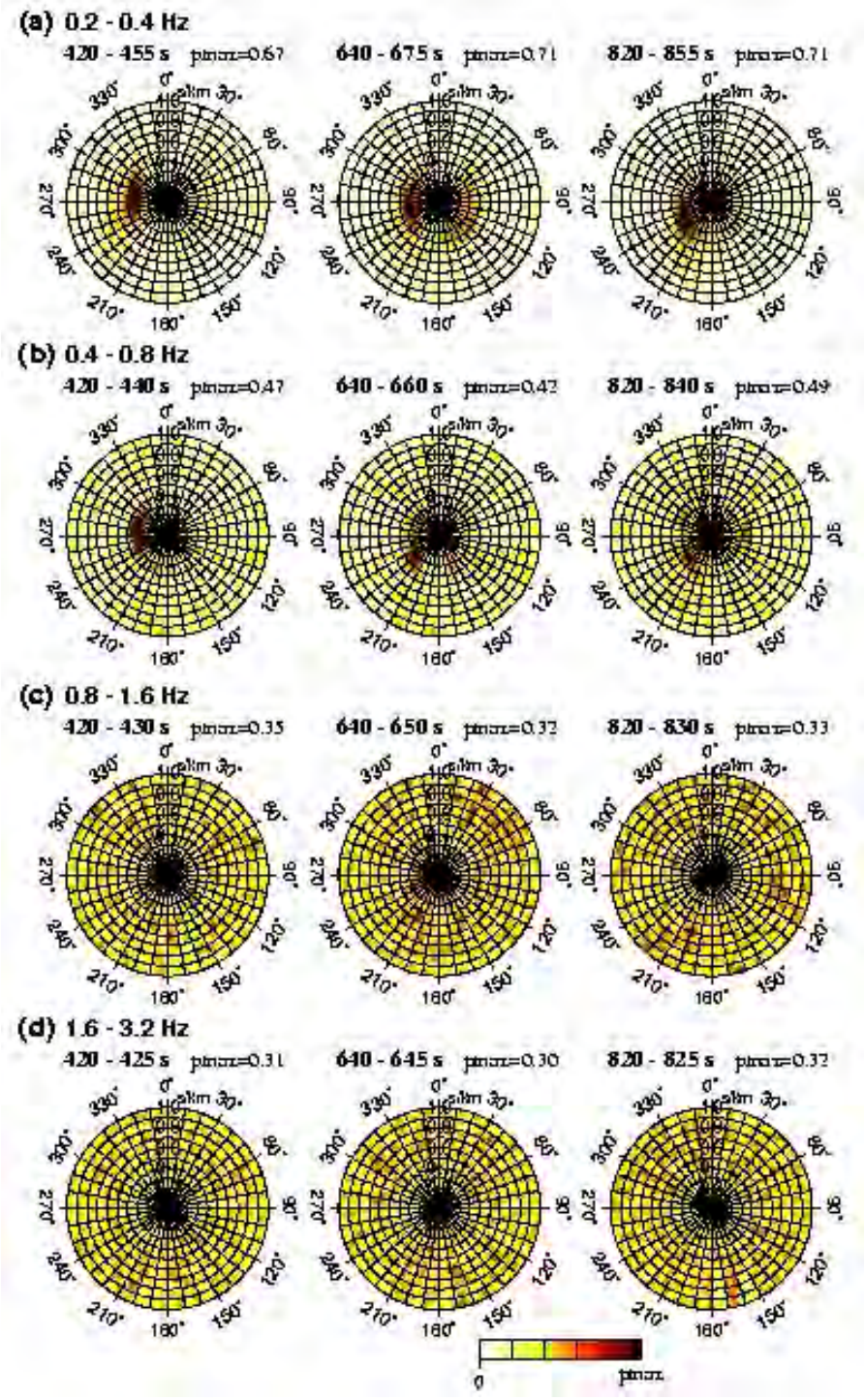


Figure 5. Slowness power spectra of bandpass filtered coda from F-K source-array analysis. The bandpass filter ranges are 0.2-0.4 Hz, 0.4-0.8 Hz, 0.8-1.6 Hz, and 1.6-3.2 Hz. Strong *Rg*-origin energy with a phase velocity of 3.0 km/s is observed in low-frequency regimes of 0.2-0.4 Hz and 0.4-0.8 Hz, while the phase composition of high-frequency coda (0.8-1.6 Hz, 1.6-3.2 Hz) appears to be diffusive. The phase velocity of *Rg* is 3.0 km/s at frequencies between 0.5 and 0.8 Hz, which is the dominant frequency range of coherent *Rg* signal.

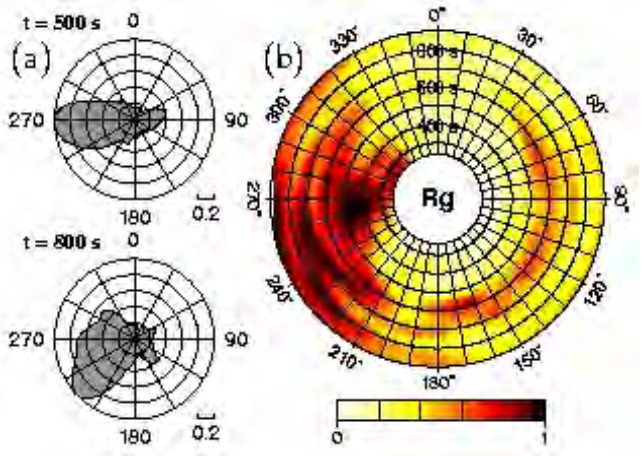


Figure 6. (a) Azimuthal distributions of normalized *Rg* scattered energy at lapse times of 500 and 800 s. The *Rg* scattered energy is quantified using a slant-stacking. (b) Collective results of normalized *Rg* scattered energy at lapse times from 245 to 900 s. The azimuths of maximum strength, which indicate the initial radiation directions from the source, vary with time. The temporal variation of azimuths indicates that *Rg* waves are scattered from various sources of lateral heterogeneities distributed over regional and teleseismic distances.

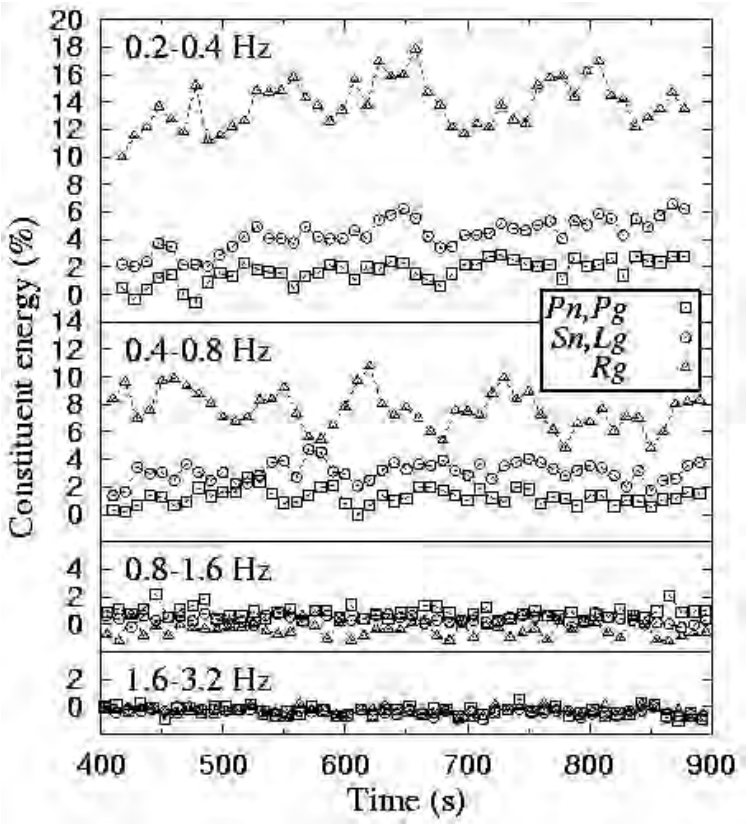


Figure 7. Constituent energy of seismic coda in terms of regional phases. *Rg*-origin energy dominantly constitutes low-frequency coda (0.2-0.4Hz, 0.4-0.8 Hz). In higher frequencies, the phases of origin is not identified which may be associated with multiple scattering by small-scale heterogeneities in the crust. The high-frequency coda appears to be diffusive.

CONCLUSIONS

We investigated the near-source phase composition of regional seismic waves leaving underground nuclear explosions at the Balapan and Degelen test sites by applying a slowness power spectral analysis to source array records under the reciprocity theorem. The properties of regional phases are consistent between the two test sites. The dominant *Pn* phase velocity (v_h) is about 8.0 km/s. The energy in the expected *Sn* window is composed of scattered crustal *Pg* waves with a v_h of 7.1 km/s and the mantle shear waves with a v_h of 4.8 km/s. The *Lg* wave in a frequency range of 0.5-2.0 Hz has a phase velocity of 4.2 km/s that is typical for super-critically reflected crustal *S* waves. On the other hand, the expected *Rg* window is dominated by a fundamental mode Rayleigh wave with a v_h of 3.0 km at frequencies below 0.8 Hz. Above 0.8 Hz the phase coherency degrades drastically owing to a strong attenuation of Rayleigh wave during propagation.

In the analysis of phase composition of seismic coda from the Balapan UNEs, we observed strong and coherent *Rg*-origin energy with variational azimuths, which is consistently observed over 900-s coda record sections in a frequency range of 0.2-0.8 Hz. This *Rg* energy is originated by scattering of *Rg* on lateral heterogeneities in the crust. In the high frequency range over 0.8 Hz, the phases composing the coda are diffusive. The observation of *Rg* scattered waves supports the presence of *Rg* scattering, one of the mechanisms proposed for explanation of shear-wave excitation from UNE. The coherent *Rg*-origin scattered waves, however, are observed only after the main *Rg* phase. The observations of *Rg*-origin energy in coda and different phase velocities between *Lg* and *Rg* suggest that *Rg*-to-*S* scattering may not be responsible for the excitation of regional shear waves (*Sn*, *Lg*) from the Balapan and Degelen UNEs.

ACKNOWLEDGEMENTS

We thank Won-Young Kim for information on data and instrument response and Vitaly Khalturin for information on nuclear explosions in Kazakhstan.

REFERENCES

Adushkin, V.V., V.A. An, V.M. Ovchinnikov, and D.N. Krasnoshchekov (1997). A jump of the density on the outer-inner core boundary from the observations of PKiKP waves on the distance about 6 degrees, *Doklady Akademii Nauk*, 354: (3), 382–385.

Bonner, J.L., D.C. Pearson, W.S. Phillips, and S.R. Taylor (2001). Shallow velocity structure at the Shagan River test site in Kazakhstan, *Pure Appl. Geophys*. 158: 2017–2039.

Der, Z., M.E. Marshall, A. O'Donnell, and T.W. McElfresh (1984). Spatial coherence structure and attenuation the *Lg* phase, site effects, and interpretation of the *Lg* coda, *Bull. Seism. Soc. Am.* 74: 1125–1148.

Gupta, I.N., W.W. Chan, and R.A. Wagner (1992). A comparison of regional phases from underground nuclear explosions at east Kazakh and Nevada test sites, *Bull. Seism. Soc. Am.* 82: 352–382.

Hong, T.-K. (2004). Scattering attenuation ratios of P and S waves in elastic media, *Geophys. J. Int.* 158: 211–224.

Hong, T.-K. and J. Xie (2005). Phase composition of regional seismic waves from underground nuclear explosions, *J. Geophys. Res.* 110: B12302, doi:10.1029/2005JB003753.

Kanasewich, E.R. (1981). *Time Sequence Analysis in Geophysics*, Third Edition, The University of Alberta Press, Alberta, Canada.

Kennett, B.L.N. (2002), *The Seismic Wavefield*, Volume II, Interpretation of Seismograms on Regional and Global Scales, Cambridge University Press, New York.

Kim, W.-Y., P.G. Richards, V. Adushkin, and V. Ovtchinnikov (2001). Borovoye digital seismogram archive for underground nuclear tests during 1966-1996, Technical Report, Lamont-Doherty Earth Observatory of Columbia University.

Levashova, N.M., K.E. Degtyarev, M.L. Bazhenov, A.Q. Collins, and R. van der Voo (2003), Permian palaeomagnetism of East Kazakstan and the amalgamation of Eurasia, *Geophys. J. Int.* 152: 677–687.

Marshall, P.D., T.C., Bache, and R.C., Lilwall (1985). Body wave magnitudes and locations of Soviet underground nuclear explosions at Semipalatinsk Test Site, *AWRE Report,* No. O 16/84, H.M. Stationery Office, London.

NNCRK (1999). Technical Report, Proceedings of the Workshop on IMS Location Calibration, contributed by the National Nuclear Centre of the Republic of Kazakhstan, Olso, Jan 1999.

Quin, H.R. and C.H. Thurber (1992). Seismic velocity structure and event relocation in Kazakhstan from secondary *P* phases, *Bull. Seism. Soc. Am.* 82: 2494–2510.

Ringdal, F., P.D. Marshall, and R.W. Alewine (1992). Seismic yield determination of Soviet underground nuclear explosions at the Shagan River test site, *Geophys. J. Int.* 109: 65–77.

Spudich, P. and T. Bostwick (1987). Studies of the seismic coda using an earthquke cluster as a deeply buried seismograph array, *J. Geophys. Res.* 92: (B10), 10,526–10,546.

Thurber, C., C. Trabant, F. Haslinger, and R. Hartog (2001). Nuclear explosion locations at the Balapan, Kazakhstan, nuclear test site: the effects of high-precision arrival times and three-dimensional structure, *Phys. Earth Planet. Inter.* 123: 283–301.

Xie, J., L. Cong, B.J. Mitchell, and J.-M. Chiu (1996). Complexities in high-frequency seismic waveforms due to three-dimensional structure in the New Madrid Seismic Zone, *J. Geophys. Res.* 101: (B3), 5751–5778.

POSSIBLE EFFECTS OF FROZEN ROCK ON EXPLOSIVE COUPLING

Mark Leidig[1], Vladimir Romanovsky[2], Roger Hansen[2], Randy Martin[3], Robert Grove[2], Jessie Bonner[1], and Jim Lewkowicz[1]

Weston Geophysical Corp.[1], Univ. of Alaska at Fairbanks[2], New England Research, Inc.[3]

Sponsored by Air Force Research Laboratory

Contract No. FA8718-04-C-0026

ABSTRACT

Laboratory studies have demonstrated that frozen rock is significantly stronger than unfrozen rock, and it has been hypothesized that this increased strength can significantly alter seismically estimated yield. Weston Geophysical Corporation, University of Alaska at Fairbanks, and New England Research, Inc. formed a consortium to perform a field experiment to provide empirical data in order to test the hypothesis. The results of this experiment will aid the monitoring community in determining actual yield for explosions in permafrost regions.

The experiment is being conducted at a gold mine in central Alaska that has abrupt lateral boundaries in discontinuous permafrost. We are detonating a series of small, repeated explosions ranging in size from 2 to 800 lb of explosives at 20–30 m depth. We conducted laboratory tests on rock samples collected at the test site and found increased *P*-wave (primary wave) velocities when the rock temperature was decreased from +21°C to –12°C. The increase in *S*-wave velocities was even more significant.

The explosions are being recorded on a near-source network of 18 accelerometers and velocity seismometers along with a large array of seismometers at local distances. The mine is located near several stations of the Alaska Earthquake Information Center network and is within 100 km of the ILAR and ALPA seismic arrays, thus the explosions are being recorded by an extensive regional network.

Borehole temperature measurements at 10 m depth indicate frozen (–0.5°C) and unfrozen (1.5°C) rock within 300 m of each other. To examine the temperature at the planned depth of explosive emplacement, 50 m boreholes were drilled at the test site and indicate frozen (–0.2°C) with ice-filled fractures and unfrozen (0.1°C) rock at 30 m depth. A nearby shallow borehole located warmer unfrozen rock. We will locate the experiment explosive holes to achieve the largest possible temperature difference in the frozen and unfrozen rock. Time-dependent temperature logging indicates drilling has very little effect on the steady-state temperature regime and the experiment can be conducted shortly after the explosive boreholes are drilled. A shallow geophysical survey is being conducted to develop a high-resolution velocity profile of the test site. Borehole coring is also being conducted to examine the emplacement media's physical properties. To determine how the natural fracture field is modified by the explosions, we will obtain fracture orientation and extent from borehole cores before and after the detonations.

A broadband seismometer was deployed for 3 months approximately 12 kilometers from active blasting at the gold mine. Examination of waveforms from the blasting shows large signal-to-noise ratio body and surface waves. This data is aiding in the experiment design and providing background noise levels. Teleseismic earthquakes recorded at this station are being used to generate receiver functions for constraining the lower crustal velocity structure and Moho depth.

OBJECTIVES

Weston Geophysical Corp., the University of Alaska at Fairbanks, and New England Research, Inc., have formed a consortium to conduct the Frozen Rock Experiments (FRE) in central Alaska to characterize the variations in ground motion scaling and coupling for explosions in frozen and unfrozen rocks. The experiment is helping to quantify the variations in estimated seismic yield of explosions in frozen rock due to changes in coupling. The consortium is detonating and recording the explosions on a large array of near-source and local stations deployed specifically for the experiment. The data is also being recorded on permanent regional stations of the Alaska Earthquake Information Center (AEIC) network and nearby ILAR and ALPA seismic arrays. In the final phase, we will analyze the data to quantify the source function variations for equal yield explosions detonated in frozen and unfrozen rocks.

RESEARCH ACCOMPLISHED

Experiment Background

A critically important aspect of nuclear test monitoring is yield estimation. United States monitoring agencies must be able to accurately estimate yields for nuclear explosions detonated in regions of monitoring concern. If frozen-rock emplacement conditions create a circumstance favorable for biased yields, data must be available such that any bias can be accounted for when the yield is estimated. Prior studies (Mellor, 1971) have established that frozen-rock properties are considerably different from unfrozen-rock properties. Moreover, it has been hypothesized that these altered properties may be sufficient to cause significant variations in seismic coupling, which in turn, significantly alters seismic yield estimates.

Sammis and Biegel (2004) have noted that an increase in low-temperature uniaxial strength is related to the ice in the initial pores and cracks. The ice increases the apparent coefficient of sliding friction on these initial cracks. Since the strengthening is strain-rate dependent, for nuclear explosions the full strengthening should occur in a small range near 0°C. This is important given that our experiment test site region has frozen ice in the cracks at temperatures of –0.5°C.

Sammis and Biegel (2005) successfully approximated the stresses around the 1993 NPE explosion. They found that increasing the static friction and reference strain, which simulates ice-filled cracks, each caused more rock damage at greater distance from the explosion and an increase in radial crack length. For the increased static friction case, there was actually less damage at very close-in distances. In addition, increasing the seismic velocity and/or rock strength caused reduced seismic amplitudes in the far-field for explosions in frozen rock, which would result in an underestimated yield.

Experiment Location and Design

We chose to conduct the experiment north of Fairbanks, AK (Figure 1) because that region contains discontinuous permafrost, with frozen and unfrozen rock in close proximity. Farther north, it is difficult to find unfrozen rock and farther south, it is difficult to find frozen rock. In addition, this area is also in close proximity to permanent regional seismic stations and allows for relatively easy placement of near-source and local instruments to record the experiment.

A series of repeated explosions will be detonated within 300 m of each other in frozen rock and unfrozen rock. These explosions will include shots of 200, 400 (two are planned), and 800 lb of ammonium nitrate fuel oil (ANFO). The emplacement depth is designed to approximate a nuclear-scaled depth of burial for a fully contained and confined explosion. This allows all rock damage to be confined to frozen or unfrozen rock, depending on the location of shot.

High-g accelerometers and broadband and short-period seismometers will be deployed at near-source and local distances to record the explosions. Accelerometers will be placed within 5 m of the explosions. The instruments will provide complete azimuthal coverage and span the distance to the permanent regional seismic network of the Alaska Earthquake Information Center (AEIC). High-speed and resolution videographic data will be recorded to verify the explosions detonate as planned and are fully confined and contained.

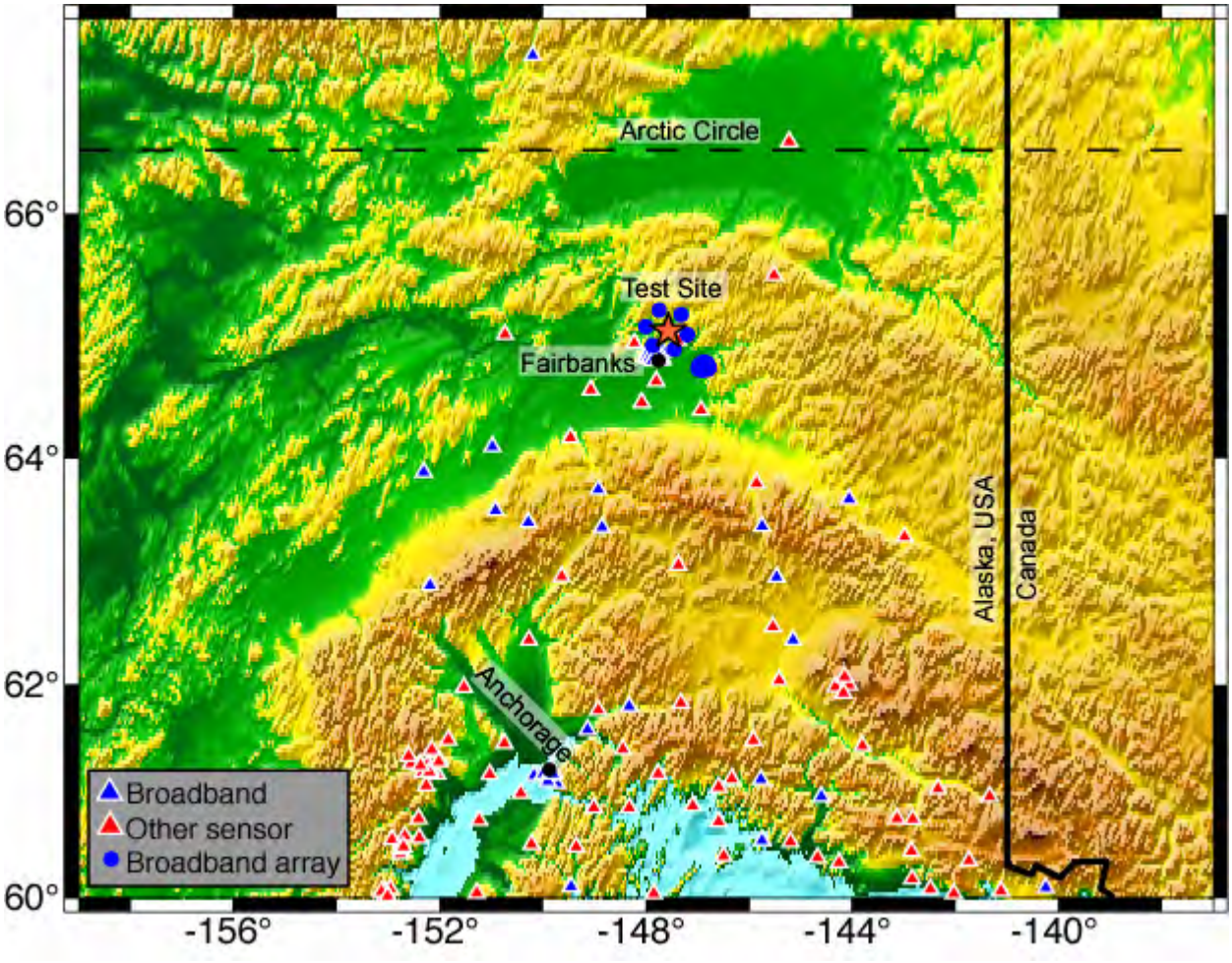


Figure 1. Location map of the test site region (star) and nearby seismic stations.

Temperature Profiles

Existing permafrost monitoring wells were logged to verify the test site contained sufficient quantities of frozen rock. This logging indicates frozen rock around –0.5°C (Figure 2). We drilled two 50 m boreholes to locate frozen and unfrozen rock in close proximity on our test site. Temperature measurements from these holes are shown in Figure 3 (left and center). The unfrozen rock borehole is located in marginally unfrozen ground, but logging of another nearby shallow borehole located a warmer unfrozen zone. The frozen rock hole is below 0°C between approximately 10 to 50 m depth. Temperature measurements were taken shortly after drilling so the values may have a slight variation above steady state due to drilling disturbance. Time-dependent temperature logging in the unfrozen well indicates the drilling disturbance is minimal though.

These four boreholes indicate our test site has discontinuous zones of frozen and unfrozen rock. In order to locate the best sites to conduct the experiment, we need to find the coldest and warmest regions. To accomplish this, we will conduct a 2-dimensional DC resistivity tomography of the test site before choosing the locations for the explosive boreholes. Temperature logging of the explosion boreholes will be conducted before loading them with explosives. We will require at least –0.4°C, with visible ice in fractures, for the frozen site and +1.0°C or greater in the unfrozen site before conducting the explosions.

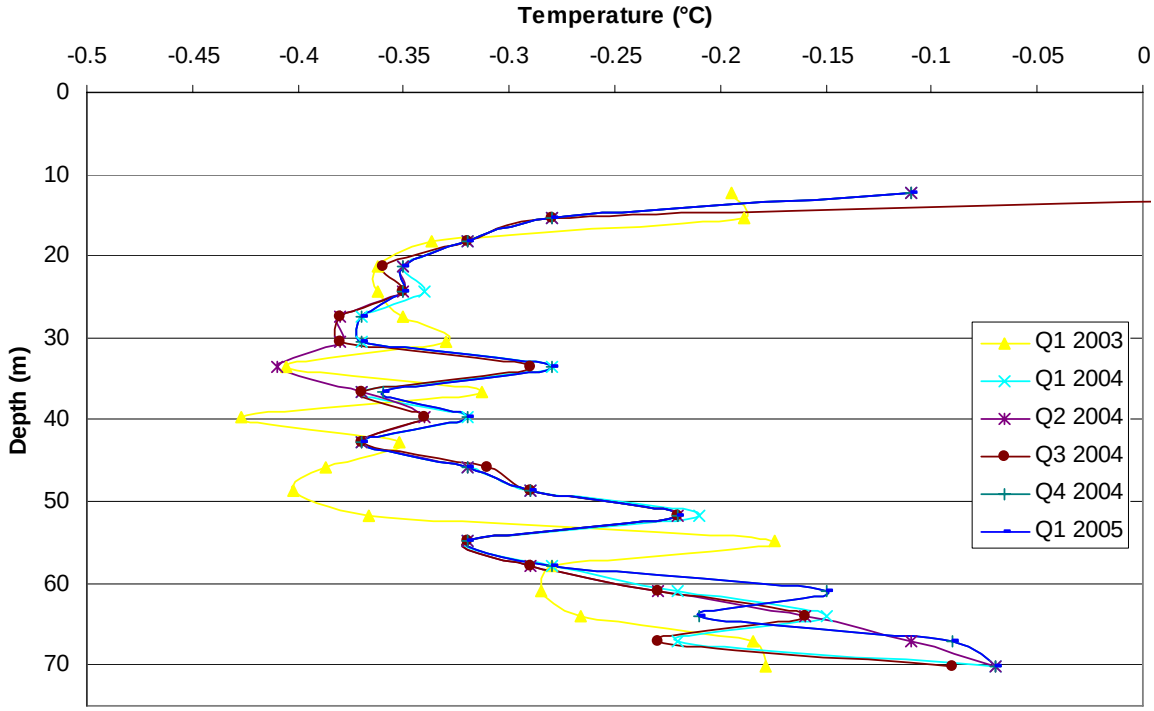


Figure 2. Temperature logs acquired from a permafrost monitoring well near the frozen rock test site. These logs allow us to examine the steady-state temperature profile.

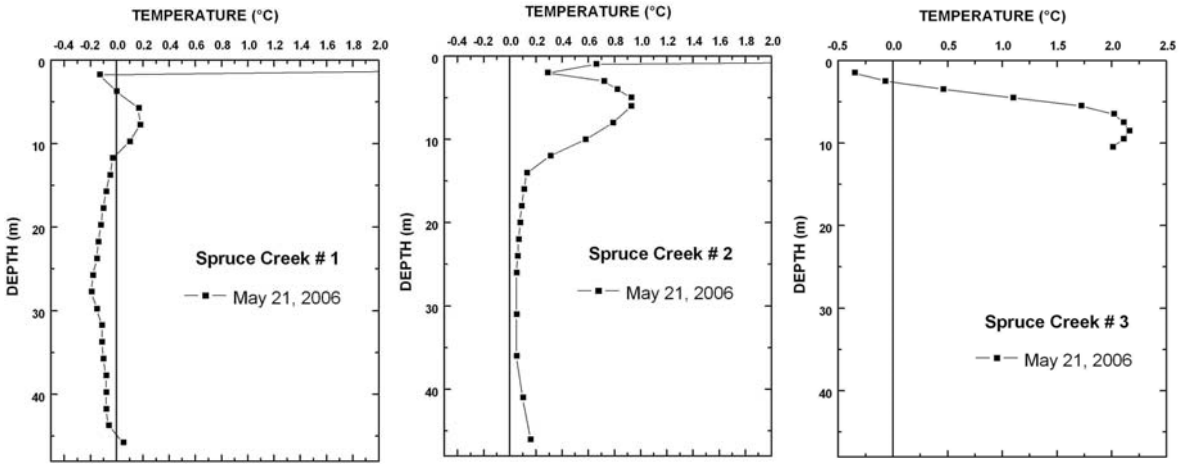


Figure 3. Temperature profiles of the test site from our initial characterization. We drilled two 50 m boreholes and located frozen rock (left) and unfrozen rock (center) sites in close proximity. A fourth borehole on the test site (right) located warmer rock for the unfrozen tests.

Test Site Rock Properties

Laboratory testing of rock samples collected at the test site indicates both *P*- and *S*-wave velocities increase when saturated rocks are frozen at –12°C. Figure 4 plots the results for *P* velocity on the left and the results for *S* velocity at two different confining pressures on the right. Velocities increase by 3%–5% in the frozen samples. Sammis and Biegel (2005) determined that an increase in velocity related to ice-filled cracks would decrease observed seismic amplitudes causing a smaller estimated yield.

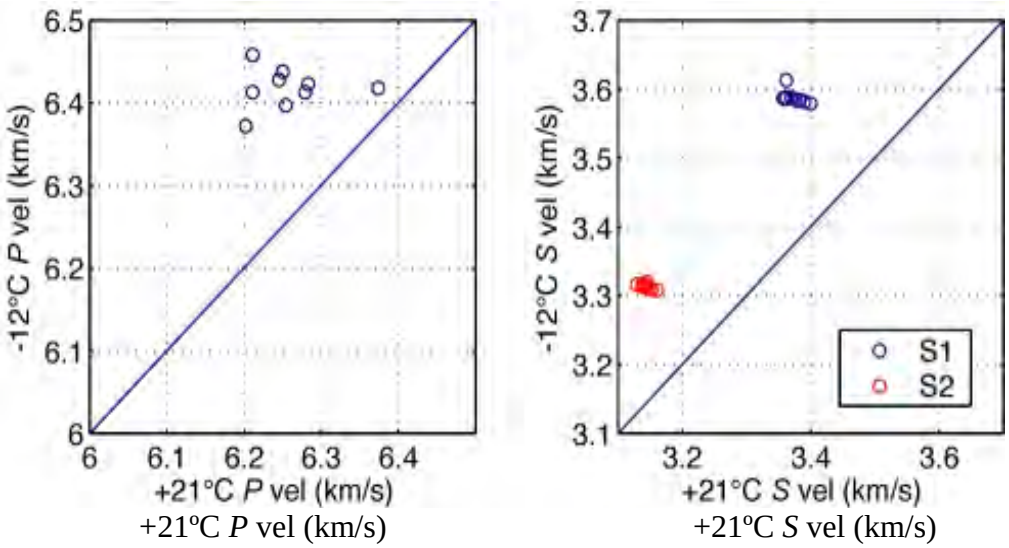


Figure 4. Empirical laboratory results comparing the *P*- (left) and *S*- (right) wave seismic velocities of frozen and unfrozen rocks collected at the test site.

A series of preliminary experiments are being conducted to determine the elastic moduli, strength, and coefficient of friction in frozen and unfrozen rock samples. Coring of the explosive boreholes before and after the explosions will provide rock samples from the explosive emplacement depth. Laboratory tests will then be conducted on these samples. Shallow seismic refraction experiments are being carried out across the test site to develop a velocity and structure profile. A DC resistivity tomography survey is being conducted to map the extent of permafrost across the test site. This will also aid in locating the explosive boreholes in the coldest and warmest rock at the test site.

Local Mining Explosions and Earthquakes

A broadband seismometer was deployed for three months less than 1 km from the test site. The station recorded nearby delay-fired mining activity and earthquakes, including a number of small local events. A map of the local events recorded is shown in Figure 5. Open pit delay-fired mine blasting designed to fracture the hard granitic rock occurred 12 km to the east-southeast of the station and forms a cluster of events. Small earthquakes or other man-made events (ML<2) at local distances were also recorded and make up the rest of the events in the plot. Body and surface-waves from the local events were well recorded by this station even for the smallest events. The station will record the experiment blasts for a direct comparison of local earthquakes and single-and delay-fired explosions.

Many regional and teleseismic earthquakes were also recorded. These events are being used in a joint surface wave dispersion and receiver function study to determine the crustal velocity structure of the area. Combining this model with the data obtained from the shallow seismic refraction and resistivity tomography will provide an extremely detailed model of the test site structure from the shallow sub-surface to the Moho depth.

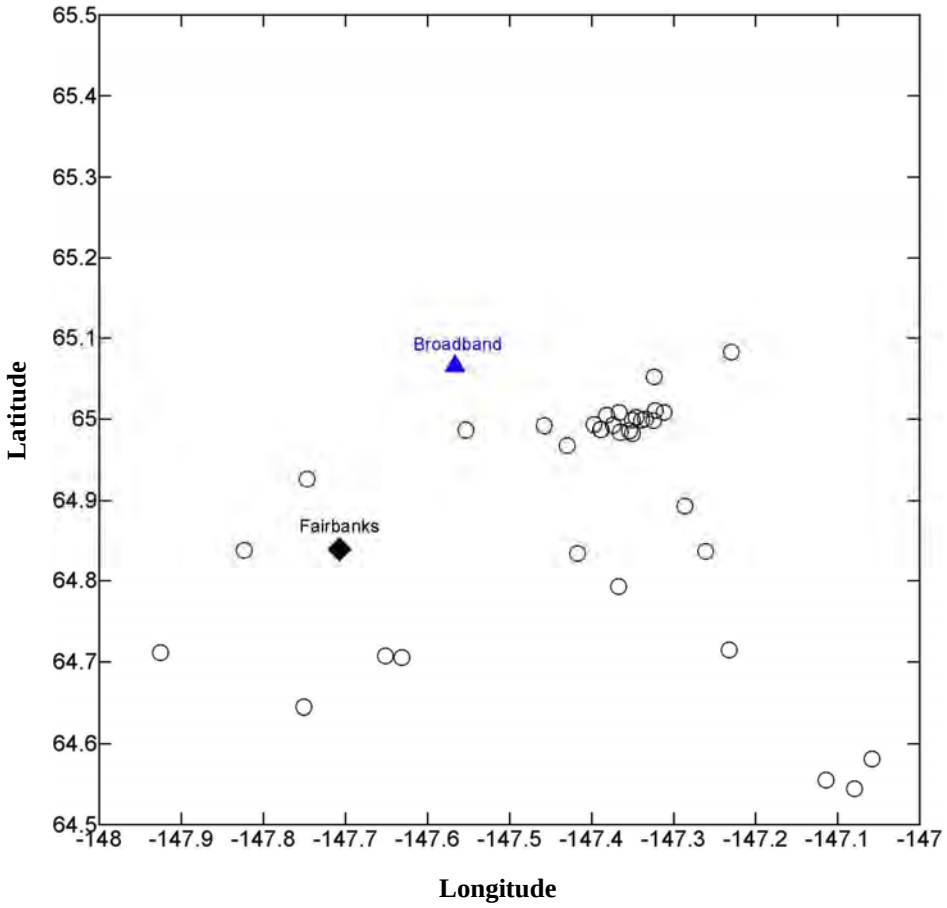


Figure 5. Location of the deployed broadband station (blue triangle) and nearby seismic events (black open circles). Mine blasts are clustered ESE of the broadband.

CONCLUSIONS AND RECOMMENDATIONS

A series of single-fired explosions is being conducted in Alaska the last week of August to advance the understanding of phenomenology and estimated yield differences from explosions in frozen and unfrozen rock. Sammis and Biegel (2005) concluded that estimated seismic yield will be reduced by increased seismic velocities and compressive strength of the explosive source rock related to ice-filled cracks. We plan to obtain empirical data to compare with their theoretical values.

REFERENCES

Mellor, M. (1971). Strength and deformability of rocks at low temperatures, Hanover, NH, Cold Regions Research and Engineering Laboratory (CRREL), U. S. Army Corps of Engineers, Research Report 294.

Sammis, C. and R. Biegel (2004). Mechanics of strengthening in crystalline rock at low temperatures: a preliminary assessment, in *Proceedings of the 26th Seismic Research Review: Trends in Nuclear Explosion Monitoring*, LA-UR-04-5801, Vol. 2, pp. 475–484.

Sammis, C. G. and R. L. Biegel (2005). Seismic radiation from explosions in frozen crystalline rock, in *Proceedings of the 27th Seismic Research Review: Ground-Based Nuclear Explosion Monitoring Technologies*, LA-UR-05-6407, Vol. 1, pp. 642–652.

REGIONAL *P*-CODA FOR STABLE ESTIMATES OF BODY WAVE MAGNITUDE: EXTENDING THE M_S:m_b DISCRIMINANT TO SMALLER EVENTS

Kevin Mayeda, Jessie Bonner, and Heather Hooper

Weston Geophysical Corporation

Sponsored by Air Force Research Laboratory

Contract No. FA8718-06-C-0027

ABSTRACT

The most successful teleseismic discriminant is M_s:m_b, and many studies are underway to try and extend surface wave magnitude (M_s) estimation to regional distances. A problem that is encountered at regional distances and small magnitudes is how to estimate m_b so that the M_s:m_b discriminant is meaningful and consistent with teleseismic measures.

Over the past several years, a regional *S*-coda wave methodology has been developed that provides for the lowest variance estimate of the seismic source spectrum. Thus, regional M_W and m_b estimates derived from *Sn* and *Lg* coda are very stable, even when only a single station is used. However, these m_b's are inherently biased for earthquakes because they are an *S*-based measurement, and explosions are relatively depleted in *S*-waves. Previous research projects have used region-specific m_b scales based on direct measurements of *Pn* and *Pg* to improve the M_s:m_b discrimination, even though the m_b estimates often had a large variance.

The next obvious step to be implemented in the coda wave methodology is the use of *P* coda for m_b estimates. This study focuses on developing a regional *P*-coda methodology to earthquakes and explosions on or near the Nevada, Shagan, Lop Nor, and Novaya Zemlya (NZ) test sites. We will use the *P*-coda spectra to derive estimates of m_b and yield. The new m_b estimates will then be compared with regional M_s measurements to examine possible discrimination improvements. As this project is new, we have only preliminary results using far-regional and teleseismic *P*-coda using Atomic Weapons Establishment (AWE) Blacknest data for NZ explosions and near-regional results for Nevada Test Site (NTS) explosions. Our goal will be to test whether *P*-coda magnitudes scale with the teleseismic m_b for both earthquakes and explosions. Second, we want to know if these *P*-coda magnitudes exhibit less variance than their direct wave counterparts. Paths from NZ to NORSAR are still at regional distance and one might expect the *P*-wave and its coda to be comprised of waves that sample the crust and upper mantle over a range of take-off angles from the source. At teleseismic distances however, we might expect the averaging nature observed for local and regional coda waves to breakdown. At these distances, first arriving *P*-waves are likely emanating from a limited range of take-off angles near the bottom of the focal sphere. To investigate this, we processed roughly 30 NZ explosions recorded at the U.K. arrays, Eskdalmuir in Scotland (EKA) and Yellowknife in Canada (YKA) located at ~30 and 44 degrees from NZ, respectively.

OBJECTIVES

Our research will determine whether *P*-coda can be used to estimate stable m_b estimates. Our objectives include:

- Developing a new technique for estimating *P*-coda-based m_b's at regional and near-teleseismic distances for sparse networks or at a single station,
- Improving M_S:m_b discrimination at lower magnitudes based on combining new *P*-coda-based m_b's with the current regional, variable period M_s estimation technology, and
- Providing an estimate of yield from *P*-coda-derived spectra that can complement similar estimates based on *Lg* and *Sn* coda.

We are in the preliminary phases of this project and are currently examining the characteristics of *P-coda* for the NTS. The preliminary results are presented in the following paragraphs.

RESEARCH ACCOMPLISHED

Background

For sparse local and regional seismic networks, a stable method of determining magnitude is necessary for the development of discriminants, yield estimation, and detection threshold curves. Over the past several years, the Department of Energy (DOE) labs have developed a regional coda wave methodology that obtains the lowest variance estimate of the seismic source spectrum (Mayeda et al., 2003; Phillips et al., 2003; Mayeda et al., 2005). Unlike traditional magnitudes such as M_L and m_b, which are relative, narrowband measurements that often have regional biases, the coda methodology provides stable, absolute source spectra that are corrected for *S*-to-coda transfer function, scattering, inelastic attenuation, and site effects. The spectra have been used to calculate stable moment estimates (M_w), short-period magnitudes (m_b, M_L), explosion yields, and radiated seismic energy, E_R (Mayeda and Walter, 1996) from as few as one station. The coda-derived spectra are calibrated for the particular region of interest and are in turn used as input into the Magnitude and Distance Amplitude Correction (MDAC) discrimination procedure outlined by Walter and Taylor (2002).

In addition to MDAC's regional high frequency discriminants, the traditional teleseismic discriminant, M_S:m_b, is currently being extended to smaller events at regional distances. For example, detailed global group velocity measurements are being used to develop models for Rayleigh waves (Pasyanos et al., 2003; Stevens et al., 2001; Ritzwoller et al., 2002; Levshin et al., 2002) that aid in the development of phase-match filters. These models are now being extended to periods as short as 7 s. New surface wave magnitude formulas (Russell, 2006) and measurement techniques [M_s Variable-Period, Maximum Magnitude Estimation (VMAX)] by Bonner et al., 2006) are being developed that allow estimates at these shorter periods that are unbiased with respect to teleseismic M_s estimates. The problem that we are experiencing at the lower magnitudes ($m_b < 4$) is the lack of unbiased body wave magnitudes for discrimination purposes.

For small-to-intermediate sized events, we have found that the discriminant performance decreases because of variance in the m_b magnitudes. Figure 1 shows the difference in performance between United States Geological Survey (USGS) and International Data Center (IDC) magnitudes for earthquakes near the Lop Nor test site. The event screening lines are based on research by Murphy et al. (1997). Events above the line are assumed to be earthquakes, thus more would be screened using the IDC magnitudes than the USGS magnitudes. Rather than argue which m_b estimate is most correct, our objective is to find a more stable estimate of m_b using regional and near-teleseismic *P*-coda-wave data.

We could use *Lg* and *Sn* coda-derived m_b estimates; however, this *may actually hinder* the M_S:m_b discrimination performance. Though m_b derived from regional *Lg* (e.g., Nuttli, 1973; Patton, 2001) and *Lg* coda (e.g., Mayeda, 1993) have been calibrated for certain regions, both are *S*-based measures, and thus will be biased with respect to earthquakes. Figure 2 shows m_b(*Lg* coda) from Mayeda (1993) for NTS explosions. The same path and site corrections applied to earthquakes in the region would result in almost an order of magnitude bias. This bias is also observed for direct *Lg*. For example, the Little Skull Mountain earthquake at NTS had an M_w of 5.5, but would have an m_b(*Lg*) of ~6.5, whereas the National Earthquake Information Center (NEIC) and International Seismological Center (ISC) m_b's for this event are 5.3. Likewise, if we calibrate m_b(*Lg*) to teleseismic estimates of m_b for

earthquakes, we will underestimate the m_b's for explosions. The use of *S*-based m_b's in the traditional M_S:m_b discriminant significantly degrades the discriminant's performance, since it tends to move the explosion and earthquake populations closer together.

Regional m_b's have been calculated based on the *P*-based phases, such as *Pn* (e.g., Denny et al., 1987) and Pg (e.g., Tibuleac et al., 2001). However, Mayeda (1993) has shown that these regional measures have significant scatter associated with them, and thus significant numbers of recordings would be required to reduce the variance.

The questions that we are addressing through this research project include the following: Can we reduce the variance in regional m_b estimates using a sparse-station *P*-coda methodology, as opposed to using multitudes of direct *Pn* and *Pg* measurements, how will the stability of these m_b(*P*-coda) estimates compare to the highly successful and stable (but unfortunately biased) methods involving *Lg* and *Sn* coda, how many stations will be needed, and will the use of m_b(*P*-coda) improve M_S:m_b discrimination at regional distances?

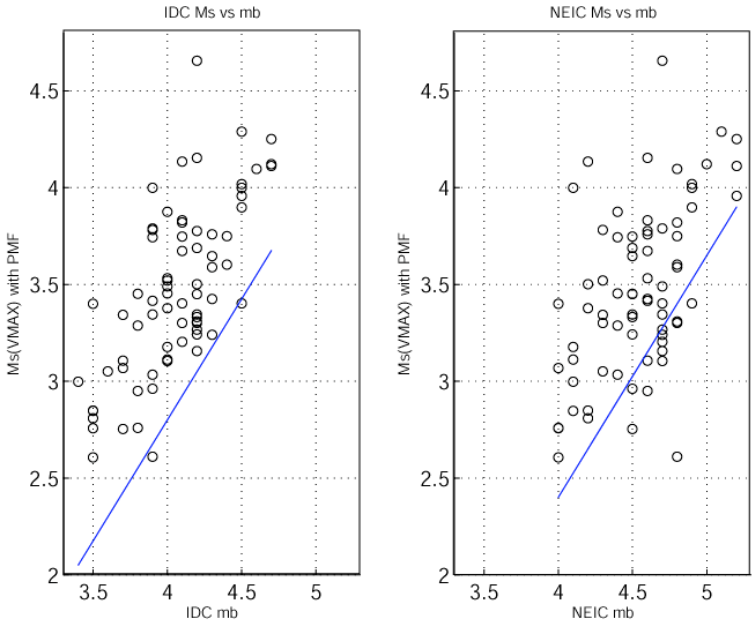


Figure 1. Comparison of event screening using M_s(VMAX):m_b(*P*) for small-to-intermediate sized events in Asia. (Left) IDC m_b. (Right) USGS NEIC m_b. The dashed line is the Murphy et al. (1997) criterion for event screening, which is M_s = 1.25 * m_b (USGS)–2.6 and M_s = 1.25 * m_b (IDC)–2.2.

Coda Window Length

Mayeda et al. (2003) showed that the variance of coda envelope measurements reached a constant value for *Lg* coda after a certain length of measurement window. Figure 3 shows the interstation variance plotted as a function of coda window length. This figure shows that any length of coda is preferable over measuring the direct phase. We plan to systematically test the regional and near-teleseismic *P*-wave coda's dependence on window length. Examples of the *P*-coda window lengths for NTS nuclear explosions recorded on the Livermore Network are shown in Figure 4. These windows show that approximately 20–30 s of coda can be used for magnitude estimates at these near-regional distances. Based on the results in Mayeda et al. (2003), using *P*-coda could reduce the interstation standard deviations in regional m_b*s* by between 20% and 50% depending upon the frequency band under consideration. We note that these percentages are based on *Lg* data, and may differ for P-coda.

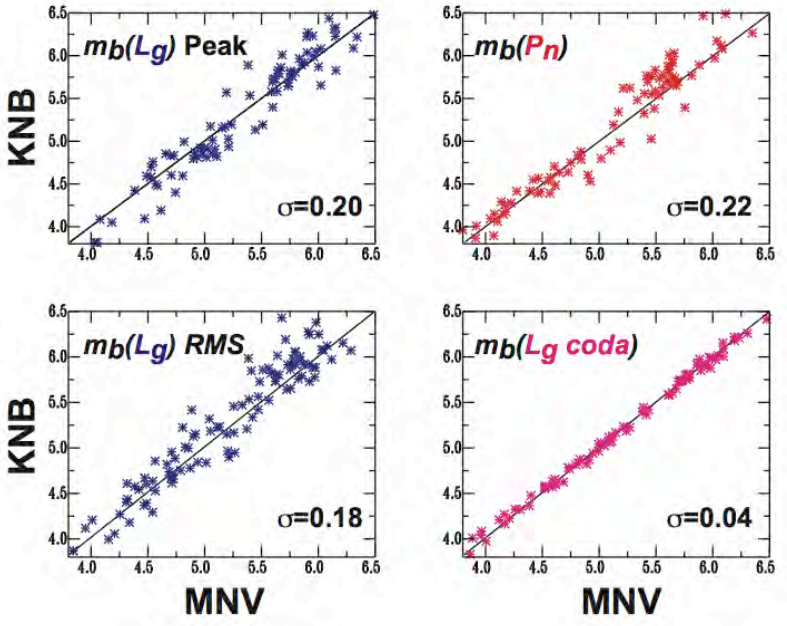


Figure 2. A comparison of four different m_b estimation techniques for NTS explosions recorded at MNV and KNB. The interstation standard deviation is roughly five times smaller for the m_b(Lg coda) than for the m_b(*Pn*) and m_b(*Lg*) methods.

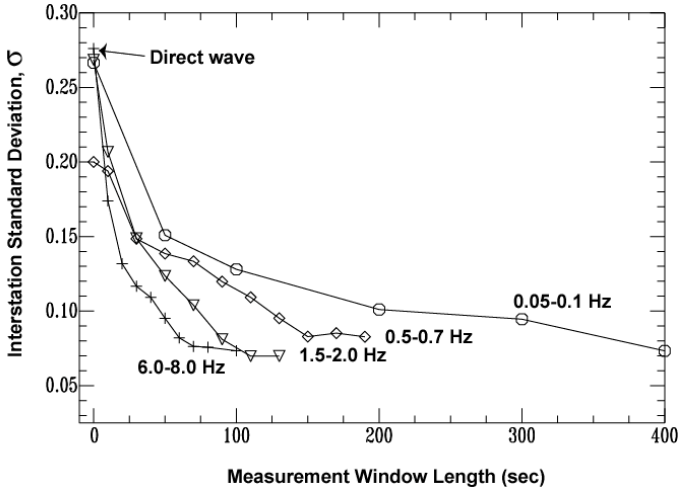


Figure 3. Interstation standard deviation, σ, is shown for a range of frequencies as a function of coda measurement window length using Gulf of Aqaba earthquakes. For longer periods, the critical window length, where further reduction in scatter is minimal, becomes larger, ranging from about 60 s at 6.0–8.0 Hz to about 200 s for 0.05–0.1 Hz.

What Composes *P*-Coda?

It is important to ensure that the *P*-wave coda is actually composed of coherent scattered *P*-wave energy and not direct arrivals or random scattered arrivals. Morozov and Smithson (2000) show that near-teleseismic coda phases can be explained by the excitation of short-period scattered waves within the crust by the waves incident from the mantle. Wagner (1997) found that the *P*-coda is a continuous succession of coherent, forward scattered/multipathed arrivals, not just the occasional deterministic regional phase immersed in "randomly" scattered coda. The number of coherent arrivals in the *P*-coda shown in Figure 5 is more than what would be expected from crustal multiples like *PmP*. Stacked coda envelopes from a Nevada earthquake (Figure 6) recorded on the Seismic Array in Mina, Nevada (NVAR) show that the *P*-coda has different characteristics (e.g., slopes) than the *Lg* coda, although both show little interstation scatter.

Characteristics of NTS *P*-Coda

We are processing over 240 nuclear tests from NTS using regional stations from the Lawrence Livermore National Laboratory (LLNL) digital seismic network along with far-regional and near-teleseismic stations (e.g., TUC, CMB, PAS, PDAR, TXAR). For NTS, we are in the process of examining the characteristics of the near-regional coda by deriving empirical envelope functions for selected regional and near-teleseismic stations. For this analysis, we have considered 5 narrow bands ranging between 0.5 and 3.0 Hz (e.g., 0.5 to 0.7, 0.7 to 1, 1 to 1.5, 1.5 to 2, and 2–3 Hz). Examples of the envelopes between 2 and 3 Hz are shown in Figure 7. We note that for this station (ELK) at approximately 400 km from most of the NTS explosions, the appropriate coda window starting time would be after *Pg*.

We are also compiling the characteristics of the *P*-coda spectra for NTS earthquakes and explosions (Walter et al., 2003). Corner frequency effects must be considered in our analysis, as must any possible differences in site response between stations. Since our proposed methodology will be to normalize each *P*-coda-derived source spectra to an absolute scale, site and path effects will be eliminated. In Figure 8, which shows coda spectra formed at ELK and MNV for Yucca Flat explosions, the corner frequency decreases as a function of increasing event size. We note however that the emplacement conditions also change with event size, since bigger events are shot at deeper depths where velocity and density are higher and gas-filled porosity is lower. As we continue this research, we plan to determine interstation magnitude scatter as a function of frequency band in order to find the optimal band for measuring m_b from *P*-coda spectra.

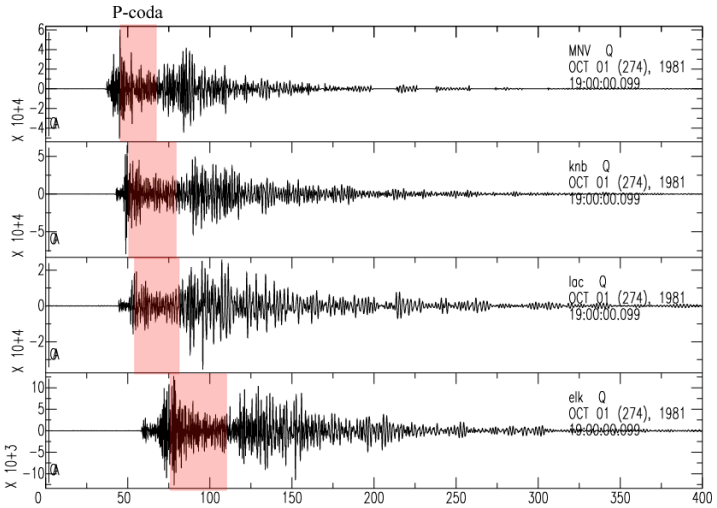


Figure 4. Plot showing regional *P*-coda windows for near-regional recordings of an NTS nuclear explosion.

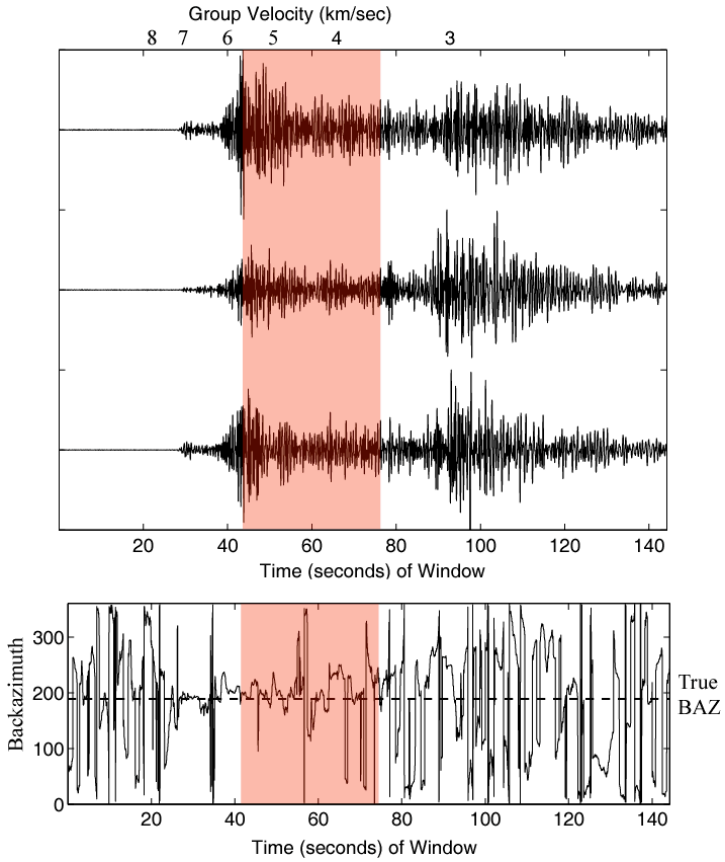


Figure 5. (Top) Seismic waveforms from an NTS nuclear explosion recorded at the ELK 3C station. (Bottom) A bearing-time recording for the three-component seismograms shows that the *P*-coda is not made up of random scattering with a few on-azimuth arrivals (the true back azimuth is the dashed line). Instead, the *P*-coda is composed of a continuous succession of coherent, forward scattered/multipathed arrivals, which will retain some "memory" of the original source strength.

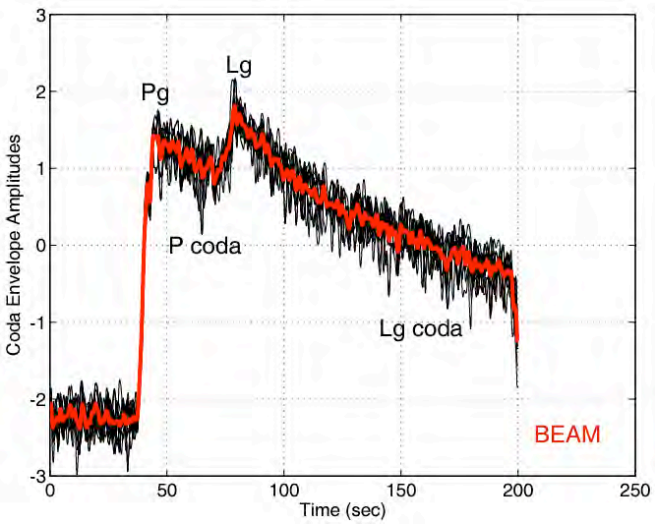


Figure 6. Coda envelopes at NVAR for a southern Nevada earthquake. The individual elements are shown as thin black lines, while the beam is shown as the red line. The results suggest that the *P*- and *Lg* coda are different, but both have small interstation scatter.

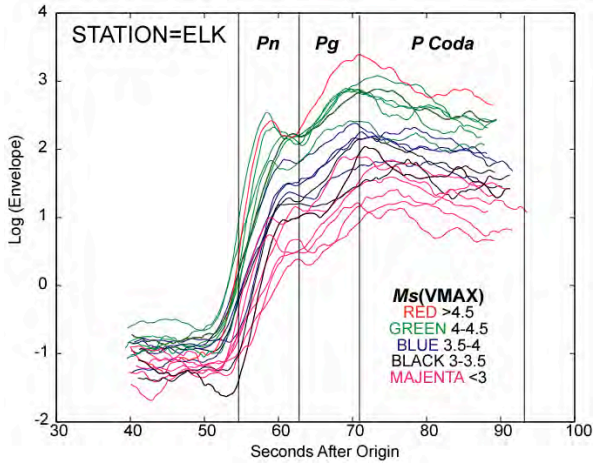


Figure 7. Narrowband envelopes (2–3 Hz) for *Pn*, *Pg*, and *P*-coda for explosions recorded at the Lawrence Livermore Network station ELK (~400 km). The envelopes have been binned based on M_s(VMAX) estimates for each event. We propose to use these coda envelopes to determine m_b.

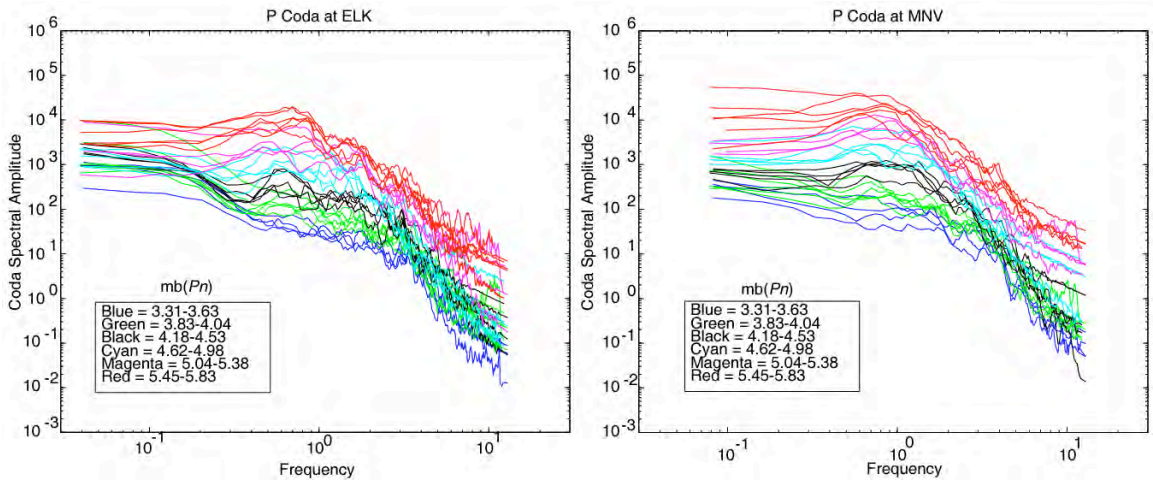


Figure 8. Observed *P*-coda spectra for Yucca Flat explosions at ELK (left) and MNV (right).

Characteristics of Novaya Zemlya *P*-Coda

The following section describes preliminary results using far-regional and teleseismic *P*-coda waveforms from the AWE Blacknest array stations. We specifically wanted to determine whether *P*-coda magnitudes would scale with the teleseismic m_b for both earthquakes and explosions. Second, we wanted to ascertain whether these *P*-coda magnitudes exhibited less variance than their direct wave counterparts. Figure 9 shows array-averaged envelopes (2–3 Hz) for two NZ explosions (m_b~5.8) recorded at NORSAR, at an epicentral distance of roughly 2200 km. Notice that both *P*- and *S*-codas are very similar in character. (Note: Pre-event noise level differences reflect seasonal variations.)

We measured relative *P*-coda envelope amplitudes using the October 24, 1990, NZ explosion as a reference event. By scaling narrowband envelopes between our reference event and the other explosions and earthquakes, we were able to tabulate relative coda amplitudes. Figure 10 shows coda envelope amplitude residuals (y-axis) relative to the maximum likelihood magnitude m_b(ML) for explosions (red squares) and earthquakes (blue triangles) (Lilwall and Marshall, 1986; Marshall et al., 1989; Bowers, 2002). This regression was done using roughly 100 s of *P*-coda in the 2–3 Hz band. These preliminary results are very promising in that earthquake m_b's are also in good agreement with m_b (ML). This is in sharp contrast to results from regional m_b(*Lg*) and m_b(*Lg* coda) (e.g., Mayeda, 1993). In those

studies, m_b was tied to explosions at the NTS, however applying the same formulas to earthquakes resulted in an overestimation of ~1 magnitude unit.

Paths from NZ to NORSAR are still at regional distance, and one might expect the *P*-wave and its coda to be comprised of waves that sample the crust and upper mantle over a range of take-off angles from the source. At teleseismic distances however, we might expect the averaging effect observed for local and regional coda waves to break down. At these distances, first arriving *P*-waves are likely emanating from a limited range of take-off angles near the bottom of the focal sphere. To investigate this, we processed roughly 30 NZ explosions recorded at the U.K. arrays Eskdalmuir in Scotland (EKA) and Yellowknife in Canada (YKA) located at ~30 degrees and 44 degrees from NZ, respectively.

Figure 11 shows envelopes at EKA for 4 NZ explosions with roughly the same magnitude that were located within a few kilometers of each other. (Note: The pre-event noise is lower for the October 11, 1982, event because of improvements to the electronics in late 1979.) We see an immediate discrepancy for the September 24, 1979, event. Though it has the largest m_b(ML), it is roughly a factor of 3 smaller in amplitude (0.5 in $\log_{10}$) at EKA relative to the other three events. The direct *P*-wave, coda, and *PcP* phase (not shown) are all small. In fact, the EKA station magnitude for this event is low relative to the global m_b(ML) estimate, as well as the NORSAR and YKA estimates. Careful inspection of the raw data shows nothing unusual. The closest event is the September 27, 1978, event, but this event does not appear to be anomalous. Assuming that this anomalous behavior is real, it suggests a near-source process such as focusing directly beneath the event. Moreover, the scale-length must be small since a nearby event is not affected. This supports the notion that teleseismic *P*-codas will not have the same averaging properties that local and regional codas exhibit.

We also made relative coda envelope measurements for YKA and EKA for three bands (1.0–1.5, 1.5–2.0, and 2.0–3.0 Hz). In all cases we used the explosion envelopes for the August 18, 1983, event as our reference. The left side of Figure 12 shows *P*-coda amplitudes (relative to the reference envelope) for common events at YKA and EKA for all three frequency bands. We see that in general, there is good agreement between the *P*-coda amplitudes at the two stations (interstation scatter is ~0.17), though regional *Lg* coda at NTS has interstation scatter of only ~0.04 (see Figures 2 and 3).

The right side of Figure 12 shows *P*-coda amplitudes plotted against m_b(ML) for the 1.0–1.5 Hz band (again, these are relative amplitudes using the August 18, 1983, event as the reference). The solid line has a slope of 1. We note that 16 events at YKA and 10 events at EKA had clipped *P*-waves, however coda envelope measurements could still be made by measuring a few 10s of seconds past the clipped direct arrival.

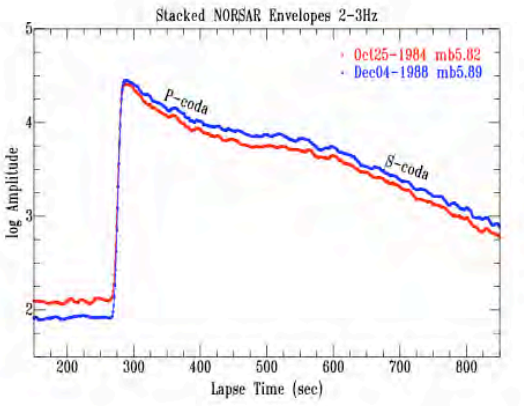


Figure 9. Array-averaged envelopes (2–3 Hz) for two NZ explosions (m_b~5.8) recorded at NORSAR.

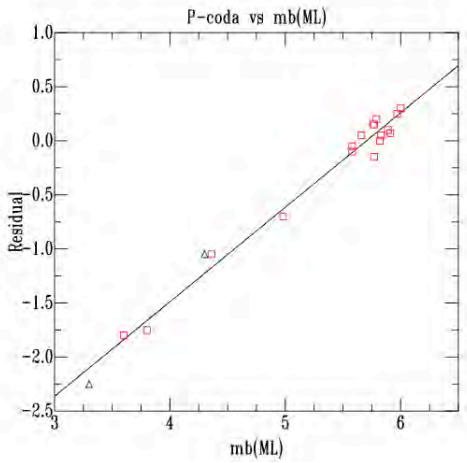


Figure 10. *P*-coda envelope amplitude residuals relative to the maximum likelihood magnitude m_b(ML) for NZ explosions (red squares) and earthquakes (blue triangles) measured at NORSAR.

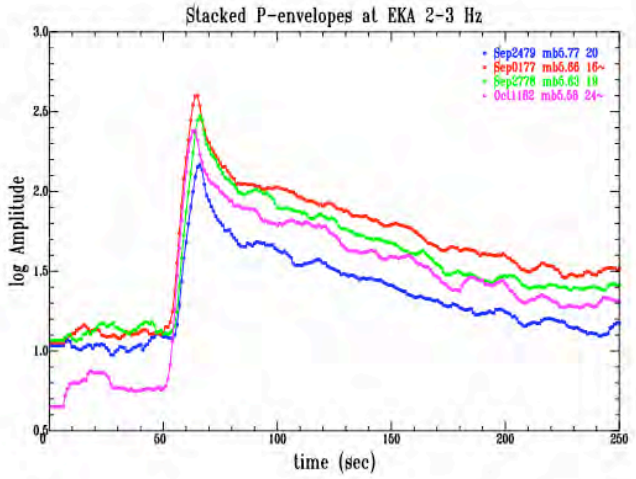


Figure 11. *P*-coda envelopes at EKA for 4 similar-magnitude NZ explosions.

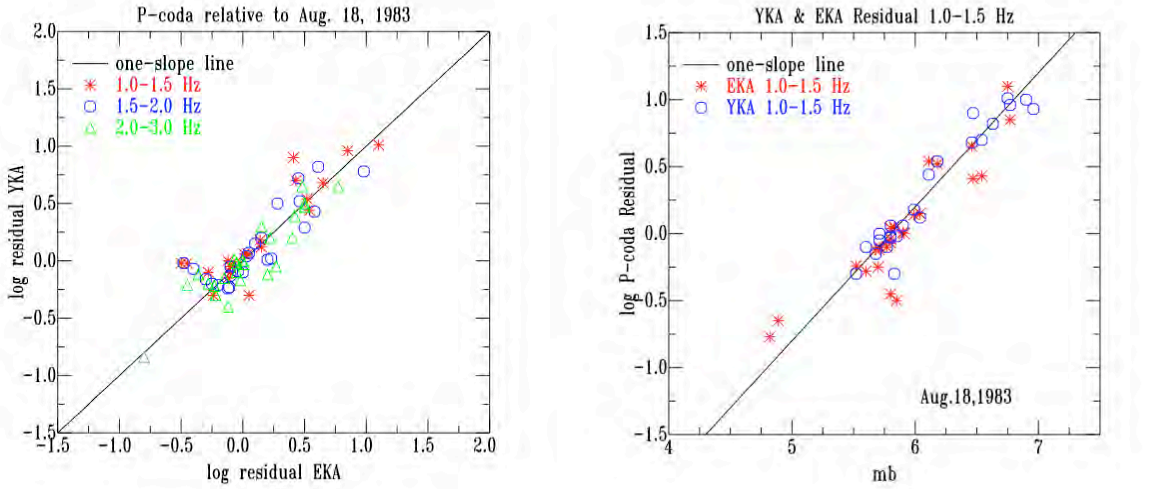


Figure 12. (Left) *P*-coda amplitudes (relative to the reference envelope) for common events at YKA and EKA for three frequency bands. (Right) *P*-coda amplitudes plotted against m_b(ML) for the 1.0–1.5 Hz band.

Our preliminary findings suggest that at regional distances the *P*-coda can be used as a surrogate for teleseismic m_b for both earthquakes and explosions based on the findings at NORSAR for NZ events (e.g., Figure 10). We plan to do a more rigorous test by looking at inter-station scatter and comparing directly with *P*-waves. To accomplish this, we will use NTS explosions and earthquakes recorded at multiple stations at progressively larger distances from NTS (e.g., BKS, YKA, EKA, NORSAR etc.). At teleseismic distances, the *P*-coda appears to share the same radiation pattern as the direct *P*-wave and does not appear to average over the focal sphere, as is observed for local and regional shear waves. Nonetheless, the derived body wave magnitude m_b(*P*-coda) at EKA and YKA for NZ explosions is in good agreement with the globally averaged results using direct teleseismic *P* (e.g., Figure 12). Furthermore, m_b(*P*-coda) can be computed on clipped data, which is quite common for the larger NZ explosions recorded at EKA and YKA.

CONCLUSIONS AND RECOMMENDATIONS

In our preliminary research, we have determined characteristics of *P*-coda, which suggest that we can use it to obtain regional body wave magnitudes with decreased interstation variance. During the next stage of the research, we will measure *P*-coda envelope amplitudes and derive path and site corrections. Since we will be considering events clustered at test sites, the corrections are expected to be minimal; however, for broad areas the corrections will be significant. We will compare interstation scatter of distance-corrected amplitudes as a function of window length. This will provide an empirical measure of error based on window length for each frequency band. For each frequency band, we will regress our coda envelope amplitudes against regional and teleseismic estimates of m_b (e.g., m_b(*Pn*), m_b(*P*)) to determine which band provides the lowest variance. This will yield slope and intercept values for each frequency band. We will then derive m_b(*Pn*) and m_b(*P*) (following Denny et al. 1987) to compare against m_b(*P*-coda) to assess performance at the network and single-station level. Most of the nuclear explosions already have an m_b(*Pn*) compiled by Vergino and Mensing (1989). Patton (2001) has estimated m_b(*Pn*) for many historic NTS earthquakes. For recently recorded earthquakes, we will need to estimate m_b(*Pn*) and m_b(*P*). Finally, we will compute M_s(VMAX) from the regional stations and form an M_s(VMAX)*:*m_b(Pcoda) discriminant; compare against teleseismic values and trends.

ACKNOWLEDGEMENTS

We wish to thank Drs. Howard Patton and Scott Phillips for fruitful discussions regarding coda generation and propagation. We also thank Dr. William Walter for assistance in acquiring NTS data for this project.

REFERENCES

Bonner, J. L., D. Russell, D. Harkrider, D. Reiter, and R. Herrmann (2006). Development of a time-domain, variable-period surface wave magnitude measurement procedure for application at regional and teleseismic distances—Part II: Application and Ms-mb performance, *Bull. Seism. Soc. Amer.* 96: 678–696.

Bowers, D. (2002). Was the 16 August 1997 seismic disturbance near Novaya Zemlya an earthquake? *Bull. Seism. Soc. Am*. 92: 2,400–2,406.

Denny, M. D., S. R. Taylor, and E. S. Vergino (1987). Investigation of m_b and M_s formulas for the western United States and their impact on the M_s/m_b discriminant, *Bull. Seism. Soc. Am*. 77: 987–995.

Levshin, A., J. Stevens, M. Ritzwoller, and D. Adams (2002). Short-Period (7 s to 15 s) group velocity measurements and maps in Central Asia, in *Proceedings of the 24th Seismic Research Review—Nuclear Explosion Monitoring: Innovation and Integration*, LA-UR-02-5048, Vol. 1, pp. 97–106.

Liwall, R. C. and P. D. Marshall (1986). Body wave magnitudes and locations of Soviet underground explosions at the Novaya Zemlya test site, AWRE report No. 0 17/86, HMSO, London.

Marshall, P. D., R. C. Stewart, and R. C. Liwall (1989). The seismic disturbance on 1986 August 1 near Novay Zemlya: A source of concern? *Geophys. J*. 98: 565–573.

Mayeda, K. (1993). m_b(*Lg*Coda): A stable single station estimator of magnitude, *BSSA* 83: 851–861.

Mayeda, K. and W. Walter, (1996). Moment, energy, stress drop, and source spectra of western U.S. earthquakes, *JGR*, 101: 11,195–11,208.

Mayeda, K., A. Hofstetter, J. L. O'Boyle, and W. R. Walter (2003). Stable and transportable regional magnitudes based on coda-derived moment-rate spectra, *BSSA* 93: 224–239.

Mayeda, K. L. Malagnini, W. S. Phillips, W. R. Walter, and D. Dreger (2005). 2-D or not 2-D, that is the question: A northern California test, *Geophys. Res. Lett*. 32: L12301.

Morozov, I. B. and S. B. Smithson (2000). Coda of long-range arrivals from nuclear explosions, *Bull. Seism. Soc. Am.* 90: 929–939.

Murphy, J. R., B. W. Barker, and M. E. Marshall (1997). Event screening at the IDC using the M_s/m_b discriminant, Maxwell Technologies final report.

Nuttli, O. W. (1973). Seismic wave attenuation and magnitude relations for eastern North America, *J. Geophys. Res*. 78: 879–885.

Pasyanos, M., W. Walter, and M. Flanagan (2003). Geophysical models for nuclear explosion monitoring, in *Proceedings of the 25th Seismic Research Review—Nuclear Explosion Monitoring: Building the Knowledge Base*, LA-UR-03-6029, Vol. 1, pp. 125–134.

Patton, H. J. (2001). Regional magnitude scaling, transportability and M_s:m_b discrimination at small magnitudes, *Pure Appl. Geophys.* 158: 1,951–2,015.

Phillips, W., H. Patton, C. Aprea, H. Hartse, G. Randall, and S. Taylor (2003). Automated broad area calibration for coda based magnitude and yield, in *Proceedings of the 25th Seismic Research Review—Nuclear Explosion Monitoring: Building the Knowledge Base*, LA-UR-03-6029, Vol. 2, pp. 437–444.

Ritzwoller, M. H., N. M. Shapiro, M. P. Barmin, and A. L. Levshin (2002). Global surface wave diffraction tomography, *J. Geophys Res.* 107: B12, 2335.

Russell, D. R. (2006). Development of a time-domain, variable-period surface wave magnitude measurement procedure for application at regional and teleseismic distances—Part I: Theory, *Bull. Seism. Soc. Amer.* 96: 665– 677.

Stevens, J. L., D. A. Adams, and E. Baker (2001). Surface wave detection and measurement using a one-degree global dispersion grid, SAIC final report SAIC-01/1085.

Tibuleac, I. M, E. T. Herrin, and P. Negraru (2001). Calibration studies at NVAR, *Seis. Res. Lett.* 72: 754.

Vergino, E. S. and R. W. Mensing, (1989). Yield estimation using regional m_b(*Pn*), Lawrence Livermore National Laboratory report UCID-101600.

Wagner, G. S. (1997). Regional wave propagation in southern California and Nevada: Observations from a three-component seismic array, *J. Geophys. Res*. 102: 8,285–8,311.

Walter, W. R. and S. R. Taylor (2002). A revised magnitude and distance amplitude correction (MDAC2) procedure for regional seismic discriminants, Lawrence Livermore National Laboratory report UCRL-ID-146882.

Walter, W. R., K. D. Smith, J. L. O'Boyle, T. F. Hauk, F. Ryall, S. Ruppert, S. C. Myers, M. L. Anderson, and D. A. Dodge (2003). The fundamental understanding of regional seismic signal processing with a unique western United States dataset, in *Proceedings of the 25th Annual Seismic Research Review—Nuclear Explosion Monitoring: Building the Knowledge Base*, LA-UR-03-6029, Vol. 2, pp. 486–494.

A SCALING ANALYSIS OF FREQUENCY-DEPENDENT ENERGY PARTITION FOR LOCAL AND REGIONAL SEISMIC PHASES FROM EXPLOSIONS

John R. Murphy[1], Brian W. Barker[1], and Jamil Sultanov[2]

Science Applications International Corporation[1] and Institute for Dynamics of the Geospheres[2]

Sponsored by Air Force Research Laboratory

Contract No: FA8718-04-C-0030

ABSTRACT

It has long been recognized that seismic identification of underground nuclear tests with $m_b < 4$ will have to be based largely on discriminants that are effective in the regional distance range. Research conducted over the past 20 years has demonstrated that the most reliable of the regional discriminants considered to date are those based on high-frequency spectral ratios of the amplitudes of the seismic shear phases Sn and Lg to those of the corresponding direct P phases Pn and Pg. While much observational evidence supporting the general applicability of these regional discriminants has now been accumulated, a problem remains in that there is currently no deterministic model of shear wave generation by explosions that has been shown to be quantitatively consistent with the wide range of Sn and Lg observations from explosion sources. Consequently, extrapolation of these discrimination criteria to previously untested locations and source conditions is still subject to considerable uncertainty. The technical objectives of this research program are to determine frequency-dependent source-scaling relations for the regional phases Pn, Pg, Sn, and Lg through statistical analyses of data recorded from underground explosions at the Semipalatinsk, Novaya Zemlya, Lop Nor, and Nevada Test Site (NTS) nuclear test sites and to apply these derived scaling relations to a quantitative evaluation of the plausibility of various proposed physical source mechanisms for the regional shear phases Sn and Lg observed from underground explosion sources.

During the initial year of the program, the study effort focused on analyses of regional seismic data recorded from explosions at the Degelen Mountain and Balapan testing areas of the Semipalatinsk test site. Digital data recorded at the Borovoye Geophysical Observatory in North Kazakhstan from large samples of Semipalatinsk explosions were processed and analyzed to define frequency-dependent source-scaling relations for these observed regional P and S wave data. The source-scaling results indicated that both the Sn/Pn and Lg/Pn spectral ratios show some modest yield dependence in the 1-3 Hz band but no statistically significant yield dependence at the higher frequencies typically used for discrimination purposes. Subsequent analyses have demonstrated that these yield-scaling observations are remarkably consistent with a simple explosion S wave source that is directly proportional to the Mueller/Murphy source for P, with the corner frequency reduced by the S/P velocity ratio of the source medium. One S wave generation mechanism that could be consistent with these observations is release of tectonic strain energy by the explosion. However, it has been found that the observed S wave source strengths for Balapan explosions show no obvious correlation with the documented long-period tectonic release for these explosions.

Current effort is focusing on an extension of the Semipalatinsk analysis to consider explosions at the Chinese Lop Nor test site. Digital data recorded from Lop Nor explosions at 14 different regional stations have now been collected and processed. These multi-station data have been analyzed to define frequency-dependent source scaling for the observed Lg/Pn spectral ratios using a covariance statistical analysis technique in which the source scaling is assumed to be common to all stations. Preliminary results of these analyses are generally consistent with the previous Semipalatinsk analysis results in that the observed Lg/Pn spectral ratios have been found to be essentially independent of source size over the analyzed frequency band extending from 0.5 to about 8 Hz. Regional peak amplitude data recorded from these same explosions at 7 former Soviet network stations have also been analyzed and, as at Semipalatinsk, it has been found that the regional phase amplitude ratios show no statistically significant dependence on azimuth. These observations place strong constraints on the possible S wave generation mechanisms for these explosions, but the search continues for specific physical mechanisms that can be shown to be quantitatively consistent with all of them.

OBJECTIVES

The technical objectives of this research program are to determine frequency-dependent source-scaling relations for the regional phases Pn, Pg, Sn, and Lg through statistical analyses of data recorded from underground explosions at the Semipalatinsk, Novaya Zemlya, Lop Nor, and NTS nuclear test sites and to apply these derived scaling relations to a quantitative evaluation of the plausibility of various proposed physical source mechanisms for the regional shear phases Sn and Lg observed from underground explosion sources. The ultimate objective is to improve U.S. operational monitoring capability by providing a quantitative framework that can be used for confidently evaluating expected regional event discrimination performance as a function of the ranges of explosion source size and emplacement conditions that must be considered in global nuclear monitoring.

RESEARCH ACCOMPLISHED

A number of focused research studies have been conducted in recent years in attempts to better define the source of the S waves observed from underground nuclear explosions, particularly as they relate to the generation of the Lg regional phase that has come to play a central role in the identification and yield estimation of small explosions. In early studies of the seismic waves generated by underground nuclear explosions, it was generally assumed that the observed S waves were produced by linear conversion of the primary explosion P waves by the layered geology in the source region and along the propagation path between the source and the receiver. However, it was soon recognized that relatively strong S arrivals were also observed on the transverse components of motion at regional distances, and this necessitated the addition of a nonisotropic scattering mechanism to the simple linear conversion model. Subsequent deterministic simulations of the Lg phases produced by point source explosions in planar multilayered approximations of the crustal waveguide raised further questions regarding the plausibility of the linear P-to-S conversion mechanism in that isotropic explosions in high-velocity source media such as granite were predicted to generate very little Lg energy (e.g., Jih and McLaughlin, 1988).

These inconsistencies prompted intensive searches for alternate sources of Lg that generally focused on either scattering of the Rg phase induced by the isotropic explosion into Lg (e.g., Gupta et al., 1991, 1997), or on direct generation of S and Rg waves by the nonisotropic components of the explosion source associated with spall and other nonlinear interactions of the primary explosion source with the overlying geology and free surface (e.g., Stevens et al., 1991, 2003). Although significant theoretical and observational evidence has been marshalled to support the plausibility of both of these hypothetical sources of Lg, problems remain in that neither seems completely consistent with the wide range of Lg observational data that is currently available (Stevens et al., 2003). For example, it has been observed that Lg amplitude level correlates remarkably well with the known yields of underground explosions over broad source regions, and this fact seems difficult to reconcile with the Rg scattering hypothesis. Moreover, both of these proposed sources would predict a pronounced dependence of Lg excitation on source depth, and this seems inconsistent with the results of Nuttli (1986) and others who have obtained reliable Lg-based yield estimates for very deep explosions, including the U.S. Peaceful Nuclear Explosion (PNE) RULISON which was detonated at a scaled depth more than six times larger than the nominal NTS containment depth. It follows that additional research is needed to identify potential sources of explosion S and Lg phases that satisfy all available constraints.

One potentially powerful constraint on the source of S waves from explosions is provided by their frequency-dependent scaling as a function of explosion yield, depth of burial, and source medium relative to the well-documented scaling of the associated direct P wave phases. That is, since it is well established that the scaling of the direct P waves observed from explosions can be explained to first order by a simple isotropic source model (Mueller and Murphy, 1971), the degree to which the scaling of secondary regional phases such as Sn and Lg is similar to that of the corresponding Pn phases provides direct evidence of any significant departures from the isotropic source model. Thus, while a scaling analysis in itself will not specifically identify a physical mechanism for Lg generation, it will nonetheless provide powerful quantitative constraints that would have to be met by any proposed source mechanism.

During the first year of this study program, our analyses focused on the source scaling of regional phase data recorded at the Borovoye digital seismic station in Kazakhstan from underground nuclear explosions at the Degelen and Balapan testing areas of the former Soviet Semipalatinsk test site. The basic methodology can be briefly summarized as follows. Let $A_i(\omega)$ denote the observed regional phase spectral amplitude from explosion i with

known yield (W_i) and depth of burial (h_i). Then, according to the Mueller/Murphy explosion source model, for tests in a fixed source region, we can approximate the dependence of A_i on W_i and h_i by using a power law functional relation of the form

$$A_i(\omega) = K(\omega) W_i^{n(\omega)} h_i^{m(\omega)}, \quad (1)$$

where $n(\omega)$ and $m(\omega)$ are the frequency-dependent yield and depth scaling exponents, respectively, and $K(\omega)$ is a station-specific intercept function. It follows from Equation 1 that

$$\log A_i(\omega) = K'(\omega) + n(\omega) \log W_i + m(\omega) \log h_i, \quad (2)$$

from which we can estimate $n(\omega)$, $m(\omega)$, and $K(\omega)$, given a set of observations of $A(\omega)$ from explosions of known yield and depth of burial. This was the model employed by Murphy et al. (2001) in their source-scaling analysis of Soviet PNE data. However, for explosions at the nuclear weapons test sites being considered in this study, the sampled ranges of source depth are generally too restrictive to permit confident estimation of the depth-scaling exponents and, consequently, for the purposes of the present analysis, Equation 1 has been simplified to express the regional phase spectral ratios in the form

$$\frac{S_i(\omega)}{P_i(\omega)} = \tilde{K}(\omega) W_i^{n'(\omega)}, \quad (3)$$

where here S corresponds to Sn or Lg and P to Pn or Pg, and $n'(\omega)$ denotes the difference in the frequency-dependent yield-scaling exponents, $n_s(\omega)$ - $n_p(\omega)$, between the S and P phases. It follows that if the S wave source scales with yield in the same manner as the P wave source, the estimated $n'(\omega)$ values are expected to be close to zero, independent of frequency. Any differences in depth dependence between the different regional phases can then be assessed in terms of observed departures from the average ratios predicted by Equation 3.

Equation (3) is directly applicable to a testing area like Degelen, where yields of individual explosions encompassing a wide yield range are known. However, little or no individual explosion-yield data are available from the Balapan testing area of Semipalatinsk or the Chinese Lop Nor test site discussed below. For such test sites, we use m_b as a surrogate for yield, assuming that the slope, b, of the average m_b/yield relation

$$m_b = C + b \log W, \quad (4)$$

is known. That is, the dependence of the observed regional-phase spectral-amplitude ratios on m_b is estimated statistically to obtain $n'(\omega) / b$, and the corresponding frequency-dependent yield-scaling exponents, $n'(\omega)$, are approximated using the known value of b.

The regional-phase spectral-amplitude estimates used in this study have been obtained by bandpass filtering the observed vertical component seismograms through a Gaussian comb of filters spaced at intervals of 0.25 Hz between 0.5 and 10 Hz, where each filter is characterized by a Q value of $6f_c$, with f_c being the filter center frequency. Figure 1 shows an example of filter outputs encompassing this frequency range for the 1.8 kt Degelen Mountain explosion of 10/04/89, where the selected time windows for the Pn, Sn, and Lg regional phases are indicated. It can be seen that these data indicate large Lg/Pn ratios out to about 2 Hz, above which the Lg spectral-amplitude level decreases quite rapidly to the P coda level at about 5 Hz. The observed Sn spectral-amplitude levels are also greater than those of Pn out to about 3 Hz but decrease less rapidly than those of Lg at higher frequencies, showing spectral-amplitude levels above the P coda levels out to 10 Hz. For purposes of the source-scaling analysis, the spectral-amplitude levels at each filter center frequency were estimated by computing root mean square (RMS) values from the instrument-corrected filter outputs in each of the designated regional-phase time windows.

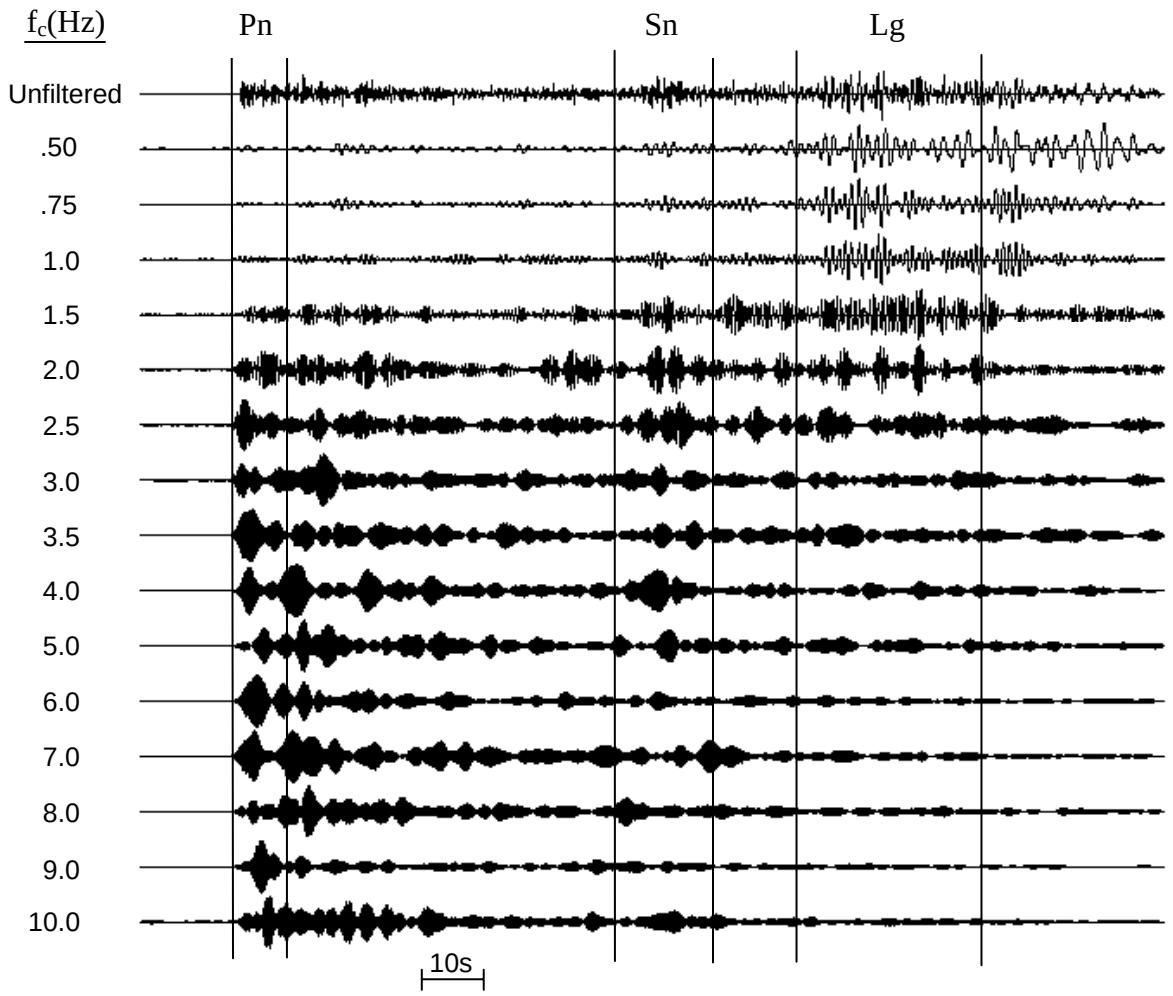


Figure 1. Bandpass filter processing results for the Borovoye recording of the 1.8 kt Degelen Mountain nuclear explosion of 10/04/89.

The yield-scaling exponents as functions of frequency for the Sn/Pn and Lg/Pn spectral ratios estimated from large samples of Degelen and Balapan explosion data recorded at Borovoye are compared in Figure 2. It can be seen from this figure that the estimated yield scaling exponents for these two Semipalatinsk testing areas are very similar and are generally quite small, ranging between only about –0.25 and +0.10. In fact, the dashed lines on these figures denote the 95% confidence intervals about the derived Degelen estimates, and it can be seen that they differ significantly from zero only in a narrow frequency band between about 1 and 3 Hz. It follows that the observed Sn and Lg spectral amplitudes must scale with yield in a very similar manner to the corresponding direct Pn spectral amplitudes, particularly in the higher frequency ranges used for regional discrimination purposes.

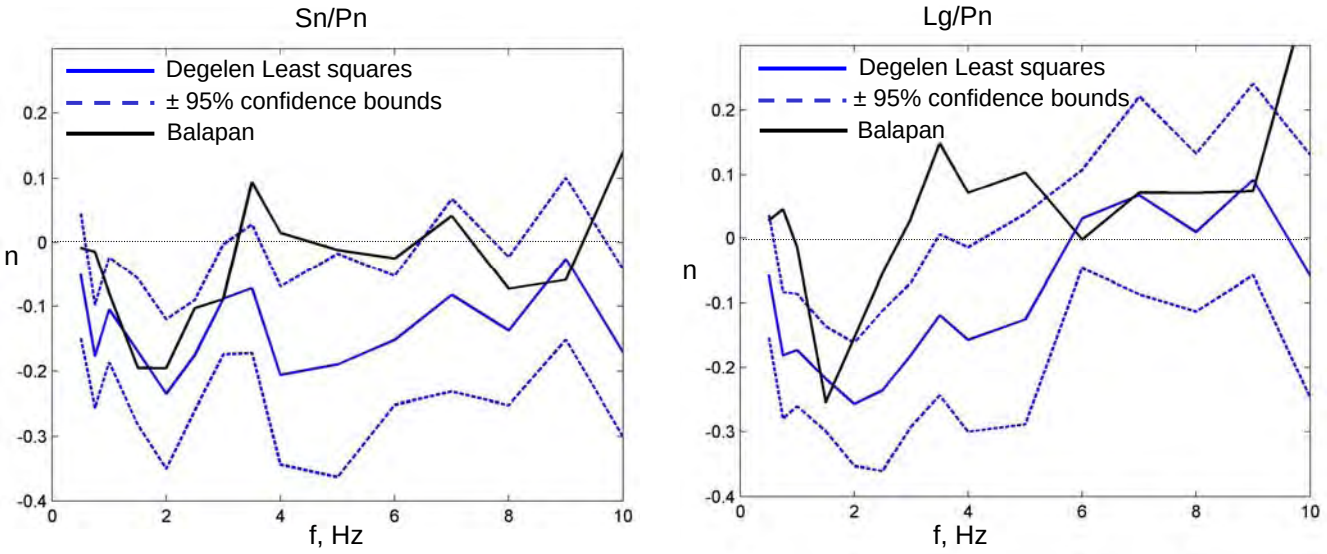


Figure 2. Comparison of Balapan and Degelen explosion yield-scaling exponents (n) as functions of frequency for the Sn/Pn (left) and Lg/Pn (right) regional phase spectral ratios. It can be seen that the Balapan scaling results are generally consistent (within the uncertainty bounds) with the corresponding Degelen scaling results, indicating that the Sn and Lg yield scaling is very comparable to that associated with the direct Pn phase for explosions at these two Semipalatinsk testing areas, particularly in the higher frequency ranges used for regional discrimination purposes.

These yield-scaling results provide some strong, quantitative constraints for use in evaluating proposed S wave generation mechanisms. For example, Fisk et al., (2005) have recently demonstrated some success in modeling observed Sn and Lg amplitude spectra using a simple S wave source model that was obtained from the corresponding Mueller/Murphy P wave source model by scaling the corner frequency by the S/P velocity ratio of the source medium. In an attempt to determine whether this proposed S wave source model is consistent with our derived yield-scaling exponents for the Degelen and Balapan testing areas, the observed S/P ratios corresponding to the explosions in our selected sample were theoretically simulated using this Mueller/Murphy-based model, and the resulting synthetic S/P spectral ratios were statistically analyzed as a function of yield in the same manner as were the observed data. The results are shown in Figure 3, where it can be seen that these theoretical yield-scaling exponents, as a function of frequency, are remarkably consistent with the experimental Semipalatinsk values, within the approximate ±0.1 uncertainty bounds on those yield-scaling estimates. That is, these comparisons are consistent with an S wave source for Semipalatinsk explosions, which is directly related to the corresponding P wave source. One physical S wave source that could produce such source scaling is tectonic release within the nonlinear zone surrounding the explosion. Now the long-period tectonic release characteristics of a number of Balapan explosions were previously analyzed using formal moment tensor inversion techniques to estimate the relative strengths (i.e., F factors) of the explosion and tectonic components of the observed long-period radiations from these explosions (e.g., Given and Mellman, 1986). To test the tectonic release hypothesis, F factors were collected for a sample of 35 Balapan explosions that were included in our source-scaling analysis, and an attempt was made to correlate them with the observed S/P spectral ratios for these explosions. However, evaluation of the observed, frequency-dependent Sn/Pn spectral ratios revealed no systematic dependence on the associated F values, indicating that the S wave generation efficiency for these explosions does not correlate with the strength of the accompanying tectonic release, at least as measured by the long-period F factor. This fact is illustrated in Figure 4, which shows a comparison of the observed Borovoye Sn/Pn spectral ratios for two Balapan explosions of comparable yield but significantly different long-period tectonic release characteristics. It can be seen that these two spectral ratios are essentially identical over the 0.5 to 10 Hz frequency band, despite the large difference in the inferred F factors for these two explosions. Thus, while the frequency-dependent source-scaling characteristics of the S wave generation by these Semipalatinsk explosions have now been quantitatively defined, identification of a specific physical mechanism that is consistent with these constraints continues to be elusive.

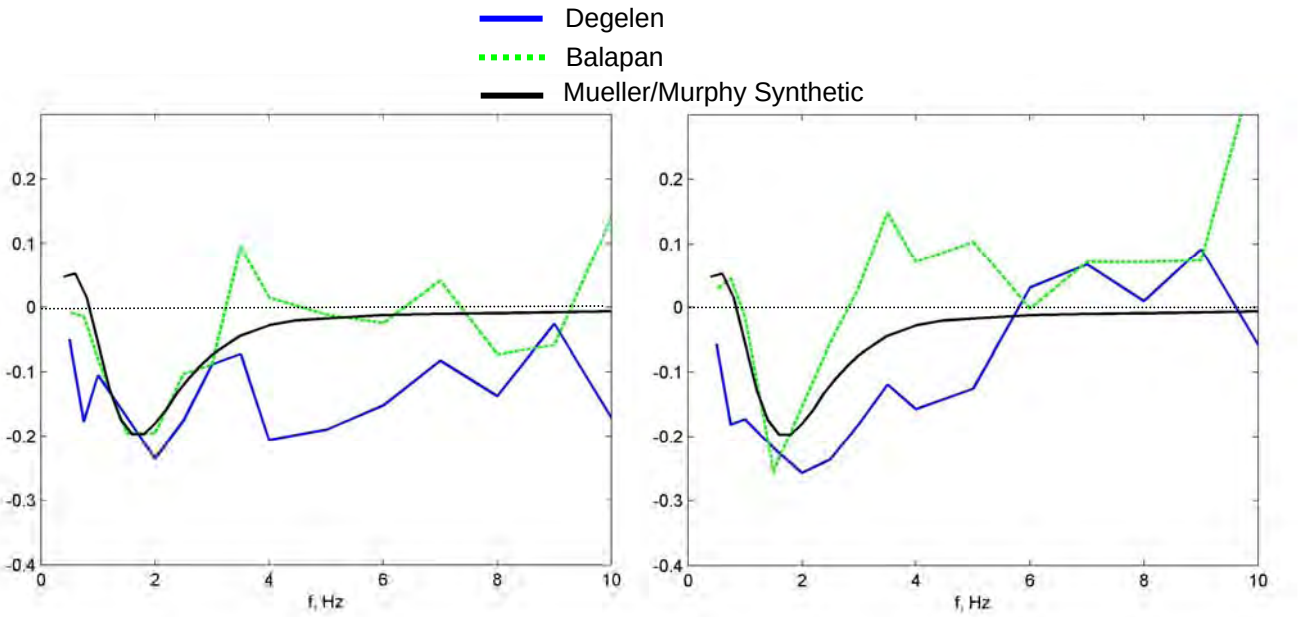


Figure 3. Comparison of observed Degelen and Balapan frequency-dependent yield-scaling exponents for Sn/Pn (left) and Lg/Pn (right), with the theoretical exponents predicted by a simple source model based on Mueller/Murphy, with Sn(f) = Pn(*k*f), where *k* represents the ratio of the P to S wave velocities of the source medium.

Our current investigations are focusing on extending the source-scaling analyses to explosions at the Chinese Lop Nor test site. Figure 5 shows the map locations of the regional stations for which we have assembled data recorded from Lop Nor explosions, encompassing a range in m_b extending from 4.8 to 6.6 (i.e., a yield range of approximately 3–735 kt). In this case, digital data are available from a number of stations, but unlike Semipalatinsk, no one station recorded explosions sampling the entire range of energy release. Consequently, for this test site we employed a modified covariance statistical analysis approach in which the S/P spectral amplitude ratio at station i from explosion j is represented in the form

$$\frac{S_{ij}(\omega)}{P_{ij}(\omega)} = \tilde{K}_i(\omega) W_j^{n'(\omega)}, \qquad (5)$$

where $n'(\omega)$ is assumed to be common to all stations for a given phase ratio. As at Balapan, m_b was used as a surrogate for yield at Lop Nor, and $n'(\omega)$ was estimated from the statistically determined value of $n'(\omega)/b$, using the value of b inferred from previous teleseismic analyses.

Sample bandpass filtering processing results for a station AAK ($\Delta \approx 10°$) recording of a Lop Nor explosion are shown in Figure 6. This example is typical of our Lop Nor data sample in that, unlike the Borovoye recordings of Semipalatinsk explosions, there is no obvious Sn arrival that can be correlated across the frequency range of interest. Moreover, although Lg is relatively strong at low frequencies, its amplitude level decreases quite rapidly to the P coda level above about 3 Hz. Although these results vary somewhat from station to station, there is no evidence of Lg energy above the P coda level at frequencies above 5 Hz at any of these stations except WMQ, for which only a single explosion recording is available. Consequently, we have limited our Lop Nor source scaling analysis to the Lg/Pn spectral ratio at frequencies below 5 Hz.

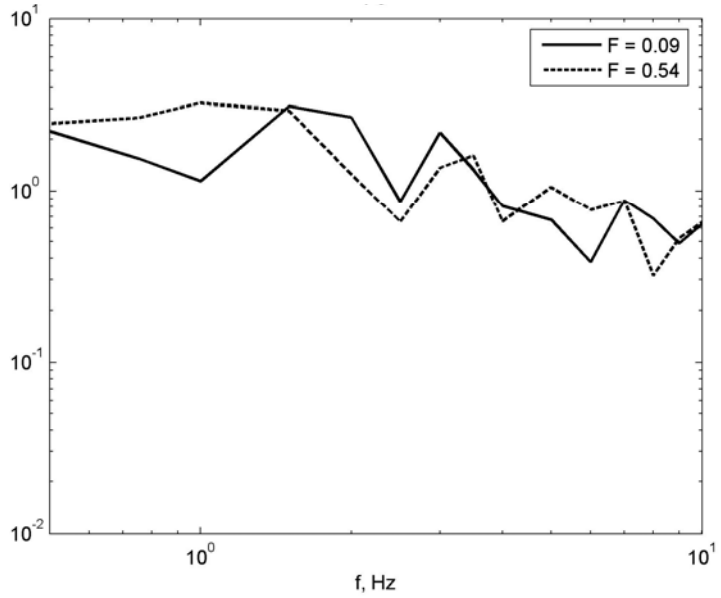


Figure 4. Comparison of observed Sn/Pn spectral ratios for two Balapan explosions of comparable yield but significantly different long-period tectonic release characteristics (i.e., F factors).

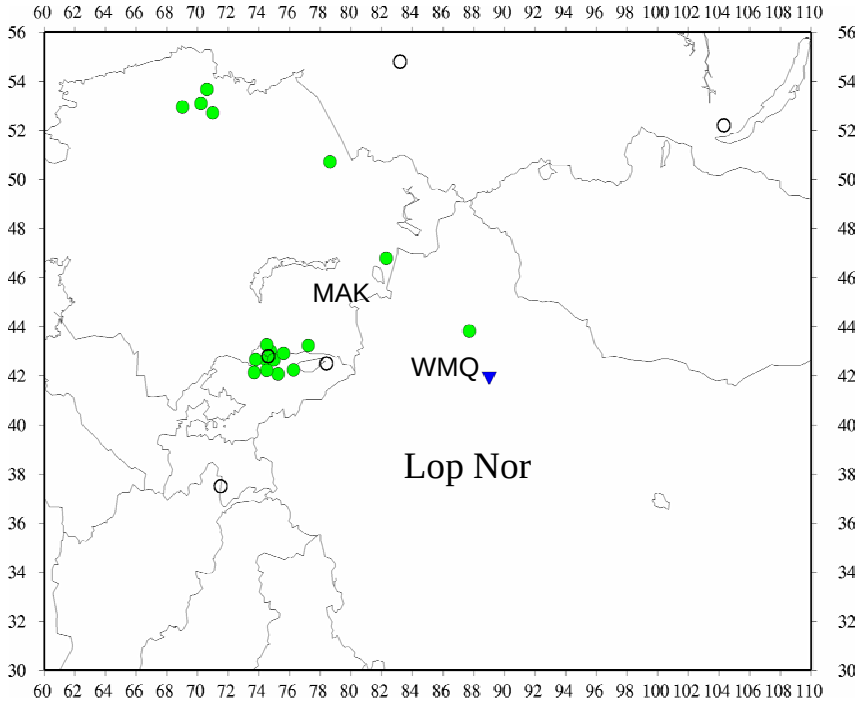


Figure 5. Distribution of seismic stations used in the analysis of seismic source scaling of regional phases from Lop Nor explosions. Filled circles denote stations for which digital data are available, and open circles denote Soviet network stations for which only peak amplitude readings are available.

The Lg/Pn frequency-dependent yield-scaling exponents estimated from the Lop Nor explosion data are shown in Figure 7 where they are compared with the corresponding Balapan exponents over the frequency range extending from 0.5 to 5.0 Hz. It can be seen that these Lop Nor source-scaling results are remarkably similar to those for Balapan, again indicating that the difference in yield-scaling exponents between the S and P wave sources are

significantly different from zero in a narrow band from 1 to 2 Hz only. As at Semipalatinsk, these observed Lop Nor S/P spectral ratios have been theoretically simulated using the simple Mueller/Murphy-based S wave source model, and the frequency-dependent yield-scaling exponents derived from these synthetic ratios are compared with those estimated from the observed Lop Nor Lg/Pn ratios in Figure 8. Once again, the agreement is excellent, indicating that the observed Lop Nor source scaling for Lg/Pn is consistent with a simple S wave source that is directly related to the corresponding P wave source.

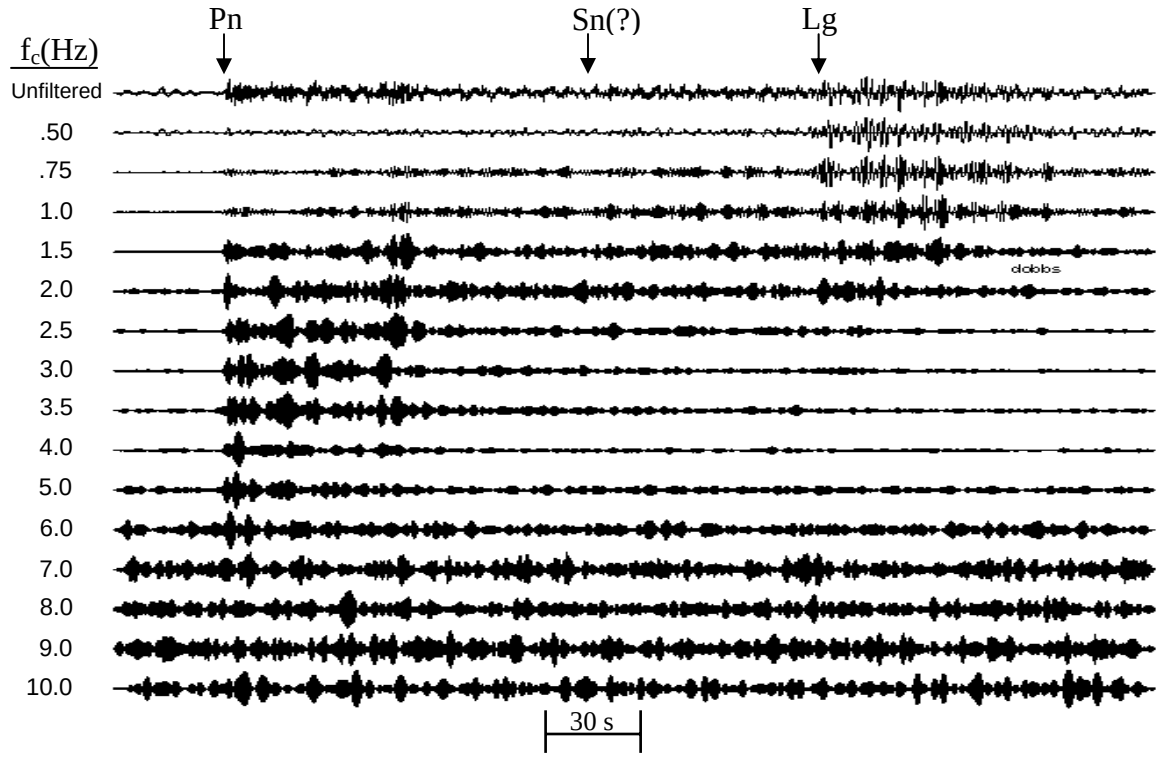


Figure 6. Bandpass filter processing results for the station AAK recording of the Lop Nor explosion of 29 July 1996. While there is evidence of a relatively strong Lg arrival at low frequencies, no clear Sn arrival is evident.

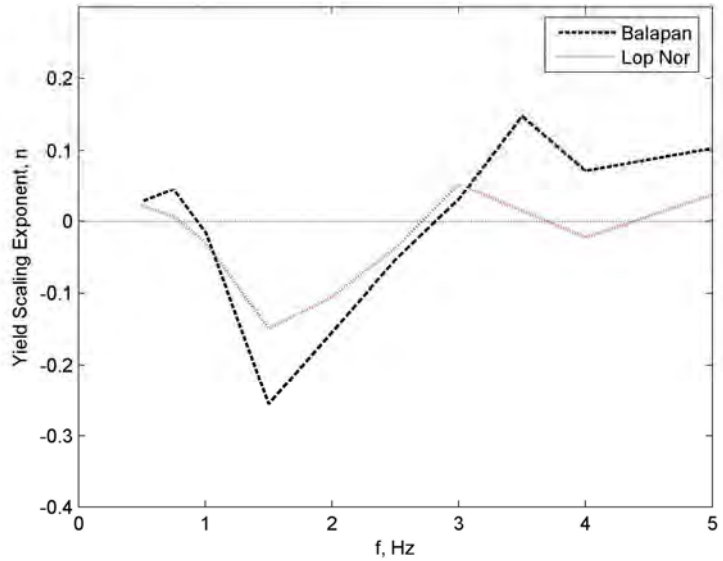


Figure 7. Comparison of observed Lop Nor and Balapan frequency-dependent yield-scaling exponents for Lg/Pn.

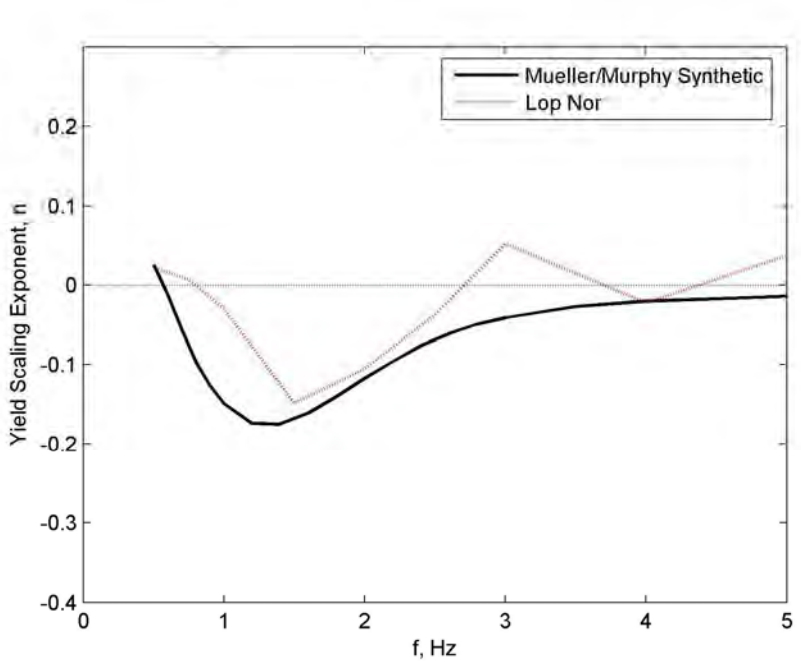


Figure 8. Comparison of observed Lop Nor frequency-dependent yield-scaling exponents for Lg/Pn, with the theoretical exponents predicted by a simple source model based on Mueller/Murphy, with S(f) = P(kf), where k represents the ratio of the P to S wave velocities of the source medium.

CONCLUSIONS AND RECOMMENDATIONS

Frequency-dependent seismic source-scaling analyses of regional phase data recorded from underground nuclear explosions at the Degelen and Balapan testing areas of the former Soviet Semipalatinsk test site and the Chinese Lop Nor test site have now been completed. The results from these three testing areas are very consistent and indicate that the observed Sn and Lg phase spectra scale with yield in a manner that is very comparable to that of the corresponding direct Pn phase spectra, differing significantly only in a narrow frequency band between about 1 and 3 Hz. Moreover, direct comparisons of Sn/Pn and Lg/Pn spectral ratios over the sampled ranges of depth and scaled depth indicate that any differences in the frequency-dependent source-depth dependencies of Pn, Sn, and Lg must be quite small. These source-scaling results provide strong constraints on any proposed S wave generation mechanisms for explosions. For example, the frequency dependent source scaling results for these three testing areas have been shown to be remarkably consistent with a simple explosion S wave source that is directly proportional to the corresponding Mueller/Murphy P wave source, with a corner frequency reduced by the S/P velocity ratio of the source medium. As Fisk et al. (2005) have noted previously, these results seem to indicate that the explosion S wave source has a characteristic length that is very similar to that of the corresponding P wave source. Although this result could be consistent with a tectonic release mechanism for S, it has been found that the observed S wave source strength shows no obvious correlation with previously inferred tectonic release characteristics of these explosions, at least as quantified by the long-period F factor. Consequently, the search continues for a physically plausible S wave generation mechanism that is consistent with the frequency-dependent source scaling of observed regional shear phases from explosions. These source-scaling results are currently being extended to encompass underground nuclear explosions at the Russian Novaya Zemlya test site.

REFERENCES

Fisk, M. D., S. R. Taylor, and T. Lay (2005). Modeling and empirical research on energy partitioning of regional seismic phases used for explosion monitoring, in *Proceedings of the 27th Seismic Research Review*, LA-UR-05-6407, Vol. 1, pp. 539–549.

Given, J. W., and G. R. Mellman, (1986). Estimating explosion and tectonic release source parameters of underground nuclear explosions from Rayleigh- and Love-wave observations, Sierra Geophysics Final Report to Air Force Geophysics Laboratory, Part 1, AFGL-TR-86-0171, SGI-R-86-126, July.

Gupta, I. N., T. W. McElfresh, and R. A. Wagner (1991). Near-source scattering of Rayleigh to P in teleseismic arrivals from Pahute Mesa NTS shots, in *Explosion Source Phenomenology,* AGU Geophysical Monograph 65, ISBN 0-87590-031-3: pp. 151–159.

Gupta, I. N., T. Zhang, and R. Wagner (1997). Low-frequency Lg from NTS and Kazakh nuclear explosions–observations and interpretations, *Bull. Seism. Soc. Am*., 87: 1,115–1,125.

Jih, R. S. and K. L. McLaughlin (1988). Investigation of explosion generated SV Lg waves in 2-D heterogeneous crustal models by finite-difference method, Report No. AFGL-TR-88-0025.

Mueller, R. A. and J. R. Murphy (1971). Seismic characteristics of underground nuclear detonations, I: Seismic spectrum scaling, *Bull. Seism. Soc. Am*., 61: 1,675-1,692.

Murphy, J. R., I. O. Kitov, B. W. Barker, and D. D. Sultanov (2001). Seismic source characteristics of Soviet peaceful nuclear explosions, monitoring the comprehensive nuclear-test-ban treaty, in *Source Processes and Explosion Yield Estimation, PAGEOPH Topical Volume*, Birkhauser, pp. 2,077–2,101.

Nuttli, O. W. (1986). Yield estimates of Nevada Test Site explosions obtained from seismic L_g waves, *J. Geophys. Res*., 91: 2,137–2,151.

Stevens, J. L., T. G. Barker, S. M. Day, K. L. McLaughlin, N. Rimer, and B. Shkoller (1991). Simulation of teleseismic body waves, regional seismograms, and Rayleigh wave phase shifts using two-dimensional nonlinear models of explosion sources, in *Explosion Source Phenomenology*, AGU Geophysical Monograph 65, ISBN 0-87590-031-3: 239–252.

Stevens, J. L., G. E. Baker, H. Xu, T. J. Bennett, N. Rimer, and S. M. Day (2003), The physical basis of Lg generation by explosion sources, in *Proceedings of the 25th Seismic Research Review–Nuclear Explosion Monitoring: Building the Knowledge Base*, LA-UR-03-6029, Vol. 2, pp. 456–465.

REGIONAL MAGNITUDE RESEARCH SUPPORTING BROAD-AREA MONITORING OF SMALL SEISMIC EVENTS

Howard J. Patton and W. Scott Phillips
Los Alamos National Laboratory

Sponsored by National Nuclear Security Administration
Office of Nonproliferation Research and Development
Office of Defense Nuclear Nonproliferation

Contract No. W-7405-ENG-36

ABSTRACT

The Nuclear Explosion Monitoring Research and Engineering (NEM R&E) Program has a long-standing magnitude research project in support of regional yield estimation and seismic discrimination. This project has developed magnitude-yield scaling relationships based on regional *P, S* phases and coda waves to improve the capabilities to monitor nuclear explosions over broad areas and at low yields. Due to the great variability of regional seismograms, the methods developed for broad-area monitoring must be adaptable to different phases and frequency bands. These requirements, along with an understanding of the transportability of scaling relationships, pose significant challenges, both in practice and theoretically, since any broad-area method needs a sound physical basis to be ultimately successful.

We continue to study multi-frequency scaling observations of *Pn* and *Lg*-coda waves for explosions detonated at the Nevada (NTS) and Semipalatinsk (STS) test sites. Observations for both test sites show that *Pn* amplitudes scale with yield ~10-40% higher than coda amplitudes for frequencies between 2-8 Hz. For NTS explosions, the contrast in scaling is even greater (as much as 50-60%) for frequencies < 2 Hz, except for the lowest frequency band analyzed, 0.3-0.5 Hz, where scaling differences are not significant. On the other hand, *Pn* and coda amplitudes for STS explosions do not scale differently for any band < 2 Hz. These observations have implications for yield estimation and seismic discrimination, among them being that high-frequency phase ratios should display yield dependence.

An analytical source model for explosions generating *S* waves is under development in order to study the physical basis for scaling differences between *P* and *S* waves. The model has three essential elements: (1) a monopole source characterized by emplacement depth, source function, and yield, (2) a shallow conical source of tensile failure described by a compensated linear vector dipole (CLVD) and spallation-like source function, and (3) seismic scattering off topography and structural heterogeneities in the source region. We test the importance of near-source *Rg*-to-*S* scattering with this model. The model predicts that the excitation of high-frequency *Rg* waves is much greater for the CLVD compared to the monopole due mainly to differences in centroid depths. This prediction raises the interesting possibility that high-frequency *P* and *S* waves scale differently because under the Rg→S scattering scenario, *S* wave generation is mediated by the excitation of *Rg* waves from the CLVD, while *P* waves are excited directly by the monopole source. Our preliminary model calculations of this scenario do indeed show scaling differences consistent with the observations at high frequencies.

We are also exploring observational evidence of coupling differences between *P* and *Lg*-coda waves related to depth of burial (DOB), since such evidence provides clues about the physical basis of coda (*S*) generation and has implications for yield estimation. The well-known effect of overburden on cavity radius reduces seismic amplitudes for overburied explosions. As DOB decreases from overburied to more normal scaled depths of burial (sDOB), ~150 m/kt$^{1/3}$, amplitudes increase to a broad plateau. If sDOB continues to decrease below ~100 m/kt$^{1/3}$ the competing effects of confinement begin to dominate over the overburden effects with the opposite result, reducing seismic amplitudes as more and more energy is lost to severe spallation, cratering, and to the atmosphere. We are attempting to identify differences in the coupling of *P* and *Lg*-coda waves for small sDOB. Our methods must account for the effects of material properties on amplitudes of *P* and *Lg*-coda waves since such effects depend on depth too.

OBJECTIVE

We seek to improve yield estimation and seismic discrimination capabilities for broad areas and small events through the development of regional magnitude methodologies and data sets of direct phases and coda waves. Our research advances the state of the art in nuclear monitoring through (1) characterization of the scaling behavior and transportability of regional magnitudes based on path-corrected amplitudes using advanced calibration techniques and (2) development of physical models to interpret the observations and to lay a physical basis supporting operational techniques.

RESEARCH ACCOMPLISHED

In recent years we have witnessed exciting technical advances with great promise for increasing the precision of seismic yield estimates and extending M_s-m_b discrimination to small magnitudes through the use of amplitudes measured off regional seismograms. With these advances has come an extraordinary change in the measurements seismologists rely upon to do monitoring. They are now often based on the amplitudes of shear phases (*Lg*, *Sn*) and codas following these phases, and to a lesser degree on the compressional phases that explosions excite with great efficiency. This is because shear phases are usually the largest on regional seismograms and hence are the best recorded as source sizes decrease and noise levels increase, an important consideration for the ability to do low-yield monitoring. The reliance upon regional shear phases represents a major paradigm change from the way seismologists monitor nuclear explosions at teleseismic distances, and this change is a driver for much new, innovative research in our community today.

In order to address the challenges confronted by monitoring small events in broad areas, a significant component of this project's research is directed at characterizing the scaling behavior of regional magnitudes over a broad yield range and in different frequency bands. In the process, we are forming an observational basis from which to draw new insights for improving yield estimation and extending M_s-m_b to smaller magnitudes. Equally important is the need to develop a physical model for shear-wave generation by underground explosions and to lay a theoretical foundation supporting the empirical methods in operational use. We believe that both components, empirical characterization of scaling behavior and development of a physical basis, are essential for the success of new, improved methods for broad-area monitoring at small yields.

The ability to estimate yields and discriminate seismic events especially at small magnitudes depends in large part on understanding the energy partitioning between *P* and *S* phases and the manner in which the phases scale with yield or source size. Another important consideration is the portability of seismic measurements across broad areas. Scatter between areas could be a sign that path effects are not being adequately corrected for in our measurements and/or it could be a sign of intrinsic source effects. This is one reason that so much research has been invested in the calibration of regional path effects and the development of tomographic models for 1- and 2-D path corrections. In many areas of monitoring concern, these models are mature to the point that we are confident the path effects are effectively removed. We believed this is true for the corrected amplitudes used to measure magnitudes in this study.

Much effort has been spent developing methodologies to estimate regional magnitudes and building magnitude databases of historic explosions in Asia, as well as at NTS where so much ground truth information is available. Over the years, our efforts, joint with Livermore's, have investigated coda amplitudes of *Lg* and *Sn* waves, tied to seismic moment through an innovative calibration method (Mayeda and Walter, 1996); the results of this method have shown great promise. The corrected coda measurements are referred to as "apparent coda source amplitudes" (ACSA) with units of Newton-meters (Nm), and they are measured through a bank of narrowband filters with set bandwidths. The most extensively-studied bands to date are 0.3-0.5, 0.5-0.7, 0.7-1.0, 1.0-1.5, 1.5-2.0, 2.0-3.0, 3.0-4.0, 4.0-6.0, and 6.0-8.0 Hz.

A remarkable finding discovered early in our studies is the fact that *Lg* and *Sn* 1.0-1.5 ACSA yield scale differently compared to teleseismic m_b(*P*). Apparently, teleseismic 1-Hz *P* wave amplitudes yield scale ~15% faster than shear-based coda-wave amplitudes. Similar differences were noticed in m_b(*Lg*) and m_b(*Pn*) observations of NTS explosions for the traditional 1-Hz short-period passband of the World-Wide Standard Seismographic Network response (Patton, 2000). At the 2005 Seismic Research Review (SRR) meeting, Patton and Phillips (2005) documented the differences in scaling between *Pn*- and *Lg*-coda amplitudes for a range of frequencies and for NTS and STS. Further work this

year has served to validate the method we used to detect these scaling differences. Below we present the scaling results, and discuss the initial work developing a new explosion source model that may provide a physical basis for differences in the scaling and new insights into *S* wave generation by underground explosions.

Observations of Pn, Lg-Coda scaling differences. The interested reader is referred to our extended abstract from last year's SRR meeting for background on the relative-scaling analysis that we use to detect differences in the scaling of *Pn*- and *Lg*-coda waves. Briefly, relative scaling slopes were estimated using two methodologies summarized in the following equation:

$$slope = (\Delta \log A_{Pn}) / (\Delta \log A_{LgC}) \cong \left(\frac{\Delta \log A_{Pn}}{\Delta \log W}\right) / \left(\frac{\Delta \log A_{LgC}}{\Delta \log W}\right),$$

where A_{Pn} and A_{LgC} are amplitudes of *Pn*- and *Lg*-coda waves passed through identical narrowband filters, W is yield, and base-10 logarithms are used. The first method determines the scaling slope on log-log plots of A_{LgC} versus A_{Pn} for a common station and for many explosions spanning several orders of magnitude in yield. If the explosions are located in small test areas, the path effects on A_{Pn} and A_{LgC} to a given station should be the same. This method was applied to both NTS and STS explosions. If ground-truth information on yields and emplacement conditions are available, amplitude-yield regressions can be performed, estimates of the yield coefficient for *Pn*- and *Lg*-coda waves determined, and the relative yield scaling calculated by taking the ratio. This second method was applied to NTS explosions to validate the results from the first method. The results from method 1 do not necessarily have to equal the ratio of yield coefficients if other excitation factors come into play such as the effects of depth burial alluded to in the abstract and discussed in our 2005 SRR paper. In carrying out the yield regressions, the effect of gas porosity was accounted for, and for both methods, overburied explosions were avoided.

All amplitudes were subjected to signal-to-noise checks. It should be noted that the signal-to-noise ratios for *Lg*-coda waves decrease rapidly above ~6 Hz for recordings off the Livermore NTS Network. Nevertheless, it is clear that the codas are those of *Lg* waves for all bands, as *Sn* is not as well recorded on this network compared to *Lg*. On the other hand, *Lg* amplitudes recorded at Borovoye for STS explosions can drop below the level of *Sn*-coda waves for frequency bands above the 2-3 Hz passband. Thus, even though many recordings of the Borovoye archive (Kim et al., 2001) are well above the noise levels at high frequencies, our measurement windows contain a superposition of *Sn* and *Lg* codas, where *Lg* codas appear more important for frequencies below the 2-3 Hz passband, while *Sn* codas may dominate the higher frequency bands.

Figure 1 is a summary of scaling results for NTS explosions. The results from method 1 are shown with open symbols, and those involving yield regressions (method 2) with solid symbols. The various frequency passbands are denoted with horizontal lines on the abscissa. The results for both methods are in reasonably good agreement for stations Elko and Kanab. Both stations have similar frequency dependence, showing rapid change at low frequencies, going from no scaling differences in the lowest band to 50-60% faster scaling for *Pn* relative to *Lg* coda in the next band, 0.5-0.7 Hz. The differences lessen for the traditional bands between 1 and 2 Hz. Above 2 Hz, there is a suggestion that the differences increase again, but discrepancies between stations (3-4 Hz band) and between methods (6-8 Hz band) make such a determination difficult. With the exception of the lowest band, the results of all bands indicate that *Pn* amplitudes scale at a higher rate than *Lg* coda amplitudes, and the close agreement between results of both methods strengthen the reliability of these findings.

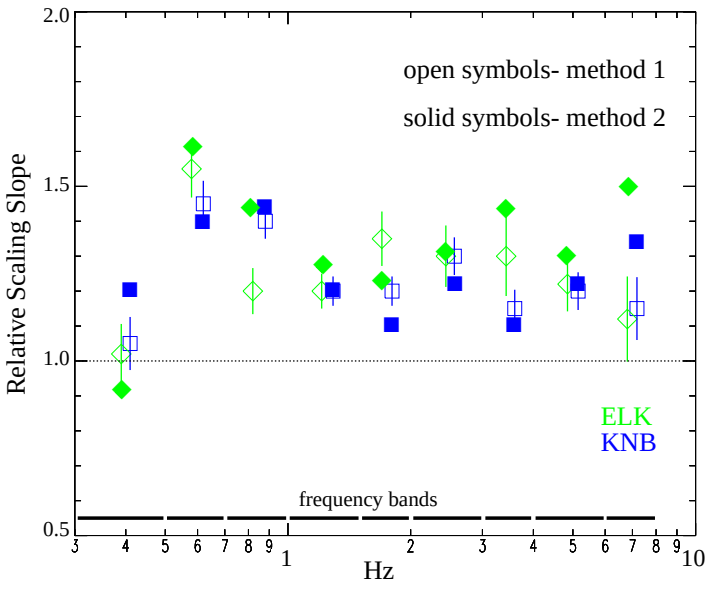


Figure 1. Relative scaling slope results for NTS explosions.

NTS results were based on just explosions detonated on Yucca Flats. Our analysis of STS explosions drew on explosions from Balapan and Degelen Mountain test areas, as data from both test areas were necessary in order to provide adequate sampling over a broad enough yield range to ensure that slopes were well determined using method 1. Paths to Borovoye are similar enough between the two test areas that we believe the common path assumption still holds. However, these test areas are geophysically distinct and that raises the possibility that energy partitioning differences could bias the slopes since explosions conducted in the Degelen tunnels tend to be smaller than explosions fired in shafts at Balapan. Thus, to address these concerns and the possibility that there could be some path differences, the data from each test area were made zero-mean before the data sets were combined for regression analysis. Zero-mean data sets decouple the slope determination from a systematic offset that may pre-exist between the test sites.

Relative scaling slopes from zero-mean regressions on combined data sets are plotted in Fig. 2, along with the NTS results (blue shaded region). The frequency dependence of STS results show marked contrast to NTS, particularly at low frequencies below 1.5 Hz where scaling differences are negligible. The most stable results are found for the 2-3 Hz band. A perusal of Fig.1 reveals that the shaded region greatly exaggerates the spread in the observations for this band, and the stability/agreement of 2-3 Hz results is excellent for both test sites. Interestingly, the trend in STS results changes abruptly above the 2-3 Hz band. This might be related to the fact noted above that *Lg* drops below the amplitude level of *Sn* coda in the higher frequency bands, so *Sn* might control the scaling, while the lower bands are controlled by *Lg*. In any case, both *Sn* and *Lg* codas are shear-dominated and both show lower scaling relative to *Pn* waves at high frequencies for NTS and STS explosions.

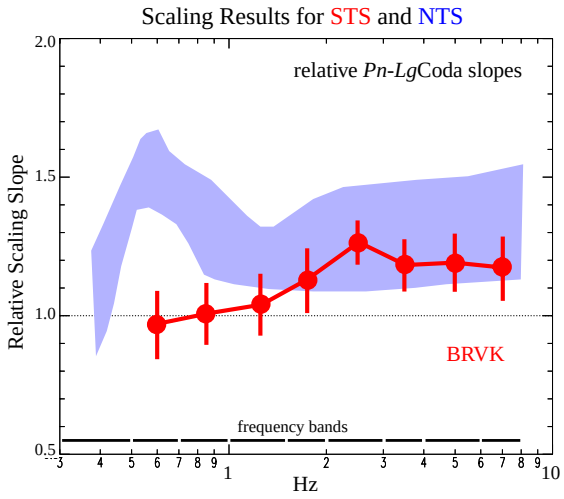


Figure 2. Relative scaling slopes for NTS (methods 1 and 2; shaded area) and for STS (method 1).

The observations in Fig. 2 are of fundamental importance, not just for the implications related to yield estimation and seismic discrimination, but also for the potential information about the mechanisms of S wave generation. For this reason, we are continuing work to improve these scaling observations by adding new measurements. Analysis of new STS measurements will be done with hopes of placing better control on the high-frequency scaling observations. Another team of researchers led by J. Murphy has failed to detect significant differences in the scaling at high frequencies for STS explosions using an approach similar to method 2 but employing amplitude ratios instead of straight amplitudes. Since similar data sets were used by both teams, this suggests the cause of differences in our results and Murphy's might be methodological.

In the case of NTS explosions, both methods gave similar results, and both show significant differences in the scaling of *P* and *S* waves, *P* waves scaling ~30% higher on average. In light of the good agreement for the 2-3 Hz band and the apparent differences at low frequencies between the test sites (here Murphy's STS results and ours agree), an effort to interpret the higher frequency observations in terms of a new source model has been initiated. Simple extensions of existing source models are not adequate for this purpose. For example, the Fisk conjecture (Fisk, 2006) that *S* wave spectra may be modelled with the same functional form as *P* wave spectra predicted by the Mueller-Murphy (MM) model is not consistent with the high-frequency observations in Figs. 1 and 2. This year we started development of a next generation analytical model in the mold of MM but incorporating more phenomenology. In particular, secondary sources exist to some degree on virtually every explosion owing to strong interactions of the stress waves with the free surface. Even the most overburied NTS explosions spall, and a chemical explosion at STS with sDOB of ~1400 m/kt$^{1/3}$ was documented to have spalled (Patton et al., 2005). Thus the new model builds on the MM model incorporating free surface phenomenology and new insights into the near-source scattering of *Rg* waves. The following subsection summarizes the progress made to date on a new analytical explosion source model to support further development of regional seismic discrimination and yield estimation technologies.

Explosion source model. Three essential elements of the source model are: (1) the explosion, modelled as a monopole source and characterized by emplacement depth h_x, moment source spectrum $M_x(\omega,W)$, and W, (2) non-linear free surface interactions resulting in a shallow conical source of tensile failure which spallation is a part of and is kinematically described by a CLVD with centroid depth h_{clvd} and source spectrum $M_{clvd}(\omega,W)$, and (3) near-source scattering of P, $Rg \rightarrow S$, P waves off topography and material heterogeneities (faults, basins, etc). The combined source is assumed to be a linear superposition of monopole and CLVD point sources and is axisymmetric. M_x is related to the reduced displacement potential $\Psi(\omega,W)$; we have used the RDP development of Denny and Johnson (1991) throughout this study. M_{clvd} is related to particle displacements on/within the conical source volume. We have adopted a variant of the spall time histories developed by Stump (1985) to provide an analytical expression for this source spectrum. The moment rate spectrum falls off as ω^{-3} (as opposed to ω^{-2} for the explosion) and has no net moment (i.e., ω slope at low frequencies). Thus no residual particle displacement is associated with the CLVD. This is an assumption, although we have evidence to believe that it is indeed the case for NTS explosions, while studies of chemical explosions at STS come to the opposite conclusion (Patton et al., 2005). The fact that explosions in hard rock media are characterized by residual displacements while explosions in weak rock are not suggests that shear-dilatancy may play a role in the free-surface interactions in hard-rock media.

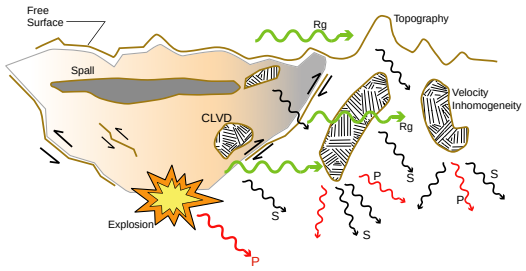


Figure 3. A cartoon depicting the essential elements of a new explosion source model. Two sources, the explosion plus a CLVD representing a conical zone of extensional deformations, excites *P*, *S*, and *Rg* waves. High-frequency *Rg* waves propagate near the Earth's surface and scatter mainly into *S* waves off topography and material heterogeneities in the source region.

Nearfield scattering is assumed to be dominated by $Rg \rightarrow S$, and at this stage the model ignores contributions from $Rg \rightarrow P$ and $P \rightarrow S$ scattering. Furthermore, P and S waves excited directly by the CLVD are ignored, which might be justified for P by cancellation with a depth phase (pP) and relatively large P waves from the explosion, and for S by radiation pattern effects. The details of these assumptions have yet to be verified, but for purposes of initial model development, Rg waves are the sole mediator of S wave generation, while the only source of P waves is the explosion.

If all explosions occur in a localized test area where the scattering transfer function is in common, then the relative scaling slope can be related to spectral quantities of the model,

$$(\Delta \log A_{Pn}) / (\Delta \log A_{LgC}) \cong \left(\frac{\Delta \log A_{Pn}}{\Delta \log W}\right) / \left(\frac{\Delta \log A_{LgC}}{\Delta \log W}\right) = \left(\frac{\Delta \log |\Psi(\omega, W)|}{\Delta \log W}\right) / \left(\frac{\Delta \log |A_{Rg}(\omega, W)|}{\Delta \log W}\right),$$

where $|A_{Rg}(\omega,W)|$ is the Rg amplitude spectrum of the composite source. Thus linear scattering is invoked and the shape and indeed the scaling of the Rg spectrum are imprinted onto the scattered S waves. This is a fundamental tenet of the model, and is motivated by the results of Patton and Taylor (1995). Based on the model outlined in the paragraphs above, an expression for A_{Rg} is

$$A_{Rg}(\omega, W) = M_x(\omega, W) \cdot G_{Rgx}(\omega, h_x(W)) + M_{clvd}(\omega, W) \cdot G_{Rgclvd}(\omega, h_{clvd}(W)) \cdot e^{i\omega t_s},$$

where the yield dependence of the spectral Rg Green's functions G_{Rgx} and G_{Rgclvd} enters through the source depth scaling, and the origin of CLVD source is delayed t_s seconds since the stress wave must propagate to and reflect off the free surface before tensile failure can occur (e.g., $t_s = (h_x + h_{clvd})/\alpha$, where α is the P wave speed). We have chosen to use analytical expressions for Rg Green's functions in a halfspace to start with to keep the model strictly analytical. This allows for simplified analysis of the high frequency scaling in the next subsection. But first, we discuss key source parameters of the CLVD and revisit spectral ratio modeling of Patton and Taylor (1995).

CLVD source parameter scaling. Three key source parameters are (1) the source process time T, (2) the relative source strength Φ_o / M_x, where Φ_o is the "zero-frequency" strength of the CLVD source and M_x the scalar moment of the explosion, and (3) the centroid depth h_{clvd}. In our model T is identified with the duration of a source located just beneath the spall-parting depth where ground motions are in a state of "incipient spall"; this state is modelled by Stump's time histories when the rise time and dwell time are set equal. Thus h_{clvd} corresponds to the deepest extent of

spall. Yield scaling relationships for these source parameters must be developed, and this is work in progress. To date, we have drawn upon published information related to close-in ground-motion measurements of spall. We have found the best constraints are on the scaling relationships for T and h_{clvd}.

The relative source strength Φ_o/M_x can be estimated from modeling *Lg* spectral ratios as in Patton and Taylor. It has come to our attention that the Rayleigh wave source phase was violated by models in the 1995 study because the estimates of Φ_o/M_x are too large and the CLVD source, which looks like an impulse at long periods, perturbs the phase. Long-period observations on typical NTS explosions are consistent with a step function of the monopole source, not an impulse. The new modeling results discussed below do not violate the long-period phase owing to smaller estimates of Φ_o/M_x. Importantly, these revisions have led to a new interpretation of the spectral null in the *Lg* spectral ratios identified by Patton and Taylor. The revised model suggests that the null is caused by interference between *Rg* waves emitted by the CLVD and monopole sources, not by an *Rg* excitation null related to the CLVD source depth.

Network-averaged *Lg* spectral ratios for BASEBALL/BORREGO modelled in Patton and Taylor are plotted in Fig. 4a along with a prediction based on the source model developed herein. This prediction was computed by taking the amplitude ratio of *Rg* spectra plotted in Fig. 4b under the assumption that the *Rg* spectrum is imprinted on the scattered *S* waves making up *Lg* at regional distances. I have used "order-of-magnitude" yields 100 and 1 kt for this generic calculation. Located within 1 km of BASEBALL at the same emplacement depth, the overburied explosion BORREGO serves as an empirical Green's function source. BORREGO's source effects are dominated by the monopole at low frequencies due to a much-reduced relative source strength Φ_o/M_x. Indeed, based on displacements measured over ground-zero on BASEBALL and BORREGO and on estimates of the CLVD source dimensions, the relative source strength is roughly a factor of 50 less than BASEBALL's.

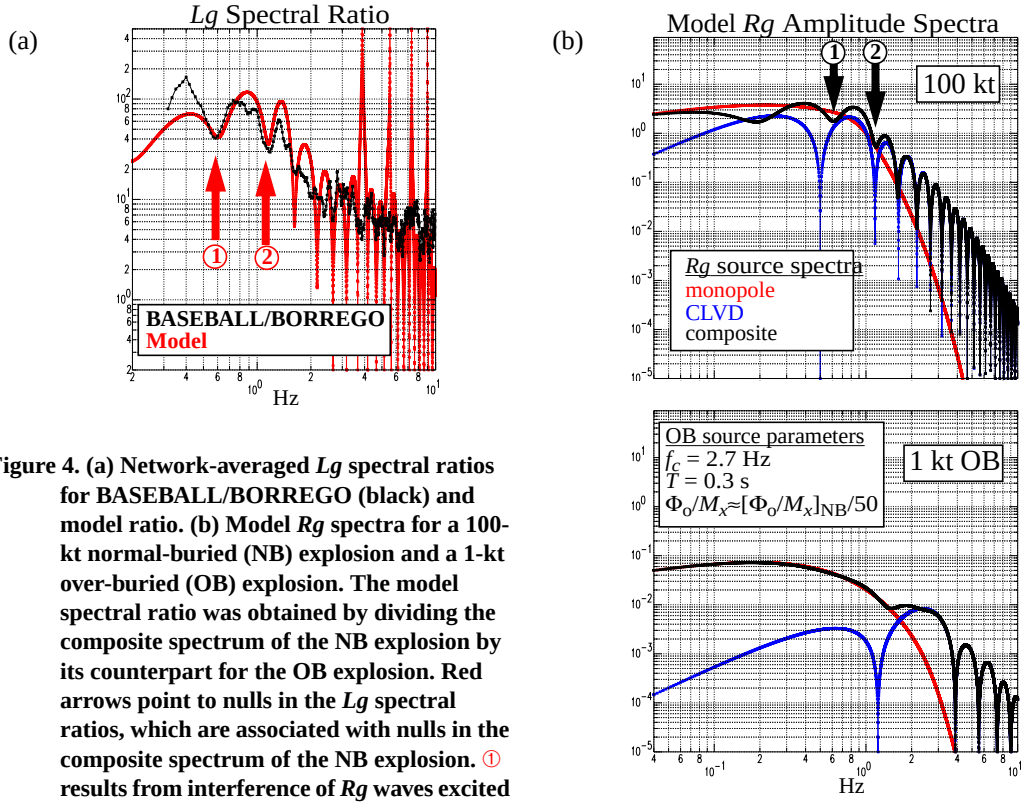


Figure 4. (a) Network-averaged *Lg* spectral ratios for BASEBALL/BORREGO (black) and model ratio. (b) Model *Rg* spectra for a 100-kt normal-buried (NB) explosion and a 1-kt over-buried (OB) explosion. The model spectral ratio was obtained by dividing the composite spectrum of the NB explosion by its counterpart for the OB explosion. Red arrows point to nulls in the *Lg* spectral ratios, which are associated with nulls in the composite spectrum of the NB explosion. ① results from interference of *Rg* waves excited by monopole and CLVD sources and ② is the lowest frequency null in the spectrum of the CLVD time function.

Scaling relations for corner frequency f_c and M_x for normal-buried explosions were taken from Denny and Johnson (1991). For a 100 kt explosion, f_c equals 0.91 Hz. The moment scaling has no impact on our estimate of Φ_o/M_x for

BASEBALL, and was used for the sole purpose of scaling unit-moment spectra A_{Rg}/M_x upward for a 100 kt explosion in order to calculate the model spectral ratios. Thus the first term in the expression for A_{Rg}/M_x (see equation for A_{Rg}) is completely specified for BASEBALL and utilizing scaling relationships for T and h_{clvd}, the second term can be specified to within a constant (Φ_o/M_x). We are able to model the first spectral null in the *Lg* spectral ratio (see Fig. 4a) without violating the long-period phase with Φ_o/M_x set equal to 0.17 s. The second spectral null is also modeled well because the lowest frequency notch in the spectrum of the CLVD time function occurs very close to 1.1 Hz.

A remarkable feature of the composite spectrum for the 100-kt explosion is that the high frequencies are controlled by the CLVD in spite of the fact that the source spectrum rolls off faster than the monopole source spectrum (ω^{-3} versus ω^{-2} for moment-rate spectra). This result is a consequence of (a) differences in the *Rg* Green's function response for the respective sources and (b) the centroid depth of the CLVD being shallower than the monopole's. The net effect of the Green's functions more than compensates for the differences in the spectral roll-offs. This feature is true for the over-buried explosion as well, and appears to be a robust characteristic of *Rg* excitation in this source model. This prediction raises the interesting possibility that high-frequency *P* and *S* waves scale differently because *S* wave generation is mediated by *Rg* waves from just the CLVD source, while *P* waves are excited directly by the explosion.

To explore this possibility, we can write simple expressions for the high frequency scaling slopes of *P* and *S* waves using our analytical source model. For *P* waves, yield slope *YS*(*P*) is

$$YS(P) = a + m \cdot b \quad ,$$

where a is the yield exponent on M_x scaling, m is the high frequency roll-off, and b is the yield exponent on corner frequency scaling. The results of Denny and Johnson (1991) for normal-buried explosions give $a \approx 0.85$, $b \approx -0.15$, and $m = 2$, or $YS(P) \approx 0.55$. For *S* waves mediated by the excitation of *Rg* waves, the yield slope *YS*(*S*) involves the CLVD source function and a high-frequency asymptotic expression for G_{Rgclvd},

$$YS(S) = a + \kappa + n \cdot b' - \omega \cdot \hat{\eta}_\beta \cdot h_{clvd} \cdot c \quad ,$$

where κ is the yield exponent on Φ_o/M_x scaling, n is the high frequency roll-off, b' is the yield exponent on corner frequency, $\hat{\eta}_\beta$ is a slowness parameter, and c is the yield exponent on h_{clvd} scaling. The first three terms are completely analogous to *YS*(*P*) since the sum of exponents a and κ is nothing more than the yield exponent on Φ_o scaling. The last term is contributed from *Rg* excitation and introduces frequency and yield dependences. Using the scaling relationship for h_{clvd} and 2×10^{-4} s/m for $\hat{\eta}_\beta$, the last term can be written $-3\times10^{-2} \cdot W^{1/3} \cdot f$, where f is frequency in Hz and $W^{1/3}$ comes from the h_{clvd} scaling relation. b' equals the exponent on $1/T$, or -0.1, and $n = 4$ in the case of Rayleigh wave excitation. At this stage is our research, our best estimate of κ is ~0.2-0.3 based on self-similarity analysis of synthetic *Rg* spectra, like the analysis Jones and Taylor (1996) performed on *Lg* spectra for NTS explosions. Summarizing, for frequencies >3 Hz and for yields distributed around 10 kt, *YS*(*S*) is bounded from above,

$$YS(S) < 0.85 + 0.25 + 4 \cdot (-0.1) - 3\times10^{-2} \cdot 10^{1/3} \cdot 3 \approx 0.5 \quad .$$

The model predicts the yield scaling slope of *S* waves *YS*(*S*) is less than 0.5 at high frequencies and thus smaller than the *P* scaling slope *YS*(*P*), consistent with the observations we reported on earlier in this paper.

CONCLUSIONS AND RECOMMENDATIONS

The NEM R&E magnitude research project is focused on improving yield estimation and seismic discrimination capabilities for broad areas and small events through the development of regional magnitude methodologies and data sets of direct seismic phases and coda waves. A significant component of the research empirically characterizes the yield scaling behavior of regional magnitudes in different frequency bands under a variety of underground testing environments, both in terms of containment and geology. Equally important is the development of physical models for shear-wave generation by underground explosions to lay a theoretical foundation supporting the empirical methods in operational use. We believe that both components, empirical characterization of scaling behavior and development of a physical basis, are essential for the success of new, improved methods for broad-area monitoring at

small yields. We have summarized some research results from the past year in this paper, and are excited by the prospects of coda-based methodologies in operational use. At the same time, there are many open questions about the operational performance of coda-wave techniques, and full confidence to monitor broad areas effectively will only come with continued research on both empirical and theoretical fronts.

REFERENCES

Denny, M. D. and L. R. Johnson (1991). The explosion seismic source function: models and scaling laws reviewed, in *Explosion Source Phenomenology, Am. Geophys. Monograph* 65: 1–24.

Fisk, M. D. (2006). Source spectral modeling of regional *P/S* discriminants at nuclear test sites in China and the Former Soviet Union, *Bull. Seism. Soc. Am.* 96: in press.

Jones, E. M. and S. R. Taylor (1996). Are *Lg* spectra from NTS explosions self-similar? *Bull. Seism. Soc. Am.* 86: 445–456.

Kim, W.-Y., P. G. Richards, V. Adushkin, and V. Ovtchinnikov (2001). Borovoye digital archive for underground nuclear tests during 1966–1996, Data report on the web at http://www.ldeo.columbia.edu/res/pi/Monitoring/Data/brv_exp_archive.html, Borovoye Archive for UNT (information product in PDF).

Mayeda, K. and W. R. Walter (1996). Moment, energy, stress drop, and source spectra of western United States earthquakes from regional coda envelopes, *J. Geophys. Res*. 101: 11,195–11,208.

Patton, H. J. (2000). M_S:m_b relationships for small magnitude events: Observations and physical basis for m_b based on regional phases, in *Proceedings of the 22nd Seismic Research Review: Planning for Verification of and Compliance with the Comprehensive Nuclear-Test-Ban Treaty (CTBT)*, LA-UR-00-2436, Vol. 2, pp. 293.

Patton, H. J. and S. R. Taylor (1995). Analysis of *Lg* spectral ratios from NTS explosions: implications for the source mechanism of spall and the generation of *Lg* waves, *Bull. Seism. Soc. Am.* 85: 220-236.

Patton, H. J., J. L. Bonner, and I. N. Gupta (2005). *Rg* excitation by underground explosions: insights from source modelling the 1997 Kazakhstan depth-of-burial experiment, *Geophys. J. Int*. 163: 1006-1024.

Patton, H. J. and W. S. Phillips (2005). Regional magnitude research supporting broad-area monitoring of small seismic events, in *Proceedings of the 27th Seismic Research Review: Ground-based Nuclear Explosion Monitoring Technologies*, LA-UR-05-6407, Vol. 1, pp. 606.

Stump, B. W. (1985). Constraints on explosive sources with spall from near-source waveforms, *Bull. Seism. Soc. Am.* 76: 361-377.

REGIONAL EVENT IDENTIFICATION RESEARCH IN ASIA

George Randall[1], Xiaoning (David) Yang[1], Hans Hartse[1], Monica Maceira[1], Marie Arrowsmith[1], and Steven Taylor[1,2]

Los Alamos National Laboratory[1] and Rocky Mountain Geophysics, LLC[2]

Sponsored by National Nuclear Security Administration
Office of Nonproliferation Research and Development
Office of Defense Nuclear Nonproliferation

Contract Nos. W-7405-ENG-36[1] and DE-AC52-06NA25396[2]

ABSTRACT

We present results of new and ongoing studies of regional-event identification in Asia, emphasizing accurate identification, with a clear physical basis and a sound statistical framework having proper uncertainty estimates for clear reporting to decision makers with either non-technical or scientific background.

To expand our ongoing event identification research we have been acquiring ground-truth mining event data sets from eastern Kazakhstan. From Kazakh National Data Center (KNDC) bulletins we have observed that many small events occur during local daytime. Through cross-correlations, we have grouped many near-regional waveforms associated with these daytime events into individual clusters, and we are in the process of tying these event clusters to satellite images of open-pit mines. For event identification our goal is to use these mining events to test traditional P/S discriminants and explore coda-based and other discriminants.

We validated a method that uses the probability of detection model (PXD) to estimate the probability that a surface wave detection came from an underground explosion. We gathered and analyzed signals from a set of more than 1,000 earthquakes and explosions in Eurasia recorded at the Urumqi (Wulumuchi) seismic station (WMQ). The results of the signal detection formulation using short period Rayleigh waves in the bandwidth 6–12 s show an improvement over the traditional m_b-M_s discriminant. False alarm rates are reduced from 22% for m_b-M_s to 15% using the probability of detection model for the mentioned data set. We also measured multi-frequency surface wave magnitudes Ms for the same dataset using the methodologies of Marshall and Basham (1972) and Russell (2004). Five frequency bands with center periods of 20, 16, 12, 10, and ~7 s were chosen, and the final M_s corresponds to the band giving the largest M_s or the largest amplitude. We found out that using the Ms computed in this way, the amount of false alarms decreases and the PXD method is not needed.

In parallel to a project between University of California, Santa Cruz (UCSC) and Los Alamos National Laboratory (LANL) to develop 1-Hz, two-dimensional (2D) regional-phase attenuation models for Eurasia to improve the magnitude and distance amplitude correction (MDAC) discrimination methodology, we are working on developing regional-phase attenuation models for Eurasia for a broad range of frequencies between 0.5 and 10 Hz. We have finished an initial phase of data collection and amplitude measurement for around 100 stations in the region. Analysis of the measurements indicates that further data collection, phase picking and amplitude measurements are required especially for certain areas in the region. We have also conducted synthetic simulations to investigate the geometric spreading of Pn phase in a spherical earth. Preliminary results indicate that the sphericity of the earth has a controlling effect on Pn geometric spreading. A new, frequency dependent model is required to adequately represent the realistic Pn geometric spreading.

OBJECTIVES

We have carried out studies to collect ground truth for Kakakh mining seismicity, regional MS discrimination and regional Pn spreading and attenuation tomography. The results of these efforts are all directed toward improved discrimination between earthquakes and explosions with regional seismic data.

RESEARCH ACCOMPLISHED

Kazakh Mining Ground Truth Study

We have been expanding our seismic ground truth data collection efforts for central Asia by identifying mines and mining explosion seismograms. Working with the KNDC bulletins (2002–2005), waveform cross correlation and clustering methods, and satellite imagery we have been studying the area between array MKAR and station Kurchatov Auxiliary Seismic Station (KURK) in eastern Kazakhstan. Most of the events within this area occur during daytime (Figure 1), are usually small (recorded at only 2 or 3 stations or arrays), and therefore tend to be poorly located. Our objective is to identify active mines and use the seismograms associated with those mines to test discriminants and develop better event location correction surfaces. To date we have identified three clusters of similar waveforms representing about 200 events. With our new event set we plan to test regional P/S discriminants and explore coda-based and other discriminants.

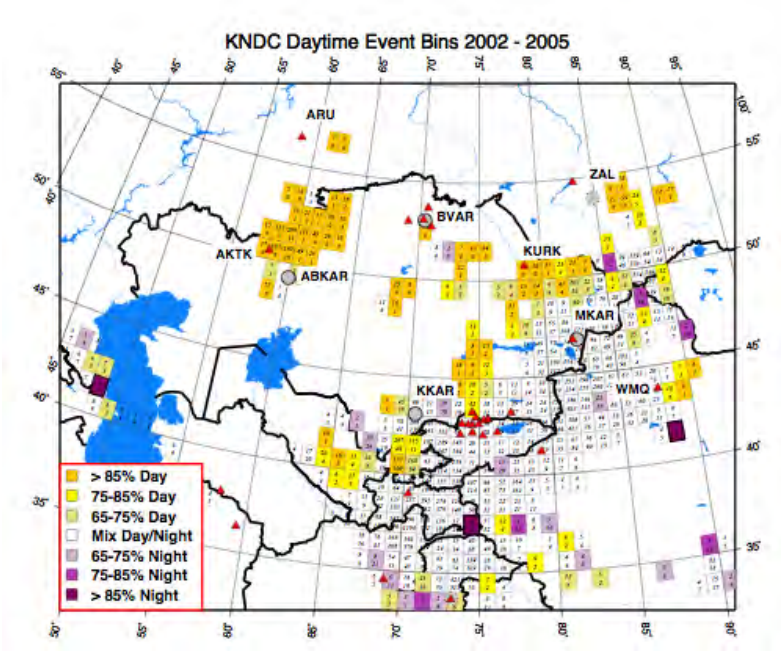


Figure 1. Time of day event map for Kazakhstan based on KNDC bulletins from 2002–2005. Gold and yellow areas are dominated by daytime events, which we presume to primarily be mining explosions. Our study area is currently focused between array MKAR and station KURK.

Regional Ms Discrimination

Taylor and Patton (2006) presented an alternative to the traditional M_s:m_b discriminant. They developed an innovative technique using a PXD to estimate the probability that a detected surface wave came from an underground explosion. In the following we validate their method and present some findings about it. We also test a new methodology to obtain amplitude and M_s magnitude measurements and show that Russell's formula (2004) to compute M_s magnitudes is more efficient for seismic discrimination problems. With this new methodology seismologists working on seismic discrimination problems can be certain to measure the maximum peak-to-peak

Rayleigh wave amplitude and not the amplitude of any other phase arriving in the same time window. Also the finding about the efficiency of Russell's formulation is of great importance to tackle seismic discrimination problems because Russell's formula (2004) is simple and can be applicable to different bandwidths avoiding when possible the more complicated and noisy waveforms that dominate the shorter periods.

A Probability of Detection Method Validation

In their paper, Taylor and Patton (2006) describe the PXD used to quantify the probability that, at a given significance level, the signal came from a nuclear explosion based on probability of detection models using only the amplitude of the recorded signal and noise. They computed this conditional probability using a p-value formulation (Anderson et al., 2004). No additional assumptions are necessary for the signal from the alternative source (earthquake) other than its maximum amplitudes are expected to be larger than those of the explosion for a given m_b magnitude. Therefore, the detection classifier is applicable when there is a signal detection (A_0) above a specified signal-to-noise ratio (N_0) and the detection is of greater amplitude than the maximum expected explosion amplitude (A_x^a). The computed p-values range from 0 to 1. When near zero, the p-value indicates a low probability that the detected signal originated from an explosion. Meanwhile a large to moderate value indicates consistency with explosion characteristics.

To validate the PXD method of Taylor and Patton (2006), we measured noise and signal levels of over 1,300 earthquakes and 26 underground explosions recorded at the broadband, digital station WMQ in western China. We requested all the events recorded at station WMQ between 1997 and 2001 which occurred in the region between 29° and 54° N and 69° and 108° E, and with a United States Geological Survey (USGS) preliminary determination of epicenters (PDE) catalog m_b. With these criteria, we retrieved waveforms from more than 1,300 earthquakes with epicentral distances between 224 and 2,300 km, and with m_b magnitudes ranging between 3.0 and 6.2. Twenty-six nuclear explosions from the former Soviet Union test site in Kazakhstan (KTS) were also recorded at WMQ between 1987 and 1989. Their magnitudes range between 4.6 and 6.1, and the maximum event-station distance is 1,007 km.

For consistency with the PXD application shown in Taylor and Patton (2006), we followed the event processing described in Hartse et al. (1997). We first removed the instrument response and decimated the seismograms to 1 sample/s. We removed the signal mean and applied a short (~5%) Hanning window taper. Since we are interested in evaluating the PXD performance at short-periods, we bandpassed the seismograms between 6 and 12 s period. We defined the measurement window following the velocity table used for data processing from Hartse et al (1997). For Rayleigh waves, they used a minimum velocity of 2.20 km/s and a maximum velocity of 3.15 km/s to constrain the measurement window. The noise window starts at the beginning of the bandpass filtered trace until a time that is based on a velocity value of 9 km/s. For each data window, we measured the maximum peak-to-peak amplitude and the signal-to-noise ratio. These peak-to-peak amplitude measurements were converted to M_s using Rezapour and Pearce (1998). Once the M_s magnitudes were computed, we analyzed the performance of the PXD method and compare it with the short-period single station m_b-M_s discriminant at WMQ. We first assigned a critical value of m_b-M_s to be that of the lowest explosion below which all events are declared earthquakes. This is shown in the histogram of m_b-M_s values at the top of Figure 2. For this case, the critical value is 0.63, which results in a false alarm (calling an event an explosion when it is actually an earthquake) rate of 22%. Using the equation from Taylor and Patton (2006) to compute the maximum expected explosion amplitude based on the m_b and distance to WMQ, we obtain the plots at the bottom of Figure 2. In these m_b-M_s versus m_b and distance plots, P(X|Q) indicates a false alarm (green circles), and P(Q|Q) (yellow circles) and P(X|X) (red stars) indicates correctly classified earthquakes and explosions respectively. The blue triangles represent events that were false alarms with the m_b-M_s discriminant but were assigned a low p value with the PXD analysis, and therefore are correctly identified as earthquakes. This implies a reduction of the false alarm rate from 22% to 17%. The values in Figure 2 were obtained assuming a Q value of 220 and a U value of 3 km/s. The Q value is based on the average value of 20 s Rayleigh-wave attenuation models of Yang et al. (2004). However, from Taylor and Patton (2006), it is evident that attenuation and group velocity tomography can be used in the estimation of the maximum expected explosion amplitudes. Using path-dependent attenuation and group velocity values should improve the detections and decrease the false-alarm rate. We calculated path-dependent attenuation values from the study of Yang et al. (2004). We used the slowness tomographic models from Maceira et al. (2005) to compute path-dependent group velocity values. Using these refined values we got the false alarm rate to decrease even more to 15%.

Then the PXD method seems to be effective and for the described dataset the application of Taylor and Patton methodology can reduce the false alarm rate from 22% to 15%. However, we noticed that if instead of a bandwidth from 6 to 12 s, we repeated the analysis between 8 to 12 s period, the PXD method is not so effective and it only reduces the false alarm rate from 23% to 22%. This illustrates how complicated the short period waveforms can be in areas of complex geology and tectonics. Therefore, the results shown from applying the PXD method are somehow sensitive to the bandwidth of study.

New Amplitude and M_s Magnitude Measurements

In the previous section, we described the PXD method of Taylor and Patton (2006) and we validated it with a new and independent dataset. However, during the analysis, some very interesting findings came out which can be very helpful to scientists working on seismic discrimination problems. They are related to the way amplitudes are measured and the formulation used to compute a M_s.

Using the same data set described above, we computed new amplitude measurements with a new method and obtained multi-frequency surface wave magnitudes M_s following the methodologies of Marshall and Basham (1972) (M-B M_s) and Russell (2004) (DR M_s). Figure 3 shows a flowchart of the procedure used to perform the amplitude measurements and compute the surface wave magnitudes. Preprocessing of the dataset involves correcting for instrument response to ground displacement in nm, and rotating to the great circle path using a known epicentral location. Then we filtered the displacement waveforms into five passbands with center periods of 20, 16, 12, 10, and 7 s. For each filtered trace, we computed a particle motion window and a group velocity time window. The particle motion window is obtained by multiplying the Hilbert-transformed radial component by the vertical component. Passing the absolute value of the resulting time series through a band-reject filter, we get a smooth envelope function where the largest amplitudes correspond to times consistent with Rayleigh particle motion. The group velocity time window is computed using minimum and maximum slowness values for the frequency band of interest from the tomographic models developed by Maceira et al. (2005) for central Asia. Finally, the measurement window is defined by intersection of these two time windows. An amplitude measurement is made only on that portion of the waveform lying inside the measurement window. If there is no intersection between the arrival time window and the particle motion window, the result is a null trace and no amplitude measurement is made. This is illustrated in Figures 4 and 5, which show the filtered waveforms for M-B M_s and for DR M_s respectively.

Once amplitudes and periods for each bandpass are measured, we computed the associated M_s following the methodologies of Marshall and Basham (1972) and Russell (2004). We computed a M-B and DR M_s for each of the five passbands for each earthquake and explosion in the dataset. The final M-B M_s is the magnitude from the band yielding the largest magnitude. The final DR M_s is based on the passband with the largest amplitude. If we now apply the analysis described in the previous section comparing the performance of the traditional m_b-M_s discriminant with the PXD method, but now using the new amplitude and magnitude measurements (see Figure 6), it can be observed that the m_b-M_s discriminant using Russell formulation (2004) performs better as an earthquake identifier (21% false alarm rate) than Rezapour and Pearce (1998) formulation (45% false alarm rate), and meanwhile the PXD analysis seems to improve the results for the formula of Rezapour and Pearce (1998) reducing the false alarm rate to 31%, it does not improve the results for the Russell formulation (still 21% false alarm rate).

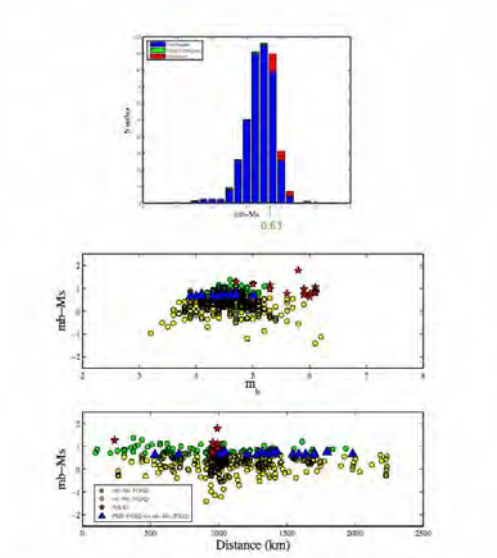


Figure 2. (Top) Histogram of m_b-M_s values for the data set under study, showing the lowest explosion value of 0.63. (Bottom) Performance comparison of traditional m_b-M_s discriminant and PXD results. See text for explanation.

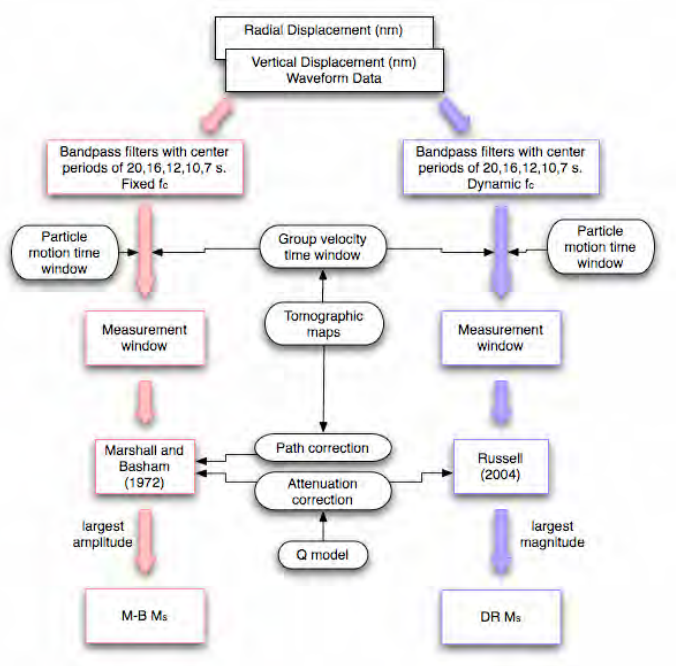


Figure 3. Flowchart of the procedure followed to perform time domain amplitude measurements and posterior computation of surface wave magnitudes M_s.

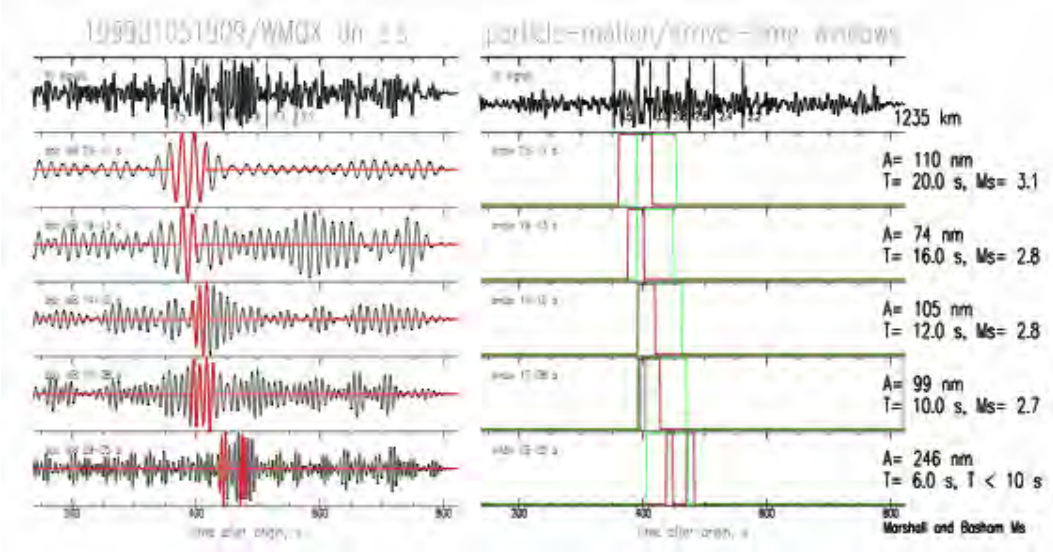


Figure 4. Example of waveform processing for the computation of M-B M_s. For reference, broadband (25 to 4 s) waveforms are plotted at the top of each column, vertical component on the left, radial component on the right. Filtered, vertical component waveforms are plotted on the left, while the corresponding boxcar traces are plotted to the right. The green boxcar shows the predicted Rayleigh wave arrival window, the black boxcar shows Rayleigh wave particle motion window(s), and the red boxcar shows the measurement window(s). The unit boxcar measurement traces are multiplied into the filtered waveforms (to the left), and the resultant windowed traces are overlaid in red on the bank of filtered waveforms.

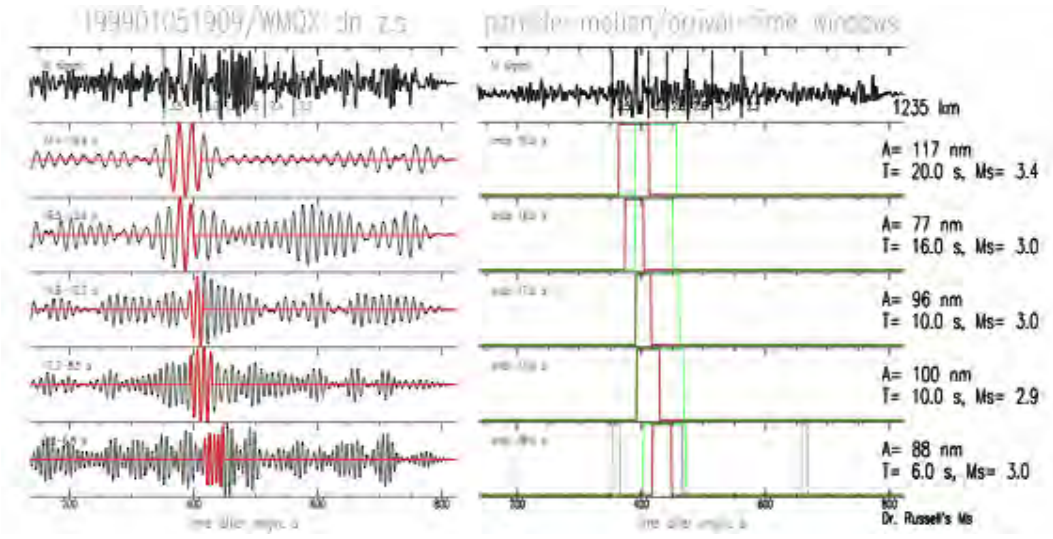


Figure 5. Example of waveform processing for the computation of DR M_s for the same event shown in Figure 3. See Figure 3 for explanation.

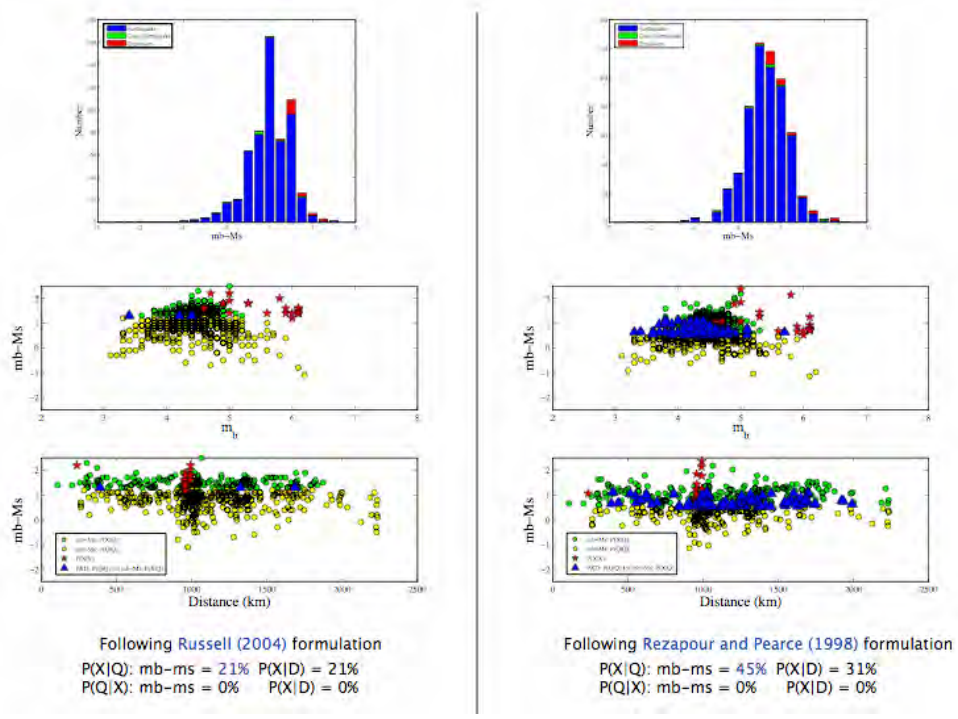


Figure 6. Performance comparison of traditional m_b-M_s discriminant, with the M_s values computed following Russell (2004) and Rezapour and Pearce (1998) formulations, and the PXD analysis. The symbols indicate the same as in Figure 1.

Regional-Phase Attenuation Tomography between 0.5 and 10 Hz

Two-dimensional (2D) regional-phase (Pn, Pg, Sn and Lg) attenuation models can improve the performance of the MDAC methodology in discriminating underground nuclear explosions from earthquakes. Since MDAC works on amplitude data in different frequency bands, regional-phase attenuation models for corresponding frequency bands are desired. One method of obtaining the models at different frequencies is to derive the model at 1 Hz and then use an assumed relationship between frequency and attenuation to deduct attenuation models at other frequencies. A second approach is to develop attenuation models at multiple frequency bands directly from observed data. Based on the second approach, we are working on developing regional-phase attenuation models for Eurasia for a broad range of frequencies between 0.5 and 10 Hz. Our focus has been on the Pn attenuation investigation. This effort is in parallel to a BAA project between UCSC and LANL to develop 1-Hz, 2D regional-phase attenuation models for the same region (Lay, et al., 2006).

We have finished the initial phase of data collection and amplitude measurement. We have collected waveform data from over 3,000 events recorded by 84 stations in Eurasia. Figure 7 displays the event and station distribution. These data were requested from the Data Management Center (DMC) of the Incorporated Research Institutions for Seismology (IRIS). From this data set, we have made regional-phase amplitude measurements at frequencies of 0.5, 0.75, 1.0, 1.25, 1.5, 2.0, 2.5, 3.0, 4.0, 6.0, and 8.0 Hz. We used a semi-automatic procedure based on analyst picks and nominal regional-phase travel times to window different phases for amplitude measurement. Figure 8 shows, at selected frequencies, the path coverage of Pn amplitudes that have signal-to-noise ratio of 2 or larger and a source-receiver distance of 2,000 km or shorter. The coverage is decent for 1-Hz data for certain parts of the region and degrades toward higher frequencies. This is a common phenomenon for all the phases that we measure. It suggests that attenuation maps developed from these measurements will have different coverage areas for different frequencies

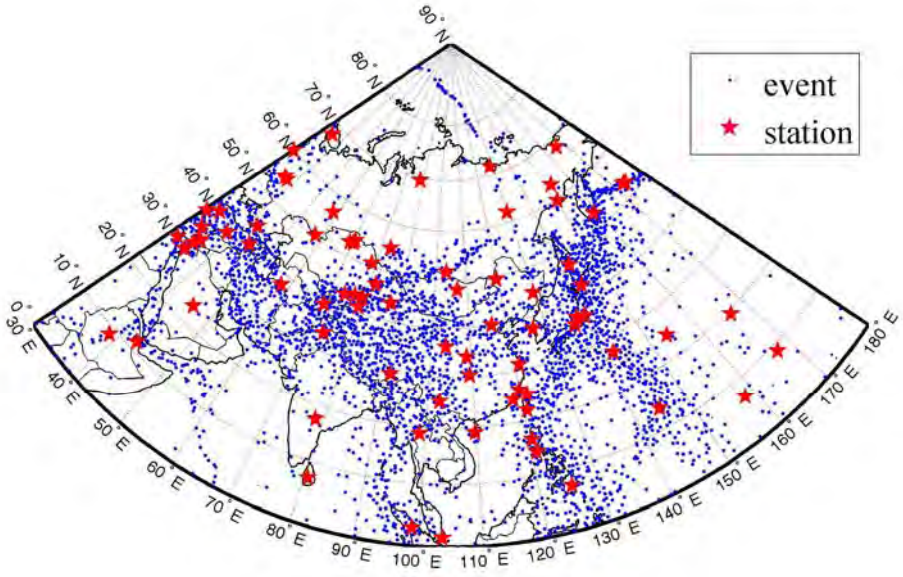


Figure 7. Event and station distribution for the initial phase of data collection and amplitude measurement.

We are conducting the second phase of data collection, phase picking and amplitude measurement to improve the coverage. During the second phase, we focus on the data residing in the LANL Ground-Based Nuclear Explosion Monitoring (GNEM) database. The LANL GNEM database contains a multitude of arrivals, amplitudes and waveforms. From the database, we gathered analyst-picked Pn amplitudes that were not in the measurements from the first phase of the data collection. This amounted to 1,800 events recorded by 25 stations (Figure 9). We also sought to take advantage of the extensive waveform coverage in the database by combining arrival information with waveform data to subsequently make amplitude measurements. Using a subset of event location tables within the GNEM database (Begnaud et al., 2002), we were able to extrapolate the most reliable catalog pick information for a given station and event to then calculate regional-phase amplitude measurements at the aforementioned frequencies. There were approximately 22,000 (vertical component) waveforms with a corresponding catalog pick. Utilizing this information allowed us to add another 12,000 events recorded by 32 stations to our dataset (Figure 10).

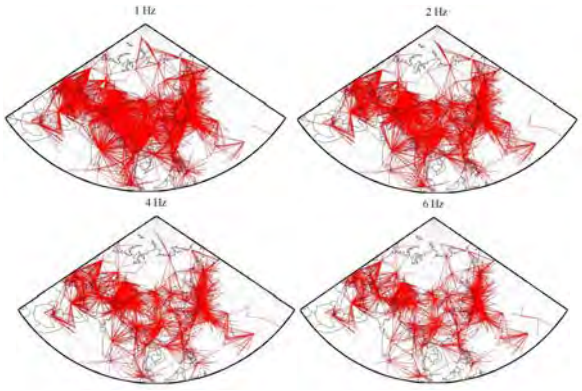


Figure 8. Path coverage of Pn amplitude measurements at different frequencies with path lengths of 2,000 km or less.

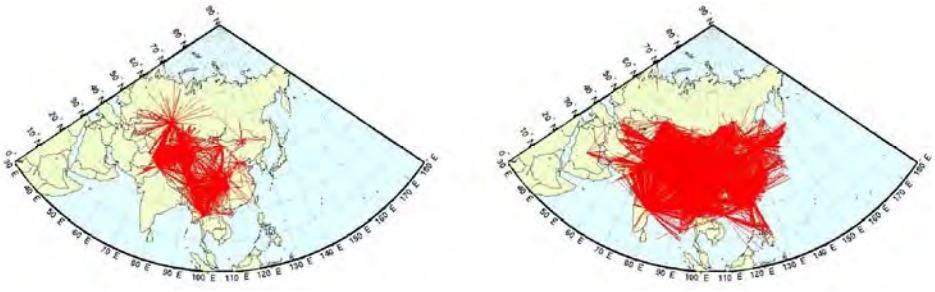


Figure 9. Summary of data obtained for the second round of Pn amplitude acquisition. The left-hand map shows Pn (1 Hz) path coverage for existing amplitudes in the GNEM database. The right-hand map shows path coverage for which the GNEM database contained waveforms and reliable Pn arrival information that will be used to measure additional amplitudes.

Because of the tradeoff between geometric spreading and attenuation, it is necessary to accurately constrain the geometric spreading of the regional phases in order to develop reliable regional-phase attenuation models. Whereas the geometric spreading of crustal phases Pg and Lg may be relatively simple (Yang, 2002), the geometric spreading of upper-mantle phases Pn and Sn is more complex due the sensitivity of these phases to the upper-mantle velocity structure and the Earth's sphericity. Synthetic simulations (Sereno and Given, 1990; Lay, et al., 2006) show that the Earth's sphericity alone causes the 1-Hz Pn geometric spreading to change dramatically from that of a head wave. The effects are frequency dependent as well. Figure 10 shows the modeling results of Pn amplitude decay at different frequencies for a one-layer crustal velocity model used by Lay et al. (2006). The Earth's sphericity causes the Pn amplitudes to decay much slower and to even increase as the distance increases. The higher the frequency is, the larger the effects become. Although the effects of the Earth's sphericity are different in degrees at different frequencies, they can all be modeled by the same polynomial model proposed by Lay et al. (2006):

$$A(\log_{10}\Delta)^2+B(\log_{10}\Delta) \qquad (1)$$

for the logarithm of the amplitude. The Δ in (1) is source-receiver distance, and A and B are constants. The coefficients of model (1) will depend on frequency. Table 1 lists the coefficients A and B of the model for different frequencies from fitting the data in Figure 10.

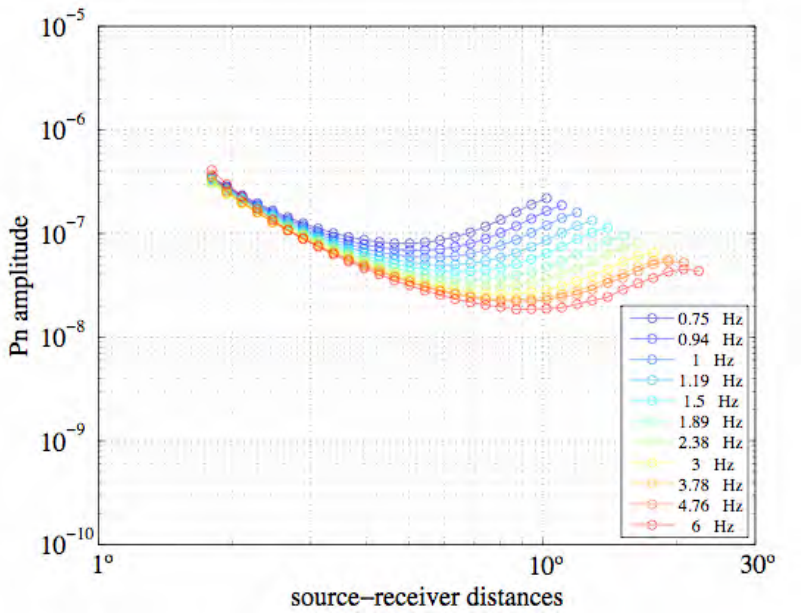


Figure 10. Pn amplitude decay in a spherical one-layer crust model.

Table 1. Coefficients of the polynomial model (1) from fitting the curves in Figure 10

Frequency (Hz)	A	B
0.75	2.72	-5.16
0.94	2.67	-4.92
1.0	2.68	-4.88
1.19	2.71	-4.80
1.5	2.83	-4.83
1.89	3.00	-4.93
2.38	3.16	-4.99
3.0	3.29	-5.00
3.78	3.46	-5.04
4.76	3.61	-5.05
6.0	3.78	-5.06

CONCLUSION(S) AND RECOMMENDATIONS

We have an ongoing program to identify mining seismicity clusters in Kazakhstan from waveform correlation and tie these to overhead imagery for ground truth. We have presented a new method for regional Ms discrimination based on a probability of detection. We have presented results for regional phase attenuation tomography and Pn spreading to make path corrections for regional discrimination. These efforts show promise, and we will continue to develop the methods for improved performance of regional discriminants.

ACKNOWLEDGEMENTS

We thank the LANL GNEM Research and Engineering team for supporting efforts that make this work possible.

REFERENCES

Anderson, D. N., D. K. Carlson, G. D. Kraft, K. D. Hutchenson, M. A. Tinker, F. R. Schult, D. R. Russell, M. T. Woods, J. K. Schrodt, and S. R. Taylor (2004). A mathematical alternative to voting procedures for seismic event identification, Pacific Northwest National Laboratory report, PNNL-14600.

Begnaud, M. L., J. C. Aguilar-Chang, A. A. Velasco, and L. K. Steck (2002). Developing regional seismic databases for improving event location and ground truth data sets in Asia, in *Proceedings of the 24th Seismic Research Review—Nuclear Explosion Monitoring: Innovation and Integration*, LA-UR-02-5048, Vol. 1, 839–844.

Hartse, H. E., S. R. Taylor, W. S. Phillips, and G. E. Randall (1997). A preliminary study of regional seismic discrimination in central Asia with emphasis on western China, *Bull. Seismol. Soc. Am.* 87: 551–568.

Lay, T., X. Yang, X. B. Xie, and M. D. Arrowsmith (2006). Development of regional tomographic attenuation models for Eurasia (these Proceedings).

Maceira, M., S. R. Taylor, C. J. Ammon, X. Yang, and A. A. Velasco (2005). High-resolution Rayleigh wave slowness tomography of central Asia, *J. Geophys. Res.* 110: B06304, doi:10.1029/2004JB003429.

Marshall, P. D. and P. W. Basham (1972). Discrimination between earthquakes and underground explosions employing an improved M_s scale, *Geophys. J. R. Astr. Soc.* 29: 431–458.

Rezapour, M. and R. G. Pearce (1998). Bias in surface-wave magnitude M_s due to inadequate distance correction, *Bull. Seismol. Soc. Am.* 88: 43–61.

Russell, D. R. (2004). Theoretical analysis of narrow-band surface wave magnitudes, Air Force Technical Applications Center technical report, Patrick Air Force Base, AFTAC-TR-04-004.

Sereno, T. J. and J. W. Given (1990). Pn attenuation for a spherically symmetric earth model, *Geophys. Res. Lett.* 17: pp. 1,141–1,144.

Taylor, S. R. and H. J. Patton (2006). A probability of detection method for reducing short-period m_b-M_s false alarm rates, *Bull. Seismol. Soc. Am.* 96: 1,078–1,090.

Yang, X., S. R. Taylor, and H. J. Patton (2004). The 20-s Rayleigh wave attenuation tomography for central and southern Asia, *J. Geophys. Res.* 109: doi:10.1029/2004JB003193.

Yang, X. (2002). A numerical investigation of Lg geometrical spreading, *Bull. Seismo. Soc. Am.* 92: 3,067–3,079.

PREPARING FOR THE 2006 ALASKA PERMAFROST EXPERIMENT

Charles G. Sammis and Ronald L. Biegel

University of Southern California

Sponsored by Air Force Research Laboratory

Contract No. FA8718-04-C-0012

ABSTRACT

The objective is to measure the effect of ice in rock on the seismic coupling of explosions. This study is motivated by discrepancies in modeling Soviet explosions at their arctic test site at Novaya Zemlya. In support of the Alaska field experiment, we have used the damage mechanics model developed by Ashby and Sammis (1990) to interpret laboratory data on the strength of frozen rock (Sammis and Biegel, 2004). In this model the increase in rock strength as a function of decreasing temperature is explained by the increase in the flow strength of ice asperities in the cracks as the temperature drops. Since the flow stress in ice is also strain dependent, we expect frozen rock to reach its low-temperature strength limit at the high strain rates in an explosion source region, even though its temperature is not very far from the freezing point. However, if the ice temperature is too near 0ºC, then this strain-rate-dependent strengthening may be limited by pressure melting, a phenomenon we explore in this paper. The elasticity model of O'Connell and Budianski (1974) was used to calculate the increase in the elastic moduli caused by ice in the cracks (Sammis and Biegel, 2005). We have used the "equivalent elastic medium model" for an explosive source developed by Johnson and Sammis (2001) to explore the effect of an increase in both elastic stiffness and compressive strength on the amplitude of far-field seismic radiation. We found that an increase in the elastic moduli produces a decrease in the far-field amplitudes, as does an increase in the coefficient of static friction and the consequent increase in compressive strength. Our conclusion is that an explosion in frozen rock should have a smaller apparent yield than the same explosion in rock at temperatures above the freezing point and that the effect should be larger in limestone than in granite, although these effects can be reduced by pressure melting at rock temperatures near 0ºC.

OBJECTIVES

The objectives of this research program are to accomplish the following:

1. Build the micromechanical damage mechanics developed by Ashby and Sammis (1990) into source models for underground explosions.
2. Use this model to explore the influence of site effects such as rock type, groundwater saturation, permafrost, and depth of burial on the seismic signature generated by the explosion.
3. Use this model to help interpret laboratory measurements and field experiments.
4. Explore the possibility that secondary radiation generated by the damage contributes to the regional seismic phases.

RESEARCH ACCOMPLISHED

Introduction

The Soviet test site at Novaya Zemlya at $73°$ north latitude lies well above the Arctic Circle. Rock at this site is probably below the freezing point of water to a considerable depth. Permafrost thickness is greatest in non-glaciated polar regions like Siberia, where a record depth of 4,900 feet to the permafrost base has been reported. Permafrost thickness in arctic Canada has been estimated to exceed 3,000 feet, and in arctic Alaska it may exceed 2,000 feet. The question has therefore arisen as to how frozen water in cracks and pores might affect the seismic signature of an underground explosion.

Sammis and Biegel (2004) interpreted uniaxial compressive and tensile strength data on frozen rock from Mellor (1973) using the micromechanical damage model developed by Ashby and Sammis (1990). In this model, sliding on preexisting cracks in rock induces additional fracture damage and ultimate failure. The effect of ice in the damage model is to increase the effective coefficient of sliding friction on the preexisting cracks, thus inhibiting the generation of new damage and strengthening the rock. In addition to strengthening, the damage model was also able to explain some of the subtler phenomenology in the frozen rock data, such as the differences between porous and crystalline rock and the progressive strengthening observed to occur as the temperature was lowered from $0°\,\mathrm{C}$ to $-150°\,\mathrm{C}$. A second effect of ice in cracks in rock is to increase the elastic moduli by sealing small cracks and shortening longer cracks by ice bridging.

Sammis and Biegel (2005) used the “equivalent elastic medium source model” developed by Johnson and Sammis (2001) to investigate the effects of frozen water in the cracks of crystalline rock on the seismic radiation from an underground explosion. They found that an increase in the elastic moduli produces a decrease in the far-field amplitudes. This was not surprising because it is well known that the apparent yield of an explosion decreases as the inverse of the shear-wave velocity in the source rock. An increase in the coefficient of static friction in the cracks, and consequent increase in compressive strength, also reduces the amplitude of the far-field seismic radiation. Their conclusion was that an explosion in frozen rock should have a smaller apparent yield than the same explosion in rock at temperatures above the freezing point, and that the effect should be larger in limestone than in granite.

In order to test these ideas, an initiative has been launched to detonate identical chemical explosions above and below the permafrost layer in Alaska to see if the expected differences in seismic coupling are observed. There is some concern that temperatures in the permafrost hole are only –0.2ºC which because of an interaction between the water and minerals, may not be cold enough to form ice in the cracks. There is also some concern that ice this near its melting temperature may not significantly strengthen the rock. We address the latter concern in this report by showing that significant strengthening should occur near 0ºC at the high strain rates in the nonlinear region of an explosion. We begin with a brief review of the mechanical effects of ice in the cracks of crystalline rock and then present a simulation of an 800 lb explosion at a depth of 20 m in hard rock.

The Mechanical Effects of Ice in the Cracks of Crystalline Rock

When water in the cracks of crystalline rock freezes, it affects the mechanical properties in two ways: (1) it increases the elastic moduli, and (2) it increases the strength. Both effects can be understood in the context of the micromechanical damage mechanics developed by Ashby and Sammis (1990).

The Effect of Ice on Elastic Properties

In the Ashby and Sammis (1990) damage mechanics, the size and density of fractures in crystalline rock are characterized by a single parameter called damage. The initial damage, before loading, is defined as

$$D_0 = \tfrac{4}{3}\pi\left(a\cos\chi\right)^3 N_V \quad , \tag{1}$$

where a is the half-length of the cracks, N_V is the number of cracks per unit volume, and χ is an angle describing their orientation (see Figure 1).

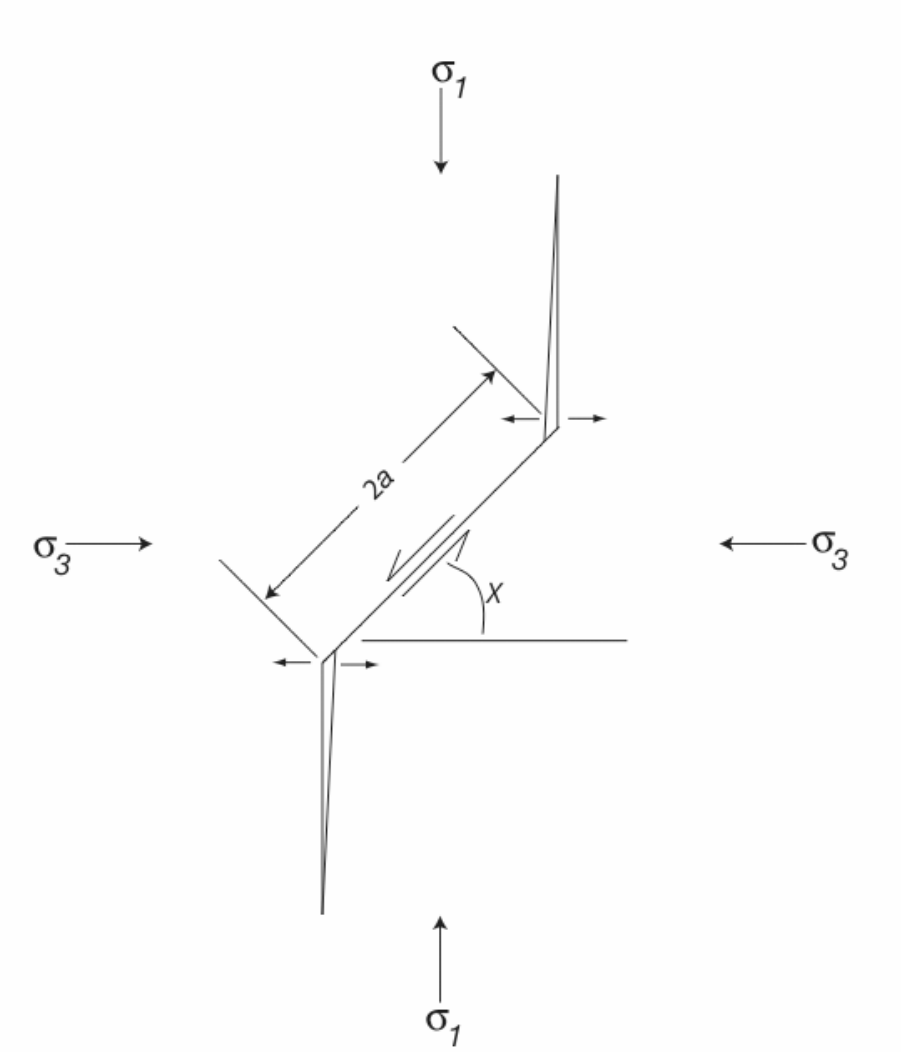


Figure 1. Crack geometry used in the Ashby and Sammis (1990) damage mechanics. Sliding on an inclined crack of length 2*a* nucleates tensile wing-cracks at its ends. Interaction between such cracks in an array of *Nv* cracks per unit volume leads to failure and fragmentation.

The effect of ice in the inclined crack in Figure 1 is to either totally immobilize it, thus reducing *Nv* in Eq. (1), or, if saturation is not total, to form ice bridges, thus reducing *a* in Eq. (1). The net effect of both is to reduce the initial damage *Do*.

The elastic moduli of rock are extremely sensitive to *Do*. Figure 2, from O'Connell and Budiansky (1974), shows the effect of changing *Do* on the P and S wave velocities in dry and water-saturated rock. Note that the x-axis in Figure 2 is $\varepsilon = N\left\langle a^3 \right\rangle$, where N is the number of cracks per unit volume and a is the half-length of the crack. Comparison with Eq. (1) shows that ε can be written in terms of the initial damage as

$$\varepsilon = \frac{3}{4\pi}\left(\frac{1}{\cos\chi}\right)^3 D_o \approx 0.68 D_o \quad . \tag{2}$$

The effect of freezing water in the cracks is to move to the left (toward lower damage) on the curves in Figure 2. This will produce an increase in elastic wave velocity. The effect is larger for S waves than for P waves in saturated rock.

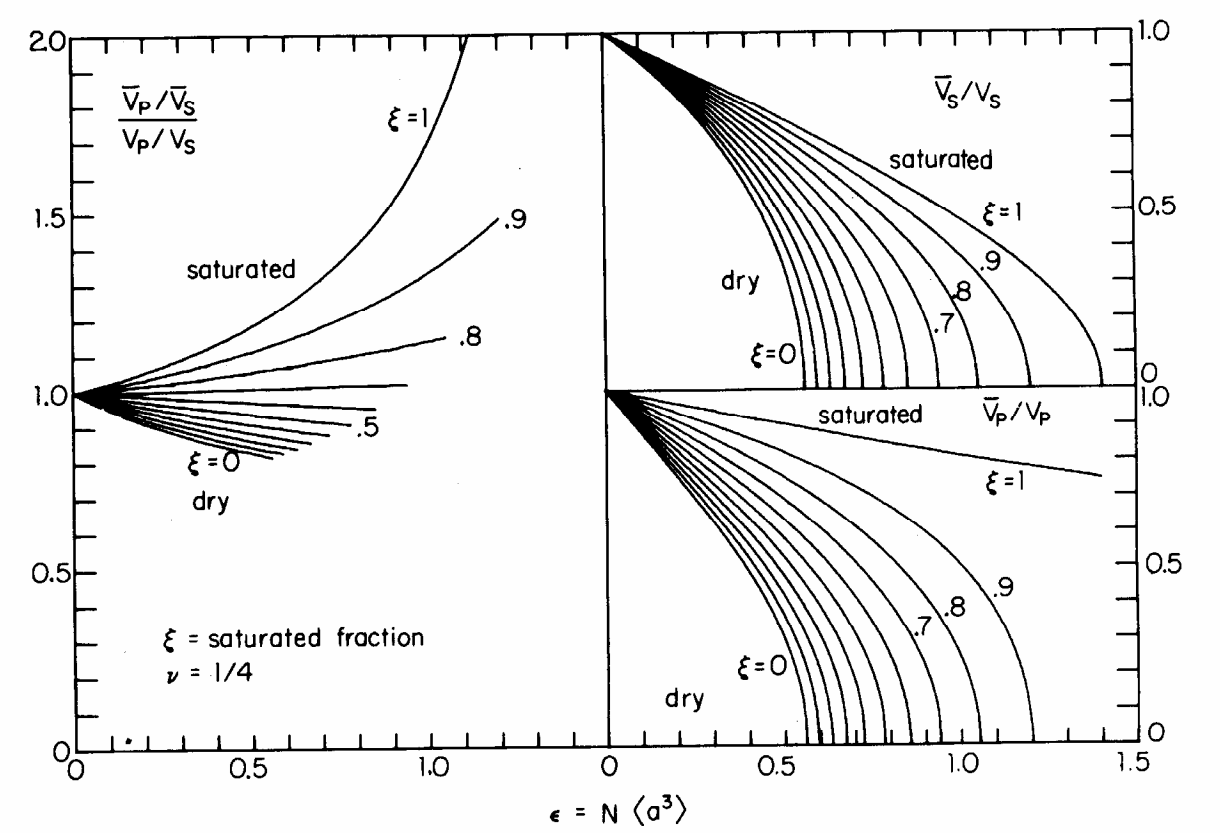


Figure 2. The effect of fractures on the elastic wave velocities in wet and dry rock (from O'Connell and Budiansky, 1974). The crack density parameter ε is closely related to the damage parameter in the Ashby and Sammis (1990) damage mechanics, differing only by a constant. See Eq. (2).

The Effect of Ice on Strength

Sammis and Biegel (2004) used the Ashby and Sammis (1990) damage mechanics to explain measurements by Mellor (1973) of the uniaxial strength of saturated rock as a function of temperature from 20 °C to –197°C. They found that Mellor's data for the compressive strength (replotted here as Figure 3) could be fit by the Ashby-Sammis model if the coefficient of friction in the sliding cracks is temperature dependent. The required temperature dependence is shown in Figure 4. Sammis and Biegel (2004) then showed that a simple Bowdin and Tabor (1950, 1964) asperity model consisting of a combination of rock and ice asperities could explain the temperature

dependence of the coefficient of static friction in Figure 4, using the known temperature dependence of the creep strength of ice.

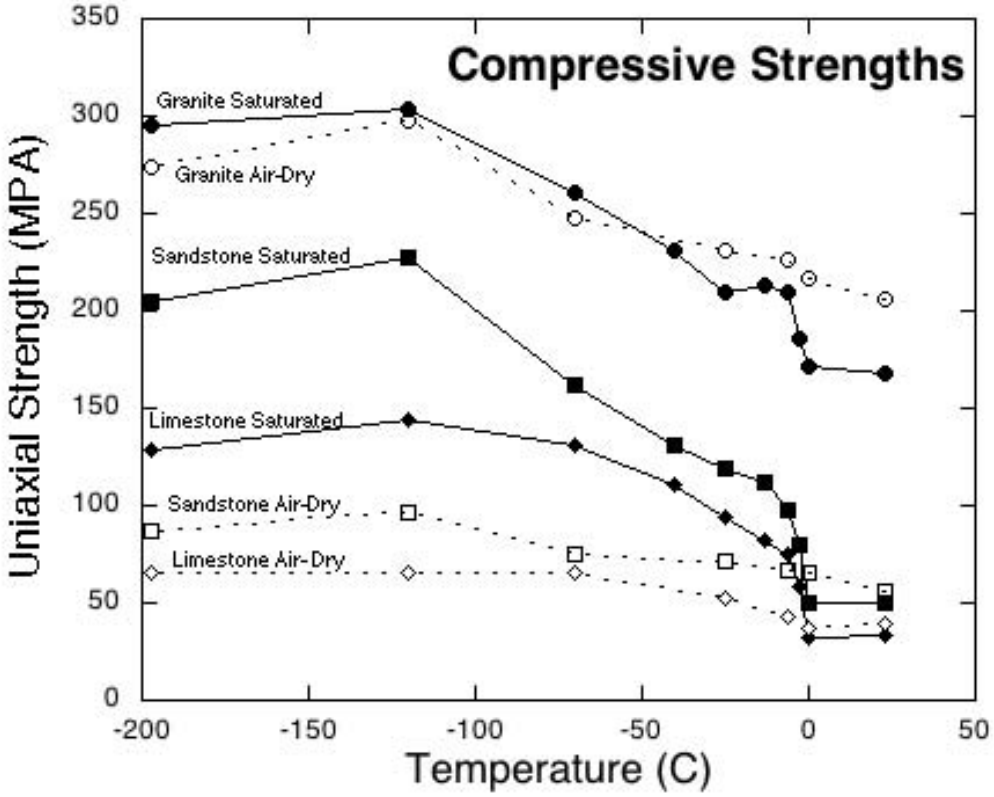


Figure 3. Strength of granite, limestone, and sandstone in uniaxial compression at low temperatures from Mellor (1973). Note that the strengths of saturated and air-dry granite samples are nearly the same at all temperatures, indicating that the thin cracks in granite are saturated under air-dry conditions (from Sammis and Biegel, 2004).

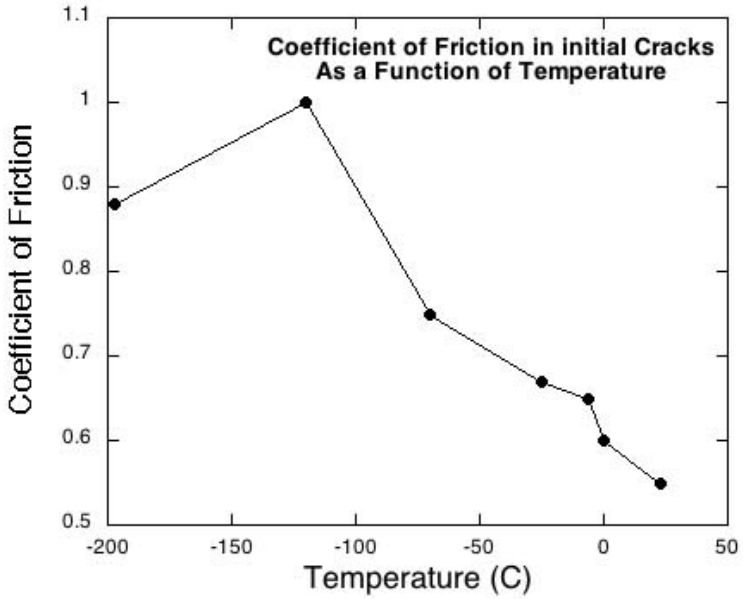


Figure 4. Coefficient of friction on starter cracks required if the damage mechanics model is to explain the increase in compressive strength at low temperatures in Figure 3 (from Sammis and Biegel, 2004).

The Effect of Strain Rate on the Strength of Frozen Rock

The effect of strain rate on the strength of frozen rock is illustrated by the deformation-mechanism map for ice in Figure 5. Temperatures near melting are at the right edge of the map, where it can be seen that increasing the strain rate produces a significant increase in the flow stress. At an effective shear stress of about 10 MPa, this trend is reversed by the onset of pressure melting, which weakens the ice.

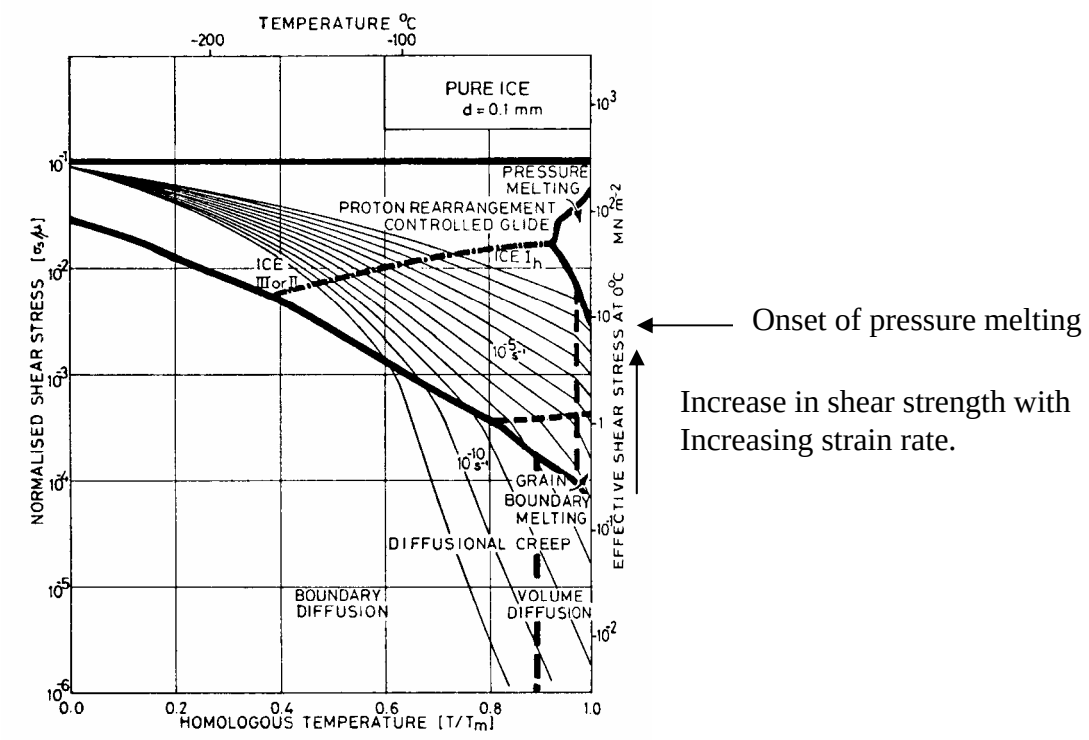


Figure 5. Deformation-mechanism map for ice. Note that increasing the strain rate by 5 orders of magnitude near 0ºC increases the shear strength (effective shear stress) by a factor of 10. This increase in strength is limited by pressure melting that occurs at an effective shear stress of about 10 MPa (from Frost and Ashby, 1982).

The Effects of Ice in the Cracks of Crystalline Rock on Seismic Radiation from an Explosion

In order to model the effect of ice on the damage generated by an explosion and on the seismic radiation, we require the principal stresses generated by the explosion as a function of distance and time. This is made difficult by the existence of the nonlinear processes between the cavity radius and the effective elastic radius, beyond which the assumptions of ordinary linear elasticity are valid. Sophisticated computer codes have been developed that include hydrodynamic effects, shock waves, and nonlinear equations of state (see, for example, Rodean, 1971; King et al., 1989; Glenn, 1993; Glenn and Goldstein, 1994, for discussion and further references). We use here an approximate method to calculate the stresses surrounding an explosion that is based on the equivalent elastic method developed by earthquake engineers to model the nonlinear behavior of soils that occurs during strong ground motion. The central idea is to make the material properties a function of the stress in the outward propagating pressure pulse and then to adjust these material properties in an iterative process until the appropriate values are present at all distances from the source. In effect, the nonlinear stress-strain behavior is approximated by a series of linear relationships that

change with the level of stress. The present formulation, described by Johnson (1993), relates density and bulk elastic properties to the peak pressure and shear and anelastic properties to the maximum shear strain.

The details of this model are published in Johnson and Sammis (2001) and will not be repeated here. In that paper we modeled the 1 kt chemical explosion detonated in September 1993 as part of the Non-Proliferation Experiment (NPE) (see Denny, 1994). Last year Sammis and Biegel (2005) explored the effect of an increase in both elastic stiffness and compressive strength on the amplitude of far-field seismic radiation that would be expected if ice were present in the source rock of the NPE explosion. Both produced a decrease in the far field amplitudes. Our conclusion was that an explosion in frozen rock should have a smaller apparent yield than the same explosion in rock at temperatures above the freezing point and that the effect should be larger in limestone than in granite.

The Expected Effects of Ice in the Cracks of Crystalline Rock in the Proposed Alaskan Experiment

The question here is how much strengthening we can expect in the much smaller explosions planned for the Alaskan experiment. To explore this question, we simulated an 800 lb explosion at 20 m depth in crystalline rock in order to see whether the peak shear stresses (and associated strain rates) are large enough to significantly strengthen ice in the source region and whether they are high enough to induce pressure melting. The results are summarized in Figure 6.

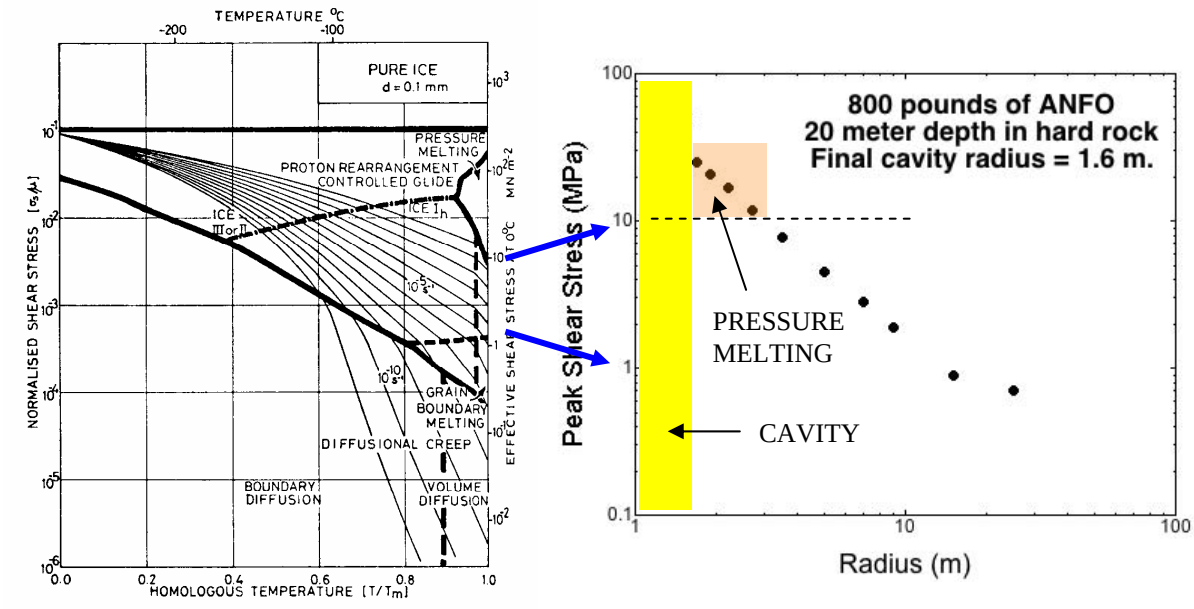


Figure 6. Simulation of 800 lb explosion in hard rock. Note that pressure melting is expected out to a radius of about 3 m and that significant strengthening should extend out to about 10 m.

The shear stresses are sufficiently high to cause pressure melting out to a radius of about 3 m and to significantly strengthen the ice out to a radius of about 10 m. We did not feed the new ice parameters back into the model and iterate to find a self-consistent solution, as we will do when we model the actual experiments. The objective here was simply to see if the peak shear stresses are sufficiently high to significantly strengthen the ice. They are.

CONCLUSIONS AND RECOMMENDATIONS

Inclusion of the mechanical effects of ice in the cracks of crystalline rock in the explosion source formulated by Johnson and Sammis (2001) has led to the following conclusions:

1. The increase in elastic wave velocities associated with ice in the cracks will decrease the seismic amplitudes in the far field, resulting in an apparently smaller yield.

2. The increase in compressive strength caused by ice in the cracks will also decrease seismic amplitudes in the far field, also resulting in an apparently smaller yield.

3. Near 0ºC, significant strengthening should occur at high strain rates in the nonlinear regime of an 800 lb explosion of the type planned for the Alaska experiment. However this increase is limited by the onset of pressure melting. The rock should be weak close to the detonation point, but strong farther out.

The following recommendations are based on the analysis in this paper and our previous analysis of the frozen rock data (Sammis and Biegel, 2004, 2005). Many of these recommendations may already have been implemented in Randy Martin's laboratory work to be presented at this year's SRR meeting.

1. The uniaxial data from Mellor (1973) should be supplemented with a full set of triaxial data in granite at low temperatures. Uniaxial data typically shows large experimental scatter, mostly because the strength is extremely sensitive to the initial flaw distribution in the absence of confining stress. A set of triaxial data would allow a more comprehensive assessment of the extent to which the damage model can represent the strength of rock at low temperatures.

2. The triaxial data set should be supplemented with measurements of the coefficient of friction as a function of temperature under saturated and air-dry conditions. These measurements can be made either on saw-cut samples as part of the triaxial set of experiments or in Jim Dieterich's double-shear apparatus at the United States Geological Survey laboratory in Menlo Park, California.

3. Both the triaxial measurements and friction measurements should be performed at different strain rates to further test the hypothesis that the strengthening is associated with ice asperities.

4. Seismic velocities should be measured in frozen and thawed rock at the same field location as part of any pending field study of explosions in frozen rock. The differences between the seismic velocities above and below the permafrost should lead to a constraint on the nature and density of the native fractures.

5. The equivalent elastic source model of Johnson and Sammis (2001) should be improved to make the nonlinearity depend explicitly on the damage. This nonlinearity is now given by an analytic approximation that depends on only the peak stress (or, equivalently, on the reference strain).

6. The issue of the actual freezing temperature of water in cracks in rock needs to be resolved, as does the amount of strengthening achieved by increasing the strain rate near 0ºC. These issues are vital to the success of the pending field test where the permafrost temperature in the proposed hole is only –0.2ºC.

ACKNOWLEDGEMENTS

We thank Professor Lane Johnson for many helpful discussions and for computational assistance with the equivalent elastic medium source model.

REFERENCES

Ashby, M. F. and C. G. Sammis (1990). The damage mechanics of brittle solids in compression, *Pure Appl. Geophys*: 133, 489-521.

Bowden, F. P. and D. Tabor. (1950). *The Friction and Lubrication of Solids. Part I.* Oxford: Clarenden Press.

Bowden, F. P. and D. Tabor. (1964). *The Friction and Lubrication of Solids. Part II.* Oxford: Clarenden Press.

Denny, M. D. (1994). Introduction and highlights, in *Proceedings of the Symposium on the Non-Proliferation Experiment (NPE): Results and Implications for Test Ban Treaties*, M. D. Denny (editor), CONF-9404100, Department of Energy.

Frost, H. J. and M. F. Ashby (1982). *Deformation-Mechanism Maps*, New York: Pergamon Press.

Glenn, L. A. (1993). Energy-density effects on seismic decoupling, *J. Geophys. Res.*: 98, 1933-1942.

Glenn, L. A. and P. Goldstein (1994). Seismic decoupling with chemical and nuclear explosions in salt, *J. Geophys. Res.*: 99, 11,723-11,730.

Johnson, L. R. (1993). Wave propagation near explosive sources, PL-TR-93-2118, Phillips Laboratory, 22 pp.

Johnson, L. R. and C. G. Sammis (2001). Effects of rock damage on seismic waves generated by explosions, *Pure Appl. Geophys.*: 158, 1869-1908.

King, D. S., B. E. Freeman, D. D. Eilers, and J. D. Johnson (1989). The effective yield of a nuclear explosion in a small cavity in geologic material: enhanced coupling revisited, *J. Geophys. Res.*: 94, 12,375-12,385.

Mellor, M. (1973). Mechanical properties of rocks at low temperatures, in *Second International Conference on Permafrost*, Washington, D.c., National Academy of Sciences, 334-343.

O'Connell, R. J. and B. Budiansky (1974). Seismic velocities in dry and saturated cracked solids, *J. Geophys. Res.*: 79, 5412-5426.

Rodean, H.C. (1971), Nuclear-Explosion Seismology, U.S. Atomic Energy Commission, TID-25572, 156 pp.

Sammis, C. G. and R. L. Biegel (2004). Mechanics of strengthening in crystalline rock at low temperatures: A preliminary assessment, in *Proceedings of the 26th Seismic Research Review: Trends in Nuclear Explosion Monitoring*, LA-UR-04-5801, Vol 2, pp. 475-484.

Sammis, C.G. and R.L. Biegel (2005). "Seismic radiation from explosions in frozen crystalline rock," in *Proceedings of the 27th Seismic Research Review Ground-Based Nuclear Explosion Monitoring Technologies*,LA-UR-05-6407, Vol. 2, pp. 642-652.

SPECTRAL STUDIES OF SHALLOW EARTHQUAKES AND EXPLOSIONS IN SOUTHERN CALIFORNIA

Peter M. Shearer and Bettina P. Allmann

University of California San Diego

Sponsored by Air Force Research Laboratory

Contract No. FA8718-06-C-0004

ABSTRACT

We compute and analyze *P*-wave spectra from over 300,000 earthquakes and 23,000 explosions recorded by over 300 seismic stations in southern California. We use an online waveform database stored on a RAID system at Caltech, which provides complete access to the Southern California Seismic Network (SCSN) seismogram archive. We compute spectra using a multi-taper method on 1.28 s noise and signal windows, positioned immediately before and after the *P* arrivals. After applying a signal-to-noise cutoff, we process the spectra using an iterative robust least-squares method to isolate source, receiver, and propagation path contributions. This corrects for first-order attenuation structure, as well as near-receiver site effects and any errors in the instrument response functions. Using the earthquake spectra and a simple source model, we compute an empirical Green's function to remove the tradeoff between the source terms and other terms in our model. Our observed earthquake spectra are fit reasonably well with a constant stress drop model over a wide range of moment. However, the explosion spectra show significant differences from the earthquake spectra, and often have a peak in their displacement spectra between about 3 and 8 Hz. Using this result, we develop and test a method to discriminate between shallow earthquakes and explosions using the relative amplitudes of the spectra within several different frequency bands. We compare results obtained for single explosions and ripple-fitted quarry blasts.

OBJECTIVES

The goal of this project is to systematically analyze and compare source spectra from over 340,000 earthquakes and explosions in southern California (Figure 1) to develop new insights into discrimination methods. Advances in data storage and computer capabilities make possible much more extensive analyses than have been performed in the past, which will provide a better picture of the distribution of source spectral properties and amplitudes. By examining tens of thousands of events, we will quantitatively characterize differences between earthquakes and explosions in terms of their spectral content and their P/S energy ratios. We also will identify and examine anomalous events, in particular earthquakes that may appear like explosions in spectral discrimination methods to determine how common they are and whether alternate discrimination techniques can be applied.

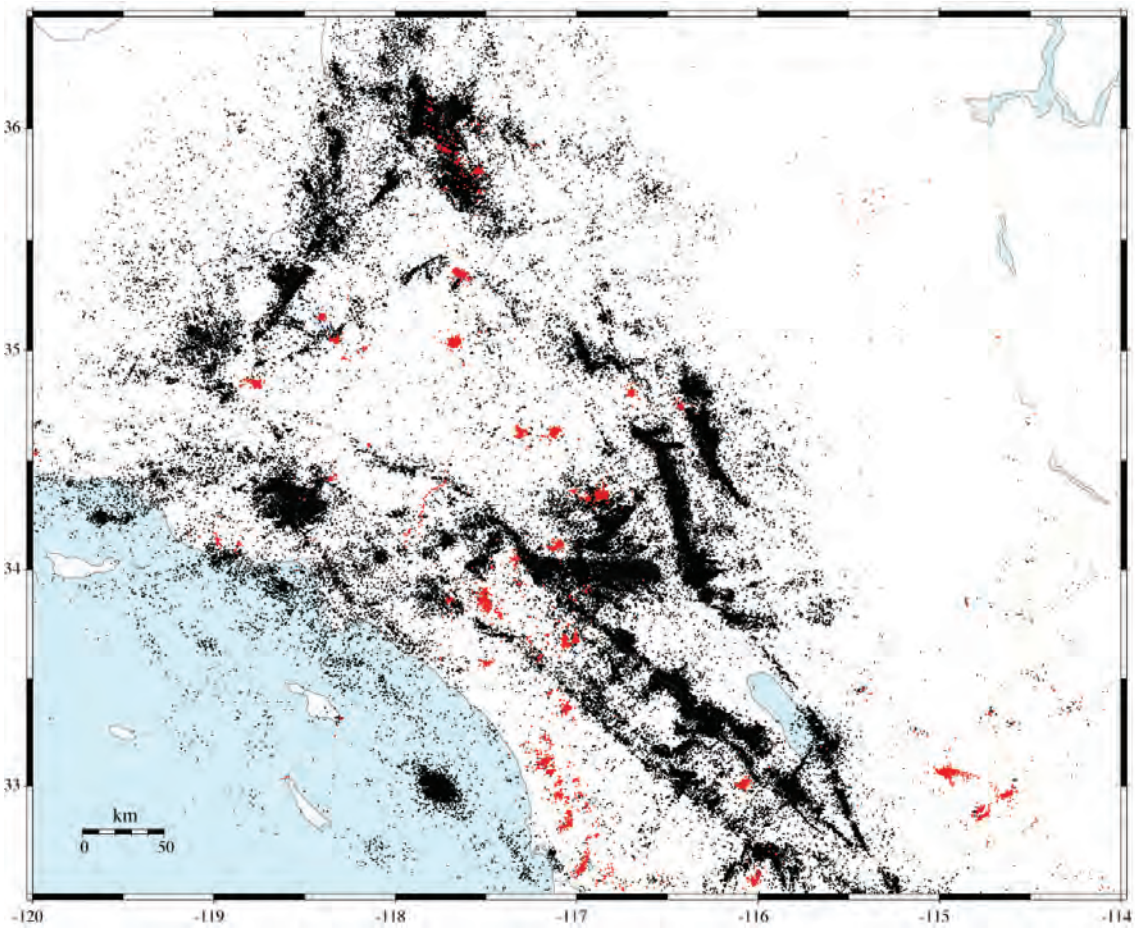


Figure 1. Locations of 319,750 earthquakes (black) and 23,748 explosions (red) in southern California from 1984 to 2002 as recorded by the SCSN. Figure adapted from Lin et al. (2006).

The project builds upon a recently completed large-scale analysis of southern California earthquake spectra (Shearer et al., 2006), to include a set of over 23,000 mining and other explosions between 1984 and 2004. The Shearer et al. earthquake study has already provided the largest set of earthquake spectra and stress drops computed to date, showing that individual event stress drops range between 0.2 and 20 MPa. The large number of stations and events available in southern California make possible empirical calibration methods to remove receiver response and path propagation effects. Our efforts focus on southern California because of the unmatched size and quality of the available data, but the results and insights will be applicable to other regions of more direct interest to nuclear monitoring programs.

In addition to computing and comparing stress drops between earthquakes and explosions, we will systematically analyze S-to-P amplitude ratios as a function of frequency and evaluate different discrimination strategies

(e.g., Hedlin et al., 1990, 2004; Su et al., 1991; Walter et al., 1995; Stump et al., 2002; Leidig et al., 2004; Tibuleac et al., 2004). The large number of available events will make possible quantitative measures of the uncertainties in all of our computed parameters as well as missed and false detection rates in explosion discrimination methods.

RESEARCH ACCOMPLISHED

The SCSN has several hundred stations and records about 12,000 to 35,000 earthquakes each year. Recently, we began storing seismograms from all archived events in an online RAID system that provides rapid and random access to the data (Hauksson and Shearer, 2005). Spectra are computed as follows. For each seismogram, we pick the P and S arrivals. This is done using the operator pick, if available, or using the output of an automatic picking algorithm for a window around the predicted arrival time (based on the catalog event location and a 1-D velocity model). Traces are resampled to a uniform 100-Hz sample rate. Spectra are computed using a multitaper algorithm (e.g., Park et al., 1987) for 1.28 s noise and signal windows, immediately before and after the pick time. We compute results for all available channels and components for both P and S, including rotation of the horizontals (if present) into transverse and radial records. However, so far we have analyzed only P waves from the vertical EH (short-period) component. Both signal and pre-event noise spectra are corrected to displacement and stored in a special binary format. We note that these records generally clip for $M_L > 3.5$ earthquakes.

We apply a signal-to-noise (STN) cutoff to the spectra, requiring that the STN amplitude ratio be at least 5 for three separate bands of 5 to 10 Hz, 10 to 15 Hz, and 15 to 20 Hz. Next, we process the spectra to isolate source, receiver, and propagation path effects. This is an important step because individual spectra tend to be irregular in shape and difficult to fit robustly with theoretical models. However, by stacking and analyzing thousands of spectra, it is possible to obtain more consistent results. The basic approach is illustrated in Figure 2 and is similar to that used by Warren and Shearer (2000 and 2002) and Prieto et al. (2004). Each observed displacement spectrum $d_{ij}(f)$ from source i and receiver j is a product of a source term e_i (which includes the source spectrum and near-source attenuation), a near-receiver term s_j (which includes any uncorrected part of the instrument response, the site response, and the near-receiver attenuation), and a travel-time-dependent term $t_{k(i,j)}$ (which includes the effects of geometrical spreading and attenuation along the ray path). In the log domain, this product becomes a sum: $d_{ij} = e_i + s_j + t_{k(i,j)} + r_{ij}$ where r_{ij} is the residual for path ij. We parameterize t in terms of the predicted P travel time between the source and receiver, using the event locations and velocity model from Shearer et al. (2005). This accounts for both the event depth and the source receiver distance. The travel-time term $t_{k(i,j)}$ is discretized by its index k at 1 s increments in travel time. Because each station records multiple events and each event is recorded by multiple stations, this is an over-determined problem. We solve this equation using a robust, iterative, least-squares method in which we sequentially solve individually for the terms t_k, s_j, and e_i, keeping the other terms fixed at each stage. We suppress outliers by assigning L1-norm weights to misfit residuals greater than 0.2 s (or less than -0.2 s). This weighting scheme is necessary to ensure robustness with respect to a small number of spectra with large excursions compared to the bulk of the data. In practice, we found that the method converged rapidly to a stable solution after a few iterations.

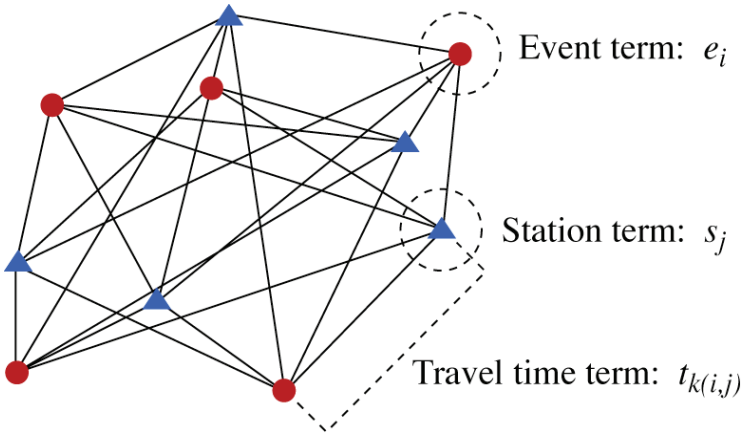


Figure 2. A cartoon showing how measured spectra can be modeled as a product of event, station, and travel-time-dependent terms.

Radiation pattern differences are not included in the previous equation and would be difficult to include in our processing because they are not generally available for the smaller-magnitude events. By using multiple stations for each source, however, radiation pattern effects will tend to average out. Note that this method resolves only differences in the relative shapes of the spectra. Without additional modeling assumptions, it cannot, for example, resolve how much of the spectral falloff is due to source effects and how much is due to attenuation common to all paths. The advantage of the method, however, is that it identifies and removes anomalies that are specific to certain sources or receivers. Because there may be difficulties in obtaining reliable and accurate instrument response functions for many of the stations in the archive, this is an important processing step that provides a way to correct for some of these problems.

Our focus has been on the stacked source spectra, e_i, which we ultimately use to estimate the moment and corner frequency of each event. At this stage, however, the source spectra only contain relative information among the different events. In order to estimate absolute spectra from our source stacks, we use the local magnitude M_L to obtain the scaling factor necessary to convert our relative moment estimates to absolute moment and we use an empirical Green's function approach to correct the spectral shapes for attenuation and other path effects (for details, see Shearer et al., 2006).

To study the average shape of the spectra, we stack our results within equally spaced bins in estimated seismic moment (obtained from the low-frequency part of the spectrum). Figure 3 shows these stacked spectra for both earthquakes and quarry blasts during 1994. The dashed lines show the best-fitting constant stress drop model of Madariaga (1976). One of the most active quarries is particularly anomalous and produces a bump in the spectra between about 3 and 8 Hz (seen in the middle panel of Figure 3). This bump largely disappears if this quarry is excluded from the analysis (see right panel of Figure 3).

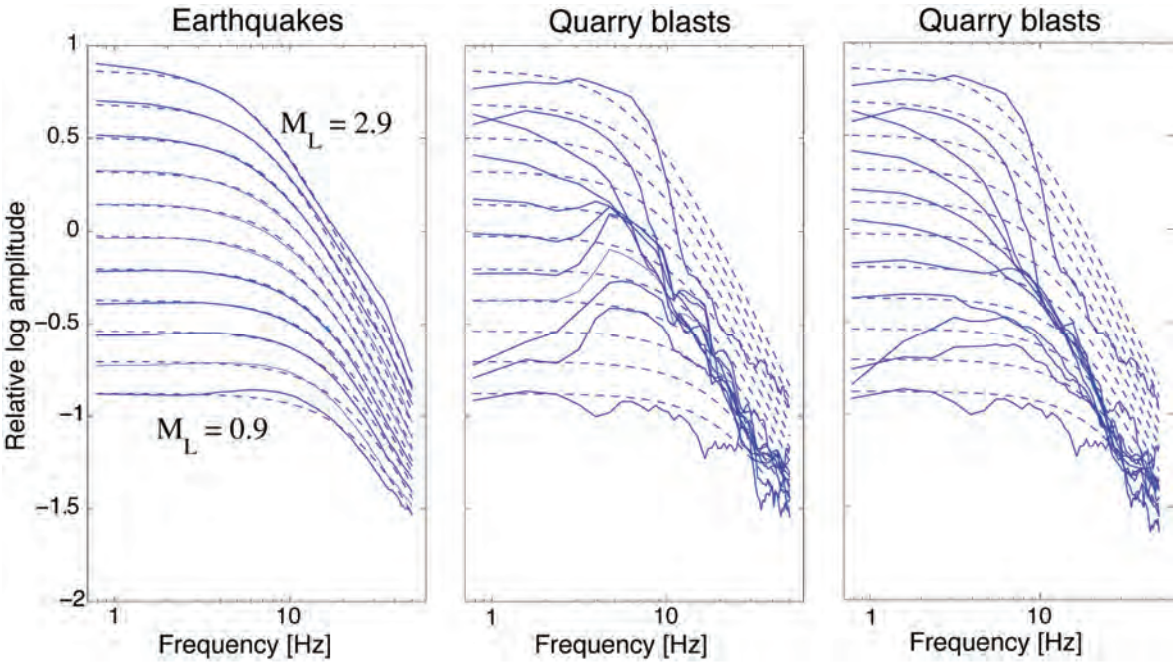


Figure 3. Stacked P-wave source displacement spectra from 1994 within bins of estimated seismic moment for: (left) 14,280 earthquakes, (middle) 360 quarry blasts, (right) 213 quarry blasts, excluding one particularly anomalous quarry. The spectra have been corrected for attenuation and other path effects using the empirical Green's function (EGF) method of Shearer et al., (2006). The dashed lines show the best-fitting constant stress drop model of Madariaga (1976).

Figure 3 shows that averaged earthquake spectra in southern California are well fit by a standard source model. However, the averaged quarry spectra appear anomalous in at least two respects: (1) they exhibit large misfit

compared to the source model predictions, and (2) they have generally steeper falloffs at high frequencies than the model predictions, which will lead to lower corner frequencies and stress drop estimates. The lack of high-frequency radiation from the quarries is somewhat surprising and may reflect ripple firing and/or strong near-surface attenuation. In any case, we attempt to use these two differences to discriminate between earthquakes and quarry blasts in southern California.

Figure 4 plots root mean squared (RMS) misfit versus estimated stress drop for the Madariaga model. The quarry blasts have generally higher misfit and smaller estimated stress drops than the explosions. However, the two populations are not completely separated and there is a region of overlap. Figure 5 plots estimated moment versus corner frequency for the two sets of events. The quarry blasts exhibit a smaller range of moment and generally lower corner frequencies at the same moment, but again there is some overlap between the two groups.

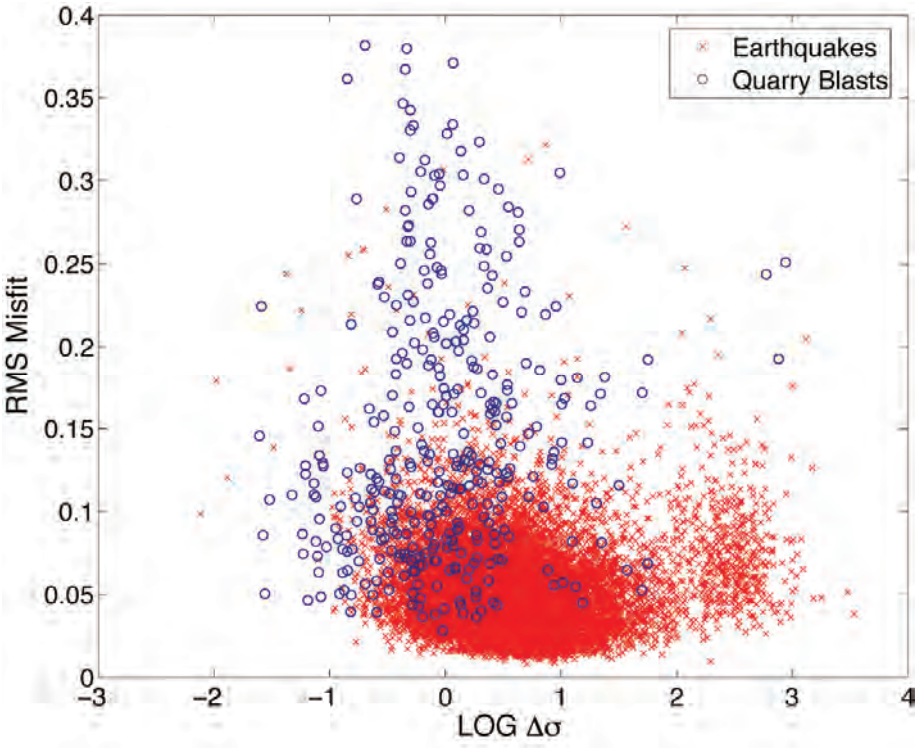


Figure 4. Spectral misfit to a standard source model versus estimated stress drop for southern California earthquake and quarry blasts during 1994. Earthquakes are shown in red, explosions in blue.

CONCLUSIONS AND RECOMMENDATIONS

Earthquakes and explosions in southern California exhibit significant differences in their average P-wave spectral properties. Quarry blast spectra are not well-fit by standard source models and typically have lower corner frequencies and anomalously steep falloffs at high frequencies compared to earthquakes of the same estimated moment. However, spectra from individual events have large variations and do not always permit an unambiguous identification of event type. Future results from analysis of S-wave spectra may provide additional discriminants.

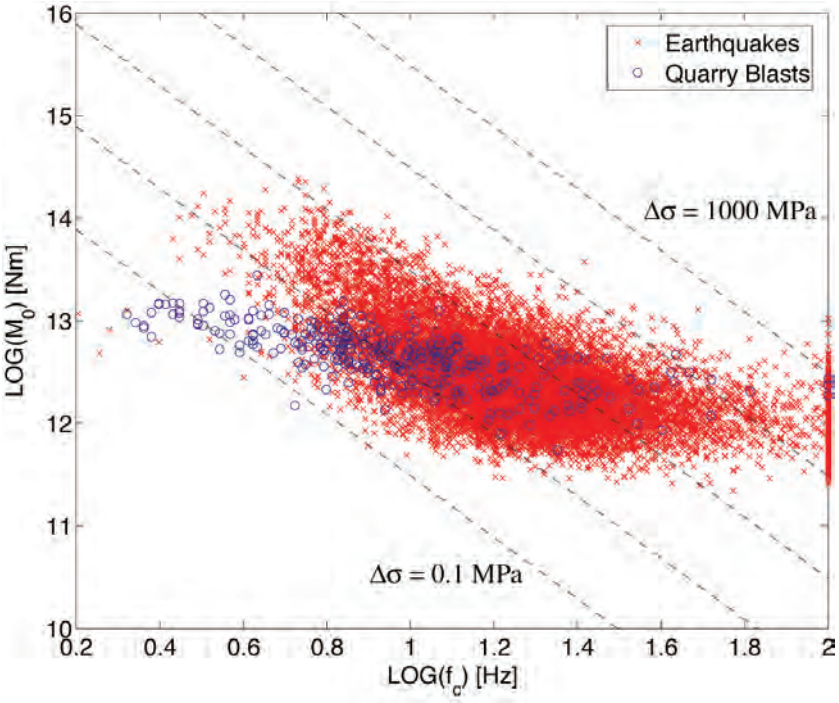


Figure 5. Moment versus observed corner frequency for southern California earthquakes and quarry blasts during 1994. The dashed lines show corresponding stress drop values from the Madariaga (1976) model. Earthquakes are shown in red and explosions in blue.

ACKNOWLEDGEMENTS

We thank Egill Hauksson for his help in maintaining the waveform database and computing the spectra and German Prieto for assistance in implementing the multi-taper algorithm.

REFERENCES

Hauksson, E. and P. Shearer (2005). Southern California hypocenter relocation with waveform cross-correlation, Part 1: Results using the double-difference method, *Bull. Seismol. Soc. Am.* 95: 896–903, doi:10.1785/0120040167.

Hedlin, M. A. H., J. -B. Minster, and J. A. O. Orcutt (1990). An automatic means to discriminate between earthquakes and quarry blasts, *Bull. Seismol. Soc. Am*. 80: pp. 2143–2160.

Hedlin, M. A., B. W. Stump, S. Arrowsmith, and M. D. Renwald (2004). A comparative test of seismic discriminants for mining explosions, in *Proceedings of the 26th Seismic Research Review*: *Trends in Nuclear Explosion Monitoring*, LA-UR-04-5801, Vol. 1, pp. 407–416.

Leidig, M. R., B. W. Stump, J. L. Bonner, C. T. Hayward, A. A. Velazco, D. F. Baker, H. Hooper, W. R. Walter, X. Yang, R. Zhou, C. L. Edwards, M. D. Renwald, and J. F. Lewkowicz (2004). Source phenomenology experiments in Arizona, in *Proceedings of the 26th Seismic Research Review: Trends in Nuclear Explosion Monitoring*, LA-UR-04-5801, Vol. 1 pp. 366–374.

Lin, G., P. Shearer, and Y. Fialko (2006). Obtaining absolute locations for quarry seismicity using remote sensing data. *Bull. Seismol. Soc. Am*. 96: pp. 722–728.

Madariaga, R. (1976). Dynamics of an expanding circular fault. *Bull. Seismol. Soc. Am*. 66: pp. 639–666.

Park, J., C. R. Lindberg, and F. L. Vernon, (1987). Multitaper spectral analysis of high frequency seismograms, *J. Geophys. Res*. 92: pp. 12,675–12,648.

Prieto, G. A., P. M. Shearer, F. L. Vernon, and D. Kilb (2004). Earthquake source scaling and self-similarity estimation from stacking P and S spectra, *J. Geophys. Res.* 109: doi:10.1029/2004JB003084.

Shearer, P., E. Hauksson, and G. Lin (2005). Southern California hypocenter relocation with waveform cross-correlation: Part 2. Results using source-specific station terms and cluster analysis, *Bull. Seismol. Soc. Am*. 95: pp. 904–915.

Shearer, P. M., G. Prieto, and E. Hauksson (2006). Comprehensive analysis of earthquake source spectra in southern California, *J. Geophys. Res*. 111: B06303, doi:10.1029/2005JB003979.

Stump, B., M. A. H. Hedlin, D. C. Pearson, and V. Hsu (2002). Characterization of mining explosions at regional distances, *Reviews of Geophysics*, 40: (4), 1011, doi:10.1029/1998RG000048.

Su, F., K. Aki, and N. N. Biswas (1991). Discriminating quarry blasts from earthquakes using coda waves, *Bull. Seismol. Soc. Am*. 81: pp. 162-178.

Tibuleac, I. M., J. Britton, D. B. Harris, T. Hauk, H. Hooper, and J. L. Bonner (2004). Detection methods for mining explosions in southern Asia, in *Proceedings of the 26th Seismic Research Review*: *Trends in Nuclear Explosion Monitoring*, LA-UR-04-5801, Vol. 1, pp. 427–438.

Walter, W. R., K. M. Mayeda, and H. J. Patton (1995). Phase and spectral ratio discrimination between NTS earthquakes and explosions, Part I: Empirical observations, *Bull. Seism. Soc. Am.* 85: pp. 1050–1067.

Warren, L. M. and P. M. Shearer (2000). Investigating the frequency dependance of mantle Q by stacking P and PP spectra, *J. Geophys. Res*. 105: 25, pp. 391–25, 402.

Warren, L. M. and P. M. Shearer (2002). Mapping lateral variations in upper mantle attenuation by stacking P and PP spectra, *J. Geophys. Res*. 107: pp. B12, 2342, doi:10.1029/2001JB001195.

THE PHYSICAL BASIS OF THE EXPLOSION SOURCE AND GENERATION OF REGIONAL SEISMIC PHASES

Jeffrey L. Stevens, G. Eli Baker, and Heming Xu

Science Applications International Corporation

Sponsored by Air Force Research Laboratory

Contract No. FA8718-04-C-0025

ABSTRACT

A longstanding nuclear monitoring problem is prediction of regional S phases, particularly Lg. Observed Lg is generally larger than predicted from a point source in a plane-layered earth model, particularly in high-velocity source regions. Direct generation of shear waves by a realistic explosion source is a likely explanation of the Lg amplitudes, although other explanations such as redirection of pS or scattering of Rg into Lg have been proposed, and to date it has not been possible to conclusively and quantitatively resolve the mechanisms responsible. We analyze several distinct sets of nuclear explosion records, complemented by nonlinear source and near field scattering calculations, which are coupled to regional waveform calculations, to quantify the effect of separate mechanisms.

We use local records obtained under this contract by the Institute for the Dynamics of the Geospheres (IDG) for 15 Degelen and Balapan explosions to investigate the effect of source depth and location within the Semipalatinsk Test Site (STS) on local generation of Sg and Rg relative to P. The local Sg/Pg ratios span a broad range and correlate well with regional S/P amplitudes recorded at the Borovoye auxiliary seismic station BRVK, at 650 km, suggesting that the local Sg may be the major contributor to regional S. IDG has also delivered parametric information, including depths and yields for nearly all of these events, and depths, yields, and near field waveform parameters (peak velocity, rise time, positive pulse width, and arrival time) for 19 STS nuclear explosions from the 1960s and 1970s.

We also have extended previous work on Nevada Test Site (NTS) and Kazakh depth of burial experiments. Specifically, we extend a comparison of vertical component P and Lg spectra of co-located overburied and normally buried explosions at NTS to 3-components and to Lg coda. Interpretation of a null previously observed in vertical component Lg spectral ratios is complicated by a corresponding peak in the Lg spectra of the overburied events. The null, however is clearly observed in the raw vertical component Lg spectra of normally buried events. It is somewhat inconsistent in the horizontal component Lg, and it is not present at all in the Lg coda. Rg scattered to Lg in modal scattering calculations for an NTS structure, however, is more prominent in the Lg coda time window (due to excitation of slower modes) than in the Lg. Wave number synthetics for spherical and CLVD point explosions and the modal scattering calculations also indicate that directly generated S and trapped pS in an NTS structure have similar nulls and contribute more to the Lg spectra than does scattered compensated linear vector dipole (CLVD) Rg. We are currently analyzing results of nonlinear source calculations for a normally buried and overburied explosion.

We also extend analysis of Kazakh depth-of-burial explosion data to 3-components. We find distinct Sg, separate from Rg, and extending to higher frequencies than Rg, on all 3-components of the local records of all three events. The local Sg is most prominent on the records of the two shallower events. Rg is still the dominant phase in near regional (85 km) records at KUR, where it is again preceded by a distinct S phase. These observations are consistent with S generated by the source, trapped pS, and possibly S* being major contributors to Lg.

OBJECTIVE

The objective of this project is to determine the source physics and corresponding generation and evolution of local and regional seismic waves from nuclear explosions. This is a joint project between the Science applications International Corporation (SAIC) and the Institute for the Dynamics of the Geospheres (IDG) in Moscow, Russia.

RESEARCH ACCOMPLISHED

Introduction

Lg is important to explosion yield estimation and earthquake/explosion discrimination, but the source of explosion generated Lg is still an area of active investigation. A spherical explosion in a whole space generates no shear waves. Thus, in the earth, shear waves from explosions must be generated by non-spherical components of the source, due to some asymmetry of the source or source conditions, or tectonic strain release, or by conversion of P and/or Rg waves to S, particularly though surface Rg scattering and surface P-to-S conversion including generation of S* (the strongly depth dependent nongeometric phase generated by conversion of the curved P wavefront).

In this project, we have been trying to constrain the source of Lg and other regional phases by examination of unique data sets from historical Soviet nuclear explosions, combined with theoretical analysis and numerical modeling. We examine local and regional data from these explosions to directly observe the generation, propagation and attenuation of S phases and the Rg phase. Most of the proposed mechanisms for Lg generation have a significant dependence on depth and/or scaled depth. We have excellent constraints on the yield and depths of the Soviet explosions and so can examine this dependence directly. In addition to regional phase generation, we also use new Soviet data from explosions detonated close to earlier explosions to determine the effect of proximity to an earlier event on coupling efficiency.

New Local Semipalatinsk Data: Description and Analyses

The Russian Institute for the Dynamics of the Geospheres (IDG) has provided two types of data. First is parametric data, depth, yield, peak velocities, and rise times for 25 Semipalatinsk nuclear explosions (Table 1). Event selection focused on sets of adjacent events to enable analysis of the effect of previous nearby events on the waveforms. IDG also provided 275 unique seismograms for 17 nuclear explosions with time series extending past the Rg arrival (Table 2). We are comparing local P, S, and Rg amplitudes with depth, yield, scaled depth, and with corresponding measurements at regional distance (BRVK, 650 km).

The near field data from some events in close proximity to earlier events were indistinguishable from the earlier events; however, a few events that were detonated close to an earlier event have distinctly different near field data. In Table 1, those events that were both close to an earlier event and which had significantly different near field peak velocity measurements than the earlier event are marked.

Figure 1 shows a map of part of the Degelen test site with 5 events marked (listed by number in Table 1). Peak velocity vs. scaled range measurements (Figure 1, right side) show that events 13 and 14 have significantly lower peak particle velocities than the earlier event that they were very close to: event 11. Event 15 was also close to event 12, but the effect on particle velocity is less clear than for events 13 and 14. The other two events marked in Table 1 were also close to an earlier event and had significantly reduced peak velocities.

Despite the significant effect on peak velocities for some events in the near field, there is no apparent effect on m_b. The events with reduced near field peak velocity fall right into the population of other explosions in a plot of m_b vs. yield (Figure 2) and are quite close to the magnitude/yield curve for this region ($m_b = 0.75\log Y + 4.45$, where Y is yield in kilotons; Murphy, 1995).

Table 1. Near field tabular data collected by IDG.

Date	Yield (kt)	Depth (m)	m_b	Event No.	Near Earlier Event	Lat	Lon
61/10/11	1.16	141	[K]4.78			49.772	77.995
62/02/02	16.9	265	[K]5.63			49.778	78.002
64/03/15	23.6	245	[A]5.56			49.808	78.102
64/05/16	23.7	266	[A]5.55	11		49.775	77.988
64/06/06	1.05	75	[K]4.42			49.809	78.093
64/11/16	23	203	[A]5.64			49.809	78.133
65/02/04	17	262	[A]5.10		X	[2]49.773	[2]77.991
65/07/29	1.0	126	[I]4.5			[2]49.773	[2]77.991
65/06/17	12	178	[A]5.24			49.828	78.067
65/09/17	10	148	[A]5.22			49.812	78.147
65/10/08	15	204	[A]5.47	12		49.826	78.111
65/11/21	29	303	[A]5.61			49.819	78.064
65/12/24	6	228	[A]4.94	13	X	49.805	78.107
66/02/13	109-125	343	[A]6.26			49.809	78.121
67/12/08	12.5	166	[A]5.31			49.817	78.164
68/09/29	75	358	[A]5.8			49.812	78.122
73/02/16	25	225	[A]5.48	14	X	49.816	78.116
79/05/31	8.5	183	[A]5.27		X	49.830	78.087
80/06/25	0.3	152	[K]3.70	15		49.826	78.099

m_b from AWE, Khalturin et al (2001) or ISC

Table 2. Local/near regional data collected by IDG that contain Rg arrivals. SD stands for scaled depth, column 6 lists the number of distinct seismograms for each component (there are multiple recordings at many distances—we count these only once). The last column lists location within Semipalatinsk, D for Degelen or B for Balapan.

Date	Time	Yield	Depth	SD	Data t/r/z	Range (km)	m_b	Lat	Lon	Loc
[1]71/12/15	07:52:59	1.3-1.5	146	1.07	3/9/9	7-77	[A]4.68	50.031	77.972	D
85/06/30	02:39:05	100	527	0.93	0/6/5	49-88	[A]5.92	49.857	78.659	B
85/07/20	00:53:16	76	466	0.90	0/8/7	56-86	[A]5.89	49.943	78.783	B
[1]87/05/06	04:02:08	18	174	0.54	0/9/9	13-83	[I]5.6	49.777	77.984	D
[1]87/07/17	01:17:09	78	267	0.51	1/7/6	15-84	[I]5.8	49.769	78.035	D
[1]87/10/16	06:06:07	1.1	82	0.65	0/8/8	19-76	[I]4.6	49.802	78.14	D
87/12/13	03:21:07	130	530	0.86	0/5/5	57-60	[A]6.06	49.957	78.792	B
[1]88/04/22	09:30:09	2	---	---	0/3/3	57-81	[I] 4.9	49.824	78.102	D
88/05/04	00:57:06	134	530	0.85	0/6/4	53-84	[A]6.09	49.931	78.741	B
88/06/14	02:27:09	5	271	1.30	0/7/6	67-89	[A]4.8	50.034	78.964	B
88/09/14	04:00:00	140	651	1.03	3/7/7	60-94	[A]6.03	49.879	78.823	B
88/11/12	03:30:06	17	---	---	5/6/7	68-88	[A]5.24	50.048	78.96	B
[1]88/11/23	03:57:09	19	204	0.63	6/9/9	14-83	[I]5.4	49.765	78.029	D
88/12/17	04:18:09	84	642	1.20	6/6/6	67-98	[A]5.83	49.879	78.924	B
89/01/22	03:57:09	108	580	1.00	6/9/9	58-88	[A]6.10	49.934	78.815	B
89/02/12	04:15:09	74	572	1.12	4/7/9	51-85	[A]5.86	49.911	78.704	B
[1]89/10/04	11:29:57	1.8	94	0.63	5/8/7	16-85	[I]4.6	49.751	78.005	D

[1] More data from previously reported event, with longer time series that include Rg.
[A] and [I] indicate m_b from the United Kingdom's Atomic Weapons Establishment (AWE) and the International Seismological Centre (ISC), respectively.
Locations from Geoscience Australia's database (http://www.ga.gov.au/oracle/nukexp_form.jsp)

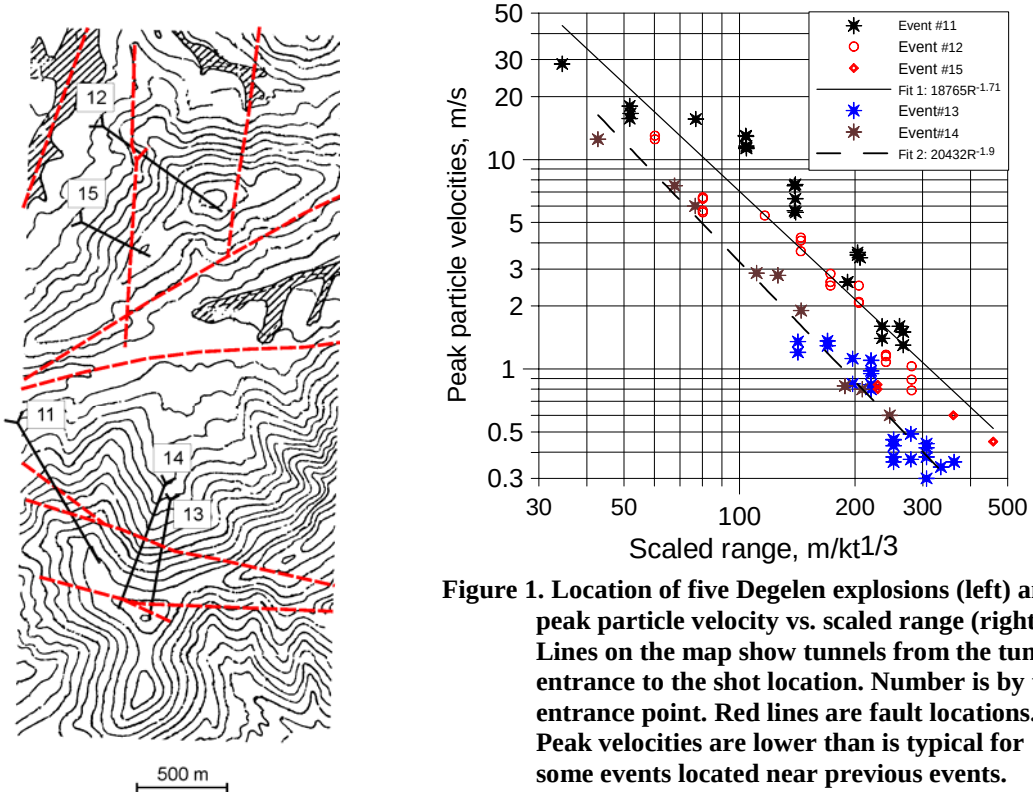


Figure 1. Location of five Degelen explosions (left) and peak particle velocity vs. scaled range (right). Lines on the map show tunnels from the tunnel entrance to the shot location. Number is by the entrance point. Red lines are fault locations. Peak velocities are lower than is typical for some events located near previous events.

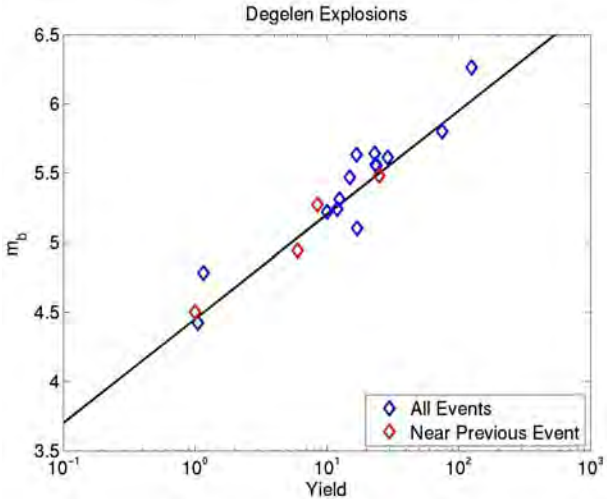


Figure 2. m_b vs. yield for the events in Table 1. Red triangles mark the four events marked in Table 1 as close to another event and having reduced near field peak velocities. The solid line is the nominal m_b/yield curve for this region from Murphy (1995). The effect of previous events on local peak velocities (Figure 1) is not observed in m_b.

Figure 3 shows local records of each of the Balapan explosions recorded at approximately 80 km (left) vs. the corresponding record from BRVK, at approximately 685 km. Figure 4 shows the same for the Degelen explosions. Both the local and regional records are normalized by the P-wave amplitudes. The Degelen records have much larger Sn and Lg amplitudes relative to P, which may be explained by the relative source spectra of S and P. That is, the Balapan explosions are mostly at yields and depths where the corner frequencies of the predicted P and S source spectra fall toward the left edge of the 0.5 to 2 Hz frequency band. The S spectral corners of the smaller Degelen explosions are more likely to be to the right of the frequency band we are examining. Figure 5 shows the predicted P and S-wave source spectra in granite (Mueller and Murphy, 1971; Murphy 2006) for the 74 and 5 kt Balapan explosions. The predicted source spectra are consistent not only with larger regional S/P for Degelen than for Balapan events, but also with the more distinct Sn and larger Lg from the smallest Balapan explosion (Figure 3,

bottom trace) and smaller Sn and Lg for the largest Degelen explosion (Figure 4, top trace). It is also consistent with the observations and conclusions of Fisk et al. (2005) regarding regional S/P from Lop Nor explosions. A second important observation made from these new data is that local Sg/Pg ratios are positively correlated with regional S/P ratios.

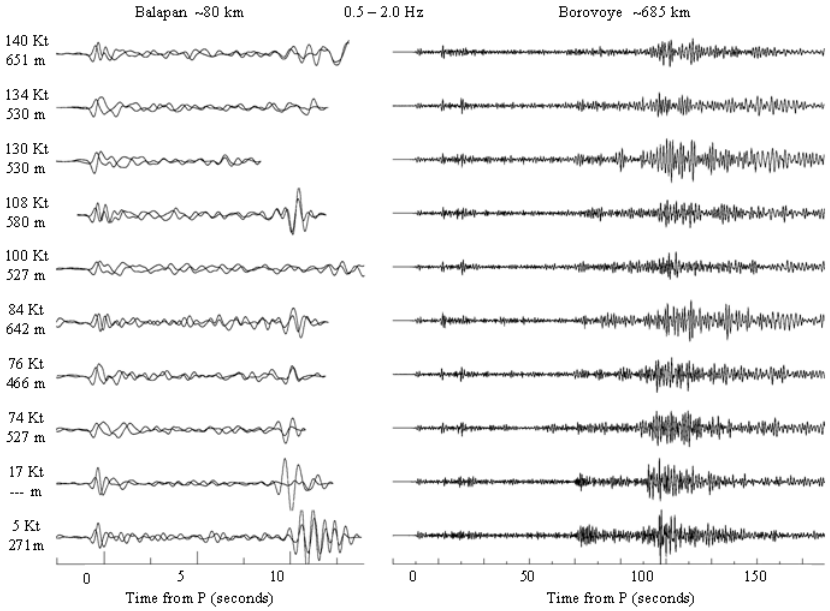


Figure 3. Overlain vertical and Hilbert transformed radial records of Balapan explosions (the closest record to 80 km distance for each event is plotted). To highlight S the large Rg is not plotted (left). Vertical records of the same events at BRVK, at 680 to 690 km, are plotted on the right. Both local and regional records are normalized by their P-wave amplitudes. Yields and depths are noted to the left of the traces. Sn is not prominent, and Lg is relatively small except for the smallest events.

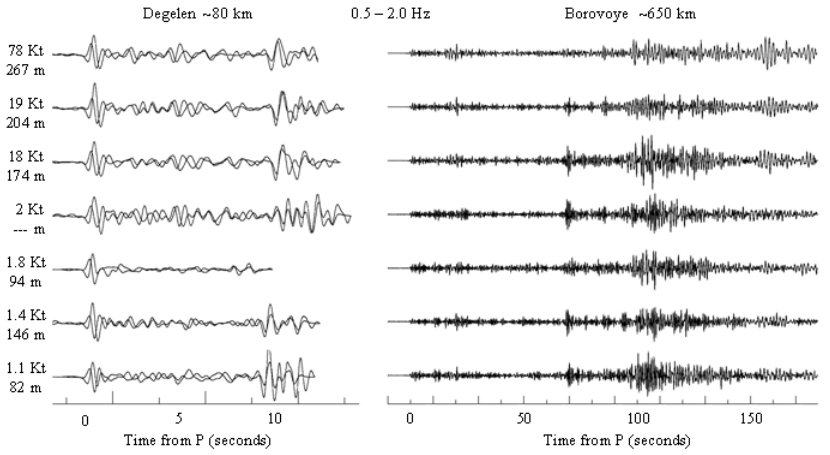


Figure 4. Same as Figure 2, but for Degelen explosions. Sn and Lg are prominent and large, except for the largest events, which appear more similar to the Balapan explosion records. The difference in S/P ratios may be accounted for by P and S source scaling (Figure 5).

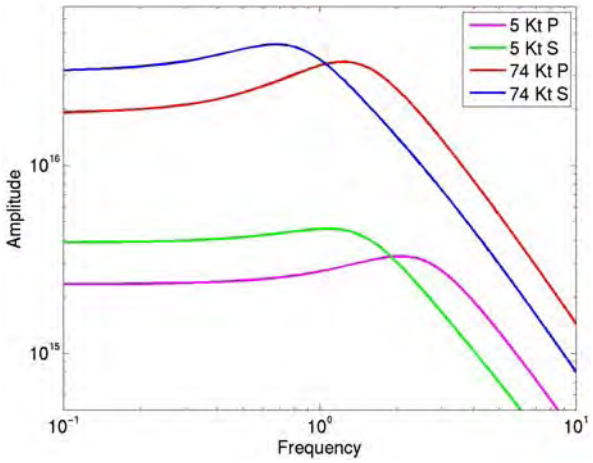


Figure 5. P and S source spectra for the 74 Kt, 572 m depth (2/12/89) and the 5 Kt, 271 m depth (6/14/88) Semipalatinsk explosions. The P spectrum is a Mueller Murphy granite source; the S spectrum is the Mueller Murphy source with the P wave speed replaced by the S wave speed, which shifts the spectrum to lower frequency for the S phase. This causes the S waves to appear to grow relative to P with decreasing explosion yield.

New Analysis of NTS Records

Patton and Taylor (1995) attribute a consistent spectral null at 0.55 Hz in the ratio of Lg spectra from normally buried to overburied explosions to CLVD generated Rg scattering to Lg. We extend analysis of the data used by Patton and Taylor to 3-components and to coda spectra, and use nonlinear source calculations, modal calculations, and wavenumber integration to model the results. Patton and Taylor (1995) normalized the vertical component Pg and Lg spectra of three normally buried explosions by those of two nearby overburied explosions to isolate the effects of spall. We do not use spectral ratios, because a spectral peak at 0.55 Hz in the overburied events' spectra causes a corresponding null in spectral ratios, which makes interpretation ambiguous. Table 3 lists the distances from the normally buried events to each of the overburied events, yields based on m_b(Lg), depths, scaled depths, and which components were available at each of the four Lawrence Livermore National Laboratory (LLNL) stations used for the five events used by Patton and Taylor.

Figure 6 shows the network averaged spectra for Pg, Lg (3.6 to 3.0 km/s), and Lg coda (3.0 to 2.0 km/s), for all three components. There is a clear spectral null in the vertical component Lg, and less distinct but similar nulls in Baseball and Caprock's, but not Glencoe's radial Lg. There is no clear corresponding null in the tangential Lg spectra, although Baseball has a null at slightly higher frequency. There are no corresponding nulls in any component of the Lg coda for any of the events.

Table 3. Metadata and availability of 3-component data from NTS events used in Taylor and Patton (1995) to investigate the effects of spall. The fifth column, SD, indicates scaled depth.

	Dist[1] (km)	Dist[2] (km)	Y=y(m_b)	Depth (m)	SD	ELK 412 km	MNV 238 km	LAC 301 km	KNB 287 km
Caprock	0.34	1.36	264	600	0.77	-	T,R,Z	T,R,Z	N,Z
Baseball	2.14	0.45	117	564	0.94	T,R,Z	T,R,Z	T,R,Z	T,R,Z
Glencoe	2.97	2.06	101	610	1.07	N,Z	T,R,Z	T,R,Z	E,Z[3]
Techado	-	1.70	2.89	533	3.07	T,R,Z	T,R,Z	T,R,Z	Z
Borrego	1.70	-	0.868	564	4.85	T,R,Z	T,R,Z	T,R,Z	T,R,Z

[1] Distance from Techado
[2] Distance from Borrego
[3] East component exists but is extremely poor quality

Modal simulations for an NTS structure indicate that, even for instantaneous scattering of all Rg to higher modes, the scattered Rg contributes more to the Lg coda time window than it does to Lg. This suggests that if the observed null is due to scattered CLVD Rg, the null should also be prominent in the Lg coda. The absence of the null in the coda spectra raises the question of which other sources of Lg could account for the observed null. Figure 7 shows the contributions to Lg from trapped pS, direct S from a CLVD source, scattered explosion Rg, and scattered CLVD Rg, all calculated for an NTS structure. The spherical explosion source is at 500 m depth, and the CLVD is half the moment of the explosion and is at 300 m depth. The scattered Rg contributions assume instantaneous scattering of all Rg energy into higher modes, with the distribution determined by a vertical point force (Stevens et al., 2005).

Time series are on the left and spectra on the right. Each of the contributions has a null in the same frequency band, but the amplitude of CLVD Rg contribution is approximately an order of magnitude smaller than that of other sources of Lg.

Actual nuclear explosion sources have some spatial and temporal distribution, which could affect their spectral shape. Figure 8 shows the regions of permanent nonlinear deformation and cracking from 2D nonlinear calculations of the Baseball and Techado sources. It also shows the Lg spectra of the Baseball (blue) and Techado (red) calculations compared with the sum of a spherical point explosion and a CLVD of half the explosion's size (black, dashed). The Lg of all three share a 0.55 Hz null. The common Lg spectral nulls demonstrate that the trapped pS and direct S from the nonspherical parts of the source are sufficient to explain the observed spectral nulls, and that the nulls persist for a more realistic distributed source. This analysis demonstrates that Lg spectral nulls can be generated by direct S and pS in an NTS structure, but, because increased scattering in the coda could obscure nulls there, the lack of nulls in Lg coda alone is insufficient to rule out other possible mechanisms.

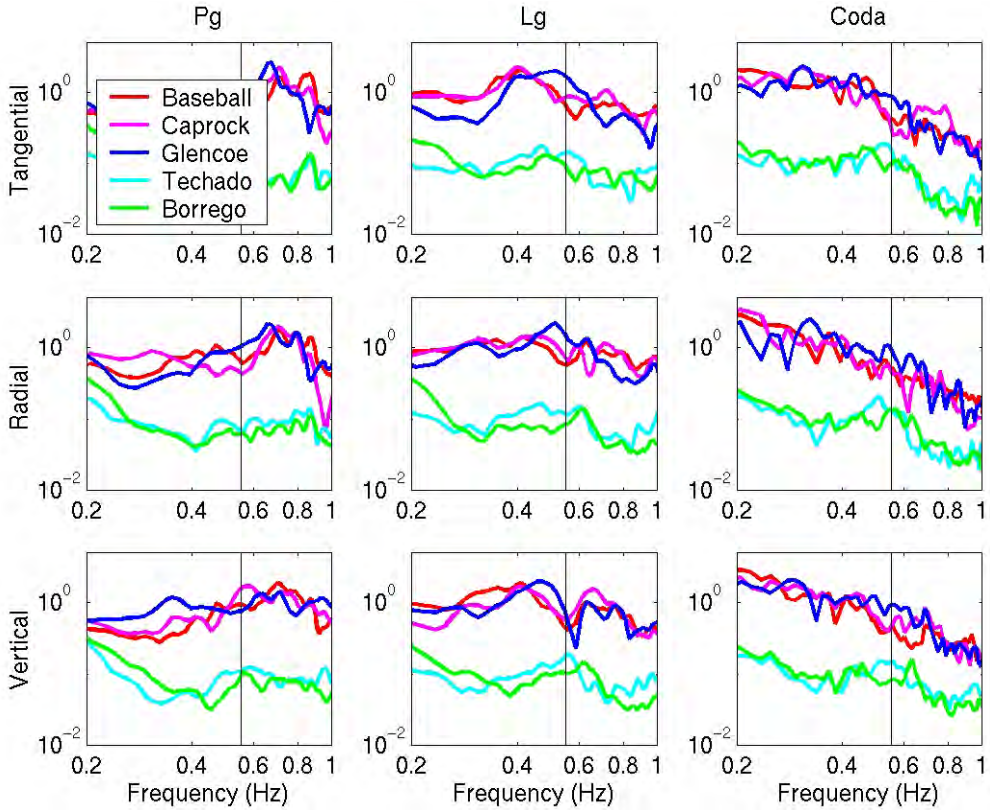


Figure 6. Network average Pg, Lg, and Lg coda spectra for all 3-components for Baseball (red), Caprock (purple), Glencoe (blue), Techado (aquamarine), and Borrego (green). The 0.55 Hz, black, vertical line shows the vertical component Lg spectral null position for the normally buried events. The null is not observed in the Lg coda, or as consistently in other components of Lg.

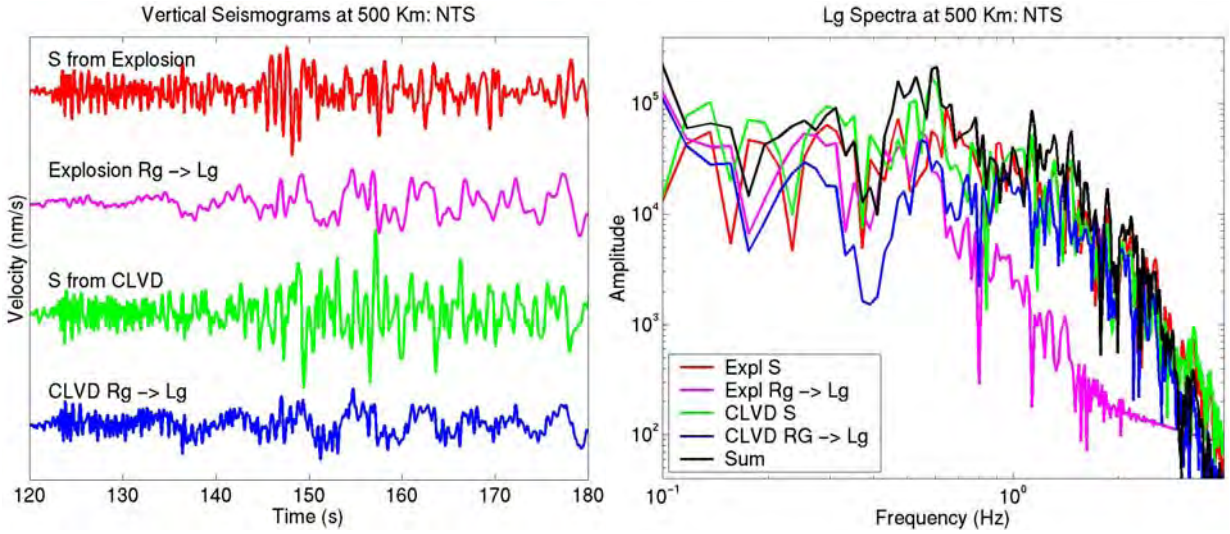


Figure 7. Contributions to the time series within the Lg window (left) and their spectra (right). Trapped pS (red), spherical explosion Rg to Lg scattering (maroon, upper bound), direct S from a CLVD (green), and CLVD Rg to Lg scattering (blue, upper bound) share a common spectral null, but the scattered CLVD Rg contributes less than the others. The black spectral curve is the sum of all the contributions.

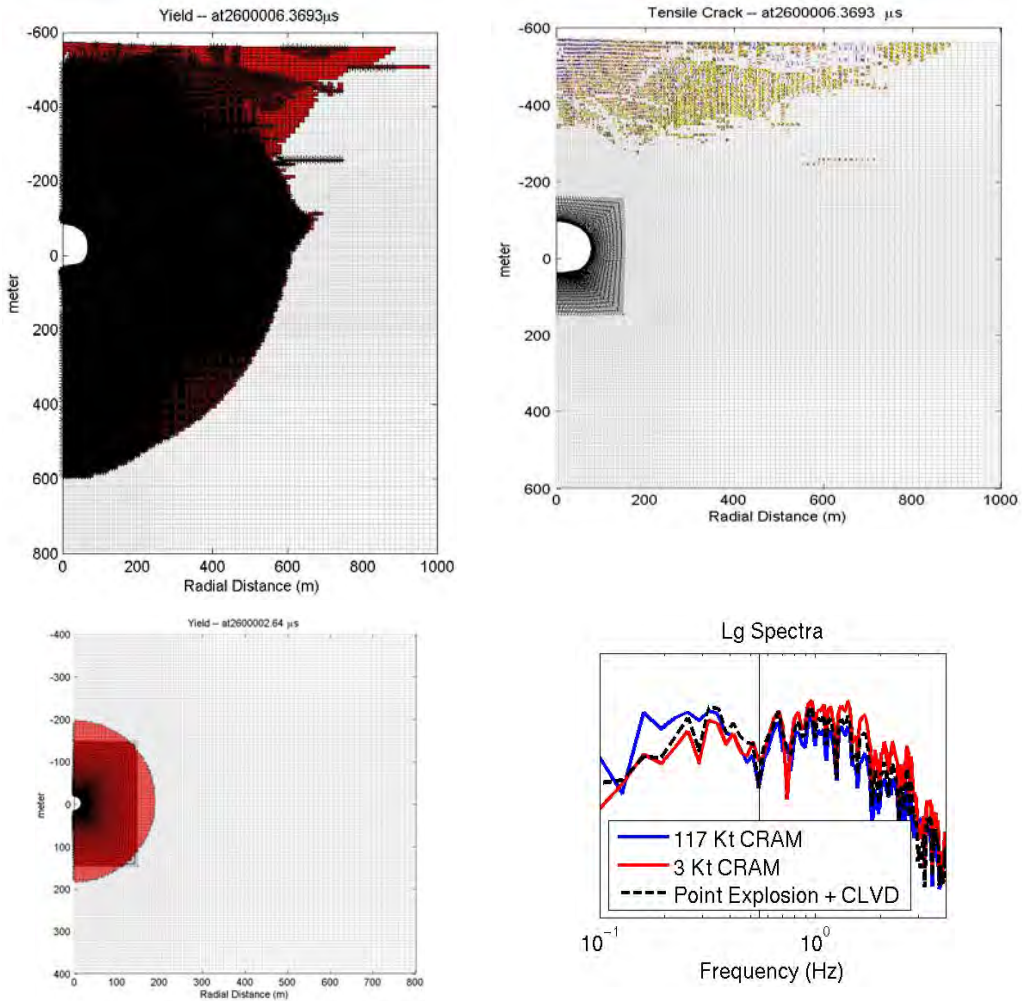


Figure 8. Permanent nonlinear deformation (left column) produced by 2D Lagrangian finite-difference simulations of the sources of Baseball (top) and Techado (bottom). The simulation for Techado produces a nearly spherical area of permanent deformation and no cracks. Cracks predicted by the Baseball simulation are shown in the upper right. Lg from these nonlinear source calculations for the Baseball (blue), Techado (red), and the sum of an explosion and a CVLD of half the explosion's size (black, dashed). The vertical black line indicates 0.55 Hz.

New Analysis of Kazakh Depth of Burial Experiments

Three 25-ton explosions were detonated at Balapan to investigate the effect of burial depth (Glenn and Myers, 1997). Myers et al. (1999) attribute spectral differences between regional P/S amplitude ratios to depth dependent differences in Rg, which is assumed to scatter to S. Patton et al. (2005) suggest that m_b(Lg) differences they observe at 415 km are due to differences in the amount of Rg available from each explosion for scattering to Lg near the source. The observed regional phase amplitudes may also be explained by differences in S directly generated at the source, due to structure and lack of containment for the shallow event. Direct generation of S from the explosions that reproduces the observed regional S/P ratios would predict Sg distinct from Rg near the source, and local S/P ratios consistent with regional S/P. To evaluate this prediction, we extend the previous work by examining 3-component local records to identify local Sg. We also examine an additional record at 85 km to investigate the persistence of Rg.

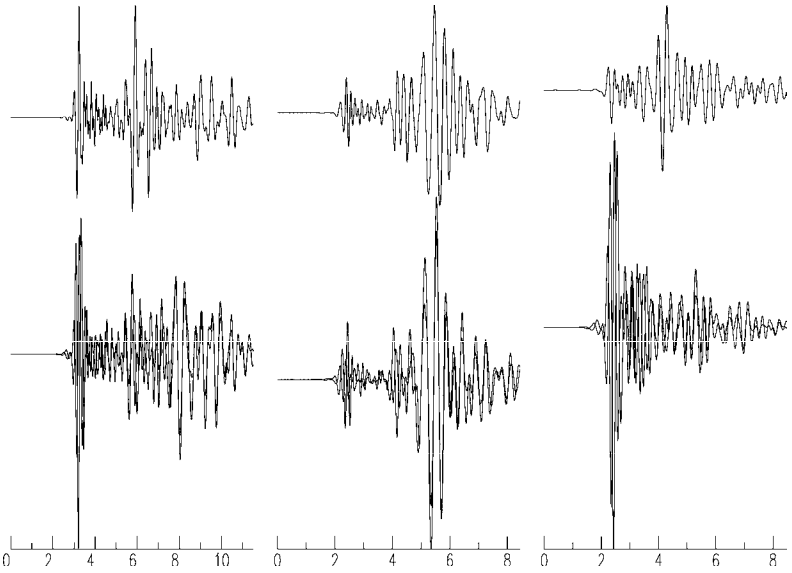


Figure 9. Tangential (upper) and overlain vertical and Hilbert transformed radial (lower) records of the 50, 300, and 550 m depth events (from left to right), filtered from 2 to 5 Hz. All three records in each set share the same scale. Records are at 17.3, 12.7, and 12.7 km respectively, and are plotted from origin time to 1.5 km/s group velocity. In each, a distinct Sg precedes the Rg (off azimuth for the 300 m depth event). Sg is more commonly observed and larger for the two shallowest explosions. Rg is smallest for the deepest event.

Figure 9 shows one 3-component set of local records for each event, filtered from 2 to 5 Hz, at 17.3, 12.7, and 12.7 km distance respectively for the 50, 300, and 550 m depth events. All records for each 3-component set are plotted on the same scale. Sg is distinguishable on all three components of records from all three events. Record sections (not shown due to space limitations) show that these Sg observations are not unique to just the records shown, and that Sg is generally most prominent on the records of the two shallower events. The Sg persists to frequencies greater than those of Rg, suggesting that they are not merely scattered from Rg.

Differences in source parameters besides depth, and the multiplicity of mechanisms that have some depth dependence complicate interpretation of the observed differences in S-wave generation between explosions. The shallowest explosion, which cratered, took place in “a weak shale” (Glenn and Myers, 1997), while the other two explosions were in granite. For the shallowest explosion, S*, the cratering, and more generally the asphericity of the yielding region, which generates shear waves directly, should all contribute to generate more shear waves than come from the deeper explosions. Although the two deeper explosions are very overburied, so we might not normally expect much asphericity, acceleration records show evidence of spall at depths associated with weak zones in both cases (Patton et al., 2005). Also, the P-wave velocity of the weak shale is less than the mantle shear wave velocity, and so the surface pS converted phase should be trapped and contribute significantly to Lg. Trapping of pS is less certain for the deeper sources, where source P-wave velocities are near the mantle S-wave velocity.

The importance of scattered Rg as a source of S depends on the rate of near source Rg scattering. Modal scattering upper bound calculations for a Degelen structure, similar to those in Figure 6, indicate that even if all CLVD Rg is scattered instantaneously at the source, it contributes less to Lg above 0.5 Hz than does direct S from the same CLVD. Ongoing work includes similar calculations for the structure local to these events at the event depths with more realistic rates of Rg scattering. Myers et al. (1999) observe that Rg is rapidly attenuated at < 20 km. We however observe that for all three explosions, below 2 Hz, Rg is still the dominant phase at KUR, 85 km distance (Figure 10). The Rg, arriving at approximately 30 s, is so dominant at 0.5 to 1 Hz that it is almost the only phase visible. At 1–2 Hz it is still larger than P and as large as the S phase, which arrives at approximately 20 s. This observation provides a limit on the energy available for near source scattering of Rg to regional S.

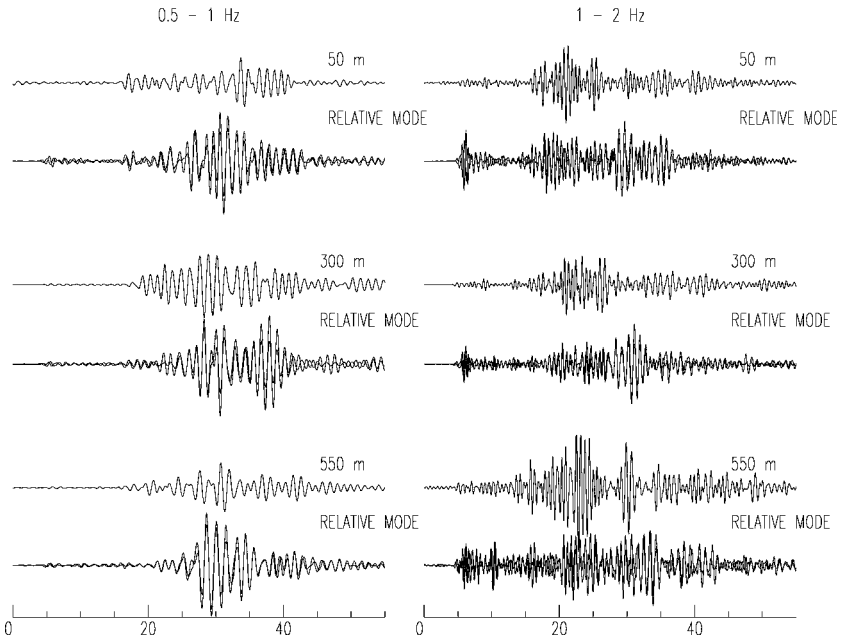


Figure 10. Shown here are 3-component seismograms for the 50 (upper set), 300 (middle), and 550 (lower) m depth of burial explosions at 85 km distance, at station KUR, from 0.5–1 Hz (left) and 1–2 Hz (right). Sg (at ~20 s) is distinct from the large Rg (~30 s) is apparent on the tangential component (upper traces of sets) and the overlain vertical and the Hilbert transformed radial seismograms (lower traces).

CONCLUSION AND RECOMMENDATIONS

We have collected extensive new data sets, including depths and yields, from the Semipalatinsk test site. These have proven useful in demonstrating decreased local peak velocities for some events located near previous explosions, although there is no apparent corresponding effect on m_b. Comparison of the new local records with regional data indicates that local Sg/Pg amplitudes correlate positively with regional S/P. That and the existence of distinct Sg, separate from Rg, for all events suggest that the source of Sg could be the same as that of Sn and Lg. Decreased S/P ratios for larger events can be explained by yield and depth dependent differences in source spectra.

Analysis of data from adjacent normally and overburied NTS events, and of the Kazakh depth of burial experiments, both previously interpreted as supporting Rg scattering to Lg, indicates that direct generation of S at the sources could also explain the observations. Numerical simulations, including modal scattering calculations, indicate that for the NTS events, both pS and direct S from a CLVD should contribute more to Lg than does scattered Rg from a CLVD. Nonlinear source calculations demonstrate that spectral nulls associated with pS and direct S from a CLVD are preserved for a more realistic distributed source. For the Kazakh depth of burial explosions, similar calculations indicate the same conclusion for the direct CLVD S, but further simulations at the depth of each explosion should be performed. For these calculations, Rg decay from local records and KUR should be employed to constrain the upper bound on Rg energy available for scattering to Lg.

REFERENCES

Fisk, M., T. Lay, and S. Taylor (2005). Modeling and empirical research on energy partitioning of regional seismic phases used for explosion monitoring, in *Proceedings of the 27th Seismic Research Review: Ground-Based Nuclear Explosion Monitoring Technologies*, LA-UR-05-6407, Vol. 1, pp. 539–549.

Glenn., L. and S. Myers (1997). Depth of Burial Experiments at Balapan, Univ. of CA, LLNL Report.

Khalturin, V., T. Rautian, and P. Richards (2001). A study of small magnitude seismic events during 1961-1989 near and on the Semipalatinsk Test Site, Kazakhstan, *Pure and Applied Geophysics* 158: 143–171.

Myers, S. C., W. Walter, K. Mayeda, and L. Glenn (1999). Observations in support of Rg scattering as a source for explosion S-waves: regional and local recordings of the 1997 Kazakhstan depth of burial experiment, *Bull. Seism. Soc. Am.* 89: 544–549.

Mueller, C. and J. Murphy (1971). Seismic characteristics of underground nuclear detonations Part I: seismic spectrum scaling, *Bull. Seis. Soc. Am.* 61: 1675–1692.

Murphy, J. R. (1995). Types of seismic events and their source descriptions, in monitoring a comprehensive test ban treaty, ed. E. Husebye and A. Dainty, pp. 225–245, Kluwer Academic Publishers, Boston.

Murphy, J. R. (2006). Source scaling analyses of frequency dependent energy partition for regional P and S phases from explosion sources, *Seis. Res. Lett.* **77**: March/April, p. 196.

Patton H. and S. Taylor (1995). Analysis of Lg spectral ratios from NTS explosions: implications for the source mechanisms of spall and the generation of Lg waves, *Bull. Seism. Soc. Am.* 85: 220–236.

Patton, H., J. Bonner, and I. Gupta (2005). Rg excitation by underground explosions: insights from source modeling the 1997 Kazakhstan depth-of-burial experiment, *Geophys. J. Int*. 163: 1006–1024.

Stevens, Jeffry L., G. Eli Baker, Heming Xu, and Theron J. Bennett (2005). The physical basis of the explosion source and generation of regional phases, in *Proceedings of the 27th Seismic Research Review: Ground-Based Nuclear Explosion Monitoring Technologies*, LA-UR-05-6407, Vol. 1, pp. 663–672.

ANALYSIS OF SHEAR WAVE GENERATION BY DECOUPLED AND PARTIALLY COUPLED EXPLOSIONS

Jeffry L. Stevens, Heming Xu, and G. Eli Baker

Science Applications International Corporation

Sponsored by Air Force Research Laboratory

Contract No. FA8718-06-C-0007

ABSTRACT

The objective of this new project is to investigate the sources of shear wave generation by decoupled and partially coupled explosions, and the differences in shear wave generation between tamped and decoupled explosions, using data analysis and numerical modeling of decoupled and partially coupled explosions.

During the first phase of this project, we focused on three theoretical mechanisms for generation of shear waves from decoupled and partially coupled explosions. The first mechanism is offset of the explosion from the center of the cavity, causing impact on the sides to vary in both amplitude and time. We worked out the general solution to this problem, and then performed calculations of an airshock propagating in the cavity and impacting the cavity wall. We find that the offset explosion acts like a dipole source and can generate significant shear waves with a modest offset from the center. The second physical mechanism is an explosion in an aspherical cavity, in this case a cylindrical tunnel.

The third physical mechanism we considered is crack growth outside of a partially coupled explosion. We are investigating two types of crack distributions: (1) small hydrofractures distributed broadly around the explosion in response to tensile stresses and (2) generation of a smaller number of larger hydrofractures. We are performing these calculations using the nonlinear axisymmetric finite difference code CRAM, with crack propagation algorithms developed by Nilson et al. (1991). We use the representation theorem to calculate outgoing P and S waves to determine the additional S waves generated by the cracks.

To complement these calculations, we are examining existing records of and reports on historical decoupled explosions, in particular, data from Khirgizhia decoupling experiments and Azgir decoupled nuclear explosions in the former Soviet Union, the U.S. Salmon/Sterling experiment, and extensive reports on the British Orpheus decoupling experiments. A consistent result between all data sets for which such data is available is that at low frequencies (<~2 Hz) local records of collocated tamped and decoupled explosions scaled for yield have significant and identical shear waves. At higher frequencies (~5–15 Hz), however the tamped explosions generate larger shear waves than the collocated decoupled explosions. Near field records of the decoupled explosion Sterling are found to have strong shear waves at frequencies above 20 Hz, while the records show pure radial P-wave motion at lower frequencies. In contrast, records at similar ranges for Salmon show pure radial P-wave motion at all frequencies. We are in the process of performing two-dimensional axisymmetric finite difference calculations of the Salmon and Sterling explosions. The Salmon calculation has been completed and provides an excellent match to the near field data.

OBJECTIVES

The objective of this project is to investigate the sources of shear wave generation by decoupled and partially coupled explosions, and the differences in shear wave generation between tamped and decoupled explosions. This is being accomplished through a program of data analysis and numerical modeling of decoupled and partially coupled explosions.

RESEARCH ACCOMPLISHED

Introduction

Detonation of a nuclear explosion in a large cavity to decouple the source from the surrounding medium and so evade detection has been a concern for nuclear monitoring for many decades (e.g., Latter et al., 1961). Most previous work on decoupling has focused on the empirical evaluation and numerical modeling of frequency dependent decoupling of explosions in cavities to address evasion. The "decoupling factor," which is the amplitude ratio of the seismic signals of the tamped to the decoupled explosions, depends on the emplacement media, but can be as large as two orders of magnitude. Consequently while decoupled explosions of less than a kiloton may be detected by a capable seismic network, the seismic signal is small enough that it may be difficult to distinguish from the large number of small earthquakes and mining explosions that occur in the same magnitude range (< ~2.5). Discrimination of decoupled explosions from this background noise is therefore an important issue.

The most reliable discriminants for events in the magnitude range of decoupled explosions are high frequency spectral ratios of the amplitudes of the seismic shear phases Sn and Lg to Pn or Pg, with explosions in general having lower S/P ratios than earthquakes. It is therefore very important to understand the shear wave generation by decoupled and partially coupled explosions in order to ensure that they are identified correctly by the discriminants that depend on shear wave amplitudes, and to identify any circumstances under which the discriminants could fail.

At first glance, generation of shear waves by a decoupled explosion might appear to be an easy problem, since a nuclear explosion detonated at the center of a perfect spherical cavity large enough to decouple the explosion would generate no shear waves (other than conversions due to the earth's surface and scattering). However, there are several problems with this simple picture:

1. shear waves have been observed from all decoupled explosions, even quite close to the source;
2. no cavity actually has perfect spherical symmetry; and
3. partially coupled explosions generate cracks more readily than tamped explosions.

Our research program follows these three points. First, we review existing data for decoupled and partially coupled nuclear explosions. As pointed out above, this data has been extensively studied to understand decoupling, but much less has been done with the shear wave data. We find that there is one consistent difference between data from tamped and decoupled explosions: S/P ratios at high frequencies are larger for tamped explosions than for decoupled explosions. This is not the case at lower frequencies, where S/P ratios are observed to be nearly identical for tamped and decoupled explosions. This puts some constraints on shear wave generation mechanisms that may be operating in each case. Second, we model shear waves generated by explosions with two types of source asymmetry: non-spherical cavities and offset or asymmetric explosion sources. Our particular interest is in determining how much asymmetry is necessary to generate significant shear waves. We investigate this in two ways: (1) using nonlinear calculations of an explosion source in a non-spherical cavity and (2) using a modification of the method of Stevens (1980) to predict non-spherical oscillations of the cavity due to asymmetries in the incident stress field. Third, we model seismic waves caused by cracks generated by partially coupled explosions. Such cracks could substantially increase the shear waves generated by the explosion, complicating the discrimination problem. Finally, we are performing full two-dimensional axisymmetric finite difference calculations of the Salmon and Sterling explosions in order to understand the shear waves generated by those two important events.

Observed Frequency Dependent Differences in Shear Waves between Decoupled and Tamped Explosions

Recordings on the same instruments, from co-located tamped and decoupled explosions, normalized by the P wave to account for absolute amplitude differences due to yield and decoupling, have nearly identical shear waveforms below 2 Hz, but have relatively more S with increasing frequency. Figure 1 shows such records for Salmon, a tamped 5.3 kt nuclear explosion at 828 m depth in salt, and Sterling, the 0.38 kt nuclear explosion detonated in Salmon's 17 m radius cavity. Figure 2 is similar, but for a 64 kt tamped Azgir nuclear explosion at 987 m depth in salt and the 10 kt nuclear explosion detonated in the first explosion's 38 m horizontal radius by 33 m vertical radius cavity. Figure 3 shows records at 5 km from adjacent one ton decoupled (red) and tamped (blue) chemical explosions in limestone in Kirghizia. The decoupled explosion was suspended in a 4.92 m radius cavity.

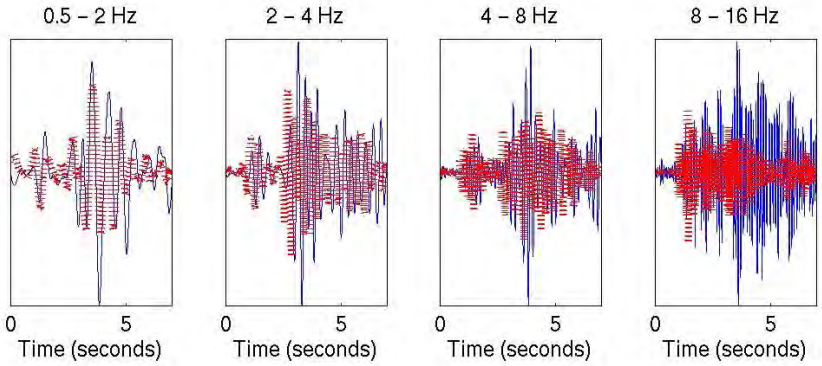


Figure 1. Salmon (blue) and Sterling (red, dotted) vertical records at 16 km, scaled by the first second of P.

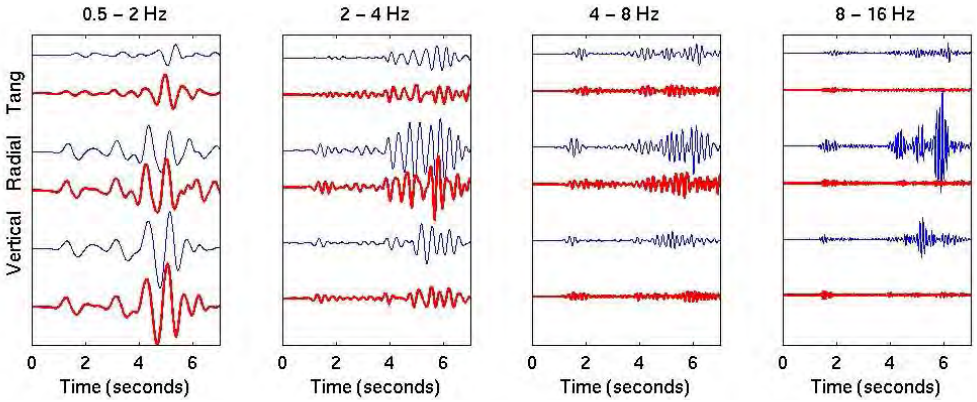


Figure 2. Tangential (upper 2 traces), radial (middle 2 traces), and vertical (bottom 2 traces) records at 18 km for tamped (blue) and decoupled (red) Azgir nuclear explosions in 4 passbands, scaled by the vertical P-wave rms amplitude. Time relative to origin is unknown. Initial P arrival is set at 1 s.

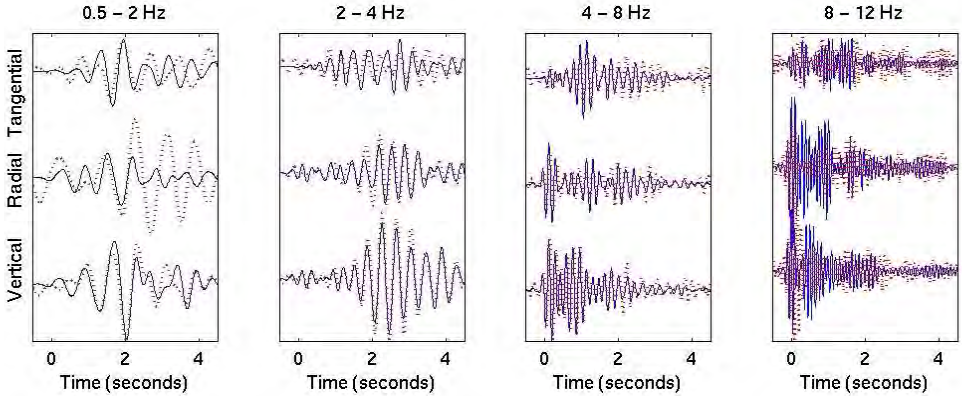


Figure 3. Tangential, radial, and vertical (top to bottom) seismograms 5 km from one ton decoupled (red) and tamped (blue) explosions, scaled by the vertical P amplitude. All three components for each event are on the same scale. Time is from the initial P arrival. SV arrives ~0.5 s after P.

Shear Waves from a Non-Isotropic Explosion Source

Stevens (1980) developed a solution for the seismic waves generated by an explosion in an arbitrarily prestressed elastic medium. Here we generalize the solution to allow for cases where the explosion is non-isotropic. In particular, we consider cases where the explosion is offset from the center of the cavity so that the amplitude and arrival time of the explosion vary as a function of position on the cavity wall. The general solution for the seismic wave field from a set of tractions applied to the inside of a spherical cavity is given by

$$u = -\int_{\Sigma} u \cdot T(G) \cdot \hat{n} dA + \int_{\Sigma} G \cdot T(u) \cdot \hat{n} dA - \frac{1}{i\omega} \int_{\Sigma} G \cdot T(u^*) \cdot \hat{n} dA \,, \tag{1}$$

where Σ is the cavity surface, u on the left side of the equation is the displacement at any location outside the cavity, and u inside the integral is the displacement on the cavity wall. G is the elastic Green's tensor in spherical coordinates, and T is the stress operator; u^* is the difference in the static displacement field before and after the explosion due to changes in the static stress field, and so will vanish for a decoupled explosion where the prestress does not change, but will be non-zero for a tamped explosion with tectonic strain release. The third integral therefore represents the response of the medium to a change in prestress, the second term represents the response of the medium to the applied stress from the explosion, and the first term represents the additional motion due to the response of the cavity wall.

Equation 1 can be solved by expanding the displacement, traction and Green's tensor in vector spherical harmonics. The case of interest here is shown in Figure 4 (left), where the explosion source is initially offset from the center of an air-filled cavity of radius R by a distance d. The right side of Figure 4 shows the calculated P and S waves from the explosion. The offset from the center causes the shock wave to impact the side of the cavity closest to the explosion earlier and with greater force than the opposite side of a cavity. This is equivalent to a dipole source acting in the direction of the offset, and as illustrated, can generate S waves comparable in amplitude to the initial P wave.

Note that the offset in origin breaks the symmetry of the problem except for axisymmetry about the offset axis. If the offset is oriented horizontally relative to the surface, strong SH waves will be generated. Zhou and Harkrider (1992) similarly found that a point explosion offset from the center in a solid-filled spherical region embedded in a whole space acts primarily as a dipole source.

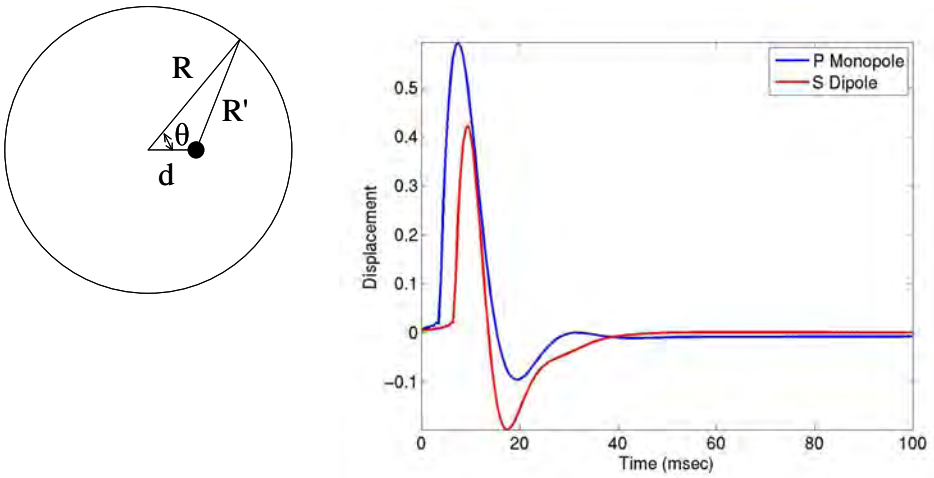


Figure 4. Calculated P and S waves (right) for an explosion in an air-filled cavity with the origin of the explosion offset from the center (left). In this example the cavity radius is 17 m and the offset from the center is 8.5 m.

Shear Waves from an Explosion in a Tunnel

Shear waves from an explosion in a tunnel are calculated using the procedure described by Rimer et al. (1994). The axisymmetric Eulerian finite difference code STELLAR is used to calculate the propagation of the air shock in the cylindrical tunnel. Just before the air shock impacts the end of the tunnel, the solution is overlaid onto a new grid that is used by the axisymmetric Lagrangian finite difference code CRAM. The calculation continues in CRAM until it reaches the linear elastic region. The representation theorem is then used to propagate the solution to the far field. In this example, we show a calculation of a 1.52 kt explosion in a cylindrical tunnel in granite with a length of 220 m and a radius of 5.4 m. Figure 5 shows the pressure field in the STELLAR computational grid at 6.6 ms and the velocity field in the CRAM grid at 10 ms.

Far-field body waves were calculated using the representation theorem to integrate the displacements and stresses on the monitoring surface together with a far-field body wave Green's function. Both P and S waves were calculated by integrating with the appropriate Green's function. Figure 6 shows the P and S waves both calculated at a 45 degree takeoff angle. The takeoff angle is measured with respect to the long axis of the cylinder, so zero is in the direction of the axis and 90 degrees is perpendicular to the long axis. S waves are largest at 45 degrees and are about ½ the amplitude of the P wave at the same takeoff angle.

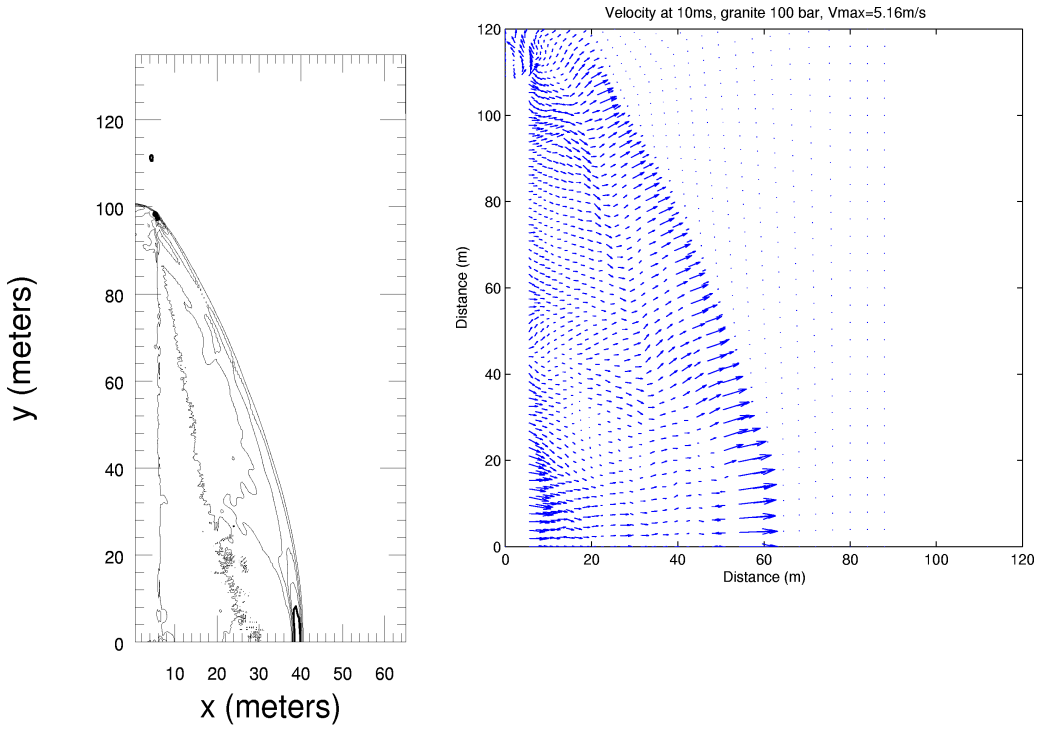


Figure 5. Pressure contours from STELLAR calculation (left) at the overlay time of 6.6 ms, and velocity field from CRAM calculation (right) at 10 ms. Only ¼ of the computed fields are shown because of symmetry about the y=0 plane and the axisymmetric x=0 line.

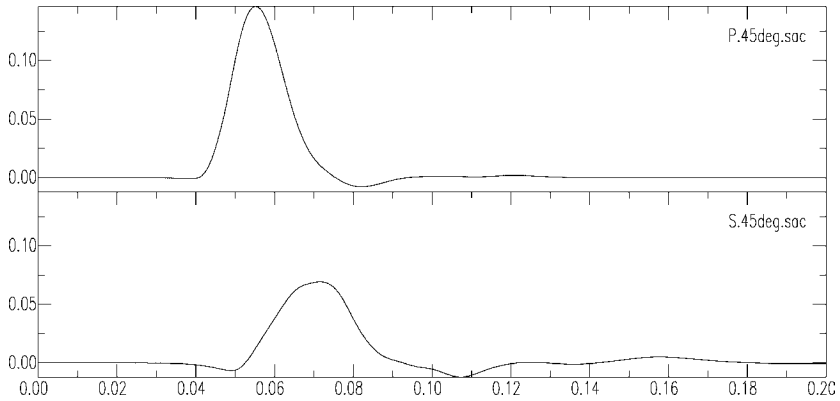


Figure 6. Far-field P (top) and S (bottom) displacement for the tunnel calculation at a takeoff angle of 45 degrees. Waveforms were lowpass filtered at 40 Hz.

Shear Waves from Hydrofractures

Crack generation has long been a concern for containment of underground nuclear explosions. During the nuclear testing program considerable effort was expended on prediction of crack generation and propagation during explosions. One of the programs developed for this purpose as part of the containment program is F-Cubed (Nilson et al., 1991). F-Cubed combines the CRAM Lagrangian finite difference code with the FAST fracture propagation code, and can predict crack generation and propagation outside of tamped or partially coupled explosions. It can be used in either of two ways: (1) to predict where cracks will occur and (2) to predict the opening and propagation of known cracks or cracks along suspected zones of weakness. Here we use it to predict crack generation.

Nonlinear stress wave dynamics of rock are affected by the penetration of gases into fractures, which fragments the rock and changes the burden. We model the interaction between stress waves and fully-pressurized fractures by assuming that the pressure within the crack is everywhere equal to the instantaneous cavity pressure. The growth of a swarm of hydrofractures is calculated by allowing the fluid to enter any computational cell having a minimum compressive stress less than the cavity pressure, subject to the connectivity, angular orientation and propagation speed restrictions. The following figures compare the characteristics of wave generation in a Nevada Test Site (NTS) structure with and without hydrofracturing. The partially coupled explosion has an initial cavity radius of 10 m, and an explosion yield such that the vaporization radius is also approximately 10 m. Although this is almost large enough to be considered tamped, the air-filled cavity makes it more subject to cracking than a fully tamped explosion. Figures 7–11 illustrate the effects of a swarm of hydrofractures on the far field seismogram and the compressional and shear waves. Figure 11 shows amplification of the S and higher mode surface waves relative to P and the fundamental mode surface wave.

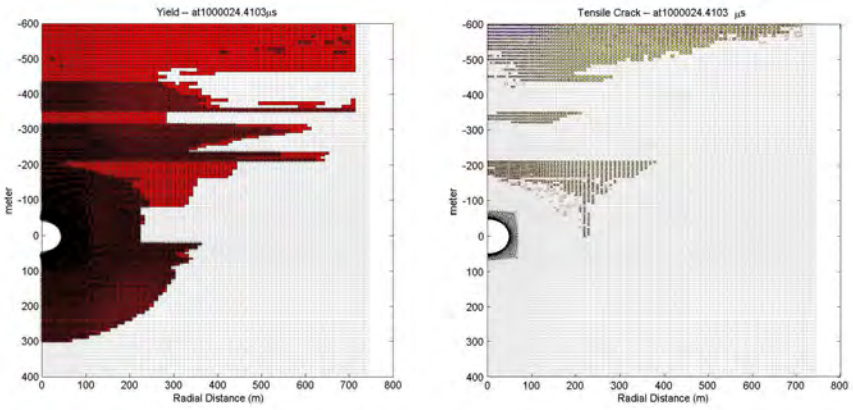


Figure 7. Yield and tensile cracks in the absence of hydrofracturing. The left panel shows the yield extent at 1 s and the right shows the tensile crack distribution.

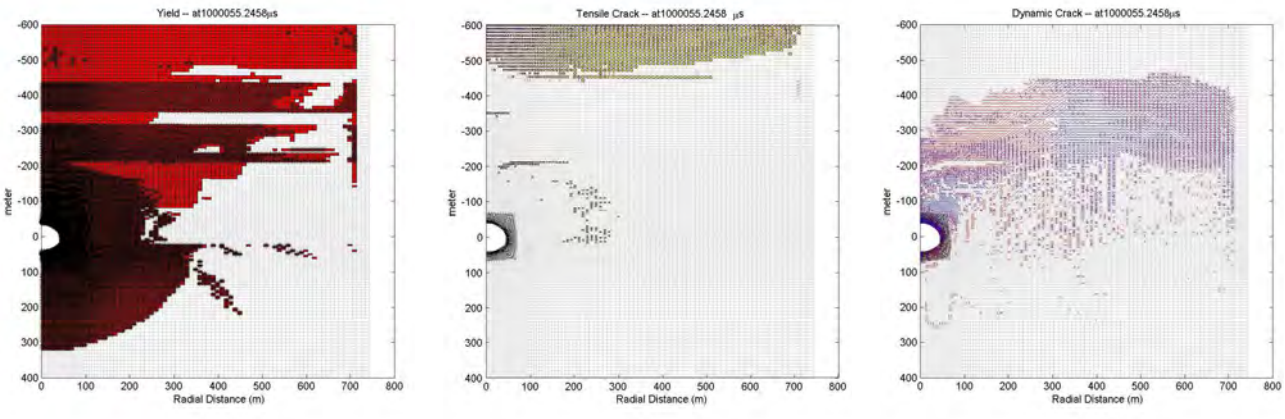


Figure 8. Yield (left), tensile cracks (middle) and hydrofractures (right) from a calculation including prediction of hydrofractures.

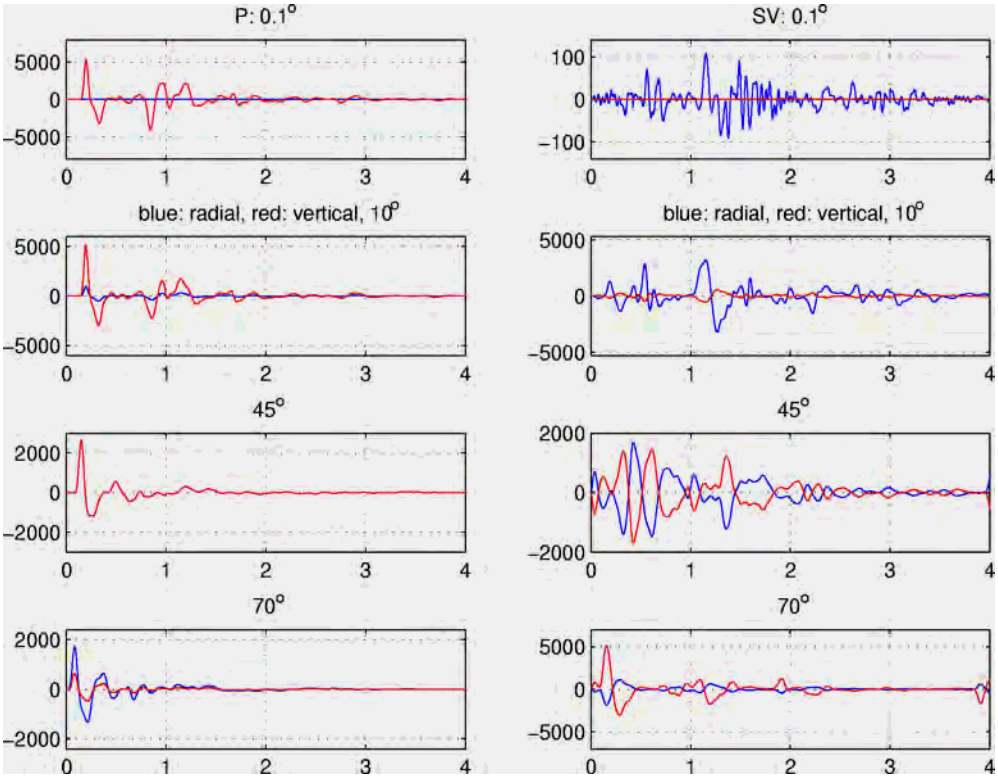


Figure 9. Body waves in the absence of hydrofracturing. The left panel shows the compressional body waves at different take-off angles and the right shows the shear waves. The red lines denote the vertical component and the blue lines the radial component.

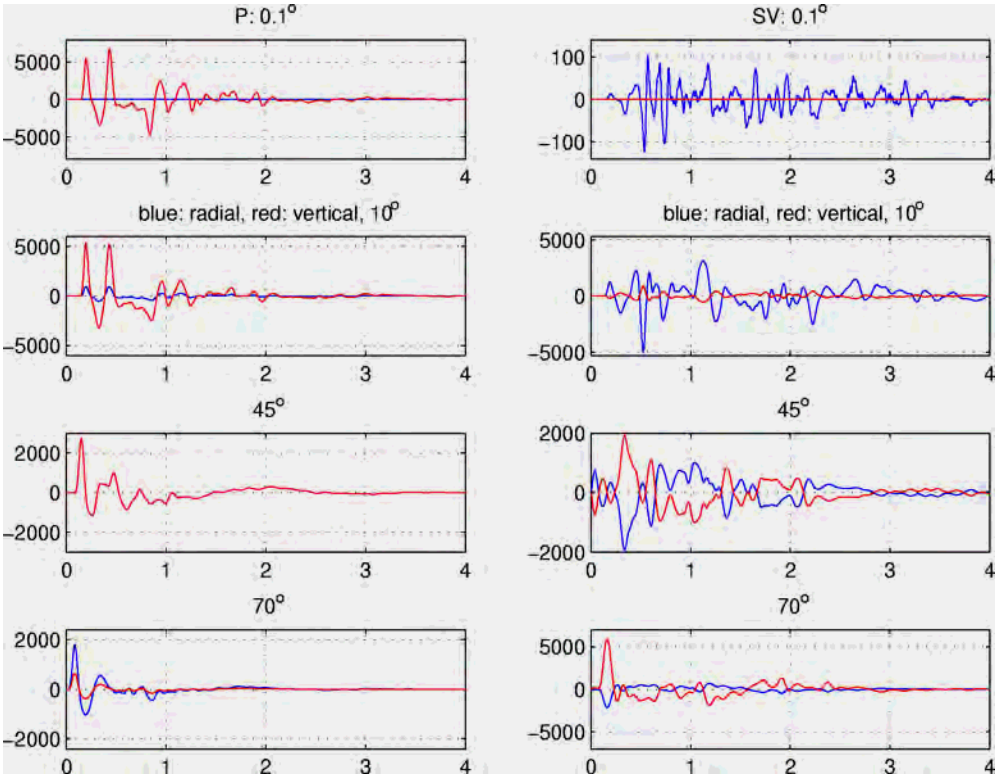


Figure 10. Similar to Figure 9 but in the presence of hydrofracturing.

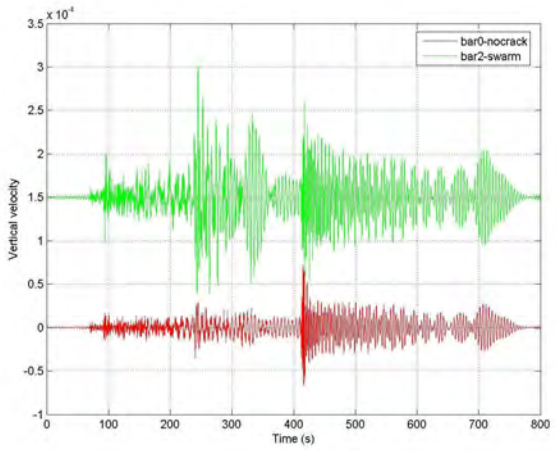


Figure 11. Comparison of seismograms at 500 km with and without hydrofracturing. The green line represents the seismogram in the presence of hydrofracturing.

Salmon/Sterling Axisymmetric Calculations

Salmon was a tamped 5.3 kt nuclear explosion detonated at 828 m depth in the Tatum salt dome. Rimer and Cherry (1982) successfully modeled the explosion event in the spherical case and found that ground motion data were best modeled by using the salt work-softening-hardening model, which is required in order to explain the small amplitude "elastic" precursor which is inconsistent with the laboratory strength measurements. The implementation in the finite-difference method is to calculate the strength as a function of the inelastic energy deposited in the material during yielding, i.e., $(Y = Y_0(1 + e_1 E - e_2 E^2) \le Y_{Lim})$, where Y_0 is the initial strength and e_1 and e_2 are respectively work hardening and work softening material constants.

We use the same parameters obtained in the spherical case to model the Salmon explosion in cylindrical symmetry with four layers (sediment, limestone, anhydrite and salt, see Murphy, 1991) and a free surface. The calculated final cavity radius is about 22 m. The middle panel in Figure 12 shows the calculated nonlinear deformation region extent. The 3 red lines mark the boundaries of materials, i.e., from top to bottom, sediment, limestone, anhydrite and salt. Both limestone and anhydrite are strong materials and did not yield in the Salmon explosion simulation. Salt yielded out to a range of about 950 m, consistent with the spherical calculation (Rimer and Cherry, 1982). The weak sediment also yielded near the surface. The right panel in Figure 12 shows tensile cracking in salt and sediment. Cracks in salt are opened out to about 200 m from the explosion, and the sediment surface also shows some tensile cracking due to spall.

The calculated ground motions are compared with the Salmon data on the surface and in the salt layer in the near field in Figure 13. The stations are shown in the left panel in Figure 12. In Figure 13, the solid lines denote Salmon data and the dashed lines denote calculations. The bottom curves represent the radial components and the upper ones represent the vertical components. The two dimensional (2D) results are also in good agreement with the recordings at these locations. At the surface gauge (E-6-S), both the data and calculation show spall caused by the tensile wave reflected from the free surface, although the calculation shows somewhat earlier free fall of the uplifted surface than the data.

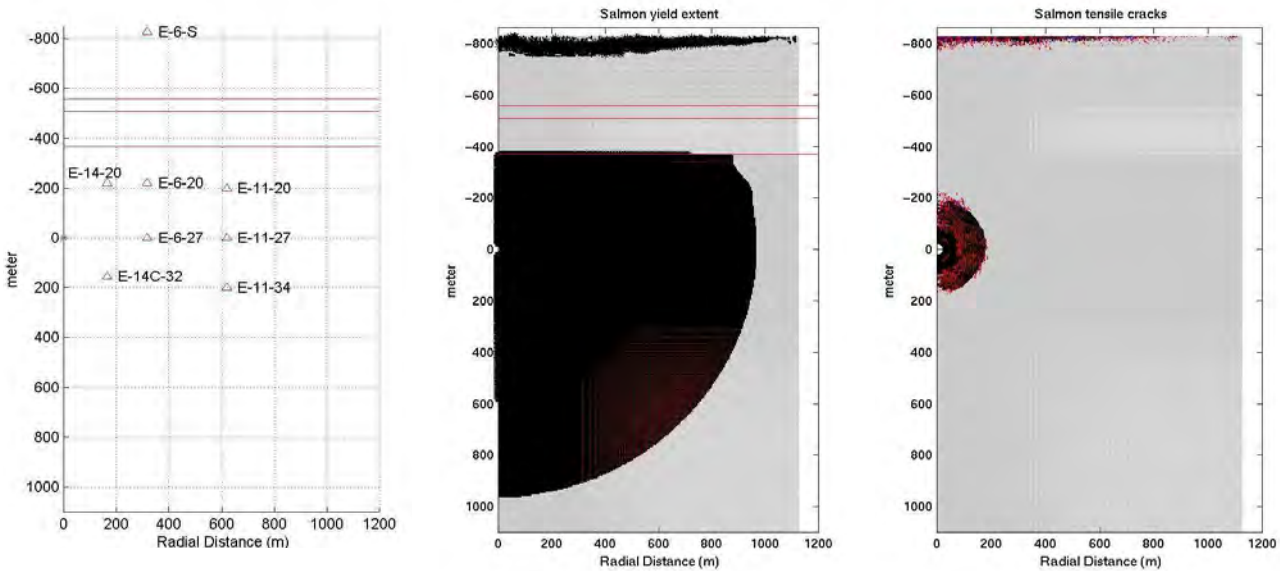


Figure 12. Left: Stations used for comparison of data and calculations. Middle: Nonlinear deformation distribution due to the Salmon explosion. Salt is yielded out to about 950 m, sediment top is partially yielded but limestone and anhydrite are not yielded. Right: Tensile crack distributions due to the Salmon explosion. Cracks open in the vicinity of the cavity within salt and near the free surface within sediment.

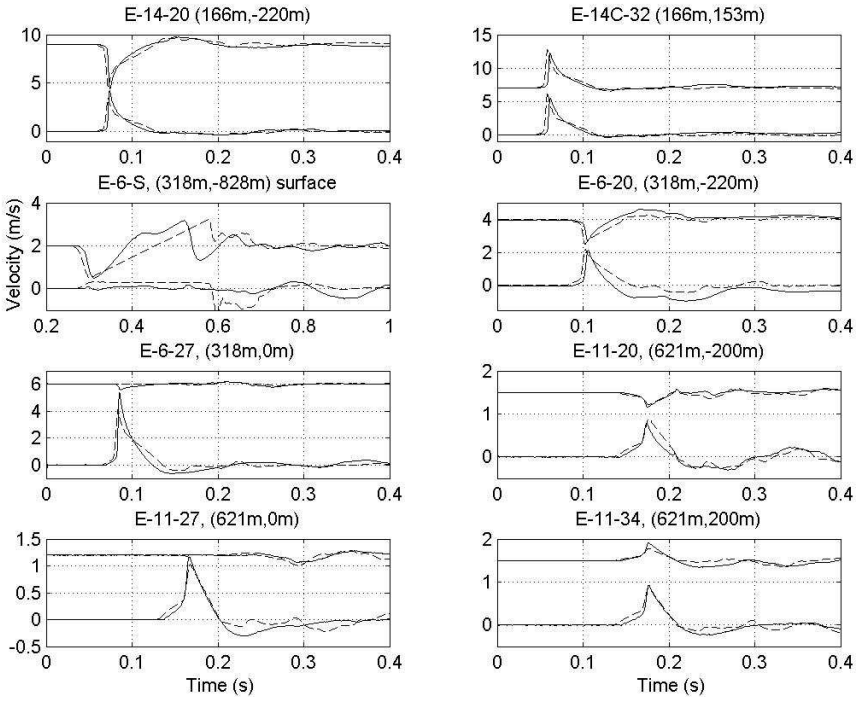


Figure 13. Comparison between the Salmon data and calculations. Spall is apparent from the –g slopes in the velocity waveform (E-6-S).

CONCLUSIONS AND RECOMMENDATIONS

In the first few months of this project, we have concentrated on numerical modeling of sources of shear waves from decoupled explosions. Specifically, we have modeled an explosion in an air-filled cavity offset from the center, an explosion in a cylindrical cavity, and explosion-generated hydrofractures. We plan to use these calculations together with analysis of data from decoupled explosions to assess which mechanisms are operating. We have also performed a detailed nonlinear finite difference calculation of the explosion Salmon, and plan to perform a detailed calculation of the decoupled explosion Sterling using the same model with a 17 m cavity (although the Salmon calculation generated a 22 m cavity, the observed cavity radius by the time Sterling was detonated was 17 m, probably because of creep during the intervening time).

In addition to the research program described above, we also plan to use data from Russian experiments in water-filled cavities (Murphy et al., 2001). Although explosions in the water-filled cavities generate signals as strong as tamped explosions of the same yield, they are similar to air-decoupled explosions in that they generate little nonlinear deformation of the cavity—the stronger signal comes from the much higher pressure generated by the water-filled cavity compared to the air-filled cavity. These data sets are useful because they provide data in which the seismic signal from tamped and decoupled explosions are approximately the same size, reducing uncertainty that observed differences are caused by source size rather than tamped/decoupled differences.

REFERENCES

Latter, A. L., R. E. Lelevier, E. A. Martinelli, and W. G. McMillan (1961). A method of concealing underground nuclear explosions, *J. Geophys. Res.* 66: 2,929.

Murphy, J. R., D. D. Sultanov, N. Rimer, and B. W. Barker (2001). Seismic source characteristics of nuclear explosions in water-filled cavities, *Pure Appl. Geophys.* 158: 2,105–2,121.

Murphy, J. R. (1991). Free-field seismic observations from underground nuclear explosions, Explosion Source phenomenology, S. R. Taylor, H. J. Patton, and P. G. Richards (Eds). American Geophysical Union, pp. 25–33

Nilson, R, N. Rimer, and E. Halda (1991). Dynamic modeling of explosively driven hydrofractures, *J. Geophys. Res.,* 96: B11, 18,081–18,100.

Rimer, N., T. Barker, S. Rogers, J. Stevens, and D. Wilkins (1994). Simulation of seismic signals from partially coupled nuclear explosions in cylindrical tunnels, Defense Nuclear Agency report DNA-TR-94-136.

Rimer, N. and J. T. Cherry (1982). Ground motion predictions for the Grand Saline experiments, S-CUBED VSC-TR-82-25.

Stevens, J. L. (1980). Seismic radiation from the sudden creation of a spherical cavity in an arbitrarily prestressed elastic medium, *Geophys. J. R. Astr. Soc.* 61: 303–328.

Zhou, L. and D. G. Harkrider (1992). Wave fields from an off-center explosion in an embedded solid sphere, *Bull. Seism. Soc. Am*. 82: 1,927–1,955.

REGIONAL SEISMIC CHEMICAL AND NUCLEAR EXPLOSION DISCRIMINATION: WESTERN U.S. EXAMPLES

William R. Walter[1], Steven R. Taylor[2], Eric Matzel[1], Rengin Gok[1], Sam Heller[1], and Virginia Johnson[1]

Lawrence Livermore National Laboratory[1] and Rocky Mountain Geophysics, LLC[2]

Sponsored by National Nuclear Security Administration
Office of Nonproliferation Research and Development
Office of Defense Nuclear Nonproliferation

Contract No. W-7405-ENG-48[1,2]

ABSTRACT

We continue exploring methodologies to improve regional explosion discrimination using the western U.S. as a natural laboratory. The western U.S. has abundant natural seismicity, historic nuclear explosion data, and widespread mine blasts, making it a good testing ground to study the performance of regional explosion discrimination techniques. We have assembled and measured a large set of these events to systematically explore how to best optimize discrimination performance. Nuclear explosions can be discriminated from a background of earthquakes using regional phase (Pn, Pg, Sn, Lg) amplitude measures such as high frequency P/S ratios. The discrimination performance is improved if the amplitudes can be corrected for source size and path length effects. We show good results are achieved using earthquakes alone to calibrate for these effects with the magnitude and distance amplitude corrections (MDAC) technique (Walter and Taylor, 2002) We show significant further improvement is then possible by combining multiple MDAC amplitude ratios using an optimized weighting technique such as Linear Discriminant Analysis (LDA). However this requires data or models for both earthquakes and explosions. In many areas of the world, regional distance nuclear explosion data is lacking, but mine blast data is available. Mine explosions are often designed to fracture and/or move rock, giving them different frequency and amplitude behavior than contained chemical shots, which seismically look like nuclear tests. Here we explore discrimination performance differences between explosion types, the possible disparity in the optimization parameters that would be chosen if only chemical explosions were available and the corresponding effect of that disparity on nuclear explosion discrimination.

Even after correcting for average path and site effects, regional phase ratios contain a large amount of scatter. This scatter appears to be due to variations in source properties such as depth, focal mechanism, stress drop, in the near source material properties (including emplacement conditions in the case of explosions) and in variations from the average path and site correction. Here we look at several kinds of averaging as a means to try and reduce variance in earthquake and explosion populations and better understand the factors going into a minimum variance level as a function of epicenter (see Anderson et al., 2006, these Proceedings). We focus on the performance of P/S ratios over the frequency range from 1 to 16 Hz finding some improvements in discrimination as frequency increases. We also explore averaging and optimally combining P/S ratios in multiple frequency bands as a means to reduce variance. Similarly we explore the effects of azimuthally averaging both regional amplitudes and amplitude ratios over multiple stations to reduce variance. Finally we look at optimal performance as a function of magnitude and path length, as these put limits the availability of good high frequency discrimination measures.

OBJECTIVES

Monitoring the world for potential nuclear explosions requires characterizing seismic events and discriminating between natural and man-made seismic events, such as earthquakes and mining activities, and nuclear weapons testing. We continue developing, testing, and refining size-, distance-, and location-based regional seismic amplitude corrections to facilitate the comparison of all events that are recorded at a particular seismic station. These corrections, calibrated for each station, reduce amplitude measurement scatter and improve discrimination performance. We test the methods on well-known (ground truth) data sets in the U.S. and then apply them to the uncalibrated stations in Eurasia, Africa, and other regions of interest to improve underground nuclear test monitoring capability.

RESEARCH ACCOMPLISHED

As part of the overall National Nuclear Security Administration Ground-based Nuclear Explosion Monitoring (GNEM) Research and Engineering program, we continue to pursue a comprehensive research effort to improve our capabilities to seismically characterize and discriminate underground nuclear tests from other natural and man-made sources of seismicity. To reduce the monitoring magnitude threshold, we make use of regional body and surface wave data to calibrate each seismic station. Our goals are to reduce the variance and improve the separation between earthquakes and explosion populations by accounting for the effects of propagation and differential source size, and by optimizing the types and combinations of amplitude measurements used.

Western U.S Data Corrected for Magnitude and Distance Effects

We continue re-examining the large database of western U.S. underground nuclear tests and earthquakes we assembled under a prior project (Walter et al., 2003). This western U.S. nuclear explosion data covers a wide range of depths and material properties and has excellent ground truth information (Springer et al., 2002). This is unlike the situation in most of the world where regional recordings of nuclear tests are scarce and discrimination optimization needs to be done in their absence. In addition we have chemical explosions recorded at the same stations from the Arizona Source Phenomenology Experiment (AZSPE). The AZSPE carried out dedicated single shot chemical explosions under a variety of depth and confinement conditions in two mining regions, a soft rock coal mine and a hard rock copper mine (e.g., Bonner et al., 2005). These mining regions also routinely detonate ripple-fired production blasts that can be observed at regional distances. The availability of both nuclear and chemical explosions lets us examine the differences in optimization and performance of the two source types relative to the earthquakes. The locations of the data and stations discussed in this paper are shown in Figure 1.

Effective earthquake-explosion discrimination has been demonstrated in a broad variety of studies using ratios of regional amplitudes in high-frequency (primarily 1- to 20-Hz) bands (e.g., Walter et al., 1995; Taylor, 1996; Hartse et al., 1997; Rodgers and Walter, 2002; Taylor et al., 2002; Battone et al., 2002; and many others). When similar-sized earthquakes and explosions are nearly co-located, we can understand the observed seismic contrasts, such as the relative P-to-S wave excitation, in terms of depth, material property, focal mechanism, and source time function differences. However, it is well known that path propagation effects (e.g., attenuation, blockage) and source scaling effects (e.g., corner frequency scaling with magnitude) can make earthquakes look like explosions and vice versa. We have developed a technique called MDAC (Magnitude and Distance Amplitude Corrections, Walter and Taylor, 2002) that can account for these effects with proper calibration. We use the earthquakes alone to determine the MDAC parameters such as geometrical spreading, frequency dependent Q, and the average apparent stress. After calibration, the MDAC formulation provides expected spectral amplitudes as a function of phase, magnitude, and distance. These can then be subtracted from the actual observations. For earthquakes, the corrected data should be zero mean, and trends should be removed as a function of distance and magnitude. Explosions should have significant non-zero mean residuals, leading to improved discrimination.

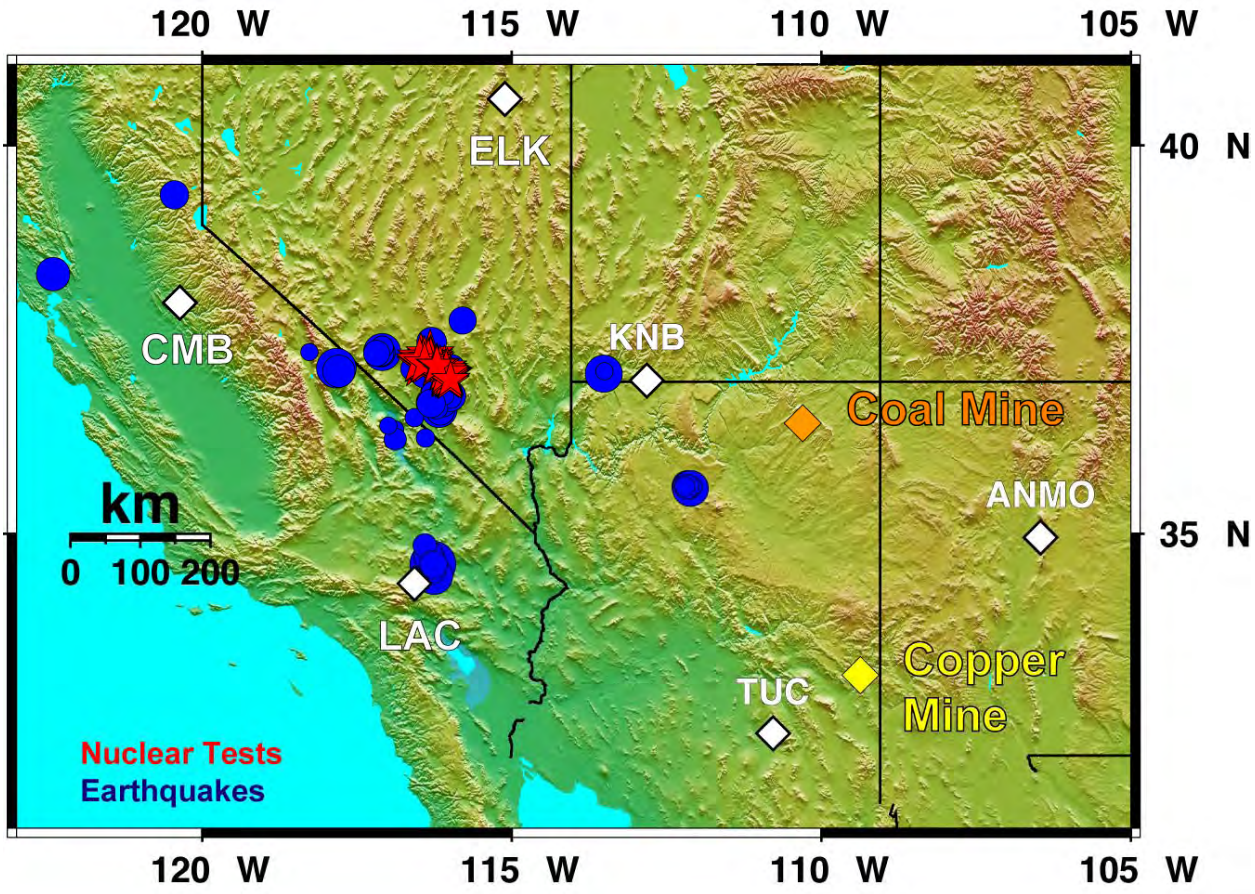


Figure 1. Map showing the location of earthquakes, historic nuclear explosions, mining explosions and stations used in this paper.

After the MDAC correction we can explore optimal combinations of particular regional discriminants (e.g., Taylor, 1996). We use the linear discriminant analysis method (LDA) to find the optimal coefficients to combine the measurements. Last year we showed an example of this at KNB of three different regional phase and spectral ratios (Walter et al., 2005). The metric of performance we use is the equiprobable point, which provides a measure of the overlap of the earthquake and explosion populations. It is the point on a receiver operating characteristic (ROC) tradeoff curve where the error rates are equal. For example an equiprobable point of 0.1 implies that 10% of the earthquakes are misclassified as explosions and 10% of explosions are misclassified as earthquakes. In practice one might chose a decision line with unequal error rates, such as by picking a low probability of misclassifying an explosion. The equiprobable point provides a single numerical measure of performance that is much more intuitive than other measures such as Mahalanobis distance, though it can be related to that measure.

Chemical versus Nuclear Explosion Discrimination

Routine industrial mining explosions play two important roles in seismic nuclear monitoring research: (1) they are a source of background events that need to be discriminated from potential nuclear explosions; (2) as some of the only explosions occurring in the current de facto global moratoria on nuclear testing, their signals should be exploited to improve the calibration of seismic monitoring systems. A common issue arising in both of these roles is our limited physical understanding of the causes behind observed differences and similarities in the seismic signals produced by routine industrial mining blasts and small underground nuclear tests. The AZSPE

provides an opportunity to compare chemical and nuclear explosion regional amplitudes at common stations to better understand their similarities and differences.

The two different types of chemical explosions (single contained shots versus ripple fired production blasts) show some interesting similarities and differences to the nuclear explosions. They all have similar high frequency P/S ratios, as the 6-8 Hz Pg/Lg example in Figure 2 shows. However in looking at regional seismic coda derived spectra (e.g., Mayeda and Walter, 1996; Mayeda et al., 2003) in Figure 2 we find the production shots have steeper spectral decay between 1-8 Hz, and this accounts for the differences we see in the low to high frequency ratios. For this reason it is clear that optimizing discrimination performance (such as finding LDA coefficients) using industrial explosions may not be optimal when low to high frequency spectral or cross spectral ratios are involved. This is an area of research we are actively exploring.

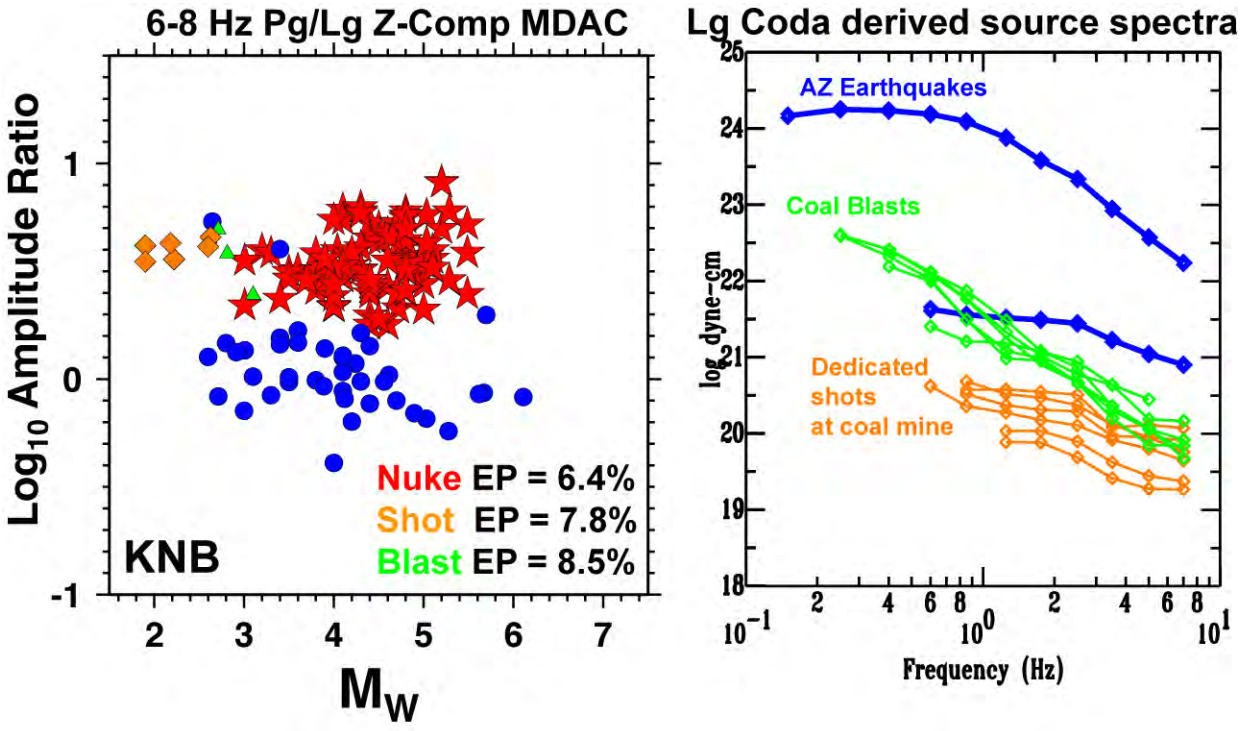


Figure 2. Here we compare the behavior of various explosion types against earthquakes (blue circles and lines) at station KNB. On the left-hand side we show explosion discrimination from earthquakes for the 6–8 Hz Pg/Lg ratio after MDAC corrections were applied. The equiprobable measure of discrimination of each explosion type relative to earthquakes is given, and they are quite similar for this ratio. On the right-hand side we show regional coda envelope derived S-wave spectra of earthquakes (blue) and dedicated single shot chemical explosions (orange) and normal mine production blasts (green). The coda calibrations were done using the Colorado Plateau earthquakes shown. Note that most of the ripple-fired shots have much steeper spectral falloff than the single shots.

P/S Discrimination versus Frequency

Many previous studies of regional nuclear explosion discrimination using P/S ratios have noted that discrimination improves as the frequency increases, with the largest improvement often occurring as frequencies get above about 4 Hz (e.g., Dysart and Pulli, 1987; Baumgardt and Young, 1990; Walter et al., 1995; Taylor, 1996; Hartse et al., 1997; and many others). Few of these studies looked at frequencies above 10 Hz. Some studies utilizing chemical explosions have looked at discrimination at frequencies above 10 Hz (e.g.,

Kim et al., 1993; Kim et al., 1997) finding good separation at all frequencies above about 5 Hz. However, for the western U.S. nuclear data, we have previously limited our analysis to 10 Hz and less (Walter et al., 1995; Taylor et al., 1996) due both to quality control issues at the higher frequencies and an eye towards the limited number of stations at that time with sample rates greater than 20 sps. As the number of stations with sample rates of 40 sps continues to increase it is worth revisiting the behavior of the P/S ratio discriminants with frequency for the western U.S. nuclear explosion dataset.

Great care must be taken when using historical data to look at high frequency discrimination. Because most of the nuclear testing occurred prior to the deployment of 24 bit recorders, much high frequency amplitude data is corrupted. For example while the Lawrence Livermore National Laboratory (LLNL) Nevada Network (LNN) stations sampled at 40 sps since digital telemetry was started in 1979, they utilized 12-bit gain ranging prior to September 1987 (Jarpe, 1989). This works fine for data up to 8–10 Hz in most cases, but above that frequency the data shows signs of signal generated noise that we suspect is related to the gain ranging. In September 1987 the LNN recorders were upgraded to 16 bit and S-13 seismometers installed with a concerted effort to record good high frequency data. For this reason we have focused our analysis only on the LNN nuclear explosion data from September 1987 to the end of testing in 1992. In the summer of 1992 the instruments were upgraded to 24 bit recorders and Guralp broadband 3T seismometers giving very high quality data. We make use of earthquakes from 1987 through 2005. Finally there still remain problems with glitches, clipping, and dropouts. Each seismogram was carefully reviewed by a seismologist; problem data were identified and not used. We are still analyzing data and here show results only for station ELK. The results for Pn/Lg in 8 frequency bands from 0.5 up to 16 Hz are given in Figure 3, and similar results for Pg/Lg are given in Figure 4. We used a signal to pre-event noise threshold of 2.0 for the P-wave phases and 1.3 for the S-wave phases. Note that there is a general improvement in discrimination as the frequency increases as measured by the equiprobable point. However the number of events at the lowest and highest frequency bands drops off due to poor signal to noise.

In order to make a fairer comparison of the effect of frequency on P/S discrimination we restricted the data to those events where all 8 frequency bands were available. In general this raises the threshold to about magnitude 4 and greater. These results are shown in Figure 5 and indicate that the big improvement in both P/S ratios occurs at 4 Hz and higher. In fact the frequency bands between 4 and 10 Hz seem to occupy an effective niche for discrimination without big drop off in the number of events that can be measured. At frequencies above 10 Hz we see two complications start to become significant. First the number of events starts to decease substantially due to signal to noise issues. This is a problem in tectonic regions like the western U.S. with relatively strong regional phase attenuation. Use of frequencies above 10 Hz at ELK will tend to be limited to closer and/or larger events, such as within 300 km or greater than magnitude 4. The second issue is that the Pg/Lg discrimination starts to worsen. Looking at Figure 4 we can see this is primarily due to just two earthquakes. These two events occur in California; one is the Hector Mine mainshock and the other occurs near Lake Tahoe. We believe these events are showing us the limits of the one-dimensional (1-D) power law distance correction above 10 Hz, as they are not outliers at lower frequencies. These are the only events above 10 Hz passing our SNR tests that are not within 100 km of the test site. We suspect that using a two-dimensional (2-D) attenuation correction could probably reduce the variance (e.g., Mayeda et al., 2005), and expect that P/S has the potential to be a little better discriminant at high frequencies when events are nearly co-located. However in practice getting good 2-D attenuation maps at high frequencies may not be easy unless the region is well instrument and seismically active.

For these reasons, frequencies of 4–10 Hz, including the commonly used 6–8 Hz, seem to make good practical discriminants. We should note that LDA analysis shows us that there is useful discrimination information even in mediocre discriminants and the best performance comes from combining multiple discriminant ratios. We are currently exploring techniques that average P/S ratios over multiple frequency bands, as averaging multiple bands appears to reduce variance and improve discrimination. Finally, we should note that the Pg/Lg discriminant seems to work better than Pn/Lg at most frequencies, particularly the lower frequencies, and the reasons for this need further investigation, but may have to do with amplitude averaging over the source.

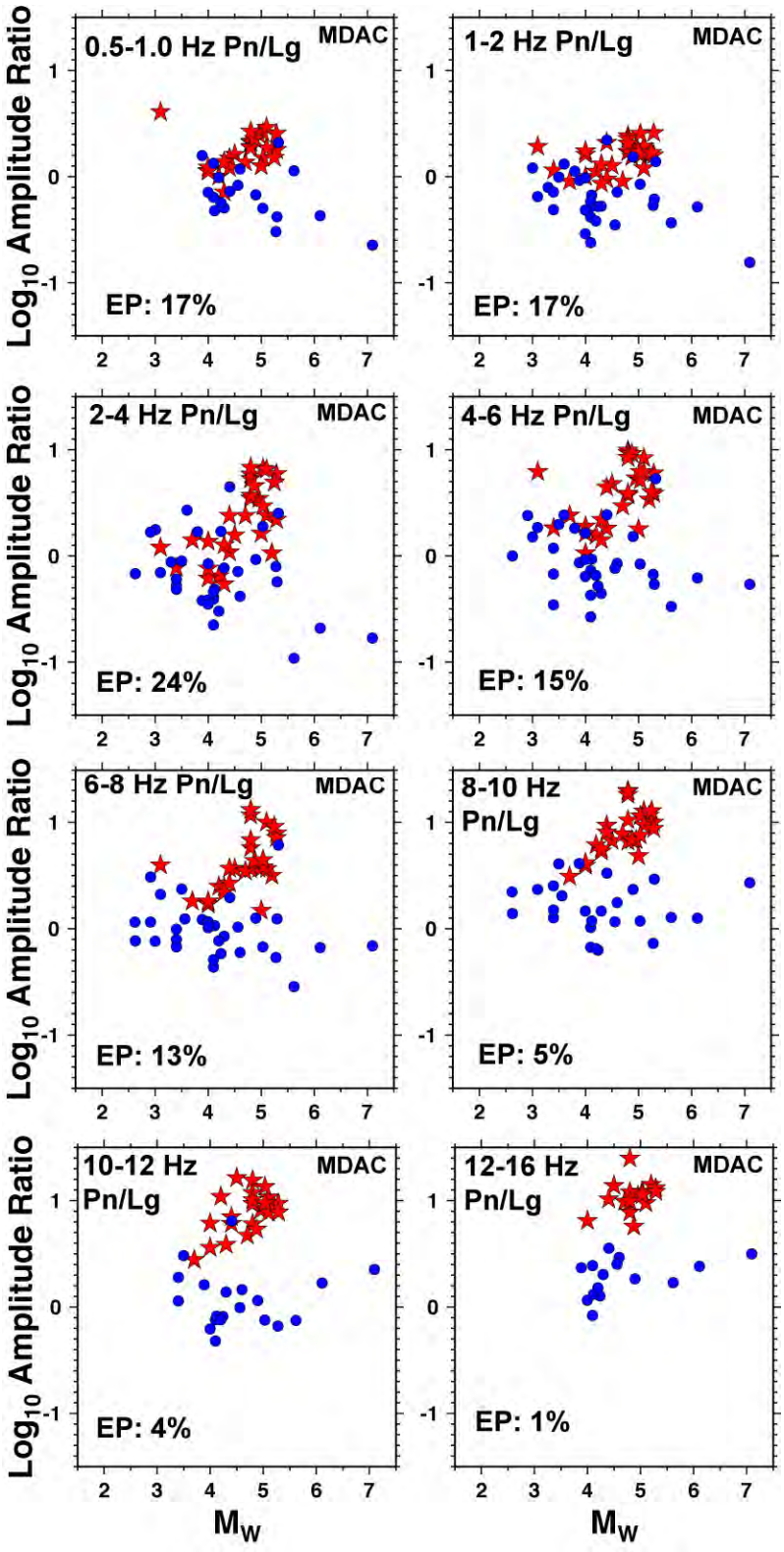


Figure 3. Earthquake (blue circles) and explosion (red stars) discrimination at station ELK for Pn/Lg in eight different frequency bands from 0.5 to 16 Hz. Note the general improvement as frequency increases as measured quantitatively by the equiprobable value, although the number of events decreases.

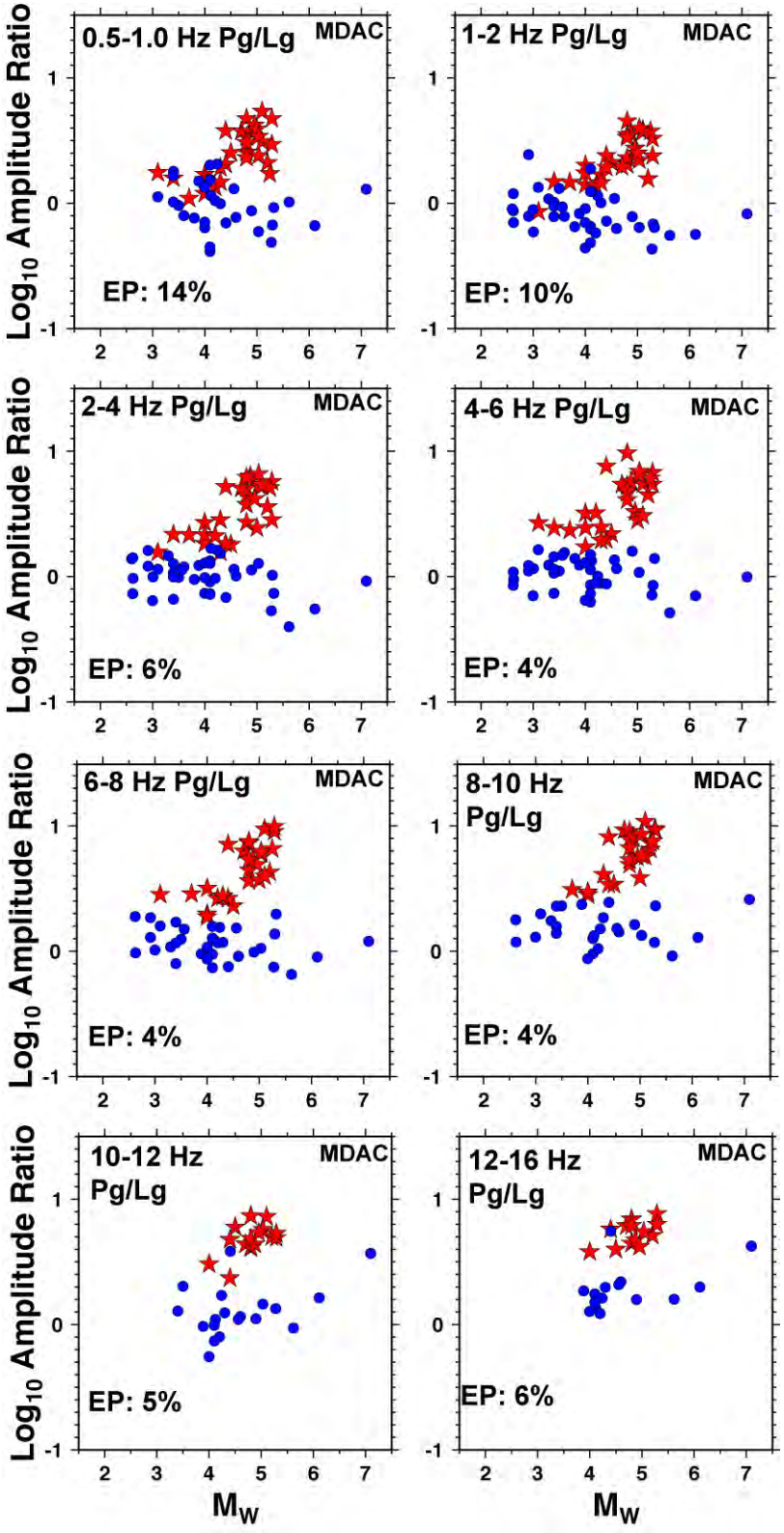


Figure 4. Same as Figure 3, except for Pg/Lg at ELK.

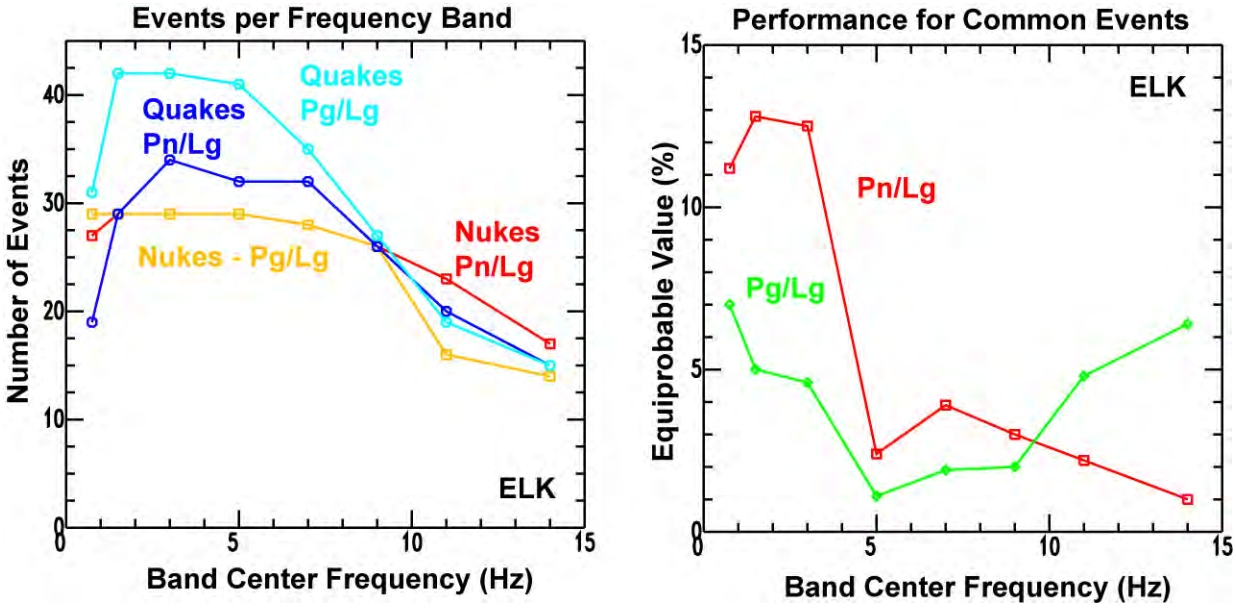


Figure 5. Left-hand side shows the number of events passing the SNR criteria for each ratio at each frequency band. The right-hand side shows the ELK P/S discrimination performance as measured by the equiprobable value for each ratio as a function of frequency using only events where all frequency measures are available.

Averaging Stations

It has been observed that events that appear problematic to discriminate at one station may not be a problem at other stations in the same region. We have previously argued qualitatively (e.g., Walter et al., 1995) that averaging over stations improves discrimination performance. We are currently working to quantify this effect. We show a simple two-station example in Figure 6 using just the data from 1987 and later. We are currently testing all 4 LNN stations and other long-standing western U.S. stations to better understand the value of multiple station averaging for regional discrimination.

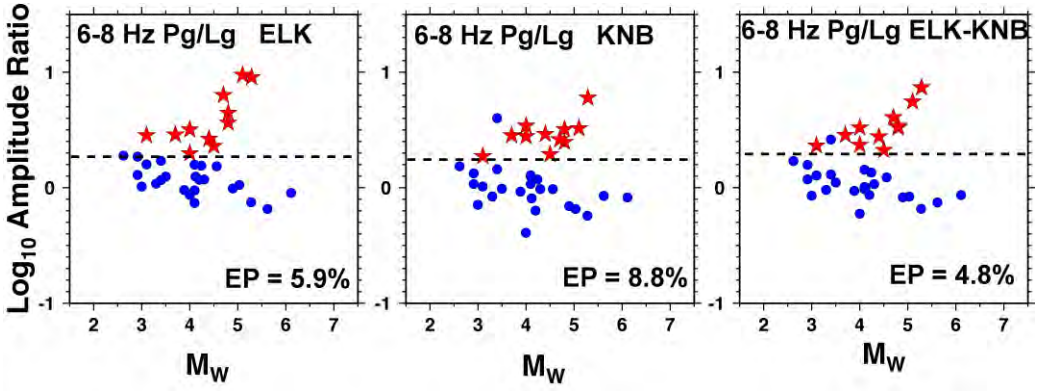


Figure 6. Comparison of 6–8 Hz Pg/Lg discrimination performance at stations ELK and KNB for the same events. ELK has better performance than KNB. An earthquake outlier at KNB is not an outlier at ELK indicating that averaging should help reduce variance. A hypothetical decision line has been drawn just below the lowest explosion value in each case. Note that the average of the two stations performs better than either alone as measured by equiprobable value.

CONCLUSIONS AND RECOMMENDATIONS

Regional discrimination algorithms require calibration at each seismic station to be used for nuclear explosion monitoring. We apply a Magnitude and Distance Amplitude Correction procedure to remove source size and path effects from regional body-wave phases. This allows the comparison of any new regional events recorded at a calibrated station with all available reference data and models. This also facilitates the combination of individual measures at multiple stations to form multivariate discriminants that can significantly improve performance over single station individual measures. We are working to quantify the performance of P/S ratio discriminants as a function of frequency and number of stations. We are using the AZSPE data to explore the use of industrial chemical explosions to help calibrate regional discriminants in areas where nuclear explosion data is not available.

ACKNOWLEDGEMENTS

We thank Stan Ruppert and Terri Hauk for loading and maintaining the LLNL database. We thank Doug Dodge and Mike Ganzberger for developing and maintaining Regional Body-wave Amplitude Processor (RBAP), which was used to make the regional measurements. We thank Veronica Parker and Flori Ryall for picking phase onsets for much of this data.

REFERENCES

Anderson, D. N., W. R. Walter, D. K. Carlson, T. M. Mercier, and S. R. Taylor (2006). A lower bound on the standard error of an amplitude-based regional discriminant, in *Proceedings of the 28th Seismic Research Review: Ground-Based Nuclear Explosion Monitoring Technologies*, LA-UR-06-5471.

Battone, S., M. D. Fisk, and G. D. McCarter (2002). Regional seismic-event characterization using a Bayesian formulation of simple kriging, *Bull. Seism. Soc. Am.* 92: 2,277–2,296.

Baumgardt, D. R. and G. B. Young (1990). Regional seismic waveform discriminants and case-based identification using regional arrays, *Bull. Seism. Soc. Am.* 80: 1,874–1,892.

Bonner, J., B. Stump, M. Leidig, X. Yang, R. Zhou, T. S. Kim, W. R. Walter, A. Velasco, C. Hayward, D. Baker, C. L. Edwards, S. Harder, H. Hooper, Travis Glenn, C. Zeiler, J. Britton, and J. F. Lewkowicz (2005). Source phenomenology experiments in Arizona, in *Proceedings of the 27th Seismic Research Review: Ground-Based Nuclear Explosion Monitoring Techniques*, LA-UR-05-6407, Vol. 1, pp. 519–528.

Dysart, P. S. and J. J. Pulli (1987). Spectral study of regional earthquakes and chemical explosions recorded at the NORES array, SAIC technical report C87-03.

Hartse, H., S. R. Taylor, W. S. Phillips, and G. E. Randall (1997). A preliminary study of regional seismic discrimination in Central Asia with an emphasis on Western China, *Bull. Seism. Soc. Am.* 87: 551–568.

Jarpe, S. (1989). Guide for using data from the LNN seismic monitoring network, Lawrence Livermore National Laboratory report UCID-21872.

Kim, W.-Y., D. W. Simpson, and P. G. Richards (1993). Discrimination of earthquakes and explosions in the eastern United States using regional high frequency data, *Geophys. Res. Lett.* 20: 1507–1510.

Kim, W.-Y., V Aharonian, A. L. Lerner-Lam, and P. G. Richards (1997). Discrimination of earthquakes and explosions in southern Russia using regional high frequency three-component data from the IRIS/JSP Caucasus network, *Bull. Seism. Soc. Am.* 87: 569–588.

Mayeda, K. M. and W. R. Walter (1996). Moment, energy, stress drop and source spectra of western U.S. earthquakes from regional coda envelopes, *J. Geophys. Res.* 101: 11,195–11,208.

Mayeda, K., A. Hofstetter, J. L. O'Boyle, and W. R. Walter (2003). Stable and transportable regional magnitudes based on coda-derived moment-rate spectra, *Bull. Seis. Soc. Am*. 93: 224–239.

Mayeda, K., Malagnini, L. W. S. Phillips, W. R. Walter, and D. Dreger (2005). 2-D or not 2-D, that is the question: A northern California test, *Geophys. Res. Lett.* 32: doi:10.1029/2005GL022882.

Rodgers, A. J. and W. R. Walter (2002). Seismic discrimination of the May 11, 1998 Indian nuclear test with short-period regional data from station NIL (Nilore, Pakistan), *Pure Appl. Geophys.* 159: 679–700.

Springer, D. L., G. A. Pawlowski, J. L. Ricca, R. F. Rohrer, and D. K. Smith (2002). Seismic source summary for all U.S. below-surface nuclear explosions, *Bull. Seism. Soc. Am.* 92: 1,806.

Taylor, S., (1996). Analysis of high-frequency Pg/Lg ratios from NTS explosions and Western U.S. earthquakes, *Bull. Seism. Soc. Am.* 86: 1042–1053.

Taylor, S., A. Velasco, H. Hartse, W. S. Philips, W. R. Walter, and A. Rodgers (2002). Amplitude corrections for regional discrimination, *Pure. App. Geophys*. 159: 623–650.

Walter, W. R. and S. R. Taylor (2002). A revised magnitude and distance amplitude correction (MDAC2) procedure for regional seismic discriminants, Lawrence Livermore National Laboratory report UCRL-ID-146882.

Walter, W. R., K. Mayeda, and H. J. Patton (1995). Phase and spectral ratio discrimination between NTS earthquakes and explosions—Part 1: Empirical observations, *Bull. Seism. Soc. Am*. 85: 1,050–1,067.

Walter, W. R., K. D. Smith, J. L. O'Boyle, T. F. Hauk, F. Ryall, S. D. Ruppert, S. C. Myers, M. Anderson, and D. A. Dodge (2003). Improving the fundamental understanding of regional seismic signals with a unique western United States dataset, in *Proceedings of the 25th annual Seismic Research Review—Nuclear Explosion Monitoring: Building the Knowledge Base*, LA-UR-03-6029, Vol. 2, pp 486–484.

Walter, W. R., K. Mayeda, R. Gok, A. J. Rodgers, A. Sichermann, T. Hickling, D. Dodge, E. Matzel, M. Ganzberger, and V. Parker (2005). Regional seismic discrimination optimization with and without nuclear test data: Western U.S. examples, in *Proceedings of the 27th annual Seismic Research Review: Ground-Based Nuclear Explosion Monitoring Technologies*, LA-UR-05-6407, Vol. 1, pp. 693–703.

Proceedings of the 28th Seismic Research Review: Ground-Based Nuclear Explosion Monitoring Technologies

September 19–21, 2006

Orlando, Florida

Volume II

Hydroacoustic Monitoring
Radionuclide Monitoring
Infrasound Monitoring
Data Processing and Analysis

Approved for Public Release; further dissemination unlimited.

National Nuclear Security Administration

AIR FORCE RESEARCH LABORATORY

LA-UR-06-5471

2006

Proceedings of the 28th Seismic Research Review: Ground-Based Nuclear Explosion Monitoring Technologies

Vol. II

To view these Proceedings online, visit
https://www.nemre.nnsa.doe.gov/review2006

Table of Contents - Volume II

4. Hydroacoustic Monitoring 715

4-01 **Graeber, F., J. Coyne, and E. Tomuta**
The Current Status of Hydroacoustic Data Processing at the International Data Centre 717

4-02 **Hanson, J., C. Reasoner, and J. Bowman**
Hydroacoustic Propagation Loss from Reflection and Transmission over Shallow Bathymetry in the Indian Ocean 725

4-03 **Matzel, E. and P. Harben**
Propagation, Attenuation and Blockage of Hydroacoustic Waves in the Earth's Oceans 736

4-04 **Pulli, J., Z. Upton, J. Wagoner, and P. Harben**
Dynamic Modeling of Hydroacoustic Reflections and a First Look at the Data from the New Hydroacoustic Arrays at Ascension Island 742

4-05 **Upton, Z., J. Bhattacharyya, J. Pulli, and M. Collins**
Hydroacoustic Blockage Studies Using HydroCAM Version 5 Propagation Models and Kriging Techniques 752

5. Radionuclide Monitoring 763

5-01 **Beyerle, A. and D. Walker**
Evaluation of HPXe Nuclear Explosion Monitor Applications 765

5-02 **Biegalski, K., S. Biegalski, and D. Haas**
Further Development of the Spectral Deconvolution Analysis Tool (SDAT) to Improve Counting Statistics and Detection Limits for Nuclear Explosion Radionuclide Measurements 774

5-03 **Farsoni, A. and D. Hamby**
Study of a Triple-Layer Phoswich Detector for Beta and Gamma Spectroscopy with Minimal Crosstalk 784

5-04 **Hayes, J., P. Doctor, T. Heimbigner, C. Hubbard, L. Kangas, P. Keller, J. McIntyre, B. Schrom, and R. Suarez**
Application of Artificial Neural Network Modeling to the Analysis of the Automated Radioxenon Sampler-Analyzer State of Health Sensors 793

5-05 **Hennig, W., H. Tan, A. Fallu-Labruyere, W. Warburton, J. McIntyre, and A. Gleyzer**
Design of a Phoswich Well Detector for Radioxenon Monitoring 801

5-06 **Hull, E., R. Pehl, J. Lathrop, G. Martin, R. Mashburn, H. Miley, C. Aalseth, and T. Hossbach**
Segmentation of the Outer Contact on P-Type Coaxial Germanium Detectors 811

5-07 **Hull, E., R. Pehl, J. Lathrop, G. Martin, R. Mashburn, H. Miley, C. Aalseth, T. Hossbach, and T. Bowyer**
Mechanically Cooled Large-Volume Germanium Detector Systems for Nuclear Explosion Monitoring 822

5-08 **Orrell, J., C. Aalseth, A. Day, J. Fast, T. Hossbach, L. Lidey, H. Miley, M. Ripplinger, and B. Schrom**
A Beta-Particle Hodoscope Constructed Using Scintillating Optical Fibers and Position Sensitive Photomultiplier Tubes 832

5-09 **Warburton, W. and B. Dwyer-McNally**
Time Projection Chamber for Locating Fission Fragments in RASA Filters 841

5-10 **Waye, S., S. Biegalski, and O. Ezekoye**
Design of Aerosol Sampler to Remove Radon and Thoron Progeny Interference from Aerosol Samples for Nuclear Explosion Monitoring 851

6. Infrasound Monitoring 861

6-01 **Bahavar, M., J. Bowman, H. Israelsson, B. Kohl, R. North, M. O'Brien, and G. Shields**
Infrasound Resources of the SMDC Monitoring Research Program 863

6-02 **Brachet, N. and J. Coyne**
The Current Status of Infrasound Data Processing at the International Data Centre 873

6-03 **Christie, D., B. Kennett, and C. Tarlowski**
Detection of Atmospheric Explosions at IMS Monitoring Stations Using Infrasound Techniques 882

6-04 **de Groot-Hedlin, C.**
Finite Difference Methods for Acoustic and Acousto-Gravity Wavefields: Application to Low Frequency Infrasound Propagation 893

6-05 **Gibson, R., D. Drob, and D. Norris**
Advancement of Infrasound Propagation Calculation Techniques Using Synoptic and Mesoscale Atmospheric Specifications 900

6-06 **Herrin, E., P. Golden, P. Negraru, W. Andre, H. Bass, M. Garces, M. Hedlin, M. McKenna, D. Norris, D. Osborne, and R. Whitaker**
Infrasound Calibration Explosions from Rockets Launched at White Sands Missile Range 910

6-07 **Norris, D., J. Bhattacharyya, and R. Whitaker**
Development of Advanced Propagation Models and Application to the Study of Impulsive Infrasonic Events 919

6-08 **O'Brien, M., J. Bowman, and D. Drob**
Improved Infrasound Locations Through Refining Atmospheric Models Using Wind Data and Ground-Truth Infrasound Events 926

6-09 **ReVelle, D.**
Earthquake Depth Predictions Using Infrasonic Waves 936

6-10 **Walker, K., M. Zumberge, J. Berger, and M. Hedlin**
Determining Infrasound Phase Velocity Direction with a Three-Arm OFIS 947

6-11 **Whitaker, R. and J. Mutschlecner**
Revisiting Yield, Direction, and Signal Type 957

7. Data Processing and Analysis 965

7-01 **Elliott, A., D. Dodge, M. Ganzberger, T. Hauk, E. Matzel, and S. Ruppert**
Enhancing Seismic Calibration Research Through Software Automation and Scientific Information Management 967

7-02 **Jensen, L., J. Hipp, R. Villanueva, D. Myers, B. Ammons, and J. Gauthier**
PGL Server: Development of a Stand-Alone Server-Based Earth-Model Library for Seismic Monitoring 976

7-03 **Kromer, R. and D. Hart**
Integrated Seismic Sensor/Digitizer Evaluation 987

7-04 **Kvaerna, T., S. Gibbons, F. Ringdal, and D. Harris**
Integrated Seismic Event Detection and Location by Advanced Array Processing 997

7-05 **Le Bras, R., T. Hampton, J. Coyne, and A. Boresch**
SELO: A Fast Prototype Bulletin Production Pipeline at the CTBTO 1007

7-06 **Ringdal, F., T. Kvaerna, S. Mykkeltveit, S. Gibbons, and J. Schweitzer**
Basic Research on Seismic and Infrasonic Monitoring of the European Arctic 1017

7-07 **Stead, R., M. Begnaud, and J. Aguilar-Chang**
Advances in Data Integration and Quality Control in Support of the NNSA Knowledge Base 1028

Acronyms, Etc. 1039

Acronym - Definition 1041

Guide to Seismic Phases 1045

Hydroacoustic Monitoring

THE CURRENT STATUS OF HYDROACOUSTIC DATA PROCESSING AT THE INTERNATIONAL DATA CENTRE

Frank M. Graeber, John Coyne, and Elena Tomuta

Provisional Technical Secretariat of the Preparatory Commission for the
Comprehensive Nuclear-Test-Ban Treaty Organization (CTBTO)

ABSTRACT

After the installation of Release 3 of the International Data Centre (IDC) application software, development and maintenance of the existing and new software modules was taken over by the IDC. In 2002, when only three IMS hydroacoustic stations were operational, an Ad Hoc Expert Group for the Evaluation of Hydroacoustic Data Processing at the IDC was formed under the auspices of the Provisional Technical Secretariat of the CTBTO. The report and recommendations of the Expert Group list various areas of potential improvement and are used as guidance for IDC hydroacoustic software development. Progress was made in several of these areas.

A software package, including environmental data sets, for long range hydroacoustic propagation modeling was acquired, which is primarily used to compute seasonally varying radial 2D (or Nx2D) tables of travel-times and transmission loss for hydrophone and land-based T-phase stations. Some of the travel-time tables display deviations of up to about 100 s compared to the previously used constant wave speed model. A new software module along with parameter changes was implemented as part of the detection and feature extraction sub-system. It includes cepstral analysis used for identification of bubble pulses from explosive in-water sources. In order to improve the performance of the automatic phase identification sub-system for hydrophone stations, a wider range of frequencies is now used to compute hydroacoustic arrival features. Parameters of the rule-based phase identification sub-system were tuned and a significant reduction of erroneous identifications was achieved. A number of upgrades of the azimuth estimator were inspired by the Progressive Multi-Channel Correlation (PMCC) algorithm. In a related effort, relative hydrophone positions were refined to improve the accuracy of azimuth and slowness estimates. The new version of the azimuth estimator can also compute a slowness outside the typical range of hydroacoustic phases; hence, it is now called the Hydroacoustic Azimuth and Slowness Estimator (HASE) and thus contributes to the automated identification of seismic arrivals on records of hydrophone triad stations, which is currently being tested. Other synergy effects between the three waveform technologies are being studied and will contribute to data fusion processes. New interactive review tools for hydroacoustic data are being developed to be compatible with the methods used in automatic processing.

OBJECTIVES

The International Data Centre's (IDC's) automatic hydroacoustic data processing pipeline consists of the following subsystems (excluding applications which handle data formatting, storage, dissemination and the like): Detection and feature extraction (DFX), channel based phase identification (StaPro), multi-channel processing for azimuth and slowness estimation (HASE), network processing/data fusion (GA – Global Association). This basic structure has not been changed since the delivery of the original software suite from the Prototype International Data Centre (Hanson et al., 2001) and—except for the HASE application—is in principle also used for processing seismic and infrasound data. IDC interactive review is performed using the Analyst Review Station (ARS) as the core application.

RESEARCH ACCOMPLISHED

Areas of Hyroacoustic Development

Parametric Information

A software package—including environmental data sets—for long range hydroacoustic propagation modeling was acquired, which is primarily used to compute seasonally varying radial 2D (or Nx2D) tables of travel-times and transmission loss for hydrophone and land-based T-phase stations. A Matlab based GUI is used to prepare a series of input files for the hydroacoustic propagation model Kraken to compute all radials. Some of the travel-time tables display deviations of up to about 100s compared to the previously used constant wave speed model. An example table for the northern triad of IMS hydrophone station HA10 is shown in Figure 1.

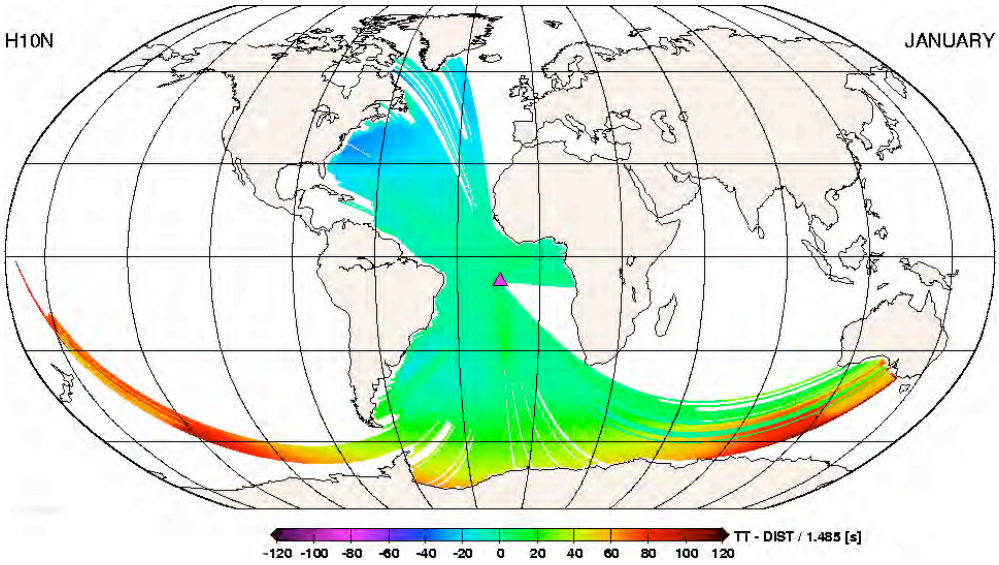


Figure 1. Reduced radial 2-D travel-time table for the northern triad IMS hydrophone station HA10 valid for the month of January.

Detection and Feature Extraction

A new software module along with parameter changes was implemented as part of the detection and feature extraction sub-system. It calculates a number of timing estimates (arrival time, start time, termination time, peak time, etc.) and includes cepstral analysis (see Figure 2) used for identification of bubble pulses from explosive in-water sources. In order to enhance the performance of the subsequent automatic phase identification for hydrophone stations, a wider range of frequencies (1–110Hz) is now used to compute hydroacoustic arrival features.

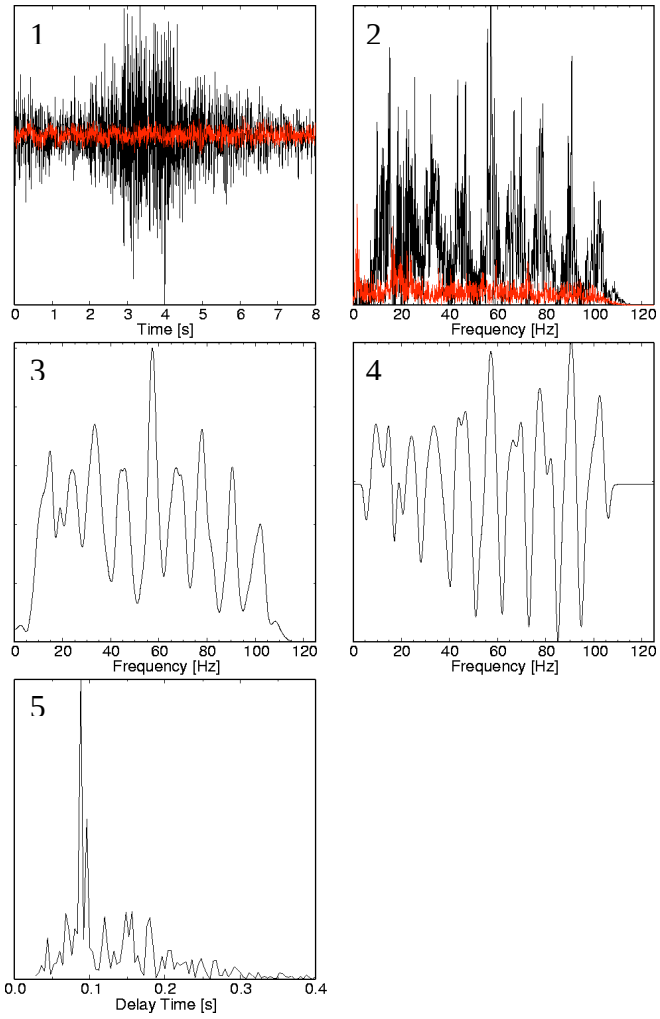
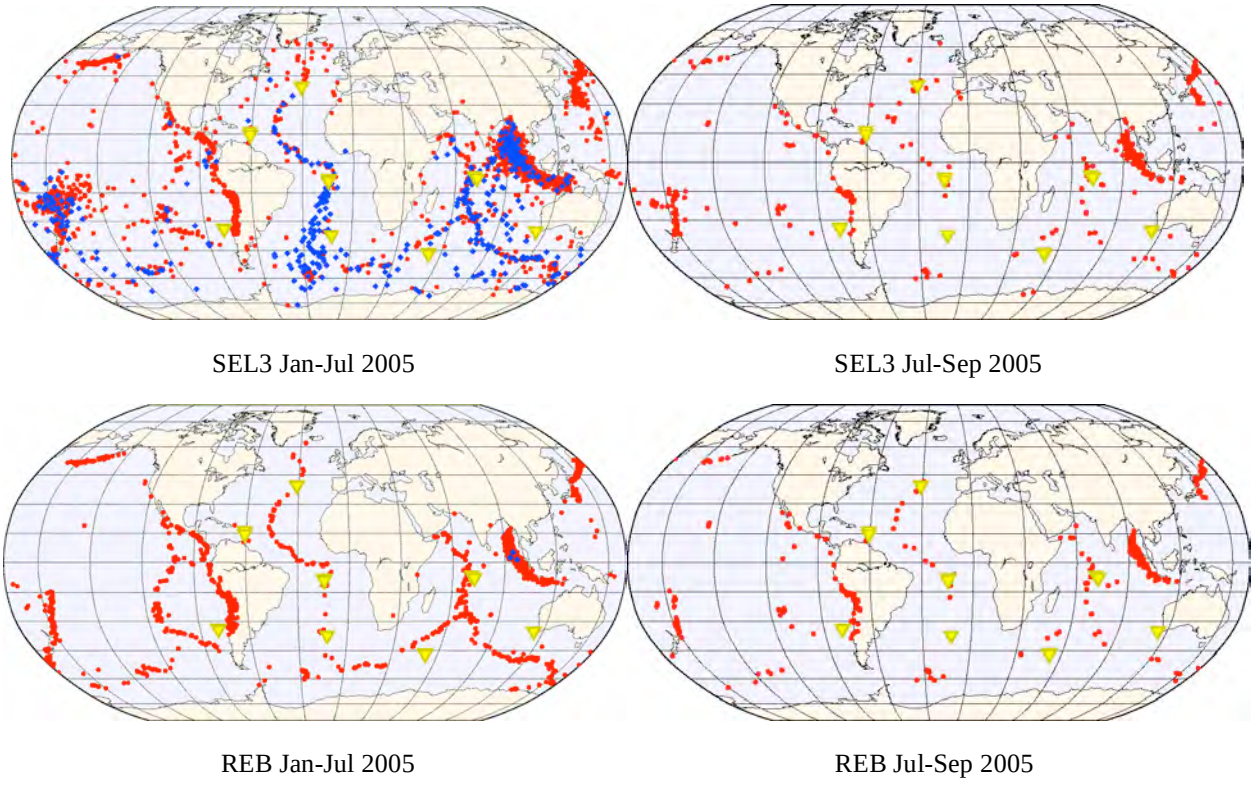


Figure 2. Data example showing five stages of cepstral analysis performed by DFX: (1) raw signal (black) and leading noise (red), (2) spectra of signal (black) and noise (red), (3) smoothed and noise corrected spectrum, (4) logarithm of the detrended spectrum, and (5) cepstrum showing the period of the bubble pulse.

Phase Identification

Parameters of the rule based phase identification sub-system were tuned on the basis of extensive data analysis and supported by an external contract. A significant reduction of wrong identifications was achieved. In particular, fewer ground coupled T phases are now wrongly identified as H phases, which by definition originate from in-water sources. This has a major impact on the automatic network processing since H phases, in contrast to T phases, contribute to defining and locating event hypotheses (see Figure 3). Today fewer false events are built on the basis of H phases.



SEL3 Jan-Jul 2005 SEL3 Jul-Sep 2005

REB Jan-Jul 2005 REB Jul-Sep 2005

Figure 3. Epicentre distribution with information on associated phases for the periods before (left frames) and after (right frames) the implementation of changes to the configuration of the rule-based phase identification. Only events with associated hydroacoustic phases are displayed. The upper frames show epicenters from the automatic bulletin (SEL3) and the lower frames epicenters from the reviewed event bulletin (REB). Red dots: Events with no associated defining H phases. Blue dots: Defining H phases associated. After the changes to the phase identification were implemented the automatic bulletin started to resemble the reviewed bulletin more closely.

Multi-Channel Processing/Azimuth and Slowness Estimation

When detailed analysis of hydrophone triad data started at the IDC, a systematic bias in azimuth and wave speed residuals was observed for some stations when the original receiver positions of hydrophone triads from the deployment cruises were used in multi-channel processing. In order to eliminate this bias, azimuth and wave speed residuals from a set of well constrained events were inverted for the relative receiver positions (one element was fixed at its position), leading to a considerable improvement of the accuracy of azimuth and wave speed estimation. The standard deviation of azimuth residuals is now on the order of 1 degree. So far the relative receiver positions of the hydrophone triads HA01, HA08 (north and south), HA03 (north only) and HA10 (north and south) were reviewed. The example given in Figure 4 shows the input and output residuals as well as resulting receiver positions for the hydrophone station HA01.

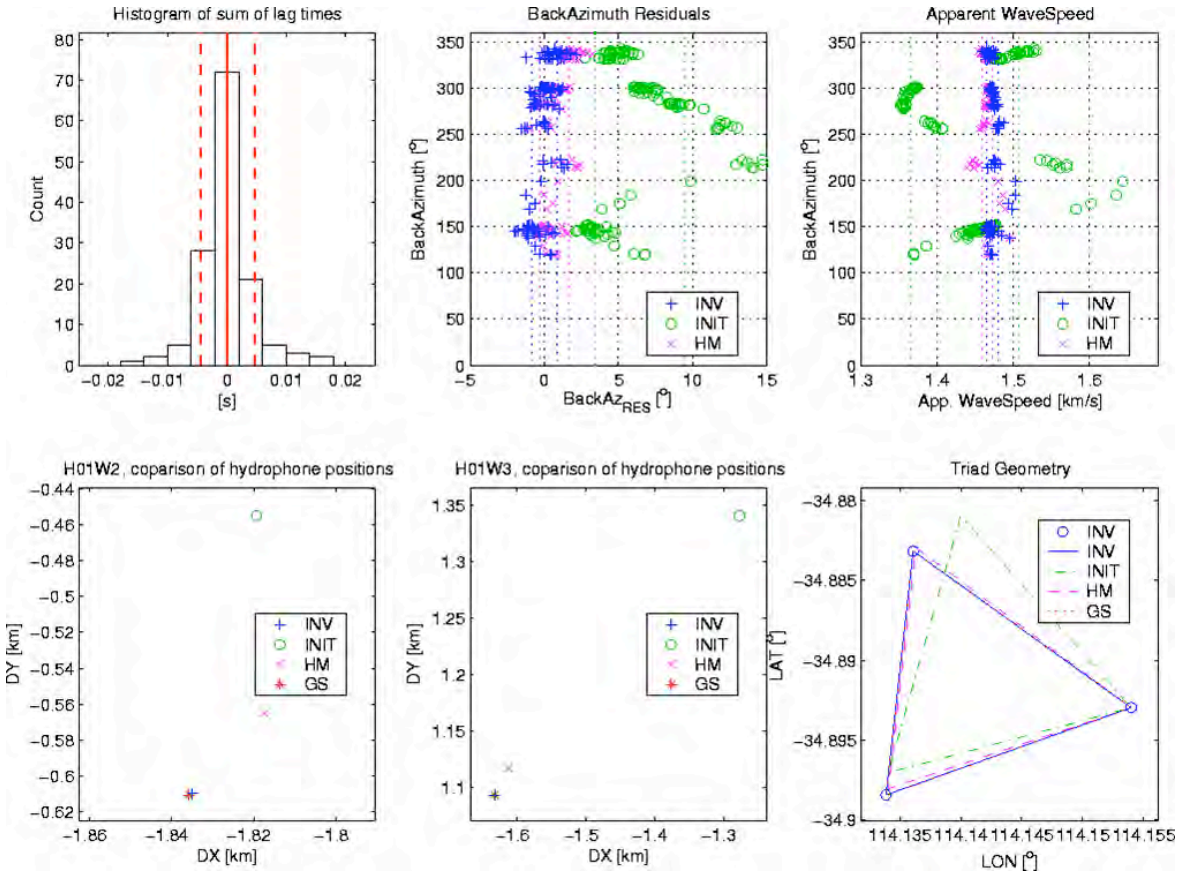
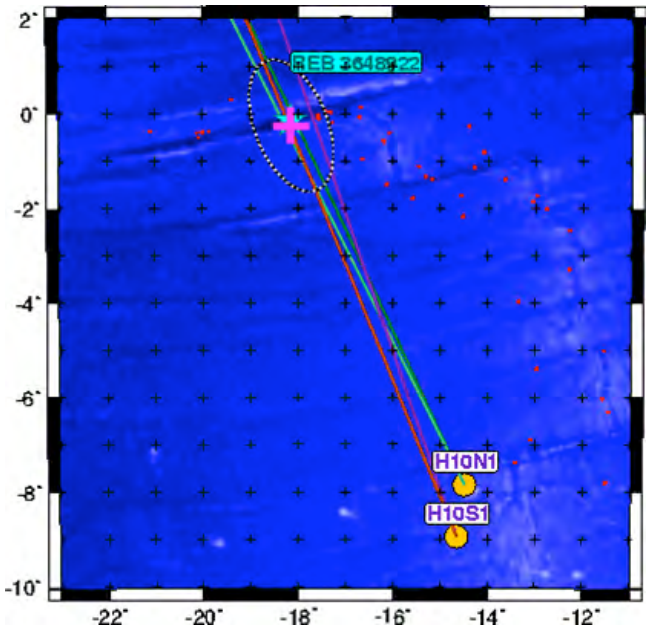


Figure 4. Refinement of the relative hydrophone positions of HA01 (Cape Leeuwin, AU). Top left: Consistency of lag times of the data used in the inversion procedure. Top centre/right: Back-azimuth and wave speed residuals before (green circles) and after (blue plus symbols) the inversion, compared with the results of a study done by Newton and Grenard (purple crosses). Bottom left/centre: Differences in relative receiver positions, also compared with the results of a grid search approach. Bottom right: Comparison of original and resulting triad geometries. The blue circles depict the positions that are now used in IDC operations.

A number of upgrades of the azimuth estimator were inspired by the PMCC algorithm (Cansi, 1995; Graeber and Piserchia, 2004). A derivative of PMCC has previously been implemented in DFX to process infrasound data at the IDC. As in PMCC, sliding correlation windows in different frequency bands are employed to find the most consistent azimuth and slowness estimates and only data windows which display a high degree of consistency (or a small sum of lag times) are considered. However, while PMCC declares detections on the basis of consistent signal coherency and is thus applied to continuous streams of data, HASE uses the conventional DFX detections to focus the analysis on relatively short data segments, which greatly reduces the resources required to process the data.

The new version of the azimuth estimator may also compute a slowness value outside the typical range of hydroacoustic phases and thus contributes to the automated identification of seismic arrivals, which is currently being tested at the IDC. So far, using rather conservative thresholds, about 30 seismic arrivals have been successfully detected per month on the stations HA08, HA01, and HA10. Very few (1–2) false identifications were made. Lag time corrections for the hydrophone mooring geometry were introduced to improve azimuth and slowness estimates of seismic phases and the preliminary results are encouraging (Figure 5). Further systematic differences between observed and predicted azimuth and slowness (Figure 6) are attributed to unknown properties of the seafloor and will be corrected in a way that is similar to what is currently done for seismic stations.



O-time	O-lat	O-lon	O-depth	smajax	sminax	strike	GAP
2006/04/08 22:03:04.9	-0.2550	-18.1340	0.0	162.9	84.8	158.9	356.1

Figure 5. A single hydroacoustic station (HA10) location using arrival times and azimuth estimates (given by the coloured lines) from Pn and T phases compared to the corresponding location of the IDC's reviewed event bulletin (REB). Note the very good agreement of the two independent locations and the highly consistent azimuth estimates obtained for the four arrivals.

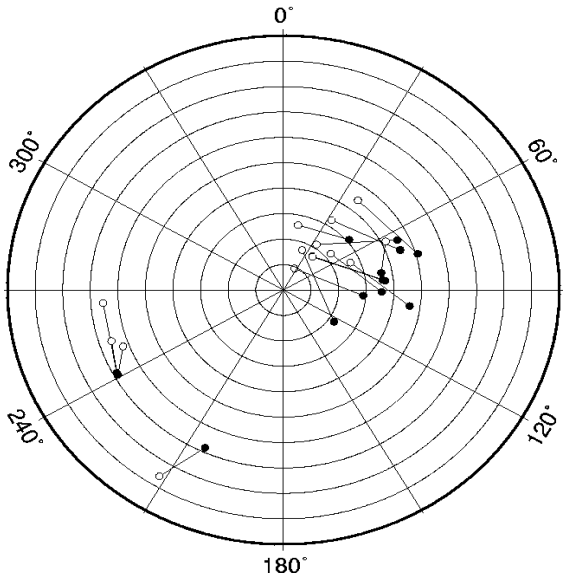


Figure 6. Polar plot showing the systematic differences between observed and predicted azimuth and slowness for the southern hydrophone triad of HA08. The concentric rings depict the slowness at intervals of 2 s/deg. Black circles show the predicted values, white circles the measured values.

Network Processing

Some minor changes were made to the global association (GA) sub-system, which was initially designed for seismic data, to facilitate the creation of events from hydroacoustic associations only. The need for the changes became obvious when a comparably strong in-water explosion was clearly observed at all three Indian Ocean hydrophone stations in May 2004 (Figure 7), while the event was not built by the automatic system. After the changes were implemented, the event was successfully built when the data was reprocessed off-line. Events like this are often used for testing purposes, even though the ground truth information is unfortunately not available.

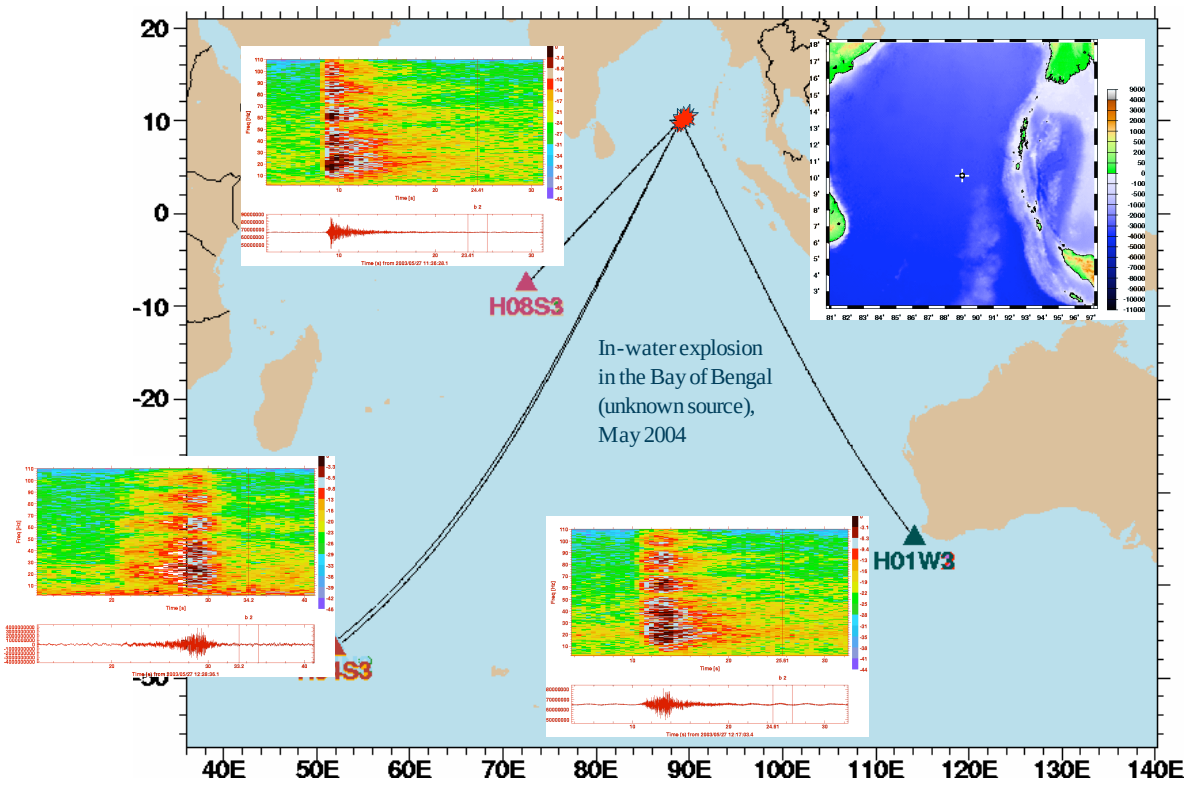


Figure 7. In May 2004 strong signals from an in-water explosion were observed at all Indian Ocean hydrophone stations. The event was formed automatically once some minor changes to GA were implemented. The location shown here was obtained off-line using the modified software.

Interactive Review Tools

New interactive review tools are being developed to enhance processing of hydroacoustic data and to be compatible with the methods used in automatic processing. A spectrogram tool, which is of essential importance for hydroacoustic phase identification and arrival time estimation, has been included in ARS. A prototype interactive cepstral review tool has been developed on the basis of the software module that was developed for automatic detection and features extraction (Figure 8). A new azimuth and slowness review tool will be developed using the experiences made with HASE and DFX-PMCC.

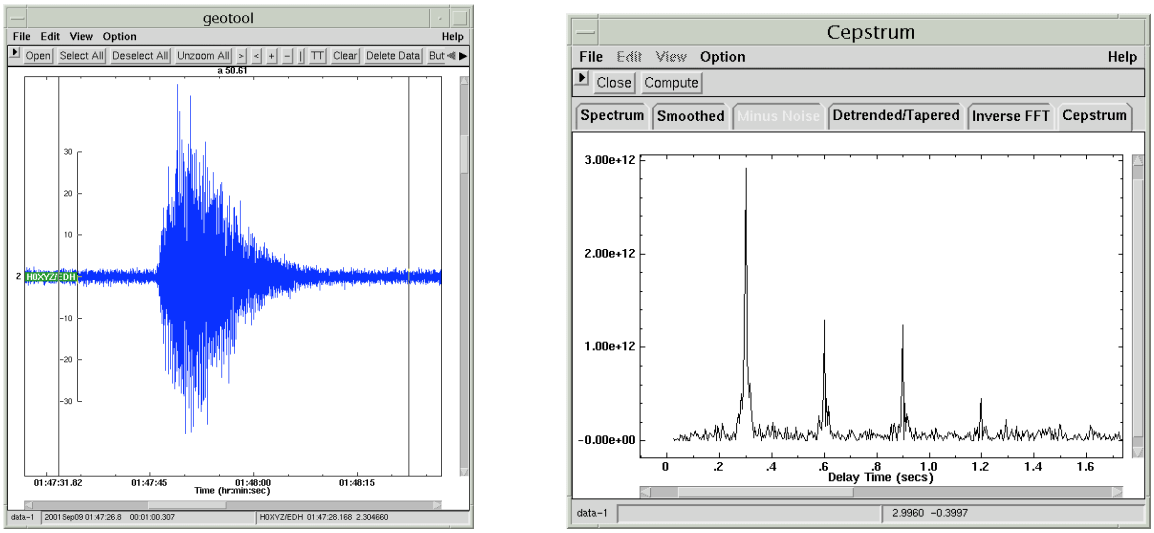


Figure 8. Screen shots of the prototype cepstral review tool. Processing parameters may be changed and intermediate stages of cepstral analysis can be displayed for better control of the final results.

CONCLUSIONS

Development of hydroacoustic data processing has made significant progress since the first IMS hydroacoustic stations became operational. Several pieces of the original software were upgraded or replaced. Parametric information such as the travel-time tables and the relative hydrophone positions was added or tuned. Today the results of the automatic processing more closely resemble the reviewed event bulletin, which implies that there is less work to be done on hydroacoustic data during interactive analysis. Future development may result in a major reorganization of the processing sequence in order to further enhance multi-channel processing and to facilitate the use of synergy effects between the three waveform technologies. Interactive review tools will be designed to not only provide the required functionality and accurate results, but also to streamline the routine processing.

DISCLAIMER

The views expressed herein are those of the authors and do not necessarily reflect the views of the CTBTO Preparatory Commission.

ACKNOLEDGEMENTS

We would like to recognize valuable communications with J. Newton and P. Grenard.

REFERENCES

Cansi, Y. (1995). An automatic seismic event processing for detection and location: The P.M.C.C. method, *Geophys. Res. Lett*. 22: 1021–1024.

Graeber, F. M. and P.-F. Piserchia, (2004). T-phase excitation in the NE Indian Ocean mapped using variations in backazimuth over time obtained from multi-channel correlation of IMS hydrophone triplet data, *Geophys. J. Int.* 158: 239–256.

Hanson J., R. Le Bras, P. Dysart, D. Brumbaugh, A. Gault, and J. Guern (2001). Operational processing of hydroacoustics at the Prototype International Data Center, *Pure Appl. Geophys*. 158: 425–456.

HYDROACOUSTIC PROPAGATION LOSS FROM REFLECTION AND TRANSMISSION OVER SHALLOW BATHYMETRY IN THE INDIAN OCEAN

Jeffrey A. Hanson, Colin L. Reasoner, and J. Roger Bowman

Science Applications International Corporation

Sponsored by Army Space and Missile Defense Command

Contract No. W9113M-05-C-0138

ABSTRACT

We examine direct and reflected hydroacoustic waves from natural sources throughout the Indian Ocean recorded at the IMS hydroacoustic stations to help plan an experiment in the Indian Ocean using explosions deployed offshore of Western Australia. Signals have been analyzed from events with paths that cross prominent bathymetric features similar to expected experiment-to-receiver paths. Theoretical models are used to gain insight into expected experimental received levels. In addition, reflection analysis has been conducted to better understand the variables affecting signal levels from various types of reflector surfaces.

To study direct propagation over basinwide distances, waveforms from natural sources (earthquakes) are analyzed in lieu of man-made explosions. Because of the limited distribution of earthquakes along active plate boundaries within the Indian Ocean, events are used with paths that are sometimes orthogonal to the expected experiment-receiver path, but cross the same shallow bathymetric features. These include the Osborn Plateau (along the Ninety-East Ridge), Broken Ridge, and Cuvier Plateau off Western Australia. Measurements comparing hydrophone received levels at independent hydrophone stations are used to assess frequency-dependent transmission loss. The frequency-dependent attenuation is observed and quantified for hydroacoustic waves traversing the bathymetric features. Attenuation of low frequencies (2 to 15 Hz) increases as source-receiver paths shoal. A parabolic equation code is used to estimate propagation loss along the event-station path using range-dependent environmental variables. The low-frequency attenuation estimated from the models is less than observed, perhaps indicating the need to use a more complicated ocean sediment model including an elastic seafloor. The higher frequency attenuation models indicate that the starting modal structure of the signal is an important factor in the attenuation of these signals.

One key objective of the active source experiment is to improve our understanding of the factors influencing reflections of high-frequency energy. To bound the various factors, we have begun by analyzing signals from events along the Carlsberg Ridge. These shallow ridge events provide many advantages over other earthquake source regions within the Indian Ocean. The direct hydroacoustic signal is less complicated than for trench events because of the more limited area of coupling of seismic energy to hydroacoustic energy. The coupling is stronger because the sound channel axis nearly coincides with the mid-ocean ridge in this area, and the signals generally contain higher frequencies than observed elsewhere. The steep continental shelf and the seamounts that surround this area provide ample reflector surfaces to study. Reflected signals are identified and associated to reflector surfaces based on azimuth and time of arrival measurements. The power spectra of observed reflections vary between 12 and 30 dB below the direct arrival power spectrum, and reflections vary in their relative frequency content. We predict reflection strengths based on bathymetry and the source/reflector/receiver geometry. Estimates are made for both specular and diffuse type reflections. Specular reflection estimates predict much of the relative variation in peak signal strength, but the geometric model does not account for all observed variations. This discrepancy and the differences in relative frequency content indicate variations in the roughness or material properties at the reflectors.

OBJECTIVES

This project is designed to improve discrimination of underwater seismic events and improve location of hydroacoustic sources in or just above the water column. Improvement in discrimination will be achieved by empirically quantifying and theoretically modeling high-frequency (>30–50 Hz) loss of hydroacoustic energy propagating in the Sound Fixing and Ranging (SOFAR) channel from reflections off coastlines and interaction with bathymetric obstacles along path. We will also use variations in the observed residual amplitudes to identify important environmental factors that most impact high-frequency transmission loss. We will localize coastal reflector locations that will allow for better prediction of the reflected wave field. We will examine the robustness and accuracy of measuring bubble pulses from reflected or highly attenuated signals.

RESEARCH ACCOMPLISHED

A series of investigations was conducted using natural sources to address the project objectives by beginning to quantify and model loss of hydroacoustic energy propagating in the SOFAR channel from reflections off coastlines and interaction with bathymetric obstacles along path. These investigations also support detailed design of the Indian Ocean experiment, which is planned for late 2006 or early 2007.

Data are taken from recordings made by the three hydrophone stations of the International Monitoring System (IMS) that monitor the Indian Ocean basin. These stations are Cape Leeuwin, Australia, Crozet Island, and Diego Garcia (Figure 1). The Cape Leeuwin station (H01W) consists of a single triad of hydrophones, while the Crozet (H04N and H04S) and Diego Garcia (H08N and H08S) stations have two hydrophone triads each to minimize signal blockage by near-station bathymetry. Four months of continuous data for all three stations, from December 2004 to March 2005, have been made available at the U.S. Army Space and Missile Defense Command (SMDC) Monitoring Research Program (MRP) website. The majority of earthquakes used in this study are gathered from that time period, but recordings for earlier time periods when only the Cape Leeuwin and Diego Garcia stations were operational are also used. Earthquake selection is complicated by the great Sumatra earthquakes of December 26, 2004, and March 28, 2005. We attempt to limit overlapping signals by excluding earthquakes occurring in the five days after the December 2004 event, and we also select events with T-phases that have a signal-to-noise ratio (SNR) of 25 dB or greater at least one hydrophone.

Direct Transmission Paths

In order to plan the Indian Ocean experiment we would like to predict signal losses from major bathymetric features that the hydroacoustic signals will cross. A two-prong approach is taken. Observations from natural sources are analyzed, and model predictions are estimated for similar paths. Because there are few earthquakes in the experimental region, we use earthquake/station paths that cross the same features albeit at different angles. For example, a feature along the Ninety-East Ridge that we expect the experimental generated signals to cross before reaching Diego Garcia is examined using earthquakes off Sumatra recorded at Crozet. The earthquakes examined are located along the Java/Sumatra trench. There are three major clusters of events (Figure 1). The central group of events simulates paths from the experiment location to Cape Leeuwin, the northern group of events simulates the experiment location to Diego Garcia by crossing the Osborn Plateau and being recorded at Crozet, and the eastern group of events simulates the experiment location to Crozet paths that cross the Broken Ridge. The source areas have relatively unblocked paths to the southern Diego Garcia triad, H08S, and this triad is used to provide a reference signal strength.

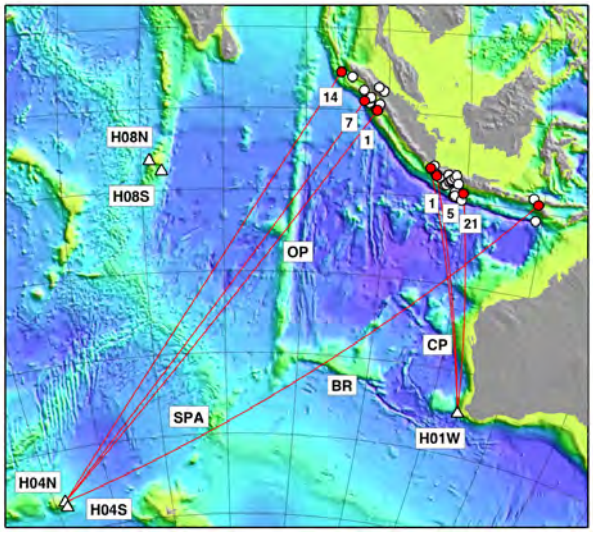


Figure 1. Earthquake and station locations. Hydrophone triads (triangles) and event locations (circles) are shown. Bathymetric features discussed in the text are also labeled: BR–Broken Ridge, CP–Cuvier Plateau, OP–Osborn Plateau, SPA–St. Paul-Amsterdam Plateau. Events plotted in red with ray paths are examined in more detail in the paper. The numbers along the ray paths correspond to event numbers used in the discussion.

Figure 2 shows the process used to estimate frequency-dependent signal loss. For each earthquake, the frequency spectrum of the direct T-phase recorded at H01W is compared with the spectrum recorded at H08S. The spectra are corrected for instrument response and a cylindrical spreading factor is included to account for the differing distances traveled from source to the different hydrophones. The signal loss estimation is considered valid where the signal level at H08S is 3 dB or greater above the noise level and the signal level at H01W is 1 dB or greater above the noise level. When the SNR at H01W falls below 1 dB, but there is still observable energy at H08S, then the estimated signal loss is considered a lower bound. The actual signal losses could be greater, but the noise level prevents us from knowing by how much. The same analysis is conducted for signals recorded at H04N.

Cuvier Plateau: Paths from the Java Trench to H01W

We selected events to provide a transect from west to east across the Cuvier Plateau that allows examination of T-phase attenuation as the water depth decreases. The event-station paths are shown in Figure 1. Figure 2 compares the signal received at H01W with the signal received at H08S for two events. The plots for event 1 show that frequencies below about 3 Hz are blocked by bathymetry along the path. For event 5, the corner of the attenuation plot moves to about 6 Hz, while all energy for event 21 (not shown) is blocked. We hypothesize that this blockage is due to the very shallow water depths (150 m) encountered along that path. By contrast, the shallowest water depth at the Cuvier Plateau for the path from event 1 is 2,600 m, and the shallowest depth for the path from event 5 at the Cuvier Plateau is 1800 m. This variation in the attenuation "corner frequency" implies that the Cuvier Plateau acts as a high pass filter with increasing higher frequency attenuation as the water depth decreases. Figure 3 shows the relationship between the mean attenuation between 1.5 and 4 Hz and the minimum water depth corresponding to the source-receiver path crossing the Cuvier Plateau. Figure 4 shows the plateau's bathymetry along a west-east transect with ray path crossing points color-coded by the attenuation corner frequency. We see from these figures that, in general, attenuation increases as water depth decreases. Once the water depth decreases to 1,000 m, nearly all T-phase energy is blocked.

These observations are complicated because attenuation determined for the paths might not be due solely to the Cuvier Plateau when the plateau's water depth is greater than about 1,200 m. The H01W bathymetry profiles in Figure 2 show that the ray paths cross shallow bathymetry (approximately 1,200 m) close to the hydrophones. Some signal is likely lost in this shallower water, and this may be the cause of some of the 1–3 Hz attenuation for events 1 to 6. This likely explains the nearly constant (and generally positive) level of attenuation for water depths at the Cuvier Plateau between 1,500 and 2,500 m in Figure 3.

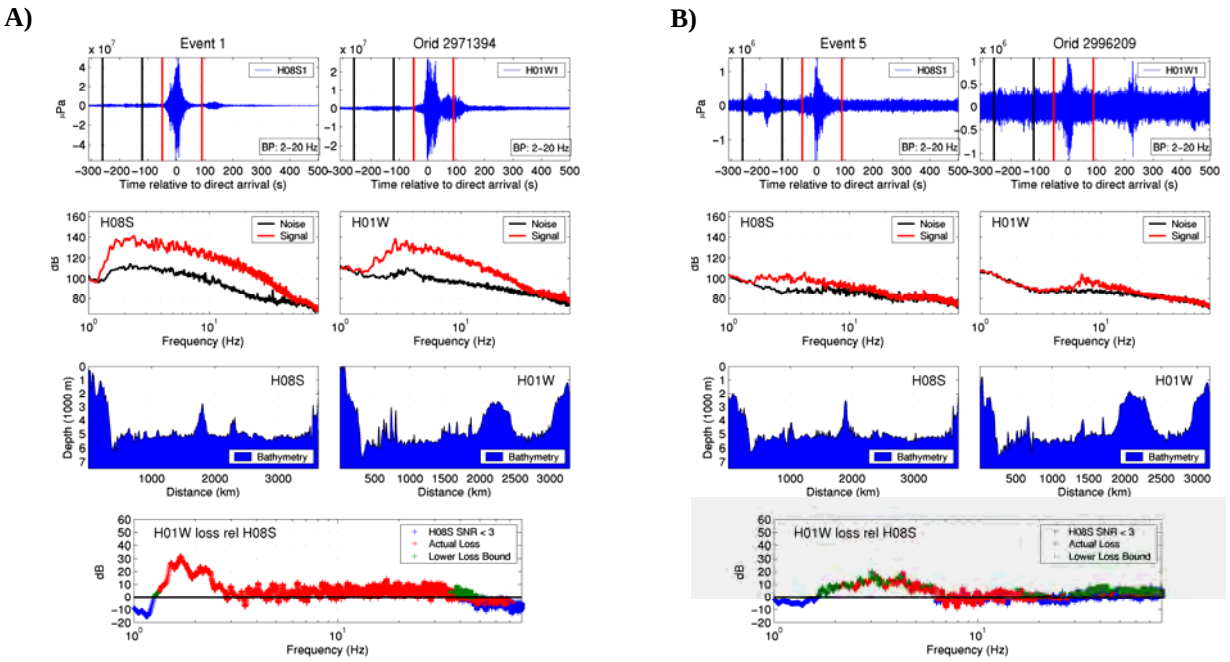


Figure 2. Signal loss for selected paths to H01W that cross the Cuvier plateau. Each sub-panel shows the waveforms at H08S1 and H01W1 (top panels), the triad-averaged signal and noise spectra (second row of plots), the bathymetry between the receivers and sources with the receivers on the right (third row of plots), and the computed signal loss at H01W relative to H08S (lowermost plots). Signal loss is color-coded. The three categories differentiate between valid signal loss estimations (red), lower bound signal loss estimations (green), and indeterminate estimates due to low SNR at H08S (blue). (A) The path for an event that crosses the Cuvier Plateau (distance from H01W is about 1,000 km) where the water depth is nearly 2,600 m, and frequencies below 3 Hz are blocked. (B) The path for an event that crosses the plateau where its depth is about 1800 m, and frequencies below 5–6 Hz are blocked.

We used RAM to estimate transmission loss between the Java Trench events and Cape Leeuwin. RAM is a parabolic equation code for computing range-dependent propagation loss (Collins, 1994). The along path environmental parameters were extracted from the World Ocean Atlas and the Sandwell and Smith global bathymetry database using BBN's Matlab interface HydroCAM. This implementation assumes a point source, which is not entirely appropriate for Java Trench earthquakes. To compensate for this approximation, transmission loss models were computed at several depths including the sound channel axis depth. Figure 5 shows results for a path that crosses the Cuvier Plateau for sources at 1,000 m and 2,000 m depths. For the 1,000 m depth simulation, which is near the sound channel axis, multiple modes are excited, but only mode 1 continues past the plateau. The deeper source excites a different set of modes, with what appears to be mode 2 continuing past the plateau. These indicate that all but the low-order modes will be stripped by the plateau bathymetry. For paths crossing over shallower portions of the plateau, the signal attenuation becomes highly dependent on bottom parameters. This is especially true for depths shallower than the sound channel axis because all modes will interact strongly with the seafloor. This leads to higher attenuation of the in-water signal due to energy leaking into the seafloor.

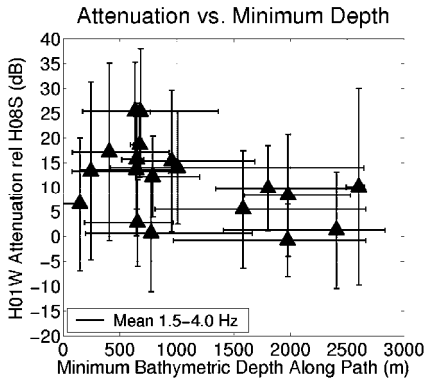


Figure 3. Attenuation vs. minimum depth at the Cuvier Plateau. The mean attenuation between 1.5 and 4 Hz is plotted. Vertical error bars represent two times the standard deviation, and horizontal error bars on bathymetry depth are computed by assessing the possible range of water depth that might be encountered given origin location errors.

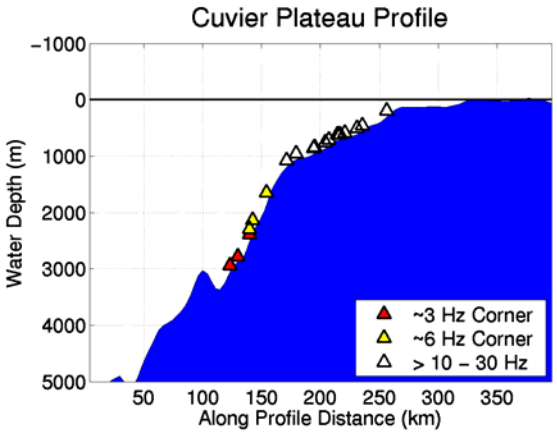


Figure 4. Changes in attenuation with bathymetry. The bathymetric profile for a transect across the Cuvier Plateau is shown (blue). The crossing points of rays to H01W are plotted as triangles color-coded to the corner frequency of the attenuation relative to H08S. The bathymetry of the Cuvier Plateau acts as a high-pass filter with increasing amounts of blockage as the water depth decreases.

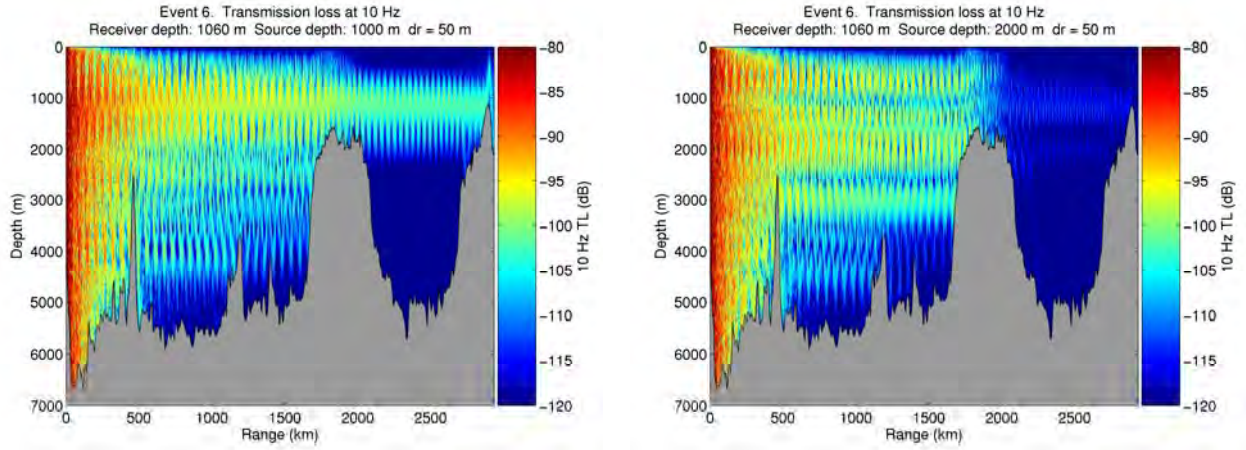


Figure 5. Transmission loss at 10 Hz modeled using RAM for a path from the Java Trench to H01W. Two different source depths are shown: 1,000 m (left panel) and 2,000 m (right panel). Propagation is dominated by mode 1 for the 1000 m source depth, while mode 2 and higher modes dominate for the 2000 m source depth. Interaction with the shallower bathymetry of the Cuvier Plateau at ranges 1,700–2,100 km increases transmission loss for both source depths, though the amount of transmission loss is greater for the deeper source.

Osborn Plateau: Paths from the Java Trench to H04N

Figure 6 shows attenuation observations for T-phases crossing the Osborn Plateau similar to the Cuvier Plateau results above. The mean attenuation in the 1.5 to 4 Hz band is shown versus the shallowest water depth encountered along path. There we focus on three events (see Figure 1). The path from event 1 crosses the eastern edge of the plateau, the path from event 7 crosses the middle of the plateau, and the path from event 14 passes to the north of the plateau. Attenuation is greatest for the path from event 7, and we hypothesize that the shallower water depth at the

Osborn Plateau is responsible for this attenuation. However, since the shallowest bathymetry encountered along this path is about 1,770 m, only energy between approximately 1 and 4 Hz is blocked. Higher frequency energy propagates over the plateau with little loss. Figure 6 shows a similar relationship as in Figure 3 with generally increased attenuation for shallower water. Also, the level of attenuation for 1,500 to 2,000 m water depths is similar, although the attenuation observations are complicated by near-receiver water depths of about 1,200 m.

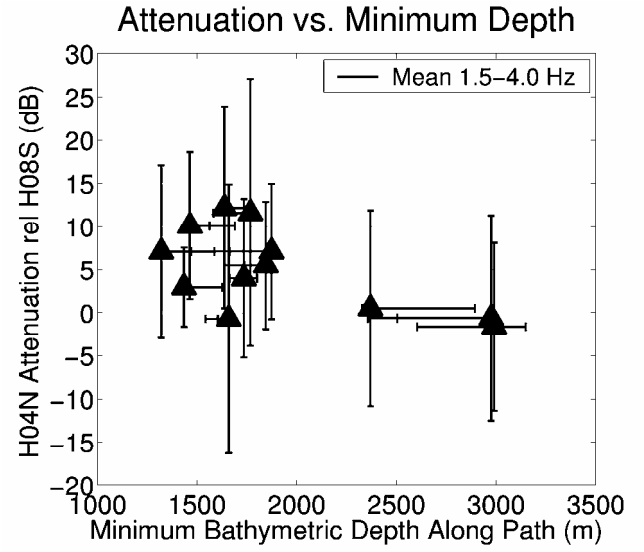


Figure 6. Attenuation vs. minimum depth for paths to H04N that cross the Osborn Plateau. Error bars are computed as in Figure 3.

Reflected Transmission Paths

A goal of this research is to correlate reflection strength to physical attributes of the reflector surfaces. Reflected signals were identified from several earthquake sources along the Java Trench at the Diego Garcia hydrophones. We used the direct arrival measurement seen at H08S and cylindrical spreading attenuation to normalize the other reflected signal strength and estimate reflection loss for different reflector surfaces. Reflector loss for various source reflector pairs were examined. However, the reflector strengths are highly correlated to the event location as opposed to the reflector location. Because the paths traverse deep water, we believe that this source dependence is more likely a function of the near-source hydroacoustic coupling than reflector attributes. The complicated nature of seismic-to-hydroacoustic coupling for trench events is well known (Graeber and Piserchia, 2004; de Groot and Orcutt, 2001), and it appears to dominate our observations, making trench events poor source candidates for this analysis. Instead we have analyzed several mid-ocean ridge events.

Signals from events along the Carlsberg Ridge northwest of Diego Garcia were studied for propagation and reflection loss characteristics. The events from this ridge are advantageous because their shallow locations and relatively simple bathymetry provide some of the most point like natural sources in the Indian Ocean basin (Hanson and Bowman, 2005). In addition many reflections from these events are commonly observed at the northern Diego Garcia triad. The shallow nature of the events and the proximity of the bathymetric ridge highs to the sound channel axis result in more high-frequency energy traveling through the SOFAR channel. Direct-T phases are often seen with energy at greater than 50 Hz. The reflection strengths also appear to be less source-dependent than for trench events.

Figure 7 shows events from the Carlsberg Ridge in the northwestern Indian Ocean that we examined for reflections. These events have clear paths to the northern Diego Garcia triad. Many reflections are observed from the surrounding continental slope and other prominent bathymetric features. Reflection losses were estimated for the 2 to 6 Hz frequency band by normalizing the reflected signal strength with the direct arrival and accounting for additional attenuation with distance. Reflector strengths are correlated by the reflector type/location although there is still scatter within each group (right panel). The differences in reflection strength within a group are most likely caused by differences due to near source bathymetry or earthquake source parameters, differences in the path attenuation of the direct source, and/or unresolved details in the reflector surfaces. The source coupling effect should be minimized because of the shallow nature of mid-ocean ridge earthquakes and the general coincidence of earthquakes with the shallowest bathymetry. The direct path attenuation might be significant because the source-to-receiver path often follows the relatively shallow and rough Carlsberg Ridge. However, if this factor was significant we would expect a decrease in inferred reflector loss for earthquakes occurring farther from H08N, which is not observed. Transmission loss along reflector paths should be minimal because reflector paths are generally orthogonal to the ridge and hence traverse fairly deep (nonattenuating) ocean paths. The possibility that the variation can be explained by more detailed reflector categorization is examined below.

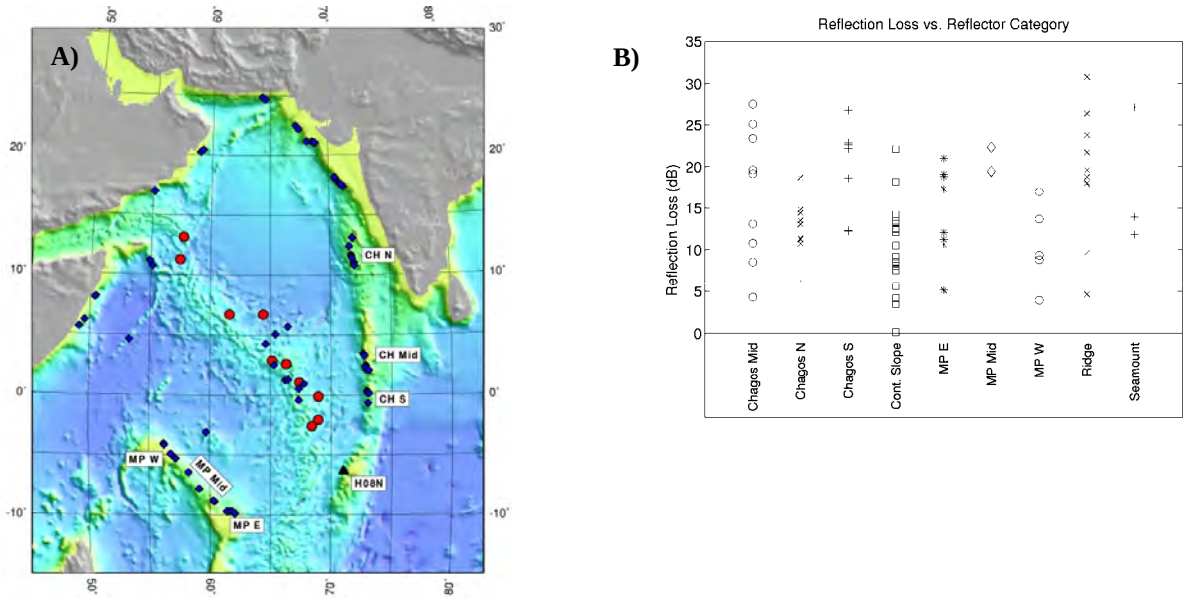


Figure 7. Reflection observations for events occurring along the Carlsberg Ridge recorded at H08N. A) Location map of earthquakes (circles) and reflection points (diamonds). The labels indicate groups of reflections. B) Reflection losses grouped by reflector category for the Carlsberg Ridge events. Reflector categories are defined by type (Continental Slope, Mid-Ocean Ridge, Seamount) or by geographic location (Chagos Archipelago north, middle, south and Mascarene Plateau (MP) east, middle, west). Losses are computed as the mean difference between reflected and direct arrivals in the 2–6 Hz band. Although each reflector category has a wide range of reflection losses, the continental slope reflectors show less signal loss than mid-ocean ridge reflectors. The Chagos Archipelago and Mascarene Plateau reflectors behave more like continental slope than mid-ocean ridge reflectors, probably due to their shallow bathymetry compared to ridges.

Reflections were analyzed for select Carlsberg ridge earthquakes described above. The time-bearing analysis of Hanson and Bowman (2006) was used to determine reflector locations based on azimuth and travel time estimates. The analysis estimated azimuths using a running 8 second time window with 50% overlap. Coherent arrivals that are continuous in the time-bearing domain were grouped together as a single reflector. An example from an earthquake that occurred in June 2003 is presented here. The reflectors found for this event are shown in Figure 8. This reflection analysis is only dependent on the earthquake location and time, the ocean sound speed, and the time-bearing measurements at H08N. At this stage information of the bathymetry has not been used. However, all reflector groups fall along distinct bathymetric features. By comparing reflections from a single source, we eliminate most of the source-dependent effects, especially the direct path attenuation. We compare these to reflection strength predictions estimated below.

Reflection strengths at H08N are predicted for a given source using the source/receiver geometry and bathymetric features. The reflections are clearly associated to bathymetric features. The analysis here attempts to establish how much of the reflector strength can be estimated from geometric factors computed from a global bathymetric map. We used the 2 minute resolution global bathymetric map of Smith and Sandwell (1997). Our analysis computed a reflector strength at each bathymetry point based on a composite of functions that depend only on the bathymetry, source location, and receiver location. These functions are blockage from source to reflector, blockage from receiver to reflector, depth relative to sound channel axis, reflector slope, transmission loss along source-reflector-receiver path, and a specular reflection coefficient. The strengths predicted from each function are multiplied to obtain a composite reflector strength.

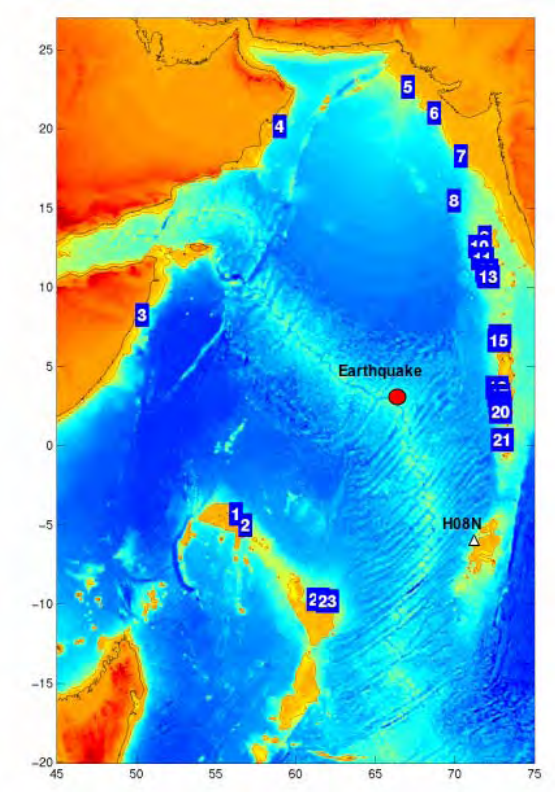


Figure 8. Map showing the inferred reflectors (numbers) of signals from a shallow earthquake on the Carlsbad Ridge (red circle) that occurred on June 22, 2003. Reflectors were identified based on the signal back azimuth measured at H08N and their time delay relative to the direct arrival.

These steps are demonstrated in Figure 9. Blockage is computed based on a bathymetric contour (currently 500 m). Two masks are computed with the source at center and the receiver at center. Instead of using a step function at the blockage contour, a 100 km transition zone is created using a sigmoid function. Reflection strength is assumed to be maximum at the sound speed channel axis. We assume the axis is a constant at 1200 m depth. The reflector strength is then estimated using a Gaussian centered on the axis. The width of the Gaussian is currently selected to be consistent with our general observations. The next factor affecting our prediction is the slope of the reflector. The slope is estimated at a particular bathymetry node in the database using the four closest nodes to compute an average slope. The cosine of the angle the normal makes with the horizontal is used to determine the slope's contribution to reflector strength with the constraint that the upward facing normal must be within 90 degrees of the reflector-to-receiver direction, i.e., the reflector must face the receiver. Finally, a reflection coefficient is computed that is a function of both the incidence angle from the source and the take off angle to the receiver. In purely specular reflection this function is zero when the incidence angle does not equal the take off angle. In purely diffuse reflection this function is independent of the take off angle. We compute a reflection function that allows for a trade-off between purely diffuse and purely specular reflection.

Figure 9 shows an example of estimating reflector strength from the various factors described above for the earthquake in Figure 8. The maps cover reflectors 9 through 13 in Figure 8. The depth based reflector strength function (Figure 9a) is necessary, but not sufficient in estimating the reflector strength. The inclusion of the bathymetric gradient and high specular reflectivity index explains many of the observed reflections. At this stage many of the strong reflectors that are predicted but not observed in the data are due to blockage.

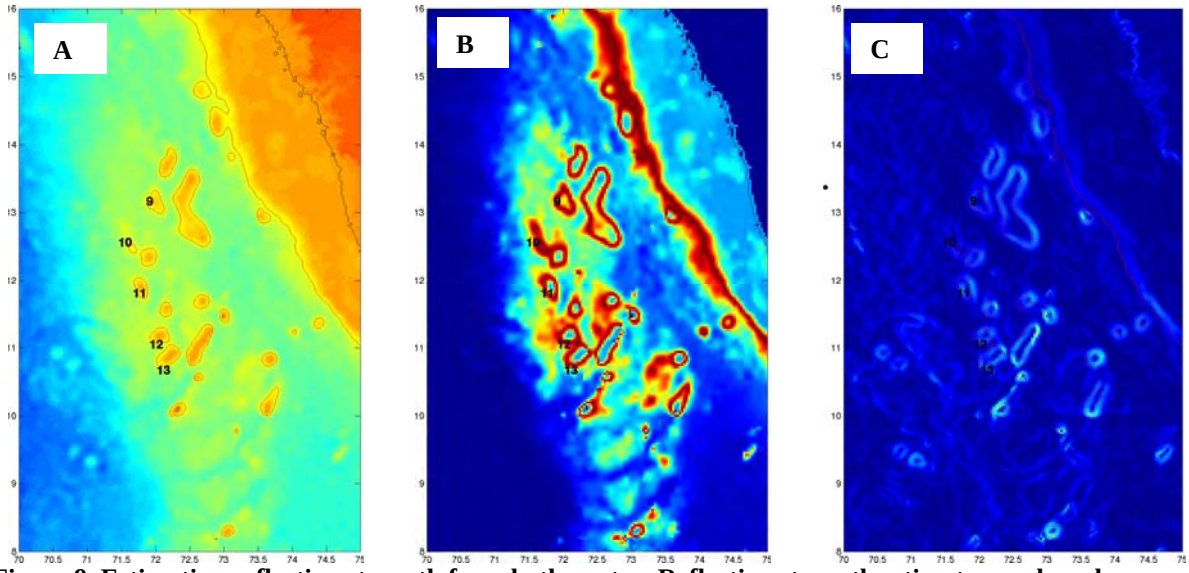


Figure 9. Estimating reflection strength from bathymetry. Reflection strength estimates are based on geometrical properties using the Smith and Sandwell (1997) global bathymetry database. The panels show some of the intermediate values that are used in estimating reflector strength. The bathymetry shown covers reflectors 9 through 13 from Figure 8. (A) Bathymetry with the 0 meter (black) and 1000 meter (red) bathymetry contours drawn. (B) Strength function based on water depth relative to sound channel axis. (C) Relative strength based on the average slope of the bathymetry.

The reflector strengths estimated at each bathymetry grid point are translated into an azimuth/time space corresponding to the expected angle and time of arrival at the hydrophone station. This results in a plot showing predicted arrival strength as a function of time and azimuth (Figure 10). This is compared to the measured angle of arrival with time from our standard time/bearing analysis (x's in Figure 10). Generally, measured arrivals coincide with the predicted energy. Energy arriving between 0 and 40 degrees corresponds to reflections from the Chagos Archipelago and the Indian continental slope. Energy arriving at 1,000 s between –120 and –60 degrees corresponds to reflectors from the Mascarene Plateau. However, there is also predicted energy with no corresponding observed arrivals. There are a number of reasons why this might happen. Energy arriving from different azimuth simultaneously will interfere with the coherence measures used to estimate azimuth. But the energy should be visible in an incoherent beam. This is not the case for the predicted energy arriving between 2,250 and 2,500 s, which corresponds to predicted energy from the coast of Africa. Because of the generally deep bathymetry, it is unlikely that this is due to unmodeled propagation loss. It is more likely that the continental slope in this area is a poor reflector.

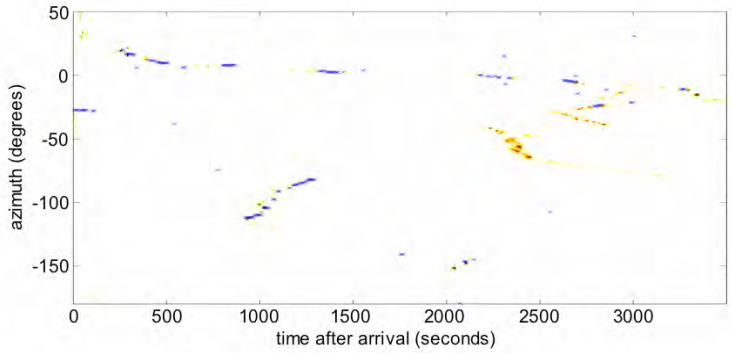


Figure 10. Comparison of predicted reflected energy (shading) and observed reflections (crosses) for the event in Figure 8. The shading represents predicted intensity based on bathymetry (dark red is high intensity, white is no energy).

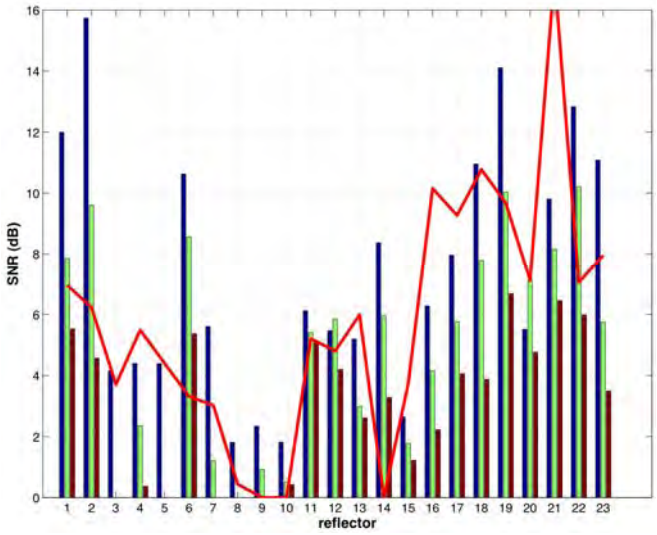


Figure 11. Histogram showing the signal-to-noise ratio (SNR) of reflected signals for 3–6 Hz (dark blue), 6–12 Hz (green), and 12–24 Hz (brown) frequency bands for the earthquake and numbered reflections in Figure 8. The red line shows the SNR predicted based on bathymetric factors. Low-frequency received levels are fairly consistent with prediction, with a few exceptions.

Figure 11 compares predicted reflection strengths versus observations with power spectra estimates. The bars represent observation power in three frequency bands. The red line is a relative measure of predicted reflector strength. Our predictions are frequency independent so there is only a single value per reflector. The predicted strengths correspond fairly well to the observations, especially considering the predictions have not included any sediment or surface roughness parameters.

The observations for each frequency band are represented as different color bars in Figure 11. The frequency bands are: 3–6 Hz, 6–12 Hz, and 12–24 Hz. The signal levels generally decrease with frequency as expected from the drop off in source level, but some reflectors lose more energy at high-frequency faster than others. This is independent of overall reflection strength levels. Figure 12 shows power spectra for the direct arrival and two reflections (6 and 7). The reflections are from two locations along the Indian sub-continent's continental slope. The frequency contents of the two reflections are strikingly different. The reflectors' surfaces are within 200 km of each other along steep portions of the continental slope. The major geometrical difference is the incidence and reflection angle between source and receiver. This difference may indicate a frequency-dependent scattering mechanism.

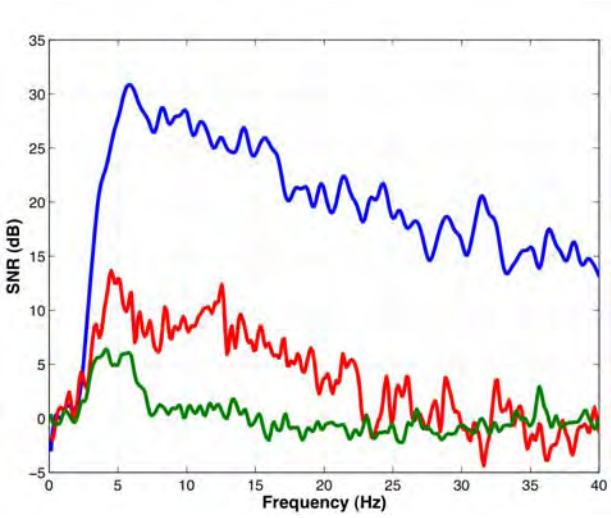


Figure 12. Power spectra for main and reflected signals. The blue line is an estimate of the power spectrum of the direct hydroacoustic arrival. The red and green lines are power spectra estimates for reflections 6 and 7 (from Figure 8), respectively. Note the difference in frequency content of the two reflections.

CONCLUSION AND RECOMMENDATION

We examined transmission and reflection losses for various source/receiver paths to better prepare for the Indian Ocean active source experiment. Natural sources were used in place of the controlled experiment sources. This limits the certainty that can be derived from the analysis. However, general conclusions can be reached. The experimental paths considered here appear to act as high pass filters with the corner frequency determined by the shallowest bathymetry along path. Higher frequency energy propagates over the bathymetric features relatively unattenuated until depths approach the SOFAR channel axis.

Many reflected signals have been observed. The trench earthquakes are not well suited for studying the properties of individual reflectors because the complicated hydroacoustic source region dominates the data variance. Ridge earthquakes are much better candidates for reflector analysis. Many reflections have been observed from Carlsberg Ridge earthquakes. The amplitudes of these reflected signals can be predicted to a large extent using simple functions that depend only on bathymetry, sound channel axis depth, and source and receiver locations. However, these predictions are not able to predict observed frequency variations, which may require the use of seafloor bottom properties.

ACKNOWLEDGEMENTS

We thank Dr. Jay Pulli and Mr. Zach Upton for their help in obtaining and running HydroCAM.

REFERENCES

Collins, M. D. (2004). Generalization of the split-step Padé solution, *J. Acoust. Soc. Amer.* 96: 382-385.

de Groot-Hedlin, C. D. and J. A. Orcutt (2001). Excitation of T-phases by seafloor scattering, *J. Acoust. Soc. Amer.* 109: 1,944–1,954.

Graeber F. M. and P.-F. Piserchia (2004). Zones of T-wave excitation in the NE Indian Ocean mapped using variations in backazimuth over time obtained from multi-channel correlation of IMS hydrophone triplet data. *Geophys. J. Int.* 158: 239–256.

Hanson, J. A. and J. R. Bowman (2005). Indian Ocean Ridge seismicity observed with a permanent hydroacoustic network, *Geophys. Res. Lett*. L06301, doi:10.1029/2004GL021931.

Hanson, J. A. and J. R. Bowman (2006). Methods for monitoring hydroacoustic events using direct and reflected T-waves in the Indian Ocean, *J. Geophys. Res*. doi:10.1029/2004JB003609.

Smith, W. H. F. and D. T. Sandwell (1997). Global seafloor topography from satellite altimetry and ship depth soundings, *Science* 277: 1957–1962.

PROPAGATION, ATTENUATION AND BLOCKAGE OF HYDROACOUSTIC WAVES IN THE EARTH'S OCEANS

Eric Matzel and Philip E. Harben

Lawrence Livermore National Laboratory

Sponsored by National Nuclear Security Administration
Office of Nonproliferation Research and Development
Office of Defense Nuclear Nonproliferation

Contract No. W-7405-ENG-48

ABSTRACT

We are investigating the nature of hydroacoustic wave propagation in the Earth's oceans, with a focus on the attenuation of signal over long distances and the blockage of signal by shallow features and islands along the source-receiver path. The objective of this research is to enhance discrimination capabilities for events located in the world's oceans. Two research and development efforts are needed to achieve this: (1) improvement in discrimination algorithms and their joint statistical application to events, and (2) development of an automated and accurate blockage prediction capability that will identify all stations and phases (direct and reflected) from a given event that will have adequate signal to be used in a discrimination analysis. Our current research involves measuring signal amplitude at hydroacoustic stations and comparing the results to predictions for a variety of models. To this end, we are continuing with the development of the Hydroacoustic Blockage Assessment Tool (HABAT) which is designed for use by analysts to predict which hydroacoustic monitoring stations can be used in discrimination analysis for any particular event. HABAT has been upgraded to allow measurements of the spectra and the signal amplitude from oceanic sources. Waveform data are read in and the signal and noise amplitudes are measured for a number of frequency bands. Several measures are taken. First, can the event be observed at a station above background noise? Second, can we establish backazimuth from the station to the source? Third, what is the decibel drop at one station relative to other stations? Finally, how do the measurements vary among the individual elements of each hydroacoustic array? From these results we can create blockage maps as a function of frequency that are then compared with the model-based blockage maps generated by Hydroacoustic Coverage Assessment Model (HydroCAM) to assess blockage criteria.

OBJECTIVE

The objective of this research is to enhance discrimination capabilities for events located in the world's oceans. We intend to characterize the propagation of acoustic waves across the oceans, estimate the attenuation of seismic signals along the source-receiver path, and establish whether the signal will be blocked by obstacles along the way. Once the physical processes are understood, we will be able to define the sensitivity of each hydroacoustic station to sources occuring at any point in the ocean. The strategy for improving source detection in the world's oceans is to improve model-based prediction of blockage and to develop a ground-truth database of reference events to assess blockage. Currently, our research is focused on the development of a hydroacoustic assessment software tool and the measurement of signal and noise amplitudes for earthquakes and experimental sources. The tool is envisioned to develop into a sophisticated and unifying package that optimally and automatically assesses both model and data-based blockage predictions in all ocean basins for all National Data Center (NDC) stations, and to account for reflected phases (Pulli et al., 2000).

RESEARCH ACCOMPLISHED

We are continuing with the development of the Hydroacoustic Blockage Assessment Tool (HABAT) which is designed for use by analysts to predict which hydroacoustic monitoring stations can be used in discrimination analysis for any particular event. HABAT employs both a model-based and a data-based approach to establish hydroacoustic station resolution. Originally written to interact with HydroCAM results to evaluate propagation models, the code has been upgraded to allow measurements of the spectra and the signal amplitude from oceanic sources. Waveform data are read in and the signal and noise amplitudes are measured for a number of frequency bands. A source is considered detected in a specific frequency band if the signal amplitude is noticeably above the pre-event noise amplitude. The amplitude measurements for specific sources are compared from one station to the next to assess how well an event is characterized by the entire network. Differences in resolution are affected by scattering and attenuation along the different paths. From these measurements we create frequency-dependent blockage maps which are then compared with the model-based blockage maps generated by HydroCAM to assess blockage criteria.

An example of the differences in source detectability is illustrated in Figure 1. The 2003 Indian Ocean cruise sailed along a track from Cape Town, South Africa to Darwin, Australia (Harben et al., 2004; Figure 1). The experiment resulted in 13 ground truth events which were detected at 1 or more of the hydroacoustic stations, including 40–50 individual waveforms of both stationary uncorrelated scattering or signals, underwater sound (SUS) and imploding sphere sources. We measured the spectra from each of the explosive source charges at each of the Indian Ocean stations (Diego Garcia North (DGN) and South (DGS), Cape Leeuwin, and Crozet Island). Because a nondetection of a source could be due either to blockage along the source-receiver path or attenuation of the signal over distance, it's helpful to have measurements at several stations to compare with one another. DGN and DGS are an excellent pair of stations to evaluate blockage criteria because they are located close to one another, but are in a region with significant bathymetric features which result in very different blockage predictions for each. An event that is observed at one site should be observed at the other, unless there is a true blockage along the path. This allows us to evaluate blockage as a function of frequency and bathymetry.

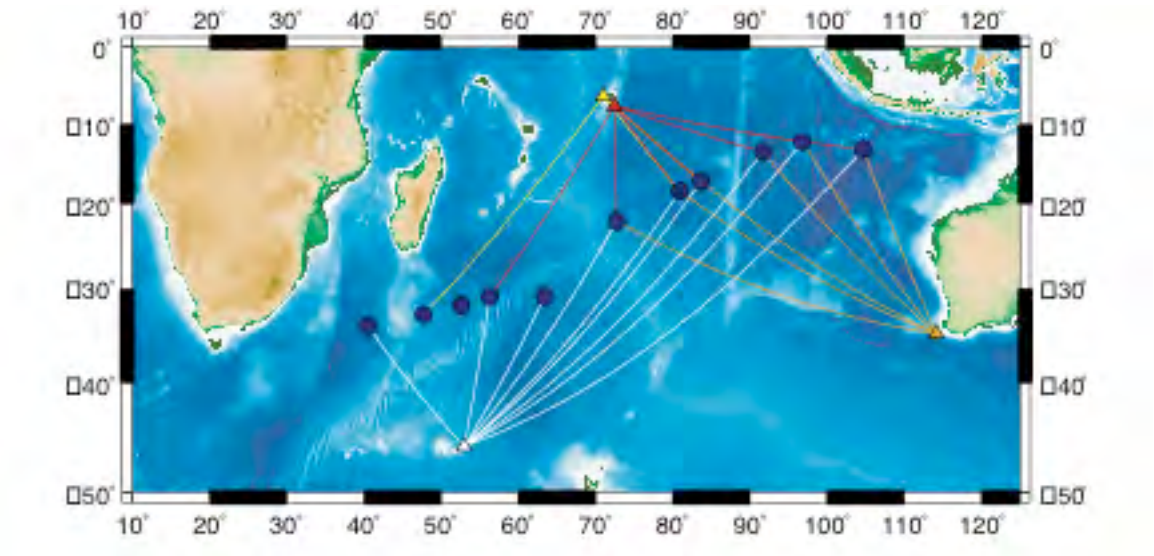


Figure 1. The 2003 cruise sailed along a track from Cape Town, South Africa to Darwin, Australia (Harben, et al., 2004). The experiment produced a series of ground truth events that were detected at 1 or more of the hydroacoustic stations; 40–50 individual waveforms for both SUS and imploding sphere sources resulted. We measured the spectra from each of the explosive source charges at each of the Indian Ocean stations (Diego Garcia North (yellow triangle), Diego Garcia South (red triangle), Cape Leeuwin (orange triangle) and Crozet Island (white triangle)). Source locations are indicated by blue circles (A01 on the left, through A11 on the right). Paths for which there was a detection are illustrated in color (white to Crozet, orange to Cape Leeuwin, yellow to DGN and red to DGS). Note that most of the paths were blocked to DGN.

Since we have only a limited number of small experimental sources available, we also take measurements of waveform data from oceanic earthquake events. These larger events are much more likely to be detected over long distances and comparisons between stations still let us evaluate attenuation and propagation criteria. Figure 2 illustrates the differences in detection of T-phases at DGN and DGS for a collection of oceanic earthquake sources. Here we've plotted signals detected above the noise at 20 Hz, which is on the lower end of the frequencies of interest (usually between 5–120 Hz). Note the significant differences in detection due to near station bathymetry. Notice, however, that a simple ray-based blockage criteria is not correct. Energy from a large source can get past an island, although it will be significantly attenuated (Figure 3). Blockage becomes more significant at higher frequencies with islands and shallow bathymetry changing from highly attenuating features into true barriers to detection (Figure 4).

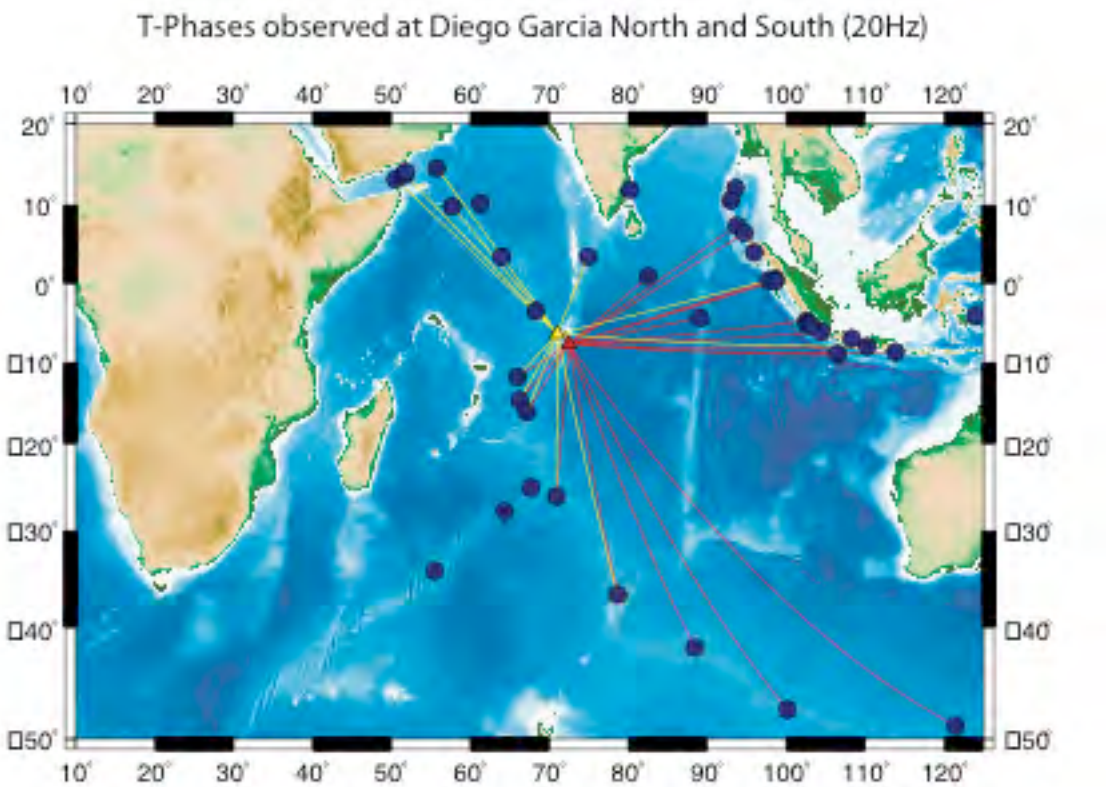


Figure 2. T-phases observed at Diego Garcia North and South. Blue circles indicate the locations of earthquake sources in the Indian Ocean in 2001 (courtesy BBN). Diego Garcia North (yellow triangle) and Diego Garcia South (red triangle) have different coverage due to the nearby bathymetry. By comparing measurements at each station to the same sources, we can define the blockage effects of the near station region. Above, we have drawn source-receiver paths for each event observed at 20 Hz.

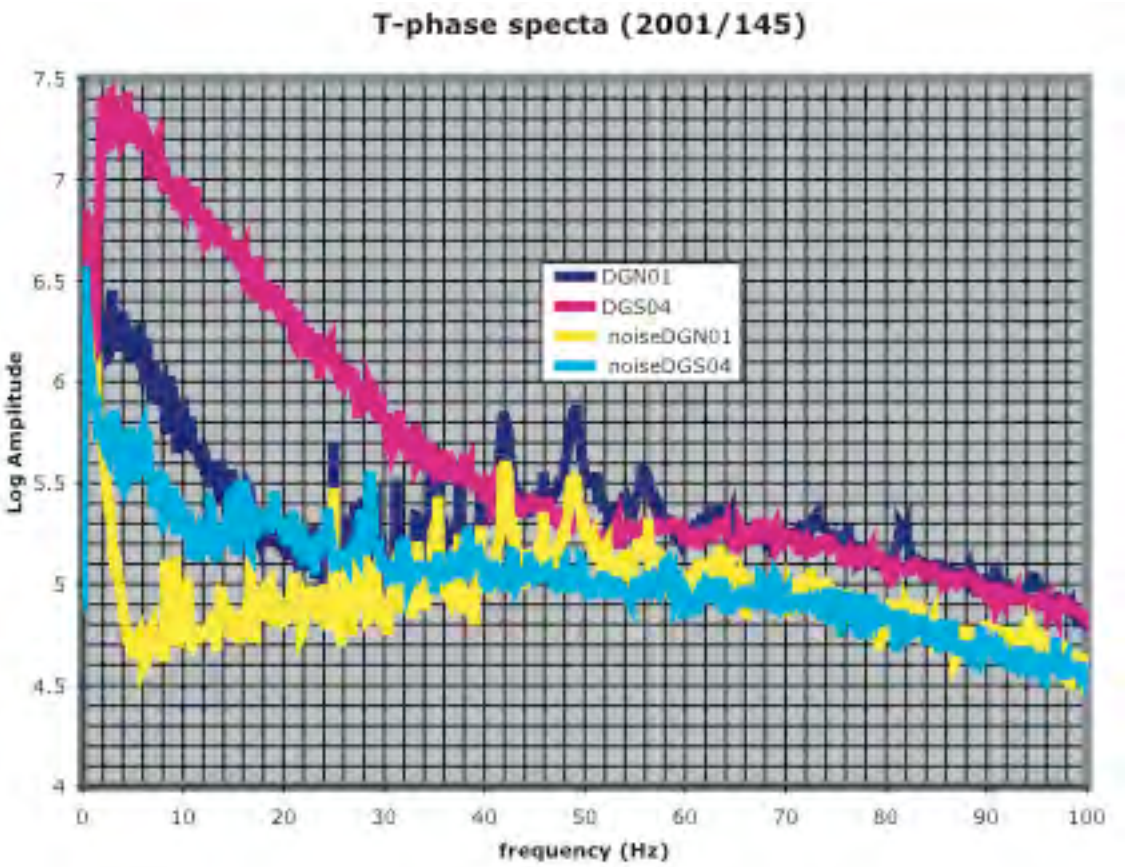


Figure 3. Spectra for a T-Phase event observed at DGN and DGS. This source was located in Java along a path expected to be blocked to DGN (it passes through the island itself). Not that there is a significant drop in amplitude at DGN relative to DGS, but the signal is still well above the noise even at 20 Hz.

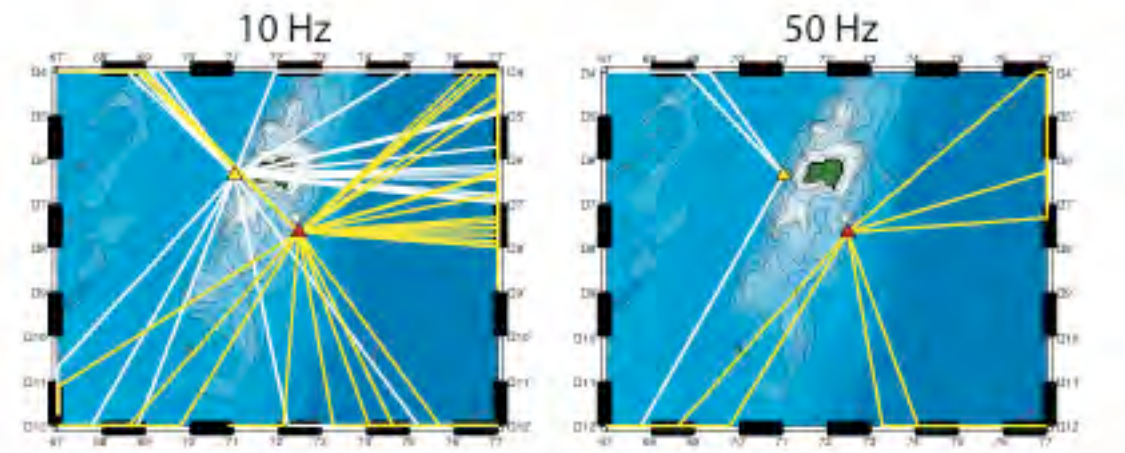


Figure 4. Here we have plotted the sensitivity of DGN and DGS to earthquake sources as a function of frequency. Each panel illustrates the local portion of the source-receiver path for sources that were observed at DGN (yellow triangle) and DGS (red triangle). The paths are plotted in white for DGN and yellow for DGS respectively. Depth contours are plotted at 0, 100, 500, 1000, 1500 and 2000 m.

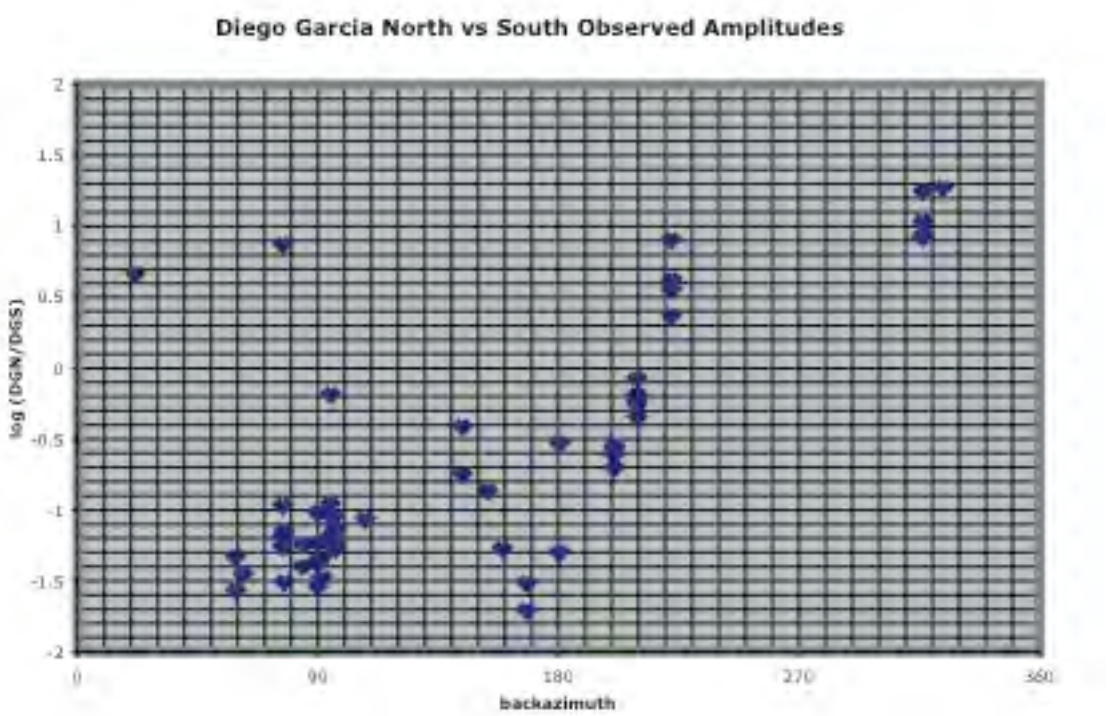


Figure 5. T-phase observations at DGN and DGS as a function of backazimuth from DGN to the source. (Only points for signals detected at both stations are plotted.)

CONCLUSIONS AND RECOMMENDATIONS

We are continuing the development of the Hydroacoustic Blockage Assessment Tool and using it in conjunction with data to define propagation, attenuation, and blockage properties of acoustic waves in the ocean. The fundamental objective is to provide a robust prediction about which hydroacoustic monitoring stations can be used in discrimination analysis for any particular event. Currently, we are limited by the small set of ground-truth data and the limitations of ray theory in defining path-stop conditions. It is apparent that blockage is not a simple phenomenon, but as we continue to collect network data we should be able to develop coverage, propagation and attenuation maps for each of the hydroacoustic stations and develop the basic criteria for establishing blockage in the ocean at large.

REFERENCES

Harben, P. E., E. Matzel, D. K. Blackman, and D. Clarke (2004). Diego Garcia reflections and implosion source development, in *Proceedings of the 26th Seismic Research Review: Trends in Nuclear Explosion Monitoring*, LAUR-04-5801, Vol. 2, pp. 553–562.

Pulli, J. J., Z. Upton, R. Gibson, J. Angell, T. Farrell, and R. Nadel (2000). Characterization of reflected arrivals and implications for hydroacoustic test-ban-treaty monitoring, BBN technical memorandum W1380.

DYNAMIC MODELING OF HYDROACOUSTIC REFLECTIONS AND A FIRST LOOK AT THE DATA FROM THE NEW HYDROACOUSTIC ARRAYS AT ASCENSION ISLAND

Jay J. Pulli[1], Zachary M. Upton[1], Jeff Wagoner[2], and Phil Harben[2]

BBN Technologies[1] and Lawrence Livermore National Laboratory[2]

Sponsored by Army Space and Missile Defense Command

Contract No. W9113M-05-C-0136[1,2]

ABSTRACT

We report on two of our efforts to better understand hydroacoustic signals for the purpose of event discrimination. The first effort involves the dynamic modeling of hydroacoustic reflections. The goal is to have a frequency dependent model-based predictive tool for assessing where consistent reflections will occur and the frequency dependence of the reflected energy that becomes trapped in the SOFAR channel. This will be a necessary capability if reflected signals are used in event discrimination. The second effort is a preliminary examination of the new hydroacoustic data coming from Ascension Island.

A specific bathymetric feature was chosen for the reflection modeling—the steep bathymetry on the eastern side of the Seychelles-Mauritius Plateau in the western Indian Ocean. This site was chosen to coincide with a known zone of reflections that have been observed from both earthquake and explosive sources. Lawrence Livermore National Laboratory (LLNL) set up the base model for dynamic reflection analysis using data from the General Bathymetric Chart of the Oceans (GEBCO) website. These data are in a format of one arc-minute grid spacing and are available as 20X20 degree tiles in netCDF format. The bathymetry data were imported into EarthVision, a 3-D surface modeling code developed by Dynamic Graphics, Inc. The geographic coordinates were then converted to a Universal Transverse Mercator (UTM) projection in the model area. The data were gridded using minimum tension gridding with a bi-harmonic cubic spline function. The basal grid elevation ranges from 18 to -4268 meters. This binary grid is then converted into a format that can be read by the Wave Propagation Project code (WPP). HydroCAM is used to predict propagation along the source-to-reflector path, which is used as input to the WPP code. The WPP code will initially be run in 3-D at low frequencies (less than 10 Hz) and compared to reflected signals from earthquake sources. Dynamic runs will be conducted in July 2006. These calculations will then be handed back to HydroCAM, where the signals will be propagated to longer distances. These modeling calculations will be compared to observed earthquake reflections to help validate the modeling and quantify the effects of parameters such as bathymetry slope at reflection depths.

In the second effort, we report on an analysis of the data from the new hydroacoustic arrays around Ascension Island. As part of this effort, the Air Force Technical Applications Center (AFTAC) data mirror at LLNL was modified to allow BBN to access data from the International Monitoring System hydroacoustic stations at Diego Garcia, Cape Leeuwin, Crozet Island, and Ascension Island. Blockage calculations at Ascension Island predict that both arrays will simultaneously record events in most of the southern Atlantic Ocean, with the exception of a small wedge of azimuths to the southeast. The azimuth that is blocked at the north array is covered by the south array. Hence, two back azimuth calculations can be used to locate an event in most areas. The arrays record numerous events along the southern Mid-Atlantic Ridge, and reasonably accurate locations and origin times are available for most of these events above magnitude 4.5 from the United States Geological Survey. These events often produce acoustic energy up to at least the anti-alias frequency of 100 Hz. We attribute this high-frequency energy to the shallow focal depths and hence the short seismic propagation path. Additionally, airgun signals and biological signals are often seen at the arrays.

OBJECTIVES

The overall goal of this project is to further our understanding of hydroacoustic blockage and reflections, and assess how these processes affect the discrimination of underwater events. An additional goal is to provide a quick-look assessment of data from the new hydroacoustic arrays as they come online in the Atlantic and Pacific Oceans. Specific objectives during this reporting period include:

- The dynamic modeling of hydroacoustic reflections from the eastern side of the Seychelles-Mauritius Plateau in the western Indian Ocean. Here, we are using the WPP being run at LLNL. Reflections are often observed from this bathymetric feature at the Diego Garcia hydroacoustic array.

- An examination of data from the new hydroacoustic arrays at Ascension Island, which became available to us during 2006. We have examined signals from 15 earthquakes during this time period, as well as numerous airgun and biological signals.

RESEARCH ACCOMPLISHED

Dynamic Modeling of Hydroacoustic Reflections

In earlier studies (Upton et al., 2006) we developed a model that estimates the impulse response of the ocean basins based on high-resolution bathymetry. For a given source-receiver pair, the model uses travel-time ellipses to predict which bathymetric features will contribute reflections to the impulse response. The strength of each reflection was based on the area of the bathymetric feature that intersects the sound channel axis, and its orientation with respect to the source-receiver travel-time ellipse. This model has been successfully applied in a matched-field approach to event localization based on a single station received wave train (Upton and Pulli, 2002). Although the travel times of the reflections match observed data very well, the simple model does not do well at predicting their amplitudes. In this study, we use a dynamic modeling technique at the bathymetric reflector, in combination with long-range predictions using HydroCAM, to more accurately model the reflection process.

A specific bathymetric feature was chosen for the reflection modeling: the steep bathymetry on the eastern side of the Seychelles-Mauritius Plateau in the western Indian Ocean (Figures 1 and 2). This site was chosen to coincide with a known zone of reflections that have been observed from both earthquake and explosive sources (Harben and Boro, 2001). LLNL has set up the base model for dynamic reflection analysis using data from the GEBCO website. These data are in a format of one arc-minute grid spacing and are available as 20X20 degree tiles in netCDF format. The bathymetry data were then imported into EarthVision, a 3-D surface modeling code developed by Dynamic Graphics, Inc. The geographic coordinates were then converted to a UTM projection in the model area. The data were gridded using minimum tension gridding with a bi-harmonic cubic spline function. The basal grid elevation ranges from 18 to -4268 meters. Four perspective views of this region are shown in Figure 3.

This binary grid is then converted into a format that can be read by the WPP code. HydroCAM is used to predict propagation along the source-to-reflector path, which is used as input to the WPP code. The WPP code will initially be run in 3-D at low frequencies (less than 10 Hz) and compared to reflected signals from earthquake sources. These calculations will then be handed back to HydroCAM, where the signals will be propagated to longer distances. These modeling calculations will be compared to observed earthquake reflections to help validate the modeling and quantify the effects of parameters such as bathymetry slope at reflection depths.

As of this writing, the first runs of the dynamic modeling are being conducted at LLNL and will be shown on the accompanying poster in September at the 2006 Seismic Research Review (SRR).

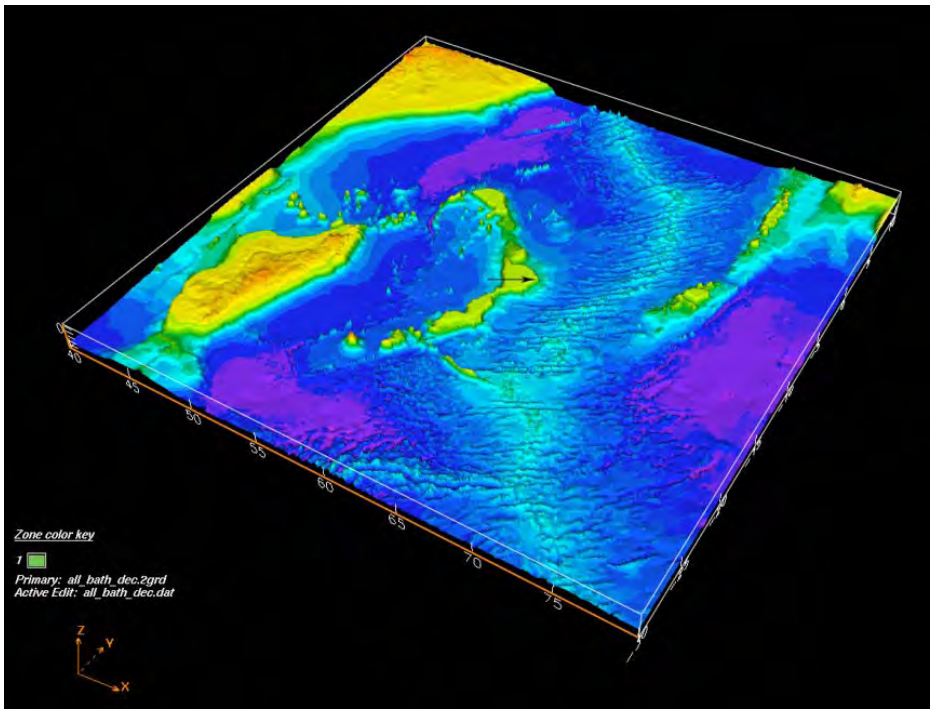


Figure 1. Map of the western Indian Ocean downloaded from GEBCO, showing the Seychelles-Mauritius Plateau. The study area is identified by an arrow at the center of the map.

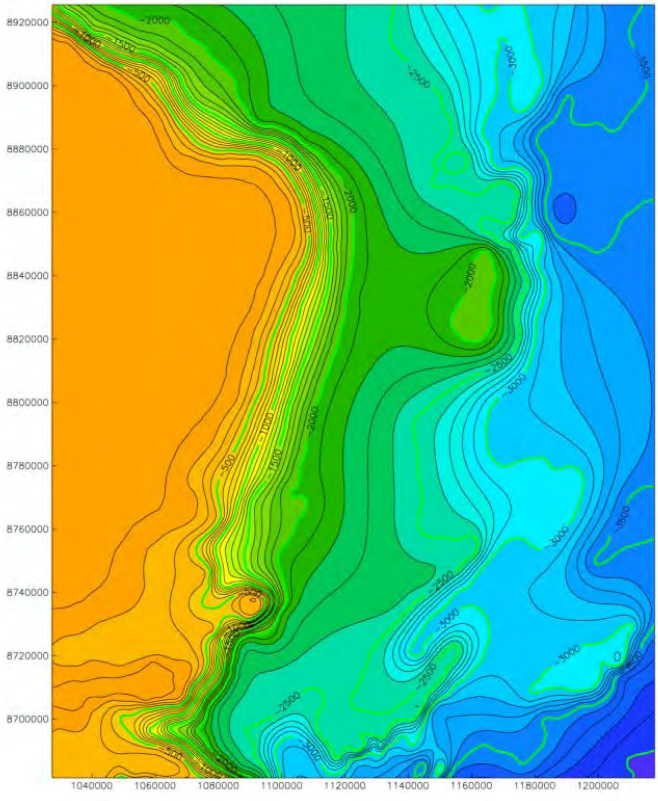


Figure 2. Detailed bathymetry of the area of interest. These data have been converted to UTM coordinates (Zone 40). Note the sharp definition of the northeastern tip of the Seychelles-Mauritius Plateau.

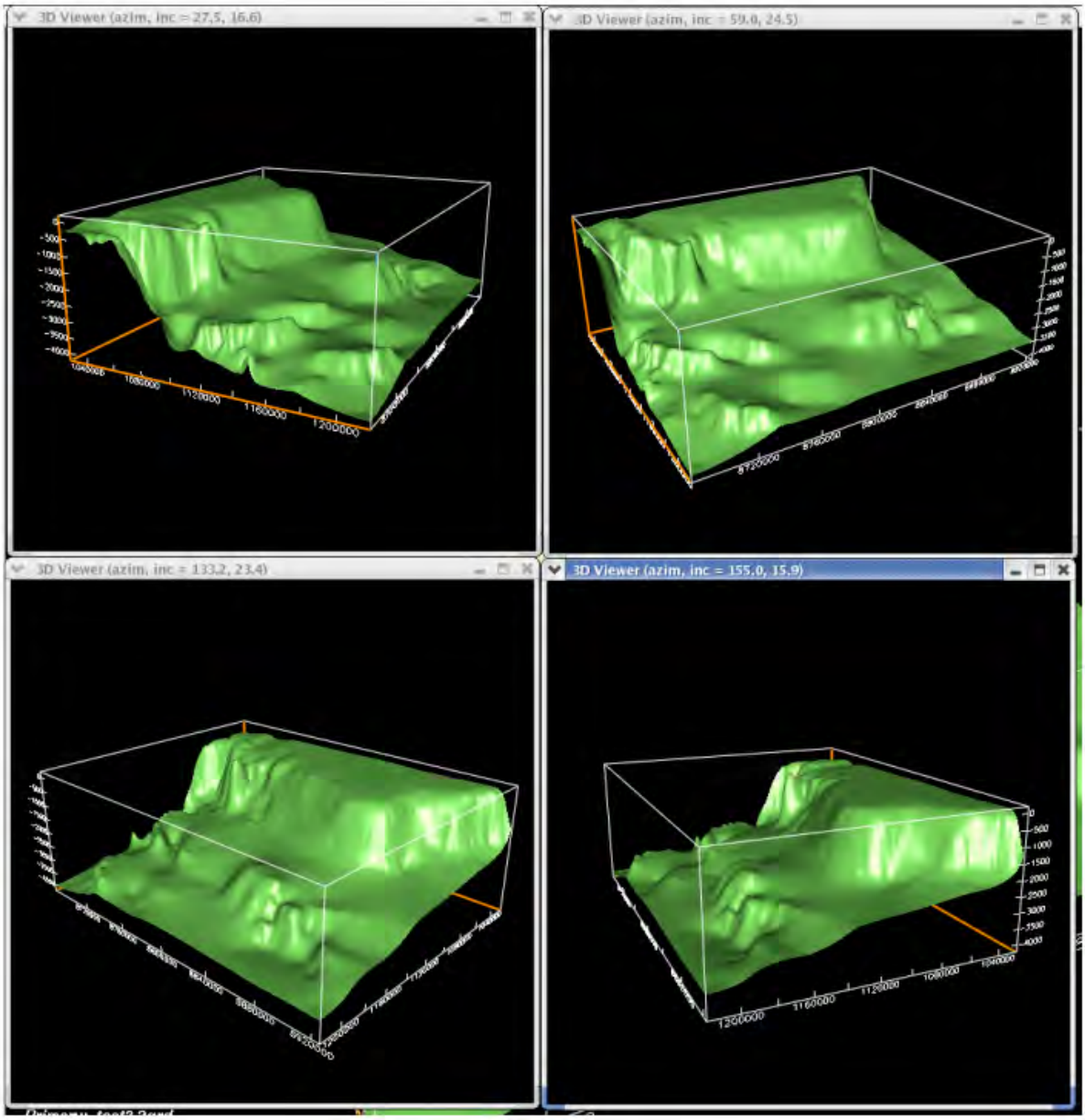


Figure 3. Four perspective views of the Seychelles-Mauritius Plateau. The intersection of the 2 orange axes represents the southwest corner of the diagram. Each plot has been rotated slightly to give the viewer a different angle of the plateau. These plots have a vertical exaggeration of 20X.

First Look at Ascension Island Hydrophone Data

Hydrophones were first installed around Ascension Island in the 1960's. These hydrophones recorded many of the large underwater explosions detonated in the Atlantic Ocean in the 1960's and 70's (Pulli et al., 2000). These hydrophone channels were of low dynamic range, so multiple gain channels were used to record the direct arrivals of the large explosions on scale. Many of these hydrophones remained operative through 2001, until equipment failures eventually rendered all of them inoperative. The new installations, which were installed in 2005 and whose data became available to us in 2006, are of the same high dynamic range configurations as those in the Indian Ocean. The geometries of these arrays are shown in Figure 4.

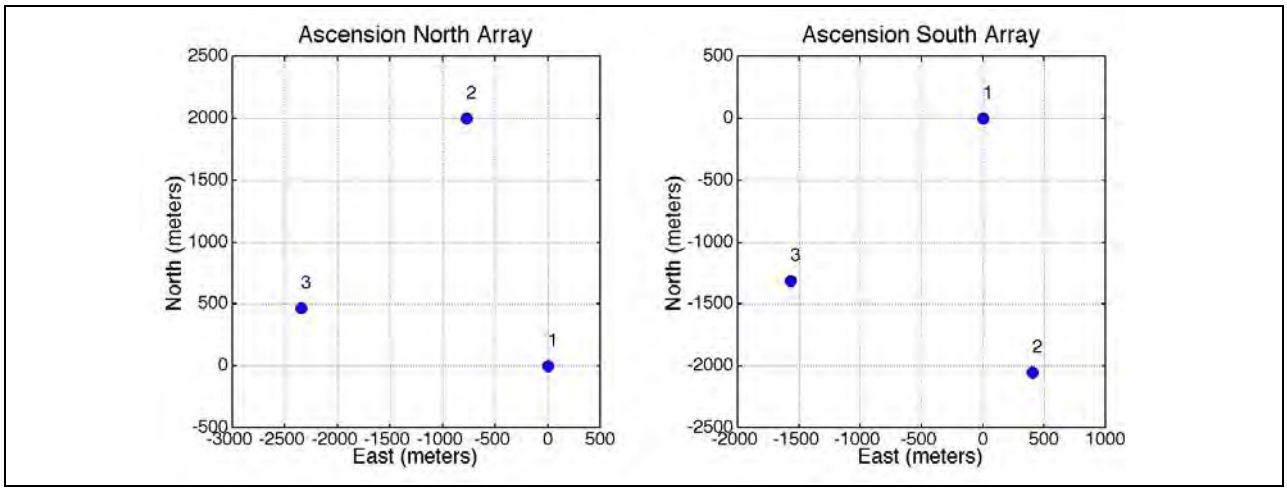


Figure 4. Geometric configurations of the North and South Arrays at Ascension Island.

In order to better understand the geographic coverage of these new arrays, blockage calculations were performed using HydroCAM. These calculations are made by shooting fans of rays from the center of each array over 360 degrees at 1-degree increments. Two different criteria are currently used to end the ray path. Figure 5 shows the calculations using the stop criteria of when the sound channel axis depth reaches the surface and becomes nonexistent. Here we see that both arrays provide detection coverage over most of the western North and South Atlantic Oceans. The wedge of blocked signal paths to the southeast for the north array is covered by the south array. Work to better understand the blockage process using an adapted version of the Naval Research Laboratory's Adiabatic Mode Parabolic Equation (Collins, 1993) model is currently being undertaken on a separate project during this SRR (Upton et al., 2006).

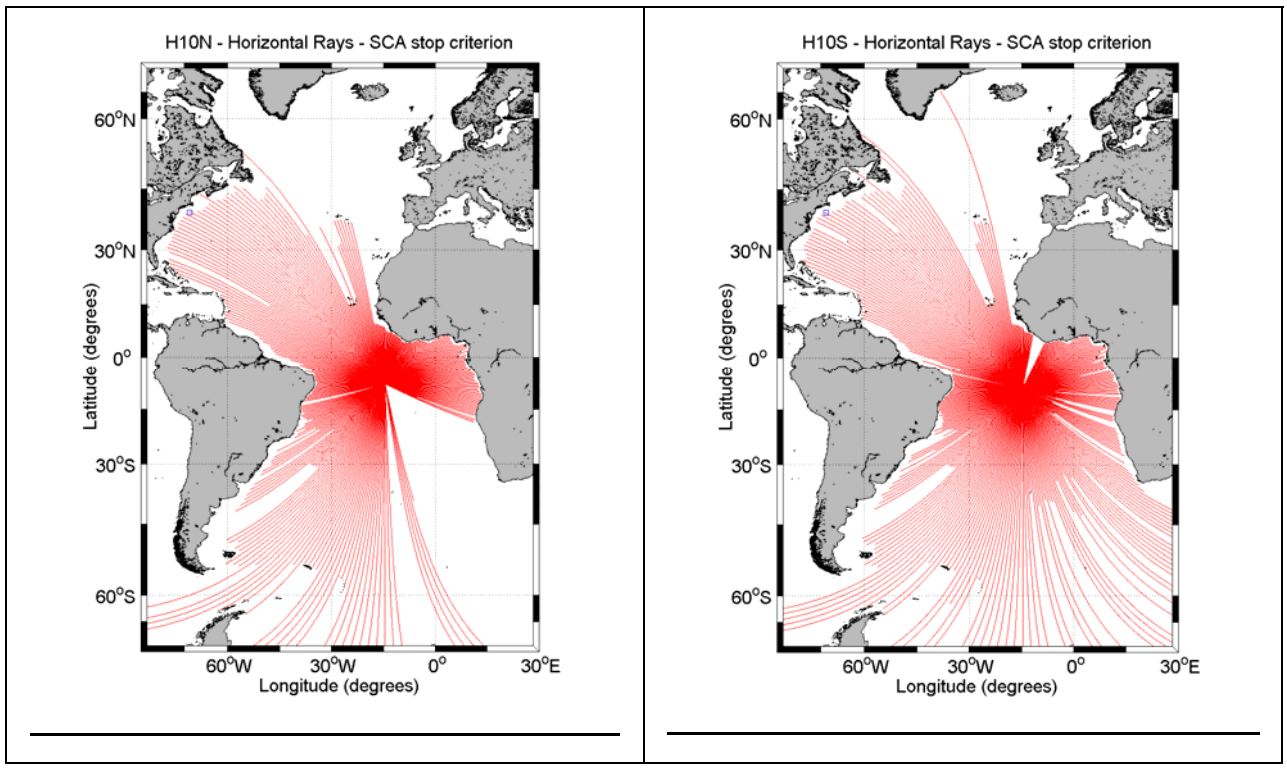


Figure 5. Hydroacoustic blockage calculations for the Ascension North (left) and South (right) arrays.

Access to the Ascension data is provided to us via two mechanisms. One is an AutoDRM message to the AFTAC data server. We perform this type of access on an event basis, typically acquiring two hours of data per event starting at the event origin time. Data access is also provided via secure ftp connection to the continuous data archive at LLNL. Most of the events recorded at Ascension have occurred along the Mid Atlantic Ridge. Fifteen events have been examined as of this writing (see Table 1 and Figure 5). These events range in magnitude from 4.6 to 6.0, although aftershocks of these events are frequently observed which are less than magnitude 4.6. In addition, airgun signals are often observed coming from the east of the arrays.

Table 1. Events analyzed at the Ascension hydroacoustic arrays. Epicentral references are from IRIS.

Date	O.T.	Lat.	Lon.	Mag.	Depth (km)	AREA
17-Feb-06	13:24:04	-1.85	-15.07	5.1	10	NO OF ASCENSION ISLAND
18-Feb-06	14:59:04	-6.48	-11.08	4.9	10	MID ATLANTIC RIDGE
4-Mar-06	00:53:32	0.9	-28.04	5.1	10	CENTRAL MID-ATLANTIC RIDGE
27-Mar-06	01:10:33	7.17	-34.26	5.3	10	CENTRAL MID-ATLANTIC RIDGE
30-Mar-06	03:14:43	-1.23	-15.89	5.0	30	NO OF ASCENSION ISLAND
8-Apr-06	22:03:04	-0.12	-18.13	5.0	10	CENTRAL MID-ATLANTIC RIDGE
10-Apr-06	06:26:13	7.45	-37.02	4.8	10	CENTRAL MID-ATLANTIC RIDGE
28-Apr-06	07:22:42	3.83	-31.5	4.9	10	CENTRAL MID-ATLANTIC RIDGE
23-May-06	07:24:23	-30.93	-13.37	4.7	10	SOUTHERN MID-ATLANTIC RIDGE
5-Jun-06	06:34:31	1.02	-28.17	5.6	10	CENTRAL MID-ATLANTIC RIDGE
5-Jun-06	06:27:08	1.18	-28.06	6.0	10	CENTRAL MID-ATLANTIC RIDGE
5-Jun-06	06:18:44	1.05	-28.12	4.9	10	CENTRAL MID-ATLANTIC RIDGE
8-Jun-06	16:29:12	4.55	-51.93	5.2	10	FRENCH GUIANA
18-Jun-06	18:28:02	32.96	-39.62	5.9	10	NO MID-ATLANTIC RIDGE
23-Jun-06	08:02:47	19.1	-46.08	4.6	10	NO MID-ATLANTIC RIDGE

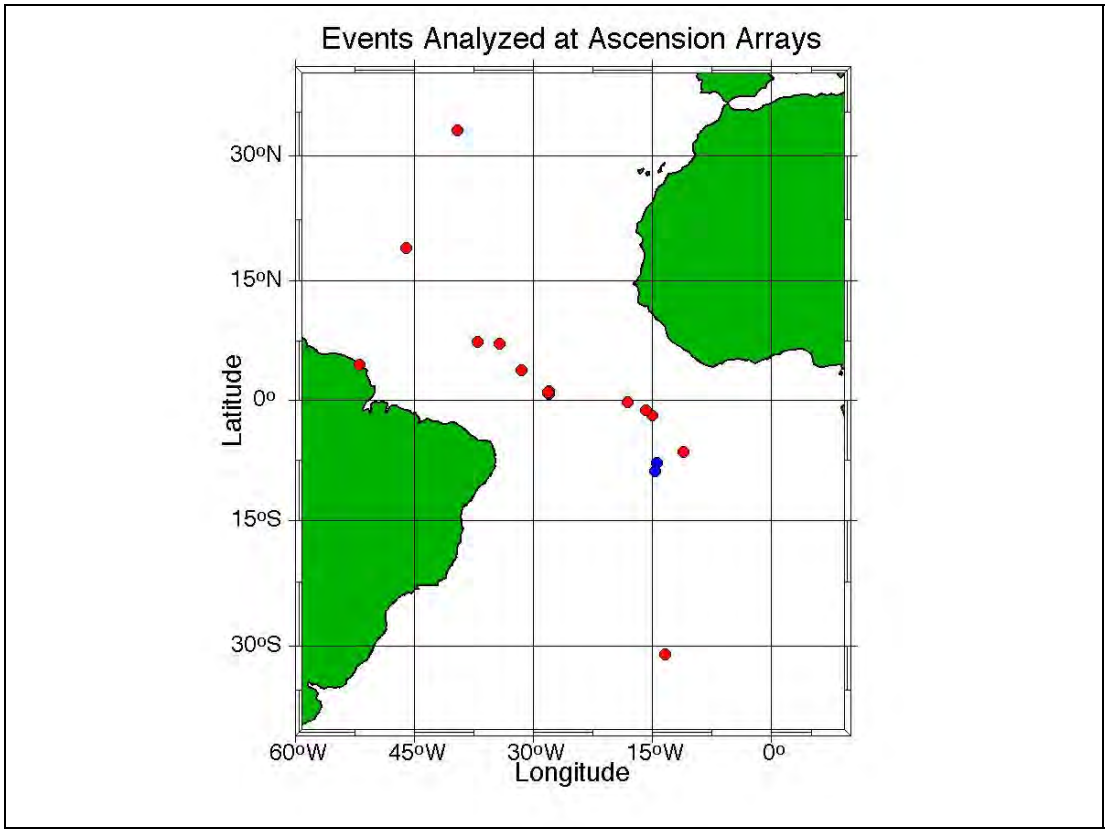


Figure 6. Map of events studied at the Ascension Island arrays (blue dots). Origin information is in Table 1.

We now show four examples of events recorded at the Ascension arrays. The first example (Figure 7) is of a magnitude 4.9 event that was located 405 km to the northeast of the north array. The P wave and T wave from this event are seen in the data, as well as some small aftershocks. In addition, airgun signals are seen in the background. Frequencies up to 70 Hz are seen in the P and T waves. The computed back azimuth from the f-k solution for the T waves is 66.45 degrees, whereas the actual back azimuth is 68.62 degrees. The apparent velocity of the T wave is 1.567 km/sec, which is faster than the actual sound speed at this depth and location (1.482 km/sec, see Figure 8). This may mean that the T-wave arrival is bending away from the horizontal as it approaches the array. Although there is adequate signal-to-noise ratio on the south array, the f-k solution is not as sharply defined as it is on the north array. This may be due to the interference of the louder airgun signals on the south array.

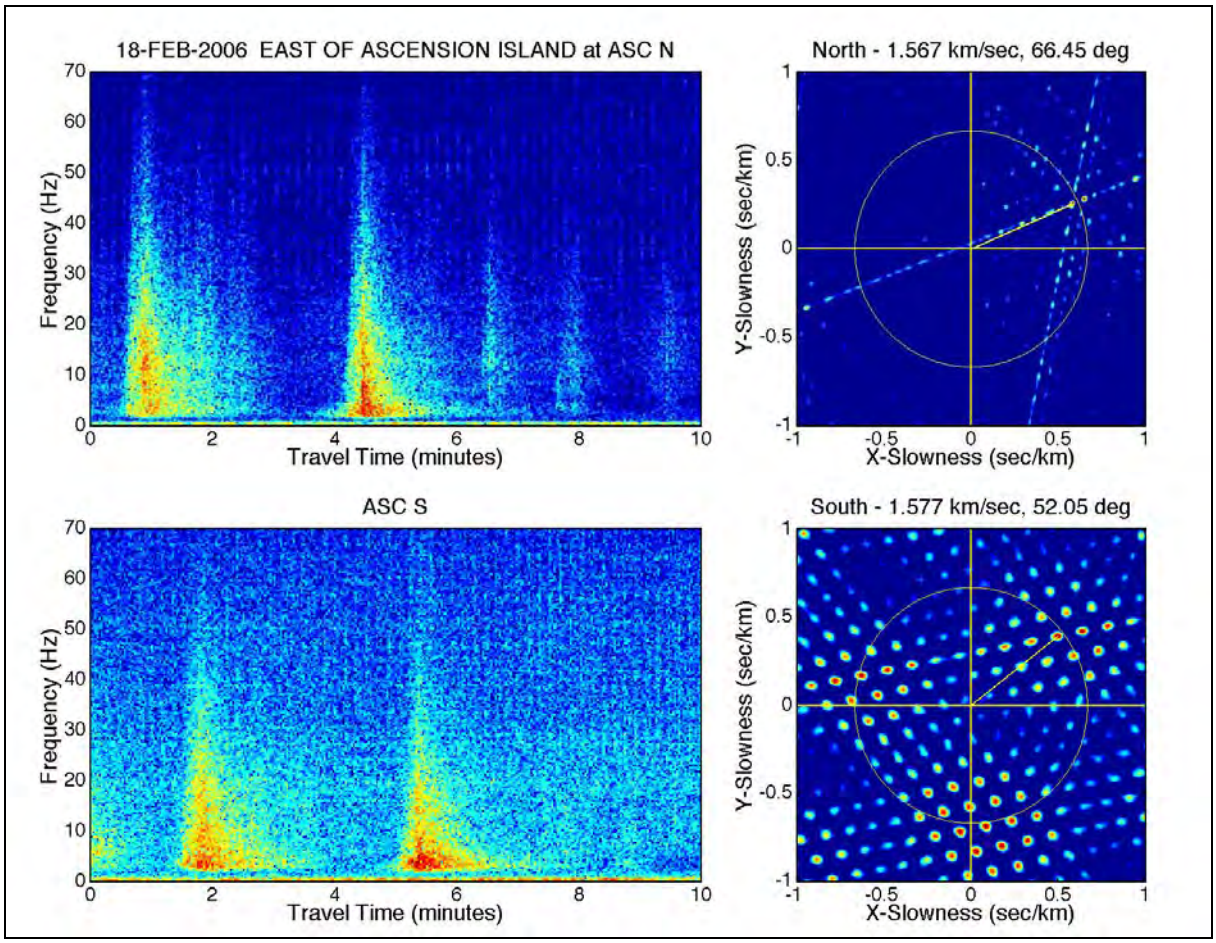


Figure 7. Time-frequency and frequency-wavenumber spectra of a magnitude 4.9 event to the northeast of Ascension Island. Origin information is given in Table 1.

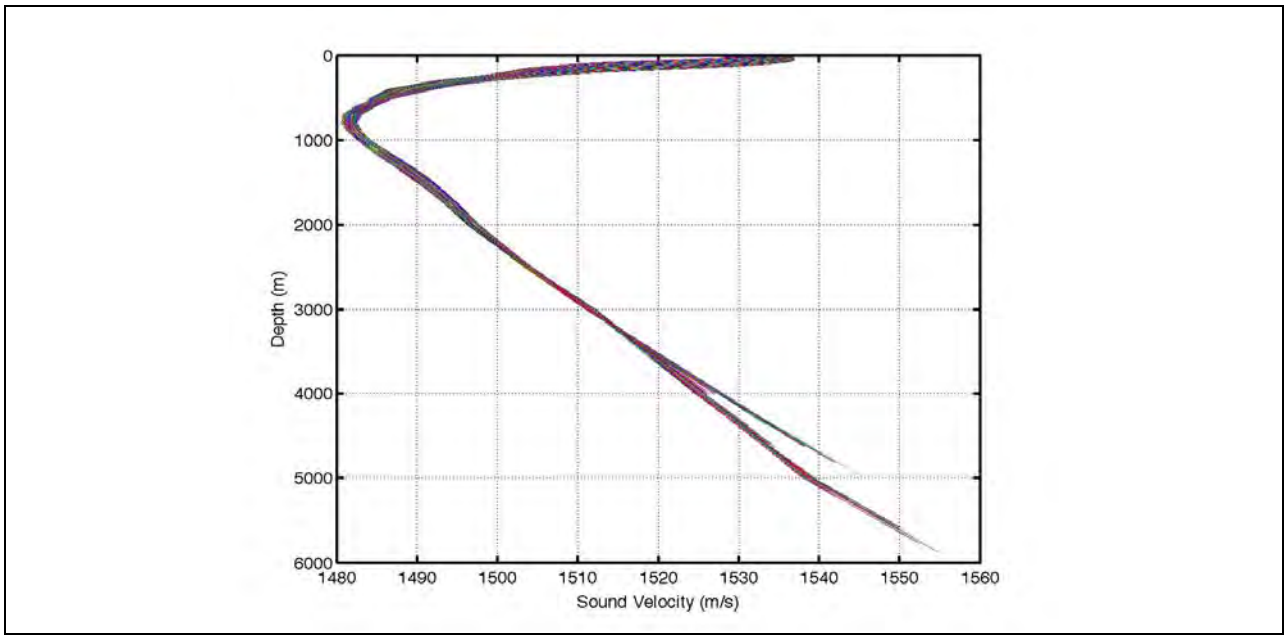


Figure 8. Sound velocity profiles in the vicinity of the Ascension arrays, from the Generalized Digital Environmental Model database.

Two other examples of events from the Mid-Atlantic Ridge are shown in Figures 9 and 10. Here we see the high-frequency content of T waves from mid-ocean ridges, due to the very shallow depths and hence short distances of seismic propagation (Salzberg, 2006). In both of these cases, the f-k solutions for the T phases point back to the source locations, however on the south array we find that the apparent velocity of the wavefront is again faster than the actual propagation velocity.

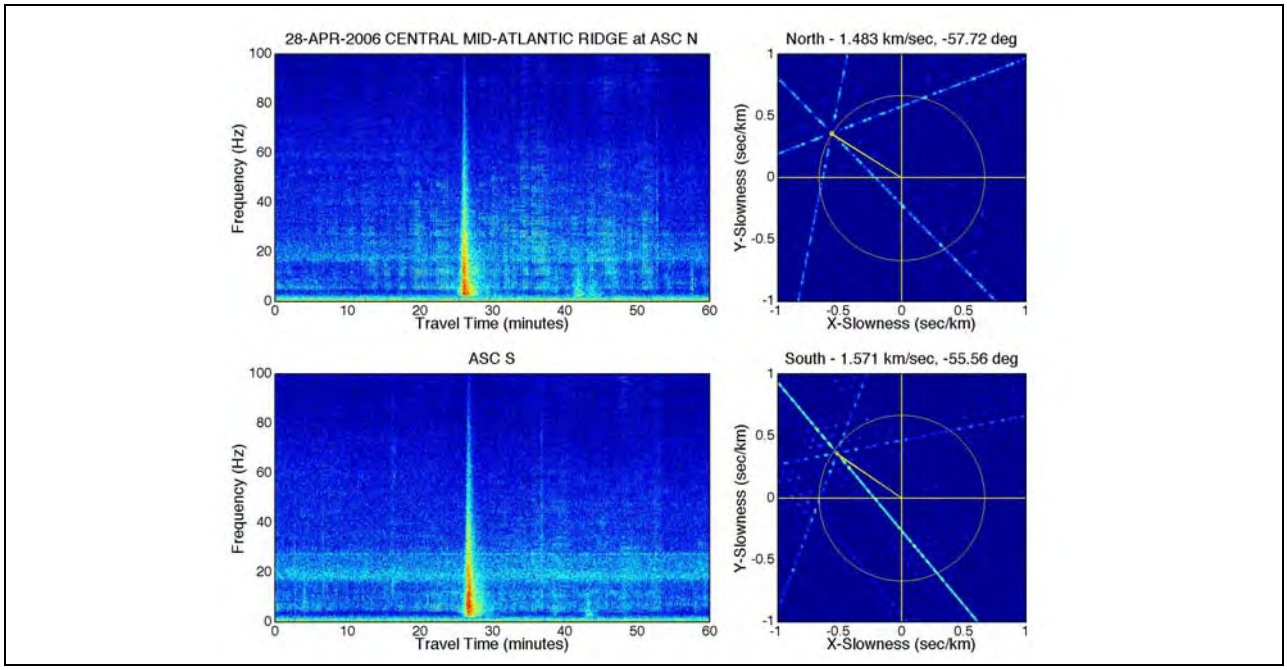


Figure 9. Time-frequency and frequency-wavenumber spectra of a magnitude 4.9 event to the northwest of Ascension Island along the Central Mid Atlantic Ridge. Origin information is given in Table 1.

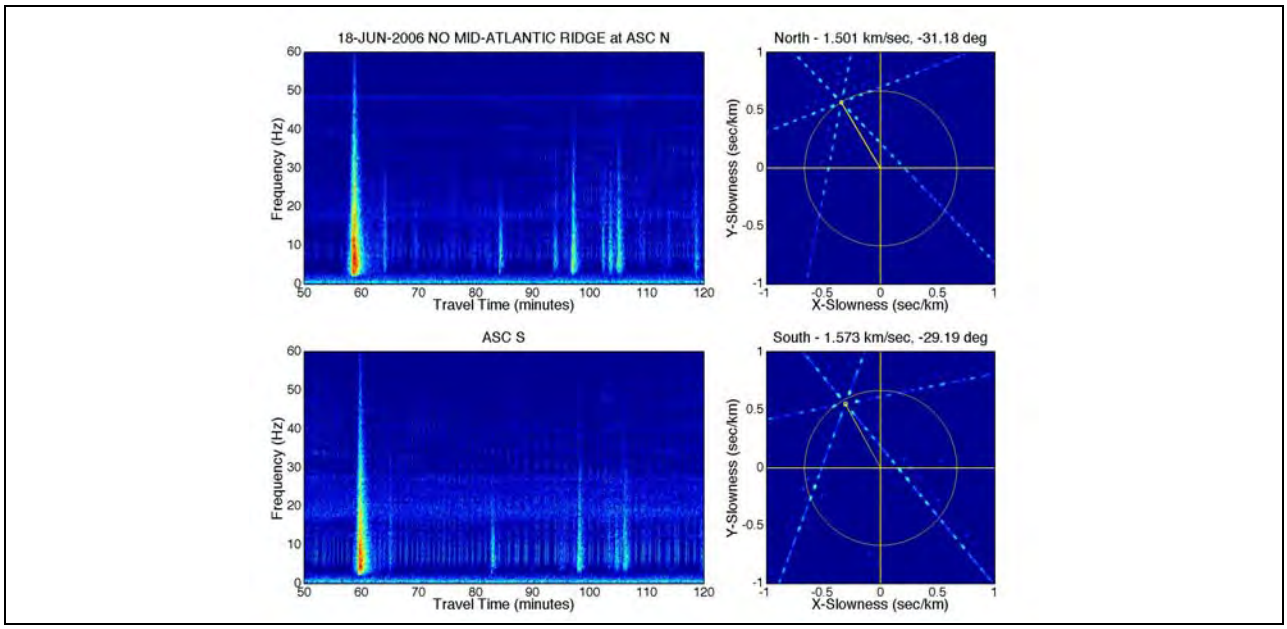


Figure 10. Time-frequency and frequency-wavenumber spectra of a magnitude 5.9 event to the northwest of Ascension Island along the Central Mid Atlantic Ridge. Origin information is given in Table 1.

The final example is an event that occurred on the coast (in continental crust) of French Guiana on June 8, 2006, (Figure 11). T waves from this event arrived at Ascension approximately 48 minutes after the event origin. Two groups of T waves were observed, separated by approximately 3 minutes. The second T-wave arrival could be from an aftershock or from a second seismic-to-acoustic conversion point. Because this is a continental earthquake, the bandwidth of the T waves is lower, and is limited to less than 15 Hz by the time the signals reach Ascension. In this case, there are no seismic stations to the east of the event, which may bias the computed location. But this T-wave recording could be used to provide azimuthal constraint on the location.

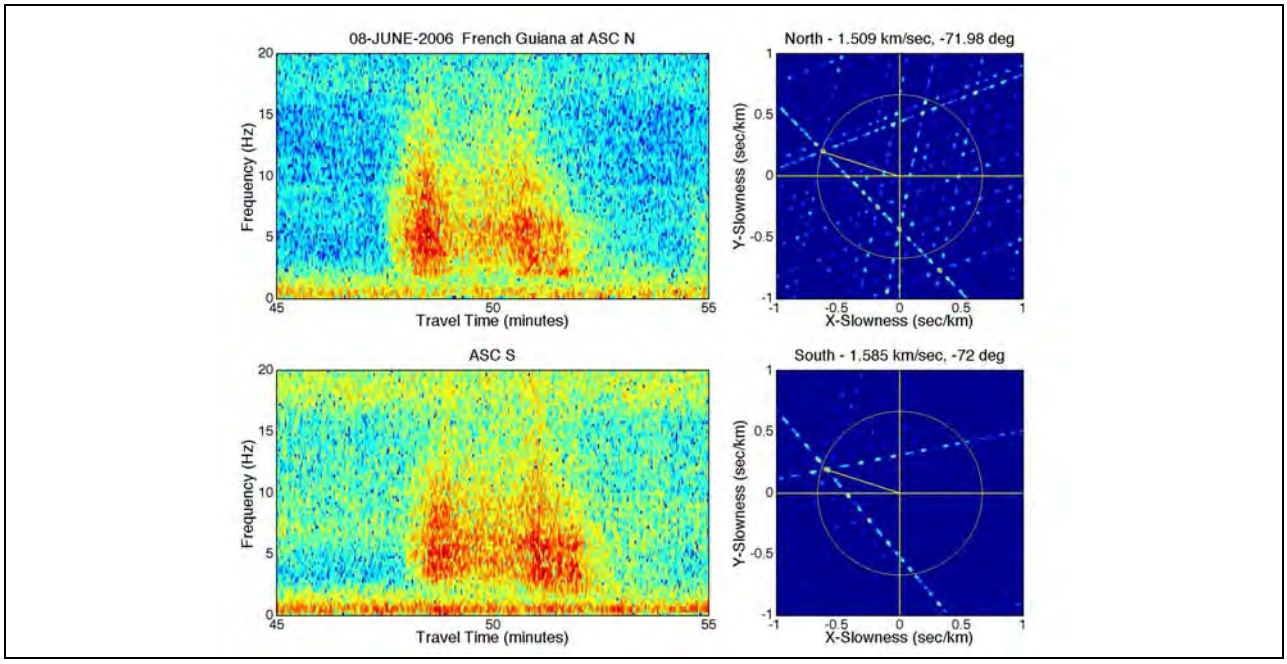


Figure 11. Time-frequency and frequency-wavenumber spectra of the T-waves from a magnitude 5.2 event on the coast of French Guiana, recorded at the Ascension arrays. Origin information is given in Table 1.

CONCLUSIONS AND RECOMMENDATIONS

Long-range hydroacoustic reflections have been reported in the literature for nearly forty years (e.g., Northrop, 1968). With the advent of modern high dynamic range acoustic arrays, we are now beginning to understand how to use these signals to supplement hydroacoustic locations and discrimination analysis (Upton et al., 2006). Our present study seeks a better understanding of the reflection process by modeling one particular bathymetric reflector, the eastern side of the Seychelles-Mauritius Plateau in the western Indian Ocean. We are currently using the WPP at LLNL. Calculations are being performed by LLNL during July and will be reported at the SRR meeting in September.

We have also been examining the data from the new hydroacoustic arrays around Ascension Island, which have replaced the hydrophones that operated in this area since the 1960's. These combined arrays have a detection coverage area that spans the western North Atlantic Ocean and nearly all of the South Atlantic Ocean, with the exception of a few small areas behind islands. So far, we have examined fifteen earthquakes in the Atlantic Ocean that have been recorded at Ascension Island. High frequency T-wave signals are observed from the shallow events along the Mid-Atlantic Ridge. A coastal event in French Guiana was also recorded by the arrays. In addition, airgun signals are often observed coming from the area east of the arrays.

ACKNOWLEDGEMENTS

The authors would like to acknowledge the cooperation of the Air Force Technical Applications Center in providing access to the Ascension Island hydrophone array data.

REFERENCES

Collins, M.D. (1993). The Adiabatic Mode Parabolic Equation, *J. Acoust. Soc. Am.* 94: (4), pp. 2269–2248.

Harben, P. and C. Boro (2001). Implosion source development and Diego Garcia reflections, in *Proceedings of the 23rd Seismic Research Review: Worldwide Monitoring of Nuclear Explosions*, LA-UR-01-4454, Vol. 2, pp. 23–31.

Northrop, J. (1968). Submarine topographic echoes from Chase V, *J. Geophys. Res.*,73: 3,909–3,916.

Pulli, J. J., Z. Upton, R. Gibson, J. Angell, T. Farrell, and R. Nadel (2000). Characterization of reflected arrivals and implications for hydroacoustic test-ban treaty monitoring, Defense Threat Reduction Agency Report DTRA-TR-00-36, 85 pp.

Salzberg, D. (2006). Hydroacoustic estimates of earthquake source depth: applications to tsunami warning, submitted to *Geophys. Res. Letters*.

Upton, Z. M. and J. J. Pulli, (2002). Localization of sub-sea earthquakes using hydroacoustic reflections and matched field processing, in *Proceedings of the 24th Seismic Research Review—Nuclear Explosion Monitoring: Innovation and Integration*, LA-UR-02-5048, Vol. 2, pp. 676–685.

Upton, Z.M., J. J. Pulli, B. Myhre, and D. Blau (2006). A reflected energy prediction model for long-range hydroacoustic reflections in the oceans, *J. Acoustical Soc. Amer. Union* 119: (1), 153–160.

HYDROACOUSTIC BLOCKAGE STUDIES USING HYDROCAM VERSION 5 PROPAGATION MODELS AND KRIGING TECHNIQUES

Zachary Upton[1], Joydeep Bhattacharyya[1], Jay J. Pulli[1], and Michael Collins[2]

BBN Technologies[1] and Naval Research Laboratory[2]

Sponsored by National Nuclear Security Administration
Office of Nonproliferation Research and Development
Office of Defense Nuclear Nonproliferation

Contract No. DE-ACO3-02SF22560[1,2]

ABSTRACT

The Hydroacoustic Coverage Assessment Model (HydroCAM) was designed to analyze hydroacoustic network coverage and long-range hydroacoustic propagation. To that end, the models and databases that made up the initial versions of HydroCAM were focused on general propagation studies, such as horizontal ray-based travel time studies and vertical normal mode/parabolic equation studies. The long-term vision was to add more-detailed models as the needs of HydroCAM users changed. For HydroCAM Version 5.0, we have adapted the Naval Research Laboratory's Adiabatic Mode Parabolic Equation (AMPE) model to the specific needs of hydroacoustic nuclear monitoring and integrated it into HydroCAM. In addition, we have applied established statistical kriging techniques to our large-event data set in the Indian Ocean to create an empirical model of blockage.

In 2001, BBN observed that at the Diego Garcia hydrophone arrays (H08N and H08S), an absolute assessment of blockage (i.e., blocked or not blocked) was not appropriate. Many signals that a ray model would predict as blocked were clearly detected but attenuated. This year, we have integrated the AMPE model into HydroCAM to improve its capability to analyze the complicated effects of blockage. The AMPE model is a three-dimensional model that accounts for the effects of diffraction around and over bathymetric features. The model also predicts the possible acoustic-seismic-acoustic propagation through small bathymetric features. BBN has enhanced the model to make it range dependent in sound velocity and has optimized the model to run more efficiently. We report on the integration and show several model-to-data comparisons carried out to validate the new model and analyze the blockage at Diego Garcia.

Over the past six years, BBN has built a database of hydroacoustic ground truth events from the Indian Ocean region recorded on at least one of the Diego Garcia arrays. The past two years have yielded a number of important events. For example, events related to the Sumatra earthquakes in 2004–2005, following the Tsunami event, greatly increase our data coverage in that region. Such enhanced coverage allows us to robustly predict the recorded amplitude over much of the Indian Ocean region from a combination of empirical and model-based calculations using the kriging technique. Further, an expanded data set is optimal for us to explore one of our prime assumptions: the amplitude variation can be well modeled by a stationary random function model for large search windows. For certain regions such as Sumatra and the Carlsberg Ridge, we have an adequate coverage that lets us test for local stationarity and explore the pattern of anisotropy in our variogram modeling. A combination of such models will allow us to explore non-stationary kriging for the Indian Ocean.

OBJECTIVES

Our primary objective in this program is to provide the Department of Energy (DOE) and the Air Force Technical Applications Center (AFTAC) with a detailed understanding of the blockage of hydroacoustic signals near the International Monitoring System's (IMS) hydrophone stations. We accomplish this goal by integrating advanced hydroacoustic propagation models into HydroCAM and by combining predictions with observed data using geostatistical techniques to provide new insights into blockage that can be integrated into the DOE Hydroacoustic Blockage Analysis Tool.

We have updated our data set of earthquake amplitude measurements at Diego Garcia to include events from 2005 and 2006. This database now includes over 190 events. These data are used as input to the data analysis process as well as in our blockage modeling studies to conduct model-to-data comparisons. The AMPE model has been improved to make it more efficient and to include changing sound velocity profiles with geographic location. To begin to validate the model, we have conducted a model and data study at 5 Hz at H08. HydroCAM Version 5.0, which will be released in September, will include the improved AMPE model.

We have also used our data set to analyze blockage statistically. We have implemented the well-known kriging technique to smoothly extrapolate the empirical constraints to regions of sparse data coverage. We validate that kriging can indeed be used to improve predictions of amplitude in the Indian Ocean.

RESEARCH ACCOMPLISHED

Amplitude Measurement and Analysis

We have conducted an analysis of recorded signal amplitudes to map T-phase blockage at the Diego Garcia hydroacoustic station. The recorded data are from a distribution of shallow- and intermediate-depth Indian Ocean earthquakes for which the source location and origin times are relatively well known, i.e., they can be considered to be reference events. We consider blockage as an amplitude estimation problem, i.e., the difference in amplitude from events recorded in the South and North. We use the empirical data to estimate the amplitudes of signal and noise for these events. Our data set consists of 191 measurements. To avoid exceptionally long propagation distances, we limit our analysis to events within the following geographical boundary: latitude = [-70 30]° N, longitude = [20 120]° E. After removing measurements with low SNR, our final data set consists of 153 events, recorded at both of the Diego Garcia arrays (H08N and H08S). We have used this reference event data set to measure signal and noise amplitudes at DGN and DGS over a set of frequencies between 5 and 100 Hz. We present analysis of data set-scale variation in signal amplitudes with frequency and depth of the events to identify some of the source effects in our analysis of blockage.

Variation of Signal Amplitude with Event Depth

One of the outstanding issues of hydroacoustic propagation is the location of the T-phase conversion region. One of the factors that can affect this location is the depth of the seismic source, as that would control the incidence angle at the crust-water interface. In this section, we investigate the large-scale variation of signal spectra with source depth for events recorded at H08N and H08S. We note that for a significant number of the events in our database, the source depth is known only to a default value, i.e., 10 km or 33 km, depending on the catalog. To decrease the sensitivity of our analysis to such values, we have divided our event into two subsets: deep (depth >40 km) and shallow. Figure 1 shows the variation of signal amplitude and blockage, with frequency and source depth. We believe that the significant variation between deep and shallow earthquakes is due to the geographical variation of earthquake depths.

Variation of Signal Blockage with Frequency

We define blockage as those observations for which the amplitudes differ by more than 10 dB between the North and South stations for a particular frequency. Figure 2 shows the locations of the events for the blocked paths at 20 Hz; a positive value signifies blockage on the North station. We note that the signals are blocked at the North station from events near Sumatra and some near the mid-Indian ridge. Events located close to the North station (Carlsberg Ridge, Chagos Archipelago) are mostly blocked at the South. Next, we separate the paths that are blocked at either the North or the South stations and estimate the variation with frequency.

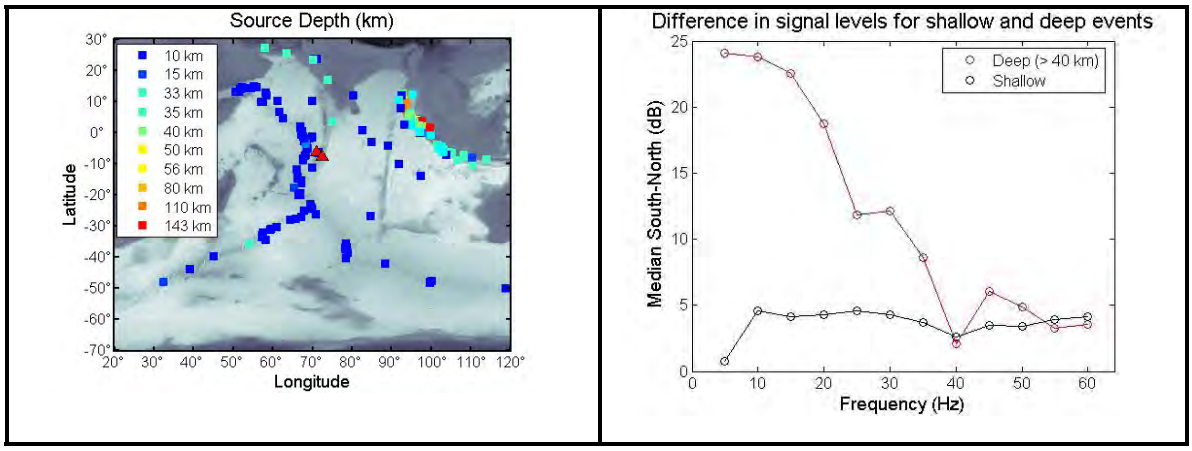


Figure 1. Distribution of source depths in our data sets and the variation of signal blockage with frequency and earthquake source depth. We note that though the event depth does not affect the amplitudes significantly for the southern station (H08S); shallow events have larger amplitude at H08N for frequencies up to about 40 Hz. The signal-to-noise ratios for the deep events are significantly larger at the South station; however, we do not observe this difference for the shallow events. Some of the aforementioned amplitude variations might be accounted for by the differences in typical source depths, sometimes specific to regions, with blocked or unblocked paths.

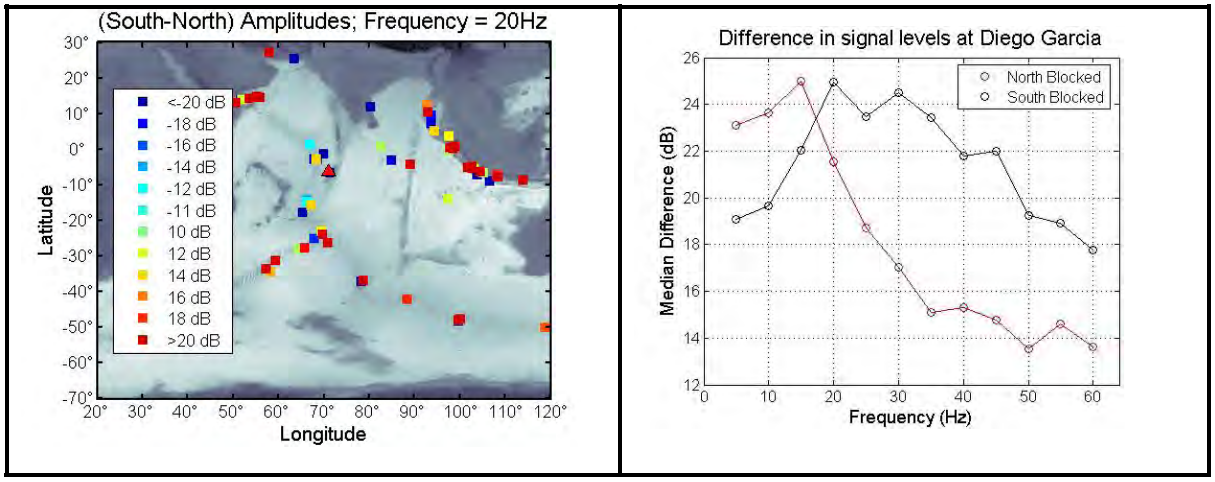


Figure 2. Variation of blockage with source location at 20 Hz (left) and signal frequency.

Blockage Modeling

When HydroCAM was first designed, the intent of the included propagation models was to provide global and ocean basin scale assessment of hydroacoustic propagation and International Monitoring System (IMS) network coverage. To that end, horizontal ray trace models were used to predict travel time, transmission loss, detection statistics, localization areas of uncertainty, etc. An assumption in this design was that, as the modeling requirements evolved, more detailed models and databases could be integrated into the existing HydroCAM framework. Modeling the blockage of hydroacoustic signals by islands and seamounts is a scenario that requires a more-detailed model. Studies by Pulli and Upton (2001); Harben, et al. (2004); and others compared horizontal ray trace blockage predictions with data observations at Diego Garcia and established that the binary prediction of blockage (blocked or not blocked) that resulted from the models was not sufficient to provide an accurate measure of blockage.

In our last SRR paper (Upton, et al. 2005), we reported on an initial study of the U.S. Naval Research Lab's AMPE model (Collins, 1993). This model includes the effects of vertical and horizontal diffraction, as well as acoustic-to-seismic-to-acoustic propagation. The initial study demonstrated several things:

- The AMPE model could reasonably predict blockage at Diego Garcia when compared with observed data. Predictions for the January 26, 2001 earthquake in Western India and the December 26, 2004, Great Sumatran Earthquake were within 6 dB of the observations at Diego Garcia's H08 IMS hydrophone station.

- The AMPE model was not spatially dependent in sound velocity. It used one sound velocity profile for the entire prediction, regardless of location.

- The AMPE model used a uniform azimuthal spacing, regardless of range. In order to avoid spatially undersampling the space at long range, the closer ranges were oversampled, thus slowing down the model.

- The AMPE model used the DBDB5 5-minute resolution bathymetry. Higher-resolution bathymetry exists and could be used to make the model more accurate near islands, where bathymetry can change rapidly.

We report here on improvements to the first three of these bullets. Work to integrate the AMPE model into HydroCAM is underway. With that integration, all of HydroCAM's bathymetric databases will be available to the AMPE model.

AMPE Improvements

In the initial design of the AMPE model, Collins used a single sound velocity profile to predict propagation on a global scale. To improve the model's capability, especially at higher frequencies, BBN redesigned the model to take advantage of the global databases of the ocean environment that are available in HydroCAM. Figure 3 shows all of the sound velocity profiles from the World Ocean Atlas database for the Indian Ocean. There is significant variation in these profiles that can affect the direction and depth at which acoustic energy will propagate.

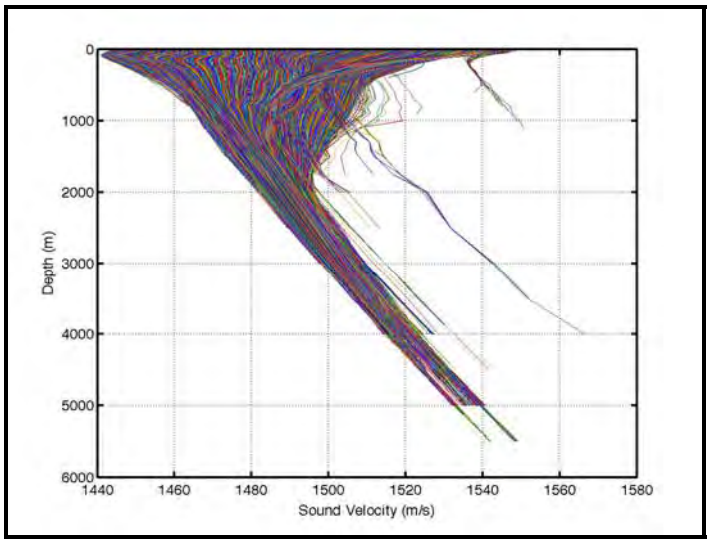


Figure 3. Annual mean sound velocity profiles in the Indian Ocean (70S to 30N, 20E to 120E) from the World Ocean Atlas database. These profiles demonstrate the need to have a model that is spatially dependent in sound velocity as well as bathymetry.

The AMPE model begins at the source location and then makes its predictions in spherical coordinates (r, θ, ϕ) that are then projected onto a polar coordinate grid (r, θ). The original version of the model used a uniform spacing in θ, regardless of range. The azimuthal spacing required to produce accurate results at the maximum range oversampled the space at short and intermediate ranges. We have modified the model so that the user specifies the azimuthal spacing as a fraction of the wavelength of sound at a given frequency. At a user-defined range step (i.e., 50 km), the spacing is recalculated, maintaining the azimuthal sampling at an arc length of the specified fraction of a wavelength. This modification tripled the speed of an AMPE run with no degradation of the result.

Results and Model-to-Data Comparison

To verify our improvements to the AMPE model and to begin to validate its use for the prediction of hydroacoustic blockage, BBN has begun a model-to-data comparison study using the amplitude measurements described above. We have used this new version of the AMPE model to predict the blockage at Diego Garcia at 5 Hz in 10-degree increments around the atoll. For source positions, we simulate sources at 500 km range. Since this blockage prediction is a differential measurement of blockage across the Chagos Archipelago (i.e., amplitude at H08N minus mplitude at H08S), these relatively short-range predictions should represent the blockage of plane wave signals arriving from much longer ranges. Figure 4 shows a map of the Diego Garcia area, the H08N and H08S tripartites, and the 36 source positions used in this model study.

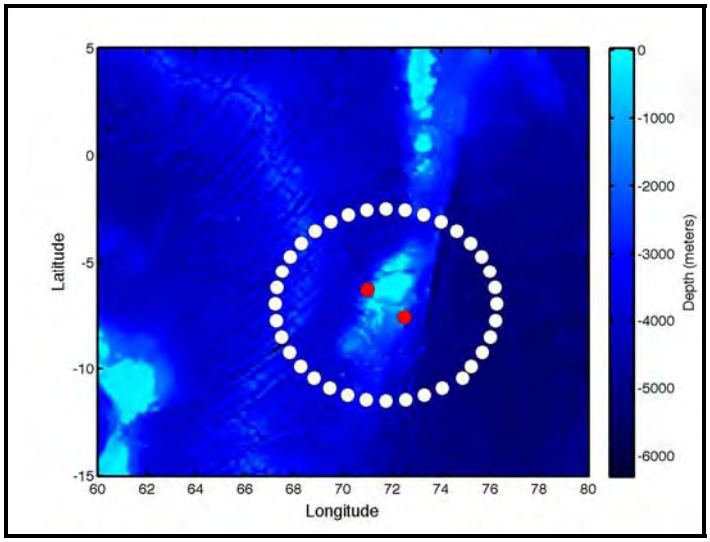


Figure 4. Map of the source positions used in this study relative to the H08 IMS hydrophone tripartites.

As an example, Figure 5 shows the AMPE result at 80-degree azimuth. Note that the horizontal diffraction pattern around the shallower parts of the Chagos Archipelago shadows H08N, but there is still energy that diffracts over and/or transmits through the archipelago. At this back azimuth, the predicted blockage is about 33 dB.

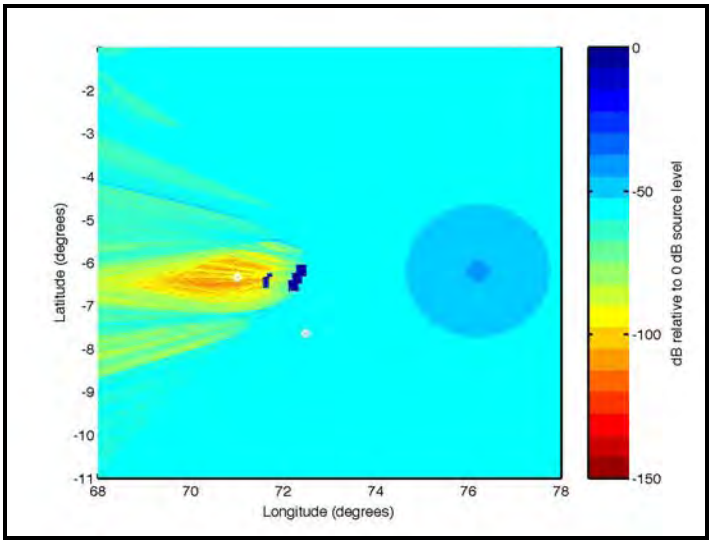


Figure 5. AMPE result for a source 500 km away at an 80-degree back azimuth. The color scale represents the attenuation in dB relative to a source level of 0 dB. The white circles represent the postions of the H08N and H08S tripartites.

The AMPE blockage predictions as a function of azimuth are shown in Figure 6 as a red line. The blue dots in the figure represent recorded blockage at 5 Hz from the amplitude measurements described above. Although there is a lot of scatter in the measurements, general trends and regional clusters show good correlation with the model predictions. These predictions could improve with a more-accurate estimate of the bottom characteristics and the use of higher-resolution bathymetry. At this stage of the study, the AMPE model results seem to correlate well with the data.

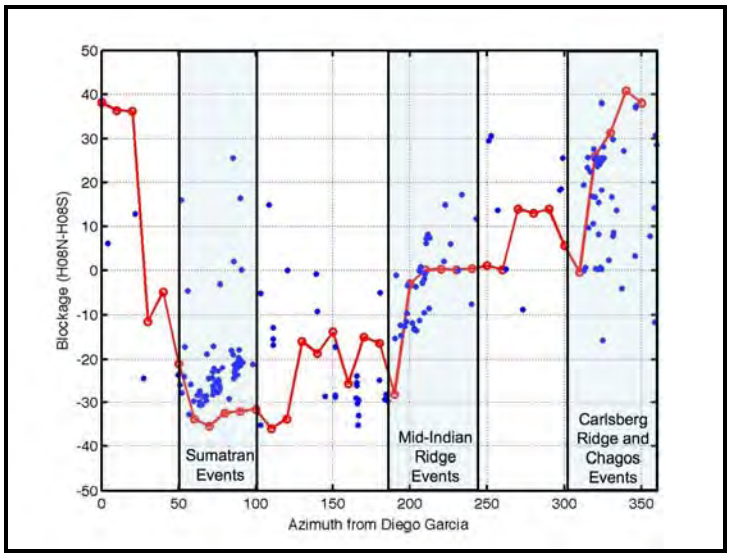


Figure 6. Model-to-data comparison for AMPE at 5 Hz. All data are plotted in terms of subtracting the signal amplitude at H08S from that at H08N. The blue dots represent the blockage as measured in our amplitude measurement task. The red line shows the blockage as predicted by the AMPE model.

Over the remainder of the period of this contract, BBN will focus its blockage modeling efforts on two tasks:

- Integrating the AMPE model into HydroCAM for the Version 5.0 release
- Completing the AMPE model study

To complete the AMPE model study at Diego Garcia, we intend to refine the model input parameters (bottom characteristics, sound velocity profiles, and bathymetry) and to conduct a study similar to the one shown above, at a variety of frequencies.

Geostatistical Analysis Using the Ordinary Kriging Technique

Robust predictions of amplitudes of hydroacoustic T-phases are essential in nuclear explosion monitoring. In this study, we are augmenting our group's earlier theoretical estimates with measurements from our reference-event data set. These measurements, described above, can be used to map out the spatial variation of blockage at Diego Garcia as a function of the source locations. However, the geographical distribution of our data set is inadequate for ocean basin analysis of spatial variation. To use such a sparse data set to extract robust amplitude predictions, we will use the well-established kriging technique, which allows us to combine the information from our measured and predicted amplitude estimates. Using kriging, we obtain both the amplitude and its formal error on a grid of geographical locations. The kriging analysis is carried out with the blockage estimates and can predict the blockage levels all through the Indian Ocean region. By systematically removing data points in our analysis and then using them to compare measurements and predictions, we validate our kriging model in this study. In this analysis, we show results for omnidirectional variograms for which the directional tolerance is large enough that the direction of any particular data pair separation vector becomes unimportant. Figure 7 shows the best-fitting variogram for Diego Garcia at 5, 20, and 45 Hz. The lag is the normalized range that is normalized by the maximum (diagonal) distance of the rectangular data observation region (75 degrees). We observe some scatter in the fits to a semi-variogram model. We expect the inclusion of non-stationarity, realistic error estimates, and the removal of the distance and

magnitude bias will decrease the scatter. We use the general exponential-Bessel variogram model to fit the data. The parameters for the data fits (nugget, sill, and range) are given in the figure legend. The nugget values are nearly the same in all plots, suggesting that the variance induced from measurement errors and non-uniform sampling is similar for our whole data set. The range values are approximately similar, suggesting that the correlation length of the amplitude variations in the Indian Ocean region is consistent across frequencies for Diego Garcia.

We can use the results of our variogram modeling to develop empirically constrained amplitude prediction surfaces. We use ordinary kriging (OK) for our modeling (Isaaks and Srivastava, 1989). OK is *linear* because its estimates are weighted linear combinations of the available data. OK is *unbiased*, as it tries to make the mean residual or error to zero. However, OK can handle the situation of an unknown, constant, non-zero mean. OK is an attractive technique, as it aims to minimize the variance of the errors. In OK, the error variance is minimized with the constraint that the kriging weights sum-up to 1. Figure 8 shows the results from our kriging analysis, i.e., it maps the variation of amplitudes recorded at the South station minus the one from the North station. We note that the kriged surfaces clearly delineate the blockage for events from the west and northwest (i.e., blocked at the South station) while events from the northeast and southeast are expected to be blocked at the North station. We validate that the kriging analysis can indeed model for the blockage. For instance, we carried out separate kriging modeling by deleting one data point and then estimated the kriged value for that data point. We observe a 29.7% variance reduction for blockage for the 5 Hz using kriging.

CONCLUSION(S) AND RECOMMENDATIONS

In this year's effort to date, we have added 60 events to our database of amplitude measurements at Diego Garcia, bringing the total number of events to nearly 200. These reference measurements are from earthquakes, and therefore are located mostly along the plate boundaries. They sparsely sample the entire ocean but have a good distribution in azimuth around the H08 IMS station. These data are used in our efforts to develop a detailed blockage modeling capability for HydroCAM. We can also apply geostatistical techniques to this data to extrapolate the blockage over the entire ocean basin.

The AMPE model has been modified to scale its azimuthal resolution with range. The result is that the model can run three times faster because it is not oversampling the short and intermediate ranges of a model run. In addition, the model has been modified to take into account the changes in sound velocity with geographic position. A 360-degree study has been conducted at 5 Hz to evaluate these model upgrades. A model-to-data comparison shows good correlation between the model results and the amplitude measurements discussed above.

In addition to integrating this model into HydroCAM Version 5, we will complete this model study, predicting blockage at a variety of frequencies and comparing the results with our amplitude measurement data set. We will also investigate the bottom characteristics (attenuation, density, etc.) and other bathymetry databases to attempt to gain an even better match to the recorded data.

This version of the AMPE model holds promise for predicting blockage at IMS hydroacoustic stations. We recommend future modeling studies at the other hydrophone stations of the IMS to assess blockage and further advance this modeling capability.

This year's effort has resulted in a second prediction at H08 of how the blockage varies spatially for sources over the entire ocean. Using our reference event database of amplitude measurements and HydroCAM predictions of amplitude, we have applied kriging techniques to produce extrapolated blockage predictions over the entire Indian Ocean, not just where we have event data. We will refine these results over the next few months and provide our final delivery to DOE for integration into the DOE Knowledge Base and the DOE Hydroacoustic Blockage Analysis Tool.

As data are collected on the other stations of the IMS, we recommend that these kriging techniques be applied to predict blockage in areas where events are sparse. In addition, we recommend integrating the results of more-accurate models like the AMPE model to make the kriging extrapolation more accurate.

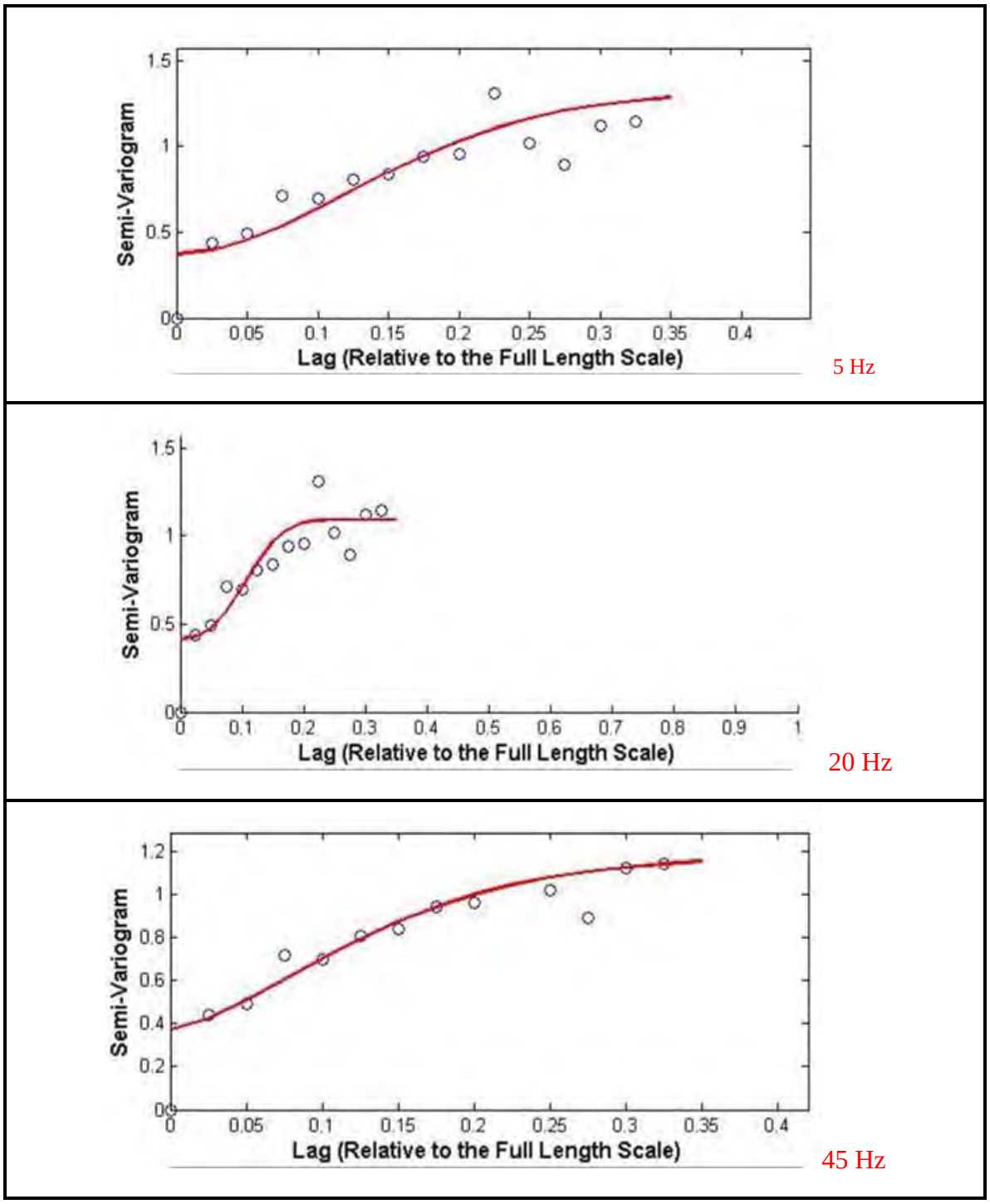


Figure 7. Variogram modeling for signal blockage at Diego Garcia at 5, 20, and 45 Hz. The lag is normalized by the maximum range, which is approximately 75° for our data set. The nugget, sill, and range values for the three frequencies are as follows: (a) 5 Hz—0.37, 0.91, and 0.36; (b) 20 Hz—0.410, 0.92, and 0.36; and (c) 45 Hz—0.37, 0.91, and 0.36, respectively.

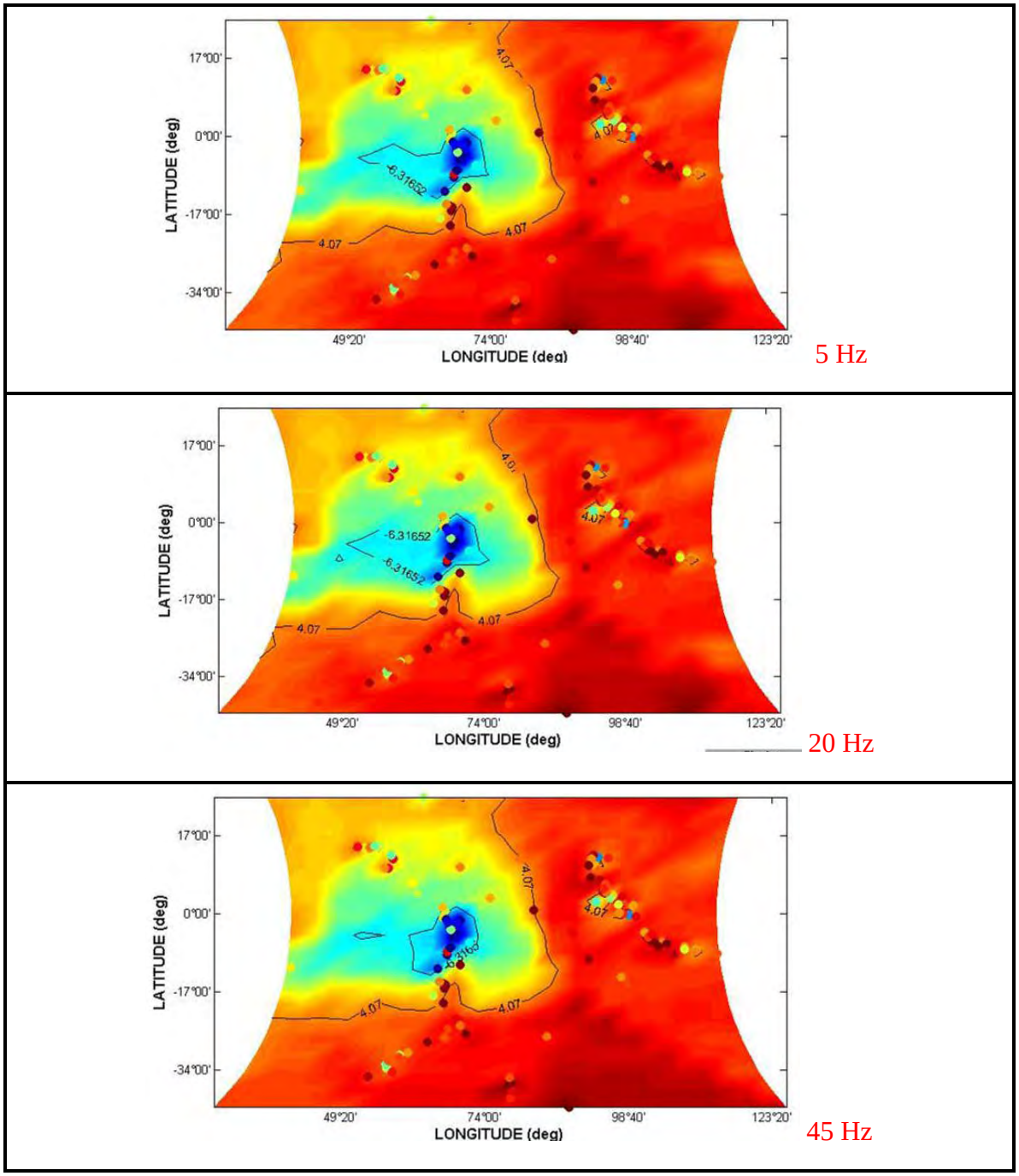


Figure 8. Results of ordinary kriging of measured amplitudes, mapping the variation of amplitudes in dB recorded at the South station minus the amplitudes from the North station. The measured values are plotted on the map using the same scale as that for the kriging map. The predicted values are significantly larger for the 20 Hz case.

REFERENCES

Collins, M.D. (1993). The adiabatic mode parabolic equation, *J. Acoust. Soc. Am*. 94: 2269–2248

Harben, P., E. Matzel, D. Blackman, and D. Clarke (2004). Hydroacoustic blockage calibration for discrimination: Results from 2003 Indian Ocean cruise and imploding sphere calibration source development, in *Proceedings of the 26th Seismic Research Review: Trends in Nuclear Explosion Monitoring*, LA-UR-04-5801, Vol. 2, pp. 553–559.

Isaaks, E. H. and R. M. Srivastava (1989). *An Introduction to Applied Geostatistics*. New York: Oxford University Press.

Pulli, J. J. and Z. M. Upton (2001). Hydroacoustic blockage at Diego Garcia: Models and observations, in *Proceedings of the 23rd Seismic Research Review: Worldwide Monitoring of Nuclear Explosions*, LA-UR-01-4454, Vol. 2, pp. 45–54

Upton, Z. M., J. Bhattacharyya, J. Pulli, S. Shah, and M. Collins (2005). Improving the physical understanding of hydroacoustic blockage: Statistical and model based studies, in *Proceedings of the 27th Seismic Research Review: Ground-Based Nuclear Explosion Monitoring Technologies*, LA-UR-05-6407, Vol. 2, pp. 749–758.

Radionuclide Monitoring

EVALUATION OF HPXe NUCLEAR EXPLOSION MONITOR APPLICATIONS

Albert G. Beyerle[1] and David M. Walker[2]

Mirmar Sensor, LLC[1] and Quantum Technology, LLC[2]

Sponsored by National Nuclear Security Administration
Office of Nonproliferation Research and Development
Office of Defense Nuclear Nonproliferation

Contract No. DE-FG02-06ER84636[1,2]

ABSTRACT

The selection of a detector type for field gamma-spectroscopy monitoring applications is usually based on achieving an acceptable balance of detector energy resolution, efficiency, practicality in the measurement environment, and cost. Because energy resolution and photopeak efficiency of the detector are key factors in determining the detection sensitivity limit, these parameters usually must be addressed first to ensure that the measurement objectives of the mission can be met by the system. For automated spectroscopy systems viewing a complex radionuclide mixture, the unmatched resolution of germanium detectors frequently makes the High Purity Germanium (HPGe) the detector of choice, in spite of the relatively high cost, requirements for cryogenic cooling, and limitations on size and ruggedness of germanium detectors. Promising results are being realized for improvements in the performance of several alternate room temperature detector types in areas of compound semiconductors, halide scintillators and high pressure gas detectors.

One detector type that has shown recent progress as a rugged high-temperature detector with better energy resolution is the high pressure xenon (HPXe) detector. Current HPXe detectors deliver energy resolutions in the range of 1.7%–2.0 % at 662 keV and 7–8 keV FWHM for low-energy gamma rays. Although HPXe detector resolution will likely never match the 0.3-0.5 % resolution of large HPGe detectors, the resolution is quite acceptable for many field applications, and provides other benefits for field systems such as large volume and extended stable operation without cooling. Excellent temperature stability (0.2% total over 23°C–80°C) and negligible drift over time are now being achieved, thus facilitating energy calibration and long-term operation of unattended systems. Current R&D programs are expected to produce HPXe detectors with active detector mass in the few Kg range, and surface areas of 1–3 square feet. These promising developments have prompted recent consideration of HPXe systems for specific harsh environment applications in homeland security, power reactor fuel failure monitors, environmental monitoring stations and “bore hole” measurements at nuclear facility cleanup sites.

In this present work, the performance potential for HPXe-based systems for Nuclear Explosion Monitoring (NEM) applications will be evaluated. A candidate HPXe detector is being selected and characterized in a series of test measurements. A NEM-specific Monte Carlo N-Particle (MCNP) model will be developed for use in optimizing and evaluating the performance of promising NEM configurations. Data from the test measurements will be used to verify the accuracy of the MCNP model and to predict detection sensitivity capabilities for selected radionuclides in the presence of expected NEM interference. If warranted by the performance predictions for HPXe-based nuclear explosion monitors, the MCNP model will be used to define an optimized design of an HPXe-based NEM prototype system.

OBJECTIVES

Note: The research and development project described in this publication has been approved for funding, and a contract to initiate the project is expected by mid-July 2006. This paper is a description of the technical basis and objectives of the program, and of the method by which it will be accomplished.

Background

In defining the detector and auxiliary components for a gamma spectroscopy measurement system, the energy resolution, photopeak efficiency, and peak-to-Compton ratios over the gamma energy range of interest are of primary concern in ensuring that the measurement system will have the inherent capability to meet the required detection sensitivity. For an applied gamma spectroscopy system that must perform a single specific mission in a severe environment with limited access to skilled personnel, other detector features such as room temperature operation, system stability, ruggedness, reliability, and ease of maintenance can also be crucial to success. A recent International Atomic Energy Agency (IAEA) program to review the effectiveness of existing field spectroscopy measurement instruments and fixed monitors identified several major applied systems with state-of-the-art measurement capabilities that were removed from operation because their sensitivity provided too many false positives or provided information in a manner than could not be interpreted and constructively used by field personnel (Arlt, 2005). The IAEA report indicated that a system that requires support and maintenance to the extent of interfering with the primary role of the operator will likely have a very poor availability record. The different criteria for success in a laboratory system and a field gamma spectroscopy system requires that much more consideration of operational issues must be included in the design of a field system if it is to successfully meet the mission role for which it was intended.

If the purpose of a gamma spectroscopy system is to provide a variety of low level measurements in the presence of interference from multiple radionuclides, the excellent energy resolution of an HPGe detector system usually makes it the detector of choice because it offers superior detection sensitivity that simplifies the data analysis process. In a research laboratory environment, resources are normally available to provide cryogenic cooling, background reduction, stable power, minimal shock and vibration, access to replacement parts, and a support staff of experts in detectors and instrumentation. Also, in the laboratory research environment, spectroscopy system downtime is inconvenient, but does not represent a potentially life-threatening emergency that can be associated with unavailability of crucial applied nuclear monitoring systems.

By contrast, NEM, and homeland security and nuclear plant applications of automated gamma spectrometer monitors are examples of systems that must perform a fixed crucial mission with very little downtime over a wide range of severe environmental and logistical conditions. In several field applications of automated gamma spectrometry based monitoring, HPGe detector-based systems have been used successfully to demonstrate that the desired measurement can be made in the field if adequate resources for support can be provided. The Radionuclide Aerosol Sampler Analyzer (RASA) system for nuclear explosion monitoring clearly has demonstrated the inherent capability of that system to identify and quantify radionuclides from an nuclear explosion (Miley, 1998). RASA operational problems related to the reliability of the HPGe detectors and the filter system have been addressed and mitigated (Miley et al., 2000).

Tests of several HPGe based Advanced Spectroscopic Portal Monitors have demonstrated the ability to resolve complex spectra, but the HPGe system is not recommended as the detection system of choice by Arlt (2005). For nuclear power plant applications, automated HPGe based systems have provided fuel failure detection (Walker and Mullin 1996) and post accident sampling (Serpa et al., 1981) capabilities for more than two decades. These nuclear plant systems provide regulatory compliance and operational benefit that justifies the added manpower and radiation dose for providing maintenance and continuous cryogenic cooling of the automated HPGe-based systems in high radiation areas.

For each of these field based automated gamma spectroscopy systems, the practical advantages of a rugged room temperature detector of sufficient resolution and efficiency would be significant. Within the last few years, several promising detector candidates have emerged that offer resolution between that of HPGe (0.2%–0.5% at 662 keV) and NaI (6%–8%) (Park et al., 2006). In particular, three alternate room temperature detector types are now available as commercial detector products offering energy resolution in the range of 1.5% to 3% with acceptable

efficiency for many field monitoring applications. CdZnTe semiconductor detectors have been reported with an energy resolution of 1.9% for a 2.25 cc detector, and of 4% for an 11 cc detector (Gostilo et al., 2005). A commercial scintillation supplier recently reported the availability of a 3" x 3" $LaBa_3$(Ce) scintillation detector with resolution of 2.8%, and the production of a 10.5 cm x 10.5 cm (4.1" x 4.1") detector (Rozsa et al., 2006). HPXe detectors of 1.5" diameter x 3" active length and 1.7% resolution are commercially available from Mirmar Sensor, as are detectors as large as 4.5" diameter by 24". Park et al., (2006) states that, "A recent demonstration at Los Alamos National Laboratory (LANL) showed HPXe detector performance may be superior to that of NaI, plastic scintillators, high-purity germanium, or lanthanum halide/bromide detector materials for many homeland security applications."

Each of the three room temperature detector types now appear to have useful field applications in nonproliferation monitoring, homeland security, nuclear power, and nuclear site cleanup. Their application to practical field systems will require a careful matching of detailed mission requirements with the performance capabilities and operational advantages of these detectors with intermediate resolution. In many cases, the design freedom offered by room temperature detectors will present opportunities for improved sampling systems and shielding configurations to boost detection sensitivity and system reliability.

Specific Objectives of this Project

The general purpose of this R&D project is to determine how to best apply higher resolution, room temperature HPXe detectors to produce rugged, user-friendly field gamma spectroscopy for the NEM program. The project will focus on matching the present capabilities of HPXe detector systems with both the measurement requirements and operational considerations for specific NEM applications. The HPXe system development program will draw heavily on the source description data, operating experiences and lessons-learned from the decade of experience of National Nuclear Security Administration (NNSA) and its contractors in the worldwide deployment of RASA and Automated Radioxenon Analyzer/Sampler (ARSA) systems.

Specific objectives of this project are as follows:

1. Identify an optimum HPXe detector for a NEM application, and to produce measured parametric detector performance data for the detector to allow calculations of detection sensitivity limits for evaluating various NEM applications,
2. Develop and verify an MCNP model for HPXe-based systems that can provide quantitative evaluation of the performance of a variety of HPXe-based system designs for specific NEM applications,
3. Define and optimize a conceptual design for the most promising application of HPXe detectors to an NEM program need, and to propose and predict the performance of a prototype HPXe system to be constructed and tested in a field environment situation.

RESEARCH ACCOMPLISHED

This section will describe portions of previous HPXe detector development results and detector performance of HPXe detectors developed and produced by Mirmar Sensor (Mirmar). The R&D program in basic HPXe detector technology is still in progress at Mirmar, and the HPXe detectors for this pending project will be supplied from the inventory of detectors at the Mirmar facility. The purpose of this current project for NNSA is to define and evaluate the performance of HPXe-based spectroscopy systems for applications in nuclear explosion monitoring. It is being conducted under a joint venture agreement between Mirmar and Quantum Technology, an applied spectroscopy systems company.

Status of Mirmar HPXe Detector Development

Mirmar Sensor now builds xenon detectors in the USA in standard active volume sizes (diameter and length) of 1.5" by 3.0", 1.5" by 6.0", 4.5". by 8.0", and 4.5" by 24". Typical energy resolution is less than 2%, and detectors in the 1.7% range are routinely produced. The Model 121 detectors shown in Figure 1 have an integral preamplifier and high-voltage power supply, and are self-contained in that they requires only ±12 V to operate. They have active detector dimensions of 1.5" diameter by 3" length, and overall dimensions of 1.75" diameter by 19" long. The internal microprocessor raises the high-voltage, then signals (via an LED) that the detector is ready for operation.



Figure 1. Mirmar Model 121 High-Pressure Xenon Detectors.

Figure 2 shows a measured spectrum of a ^{137} Cs source taken with the Model 121 HPXe detector shown in Figure 1. The FWHM resolution at the 662 keV peak is 11.0 keV, or less than 1.7%. Note the distinct xenon x-ray peak at 30 kev below the 662 keV line, which shows that low-energy tailing is not significant for this detector.

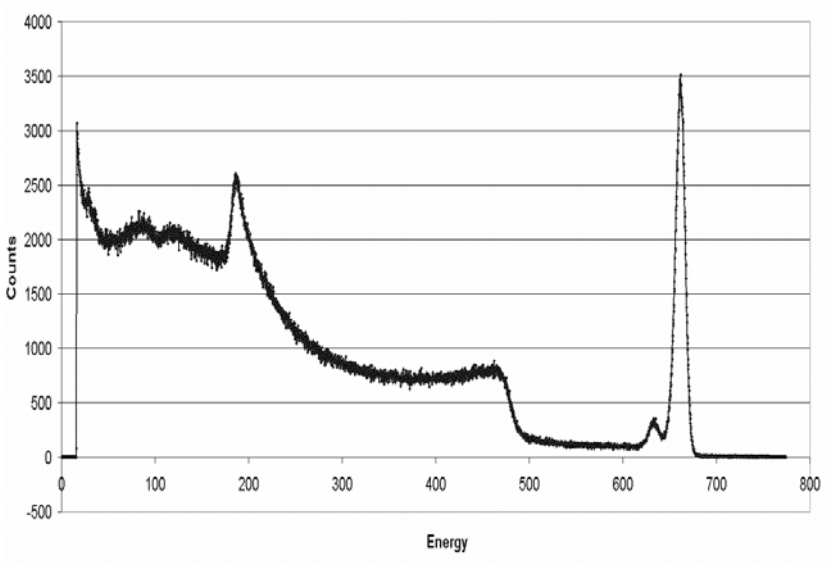


Figure 2. Measured ^{137}Cs spectrum with HPXe Detector Model 121 (Beyerle, 2005).

Stability

The gain of the xenon detectors is quite stable as shown in Figure 3. The time variance of the gain is about 0.02% over a week. This stability eliminates the need for periodic calibration. More importantly, the stability allows the peak location to be very accurately known, which can be useful in quantitative analysis of unresolved peaks. This is important in this application because there are several cases of unresolved or barely resolved doublets.

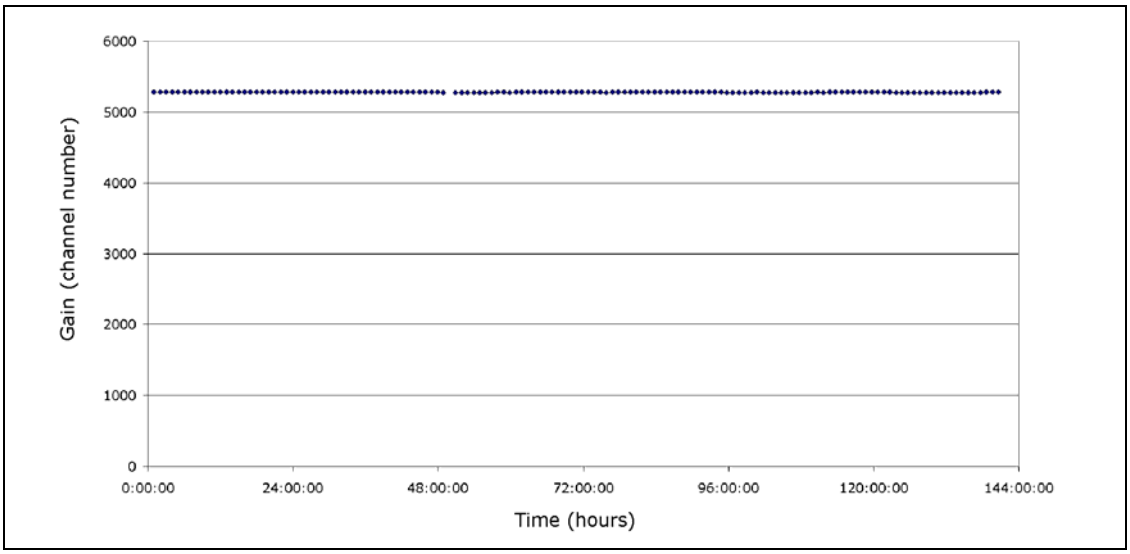


Figure 3. Gain variation over a week for an HPXe detector (Beyerle, 2005).

The temperature stability of the HPXe detector is shown in Figure 4. The temperature stability is about 0.2% over the entire range 25°C–80°C (77°F–176°F). Even this excellent stability range is an upper limit since the precision of the measurement is comparable to the measured variation. Temperature stability is important in applications such as outdoor air monitoring or vehicle portal monitoring systems where the detector temperature may change significantly on a daily and seasonal basis.

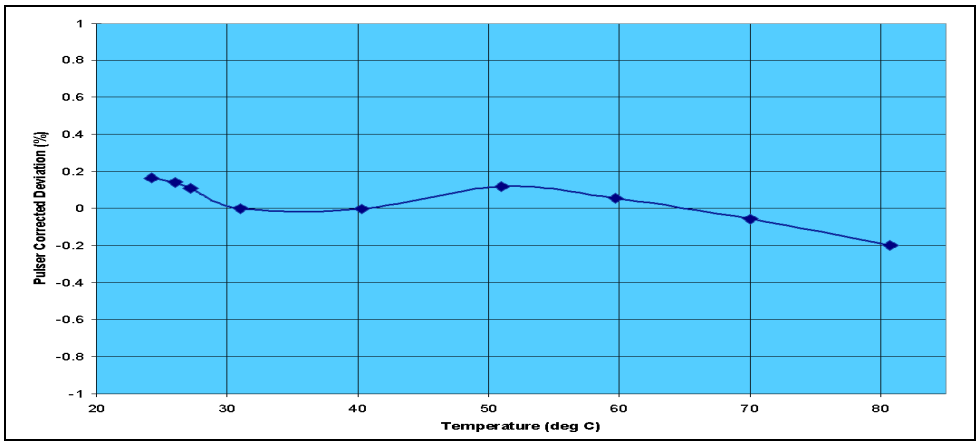


Figure 4. Temperature Stability of HPXe (Beyerle, 2005).

Figure 5 shows a ^{133}Ba spectrum taken with the Model 121 HPXe detector. Significant features of the spectrum include the following:

- The peak at 30 keV is nearly entirely due to the xenon x-ray at 30 keV. The vessel wall is not very transparent at 30 keV. A carbon fiber or aluminum vessel would alleviate this problem.
- The peak at 50 keV is a combination of the x-ray escape from the 81.0/ 79.6 keV peak and the ^{133}Ba 53.17-keV peak.
- The peak at about 80 keV is the ^{133}Ba 81.0 and 79.6 keV peaks. The resolution is not nearly good enough to separate the peaks but the excellent symmetry of the peaks allows some distinction of the closely separated small peak immediately lower in energy than a larger peak.
- The ^{133}Ba peak at 160.6 keV is obscured by the Compton backscatter. This is a reason to use larger diameter detectors.
- The ^{133}Ba peak at 223-keV is barely visible due to its small intensity.
- The standard four ^{133}Ba lines at 276, 303, 356, and 384 are clearly separated. Each has an x-ray escape. Especially noticeable is the x-ray escape of the largest 356-keV peak at 326 keV.
- Higher energy peaks are pile-up.

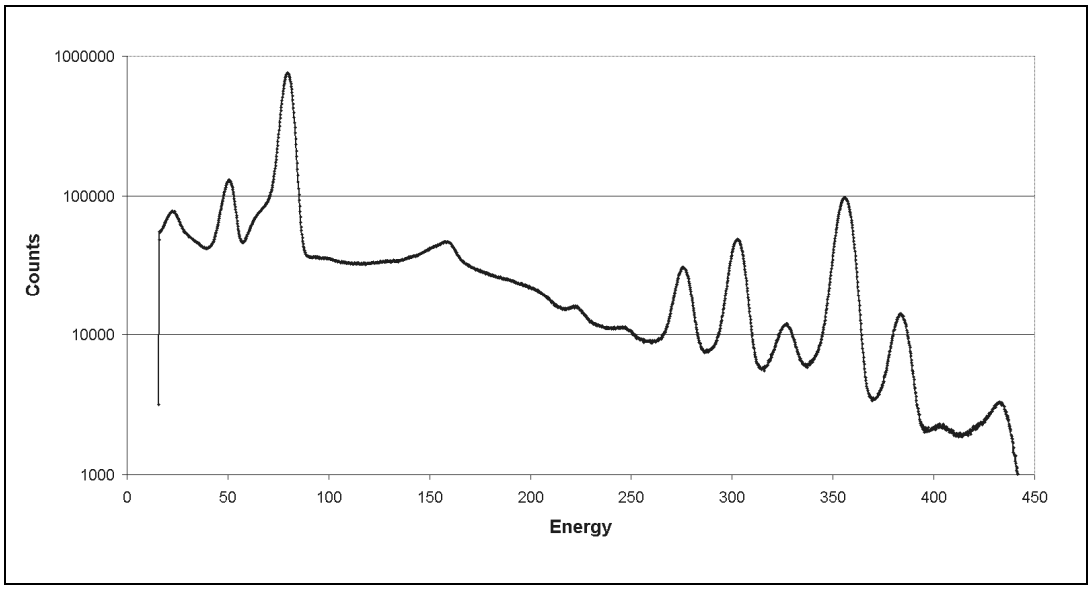


Figure 5. The ^{133}Ba spectrum from a small xenon detector. Low-energy FWHM is 6–7 keV (Beyerle, 2005).

Vibration Issues

Mirmar Sensor has developed a patented technology to greatly reduce the vibration sensitivity of the HPXe detectors. Detectors are generally unaffected by vibration up to about 0.2–0.5 G vibration at any frequency. External damping can further reduce this sensitivity.

Nuclear Test Monitoring

We have performed a first order simulation of the nuclear test air monitoring spectra. This simulation was accomplished by taking a ^{133}Ba spectrum with its gamma-ray lines in the relevant energy regime, and simultaneously fitting all of the peaks. The gamma-ray energies of the ^{133}Ba were replaced with the energies of the actual fallout gamma-rays from Miley (1999). with all of the intensities equal. The resulting spectra are shown in Figures 6 and 7. This was fit over an actual depleted uranium spectrum, hence the fitted peaks (red/solid) bear no

resemblance to the real peaks (blue/dotted) except to give an idea of the statistical noise and the quality of the fit in the one case (U-238 at 1001 keV) where there is alignment.

Note that in each case, there is an irresolvable overlap between the ^{147}Nd and ^{140}Ba at 537 and 531 keV that must be resolved by the ^{140}Ba at 487 keV. The ^{95}Zn (in the fit in red/solid) at 768 keV has a conflict with the natural Thorium line (from the data in blue/dotted), which is resolved by the ^{95}Zn peak at 739 keV.

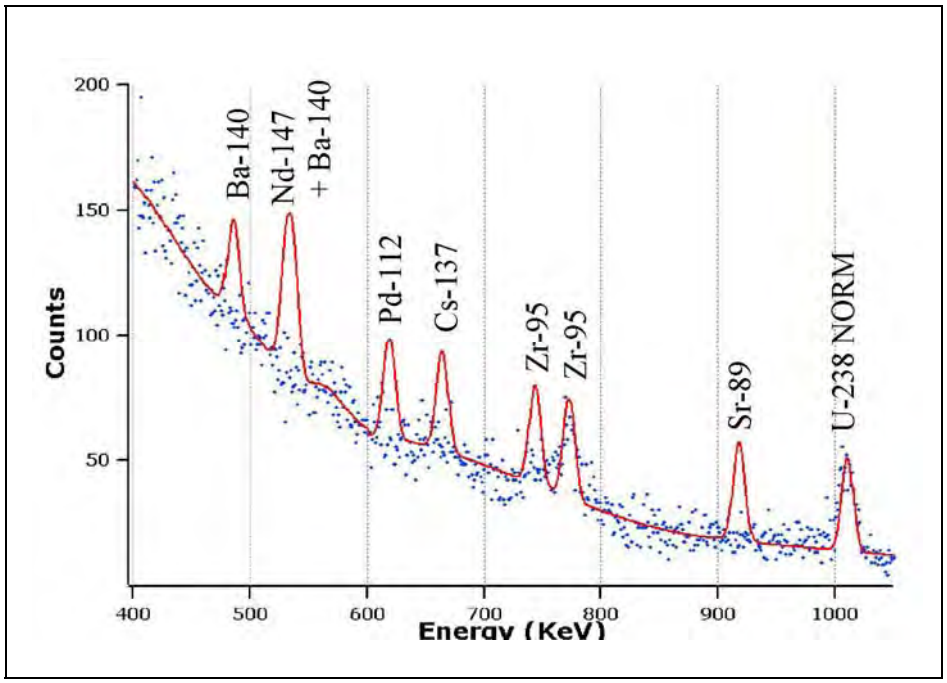


Figure 6. Simulated portion of a spectrum for filter collection 14 days after a nuclear event.

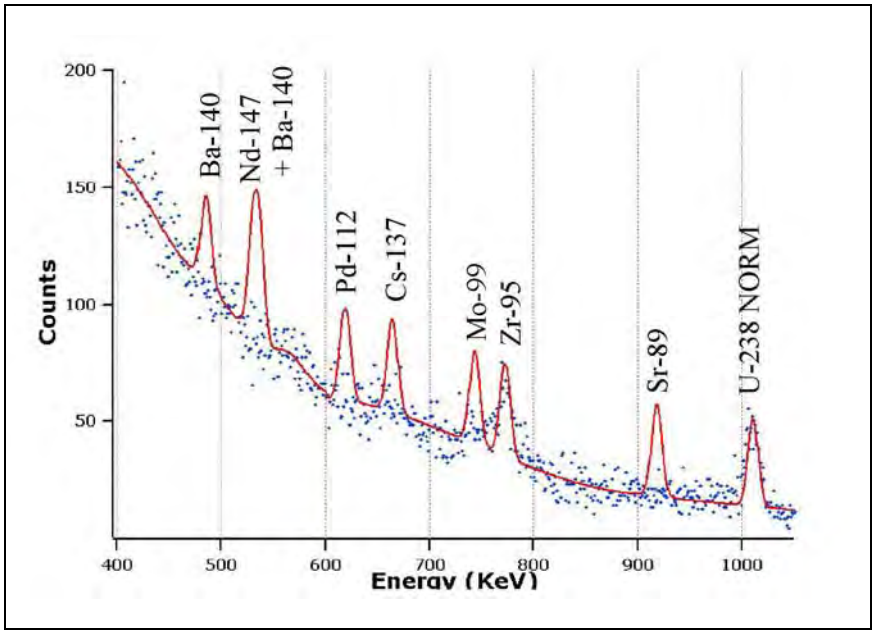


Figure 7. Simulated spectrum for filter collection 2 days after a nuclear event.

Project Plan

The purpose of this project is to evaluate the performance of HPXe-based field spectroscopy systems for nuclear explosion monitoring applications and to advance a selected applied HPXe monitor to the system prototype stage. The first phase of the effort will consist of the following tasks that will be executed in parallel:

1. HPXe Detector Selection and Characterization—HPXe detectors will be selected and used in a series of test measurements with National Institute of Standards and Technology (NIST) traceable sources to generate parameterization data of energy resolution vs. energy, efficiency vs. energy, and Compton baseline over the energy range of 60 keV to 2,000 keV. Data will also be recorded with selected sources representative of NEM and interference sources in field applications. These data will be used to calculate detection sensitivity for cases of interest, and to test the accuracy of Monte Carlo models of HPXe based measurement systems. Data will also be collected to allow prediction of stability vs. time, microphonic effects, and to evaluate optimum pulse processing and data analysis methods for HPXe spectra.
2. Development and Verification of a Monte Carlo Model for Applied HPXe-Based Measurement Systems—A Monte Carlo model will be developed for applied HPXe systems based on the MCNP-5 code. The experimental results from Task 1 will be used to verify the accuracy of the Monte Carlo model, and to estimate the error bounds of the calculated results. Auxiliary programs will be written to transfer calculated spectra into commercial spectroscopy programs to facilitate evaluation of MDC performance and resolution of interference components in the HPXe spectra.
3. Identification and Evaluation of promising NEM applications using HPXe Systems—Promising NEM applications for which HPXe based field systems may offer advantages will be identified based on NEM mission requirements and the data, and operating experiences and lessons learned of the NEM community. Alternate sample collection and data processing and analysis methods will be examined that take advantages of the large size, ruggedness, and flexibility of shielding of HPXe detectors. The MCNP model will be used to quantify the performance of various system configurations, and to optimize system designs for maximum performance. This collective information will be used to select and optimize a prototype design for an HPXe NEM system for specific field applications. The prototype system will be constructed and tested in a field environment situation in subsequent phases of this project.

CONCLUSION(S) AND RECOMMENDATIONS

HPXe detector technology has progressed to a point that justifies an authoritative evaluation of HPXe systems for specific applications in nuclear explosion monitoring. HPXe detectors are viable candidates for nuclear test monitoring because large area spectrometers with excellent stability are available. Detectors have been operated out of doors in air sampling systems successfully for more than a year maintaining 2% resolution, with excellent stability. Their large area makes them the most sensitive choice where a large area sample, such as a large filter, is involved.

This study is a focused program to develop and apply tools to define and optimize HPXe systems that provide effective, practical field systems for NEM applications.

REFERENCES

Arlt, R. A. (2005). Automated gamma spectrometry in radiation monitoring at borders and in a country, IEEE-NSS 2005, special IAEA presentation of session chairman.

Beyerle, A. G. (2005). Stability of high-pressure xenon gamma-ray spectrometers, in *Proceedings of Hard X-ray and Gamma-Ray Detector Physics VII, International Society for Optical Engineering.* Vol. 5, pp. 922–928.

Gostilo V., Z. He, V. Ivanov, L. Li, A. Loupilov, and I. Tsirkounova (2005). Preliminary results of large volume multi-pair coplanar grid CdZnTe detector fabrication, in *2005 IEEE Nuclear Science Symposium Conference Record*, N35-58, pp. 1,402–1,407.

Miley, H. S., D. N. Anderson, R. J. Arthur, J. E. Ellis, T. W. Haimbinger, G. R. Kiebel, and R. C. Thompson (2000). Radionuclide operational research & development, in *Proceedings of the 22nd Seismic Research Symposium: Planning for Verification of and Compliance with the Comprehensive Nuclear-Test-Ban Treaty (CTBT)*, Vol. 2, pp. 121–128.

Miley, H. S. (1999). Evaluation of fission product isotopes for field or laboratory detection, in Proceedings of the 21st Seismic Research Symposium: Technologies for Monitoring the Comprehensive Nuclear-Test-Ban Treaty, LA-UR-99-470, Vol. 1, pp. 261–266.

Miley, H. S., S. M. Bowyer, C. W. Hubbard, A. D. McKinnon, R. W. Perkins, R. C. Thompson, and R. A. Warner (1998). A description of the DOE radionuclide aerosol sampler/analyzer for the Comprehensive Test Ban Treaty, *JRNC* 235: 83–87.

Park, B. K., J. M. Backadar, I. H. Campbell, J. D. Danneskiold, R. J. Estep, G. H. Gardner, M. W. Johnson, M. D. Martinez, E. A. McKigney, W. L. Myers, C. J. Sullivan, and G. J. Van Tuyle (2006). Advances in nuclear monitoring technologies, in *Forum Phys. Soc.* (American Physical Society). Vol. 35, No. 3.

Rozsa, C. M., M. R. Mayhugh, and P. R. Menge (2006). Two new scintillators: $LaCl_3$(Ce) and $LaBr_3$(Ce), 51st HPS Annual Meeting, June 25–29, 2006, Paper No. TMP-C.4.

Serpa, D. P., D. M. Walker, and T. A. Jenckes (1981). Emergency monitoring, assessment and response system for Diablo Canyon power plant, *IEEE Trans. Nuc. Sci.* NS-28: No. 1–Part I, 236–241.

Walker, D. M. and D. S. Mullin (1996). Updating of a gamma dpectroscopy-based failed fuel monitor, in *IEEE Nuclear Science Symposium Conference Record*, Vol. 2, pp. 950–954.

FURTHER DEVELOPMENT OF THE SPECTRAL DECONVOLUTION ANALYSIS TOOL (SDAT) TO IMPROVE COUNTING STATISTICS AND DETECTION LIMITS FOR NUCLEAR EXPLOSION RADIONUCLIDE MEASUREMENTS

K. M. Foltz Biegalski, S. R. Biegalski, and D. A. Haas

The University of Texas at Austin

Sponsored by Army Space and Missile Defense Command

Contract No. W9113M-05-1-0017

ABSTRACT

The Spectral Deconvolution Analysis Tool (SDAT) software was developed to improve counting statistics and detection limits for nuclear explosion radionuclide measurements. SDAT utilizes spectral deconvolution spectroscopy techniques and can analyze both β–γ coincidence spectra for radioxenon isotopes and high-resolution HPGe spectra from aerosol monitors.

Spectral deconvolution spectroscopy is an analysis method that utilizes the entire signal deposited in a γ-ray detector rather than the small portion of the signal that is present in one γ-ray peak. This method shows promise to improve detection limits over classical γ-ray spectroscopy analytical techniques; however this hypothesis requires study. To address this issue, three tests were performed utilizing HPGe spectra to compare the detection ability and variance of SDAT results to those of commercial-off-the-shelf (COTS) software that utilizes a standard peak search algorithm.

To test the applicability of the SDAT to β–γ coincidence spectra, Monte Carlo N-Particle eXtended (MCNPX) is used to simulate the detector response in an Automated Radioxenon Sampler-Analyzer (ARSA) detector for all the electrons and photons emitted from ^{131m}Xe, ^{133}Xe, ^{133m}Xe, ^{135}Xe, and ^{137}Cs. A MatLab code was written to incorporate the MCNPX results in the calculation of β-γ coincidence spectra. These will aid in the development of the SDAT and to calibrate β-γ coincidence systems. The models developed for this work include improvements over previous models in their ability to address Compton scattering in the β cell, and the β distribution offset in the 30 keV γ-ray region for ^{133}Xe.

OBJECTIVES

This work aims to develop a spectral analysis tool that utilizes deconvolution to quantitatively calculate fission product concentrations in nuclear explosion monitoring radionuclide samples. The project was divided into two tasks for the year. The first task was to develop the Spectral Deconvolution Analysis Tool (SDAT). The second task was to develop models of both β–γ coincidence radioxenon spectra and HPGe fission product spectra in MCNP. These MCNP models were used to calibrate and test the SDAT code.

RESEARCH ACCOMPLISHED

SDAT Development

A good portion of the main SDAT analysis algorithm was written and discussed during the last SRR. This year, the focus was on testing, documentation, and development of peripheral software to improve analysis results.

Testing

The purpose of the first tests was to evaluate how well SDAT improves counting statistics and detection limits for explosion radionuclide measurements compared to COTS software that uses a standard peak-search and peak integration algorithm. SDAT results were compared with those from Canberra's Genie-PC program. Three experiments were performed. In the first test, the variance properties of several sparse ^{137}Cs spectra were determined. For the second test, small ^{137}Cs peaks were superimposed on the Compton continuum of a ^{60}Co spectrum and we compared how well each software package detected the small peaks. For the third test, ^{137}Cs spectra of varying count times were superimposed onto ^{60}Co spectra of varying count times such that the ^{137}Cs peak occurs at the first gamma-line of ^{60}Co: 1172 keV. In this case, the ability of each software package to deconvolve the multiplet peak signal was studied. For experimental details of these tests, see the Foltz-Biegalski, Biegalski, and Haas paper presented at the Methods and Applications of Radioanalytical Chemistry conference in Kona, Hawaii in April 2006.

Conclusions of the test results were as follows. First, SDAT performs better than standard peak search and peak integration routines when the total spectrum count rates are relatively low, e.g., as in the ARSA histograms. This result was expected, but tests were needed to confirm this hypothesis. Not expected was the poor performance seen from the spectral deconvolution algorithm for spectra with high total counts. In these cases, peak-weighting significantly improved SDAT results; however, not consistently enough to achieve better results than the standard peak search and peak integration routine in cases of multiplet interference. The standard peak search and peak integration routine outperformed SDAT in these cases and gave more accurate results with lower errors. Consequently, we cannot recommend spectral deconvolution to replace standard peak search and peak integration algorithms, but to serve as a supplementary tool for analyzing atmospheric samples with low count rates or for analyzing samples with higher backgrounds when multiplets are not a concern. In the latter case, peak weighting must be used in conjunction with the with the spectral deconvolution algorithm.

Additional testing was performed using four detector response histograms created using the MCNPX ARSA model, one for each radioxenon isotope of interest. A weighting matrix was created using the SDAT program, "`Create_weighted_matrix.m`". Several experimental sample histograms were created by combining the radioxenon detector response files in different amounts. The `SDAT` analysis program was then used to deconvolve the experimental samples. The coefficients calculated by SDAT were as expected with very low residual.

Documentation

The SDAT software suite is described in a document titled "SDAT Software Documentation."
This document gives an overview of the software package, includes installation information, and describes basic procedures and detailed operations. Additional scientific documentation on the software can be found in the final report prepared for SMDC.

Further Software Development

Two important additions were made to the SDAT software suite this year. These included the ability to calculate uncertainty values for the multiplier coefficients and the ability to determine a weighting matrix using the four radioxenon library files and a user-defined sensitivity index. The weighting matrix is used to improve the results of the deconvolution algorithm as discussed above in the section on software testing.

The uncertainty of the multiplier coefficients was determined according to multiple linear regression theory as discussed in *Statistical Analysis for Engineers and Scientists* by J. Wesley Barnes, 1994 on page 250. The theory is summarized below. The [*Coefficients*] matrix will be referred to as β to match the reference. Other symbolic replacements that will be used in this discussion are listed below.

[*Response*] = X_{nxp}

[*Sample*] = y

$\ddot{\beta}$ is an unbiased estimate of β. The variance-covariance matrix of $\ddot{\beta}$ is $\sigma^2(\ddot{\beta}) = (X^T X)^{-1}\sigma^2$. The mean square of errors, or MSE, is the best unbiased estimate of σ^2. Therefore,

$$\sigma^2 = \mathrm{MSE} = \frac{\mathrm{SSE}}{(n-p)}$$

where *SSE* is the sum of squares for error, *n* is the number of samples in the data set, and *p* is the number of parameters in the model. In our case, n = 255 x 255 = 65025 and p = 4 for the four radioxenon isotopes (p =6 if radon background and detector background are included). SSE is determined using the equation below.

$$\mathrm{SSE} = y^T y - b^T X^T y - y^T X b + b^T X^T X b.$$

Therefore

$$\sigma^2 = \frac{y^T y - b^T X^T y - y^T X b + b^T X^T X b}{(n-p)}.$$

As mentioned in the Testing section, it was found that, in most cases, signal weighting reduced the residual of the [*coefficients*] matrix [Foltz Biegalski, Biegalski, and Haas, 2006]. To create a weighting histogram, a program that comes with the SDAT software called "`Create_weighted_matrix.m`" is used. This program uses all the detector response files to create the weighting histogram. For β-γ coincidence data, the weighting file contains a 255 x 255 matrix of zeroes and ones that is used to weight the areas of the sample spectrum in which a radioxenon signal is expected. The interesting areas of the sample histogram can be weighted in different amounts by changing a sensitivity number within the program. See the *SDAT Software Documentation* for more information on the setup and execution of this program.

MCNPX Model Development

For the last SRR, MCNPX models for both the ARSA β–γ coincidence detector and a HPGe detector were created. This year, Compton scattering was added to the ARSA detector model as well as the 45 keV β energy shift at 30 keV on the γ energy scale caused by an additional coincident photon during conversion electron decay (Figure 1). All models were transferred to MCNPX this year due to improved decay libraries. As a result of the improved models, more accurate representations were made of the individual radioxenon histograms (Figures 1-5). A model was also produced for the β-γ coincidence response expected from Compton scattering of ^{137}Cs–a proposed method for calibrating the energy vs. channel response of the ARSA. (Figure 6) In addition, decay signals of the four radioxenon isotopes of interest—^{131m}Xe, ^{133}Xe, ^{133m}Xe, and ^{135}Xe —and other fission products including ^{137}Cs, ^{140}Ba, and ^{140}La were modeled using the HPGe detector model. (Figures 7–13) More information on the scientific details behind the creation of the radioxenon histograms can be found in the Haas, Biegalski, Foltz-Biegalski paper, "Modeling β-γ coincidence spectra of ^{131m}Xe, ^{133}Xe, ^{133m}Xe, and ^{135}Xe," presented at the Methods and Applications of Radioanalytical Chemistry conference in Kona, Hawaii in April 2006. Additional details are provided in this year's final report for this project provided to SMDC.

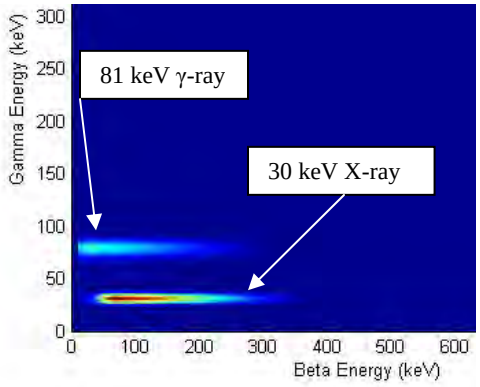


Figure 1. β-γ coincidence data for ^{133}Xe produced through MCNPX simulation. Note the endpoint of the β spectrum coincident with the 30 keV X-ray is approximately 45 keV greater than that coincident with the 81 keV γ-ray.

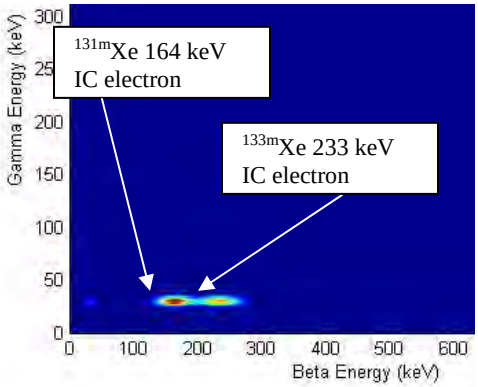


Figure 2. β-γ coincidence data for ^{131m}Xe and ^{133m}Xe produced through MCNPX simulation.

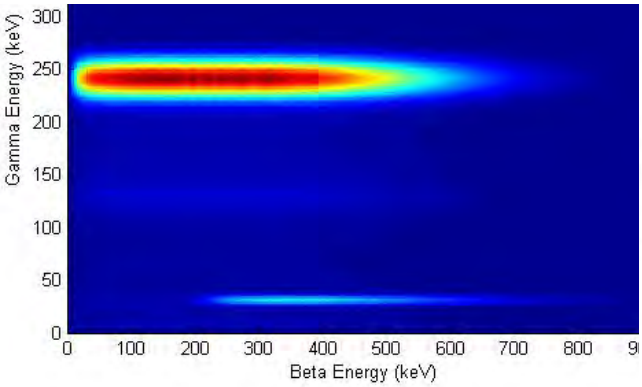


Figure 3. β-γ coincidence data for ^{135}Xe produced through MCNPX simulation.

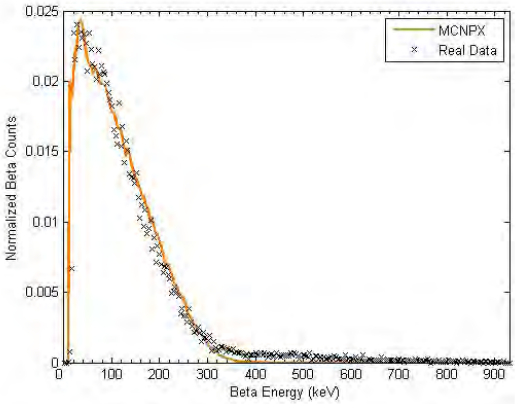


Figure 4. Plot of the β spectra in coincidence with the 81 keV γ-ray of ^{133}Xe from the real sample and MCNPX model.

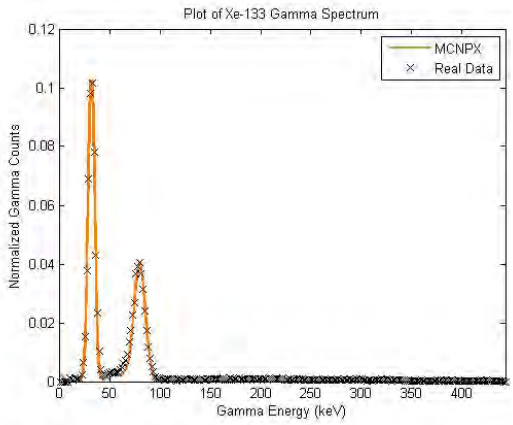


Figure 5. Plot of the γ spectra in coincidence with β particles from the decay of ^{133}Xe.

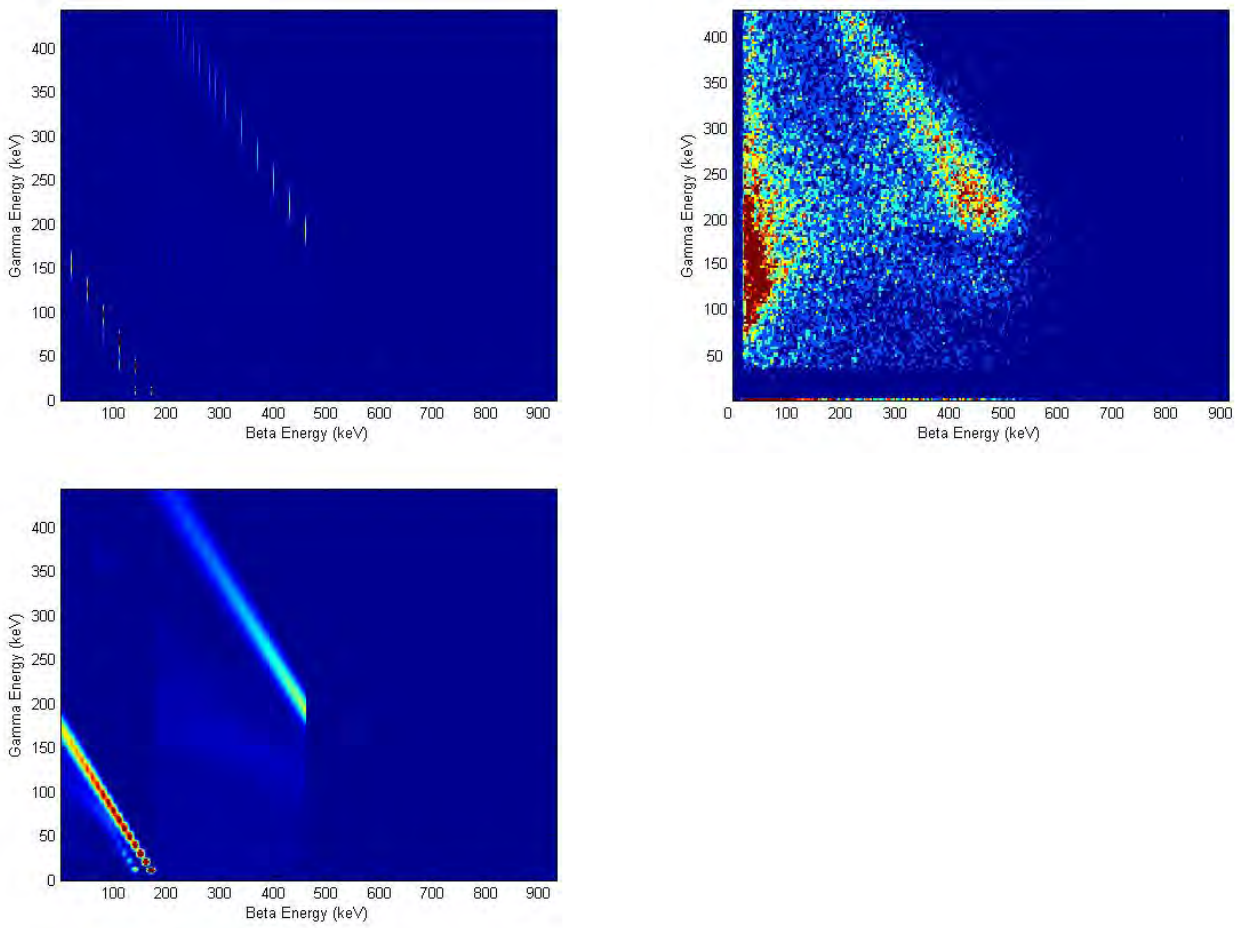


Figure 6. β-γ coincidence spectrum of the ^{137}Cs calibration source. Top - MCNPX model of the gamma spectra coincident with different energy events in the β cell. Middle—interpolation of the top image gives a complete model. Bottom—an experimental result.

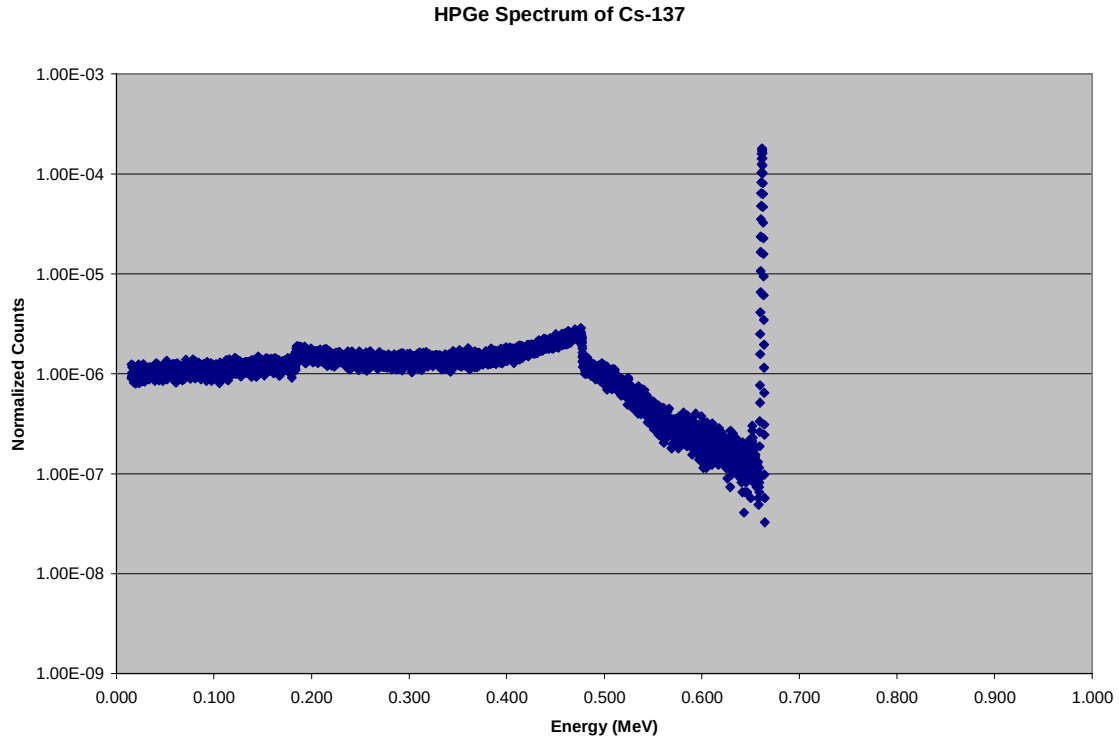


Figure 7. Modeled plot of ^{137}Cs γ spectra acquired with a HPGe detector.

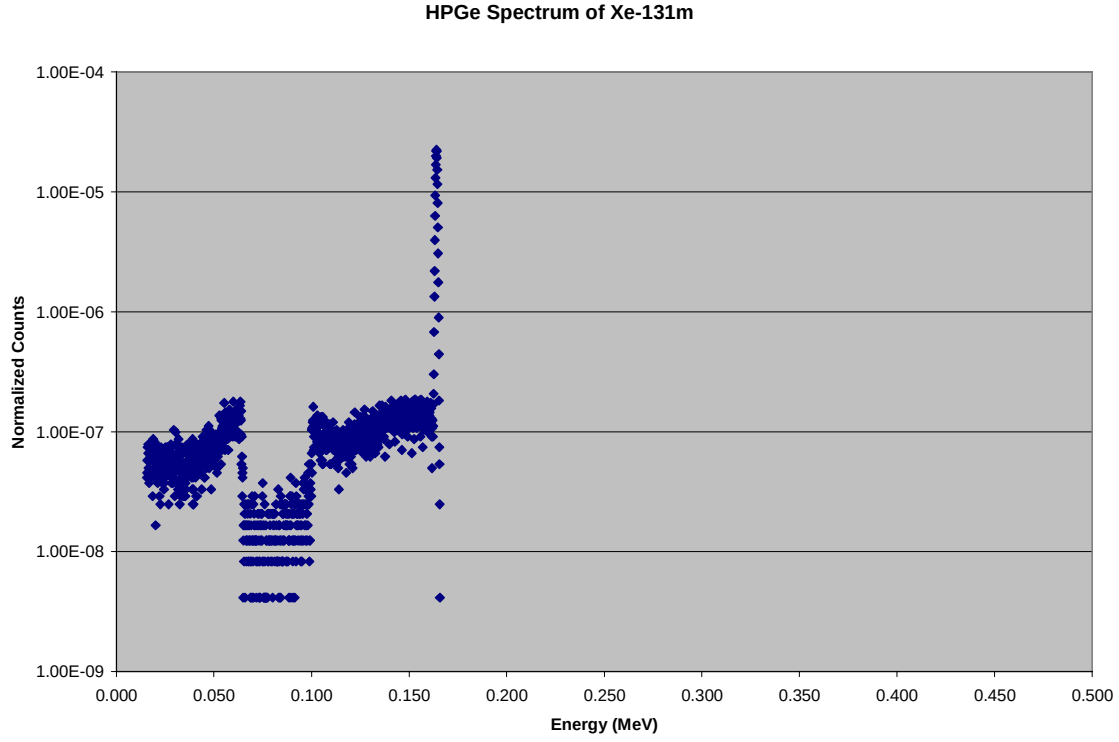


Figure 8. Modeled plot of ^{131m}Xe γ spectra acquired with a HPGe detector.

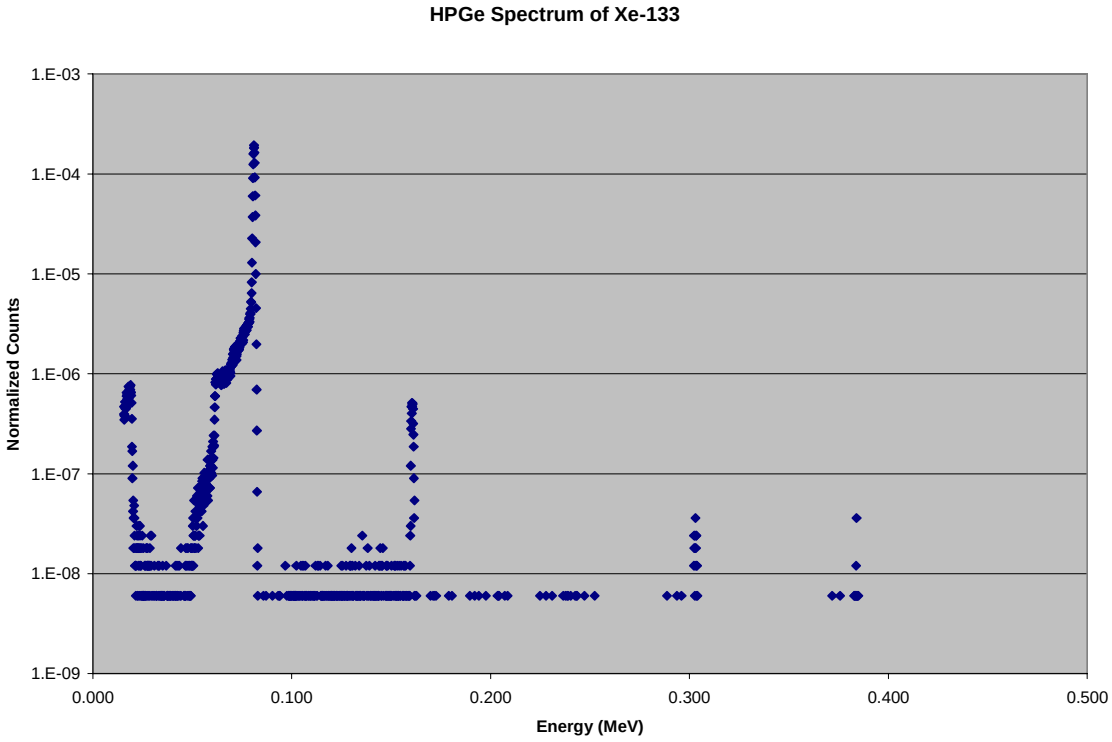


Figure 9. Modeled plot of ^{133}Xe γ spectra acquired with a HPGe detector.

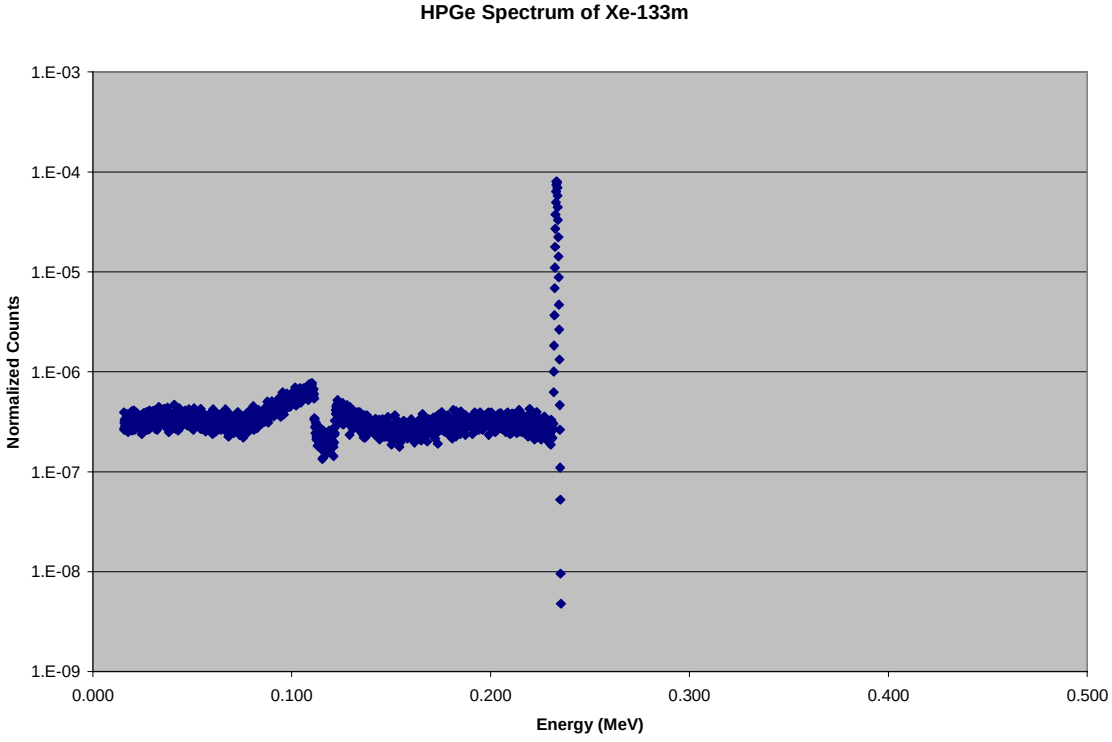


Figure 10. Modeled plot of ^{133m}Xe γ spectra acquired with a HPGe detector.

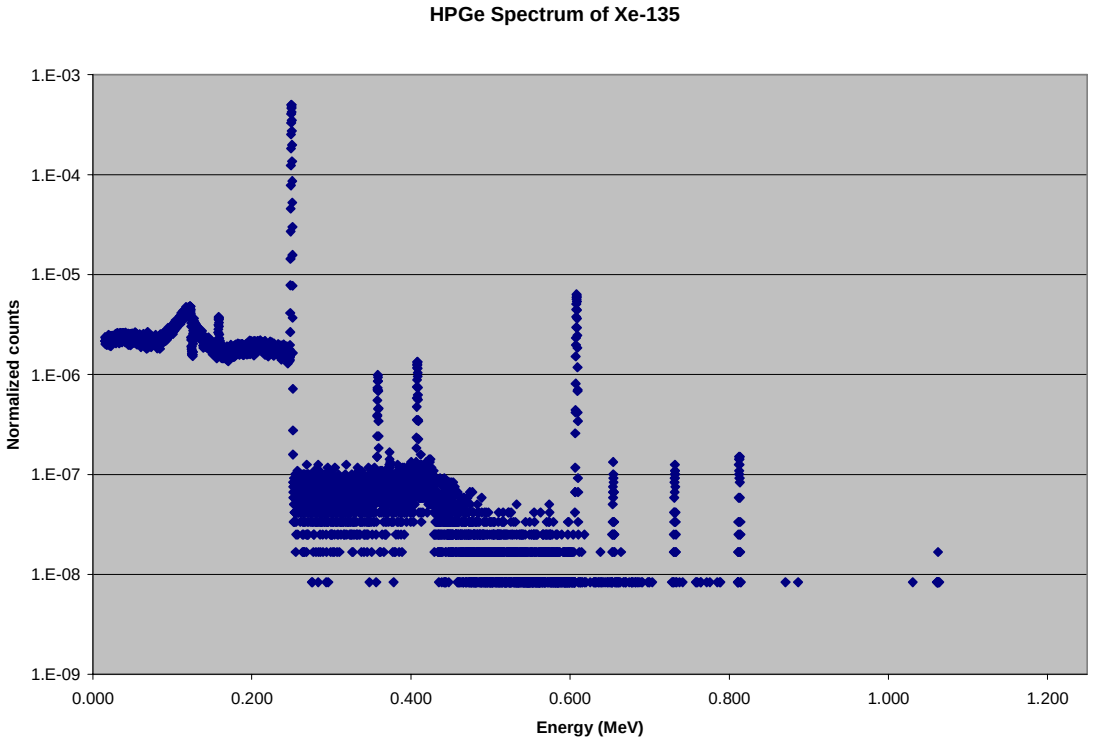


Figure 11. Modeled plot of ^{135}Xe γ spectra acquired with a HPGe detector.

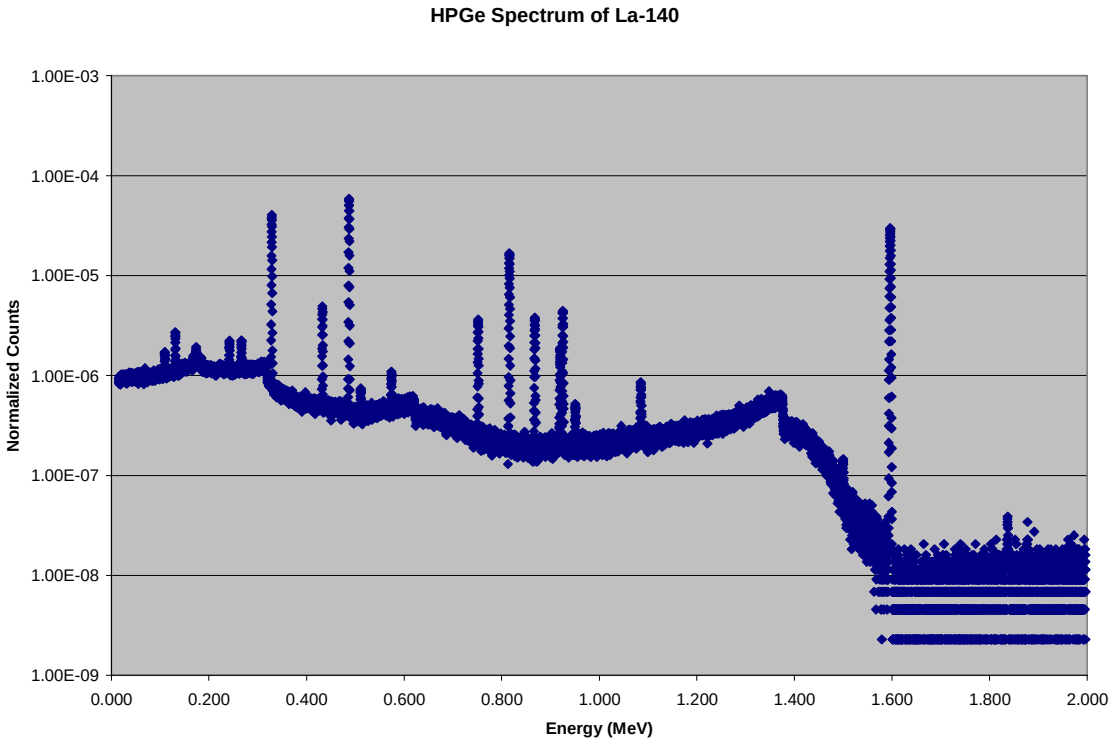


Figure 12. Modeled plot of ^{140}La γ spectra acquired with a HPGe detector.

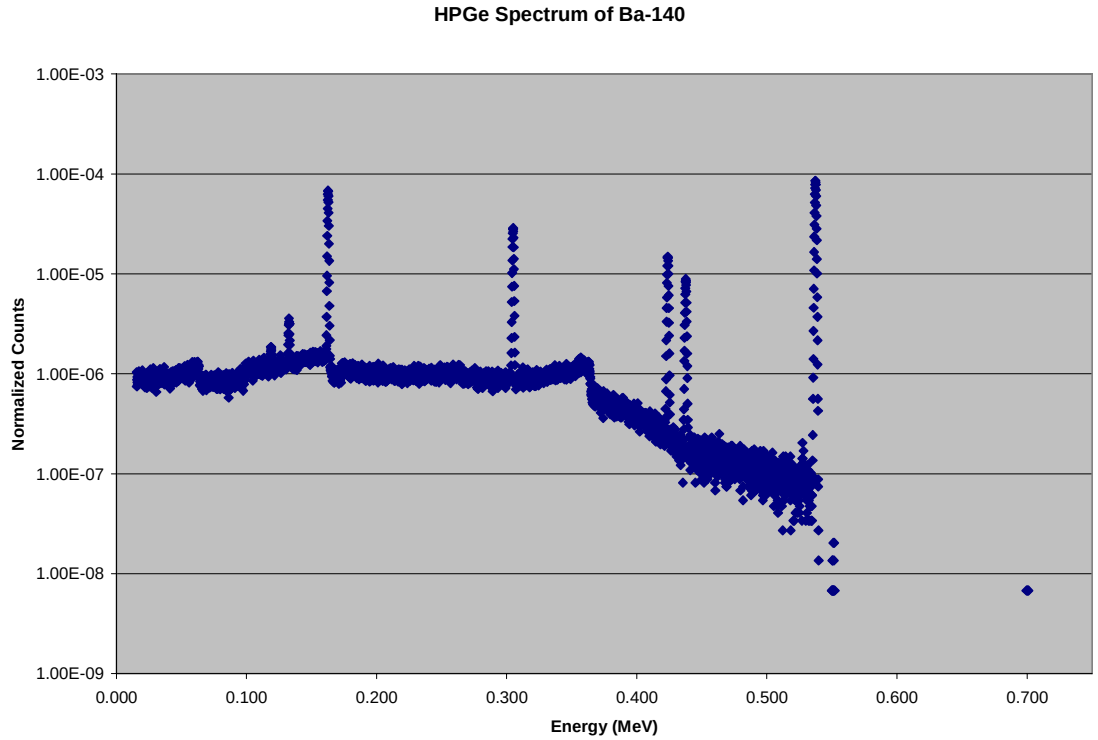


Figure 13. Modeled plot of ^{140}Ba γ spectra acquired with a HPGe detector.

CONCLUSIONS AND RECOMMENDATIONS

Future work will include purchase of a β-γ coincidence detector similar to what is utilized in an ARSA or Swedish SAUNA system. We have begun constructing equipment for creating and separating radioxenons. The radioxenon will be produced through irradiation of uranium in the 1.1 MW TRIGA Mark II research reactor at UT. The samples produced will provide greater activity samples for counting in the detector which will give better counting statistics. The goal will be the development of an accurate and reliable deconvolution tool for determining isotopic abundances of radioxenon for use in support of the Comprehensive Nuclear-Test-Ban Treaty (CTBT). It is planned to incorporate the SDAT software into a user-friendly GUI during the summer of 2006.

REFERENCES

Foltz-Biegalski, K. M. (2006). Spectral Deconvolution Assessment Tool (SDAT) software documentation, developed for SMDC as part of this contract.

Foltz-Biegalski, K. M., S. R. Biegalski, and D. A. Haas (2006). Performance evaluation of Spectral Deconvolution Analysis Tool (SDAT) software used for nuclear explosion radionuclide measurements," Methods and Applications of Radioanalytical Chemistry Conference, April 2006 (to be published in the 2008 *J. Radioanal. Nucl. Chem.*).

Foltz-Biegalski, K. M., D. A. Haas, and S. R. Biegalski (2006). SDAT final report, developed for SMDC as part of this contract.

Haas, D. A., S. R. Biegalski, and K. M. Foltz Biegalski (2006). Modeling β-γ coincidence spectra of ^{131m}Xe, ^{133}Xe, ^{133m}Xe, and ^{135}Xe signals, Methods and Applications of Radioanalytical Chemistry Conference, April 2006 (to be published in the 2008 *J. Radioanal. Nucl. Chem.*).

Lawson, C. L. and R. J. Hanson (1974). *Solving Least Squares Problems*. Englewood Cliffs, New Jersey: Prentice-Hall.

STUDY OF A TRIPLE-LAYER PHOSWICH DETECTOR FOR BETA AND GAMMA SPECTROSCOPY WITH MINIMAL CROSSTALK

A. T. Farsoni and D. M. Hamby

Oregon State University

Sponsored by National Nuclear Security Administration
Office of Nonproliferation Research and Development
Office of Defense Nuclear Nonproliferation
and
Department of Energy

Contract Nos. DE-FC52-06NA27322 and DE-FG07-02ID14331

ABSTRACT

The Automated Radioxenon Sampler/Analyzer (ARSA) has been developed at Pacific Northwest National Laboratory for the Comprehensive Nuclear-Test-Ban Treaty (CTBT) to monitor radioactive xenon. Employing 12 photomultiplier tubes in the present ARSA technology makes it calibration intensive and power hungry. Therefore, to be used at remote distances and as an unattended system, simplification of the current ARSA is essential.

A triple-layer phoswich detector has been developed at Oregon State University to collect separate beta and gamma energy spectra with minimal crosstalk. By utilizing a digital pulse processing scheme, the detector is also capable of recording coincidence events and therefore can be used to simplify the ARSA technology. The first two layers, CaF_2 and BC400, are chosen specifically for beta spectroscopy and the third layer, NaI, is intended for gamma-ray spectroscopy. The Monte Carlo n-particle (MCNP) code was used to simulate energy deposition in each layer from gamma-rays and monoenergetic electrons. In this paper, we discuss the MCNP analysis and preliminary experimental results, in which digital signal processing techniques are employed.

OBJECTIVE

The ARSA has been developed at the Pacific Northwest National Laboratory to measure the four radioxenons ^{131m}Xe, ^{133m}Xe, ^{133}Xe and ^{135}Xe released after a nuclear weapons test (Reeder and Bowyer, 1998). The ARSA system is intended to be employed in the International Monitoring System (IMS) as part of the Comprehensive Nuclear-Test-Ban Treaty. The ARSA system uses two separate channels for beta and gamma detection in a coincidence scheme to significantly reduce the natural background. The beta channel includes two photomultiplier tubes (PMTs) per gas cell, a total of 8 PMTs, for detecting beta absorption in cylindrical plastic scintillators. The gamma channel has four photomultiplier tubes for detecting any gamma deposition in two NaI(Tl) crystals. Although very sensitive, employing 12 photomultiplier tubes in one compact system requires a continuous and precise calibration. In addition to the calibration difficulties, the ARSA system needs a substantial source of power. To overcome these limitations, several efforts were initiated to investigate employing one single channel for both beta and gamma detection using phoswich detectors.

A phoswich detector developed by Ely et al., (2003) consisted of two scintillation layers, a CaF_2(Eu) layer (decay constant 940 ns) and a NaI(Tl) layer (decay constant 230 ns) intended for beta and gamma detection, respectively. The scintillation layers were optically coupled to a single PMT with an integrating preamplifier. Then rising pulses from the preamplifier were digitally captured and analyzed. Another phoswich detector design was introduced by Hennig et al., (2005). This phoswich design also had two layers, plastic scintillator BC-404 (decay constant 1.8 ns) and CsI(Tl) crystal (with two decay constants of 0.68 and 3.34 μs) optically coupled to a single PMT. The signal output from the PMT was directly connected to a digital pulse processor. Because radiation pulses are not integrated but are directly captured, the timing profile of pulses represents the timing profile of light produced in each scintillation layer.

By choosing a sufficient density thickness of CaF_2(Eu), 324 mg/cm^2, Ely's phoswich is designed to stop nearly the highest beta particle energies from radioxenon decay (905 keV from ^{135}Xe). This enhances the beta spectroscopy capability, but increases the Compton scattering probability and introduces some degree of crosstalk from the incident gamma rays in that layer. On the other hand, to reduce the probability of interaction of the incident gamma rays with the plastic scintillator in the design of Hennig et al., (2005) the density thickness is reduced to 103 mg/cm^2, stopping 362 keV electrons.

In this paper, we introduce a triple-layer phoswich detector which is able to collect separate gamma and beta energy spectra simultaneously with minimal crosstalk. The MCNP code was used to predict the probability of possible pulse shapes from gamma and beta interactions with the detector layers. We also discuss the preliminary results in which the detector was exposed to pure beta (^{90}Sr/^{90}Y) and gamma (^{137}Cs) sources to examine the ability of the detector to separate beta-only and gamma-only pulses.

RESEARCH ACCOMPLISHED

Phoswich Detector Design

A triple-layer phoswich detector is designed for simultaneous gamma and beta spectroscopy. Having sufficient timing contrast and low Z elements, the first two layers, BC-400 and CaF_2(Eu), are chosen specifically for beta particle spectroscopy. The third layer, NaI(Tl), is intended for gamma-ray spectroscopy. The schematic arrangement of the detector and the physical properties of the scintillation materials are shown in Figure 1 and Table 1, respectively.

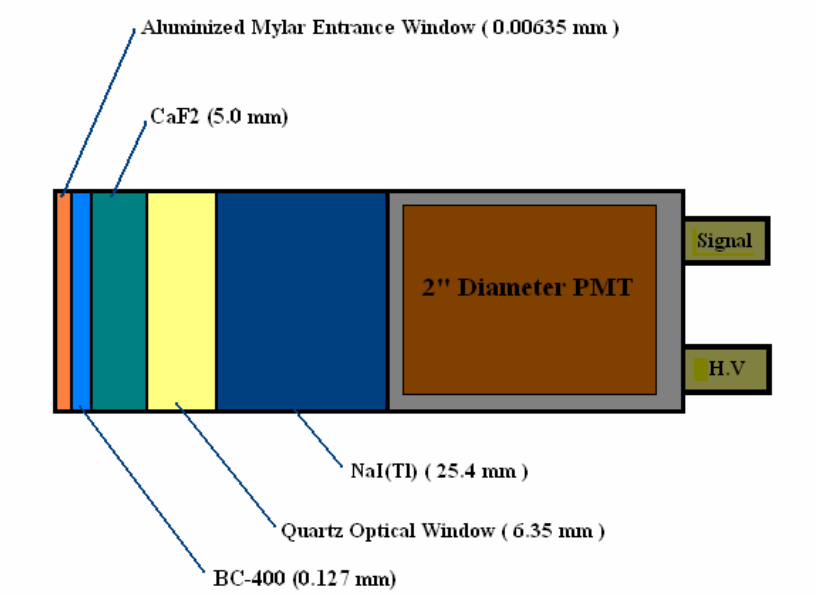


Figure 1. Schematic arrangement of the phoswich detector.

Table 1. Physical properties for scintillation materials used in the phoswich detector.

Scintillator	Density (g/cm^3)	Max. Emission Wavelength (nm)	Light Output (% of NaI)	Index of Refraction	Principle Decay Constant (ns)
BC-400	**1.032**	**423**	**26**	**1.58**	**2.4**
CaF_2:Eu	**3.19**	**435**	**50**	**1.47**	**900**
NaI:Tl	**3.67**	**415**	**100**	**1.85**	**230**

Since NaI(Tl) is a hygroscopic crystal, it is isolated from the other two components by a quartz optical layer. The density thickness of BC-400 and CaF_2(Eu) together are such that electrons with energies up to 3.2 MeV are stopped in these layers. As it will be shown in MCNP simulation of the detector, the light component from the fast scintillator, BC400, acts as a passive signature of the beta-induced pulses. If the incident electron has enough energy to penetrate into the slow scintillator, CaF_2(Eu), the two simultaneous light pulses form a double-component pulse at the photomultiplier output. Employing an appropriate digital pulse processing algorithm, this type of pulse can be separated from gamma-induced-pulses which are generated from interaction of gamma rays either in CaF_2(Eu) (mostly from Compton scattering) or in NaI(Tl). Since only very high energy electrons (6.7 MeV) can penetrate into the NaI(Tl) crystal, the light pulses (decay time 230 ns) generated in this layer represent only gamma ray interactions with no crosstalk from beta particle energy absorption.

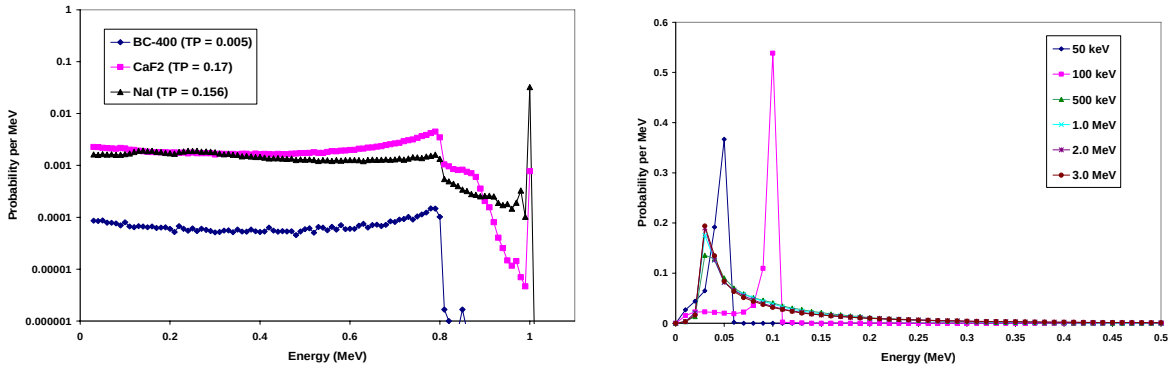
MCNP Simulation

The MCNP code was used to simulate energy deposition from gamma-rays and monoenergetic electrons in each layer of the detector. It should be noted that, for all probability calculations using MCNP, the energy threshold was assumed to be 10 keV so that events with energies less than this amount were excluded.

Figures 2(a) and 2(b) show two simulated energy deposition spectra from 1 MeV gamma rays in the three scintillation layers and from different monoenergetic electrons in BC-400, respectively. From Figure 2(a) as expected, Compton scatter is the prominent interaction from incident gamma rays in BC400 and CaF_2(Eu). The legend in Figure 2(a) also shows the total interaction probabilities (TP) from 1 MeV gamma rays in each layer.

Since the CaF_2(Eu) layer is thick enough to accommodate electrons up to 3.2 MeV, the unwanted events (mostly Compton scattering) in the beta-side of the detector (CaF_2 (Eu)) are comparable to that of the gamma-side, the NaI(Tl) layer. However, since common beta particles have much shorter mean free paths than gamma rays in scintillation materials, events in the first layer can be used to identify the beta-induced pulses from beta interactions with CaF_2 (Eu), and so the Compton events can be distinguished quite easily. Figure 2(b) shows how the fast light component (2.4 nsec) from the first layer behaves when the layer is exposed to different monoenergetic electrons. With increasing energy of electrons above 100 keV, the most significant component of the spectra shifts towards lower energies. In terms of anode pulse shape, this means that electrons with energies higher than a threshold most likely add a small amount of fast decay component to the generated signal pulse.

By combining three timing components corresponding to the decay constants of three scintillation layers and depending on how a given incident beta or gamma ray releases its energy within each layer, seven possible interaction scenarios for either beta or gamma interactions could occur (Farsoni and Hamby, 2005). Corresponding to these scenarios, seven possible pulse shapes can be generated. The occurrence probabilities for seven possible gamma- and beta-induced pulse types, calculated using the MCNP code, are given in Table 2. These results provide the criteria for acceptance of a pulse as a beta only, gamma only or beta/gamma coincidence pulse.



(a) (b)

Figure 2. Simulated energy spectra from (a) 1.0 MeV gamma rays in three layers and (b) different monoenergic electrons in BC-400.

Table 2. Pulse acceptance/rejection criteria calculated using MCNP simulation. *Total probabilities are calculated for 1.0 MeV photon/electron events. Events with energies less than 10 keV were excluded as electronic noise.

Scenario	Scintillation Layers			Total Probability (%)*		Pulse Recorded as:
	BC-400	CaF2	NaI:Tl	Gamma	Beta	
1	×			0.35	**12.30**	**Beta Only**
2	×	×		0.07	**81.70**	
3		×		14.40	4.60	Rejected
4	×		×	0.06	0.08	**B/G Coincidence**
5		×	×	2.65	0.03	Rejected
6	×	×	×	0.01	0.57	**B/G Coincidence**
7			×	**12.87**	0.00	**Gamma Only**

For example, if a pulse is observed with only the fast component (pulse type 1) or both fast and slow components (pulse type 2, Figure 3(a)), the probability that the pulse is gamma-induced is 0.35% or 0.07%, respectively, whereas the probability for a beta particle with the same energy producing the same pulse type is 12.30% or 81.70%, respectively. Therefore, these types of pulses update the corresponding beta particle energy histogram. However, if a pulse is observed as having only a decaying component corresponding to the energy deposition in the NaI(Tl) (pulse type 7, Figure 3(b)), the probability that the pulse is from a 1 MeV gamma ray or beta particle is 12.87% or 0.00%, respectively. This type of pulse, therefore updates the corresponding gamma-ray energy histogram. When the radionuclide emits both beta and gamma rays, gamma/beta coincident pulses can be detected from pulse types 4 and 6. Since there is no useful information in pulse types 3 and 5, these pulses are not recorded.

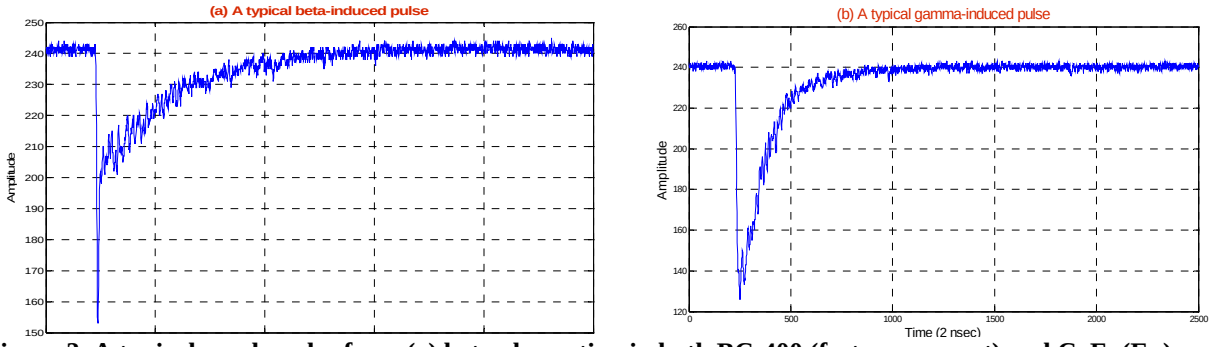


Figure 3. A typical anode pulse from (a) beta absorption in both BC-400 (fast component) and CaF_2 (Eu) (slow component), and (b) gamma absorption in NaI(Tl).

Development of an Algorithm for Gamma/Beta Separation

Based on the MCNP simulation results, an off-line algorithm is developed to digitally process the anode pulses and collect separate beta and gamma energy spectra. To develop the algorithm at this phase of our study, pulse types 1, 2 and 7 (beta- and gamma-only events) are detected but pulse types 4 and 6 (beta/gamma coincidence events) are not considered.

For each pulse, four sums, Base, A, B and C, are calculated (Figure 4). For the baseline determination, the average of Base is used. A simplified flowchart of the algorithm is shown in Figure 6. After loading the waveform and the baseline correction, using the peak of waveform and the average of sum B, the fast ratio (FR) of the pulse is measured. The FR quantity indicates the presence of a fast component in the pulse. Then FR is compared with a threshold value, FR_th. If the pulse passes the inspection, the pulse is considered to be a beta-induced candidate pulse, otherwise it is processed as a gamma-induced pulse candidate. Figure 5 shows the measured FR distribution from two pure beta emitters, $^{90}Sr/^{90}Y$ and ^{36}Cl, and two gamma sources, ^{137}Cs and ^{60}Co. For the preliminary experiments, FR_th was chosen to be around 0.35.

To be accepted as a beta- or gamma-induced pulse, the pulse should pass another inspection, the fall time measurement. In the beta case, the fall time measurement is done only on the slow part of the pulse and then the result is compared with a fall time threshold. If the result is positive, using sums A and C, the corresponding beta energy deposition in BC-400 and CaF_2(Eu) is calculated and the beta energy histogram is updated. In the gamma case, if the fall time is within a fall time window, using sum C, the corresponding gamma energy deposition in NaI(Tl) is calculated and the gamma energy histogram is updated.

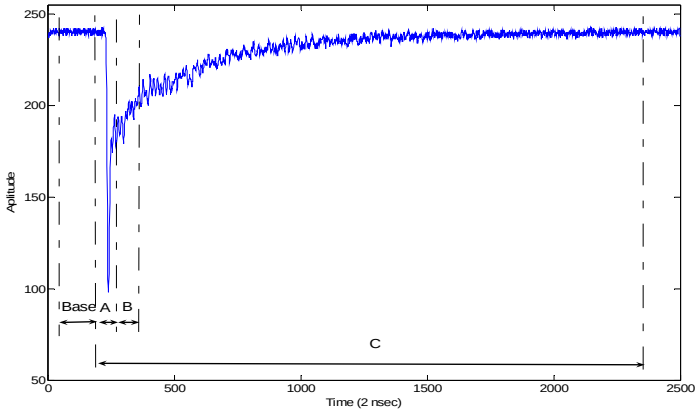


Figure 4. Four sum regions—Base, A, B and C—used to analyze the anode pulses.

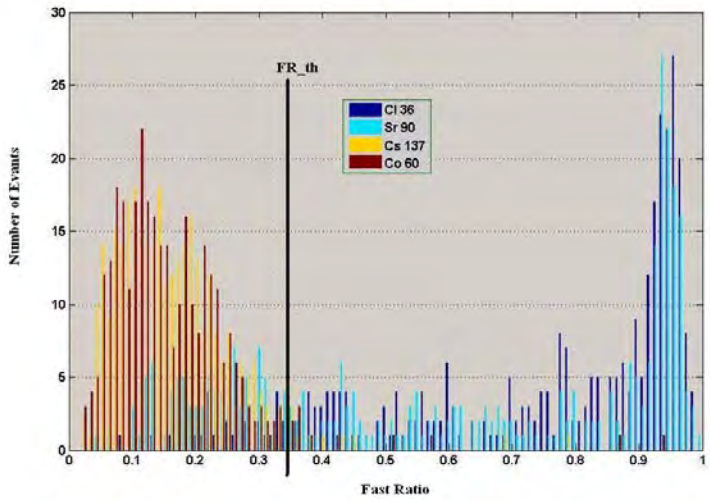


Figure 5. FR distribution from four beta and gamma sources. Detector was shielded against beta/conversion electrons when exposed to gamma sources.

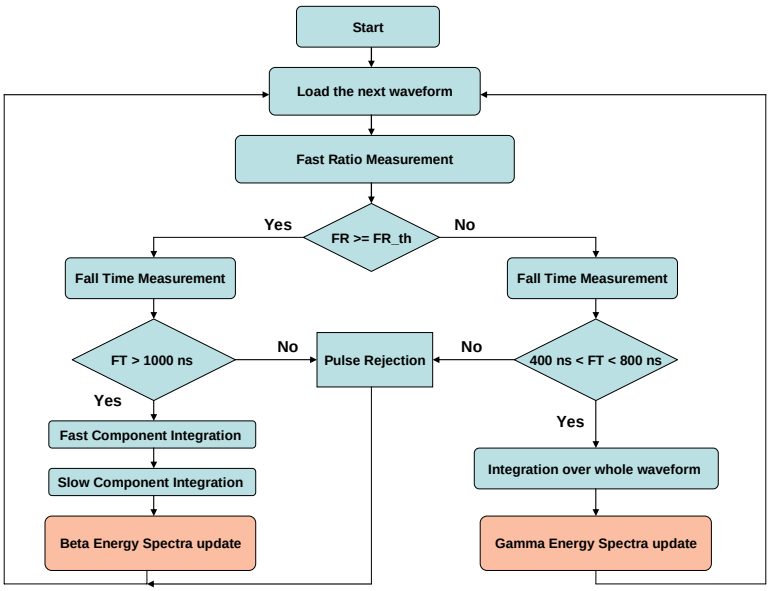


Figure 6. The algorithm developed to collect separate gamma and beta energy spectra.

Simultaneous Beta/Gamma Spectroscopy

Using a digital oscilloscope with 500 MSPS sampling rate and 8-bit resolution, anode pulses were captured directly and then transferred to the PC through the serial (RS-232) port. To evaluate how the algorithm separates gamma and beta events, the phoswich detector was exposed on separate occasions to $^{90}Sr/^{90}Y$, ^{14}C and ^{137}Cs sources. Beta particles and conversion electrons from ^{137}Cs were blocked using an appropriate shield during counting. Results are shown in Figure 7.

Three scintillation layers with relatively high light output differences (in Table 1, max light output ratio is 100/26) in a single light channel expands the dynamic range of the anode output. Therefore, for a higher degree of precise digital measurements, employing an analog-to-digital converter (ADC) with lower quantization errors is necessary. We believe that the relatively high fraction of accepted gamma and beta events, respectively from pure beta and gamma sources, results from over-or-under estimation of either the FR or fall time measurements.

The high difference in the percentage of rejected gamma events in Figures 7(a) and 7(b) can be explained using the MCNP analysis presented in Figure 2(b). On average, beta particles from $^{90}Sr/^{90}Y$ deposit less energy than that of ^{14}C in the BC-400 layer. This produces relatively smaller fast components in the induced pulses from $^{90}Sr/^{90}Y$ and subsequently causes the Fast Ratio algorithm to misclassify some of them as a gamma candidate pulse. Eventually, the misclassified pulses are rejected in the fall time inspection. These fractions, however, can be significantly modified using a digital data acquisition system with higher resolution, i.e., 12 bits. The rejected gamma events from the gamma source, 10.7%, are believed to be mostly from Compton scatter in $CaF_2(Eu)$.

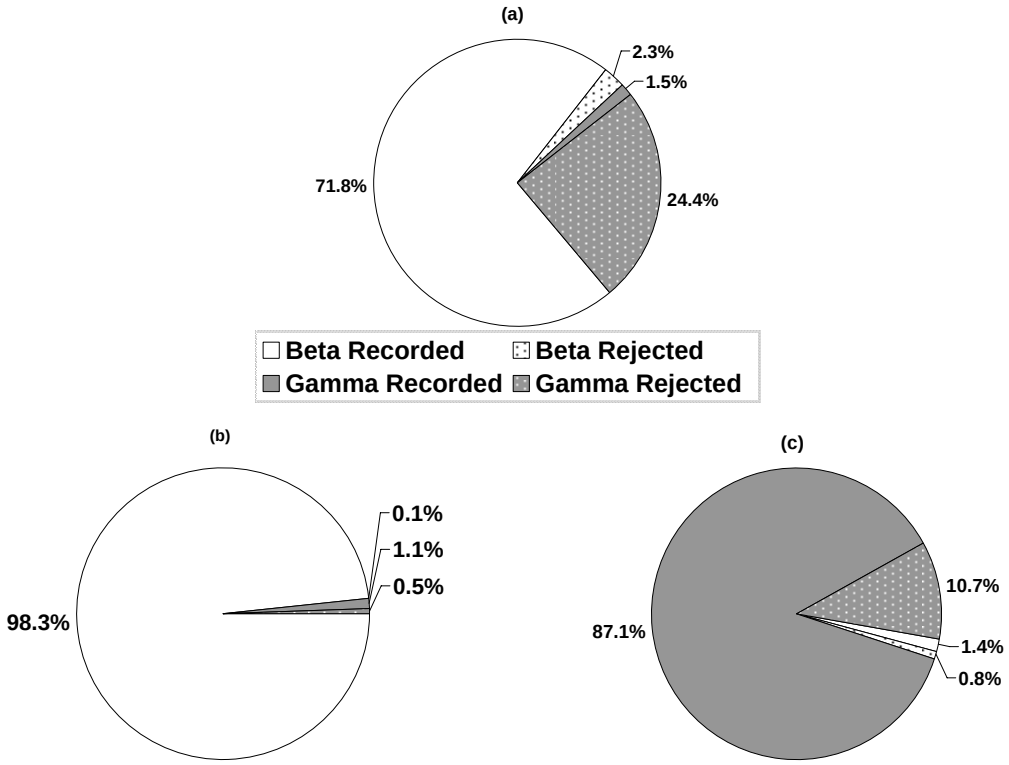


Figure 7. Percentage of events when the detector was exposed separately to (a) pure beta $^{90}Sr/^{90}Y$, (b) ^{14}C, and (c) shielded gamma (^{137}Cs) sources.

Figure 8 shows the separated beta and gamma spectra when the phoswich detector is exposed to both $^{90}Sr/^{90}Y$ and ^{137}Cs sources simultaneously. Again beta particles and conversion electrons from ^{137}Cs were blocked during spectroscopy.

The beta and gamma energy absorption spectra in Figure 8 possess details as expected. For example, in the gamma spectrum, the photopeak has a nearly symmetric shape (FWHM ~ 8%) and the Compton continuum and Compton edge are prominent. The shape of the beta spectrum is similar to that expected from $^{90}Sr/^{90}Y$ in that two components can be seen. Some energy degradation is apparent and could result from energy absorption in air and the Mylar layer, energy absorption in the gap between the BC-400 and $CaF_2(Eu)$ scintillators, and incomplete beta particle absorption and backscattering in the material interfaces.

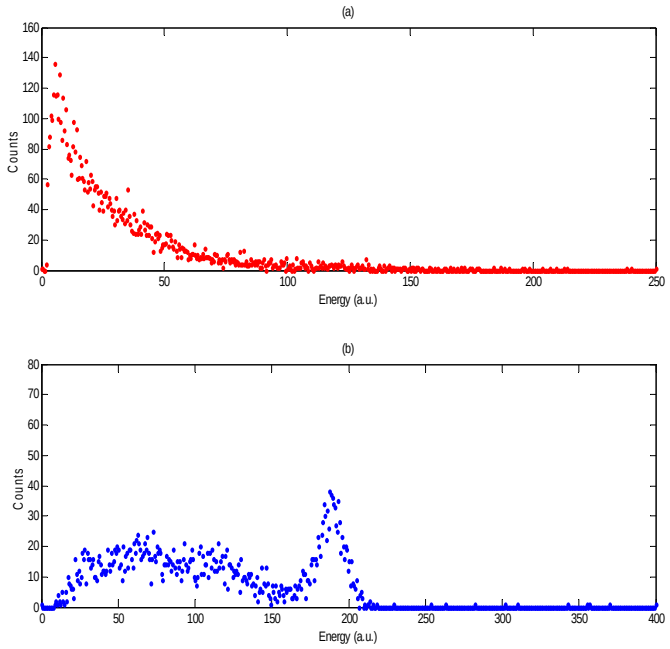


Figure 8. Simultaneous beta (a) and gamma (b) energy spectra digitally collected and processed from 15,000 anode pulses when the detector was exposed to both $^{90}Sr/^{90}Y$ and ^{137}Cs sources.

CONCLUSION

A triple-layer phoswich detector for simultaneous beta and gamma ray spectroscopy was simulated and built. Based on the criteria extracted from the MCNP analysis, an algorithm was developed to separate beta- and gamma-induced pulses in the BC-400/CaF_2(Eu) and NaI(Tl), respectively. A fast digital oscilloscope was used to capture and transfer anode pulses to the PC. The preliminary experimental results proved the overall concept of the detector design as a general purpose beta/gamma detector. The second phase of this research includes optimizing the phoswich detector for radioxenon detection and employing a customized digital pulse processor with 100 MSPS and 12-bit resolution to apply the detector capabilities for radioxenon beta/gamma coincidence.

ACKNOWLEDGEMENTS

We would like to thank the United States Department of Energy, Nuclear Engineering Education Research and the National Nuclear Security Administration, for sponsorship of portions of this work.

REFERENCES

Reeder, P. L., T. W. Bowyer, and R. W. Perkins (1998). Applications of nuclear techniques to non-proliferation treaties and weapons detection—Beta-gamma counting system for Xe fission products, *J. Radioanal. Nucl. Chem.* 235: 89–94.

Ely, J. H., C. E. Aalseth, J. C. Hayes, T. R. Heimbigner, J. I. McIntyre, H. S. Miley, M. E. Panisko, and M. Ripplinger, (2003). Novel beta-gamma coincidence measurements using phoswich detectors, in *Proceedings of the 25th Seismic Research Review–Nuclear Explosion Monitoring: Building the Knowledge Base*, LA-UR-03-6029, Vol. 2, pp. 533–541.

Hennig, W., H. Tan, W. K. Warburton, and J. I. McIntyre (2005). Digital pulse shape analysis with phoswich detectors to simplify coincidence measurements of radioactive xenon, in *Proceedings of the 27th Seismic Research Review–Nuclear Explosion Monitoring Technologies*, LA-UR-05-6407, Vol. 2, pp. 787–794.

Farsoni, A. T. and D. M. Hamby (2005). MCNP analysis of a multilayer phoswich detector for beta-particle dosimetry and spectroscopy, *Nucl. Instrum. Methods Phys. Res., Sect. A*. 555: 553–559

APPLICATION OF ARTIFICIAL NEURAL NETWORK MODELING TO THE ANALYSIS OF THE AUTOMATED RADIOXENON SAMPLER-ANALYZER STATE OF HEALTH SENSORS

James C. Hayes, Pamela G. Doctor, Tom R. Heimbigner, Charles W. Hubbard, Lars J. Kangas, Paul E. Keller, Justin I. McIntyre, Brian T. Schrom, and Reynold Suarez

Pacific Northwest National Laboratory

Sponsored by National Nuclear Security Administration
Office of Nonproliferation Research and Development
Office of Defense Nuclear Nonproliferation

Contract No. DE-AC05-RLO1830

ABSTRACT

The Automated Radioxenon Analyzer/Sampler (ARSA) is a complex gas collection and analysis system operating autonomously under computer control. The instruments are part of a network of sensors, some located in remote areas that feed concentration data to a central data center. Because the ARSA instrument is complex, it requires constant monitoring to verify that it is operating according to specifications. System performance monitoring is accomplished by over 200 internal sensors, some of which also send their readings to the data center. Several of those sensors are designated as safety sensors that can automatically shut down the ARSA when unsafe conditions arise, in which case the data center is advised of the shutdown and the cause, so that repairs may be initiated. However, the other sensors, called state of health (SOH) sensors, provide valuable information on the functioning of the ARSA and it would be desirable to detect impending malfunctions before they occur to avoid unscheduled shutdowns. Any of the sensor readings can be displayed by the ARSA Data Viewer, but the interpretation of the data requires specialized technical knowledge that is not routinely available at the data center. Therefore, it would be advantageous to have the sensors automatically monitored and evaluated for the precursors of malfunctions and the results transmitted to the data center. With more automated analysis, the operation of the data center would not require as much detailed technical expertise. Artificial Neural Networks (ANN) are data analysis methods that have shown wide application to monitoring systems with large numbers of information inputs, such as the ARSA. Structured and unstructured ANN methods were applied to ARSA SOH data recording during normal operation of the instrument.

OBJECTIVES

The objectives of the study are first to select and evaluate data analysis methods that are capable of automated real-time monitoring and analysis of the output of the SOH sensors to provide early warning of a potential malfunction before the system is forced to shut down. Second, benefits of this research would mean the ARSA could be operated by less technically trained personnel. The third objective was to develop an automated method to identify the fewest number of sensors that contain the most information for determining the state of health of the ARSA instrument.

The ARSA is a complex gas collection and analysis system operating autonomously under computer control (Hayes et al., 1999; Heimbigner et al., 2002). There are in excess of 80 digital outputs used to control valves, apply power to various pumps and compressors, reset various components, and shuttle calibration sources in and out of the system's nuclear detector. The 10 analog output signals are used to adjust three mass flow controllers as well as control the system's seven heaters.

The ARSA requires constant online monitoring of system operations and overall system health (Heimbigner et al., 2004**).** The software control system records and monitors over 200 different system sensors (temperature, pressures, voltages, etc.). Approximately 20 digital input signals are used to monitor source transfer and safety related sensors, such as heater over-temperature signals. A real-time record of the system state allows the system to monitor for unsafe conditions and maintain a safe state regardless of external or internal failures (e.g., vacuum pump, valve, or power failures and runaway temperatures). If the readings from safety-related sensors deviate from safe levels, the system shuts down in an orderly fashion, and a message is sent to the data center describing the cause of the shutdown, which initiates repair activities.

Figure 1 shows the capability of the ARSA system data viewer to display the values of multiple sensors simultaneously. When viewing SOH data, the user can select any combination of analog and digital sensors for simultaneous display. This capability allows a user who is familiar with the operations of the ARSA to evaluate the health of the system. With the inherent zoom capability, the user can examine specific regions of the data in more detail. Another function of real-time monitoring allows the user to troubleshoot the system when a problem arises should a minor sensor or a major system failure occur.

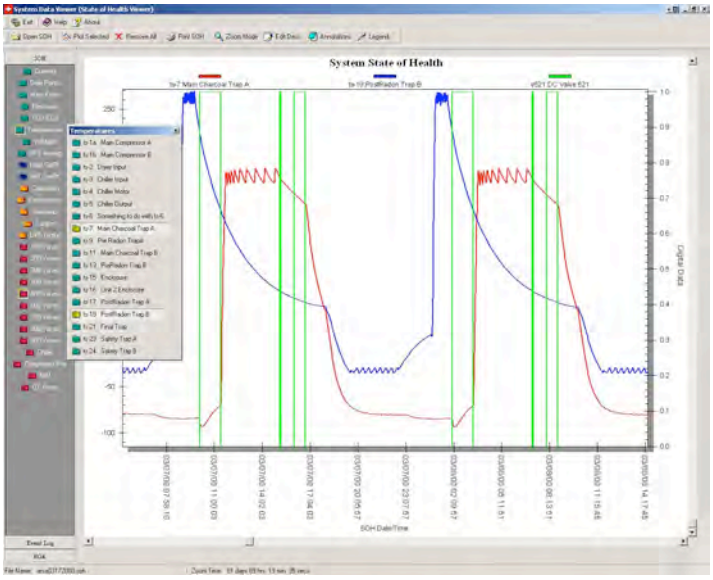


Figure 1. Three of the 46 ARSA analog SOH traces as seen in the ARSA data viewer.

In Figure 1, the behavior of the three sensors represents normal operations. The figure shows that sensor behavior repeats from one cycle to the next with some sensors more consistent than others. These cycles vary at 8-, 16-, and 32-hour intervals for different subsystems (and sensor behavior). Due to the complexity of the plots, as in this example, only three sensor outputs can be represented clearly, so it is difficult to monitor a large number of sensors simultaneously. It would be advantageous to have software algorithms that could continuously monitor the sensors simultaneously to identify subtle changes in multiple sensors that can be indicative of impending malfunctions but are difficult to see by viewing the behavior of one or a few sensors. When detected, the system could send a message to the data center describing the impending malfunction and request service before the system is shut down. The added advantage of an automated SOH monitoring system is that there would be less need to rely on trained personnel to monitor the ARSA operations.

In addition, the data transmission infrastructure restricts the throughput of SOH sensors readings to the data center on a continuous basis. Currently, the data transmission limit is six SOH sensors that can be sent to the data center. Therefore, it would be desirable to have an analytical method to determine which of the sensors provides the most information for predicting failures and transmit only those data to the data center.

RESEARCH ACCOMPLISHED

In this study, we used the feed-forward ANN as an Auto-Associative (AA) ANN to model the relationship between the ARSA sensor values by reducing the values to principal components (PCs) and then expanded the same components to predict sensor values. ANNs are a class of analytical techniques that can potentially address our objectives and will be the focus of this report. The ability of the ANN methodology to address the three objectives was evaluated by using several ANN modeling approaches. The data used in the evaluation of ANN methodologies consisted of sensor readings taken every two minutes from 51 SOH sensors over a three-week period in 2001. Each two-minute reading had a date/time stamp. During this period the ARSA instrument was considered to be operating normally.

Supervised Artificial Neural Networks

ANN modeling is an equation-free, data-driven modeling technique that tries to emulate the learning process in the human brain by using many examples. It is an information processing paradigm that is different from conventional computer programs in that it learns by example rather than by following instructions. It is thus a data-driven methodology that learns to model a system from historical data.

An ANN consists of simple mathematical “neurons” connected by weights. Figure 2 shows the structure of a simple ANN, in this case a feed-forward ANN composed of a set of highly interconnected neurons or nodes, and these neurons work in parallel to solve a complex problem. One input layer, zero or more hidden layers, and one output layer make up the architecture. Each layer contains nodes (circles in the figure), and the nodes in each layer are fully or partially connected to the nearest layers above or below by the lines. A weight is associated with each connecting line. The nodes in the input layer receive the input vectors, and nodes in the output layer produce the output vectors in response to the input vectors. The layers are connected through the weighted connections. Nodes in hidden layers and the output layer perform two calculations: they sum the products of connection weights and the signals from the previous layer, and pass that sum through a transfer function—often a sigmoid function.

A supervised ANN model is trained from known, labeled examples. The network learns a mapping from one vector space to another and is often employed in classification or regression (prediction) problems. Examples of inputs and outputs are presented to the ANN, and the values of the weights between the “neurons” in the hidden layer in the figure are estimated during the training of the ANN by “back-propagation” of the errors between the ANN outputs and the known data output (Werbos, 1974, 1994; Rumelhart et al. 1986). Once the ANN is trained and verified by presenting examples not used in the training but used for validation, it is used to predict the model outputs from the new input examples presented to it.

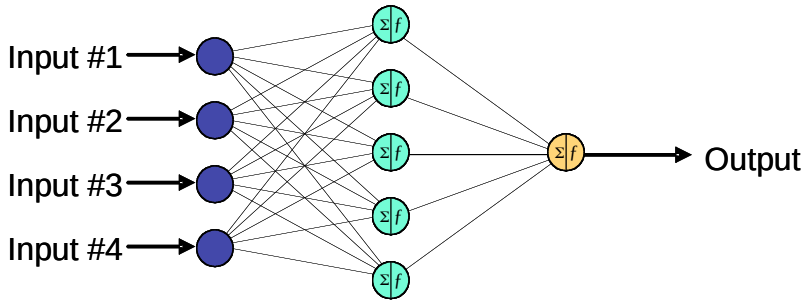


Figure 2. Diagram of a simple feed-forward ANN with a single hidden layer.

Auto-Associative Artificial Neural Networks

AA-ANNs are a special form of ANN models. They are trained to reproduce the input data as an identical vector at the output. To efficiently perform this task, they learn the interrelationships among the input variables. When trained successfully, a small number of "hidden neurons" is sufficient to recreate the input values as the output of the AA-ANN model. Also, through the same mechanism, they have some capability to reproduce data from incomplete data, i.e., to "fill in" missing variables.

Principal Component Analysis Artificial Neural Networks

An AA-ANN can be used to develop an ANN that performs a data reduction similar to that of PC analysis (PCA). When the AA-ANN is used in this manner, it is often called a PCA-ANN. The data are compressed to a few dimensions, and the subsequent prediction of the original values is only successful if the ANN learns the relationship among the values. Thus, the network learns to efficiently represent the sensor values in PCs. The ANN used in the study was not enforced with certain restrictions that would produce "true" PCs, although they are similar. See Karhunen et al., 1995 and 1997 for discussions on using ANNs for PCA.

A PCA-ANN is trained as one network but should conceptually be considered two networks. Once the AA-ANN is trained to reproduce the inputs on the outputs, the ANN is broken apart. The first network compresses the data vectors into PCs, the other expands the PCs to a vector with the original number of dimensions that is a reconstruction of the vector from its PCs. The part that connects the input to the bottleneck layer forms an ANN that maps the input sensor values to a reduced representation analogous to PCs. It also can be considered an encoder network that takes many inputs and compresses them into a few encoded components. The encoded components can then be decoded with the second half of the AA-ANN. This is illustrated in Figure 3. If the PCA-ANN is separated into two networks, as it is when it is used, a single hidden layer network will become two networks with one input layer and one output layer each. A three-hidden-layer PCA-ANN will separate into two networks with one hidden layer each. This type of network (a feed-forward network) requires at least one hidden layer to perform nonlinear mapping from input to output space. Thus, the single hidden layer PCA-ANN is limited to linear PCA, but the three-hidden-layer PCA-ANN performs nonlinear PCA, which captures the nonlinear relationships between the dimensions of the data. We chose to call the common mathematical definition of PCA a "linear" PCA to separate it from the other type, often called nonlinear PCA in the literature.

The PCA-ANN has two or more possible applications for ARSA. First, it allows the data to be compressed into fewer dimensions, benefiting both transmission and storage. Second, the PCA-ANN models the relationship between the different sensors where they exist. As such it can be used to detect when the sensor relationships deviate from the modeled values in sensor validation. In general, the PCA-ANN also functions as an anomaly detector if it is evident that several sensor values differ from those modeled. This latter use can be advanced to different levels of model based reasoning for diagnostics to determine causal origins to anomalies.

Nonlinear PCA Application to ARSA Data

A nonlinear PC neural network model was applied to the ARSA data. In this approach, three hidden layers are used in the AA training so that the final PCA-ANN has an input layer, a hidden layer, and an output layer to fully represent any nonlinear relationships in the data.

Figure 4 shows root-mean-square errors (RMSEs) for different numbers of PCs for two configurations of the PCA-ANN used in this study. One had a single hidden layer corresponding to PCs; the other had three hidden layers, with the middle layer corresponding to the PCs. The figure shows that the prediction error for a set of 46 ARSA sensors decreases as the data set is reduced to an increasing number of PCs, as expected. It also shows that the three-hidden-layer PCA-ANN performs significantly better than a single-hidden-layer PCA-ANN. The better PCA-ANN reduces the 46-sensor set to the PCs in two steps and also expands the PCs back to predicted sensor values in two steps; therefore, it captures more of the relations among the sensors. The one-hidden-layer PCA-ANN uses one step each to compress and expand the data vectors.

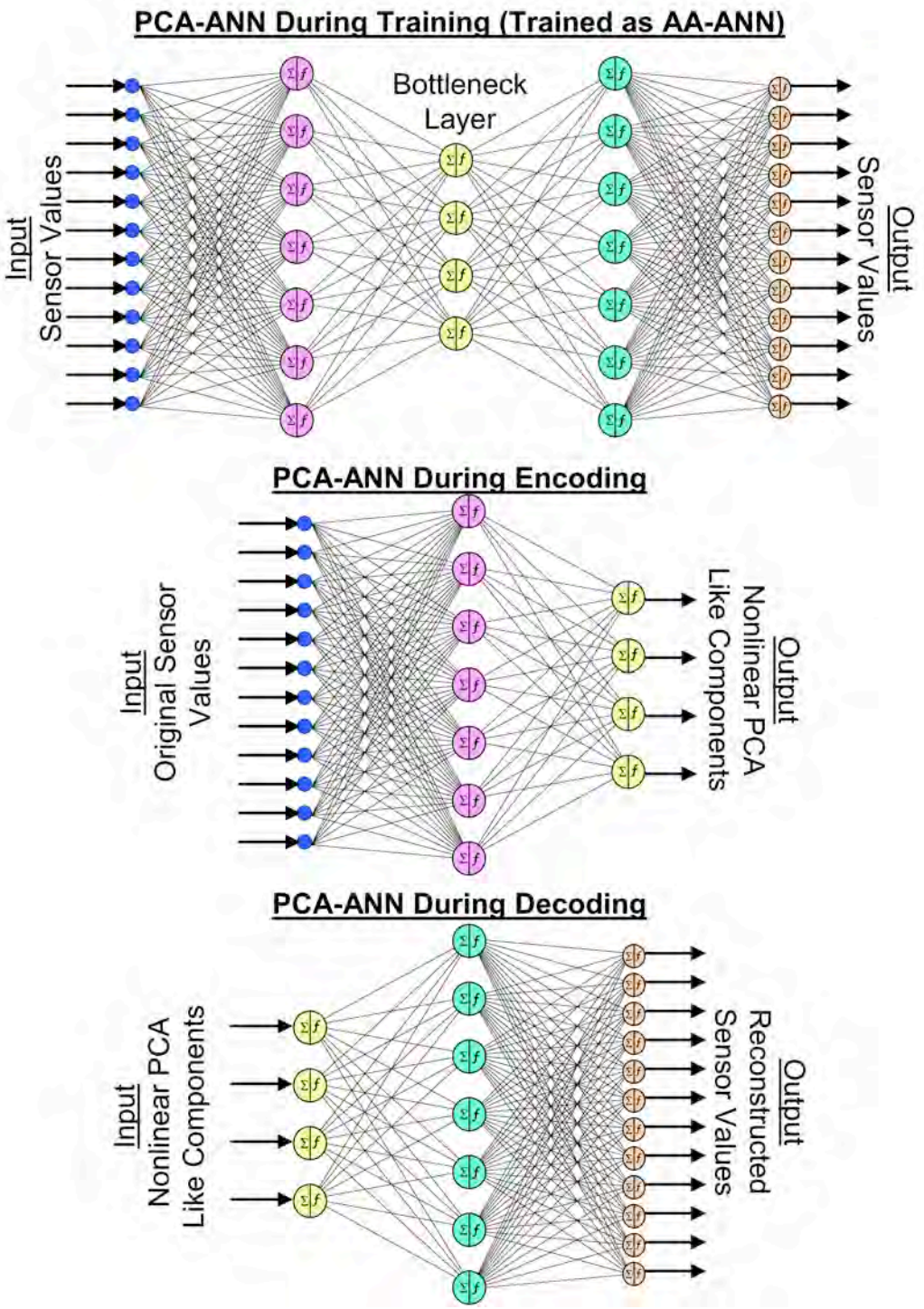


Figure 3. Top—illustration of a PCA-ANN configuration as it is trained to reproduce the input at the output (i.e., AA-ANN); middle—illustration of a PCA-ANN that encodes input sensor values to a set of nonlinear PCA-like components at the bottleneck layer; bottom—illustration of a PCA-ANN that decodes nonlinear PCA-like components and reconstructs the original sensor values.

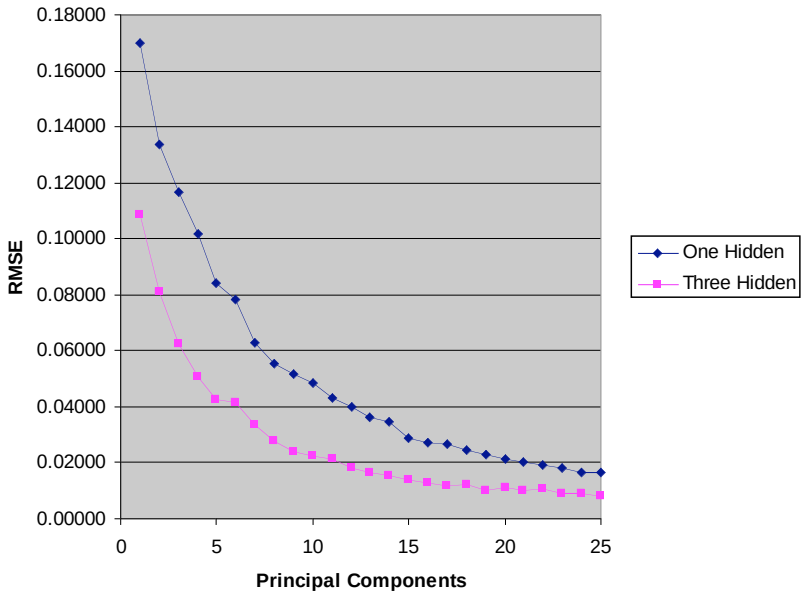


Figure 4. Two configurations of PCA-ANN to compress a set of 46 ARSA sensors to PCs. One ANN has a single hidden layer; the other has three hidden layers for more efficient data compression.

Figure 5 illustrates the ability of a nonlinear PCA-ANN to reproduce the sensor values at the output. The actual values of two cycles of the ps-5 sensor are shown with the decoded sensor values from the nonlinear PCA-ANN. The plots were staggered and offset to facilitate the comparison of the fine detail.

The prediction errors for a PCA-ANN, i.e., how well the network reproduces the data after it has been represented in a few PCs, was calculated for 46 ARSA sensors with six PCs. The errors were calculated for the set from approximately 1,700 test samples. In this case, 14,800 samples were used in developing the PCA-ANN. The mean error for all sensors as a percentage of their individual ranges is 3.8%.

As discussed above, deviations between actual and predicted individual sensors or groups of sensors can be incorporated in sensor validation and model based diagnostics. Most sensors in this study were modeled with high accuracy, such as the pressure sensor shown in Figure 5, making these models attractive in a health monitoring system for ARSA.

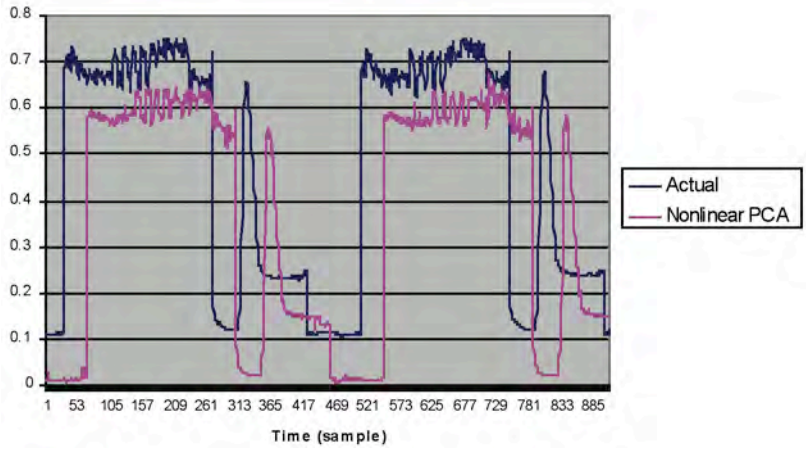


Figure 5. Actual values for sensor ps-5 and those decoded from the 46-60-6-60-46 five-layer PCA-ANN (the two traces are staggered for clarity).

CONCLUSION(S) AND RECOMMENDATIONS

The PCA–ANN successfully compressed the information from over 40 ARSA sensors into 6 nonlinear PCs that were then expanded into reasonable estimates of the original sensor data values with high accuracy. This research indicates that it would be possible to compress all of the ARSA SOH data into as few as six PCs that can then be sent to the data center where an accurate representation of the SOH data can be viewed. Current methodology relies on trained analysts to determine the six best sensors to be sent to the data center, losing most of the SOH information.

Monitoring systems with neural network algorithms can also be used to monitor the system real time for failures as they occur. Currently, most system failures are recognized days after the failure has occurred.

REFERENCES

Hayes, J. C., K. H. Abel, T. W. Bowyer, T. R. Heimbigner, M. E. Panisko, P. L. Reeder, J. I. McIntyre, R. C. Thompson, L. C. Todd, and R. A. Warner (1999). Operations of the Automated Radioxenon Sampler/Analyzer—ARSA, in *Proceedings of the 21st Seismic Research Symposium: Technologies for Monitoring the Comprehensive Nuclear-Test-Ban Treaty*, LA UR-99-4700, Vol. 2, pp. 249–260.

Heimbigner, T. R., J. I. McIntyre, T. W. Bowyer, J. C. Hayes, and M. E. Panisko (2002). Environmental monitoring of radioxenon in support of the radionuclide measurement system of the International Monitoring System, in *Proceedings of the 24th Seismic Research Review—Nuclear Explosion Monitoring: Innovation and Integration*, LA-UR-02-5048, Vol. 2, 694–700.

Heimbigner, T. R., T. W. Bowyer, J. C. Hayes, C. R. Hubbard, J. I. McIntyre, M. Panisko, M. Ripplinger, and R. Suarez (2004). State-of-health software for the Automated Radioxenon Sampler/Analyzer, in *Proceedings of the 26th Seismic Research Review: Trends in Nuclear Explosion Monitoring*, LA-UR-04-5801, Vol. 2, 710–718.

Karhunen, J. and J. Joutsensalo (1995). Generalizations of principal component analysis, optimization problems, and neural networks, *Neural Networks* 8: 549–562.

Karhunen, J., E. Oja, L. Wang, R. Vigaro, and J. Joutsensalo (1997). A class of neural networks for independent component analysis, *IEEE Trans. Neural Networks*, 8: 486–504.

Rumelhart, D. E., G. E. Hinton, and R. J. Williams (1986). *Learning Internal Representations by Error Propagation, Parallel Distributed Processing: Explorations in the Microstructures of Cognition*, Vol. 1, Foundations, D. D. Rumelhart and J. L. McClelland (Eds.). Cambridge, Massachusetts; MIT Press, pp. 318–362.

Werbos, P. J. (1974). Ph.D thesis, Harvard University, Cambridge, Massachusetts.

Werbos, P. J. (1994). *The Roots of Back-Propagation*. New York: John Wiley & Sons.

DESIGN OF A PHOSWICH WELL DETECTOR FOR RADIOXENON MONITORING

W. Hennig[1], H. Tan[1], A. Fallu-Labruyere[1], W. K. Warburton[1], J. I. McIntyre[2], A. Gleyzer[3]

XIA, LLC[1], Pacific Northwest National Laboratory[2], and PhotoPeak, Inc.[3]

Sponsored by National Nuclear Security Administration
Office of Nonproliferation Research and Development
Office of Defense Nuclear Nonproliferation

Contract No. DE-FG02-04ER84121[1,2,3]

ABSTRACT

The network of monitoring stations established through the Comprehensive Nuclear-Test-Ban Treaty includes systems to detect radioactive xenon released into the atmosphere from nuclear weapons testing. One such monitoring system is the Automated Radio-xenon Sampler/Analyzer (ARSA) developed at Pacific Northwest National Laboratory. For high sensitivity, the ARSA system currently uses a complex arrangement of separate beta and gamma detectors to detect beta-gamma coincidences from characteristic radioxenon isotopes in small samples of xenon extracted from large volumes of air. The coincidence measurement is very sensitive, but the large number of detectors and photomultiplier tubes requires careful calibration.

A simplified approach is to use a single phoswich detector, consisting of optically coupled plastic and CsI scintillators. In the phoswich detector, most beta particles are absorbed in the plastic scintillator and most gamma rays are absorbed in the CsI, and pulse shape analysis of the detector signal is used to detect coincidences. As only a single detector and electronics readout channel is used, the complexity of the system is greatly reduced. Previous studies with a planar detector have shown that the technique can clearly separate beta only, gamma only and coincidence events, does not degrade the energy resolution, and has an error rate for detecting coincidences of less than 0.1%.

In this paper, we will present the design of a phoswich well detector, consisting of a 1" diameter plastic cell enclosed in a 3" CsI crystal. Several variations of the well detector geometry have been studied using Monte Carlo modeling and evaluated for detection efficiency, effects on energy resolution, and ease of manufacturing. One prototype detector has been built and we will present here some preliminary experimental results characterizing the detector in terms of energy resolution and its ability to separate beta only, gamma only, and coincidence events.

OBJECTIVES

The network of monitoring stations established through the Comprehensive Nuclear-Test-Ban Treaty includes systems to detect radioactive xenon released into the atmosphere from nuclear weapons testing. One such monitoring system is the ARSA developed at Pacific Northwest National Laboratory (Reeder et al., 1998). The ARSA system consists of a pair of large NaI(Tl) scintillator crystals holding four cylindrical fast plastic scintillator (BC-404) cells which are optically isolated from the NaI(Tl). The cells are filled with the xenon gas to be counted, which decays by emitting gamma rays or X-rays in coincidence with beta particles or conversion electrons. The plastic scintillator is meant to absorb all beta particles and conversion electrons, while the longer range gamma rays and X-rays will mainly be absorbed in the NaI(Tl) scintillator. Each BC-404 cell and each NaI(Tl) crystal is coupled to a pair of photomultiplier tubes (PMTs) and is read out by independent electronic channels. The sensitivity for detecting xenon isotopes is greatly increased by requiring coincidence between the signals from the PMTs coupled to the NaI(Tl) and the signals from the PMTs coupled to the BC-404.

While obtaining high coincidence detection efficiency and resolutions of about 25% for characteristic 80keV gamma rays, the current ARSA system design is operationally complex. The principle of time based coincidence, while effective in suppressing the background, requires separate signals from the NaI(Tl) and the BC-404, i.e. separate PMTs and readout electronics. In particular, the 12 PMTs require careful gain matching and calibration, and as the PMT gains change with time, voltage and temperature, the system easily drifts out of calibration. A simplified approach is to use a single phoswich detector (Ely et al., 2003), in the most recent implementation consisting of optically coupled plastic and CsI(Tl) scintillators (Hennig et al., 2006). The plastic scintillator is meant to absorb all beta particles and conversion electrons, while the longer range gamma rays and X-rays are mainly absorbed in the CsI(Tl) scintillator. Beta-gamma coincidences are then detected using pulse shape analysis of the detector signal. As only a single detector and electronics readout channel is used, the complexity of the system is greatly reduced.

Previous studies with a small planar detector showed that the technique can clearly separate beta only, gamma only and coincidence events, does not degrade the energy resolution, and has an error rate for detecting coincidences of less than 0.1%. In this paper, we will present the design of a phoswich well detector, consisting of a 1" diameter plastic cell enclosed in a 3" CsI crystal.

RESEARCH ACCOMPLISHED

1. Geometry of Phoswich Well Detector

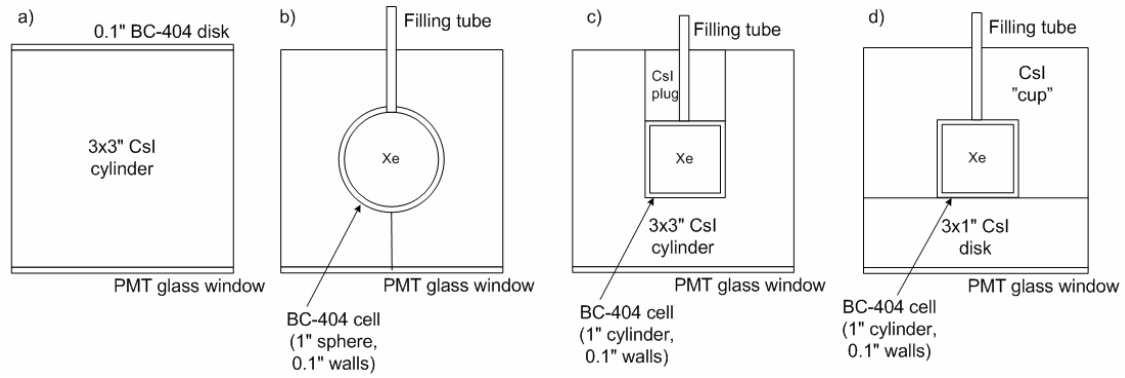


Figure 1. Geometries of detector designs studied. All outer surfaces have a diffuse reflective coating, all interfaces between CsI and BC-404 or CsI and CsI have optical couplant.

The geometry of the well detector has the following design constraints: i) to contain the volume of a typical radioxenon sample of 2-3 cm^3, the inner volume of the plastic cell should be 6-10 cm^3; ii) according to radiation transport simulations described in (Hennig, 2006), in order to stop all beta radiation but not absorb a significant amount of X-rays or gamma rays, the cell wall thickness should be 0.1”; iii) to absorb most of the X-rays and gamma rays, the cell must be surrounded by 1” of CsI on all sides. These constraints can be met with a variety of detector designs. The designs studied so far in detail are shown in Figure 1: a) a planar geometry, scaled up in size from the detector used in the previous work, b) a spherical cell with a vertical split, c) a cylindrical cell with a 1" plug, and d) a cylindrical cell with a horizontal split.

Figure 2 shows the results of Monte Carlo light collection simulations (using DETECT2000) for these geometries, assuming an index of refraction of 1.50 for the PMT glass window and the optical couplant, 1.58 for the BC-404 and 1.85 for the CsI. Variations in collection efficiency causes different amounts of light to be collected for gamma rays of the same incident energy interacting in different locations of the detector. Weighting the light collection efficiency data obtained in the simulation according to the volume each point represents (i.e. in first approximation, the probability of interaction), we obtain an estimate of the contribution of the crystal non-uniformity to the broadening of peaks in the energy spectrum. The probability distributions for each simulated detector are shown in Figure 3 and the peak resolutions range from 1.3% for geometry a) with a reflective constant of RC = 0.99 on the outer surface of the detector to double peaks with an overall ~6% width for geometry d) with RC = 0. 90, as listed in Table 1. This peak broadening due to light collection non-uniformity is only one contribution to the overall energy resolution of the detector, adding in quadrature to contributions from other effects such as photostatistics, crystal non-uniformities and energy non-linearities. In a good quality CsI detector, the overall energy resolution is typically ~17% for characteristic 80 keV gamma rays emitted from radioxenon. Therefore, as long as the changes in the light collection efficiency due to the embedded cell or the crystal geometry are minor, the energy resolution of the detector will not worsen significantly.

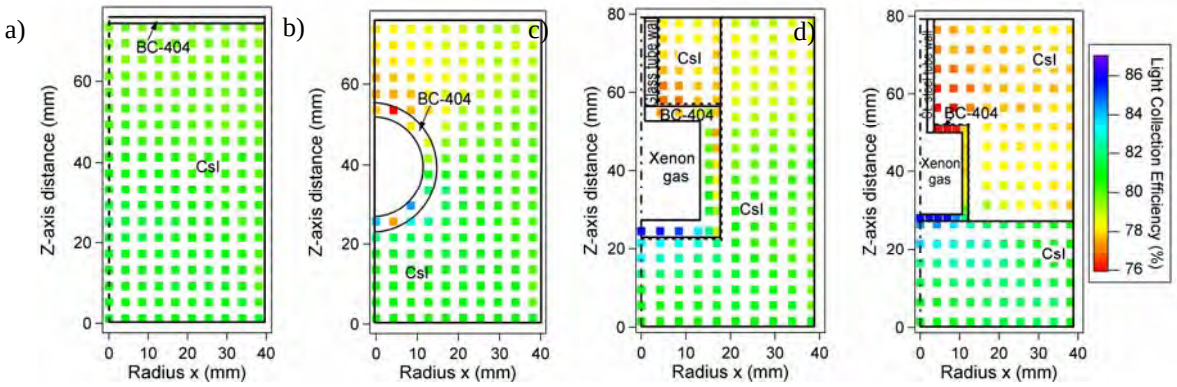


Figure 2. Geometric distribution of light collection efficiency for outer reflection coefficients = 0.95. By symmetry, only half of the crystal is simulated (from radius x=0 to 38mm).

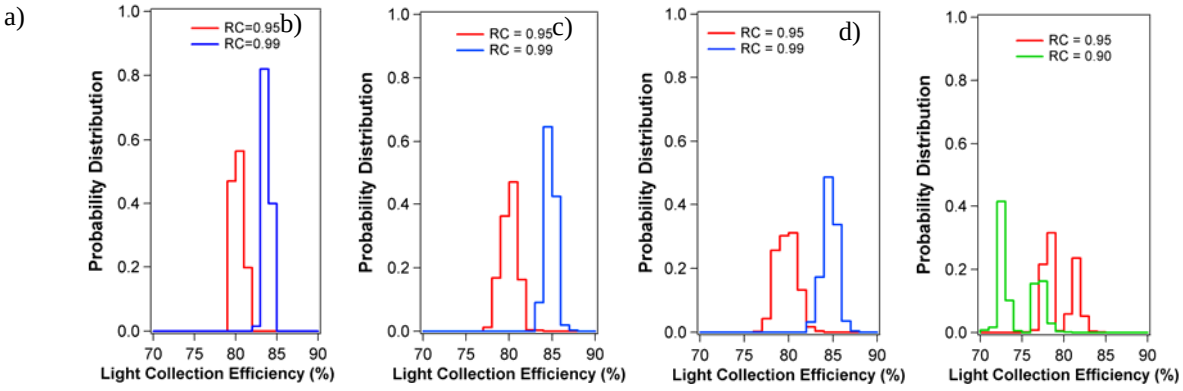


Figure 2. Volume-weighted distribution of light collection efficiency.

Table 1. Resolution due to non-uniformity of light collection for the detector geometries studied, with various values for the reflective constant RC on the outer surface of the detector

	Resolution (RC = 0.99)	Resolution (RC = 0.95)	Resolution (RC = 0.90)
Detector a)	1.3%	2.4%	--
Detector b)	1.8%	2.9%	--
Detector c)	2.3%	3.8%	--
Detector d)	--	~5%	~6%

The detection efficiency for beta-gamma coincidences in geometry a) is poor since a source in front of the detector will emit at least half of the beta particles and half of the gamma rays or X-rays away from the detector and thus at most 25% of coincidences will be detected. This geometry, used on a smaller scale in the previous work to study the principle of the phoswich detector and pulse shape analysis, here serves only as a comparison for the other geometries. In all geometries b) – d), the thickness of the plastic cell is the same and differences in cell geometry are minor which means that beta particles and conversion electrons have the same probability to be detected. The shape of the surrounding CsI varies somewhat in the different geometries. However, in each geometry there is at least 1″ of CsI in any direction of the plastic cell, absorbing 88 % of the highest energy gamma rays (~250 keV) and 99% or more for X-rays and gamma rays up to 164 keV. In some directions the radiation will have to travel through more CsI before escaping the detector and thus have a higher chance to be fully absorbed. For example, radiation emitted at the center of the detector towards the corner of the outer cylinder will travel through up to 1.41" of CsI in geometries c) and d), but 1.62" in geometry b). However, the increase in absorption efficiency is relatively small (e.g. to 95% for 1.5" of CsI for 250 keV), lower energy gamma rays are almost fully absorbed in 1″ already, and the variations between the geometries b) to d) are minor. Therefore, we can also assume the probability to absorb and detect X-rays and gamma rays to be essentially equal. Thus for geometries b) – d), the coincidence detection efficiency is the same as estimated in (Hennig, 2006); it is between 82% and 92% for the various radioxenon isotopes.

A further concern is ease of manufacturing. While geometry a) is a commonly used shape and easy to manufacture, geometries b) – d) require custom machining of the CsI; especially challenging for geometry b). In addition, during assembly of the well detector, it is important not to trap any air at the interfaces of the CsI and the plastic cell which will obstruct the light collection. For planar surfaces within the detector, such as the interface below the plastic cell in geometry c), trapping of air is in practice almost impossible to avoid.

Therefore, even though geometry d) has the highest non-uniformity of light collection, it was considered the easiest to manufacture and assemble, and was subsequently built as the first prototype of the well detector. Since for a given geometry, the two key parameters that increase uniformity of light collection are the outer reflectivity and the index of refraction of the optical couplant, care was taken during manufacturing to make them at least equal to 0.95 and 1.50, respectively. Experiments are under way to quantify the penalties associated with the less uniform light collection of design d) and additional geometries are being studied for future prototypes.

2. Measurements with Prototype Well Detector

The prototype detector (geometry d) was tested first with a weak ^{137}Cs needle source inserted into the detector through the filling tube, second with a stronger external ^{137}Cs source, and third with Xe gas sources at PNNL. The ^{222}Rn source was placed into a container connected to the filling tube and the ^{222}Rn gas gradually diffused into the detector. The PMT was read out with a DGF Pixie-4 (Hennig, 2005) that also calculated filter sums for further offline analysis as described previously (Hennig, 2006). In the analysis, pulses were categorized as 1) CsI only, 2) plastic only, and 3) combination pulses (see Figure 4) and their energy contributions in each part of the detector were calculated.

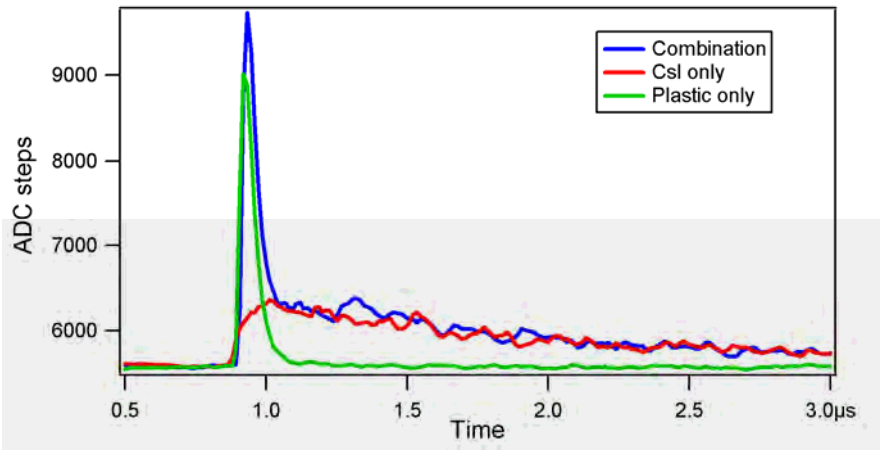


Figure 4. Pulse waveforms from the phoswich well detector.

In the small planar phoswich detector in the previous work, we measured a resolution of ~7% at 662 keV, a typical value for high quality CsI. For the well detector, using the external source, we measured between 11.5% and 12.8% resolution depending on the position of the source (see Figure 5). In addition, the peak position shifted by about 6.8% from the measurement with the source at the front to the measurement with the source at the back. The shift is expected from our light collection simulations, since the different source positions cause different parts of the detector to be irradiated, The measured value of 6.8%, though, is slightly higher than the 5-6% expected from the light collection simulations.

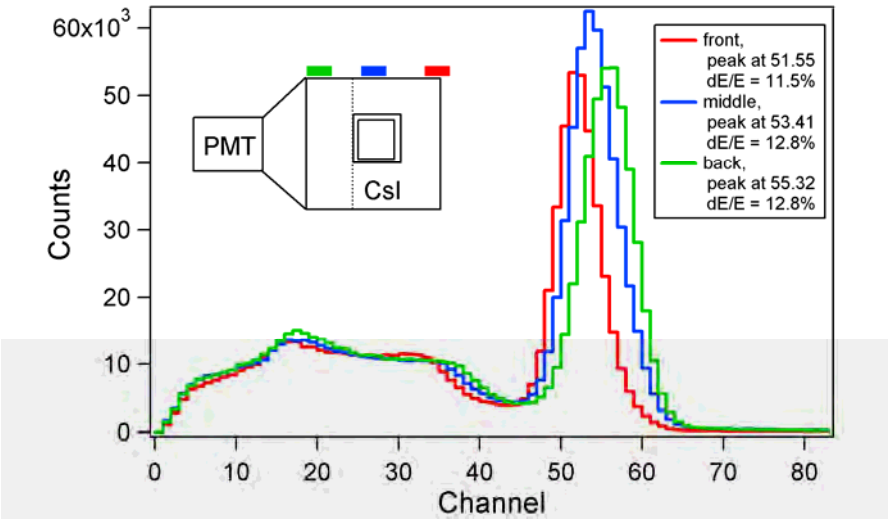


Figure 5. MCA spectra of ^{137}Cs source placed in various positions on the phoswich well detector. The output count rate was 12,000 – 14,000 cps.

With the ^{137}Cs needle source, the count rate is ~150 cps with lead shielding around the detector. The pulse shape analysis categorized ~53% of the events as CsI only, 41% as plastic only, and 2% as combination events. The resolution of the 662 keV peak for CsI only events is 12.8%. In the measurements with ^{137}Cs, there are no beta-gamma coincidences, but gamma rays are Compton scattered between CsI and the plastic scintillator, so the combination events form a line of constant energy in the scatter plot of energy deposited in the CsI vs energy deposited in the plastic (Figure 6).

To get a first estimate of the background rejection rate of the detector and pulse shape analysis (PSA) algorithms, we took a further measurement without sources. With the lead shield, the background rate is about 12 cps, of which 91.3% were categorized as CsI only, 0.4% as plastic only and 0.7% as combination events. The remaining ~7.7% of events could not be categorized. (Without lead shield, the background rate is ~127 cps.). Though some of the

combination events may come from contaminants inside the detector (e.g. the natural radon present in air) and thus be true beta-gamma coincidences, as a worst case estimate we assume all combination events to be false coincidences, for example external gamma rays interacting with both parts of the detector or events wrongly categorized by the PSA. Thus we obtain the upper limit of false beta-gamma coincidences to be 0.7%, which means the background rejection rate is at least 99.3%.

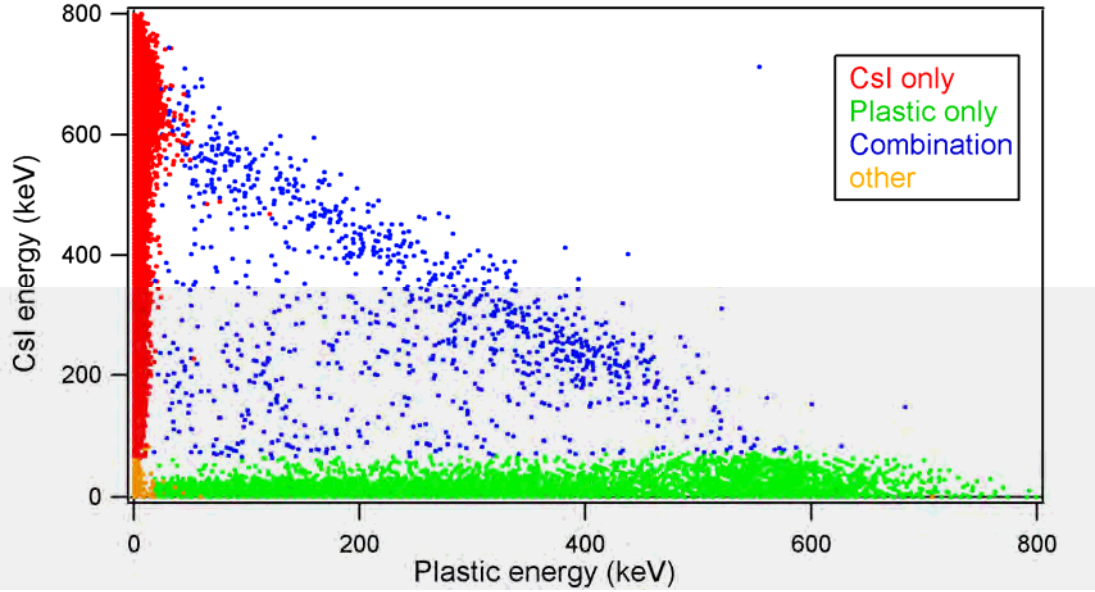


Figure 6. Two-dimensional energy scatter plot for ^{137}Cs. Note the diagonal line of constant total energy which is used for calibration of the plastic energy.

In the measurements with Xe sources at PNNL, the detector's filling tube was connected to a small pumping system. After background measurements, the cell was evacuated and filled with ^{131m}Xe. After several hours of data acquisition, the cell was evacuated again and flushed with air several times, later filled with ^{135}Xe for further measurements.

Fig. 7 shows a 2D energy scatter plot from measurements with ^{131m}Xe. Since ^{131m}Xe emits a conversion electron (with a fixed energy) in coincidence with an X-ray, the detector acquired a large number of combination events corresponding to beta-gamma coincidences. Most coincidence events fall into an area centered around 129keV plastic energy and 30keV CsI energy. Some conversion electrons loose a portion of their energy (e.g. due to absorption in the Xe itself) and thus fall in a band of varying plastic energy and a fixed CsI energy of 30keV. A second, weaker band is visible at ~80 keV, probably due to impurities from ^{222}Rn or ^{133}Xe. In some cases, conversion electron pass through the plastic cell and deposit part of their energy in the CsI, forming a diagonal band of events with constant overall energy.

CsI only events (not in coincidence with betas) fall on the vertical axis. Plastic only events (no coincidence with beta) fall on the horizontal axis and cluster at ~164 keV, corresponding to a non-coincident conversion electron emission from ^{131m}Xe.

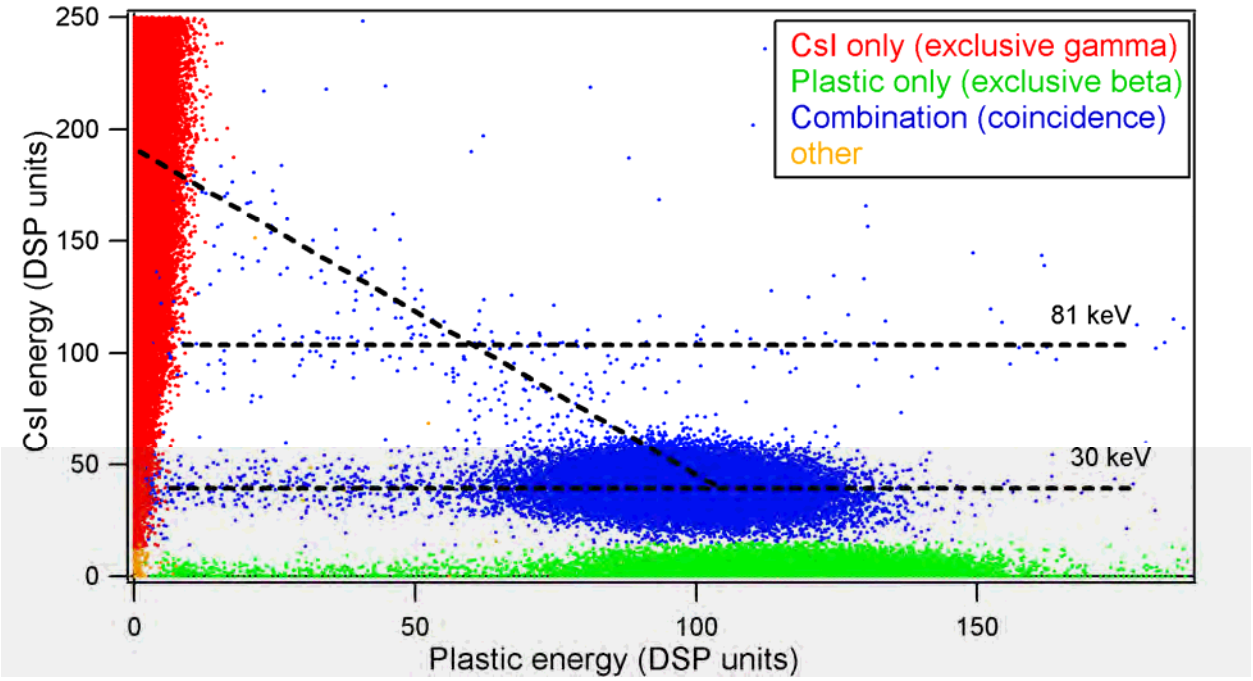


Figure 7. 2D energy scatter plot of events acquired with the phoswich well detector using a ^{131m}Xe source.

Figure 8 shows the spectra of energies deposited in the CsI (top, projection on vertical axis of Fig. 7) and the BC-404 (bottom, projection on horizontal axis). The resolution for the beta peaks is about 27%. Resolution for the 30 keV peak is about 45.8%, for the 81 keV peak about 29.6%. The 30 keV peak contains ~4.43×10^5 events in the histogram of all gammas and ~4.34×10^5 events in the histogram of coincident gammas (sum over peak minus background). Thus a first estimate for the coincidence detection efficiency at 30 keV is 97.9%.

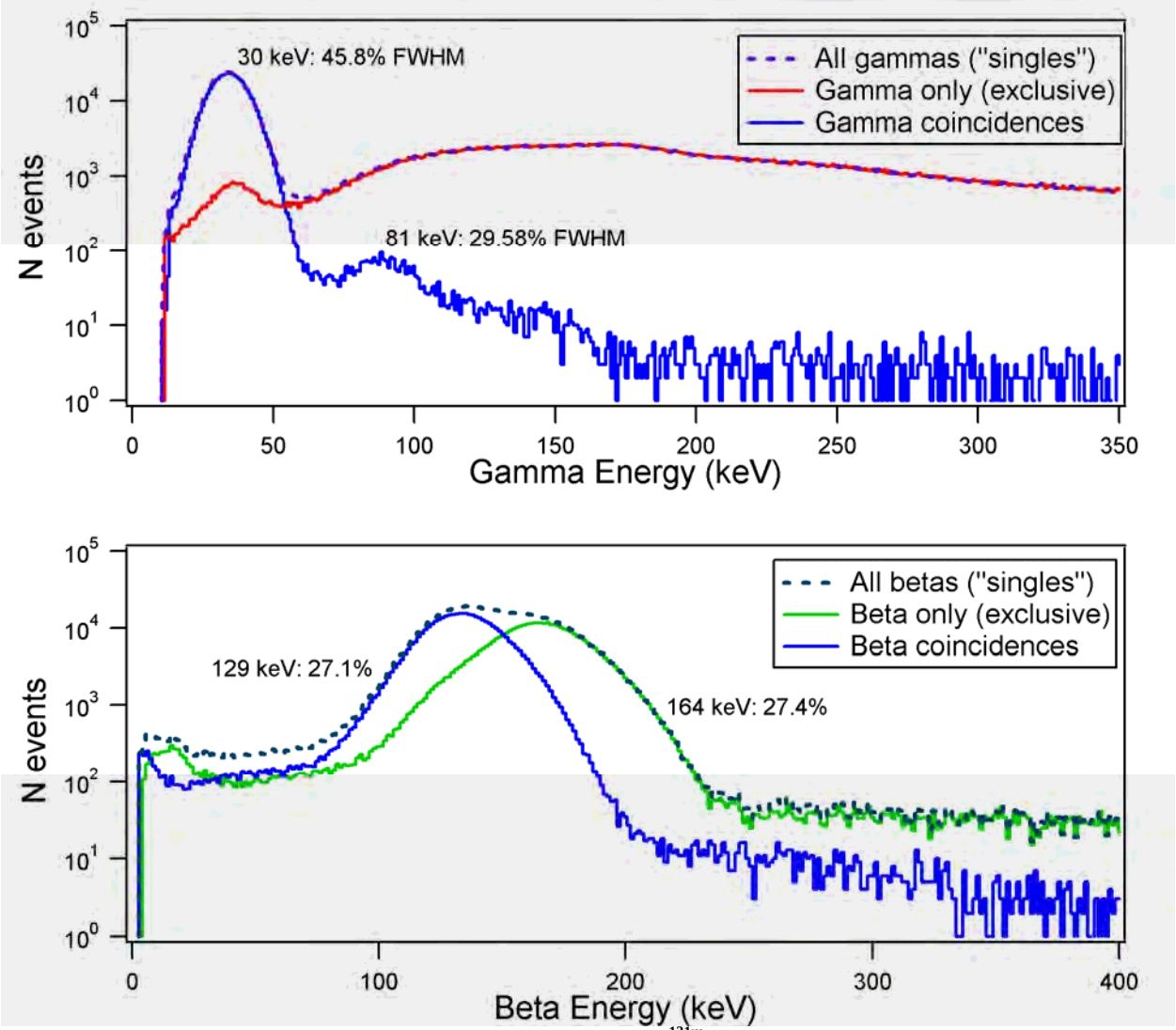


Figure 8: Energy histograms from the phoswich well detector with a ^{131m}Xe source. Top: Gamma/X-ray energy deposited in the CsI. Bottom: Beta energy deposited in the BC-404.

The ^{135}Xe source used in the later measurements at PNNL was much weaker than the previously used ^{131m}Xe source. Therefore the count rate and consequently the statistics are much lower in the ^{135}Xe measurements. In addition, some of the ^{131m}Xe remained trapped in the walls of the plastic cell (memory effect) and thus added a "background" of ^{131m}Xe events to the ^{135}Xe measurements. However, the band of combination events corresponding to coincidences of a 250 keV gamma with a beta particle of varying energy (max. 905 keV) is clearly visible (see Fig. 9). The resolution of the 250 keV peak in the gamma energy spectrum of coincidence events is about 17.6 % (see Figure 10).

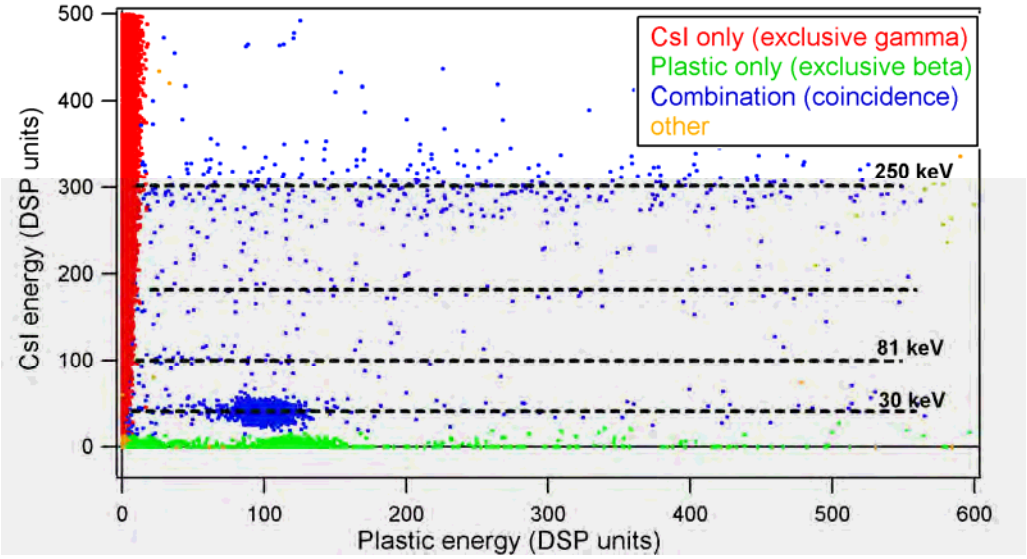


Figure 9: 2D energy scatter plot of events acquired with the phoswich well detector using a ^{135}Xe source. Some ^{131m}Xe from the previous measurement still remains due to the memory effect in the plastic cell.

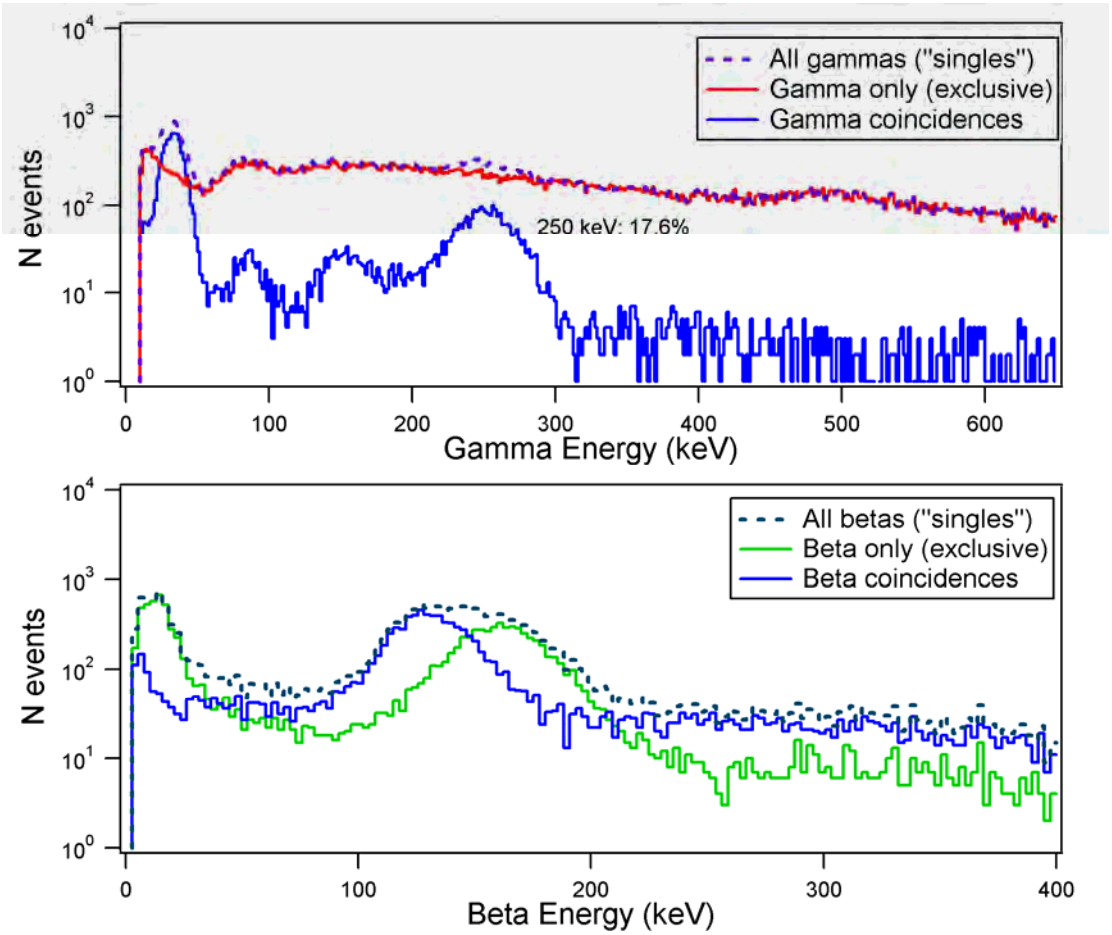


Figure 10: Energy histograms from the phoswich well detector with a ^{135}Xe source, but with some ^{131m}Xe remaining in the detector from the previous measurement. Top: Gamma/X-ray energy deposited in the CsI. Bottom: Beta energy deposited in the BC-404.

CONCLUSIONS AND RECOMMENDATIONS

In summary, a prototype phoswich well detector has been designed, modeled and manufactured. Preliminary test results using radioactive sources were presented. While the effects of crystal non-uniformity on the light collection in the detector and their possible limitations for the achievable energy resolution have to be studied further, preliminary measurements show that the detector is capable of detecting beta-gamma coincidences with high efficiency and separately measuring the energy deposited in each part of the detector. Further, as in our earlier work, the energy resolution of the CsI scintillator is not excessively degraded by application of the phoswich PSA algorithms. Work to date suggests that our models provide relatively accurate descriptions of phoswich detectors as built. The models, moreover, strongly suggest that it will be necessary to move toward a design more like geometry b), which has uninterrupted light paths between all parts of the CsI crystal and the PMT if we wish to achieve the highest energy resolution the technique is capable of. The prototype phoswich well detector will be used to further test the technology and to refine the PSA algorithms for better separation of event types. Our next goals are to develop a final detector design, based both on the geometry b) and on manufacturability issues, that will then be combined with designated readout electronics to create a replacement module for existing the ARSA detector and its readout electronics.

REFERENCES

Ely, J. H., C. E. Aalseth, J. C. Hayes, T. R. Heimbigner, J. I. McIntyre, H.S. Miley, M. E. Panisko, and M. Ripplinger (2003). Novel Beta-Gamma coincidence measurements using phoswich detectors, in *Proceedings of the 25th Seismic Research Review – Nuclear Explosion Monitoring: Building the Knowledge Base*, LA-UR-03-6029, Vol. 2, pp. 533–541.

Hennig, W., H.Tan, W. K. Warburton, and J. I. McIntyre, (2006). Single channel beta-gamma coincidence detection of radioactive Xenon using digital pulse shape analysis of phoswich detector signals, *IEEE Transactions on Nuclear Science* 53: (2) p. 620.

Hennig, W., Y.X. Chu, A. Fallu-Labruyere, W. K. Warburton, and R. Grzywacz, (2005). The DGF Pixie-4 spectrometer - compact digital read-out electronics for HPGe Clover detectors, presented at the IRRMA IV conference, Hamilton, ON, Canada, June 2005, submitted to *NIM B*.

Reeder, P. L., T.W. Bowyer, and R. W. Perkins, (1998). Beta-gamma counting system for Xe fission products, *Journal of Radioanalytical and Nuclear Chemistry*, 235: (1-2), 89–94.

SEGMENTATION OF THE OUTER CONTACT ON P-TYPE COAXIAL GERMANIUM DETECTORS

Ethan L. Hull[1], Richard H. Pehl[1], James R. Lathrop[1], Gregory N. Martin[1], Ronnie B. Mashburn[1], Harry S. Miley[2], Craig E. Aalseth[2], and Todd W. Hossbach[2]

PHDs Co.[1] and Pacific Northwest National Laboratory[2]

Sponsored by DOE Office of Nuclear Physics

Contract Nos. DE-FG-02-05ER84157[1] and DEAC05-RLO1830[2]

ABSTRACT

Germanium detector arrays are needed for low-level counting facilities. The practical applications of such user facilities include characterization of low-level radioactive samples. In addition, the same detector arrays can also perform important fundamental physics measurements including the search for rare events like neutrino-less double-beta decay. Coaxial germanium detectors having segmented outer contacts will provide the next level of sensitivity improvement in low background measurements. The segmented outer detector contact allows performance of advanced pulse shape analysis measurements that provide additional background reduction. Currently, n-type (reverse electrode) germanium coaxial detectors are used whenever a segmented coaxial detector is needed because the outer boron (electron barrier) contact is thin and can be segmented. Coaxial detectors fabricated from p-type germanium cost less, have better resolution, and are larger than n-type coaxial detectors. However, it is difficult to reliably segment p-type coaxial detectors because thick (~1 mm) lithium-diffused (hole barrier) contacts are the standard outside contact for p-type coaxial detectors. During this Phase 1 Small Business Innovation Research (SBIR) we have researched the possibility of using amorphous germanium contacts as a thin outer contact of p-type coaxial detectors that can be segmented. We have developed amorphous germanium contacts that provide a very high hole barrier on small planar detectors. These easily segmented amorphous germanium contacts have been demonstrated to withstand several thousand volts/cm electric fields with no measurable leakage current (<1 pA) from charge injection over the hole barrier. We have also demonstrated that the contact can be sputter deposited around and over the curved outside surface of a small p-type coaxial detector. The amorphous contact has shown good rectification properties on the outside of a small p-type coaxial detector. These encouraging results are the first fundamental steps toward demonstrating the viability of the amorphous germanium contacts for much larger segmented p-type coaxial detectors. Large segmented p-type coaxial detectors based on this technology could serve as the gamma-ray spectrometers on instruments such as the Radionuclide Aerosol Sampler/Analyzer (RASA). These detectors will provide a more sensitive, lower background measurement than currently available unsegmented p-type coaxial detectors.

OBJECTIVES

Germanium detector arrays are needed for low-level counting facilities. The practical applications of such user facilities include characterization of low-level radioactive samples. In addition, the same detector arrays can also perform important fundamental physics measurements including the search for rare events like neutrino-less double-beta decay (Miley et al., 1991; Miley, et al., 1990; Majorana Collaboration White Paper, 2003; and Goulding et al., 1984). Coaxial germanium detectors having segmented outer contacts will provide the next level of sensitivity improvement in low background measurements. The segmented outer contact allows performance of advanced pulse-shape analysis measurements. These techniques can be used to discriminate between multiple Compton-scattered gamma-ray events and single-point beta-decay events. Recently, such techniques have been demonstrated with Clover detectors at Los Alamos National Laboratory (LANL) and confirming simulations done at Pacific Northwest National Laboratory (PNNL), Lawrence Berkeley National Laboratory (LBNL), and Oak Ridge National Laboratory (ORNL). Because of their complexity, the segmented coaxial detectors are expensive and available only after relatively long lead times. Improved detector segmentation techniques would be both important and timely. Such technological advances will reduce fabrication costs and improve availability of these detectors for the low-level counting community.

Currently, n-type (reverse electrode) germanium coaxial detectors are used whenever a segmented coaxial detector is needed. To obtain reasonably accurate coaxial detector segmentation, the outer detector contact must be the segmented contact. The most conveniently segmented outer contact is the boron-implanted outer contact of an n-type coaxial detector. The ability to segment the outer boron contact is the reason segmented n-type coaxial detectors are suggested for use in low background gamma-ray measurements. N-type coaxial detectors should be used in environments where radiation damage is a concern and/or a thin outer detector contact is desired. However, segmented p-type (conventional electrode) coaxial detectors would have technical and financial advantages in low background counting experiments.

P-type coaxial detectors are significantly less expensive and have better gamma-ray energy resolution than n-type coaxial detectors. Fundamentally, this is due to the presence of electron-trapping sites found in even the best detector-quality germanium. A small percentage of the electrons arising from gamma-ray interactions in the detector are trapped before reaching the electron-collecting contact. The charge is trapped for a sufficient duration and is not included in the processed signal for that event. The resulting pulse-height deficits cause broadening of gamma-ray peaks. The magnitude of this energy-resolution degradation from electron trapping is strongly dependent on the geometry of the detector. In detectors of coaxial geometry, the charge carriers collected on the inner contact are responsible for inducing most of the total signal from gamma-ray interactions occurring in most of the volume of the detector. In n-type coaxial detectors, electrons are collected on the inner contact. Consequently, the gamma-ray energy resolution of n-type coaxial detectors is degraded by even small amounts of electron trapping. On the other hand, the spectroscopy of p-type detectors of coaxial geometry relies more heavily on the collection of holes on the inner contact. As a result, electron trapping causes much less resolution degradation in a p-type coaxial detector than in an n-type coaxial detector. The decreased sensitivity to electron trapping makes a greater fraction of the germanium crystals viable for fabrication into p-type coaxial detectors having excellent energy resolution. The lesser importance of electron trapping also allows fabrication of larger diameter p-type coaxial detectors. Thus fewer detectors are needed to make an array of a given total volume. In a detector array like Majorana, we estimate the cost savings associated with the use of segmented p-type coaxial detectors, rather than n-type detectors, to be about $13M. It is important to note that electron trapping is still not thoroughly understood and difficult to control in the growth of detector-quality germanium. Any large-scale low-level counting facility employing segmented coaxial detectors would greatly benefit, both technically and financially, from the use of p-type coaxial detectors.

Currently the segmentation of the outer lithium-diffused n+ contact of a p-type coaxial detector is a nontrivial operation. The outer contact of a p-type coaxial detector is conventionally made using a rather thick (as much as ~1 mm thick) lithium-diffused layer as the hole barrier contact. Thick lithium-diffused contacts are very rugged and reliable but require rather drastic techniques for segmentation. Some techniques involve cutting through the lithium-diffused layer with a saw to segment the contact. Although it can work, such detector fabrication techniques are expensive, time consuming, and mechanically cumbersome. In the event that a saw-cut lithium contact does not successfully function, successive fabrication attempts may prove difficult. Accommodating the saw-cut grooves during the subsequent fabrication attempts may be sufficiently complicated to compel regrinding the crystal to a smaller diameter or even starting over again with a new crystal. In addition, such saw cuts can cause

charge-collection and surface-channel problems in the vicinity of the grooves between the segments. Grooves often result in effectively "dead" germanium near the grooves. The initial saw cuts and electronically "dead" germanium consume valuable isotopically enriched germanium. Some recent data has proven that this is a significant issue. A side-by-side comparison between saw-cut lithium contacts and thin amorphous germanium contacts on planar strip detectors show that charge-collection problems associated with saw-cut lithium can be quite significant (Gros and Lister, 2006).

To make segmented p-type coaxial detectors viable, better outer contacts must be developed to replace saw-cut segmented thick lithium contacts. There are other contact technologies with the potential to provide hole-barrier contacts that are more easily segmented than thick-lithium n+ (hole barrier) contacts. This study seeks to determine the best solution for producing thin-segmented hole barrier contacts on p-type germanium detectors. This will make p-type coaxial detectors viable for large-scale low-level counting arrays. We have started investigating alternative techniques for making segmented hole-barrier contacts in lieu of conventional thick lithium-diffused n+ contacts. Amorphous germanium contacts represent one possible alternative. During this Phase I SBIR we fabricated and tested many small planar test detectors (~2-4 mm thick, ~30 mm diameter) having segmented amorphous germanium contacts as the hole-barrier (+ biased) contacts. We focused on making the amorphous germanium hole barrier as high as possible. A larger hole barrier provides better rectification and a higher probability of successful fabrication of large diameter p-type coaxial detectors using the thin amorphous germanium contact over the entire outside area of the detector. Amorphous germanium contact technology naturally lends itself to the simple fabrication of finely segmented germanium detectors (Luke et al., 1992; Hull et al., 2002; and Hull et al., 2003). By making many planar test detectors, we studied the rectification and segmentation of amorphous germanium contacts with a focus on increasing the hole barrier contact. Our detector processing parameters have been tuned to make reliable segmented amorphous germanium contacts having a large hole-injection barrier specifically for large diameter p-type coaxial detectors. We demonstrated the viability of our fabrication techniques by fabricating a small p-type coaxial detector (MJ1) having an amorphous germanium outer contact. The successful rectification of this contact over the large curved outer contact of MJ1 serves as a first step toward a viable manufacturing process for segmented p-type coaxial detectors. Segmented planar germanium detector technology is our specialty. We believe that the best way to approach the fabrication of segmented coaxial detectors is to first understand the fabrication processes for planar detectors. With the fundamental physics and technology well in hand, the technology can be extended to accommodate the nonplanar geometry issues arising in coaxial detector fabrication.

RESEARCH ACCOMPLISHED

The progress made during the Phase I is described here. Extremely important strides were made toward the commercialization of large p-type coaxial detectors having highly segmented outer contacts for low-level counting arrays. The use of p-type germanium detectors will greatly decrease the cost and difficulty associated with the production of segmented coaxial detectors for such arrays. We have made the first steps toward demonstrating the viability of segmented p-type coaxial detectors. This has been done through fabrication and evaluation of many small planar test detectors and a small p-type coaxial detector. We focused on the amorphous germanium contact as the hole barrier contact. We presented some of our early Phase I results at the 2005 Seismic Research Review meeting in Rancho Mirage, CA, in September 2005 (Hull and Pehl, 2005).

We made a number of small planar test germanium detectors with the goal of increasing the hole barrier formed by the amorphous germanium contact. A larger amorphous germanium hole barrier contact recipe should provide the best rectification characteristics possible under the high electric fields present in large p-type coaxial detectors. Four planar test detectors were made and tested to evaluate each fabrication process. The detectors were etched in a mixture of 3:1 HNO_3:HF for approximately 30 s each. The detectors were rinsed with methanol and blown dry with N_2 gas. The detectors were placed into our RF sputtering chamber and a layer of amorphous germanium was sputter deposited onto the test detectors. After that, the detectors were placed in our thermal evaporator and a layer of aluminum was evaporated through a shadow mask to establish the active areas of the segmented amorphous germanium contact. A center and guard-ring are the two segments on our test detectors. The detectors were then placed in a four-detector test cryostat, pumped, cooled, and tested the following day. Figure 1 shows a set of the test detectors in the four-detector test cryostat. The segmentation is created by evaporating aluminum through a shadow mask, establishing the center and guard-ring features.



Figure 1. A four-detector test cryostat contains planar test detectors. The detectors in the picture have segmented amorphous germanium contacts.

We repeated fabrication and testing on both n- and p-type planar test detectors. The amorphous germanium contact was finely tuned to maximize the rectifying hole barrier height. Rectifying charge-injection barriers exponentially decrease the leakage current from thermionic charge injection over the contact barriers. This is apparent when comparing our new amorphous germanium contact barrier with our earlier detector fabrication recipe. Figure 2 shows a plot of leakage current vs. bias voltage for detectors made with our earlier amorphous germanium detector recipe. The data show the standard linear (exponential) voltage dependence that we have observed repeatedly from the contacts on many detectors. The solid curves in the figure are produced by the amorphous-crystalline heterojunction equation for fully depleted devices: $j = j_{\infty} \exp(-\{\varphi - [(\varepsilon_0\varepsilon_{Ge}/N_F)^{1/2}(V+V_{depl})/d]\}/k_BT)$ (Hull et al., 2005). The critical values used in the expression are the barrier height $\varphi = .30$ eV and density of states $N_F = 5x10^{17}$ /eVcm^3. The barrier height dictates the temperature dependence and the density of states dictates the slope of the voltage dependence of the leakage current. These leakage currents were rather high due to the relatively low hole barrier height. By repeatedly fabricating and testing many detectors we successfully increased the barrier height enough to eliminate all measurable leakage current thermionically emitted over the hole barrier.

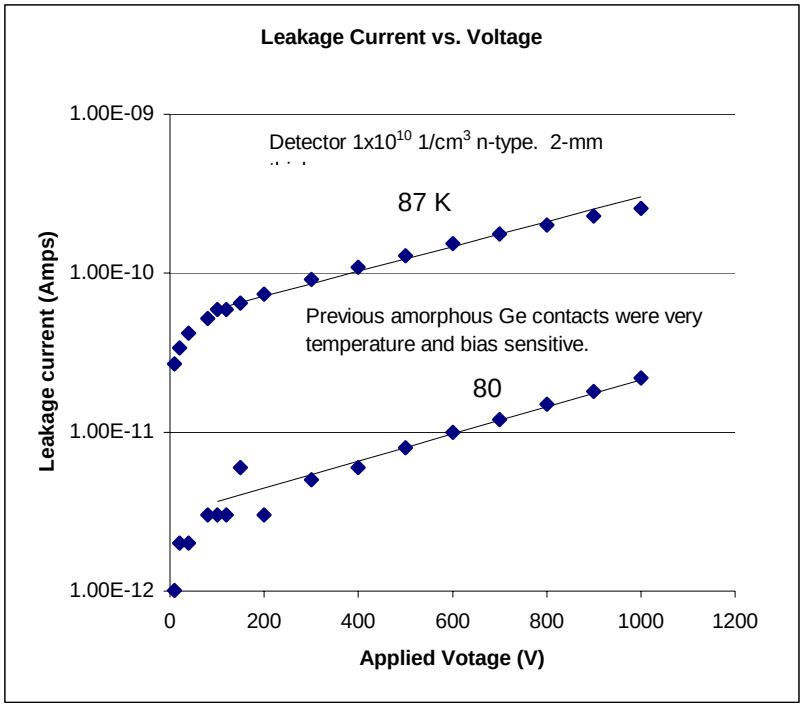


Figure 2. This plot shows the leakage current from a detector fabricated using our previous amorphous germanium contacts. The high leakage current results from relatively low (~.30 eV) hole barriers.

We tuned the amorphous germanium contact to form the very highest hole barrier possible for the sake of eventually making large p-type coaxial detectors. Many sets of planar test detectors were made and tested. We varied the sputter chamber pumpdown time and the percentage of hydrogen in the argon sputter gas in an attempt to fabricate an amorphous germanium contact having a very high hole barrier. Eventually we were routinely able to make planar test detectors that withstood several thousand volts/cm with no measurable leakage current! This is plenty of electric field for a large p-type coaxial detector. Figure 3 shows a plot of leakage current as a function of bias voltage for a detector fabricated using our new amorphous germanium contact recipe for p-type coaxial detectors. These detectors were 2.8 mm thick. There is no measurable leakage current from the center section of the detector at 1,000 V. Leakage currents below 1 pA are difficult for us to measure and are insignificant for the operation of a germanium detector. We assign a value of .01 pA to make the data points appear on the logarithmic plot. The center section of this detector withstood 1,000 V with no measurable leakage current. This corresponds to an electric field of ~1,000 V/.28cm = 3,571 V/cm, plenty to make a large p-type coaxial detector.

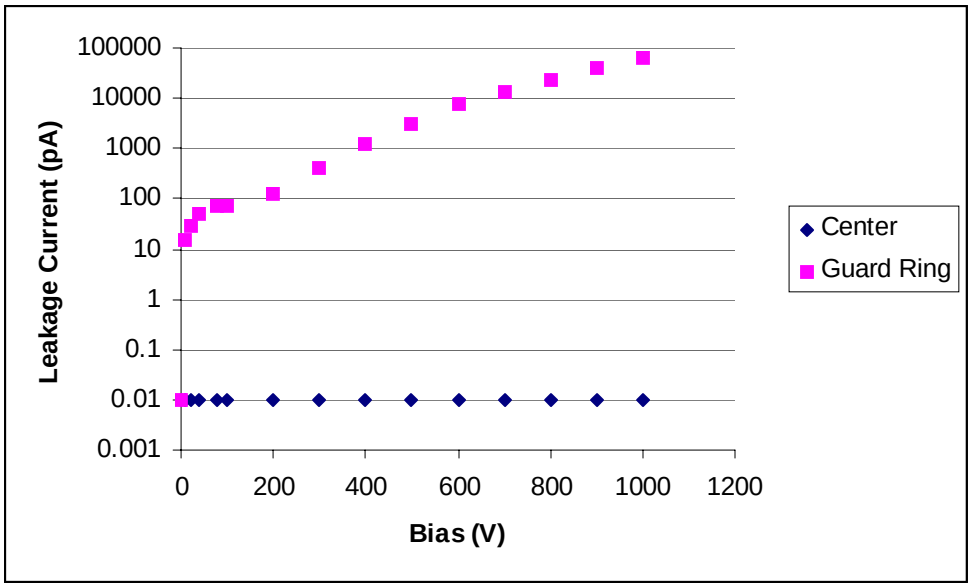


Figure 3. The leakage current from a the center and guard ring sections of a planar test detector. The center contact shows no measurable leakage current up to 1,000 V. This detector is only 2.8 mm thick. The guard ring shows a large amount of surface leakage current.

The leakage current measured on the guard ring of the detector is very high. Unfortunately, this is typical of detectors having our new α-Ge contacts. The current measured on the guard ring is "intrinsic surface" leakage current caused by conductive surface channels (Hull et al., 1995). We have carefully tuned the amorphous germanium sputtering process to produce a high hole barrier contact. Unfortunately, the contact wraps around the sides of the planar test detector during the sputtering process. Most likely, this layer forms a fairly strong n-type surface channel on the intrinsic surface. We normally have a guard ring on our planar strip detectors; consequently, surface channels of this magnitude do not affect the performance of the electrodes within the guard ring. In the future, we may treat this surface with an acid etch after the contacts are deposited on the detector to eliminate this strong n-type surface channel. If high surface leakage currents continue to be a problem we also have the capability to make a thin guard-ring on the inside contact of coaxial detectors to eliminate the ill effects of surface leakage current.

A major accomplishment of this work was the establishment of the fact that the amorphous germanium contact can be made to form a very high hole barrier contact. The amorphous-germanium contact can be a candidate for the outer-segmented contact on large diameter p-type coaxial detectors. As far as we can tell, the detector contacts do not contribute to the leakage current of the detector. In fact, the dominant observed leakage current appears to be bulk generation current from generation-recombination sites near the mid-band-gap region in crystal. If these mid-gap sites are responsible for the leakage current, the leakage current should be proportional to ~exp(-(E_{gap}/2)/kT), where E_{gap} is the band gap (E_{gap} = .7 eV) (Grove, 1967). To investigate this, the leakage current from the center and guard-ring sections of the detector were monitored as a function of temperature of the detector mounting plate in the cryostat (Pehl et al., 1989). Figure 4 shows a plot of the leakage current from the center segment of a test detector having the new amorphous germanium contacts optimized for p-type coaxial detectors. These data were taken with 200 V on the detector. The leakage current on the center contact is not measurable (< 1 pA) until the detector reaches the 125-130 K region. Above the 125 K region, the leakage current follows the ~exp(-.35eV/kT) behavior expected from bulk leakage current due to generation-recombination sites near the mid-gap position. These data are consistent with the results in the seminal work by Pehl, Haller, and Cordi (Pehl et al., 1973).

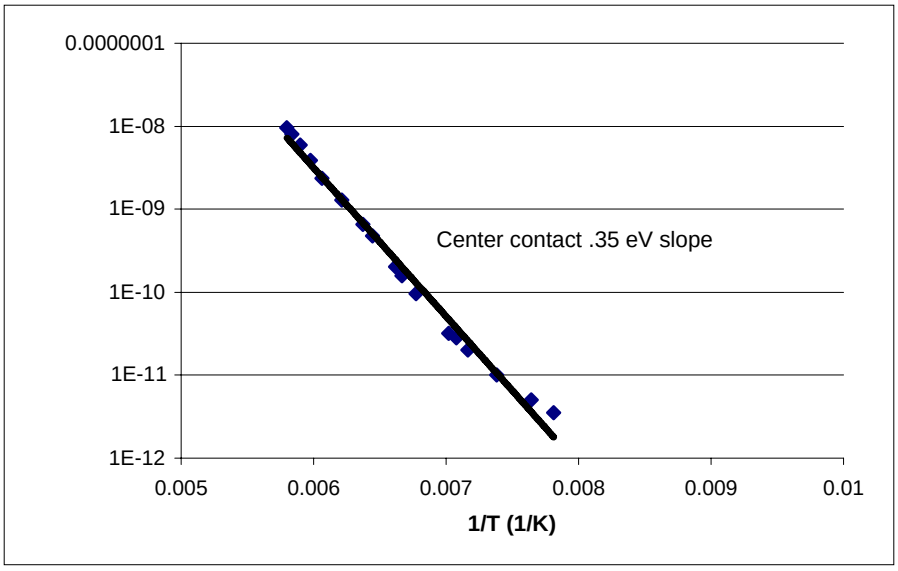


Figure 4. The leakage current from the center segment of a planar test detector as a function of temperature shows the characteristics of bulk generation current. The detector contacts contribute no measurable charge injection.

If the contacts had hole barriers that were low enough to contribute to the leakage current, we would measure leakage current increases at much lower temperatures. This is why we see the temperature dependent leakage current plotted in Figure 2 in the 80–87 K region from the earlier amorphous germanium contacts. According to our calculations, an amorphous germanium hole barrier height greater than .42 eV is sufficient to prevent the contact from injecting a measurable amount of leakage current. With contact barrier heights greater than .42 eV, the dominant leakage current arises from bulk charge generation. Using capacitance vs. pulser voltage techniques, we have measured the amorphous germanium hole barrier height to be ~.6 eV. If we had not been able to make an amorphous germanium contact with such a high barrier height, we could not have hoped to make large diameter p-type coaxial detectors with this technology.

Having this detector recipe in hand, we began trying to fabricate MJ1. We obtained a right cylindrical piece of p-type germanium of 4 cm diameter and 2 cm length having a net electrically-active impurity concentration of ~$9x10^9$ /cm^3 at 77 K. The more impure (seed) end of the crystal was lapped from a sharp 90-degree angle into a smooth curve of approximately 7-mm radius. This end would be the top or closed end of the detector. The other side of the detector was left flat. The detector was polish etched in 3:1 HNO_3:HF for about 2 minutes to eliminate any damage done by the lapping. Figure 5 shows a photograph of the MJ1 detector after etching.

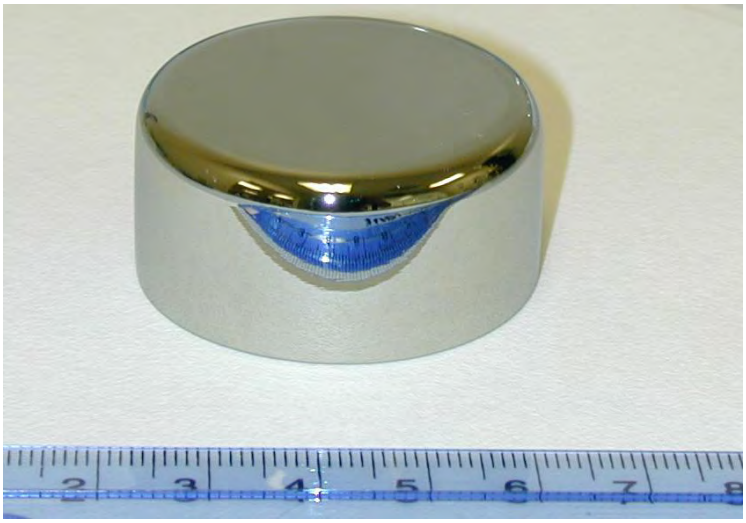


Figure 5. The MJ1 germanium crystal after lapping and etching. The ruler in the foreground is in centimeters. The flat side is face down and the closed end of the detector is face up.

The outer contact was made by sputtering amorphous germanium on the outside of the crystal while it was sitting in the sputter chamber on the intrinsic surface just as pictured in Figure 5. We hoped that the atomic germanium scattering that occurs in the argon during the sputter-deposition process would be sufficient to coat the sides and top of MJ1 evenly in one deposition step. Then the amorphous germanium was covered with evaporated aluminum. A special motorized turntable was built inside our thermal evaporator to rotate the detector during evaporation. This allows the amorphous germanium contact to be coated evenly with aluminum during a single vacuum evaporation. With these physical modifications to the fabrication process, the same amorphous germanium deposition parameters used to make excellent planar test detectors were used to make the small p-type coaxial detector. The amorphous germanium contact forms a rectifying amorphous crystalline heterojunction with the p-type crystalline germanium at the outside diameter of the detector. Positive bias applied to the outer contact depletes the detector from the outside toward the small p+ dot contact in the center of the flat intrinsic surface making a hemispherical or pseudo-coaxial detector. We attempted this process three times with very poor results. The leakage current measured from the flat center contact was several hundred nanoamperes with the application of only 100 Volts, far too high to make a functional detector. Between these three fabrication attempts, we fabricated sets of planar test detectors using the same amorphous germanium deposition parameters to check the integrity of our process. The process appeared to be fine in all cases. We suspected that the dot-like center contact in the middle of the intrinsic surface might be the problem. Generally, such a detector would have some physical indentation into the flat surface. The p+ contact would usually be deposited down in the hole. We used our glass bead blaster to make a 7-mm diameter hole approximately 7-mm deep at the center of the intrinsic surface to accommodate the p+ contact. We etched and fabricated the detector again achieving far better results. After a fourth fabrication attempt, the detector depleted at about 650 V, corresponding to a p-type net electrically active impurity concentration approximately $9x10^9$ /cm^3. The capacitance and leakage current were measured as a function of voltage to establish the diode performance of the detector. The capacitance-C(V) and leakage current-I(V) curves are shown in Figure 6.

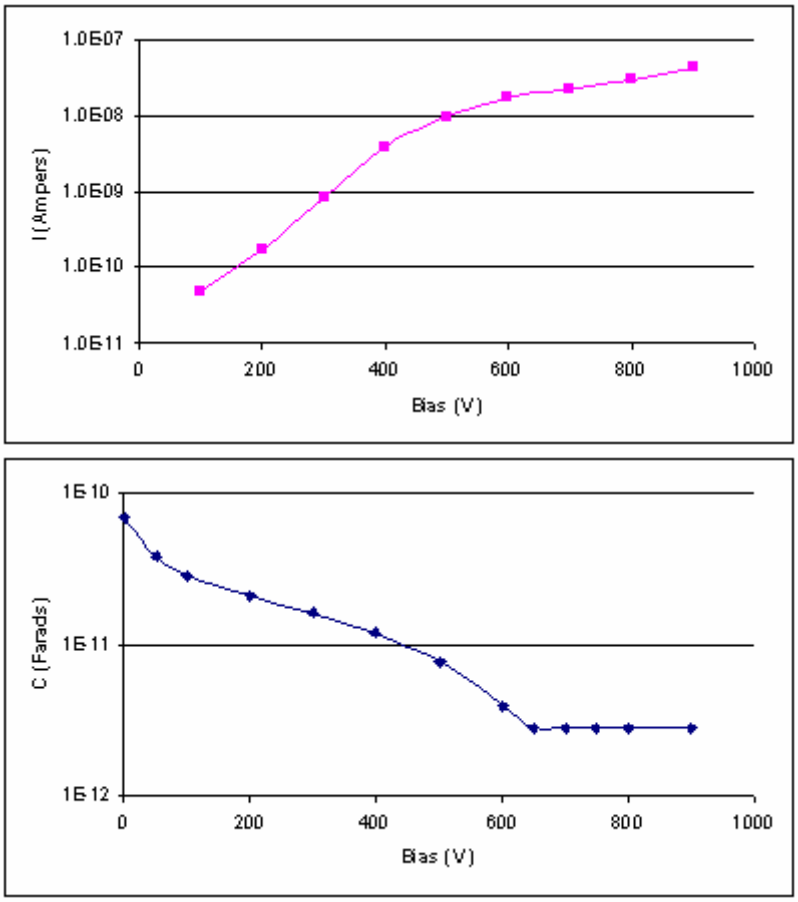


Figure 6. The leakage current-I(V) and capacitance-C(V) curves from MJ1 as a function of bias voltage. The outer amorphous germanium contact is rectifying on the small p-type coaxial detector. The rather high leakage current is due to surface-channel leakage surface. The C(V) curve indicates a very abrupt depletion at ~650 V. The depleted capacitance of the detector was 2.8 pF.

CONCLUSIONS AND RECOMMENDATIONS

Admittedly, the leakage current is somewhat high to call this a tremendously good germanium detector. This leakage current is due to surface-channel leakage currents. The shape of the I(V) curve looks very much like normal surface leakage current we observe with our planar detectors. It can be eliminated with changes in the detector processing, including a simple post-processing surface etch. The important feature to note is the absence of any sharp jumps in the I(V) curve. When an amorphous germanium contact ceases to rectify on a germanium detector, it instantly injects very large currents into the detector. This shows up in the I(V) curve as an abrupt step increase in the leakage current. There are no such features in this I(V) measurement curve. The contact is rectifying. The leakage current here is due to surface channel current. This proves that the amorphous germanium contact does rectify well when sputtered around the curved closed end of a small pseudo-coaxial p-type detector.

The C(V) curve shows a very sharp change in slope at the point of full depletion, ~650 V. Once the detector is fully depleted, there is no measurable additional decrease in detector capacitance as is often observed in detectors having thick lithium contacts. The diffuse junction formed by a thick lithium contact causes the depletion point to have a less sharp discontinuity in slope. This is often called a “soft C(V).” The MJ1 detector clearly shows a very “hard C(V)” because both contacts are very thin and well defined. When fully depleted, this detector represents only

2.8 pF of input capacitance. The low capacitance plus the thin (~2,000 angstroms) amorphous germanium contact would make this a nice p-type x-ray detector if the leakage current were lower.

Although the detector did have rather high leakage current, it was still a functional gamma-ray detector. When operated at 500 V with a unipolar peaking time of 6 μs, the leakage current was low enough to make the gamma ray spectrum shown in Figure 7. Closer analysis of the shapes of the gamma-ray peaks indicate very little asymmetry from poor charge collection. Although the ~3 keV full width at half maximum (FWHM) noise makes the measurement somewhat insensitive to poor charge collection from trapping, the higher energy gamma-ray peaks show no noticeable tailing associated with trapping. The electric field is rather low in the detector at 500 V, so this is a worst-case scenario with respect to charge collection. We believe that this is due to the fact that holes (rather than electrons) are the charge carrier collected on the inner contact. Holes are responsible for most of the signal. Hole trapping generally occurs less than electron trapping in germanium detectors. We would almost certainly see tailing of the 1,332 keV peak if this were an n-type coaxial detector collecting electrons on the inner contact. This observation is in line with the supposition on which this work is based.

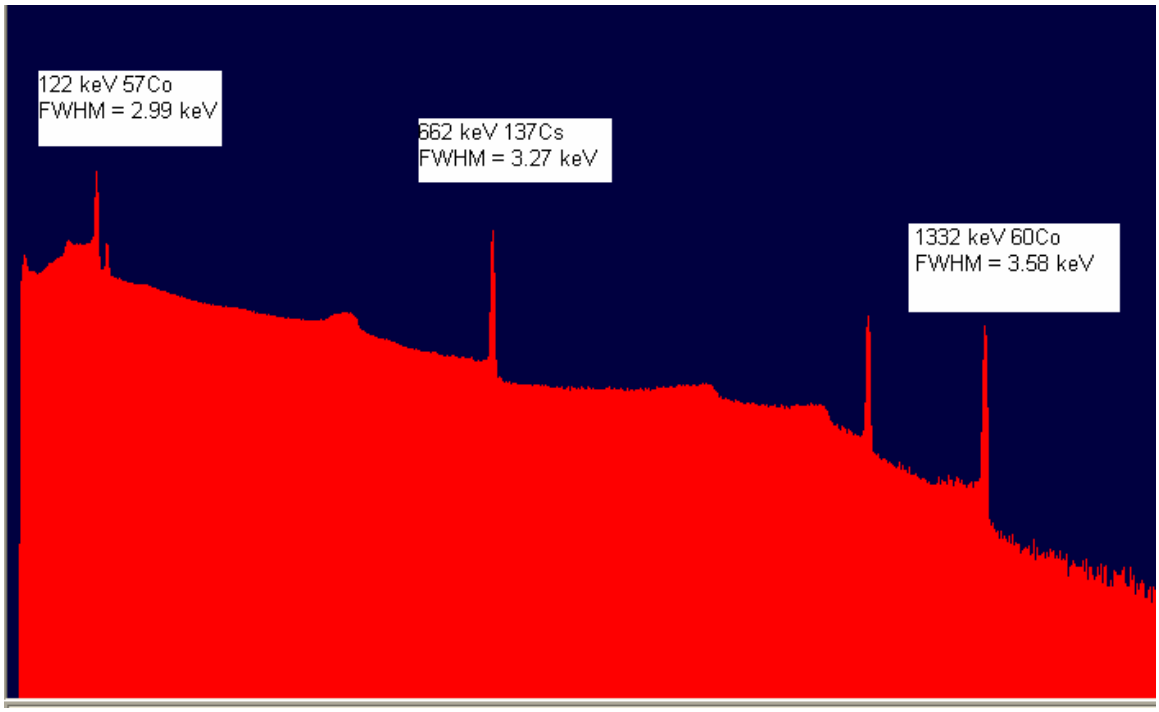


Figure 7. An energy spectrum shows the performance of the detector. The noise of the system was FWHM ~3 keV due to noise from intrinsic surface leakage current.

REFERENCES

Goulding, F. S., D. A. Landis, P. N. Luke, N. W. Madden, D. F. Malone, R. H. Pehl, and A. R. Smith (1984). Semiconductor detectors and double beta decay, *IEEE Trans Nucl. Sci*. NS-31: 285–299.

Gros, S. and C. J. Lister (2006). A Comparison of performance of large area planar germanium detectors with amorphous or lithium-drifted contacts, 2006 Symposium on Radiation Measurements and Applications University of Michigan, Ann Arbor, Michigan, *Nucl. Instrum. Methods* (to be published).

Grove, A. S. (1967). *Physics and Technology of Semiconductor Devices*. Wiley International.

Hull, E. L., H. Miley, R. Pehl, C. Aalseth, and T. Hossbach (2005). Segmentation of the outer contact on p-type coaxial germanium detectors, in *Proceedings of the 27th Seismic Research Review: Ground-Based Nuclear Explosion Monitoring Technologies*, LA-UR-05-6407, Vol. 2, pp. 795–804.

Hull, E. L. and R. H. Pehl (2005). Amorphous germanium contacts on germanium detectors, *Nucl. Inst. Methods A*. 538: 651–656.

Hull, E. L., R. H. Pehl, N. W. Madden, P. N. Luke, C. P. Cork, D. F. Malone, J. S. Xing, K. Komisarcik, J. D. Vanderwerp, and D. L. Friesel (1995). Temperature sensitivity of surface channel effects on high-purity germanium detectors, *Nucl. Instrum. Methods A*. 364: 488.

Hull, E. L. (2003). Germanium detectors for gamma-ray imaging, in *Radiation Detection Technologies Program, R&D Portfolio*, D. P. Spears and G. M. Alonzo (Eds.). NNSA Office of Nonproliferation Research and Engineering.

Hull, E. L., M. T. Burks, C. P. Cork, W. Craig, D. Eckels, L. Fabris, A. Lavietes, P. N. Luke, N. W. Madden, R. H. Pehl, and K. P Ziock (2002). A germanium orthogonal strip detector system for gamma-ray imaging, in *Proceedings of the AIP Conference 632: Unattended Radiation Sensor Systems for Remote Applications*, p. 118.

Luke, P. N., C. P. Cork, N. W. Madden, C. S. Rossington, and M. F. Wesela, (1992). Amorphous Ge bipolar blocking contacts on Ge detectors, *IEEE Trans. Nucl. Sci*. NS-39: 590.

Majorana Collaboration White Paper (2003). The Majorana zero-neutrino double-beta decay experiment, LA-UR-2003-7709 and PNNL-14420, http://majorana.pnl.gov/MajoranaWhitePaper.pdf.

Miley, H. S., R. J. Arthur, R. L. Brodzinski, W. K. Hensley, J. H. Reeves, and F. T. Avignone (1991). Low background detectors for exotic physics experiments, in *Proceedings of the 4th International Workshop on Low Temperature Particle Detectors*.

Miley, H. S., F. T. Avignone, R. L. Brodzinski, J. I. Collar, and J. H. Reeves (1990). Suggestive evidence for the 2-neutrino double-beta decay of Ge-76, *Phys. Rev. Lett.* 65: 3092–95.

Pehl, R. H., E. E. Haller, and R. C. Cordi (1973). Operational characteristics of germanium detectors at higher temperatures, *IEEE Trans. Nucl. Sci*. 20: 494.

Pehl, R. H., N. W. Madden, D. F. Malone, C. P. Cork, D. A. Landis, J. S. Xing, and D. L. Friesel (1989). A variable temperature cryostat that produces in situ cleanup of germanium detector surfaces. *IEEE Trans. Nucl. Sci.* NS-36: 190–193.

MECHANICALLY COOLED LARGE-VOLUME GERMANIUM DETECTOR SYSTEMS FOR NUCLEAR EXPLOSION MONITORING

Ethan L. Hull[1], Richard H. Pehl[1], James R. Lathrop[1], Gregory N. Martin[1], Ronnie B. Mashburn[1], Harry S. Miley[2], Craig E. Aalseth[2], Todd W. Hossbach[2], and Theodore W. Bowyer[2]

PHDs Co.[1] and Pacific Northwest National Laboratory[2]

Sponsored by National Nuclear Security Administration
Office of Nonproliferation Research and Development
Office of Defense Nuclear Nonproliferation

Contract Nos. DE-FC52-06NA27323[1] and DE-AC05-RLO130[2]

ABSTRACT

Compact maintenance free mechanical cooling systems are being developed to operate large volume (~570 cm^3, ~3 kg, 140% or larger) germanium detectors for field applications. We are using a new generation of Stirling-cycle mechanical coolers for operating the very largest volume germanium detectors with absolutely no maintenance or liquid nitrogen requirements. The user will be able to leave these systems unplugged on the shelf until needed. The flip of a switch will bring a system to life in ~1 hour for measurements. The maintenance-free operating lifetime of these detector systems will exceed five years. These features are necessary for remote long-duration liquid-nitrogen free deployment of large-volume germanium gamma-ray detector systems for Nuclear Explosion Monitoring (NEM). The Radionuclide Aerosol Sampler/Analyzer (RASA) will greatly benefit from the availability of such detectors by eliminating the need for liquid nitrogen at RASA sites while still allowing the very largest available germanium detectors to be utilized. These mechanically cooled germanium detector systems being developed here will provide the largest, most sensitive detectors possible for use with the RASA. To provide such systems, the appropriate technical fundamentals are being researched. Mechanical cooling of germanium detectors has historically been a difficult endeavor. The success or failure of mechanically cooled germanium detectors stems from three main technical issues: temperature, vacuum, and vibration. These factors affect one another. There is a particularly crucial relationship between vacuum and temperature. These factors will be experimentally studied both separately and together to insure a solid understanding of the physical limitations each factor places on a practical mechanically cooled germanium detector system for field use. Using this knowledge, a series of mechanically cooled germanium detector prototype systems are being designed and fabricated. Our collaborators at Pacific Northwest National Laboratory (PNNL) will evaluate these detector systems on the bench top and eventually in RASA systems to insure reliable and practical operation.

OBJECTIVES

Mechanical cooling systems will be developed to operate large volume (~570 cm^3, ~3 kg, ~140% or larger) germanium detectors for field use in rugged conditions. The hand-held "Detective" is an elegant example of a currently available mechanically cooled germanium detector system manufactured by Ortec (Keyser et al., 2003). This system uses a small Stirling-cycle cooler to cool a modest sized germanium detector to operating temperature overnight (~12 hours). Our project proposes to utilize a newer and larger generation of Stirling-cycle mechanical coolers to produce systems that will reliably cool the very largest germanium detectors while requiring no maintenance. The detectors will be cooled to a lower temperature, resulting in much more reliable detector operation. These new coolers have operating lifetimes in excess of five years. The coolers require no maintenance. We intend to develop germanium detector systems that can be left unattended, running or not, for several years with no maintenance. The flip of a switch brings the system to life. The relatively large heat lift of these coolers can cool a detector to operating temperature for gamma-ray measurements in ~1 hour. These features will make liquid-nitrogen free operation of the largest (~200%) germanium gamma-ray detectors viable and convenient for NEM. RASA is one system than will benefit from the availability of such detectors (Bowyer et al., 1997; Miley et al., 1998).

Mechanical cooling of germanium detectors has historically been a difficult endeavor. The success or failure of mechanically cooled germanium detectors stems from three main technical issues: temperature, vacuum, and vibration. These factors affect one another. There is a particularly crucial relationship between vacuum and temperature, as we shall explain. These three factors must be studied both separately and together to fully realize the most practical means of addressing their technical limitations.

Temperature is the most important fundamental parameter in the operation of any semiconductor detector. The temperature must be low enough to operate a large volume coaxial germanium detector with tolerable leakage current. Excessive leakage current, usually more than ~100 pA, causes noise in the spectroscopy of germanium detectors. Detector operating temperatures are usually below 100 K. Leakage current becomes more important for very large coaxial detectors. Large diameter germanium detectors have optimum energy resolution at relatively long shaping amplifier peaking times (6-12 μs). Leakage current affects the measured noise of germanium spectrometers more adversely at longer peaking times. These large p-type coaxial detectors should be operated as cold as possible to reduce the leakage current.

For the vast majority of germanium detector systems, a Dewar of liquid nitrogen provides a 77 K heat reservoir for cooling. The detector is usually coupled to the liquid nitrogen with a copper rod or braid. The detector temperature is always somewhat higher than 77 K, perhaps 82 K at the coldest and 100 K at the highest. The authors have personally built liquid-nitrogen cooled systems having a copper cooling path of approximately 0.8 W/K and a detector temperature of 82.5 K (Hull et al., 2002). That corresponds to about 4 W of cooling power (or heat lift) at 77 K. This is a reasonable (conservative) heat load for a recently pumped cryostat holding a large detector. The heat load stems from emissive (or infrared) load, conductive load from cryostat parts such as wires, and conductive gas load from the imperfect vacuum in the cryostat. However, the liquid nitrogen will always provide a 77 K heat sink and vacuum getter regardless of thermal load. The same is not true for a mechanically cooled detector system. In a mechanically cooled system the coldest temperature is created at the cold tip of the cooler as a result of the refrigeration cycle. The cold tip temperature is not a constant and is directly affected by the heat load placed on the cold tip. Fundamental thermodynamics dictate that all mechanical coolers remove less heat as the cold tip temperature decreases. This point can present difficulty in cooling a germanium detector. An increase in heat load will always increase the temperature of the cooler cold tip, the detector, and the cold vacuum getter surfaces. The heat-sink temperature does not remain constant as it does with liquid nitrogen. Over the long term, the imperfect vacuum in the cryostat can degrade causing an even larger conductive gas heat load on the cold tip. The cold tip warms up making it a poorer vacuum getter, hence, the detector temperature increases. If the temperature increases sufficiently, the detector leakage current increases; causing noise that degrades the spectroscopy.

Lower temperature operation decreases the detector leakage current providing a more reliable detector. In many cases, a few degrees can make the difference between acceptable and intolerable performance. We always make our detector systems as cold as possible. The leakage current of a rectifying semiconductor device (such as a germanium detector) arises from intrinsic-surface charge generation, rectifying-contact thermionic emission, and bulk generation (Sze, 1981; Malm, 1975; Grove, 1967; Hull and Pehl, 2005; and Pehl et al., 1973). All these current

sources are proportional to $exp(-\varphi/kT)$. Here φ is some characteristic energy on the order of the germanium band gap ($\varphi \leq .7$ eV), k is the Boltzman constant, and T is the Kelvin temperature. This is an extremely strong function of temperature. More importantly, as a detector becomes larger, the larger area increases the emissive and gas conductive heat loads. In addition, all three sources of detector leakage current are proportional to either the volume or surface area of the detector. The leakage current will be higher for a larger detector than a smaller detector at any given temperature.

To operate a large mechanically cooled detector we must get the detector as cold as possible while under a heat load in the region of 3-5 W. Fortunately, we have identified a new generation of Stirling-cycle mechanical coolers having tremendous heat lift (cooling capacity), even at very low temperatures, approximately 6 W at 60 K. Produced for the telecommunications industry, these coolers claim operating lifetimes in excess of 5 years atop cell phone towers. A good deal of the inspiration for this project comes from the availability of this new generation of relatively inexpensive mechanical coolers. We are adapting these coolers for use with germanium detectors. Preliminary tests of one such cooler have been very encouraging. We purchased a Cryotel CT Stirling-cycle cooler from Sunpower. We never intended to use this cooler for large coaxial detectors but the following results were so impressive that we now have to consider such an application. Figure 1 shows a technical drawing of the cooler with the test cryostat we designed and built to evaluate the cooler. Figure 2 shows a photograph of the cooler and test cryostat.

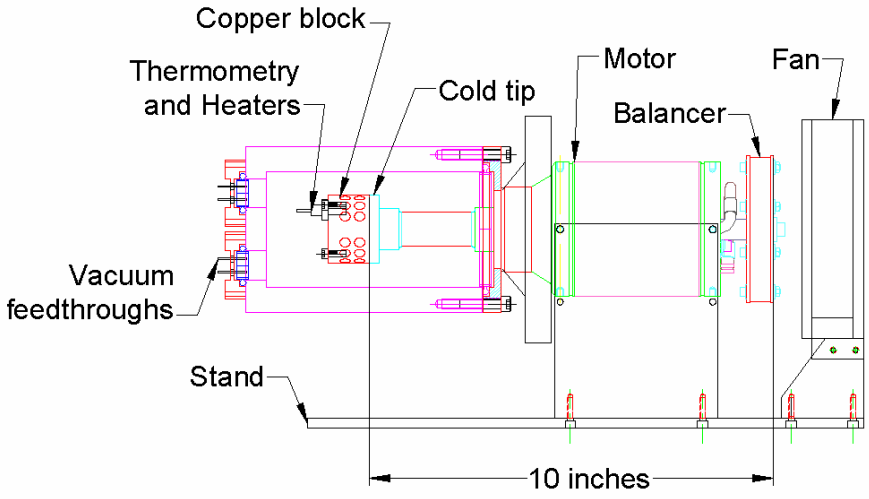


Figure 1. A technical drawing of the cooler and cryostat shows the basic test setup constructed for preliminary measurements. From left to right the diagram shows the cryostat body with vacuum feed throughs, the cold tip with copper block, the cooler motor, passive balancer, and finally the fan for air cooling. The entire structure has been mounted on an aluminum stand. The cooler is 10 inches long and 3 inches in diameter, far smaller than any useful liquid nitrogen Dewar.

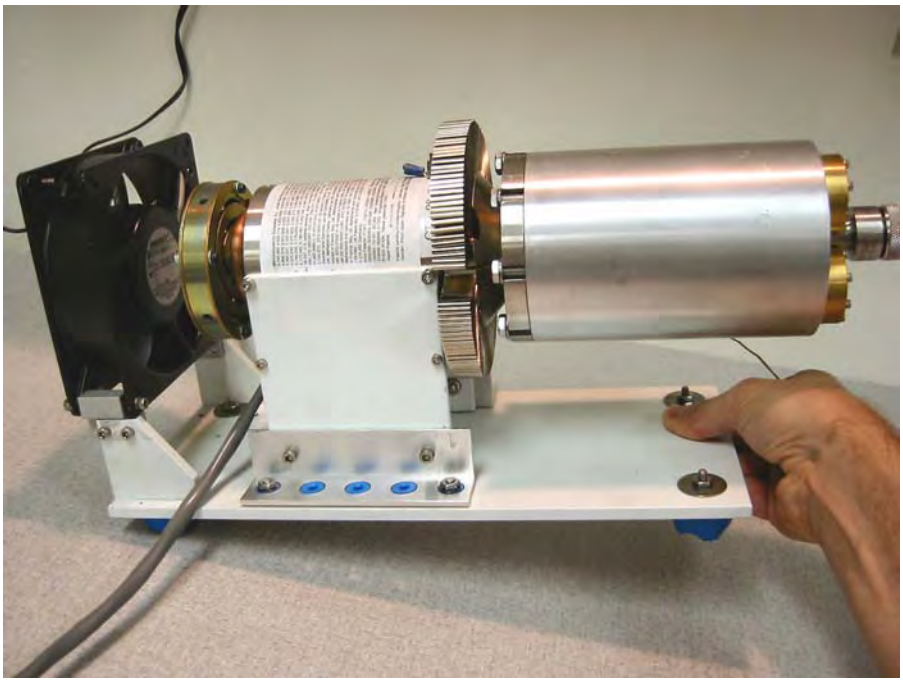


Figure 2. A photograph of the cooler and cryostat shows the basic test setup constructed for preliminary measurements. The cooler alone weighs only 3 kg. The only connection needed is power from the gray cable in the left foreground of the photo. The future germanium detector systems will be only a few inches longer than the cryostat pictured here.

A copper block was machined to fit on the cold tip of the cooler. The 500 g copper block has a cavity in the middle with many holes leading from the cavity to the outside of the block. The cavity was filled with molecular sieve held in with a fine-mesh stainless steel screen. The copper block was instrumented with silicon diodes calibrated for accurate (less than +/- .5 K) temperature monitoring. A power Zener diode on the copper block can apply power to simulate the heat load of a detector. The first time we cooled the system we were very pleased with the surprisingly short cool-down time. The copper block was cooled from room temperature to 77 K in 8 minutes and down to 40 K in 10 more minutes! With 4 W of heat load power applied to the copper block, it cooled from room temperature to 77 K in 20 min, and down to 54 K in an additional 15 minutes. This cooler has tremendous heat lift, even at very low temperatures. The cooler has cycled from room temperature down to under 40 K tens of times with perfect repeatability and no measurable degradation in performance. Figure 3 shows these cool-down curves. The cold tip cools a reasonable mass of copper (500 g) down to very low temperatures very quickly while fighting a realistic heat load. There is no infrared thermal shield in this test cryostat. Normally, a reflective infrared shield would be placed between the cold tip and the cryostat walls to diminish the infrared heat load on the system. With some cryostat engineering, these coolers are viable candidates for cooling large germanium detectors quickly and to very cold temperatures.

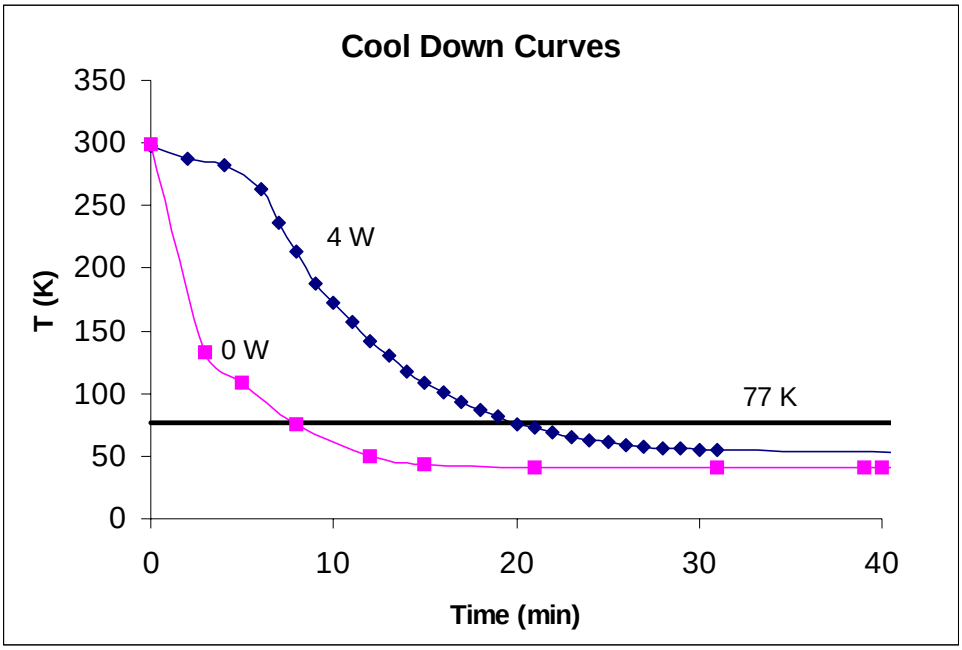


Figure 3. The lower cool-down curve represents the temperature of the copper block as a function of time after the cooler is turned on at room temperature with 0 W of applied heat load. The copper block reached 77 K in 8 minutes and the lowest temperature reached was ~40 K. The upper cool-down curve was measured with 4 W of power applied to the copper block. The copper block reached 77 K in 20 minutes.

The quality of the vacuum in the cryostat is extremely critical. Vacuum and temperature are inseparable factors in the operation of a mechanically cooled detector system. We have already found that the larger heat lift and colder temperature of the Sunpower cooler provides a good deal of passive vacuum pumping by cooling molecular sieve. However, there remain vacuum issues that are crucial for long duration operation. The cryostat vacuum must be of sufficient quality that no substantial thermally conductive gas heat load is placed on the cooler. This vacuum quality must remain for the intended lifetime of the instrument. This is more difficult and critical than apparent at first. Because the heat lift of a mechanical cooler decreases with lower temperature, it takes surprisingly little gas heat load to measurably increase the temperature of a mechanically cooled detector. With the temperature increase, more gases evolve from the cold surfaces further degrading the vacuum. This positive outgassing feedback can eventually degrade the vacuum until the detector temperature is too high for stable operation. The authors are aware of numerous detector systems that function for a period of many months before failing mysteriously. In most cases, the cause is almost certainly degradation of the vacuum in the cryostat.

In liquid-nitrogen cooled systems, the constant 77 K temperature of the walls of the cryostat and molecular sieve cover many vacuum sins that cannot be tolerated in a mechanically cooled system. Liquid nitrogen is always 77 K regardless of heat load. An increase in heat load only boils the liquid nitrogen faster but the temperature is always 77 K. The cold tip of a mechanical cooler can very quickly exceed 77 K with sufficient gas load. In this temperature range, condensed O_2, N_2, and Ar begin evolving from the cold surfaces and molecular sieve. Our preliminary tests have shown that vacuum remains an issue, even with the immense heat lift and low temperature of the Cryotel CT. The vacuum must be properly studied and handled in the context of a long-lived germanium detector system.

Any vacuum system is a dynamic situation. Atmospheric gases are constantly diffusing through vacuum seals. Internally, gases evolve from surfaces in the vacuum. These gas sources must be constantly pumped by something in the chamber or the vacuum degrades. Liquid-nitrogen cooled germanium detector systems use the 77 K walls of the cryostat combined with molecular sieve, activated charcoal, and other chemical gettering schemes to maintain the vacuum. Although elastomer o-rings make a vacuum seal that is considered to be “leak tight,” significant atmospheric gas can still diffuse through the o-rings. Metal seals reduce the diffusion by several orders of

magnitude. However, standard metal seals generally require more sealing force and bolting infrastructure requiring a much bulkier cryostat. The question to be addressed here is: "What combination of vacuum seals, cryostat materials, design, and vacuum gettering is appropriate for a long-lived large volume mechanically cooled germanium detector?" This question must be addressed in the context of a viable detector system. For example, having a turbo molecular pumping station attached to the system at all times is not a viable option. The system must maintain its vacuum in a convenient and compact manner. The first step toward accomplishing this is better understanding of the constituents and sources of the gases spoiling the vacuum.

Figure 4 shows a plot reflecting the impact of vacuum degradation on our mechanically cooled test system. The plot shows the coldest obtainable temperature achieved with the cooler running at full power as a function of time after the system was last pumped with a high vacuum system. After the initial pump, the system is sealed off, cooled, tested, and allowed to sit in the air with no further external pumping. Every few days the system is cooled again to note any changes. The data curve shows the impact of allowing our system to sit in air for 3 weeks with Viton o-rings used for vacuum seals. The temperature increased from 38 K up to 56 K. The cooler is capable of lifting approximately 1 W at 38 K and 5 W at 56 K. Enough gas diffused into the system to cause a 4 W heat load in only three weeks. A brief pump with the high vacuum system eliminated the heat load and the cold tip cooled immediately back down to about 38 K, proving that the problem is a conductive gas heat load. The next questions are: Which gas species are present? and Where are these gasses coming from? The molecular sieve packed in the copper block should adsorb the common atmospheric gases quite well at these temperatures (Stern and DiPaolo, 1967).

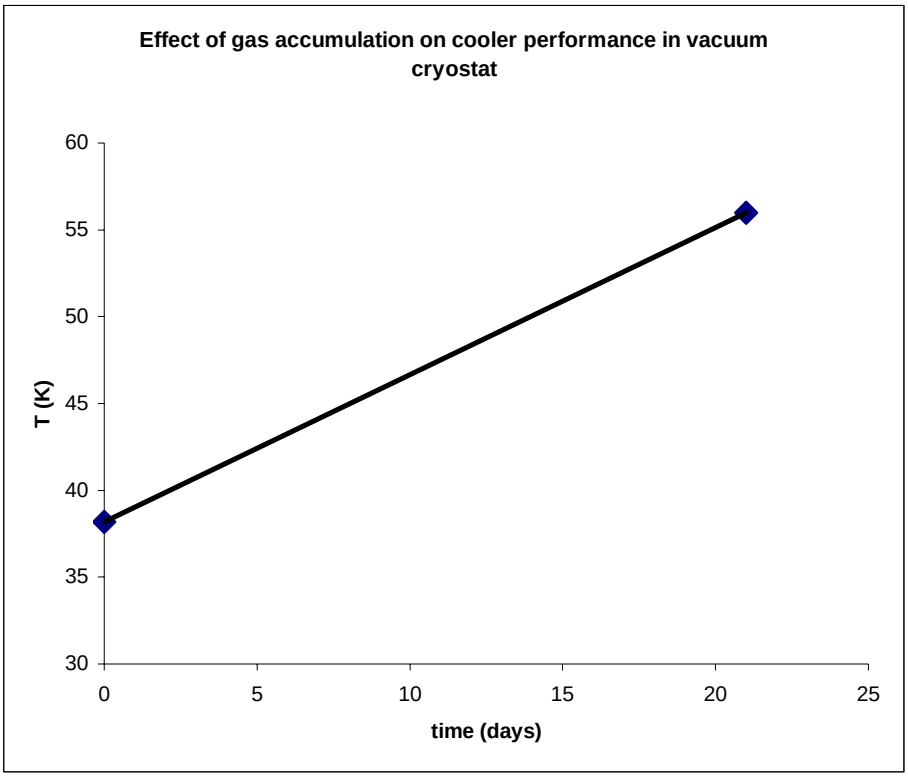


Figure 4. The temperature of the cooler increases as gases accumulate in the vacuum cryostat. The copper block (filled with molecular sieve) is at the temperatures shown. There is clearly some gas load accumulating that is not pumped by the cold molecular sieve. This degradation could eventually compromise the performance of a mechanically cooled germanium detector.

We have heard and discussed many different, semi-plausible arguments for these gas sources. Some of the explanations are very interesting and creative but none fully explain the data we have. An example of one explanation is: "The stainless steel in the chamber is reducing water vapor into H_2 and O_2, the H_2 is not gettered by your sieve even at 40 K so that is the source of this additional heat load." We have also been told the gas is oxygen from water vapor, although we would expect that oxygen and water vapor should be pumped very well by the cold molecular sieve. Some say it is H_2 coming from the aluminum cryostat walls. We ponder that it might even be helium diffusing through the braze joint in the mechanical cooler itself, although diffusion through metals is very small. These Stirling-cycle coolers have several atmospheres of helium inside as the working gas. There could also be helium diffusing into the vacuum from the atmosphere through the seals. Clearly some high quality quantitative measurements of the gas species present in such systems would be an excellent first step in properly addressing this issue. The very slight accumulation of gasses in a sealed vacuum chamber over long time periods must be studied quantitatively to understand this issue.

During this study we are assembling a vacuum pumping station with a Residual Gas Analyzer (RGA). The RGA will be used to monitor the quantity and species of these accumulating gases. We will monitor the gas quantity and species as a function of time and the temperature of the molecular sieve. We are making some simple vacuum boxes out of different common metals to see what gases accumulate as a function of the chamber wall materials. We have heard that H_2 comes out of some grades of aluminum and that Ar comes out of some stainless steel. There is surely some truth to many of these suggestions, particularly at ultra high vacuum levels ($< 10^{-9}$ Torr). However, we are seeing gas accumulations on the order of 10^{-4} Torr in a relatively short time. We need to know the dominant gas species so we can build our detector systems accordingly. This effort will result in good practical vacuum technology and better mechanically cooled germanium detectors.

The remaining issue to be addressed is the vibration of the mechanical cooler. Vibration of the mechanical cooler can cause microphonic noise adversely affecting the energy resolution of the detector. Microphonic noise can be devastating in some cases. In every other mechanically cooled detector we know of, the mechanical cooler contributes some measurable noise to the overall energy resolution of the system. Germanium detectors have such excellent energy resolution that their front-end electronics must necessarily be sensitive to small vibrations in the leads on either side of the detector. Since we want to mechanically cool the very largest diameter germanium detectors, microphonic considerations are very important. With larger diameter coaxial detectors come ballistic deficit concerns. Higher bias voltage must be used to operate the detector along with longer amplifier peaking times for optimum spectroscopic energy resolution. Longer peaking times are more susceptible to the generally low frequency microphonic noise caused by mechanical coolers. The cooler we have been testing does vibrate. We have been able to lessen the vibration somewhat with rubber isolation pads on the cooler stand. There are certainly other mechanical adjustments that can reduce the primary vibration source. In fact, the cooler vendor even sells an "active balancer" that can be tuned to dampen the vibrations characteristic of the particular cryostat. In addition, there are electronic tricks one can employ to lessen the effect on the final energy resolution of the system. If the frequency structure of the microphonic noise is known, it can be subtracted from the signal to lessen the impact on the system noise. Such additions will only be added if deemed necessary. We would like to keep the system as simple as possible. To evaluate the severity of the microphonics problem, we will fabricate and instrument a small guard-ring planar germanium detector in our test system. We make and use these small simple detectors to evaluate all kinds of detector, electronic, and cryostat issues. Using this detector we can evaluate the effect of the vibrating cooler on the spectroscopy of the system. This is a fast, inexpensive way to evaluate such things before loading a large expensive coaxial detector into the system.

We do not think microphonic noise will be an insurmountable problem for this system. In fact, we have made preliminary bench top measurements indicating the problem is not too significant. Five-inch long wires and various capacitors (to simulate the detector capacitance) were allowed to vibrate on the input junction gate field-effect transistor (JFET) of an operating preamplifier at room temperature. The box holding the preamplifier was clamped rigidly to the body of the mechanically cooled test cryostat. The output of the preamplifier was processed by a TC-244 spectroscopy amplifier and was calibrated with test capacitors and a pulser. The noise increased very slightly when the cooler was turned on. There is a brief burst of noise when the cooler starts. After that, the noise settles down. The cooler running at full power increased the root mean square (RMS) noise value only a few percent using a peaking time of 4-6 μs. Below 4 μs, the microphonic noise was not measurable. To be fair, we had no bias on the test capacitor. Detector bias voltage can greatly increase the measured microphonic noise. However, we have made side-by-side tests of small planar detectors (with bias voltage) in one of our liquid-nitrogen cooled test

cryostats indicating further microphonic noise reduction when the JFET is cooled. These detectors use several hundred volts of bias for operation. In the same cryostat, we instrumented some detectors with cooled JFETs and some with room temperature JFETs. The detectors having cooled JFETs showed much less (~100x less) microphonic noise response when tapping on the side of the cryostat. The cooled JFET is much closer to the detector, providing a shorter sensitive gate lead between the detector and JFET. Since we will be cooling the JFET in our mechanically cooled detector system, we are optimistic about overcoming microphonic problems in a practical detector system.

For a mechanically cooled large volume coaxial detector to be viable, the temperature, vacuum, and noise caused by vibration must be under control for the lifetime of the detector system—several years. These factors are being studied in the laboratory at the most fundamental levels to insure a solid understanding. Based on these fundamental measurements, the best possible prototype detector-cooler systems will be fabricated for practical tests. Any changes in performance will be studied as a function of time. A prototype detector system will be field tested in RASA systems to insure reliable and practical operation. Our PHDs-PNNL team brings together vacuum, cryogenic, detector, electronic, and field-application expertise. With support for this project, the stage is set for the development of a new generation of mechanically cooled germanium detector systems. These systems promise fast reliable cooling and operation of the very largest germanium detectors. At the end of this project we will offer a new product line, the MCX mechanically cooled detector product line for use with RASA and similar detection systems.

RESEARCH ACCOMPLISHED

This project has just started. These are a few of the accomplishments to date.

A new mechanically cooled cryostat is being designed for this project. We call the cryostat MC0-a. This cryostat is slightly larger than our test cryostat described above. It will hold a brass detector dummy to simulate the heat capacity and area of a large coaxial germanium detector. Of course, a real germanium detector will eventually replace the brass dummy. The brass detector dummy will be 10-cm in diameter and 10-cm long. This is the size of the largest germanium detector conceivable at this time corresponding to a ~200% germanium coaxial detector. This cryostat will be used to determine the correct materials, seals, and design to be used for large mechanically cooled coaxial detectors.

At the same time, we have ordered the critical components of a vacuum pumping station suitable for quantitative analysis of the accumulating gas constituents in a sealed cryostat volume. We have ordered a Pfeiffer TSU 521 (6” nominal diameter) turbo-molecular pumping station and received an Ametek LC100M RGA with 100-amu range. We have ordered several vacuum valves and connection flanges. We will assemble these components to form a high-vacuum pumping station with the ability to quantify the species and pressure of numerous different gas species accumulating in our cryostats. A small-diameter bleeder valve will bypass the detector pumping port to further limit the conductance between the pump and the cryostat. The total pressure at the RGA head must be maintained below the high 10^{-5} Torr range to allow the RGA to operate properly. At the same time, we want to be able to measure the gases coming out of our test cryostat without them being pumped away immediately. The RGA needs time to sweep through the different atomic masses of the different possible accumulated gas species. Although common RGAs measure all gas species down to the 10^{-11} Torr level, dry gases (N_2, O_2, etc) are pumped off very quickly by a wide-open high vacuum pump. With the main vacuum valve open, the pumping station will also be used to pump the mechanically cooled cryostats before testing. We have decided to mount a series of different metal chambers on outer flanges of the vacuum pumping station. Each metal chamber will be a machined and cleaned right cylinder having an inside volume of 1 liter, comparable to the volume inside a germanium detector cryostat. We will fabricate three identical chambers, one each made of aluminum, brass, and stainless steel. Each of these three chambers will be pumped out over a several day period on the pumping station. The chambers will be individually sealed off (using a metal seal inside the vacuum chamber) from the rest of the vacuum system and allowed to sit for various amounts of time. Gasses evolving from the surfaces of these metals will accumulate in the chamber. With the RGA and pumping station based out in the 10^{-7} Torr range, the valves will be opened and the accumulated gas species will be released and measured. In this manner, any gasses coming from these common cryostat materials will be measurable. Once these gasses have been quantified, the lowest gas emitting metal cylinder will be removed and various materials, including high-purity germanium, will be placed in the cylinder and allowed to outgas for a period of time to determine any gasses coming from common materials (like Teflon) used in the cryostat.

Depending on the type and predominance of various gas species, we will react by modifying MC0-a to prevent these species from accumulating to as large a degree as possible. For example, if we see a predominance of hydrogen we will place palladium packets in the vacuum. Palladium is an excellent getter of hydrogen. There are also chemical getters for oxygen. If we see a predominance of other light gases like helium we may need to use a small (~1 cm^3) appendage ion pump on the system to remove this gas. It would be nice to avoid the additional complexity of such appendages if possible, unless they are deemed absolutely necessary by solid measurements. It is also possible that our molecular sieve is slowly outgassing small amounts of helium and neon. We will study this possibility by baking and pumping the entire system and the molecular sieve on the turbo pump for much longer periods of time (like weeks) before sealing and cooling the system. We will note any changes in the amount and type of gas accumulation.

The test cryostat, MC0-a, will be cooled down with the mechanical cooler to evaluate the impact of gasses on the temperature of the cold tip. First we will operate MC0-a with the copper block (with thermometry) only on the cooler cold tip while pumping on the cooler with the turbo pump. This will give us the baseline, lowest temperature to be expected. All gases accumulated after the seal-off valve is closed will add a heat load that is measurable by an increase in the coldest achievable temperature. The heat lift of the cooler is well known as a function of operating temperature. To a very good approximation, the power is: P = (.224W/K)*(T-32K). Next we will seal off the test cryostat and operate the cooler. We will measure the temperature of the copper block as a function of time after the test cryostat has been allowed to sit in air. After a few weeks, we should measure a temperature increase with time similar to that discussed in our preliminary measurements. We will then open the cryostat to the RGA-turbo pump system to measure the accumulated gas species. This will be our first quantitative data on the important gas constituents affecting the vacuum and temperature of a large mechanically cooled germanium detector system.

CONCLUSION(S) AND RECOMMENDATIONS

This project has only just begun. As of yet, we have no sweeping conclusions or recommendations.

ACKNOWLEDGEMENTS

We would like to thank the Office of Nonproliferation Research and Development (NA22) for the opportunity to make contributions to enabling technologies for better, more sensitive radioisotope measurements for nuclear explosion monitoring.

REFERENCES

Bowyer, S. M., H. S. Miley, R. C. Thompson, and C. W. Hubbard. 1997. Automated particulate sampler for comprehensive test ban treaty verification (the DOE radionuclide aerosol sampler/analyzer). *IEEE Transactions on Nuclear Science* 44: (3), 551–6.

Grove, A. S., (1967). *Physics and technology of semiconductor devices*, John Wiley & Sons, Inc. (1967).

Hull, E. L., Morgan T. Burks, Chris P. Cork, William Craig, Del Eckels, Lorenzo Fabris, Anthony Lavietes, Paul N. Luke, Norman W. Madden, Richard H. Pehl, and Klaus P. Ziock, (2002). A germanium orthogonal strip detector system for gamma-ray imaging, AIP Conference Proceedings 632**,** *Unattended Radiation sensor systems for remote application*, Washington, DC. 2002, p.118.

Hull, E. L., R. H. Pehl, (2005) Amorphous germanium contacts on germanium detectors, *Nucl. Inst. and Meth*. A, 538: Issues 1-3, (2005), pp. 651–656.

Keyser, R. M., T. R. Twomey, D. L. Upp (2003). Performance of light-weight, battery-operated, high-purity germanium detectors for field use, presented at INMM, July 2003.

Malm, H. L., (1975) Properties of metal surface barriers on high purity germanium, *IEEE Trans. Nucl. Sci*., NS-22, p. 140.

Miley, H. S., S. M. Bowyer, C. W. Hubbard, A. D. Mckinnon, R. W. Perkins, R. C. Thompson, and R. A. Warner. 1998. A description of the doe radionuclide aerosol sampler/analyzer for the comprehensive test ban treaty. *Journal of Radioanalytical and Nuclear Chemistry* 235: (1-2): 83–87.

Pehl, R. H., E. E. Haller, and R. C. Cordi, (1973). Operational characteristics of germanium detectors at higher temperatures, *IEEE Trans. Nucl. Sci.* 20: p. 494.

Stern, S. A. and F. S. DiPaolo, (1967). The adsorption of atmospheric gases on molecular sieves at low pressures and temperatures, *Journal of Vacuum Sciences and Technology*, 4: (6), 347.

Sze, S. M., (1981). *Physics of Semiconductor Device*s, 2nd Edition, John Wiley & Sons, Inc.

A BETA-PARTICLE HODOSCOPE CONSTRUCTED USING SCINTILLATING OPTICAL FIBERS AND POSITION SENSITIVE PHOTOMULTILPLIER TUBES

John L. Orrell, Craig E. Aalseth, Anthony R. Day, James E. Fast, Todd W. Hossbach, Lance S. Lidey, Harry S. Miley, Michael D. Ripplinger, and Brian T. Schrom

Pacific Northwest National Laboratory

Sponsored by National Nuclear Security Administration
Office of Nonproliferation Research and Development
Office of Defense Nuclear Nonproliferation

Contract No. DE-AC05-RLO1830

ABSTRACT

A hodoscopic detector was constructed using scintillating optical fibers and position sensitive photomultiplier tubes to determine the location of beta-active micron-sized particulates on air filters. The ability to locate beta active particulates on air-sample filters is a tool for environmental monitoring of anthropogenic production of radioactive material. A robust, field-deployable instrument can provide localization of radioactive particulate with position resolution of a few millimeters. The detector employs two crossed layers of scintillating optical fiber on which a filter is placed for assay. The detector is intended to be sensitive to activity greater than 1 Bq. To reduce power and the number of electronic read-out channels, position sensitive photomultiplier tubes are used to determine those fibers transmitting scintillation light. The physical design, position reconstruction method, and expected detector sensitivity are reported.

OBJECTIVE

The filter activity survey technique (FAST) is intended to provide a method of detection for beta active particulates collected on air filters used in treaty monitoring programs. The FAST system is intended to extend the filter triage efficacy by identifying filters with beta-active particulates with greater than approximately 0.75 Bq events (1 Bq = one disintegration per second). The identification of these lower-activity laden filers can then be given higher high-purity germanium (HPGe) counting priority and used for planning of follow-on sampling activities.

The FAST system provides additional sensitivity by taking advantage of the particulate nature of the beta-active particles of interest to treaty monitoring programs. A filter is expected to have a predominately uniform background of activity 2 Bq/cm^2 coming from radon daughters or other radioisotopes naturally present in the atmosphere. The detection goal is to identify a particle having an activity of 0.75 Bq that is essentially a point source of beta radiation. Using two crossed arrays of scintillating optical fibers, it is possible to create radiation detection elements of approximately 10 mm^2, depending on the exact width of the optical fibers used and the resolution of the instrument. These 10 mm^2 detection elements would see an effective signal-to-noise ratio equal to 3.75 from the 0.75 Bq signal and a background of 0.2 Bq per 10 mm^2. Counting a typical 16-in. diameter filter without position sensitivity that has ten of these 0.75 Bq activity particles gives a signal-to-noise ratio of 0.0029, approximately a factor of 1300 worse than expected for the FAST system.

The active element of the FAST apparatus is constructed using two single-fiber think arrays of scintillating optical fibers crossed at right angles. The fibers in the top layer, closest to the filter, have a 0.5 mm by 0.5 mm square cross-section. The bottom layer is composed of 1.0 mm by 1.0 mm square cross-section fibers. Each of the two crossed arrays of fibers defines one coordinate axis on the filter plane. The scintillating optical fibers are connected to a position sensitive photomultiplier tube (PMT), with one PMT per layer. Thus each PMT provides information along a single axis of the filter plane. Combining coincident information from each of the two PMTs allows for the two-dimensional reconstruction of the location of activity on the filter. The critical components (plastic optical fibers and PMTs) of the system are robust in transport allowing for field deployment of the system in a large luggage-sized case. To make the FAST system as effective and sensitive as possible, a number of issues were investigated in the construction of the detection components and the integration of the software reconstruction. Design schematics are shown in Figure 1.

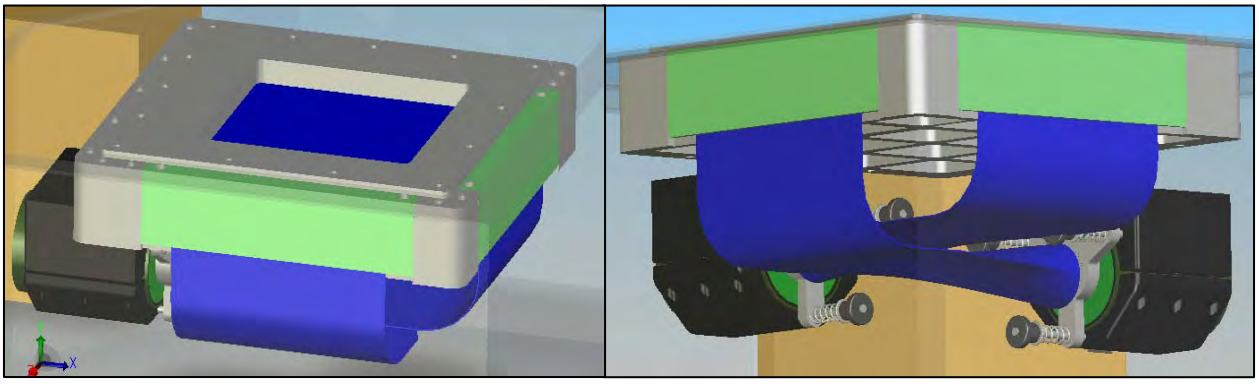


Figure 1. Design schematics of the internal components of the FAST apparatus. The fiber layers are blue. Position sensitive photomultiplier tubes (PS-PMTs) are held by black support blocks. Grey and green parts are plastic superstructure.

RESEARCH ACCOMPLISHED

The work done to make a field ready FAST system focuses on studying the light collection properties of the underlying detection mechanism and implementing a design approach in response to the component-by-component requirements.

Introduction: Position Sensitive Photomultiplier Tubes

The use of position sensitive photomultiplier tubes (PS-PMTs) dramatically reduces the number of electrical components and electrical read-out channels needed for the FAST system. The information from hundreds of optical fibers are collected by two PS-PMTs and reduced two four electrical read-outs per PS-PMT. The position of light on the face of the PS-PMT is determined from ratios of these electrical signals. The "energy" measured on each of the four PS-PMT channels (A, B, C, and D) are used to reconstruct the location of the light on the PMT's front window. The equations used to calculate the x and y coordinates are:

$$x = \frac{(A-B)}{(A+B)} \qquad\qquad y = \frac{(C-D)}{(C+D)}$$

A two-dimensional histogram is then filled using the calculated x and y coordinates. The entries in the histogram are given a weight equal to the sum of the four channels, E = A + B + C + D, which properly represents the total energy of the event seen by the PS-PMT.

Fiber Resolution

The response of the PS-PMT to light traveling down a single 1 mm by 1 mm cross-sectional optical fiber determines the ability of the PS-PMT to resolve the physical location of the fiber on the face of the tube. Greater ability to identify light from individual fibers in the fiber array is directly related to the ability of the FAST system to resolve locations of activity on the air filter. Conversely, restated as a design requirement, the reconstruction resolution of a single optical fiber on the face of the PS-PMT defines the proximity beyond which fibers are individually identifiable. In simple terms, the size of the reconstructed spot generated by a fiber on the face of the PS-PMT defines how far apart fibers should be spaced. Figure 2 shows two scintillating optical fibers having a physical separation (denoted by the subscript "mm") of Δ_{mm} = 14.19 mm center-to-center on the face of the PS-PMT. This value sets the scale to convert between the PS-PMT's coordinate (dented by the subscript "PMT") and physical coordinates measured in millimeters. A two-dimensional fit was applied to the histogram of two irradiated fibers shown in Figure 2 to extract the *x* and *y* coordinates of the centers of the peaks and to determine a (Gaussian based) measure of the peak widths. This fit has the form

$$\begin{aligned} z \;=\; & a_0 + a_1 e^{-\frac{1}{2}\left[\left(\frac{x-x_1}{\sigma_{x_1}}\right)^2+\left(\frac{y-y_1}{\sigma_{y_1}}\right)^2\right]} \\ & + a_2 e^{-\frac{1}{2}\left[\left(\frac{x-x_2}{\sigma_{x_2}}\right)^2+\left(\frac{y-y_2}{\sigma_{y_2}}\right)^2\right]} \\ & + a_3 e^{-\frac{1}{2}\left[\left(\frac{m_{xy}x+b-y}{\sigma_{xy}}\right)^2+\left(\frac{m_{yx}x+b-y}{\sigma_{yx}}\right)^2\right]} \end{aligned} \qquad [1]$$

where *z* is the color-height of the histogram, a_n are height-magnitudes, and the exponential functions define two, 2-dimensional Gaussian peaks and a saddle region bridging between the two peaks. The fit variables are constrained such that specific peaks and the saddle region are selected by each portion of the formula. The fit determined the following tabulated values; only variables relevant to determining the fiber resolution are shown.

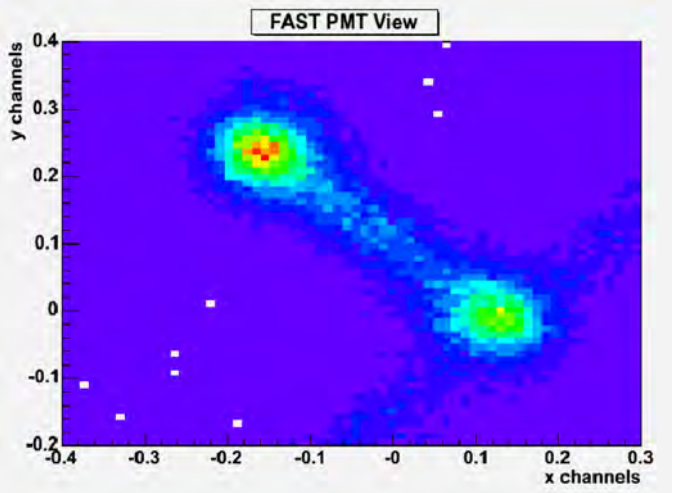


Figure 2. Reconstruction of a single position sensitive photomultiplier tube (PS-PMT) having two scintillating optical fibers attached to the face of the tube. Red indicates greater intensity.

Table 1. Resulting parameters from a two Gaussian fit to the histogram in Figure 2

Parameter		**Value (PMT)**
Large, Upper Left Peak	Center (x_1 , y_1)	(-0.1560 , 0.2330)
Large, Upper Left Peak	Widths (σ_{x1} , σ_{y1})	(0.0398 , 0.0406)
Smaller, Lower Right Peak	Center (x_2 , y_2)	(0.1310 , -0.0050)
Smaller, Lower Right Peak	Widths (σ_{x2} , σ_{y2})	(0.0443 , 0.0409)

From these we determine an average resolution, $\langle\sigma_{PMT}\rangle = 0.0414$, and the separation between the centers of the two peaks, $\Delta_{PMT} = 0.373$, both measured in the PMT's coordinate system. Using a ratio, we can now determine the absolute physical resolution of the peaks:

$$\frac{\langle\sigma_{mm}\rangle}{\langle\sigma_{PMT}\rangle} = \frac{\Delta_{mm}}{\Delta_{PMT}} \quad \rightarrow \quad \frac{\langle\sigma_{mm}\rangle}{0.0414} = \frac{14.19}{0.373} \quad \Rightarrow \quad \langle\sigma_{mm}\rangle = 1.58\text{mm} \qquad [2]$$

Light Sharing

In Figure 2 from the previous section, it is noted there is a raised saddle region of events spanning between the two fibers shown. This is the blue-ridge generally following a y = x–0.1 formula through the green peak in the lower right corner. This saddle region is a ridge created due to light sharing between fibers that are physically adjacent to one another *at the location of the radiation interaction*. The reason the ridge appears is because the PS-PMT is an analog instrument: if there is light coming out of two fibers, the PS-PMT responds with a set of four output signals that is a light intensity weighted average. That is, if two fibers have the same intensity of light, then the PS-PMT will give an output signal that is exactly between the two fibers on the face of the tube. In general, this is a hindrance to being able to distinguish single fiber illumination. To address this issue it is important to understand the source of the light sharing.

When radiation interacts in the scintillating optical fibers, the end result is the production of light. The light produced is isotropic. In fact only 3% to 4% of the scintillation light is captured and transmitted by the optical fibers Saint-Gobain (2005). The remaining greater than 95% of the scintillation light leaves the fiber in which is was generated. Secondary fibers, physically adjacent to the primary fiber, have the possibility to capture and transmit some fraction of the isotropic scintillation light leaving the primary fiber. This is the process by which light sharing

among fibers is created. To combat light sharing between fibers, a series of tests were conducted looking for fiber coatings that could both serve to first reduce or eliminate light sharing and second act as an adhesive to bond the together into arrays. The secondary adhesion requirement for the coating was a design consideration to minimize the amount of material between the source of the beta particles and the active scintillating core of the optical fibers. That is, the coating should not attenuate a large fraction of the beta particles the FAST system is intended to detect. The two best coating are shown in Figure 3. The best coating scheme was to aluminize the optical fibers and then coating then in a white, urethane based extramural absorber. However, this process was time consuming and only moderately better than only using the white extramural absorber. Since the extramural absorber coating acts as a bonding agent it was the chosen coating scheme.

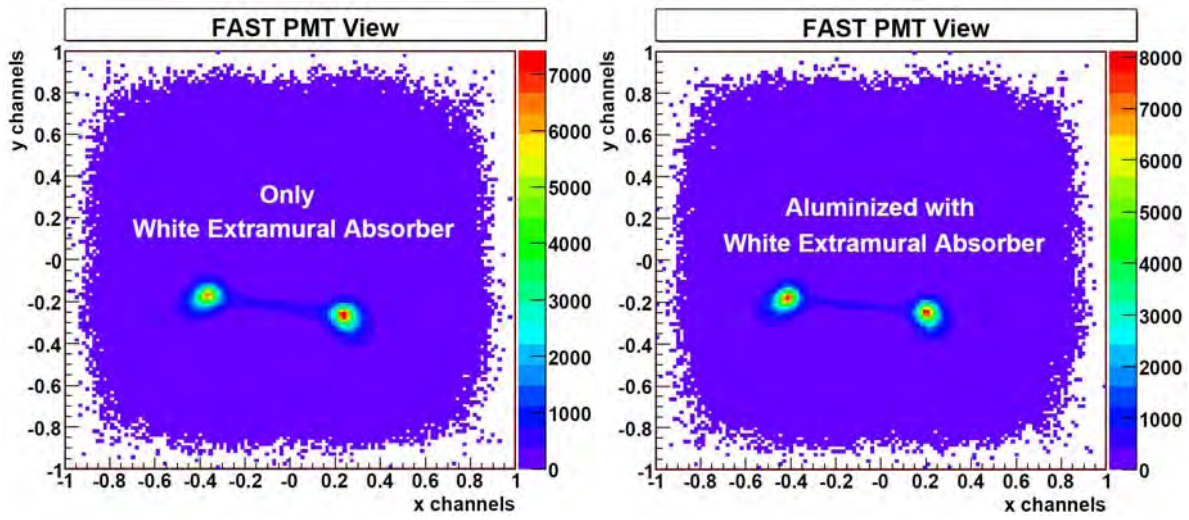


Figure 3. Light sharing between adjacent fibers and the reduction thereof by coatings.

Fiber Puck Design

From the requirements of the preceding sections, several hundred fibers from one layer are attached to a single PS-PMT. The design takes into account several features of the components. The analog nature of the PS-PMTs and the residual light sharing among fibers calls for placement of fibers adjacent to another on the face of the tube. In this way, if there is light sharing or incorrect reconstruction of the PS-PMT, the induced error will only contribute to a small shift in the estimation of the location of the beta activity on the assayed filter, on the order of a few millimeters. Likewise, fibers that are physically distant from one another on the filter measure surface, should be physically distant from one another on the face of the PS-PMT. These considerations lead to a fiber layout on the face of the PS-PMT having a snaking pattern across to the tube face, placing adjacent fibers closer together and columns of the pattern further apart. This is diagrammed in Figure 4.

Beta Attenuation Simulation

To determine the location of beta activity on an air filter, an emitted beta particle must interact and produce scintillation light in *both* of the crossed layers of optical fibers. For this to take place the beta particle must not be stopped by the top layer of fibers before reaching the bottom layer of fibers. To understand the effect of beta attenuation in the FAST detection elements a FLUKA (http://www.fluka.org/) simulation was performed. The simulation determined when more than 10 keV of energy is deposited in both fiber layers for a series of mono-energetic electrons incident perpendicular to the crossed-array. The effect of variable thickness aluminum entrance windows was also studied. The result of the simulation, shown in Figure 5, clearly demonstrates there is approximately a 200 keV energy threshold reduction (from ~500 keV to ~300 keV) availed by using 0.5 mm by 0.5 mm cross-sectional fibers. Over the range of expected thicknesses of the aluminum entrance windows, the change in apparatus is comparatively small.

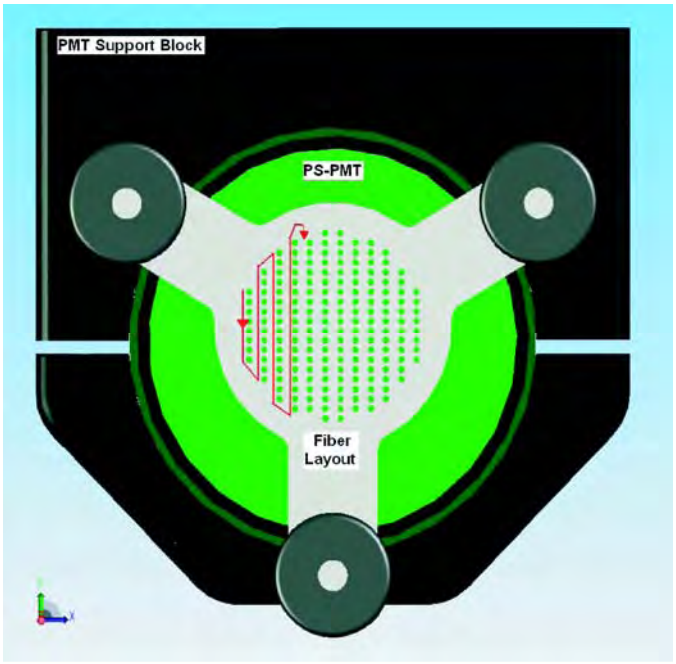


Figure 4. Fiber puck design schematic. Individual fibers are positioned in the holes. The "snaking" red path shows the fiber layout relative to the flat filter assay surface.

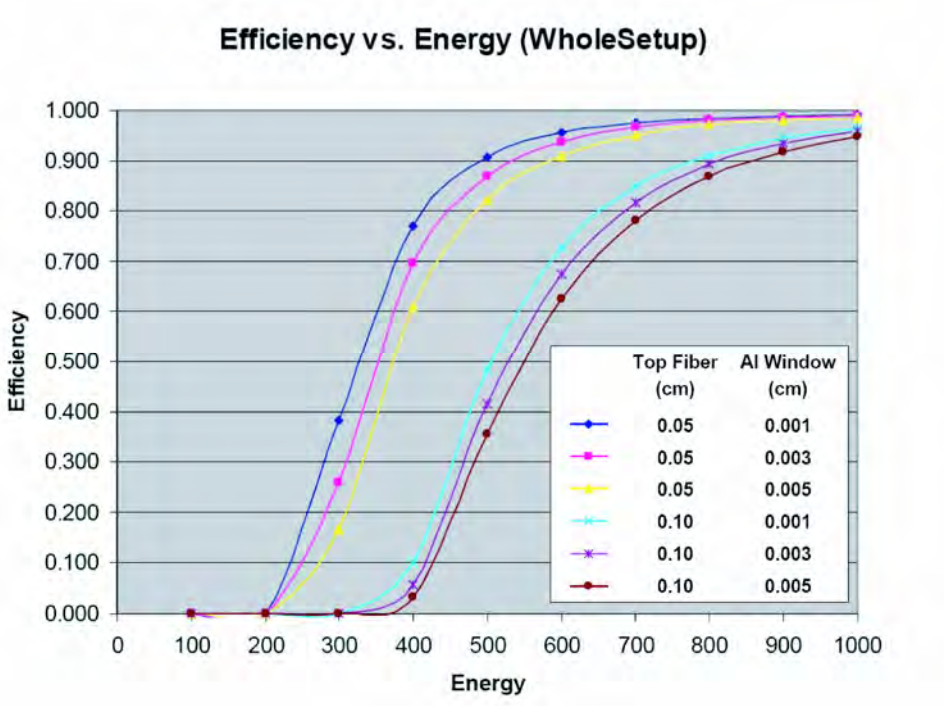


Figure 5. Total beta detection efficiency as a function of the initial beta particle energy for various thicknesses of the FAST detection components.

First Filter Map Reconstruction

The hardware assembly complete, the developing calibration tools necessary for the full reconstruction of the filter activity map provide a glimpse of the operational capability of the FAST system. Figure 6 is a screen image of the analysis program showing the FAST system's response to a beta source collimated to 1 mm diameter. The mirror/ghost images appearing in the filter activity map of the known *single* collimated source are due to both the yet to be optimized hardware configuration and the scaling symmetry present in the reconstruction algorithm. Once the already demonstrated resolution (see Figures 2 and 3) is obtained, it is clear from this initial filter activity map that 4 mm full width at half maximum resolution will be achieved.

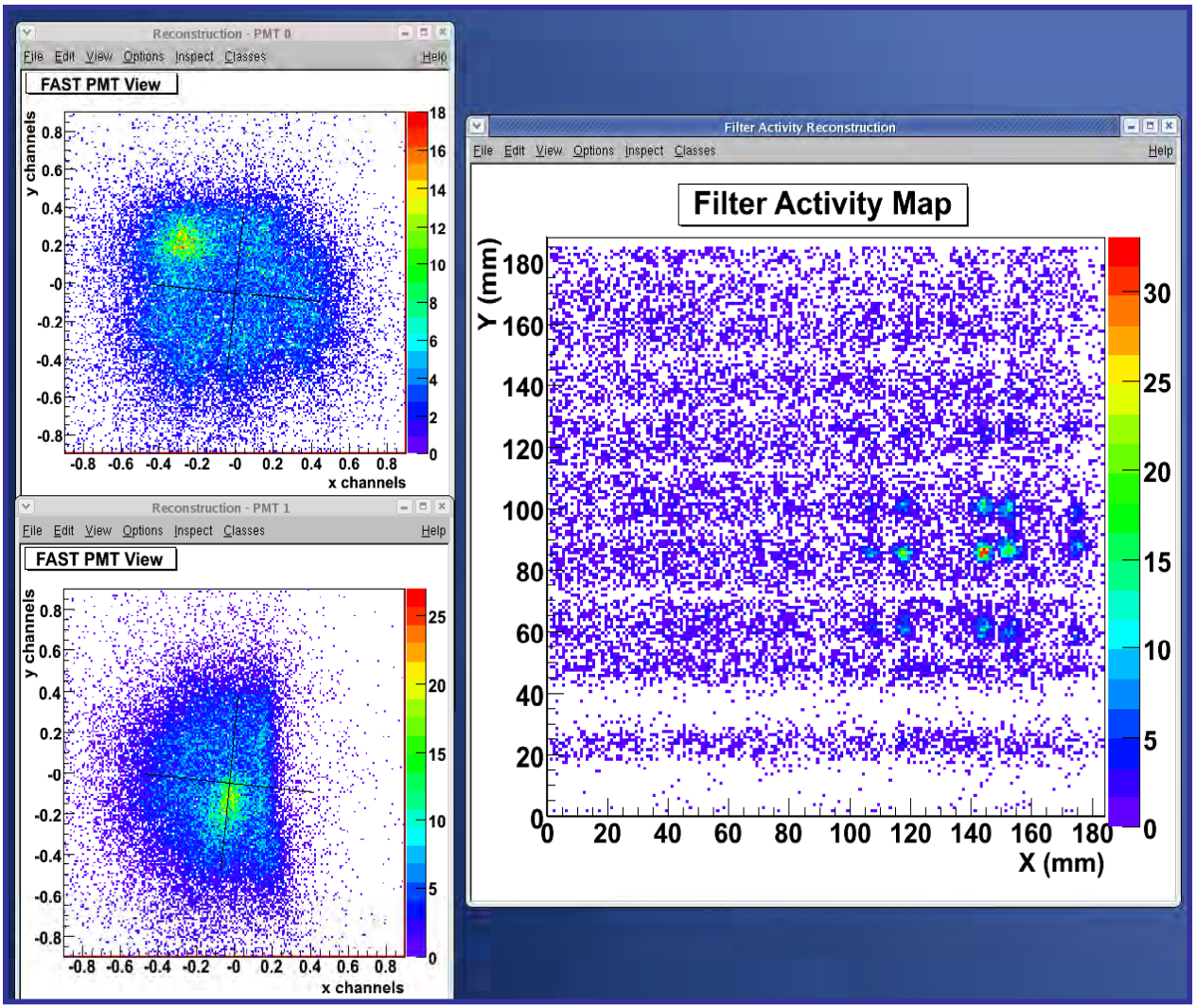


Figure 6. Screen capture of an early full two-dimensional reconstruction of the filter assay area. A 1 mm diameter Sr-90 source is located on the detection surface. Mirror images seen in the filter activity map are due to less than optimal single PS-PMT resolution and scale symmetries in the calibration program.

CONCLUSIONS AND RECOMMENDATIONS

The FAST system has demonstrated the ability to identify beta activity and is expected to provide particulate location information on the few millimeter scale. The technology employed is similar to that applied to particle detectors located at high-energy physics accelerator facilities (Baehr et al., 1994 and Kuroda, 1989). The technical challenge was optimizing these components to operate effectively at particle energies six orders of magnitude lower. The detection portion of the apparatus is composed solely of plastic optical fibers, two position sensitive photomultiplier tubes, and one small electronics crate with an on-board central processing unit (CPU). These components are expected to be robust in field deployment.

Work continues on the optimization of the automated diagnostics and calibration routines to streamline the user interface. Analysis software is progressing past the most simplistic reconstruction algorithms to provide greater fidelity and result reliability. Figure 7 shows the FAST apparatus on a test bench where this work is being conducted. The coming year will transition this instrument to the end users for true field deployment.

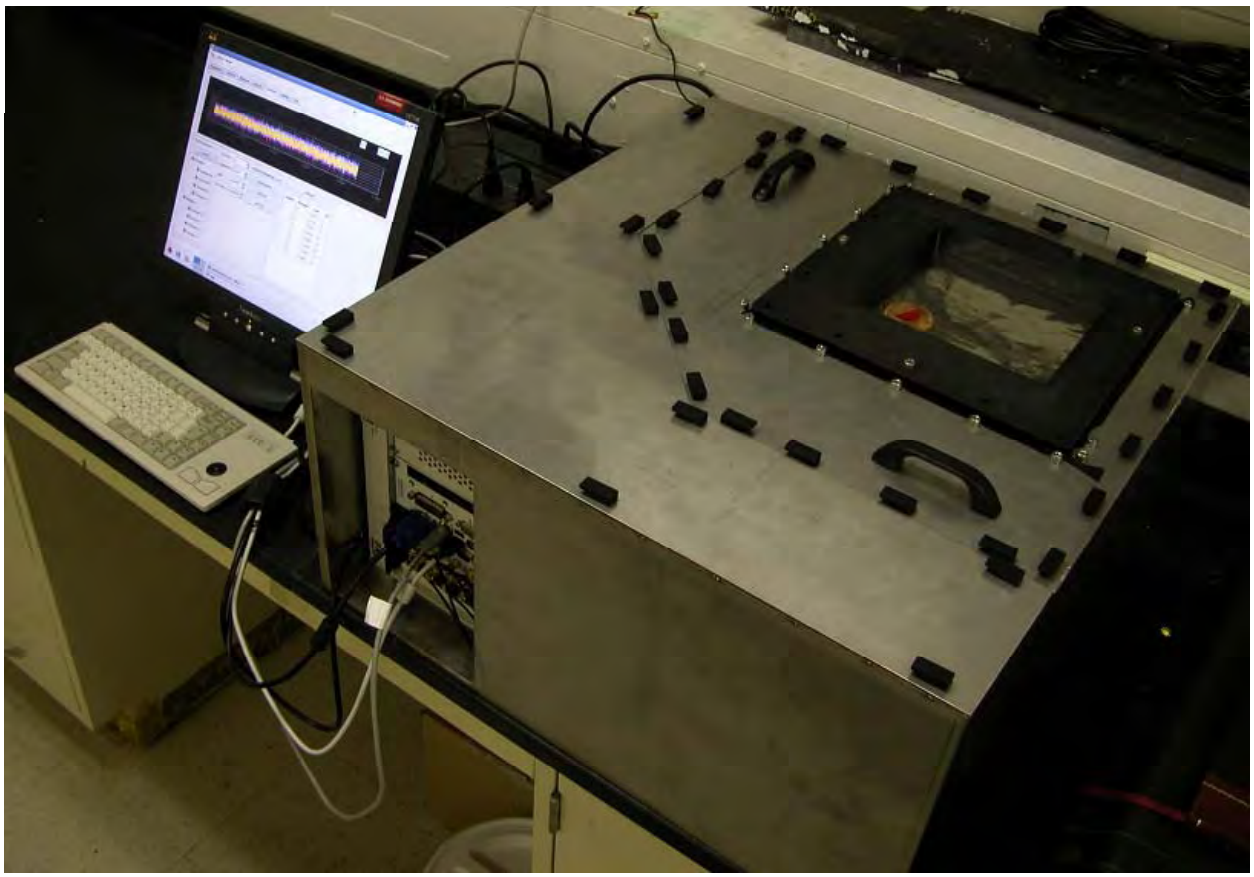


Figure 7. All components of FAST are self-contained except for the keyboard and monitor. The filter assay surface, redesigned for quarter folded filters, is inside the black rectangle at the upper right.

REFERENCES

Baehr, J., K. Hiller, B. Hoffmann, H. Lüdecke, R. Nahnhauer, A. Menchikov, M. Pohl, H. E. Roloff, and R. Völkert (1994). Test of fiber detector readout by position-sensitive photomultipliers, *Nucl. Instrum. Methods Phys. Res.* A348: 713–718.

The FLUKA particle physics Monte Carlo simulation software package. http://www.fluka.org/.

Kuroda, K. (1989). A new trend in photomultiplier techniques and its implications in future collider experiments, *Nucl. Instrum. Methods Phys. Res.* A. 277: 242–250.

Saint-Gobain Crystals (2005). Scintillation Products, Scintillating Optical Fibers Brochure, Version 605.

TIME PROJECTION CHAMBER FOR LOCATING FISSION FRAGMENTS IN RASA FILTERS

William K. Warburton and Brendan J. Dwyer-McNally

XIA, LLC

Sponsored by the National Nuclear Security Administration
Office of Nonproliferation Research and Development
Office of Defense Nuclear Nonproliferation

Contract No. DE-FG02-04ER84179

ABSTRACT

Detecting nuclear debris vented to the Earth's atmosphere from a nuclear explosion can provide highly reliable corroborative evidence that an explosion detected by other means (e.g., seismically) was in fact nuclear. The DOE's Pacific Northwest National Laboratory (PNNL) has developed a highly sensitive, automated system (RASA: Radionuclide Aerosol Sampling and Analysis) to capture such debris from the atmosphere and prescreen it for evidence of radioactivity. RASA is capable of detecting that it has captured as few as 10 fragments, each having only 10^5 fission atoms, in one of its 60 cm x 40 cm polypropylene filters. Having done so, however, RASA lacks the capability of locating these particles, whose sizes will typically be in the 0.3–0.5 μm range, so that they can be excised and distributed to certified laboratories for confirmatory measurements.

In this project we are working to develop an ultra-low background "time projection chamber" to determine the locations of alpha-particle-emitting fragments with a positional accuracy of better than 1 cm. Our work builds upon a commercial product being developed at XIA that is capable of measuring the alpha emissivity of Pb at the 0.0005 α/cm^2/hour level for the electronics industry. Operating as an ionization counter filled with pure N_2, this instrument employs pulse shape analysis to determine if detected alpha particles emanated from the 45 x 45 cm^2 Pb sample or the counter's electrode. This discrimination allows the counter to achieve detection limits that would otherwise require counter construction using hyper-pure materials.

In the time projection chamber we replace the single electrode with an electrode of "flattened" cross-strips that are 1 cm wide. When an alpha particle produces an ionization track in the N_2, the electrons in the track drift to the electrode, inducing currents in the strips as they move. After integration by charge sensitive preamplifiers, the resultant time dependent charge signals are captured by digital signal processors for analysis. Each strip captures the track charge projected on it, and the time of arrival of that charge increases with the distance between its original location along the track and the electrode. By using the complete set of charges and arrival times captured from all the electrode strips, it then becomes possible to reconstruct the original charge track in 3 dimensions. In this paper we present results, computed using an accurate charge induction model, that show the time evolution of the counter's signals and indicate that the method should be able to locate track origins (and hence particle locations) within 0.5 cm using 1 cm strip widths.

OBJECTIVE

XIA, LLC, is currently working to develop an ultra-low background time projection chamber (TPC) to spatially locate the ionization tracks produced by alpha particles emitted from samples placed within it. Accomplishing this project will require meeting multiple objectives including designing and fabricating an experimental TPC, developing electronics to cost-effectively instrument its crossed strip electrode; and, most critical, developing analysis software to extract the track locations from captured signals. In support of the latter effort, we have the objective reported here: to develop a computational procedure capable of producing realistic model electrode signals that we can use both to develop our intuition about the expected signals and, particularly, to provide well characterized input signals for the track location software. Specifically, to test our track location algorithms, we would like to be able to generate expected signals from an alpha particle track emitted from a random location in a random direction within the TPC. Once we can reliably recover track locations from noisy theoretical electrode signals, then we will be ready to move on to examining track signals from point alpha sources—comparing these signals to the theory in order to refine the theory and adapting our location algorithms to accommodate the differences between theoretical and practical signals. In this paper we report that we have successfully developed the theoretical model and present some example signal traces that both elucidate the physical nature of the problem and suggest algorithms that can be developed to extract track locations.

RESEARCH ACCOMPLISHED

Project Background

Detecting nuclear debris vented to the Earth's atmosphere from a nuclear explosion can provide highly reliable corroborative evidence that an explosion detected by other means (e.g., seismically) was in fact nuclear. Under the Comprehensive Nuclear-Test-Ban Treaty (CTBT), the Provisional Technical Secretariat has been building up the International Monitoring System (IMS), including a network of 80 air filtering stations to monitor for radioactive particulate matter. A good example of the instrumentation found at such stations is the highly sensitive, automated RASA (Radionuclide Aerosol Sampling and Analysis) system, developed by DOE's Pacific Northwest National Laboratory (PNNL), which is designed to capture such debris from the atmosphere and prescreen it for evidence of radioactivity (Bowyer et al., 1997; Miley et al., 1998). RASA operates by filtering approximately 20,000 m^3 of air per day through a 60 cm x 40 cm polypropylene filter composed of six 10 cm x 40 cm strips. These strips are piled into a single 10 cm x 40 cm sandwich and wrapped around a 40% HPGe detector to determine if any fission products are present. If any are detected, then the filter is supposed to be divided into 2–3 pieces of nearly equal activity, with 1–2 pieces being sent to certified laboratories for confirmatory measurements and 1 piece being archived. Only this last step (dividing the pieces) is not automated. Personnel have to actually travel to the station to make the division.

RASA is extremely sensitive, being able to detect about 10^6 fission atoms collected in 24 hours, which corresponds to 30 mBq/m^3 of air, for a 20,000 m^3 sample. Its sensitivity is limited by both the efficiency of the HPGe detector and the ubiquitous background of airborne radon daughters (^{214}Pb, ^{214}Bi, ^{212}Pb, ^{212}Bi, and ^{208}Tl) that are also trapped in the filter. The system has no spatial sensitivity. This becomes an issue in the event that a filter needs to be divided, because RASA is sensitive enough to detect as few as 10 particles each containing only 10^5 fission atoms and ranging in size between 0.1 to 10 μm (typically 0.3–5.0 μm). Knowing the locations of these particles then becomes critical: first to know that the number is indeed small, which may require special handling; second, to ensure that each certified laboratory gets an appropriate (and known) fraction of the particulates; and third, because signal to noise in the counting measurements can be increased by over 2 orders of magnitude if the particles can be excised from the radon daughter–laden filter. DOE has therefore included a request in their recent SBIR solicitations for an instrument capable of locating such particles with an accuracy of approximately 1 cm. XIA, LLC, responded to one of these solicitations and is currently doing Phase I research to develop a TPC to meet this need.

Instrument Design

Our TPC design is an extension of an ultra-low background alpha particle counter originally developed to measure alpha particle emissivity from Pb and other materials of interest to the semiconductor industry (Warburton et al., 2004; Warburton and Dwyer-McNally, 2006). The counter is fundamentally a parallel plate ionization chamber with a guard ring enclosing its anode electrode, as shown in the sketch in Figure 1. Both the anode and guard ring are

instrumented with charge integrating preamplifiers whose outputs are digitized and captured for offline analysis. The counter is filled with dry N_2 gas, and 1000 V are applied between the sample tray and the electrodes. When an alpha particle is emitted into the chamber, it deposits energy in the N_2, creating an ionization track. The electrons in the track then drift toward the anode. The operation of the counter is based on the principles of charge induction. As described in the references, in the parallel plate geometry, as long as each electron is drifting toward the anode, it induces a constant current in the anode that, when integrated onto the preamplifier's feedback capacitor, results in a uniformly rising preamplifier output signal. When the electron reaches the anode, the induction stops, no more current flows, and the preamplifier signal either becomes constant or starts decaying (in radiochemical feedback configurations). Thus, the farther the electron drifts, the longer the preamplifier signal risetime and the larger its final value.

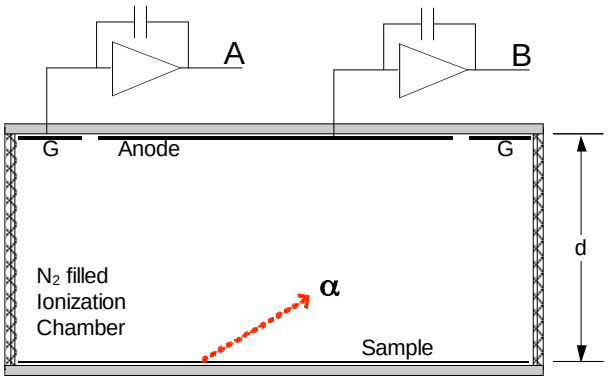


Figure 1. Sketch of the original XIA ultra-low background alpha particle counter.

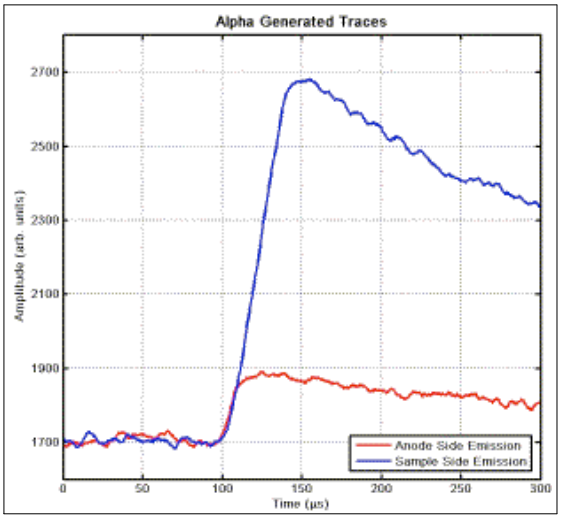


Figure 2. Signal traces captured from the alpha particle counter shown in Figure 1.

In particular, this means that ion tracks emanating on the sample side, which have to drift all the way across the chamber, produce long (45–50 μs) signal risetimes and large output signals. On the other hand, ion tracks that emanate from the anode itself merely have to drift the short distance back to the anode, producing short (10–15 μs) risetimes and small output signals. Figure 2 shows typical traces for both cases. Thus, by measuring signal risetimes and amplitudes, it becomes possible to use pulse shape analysis to discriminate between the two cases and electronically reject signals that do not originate from the sample. By this means it becomes possible to obtain ultra-low background counting without having to construct the counter out of expensive materials having ultra-low alpha particle emissivities. Because alpha particles emanating from the sidewalls can produce signals whose risetimes can have any values lying between the extremes noted above, they cannot be completely rejected based on pulse shape alone. This problem is solved by the use of a guard ring, which is placed to collect a significant fraction of the track charges from all sidewall events. Good anode signals are then required to be in anti-coincidence with guard ring signals. Using these methods we have reduced background counting rates in a commercial prototype having a 45 cm x 45 cm anode area, the Ultra-Lo-1800, to below 0.0001 α/cm^2/hour. This instrument, like the RASA, has no position sensitivity.

In order to add that position sensitivity, we needed to replace the Ultra-Lo's single anode with some type of segmented anode array. After considering the alternatives, we developed the "flattened" cross strip array electrode design shown in Figure 3. The following issues were involved in this decision. First, in order to achieve 1 cm spatial resolution or better, we estimated that we would need pixel dimensions of order 1 cm x 1 cm, or 2400 pixels for the 40 cm x 60 cm RASA filters. However, even at a reduced electronics cost of $500/pixel, this is clearly an enormously expensive approach. At low event rates, where there is never more than a single track in the TPC, a crossed strip design can produce nearly as much tracking information but would require only 100 channels of electronics (40 + 60). While crossed strip anodes are traditionally made of strung wires, our experience with the

Ultra-Lo 1800 showed an extreme sensitivity to microphonics, to which strung wires are particularly prone. The Figure 3 design is fabricated using printed circuit board technology and can be solidly attached to a rigid backing surface, essentially eliminating all but very low frequency pickup. As shown in Figure 3, in one direction there are row electrodes that are actually perforated strips, with preamplifier contacts at one end. The perforations are filled with electrically isolated secondary electrodes that are connected in columns via traces on the board's backside to form the orthogonal set of strips. As the electrons in an ionization track drift toward this anode, they will induce different amounts of charge in different column and row "strips," from which we will attempt to reconstruct the original track location. Our next step, therefore, and the topic of this report, is to develop a model explicitly describing the charge induction process relating the original track location to the strip output signals.

Charge Induction Model

We begin by considering an isolated electron of charge $-q$ located at a distance z from an infinite conducting plane. We know that electric field lines must be everywhere normal to the conductor and that the magnitude of the field as a function of location is easily found using the method of image charges, i.e., by reflecting an image charge $+q$ at a distance $-z$ on the opposing side of the conducting plane. Gauss's Law then provides the connection between the local electric field strength at any point on the conducting plane and the surface charge density σ required to support it. In particular, if we subdivide the conducting plane into a set of strips, pixels, or other shapes, then we can integrate σ_i over any particular isolated shape i to compute the total charge Q_i induced on it.

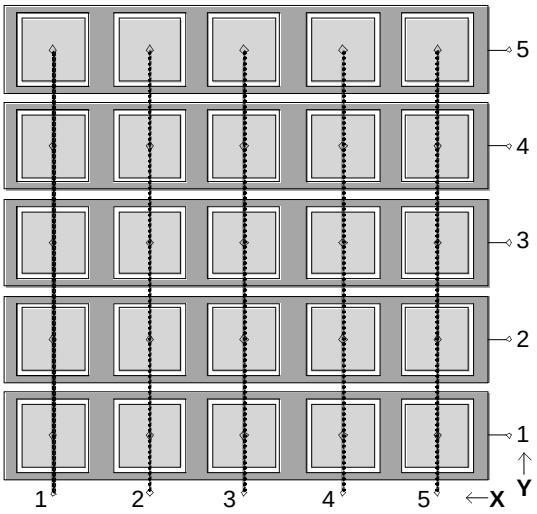


Figure 3. Sketch of the "flattened" cross strip anode.

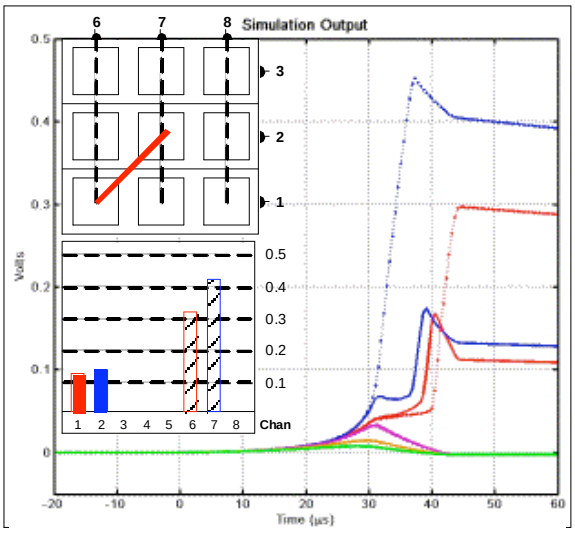


Figure 4. Computed output traces and collected charges for the indicated alpha particle track.

If the separation z is now a function of time $z(t)$, the same procedure can be employed to compute $\sigma(t)$ and hence $Q_i(t)$. The time derivative of $Q_i(t)$ is the current $I_i(t)$ that must flow to the pixel i to allow $Q_i(t)$ to change with time. If this current is integrated by a charge integrating preamplifier, then its output in time will be $Q_{pi}(t) = Q_i(t) - Q_i(0)$. In the case of an ionization track, equal densities of electronic and ionic charge will be created at z at time $t = 0$, but only the electrons will move significantly over the time scales of interest. Thus, the above expression for $Q_{pi}(t)$ will still be valid since only *changes* in surface charge density σ_i cause currents to flow through the external circuit.

When the test charge is placed *between* two planes separated by a distance d, as in our counter, where it lies between the anode plane and the conducting plane of the sample tray, the problem becomes more complex. This is because, while the test charge generates two primary image charges by reflection in the two planes, each of these generates a secondary image charge by refection in the other plane, the secondary charges generate tertiary image charges by reflection and so forth to produce an infinite set of image charges. Luckily, however, when the dimension d is large compared with the pixel or strip dimension, the series converges rather quickly, and typically only the first two or three orders are required to compute σ_i values to better than 1% accuracy. In this case (Warburton, 1998), when the

initial charge is located at (x, y, z) and the ij^{th} rectangular pixel is bounded by the values $(x_{in}, x_{ip}, y_{in}, y_{ip})$, the contribution to the induced charge on the pixel from the k^{th} image charge pair is given by Equation 1, where the fences represent the 4 signed terms from the four limits of integration:

$$Q_{ijk} = \frac{qz}{2\pi}\int_{x_{in}}^{x_{ip}} dx \int_{y_{in}}^{y_{ip}} \frac{dy}{\left(x^2 + y^2 + z_k^2\right)^{.5}} = \frac{q}{2\pi}\left|\left| \sin^{-1}\left(\frac{x_{i\pm}^2 \left(y_{j\pm}^2 - z_k^2\right) - z_k^2 \left(y_{j\pm}^2 + z_k^2\right)}{x_{i\pm}^2 \left(y_{j\pm}^2 + z_k^2\right) + z_k^2 \left(y_{j\pm}^2 + z_k^2\right)} \right) \right|\right|_{x_n}^{x_p} \Bigg|_{y_n}^{y_p} . \quad (1)$$

Q_{ijk} must then be summed over an adequate number of image charge pairs k to obtain the induced charge on pixel ij. In the present work we used three values of k. Because our strips are not simple rectangles, we computed the induced charge on unperforated strips and on the perforation areas separately. We then subtracted the perforation charges along the row strips to obtain induced charges on the row electrodes and summed perforation charges appropriately to obtain the induced charges on the column electrodes, in both cases from a simple test charge $-q$ at location (x,y).

Having created, in Equation 1, the basic machinery required to compute induced charges on our electrodes, we are now ready to generate signal traces from the drifting charges associated with ionization tracks. We assume that the track emanates from the sample plane at (x_0, y_0), has length L, and forms the angles ϕ with the z axis and θ with the x axis. For want of more-precise knowledge at this time, we assume a uniform charge density along the length L, which will typically be of order 5 cm for typical alpha energies in the 4–6 MeV range. Knowing the energy ε required to form an electron-ion pair in N_2, then gives the charge density ρ along the track. For purposes of computation, the track was subdivided into N equal segments, each of which was then treated as a point charge using Equation 1. A typical value of N in our model was 50. Since the track emanates from the sample surface, there is always at least one track segment that has to drift across the entire distance d = 150 mm, setting a constant maximum drift time T_d = 45 μs at a drift velocity of 0.3 μs/mm. For the purpose of computation, we then divided T_d into M steps, where M was typically 100.

The computation of the electrode signals then was carried out as indicated in the following pseudo code.

For each time step *m* between *1* and *M*, where time step 1 corresponds to the initial condition,
  Transfer $Q_{ij}(m)$ to $Q_{ij}(m\text{-}1)$ for all strip electrodes *ij*
  Zero $Q_{ij}(m)$ for all strip electrodes *ij*
 For each strip electrode *ij*
  For each track segment *n* between *1* and *N*
   Compute *z* of track segment
   If track segment *n* has not reached the anode
    For each image charge pair *k*
     Compute Q_{ijk} using Equation 1 and add to $Q_{ij}(m)$
    End For
   Else If track segment *n* annihilated with its image charge on this electrode
    Add the same charge contribution to $Q_{ij}(m)$ as in previous step *m-1*
   End If
  End For
 End For
  Compute $Q_{pij}(m) = Q_{ij}(m) - Q_{ij}(1)$
End For

Results—Introduction

Figure 4 shows the results of a sample computation using our model code. The inset in the upper left of the figure shows a sketch of a small section of the anode, with three horizontal Row electrodes labeled “1” through “3” and three vertical Column electrodes labeled “6” through “8”. Superimposed on this sketch is the upward projection, along the *z* axis, of the alpha particle ionization track being computed. Track locations are specified by their *x* and *y* point of emanation, measured in millimeters, from the origin (lower left-hand corner of the electrode), their angle θ

from the *x* axis, and their angle ϕ from the vertical. All tracks are 4.5 cm long. This particular track is designated (5.00, 5.00, 45, 20), meaning that it originated at a point located 5 mm in both *x* and *y* (i.e., centered on the first perforation in Column 6) and made angles 45° with the *x* axis and 20° with the *z* axis. The superimposed image clearly shows the *x*, *y*, and θ values; ϕ can be inferred from the relative track length.

The traces on the right-hand side of the image are the computed preamplifier output signals. The track starts drifting at time $t = 0$, but as is clear from the traces, no significant signals can be seen until approximately 25 μs have passed (i.e., the closest part of the track to the anode has moved over half way across the chamber). This is a manifestation of the well known "small pixel effect" (Barrett et al., 1995), which arises from the fact that until the charge is relatively close to the anode, most of its field lines terminate on other points on the (semi-infinite) anode plane. As may be seen from the figure, the uppermost charges in the track, which lie under Column 7, arrive first, followed by the charges lying under Row 2, Row 1, and Column 6. The sharp rising edges on these traces make it easy to determine which parts of the track arrive first and, thereby, which end of the track is up. The declines on Traces 1, 2, and 7 before they reach their final values at 44 μs is due to the loss of charge induced on their associated electrodes by the charge under Column 6, as that charge is eventually collected onto Column 6. Similarly, the moving track charges temporarily induce charges on Row 3 and Column 8 but leave no net charge on them because no part of the track finally reaches them. The bar graph inset in the lower left of the figure shows the final charges collected by the different electrodes at time 45 μs, just after the last charges in the track complete drifting to the anode.

Results—Variations with Track Orientation and Location

The following figures show how the output traces and collected charges vary as we systematically adjust the location and orientation of the ionization track. In Figures 5A–5C, we move the origin of the track by plus and minus increments of 2.13 mm with respect to a track similar to the one shown in Figure 4, leaving its orientation unchanged. As is immediately obvious, even these relatively small motions produce large changes in the output traces. Thus, compared with the central trace from a (5.00, 5.00, 32, 20) track, the trace from the (2.87, 5.00, 32, 20) track has nearly halved the charge collected on Row 1 and doubled the charge collected on Column 6, while leaving the order of arrival unchanged. On the other hand, the trace from the (7.13, 5.00, 32, 20) track has nearly doubled the charge collected on Row 2, while greatly reducing the charges collected on Columns 6 and 7, the former by a factor of nearly 3. The order of arrival has also changed, with Row 2 arriving before Column 7. The complex time structure of the traces can be understood by looking at the projection and noting that, due to the particular projection of the track onto the anode, parts of the Row 2 charge arrive both before and after the Column 7 charge. In noting changes in the traces with track translation, it is also worth noting that a translation of a full 10 mm, the pitch of the anode, will produce identical traces, but with the electrode numbers incremented appropriately by 1.

Figures 6A–6C document the trace changes that result from changing the angle θ by increments of 10° relative to a (7.13, 5.00, 32, 20) track. What is interesting here is that, while the ±10° motions produce fairly large changes in trace amplitudes compared with the central trace, they are not nearly so different from each other. Whether these cases could be distinguished by pulse amplitude alone will depend upon what signal-to-noise we can achieve in the detector. However, when we look at times of arrival, the two cases are clearly distinct, with the order of charge arrival being (2, 1, 7, 6) in the $\theta = 22°$ case and (7, 2, 1, 6) in the $\theta = 42°$ case. We also note the particular details of the trace shapes also vary considerably. However, until we know more about what signal-to-noise we can obtain, we do not wish to speculate about whether this information will also be usefully available to aid in our analysis.

Figures 7A–7C document the trace changes that result from changing the angle ϕ by increments of ±10° relative to a (7.13, 5.00, 32, 30) track. These variations produce even larger changes in the output traces than do the other two cases, primarily because changing ϕ effectively changes the projected track length, which changes the number of electrodes that collect induced charge. Thus, in addition to the observed changes in collected charge on Rows 1 and 2 and on Columns 6 and 7, between $\phi = 30°$ and $\phi = 20°$, we also see collected charge disappear from Column 8, whereas, between $\phi = 30°$ and $\phi = 40°$, we also see collected charge appear on Row 3. We further notice that the *range* of arrival times collapses as the angle ϕ increases and the range of distances between track segments and the anode similarly collapses.

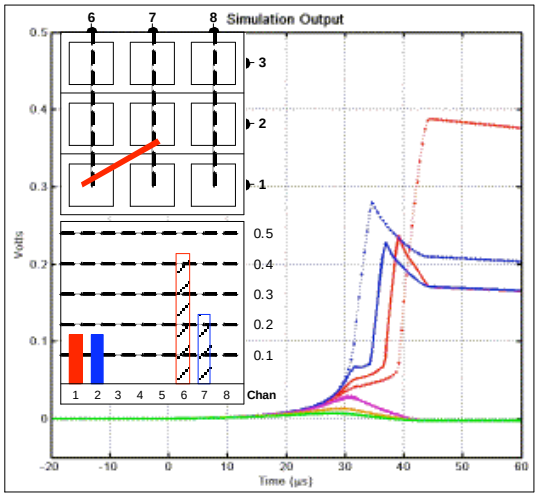


Figure 5A. Traces from a (2.87, 5.00, 32, 20) track.

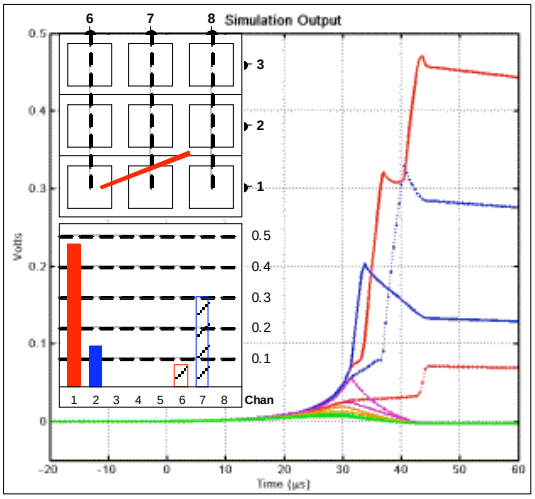


Figure 6A. Traces from a (7.13, 5.00, 22, 20) track.

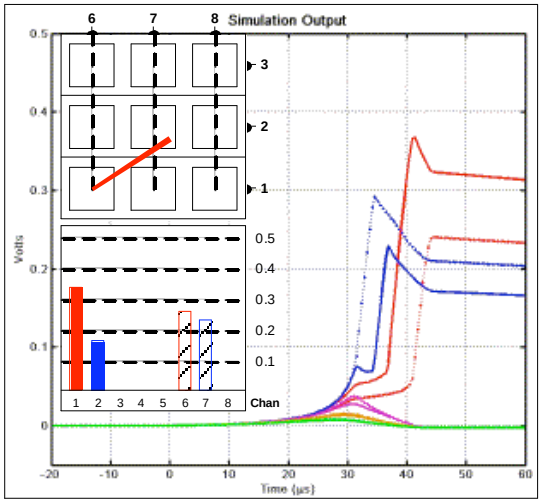


Figure 5B. Traces from a (5.00, 5.00, 32, 20) track.

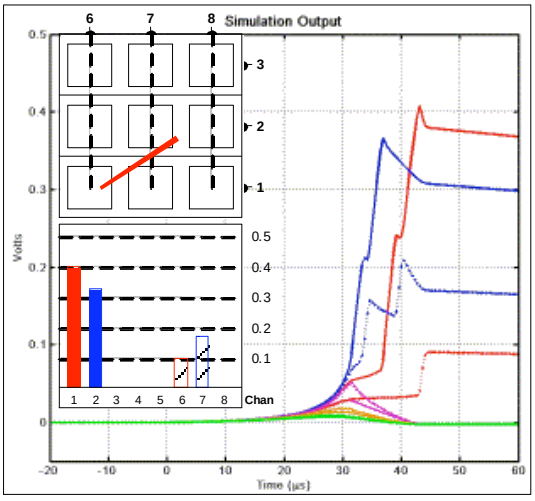


Figure 6B. Traces from a (7.13, 5.00, 32, 20) track.

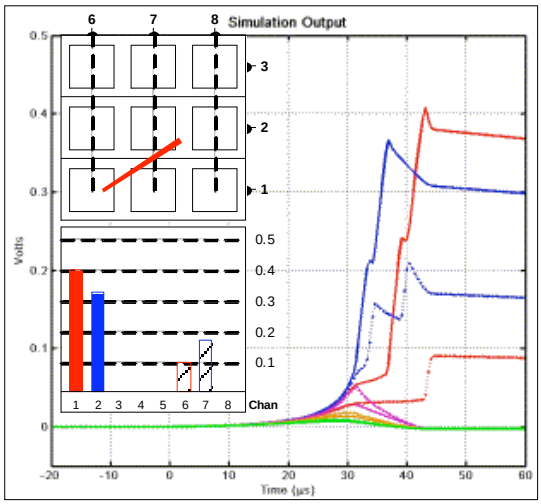


Figure 5C. Traces from a (5.00, 7.13, 32, 20) track.

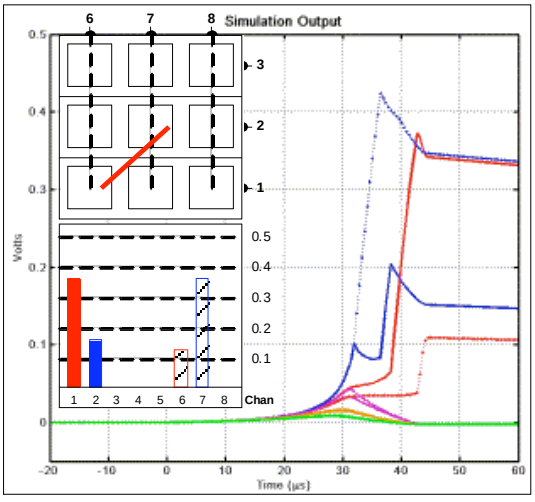


Figure 6C. Traces from a (7.13, 5.00, 42, 20) track.

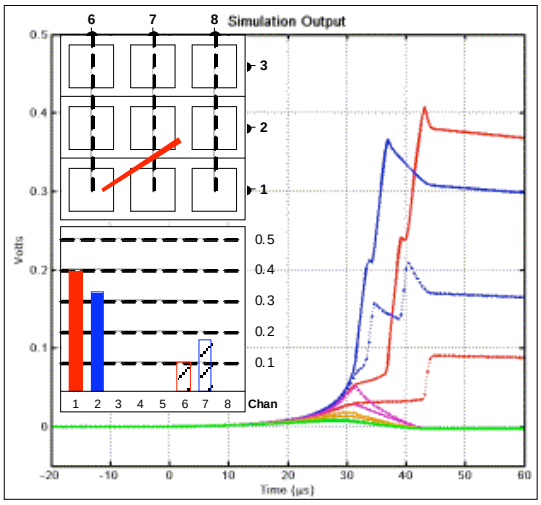


Figure 7A. Traces from a (7.13, 5.00, 32, 20) track.

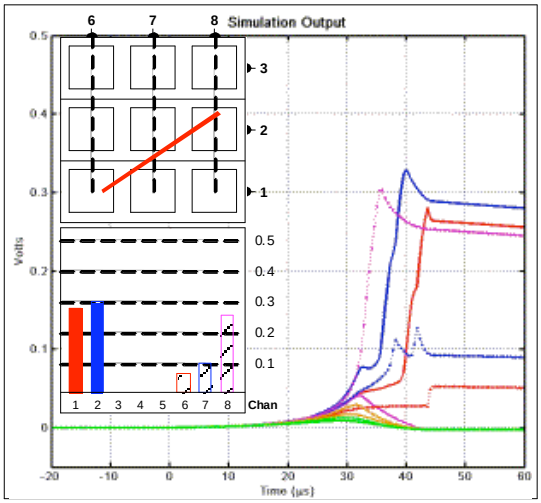


Figure 7B. Traces from a (7.13, 5.00, 32, 30) track.

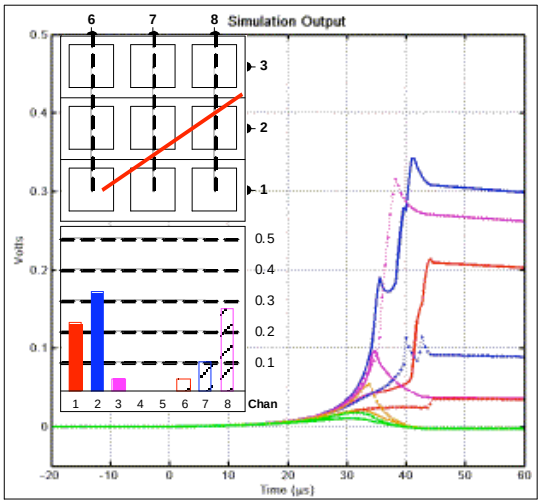


Figure 7C. Traces from a (7.13, 5.00, 32, 40) track.

Results—Analysis

The large trace changes observed from track translations of less than 1/4th of the anode pitch imply that the TPC method is sensitive enough to allow us to be able to easily detect and extract track locations with a precision that is significantly smaller than the strip pitch and may even approach 1 mm for 10 mm pitch strips. We further observe that, if in addition, we also use time of arrival information, we can significantly extend our capability to determine track locations. We therefore consider how captured traces might best be analyzed to extract track locations and orientations.

Since, in general, the further a charge drifts toward an electrode the more charge it induces, we might not expect there to be any simple relationship between the amount of projected charge under an electrode and the final charge induced on it. We have discovered, however, that due to the small pixel effect noted above, this generalization is not true in the present design. Thus, because a given electrode does not begin to effectively "see" a drifting charge segment until it is within about 5 cm, all charge segments have effectively identical drift lengths (i.e., 5 cm) and induce charges on the electrodes that are strictly proportional to their own charge. As a result, we find that the preamplifier signal amplitudes just after all charges have finished drifting (i.e., at 45 μs) are directly proportional to the charges in the track projected onto their respective electrodes. As an example, we look at Figure 4, where the ionization track has projected charge only on Rows 1 and 2 and Columns 6 and 7. Table 1 shows the measured voltages at 45 μs, their values normalized to unity, and the projected fractions of the tracks over the same electrodes. As may be seen, the agreement between the normalized and projected values is very good.

Table 1. Comparison of measured signal values to projected track lengths in Figure 4

Electrode	Measured Trace at 45 μs	Normalized Trace at 45 μs	Projected % Track on Electrode
#1	0.1118	0.118	0.12 ± 0.01
#2	0.1397	0.140	0.14 ± 0.01
#6	0.2973	0.314	0.32 ± 0.01
#7	0.4044	0.428	0.42 ± 0.01

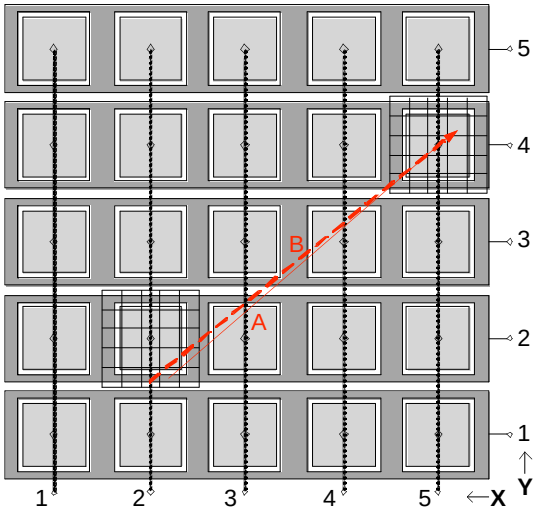


Figure 8. Method for generating tracks and projected charges for fitting to experimental data.

The result established in Table 1 is very important to our analysis because it means that we can use simple geometric analysis to extract track locations from signal traces. Figure 8 shows the proposed method. First we establish the Row-Column intersections where the track starts and stops. In Figure 4 this would be Row 1/Column 6 and Row

2/Column 7 and use times of arrival to establish which end was up (here Row 2/Column 7). We then compute the normalized trace fractions for each electrode as in Table 1. We then divide the starting and stopping intersections into a grid of squares of desired spatial resolution (here 2 mm). For each pair of starting and stopping squares we then geometrically compute the projected track on the electrode and make a weighted least squares comparison of these values to our measured values and select the globally best value as our best estimate of the track location. As may be seen by the comparison between tracks A and B in the figure, and their projections onto the electrodes, we expect the differences between the various tracks to be easily discernable.

CONCLUSIONS AND RECOMMENDATIONS

We have developed a computer model, based on the principles of electrostatics, that accurately produces expected output signals as the electrons in charge tracks generated in N_2 by alpha particles drift to our crossed strip anode. Our examination of these signals suggests that it will be possible to locate the origins of the trajectories of these tracks with an accuracy of better than 0.5 cm within a counter large enough to hold an entire RASA filter. Noting that Rn decay products will only emit one or two alpha particles, we can use the intersections of a larger number T of tracks (e.g., 3) to locate fission fragments or other radioactive particles trapped in the filters. Thus, by employing the number T as a "spatial coincidence" test, we can greatly reduce the counter's random background and enhance its sensitivity to even very tiny fission fragments.

At XIA we are continuing to develop this counter with the remainder of our Phase I SBIR funding and expect to have a small prototype working within the next 2–3 months, at which time we will be able to make first comparisons between the model traces presented here and actual traces captured from a counter with real electronics and their concomitant noise sources.

REFERENCES

Barrett, H. H., J. D. Eskin, and H. B. Barber (1995). Charge transport in arrays of semiconductor gamma-ray detectors, *Phys. Rev. Lett.* 75: 156–159.

Bowyer, S. M., H. S. Miley, R. C. Thompson, and C. W. Hubbard (1997). Automated particle sampler for Comprehensive Test Ban Treaty verification (The DOE Radionuclide Aerosol Sampler/Analyzer), *IEEE Trans. Nucl. Sci.* 44: 551–556.

Miley, H. S., S. M. Bowyer, C. W. Hubbard, A. D. Mckinnon, R. W. Perkins, R. C. Thompson, and R. A. Warner (1998). Automated aerosol sampling and analysis for the Comprehensive Test Ban Treaty, *IEEE Trans. Nucl. Sci.* 45: 1034–1039.

Warburton, W. K. (1998). An approach to sub-pixel spatial resolution in room temperature x-ray detector arrays with good energy resolution, in *Semiconductors for Room Temperature Radiation Detector Applications II*, R.B. James et al. (Eds.), *Mat. Res. Symp. Proc.* 487: 531–535.

Warburton, W. K., B. Dwyer-McNally, M. Momayezi, and J. E. Wahl (2004). Ultra-low background alpha particle counter using pulse shape analysis, in *Nuclear Science Symposium Conference Record, 2004 IEEE*, 1: 577–581. Digital Object Identifier 10.1109/NSSMIC.2004.1462261.

Warburton, W. K. and B. Dwyer-McNally (2006). Electronic background rejection in a new, ultra-low background alpha particle counter, *Nucl. Instrum. Methods Phys. Res. B* (accepted).

DESIGN OF AEROSOL SAMPLER TO REMOVE RADON AND THORON PROGENY INTERFERENCE FROM AEROSOL SAMPLES FOR NUCLEAR EXPLOSION MONITORING

Scot K. Waye, Steven R. Biegalski, and Ofodike A. Ezekoye

The University of Texas at Austin

Sponsored by Army Space and Missile Defense Command

Contract No. W9113M-05-1-0016

ABSTRACT

An aerosol sampler is being developed to physically separate naturally occurring radionuclides from anthropogenic radionuclides produced in nuclear weapons explosions. Studies show that aerosols with natural activity have an aerodynamics diameter in the range of 0.1 to 1.0 μm. In contrast, atmospheric nuclear explosions produce radioactive aerosols with aerodynamic diameters less than 0.1 μm. Surface nuclear explosions produce a bimodal distribution of radioactive aerosol particles with aerodynamic particles greater than 1.0 μm and less than 0.1 μm. A high volume (70 m^3hr^{-1}), low pressure aerosol impactor has been designed that will separate the particles into the three size distributions: aerosols with aerodynamic diameters greater than 1.0 μm, between 0.1 and 1.0 μm, and smaller than 0.1 μm. Computational fluid dynamics (CFD) modeling was implemented in order to examine sampler inlet velocities and cutoff efficiencies. An interactive design tool was developed to obtain the impactor geometry that yields the desired aerodynamic particle diameters. Filters were chosen that had good collection efficiencies for small particles and had very low natural radioactivity. The components of the aerosol impactor were manufactured or obtained and then assembled. Sample aerosols of known aerodynamic diameters were introduced to verify the aerosol cut-off diameters achieved by the sampler.

OBJECTIVES

This work seeks to develop an aerosol sampler that physically separates aerosols containing radioactivity from natural origin from aerosols containing radioactivity produced in a nuclear weapons explosion. Aerosols with natural radioactivity have been shown to have a size distribution predominantly between 0.1 and 1.0 μm. Grundela and Porstend (2004) showed this was the case for data collected in Göttingen, Germany for thoron and radon progenies. Similar studies, including Bondietti, et al. (1987) also found this size range for thoron progeny. Aerosols with radioactivity from nuclear explosions were found to have a bimodal size distribution depending on the type of detonation. Aerosols were collected after a 20 kt nuclear explosion. For air explosions, the aerosol particles had a diameter less than 0.1 μm and for surface explosions, the particle size was larger than 1.0 μm (Storebø, 1974). This data was consistent with aerosols collected in Sweden from a September 26, 1976 Chinese 20-200 kt nuclear explosion conducted above-ground (De Geer et al., 1978). It is therefore advantageous to separate aerosol particles into at least three size groups by particle diameter: greater than 1.0 μm, between 0.1 and 1.0 μm, and less than 0.1 μm.

There are many designs of aerosol samplers that separate the particles by size. Inertial impactors, especially cascade impactors, are ideal for this task. Particle inertia in a curved flow makes the particles deviate from the streamline, impacting a collection surface (Willeke and Baron, 1993). By controlling the fluid flow through the geometry of the sampler, particular sizes can be separated. When multiple single-stage impactors are placed in series, particle sizes of decreasing diameter may be collected. One difficulty with the current study is the small particle size of radioactive aerosols from above-ground nuclear explosions (particle size is less than 0.1 μm). Conventional impactors normally only have a particle diameter limit of 0.3-0.4 μm (Vanderpool et al., 1990). Two methods that have been used previously to obtain lower particle diameters are using a Micro-Orifice Uniform Deposit Impactor (MOUDI) or using a low-pressure impactor. The nozzles in a MOUDI are difficult to manufacture, especially for the case of a high volume flow since thousands of nozzles are needed for the lower stages. Lowering the pressure in a stage changes the mean free path between fluid particles and allows for smaller diameter particles to be collected. A critical stage is needed to create a pressure drop and a vacuum pump is needed in order to pull the desired pressures.

Once the aerosols containing radioactivity from natural sources are separated from those with radioactivity from nuclear explosions, the samples are analyzed. With the reduced background, gamma-ray spectroscopy of the aerosol filters will result in detection limit improvements. The filters will not need significant decay times between collection and gamma-ray spectrum acquisition. These improvements will be most notable where radon and thoron levels are high. The size distribution will also enable identification of a surface or atmospheric explosion.

The current focus of the study is the design and validation of the before mentioned aerosol sampler. A generic impactor was modeled using a CFD program, FLUENT 6.1 (2002). Both circular and rectangular nozzles were modeled and benchmarked with previous studies. This provided insight into the physics of the fluid flow and particle behavior. By calculating the necessary geometries and pressures needed to obtain the desired aerosol particle sizes, the cascade impactor was manufactured and assembled. In order to verify the size distribution for each stage, fluorescent test aerosol particles of known size were produced and collected by the sampler onto the filters of each stage. The filters were then analyzed for size distribution for design validation.

RESEARCH ACCOMPLISHED

Various geometries of impactor stages were modeled in FLUENT and benchmarked with previous literature. Both Lagrangian and Eulerian modeling approaches were attempted. For the Lagrangian approach, the fluid flow was solved and then discrete particles were introduced into the flow and tracked. This approach yielded particle paths, and by varying the particle size, collection efficiencies were obtained. The collection efficiency of a stage is defined as the percentage of particularly sized particles introduced into the flow that was collected. Each stage is designed to have a particle efficiency of 50%, although the curve is steep around this design point. In the Eulerian approach, user defined scalar transport equations were introduced into FLUENT and the scalars (particle density) were solved simultaneously with the fluid flow. Due to numerical diffusion and a poor resolution of particle fronts, this approach did not produce results that were as accurate, although it provided qualitative results. Many of the computational studies in the literature use the Lagrangian approach in order to determine the collection efficiency of an impactor stage.

Two stages of a round nozzle cascade impactor were modeled in FLUENT and benchmarked with the experimental and numerical results found in Huang and Tsai (2001). Grid independence was carefully monitored in order to ensure that the grid was properly discretized to obtain an accurate fluid flow, as seen in Figure 1. The resulting cutoff diameters changed very little between the grids with 40000 cells and 160000 cells. Each of the two stages was modeled independently with boundary conditions matching Huang and Tsai (2001). The results compared well, as shown in Table 1. Stages 1 and 2 of the cascade impactor yielded cutoff diameters (50% efficiency) of 8.9 and 6.0 μm for the current study, respectively, as compared to 9.0 and 5.5 μm for Huang and Tsai's (2001) experimental results and 9.1 and 6.1 μm for their numerical results, respectively. Figure 2 shows the particle paths and density using the Lagrangian and Eulerian approaches for stage 1.

A second benchmark of FLUENT for aerosol sampling applications was completed. An impactor with rectangular nozzles was more desirable for this study due to available commercial products and high volume flow. A computational study that simulated rectangular nozzles (Hari et al., 2005) was benchmarked in FLUENT using the Lagrangian approach with equal success to the round nozzle impactor, as shown in Figure 3. Hari et al., (2005) used CFX, a CFD program supported by ANSYS. The cutoff diameter was 0.84 μm, while the current study, using FLUENT, found a cutoff diameter of 0.80 μm. The efficiency curve was steeper in the current study, which provides a more accurate analysis and a larger certainty of the particle size. The benchmarking proved useful in order to show that FLUENT could be successfully implemented for aerosol impactor applications.

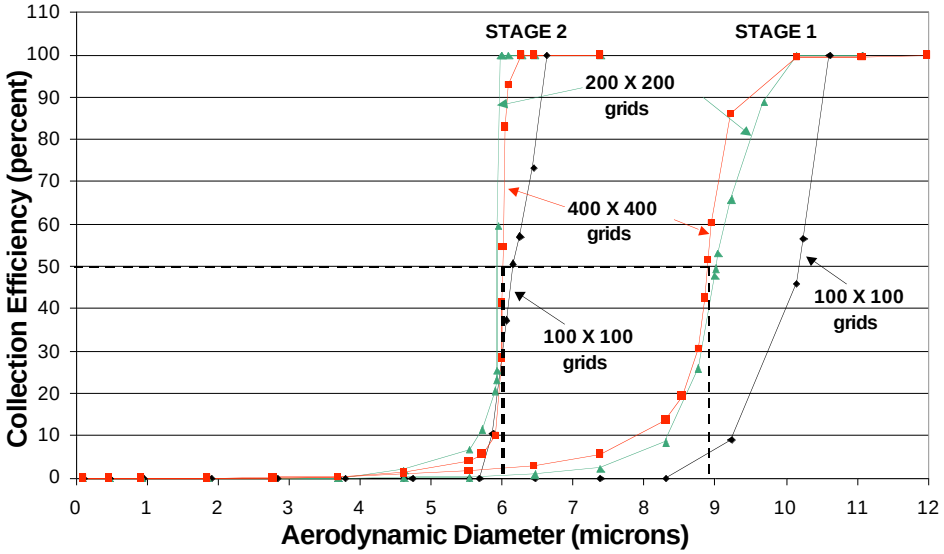


Figure 1. Grid independence study to find particle cutoff diameters for two stages of a round nozzle cascade impactor modeled with the same geometry as Huang and Tsai (2001).

Table 1. Comparison of particle aerodynamic cutoff diameters from current numerical study with Huang and Tsai (2001).

	Stage 1	Stage 2
	Particle aerodynamic diameter (μm)	
Experimental [Huang and Tsai (2001)]	9.0	5.5
Numerical [Huang and Tsai (2001)]	9.3	6.1
FLUENT CFD [Current Study]	8.9	6.0

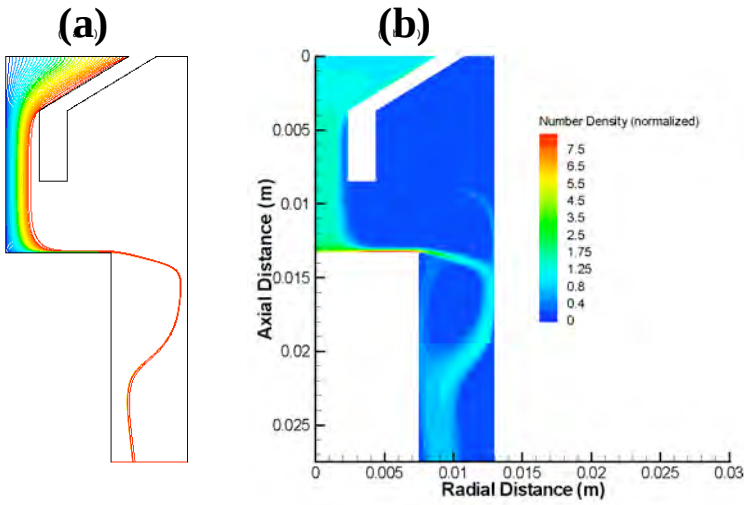


Figure 2. Particle paths and density for Stage 1 using (a) Lagrangian approach and (b) Eulerian approach. The particle diameter used for these figures was 9.0 µm.

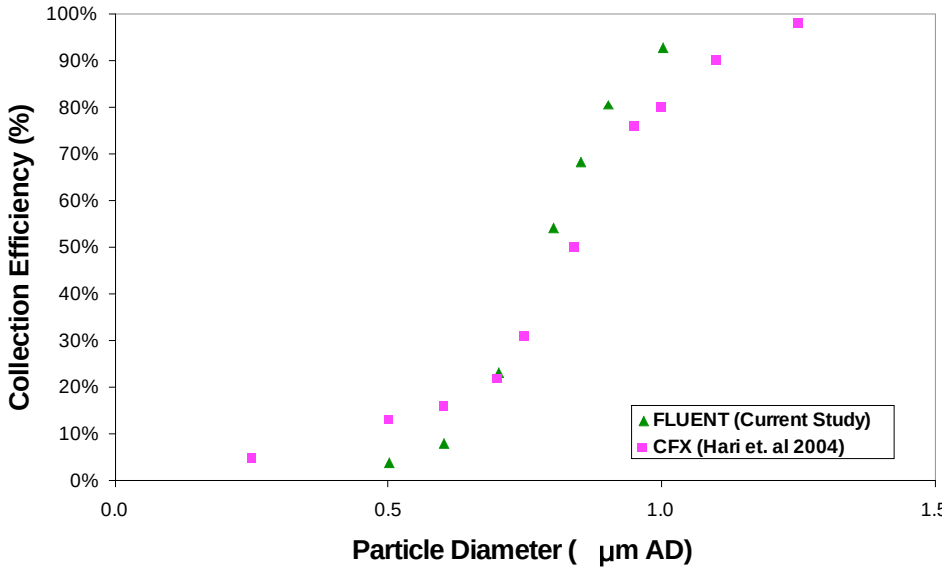


Figure 3. Collection efficiency curve for rectangular slot impactor for current study compared to Hari et al. (2004). The geometry for the current study was modeled after Hari et al., (2004).

The Stokes number characterizes the particle motion in the flow field and the Reynolds number characterizes the flow field (Hinds, 1999). The Stokes number is defined as the ratio of the relaxation time of the particle to the fluid (Crowe et al., 1998). Using the Stokes number (St) definition and the concept of a slip correction factor (C), which is a function of the mean free path of the air molecules (which conversely is a function of pressure only) (Marple and Willeke, 1976), some of the parameters in these definitions may be manipulated in order to yield the desired values for the other variables.

$$\mathrm{St} = \frac{\tau_p}{\tau_f} = \frac{\rho_p C D_p^2}{18\mu} \Big/ \frac{W/2}{V_0} = \frac{\rho_p V_0 C D_p^2}{9\mu W} \qquad \text{Eq. [1]}$$

$$C = 1 + \frac{0.163}{D_p P} + \frac{0.0549}{D_p P}\exp(-6.66 D_p P)$$

Smaller cut-off diameters may be attainable while maintaining a constant Stokes number by increasing the jet velocity in an impactor stage (V_0), or by increasing the Cunningham slip factor (C). The Cunningham slip factor is

related to inverse pressure, so by lowering the pressure, raising the Cunningham slip factor can be achieved. Low-pressure impactors implement one or more critical stages that lower the pressure across the stage, usually by choking the flow (making the jet approach the sonic speed). This can be achieved by limiting the nozzle area while using holes or slits that are more easily manufactured with traditional tooling.

An interactive electronic design tool to determine the stage parameters has been developed, based on the design methodology of Marple and Willeke (1976). If the cut-off diameter, Reynolds number, and flow rate are known, the geometry of the round or rectangular nozzles is calculated. If the geometry of the nozzles and the flow rate (or Reynolds number) is known, the cut-off diameter is calculated. This cascade impactor design tool was benchmarked with various pieces of literature and the documentation of the commercial cascade impactor that we own (Tisch Environmental, Inc. TE-230 High Volume Cascade Impactor). These comparisons and validation are found in Tables 2–5. The agreement is generally good with slight deviations in some geometry due to limited tooling dimensions as opposed to a theoretical dimensions calculated with the design tool.

Table 2. Validation of aerosol impactor calculator geometry predictions with specifications for Tisch Environmental, Inc. Series 230 High Volume Cascade Impactor for Q = 20 cfm.

		Stage 1		Stage 2		Stage 3		Stage 4		Stage 5		Stage 6	
		Tisch	Waye	Tisch	Waye	Tisch	Waye	Tisch	Waye	Tisch	Waye	Tisch	Waye
Given	D_p (µm)	10.2	10.2	4.2	4.2	2.1	2.1	1.4	1.4	0.73	0.73	0.41	0.41
	Re	2245	2245	2005	2005	2005	2005	2005	2005	2005	2005	602	602
	Q (cfm)	20	20	20	20	20	20	20	20	20	20	20	20
Calculated	W (mm)	3.96	4.49	1.63	1.85	0.91	0.94	0.46	0.64	0.25	0.35	0.15	0.12
	L (cm)	110.5	59.4	124	60.7	124	60.7	124	60.7	124	60.7	120	201.7
	V (m/s)		3.5		8.4		16.5		24.3		44.5		40.5

Table 3. Validation of aerosol impactor calculator geometry predictions with specifications for Tisch Environmental, Inc. Series 230 High Volume Cascade Impactor for Q = 40 cfm.

		Stage 1		Stage 2		Stage 3		Stage 4		Stage 5	
		Tisch	Waye	Tisch	Waye	Tisch	Waye	Tisch	Waye	Tisch	Waye
Given	D_p (µm)	7.2	7.2	3.0	3.0	1.5	1.5	0.95	0.95	0.49	0.49
	Re	2245	2245	2005	2005	2005	2005	2005	2005	2005	2005
	Q (cfm)	40	40	40	40	40	40	40	40	40	40
Calculated	W (mm)	3.96	3.18	1.63	1.33	0.91	0.68	0.46	0.45	0.25	0.25
	L (cm)	110.5	119	124	121	124	121	124	121	124	121
	V (m/s)	4.3	5.0	9.4	11.7	16.7	22.8	33.4	35.0	60.1	63.4

Table 4. Validation of aerosol impactor calculator geometry predictions with specifications for round nozzle impactor stages used in Huang and Tsai (2001).

		Stage 1		Stage 2	
		Huang	Waye	Huang	Waye
Given	D_p (µm)	9.3	9.3	6.1	6.1
	Re	784	784	588	588
	Q (cfm)	2	2	2	2
Calculated	D_j (cm)	0.48	0.51	0.36	0.29
	# jets	1	0.7	1	1.6
	V (m/s)	1.84	2.4	3.27	3.16

Table 5. Validation of aerosol impactor calculator geometry predictions with specifications for rectangular nozzle impactor stage used in Hari et al. (2004).

		Stage 1	
		Hari	**Waye**
Given	**D_p (μm)**	0.84	0.84
	Re	1100	1100
	Q (cfm)	2.2072	2.2072
Calculated	**W (mm)**	0.254	0.293
	L (cm)	12.7	12.3
	V (m/s)	32.3	28.8

With this design tool, stages were designed for the specific purpose of separating particles with diameters greater than 1.0 μm, between 0.1 and 1.0 μm, and less than 0.1 μm. The specifications of the cascade are found in Table 6. The majority of radioactive aerosol particles from a surface or below ground explosion (particle diameter greater than 1.0 μm) is separated by Stage 1 and collected on a filter before Stage 2. The type of filter is critical in order to control the amount of background gamma-ray spectra. A glass fiber filter will be used since it has a lower level of background radiation when compared to the cellulose filters. Stage 5 separates the aerosol particles with radioactivity occurring from natural origins (particle diameter between 0.1 and 1.0 μm). Stage 7 is a filter that would collect all remaining particles that include aerosol particles with radioactivity from atmospheric explosions (smaller than 0.1 μm). Two critical stages, stages 3 and 4, drawn in Figures 4 and 5 create a pressure drop to 0.29 atm.

Table 6. Cascade impactor specifications.

Stage	**1**	**2**	**3**	**4**	**5**	**6**	**7**
P_{inlet} (atm)	1.0	0.994	0.994	0.549	0.290	0.173	0.136
Q (scfm)	40	40	40	40	40	40	40
L (cm)	124.0	124.0	14.9	97.5	97.5	124.0	---
Re	1950	2005	---	---	2480	1968	---
W (mm)	0.460	1.63	0.635	0.254	0.254	0.460	---
V_0 (m/s)	33.4	9.38	289	253	251	33.4	---
Cut-off diameter (μm)	1.0	---	---	---	0.10	---	< 0.10
P_{exit} (atm)	0.994	0.994	0.549	0.290	0.173	0.136	---

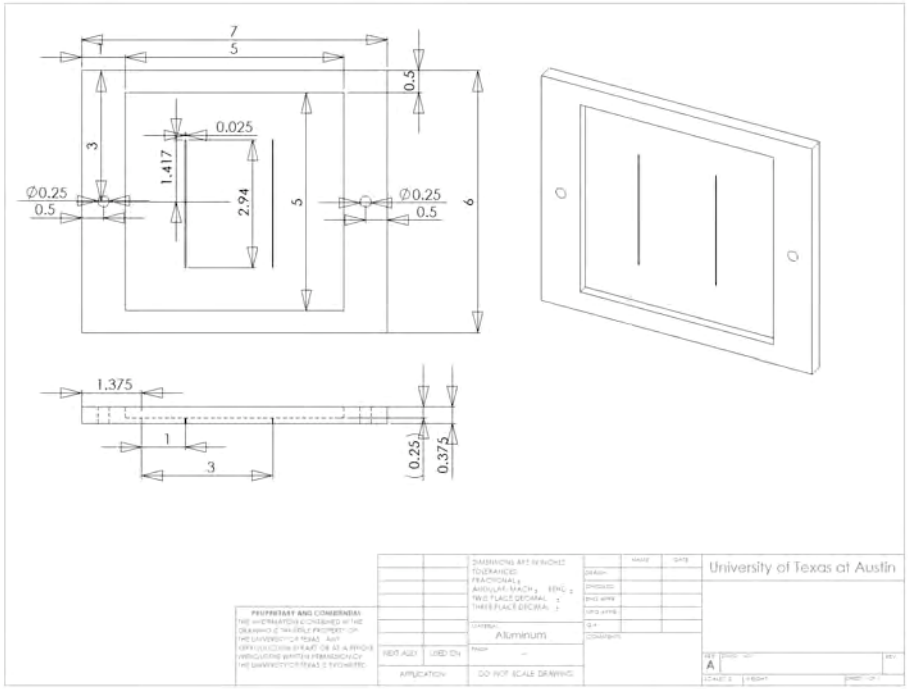


Figure 1. Critical Stage 1.

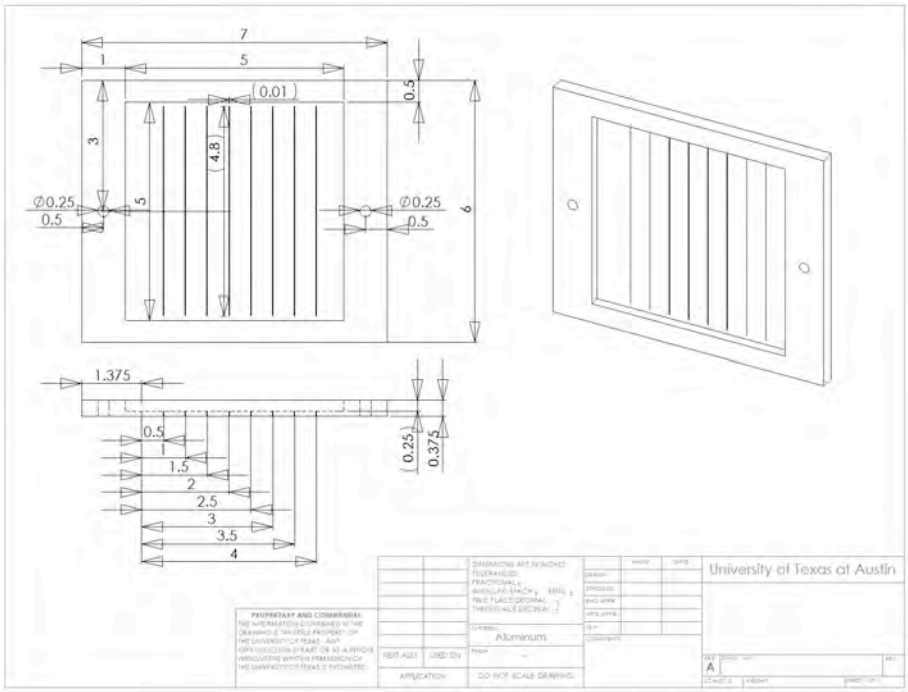


Figure 5. Critical Stage 2.

A six-stage cascade impactor was purchased that used parallel rectangular nozzles (TE-230 high volume cascade impactor with TE-5000 high volume air sampling system made by Environmental Tisch). The TE-230 impactor has a variable motor that can vary the volumetric flow rate. At 20 cfm, the cutoff diameters are 10.2, 4.2, 2.1, 1.4, 0.73, 0.41, and 0 μm. At 40 cfm, the cutoff diameters are 7.2, 3.0, 1.5, 0.95, 0.49, and 0 μm (the 6th stage is not used because the pump cannot handle the pressure drop). For the current study, this impactor setup was extensively modified. New plates were machined as mentioned above and a new pump was obtained that would accommodate the high flow rate and large pressure drop. In order to attain the relatively high flow rate of 40 scfm (1133 L/min)

with the low pressure of approximately 0.2 atm (absolute) after the last stage, a Rietschle Thomas Zephyr DLR60 dry compression claw compressor with a 5 HP motor was acquired. This vacuum pump has a capacity of up to 2 atm gage pressure at 42.4 cfm. With the addition of a pressure regulating kit, the pressure can be adjusted. Figure 6 shows a schematic of the new set up that regulates the flow. The cascade impactor assembly is shown in Figure 7, showing the particle cutoff diameters and the pressures at critical points through the impactor.

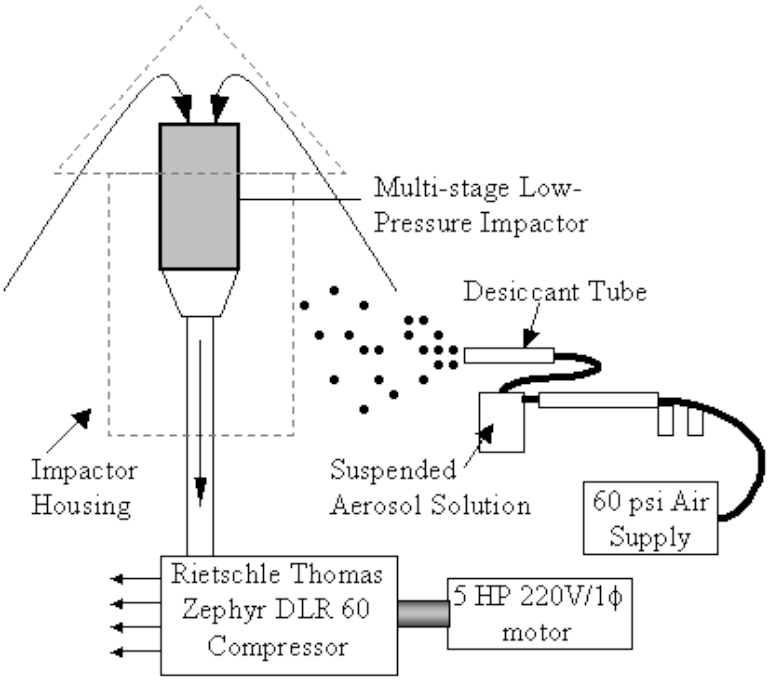


Figure 6. Schematic of modified experimental setup of cascade impactor and aerosol generator.

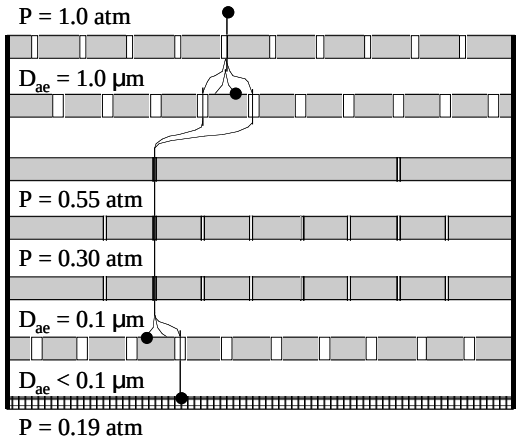


Figure 7. Cascade impactor specifications. Cutoff diameters given for separation stages and absolute pressure given where pertinent.

A submicrometer monodisperse aerosol generation system was procured, as shown in Figure 8 (TSI, 2005). A TSI Model 2076 constant output atomizer creates submicrometer aerosols from solutions or suspension. Compressed air expands through an orifice, forming a high-velocity jet, as shown in Figure 9a (TSI, 2005). As the liquid is drawn through the atomizing section, the large droplets impact on the wall opposite the jet and drain back. A fine spray leaves the atomizer and is dried by silica gel in an annular tube (TSI Model 3063 diffusion dryer), shown in Figure 9b (TSI, 2003). Fluorescent particles with particle sizes of 0.051, 0.10, 0.20, 0.92, 1.0, and 2.1 μm were obtained, which are suspended in solution and bracket the designed particle sizes. By releasing these particles for collection, the designed cutoff diameters are verified.

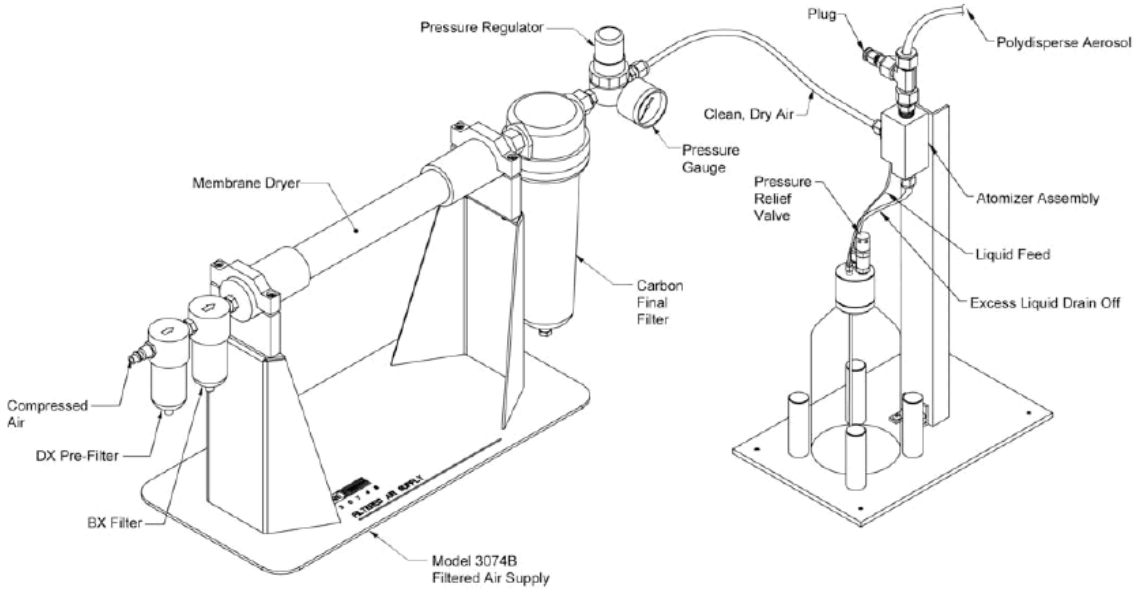


Figure 8. Diagram of submicrometer monodisperse aerosol generation system.

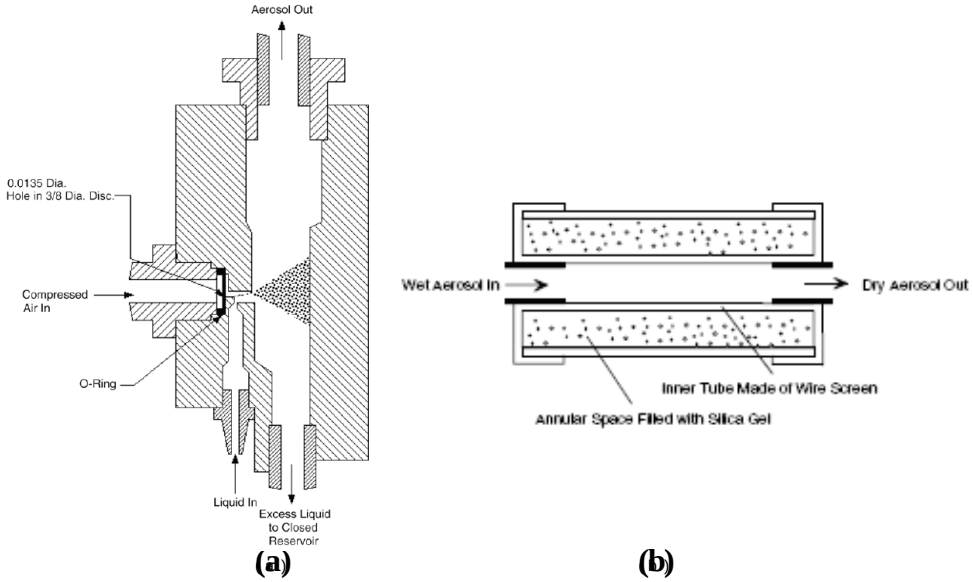


Figure 9. (a) TSI Model 2076 constant output atomizer, (b) TSI Model 3063 diffusion dryer.

CONCLUSIONS AND RECOMMENDATIONS

A high-volume, low-pressure impactor was designed to physically separate radioactive aerosol particles by size in order to separate the radionuclides from natural origins from those from nuclear explosions. In order to separate ultra fine particles, down to 0.1 μm, custom impactor stages and a low-pressure flow field were used. A stronger vacuum pump and impactor stages were assembled. Fluorescent test particles of known size that bracket the desired particle cutoff diameters (0.1 and 1.0 μm) will be released near the impactor to validate the cutoff diameters of each stage. This will further demonstrate that the design tool correctly calculated the geometry for a particular particle size.

In the next year The University of Texas at Austin will run the sampler in an outdoor environment and measure the activity on each of the three filters from the three size distributions. A Geiger Muller detector will be used

immediately after sample collection. This will provide a quantitative evaluation of the activity on each of the filters. This data will be compared to previous samples and correlated to the environmental conditions. System performance and reliability will also be monitored. Gamma-ray spectroscopy will be used using hyperpure germanium detectors to determine the fraction of natural radioactivity collected on the second filter in comparison with the first and third filters. Thoron and radon progeny daughter products from aerosols with radioactivity from natural origins will also be identified. Detection limits will be calculated and the sampling methodology will be optimized. Variations of collection and run times will be implemented to minimize the background interference from naturally occurring radionuclides. The flow rates and geometry of the impactor stages may also be adjusted according to the results of the environmental testing to best match the particle size distribution of the collected radionuclide aerosol particles. Testing will also be conducted in parallel with an Anderson 5-stage impactor. The samples for the two impactors will be compared using gravimetric analysis, gamma-ray spectroscopy, Geiger Muller measurements, and neutron activation analysis to determine elemental content on the filters.

REFERENCES

Bondietti, E. A., C. Papastefanou, and C. Rangarajan (1987). Aerodynamic size associations of natural radioactivity with ambient aerosols, in *Radon and Its Decay Products—Occurrence, Properties and Health Effects*, P. K. Hopke (Ed.), ASC-Symposium Series 3131, pp. 377–397.

Crowe, C., M. Sommerfield, and Y. Tsuji (1998). *Multiphase Flows with Droplets and Particles*. Boca Raton, Florida: CRC Press, pp. 67–101.

De Geer, L.-E., R. Arntsing, I. Vintersved, J. Sisefsky, S. Jakobsson, and J.-A. Engstrom (1978). Particulate radioactivity, mainly from nuclear explosions, in air and precipitation in Sweden mid-year 1975 to mid-year 1977, FOA Report, FOA-C—40089.

FLUENT 6.1, Fluent USA Inc., 2002. Lebanon, NH, USA.

Hari, S., Y. A. Hassan, and A. R. McFarland (2005). Computational fluid dynamics simulation of a rectangular slit real impactor's performance, *Nucl. Eng. Des.* 235:1015–1028.

Hinds, W. C. (1999). *Aerosol Technology: Properties, Behavior, and Measurement of Airborne Particles*. New York: Wiley, pp. 121–128.

Huang, C. H. and C. J. Tsai (2001). Effect of gravity on particle collection efficiency of inertial impactors, *J. Aerosol Sci.* 32: 375–387.

Grundela, M., J. Porstend (2004). Differences between the activity size distributions of the different natural radionuclide aerosols in outdoor air, *Atmos. Environ.* 38: 3723–3728.

Marple, V. A. and K. Willeke (1976). Impactor design, *Atmos. Environ.* 10: 891–896.

Storebø, P. B. (1974). Formation of radioactivity size distributions in nuclear bomb debris, *Aerosol Sci.* 5: 557–577.

TSI Model 3062 *Diffusion Dryer Instruction Manual*, P/N 1933062, Revision G (2003).

TSI Model 3076 *Constant Output Atomizer Instruction Manual*, P/N 1933076, Revision J (2005).

Vanderpool, R. W., D. A. Lundgren, and P.E. Kerch (1990). Design and Calibration of an in-stack low-pressure impactor, *Aerosol Sci. Technol.* 12: 215–224.

Willeke, K. and P. A. Baron (1993). *Aerosol Measurement: Principles Techniques and Applications*. New York: Van Nostrand Reinhold.

Infrasound Monitoring

INFRASOUND RESOURCES OF THE SMDC MONITORING RESEARCH PROGRAM

Manochehr Bahavar, J. Roger Bowman, Hans G. Israelsson, Benjamin C. Kohl,
Robert G. North, Michael S. O'Brien, and Gordon Shields

Science Applications International Corporation

Sponsored by Army Space and Missile Defense Command

Contract No. DASG60-03-C-0009

ABSTRACT

The Research and Development Support Services (RDSS) project of the Space Mission Defense Command (SMDC) Monitoring Research Program provides a variety of resources for nuclear explosion monitoring R&D. A large archive of continuous hydroacoustic, infrasound and seismic data can be viewed and downloaded from the RDSS web page (www.rdss.info), and a number of research datasets have been developed and are also available from the RDSS. These resources are particularly well-developed for infrasound. The RDSS has an extensive archive of infrasound waveform data including continuous waveform data from International Monitoring System (IMS) and non-IMS stations over the period 1995–2006. At present, data from 36 infrasound stations located on seven continents are being received and made available in near-real time

As the availability of infrasound data from a global network grows, increasing numbers of source events are being discovered. Such events are identified from the scientific literature, press reports (accidental explosions) and by routinely searching the waveform archive for signals from recent events listed in bulletins of seismic, volcanic, mining, bolide and rocket launch activity. Source information for several hundred events with infrasound signals is given on the RDSS web page, together with the associated signal waveforms. Some events are recorded on several infrasound stations, and thus can be used to develop and test techniques for locating infrasound events, and there are a number of instances of repeated observations over the same source-receiver path. The latter are particularly useful for modeling the atmospheric propagation of infrasound in a wide variety of meteorological conditions, and examples include mining explosions in North America and Eurasia, volcanic eruptions in South America, the southwest Pacific and Alaska, and rocket launches from a variety of locations around the globe. The RDSS is also responsible for the collection and distribution of data and metadata for the rocket experiments at White Sands Missile Range during 2005–2006.

A systematic effort to characterize all these signals is now underway. A standardized procedure is being applied to measure signal onset time, azimuth, slowness, duration, frequency content, amplitude and dominant period, coherence, and other measures. These parameters will be stored in the infrasound database and a subset included in infrasound event bulletins that will be provided on the RDSS web page. Statistical analyses of azimuth and slowness residuals, and such relationships as frequency versus distance, should provide insights into the detection and identification of infrasound signals, and their use for event location.

OBJECTIVES

The objective of the RDSS is to support the nuclear explosion monitoring research and development community with a wide range of data, state-of-the-art data access tools, and value-added datasets.

RESEARCH ACCOMPLISHED

Archive of Continuous Infrasound Data

The RDSS has been acquiring infrasound data since 1996. Initial holdings are from research arrays in the United States, and the archive has been greatly enlarged by the growth of the IMS, with over 35 stations installed on all seven continents and many remote islands. Figure 1 summarizes the infrasound archive.

Figure 2 shows the location of the infrasound arrays for which data are available from the RDSS. The arrays range in aperture from 0.5 to 3 km, and consist of 4 to 9 elements. Detailed metadata, including array layout and instrumentation, are available from the RDSS web site for each array. The IMS infrasound network is now more than 50% complete (the full network will comprise 60 arrays) and, except for Eurasia, already provides very good coverage.

Infrasound Ground Truth Database (IDB)

The IDB draws on a unique collection of waveforms (many of which are not archived anywhere else) from infrasound arrays operated by the Department of Energy (DOE), IMS, and other organizations. In addition to events recorded on the arrays shown in Figure 2, it also includes historical recordings of Soviet and U.S. atmospheric nuclear explosions. These older recordings are digitized from the original analog records, and thus are of variable quality, but nevertheless are invaluable representations of their source type.

More recent events in the IDB were identified from scientific publications, bulletins of earthquake, mining and volcanic activity, and media reports, particularly of industrial accidents. Source types include

- Chemical explosions, both surface and in the upper atmosphere (White Sands rocket grenade experiments, described elsewhere in this volume). Some of these have ground truth location and origin time, but others are the results of industrial accidents and, while the location can be determined fairly accurately, there may be uncertainty in the origin time.
- Known and suspected mine blasts. Known mine blasts are identified from publications and bulletins such as the United States Geological Survey (USGS) list of U.S. mining events, while suspected ones are inferred (e.g., the vast majority of seismic events reported from northeast Wyoming and from mining areas of Russia, the Ukraine and Australia can reasonably be assumed to be related to mining, particularly if a corresponding infrasound signal is observed). Origin times and locations can be quite well constrained if provided by seismic locations.
- Volcanoes. Explosive eruptions on all continents have been well recorded; as for many of the other source types above, location is well-established but origin time often uncertain.
- Earthquakes. Both large (e.g., International Data Center [IDC] bulletins occasionally include infrasound observations) and small (e.g., Revelle, 2005) earthquakes can generate infrasound.
- Bolides. These can produce very large signals recorded around the globe.
- Avalanches. The Mt. Steller avalanche in Alaska (Arnoult et al., 2005) was well-recorded at three infrasound arrays.
- Rocket launches. Large launches such as those of the space shuttle are routinely recorded at considerable distances. The observed signals may however originate over several hundreds of km of the initial flight path, and often correspond to the ignition of secondary stages.

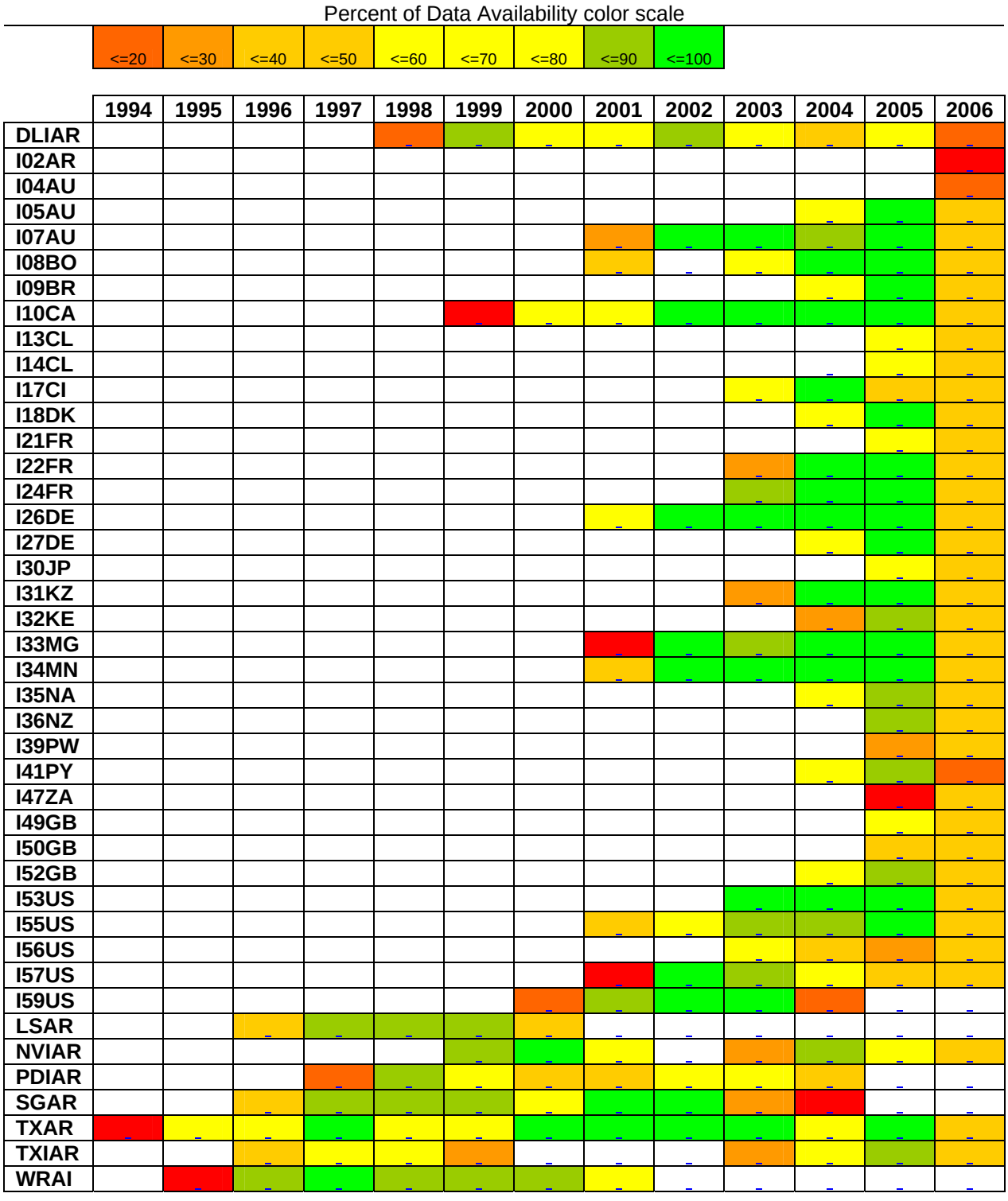


Figure 1. Summary of infrasound data available from the RDSS. The color coding (legend at top) indicates the overall availability of data for each station and year. Availability for 2006 appears low only because the year is not yet complete.

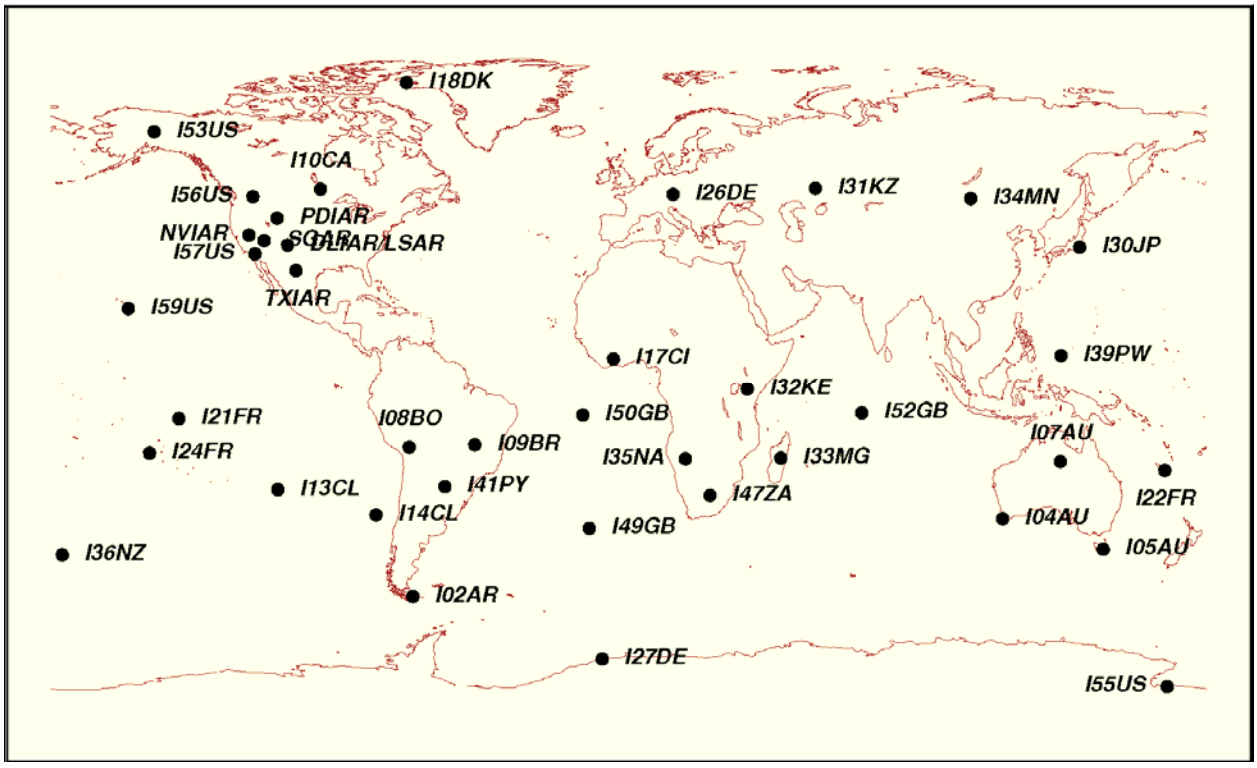


Figure 2. Location of arrays for which infrasound data are available from the RDSS archive (see Figure 1).

Figure 3 shows events in the IDB, together with the great-circle paths of the associated signals. While many of the events, such as bolides and accidental explosions are "one-off," a surprising number are repeated occurrences at the same location. Repeated observations over the same path provide an opportunity to model the variability of atmospheric propagation (for an example, see the last section of this paper). Multiple observations over the same path have been made for the following:

- Volcanic eruptions—For example, the many episodes of the early-2006 eruption of St. Augustine (Alaska) and several eruptions of Lascar (Chile).

- Mine blasts—Many tens of observations of mine blasts in Wyoming have been made at I10CA, and a similar number of observations of events at a large Russian mine are described later in this paper.

- Repeated experiments—Some (such as those at White Sands during 2005–2006) are expressly designed to facilitate propagation studies.

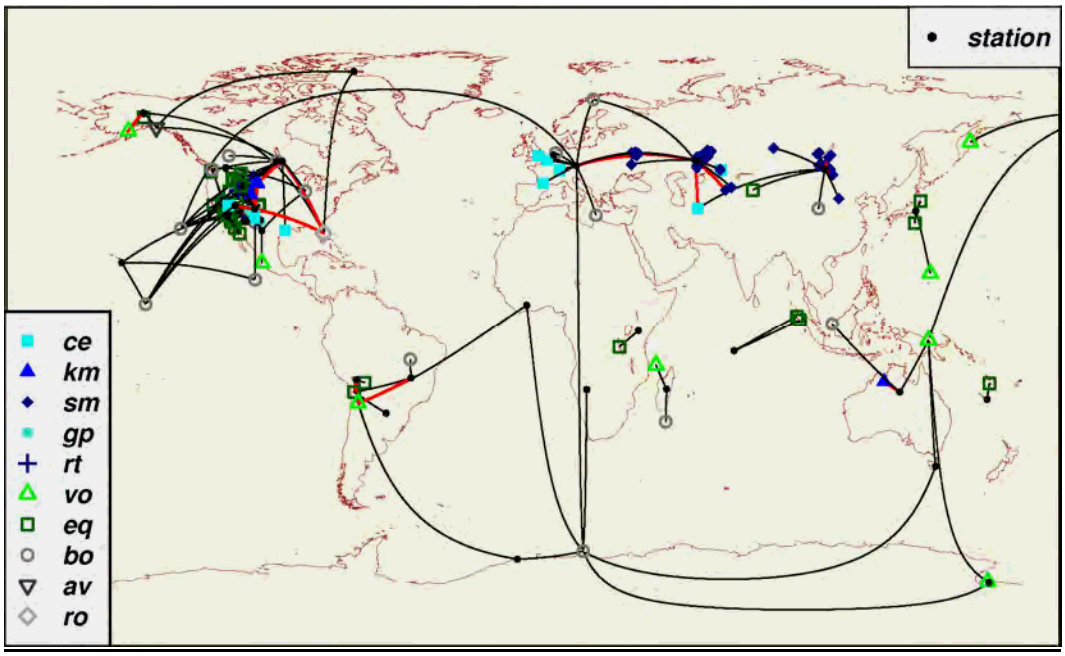


Figure 3. Great-circle paths for signals included in the IDB. Paths over which multiple observations have been made (repeated sources at the same location) are shown in red. Source types are chemical explosions (ce), known mine blasts (km) and suspected mine blasts (sm), gas pipeline accidents (gp), static rocket tests (rt), volcanic eruptions (vo), earthquakes (eq), bolides (bo), avalanches (av) and rocket launches (ro). Details of paths in North America are shown in Figure 4.

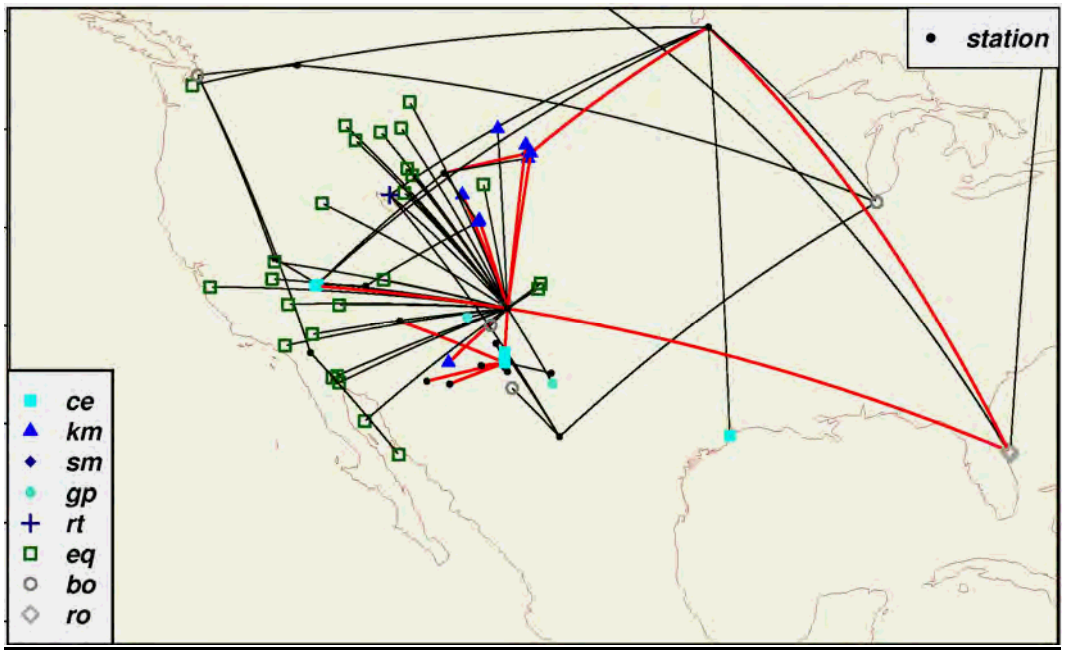


Figure 4. As Figure 3, but scaled to show details of paths in North America.

Infrasound Signal Characterization

Standardized measurements have been defined for seismic observations for more than half a century, but no such standards exist for infrasound signal measurements. As a result, it is hard to interpret, and almost impossible to reproduce, measurements of infrasound signals that are reported in the literature. We have embarked upon a process of systematically measuring signals in the IDB (previous section) and storing the results, some of which are also reported as the characteristics of "phase arrivals" given for each event on the IDB section of the RDSS web page. These arrivals are reported in a format that was developed for seismic bulletins, and is not really appropriate for infrasound; a new infrasound "bulletin" format is being developed and will be used in the future.

Procedures have been defined and are being employed to measure the following parameters for each distinct infrasound signal (several signals may be identified at one array from a given source event):

- Onset time*
- Signal duration
- Slowness* (and slowness "slope", where values change over the signal duration)
- Azimuth* and azimuth slope
- High- and low-frequency limits of the signal
- Dominant period*
- Peak amplitude* and corresponding time
- Signal-to-noise ratio (SNR)*
- Coherence and corresponding coherence SNR
- Fstat

Parameters above that are followed by an asterisk are included in the "bulletin" listing for each event on the IDB portion of the RDSS web page. Most parameters are also accompanied by an error estimate.

At the time of writing, parameters had been measured for approximately one third of the events in the IDB.

Infrasound from Mining Explosions in Eurasia

It is well known that many of the signals recorded on infrasound stations are from chemical explosions detonated in mines and quarries in the region (typically within a few hundred, occasionally a few thousand kilometers of the stations). The IMS infrasound stations I31KZ at Aktyubinsk, Kazakhstan, I34MN at Songino, Mongolia and I26DE at Freyung, Germany, have been operating and recording such signals from events in Eurasia since September 2003, July 2001, and April 2001, respectively. Here we report on the development of a database of several hundred infrasound signals from presumed mine explosions with source-receiver propagation paths ranging from 50 to 1,500 km. These events and associated signals will be incorporated into the IDB (see above).

First we looked for evidence of mining operations at locations known from published sources to be mines or quarries generating infrasound or seismic signals. For example Bayarsaikhan et al. (2002) yielded approximate location information on seven mines in Mongolia, and Richards et al. (2004) provided information on mines in Kazakhstan. (For a comprehensive list of over a dozen references, see Kohl, 2006). We examined medium resolution LandSAT imagery (14.25 m/pixel) to confirm above ground mining activity at these sites and obtained accurate absolute locations. Much of the imagery analysis was done using false-color LandSAT imagery. In our preferred spectral combination, freshly exposed rock appears blue or magenta in the images allowing for ready identification of recent mining activity. We exploited the knowledge gained by examining known sites to scan the imagery for new sites with the same type of features, e.g., large pits, extensive tailing piles, roads. In total we

identified 104 distinct mining operations, 37 of which were not previously identified in published sources. Figure 5 shows the locations of these features with respect to the infrasound stations.

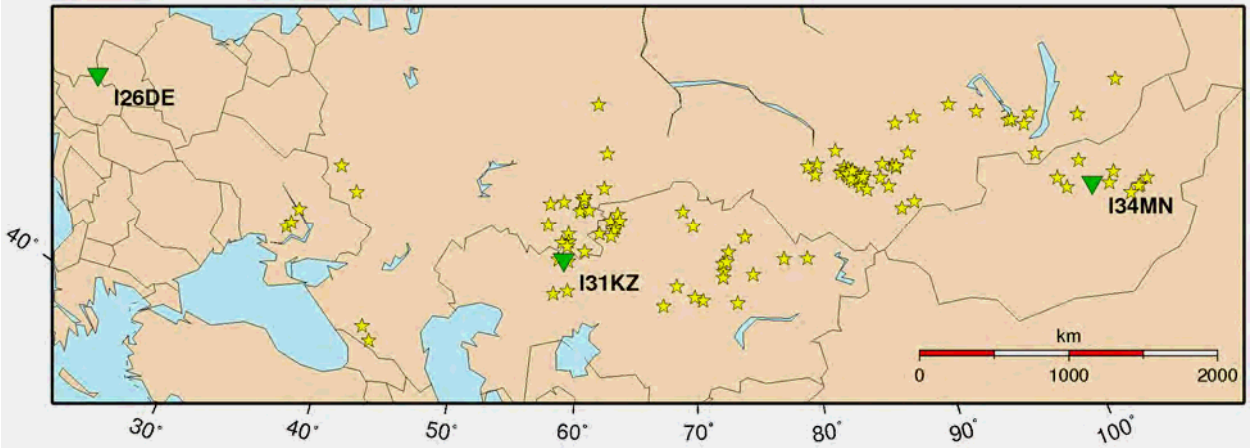


Figure 5. Map of 104 mines (yellow stars) in Eurasia observed in LandSAT imagery. All these sites are candidate sources of infrasound signals recorded at IMS infrasound stations (green inverted triangles).

In the second phase of our effort we exploited the fact that mine explosions large enough to generate infrasound that propagates over large distances are often detected and located seismically. We associated infrasound with events in seismic bulletins by looking for signals in a predicted time window with appropriate signal features (e.g., azimuth). The REB and the SEL1 and SEL3 automated events lists of the IDC and the bulletin of the Kazakhstan National Data Center (KNDC) were used as driver seismic bulletins. Further we exploited the automated detection list of the IDC for both infrasound and seismic signals and performed automated joint seismic/infrasound association based on the principles of the IDC's Global Association (GA) algorithm with the variation of using the infrasound signals as the driver arrivals and looking for corroborating seismic detections. In total this yielded several thousand candidate seismic/infrasound events. Given that many of these were based on automated processing, this included many false associations. To identify the seismic/infrasound events associated with mining activity we performed a nearest neighbor cluster analysis using epicentral distance and time-of-day in the distance metric. Further analysis of both the seismic and infrasound recordings of these events is underway to ensure that false associations are not included in the final database. Figure 6 shows a map of all the currently identified seismic/infrasound events plotted using these seismically determined location. Note that all these events are in the vicinity of a known feature.

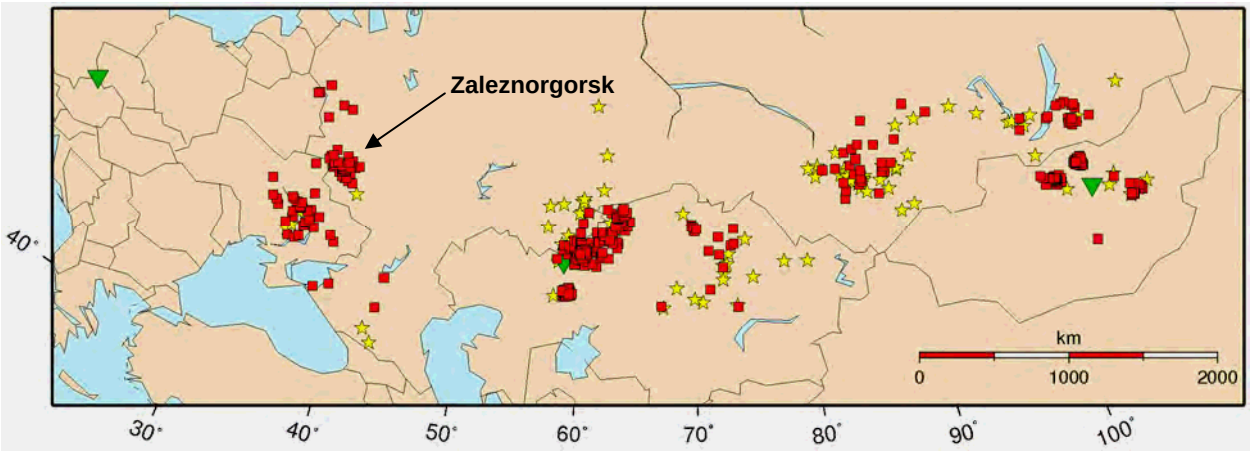


Figure 6. Map of infrasound generating events (red squares) in Eurasia.

Over 50 seismic/infrasound events were associated with the large iron mine (Figure 7) near Zaleznogorsk in western Russia. Propagation modeling using InfraMap (Norris and Gibson, 2004) is reasonably successful at predicting detection/non-detection of infrasound signals from these events. Figure 8 compares arrival times of eigenrays computed with InfraMap with observed arrivals at I31KZ and I26DE from Zalesznogorsk events reported in the IDC Reviewed Event Bulletin (REB) between 2004 and the first half of 2006. The patterns of detections and non-detections at the two stations vary with season and are almost opposite - events occurring during summer and winter are observed only at I26DE and I31KZ, respectively. This effect is good agreement with the modeled results for eigenrays and is due to the seasonal variation of the horizontal wind velocity along the paths to the two stations.

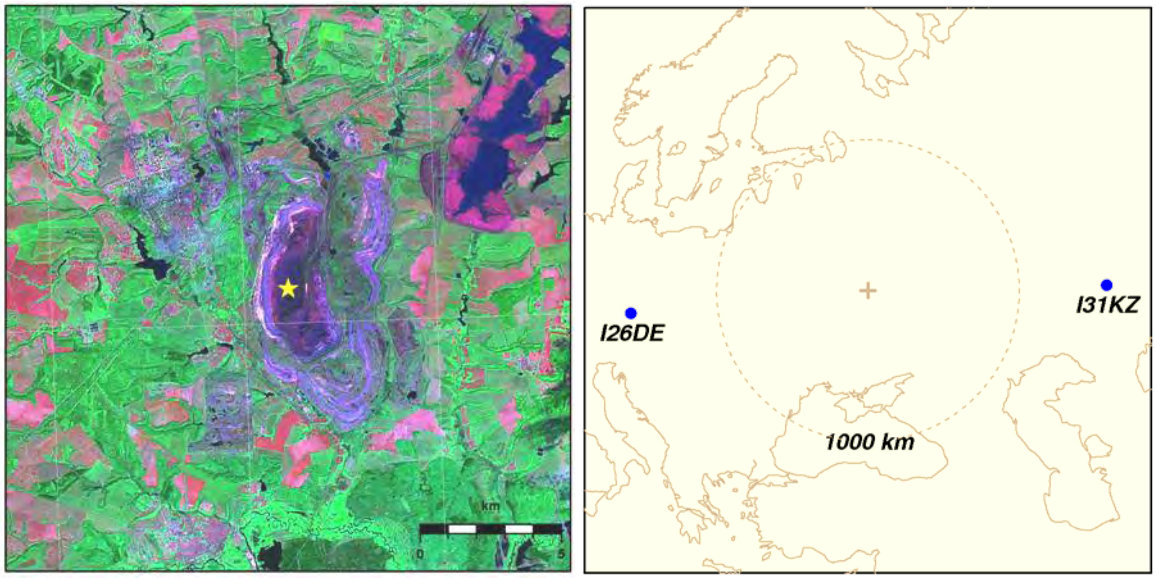


Figure 7. LandSAT image of the Zaleznogorsk iron mine (left panel) and map of mine location (right panel) with respect to the recording stations.

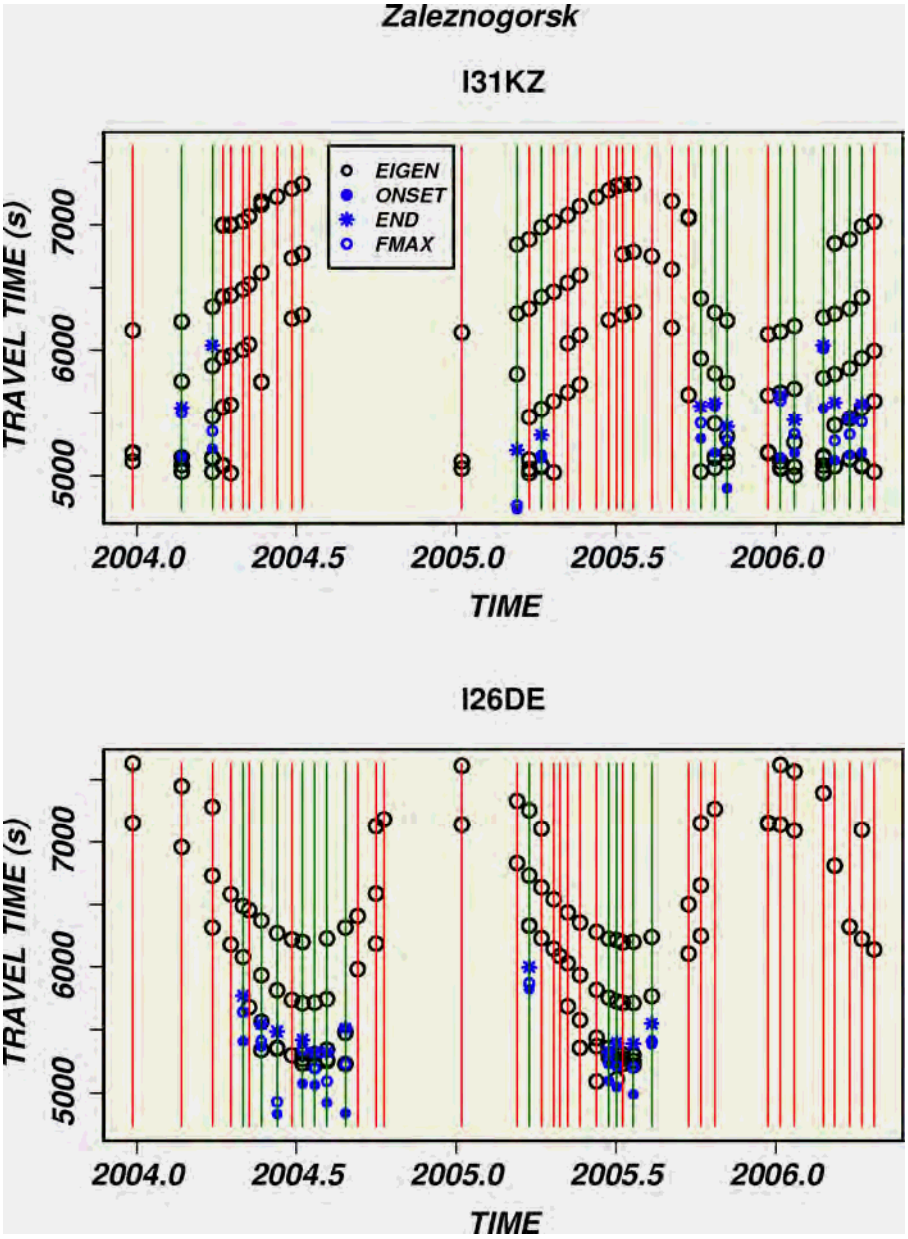


Figure 8. The diagrams show detection and non-detection at I31KZ (top) and I26DE (bottom) of Zalesznogorsk events as a function of season between 2004 and the first half of 2006. Green and red vertical bars indicate detection and non-detection respectively. Observed arrival times of detected signals are marked with blue symbols—filled circles for onset, stars for end of signals and open circles mark the time of maximum of the F trace. The black open circles indicate the arrival times of eigenrays calculated with InfraMap using the standard HWM-93 and MSIS models (Norris and Gibson, 2004). Note that signals are usually observed when eigenrays with early arrivals (~5,000 s) or stratospheric phases are predicted.

CONCLUSIONS AND RECOMMENDATIONS

An extensive archive of infrasound data has been assembled by the RDSS and continues to grow. An increased number of stations provides an opportunity to search for signals from many types of events and to characterize them so that the results may be used to improve both automatic processing and analysis of infrasound. As an example, semi-automated processing of infrasound and seismic data has identified many hundreds of events with infrasound signals in Eurasia.

REFERENCES

Arnoult, K. M., C. R. Wilson, J. V. Olson, and C. A. L. Szuberla (2005). Infrasound associated with Mt. Steller avalanche, *Inframatics* 12: 4–7.

Bayarsaikhan, Ch., M. Ulzibat, A. Le Pichon, and A. Schlupp (2002). Seismo-acoustic data analysis at I34MN Mongolia – Songino, 2002 Infrasound Technology Workshop, De Bilt, The Netherlands.

Kohl, B. (2006). Database of aeatures in central Asia: Locations of mines and quarries that generate infrasound recorded at I31KZ and I34MN, Science Applications International technical report, SAIC-06/2201.

Norris, D. and R. Gibson (2004). User's guide for InfraMap (Infrasonic Modeling of Atmospheric Propagation), Version 4, BBN Technologies technical memorandum W2034.

Revelle, D. O. (2005). Additional infrasonic studies of earthquakes and mining blasts discrimination, in *Proceedings of the 27th Seismic Research Review: Ground-Based Nuclear Explosion Monitoring Technologies,* LA-UR-05-6407, Vol. 2, pp. 845–854.

Richards, P., W.-Y. Kim, M. Hagerty, V. Khalturin, T. Rautian, and P. Martysevich (2004). Integrated study of seismic and infrasonic signals from sources in southern Siberia, eastern Kazakhstan and western China, DTRA technical report, DTRA-TR-01-38.

THE CURRENT STATUS OF INFRASOUND DATA PROCESSING AT THE INTERNATIONAL DATA CENTRE

Nicolas Brachet and John Coyne

Provisional Technical Secretariat of the Preparatory Commission for the
Comprehensive Nuclear-Test-Ban Treaty Organization (CTBTO)

ABSTRACT

One component of the Comprehensive Nuclear-Test-Ban Treaty Organization (CTBTO) Preparatory Commission is the International Data Centre (IDC), which receives and processes data from a globally distributed network of seismic, hydroacoustic, infrasound, and radionuclide stations. Currently the Operational system at the IDC makes only limited use of infrasound data during routine processing. However, active development and testing is being done in the development environment, as described in this paper. Infrasound data at the IDC are processed at the station level using the Progressive Multi-Channel Correlation (PMCC) algorithm, which calculates the correlation between sensors at an infrasound array station. If the signal is sufficiently correlated and consistent over an extended period of time and frequency range, a detection is created. Groups of detections are then categorized, and detections are assigned the phase name I (infrasound), IPx (seismic P), ISx (seismic S), or N (noise). Currently, around 90% of detections are identified as noise. Non-noise detections are then used in network processing, along with detections from seismic and hydroacoustic technologies. The result is an automatically generated bulletin that includes phases detected at seismic, hydroacoustic, and infrasound stations. This automatic bulletin including all waveform technologies is planned to be routinely reviewed by analysts during the interactive review process. Specialized software is being developed that allows analysts to visualize the PMCC results that were automatically calculated and stored during station processing. These results are presented in plots of azimuth and speed versus time and frequency. This form of display is very powerful, especially for low signal-to-noise ratio (SNR) signals, which may be very difficult to visualize with only waveform data. Procedures for the routine interactive review of infrasound data are currently being explored and developed at the IDC.

INTRODUCTION

The CTBTO is tasked with monitoring compliance with the Comprehensive Nuclear-Test-Ban Treaty (CTBT), which bans nuclear weapon explosions underground, in the oceans, and in the atmosphere. The verification regime includes a globally distributed network of seismic, hydroacoustic, infrasound, and radionuclide stations that collect and send data to the IDC in Vienna, Austria, shortly after the data are recorded at each station. Upon receipt at the IDC, the time series data from each seismic, hydroacoustic, and infrasound station are automatically processed (Figure 1) at the station level (station processing). The results of station processing serve as input to network level (network processing). Network processing results in automatic event locations, which are reported in bulletins knowns as Standard Event Lists (SELs). Three SELs are successively made at the IDC: SEL1 includes seismic and hydroacoustic data, and is produced two hours after real time; SEL2 includes seismic, hydroacoustic, and infrasound data and is available six hours after real time; SEL3 also includes seismic, hydroacoustic, and infrasound data and is available twelve hours after real time. Seismic data from auxiliary seismic stations are requested after each SEL and are used to refine event locations in subsequent bulletins. The bulletin production deadlines are staggered to accommodate late-arriving data and the signal propagation times for all technologies.

The SEL3 bulletin is reviewed by human analysts, during which the automatic results are corrected and any late-arriving data not available for SEL3 processing are considered. The result of the interactive review process is the Reviewed Event Bulletin (REB), which is typically available in less than 10 days after real time. The creation of the REB triggers a post-location processing pipeline, which includes processes such as surface wave magnitude estimation and event characterization. Additional bulletins are formed as a result of these processes. After Entry Into Force (EIF) of the CTBT, the delay for producing the REB is planned to be two days.

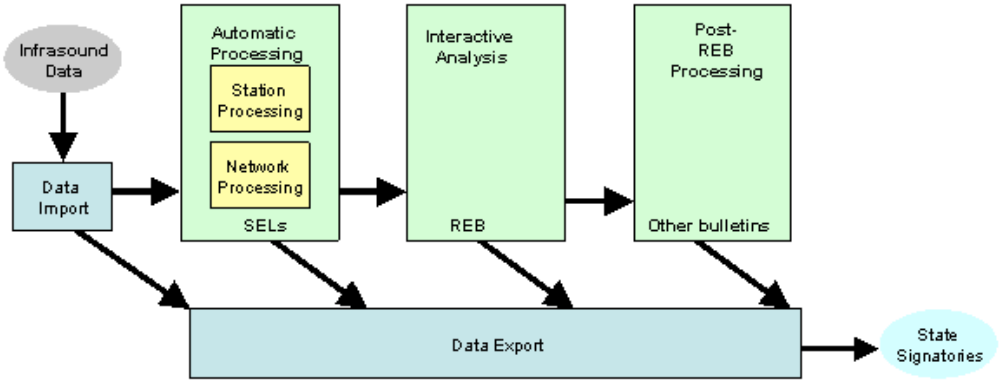


Figure 1. Schematic overview of data processing at the IDC.

The IDC is actively developing software and procedures that will be used to routinely process infrasound data at the IDC. Currently, in the IDC Operational System, infrasound data are routinely processed at the station level but are not considered during network processing and consequently do not contribute to any SEL bulletin. Analysts may manually associate infrasound data during interactive review, but this is currently done only on an exceptional basis. Consequently, infrasound stations rarely appear in the REB at the current time. The remainder of this paper discusses the current status of infrasound processing in the IDC development environment.

RESEARCH ACCOMPLISHED

IDC Development Environment

Development at the IDC is done in a mixed Solaris and Linux environment, where the full suite of IDC application software is routinely operated 24 x 7. All development and maintenance activities are initially tested and refined in this environment before promotion into the Operational System. The full set of IMS data available in Operations is present in the development environment, as well as stations that are still being tested and have not yet been promoted into Operations. As of June 2006, data from 35 infrasound stations are processed in the IDC development environment (Figure 2). This accounts for 58% of the planned infrasound network of 60 stations, as defined in Annex 1 to the Protocol of the CTBT. Thirty-four of these stations are in the IDC Operational System.

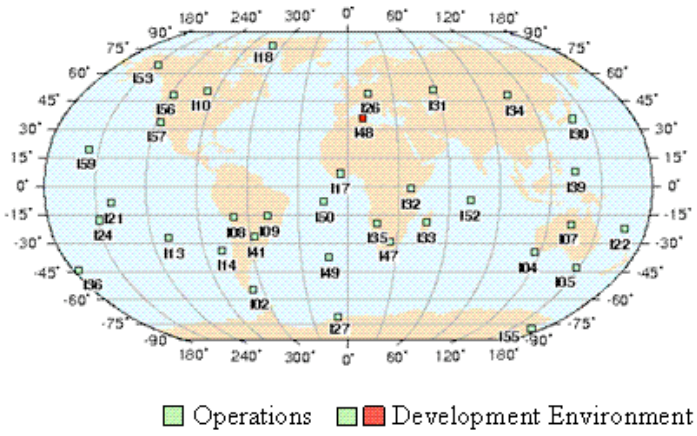


Figure 2. Status of CTBTO infrasound network at the IDC in June 2006.

Infrasound Station Processing

Note: Throughout this text, when specific values are given, it is important to remember that many of the values are interrelated and must be considered in the proper context. Changing a value may have unforeseen consequences elsewhere. In addition, active development is being done in many of these areas, and values are subject to change and refinement. The incentive for including these values is to provide a technical insight into the infrasound processing currently being done at the IDC.

Signal Detection

Signals recorded at infrasound stations are detected at the IDC using the PMCC algorithm (Cansi, 1995). PMCC is an array processing technique that detects coherent energy crossing the array. This algorithm initially calculates the correlation of signals between triplets of sensors at an infrasound station. If the signals are correlated and consistent, waveforms from other sensors at the station are progressively considered and are retained if the signals are sufficiently correlated and consistent. As additional sensors are added, the obtained results are refined and improved. Correlation is performed for overlapping time windows and multiple frequency bands. Currently, due to limited processing capacity, processing is done using time windows 50 s long with a 10 s increment between adjacent windows and 10 frequency bands between 0.1 and 4.0 Hz. There are plans to introduce new hardware and the Linux operating system, where processing will be done using variable window lengths and 15 frequency bands between 0.02 and 4.0 Hz.

If waveforms are sufficiently correlated and consistent for a specific time window and frequency band, the results are stored in a so-called **pixel**, which provides an insight into how the results are subsequently visualized. The pixel height represents the processing bandwidth, while the pixel width represents the time increment between adjacent windows. Each pixel also includes detection attributes such as azimuth, speed (trace velocity), consistency, root mean square (rms) amplitude, and Fisher statistic values (F-stat).

The next stage of the detection processing consists of aggregating pixels with similar attributes into larger groups that are referred to as **families**. Attributes that factor into the family grouping process include time, frequency, azimuth, and speed. If there are a sufficient number of pixels in a family, the family will give rise to a **detection**. When a detection is formed, a number of attributes are calculated for the family, including time duration of the family, frequency bandwidth, centre frequency, speed, azimuth, and F-stat.

Figure 3 shows a typical display of PMCC processing results. The top two panels show azimuth and speed, respectively. Individual PMCC pixels can be seen, as well as groups of similar pixels that form a family. The lower panel shows waveform data and includes the detections that were identified as I phases. The phases are positioned at the start of each family.

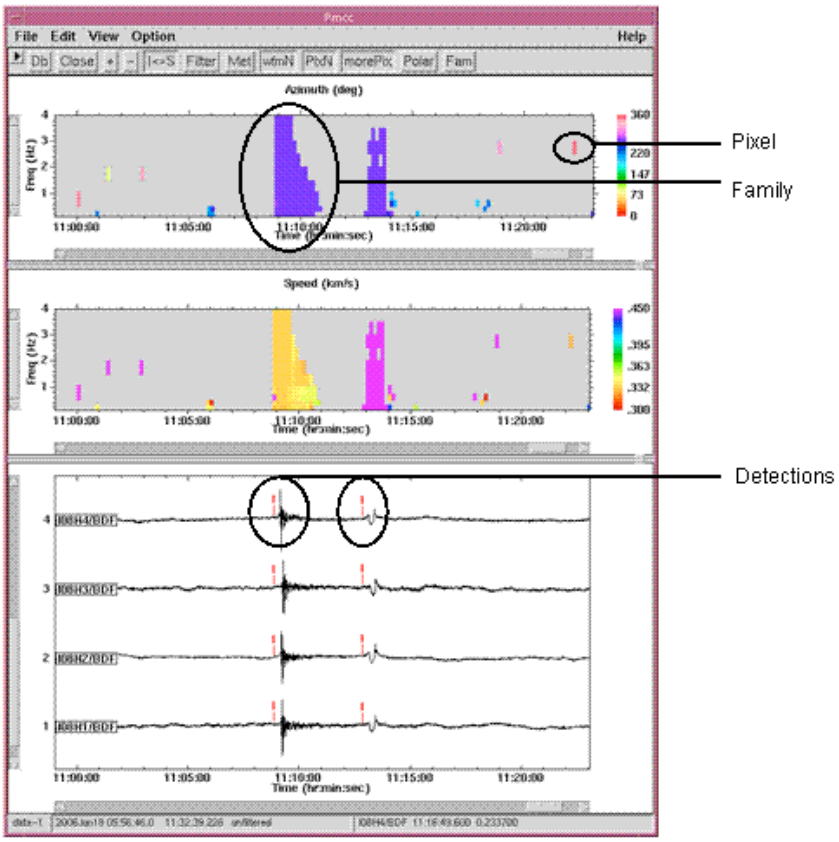


Figure 3. Visualization of PMCC results, illustrating azimuth and speed pixels, and waveforms (unfiltered) with detected infrasound arrivals.

Detection Categorization

After events are detected, the next step of station processing is detection categorization, followed by phase identification. It is instructive to consider the mission of the CTBTO to understand and appreciate the phase identification process applied to infrasound data at the IDC. The overall mission is to monitor compliance with the CTBT, and this is accomplished by routinely producing, daily, a global bulletin of events that were observed by a global network of seismic, hydroacoustic, and infrasound stations. The reported events are usually impulsive and are observed on multiple stations. If the bulletin included single-station events, the uncertainty for those events would be extremely large, and the number of events in the bulletin would increase substantially.

Given these requirements of a global bulletin of events recorded by multiple stations, there are a number of signals recorded at infrasound stations that are not of interest for CTBT monitoring. Such signals include ocean activities (offshore microbaroms or surf on the coast), thunderstorms, small mine blasts in the near vicinity of the station, and aircraft takeoffs and landings. The phase identification process at the IDC is designed to identify such signals as noise (N phase), so these phases are not considered during network processing. If this were not the strategy, there would be a good chance that such signals would be misassociated with other phases (e.g., with seismic phases) during network processing, and the automatic bulletins would be overwhelmed with these false events, which would need to be reviewed and discarded during the interactive review process.

Detection categorization is accomplished in the following two steps.

1. Apply categorization on individual detections

Any detection that is high frequency or that does not have an infrasonic speed is identified as noise. This is accomplished with the following tests:

- min_freq > 1.75 Hz
- speed < 290 m/s
- speed > 500 m/s

2. Apply categorization on clusters of detections

The first step is to build clusters of detections with similar characteristics. Two detections (or families) are clustered together if the two detections are close in time, azimuth, and frequency. This is accomplished with the following tests:

- abs (time2 – (time1 + durations1)) ≤ 5400 s
- abs (az2 – az1) ≤ max (1., 2 * max(std dev az1, std dev az2)
- abs (cfreq2 – cfreq1) ≤ max(2 * std dev freq1, 0.5 * bandwidth1)
- abs (cfreq2 – cfreq1) ≤ max(2 * std dev freq2, 0.5 * bandwidth2)
- min(common_bandwidth / bandwith1, common_bandwidth/bandwidth2) ≥ 30%

A cluster is identified as noise for long-duration clusters, short-duration clusters, and repetitive clusters. This is accomplished if any of the following criteria are met:

Criterion 1 (long-duration clusters)

- Detection is not the first in a cluster,
- Cluster duration is ≥ 3600 s, and
- (detection_fstat – min_cluster_fstat) ≤ (3 * std_dev_cluster_fstat)

Criterion 2 (short-duration clusters)

- Cluster duration < 60s

Criterion 3 (repetitive clusters)

- Detection is not the first in a cluster,
- Cluster is composed of more than 5 detections, and
- (detection_fstat – min_cluster_fstat) ≤ (3 * std_dev_cluster_fstat)

Note: Non-infra detections (detections with speeds ≥ 2900 m/s) are incompatible with the categorization process, and consequently are not considered at this stage, and are directly put into the phase identification process.

Phase Identification

During the phase identification process, phase names are assigned to detections. Detections that have been identified as noise during the categorization process are named N. Detections with speeds over 5700 m/s are interpreted as P-type signals and are named IPx. Detections with speeds between 2900 m/s and 5700 m/s are named ISx. All other detections are interpreted as infrasound arrivals and are named I.

Figure 4 shows two views of the IDC detection list for the station I04AU for the time period 22 May 2006 through 28 May 2006. Each panel of data contains the detections for one day. The display shows the azimuth for the detections, and the azimuth scale is at the bottom of each side. The plots on the left-hand side show all PMCC detections for this time period, including many long-duration signals caused by surf noise and microbaroms. The plots on the right-hand side show the non-noise detections after the detection characterization and phase identification process. The numbers between the plots show the number of detections for each day before and after this process.

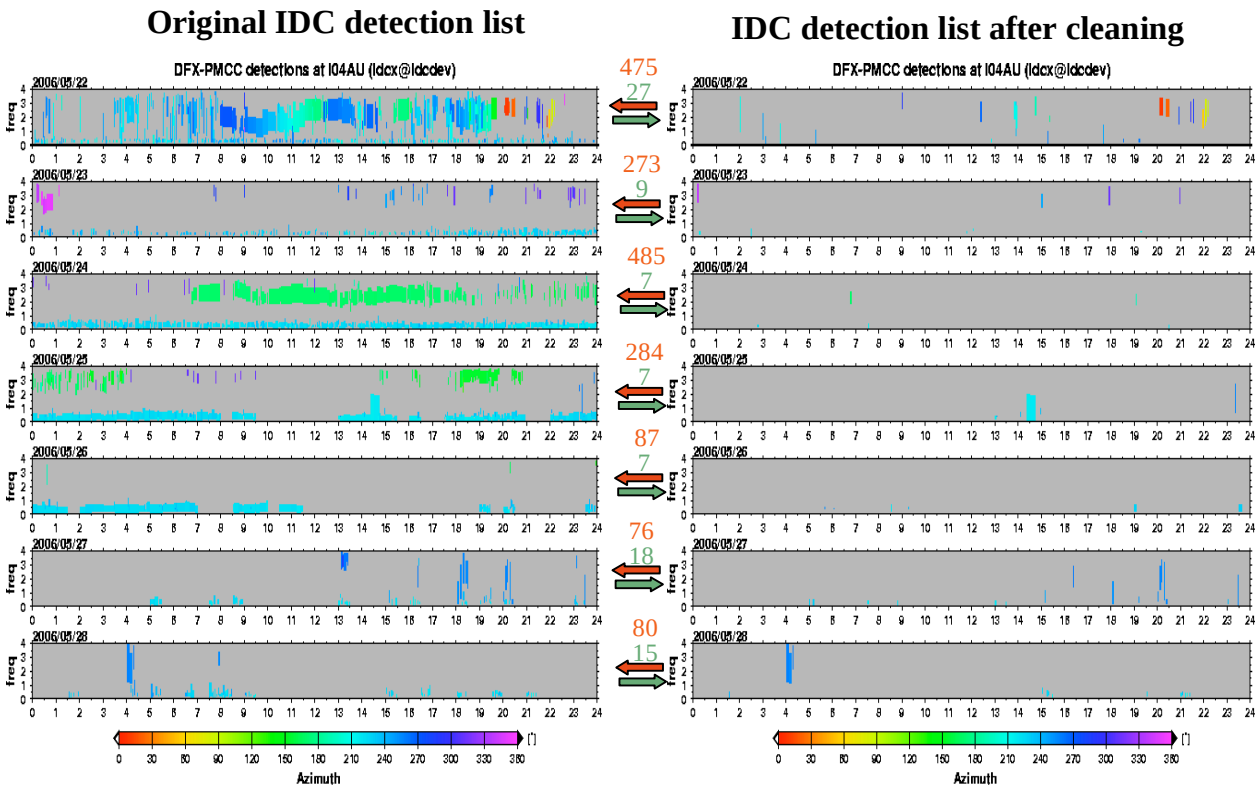


Figure 4. Example of IDC detection list before and after detection characterization and phase identification. Detections which were identified as noise are removed from the display on the right-hand side.

Network Processing

During network processing, non-noise phases are used as candidates for forming events that appear in the automatic bulletins. The location algorithm used at the IDC is an iterative non-linear least-squares inversion originally developed by Jordan and Sverdrup (1981) which was later modified by Bratt and Bache (1988) to include azimuth and slowness observations. An event with only infrasound observations will appear in an automatic IDC bulletin if the event is seen by at least two infrasound stations. At the current time, infrasound phases can be associated with events that are up to 60 degrees from a station. During network processing, the time, azimuth, and slowness attributes from arrivals are considered for different hypothetical events. If a candidate event is found, it is saved and will appear in the automatic SEL2 and SEL3 bulletins. Network processing in the development environment currently builds mixed technology events using seismic, hydroacoustic and infrasound phases.

The automatic association algorithm uses the same infrasound travel time model that was originally introduced by the Prototype International Data Center (PIDC) in Arlington, USA. This velocity model basically uses a constant slowness of 350s/deg (i.e., celerity of 318m/s) regardless of the range between source and receiver. Some work is currently underway to refine this propagation model using a dataset of reference events collected by the IDC during the last 5 years.

Large efforts have been produced to decrease the number of false associations with infrasound arrivals. The introduction of the detection categorization strategy (previously described) has contributed to significantly lowering the number of automatic events with infrasound down to a manageable level. The experimental SEL3 bulletin currently produces about 60 events per day, including arrivals from one or several of the 34 infrasound stations. Currently, infrasounds contribute to about 35% to the total events formed with seismic and hydroacoustic technologies. These results are encouraging, but the proportion of false infrasound associations is still too high and unacceptable for an analyst's interactive review in Operations. Work is currently underway to explore additional techniques to limit infrasound associations based on a distance/frequency relationship. This process may be further refined by considering other attributes such as duration and amplitude.

Interactive Review

The primary tool used by analysts at the IDC to routinely review waveform data is the Analyst Review Station (ARS). ARS allows an analyst to review each SEL3 event and to make corrections and additions as needed. The majority of the ARS interface is occupied with waveform data. During seismic data review, FK results are visualized using another tool. This set up of ARS and the FK tool has worked well for reviewing seismic data.

After data are processed using PMCC, it is critical to visualize the PMCC pixels in time and frequency along with the waveforms, in order to correctly comprehend and interpret the results. This is especially true for low SNR arrivals, which may be very difficult to visualize with only waveform data. In order to accommodate this need, a software tool has been developed that allows the PMCC pixels that were calculated during station processing to be visualized during the interactive review process.

This tool has a number of innovative features, including the following:

- Plots of azimuth and speed pixel information as a function of frequency and time, as well as the original time series data, phases identified during station processing, and meteorological observations at the station.
- Ability to toggle the pixel display between all pixels, only pixels that are members of a family, or only pixels that are members of a non-noise family.
- Polar diagram plot that is integrated with the main window and displays pixel information in polar coordinates of azimuth and speed. Figure 5 shows the waveforms recorded at I07AU when a fast-moving object passed over the array. The polar diagram shows the azimuth and change of speed for this fast-moving object.
- Integration with ARS.

Analysts typically use ARS to review all waveform data from an event. In ARS, a user may select a phase recorded at an infrasound station and press a button to send a message to the PMCC tool, which displays the PMCC results surrounding the arrival. Once those results are displayed, a user may retime, rename, or delete the phase, where each action is synchronized with ARS.

The tool can also be used independently of ARS to directly read and display PMCC results of station for a specific time interval. In all cases the tool reads data from the relational database management system, including the pixel and arrival information that was calculated and stored during station processing.

Work is currently underway at the IDC to develop procedures for the routine interactive review of infrasound data. Currently, in the Operational System, interactive review is done by an analyst who selects a 4-hour time block and analyzes all events and waveforms in that time period. Events that are toward the beginning of the time block sometimes require data from the previous time block to be reviewed.

The process of analyzing infrasound data may require a different procedure for a number of reasons, including the following:

- Different types of display needed to visualize and comprehend the results of station processing.
- Much slower wave propagation times so that associated infrasound arrivals are often outside the time block being reviewed.
- A significant number of additional stations, which could have a severe impact on ARS performance.
- The infrasound channels to display for each station in ARS is still an open issue. For seismic arrays, a beam is typically displayed in ARS; however, beams are not currently made during infrasound station processing.

Given these reasons, different approaches for reviewing infrasound data are being considered and are in various stages of implementation and testing. In one approach, infrasound data are treated the same as other waveform data, and selected channels are displayed for a time block in ARS. Data outside the time block are displayed as needed. In the second approach, infrasound waveforms are not displayed in ARS. When an event is reviewed that contains infrasound arrivals, the arrival is selected in the location dialog window of ARS and is sent to the PMCC review tool which displays the data. The results can be modified in the tool and sent back to ARS. The third approach is to do a "first pass" review of infrasound data using only the PMCC review tool in order to validate or discard the infrasound arrivals contributing to SEL3 events. After this step, arrivals and events that have a reasonable probability of being genuine are reviewed in the context ARS.

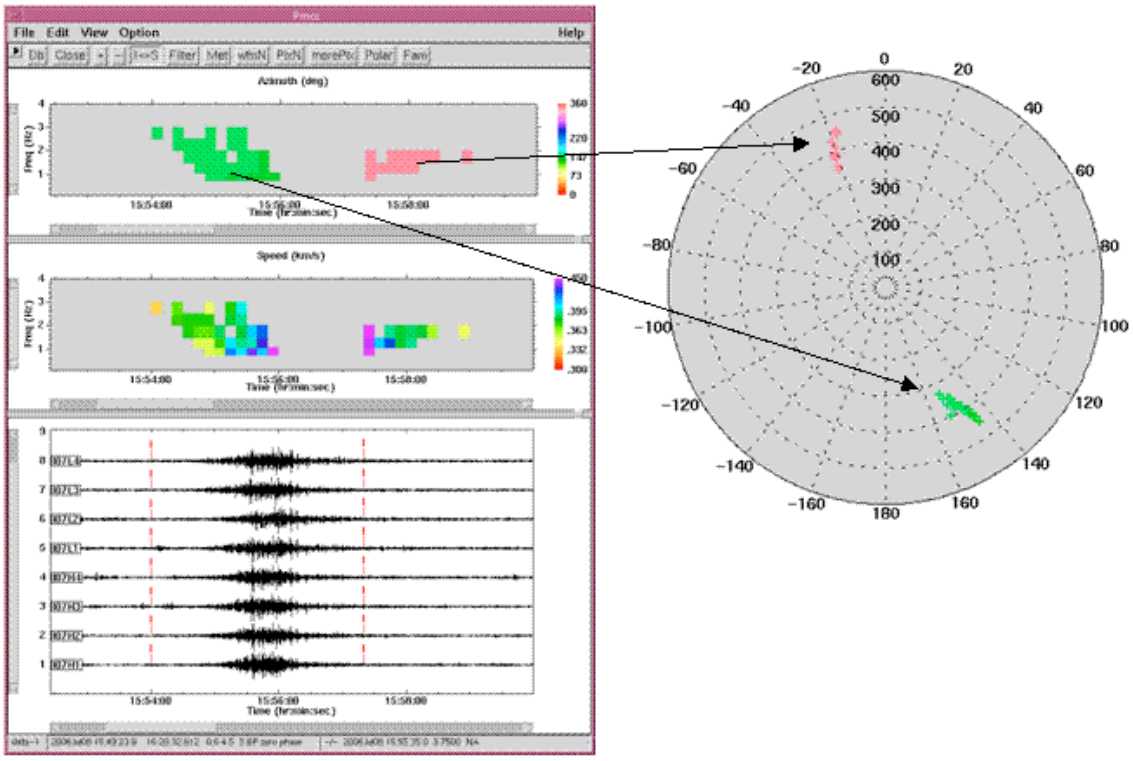


Figure 5. Example of PMCC pixel display and polar diagram, showing a fast-moving aircraft traveling from the southeast to the northwest across the array. The units in the polar display are azimuth (deg) and speed (m/s).

CONCLUSION(S) AND RECOMMENDATIONS

This paper describes the current status of infrasound processing in the development environment at the IDC. The PMCC algorithm is being used to routinely detect signals observed at infrasound stations. Detections with similar characteristics are categorized into clusters, which facilitates the assignment of phase names to similar detections. Infrasound signals are then assigned the phase names N, I, IPx, or ISx. Around 90% of infrasound detections are currently identified as noise. Non-noise arrivals are considered during network processing, which considers arrivals from all waveform technologies. Currently, about 35% of the SEL3 events in the development environment include infrasound arrivals. A specialized tool has been developed to interactively review the results of infrasound station processing, and procedures are currently being developed for the routine interactive review of infrasound data.

DISCLAIMER

The views expressed herein are those of the authors and do not necessarily reflect the views of the CTBTO Preparatory Commission.

ACKNOWLEDGEMENTS

We would like to thank the members of the infrasound specialist group at the IDC, who have provided valuable feedback concerning the interactive review software. The members of this group are Abdou Ndiath, Misrak Fisseha, Feyza Ocal, Kirill Sitnikov, and Gadi Turyomurugyendo.

REFERENCES

Bratt, S. R. and T. C. Bache (1988). Locating events with a sparse network of regional arrays, *Bull. Seism. Soc. Am.* 78: 780–798.

Cansi, Y. (1995). An automatic seismic event processing for detection and location: The P.M.C.C. method, *Geophys. Res. Lett*. 22: 1021–1024.

Jordan, T. and Sverdrup (1981). Teleseismic location techniques and their application to earthquake clusters in the South-Central Pacific, *Bull. Seism. Soc. Am*. 71: 1105–1130.

DETECTION OF ATMOSPHERIC EXPLOSIONS AT IMS MONITORING STATIONS USING INFRASOUND TECHNIQUES

Douglas R. Christie, Brian L. N. Kennett, and Chris Tarlowski

Australian National University

Sponsored by Air Force Research Laboratory

Contract No. FA8718-04-C-0032

ABSTRACT

Work is continuing on the development of infrasound techniques that can be used to improve detection, location and discrimination capability for atmospheric nuclear explosions at International Monitoring System (IMS) infrasound monitoring stations. In particular, we are continuing to focus on the detection of atmospheric explosions in the distance range from about 500 to 4500 km. We note that good detection capability in this distance range is essential to ensure that the global IMS infrasound network has acceptable monitoring capability, including good capability for the detection of explosions that occur over the vast open ocean areas in the Pacific, Indian and Southern Oceans. This investigation has therefore been primarily concerned with a detailed study of the properties of infrasound generated by regional and distant atmospheric explosions and the development of techniques that can improve detection capability for regional and distant sources at infrasonic monitoring stations. The database for this study has been expanded to include, in addition to data from IS05 Hobart, Tasmania and IS07 Warramunga in northern Australia, all data from IMS infrasound station IS04 Shannon in southwest Australia, and also data from a number of portable infrasonic array experiments carried out in eastern and northern Australia.

We are continuing to study the influence of the spatial correlation properties of infrasound from distant explosions on the detection capability at IMS infrasound monitoring stations. These studies show that a low degree of correlation between signals at different array elements at frequencies above 0.5 Hz is clearly a significant problem for the detection of infrasound from distant sources at monitoring stations with a small number of widely separated array elements. We also find that the degree of spatial correlation of infrasonic signals, even from sources in the same distance range, is quite variable, which may reflect seasonal variations in waveguide structure and variations in source characteristics. A technique has been developed that allows a direct comparison of the predictions from spatial coherence theory with array averaged coherence observations at all azimuths for any specified infrasonic array configuration.

A high-sensitivity portable infrasonic array has been deployed at a number of sites in the Australian region during the second year of this project. The first experiment with this portable array was carried out at a location between IS05 Hobart and IS07 Warramunga in order to assess the combined detection capability of these neighbouring IMS stations for surface mining explosions in the distance range from 1000 to 2000 km. Three additional experiments have been carried out using the portable array at locations in the Northern Territory and northern Queensland. These experiments were designed to provide data that will assist with the positive identification of local and distant infrasound sources observed at IS07 Warramunga.

Work has also started on the identification of the fundamental physical processes that result in background noise at IMS infrasound stations. These processes include both infrasonic and sub-sonic noise sources. It is clear that any technique that will improve signal-to-noise ratios (even by a factor of two) will significantly improve the monitoring capability of the IMS infrasound network. We recognize that wind-generated turbulence is usually the most significant source of background noise at infrasound monitoring stations and we have therefore started experimental work on techniques that will reduce the influence of wind-generated noise at frequencies in the principal infrasound monitoring passband.

OBJECTIVES

The primary goals of this research project are

- To identify problems with the detection, location, and discrimination of atmospheric nuclear explosions and
- To develop techniques using infrasound technology that will improve detection, location, and discrimination capability for nuclear explosions in the atmosphere.

Since this project is primarily concerned with the detection capability of the global IMS infrasound network, this research continues to be focused on an investigation of the properties of infrasonic signals observed at typical IMS monitoring stations. The average separation between nearest neighboring IMS infrasound stations is 1920 km in the Northern Hemisphere and 2020 km in the Southern Hemisphere. The distances between stations on opposite sides of the vast open ocean areas in the Southern Hemisphere may, however, exceed 7000 km. Stations that monitor the vast open ocean areas in the Southern Hemisphere therefore need to have good detection capability for explosions that occur at distances of at least 4000 km. This project is therefore focused on monitoring capability for atmospheric explosions at distances in the range from about 500 to 4500 km.

RESEARCH ACCOMPLISHED

Introduction

The research in this project is based on a detailed study of signal and noise properties derived from infrasonic data recorded at Australian IMS monitoring stations and data recorded during a number of carefully designed portable infrasonic array experiments. This work is divided into two separate, but closely linked, investigations. The first part is concerned with an ongoing investigation of the properties of infrasonic signals recorded at typical IMS stations, with emphasis on problems associated with the detection, location, and discrimination of regional and distant atmospheric explosions. These results are used to determine techniques that will improve existing infrasonic array designs and currently used analysis procedures. It has been noted (Christie et al., 2005a, b) that the optimum analysis passband for the detection of infrasound from distant explosions is generally centered on frequencies below 1.0 Hz. Up to this point, it has been tacitly assumed that the optimum passband for the detection of a 1-kT explosion at distances in the range from 1000 to 4500 km is centred at or above 1.0 Hz. However, research carried out to date shows that signal components with frequencies of 1 Hz or higher may have eroded away completely when the source lies at distances of more than 1500 km. In this case, the optimum detection passband usually extends from about 0.4 to 1.0 Hz. In some cases, especially when only thermospheric waveguide propagation is possible, detectable infrasound components from distant explosions are found only at frequencies below 0.1 Hz. The detection capability at an infrasound monitoring station is also found to be critically dependent on array design. Two specific problems can be identified: a) spatial aliasing of higher frequency signals and b) problems with signal coherence between array elements. Spatial aliasing of higher frequency signals has been extensively studied in recent years and the use of arrays with eight or nine elements has largely eliminated this problem. The results from the continuing investigation of signal coherence are proving to be surprisingly complex. It is clear, however, that the low degree of signal coherence between array elements at some existing larger-aperture 4-element infrasound monitoring stations will severely limit detection capability for infrasound generated by regional and distant explosions. Some of the results from the survey of signal coherence properties are described below.

The second part of this project is focused on a detailed study of the physical processes that generate infrasonic background noise and the development of techniques that will improve the signal-to-noise ratio for infrasonic signals from regional and distant atmospheric explosions. Detection capability at many infrasonic monitoring stations is limited by background noise usually associated with wind-generated turbulent eddies in the atmospheric boundary layer. Wind-generated noise is a particularly significant factor in the case of monitoring stations located in open exposed environments with little protection from the ambient winds. However, background noise at infrasonic monitoring stations is not limited to turbulent-eddy-generated micropressure fluctuations; there are also a number of other significant sources of background noise ranging from continuous or semi-continuous infrasonic signals to longer period noise components of unknown origin. It is clear that any technique that will reduce the effective background noise level at an infrasound monitoring station has the potential to significantly improve the monitoring capability of the global infrasound network. We have now started experimental work on the development of new techniques, which we hope will lead to a significant reduction in background noise in the primary monitoring

passbands. A brief description of the results of a preliminary experimental investigation of a potentially useful noise reducing technique is presented below.

IMS Infrasound Stations, Temporary Infrasonic Arrays, and Explosion Sources in the Australian Region

Five IMS infrasound monitoring stations are located on Australian territory. Two of these stations, IS05 Hobart and IS07 Warramunga have been in operation and certified for some time. IS04 Shannon in southwest Australia has recently been certified and data from this station is now being analyzed continuously in conjunction with data from IS05 and IS07 in an attempt to detect, locate, and identify all significant explosions in the Australian region. Work on the construction of a 4th Australian station, IS06 Cocos Islands, is underway and it is anticipated that the last Australian station in the IMS network, IS03 Davis Base in Antarctica, will be established in late 2007. The locations of the three certified infrasound stations on the Australian mainland, along with the location of the most important open-cut mines are shown in Figure 1. The locations of the New South Wales bolide on 5 December 2004 and the Manam Volcano explosion on 27 Jan 2005 are also shown on this map, along with the location of a 0.027-kT chemical explosion at the Woomera Test Range. The analysis of infrasonic waves generated by these three events has provided considerable insight into the properties of infrasound from distant sources. Only the most significant open-cut mines and mining areas are shown in Figure 1. A large number of smaller mines have been omitted since explosions at these mines tend to be of lower yield and signals from these explosions are usually detected only at local or near-regional distances.

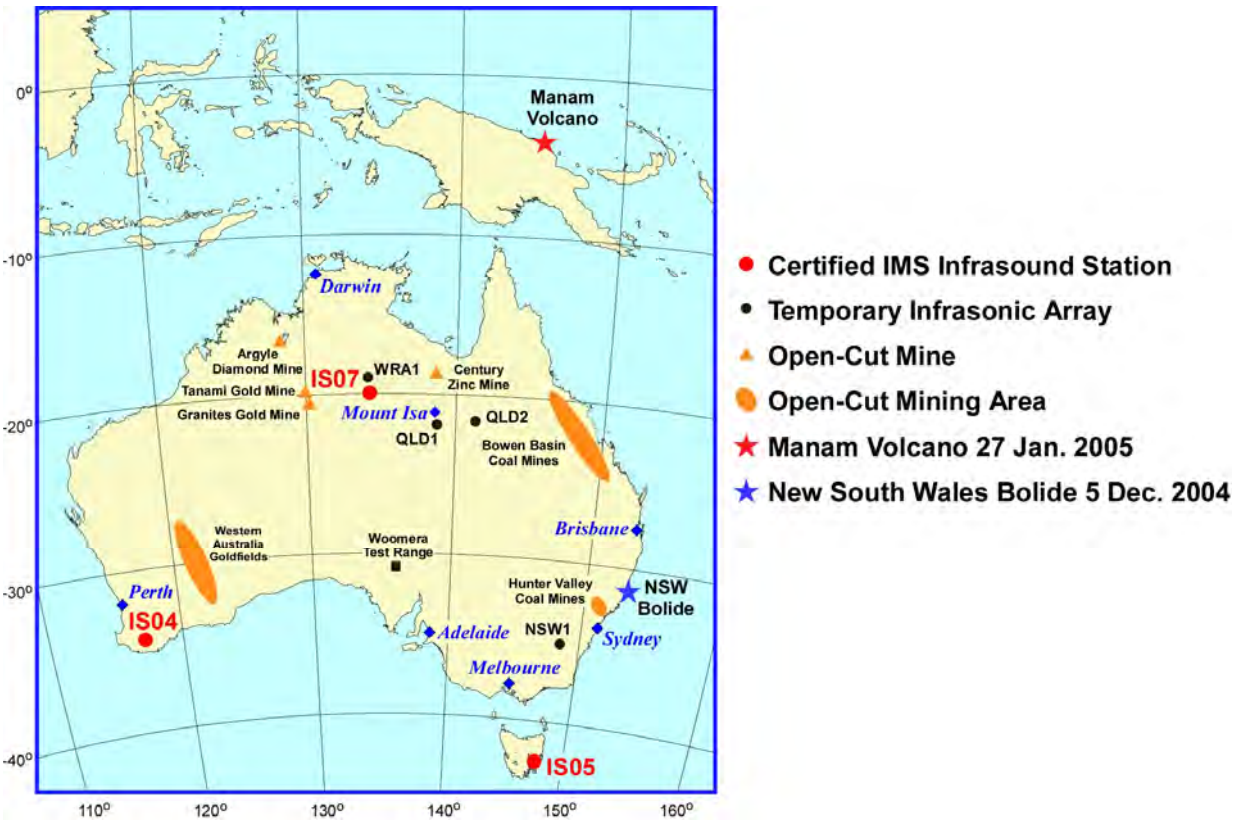


Figure 1. Map of the Australian region showing the locations of certified IMS monitoring stations IS04, IS05, and IS06, the locations of the most significant open-cut mines and open-cut mining regions, the sites of temporary infrasonic arrays (NSW1, WRA1, QLD1 and QLD2) used in this study, and the locations of the 0.027 kT chemical test explosion on 20 September 2002 at the Woomera Test Range, the explosive eruption of Manam Volcano on 27 January 2005 and the New South Wales bolide on 5 December 2004.

A 4-element high sensitivity portable infrasonic array has been constructed and deployed at a number of experimental sites as shown in Figure 1. The sensor used at each array element is a Chaparral Physics Model 5 microbarometer with specifications that exceed those required for IMS infrasound monitoring stations. Data is recorded on RefTek 24-bit model 130-01 digital recorders. Power is supplied at each array element by a solar power system and time is maintained to within 5 microseconds using independent GPS clocks. The portable array is usually deployed in a slightly irregular centered triangle configuration with an aperture of about 300 m. Noise reduction is achieved by connecting four 15-m porous hoses, arranged in a spiral configuration, to the inlet manifold on each microbarometer. Results from the portable array experiments are used to identify sources, to extend the database for the study of infrasonic wave properties to new sources and source distances, to measure the properties of background noise, and to test procedures that can be used to minimize background noise. NSW1 in New South Wales was installed to evaluate the performance of IS05. WRA1 was located near Warramunga to identify local sources at IS07. QLD1 was established near Mount Isa to observe infrasound generated by a large industrial mining complex and QLD2 was installed midway between the coal mining region in the Bowen Basin and IS07.

The detection characteristics, array configurations, and background noise properties of IS04 Shannon, IS05 Hobart, and IS07 Warramunga differ substantially. IS04 is located inside one of the tallest forests in Australia (trees to a height of more than 60 m) dominated by giant kari trees. The array elements are well sheltered from the ambient winds and noise levels tend to be quite low at most times of day. It is worth noting that the noise levels in the low-frequency monitoring passband from about 0.03 to 0.1 Hz are significantly lower on average than the levels observed at other IMS infrasound monitoring stations. Microbaroms generated by storms over the Southern Ocean tend to have large amplitudes and can be detected in the data at any time of day. Surf noise is seen on occasion at frequencies above 1 Hz. Longer period semi-continuous auroral-generated infrasonic signals are also observed at IS04 from time to time. The low-noise conditions at IS04 suggest that this station will play a valuable role in the monitoring of the open ocean regions in the South Indian and Southern Oceans. The noise conditions at IS05 in Tasmania are not nearly as good as those found at IS04. This station is located in a fairly open eucalypt forest which provides some shelter from the ambient winds, but noise levels tend to be relatively high at all times of day and to vary significantly from one array element site to the next. High frequency noise associated with surf activity along the eastern coast of Tasmania is frequently observed. As with IS04, microbaroms generated by intense storms over the Southern Ocean tend to have high amplitudes, but, in contrast with IS04, microbaroms cannot be detected at all times due to relatively high levels of background noise. Numerous local explosions generated by mining activity on the island of Tasmania have been detected. However, it is a matter of some concern that signals from large mining explosions on the Australian mainland are seldom detected at IS05. This may be due to the relatively high levels of background noise at IS05. It may also be due to the fact that most signals from sources on the Australian mainland can only propagate to IS05 in a thermospheric waveguide. IS07 at Warramunga in the Northern Territory is located in a semi-desert environment. Some protection from the ambient winds is provided by long grass, bushes and a few small trees, but wind-noise levels are almost always high during the daytime. Winds in the boundary layer are decoupled from the surface shortly after sunset with the rapid development of an intense radiation inversion. Noise levels therefore tend to be very low at night except when the radiation inversion is destroyed by thunderstorm activity or by propagating highly nonlinear mesoscale solitary waves and internal bore wave disturbances (Christie, 1989). Highly nonlinear gravity waves of this type are frequently observed at IS07 but have not been identified in the data from IS04 and IS05. They probably occur with reasonable frequency at IS04 Shannon, but only rarely at IS05 Hobart.

The array configurations and responses for IS04, IS05, and IS07 are compared in Figure 2. As can be seen from this illustration, the overall aperture of each of these arrays is approximately the same, but the configurations of the array elements differ substantially. The array elements at IS07 Warramunga are configured in a “high-frequency” small aperture triangular sub-array enclosed by a larger aperture “low-frequency” triangular main array. This configuration is typical of the array configurations used during the early stages in the construction of the IMS. IMS arrays that are currently being installed are usually configured in the form of a small aperture tripartite sub-array centered inside a larger aperture pentagon array, a design with very good side-lobe suppression characteristics. It is not always possible to install an IMS monitoring station with an ideal array configuration. The somewhat unusual array configurations at IS04 and IS05 have been installed to accommodate local conditions at each of these stations. The array response for all of the IMS arrays on the Australian mainland is quite good with fairly reasonable side-lobe suppression. Spatial aliasing will not be a problem except in the case of higher frequency signals with low signal-to-noise ratios. In this case, the technique described by (Kennett et al., 2003) can be used to minimize spatial aliasing and lower detection thresholds.

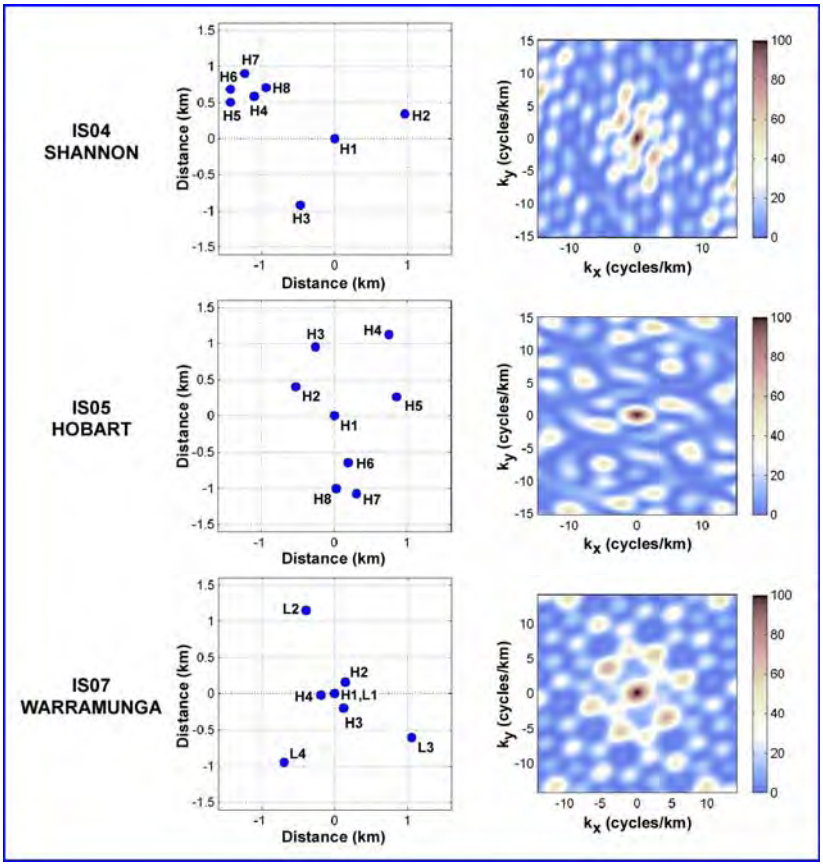


Figure 2. Comparison of the array configuration and response at IS04 Shannon, IS05 Hobart, and IS07 Warramunga. The overall aperture of each array is similar and each array includes both small and large aperture sub-arrays. The array response at all stations exhibits fairly reasonable side-lobe suppression.

Spatial Correlation of Explosion-Generated Infrasonic Signals

The spatial coherence of infrasonic signals has been studied extensively since the pioneering work of Gossard (1969), Gossard and Sailors (1970) and Mack and Flinn (1971) (see also Gossard and Hooke (1975). Mack and Flinn (1971) developed a relatively simple model for spatial coherence as a function of sensor separation and frequency and compared the predictions of this model with observations of relatively long-period infrasonic signals from very large explosions observed at great distances at a large aperture array. The model provided a very good fit to the observed data. Interest in recent years has focused on the spatial coherence of higher frequency infrasonic signals generated by relatively small explosions at distances ranging from a few hundred to a few thousand kilometers. The design of modern infrasound monitoring arrays is critically dependent on the results of these investigations. The first work on this subject was presented by Blandford (1997) in a sophisticated design study based on an extrapolation of the results of Mack and Flinn (1971). Further attempts to apply the theoretical treatment of Mack and Flinn to higher frequency infrasound observations have been reported by Armstrong (1998), Blandford (2000, 2004), McCormack (2002), and Christie et al. (2005a, b). In all cases, the results indicate that the degree of spatial coherence decreases rapidly with increasing frequency and with increasing sensor separation. In particular, the results suggest that a low degree of spatial coherence is likely to be a significant problem for the reliable detection of infrasound from distant sources at frequencies above 1.0 Hz at arrays with large apertures and few array elements. Coherence observations are usually compared with the predicted upper and lower limits defined by the Mack and Flinn theory for sensor pairs aligned normal to and parallel to the wavefront, respectively, as a function of sensor spacing. The measured coherence values generally exhibit large variations. It has been noted by Christie et al. (2005a,b) that the initial results from an on-going investigation of signal coherence at IMS infrasound stations suggest that the optimum passband for the detection of regional and distant explosions is centered below 1.0 Hz.

Here, we extend the observations of signal coherence at IMS infrasound stations and compare the directly observed *array-averaged* correlation coefficients with the array-averaged values predicted by Mack and Flinn theory.

Gossard (1969), Mack and Flinn (1971), and Blandford (1997) provide evidence to show that the observed loss of signal coherence along the direction of wave propagation is due to a small variation, $\pm \Delta c$, in wave velocity while the observed loss of coherence along the wavefront is due to a small variation, $\pm \Delta\theta$, in wave azimuth. The coherence parameters Δc and $\Delta\theta$ are range (and probably frequency) dependent. These parameters are adjusted by Mack and Flinn (1971) and Blandford (1997) to fit the observed loss in coherence both along and perpendicular to the wavefront. The precise physical processes that give rise to spatial decorrelation of infrasonic signals remain poorly understood. It seems reasonable, however, to assume that part of the observed decorrelation may be due to the specific characteristics of the source and part is due to scattering associated with wave propagation through an inhomogeneous medium with turbulence and/or small-scale variations in wind speed. Mack and Flinn consider three possible distributions, $F(\mathbf{k},f)$, for amplitudes in the wavenumber domain, two with symmetrical continuous distributions around a central maximum, and a third with constant amplitudes defined by the windows $\pm \Delta c$ and $\pm \Delta\theta$ in frequency-wavenumber space. As noted by Mack and Flinn, the results for all distributions are essentially the same. Since the precise form of the amplitude distribution in wavenumber space is not known, we shall adopt the basic uniform distribution model proposed by Mack and Flinn (1971). Mack and Flinn obtain an expression for the squared coherency, γ^2, at a given frequency, f, by integrating the spatial Fourier transform of the wavenumber spectrum $F(\mathbf{k},f)$ over the area where $F(\mathbf{k},f) \neq 0$, and normalizing the result to unity when $|\mathbf{r}| = 0$. The signal correlation, *C*, between two sensors separated by vector **r** is given, at a specified frequency, by the square root of the squared coherency (Blandford, 2000). For convenience, we write the expression for *C* in the following form:

$$C(\mathbf{r},T) = \sqrt{\gamma^2(\mathbf{r},T)} = \sqrt{\left|\frac{\sin(2\pi x \sin(\Delta\theta)/cT)}{2\pi x \sin(\Delta\theta)/cT}\right|^2 \cdot \left|\frac{\sin(2\pi y \Delta c/(cT(c+\Delta c))}{2\pi y \Delta c/(cT(c+\Delta c)}\right|^2} \qquad (1)$$

Here, *T* is period, *c* is the mean phase velocity and *x* and *y* are the components of the vector separation **r**. The coherence parameters used in this investigation (Δc = 15 m/s and $\Delta\theta$ = 5º) are taken from the results of Blandford (1997) for higher frequency infrasonic waves. Expression (1) can be plotted for $y = 0$ to give the Mack and Flinn limiting curve for the correlation between two sensors at a specified period as a function of sensor separation for sensors aligned parallel to the wavefront. Similarly, a plot of expression (1) with x = 0 gives the Mack and Flinn limiting curve for the variation of correlation at a given period as a function of sensor separation for sensors aligned normal to the wavefront.

A useful comparison of observations with the predicted Mack and Flinn limiting curves can be carried out directly when it is possible to find pairs of array elements in a large array separated by a range of distances and aligned along or perpendicular to the wavefront. The method is less useful when the comparison is based on data from a fixed array with a small number of array elements where few, if any, array element pairs are aligned normal and perpendicular to the wave propagation direction. In this case, corrections can be applied to the observed coherences to give estimates of the normal and perpendicular values, but this is a potential source of error. We have therefore decided to use a different comparison method that can be applied directly to any array configuration and which includes a contribution from all array element pairs. The method also allows the theoretical predictions at a specified frequency to be compared directly on the same plot with observed infrasonic wave correlation data corresponding to sources located at any azimuth.

Consider first the azimuthal variation of the signal correlation between two sensors as given by expression (1). The predicted azimuthal variation is plotted in Figures 3a and 3b in polar coordinates as a function of both sensor separation and wave period. The curves shown in Figure 3a correspond to a sensor separation of 1.0 km. As can be seen from this diagram, the degree of anisotropy in the azimuthal distribution increases rapidly as period decreases below 2.0 seconds. This indicates that the dominant contribution to the overall array-averaged correlation coefficient at higher frequencies will come from array element pairs that are aligned more or less in the wave propagation direction and suggests that some array configurations may exhibit azimuthally-dependent detection characteristics. This will be illustrated further in the results presented below. The results presented in Figure 3b for the azimuthal variation of the correlation between two sensors at constant period as a function of sensor spacing are similar in

form to those shown in Figure 3a. The azimuthal distribution is essentially isotropic at a period of 1 second when the sensor separation is less than about 0.3 km and highly anisotropic when the separation is more than about 1.0 km. Again these results suggest that certain array configurations may exhibit detection characteristics that are azimuthally biased at higher frequencies.

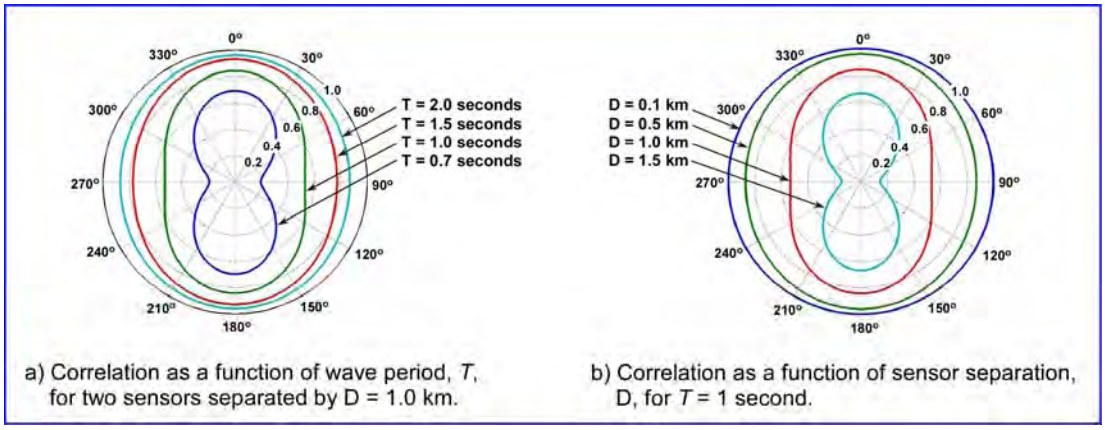


Figure 3. Predicted azimuthal variation of signal correlation between two sensors aligned along the 0º direction as a function of a) wave period, *T*, and b) station separation, D. The azimuth is the angle between the wave propagation direction and the vector separation between the sensors. Δc = 15 m/s and $\Delta\theta$ = 5º.

The predicted correlation between two sensors for all signal azimuths is specified, at a given period, by expression (1) in a coordinate system where azimuth is measured from the direction defined by the separation vector **r**. Thus, the predicted correlations for each individual sensor pair in an array can be calculated in a common polar coordinate system where azimuth, φ, is measured from geographic north by rotating the azimuthal distribution defined by (1) to the direction of the pair separation vector $\mathbf{r}_{ij}$ in the common coordinate system. The results for each sensor pair, $\tilde{C}_{ij}(\varphi, T)$, in rotated coordinates can then be averaged over all pairs of elements in the array to give a predicted normalized array-averaged correlation coefficient for all wave back-azimuths:

$$\bar{C}(\varphi, T) = \frac{2}{N(N-1)} \sum_{j>i}^{N} \tilde{C}_{ij}(\varphi, T) \qquad (2)$$

The resulting polar distribution of the array-averaged correlation coefficient is a unique characteristic of the array configuration, the parameterisation of Mack and Flinn theory, and the specified period. As noted above, each sensor pair in the array contributes to the predicted normalized array-averaged correlation coefficient for all wave back-azimuth directions and thus the observed normalized array-averaged correlation coefficients from all sources can be compared directly with the theoretical predictions on the same diagram.

Problems with the detection of higher frequency infrasonic signals on large aperture arrays can be illustrated by comparing the Mack and Flinn theoretical predictions with observations of array-averaged correlation coefficients corresponding to explosion-generated infrasonic wave detections on both small and large aperture arrays specified by sub-arrays at IS07 Warramunga. Examples of this procedure are illustrated in Figure 4 for the detection of infrasonic waves from regional and distant sources at a period of 1.0 seconds. The predicted azimuthal distribution of the normalized array-averaged correlation coefficient for a small aperture (~ 300 m) 3-component array defined by IS07 sites H2, H3, and H4 (see Figure 2) is given by the blue curve in each of the polar diagrams shown in Figure 4. Since the individual pair correlation coefficients are uniformly high for all pairs in this small aperture sub-array, the relatively minor azimuthal variations for each individual pair are integrated out in the averaging process leaving an isotropic overall predicted array-averaged correlation coefficient of about 0.94. In contrast, the azimuthal distribution of the predicted array-averaged correlation coefficient for a larger aperture (~ 2 km) three-component array defined by IS07 sites L2, L3, and L4 exhibits significant anisotropy as shown by the solid red curve in Figure 4. In this case, the predicted array-averaged correlation coefficients are less than the detection threshold.

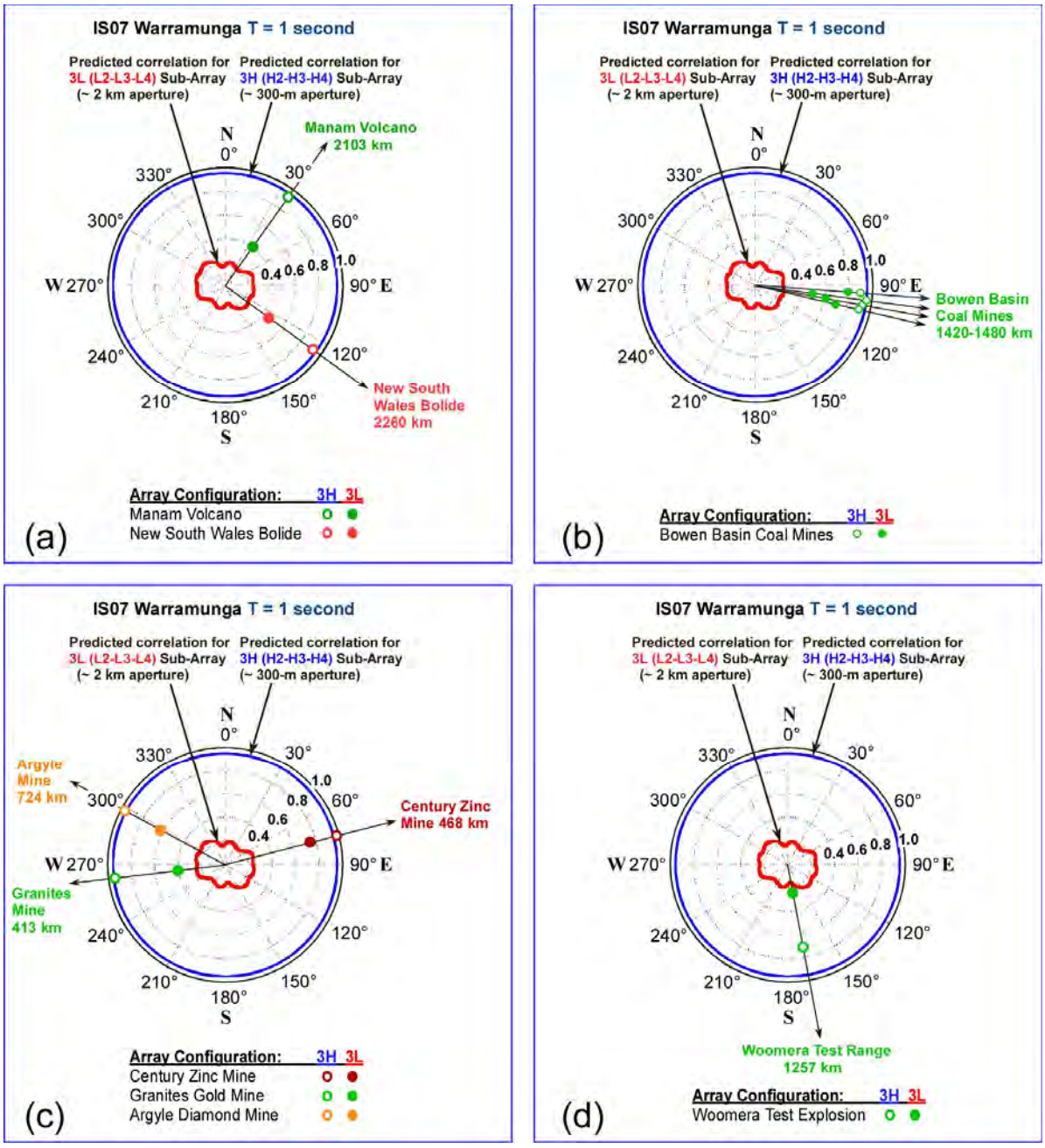


Figure 4. Array-averaged correlation coefficients observed at IS07 on large and small aperture arrays at a period of 1 second for explosion-generated signals compared with predictions based on the theory of Mack and Flinn (1971). The blue curve corresponds to the theoretical prediction for the 3-component small aperture sub-array H2, H3, and H4 (see Figure 2). The azimuthally anisotropic theoretical distribution specified by the red curve is computed for a larger aperture 3-component sub-array defined by L2, L3, and L4. Δc = 15 m/s and $\Delta\theta$ = 5°. (a) Results for two naturally occurring distant explosions: Manam Volcano on 27 January 2005 and the New South Wales bolide on 5 December 2004. (b) Results for distant coalmine explosions in the Bowen Basin. (c) Comparison of results for regional mining explosions. (d) Results for a chemical test explosion at the Woomera Test Range on 20 September 2002. Open circles are array-averaged correlation coefficients observed for signals detected on the small aperture 3H sub-array. Filled circles are observed array-averaged correlation coefficients for signals detected on the large aperture 3L sub-array.

The large amplitude infrasound signals generated by the New South Wales bolide on 5 December 2004 and signals from the explosive eruption of Manam volcano on 27 January 2005 are very easily detected on the small aperture 3H sub-array at IS07 with high array-averaged correlation coefficients (see Figure 4a) comparable to those predicted by the theoretical model. Observed correlation coefficients for the large aperture 3L sub-array are much smaller and detection is limited to a few time intervals with correlation coefficients close to the detection threshold. As noted above the predicted correlation coefficients for the large aperture array are substantially below the detection threshold. This low degree of correlation may be an artifact of the simple constant amplitude model used in the wavenumber domain. Alternatively, the results may indicate that the attenuation of the degree of spatial correlation predicted by the model is too high. In any case, the observed degree of correlation between array elements in the large aperture array is significantly attenuated and signal detection is marginal. These comments apply to all other results shown in Figure 4. In most cases, the array-averaged correlation coefficient observed on the large aperture array for infrasonic signals at 1 Hz is generally very close to the detection threshold. Some infrasonic signals observed on the large aperture array from distant coal mining explosions in the Bowen Basin have higher than expected correlation coefficients which suggests that the parameters used in Mack and Flinn predictions may give results that are slightly too restrictive. On the other hand, we note that the degree of correlation over the large amplitude array for signals from the Woomera test explosion is too small to allow any automatic detections. The essential conclusion is that regional and distant explosions will not be reliably detected using standard automatic data processing algorithms based on correlation techniques at a frequency of 1.0 Hz or higher at infrasonic array stations which have a small number of array elements and array element spacings of about 1.5 km or more.

Development of New Noise-Reducing Techniques

As noted above, high levels of wind-generated background noise continue to be the primary limiting factor on the performance of many infrasound stations. Traditionally, noise reduction has been achieved by using pipe arrays constructed either from porous hoses or from a series of pipes with discrete inlet ports. Both methods are in use at infrasound stations in the IMS. However, it seems unlikely that significant noise-reduction improvements can be achieved by simply refining existing pipe array designs since the size and number of inlet ports in these designs has reached practical limits. It has been proposed that substantial improvements might be achieved by replacing the noise-reducing pipe system at each monitoring array element with a compact array of individual sensors (Talmadge et al., 2001; Bass and Shields, 2004; Shields, 2005) The digital output from all sensors in each of these compact arrays would then be analyzed adaptively to discriminate against wind-generated noise and thus provide improved noise reduction. It seems very likely that this technique could indeed be used to achieve better signal-to-noise ratios, but the number of sensors and digitizers required at each array element is likely to be quite large and the cost for an installation of this type could be fairly high. Noise reduction in the monitoring passband can also be achieved by using techniques to attenuate the ambient winds and/or transform noise-producing eddies into smaller scale eddies that generate micropressure fluctuations at frequencies that lie well outside the monitoring passband. Significant noise reduction has been achieved at higher frequencies (> 1 Hz) using this technique in the form of relatively small-scale porous wind fence structures. We emphasize that the results to date from the present research project suggest that the optimum passband for the detection of infrasound from regional and distant explosions is centered at frequencies below 1.0 Hz. We have therefore decided to focus on techniques that can potentially enhance existing noise-reducing techniques at frequencies below 1 Hz. Our preliminary attempts in this regard are based on the results of a limited series of experiments described briefly by Christie (2000). In this report it was shown experimentally that noise levels obtained using a single inlet port mounted close to the surface can be significantly reduced at higher frequencies by effectively lifting the turbulent boundary layer over the port by covering the port with a fine 80-cm diameter screen carefully positioned to ensure that the screen does not interfere with the ambient flow. Noise levels in this single port experiment were reduced by nearly an order of magnitude at 5 Hz, but there was only a small improvement at a frequency of 1 Hz as could be expected, considering the small diameter of the surface screen. However, it seems likely that this noise-reducing technique can be extended to lower frequencies by increasing the diameter of the surface screen. A larger scale experiment has therefore been carried out and the results appear to be promising.

We emphasize that in the present technique we attempt to place the inlet port (or an array of ports) in a stagnant turbulence-free layer at the surface created by lifting the turbulent boundary layer over the inlets without disturbing the flow. This procedure should minimize dynamic pressure contributions to background noise. It is important to avoid any perturbation to the surface flow, since any obstacle will potentially generate further unwanted turbulence.

This is achieved by using very low profile surface screens. The results described here are of an essentially exploratory nature since the scale used in these preliminary experiments is small in comparison to the effective wavelengths of turbulent eddies associated with longer period micropressure fluctuations and small in comparison to the scale of currently used pipe arrays. We have decided to use a distributed porous hose in these experiments, since any improvement in noise-reducing performance will indicate the potential for improvement over conventional pipe array systems when the scale of the system is increased to the scale of current pipe arrays.

A diagram illustrating the dimensions of the relatively small-scale low-profile screened noise-reducing system used in this preliminary experiment is given in Figure 5. A section of porous hose was arranged in a 3-m diameter circle and connected by a short section of impervious hose to the microbarometer. Two low-profile screens constructed from 3.6 m^2 sheets of 60% porous shade cloth were then carefully fastened in place over the circular section of porous hose and background noise measurements were carried out over a period of several days. For comparison, measurements were also made simultaneously on an identical conventional unscreened 3-m diameter porous hose system located about 5 m away from the screened porous hose system. The results are also shown in Figure 5 for an average wind speed of about 3.5 m/s. As can be seen, the surface boundary layer screen used in this small-scale experiment does provide improved noise reduction capability over that obtained with a conventional noise reducing system at all frequencies above about 0.3 Hz. Rather unexpectedly, we found that the addition of the second low-profile surface screen layer did not lead to any improvement. We note that noise suppression has been extended to lower frequencies by the use of a larger diameter screen. These preliminary measurements appear to indicate that large-scale low-profile boundary layer surface screens may prove to be an effective means for enhancing noise-reducing capability at infrasonic stations located in high wind environments.

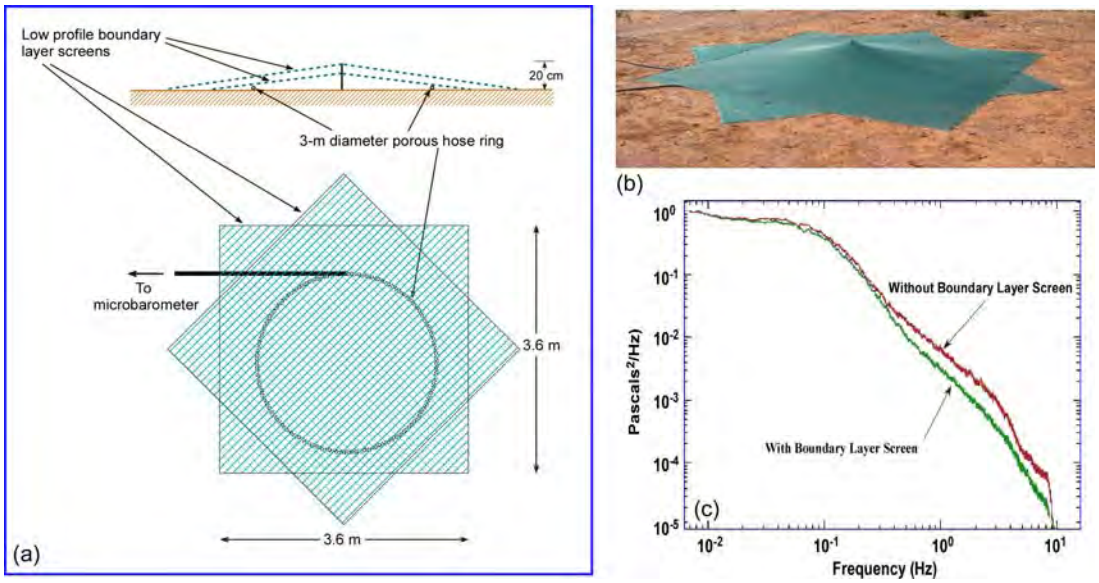


Figure 5. (a) Schematic diagram illustrating the layout and construction of the boundary layer screens used in the preliminary noise-reducing experiments. (b) Photograph of boundary layer screens in place over a 3-m diameter porous hose noise-reducing system. (c) Comparison of power spectral density of micropressure noise data recorded simultaneously from the screened porous hose system and an identical conventional unscreened porous hose system. The average wind speed is about 3.5 m/s.

CONCLUSIONS AND RECOMMENDATIONS

It is clear, from the results presented here, that detection capability for regional and distant explosions at some existing larger-aperture 4-element infrasound monitoring stations in the global infrasound monitoring network will be severely limited by the low degree of signal coherence between array elements. The results from the on-going investigation of signal coherence are proving to be surprisingly complex. This can probably be attributed in part to source characteristics, but variations in waveguide properties will also contribute to the observed variation in the degree of observed signal coherence. It seems likely at this point that observed spatial coherence will not prove to be a reliable discriminant. The main conclusions are as follows:

a) Infrasound monitoring stations should have at least eight array elements configured in both large and small aperture sub-arrays designed to eliminate spatial aliasing and signal coherence problems at higher frequency. The overall aperture of the array should be at least 1 km in order and to ensure accurate azimuthal measurements.
b) Automatic data processing should be carried out in passbands that span both high and low frequencies.

REFERENCES

Armstrong, W. T. (1998). Comparison of infrasound correlation over differing array baselines, in *Proceedings of the 20th Annual Seismic Research Symposium*, Sept. 21–23, 543–554.

Bass, H. E. and F. D. Shields (2004). The use of arrays of electronic sensors to separate infrasound from wind noise, in *Proceedings of the 26th Seismic Research Review*: *Trends in Nuclear Explosion Monitoring*, LA-UR-04-5801, Vol. 2, pp. 601–607.

Blandford, R. R. (1997). Design of Infrasonic Arrays. Air Force Technical Applications Center Report, AFTAC-TR-97-013.

Blandford, R. R. (2000). Need for a small subarray at IMS infrasound stations – Implications of shuttle and S. Pacific nuclear signals, in *Proceedings Infrasound Workshop*, Passau, Germany.

Blandford, R. R. (2004). Optimal infrasound array design for 1kt atmospheric explosions, in *Proceedings Infrasound Technology Workshop*, Hobart, Australia.

Christie, D. R. (1989). Long nonlinear waves in the lower atmosphere, *J. Atmos. Sci*. 46: 1462–1491.

Christie, D. R. (2000). Establishment of the CTBT IMS infrasound network: wind noise reduction, optimal array configuration and other technical issues, in *Proceedings Infrasound Workshop*, Passau, Germany

Christie, D. R., B. L. N. Kennett and C. Tarlowski (2005a). Detection of distant atmospheric explosions: Implications for the design of IMS infrasound array stations, in *Proceedings Infrasound Technology Workshop*, Papeete, Tahiti.Christie, D. R., B. L. N. Kennett and C. Tarlowski (2005b). Detection of regional and distant atmospheric explosions, in *Proceedings of the 27th Seismic Research Review*: *Ground-Based Nuclear Explosion Monitoring Technologies*, LA-UR-05-6407, Vol. 2, pp. 817–827.

Gossard, E. E. (1969). The effect of bandwidth on the interpretation of the cross-spectra of wave recordings from spatially separated sites, *J. Geophys. Res.* 74: 325.

Gossard, E. E. and Sailors, D. B. (1970). Dispersion bandwidth deduced from coherency of wave recordings from spatially separated sites, *J. Geophys. Res.* 75: 1324–1329.

Gossard, E. E. and Hooke, W. H. (1975). Waves in the Atmosphere. Elsevier, New York. Chapter 9, Section 65.

Kennett, B. L. N., D. J. Brown, M. Sambridge, and C. Tarlowski (2003). Signal parameter estimation for sparse arrays, *Bull. Seism. Soc. Am.* 93: 1765–1772.

Mack. H. and E. A. Flinn (1971). Analysis of the spatial coherence of short-period acoustic-gravity waves in the atmosphere, *Geophys. J. R. Astr. Soc*. 26: 255–269.McCormack, D. (2002). Towards characterization of infrasound signals, in *Proceedings Infrasound Technology Workshop*, De Bilt, The NetherlandsShields, F. D. (2005). Low-frequency wind noise correlation in microphone arrays, *J. Acoust. Soc. Am.* 117: 3489–3496.

Talmadge, C. L., D. Shields and K. E. Gilbert (2001). Characterization and suppression of wind noise using a large-scale infrasound sensor array, in *Proceedings Infrasound Technology Workshop*, Kailua-Kona, Hawaii.

FINITE DIFFERENCE METHODS FOR ACOUSTIC AND ACOUSTO-GRAVITY WAVEFIELDS: APPLICATION TO LOW FREQUENCY INFRASOUND PROPAGATION

Catherine de Groot-Hedlin

University of California, San Diego

Sponsored by Army Space and Missile Defense Command

Contract No. W9113M-06-1-0003

ABSTRACT

A finite difference (FD) method is derived for the frequency-domain acoustic and acousto-gravity equations as expressed in cylindrical coordinates. First, it is shown analytically that for an isovelocity atmosphere in which the density decreases exponentially with altitude, the acoustic wave equations (i.e., neglecting gravity) indicate that (1) the pressure varies with the square root of the density and (2) the acoustic wavelength depends not only on the frequency and velocity but also on the rate of exponential decrease of the density with altitude. Discretization of the linear equations relating acoustic particle velocities and pressures is straightforward except near the source. At $r = 0$, a singularity exists for the acoustic wave equation as expressed in cylindrical coordinates. In this case, l'Hopital's rule is used to transform the singularity at $r = 0$ into a determinate form. The FD equations must be solved simultaneously, which requires the solution of a very large, sparse matrix equation, which is accomplished using a quasi-minimum residual method. The resulting FD algorithms can be used to solve for sound intensities in arbitrarily complex models that may include high material contrasts and arbitrary topography.

The FD method is also extended to handle the effects of gravity on the acoustic wavefields. It is shown that the acousto-gravity equations require the simultaneous solution of the pressure and density perturbations caused by the passage of a sound wave. Acousto-gravity waves are relevant at very low frequencies, especially in the upper atmosphere where densities are very low.

OBJECTIVES

A FD method of solving the acoustic wave equation in cylindrical coordinates has been developed. The FD method yields the solution to a discretized version of the full acoustic wave equation for arbitrarily complex media. It is a full spectrum approach and is thus reliable at all angles of propagation, including backscatter. This offers an advantage over other standard propagation methods in wide use, as it allows for accurate computation of acoustic energy levels in the case where significant scattering can occur near the source, such as may happen for an explosion near the surface, or underground. This fits in with nuclear monitoring goals in that it allows for an improved understanding of the generation and propagation of infrasound energy from underground and near-surface explosions.

At high frequencies, the atmospheric density varies insignificantly over the scale of the acoustic wavelength and hence computation of the acoustic propagation is quite straightforward. However, atmospheric density drops off by an order of magnitude with approximately every 15–20 km in altitude. As will be shown in this paper, these variations in density strongly affect acoustic propagation at very long periods—over 100 s—for which the acoustic wavelength is greater than 30 km. FD solutions are presented for very low frequency sources for the acoustic wave equation. An FD computational method is sketched out for acousto-gravity propagation.

RESEARCH ACCOMPLISHED

Equations Governing Acoustic and Acousto-Gravity Propagation

The standard equations governing sound propagation may be written in the frequency domain as

$$-i\omega p = -\rho_0 c^2 \nabla \cdot \mathbf{v} \qquad (1a)$$

$$-i\omega \mathbf{v} = -\frac{1}{\rho_0}\nabla p \qquad (1b)$$

where the convention $p = p\ exp(-i\omega t)$ has been used to transform from the time to the frequency domain. In the above equations, p denotes the acoustic pressure, $\mathbf{v}$ is the acoustic particle velocity vector, ρ_0 is the ambient density in the absence of perturbations caused by the sound wave, c is the propagation speed of the medium, and ω is the circular frequency.

Buoyancy effects are significant in the propagation of acoustic energy at very low frequencies. The following acousto-gravity equations combining buoyancy and compressibility effects govern sound propagation at very low frequencies:

$$-i\omega p = \mathbf{v} \cdot (\rho_o \mathbf{g}) - \rho_o c^2 \nabla \cdot \mathbf{v} \qquad (2a)$$

$$-i\omega \mathbf{v} = -\frac{1}{\rho_o}\left[\nabla p + \rho_s \mathbf{g}\right] \qquad (2b)$$

$$-i\omega \rho_s = -\mathbf{v} \cdot \nabla \rho_o - \rho_o \nabla \cdot \mathbf{v} \qquad (2c)$$

where $\mathbf{g} = (0,0,9.8)$ is the acceleration that is due to gravity and ρ_s is the density perturbation caused by the passage of the sound wave. The term $\rho_s \mathbf{g}$ in Eq. (2b) is a buoyancy force (Gill, 1982); note that a negative density perturbation yields an upward acceleration that is due to the effect of gravity. Note that, in the case where gravity contributes negligibly, Eqs. (2) reduce to Eqs. (1). In that case, the density perturbations are approximately a scalar multiple of the acoustic pressure, i.e., $\rho_s = p/c^2$, since the second term in Eq. (2c) dominates.

The standard FD method relies on replacing linear partial differential equations with a set of discrete equivalents. Field solutions are then computed over a discrete set of nodes that compose the spatial grid. Figure 1 indicates how the field variables are defined and how the medium is discretized for the solution method presented in this paper.

The FD method is formulated in cylindrical coordinates here. A radially symmetric model is assumed, allowing for the response to a continuous wave point source to be computed using only two coordinate directions.

The model is decomposed into a set of discrete cells of dimension $\Delta r \times \Delta z$, each with a uniform propagation speed c and ambient density ρ_0. Pressure nodes are defined at the center of each cell, and the velocity variables are located midway between the pressure nodes. The staggered grid formulation increases the accuracy of the FD solution, since central differences are used to compute the discrete derivatives (Taflove and Hagness, 2000). A column of cells of width $\Delta r/2$ bounds the model at the axis of symmetry at $r = 0$; these become full cells when reflected about the axis. This choice allows pressure nodes, and hence the source, to be defined along the axis of symmetry. The locations of the vertical velocity nodes are defined in such a way as to allow a rigid surface ($v_z = 0$) to be defined at the bottom of the model.

Variables for the density perturbations must also be introduced when buoyancy effects are included in the FD solution. In the first-order equations above, both the density and pressure perturbations are dependent on each other only through the equation for the velocity perturbations. Therefore, the density variables ρ_s may be located at the same points in space and time as the pressure variables p.

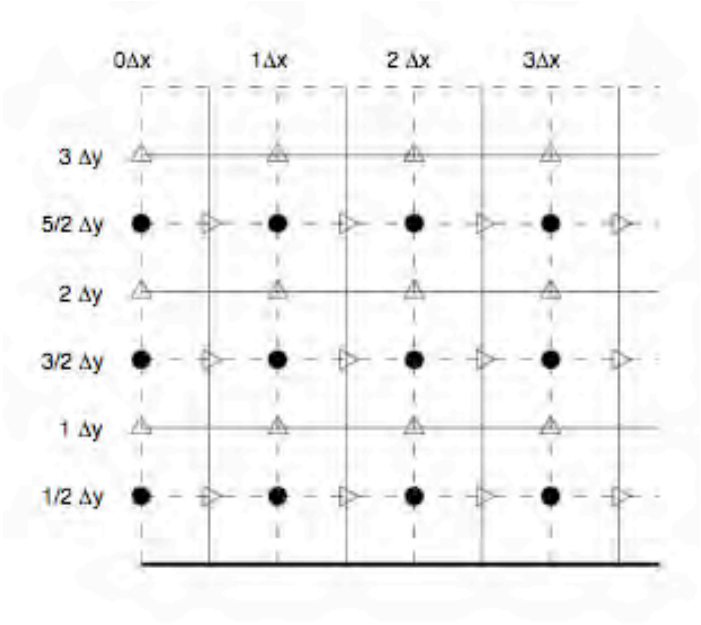


Figure 1. The FD model is decomposed into a set of discrete cells, indicated by the solid lines, each with uniform velocity c and ambient density ρ_0. The acoustic pressure and density perturbations are defined by the nodes at the center of each cell, indicated by the filled circles. When gravitational effects are neglected, only pressure perturbations need to be computed. The locations of the horizontal velocity v_r (triangles pointing right) and vertical velocity variables v_z (triangles pointing up) are defined on a spatially staggered grid, as shown.

Analytic Solution for an Isovelocity Model with Exponentially Decreasing Density

In a realistic atmospheric model, the ambient density decreases exponentially with altitude. An example of a realistic velocity and density profile is shown in Figure 2. In this section an analytic solution is derived for an isovelocity atmospheric model in which density decreases exponentially with altitude.

It can be shown that for a model with uniform velocity and exponentially decreasing density, where $\rho_0(z)=\rho_0(0)\, e^{-az}$, Eqs. (1) can be combined to yield

$$k^2 p - a\frac{\partial p}{\partial z} + \nabla^2 p = 0, \tag{3}$$

where k = ω/c is the wave number. Using a change of variables $p(r,z) = e^{-az/2} q(r,z)$, where the exponential term is equal to the square root of the density, Eq. (3) becomes

$$(k^2 - a^2/4)q + \nabla^2 q = 0, \tag{4}$$

after some manipulation. The *q* field values depend only on distance from the source (variability in depth was removed by the change of variables). By solving Eq. (4) in spherical coordinates (Jensen et.al., 1994) and converting back to cylindrical coordinates, it can be shown that

$$q(r,z) = A_1 \frac{e^{ik_m R}}{R} + A_2 \frac{e^{-ik_m R}}{R}; \tag{5}$$

where

$$k_m = \sqrt{k^2 - a^2/4}; \quad R = \sqrt{r^2 + (z - z_s)^2}$$

are the modified wave numbers and distance from source, respectively, and z_s is the source altitude. The pressure for an isovelocity whole-space with exponentially decreasing density, bounded by a rigid halfspace is given by

$$p(r,z) = \sqrt{\rho_0}\left[A_1 \frac{e^{ik_m R}}{R} + A_2 \frac{e^{-ik_m R}}{R}\right]; \tag{6}$$

where the first term corresponds to diverging spherical waves and the second term to converging spherical waves. For a wholespace, $A_2 = 0$. Strictly, this is not a physically realistic model since the density is defined as exponentially decreasing with z, or equivalently, exponentially increasing as z approaches negative infinity. The pressure thus also approaches infinity in this direction. A realistic analytic model would have to include a lower boundary with a realistic density; such a model is examined in the section on the FD method.

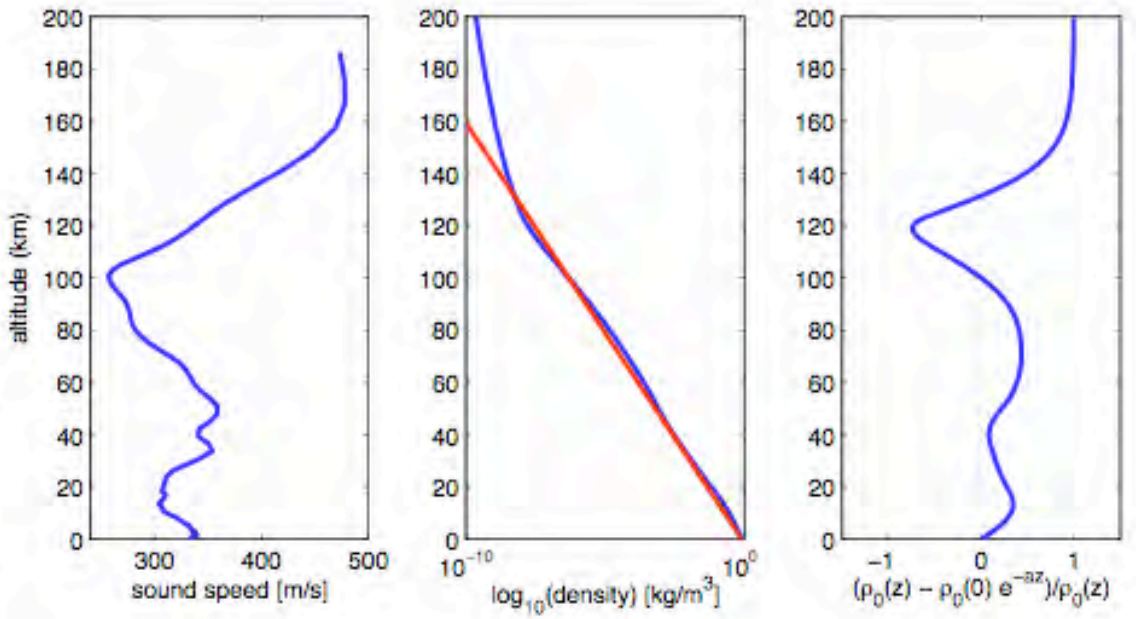


Figure 2. Profiles for atmospheric sound speed (left) and density (blue line, center). The red line at center shows the density profile corresponding to an exponentially decreasing density profile of e^{-az} profile, where a = 1.457 x 10^{-4}. The profile at right shows the fractional difference between the actual and exponential profiles. As indicated, the exponential approximation is adequate to an altitude of nearly 150 km.

Note that the pressure solution indicates that the acoustic wavelength, which is inversely proportional to the wave number, depends not only on the frequency and sound speed but also on the exponential decrease of density with altitude, which is characterized by the value of *a*, as defined in Eq. 3. Figure 3 shows a plot of wavelength λ vs. period, for a medium with a uniform velocity of c = 300 m/s. The relation is linear until *k* is on the same order of magnitude as *a*. For very, very low frequencies, Eq. (6) suggests that the acoustic wavefield should undergo exponential decay as k_m becomes imaginary. However, note that this derivation neglects the effects of gravity; these effects are discussed in the section on the FD solution to the acousto-gravity problem.

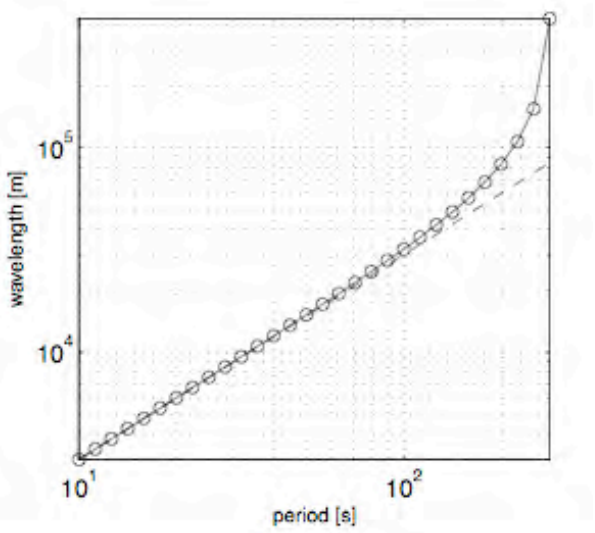


Figure 3. **Wavelength k_m vs. period for an isovelocity medium (c = 300 m/s), with exponentially decreasing density. The solid line indicates the acoustic wavelength for an atmosphere with exponentially decaying density, where the decay rate *a* is set to 1.457 x 10^{-4}, i.e., the same value as for the realistic density profile shown in Figure 2. The dotted line indicates the wavelength for *a = 0*. In the latter case, the period and wavelength vary linearly. At even longer periods, the k_m becomes an imaginary value.**

FD Solution for Acoustic Propagation in the Atmosphere

In cylindrical coordinates, the FD solution of the frequency-domain acoustic wave equations involves solving the discretized equivalents of Eq (1), i.e.,

$$0 = i\omega p_{i,j} - \rho_{o_{i,j}} c_{i,j}^2 \left[\frac{v_{r_{i,j}} - v_{r_{i-1,j}}}{\Delta r} + \frac{v_{r_{i,j}} + v_{r_{i-1,j}}}{r} + \frac{v_{z_{i,j}} - v_{z_{i,j-1}}}{\Delta r} \right] \qquad (7a)$$

$$0 = i\omega v_{r_{i,j}} - \frac{2}{\rho_{o_{i+1,j}} + \rho_{o_{i,j}}} \left[\frac{p_{i+1,j} - p_{i,j}}{\Delta r} \right] \qquad (7b)$$

$$0 = i\omega v_{z_{i,j}} - \frac{2}{\rho_{o_{i,j+1}} + \rho_{o_{i,j}}} \left[\frac{p_{i,j-1} - p_{i,j}}{\Delta z} \right] \qquad (7c)$$

where *i* indicates the row index and *j* indicates the column index, and v_r and v_z are the radial and vertical components of the velocity, respectively.

All equations must be solved simultaneously, which implies that a matrix equation of the type

$$\mathbf{A}\,\mathbf{x} = \mathbf{b} \qquad (8)$$

must be solved, where **x** is the *N x 1* vector of field components sought (in this case, the pressure variables at each node); **b** is the *N x 1* source vector, mainly composed of zeros; and **A** is a large, sparse matrix of size *N x N*. The problem is made feasible by the fact that only approximately *5 x N* variables of **A** are non-zero and need to be stored. For large models, the total number of variables can be on the order of tens to hundreds of thousands; therefore, a highly efficient method is required for solving this problem. The quasi-minimal residual (QMR) algorithm, developed to handle large, linear systems that have only a few non-zero entries per row (Freund et.al., 1991), was used to solve the examples presented in this paper.

In Figure 4, solutions of these equations are shown for 3 simple cases. In each case the bottom boundary is a flat, rigid surface representing the air/Earth boundary. The sound speed and density profiles within the atmosphere are as shown in Figure 2, and the source is located at an altitude of 35 km. Acoustic field solutions are derived for source periods of 100 s, 200 s, and 300 s. There periods were chosen because, as indicated in Figure 3, the acoustic wavelength k_m , defined in Eq. (5), is approximately equal to $k = \omega/c$ at a period at 100s; at T = 200 s, k_m differs significantly from k, and at T = 300 s, the acoustic wavelength is predicted to have an imaginary value. The transmission loss solutions are shown in Figure 4. The results suggest that the low-frequency acoustic fields would undergo significant attenuation with increasing distance from the source. Note that these computations neglect the effects of gravity.

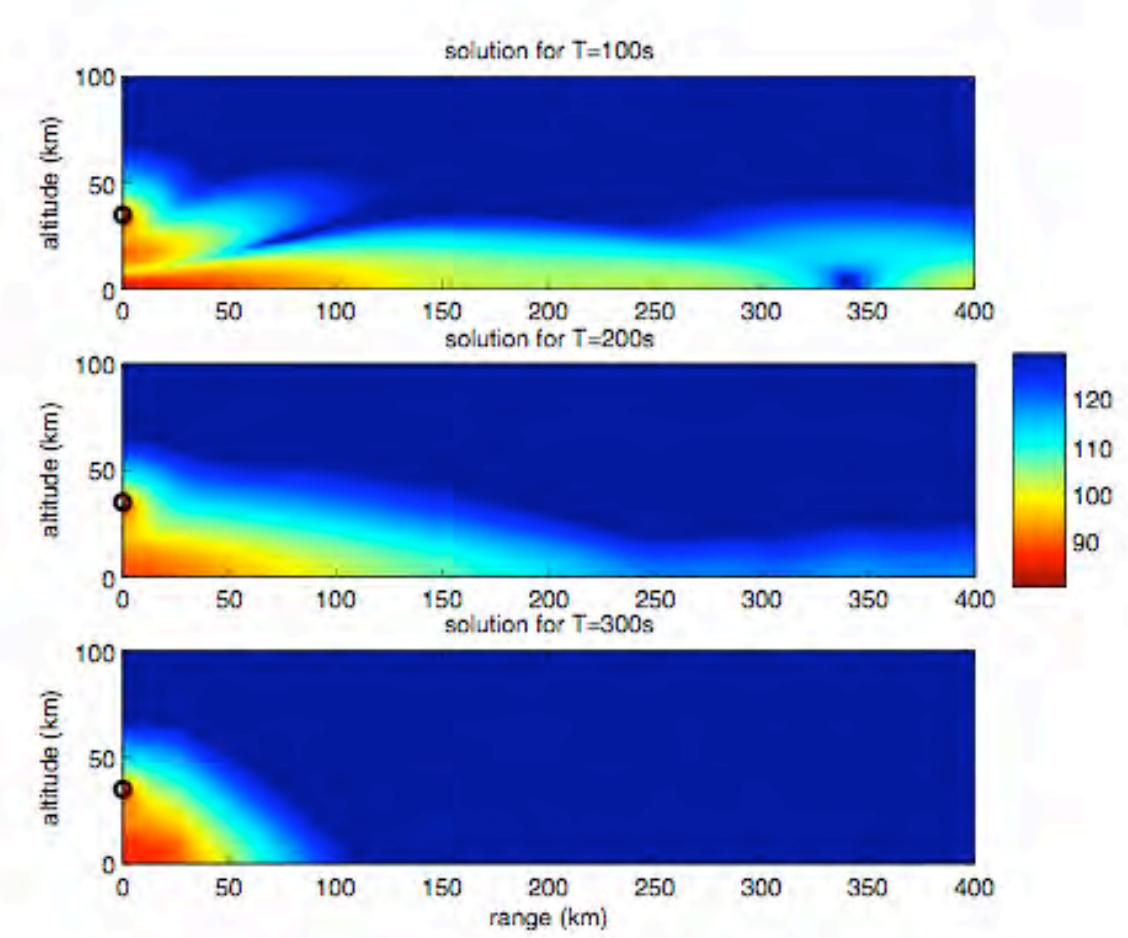


Figure 4. Finite difference transmission loss solutions for source periods of T = 100 s (top), T = 200 s (center) and T = 300 s (bottom). The model velocities and densities are as shown in Figure 2 (the density profile is given by the blue line in the center of Figure 2) and is terminated at the bottom by a rigid boundary. Absorbing boundary conditions are used to simulate a model with infinite extent with both increasing range and altitude. The color scale is identical for each plot.

FD Solution for Acousto-Gravity Propagation in the Atmosphere

An FD computation of acousto-gravity fields involves discretizing Eqs. (2). The density and pressure perturbations caused by the passage of a sound wave are computed simultaneously in this formulation so that the acousto-gravity formulation is more computationally intensive than is the acoustic-only solution. However, the model discretization in each coordinate direction scales with the acoustic wavelength—approximately 15 nodes per wavelength are required for an accurate solution. Acousto-gravity effects are significant only at very low frequencies—for wavelengths on the order of 100 km. Therefore, realistic atmospheric models for acousto-gravity effects have spatial scales on the order of several wavelengths in the *z* direction. Thus, the FD approach can handle acousto-gravity problems with reasonable computational efficiency.

CONCLUSIONS AND RECOMMENDATIONS

It was shown that the exponential decrease in atmospheric density plays an important role in acoustic propagation at very long periods. For periods of T >100 s. the ratio of the acoustic wavelength to the period increases rapidly. At periods greater than T = 300 s, the acoustic wave equations predict that the wave number is imaginary; thus, acoustic propagation dissipates rapidly away from the source. However, these results ignore the effects of gravity. At very long periods, buoyancy effects become significant, as density perturbations caused by the passage of a sound wave play an increasingly important role. Including gravity in the FD equations reduces the stability of the algorithm; methods of increasing the stability are under investigation.

REFERENCES

Freund, R. W. and N. M. Nachtigal (1991). QMR: A quasi-minimal residual method for non-Hermitian linear systems, *Num. Math*. 60: 315–339.

Gill, A. E. (1982). *Atmosphere-Ocean Dynamics*. San Diego: Academic Press.

Jensen, F. B., W. A. Kuperman, M. B. Porter, and H. Schmidt (1994). *Computational Ocean Acoustics*. Woodbury, New York: AIP Press.

Taflove, A., S. C. Hagness (2000). *Computational Electrodynamics: The Finite-Difference Time-Domain Method*, 2nd edition. Norwood, Mass.: Artech House.

ADVANCEMENT OF INFRASOUND PROPAGATION CALCULATION TECHNIQUES USING SYNOPTIC AND MESOSCALE ATMOSPHERIC SPECIFICATIONS

Robert G. Gibson[1], Douglas P. Drob[2], and David E. Norris[1]

BBN Technologies[1] and Naval Research Laboratory[2]

Sponsored by U.S. Army Space and Missile Defense Command

Contract No. W9113M-05-C-0132[1,2]

ABSTRACT

Numerical calculation of infrasound propagation paths is necessary to support accurate infrasound source location and phase identification. Predicting the details of infrasound propagation relies both on propagation models that capture the fundamental physical processes and on characterization of the propagation medium, namely the global atmosphere from the ground to altitudes above 100 km. The accuracy of propagation modeling depends in part on the fidelity of the atmospheric characterization. The analysis tool kit InfraMAP (*Infra*sound *M*odeling of *A*tmospheric *P*ropagation) integrates infrasound propagation models and environmental representations, including synoptic updates of the atmospheric specification, such as the output from numerical weather prediction models that supplement the baseline climatological characterization of temperature, wind and air composition. These capabilities allow infrasound researchers to investigate critical propagation phenomena, conduct sensitivity studies, and compare results of numerical modeling with observed signals.

Recent efforts investigate combining accurate, high-resolution regional atmospheric specifications with infrasound propagation modeling codes. Mesoscale models, which focus on the meteorology of a specific region, can account for and resolve important meteorological phenomena relevant to regional and local infrasound propagation. By investigating realistic spatial and temporal atmospheric models at a range of resolutions, we seek insight into the appropriate spatial and temporal scales that are necessary for achieving improved infrasound predictions at the relevant frequencies. Approaches are being developed to assess performance of candidate techniques for incorporating mesoscale atmospheric models and terrain specifications with propagation models and to evaluate the benefits for infrasound monitoring.

OBJECTIVES

In order to advance the state of the art for high-fidelity infrasound predictions, it is necessary to develop both propagation models and atmospheric characterizations that capture more of the fundamental physics that affect infrasound. The overall objective of this effort is to improve understanding of the effects of atmospheric dynamics on the propagation of infrasound, thus improving infrasonic source localization, phase identification, and discrimination. This will be accomplished by developing and analyzing advanced atmospheric specifications for use with propagation models and applying them in comparison studies using ground truth infrasound events. Specific objectives include the following:

- Comparing ground truth observations to propagation predictions using existing atmospheric specifications and propagation models. This will include sensitivity studies using the Naval Research Laboratory (NRL) Ground-to-Space (G2S) specification at various resolutions and statistical uncertainty studies to address atmospheric model biases and error budgets.
- Developing a multi-resolution, regional environmental specification capability, based on the NRL G2S framework, for use in propagation calculations. This will include assimilation of mesoscale atmospheric models that provide high resolution meteorological information on local and regional scales.
- Comparing ground truth observations to propagation predictions using the newly developed regional specifications that incorporate mesoscale atmosphere and terrain elevation.
- Investigating effects of including variable terrain elevation in ray-tracing propagation predictions.
- Developing research products that are useful for improving nuclear explosion monitoring capability.

This paper discusses recent progress in providing accurate atmospheric specifications for ground-based nuclear explosion monitoring via infrasound. The propagation properties of infrasound in the atmosphere are driven, in part, by the atmosphere, which has significant spatiotemporal variations. Therefore, in order to accurately relate regional infrasound propagation calculations to microbarograph array observations, the use of adequate atmospheric specifications is required. If the initial conditions for an infrasound propagation calculation (e.g., source altitude and surface conditions) or specifications of the intervening medium are specified inaccurately, then erroneous estimates of ducting heights, travel times, and amplitudes will result. In shifting away from current climatological characterizations, a great deal of complexity is introduced into atmospheric specification. This complexity arises from the natural variability of the atmosphere over all heights.

Prior work by Drob et al., 2003, has provided a simple framework to account for this complexity over certain height ranges. The NRL Ground to Space (NRL G2S) semi-empirical spectral model combines numerous sparse data sets using global spectral methods to specify the details of the entire atmosphere for use in infrasound propagation calculations. The infrasound analysis tool kit InfraMAP (Infrasound Modeling of Atmospheric Propagation) allows options for specifying the propagation environment by incorporating the output from numerical weather prediction models to supplement the baseline climatological characterization of temperature, wind and air composition (Gibson and Norris, 2003, 2004). These synoptic specifications are used with infrasound propagation models in order to improve predictions compared to those based on climatology. However, observed infrasound phases have not been well predicted by state of the art propagation models for several ground truth events (e.g., Bhattacharyya et al., 2003). Therefore, modeling advances that address the fundamental physical processes that affect infrasound are required. Also required, in parallel, are advances in specification of the propagation environment that address fundamental atmospheric physics at appropriate spatial and temporal scales and that can be utilized to improve the performance of advanced propagation models. This paper discusses recent research that will result in improved accuracy and understanding of the underlying physics of infrasound propagation calculations for nuclear explosion monitoring at regional and local ranges.

RESEARCH ACCOMPLISHED

Improving NRL G2S with Mesoscale Atmospheric Specifications

Fine scale atmospheric structures, both resolvable and irresolvable, can be responsible for acoustic wave scattering. Furthermore, the resulting specifics of computational modeling of infrasound from source to receiver are sensitive to the initial and final environmental boundary conditions, as well as conditions at points along the propagation path.

The atmospheric structure responsible for the refraction of infrasonic energy from the surface to the stratosphere and above may change rapidly. Below 55 km these structures are now being resolved on an hourly basis in real-time for civilian and defense applications by powerful operational global and regional scale data assimilation systems that synthesize huge amounts of data from a diverse network of operational satellite-, ground-based, and in-situ sensors. If technologically feasible, use of such atmospheric characterizations is likely to result in higher precision infrasound propagation predictions than are possible using climatology. These observationally based meteorological analysis fields are being produced on a routine basis the by the combined efforts of the National Oceanic and Atmospheric Administration (NOAA), National Aeronautics and Space Administration (NASA), Department of Defense (DoD), and the World Meteorological Organization.

The NRL G2S model of Drob et al. (2003) took the first step toward combining the available global operational lower atmospheric specifications from NOAA (Kanamitsu, 1998; Kalnay et al., 1990) and NASA (Bloom et al., 2005) with the NRLMSISE-00/HWM-93 models (Picone et al., 2002, Hedin et al., 1996) of the upper atmosphere for historical and, subsequently, near-real-time infrasound event analysis. A number of realizable technical improvements to the existing G2S environmental prediction system, theoretically shown to be significant to infrasound propagation calculations, are now being implemented. One of these is the incorporation and utilization of operational, high-resolution, mesoscale (regional) atmospheric specifications.

National and DoD weather centers can provide regional atmospheric specifications that have a very high spatiotemporal resolution and accuracy compared to comprehensive global specifications. This is achieved by focusing additional efforts on the meteorological observations and atmospheric physics specific to a given geographic region. To illustrate this increase in information content, Figure 1 shows a comparison of zonal and meridional wind profiles from the HWM-93 empirical wind model, the global NRL G2S system, and the Weather Research and Forecasting (WRF) mesoscale specifications at two locations, I31KZ and Baghdad, Iraq. Improved resolution of the vertical structure can be seen in the 0 to 20 km region.

Utilization of these mesoscale specifications should generally be superior to the utilization of an individual radiosonde profile obtained in the immediate vicinity of a ground-truth event for infrasound propagation calculations for all but very short range (< 25 km) propagation calculations. The operational assimilative analysis serves to remove any instrument calibration biases, as well as reduce statistical measurement errors by corroboration with overlapping and adjacent satellite, radar, and ground-based measurements, as well through known fluid dynamical constraints. In addition, by self-consistently combining all of the available meteorological observations in the immediate vicinity of a ground-truth event into a unified specification, range variations (i.e., horizontal gradients) that are important for infrasound propagation over distance of about 100 km can be resolved and provided. To illustrate this point further, the zonal and meridional wind profiles along a 300 km north-south path at 10 km intervals centered on I31KZ are shown in Figure 2 along with a single G2S profile for comparison. Improvement in the information content of the atmospheric specifications over the lower resolution G2S global specifications is clearly apparent. The significance of topographic variations relative to the vertical scale of the meteorological variations also becomes evident.

Model Domains and Initial Implementations

A potential disadvantage of the development and utilization of mesoscale or regional atmospheric specifications is that the available background fields are limited to a specific model domain. These domains generally encompass important regions of interest, but the domains can also be customizable to some extent. By design, the boundary conditions (including the upper level boundary condition) of these mesoscale specifications are provided by the corresponding global atmospheric specifications.

NOAA operates and provides atmospheric specifications at 13 and 20 km horizontal resolution on an hourly basis for the continental US (CONUS) in a reliable and straightforward manner, and the specifications can be used to investigate infrasound propagation from ground-truth events. The NOAA mesoscale system is called the Rapid Update Cycle (RUC). The RUC specifications extend to an altitude of approximately 20 km and are widely used by the commercial aviation and weather forecasting industries. The provision of operational and/or custom mesoscale atmospheric specifications for infrasound propagation calculations is discussed further below.

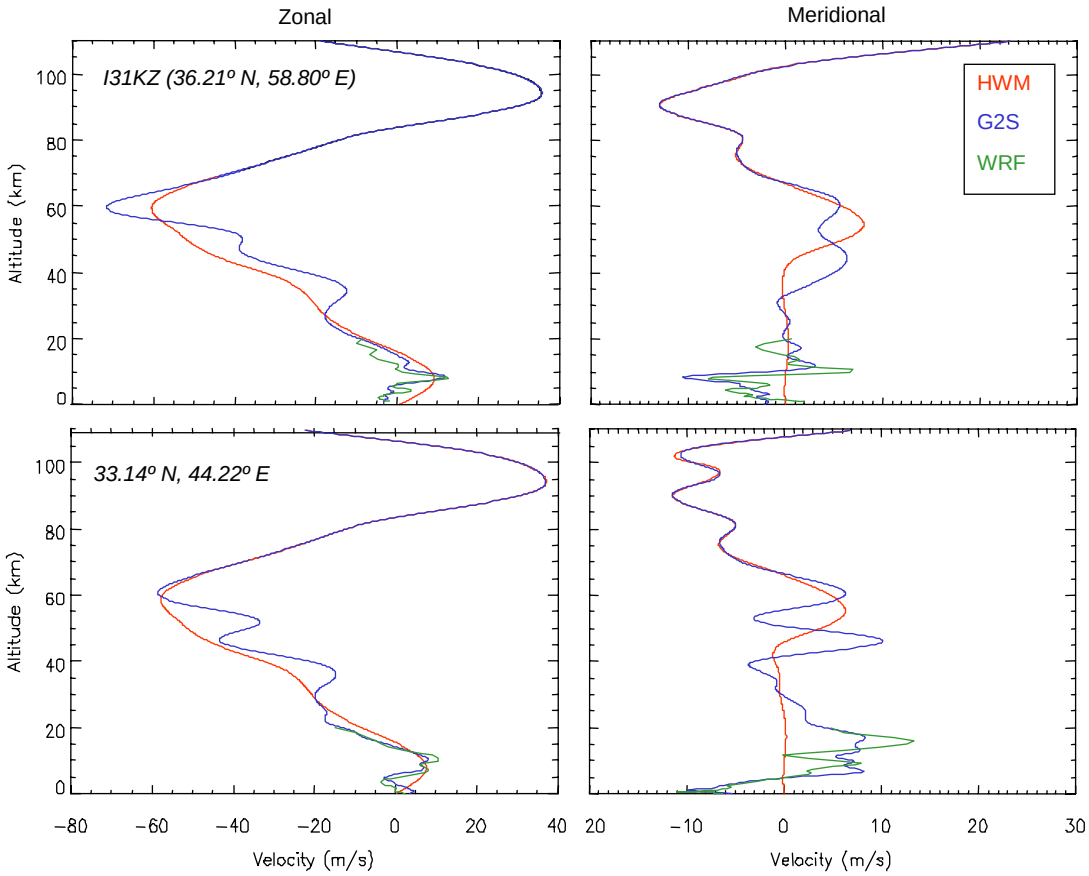


Figure 1. A comparison of zonal and meridional wind profiles from the HWM-93 empirical model (red), NRL Global G2S (blue), and the NRL Mesoscale G2S specifications (under development) that incorporate WRF (green), at two locations, I31KZ (above) and Baghdad, Iraq (below).

One of the challenges in utilizing the NOAA CONUS RUC for infrasound propagation calculations is related to the handling of the horizontal coordinate system. The NOAA RUC specifications are provided on a 301 x 225 Lambert equal area projection. This horizontal grid system is problematic because bivariate interpolants that are continuous in the first derivative across the grid cells are computationally expensive to approximate from the unequally spaced grid points as compared to equally spaced grid points. Interpolation of the unequally sampled fields for use by propagation codes would increase computational times significantly. An alternate approach is to interpolate from the RUC coordinates to an equally spaced coordinate system in advance. This requires a significant amount of computational time compared to other aspects of the G2S mesoscale data fusion process.

In the current implementation of the G2S-mesoscale model merging process, the NOAA Global Forecast System (GFS) and NASA GEOS-4 stratospheric specifications, which provide information content in the 25 to 55 km region, and the corresponding global G2S specifications, which provide information content in the 55 km region, are interpolated to the RUC grid points before merging all of the data sets in the vertical direction. Because the NOAA RUC fields are self-consistent with the NOAA GFS specifications, and because the NOAA GFS and NASA GOES-4 are implicitly self-consistent with the corresponding global G2S specification in the 45 to 55 km region, no

significant discontinuities arise between various data sets in the overlap region. As a result, merging of the various fields in the vertical can be performed by averaging the last four grid points of the RUC specification with the other overlapping data sets. The resulting unified specification has 96 vertical levels, with the majority of levels in the first 25 km. These specifications are then interpolated to a regularly spaced latitude and longitude grid at 0.125° intervals using a cubic Shepard method for bivariate interpolation of scattered data, as outlined by Renka, 1999.

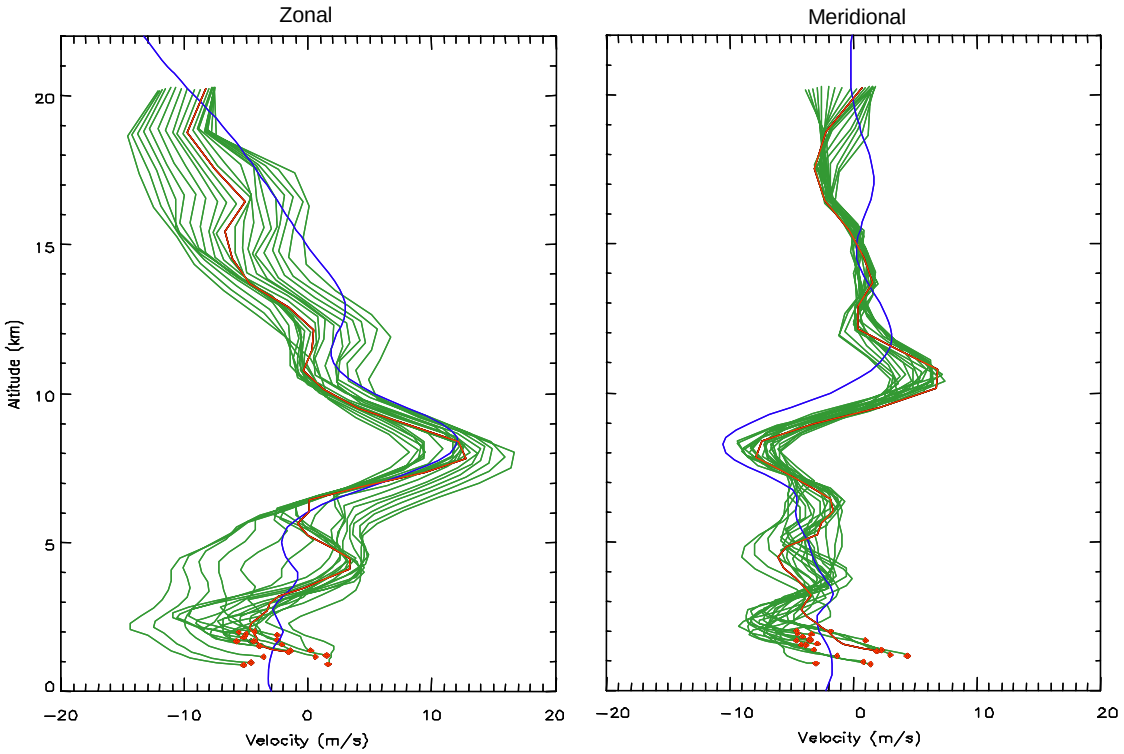


Figure 2. Mesoscale wind profile specifications along a +/- 150 km north/south meridian centered at I31KZ (green). The red profile indicates the profile at I31KZ. The blue profile represents the corresponding G2S global specification. The red dots at the bottom of each profile indicate the surface altitude variation at each location relative to mean sea level.

For practical reasons, the resulting G2S mesoscale grid that has been used for current software integration and testing purposes, systems automation development, and ground-truth validation efforts has been limited to the western half of CONUS. This domain encompasses the regional US infrasound network and includes I57US, I56US, and I10CA, as well as the source regions of White Sands Missile Range (WSMR) and Nevada Test Site (NTS). The domain is shown in Figure 3.

Another aspect of the effort has been to address the issue of the mesoscale vertical coordinate system. Effects ranging from the direct influence of mountain ridges on local wind patterns to the altitude-dependent interaction of humidity with precipitation, soil moisture, and ground cover content are all considered by meteorologists and by the current mesoscale numerical specification and prediction systems. Moderate- to high-resolution terrain models are thus an integral part of mesoscale meteorological specifications that are used to update and initialize operational numerical forecast models. To simplify numerical integration of the dynamical fields, as well as specification of the lower boundary conditions, operational mesoscale atmospheric data fields utilize what is known a sigma vertical coordinate system. This coordinate system is defined relative to the earth's surface and is thus terrain following. This makes direct utilization of existing mesoscale (and global) fields in infrasound propagation calculation difficult because these calculations are almost always performed in altitude coordinates. To illustrate the nature of this coordinate system as it relates to infrasound propagation, a vertical cross section of the first 25 kilometers of the G2S mesoscale atmospheric specification for zonal wind fields at 15 UTC on March 25, 2006, is shown in Figure 4. Each horizontal line represents a data specification level on which the wind and temperature fields are provided.

Note that the vertical resolution of the mesoscale system is on the order of 20 to 50 meters near the surface, increasing to larger, yet variable values with altitude. Being regularly gridded in horizontal directions, these specifications can be interpolated over one dimension in the vertical direction with cubic splines. Efficient vertical interpolation of these fields for infrasound propagation calculations is currently being investigated.

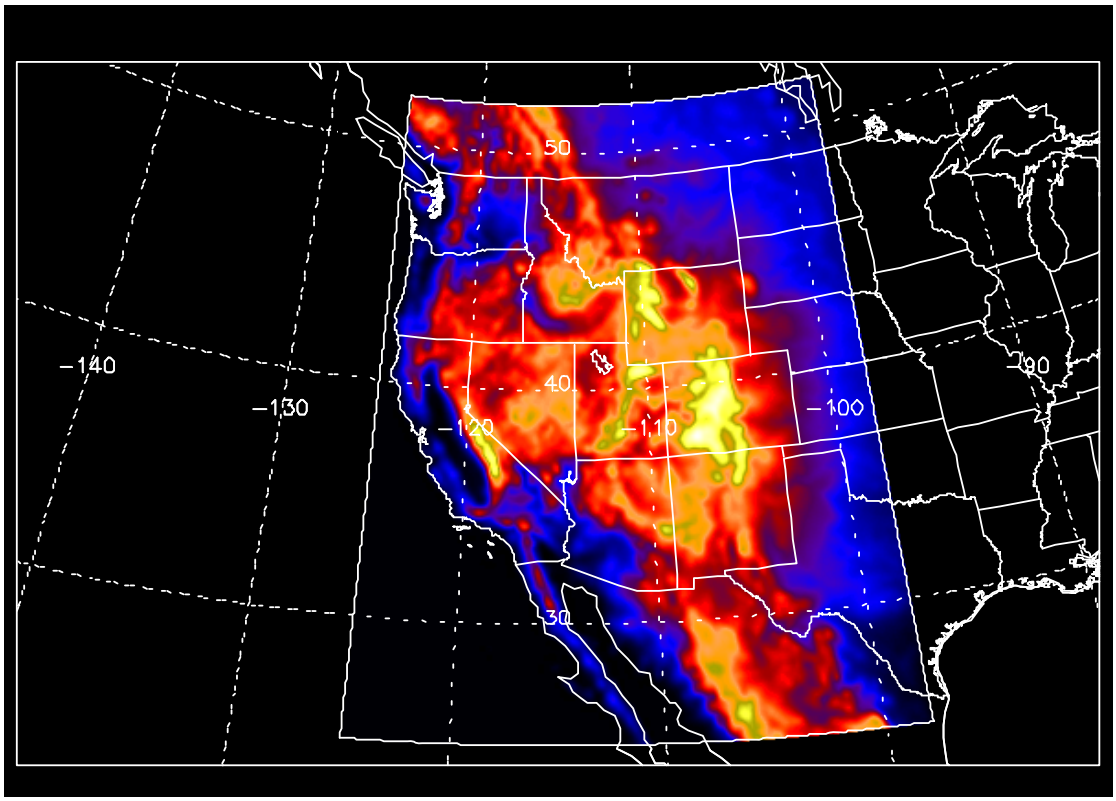


Figure 3. The prototype NRL G2S CONUS-WEST mesoscale specification domain. The image represents the 20 x 20 km terrain elevation model used to specify the lower boundary of the model domain. The color scale ranges from black for mean sea level within the domain, to white in the Colorado Rocky Mountains with an altitude of 3551 meters above sea level.

A static digital terrain elevation model is required to combine mesoscale and recent global atmospheric specification fields with the HWM/thermospheric atmospheric model (MSIS) empirical models in order to translate them into altitude coordinates so that they can be used in infrasound propagation calculations. In addition, detailed range dependent propagation calculations by a number of researchers have clearly demonstrated that terrain scattering effects should not be ignored in mountainous regions. The new G2S mesoscale specifications are being designed to address these issues simultaneously. As a result, in addition to the atmospheric specifications, new capabilities were built into the G2S client software to provide terrain elevation estimates at 30′ resolution (1 km) for any location on the globe to support infrasound propagation models. The NOAA Global Land One-km Base Elevation (GLOBE) digital terrain model provides the underlying data (Hastings and Dunbar, 1998).

Using these mesoscale fields and new tools described above we have now begun to investigate the information content and consequences of G2S-mesoscale specifications for infrasound signal propagation for several ground-truth events. This includes the examination of the fine scale structure of vertical and horizontal gradients in the G2S-mesoscale sound speed and wind fields to assess geophysical significance.

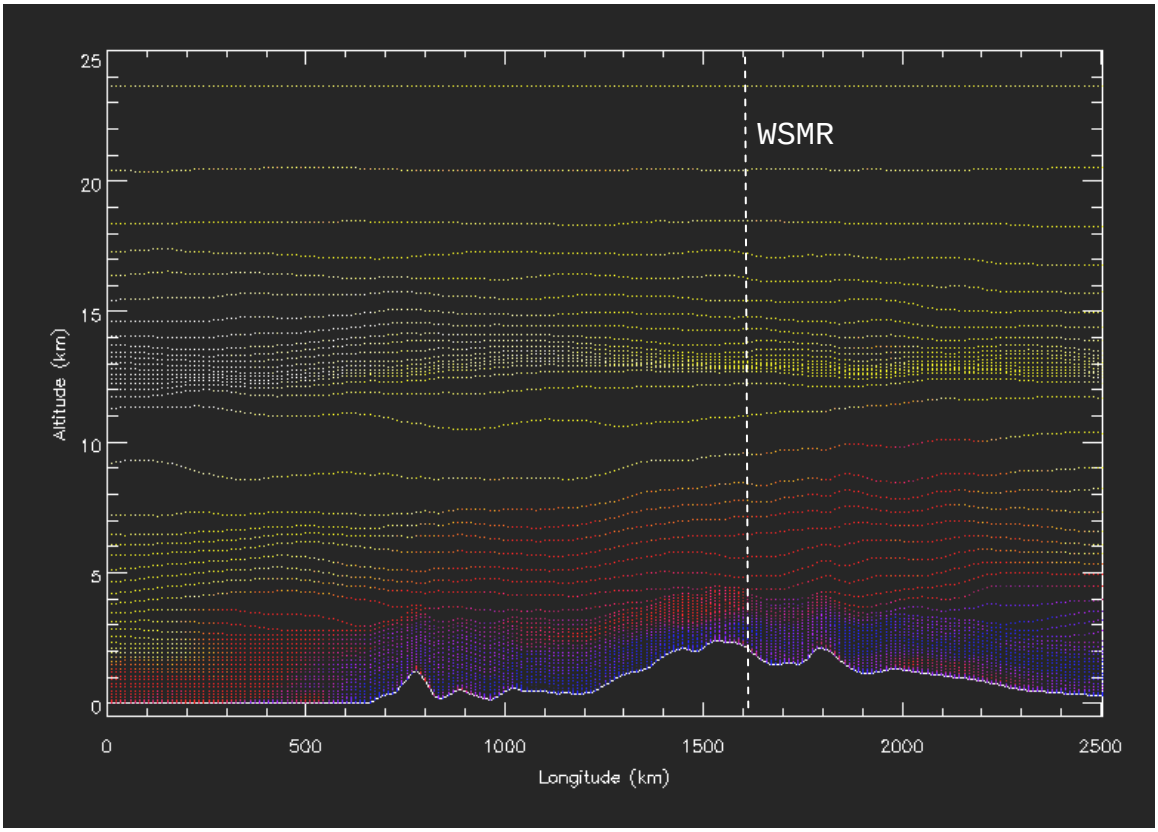


Figure 4. A vertical cross section of the first 25 km of the G2S mesoscale atmospheric specification, zonal wind fields at 15 UTC on March 25, 2006, at a latitude of 33° N. The color scale ranges from 40 m/s eastward (white) to -10 m/s (dark blue). The horizontal axis represents the distance in km from the left edge of the specification domain. The approximate location of WSMR is indicated with a vertical line.

Variable Terrain Elevation and Ray Tracing

Existing ray tracing propagation models for infrasound are limited in how well they characterize the interaction with the earth's surface. In general, a flat surface is assumed and defined using either an equivalent spheroid earth or ellipsoidal earth. As the propagation range decreases, the importance of ray interaction with variable terrain increases. Thus, we are pursuing an effort to integrate variable terrain elevation into ray tracing.

One of the key issues in this effort is identifying the relevant spatial scales over which the variable terrain elevation needs to be resolved for infrasound propagation calculations. To support the evaluation of this issue, we have integrated additional Earth Topographic (ETOPO) databases into the InfraMAP tool kit. Previously, only the ETOPO30 and ETOPO5 databases were available. ETOPO30 provides 30 minute resolution, which translates to approximately 55 km between grid points. ETOPO5 provides 5 minute resolution, or approximately 9 km between grid points. We have integrated the 2 minute ETOPO2 database, with ~4 km grid spacing, and are evaluating the integration of the 30 arc second GLOBE database, which provides very high resolution of order 1 km. Once integrated, each of these databases will be available for use with the ray tracing propagation model. This capability will enable detailed evaluation of the spatial scale issue.

At this time, the ray tracing model integration with ETOPO5 has been completed. At local interactions between the rays and ground, the ETOPO5 database is used to compute the local terrain height and the local first and second derivatives in latitude and longitude. These data are needed in the ray tracing formulations to resolve the angle of reflection of the ray at the surface.

They are computed using cubic spline interpolation. A 4x4 data grid is loaded surrounding the bounce position. Second derivatives at the grid boundaries are computed using central finite differencing over an expanded 16x16 grid. Then cubic interpolation uses these values to compute the local terrain height and associated derivatives needed for the ray calculations.

As an example of this new ray tracing capability, consider the scenario shown in Figure 5. In the background image (left panel) and profile (right panel), the ETOPO5 topography is displayed. The source-receiver path is defined over a 450 km path, providing ample opportunity for interaction between rays and the complex terrain surface.

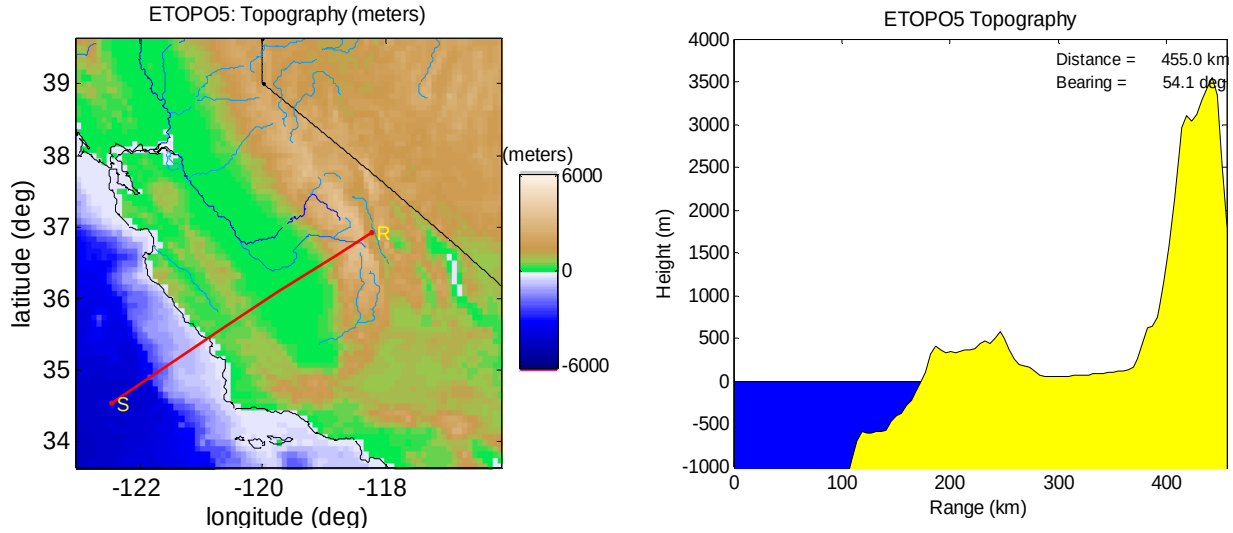


Figure 5. Modeling scenario with source (S) off coast of California and receiver (R) in the Sierra Nevadas. The ETOPO5 database is shown over the region (left) and along the source-receiver great circle path (right).

Figure 6 gives the solution for a ray launched with an initial elevation angle of 15 degrees. There are two bounce points, one at a range of approximately 230 km and the other near the receiver. The first bounce point is shown in more detail in the right panel of the figure. For this resolution and plot scale, the ray appears to reflect specularly, although a more comprehensive comparison with flat earth predictions is needed to fully quantify the effect. In addition to reflection angle, the ray path shape and ray path travel time will vary due to the incorporation of complex terrain.

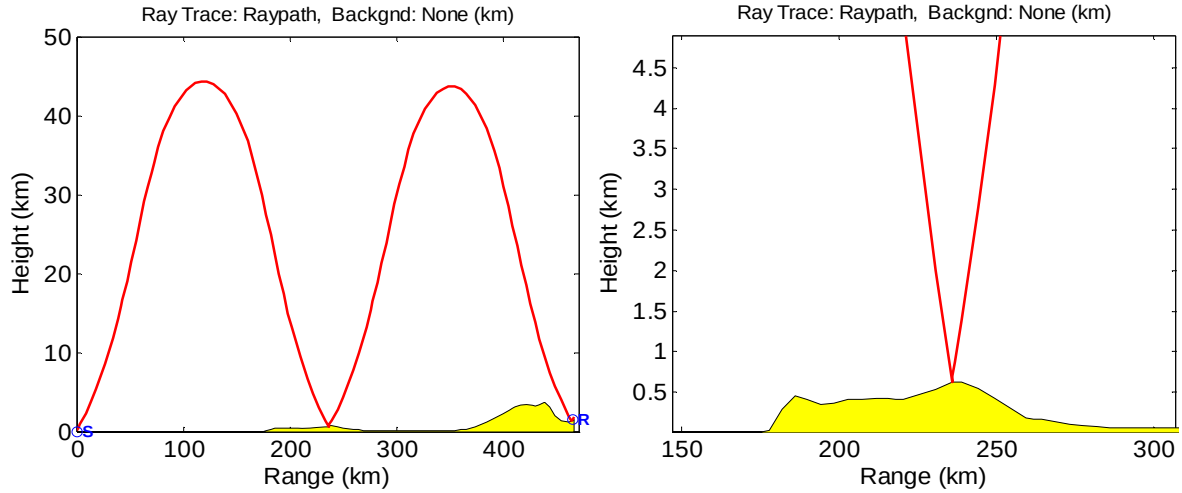


Figure 6. Ray solution for scenario illustrated in Figure 5. The full path of the ray is shown (left) along with the interaction with the complex surface at the first bounce (right).

CONCLUSIONS AND RECOMMENDATIONS

Synoptic specifications are used with infrasound propagation models in order to improve predictions compared to those based on climatology. However, observed infrasound phases have not been well predicted by state of the art propagation models for several ground truth events. Therefore, modeling advances that address the fundamental physical processes that affect infrasound are required. Also required, in parallel, are advances in specification of the propagation environment that address fundamental atmospheric physics at appropriate spatial and temporal scales and that can be utilized to improve the performance of advanced propagation models.

Study of long-range events will improve understanding of the strengths and weaknesses of global synoptic specifications. Mesoscale atmospheric models and terrain databases, used to improve characterization of the lower regions of the atmosphere, will enable improved understanding of local and regional propagation of infrasound signals. Study of local and regional events will improve understanding of the importance of mesoscale phenomena.

One of the important aspects of the work is to consider the uncertainties introduced by the various physical assumptions and environmental specifications that relate the infrasonic observable back to source characteristics. The significance of these assumptions and uncertainties must be compared to uncertainties in the measurement techniques and statistics of the ground truth event database. Assumptions about the spatiotemporal resolution of environmental specifications can be further quantified deterministically in this line of research. There are a number of known biases and irresolvable atmospheric phenomena that also need to be considered in the evaluation of the performance of infrasonic monitoring systems.

Research investigations are underway regarding the effects of terrain elevation on infrasound propagation, and the development of calculation techniques for predicting terrain effects will continue.

REFERENCES

Bhattacharyya, J., H. Bass, D. P. Drob, R. Whitaker, D. Revelle, and T. Sandoval (2003). Description and Analysis of Infrasound and Seismic Signals Recorded from the Watusi Explosive Experiment, on September 28, 2002, in *Proceedings of the 25th Seismic Research Review - Nuclear Explosion Monitoring: Building the Knowledge Base*, LA-UR-03-6029, Vol. 2, pp. 587–596.

Bloom, S., A. da Silva, D. Dee, M. Bosilovich, J.-D. Chern, S. Pawson, S. Schubert, M. Sienkiewicz, I. Stajner, W.-W. Tan, M.-L. Wu (2005). Documentation and Validation of the Goddard Earth Observing System (GEOS) Data Assimilation System - Version 4**.** *Technical Report Series on Global Modeling and Data Assimilation*, NASA/TM-2005-104606.

Drob, D. P., J. M. Picone, and M. A. Garcés (2003). The Global Morphology of Infrasound Propagation, *J. Geophys. Res.* 108: doi: 10.1029/2002JD003307.

Gibson, R. and D. Norris (2003), Integration of InfraMAP with near-real-time atmospheric characterizations and applications to infrasound modeling, in *Proceedings of the 25th Seismic Research Review - Nuclear Explosion Monitoring: Building the Knowledge Base*, LA-UR-03-6029, Vol. 2, pp. 638–645.

Gibson, R. and D. Norris (2004), Integration of InfraMAP Software with Near-Real-Time Atmospheric Characterizations, BBN Technologies Final Report for Air Force Research Laboratory (AFRL/VSBYE) under Contract DTRA01-01-C-0084.

Hastings, D.A. and P.K. Dunbar (1998), Development & Assessment of the Global Land One-km Base Elevation Digital Elevation Model (GLOBE), *International Society of Photogrammetry and Remote Sensing | Commission IV | Symposium in September, 1998, ISPRS Archives*, Vol.32, number 4, pp. 218–221.

Hedin, A. E, E. L. Fleming, A. H. Manson, F. J. Schmidlin, S. K. Avery, R. R. Clark, S. J. Franke, G. J. Fraser, T.Tsuda, F. Vial, and R. A. Vincent (1996), Empirical wind model for the upper, middle, and lower atmosphere, *J. Atmos. Terr. Phys.*, 58, 1421-1447.

Kanamitsu, M. (1989), Description of the NMC global data assimilation and forecast system. *Wea. and Forecasting*, 4, 335-342.

Kalnay, M. Kanamitsu, and W.E. Baker (1990), Global numerical weather prediction at the National Meteorological Center, *Bull. Amer. Meteor. Soc.*, 71, 1410-1428.

Picone, J. M., A. E. Hedin, D. P. Drob, and A. C. Aikin, (2002), NRLMSISE-00 Empirical Model of the Atmosphere: Statistical Comparisons and Scientific Issues, *J. Geophys. Res.*, 107(A12), art. no. 1468.

Renka, R. J. (1999), Algorithm 790: CSHEP2D: Cubic Shepard Method for Bivariate Interpolation of Scattered Data. *ACM Trans. Math. Softw.*, 25, 1, 70-73.

INFRASOUND CALIBRATION EXPLOSIONS FROM ROCKETS LAUNCHED AT WHITE SANDS MISSILE RANGE

Eugene Herrin[1], Paul Golden[1], Petru Negraru[1], William Andre[2], Henry Bass[3], Milton Garces[4], Michael Hedlin[5], Mihan McKenna[6], David Norris[7], Daniel Osborne[8], and Rodney Whitaker[9]

Southern Methodist University[1], US Army Space and Missile Defense Command[2], University of Mississippi[3], University of Hawaii, Manoa[4], University of California, San Diego[5], US Army Engineer Research and Development Center-GSL[6], BBN Technologies Inc.[7], University of Alaska, Fairbanks[8], and Los Alamos National Laboratory[9]

Sponsored by Army Space and Missile Defense Command

Contract No. W9113M-05-1-0018[1–9]

ABSTRACT

A national infrasound research team has been established to conduct large-scale experiments utilizing atmospheric explosions to study infrasound propagation phenomenology and to calibrate a network of infrasound arrays. In the last two years, calibration experiments were carried out at the White Sands Missile Range (WSMR) in which explosions with yields of 70 lb TNT equivalent were conducted at altitudes greater than 30 km. The next calibration experiment is scheduled to take place in late July 2006. Infrasound data from the explosions were collected by the team members at more than 20 locations in the southwest US. The recorded waveforms represent a truly unique dataset due to the high source altitude, and yield information availability.

The primary goal of the project is to improve understanding of the fundamental physics of the atmospheric properties affecting propagation of infrasound signals. A secondary goal is to validate the yield/dominant frequency and yield/pressure amplitude scaling relationships. To a first order approximation, both goals have been achieved. The signal detection pattern of the experiments related to receiver location is in agreement with the predictions based on average atmospheric models. The validity of yield/frequency and yield/pressure relationships is currently being investigated.

OBJECTIVES

An infrasound research team has been established to conduct a large-scale experiment utilizing high altitude atmospheric explosions to study infrasound propagation phenomenology. Two infrasound calibration experiments involving explosions of 70 lb TNT at altitudes greater than 30 km over White Sands Missile Range, New Mexico, were successfully conducted in the fall of 2005 and spring of 2006. A third experiment is scheduled for late July 2006. Infrasound data from the explosions were collected by the team members at many locations in the southwest US. The resulting waveforms represent a truly unique dataset in terms of ground truth information including source location and yield. The efforts of the team to date included only acquisition and quick-look analysis of the data, but in-depth analysis will focus on atmospheric and propagation modeling, and validating those models. An additional goal of this project is to validate the yield/dominant frequency and yield/pressure scaling relationships.

RESEARCH ACCOMPLISHED

Atmospheric modeling has played a key role in determining the schedules and locations of portable deployments of infrasound arrays for the previous explosion experiments. Figure 1 illustrates atmospheric modeling showing seasonal trends in effective sound profiles at the WSMR source site. These profiles are based entirely on climatology and attempt to resolve mean seasonal and diurnal atmospheric trends. In the northern hemisphere, strong westward ducts form during the summer months, with a peak in July. To take advantage of the possibility of strong ducting, which could provide increased distance for recording signals to the west, a third test (WSMR3) was scheduled for July 2006.

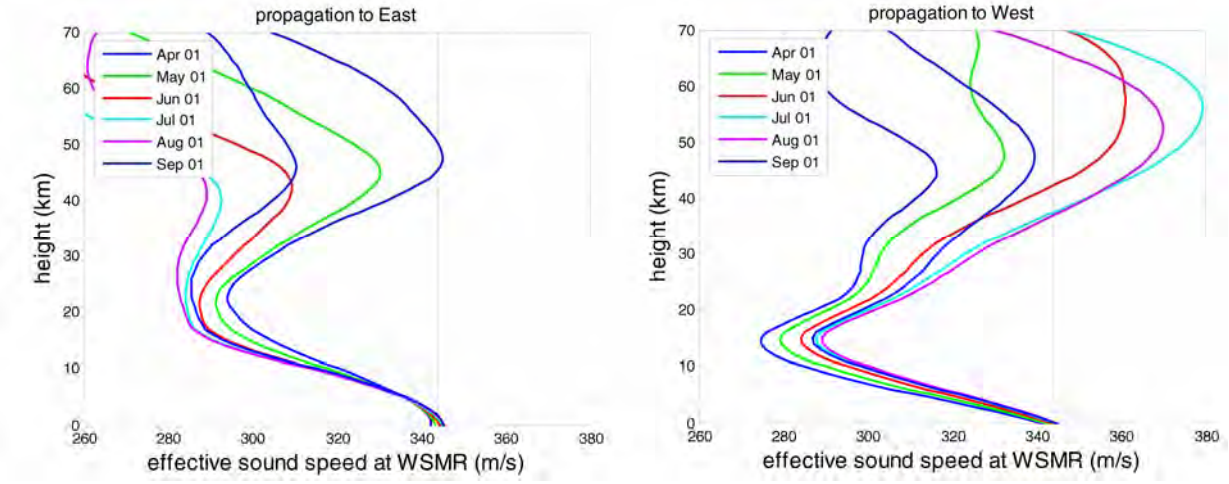


Figure 1. Effective sound speed profiles used in selecting optimal test dates.

As a second example of planning research, Figure 2 shows parabolic equation (PE) predictions from the WSMR source to the Los Alamos station, DLIAR 260 km to the north. This prediction was part of a pre-test study in support of the September 2006 WSMR1 explosive experiment. The source level was predicted using the ANSI S2.20-1083 standard and then combined with PE model predictions of signal attenuation at each station to compute theoretical station signal-to-noise levels.

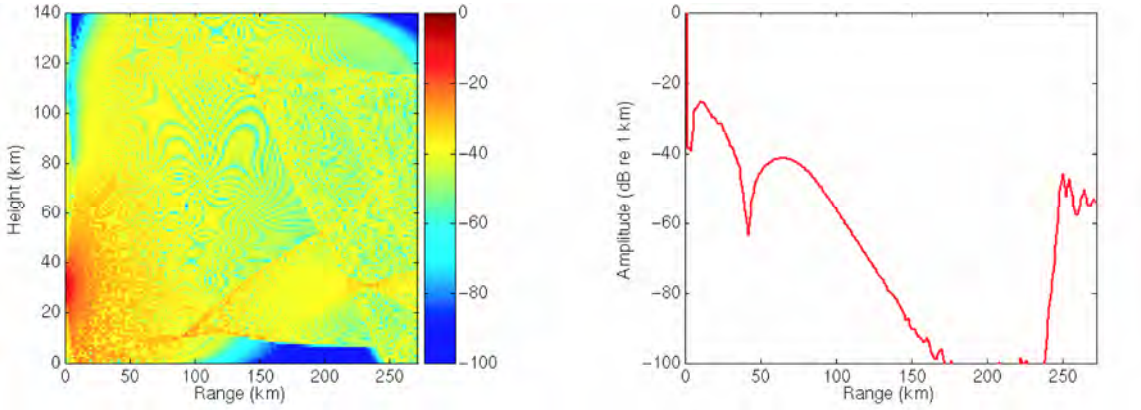


Figure 2. Pre-test Parabolic Equation (PE) predictions from source to station at Los Alamos, New Mexico (DLIAR).

The resulting signal-to-noise ratio (SNR) predictions for all preliminary station locations are given in Figure 3. The uncertainty bars were based upon the difference between predictions using climatology and those using NRL-G2S characterizations. Also shown are expected signal-to-noise levels for low, moderate and high wind noise. This modeling study was instrumental in selection of the temporary station locations and in providing an analytical basis for expected detection ranges.

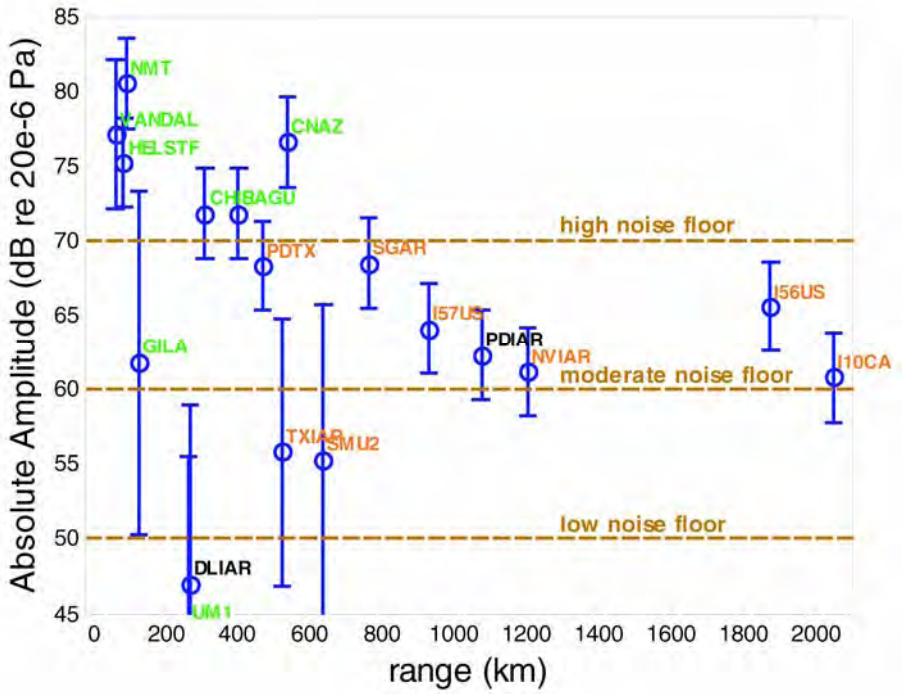


Figure 3. SNR predictions of pre-test station configuration for the September 2006 WSMR rocket test. Permanent stations are in orange and temporary station in green.

Based on the expected climatic conditions, two infrasound calibration experiments were conducted at White Sands Missile Range, New Mexico, on September 9, 2005, and March 25, 2006. During each experiment two missiles were launched at approximately 4-hour intervals. Although plans were for detonations at 40 km altitude WSMR1, detonations were limited to approximately 30 km due to range safety concerns. WSMR2 detonations were allowed at an altitude of approximately 35 km after additional debris modeling was completed. We anticipate detonation at 35 km for the experiment planned for July 2006. The main goal of the experiments is to provide further understanding of the atmosphere propagation of infrasound signals during different atmospheric conditions. A second goal was validating the yield/dominant frequency and yield/pressure scaling relationships. Preliminary analyses suggest that to a first order approximation both goals were achieved.

Figure 4 shows the location of the permanent and temporary infrasound arrays deployed for the first experiment, in September 2005. In total there were 20 arrays or stations at ranges from 63 to 2049 km. For the second experiment, the number of arrays increased to 23, covering the same distance ranges. The temporary infrasound arrays were placed mostly west of the source for the September 2005 experiment, and east of the source for the March 2006 experiment. This pattern was chosen in agreement with the direction of the zonal stratospheric winds. Past observations of the zonal stratospheric winds are predominantly westward (at around 10 m/s) for the beginning of September, while at the end of March the winds are predominantly eastward, with variable strength. However, observations suggest the second experiment was carried out close to the time when the zonal winds were turning to the west.

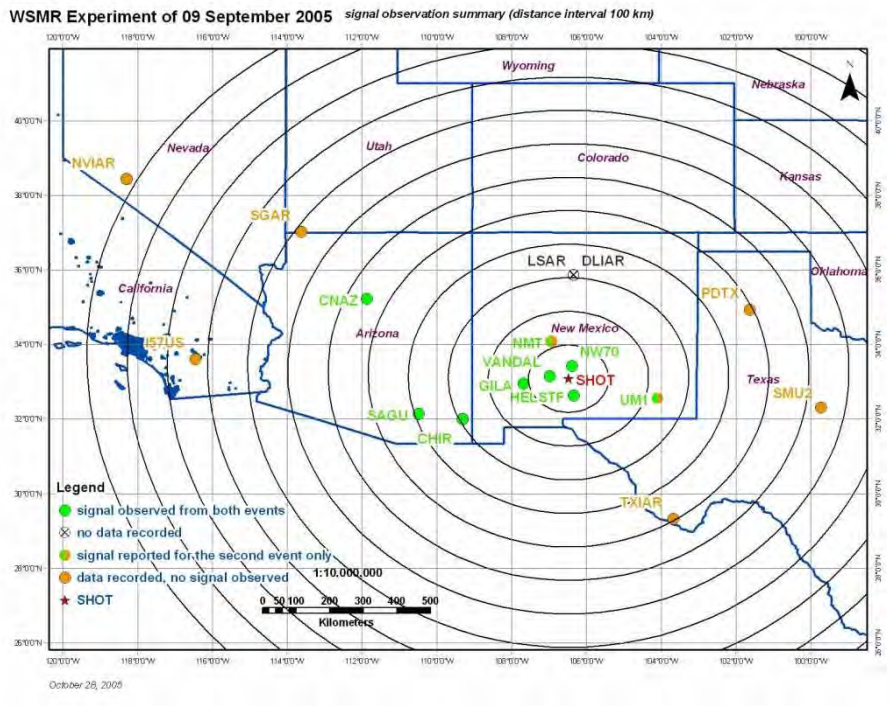


Figure 4. Map showing locations and distances from the source for infrasound arrays and stations deployed during the WSMR1 explosion experiment.

The detection pattern of the first calibration event was strongly dependent on the zonal winds, as the preliminary modeling suggested (see Figure 1). In September, when the winds were predominantly westward, detections to the west were recorded as far as Camp Navajo in Arizona (at a distance of 563 km), while to the east, except for the very close arrays, only UM1 (265 km) has a possible detection of a signal. Because the second calibration experiment was carried out recently, quick-look data analysis has not been finalized.

Quick-look analysis of data collected at Ft. Davis, Texas, during the WSMR2 experiment yielded interesting results. An event from an unknown source was recorded only minutes after the signal from the explosion. At first, this was thought to be a late thermospheric arrival, but this was ruled out after initial analysis. Figure 5 shows the signal recorded at Ft. Davis from the second explosion of WSMR2.

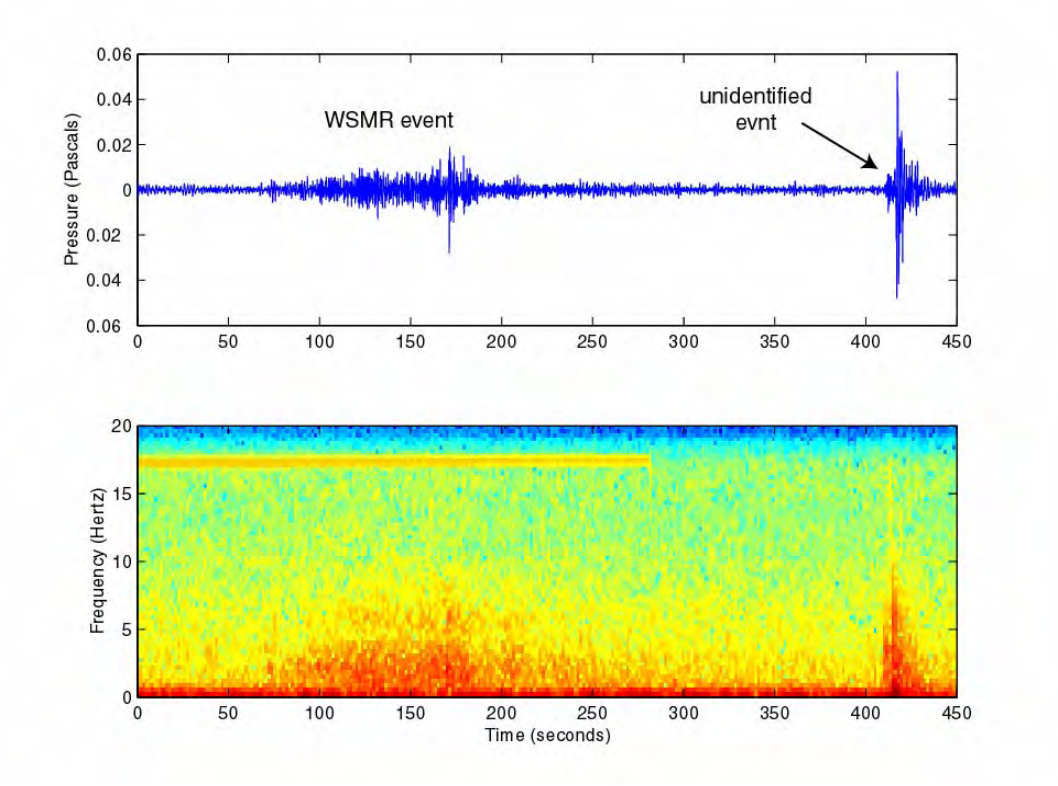


Figure 5. WSMR2 second explosion data (upper plot) recorded at Fort Davis and corresponding spectrogram (lower plot).

The unidentified event begins approximately 5 minutes after the signal associated with the calibration experiments. Both the frequency content and estimated azimuth suggest the second event has a different origin, which has not yet been identified. The WSMR calibration experiments have little or no energy above 5 Hz, while the unidentified event shows a broader spectrum, with energy above 8 Hz. In addition, the difference in the estimated azimuths for the two signals is more than 10°, which suggests that they have different source locations.

A few interesting observations have been made for both sets of experiments. First, although the explosions of the individual experiments were carried out approximately four hours apart, signals show significant waveform variations. This suggests that dynamics of the atmosphere can change quickly and do strongly affect the amplitudes and arrivals of signals. Figure 6 is an example of waveforms from the first and second explosions recorded from WSMR1 recorded at Camp Navajo, Arizona. The first shot is clearly more impulsive than the second one, while on the second shot more arrivals could be identified. It is important to note that the peak frequency of the signals is almost the same. Therefore only the phase of the signals appears to be strongly distorted by the short-term dynamics of the atmosphere.

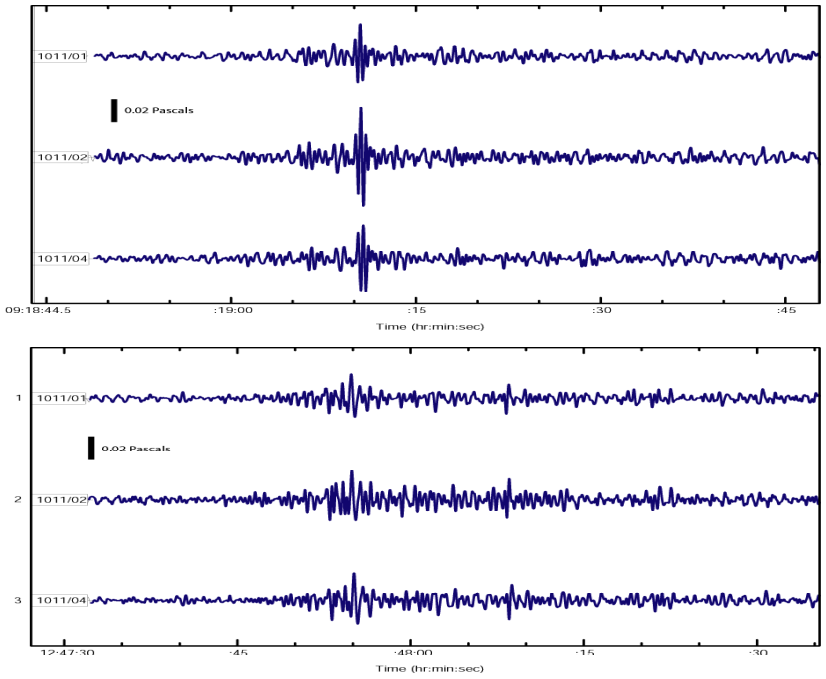


Figure 6. Recordings of the WSMR 1 experiment at Camp Navajo, Arizona. Although the shots were only 4 hours apart and the source is not believed to vary significantly, the differences in the phase of the signal is significant.

In addition, the dominant period/yield scaling relationship for the explosions shows consistent results. Figure 7 shows the frequency estimates for signals recorded by SMU for the first two WSMR experiments. For comparison purposes the unidentified event recorded at Fort Davis is also shown.

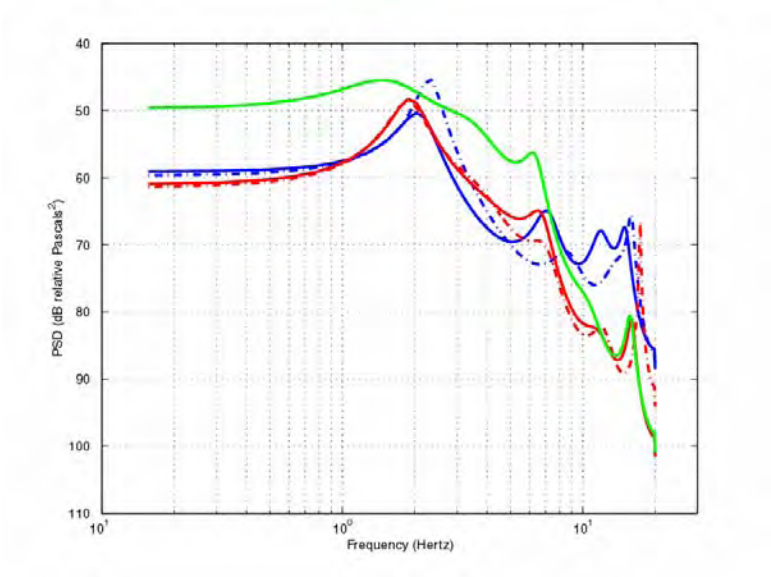


Figure 7. Power Spectra of the WSMR experiments and the unidentified event. The WSMR1 experiments are shown as blue and dash-dot blue lines, WSMR2 are shown as red and dash-dot red lines and the unidentified event is the green line.

The power spectral estimates were obtained using an autoregressive process of order 10 via Burg's method. Pre-filtering of the data with a high pass (1 Hz) zero-phase Butterworth filter was required due to the fact that the roots of the polynomial are dominated by the long period background pressure variations. Shown on the graph are the power spectra of the WSMR1 experiments (blue and dash-dot blue lines) recorded at Camp Navajo, Arizona, WSMR2 experiments (red and dash-dot red lines) recorded at Fort Davis, Texas (site SMU4), and the unidentified event (green line) clearly showing the difference in dominant period. Table 1 gives the dominant frequencies for the different arrivals. The dominant frequency is dependent on the altitude and yield of the event as predicted by the scaling relationship. A secondary conclusion is the difference in the dominant frequency of the peak between the WSMR experiments and the unidentified event. The WSMR signals have predominant frequencies around 2 Hz, while the unidentified event has strong frequencies between 1 and 8 Hz.

Table 1. Altitudes and dominant frequencies of arrivals recorded by SMU for both WSMR experiments

Signals	Dominant Frequency (Hz)	Altitude (km)
WSMR1, shot 1	2.3	31.1
WSMR1, shot 2	2.1	31.6
WSMR2, shot 1	1.9	35
WSMR2, shot 2	1.9	35.18
Unidentified event	1.4	?

An additional goal of this proposal is to validate empirical formulas for the frequency/yield and pressure amplitudes/yield developed by Air Force Technical Applications Center (AFTAC) and Los Alamos respectively. The AFTAC yield/dominant frequency scaling relationship is based on surface or low altitude nuclear explosions. The formula is written as

$$Y \approx (2) \times 2.63 \times T^{3.34} \ ,$$

where Y is the yield in metric tons and T is the dominant period of the signal (seconds). An altitude correction was provided by Armstrong, (1998). For a constant period the yield estimate (Y) is proportional to ambient pressure $P(z) = P_o e^{-Z/H}$, where H is the pressure scale height of atmosphere. However, the correction was based on surface or low altitude nuclear explosions, and scaling to higher altitudes was not verified by ground truth data. The only recorded event at a known location at such high altitude was the Columbia shuttle disaster, but this event provided ground truth only in terms of location (x, y, z position), not in terms of yield. The height was just over 63 km, and using the altitude correction of Armstrong, the estimated yield of the explosion was between 2 and 3 lb of TNT equivalent (McKenna and Herrin, 2006).

A second approach was developed at LANL using data based on high-explosive (HE) shots covering charge weights of ~20 to 4,880 tons, (Mutschlecner and Whitaker, 2005). The formula uses wind corrected pressure amplitudes and scaled ranges. The data are shown in Figure 8.

The range, R, in km, is scaled as: $(R/(2*\text{charge weight})^{0.5,}$, charge weight in kilotons of HE. Pressures are in microbars. The observing stations had distances of 250 km to 5330 km, but the 5330 km station was only on for one event. The regression fit for these data is

$$P_{wca} = 5.95E04*(SR)^{-1.4072} \text{ with an } R^2 \text{ of } 0.93 \ .$$

The raw amplitudes are normalized for the effects of the seasonal stratospheric winds, using the wind speed at 50 km altitude, in the direction of propagation.

$$\log\left(P_{wca}\right) = \log\left(P_{raw}\right) - kV_d$$
$$V_d = -\left(V_z \sin\left(\Theta\right) + V_m \cos\left(\Theta\right)\right) \ ,$$

where the empirically derived wind parameters (in meters/second) are as follows: V_d - wind component directed, source to array; V_z - zonal component of stratospheric wind; V_m - meridional component of stratospheric wind, θ is azimuth to source, and k = 0.018. Pressure amplitudes are measured peak to peak, at the dominant period.

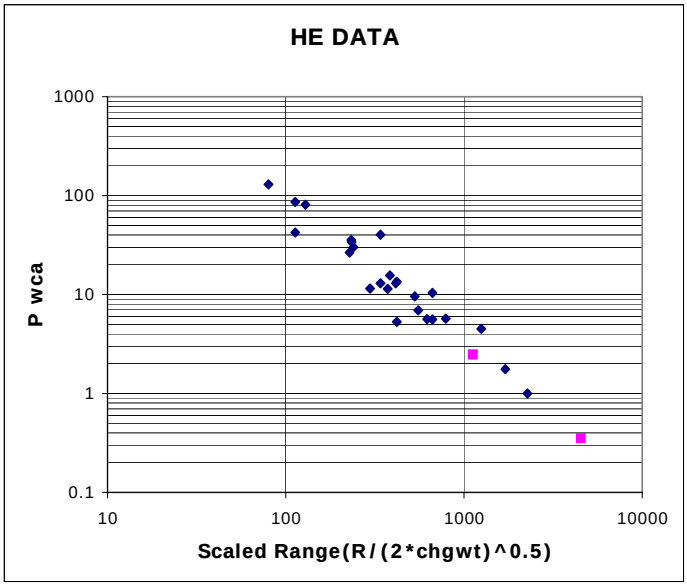


Figure 8. Wind corrected pressure amplitudes vs range for observed data for HE tests provided by Los Alamos National Laboratory. The blue diamonds are DNA explosions at WSMR from 1981–1992; the red squares are for Watusi experiments at the Nevada Test Site.

The purpose of wind normalization is to estimate signal amplitudes as if there were a zero wind condition. Thus, if one is in favorable wind propagation, the normalized amplitude would be less than observed. If in an unfavorable wind propagation, the normalized amplitude is greater than the observed. In the northern hemisphere, favorable conditions would be a source west of the receiver in the winter, because winds would be west to east, and in this case the receiver is downwind of the source. Unfavorable conditions would be a source west of the receiver in summer months.

The energy of the source is folded into the scaled range term. So here one would take the observed raw peak-to-peak amplitude, do the wind normalization to get P_{wca}, and then with the range to the source, use the regression relation to calculate the yield of the explosion.

CONCLUSIONS AND RECOMMENDATIONS

Successful calibration experiments were carried out at WSMR in fall 2005 and spring 2006 with the main purpose of understanding the temporal dynamics of the atmosphere. The calibration experiments involved high altitude atmospheric sources for which the locations and yields were known with a high degree of accuracy. The initial goal of the calibration experiments was achieved, and detection patterns of the signals relative to the source locations were in agreement with predicted atmospheric conditions. Post-event modeling will use atmospheric observations at the time of the shot, and will try to relate the observed signal to the atmosphere variations. As a byproduct of the modeling technique, the current infrasound modeling codes developed by BBN Technologies will be tested and validated.

There are established procedures for estimating the yield of an atmospheric explosion from the recorded infrasound signal. However, a problem could arise from the fact that the scaling relationships were developed using surface or low altitude explosions. Using the new ground truth data acquired during the WSMR experiments the formulas can be validated for higher altitudes.

ACKNOWLEDGEMENTS

We wish to thank the Naval Surface Warfare Center at WSMR for all their efforts in preparing the rockets and successfully conducting the launches, in particular Mr. John Winstead, Head, Test Planning Branch; Navy Project Engineer Ms. Kathie Hoffman; Navy Flight Engineer Mr. Sal Rodriguez; and, for Missile Systems, Mr. Troy Gammill from New Mexico State University.

REFERENCES

Armstrong, W. T. (1998). Comparison of infrasound correlation over differing array baselines, in *Proceedings of the 20th Annual Seismic Research Symposium: On Monitoring a Comprehensive Test Ban Treaty (CTBT*), 526–537.

McKenna, M. H. and E. T. Herrin (2006). Validation of infrasonic waveform modeling using observations of the STS107 failure upon reentry, *Geophys. Res. Lett*. 33: LXXXXX, doi:10.1029/2005GL024801.

Mutschlecner, J. P. and R. W. Whitaker (2005). Infrasound from earthquakes, *J. Geophys. Res.* 110: D01108, doi:10.1029/2004JD005067.

DEVELOPMENT OF ADVANCED PROPAGATION MODELS AND APPLICATION TO THE STUDY OF IMPULSIVE INFRASONIC EVENTS

David Norris[1], Joydeep Bhattacharyya[2], and Rodney Whitaker[2]

BBN Technologies[1] and Los Alamos National Laboratory[2]

Sponsored by Army Space and Missile Defense Command

Contract No. W9113M-05-C-0135[1,2]

ABSTRACT

State-of-the-art advances have been made in the areas of advanced model development, GT event studies, and model validation. Through these efforts, some of the driving mechanisms affecting the measured waveforms have been identified, and the prediction performance of the new models quantified. These advances ultimately increase event localization capabilities. More robust prediction of infrasonic arrivals, such as those that reach the ground through diffraction, more accurate travel-time predictions, and more robust amplitude predictions all improve localization. In addition, these advances support discrimination between various infrasonic impulsive events.

A baseline ground truth (GT) event list has been created, which can be used for testing infrasound propagation models, the effect of meteorological conditions on recorded signals, and localization algorithms. This list builds on some of the prior analysis that we have done and incorporates some of the recent information that has been compiled from LANL and other sources in the infrasound community, e.g., International Data Center (IDC), Research and Development Support Services (RDSS), Defense Threat Reduction Agency (DTRA), Koninklijk Nederlands Meteorologish Instituut (KNMI), Commissariat á l'Energie Atomique—Departement Anahise, Surveillances Environement (CEA/DASE), Geoscience Australia, Southern Methodist Univ., Univ. of Mississippi, Univ. of Alaska, Univ. of Hawaii and Univ. of Western Ontario.

New propagation modeling capabilities include a ray model that incorporates the effects of diffraction, PE/TDPE models that account for non-zero density gradients, and PE/TDPE models that incorporate small-scale atmospheric variability. Examples applications of these new models applied to specific GT events are presented in detail.

OBJECTIVES

The objective of this research is to improve our ability to understand and characterize infrasonic propagation. This objective will be accomplished by developing advanced propagation models and applying them in comparison studies with GT data sets of various infrasonic events.

Through these efforts, the driving mechanisms affecting the measured waveforms will be identified, and the prediction performance of the new models will be quantified. These advances will ultimately improve event localization capabilities. More robust prediction of infrasonic arrivals, for example, those that reach the ground through diffraction, more accurate travel-time predictions, and more robust amplitude predictions will improve localization. Variability bounds placed on travel time and amplitude predictions will provide physics-based predictions that will greatly improve the accuracy of confidence bounds placed around event localizations. In addition, these advances will support discrimination between various infrasonic impulsive events. Waveform synthetics will be generated and compared to measurements, and the physical processes relevant to different sources studied.

Modeling

Advanced propagation models are proposed in areas that will support an improved understanding of the propagation and an improved ability to predict travel times, amplitudes, other waveform metrics, and associated uncertainty bounds. The specific modeling advances are listed in the left column of Table 1. They will focus on diffraction, variability, terrain, and nonlinear effects. Specifically,

- Ray tracing capabilities will be advanced by integrating a diffraction model for shadow zone regions;
- Variable terrain will be integrated into PE and TDPE models;
- Atmospheric density gradients and their effect on refraction will be modeled and evaluated;
- Small-scale atmospheric variability characterizations will be integrated into the PE and TDPE models;
- A version of the Nonlinear Progressive Equation (NPE) model will be developed that addresses the nonlinearities associated with a weak shock front.

Table 1. Events parameters of near surface nuclear explosions with available waveforms.

Event	Date	Time	Location	Latitude (°N)	Longitude (°E)	Height (km)	Size (kT)
Yankee	5/4/1954	18:10:00	Bikini	11.6655	165.3869	N/A	13500
Wasp	2/18/1955	19:59:59	NTS	37.0867	-116.0219	0.2	1
Turk	3/7/1955	13:20:00	NTS	37.1383	-116.1175	0.2	43
Hornet	3/12/1955	13:20:00	NTS	37.0403	116.0253	0.1	4
Bee	3/22/1955	13:05:00	NTS	37.0947	-116.0239	0.2	4
Ess	3/23/1955	20:30:00	NTS	37.1683	-116.0439	0	1
Wasp Prime	3/29/1955	17:59:55	NTS	37.0867	-116.0578	0.2	3
HA	4/6/1955	18:00:04	NTS	37.0286	-116.0578	11.2	3

Ground Truth Data Sets

A repository of GT data sets will be created and maintained, consisting of both nuclear and nonnuclear events. Additional data will be compiled from archived Nevada Test Site (NTS) records that are becoming available, and new events of opportunity will also be used. The GT data sets will be used to compare arrival times, amplitudes, and other waveform metrics with model predictions. The comparison studies will leverage state of the art environmental characterizations that are now available, including near real-time formulations.

Model validation

As the propagation modeling advances are developed they will be applied to study Ground Truth events. The main goals of these model validation studies are to

- Quantify the accuracy and applicability of the model predictions
- Estimate of the uncertainty associated with the modeling predictions, including contributions from both the modeling assumptions and unresolved atmospheric structure.
- Identify the relevant physical mechanism affecting the propagation for specific ranges and source types

These test goals will be met by laying out the framework for the validation, developing an event list from which the tests will be performed, and listing the hypotheses to be tested.

RESEARCH ACCOMPLISHED

Ambient Density Gradient Effects and Reference Sound Speed Sensitivity

Derivations of linear continuous wave Parabolic Equation (PE) models start with the Helmholtz equation. Implicit in this formula is the assumption that the ambient density gradient is either zero or negligible. For variable ambient density, ρ, the Helmholtz equation takes the form

$$\rho\nabla\bullet\left(\frac{1}{\rho}\nabla p\right)+\kappa^2 p=0$$

.

With a substitution of variables, this equation can be reformulated into the standard Helmholtz equation but with an "effective" index of refraction. Variable density models in ocean acoustics have been carried out to improve propagation predictions in regions such as littoral zones (Collins, 1988). This transformation allows us to estimate the effect of variable density on atmospheric propagation.

The ambient density for a standard atmosphere falls off exponentially with height and it can be equated to a change in the index of refraction. This change can potentially alter predictions of travel times, shadow zone regions, and ground bounce locations. In this task, we have developed PE and TDPE models based on the more rigorous Helmholtz equation that captures the nonlinear physical effect of variable density.

Model-to-model comparisons over infrasound frequencies in the range of 0.01 to 5 Hz have been completed. They suggest that variable density has no discernable effect on travel times, amplitude, or ground-bounce locations. This insensitivity is likely due to the nature of the density profile. Although density changes by several orders of magnitude over the range from the ground to the thermosphere, the density gradient at any given height is relatively small. Thus, the resulting effect on the propagation is minimal.

PE model formulations include the specification of a reference sound speed. It is typically constant and set to a value at the ground. PE predictions have been shown to be sensitive to reference sound speed. A sound-speed insensitive version of the PE has been developed which minimizes this dependence (Tappert et al., 1995).
Model-to-model comparisons have been made to quantify the improvement.

Figure 1 shows a comparison of predictions at 5.0 Hz for the sound-speed insensitive and reference PE models. There are significant differences between the two predictions. Within the thermosphere, the baseline predictions have an upper turning height in the range of 120 km, while the sound-speed insensitive predictions have energy penetrating well above 150 km. These differences can effect both absorption calculations and ground bounce ranges.

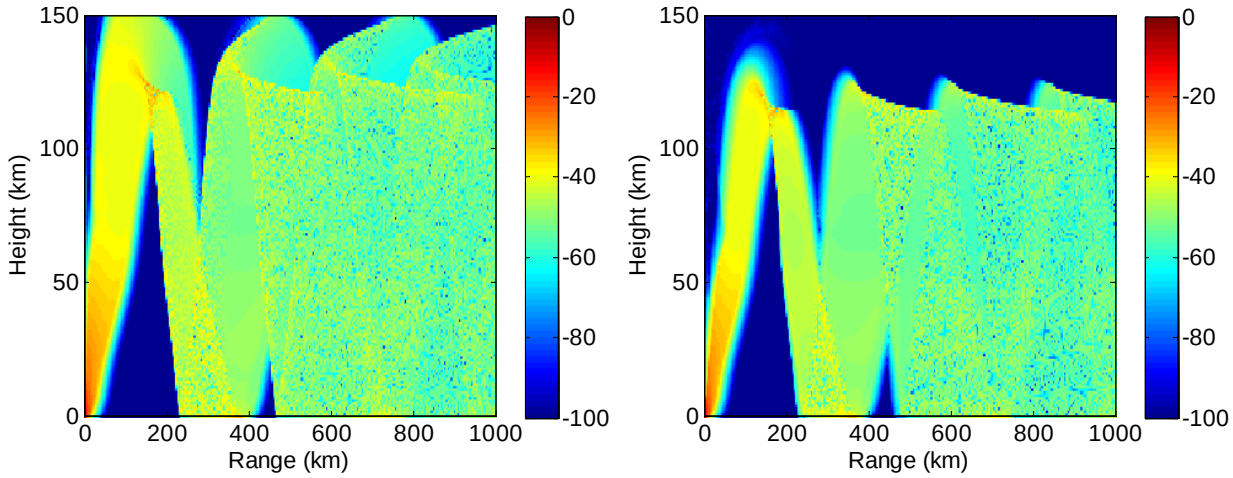


Figure 1. PE amplitude field predictions at 5.0 Hz for baseline formulation (left) and that including variable density term (right).

To quantify the effect of the reference sound speed over a band of frequencies, TDPE waveform predictions were computed. Significant differences in amplitude, waveform shape, and arrival time are observed. Stratospheric energy for the sound-speed insensitive PE arrives approximately 3 percent later, while the thermospheric arrival difference is approximately 2 percent. Differences in amplitude and waveform shape are also observed. They need to be quantified further in relation to each other and with respect to observations.

Propagation Variability

In this task, we have extended propagation modeling capabilities by integrating atmospheric variability models into the PE and TDPE models. The model predictions can be made through atmospheric snapshots of the inhomogeneities. These predictions capture the effects of the atmospheric variability on the waveform metrics such as amplitude, travel time, duration, and spectral content.

Small-scale atmospheric structure not characterized by near-real-time atmospheric models, such as NRL-G2S, has been identified as a likely source of diffraction and scattering effects that may play a significant role in accurate propagation predictions. In particular, gravity waves are of interest because their spatial scales are of the same order as infrasonic wavelengths. They have been modeled spectrally (Norris and Gibson, 2002), based on a horizontal wave number model (Gardner, 1993). An example realization of wind fields associated with the Watusi effect, discussed below, is shown in Figure 2. The gravity waves are seen as thin layers of coherent wind anomalies. The total atmospheric wind realization is seen to be the sum of the mean NRL-G2S specification and fine-scale gravity wave structure.

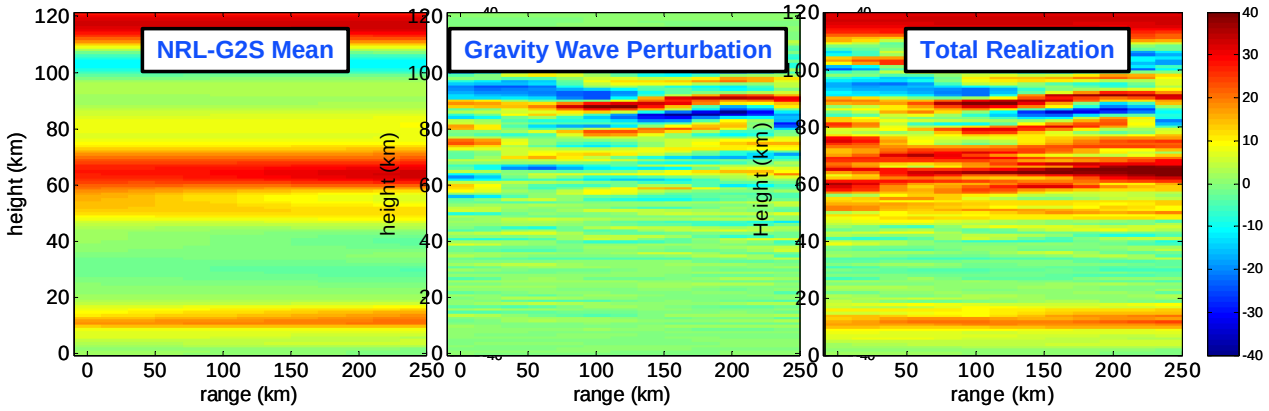


Figure 2. Atmospheric specification for Watusi study showing the NRL-G2S mean wind fields (left panel), wind perturbations from gravity waves (middle panel), and resulting total realization (right panel).

As a first step in quantifying the effects of the atmospheric variability, the Watusi event of 2002 is studied. This event was a surface explosion of 38,000 pounds (0.019 kT) of TNT equivalent. It was detonated at 21:25:17 UTC on 28 Sept 2002 and located at Nevada Test Site (NTS) (37.099º N, 116.092º W). Here we consider the 219 km path to the SGAR infrasound station. Figure 3 shows the PE predictions at 0.5 Hz for the cases in which small-scale gravity wave perturbations are excluded and included. Without gravity wave perturbations, no energy penetrates the shadow and reaches the receiver locations. With the gravity wave perturbations, scattered energy is predicted to penetrate the shadow zone and reach the receiver.

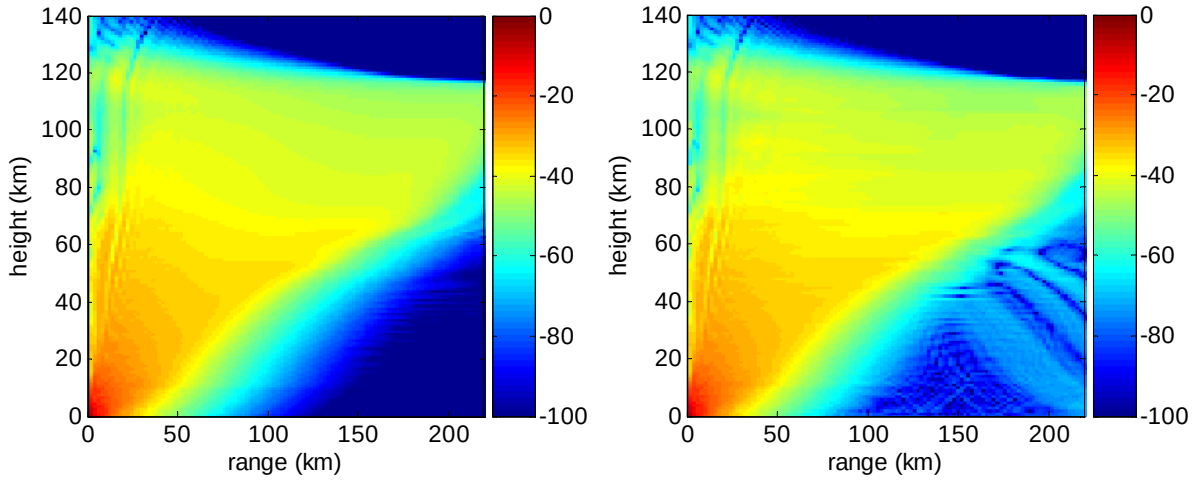


Figure 3. PE predictions at 0.5 Hz without gravity waves (left panel) and with gravity waves (right panel).

Substantial proof in the importance of small-scale variability is indicated by TDPE waveform predictions along the same propagation path. TDPE waveform predictions without gravity wave perturbation predict no received energy. However, with gravity waves, waveform predictions show substantial received energy. The comparison between predicted and observed waveforms is shown in Figure 4. The agreement in arrival time is excellent and that for amplitude differ by approximately 3 dB.

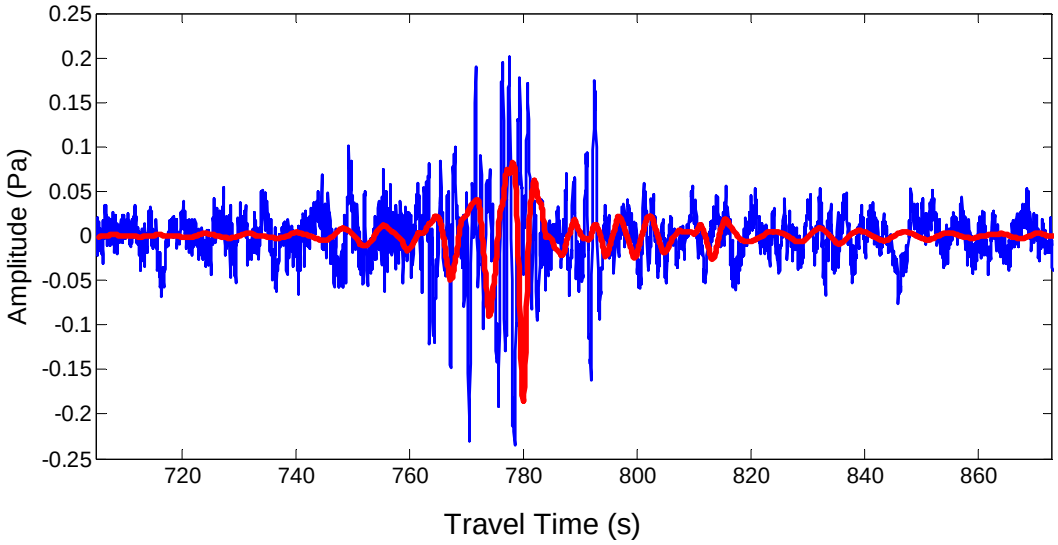


Figure 4: Observations (blue) and TDPE predictions (red) for the Watusi event at SGAR.

Ground Truth Database Compilation

The members of the BBN and LANL teams have been developing a Ground Truth data set repository that spans different propagation ranges and event types. Over the last year, progress has been made by adding the following data sets to the repository.

Underground nuclear explosion
We have obtained digital archives from infrasound arrays operated by Los Alamos National Laboratory in Nevada, New Mexico, and Utah since the early 1980s. These were mostly four-element arrays, with three sensors arranged in a triangle and the fourth at the center. In some cases, seismic data were also recorded at the same sites. Over the years, these arrays have recorded a variety of acoustic events, including underground nuclear tests at NTS and subsequent cavity collapses, and conventional explosions both above and below ground.

Near-surface nuclear explosion
We have obtained digital waveform data for the near surface nuclear explosions from Operation Teapot carried out in the spring of 1955 from Eric Chael of SNL (Chael and Whitaker, 2004). This series included several events with yields from 1 kt to 43 kt, all detonated a few hundred feet aboveground (Table 1). Chael has extracted about 15 traces per test from the available stations, some of which used two sensors separated about 1 mile along the direction from NTS. For the larger events, detected signals are distinct at frequencies between 0.5–3.0 Hz; for the smaller events (<20kT), higher frequencies are observed (Chael and Whitaker, 2004). The smaller yield, higher frequency events are more compatible with current array configurations and monitoring goals, and therefore they will be the primary focus.

CONCLUSIONS AND RECOMMENDATIONS

The results of this research effort will improve state of the art capabilities in accurately predicting infrasonic propagation parameters and assessing the influence of fundamental physical processes. Recent improvements in environmental characterization, particularly with near-real-time model, enable the ability to generate high-fidelity, global environmental fields for a specific event time. Advanced model developments described here fully leverage these existing atmospheric capabilities in prediction performance.

Variable atmospheric density does not appear to have a discernable effect on infrasound propagation, likely due to the gradual change in density with height. Model-to-model comparisons suggest the sound-speed insensitive PE algorithm provides higher-fidelity predictions of ground bounce range and arrival time. The relative improvements with respect to absorption and waveform characteristics still need to be quantified.

Integrating small-scale atmospheric structure into PE and TDPE models have been shown to influence the predictions of waveform structure. Additional comparison studies need to be completed to further quantify the influence of this physical phenomenon over various propagation scenarios.

Expanding the Ground Truth database has enabled careful comparison of model predictions with ground-truth data sets, enabling assessment of model performance. The data sets support evaluation of the strengths and weaknesses of the models and recommendations as to an analyst's course of action with respect to which models to apply for specific scenarios and ranges of interest.

REFERENCES

Chael, E. and R. Whitaker (2004). Infrasound Signal Library, in *Proceedings of the 26th Seismic Research Review: Trends in Nuclear Explosion Monitoring*, LA-UR-04-5801, Vol. 2, pp. 618–623/.

Collins, M. (1988). The time-domain solution of the wide-angle parabolic equation including the effects of sediment dispersion, *J. Acoust. Soc. Am.* 84: 2114–2125.

Gardner, C. (1993). Gravity Wave Models for the Horizontal Wave Number Spectra of Atmospheric Velocity and Density Fluctuations, *J. Geophys. Res.* 98: D1, 1035–1049.

Norris, D. and R. Gibson (2002). InfraMAP enhancements: Environmental/propagation variability and localization accuracy of infrasonic networks, in *Proceedings of the 24th Seismic Research Review—Nuclear Explosion Monitoring: Innovation and Integration,* LA-UR-02-5048, Vol. 2, pp. 809–813.

Tappert, Frederick, John L. Spiesberger, and Linda Boden (1995). New full-wave approximation for ocean acoustic travel time predictions, *J. Acoust. Soc. Amer.* 97: (5), part 1, 2771–2782.

IMPROVED INFRASOUND LOCATIONS THROUGH REFINING ATMOSPHERIC MODELS USING WIND DATA AND GROUND-TRUTH INFRASOUND EVENTS

Michael S. O'Brien[1], J. Roger Bowman[1], and Douglas P. Drob[2]

Science Applications International Corporation[1] and Naval Research Laboratory[2]

Sponsored by Army Space and Missile Defense Command

Contract No. W9113M-06-C-0027[1,2]

ABSTRACT

One of the principal functions of infrasound in nuclear-explosion monitoring is to locate low atmospheric and near-surface nuclear explosions in areas that have relatively poor coverage by other sensor technologies (e.g., the southern oceans). This includes regional scenarios for which accurate location is an important discriminant. Recent infrasound studies suggest that the ability to locate events accurately is often limited by erroneous predictions of infrasound observables (arrival time and back azimuth) from which location is estimated, even when advanced atmospheric state specifications are available. A wealth of new atmospheric wind measurements reveals significant inaccuracy in the atmospheric Horizontal Wind Model (HWM-93) and Ground to Space (G2S) wind model between elevations of 60 and 120 km as likely the single largest source of these infrasound prediction errors. To address this problem, we will revise these wind models with a voluminous database of recently available and validated upper atmospheric wind measurements. Our approach will be novel in that we will use the growing number of ground-truth infrasound events in the Space Missile Defense Command (SMDC) Monitoring Research Program databases as atmospheric soundings. These infrasonic ground-truth events will be used to complement the wind measurements in constraining new models, as well as to assess their overall predictive accuracy. We will improve both HWM-93 and G2S but will emphasize the HWM climatological models and corrections because they apply to all locations and times and, thus, will improve our general infrasound event location capability. Here we describe both the atmospheric wind data and infrasound data that will be used to generate and validate new models and subsequent performance in event analysis. We also describe the procedures for data analysis and preparation, the process for assimilating the data into new wind models, and the approach we will employ for assessing the new models.

OBJECTIVES

The primary purpose of this project is to improve our general ability to locate infrasound events by improving the Horizontal Wind Model used in the prediction of infrasound observables using recent wind measurements and direct infrasound observations.

A second purpose of this project is to evaluate statistically, i.e., against a large set of infrasound observations, the ability of the old and new atmospheric models to locate infrasound events and to predict the principal infrasound observables, arrival time and back azimuth.

RESEARCH ACCOMPLISHED

Background

The ability to locate event sources accurately is a central element of nuclear explosion monitoring. In regional scenarios, it can provide important corroboration of explosive events but only if signals can be reliably attributed. Location and, thus, location-related observables are central to source attribution. In remote regions that are not well monitored by other land-based technologies, such as the southern oceans, infrasound may provide the only information that constrains location.

The reliability of infrasound source locations depends on the reliability with which signal features can be predicted from source properties. This requires detailed knowledge of sound propagation in the atmosphere and the physical properties that control it, in particular, the sound speed. The state of the art in representing the atmospheric properties pertinent to infrasound propagation is the Naval Research Laboratory (NRL) Ground to Space (G2S) model (Drob and Picone, 2000; Drob et al., 2003). This model combines climatological data captured in NRL's total atmospheric model (NRLMSISE-00) and HWM-93 with numerical weather prediction (NWP) data such as the Navy Operational Global Atmospheric Prediction System (NOGAPS) and the National Oceanic and Atmospheric Administration (NOAA)-National Center for Environmental Prediction Global Forecast System (NCEP-GFS). The inclusion of the NWP data in G2S significantly improves estimates of tropospheric and stratospheric wind jets that profoundly influence sound speed at lower altitudes (<50 km). Wind models that are based solely on climatology often substantially underestimate tropospheric and stratospheric wind jets, which leads to significant under prediction of the fraction of energy that is ducted through these layers (Drob and Picone, 2000; Drob et al., 2003).

While the G2S models are the most comprehensive atmospheric representation available, significant infrasound residuals are still obtained using them. Le Pichon et al. (2005) found that back-azimuth residuals using G2S models averaged several degrees for repeated thermospheric propagation paths. O'Brien and Shields (2004) compared G2S predictions to observations from 21 ground-truth (GT) events at different locations. They assumed that one could unambiguously identify the duct in which a signal propagated but not the specific path traveled, as when one does not know the location of a source. So, they compared observations to model predictions averaged over each duct. They found that the additional ambiguity raised travel-time and back-azimuth residuals to almost 10% and 7°, as illustrated in the histograms of Figure 1.

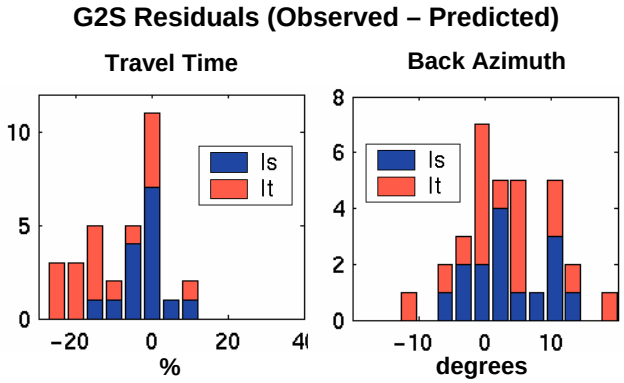


Figure 1. Residuals between infrasound observations and G2S model predictions indicate typical discrepancies of 10% in travel time and 7º in back azimuth.

The principal source of these discrepancies appears to be the wind model in the mesospheric / lower thermospheric (MLT) region where weather data cannot assist. Recent direct measurements of winds at higher elevations indicate that HWM-93 significantly underestimates winds there. This is illustrated by the two independent sets of optical satellite-based wind measurements in Figure 2, which consistently and substantially exceed the HWM-93 predictions, at times by up to 65 m/s. Similar wind corrections were also obtained by Le Pichon et al. (2005) who used the infrasound residuals to constrain the MLT region winds.

In this project, we use the extensive measurements of MLT winds made since HWM-93 and GT infrasound observations to improve the wind model, thereby improving our infrasound prediction capability. Our goal is to create two new HWMs: one constrained only by the new set of atmospheric data, the other constrained by atmospheric and infrasound data. We will also derive corresponding G2S models from the new HWMs.

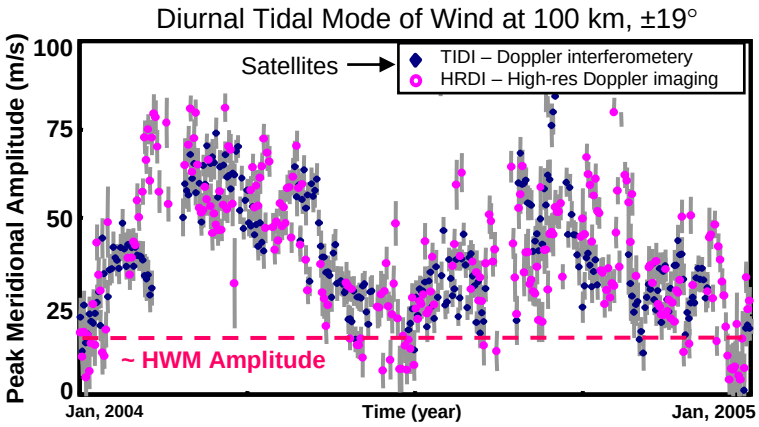


Figure 2. Meridional winds associated with the diurnal tidal mode at an elevation of 100 km measured globally between ±19°. Wind measurements made since HWM-93 was created (Hedin et al., 1996; Picone et al., 2002) disagree with the model predictions consistently and substantially, at times by as much as 65 m/s.

To generate and vet these models we will follow an iterative process along two tracks as illustrated in Figure 3 below. On one track, we will prepare atmospheric data and use them to generate and refine atmospheric wind models. On the second track, we will assemble an event data set, derived largely from events and waveforms already available in the SMDC Monitoring Research Program's Infrasound Database (IDB) and waveform archives and then analyze signals to measure arrival time, back azimuth, slowness, amplitude, etc. The two tracks converge when we evaluate models by comparing predictions from the atmospheric models with the measured observables. The results of the evaluation will then be used to refine our understanding of propagation paths analyzed signals. The components of this process and progress are described in the following subsections.

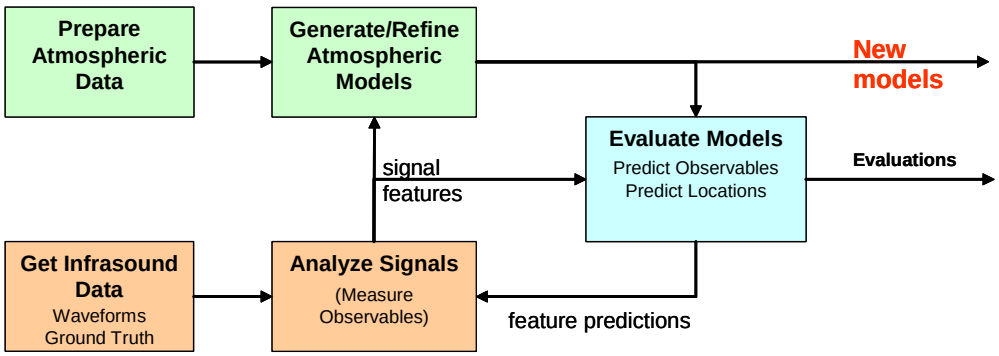


Figure 3. Process for refining atmospheric wind models using wind and infrasound data. The process iteratively refines the atmospheric models as the data sets are expanded and refined and the inversion methodology is developed.

Atmospheric Data

The NRL has been collecting and validating atmospheric data for the past ten years. The current NRL database represents more than 30 times the number of individual atmospheric observations than available when HWM-93 was created. More importantly, the new observations fill a number of critical gaps in the spatiotemporal distribution of the previous database, particularly in the 90 to 120 km region. A partial list of the recent satellite and ground-based data sets that have been assembled at NRL and that we will bring to bear is shown in Table 1. The details on each of these data sets are beyond the scope of this paper. All of these data sets have been well vetted and validated in the open scientific literature (Drob et al., 2000; Swinbank and Ortland, 2003; Larsen et al., 2003) and are available for use. However, these data must be carefully selected, partitioned, and weighted to ensure that the number of data points is distributed as evenly as possible over the represented ranges of altitude, latitude, local time, day-of-year, etc., before application of the parameter estimation process.

Table 1. Atmospheric wind measurements made available since HWM-93 was developed.

Data Type	Experiment	Years	Altitude (km)	Location	Local Time Coverage	Field
NWP Synthesis	NCEP/GFS, GEOS4, ...	93 – now	0 – 60	Global	4x daily	T, U, V
NASA/UARS (satellite)	HRDI (Level 2B)	92 – 98, 05	50 – 110	± 60º	Day/Night	T, U, V
	WINDII	92 – 98	80 – 300	± 70º	Day/Night	T, U, V
	HALOE	92 – 98	35 – 90	± 70º	Twilight	T
NASA/TIMED (satellite)	TIDI	00 – now	60 – 110	± 85º	Day/Night	U, V
	SABER	00 – now	35 – 95	± 85º	Day	T
LIDAR	Colorado State (Na)	93 – now	80 – 105	41 N, 103 W	Night	T, U, V
	Urbana (Na)	96 – 98	80 – 105	40 N, 88 W	Night/Day	T, U, V
	Bear Lake (Rayleigh)	94 – 96	30 – 80	41 N, 111 W	Night	T
	Urbana (Rayleigh)	95 – 96	30 – 80	40 N, 88 W	Night	T
MF RADAR	Christmas Island, Kiribati	92 – 93	70 – 96	2 N, 157 W	Continuous	U, V
	Bribe Island, Australia	95	70 – 96	28 S, 153 N		
	Adelaide, Australia	01 – 04	70 – 98	34 S, 138 E		
	Davis, Antarctica	01 – 04	50 – 100	68 S, 77 E		
	Poker Flat, Alaska	98 – 04	44 – 108	65 N, 147 W		
	Yamagawa, Japan	98 – 03	60 – 98	31 N, 130 E		
	Wakkanai, Japan	97 - 03	60 – 108	45 N, 141 E		
	Titunelveli, India	01 – 02	68 – 98	8 N, 77 E		
ISR RADAR	Arecibo, Puerto Rico	83 – 99	100 – 170	18 N, 67 W	Day	V
	Millstone Hill, Mass.	88 – 99	105 – 135	43 N, 72 W		
	Sondrestrom, Greenland	87 – 91	105 – 135	67 N, 147 W		
Rocket	TMA chemical trails	58 – 02	85 – 150	Sparse/Global	Day/Night	U, V
	Falling sphere	58 – 02	75 – 110	Sparse/Global	Day/Night	T

Generation of Horizontal Wind Models

The NRL data assimilation process is illustrated in Figure 4. In HWM-93 vertical, horizontal, and temporal variations are represented with associated Legendre polynomials, polynomials, and Fourier harmonics, respectively (Hedin et al., 1996). Its approximately 1000 model coefficients were computed using a subset of only 9000 data points (from a much larger population of measurements from over 20 different instruments) because of the computational limitations at the time. This limited spatiotemporal coverage meant that higher order spectral terms could not be resolved, so the model resolution was effectively limited to a relatively low order (harmonic degree and order six). Subsequent advances in computing, and the availability of new data sets, mean that we can now fuse 100 times the number of data into a new HWM. This will dramatically improve HWM resolution and accuracy, and thus infrasound predictions.

Our HWM/MSIS data assimilation routines are based on Levenberg-Marquardt fitting (Press et al., 1994) extended by modification of the convergence parameter trust region. Subsets of parameters are matched with constraining data (i.e., geographically and temporally nearby) and fitted to those data individually to increase efficiency and stability. The ability to specify limiting constraints is provided through the method of target values. The fitting process iterates until the chi-squared for each parameter subset changes less than 0.1%. Statistical diagnostics allow us to assess the quality of the fit by analyzing the influence of different data on different parameters, data cross correlations, etc.

The data assimilation process accommodates multiple, diverse datasets of varying space-time densities to achieve the most comprehensive coverage. We will explicitly address the issues of statistical independence and data quality within each data subset. This is important for ensuring that the small set of high quality infrasound observations is not overwhelmed by the comparatively vast but statistically dependent (i.e., repetitive) sets of atmospheric data. We pre-balance the content of independent information among the data that go into the fitting process through a combination of subsampling and error-weighted averaging over evenly spaced bins in space-time. We also

determine optimal observational error scaling or weighting factors (σ_i) for each dataset by instrument and wind component. This will allow us to let the infrasound observations control the parameter estimation process, whether for reasons of higher data quality or relative statistical independence, of those model parameters for which information is provided.

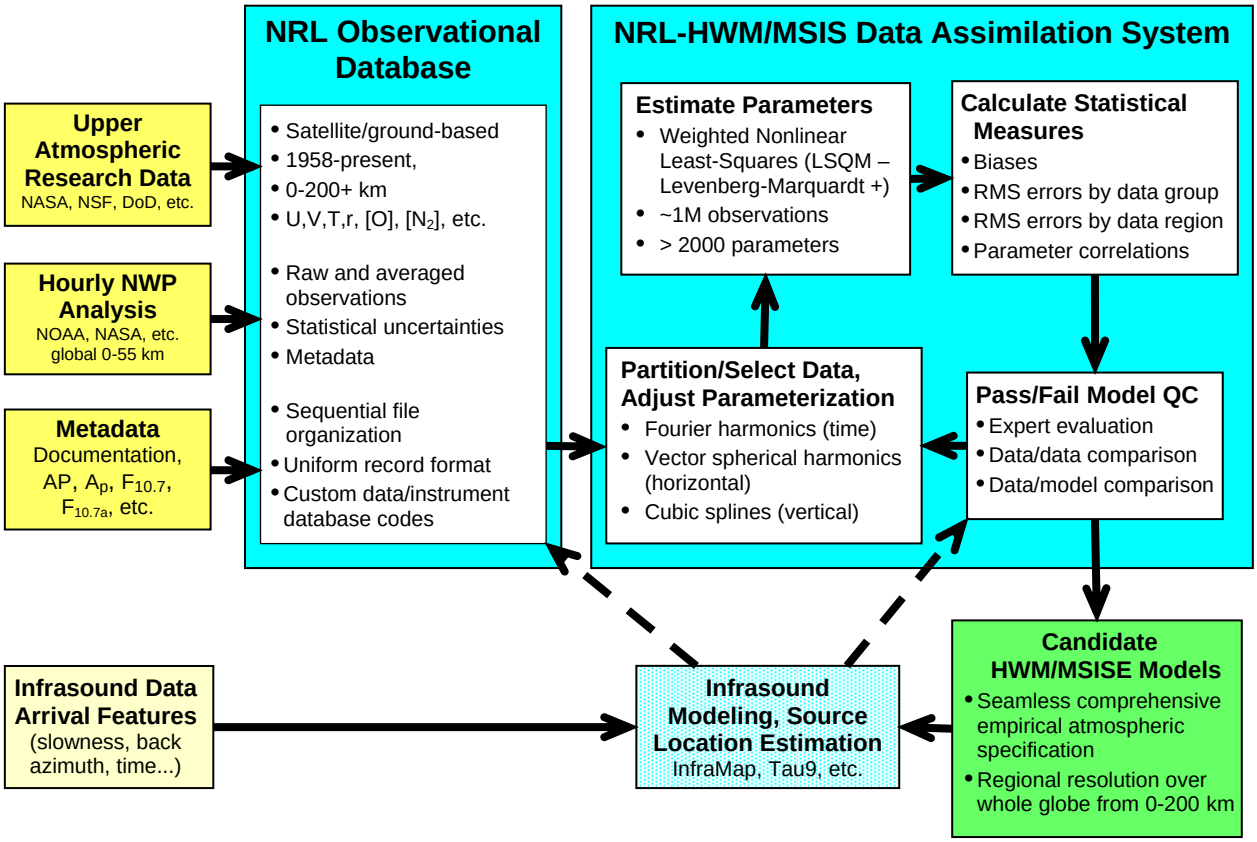


Figure 4. Process for assimilation of wind and infrasound data into new HWM models.

Infrasound Ground-Truth Events

Given the extensive space-time complexity of the atmospheric winds, we seek as many infrasound observations as possible with which to constrain or validate models. We have begun the collection of our GT data set for validating and constraining existing and new models by building on SMDC's existing IDB, which contains events from a variety of source types spanning several decades. We consider here a superset of the IDB, augmented with recent events. We will continue to augment our data set as events are identified and data become available. Figure 5 illustrates the global distribution of 264 events currently in the set.

However, prediction residuals, specifically in the travel time T (the difference between arrival and source times) and back azimuth deflection A (the difference between arrival and source-receiver back azimuths) are partly the result of errors in measured arrival properties, time t and back azimuth a, and GT source parameters, time τ, location r, and elevation e. Many events in our data set will have little utility for model constraint or assessment because the measurement- and ground-truth-related errors are too large compared to the model-related errors – from the background discussion, that will start to be the case when the errors are more than a few percent in T or a few degrees in A. We can estimate the fractional uncertainty σ_T in T and the total uncertainty σ_A in A in terms of the arrival measurement uncertainties σ_t and σ_a in t and a, and the source parameter uncertainties σ_τ, σ_r and σ_e in τ, r, and e. Letting R represent source-receiver range and $V=R/T$ the group velocity:

$$\sigma_T^2 \approx \left(\sigma_t^2 + \sigma_r^2/V^2 + \sigma_e^2/V^2 + \sigma_\tau^2\right)/T^2$$
$$\approx \sigma_t^2 V^2/R^2 + \sigma_r^2/R^2 + \sigma_e^2/R^2 + \sigma_\tau^2 V^2/R^2 \quad (1)$$

$$\sigma_A^2 \approx \sigma_a^2 + \sigma_r^2/R^2 \quad (2)$$

Note that the source-related parts of both errors are range dependent. Thus, we cannot assess the constraining value of data on an event basis, even if we assign measurement errors σ_a and σ_t uniformly – we must do so signal by signal. Since the effects of the errors diminish with range, it is possible for less well-characterized sources to constrain the wind models if observed at long enough range. Note also that travel times contain more source-related errors than back-azimuth deviation, so in general, arrival-time data will be less useful than back-azimuth data.

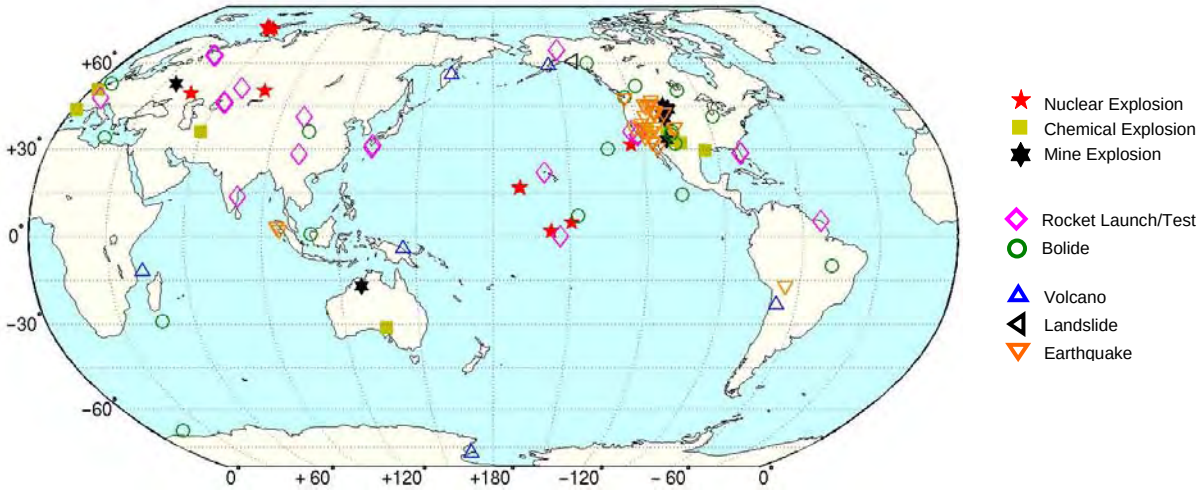


Figure 5. The distribution of sources in the expanded data set.

Equations 1 and 2 ultimately make their way into the significance statistics in the next section, as a continuous mechanism for weighting data in proportion to their constraining power. However, we can make a preliminary assessment of which event data have enough accuracy to be worth considering at all, by assigning values to the source errors σ_τ, σ_r and σ_e for each event and setting liberal upper thresholds on σ_A and σ_T for rejecting the arrival data outright. Figure 6 illustrates the travel paths for the remaining signals in the data set where either threshold σ_T < 3% and σ_A < 3° was passed for our preliminary assignment of source errors discussed next. We neglect arrival property errors σ_a and σ_t to focus only on the effects of source parameter errors. For the purpose of display, we have used colors to represent the number of paths whose endpoints fall within the same pair of 1° bins.

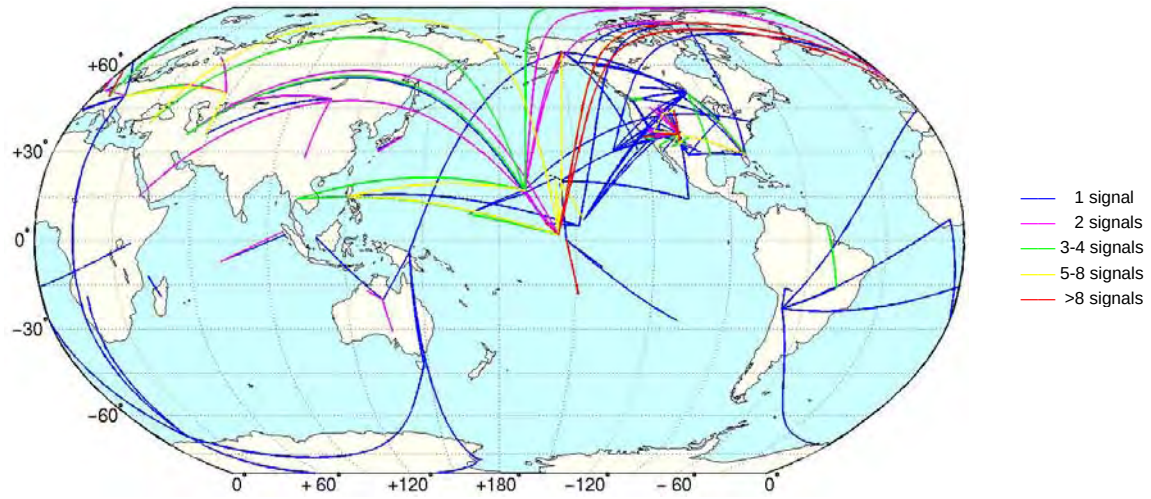


Figure 6. The distribution of signal paths for which source-related errors are σ_T < 3% and σ_A < 3°.

The accuracy assessment depends strongly on the assignment of source uncertainties, a laborious undertaking that often requires significant detective work. Three broad categories of events fall out of the related considerations. The rough distribution of events among them is summarized in Table 2. The first category is composed of well-known, impulsive, stationary events – mostly nuclear explosions (e.g., Operation Dominic, 1961) and controlled chemical explosions (e.g., Watusi, 2003; White Sands Missile Range Infrasound Calibration Experiments, 2005, 2006), and some mining explosions, where source location and time were independently measured and recorded. Source parameters for these events are generally constrained well enough that their contributions to σ_A and σ_T are much smaller than those from the models or the arrival measurements. For this group of events we set σ_r, σ_e, and σ_τ to half the least significant digit of officially stated source parameters where we believe precision is reflective of accuracy (generally the case), although we set floors of σ_r, σ_e=1 m on location and σ_τ=1 s on time.

Table 2. Distribution of event sources and qualities.

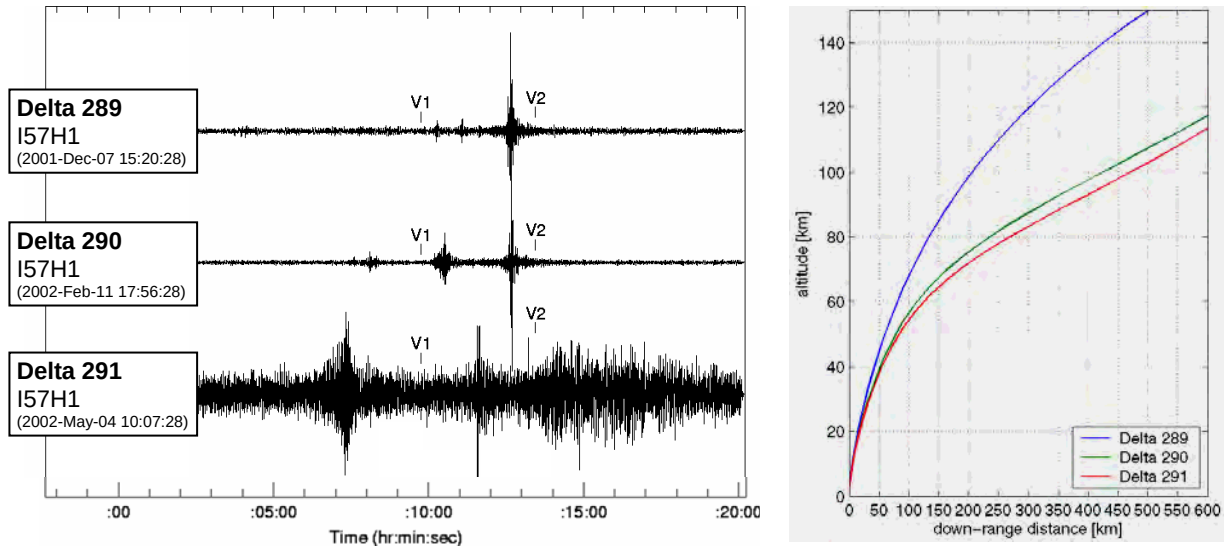
Event Source Type	1	2	3
Nuclear test explosion	31	22	
Chemical explosion	14	7	
Mine explosion		40	
Rocket launch/re-entry/test	1		77
Bolide			21
Volcano/Earthquake		51	
Total	**46**	**120**	**98**

1 – Well constrained, impulsive, stationary
2 – Partially constrained, stationary, possibly non-impulsive
3 – Moving

The second category is the much broader collection of partially constrained sources for which errors must be evaluated on a case-by-case basis. Locations for many accidental explosions can be determined precisely after the fact. However, the best time constraints come from eyewitness accounts, post-accident reports, etc., which are often of poor or marginal quality. For these events we conservatively set σ_τ to a minimum of 120 s, even in cases where time was specified to the minute. For earthquakes and mining explosions whose locations are estimated seismically we uniformly set σ_r=20 km, σ_τ=10 s and σ_e=0 km; case-specific assessments will be made in the future. Volcanic eruptions are generally well located so we set σ_r=0.5 km. For isolated explosive eruptions we set σ_τ=60–600 s depending on available accounts. We have not yet added continuous eruption data such as those from Vanuatu observed at station I22FR (Le Pichon et al., 2005). For these event sequences, energy cannot be matched up one-to-one with specifically timed sources, so we will likely set σ_τ large, essentially discarding time data.

Events in the third category have moving sources: rocket launches, re-entries, and bolides. This may be a controversial set of events because it is difficult to constrain the space-time-amplitude function of the objects as infrasound sources. On the other hand, it is a potentially important set because bolides and rocket launches are frequent compared to controlled, stationary sources of appreciable size. Bolides typically traverse the atmosphere in several seconds, traveling tens to hundreds of kilometers laterally and release significant energy as they disintegrate, sometimes explosively. While their source durations are brief, their exact times are often known only through eyewitness accounts. In such cases we have assigned large source errors σ_τ =60–120 s, σ_r =100 km, σ_e =5–20 km, depending on the quality of accounts, which eliminates most of their data against any reasonable thresholds on σ_A and σ_T. However, optical satellite imagery has fixed the precise time and location of detonation of some bolides, which we have equated to the predominant time and location of infrasound production and assigned σ_t as low as 2–5 s, and σ_r and σ_e as low as 1 km.

In contrast, rocket launches take minutes to exit the atmosphere while traveling hundreds of kilometers laterally. Where only launch time and location constrain the source, we have respectively assigned σ_τ =120 s, σ_r =100 km and σ_e=30 km, effectively eliminating all of their data. However, as with bolides, there are theoretically favorable points along the path for the rockets to generate infrasound, such as sonic/supersonic transition points. Impulsive signals, such as those for Delta 289 or Delta 290 in Figure 7(a) serve as evidence that this is the case. Approximate trajectories can be constructed for some rocket launches, (e.g., Gibson and Norris, 2002, 2004b) allowing these points to be more closely located. Profiles for three launches from Vandenberg AFB detected at I57US are illustrated in Figure 7(b). Trajectory information also allows sources to be modeled as lines, as Arrowsmith et al. (2003) did for the Washington state fireball. Then arrival features can be compared as whole sets to predictions, thereby providing not only the properties of individual arrivals as validation data, but also their progressions with time and values relative to one another. In these cases we have been more optimistic, setting σ_t =30 s, σ_r =5 km and σ_e ~5 km.



(a) (b)

Figure 7. (a) Infrasound traces at I57US from three rocket launches from Vandenberg AFB and (b) corresponding flight profiles constructed from launch parameters.

For the 632 signals currently in the expanded IDB data set, about half of the arrival-time data and a third of the back-azimuth data failed to pass the preliminary winnowing thresholds of σ_T < 3% and σ_A < 3°. However, this set will change, perhaps substantially, as knowledge of source parameters and our uncertainties in them is improved, as the IDB is expanded with new events and data, and as signal properties are measured and their accuracies systematically assessed.

Infrasound Validation of Wind Models

For the purposes of nuclear explosion monitoring, the new wind models must be evaluated in terms of accuracy with which they make infrasound predictions. Given the highly variable nature of the atmosphere and the dramatic effects that the variability has on infrasound propagation, it can be difficult to assess how one model improves prediction over another, so a statistical approach is essential. We follow the approach of O'Brien and Shields (2004) by formulating statistical hypothesis tests from the residuals between GT data and the predictions of each model.

Where possible, we evaluate the location accuracy associated with a given atmospheric model by directly comparing the source locations and times it predicts from arrival measurements to GT values. Generally, this is a multiple arrival problem, since a single arrival cannot uniquely specify the four space-time source coordinates, even if all of arrival time, back azimuth and slowness are usable data. However, the formulation of tractable statistics for multiple arrivals is dependent on the particular way in which data are combined with one another. Here we consider an alternative approach, in which we specify the least variable of the source parameters, elevation, and define measures of fit for the other three that sum over the predictions from all the arrivals. From those, we create statistics with approximate F distributions with which to test the significance of the differences between predictions of pairs of models. The residuals Δ, sample measures of fit s^2, and significance statistics F are listed below, where along- and cross-path location error components are denoted by $\parallel$ and $\perp$, the number of arrivals by N, and wind models by i and j. As above, uncertainty is denoted by σ, source location and time by r and τ, arrival time and back azimuth by t and a, and travel time by T. Following O'Brien and Shields (2004), we normalize travel-time residuals by the observed travel time (measured arrival time less the GT source time) and location residuals by the source-receiver range. This removes the expected dependence of the model-related errors, hence the residuals, on source-receiver range. After normalization, the residuals have roughly the same expected size and distribution so they can be combined to form statistics s^2 that are approximately distributed as χ^2, and statistics F that are approximately distributed as F.

Residuals		***Measure of Fit***		***Significance Test Statistic***	
$\Delta_{\tau k} = \dfrac{\left(\tau_{pred} - \tau\right)_k}{\left(t_{obs} - \tau\right)_k}$	$\Rightarrow$	$s_\tau^2 = \dfrac{1}{N-1}\sum_{k=1}^{N}\dfrac{\Delta_{\tau k}^2}{\sigma_{Tk}^2}$	$\Rightarrow$	$F_{\tau ij} = \dfrac{s_{\tau i}^2}{s_{\tau j}^2} \sim \mathrm{F}_{N,N}$	(3)
$\Delta_{\parallel k} = \dfrac{\left(r_{pred} - r\right)_{\parallel k}}{\left\lvert \mathbf{r}_{sta} - \mathbf{r}_k \right\rvert}$	$\Rightarrow$	$s_\parallel^2 = \dfrac{1}{N-1}\sum_{k=1}^{N}\dfrac{\Delta_{\parallel k}^2}{\sigma_{rk}^2}$	$\Rightarrow$	$F_{\parallel ij} = \dfrac{s_{\parallel i}^2}{s_{\parallel j}^2} \sim \mathrm{F}_{N,N}$	(4)
$\Delta_{\perp k} = \dfrac{\left(r_{pred} - r\right)_{\perp k}}{\left\lvert \mathbf{r}_{sta} - \mathbf{r}_k \right\rvert_k}$	$\Rightarrow$	$s_\perp^2 = \dfrac{1}{N-1}\sum_{k=1}^{N}\dfrac{\Delta_{\perp k}^2}{\sigma_{rk}^2}$	$\Rightarrow$	$F_{\perp ij} = \dfrac{s_{\perp i}^2}{s_{\perp j}^2} \sim \mathrm{F}_{N,N}$	(5)
			$\Rightarrow$	$F_{rij} = \dfrac{s_{\parallel i}^2 + s_{\perp i}^2}{s_{\parallel j}^2 + s_{\perp j}^2} \sim \mathrm{F}_{2N,2N}$	(6)

However, not all of the arrival measurements, time, back azimuth, and slowness are always available or used for estimating location. Often, slowness is disregarded altogether because it provides only weak constraint on the source-receiver geometry; in single detection scenarios, which is often the case for small local or regional events. That leaves only arrival time and back azimuth as reliable data. In some multiple station scenarios, arrival times are dropped also, in favor of back azimuth data because the effects of error in source parameters and assumed propagation path are more pronounced in travel time than back azimuth deflection. Thus, to exploit all GT infrasound observations fully, we must also be able formulate an evaluation in terms of the observables themselves.

Again, following O'Brien and Shields (2004), we formulate measures of fit and model comparison statistics for travel time and back azimuth deflection residuals, *T* and *A*. Note that these are numerically equivalent to residuals in arrival time and back azimuth. Travel-time residuals are normalized as described above. Back azimuth deflection residuals are not, since the model-related back-azimuth errors lack the same systematic dependence on source-receiver range. These statistics allow all arrival time and back-azimuth data to participate in model assessment, whether or not they can be combined into actual location estimates.

Residuals		***Measure of Fit***		***Significance Test Statistic***	
$\Delta_{Tk} = \dfrac{\left(T_{pred} - T_{obs}\right)_k}{\left(T_{obs}\right)_k}$	$\Rightarrow$	$s_T^2 = \dfrac{1}{N-1}\sum_{k=1}^{N}\dfrac{\Delta_{Tk}^2}{\sigma_{Tk}^2}$	$\Rightarrow$	$F_{Tij} = \dfrac{s_{Ti}^2}{s_{Tj}^2} \sim \mathrm{F}_{N,N}$	(7)
$\Delta_{Ak} = \left(A_{pred} - A_{obs}\right)_k$	$\Rightarrow$	$s_A^2 = \dfrac{1}{N-1}\sum_{k=1}^{N}\dfrac{\Delta_{Ak}^2}{\sigma_{Ak}^2}$	$\Rightarrow$	$F_{Aij} = \dfrac{s_{Ai}^2}{s_{Aj}^2} \sim \mathrm{F}_{N,N}$	(8)
			$\Rightarrow$	$F_{ij} = \dfrac{s_{Ti}^2 + s_{Ai}^2}{s_{Tj}^2 + s_{Aj}^2} \sim \mathrm{F}_{2N,2N}$	(9)

Once we have defined the final evaluation data set, we will make corresponding predictions using each wind model, and evaluate the measures of fit. We will then evaluate the comparison statistics for each relevant model pair and determine the significance level at which each model is statistically better than the other.

CONCLUSIONS AND RECOMMENDATIONS

We have begun preparation of data for incorporation into new wind models that should dramatically improve infrasound prediction for paths that sample the mesosphere and thermosphere. This includes vast new set of atmospheric wind data, collected mostly by satellite, and warehoused by NRL since the time that HWM-93 was created. This data set, along with infrasound data, indicate that a dramatic improvement in the parameterization of mesospheric and lower thermospheric winds will be possible.

We have also begun the preparation of many infrasound observations for validating the new wind models, building on the existing SMDC infrasound event database. We have defined statistics that will allow for the limited

infrasound data to be maximally exploited to constrain and evaluate the predictive capabilities of new and existing atmospheric models. We estimate that as many as two-thirds of these will yield data that can constrain the new wind models. However, this set is not large. Thus, we recommend that continued efforts to acquire and refine our understanding of GT infrasound so that the set of useful data is expanded, improving our understanding of the winds and the accuracy of wind models we have created.

REFERENCES

Drob, D. P., J. M. Picone, and S. D. Eckerman, C. Y. She, J. F. Kafkalidis, D. A. Ortland, R. J. Niciejewski, and T. L. Killeen (2000). Mid-latitude temperatures at 87 km: Results from multi-instrument Fourier analysis, *Geophys. Res. Lett*. 27: (14), 2109-2112, 10.1029/1999GL010821.

Drob, D.P., J. M. Picone, and M. Garces (2003). Global morphology of infrasound propagation, *J. Geophys. Res*., 108 (D21), 4680, 10.1029/2002JD003307.

Drob D.P., and J.M. Picone (2000). Statistical performance measures of the HWM-93 and MSISE-90 empirical atmospheric models and the relation to infrasonic CTBT monitoring, in *Proceedings of the 22nd Seismic Research Symposium: Planning for Verification of and Compliance with The Comprehensive Nuclear-Test-Ban Treaty*, Vol. 3, pp. 161–169.

Gibson, R. and D. Norris (2002). Integration of near-real-time atmospheric models with InfraMAP and applications to modeling infrasound from rockets, *Proceedings of the 24th Seismic Research Review– Nuclear Explosion Monitoring: Innovation and Integration*, LA-UR-02-5048, Vol.2, 775–782

Gibson, R. and D. Norris (2004b). Integration of InfraMAP software with near-real-time atmospheric characterizations, BBN Technical Report DTRA01-01-C-0084.

Hedin, A.E. (1991). Extension of the MSIS thermosphere model into the middle and lower atmosphere, *J. Geophys. Res*. 96: (A2), 1159–1172, 10.1029/90JA02125.

Hedin, A. E, E. L. Fleming, A. H. Manson, F. J. Schmidlin, S. K. Avery, R. R. Clark, S. J. Franke, G. J. Fraser, T. Tsuda, F. Vial, and R.A. Vincent (1996). Empirical wind model for the upper, middle, and lower atmosphere, *J. Atmos. Terr. Phys*. 58: 1421-1447.

Larsen M. F., A. Z. Liu, R. L. Bishop, and J. H. Hecht (2003). TOMEX: A comparison of lidar and sounding rocket chemical tracer wind measurements, *Geophys. Res. Lett*. 30: (7), 1375, doi:10.1029/2002GL015678.

Le Pichon, A., E. Blanc, D. P. Drob, S. Lambotte, J. X. Dessa, M. Lardy, P. Bani, and S. Vergniolle (2005). Infrasound monitoring of volcanoes to probe high-altitude winds, *J. Geophys. Res*. 110: D13106, 10.1029/2004JD005587.

O'Brien, M. and G. Shields (2004). Infrasound source locations using time-varying atmospheric models, in *Proceedings of the 26th Seismic Research Review: Trends in Nuclear Explosion Monitoring*, LA-UR-04-5801, Vol. 2, 660–669.

Picone, J. M., A. E. Hedin, D. P. Drob, and A. C. Aikin (2002). NRLMSISE-00 empirical model of the atmosphere: Statistical comparisons and scientific issues, *J. Geophys. Res*. 107: (A12), 1468, 10.1029/2002JA009430.

Press, W. H., B. P. Flannery, S. A. Teukolsky, and W. T. Vetterling (1994). Numerical recipes: the art of scientific computing, Cambridge University Press, New York.

Swinbank R. and Ortland D. A. (2003). Compilation of wind data for the Upper Atmosphere Research Satellite (UARS) Reference Atmosphere Project, *J. Geophys. Res*. 108: (D19), 4615, 10.1029/2002JD003135.

EARTHQUAKE DEPTH PREDICTIONS USING INFRASONIC WAVES

Douglas O. ReVelle

Los Alamos National Laboratory

Sponsored by National Nuclear Security Administration
Office of Nonproliferation Research and Development
Office of Defense Nuclear Nonproliferation

Contract No. W-7405-ENG-36

ABSTRACT

Having recently examined a U.S. Geological Survey (USGS) data set of ~190 earthquakes and of ~60 mining blasts in the Western USA that occurred during 2000–2002 with corresponding local seismic magnitudes from 3–4.5 over horizontal ranges from 200–1,500 km, we have detected ~20 well defined earthquake signals at the DLIAR large-baseline infrasonic array in Los Alamos. Most of these signals were thermospherically ducted waves. Of the 20 infrasonic earthquake detections, 15 recordings were thermospheric, 11 recordings were stratospheric and 6 recordings were of both types. For infrasonic signals with only a single recorded return, 9 recordings were thermospheric and 5 recordings were stratospheric. One approach, of the numerous types of analyses performed on these waves, assumed that the earthquake signals have identical atmospheric propagation characteristics to those of near-surface atmospheric explosions, with the only exception being that the earthquake source occurred at generally shallow depths (<15 km) within the earth's crust. All of the original calibrated earthquake depths are known parameters from the individual USGS seismic wave solutions (in addition, to source origin time, latitude, longitude, etc.). From this type of analysis, we have produced a strongly correlated relationship connecting the calibrated earthquake depth and the deduced vertical depth scale factor from our infrasonic wave amplitude solutions. This vertical depth scale factor is the required vertical scaling parameter for each earthquake that is needed in order to predict the specific infrasonic wave amplitudes that are identical to those for ducted atmospheric blast waves from a near-surface point source as a function of range and source yield (or equivalently for the concomitant local seismic magnitude). This deduced vertical depth scaling factor was determined using a least-squares curve-fit of observed earthquake depths versus the vertical depth scaling factor for the simple case of a four-parameter Gaussian function. This fitting resulted in a maximum value of $r^2 = 0.831$ by utilizing the observed earthquake depths and the four-channel averages of the peak-to-peak, maximum infrasonic wave amplitudes. Our curve-fitted results can now be used to more realistically forecast earthquake depths as a function of the observed horizontal range (~207–1,370 km), as a function of the observed source yield (or for the local seismic magnitudes from ~3 to 5.5) and finally as a function of the observed infrasonic wave amplitudes (from ~0.007 to 0.12 Pa). It can also be used as a depth discriminant to reliably diagnose earthquake infrasonic signals from mining blast explosion infrasound for sources whose signals are well observed infrasonically and for which ancillary source yields are also available in the absence of simultaneously recorded seismic waveform data.

OBJECTIVES

The objective of this work was to systematically and reliably evaluate the depth of earthquakes on the basis of the detection of their infrasonic signals radiated as a function of horizontal range, source yield (or equivalently the local seismic magnitude) and of the infrasonic wave signal amplitude. Using depth as a key identified parameter, we can then pursue the successful discrimination of earthquakes from near-surface mining blasts using infrasonic waves.

RESEARCH ACCOMPLISHED

We have evaluated the infrasonic signals from ~20 earthquakes (whose seismic magnitude ranged from about 3–5.5) in order to systematically deduce earthquake depth (ReVelle, 2005). This was accomplished using the following key assumption for earthquake zones that also possess the requisite source fault mechanism:

> The propagation of infrasonic signals from earthquakes is otherwise ***identical*** to that of near-surface free air bursts in the atmosphere. The only fundamental difference between these assumed point sources is that "small" earthquakes generally originate at ***shallow*** depths within the earth (<15 km below the surface), which always degrades the recorded signal amplitude. Thus, if we can successfully evaluate a depth correction factor for each earthquake (as a function of range, yield, and infrasonic signal wave amplitude), we can also deduce an empirical relationship between earthquake depth and the vertical depth scale factor due to the source region location beneath the earth's surface.
>
> A curve-fitted analysis of this behavior will allow the general prediction of earthquake depths over a range of observing conditions. The analysis of this predicted, but admittedly overly simplified behavior, is outlined below.

Earthquake Amplitude Coupling to the Atmosphere

We have examined propagating atmospheric blast waves from near-surface "point" sources and have compared the observed earthquake amplitudes as a function of range and source energy (or equivalently in terms of local seismic magnitude), etc. The far-field, quasi-linear, semi-empirical wave propagation amplitude regression equation for free-air, near-ground-level explosions (just above ground level, but not buried) propagating in a thermospheric waveguide in the atmosphere is given by ANSI (1983):

$$\Delta p = K \cdot \{W^c / R\}^B \qquad (1)$$

where

- Δp = peak to peak wave amplitude in μbars
- K = $4.95 \cdot 10^4$ = constant for amplitudes in μbars (1 μbar = 0.10 Pa)
- W = explosive charge weight in kt: TNT equivalent
- c = ½ for far-field conditions ($R >> \lambda$, λ the wavelength at $x = 10$, i.e., $R = 10.0 \cdot R_{ps}$ with $x = R/R_{ps}$)
- R = total horizontal range from source to observation point
- B = 1.36
- $c \cdot B$ = 0.68

The original expression for a stratospheric waveguide also contained the multiplying factor 10^{-kV} on the right hand side of Equation (1), which accounted for stratospheric wind speed propagation effects whose speed regularly exhibited a seasonal direction reversal, with generally small seasonal wind speed changes (where k is a propagation constant). We have implicitly assumed in this analysis that for sufficiently large sources (such that absorption losses are sufficiently small over relatively long propagation paths) that the thermospheric waveguide amplitudes could be modeled using the Stratospheric waveguide results with the wind enhancement/decay factor having been removed.

For an atmospheric point source explosion, the blast wave relaxation radius, R_{ps} is given by Sakurai (1965):

$$R_{ps} \equiv \{E_s/p(z)\}^{1/3} \quad (2)$$

where

p(z) =the ambient atmospheric pressure at the source altitude

Es = the source energy in Joules (where 1 kt of TNT equivalent energy release = $4.185 \cdot 10^{12}$ Joules)

The corresponding wave frequency and wavelength, λ, at maximum amplitude in the atmosphere at x = 10 ($x \equiv 10\ R/R_{ps}$) are given by

$$f = c_s/\{2.21 \cdot R_{ps}\} \quad (3a)$$

$$\lambda = 2.21 \cdot R_{ps} \quad (3b)$$

More recent analyses of weakly nonlinear propagation effects (see Mutschlecner and Whitaker, 2005, for example) have suggested B = 1.45 whereas earlier analyses by Reed (1972a; 1972b) had suggested B = 1.20, so that the value we have used brackets the available measurement possibilities. Since B > 1, this means that some small accumulative weakly nonlinear propagation effects will affect the propagation of the dispersed explosion pulse through the atmosphere. At very large ranges, for sufficiently small amplitude waves compared to the background pressure (where $\Delta p/p << 1$), Δp is proportional to 1/R so that the energy "lost" from the wave has a corresponding geometrical spreading loss that exhibits an inverse square law dependence.

Next, we will also compare earthquake infrasonic propagation through a thermospheric waveguide against the results using Equation (1) by first defining an exponential decaying vertical depth coupling factor, k_{EQ} (because earthquakes deliver their energy to the atmosphere through ground "shaking" after propagation upward from the source below, from various depths below ground level, i.e., below z = 0, after a corresponding propagation time delay, Δt, from the earthquake at depth z to the surface).

$$\Delta p = K \cdot \{W^c/R\}^B \cdot \exp[-k_{EQ} \cdot z] = K \cdot \{W^c/R\}^B \cdot \exp[-z/D_{EQ}] = K' \cdot \{W^c/R\}^B \quad (4)$$

where

z = depth of the earthquake below the ground (z = 0)

k_{EQ} = D_{EQ} where D_{EQ} is the vertical depth scale factor (expressed in km) with k_{EQ} the vertical depth coupling factor (or the vertical depth coefficient), expressed in km^{-1}

K' = amplitude scaling reduction due to the earthquake depth

In essence, multiplying Equation (1) by the exponential factor is another way of saying that the purely atmospheric propagation constant K has now changed to the form $K' = K \cdot \exp[-z/D_{EQ}]$. In this way, assuming all other propagation and fault type factors, etc., are unchanged, we have prescribed a way of determining the vertical depth scale factor, D_{EQ}, assuming that all of the amplitude changes relative to an air-blast situation are due solely to the depth of the earthquake below the surface of the earth. This is obviously an extreme simplification of the complex earthquake source, but one that certainly deserves examination.

Values of k_{EQ} were extracted from the 15 infrasonically detected wave amplitudes (four-channel averaged values) for thermospheric returns using the following expression (except for the indeterminate value in the limit as $z \rightarrow 0$):

$$k_{EQ} = -\ln\{(\Delta p/K)\cdot(W^c/R)^{-B}\}/z = 1/D_{EQ} \quad (5)$$

or after inverting and explicitly solving for the earthquake depth:

$$z = \text{earthquake depth} = -D_{EQ}\cdot \ln\{(\Delta p/K)\cdot(W^c/R)^{-B}\} \quad (6)$$

Plotting the deduced vertical depth scaling factor, D_{EQ}, versus the various earthquake depths available from the seismic data analyses that were deduced automatically by the USGS (recorded over a wide range of horizontal distances, wave amplitudes, and seismic magnitudes), we have been able to determine a well-correlated regression between the earthquake depth and the vertical depth scaling factor:

$$z = y_o + a\cdot\exp[-(1/2)\cdot((D_{EQ} - x_o)/b)^2] \quad (7)$$

or

$$D_{EQ} = x_o \pm b\cdot\{-2\cdot\ln((z-y_o)/a)\}^{1/2} \quad (8)$$

where

$a =$ 24.4795 km ± 30.3779 km

$b =$ 2.1453 km ± 1.7200 km

$x_o =$ 2.1224 km ± 0.1350 km

$y_o =$ -14.9268 ± 30.8003

Of the two solutions available for the square root expression in Equation (8), the negative root is applicable for earthquake source depths < a (in km) for values of the depth scale factor ≤ x_o. For source depths < a with a depth scale factor > x_0, the positive square root of the multi-valued system is applicable.

The Scaled-Energy-Range Concept

We have chosen to plot our results derived above versus either the local seismic magnitude or versus the scaled energy-range. The seismic magnitude and its conversion to energy will be discussed next. The general relationship that was used in order to convert between the Richter (local) seismic magnitude, M_R, and the source energy expressed in kt (TNT equivalent) is as follows:

$$\log(W(\text{kt TNT equivalent})) = \{1.50\cdot M_R - 6.0\} \quad (9a)$$

or

$$M_R = (2/3)\cdot\{\log(W(\text{kt TNT equivalent})) + 6.0\} \quad (9b)$$

The dimensionless scaled-energy range concept is simply a way of simultaneously combining the two separate parameters of source energy (or equivalently, the charge weight expressed in kt, for example) and range and is contained within the amplitude relationship, Equation (1), after normalization for thermospheric returns. The scaled energy-range can be written using Equation (1) after first dividing through by K, the leading constant propagation factor:

$$\langle E_s\cdot R\rangle_{scaled} = \Delta p = \{W^c/R\}^B \quad (10)$$

This relationship is used as a diagnostic parameter for earthquakes in Figure 2. Since this expression arises directly from the pressure wave amplitude relationship, Equation (1), divided by the leading constant factor K, it can also readily be called the normalized pressure wave amplitude factor. An example of the deduced behavior as a function of these parameters (seismic magnitude, scaled energy range, etc.) is shown in Figures 1 and 2.

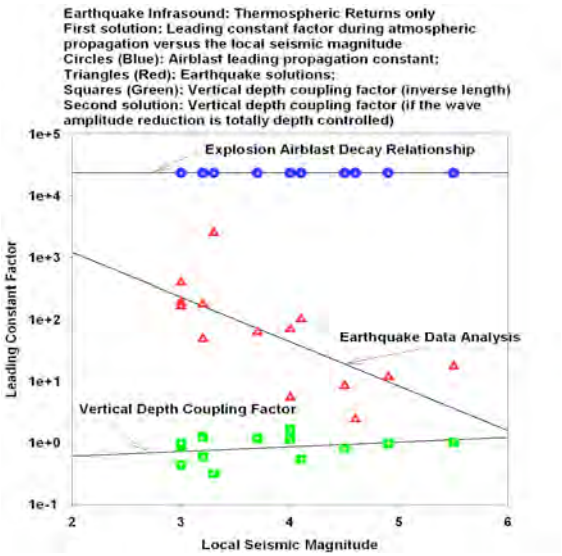


Figure 1. Leading constant propagation factor and the vertical depth coupling factor, k_{EQ} (in km^{-1}), versus the local seismic magnitude.

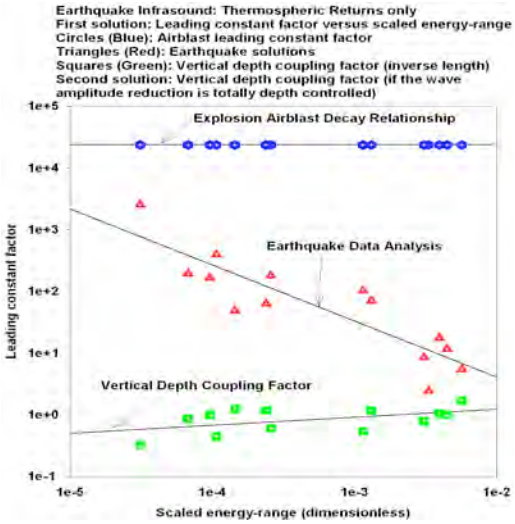


Figure 2. Leading constant propagation factor and the vertical depth coupling factor, k_{EQ} (in km^{-1}), versus the scaled energy-range.

From our analysis in Figure 1, it is evident that there is a single value of the leading constant propagation parameter for earthquakes that approaches the value of the atmospheric explosive blast wave solution propagation value, K. Presumably, this is also the local seismic magnitude where the depth of the recorded earthquakes also approaches zero (since this is observed to occur in Figure 1 at a local seismic magnitude of ~0). Similarly, the factor k_{EQ} is small for small earthquakes while its value steadily increases as the local seismic magnitude progressively increases. This is observed to be the inverse behavior of the leading constant propagation factor, whose value steadily decreases as the local seismic magnitude increases, presumably as the depth of the earthquakes also steadily increases. Equations (7) and (8) have been curve-fitted using a simple four-parameter Gaussian regression whose least squares correlation coefficient squared, $r^2 = 0.83132$ for the earthquake depth versus the vertical depth scale factor, D_{EQ}, as shown in Figure 3, whereas $r^2 = 0.6953$ was achieved for the vertical depth coupling coefficient, k_{EQ}, as shown in Figure 4 (with a single earthquake depth value at exactly $z = 0$ having first been removed from the data set to avoid division by zero and its implications).

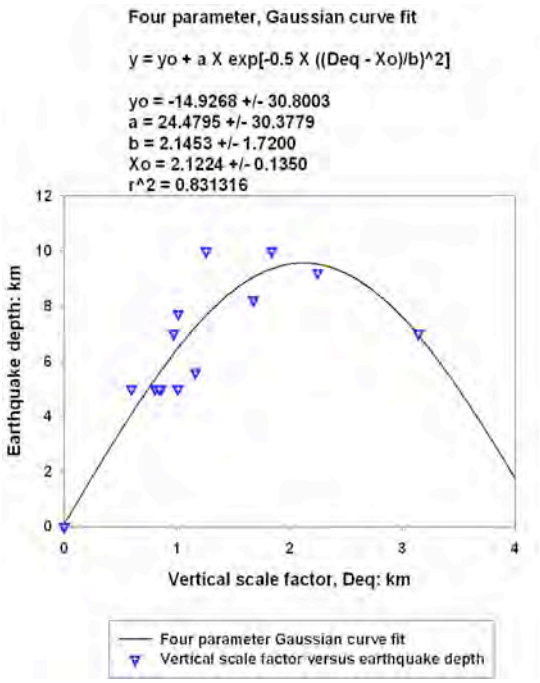


Figure 3. Earthquake depth versus the deduced vertical depth scale factor, D_{EQ} (km).

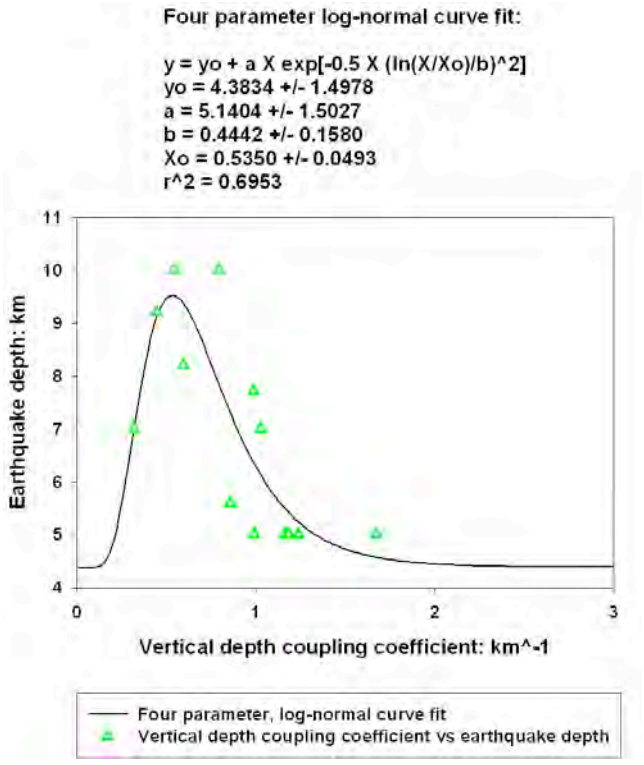


Figure 4. Earthquake depth versus the deduced vertical depth coupling coefficient, k_{EQ} (in km^{-1}).

The resulting curve-fit indicated in Equation (7) and shown in Figure 4 is only one of several regression curve-fits that we attempted, but all of our results indicated the same general form of curve-fitted behavior, with generally only small variations in (a, b, x_0), etc., and in the resulting maximum r^2 value.

Thus, the infrasonic amplitude (mean four-channel averaged value expressed in Pa) for Thermospheric returns can be now expressed in the following form:

$$\Delta p = K\cdot\{W^c/R\}^B\cdot\exp[-z/D_{EQ}] = K\cdot\{W^c/R\}^B\cdot\exp[-z/(x_0 \pm b\cdot\{-2\cdot\ln((z-y_o)/a)\}^{1/2})] \quad (11a)$$

We finally obtain the transcendental equation for the earthquake depth as a function of observed parameters:

$$z/(x_0 \pm b\cdot\{-2\cdot\ln((z-y_o)/a)\}^{1/2}) = -1.0\cdot\ln[(\Delta p/K)\cdot(W^c/R)^{-B}] \quad (11b)$$

or examining changes in z/D_{EQ}:

$$\delta(z/D_{EQ}) = z/(x_0 \pm b\cdot\{-2\cdot\ln((z-y_o)/a)\}^{1/2}) + \ln[(\Delta p/K)\cdot(W^c/R)^{-B}] \sim O(0) \quad (11c)$$

Equations (11b) and (11c) were formally solved by iterating very small values of D_{EQ}, while z, the earthquake depth, was evaluated using Equation (7). To accomplish this, we assumed that the difference between the two sides of the equation had to be less than a threshold value, which was assumed after trial and error to be ≤ 0.05 %.

From these curve fits, we have produced plots of the predicted earthquake depths (in km) as a function of range versus the local seismic magnitude for two assumed values of the wave amplitude in Figures 5 and 6 (for $\Delta p = 20$ and 2 Pa, respectively). Equivalently the same earthquake depth information is displayed in Figure 7 for $\Delta p = 20$ Pa, at various assumed horizontal ranges versus the source energy. These plots are presented directly below and were purposely computed for values slightly outside the original range of measurements that were documented in earlier reports.

In Figure 5 we have plotted our numerical solutions of Equations (11b) and (11c) for ***positive*** earthquake depths for the following extrapolated range of parameters with the observed earthquake parameters indicated in parentheses:

(1) $\Delta p = 0.02$ to 20.0 Pa (Observed amplitudes: 0.007 to 0.118 Pa)

(2) R = 320.0 to 5,000 km (Observed horizontal range: 206.9 to 1370.0 km)

(3) $W = 0.01$ to $1.0\cdot10^4$ kt (Observed source yield range: 0.0316 to 177.83 kt)

(4) M = 2.6667 to 6.6667 (Observed magnitude range: 3.0 to 5.5)

Numerical solutions of the earthquake depth as a function of the above parameters clearly show the following:

(1) Earthquake depths maximize at larger seismic magnitudes as either range increases or amplitude increases.

(2) The multi-valued nature of the solution is clearly evident in these plots since earthquake depths maximize as a function of the seismic magnitude and infrasonic amplitude at all selected ranges. This maximized behavior is produced by our simple Gaussian regressions expressed in curve-fit form in Equation (7).

It should be noted that the final values of the earthquake depths are slightly sensitive to all of these assignments but especially for the product c·B (see below for further discussion on this point). A complete sensitivity analysis of this system of equations will be performed shortly.

To illustrate the interpretation of the results, we will choose an example. If we have an infrasonic $\Delta p = 20.0$ Pa for R = 320 km and for $M_R < \sim 2.67$ (0.01 kt), all computed earthquake depths are very shallow, and the event could possibly be of man-made origin. Conversely, at the same range, if $M_R > \sim3.0$ (0.032 kt), but $M_R < \sim6.67$ ($1.0\cdot10^4$ kt), all computed depths are quite large, which effectively rules out a man-made source origin. However, for still larger observed seismic magnitudes, a significant decrease in the predicted depths again appears and the possibility of man-made sources again arises.

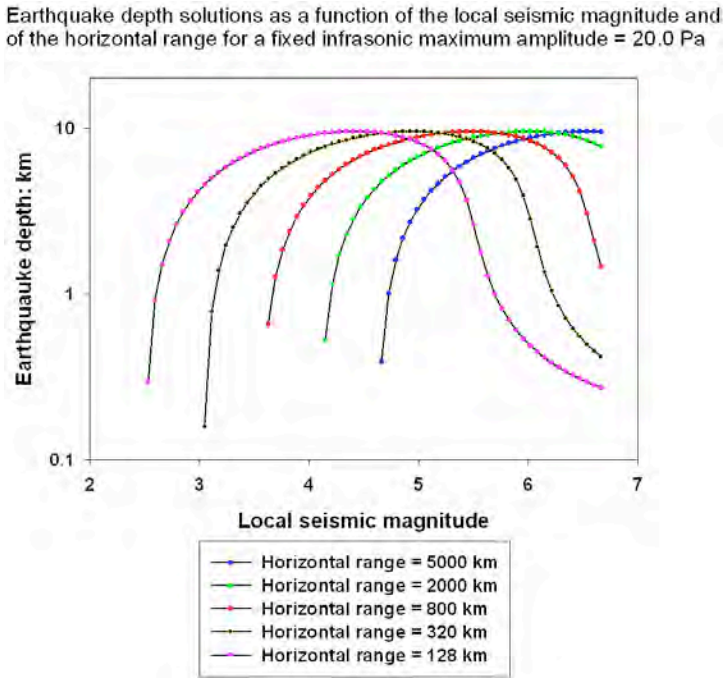


Figure 5. Earthquake depth (in km) versus the local seismic magnitude and the horizontal range for a fixed maximum infrasonic wave signal amplitude = 20 Pa.

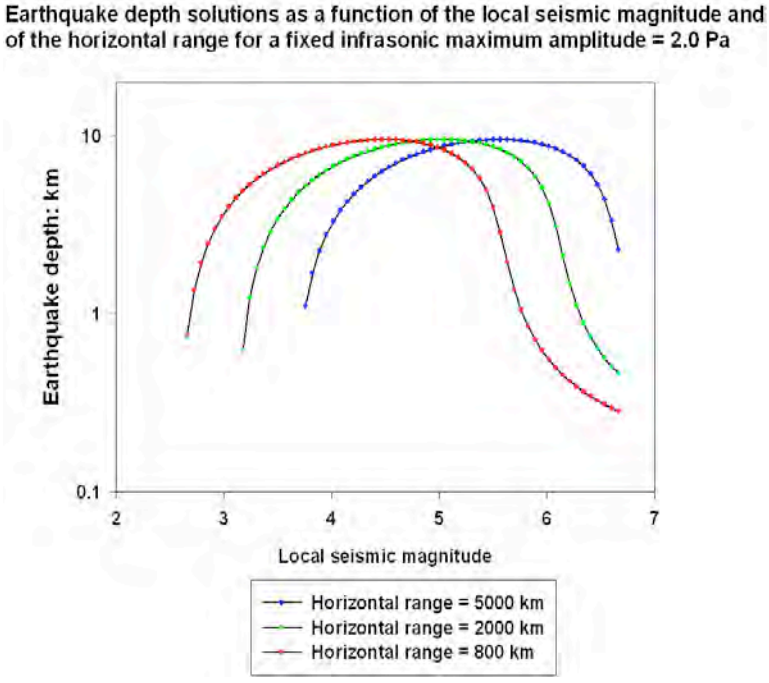


Figure 6. Earthquake depth (in km) versus the local seismic magnitude and the horizontal range for a fixed infrasonic maximum signal amplitude = 2.0 Pa.

Finally, we also have plotted these solutions as a function of the source energy in Figure 7.

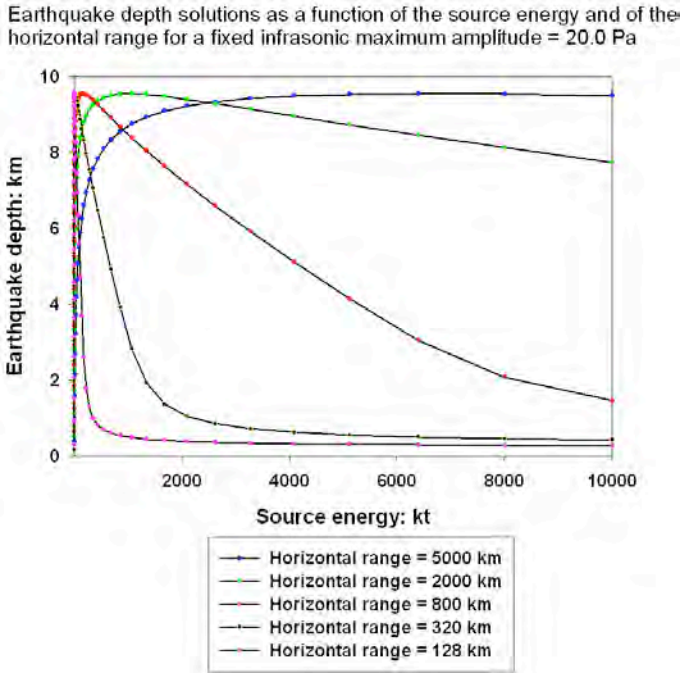


Figure 7. Earthquake depth (in km) versus the source yield (in kt) and the horizontal range for a fixed infrasonic maximum signal amplitude = 20.0 Pa.

For comparison, we present a bubble plot of the original 15 observed earthquake depths available from the USGS 2000–2002 database from our infrasonic detections at DLIAR. Depths are indicated within each bubble, while the relative bubble size is also indicative of the earthquake depth.

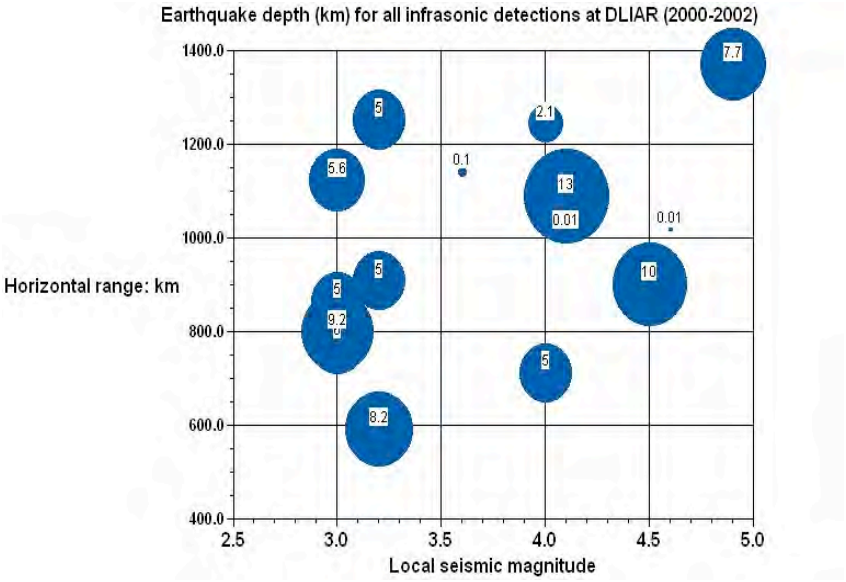


Figure 8. Observed earthquake depth (in km) versus the horizontal range and local seismic magnitude.

As a further example of the predicted behavior, consider a signal arriving from an unknown source that has been detected only infrasonically so that the source depth is fundamentally unknown except for the predictions for the set of equations developed in this paper. If the type of the signal is also unknown and if we assume that it is from an earthquake, we can still deduce the depth, knowing the horizontal range to the source, the maximum infrasonic wave amplitude, and the local seismic magnitude—or equivalently, a source energy estimate related to either a seismic magnitude, as shown earlier in Equations (9a) and (9b), or from the infrasonic wave period at maximum amplitude, etc. Assume the following observed parameters (for horizontal range, seismic magnitude, and wave amplitude):

Horizontal range = 1,500 km

Local seismic magnitude = 3.70 (W = 0.3548 kt)

Infrasonic amplitude = 10.0 Pa

From these parameters, we can deduce the vertical depth scaling factor, D_{EQ} = 4.160 km (k_{EQ} = 0.2404 km^{-1}) and the source depth = 0.662 km, if the source was an earthquake. It is very unlikely that a mining blast could be detonated at such a depth (662 m). As an alternative, consider the following set of recorded parameters:

Horizontal range = 100 k

Local seismic magnitude = 6.66 (W = 10^4 kt)

Infrasonic amplitude = 300.0 Pa

From these parameters, we can deduce the vertical depth scaling factor D_{EQ} = 0.1565 km (k_{EQ} = 6.39 km^{-1}) and the source depth = 1.159 km, if the source was an earthquake. It is extremely unlikely that a mining blast could be detonated at such a depth. If we further increase the amplitude to 3000 Pa (= 300 μbars) and keep all other factors held fixed, the source depth = 9.319 km, which certainly rules out a man-made underground explosion source. Further increases in amplitude, with all other parameters fixed, produce a decrease in the source depth, however. The reliability of the deduced infrasonic depth is only as good as the initial seismic calibration of the earthquakes analyzed earlier (for full details see ReVelle, 2005). If no seismic data are available for a set of infrasonic signals, we can still estimate the depth for the unknown signals by "crossing the beams" from multiple infrasonic arrays. This leads to the relative location as well as the horizontal range to the source, using the back azimuths of the analyzed signals. We can also measure other signal parameters and determine an independent source energy estimate, perhaps from the wave period at maximum amplitude of the signals or information that may be available from other external sources. Our final results are somewhat sensitive to the input parameters utilized but especially to the product, c·B, which has the possible ***far-field*** values $0.60 \leq c \cdot B \leq 0.725$, while we have used c·B = 0.68.

CONCLUSIONS AND RECOMMENDATIONS

On the basis of our results, we can say with confidence that given an infrasonic impulsive signal observation, we can reliably evaluate the value of the depth of the source if it was an earthquake. For sufficiently great depths, the event in question cannot be due to mining blasts, which are normally detonated quite close to the earth's surface.

REFERENCES

American National Standards Institute (1983). Estimating airblast characteristics for single point explosions in air, with a guide to evaluation of atmospheric propagation and effects, ANSI S2.20-1983 (New York: AIP).

Mutschlecner, J. P., and R. W. Whitaker (2005). Infrasound from earthquakes, *J. Geophys. Res*. 110: D01108, 1–11.

Reed, J. W. (1972a). Attenuation of blast waves by the atmosphere, *J. Geophys. Res.* 77: 1,616–1,622.

Reed, J. W. (1972b). Airblast overpressure decay at long range, *J. Geophys. Res*. 77: 1,623–1,629.

ReVelle, D. O. (2005). Additional infrasonic studies of earthquakes and mining blast discrimination, in *Proceedings of the 27th Seismic Research Review: Ground-Based Nuclear Explosion Monitoring Technologies*, LA-UR-05-6407, Vol. 2, pp. 845–854.

Sakurai, A. (1965). Blast wave theory, in *Basic Developments in Fluid Dynamics*, M. Holt (Ed.). New York: Academic Press), Vol. 1, pp. 309–375.

DETERMINING INFRASOUND PHASE VELOCITY DIRECTION WITH A THREE-ARM OFIS

Kris Walker, Mark Zumberge, Jon Berger, and Michael Hedlin

University of California, San Diego

Sponsored by Army Space and Missile Defense Command

Contract No. W9113M-05-1-0020

ABSTRACT

Optical fiber infrasound sensors (OFIS) are long, compliant tubes wrapped with two optical fibers that interferometrically measure pressure change. Because the differential pressure variation is integrated along the length of the tube, the instrument response is a function of the orientation of the OFIS relative to the orientation of the wavefront. We show with real data recorded at Pinion Flat Observatory in southern California and in the 2006 White Sands Missile Range II experiment in New Mexico that this spectral property can be exploited with multiple OFIS in different ways to determine the phase velocity of infrasound signals. We identify the strengths and weaknesses of such techniques, and compare them to time-delay techniques used with traditional microbarometer arrays. We also introduce two new techniques that should be significant improvements upon the technique we use to estimate phase velocity direction from OFIS data. As this research is ongoing, this paper is written as a progress report.

OBJECTIVES

The overall objective of our research is to further the development of OFIS. The original motivation for this research was to reduce the detrimental effects of wind noise by averaging pressure change along a line. However, we also recently became interested in how well an OFIS can obtain signal orientation parameters (phase velocity direction) as the signal propagates across the recording site because a multi-arm OFIS occupies less space than a traditional microbarometer array (Figure 1).

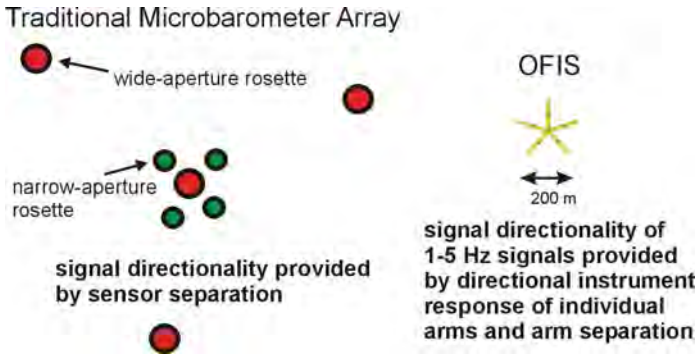


Figure 1. A typical 8-element infrasound array (left) and a 5-arm OFIS on the right. Rosettes are spatial filters created by an array of inlets connected to underground pipes that all connect to a centrally located microbarometer.

The specific objective of this research that we report on here is to develop and test techniques for resolving infrasound signal phase velocity direction with a 3-arm OFIS. We deploy and collect real signals at Pinion Flat Observatory (PFO) and as part of the March 2006 White Sands Missile Range (WSMR) controlled-source infrasound experiment to validate the theory we base our algorithms on, and to determine if an *n*-arm OFIS can resolve phase velocity direction better than an *n*-arm microbarometer array.

RESEARCH ACCOMPLISHED

We present below the most current details of our phase velocity determination research with a multi-arm OFIS. But we present first the obstacles that we encountered, what we learned from them, and how we dealt with them during our research.

Obstacles and Miscellaneous Accomplishments

Several obstacles developed during this research. In the past we relied on a commercial software package called Progressive Multi-Channel Correlation (PMCC) to obtain phase velocity direction for real signals. We generally assumed these PMCC results to be accurate and therefore be the "ground truth" in our comparisons (Walker et al., 2005). The PMCC software package gives results in a compact form, leaving out a lot of additional information about how well constrained the results are. Because our research requires us to make precise comparisons between the "ground truth" and the results of our algorithms, we developed a beamforming software package that provides the additional information about accuracy and resolution not available in our PMCC package. Using this new software, we discovered that we were not accounting for a known timing error associated with one of the elements of the I57US array. We confirmed that this error could have significantly degraded our previous PMCC-derived calculations. With our new beamforming software, we have calculated the phase velocity direction for 327 new high-quality signals at PFO as well as the signals obtained at station BACA during the WSMR II experiment.

Another obstacle that we encountered in our research was a source of noise that we needed to better understand because it is quite pervasive in the time series. In previous reports (Walker et al., 2005) we called this problem "spiking," and suggested it was due to creaking between the fiber and silicone tube, which gave rise to sharp steps in the optical fiber path length difference and resulting pressure change. We call this "spiking" because we often observe the filtered version of these offsets, which resemble spikes in the time series. This spiking problem occurs

when the sun begins to set and lasts for many hours. We also see spikes during the morning, although they are not as pronounced. We needed to better understand this problem because about half of the signals detected at PFO occur during these spiking periods. Unfortunately this was a lengthy experimentation process. We created some new OFISs, modified the design, and performed some pressure and controlled-temperature tests. The problem generally revealed itself when we suspended an OFIS above the ground—the spikes are most likely due to the relative motion of the silicone tube on the ground itself as the tube expands and contracts with temperature change.

A minor issue that affects uptime is polarization change in the fibers wrapped around the OFIS, which is strongly correlated with temperature change. We briefly performed an experiment on a variation of a polarization diversity detector to determine if one could obtain a stable ellipse by splitting the recombined signal into two different orthogonal polarizations and photodetectors, then using the lock-in amplifier to lock in to the summation of the photodetector outputs. The idea was that when one ellipse was collapsing, the other was getting larger, but the summation of the two would always produce a well-formed ellipse. Our brief experiment suggested that this technique does not yield the results we desire.

Sensor Directivity

The instrument response, *R*, of an OFIS relative to a point detector is a function of the orientation of the signal propagation with respect to the length of the OFIS:

$$R(f) = \left| sinc\left(\frac{L^1 f}{V_a} cos(\theta) \right) \right| \tag{1}$$

where f is frequency, L is the length of the OFIS, V_a is the sound speed at the Earth's surface (~330-350 m/s), and θ is the angle between the incident ray path and the OFIS

$$\theta = \cos^{-1}(\cos(\theta_b)\cos(\theta_e)) \tag{2}$$

where θ_b is the back azimuth, and θ_e is the elevation angle. For typical infrasound signals from distance sources, θ_e is 0–30° (subhorizontal) and θ *E* θ_b. Figure 2a shows a polar plot of *R* as a function of angle from the long axis of the OFIS for three typical infrasound signal frequencies.

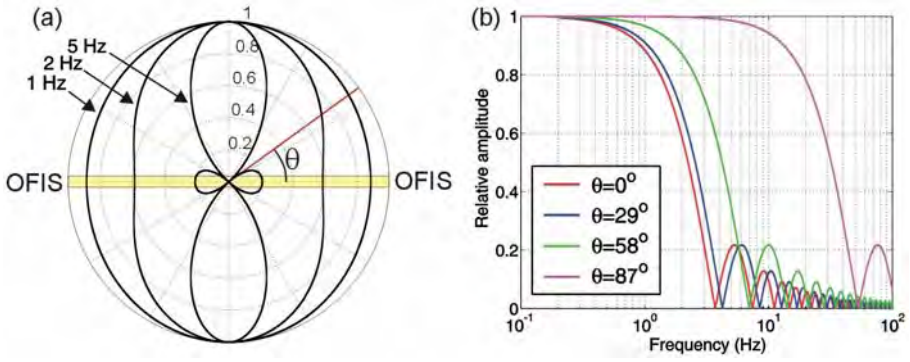


Figure 2. Frequency response *R* for a 90 m long OFIS as a function of frequency and angle θ from the length of the OFIS (Eqs. 1–2).

The response *R* is dependent on the ratio of the OFIS length to the frequency (Figure 2b). For low frequencies and long wavelengths relative to the OFIS length, the OFIS is effectively a point sensor and records the wavefront perfectly. For higher frequencies and shorter wavelengths, the OFIS attenuates some part of the signal because many of the peaks and troughs in the wavefront tend to average out along the length of the OFIS. The sinc form of this response can be thought of as the Fourier transform of a boxcar time series function, which represents the averaging of an impulse function signal as it propagates across the OFIS. For rays perpendicular to the OFIS, the impulse signal is recorded perfectly (flat amplitude spectrum) since the wavefront is parallel to the OFIS. For rays at lower angles to the OFIS, the impulse is smeared in time into a boxcar shape with a lower amplitude, resulting in the sinc function for the amplitude spectrum.

Typical power spectral densities (PSDs) of infrasound signals show modest levels of microbarom and wind noise. Figure 3a shows a hypothetical PSD example of a signal recorded by an OFIS oriented 29 degrees from the signal phase velocity direction. Although infrasound signals from distance sources have been observed in the ~0.7–15 Hz range on microbarometers, this OFIS only detects the signal in the ~0.7–7 Hz band because of the averaging property (*R*, Figure 3b). The slope as a function of frequency of the PSD from about 2–7 Hz provides valuable information about the true signal spectrum and the signal propagation direction with respect to the OFIS orientation. However, we have found that for the signals recorded on the 90 m OFIS at PFO, the most practical bandwidth to isolate this slope information is ~ 2–5 Hz. For longer and shorter OFIS lengths, this optimum range will shift to lower and higher frequencies, respectively, but will also be dependent on the bandwidth of the signals of interest.

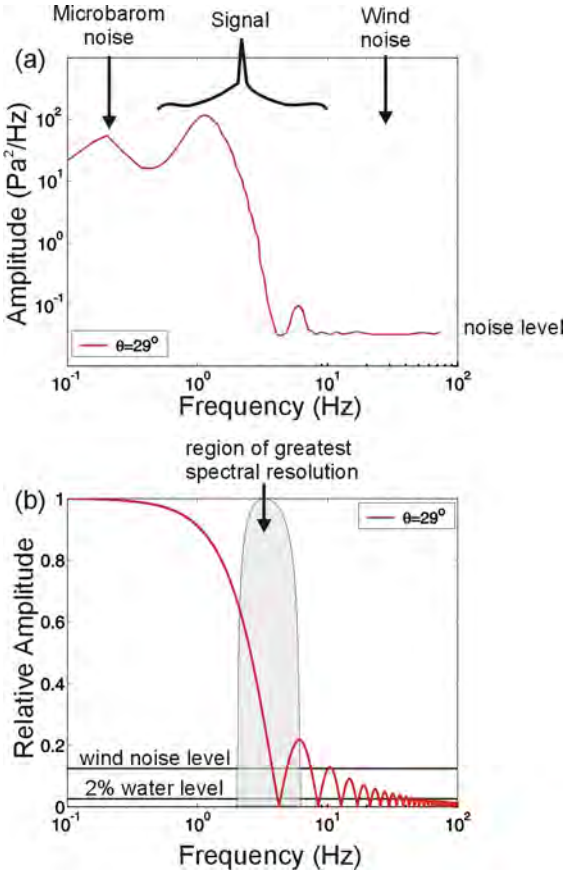


Figure 3. Details of the relationship between recorded signals and the instrument response function. A hypothetical infrasound signal recorded by an OFIS that is oriented 29 degrees from the propagation direction shows two peaks in the power spectral density (a) due to the directional instrument response (b).

Since θ is known in this case to be 29 degrees, one could deconvolve R from the recorded signal S_r in frequency space to determine the actual signal spectrum and waveform $S_w = S_r / R$. Ideally what is left is the signal spectrum, which is a convolution of the source and path term, in the 2–5 Hz band for a 90 m OFIS. However, traditional deconvolution is unstable in this case because the denominator R has near-zeros for certain frequency bands. To get around this problem, we have been using a water-level deconvolution method, which increases the amplitude of R in these troughs to 2% of the maximum (Figure 3b). This water-level technique introduces noise into S_w, but we have developed a better deconvolution technique that uses a least-squares inversion of the recorded frequency spectra of several OFIS (discussed later).

Phase Velocity Direction Determination Techniques

We typically want to obtain θ and the signal source spectrum from our infrasound sensors. One obvious way to do this is to have an array of several circular OFIS in a configuration optimized for time-delay beamforming in the frequency band of interest (Figure 4). However, the instrument response of a linear OFIS is highly dependent on the ray orientation, and so we can exploit this dependence by forming an array comprised of linear OFIS arms in different orientations. Therefore, for each possible ray orientation, there is a transfer function R that is unique to each OFIS that relates the signal spectrum S_w to what should be recorded by that OFIS. Quantitatively, the recorded OFIS signal is $S_r = f(S_w, \theta, L)$, where only S_w and θ are the unknowns. One can therefore estimate S_w and θ if one records the signal on two OFIS with different orientations (Figure 4a)

$$S_{r1} = f(S_w, \theta_1, L, V_a) \qquad (3)$$

$$S_{r2} = f(S_w, \theta_2, L, V_a)$$

where θ_1 and θ_2 are related by the array configuration. One can do this by substitution, i.e., using S_{r1} to predict S_w^p, and then S_{r2}^p

$$S_{r2}^p = S_w^p R_2, = S_{r1} R_2 / R_1. \qquad (4)$$

We perform a grid search over trial θ (back azimuth and elevation angle; Eq. 2) to minimize the L2 misfit between the inverse Fourier transforms of S_{r2} and S_{r2}^p. The global minimum corresponds with the phase velocity direction. Knowledge of the L2 misfit function allows us to calculate formal 2σ error bars by assuming the misfit function is the sum of squares of a random chi-squared noise process. We determine the number of degrees of freedom based on the average recorded signal bandwidth, which frees us from the typical assumption that the observed signal samples are independent of each other (white spectrum). This method calculates the misfit function by using one OFIS (e.g., OFIS 1) to predict what the other OFIS (e.g., OFIS 2) is observing. We have verified that the method is more stable by also calculating the misfit function in the other direction (using OFIS 2 to predict OFIS 1) and summing the two misfit functions.

The above method is ideal for two OFIS separated by 90 degrees (Figure 4a). The 90 degree separation offers identical spectral resolution for phase velocity directions in all of the quadrants. In addition, it is computationally fast because one only needs to do the grid search within one of those quadrants to get the spectral resolution. For each trial, we can therefore obtain the spectral constrains, and then the time shift constraints (since the centers of the OFIS arms are separated) by time shifting the resulting inverse Fourier transformed waveform four times (corresponding to the four possible quadrants) to calculate four separate misfit values. It can be shown that the amount to time shift is

$$dt = (h_2 \cos\alpha_2 - h_1 \cos\alpha_1) \cos\theta_e / V_a \qquad (5)$$

where α is the angle between the trial θ_b and the OFIS azimuth and h is the distance from the array center to the center of the OFIS arms.

The 2-90 configuration has been tested on real signals recorded at the PFO (Walker et al., 2004; 2005). A 2-90 works well for sub-horizontally propagating signals with a good amplitude signal-to-noise ratio (SNR>2). However, it does not work as well for signals that are propagating close to, but not quite parallel to the OFIS, because the

predicted difference in the time shift that distinguishes between two of the four possible quadrants is very small (Figure 4a). A fundamental limitation of any two-arm OFIS configuration is that it cannot be used to determine a phase velocity direction within the vertical plane defined by the azimuth in between the two OFIS.

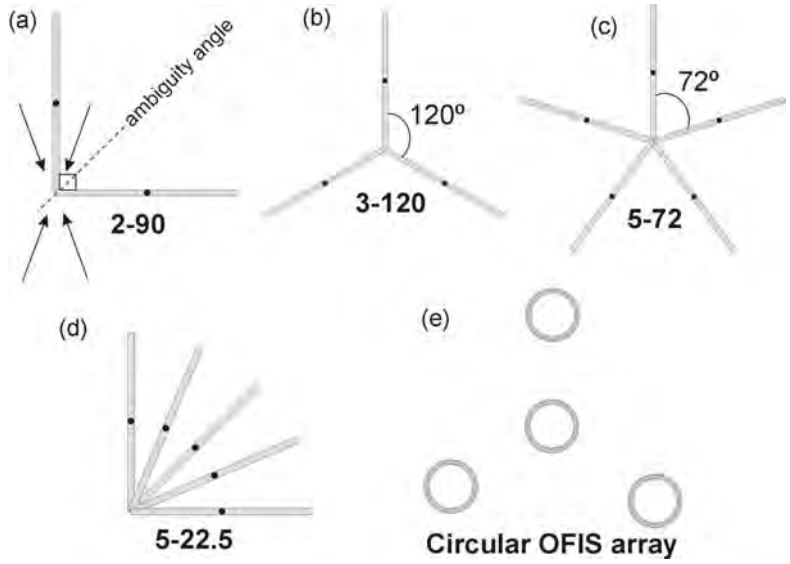


Figure 4. Possible OFIS configurations. Configurations a–d could be used in directional instrument-response dependent beamforming, and could provide a better phase velocity direction estimate if the wind noise suppression is good. Configuration e could be used in the same sense as pipe rosette filters or hose arrays. Configuration a, b, and e has been tested against pipe and hose arrays. For some signals the SNR is better on the OFIS. For other signals the SNR is better on the pipe and hose arrays.

We refer to the technique above as the "water-level deconvolution-predicted-OFIS comparison" (WLD-POC) technique. WLD-POC can be applied to OFIS in different configurations (Figure 4a–d), but the computational time for the above method is proportional to $n(n-1)$ and there is an additional doubling of CPU time associated with going from a 2-90 configuration to 3-120 or 5-72 configuration because one does not have quadrant symmetry anymore with regard to spectral resolution, but rather hemisphere symmetry. A 5-22.5 configuration still benefits from quadrant symmetry, but does not have the same degree of time separation resolution as the 3-120 and 5-72 configurations. For lower frequency signals (e.g., 0.5-2.0 Hz for 90 m OFIS), the time shift information is critical in determining the phase velocity direction.

Promising New Techniques

The WLD-POC technique is inherently unstable because of the deconvolution step. We have developed two new algorithms that avoid this step, but we have yet to confirm that they work better than the above method. The first method we call the "array response comparison" (ARC). We recall that the observed signals for two OFIS are $S_{r1}= S_wR_1$ and $S_{r2}= S_wR_2$. We can multiply both sides of these equations by the opposite response function $S_{r1}R_2= S_wR_1R_2$ and $S_{r2}R_1= S_wR_2R_1$. Because of the commutative property of multiplication in the frequency domain, the right hand side of these two equations are equal, and therefore $S_{r1}R_2= S_{r2}R_1$. We call this quantity the "array response" to the signal waveform. Each OFIS can be used to generate an array response for some given phase velocity direction. For the correct phase velocity direction, the array responses estimated from each OFIS should be equal. Therefore, we can perform a grid search over trial phase velocity direction and minimize the misfit between the estimated array responses. One could do this for n OFIS arms, where for each trial direction each OFIS recording would be convolved with n-1 instrument responses before being inverse Fourier transformed back to the time

domain where the misfit is evaluated. The ARC technique completely avoids deconvolution in determining the phase velocity direction. However, it does not inherently provide us with an estimate of the true signal spectrum.

Another technique we have developed is called the concurrent array deconvolution (CAD) technique, which replaces the water-level deconvolution step in the WLD-POC method. CAD is used in the POC grid search approach to estimate the signal spectrum by weighting, as a function of frequency and trial phase velocity direction, the recorded spectra of the OFIS arms such that only those OFIS arms that are in a good position to estimate S_w are effectively used. For example, if one had a 4-arm OFIS that recorded a signal with a phase velocity direction that was 0, 29, 58, and 87 deg from the OFIS arms, respectively (Figure 2b), at a frequency of 7 Hz, CAD would determine the signal spectrum from the OFIS spectra weighted from heaviest to least in this order: OFIS 4, OFIS 2, OFIS 3, and OFIS 1. Due to length restrictions, we postpone deriving this technique until we have tested it on real signals.

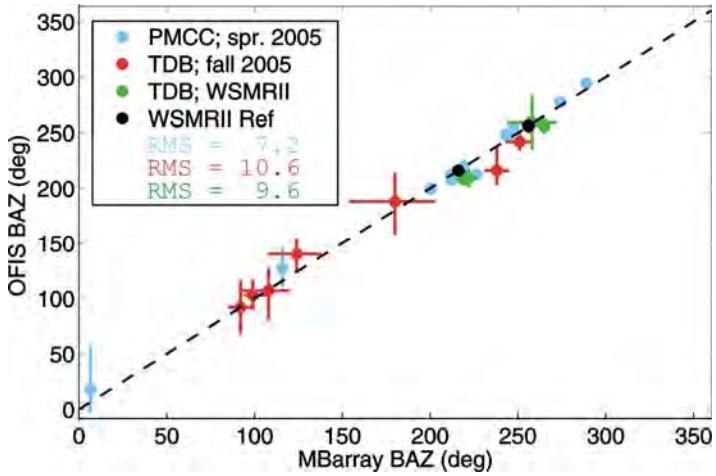


Figure 5. Back azimuth comparison.

Three-Arm OFIS: Analyzing Real Data

Using the WLD-POC method, we tested the 3-120 configuration and WLD-POC algorithm on many infrasound signals of good signal-to-noise ratio recorded during 2005-06 (Figure 5). Some of these results were reported in Walker et al. (2005); however, those previous results were not plotted correctly and we replot them correctly here along with some new measurements. We compare our estimated phase velocity directions with those obtained from the co-located I57US with the PMCC algorithm and our newly developed time-domain beamforming (TDB) software. The blue symbols indicate PFO signals that were analyzed by WLD-POC and PMCC. The PMCC results may have been affected by a timing error on one of the array elements (H2), and have questionably small error bars. The red symbols are PFO signals that were analyzed by WLD-POC and TDB (shown in more detail later). These signals are known to have signal-to-noise ratios greater than two and are from the analysis of eight time windows that comprise an infrasound wavetrain originating from an airplane above PFO. The green symbols represent WSMR II (BACA) signals that were analyzed by WLD-POC and TDB (also shown later). The WSMR II line-of-sight back azimuths to the launch pad and explosions provides some measure of ground truth. In all non-PMCC estimates, the 2σ error bars are shown. We do not know what level of certainty the PMCC error bars represent. In general there is a root mean square (RMS) deviation of about +/-10 deg. If we assume that the non-OFIS measurements represent the true back azimuths, then the error bars associated with the OFIS azimuths are consistent with the deviations. Based on some previous synthetic tests, this deviation would likely be less if we were using a 5-72 or 5-22.5 configuration.

An airplane that flew above PFO created an infrasound wavetrain that was recorded on both the 3-120 OFIS and three elements of the co-located I57US array (Figure 6). The three elements used at PFO were the 18 m underground rosettes, which are separated by 150–180 m, for a footprint of ~220 m. Each of the three OFIS arms is 90 m long,

for a footprint of about 180 m. The footprints are about the same in size. The phase velocity direction and 2σ error bars are obtained for each of the eight 6 sec time windows. The back azimuths of these measurements are also presented in Figure 5. Both sensor systems tracked the plane fairly well. Although the OFIS error bars include the pipe array estimate most of the time, the pipe array consistently yielded smaller error bars, even though the method for obtaining these error bars was the same for both. This is also reflected by the linearity of the pipe-array flight path (red line) as compared to the more rugged OFIS flight path (blue line), and is consistent with measurements of the signal-to-noise ratio for each of the time windows. Unfortunately the array elements are not co-located with the OFIS. Although this could explain the signal-to-noise differences, the rosette filters could also be reducing wind noise better than the OFIS arms. At such high elevation angles, the instrument response is almost flat for all three OFISs, so the OFIS instrument response is not the reason the signal-to-noise is lower. These results prove that not only is the back azimuth constrained by a 3-120 OFIS array, but the elevation angle is also constrained.

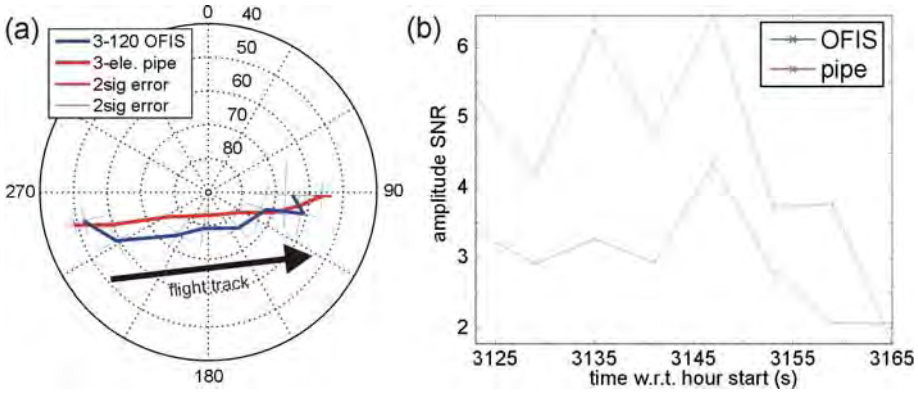


Figure 6. The results of the analysis of the airplane-induced infrasound wavetrain. The flight track defined by the 3-arm OFIS results and the 3-element pipe array is shown in (a). The average (for all sensors) signal-to-noise ratio of the time windows are shown in (b).

Figure 7 shows the analyzed waveforms and corresponding misfit functions for one of the time windows of the airplane signal in Figures 5 and 6. The grid shown is the log10 of the misfit for presentation purposes. The OFIS misfit function is more complex, although the misfit region is still fairly well defined and includes the pipe array solution. On the right hand side of Figure 7a are the predicted OFIS waveforms compared with the observed OFIS waveforms. For example, the bottom trace (OFIS 1->2 p/o) is OFIS 2 predicted from OFIS 1 (red) as compared with the observed OFIS 2 (black) for the optimum OFIS solution. The correlation coefficient between the two is shown on the left of the traces. The average is shown at the bottom and ideally should be 1.0 in the presence of no noise and with a perfect deconvolution technique. The estimated signal waveforms and the result of stacking these traces are shown in blue. For the pipe array, the time-shifted signals are also stacked together, and the correlation coefficients are with respect to this stack.

White Sands Missile Range II (WSMR II) Experiment Results

We deployed a new 4-arm OFIS, a 50 ft circular OFIS, and some array sensors at a remote site in New Mexico (BACA) during the 2006 WSMR II controlled-source infrasound experiment. Two small rockets were launched in the early morning hours from White Sands to 35 km altitude where they exploded. BACA was located about 115 km from the explosion epicenters. We used the WLD-TOC and TDB to analyze the several detected signals (Table 1; see also Figure 5). For both techniques, we assumed a velocity of 330 m/s based on the ambient temperature, and bandpass filtered the signals between 1 and 6 Hz. There were two suites of detected signals. Signals of around 0.2 Pa before the predicted explosion arrival time, with a back azimuth between 208 and 221 degrees, are interpreted as due to shockwaves associated with the acceleration of the rocket to supersonic speeds above the launch pad, which had a predicted azimuth (paz) of 216 degrees. The second suite of signals arrived at the predicted travel time for the explosions with amplitudes of 0.33 and 1.0 Pa for shot 1 and 2. The phase velocity directions are similar, but significantly different in some cases (bold). Some measurements are significantly different than the line-of-sight estimate (red). In general, the OFIS error bars are larger than those for the hose array. However, the hose array used 4 sensors as compared to 3 sensors for the OFIS, so this likely contributed to the smaller error bars.

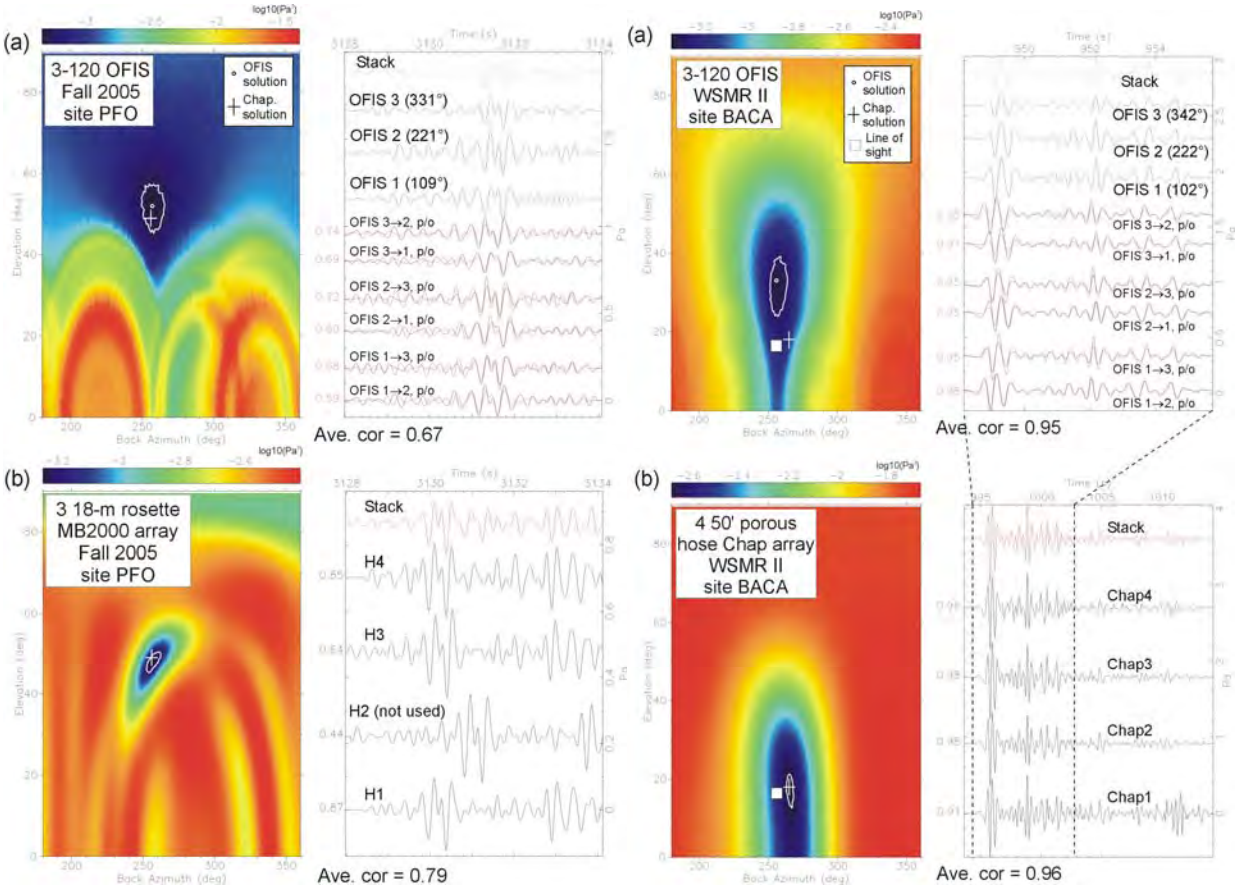


Figure 7. Comparison between the resolution of a 3-arm OFIS (a) and a 3-element pipe array (b) for a time window of an airplane infrasound signal at PFO (left) and a signal during the WSMR II experiment (right).

Table 1. WSMR II phase velocity direction comparison between OFIS and hose array results at station BACA

Signal	UTC (hr:sec)	Max Amp (Pa; p-to-p)	Paz	OFIS az	OFIS az 2σ	OFIS cor	OFIS snr	HOSE az	HOSE az 2σ	HOSE cor	HOSE snr
1-lnch	09:0538	0.21	216	**209**	6.5	0.63	13.8	**221**	3.5	0.88	8.8
1-exp.	09:0555	0.06	256	259	24.0	0.86	2.6	258	14.0	0.85	3.4
1-exp.	09:0561	0.33	256	258	7.5	0.91	8.0	264	3.5	0.97	11.5
2-lnch	13:0978	0.23	216	209	8.0	0.78	5.3	222	5.0	0.93	6.5
2-lnch	13:0981	0.20	216	**208**	4.0	0.71	4.1	**219**	4.5	0.95	8.9
2-exp.	13:1003	1.0	256	256	6.5	0.95	26.0	265	3.0	0.96	30.1

The analysis for the 1.0 Pa explosion signal for shot 2 is shown in Figure 8. Although the 95% confidence region is smaller for the hose array, it is significantly different than the line-of-sight back azimuth, but much closer than the OFIS to the line-of-sight elevation angle of 17 degrees. We note here that the azimuths of the OFIS were well determined with a Brunton compass, and the lengths were well determined in the lab. The array elements were positioned with a handheld GPS without a wide area augmentation system (WAAS) correction, which likely had a horizontal error bar of 5–10 m. We performed a simple experiment by randomly mislocating each array element by up to 5 m to determine the impact on the resulting TDB solution. The deviation from 265 was as much as 4 degrees, with no significant modification of the 3 degree error bar. We repeated this experiment with random mislocations of up to 10 m and found deviations by as much as 7 degrees. However, for such large deviations the 95% confidence region also expanded in size to include 265 degrees. If the elements were mislocated in a non-random manner, it may be possible to achieve a 9 degree mislocation without a significant increase in the error bar. This demonstrates the importance of accurate element positioning.

A noise study was also performed at site BACA. Preliminary results suggest that the 4 OFISs that were out in an open area were quieter than the hose array elements, most of which were beneath a short tree canopy. In addition, the amplitude envelope of those hose array elements was highly correlated with the wind speed whereas there was no significant correlation with the OFISs.

CONCLUSIONS AND RECOMMENDATIONS

The spiking problem is due to slip between the fibers and the ground as the OFIS moves during temperature fluctuations. The TDB algorithm we wrote works better for our comparisons than the PMCC software package. An OFIS is rugged, can be used for temporary deployments, and does not require thermally stable conditions for the electronics. A 3-120 OFIS configuration can resolve the back azimuth and elevation angle (phase velocity direction) of typical infrasound signals from distance or local sources using the WLD-POC method. The confidence region is usually better defined by using simple time-domain beamforming with a 3-element microbarometer array. The TDB solution also appears to be the most accurate based on analysis of a PFO airplane signal. The RMS difference in the back azimuths between the two methods appears to be about 10 deg for signals with SNR > 1.5. We currently interpret this discrepancy to be due to noise introduced by the WLD technique, and are in the process of evaluating two new techniques. We will also investigate in more detail the wind-noise reducing properties of the OFIS, and will create a very long OFIS to record the WSMR III signal at PFO and compare it with the co-located I57US array. We also plan on testing a 5-22.5 OFIS configuration if we obtain favorable wind-noise reduction results.

ACKNOWLEDGEMENTS

We thank P. Durdevic, P. Walsh, and R. Matoza for their assistance, and P. Shearer for his array deconvolution idea.

REFERENCES

Walker, K., M. Zumberge, J. Berger, and M. Hedlin (2005). An improved method for determining infrasound back azimuth with optical fiber sensors, *Proceedings of the 27th Seismic Research Review: Ground-Based Nuclear Explosion Monitoring Technologies*, Vol. 2, pp. 855–865.

Walker, K. T., S. Arrowsmith, J. Berger, M. Hedlin, and M. Zumberge (2004). Resolving infrasound signal back azimuths with arrays of optical fiber sensors, in *Proceedings of the 26th Seismic Research Review: Trends in Nuclear Explosion Monitoring*,LA-UR-04-5801, Vol. 2, 680–687.

REVISTING YIELD, DIRECTION, AND SIGNAL TYPE

Rodney W. Whitaker[1] and J. Paul Mutschlecner[2]

Los Alamos National Laboratory[1] and ComForce, Inc.[2]

Sponsored by National Nuclear Security Administration
Office of Nonproliferation Research and Development
Office of Defense Nuclear Nonproliferation

Contract No. W-7405-ENG-36[1,2]

ABSTRACT

Herein we present a review of three topics regarding infrasound signal analysis. For atmospheric nuclear explosions we review empirical yield estimates and bearing estimates for events at the Nevada Test Site. The events discussed have announced yields. Data were recorded by infrasound array stations operated by the United States during atmospheric testing.

In the third area we compare several characteristics of observed infrasound signals returned from stratospheric heights and thermospheric heights. The data come from four source types: atmospheric nuclear explosions, high explosive (HE) chemical explosions on the surface, earthquakes with previously detected stratospheric signals, and earthquakes for which stratospheric signals were not detected. The signal characteristics compared include: amplitude, travel velocity, azimuth and duration. In addition rough estimates of thermospheric-signal frequency of detection are presented.

OBJECTIVES

We present information about characteristics of infrasound signals from nuclear and conventional explosions and from moderate earthquakes. A comparison of stratospheric signals and thermospheric signals for three infrasound data sets is made that highlights some interesting relations. Finally we show some period-yield data for a set of atmospheric nuclear tests.

RESEARCH ACCOMPLISHED

Comparison of Some Characteristics for Stratospheric and Thermospheric Infrasound Signals

As more infrasound signals are reported, the opportunity for comparison of different signal types becomes obvious. Two types of interest are the signals that represent energy returning from the stratosphere and from the thermosphere, S and T signals respectively. Generally these two will exhibit different travel velocities as is well known. Other characteristics of the received signals would be of interest as well, such as azimuth deviation, duration and detection frequency. Here we will summarize results from a comparison S and T signals from three data sets, (Mutschlecner and Whitaker, 2006). These comparisons are of interest for purposes of identifying observed signals and for use in propagation studies. As researchers add to the observed signal database, such comparisons can be extended to additional sources and observations. Mutschlecner and Whitaker, 2006, then is a first step in this area. Future work may change some of the results we present, as would be expected for a field of active research.

For this investigation three data sets have been employed: (1) atmospheric nuclear explosions, (2) HE chemical explosions on the surface, (3) earthquakes with previously detected S signals.

Atmospheric Nuclear Explosions

The Nevada Test Site (NTS) nuclear explosion data used here were reported in Reed (1969). This data set covers observations for the period 1951 to 1958 and is one of the best sets available for completeness and consistency. The yields range from 0.6 to 74 kilotons. Signals were observed with single microphones at 12 stations. Only the data from the stations at St. George, UT; Bishop, CA; and China Lake (Inyokern), CA were used, all of which are at about one-bounce locations. Reed reports both S and T signals which he refers to respectively as ozonospheric and ionospheric signals. Mutschlecner et al., 1999, (hereafter MWA) have provided a detailed review of these data with an emphasis on the seasonal variations and normalization for the effect of wind on the S signals. The seasonal effect on amplitude is shown in Figure 1 for data at Bishop.

The average travel velocities for the T arrivals are: St. George, 228m/s; Bishop, 218 m/s; and China Lake, 209 m/s. There is reasonable consistency, especially to the east and west. The values of cover a fairly large range from about 200 to 260 m/s; there is no indication of seasonal variation. By comparison S signal average velocities were shown (MWA) to have an average value of 294 m/s.

The percentage of events with T signals is only 40% for St. George, 57% for Bishop, and 67% for China Lake. By contrast, S signals were detected on average at 95%. At St. George there were five T signals observed with no corresponding S signals or 5 %. All of those were during the "summer" or counter-wind period for the station when the S signals have greatly reduced amplitudes. For Bishop three T signals had no corresponding S signals or 5 %. These occurred during the counterwind or "winter" period for Bishop. At China Lake only one T signal had no accompanying S signal. For Bishop three T signals had no corresponding S signals or 5 %. These occurred during the counterwind or "winter" period for Bishop. At China Lake only one T signal had no accompanying S signal.

We compare S and T amplitudes (reported in the Reed report) by normalizing the S signal amplitudes for the stratospheric wind as discussed in MWA using the Stratospheric Circulation Index from Webb (1966), then taking the ratio of normalized S amplitude to T amplitude, A_S/A_T. Figure 2 shows the results for St. George and Bishop. Overall the average ratios are for Bishop, 4.7; for St George, 3.3; and for China Lake 7.4. We see that the normalized S amplitudes (equivalent to a zero wind value) are larger than the T amplitudes.

The Reed data were taken with single sensor stations so no azimuth data are available.

HE Data

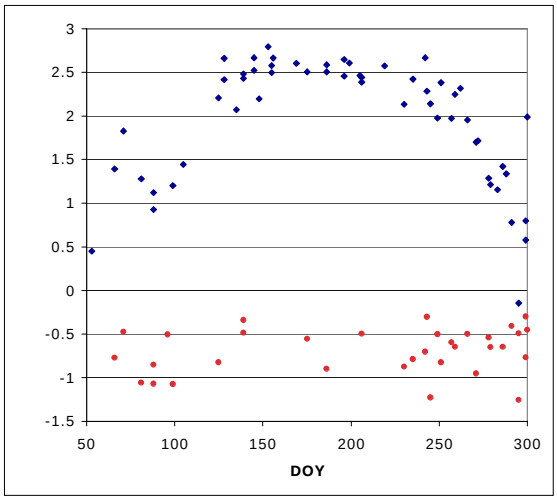


Figure 1: Log of A_S (diamonds) and A_T (dots) signal amplitudes versus day of year for nuclear explosions observed at Bishop, CA. Both amplitudes are normalized to 1 kT; the T log amplitudes have been shifted by -2 to provide clarity. While the S signal values show a clear seasonal variation, the T signals values appear to have no seasonal changes.

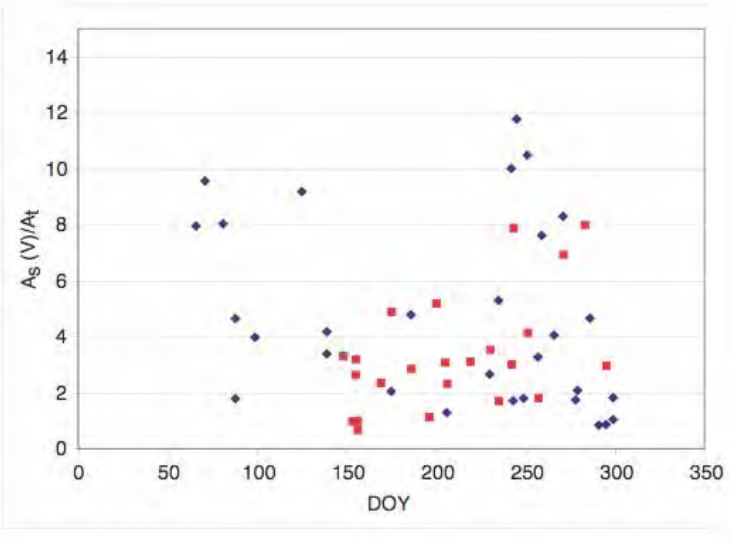


Figure 2. The ratios of wind-normalized S signal amplitudes, A_S, to T signal amplitudes, A_T, are shown versus day of year for the St. George UT (squares), and Bishop CA (diamonds), nuclear data.

A number of high explosive tests have been monitored for infrasound signals by the Los Alamos National Laboratory. The tests were conducted at the White Sands Missile Range in New Mexico by the Defense Nuclear Agency (now the Defense Threat Reduction Agency). The test explosives were on the surface except for one at a small elevation and varied in size from 0.04 to 4880 tons of explosive (ANFO). Observations were carried out at both fixed and specially deployed temporary infrasound arrays. The arrays typically consisted of four microphones. Unlike the nuclear explosion data, these include a wide range of distances from 250 to 5300 km. A portion of these data previously were discussed by Davidson and Whitaker (1992), and Whitaker et al. (1990). A set of 24 measurements, all of which had well-defined S signals, were investigated for T signals. The events are listed in Table 1.

Table 1: List of HE events.

EVENT	DATE: DOY	WEIGHT (TONS)	SITES
MILL RACE	9/16/81: 259	600	1
PRE-DIRECT COURSE	10/7/82: 280	24	2
DIRECT COURSE	10/26/83: 299	600	4
MINOR SCALE	6/27/85: 178	4800	2
MISTY PICTURE	5/14/87: 134	4880	5
MISERS GOLD	6/01/89: 152	2400	8
DISTANT IMAGE	6/20/91: 171	2400	2
MINOR UNCLE	6/10/93: 161	2400	3

The S signal travel velocities were in the range of 280 to 300 m/s, while the average for T signals was 228 m/s, all quite comparable to the nuclear data.

The T signals data came from examination of hardcopy records because the digital data are no longer available. Our detection frequencies for T signals are more likely lower bounds because, for some of the data, analysis was not carried out at lower frequency and some contributions may have been missed. With this caveat, the frequency of observation with T signals was found to be 42%, 10 T signals and 24 S signals.

The average normalized S amplitude to T amplitude ratio was found to be 2, a little less than the nuclear set. Average S signal duration was 7.9 minutes and 1.0 minute for T signals. For azimuth deviation, S signals averaged 5.1 degrees and T signals averaged 6.0 degrees.

Earthquake Data

A set of 24 earthquakes with well-determined S signals was selected from a larger set previously investigated by Mutschlecner and Whitaker (2005). The selection was based primarily upon earthquakes for which the predicted arrival time for possible T signals was larger than that of the ending times of the observed S coda. This was done to avoid, as much as possible, the difficulty of clearly separating a T signal from the preceding S signal. The earthquakes were observed by infrasound arrays at Los Alamos, NM, and at St. George, UT, over the period of 1985 to 2002. The range of magnitudes is from 4.4 to 7.9 and the distances from about 400 to 4000 km.

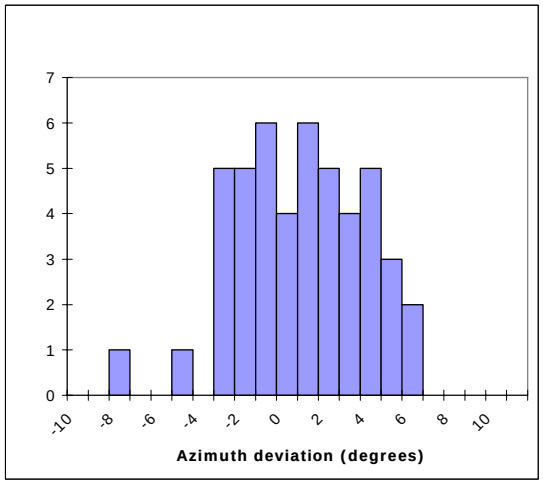


Figure 3: Distribution of azimuth deviations for earthquakes in Mutschlecner and Whitaker, 2005.

The S signals travel velocities were in the normal stratospheric range, while those of the T signals average 243 m/s with a full range of 200 to 270 m/s. T signal detection frequency was 37%, and is probably a lower bound. Azimuth deviations were 2.5 degrees for S signals and 3.3 degrees for T signals, similar to other data sets. Average durations were 18 minutes for S signals and 58 seconds for T signals. In Figure 3, we show the distribution of azimuth deviation for the S signals.

Interestingly the earthquake data for the ratio of normalized S amplitude to T amplitude show a departure from the other sets. Here the ratio averaged 0.4 with a range from close to 0.1 to 0.7. This difference in ratio may be due in part to source differences because explosions are point sources and the earthquakes have extended areas of ground motion. Earthquakes may have more energy at larger elevation angles than explosions. This could be examined with detailed ground motion data for some earthquakes and deriving emission patterns. It should be noted, the ratio here is that using the normalized S amplitude, adjusted to zero wind. Because of wind effects, there are times when the raw S amplitude will be larger than the T amplitude.

Azimuth Deviations from Some NTS Events

Olmstead (1951, 1953, and 1954 reports de-classified) gives data on azimuth deviations and other characteristics for atmospheric nuclear events in three operations. The azimuth results are shown in Figure 4 below. The operations were Buster Jangle (B-J), 1951 at the Nevada Test Site; Ivy, 1952 in the Pacific; and Upshot Knothole (U-K), 1953, at the NTS

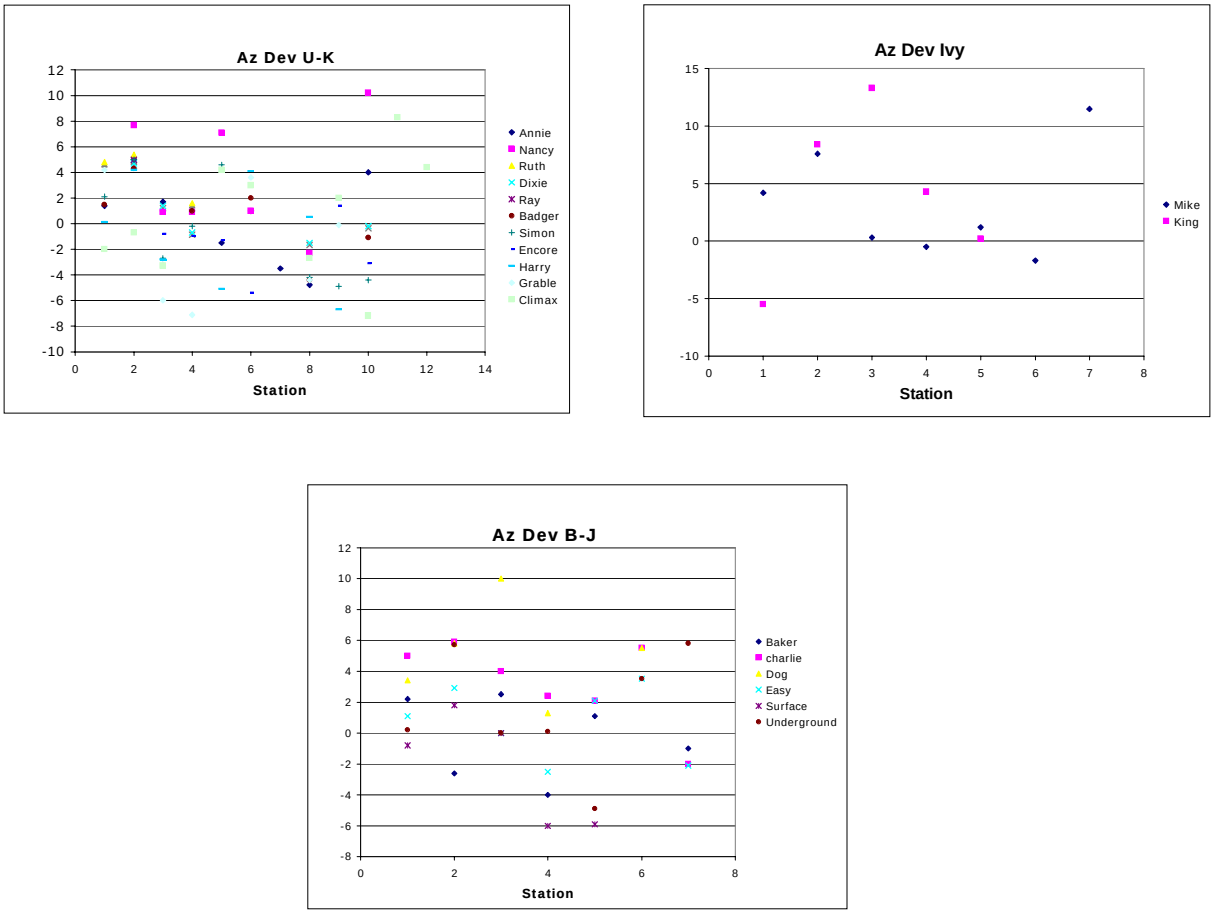


Figure 4: Observed azimuth deviations for three operations.

For illustration, we have taken the observations for each operation and determined a standard azimuth deviation for the operation. The results are shown in Table 2.

Table 2: Summary standard deviations in azimuth for three atmospheric test operations.

	U-K	B-J	Ivy
Std dev azimuth (degrees)	3.96	3.75	5.66

These are quite similar to deviations seen for other data sets. The value for Operation Ivy is larger because of one large deviation for each event, though not from the same station.

Period and Yield

We have gathered some period-yield for six US atmospheric nuclear test operations. Some of the data appear in the reports by Olmstead in the references, while other data are in old records that are not easily available. All events used had announced yields taken from the test summary report DOE/NV-209-Rev 15. Periods were averaged over the results for stations reporting. The period is that of the main acoustic arrival, interpreted as that from stratospheric heights. Earlier, ReVelle (1997) had given two representation of the period yield relation, applicable for two ranges of source size. For comparison, here we use just one fit over all the events considered. Test operations from which data came are shown in Table 3. The data are shown, with the regression line, in Figure 5.

Table 3: Operations used in period – yield relation.

OPERATION	ABBREVIATION	YEAR	TEST AREA
Greenhouse	G-H	1951	Pacific
Buster-Jangle	B-J	1951	NTS
Tumbler-Snapper	T-S	1952	NTS
Ivy	Ivy	1952	Pacific
Upshot-Knothole	U-K	1953	NTS
Redwing	R-W	1956	Pacific

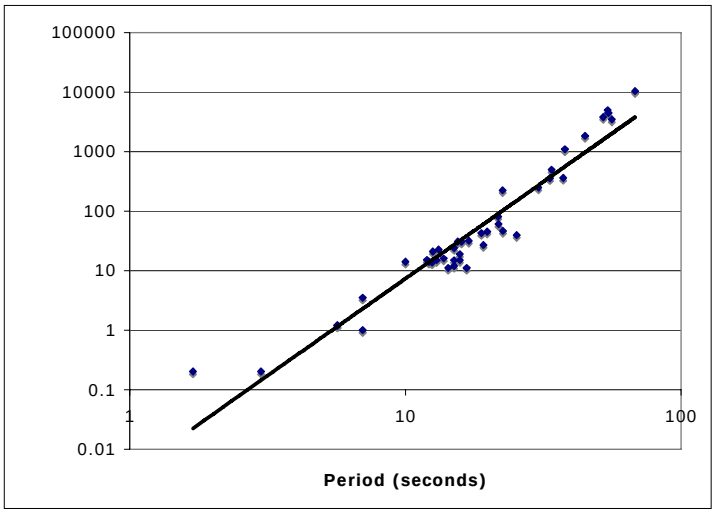


Figure 5: Infrasonic yield vs period for some atmospheric nuclear tests.

The regression gives, independent of other fits:

$$Y = 4.0 \times 10^{-3} P^{3.26} \qquad \text{or} \qquad \log(Y) = -2.4 + 3.26\log(P) \qquad (1)$$

where Y is in kilotons and P is in seconds. The regression has a R^2 of 0.93 and a standard deviation of the fit (log) of 0.15, or a factor of 1.41 in physical units. These apply to this particular analysis.

It should be noted that the relation is for surface and low altitude explosions, essentially point sources. High altitude events would require some adjustment for altitude scaling (Baker, 1973). In addition for moving sources, such as

bolides, accounting for the line source physics must be made. Two recent contributions addressing this for meteors and bolides are Edwards et al., 2004, and Edwards et al., 2006.

CONCLUSIONS AND RECOMMENDATIONS

We have summarized data on the period yield relationship for atmospheric explosions, reviewed azimuth deviations for explosions and moderate earthquakes and compared characteristics of stratospheric returns and thermospheric returns. Because data and analysis limitations with some of the data, we could have missed some thermospheric signals. In terms of frequency of detection, duration, and azimuth deviation, the sets are reasonably consistent. From a number of source types, we find azimuth deviations to be within six degrees (standard deviation) and apply to S or T signals. Average travel velocities for T signals range from 200 m/s to 270 m/s. The fit to the yield period relation shown here is within a factor of two (from the standard deviation of this regression).

REFERENCES

Baker, Wilfred E. (1973). *Explosions in Air*, University of Texas Press, Austin, Texas.

Davidson, M. and R. W. Whitaker (1992). Miser's Gold, Tech. Rep. LA-12074-MS, Los Alamos National Laboratory, Los Alamos, N.M.

Edwards, Wayne N., Peter G. Brown and Douglas O. ReVelle (2004). Bolide energy estimates from infrasonic measurements, *Earth, Moon and planets, 95*,501-512, DOI:10.1007/s11038-005-2244-4.

Edwards, Wayne N., Peter G. Brown and Douglas O. ReVelle (2006). Estimates of meteoroid kinetic energies from observations of infrasonic airwaves, *Journal of Atmospheric and Solar-Terrestrial Physics*, in press, doi:10.1016/j.jastp.2006.

Mutschlecner, J.P. and R. W. Whitaker (2006). Thermospheric Infrasound, LA-UR-06-4581, Los Alamos National Laboratory, (submitted to *J. of Geophy. Res*).

Mutschlecner, J.P. and R. W. Whitaker (2005). Infrasound from earthquakes, *J. of Geophy. Res.*110: D01108.

Mutschlecner, J. P., R. W. Whitaker and L. H. Auer (1999). An empirical study of infrasonic propagation, *Tech. Rep.* LA-13620-MS, Los Alamos National Laboratory, Los Alamos, N.M.

Olmstead, G. B. (1951). Detection of airborne low frequency sound from nuclear explosions, Operation Buster-Jangle, WT-322, Headquarters United States Air Force, (DTIC AD-A995156).

Olmstead, G. B. (1953). Detection of airborne low frequency sound from nuclear explosions, Operation Ivy, WT-632, Headquarters United States Air Force, (DTIC AD0363576).

Olmstead, G. B. and Major E. H. Nowak (1954). Detection of airborne low frequency sound from nuclear explosions, Operation Upshot Knothole, WT-763, Headquarters United States Air Force, (DTIC AD-A995499).

Reed, J. W. (1960). Climatology of airblast propagations from Nevada Test Site nuclear airbursts, *Tech. Rep.* SCRR-69–572, Sandia Lab., Albuquerque, N. M.

ReVelle, Douglas O. (1997). Historical detection of atmospheric impacts by large bolides using acoustic gravity waves, *Annals of the New York Academy of Sciences* 822: 284–302.

United States Nuclear Tests July 1945 through September 1992, DOE/NV-209 Rev 15, December, 2000, National Technical Information Center.

Webb, W. L., (1966). *The Structure of the Stratosphere and Mesosphere*, pp 141–145, Elsevier, New York.
Whitaker, R. W., J. P. Mutschlecner, M. B. Davidson and S. D. Noel, (1990), Infrasonic observations of large-scale HE events, Fourth International Symposium on Long Range Sound Propagation, NASA Conf. Pub. 3101.

Data Processing and Analysis

ENHANCING SEISMIC CALIBRATION RESEARCH THROUGH SOFTWARE AUTOMATION AND SCIENTIFIC INFORMATION MANAGEMENT

Annie B. Elliott, Douglas A. Dodge, Michael D. Ganzberger, Teresa F. Hauk, Eric M. Matzel, and Stanley D. Ruppert

Lawrence Livermore National Laboratory

Sponsored by National Nuclear Security Administration
Office of Nonproliferation Research and Development
Office of Defense Nuclear Nonproliferation

Contract No. W-7405-ENG-48

ABSTRACT

The National Nuclear Security Administration (NNSA) Ground-Based Nuclear Explosion Monitoring Research and Engineering (GNEM R&E) Program has automated significant portions of the processes of both seismic data collection and processing, and of determining seismic calibrations and performing scientific data integration by developing state-of the-art tools. We present an overview of our software automation and scientific data management efforts and discuss frameworks to address the problematic issues of very large datasets and varied formats utilized during seismic calibration research. The software and scientific automation initiatives directly support the rapid collection of raw and contextual seismic data used in research, provide efficient graphics-intensive and user-friendly research tools to measure and analyze data, and provide a framework for research dataset integration. The automation also improves the researcher's ability to assemble quality-controlled research products for delivery into the NNSA Knowledge Base (KB). The software and scientific automation tasks provide the robust foundation upon which the synergistic and efficient development of GNEM R&E Program seismic calibration research may be built.

The task of constructing many seismic calibration products is labor intensive and complex, hence expensive. However, certain aspects of calibration product construction are susceptible to automation and future economies. We are applying software and scientific automation to problems within two distinct phases or "tiers" of the seismic calibration process. The first tier involves initial collection of waveform and parameter (bulletin) data that comprise the "raw materials" from which signal travel-time and amplitude correction surfaces are derived, and is highly suited for software automation. The second tier in seismic research content development activities, which we focus on in this paper, includes development of correction surfaces and other calibrations. This second tier is less susceptible to complete automation, more complex and in need of sophisticated interfaces, as these activities require the judgment of scientists skilled in the interpretation of often highly unpredictable event observations. Even partial automation of this second tier, through development of tools to extract observations and make many thousands of scientific measurements, has significantly increased the efficiency of the scientists who construct and validate integrated calibration surfaces. This achieved gain in efficiency and quality control is likely to continue and even accelerate through continued application of information science and scientific automation.

Data volume and calibration research requirements have increased by several orders of magnitude over the past decade. Whereas it was possible for individual researchers to download individual waveforms and make time-consuming measurements event by event in the past, with the terabytes of data available today, a software automation framework must exist to efficiently populate and deliver quality data to the researcher. This framework must also simultaneously provide the researcher with robust measurement and analysis tools that can handle and extract groups of events effectively and isolate the researcher from the now onerous task of database management and metadata collection that is necessary for validation and error analysis. Lack of information management robustness or loss of metadata can lead to incorrect calibration results in addition to increasing the data management burden. To address these issues we have succeeded in automating several aspects of collection, parsing, reconciliation and extraction tasks, individually. We present several software automation tools that have resulted in demonstrated gains in efficiency of producing scientific data products.

OBJECTIVES

The NNSA GNEM R&E Program has made significant progress enhancing the process of deriving seismic calibrations and performing scientific integration with automation tools. We present an overview of our software automation efforts and framework to address the problematic issues of improving the workflow and processing pipeline for seismic calibration products, including the design and use of state-of-the-art interfaces and database-centric collaborative infrastructures. These tools must be robust, intuitive, and reduce errors in the research process. This scientific automation engineering and research will provide the robust hardware, software, and data infrastructure foundation for synergistic GNEM R&E Program calibration efforts. The current task of constructing many seismic calibration products is labor intensive and complex, expensive and error prone. The volume of data and calibration research requirements have increased by several orders of magnitude over the past decade. The increase in quantity of data available for seismic research over the last two years has created new problems in seismic research; data quality issues are hard to track given the vast quantities of data, and this quality information is readily lost if not properly tracked in a manner that supports collaborative research. We have succeeded in automating many of the collection, parsing, reconciliation and extraction tasks individually. Several software automation tools have also been produced and have resulted in demonstrated gains in efficiency of producing derived scientific data products. In order to fully exploit voluminous real-time data sources and support new requirements for time-critical modeling, simulation, and analysis, continued expanded efforts to provide scalable and extensible computational framework will be required.

RESEARCH ACCOMPLISHED

The primary objective of the Scientific Automation Software Framework (SASF) efforts are to facilitate development of information products for the GNEM R&E regionalization program. The SASF provides efficient access to, and organization of, large volumes of raw and derived parameters, while also providing the framework to store, organize, integrate and disseminate derived information products for delivery into the NNSA KB.

These next generation information management and scientific automation tools are used together within specific seismic calibration processes to support production of tuning parameters for the United States National Data Center run by the Air Force (Figure 1). The calibration processes themselves appear linear beginning with data acquisition (Figure 1) extending through reconciliation, integration, measurement and simulation through to the construction of calibration and run-time parameter products. However, efficient production of calibration products requires extensive synergy and synthesis not only between large datasets and a vast array of data types (Figure 1), but also between measurements and results derived from the different calibration technologies (e.g., location, identification, and detection) (Figure 1). This synergy and synthesis between complex tools and very large datasets is critically dependent on having a scalable and extensible unifying framework. These requirements of handling large datasets in diverse formats and facilitating interaction and data exchange between tools supporting different calibration technologies has led to an extensive scientific automation software engineering effort to develop an object oriented database-centric framework (Figure 3), using proven research driven workflows and excellent graphics technologies as an unifying foundation.

The current framework supports integration, synthesis, and validation of the various different information types and formats required by each of the seismic calibration technologies (Figure 1). For example, the seismic location technology requires parameter data (site locations, bulletins), time-series data (waveforms), and produces parameter measurements in the form of arrivals, gridded geospatially registered corrections surfaces and uncertainty surfaces. Our automation efforts have been largely focused on research support tools, RBAP (Regional Body-wave Amplitude Processor) and KBALAP (Knowledge Base Automated Location Assessment and Prioritization). Further, increased data availability and research requirements have driven the need for multiple researchers to work together on a broad area, asynchronously. Interim results and a complete set of working parameters must be available to all research teams throughout the entire processing pipeline. Finally, our development staff has continually and efficiently leveraged our proprietary Java code library, achieving 45% code reuse (in lines of code) throughout several thousand Java classes.

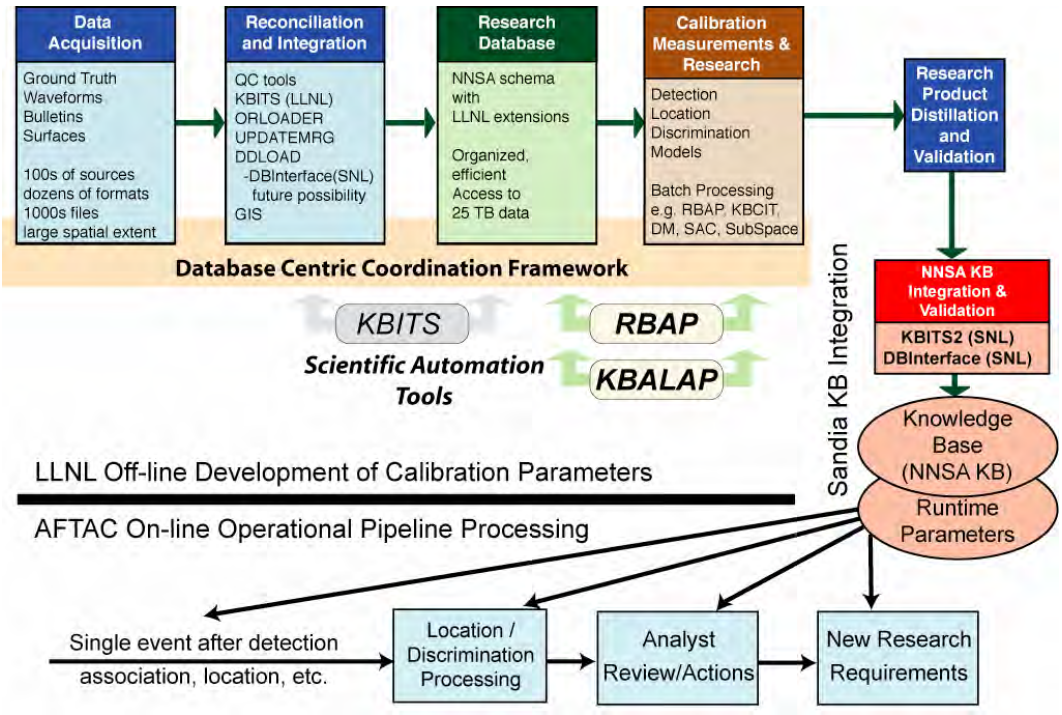


Figure 1: Summary of the processes of data collection, research and integration within the LLNL calibration process that result in contributions to the NNSA KB. The relationships of the current LLNL calibration tools, scientific automation tools, and database coordination framework to those involved in the assembly of the NNSA KB or within the Air Force Technical Applications Center (AFTAC) operational pipeline are delineated.

Database-Centric Coordination Framework

As part of our effort to improve our efficiency we have realized the need to allow researchers to easily share their results with one another. For example, as the location group produces GT information, that information should become available for other researchers to use. Similarly, phase arrival picks made by any qualified user should also become immediately available for others to use. This concept extends to sharing of information about data quality. It should not be necessary for multiple researchers to have to repeatedly reject the same bad data, or worse, miss rejecting bad data. Rather, once data are rejected because of quality reasons, they should automatically be excluded from processing by all tools. We are implementing this system behavior using database tables, triggers, stored procedures and application logic. Although we are at the beginning of this implementation, we have made significant progress over the last year with several kinds of information sharing using the new database-centric coordination framework. These are discussed below.

Significant software engineering and development efforts have been applied successfully to construct an object-oriented database framework that provides database-centric coordination between scientific tools, users, and data. A core capability this new framework provides is information exchange and management between different specific calibration technologies and their associated automation tools such as seismic location (e.g. KBALAP), seismic identification (e.g. RBAP), and data acquisition and validation (e.g. KBITS). A relational database (Oracle) provides the current framework for organizing parameters key to the calibration process from both Tier 1 (raw parameters such as waveforms, station metadata, bulletins etc) and Tier 2 products (derived measurements such as ground-truth, amplitude measurements, calibration and uncertainty surfaces etc.). Efforts are underway to augment the current relational database structure with structured queries based on semantic graph theory for handling complex queries. Seismic calibration technologies (location, identification, etc.) are connected to parameters stored in the relational database by an extensive object-oriented multi-technology software framework that includes elements of schema design, PLSQL (extension to Oracle), real-time transactional database triggers, constraints, as well as coupled Java

and C++ software libraries to handle the information interchange and validation requirements. This software framework provides the foundation upon which current and future seismic calibration tools may be based.

Sharing of Derived Event Parameters

We have long recognized the inadequacies of the CSS3.0 origin table to serve as a source of information about the "best" parameters for an event. One origin solution may have the best epicenter but poor information on other parameters.

Another may have the correct event type, but be poor in other respects, and so on. We have discussed producing origin table entries with our organization as the author, but that approach has difficulties. Different groups would have responsibility for different fields in the origin. Because their information would not be produced in synchronization, we would either have to always be updating the preferred origin or else producing new preferred origins. Also, there would be difficulties in tracking the metadata associated with each field of the preferred origin. Our solution was to create a set of new tables and associated stored procedures and triggers that collectively maintain the "best" information about events.

In order to calibrate seismic monitoring stations, the LLNL Seismic Research Database (SRDB) must incorporate and organize the following categories of primary and derived measurements, data and metadata:

Tier 1: Contextual and Raw Data
- Station Parameters and Instrument Responses
- Global and Regional Earthquake Catalogs
- Selected Calibration Events
- Event Waveform Data
- Geologic/Geophysical Data Sets
- Geophysical Background Model

Tier 2: Measurements and Research Results
- Phase Picks
- Travel-time and Velocity Models
- Rayleigh and Love Surface Wave Group Velocity Measurements
- Phase Amplitude Measurements and Magnitude Calibrations
- Detection and Discrimination Parameters

Automating Tier 1

Corrections and parameters distilled from the calibration database provide needed contributions to the NNSA KB for the Middle East, North Africa and Western Eurasia region and will improve capabilities for underground nuclear explosion monitoring. The contributions support critical functions in detection, location, feature extraction, discrimination, and analyst review. Within the major process categories (data acquisition, reconciliation and integration, calibration research, product distillation) are many labor intensive and complex steps. The previous bottleneck in the calibration process was in the reconciliation and integration step. This bottleneck became acute in 1998 and the KBITS suite of automated parsing, reconciliation, and integration tools for both waveforms and bulletins (ORLOADER, DDLOAD, UpdateMrg) were developed. The KBITS suite provided the additional capability required to integrate data from many datasources and external collaborations. Data volumes grew from the 11,400 events with 1 million waveforms in 1998 to the 6 million events with 70 million segmented waveforms and terabytes of continuous data today (e.g. Ruppert et al.; 1999, Ruppert et al. 2005). This rapid increase in stored parameters soon led to two new bottlenecks hindering rapid development and delivery of calibration research.

Automating Tier 2

As the number of data sources required for calibration have increased in number and source location, it has become clear that the manual, labor intensive process of humans transferring thousands of files and unmanageable metadata cannot keep the KBITS software fed with data to integrate, nor could the seismic researcher consistently find, retrieve, validate, or analyze the raw parameters necessary to effectively produce seismic calibrations in an efficient

manner. Significant software engineering and development efforts were applied to address this critical need to produce software aids for the seismic researcher. Thus, our development efforts are focused on the development of two scientific automation tools, RBAP and KBALAP, for seismic location and seismic identification calibration tasks, respectively.

Both of these tools include methods and aids for efficiently extracting groups of events and waveforms from the millions contained in the SRDB, and for making large numbers of measurements with metadata in a batch mode. The concept of event sets (groups of related seismic events or parameters that can be processed together, e.g. either station-centric or event-centric) was introduced, as previous seismic analysis code (SAC) scripts and macros could not scale to the task.

All analysis results go directly into the LLNL production schema where they become available for other users. Because users of KBALAP and RBAP may be able to write to our core tables, these tools implement a rule system that uses database roles to control which users can modify data, and which users can modify other users data or modify bulletin data. For example, some users may be able to rank picks, but not save new origin solutions. Some users may be able to perform an array analysis, but not rank picks, etc. By this means we are able to support use of RBAP and KBALAP by analysts with different skill sets and different research priorities. Users get the convenience of being able to produce the results they want and have them immediately available in the production schema without worrying about the impact of their work on a different research group.

The RBAP Program

The Regional Body-wave Amplitude Processor (RBAP) is a station-centric Tier 2 automation tool; it is an interactive, graphical (Figure 2) and highly specifiable software program that acts as a picker and a magnitude and distance amplitude corrections (MDAC) calculator. RBAP helps to automate the process of making amplitude measurements of regional seismic phases for the purpose of calibrating seismic discriminants at each station. RBAP generates station-centric raw, and MDAC-corrected Pn, Pg, Sn and Lg amplitudes along with their associated calibration parameters (e.g. phase windows, MDAC values, reference events, etc.) in database tables. It strictly follows standardized MDAC processing, and it replaces the original collection of LLNL scripts described by Rodgers (2003). RBAP has a number of advantages over the previous scripts. It is much faster, significantly easier to use, allows for collaboration, scales more easily to a larger number of events and permits efficient project revision and updating through the database.

RBAP integrates the functions of the modules in the previous LLNL scripts into a single, unifying program that is designed to both perform the amplitude measurement task efficiently and to require a minimum effort from the users for managing their data and measurements. For well-located events with pre-existing analyst phase picks, the user reviews for quality control and then generates all the amplitudes with just a few mouse clicks. For events needing more attention, the user has complete control over the process (e.g. window control, ability to mark bad data, define regions, define MDAC parameters and define the events to be used in the overall calibration process). RBAP shortens the time required for the researcher to calibrate each station while simultaneously allowing an increase the number of events that can be efficiently included. RBAP is fully integrated with the LLNL research database. Data is always read directly from the appropriate tables in the research database rather than from a snapshot as was done in the previous system. All RBAP result tables have integrity constraints on the columns with dependencies on data in the LLNL research database. This design makes it very difficult for results produced by RBAP to be stale and also ensures that as the research database expands, RBAP automatically becomes aware of new data that should be processed, as well as data marked as unusable by other applications (such as KBALAP), which should no longer be used for processing. In a like manner, when a segment is marked as bad in RBAP, it is excluded from further processing in KBALAP.

RBAP projects are station-centric; stations can be either single stations or arrays, where arrays focus on a reference element. Each project also specifies one or more regions, which can be simple rings or user-defined polygons; each region may be assigned its own velocity model. Once defined, concepts such as geographic regions are available to other researchers and other projects; interfaces include extensive use of modern mapping technologies and data tables the design of which are driven by research workflows. RBAP makes use of the data type manager concept extensively, and includes separate managers for velocity models, regions and events. Events are shown color-coded on a map for ease of use. RBAP also includes a graphical phase picker that generates windows automatically for the

Pn, Pg, Sn and Lg phases using times predicted by the velocity model. The picker is geared towards using signal-to-noise ratios for regional body wave amplitude measurements, and picks are automatically advanced according to applied velocity models.

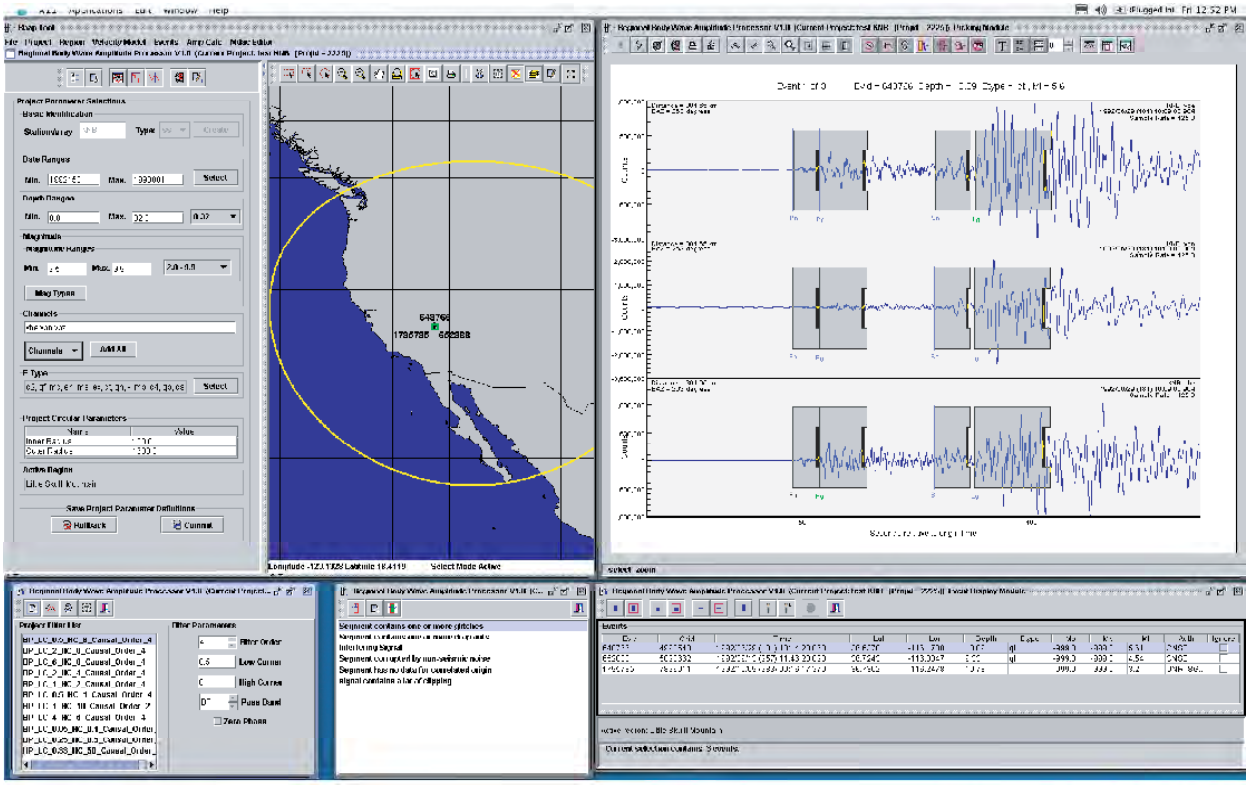


Figure 2: A sample of some of the RBAP graphical and data manager windows.

Some key features of RBAP are listed below:

• *Based on WG 2 Standardized Algorithm*
-RBAP is built on the standardized MDAC body-wave amplitude measurement algorithms. Its results are completely consistent with the last version of the LLNL scripts (Rodgers, 2003) that were vetted in the February 2003 exercise between LLNL, LANL, and AFTAC.

• *Fast and Efficient Calibration*
-RBAP is self-contained and optimized for station-centric body-wave processing. “Good” events can be handled with just few mouse clicks. The researcher has direct control over key calibration parameters within the tool such as phase amplitude windows and migration, marking bad segments, defining distinct geophysical regions, event types to process, etc. We expect RBAP, when fully developed, to provide roughly a factor of 5 increase in calibration speed compared with the original scripts, enabling us to calibrate more stations, with more events per station.

• *Project Management*
- RBAP is designed so that a calibration project can be put down for a day, month or a year, and easily picked up, by the same researcher or a new one. All processing metadata is saved and events are easily tracked as processed, unprocessed or outside the current project definitions. This allows a researcher to efficiently work through a huge data list without repetition and to easily identify and incorporate new events as they become available in the database.

• *Utilizes Database for Up-to-Date Results*
- RBAP can draw on the latest calibration parameters being generated by other working groups, such as the most recent phase picks, relocations, magnitudes, instrument response information, or event type ground truth.

• *Batch Processing*
- RBAP is designed to allow simple batch updating of the amplitude results, whether the change is small (e.g. one-event is relocated) or large (instrument response is changed affecting all events).

• *Engenders Collaboration, Consistency and Efficiency*
- RBAP's complete database integration allows multiple researchers to access the finest-grained tuning parameters for all projects; no data is lost in collaboration, and parameters may be reused.

The KBALAP Program

The KBALAP program is another Tier 2, event-centric automation effort in the GNEM program. It is a highly interactive, graphical tool (Figure 3) which uses a set of database services and a client application based on data selection profiles that combine to efficiently produce location ground truth data which can be used in the production of travel time correction surfaces, and as part of the preferred event parameters used by other tools in our processing framework.

KBALAP's database services are responsible for evaluating bulletin and pick information as it enters the system to identify origin solutions that meet pre-defined ground-truth criteria with no further processing, and for identifying events that would likely meet a predefined ground truth level if a new origin solution was produced using available arrivals. The database service is also responsible for identifying events that should have a high priority for picking based on their existing arrival distribution, and the availability of waveform data for stations at critical azimuths and distances.

The interactive portion of KBALAP has the following principal functions:

- production of GT origins through prioritized picking and location,
- specification of GT-levels for epicenter, depth, origin time, event type,
- batch-mode location of externally-produced GT information,
- production of array azimuth-slowness calibration data, and
- easy review and modification of event parameters used by all GNEM researchers.

Users of KBALAP are able to easily search for data relevant to the production of GT and filter the results by processing status, GT level or potential GT level. The user can select any GT or potential GT event and observe the distribution of stations with picks and stations which have available waveforms. The tool can indicate whether a selected event has the potential to become a GT event if appropriate picks were made on available waveforms that currently have no suitable picks. The user can also select any station with available waveforms and open a picker with any current picks displayed, and adjust existing picks, add new picks, mark bulletin picks as unusable, and relocate the event. When a new GT level is calculated, the user can choose to accept that origin solution and GT level, or continue working with other stations. Traces marked as unusable in KBALAP are automatically viewed by RBAP as bad, and thus not used in processing in that program as well.

With a single mouse click, the user can open a selected event for review and further analysis. In this review mode the user can review and rank existing picks, calculate new origin solutions, and, if appropriate, produce calibration origins. At any point in this process, the user can see the current spatial distribution of arrivals and stations with

waveforms. The tool can also guide the user toward analyzing stations that are important to achieving an origin solution with the best possible GT level.

The interactive GT entry mode of KBALAP allows the user to retrieve information about a specific event and add or update that event's GT parameters. The program can also create a new event with a GT level for cases where epicenter, time, depth and magnitude GT data are available. Similarly, KBALP's batch mode allows for the specification of flat files containing GT data for events already in the database. KBALAP's research driven interface design includes dedicated graphical user interfaces (GUIs) for station filtering, event selection and single and multi-station phase-onset pick windows. Further, there are GUIs that allow users to specify, store and apply different types of bandpass filters. Finally, there is a waveform pick editor window, as well as multiple pick "views," including band filtered views for low signal-to-noise problems and filtering by attributes such as analyst or load date.

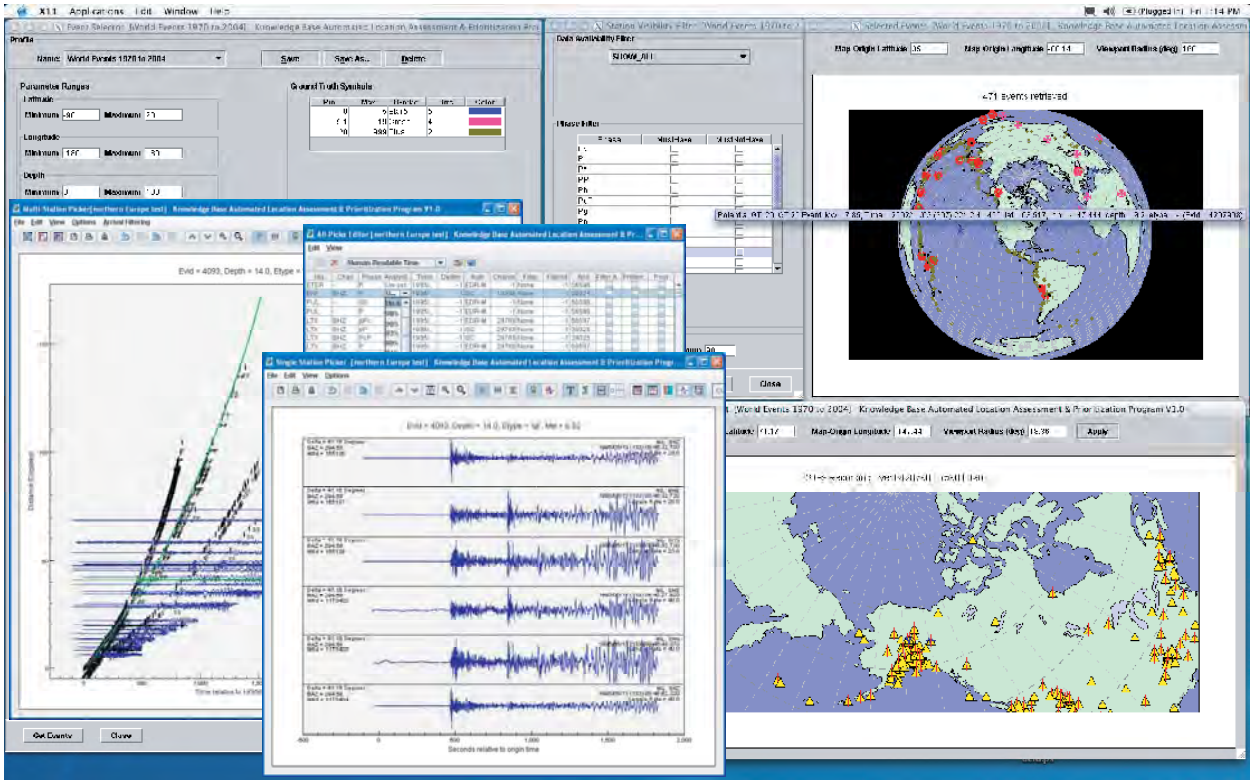


Figure 3: A sample of some of the KBALAP graphical and data manager windows.

Some key KBALAP features are listed below:

• *Fast and Efficient Location*
-KBALAP data selection profiles are self-contained and optimized for the event-centric task of location. KBALAP displays all available picks with available waveforms, and allows picks with waveforms to be modified.

• *Project Management and Collaboration*
- KBALAP is designed so that a profile can be put down for a day, month or a year, and easily picked up by the same researcher or a new one. All processing metadata is saved, and events are easily tracked as processed, unprocessed or outside the current project definitions. This allows researchers or research teams to efficiently work through a huge data list without repetition and to easily identify and locate new events as they become available in the database. Once a senior researcher has reviewed a profile's picks, these picks are finalized and the arrivals and associated metadata made available to other researchers and tools.

• *Batch Processing*
- KBALAP is designed to allow simple batch loading of externally produced GT information.

Further Enhancements to Efficiency Through Cluster-Based Computing

We have begun to leverage scalable and reconfigurable cluster computing resources to improve the efficiency of our computational infrastructure. Just as the database-centric approach to information management provided important gains in efficiency, we have realized the need to move to a different computational paradigm to provide the computational power necessary during calibration production and research. We have begun developing a set of flexible and extensible tools with platform independence that are parallelizable. These research tools will provide an efficient data processing environment for all stages of the calibration workflow, from data acquisition through making measurements to calibration surface preparation. We are also scheduled to implement Oracle 10g's clustering capabilities to further push the performance envelope for our production database. This scalable and extensible approach will result in more coupled and dynamic work flow in contrast to the linear work flow of the past, and allow more interaction between data, model creation, and validation processes.

Initial development and modification of existing codes and algorithms of the cluster based computing environment has yielded significant efficiency improvements in RBAP and other measurement tools. Modification of RBAP to incorporate threads to isolate computationally intensive operations has provided a more interactive and responsive environment for the researcher, as well as laid the ground work for moving the threads to cluster-based computing resources. Other areas under investigation that leverage cluster resources are waveform correlation and subspace detector operations, as well as large-scale event relocations to support the evaluation of ground truth and model calibrations.

CONCLUSIONS AND RECOMMENDATIONS

We present an overview of our software automation efforts and framework to address the problematic issues of consistent handling of the increasing volume of data, collaborative research efforts and researcher efficiency, and overall reduction of potential errors in the research process. By combining research driven interfaces and workflows with graphics technologies and a database-centric information management system coupled with scalable and extensible cluster based computing, we have begun to leverage a high performance computational framework to provide increased calibration capability. These new software and scientific automation initiatives will directly support our current mission including rapid collection of raw and contextual seismic data used in research, provide efficient interfaces for researchers to measure and analyze data, and provide a framework for research dataset integration. The initiatives will improve time-critical data assimilation and coupled modeling and simulation capabilities necessary to efficiently complete seismic calibration tasks. This scientific automation engineering and research will provide the robust hardware, software, and data infrastructure foundation for synergistic GNEM R&E Program calibration efforts.

ACKNOWLEDGEMENTS

We acknowledge the assistance of the LLNL computer support unit in implementing and managing our computational infrastructure. We thank Jennifer Aquilino, John Hernandez and Laura Long for their assistance in configuration and installation of our Linux cluster and workstations.

REFERENCES

Ruppert, S., T. Hauk, J. O'Boyle, D. Dodge, and M. Moore (1999). Lawrence Livermore National Laboratory's Middle East and North Africa Research Database, in *Proceedings of the 21st Seismic Research Symposium: Technologies for Monitoring The Comprehensive Nuclear-Test-Ban Treaty*, Vol. 1, pp. 234–242.

Ruppert, D. Dodge, A. Elliott, M. Ganzberger, T. Hauk, E. Matzel (2005). Enhancing Seismic Calibration Research Through Software Automation, in *Proceedings of the 27th Seismic Research Review: Ground-Based Nuclear Explosion Monitoring Technologies*, LA-UR-05-6407, Vol. 2, pp. 937-945.

PGL SERVER: DEVELOPMENT OF A STAND-ALONE SERVER-BASED EARTH-MODEL LIBRARY FOR SEISMIC MONITORING

Lee A. Jensen, James R. Hipp, Rose Q. Villanueva, Daniel S. Myers, Breanna Ammons, and Jack H. Gauthier

Sandia National Laboratories

Sponsored by National Nuclear Security Administration
Office of Nonproliferation Research and Development
Office of Defense Nuclear Nonproliferation

Contract No. DE-AC-04-94-AL85000

ABSTRACT

Sandia National Laboratories is developing a server version of the Parametric Grid Library (PGL), a shared-object library that allows storing and accessing Earth models for the National Nuclear Security Administration (NNSA) Knowledge Base. Creation of a server version of the PGL—PGL Server—allows several improvements when compared with the existing version of the PGL, which bundles an Earth model directly with an application.

(1) Computational efficiency. From a practical viewpoint, currently when an application calls or starts up (i.e., instantiates) the PGL, there is a significant startup delay while the PGL reads in the Earth-model data. This delay can occur frequently if the application is not always in use. The PGL Server has the advantage of always having the Earth-model data available, thus there is no delay. However, the PGL Server does accrue delays from message passing.

(2) Platform independence. A server-based Earth model allows applications to talk to the server across a network; thus the Earth model and the applications can run in a heterogeneous computing environment.

(3) Architectural flexibility. A server-based Earth model can support many architectures, including client-server architectures, service-oriented architectures, and distributed-objects architectures. A server-based Earth model can also support parallelism, either with a single server for multiple applications or multiple servers for one or more applications.

Several issues are still being addressed with the PGL Server. These issues include assessing network communication performance between applications and the PGL Server, managing application state in order to manage simultaneous requests from multiple applications, and evaluating parallel distributed architectures that allow the PGL Servers to scale for large problems and large numbers of applications. Architectural issues are also being addressed, including the most appropriate service level for an Earth model. The PGL Server used at its lowest level (atomic components) can require many small messages to be passed. But defining a server at a higher interface level (e.g., the level where event-locations are calculated) might require only a few large messages (a server-based event locator would have the Earth model instantiated with it). Because of the message-passing overhead, a higher-level server could provide performance improvements in many circumstances.

OBJECTIVE

We are developing a server version of the PGL called the PGL Server. The PGL is a shared-object library used in seismic analysis and seismic monitoring to store, access, and manipulate geophysical data representing the Earth. With the PGL Server, we want to improve a delay problem when the PGL is instantiated. In addition, we want to use the PGL Server to investigate advanced computing architectures that might be used in future seismic-monitoring systems.

RESEARCH ACCOMPLISHED

Background

The PGL is a shared-object library used to store, access, and manipulate geophysical data representing the Earth—spatial dimensions (lat, lon, and depth), density, travel time of seismic waves, the difference between observed and actual travel times, etc (Hipp et al., 2005). These "Earth models"—the geophysical datasets—are used in seismic monitoring to identify, locate, and measure the yield of nuclear explosions. There are many Earth models and they are often updated.

The PGL can be used in research to build Earth models and in operations to monitor seismicity in near real time. It works with many Earth models, and it incorporates features that allow it to be readily modified. It is used by many applications, including tools to create and modify Earth models (e.g., KBCIT) and seismic-event locators (e.g., LocOO). It is an object-oriented program, written in C++, designed to be flexible, modifiable, and computationally efficient. The PGL contains approximately 250,000 lines of code, of which approximately 150,000 lines are source code. It has almost 200 classes, with several thousand public methods.

Currently, an application must instantiate the PGL directly. This situation requires that the PGL be on the same machine as the application, and that the application be in the same language as the PGL (although applications written in Java can also access the PGL through special Java Native Interface calls). This situation also typically necessitates a lengthy startup delay while the PGL reads the Earth model dataset and constructs the appropriate objects. This "startup problem" can occur frequently if the application uses the PGL in a repetitive start/stop execution cycle.

The PGL Server was initially conceived as a means of circumventing the startup problem. A PGL Server runs all of the time; thus, the Earth model is always loaded and the objects always instantiated. An application—or several applications—can access the PGL immediately, whether the application is in constant use or not. Figure 1 shows the fundamentally different way that the PGL and the PGL Server can be used.

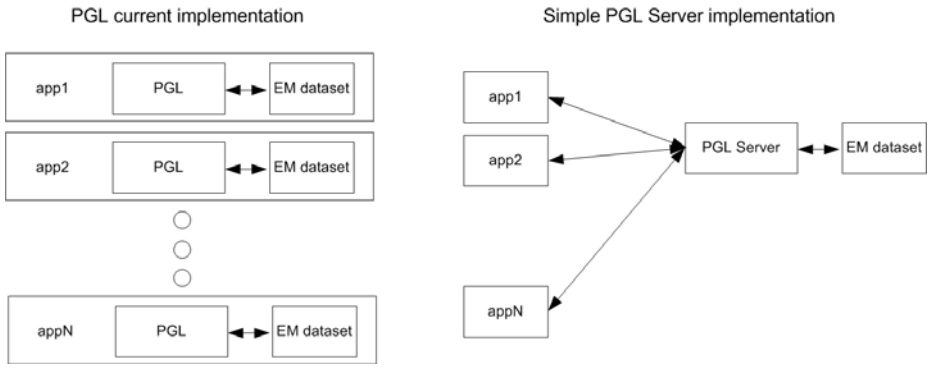


Figure 1. Comparison of current the PGL implementation with a simple the PGL Server implementation.

Although the initial impetus for a server version of the PGL was the startup problem, the PGL Server also offers the opportunity of investigating more advanced architectures that could be used in a seismic-monitoring system. Server versions of software products are seeing widespread use in industry, for example enterprise databases, which are often used in seismic monitoring, are typically server-based products. Architectures built on server-based products

(e.g., service-oriented architectures [SOA] and web services [SOA over the Internet]), are of increasing interest (Binstock, 2005; Reuters, 2006). These advanced architectures are being developed because they offer advantages in cost, reliability, upgradeability, and performance. As a component within an advanced architecture, the PGL Server could offer similar benefits to seismic monitoring.

(1) Cost: the PGL Server can run on a variety of platforms, allowing use of commercial-off-the-shelf (COTS) hardware. Also, applications can be located on the same or different machines. The ability to operate in a heterogeneous computing environment not only allows reduction in capital costs, but protects against obsolescence.

(2) Availability, reliability, and maintainability. Multiple PGL Servers could be implemented redundantly so that if one fails, the job can be completed by another. Such a configuration could also allow a machine running the PGL Server to be disconnected from the network without failure of the system, thus simplifying maintenance.

(3) Upgradeability: Legacy code is difficult to upgrade for two reasons. First, it usually requires single-supplier hardware. Second, it usually requires a transition that cannot be easily performed within the existing system. The PGL Server is platform independent. And multiple PGL Servers can be readily deployed, including upgraded versions, so that transitions can be done easily.

(4) Design flexibility: As a stand-alone component with access through an application programming interface (API), the PGL Server can fit into many system designs, including client-server, distributed-objects, and SOA. This flexibility is important because many applications have need of an Earth model, and these applications might have different design requirements; therefore, the PGL Server would not interfere with design decisions. In this manner the PGL Server also allows ease of upgrading.

(5) Data and parameter control: The separate, stand-alone nature of the PGL Server allows different applications to have the same or different datasets or parameters.

(6) Performance. Not only could the PGL Server fix the startup problem, but increased speedup and higher throughput could be achieved by implementing multiple distributed PGL Servers or by having a PGL Server running on a faster machine. Different configurations are possible, as discussed later.

Several issues need to be addressed before an efficient and effective PGL Server can be realized. These issues include understanding (1) the design of a PGL Server, (2) the delays incurred from message passing, (3) how a PGL Server should keep track of multiple client applications, (4) what is the most appropriate service level for an Earth model, and (5) how to best implement parallelism. These issues are interrelated. We have conducted and continue to conduct experiments to examine these issues. This paper presents our work and conclusions.

Basic Design of the PGL Server

The PGL Server is a stand-alone, continuously running program. It instantiates one or more Earth models from File Databases (FDB) as specified by clients accessing the models. In addition to the objects instantiated from the FDB, the PGL Server also contains a set of stub classes and methods that match one-to-one with PGL classes and methods. These stubs contain the processes necessary to create, send, receive, and decipher messages. In the case of the version of the PGL Server that we are currently using, the messages are in eXtensible Markup Language (XML) and the message passing is handled by XML-Remote Procedure Call (XML-RPC). The PGL Server is written in C++ and uses an XML-RPC library for C++.

XML-RPC was chosen as the message-passing protocol for this work after we performed a survey of existing distributed-system software. The XML-RPC protocol makes use of two well-established technologies: XML and HTTP. XML-RPC has several desirable properties. In particular, the protocol is lightweight and is specifically designed to emphasize compatibility between different platforms and programming languages. This is important, since we have many Java applications that need to communicate with the C++ PGL library.

When a request is generated, XML-RPC parses the relevant information—such as the name of the procedure, argument types, and argument values—and generates an XML document with all of the necessary information. This document is transmitted to the server using the HTTP protocol. After the server receives the message, it parses the XML document to reconstruct all the information it needs to complete the request. In order to handle complex objects, the PGL Server creates an object map to retain the information on any instantiated object. In this map, the PGL Server saves the object and a unique identifier as its key. This key, in most situations, is provided by the client. Usually the client is the one creating objects (e.g., it can use Java's toString() method to create a unique key), which it then sends to the server for the object map. This work is all done in the stub classes, so use of XML-RPC is completely transparent to the user, and the user interface to PGL is almost, if not exactly, the same.

A client using the PGL Server can run on the same computer or on a different computer. It can be written in any computer language that has support for the same message passing protocol as the PGL Server. Among other languages, XML-RPC has libraries for C/C++, Java, Lisp, and a number of scripting languages including Perl, Python, PHP, and Tcl (XML-RPC, 2003; Apache, 2006). The client must have a set of stub classes and methods that represent the PGL classes and methods that it uses. These stubs are similar to the PGL Server stubs; they contain the processes to create, send, receive, and decipher messages.

Currently, a version of the PGL Server exists that runs on Sun servers with the Solaris operating system, and clients have been written that run on Sun servers, Linux servers, and personal computers.

Figure 2 contains an illustration of how a PGL Server interacts with the PGL and with client stubs.

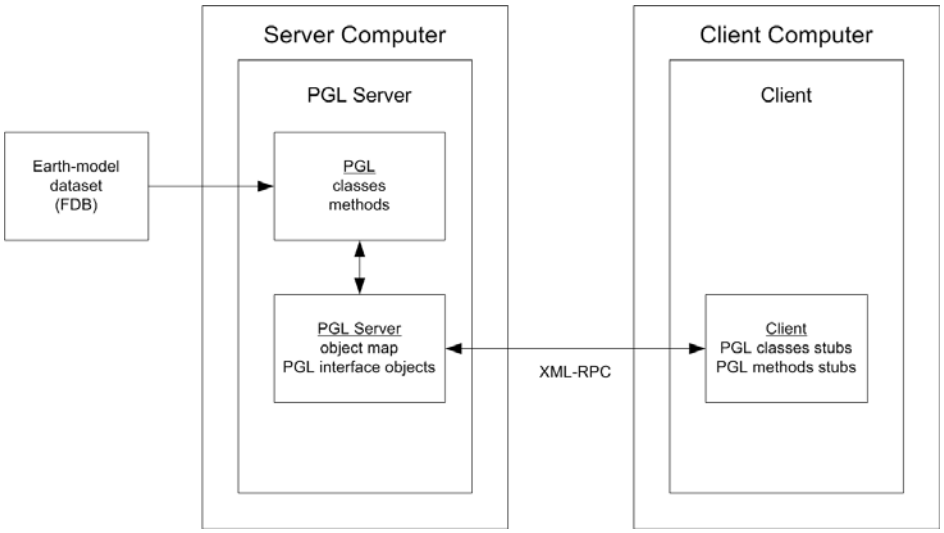


Figure 2. Basic design of the PGL Server.

Because the PGL has over 5,000 methods, programming all of the necessary stubs is a daunting task, compounded by the prospect of making stubs for different interfaces (e.g., XML-RPC, sockets, and Java Native Interface [JNI]). The PGL also has several Java-based clients, which interface to PGL in a manner similar to that shown in Figure 2, but using Java Native Interface. For the PGL Server project, we also developed a method for automatically generating the PGL interface stubs. Automatic stub generation consists of three parts: Doxygen (an open-source documentation tool) (van Heesch, 2006), a specialized parser, and the generating programs themselves.

First, the Doxygen program scans each of the PGL source files and produces an XML document summarizing the information in each class: methods, members, arguments, etc. Next, this XML document is processed by a specialized parser that examines each XML document and produces a tree data structure containing the same information as the raw XML, but in a more convenient form. Finally, the tree is processed using a standard pre-order traversal. As it encounters each new class, the code-generating program creates a new source file, and applies its rules to create XML-RPC interfaces to each of the PGL functions.

As mentioned previously, the XML-RPC protocol has no innate method of dealing with complex objects. The PGL library is object-based, so this is an obstacle to fully implementing the new system. Our solution to this problem is to create all objects in pairs, with one object created on the server-side, and one on the client-side. The server-side object is the "real" copy that maintains its state and actually executes any RPC requests. The client-side object is only a stub, and is used only to supply an interface from the client to the server. The two objects are linked by a common handle, created during the construction process. When an RPC request involves an object, the client will collect the appropriate stub object and extract the handle linking it to a server-side object. The handle is sent with the other data as part of an XML-RPC request. When the server unpacks the handle, it uses a hash-table data structure to look up the corresponding "real" object. This server object performs any requested work, saves its state, and is then re-hashed until it is needed again. This approach does require more sophisticated methods to manage object life-cycles, so that objects are correctly discarded when their useful lives are over, but this functionality is already part of the PGL, so we do not have to manage object life-cycles explicitly.

Delays Incurred by Message Passing

One of the potential problems with the PGL Server (and indeed all server-based software and SOAs) is the overhead associated with message passing. We are interested in understanding the best method for implementing message passing (a lower-level technique, such as sockets, or a higher-level system, such as XML-RPC). Delays incurred by message passing can also be mitigated by choosing the appropriate level of service of an Earth model. This issue is discussed below.

Important variables in this problem are the format of the message, size of the message, the compression of the message, and the platforms that the client and PGL Server are running on. Preliminary work showed that binary (unformatted) messages without any compression are transferred the most efficiently. Binary messages are shorter and generally require less processing than formatted (ASCII or unicode) messages, although the communicating processes must know how to decipher the message. Our investigation confirmed fewer large messages are more efficient than numerous small messages. This preliminary work also showed that compression only helped with formatted messages, and then only with a low level of compression. Additional preliminary work also showed that Fast Infosets (Sandoz and Pericas-Geertsen, 2005), a binary XML implementation, show promise in speeding message passing under some circumstances.

For the work presented here, we programmed a client in Java that communicates with the PGL Server. The client is based on an original test code for the PGL. The client calls the same methods using the same PGL interface as the original, but it can be running on the same or a different machine. The Java client sends method parameters to the server via XML-RPC, and the C++ PGL Server sends responses back to the client in the same way. The major complication occurs when the original test code passes pointers to large datasets. Pointers have no meaning on a different machine, so what the pointers are pointing to - generally large data vectors - have to be passed back and forth.

To address this complication, the client calls the PGL stub classes (Figure 2). The purpose of these stubs is to execute the PGL method calls via XML-RPC, performing whatever manipulations are necessary to make communication between it and the server as simple as possible. An object map on the server side retains the information on any instantiated object. In this map, the server saves the object and a unique identifier as its key. This key is provided by the client, using Java's toString() method, which it then sends to the server for the object map. This work is all done in the stub classes, so use of XML-RPC is completely transparent to the user, and the user interface to the PGL is almost if not exactly the same.

The first step of the performance testing is to determine the baseline performance. Of particular importance is the total amount of time spent doing XML-RPC-related processing. The baseline times are used below to adjust the the PGL Server times to determine the additional fraction of time spent on XML-RPC-related processing. To determine the baseline times, the original C++ test code, directly connected to the PGL, was timed performing operations on various sized data vectors. For the test, the PGL was actually exchanging six vectors of doubles of the indicated size between the client and server: two containing interpolatory coordinate information and four containing interpolation results vectors for some arbitrary attributes. The results of the baseline PGL performance testing are given in Figure 3.

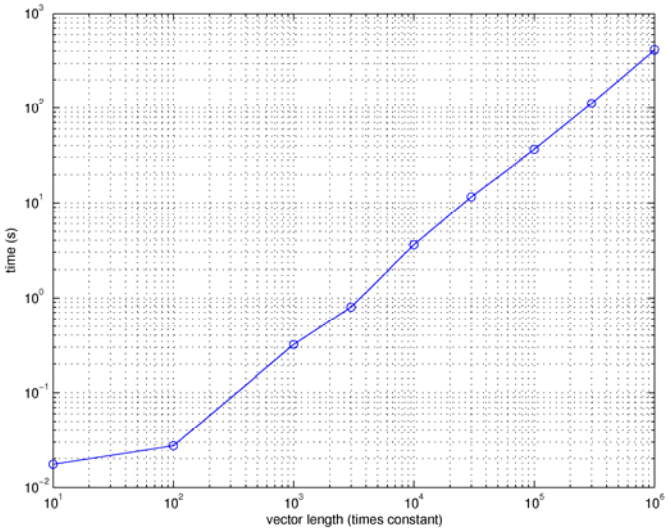


Figure 3. Baseline processing times for various data lengths using the PGL and the original test code.

The same tests were then conducted with the PGL Server and the Java client. The data messages were passed as uncompressed binary payloads, as the preliminary testing indicated that this type of message would give the best performance. Performance testing was conducted with the PGL Server running on a Sun server. The Java client communicating with the PGL Server was tested running on the same Sun server, a Linux server and a Windows XP workstation. The network connection to the Sun server was 100 Mbps.

The results of the testing are presented in Figure 4. The plot shows the fraction of XML-RPC-related processing time required for various message sizes. The metric shown on the Y-axis was calculated as the time it took to execute with the PGL Server minus the baseline time (Figure 3), normalized by the baseline time: [(XML-RPC time) – (baseline time)] / (baseline time). The result is the additional fraction of time spent doing XML-RPC related processing, such as parsing and serializing XML documents and sending these over the network.

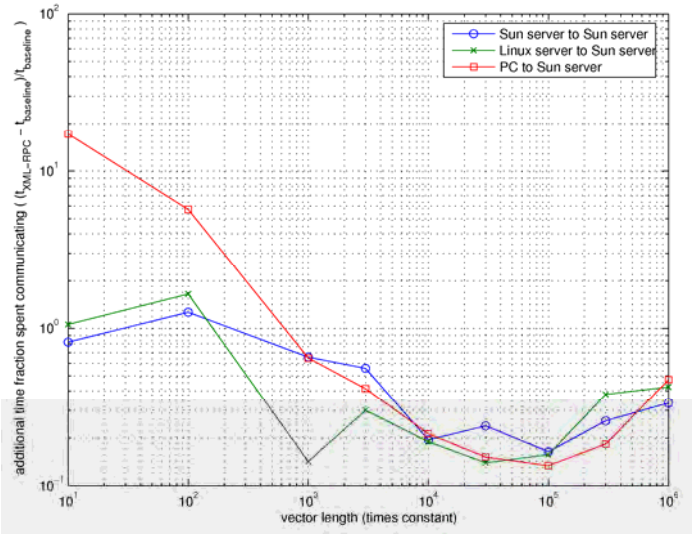


Figure 4. The additional fraction of processing time required by the PGL Server compared with the PGL.

As shown in Figure 4, in all cases XML-RPC related processes reduce performance of the PGL. This finding is especially true when dealing with short data-vector lengths, with the total run times taking more than twice as much time as the baseline. Note however, that the total run times for these short data-vector lengths are typically small fractions of a second. For larger amounts of data, the performance suffers by only 20 to 40 percent.

These results indicate that there is a penalty associated with using the PGL Server. However, the additional time needed for passing short data vectors is small in absolute terms, and the additional time needed for passing long data vectors is small in relative terms. And these delays are much less than the typical 30-second or more startup time for the PGL with a large Earth-model FDB.

How the PGL Server Should Keep Track of Multiple Client Applications

Server software should be able to handle multiple clients. Thus, the software should be able to save the state of each process for the clients that are being served. However, the PGL was not designed with this specific capability as it was originally intended to be bound to a single client for its entire execution lifetime. In the future, however, we plan to modify the PGL Server to support a message queue that tags each client's requests with a unique identifier. The PGL Server will then use the identifier with an object map to determine various "state" settings associated with a particular client. With this approach the PGL Server will be able to change its state settings, process a request, and store the results for each client that it is serving. The client will be able to request these tasks be performed in separate asynchronous functional calls, if desired, without having to worry about other clients modifying the server's state and thus producing a result that is different than the original request submitted by the client.

The Most Appropriate Service Level for an Earth Model

An outstanding architectural issue is whether the most appropriate service level for an Earth model is the PGL Server. Consider that the PGL Server, used at its lowest level (atomic components), can require many small messages to be passed. But defining a server at a higher interface level (e.g., the level where event-locations are calculated), might require only a few large messages. In this case, a server-based event locator would have the PGL and the Earth model instantiated with it. Because of the message-passing overhead, a higher-level server could provide performance improvements in many circumstances. This architectural issue is illustrated in Figure 5.

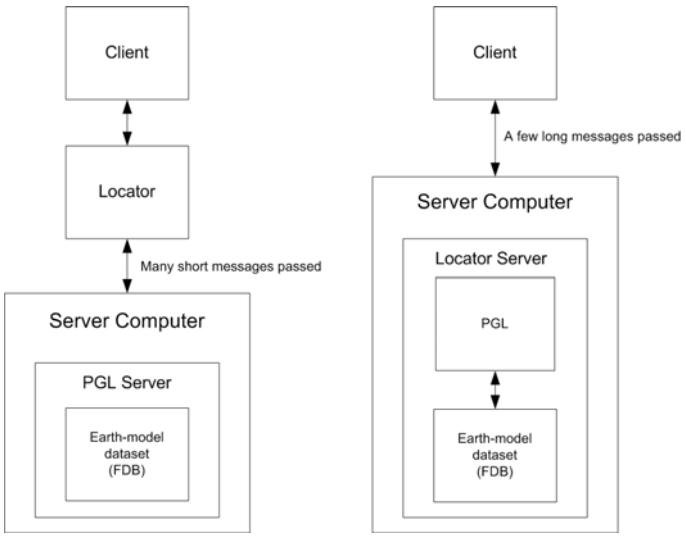


Figure 5. Comparison of architectures at the PGL/Earth model level and the event-locator level.

To address this issue, we have programmed a server version of the event-locator LocOO (Ballard, 2003). LocOO takes as input data for one event and (based on a given FDB) returns the location. LocOO calculates locations by repeated successive queries to the PGL, continually refining its estimate of the event's hypocenter and epicenter and the error volumes associated with these locations. Many requests for small collections of data are made. The version of LocOO that is typically used instantiates its own copy of the PGL to access Earth-model data, so these numerous requests to the PGL carry little overhead. LocOO can also use the PGL Server, but when it does the numerous message-passings that occur cause substantial overhead.

Contrast this situation with LocOO Server. An instance of the PGL is created within LocOO Server when LocOO Server is started. LocOO Server takes the same input data as LocOO. LocOO Server then calculates the location by repeated successive queries to the PGL, but because the PGL is bound directly to LocOO Server on the same machine, the communication overhead is minimal.

We are currently defining tests to quantify the differences between using the PGL Server and LocOO Server in typical location problems. We are also interested in looking at implementing parallelism in the PGL Server and LocOO Server (see the next section), because LocOO is often used to locate or relocate hundreds of events. Location, however, is only one specific problem where Earth-model data are needed. Earth models are also used in phase identification, magnitude, discrimination of explosions from earthquakes, etc. It is possible that a next-generation data center for seismic event monitoring could have Earth models available at several different service levels within the processing system.

How to Best Implement Parallelism

Parallelism, the execution of two or more similar processes concurrently, is one technique for improving processing speed and achieving higher processing throughput in a system. It is possible that next-generation data centers for seismic event monitoring will have to deal with many difficult processing issues (e.g., 3D Earth models). At this time, we have only dealt with parallelism primarily at a theoretical level. However, the PGL Server and other server-based components of a seismic event monitoring system lend themselves immediately to parallelism. Here we discuss some ideas concerning parallelism, including running the PGL Server in parallel processes.

There are two ways of implementing parallelism in an Earth-model tool such as the PGL Server: “internal” parallelism, where subprocesses within a single instance of the PGL Server can execute in parallel, and “external” parallelism, where multiple instances of the PGL Server work on the same job in parallel. Examples of these types of parallelism are outlined in Figure 6. Note that in the figure the job being processed is implied within the PGL Server. In both types of parallelism, a single job is split into parts, the parts are worked at the same time, and then the results from each part are collected (the parts of the job cannot be dependent on one another).

Internal parallelism is the type of parallelism that is usually envisioned. Several software systems have been developed to implement this type of parallelism, including Message Passing Interface (MPI) and Parallel Virtual Machine (PVM). Although not strictly necessary, this type of parallelism tends to work best on multi-processor computers or a network of homogeneous computers with exotic network hardware. We believe there are processes that the PGL performs that are amenable to distributed parallel processing (e.g., loop oriented numerical processes such as matrix solvers). In addition to implementing MPI parallelism within the PGL for multiprocessor machines, we are investigating how to implement the PGL Server parallelism using a network of heterogeneous computers and standard gigabit Ethernet hardware.

More germane to this paper is how to implement parallelism using multiple instances of the PGL Server. Two basic questions arise: (1) Would there be an improvement in speedup or throughput; and, (2) how would multiple PGL Servers be controlled? This second question includes issues such as how would the job be divided among multiple servers, how would load balancing be performed, how many servers would be running, and how would errors be handled (e.g., fault tolerance). Answering the second question involves theoretical work and creating prototypes of controllers. In our initial approach, each the PGL Server instance has an agent that communicates with agents at each client to manage these issues. This work is in the formative stages, and we will only address the first question here.

Using the Condor batch-job-farming software (Condor, 2006), we investigated the extent of the speedup afforded by using multiple instances of the PGL on different processors. The problem was to visualize a travel-time model by using kriging to interpolate on a grid of given resolution (e.g., two degree spacing over some extent). By varying the grid resolution and the number of processors, it was possible to investigate performance improvements afforded by using Condor to facilitate parallel processing with the PGL. In this particular test with the interpolation of grid points was split between 9 processors, we see parallel performance bettering single processor performance at a grid resolution of 0.5 degrees (approximately 2,000 total grid points in this test). The performance improvement approaches linear speedup when the grid resolution is 0.025 degrees (approximately 750,000 total grid points in this

test). These results are shown in Figure 7. Thus, to answer the first question, we have shown that multiple instances of the PGL (or PGL Server) can improve speedup under certain circumstances within a seismic monitoring system.

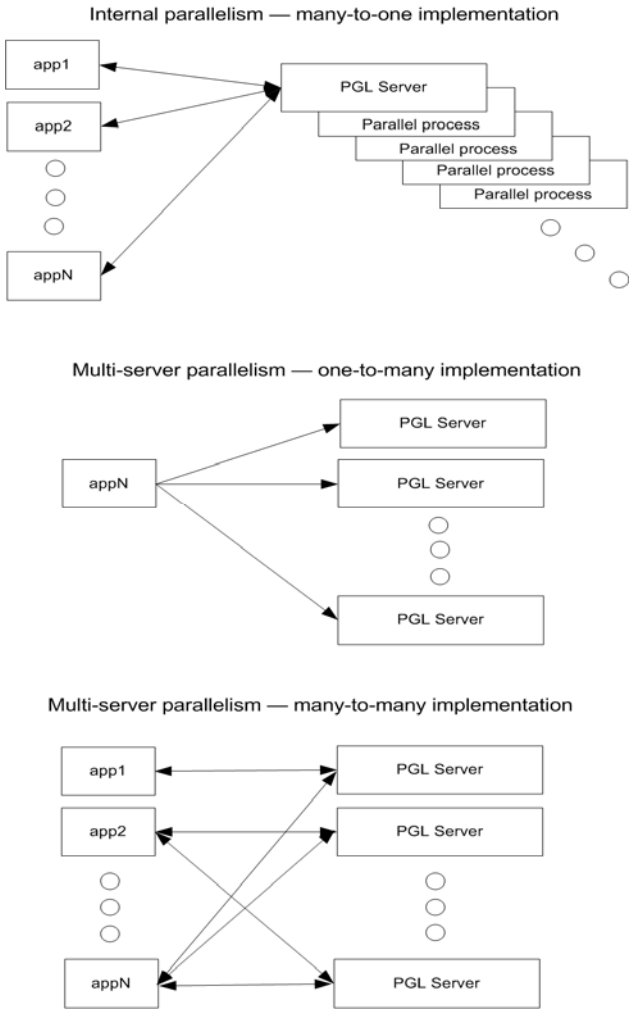


Figure 6. Potential ways of implementing parallelism with the PGL Server.

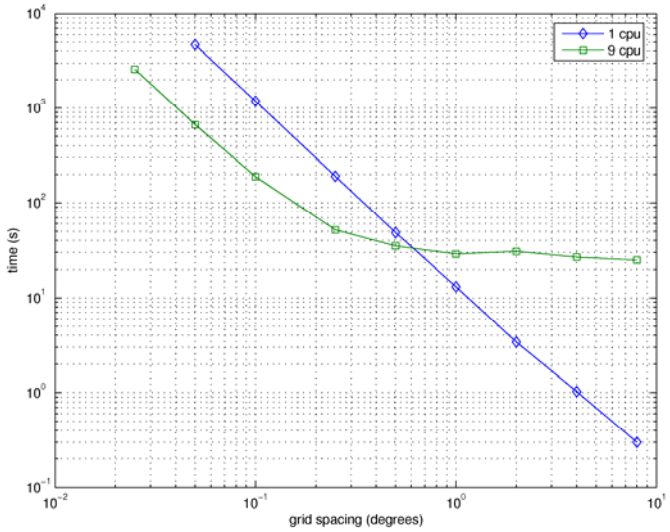


Figure 7. Linear speedup can be achieved on high-resolution problems using multiple instances of PGL.

CONCLUSIONS AND RECOMMENDATIONS

We currently have a version of the PGL Server that uses XML-RPC for communications. The PGL Server can be used to solve the PGL startup problem. In the process of developing this version of PGL Server, we are also developing an automatic method for generating the PGL Server stub libraries (e.g., using XML-RPC, sockets, JNI). We also developed a server version—LocOO Server—for the event-location program LocOO.

With these programs, we investigated issues associated with advanced system architectures, in particular SOAs. We conducted performance testing that indicated the best way to conduct message-passing and the best form of the messages. Using LocOO Server, we have begun to investigate the structure of different architectures, including whether it is better to have a service level at the Earth model or at the locator. This preliminary work suggests that different processes might require different service levels. In anticipation of more computation-intensive operations being required for seismic monitoring in the future, we began to study ways of parallelizing Earth models. A preliminary finding from this work is that many PGL calculations scale linearly with the number of PGL instances (e.g., PGL Servers) running.

Much of this work is in the initial stages. We would like to implement a method for saving state within the PGL Server. We would like to better understand how to manage multiple PGL Servers and how to best implement parallelism with the PGL Server. Additionally, we would like to test the concepts that we are developing on real-world problems.

In performing this work, we understand that architecture development is not accomplished by introspection, and it is not just a paper study. Development of an advanced architecture requires construction of prototypes and testing the behaviors of these prototypes in realistic situations. Ultimately, we believe that the knowledge that we have gained from this work can be applied to the design of an advanced-architecture for a seismic monitoring system.

ACKNOWLEDGEMENTS

We would like to thank David Gallegos, Mark Harris, and Chris Young; without their support and guidance this work would have never been accomplished.

REFERENCES

Apache (2006), http://ws.apache.org/xmlrpc/, Apache Software Foundation.

Ballard, S. 2003, Seismic event location: Dealing with multi-dimensional uncertainty, model non-linearity and local minima, in Proceedings from the 25th Seismic Research Review, LA-UR-03-6029, Vol. 1, pp. 193-202.

Binstock, A. (2005), What's next in software, www.infoworld.com.

Condor (2006), Condor high throughput computing, http://www.cs.wisc.edu/condor.

Hipp, J.R., Ballard, S., Chang, M.C., and Jensen, L.A. (2005), "Representing Kriged Travel Time Correction Surfaces with Optimal Tessellations," in *Proceedings of the 27th Seismic Research Review: Ground-Based Nuclear Explosion Monitoring Technologies*, LA-UR-05-6407, pp. 352-361.

Reuters (2006), Microsoft CEO sees Web services as top R&D priority, www.computerworld.com/developmenttopics/development/webservices/story/0,10801,111195,00.html.

Sandoz, P. and S. Pericas-Geertsen (2005), Fast Infoset @ Java.net, http://www.idealliance.org/proceedings/xtech05/papers/04-01-01.

van Heesch, D. (2006), Doxygen, http://www.stack.nl/~dimitri/doxygen.

XML-RPC (2003), http://www.xmlrpc.com/, UserLand Software, Inc.

INTEGRATED SEISMIC SENSOR/DIGITIZER EVALUATION

Richard P. Kromer and Darren M. Hart

Sandia National Laboratories

Sponsored by National Nuclear Security Administration
Office of Nonproliferation Research and Development
Office of Defense Nuclear Nonproliferation

Contract No. DE-AC04-94AL85000

ABSTRACT

Sandia National Laboratories have tested and evaluated an integrated seismic sensor/digitizer from Science Horizons Inc. (SHI), Melbourne, FL. A Geotech GS21 single component short-period vertical borehole seismometer was integrated with a SHI AIM24-S1/GS21 modified borehole digitizer. The integrated seismometer/digitizer concept may provide a lowered system noise due to the elimination of long analog cables (up to 100 m), digitizer cable harness, and potentially quieter pre-amplifier design.

The modified SHI AIM24-S1/GS21 digitizer was compared to a standard configuration AIM24-S1/GS21 digitizer with a 30-m analog cable for self-noise measurement comparison. A sensor impedance simulator was used as a digitizer load.

OBJECTIVE

Introduction

The Air Force Technical Applications Center (AFTAC) is tasked with monitoring compliance of existing and future nuclear test treaties. To perform this mission, AFTAC uses several different monitoring techniques to sense and monitor nuclear explosions, each designed to monitor a specific domain (e.g. space, atmosphere, underground, oceans, etc.) Together these monitoring systems, equipment and methods form the United States Atomic Energy Detection System (USAEDS). Some USAEDS seismic stations may be included in the International Monitoring System (IMS). Some of these monitoring systems are deployed in extremely quiet locations that challenge the performance of the digitizing waveform recorder (DWR).

Some Sensor Sub-Systems (SSS) built for AFTAC applications use passive sensors such as the Geotech GS21, 23900, GS21a and GS13. These sensors are typically installed in a borehole at up to 100 meters depth. A DWR is typically installed at the top of the borehole in a Wellhead Terminal Unit (WTU). A long analog cable connects the seismometer output to the DWR input through an Interface Box (IB). The sensor impedance is terminated using a programmable resistance in the DWR. The DWR provides an internal preamplifier to set the seismic signal level appropriate to the application.

A set of tests has been developed to (1)determine if the long analog cable contributes noise to the separated sub-system and (2)determine if an integrated sensor/DWR can lower sub-system noise.

Evaluations Performed

Evaluations include determination of the GS21seismometer impedance model, construction of a seismometer impedance simulator and tests to determine sensor sub-system performance.

Tests included:
DWR Seismic Sensor Application Tests
- Seismic System Static Performance Tests
- DWR Seismic System Noise (DWR-SSN)

Sensor Sub-Systems Seismic Sensor Application Tests
- Sensor Sub-Systems Seismic System Static Performance Tests
- Sensor Sub-Systems Seismic System Noise (SS-SSN)

RESEARCH ACCOMPLISHED

Determination of Seismometer Impedance Model

The complex impedance of a seismometer can be modeled using equation 1.

$$Complex_impedance(\omega) = \frac{R_1 + \left[\frac{R_2 * G_c^{\,2}}{M}\right] * \omega}{\omega^2 + 2 * D_c * \omega_0 + \omega_0^{\,2}} \qquad \text{Equation 1}$$

Where

$R_1 = \frac{R_{DC} * R_{ED}}{R_{DC} + R_{ED}}$ and $R_2 = \left[\frac{R_{ED}}{R_{DC} + R_{ED}}\right]^2$, R_{ED} is the external damping resistor (ohms), R_{DC} is the data coil resistor (ohms), M is the seismometer mass (kg), D_c is the seismometer damping coefficient, G_c is the seismometer generator constant (V/m/s), ω_0 is the natural frequency (radians/second) of the seismometer. These parameter values for the seismometers used in this study are shown in Table 1.

Table 1. List of seismometer parameters used to calculate complex impedance.

Seismometer Type	Generator Constant (V/m/s)	External Damping Resistor (ohms)	Damping Coefficient	Data Coil Resistance (ohms)	Natural Frequency (Hz)	Seismometer Mass (kg)
GS21	458.0	4255	0.707	467	1.0	5.0

The complex impedance plot for the GS21 seismometer is shown in Figure 1. The plot shows at low and high frequencies the seismometer impedance is approximately equal to R_1 (~420 ohms) and the seismometer impedance rises to the value of the external damping resistance at the natural frequency of the seismometer.

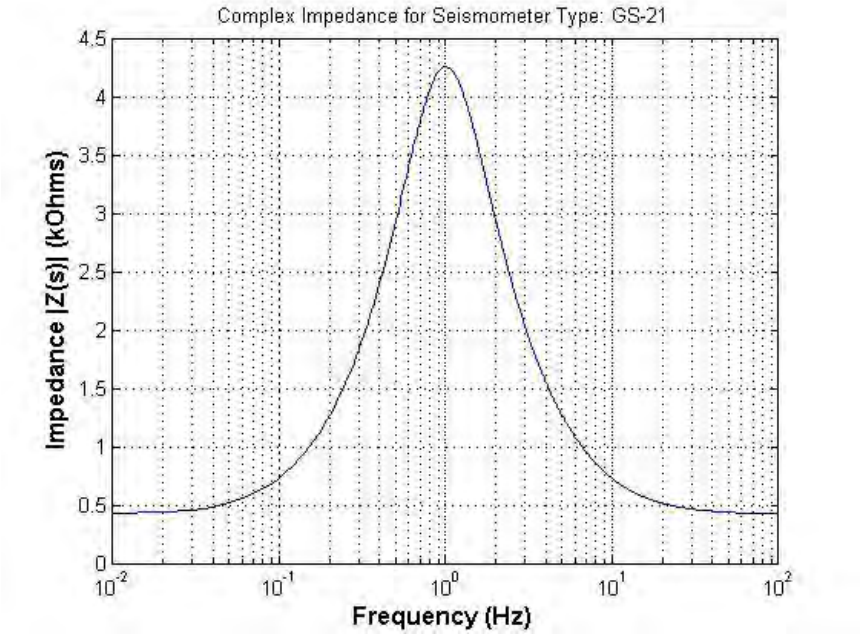


Figure 1. GS21 Complex Impedance.

Table 2. Impedance terminators used to model GS21 seismometer's complex impedance. X's indicate impedance values used to model specific seismometers complex impedance. For this report the best and worst case impedances were used (XX).

Impedance Termination (ohms)	402	1050	1500	2100	2500	3010	3480	4420
GS-21	**XX**	X	X	X	X	X	X	**XX**

Construction of Seismometer Impedance Simulator
A Seismometer Impedance Simulator was constructed using parts of an old seismometer. Changeable resistor terminations are installed on the inside. This simulator, shown in Figure 2, was used in place of the seismometer.



Figure 2. Sensor Impedance Simulator with interchangeable loads.

Evaluation of AFTAC Typical Sensor Sub-System and Alternative Integrated Sensor Sub-System
An AFTAC Typical Sensor Sub-System consists of a Geotech GS21 sensor installed at the bottom of a borehole and connected to a DWR installed in a WTU. Analog signals from the seismometer are connected by borehole cable to the WTU Interface Box and distributed to the DWR installed at the top of the borehole. This is shown in Figure 3, left.

The Alternative Integrated Sensor Sub-System consists of a Geotech GS21 sensor directly integrated to a DWR installed at the bottom of a borehole. Digital signals from the integrated DWR/seismometer are connected by borehole cable to the WTU breakout box. This is shown in Figure 3, right.

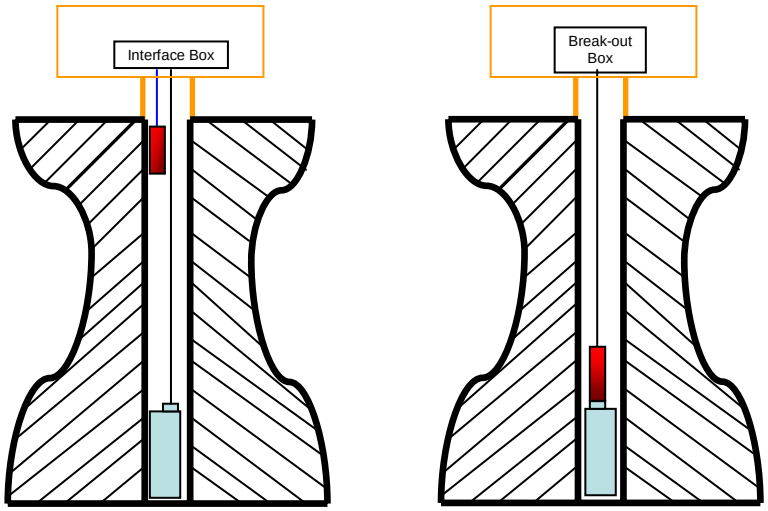


Figure 3. A cartoon drawing of the two deployment configurations tested in this study. The boxes in red represent the digitizer, light blue boxes represent the seismometer and the orange objects represent the WTU. The drawing on the left is the typical deployment configuration. The drawing on the right shows the alternative configuration where the digitizer is directly connected to the seismometer.

Evaluation of AFTAC Typical Sensor Sub-System using Science Horizons AIM24S1 DWR separate from Geotech GS21 Short-period Vertical Borehole Seismometer (Figure 4).



Components of AFTAC Typical SSS



Installation of Sensor Simulator in WTU Borehole



Installation of DWR in WTU Borehole

Figure 4. Installation of AFTAC Typical Sensor Sub-System

The following tests were conducted on the AFTAC Typical SSS DWR.

DWR Seismic Sensor Application Tests
- Seismic System Static Performance Tests
- DWR Seismic System Noise (DWR-SSN)

The following tests were conducted on the AFTAC Typical SSS.

Sensor Sub-Systems Seismic Sensor Application Tests
- Sensor Sub-Systems Seismic System Static Performance Tests
- Sensor Sub-Systems Seismic System Noise (SS-SSN)

DWR Seismic System Noise (DWR-SSN) Test
Purpose: The purpose of the DWR seismic system noise test was to determine ability of the DWR to resolve the expected seismic background using a specific seismometer. The DWR self-noise should be below the expected seismic background.

Configuration: The DWR sensor input connector was terminated with the equivalent output impedance of the application sensor. For the GS21 comparison purposes, the range of values was chosen to approximate the minimum (402 ohms) and maximum (4.4 K ohms) impedance.

Evaluation: For GS21 sensor application, the system noise of the DWR was converted to ground motion using the GS21 seismometer response mathematical model. The results of this computation were overlaid with the USGS New Low Earth Noise Model (NLNM) to demonstrate the ability of the DWR to resolve the local seismic background.

Sensor Sub-System Seismic System Noise (SS-SSN) Test
Purpose: The purpose of the SSS seismic system noise test was to determine ability of the SSS to resolve the expected seismic background using a specific seismometer. The SSS self-noise should be below the expected seismic background.

Configuration: The SSS Sensor Simulator at the sensor end of the SSS sensor cable was terminated with the equivalent output impedance of the application sensor. For the GS21 comparison purposes, the range of values was chosen to approximate the minimum (402 ohms) and maximum (4.4 K ohms) impedance.

Evaluation: For GS21 sensor application, the system noise of the SSS was converted to ground motion using the GS21 seismometer response mathematical model. The results of this computation were overlaid with the USGS New Low Earth Noise Model (NLNM) to demonstrate the ability of the DWR/SSS to resolve the local seismic background. Comparisons were made between the two configurations.

Results: DWR-SSN and SS-SSN results are shown in Figure 5. There were no appreciable differences between the two test configurations.

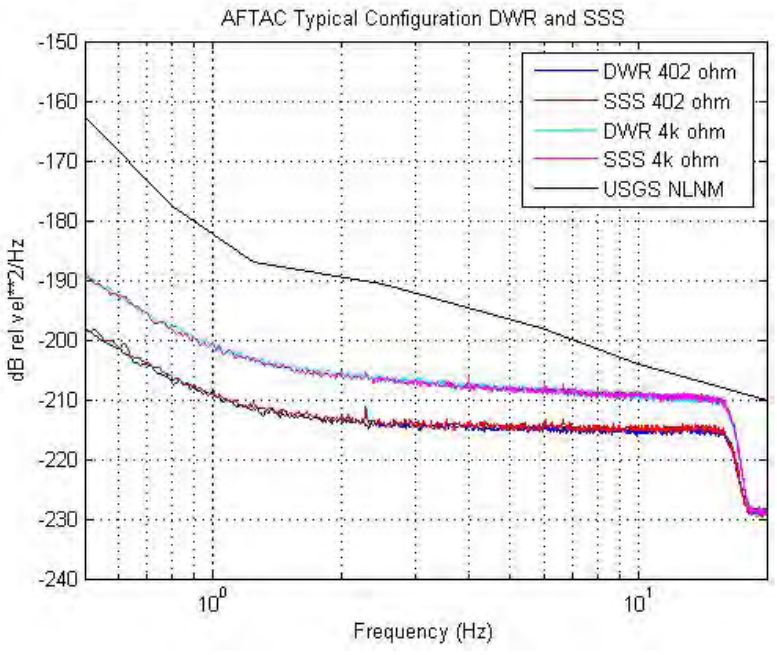
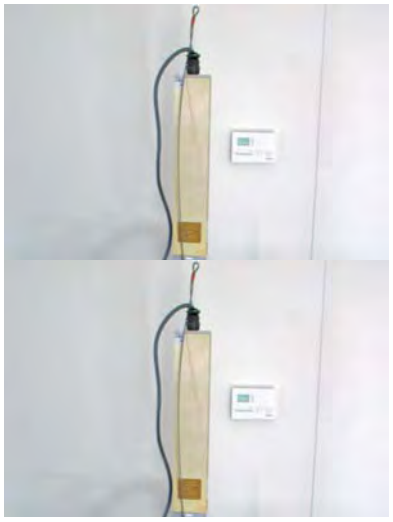


Figure 5. DWR Seismic System Noise (DWR-SSN) Test and Sensor Sub-Systems Seismic System Noise (SS-SSN) Test Results.

Evaluation of Alternative Integrated Sensor Sub-System using Science Horizons AIM24S1 DWR integrated with Geotech GS21 Short-period Vertical Borehole Seismometer (Figure 6).



Components of Alternative Integrated SSS



Installation of Integrated Sensor Simulator with DWR in WTU Borehole

Figure 6. Installation of Alternative Integrated Sensor Sub-System.

The following tests were conducted on the Alternative Integrated SSS.

Sensor Sub-Systems Seismic Sensor Application Tests
- Sensor Sub-Systems Seismic System Static Performance Tests
- Sensor Sub-Systems Seismic System Noise (SS-SSN)

Sensor Sub-System Seismic System Noise (SS-SSN) Test
Purpose: The purpose of the SSS seismic system noise test was to determine ability of the SSS to resolve the expected seismic background using a specific seismometer. The SSS self-noise should be below the expected seismic background.

Configuration: The Alternative Integrated SSS DWR/Sensor Simulator was terminated with the equivalent output impedance of the application sensor. For the GS21 comparison purposes, the range of values was chosen to approximate the minimum (402 ohms) and maximum (4.4 K ohms) impedance.

Evaluation: For GS21 sensor application, the system noise of the SSS was converted to ground motion using the GS21 seismometer response mathematical model. The results of these computations were overlaid with the USGS New Low Earth Noise Model (NLNM) to demonstrate the ability of the DWR/SSS to resolve the local seismic background.

Results: SS-SSN results are shown in Figure 7.

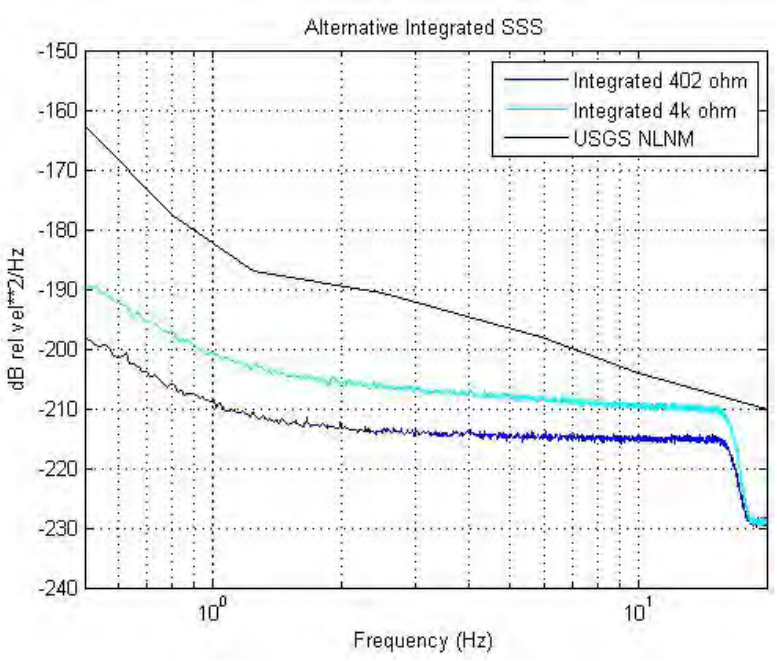


Figure 7. Alternate Integrated Sensor Sub-Systems Seismic System Noise (SS-SSN) Test Results.

Comparison of AFTAC Typical Sensor Sub-System and Alternative Integrated Sensor Sub-System Seismic System noise

Sensor Sub-System Seismic System Noise (SS-SSN)
Purpose: The purpose of the SSS seismic system noise test was to determine ability of the SSS to resolve the expected seismic background using a specific seismometer. The SSS self-noise should be below the expected seismic background.

Configuration: The Alternative Integrated SSS DWR/Sensor Simulator was terminated with the equivalent output impedance of the application sensor. For the GS21 comparison purposes, the range of values was chosen to approximate the minimum (402 ohms) and maximum (4.4 K ohms) impedance.

Evaluation: For GS21 sensor application, the system noise of the SSS was converted to ground motion using the GS21 seismometer response mathematical model. The results of these computations were overlaid with the USGS New Low Earth Noise Model (NLNM) to demonstrate the ability of the DWR/SSS to resolve the local seismic background.

Results: SS-SSN results are shown in Figure 8. There were no appreciable differences between the two test configurations.

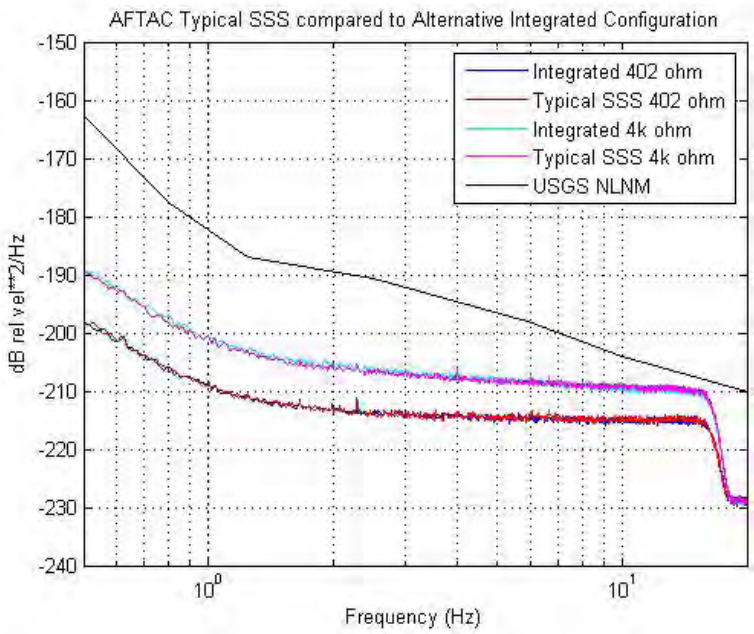


Figure 8. Comparison of Seismic System Noise (SS-SSN) between AFTAC Typical Sensor Sub-System and Alternate Integrated Sensor Sub-Systems.

CONCLUSIONS

Evaluation of AFTAC Typical Sensor Sub-System
The DWR seismic system noise was not degraded or increased by installation into an AFTAC Typical SSS installation for either sensor impedance. SSS seismic system noise was equivalent to within 0.2 dB.

Evaluation of Alternative Integrated Sensor Sub-System
The Alternative Integrated SSS seismic system noise was measured without difficulty.

Comparison of AFTAC Typical Sensor Sub-System and Alternative Integrated Sensor Sub-System
The Alternative Integrated SSS seismic system noise was not improved over the AFTAC Typical SSS installation for either sensor impedance.

The pickup of unwanted electronics noise can be a problem when separating a passive seismometer like the Geotech GS21 and the application DWR with up to 100 meters of cable. The AFTAC Typical installation technique for this configuration including power, cable interconnection and radio communications does not appear to contribute electronics noise to the SSS.

The DWR/Seismometer tested is the least affected impedance match. Other passive sensors can have impedances to greater than 100K ohms. This series of tests could be applied to these sensors to confirm rejection of unwanted electronics noise.

RECOMMENDATIONS

The present generation of AFTAC DWR components have inherent rejection of common mode electronics noise of up to the analog power supply voltages (+/- 12 volts). The next generation of low power DWR component technology utilizes electronics components shared with the cell phone and similar industry. The typical power supply voltages are +/- 3 volts or even lower. These components will not have the electronic noise rejection of the present technologies.

The use of the alternative integrated technique should continue to be evaluated as next-generation electronics components become more common in DWR design. This design might require more integrated functions into the DWR/SSS design such as internal GPS, integrated power systems and direct digital communication to the downhole integrated sub-system.

INTEGRATED SEISMIC EVENT DETECTION AND LOCATION BY ADVANCED ARRAY PROCESSING

T. Kvaerna[1], S. J. Gibbons[1], F. Ringdal[1], and D. B. Harris[2]

NORSAR[1] and Lawrence Livermore National Laboratory[2]

Sponsored by National Nuclear Security Administration
Office of Nonproliferation Research and Development
Office of Defense Nuclear Nonproliferation

Contract Nos. DE-FC52-03NA99517[1] and W-7405-ENG-48[2]

ABSTRACT

As the trend in nuclear explosion monitoring continues in the direction of detecting and locating seismic events of ever smaller magnitudes, the number of events which are detected and which require processing increases enormously. With more candidate phase determinations and event hypotheses, it is of paramount importance that the accuracy of parameter estimates and automatic event locations is good enough to prevent analyst time being used on examining signals which can, with a high level of confidence, be attributed to known industrial seismic sources. It is similarly important to try to maintain a low false alarm rate. Many seismic arrays of the International Monitoring System (IMS) are within regional distances of many sources of repeating seismic events. In recently funded studies, large numbers of events from known sources of seismicity have been identified providing an excellent basis of ground-truth (GT) events by which we have been able to benchmark phase determinations and subsequent event location estimates. Some of these events are mining events for which the mine operators have provided explosion times and locations, and other events have been attributed to source locations on the basis of waveform correlation studies.

The aim of the current project has been to construct a prototype system for the automatic monitoring of seismic events from sites of interest using regional seismic arrays. Current automatic location procedures frequently show rather large mislocations. In many cases, this is due to multiple events whereby several sequences of similar regional phases may reach a given seismic array within a short time period and be subsequently associated incorrectly. The prototype system is designed to mitigate errors of this kind by considering a system of *site-templates* whereby, under the hypothesis of an event at a given time from a calibrated source location, we consider only the observation of wavefield parameters in a number of very carefully defined time-windows relative to the hypothetical origin time. Another major source of error in the current automatic location estimates is a result of the use of azimuth and slowness estimates measured using variable frequency bands which show a demonstrably greater spread than the corresponding estimates measured in fixed frequency bands. The prototype system is designed to mitigate these errors by using a calibrated *phase-template* for each of the time-windows specified by the site-template. Azimuth and slowness are measured in one or more fixed frequency bands which are demonstrated to give the most stable estimates for a given phase from a given site, and appropriate corrections are applied prior to the location procedure. The template-based system gives automatic location estimates which are demonstrably better for the sites considered than the corresponding generalized beamforming (GBF) solutions. Anticipated and observed azimuth values can vary dramatically, emphasizing the need for calibration.

An additional problem with site- or phase-templates relying upon conventional frequency wavenumber (F-K) analysis and beamforming is the loss of coherence across an array aperture. Conventional algorithms assume that the wavefields incident upon an array satisfy a plane-wave model. When they do not, as happens when refraction and scattering are significant, especially in higher frequency bands, empirical matched-field processing may improve performance. In the matched-field processing approach, narrowband plane-wave steering vectors are replaced with empirical steering vectors derived from many observations of the array signal of interest. Last year we demonstrated empirical steering vectors for the ARCES array for the Pn phase from mines of the Khibiny Massif. These calibrations provided up to a factor of 3 improvement in energy detection at frequencies above 10 Hz. This year we report progress on extending the calibration from a single phase to the entire seismogram. The innovation is a non-stationary calibration or set of steering vectors that changes continuously throughout the duration of the seismogram as different phases come and go.

OBJECTIVE

This two year collaboration between the Norwegian Seismic Array (NORSAR) and Lawrence Livermore National Laboratory (LLNL) has explored improvements to the automatic detection and location of seismic events using regional arrays. At the heart of the study has been the calibration of processing parameters for the detection and location of events from a specific region using observations of previous ground-truth events at the sites of interest. The goal is to attribute, with a high degree of confidence, automatically located events to active mines or areas with known recurring seismicity. The study has examined sites in Fennoscandia and Kazakhstan using the seismic arrays in these regions.

The signals at a given array station, resulting from a set of events from a site with recurring seismicity, are likely to display common characteristics which may be exploited in order to identify subsequent events from the same region. A template describing the measurements which can be anticipated at a given station at a given time can be used to judge whether or not a detected signal is the likely result of an event from the site of interest. Such templates must be calibrated by investigating the variability of measurements made from events confirmed to have taken place at the sites; such calibrations have been the main focus of this investigation. We have, in addition, explored the potential of applying advanced new “matched field” array processing methods in order to compensate for array processing loss due to refraction and scattering, thus enhancing array gain at high frequencies.

RESEARCH ACCOMPLISHED

Automatic Event Detection and Location Procedures

The aims of nuclear explosion monitoring are being widened continually to encompass the detection, location, and identification of seismic events of ever smaller magnitude. This leads to a dramatic increase in the number of seismic events which require processing which in turn leads to increased demands upon automatic processing procedures. Such procedures need to be sensitive (to ensure that no events are missed), with a low false-alarm rate, and accurate. In particular, the large number of routine industrial seismic events should be associated (fully-automatically and with a high level of confidence) with the correct source location. Recent improvements in GT information for repeating seismic sources have improved dramatically our ability to assess the quality of fully automatic event location estimates. Figure 1 shows the location of numerous sites of repeating seismicity in northern Fennoscandia and north-west Russia for which we have excellent GT information. The four regions indicated in Russia are all sites of several different mines and information regarding the location and origin times of explosions has been collected from all these sites under the NNSA-funded contract “Ground-truth Collection for Mining Explosions in Northern Fennoscandia and Russia” (Harris et al., 2003). Explosions at the Finnish ammunition destruction site were identified largely from the GBF (Kvaerna and Ringdal, 1989) automatic event bulletin due to the characteristic explosion times; their identification was subsequently confirmed using array-based waveform correlation (Gibbons and Ringdal, 2006) which also provided excellent constraints upon the origin time of each event. For the remaining sites (all large-scale mining operations in the north of Sweden), information regarding a few selected events was provided by the mining companies, and large numbers of additional events were subsequently identified using waveform correlation methods. Figure 1 (a,b) allows a direct comparison of known event locations and fully-automatic GBF location estimates. Whilst the location accuracy is generally sufficiently good for an analyst to take an event and relocate it interactively, it is clear that associating signals with a specific source region is not possible without some form of post-processing algorithm. The reasons for the large spread in the GBF solutions are well-understood and motivate the development of a template-based system as depicted in Figure 2. Observations of many events from the same source region allow for a very good evaluation of which phases are well-observed at which stations and at which times following a seismic event; this is the concept of a site template. Within a carefully defined time-window for each such phase, we can define a set of diagnostic tests together with a range of accepted values by which we can determine whether or not the observed phase is consistent with corresponding observations from previous events at the same site. This is the concept of a phase template (see Figure 3). Gibbons et al. (2005) describe in detail the algorithm and results for such a system for the identification and location of events from the Kovdor mine. In this case, observations from only a single array station are used. This is a case of increasing relevance in the observation of increasingly small events using a relatively sparse international seismic network.

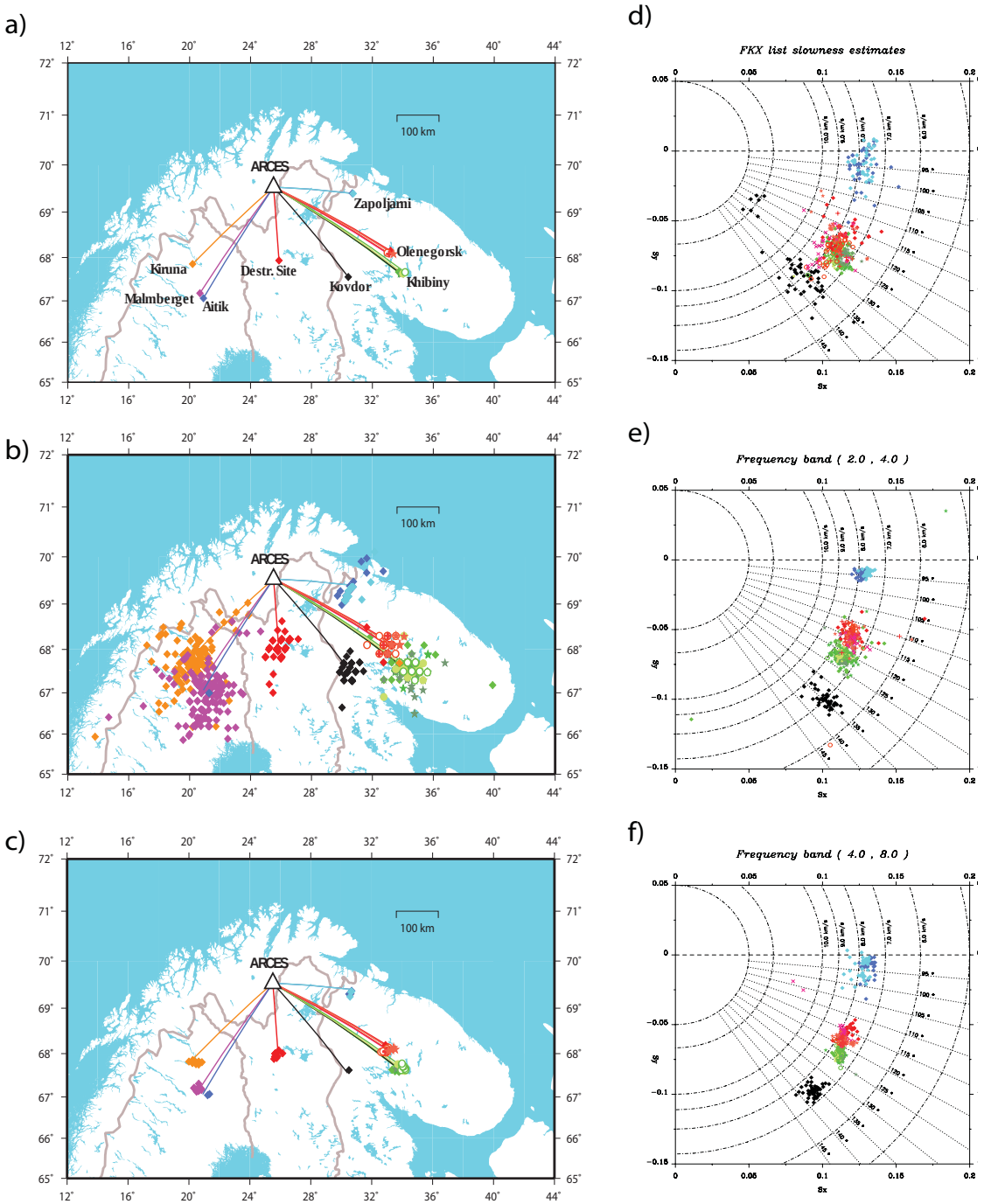


Figure 1. (**a) Sites of repeating seismicity in the vicinity of the ARCES primary IMS array. (b) Fully automatic location estimates (Kværna and Ringdal, 1989) for events known to have taken place at the sites in (a). (c) Analyst reviewed location estimates for selected events from (b). (d) fully automatic slowness vector estimates for initial P-arrivals for events from the mining sites on the Kola Peninsula in North West Russia (Zapoljarni, Olenegorsk, Khibiny, Kovdor). (e) Fixed frequency band slowness estimates (2.0 - 4.0 Hz) for the arrivals displayed in (d). (f) the same phase arrivals processed in the fixed frequency band 4.0 - 8.0 Hz.**

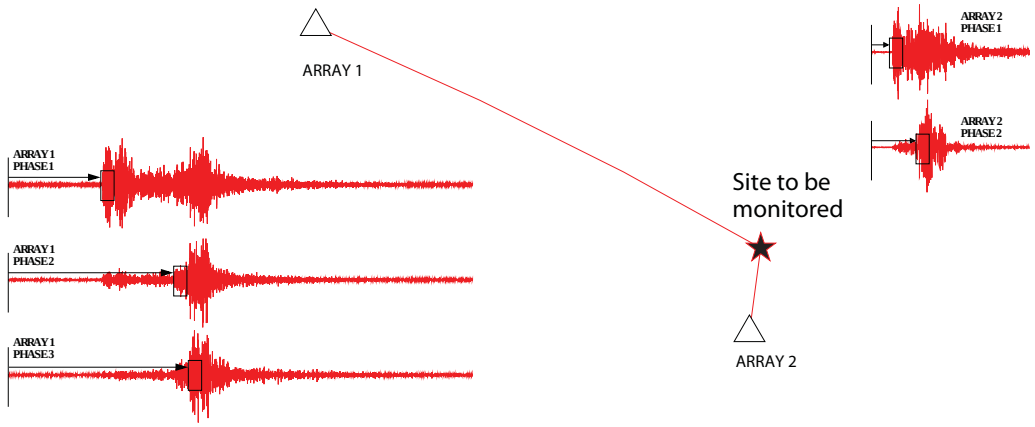


Figure 2. Schematic representation of a template-based event identification and location algorithm. The site template specifies which seismic phases should be observed at which times at which stations, given a hypothesis of a seismic event at a site of interest at a given time. For each such phase, a phase-template (symbolized by the black boxes) defines a set of test parameters, evaluation criteria and, optionally, calibration information which determine whether or not the observed phase is consistent with observations of that phase from previous events at that site (see Figure 3).

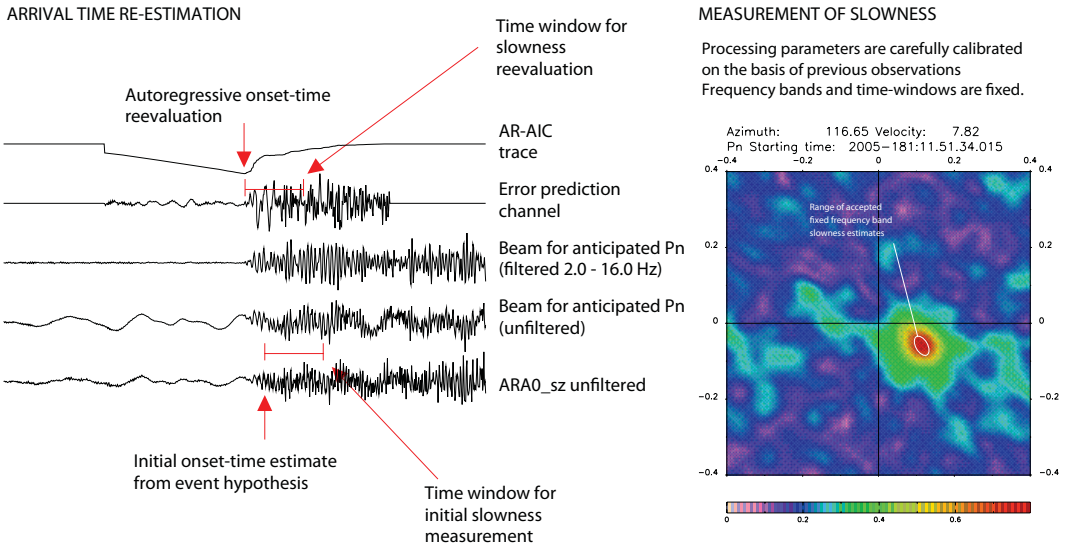


Figure 3. The principal components of a site template in regional array event identification and location algorithms: autoregressive arrival time re-estimation (left) and measurement of backazimuth and apparent velocity using broadband F-K analysis in fixed frequency bands. As displayed in Figure 1 (d,e,f), the use of carefully chosen fixed frequency bands can lead to a great improvement in the stability of slowness estimates and allows for far tighter hypothesis acceptance criteria.

Under the current project (Kværna et al. 2004, 2005), the principles applied in Gibbons et al. (2005) have been extended to encompass a far wider range of sites and station configurations. In all cases, the application of template-based algorithms has led to an improvement in fully-automatic event location estimates. In almost all cases in which the procedure failed, the reason for failure was the rejection of event hypotheses due to the inability to measure a phase arrival time with a sufficient level of confidence (signal-to-noise ratio [SNR] or Akaike Information

Criterion measurements did not satisfy required thresholds) or the failure of F-K analysis to return a slowness estimate within the required time-window. In almost all cases, this was the result of “interfering signals” which were almost invariably multiple events from the same site. Such multiple event sequences are unfortunately very characteristic of the type of event we are attempting to classify in the current investigation. In the GBF algorithm, this typically leads to a spurious association of P- and S- phases from distinct events and a corresponding location estimate at the wrong site (see Figure 1b). This eventuality is precluded from the template-based system since we only consider observations within the time-windows defined by the site-template (Figure 2); phases observed outside of these time intervals have no influence on the evaluation of the event hypothesis. Gibbons et al. (2005) found that approximately 40% of the confirmed Kovdor events could not be located automatically due to such interfering phases. To deal with this eventuality, a new category “very likely Kovdor events” was defined; these are signals which show many characteristics of events from the site of interest, albeit not sufficiently many that the event can be located automatically. This category is useful but a setback in our quest to mitigate the need for analyst interaction. It is useful to note that in the cases where a fully automatic location was not possible, the analyst location was also subject to a far higher degree of error. This failure rate (40% of events not locatable) turned out to be quite typical for all the sites covered.

Considerations in the Use of Small-Aperture Arrays for Slowness Measurements and Consequences for Event Location Etimates

Whilst the majority of the location estimates in Figure 1b which are “qualitatively incorrect” are the result of spurious phase association, the general large spread in location estimates is primarily the result of applying slowness and azimuth estimates which are measured in variable frequency bands. Figure 1d shows slowness estimates for the initial P-arrivals from the Russian events in the dataset, measured in a frequency band optimized on an event-by-event basis, as they appear in the NORSAR detection lists. Figure 1 e) and f) show the slowness estimates for exactly same arrivals when measured in the fixed frequency bands 2.0-4.0 Hz and 4.0-8.0 Hz respectively. Two results are immediately evident:

1. The fixed frequency band estimates are far more stable than the variable band estimates.
2. The frequency band offering the most stable estimate is not the same for all sites.

It is, for example, clear how the spread in slowness estimates for the Zapoljarni mines (blue symbols) in Figure 1d translates directly into the spread in event location estimates observed in Figure 1b. It is likely that if only slowness estimates obtained in the 2.0 - 4.0 Hz band were applied, then the corresponding spread in location estimates would decrease dramatically. If the slowness estimates obtained between 4.0 and 8.0 Hz were used instead, the spread in location estimates would probably remain large. The situation is reversed for the Khibiny mines with the higher frequencies resulting in more stable estimates.

The set of Finnish explosions provides a nice example case since, due to the simpler source-time functions, none of the events were subject to interfering phases and the spread in event location estimates can be attributed almost entirely to variable slowness estimates and error in phase onset-time measurements. Figure 4 shows the fully-automatic P-phase slowness estimates (left) and the same estimates made in the fixed frequency bands as indicated (right). The fixed-band estimates not only display a significantly lower spread for each band applied, but also display almost no overlap between the different bands. It is important to note that at this epicentral distance, a triplication occurs whereby the Pg crustal phase and the higher frequency Pn phase arrive essentially at the same time; this may explain why the velocity in the 4.0-8.0 Hz band is higher than the velocity at lower frequencies. At even higher frequencies, waveform incoherence over the array is probably significant. However, what is not explained by this triplication is how the azimuth varies with the frequency band. The smallest spread is observed for the 2-4 Hz band and restricting location estimates to these values results in location estimates for the fully-automatic template-based method which are superior to the analyst interactive location estimates (Figure 5). The reason for this is evident from Figure 4; the analyst picks a frequency band on an event-to-event basis and locates the event using velocity and azimuth measured in the chosen band. The analyst does not (currently) have the calibration information available and is not aware that the 2-4 Hz band gives by far the most stable azimuth estimates for events from this site. It must also be stressed that this result is by no means intuitive since the SNR is significantly lower in this frequency band than it is at higher frequencies. The temptation will be to use a frequency band which produces an optimal combination of SNR and high F-K power (beam gain) - this is judged subjectively by the analyst for each

event encountered and results consequently in a directional estimate which is a direct function of the frequency band applied.

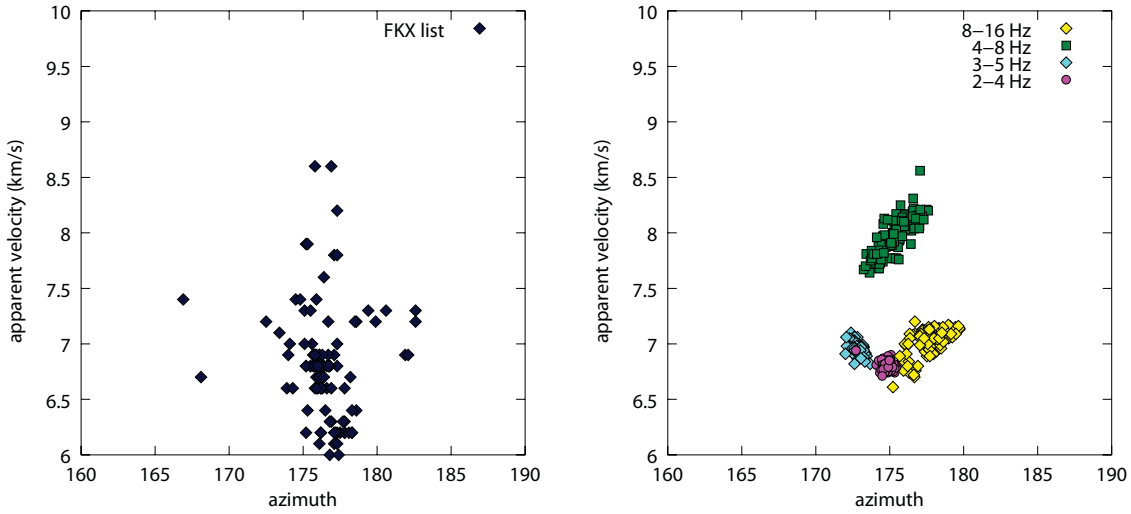


Figure 4. (Left) slowness estimates in the routine automatic processing for the defining P-arrival at the ARCES seismic array for each of 108 ammunition destruction explosions at a military site in the north of Finland, at a distance of approximately 175 km. (Right) slowness estimates for in the indicated fixed frequency bands for the same arrivals, albeit measured in an identical time window for each event.

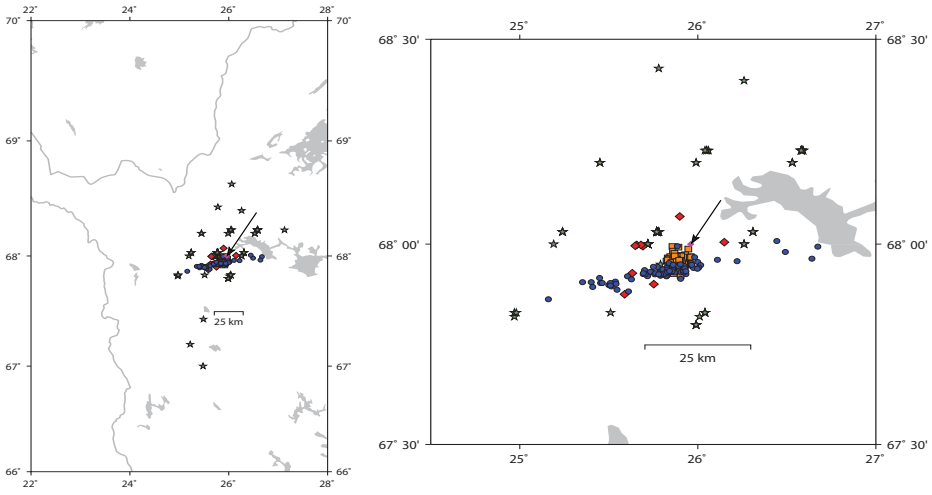


Figure 5. Locations of Finnish explosions using different location methods. The exact explosion site coordinates are not known but are assumed to be approximately 68°N, 26°E (see arrow), the green stars represent the GBF fully-automatic location estimates, the red diamonds indicate the NORSAR analyst reviewed location estimates, the orange squares indicate the single array (ARCES) template-based location estimates, and the blue circles indicate the 3-component station network solutions using the Finnish National Seismic Network (courtesy of the seismic bulletin of the University of Helsinki). Note in particular how the template-based fully automatic solutions have a far lower standard error (approximately 5 km) than either the NORSAR reviewed analyst solutions (approximately 15 km) or the Finnish network solutions.

Matched Field Processing

Last year, we tested the concept of applying empirical matched field processing to a single phase (Pn) at high frequencies (above 10 Hertz) for a small aperture array (ARCES). For a single phase it is reasonable to make the assumption that the spatial statistics of the signal are stationary. Using a narrowband (essentially monochromatic) assumption, we made the approximation that the complex analytic form of the array signal in a narrow band centered on frequency $\mathbf{f}_0$ has the form:

$$\underline{\mathbf{r}}(\mathbf{t}) = \begin{bmatrix} \mathbf{r}(\underline{\mathbf{x}}_1, \mathbf{t}) \\ \mathbf{r}(\underline{\mathbf{x}}_2, \mathbf{t}) \\ \\ \mathbf{r}(\underline{\mathbf{x}}_N, \mathbf{t}) \end{bmatrix} = \underline{\varepsilon}(\mathbf{f}_0)\mathbf{s}(\mathbf{t}, \mathbf{f}_0)\mathbf{e}^{-\mathbf{i}2\pi\mathbf{f}_0\mathbf{t}} \qquad (1)$$

where the signals $\mathbf{r}(\underline{\mathbf{x}}_\mathbf{i}, \mathbf{t})$ are the signals recorded by individual sensors in the array located at positions $\underline{\mathbf{x}}_\mathbf{i}$. The baseband signal $\mathbf{s}(\mathbf{t}, \mathbf{f}_0)$ is a slowly-varying complex envelope. This narrowband approximation has the effect of separating the spatial and temporal variations of the signal into multiplicative factors. The so-called steering vector $\underline{\varepsilon}(\mathbf{f}_0)$ encodes all of the spatial variation of the signals across the array, and the baseband signal encodes the remaining temporal structure. This approximation becomes more accurate the narrower the processing band and becomes exact for monochromatic signals.

In the plane-wave approximation, the steering vector embodies the complex phase factors induced by propagation delays across the array. In a reality, effects of refraction (e.g. focusing), diffraction, and scattering cause the steering vector to depart from this simple model. As a consequence, we advocate measuring the steering vector for particular source regions as a calibration and applying the measured steering vector in FK and beamforming operations instead of its theoretical plane-wave counterpart. Measuring the steering vector is conceptually straightforward using a large number (*M*) of waveforms from events in the target region of interest. We recommend estimating the spatial covariance matrix over the ensemble of events as:

$$\underline{\mathbf{R}}(\mathbf{f}_0) = \overline{\underline{\mathbf{r}}(\mathbf{t})(\underline{\mathbf{r}}(\mathbf{t}))^{\mathbf{H}}} \sim \frac{1}{\mathbf{M}} \sum_{\mathbf{j}=1}^{\mathbf{M}} \int \underline{\mathbf{r}}_\mathbf{j}(\mathbf{t})(\underline{\mathbf{r}}_\mathbf{j}(\mathbf{t}))^{\mathbf{H}} \mathbf{dt} = \alpha \underline{\varepsilon}(\mathbf{f}_0)(\underline{\varepsilon}(\mathbf{f}_0))^{\mathbf{H}} \qquad (2)$$

where $\alpha = \frac{1}{\mathbf{M}} \sum_{\mathbf{j}=1}^{\mathbf{M}} \int \left|\mathbf{s}_\mathbf{j}(\mathbf{t}, \mathbf{f}_0)\right|^2 \mathbf{dt}$.

If the assumption that a single phase is present is correct, the covariance matrix as shown in equation (2) is rank one and the steering vector may be obtained as the principal eigenvector of the matrix. This line of reasoning can be extended to calibrate the entire wavetrain for events from a particular region. However, the signal can no longer be considered to be stationary, even approximately. The signal model must be extended to permit changing spatial covariance structure along the wavetrain. We propose the following narrowband model:

$$\underline{\mathbf{r}}(\mathbf{t}) = \underline{\mathbf{E}}(\mathbf{f}_0)\underline{\mathbf{S}}(\mathbf{t}, \mathbf{f}_0)\mathbf{e}^{-\mathbf{i}2\pi\mathbf{f}_0\mathbf{t}} = \left[\underline{\varepsilon}_1\ \underline{\varepsilon}_2\ \cdots\ \underline{\varepsilon}_\mathbf{d}\right]\begin{bmatrix}\mathbf{s}^1(\mathbf{t})\\ \mathbf{s}^2(\mathbf{t})\\ \cdot\\ \cdot\\ \cdot\\ \mathbf{s}^\mathbf{d}(\mathbf{t})\end{bmatrix}\mathbf{e}^{-\mathbf{i}2\pi\mathbf{f}_0\mathbf{t}} \tag{3}$$

This is a collection of $\mathbf{d}$ signals representing all of the phases present, which may be a great number if multipath arrivals are considered. For simplicity, the frequency dependence of the model has been suppressed, but it is understood that the $\mathbf{d}$ individual steering vectors and baseband signals are functions of $\mathbf{f}_0$. The support of the individual baseband phase signals $\mathbf{s}^\mathbf{i}(\mathbf{t})$ may be expected to be transient. With phases coming and going, the spatial structure of the signals will vary as first one steering vector, then another comes to dominate array signal. At higher frequencies, as scattering becomes more significant, it is likely that multiple steering vectors will be required simultaneously to capture the range of spatial structure of signals originating from a specific source region.

$$\underline{\mathbf{R}}(\mathbf{t}_1, \mathbf{t}_2) = \overline{\underline{\mathbf{r}}(\mathbf{t}_1)(\underline{\mathbf{r}}(\mathbf{t}_2))^\mathbf{H}} \sim \left[\underline{\varepsilon}_1\ \underline{\varepsilon}_2\ \cdots\ \underline{\varepsilon}_\mathbf{d}\right]\left(\frac{1}{\mathbf{M}}\sum_{\mathbf{j}=1}^{\mathbf{M}}\begin{bmatrix}\mathbf{s}_\mathbf{j}^1(\mathbf{t}_1)\\ \mathbf{s}_\mathbf{j}^2(\mathbf{t}_1)\\ \cdot\\ \cdot\\ \cdot\\ \mathbf{s}_\mathbf{j}^\mathbf{d}(\mathbf{t}_1)\end{bmatrix}\begin{bmatrix}\mathbf{s}_\mathbf{j}^1(\mathbf{t}_2)\\ \mathbf{s}_\mathbf{j}^2(\mathbf{t}_2)\\ \cdot\\ \cdot\\ \cdot\\ \mathbf{s}_\mathbf{j}^\mathbf{d}(\mathbf{t}_2)\end{bmatrix}^\mathbf{H}\right)\left[\underline{\varepsilon}_1\ \underline{\varepsilon}_2\ \cdots\ \underline{\varepsilon}_\mathbf{d}\right]^\mathbf{H} \tag{4}$$

It is convenient to compute and represent samples of the covariance function of equation (4) in discrete form as a matrix

$$\underline{\mathbf{R}} = \begin{bmatrix}\underline{\mathbf{R}}(0,0) & \underline{\mathbf{R}}(0,\Delta\mathbf{t}) & \underline{\mathbf{R}}(0,2\Delta\mathbf{t}) & \cdots & \underline{\mathbf{R}}(0,\mathbf{P}\Delta\mathbf{t})\\ \underline{\mathbf{R}}(\Delta\mathbf{t},0) & \underline{\mathbf{R}}(\Delta\mathbf{t},\Delta\mathbf{t}) & \underline{\mathbf{R}}(\Delta\mathbf{t},2\Delta\mathbf{t}) & \cdots & \underline{\mathbf{R}}(\Delta\mathbf{t},\mathbf{P}\Delta\mathbf{t})\\ \underline{\mathbf{R}}(2\Delta\mathbf{t},0) & \underline{\mathbf{R}}(2\Delta\mathbf{t},\Delta\mathbf{t}) & \underline{\mathbf{R}}(2\Delta\mathbf{t},2\Delta\mathbf{t}) & \cdots & \underline{\mathbf{R}}(2\Delta\mathbf{t},\mathbf{P}\Delta\mathbf{t})\\ \cdots & \cdots & \cdots & \cdots & \cdots\\ \underline{\mathbf{R}}(\mathbf{P}\Delta\mathbf{t},0) & \underline{\mathbf{R}}(\mathbf{P}\Delta\mathbf{t},\Delta\mathbf{t}) & \underline{\mathbf{R}}(\mathbf{P}\Delta\mathbf{t},2\Delta\mathbf{t}) & \cdots & \underline{\mathbf{R}}(\mathbf{P}\Delta\mathbf{t},\mathbf{P}\Delta\mathbf{t})\end{bmatrix} \tag{5}$$

An example covariance matrix for the signals from the Kirovsk mine observed by four of the channels (ARA0, ARD1, ARD4, ARD7) of ARCES is shown in Figure 6. This covariance matrix was computed for a narrow band around 2.5 Hz using 236 events. The moduli of the individual (complex) elements of the matrix are represented in grayscale in the image with the darker elements having larger moduli. The individual phases (Pn, Pg, Sn and Lg) are apparent in the matrix. It is interesting to note that the separate phases are correlated. Some decorrelation might be expected given the relative moveout of the different phases as the events are distributed over some source region. In

this case, the source region is small (several kilometers in extent), which may account for the relatively high cross-correlations among the phases.

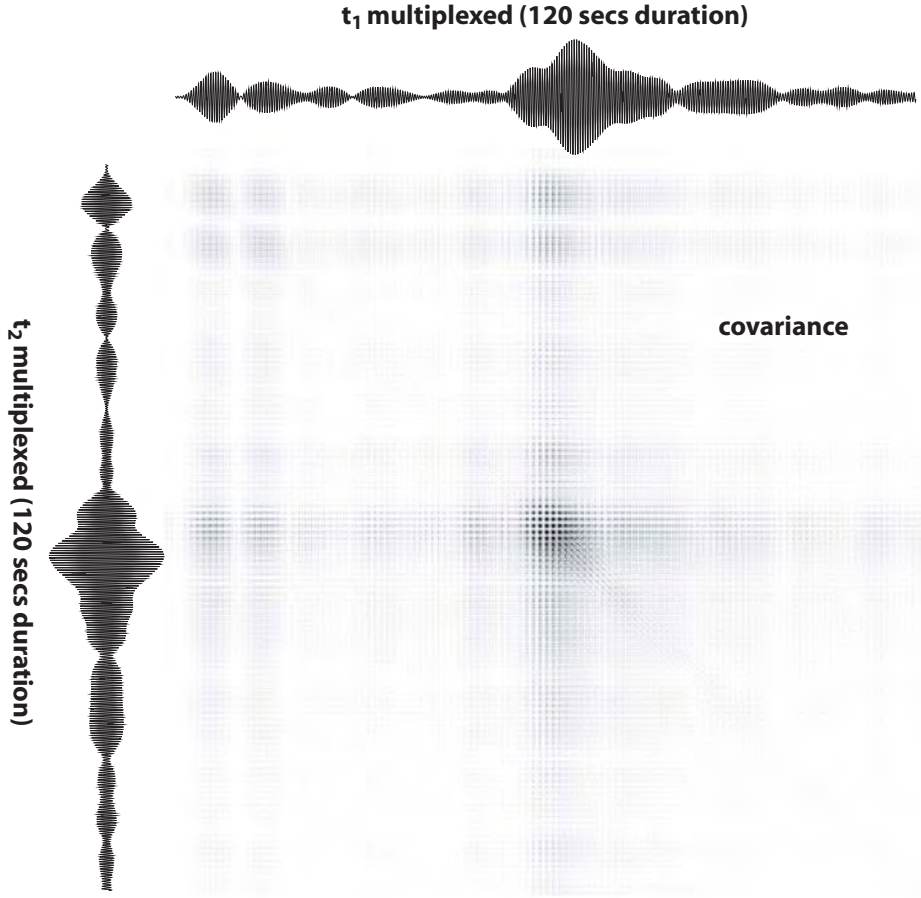


Figure 6. Example covariance matrix for 236 events from the Kirovsk mine on the Khibiny massif as recorded by a subset of the ARCES array. Note the correlations between the different phase types: Pn, Pg, Sn, and Lg.

It is our intention to extract systematically from covariance matrices of the type shown time-varying steering vectors for particular source regions and for a large number of narrow bands. We anticipate using these steering vectors in beamforming operations that use the entire time-history of the signal in an temporally incoherent, but spatially coherent detection operation.

CONCLUSIONS AND RECOMMENDATIONS

We have constructed a prototype algorithm for the fully-automatic identification and location of seismic events from a given source region. This has been applied to a wide range of sources of repeating seismicity in Fennoscandia and North West Russia, and in Kazakhstan. The use of carefully calibrated processing parameters has led to greatly increased stability in location estimates which in many situations are comparable to solutions obtained interactively by an analyst. We have also documented a situation whereby the fully automatic template-based location estimates were significantly better than those obtained by an analyst. This is due to the fact that the solutions obtained are heavily influenced by the backazimuth estimates obtained from a regional array station and these are estimates vary with the applied frequency band. For each phase analyzed, the analyst makes a decision of which frequency band to use and does not have available information regarding which frequency band is optimal for that particular site (we have also demonstrated that the optimal frequency band varies significantly from site to site). The template-based automatic system also applies a calibrated correction term to the backazimuth measurement prior to the location

procedure which takes into account the azimuth bias associated with the specific frequency band applied. An analyst would require detailed calibration information for the site involved in order to know how great a correction to apply for the processing parameters chosen. This scenario motivates a completely different approach whereby the steering vectors applied during F-K analysis are modified to take account of the demonstrable apparent curvature of the wavefield with frequency, in order to provide a slowness estimate with a zero bias for all frequency bands. It is not yet known to which degree such a calibration is possible. The greatest unknown is the extent to which the time-delay corrections are a continuous function of the theoretical slowness vector.

Towards the aim of source-region-specific detection procedures, in situations where complicated and highly heterogeneous source-time functions preclude the effective use of waveform correlation detectors, we anticipate that time-varying steering vectors calculated from multiple narrow-band observations of large numbers of events from that region will facilitate an effective beamforming operation which utilizes the full wavetrain.

ACKNOWLEDGEMENTS

We are grateful to Vladimir Asming and colleagues at the Kola Regional Seismological Center in Apatity, Russia, for collecting Ground Truth information from the Russian mine-operating companies as to the sites and times of routine industrial explosions. We would also like to thank staff at the Kazakhstan National Data Center for providing data from the Kazakhstan array network together with automatic and reviewed event bulletins.

REFERENCES

Gibbons, S. J., T. Kværna and F. Ringdal (2005), Monitoring of seismic events from a specific source region using a single regional array, in *J. Seismol.* 9: 277-294.

Gibbons, S. J. and Ringdal, F. (2006), The detection of low magnitude seismic events using array-based waveform correlation, in *Geophys. J. Int*. 165: 149-166.

Harris, D. B., F. Ringdal, E. O. Kremenetskaya, S. Mykkeltveit, J. Schweitzer, T. F. Hauk, V. E. Asming, D. W. Rock and J. P. Lewis (2003). Ground-truth collection for mining explosions in Northern Fennoscandia and Russia, in *Proceedings of the 25th Seismic Research Review - Nuclear Explosion Monitoring: Building the Knowledge Base*, LA-UR-03-6029, Vol. 1, pp. 54-63.

Kværna, T., S. J. Gibbons, F. Ringdal, and D. B. Harris (2004). Integrated seismic event detection and location by advanced array processing, in *Proceedings of the 26th Seismic Research Review - Trends in Nuclear Explosion Monitoring*, LA-UR-04-5801, Vol. 2, pp. 742-751.

Kværna, T., S. J. Gibbons, F. Ringdal, and D. B. Harris (2005). Integrated Seismic Event Detection and Location by Advanced Array Processing, in *Proceedings of the 27th Seismic Research Review - Ground-based Nuclear Explosion Monitoring Techniques*, LA-UR-05-6407, Vol. 2, pp. 927-937.

Kværna, T. and F. Ringdal (1989), A multichannel processing approach to real time network detection, phase association and threshold monitoring, in *Bull. Seism. Soc. Am.* 79: 1927-1940.

SEL0: A FAST PROTOTYPE BULLETIN PRODUCTION PIPELINE AT THE CTBTO

Ronan J. Le Bras[1], Tim Hampton[1], John Coyne[1], and Alexander Boresch[2]

Provisional Technical Secretariat of the Preparatory Commission for the Comprehensive Nuclear-Test-Ban Treaty Organization (CTBTO)[1] and Angewandte Wissenschaft Software und Technologie GmbH (AWST)[2]

Sponsored by Comprehensive Nuclear-Test-Ban Treaty Organization

Contract No. 2005-0376[1,2]

ABSTRACT

The Preparatory Commission for the Comprehensive Nuclear-Test-Ban Treaty Organization (CTBTO) is exploring and assessing which data and products, beyond the raw waveform data from the International Monitoring System (IMS), might be useful and can be provided by the CTBTO's Provisional Technical Secretariat (PTS) as input to tsunami warning centers. One of the critical features of such input is the timeliness of the delivery. The earliest standard automatic network processing at the International Data Centre (IDC), standard event list 1, or SEL1, forms events 1 hour and 40 minutes after they occur. This is too late for consideration by a tsunami warning system. Starting in February 2005, the PTS has conducted a technical test in its IDC development environment where the standard IDC software was tuned and improved to minimize the time difference between occurrence of the event and writing into a new standard event list in the database. This new standard event list is called SEL0. Time differences on the order of 20 minutes are routinely achieved between event occurrence and the writing of an event into the database, which should make it a usable input to an organization tasked with generating a tsunami warning. We present the basic characteristics of the configuration of this new processing pipeline, some statistics on the results achieved with this prototype, and future work to be conducted under this project. The basic conclusions are that, under stable conditions, no large events of interest are missed by the SEL0 pipeline and that the false alarm rate has shown some improvement during the last year of development of the pipeline.

OBJECTIVES

The objectives of this project are to develop a prototype processing pipeline using the IMS network that can produce a timely bulletin useful as input for agencies charged with warning the general public about impending disasters such as tsunamis.

Specifically, the elements of interest in a bulletin for such an agency would be as follows:

- Timeliness of the bulletin. This is the most critical element of the prototype system, as the warning has to be issued as early as possible to allow sufficient time for civil authorities to proceed with such actions as evacuation. We set this objective at an indicative time of 20 minutes after the occurrence of the event, given that the IMS network is not sufficiently dense to provide a faster bulletin uniformly on the surface of the globe.

- Minimal missed event rate. This is another critical element of the prototype system, as missing a large event would be unacceptable. There are several stages in an operational system that would be prone to failure leading to missed events. This includes failures of the acquisition system, hardware failures, database problems, or failures of the software system to detect a large event. At this stage of the prototype, since we have operated using minimal resources and in a development environment (where interruptions to processing are not uncommon), we have concentrated on the ability of the software to detect the large events when the acquisition and the hardware environment were stable.

- Location accuracy of the bulletin. This is an important element in determining whether the event is offshore or close to the shore and thus has the potential to generate a tsunami.

- Minimal false alarm rate. This is important in order to minimize disruption in the overall warning mechanism (it is important to remember that civil actions, such as evacuations ordered as a result of a tsunami warning, are themselves not without risk and often result in injuries or event deaths.)

- Accurate sizing and focal mechanism for events in the bulletin. The IDC automatic bulletins produce a measure of the size of the event based on the *mb* magnitude. It is well known that this magnitude scale saturates for events larger than about 6.5 (e.g., Abe, K, 1995). It is therefore important to develop other methods of assessing the size of large events in a timely manner. We have investigated the possibility of performing moment tensor inversion on long period P waves. This is currently at the development stage. The focal mechanism would also provide additional information for the tsunamigenic potential of the event.

RESEARCH ACCOMPLISHED

Configuration of the SEL0 Pipeline

The software used to produce the SEL0 bulletin is identical to the standard IDC software. The difference is that processing includes an additional set of auxiliary seismic stations received continuously in addition to the IMS primary stations. The configuration of the software is the main difference with the standard IDC processing. The main adjustments to data processing are that station processing intervals are 2 minutes instead of 10 minutes long in standard IDC processing, and network processing is run every 5 minutes instead of every 20 minutes in standard processing. The timing of network processing is also moved from 1 hour and 40 minutes to 20 minutes after the time of the event. An additional feature of SEL0, compared with the standard IDC processing, is that it keeps track of all instances of events written to the database as soon as they are written to the origin database table. To achieve this, in addition to the standard ORIGIN table, the ORIGIN_EWS table contains all versions of events and may contain the same event several times.

SEL0 processing is currently done in a non-operational context, on the IDC development environment, using a mixed Solaris-Linux environment, where most of the heavy-duty processing is done under Linux (detection

processing, phase identification, and network processing.) This non-operational mode implies that processing stops when forwarding of data is interrupted. To ensure timeliness of results, the SEL0 pipeline is configured to ignore data arriving more than 30 minutes after real time. This is in contrast to the normal IDC Operations where "catch up" after an extended outage significantly delays automatic bulletin production. Maintaining a constant data flow to the SEL0 pipeline would be a high priority if it were to become operational. In the current context, events are missed when the data are late or interrupted, which is not acceptable for an operational system.

Reporting on a Monitoring Web Page

Figure 1 shows the web interface through which detailed information about events generated by the SEL0 pipeline can be accessed. The page is continually updated by the processing to display the most recent events built by the processing. The final column of the figure shows the delay in minutes between the origin time of the event and the time at which it was written to the database.

#	Origin Time (hum)	Origin Time (ep)	Orid	Latitude	Longitude	Depth	Magnitude	Nass	Ndef	Region	Delay(m)
1	2006-07-04 03:56:32	1151985392.4	227315	42.8499	114.6850	0.0	4.5	9	6	NORTHEASTERN CHINA	23.62
2	2006-07-04 03:56:25	1151985385.5	227313	39.1289	116.1712	0.0	4.6	39	14	NORTHEASTERN CHINA	18.75
3	2006-07-03 16:33:36	1151944416.1	227152	-6.6526	129.1601	41.4	4.6	13	6	BANDA SEA	21.67
4	2006-07-03 13:39:51	1151933991.8	227099	-20.3941	-176.1112	123.0	4.8	26	8	FIJI ISLANDS REGION	15.43
5	2006-07-03 08:05:45	1151913945.0	227004	-40.8960	-72.4163	0.0	4.7	3	3	CENTRAL CHILE	19.42
6	2006-07-03 04:22:10	1151900530.9	226954	-15.1054	-177.5331	0.0	4.6	8	5	FIJI ISLANDS REGION	18.00
7	2006-07-03 04:12:37	1151899957.6	226950	-10.3630	-177.3580	0.0	4.5	6	4	NORTH OF FIJI ISLANDS	17.60
8	2006-07-02 17:20:28	1151860828.1	226788	55.2614	178.9313	0.0	4.7	9	6	BERING SEA	24.85
9	2006-07-02 17:20:34	1151860834.8	226786	51.0903	-179.4801	132.4	4.6	37	13	ANDREANOF ISLANDS, ALEUTIAN IS.	19.57
10	2006-07-02 16:57:06	1151859426.5	226776	42.4556	-170.5177	0.0	4.5	10	4	NORTH PACIFIC OCEAN	23.05
11	2006-07-02 16:58:10	1151859490.9	226774	51.0166	-179.3487	151.4	4.6	26	8	ANDREANOF ISLANDS, ALEUTIAN IS.	17.02

Figure 1. Example of a web page on July 3, 2006, showing the most recent SEL0 events at that date with mb magnitude larger than 4.5.

Events with M_w > 6 for Test Periods between June 7 and June 21, 2005, and between June 14 and June 30, 2006

The events of interest for a warning system are large events. Our testing has concentrated on events with M_w larger than 6.0 as reported in the Preliminary Determination of Epicenters (PDE) bulletin of the U.S. Geological Survey (USGS). During the 15 days between June 7 and 21, 2005, processing was relatively stable, with the exception of 13.5 hours between 02:30 and 16:00 on June 13, 2005, caused by a hardware failure. Similarly, during the period between June 14 and 30, 2006, processing was stable with the exception of a slowdown on June 27 between 18:00 and 19:00. Table 1 shows the 15 events published in the PDE (USGS) catalog with M_w magnitude larger than 6.0 during these time intervals. Note that one of them, event 3, grayed in the table, falls in the SEL0 processing gap previously mentioned, whereas event 15 could not be obtained because data acquisition was delayed by more than 30 minutes. Event 6, offshore California, prompted a tsunami warning (issued, but subsequently cancelled) and resulted in maximum wave heights (peak-to-trough) of between 26.0 cm at Crescent City down to 2.0 cm at Bamfield, Vancouver Island, Canada.

Table 2 shows the SEL0 events corresponding to the PDE events during the two time periods. The last column in the table shows the delay time between the origin time of the event and the time at which the event was written to the

database. Note that all the events were formed in the SEL0 bulletin at the exception of events 3 and 15, when the SEL0 processing was disrupted.

Table 1. PDE events with M_w > 6.0 from June 7 to 21, 2005, and from June 14 to 30, 2006 (see Figure 2). The grayed events fall in a processing gap due to hardware failure or late processing

Event number	Latitude	Longitude	Depth (km)	USGS M_w	Date	Time
1	2.21	96.74	46	6.1	08-Jun-2005	06:28:13.90
2	-56.24	-27.04	94	6.0	12-Jun-2005	19:26:24.81
3	2.09	126.61	10	6.0	13-Jun-2005	07:02:33.11
4	-19.93	-69.03	117	7.8	13-Jun-2005	22:44:33.86
5	51.23	179.39	51	6.8	14-Jun-2005	17:10:16.35
6	41.28	-125.98	10	7.2	15-Jun-2005	02:50:53.01
7	-4.59	153.19	75	6.3	15-Jun-2005	10:13:59.10
8	-44.97	-80.57	10	6.5	15-Jun-2005	19:52:24.31
9	40.76	-126.60	10	6.7	17-Jun-2005	06:21:41.92
10	51.78	177.07	14	6.4	14-Jun-2006	04:18:42.44
11	45.41	149.35	95	6.0	22-Jun-2006	10:53:11.63
12	-0.44	123.30	53	6.3	24-Jun-2006	21:15:04.94
13	52.24	176.23	37	6.2	27-Jun-2006	02:39:36.02
14	-19.87	-178.31	571	6.2	27-Jun-2006	02:59:15.72
15	6.53	92.72	32	6.2	27-Jun-2006	18:07:23.05

Table 2. SEL0 events matching PDE with M_w > 6.0 from June 7 to 21, 2005, and from June 14 to 30, 2006 (see Figure 2)

Matching PDE Event	Latitude	Longitude	Depth (km)	IDC mb	Date	Time	Delay time (min.)
1	2.21	96.79	67	5.07	08-Jun-2005	06:28:16	17.7
2	-56.34	-27.19	55	5.22	12-Jun-2005	19:26:22	19.4
4	-18.83	-71.74	0	6.66	13-Jun-2005	22:44:26	21.6
5	51.31	179.48	99	5.51	14-Jun-2005	17:10:22	20.2
6	41.67	-125.51	0	5.03	15-Jun-2005	02:50:54	26.5
7	-4.60	152.91	96	5.48	15-Jun-2005	10:14:02	17.4
8	-44.89	-80.75	0	4.89	15-Jun-2005	19:52:23	18.9
9	40.91	-126.27	19	5.46	17-Jun-2005	06:21:44	18.8
10	51.76	177.21	0	5.05	14-Jun-2006	04:18:40	16.6
11	45.45	149.21	73	5.61	22-Jun-2006	10:53:09	17.0
12	-0.28	123.31	0	5.37	24-Jun-2006	21:14:56	20.2
13	52.06	176.19	112	4.74	27-Jun-2006	02:39:43	15.5
14	-19.77	-178.25	556	5.04	27-Jun-2006	02:59:15	15.9

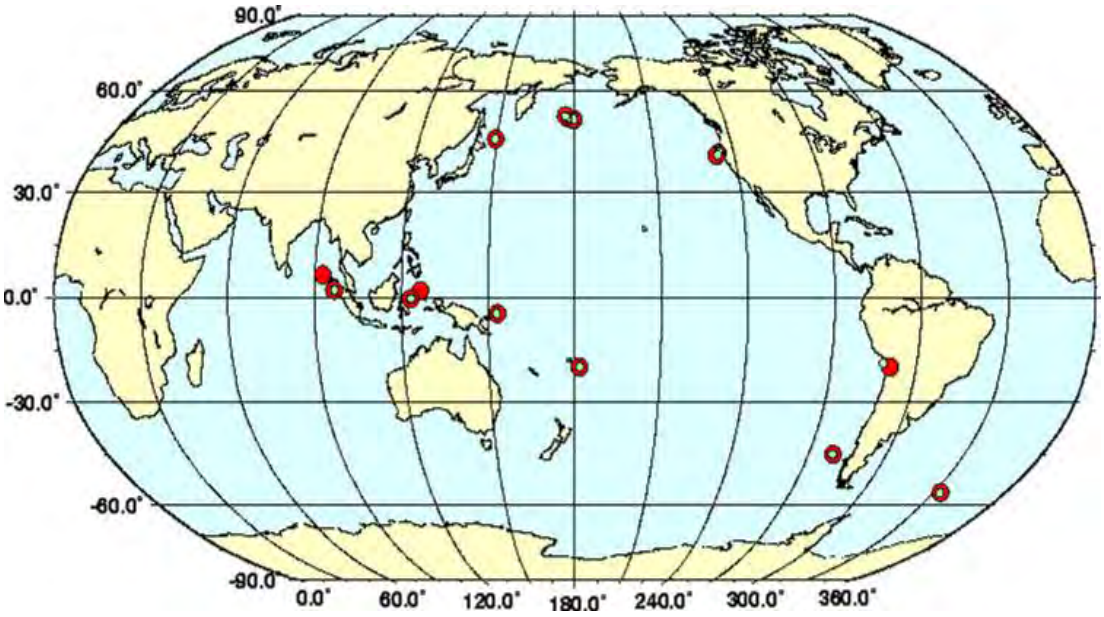


Figure 2. This map shows the 15 PDE events (in red) with Mw >6 during the time period between June 7 and 21, 2005, and between June 14 and 30, 2006. The matching SEL0 events are shown in green. Owing to a hardware failure, the SEL0 processing could not process the time period including the Molucca Sea event. Similarly, due to late processing, one Indonesian event on June 27, 2006, was not obtained by SEL0. All other 13 PDE events were matched by corresponding SEL0 events. Note that some of the events are close together and that the symbols are superimposed on the map.

False Alarms for Test Periods between June 7 and 21, 2005, and between June 14 and 30, 2006

The rate of false alarms observed for SEL0 magnitudes mb 5 and above (IDC mb magnitude) was 40% for the time period in June 2005 (see Figure 3). This was significantly less than the false alarm rate observed for standard IDC operations (including all magnitudes) but not sufficient to reliably issue an alert based purely on this magnitude estimation. Most of the false alarms (14 out of 16) have only 1 or 2 defining station mb magnitudes (9 have 1 defining station mb, and 5 have 2 defining station mb).

In the meantime, we have implemented a quality control module in network processing to eliminate false alarms based on the difference between an estimated local station magnitude Ml and an estimated mb. If an event is defined by fewer than three stations and the difference between an estimated mb and Ml is larger than one magnitude unit, the event is considered to be a false event due to incompatibility in amplitudes between the stations. In addition to this module, we are screening detections based on SNR in the frequency band 0.8 to 4.5 Hz and identifying more of the low signal-to-noise ratio (SNR) detections as noise (Jia, 2006).

The false alarm rate at the level of SEL0 magnitude mb 5 and above has decreased significantly between June 2005 and June 2006, with just 2 false alarms out of a total of 21 events above magnitude 5 (see Figure 4). This is slightly under 10%. We attribute this improvement in part to the introduction of the quality control module eliminating small events with large discrepancies between Ml and mb and in part to an improvement in identifying low SNR detections as noise.

It is still desirable to improve on this magnitude estimation, for instance, by rapidly estimating an M_w magnitude for SEL0 events, given that we know that the IDC mb magnitude scale saturates rapidly for events with $M_w > 6$. Furthermore, a comparison between IDC and International Seismological Centre (ISC) magnitudes has shown that the IDC estimate of mb is on average smaller than the ISC estimate. We believe that the SEL0 bulletin at this stage could be a useful input to a decision-making process prior to issuing an alert. Its main advantage is its timeliness and

the fact that we have not observed at this stage any missed event (for confirmed events with $M_w > 6$). It would be very advisable to include a quick expert review of the SEL0 results before an alert is released to discard potential false alarms.

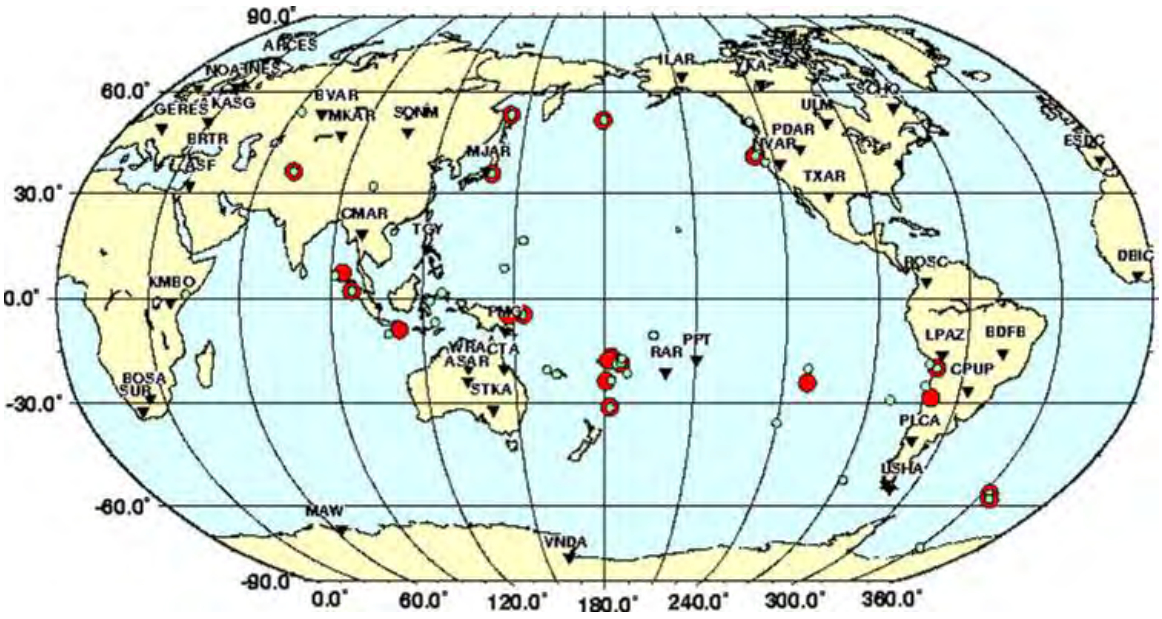


Figure 3. This map shows all 40 SEL0 events (in green) with mb > 5.0 during the time period June 7 to 21, 2005, and the matching PDE events (in red). Note the false alarm rate of about 40%. The SEL0 bulletin was using data from 41 stations, including some IMS auxiliary stations whose data was requested continuously.

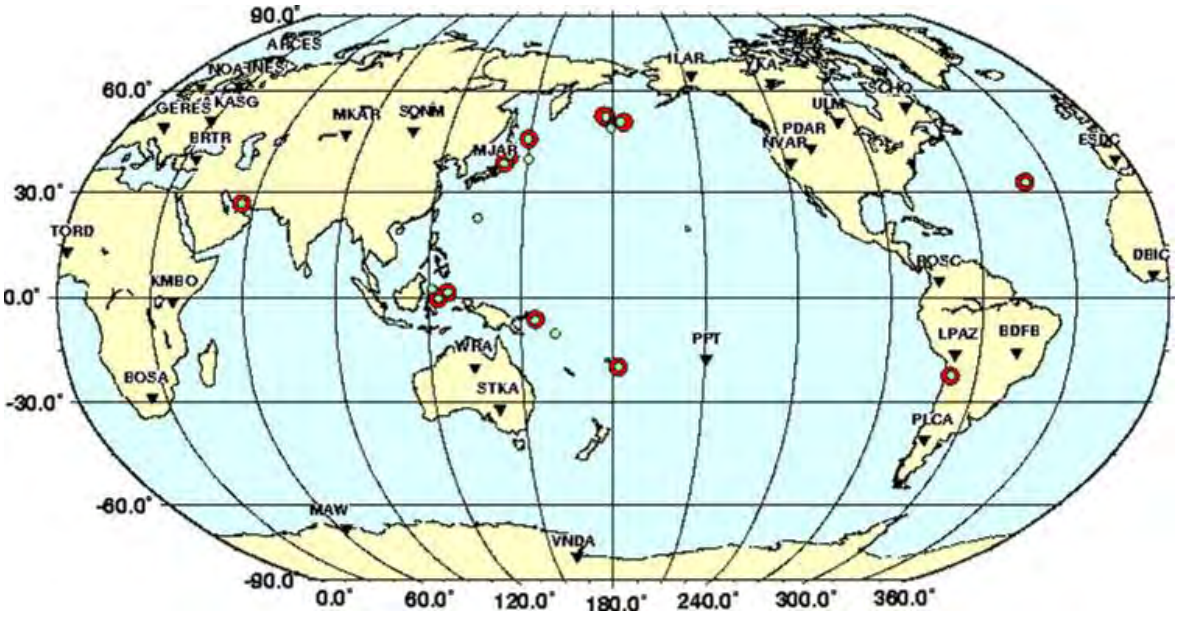


Figure 4. This map shows all 21 SEL0 events (in green) with mb > 5.0 during the time period June 14 to 30, 2006, and the matching PDE events (in red). Note that there are few false alarms during that time period. The SEL0 was using 30 stations during that time period.

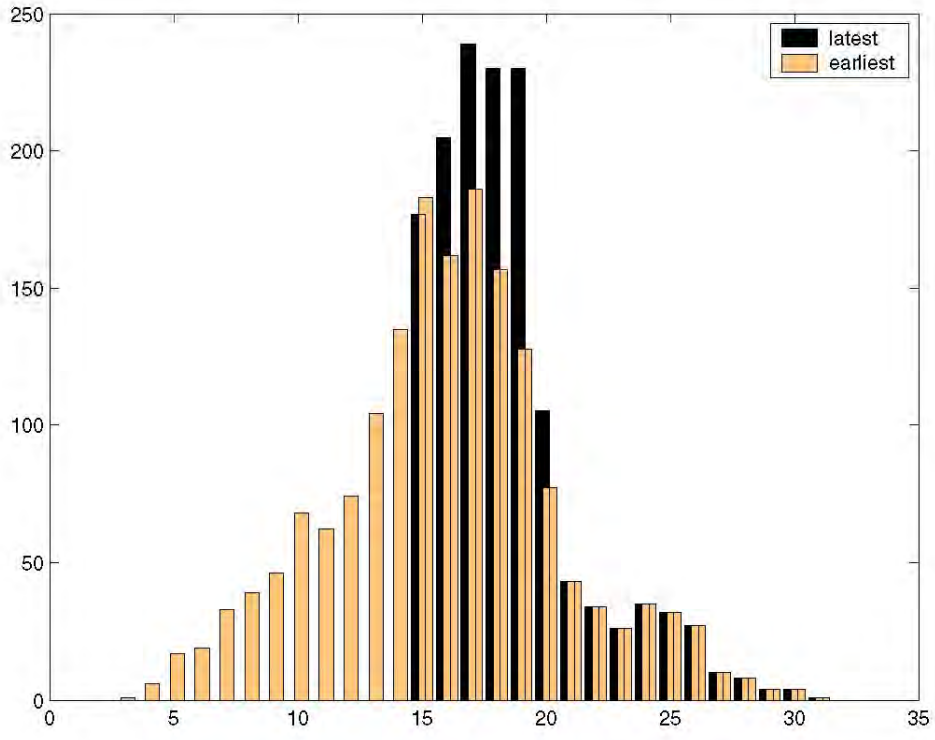


Figure 5. This histogram shows the distribution of events during the time period June 14 to 30, 2006. according to the time delay at which they were written in the SEL0 origin database table. Note that the majority of events are in the database 20 minutes after they occur.

Figure 5 shows the statistics of the time delays between the origin time and the time at which the events are written to the SEL0 origin database table, as well the equivalent statistics for an intermediate table (SEL0-EWS) that contains all events ever built by the system, as soon as they are built. The average delay is 16.4 minutes for the SEL0-EWS events and 18.9 minutes for the SEL0 events.

CONCLUSION(S) AND RECOMMENDATIONS

We have shown that it is possible to make adjustments to the CTBTO IDC software in order to produce a bulletin that can be useful as input to tsunami or other natural disaster warning centers. During relatively stable processing windows in June 2005 and June 2006 in a developmental context, we have shown that the timeliness objective can be obtained with a global bulletin produced within 20 minutes of real time. The SEL0 bulletin did not miss any event with M_w of 6 or more reported by the PDE bulletin during these two time windows with the exception of two events occurring during hardware failure and acquisition delay, respectively. We have seen an improvement in terms of false alarm rate for mb > 5 between June 2005 and June 2006. We are working on further reducing this false alarm rate and adding automatic fast computation of an M_w magnitude based on long-period P waves, which will give a better estimate of size for large events.

ACKNOWLEDGEMENTS

We thank Lassina Zerbo, IDC Director, for allowing us to publish this research and for his constant support during the project.

DISCLAIMER

The views expressed in this paper are those of the authors and do not necessarily reflect the views of the CTBTO Preparatory Commission.

REFERENCES

Abe, K. (1995). Magnitudes and moments of earthquakes, in *Global Earth Physics, A Handbook of Physical Constants*, AGU Reference Shelf 1: 206, 213.

BASIC RESEARCH ON SEISMIC AND INFRASONIC MONITORING OF THE EUROPEAN ARCTIC

Frode Ringdal, Tormod Kværna, Svein Mykkeltveit, Steven J. Gibbons, and Johannes Schweitzer

NORSAR

Sponsored by Army Space and Missile Defense Command

Contract No. W9113M-05-C-0224

ABSTRACT

This project represents a three-year research effort aimed at improving seismic and infrasonic monitoring tools at regional distances, with emphasis on the European Arctic region, which includes the former Novaya Zemlya test site. The project has two main components: a) to improve seismic processing in this region using the regional seismic arrays installed in northern Europe and b) to investigate the potential of using combined seismic/infrasonic processing to characterize events in this region. In the latter case, we plan on using the northern European seismic array network in combination with infrasonic stations either installed or scheduled for installation in the near future.

During this reporting period, we have implemented basic infrasonic processing software for the Apatity infrasonic array and for the ARCES seismic array. In the case of ARCES, there are currently no infrasonic sensors available (the plans are to install an infrasound array in 2006/2007), but the seismic sensors have proved useful as an initial substitute for detecting and processing infrasonic signals from explosions at local and regional distances. We have developed an algorithm for associating detected infrasonic phases (either by ARCES or Apatity) with regional seismic events detected and located by the on-line Generalized Beamforming (GBF) process which is currently in experimental operation at NORSAR. We searched the GBF bulletin for approximately one full year of data for seismic events at local or near regional epicentral distances to ARCES or the Apatity infrasound array. We found that 944 infrasound signals could be associated with 651 different seismic events from the GBF bulletin. The large majority of these events were confirmed mining explosions, mainly on the Kola Peninsula.

We present results from an analysis of seismic and infrasonic signals from a set of 108 surface explosions in northern Finland, carried out for the purpose of destroying old ammunition. We have used waveform cross-correlation on ARCES seismic recordings to determine very accurate origin times for the explosions. The extremely high correlation coefficients observed for this data set indicate that these explosions are all very closely spaced, probably within an area of some hundreds of meters in diameter. We have used this database to study the stability of slowness estimates for both seismic and infrasonic phases, using ARCES and Apatity array recordings. By analyzing various subconfigurations of the ARCES array, we find that the scatter (standard deviation) in the azimuth estimates for the explosions is about inversely proportional to array aperture. When carrying out a similar analysis of infrasonic data, we find that, in contrast to the case for the seismic P-waves, the azimuth scatter using our f-k estimation process does not decrease when the array aperture increases. Furthermore, the average azimuth remains essentially unbiased both with varying array aperture and with varying filter bands. This is also in contrast to the situation for seismic P-waves, where we have found strong frequency dependent and configuration dependent azimuth anomalies.

The recent upgrade of the Spitsbergen seismic array, which has included installation of five new three-component seismometers, has resulted in a significant improvement of S-phase detection. We demonstrate this improvement by presenting analysis of recent small seismic events on Novaya Zemlya, where three events (of m_b=2.2, 2.3 and 2.7) were detected by the GBF process during March 2006.

OBJECTIVE

The objective of the project is to carry out reseach to improve the current capabilities for monitoring small seismic events in the European Arctic, which includes the former Russian test site at Novaya Zemlya. The project has two main components: a) to improve seismic processing in this region using the regional seismic arrays installed in northern Europe and b) to investigate the potential of using combined seismic/infrasonic processing to characterize events in this region. In the latter case, we plan on using the northern European seismic array network in combination with infrasonic arrays either installed or scheduled for installation in the near future

RESEARCH ACCOMPLISHED

Infrasound Data Processing using Apatity and ARCES Array Data

The Apatity infrasound array is a three-element array co-located with the nine-element Apatity short-period regional seismic array, which was installed in 1992 on the Kola Peninsula, Russia by the Kola Regional Seismological Centre (KRSC). For further details see Baryshnikov (2004).

The 25 element ARCES array is a short-period regional seismic array, located in northern Norway. ARCES has no infrasound sensors, but because of special near surface installation conditions, many of its seismic sensors are also sensitive to infrasound signals. The seismic sensors have therefore proved useful as an initial substitute for detecting and processing infrasonic signals from explosions at local and regional distances (see e.g., Ringdal & Schweitzer, 2005). Current plans are to install an infrasound array near the ARCES site in 2006/2007.

In this study, we have developed an initial STA/LTA-based infrasonic processing system for the Apatity infrasound array and for the ARCES seismic array. We have also developed an algorithm for associating detected infrasonic phases (either by ARCES or Apatity) to regional seismic events generated in the on-line Generalized Beamforming process which is currently in experimental operation at NORSAR. Some preliminary results are summarized in the following (for details, see Schweitzer et. al., 2006).

On the average, 23.4 infrasound signals per day were observed with the Apatity infrasound array and 7.6 signals per day with the ARCES array. These numbers of observations result from applying only an initial set of infrasound signal processing rules. We want to determine how many of these infrasonic signals can be associated to sources already known from their seismic signals. To investigate this question in more detail the following test was performed:

The Generalized Beamforming (GBF) algorithm (Ringdal and Kværna, 1989) integrates automatically all observations of local and regional phases from all seismic arrays analyzed at the NORSAR data center in one common bulletin, associates these observations to their common sources, and locates these seismic sources. It can be assumed that this bulletin is quite complete and that it is representative for local and regional seismic events in Fennoscandia and the European Arctic with local magnitudes above 1.5 in on-shore regions and above 2.5 overall. At large distances from the arrays, the threshold could be higher. We searched the GBF bulletin for the first 351 days of the year 2005 (until the 17th of December) for seismic events at local or near regional epicentral distances to ARCES or the Apatity infrasound array. The following association criteria were used to correlate seismic events with presumed, corresponding infrasound signals:

- The epicentral distance of the event must be within 500 km from the array.
- The possible onset time of the infrasound signals was set to be within the time window spanned by group velocities between 0.2 and 0.7 km/s.
- The difference between the event backazimuth and the backazimuth observed for the infrasound signal should not be larger than 20 degrees.

BALTIC STATES-BELARUS-NW RUSSIA REGION

Origin time	Lat	Lon	Azres	Timres	Wres	Nphase	Ntot	Nsta	Netmag
2005-074:14.49.38.0	67.70	34.84	5.36	0.62	1.96	6	13	3	1.28

Sta	Dist	Az	Ph	Time	Tres	Azim	Ares	Vel	Snr	Amp	Freq	Fkq	Pol	Arid	Mag
APA	79.0	81.5	Pg	14.49.50.2	-0.5	87.3	5.8	7.3	31.0	494.1	4.32	1	1	743613	
APA	79.0	81.5	Lg	14.50.00.1	-0.5	81.4	-0.1	4.2	11.7	1577.1	3.67	1		743619	0.74
APA	79.0	81.5	s	14.50.03.0		83.2	1.7	3.4	6.4	1414.3	2.51	1		743620	0.87
APA	79.0	81.5	Ix	14.51.24.3		78.6	-2.9	0.325	14.2	5676.4	1.08	4		16005	
APA	79.0	81.5	Ix	14.54.24.6		73.3	-8.2	0.329	21.5	8792.5	9.88	6		16010	
APA	79.0	81.5	Ix	14.55.24.6		73.8	-7.7	0.338	116.5	66643.0	4.90	3		16015	
ARC	431.5	114.0	Pn	14.50.40.5	2.0	123.6	9.6	7.8	47.9	210.7	4.92	1		744345	
ARC	431.5	114.0	p	14.50.44.9		119.4	5.4	7.9	4.9	29.0	5.07	1		744348	
ARC	431.5	114.0	p	14.50.50.0		119.4	5.4	7.0	7.6	93.6	3.36	1	1	744349	
ARC	431.5	114.0	Sn	14.51.23.0	0.2	124.0	10.0	4.7	6.0	147.3	4.16	2	1	744357	1.25
ARC	431.5	114.0	s	14.51.27.2		116.4	2.4	3.7	3.5	80.1	4.28	3		744362	
ARC	431.5	114.0	s	14.51.33.6		111.3	-2.7	3.5	11.5	307.3	2.66	1	-3	744363	
ARC	431.5	114.0	s	14.51.38.1		129.2	15.2	4.6	11.3	378.2	3.90	1	-3	744369	1.69
ARC	431.5	114.0	Lg	14.51.41.5	0.3	117.9	3.9	5.1	4.7	216.0	2.74	1		744374	1.51
ARC	431.5	114.0	Ix	15.12.01.0		104.7	-9.3	0.319	10.7	130.4	4.17	2		97910	
ARC	431.5	114.0	Ix	15.12.52.6		104.0	-10.0	0.320	4.9	42.9	3.73	3		97915	
ARC	431.5	114.0	Ix	15.12.58.3		104.4	-9.6	0.319	4.3	59.1	3.45	3		97920	
ARC	431.5	114.0	Ix	15.13.54.4		102.3	-11.7	0.325	11.2	256.5	2.69	3		97925	
SPI	1304.8	143.5	p	14.52.21.8		163.0	19.5	5.6	6.4	72.3	5.89	2		743922	
SPI	1304.8	143.5	Pn	14.52.24.8	0.3	146.2	2.7	7.8	5.1	62.2	5.92	1		743925	

Figure 1. GBF bulletin of an event in the Khibiny Massif, Kola Peninsula with associated infrasound signals (marked as Ix) observed at the Apatity infrasound array and at ARCES.

Applying these rules, 944 infrasound signals could be associated to 651 different events of the GBF bulletin. For these 651 events we obtained the following statistics:

- 333 events could be associated only with infrasound signals observed at the Apatity infrasound array.
- 250 events could be associated only with infrasound signals observed at the ARCES seismic array.
- 68 events could be associated with infrasound signals at both arrays, the ARCES seismic array and the Apatity infrasound array.

Figure 1 shows the GBF bulletin entry for an event in the Khibiny Massif, Kola Peninsula, for which infrasound signals were observed at both arrays. The source area is known to have numerous large explosions in open pit mines. The associated infrasound signals show quite small backazimuth residuals, the SNR of the observed infrasound signals at both arrays is of the same order as for the seismic signals, and at both arrays, the infrasound waves are arriving in different onset groups within a time window of 1 to 2 minutes.

Figures 2 and 3 show the results of the associations described above. We note that the seismic events with associated infrasound observations are concentrated around known mining areas. We further note that all of these associations are automatic, and have not been reviewed by an analyst. Nevertheless, we are confident that the vast majority of these associations are in fact real. Further work will include detailed review and statistical analysis of results from this association process.

Case Study of Explosions in Northern Finland

Each year between mid-August and mid-September, a series of explosions in the north of Finland is recorded by the stations of the Finnish national seismograph network and also by the seismic arrays in northern Fennoscandia and NW Russia. Based upon event locations given in the seismic bulletin of the University of Helsinki, the geographical coordinates of the explosion site are assumed to be approximately 68.00^{o}N and 25.96^{o}E. The explosions are carried out by the Finnish military in order to destroy outdated ammunition and are easily identified from the automatic seismic bulletins at NORSAR for several reasons. Firstly, they are always detected with a high SNR on the ARCES array, secondly they register very stable azimuth estimates on the detection lists, and thirdly they take place at very characteristic times of day (the origin time indicated by the seismic observations almost invariably falls within a few seconds of a full hour, or half-hour in the middle of the day). A preliminary list of candidate events was obtained by scanning the GBF automatic detection lists for events which appeared to come from the correct region at appropriate times of day.

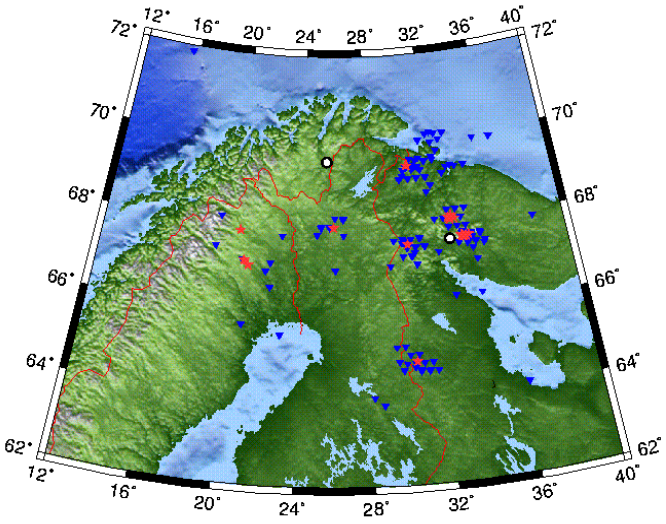


Figure 2. The map shows the 651 automatically located events (GBF) for which either the ARCES seismic array or the Apatity infrasound array observed infrasound signals. The blue triangles show the GBF event locations and the red stars show the location of known sites with explosions either at the Earth's surface or in the atmosphere. Note that the automatic GBF locations usually scatter over a larger area around these source regions. Also note that the GBF locations employ a fixed grid, and that many of the grid points shown on the map have a large number of corrsponding events.

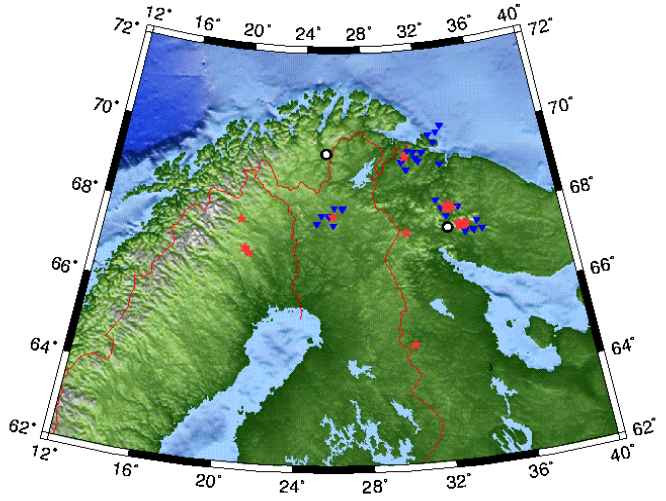


Figure 3. This map is similar to Figure 2, and shows the 68 automatically located events (GBF) for which both the ARCES seismic array and the Apatity infrasound array observed infrasound signals. The blue triangles show the GBF event locations and the red stars show the location of known sites with explosions either at the Earth's surface or in the atmosphere.

Between 2001 and 2005, a total of 108 events were found which appeared to fit the general attributes of explosions from this site; the GBF location estimates for these events are displayed in Figure 4. These fully automatic estimates display a somewhat surprisingly large geographical spread and, assuming that these events are in fact essentially co-located, the origin times will be correspondingly spurious. Before we proceed in attempting to detect and analyse infrasound signals produced from these explosions, we must first confirm that all of our candidate events are in fact from essentially the same location and then obtain the best possible origin time for each event. To this end, we applied a waveform correlation procedure, which confirmed that the explosions were indeed closely spaced, probably within an area of some hundred meters in diameter (for details, see Ringdal and Gibbons, 2006).

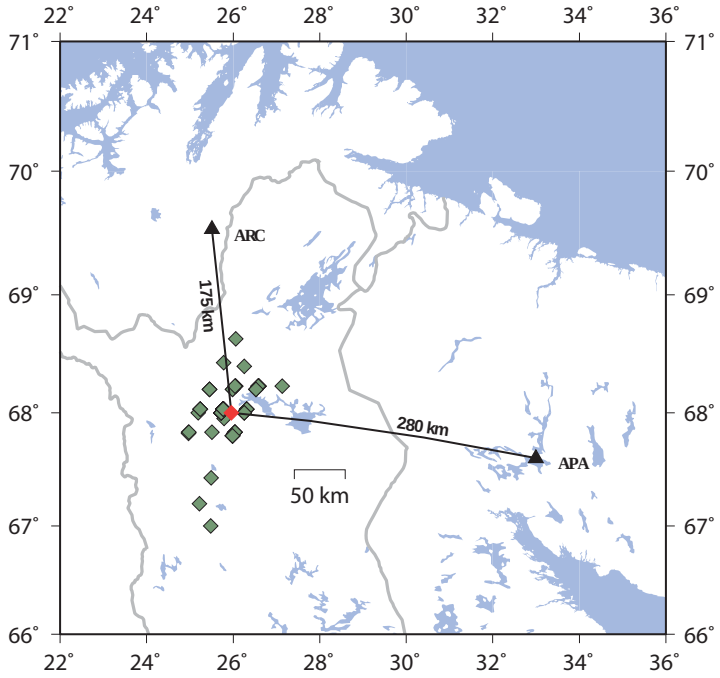


Figure 4. Estimated location of the explosion site in northern Finland (orange diamond) in relation to the seismic arrays ARCES and Apatity together with the GBF fully automatic location estimates for 108 candidate events between August 2001 and September 2005 (green diamonds). The regular pattern of event location estimates is due to the fixed-grid trial epicenter procedure employed by the GBF.

Thus, this data set of more than 100 surface explosions in almost exactly the same place recorded by the ARCES and Apatity arrays provides an excellent opportunity to investigate the stability of slowness estimates, both for the seismic and infrasonic recordings. The paper by Ringdal and Gibbons (2006) presents results on the effects of filter frequency band, array aperture and number of sensors at both the Apatity and ARCES arrays. In this paper we will focus on using various sub-configurations of ARCES to simulate array configurations of various diameters and number of sensors.

Figure 5 shows the ARCES slowness estimates for the event set as a function of various sub-configuration of vertical-component seismometers. These are, in increasing sizes:

- The 4-element A-ring configuration (seismometers A0, A1, A2, A3)
- The 9-element A,B-ring configuration (by adding the seismometers B1-B5)
- The 16-element A,B,C-ring configuration (by adding the seismometers C1-C7)

- The 25-element A,B,C,D-ring configuration (comprising the full ARCES vertical-component array)

As expected, the scatter of the estimates decreases as the array size and number of seismometers increases, and the amount of decrease in the standard deviations is about proportional to the increase in array diameter. We note that the mean azimuth estimates show significant differences among the array configurations, even if we are applying the same bandpass filter (3-5 Hz) throughout.

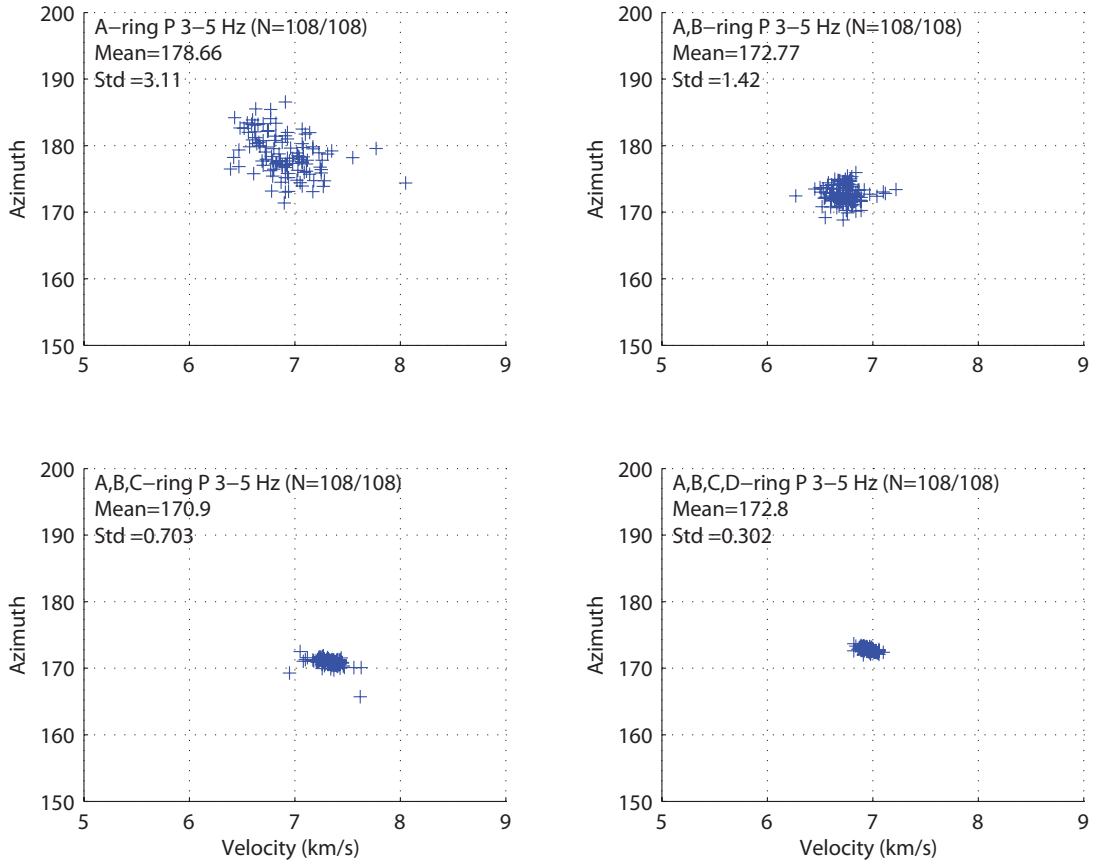


Figure 5. Seismic slowness estimates of the 108 events in the data base. The figure corresponds to estimates for the seismic P-phase (25-35 seconds after the event origin time), in the filter band 3-5 Hz. The four subconfigurations are as described in the text. For each subconfiguration, the mean and standard deviation of the azimuth estimates are indicated.

We carried out a similar study of slowness estimates for infrasonic waves recorded at the ARCES seismic array. In this case, we used throughout a 60 second window beginning 620 seconds after the event origin time. Figure 6 shows the ARCES slowness estimates for the infrasonic phases (named Ix) as a function of the same sub-configuration of vertical-component seismometers as used in our studies of P-waves described above.

In contrast to the P-wave analysis, we were not able to make reliable slowness estimates for the infrasonic phases of all the events. This is mainly due to low infrasonic SNR for a number of the events in the database. This makes a

comparison between the performances of different filters and subconfigurations more complicated, and we need to consider both the number of successful estimates and the variance reduction when evaluating the results.

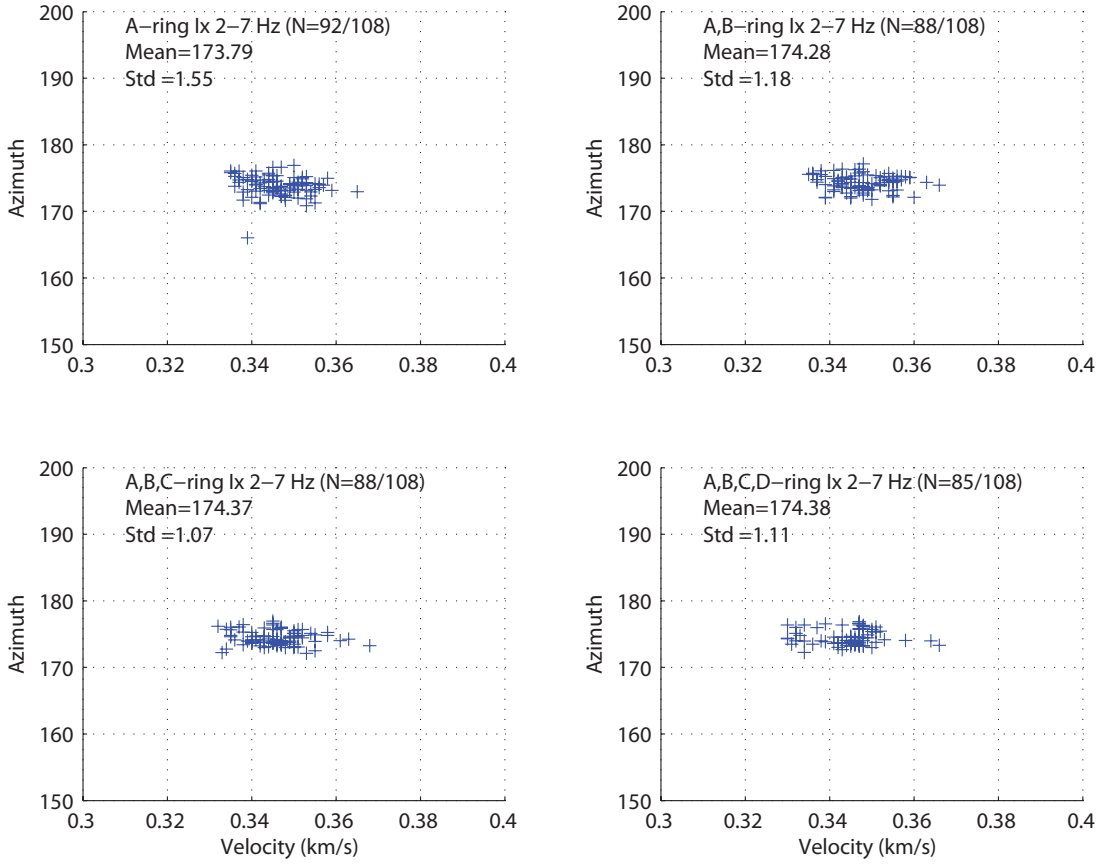


Figure 6. Infrasonic slowness estimates of the 108 events in the data base. The figure corresponds to estimates for the infrasonic phase (620-680 seconds after the event origin time), in the filter band 2-7 Hz. The number of events for which reliable estimates could be made is indicated on each plot. The four subconfigurations are as described in the text. For each subconfiguration, the mean and standard deviation of the azimuth estimates are indicated.

When comparing the infrasonic results to those obtained for seismic P-waves, we see some interesting differences. For example, we see no significant variance reduction as the array aperture and number of sensors increases. Although there appears to be a slight reduction in the standard deviations, the largest number of successful estimates were in fact made using the smallest configuration. Therefore we consider that there is essentially no difference in the stability of the slowness estimates for these four configurations. It is of course possible that other estimation techniques could show such improvements, but it may also be that the variance in estimates is dominated by factors such as varying atmospheric conditions over the 5 years covered by this study. Another important observation is that the average azimuth values are essentially independent of the subconfiguration chosen. This also contrasts to our observations from seismic P-waves.

Detection of Small Seismic Events near Novaya Zemlya

The recent upgrade of the Spitsbergen seismic array, which has included installation of five new three-component seismometers as well as an upgrading of the sampling rate from 40 to 80 Hz, has resulted in a significant improvement of S-phase detection. We demonstrate this improvement by presenting analysis of recent small seismic events near Novaya Zemlya, where three events (of m_b=2.2, 2.3 and 2.7) were detected by the GBF process during March 2006 (Table 1).

Table 1. Seismic events near Novaya Zemlya detected during March 2006

Date	Origin time	Latitude (N)	Longitude (E)	Magnitude (mb)
05/03/2006	**23.17.35.7**	**76.80**	**66.04**	**2.65**
14/03/2006	**20.57.02.4**	**75.07**	**53.05**	**2.23**
30/03/2006	**10.46.02.8**	**70.79**	**51.50**	**2.30**

Figure 7 shows spectrograms of the Spitsbergen B1 seismometer (vertical, radial and transverse components) for the Novaya Zemlya event on 5 March 2006. The most noticeable feature is the high SNR of the P-phase for this small (m_b=2.65) event. In fact, the SNR on the array beam is above 100, indicating that even an event at this site more than an order of magnitude smaller could have been detected. This should not, however, be extrapolated to a general statement about detection thresholds for the Spitsbergen array, since the SNR to a large extent depends upon path-specific focussing effects. Nevertheless, the amount of high-frequency energy is remarkable, taking into account the large epicentral distance (more than 1000 km). We note that the vertical and radial components have significant P-wave energy even above 20 Hz. The transverse component shows (not unexpectedly) a small P-wave and a much larger S-wave, indicating that the use of transverse components could be useful in detecting S-phases.

This is further illustrated in Figure 8, which shows selected Spitsbergen array beams for the 5 March 2006 Novaya Zemlya event. The top trace is a beam steered to the epicenter with a P-wave velocity, and using a typical detection filter (3-16 Hz). Note that the S-wave on this trace is fairly small, and would give a fairly marginal detection by the automatic process. The middle trace is an “optimum” beam designed to detect the S-wave. It represents the beams of the transverse components of the six three-component seismometers in the array, filtered in the band 2-4 Hz and steered to the epicenter with an S-phase velocity. Note the greatly improved SNR gain on this trace. The bottom trace shows, for comparison, a P-beam of vertical sensors using the same (2-4 Hz) filter. Clearly, the detection of S-phases could be greatly improved by augmenting the beam deployment with several steered beams , rotated so as to provide transverse components, toward the grid points in the beam deployment system.

CONCLUSIONS AND RECOMMENDATIONS

The initial results from associating infrasonic observations to seismic events are promising. We plan in the future to compare in more detail the infrasound observations with analyst reviewed event locations. This will require a review by an analyst of each infrasound signal, in order to confirm their validity and to identify possible misassociations if appropriate. Furthermore, we will implement ant test additional infrasonic array detectors, such as the PMCC detector (Cansi, 1995).

The data set of more than 100 surface explosions in northern Finland in almost exactly the same place recorded by the ARCES and Apatity arrays has provided an excellent opportunity to investigate the stability of slowness estimates for seismic and infrasonic recordings as a function of array geometry, number of sensors and filter frequency band. Future work will focus using this database as well as the ground truth data base of mining explosions in the Kola Peninsula to assess the detectability of infrasonic phases under various atmospheric conditions.

The new Spitsbergen array configuration has shown excellent recordings of high-frequency data from Novaya Zemlya events. The new three-component instrumentation provides a great potential for improving S-phase detection at this array, and an enhanced S-phase detector will be implemented in the near future.

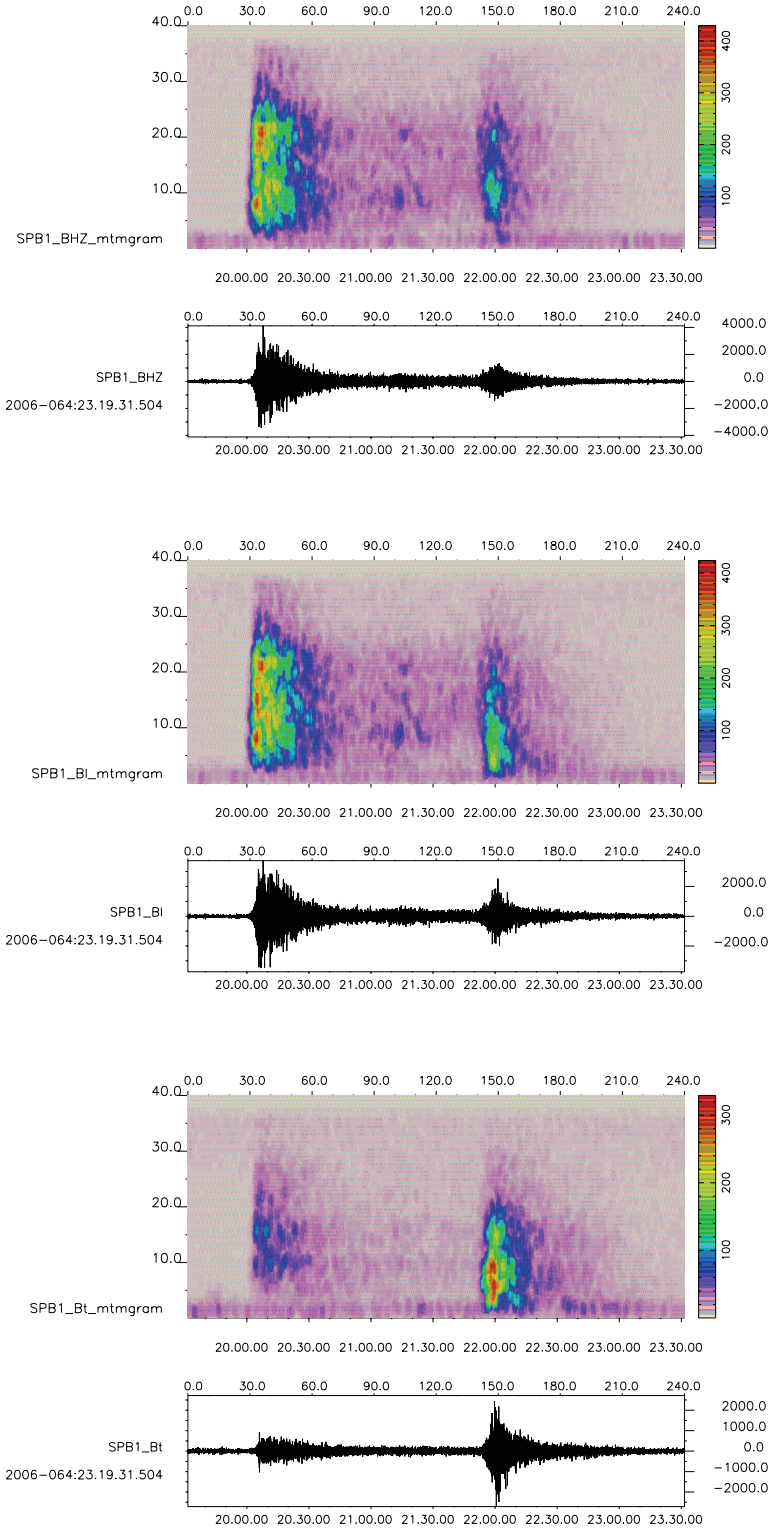


Figure 7. Spectrograms for the Spitsbergen B1 seismometer (vertical, radial and transverse components) for the Novaya Zemlya event on 5 March 2006.

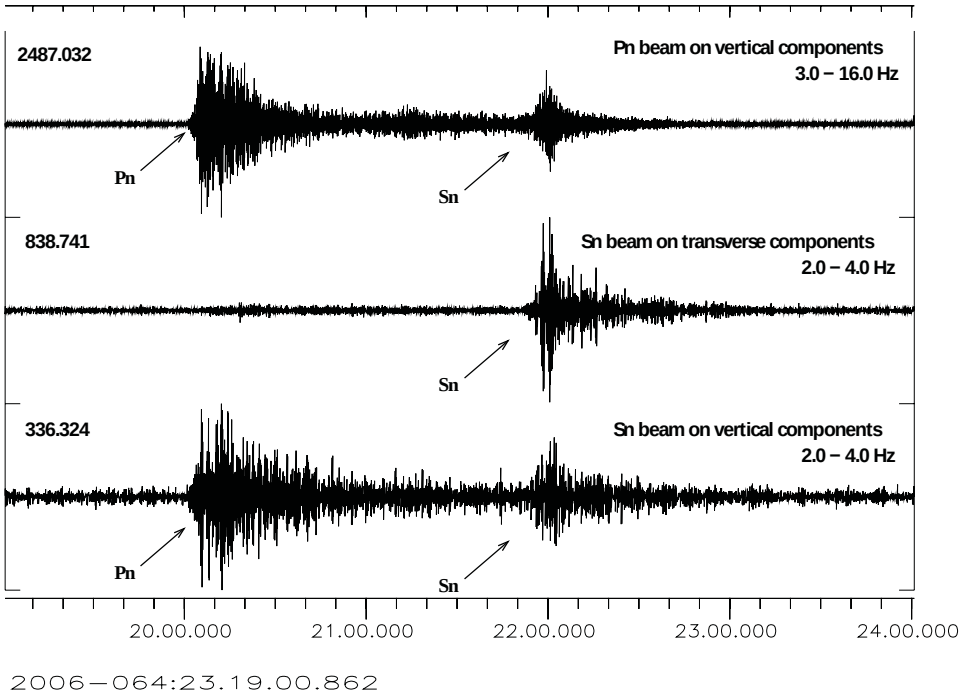


Figure 8. Spitsbergen array waveforms for the 5 March 2006 Novaya Zemlya event. Note the greatly improved SNR gain for the Sn phase shown in middle trace, which represents the beams of the transverse components of the six three-component seismometers in the array.

REFERENCES

Baryshnikov, A.K. (2004). Research of infrasound background characteristics for estimation of threshold sensitivity of infrasound method for nuclear test monitoring. Final Technical Report ISTC 1341-01 (Part 1 of total 2), International Science and Technology Center (ISTC), Moscow, 255 pp.

Cansi, Y. (1995). An automatic seismic event processing for detection and location: The P.M.C.C. method, *Geophys. Res. Lett.* 22: 1021–1024.

Ringdal, F. and S.J. Gibbons (2006). Seismic/Infrasonic Processing: Case study of explosions in north Finland. Semi-annual Technical Summary, 1 July – 31 December 2005, NORSAR Sci. Rep. 1-2006: 54–68.

Ringdal, F., and T. Kværna (1989). A multi-channel processing approach to real time network detection, phase association, and threshold monitoring, *Bull. seism. Soc. Am.* 79: pp. 1927-1940.

Ringdal, F. & J. Schweitzer (2005). Combined seismic/infrasonic processing: a case study of explosions in NW Russia. Semiannual Technical Summary, 1 January – 30 June 2005, NORSAR Sci. Rep. 2-2005: 49–60.

Schweitzer, J., F. Ringdal, T. Kværna, V asming and Yu. Vinogradov (2006). Infrasound data processing using Apatity and ARCES array data. Semiannual Technical Summary, 1 July – 31 December 2005, NORSAR Sci. Rep. 1-2006: 42–53.

ADVANCES IN DATA INTEGRATION AND QUALITY CONTROL IN SUPPORT OF THE NNSA KNOWLEDGE BASE

Richard Stead, Michael Begnaud, and Julio Aguilar-Chang

Los Alamos National Laboratory

Sponsored by National Nuclear Security Administration
Office of Nonproliferation Research and Development
Office of Defense Nuclear Nonproliferation

Contract No. W-7405-ENG-36

ABSTRACT

The goal of the NNSA Ground-based Nuclear Explosion Research and Engineering program (GNEM R&E) is to develop, demonstrate, and deliver advanced technologies and systems to operational monitoring agencies to support ground-based detection, location, and identification of nuclear explosions. One such system is a custom-designed data storage and access system known as the NNSA Knowledge Base (KB), primarily based on relational database schemas (sets of table structures). The GNEM R&E research conducted at the national laboratories to populate the KB requires collection and integration of a remarkably large and diverse collection of geophysical data to develop the types of products needed to improve monitoring capability. The size and diversity of these data present substantial technical challenges to achieve complete, correct, consistent, useful, and accessible information. These data are processed by the labs to produce the higher-level engineering products (e.g., travel time correction surfaces) that are needed for operational monitoring, but the basic data must also be included in the KB to fully test and verify the operational products. Without the supporting data and metadata capturing the processing details, the operational engineering products cannot be validated and thus will not be used for operations. Los Alamos National Laboratory (LANL) has developed and contributed to several versions of the Knowledge Base and in the process we have developed and refined a substantial foundation of software, structures, and procedures to assure high-quality integration of diverse data sets. Software advances include generalized database interfaces and generalized quality assurance/quality control (QA/QC) software. Structural advances include a metadata abstraction of supporting structures (themselves metadata) that we refer to as the schema schema. Procedural advances leverage the software and structures to create robust procedures for definition and transfer of data between groups.

The development and application of automated QC software is the primary topic of this paper. Attention to quality, particularly in the supporting data, has been a subject of growing importance and focus recently. Dealing with data quality in an established KB is difficult and time-consuming. A better approach is automated QC of supporting data before they are integrated into the KB. We have taken several steps in this area over the past year, including the development of automated quality-inspection software. The first critical step in automating QC was to make the information about the schema readily available to the QC software, which was done by developing a set of tables describing the schema itself, or a "schema schema." The schema schema captures information about the content of each table (what the columns are), the relationships between the tables, and information about each column (definition, acceptable range of values). With this in hand, we then developed a Perl-based QC tool to check the content of any set of tables against what is in the schema schema. The software performs three basic types of checks: 1) validity of column data within each table, 2) consistency of column data between related tables, and 3) more complicated consistency relationships between related tables. Because the software makes use of the schema schema, it was written in a generic manner and thus can be used for virtually any sort of check without modifying code. A user sets up a parameter file to designate the database tables that will be checked, writes the specific checks for #2 and #3 above, and then initiates the QC check. The output can then be used to direct the KB integrator to problems in the incoming data. The QC tool was used extensively for the production of the latest KB release with excellent results. Thousands of problems were found and fixed prior to integration thereby greatly improving the quality of the KB and dramatically reducing the amount of post-delivery editing.

OBJECTIVES

The GNEM R&E program has made recent progress in developing and automating QC of the NNSA KB and in the supporting metadata architecture. The goal is to improve the quality of data and derived calibration results in the KB, as well as improving the speed and accuracy of the procedures for incorporating new data and derived calibration results. A related goal is to improve human interfaces to increase the efficiency and effectiveness of KB integrators.

RESEARCH ACCOMPLISHED

Background: The Need for Quality Control

Quality control in this paper will refer to the quality assurance and quality control of both geophysical data and research products derived from those data. QC for the GNEM R&E KB is an issue that has increased in priority and significance recently. While QC has never been ignored, the increased maturity of various processes and products developed under GNEM R&E and advancing toward operations has brought necessary scrutiny. This scrutiny is different and far more intense in many ways than that typically experienced in the research community. At the same time, the volume and diversity of data and products is challenging by any standard (Stead, 2006).

A variety of typical methods of QC exist that are adopted in smaller research efforts. One is to include manual review of every field for every element of data and products by the researchers. This method works well, since the researchers are the experts and will immediately recognize errors, but it is only viable for very small and focused collections of data and products. A second method is sampling, where the expert examines a small sample of data and results to verify the correctness of these, and projecting the QC result to the whole. If properly applied, this can be a viable method for the QC of data, even large data sets. But it takes an intimate knowledge of the particular data source to know how best to properly sample the data and have confidence in the results. It is not a good approach for research products, since it implicitly assumes random errors and normal distributions. A third method is to develop a dedicated application to QC a particular type of data or research product. But this exercise then must be repeated for every new type of data or research product, and the dedicated applications require constant maintenance to account for changes in data or products. This is not meant to be an exhaustive list, but merely a representative sampling to indicate the disadvantages of such ad-hoc approaches when the QC problem deals with very large and diverse data and research products, many of which are inter-dependent, where there are frequently new kinds of information or important changes to existing information, and where much of the information is targeted for operational purposes (see Figure 1).

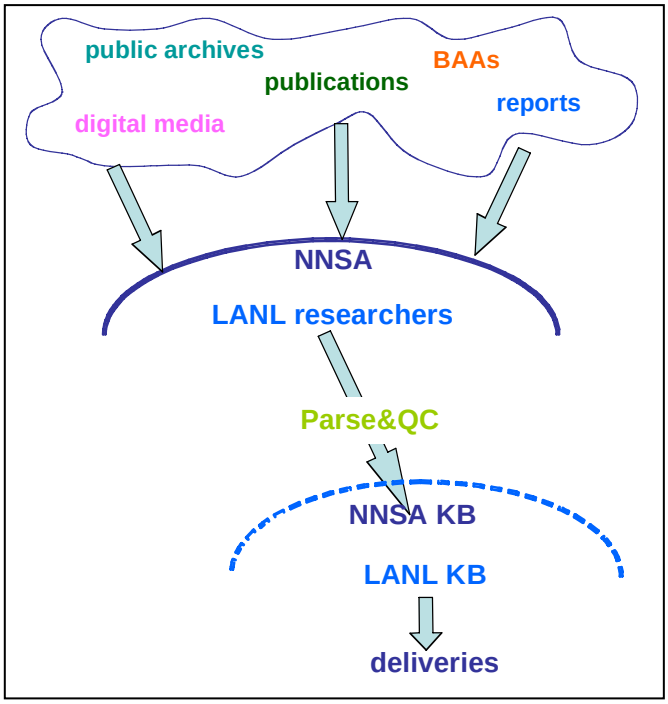


Figure 1. Generalized data acquisition and integration process. External resources of data are obtained or received by LANL researchers, then, after review and prioritization, are parsed into the standard KB structures and QC'd before being integrated into the LANL KB. The LANL KB is part of the larger NNSA KB. The formal NNSA KB, maintained by SNL, comes from the delivered portions, which undergo further review and QC at SNL before delivery to AFTAC. This view of the process is notional, and the actual procedures may involve multiple iterations and even loops among the kind of operations depicted.

Faced with this situation, LANL has been developing more comprehensive and flexible QC that can be automated. We have also worked closely with Sandia National Laboratories (SNL) on these issues, but this paper will primarily deal with the work done at LANL.

Infrastructure for QC

Any generalized, automated QC capability will require a certain amount of information infrastructure to support the process. At a fundamental level, such QC will require information that describes what qualified data and products are. A generalized QC process then merely has to match the data and products to the information and indicate which elements violate the qualification. The automated, generalized QC will only reach a level of achievement that the information infrastructure on which it is built will permit. Therefore, careful consideration must go into the construction and population of the infrastructure.

Some requirements for the infrastructure are that it be

- sufficiently general to describe all conceivable types of data and products;
- simple to understand and populate, directly or through user interfaces;
- simple to maintain, directly or through user interfaces;
- capture as much information about what qualifies data and products as possible; and
- multipurpose, so that any effort in populating and maintaining it can benefit other work.

To this end, LANL initiated the development of a database-based metadata model to support QC and other database development work beginning about two years ago. The basic concept behind this metadata model is that it is a metadata model to describe other metadata, and because of this design, it has come to be referred to as the "schema schema" (i.e., a schema to describe schemas). It is simple in that it has only four objects in the schema: an object to

describe tables, an object to describe columns, an object to describe the association between tables and columns, and an object to provide definitions of fixed values that columns may take. Additional objects can be added that relate to these basic four, to handle other special-purpose tasks (one is the **complexjoin** table which will be described below).

This concept was deliberately designed to have a close relationship to the Oracle data dictionary, to make the use and understanding of the schema schema simple and straightforward. However, it does go well beyond the Oracle data dictionary in various ways. In particular, because it exists apart from the tables it describes, it exists at all times regardless of which objects are currently defined or how they are defined. It also supports all of the concepts embedded in earlier documentation of the KB schema, including external flat-file formats and NA values.

The structure is quite amenable to web-based interfaces, making the population, maintenance, and visual interface simple to use and understand.

The structure is also multipurpose. By designing it to capture the information in previous database description documents, providing the capability to maintain multiple versions of such information in a single place and with a single interface, and providing simple tools to maintain the information, the schema schema has replaced the flat-file documentation as the medium of choice for direct maintenance of all schema information and documentation. LANL has developed web-based interfaces that allow users to quickly view database documentation in a familiar format, directly out of this schema, eliminating the piles of massive paper documents that had to be used in the past. SNL has also developed additional interfaces for viewing and maintenance. In addition, the schema provides a direct and simple means for software of all types to determine the objects and there structure at run time, as opposed to maintaining software-based descriptions of all of this information. SNL has made extensive use of this feature in the development of their Java-based **dbtoolkit**. LANL is using this feature in a variety of Perl-based software.

Figures 2–4 show the LANL-developed web interface for viewing the table descriptions and column associations, the column descriptions, and the glossary (the 4 core schema schema tables). See Begnaud, et al., 2005 for additional information on the schema schema and the web interfaces to the KB.

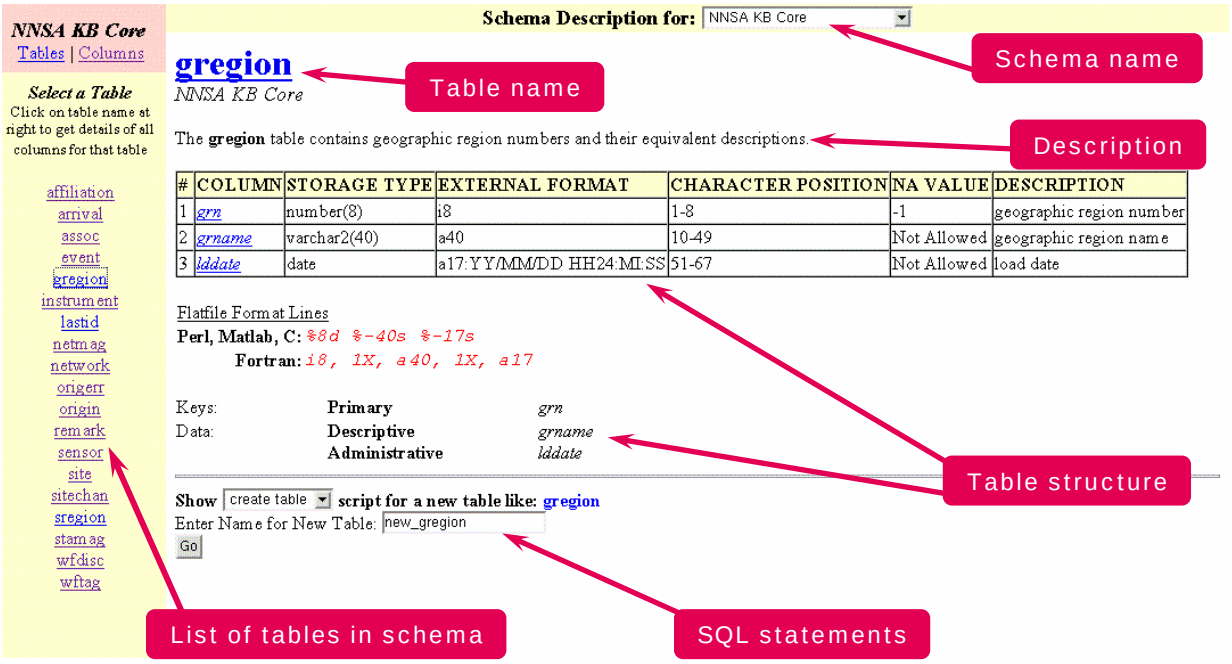


Figure 2. Table description web GUI. This web panel shows the complete description of a table from a particular schema, along with the column associations for the table and SQL statements and format lines that correspond to the table.

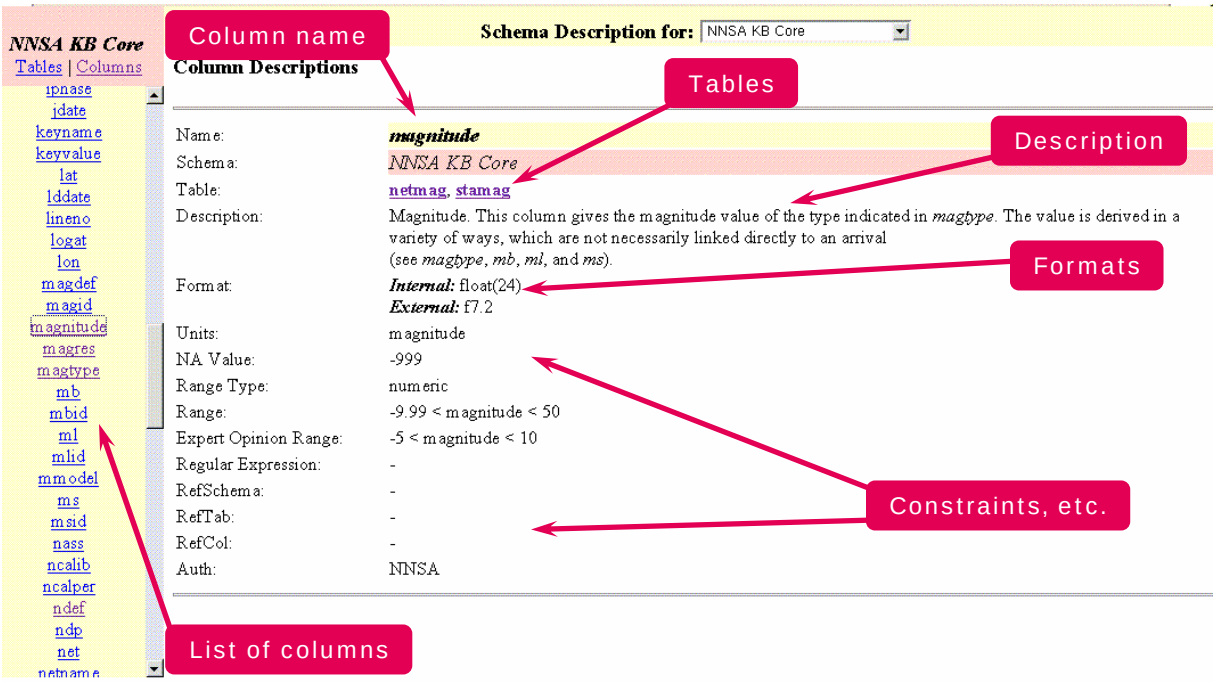


Figure 3. Column description web GUI. This web panel shows the complete description of a column from a particular schema, along with the table associations for the column.

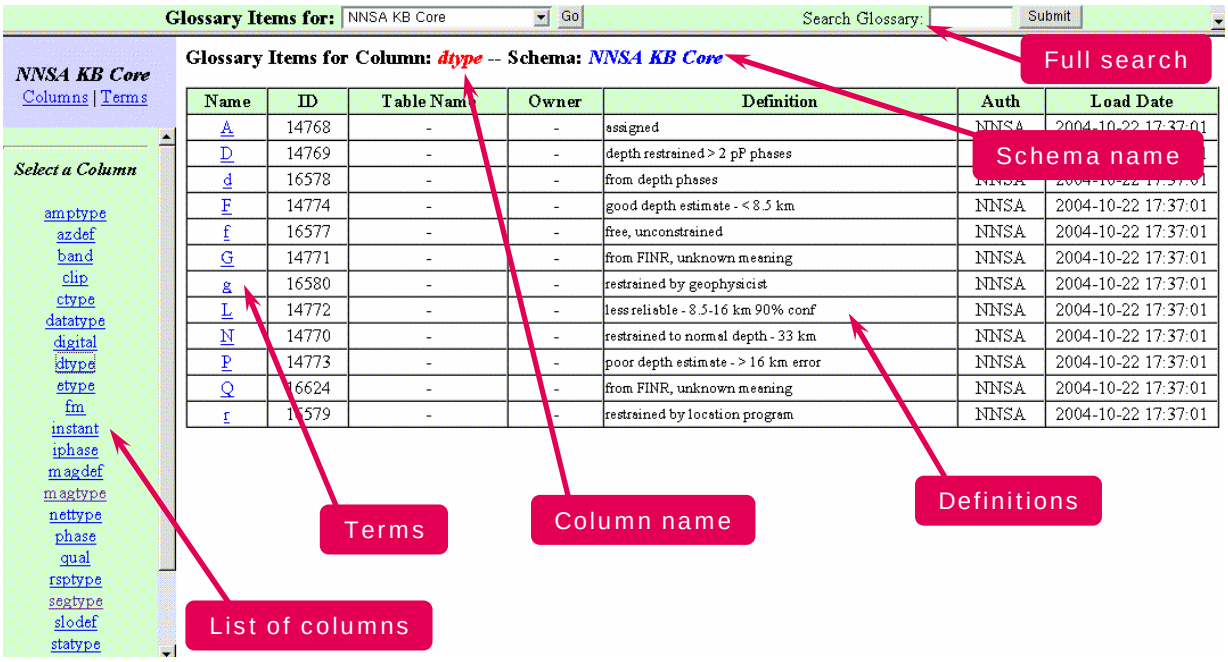


Figure 4. Glossary web GUI. This web panel shows the complete description of selected glossary entries. The entries may be selected by schema name, table name, and column name, or by the search feature.

Automated QC

A first-generation QC tool has been developed at LANL. The tool leverages the schema schema described above to facilitate automated inspection of data and derived products that exist in database tables. The tool can operate on any collection of tables, but it can only do the most basic kinds of inspection unless the tool can match each table to a corresponding description in the schema schema. The tool is applicable in a variety of situations. A version has been adopted by the DOE labs, as a group, to handle QC of deliveries between the two science labs and SNL. LANL has found the tool to be of considerable use in dealing with raw or 'roughed-in' data sets and research products. Running the tool on such information allows a wide variety of issues to be identified quickly and corrections then planned and made separately. The results also then are used as feedback to improve the conversion of data sets from their raw form into the KB, and also to improve both the structure of research products, and even the processes that generate research products. The tool has significant advantages over ad-hoc QC, in that it adapts automatically to changes in the underlying schemas, no specialized software is required if new data or products become available, and there is no need for tedious manual inspection or for experts to remember or track all of the possible QC errors that may arise.

The automated tool requires very little information to run. The basic run-time parameters are the connection to the database and the list of tables to be examined. Currently, if cross-reference checks are desired, these must also be specified individually, since there is no generalized table in the schema schema to describe these. In practice, a user of the tool will keep a list of cross-reference parameters, and copy them as needed into a run-time parameter file for a particular set of tables to be examined. The tool learns everything else it needs from the database. The tool executes three stages of QC checks: single-table checks, cross-reference checks, and complex joins.

The single-table checks consist of four table-based checks (beyond simple existence of the table), followed by a large number of column-by-column checks (that depend on the type of column), for each table specified. First, the tool determines the standard names of the schema and table. This verifies that the table matches a documented table structure and provides the tool access to a complete description of that table and its columns, glossary entries and complex joins. It counts the number of rows (a primitive check – a lack of rows or too many may indicate a problem), and then validates the table's primary key, and its unique key (if any). That completes the table-based checks. The column-based checks may be basically divided into general checks and then checks performed only on string columns and only on numeric columns. The general column checks include counting the unique values, NA values and nulls, determining the minimum and maximum of the column, and finding duplicated values. None of these may be errors, but they can indicate errors when subsequently reviewed. The character column checks include checks for bad character strings, strings that do not fit a columns regular expression (if any), and comparisons to the glossary for columns that have defined or reference set values. The numeric column checks include various range checks, checks for NA values other than that defined for a column, and checks for negative values.

The multi-table or cross-reference checks are individually specified and executed. There is no need for the tables in the cross-reference checks to be specified in the list of tables to check. This allows checks against reference tables, without having the tool perform full checks (single table and complex join) of the reference table itself. There are three basic kinds of checks: single column cross-references between tables, two-column cross-references between tables, and indirect cross-references. A single-column cross reference requires that every value in the specified column of the table being checked is also found in the specified column of the table that the first table is to be compared against. There are different versions of this check, since the underlying queries may be faster or slower under different circumstances. The two-column check is the same as the single-column check, except that each unique pair of values from two specified columns in the table being checked must be found in the two column specified for the comparison table. The indirect cross-reference check handles cases where the reference for a column in a table being checked is specified by a second column in the same table. The archetypical example of this is the **wftag** table, where the reference for the **tagid** column is specified by the **tagname** column; that is, if **tagname** equals 'evid', then **tagid** contains an **evid** and should be compared to columns in other tables that are **evids** (like **event.evid**), but if **tagname** equals 'arid', then the contents of **tagid** must be compared to **arids** (like **arrival.arid**).

The third and final checks are the complex joins. These are specified in an auxiliary table to the schema schema. This table can specify up to three tables to be involved in the join from the list of tables being checked. The QC tool will automatically format and run a check if the kinds of tables the check requires are among the list of tables the user provided. Since the table contains a generalized SQL query, these checks can be as complex as SQL permits. Some simple examples include verifying that a date in a table corresponds to the time specified in the same table,

verifying that the contents of a field in one table correspond to those in another, when the is no direct link between the tables (such as **wfdisc.instype** versus **instrument.instype**), and verifying that a count listed in a field of one table equals the count of those objects in another table (such as **origin.ndef** versus the count of time-defining arrivals in **assoc**).

Figures 5 and 6 provide examples of the QC tool output.

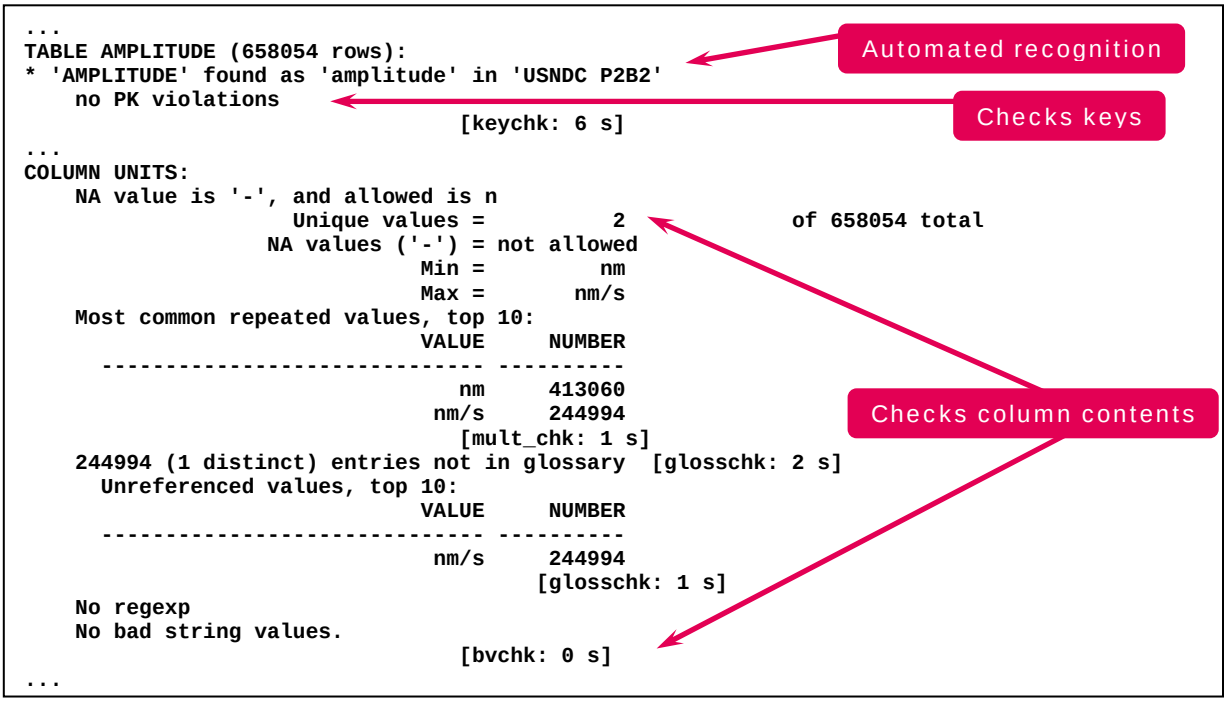


Figure 5. QC tool: single-table check stage: example output.

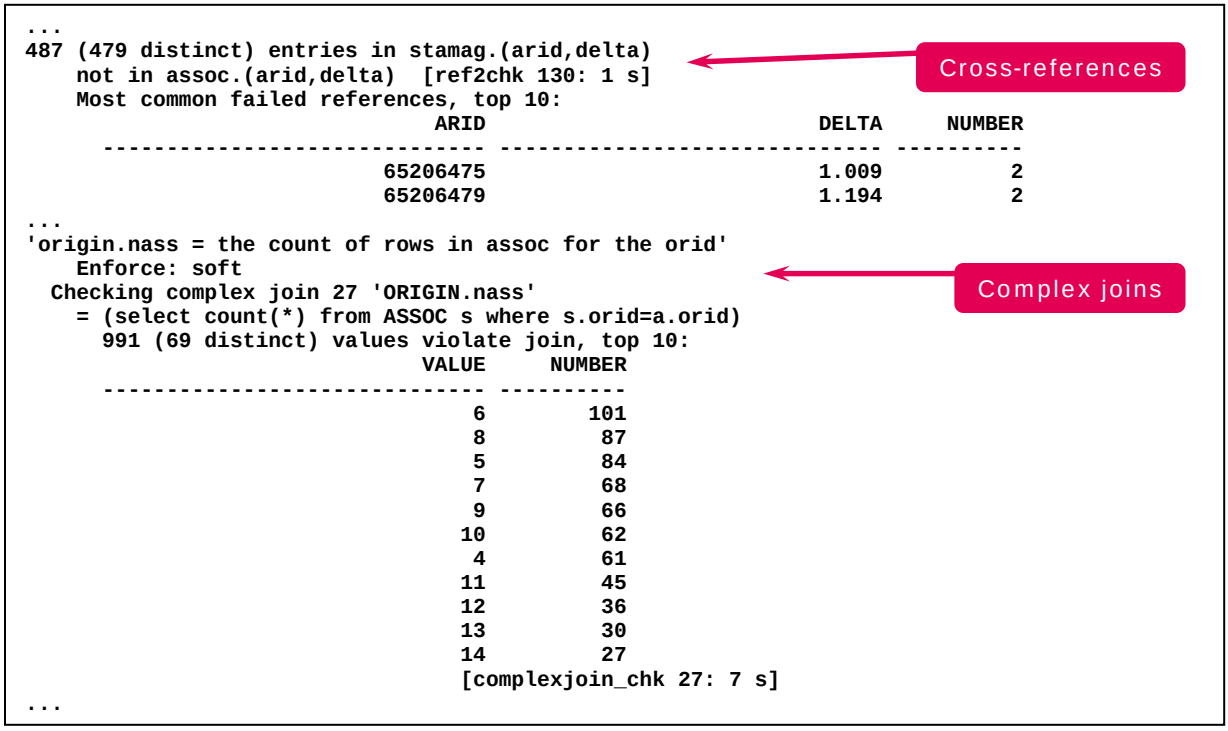
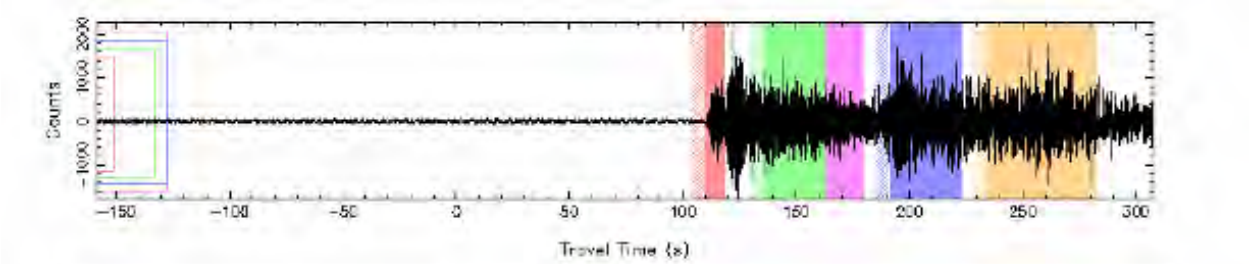


Figure 6. QC tool: cross-references and complex joins: example output.

Limitations

This is a first-generation QC tool and there are a variety of limitations. Two limitations are prominent. The first is that this is a QC inspection tool, not a QC inspection and repair tool. The second is that this QC tool is limited to inspection of data that are in the database. The NNSA KB schema (Carr, 2005) contains objects, principally **instrument** and **wfdisc**, which point to and describe external data. Other tools are required to incorporate these data into overall QC review.

Some tools exist to handle these limitations. In particular, we have recently extended the LANL web interface to the KB to include waveform review. Waveforms may be viewed in a browser, using basic selection criteria, and other information, such as amplitude measurement windows may be overlain on these images to provide a simple visual inspection (see Figure 7).



NNSA Amp_descript Holdings

ORID: 572381, WFID: 1371

Station: MAKZ, Channel: BHZ10, Delta: 7.603, SEAZ: 128.741

(click WINDOWID to view Amplitudes for that window) (click on CLR to Zoom To that phase window)

CLR	WINDOWID	PHASE	GVLO	GVHI	TOFF	START_TIME	DURATION	ALOGID	AUTH	LDDATE ▼	ARID	ARRIVAL.CHAN	ARRIVAL.LDDATE
	521779	P	7.6	8.2	0	110.08	8.13	-1	LANL	2003-01-13 18:37:54	-1		
	521786	S	4	4.7	0	191.8	51.47	-1	LANL	2003-01-13 18:37:54	-1		
	521791	Lg	3	5.6	0	234.74	86.95	-1	LANL	2003-01-13 18:37:54	-1		
	521785	Pc	4.7	5.7	0	148.26	31.54	-1	LANL	2003-01-13 18:37:54	-1		
	521782	Pg	5.2	6.2	0	136.5	26.21	-1	LANL	2003-01-13 18:37:54	-1		
	521792	PrEvNLg	-1	-1	-999	-159.22	86.95	-1	LANL	2003-01-13 18:37:54	-1		
	521780	PrEvNP	-1	-1	-999	-159.22	8.14	-1	LANL	2003-01-13 18:37:54	-1		
	521788	PrEvNPc	-1	-1	-999	-159.22	31.55	-1	LANL	2003-01-13 18:37:54	-1		
	521783	PrEvNPg	-1	-1	-999	-159.22	26.22	-1	LANL	2003-01-13 18:37:54	-1		
	521789	PrEvNS	-1	-1	-999	-159.22	51.47	-1	LANL	2003-01-13 18:37:54	-1		
	521793	PrPhNLg	-1	-1	-999	228.74	5	-1	LANL	2003-01-13 18:37:54	-1		
	521781	PrPhNP	-1	-1	-999	104.09	5	-1	LANL	2003-01-13 18:37:54	-1		
	521787	PrPhNPc	-1	-1	-999	142.26	5	-1	LANL	2003-01-13 18:37:54	-1		
	521784	PrPhNPg	-1	-1	-999	130.5	5	-1	LANL	2003-01-13 18:37:54	-1		
	521790	PrPhNS	-1	-1	-999	185.8	5	-1	LANL	2003-01-13 18:37:54	-1		

Figure 7. Web-based frame for visual inspection of amplitude measurements relative to the waveform.

CONCLUSIONS AND RECOMMENDATIONS

We have developed a metadata schema to describe metadata, which has matured to the point now that it undergirds a variety of software within the GNEM program. It is now a component that is helping to meet a variety of tasks and requirements in a manner that improves efficiency and allows work done in documenting and maintaining metadata information to have immediate benefits elsewhere.

We have developed a first-generation QC inspection tool that relies in the schema schema. QC, which is always important, has become prominent in GNEM recently. Metadata and the proper handling of metadata are the keys to getting a handle on QC, particularly for large and diverse collections of data and research products like the GNEM KB. The QC tool has proven to be very useful in a variety of situations, and has now been deployed throughout the GNEM labs. We expect that the tool will undergo further development, based on experience, to increase both ease of use and automation.

The QC efforts have not yet extended to automated or semi-automated correction of errors. This is an obvious next step. We plan to investigate this subject as well, and we expect to find that a variety of QC problems can be addressed at least in a semi-automated fashion. By semi-automated, we mean that general rules for the repair of problems can be created that can then be adapted to particular problems in software, and applied to those problems

given simple approval by an expert. This differs from manual repair in that the repair does not need to be formulated from scratch each time.

ACKNOWLEDGEMENTS

The authors wish to acknowledge LANL personnel who are making or have made important contributions to the development and maintenance of the LANL KB, and have provided helpful discussions on these and related topics: Diane F. Baker, Hans E. Hartse, W. Scott Phillips, George E. Randall, and Marian D. Romero-Yeske. We also wish to acknowledge helpful discussions with SNL personnel, which improved the work reported here and its more general application: Sandy Ballard, Dorthe Carr, Marcus Chang, Jennifer Lewis, and Chris Young.

REFERENCES

Begnaud, M. L., R. J. Stead, J. Aguilar-Chang, and H. Hartse (2005). Optimizing data Access and availability for seismic calibration research, in *Proceedings of the 27th Annual Seismic Research Review: Ground-Based Nuclear Explosion Monitoring Technologies*, Vol II, p.888-897.

Carr, D. (2005). National Nuclear Security Administration Knowledge Base Core Table Schema Document, Sandia National Laboratories report SAND2002-3055.

Stead, R. J. (2006). Data Collection and Integration in Support of the NNSA Knowledge Base, *Eos Trans. Am. Geophys. Union* 87: 36, Joint Assembly Supplement, Abstract S31B-03.

Acronyms, Etc.

Acronyms

Acronym	Definition
2-D, 2D, 3-D, 3D	two-dimensional, three-dimensional, etc.
ABCE	Annual Bulletin of Chinese Earthquakes
ACD	advanced concept demonstration
AEDS	Atomic Energy Detection System
AFRL	Air Force Research Laboratory
AFTAC	Air Force Technical Applications Center
AIC	Akaike Information Criterion
AK135	seismic travel time model
AMPE	adiabatic mode parabolic equation
ANFO	ammonium nitrate fuel oil
ANOVA	analysis of variance code
ArcView	commercial GIS software
ARS	analyst review station
ARSA	Automated Radioxenon Sampler/Analyzer
ATOC	acoustic thermometry of the ocean climate
BB	broad band
BDSN	Berkeley Digital Seismic Network
BEM	boundary element method
Be-7	beryllium-7
CC	cross-correlation coefficient
CDSN	Chinese Digital Seismic Network
CEA	Commissariat l'Energie Atomique (French bulletin)
ChISS	Russian abbreviation for multichannel spectral seismometer
CLVD	compensated linear vector dipole
CMT	Harvard centroid moment tensor
CodaMag	tool to implement magnitude calculations (Mayeda, 1993; Mayeda and Walter, 1996)
CRUST2.0	crustal model (Bassin et al., 2000)
CSEM	coupled spectral element method
CTBT	Comprehensive Nuclear-Test-Ban Treaty
CTBTO	Comprehensive Nuclear-Test-Ban Treaty Organization
CU	University of Colorado
CUB2.0	3D global models (Shapiro et al., 2002)
CU-Boulder	University of Colorado, Boulder
DD	double-difference
DEM	digital elevation model
DMC	Data Management Center
DOB	depth of burial
DoD	Department of Defense
DOE	Department of Energy
DOS	Department of State
DSS	deep seismic sounding
DTRA	Defense Threat Reduction Agency
EDR	Earthquake Data Reports - a USGS publication
EHB	Engdahl, E.R., van der Hilst, R. & Buland, R., 1998. Global teleseismic earthquake relocation with improved travel times and procedures for depth determination, Bull. Seismol. Soc. Amer.,
EM	electromagnetic
ERL	Earth Resources Laboratory
ERS	European Remote Sensing (satellites)
ESRI	Environmental Systems Research Institute (makers of ArcInfo, ArcIMS, ArcGIS, etc. [http://www.esri.com/company/about/history.html]

Acronyms

Acronym	Definition
ETOPO	earth topographic (database)
ETOPO5	terrain model
EventID	tool to implement event discrimination (Hartse et al., 1997; Walter et al., 1999)
EvLoc	location software
FDSN	Federation of Digital Seismic Networks
FD	finite difference
FE	finite element
F-K	frequency wavenumber
Fstat, F-stat	F-statistic
FSU	Former Soviet Union
GEON	Center for Geoecological Studies
GII	Geophysical Institute of Israel
GIS	geographical information system
GMT	generic mapping tool
GNEMRE	Ground-Based Nuclear Explosion Monitoring Research and Engineering Program
GSEL	grid single-event location or single-event location algorithm
GSN	global seismographic network
GT	ground truth
GTx	ground truth information of accuracy x km
GUI	graphical user interface
HDC	hypocentroidal (or hypocentral) decomposition
HE	high explosive
HPGe	high purity germanium
HydroCAM	Hydroacoustic Coverage Assessment Model
Hz	hertz
IAEA	International Atomic Energy Agency
IASPEI	International Association of Seismology and Physics of the Earth's Interior
IASPEI91	standard earth model
IDC	International Data Centre
IDG	Russian Institute for the Dynamics of the Geospheres
IMS	International Monitoring System
InfraMAP	Infrasound Modeling of Atmospheric Propagation
InSAR	Interferometric Synthetic Aperture Radar
IRIS	Incorporated Research Institutions for Seismology
IRP	integrated research product
ISC	International Seismological Centre
ISTC	International Science and Technology Center
JHD	joint hypocenter determination
KB	Knowledge Base
KBCIT	Knowledge Base Calibration Integration Tool
LANL	Los Alamos National Laboratory
LBNL	Lawrence Berkeley National Laboratory
LDA	linear discriminant analysis
LDRD	laboratory directed research and development project
LLNL	Lawrence Livermore National Laboratory
LVZ	low velocity zones
Ma	million years ago
Matlab	commercial software application
MatSeis	seismic analysis package developed by SNL using Matlab
mb	body wave magnitude

Acronyms

Acronym	Definition
Md	duration magnitude
MDAC	magnitude and distance amplitude corrections
MIT	Massachusetts Institute of Technology
Ms	surface wave magnitude
MSE	mean squared error
MSU	Michigan State University
MUSIC	MULtiple Signal Classification
Mw	moment magnitude
NA-22	Office of Nonproliferation Research and Engineering
NASA	National Aeronautics and Space Administration
NCEDC	Northern California Earthquake Data Center
NEIC	National Earthquake Information Center
NEM R&E	Nuclear Explosion Monitoring Research and Engineering
Nm	newton-meters
NNSA	National Nuclear Security Administration
NOAA	National Oceanic and Atmospheric Administration
NOGAPS	Navy Operational Global Atmospheric Prediction System
NORSAR	Norwegian Seismic Array
NPE	Nonproliferation Experiment
NRL	Naval Research Laboratory
NTS	Nevada Test Site
PDE	Preliminary Determination of Epicenters - a USGS publication
PDF	portable document format
PNE	peaceful nuclear explosions
PNNL	Pacific Northwest National Laboratory
PREM	Preliminary Reference Earth Model (Dziewonski and Anderson, 1981)
PrepCom	Preparatory Commission
PSD	power spectral density
PSU	Penn State University
Q	Q factor
QDA	quadratic discriminant analysis
RASA	Radionuclide Aerosol Sampler Analyzer
REB	Reviewed Event Bulletin - an IDC report
RF	receiver functions
RGA	residual gas analyzer
RMS	root mean square (errors)
ROC	receiver operating characteristic
RSS	residual sum of squares
RUM	mantle velocity model
SAC	seismic analysis code
SASC	slowness-azimuth station correction
SBIR	Small Business Innovation Research
SCSN	Southern California Seismic Network
SEM	spectral element method
SLU	Saint Louis University
SMDC	Space Missile Defense Command (Army)
SNR	signal-to-noise ratio
SOFAR Channel	SOund Fixing And Ranging - primary sound channel in the ocean
SP	short period
STA/LTA	short-term average/long-term average

Acronyms

Acronym	Definition
SVD	singular value decomposition
T-phase	hydroacoustic phase
UCB	University of California, Berkeley
UCSD	University of California, San Diego
UNE	underground nuclear explosions
UNR	University of Nevada, Reno
USAEDS	United States Atomic Energy Detection System
USGS	United States Geological Survey
USNDC	United States National Data Center
VELEST	software program for determining seismic locations and velocities
WINPAK3D	P-wave velocity model for India and Pakistan
WSMR	White Sands Missile Range
WWSSN	World Wide Standard Seismograph Network

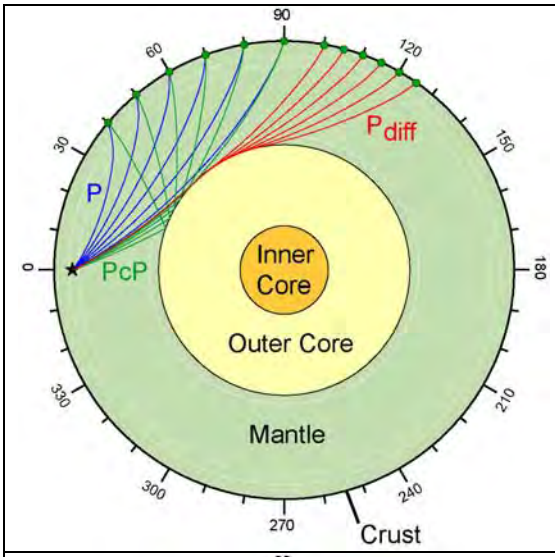
Guide to Seismic Phases

The change of seismic velocities within Earth, as well as the possibility of conversions between compressional (P) waves and shear (S) waves, results in many possible wave paths. Each path produces a separate seismic phase on seismograms. Seismic phases are described with one or more letters, each of which describes a part of the wave path. Upper case letters denote travel through a part of the earth (e.g. P or S), and lower case letters denote reflections from boundaries. A complete, standardized nomenclature for seismic wave paths is available at the web site: http://www.isc.ac.uk/Documents/IASPEI/sspl.html. This information has also been published [Storchak, D.A., J. Schweitzer, P. Bormann (2003), "The IASPEI Standard Seismic Phase List", Seismol. Res. Lett. 74, 6, 761-772], and a pdf file of this publication is available from the same web site.

In the verification context, wave propagation in Earth is divided into *teleseismic* (distances greater than 2000 kilometers) paths and *regional* (distances less than 2000 kilometers) paths.

Teleseismic Phases

In these plots, the seismic event is at the left, and seismic ray paths are shown to possible stations at several angular distances from the event.

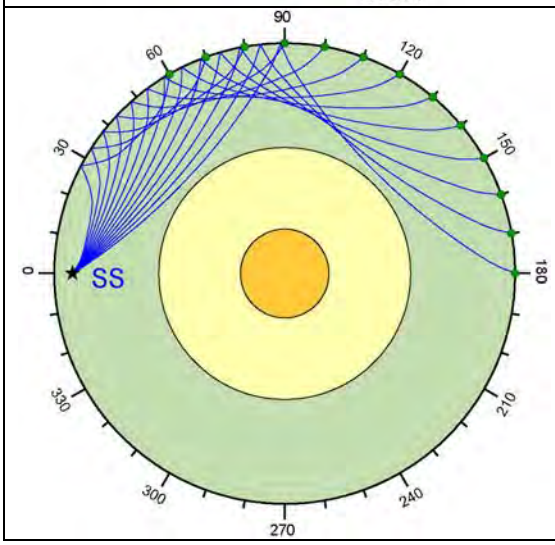


P A primary (compressional) wave that follows a simple path from event source to the station.

PcP A P wave that goes downward through the mantle (the first "P"), is reflected from the top of the outer core ("c") and goes upward through the mantle to the station (second "P").

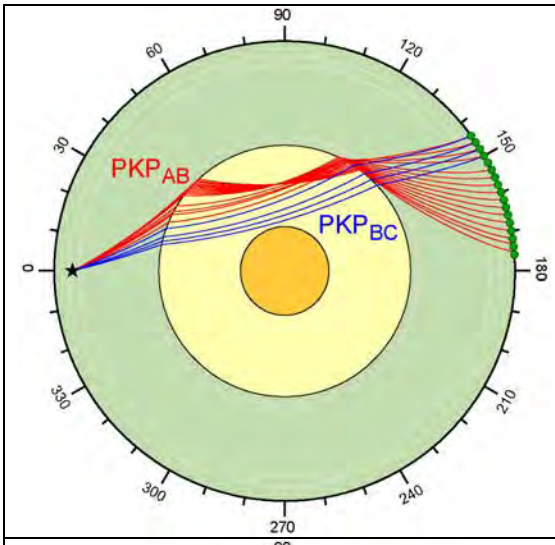
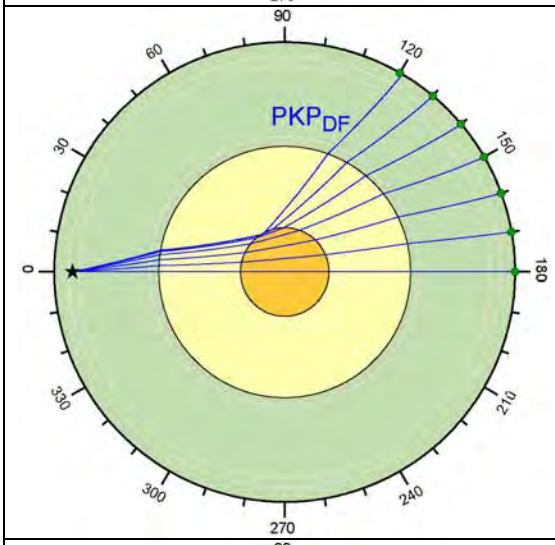
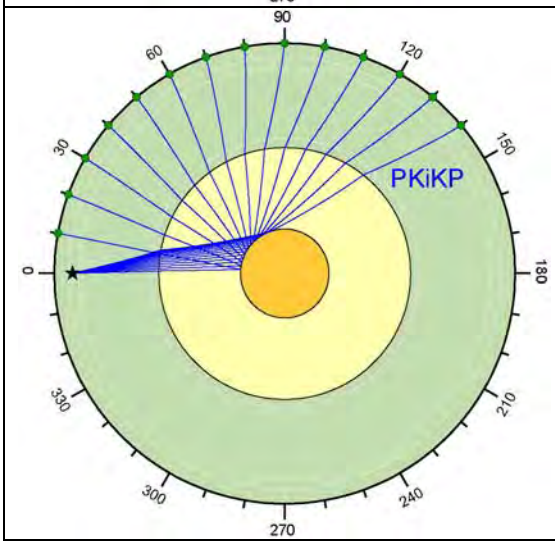
P_{diff} A P wave that has been bent (diffracted) around the outer core boundary and arrives at a station in the ray "shadow" of the outer core.

S A secondary (shear) wave that follows a path similar to the P wave (not shown).



SS A shear wave that has traveled through the mantle ("S"), undergone one reflection from the underside of Earth's surface and traveled again through the mantle (second "S"). Unlike with most other reflected waves, there is no separate letter to denote the reflection at the surface; it is implicit.

PP A compressional wave that follows paths similar to those of SS (not shown).

	**PKP**	A P wave that has traved through the mantle ("P"), been transmitted across the mantle-outer core boundary and traveled through the outer core ("K"), transmitted back across the outer core-mantle boundary and traveled as a P wave to the station ("P"). Because of the large difference between the P wave velocity in the mantle and the outer core, this wave is bent (refracted) strongly at the boundary. Seismic waves can follow slightly different paths (labeled PKP_{AB}, PKP_{BC}) and still arrive at about the same time.
	**PKIKP**	A P wave that has traveled through the mantle ("P"), been transmitted across the mantle-outer core boundary ("K"), crossed the outer-core inner-core boundary and traveled through the inner core as a P wave ("I"), then followed a similar path in reverse to get from the inner core to the station (the second "KP"). An alternate name for this phase is PKP_{DF} (shown in the path illustration).
	**PKiKP**	This phase has followed a series of paths similar to the PKIKP phase, except it was reflected off the top of the inner core-outer core boundary (this is the "i" part of the path), rather than being transmitted through the inner core.

Figures courtesy of Ed Garnero, Arizona State University (http://garnero.asu.edu/research_images/index.html)

Depth Phases

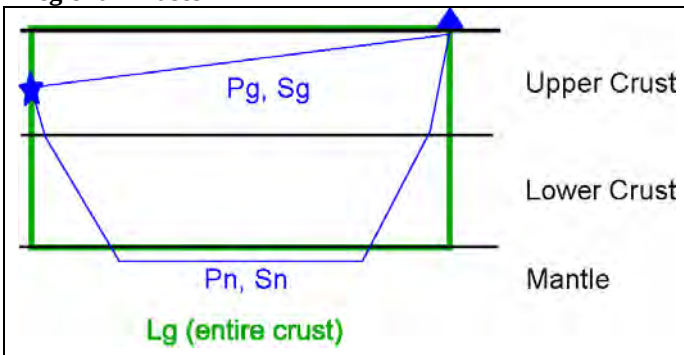
A number of "depth" phases are referred to in the proceedings. The paths of these phases are nearly the same as P waves. The depth phases all result from a reflection from the Earth's surface near the epicenter of the event. The time delay between the P wave and the depth phase is proportional to the depth of the event (hence the term "depth" phase).

pP A P wave that started out upward from the source ("p"), reflected off the Earth's surface, and traveled to the station as a P wave ("P").

sP An S wave that started out upward from the source ("s"), reflected off the earth's surface and also converted to a P wave, which then traveled to the station as a P wave ("P").

pwP Similar to the pP phase. A P wave that started out upward from the source ("p"), reflected off the ocean surface ("w" - water) and traveled to the station as a P wave ("P").

Regional Phases



A highly simplified representation of the crust of Earth, which is seldom so simple and flat. Changes of crustal thickness and velocities can disrupt crustal phases, notably Lg.

Pg (Sg) At short event-station distances, an upgoing P (S) wave from a source in the upper crust (depicted here) or a P (S) wave bottoming in the upper crust. At larger distances the Pg phase includes arrivals resulting from multiple P-wave reverberations within the entire crust that propagate at a group velocity around 5.8 km/s.

Pn (Sn) A P (S) wave bottoming in the uppermost mantle or an upgoing P wave from a source in the uppermost mantle

Lg A wave group observed at larger regional distances and caused by superposition of multiple S-wave reverberations and S to P and/or P to S conversions inside the whole crust. The maximum energy travels with a group velocity around 3.5 km/s